AFRL-RV-PS-
TR-2021-0080

AFRL-RV-PS-
TR-2021-0080

HIGH SPECIFIC POWER MULTI-JUNCTION THIN FILM PV

Randy J. Ellingson, et al.

The University of Toledo
2801 W. Bancroft St.
Toledo, OH 43606

17 Nov 2021

Final Report

APPROVED FOR PUBLIC RELEASE; DISTRIBUTION IS UNLIMITED.



AIR FORCE RESEARCH LABORATORY
Space Vehicles Directorate
3550 Aberdeen Ave SE
AIR FORCE MATERIEL COMMAND
KIRTLAND AIR FORCE BASE, NM 87117-5776

NOTICE AND SIGNATURE PAGE

Using Government drawings, specifications, or other data included in this document for any purpose other than Government procurement does not in any way obligate the U.S. Government. The fact that the Government formulated or supplied the drawings, specifications, or other data does not license the holder or any other person or corporation; or convey any rights or permission to manufacture, use, or sell any patented invention that may relate to them.

This report is the result of contracted fundamental research which is exempt from public affairs security and policy review in accordance with AFI 61-201, paragraph 2.3.5.1. This report is available to the general public, including foreign nationals. Copies may be obtained from the Defense Technical Information Center (DTIC) (http://www.dtic.mil).

AFRL-RV-PS-TR-2021-0080 HAS BEEN REVIEWED AND IS APPROVED FOR PUBLICATION IN ACCORDANCE WITH ASSIGNED DISTRIBUTION STATEMENT.

//SIGNED//

ALEC JACKSON
Program Manager

//SIGNED//

ANDREW SINCLAIR
Tech Advisor, Space Control Technologies Branch

//SIGNED//

JOHN BEAUCHEMIN
Chief Engineer, Spacecraft Technology Division
Space Vehicles Directorate

This report is published in the interest of scientific and technical information exchange, and its publication does not constitute the Government's approval or disapproval of its ideas or findings.

Approved for public release; distribution unlimited.

REPORT DOCUMENTATION PAGE

Form Approved
OMB No. 0704-0188

Public reporting burden for this collection of information is estimated to average 1 hour per response, including the time for reviewing instructions, searching existing data sources, gathering and maintaining the data needed, and completing and reviewing this collection of information. Send comments regarding this burden estimate or any other aspect of this collection of information, including suggestions for reducing this burden to Department of Defense, Washington Headquarters Services, Directorate for Information Operations and Reports (0704-0188), 1215 Jefferson Davis Highway, Suite 1204, Arlington, VA 22202-4302. Respondents should be aware that notwithstanding any other provision of law, no person shall be subject to any penalty for failing to comply with a collection of information if it does not display a currently valid OMB control number. **PLEASE DO NOT RETURN YOUR FORM TO THE ABOVE ADDRESS.**

1. REPORT DATE *(DD-MM-YYYY)*	**2. REPORT TYPE**	**3. DATES COVERED** *(From - To)*
17-11-2021	Final Report	17 Aug 2018 – 17 Nov 2021

4. TITLE AND SUBTITLE
High Specific Power Multi-Junction Thin Film PV

5a. CONTRACT NUMBER
FA9453-18-2-0037

5b. GRANT NUMBER

5c. PROGRAM ELEMENT NUMBER
62203F

6. AUTHOR(S)
Randy Ellingson, Jacques Amar, Robert Collins, Michael Heben, Sanjay Khare, Nik Podraza, Yanfa Yan, Adam Phillips, Zhaoning Song, Shan Ambalanth, Ebin Bastola, Indra Subedi, Abudulimu Abasi

5d. PROJECT NUMBER
3145

5e. TASK NUMBER
EF130941

5f. WORK UNIT NUMBER
V19M

7. PERFORMING ORGANIZATION NAME(S) AND ADDRESS(ES)
The University of Toledo
2801 W. Bancroft St.
Toledo, OH 43606

8. PERFORMING ORGANIZATION REPORT NUMBER

9. SPONSORING / MONITORING AGENCY NAME(S) AND ADDRESS(ES)
Air Force Research Laboratory
Space Vehicles Directorate
3550 Aberdeen Avenue SE
Kirtland AFB, NM 87117-5776

10. SPONSOR/MONITOR'S ACRONYM(S)
AFRL/RVSV

11. SPONSOR/MONITOR'S REPORT NUMBER(S)
AFRL-RV-PS-TR-2021-0080

12. DISTRIBUTION / AVAILABILITY STATEMENT
Approved for public release, distribution is unlimited.

13. SUPPLEMENTARY NOTES

14. ABSTRACT
The University of Toledo focused research and development on materials and devices to advance photovoltaic (PV) technology and knowledge of "High Specific Power Multi-Junction Thin film PV." Studied PV technologies focused on materials capable of both high efficiencies and low total weight – including perovskites, III-V, II-VI, and I-III- V-12 absorbers – with the goal of optimizing and combining absorbers to create highly efficient tandem solar cells. UT refined and applied unique diagnostic instrumentation for optical, electrical, and energy phenomena fundamental to understanding material properties and behavior as they depend upon surface and interface chemistry, electronic band structure, structural and impurity defects, energy barriers, and the intrinsic relationships between electronic/structural properties and device performance. These studies advanced the knowledge of these thin film technologies to enable breakthroughs in photovoltaic power sources' reliability and efficiency.

15. SUBJECT TERMS
Photovoltaics, perovskites, CdTe, CIGS, perovskites, III-V, spectroscopic ellipsometry, thin film, optical spectroscopy, transparent contacts, materials/device modeling

16. SECURITY CLASSIFICATION OF:			**17. LIMITATION OF ABSTRACT**	**18. NUMBER OF PAGES**	**19a. NAME OF RESPONSIBLE PERSON**
a. REPORT	**b. ABSTRACT**	**c. THIS PAGE**			Alec Jackson
Unclassified	Unclassified	Unclassified	Unlimited		**19b. TELEPHONE NUMBER** *(include area code)*

--- This Page Intentionally Left Blank ---

Approved for public release; distribution unlimited.

TABLE OF CONTENTS

Page

LIST OF FIGURES vi

LIST OF TABLES xvii

FOREWORD xix

PREFACE xx

ACKNOWLEDGMENTS xxii

1. EFFICIENT PEROVSKITE SOLAR CELLS USING A DOPANT-FREE HOLE TRANSPORT MATERIAL 1
   1.1 SUMMARY 1
   1.2 INTRODUCTION 1
   1.3 METHODS, ASSUMPTIONS, and PROCEDURES 1
   1.4 RESULTS and DISCUSSION 2
   1.5 CONCLUSIONS 6

2. CORRELATING HYSTERESIS AND STABILITY WITH ORGANIC CATION COMPOSITION IN TWO-STEP SOLUTION-PROCESSED PEROVSKITE SOLAR CELLS .. 7
   2.1 SUMMARY 7
   2.2 INTRODUCTION 7
   2.3 METHODS, ASSUMPTIONS, and PROCEDURES 8
   2.4 RESULTS and DISCUSSION 9
   2.5 CONCLUSIONS 16

3. INVESTIGATION OF MIXED-CATION FA/MA PB/SN I3 PEROVSKITE THIN FILMS AND SOLAR CELLS 17
   3.1 SUMMARY 17
   3.2 INTRODUCTION 17
   3.3 METHODS, ASSUMPTIONS, and PROCEDURES 18
   3.4 RESULTS and DISCUSSION 19
   3.5 CONCLUSIONS 24

4. PROTECTING PEROVSKITE SOLAR CELLS AGAINST MOISTURE-INDUCED DEGRADATION WITH SPUTTERED INORGANIC BARRIER LAYERS 25
   4.1 SUMMARY 25
   4.2 INTRODUCTION 25
   4.3 METHODS, ASSUMPTIONS, and PROCEDURES 26
   4.4 RESULTS and DISCUSSION 27
   4.5 CONCLUSION 31

TABLE OF CONTENTS (Continued)

Page

5. EFFECTS OF CU PRECURSOR ON THE PERFORMANCE OF EFFICIENT CDTE SOLAR CELLS 32
5.1 SUMMARY 32
5.2 INTRODUCTION 32
5.3 METHODS, ASSUMPTIONS, and PROCEDURES 33
5.4 RESULTS and DISCUSSION 34
5.5 CONCLUSIONS 42

6. SYNTHESIS OF TELLURIUM AND COPPER TELLURIDE NANOWIRES 43
6.1 SUMMARY 43
6.2 INTRODUCTION 43
6.3 METHODS, ASSUMPTIONS and PROCEDURES 44
6.4 RESULTS and DISCUSSION 44
6.5 CONCLUSIONS 48

7. SOLUTION PROCESSED LEAD TELLURIDE NANOWIRES AS A PASSIVATING LAYER TO CDTE PHOTOVOLTAICS 49
7.1 SUMMARY 49
7.2 INTRODUCTION 49
7.3 METHODS, ASSUMPTIONS, and PROCEDURES 51
7.4 RESULTS and DISCUSSION 52
7.5 CONCLUSIONS 60

8. BACK SURFACE PASSIVATION OF CDTE SOLAR CELLS USING SOLUTION-PROCESSED OXIDIZED ALUMINUM 61
8.1 SUMMARY 61
8.2 INTRODUCTION 61
8.3 METHODS, ASSUMPTIONS, and PROCEDURES 62
8.4 RESULTS and DISCUSSION 63
8.5 CONCLUSION 71

9. SOLUTION BASED Cu-DOPED ALUMINUM OXIDE AS A BACK INTERFACE LAYER FOR CDTE SOLAR CELLS 73
9.1 SUMMARY 73
9.2 INTRODUCTION 73
9.3 METHODS, ASSUMPTIONS, and PROCEDURES 74
9.4 RESULTS and DISCUSSION 76
9.5 CONCLUSIONS 86

10. SILAR DEPOSITED TRANSPARENT CU-ZN-S NANOCOMPOSITES AS HOLE TRANSPORT MATERIALS IN CDTE PHOTOVOLTAICS 87
10.1 SUMMARY 87
10.2 INTRODUCTION 87
10.3 METHODS, ASSUMPTIONS, and PROCEDURE 89

Page

10.4 RESULTS and DISCUSSION 90
10.5 CONCLUSIONS 98

11. MICROSTRUCTURAL CONTROL OF THIN FILM CDTE BY GLANCING ANGLE DEPOSITION 99
11.1 SUMMARY 99
11.2 INTRODUCTION 99
11.3 METHODS, ASSUMPTIONS, and PROCEEDURES 100
11.4 RESULTS and DISCUSSION 102
11.5 CONCLUSIONS 109

12. SYNTHESIS AND CHARACTERIZATION OF COLLOIDAL II-VI QDS FOR PASSIVATION STUDIES RELEVANT TO CDTE PHOTOVOLTAICS 110
12.1 SUMMARY 110
12.2 INTRODUCTION 110
12.3 METHODS, ASSUMPTIONS, and PROCEDURES 111
12.4 RESULTS and DISCUSSION 112
12.5 CONCLUSIONS 118

13. OPTICAL STUDIES OF III-V THIN FILMS 119
13.1 SUMMARY 119
13.2 INTRODUCTION 119
13.3 METHODS, ASSUMPTIONS, and PROCEEDURES 120
13.4 RESULTS and DISCUSSION 123
13.5 CONCLUSIONS 129

14. DECREASING THE RESOLUTION LIMIT OF LASER BEAM INDUCED CURRENT MEASUREMENTS BELOW THE BEAM SIZE WITHOUT CONFOCAL OPTICS: DETERMINING LASER SCRIBE WIDTHS 131
14.1 SUMMARY 131
14.2 INTRODUCTION 131
14.3 METHODS, ASSUMPTIONS, and PROCEDURES 132
14.4 RESULTS and DISCUSSION 134
14.5 CONCLUSION 139

15. DEVELOPMENT OF INTEGRATED INSTRUMENTATON FOR VARIABLE ANGLE, POLARIZATION-DEPENDENT EQE/SE/SR MEASUREMENT 140
15.1 MOTIVATION AND SUMMARY 140
15.2 INTRODUCTION 141
15.3 METHODS, ASSUMPTIONS, and PROCEDURES 141
15.4 RESULTS and DISCUSSIONS 147
15.5 CONCLUSIONS 179

TABLE OF CONTENTS (Continued)

Page

16. DEVELOPMENT OF AN EXPERIMENTAL SET-UP TO MEASURE AN IMPLIED OPEN-CIRCUIT VOLTAGE OF SOLAR CELLS 181
16.1 SUMMARY 181
16.2 INTRODUCTION 181
16.3 METHODS, ASSUMPTIONS, and PROCEDURES 182
16.4 RESULTS and DISCUSSION 184
16.5 CONCLUSIONS 186

17. IRRADIANCE AND TEMPERATURE CONTROL CHAMBER FOR ELECTRONIC MEASUREMENTS 187
17.1 SUMMARY 187
17.2 INTRODUCTION 187
17.3 METHODS, ASSUMPTIONS, and PROCEDURE 188
17.4 RESULTS and DISCUSSION 201
17.5 CONCLUSIONS 204

18. APPLICATION OF OPTICAL HALL EFFECT 206
18.1 SUMMARY 206
18.2 INTRODUCTION 206
18.3 METHODS, ASSUMPTIONS, and PROCEDURES 208
18.4 RESULTS and DISCUSSION 209
18.5 CONCLUSIONS 214

19. INVESTIGATING THE ROLE OF BAND ALIGNMENT AT THE TRANSPARENT CONDUCTOR/ELECTRON TRANSPORT LAYER INTERFACE IN WIDE-BANDGAP PEROVSKITE SOLAR CELLS 215
19.1 SUMMARY 215
19.2 INTRODUCTION 215
19.3 METHODS, ASSUMPTIONS, and PROCEDURES 217
19.4 RESULTS and DISCUSSION 218
19.5 CONCLUSION 223

20. MATERIALS REQUIREMENTS FOR IMPROVING THE ELECTRON TRANSPORT LAYER/PEROVSKITE INTERFACE OF PEROVSKITE SOLAR CELLS DETERMINED VIA NUMERICAL MODELING 224
20.1 SUMMARY 224
20.2 INTRODUCTION 224
20.3 METHODS, ASSUMPTIONS, and PROCEDURES 225
20.4 RESULTS and DISCUSSION 226
20.5 CONCLUSION 229

21. UNDERSTANDING V_{OC} AND PERFORMANCE DEFICIT IN WIDE BANDGAP PEROVSKITE PHOTOVOLTAIC DEVICES 230
21.1 SUMMARY 230

TABLE OF CONTENTS (Continued)

Page

21.2 INTRODUCTION 230
21.3 METHODS, ASSUMPTIONS, and PROCEDURES 231
21.4 RESULTS and DISCUSSION 231
21.5 CONCLUSION 237

22. ENERGY, TEMPERATURE, AND DEPOSITION ANGLE DEPENDENCE OF CD AND TE_2 DEPOSITED ON CDTE 238
22.1 SUMMARY 238
22.2 INTRODUCTION 238
22.3 METHODS, ASSUMPTIONS, and PROCEDURES 238
22.4 RESULTS and DISCUSSION 240
22.5 CONCLUSIONS 243

23. ENERGY BARRIERS AND PREFACTORS FOR CD AND TE_2 DESORPTION FROM THE CDTE(100) SURFACE 245
23.1 SUMMARY 245
23.2 INTRODUCTION 245
23.3 METHODS, ASSUMPTIONS, and PROCEDURES 245
23.4 RESULTS and DISCUSSION 247
23.5 CONCLUSIONS 250

24. PHYSICALLY REALISTIC PARAMETRIC OPITCAL MODEL DEVELOPMENT FOR POLYCRYSTALLINE SEMICONDUCTORS 251
24.1 SUMMARY 251
24.2 INTRODUCTION 251
24.3 PROCEDURES and DISCUSSION 252
24.4 CONCLUSIONS 254

25. CHARACTERIZING THE PHASES OF TERNARY NITRIDE $MgSnN_2$ AND THE ALLOYS OF $Zn_xCd_{1-x}Te$, ($\mathbf{0 \leq x \leq 1}$). 255
25.1 SUMMARY 255
25.2 INTRODUCTION 255
25.3 METHODS, ASSUMPTIONS, and PROCEDURES 255
25.4 RESULTS and DISCUSSION 255
25.5 CONCLUSIONS 258

26. REFERENCES 259

LIST OF ACRONYMS, ABBREVIATIONS, AND SYMBOLS 302

APPENDIX - PUBLICATIONS FUNDED UNDER AFRL #FA9453-18-2-0037……..…306

LIST OF FIGURES

Page

Figure 1. (a) Computed ESP of DTP-C6Th. (b) Energy levels of spiro-OMeTAD and DTP-C6Th. (c) SCLC J–V characteristics of DTP-C6Th or spiro-OMeTAD based devices. (d) Cross-sectional SEM image of device with DTP-C6Th HTM. (e) PL intensity and (f) TRPL decays of perovskite films 3

Figure 2. Photovoltaic parameters of PVSCs using DTP-C6Th or spiro-OMeTAD as HTM. Histograms of (a) V_{OC}, (b) J_{SC}, (c) FF, and (d) PCE of corresponding devices 4

Figure 3. (a) SEM image of a $MA_{0.7}FA_{0.3}PbI_3$ film. (b) SEM image of a $MA_{0.7}FA_{0.3}Pb(I_{0.925}Br_{0.075})_3$ film. (c) Absorbance, (d) PL, (e) TRPL and (f) XRD patterns of $MA_{0.7}FA_{0.3}PbI_3$ and $MA_{0.7}FA_{0.3}Pb(I_{0.925}Br_{0.075})_3$ films 5

Figure 4. Photovoltaic parameters of the best performing PSCs (W/ PMMA & Br). (a) J–V curves. (b) EQE plots. (c) Steady-state efficiency over 1200 s. (d) Histogram of PCEs for 20 cells 6

Figure 5. SEM images of $FA_xMA_{1-x}PbI_3$ films with x = (a) 0.0, (b) 0.2, (c) 0.4, (d) 0.6, (e) 0.8, and (f) 1.0. 10

Figure 6. (a) XRD, (b, c) normalized XRD, (d) absorbance and (e) PL spectra, and (f) PL decays of $FA_xMA_{1-x}PbI_3$ films with x = 0.0, 0.2, 0.4, 0.6, 0.8, and 1.0. 11

Figure 7. PV parameters including (a) PCE, (b) JSC, (c) VOC, and (d) FF for $FA_xMA_{1-x}PbI_3$; R and F represent reverse and forward scans 12

Figure 8. EQE spectra of perovskite solar cells with different FA fractions 13

Figure 9. J-V curves of $FA_xMA_{1-x}PbI_3$ solar cells with x = (a) 0.0, (b) 0.2, (c) 0.4, (d) 0.6, (e) 0.8, and (f) 1.0. 14

Figure 10. Dark J-V analysis of PSCs with different FA fractions: (a) FA = 0.0, (b) FA = 0.2, (c) FA = 0.4, (d) FA = 0.6, (e) FA = 0.8, and (f) FA = 1.0. 14

Figure 11. MPP tracking of unencapsulated $FA_xMA_{1-x}PbI_3$ solar cells under (a) dry nitrogen and (b) high relative humidity (>70%) conditions 16

Figure 12. Complex dielectric function ($\varepsilon = \varepsilon_1 + i\varepsilon_2$) spectra of $(FASnI_3)_x(MAPbI_3)_{1-x}$ ($0.3 \leq x \leq 0.8$) perovskite films 20

Figure 13. Absorption spectra for $(FASnI_3)_x(MAPbI_3)_{1-x}$ ($0.3 \leq x \leq 0.8$) films (a) exposed to air, measured by SE and (b) unexposed, measured by PDS 21

LIST OF FIGURES (Continued)

Page

Figure 14. (a) Bandgap (E_g) and (b) Urbach energy (E_U) as a function of composition for $(FASnI_3)_x(MAPbI_3)_{1-x}$ perovskite films 21

Figure 15. Defect densities calculated using the optical sum rules for $(FASnI_3)_x(MAPbI_3)_{1-x}$ protected (open circles) and exposed perovskite films 22

Figure 16. V_{OC}, FF, J_{SC}, and PCE for $(FASnI_3)_x(MAPbI_3)_{1-x}$ solar cells 22

Figure 17. (a) PCE of $(FASnI_3)_x(MAPbI_3)_{1-x}$ perovskite solar cells as function of E_U and composition; (b) V_{OC} deficit as a function of E_U 23

Figure 18. (a) Diagram of encapsulated device; (b) JV for 1 cm^2 PSC without and with 45 nm SiO_2 layer; (c) J-V data with SiO_2, as-fabricated and after two months 28

Figure 19. LBIC data for (a) no SiO_2 and (b) a 45 nm SiO_2 protection layer; (c) corresponding J-V curves for panels (a) and (b), before and after LBIC 29

Figure 20. LBIC data for PSCs exposed to 85% RH at 25 °C with (a) no protection, and (b-e) protection layers of 45 nm, 60 nm, 140 nm, and 300 nm, respectively. (f) normalized, integrated LBIC signal vs. exposure time. 30

Figure 21. (a, c) J-V curves and (b, d) EQE spectra of representative (a, b) CdS/CdTe and (c, d) ZMO/CdTe devices treated with different Cu precursors 35

Figure 22. (a) PL spectra and (b) TRPL decays for CdS/CdTe-Cu and CdS/CdTe-CuCl devices (PL excitation with 633 nm laser 37

Figure 23. (a) MS plots measured at room temperature for devices with Cu and CuCl treatment (Inset: MS plots). (b) Carrier densities extracted from C-V measurements. 38

Figure 24. Differential capacitance spectra ($-\omega dC/d\omega$) for (a) CdTe-Cu and (b) CdTe-CuCl devices. (c) Arrhenius plots and (d) defect distributions from (a) and (b). Inset shows trap defect activation energies (E_A), capture cross-section (σ_t) and trap state densities (N_t) 39

Figure 25. Degradation test results: ambient for 60 days, varied window layers and Cu precursors. Degradation of (a) V_{OC}, (b) J_{SC}, (c) FF, and (d) Efficiency. 40

Figure 26. SEM images of Te NWs for (a, b) 0.1 gm PVP , 0.75 mL ascorbic acid (c, d) 0.2 gm PVP, 1.5 mL ascorbic acid; (e, f) STEM images of Te NWs for 0.1 gm, 0.75 mL 45

Figure 27. Diameter, length and aspect ratio distribuiton of Te NWs, 120°C for 21 hrs. (a, b, e) 0.1 g PVP and 0.75 mL ascorbic acid (c, d, f) 0.2 g and 1.5 mL 46

Page

Figure 28. (a) XRD pattern, Te NWs of high-purity hexagonal crystal structure (reference from PDF #97-004-0042, MDI JADE software); (b) Raman scattering spectrum of Te NWs, 632.8 nm laser excitation, 0.1 gm PVP, 0.75 mL ascorbic acid. 47

Figure 29. (a) SEM image and (b) XRD pattern of synthesized Cu_7Te_4 NWs, with hexagonal crystal structure. 48

Figure 30. (a) XRD pattern and (b) Raman spectrum for PbTe NWs 52

Figure 31. Surface SEM images of (a) PbTe NWs, (b) $CdCl_2$ activated CdTe device, and (c) with PbTe NWs on device; (d) band alignment of CdS, CdTe, PbTe and Au 53

Figure 32. PL and TRPL spectrum of CdS/CdTe device (a, b) glass side illumination and (c, d) film side illumination 54

Figure 33. (a) J-V results; (b) EQE results of CdS/CdTe devices, varied back contacts; for JV, solid lines are light, and dotted lines are dark 56

Figure 34. Statistical distribution of V_{OC}, J_{SC}, FF, and PCE of CdS/CdTe solar cells, various back contacts 57

Figure 35. (a) Temperature-dependent JV for CdTe devices, two different back contacts; (b) plots of ln (J_o/T^2) versus $1/k_BT$ to evaluate back barrier height 58

Figure 36. $CuCl_2$/Au, $CuCl_2$/PbTeNWs/Au back contacts: (a) dark J-V, (b) R_{sh} characterization (c) dV/dJ versus 1/J for A and R_S; (d) V-R_sJ for A and J_0 59

Figure 37. (a) JV results for CdTe device, varying number of spin/heat cycles; (b) Average PCE and FF; (c) average V_{OC} and long lifetime τ_2 of the TRPL 64

Figure 38. SEM images of CdTe surface (a) without and with (b) one or (c) five cycles of Al_2O_3 processing; (d) Al 2p XPS data without (green), with one (red) and with five (black) cycles 67

Figure 39. (a) JV data of CdTe devices, varied back contacts; (b) EQE results for short circuit and maximum power point bias 69

Figure 40. (a) JV data, CdTe devices with varied back contacts; (b) SEM image, CdTe surface with $Al(acac)_3/CdCl_2$ 71

Figure 41. Schematic diagram of CdS/CdTe solar cell devices with CuAlOx as a back buffer layer 75

Figure 42. (a) Thermogravimetric analysis (b) decomposition profile of aluminum nitrate nonahydrate (aluminum source) chemical 76

Page

Figure 43. (a) Transmittance and (b) reflectance spectra; (c) Tauc plot from SE data; (d) *n* and *k* spectra for CuAlOx, SE data 77

Figure 44. Surface morphology of (a) CdTe (b) CdTe/ Al_2O_3, and (c) CdTe/ CuAlOx 77

Figure 45. TRPL data for CdTe devices with Al_2O_3 at different annealing temperature, film side illumination by 532 nm laser 78

Figure 46. (a) J -V characteristics of CdS/CdTe/Al_2O_3 vs. Cu concentration; (b) control device data, various back contacts 79

Figure 47. Steady state PL spectra and TRPL decays of CdTe devices with Al_2O_3 and varied Cu concentrations: (a) film side PL, (b) glass side PL; (c) film side TRPL; (d) glass side TRPL 81

Figure 48. PL spectra of CdS/CdTe film (a) standard and (b) CdS/CdTe/Al_2O_3(30 % Cu). Gaussian fits shown as solid blue curves; dotted curve represents the fit sum 82

Figure 49. JV results for CdS/CdTe sample with Al_2O_3 (30% Cu) 83

Figure 50. Statistical results of solar cell performance for Al_2O_3(2% Cu), Al_2O_3(50% Cu) as a passivating interface layer on CdS/CdTe solar cells 84

Figure 51. SCAPS simulation: relationship between the front SRV and the minority carrier lifetime using the CuAlOx as the back buffer layer 85

Figure 52. (a) T and R (dotted) spectra of CZS NC thin films prepared by SILAR; (b) plots of $(\alpha h\nu)^2$ v.s energy (hν, eV) for band gap estimation 91

Figure 53. SEM images, Cu-Zn-S thin films (a) CZS-10 (b) CZS-30 (c) CZS-50 and (d) CZS-80 92

Figure 54. Schematic device diagram and cross-sectional SEM image of CdTe solar cells with Cu-Zn-S (CZS-50) as a back-contact interface layer. 94

Figure 55. J-V characteristics of CdTe photovoltaics with and w/o Cu-Zn-S (CZS) nanocomposites as HTMs. 94

Figure 56. SEM images of CdTe surface (a) without CZS NCs and (b) with CZS NCs; (c) XRD pattern of CdTe/CZS-30 (references to CdTe and CuS are PDF #97-005-2840 and PDF #98-001-3414) 95

Figure 57. (a) Average PCE vs. cycles; best JV curves vs. deposition cycles of CZS-30 NCs; (c) *J-V* characteristics of the best cells, $CuCl_2$ treated devices with CZS NCs 97

Figure 58. Schematic of glancing angle deposition (GLAD) sputtering 100

Page

Figure 59. Schematic of CdS/CdTe solar cells with and without thin GLAD wurtzite CdTe interlayer 101

Figure 60. Cross-sectional and plan-view SEM images, as-deposited RT GLAD CdTe films vs. source flux angles with respect to substrate normal [308]..... 102

Figure 61. XRD patterns of as-deposited (left) RT [308] and (right) 250°C [309] CdTe sputtered on soda-lime glass at different source flux angles (Φ) 103

Figure 62. Crystallite size of CdTe deposited at different source flux angle and substrate temperature [309]..... 104

Figure 63. (a), (b) $\varepsilon = \varepsilon 1 + i\varepsilon 2$ spectra of as-deposited RT GLAD polycrystalline CdTe films vs. source flux angle; [308] inset: the structural model..... 105

Figure 64. Comparison of ε for GLAD prepared at different temperatures and source flux angles [309]..... 105

Figure 65. Anisotropic optical properties parallel (extra-ordinary, e) and perpendicular (ordinary, o) to the columnar principal axes in (top) ε1 and (bottom) birefringence, ne-no in the transparent spectral range [308]..... 106

Figure 66. Crystallite size deduced via the Scherrer equation as a function of $CdCl_2$ treatment time for CdTe deposited at different source flux angles [308] 107

Figure 67. (a) JV and (b) EQE performance data best CdS/CdTe cells with and without a 100 nm GLAD wurtzite CdTe interlayer [308]..... 108

Figure 68. X-ray diffraction pattern of as-synthesized CdTe QDs 112

Figure 69. UV-Vis spectrum of CdTe QDs with excitonic transitions annotated 113

Figure 70. (a) PL spectra of syntheses #6 and #9, CdTe QDs; (b) TRPL of these same samples. 114

Figure 71. UV-Vis spectra of CdTe and alloyed $CdSe_xTe_{1-x}$ QDs..... 115

Figure 72. PL spectra of QD samples at three excitation wavelengths: 405 nm, 532 nm, and 633 nm 115

Figure 73. PL spectra of QD samples vs. Cd precursor amount, measured at three different excitation wavelengths: 405 nm, 532 nm, and 633 nm..... 116

Figure 74. Optical absorption spectra of CdTe and CdSeTe QDs 117

Page

Figure 75. Time-resolved PL decays of CdTe (left) and CdSeTe (right) QD samples excited at 633 nm 118

Figure 76. Schematics of (left) InGaAs and (right) InAlAs epitaxial film stacks 121

Figure 77. Estimations of penetration depth using Beers Law to (left) InGaAs and (right) InAlAs layers corresponding to the samples described in Figure 76. 122

Figure 78. Experimental SE spectra (open blue circles) and model fit (solid red lines) for multilayer sample as in Figure 76 (left) 126

Figure 79. $\varepsilon = \varepsilon_1 + i\varepsilon_2$ spectra from 1.53 meV to 4.11 meV (left), and 0.055 eV to 3 eV (right) of the 1500 nm thick epitaxial InGaAs. 126

Figure 80. Experimental SE spectra (open blue circles) and model fit (solid red lines) for multilayer sample as described in Figure 76 (right) 127

Figure 81. $\varepsilon = \varepsilon_1 + i\varepsilon_2$ spectra from 0.45 meV to 3.95 meV (left), and 0.055 eV to 2.5 eV (right) of 1500 nm thick epitaxial InAlAs..... 127

Figure 82. (a) Diagram of LBIC measurement across a scribe line. (b) Expected normalized induced current vs. laser center position..... 133

Figure 83. (a) Laser beam intensity map and corresponding intensity profiles as depicted in (b) and (c) 134

Figure 84. (a) Top and (b) cross-sectional schematic diagrams of the sample investigated with 14 scribe lines of increasing scribe beam power 135

Figure 85. LBIC results along the beam's (a) short axis, parallel and (b) long axis perpendicular to the scribe line, obtained from scribed lines formed with laser powers of 0.25, 0.55, 0.9 W.. 136

Figure 86. (a) Chi-squared (χ^2) test of simulation results of the electrical dead width of scribed lines; (b), (c), (d) simulations and corresponding measurements, short axis; (e), (f) and (g) show the same for the long axis 137

Figure 87. (a) Scribe widths measured by LBIC and optical microscopy; (b) Power distribution for low- and high-power; (c) and (d) scribe profiles corresponding to (b)..... 138

Figure 88. (a) LBIC measurements across a square defect (blue); (b) Expected normalized LBIC response vs. laser center position for the illustration in panel (a)..... 139

Figure 89. Schematic of the integrated EQE/SR/SE system; inset shows the rotated sample stage 142

Page

Figure 90. Schematic of the Krasilov compensator, depicting beam path and dimensions..... 143

Figure 91. Photograph of the unmounted Krasilov compensator in which the two prisms have been assembled per the schematic design but inverted..... 143

Figure 92. Photograph of the Krasilov compensator mounted within a hollow rotatable holder.. 144

Figure 93. ε_2 spectrum generated from the Ashcroft and Sturm parameters and individual contributions (broken lines) plotted with ε_2 from Ref. [358]..... 146

Figure 94. ε_1 spectrum generated from the Ashcroft and Sturm parameters and individual contributions (broken lines) plotted with ε_2 from Ref. [358]..... 146

Figure 95. Fit of the Ashcroft and Sturm parameters to the measured ψC of the Krasilov compensator..... 147

Figure 96. Difference between measured and best fit dichroism parameter ψC obtained from the Ashcroft and Sturm model..... 149

Figure 97. Final dielectric function of the aluminum coating used in the characterization of the Krasilov compensator, Ashcroft and Sturm model..... 149

Figure 98. (ε_1, ε_2) spectra of the modeled Al dielectric function in comparison with the values available in the Woollam Co., Inc software database..... 150

Figure 99. Cross-section of the Krasilov compensator, closed circles indicate mounting locations. In the figure, red lines identified (odd numerals) represent optical beam paths, and even numerals represent internal reflections..... 152

Figure 100. Average stress angle α measured as a function of the compensator fast axis (C′), and angle (α) for the unmounted compensator (left-most data point)..... 152

Figure 101. Plot of total stress induced retardance δn along all respective beam paths in the compensator measured vs. fast axis angle (C′)..... 153

Figure 102. Stress induced retardance spectra of the unmounted and mounted Krasilov compensator vs. a King-Downs rhomb compensator..... 154

Figure 103. Final results for the spectra in the complete normalized Mueller matrix of the unmounted Krasilov compensator measured experimentally and the best simulated fit..... 156

Figure 104. Retardance of the Krasilov compensator, as the sum of retardances from reflections from two fused-silica/ambient interfaces (δ_2 and δ_6) and a reflection from a fused-silica/aluminum (δ_4) interface..... 158

Page

Figure 105. Retardance of the Krasilov compensator and the MgF_2 biplate compensator currently used in the EQE-SE system 158

Figure 106. Photograph of the Krasilov compensator attached to the stepper motor and all the alignment stages upon which the compensator is mounted 160

Figure 107. Photograph of the motor with all stages, designed for aligning the motor rotational axis to superimpose onto the beam path 161

Figure 108. Photograph of the rotating compensator ellipsometer in straight-through configuration using the Krasilov compensator 161

Figure 109. Irradiance spectra (eight scans) for the single rotating compensator in the straight-through configuration with P = 0° and A = 45° 162

Figure 110. Normalized Fourier coefficients incorporating the Krasilov compensator in straight-through configuration with P = 0° and A= 0°. 164

Figure 111. Normalized Fourier coefficients incorporating the Krasilov compensator in straight-through configuration with P = 0° and A = 45°. 165

Figure 112. Dichroism of the Krasilov compensator measured in the rotating compensator configuration PCR(Kr)A; spectroscopic variation of the dichroism is small, yielding apparently noisy data on this scale of the ordinate 166

Figure 113. Retardance of the Krasilov compensator in comparison with the measurement by the J. A. Woollam Co., Inc model RC2 ellipsometer 167

Figure 114. SE results at 50°, 60°, and 70° incidence angles with best fits for the Hamamatsu S1337-21 silicon photodiode measured with EQE-SE system 168

Figure 115. (a) Hamamatsu S1337-21 silicon photodiode SE data (incidence angle = 60°) with fits; (b) Structural model and layer thicknesses, from the fits 169

Figure 116. (a) Normal incidence EQE data and simulation for best fit thicknesses $\boldsymbol{tSiO2 = 31\ nm}$, $\boldsymbol{tSi = 429\ \mu m}$, $\boldsymbol{tSi/Au = 80\ nm}$; (b, c, d) show sensitivity analysis for the effects of the thicknesses on the modeled EQE spectrum 170

Figure 117. Plots of angular EQE data with the corresponding best fit simulated EQE with $\boldsymbol{tSiO2}$ as the fit parameter. 172

Figure 118. J-V results of sample #3, under detailed investigation by the EQE-SE system 173

Figure 119. SE spectra for the CIGS solar cell measured in the EQE-SE system at angles of incidence of 50°, 60°, and 70° 174

Page

Figure 120. Multilayer structural model of the CIGS solar cell under study 175

Figure 121. Bandgap profile of CIGS bulk layer..... 176

Figure 122. Compositional depth profile of the 2.4 μm thick CIGS absorber layer obtained from Auger electron spectroscopy..... 176

Figure 123. Plot of measured normal incidence EQE and the simulated EQE based on a best fit collection model..... 177

Figure 124. EQE spectra measured at 50° angle of incidence for both p and s polarizations along with corresponding simulations 178

Figure 125. EQE spectra measured at 60° angle of incidence for both p and s polarizations along with corresponding simulations 178

Figure 126. EQE spectra measured at a 70° angle of incidence for both p and s polarizations along with corresponding simulations 179

Figure 127. iV_{oc} experimental set up..... 183

Figure 128. PL spectra of $MAPbI_3$ films taken at room temperature 185

Figure 129. (Left) Chamber design in Solidworks, (Right) Chamber construction status from the previous group 188

Figure 130. Finalized irradiance and temperature control chamber 189

Figure 131. Initial TEC device arrangement..... 189

Figure 132. Current TEC device arrangement..... 190

Figure 133. (left) Mounted thermal stage inside the test chamber; (right) Solar cell placement on the thermal stage 191

Figure 134. Power chamber, power supplies, and bus bar..... 192

Figure 135. (Left) Multi-array hybrid light source; (Right) mirror assembly and the mounted light source..... 193

Figure 136. Lamp controlling, temperature controlling, and VI measurement controlling LabVIEW program user interface..... 194

Figure 137. Spec sheet of the irradiance variation of each light type with its intensity percentage 197

Page

Figure 138. Superposition and individual irradiance spectra for each bulb type used to simulate the AM 1.5 spectrum 198

Figure 139. (Left) spectrometer positioning on the sample stage; (Right) fast and accurate target temperature landing 198

Figure 140. Device performance comparison between in-house solar simulator and control chamber 202

Figure 141. Device performance parameters as a function of temperature 203

Figure 142. Current density vs. voltage curves for different temperatures 204

Figure 143. Schematic of a Si PV cell mounted on a magnet for optical Hall effect measurements based on THz range SE [382] 207

Figure 144. Experimental (symbols) spectra at 0 T (top-left), +1.48 T (top-right), –1.48 T (bottom-left) and difference spectra at ±1.48 T (bottom-right) with their corresponding calculated models (solid lines) of normalized Mueller matrix elements for the Al-BSF Si solar cell [382] ..210

Figure 145. $\varepsilon = \varepsilon_1 + i\varepsilon_2$ spectra for n-type Si:P emitter layer and p-type Si :B bulk wafer from optical Hall effect measurements [382] 211

Figure 146. (a) Simulated JV and J_rV curves; (b) mpp band diagrams at the front interface vs. TCO electron affinity 219

Figure 147. (a) V_{OC}, (b) J_{SC}, (c) FF, and (d) PCE vs. perovskite bandgap and TCO electron affinity 220

Figure 148. JV and J_rV for a TCO electron affinity of (a) 4.25 eV and (b) 3.8 eV for various ETL/perovskite CBOs. MPP band diagrams at the front interface for TCO electron affinity of (c) 4.25 eV and (d) 3.8 eV 222

Figure 149. (a) V_{oc}, (b) FF, and (c) PCE as a function of changing conduction band offset 226

Figure 150. (a) JV and J_rV curves for three CBOs. (b) Energy bands at the ETL/perovskite interface, V_{mpp}, with reduced HTL interface influence 227

Figure 151. Contour plots of (a) PCE and (b) Voc for ETL conduction band offsets of -0.35, -0.25, and -0.05 eV 228

Figure 152. (a), (b) simulated J-V curves, varied CBO and VBO; (c), (d) J_r for ETL and HTL interfaces; (e), (f) energy bands for the ETL/conduction band and the HTL/valence band interfaces, respectively, at MPP 232

Page

Figure 153. (a) V_{OC}, (b) FF and (c) PCE of perovskite devices with 1.6 eV, 1.7 eV and 1.8 eV absorbers vs. VBO and CBO 235

Figure 154. (a) PCE and (b) V_{OC} relative to the internal SQ limit as a function of bandgap for absorber with 10 μs carrier lifetimes 237

Figure 155. Illustration of 8 possible cases of the final states after impact. Single atoms correspond to Cd while dimers correspond to Te_2 239

Figure 156. (a) Sticking probability vs. deposition angle, temperature, and kinetic energy for Cd atoms (dashed lines) and Te_2 clusters (solid lines) on (100) Cd-terminated surface. (b) Same, but for (100) Te-terminated surface 241

Figure 157. (a) Sticking probability vs. deposition angle, temperature, and kinetic energy for Cd atoms (dashed) and Te_2 dimers (solid) deposited on (111) Cd-terminated surface; (b) Same, but for (111) Te-terminated surface..... 242

Figure 158. Excess Te sticking probability vs. temperature and kinetic energy..... 243

Figure 159. Top views of (a) equilibrated Te-terminated surface and (b) Te_2 dimer (white circle) leaving surface; (c) side view of Te_2 dimer leaving surface 247

Figure 160. (a) Velocity z-component distribution of desorbing Te_2 dimers; (b) dependence of kTST on window width b for vs. extrapolation factor s 248

Figure 161. (a) Semi-log plot of Te2 desorption rate as function of 1/kBT for full Te(100) ML. (b) Semi-log plot of Cd desorption rate as function of 1/kBT for Cd-terminated (100) surface. 249

Figure 162. Absorption coefficient, α (top) and reflectivity (bottom) vs. energy, of $MgSnN_2$ based on rock-salt structure 257

Figure 163. (a) Frequency of occurrence for all possible Zn-Cd coordination numbers relative to their completely random configuration; (b) Bond angle distributions of ∡Zn-Te-Cd in $Zn_{0.25}Cd_{0.75}Te$ simulated at 400 K and 1000 K. 258

LIST OF TABLES

Page

Table 1. JV parameters for the best CdS/CdTe and ZMO/CdTe devices, varied precursors 36

Table 2. Lifetime measurements of the CdS/CdTe solar cells with different form of back contacts 55

Table 3. The device performance parameters (V_{OC}, J_{SC}, FF and η) of the best cells of CdS/CdTe devices with different back contacts 56

Table 4. J-V data, devices fabricated with and without Cu and Al_2O_3 deposition/heating cycles. Data is for best PCE 65

Table 5. J-V parameters for best devices (PCE), with and without 1 cycle of Al_2O_3 followed by $CdCl_2$ activation, standard Cu/Au back contact 70

Table 6. JV parameters, including Al_2O_3 with varied Cu concentration (active device area = 0.06 cm^2), and including standard back contact values 80

Table 7. JV parameters for CdTe solar cells with Al_2O_3(30% Cu) back buffer layer, varied annealing times 84

Table 8. Properties of Cu-Zn-S Thin Films 93

Table 9. Average JV parameters with and without CZS NC for $CuCl_2$ treated CdTe devices 98

Table 10. Best (based on PCE) and average JV parameters of CdS/CdTe solar cells with and without a 100 nm thick GLAD wurtzite CdTe interlayer [308] 108

Table 11. Thicknesses obtained from SE analysis of ~1500 nm thick InGaAs epitaxial layers in multilayer stacks 128

Table 12. Model fit parameters for ~1500 nm thick epitaxial InGaAs in a multilayer stack; CP = critical point 128

Table 13. Thicknesses obtained from SE analysis 128

Table 14. Complex dielectric function parameters for epitaxial InAlAs in a multilayer stack . 129

Table 15. Drude complex dielectric function parameters describing the for epitaxial InGaAs and InAlAs in their corresponding multilayer stack 129

Table 16. I_{min} values as a function of dead area square. I_{min} are calculated through the model for alignment of the center of the beam with the center of the feature 139

LIST OF TABLES (Continued)

Page

Table 17. Ashcroft and Sturm (A&S) parameters determined by fitting the measured ψC of the Krasilov compensator 148

Table 18. Expressions for the Mueller matrix elements of the Krasilov compensator, to first order in beam path retardances and in deviation of the dichroic angle from 45°..... 157

Table 19. Fit results for the SiO_2 layer thickness at various angles for p and s polarization states. 171

Table 20. Constant parameters used in the calculation of implied open-circuit voltage 185

Table 21. Luminescence quantum efficiency and implied open-circuit voltage of $MAPbI_3$ 186

Table 22. Configuration file format of the light source 195

Table 23. Irradiance deviation between simulated spectrum and AM1.5G standard spectrum .. 197

Table 24. Integrated irradiance measurements for the homogeneity calculation..... 199

Table 25. Irradiance deviation between simulated spectrum and AM1.5G standard spectrum. 200

Table 26. Thermal stage temperature variation results with time (heating)..... 200

Table 27. Thermal stage temperature variation results with time (cooling). 200

Table 28. J-V-T measurements..... 202

Table 29. Dark and light carrier transport properties for Si phosphorus-doped n-type emitter and boron-doped p-type wafer in the Al-BSF solar cell [382] 212

Table 30. Electronic properties of simulated semiconductor materials. 217

Table 31. Materials properties used in the simulations..... 225

Table 32. Activation barriers E_d, prefactors ν_d, and binding energies B.E. for desorption of Cd and Te_2 from the (100) Cd- and Te-terminated surfaces 249

FOREWORD

The scientific research on photovoltaic (PV) materials and devices carried out by The University of Toledo on this project has advanced our country's knowledge of the most important, relevant, and impactful technologies to support our clean energy future. Thin film solar cells will play an increasingly important role in society's power-generating capacity. The PV R&D field has now focused on the need for viable tandem solar cell technology, for which two complementary semiconductors serve as the upper and lower layers to more efficiently utilize sunlight's broad spectrum. Although many challenges and opportunities remain, our advances in scientific understanding move us substantially closer to the energy technologies necessary to economically boost PV power capacity. We are proud to have executed this R&D on behalf of the Air Force Research Laboratory's Space Vehicles Directorate. Our vigorous and collaborative pursuit of scientific and technical excellence in solar power helps assure our nation's preparedness for current and future solar energy needs, and begins to address Earth's climate change crisis.

The intense pressure exerted on Earth's ecosystem, by the side-effects of humanity's pursuit of energy, water, and materials resources, demands amelioration to both maintain safe living conditions for people and to sustain Earth's biodiversity against species and habitat loss. Decarbonization of energy represents the key to solving climate change, as well as other environmental crises evident for the health of Earth's oceans, forests, and natural habitat. Solar energy converts the radiant energy of sunlight to electrical, thermal, and chemical energy, obviating the hydrocarbon combustion process and thereby avoiding the vast majority of carbon contributions, which today continue to drive record atmospheric CO_2 concentrations.

Generation of electricity directly from sunlight, the process known as photovoltaic energy conversion, uses semiconductors in a carefully engineered assembly to harvest photons of sunlight, which drive electrons to flow through an external circuit such as the power grid. Photovoltaic technology operates fundamentally with no mechanical motion, in silence, for decades with minimal maintenance required, and with minimal impact on the surroundings (the absorption of sunlight by solar modules creates shadows beneath the solar array). PV technology has advanced considerably over the past three to four decades and now competes economically with fossil-based electricity – even when omitting the costs to society of air and water pollution implicit to the wide scale mining and combustion of oil, coal, and gas. These substantial externalized costs to society must not be ignored as we weigh our energy options. The University of Toledo remains engaged in R&D to expand our options in affordable PV electricity.



Gregory C. Postel, M.D.
President, The University of Toledo

PREFACE

This Final Report presents the results of a concentrated three-year-long effort, beginning in August of 2018, to develop key materials and analytical capabilities and understanding in support of the development of thin film tandem solar cells. Such technology offers strength to our nation's decarbonized energy technology and environmental stewardship, and serves as the foundation for advanced energy infrastructure for our nation's defense forces.

The University of Toledo (UT) carried out the planned R&D, focused on materials and devices to advance photovoltaic (PV) technology and knowledge, for broad public use and benefit. This project, "High Specific Power Multi-Junction Thin Film PV", focused on thin film PV R&D in areas including technologies based on Group III-V, II-VI, and I-III-VI2 absorber materials, with the ultimate goal of optimizing and combining absorbers to create highly efficient tandem solar cells to serve society in numerous ways. In addition, UT refined and applied unique diagnostic instrumentation to investigate the optical, electrical and energy phenomena fundamental to understanding material properties and behavior as they depend upon surface and interface chemistry, electronic band structure, structural and impurity defects, energy barriers, and the intrinsic relationships between electronic/structural properties and device performance.

These studies, designed to advance the knowledge of thin film PV technologies to enable breakthroughs in PV power sources' reliability and efficiency, included efforts on perovskites, III-V's, CdTe, PV Diagnostics, and Computational/Theoretical Studies. The project principally addressed development of thin-film PV technologies, including those based on CdTe and CIGS, novel III-V device architectures, nanomaterials, and the rapidly improving perovskite-based materials systems. In addition to materials science, solar cell fabrication and testing, and investigations intended to establish new avenues to increase performance; specialized instrumentation has been developed to enable novel insights into materials, thin films, and online and real-time assessment of manufacturing quality and solar cell performance. Dr. Randall (Randy) Ellingson served as Principal Investigator during the three-year long project, with equally substantial contributions from co-Investigators Jacques Amar, Robert Collins, Michael Heben, Sanjay Khare, Adam Phillips, Nikolas Podraza and Yanfa Yan.

The 49 direct UT contributors to this project, some of whom may not be listed elsewhere as authors, are listed here:

Abudulimu, Abasi
Adhikari, Dipendra
Ahangharnejhad, Ramez H.
Al Fadhili, Fadhil Khalaf Dahash
Amar, Jacques G.
Anwar, Bhuiyan Muhammad Muktashif
Awni, Rasha
Bastola, Ebin
Bista, Sandip Singh
Bordovalos, Alexander Vasilis
Collins, Robert W.
Dulal, Prabin
Dumre, Bishal Babu
Ellingson, Randall J
Friedl, Jared D.
Ghimire, Kiran
Gibbs, Jacob Michael
Grice, Corey
Heben, Michael J
Jamarkattel, Manoj K
Jayswal, Niva
Junda, Maxwell Myles

Khanal Subedi, Kamala
Khare, Sanjay V.
Khatri, Indiras
Koirala, Prakash
Li, Chongwen
Li, Dengbing
Liyanage, Geethika Kaushalya
Lopez, Eulogio
Mainali, Madan
Mariam, Tamanna
Phillips, Adam B
Podraza, Nikolas Jacob
Pokhrel, Dipendra
Pradhan, Puja
Quader, Abdul
Ramanujam, Balaji
Rijal, Suman
Shrestha, Niraj
Snyder, Austin Jon
Song, Zhaoning
Subedi, Biwas
Subedi, Indra
Tatum, Jackson Ford
Tumusange, Marie Solange
Uprety, Prakash
Wu, Zhifang
Yan, Yanfa

In addition, we at The University of Toledo's Wright Center for Photovoltaics Innovation and Commercialization recognize and credit the technical contributions of our many external collaborators -- at U.S. National Labs, universities, and from the global community – without whom the advances achieved would be fewer. All peer-reviewed publications resulting from this effort are compiled in final published form (as Adobe Acrobat .pdf files, *appended only for the PDF version of this report*) in the Appendix of Publications appearing at the end of this report. This Final Report presents the key findings from the research topics addressed over the course of the project.

ACKNOWLEDGMENTS

We would like to thank the many people at The University of Toledo, and at Kirtland Air Force Base and elsewhere within our armed forces, who work diligently to ensure that this type of research and development project proceeds efficiently. Some of the numerous essential responsibilities necessary for this type of project to succeed include contracting, human resources, grants accounting, property management, financial reporting, security, laboratory and environmental safety, and purchasing. The investigators greatly appreciate the interactions between those overseeing this project and those working to ensure its success. The efficiency and care with which these functions have been carried out enabled an exceptional focus on developing the scientific insights and materials advances important to building a formidable foundation for a bright future in PV energy conversion.

In addition, the personnel at The University of Toledo and our partner institutions wish to thank the program management staff at Kirtland AFB for their assistance, including answering practical questions, clarifying acronyms and abbreviations specific to AFRL or DOD, and engaging scientifically. In particular, the program managers have included David Wilt and Alec Jackson, with substantial oversight and support also provided by Mariano Grinbank. In particular, the level of interest and engagement shown to the project and researchers by the program managers has clearly supported high quality research results and very high technical productivity. In addition, we wish to thank Kevin McCormick of the ONR Chicago Field Office for his oversight and input with regard to proper equipment procurement and management practices.

The authors thank Drs. Ebin Bastola and Abudulimu Abasi at The University of Toledo for assistance with report formatting requirements and preparation of certain aspects of the report including the list of acronyms and abbreviations.

The PVIC faculty, staff, and students who have conducted the research at The University of Toledo wish to thank our co-workers for their diligent and dedicated efforts to allow the project to run smoothly, including (but not limited to) Robin Lanz, Lori Burkholder, Lynda Obee, Lisa Selmek, Paula Minor, Laura Hallauer, Jeremy Archer, Gary Andres, Anne Izzi, Marcie Ferguson, Pamela Moore, Gary Rafe, Jamie Fager, Sara Lockett, and Frank Calzonetti.

1. EFFICIENT PEROVSKITE SOLAR CELLS USING A DOPANT-FREE HOLE TRANSPORT MATERIAL

1.1 SUMMARY

Dopant-free hole transport materials (HTMs) are essential for commercialization of perovskite solar cells (PSCs), however, the state-of-art power conversion efficiency (PCE) for small molecule dopant-free HTMs is only around 20%. We have studied a simple dithieno[3,2-b:2′,3′-d]pyrrol-cored small molecule, DTP-C6Th, synthesized by our collaborator, which is a promising dopant-free HTM. Compared with commonly used spiro-OMeTAD, DTP-C6Th exhibits a similar energy level, a better hole mobility of 4.18×10^{-4} cm^2 V^{-1} s^{-1}, and enhanced hole extracting capability. Using an ultra-thin poly (methyl methacrylate) passivating layer and careful composition adjustment of perovskite, we fabricated planar n-i-p PSCs achieving a champion PCE of 21.04% and good long-term stability with dopant-free DTP-C6Th as HTM, which is the highest conversion efficiency for small molecule dopant-free HTM based PSCs to date.

1.2 INTRODUCTION

2,2′,7,7′-tetrakis(N,N-di-p-methoxyphenylamino)-9,9′-spirobifluorene (spiro-OMeTAD) is the most widely used and successful hole-transporting material (HTM) for achieving high efficiency in halide perovskite solar cells (PSCs). [1-6] However, to improve the electrical conductivity, spiro-OMeTAD film must be doped with dopants including 4-tert-butylpyridine (t-BP), lithium bis(trifluoromethyl sulfonyl)imide (Li-TFSI) and cobalt(III) complexes. [7-9] These additive salts are hygroscopic and have a strong tendency to diffuse, thereby limiting long-term stability of PSCs. [10-12] Furthermore, the additional steps of adding dopants and oxidation increase total cost and complexity. For these concerns, developing dopant-free HTMs is urgently demanded.

In this work, we report DTP-C6Th, a simple dithieno[3,2-b:2′,3′-d]pyrrol-cored small molecule, as a promising dopant-free HTM for n-i-p type PSCs. [13] Compared with doped spiro-OMeTAD, dopant-free DTP-C6Th shows similar energy level and enhanced hole extracting/transporting property. Planar n-i-p PSCs using pristine DTP-C6Th as HTM reach a PCE of 18.56%, after interface passivation and component adjustment of perovskite layer, a champion PCE of 21.04% is acquired with a steady-state efficiency of 20.36%, which was the highest efficiency for PSCs based on small molecule dopant-free HTMs.

1.3 METHODS, ASSUMPTIONS, and PROCEDURES

Perovskite precursor solution preparation

$MA_{0.7}FA_{0.3}PbI_3$ precursor: 1 mmol PbI_2 (Alfa Aesar), 0.7 mmol methylammonium iodide (MAI, Dyesol), 0.3 mmol formamidinium iodide (FAI, Dyesol) and 9.22 mg $Pb(SCN)_2$ (Sigma-Aldrich, 99.5%) were added to 600 μL N,N-dimethylformamide (DMF, Sigma-Aldrich), then 1 mmol dimethyl sulfoxide (DMSO, Sigma-Aldrich) was added. The precursor solution was stirred on a hotplate at 60 °C for 1 h and then purified using a 0.45 μm filter before deposition.

$MA_{0.7}FA_{0.3}Pb(I_{0.925}Br_{0.075})_3$ precursor: 0.8875 mmol PbI_2, 0.1125 mmol $PbBr_2$ (TCI), 0.7 mmol MAI, 0.3 mmol FAI and 9.22 mg $Pb(SCN)_2$ were added to 600 μL DMF, then 1 mmol DMSO was

added. The precursor solution was stirred on a hotplate at 60 ℃ for 1 h and then purified using a 0.45 μm filter before deposition.

Perovskite solar cell fabrication

FTO substrates were sequentially cleaned by ultra-sonication with diluted Micro-90 detergent, deionized water, acetone, and isopropanol for 30 min, respectively. A SnO_2 layer was deposited on the FTO using plasma-enhanced atomic layer deposition (PEALD) method with a thickness of 15 nm. [14] The SnO_2 layer was annealed at 100 ℃ for 1 h in ambient air. A C_{60}-SAM solution was then spin-coated onto the SnO_2 layer at 3000 rpm for 1 min. The perovskite precursor solution was spin-coated on the PEALD SnO_2 /C_{60}-SAM layers at 500 rpm for 3 s and at 4000 rpm for 60 s. At the 8 s of the spinning process, 700 μL diethyl ether was then dropped onto the perovskite surface in one portion. After spin-coating, the perovskite film was annealed at 100 ℃ for 5 min. All of these processes were carried out in a N_2 filled glove box. After the deposition of the perovskite layer, a PMMA passivation layer was spin-coated on the top of the perovskite film at a speed of 6000 rpm, then annealed at 100 ℃ for 10 min. For the HTM, a DTP-C6Th layer was spin-coated on the perovskite film at 3500 rpm for 50 s, resulting in an approximately 40 nm layer. Alternatively, Spiro-OMeTAD was deposited on the perovskite film at 3000 rpm for 60 s. Finally, a 100 nm gold (Au) lay was then deposited on the top of HTMs using thermal evaporation. The working area of the devices was 0.08 cm^2 as defined by the overlapped area of FTO and Au electrodes.

1.4 RESULTS and DISCUSSION

Figure 1(a) shows the calculated electrostatic surface potential (ESP) results, the negative electrostatic potential (in red color) concentrates on the S atoms of DTP core and thiophene spacer, while the positive electrostatic potential (in blue color) mainly localizes on triphenylamine arms. This kind of charge polarization could facilitate the intramolecular charge transfer. Moreover, S heteroatom of DTP may benefit interface passivation of perovskite due to strong Pb^{2+}-S interaction.

Cyclic voltammetry (C-V) and ultraviolet photoelectron spectroscopy (UPS) were used to determine the energy levels of HTMs. The results are shown in Figure 1(b) C-V was conducted by dissolving HTMs in dichloromethane with tetrabutylammonium hexafluorophosphate (0.1 M) as electrolyte. After calibrating redox potentials with ferrocene, the highest occupied molecular orbital (HOMO) levels of spiro-OMeTAD and DTP-C6Th were calculated to be -4.82 eV and -4.87 eV, respectively. The ionization potential (IP) for spiro-OMeTAD and DTP-C6Th were -5.03 eV and -4.94 eV, indicating the open circuit voltage (V_{OC}) of spiro-OMeTAD based PVSCs may be higher than DTP-C6Th based devices. Since the normal bandgap perovskite used in our investigation ($MA_{0.7}FA_{0.3}PbI_3$, MA = methylammonium, FA = formamidinium) has a valence band edge around -5.40 eV, both spiro-OMeTAD and DTP-C6Th have sufficient driving force for hole extraction.

Figure 1(c) shows space-charge-limited-current (SCLC) method was adopted using a hole only device structure of ITO/poly(3,4-ethylenedioxythiophene):poly(styrenesulfonate) (PEDOT:PSS)/HTM/Au. The hole mobility value of DTP-C6Th is estimated to be

4.18×10-4 cm2 V^{-1} s^{-1}, which is one order of magnitude higher than spiro-OMeTAD (3.43×10^{-5} cm^2 V^{-1} s^{-1}). The high mobility enables DTP-C6Th to act as efficient HTM for PVSCs with no doping process.

Figure 1(d) shows a cross sectional scanning electron microscopy image of a PSC using a 40 nm thick DTP HTL. To evaluate the hole extracting capability of DTP-C6Th and spiro-OMeTAD at perovskite/HTM interface, steady-state photoluminescence (PL) and time resolved photoluminescence (TRPL) measurements were carried out. It is clearly seen in Figure 1(e) that bare perovskite film exhibited strong PL intensity upon excitation. After capping perovskite with spiro-OMeTAD, the PL intensity decreased to around one third of original level. Furthermore, DTP-C6Th coated on perovskite showed the most significant PL quenching, indicating a more effective hole extraction at the perovskite/DTP-C6Th interface than perovskite/spiro-OMeTAD. From the TRPL results shown in Figure 1(f), the mean carrier lifetime for pristine perovskite, perovskite covered with spiro-OMeTAD and DTP-C6Th is 777 ns, 158 ns and 10 ns, respectively. The shortest lifetime of perovskite/ DTP-C6Th proves the fastest charge carrier dynamics at interface.

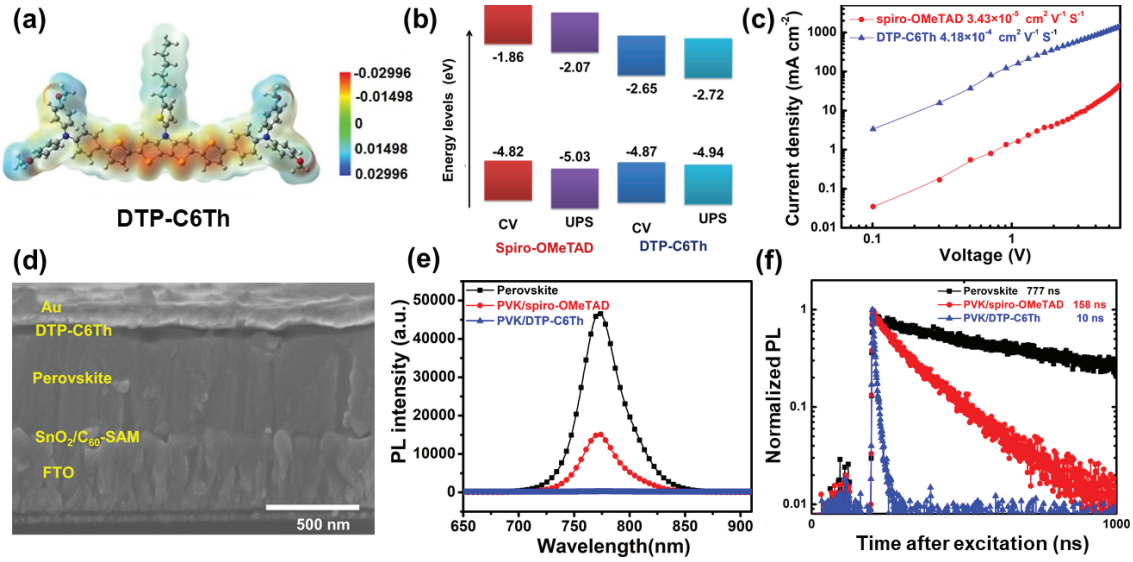


Figure 1. (a) Computed ESP of DTP-C6Th. (b) Energy levels of spiro-OMeTAD and DTP-C6Th. (c) SCLC J–V characteristics of DTP-C6Th or spiro-OMeTAD based devices. (d) Cross-sectional SEM image of device with DTP-C6Th HTM. (e) PL intensity and (f) TRPL decays of perovskite films

We adopted a surface passivation strategy by incorporating an ultra-thin layer of poly(methyl methacrylate) (PMMA) and optimized the processing conditions. The changes in photovoltaic parameters of PVSCs under different optimization conditions are shown in Figure 2(a-d). With the help of PMMA, DTP-C6Th based PVSCs achieve a high PCE of 20.42%, which is comparable with control devices using doped spiro-OMeTAD as HTM. To further improve the device performance, we turn to composition tuning of perovskite layer by adding small amount of bromine (Br). It is well known that adding Br can effectively tune bandgap and bring higher V_{OC},

at a cost of reducing JSC. By carefully tuning the V_{OC}/J_{SC} trade-off, a maximum efficiency can be acquired. For optimal results, 7.5% Br is added, leading to a new composition of $MA_{0.7}FA_{0.3}Pb(I_{0.925}Br_{0.075})_3$ (referred to as W/ PMMA & Br).

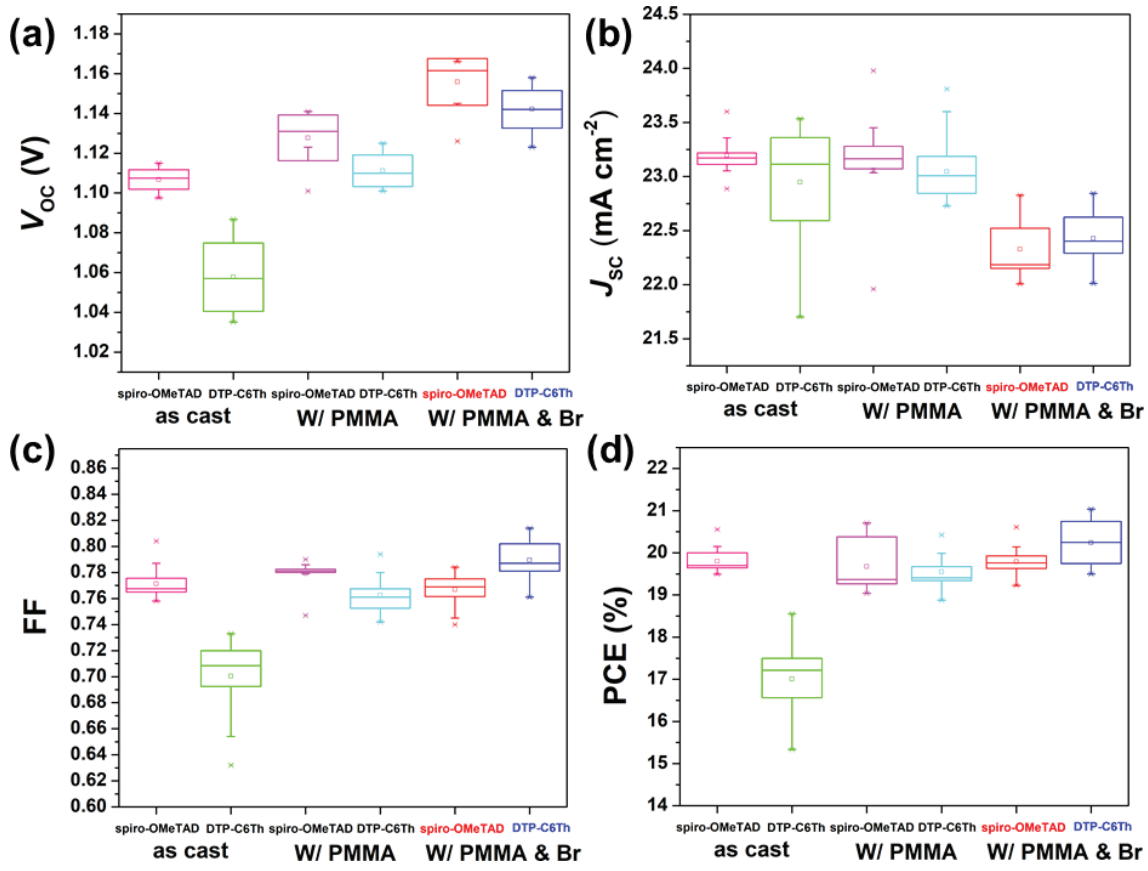


Figure 2. Photovoltaic parameters of PVSCs using DTP-C6Th or spiro-OMeTAD as HTM. Histograms of (a) V_{OC}, (b) J_{SC}, (c) FF, and (d) PCE of corresponding devices

Figure 3(a) shows the top-view SEM image of a $MA_{0.7}FA_{0.3}PbI_3$ film with a compact and smooth morphology, the calculated average grain size is 1.75 μm. For $MA_{0.7}FA_{0.3}Pb(I_{0.925}Br_{0.075})_3$, the average grain size is 1.52 μm (Figure 3(b)). This kind of large size (>1 μm) crystals with PbI_2 passivation at the grain boundaries are beneficial for the performance of PVSCs. As expected, the absorption onset and PL peak of $MA_{0.7}FA_{0.3}Pb(I_{0.925}Br_{0.075})_3$ film show a small blue shift due to the introduction of Br (Figure 3(c)), indicating the increasement of bandgap, which is consistent with previous reports. As shown in Figure 3(d-f), perovskite with 7.5% Br shows enhanced PL intensity, longer carrier lifetime and improved crystallinity, indicating better perovskite quality than $MA_{0.7}FA_{0.3}PbI_3$. Thus, PSCs using $MA_{0.7}FA_{0.3}Pb(I_{0.925}Br_{0.075})_3$ as absorbers may have better device performance.

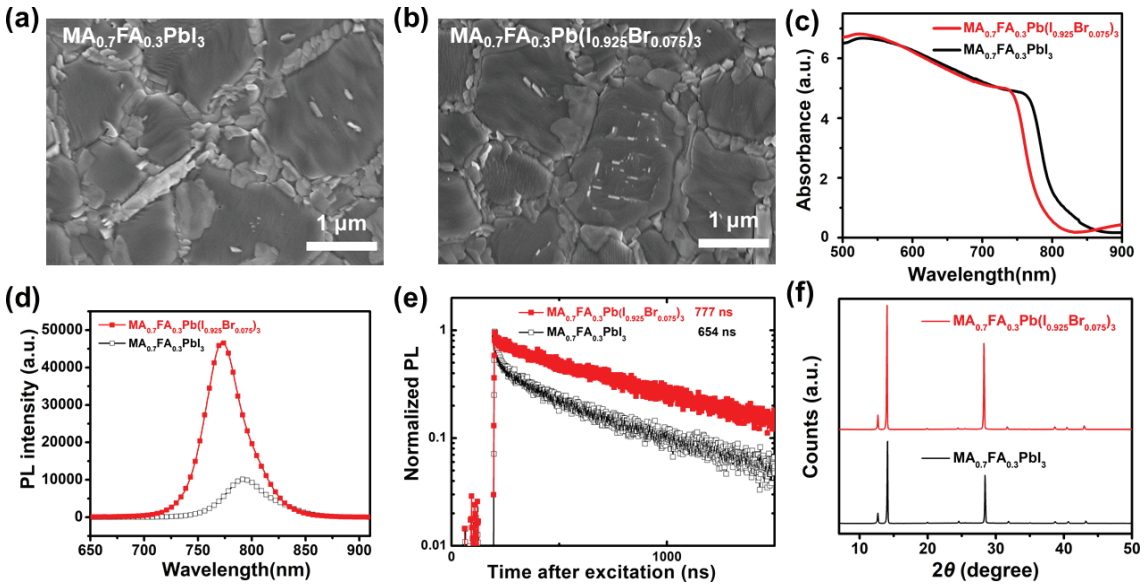


Figure 3. (a) SEM image of a $MA_{0.7}FA_{0.3}PbI_3$ film. (b) SEM image of a $MA_{0.7}FA_{0.3}Pb(I_{0.925}Br_{0.075})_3$ film. (c) Absorbance, (d) PL, (e) TRPL and (f) XRD patterns of $MA_{0.7}FA_{0.3}PbI_3$ and $MA_{0.7}FA_{0.3}Pb(I_{0.925}Br_{0.075})_3$ films

Figure 4(a) shows the J-V curves under reverse or forward voltage scan of our best-performing PSCs (W/ PMMA & Br) with dopant-free DTP-C6Th or doped spiro-OMeTAD as HTMs. Our champion cell with DTP-C6Th achieves a maximum PCE of 21.04% with a V_{OC} of 1.157 V, a J_{SC} of 22.76 mA cm^{-2}, and a FF of 79.9% under reverse scan, which is the highest PCE for dopant-free HTM based PVSCs at the time. For reference, PSC based on spiro-OMeTAD exhibits a slightly lower PCE of 20.61% under the same conditions. Devices based on both HTMs show similar hysteresis, thus the J–V hysteresis might be ascribed to perovskite problem including trap states, ion migration, or ferroelectricity. The integrated J_{SC}s from EQE (Figure 4(b)) for DTP-C6Th or spiro-OMeTAD device are 22.20 mA cm^{-2} and 21.92 mA cm^{-2}, which are in good agreement with J-V measurements. Additionally, the stabilized output PCE of DTP-C6Th-based champion PVSC (W/ PMMA & Br) was recorded (Figure 4(c)) in air without encapsulation, a PCE of 20.36% was obtained under 1200s continuous illumination. This indicates the device works well under real working conditions. For 20 individual devices, the histograms of PCE distribution are shown in Figure 4(d). Good reproducibility can be realized using either dopant-free DTP-C6Th or doped spiro-OMeTAD hole transfer materials, giving an average PCE of 20.24% and 19.79%, respectively.

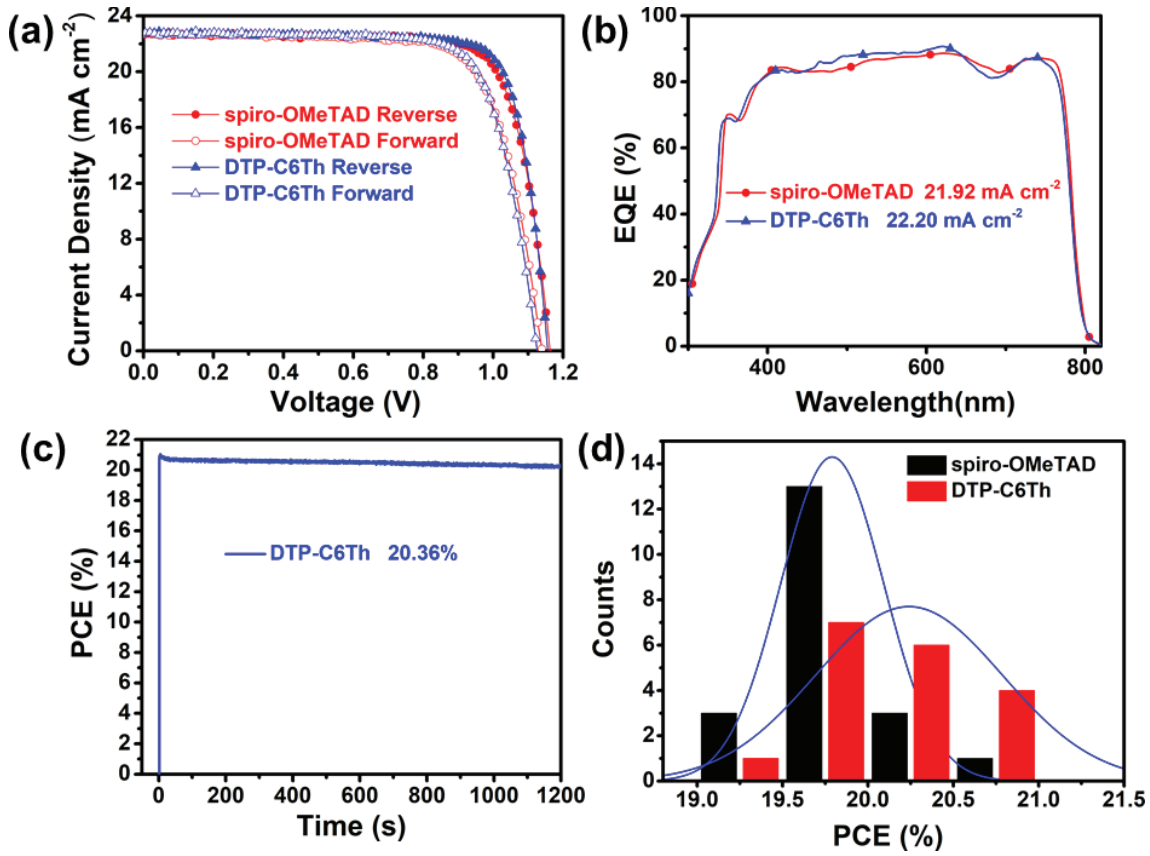


Figure 4. Photovoltaic parameters of the best performing PSCs (W/ PMMA & Br). (a) J–V curves. (b) EQE plots. (c) Steady-state efficiency over 1200 s. (d) Histogram of PCEs for 20 cells

1.5 CONCLUSIONS

We found that the new small molecule dopant-free HTM material with a simple dithieno[3,2-b:2′,3′-d]pyrrol core, i.e. DTP-C6Th, exhibits an suitable IP of -4.94 eV and a good hole mobility of 4.18×10^{-4} cm^2 V^{-1} s^{-1} (3.43×10^{-5} cm^2 V^{-1} s^{-1} for spiro-OMeTAD). After careful device optimization by inserting ultra-thin PMMA passivating layer and tuning perovskite composition with Br, an impressive PCE of 21.04% with a steady-state efficiency of 20.36% is obtained, which is the best value for small molecule dopant-free HTM based PVSCs. Therefore, DTP-C6Th could be a promising dopant-free HTM for PVSC commercialization.

2. CORRELATING HYSTERESIS AND STABILITY WITH ORGANIC CATION COMPOSITION IN TWO-STEP SOLUTION-PROCESSED PEROVSKITE SOLAR CELLS

2.1 SUMMARY

Organic cation composition used in the two-step solution processing of mixed-cation lead halide perovskite solar cells plays a critical role in the perovskite film formation and the resultant device performance. However, little is understood about the impacts of organic cation composition on the current density-voltage (J-V) hysteretic behavior and stability of perovskite solar cells. To address this need, we study the effect of mixed organic cations, i.e., the fraction of formamidinium (FA) and methylammonium (MA) contents, used for the two-step solution-processed perovskite thin films on solar cell performance, including efficiency, J-V hysteresis, and stability. In addition to the efficiency variations, we find that perovskite solar cells based on FA-rich and MA-rich stoichiometries show distinct characteristics in J-V hysteresis and stability. The origins of such a discrepancy are attributed to the thermodynamically driven conversion from lead iodide to perovskites, which is determined by the combination of organic cations. The perovskite solar cells based on the mixed cation $FA_{0.6}MA_{0.4}PbI_3$ composition show a champion power conversion efficiency of over 21% and robust stability under maximum power point tracking conditions. Our work provides insights on understanding the formation of perovskite films in the two-step process, which may benefit further investigation on perovskite solar cells.

2.2 INTRODUCTION

With the revolutionary progress in perovskite solar cells (PSCs), a variety of solution-based deposition methods, including antisolvent-assisted single-step spin-coating [15-18] and two-step sequential deposition, [6, 19-22] have been successfully developed and widely used to prepare perovskite absorber layers for high-efficiency PSCs. Compared with the single-step antisolvent dripping technique, the two-step solution process has some unique advantages, such as more precise and reproducible process control, more suitable for scale-up fabrication, and vertical-columnar grain formation that enables the preparation of thicker perovskite absorber layer. [6, 20-22] Because of these merits, the two-step method is more preferred than the single step antisolvent dripping method for the commercialization of PSCs.

Despite the success in fabricating high-efficiency PSCs, the underlying mechanisms that govern the formation of perovskite films in the second step and corresponding device performance are yet to be fully understood. Since the PV performance of PSCs can be influenced by the synthesis approach and stoichiometry of the perovskite absorber layers, it is critical to understand and precisely control the crystal growth process during the formation of perovskite films. Over the years, the nucleation dynamics and growth of perovskite films were manipulated by various approaches. [23-32] Among them, the organic cation composition of perovskites plays a critical role in the perovskite film formation and the resultant device performance and stability. Particularly, mixing organic cation can adjust the Goldschmidt tolerance factor of FA-based perovskites and thus stabilize FA-rich perovskites. [33] The MA to FA ratio can also influence the microstructure and crystal orientation of perovskite crystallites. [23] However, the two-step solution-processed mixed-cation perovskites have rarely been explored in the full MA-FA

compositional space. Furthermore, little is known about the impacts of organic cation composition on the current density-voltage (J-V) hysteretic behavior and stability of perovskite solar cells. To address this need, we investigated the effect of mixed organic cations, i.e., the fraction of FA and MA contents, used for the two-step solution-process perovskite thin films on solar cell performance, including efficiency, J-V hysteresis, and stability. [34] Additionally, the origins of the different hysteresis and stability behaviors were also explored.

2.3 METHODS, ASSUMPTIONS, and PROCEDURES

Materials

Acetone used to clean the substrates was purchased from Fisher Scientific. Tin (IV) oxide (15% in H_2O colloidal dispersion) was purchased from Alfa Aesar. Lead iodide (99.999%), spiro-OMeTAD (99%), Bis(trifluoromethane)sulfonimide lithium salt (99.95%), FK102 Co(III) TFSI salt (98%), N,N-dimethylformamide (DMF, 99.8%), dimethyl sulfoxide (DMSO, 99.9%), isopropanol (IPA, 99.5%), chlorobenzene (99.8%), 4-tert-butylpyridine (TBP, 98%) and acetonitrile (99.8%) were bought from Sigma-Aldrich. Formamidine iodide (FAI), methylammonium iodide (MAI), methylammonium chloride (MACl) were bought from Greatcell Solar.

Preparation of perovskite precursor solutions

The PbI_2 solution was prepared by dissolving 1.3 M PbI_2 in a mixed solvent of 950 μL DMF and 50 μL DMSO. The mixed organic halide solution was prepared by dissolving FAI and MAI at a total concentration of 0.45 M in IPA solution. MACl additive with a concentration of 7 mg/mL was added to the organic halide solution to assist the perovskite conversion. The molar ratio of FA to FA+MA was varied from 1, 0.8, 0.6, 0.4, 0.2 to 0, denoted as $FA_xMA_{1-x}PbI_3$. All the solutions were stirred on a hotplate at 60 ℃ for 3 h and filtered with a 0.45 μm PTFE filter before using.

Perovskite solar cell fabrication

ITO substrates were sequentially cleaned with deionized water, acetone, IPA in an ultrasonic bath and then dried with a nitrogen flow. The substrates were then treated with UV-ozone for 20 min. A diluted SnO_2 solution (SnO_2: DI water = 1: 6) was spin-coated on the substrates at 3000 rpm for 30 s and then annealed at 150 ℃ for 30 min in ambient air. After cooling down, the substrates were transferred to an N2-filled glovebox. The PbI_2 solution was spin-coated on the ITO/SnO_2 substrates at 2000 rpm for 30 s and annealed at 70 ℃ for 2 min. After that, the organic halide precursor solutions with different FAI/MAI ratios were spin-coated on the substrates at 2000 rpm for 30 s. All the substrates were then annealed at 150 ℃ for 15 min in the air with 30% - 40% relative humidity, except for $MAPbI_3$ that was annealed at 100 ℃. The spiro-OMeTAD was spin-coated on perovskite layers at 3500 rpm for 60 s. Finally, 80 nm of gold was deposited by the thermal evaporation to complete the devices. The active area of 0.12 cm^2 was defined by the overlap area of the ITO and gold electrodes.

Material and Device characterization

SEM images were taken with a Hitachi S-4800 high-resolution field-emission microscope. Absorbance spectra of perovskite films were measured by employing an ultraviolet-visible (UV-vis) spectrophotometer (PerkinElmer Lambda 1050). X-ray diffraction (XRD) spectra were obtained by using Rigaku D/MAX 2400 diffractometer with Cu $K_ς$ radiation. J-V curves were measured by adopting a Keithley 2400 source meter under AM1.5G (100 mW/cm^2) illumination

(PV Measurements Inc.). Photostability measurement was performed at room temperature in an environmental control box using a white LED light source calibrated to 100 mW/cm^2 light intensity with a silicon photodiode. External quantum efficiency (EQE) spectra from 300 nm to 860 nm were obtained with a QE system (PV Measurements Inc.) All the characterizations were measured under the ambient at room temperature.

2.4 RESULTS and DISCUSSION

The PV performance and stability of PSCs are mainly determined by the quality of the perovskite absorber layer. To evaluate the structural and optoelectronic properties of MA-FA mixed cation perovskites prepared by the solution-based two-step deposition approach, we prepared a series of perovskite thin films. Figure 5 shows false-color scanning electron microscopic (SEM) surface images of the perovskite films with different FA ratios in the organic halide precursor solution. The pure $MAPbI_3$ film (FA = 0.0) shown in Figure 5(a) exhibits a dense and smooth surface morphology but slightly nonuniform distribution in grain sizes ranging from ~0.3 to ~1 μm. The small grain size is attributed to the relatively low annealing temperature (100 ˚C), particularly used for $MAPbI_3$. The yellow highlighted regions in Figure 5 are attributed to formation of PbI_2.

With the incorporation of FA cations into perovskites, a higher annealing temperature of 150 ˚C was enabled, promoting significant grain growth with average grain sizes reaching more than 1 μm (Figure 5(b-f)). However, the higher annealing temperature also leads to the partial decomposition of perovskite into PbI_2, especially on the top surface. The PbI_2 particles are identified on the surface of perovskite films, as is evident from the high contrast (low conductive) areas, which are highlighted in yellow in the SEM images. The thermal decomposition is more severe for the compositions with higher MA content (FA = 0.2 and 0.4 in Figure 5(b, c), respectively). Increasing the FA content makes perovskite more thermally stable, suppressing the formation of PbI_2 on the perovskite surface (Figure 5(d-f)). It is worth noticing that the PbI_2 particles are mostly distributed at grain boundaries where perovskites are prone to decomposition. It is known that the proper amounts of PbI_2 help passivate defect centers at grain boundaries, leading to enhanced V_{OC} and FF. However, too much of PbI_2 adversely affect the charge collection at the interface, resulting in lower J_{SC} and FF. The MA-rich (FA < 0.5) perovskite films (Figure 5(b, c)) contain significant quantities of PbI_2 particles on the top surface due to thermal decomposition of perovskites, whereas the high FA (FA > 0.7) content films (Figure 1(e, f)) show a limited coverage of PbI_2. The FA = 0.6 sample (Figure 5d) possesses a proper amount of PbI_2 that only existed at grain boundaries, which provides effective surface passivation.

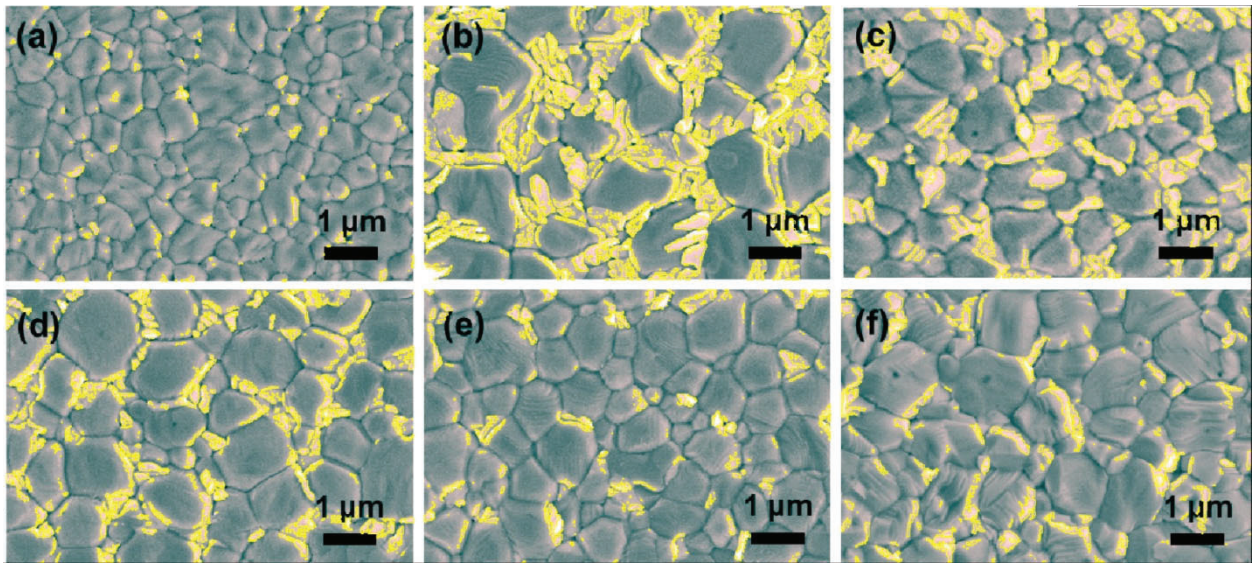


Figure 5. SEM images of $FA_xMA_{1-x}PbI_3$ films with x = (a) 0.0, (b) 0.2, (c) 0.4, (d) 0.6, (e) 0.8, and (f) 1.0

Turning to the XRD patterns of perovskite films with various FA contents, as shown in Figure 6(a-c), perovskite films with different organic cation compositions show different combinations of chemical phases and crystal orientations. The $MAPbI_3$ film (FA = 0.0) shows the almost pure tetragonal (β) perovskite phase (space group: I4/mcm) without a clear trace of PbI_2 (Figure 6(b)). The tetragonal phase is revealed by the shoulder peak of the (002)/(110) planes at 14.1˚ and the (211) plane at 23.5˚ which has the reflection position inconsistent with cubic symmetry. In contrast, perovskites with FA cations show the cubic (α) phase (space group: Pm-3m) with the presence of PbI2 peak at ~12.6˚. The hexagonal non-perovskite (δ) phase $FAPbI_3$, which is photoinactive and detrimental to the device performance if in bulk, is not observed in any perovskite films. With the increase of FA content, the characteristic XRD peaks shift to a lower angle (Figure 2(b)), corresponding to larger lattice spacing due to the larger size of FA as compared to the MA cation.

The crystal orientation in perovskite films can also influence the optoelectronic of the films. Interestingly, the perovskite films with high FA content (FA = 0.8 and 1.0) exhibit a strongly preferred (111) orientation compared with other films. The different preferred orientation indicates that the nucleation and growth of FA-rich perovskites follow a crystal orientation that is more thermodynamically favorable. Note that the lattice displacement of iodine atoms in the (111) orientation closely matches the (001) plane of the hexagonal PbI_2, resulting in a quasi-epitaxial growth of perovskite on the PbI_2. Therefore, it is likely that a thin PbI_2 template layer may remain at the interface between SnO_2 and perovskite layers which assists the growth of (111) oriented FA-based perovskites. When FA content is high, the reaction between PbI_2 and organic halide salts is retarded due to less reactivity of FA than MA. The conversion may not be completed, leaving some unreacted PbI_2 at the SnO_2/perovskite interface. The hypothesis is in good agreement with the XRD (Figure 6(b)) and SEM (Figure 5(e, f)) results of high FA content films. The XRD patterns

(Figure 6(b)) show a significant amount of PbI_2 phases (10% to 24%) in these films. The remaining PbI_2 at the bottom can passivate the perovskite interface but may hinder the charge collection.

Figure 6(d) shows the optical absorption spectra of mixed cation perovskite films. The absorption edge of perovskite shows a redshift from 760 to ~800 nm with increasing FA fraction from 0 to 1. The pure $FAPbI_3$ film (FA = 1.0) shows lower optical absorption than others, indicating an uncompleted perovskite conversion with poor crystal quality in the resulting perovskite film. In good agreement with the optical absorption, PL emission (Figure 6(e)) shows the same trend of bandgap redshift with a higher FA fraction. To quantitatively analyze the carrier lifetime in different mixed cation perovskites, perovskite thin films were prepared directly on bare soda-lime glass substrates, and the TRPL data was acquired via the through-glass photoexcitation, as shown in Figure 6(f). All the perovskite films show decent carrier lifetimes of more than 700 ns. Particularly, the FA-rich (FA > 0.5) perovskite films show longer lifetimes than MA-rich (FA < 0.5) samples, likely due to the remaining unreacted PbI_2 at the bottom of the perovskite films, which passivate the perovskite interfaces.

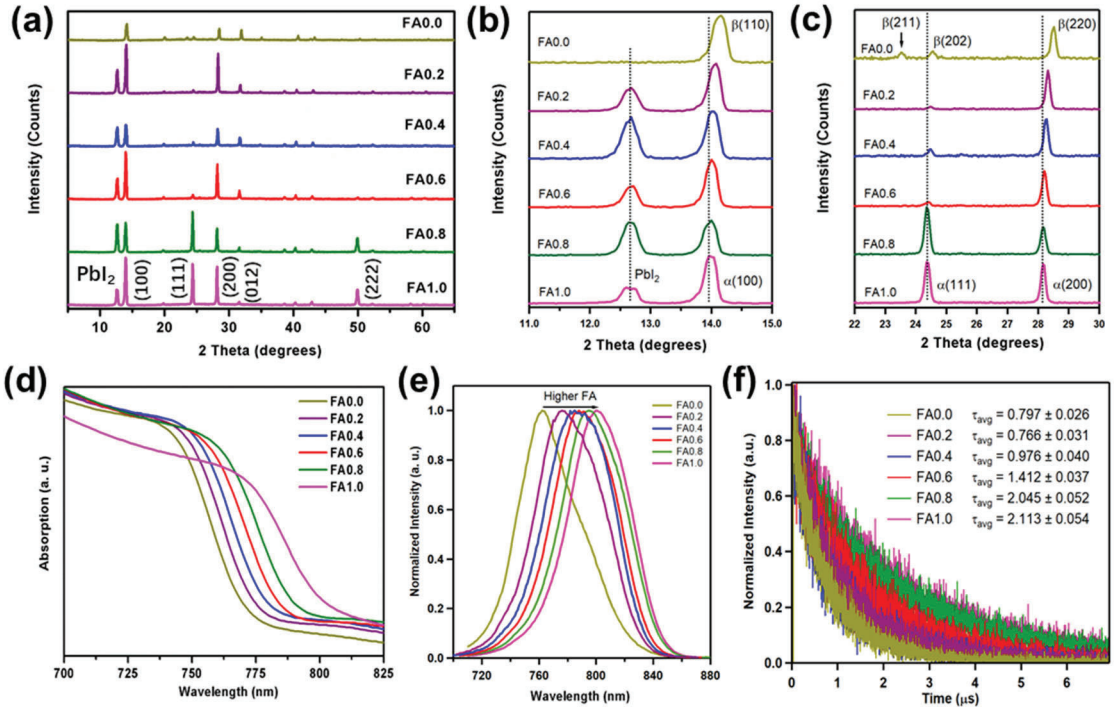


Figure 6. (a) XRD, (b, c) normalized XRD, (d) absorbance and (e) PL spectra, and (f) PL decays of $FA_xMA_{1-x}PbI_3$ films with x = 0.0, 0.2, 0.4, 0.6, 0.8, and 1.0

To evaluate the PV performance of PSCs based on different mixed cation perovskite films, planar PSCs with the structure of glass/ITO/SnO_2/$FA_xMA_{1-x}PbI_3$/Spiro-OMeTAD/Au were fabricated. Figure 7(a-d) summarizes the statistical distributions of PV parameters of more than 40 cells for each group, determined by light current density-voltage (J-V) curves under the standard AM1.5G illumination with reverse (R) or forward (F) voltage scan directions. The PCE (Figure 7(a)) increases first with increasing FA fraction from 0 to 0.6 and then decreases slightly as the FA fraction is further increased. The variations in JSC and FF (Figure 7(b, d)) follow a similar trend

as the changes in PCE. The J_{SC} values were confirmed by the external quantum efficiency (EQE) measurements, as shown in Figure 8. Notably, the EQE cutoffs at the long-wavelength side are consistent with the bandgaps of the perovskite films determined by the absorption measurements (Figure 6(d)). In contrast to the variations in J_{SC} and FF, V_{OC} from the reverse scan remains approximately constant except for the FA-free PSCs, while V_{OC} from the forward scan shows an almost monotonic increase with increasing the FA fraction. This higher V_{OC} indicates lower recombination in the FA-rich perovskites, which is likely attributed to the remaining PbI_2 in the films. It is noticeable that all the PSCs show pronounced hysteresis in PCEs, which is mainly caused by the differences in V_{OC} and FF. Particularly, the hysteresis gap in V_{OC} decreases with higher FA fraction, indicating more stable quasi-Fermi energy splitting at a forward bias voltage. This is likely due to better defect passivation in the FA-rich perovskite films, which is consistent with the longer carrier lifetime measured by TRPL (Figure 6(f)).

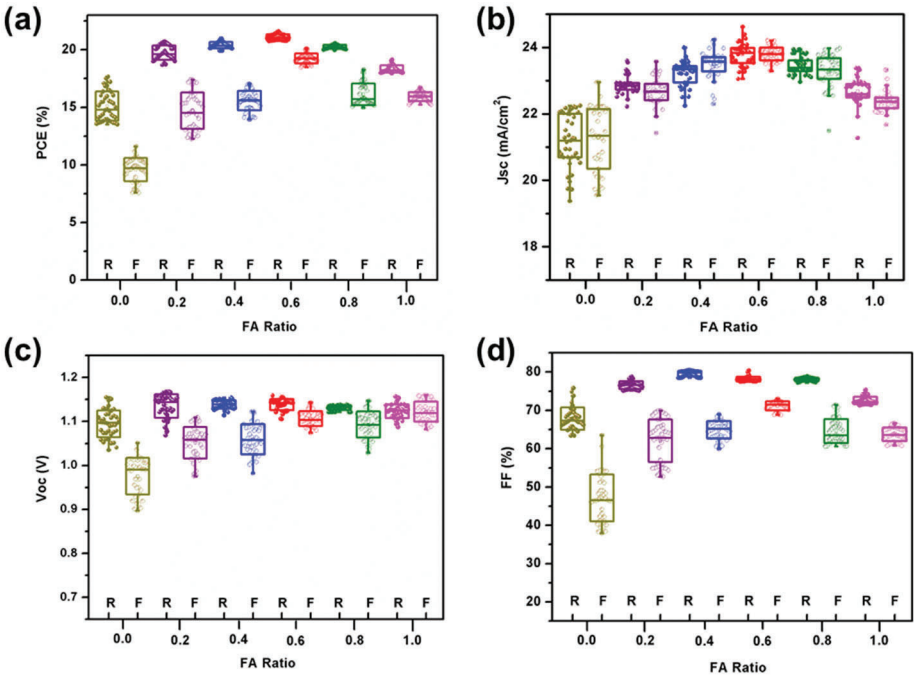


Figure 7. PV parameters including (a) PCE, (b) JSC, (c) VOC, and (d) FF for $FA_xMA_{1-x}PbI_3$; R and F represent reverse and forward scans

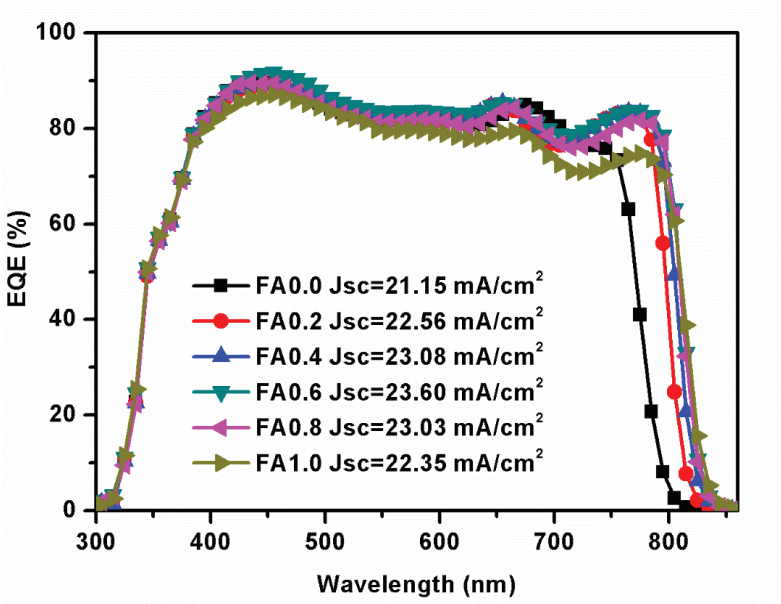


Figure 8. EQE spectra of perovskite solar cells with different FA fractions

Figure 9 plots representative J-V curves of mixed cation PSCs with various FA fractions, showing two dissimilar hysteresis characteristics for different PSCs. The MA-rich PSCs (FA < 0.5) exhibit apparent V_{OC} shifts (Figure 9(a-c)). The higher the MA fraction, the larger the difference in the V_{OC} under the opposite scan directions. The V_{OC} shift is confirmed by the J-V scans of corresponding devices in the dark (Figure 10), from which the dark saturation current density (J_0) can be calculated. J_0 is a typical parameter depending on the recombination in a solar cell and be used as an indicator of the quality of the cell. The FA-rich (FA > 0.5, see Figure 9d-f) PSCs exhibit higher J_0 values under the forward scan than that under the reverse scan, indicating more severe recombination in the device when a forward voltage sweep is applied. Such voltage-sweep induced recombination is likely related to the ion migration along the grain boundaries, which creates a significant amount of trap states. MA-rich perovskites are prone to having a higher density of non-passivated grain boundaries, resulting in lower carrier lifetimes and higher recombination rates. These non-radiative recombination centers can be filled when the device is positively biased, making a negligible impact on V_{OC} during a reverse voltage scan. However, when the device is under a forward scan, the unfilled trap states cause a high J_0, limiting the achievable V_{OC}. Particularly, the $MAPbI_3$ (FA = 0) cell shows the most severe hysteresis. The relatively small grains and possible organic residual on the top surface are likely the origins of the high hysteresis.

FA-rich (FA > 0.5) PSCs exhibit different hysteretic characteristics. The devices (Figure 9(d-f)) show a small or negligible V_{OC} shift but a more remarkable Ohmic-like behavior at low biases (low shunt resistance, R_{Sh}) under the forward scan, resulting in lower FF than that of the reverse scan. The J_0 of FA-rich PSCs shows insignificant changes under different scan directions (Figure 10), indicating good passivation and long carrier lifetime in the bulk perovskite films. The high R_{Sh} is likely related to the unfavorable azimuth angle crystal growth in the (111) orientation as well as the unreacted PbI_2 at the SnO_2/perovskite interface, both resulting in an unfavorable energy barrier at the front interface. The positive biasing condition under the reverse scan can compensate for the barrier, resulting in a decent FF. In contrast, under the forward scan, the front

barrier hinders the current extraction, resulting in lower photocurrent value at a positive voltage, and thereby lower FF.

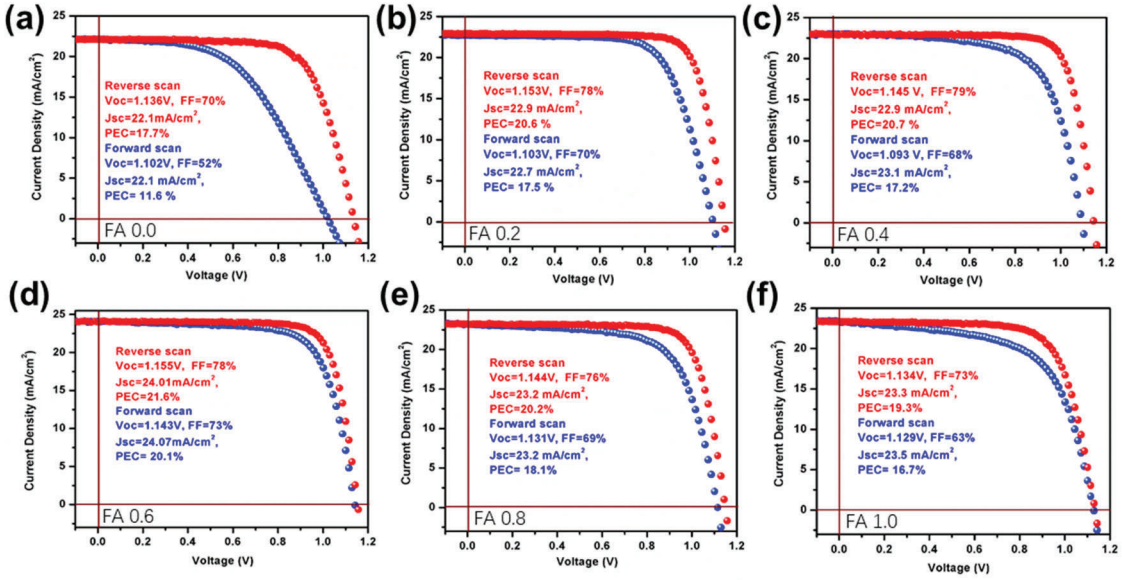


Figure 9. J-V curves of $FA_xMA_{1-x}PbI_3$ solar cells with x = (a) 0.0, (b) 0.2, (c) 0.4, (d) 0.6, (e) 0.8, and (f) 1.0

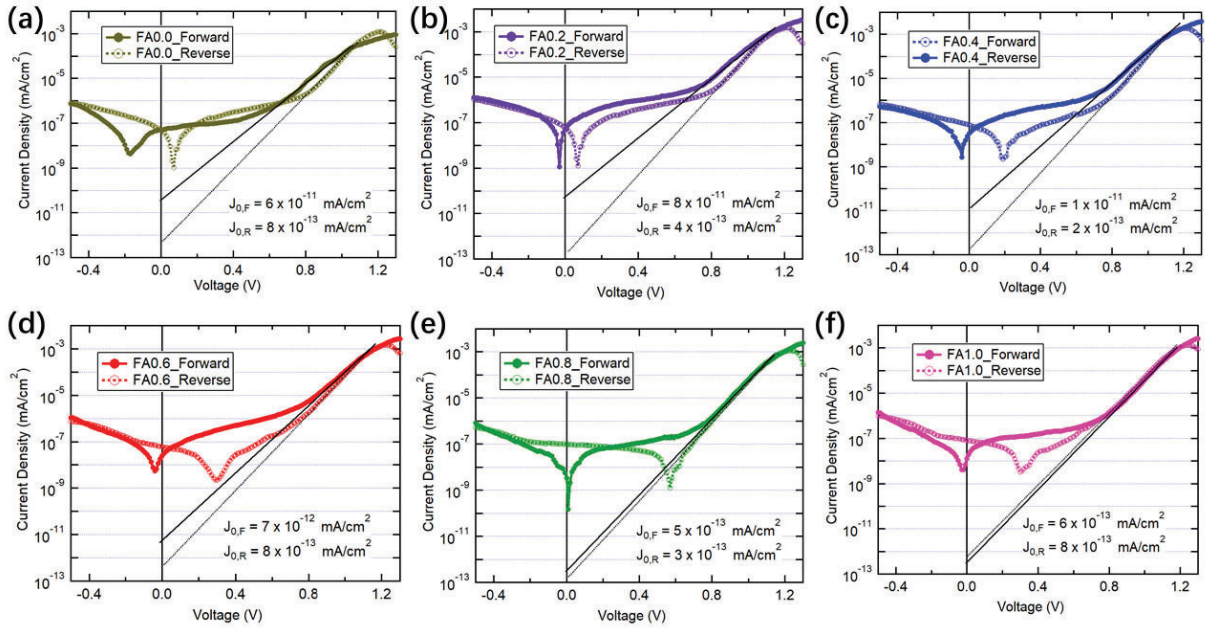


Figure 10. Dark J-V analysis of PSCs with different FA fractions: (a) FA = 0.0, (b) FA = 0.2, (c) FA = 0.4, (d) FA = 0.6, (e) FA = 0.8, and (f) FA = 1.0

Despite the high J-V hysteresis index values, PSCs with a wide range of FA fractions (FA = 0.2 to 0.8) show PCEs exceeding 20%. The best PCE of 21.6% (20.1%) under the reverse (forward) scan was achieved in a $FA_{0.6}MA_{0.4}PbI_3$ device, with a V_{OC} of 1.155 (1.143) V, a J_{SC} of 24.01 (24.07) mA/cm^2, and a FF of 78 (73) %, which also shows the lowest hysteresis value. The decent performance of this composition can be attributed to a combination of proper PbI_2 passivation and favorable crystal orientation, which results in low recombination and decent charge transport properties at the interfaces. Further improvement in the device performance and reduction of hysteresis relies on optimizing the interface between the perovskite absorber and charge extraction layers. For instance, modification on the electron and hole transport layers has been shown as a practical approach to eliminate hysteresis and achieve stable high efficiency.

The stability of unencapsulated PSCs under maximum power point tracking (MPPT) was further investigated. Figure 11(a) shows the MPPT stability of one batch of mixed cation PSCs in dry nitrogen. The FA-rich (FA > 0.5) cells retained more than 90% of their initial PCEs after working continuously under one sun illumination for 500 hours. PSCs with a high FA content (FA > 0.7) probably suffer from the excess of PbI_2, which may adversely affect the stability of perovskite. In contrast to the relatively stable FA-rich PSCs, MA-rich (FA < 0.5) devices, especially the pure $MAPbI_3$ cell (FA = 0), show more pronounced performance degradation under continuous operation. The more severe degradation of MA-rich PSCs is likely due to the photo instability of MA-contained perovskites. Therefore, a proper FA fraction benefits the stability of the perovskite absorber layer. In this stability test, the best performing device based on the $FA_{0.6}MA_{0.4}PbI_3$ composition shows the best stability, retaining 92% of its initial PCE after 500 hours.

It is known that metal halide perovskites are vulnerable to moisture due to water-induced degradation. To investigate the effect of organic cation composition on the device stability against water, an MPPT test was performed on another batch of unencapsulated PSCs with various absorber compositions under high humid (relative humidity > 70%) ambient conditions (Figure 11(b)). All the PSCs show significant device degradation in the humid air. It is noticeable that FA-rich PSCs show more pronounced degradation than MA-rich cells, due to water catalyzed phase transformation from the black cubic (α) phase to the yellow non-perovskite (δ) phase. The $MAPbI_3$ cell shows the highest remaining PCE among the group. However, the relatively lower initial PCE (13%) for the $MAPbI_3$ device compared to others (~20%) make the higher remaining PCE factor less remarkable. Considering the stability of PSCs in both dry and humid conditions, devices based on the $FA_{0.6}MA_{0.4}PbI_3$ composition still show the most robust stability. This result indicates that the perovskite films with too much excess PbI_2, either at the top or bottom interfaces, may accelerate the degradation of PSCs under high humidity.

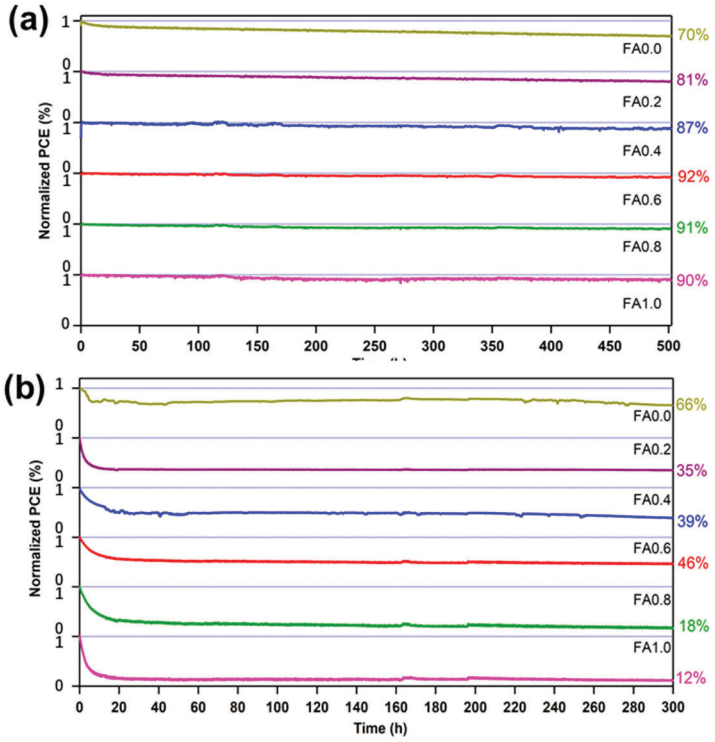


Figure 11. MPP tracking of unencapsulated $FA_xMA_{1-x}PbI_3$ solar cells under (a) dry nitrogen and (b) high relative humidity (>70%) conditions

2.5 CONCLUSIONS

In summary, we explored the impact of FA and MA fractions on structural and optoelectronic properties of perovskite thin films prepared by two-step solution methods. The thin-film properties were correlated to the device performance of PSCs, including efficiency, J-V hysteresis, and stability. We found discrepancies in J-V hysteresis and stability for the PSCs based on FA-rich and MA-rich stoichiometries, which are attributed to the thermodynamically driven perovskite conversion with different combinations of organic cations. Additionally, PSCs with a composition of $FA_{0.6}MA_{0.4}PbI_3$ demonstrated the best PCE of over 21% and robust stability (retaining more than 90% of initial efficiency) under maximum power point tracking in dry nitrogen for more than 500 hours.

3. INVESTIGATION OF MIXED-CATION FA/MA PB/SN I3 PEROVSKITE THIN FILMS AND SOLAR CELLS

Biwas Subedi, Chongwen Li, Maxwell Junda, Zhaoning Song, Yanfa Yan, and Nikolas Podraza

3.1 SUMMARY

Narrow bandgap mixed tin (Sn) + lead (Pb) perovskites are necessary as the bottom sub-cell absorber in high efficiency all-perovskite polycrystalline tandem solar cells. We report on the impact of mixed cation composition and atmospheric exposure of perovskite films on sub-gap absorption in films and performance of solar cells based on narrow bandgap mixed formamidinium (FA) + methylammonium (MA) and Sn+Pb halide perovskites, $(FASnI_3)_x(MAPbI_3)_{1-x}$. Structural and optical properties of $0.3 \leq x \leq 0.8$ $(FASnI_3)_x(MAPbI_3)_{1-x}$ perovskite thin film absorbers with bandgaps ranging from 1.25 ($x = 0.6$) to 1.34 eV ($x = 0.3$) are probed with and without atmospheric exposure. Urbach energy is tracked for pristine perovskite films as a function of composition, with $x = 0.6$ and 0.3 demonstrating the lowest and highest Urbach energies of 23 and 36 meV, respectively. Films with $x = 0.5$ and 0.6 compositions show less degradation upon atmospheric exposure than higher or lower Sn-content films having greater sub-gap absorption. The corresponding solar cells based on the $x = 0.6$ absorber show the highest device performance. Despite having a low Urbach energy, higher Sn-content solar cells show reduced device performance since degradation via oxidation is the most substantial.

Complete details of this work can be found in B. Subedi, C. Li, M. M. Junda, Z. Song, Y. Yan, and N. J. Podraza, Effects of Intrinsic and Atmospherically Induced Defects in Narrow Bandgap $(FASnI_3)_x(MAPbI_3)_{1-x}$ Perovskite Films and Solar Cells, *J. Chem. Phys.*152, 064705 (2020). [35]

3.2 INTRODUCTION

In all perovskite tandem solar cells, narrow bandgap (E_g) bottom cell absorbers based on mixed FA+MA and Sn+Pb iodide perovskites still have opportunities for improvement in morphology, stability, and device performance. To fully absorb low energy photons in the bottom sub-cell, a greater than 1 micron thick narrow-E_g perovskite absorber layer is needed. [36] However, due to the presence of impurities and defect states, this relatively thick layer is more prone than thinner layers to non-radiative recombination losses through both the bulk and interfaces. Therefore, preparation of a thick perovskite layer with high electronic quality and crystallinity has remained an issue for narrow-E_g mixed Sn+Pb perovskites solar cells. As narrow-E_g perovskite absorbers require replacing a fraction of Pb with Sn, variations in crystallinity, stability, and optical properties result. Both ≤ 30% and ≥ 80% Sn-content mixed Sn+Pb perovskites show poorer crystallinity and hence lower device performances. [37] The possible oxidation of Sn^{2+} to Sn^{4+} occurring for higher Sn-content absorbers can increase p-type self-doping [38] and result in increased recombination and decreased carrier lifetime. Several studies have shown that narrow-E_g mixed Sn + Pb perovskite films with 50-60% Sn-content (atomic %) show good crystallinity and device performance. [39, 40]

All semiconductors including perovskites show tailing in the absorption spectra below E_g due to lattice vibrations, defects, and impurities contributing to the Urbach tail. [41] Here, we use the

Urbach energy (E_u) to quantify the tailing effect and its contribution to sub-gap absorption for narrow bandgap mixed Sn+Pb $(FASnI_3)_x(MAPbI_3)_{1-x}$ perovskite films. Higher values of E_u show higher sub-gap absorption and vice versa. Defects contributing to this absorption include grain boundaries, intrinsic point defects, and various complex phases forming from the atmospheric exposure. Similarly, in perovskite solar cells, defects are also formed at interfaces due to interaction between the perovskite absorber and other device components. Varying cationic-anionic composition changes crystallinity, phase stability, charge transport, and optical properties. The amount of defect induced sub-gap absorption also depends upon cationic and anionic compositions. We have studied the complex optical property spectra of narrow-E_g $(FASnI_3)_x(MAPbI_3)_{1-x}$ perovskite films using photothermal deflection spectroscopy (PDS) and spectroscopic ellipsometry (SE) coupled with unpolarized transmittance. The variation in defect induced sub-gap absorption and stability are compared for mixed Sn+Pb compositions. Perovskite solar cells based on these absorbers are fabricated, and links between the device performance parameters and perovskite optoelectronic qualities are established. The combination of both low E_u and the least change in sub-gap absorption upon exposure to ambient air observed in intermediate x $(FASnI_3)_x(MAPbI_3)_{1-x}$ films correlate with the highest solar cell device performance. Reduced performance in devices with high and low Sn-content x are attributed to high E_u, low perovskite stability, or both.

3.3 METHODS, ASSUMPTIONS, and PROCEDURES

All perovskite thin films are fabricated in a nitrogen (N_2)-filled glove box to prevent exposure to ambient air. $(FASnI_3)_x(MAPbI_3)_{1-x}$ with $0.3 \leq x \leq 0.8$ compositions are obtained by controlling the ratio of $FASnI_3$ and $MAPbI_3$ precursor solutions. The preparation of $FASnI_3$ precursor solution consists of dissolving 372 mg of SnI_2 (Sigma Aldrich) and 172 mg of FAI (GreatCell Solar) in mixed N,N-dimethylmethanamide (DMF) (Sigma Aldrich, anhydrous) and dimethyl sulfoxide (DMSO) (Sigma Aldrich, anhydrous). Similarly, the preparation of $MAPbI_3$ precursor solution consists of dissolving 461 mg PbI_2 (Alfa Aesar) with 159 mg MAI (GreatCell Solar) in 630 µL DMF and 70 µL DMSO. The mixed precursor solutions are spin-coated on glass substrates at 5000 rpm for 60 seconds. Diethyl ether, as the anti-solvent, is dripped on to the spinning substrates after 5 seconds. To obtain the perovskite phase and most importantly to remove remaining solvents, the spin coated films are annealed at 100°C for 7 minutes inside the glove box before they are transferred to optical characterization.

While transferring the samples for PDS measurements, films are loaded into a quartz cuvette containing inert C_6F_{14} fluid (3M Fluorinert FC-72, Synquest Laboratories), inside the N_2-purged glove box to prevent unwanted exposure to laboratory ambient air. C_6F_{14} is the thermally sensitive deflecting medium for PDS also protects perovskite films from atmospheric exposure during measurements lasting for 1-2 hours. PDS is performed in a transverse configuration system [42] (PTS-3-PTD, Sciencetech Inc.) over a spectral range from 1100-800 nm (1.27-1.55 eV) for x = 0.3, 0.4, and 0.5 $(FASnI_3)_x(MAPbI_3)_{1-x}$ and from 1150-800 nm (1.08–1.46 eV) for x = 0.6, 0.7, and 0.8 $(FASnI_3)_x(MAPbI_3)_{1-x}$ in 10 nm spectral scanning steps. The pump beam in this system is the monochromatic beam modulated with a mechanical chopper at 0.5 Hz; a nominally 300 µm cross-section diameter 633 nm helium-neon laser acts a probe beam. Near infrared to ultraviolet (UV) (0.74-5.9 eV) spectroscopy ellipsometry (SE) and unpolarized transmittance measurements of films are collected using a single rotating compensator multichannel spectroscopic ellipsometer

(M-2000FI, J.A. Woollam Co., Inc.). All films are exposed for 2-3 minutes in the laboratory ambient air during data acquisition, with SE and unpolarized transmittance measurements collected at 70° and 0° angle of incidence, respectively. After unpolarized transmittance measurement, frosted tape is applied to the backside of the glass to scatter light and suppress reflections from that interface. The spot diameter of the measurement beam is ~1 mm.

Narrow-E_g perovskite solar cell devices are fabricated as described in previous work. [40] Poly(3,4-ethylenedioxythiophene)-poly(styrenesulfonate) (PEDOT:PSS) (50 nm) films are spin coated onto indium tin oxide (ITO) (150 nm) coated soda lime glass substrates at 4000 rpm for 50 seconds and annealed at 175 °C for 30 minutes. $(FASnI_3)_x(MAPbI_3)_{1-x}$ thin films are prepared as described in the beginning of this section. To complete the solar cell device structure, buckminsterfullerene (C_{60}) (20 nm) / bathocuproine (BCP) (5 nm) / silver (Ag) (75 nm) are sequentially deposited by thermal evaporation. In this solar cell configuration, ITO, PEDOT:PSS, $(FASnI_3)_x(MAPbI_3)_{1-x}$, C_{60} / BCP, and Ag act as front contact, hole selective layer, absorber, electron selective layer, and back contact, respectively. Perovskite solar cell devices are encapsulated with cover glass using UV-curable epoxy before removal from the glove box for PV device performance characterization. Current-voltage (J-V) measurements are performed in air ambient under 100 mW/cm^2 AM 1.5G solar irradiation (PV Measurements Inc.) with a Keithley 2400 Source Meter. A standard silicon cell is used as a reference for J-V measurements.

3.4 RESULTS and DISCUSSION

Ellipsometric spectra are coupled with unpolarized transmittance spectra and simultaneously fitted to a parameterized optical and structural model to extract the complex optical response for the perovskite films in terms of complex dielectric function ($\varepsilon = \varepsilon_1 + i\varepsilon_2$) spectra. The structural model consists of a glass substrate / interfacial layer / perovskite film / surface roughness. Complex optical property in terms of ε spectra (Figure 12) and structural parameters for these perovskite films including the film thicknesses, interfacial layer thicknesses, surface roughness layer thicknesses, and void fractions in both interfacial and surface roughness layers, are determined using divided spectral range analysis. [43] Both the complex optical and structural properties vary with the composition. For each film, the effective thickness (d) is determined by combining the perovskite bulk film thicknesses with the interfacial layer and surface roughness layer thickness weighted by the perovskite material fraction in each layer, respectively. Here, the d ranges from 566 to 651 nm.

Absorption coefficient (α) spectra are obtained from $\alpha = 4\pi k/\lambda$, where k is extinction coefficient in $\varepsilon = (n + ik)^2$ and λ is the wavelength. Figure 13(a) shows spectra in α near the absorption onset obtained from numerical inversion of $(FASnI_3)_x(MAPbI_3)_{1-x}$ ($0.3 \leq x \leq 0.8$) perovskite films which have been exposed to laboratory ambient air for approximately 2-3 minutes during SE and transmittance measurement. Near-E_g spectra in α for the perovskite films which have not been exposed to laboratory ambient air are obtained from PDS using $\alpha = -\ln(1-S/S_0)/d$, where S is the experimental measured signal, S_0 is the saturation signal, and d is the path length through the film and are shown in Figure 13(b). The path length through the film is assumed to equal to the

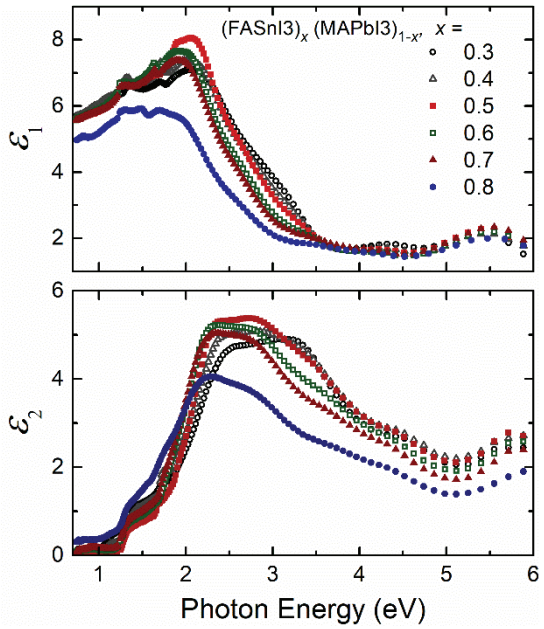


Figure 12. Complex dielectric function ($\varepsilon = \varepsilon_1 + i\varepsilon_2$) spectra of $(FASnI_3)_x(MAPbI_3)_{1-x}$ ($0.3 \leq x \leq 0.8$) perovskite films

effective film thickness of the film. From the PDS determined spectra in α, the direct gap E_g for each perovskite film is calculated using Tauc plots by linear fitting $(\alpha h\nu)^2 = 0$ over the $(1 - 7) \times 10^8$ eV^2cm^{-2} range, with the abscissa given by the photon energy ($h\nu$). The resulting E_g are shown in Figure 14(a). E_u is calculated as the inverse slope of the linear fit to $\ln(\alpha/\alpha_g)$ where α_g is the value of α spectra at corresponding E_g. E_u calculated from PDS determined spectra in α for all films are shown in Figure 14(b). Short circuit current density (J_{SC}), open circuit voltage (V_{OC}), fill factor (FF), and power conversion efficiency (PCE) for solar cells incorporating different composition perovskite absorbers are reported in Figure 16.

Perovskite films, exposed to laboratory ambient air for approximately 2-3 minutes, with $x = 0.5$ and 0.6 show relatively sharper absorption edges with lesser sub-gap absorption compared to other compositions. The amount of sub-gap absorption increases with either increasing or decreasing x, with $x = 0.8$ being the most pronounced. Finite photon energy range spectra in ε_2 is used to calculate the concentration of electrons associated with defect induced absorption using the optical rule. [44] Defect density is approximated for all perovskite films and it represents the total number of electronic transitions depending upon the nature of defects represented by absorption below E_g. Figure 15 shows the defect density for perovskite films exposed to laboratory ambient and protected against air exposure. For the films exposed to laboratory ambient air, substantial variations in defect density are observed as a function of composition. Extrinsic defects are likely to be formed by this exposure, increasing the observed sub-gap absorption and associated defect density for perovskite films. Defect densities are uniformly low in the protected films. However, the increase in defect density arising from exposure to

laboratory ambient air is smallest in x = 0.5 and 0.6 films which indicates that these compositions are less susceptible to the degradation. x = 0.6 perovskite film shows the lowest E_u among this series with increases in E_u with either decreasing or increasing x. This $(FASnI_3)_{0.6}(MAPbI_3)_{0.4}$ perovskite film exhibits the lowest sub-gap absorption and lowest associated defect density.

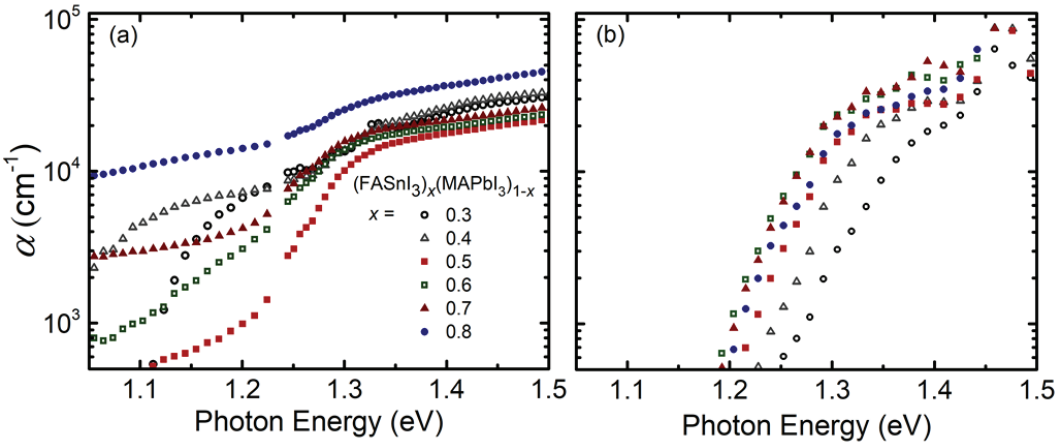


Figure 13. Absorption spectra for $(FASnI_3)_x(MAPbI_3)_{1-x}$ ($0.3 \leq x \leq 0.8$) films (a) exposed to air, measured by SE and (b) unexposed, measured by PDS

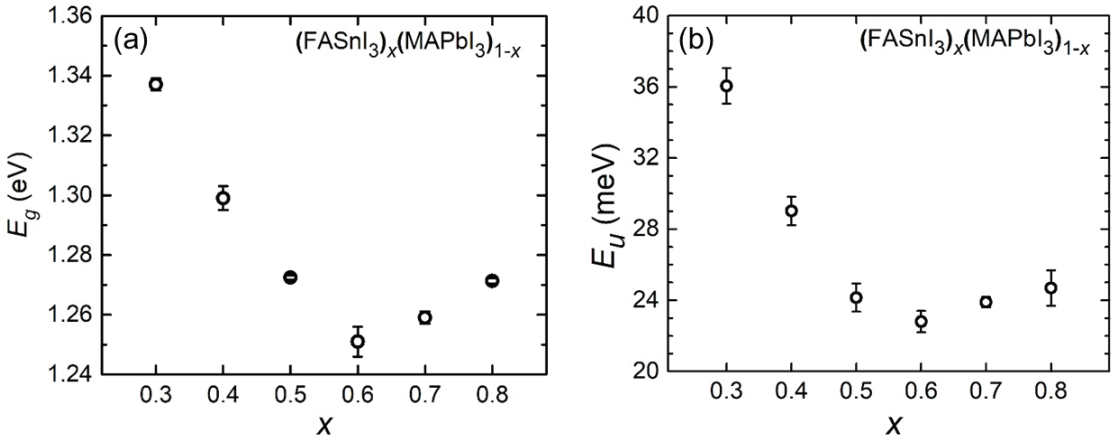


Figure 14. (a) Bandgap (E_g) and (b) Urbach energy (E_U) as a function of composition for $(FASnI_3)_x(MAPbI_3)_{1-x}$ perovskite films

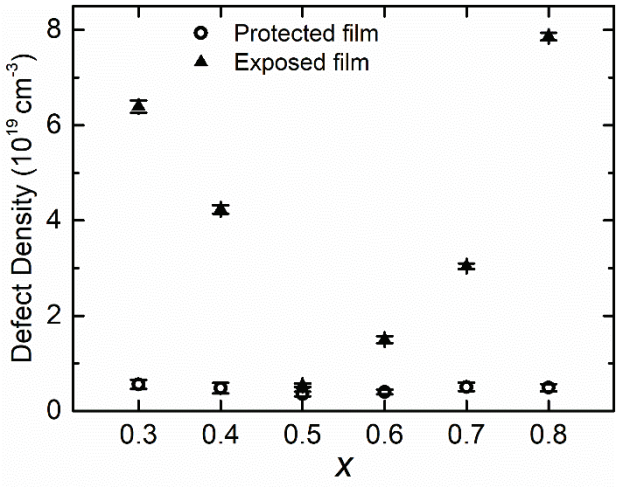


Figure 15. Defect densities calculated using the optical sum rules for $(FASnI_3)_x(MAPbI_3)_{1-x}$ protected (open circles) and exposed perovskite films

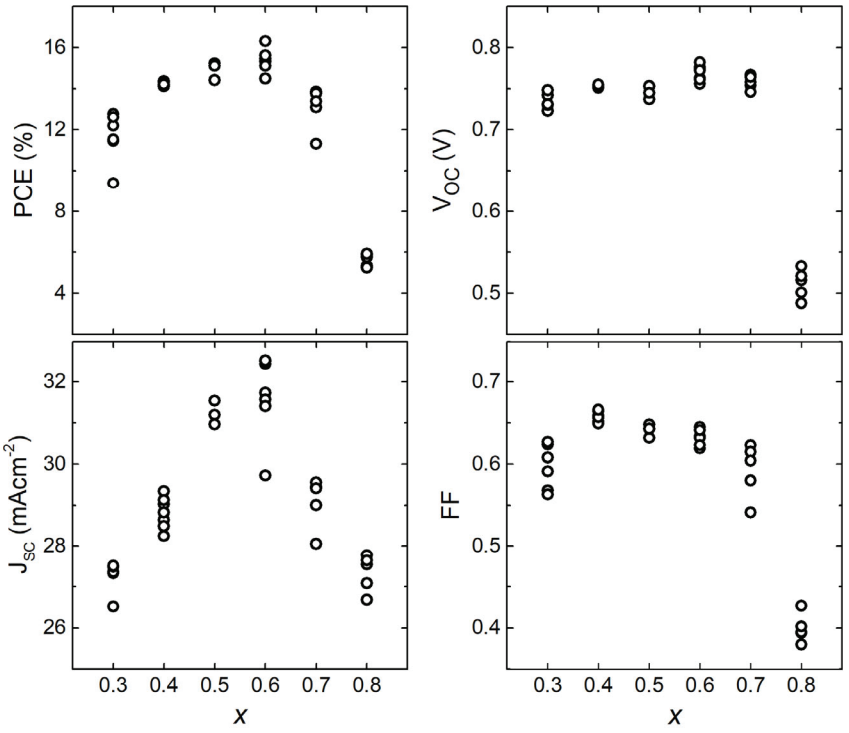


Figure 16. V_{OC}, FF, J_{SC}, and PCE for $(FASnI_3)_x(MAPbI_3)_{1-x}$ solar cells

The solar cells with $(FASnI_3)_{0.6}(MAPbI_3)_{0.4}$ absorbers show the highest J_{SC}, V_{OC}, and PCE with moderately high *FF* (Figure 17). For devices with higher or lower x relative to x = 0.6, J_{SC} decreases. Devices with $x < 0.6$ and $x > 0.6$ have increasingly higher E_g with decreasing or increasing x, hence reducing the possible optical absorption in the cell and maximum J_{SC}. Films with lower Sn content also have smaller grain size which is reflected in higher E_u. In addition, as perovskite devices are not completely protected against degradation in laboratory ambient air, possible oxidation of Sn^{2+} to Sn^{4+} occurring for higher Sn content films can increase p-type self-doping. For solar cells with $0.3 \leq x \leq 0.7$ absorbers, V_{OC} and *FF* are relatively similar without a well-defined trend as observed for J_{SC}. The resultant variation in PCE is possibly due to the variation in J_{SC}, however V_{OC} and *FF* along with J_{SC} depend upon the crystallinity and number of defects present at grain boundaries in an absorber layer. The associated composition dependent variation in absorber layer crystallinity and defect states affects the PCE of $(FASnI_3)_x(MAPbI_3)_{1-x}$ perovskite solar cells. Except for solar cell devices with higher Sn content, x = 0.7 and 0.8, average *PCE* decreases with increases in E_u of the absorber layer and vice versa as shown in Figure 17(a). For solar cells, the presence of defects is mostly reflected by the V_{OC}. Since V_{OC} of solar cells also depends upon E_g which varies with composition, it is logical to compare the V_{OC} deficit with E_u of the absorbers. V_{OC} deficit is defined as E_g/q-V_{OC} and refers to the existence of imperfections in the absorber layer linked to E_u. Figure 17(b) shows the variation of V_{OC} deficit with composition and E_u respectively, with a monotonic relationship aside from x = 0.8.

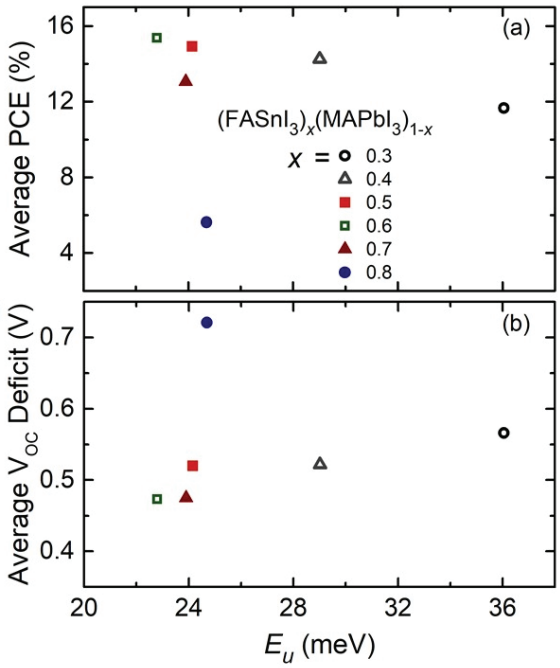


Figure 17. (a) PCE of $(FASnI_3)_x(MAPbI_3)_{1-x}$ perovskite solar cells as function of E_U and composition; (b) V_{OC} deficit as a function of E_U

Again, the highest PCE solar cell has a x = 0.6 absorber and shows the lowest E_u and lowest V_{OC} deficit, whereas devices with a x = 0.8 absorber deviates from this trend. The x = 0.8 absorber film shows a low E_u = 25 ± 1 meV, which is almost comparable to that of best-performing absorber,

x = 0.6 with E_u = 23±1 meV, but solar cell performance parameters, particularly V_{OC} and *FF*, are substantially reduced. We attribute this exception to differences in how these materials are prepared and handled as films for E_u characterization and as absorber layers in complete solar cells. During preparation of films for PDS and measurements, there is no exposure to the atmospheric moisture, oxygen, and UV light. Device performance measurements of solar cells are performed in laboratory ambient air potentially leading to atmospherically induced defects.

Even though differences exist in conditions during fabrication and characterization of thin films and devices, sensitivity to oxidation is likely the primary cause of poor performance of devices with high Sn-content absorbers. Previous studies show that excess Sn in mixed Sn+Pb perovskite is more prone to degradation via oxidation. [39] Substantially increased near-E_g spectra in α for high Sn-content material, especially x = 0.8, is observed for material exposed to laboratory ambient relative to material protected against it as seen in Figure 13. $(FASnI_3)_{0.8}(MAPbI_3)_{0.2}$ as a film exposed to laboratory ambient or as the absorber layer in a solar cell is more prone to degradation via oxidation than other compositions studied here. Even though the other device component materials are deposited over perovskite absorber layers in the solar cell device configuration preventing direct interaction with oxygen in ambient air, prolonged exposure will result in oxidation with non-ideal encapsulation.

3.5 CONCLUSIONS

Spectra in α for narrow bandgap $(FASnI_3)_x(MAPbI_3)_{1-x}$ $0.3 \leq x \leq 0.8$ perovskite thin films are obtained using SE, unpolarized transmittance, and PDS. Sub-gap absorption present in spectra in α obtained from PDS is used to identify E_u. The minimum E_u is found for x = 0.6 with $(FASnI_3)_x(MAPbI_3)_{1-x}$ perovskite films show increasing E_u with either increasing or decreasing x. In addition, solar cell devices based on $(FASnI_3)_{0.6}(MAPbI_3)_{0.4}$ absorber layers show the best overall device performance including highest PCE and lowest V_{OC} deficit which suggests the importance of absorber film quality on the solar cell performance. Even though optical characterization of perovskite films by PDS are protected from laboratory ambient exposure, layers in solar cells may undergo exposure to laboratory ambient oxygen and ultraviolet light during processing and encapsulation. $(FASnI_3)_{0.8}(MAPbI_3)_{0.2}$ perovskite-based solar cells show substantially reduced device performances despite a low E_u for the corresponding film. This behavior is attributed to the variation in optical responses of mixed Sn+Pb perovskite absorber layers with varying Sn content, meaning that at similar exposure to laboratory ambient oxygen, $(FASnI_3)_{0.8}(MAPbI_3)_{0.2}$ perovskite films show more via oxidative degradation than do the lower Sn-content compositions.

4. PROTECTING PEROVSKITE SOLAR CELLS AGAINST MOISTURE-INDUCED DEGRADATION WITH SPUTTERED INORGANIC BARRIER LAYERS

Zhaoning Song, Nikolas J. Podraza, Adam B. Phillips, Yanfa Yan and Michael J. Heben

4.1 SUMMARY

We describe a general approach for protecting metal halide perovskite solar cells against degradation in high humidity environments using a sputtered barrier coating. An SiO_2 protective layer, applied to two different types of perovskite solar cells, was deposited without strongly impacting the initial device performance. The degradation of the cells was imaged in real-time using laser beam induced current (LBIC) measurements in an accelerated test. We show that the SiO_2 barrier films can improve the tolerance of the devices to extreme humidity conditions and extend lifetimes by a factor of ~60 when a 45 nm SiO_2 barrier layer is applied to $CH_3NH_3PbI_3$ and by a factor of ~600 when a 300 nm barrier is applied to a triple-cation perovskite material. The LBIC data revealed the approach promises protection against degradation initiation at the edges of scribed lines, which will be necessary for the fabrication of monolithically integrated modules.

4.2 INTRODUCTION

Metal halide perovskite solar cells have reached power conversion efficiencies (PCE) above 25% [45, 46] in just over a decade since their debut. [47] Perovskite photovoltaics (PV) show promise for future deployment with exceptional low cost [48-52] and low environmental impacts. [52-54] Large scale commercial fabrication is being proposed, [55-57] and applications in multi-junction [36, 58-61] and bifacial configurations look promising. [62, 63] However, a major drawback associated with perovskite PV technology is the lack of stability. Perovskite devices are known to decompose due to exposure to excessive heat, [64, 65] illumination, [66, 67] and moisture, [68-70] and effective methods to protect and stabilize devices against the extreme environmental conditions that will be encountered during deployment are needed to achieve long lifetimes and a low levelized cost of electricity. [48]

Efforts to improve the stability of perovskite cells spans multiple approaches: exploring new material for higher stability transport and contact layers, [71-73] and engineering of the perovskite layer fabrication and its chemistry. [74-78] Several approaches offer significant improvements in the lifetime of unencapsulated devices, and lifetimes of a several thousand hours under moderate humidity, temperature, and irradiance conditions have been demonstrated. [72, 79-81]

Protection against degradation due to interactions with the environment can also be provided by encapsulation. [82-85] Application of ethylene vinyl acetate, which is used in Si PV, [86] has not been effective due to adverse chemical reactions with the perovskite material. [87, 88] Adverse chemical reactions have also been observed for UV curable epoxies, [89] while delamination has been the issue when Surlyn was used in glass/glass encapsulation schemes. [87, 90] Some success with glass/glass encapsulation was found with two layers of commercial polyimide adhesive and devices retained ~97% of their initial PCE under continuous illumination for 3 minutes while the sample was kept in water. [91] Also, devices encapsulated with polyisobutylene have been shown

to retain initial PCE for 540 hours of heat cycles between -40 and 85 ºC with >1 hour of relaxation time following exposure to the test conditions, before the solar cells are remeasured. [92]

Inorganic thin films as barrier layers have also been investigated. Several approaches have followed from experience with organic light emitting diodes [82, 83, 88] where water vapor transmission rates (WVTR) approaching 10^{-6} g-m^{-2}-day^{-1} are desired. Al_2O_3 layers prepared by atomic layer deposition (ALD) for organic light emitting diodes (OLEDs) and organic photovoltaic (OPV) devices show WVTR values as low as 10^{-5} g-m^{-2}-day^{-1}. [83] Al_2O_3 protection layers prepared via ALD has been applied to perovskite PV devices as well. [83, 93] Although significant protection has been reported, ALD can reduce the initial efficiency of the devices depending on the deposition temperature (*vide infra*). [93] Even if ALD could be adjusted to be less damaging, it is not likely to be amenable to the high-rate, low-cost, large-area manufacturing that is imagined for perovskite PV. Evaporation of SiO_2 has been investigated too, but such line-of-sight techniques do not offer protection of film edges, and thus supplementary epoxy was required for effectiveness. [94] Conformal coating methods are obviously preferred, and the significance of eliminating access points for moisture ingress was demonstrated in polymer encapsulation schemes that cover film edges. [92]

Sputtering is a high-rate process and SiO_2 films prepared on polyethylene terephthalate substrates via roll-roll processing have been investigated as water permeation barriers for OLED and OPV devices. Fairly low WVTR values of 7.7 x 10^{-3} g-m^{-2}-day^{-1} have been reported, [95] and it has been suggested that thin SiO_2 coatings could approach the effectiveness of bulk glass if film uniformity was appropriately controlled. [96] Surprisingly, sputtered films in general and sputtered SiO_2 in particular have not been explored for protection of perovskite solar cells. Here we introduce sputtering as means to produce SiO_2 barriers for perovskite PV. The approach conformally protects the active materials without significantly affecting the initial device performance. The degree of protection was evaluated using an accelerated degradation test in which the devices were stressed under extreme humidity conditions and the degradation mode and rate were imaged using laser beam induced current (LBIC) measurements. Thin SiO_2 barrier films significantly increase the lifetime of perovskite cells. Increasing the thickness of the SiO_2 layer improves the degree of protection, presumably due to the reduced the number and size of through-film defects in the coating.

4.3 METHODS, ASSUMPTIONS, and PROCEDURES

Perovskite cells were fabricated with both single-cation ($MAPbI_3$) and triple-cation ($Cs_{0.05}(FA_{0.85}MA_{0.15})_{0.95}Pb(I_{0.85}Br_{0.15})_3$) perovskite absorber layers, where MA is methylammonium ($CH_3NH_3^+$) and FA is formamidinium ($HC(NH_2)_2^+$), in the n-i-p structure (glass/FTO/SnO_2/Perovskite/Spiro-OMeTAD/Au). Fluorine-doped tin oxide (FTO) was the front transparent electrode, while undoped SnO_2 was employed as the electron-selective layer. Spiro-OMeTAD (2,2′,7,7′-tetrakis(N,N-bis(p-methoxy-phenyl)amino)-9,9′-spirobifluorene) was used as the hole-selective layer, and the back metal electrode was Au. The cell geometry was defined by removing cell material by laser scribing.

Although single-cation perovskite devices with the classic $MAPbI_3$ absorber composition are perhaps the simplest to fabricate, they have been shown to have significant stability issues relating to heat and moisture. [70, 97] The stability with respect to heat and illumination can be improved to some degree by the introduction of Cs and FA in triple-cation formulations, [98] but this compositional mixing [74, 99] comes at the expense of stability with respect to humidity. [100, 101] Increased moisture sensitivity is due to both the incorporation of hygroscopic Cs cations [102, 103] and the water-induced phase transitions that are possible when $FAPbI_3$ is present as the majority phase. [104-106] Indeed, a tendency towards fabrication of $FAPbI_3$-based absorbers due to the overall favorable bandgap, heat, and illumination stability calls for high tolerance to humidity for large-scale application. [107, 108]

We prepared relatively large area devices (1 cm^2) to allow time-resolved imaging of the degradation using laser beam induced current (LBIC). Champion single- and triple-cation devices yielded initial PCEs of 11.62 and 11.95%, respectively, from reverse scan measurements. Note that smaller devices (0.08 cm^2) were also prepared with champion PCE values of 18.30% and 17.5%, respectively. The larger area cells showed lower performance due to lower fill factors (FFs), presumably due to increased lateral resistance in the FTO electrodes.

Finished cells were defined by laser scribing and then over coated with SiO_2 layers deposited by RF-sputtering (150 W, 3-inch target, 10 mTorr of argon gas flowing at 12 sccm) at room temperature. The deposition system was manufactured by Kurt J. Lesker, and the base pressure is $\sim 1 \times 10^{-6}$ Torr with the integrated cryopump. The SiO_2 sputtering target was purchased from Plasmaterials, the distance from sample to target during sputtering was ~12.5 cm, and the deposition rate was ~0.5 nm/min. The thickness of the SiO_2 layer was controlled through the deposition time. The composition of the sputtered films was measured by energy dispersive X-ray spectroscopy and the ratio of silicon to oxygen was 1 to 2.04, as expected for the formation of SiO_2. A diagram of the encapsulated device is given in Figure 18(a). SiO_2 thicknesses were evaluated by spectroscopic ellipsometry on companion glass slides. The surface morphology on finished devices was investigated using atomic force microscopy. A surface roughness of ~10 nm was measured for a 45 nm SiO_2 coating on completed devices. Since the roughness is much less than the film thickness it can be assumed that the growth is conformal with full coverage. Scanning electron microscopy data presented below supports this conclusion and provides evidence that the device is fully encapsulated.

4.4 RESULTS and DISCUSSION

To determine if the SiO_2 deposition caused any damage to the device, current-voltage (J-V) measurements were performed. Figure 18(b) shows the J-V curves for 1 cm^2 single-cation cells before and after deposition of 45 nm of SiO_2. On average, the PCE decreased by 2% and 6% after deposition of SiO_2 for the single- and triple-cation perovskites, respectively. Reduction in the shunt resistance and the V_{OC} are the primary causes of the decline in PCE in devices with single cation perovskite, while a drop in FF was also observed for the triple-cation device. This could be due to the introduction of small pinholes in the films or contacts due to interactions with the energetic plasma, [109-112] or perhaps inadvertent heating that may have occurred. Note that the degree of impact of the sputter SiO_2 layer is much lower than previous reports involving atomic layer deposition of Al_2O_3 where drops in PCE of ~16%, ~20% and ~35% were seen at deposition

temperatures of 95 °C, 105°C and 120 °C, respectively. [93] Similarly, usage of Surlyn, and of ultraviolet curable epoxy, in encapsulation have shown reductions in PCE of ~32% [113] and ~25% [88, 114] respectively.

The benefit of the thin protection layer is evident in the improved shelf life of the devices. As shown in Figure 18(c), devices with a SiO_2 protection layer showed ~1.5% drop in PCE after two months of exposure to lab environment and light while the unprotected devices showed ~11.3% drop in PCE during the same time period.

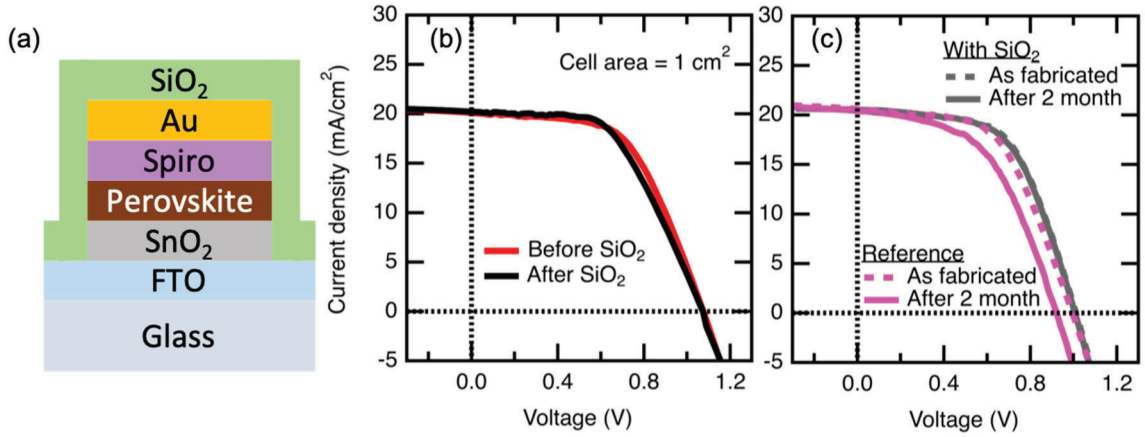


Figure 18. (a) Diagram of encapsulated device; (b) JV for 1 cm^2 PSC without and with 45 nm SiO_2 layer; (c) J-V data with SiO_2, as-fabricated and after two months

The initial evidence of improved resistance to environmental degradation prompted further investigation under more stressful conditions. Consequently, laser beam induced current (LBIC) measurements were performed while the devices were exposed to flowing N_2 containing 85% relative humidity (RH) at 25 ºC (partial pressure of water of ~20 Torr) in a controlled environment box. The LBIC measurements were done using a 532 nm laser Q-switched at 600 kHz, as previously described. [115-118] The fast raster speed was 6 mm/s, and 20 minutes was required for each image. With ~5 µW of average power incident in the ~50 µm diameter beam the power density was ~2.5 kW/m^2, which is ~2.5 times higher than the power density of the integrated AM1.5G spectrum.

Figure 19 shows snapshots in the time evolution of the LBIC data for bare and SiO_2-protected single-cation devices. Without SiO_2 (Figure 19(a)) the photocurrent generation rapidly degrades, and only ~50% of the device area is still active after 160 min. Overall, the degradation behavior is consistent with our previous observations [116] of a four-stage process wherein the first two stages are controlled by water-induced carrier extraction and transport changes in the spiro-OMeTAD layer while the second two stages are due to water-induced phase transformation and hydrolysis of the perovskite material. The dramatic reduction in LBIC current shown in Figure 19(a, b) is associated with the latter two stages. Similar to our previous observations, [70] the degradation initiates at the top left corner and continues from the edges. This is consistent with the vulnerability that was introduced by the laser scribing process used to define the device geometry (*vide supra*). It is worth noting that the scribing edges are comparable to the P3 scribing

lines that will be required for monolithic integration of perovskite modules, [48] and that protection at these locations will be critical for long-term stability. The experiment was terminated after 560 min, and the companion J-V curve (Figure 19(c)) showed severe degradation in V_{OC}, J_{SC}, and FF, with the PCE having decayed from ~11% to 0.4 % during the LBIC experiment. In contrast, a 45 nm thick SiO_2 coating allowed the device to function without significant degradation for ~10 times longer (Figure 19(b)). In this case, the PCE had declined to 7.3% from the initial value of 11.5% after 1800 min of exposure to the high humidity condition. Interestingly, the degradation was more spatially uniform, and the majority of the impact was in J_{SC} (20% loss) and FF (9.8% loss), while the V_{OC} was not strongly affected (3.7% loss).

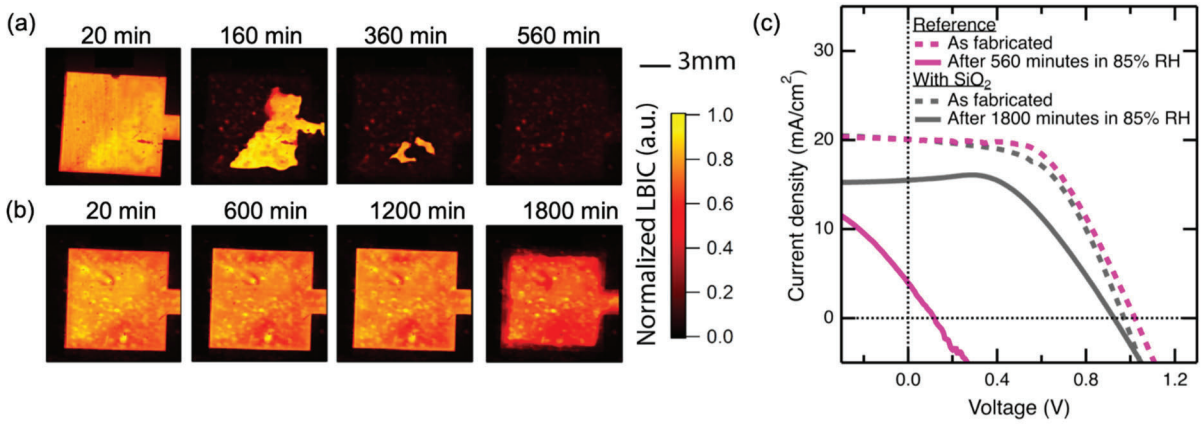


Figure 19. LBIC data for (a) no SiO_2 and (b) a 45 nm SiO_2 protection layer; (c) corresponding J-V curves for panels (a) and (b), before and after LBIC

The difference in the evolution of the LBIC data for the device over coated with SiO_2 can be understood by considering scanning electron microscope (SEM) images which in cross-section show a thin, continuous SiO_2 layer clearly seen on top of the perovskite device structure. When SiO_2 is not present, the scribed edges of the device are frayed and the layers in the stack are delaminated. However, when SiO_2 is present the film edge remains intact and the device layers retain their integrity. Our results indicate that the SiO_2 barrier layer conformally extends over the film, over the edge, and across the scribed area.

Figure 20 shows LBIC images for the water-induced degradation of devices fabricated with the $Cs_{0.05}(FA_{0.85}MA_{0.15})_{0.95}Pb(I_{0.85}Br_{0.15})_3$ absorber. Figure 20(a) shows that the unprotected triple cation device dies much more quickly than the unprotected single-cation device as expected for the greater water sensitivity (*vide supra*). Addition of 45 nm of SiO_2 imparts some protection (Figure 20(b)), but not to the same degree as seen for the single-cation formulation. The device shows some level of photocurrent generation capability after 600 minutes in 85% RH. In contrast to the fairly uniform spatial degradation observed for the single-cation device, the commonly observed mode of degradation for these samples appears to be associated with water ingress from the necked contact coupled with transport of water within the film stack. Panels (c), (d), and (e) in Figure 20 show the effects of increasing the SiO_2 protection layer thickness to 60, 140 and 300 nm, respectively. As before, the deposition of thicker SiO_2 layers did not significantly impact the J-V performance. Overall, the trend is to longer lifetimes with increased SiO_2 thickness. While

the devices with 60 nm showed degradation across the entire cell area after 10 hours of exposure, devices with 140 nm and 300 nm continued to generate current for 36 and 48 hours, respectively. Figure 20(f) shows how the time dependence of the integrated LBIC current varies for the various SiO_2 thicknesses. Clearly, the thicker layers delay the onset of degradation, which proceeds rapidly once initiated. Interestingly, the mode of degradation appears to be different for the thicker SiO_2 layers. For example, degradation is initiated at specific points for the 140 nm and 300 nm coatings (Figure 20(d-e), respectively), and these points grew in size from within the device area with further exposure time. This contrasts with the data for the 45 nm coating (Figure 20(b)), where degradation begins at the device edges. SEM investigations revealed some "snow-flake" defects in the thicker SiO_2 where the underlying device could be seen. These local imperfections in the thicker sputtered coatings likely provide access points for water. The origin of these defects is not clear, but they appear to be due to lack of nucleation, perhaps due to local differences in surface charge or impurities. The thickest films evidently had a reduced density of these access points. A greater degree of protection could presumably be achieved if these imperfections were eliminated, perhaps by using even thicker deposits. However, increasing the thickness of the coatings further could also lead to new problems associated with stress induce delamination, for example. [83]

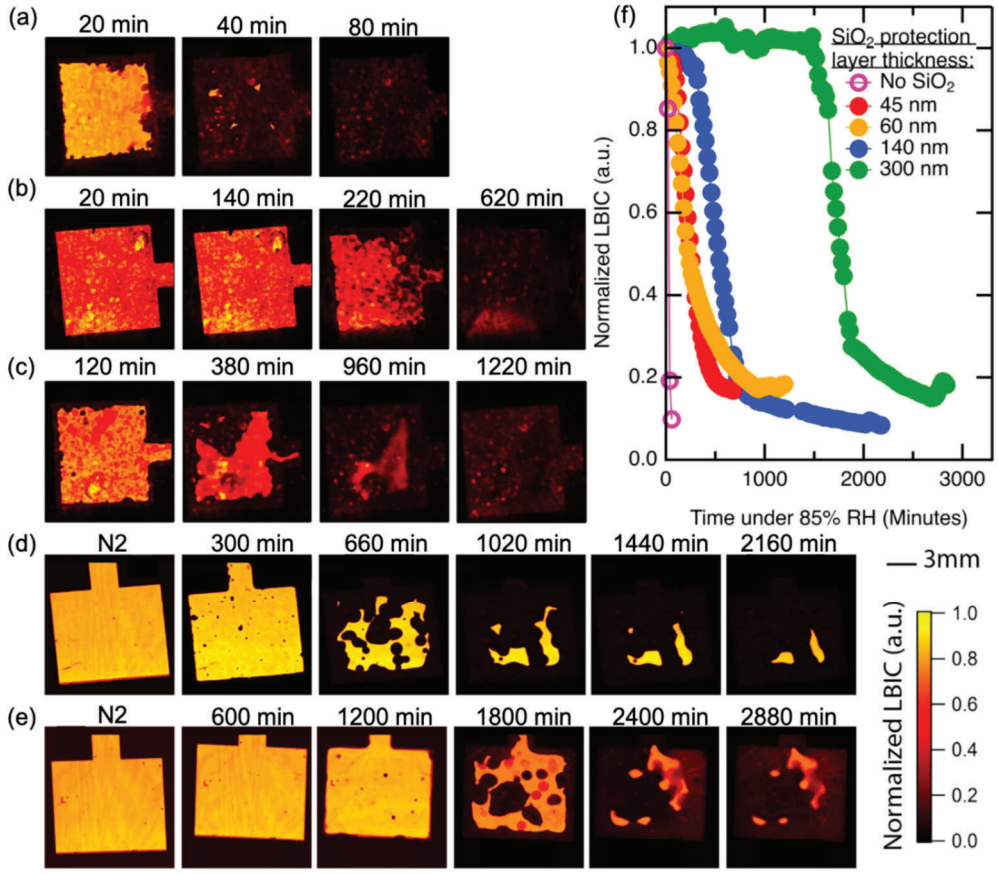


Figure 20. LBIC data for PSCs exposed to 85% RH at 25 °C with (a) no protection, and (b-e) protection layers of 45 nm, 60 nm, 140 nm, and 300 nm, respectively (f) normalized, integrated LBIC signal vs. exposure time

The results presented here suggest that more complete optimization of sputtered barrier films could dramatically enhance the stability of perovskite PV devices. In addition to preventing water ingress, complete encapsulation with an inorganic material might also provide thermal protection against the loss of high vapor pressure species. If such coatings could be perfected one might imagine, for example being able to eliminate one piece of glass and the encapsulant in a glass-glass package. Based on earlier work, [48] and assuming the SiO_2 deposition could be achieved at the same cost as other sputter deposited layers such as transparent conductive oxide films, the cost of manufacturing would be reduced by ~33%.

4.5 CONCLUSION

We investigated sputtered SiO_2 barrier films for protecting perovskite devices against humidity-induced degradation. Conformal SiO_2 layers were applied to two different absorber material compositions. The performance of the devices was not greatly affected by the deposition process. The SiO_2 barrier layer improved the stability of the device during storage under ambient conditions. LBIC was used to image the degradation across the area of the protected devices as a function of time during an accelerated test (85% RH at 25 °C). Significant improvements in the device lifetimes were observed for two different perovskite compositions, and the degree of protection scaled with the thickness of the barrier layer. Degradation proceeds through imperfections in the coating, and it is likely that greater degrees of protection could be achieved with more uniform barrier layers. The approach offers protection to film edges produced by scribing, which will be necessary for the fabrication of monolithically integrated modules.

5. EFFECTS OF CU PRECURSOR ON THE PERFORMANCE OF EFFICIENT CDTE SOLAR CELLS

5.1 SUMMARY

Copper (Cu) incorporation is a key process for fabricating efficient CdTe-based thin-film solar cells and has been used in CdTe-based solar cell module manufacturing. Here, we investigate the effects of different Cu precursors on the performance of CdTe-based thin-film solar cells by incorporating Cu using a metallic Cu source (evaporated Cu) and ionic Cu sources (solution-processed cuprous chloride (CuCl) and copper chloride ($CuCl_2$)). We find that ionic Cu precursors offer much better control in Cu diffusion than the metallic Cu precursor, producing better front junction quality, lower back-barrier heights, and better bulk defect property. Finally, outperforming power conversion efficiencies of 17.2% and 17.5% are obtained for devices with CdS and zinc magnesium oxide as the front window layers, which are among the highest reported CdTe solar cells efficiencies. Our results suggest that an ionic Cu precursor is preferred as the dopant to fabricate efficient CdTe thin-film solar cells and modules.

5.2 INTRODUCTION

Cadmium Telluride (CdTe) solar cell technology has been attracting extensive attention due to its low cost and ideal bandgap for high-efficiency photovoltaics. [119] For most efficient CdTe solar cells and modules, copper (Cu) is applied as a dopant to improve the p-type conductivity of the CdTe absorber and to reduce the Schottky-barrier height between the CdTe and the back contact. [120-123] The Cu concentration [124] and distribution in the CdTe absorber layer can significantly influence the performance of CdTe solar cells. For example, excessive Cu incorporation can introduce interstitial defects (Cu_i) and other Cu related compensation complexes, e.g., Cu_i-Cu_{Cd}, [125] which would limit the hole density in CdTe films. Additionally, Cu_i ions can diffuse at a high speed due to its high solubility at grain boundaries, [126-129] which adversely affects the long-term stability of CdTe solar cells. [130-132] More importantly, Cu at the front interfaces (e.g., the cadmium sulfide (CdS)/CdTe and zinc magnesium oxide (ZMO)/CdTe interfaces) has been thought to form recombination centers and shunting pathways, leading to the degradation of device performance. [120, 133] Therefore, the Cu dosage and distribution in CdTe films should be well controlled to minimize the nonradiative recombination related to Cu doping and maximize the device performance and long-term stability.

Here, we study the effects of Cu precursors on the performance of CdTe-based thin-film solar cells. Please note that no etching treatment is performed on the chlorinated CdTe film in this work. We fabricate CdTe thin film solar cells using a metallic Cu source (evaporated Cu) and ionic Cu sources (solution processing using cuprip chloride with Cu(I) – CuCl -- and copper chloride with Cu(II) -- $CuCl_2$). We find that the ionic Cu precursors offer much better control of Cu diffusion than the metallic Cu precursor. The statistical analysis of a large number of CdTe solar cells shows that the cells fabricated using the ionic Cu source show better front junction quality, lower back barrier heights, and better bulk defect property than the cells fabricated using the metallic Cu source. CuCl and $CuCl_2$, with different oxidation states of Cu, deliver almost the same performance for CdTe solar cells, which are much better than the cells used the metallic Cu source. Our results

show that the ionic Cu precursor plays a critical role in controlling the Cu dosage and establishing a desired Cu distribution profile.

5.3 METHODS, ASSUMPTIONS, and PROCEDURES

CdTe solar cells with two kinds of electron transport layers, i.e., CdS and ZMO, were fabricated. For the CdS/CdTe devices, fluorine doped tin oxide (FTO) coated glass (TEC 12D; NSG, US) with a 30 nm intrinsic SnO_2 layer was used as the substrate. First, an oxygenated cadmium sulfide (CdS:O) window layer with a thickness of 60 nm was deposited by radio-frequency (RF) magnetic sputtering using a 2-inch CdS target in a 2% oxygen and 98% argon environment at room temperature under 10 mTorr pressure and 50 W power. A 4-μm CdTe absorber was deposited by CSS at the source and substrate temperatures of 660 and 590 ˚C, respectively, at 10 Torr pressure, followed by a wet cadmium chloride ($CdCl_2$) treatment at 390 ˚C for 30 min in dry air. [134]

For the ZMO/CdTe devices, FTO coated glass (TEC 12; NSG, US) was used as the substrate. [120] A 80 nm ZMO window layer was deposited using a commercial ZMO target (8 wt% MgO) by RF sputtering with a flow gas of 16 sccm of pure argon and 24 sccm mixture gas of 95% argon and 5% oxygen. After a 10 min UV-ozone treatment for the as-deposited ZMO window layer, a 3.5 μm CdTe film was deposited by CSS with a source temperature of 560 ˚C and a substrate temperature of 495 ˚C under 1 Torr. Then, a $CdCl_2$ treatment was carried out at 420 ˚C for 20 min with a helium (He) flow (500 sccm) at 500 Torr.

After $CdCl_2$ treatment, the samples were rinsed with methanol to remove the residual $CdCl_2$ from the back surface. Then, three different Cu precursors were used to incorporate Cu for both CdS/CdTe and ZMO/CdTe devices. It is noted that no etching treatment was performed after $CdCl_2$ treatment for all the devices. The first Cu precursor was metallic Cu: a bilayer electrode of Cu (4 nm for CdS/CdTe and 3 nm for ZMO/CdTe devices) and Au (40 nm) was deposited by thermal evaporation with an individual cell area of 0.08 cm^2, followed by an activation treatment at 200 ˚C for 20 min. The second precursor was CuCl: a saturated CuCl (100 μL for CdS/CdTe and 80 μL for ZMO/CdTe devices) solution in ethanol was used to drop and spread on a 1.5″ ×1.5″ CdTe surface. After drying naturally, the samples were treated through rapid thermal annealing (RTA) (at 200 ˚C for CdS/CdTe and 160 ˚C for ZMO/CdTe devices) with a ramping speed ~60 ºC/min without dwelling time in a 500 sccm He flow. The third precursor was $CuCl_2$: a $CuCl_2$ solution (with Cu a concentration of 3.10 μg/mL, 100 μL for CdS/CdTe and 80 μL for ZMO/CdTe devices) solution in ethanol was used to drop and spread on a 1.5″ ×1.5″ CdTe surface. After drying naturally, the samples were treated through rapid thermal annealing (RTA) (at 200 ˚C for CdS/CdTe and 160 ˚C for ZMO/CdTe devices) with a ramping speed ~60 ºC/min without dwelling time in a 500 sccm He flow. Note that the Cu ion concentration in both CuCl and $CuCl_2$ solution was 3.10 μg/mL. After the Cu activation annealing treatment, a 40 nm Au layer was deposited on the back surface with an individual device area of 0.08 cm^2. No further annealing treatment was taken after the Au deposition. Finally, a 120 nm magnesium fluoride (MgF_2) anti-reflective layer was deposited on the glass side of the FTO substrate in an e-beam evaporation system.

Hall effect measurements were performed for our as deposited, $CdCl_2$ treated and CuCl treated CdTe films (~3 μm) deposited on soda lime glass using M91Fast Hall measurement system (LakeShore Cryotronics Advancing Science). All the as deposited, $CdCl_2$ treated and CuCl treated

CdTe films show p-type conductivity with hole concentrations in the order of 10^{12}, 10^{12}, 10^{13} cm^{-3}, respectively. Solar cell performance was characterized by measuring current density-voltage (J-V) curves under AM1.5G illumination using a solar simulator and a source meter (Keithley 2400) and the external quantum efficiency (EQE) spectra using an EQE system (PV Measurements Inc.). Dynamic secondary ion mass spectrometry (SIMS) was performed using Dynamic-SIMS5 from ION-TOF GmbH (Munster, Germany). The samples were analyzed in a dual beam profiling mode and the primary ion for analysis was 30 keV Bi^{3+} (Bi liquid metal ion source). This ion beam was applied over a 100 μm ×100 μm area at the center of the sputter crater (400 μm × 400 μm). The spectral data was acquired in a high mass-resolution mode. The energy of the sputtered ion was 1 keV Ar^{+} (Ar, electron impact ion source). Room temperature capacitance-voltage (C-V), temperature-dependent current-voltage (J-V-T), thermal admittance spectroscopy (TAS), and impedance spectroscopy (IS) measurements were performed using a Solartron Modulab potentiostat equipped with a frequency response analyzer (Ametek Inc.). Photoluminescence (PL) characteristics were investigated utilizing steady state and time-resolved PL. The detail of the electrical characterizations and PL measurement can be found in our previous publication. [120]

5.4 RESULTS AND DISCUSSION

The representative device performance of CdTe solar cells with different Cu precursors (i.e., metallic Cu, CuCl, and $CuCl_2$, named CdTe-Cu, CdTe-CuCl, and CdTe-$CuCl_2$ hereafter, respectively) is shown in Figure 21(a-d). The best J-V parameters for each type of devices are tabulated in Table 1. For the devices with CdS as the front window layer (Figure 21(a, b, d)), the best CdTe-Cu device shows a PCE of 15.20%, with a V_{OC} of 833 mV, a J_{SC} of 25.5 mA/cm^2, and a FF of 71.7%, while the CdTe-CuCl device demonstrates an overall improved performance with a V_{OC} of 870 mV, a J_{SC} of 26.4 mA/cm^2, and a FF of 75.1%, yielding a PCE of 17.2%. The CdTe-$CuCl_2$ device exhibits a similar performance to the CdTe-CuCl device with a V_{OC} of 854 mV, a J_{SC} of 26.3 mA/cm^2, and a FF of 74.3%, yielding a PCE of 16.7%. When comparing the EQE results, the CdS/CdTe-CuCl and CdS/CdTe-$CuCl_2$ devices show a significantly increased spectral response in the wavelength range from 350 to 550 nm with respect to the CdS/CdTe-Cu device (Figure 21(b)) and deliver an integrated current density of 26.7 and 26.4 mA/cm^2, respectively, higher than that of the CdS/CdTe-Cu device (25.5 mA/cm^2). The significant improvement of EQE in the whole wavelength range for the CuCl and $CuCl_2$ treated devices suggests better carrier separation and transport properties, especially at the front interface. This is can be attributed to the reduced Cu diffusion to the front junction, which will be discussed later.

The performance of ZMO/CdTe solar cells with CuCl and $CuCl_2$ (Figure 21(c)) is also significantly improved compared with that of the metallic Cu-treated device (Figure 21(c)). The devices treated with solution processed CuCl and $CuCl_2$ show higher quantum efficiencies of ~ 90% from 500 to 600 nm, yielding an integrated current of 26.2 and 25.9 mA/cm^2, respectively, which are higher than the J_{SC} of 25.5 mA/cm^2 in the ZMO/CdTe-Cu device (Figure 21(b)). The statistical comparisons also show the same improvements for the devices with the CdS and ZMO front window layers, especially the V_{OC} and FF, suggesting a better front main junction and a reduced back barrier height. Interestingly, the J_{SC} values in the CdS/CdTe devices are higher than those in the ZMO/CdTe devices although ZMO has larger bandgap than CdS. One reason is that the CdS film in this work is thinner (60 nm) than the ZMO film (80 nm), resulting in higher transmittance at the range of 300~380 nm. The other reason is the interdiffusion between CdS and CdTe at the

front interface, resulting in the formation of CdSTe alloy, which has slightly smaller bandgap. [135] Thereby, the light absorption of the CdS/CdTe device extended to longer wavelength at the range of 840~880 nm.

Note that the J-V curves of the ZMO/CdTe device with Cu metal (Figure 21(c)) shows clear distortion under a forward bias near V_{OC} (i.e., an S-kink), indicating poor heterojunction properties at the ZMO/CdTe interface. According to our SCAPS simulation results, [136] the S-kink can be attributed to the low ZMO film conductivity and the high acceptor-like defect trap concentration at the front interface, both of which are caused by the over diffusion of Cu. The diffusion of Cu into the ZMO film and the ZMO/CdTe interface can significantly decrease the ZMO conductivity [137-139] and form recombination centers at the front interface. [120, 133] The aggregation of Cu at the front interface and in the ZMO layer are identified by the dynamic-SIMS measurements. Note that in the CdTe-CuCl devices, the Cu activation can be performed by a RTA process at 160 ºC with ~150 times less Cu dosage than the treatment using metallic Cu, as in our previous report. [120] The RTA process has also been tried for the devices with metallic Cu doping. However, the traditional Cu activation process (200 °C for 20 min) always shows higher device performance than that treated with the RTA process when metallic Cu is used as the Cu source. In comparison, the CdS/CdTe devices treated with metallic Cu show no S-kink. This is probably because CdS is not as sensitive to Cu as ZMO.

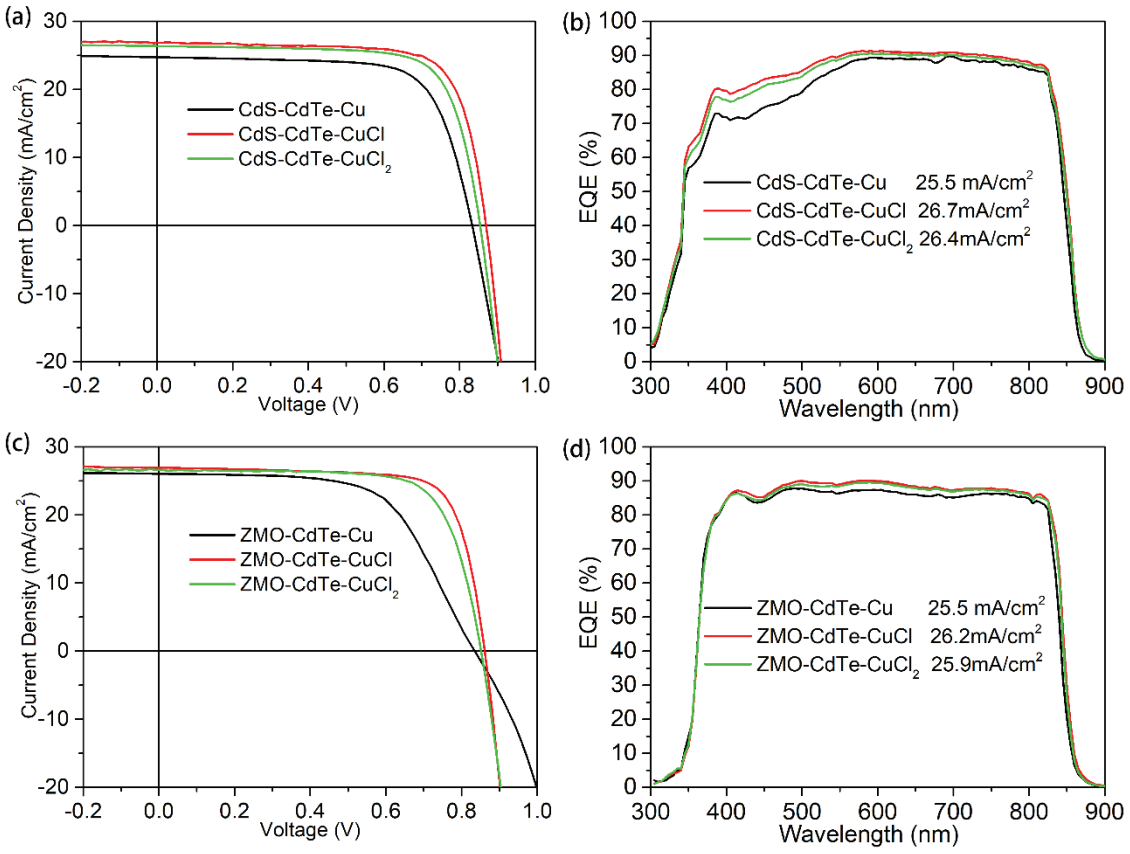


Figure 21. (a, c) J-V curves and (b, d) EQE spectra of representative (a, b) CdS/CdTe and (c, d) ZMO/CdTe devices treated with different Cu precursors

Table 1. JV parameters for the best CdS/CdTe and ZMO/CdTe devices, varied precursors

Samples	V_{OC} (V)	J_{SC} (mA/cm^2)	FF (%)	PCE (%)	R_S (Ω cm^2)	R_{SH} (Ω cm^2)
CdS-CdTe-Cu	0.833	25.5	71.7	15.2	3.8	1140
CdS-CdTe-CuCl	0.870	26.4	75.1	17.2	1.7	1421
CdS-CdTe-$CuCl_2$	0.854	26.3	74.3	16.7	2.1	1209
ZMO-CdTe-Cu	0.837	25.9	61.8	13.4	9.8	1297
ZMO-CdTe-CuCl	0.862	26.9	75.5	17.5	1.7	1455
ZMO-CdTe-$CuCl_2$	0.851	26.6	73.3	16.7	2.6	1548

To further investigate the effect of different Cu precursors on the optoelectronic properties of CdTe films, a suite of characterizations was performed. Note that the CdTe-CuCl devices show similar performances with the CdTe-$CuCl_2$ devices, implying the nonessential effect of the oxidation state of Cu. Also, the devices treated with metallic Cu show much lower device performance than those with the solution processed CuCl and $CuCl_2$ treatments, suggesting more significant effect of the ionic versus metallic Cu sources. In addition, changing the front window layer, e.g., CdS and ZMO, does not affect the influence of different Cu precursors. Therefore, CdS/CdTe-CuCl was chosen as the representative of ionic Cu treatment to make comparison with the devices with metallic Cu in the characterization hereafter.

Figure 22(a) shows the PL measurements of CdTe-Cu and CdTe-CuCl devices with CdS as the front window layer. Both samples show PL spectra with an emission peak centered at 1.501 ± 0.003 eV when excited through the FTO glass side and at 1.537 ± 0.002 eV when excited from the film side but with different emission intensities. The variation of the emission peak is due to the interdiffusion of CdS and CdTe at the front interface. [140] Higher PL intensity generally suggests a lower nonraditative recombination rate and a higher carrier lifetime. For both glass and film side excitations, the CdTe-CuCl device shows higher PL intensities than the CdTe-Cu device, indicating lower recombination rates at the CdS/CdTe and CdTe/Au interfaces in the CdTe-CuCl device. [136] The TRPL results in Figure 22(b) further confirm this conclusion by showing a much higher carrier lifetime of 9.7 ns in the CdTe-CuCl device than that of 7.4 ns in the CdTe-Cu device when exicited from the glass side. When excited from the film side, the same lifetime is obtained due to the severe recombination at the back surfaces and the equipment detection limit. The same PL and TRPL meausrements were also carried out for ZMO/CdTe devices and similar trends can be observed with higher PL intensity and lifetime in the CuCl treated ZMO/CdTe films.

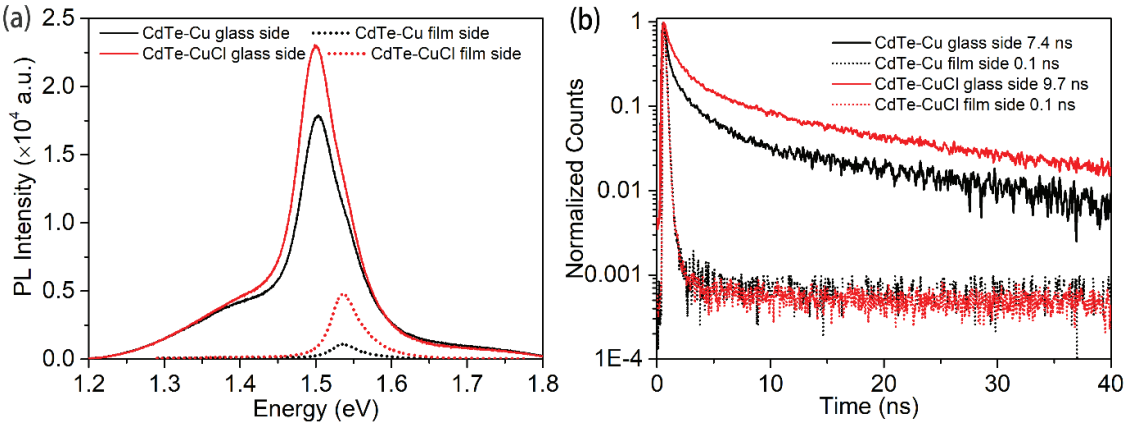


Figure 22. (a) PL spectra and (b) TRPL decays for CdS/CdTe-Cu and CdS/CdTe-CuCl devices (PL excitation with 633 nm laser

C-V measurement was used to investigate the apparent build-in potential (V_{bi}) at the front junction and extract the doping density in the CdTe absorber layer (Figure 23(a)). From the intercept of the linear fit of the Mott-Schottky plot ($1/C^2$ vs bias) with the bias axis, the V_{bi} across the depletion region formed by the CdS/CdTe junction was extracted. The CdTe-CuCl device shows a higher V_{bi} (0.58 V) than does the CdTe-Cu device (0.42 V) (Figure 23(a)). The improvement of V_{bi} suggests an improved front junction at the CdS and CdTe interface of the CdTe-CuCl device, which plays the most important role on V_{OC} and final device performance. The improvement of V_{bi} in the CdTe-CuCl device can be attributed to the improvement of hole density in the bulk CdTe absorber, the reduction of the interface trap state concentration and higher n-type conductivity of CdS film due to well-controlled Cu diffusion into the front interface and CdS film. [141] The apparent hole density N_A in the CdTe layer is calculated using the Mott Schottky plot according to the following equation: [142]

$$N_A = -\frac{2}{q\varepsilon\varepsilon_0 A^2}\left[\frac{dC^{-2}(V)}{dV}\right]^{-1} \quad (1)$$

where ε is the relative dielectric constant of CdTe, ε_0 is the absolute permittivity of vacuum, A is the surface area of a cell, C is the junction capacitance, and V is the bias voltage. As shown in Figure 23(b), the hole carrier concentration taken from the lowest point of its depth profile of CdTe-CuCl device is 5.33×10^{14} cm^{-3}, which is higher than the carrier concentration in the CdTe-Cu device (8.63×10^{13} cm^{-3}). Capacitance-voltage (CV) measurements for the ZMO-CdTe devices with varied Cu precursors were also performed and similar changes of the carrier concentration can be observed. The improvement of hole density in CdTe bulk is beneficial to the improvement of V_{bi} as discussed above and the reduction of the back-barrier height, which will be discussed later.

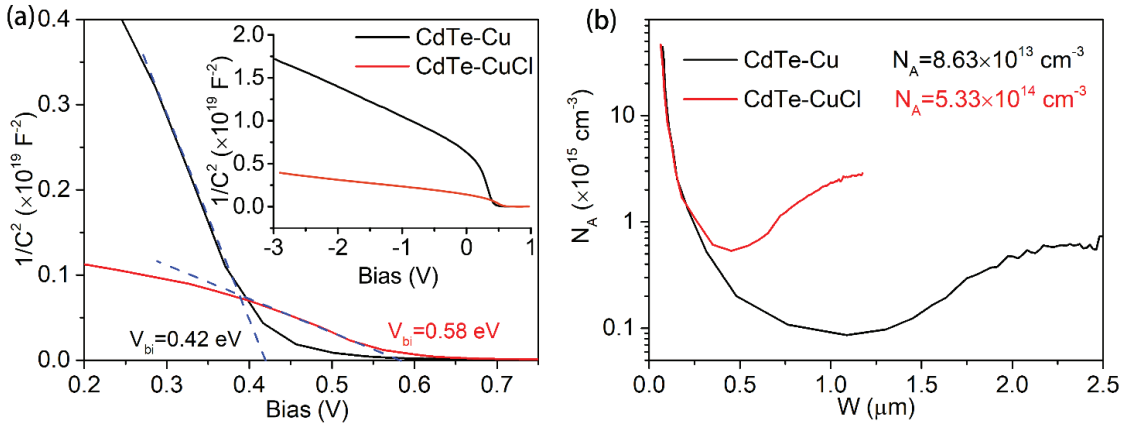


Figure 23. (a) MS plots measured at room temperature for devices with Cu and CuCl treatment (Inset: MS plots). (b) Carrier densities extracted from C-V measurements

Thermal admittance spectroscopy is an effective method to study the defect properties in CdTe solar cells. [142, 143] From the peaks of derivative of capacitance spectra ($-\omega dC/d\omega$), Figure 24(a, b), the defect characteristic frequencies as indicated by arrows were extracted and used to build the Arrhenius plots (Figure 4(c)). From the linear fit of the Arrhenius plots, the trap defect states in the CdTe-Cu and CdTe-CuCl devices were calculated. Here, three characteristics activation energies, E_{A1} = 0.398 ± 0.006 eV, E_{A2} = 0.358 ± 0.011 eV, and E_{A3} = 0.354 ± 0.031 eV for CdTe-Cu devices and two activation energies, E_{A1} = 0.323 ± 0.016 eV, and E_{A3} = 0.306 ± 0.005 eV for CdTe-CuCl devices were detected. According to our previous investigation about the TAS measurements performed at various DC biases with constant AC modulation, [142] E_{A1} corresponds to the back contact barrier, while E_{A2} and E_{A3} are considered as deep acceptor-like trap states. [143-145]

For the CdTe-Cu device, a back-barrier height of 0.398 ± 0.006 eV is obtained, which is higher than 0.323 ± 0.016 eV obtained in the CdTe-CuCl devices. This can be further demonstrated by the J-V-T measurements, which we have completed. The reduction of back-barrier height is attributed to the improvement of hole density adjacent to the electrode as shown in the C-V measurement. Besides the improvement of back-barrier height, the CdTe-CuCl devices show much shallower defect levels than that in the CdTe-Cu devices. In the CdTe-Cu device, two defects with depth of E_{A2} = 0.358 ± 0.011 eV, and E_{A3} = 0.354 ± 0.031 eV are detected. While in the CdTe-CuCl devices, E_{A2} disappeared according to the change of the features in the differential capacitance spectra (Figure 24(a, b)), and only one defect E_{A3} = 0.306 ± 0.005 eV is obtained, which is shallower than the defects in the CdTe-Cu devices. The density (N_t) and capture cross-section (σ_t) of all the defects are also calculated as shown in Figure 24(d) and the inset. The defect E_{A3} in the CdTe-CuCl device have much lower N_t (2.69×10^{14} cm^{-3}) than that in the CdTe-Cu device (6.45×10^{14} cm^{-3}, 8.78×10^{14} cm^{-3} for E_{A2} and E_{A3}, respectively). In addition, the defects with depth of E_{A2}, which exists in CdTe-Cu but misses in the CdTe-CuCl device shows a much higher σ_t value of 4.83×10^{-16} cm^{-3}, than the other two defects of 2.33×10^{-17} cm^{-3} and 8.34×10^{-17} cm^{-3}, for CdTe-Cu and CdTe-CuCl devices, respectively. The eliminating of defects with high concentration and capture cross-section in the CdTe-CuCl device can reduce the nonradiative recombination loss and improve device performance.

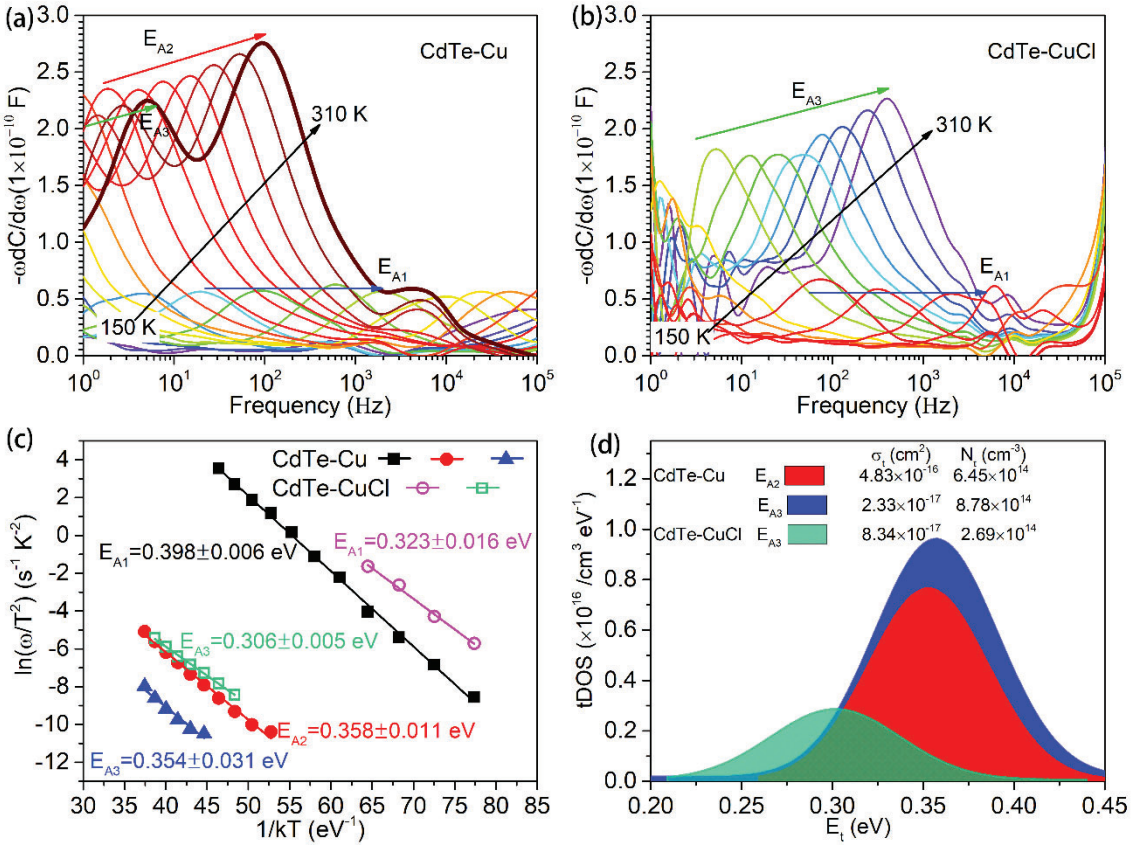


Figure 24. Differential capacitance spectra (−ωdC/dω) for (a) CdTe-Cu and (b) CdTe-CuCl devices. (c) Arrhenius plots and (d) defect distributions from (a) and (b). Inset shows trap defect activation energies (E_A), capture cross-section (σ_t) and trap state densities (N_t)

Copper ions in CdTe have a high migration rate, which is the culprit of the long-term stability issue for CdTe modules. It is worth mentioning that the CuCl treatment was performed using a RTA process owing to the ionic state of CuCl, which generated a desired Cu distribution profile, i.e., a high Cu concentration at the back surface and a low Cu concentration at the front interface. [120] At first glance, this kind of Cu distribution profile can be double edged, i.e., higher initial performance but lower long-term stability due to the gradient Cu concentration profile that can promote the diffusion of Cu from the region with high Cu concentration to the region with low Cu concentration. To study the degradation induced by the different Cu distributions, a stability test (6 cells for each group) was carried out in ambient air for 60 days (Figure 25).

For the CdTe-Cu devices, the average V_{OC} decreases by 6-7%, and the average FF decreases by 5%, yielding an average PCE relative degradation of ~14% within 60 days. On the other hand, the CdTe-CuCl devices show negligible degradation, by ~1-2%. To confirm this result, the same degradation test was performed for another CuCl-treated device with ZMO as the front window

layer instead of CdS. The degradation test shows similar stability with the CdTe-CuCl devices with CdS as the front window layer. These results further indicate that the gradient of Cu concentration does not lead to poor stability in the CdTe-CuCl devices. The robust long-term stability performance can be attributed to the low Cu dosage in the CuCl treated devices, which results in a relatively low Cu_i concentration. Cu_i has been correlated to the fast Cu redistribution in the CdTe film and at the heterojunction, while the desired Cu_{Cd} and complexes have a relatively low diffusion rate. [146, 147]

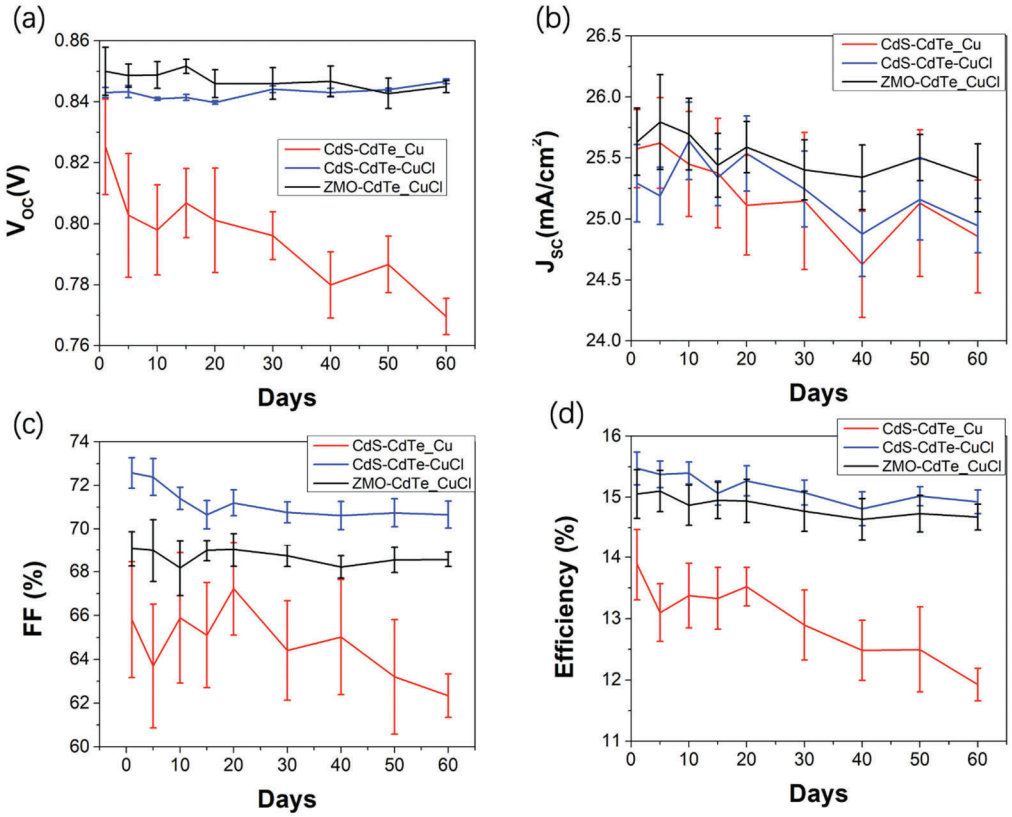


Figure 25. Degradation test results: ambient for 60 days, varied window layers and Cu precursors. Degradation of (a) V_{OC}, (b) J_{SC}, (c) FF, and (d) Efficiency

According to the device performance and characterization of the devices with different Cu precursors, the following discussions are made to understand the importance of Cu precursor in fabricating efficient CdTe solar cells:

1) Cu diffusion. CdTe solar cells shows similar performances when CuCl and $CuCl_2$ are used as the Cu precursors, with either CdS or ZMO as the front window layers. This result implies that the oxidation state of Cu in CuCl and $CuCl_2$ shows a negligible effect on the Cu incorporation. In comparison, the device with metallic Cu shows much worse device performances. These results suggest that Cu diffusion from CuCl and $CuCl_2$ into the CdTe absorber have a similar diffusion behavior and defect properties in CdTe solar cells. This is because both the CuCl and $CuCl_2$ are ionic compounds and Cu ions exist naturally in these two materials, thus, no extra energy for Cu ionization is required for the Cu diffusion into CdTe. After the diffusion into the CdTe absorber,

First-principles-based analysis indicates that Cu-related defects Cu_i^+ and Cu_{Cd}^-, both of which take Cu^+ oxidation state, have relatively low formation energies. [130, 147] We assume Cu^{2+} would change to Cu^+ and show the same diffusion rate. When metallic Cu is used as the Cu precursor, an oxidation process is needed, thus, extra energy is required to form Cu ions that can subsequently diffuse into CdTe. We suspect that this is the reason why the CuCl treatment need lower annealing temperatures or shorter annealing duration than the metallic Cu treatment.

2) Cu dosage and distribution. The Cu ion concentrations in both CuCl and $CuCl_2$ solutions are identical (3.10 μg/mL). Due to the difference of the CdTe layer thickness (3.5 and 4 μm for the CdS/CdTe and ZMO/CdTe, respectively), 100 μL chloride solution is applied to 1.5″ ×1.5″ CdS/CdTe devices and 80 μL chloride solution is applied to 1.5″ ×1.5″ ZMO/CdTe devices, which are equivalent to ~0.24 and 0.19 Å Cu layer, respectively. While, in the CdTe-Cu devices, the optimal Cu metal thicknesses applied in ZMO/CdTe and CdS/CdTe devices are 3 and 4 nm, respectively, which are much thicker than the equivalent Cu thickness in the CdTe-CuCl and CdTe-$CuCl_2$ devices. Nonetheless, the devices with the chloride treatment show a much higher carrier density than that with the metallic Cu treatment, suggesting that the Cu source in the chloride condition has a lower Cu dosage but a higher activation ratio (defined as the hole density relative to the incorporated dopant density) than metallic Cu.

3) Defect properties and long-term stability. Benefiting from the low Cu dosage, the devices treated with CuCl and $CuCl_2$ possess a higher carrier density, suppressed bulk defects with shallower levels and lower trap state capture cross section and smaller back barrier height and improved stability, simutaneously. This is because the device with a lower Cu dosage through the chloride treatment has more desired Cu_{Cd} acceptors while the device with higher Cu dosage through metallic Cu treatment has more detrimental Cu_i donors. When the Cu dosage increases, more Cu_{Cd} will be ionized, leading to the downshift of Fermi level towards the valence band maximum. In such a case, the formation energy of the charged donor defect Cu_i^+ (a compensating donor) decreases linearly as a function of Fermi energy, [148] therefore, resulting in more shallow compensating Cu_i^+ donor and lower hole concentration. Due to the formation of compensating Cu_i^+ donor, the CdTe devices with thermal evaporated Cu treatment show a larger back-barrier and a more pronounced nonradiative recombination rate at the back interface. Thereby, the device performance, specifically V_{OC} and FF, are significantly limited. In addition, the formation of Cu_i^+ also introduces fast Cu ion migration throughout the CdTe film, which is the culprit of the long-term stability issue for CdTe production facilities.

4) Effect on the devices with different front window layer. Besides the effect on the absorber bulk and at the device back interface, the diffusion of Cu toward the front interface has been widely reported in CdTe devices; this Cu diffusion can induce deep donor defect complexes at the front interface [144] and decrease the n-type conductivity of the front window layer. [124, 133, 141, 144] This effect became more notorious in CdTe solar cells with ZMO as front window layer due to its sensitivity to Cu (with several orders of magnitude reduction of window layer conductivity). [137-139] In the devices with CdS as n-type window layer, the effect of Cu at CdS/CdTe interface is weaker than that in the ZMO/CdTe devices. The solution processed chlorine treatment successfully reduces the Cu penetration into the front interface and constructs the desired Cu distribution throughout the device, thus, the diode quality of the front main junction is improved.

5.5 CONCLUSIONS

A comparison among different Cu precursors (i.e., metallic Cu, CuCl, and $CuCl_2$ solutions) as the doping source is performed on CdTe solar cells. The similar performance of the devices with CuCl and $CuCl_2$ suggests that the oxidation states of Cu^+ and Cu^{2+} show a negligible difference on device performance. Both of them show a significant improvement in device performance compared to the devices treated with the metallic Cu. The comparison of Cu activation temperature/time, dosage and device performance and characterization results concomitantly suggest that the solution-processed Cu treatment using a Cu ionic compound enables lower dopant diffusion and activation temperature/duration, less Cu dosage, more efficient Cu incorporation, and a desired gradient Cu profile in the CdTe film, resulting in improved electrical properties at both the front and back interfaces and the bulk of the absorber, leading to higher device performances than the conventical devices treated with metallic Cu doping. Finally, decent PCEs of 17.2% and 17.5% are obtained for the devices with CdS and ZMO as the front window layers, respectively, which are among the most efficient CdTe solar cells without Se.

6. SYNTHESIS OF TELLURIUM AND COPPER TELLURIDE NANOWIRES

Authors Contribution: *Dipendra Pokhrel, Ebin Bastola and Randy J Ellingson*

6.1 SUMMARY

Here, we synthesized the tellurium (Te) and copper telluride (Cu_xTe) nanowires (NWs) utilizing hot injection colloidal method. The synthetic method uses low-cost materials specifically, tellurium oxide as the tellurium source, environmentally benign ethylene glycol as a solvent and ascorbic acid as the reducing agent. Analysis of scanning electron micrographs confirm that the NWs are uniform in diameter as well as length. For example, we have prepared Te NWs exhibiting aspect ratios of 28.0 and 55.4. The X-ray diffraction pattern confirms the hexagonal crystal structure of Te and Cu_xTe NWs.

6.2 INTRODUCTION

Nanomaterials offer significant value for opto-electronic applications because of their unique structural, optical and electronic properties compared to their bulk counterparts. [149-151] Properly prepared one-dimensional semiconductors, such as nanowires (NWs), possess superior axial transport properties which make them applicable in opto-electronics including nano photonics and energy related applications. [152, 153] Shape and size of the materials play a vital role to study the properties of nanocrystal materials. NWs often exhibit low defect density, enhanced thermoelectric performance, and photoconductivity. [154-157] Tellurium (Te) is a rare earth element with narrow band gap energy (~0.35 eV) and p-type conductivity. [158] Copper telluride (Cu_xTe) is a p^+ highly degenerate semiconductor with bandgap ranges from 1.0 to 1.5 eV based on stoichiometry. [159] Here, we report on success in preparing uniform diameter and length controlled NWs of tellurium and convert into copper telluride NWs.

Although Te nanostructures such as nanowires, nanorods and nanobelts can be prepared using solution-based and vacuum based approaches, these methods typically yield product with a wide size polydispersity, particularly in length. Solution-based techniques include solvothermal and hydrothermal approaches [160-166] whereas for vacuum based technology include vapor deposition of Te such as thermal evaporation. [167, 168] Mohanty et al. have used thermal evaporation to produce Te NWs of several micron length with diameters of 100-300 nm. [168] The solution-based approaches include the use of hydrazine as a reducing agent [163, 164, 169] which is extremely hazardous and highly flammable. Thus, less hazardous, and safer chemicals are desired for the synthesis of Te NWs. The solution-based synthesis gives a freedom for the solution-processing of the material for the fabrication of devices. Silva et al. yield the Te NWs with diameter less than 30 nm and lengths varying from 600 nm to 5 μm using hypophosphorous acid. [170] Liu et al. have reported the rapid microwave assisted method to produce Te NWs with 20 nm diameter and length of tens of microns. [155] In the synthesis of nanorods and nanowires, ascorbic acid is used as a reducing agent, which is relatively less hazardous. [160, 171-173] Yang et al. reported the synthesis of Te NWs using ascorbic acid as a reducing agent and ethylene glycol as the solvent with average diameter of 9.7±2.7 nm and convert them into Cu_xTe NWs. [173] Based on the literature, all these Te NWs have relatively uniform diameters but wide distribution of lengths. Lin

et al. reported the synthesis of copper telluride nanostructures using solution based approach. [174] Uniform and controlled length of these Te NWs would provide an opportunity to improve the transport properties along the length. Here, we synthesized the Te NWs of uniform diameter and length and convert them into Cu_xTe NWs.

6.3 METHODS, ASSUMPTIONS and PROCEDURES

The synthesis is based on slightly modified version of the procedure reported by Yang et al. previously. [173] For typical synthesis of Te NWs, 1.05 mmol (0.167 gm) of tellurium oxide (TeO_2), 2.98 mmol (0.167 gm) of potassium hydroxide (KOH) and 0.1 gm of polyvinylpyrrolidone (PVP) were dissolved in 15 mL ethylene glycol under vigorous magnetic stirring to form a cloudy white solution. The temperature was set to 120 °C such that the solution becomes transparent yellow. In the meantime, 1.42 mmol (0.2496 gm) of ascorbic acid was dissolved in 0.75 ml of deionized water at 80°C to form an aqueous ascorbic acid solution. When the reaction temperature reaches to 120 °C, the ascorbic acid solution was rapidly injected resulting in a change in color to opaque black. The reaction was continued for 21 hrs. in a nitrogen (N_2) environment to complete the synthesis with high quality Te NWs. The heating mantle was removed, and the reaction flask was cooled by immersion of the three-neck flask into a cold-water bath. The product was centrifuged and cleaned with deionized water twice. To convert these Te NWs into Cu_xTe NWs, we followed the process reported previously [173] and $Cu(NO_3)_2{\cdot}3H_2O$ was used as copper precursor. As obtained Te NWs are then dispersed in 35 ml of ethylene glycol and 6 ml solution of ascorbic acid and dewater are mixed on 0.465 gm Cu $(NO_3)_2.3H_2O$ and slowly added to the Te NWs solution. The reaction continues for one hour with continuous stirring at room temperature. The product was cleaned with deionized water, centrifuged, dried, and stored in N_2 environment for further characterization.

6.4 RESULTS and DISCUSSION

The as-synthesized Te NWs and Cu_xTe NWs were dispersed in ethanol and drop cast onto soda lime glass to make a film and perform characterization. Figure 26 displays the SEM images of Te NWs prepared with varying amounts of PVP and ascorbic acid. PVP acts as a structural directing agent and stabilizing agent, [175] and therefore plays a vital role in the formation of Te NWs with uniform morphology. Along with PVP, the alkaline condition aids the growth of Te NWs. Figure 26(a, b) shows the SEM images of Te NWs prepared using 0.1 gm of PVP and 0.75 mL of ascorbic acid solution. The synthesized Te NWs are uniform in length and diameter. Figure 27(a, b) shows the diameter and length distribution of Te NWs with 0.1 gm of PVP and 0.75 ml of ascorbic acid.

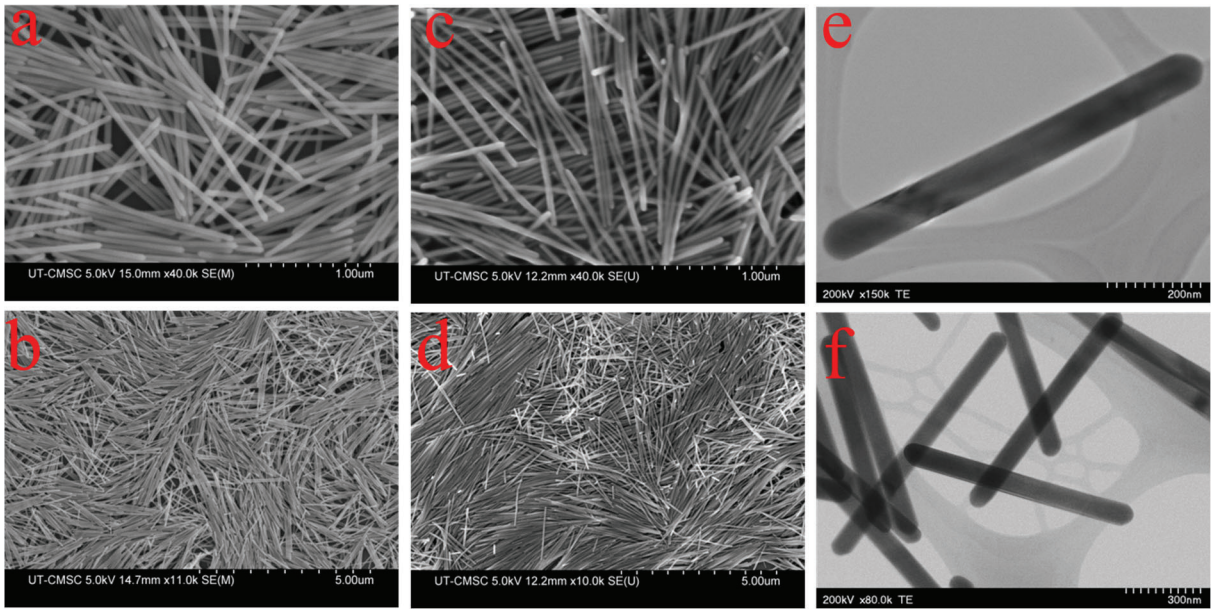


Figure 26. SEM images of Te NWs for (a, b) 0.1 gm PVP , 0.75 mL ascorbic acid (c, d) 0.2 gm PVP, 1.5 mL ascorbic acid; (e, f) STEM images of Te NWs for 0.1 gm, 0.75 mL

From SEM image Figure 26(a) and statistical analysis Figure 27(a, b), the average length and diameter of the nanowires are 1.15 ± 0.03 μm and 41.0 ± 3.0 nm respectively. The Te NWs have very narrow size distribution with standard deviation ± 0.03 μm in length and ± 3.0 nm in diameter. In this case, the aspect ratio of Te NW is 28.0 ±2.7. Upon increasing the amount of PVP to 0.2 g and ascorbic acid to1.5mL, Te NWs of uniform length and diameter were again obtained, however with decreased NW diameter and increased NW length. The SEM images are shown in Figure 26(c, d). The average length and diameter of Te NW s are 1.54 ± 0.07 μm and 27.8 ± 3.7 nm respectively. The aspect ratio of Te NWs for this case is 55.4 ±1.1. Figure 27(c, d) shows the diameter and length distribution of Te NWs with 0.2 gm of PVP and 1.5 mL of ascorbic acid. Further, we calculated the aspect ratio of the individual NWs, and plotted the graphs for aspect ratios for two synthesis conditions as shown in Figure 27(e, f). In case of the NWs synthesized by using 0.1 g PVP and 0.75 mL ascorbic acid, ~56 % of NWs have aspect ratio in the range of 26-30 while for 0.2 g PVP and 1.5 mL ascorbic acid, ~40 % of the NWs have aspect ratio in the range of 56-65 and ~36 % are in the range of 46-55. The increased in aspect ratio is due to the role of these PVP and ascorbic acid as directing agent and reducing agent. [160] Figure 26(e, f) shows the scanning transmission electron microscope (STEM) images of Te NWs formed with 0.1 gm PVP and 0.75mL ascorbic acid. It reveals that NWs are highly crystalline with uniform length and diameter. The unusual anisotropic crystal structure of Te consists of 1D helical chain of covalently bound atoms parallel to the *c*-axis. [176] Previously, Zhong *et al*. used a solvothermal technique to synthesize Te NWs with diameter 30 ± 2 nm and length 10 ± 1 μm using ethylene glycol as a solvent. [160] Qian et al. reported the synthesis of Te NWs with diameter 4-9 nm and lengths up to hundreds of μm and Wang et al. reported Te NWs with diameter 40 nm with lengths in several microns using hydrazine through hydrothermal method. [163, 164] In our case, we demonstrated the successful control of the aspect ratio of Te NWs, from 28.0 to 55.4, by varying the amount of ascorbic acid and PVP. The amount of surfactant and reducing agent are the key parameters to prepare the desired nanowires during synthesis. Potassium hydroxide to control alkalinity helps

PVP to act fully as a surfactant for the synthesis of Te NWs. Here, we developed the Te NWs with uniform length and diameter using hot injection colloidal method with small deviation in length with standard deviations of 0.03 μm and 0.07 μm respectively for two cases.

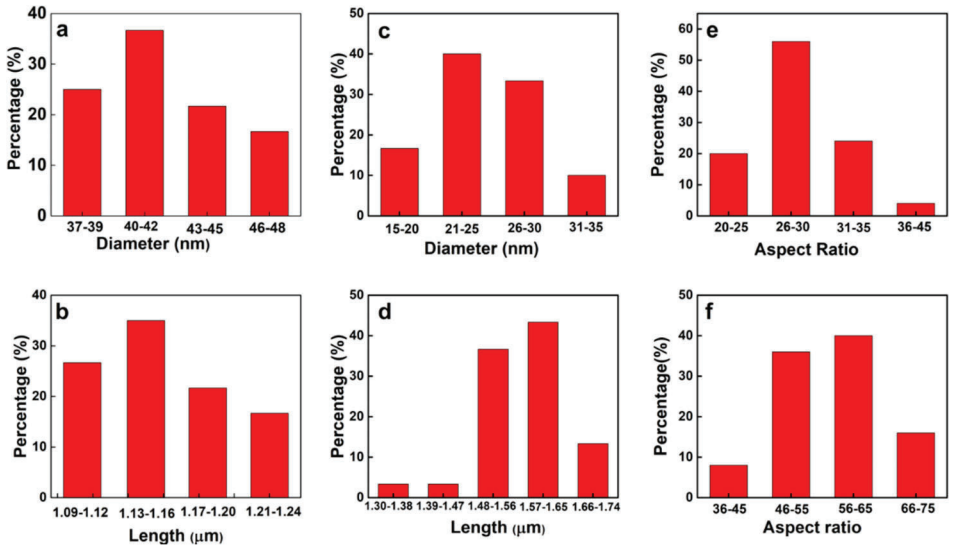


Figure 27. Diameter, length and aspect ratio distribuiton of Te NWs, 120°C for 21 hrs. (a, b, e) 0.1 g PVP and 0.75 mL ascorbic acid (c, d, f) 0.2 g and 1.5 mL

Figure 28(a) displays the typical XRD pattern of synthesized Te NWs performed in the '2θ' range of 20-70°. The diffraction peaks obtained from MDI JADE closely match with the diffraction peaks measured for our as-synthesized Te NWs. Based on the standard powder diffraction file, synthesized Te NWs are in hexagonal phase with lattice constants a = a = b = 0.4454 nm and c = 0.5924 nm. The high intensity obtained in the diffraction pattern signifies the purity of the material. Similarly, Figure 28(b) shows the Raman spectrum of Te NWs using a 632.8 nm He-Ne laser source with bands at 117.0, 136.1 and 265.9 cm^{-1}. The mode with a vibration 117.0 cm^{-1} corresponds to A_1 mode, 136.1 cm^{-1} corresponds to E_2 mode and the bands at 265.9 cm^{-1} assigned to the second-order spectra of the Te NWs, which agrees closely with previous reports. [177, 178]

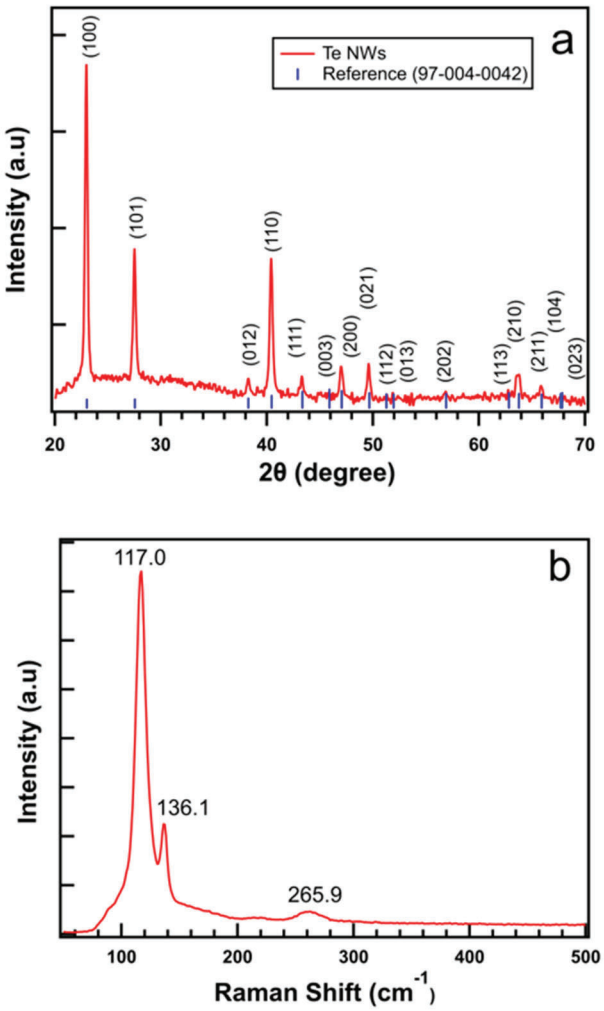


Figure 28. (a) XRD pattern, Te NWs of high-purity hexagonal crystal structure (reference from PDF #97-004-0042, MDI JADE software); (b) Raman scattering spectrum of Te NWs, 632.8 nm laser excitation, 0.1 gm PVP, 0.75 mL ascorbic acid

Figure 29 displays the SEM and XRD patter of Cu_xTe nanowires. The SEM image in Figure 29(a) indicates that the NWs grown are uniform in lengths and diameters. The EDS was carried at operating current 10 μA and voltage 20 kV. Based on EDS analysis, the elemental ratio of Cu and Te is 7:4. Figure 29(b) shows the XRD pattern of as obtained copper telluride nanowires which have hexagonal crystal structure with lattice constants a=b=0.8340 nm and c= 0.7230 nm obtained from MDI JADE software (PDF # 97-062-9337). From EDS analysis and XRD patterns, we confirm that the synthesized nanowires have chemical formula Cu_7Te_4 in hexagonal crystal structure.

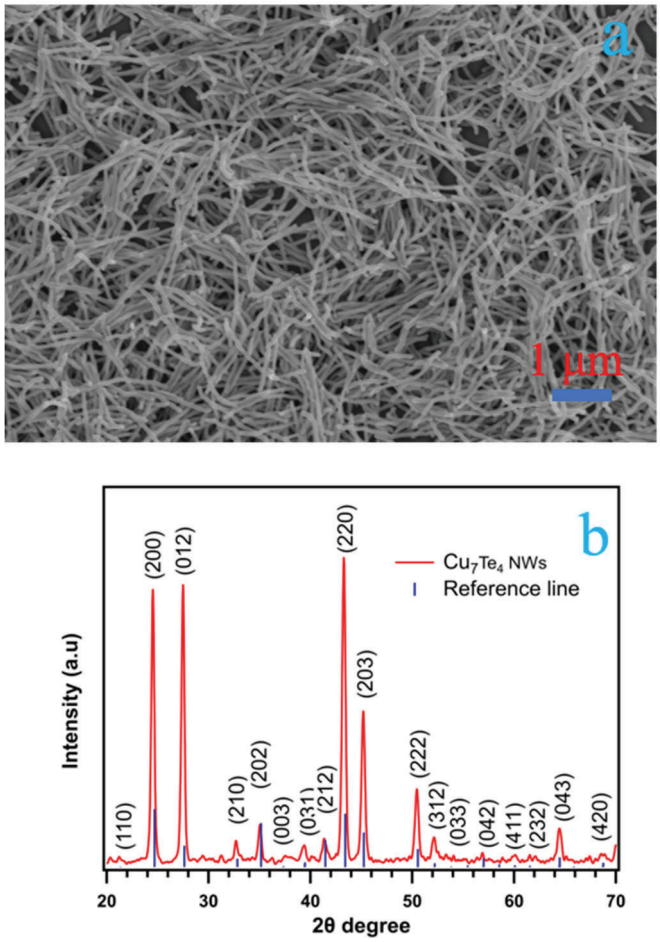


Figure 29. (a) SEM image and (b) XRD pattern of synthesized Cu_7Te_4 NWs, with hexagonal crystal structure

6.5 CONCLUSIONS

We synthesized Te NWs using hot injection colloidal method and successfully convert to Cu_xTe NWs. We successfully controlled the aspect ratio of Te NWs. The NWs are uniform in diameter as well as in length. These NWs have potential applications is sensors, detectors, and solar cells. We are planning to use these NWs as current conduits through oxide passivated interfaces for better CdS/CdTe device efficiency.

7. SOLUTION PROCESSED LEAD TELLURIDE NANOWIRES AS A PASSIVATING LAYER TO CDTE PHOTOVOLTAICS

Dipendra Pokhrel, Ebin Bastola, Kamal Khanal Subedi, Manoj K Jamarkattel, Adam B Phillips, Michael J Heben, and Randy J Ellingson

7.1 SUMMARY

Here, we report the application of lead telluride (PbTe) nanowires (NWs) as a passivating layer to cadmium telluride (CdTe) solar cells enhancing the opto-electronic properties and device performances. Utilizing hot injection colloidal method, PbTe NWs were synthesized and was spin coated as the thin film buffer layer on the back contact of CdTe solar cells. Characterization of scanning electron micrograph (SEM), X-ray Diffraction (XRD), and Raman spectra reveals the morphology, phase crystallinity, and chemical compositions of PbTe NWs. Steady state photoluminescence (PL) and time resolved photoluminescence (TRPL) measurements were performed to understand the carrier dynamics of PbTe NWs in CdTe devices. The illumination from backside of the devices shows an evidence of passivation in the form of reduced back surface recombination. With implementation of PbTe NWs as a passivating layer to CdTe solar cell, the photoconversion efficiency (PCE) of 14.8 % was measured (V_{OC} = 855 Mv and FF= 77.3 %), whereas the controlled device has 14.0 % (V_{OC} = 840 Mv and FF= 75.9 %). The PCE obtained with PbTe NWs was enhanced due to increase in minority carrier lifetime and reduced back barrier height (as measured by temperature dependent current vs voltage characteristics). Devices fabricated using these NWs demonstrate improved open-circuit voltage (V_{OC}) and fill factor (FF) in agreement with the desired effects of surface passivation of CdTe solar cells.

7.2 INTRODUCTION

Cadmium telluride (CdTe) is the most promising thin film solar cells and overall dominates the photovoltaics market with record power conversion efficiencies (PCE) of 22.1 %. [179] In CdTe solar cells, the minority carrier lifetime is very low, so the back-surface passivation of CdTe solar cells with suitable band alignment is essential, which is a major challenge to produce the record efficiency. The front and back surfaces of the solar cells are the major sources of high defect densities acting as a recombination centers, and thus device performances are suffered from low open circuit voltage and fill factor. Moreover, low doping and low carrier lifetime in polycrystalline materials are the major supporter of the loss in V_{oc}. [180] A reduction of defect states at the interface, band offsets and fixed interface charge are the strategies to passivate the semiconductor interface. [181] Previously, aluminum oxide (Al_2O_3) has shown significant improvement in carrier lifetime acting as a back surface passivating layer to CdTe solar cells. [182-184] A high density of fixed negative charge [185] or low degree of lattice mismatch [186] offer the potential for repelling minority carriers and creating the low defect density at the interface. [187] At the same time, the formation of ohmic contact by the use of p+ layer is essential to fabricate highly efficient devices. ZnTe is one of the common material that has been used for a long time as the back contact buffer layer for CdTe solar cells, however, based on the evidence that the minority carrier lifetime does not improve significantly. [188, 189] The reduction of back surface recombination is considered as the main contributor of increase in efficiency of CdTe devices.

In this section, we discuss a chalcogenide low band gap (~ 0.29 eV) material, lead telluride (PbTe), which have potential applications in polycrystalline and nanostructure thin film. [190, 191] PbTe can be p-type semiconductor with Te-rich PbTe and n-type semiconductor with Pb-rich PbTe. [192] The unique properties like narrow band gap energy, large carrier mobility ($0.329x10^{-3}$ $cm^2V^{-1}s^{-1}$) and high dielectric constant (400) [190, 193] bring attention to the researchers in various filed like thermoelectric systems, solar cells and infrared sensors etc. [194-196] Both PbTe and CdTe possess a face-centered cubic translational symmetry with rock salt and zinc blend structure. The lattice constant for CdTe is 0.648 A° and for PbTe 0.646 A°, which are nearly identical and lattice mismatch of CdTe and PbTe is only 0.3 %. The small lattice mismatch and big miscibility gap between CdTe and PbTe make them perfect heterostructure with nearly defect free and sharp interface. [197, 198] With suitable p-type doping, the fermi level of the PbTe film can be dropped and it may be possible to match the work functions of the PbTe layer and the CdTe layer. [199] A previous x-ray photoemission spectroscopy studied the lattice matched CdTe/PbTe (111) heterojunctions interface and found a valence band offset (VBO) of 0.135 eV between CdTe and PbTe, allowing hole injection into the PbTe layer. [200] Based on these properties, it is worth to consider PbTe as one of the potential materials for back buffer layer to reduce the back-surface recombination. The reduction of back surface recombination is considered as the main contributor of increase in efficiency of CdTe devices.

Nano-sized semiconductors have been extensively pursued and have great attention due to their size dependent optical and electrical properties. Various methods like chemical deposition, [201] electrochemical deposition, [202] hydrothermal, [203] and microwave-assisted [204] etc. have been used to fabricate PbTe nanostructures. As NWs can have a potential application as point contact to CdTe solar cells, we previously reported the synthesis and application of Te NWs and Cu_xTe NWs as a back interface layer to CdS/CdTe solar cells. [205, 206] Here, we used hot injection colloidal method to synthesize the PbTe NWs using environmentally benign ethylene glycol as a solvent. Matin et al. reported the numerical analysis on ultrathin CdS/CdTe with 100 nm thick back surface field (BSF) to reduce the barrier height in valence band and to minimize the recombination losses at the back contact of CdS/CdTe solar cells. [207]

In this work, we report the synthesis of PbTe NWs followed by synthesis of Te NWs utilizing hot injection colloidal method. The synthesized PbTe NWs are uniform in diameter and have cubic structure with vibrational modes at 120.2 cm^{-1} and 140.1 cm^{-1} corresponding to longitudinal optical (LO) phonon mode. Implementing these PbTe NWs to fabricate CdS/CdTe solar cells, measurements of steady state photoluminescence (PL) and time resolved photoluminescence (TRPL) show the evidence of back surface passivation and enhance the minority carrier lifetime. The temperature dependent (J-V-T) measurement shows PbTe NWs lower the back-barrier height with compared to controlled back contact. The best cell of CdS/CdTe device with PbTe NWs has an efficiency of 14.8 % with V_{OC} of 855 mV and FF of 77.3 %, an ~5 % improvement over the standard device (V_{OC} 840 mV and FF 75.9 %).

7.3 METHODS, ASSUMPTIONS, and PROCEDURES

PbTe NWs were synthesized using hot injection colloidal method. The synthesis took place in two steps. First, we prepared the Te NWs followed the process reported previously, [205] and converted these into PbTe NWs using a slight-modification of the process reported by Yang et al. [173] For a typical synthesis of PbTe NWs, 0.465 gm (1.22 mmol) of $Pb(CH_3CO_2)_2 \bullet 3H_2O$ and 0.05 gm of PVP were dissolved in 4 mL ethylene glycol by heating at 80° C in a container. At the same time, 0.2496 gm of PVP is dissolved 0.75 mL of diwater by heating at 80° C. The lead precursor was then injected into tellurium reaction solution followed by addition of 0.2496 gm of PVP that dissolved in 0.75 mL of diwater, and reaction was continued for next 24 hrs. for high quality PbTe NWs. The heating mantle was removed, and the flask temperature was lowered to room temperature using a cold-water bath. The product was centrifuged and cleaned with diwater water three times. The obtained NW product was dried and stored as a powder in a glove box in N_2 environment for characterization and applications.

To test PbTe NWs thin film as a back contact, CdS/CdTe film stack fabricated by vapor transport deposition (VTD) onto TEC^{TM}-15M (Pilkington N.A) glass substrates deposited by Willard and Kelsey Solar Group were used. Using saturated solution of $CdCl_2$ solution in methanol, the samples were activated at temperature 387°C in dry air for 30 min. Solution based $CuCl_2$/Au was considered as standard back contact to compare the device performances of CdS/CdTe devices with PbTe NWs back contact. Here, copper treatment was carried out using a procedure reported previously. [208] To fabricate a device with PbTe NWs back contact, after $CuCl_2$ treatment, 50 µL of PbTe NWs solution was spin coating onto CdTe devices with speed 1000 and 3000 rpm for 10 and 30 sec respectively. The PbTe NWs solution was prepared by dissolving PbTe NWs powder in ethanol (7mg/mL). The devices were then annealed at 200° C for 2 min and complete the back contact with 40 nm thermally evaporated gold (Au) by using the mask to make the active cells of area 0.08 cm^2.

The X-ray diffraction (XRD) pattern was performed using Rigaku Ultima III X-ray diffractometer (40 kV accelerating voltage and 44 mA currents) to examine the phase purity of PbTe NWs. The surface morphology of PbTe NWs was examined with Hitachi S-4800 scanning electron microscopy (SEM). The Raman spectra vibrational peaks of PbTe NWs was measured by using Confocal Raman Spectrometer using He-Ne laser with line excitation at 632 nm. The solar cell performance was characterized by measuring the current density-voltage (*J-V*) characteristics of the devices under AM1.5G illumination using a Keithley 2400 digital solar simulator. The external quantum efficiency (EQE) measurements were performed by PV Instruments (model IVQE8-C) system. Temperature-dependent current voltage characteristics (JV-T) were performed using a Keithley 2401 source meter for current-voltage data acquisition. Room temperature photoluminescence (PL) measurements were detected using a Horiba Symphony-II CCD detector (integration time = 0.5 s) after a 300 $g.mm^{-1}$ grating monochromator and time resolve photoluminescence (TRPL) measurements were performed with integration time 900s using TCSPC module.

7.4 RESULTS and DISCUSSION

Figure 30 shows the X-ray diffraction pattern (XRD) and Raman spectra of PbTe NWs. For these characterization, PbTe NWs were dispersed in ethanol and film was prepared on soda lime glass. Characterization of morphological and structural properties of PbTe NWs suggest the formation of high purity PbTe NWs. Figure 30(a) shows the XRD pattern of PbTe NWs in altaite phase and all the diffraction peaks can be indexed to cubic structure, which agrees well with standard (PDF 98-000-0058). The sharp peaks in XRD pattern also confirm the purity and excellent crystallinity of PbTe NWs. Raman spectroscopy measurements of PbTe NWs was performed using 632 nm excitation He-Ne laser and shown in Figure 30(b). The Raman peaks of PbTe NWs obtained at 120.2 cm^{-1} and 140.1 cm^{-1} are in close agreement with what was reported previously. [209] The vibrational mode at 120.2 cm^{-1} is attributed to the longitudinal optical (LO) phonon mode of PbTe film and peaks at 140.1 cm^{-1} is attributed to the LO phonon of TeO_2 formed on the PbTe surface due to oxidation in air ambient. [210, 211]

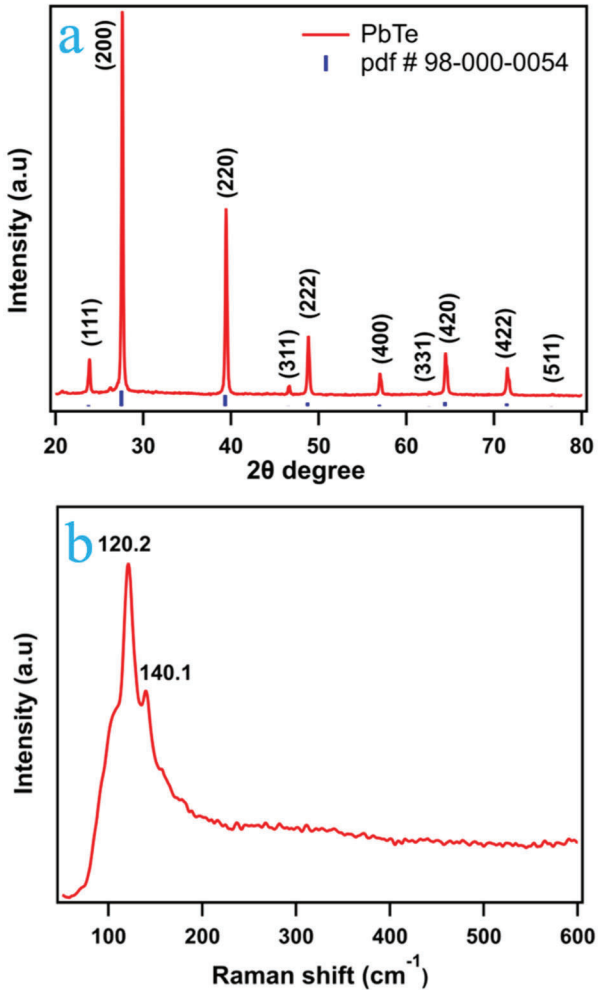


Figure 30. (a) XRD pattern and (b) Raman spectrum for PbTe NWs

Figure 31(a) shows the SEM image of PbTe NWs that was conducted at operating voltage of 10 kV. From SEM image, we can see that PbTe NWs are uniform in diameter. The average diameter of NWs is about 69 nm with standard deviation of ± 7 nm. Figure 31(b, c) display the surface SEM images of $CdCl_2$ activated CdTe device and PbTe NWs on top of CdTe respectively. The band alignment of CdS, CdTe, PbTe and Au using SCAPS simulation is shown in Figure 31(d). The insertion of PbTe NWs layer as a buffer layer between CdTe and Au decreases the contact resistance, which improves the charge collection and reduces interface recombination at the back.

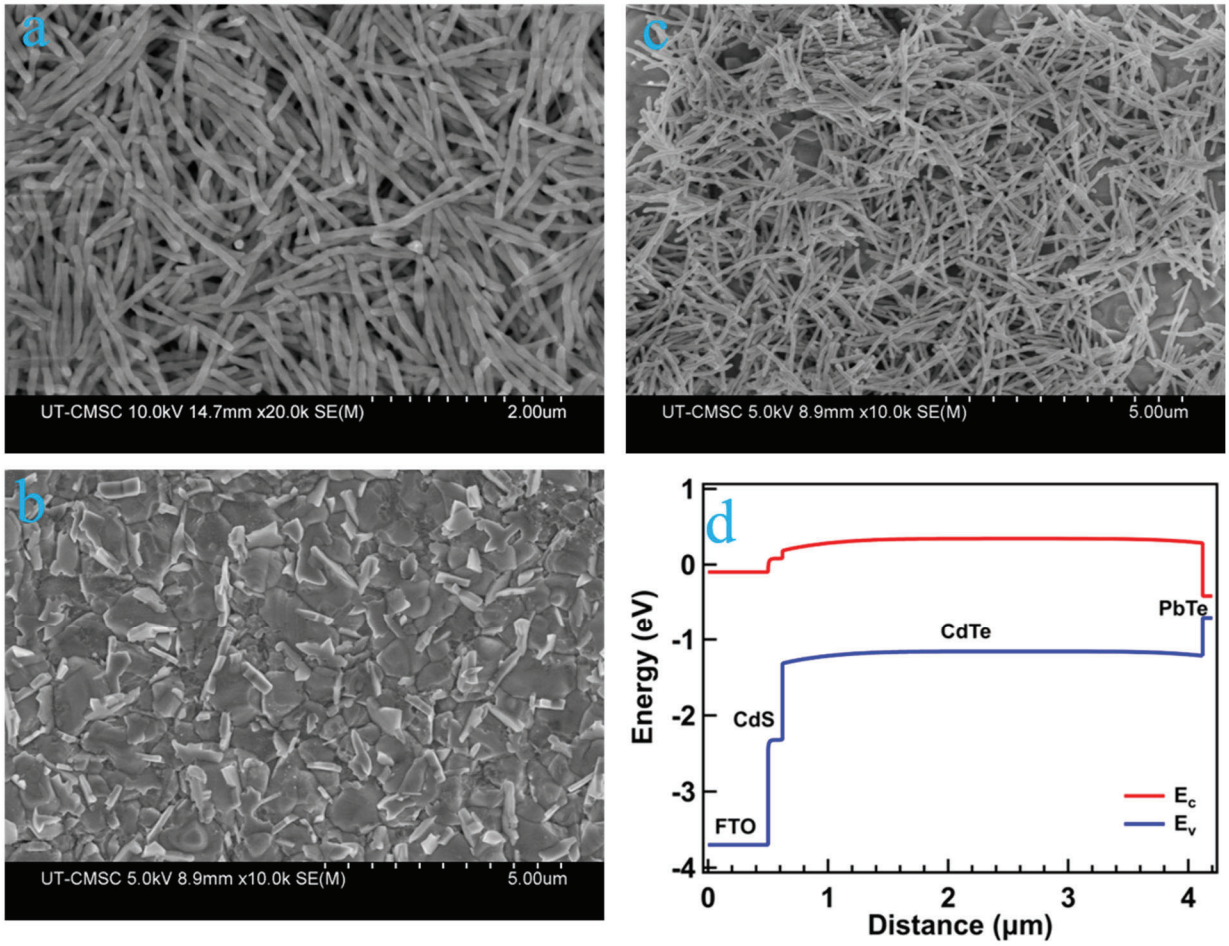


Figure 31. Surface SEM images of (a) PbTe NWs, (b) $CdCl_2$ activated CdTe device, and (c) with PbTe NWs on device; (d) band alignment of CdS, CdTe, PbTe and Au

To study the minority carrier lifetime in CdS/CdTe device, both front and back illumination steady state PL and TRPL measurements were performed. Figure 32(a-d) shows the steady state PL and TRPL measurements of CdS/CdTe devices with different back contacts. For glass side illumination, laser of excitation 633 nm and for film side laser of excitation 532 nm were used. Implementation of PbTe NWs as a back buffer layer on CdTe increases PL and photogenerated carrier lifetimes from both front and back illumination. The long component decay time (τ_2) increases significantly from 1.2 ns (without PbTe NWs) to 5.2 ns (with PbTe NWs) when measured from film side, and from 19.7 ns to 35.7 ns, when measured from glass side. The increase in minority carrier lifetime is attributed to the reduction of back surface recombination. Along with

$CuCl_2$ doping and PbTe NWs, the lifetime from glass side increases to 87.5 ns ($CuCl_2$/PbTe NWs) whereas only with $CuCl_2$ have lifetime of 55.2 ns. However, with $CuCl_2$ and $CuCl_2$/PbTe NWs do not have significant different in minority carrier lifetimes (~1.4 ns) when illuminated from the film side. The reason due to low lifetime with $CuCl_2$ is that Cu forms defect levels, which act as a recombination center. [212] The measurements of carrier lifetime are the strong indication that the recombination at the back surface has been significantly reduced. The measured τ_1 and τ_2 values with corresponding yields are presented in Table 2.

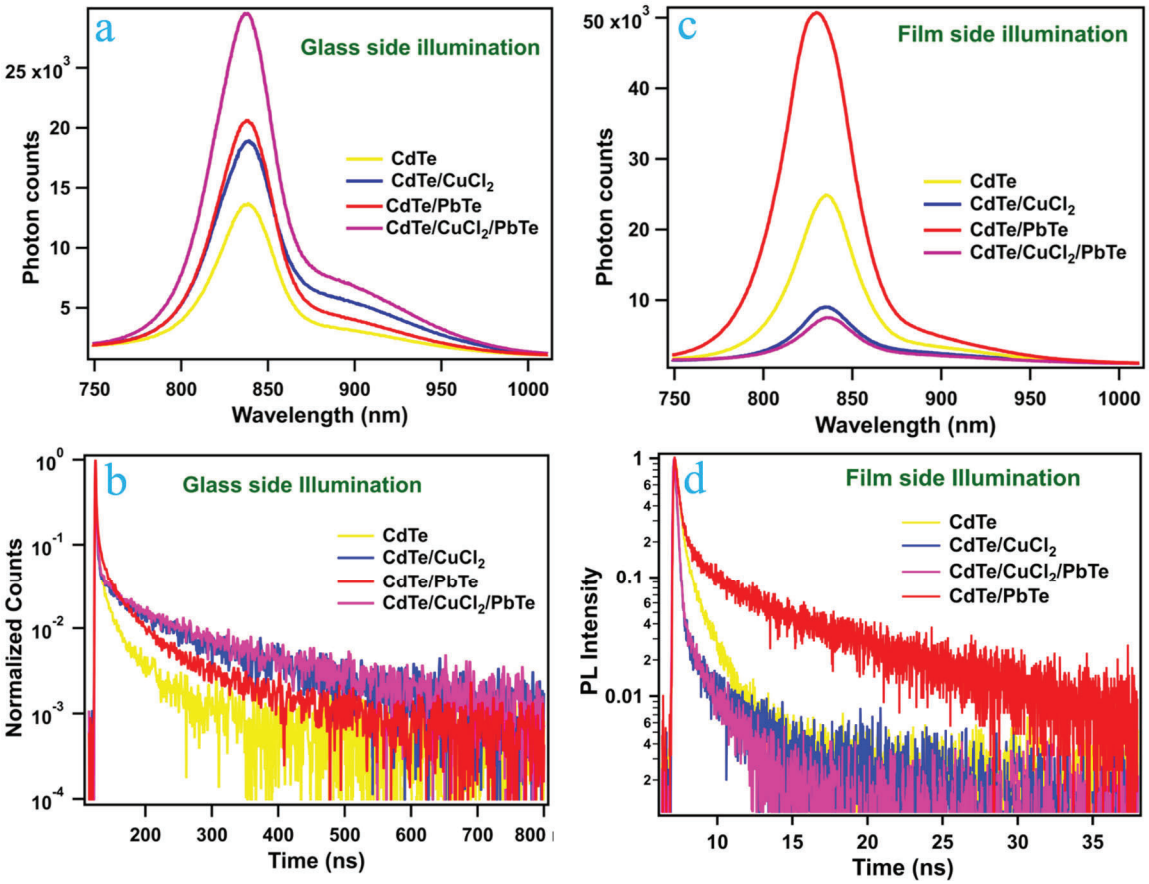


Figure 32. PL and TRPL spectrum of CdS/CdTe device (a, b) glass side illumination and (c, d) film side illumination

Table 2. Lifetime measurements of the CdS/CdTe solar cells with different form of back contacts

Samples	Glass side illumination				Film side illumination			
	τ_1(ns)	Yield (%)	τ_2(ns)	Yield (%)	τ_1 (ns)	Yield (%)	τ_2 (ns)	Yield (%)
CdTe only	1.0	59.3	19.7	40.7	0.1	51.0	1.2	48.9
CdTe/$CuCl_2$	0.9	35.8	55.2	64.2	0.05	77.1	1.3	22.8
CdTe/$CuCl_2$/PbTe	1.0	34.6	87.5	65.3	0.05	76.4	1.4	23.5
CdTe/PbTe	1.1	40	35.7	60.0	0.1	27.9	5.2	72.0

The CdTe solar cells with four different types of back contact were studied. Figure 33(a) shows the current-voltage (*J-V*) characteristics for CdS/CdTe devices with Au only, PbTe NWs/Au, $CuCl_2$/Au and $CuCl_2$/PbTe NWs/Au back contacts. The dashed lines in *J-V* curve represent the dark illumination and solid lines represent the light illumination of the devices. It should be noted that with an implementation of PbTe NWs, the V_{OC} was dramatically increased to 802 mV on an average of 15 cells, ~49 mV higher than the V_{OC} of the device with Au only back contact. The best power conversion efficiency of 13.0 % was obtained with PbTe NWs, whereas controlled device (Au only) has an efficiency of 11.8 %. The increase in V_{OC} of the device with PbTe NWs is due to increase in minority carrier lifetime of CdTe film as PbTe NWs passivate CdTe surfaces by reducing the back-surface recombination as supported by PL and TRPL measurements. It is well known that Au alone on CdTe forms a string opposing diode (Schottky barrier) that reduces device performances, and we find that the presence of PbTe NWs, even in the absence of any intentional Cu doping, modified the device performance dramatically. The efficient CdTe solar cells are based on Cu/Au back contact. [213, 214] In our lab, solution process $CuCl_2$/Au back contact is considered as controlled back contact. [208] The best cell of the CdTe device with PbTe NWs ($CuCl_2$/PbTe NWs/Au) as an interface layer yielded the open circuit voltage (V_{OC}) of 855 mV, short circuit current density (J_{SC}) of 22.4 mA cm^{-2}, fill factor (FF) of 77.3 % with PCE of 14.8 %. While as for controlled device ($CuCl_2$/Au), these values were 840 mV, 22.0 mA cm^{-2}, 75.9% with efficiency 14.0 %. For the best cell, we observed ~5% increase in PCE with PbTe NWs as an interface layer compared to controlled device. Figure 34(a-d) show the statistical distribution of V_{OC}, J_{SC}, FF, and PCE of the CdS/CdTe device with and without PbTe NWs. With incorporation of PbTe NWs as an interface layer between CdTe and Au electrode, the contact resistance decreases, which improves the carrier collection and reduce interface recombination at the back. The improvement in device performance is mainly attributed to the increase in V_{OC} and FF of the device. This statement is strongly support by the TRPL measurement discuss above. The external quantum efficiencies (EQEs) of the CdTe device with and without PbTe NWs were measured and presented in Figure 33(b) and are in close agreement with the values measured from the J-V measurements. Current-density vs. voltage measurement results for V_{OC}, J_{SC}, FF and η of the best cells of CdS/CdTe devices with different back contacts are tabulated in Table 3.

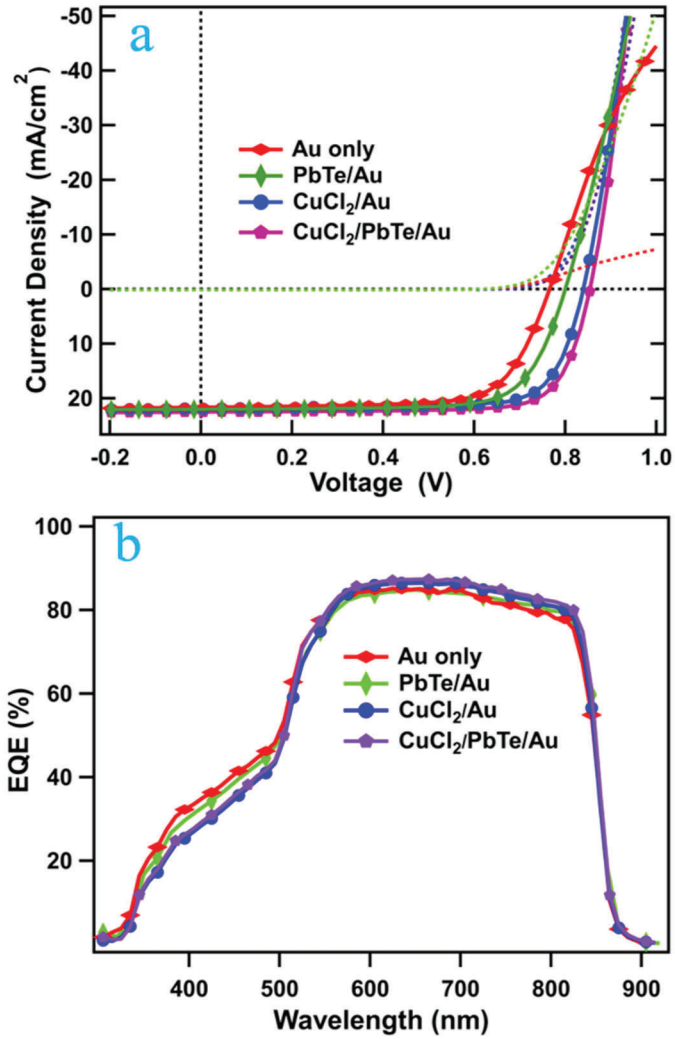


Figure 33. (a) J-V results; (b) EQE results of CdS/CdTe devices, varied back contacts; for JV, solid lines are light, and dotted lines are dark

Table 3. The device performance parameters (V_{OC}, J_{SC}, FF and η) of the best cells of CdS/CdTe devices with different back contacts

Back contacts	*V_{OC} (mV)*	*J_{SC} (mA cm^{-2})*	*FF (%)*	*η (%)*
Au only	766	21.6	71.2	11.8
PbTe/Au	797	22.1	73.8	13.0
$CuCl_2$/Au	840	22.0	75.9	14.0
$CuCl_2$/PbTe/Au	855	22.4	77.3	14.8

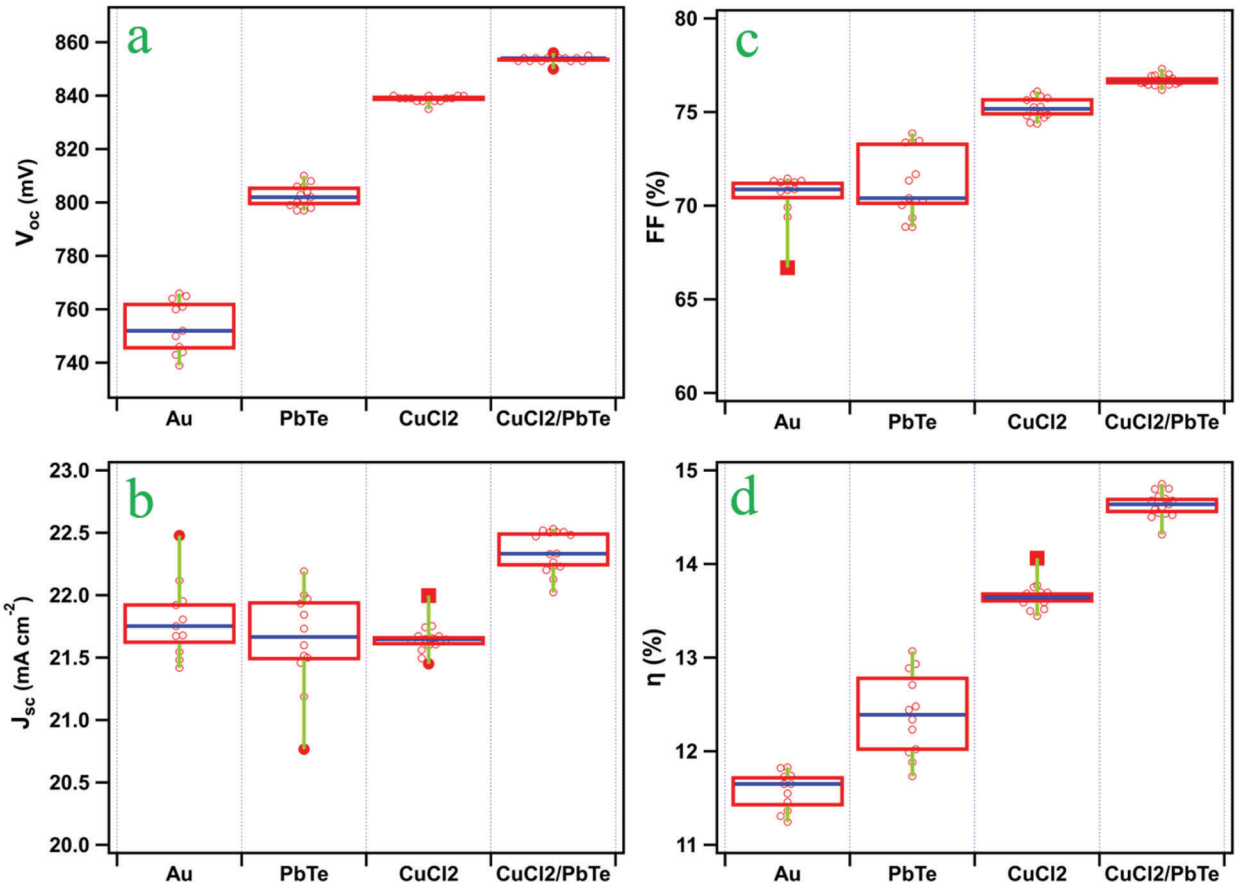


Figure 34. Statistical distribution of V_{OC}, J_{SC}, FF, and PCE of CdS/CdTe solar cells, various back contacts

To study the effect of PbTe NWs on energetic barrier (ϕ_b) created at the back interface, temperature dependent J-V characteristics were carried using thermionic emission model described by the equation: [215]

$$J_o \propto T^2 . exp\left[\frac{-q.\phi_b}{k_B T}\right] \quad (1)$$

Where J_0 is the saturation current, q is an electronic charge, k_B is the Boltzmann constant and T is the temperature. The dark curve was analyzed and the back barrier height (ϕ_b) due to effect of PbTe NWs was extracted from the Arrhenius plot of ln (J_0/T^2) versus $1/k_BT$ as shown in Figure 35(a-c). The device with PbTe NWs has barrier activation energy of 234 ± 8 meV, whereas the controlled device has 315 ± 7 meV. With an implementation of PbTe NWs as an interface layer, the back-barrier height is reduced by 81 meV over controlled device suggesting better transport of holes towards the back electrode.

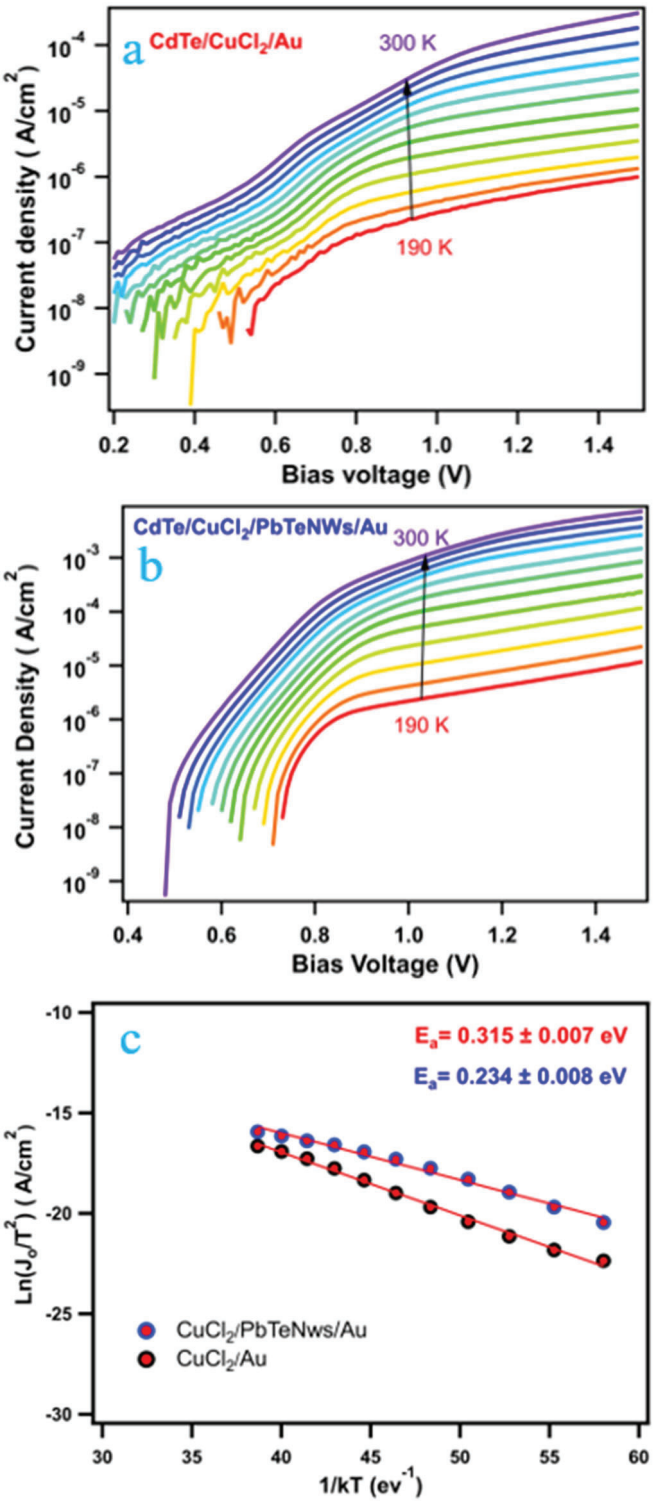


Figure 35. (a) Temperature-dependent JV for CdTe devices, two different back contacts; (b) plots of ln (J_o/T^2) versus $1/k_BT$ to evaluate back barrier height

By using single exponential diode equation given in Eq. (2), the J-V behavior of solar cells can be analyzed. [216]

$$J = J_0 \, exp\left[\frac{q}{Ak_BT}(V - R_sJ) + G_{sh}V - J_L\right] \quad (2)$$

Where J_0 is reverse saturation current, q is an electric charge, A is the diode ideality factor, k_B is Boltzmann's constant, T is temperature, R_s is series resistance, G_{sh} is the shunt conductance and J_L is the load current density at AM1.5G. The ideality factor and dark saturation current density were analyzed by fitting dark J-V curves measured at room temperature (Figure 36(a-d)). For a device with PbTe NWs, the ideality factor and dark saturation current density are 1.22 and $5.0x10^{-11}$ mA cm^{-2} respectively whereas the control device has 1.36 and $9.2x10^{-10}$ mA cm^{-2}. The ideality factor values close to 1 indicates the band-to-band recombination and is dominant, and the values close to 2 indicates the trap assisted recombination mechanism. [217] The lower values of ideality factor and dark saturation current density due to PbTe NWs indicate the better diode behavior as well as reduced recombination at the back interface over controlled device.

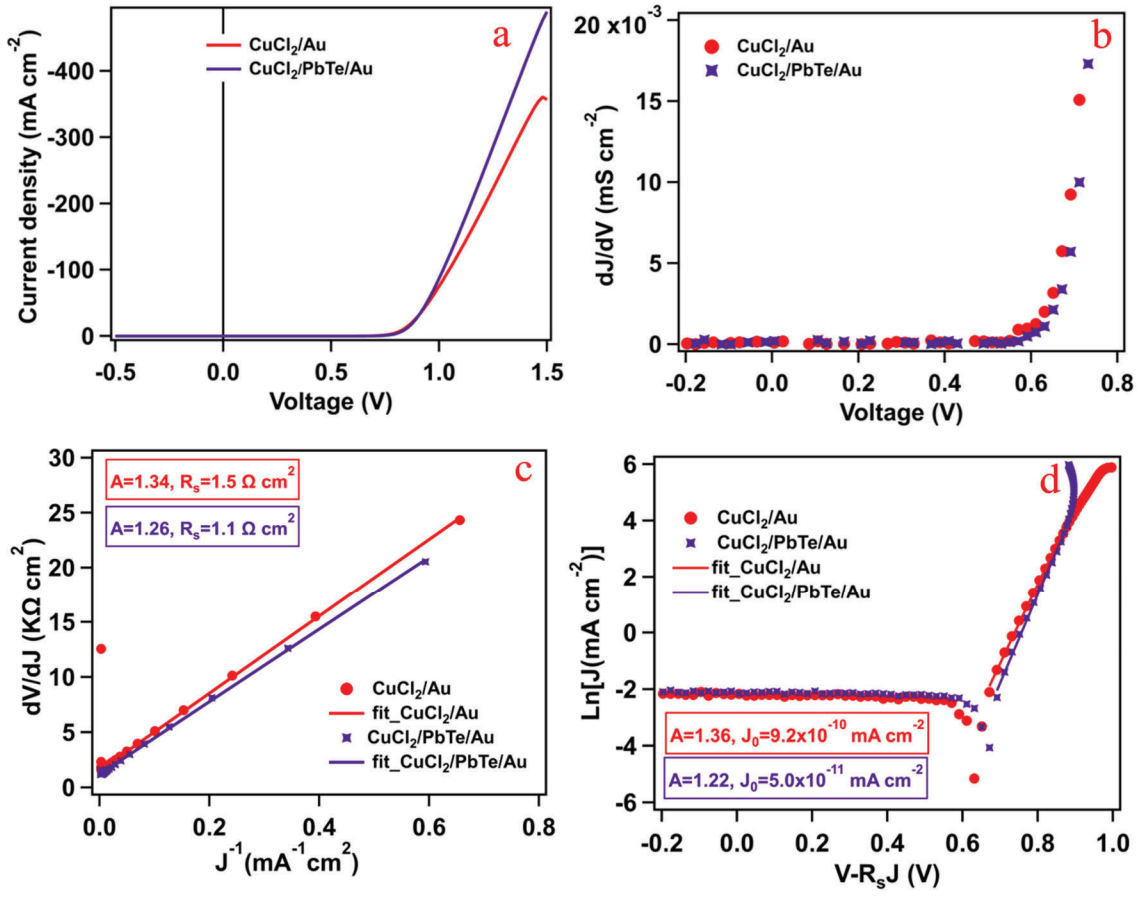


Figure 36. $CuCl_2$/Au, $CuCl_2$/PbTeNWs/Au back contacts: (a) dark J-V, (b) R_{sh} characterization (c) dV/dJ versus 1/J for A and R_S; (d) V-R_sJ for A and J_0

7.5 CONCLUSIONS

In summary, we successfully synthesized PbTe NWs employing hot injection colloidal method and demonstrated its application as a passivating layer to CdS/CdTe solar cells. As a passivating layer, it increases the minority carrier lifetime from the back as well as front of the devices and reduces the back surface recombination. Devices fabricated with PbTe NWs demonstrate improved V_{OC} and FF of the devices in agreement with the desired effects of surface passivation. With an incorporation of PbTe NWs, the PCE of 14.8 % was measured, whereas the controlled device has 14.0 %. The PCE obtained with PbTe NWs was enhanced due to increase in minority carrier lifetime and reduced back barrier height. PbTe NWs are applicable for better CdS/CdTe device efficiency as these NWs potentially allow for transport of current through oxide passivated interfaces.

8. BACK SURFACE PASSIVATION OF CDTE SOLAR CELLS USING SOLUTION-PROCESSED OXIDIZED ALUMINUM

Adam B. Phillips, Yanfa Yan, Randy J. Ellingson, and Michael J. Heben

8.1 SUMMARY

Although back-surface passivation plays an important role in high efficiency photovoltaics, it has not yet been definitively demonstrated for CdTe. Here we present a solution-based process, which achieves passivation and improved electrical performance when very small amounts of oxidized Al^{3+} species are deposited at the back surface of CdTe devices. The open circuit voltage (V_{OC}) is increased and the Fill Factor (FF) and photoconversion efficiency (PCE) are optimized when the total amount added corresponds to ~1 monolayer, suggesting the passivation is surface specific. Addition of further Al^{3+} species, present in a sparse alumina-like layer, causes the FF and PCE to drop as the interface layer becomes blocking to current flow. The optimized deposit increases the average baseline PCE for both Cu-free devices and devices where Cu is present as a dopant. The greatest improvement is found when the Al^{3+} species are deposited prior to the $CdCl_2$ activation step and Cu is employed. In this case, the best cell efficiency was improved from 12.6 to 14.4%. Time-resolved photoluminescence measurements at the back surface and quantum efficiency measurements performed at the maximum power point indicate that the performance enhancement is due to a reduction in the interface recombination current at the back surface.

8.2 INTRODUCTION

Recent improvements in the materials and interfaces in CdTe thin-film solar cells have led to increases in the photoconversion efficiency (PCE), with the record now at 22.1%. [218] While the short circuit current density (J_{sc}) is near bandgap-limited values and the fill factor (FF) has increased to 79%, [218] there is still substantial opportunity to increase the open circuit voltage (V_{oc}). [219] As further improvements in the bulk lifetime are obtained through Cl passivation [220] and Se incorporation, [221] and the interface recombination at the front surface is reduced through emitter engineering, [222, 223] both critical parameters for device improvement, [224, 225] the back interface may soon limit device efficiency. [226] Consequently, research is being focused on developing strategies to reduce back-surface minority carrier recombination while still enabling for efficient majority carrier extraction. Passivated back contacts are also required to enable bifacial operation for higher energy yields, [227] and will be required for future CdTe-based tandem solar cells.

A reduction in back surface recombination can be accomplished by reducing the concentration of electrically active defects at the interface or by creating an electric field to repel minority carriers through electrostatics, doping profiles, or band offsets. [226] Surface passivation in Si has been achieved by several approaches [228] including by depositing alumina by both vacuum and solution processing. [229, 230] Alumina has also been explored for passivation of both the rear [231] and front surfaces [232] of $Cu(In,Ga)Se_2$ solar cells. Alumina's potential to passivate CdTe surfaces was demonstrated recently when time resolved photoluminescence (TRPL) studies reported carrier lifetimes of 27 and 750 ns for CdTe (2 μm thickness) [233] and

$Cd_xSe_{1-x}Te$ (2-2.8 μm) [234] layers, respectively, in alumina double heterostructures. The mechanism of the passivation is not yet clear, but could be due to a high density of fixed negative charge [185] or the low degree of lattice mismatch (3.7%) between the unit cell of the (0001) surface of Al_2O_3 and the (111) surface of CdTe. [186] In addition, the large effective bandgap energy of alumina reduces the near-interface carrier concentration. These characteristics offer the potential for repelling minority carriers and creating a low defect density interface, respectively. [185, 233, 235, 236]

While demonstration of long carrier lifetimes via an optical measurement is promising, to date there is no clear evidence for back surface passivation in an operating CdTe device. Previous attempts have included deposition of alumina by atomic layer deposition (ALD) [237] and sputtering. [233] Liang et al. deposited alumina layers in thicknesses up to 5 nm by ALD and tracked the device performance. [237] The baseline PCE of 10.7% was improved to 12.1% when the Al_2O_3 thickness was 1 nm, while thicker deposits led to poorer device performance. A 1 nm layer was reported to be thin enough to allow holes to tunnel and thick enough to present fixed charge to repel minority carrier electrons. [237] However, the data that was presented in the paper was not consistent with this interpretation. First, an improvement in the long wavelength photoresponse at short-circuit was cited as proof of a reduced back surface recombination rate, but current collection at short circuit when the electric field is the largest is not a good indicator of back surface passivation. Second, the biggest factor leading to improved PCE (Figure 2(a) in Ref. [237]) was a flattening of the slope of the J-V curve through zero bias. This increase in the shunt resistance is more consistent with pin-hole blocking. Also, there was no evidence for current-blocking when the Al_2O_3 layers were thicker. In contrast, Kephart et al. applied Al_2O_3 by sputtering and saw pronounced kinks in the J-V characteristic at layer thicknesses of 3 and 5 nm. In this case, however, the device efficiency was not improved with the addition of Al_2O_3. [233] Thus, there has been no conclusive evidence to date for enhancement of PV performance in CdTe due to back-surface passivation. Other efforts to passivate the back surface of CdTe have included the use of TiO_2 and NiO, [238, 239] but, similarly, the results were not definitive.

Here, we present a solution-based process that reduces back-surface recombination in CdTe solar cells and increases the PCE. Following a process developed for passivating silicon solar cells by deposition of alumina, [240] we employed aluminum acetylacetonate ($Al(acac)_3$) dissolved in methoxyethanol and a spin-coating/heating procedure in an effort to deposit alumina on the back surface of CdTe solar cells. Data from current-voltage (J-V) curve analysis, time-resolved photoluminescence and external quantum efficiency (EQE) measurements made at the maximum power point and data from Auger electron and X-ray photoelectron spectroscopies provide conclusive evidence that the device improvement is indeed due to back surface passivation. The optimized process increased the average baseline efficiency for Cu-free devices from 10.4% to 11.7%, while the average PCE for devices made with Cu doping improved from 12.0% to 12.9%. Application of the $CdCl_2$ activation process after exposure to $Al(acac)_3$ with Cu-doping causes the baseline to be improved from 12.0 to 13.8%.

8.3 METHODS, ASSUMPTIONS, and PROCEDURES

CdTe device stacks were obtained from the center part of a 60 cm x 120 cm plate produced in a commercial deposition reactor by Willard and Kelsey Solar Group. The large area deposition

process produced uniform films, so the initial structure, ~100 nm of CdS and ~3 μm of CdTe on TEC^{TM}-15M coated soda-lime glass, can be considered to be constant for each experiment. The samples were activated by applying a saturated solution of $CdCl_2$ in methanol and heating to 390 °C in dry air for 30 minutes. Excess $CdCl_2$ was removed by rinsing with methanol. The aluminum acetylacetonate $Al(acac)_3$ (Sigma Aldrich Co. LLC, 99.999%) precursor solution was prepared by dissolving 400 mg of as-received powder in 20 mL of 2-methoxyethanol. 250 μl of the solution was pipetted onto a stationary sample which was then spun at 2000 rpm for 25 s. [240] Samples were then heated in laboratory air to 300 °C for 10 minutes. The spinning/heating cycle was performed 1, 3, 5, 7, and 9 times to produce increasingly thicker passivation layers. Devices were formed by depositing 40 nm of Au by thermal evaporation to form a back-metal electrode. Some samples also had a thin layer (3 nm) of Cu deposited by evaporation prior to Au deposition to enhance doping and lower the back contact barrier. In these cases, a subsequent heating step at 150 °C was performed in air to promote Cu diffusion for times ranging between 40 and 80 minutes. Individual solar cells were precisely defined by laser scribing (0.06 cm^2). Performance statistics were evaluated for relatively large data sets (n > 20).

8.4 RESULTS and DISCUSSION

Figure 37(a-c) shows the J-V curves and performance parameters as a function of the number of spin-coating/heating cycles for samples which had no copper added. Note that the standard deviation in the measured PV parameters for sets of 20 devices in each experiment showed typical variation of only 1-2% in Jsc, V_{OC}, and FF, and ~3% in PCE (Table 4). Figure 37(a) shows the J-V curves for the best devices with zero, 1, 3, 5, 7 and 9 spin-coating/heating cycles. The short circuit current density (Jsc) values are essentially constant within error, and small difference can be attributed to small deviations in the CdS emitter layer thickness. On the other hand, Figure 37(c) shows that the V_{OC} increases abruptly with the 1st cycle and stays nearly constant with additional cycles. We also note that it is surprising that the V_{OC} is already fairly high at 700 mV for zero cycles, and this may be due to Cu impurities in the CdTe source materials. The 1st cycle J-V curve also shows an improved FF but increasing the number of cycles produces first a kink, and then a strong blocking effect. Figure 37(b) shows that the overall efficiency trend is dominated by the FF, with a peak in PCE after the initial increase in the V_{OC}. Data for the full population of devices with $Al(AcAc)_3$ processing after $CdCl_2$ activation can be found in Table 4.

Figure 37(c) shows the carrier lifetimes which were extracted from biexponential fits to the PL transients. The carrier lifetime, which is associated with the longer-lived component in the PL (τ_2, see SI), followed the V_{OC} trend with spin/heating cycles. The PL was excited and detected through the back of the CdTe absorber. With a 1/e penetration depth of ~125 nm for the 532 nm light the measurement should be sensitive to recombination at the back surface. Since no Cu was used in these experiments, possible redistribution of dopants and possible changes at the front interface can be discounted. [241] Control experiments in which devices were exposed to spin/heating cycles without $Al(acac)_3$ showed different V_{OC} behavior that is more consistent with previously reported effects associated with back surface oxidation in air. [242] Thus, the increase in PL lifetime and the increase in V_{OC} can both be attributed to passivation effects, perhaps due to a reduction in the defect state surface density at the interface or a reduction in rear-surface band bending. [226, 227]

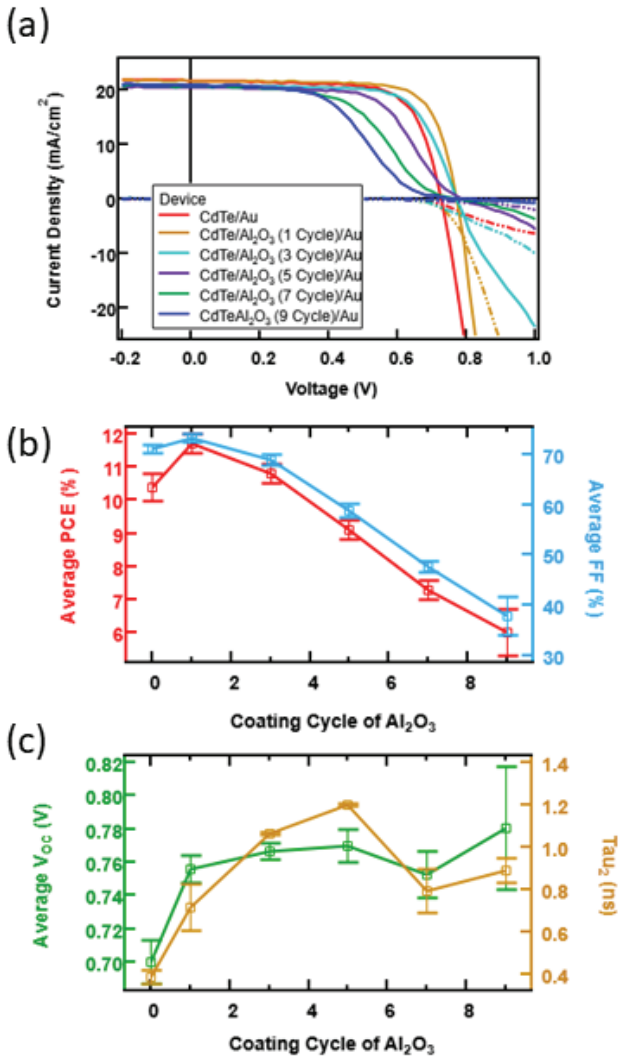


Figure 37. (a) JV results for CdTe device, varying number of spin/heat cycles; (b) Average PCE and FF; (c) average V_{OC} and long lifetime τ_2 of the TRPL

Table 4. J-V data, devices fabricated with and without Cu and Al_2O_3 deposition/heating cycles. Data is for best PCE

Device		V_{OC} (V)	J_{SC} (mA/cm^2)	FF (%)	PCE (%)
Without Cu					
CdTe/Au	Average	0.700±0.013	21.0±0.2	70.9±0.8	10.4±0.4
	Best	0.726	21.5	72.0	11.3
CdTe/Al_2O_3(1 cycle)/Au	Average	0.756±0.008	21.2±0.3	73.1±0.9	11.7±0.3
	Best	0.770	21.6	74.9	12.5
CdTe/Al_2O_3(3 cycles)/Au	Average	0.767±0.005	20.5±0.2	68.9±1.1	10.8±0.3
	Best	0.771	20.7	70.4	11.3
CdTe/Al_2O_3(5 cycles)/Au	Average	0.755±0.010	20.5±0.2	58.8±1.4	9.1±0.3
	Best	0.785	20.4	60.4	9.7
CdTe/Al_2O_3(7 cycles)/Au	Average	0.753±0.014	20.4±0.1	47.7±1.2	7.3±0.3
	Best	0.772	20.6	50.1	7.9
CdTe/Al_2O_3(9 cycles)/Au	Average	0.781±0.037	20.3±0.4	37.9±3.7	6.0±0.7
	Best	0.830	20.7	40.1	6.9
With Cu					
CdTe/Cu/Au 150 °C 40 min	Average	0.783±0.004	21.1±0.3	72.5±0.9	12.0±0.2
	Best	0.790	21.8	71.5	12.3
CdTe/Al_2O_3(1 cycle)/Cu/Au 150 °C 40 min	Average	0.800±0.008	20.8±0.5	76.4±0.8	12.7±0.2
	Best	0.806	21.8	75.6	13.3
CdTe/Al_2O_3(1 cycle)/Cu/Au 150 °C 60 min	Average	0.818±0.007	20.7±0.4	76.2±0.7	12.9±0.3
	Best	0.830	21.5	76.2	13.6
CdTe/Al_2O_3(1 cycle)/Cu/Au 150 °C 80 min	Average	0.821±0.006	20.5±0.3	75.8±1	12.7±0.3
	Best	0.829	20.7	76.4	13.1

Figure 38(a-c) show scanning electron microscopy (SEM) images of the CdTe surfaces directly after $CdCl_2$ processing and after the addition of 1 and 5 spin-casting/heating cycles, respectively. Prior to deposition (Figure 38(a)), the image is characteristic of the polycrystalline films with grain size of ~300 nm to 1 micron. The images are only subtly changed after 1 spin-casting/heating cycle (Figure 38(b)) and the grains appear to be smoothed with some edges appearing to be eroded or perhaps decorated with a thin deposit. There is no evidence of a conformal or complete coating. After five cycles, the surface morphology is significantly changed (Figure 38(c)) and small protrusions, or nodules, are evident. These are ~100 to 200 nm in extent and present on the surfaces of the grains. In some locations, it appears that the grains have developed new terraces, suggesting that the surface energy may have been reduced due to reconstruction. AES mapping yielded very poor signal-to-noise aluminum maps with no clear correlation between the Al content and the structures observed in the SEM images. However, aluminum was clearly detected in AES data that was acquired when the Al signal was integrated while scanning 2 μm x 2 μm areas of both the 1-cycle and 5-cycle samples with higher Al signal strength for the latter sample. Interestingly, not even the nodules observed in the SEM images of the 5 cycle sample were well correlated with the aluminum AES signals (Table 5).

Figure 38(d) shows Al 2p XPS data collected for zero, 1 and 5 spin/heat cycles. The aluminum signal is evident after only 1 spin/heating cycle and becomes more intense after five cycles. In an attempt to quantify the amount of Al on the surface, an alumina film prepared by ALD on a CdTe single crystal was examined as a calibration standard. The calibration standard was prepared on the CdTe native oxide using eight water/trimethylaluminum reaction cycles, resulting in an estimated thickness of 1.0 ± 0.5 nm. [243] The Al/(Cd+Te) signal ratio determined by XPS for the sample with 1 spin-casting/heating cycle was approximately $1/10^{th}$ of that measured for the calibration standard, suggesting that the amount of Al may be considered to be present in a thickness on the order of 1 monolayer. This result, coupled with the nonuniformities observed by SEM and atomic force microscopy, indicates that the passivation effect is realized through surface chemistry reactions at specific locations on the grains of the polycrystalline film. This suggest the possibility of facet-specific passivation.

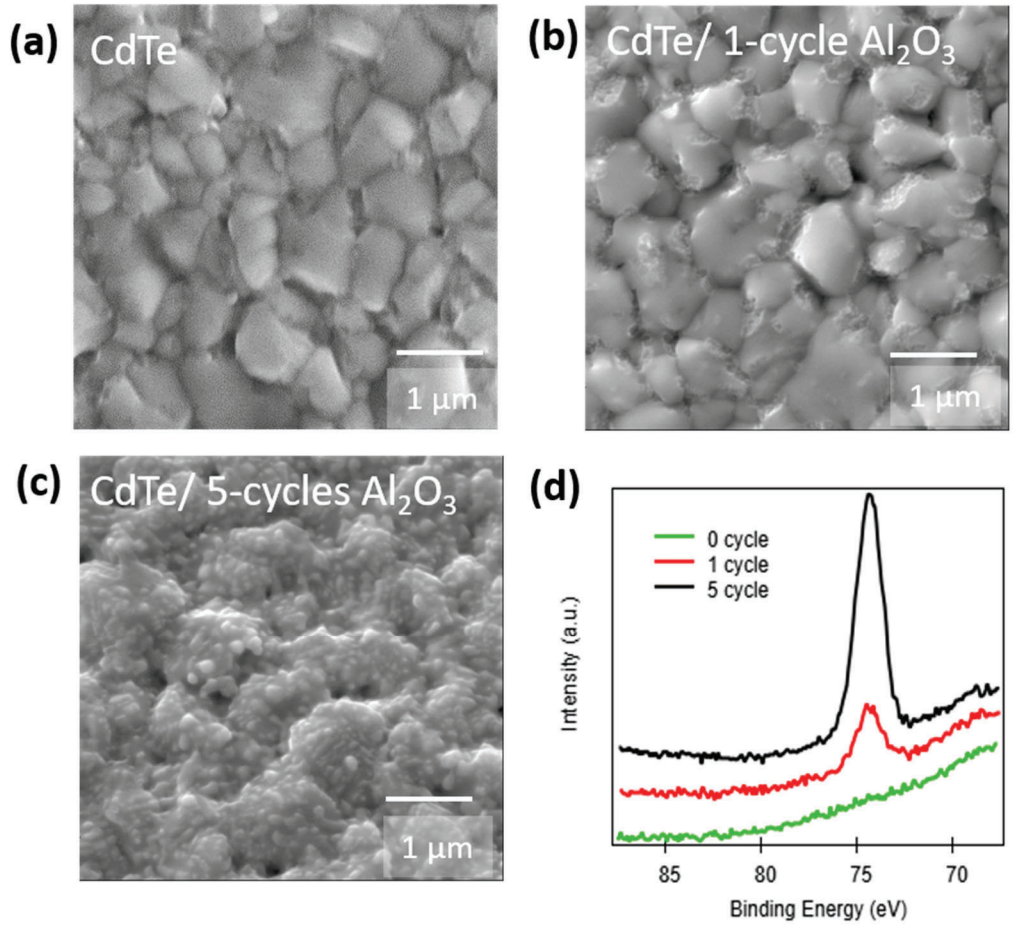


Figure 38. SEM images of CdTe surface (a) without and with (b) one or (c) five cycles of Al_2O_3 processing; (d) Al 2p XPS data without (green), with one (red) and with five (black) cycles

Maruyama and Arai produced stoichiometric Al_2O_3 films on silicon wafers by heating $Al(acac)_3$ powder to 150 ºC and introducing the entrained vapor to samples heated to temperatures between 250 and 600 ºC. [244] The films were adherent suggesting that the reaction occurred at the surface rather than in the gas phase. Our work suggests that the aluminum deposition reaction from $Al(acac)_3$ is also surface specific in the presence of polycrystalline CdTe. However, at present, due to the rough topography of the surface and the very small amounts of material involved, we have no direct evidence for the formation of Al_2O_3. Based on alignment of the spectra by setting the Te^{2-} peak to 572.4 eV, [243] the 74.3 eV binding energy for the peak rules out several possibilities including Al^0 and aluminum halides. Instead, the Al signal is consistent with Al^{3+} bonding found for several alumina oxides. [243] X-ray diffraction and infrared (IR) spectroscopy analyses were inconclusive in identifying surface Al_2O_3, even for samples made with 9 spin/heating cycles. However, when precursor layers approximately 1 µm thick were prepared on soda lime glass by blade coating and subsequently heated, infrared spectroscopy showed absorption features representative of Al_2O_3 in the range of 1000-500 cm^{-1}. [244]

In an effort to increase the PCE further, we used Cu to increase the level of p-type doping. While Cu has also been employed to reduce the height of the Schottky barrier at the back surface, the lack of roll-over in the 1 cycle Cu-free data suggested that the barrier was already low. [245] Figure 39(a) shows the J-V curves for a CdTe device with a Cu/Au back contact (3 nm evaporated Cu followed by 150 °C for 40 min in air) as compared to devices fabricated with first surface Al_2O_3 (1 cycle) and then 3 nm of Cu and 40 nm Au with Cu diffusion times (150 ºC in air) of 40, 60 and 80 minutes. After the Cu diffusion process alone (no Al_2O_3) the PCE improved from 10.4 to 12.0 % (compare Figure 37(a) and Figure 39(a), and see Table 4). Note that the performance of the devices with the optimized standard Cu/Au back contact exceeded the PCE of the devices with one Al_2O_3 cycle and no Cu (12.0 versus 11.7%, respectively). However, introducing the 3 nm of Cu on top of the 1-cycle Al_2O_3 film and employing a 40 min heating increased the best-cell PCE by a full percentage point. Extending the heating time further to 60 minutes increased the V_{OC} and the FF further without changing J_{SC}, leading to an increase of the PCE of the devices to 12.9%, and a best cell efficiency of 13.6% (Figure 39(a), Table 4).

Recent device simulations which explored the use of back buffer layers for high efficiency CdTe solar cells make it clear that a combined increase in FF and V_{OC} is one hallmark of a reduction in back surface recombination. [226] On the contrary, J_{SC} is not expected to be increased, nor should the slope of the J-V curve at zero bias change as was observed by Liang et al. [237] To further probe whether back surface passivation is indeed responsible for the improvements observed here we performed external quantum efficiency (EQE) measurements with the devices biased at their respective maximum power points (MPPs) under an AM1.5 light bias. It is most instructive to examine the wavelength-dependent carrier collection efficiency under this condition, as opposed to typical EQE measurements which are done at zero bias (short-circuit) conditions without light bias, because the energy bands in the emitter and absorber semiconductor layers will be fairly flat and poised under their normal operating condition. At MPP it is possible to examine back surface passivation effects by measuring the collection efficiency for carriers that are generated deeper in the device.

Figure 39(b) compares the data obtained at zero bias and at MPP for a device with a standard Cu/Au back contact to that obtained from a device with a 1-cycle Al_2O_3/Cu/Au back contact. Note that the zero-bias data for the two devices overlaps completely, consistent with identical J_{SC}. This result is expected since the electric field in the absorber is high at zero bias and the impact of back surface recombination should not be strongly reflected in the data.

Turning to the EQE data at the MPP, the Cu/Au contact (MPP = 650 mV) shows higher response in the short wavelength region of the spectrum (< 500 nm) presumably due to Cu compensation of donor sites in CdS window layer. [246] The absence of an increase in the short wavelength response for the 1-cycle Al_2O_3/Cu/Au (MPP- 675 mV) is consistent with the thin Al_2O_3 layer reducing Cu diffusion into the CdS. In the long wavelength portion of the spectrum (> 500 nm), the Cu/Au contact shows a reduction in the carrier collection efficiency. This is due to the downward band bending at the back surface, which causes minority carrier electrons that are generated nearby to be attracted to the back surface where they will more efficiently recombine.

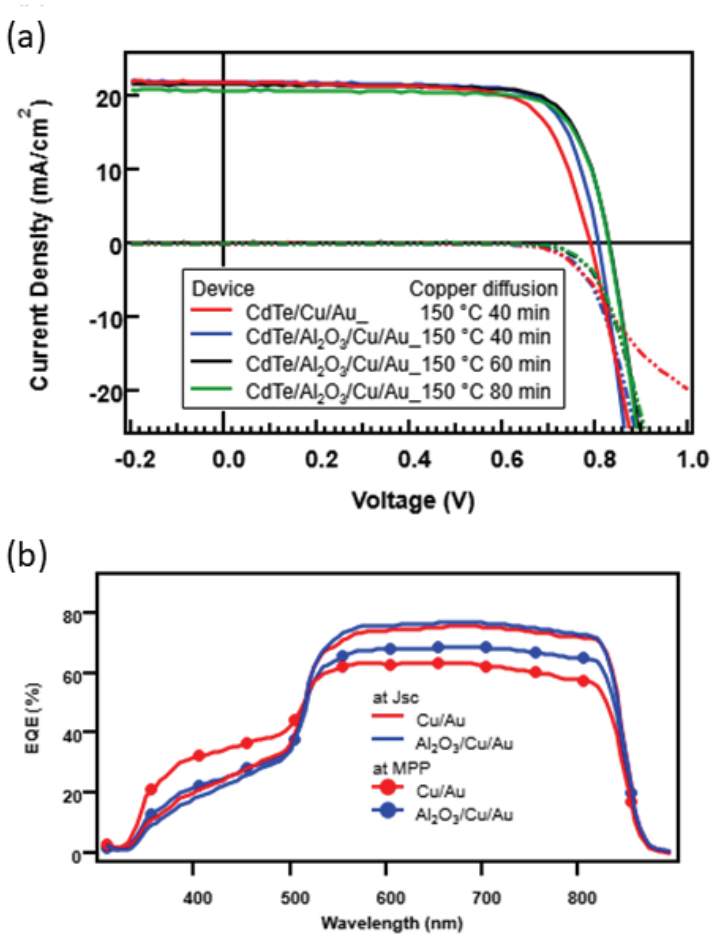


Figure 39. (a) JV data of CdTe devices, varied back contacts; (b) EQE results for short circuit and maximum power point bias

In contrast, the 1-cycle Al_2O_3/Cu/Au sample shows a long wavelength response that has the same spectral dependence (i.e. slope) as does the zero-bias data. The reduction in the EQE that is constant with wavelength in comparison to the zero-bias data is a reflection of the fact the Shockley-Read-Hall contribution to the overall recombination is larger throughout the device when the bands are flatter, as is the case at MPP. However, the fact that the spectral dependence of the EQE is the same as in the zero-bias data, where the internal field is much larger, indicates that the carriers generated throughout the device, regardless of depth, have a similar probability of being collected. Consequently, we can conclude that back-surface recombination has been measurably reduced.

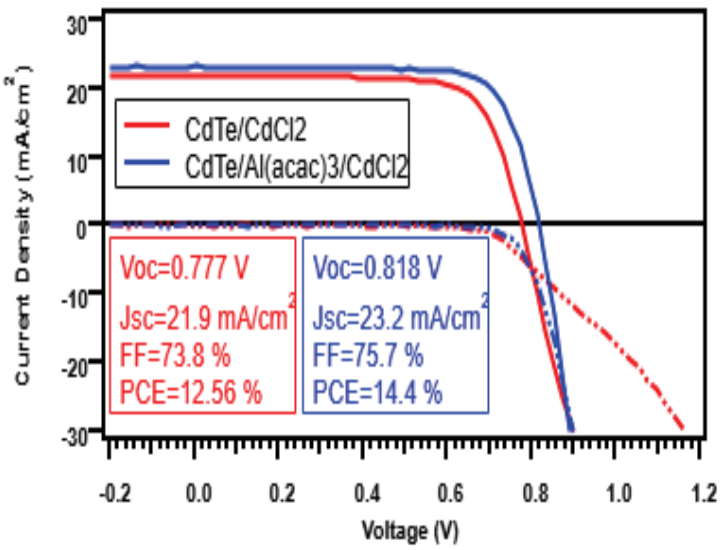
A final set of experiments demonstrated that the process could be considerably simplified. In this case, the $Al(acac)_3$ solution was first pipetted and spun onto the as-grown CdTe device stack and then the $CdCl_2$ treatment was performed. The only high temperature treatment was that used for the standard $CdCl_2$ process (387 °C for 30 min, in air). After the $CdCl_2$ treatment the Cu/Au back contact was formed as described above (with heating in air for 40 min for both samples). Table 5 shows the measured JV parameters for these $CdCl_2$/Cu/Au and $Al(AcAc)_2/CdCl_2$/Cu/Au devices.

Note that these devices stacks came from a different production run, which introduced slight differences in performance from the previous data sets. The device results were similar to those found for the single spin/heat cycle, but the performance was improved to higher values. The average V_{OC} for the sample set increased from 0.784±0.006 mV to 0.817±0.007 mV, while the FF increased from 70.6±1.5 to 76.4±1.1 and the average PCE increased from 12.0±0.3% to 13.8±0.4%. Figure 40(a) shows the J-V curves for the best performing devices of each type, while Figure 40(b) shows the SEM of the CdTe surface after the $Al(acac)_3/CdCl_2$ processing. In this data set there was a statistically significant increase in short circuit current which could be due to differences in the degree of Cu compensation.

Table 5. J-V parameters for best devices (PCE), with and without 1 cycle of Al_2O_3 followed by $CdCl_2$ activation, standard Cu/Au back contact

Device		V_{OC} (V)	J_{SC} (mA/cm^2)	FF (%)	PCE (%)
CdTe/$CdCl_2$/Cu/Au	Average	0.784±0.006	21.7±0.2	70.6±1.5	12.0±0.3
	Best	0.777	21.9	73.8	12.6
CdTe/Al_2O_3 (1 cycle) /$CdCl_2$/Cu/Au	Average	0.818±0.007	22.1 ±0.1	76.4±1.5	13.8±0.4
	Best	0.818	23.2	75.7	14.4

(a)



(b)

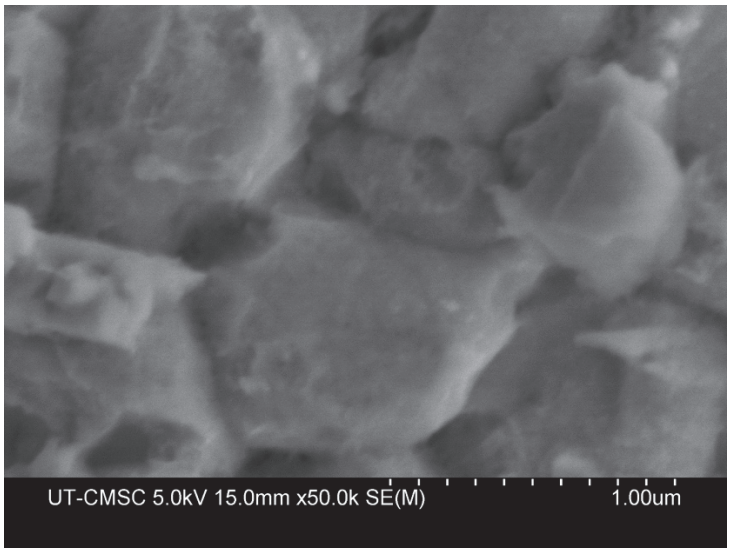


Figure 40. (a) JV data, CdTe devices with varied back contacts; (b) SEM image, CdTe surface with $Al(acac)_3/CdCl_2$

8.5 CONCLUSION

We developed a solution-based process that deposits very small amounts of oxidized aluminum (Al^{3+}) species onto the back surface of CdTe device stacks to produce increased V_{OC}, FF, and PCE in finished devices. The binding mechanisms for the Al^{3+} species appear to be site-specific and the device performance was optimized when the amount deposited corresponded to ~1 monolayer.

Time-resolved photoluminescence spectroscopy on the back surface and quantum efficiency measurements performed at the maximum power point support the conclusion that interface recombination at the back surface was reduced by back surface passivation. The mechanism is unclear at the present time, but the results could be due to either the reduction of band bending or the elimination of surface states. Further work in our laboratory will be directed toward discriminating between these two possibilities, understanding the surface chemistry in more detail, and applying the new approach to higher efficiency devices.

9. SOLUTION BASED CU-DOPED ALUMINUM OXIDE AS A BACK INTERFACE LAYER FOR CDTE SOLAR CELLS

Authors Contribution: Kamala Khanal Subedi, Adam B. Phillips, Niraj Shrestha, Indra Subedi, Zhaoning Song, Ebin Bastola, Yanfa Yan, Nikolas J. Podraza, Michael J. Heben, and Randy J. Ellingson

9.1 SUMMARY

Developing a high-quality back contact layer is the key components for achieving high efficiency II-VI polycrystalline devices. Here, we report CdS/CdTe/CuAlOx/Au device structure to increase the open circuit voltage (V_{OC}) and fill factor (*FF)*. We fabricate and characterize Cu doped aluminum oxide ($CuAlO_x$) and use as a passivating layer to CdTe based thin film solar cells by using the solution-based technique. The chemicals were analyzed by using the thermogravimetric analysis (TGA) and residual gas analyzer (RGA) technique to find out the suitable temperature for annealing. The films with ~ 10 nm thickness are highly transparent on the visible and near infrared region. Films are deposited on the CdTe polycrystalline stack by using the solution based (spin coating) process at 220˚C for 15 mins. CdTe device with this passivation layers were studied by using the steady state photoluminescence and time resolved photoluminescence to see the minority carrier lifetime increment. Our study shows that with the incorporation of the $CuAlO_x$/Au as standard back contact layer by improving both fill factor (*FF*) and open circuit voltage (V_{OC}) of the solar cells in comparison to the control sample (CdTe/Au) by making initial fermi level offset positive between CdTe and the back buffer layers. This improvement is consistent with the increment of the mean lifetime from 0.8 ns to 2.6 ns through the contact side illumination and from 4.3 ns to 37.6 ns from the glass side illumination of the CdTe devices with the inclusion of the $CuAlO_x$. These improvements show the passivation effect on the CdTe.

9.2 INTRODUCTION

Nowadays, CdTe solar cells are gathering remarkable attention due to the substantial improvement of device efficiency up to 22.5 %. [247] Efficiency improvements require reduced defects at the front interface, rear interface, in the bulk of the absorber, and at grain boundaries. Open circuit voltage (V_{OC}) is mainly limited by the rear interface defects, [248] and proper passivation of the rear interface could help to improve the V_{OC} and Fill Factor (*FF*). Previous modeling suggested that appropriate doping and lifetime increment are also essential for improvement of the V_{OC}. [180, 249, 250] Recently, Liyanage *et al.* employed numerical modeling to investigate the roll of a buffer layer for > 25% CdTe device efficiencies. They found the initial Fermi level offset should be positive to reduce the back surface recombination between the absorber and back contact buffer layers, which can be controlled by changing the doping density of the back buffer layer. [226]

The high work function of CdTe (~5.7 eV) materials, in comparison with metals, yields the rollover effect in forward bias, significantly curbing device performance. [251, 252] Commonly, CdTe solar cells employ Cu-containing back contact materials like ZnTe:Cu, [188] $(CuS)_x(ZnS)_{1-x}$, [253, 254] $BaCu_4S_3$, [255] and Cu-Al_2O_3. [256] With the incorporation of these back contact layers shows the reasonable device performance. However, these back contacts do not work effectively as required

which could be due to the downward band bending between the CdTe and back buffer interface, and interface recombination dominates the device performance.

Recently we showed that $CuAlO_x$ allows for high efficiency bifacial CdTe device. The ternary oxide $CuAlO_x$ is natural p-type, wide bandgap conductive semiconductor. [257] Our device shows the current density (J_{SC}) and fill factor (FF) is independent of thickness which means band bending at the back does not change with the bias. $CuAlO_x$ creates the upward band bending so it reduces the recombination at the back and helps to increase the device performance. This would be important for the thinner devices through the front side illumination because the depletion region is close to the front. It helps electron to repel and improve the device performance.

In this section, we report on the solution based $CuAlO_x$ back contact layer applied as the back contact layer for CdS/CdTe solar cells. The chemicals were analyzed by using thermal gravimetric analysis (TGA) and residual gas analyzer (RGA) measurement to find out the suitable annealing temperature for the formation of Al_2O_3. Usually, Al oxidizes at a higher temperature but our result shows that we could make Al oxide temperature below than 300˚C. [258] Different Cu concentration is doped into Al_2O_3 solution and applying them as a buffer layer for CdTe thin film devices. The optical properties of $CuAlO_x$ films are characterized by using UV-Vis NIR spectroscopy and spectroscopic ellipsometry. Completed devices are characterized by using scanning electron microscopy (SEM), steady state (low temperature, room temperature) photoluminescence (PL), and time resolved photoluminescence (TRPL). SCAPS simulation is done to understand the device performance from the glass side illumination Here we demonstrate that CdS/CdTe thin film solar cells with $CuAlO_x$ buffer layer to improve the minority carrier lifetime, V_{OC}, *FF,* and efficiency (η). Our CdTe thin films with Al_2O_3 (2% Cu) increase the minority carrier form 0.8 ns to 2.6 ns and 4.3 ns to 37.6 ns from the film side and glass side illumination respectively. Our best device performance is obtained when we used Al_2O_3 (30% Cu) as a buffer layer with V_{OC} = 836 mV, *FF* = 78%, and η = 14.5% which is 9% higher than the devices completed with 3 nm Cu (metal)/ Au back contact and 5% higher than the devices doped with $CuCl_2$ solution-based process/Au.

9.3 METHODS, ASSUMPTIONS, and PROCEDURES

Aluminum nitrate nonahydrate ($AlH_{18}N_3O_{18}$, 98%), copper (II) nitrate trihydrate ($CuH_6N_2O_9$, 99%), and 2-methoxyethanol ($C_3H_8O_2$) were bought from the Fisher Scientific. Aluminum nitrate nonahydrate and copper (II) nitrate trihydrate were stored in the glove box within a nitrogen environment, to improve stability.

Soda lime glass substrates were ultrasonically cleaned using detergent and deionized water (DIW) for 30 mins, rinsed several times with DIW, cleaned in methanol for 15 mins, rinsed again by acetone, and finally by DIW before drying the substrate using dry N_2 in the air.

To make the $CuAlO_x$ precursor solution, 0.04 M aluminum nitrate nonahydrate and 0.04 M copper nitrate trihydrate in 5 ml of 2-methoxyethanol. The resultant solution was stirred at 200 rpm for 5 mins at the room temperature. The final precursor will be turned into bluish. 50 µl $CuAlO_x$ was spin-coated with a rotating speed of 1000 rpm for 10 s and followed the high rotating speed of 3500 rpm for the 50s and annealed at 220ºC for 15 mins.

Unpolarized transmittance and reflectance spectra were measured by a PerkinElmer Lambda 1050 UV/Vis/NIR spectrophotometer. Room temperature ellipsometric spectra (in N = cos 2Ψ, C = sin 2Ψ cos Δ, and S = sin 2Ψ sin Δ) of $CuAlO_X$ film were collected ex situ at 50°, 60º, and 70º angle of incidence using a single rotating compensator multichannel ellipsometer [259, 260] having a spectral range from 0.735 to 5.887 eV (M-2000FI, J. A. Woollam Co.).

For the solar cell film stack, CdS (120 nm) and CdTe (3µm) layers were deposited by commercial vapor transport deposition (VTD) onto TEC^{TM}-15 glass substrates by the Willard and Kelsey Solar Group. The CdS/CdTe filmstack was treated with a saturated $CdCl_2$ solution in methanol, and the devices were annealed at 387 °C for 30 mins in dry air. This treatment helps to advance grain growth, release interfacial strain, and facilitate intermixing at the CdS/ CdTe region. $CuAlO_X$ were deposited by the spin coating method and the spin coating procedure for the device was the same as making a film on the glass substrate. Finally, 40 nm gold was thermally evaporated to complete the back contact layer.

Here we compared our device performance with the $CuCl_2$ treated and 3 nm Cu evaporated sample respectively. $CuCl_2$ treatment done on $CdCl_2$ operated CdTe device submerged in 0.1mM $CuCl_2$ solution with 24.6 ml DIW and leave it for 2 mins and rinse it thoroughly by the DIW. The $CuCl_2$ treatment carried at 200˚C for 20 mins, and the device was completed with 40 nm thermally evaporated gold. Note that this Cu doping process using solution based method is followed Bastola et al., without further optimization. [208] For thermally evaporated Cu, after deposition of 3 nm Cu followed by annealing at 150˚C for 35 mins to diffuse Cu. For both samples, 40 nm Au is thermally evaporated. Finally, the devices were scribed using 532 nm to define an array of approximately 30 cells, each with active device area 0.06 cm^2. The schematic diagram of the CdS/CdTe solar cells using $CuAlO_x$ back buffer layer is shown in Figure 41.

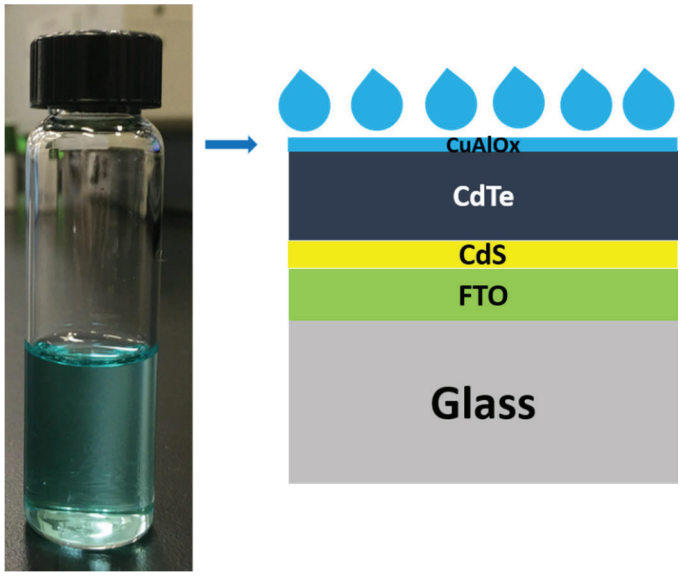


Figure 41. Schematic diagram of CdS/CdTe solar cell devices with CuAlOx as a back buffer layer

9.4 RESULTS and DISCUSSION

To determine suitable air-annealing temperature and decomposition analysis of Al_2O_3, the powder chemical aluminum nitrate nonahydrate (aluminum source) was subjected to TGA and RGA measurement. Figure 42(a) is representing the TGA measurement, and Figure 42(b) is the RGA measurement of the aluminum nitrate nonahydrate. From TGA curve, the weight loss regime before 200 ºC is very rapid and after 200 ºC, the weight loss is relatively slower because the chemicals are completely decomposing. The remaining weight % is equal to the Al_2O_3. For the further confirmation the chemicals as subjected to the RGA measurement. The chemical is completely decomposing into water (H_2O), nitric oxide (NO), nitrogen dioxide (NO_2), Nitrogen molecule (N_2), and elemental Nitrogen (N) which is shown in Figure 41(b). The decomposition is completely done until 200 ºC. Here, 2- methoxyethanol is used as a solvent and at around 210ºC solvent and other organic additives start to evaporate. [261] Therefore, the air annealing temperature is set to 220 ºC.

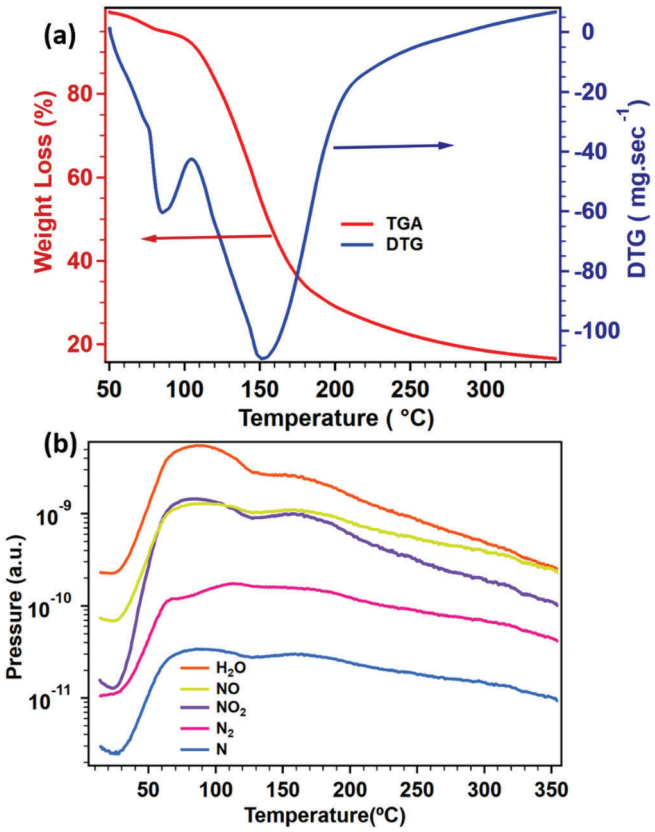


Figure 42. (a) Thermogravimetric analysis (b) decomposition profile of aluminum nitrate nonahydrate (aluminum source) chemical

Determination of the optical response of thin film $CuAlO_x$, in the form of the energy-dependent complex refractive index, $N(E) = n(E) + ik(E)$, spectra enables assessment of optical properties related to the PV devices. The transmittance and the band gap of $CuAlO_x$ is shown in the Figure 43(a, b). The band gap of $CuAlO_x$ is 3.6 eV calculated from the Tauc plot (Figure 43(c)) by

using absorption coefficient from SE analysis. Kawazoe et al. and Li et al. find the bandgap of $CuAlO_2$ is 3.5 eV [261] and 3.6 eV [262] respectively, our $CuAlO_x$ bandgap agree well with those reported literature. Figure 43(d) is the plot of refractive index (*n*) and extinction coefficient (*k*) with respect to the energy. The bulk thickness of $CuAlO_x$ films obtained from SE analysis is ~10 nm, which is in close agreement with previous reported value. [262] Note that the solution concentration is 4 times higher when we make standalone films in comparison to film in devices. Therefore, the thickness of $CuAlO_x$ on the devices is ~2.5 nm.

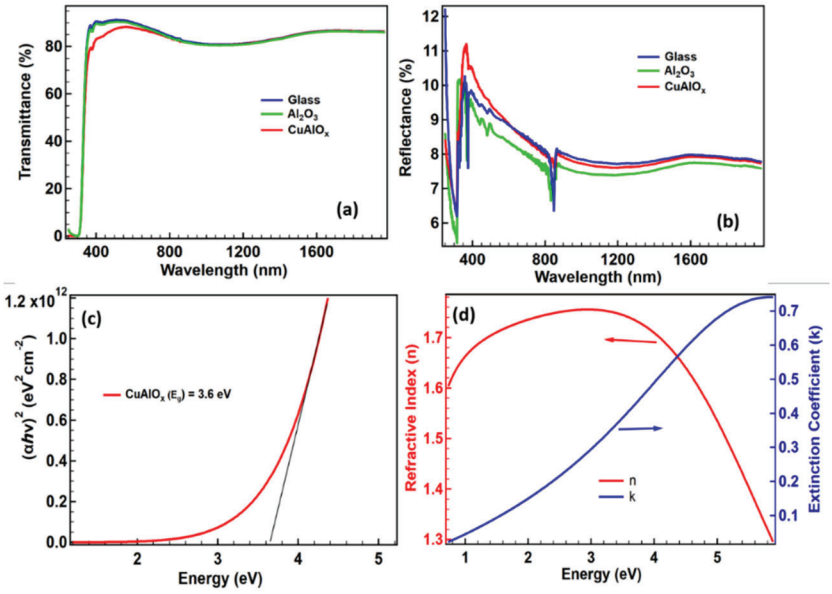


Figure 43. (a) Transmittance and (b) reflectance spectra; (c) Tauc plot from SE data; (d) *n* and *k* spectra for CuAlOx, SE data

Figure 44(a) represents the surface morphology of $CdCl_2$ treated CdTe films, Figure 44(b) represents the Al_2O_3 thin films on the CdTe surface which changes the grain morphology and grain boundaries and it made CdTe some insulating nature but, after $CuAlO_x$ the surface of the CdTe is changed into grain morphology and also the grain boundary which shows the passivating effect of $CuAlO_x$ on the CdTe thin films as shown in Figure 44(c). Furthermore, we cannot see those insulating nature after $CuAlO_x$ on the surface.

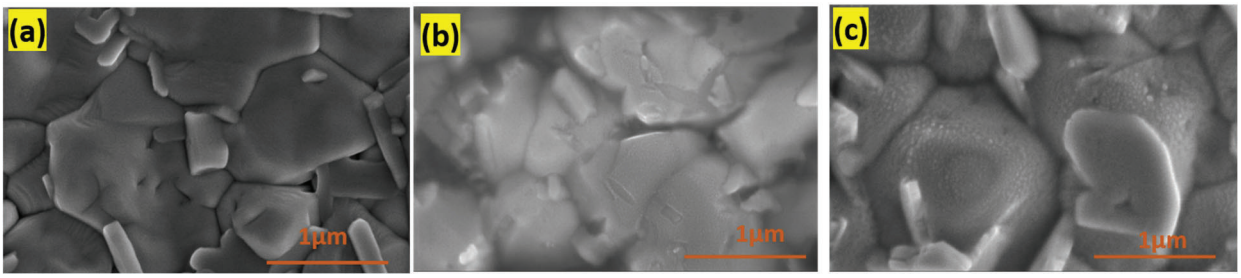


Figure 44. Surface morphology of (a) CdTe (b) CdTe/ Al_2O_3, and (c) CdTe/ CuAlOx

For the annealing time optimization, the TRPL measurement is done on the CdTe films after putting the Al_2O_3 films on the CdTe. The annealing temperature for Al_2O_3 was set to 200 ºC, 210 ºC, 220 ºC, 230 ºC, and 250 ºC for 15 mins. The laser was excited through the film side illumination and at 220 ºC the minority carrier lifetime is high from the film side that is shown in Figure 45. The bulk lifetime (τ_2) is increases to 4.6 ns where the standard samples has the bulk lifetime 1.1 ns from the film side illumination. Therefore, we fixed the annealing temperature at 220 ºC for the deposition process of Al_2O_3.

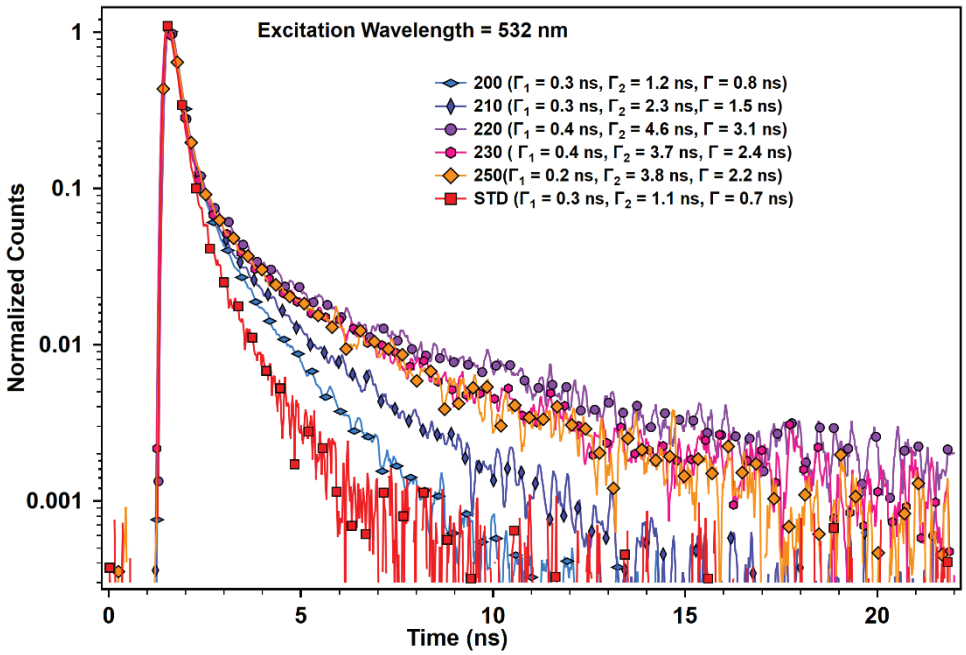


Figure 45. TRPL data for CdTe devices with Al_2O_3 at different annealing temperature, film side illumination by 532 nm laser

To get insight into the relationship between increment of lifetime and the devices performance, devices were completed with CdS/CdTe/Al_2O_3/Au structure. The devices show better performance in comparison to the CdS/CdTe/Au, exhibited remarkable improvements in V_{OC}. The best-performing CdS/CdTe/Al_2O_3/Au cell shows an efficiency 12.1% with V_{OC} = 801 mV, FF= 67.5%, J_{SC} = 22.3 mA/cm^2. In contrast, the best performing CdS/CdTe/Au cell show an efficiency 10.4% with Voc = 715 mV, J_{SC} = 22.3 mA/cm^2, FF = 66.6%. The overall efficiency is increased from 10.4% to 12.1% with relative 16.3 % improvement. The average device performance with standard deviation is shown in Table 6.

If we compare the device with CdS/CdTe/3nm Cu (metal)/Au and CdS/CdTe/Cu (solution)/Au the device performance is low which could be due to the insulating nature of Al_2O_3. We doped the Al_2O_3 precursor solution with 1%, 2%, 5%, 10%, 30%, and 50% of Cu. From Figure 46(a, b), the JV curve shows some rollover effect until 10% of Cu doping on Al_2O_3 after 30% of Cu doping the rollover effect is gone and the crossover effect is also very weak. The annealing temperature was fixed at 220 ºC for 15 mins for all the devices. The average value J-V parameter along with standard deviation is shown in Table 6. The device with Al_2O_3 with 30% of Cu doping shows the superior performance among all composition of passivating back contact. The passivating layer Al_2O_3

(30% Cu) as a back contact with CdTe could make the p + p model with p-type (CdTe) + p-type (Cu-Al_2O_3). [256, 263] The champion cell with Al_2O_3 (30% Cu) show the η =14.4% with V_{OC} = 834 mV, FF = 77.3%, and J_{SC} = 22.4 mA/cm^2 the improvement of FF and Voc is consistent with the decrease in series resistance (R_S) and increment of shunt resistance (R_{SH}). These devices performance was also higher than the devices doped with 3 nm evaporated Cu and with the devices doped with $CuCl_2$. The best cells of the standard device with evaporated metal Cu have η=13.2% with V_{OC} = 818 mV, FF = 74.0%, and J_{SC} = 21.8 mA/cm^2 and Cu doped with solution process have η =13.8% with V_{OC} = 829 mV, FF = 76.2 %, and J_{SC} = 21.8 mA/cm^2. The relative improvement is 9% with Cu metal and 4% with solution Cu. In comparison to the pronounced variation in V_{OC} and FF with and without $CuAlO_x$ passivating layer, J_{SC} variation is insignificant.

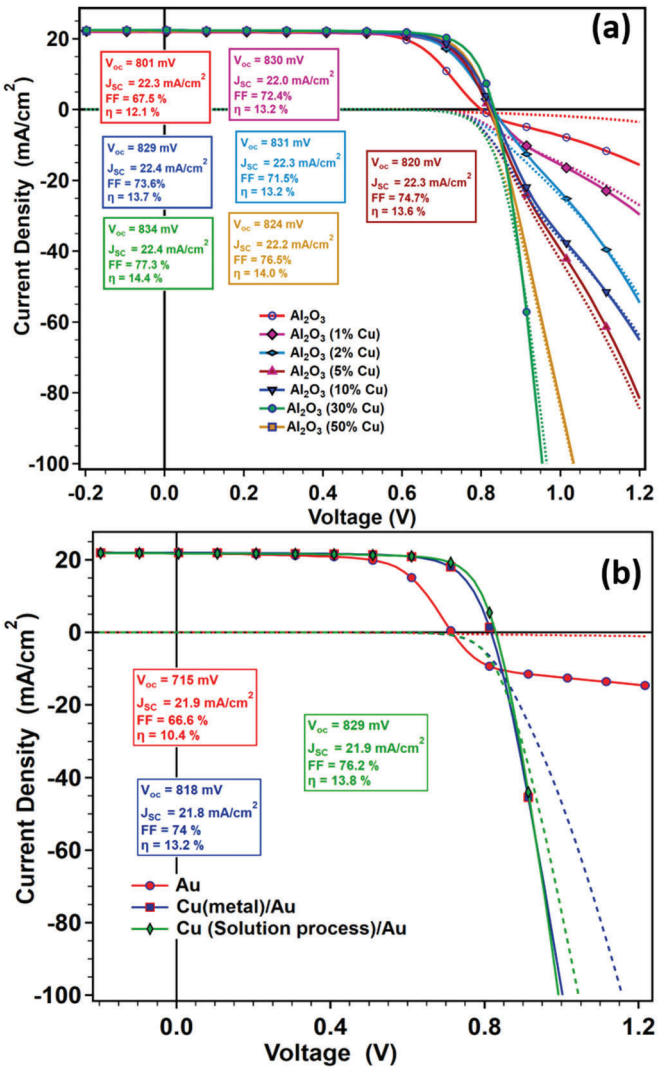


Figure 46. (a) J -V characteristics of CdS/CdTe/Al_2O_3 vs. Cu concentration; (b) control device data, various back contacts

Table 6. JV parameters, including Al_2O_3 with varied Cu concentration (active device area = 0.06 cm^2), and including standard back contact values

Cu Concentration	V_{OC} (mV)	J_{SC} (mA/cm^2)	*FF* (%)	η (%)	R_S (Ω cm^2)	R_{sh} (Ω cm^2)
0 %	790 ± 9	22.2 ± 0.1	67.0 ± 1.3	11.8 ± 0.3	23.2 ± 11.0	3511 ± 815
1% Cu	827 ± 3	21.6 ± 0.3	71.3 ± 1.5	12.8 ± 0.3	6.3 ± 0.4	2506 ± 513
2% Cu	832 ± 2	22.2 ± 0.2	68.2 ± 2.0	12.6 ± 0.4	12.1 ± 4.9	2041 ± 338
5% Cu	820 ± 5	21.8 ± 0.2	73.4 ± 1.0	13.1 ± 0.3	4.5 ± 0.6	2890 ± 342
10% Cu	822 ± 4	22.1 ± 0.4	73.2 ± 0.6	13.3 ± 0.3	4.2 ± 0.5	3191 ± 290
30% Cu	831 ± 3	22.2 ± 0.2	75.8 ± 1.6	14.0 ± 0.4	3.1 ± 0.9	4945 ± 600
50% Cu	819 ± 4	22.0 ± 0.2	75.6 ± 0.5	13.6 ± 0.3	2.5 ± 0.5	3861 ± 500
Au	718 ± 10	21.5 ± 0.2	64.8 ± 1.5	10.0 ± 0.3	8.9 ± 4.7	872 ± 230
Cu(metal)/Au	809 ± 4	21.8 ± 0.2	72.7 ± 2.3	12.8 ± 0.4	2.8 ± 0.9	3132 ± 632
Cu (Solution)/Au	827 ± 2	21.7 ± 0.3	75.2 ± 1.1	13.5 ± 0.3	2.3 ± 0.4	3407 ± 605

PL and TRPL measurements (Figure 47(a-d)) are performed on the devices with Al_2O_3 passivating layer and with devices completed with Al_2O_3 with 1%, 2%, 5%, 10%, 30%, and 50% of Cu doping. Figure 45 shows the PL and TRPL measurement of the devices completed with Al_2O_3 (2% Cu), Al_2O_3 (30% Cu), and standard devices. CdTe films with Al_2O_3 (2% Cu) shows the highest PL intensity and the higher minority carrier lifetime from both film side and glass side illumination. The PL intensity of the films with other composition also shows better intensity and lifetime in comparison with standard CdTe film except than the devices completed with Al_2O_3 (50% Cu) from the film side illumination. The mean lifetime is increased from 0.8 ns to 2.6 ns with Al_2O_3 (2% Cu) and 1.9 ns with Al_2O_3 (30% Cu) which is shown in Figure 47(c). In case of glass side illumination, the PL intensity improvement is consistent with Al_2O_3 (2% Cu) passivating interface layer and the mean lifetime is increased from 4.3 ns to 37.6 ns. With Al_2O_3 (30% Cu) the minority mean lifetime is reached to 32.6 ns which is shown in Figure 47(b, d).

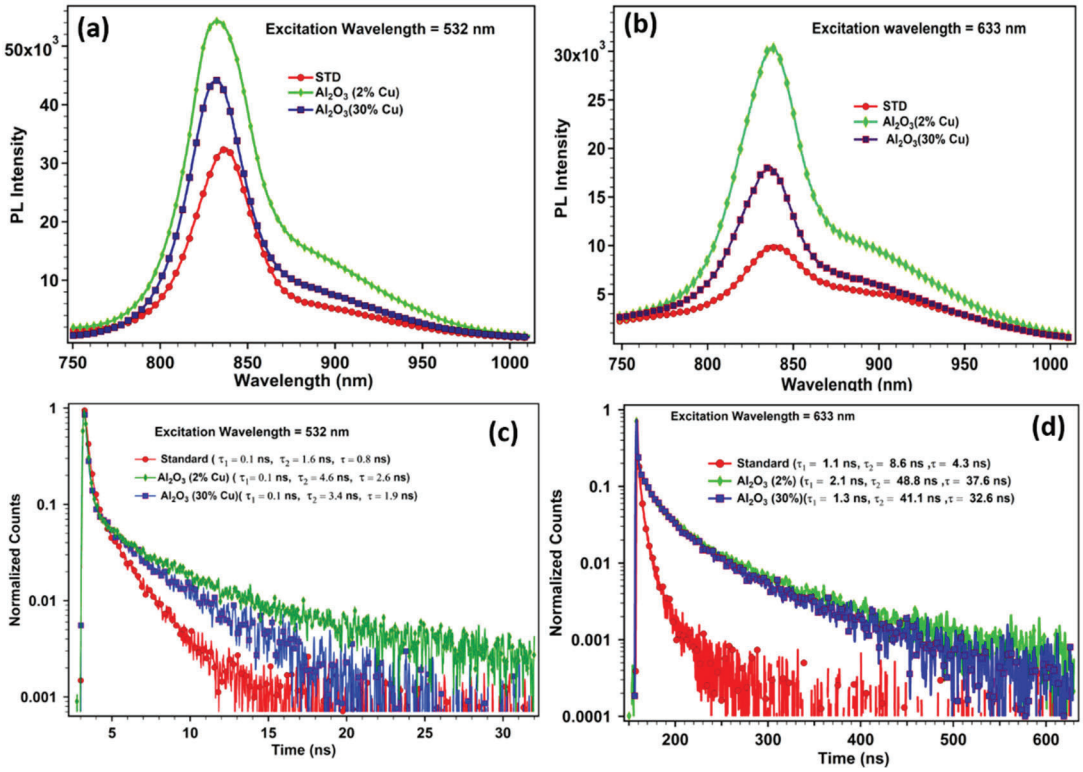


Figure 47. Steady state PL spectra and TRPL decays of CdTe devices with Al_2O_3 and varied Cu concentrations: (a) film side PL, (b) glass side PL; (c) film side TRPL; (d) glass side TRPL

Since the optoelectronic properties of the CdS/CdTe film are influenced by the presence of native defects, we have performed low temperature PL measurement on these devices to identify the type of defects associated with them. Figure 48(a, b) represent the low temperature PL measurement of standard CdS/CdTe and CdS/CdTe/Al_2O_3(30% Cu) respectively with cumulative fit of Gaussians (solid blue curves) have been fit to the observed defect peaks. After Al_2O_3(30% Cu) deposition the most prominent peaks at 1.375 eV, and shoulder peak at 1.368 eV is due to the deep defect assisted transitions [264] and 1.454 eV DAP peak (a DAP peak results due to the recombination of Cl donor to Cu_{Cd} acceptor) [265, 266], we observed on both standard CdTe thin films and with CdTe/ Al_2O_3(30% Cu) which could be due to the some presence of Cu impurities on the CdTe source. Since Cu_{Cd} has lower formation energy than any other type of defects so here 1.454 eV DAP peak however, we cannot ignore the Cu diffusion through grain boundaries into Cd vacancy site. From Figure 46(c) not much change in the PL intensity of 1.454 eV DAP peak which could indicate after the post annealing treatment Cu-Al_2O_3 makes the strong bond and effectively controlled Cu diffusion through CdTe. The higher energy peak at 1.594 eV and 1.550 eV are the free excitonic peak and DAP (recombination of some donor state to V_{Cd} acceptor) respectively. With Al_2O_3(30% Cu) deposition the peak at 1.572 eV is become more dominant, it is the convolution shallow bound exciton peak and the free electron LO peak, these features are mostly seen in high quality CdTe. [235]

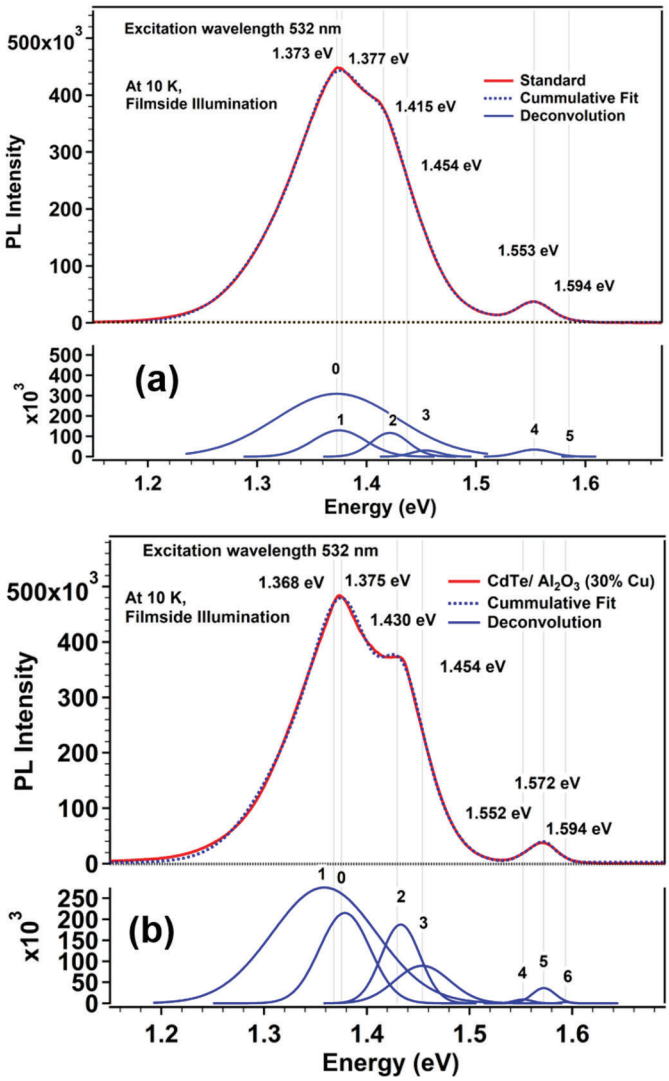


Figure 48. PL spectra of CdS/CdTe film (a) standard and (b) CdS/CdTe/Al_2O_3(30 % Cu). Gaussian fits shown as solid blue curves; dotted curve represents the fit sum

To further understand the role of the post annealing temperature on the performance of CdS/CdTe/Cu*x*AlO*y* (x = 30%) solar cells, devices were subjected to the different post annealing time at 220 ºC. The best efficiency cells of the devices annealed at different time is shown in Figure 49.

Table 7 summarizes the average device performance of the 20-25 cells with their standard deviation. The devices annealed at 15 mins shows the best average device performance, however the devices with 3 mins post annealing treatment shows the device efficiency 14.0% with V_{OC} = 805, *FF*, 77.2%, and J_{SC} = 22.6 mA/cm^2. Here the higher *FF* > 77% for all the annealing time is concur with the higher shunt resistance and lower series resistance. [267] Here we have observed very small variation on the device performance from 3 mins to 18 mins this also support the formation of Cu-Al-O after 3 mins of annealing. [268, 269] From Figure 42 and Table 6, the device completed with CuAlOx shows really high *FF* because there is no change in the band bending, which makes all the recombination due to the flat band and either interface limited with CdS or SRH. Whereas the $CuCl_2$ treated device shows relatively lower FF because it is turning on as the band bending at the back of the device due to the bias voltage. [270] Figure 50(a-d) shows JV results for CdTe devices using either Al_2O_3(2% Cu) or Al_2O_3(50% Cu) as a passivating interface layer on CdS/CdTe solar cells.

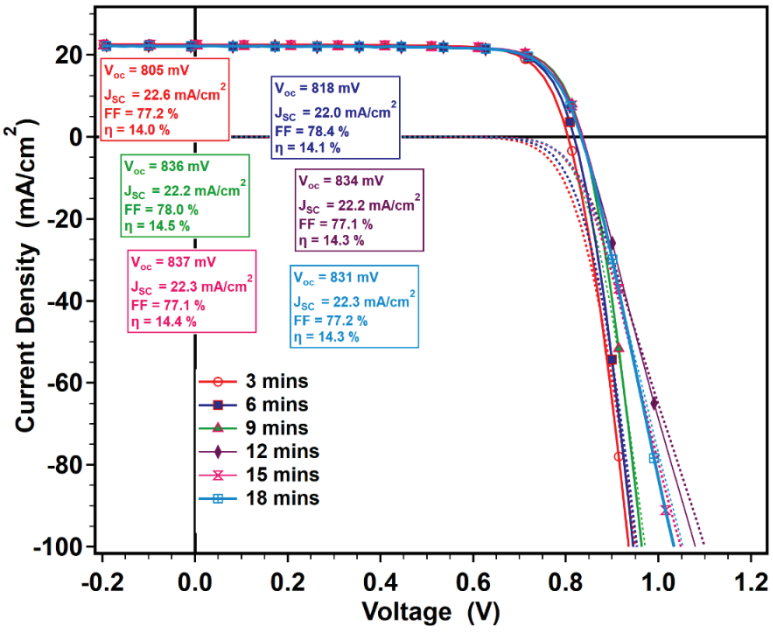


Figure 49. JV results for CdS/CdTe sample with Al_2O_3 (30% Cu)

Table 7. JV parameters for CdTe solar cells with Al_2O_3(30% Cu) back buffer layer, varied annealing times

Annealing Time	V_{OC} (mV)	J_{SC} (mA/cm^2)	*FF* (%)	η (%)	R_S (Ω cm^2)	R_{sh} (Ω cm^2)
3 mins	803 ± 3	21.9 ± 0.4	76.2 ± 1.7	13.4 ± 0.5	3.3 ± 1.0	3753 ± 780
6 mins	818 ± 2	21.9 ± 0.4	76.2± 1.1	13.8 ± 0.2	3.3 ± 0.9	7680 ± 890
9 mins	832 ± 3	22.2 ± 0.2	76.2± 1.1	13.9 ± 0.3	2.4 ± 0.7	4464 ± 593
12 mins	832 ± 3	21.9 ± 0.5	76.3 ± 0.7	13.9 ± 0.2	2.6 ± 0.4	5560 ± 580
15 mins	832 ± 4	21.9 ± 0.4	76.4 ± 0.6	14.0 ± 0.4	2.3 ± 1.1	3514 ± 1154
18 mins	830 ± 4	22.6 ± 0.4	75.8 ± 1.4	14.1 ± 0.3	2.3 ± 0.2	5589 ± 600

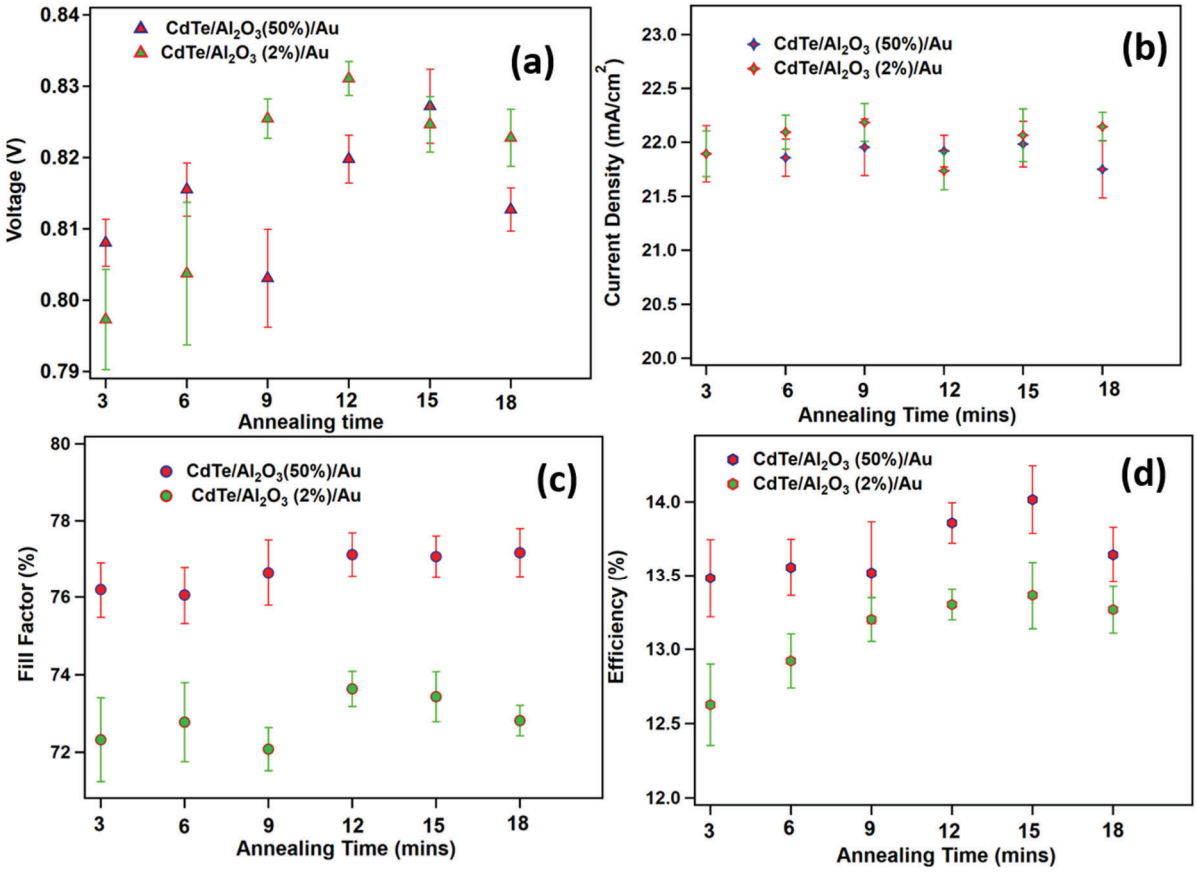


Figure 50. Statistical results of solar cell performance for Al_2O_3(2% Cu), Al_2O_3(50% Cu) as a passivating interface layer on CdS/CdTe solar cells

Since the devices with Al_2O_3 (2%) shows the best PL intensity and $CuAlO_x$ shows the impressive device performance at 220 ºC for 15 mins of annealing temperature, the device performance of the devices at different annealing time is observed. The statistical results of solar cell for CdTe/

Al_2O_3(2%)/Au and CdTe/ Al_2O_3(50% Cu) /Au is shown in Figure 48. The devices completed with CdTe/ Al_2O_3(50% Cu) /Au shows better device performance with very impressive *FF* and V_{OC} increment so overall device performance is increases where there is no such increment on the current density Al_2O_3(2%)/Au and Al_2O_3(50% Cu) with passivating interface layer. Here even though we did post annealing treatment from 3 mins to 18 mins at 3 mins interval after depositing passivating interface layer, the devices performance is very subtle. This could be due to 2% Cu doped on Al_2O_3 could not help to change the insulating nature of the Al_2O_3. Using Al_2O_3(50% Cu) as passivating layer could help to minimize the insulating nature of the Al_2O_3 so the roll over effect is minimized and device performed very nicely with the significant improvement on FF.

With the inclusion of $CuAlO_x$ lifetime is increases significantly but the device performance is limited to ~15%. The limitation of the device performance could be due to the front interface of the device. To understand the relationships between the front surface recombination velocity and lifetime SCAPS simulation [271] is done from the FSRV 1E+4 to 1E+6 and the lifetime is varied from 0.1 ns to 100 ns (Figure 51). The modeling parameters are obtained from previous models. [226, 248, 270, 272, 273] From our experimental results, our device performance is lies in 1E+5, at this condition device performance close to saturation level at lifetime 10 ns. When lifetime is increased from 10 ns to 100 ns, the device performance is only changed from 14.3% to 14.7%. Our experimental results agree well with the SCAPS simulation results. This result helps us to conclude that even though we have good back buffer layer with great lifetime, device performance can be limited by the front surface interface.

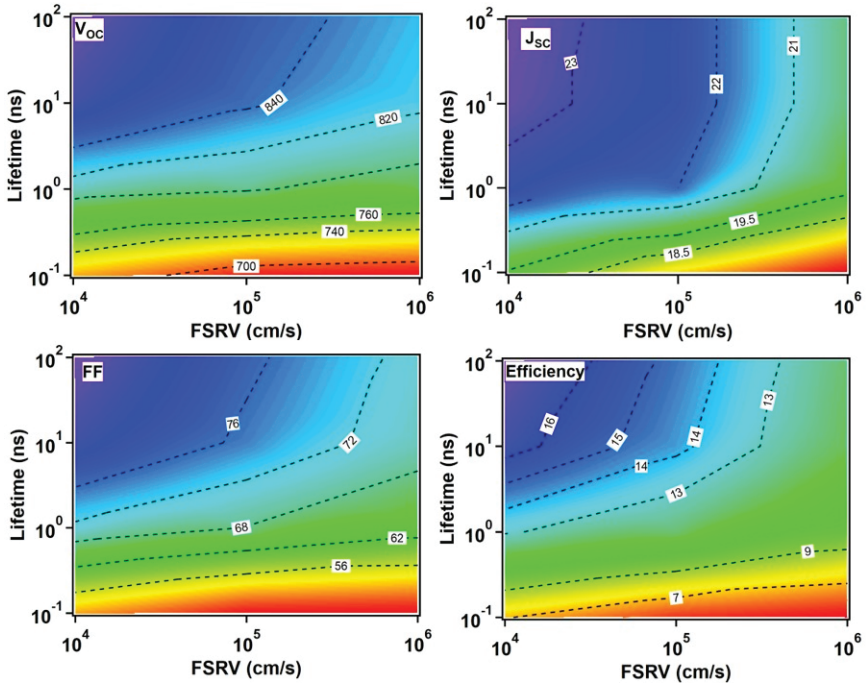


Figure 51. SCAPS simulation: relationship between the front SRV and the minority carrier lifetime using the CuAlOx as the back buffer layer

9.5 CONCLUSIONS

We have demonstrated that Al_2O_3 can be formed at low temperature can be used as a back contact layer of CdTe solar cells. With different percent of Cu doping on Al_2O_3 helps to minimize the insulating nature of Al_2O_3. The bulk lifetime is increased from 0.8 ns to 2.6 ns from the film side illumination and 4.3 ns to 37.6 ns through the glass side illumination. This passivating nature is consistent with the higher device performance with excellent increase on *FF,* $V_{OC,}$ and overall increase on the device performance. Our best cell shows the 14.5% device performance, which is 39%, 10%, and 5% relative increment over standard Au only, Cu(metal)/Au, and Cu(solution)/Au respectively. Our experiment proves that $CuAlO_x$ could serve as a promising passivating interface layer on CdS/CdTe solar cells. The development of $CuAlO_x$ by using the low cost non-vacuum solution based method and its transparency widely open the design space for bifacial and tandem PV utilizing CdS/CdTe.

10. SILAR DEPOSITED TRANSPARENT CU-ZN-S NANOCOMPOSITES AS HOLE TRANSPORT MATERIALS IN CDTE PHOTOVOLTAICS

Ebin Bastola, Kamala Khanal Subedi, Fadhil K. Alfadhili, Adam B. Phillips, Michael J. Heben and Randy J. Ellingson

10.1 SUMMARY

Evolving materials science and device architectures continue to drive improvements in photovoltaic solar cell performance. Here, we report the synthesis and application of p-type transparent copper-zinc-sulfide (Cu-Zn-S) nanocomposite thin films for application as a semi-transparent back buffer layer for cadmium telluride (CdTe) photovoltaics. Earth-abundant and low toxicity Cu-Zn-S films are prepared at room temperature using successive ionic layer adsorption and reaction (SILAR). Transparency in the range of 500 -800 nm, low resistivity, and composition-controlled bandgap energy offer a compelling material system for high performance as an electron reflector enabling bifacial cell design. Implementing the Cu-Zn-S hole transport material (HTM) at the CdTe back contact, without intentional introduction of Cu doping, converted simulated AM1.5 sunlight to electricity at an efficiency up to 13.2%, with an average device performance of 13.0%. Intentional Cu doping yielded a best efficiency of 14.3% with open-circuit voltage (V_{OC}) 848 mV, and fill factor (FF) of 77.3% (average 14.1%). Our study shows the clear promise of this material for highly efficient and semi-transparent back contact to CdTe solar cells.

10.2 INTRODUCTION

Transparent conducting materials are essential to fabricate electronic devices such as light emitting diodes [274], displays [275] and photovoltaic devices. [276, 277] The thin film solar cell device consists of transparent conducting materials as a window and/or buffer layer and a semiconductor material as an absorber layer. The transparent materials possessing both high conductivity (low resistivity) and high optical transparency are typically n-type materials. However, the buffer layers or hole transport materials (HTMs) applied at a thin film solar cell back-contact interface, such as in the case of CdTe solar cells, are p-type. The development of p-type transparent materials with high hole conductivity and optical transparency lags behind comparable n-type transparent conduction materials. [278] Common p-type transparent conducting materials, also important for the fabrication of bifacial photovoltaic devices, include oxide and sulfide compounds of copper such as Cu_xO, [279], $CuAlO_2$, [280] Cu_xS, [263] and $Cu_xZn_{1-x}S$. [281]

Cu-Zn-S (CZS) nanocomposite thin films are earth-abundant materials possessing high transparency in the visible region, high energy band gap, high conductivity and high hole concentration. [282] The optical band gap and Fermi level of the CZS material can be adjusted by changing the material composition. [283] Thus, CZS nanocomposite can serve as an effective hole selective layer in solar cells. [276] CZS materials can be prepared by vacuum [284] and solution-based techniques including chemical bath deposition (CBD) [276, 285] and successive ionic layer adsorption and reaction (SILAR) [282, 283] methods. Xu et al. have reported $(CuS)_x(ZnS)_{1-x}$ p-type transparent materials with transmission >70% in the visible region and fabricated heterojunction p-$(CuS)_x(ZnS)_{1-x}$/n-Si solar cells. [276] The $(CuS)_x(ZnS)_{1-x}$ nanocomposites served as the hole selective layers for heterojunction devices and demonstrated the application of these

earth abundant materials as HTMs in solar cells. Previously, we have fabricated CdTe devices with $(CuS)_x(ZnS)_{1-x}$ as the hole selective layer using CBD. [254] Jose et al. have synthesized and characterized CZS film using a SILAR method. [282] In a SILAR method, material gets deposited by the reactions of cations and anions producing an atomic layer thus improves the quality of the nanocomposite films. Additionally, the thin films with very small grain sizes are more compact and transparent to the visible light.

Cadmium telluride (CdTe) solar cells are well-known thin film technology to convert solar energy into an electrical energy with a suitable band gap of 1.48 eV. To fabricate CdTe solar cells, copper/gold (Cu/Au) is usually used as a standard back contact material, and the role of Cu is for doping and band bending due to a deeply located (~-5.9 eV) [286] valence band edge of CdTe. [287, 288] The work function of gold is ~5.0-5.2 eV [289] compared to the deep valence band edge of CdTe, a potential barrier is formed. To reduce this potential barrier, one utilizes a material with suitable optoelectronic properties (p-type, low resistivity, high hole concentration) and band edge location to achieve efficient extraction of holes while repelling electrons at the back interface of the CdTe devices; the desired results include a reduced forward electron current and improved open-circuit voltage. [226] Materials such as carbon nanotubes [290], copper thiocyanate (CuSCN), [291] iron pyrite (FeS_2), [292] zinc telluride (ZnTe), [188] antimony telluride (Sb_2Te_3), [293] and copper telluride (Cu_xTe), [294] have been tested as back-contact buffer layers in CdTe solar cells. First Solar has employed ZnTe as an interface layer to fabricate highly efficient CdTe solar cells on a commercial scale. [295] Some of the solution-processed back contact buffer layers include $Ni_xFe_{1-x}S_2$, chalcopyrite ($CuFeS_2$), and perovskite. [296-299] Similarly, some of the materials used as HTLs in nanocrystal based CdTe solar cells include P-TPA, Si-TPA, and Spiro to improve the hole transport properties and device efficiency. [300-302] However, most of these materials are not optically transparent to visible light for the fabrication of bifacial devices, and their doping level cannot be well controlled. We demonstrate that Earth-abundant materials such as Cu-Zn-S be an alternative HTM in photovoltaics.

Previously, we have fabricated $(CuS)_x(ZnS)_{1-x}$ thin films using a CBD method at 80 ℃ in about an hour and applied them as HTMs for CdTe photovoltaics. [254] During the deposition, Cu ions may diffuse to CdTe film and we are interested to see how room temperature processed CZS act as HTMs to CdTe photovoltaics assuming there is no Cu diffusion at room temperature. Our preliminary study of CZS HTM deposited by SILAR method on CdTe showed a promising result without additional Cu doping and inspired us to carry this investigation over a wide range of CZS compositions. [303] Here, we have fabricated and characterized transparent CZS nanocomposite thin films with various compositions using a SILAR method, and then applied them as a back-contact interface layer to CdTe solar cells. These CZS films are compact with petal like nanostructures with high transparency in the visible region and low resistivity with varying band gap energy. We found that CdTe devices with CZS layer performed better compared to the devices without CZS layer reaching an efficiency of 13.2%. With optimized doping and CZS nanocomposite as an interface layer, the best cell reached an efficiency of 14.3% (average 14.1%) with open-circuit voltage 848 mV and fill factor of 77.3%.

10.3 METHODS, ASSUMPTIONS, and PROCEDURE

Materials

Copper (II) chloride ($CuCl_2$, 99.99%), zinc acetate ($Zn(acac)_2$, 99.9%), sodium sulfide ($Na_2S.9H_2O$, 98.0%) and triethanolamine (TEA) (≥ 99.0%) were obtained from Sigma-Aldrich. Cadmium chloride ($CdCl_2$, ultra-dry, 99.996%), and methanol (CH_3OH, 98%) were obtained from Alfa Aesar™. All the chemicals were used as obtained without further purification.

Cu-Zn-S Thin Films Preparation

The CZS nanocomposite films were deposited at room temperature using a SILAR method adapting a procedure from literature. [282, 303] First, CZS thin films were deposited on a soda lime glass (SLG) substrate for characterization. For this, Micro-90 detergent was used to clean soda lime glasses by sonication for 30 mins and followed by rinsing several times with deionized water (DIW). Then, glasses were again cleaned using a sonicator in acetone, methanol and 2-propanol for 5 mins each.

CZS-30 film was deposited by preparing cationic precursor by dissolving 0.07 M $CuCl_2$, 0.03 M zinc acetate in DIW, with a total concentration of 0.1 M, and 5 mL TEA keeping the total volume 25 mL, and anionic precursor using 0.05 M Na_2S in DIW. Here, CZS-30 denotes thin films prepared using Zn precursor 30 percent (0.03 M zinc acetate) and Cu precursor 70 percent (0.07 M) of the total cations (0.1 M) used. The SLG substrate was placed in cationic precursor for 15 S, rinsed in DIW for 5 S, in anionic precursor for 15 S, and in DIW for 5 S to complete one SILAR cycle. A dip-coater from NIMA Technology was used to complete all the SILAR cycles. The same procedure was repeated to deposit CZS films on CdTe film. Similarly, for CZS-40 film (40% zinc acetate in the cationic precursor), 0.04 M zinc acetate and 0.06 M $CuCl_2$ were used as the cationic precursor keeping other chemicals same as CZS-30 film.

Device Fabrication

The CdS/CdTe device stacks received from Willard and Kelsey Solar Group were utilized for this study. Standard CdTe devices were completed using Cu/Au (3/40 nm) by thermal evaporation after $CdCl_2$ treatment in dry air environment. It was followed by thermal annealing of devices at 150 °C for about 35 mins. To fabricate CZS as HTMs, $CdCl_2$ treated CdTe devices were used and CZS films were deposited by using a SILAR method as mentioned above. Then, the devices were completed by depositing 40 nm Au. Similarly, for solution-based Cu doping, the CdTe film stack was submerged in 0.1 mmol $CuCl_2$ solution in deionized water for 2 min, rinsed with DIW, and annealed at 200 °C for 20 mins. [208]

Film and Device Characterization

Hitachi S-4800 scanning electron microscopy (SEM), energy dispersive X-ray spectroscopy (EDS), and PerkinElmer Lambda 1050 UV-Vis-NIR spectrophotometer were used to characterize the CZS thin films on soda lime glass. Rigaku Ultima III X-ray diffractometer operated at 40 KV and 44 mA was used to obtain X-ray diffraction patterns. The 4-point and Dektak profilometers

were used to measure the sheet resistance and thickness respectively. The completed devices were measured under simulated AM1.5G solar irradiance to find the photoconversion efficiency.

10.4 RESULTS and DISCUSSION

The CZS thin films were fabricated at room temperature using a SILAR method. During the first step, cations get adsorbed on the surface, and weakly bound cations are removed during the subsequent rinsing in DIW. The substrate is then immersed in anion solution resulting a reaction between cations (Zn and Cu ions) and anions (S ions) followed by an additional rinse in DIW which removes loosely bound S ions. The SILAR cycle is repeated several times to prepare a thin film of desired thickness. Figure 52(a, b) displays the transmission and reflection spectra for CZS-10, CZS-20, CZS-30, CZS-40, CZS-50 and CZS-80 nanocomposite films. Here, CZS-30 denotes thin films prepared using Zn precursor 30 percent (0.03 M zinc acetate) and Cu precursor 70 percent (0.07 M) of the total cations (0.1 M) used. As displayed in the transmission spectra, these films have greater than 50% transmittance in visible region in the range of 500-800 nm. The transmission and reflection spectra were utilized to obtain band gaps of these films. The transmission (T), reflection (R) spectra along with the thickness (t) of the films were used to calculate the absorption coefficient (α) of the thin film using an equation,

$$\alpha = -\ln(\ T/(1-R))/t \qquad (1)$$

The band gap energies for these nanocomposites were calculated by plotting $(\alpha h\nu)^2$ vs $(h\nu)$ for CZS nanocomposites. The calculated band gap values for CZS films are shown in Table 8. The energy band gap of CZS-30 film estimated by equation above is 2.50 eV.

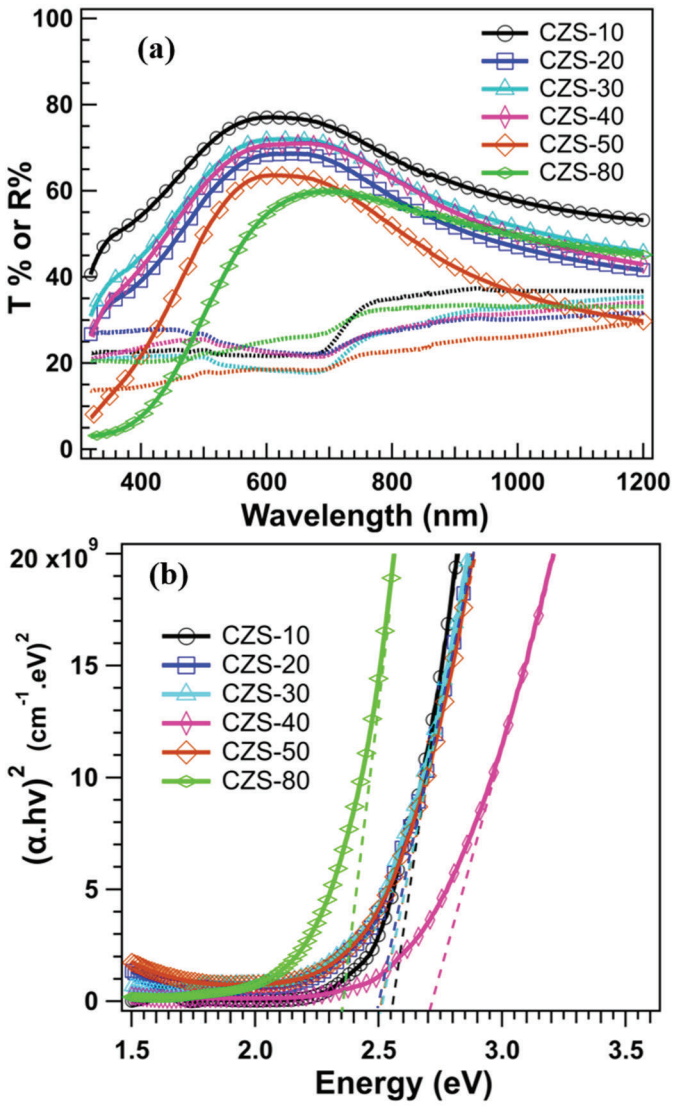


Figure 52. (a) T and R (dotted) spectra of CZS NC thin films prepared by SILAR; (b) plots of $(\alpha h\nu)^2$ v.s energy (hν, eV) for band gap estimation

Figure 53(a-d) displays the surface morphology of CZS thin films deposited on a soda lime glass for CZS-10, CZS-30, CZS-50 and CZS-80. Based on SEM images, CZS-30 and CZS-50 films have similar surface morphology with compact grains of length around 200 nm. CZS-10 film was thinner (~50 nm) compared to other films, has higher transparency, and consist of voids compared to CZS-30 and CZS-50 films. Note that all these films were deposited at the same condition and only the ratio of cations (Zn and Cu ions) were only varied. In case of CZS-80 film (Figure 53(d)), surface morphology looks different from other CZS compositions, which might be due to higher amount of Zn atoms in the cationic precursor. CZS-50 film had few diffraction peaks [303] similar to CuS whereas CZS-80 film shows amorphous nature compared to other compositions. No Zn atoms were observed in the EDS analysis for CZS-10 and CZS-20 films. The Zn percentage was increased to higher amount as the amount of Zn percentage was increased in the precursor. Here, the lower content of Zn in the film compared to precursor indicates lower reactivity of Zn atoms compared to Cu atoms as observed in $(CuS)_x(ZnS)_{1-x}$ deposition using chemical bath method. [254]

Based on X-ray diffraction patterns, as deposited CZS thin films with higher Cu (lower Zn) concentration have diffraction patterns similar to the covellite CuS (hexagonal crystal structure) but with lower Cu (higher Zn) concentration, no diffraction patterns were observed. It indicates poor crystallinity as the Zn atoms increases which is slightly different with the previous report. [282] The authors observed diffraction patterns for various compositions of CZS films. CZS-20 film has a small diffraction peak at 48.2º matching a peak of CuS (PDF #98-001-3414). In case of CZS-50 sample, its diffraction peaks match well with the standard covellite CuS peaks. However, no diffraction peaks were observed for CZS-80 film indicating amorphous nature of the materials deposited similar to the CBD deposited $(CuS)_x(ZnS)_{1-x}$ film. As the amount of Zn in the film increases, the film becomes more amorphous. [254, 276]

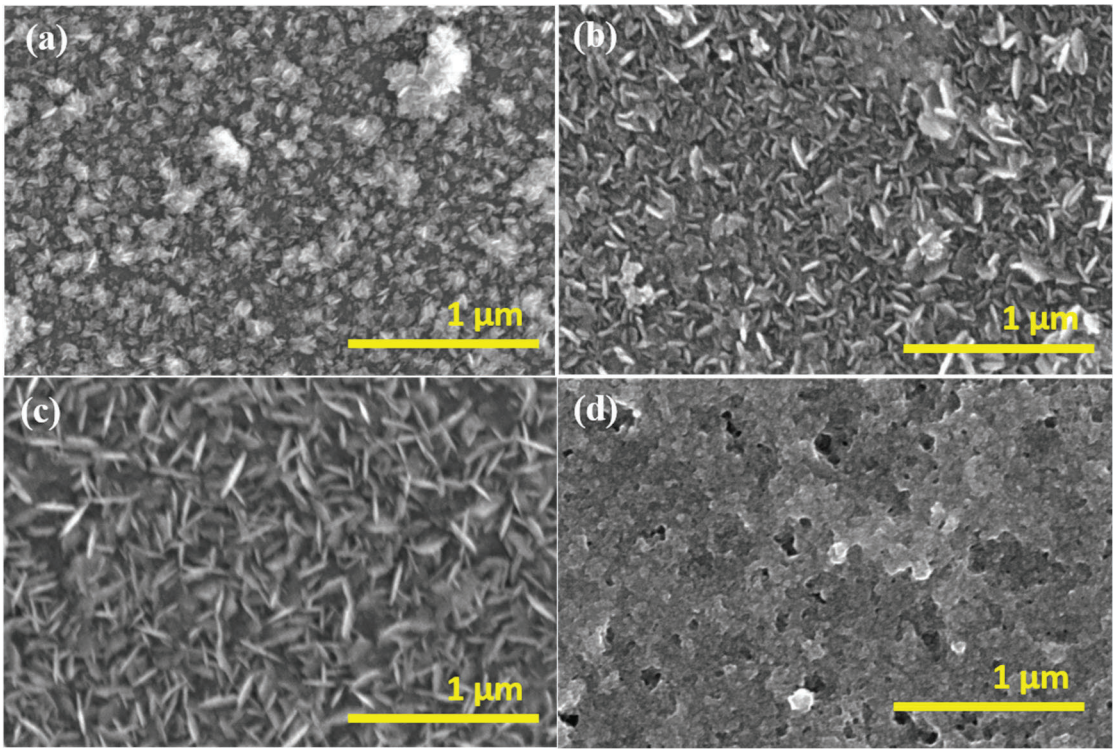


Figure 53. SEM images, Cu-Zn-S thin films (a) CZS-10 (b) CZS-30 (c) CZS-50 and (d) CZS-80

Probe and resistivities were calculated. Table 8 summarizes the various properties of these nanocomposite films including thickness, transmission at 550 nm wavelength, energy band gap, sheet-resistance and resistivity. As the amount of Zn concentration was increased, its resistivity was increased. For example, for CZS-10, the resistivity is 1.6×10^{-2} Ω cm while for CZS-80, the resistivity is 77.9×10^{-2} Ω cm. The resistivity increases due to the lower amount of Cu content and more amorphous nature of the nanocomposite film. The resistivities measured for these CZS films are similar to the values reported previously and these materials have hole concentration in the order of 10^{21} cm^{-3} thus behave like a degenerately doped semiconductors. [282] The transparency of these nanocomposite films in visible region and low resistivity make these materials promising in various optoelectronic applications including light emitting devices, displays and solar cells. As evidenced from low resistivity (high conductivity) of these CZS films, high hole concentration and

the change of its fermi level with composition, these materials can be a good contact material for solar cells. [276]

Table 8. Properties of Cu-Zn-S Thin Films

Sample	Thickness (nm)	T % at 550 nm	Band gap (E_g, eV)	Sheet Resistance (Ω/□)	Resistivity (10^{-2} Ω cm)
CZS-10	50	75.2	2.55	3143	1.6
CZS-20	100	65.3	2.50	1322	1.3
CZS-30	90	69.5	2.50	2166	2.0
CZS-40	145	67.9	2.70	6102	8.9
CZS-50	180	60.0	2.50	2918	5.3
CZS-80	200	45.1	2.35	38956	77.9

To study the hole transport properties, CZS thin films were deposited on CdTe devices and covered with 40 nm Au to complete the back-contact. Figure 54 shows a schematic and a cross-sectional image of CdTe device with a CZS layer as a hole transport layer. These devices were completed after the deposition of CZS film at room temperature and without any thermal annealing. The *J-V* characteristics for the best cells of controlled device and with CZS as HTMs under light and dark measurement conditions are shown in Figure 55. The best cell has an efficiency of 10.5% for Au only back contact with average device performance of 10.0% for 20 cells and the best back contact was CZS-30/Au with an average device performance of 12.8% with the best cell performing 13.1%. The CZS-30/Au back contact best cell has higher V_{OC} of 816 mV and FF of 74.4%. Based on the literature, Jose et al have reported that CZS-30 films deposited by a SILAR method have the highest hole density of 1.01×10^{22} cm^{-3} and mobility of 2.68 $cm^2V^{-1}s^{-1}$. [282] Thus, due to the higher doping level and hole mobility, the CZS-30 back buffer layer performed better than other CZS nanocomposites.

The device performance for CZS-30/Au film is slightly higher than the controlled device with Cu/Au (3/40 nm) deposited by a thermal evaporation. Note that, in case of devices with CZS films, no additional Cu layer was deposited. For CZS-80/Au back contact, the device efficiency was 3.9% with significant drop in the FF (31.5%) and J_{SC} (15.2 mA cm^{-2}). The higher resistivity (Table 8) of the CZS-80 film than CZS-30 and CZS-50 films reduced the device performance which is attributed to lower Cu/Zn ratio. Due to the significant increase in the resistivity of the CZS-80 layer, we observed a significant increase in the series resistance (R_S) and drop in shunt resistance (R_{SH}) of the device with CZS-80 layer, which finally reduced the device performance. Previously, CZS layers deposited by chemical bath deposition at 80 °C were also used as HTMs in CdTe devices, and the champion cell efficiency was 13.0% (V_{OC} 805 mV, J_{SC} 22.1 $mAcm^{-2}$ and FF 73.3%) with CZS layer and Cu/Au (3/40 nm) back contact. [254] During the thermal annealing after Cu evaporation, there was a loss in fill factor than the standard Cu/Au device which might be due to the over heat treatment. Here, for room temperature deposited CZS-30/Au back contact, the device efficiency is similar without an additional evaporated Cu layer and thermal

annealing (Figure 55) which indicates efficient devices can be fabricated by depositing a CZS nanocomposite at room temperature. To see the effect of annealing after the deposition of CZS layer on CdTe devices, we annealed the devices at 200 °C for 10 mins and measured after annealing, the device performance was poor compared to the unannealed device as the loss of V_{OC}, J_{SC} and FF occurs. Based on this observation, we conclude that during thermal annealing, weakly bounded Cu, Zn and S atoms from the CZS layer diffuse into CdTe film lowering the device characteristics.

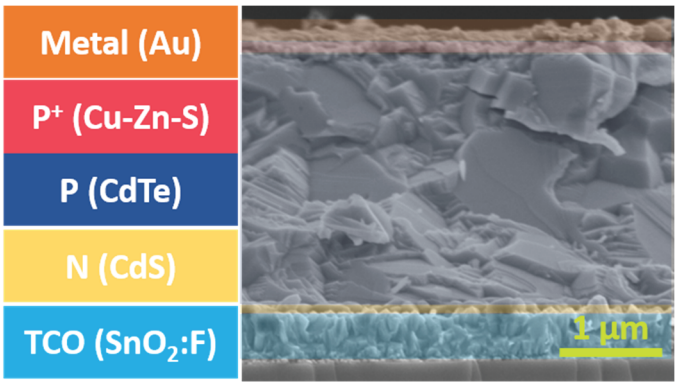


Figure 54. Schematic device diagram and cross-sectional SEM image of CdTe solar cells with Cu-Zn-S (CZS-50) as a back-contact interface layer

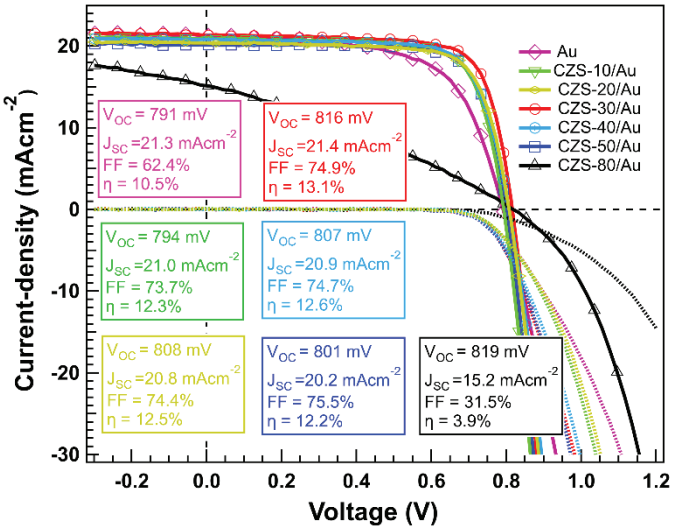


Figure 55. J-V characteristics of CdTe photovoltaics with and w/o Cu-Zn-S (CZS) nanocomposites as HTMs

Further, we analyzed the surface morphology of CdTe films with CZS layer on the top with electron microscopy, X-ray diffraction and EDS analysis. CZS nanocomposites can be observed on the top surface of CdTe indicating the change in surface morphology as shown in Figure 56(a, b). The shapes of CZS particles on CdTe surface looks slightly different from CZS nanocomposite formed on a soda-lime glass substrate. However, the elemental composition revealed Cu, Zn and S atoms in addition to Cd, Te and Cl atoms. Note that these CZS films were

deposited after $CdCl_2$ treatment on CdTe devices. XRD pattern of CdTe film with CZS layer reveals small diffraction peaks of CuS with other strong diffraction peaks of CdTe as shown in Figure 56(c). The peak marked by * is usually observed on CdTe surface after $CdCl_2$ treatment which may be due to the formation of $CdTeO_x$ present on the surface. [142, 304] The XRD pattern was compared with standard powder diffraction files (PDF) of CdTe (PDF # 97-005-2840) and CuS (PDF #98-001-3414) on the MDI ZADE software.

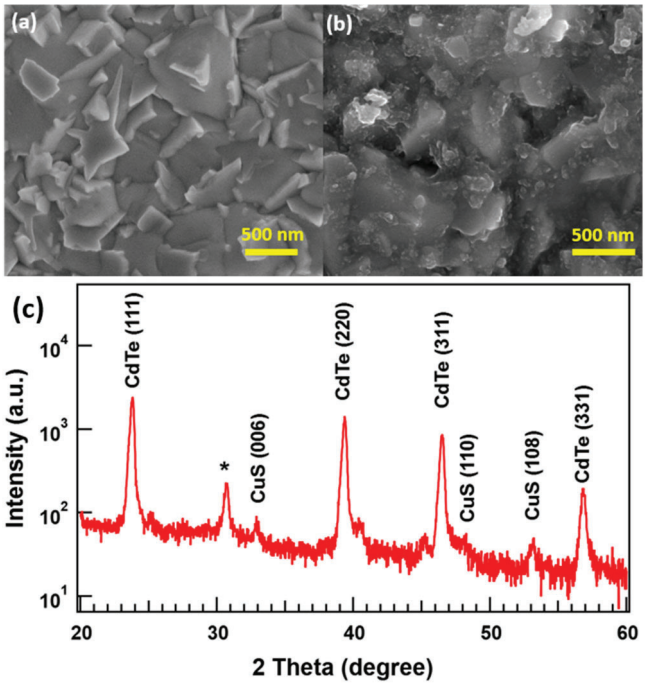


Figure 56. SEM images of CdTe surface (a) without CZS NCs and (b) with CZS NCs; (c) XRD pattern of CdTe/CZS-30 (references to CdTe and CuS are PDF #97-005-2840 and PDF #98-001-3414)

Here, we also investigated CdTe devices with CZS-30 layer of various thickness (deposition cycles) and additional Cu doped CdTe devices with $CuCl_2$ treatment. Previously, we have reported highly efficient CdTe devices can be fabricated than evaporated Cu by doping with $CuCl_2$ solution and device performance increases mainly due to the improvement in V_{OC} and FF. [208] CdTe devices with different thickness/deposition cycles of CZS-30 nanocomposites were fabricated and measured under standard AM1.5G solar spectrum. The average device performance is shown in Figure 57(a) for various deposition cycles from 0 to 60 and *J-V* characteristics of the best cells are presented in Figure 57(b) for CZS-30 nanocomposites with 0, 5, 10, 20, 40 and 60 deposition cycles. Based on these *J-V* characteristics, we found that CZS-30 with 10 deposition cycles performed the best compared to other deposition cycles. The average device efficiency is 13.0% with the best cell having an efficiency of 13.2% with V_{OC} 834 mV, J_{SC} 21.6 $mAcm^{-2}$ and FF 72.9%. We attribute the higher device efficiency, especially V_{OC}, is due to the better band alignment of CdTe with CZS nanocomposite. [226] The average efficiency of the device with higher number of deposition cycles was lower than 10 deposition cycles mainly due to the loss in FF which is due to the increase in series resistance of the device (thicker CZS composite on the back of device).

Further, we tested the effect of these CZS layer on the top of CdTe devices after copper chloride ($CuCl_2$) treatment. For this, CdTe devices after $CdCl_2$ treatment were submerged in 0.1 mmol $CuCl_2$ solution in deionized water and annealed at 200 °C for 20 mins. [303, 305] After this, CZS-30 layer with 10 deposition cycles were deposited on one of the devices and *J-V* measurement was carried. Figure 57(c) below displays the *J-V* characteristics of the best cells of the control and CZS deposited device. The average device efficiency with $CuCl_2$/Au is 13.7% with the best cell reaching 14.0% while with $CuCl_2$/CZS/Au back contact has the average device performance of 14.1%. The average device parameters are tabulated in Table 9. By using CZS layer, the average increase in PCE is 2.9 % while the FF has been improved by 2.5% for 20 cells. The best cell with $CuCl_2$/CZS/Au has V_{OC} 848 mV, J_{SC} 21.8% and FF of 77.3% with PCE of 14.3%. This efficiency is equivalent to 17.0% if other window layers (CdS:O, CdSe or MZO) were used to have J_{SC} of 26 $mAcm^{-2}$. [221, 306] Due to the CZS nanocomposite layer, the device efficiency was enhanced mainly due to the improvement of FF of the device. The better device efficiency on using CZS nanocomposite is due to a reduced back barrier height and flattening of the conduction band compared to Au only or Cu/Au back contact. [303] The *J-V-T* measurement of CdTe devices with CZS-50 nanocomposite showed a back barrier height of 0.238 eV in between CZS-50/Au which is less compared to Au only (0.395 eV) and Cu/Au (0.330 eV) back contact. [303, 307] This indicates that the CZS layer on the back of CdTe devices lowers the back barrier height increasing the device efficiency.

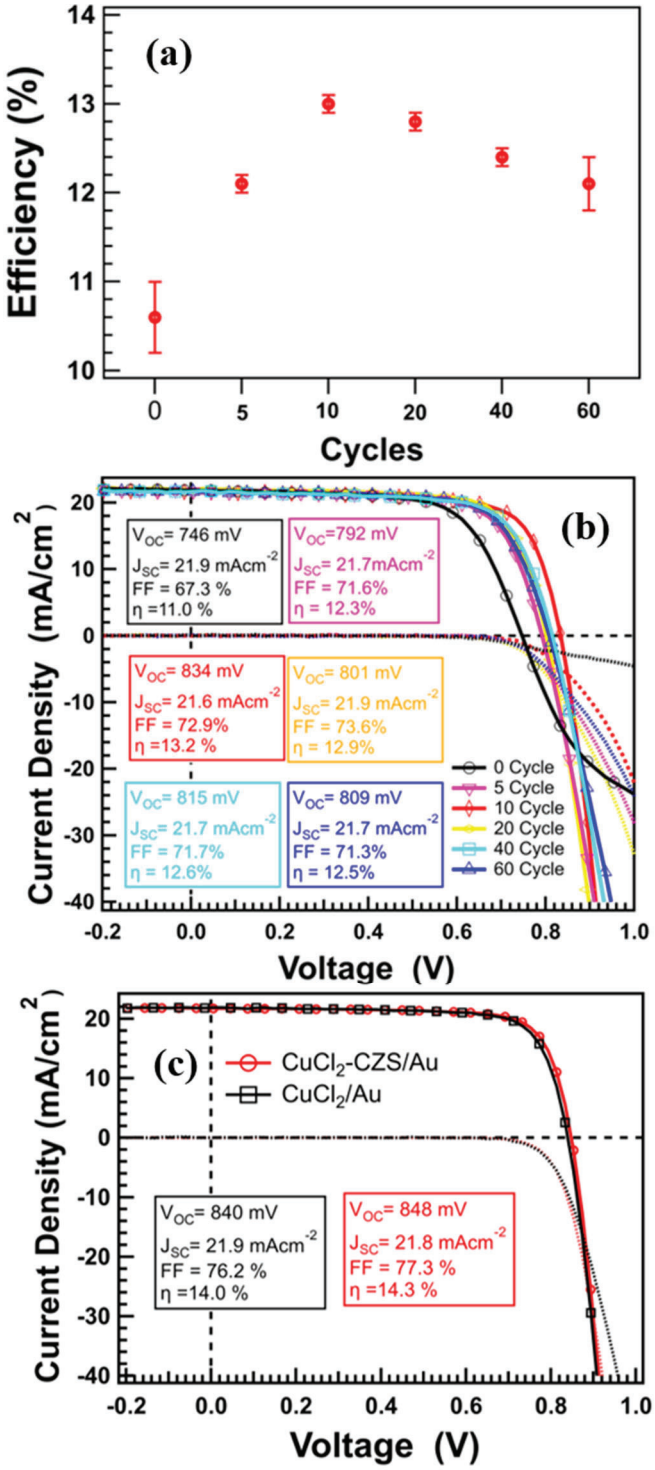


Figure 57. (a) Average PCE vs. cycles; best JV curves vs. deposition cycles of CZS-30 NCs; (c) *J-V* characteristics of the best cells, $CuCl_2$ treated devices with CZS NCs

Table 9. Average JV parameters with and without CZS NC for $CuCl_2$ treated CdTe devices

Back-Contact	V_{OC} (mV)	J_{SC} ($mAcm^{-2}$)	FF (%)	Eff. (η%)	Rs ($\Omega\ cm^2$)	Rsh ($\Omega\ cm^2$)
$CuCl_2$/Au	840±2	21.6±0.3	75.6±0.4	13.7±0.2	4.4±0.1	2717±227
$CuCl_2$/CZS/Au	845±3	21.5±0.2	77.4±0.3	14.1±0.1	2.8±1.1	3100±293

10.5 CONCLUSIONS

Here, we have successfully fabricated Cu-Zn-S nanocomposite thin films at room temperature using SILAR method, which are transparent to visible light and have low resistivity. Further, room-temperature processed transparent CZS films as the back-contact hole transport material in CdTe devices have been demonstrated. Out of the various composition of nanocomposite, CZS-30/Au as the back contact has the highest efficiency 13.1% with no additional Cu. The CZS-80 film performed poor (3.9%) due to its high resistivity and poor crystallinity. Similarly, for $CuCl_2$ treated CdTe devices with CZS interface layer, the highest efficiency observed is 14.3% with average device performance of 14.1%. Based on this study, CZS nanocomposite can be considered as a low barrier interface layer to fabricate highly efficient devices and other vacuum based approaches can be sought for deposition of these CZS films.

11. MICROSTRUCTURAL CONTROL OF THIN FILM CDTE BY GLANCING ANGLE DEPOSITION

Dipendra Adhikari, Niva K. Jayswal, Indra Subedi, Maxwell Junda, Ebin Bastola, Corey Grice, Prakash Koirala, Randy Ellingson, Robert Collins, and Nikolas Podraza

11.1 SUMMARY

To manipulate the structure of CdTe at its heterojunction with CdS, CdTe thin films with different microstructures have been produced by glancing angle deposition (GLAD) at sputter source flux angles varying from 0° to 80° with respect to substrate normal at both room temperature and 250°C. From cross-sectional micrographs for room temperature deposited material, increasingly tilted columnar structure occurs with increasing incident source flux angle for as-deposited CdTe films. Films deposited at lower source flux angles closer to normal incidence have cubic zinc blende crystal structure and those prepared at more oblique higher angles have hexagonal wurtzite crystal structure at room temperature. Films deposited at 250°C and non-normal incidence have ~20% larger crystallite size than room temperature deposited material, however these films do not show peaks unique to the hexagonal phase. Post-deposition $CdCl_2$ treated films show enhancement in crystallite size for samples prepared under all conditions prepared at room temperature. Application of wurtzite GLAD CdTe interlayers between CdS and CdTe of the standard CdS/CdTe heterojunction design solar cell shows better performance with 0.9% absolute efficiency increase.

Complete details of this work can be found in D. Adhikari, M. M. Junda, E. Bastola, P. Koirala, R. J. Ellingson, R. W. Collins, and N. J. Podraza, "Glancing Angle Deposited CdTe: Nanostructured Films and Impact on Solar Cell Performance," *Surface and Coatings Technology* **381**, 125127 (2020) [308] and N. K. Jayswal, D. Adhikari, I. Subedi, C. R. Grice, and N. J. Podraza, "Deposition Temperature Dependence of Optical and Structural Properties of Glancing Angle Deposited CdTe," submitted to *Proceedings of the 64th Annual SVC Technical Conference* (2021). [309] Additional support was provided by the National Science Foundation.

11.2 INTRODUCTION

The microstructure of CdTe films depends on deposition conditions and plays an important role in PV device performance, which depends upon the characteristics of both crystalline grains and surrounding grain boundary material. A CdS window layer is a commonly used *n*-type heterojunction partner with a *p*-type CdTe absorber. Cubic zinc blende CdTe is thermodynamically stable at room temperature, but exhibits a high lattice mismatch with room temperature stable hexagonal wurtzite CdS. Glancing angle deposition (GLAD) produces films with varying preferential grain orientations and grain boundary configurations. The dependence of crystal structure, crystallite size, crystallite orientation, and optical properties on source flux angle and deposition temperature are identified. The microstructure of CdTe films can potentially be engineered, resulting in the ability to tune opto-electronic properties for PV device optimization, such as by tailoring material structure at the *p/n* interface. This work involves study of such CdTe films deposited via radio frequency (RF) magnetron sputtering with material flux at a range of angles relative to the substrate normal and evaluation of PV device performance by incorporating GLAD CdTe. In particular, the influence of deposition angle on the microstructural and optical

properties of sputtered CdTe film are studied and potential improvement of PV device performance by incorporating a 100 nm GLAD interlayer at the *p/n* junction is demonstrated. The crystal structure and the crystallite size are obtained from x-ray diffraction (XRD), cross-section and surface microstructures are imaged from scanning electron microscopy (SEM), and complex optical properties are extracted from spectroscopic ellipsometry (SE). Source flux angle manipulates crystal structure, grain size, grain orientation, and optical properties. The effect of $CdCl_2$ post-deposition processing on grain size enhancement as a function of treatment time on GLAD CdTe is tracked. At room temperature, GLAD films may exhibit cubic zinc blende, hexagonal wurtzite, or mixed phase crystal structures depending on source flux angle. Materials prepared at 250°C do not exhibit unique diffraction peaks corresponding to only the hexagonal phase, so only cubic and potentially mixed phase crystal structures are produced. A thin nominally 100 nm structurally engineered wurtzite GLAD CdTe interlayer is introduced between the *n*-type CdS window layer and *p*-type CdTe absorber. Power conversion efficiency (*PCE*), open circuit voltage (V_{OC}), and fill factor (*FF*) improve with introduction of this GLAD CdTe interlayer between CdS and CdTe layers of a conventional CdS/CdTe heterojunction solar cell.

11.3 METHODS, ASSUMPTIONS, and PROCEEDURES

RF magnetron sputtered (frequency = 13.56 MHz) CdTe films have been deposited at room temperature (RT) and at 250°C elevated temperature onto soda-lime glass substrates using GLAD in a standalone vacuum chamber (AXXISTM, K. J. Lesker Co.). The glass substrates are cleaned ultrasonically, rinsed with deionized water, and blown dry with nitrogen before film deposition. A schematic diagram of the GLAD process is shown in the Figure 58. Films are deposited at source flux angles (Φ) of 0°, 20°, 40°, 60°, and 80° relative to the substrate normal.

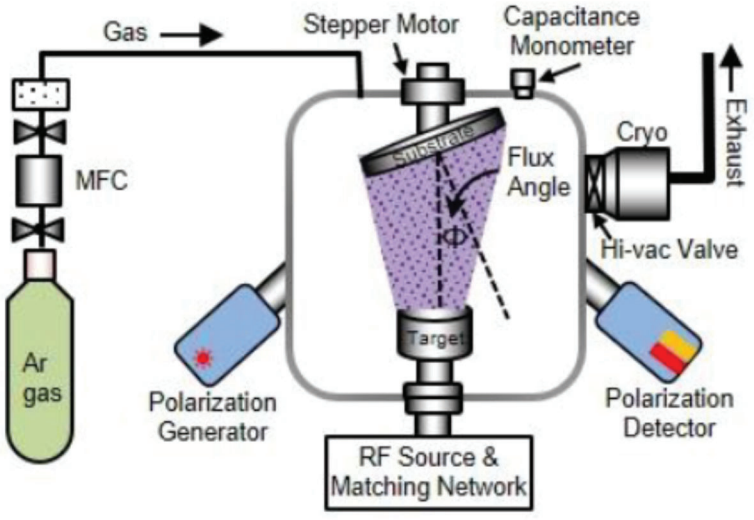


Figure 58. Schematic of glancing angle deposition (GLAD) sputtering

A 7.62 cm diameter 99.999% purity CdTe target is sputtered in a 15 mTorr pressure Ar ambient at 100 W RF target power with the substrate held at either RT or 250°C. Post-deposition $CdCl_2$ heat treatment is performed by wetting the film surface with a saturated solution of $CdCl_2$ in methanol followed by heating at 387°C in dry air ambient for 10, 20, 30, or 40 minutes. Cross-sectional and surface images are obtained from SEM (Hitachi S-4800). XRD patterns (Rigaku Ultima III diffractometer) are analyzed to obtain the crystal structure and crystallite size. *Ex-situ* spectroscopic ellipsometric and Mueller matrix spectra have been collected by using single rotating compensator (M-2000FI, J. A. Woollam Co. Inc.) and dual rotating compensator (RC2, J. A. Woollam Co. Inc.) multichannel ellipsometers. Complex optical response and optical anisotropy resulting from columnar structure are obtained from analysis of ellipsometric and Mueller matrix spectra collected for GLAD CdTe films.

CdS/CdTe heterojunction solar cells are fabricated in the superstrate configuration, as shown in the schematic diagrams in Figure 59. Solar cells are fabricated with and without a RT GLAD CdTe interlayer prepared at $\Phi = 80°$, which exhibits wurtzite crystal structure. The superstrates are 15.24 cm × 15.24 cm soda lime glass coated by 300-400 nm of SnO_2:F with an additional 100 nm of high resistivity transparent SnO_2 to form the transparent conducting oxide (TCO) front contact to the device (TEC-15M, Pilkington North America). The solar cell fabrication sequence begins with magnetron sputter deposition of 100 nm *n*-type CdS followed by a 2 μm *p*-type CdTe absorber. These layers are then subjected to the aforementioned $CdCl_2$ heat treatment for 30 mins. The solar cell is completed by RT thermal evaporation of 3 nm Cu and 40 nm Au through a dot shadow mask to form the back electrical contact. The completed cell structure is annealed at 150°C in air for 30 minutes to promote Cu diffusion into CdTe. 256 individual dot solar cells each having an active area of 0.126 cm^2 are formed for each process.

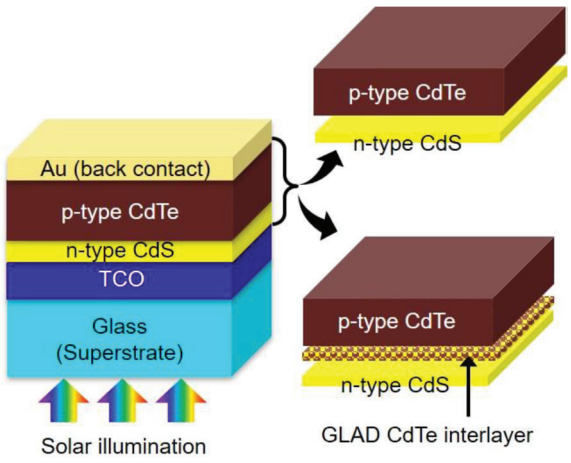


Figure 59. Schematic of CdS/CdTe solar cells with and without thin GLAD wurtzite CdTe interlayer

Photocurrent density versus voltage (*J-V*) are measured under simulated one sun AM1.5G (100 mW/cm^2) illumination from a 450 W Xenon light source (Oriel, Model 9119, Newport) with a digital source meter (Keithley 2440) in air at room temperature. External quantum efficiency

(EQE) measurements are performed (model IVQE8-C, PV Instruments) to characterize spectrally resolved device performance.

11.4 RESULTS and DISCUSSION

Full details are available in Refs. [308] and [309]. Figure 60 shows cross-sectional and surface SEM of as-deposited RT CdTe prepared at different source flux angles. The cross-sections show that the films have slanted columnar structure inclined towards the incoming material flux during sputtering. The surface morphology of the films deposited at Φ = 60° and 80° appear substantially different from other films deposited at lower Φ, which may be due to higher columnar tilt angle, crystal phase transitions from cubic to hexagonal at higher Φ, or both.

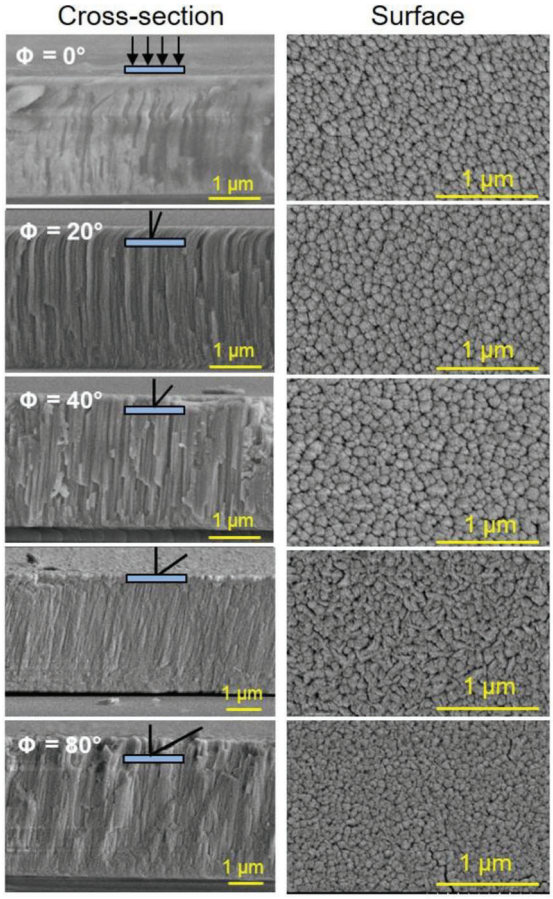


Figure 60. Cross-sectional and plan-view SEM images, as-deposited RT GLAD CdTe films vs. source flux angles with respect to substrate normal [308]

XRD patterns for the as-deposited RT CdTe films are shown in Figure 61(a, b). At lower angles with Φ < 40° the films have cubic crystal structure with lattice constant a = 6.4600 Å (MDI JADE

software, PDF# 97-010-8238) with (111) plane preferentially oriented crystallites. At higher angles with $\Phi \geq 60°$, films are predominantly hexagonal with lattice constants a = 4.5700 Å and c = 7.4800 Å (MDI JADE software, PDF# 97-015-0941) with more random crystallite orientations. The film prepared at $\Phi = 40°$ shows fewer peaks characteristic of the hexagonal structure and may be considered as mixed-phase. XRD patterns of CdTe films deposited at 250°C at different Φ are also shown. Diffraction peaks indexed to C(111) and C(311) planes of the cubic zinc blende crystal structure have been observed for all GLAD CdTe films. The C(220), C(400), and C(331) orientation peaks also exist for the film deposited at $\Phi = 0°$. The C(222) peak is observed for $\Phi \neq 0°$. No peaks attributed to only the hexagonal phase is found in films produced at this elevated temperature, although the H(002) and C(111), H(110) and C(220), and H(112) and C(311) overlap. The H(002)/C(111) and H(112)/C(311) peaks are observed for all Φ. These overlapping peaks imply that a mixed phase structure is possible; however, it is unlikely as peaks unique to solely the hexagonal phase are not observed among this high temperature series.

Diffraction peaks at $2\theta = 23.7°$ corresponding to C(111)/H(002) orientation crystallites are used to calculate average crystallite size via Scherrer's equation (Figure 62). For 250°C deposited CdTe, crystallite size is highest for the $\Phi = 40°$ film and lowest for the $\Phi = 0°$ due to lowest and highest distribution of crystallite orientations at Φ = 40 and 0°, respectively. Crystallite size of high temperature CdTe is larger than RT deposited CdTe due to more preferential orientation of crystallites at 250°C. At higher temperature, extra thermal energy facilitates the growth of the stable cubic phase as opposed to the metastable hexagonal phase. Also, the effect of atomic shelf-shadowing effect at higher Φ is decreased at high temperature due to extra thermal energy hindering formation of the tilt columnar structure and leading to larger crystallite sizes due to thermally enhanced diffusion of precursors on the surface. [310]

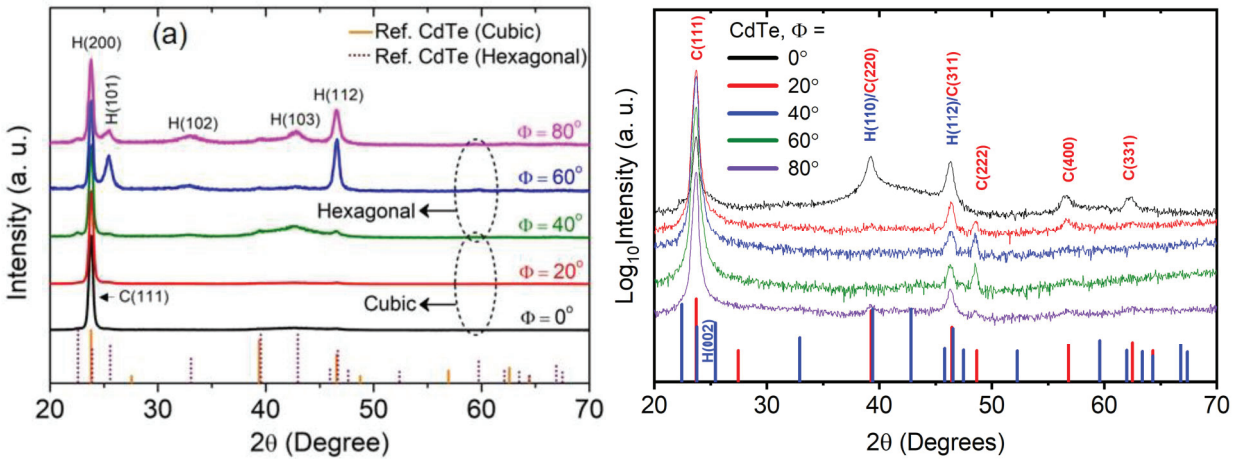


Figure 61. XRD patterns of as-deposited (left) RT [308] and (right) 250°C [309] CdTe sputtered on soda-lime glass at different source flux angles (Φ)

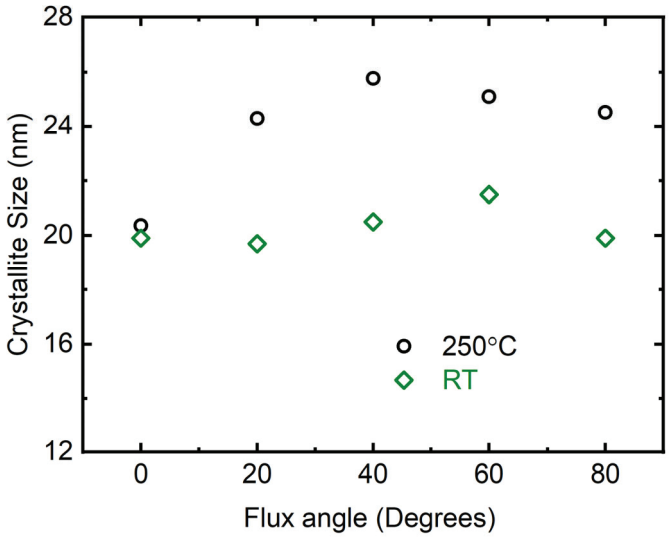


Figure 62. Crystallite size of CdTe deposited at different source flux angle and substrate temperature [309]

Isotropic optical response in the form of the complex dielectric function ($\varepsilon = \varepsilon_1 + i\varepsilon_2$) spectra and structure in the form of bulk and surface roughness thickness of all as-deposited GLAD CdTe films are obtained by fitting parametric layered optical and structural models to measured ellipsometric spectra from 0.74–5.89 eV using a least squares regression that minimizes the unweighted error function between measured and model-simulated ellipsometric spectra. Spectra in ε describing the bulk CdTe is shown in Figure 63(a, b). Comparing the optical response of these films with single crystal CdTe reveals that these films become less dense with increasing Φ due to increased columnar self-shadowing, transition in crystal structure, or both. The same approach is applied to GLAD CdTe prepared at 250°C (Figure 64). The CdTe films prepared at 250°C have sharper peaks with high amplitude compared to those prepared at RT due to the increased crystallite size of CdTe deposited at high temperature. Film stress (X) is determined using a linear stress coefficient, $C_X(E_o)$ = 0.071 eV/GPa, relative to the E_0 critical point for single crystal CdTe. [311] In-plane compressive stress of 1.26 and 0.85 GPa are found in high temperature GLAD CdTe at Φ = 0° and 80°, respectively. RT GLAD CdTe have similar compressive stress values of 1.23 and 0.65 GPa for Φ = 0° and 80°, respectively.

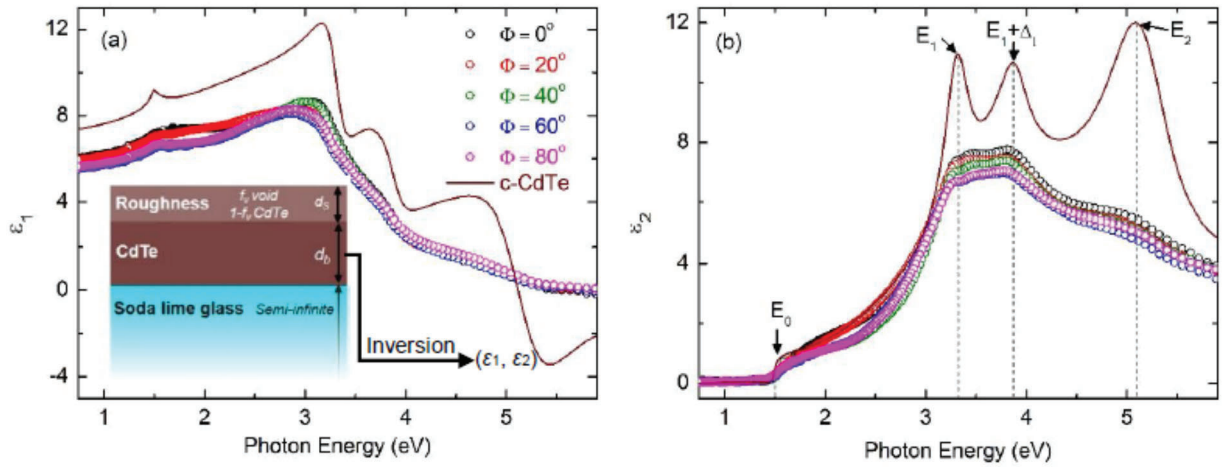


Figure 63. (a), (b) ε = ε1 + iε2 spectra of as-deposited RT GLAD polycrystalline CdTe films vs. source flux angle; [308] inset: the structural model

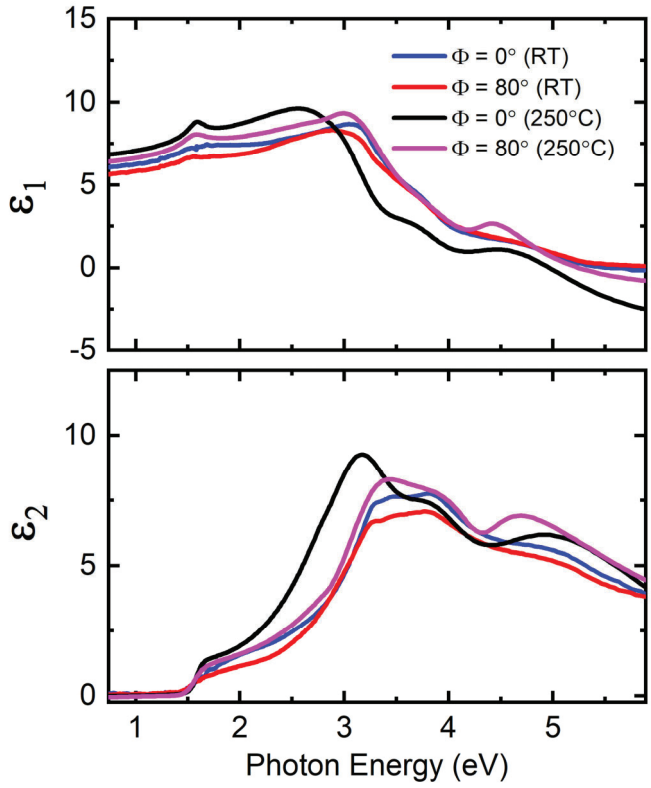


Figure 64. Comparison of ε for GLAD prepared at different temperatures and source flux angles [309]

The columnar structures of these films are substantially inclined away from substrate normal, about 12° in the cross-sectional SEMs for films deposited at Φ = 60° and 80°. In-plane optical anisotropy would be expected for the films deposited at high Φ because of the projection of sampling of the polar Euler angle rotated columns, θ = 12° in this case. Mueller matrix spectra are measured at three azimuthal angles (ϕ = 0, 45, and 90°) of rotation about the substrate normal and simultaneous modeling of all three sets of spectra is performed. Mueller matrix elements normalized to M_{11} sensitive to sample rotations (m_{13}, m_{14}, m_{23}, m_{24}, m_{31}, m_{32}, m_{41}, m_{42}) in the transparent spectral range are fit. Figure 65 shows the anisotropic optical properties over the modeled range for the two as-deposited CdTe films sputtered at Φ = 60° and 80°. The birefringence, difference in the indices of refraction in extra-ordinary and ordinary direction (n_e-n_o), is greater for Φ = 80° due to increased shadowing effects at higher angles of incidence.

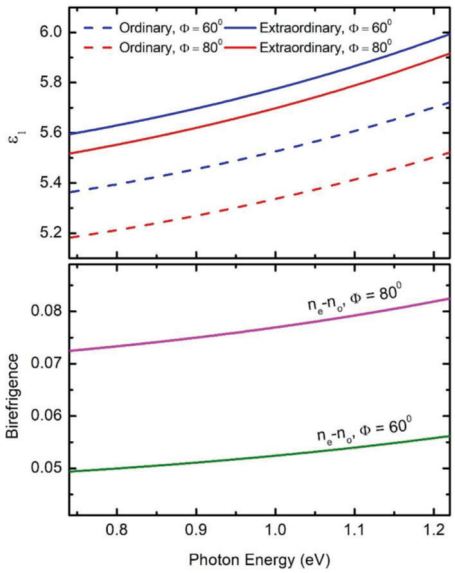


Figure 65. Anisotropic optical properties parallel (extra-ordinary, e) and perpendicular (ordinary, o) to the columnar principal axes in (top) ε1 and (bottom) birefringence, ne-no in the transparent spectral range [308]

Using XRD measurement and Scherrer's equation, the crystallite size variations with $CdCl_2$ treatment time are shown in Figure 66. Crystallite size increases after $CdCl_2$ treatment for all samples and increases with increasing treatment time. CdS/CdTe heterojunction solar cells with and without nominally 100 nm thick GLAD wurtzite interfacial layers between the *n*-type CdS window layer and *p*-type zinc blende CdTe absorber have been fabricated using Cu/Au back contacts (Figure 59). All CdTe layers are deposited at RT followed by post-deposition $CdCl_2$ treatment. Figure 67(a) shows *J-V* characteristics of the highest performing CdS/CdTe solar cells with and without the GLAD CdTe interlayer in the solar cell structure. The open circuit voltage (V_{OC}), short circuit current density (J_{SC}), power conversion efficiency (*PCE*), and fill factor (*FF*) corresponding to devices plotted in Figure 65 are shown in Table 10. The best device without the GLAD CdTe interlayer has a *PCE* = 10.05% with V_{OC} = 0.728 V, J_{SC} = 23.2 mA/cm^2, and *FF* = 59.4%. After incorporating structurally engineered GLAD CdTe between the *n*-type CdS window layer and normally sputtered *p*-type CdTe absorber, the best device has *PCE* = 11.02% with V_{OC} = 0.774 V, J_{SC} = 23.0 mA/cm^2, and *FF* = 69.1%. Using the GLAD CdTe interlayer, *PCE* increased by 0.9% absolute. The 200 (out of 256) highest performing dot cells are included in the statistical average calculation for both sets of solar cells given in Table 10. The average V_{OC}, J_{SC}, *FF*, and *PCE* of devices with GLAD CdTe interlayer are higher compared to device without GLAD interlayer. Figure 67(b) shows similar EQE spectra over the 300-1000 nm wavelength range for the same highest efficiency devices indicating that the presence of the interlayer does not reduce the spectroscopic optical performance of these solar cells.

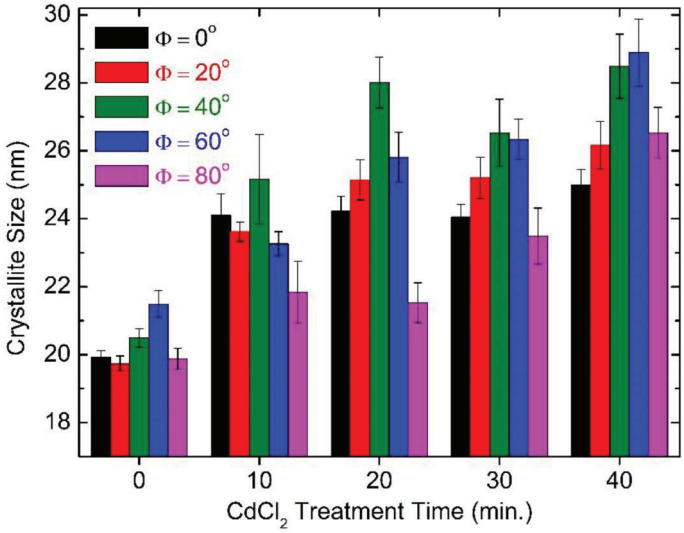


Figure 66. Crystallite size deduced via the Scherrer equation as a function of $CdCl_2$ treatment time for CdTe deposited at different source flux angles [308]

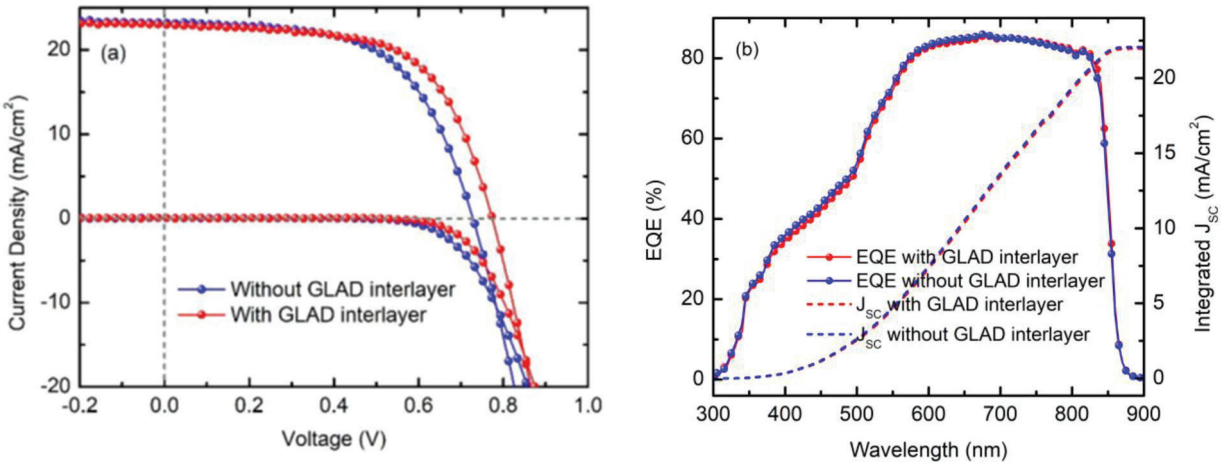


Figure 67. (a) JV and (b) EQE performance data best CdS/CdTe cells with and without a 100 nm GLAD wurtzite CdTe interlayer [308]

Table 10. Best (based on PCE) and average JV parameters of CdS/CdTe solar cells with and without a 100 nm thick GLAD wurtzite CdTe interlayer [308]

Solar cell	V_{OC} (V)	J_{SC} (mA/cm^2)	PCE (%)	FF (%)
Without interlayer (best cell)	0.728	23.2	10.1	59.4
With interlayer (best cell)	0.774	23.0	11.0	61.9
Without interlayer (average of 200 cells)	0.710	20.0	7.72	54.1
With interlayer (average of 200 cells)	0.730	20.4	8.10	54.2

The better performance of devices with the wurtzite GLAD interlayer can be attributed to improved *n*/*p* interface due to less lattice mismatch between wurtzite CdS and GLAD wurtzite CdTe, as both share the same crystal structure and more similar lattice constants when compared to zinc blende CdTe. As a result, wurtzite CdTe incorporated in these devices makes higher electronic quality, less defective interfaces with the underlying wurtzite CdS and over-deposited zinc blende CdTe. All these results indicate that the idea of incorporating a thin wurtzite CdTe interlayer between CdS and zinc blende CdTe serves as a means of interfacial tailoring at the heterojunction for improved PV device performance. This concept will be extended for devices incorporating better-optimized CdTe after deposition of the interlayer, as opposed to RT normal incidence deposited CdTe thin films.

11.5 CONCLUSIONS

GLAD magnetron sputtered CdTe shows variation in optical properties, density, and microstructure with incident source flux angle and deposition temperature. Crystal phase structure transitions from cubic zinc blende to hexagonal wurtzite with increasing source flux angle for material deposited at RT. GLAD CdTe prepared at 250°C is predominately cubic. As-deposited RT GLAD CdTe films prepared at higher source flux angles show sensitivity to in-plane optical anisotropy from the projection of the tilted columnar axes and as identified from analysis of Mueller matrix spectra. $CdCl_2$ treated CdTe shows enhanced crystallite size compared to as-deposited samples with grain size increasing with treatment time. PV devices incorporating GLAD CdTe interlayers show 0.9% absolute higher efficiency compared to devices without the interlayer. The higher efficiency of the device with GLAD CdTe interlayer is because of an improved *n/p* interface due to improved structural compatibility between CdS and GLAD wurtzite CdTe.

12. SYNTHESIS AND CHARACTERIZATION OF COLLOIDAL II-VI QDS FOR PASSIVATION STUDIES RELEVANT TO CDTEPHOTOVOLTAICS

Ebin Bastola, Trevor A. Hickle, Chandan Kadur, Dipendra Pokhrel, Scott Lambright, Abasi Abudulimu, Randy Ellingson

12.1 SUMMARY

With the eventual aim of studying surface passivation of CdTe and $CdSe_xTe_{1-x}$ photovoltaic cells, synthesis processes for colloidal CdTe and $CdSe_xTe_{1-x}$ quantum dot (QD) nanocrystals have been developed and are currently being evaluated for QD quality and batch-batch key process output (KPO) repeatability. Five separate batches of colloidal CdTe QDs and one batch of $CdSe_xTe_{1-x}$ QDs have been synthesized and characterized with optical absorption spectroscopy, steady-state photoluminescence (PL), and time-resolved photoluminescence (TRPL) lifetime in-house. For CdTe QDs, PL peaks (correlated with absorption) were found at either ~730 nm or ~720 nm with an average lifetime of 2.9 ns (with shorter wavelength PL being correlated with larger target batch size). For $CdSe_xTe_{1-x}$ QDs, PL peak was found at ~840 nm with an average lifetime of 68ns. Scanning electron microscope (SEM) and scanning tunneling electron microscope (STEM) images will be taken of these nanocrystals in the near future. Additionally, a collaboration has been initiated with the Center for Integrated Nanotechnologies (CINT), in which both groups will synthesize and characterize similar nanocrystals. This collaboration was sought after in the hope of leveraging CINT's expertise in nanotechnology to better control the synthesis process and eventually develop shell growth processes. These interface studies are a means of modeling interfaces as well as screening superior back contact materials for polycrystalline thin-film CdTe and $CdSe_xTe_{1-x}$ solar cells.

12.2 INTRODUCTION

CdTe is one of the major photovoltaic materials that is manufactured and sold on an industrial scale. Unfortunately, the commonly used back contact materials for this technology do not result in a well passivated CdTe/hole-collection layer (HCL) interface. [312] This leads to large surface recombination velocities at this interface that depress open-circuit voltage and ultimately photon conversion efficiency. In order to screen new materials and material processing methods for this photovoltaic system without the complicating imperfections of vapor-transport-deposition- (VTD) or close-space-sublimation- (CSS) deposited polycrystalline thin CdTe films, it has been determined by this research group that a replacement back contact material search would be most efficiently performed using CdTe QDs. This conclusion was informed by the assumption that the study of CdTe QDs would yield clearer KPO signals (due to lower sample-sample variation).

In the service of finding better passivating materials for the CdTe/HCL interface, a colloidal CdTe QD synthesis method has been proposed (inspired by previous work from Mulvaney *et al*. [313]), and several batches of CdTe QDs have been fabricated, in addition to one batch of $CdSe_xTe_{1-x}$ QDs. Optical absorption and PL spectrum, along with TRPL lifetimes, have been measured and compared for these QD batches. The short-term goal of this work is to minimize the variations in these KPOs batch-to-batch to facilitate maximal reproducibility during the later stages of this

project. Once we are assured that these synthesis processes are under control, shell growth methods for various candidate photovoltaic (PV) cell back contact materials will be developed, and the optoelectronic character of these core/shell interfaces will be probed.

12.3 METHODS, ASSUMPTIONS, and PROCEDURES

CdTe Quantum Dot Synthesis:

CdTe QD synthesis methodology described below is similar to a method reported by Mulvaney *et al.* [313]. Precursor masses used in a given batch varied somewhat, but the target precursor ratios were constant throughout.

1 Tellurium (and Selenium) Precursor Preparation - 1mmol (0.1276g) elemental Te powder, 6.05mmol (2.7mL, 2.2437g) trioctylphosphine (TOP), and 3.0mL octadecene (ODE) were measured and placed in single-neck flask under nitrogen in a glovebox. The flask was then sealed with a rubber septum and parafilm. This flask (tellurium precursor flask) was then removed from the glove box, placed in a sonicator, and sonicated for ~ 100minutes at 60°C.

   Note that in the case of $CdSe_xTe_{1-x}$ QD synthesis, half of the elemental Te powder, by moles, was replaced with an equivalent molar amount of elemental Se powder with no other change to this procedure.

2 Cadmium Precursor Preparation - 1mmol (128.4mg) cadmium oxide (CdO), 3.8mmol (1.2mL, 1.074g) oleic acid (OA), and 22mL ODE were measured under air and placed into a three-necked flask. A magnetic stirrer was added to this flask (reaction flask), and two of the three necks were sealed with rubber septa. The reaction flask was then placed on a heating mantle with magnetic stirring active. A thermocouple probe was inserted into the flask through one of the septa and submerged in the Cd precursor mixture. This reaction flask was then connected to a condenser and placed under vacuum, heated to 85°C, and left this way to degas for 1 hour. After degassing, the reaction flask was placed under N_2 flow. The temperature of the cadmium precursor mixture was raised to 260°C and left to dissolve for an additional 30 minutes.

3 CdTe QD Synthesis/Cleaning/Resuspension - Once the Cd precursor mixture was clear and yellow (suggesting full coordination of Cd with OA), the entirety of the tellurium precursor was injected into the reaction flask. The reaction flask's temperature was then increased to 270°C and left to react for 15 minutes. Once 15 minutes had transpired, the reaction flask was taken off of the heating mantle and submerged into a cold water bath to stop the reaction. Split product equally between several centrifuge test tubes, and copious amounts of isopropanol was added to make sure the QDs were unsoluble. These test tubes were centrifuged to precipitate the QD nanoparticles. After a first-round of precipitation, the substance that precipitated out of solution was re-dissolved into toluene using a sonicator and then precipitated a second time, again using copious isopropanol and centrifugation to drop nanocrystals out of solution. Finally, this second precipitate was dissolved in toluene using a sonicator and stored in a cool, dark place.

Optical Characterization of Quantum Dots:

1. Time-resolved Photoluminescence (TRPL) - TRPL was measured using a Horiba Scientific Deltaflex™ Modular Fluorescence Lifetime System.
2. Steady-state Photoluminescence (PL) - PL spectra were measured using a homemade system that includes a Horiba Scientific spectrophotometer and three lasers (405, 532 nm, and 630 nm excitation wavelengths).
3. Absorption – Optical absorption spectra were measured using a Perkin-Elmer Lambda 1050 ™ spectrophotometer.

12.4 RESULTS and DISCUSSION

CdTe QD synthesis work has been performed during the summer of 2021 to re-dial in a process demonstrated two years earlier in the summer of 2019. The work performed in the summer of 2019 will be briefly recounted, followed by an update concerning 2021 process modification, characterization, and control.

Summer 2019:

Figure 68 displays the XRD pattern of a film of CdTe QDs. The XRD pattern indicates the crystalline nature of these synthesized QDs, and the reference lines were obtained from MDI ZADE for PDF #98-001-4040, which clearly matches with the XRD pattern of the QDs. The CdTe has a cubic crystal structure in the zinc blende phase similar to the bulk (thin film) CdTe material. Further, we studied the absorption spectra of as-synthesized CdTe QDs using a UV-Vis-NIR absorption spectrometer, and it is shown in Figure 69. The UV-Vis spectrum shows a very strong absorption of these CdTe QDs at lower wavelength, and the absorbance is almost zero at higher wavelength (> 693 nm in Figure 69). Various excitonic features have also been observed, along with a strong first excitonic peak at 693 nm.

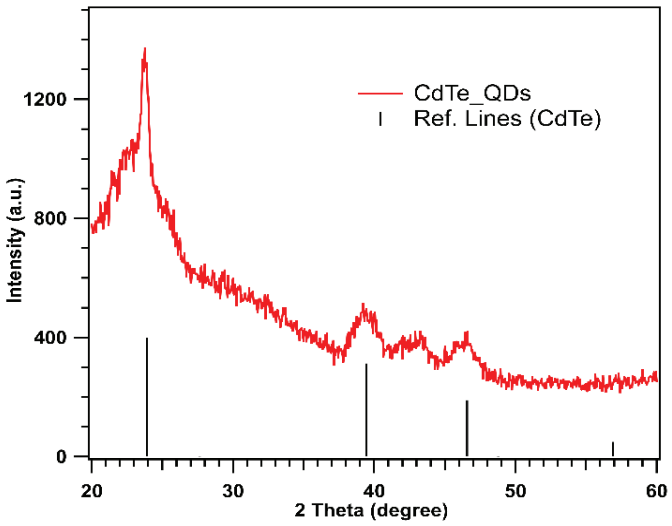


Figure 68. X-ray diffraction pattern of as-synthesized CdTe QDs

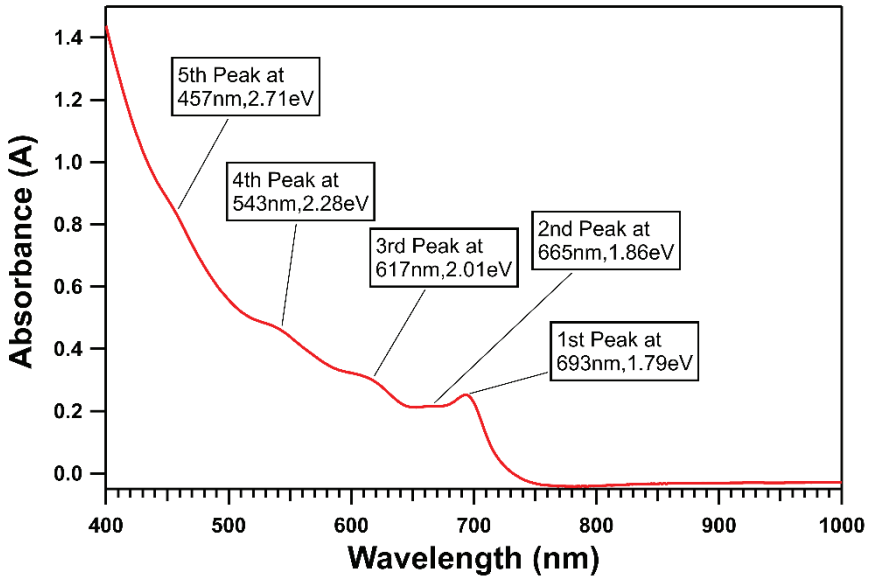


Figure 69. UV-Vis spectrum of CdTe QDs with excitonic transitions annotated

Similarly, we carried PL and TRPL measurements to these CdTe QDs, which are shown in Figure 70(a, b). The synthesis 9 produced QDs having a very high carrier lifetime of about 60 ns (average), which we believe is due to the better control of the reactants precursor before injecting Te precursor. The strong PL emission and long carrier lifetime of these QDs indicate we can synthesize very high-quality QDs material suitable for the study of surface passivation using chemical or shell growth method. The quick injection of the Te precursor to the Cd precursor, a proper amount of oleic acid for the formation of Cd-oleate, and immediate cooling of the reaction flask after removing the heating mantle helped to have a better lifetime for synthesis 9 compared to synthesis 6.

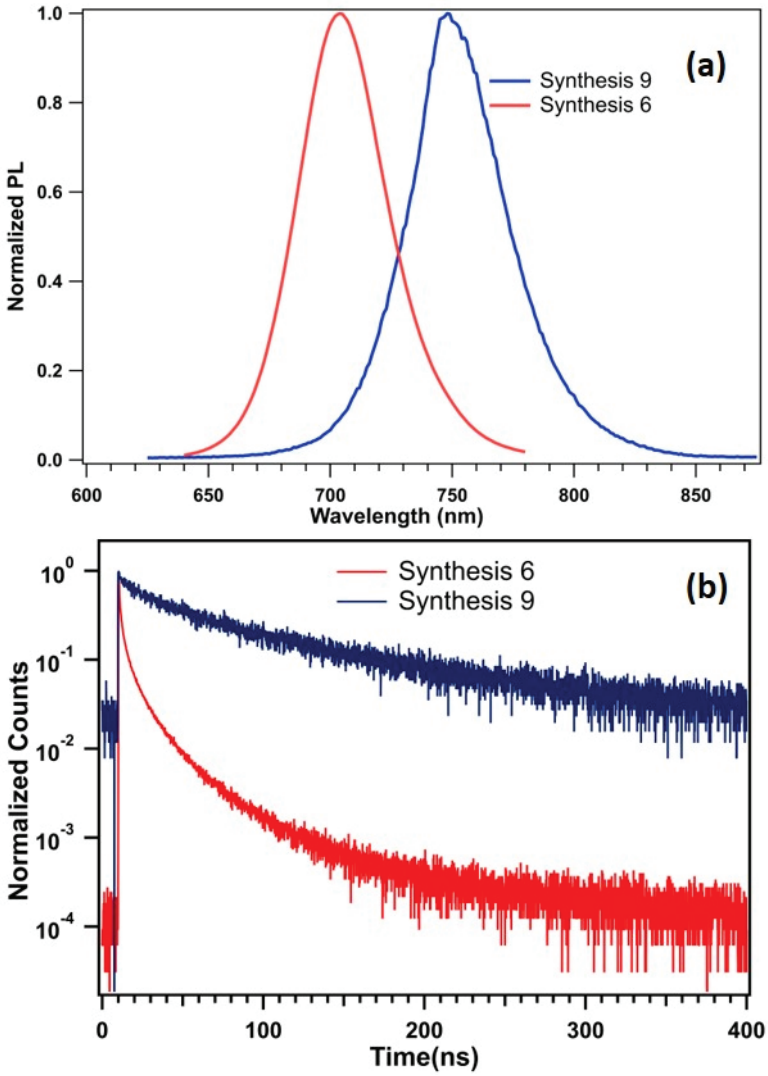


Figure 70. (a) PL spectra of syntheses #6 and #9, CdTe QDs; (b) TRPL of these same samples

Figure 71 displays the UV-Vis-NIR spectra of pure and alloyed CdTe QDs, and the alloyed CdSeTe QDs consist of various amounts of Se in the anion precursor from 0 to 20%. After we introduced the Se in the anionic precursor, the first excitation peak was shifted towards red compared to CdTe QDs, as seen in Figure 71.

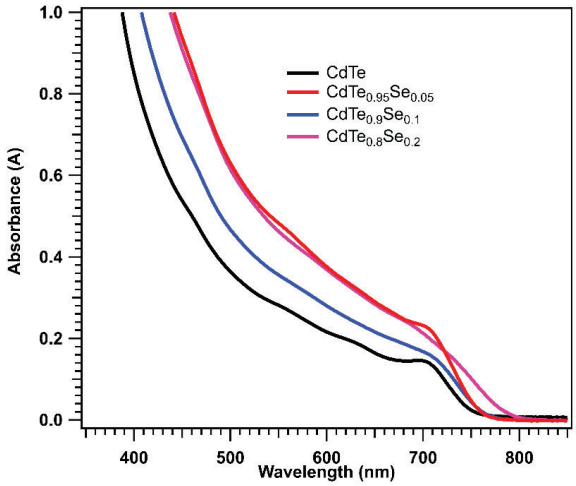


Figure 71. UV-Vis spectra of CdTe and alloyed $CdSe_xTe_{1-x}$ QDs

Summer 2021:

The PL spectra from four of the five colloidal CdTe QD batches characterized demonstrate a single signal maximum, either at ~720 nm or ~730 nm (Figure 72). The fifth of these batches demonstrates two peaks, with one peak at 720 nm and another peak at 840 nm (not shown); note that the PL peak at 840 nm is the same wavelength as the one from the batch of $CdSe_xTe_{1-x}$ QD (see Figure 72, the blue curve was measured from $CdSe_xTe_{1-x}$ sample). This suggests that the one CdTe QD batch was contaminated with $CdSe_xTe_{1-x}$ QDs, which leads us to exclude this batch from the analysis.

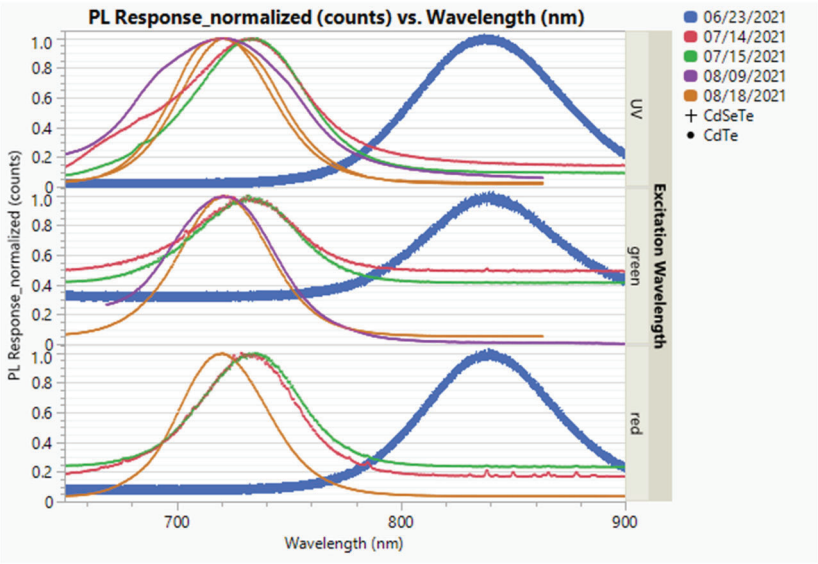


Figure 72. PL spectra of QD samples at three excitation wavelengths: 405 nm, 532 nm, and 633 nm

As seen in Figure 73, the CdTe QD PL emission peak is correlated with target batch size (i.e., Cd precursor weight, as seen in Figure 73 legend). The author believes this is due to reaction mixture heating rate differences between batches; the Te precursor in this process is at room temperature when it is injected into the reaction flask, so increased Te precursor mass could slow the heating rate of the reaction medium. This all suggests that the thermal parameters will need to be adjusted for this process if the same PL peak is to be maintained when scaling to a larger batch size.

Note that narrower PL peaks have been observed for similar synthesis processes. For similar reasons that batch-batch variation is undesirable, minimization of within-batch QD quality variation is also a goal in the optimization of this CdTe QD synthesis process. An effort will be exerted in Q4 2021 to reign in the widths of CdTe QD PL peaks, which are correlated with variation in quantum confinement within a batch of nanocrystals. [313]

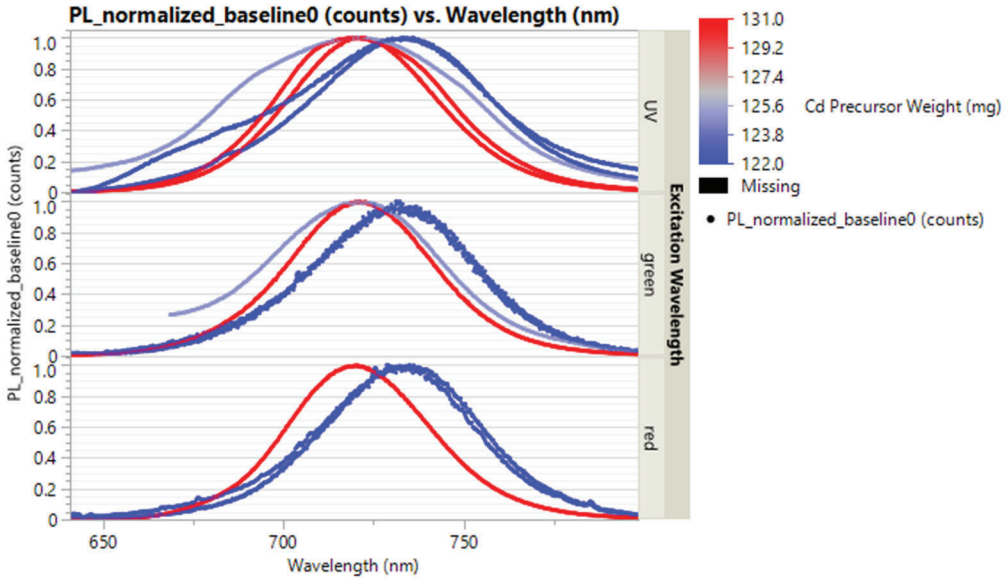


Figure 73. PL spectra of QD samples vs. Cd precursor amount, measured at three different excitation wavelengths: 405 nm, 532 nm, and 633 nm

The onset of increased absorption in CdTe QD samples for the light of 775 nm wavelength and shorter (Figure 74) agrees with PL emission peaks of these same samples. Likewise, the increased absorption of $CdSe_xTe_{1-x}$ QDs at 860 nm and shorter wavelengths (Figure 74) agrees with that sample's PL peak.

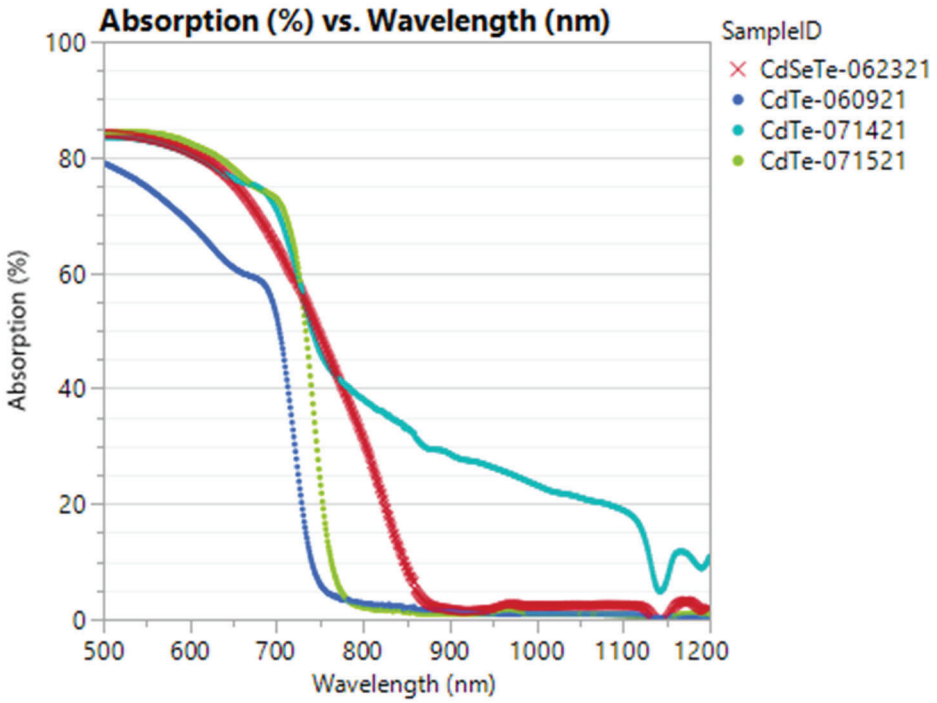


Figure 74. Optical absorption spectra of CdTe and CdSeTe QDs

The time-resolved PL decay curves (Figure 75) for the two CdTe QD batches for which it was measured overlap with each other very well, with τ_1 = 2 ns (frequently considered due to surface recombination) and τ_2 = 14 ns (frequently considered due to bulk recombination). $CdSe_xTe_{1-x}$ PL lifetimes τ_1 = 49 ns and τ_2 = 186 ns surpass CdTe QD PL lifetimes by an order of magnitude, which suggests much longer-lived excitons in the Se-alloyed system.

Theory suggests that longer lifetimes should be possible in CdTe QDs. [314] Additionally, it was demonstrated in the 2019 CdTe QD synthesis and characterization work (discussed above) that average lifetimes of 60 ns are possible with these nanocrystals -- Figure 70(b). The syntheses performed in summer 2021 followed nominally the same fabrication procedure; investigators are currently investigating what unintentionally varied process parameters could be responsible for the comparatively worse CdTe QD PL lifetime with the intention of reporting findings on this topic Q4 2021.

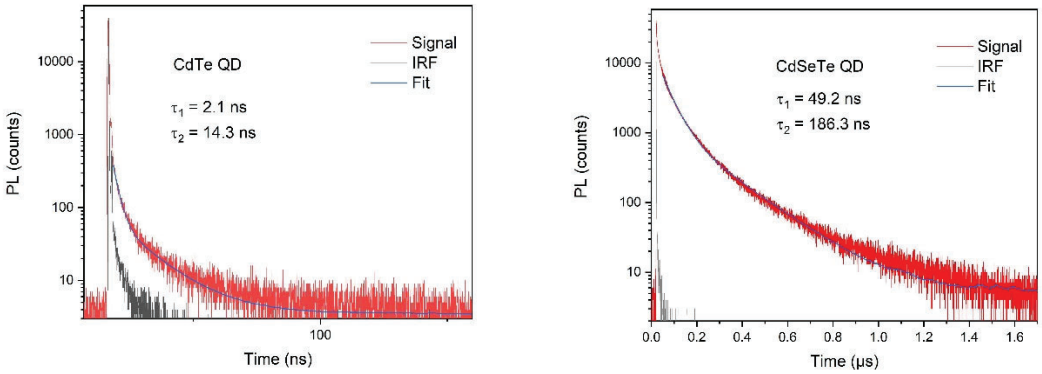


Figure 75. Time-resolved PL decays of CdTe (left) and CdSeTe (right) QD samples excited at 633 nm

12.5 CONCLUSIONS

Wide-peak PL maximums and short TRPL lifetimes suggest that the colloidal CdTe QD synthesis proposed in this update requires further optimization in order to realize narrow crystal size distribution and longer carrier lifetimes. That being said, the synthesis described above does seem imminently controllable and results in low batch-batch variation as long as target batch size (and accompanying measured precursor quantities) remain fixed. These CdTe/ $CdSe_xTe_{1-x}$ QDs will be studied using SEM and STEM imaging along with additional characterization performed by our CINT partners.

13. OPTICAL STUDIES OF III-V THIN FILMS

Madan Mainali, Indra Subedi, and Nikolas J. Podraza

*Samples provided by Prof. Seth Hubbard at RIT

13.1 SUMMARY

III-V compound semiconductor epitaxial multilayer film samples have been characterized by terahertz (THz), infrared, and near infrared to ultraviolet range spectroscopic ellipsometry using a recently developed parametric model describing the complex dielectric function spectra. This model for the complex dielectric function spectra is continuous in the first derivative with respect to photon energy, Kramers-Kronig consistent, and accounts for the direct band gap, sub-gap absorption due to Urbach tails, and higher energy critical point transitions. The infrared region absorption includes sensitivity to the phonon modes and free carrier absorption to some extent. Absorption in the THz range is predominately due to free carrier absorption and described by Drude model. It has been used to describe InP epitaxially grown on InGaAs, InGaAs epitaxial layers of different thickness grown on InP, and InAlAs epitaxially grown on InGaAs. Parametric models for the complex dielectric function spectra are generated for InP, InGaAs, and InAlAs with this method. The resulting layer thicknesses and complex dielectric function spectra obtained from analysis of ellipsometric spectra reasonably match nominal expected thicknesses and complex dielectric functions found in the literature validating the modeling approach. Differences in the complex dielectric function spectra of thin epitaxial InP grown on InGaAs relative to previous studies of films grown directly on InP:Fe wafers are attributed to differences in film stress, more prolonged oxygen exposure, or both. The magnitude of the imaginary part of the complex dielectric function of InGaAs increases with increasing layer thickness indicating an increase in electronic transition strength and reduction in lattice distortions. The electrical transport properties estimated by THz range ellipsometry and electrical Hall effect are close to each other and to that reported in literature which validates our model. The complex dielectric properties and transport properties obtained for materials in multiple layer stacks can be used as input for device performance modeling. The measurement methodology developed applies to complete III-V based solar cells.

13.2 INTRODUCTION

Multijunction solar cells based on epitaxial growth of III-V compound semiconductors already exhibit very high efficiencies, but there is a continuing desire to push the upper limits of these devices further. Like polycrystalline thin film solar cells, the performance of these epitaxial thin film solar cells depends on the opto-electronic characteristics of each component layer. In particular, ternary and quaternary compositions are often varied to change the band gap energy as well as to provide lattice matching with the underlying crystalline materials. Probing the characteristics of an individual layer within a multiple layer stack such as a solar cell is crucial to understanding deviations from expected device performance, which may arise from non-ideal optical response, electronic properties, layer stress, or a combination of these effects. Spectroscopic ellipsometry over different wavelength and photon energy ranges potentially provides sensitivity to these characteristics for thin films in all multiple layer stacks as well as measuring the complex optical response, in the form of the complex dielectric function spectra,

and multilayer stack structure, in terms of layer thicknesses and the characteristics of any native oxide and physically mixed layers. From the near infrared to ultraviolet spectral range, the complex dielectric function spectra contain information regarding the band gap energy, Urbach tail below the band gap, and above gap critical point transitions. The magnitude of the Urbach energy describing the sub-band gap absorption tail is directly related to the defect state concentration. Shifts in the band gap and critical point energies occur with variations in composition and film stress. Broadening of both the band gap and critical point transitions occurs with scattering of photo-excited charge carriers by the dominant defect mechanism. As a result, the near infrared complex optical response can be mined for information related to defects and film stress in addition to providing input for opto-electronic simulations of device performance itself. Spectroscopic ellipsometry measurements in the infrared and millimeter wavelength ranges and magnetic field dependent optical Hall effect measurements provide the ability to discern electronic transport properties of independent layers in multiple layer stacks. The combination of both near infrared to ultraviolet range spectroscopic ellipsometry and measurements at longer wavelengths provides a means of characterizing the optical properties, electronic properties, stress, and structure of layers within multilayer stacks like epitaxial III-V solar cells.

Developing physically realistic models of complex dielectric function spectra of epitaxial III-V semiconductor compounds is the most challenging part of characterizing these materials by spectroscopic ellipsometry, as the long wavelength response is already well-described using the Drude model for free charge carriers. To describe the near infrared to ultraviolet complex dielectric function spectra, a piecewise but continuous model has been developed to include the band gap, sub-gap absorption in the form of an Urbach tail, and above gap electronic transitions. These characteristics are all needed to describe the optical response of direct band gap crystalline semiconductors. Additional constraints between fit parameters have been established so that the first derivative of the complex dielectric function spectra with respect to photon energy are also continuous. This new criterion has been added to further improve the physical realism of the model. Case studies here involve epitaxial InGaAs and InAlAs films in multiple layer stacks. Near infrared to ultraviolet range spectroscopic ellipsometry is applied to characterize epitaxial layerth ickness and determine the appropriate parametric model describing the complex dielectric function spectra for InGaAs and InAlAs layers within those stacks. The optical characteristics of these films can be compared to bulk crystal reference values to discern relative stress variations. The structural information obtained from analysis of the near infrared to ultraviolet range ellipsometric spectra is fixed for the analysis of longer wavelength range infrared and THz spectra.

13.3 METHODS, ASSUMPTIONS, and PROCEEDURES

Here we have a method for characterizing the complex dielectric function spectra of III-V compound semiconductors particularly in multilayer stacks as investigated by spectroscopic ellipsometry. To describe the complex dielectric function spectra of III-V compounds, an advanced parametric model applicable from the near infrared to vacuum ultraviolet spectral range has been developed and applied to InP to deduce electronic transition critical point energies as part of an analysis procedure also yielding the optical response of its native oxide. [315] A similar analysis approach is now finalized to extract the complex dielectric function spectra and critical point energies in InGaAs and InAlAs epitaxial layers. The samples of interest consist of nominally 1500 thick InGaAs deposited on InP then over-deposited by an epitaxial InP layer, and a sample of

InAlAs deposited on InGaAs coated InP then over-deposited by InGaAs and InP epitaxial layers as shown in Figure 76. The top InP epitaxial layer is also expected to have oxidized.

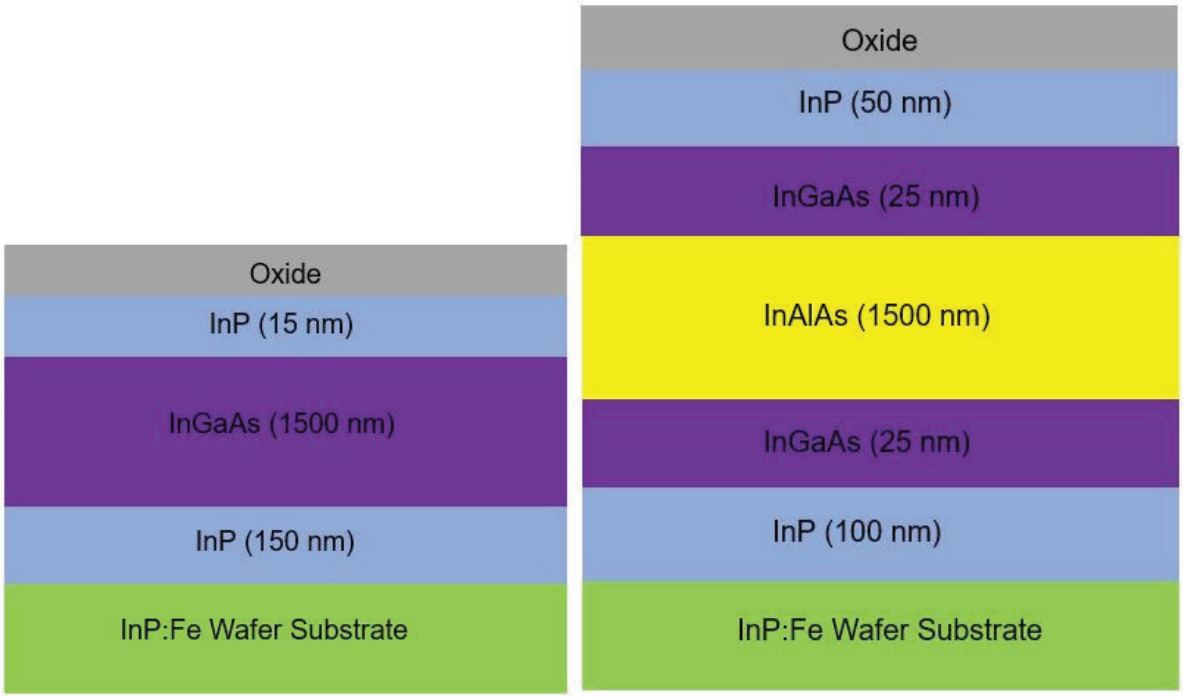


Figure 76. Schematics of (left) InGaAs and (right) InAlAs epitaxial film stacks

In general, spectroscopic ellipsometry measurements are sensitive to both sample structure in the form of layer thicknesses, interfaces, and gradients as well as optical properties in the form of the complex dielectric function ($\varepsilon = \varepsilon_1 + i\varepsilon_2$) spectra. Here we are considering spectroscopic ellipsometry measurements from the near infrared into the ultraviolet (0.74 to 5.9 eV), although the upper limit to the photon energy range in the analysis is determined by the layer of interest and the opacity of the overlying layers. To determine the optical response and critical point information contained within for a particular material beneath other absorbing layers, the upper photon energy limit is chosen so to allow at least ~20-30% of light from the initial interface of that layer with over-deposited layers as estimated by Beers Law to reach the detector as shown in Figure 77. This limit is chosen to avoid any unphysical behavior in the optical property model arising from a lack of sensitivity to underlying materials by the absorbing materials deposited on top. This approach can be adapted based on estimated layer thicknesses and reference optical properties for the layers within the III-V epitaxial multilayer stack.

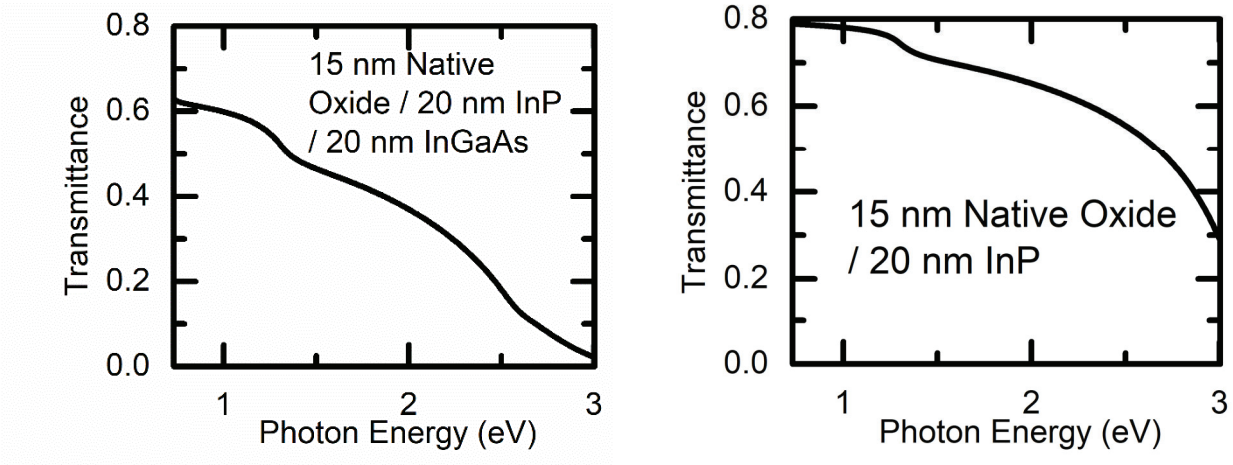


Figure 77. Estimations of penetration depth using Beers Law to (left) InGaAs and (right) InAlAs layers corresponding to the samples described in Figure 76

To describe the complex dielectric function spectra over the near infrared to ultraviolet spectral range, a parametric model has been developed which accounts for the direct band gap, an Urbach tail, and higher energy critical point electronic transitions. The complex dielectric function spectra are described as:

$$\varepsilon_2(E) = \begin{cases} e^{\frac{E-E_0}{E_u}} \operatorname{Im}\sum_{m=0}^{n} \varepsilon_{CPPB,m}(E_0) & 0 < E \le E_0 \\ \operatorname{Im}\sum_{m=0}^{n} \varepsilon_{CPPB,m}(E) & E > E_0 \end{cases}$$

$$\varepsilon_{CPPB,m}(E) = A_m e^{i\varphi_m}\left(\frac{\Gamma_m}{2E_m - 2E - i\Gamma_m}\right)^{\mu} \qquad (1)$$

$$E_u = \frac{\Delta E \operatorname{Im}\sum_{m=0}^{n} \varepsilon_{CPPB,m}(E_0)}{\operatorname{Im}\left[\sum_{m=0}^{n} \varepsilon_{CPPB,m}(E_0 + \Delta E) - \sum_{m=0}^{n} \varepsilon_{CPPB,m}(E_0)\right]}$$

$$\varepsilon_1(E) = \varepsilon_\infty + \frac{A_s}{E_s^2 - E^2} + P\int_{0.74}^{E\max} \frac{E'\varepsilon_2(E')}{E'^2 - E^2} dE'$$

where the contribution from each critical point is modeled assuming parabolic bands (CPPB) with an amplitude (A_m), broadening energy (Γ_m), critical point energy (E_m), phase (φ_m), and exponent defining dimensionality of the transition (μ_m). The direct band gap is denoted as E_0 and the Urbach energy as E_u. The parameter ΔE should be smaller than the spacing between spectral points and is used to ensure that the first derivative of the complex dielectric function with respect to photon energy is continuous. The real part of the complex dielectric function spectra from this model is calculated using Kramers-Kronig integration with additional Sellmeier (A_s, E_s) and constant additive terms (ε_∞). The resultant dielectric function model and its first derivative is continuous from above to below the band gap and Kramers-Kronig consistent by design, making it highly

physically realistic. Equation 1 represents an advance over that previously applied in Ref. [315] in that E_u is no longer an independent fit parameter and the first derivative of the complex dielectric function with respect to photon energy is now guaranteed to be continuous. It can be applied in commercial optical analysis simulation software and is also applicable to modelling the complex dielectric function spectra of both direct and indirect band gap materials.

Further, the parametric model is extended for analysis of spectroscopic ellipsometry data collected for the epitaxial multilayer stacks in the THz and infrared spectral ranges. The ellipsometric spectra collected for photon energies below 0.73 eV are analyzed by using combination of Lorentz oscillators and Drudemodels. The THz spectral range is analyzed with only the Drude contribution and infrared spectral range is analyzed using both Drude and Lorentz models. [316, 317] In both THz range and infrared range analysis, layers thicknesses are fixed from results obtained from near infrared to ultraviolet range ellipsometry analysis. A single Sellmeier expression is used to describe the optical properties of the InP:Fe substrate. Each Lorentz oscillator is described by,

$$\varepsilon(E) = \frac{A\Gamma E_0}{\left(E_0^2 - E^2\right) - i\Gamma E}, \tag{2}$$

where E_0, A, and Γ are the resonance energy, amplitude, and broadening respectively. The Drude model is expressed in terms of resistivity (ρ) and scattering time (τ):

$$\varepsilon(E) = -\frac{\hbar^2}{\varepsilon_0 \rho\left(\tau E^2 + i\hbar E\right)}, \tag{3}$$

where $\hbar$ and ε_0 are reduced Planck constant ($h/2\pi$) and permittivity of the free space respectively. The ρ and τ are related with free carrier concentration (N) and carrier mobility (μ) with the relation $N = m^*/Nq^2\tau = 1/q\mu N$ where m^* is carrier effective mass and q is the elementary charge. Electrical Hall effect measurement was also done for the InGaAs epitaxial layer and the carrier mobility and carrier concentration measured are close to the values obtained from THz range analysis.

13.4 RESULTS and DISCUSSION

Experimental ellipsometric spectra and model fits for the InGaAs samples are provided in Figure 78, the resulting spectra in ε in Figure 79, structural parameters in Table 11, and parameters describing ε in Table 12. Experimental ellipsometric spectra and model for the for the InAlAs sample are provided in Figure 80, the resulting spectra in ε in Figure 81, structural parameters in Table 13, and parameters describing ε in Table 14.

For the InGaAs samples, the model fit thicknesses reported in Table 11 are similar to the nominal expected values, with the exception of the oxide on the top InP layer. Reference spectra in ε for the underlying InP and the top InP native oxide are obtained from Ref. [315]. Spectra in ε for the InP grown on the InGaAs samples is obtained from a parameterization of

spectra in ε from Ref. [315] using equation 1. All parameters are fixed except for the InP direct band gap energy and amplitude associated with that critical point which are $E_0 = 1.273 \pm 0.005$ eV and $A_0 = 3.26 \pm 0.08$ for the nominally 1500 thick InGaAs sample. These parameters defining ε for the top InP may differ from that reported for the epitaxial film on InP:Fe wafer [315] due to strain from the underlying materials, prolonged oxidation, or both.

The critical point energies in the InGaAs epitaxial layers reported in Table 12 are quite close to those reported in literature, [318, 319] with the exception of the relatively broad weak feature near ~1.2 eV. All critical points are assumed to be one dimensional. The lowest energy critical point corresponding to the band gap is slightly outside the measured spectral range so direct conclusions on behavior cannot be drawn from these critical point values. The higher energy critical point located near 2.57 eV are within error of the value for reference InGaAs. [318, 319] The critical point near 2.8 eV is close to the reference value, however, are slightly lower in energy indicating the possibility of tensile strain. The Sellmeier position is fixed at the value of the lowest energy critical point at found at photon energies greater than the measured spectral range.

For analysis of the InAlAs sample, spectra in ε for the top InP layer and the 1500 nm thick InGaAs are used within the optical model. Model thicknesses reported in Table 14 are again close to the nominal values expected, except for the top InP layer likely due to the same reasons as for the InGaAs samples. For this sample, the maximum photon energy range measured is 2.5 eV due to the additional absorption in the ~25 nm thick InGaAs epitaxially grown on the InAlAs. All critical points are assumed to be excitonic and critical point phase φ_m are fixed to values obtained by parameterizing reference spectra in ε for InAlAs. [320] The $E_0 + \Delta$ critical point located at 1.74 eV is constrained to be 0.3 eV greater than the E_0 critical point in the model fit. The Sellmeier position is fixed at the lowest energy critical point located outside the upper photon energy limit of the analyzed spectral range. The critical point values reported in Table 14 and corresponding spectra in ε are in close agreement with that previously reported in literature indicating similar levels of strain in this epitaxial layer relative to Ref. [320] and that this parametric model reasonably represents the optical response of InAlAs. The slight blue shift in the first critical point (E_1) may indicate compressive stress near the top InAlAs surface.

Electronic transport properties of the InGaAs and InAlAs are estimated THz range ellipsometry. The Drude model with ρ and τ as fit parameters is used in the analysis. Electron effective mass are fixed at $m^* = 0.042m_e$ and $m^* = 0.075m_e$ for InGaAs and InAlAs respectively. [321, 322] Since the THz beam penetrates throughout the sample, the InP:Fe substrate thickness and the thickness of the physically mixed interfacial layer between the substrate and InP in the InGaAs epitaxial layer stack is fitted with single Sellmeier expression while the thickness of the other layers in the stack are fixed at the values obtained from near infrared to ultraviolet range analysis. THz range properties of the InP:Fe substrate is in close agreement with literature. [323] The thickness of the InP:Fe substrate and physically mixed interfacial layer in the InGaAs sample stack are found to be 353 ± 4 μm and 886 ± 138 nm, respectively. The parameters describing the spectra in ε for InP:Fe substrate are $\varepsilon_\infty = 10 \pm 2$, A_s (eV^2) $= 0.020 \pm 0.001$, and E_s (eV) $= 0.08 \pm 0.02$. In the InAlAs stack sample, the complex dielectric function spectra of the substrate are fixed with parameters estimated from the fit of the InGaAs epitaxial stack but its thickness and the thickness of the

physically mixed interfacial layer between the substrate and InP is fitted. The thickness of the InP:Fe substrate and intermix in the InAlAs sample stack is found to be 480.2 ± 0.4 μm and 374 ± 135 nm respectively. The epitaxial sample thicknesses are also measured by vernier caliper. The thickness of the InGaAs and InAlAs sample are measured to be 340 ± 10 μm and 470 ± 10 μm respectively which are close to the values obtained from the analysis of THz range ellipsometric spectra. The sample thickness is dominated by that of the substrate. The similarity of the measured thickness by two different methods and the dielectric function similar to the values reported in the literature further justify the reliability and accuracy of our modeling approach in the THz range. The Drude parameters describing complex dielectric function of the InGaAs and InAlAs in their corresponding epitaxial stacks are summarized in Table 15. N and μ for the InGaAs from the electrical Hall effect are measured to be 1.37×10^{17} cm^{-3} and 8085 cm^2/Vs respectively which are close to values obtained from the analysis using the THz range ellipsometry and the Drude model.

The infrared phonon modes are also detected in the infrared spectral range analysis. Both the Drude model and Lorentz oscillator are used to describe the dielectric functions of InGaAs and InAlAs in this range. The parameters of the Drude model are fixed at values obtained from the THz spectral range analysis. The resonance energy of the GaAs phonon mode in the InGaAs sample and the AlAs mode in the InAlAs sample are fixed at 252 cm^{-1} (0.03124 eV) and 351 cm^{-1} (0.04352 eV) respectively from Ref. [324]. Since the energy of the vibrational mode are at the lower limit of the infrared spectral range (0.055 – 0.73 eV) ellipsometer, there is high correlation between amplitude and broadening of the Lorentz oscillator. The broadening of the GaAs and AlAs mode are fixed at 8 cm^{-1} (0.00099 eV) and 5 cm^{-1} (0.00062 eV), respectively from Ref. [325, 326] to account for this correlation. The amplitude of the GaAs and the AlAs vibrational mode are found to be 88 ± 21 and 100 ± 10 cm^{-1} respectively. ε_∞ for the InGaAs and InAlAs layers are found to be 12.15 ± 0.04 and 8.7 ± 0.4, respectively. In both InGaAs and InAlAs stack, the resonance energy of the Sellmeier describing InP:Fe substrate is fixed at 0.0331 eV from Ref. [315]. In the InGaAs sample, ε_∞ and A_S (eV^2) for InP:Fe are found to be 9.92 ± 0.08 and 0.006 ± 0.001, respectively. In the InAlAs sample, ε_∞ and A_S (eV^2) for InP:Fe are found to be 10.00 ± 0.04 and 0.0037 ± 0.0007, respectively. These dielectric functions for InP:Fe are in close agreement with Ref. [315]. The carrier mobility and concentration value also depend on the material composition, temperature, doping level, and layer above and below it. [327-329]

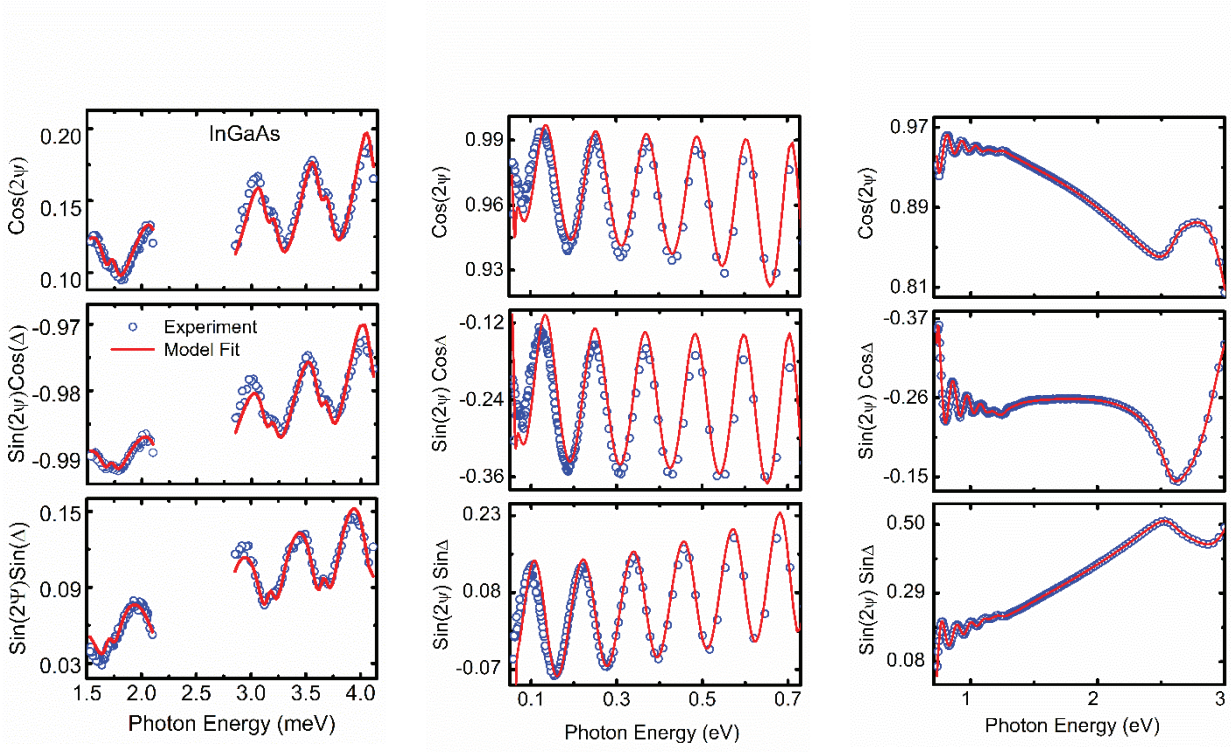


Figure 78. Experimental SE spectra (open blue circles) and model fit (solid red lines) for multilayer sample as in Figure 76 (left)

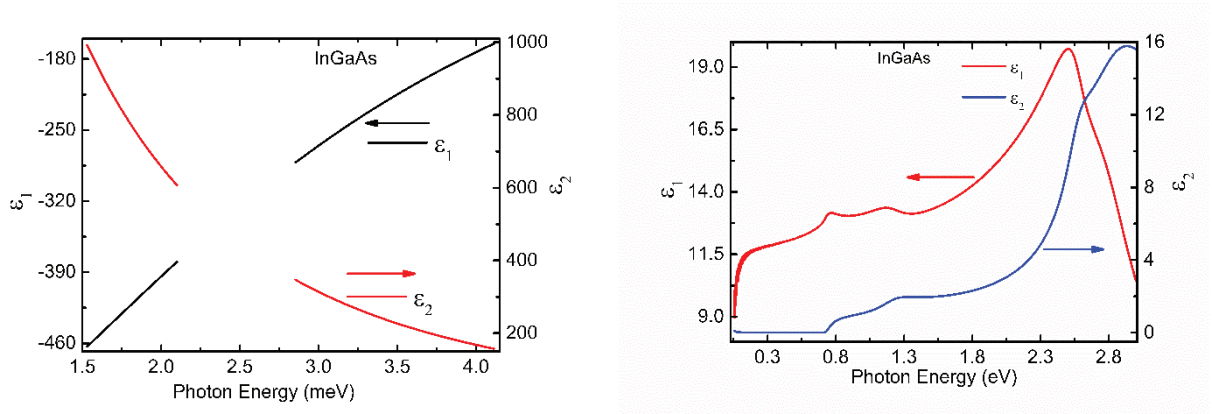


Figure 79. $\varepsilon = \varepsilon_1 + i\varepsilon_2$ spectra from 1.53 meV to 4.11 meV (left), and 0.055 eV to 3 eV (right) of the 1500 nm thick epitaxial InGaAs

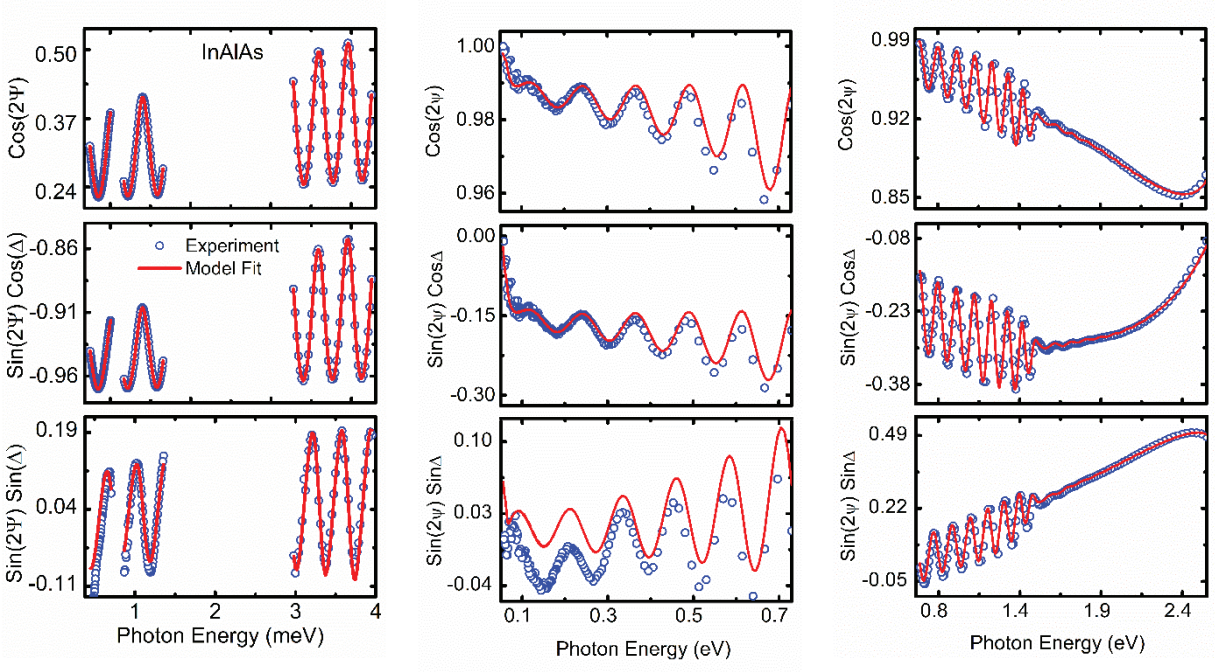


Figure 80. Experimental SE spectra (open blue circles) and model fit (solid red lines) for multilayer sample as described in Figure 76 (right)

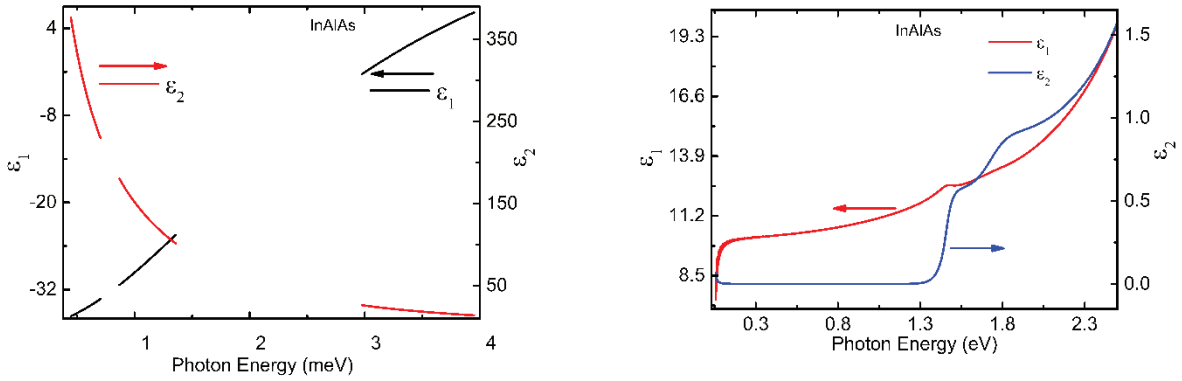


Figure 81. $\varepsilon = \varepsilon_1 + i\varepsilon_2$ spectra from 0.45 meV to 3.95 meV (left), and 0.055 eV to 2.5 eV (right) of 1500 nm thick epitaxial InAlAs

Table 11. Thicknesses obtained from SE analysis of ~1500 nm thick InGaAs epitaxial layers in multilayer stacks

Layer / Sample	~1500 nm InGaAs	Nominal
InGaAs (nm)	1516 ± 1	1500
InP (nm)	17.3 ± 0.3	15
Native Oxide (nm)	16.3 ± 0.2	

Table 12. Model fit parameters for ~1500 nm thick epitaxial InGaAs in a multilayer stack; CP = critical point

Parameter / CP	E_0	$E_0 + \Delta_0$	$E_1 - R_1$	$E_1 + \Delta_1 - R_1$
A_m (unitless)	1.14 ± 0.06	1.05 ± 0.04	6.1 ± 0.3	15.9 ± 0.4
Γ_m (eV)	0.11 ± 0.01	0.25 ± 0.02	0.205 ± 0.009	0.59 ± 0.02
φ_m (°)	−85 ± 6	359 ± 3	21 ± 5	357 ± 1
E_m (eV)	0.730 ± 0.002	1.210 ± 0.006	2.569 ± 0.004	2.80 ± 0.01
CP (eV) [318, 319]	0.75	1.05	2.57	2.82

Table 13. Thicknesses obtained from SE analysis

Layer / Sample	InAlAs	Nominal
Bottom InGaAs (nm)	24.6 ± 0.2	25
InAlAs (nm)	1514 ± 1	1500
InGaAs (nm)	20.3 ± 0.2	25
InP (nm)	21.1 ± 0.1	50
Native Oxide (nm)	14.58 ± 0.08	

Table 14. Complex dielectric function parameters for epitaxial InAlAs in a multilayer stack

Parameter / CP	E_0	$E_0+\Delta_0$	E_1
A_m (unitless)	0.38 ± 0.08	0.21 ± 0.05	182 ± 41
Γ_m (eV)	0.11 ± 0.04	0.3 ± 0.2	0.023 ± 0.005
φ_m (°)	−128	−69	21
E_m (eV)	1.44 ± 0.01	1.74 (0.3 + E_0)	2.951 ± 0.002
CP (eV) [320]	1.45	1.75	2.95

Table 15. Drude complex dielectric function parameters describing the for epitaxial InGaAs and InAlAs in their corresponding multilayer stack

Parameter	InGaAs	References	InAlAs	References
ε_∞	57 ± 4		26 ± 4	
ρ (Ω cm)	0.004 ± 0.0001		0.04 ± 0.2	
τ (fs)	225 ± 9		244 ± 103	
m^*	0.042	[321, 322]	0.075	[321, 322]
N (cm^{-3})	1.72×10^{17}		2.5×10^{16}	
μ (cm^2/Vs)	9444	12000 ref. [329]; 11400 at 300k and 4700 at 77k (undoped) ref. [328].	5714	10000 ref. [329]; 1350 at 300k (undoped) ref. [328].

13.5 CONCLUSIONS

A parametric model of spectra in ε accounting for the direct band gap, sub-gap absorption due to an Urbach tail, above gap critical point transitions, phonon mode, and free carrier absorption has been applied to describe epitaxial InGaAs and InAlAs in multiple layer stacks in the analysis of near infrared to ultraviolet, infrared, and THz range ellipsometric spectra. The structural

parameters obtained from these analyses agree reasonably with nominal expected values, and the spectra in ε obtained for these materials agree with previously reported values in literature. These results validate the physical realism of the models. Differences in InP epitaxially grown on InGaAs relative to that grown on InP:Fe wafer are attributed to strain from the underlying materials, prolonged oxidation, or both. With continued epitaxial growth these distortions may be reduced. Spectra in ε for InAlAs agree well with literature indicating similar material strain and quality. For InGaAs, InAlAs, and InP epitaxial layers physically realistic parametric models describing near infrared to ultraviolet, infrared, and THz range spectra in ε have been developed, used to identify layer thickness, track variations in material layer properties between samples. Electrical transport properties obtained from THz range ellipsometry analysis are in close agreement with that measured from electrical Hall effect and reported in the literature values.

14. DECREASING THE RESOLUTION LIMIT OF LASER BEAM INDUCED CURRENT MEASUREMENTS BELOW THE BEAM SIZE WITHOUT CONFOCAL OPTICS: DETERMINING LASER SCRIBE WIDTHS

Zhaoning Song, Adam B Phillips, and Michael J. Heben

14.1 SUMMARY

Here, we report a method using laser beam induced current (LBIC) measurements to ascertain nonresponsive features of photovoltaic devices that are smaller than the measurement beam size. To demonstrate the method, we determine the effective electrical width of laser scribed lines. Laser scribing is a critical process in producing thin-film photovoltaics modules and minimizing the effective width of the laser-scribed lines is important for closing the cell-to-module efficiency gap. However, in addition to removing material, laser scribing can also produce a heat-affected zone in which the optoelectronic properties of the remaining materials may be adversely impacted. We measured the LBIC signal across scribe lines that were produced in CdTe thin-films. The collected data was compared with the expectations based on the probing beam's shape and the profile of the scribed line. The approach allows the electrical dead width to be determined with a resolution that is substantially higher than the width of the LBIC beam. At the lowest scribing powers, where the lines were the smallest, the electrically determined widths were larger than the optically determined widths by nearly a factor of two. The ability to rapidly resolve features that are much smaller than the dimensions of the probing laser beam without the use of confocal optics may be useful in a manufacturing environment, as demonstrated here, or more generally for rapid defect identification on devices with areas ranging from centimeters up to meters.

14.2 INTRODUCTION

Laser beam induced current (LBIC) is a nondestructive method that offers spatially resolved mapping of the current output from photovoltaic (PV) devices. [330, 331] Instruments built to operate with short working distances (~1 cm) use confocal optics and microscope lens components to allow the LBIC laser to be focused to submicron diameters for high-resolution measurements. This type of LBIC instrument is applicable to local scans in the range from a few microns to a few millimeters and is typically associated with imaging submicron scale inhomogeneities in PV structures [332] or current collection in the vicinity of grain boundaries. [333-335] Such instruments have been applied to studies of the correlation between film morphology, photoluminescence, and current generation. [336-341] Short working-distance examinations are generally limited to small-scale laboratory investigations due to the relatively small scan areas and slow throughputs.

Instruments have also been designed to operate at longer working-distances (~1 m) to afford fast scan speeds for larger-scale examinations of PV devices and modules. [330] Such systems have been used to investigate degradation [116] and pinhole formation. [117] In addition, LBIC has been demonstrated as a potential quality assurance measure for fabrication lines, [342, 343] and has been applied to the characterization of large area modules and full panels. [115, 344-347] At long working distances, the resolution of the scan is typically limited by the beam size. [348]

Many defects of large area devices are smaller than the beam size of typical large area LBIC systems. Included in this is the laser scribe width, which is one of several high rate, precise, coordinated manufacturing steps on which commercialization of thin-film PV modules is predicated. Laser scribing enables the cell area to be defined, which establishes the total current of the module, [349-351] and allows multiple cells to be interconnected in series to increase the voltage output of the panel. The interconnection is accomplished using three scribe lines: P1, which, in the case of thin-film CdTe PV, isolates strips of the underlying TCO material; P2, which scribes through the absorber material through which subsequently deposited metal can create a connection between the back and front of adjacent cells; and P3, which scribes the metal back contact to complete the cell definition process. The three scribes should be placed as closely to one another as possible because the fractional area of the module that is needed for the three scribed lines does not contribute to the photovoltaic output of the module. Thus, laser scribing is critical for thin-film module production, and precise control is needed to allow series interconnection of cells while minimizing the inactive area of the panel.

The width of a laser scribe is usually determined by optical microscopy, with the assumption that the scribed trench has a rectangular cross-section and that the determined width is representative of the fraction of the material that does not contribute to the photovoltaic performance. However, a so-called heat affected zone may also be present, which can reduce electrical performance for many microns away from the boundaries of the scribe. [352-354] In these cases, the electrical dead-width, which is relevant to the photovoltaic performance, may be significantly larger than the optically determined value. Note that a three-scribe interconnect pattern results in an electrically-dead region that is at least 3 times greater than the width of the individual scribe lines, so minimizing the width of each scribe line is important for closing the cell to module efficiency gap.

As thin-film PV moves to more advanced scribing methods, precise knowledge of the scribe width as a function of scribing parameters is required. However, a fast, reliable method to determine these electrically dead-widths has not been established. Large area LBIC systems offers a compelling pathway forward if the resolution can be improved beyond the size of the beam width.

In this contribution, we describe the use of a LBIC system [115] to determine the effective electrical dead-width of laser scribe lines produced in thin-film CdTe samples. The system is operated at a working distance of 1.3 m and is compatible with high throughout measurement. The data acquired during the LBIC measurement is a convolution of the feature's photoresponse and the measurement beam's profile, and the electrical dead-width can be determined using a model that allows the two to be decoupled. The approach allows the width of scribe lines an order of magnitude smaller than the beam diameter to be determined. For the thinnest scribe lines, the electrical dead-widths were approximately a factor 2 larger than the optically determined widths. The resolution limits of the system were estimated using the model and sensitivity limits of the electronics.

14.3 METHODS, ASSUMPTIONS, and PROCEDURES

Figure 82(a, b) shows some simple considerations for understanding the photocurrent that is generated when a laser beam is scanned in the *x* direction across a previously scribed trench in a

photoactive sample. For simplicity, we assume that the cross section of the trench is rectangular, of width w, and that the probe beam is circularly shaped with uniform power density. While the beam is approaching the scribe line but is still far away, a constant, spatially independent photocurrent value is expected. This remains the case until the edge of the beam reaches the scribe line, marked as position I. With further translation, the current decreases until the center of the beam is at the center of the scribe, shown as position II. As the probe beam is moved further in the x direction the photocurrent current increases to the same initial value. The minimum normalized laser beam induced current (I_{min}) can be used to calculate the width of the dead area produced by the scribe. In this scenario I_{min} can be determined from the ratio of the active area at position II to the active area at positions I or III. Therefore, I_{min} can be formulated as:

$$I_{min} = \frac{4\times\int_{w/2}^{r}\sqrt{r^2-x^2}dx}{\pi r^2} \quad (1)$$

where w is the width of scribe line and r is the radius of the beam. Figure 82(b) shows a simulation of the LBIC that would be found during such a scan.

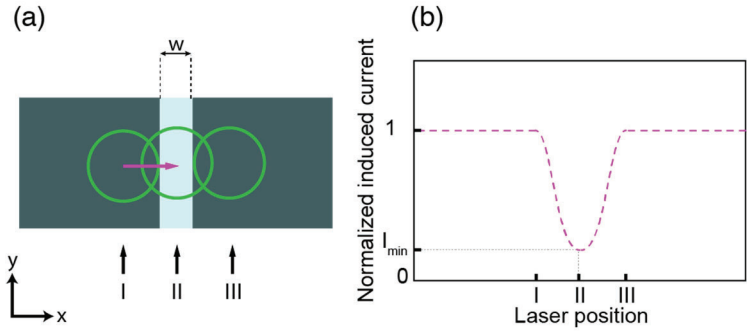


Figure 82. (a) Diagram of LBIC measurement across a scribe line. (b) Expected normalized induced current vs. laser center position

For determining the scribe width in real samples, we developed a model that simulates the experiment more accurately. The analysis becomes more complicated because the laser power density is not uniform. Here, we use a high-fidelity representation of the LBIC probe beam, including its intensity profile and dimensions. The total measured current when the center of the beam is located at coordinates (x_0, y_0) can then be expressed as:

$$I(x_0, y_0) = \sum_i \sum_j [B_x(x_i, x_0) B_y(y_j, y_0) \times H(x_i, y_j)] \quad (2)$$

Here, B_x and B_y are the Gaussian functions describing the beam's intensity projected onto the plane of the x and y axes, respectively. H is the current generation function at coordinate (x_i, y_j) which is related to the absorber layer thickness, the material under study, the laser beam wavelength, and the spatial distribution of the absorber material from which collection can occur. With a wavelength that is significantly shorter than the bandgap wavelength, the absorber is thick such that the light absorption is complete, and the collection efficiency can be assumed to be constant, the remaining information in H pertains to the geometry of the scribed lines.

To allow experimental data to be analyzed via this framework we measured the intensity distribution across the dimensions of the probe beam using a laser Spiricon SP620U profiler. The measured profile of the 532 nm beam is shown in Figure 83(a), and the intensity map shows that the beam is approximately elliptical in shape with FWHM values of 77 µm and 44 µm along the long and short axes, respectively. The power distribution is Gaussian in both dimensions. Figure 83(b) shows how this elliptical beam allows two different experiments to be performed on a given scribe depending on whether the long or short axis of the ellipse is aligned with the scribe width. Figure 83(c) shows the expected normalized current profiles with the Gaussian power distribution for the two arrangements shown in panel Figure 83(b). Similar to the circular beam case, the minimum induced current occurs when the beam is aligned with the center of the scribe (dead area) line (position II). However, the I_{min} value in the long axis scan case is higher than in the short axis scan case because the overlap area at position II is smaller in the latter case. On the other hand, the distance over which current is reduced is wider for the long axis scan because the longer axis allows the beam to reach the dead area from further away. As with the simple case of a uniform power distribution, the reduction in current begins when the beam first overlaps with the edge of the scribe line in position I. It reaches a minimum at position II, and then recovers as the beam passes through position III.

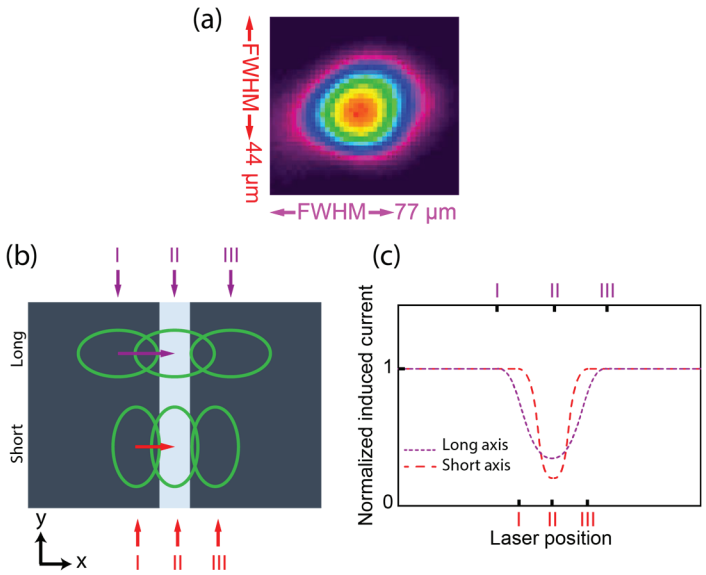


Figure 83. (a) Laser beam intensity map and corresponding intensity profiles as depicted in (b) and (c)

14.4 RESULTS and DISCUSSION

A stack of materials representative of a thin-film solar cell (glass/TCO/window layer/CdTe/metal) was used for experimentation. Figure 84(a, b) show a schematic diagram of the sample and the measurement method used in this experiment. Fourteen parallel lines were scribed into the back of the device stack using a laser beam with powers ranging from 0.25 to 0.9 W, in 0.05 W increments. Note that these powers and the resultant scribe line widths are not representative of a specific manufacturing step but are instead intended to demonstrate the value of the LBIC-based width determination technique. Further details associated with the material layers and scribing

laser operation are proprietary. This configuration is the equivalent of a P3 scribe described above, and for each scribing power the TCO remained intact under these scribing conditions. The same type of measurements could be performed to determine the width of the P1 and P2 scribe lines, though the scribing, with the specific conditions for each scribe, would need to occur before the complete stack was fabricated. Note that the configuration used here could also be used to measure the dead-widths of P2 scribes. The width of each scribe can then be used to determine the optimum scribing parameters to minimize the total dead-width between monolithically integrated cells. Contacts for LBIC measurement were made by contacting the front (TCO) and back (metal) electrodes using spring-loaded metal pins.

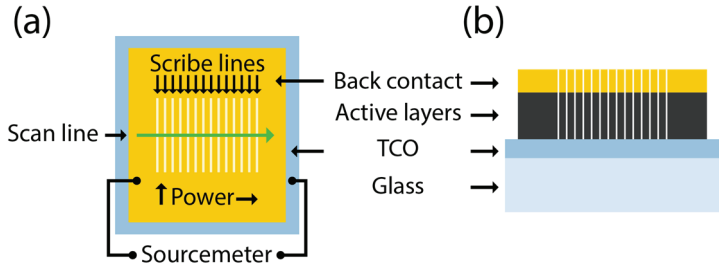


Figure 84. (a) Top and (b) cross-sectional schematic diagrams of the sample investigated with 14 scribe lines of increasing scribe beam power

For the LBIC measurements, a pulsed 532 nm laser beam with a repetition rate of 600 kHz, pulse width of 10 ns, and an average power of 0.01 mW was used. [115] The laser beam profile was as described above, and the beam was scanned perpendicular to the scribe line at a speed of 1 $cm.s^{-1}$. This pulse rate and scan speed resulted in a 17 nm translation of the beam between sequential laser pulses. Measurements were performed with both the long and short axes of the laser beam scanned perpendicular to the scribe line, as illustrated in Figure 83(b).

Figure 85(a, b) shows the normalized measured current as a function of the laser position when the short and long axes, respectively, of the laser spot were scanned perpendicularly to the scribe. The data is shown for three scribe lines that were produced with the highest, the lowest, and an intermediate scribing power. The minimum current (I_{min}) is observed to decrease as the scribing power is increased, indicating an electrical dead-width that increases with laser scribing power. As expected, I_{min} and the width of the current loss increases when the scan direction was changed from the short axis to the long axis.

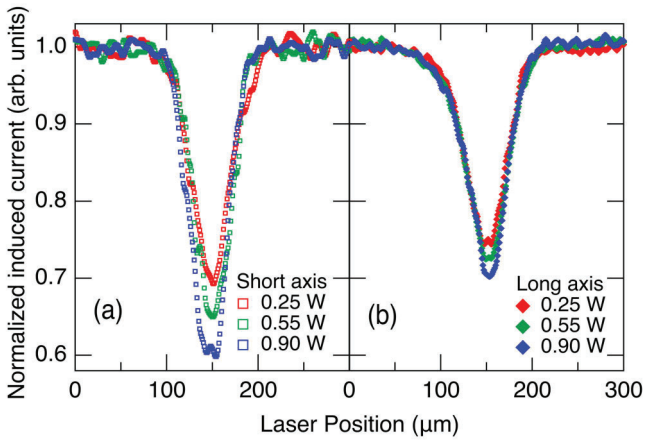


Figure 85. LBIC results along the beam's (a) short axis, parallel and (b) long axis perpendicular to the scribe line, obtained from scribed lines formed with laser powers of 0.25, 0.55, 0.9 W

To quantify the electrical dead width of the scribed trench from these measurements we used Eqn. 2 to generate simulated current scans. We then attempted to fit the experimentally obtained data by the generated data using the dead width as a fitting parameter. The width of the trench was varied from 7 µm to 30 µm in 0.1 µm steps. The simulated LBIC signals were then compared with the measured signals through a chi-squared (χ^2) test via Pearson's model. [355] The results of the χ^2 tests are shown in Figure 86(a). The value of the width that produces a minimum in χ^2 can be assigned to the effective electrical width of the scribe. Note that the values for the width determined by long- and short-axis scanning are within 0.05 µm of one another. The test showed a χ^2 minimum at 14.4 µm, 16.6 µm and 19.5 µm for scribe lines produced with 0.25, 0.55, and 0.95 W laser beams, respectively. Figure 86(b-d) show the best fit simulated LBIC signals plotted on the measured data for the short axis scans, while Figure 86(e-g) show the same data for the long axis scans.

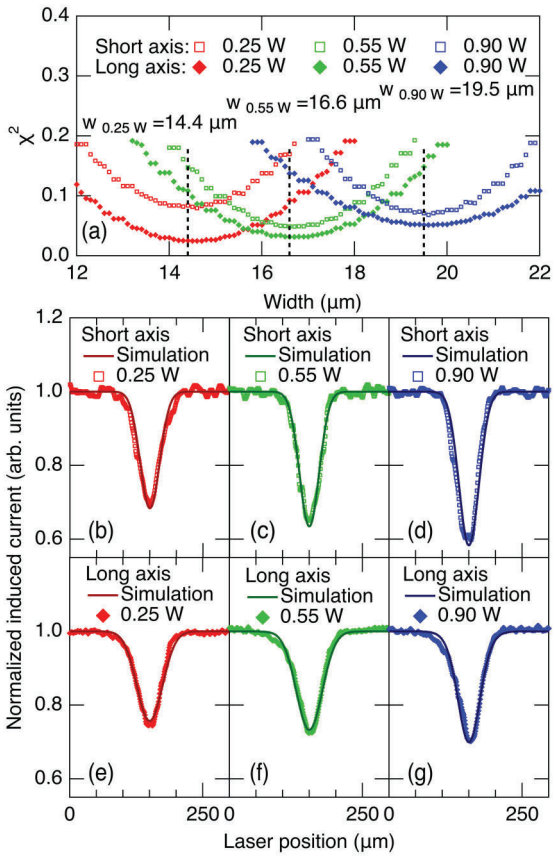


Figure 86. (a) Chi-squared (χ^2) test of simulation results of the electrical dead width of scribed lines; (b), (c), (d) simulations and corresponding measurements, short axis; (e), (f) and (g) show the same for the long axis

The electrically measured scribe widths were compared to values that were determined by optical examination. Optical widths were determined using an eye piece reticule in an optical microscope at magnification of 1000X. Figure 87(a) shows the optically- and electrical-determined dead widths and the optical scribe widths measured with LBIC and optical microscopy, respectively. The one standard deviation bars associated with each data point were determined from 10 separate measurements on a given scribe. The results show that the electrical dead width can be substantially larger than the optical width at low scribing power. This observation can be understood by considering that the threshold energy for the complete removal of the thin film and the threshold for producing electrical damage or removing the back metal can be different. Figure 87(b) shows the intensity distribution for two Gaussian beams having the same FWHM value but different total powers. In this illustration, the high-power beam is twenty times more powerful than the low-power beam. Only the portion of the beam that exceeds the removal threshold contributes to the optical width, while the portion of the beam that exceeds the damage threshold of the material contributes to the electrical width. As the scribing power increases, the measured optical and electrical widths begin to converge and are the same when the scribing power is 0.9 Watts. These results clearly show that optical measurements can be misleading, especially when scribe widths are small.

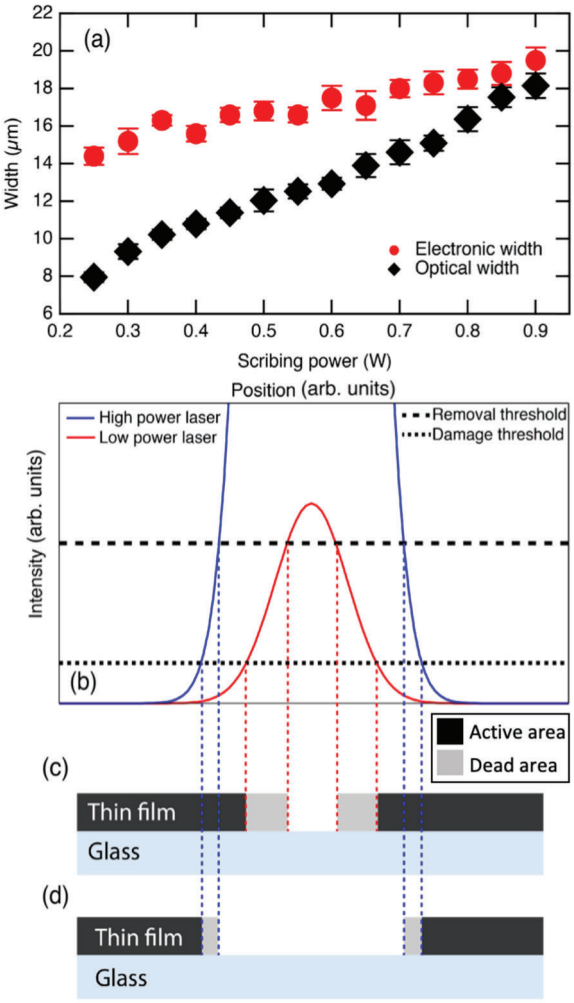


Figure 87. (a) Scribe widths measured by LBIC and optical microscopy; (b) Power distribution for low- and high-power; (c) and (d) scribe profiles corresponding to (b)

While the scribing investigations demonstrate the utility of the approach, it is interesting to consider the resolution limit on the technique. To determine this limit, we investigated the I_{min} values for square shaped dead areas with varying sizes, which could be a pinhole or some other defect in the device. Figure 88(a) shows an illustration of the LBIC measurement across a square shaped defect shown in blue with long and short axes. Figure 88(b) shows the normalized induced current for the illustration in panel Figure 88(a). At position II the defect is located at the center of the beam and the I_{min} is generated. Due to the relative size of the defect and the beam, with the former being smaller than the latter, the same I_{min} is expected regardless of scan direction. Table 16 shows the results as the dead area ranges from 0.05 μm^2 to 4 μm^2. Clearly, the detection limit will depend on the lateral resolution of the LBIC system, stability of the laser output, the sensitivity of the electronics, and the presence of any electrical noise. Based upon the data shown in Figure 85, an I_{min} of 0.955 can be distinguished, indicating that an 0.5 μm^2 feature could be resolved.

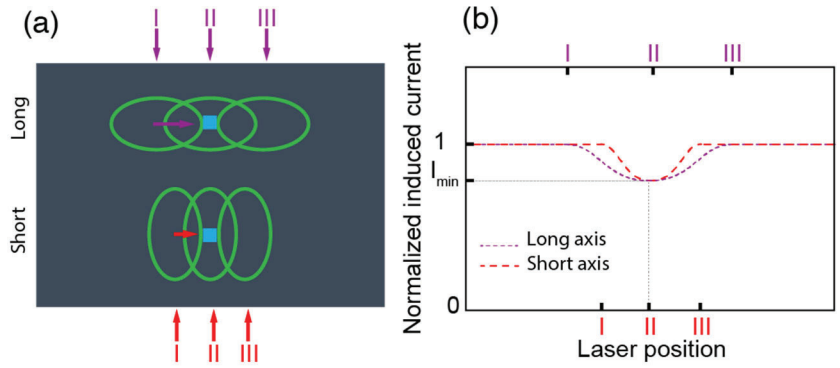


Figure 88. (a) LBIC measurements across a square defect (blue); (b) Expected normalized LBIC response vs. laser center position for the illustration in panel (a)

Table 16. I_{min} values as a function of dead area square. I_{min} are calculated through the model for alignment of the center of the beam with the center of the feature

Area (μm^2)	0.05	0.1	0.5	1	2	4
I_{min}	0.985	0.980	0.955	0.937	0.912	0.877

14.5 CONCLUSION

We have developed a method to increase the resolution of an LBIC system beyond the laser spot size and used this method to determine the effective electrical width of laser-scribed lines in thin-film solar cells. A simulation tool was developed that convolved the Gaussian profile of the probe laser beam with a laser-scribed trench of assumed shape. The width of the trench was used as a fitting parameter and a χ^2 test was applied to determine which value most closely generated the experimental data. The actual scribe width corresponded to the value with the lowest χ^2 value. Using this technique, scribe line widths an order of magnitude smaller than the LBIC beam diameter were easily resolved. For the scribing powers investigated, the optically-determined width of the scribe lines was always smaller than the electrically-determined width. The discrepancy was nearly a factor of two at the lowest powers and was reduced for increasing scribing powers. The LBIC-based method is faster, and more accurate, than the optical method. Features that are more than one order of magnitude smaller than the probing beam can be accurately measured.

15. DEVELOPMENT OF INTEGRATED INSTRUMENTATON FOR VARIABLE ANGLE, POLARIZATION-DEPENDENT EQE/SE/SR MEASUREMENT

Balaji Ramanujam, Ambalanath Shan and Robert W. Collins

15.1 MOTIVATION AND SUMMARY

An integrated system has been successfully constructed that can perform variable angle-of-incidence, polarization-dependent external quantum efficiency (EQE) measurements, along with variable angle spectroscopic ellipsometry (SE), and spectroscopic reflectance (SR), all on a complete solar cell. The details of the system development and initial results have been reported in previous annual reports for this project; however, improvements have been made over the past year enabling the system to operate at higher speed, generate higher accuracy data, and attain the robustness required to analyze different types of solar cell samples on a routine basis. This final report details the previous work as well as the latest advances made over the past year in improving and applying the system as will be summarized here.

(1) Modeling angle dependent EQE measurements of a thin film solar cell can be quite challenging because of the complexity of its multilayer structure, requiring features such as interface roughness and graded absorber layers. High accuracy of the angle dependent EQE measurement is required to model such features with confidence. In evaluations of the instrument accuracy, angle dependent EQE measurements have been performed on a Si photodiode, and such angle dependent measurements are also modeled. The results for the measured EQE and simulations are in close agreement and also in agreement with those published elsewhere. As a succeeding step on a more complicated system, angle dependent EQE measurements were performed on a thin film $CuIn_{1-x}Ga_xSe_2$ (CIGS) solar cell consisting of glass/Mo/CIGS/CdS/ZnO/ZnO:Al, and those measurements were also simulated and modeled to understand the underlying operating characteristics of the cell.

(2) The existing EQE/SR/SE instrument employs a chromatic zero-order biplate compensator as the rotating element which presents limitations in polarization analysis over a wide spectral range that extends well into the near infrared, where the retardance can decrease to angles much smaller than 90° (quarter-wave). Hence a quasi-achromatic rhomb-type compensator has been developed and investigated for this purpose. The compensator prisms have been fabricated and aligned in a mount that is nearly free of stress. Angular measurements of the compensator were performed over the complete mechanical cycle, as is required in the current application as a rotating element. These measurements were then analyzed to determine the underlying non-idealities in the compensator such as dichroism and inherent stress. The results have then been used to model the operational characteristic of the compensator at any angle with respect to plane of incidence. The constructed compensator is attached to a motor and aligned in such a way that the optical (or symmetry) axis of the compensator is in-line with the beam path; hence, such a compensator has been used as a rotating compensator in an ellipsometer in the straight through configuration. This is a significant accomplishment, given that the choice of rotatable achromatic compensators is currently limited to two varieties, the double Fresnel rhomb and the King rhomb. In the report,

this new design is referred to as the 'Krasilov compensator', as it is similar in concept to a compensator described previously [356] but incorporates key design improvements as well.

15.2 INTRODUCTION

Predictions of the annual energy yield of a solar module in the field are generally made on the basis of simulations that apply established models for the individual cell materials and their physical structures as well as various structural, optical, and electronic properties of the module materials. Such simulations must properly account for variations in output due to daily and seasonal changes in the angle of incidence of direct sunlight, its spectral distribution, the spectral and angular distributions of diffuse and direct irradiance, and even (in the future) the polarization properties of any obliquely incident sunlight. In order to verify the validity of the fundamental components of the models, laboratory measurements are needed under a variety of conditions to determine accurately the optical and electronic properties of individual solar cells and their physical structures.

To achieve a greater level of detail on the key properties, along with possible insights into performance limitations, a single unique instrument has been developed that integrates angle-of-incidence and polarization-dependent external quantum efficiency (EQE) as well as spectroscopic ellipsometry (SE) and spectroscopic reflectance (SR) measurements. This instrument has been first conceived and the concept tested and reported earlier under a previous award. Progress on its improvement and on comprehensive data analysis programs has continued under this project. In this report, the results of angle dependent EQE measurements and the corresponding simulations to characterize the performance of the instrument are reported for a Si photodiode cell and for a complete CIGS solar cell. In addition, the results of measurements and analysis for characterizing the performance and non-idealities of a novel quasi-achromatic rotatable compensator proposed for the SR/SE component of the EQE/SR/SE instrument are presented here as well.

15.3 METHODS, ASSUMPTIONS, and PROCEDURES

A single instrument has been successfully constructed that is capable of performing variable angle, polarization-dependent external quantum efficiency (EQE) and spectroscopic reflectance (SR) measurements along with variable angle spectroscopic ellipsometry (SE) on complete solar cells. The schematic of the system that has been constructed is shown in Figure 89. EQE and SE measurements of Si and CIGS solar cells were performed on the integrated EQE/SR/SE system (henceforth EQE-SE system). This report presents a detailed analysis of the EQE measurements made with that system.

Novel quasi-achromatic compensator for the SE system

The sensitivity of the polarization analysis by the system depends critically on the type of rotating compensator selected. A standard bi-plate compensator is strongly chromatic and presents limitations in polarization analysis of complex samples such as solar cells. The limitations arise because the measurement can lose sensitivity near the beginning and end of the wavelength range of the instrument, which spans from 270 nm to 1620 nm, as the compensator retardance approaches 180° (half-wave) and 0°, respectively, due to the inverse wavelength (λ^{-1}) dependence of the

retardance. Hence, a quasi-achromatic rhomb-type compensator is being investigated. By quasi-achromatic, it is meant that there is no explicit λ dependence of the retardance; however, an implicit dependence exists through the dispersion in the optical properties of the rhomb materials.

A quasi-achromatic compensator based on the improved version of that proposed by Yu. I. Krasilov [356] had been investigated in detail, and this device will be called a 'Krasilov-type quasi-achromatic compensator' or a 'Krasilov compensator' in brief. This compensator has been designed for a short total beam path so that the effects of inherent stress within the compensator would be less and, thus, the compensator performance will be closer to ideal.

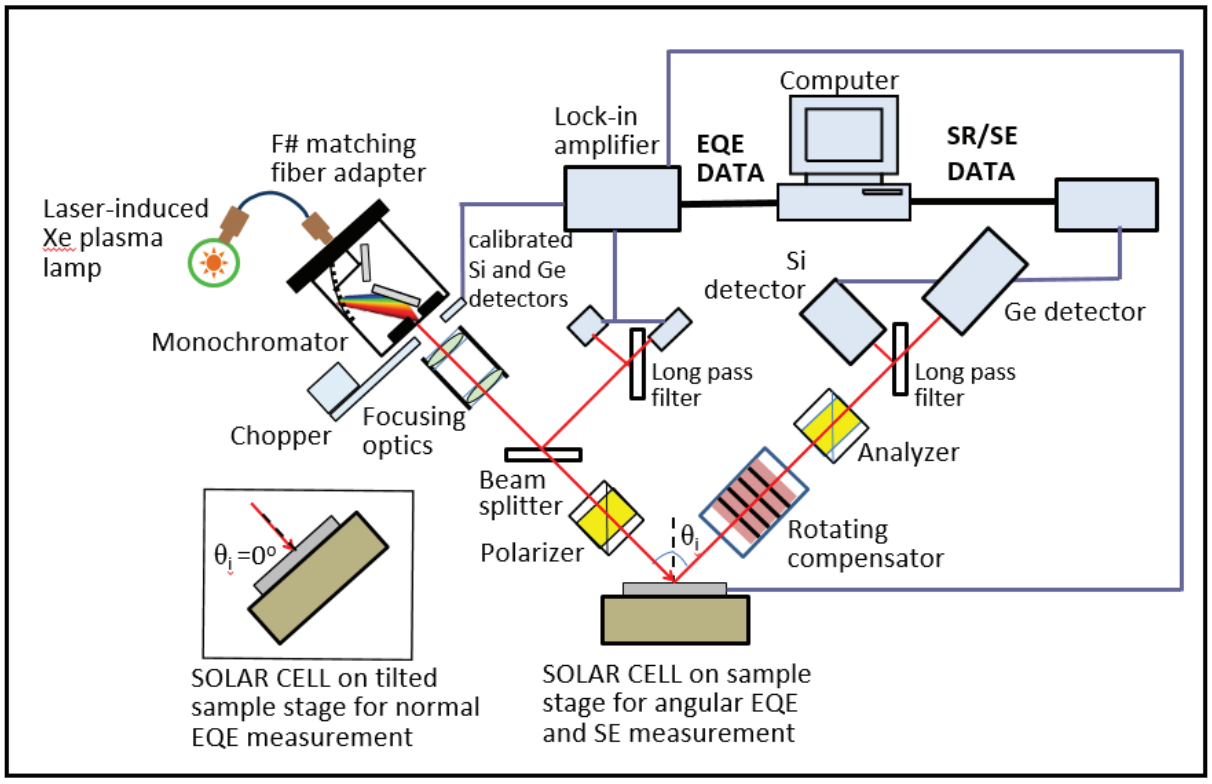


Figure 89. Schematic of the integrated EQE/SR/SE system; inset shows the rotated sample stage

Figure 90 shows a schematic along with the dimensions of the Krasilov compensator. As shown in the schematic, the compensator is constructed from a 60°-60°-60° prism and a 90°-60°-30° prism with one of the three side of the latter prism, the longer side opposite to the hypotenuse, coated with thick protected aluminum. These two prisms were obtained through special order from an optics manufacturer and were fabricated as individual matched components.

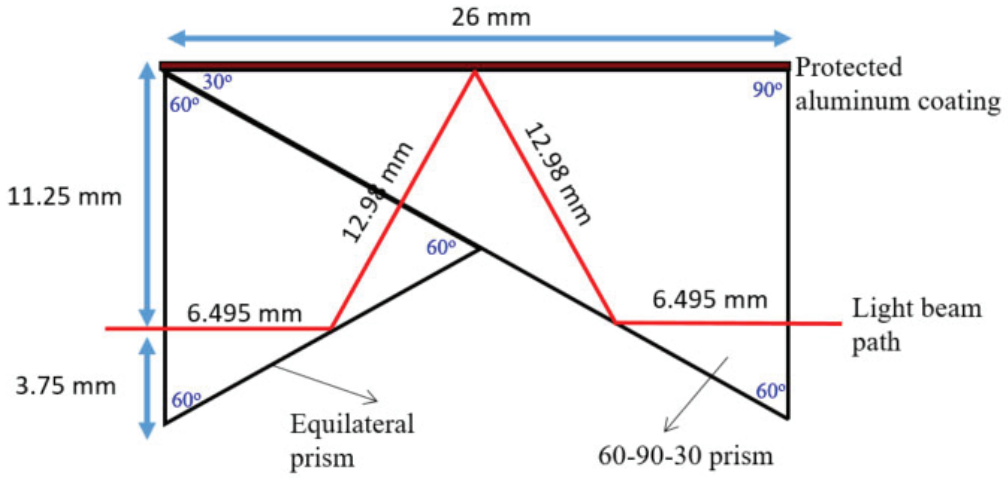


Figure 90. Schematic of the Krasilov compensator, depicting beam path and dimensions

Figure 91 shows a photograph of the unmounted Krasilov compensator in which the two prisms of the compensator were assembled as shown in the schematic but inverted. This unmounted configuration itself can behave as a complete, but not rotatable, Krasilov compensator.

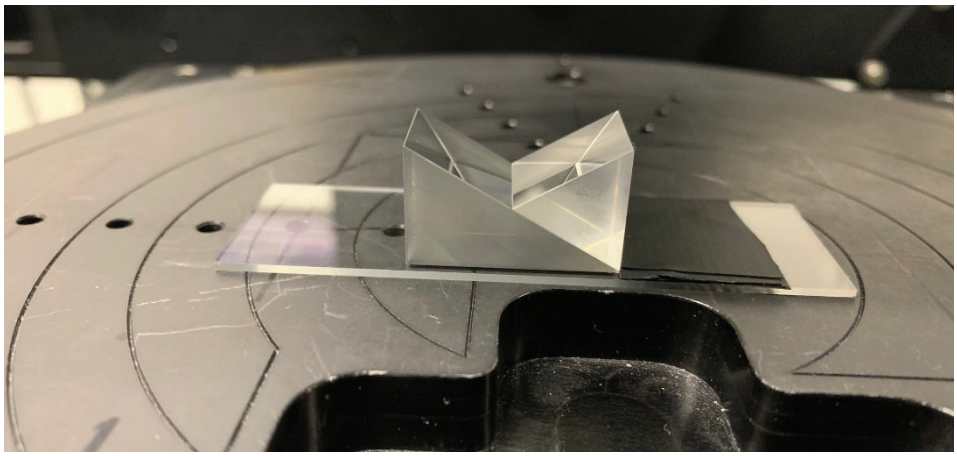


Figure 91. Photograph of the unmounted Krasilov compensator in which the two prisms have been assembled per the schematic design but inverted

Although the two prisms when placed as shown in the design diagram, but inverted, can behave as a compensator, the configuration is not useful, as it is highly unstable to movement and so not rotatable. Hence, the two prisms must be mounted together, but this mounting should be designed so as to minimize external stress on the two prisms. Multiple mounting techniques were applied and evaluated. The technique that led to minimum induced stress was finally selected. In this technique, the two prisms were held together by molten glue as in the schematic design and this mounting also enabled rotation of the compensator, a requirement of the final mounted design. Figure 92 shows the resulting mounted Krasilov compensator. This configuration shown in

Figure 92 is easily rotated and hence measurements as a function of azimuthal angle can be performed on the compensator.

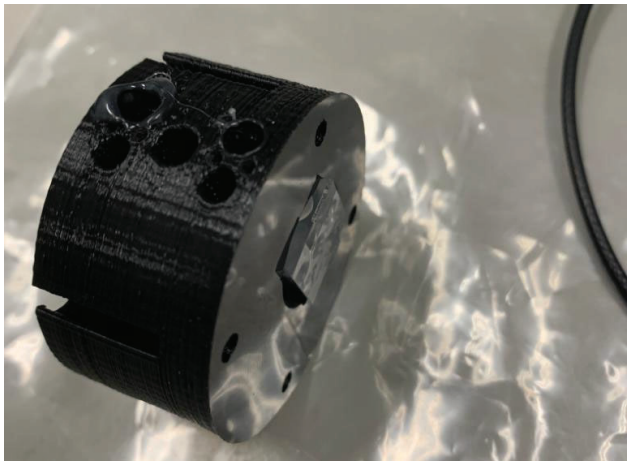


Figure 92. Photograph of the Krasilov compensator mounted within a hollow rotatable holder

Characterizing the properties of the aluminum layer in the Krasilov compensator

It was first necessary to characterize the opaque aluminum (Al) layer on the Krasilov compensator accurately in order to make reliable measurements with the compensator in a rotatable spectroscopic ellipsometry (SE) configuration. Ashcroft and Sturm in Ref. [357] have presented an analytical method for computation of the electronic band structure of aluminum and in turn a model for its dielectric function in terms of photon-energy independent parameters.

The significant advantage of the Ashcroft-Strum model is that the bulk dielectric function of Al can be expressed as a function of a relatively small number of photon-energy independent parameters. The description of Al includes a free electron or Drude contribution as well as interband contributions from two sets of transitions that dominate all others as a result of the "parallel-band" effect. In Al this effect occurs in the neighborhood of the Brillouin zone surfaces parallel to the hexagonal (111) and square (200) zone faces. These parallel-band transitions produce sharp onsets in absorption near 0.49 eV and 1.5 eV.

As a result, the dielectric function of Al derives predominantly from both Drude (intraband) and parallel-band (interband) contributions. The analytical form of these contributions is provided by Ashcroft and Sturm in Ref. [357]. The non-parallel band structure contributions can be neglected as their effect on the dielectric function is minimal. Generally, the Ashcroft-Sturm analytical form works best in a bulk-like Al layer compared to a very thin film layer, as it is derived based on the single crystal band structure.

Mathematically, the dielectric function of Al can be expressed as a sum of the intraband (D: Drude) and interband (PB: parallel band) components:

$$\varepsilon(\omega) = \varepsilon_D(\omega) + \varepsilon_{PB}(\omega) \quad (1)$$

where ω is the optical angular frequency.

The intraband contribution is described by the Drude model for a free electron gas

$$\varepsilon_D(\omega) = \varepsilon_0 - (\Omega_p^2/\,[\omega^2 + (i\omega/\tau_D)]) \quad (2)$$

where ε_0 is associated with the core interband transitions at high frequency, Ω_p is the (phenomenological) plasma frequency for the intraband transitions, and τ_D is the intraband relaxation time. A similar expression with m_{opt}/m (the optical effective mass ratio) is explained by Ashcroft and Sturm in their publication. [357]

An expression for the interband contribution has been formulated by Ashcroft and Sturm but is too lengthy to be reproduced here. Formally, the expression can be written as

$$\varepsilon_{PB}(\omega) = (4\pi i\sigma_a/\omega)\sum_K (a_0K)\, J_K(\omega,|U_K|,\tau_K) \quad (3)$$

where $\sigma_a = (e^2/12a_0h)$ with e as the electronic charge, a_0 as the Bohr radius, and h as Planck's constant. U_K is the Fourier coefficient of the crystal potential associated with the Brillouin zone face of reciprocal lattice vector K for the parallel-band transitions and τ_K is the corresponding relaxation time. The sum in Eq. (1) is performed over the two parallel-band transitions (200) and (111), and J_K are two complex-valued functions that appear in the original publication by Ashcroft and Sturm. [357]

Quantitative check of the implementation of Ashcroft and Sturm model

For the Ashcroft and Sturm model, [357] the dielectric function of Al can be defined by the following six parameters: m_{opt}/m, τ_D, τ_{200}, U_{200}, τ_{111}, and U_{111}. In general, the two parallel-band relaxation times are set equal so that $\tau_{200} = \tau_{111}$. In order to check the implementation of the model quantitatively, the same set of parameters as was adopted in Ref. [358] has been applied again in this implementation, and so the same results as found in Ref. [358] are expected here. The set of Ashcroft and Sturm parameters in Ref. [358] are used for determining the dielectric function of bulk Al and these parameters are included in Figure 93 and Figure 94. These figures clearly show that the Ashcroft and Sturm implementation established here precisely overlaps with the earlier implementation in Ref. [358], and hence this method can further be used for analysis of Al layer in the Krasilov compensator.

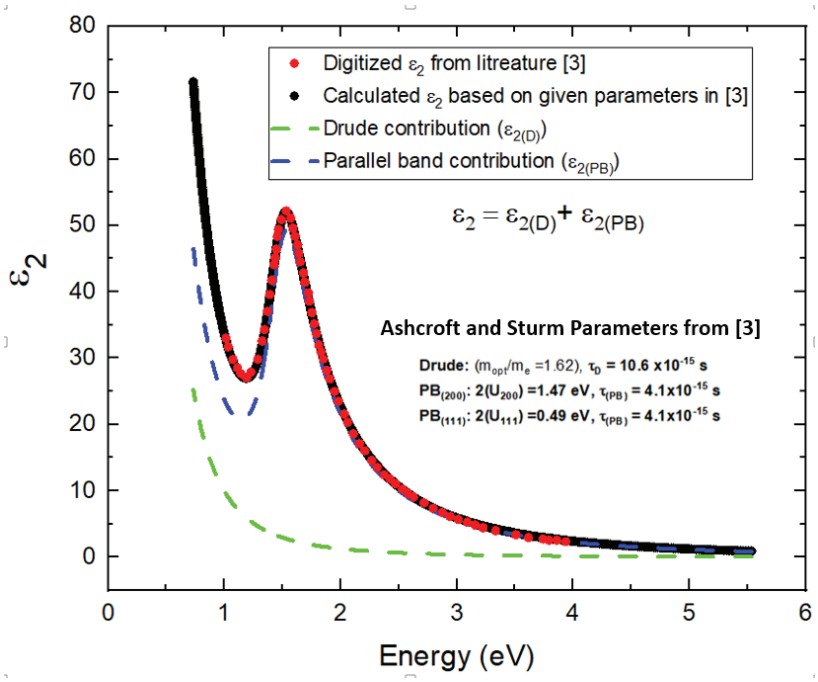


Figure 93. ε_2 spectrum generated from the Ashcroft and Sturm parameters and individual contributions (broken lines) plotted with ε_2 from Ref. [358]

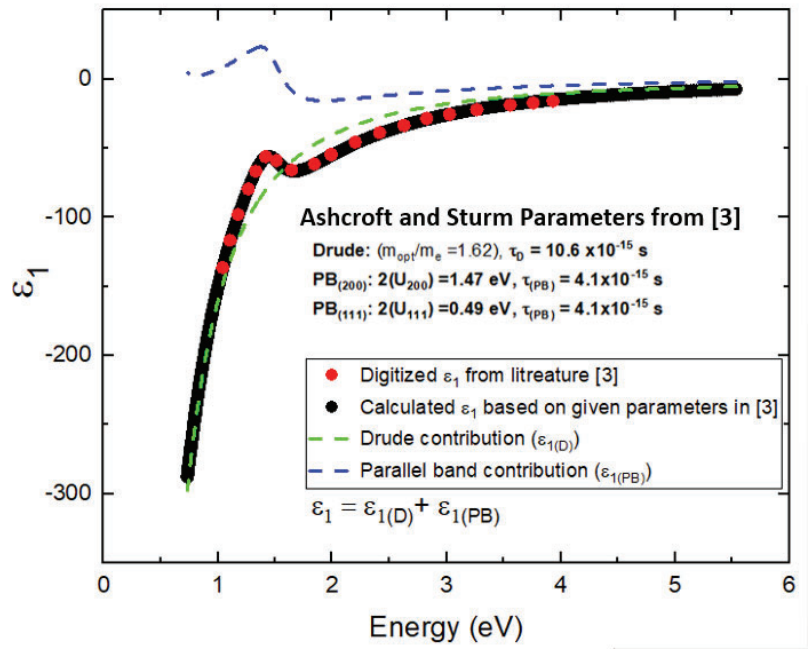


Figure 94. ε_1 spectrum generated from the Ashcroft and Sturm parameters and individual contributions (broken lines) plotted with ε_2 from Ref. [358]

15.4 RESULTS and DISCUSSIONS

Novel quasi-achromatic compensator for the SE system

Analysis of dichroism (ψ_C) of Krasilov compensator

The mounted Krasilov compensator was rotated from 0 to 360° in intervals of 10°, and the angular performance of the compensator was measured. This measurement was done on a J.A. Woollam Co., Inc model RC2 dual rotating compensator ellipsometer, hence the complete Mueller matrix of the Krasilov compensator is measured.

For the start of the analysis of the Krasilov compensator, the Al in the compensator must be characterized, so its parameters can be fixed in subsequent analysis. The Al in the compensator is the primary source of the deviation of the dichroic angle (ψ_C) in the compensator from its ideal value of 45°. Dichroism indicates a deviation in the ratio of the fast-to-slow transmission coefficients of the compensator from unity. Since $\psi_C = \tan^{-1}(|t_F|/|t_S|)$, dichroism leads to a deviation in ψ_C from 45°. The measured ψ_C of the Krasilov compensator is fitted with the Ashcroft and Sturm model to determine the photon energy independent parameters that describe the effect. Figure 95 shows the resulting best fit, and the Ashcroft and Sturm parameters determined in this fit are given in Table 17. These parameters can be used to generate the dielectric function of Al used in Krasilov compensator.

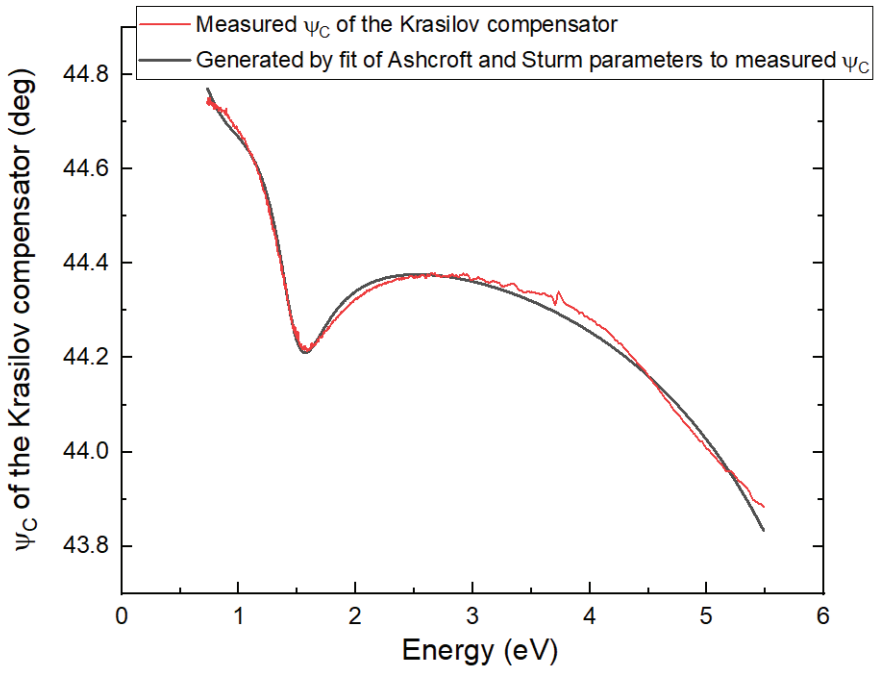


Figure 95. Fit of the Ashcroft and Sturm parameters to the measured ψC of the Krasilov compensator

Table 17. Ashcroft and Sturm (A&S) parameters determined by fitting the measured ψC of the Krasilov compensator

Ashcroft and Sturm parameters for Al in Krasilov compensator		
Parameter	**Value**	**Error (+/-)**
MSE	0.120	
Drude Parameters		
m_{opt}/m	1.292	0.002
Scattering time (τ_D) (fs)	4.898	0.006
Parallel band parameters		
$2(U_{200})$ (eV)	1.516	0.001
$2(U_{111})$ (eV)	0.755	0.004
Scattering time (τ_{PB}) (fs)	2.820	0.001
$\varepsilon_{1\text{-inf}}$	3.967	0.002
Angle (deg)	29.73	0.08

It can be seen from that the angle of incidence and $\varepsilon_{1\text{-inf}}$, which is simply a constant value added to ε_1, are varied in addition to the Drude and parallel band parameters in order to improve the fit of ψ_C for the compensator. In fact, these two additional parameters were necessary in order to get the best possible fit as shown in Figure 95.

Figure 96 shows the difference between the measured ψ_C of the compensator and the fit. The difference varies between +/– 0.02° over much of the spectral range, hence this result can be trusted as an accurate representation of ψ_C for use in developing the Mueller matrix for this element. Figure 97 shows the shows the dielectric function of Al determined from the parameters in Table 17 obtained in the fit of Figure 95.

Figure 98 shows the dielectric functions of Al from a database in comparison with that of the Al coating one face of the Krasilov compensator as determined by the parameters obtained in the fit of Figure 95 and Figure 96. These figures show that ε_1 for the Al dielectric function determined here is within the range of variation of the database dielectric functions, and hence, the Al dielectric function measured through the Krasilov compensator can be deemed as physically reasonable. The broader parallel-band feature at 1.51 eV and the higher amplitude Drude tail in ε_2 for the Al of the Krasilov compensator is attributed to the fact that the Al coating is measured at the interface to the fused silica where the film is likely to be more defective, for example with a smaller polycrystalline grain size.

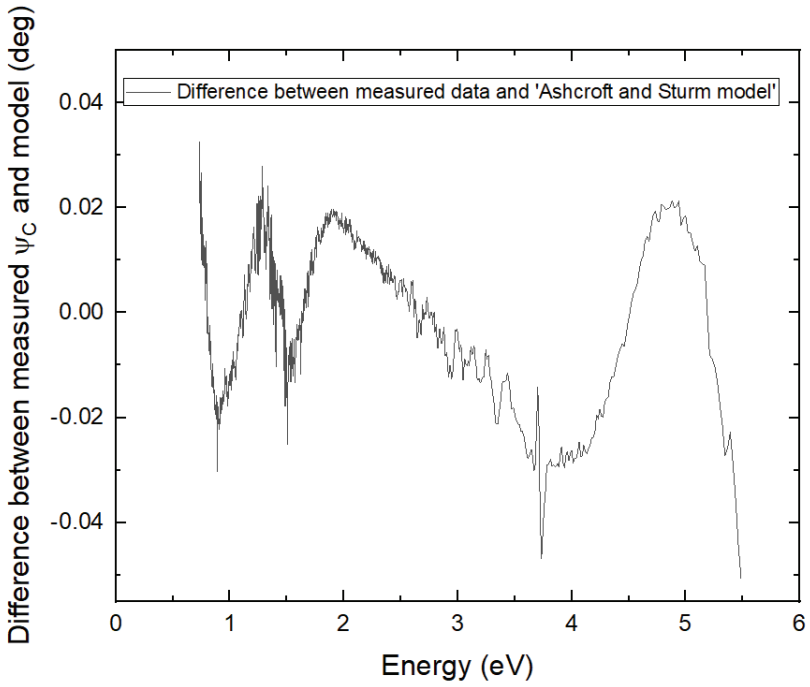


Figure 96. Difference between measured and best fit dichroism parameter ψC obtained from the Ashcroft and Sturm model

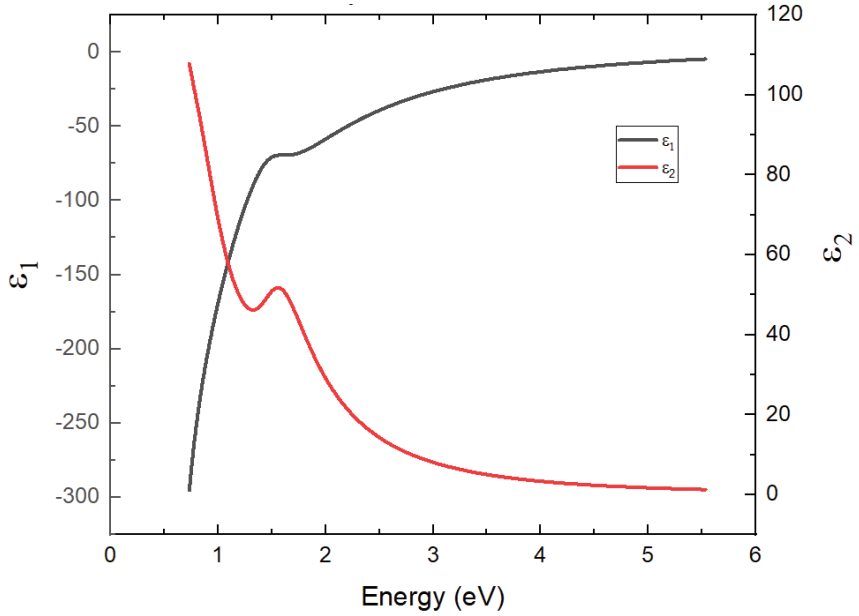


Figure 97. Final dielectric function of the aluminum coating used in the characterization of the Krasilov compensator, Ashcroft and Sturm model

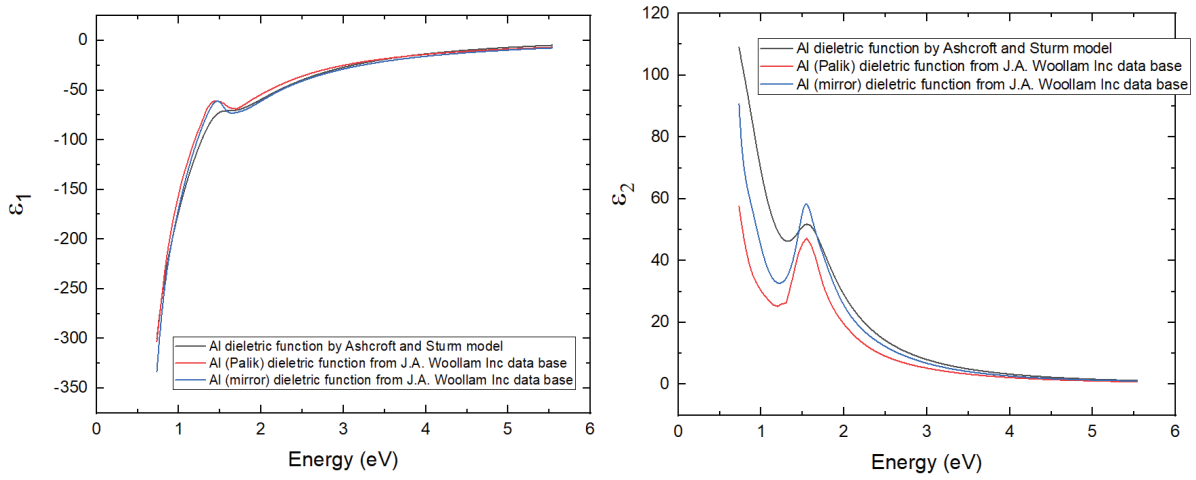


Figure 98. (ε_1, ε_2) spectra of the modeled Al dielectric function in comparison with the values available in the Woollam Co., Inc software database

Stress analysis in the Krasilov compensator

The Mueller matrix elements as determined during the measurement of the Krasilov compensator are further used for analysis of stress in the fused silica as a function of azimuthal angle as the compensator rotates about the optical axis. The following equations provide an explanation of the stress analysis performed on Krasilov compensator.

The following equation represents the normalized Stokes vector of the emergent wave at the detector $\boldsymbol{s}_D$. This Stokes vector is given in terms of the Mueller matrices that describe the four fused silica transmissions $\boldsymbol{M}_1$, $\boldsymbol{M}_3$, $\boldsymbol{M}_5$, and $\boldsymbol{M}_7$, the internal reflections at fused-silica/ambient interfaces $\boldsymbol{M}_2$ and $\boldsymbol{M}_6$, and the internal reflection at the fused-silica/Al interface $\boldsymbol{M}_4$. The sequence of these matrices and their associated rotation matrices, if needed, multiply the normalized Stokes vector of the incident wave from the source $\boldsymbol{s}_S$:

$$I_D S_D = R(-\alpha_7)\boldsymbol{M}_7 R(\alpha_7) \cdot \boldsymbol{M}_6 \cdot R(-\alpha_5)\boldsymbol{M}_5 R(\alpha_5) \cdot \boldsymbol{M}_4 \cdot R(-\alpha_3)\boldsymbol{M}_3 R(\alpha_3) \cdot \boldsymbol{M}_2 \cdot R(-\alpha_1)\boldsymbol{M}_1 R(\alpha_1) \cdot (I_S \boldsymbol{s}_S) \tag{4}$$

In Eq. (4), I_S the irradiance emitted from the source, and I_D is the irradiance incident on detector. The Mueller matrices $\boldsymbol{M}_{(1,3,5,7)}$ describing the beam paths through the fused silica of the compensator take the form

$$\boldsymbol{M}_{n=(1,3,5,7)} = \begin{bmatrix} 1 & 0 & 0 & 0 \\ 0 & 1 & 0 & 0 \\ 0 & 0 & \cos\delta_n & \sin\delta_n \\ 0 & 0 & -\sin\delta_n & \cos\delta_n \end{bmatrix} \approx \begin{bmatrix} 1 & 0 & 0 & 0 \\ 0 & 1 & 0 & 0 \\ 0 & 0 & 1 & \delta_n \\ 0 & 0 & -\delta_n & 1 \end{bmatrix} \tag{5}$$

where δ_n is the stress-induced retardance in the each of the respective beam paths, assumed to be small. In addition,

$$\boldsymbol{M}_{n=(2,6)} = \begin{bmatrix} 1 & 0 & 0 & 0 \\ 0 & 1 & 0 & 0 \\ 0 & 0 & \cos\delta_n & \sin\delta_n \\ 0 & 0 & -\sin\delta_n & \cos\delta_n \end{bmatrix} \tag{6}$$

where $\boldsymbol{M}_{(2,\ 6)}$ represent the Mueller matrices of the total internal reflections at the fused-silica/ambient interfaces and δ_n is the *p*-*s* phase shift difference for those total internal reflections. Here *p* and *s* represent the electric field directions parallel and perpendicular to the plane of incidence, respectively. The intermediate reflection Mueller matrix is given by

$$\boldsymbol{M}_4 = \begin{bmatrix} 1 & -\cos 2\psi_4 & 0 & 0 \\ 0 & 1 & 0 & 0 \\ 0 & 0 & \sin 2\psi_4 \cos\delta_4 & \sin 2\psi_4 \sin\delta_4 \\ 0 & 0 & -\sin 2\psi_4 \sin\delta_4 & \sin 2\psi_4 \cos\delta_4 \end{bmatrix} \tag{7}$$

which corresponds to the fused-silica/Al interface within the Krasilov compensator. Here ψ_4 represents the overall dichroic angle of the device. For $\psi_4 = 45°$, then the (1,2) and (2,1) Mueller matrix elements of $\boldsymbol{M}_4$ vanish and the compensator shows ideal behavior. Finally,

$$R(\alpha_{n=\{1,3,5,7\}} = \begin{bmatrix} 1 & 0 & 0 & 0 \\ 0 & \cos 2\alpha_n & \sin 2\alpha_n & 0 \\ 0 & -\sin 2\alpha_n & \cos 2\alpha_n & 0 \\ 0 & 0 & 0 & 1 \end{bmatrix} \tag{8}$$

are the rotation matrices by α_n, which is the angle of the stress plane with respect to plane of incidence over the respective beam paths.

By expanding Eq. (4), equations to first order in δ_n; n = 1, 3, 5, 7, were generated for each of the 13 Mueller matrix elements, excluding m_{11}, m_{12}, and m_{21}, as these do not carry any stress induced characteristics. The parameters α_n and δ_n in the first-order equations were varied in order to fit the measured Mueller matrix elements, and as a result, determine the angle of the stress plane α and the stress induced retardance in the respective beam paths, indicated 1, 3, 5, 7. The results are presented in Figure 99. Angular stress analysis for the compensator was performed at intervals of 30° from 0° to 360° and the results are plotted in Figure 100 and Figure 101. The average stress angle α plotted in Figure 100, is measured with respect to the angle of fast axis of the compensator. In the analysis, the stress angle is automatically corrected for *C′* which is the angle of the fast axis of the compensator measured with respect to a fixed (laboratory frame) plane of incidence. As a result, the average stress angle α should be independent of *C′* in Figure 100. It can be seen in Figure 100 that there is no significant change in α (no more than ± 0.15°) from its angular average of 1.60° for the angular measurement. A plot of total sum of the stress induced retardances combining all beam paths is shown in Figure 101. This figure shows that the stress induced retardance follows a trend with the angular variation of the compensator, and the origin of this trend needs to be understood and the results modeled.

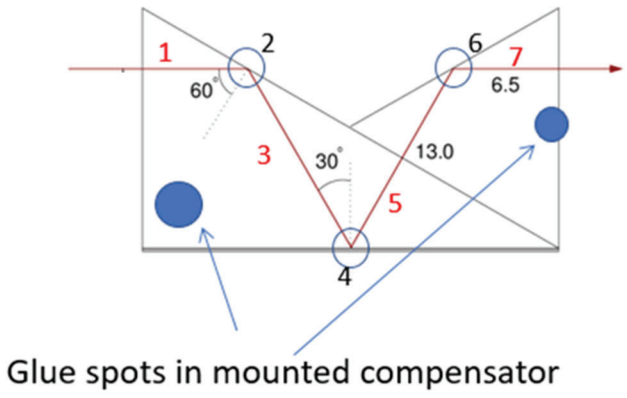


Figure 99. Cross-section of the Krasilov compensator, closed circles indicate mounting locations. In the figure, red lines identified (odd numerals) represent optical beam paths, and even numerals represent internal reflections

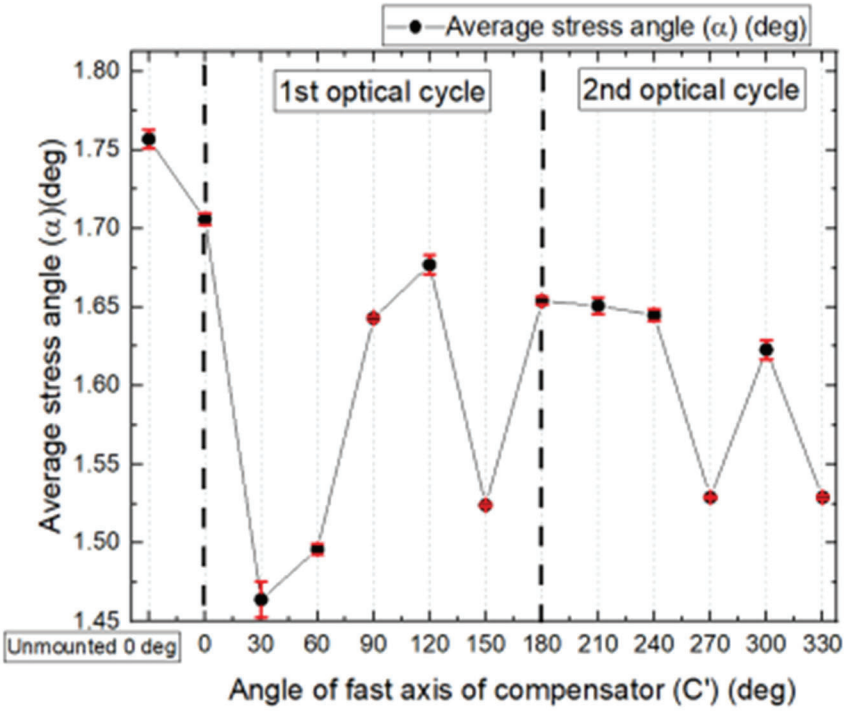


Figure 100. Average stress angle α measured as a function of the compensator fast axis (C′), and angle (α) for the unmounted compensator (left-most data point)

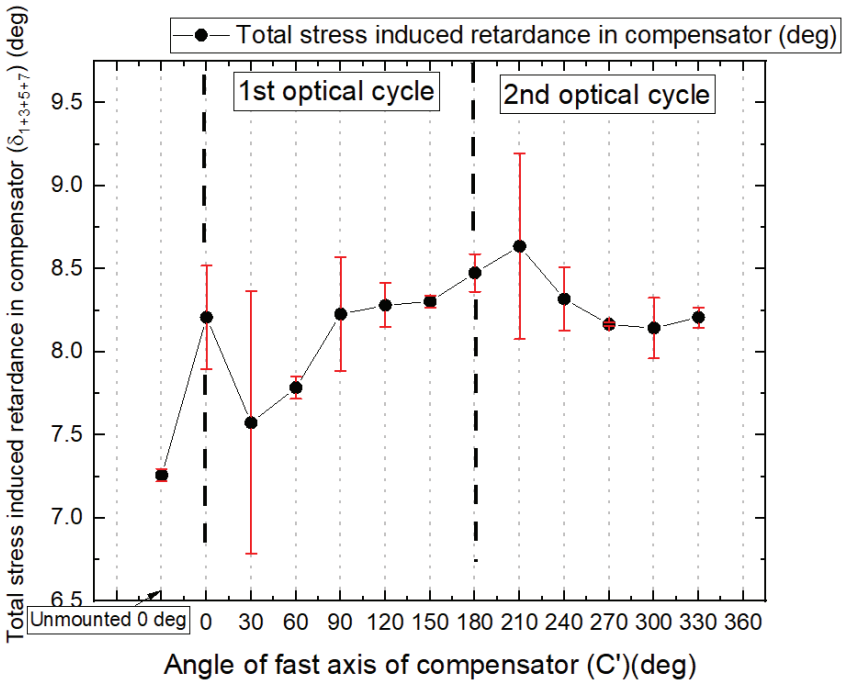


Figure 101. Plot of total stress induced retardance δn along all respective beam paths in the compensator measured vs. fast axis angle (C′)

Figure 102 presents the deduced retardance generated by the stress in the beam paths plotted as a function of photon energy. The comparison included here clearly shows that the inherent stress in the unmounted compensator is high in comparison to the additional stress induced due to mounting of the compensator. The results for a rhomb compensator in the design by King-Downs, [359] fabricated of low stress fused silica, is included in the figure. An improvement can be made to the current Krasilov compensator by fabricating the compensator prisms from low stress Heraeus Suprasil® fused silica. Compensator prisms made from Heraeus Suprasil® fused silica can show much reduced stress in the measurement, however, are more expensive. The successful proof-of-principle for this compensator design now warrants such an improvement to the device. Based on the comparison in Figure 102, where it is observed that the results for the King-Downs compensator are dominated by mounting stress, it is expected that the stress in the Krasilov design can be significantly reduced below that of the King-Down device when low stress fused silica is used for the former and both are mounted for a rotation capability.

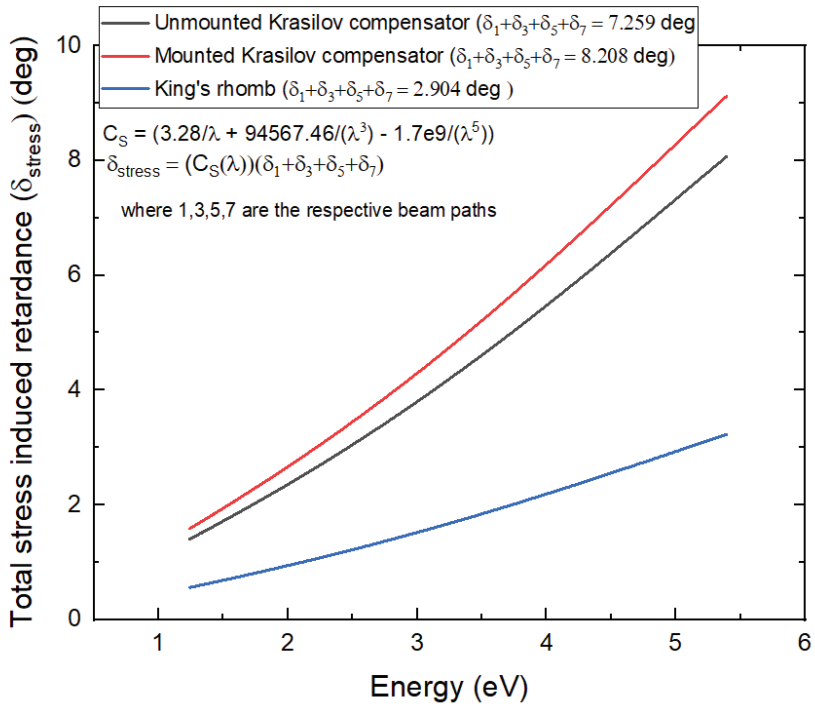


Figure 102. Stress induced retardance spectra of the unmounted and mounted Krasilov compensator vs. a King-Downs rhomb compensator

Complete Mueller matrix of the Krasilov compensator and its retardance

Now that models have been developed to describe the silica/Al reflection and the effect of stress on the polarization of the internal transmissions, the final total internal reflections at the two silica/ambient interface are easy to model based on the photon energy dependence of the index of refraction of the fused silica. Figure 103 shows the final results for the complete simulated Mueller matrix spectra of the unmounted Krasilov compensator along with the normalized Mueller matrix spectra obtained experimentally. Similar simulated and measured spectra are obtained for all angular measurements of the mounted compensator.

Table 18 provides the expressions for the Mueller matrix elements given to first order in the beam path retardances and also to first order in the deviation of the dichroic angle from 45°. Thus, this table provides information on which internal characteristics of the Krasilov compensator control each of the Mueller matrix elements in Figure 103. The clearest evidence of stress in the beam path comes from the Mueller matrix elements m_{23} and m_{24} and their transposed elements m_{32} and m_{42}, which depend only on the beam path stress. In the absence of beam path stress, these Mueller matrix elements should be zero along with m_{13} and m_{14} and the transposed elements m_{31} and m_{41}. The latter four Mueller matrix elements depend on both the stress and the dichroic angle and so are more challenging to interpret. Furthermore, because these four elements m_{13}, m_{14}, m_{31}, and m_{41} involve the product of two small quantities, the values are close to zero and the spectral variations are weak. Direct information on the dichroism, which is solely associated with the Al reflection,

derives from the m_{12} and m_{21} elements. Finally, the elements m_{33}, m_{44}, m_{34}, and m_{43} are dominated by the three phase shifts that generate the desired compensating action of the overall device.

The important operational characteristic of the Krasilov compensator is the weak wavelength dependence of the retardance δ_C which derives from the three internal reflection phase shifts according to $\delta_C = \delta_2 + \delta_4 + \delta_6$. Although the retardance of the device will show no explicit wavelength dependence owing to its design as a rhomb, it is also desirable that the retardance be smooth without any artifacts. In addition to a weak wavelength dependence without artifacts, it is important to ensure an optimum value of the retardance. Two reports have suggested different optimum retardances depending on the application. Smith [360] has suggested a retardance value of 127° as the optimum for general applications whereas Li et al. [361] has suggested that an odd integer quarterwave value such as 90° or 270° is optimum for the detection of weak anisotropies including surface induced optical anisotropies and weak stresses in glass. Our analysis seems to suggest that the 127° value arises from $\delta_C = \pm 2\tan^{-1}(2)$ which balances the magnitudes of the second and fourth order Fourier coefficients. These are the output signals of a single rotating compensator. Figure 104 shows the resulting plot of the retardance (in degrees) of the Krasilov compensator developed in this project. The plotted retardance is the sum of retardances generated by internal reflections at the two fused-silica/ambient interfaces (δ_2 and δ_6) and at a fused-silica/Al interface (δ_4). Broken lines correspond to the closest such conditions, including three-quarter wave position (270°) and a $(\frac{1}{2})\tan(\delta_C/2) = \pm 1$ condition, which is $-126.87° + 360° = 233.13°$. The results show two important characteristics of the compensator. First, the retardance is relatively flat without the strong wavelength dependence and oscillatory artifacts that occur in biplate compensators, and second, the average value of δ_C lies between the optimum values described in Refs. [360] and [361]. To emphasize the difference between this new compensator and the biplate compensator that currently exists in the EQE/SE instrument, Figure 105 provides a comparison between their retardances. These results illustrate the success achieved in this project with the new compensator design.

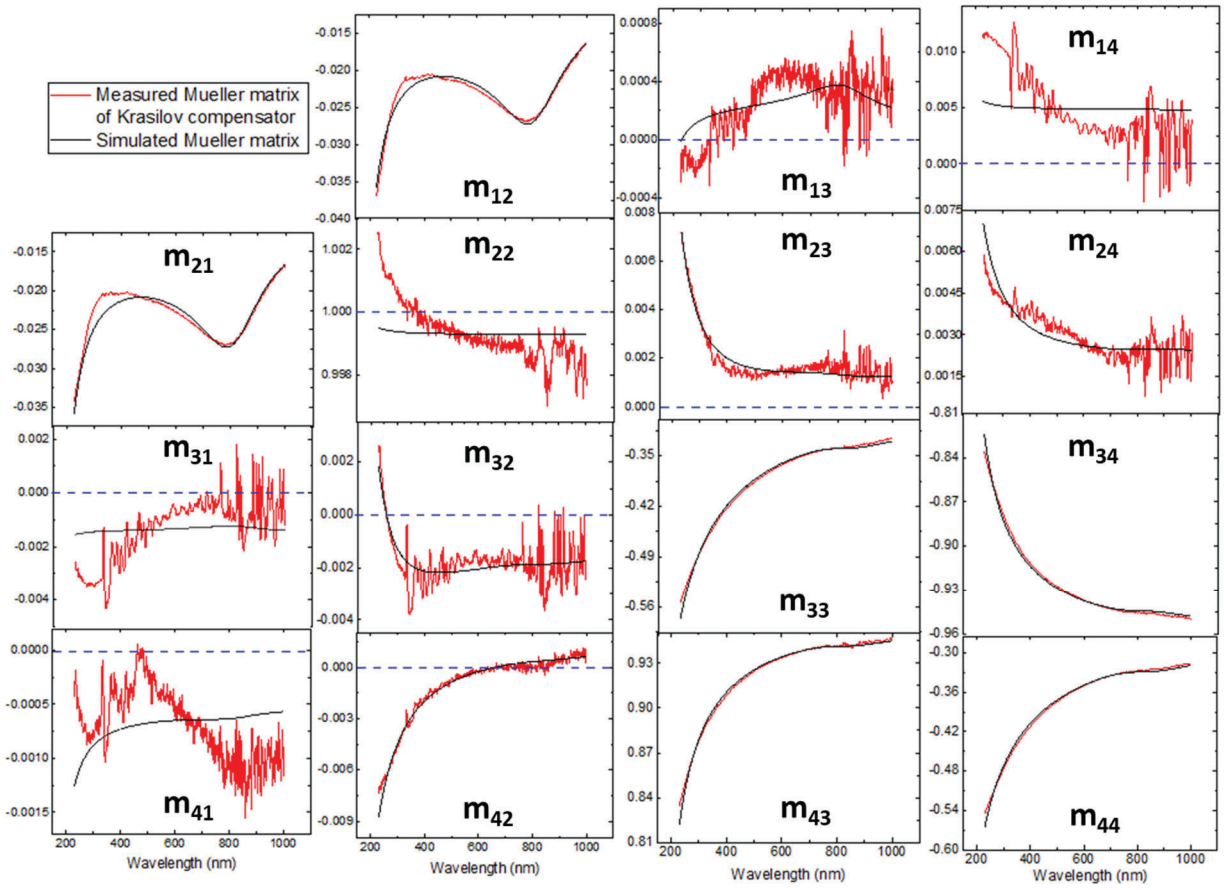


Figure 103. Final results for the spectra in the complete normalized Mueller matrix of the unmounted Krasilov compensator measured experimentally and the best simulated fit

Table 18. Expressions for the Mueller matrix elements of the Krasilov compensator, to first order in beam path retardances and in deviation of the dichroic angle from 45°

m_{11}	1
m_{12}	$-\psi'_4$
m_{13}	$-\psi'_4\,\delta_3\,sin2\alpha_3\,sin\delta_2$
m_{14}	$\psi'_4\ [\ \delta_1\,sin2\alpha_1 + \delta_3\,sin2\alpha_3\,cos\delta_2\ ]$
m_{21}	m_{12}
m_{22}	m_{11}
m_{23}	$\delta_3\,sin2\alpha_3\,\sin\delta_2 + \delta_5\,sin2\alpha_5\,\sin(\delta_2+\delta_4) + \delta_7\,sin2\alpha_7\,sin(\delta_2+\delta_4+\delta_6)$
m_{24}	$-\,[\delta_1\,sin2\alpha_1 + \delta_3\,sin2\alpha_3\,\cos\delta_2 + \delta_5\,sin2\alpha_5\,cos(\delta_2+\delta_4) + \delta_7\,sin2\alpha_7\,cos(\delta_2+\delta_4+\delta_6)\ ]$
m_{31}	$-\psi'_4\,\delta_5\,sin2\alpha_5\,sin\delta_6$
m_{32}	$\delta_1\,sin2\alpha_1\,sin(\delta_2+\delta_4+\delta_6) + \delta_3\,sin2\alpha_3\,sin(\delta_4+\delta_6) + \delta_5\,sin2\alpha_5\,\sin\delta_6$
m_{33}	$cos(\delta_2+\delta_4+\delta_6) - (\delta_1\,cos2\alpha_1 + \delta_3\,cos2\alpha_3 + \delta_5\,cos2\alpha_5 + \delta_7\,cos2\alpha_7)\,sin(\delta_2+\delta_4+\delta_6)$
m_{34}	$sin(\delta_2+\delta_4+\delta_6) + (\delta_1\,cos2\alpha_1 + \delta_3\,cos2\alpha_3 + \delta_5\,cos2\alpha_5 + \delta_7\,cos2\alpha_7)\,cos(\delta_2+\delta_4+\delta_6)$
m_{41}	$-\psi'_4\,[\ \delta_5\,sin2\alpha_5\,cos\delta_6 + \delta_7\,sin2\alpha_7]$
m_{42}	$\delta_1\,sin2\alpha_1\,\cos(\delta_2+\delta_4+\delta_6) + \delta_3\,sin2\alpha_3\,\cos(\delta_4+\delta_6) + \delta_5 sin2\alpha_5\,\cos\delta_6 + \delta_7\,sin2\alpha_7$
m_{43}	$-m_{34}$
m_{44}	m_{33}

Notes:

δ_n (n =1,3,5,7) : stress induced retardances along the respective beam paths as in Figure 13

$\delta_{2,6}$: retardances generated by fused silica total internal reflection

$\alpha_{n\ (n=1,3,5,7)}$: angle of stress plane with respect to plane of incidence as in Figure 12

ψ'_4 : dichroic angle

For $\psi_4 \sim 45°$, $sin2\psi_4 \approx 1$ and the Taylor series expansion of $cos2\psi_4$ is

$$\psi'_4 = cos2\psi_4 \approx -sgn\left(\psi_4 - {}^{\pi}/_{4}\right)2\psi_4 = \begin{cases} 2\psi_4 & ;\psi_4 < {}^{\pi}/_{4} \\ 0 & ;\psi_4 = {}^{\pi}/_{4} \\ -2\psi_4 & ;\psi_4 > {}^{\pi}/_{4} \end{cases}.$$

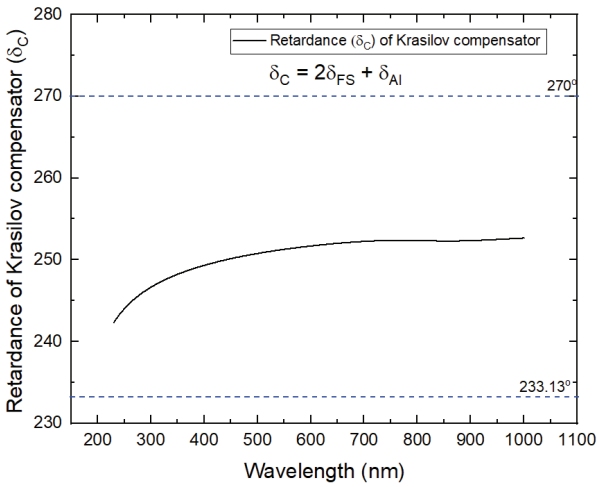


Figure 104. Retardance of the Krasilov compensator, as the sum of retardances from reflections from two fused-silica/ambient interfaces (δ_2 and δ_6) and a reflection from a fused-silica/aluminum (δ_4) interface

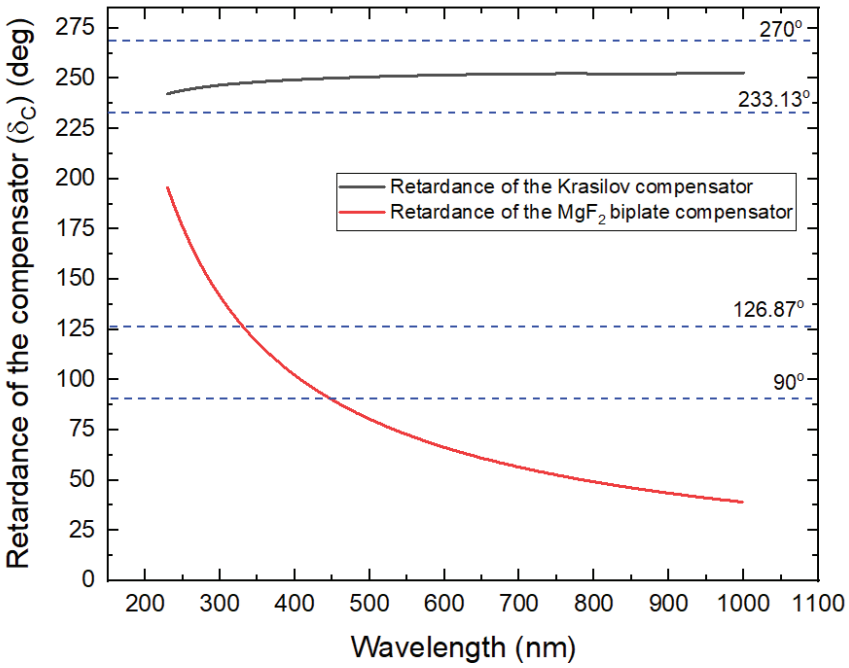


Figure 105. Retardance of the Krasilov compensator and the MgF_2 biplate compensator currently used in the EQE-SE system

Single rotating compensator ellipsometer in straight through with Krasilov compensator

The proposed Krasilov compensator for the rotation capability was constructed using an available extra set of prisms identical to those depicted earlier. This compensator is constructed in such a way that it can be easily mounted on a motor used for rotation and aligned to the motor. To facilitate

alignment and rotation, the compensator is mounted on a high-power stepper motor having the capability of stable rotation even for an asymmetric load mounted on it, as is the case here. A procedure has been developed for accurate alignment of the compensator to the beam path to achieve the desired rotating compensator configuration of an ellipsometer. Such alignment of the Krasilov compensator is a considerable challenge. In fact, for the alignment of the compensator to the beam path, two sets of alignment stages are required. One set of alignment stages with multiple degrees of freedom holds the compensator and is attached to the motor to ensure that the axis of rotation of the motor is parallel (or in-line) to the optical axis (i.e., symmetry axis) of the compensator. This optical axis lies in the desired plane of incidence that is common to the three total internal reflections within the compensator. Then the motor is attached to the second set of alignment stages to ensure that the rotation axis of the motor coincides with the beam path. Step by step, improvements in the alignment procedure and the stability of the two alignment stages helped to improve the alignment capability of the Krasilov compensator inline so that its optical axis coincides with the beam path. Once the two conditions on alignment are satisfied, the beam exiting from the compensator has minimum/no wobble and hence can be used in the rotatable compensator configuration of an ellipsometer. The photograph in Figure 106 shows the compensator at an angle, with its alignment stages attached to the stepper motor. Figure 107 shows the alignment stages attached to the stepper motor for achieving alignment of the rotation axis of the motor with the path of the beam as described above. Figure 108 shows all the optical components of the rotating compensator ellipsometer incorporating the Krasilov compensator in a straight-through configuration.

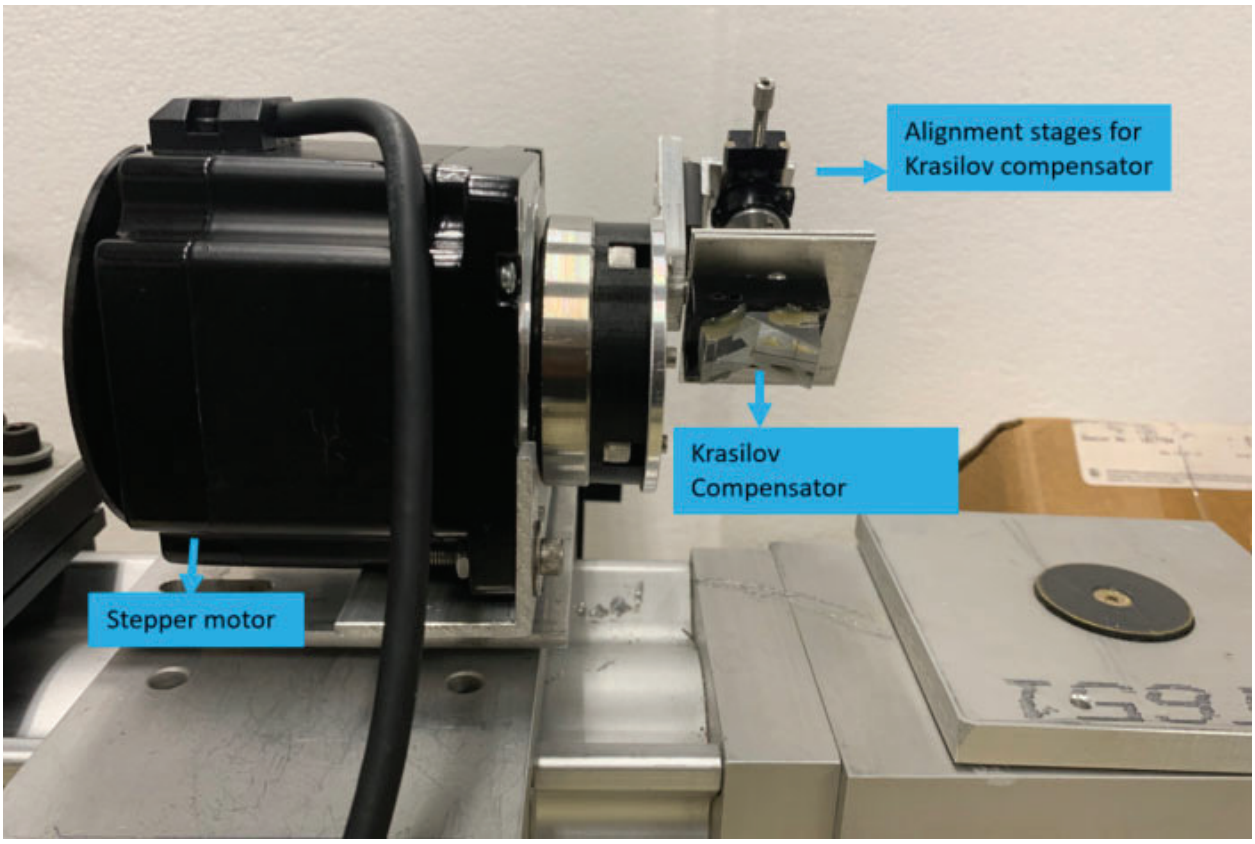


Figure 106. Photograph of the Krasilov compensator attached to the stepper motor and all the alignment stages upon which the compensator is mounted

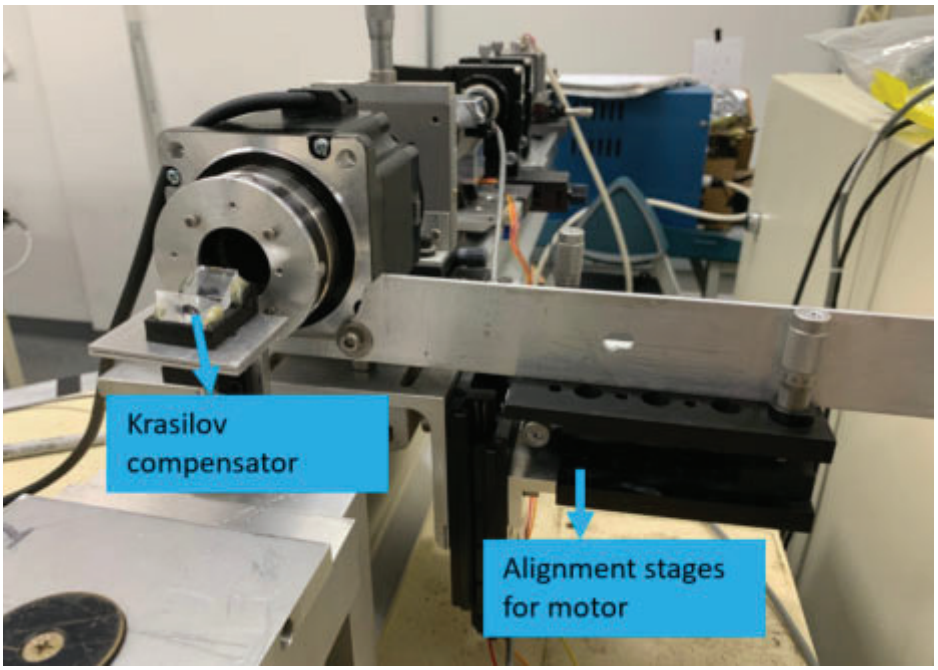


Figure 107. Photograph of the motor with all stages, designed for aligning the motor rotational axis to superimpose onto the beam path

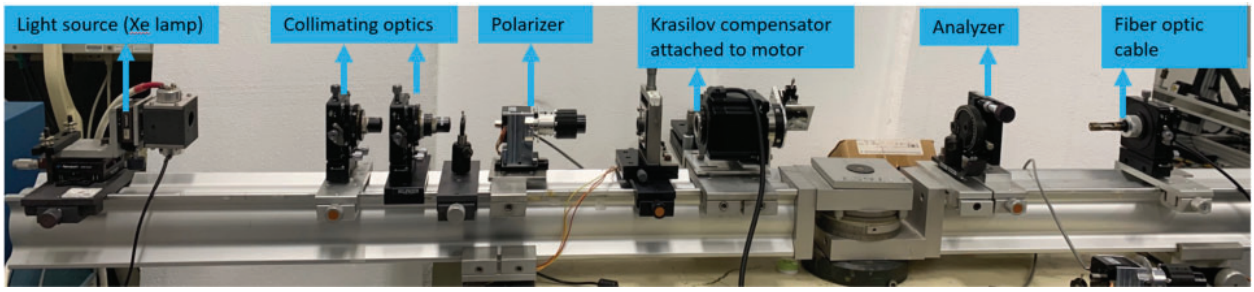


Figure 108. Photograph of the rotating compensator ellipsometer in straight-through configuration using the Krasilov compensator

For the single rotating-compensator multichannel ellipsometer, the irradiance waveform at the detector is given by:

$$I(t) = I_0 (1 + \alpha_2 \cos 2C + \beta_2 \sin 2C + \alpha_4 \cos 4C + \beta_4 \sin 4C). \quad (9)$$

Here (α_{2n}, β_{2n}; n = 1,2) are the dc-normalized cosine and sine Fourier coefficients, respectively, where C is the angle of the fast axis of the compensator. For the SE measurement in this setup, the data acquisition always starts at $C = 0$. In order to determine all the ac Fourier coefficients along with the dc coefficient, a minimum of 5 detector scans are required per optical cycle. In the configuration of Figure 108, the detector is scanned 8 times per optical cycle, and hence, 16 scans per mechanical cycle of the compensator. In a well-aligned system, the detector scans from the

two optical cycles should overlap. This condition can be used as a check to determine the quality of optical alignment of the system which impacts the accuracy of the system performance. Calibrations of the azimuthal angles of the polarizer and analyzer P and A, respectively, are completed prior to placement of the compensator. In the straight through configuration, the reference plane of incidence is set by the transmission axis of the polarizer corresponding to $P = 0°$. Calibration identifies the azimuthal angle of the analyzer transmission axis such that $A = P = 0°$. This occurs for parallel transmission axes for the polarizer and analyzer and maximum irradiance through the system. After the placement of the aligned compensator, the compensator is calibrated such that its fast axis is in-line with the plane of incidence, i.e., parallel to the transmission axis of the polarizer so that $C = 0°$. After the calibration of all the three polarization optical components, the measurement/performance of the system is tested with multiple positions of the polarizer and analyzer. Figure 109 shows the irradiance spectra in arbitrary units associated with the scans from the two optical cycles including a total of 16 scans, 8 scans each optical cycle, at polarizer an analyzer azimuthal angles of $P = 0°$ and $A = 45°$. The figure shows that the irradiance spectra from the two optical cycles overlap and hence excellent alignment of the Krasilov compensator is achieved. A similar profile of irradiance spectra is possible with any combination of P and A angles. From these irradiance spectra as in Figure 109, the Fourier coefficients are extracted as indicated in Eq. (9).

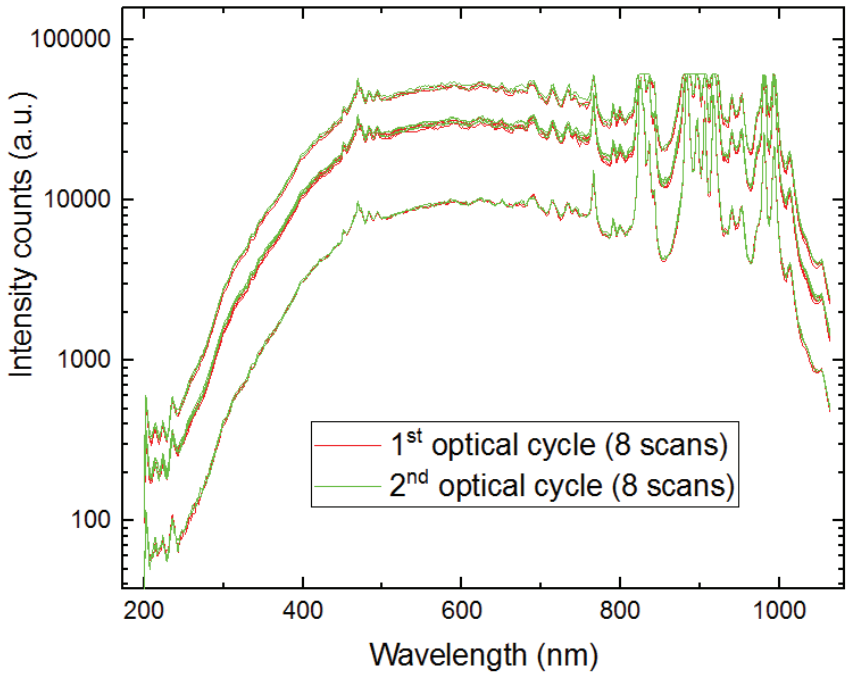


Figure 109. Irradiance spectra (eight scans) for the single rotating compensator in the straight-through configuration with P = 0° and A = 45°

The ellipsometry angles (ψ, Δ) of a sample are related to the quantities N, C, and S that appear in the Mueller matrix of the sample through $N = -cos2\psi$, $C = sin2\psi\ cos\Delta$, and $S = sin2\psi\ sin\Delta$.

In the straight through configuration used here $\psi = 45°$ and $\Delta = 0°$, and hence $N = 0$, $C = 1$, and $S = 0$. Thus, for a rotating compensator ellipsometer in straight through with fixed polarizer and analyzer azimuthal angles P and A, respectively, the unnormalized Fourier coefficients are given in terms of the dichroism and retardance ψ_c and δ_c of the compensator by

$$a_0 = I_{00}[1 + \tfrac{1}{2}(1 + \sin 2\psi_c \cos\delta_c)\cos(2P - 2A)], \quad (10a)$$

$$a_2 = -I_{00}\cos 2\psi_c\,[\cos 2P + \cos 2A], \quad (10b)$$

$$b_2 = -I_{00}\cos 2\psi_c\,[\sin 2P + \sin 2A], \quad (10c)$$

$$a_4 = \tfrac{1}{2} I_{00}(1 - \sin 2\psi_c \cos\delta_c)\cos(2P + 2A), \quad (10d)$$

$$b_4 = \tfrac{1}{2} I_{00}(1 - \sin 2\psi_c \cos\delta_c)\sin(2P + 2A), \quad (10e)$$

where I_{00} describes an irradiance factor that is common to all unnormalized Fourier coefficients. Different combinations of P and A provide the specified values of Fourier coefficients based on these values of N, C, S in straight through.

Figure 110 and Figure 111 show the Fourier coefficients generated by the two combinations of polarizer and analyzer angles $(P, A) = (0°, 0°)$ and $(P, A) = (0°, 45°)$, respectively. For all Fourier coefficient measurements shown, a stray light correction is performed for the region from 250 nm to 400 nm. A comparison of the behavior of the Fourier coefficients with expected results based on Equations (10) provides insights into the accuracy of the system performance. In the figures, the Fourier coefficient α_8 is also used as a consistency check of all eight scans. That is, if all eight scans are performed in a consistent manner by rotation of the compensator, i.e., varying only C and no other sample/rotation characteristics of the compensator, then this Fourier coefficient must vanish. If α_8 does not vanish, it is an indication of mechanical misalignment of the compensator resulting in a difference between the two optical cycles. Based on Equations (10b) and (10c), the normalized Fourier coefficients $\alpha_2 = a_2/a_0$ and $\beta_2 = b_2/a_0$ must vanish for an ideal non-dichroic compensator, but in the presence of dichroism, these Fourier coefficients can be used to provide ψ_C. In fact, in Figure 110 and Figure 111, these coefficients do not vanish in general because of the dichroism of the Krasilov compensator. For the configuration of $P = 0°$, $A = 45°$, both a_2 and b_2 of Equations (10b) and (10c) are non-zero as indicated in Figure 111, and the zero-order coefficient in Equation (10a) is simply I_{00}. Then the dichroism of the compensator under measurement can be extracted from the normalized Fourier coefficients (α_2, β_2) by using the following equation:

$$\psi_c = \tfrac{1}{2}\cos^{-1}[(|B_2|)/\sqrt{2}]\,, \quad (11)$$

where $|B_2| = \sqrt{\alpha_2^2 + \beta_2^2}$. Figure 112 shows the dichroism extracted from these Fourier coefficients.

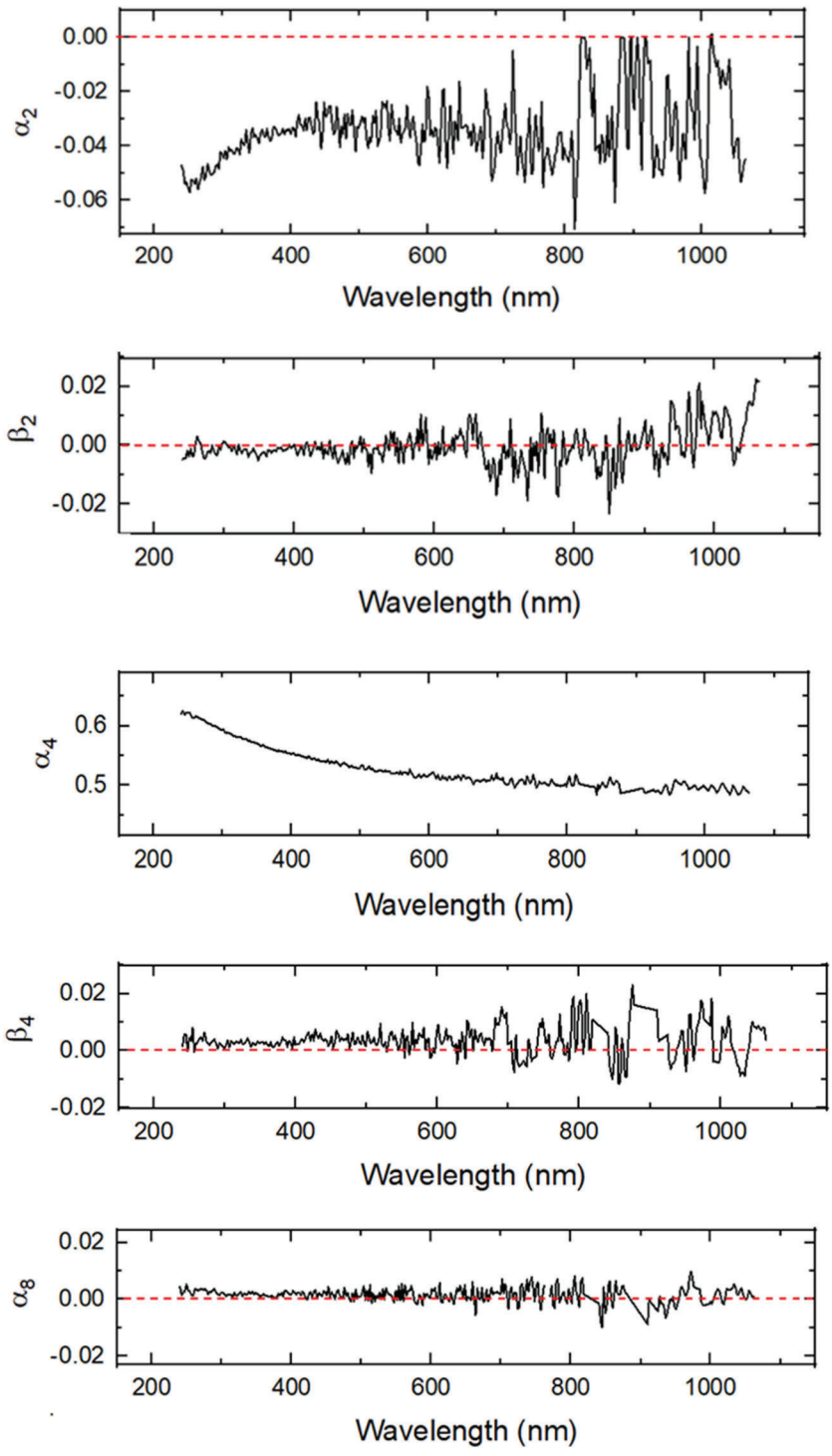


Figure 110. Normalized Fourier coefficients incorporating the Krasilov compensator in straight-through configuration with P = 0° and A= 0°

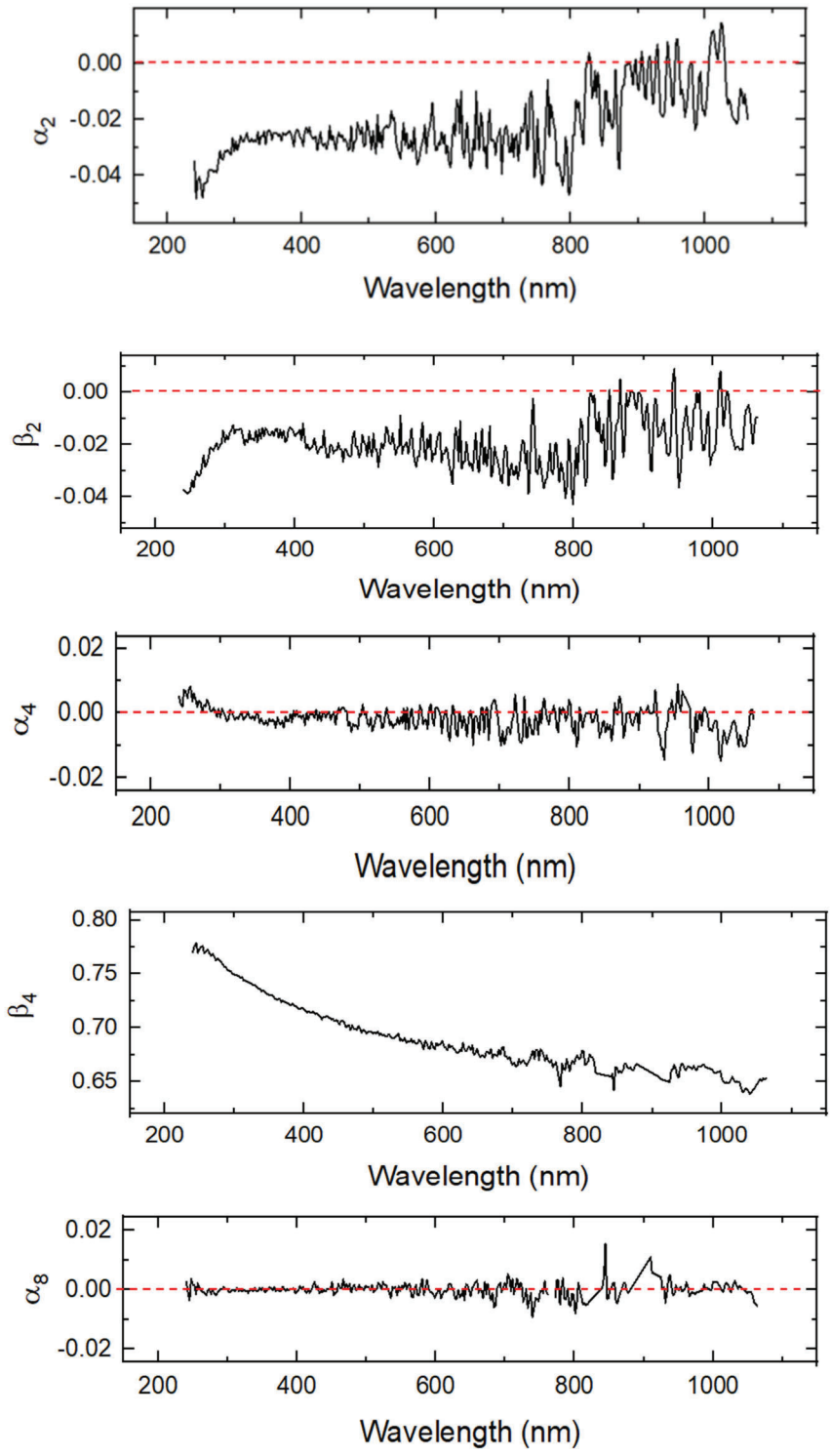


Figure 111. Normalized Fourier coefficients incorporating the Krasilov compensator in straight-through configuration with P = 0° and A = 45°

Since the Fourier coefficients are near zero due to the weak dichroism, the results for ψ_C are noisy, and so to improve the signal-to-noise ratio, the data are smoothed. The smoothed data closely overlap the dichroism measured on the compensator using a commercial J.A. Woollam Co., Inc model RC2 ellipsometer. As in the case of the dichroism, the retardance generated by the compensator is most easily extracted in the $P = 0°$, $A = 45°$ configuration of Figure 111 by using the β_4 spectrum. For this purpose, the following equation is used

$$\delta_c = cos^{-1}[(1 - 2\beta_4)/sin\ 2\psi_c] \,. \tag{12}$$

The extracted retardance spectrum is shown in Figure 113 in comparison with the results from the commercial ellipsometer. Also shown are the results from a more complicated analysis of the α_4 spectrum in the $P = 0°$, $A = 0°$ configuration of Figure 110. Reasonable agreement with the results of the commercial ellipsometer is observed over the complete spectrum. For the retardance, however, the deviations from the measurement using the commercial instrument are larger than for the dichroism and further efforts are warranted to explore these deviations. In this comparison, for example, a full analysis of stress induced retardance of the compensator is not applied and furthermore stress due to rotation of the compensator may be the origin of the differences in Figure 113 (peaks above 800 nm occur because of the high intensity peaks in the Xe spectrum). This additional stress effect due to rotation will be addressed in future studies. Generally, the results for the dichroism and retardance show that the Krasilov compensator can indeed be used as a rotating compensator (polarization modifying element) in an ellipsometer.

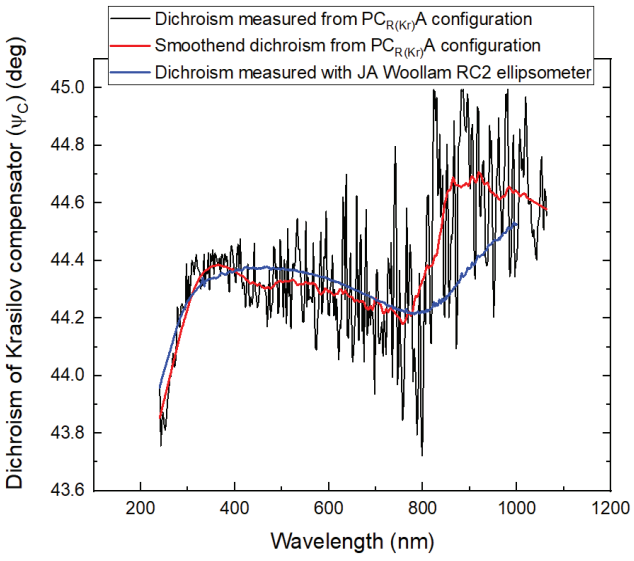


Figure 112. Dichroism of the Krasilov compensator measured in the rotating compensator configuration PCR(Kr)A; spectroscopic variation of the dichroism is small, yielding apparently noisy data on this scale of the ordinate

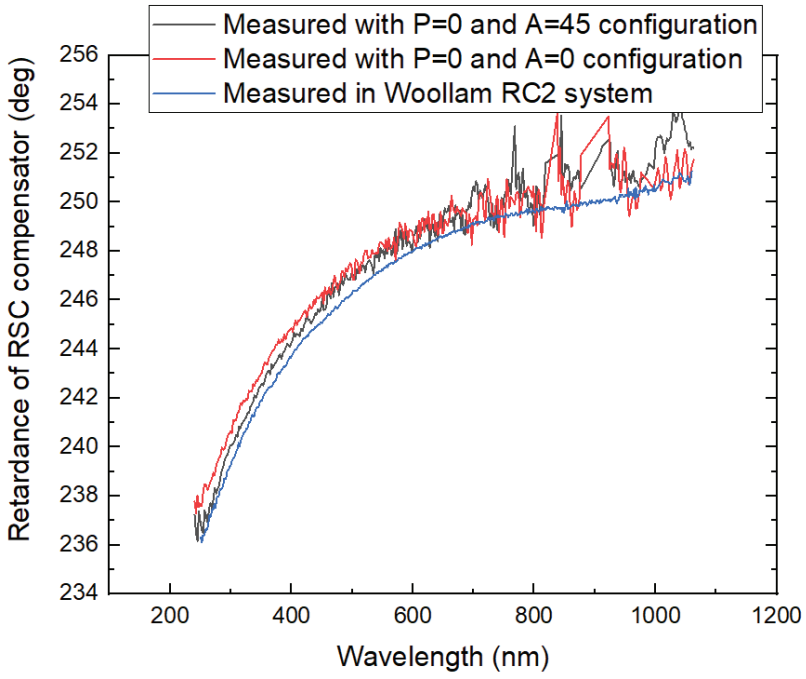


Figure 113. Retardance of the Krasilov compensator in comparison with the measurement by the J. A. Woollam Co., Inc model RC2 ellipsometer

Performance tests of the EQE-SE system

EQE analysis and fits of the Hamamatsu S1337-21 silicon photodiode

To investigate the performance of the angle dependent EQE-SE system, spectroscopic ellipsometry (SE) measurements and EQE measurements were performed on an enhanced UV sensitive (75% EQE at 200 nm) windowless silicon photodiode (Hamamatsu S1337-21) at non-normal angles of incidence of 50º, 60º and 70º. EQE was also performed at normal incidence on the photodiode. The large photosensitive area (18 mm × 18 mm) permits large oblique angle measurements with incident beam cross-sections that remain well within the detection region. Each oblique angle spectrum consists of individual *p* and *s* polarization measurements wherein the light incident on the detector is polarized with the polarizer set precisely parallel and precisely perpendicular to the plane of incidence, respectively.

The photodiode is comprised of crystalline silicon (c-Si) with a *p*-type emitter region near the surface, an *n*-type active region, and an n^+ layer at the rear contact. The *p*-layer was formed by boron diffusion with a nominal junction depth of ~ 1 µm. [362] This silicon structure is sandwiched between a silicon dioxide (SiO_2) surface passivating layer and a gold (Au) rear contact. [363] Figure 114 shows the results of SE measurements together with the fit using a corresponding model.

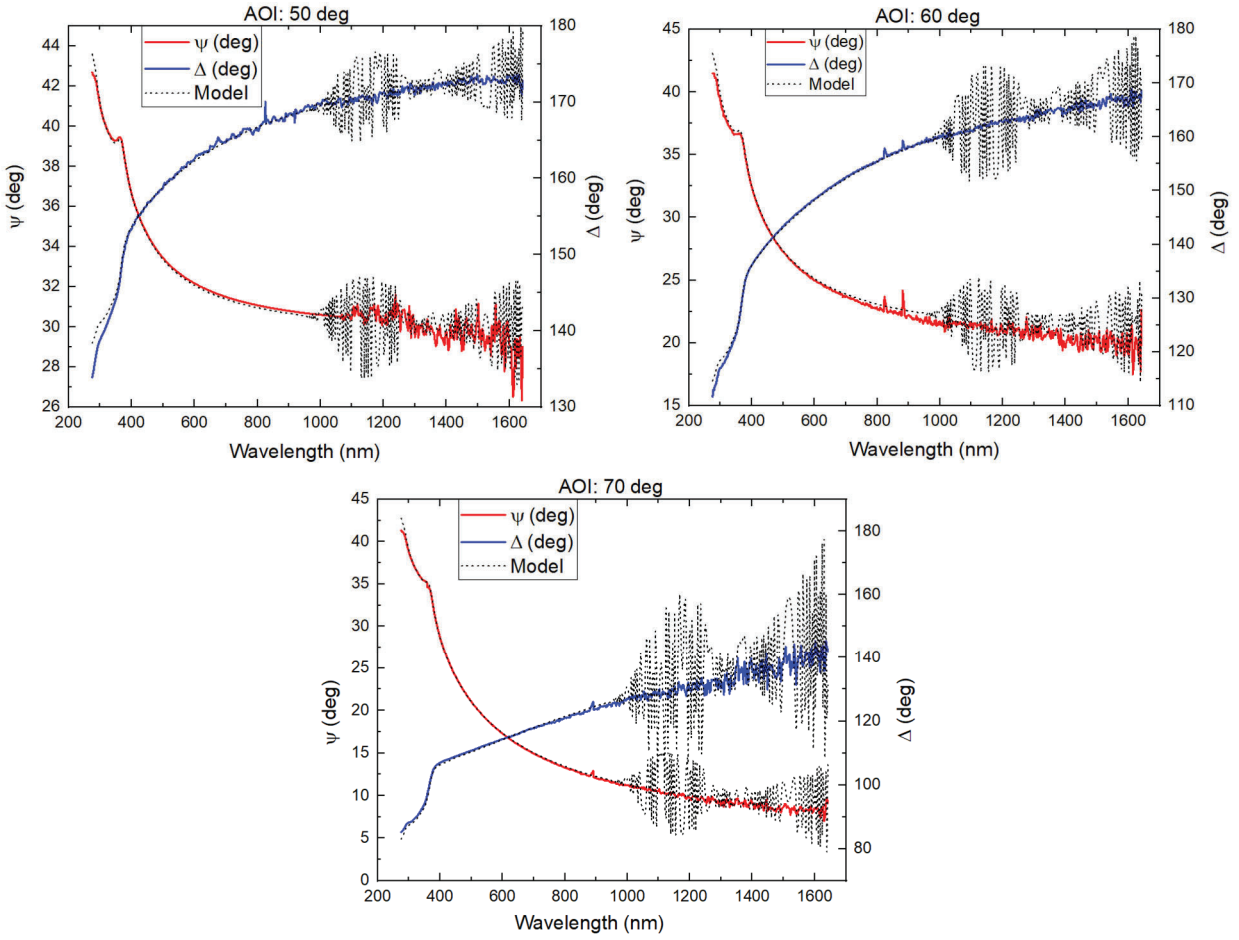
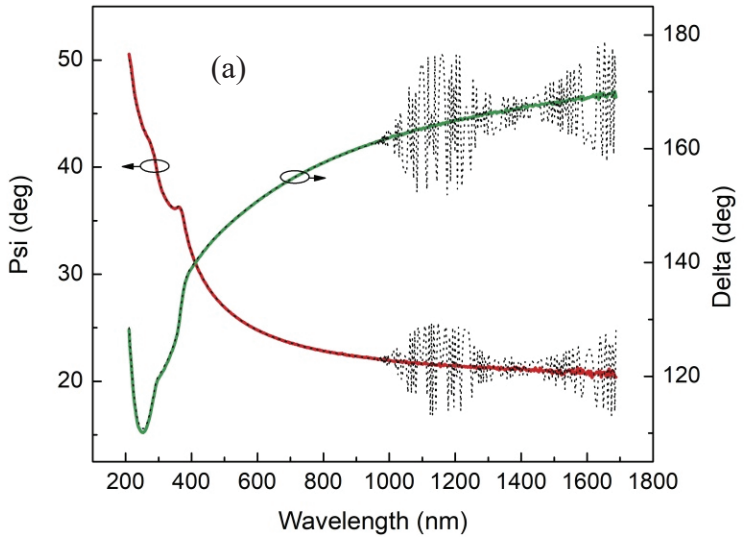


Figure 114. SE results at 50°, 60°, and 70° incidence angles with best fits for the Hamamatsu S1337-21 silicon photodiode measured with EQE-SE system

Figure 114 depicts experimental data obtained from SE measurements at angles of incidence of 50°, 60°, 70° along with corresponding best fits using a structural/optical model for the device. An increased noise in the measured spectra above 1000 nm is from the IR detector measurement system. Steps are being taken to reduce the noise in that region.

Since accuracy of measurement is required for the EQE analysis on this Si cell, a similar SE measurement is performed on a commercial J. A. Woollam Co., Inc model M2000 instrument. The measurement and corresponding fit are shown in Figure 115(a). The structural model used for SE data analysis is shown in Figure 115(b). Standard dielectric functions from the instrument's database were used for the SiO_2, c-Si, and Au layers. [364, 365] The thickness of the bulk silicon substrate was unavailable from the manufacturer and an initial guess of 250 μm was used for fits. The interface layer between the c-Si and Au was modeled using the Bruggeman effective medium theory (EMA). [366]

The SE fit routine was insensitive to the relatively large c-Si layer thickness (t_{Si}) but was sensitive to the SiO_2 thickness (t_{SiO_2}), c-Si/Au interface thickness ($t_{Si/Au}$), and volume fraction of Au (f_{Au}) in the interface. Next, the normal incidence EQE experimental data were subjected to a least squares regression routine applying the optical and structural models from SE in the EQE simulation. In this routine, t_{Si} was the only free parameter because it was not accessible from SE, and a best fit value of 429.190 ± 0.003 μm was obtained. A subsequent SE fit with the new fixed t_{Si} and the three free parameters t_{SiO_2}, $t_{Si/Au}$, and f_{Au} results in the values given in Figure 115(b). It must be noted that although a similar SE measurement and fitting method were applied to data obtained using the EQE-SE system with similar results, the data obtained by the M2000 instrument could be very closely fit, as shown in Figure 115(a), by the model simulation that yielded the minimum MSE. The fits suggest an atomically smooth interface between the passivating SiO2 layer (27 nm) and bulk doped silicon (429 μm). The interface between the gold rear-contact and cathode portion of the bulk silicon was modeled using a Bruggeman EMA layer (80 nm) resulting in a microscopically rough interface with a gold volume fraction of 15%.



(b)

Layer Composition (Properties)	Thickness
SiO_2	27.1 ± 0.1 nm
c-Si	429 μm
Si/Au (f_{Au} = 15.1 ± 0.1%)	80.1 ± 0.2 nm
Au (opaque)	

Figure 115. (a) Hamamatsu S1337-21 silicon photodiode SE data (incidence angle = 60°) with fits; (b) Structural model and layer thicknesses, from the fits

Figure 116(a) shows the result of a least squares regression fit of the normal EQE experimental data and EQE simulation with t_{SiO_2} as a fit parameter, resulting in a best fit of 30.94 ± 0.08 nm. Sensitivity analyses for the effects of the thicknesses t_{SiO_2}, t_{Si}, and $t_{Si/Au}$ on the EQE spectrum are shown in Figure 116(b-d).

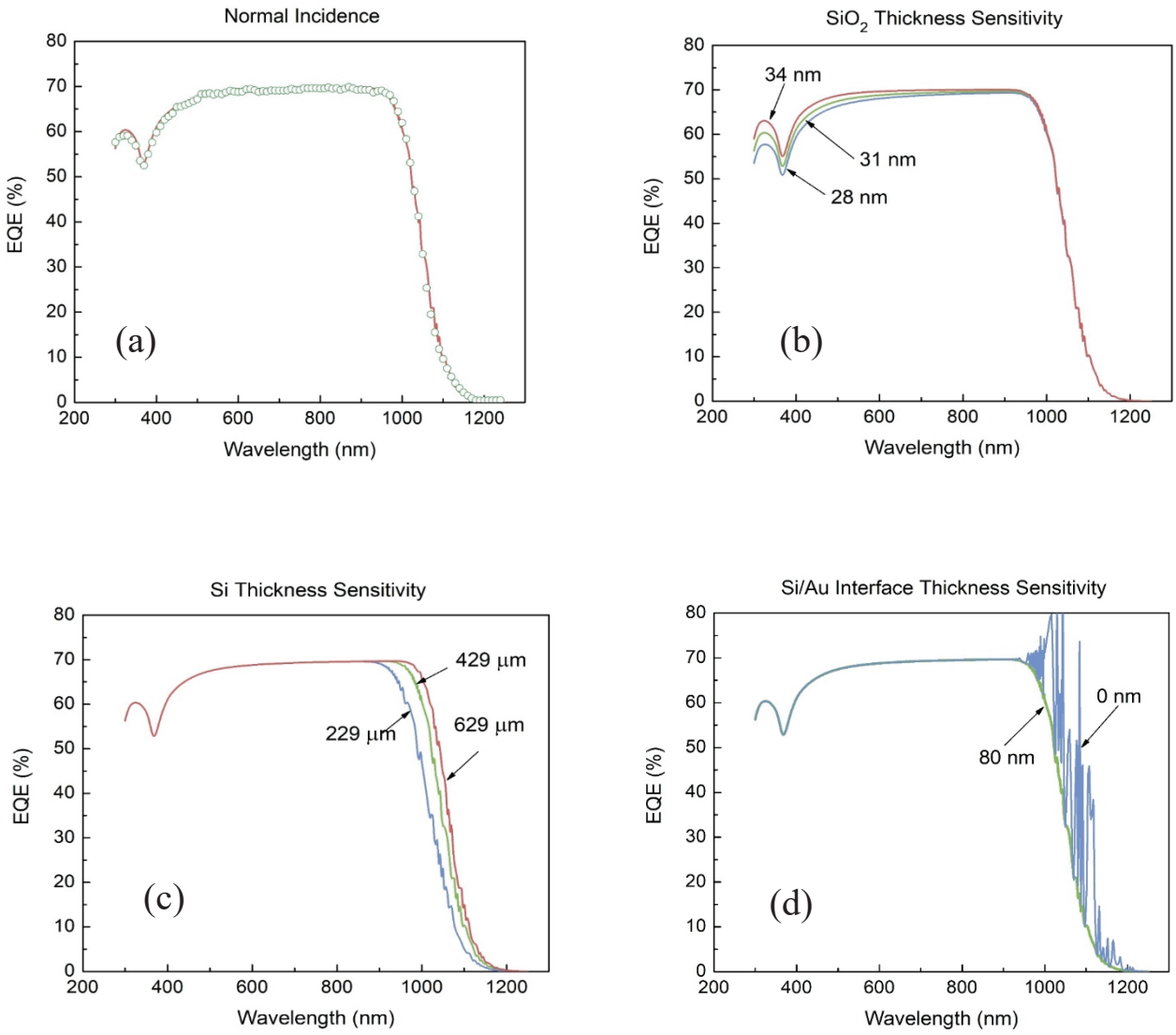


Figure 116. (a) Normal incidence EQE data and simulation for best fit thicknesses $t_{SiO_2} = 31\ nm$, $t_{Si} = 429\ \mu m$, $t_{Si/Au} = 80\ nm$; (b, c, d) show sensitivity analysis for the effects of the thicknesses on the modeled EQE spectrum

Uniformity of the top passivating SiO_2 layer across the detector factors into the measured EQE. The cross-sectional area striking the detector for angular EQE varies with respect to the area at normal angle of incidence. For the angles of incidence 50°, 60°, and 70° the area increases by factors of 1.3, 1.6, 2.0, and 2.9, respectively. Figure 116(b) suggests EQE sensitivity to the thickness t_{SiO_2} on the order of a few nanometers. Hence, EQE simulation fits for the angular data using least squares regression routines were performed with t_{SiO_2} as a free fit parameter. The results of the best fits for *p* and *s* polarizations are shown below in Table 19. The resulting angular EQE data simulation fits are shown in Figure 117.

Table 19. Fit results for the SiO_2 layer thickness at various angles for p and s polarization states

Incidence Angle (°)	$t_{SiO_2}(p)$ (nm)	$t_{SiO_2}(s)$ (nm)
0	30.94 ± 0.08	
50	30.00 ± 0.09	30.18 ± 0.05
60	31.00 ± 0.81	30.36 ± 0.12
70	29.69 ± 0.07	27.19 ± 0.05

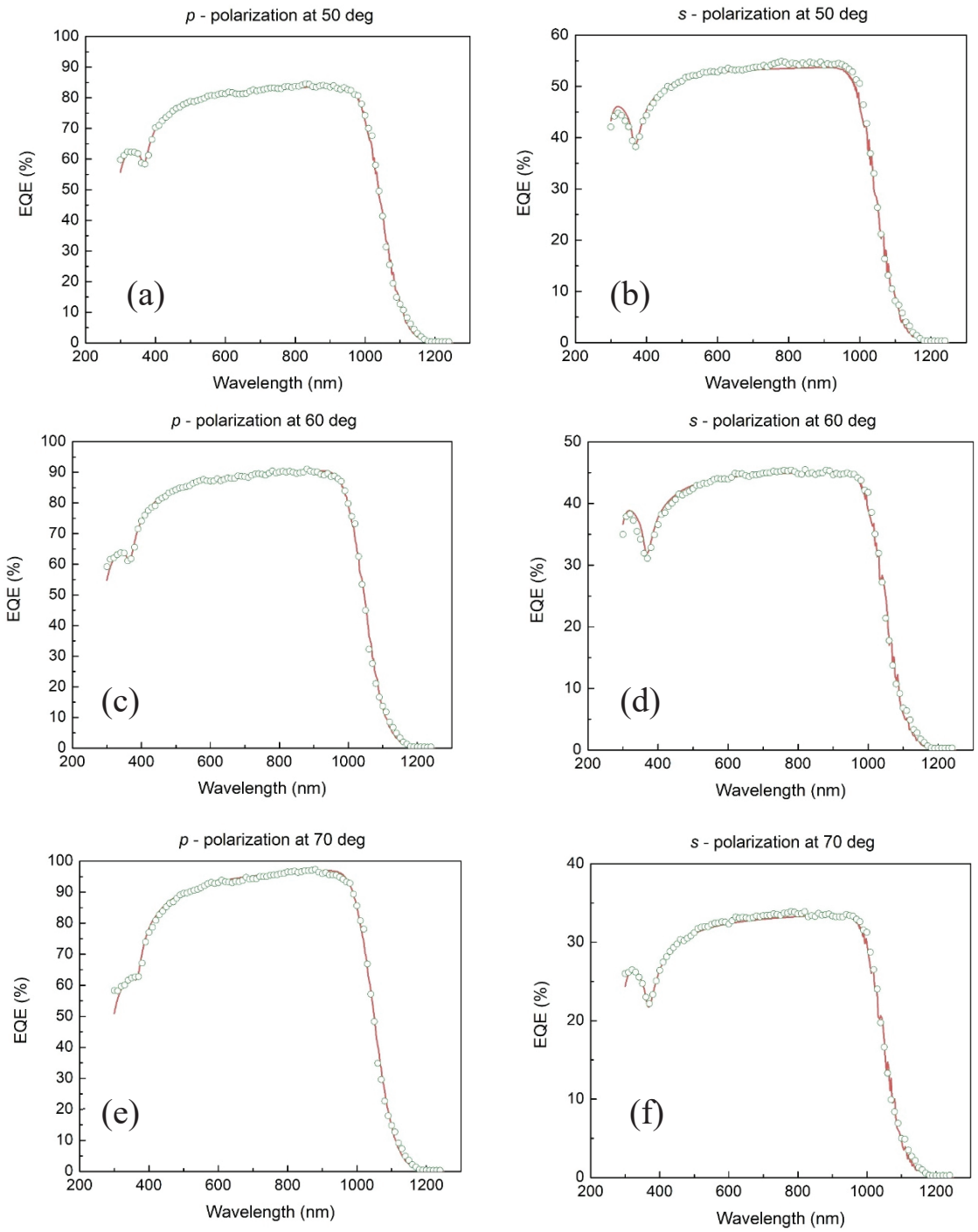


Figure 117. Plots of angular EQE data with the corresponding best fit simulated EQE with t_{SiO_2} as the fit parameter

The behavior of t_{SiO_2} with increasing angle of incidence is systematic particularly for the *p* polarization in which case t_{SiO_2} decreases with increasing angle. A possibly related discrepancy is the difference in t_{SiO_2} between the SE fit (~27 nm) and EQE fit (~30-31 nm) for 60° angle of

incidence where the probing areas are similar. Various sources of the behavior and discrepancy are possible. One possibility is non-uniformity in t_{SiO_2} over the area of the photodiode; however, such an effect would not explain the SE-EQE difference at 60° angle of incidence. Another possibility is the need for a different Si dielectric function than that in the database. Once these possibilities are explored, there will remain the possibility, unclear at this point, that front interface recombination velocity depends on the polarization of the light that excites the electron hole pair.

CIGS solar cell EQE analysis

The CIGS solar cell structure under investigation using the EQE/SE instrument was fabricated at the National Renewable Energy Laboratory and was provided by the group of J. V. Li formerly of Texas State University. The sample consisted of three cells, and the results presented in this report are for the cell marked as '3'. A spectroscopic ellipsometry (SE) measurement was performed on the cell to determine the individual structural parameters of each layer and selected optical parameters, and EQE was measured both at normal incidence and for different polarizations and different oblique angles of incidence.

The CIGS solar cell model was developed starting from available information on the sample. Then the measured SE spectra were fitted using the model via a step-by-step MSE reduction procedure in which the structural parameters were varied first starting from the nominal thickness for each layer, then selected optical parameters were also varied. For the SE analysis presented here, only the EMA volume fractions were varied in association with the optical parameter variations. All other optical parameters of the layers were kept constant at the values based on a previous similar analysis but for the cell marked as '2'. Before the SE and EQE measurements on cell #3, a current density versus voltage (J-V) measurement was performed on the cell. Figure 118 shows this cell's J-V characteristics.

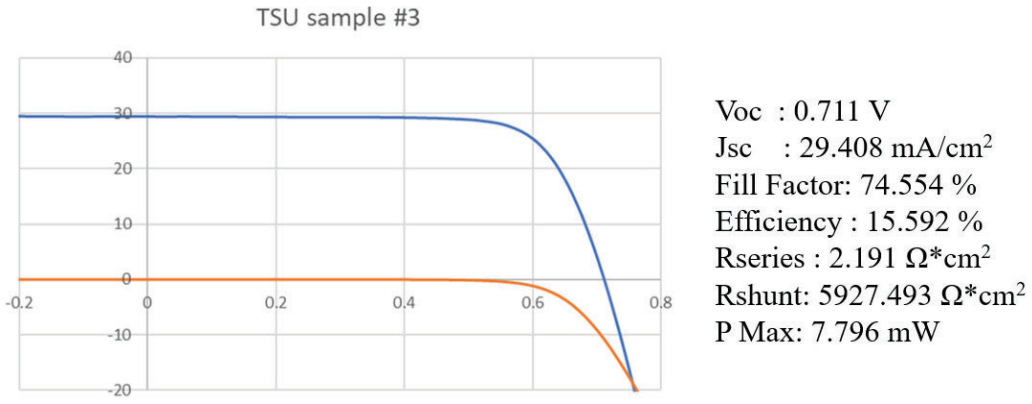


Figure 118. J-V results of sample #3, under detailed investigation by the EQE-SE system

The SE measurements were performed on the EQE-SE system along with the *p* and *s* polarization EQE measurements at 50°, 60°, and 70°. The full set of SE data is shown in Figure 119. The structural and volume fraction parameters extracted from the 60° SE measurement were used for further EQE analysis of the solar cell. The resulting best fit of the experimental data are given as

the broken line in the panels at the upper right in Figure 119, and the best fit model parameters of the layer stack are presented in Figure 119. The effective thicknesses (or film volumes/area) are shown at the right in Figure 120 and are consistent with typical intended values for CIGS. The model results at the other two angles of incidence in Figure 120 are obtained by fixing the parameters of the layer stack at the values in Figure 120.

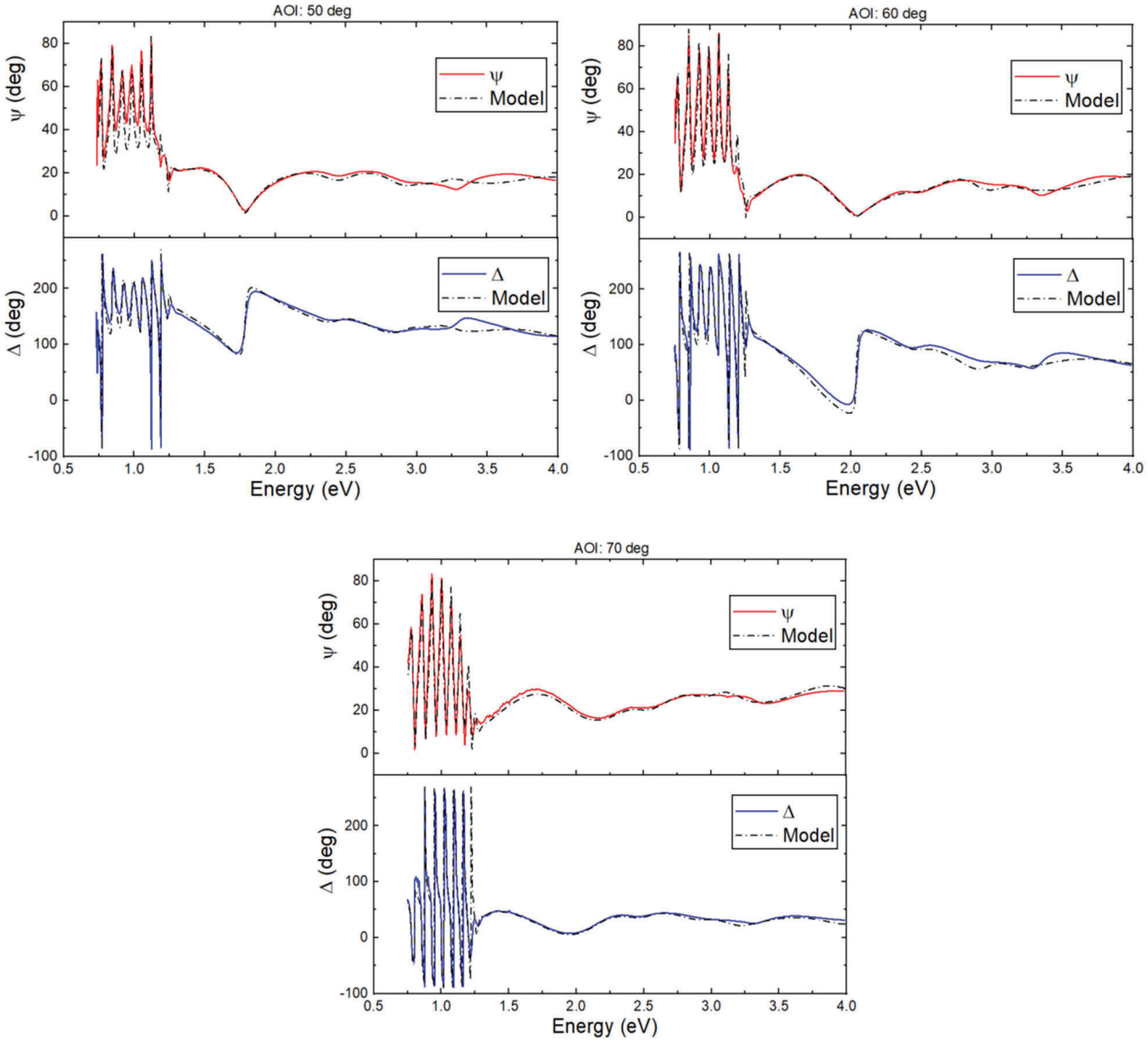


Figure 119. SE spectra for the CIGS solar cell measured in the EQE-SE system at angles of incidence of 50°, 60°, and 70°

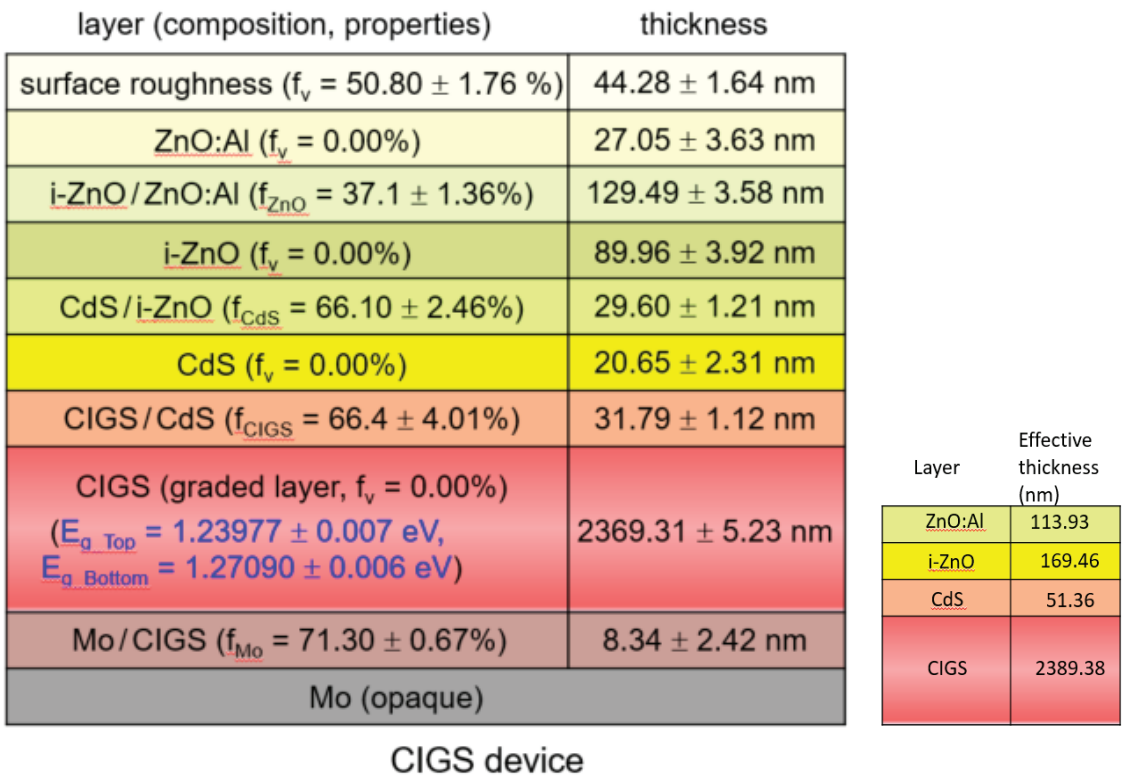


Figure 120. Multilayer structural model of the CIGS solar cell under study

Using the fixed parameters of Figure 120 in the simulation, the agreement between the data and simulation for the 70° angle of incidence is excellent. An exception is the narrow range near the bandgap where the interference fringes first develop with decreasing energy. Spectral resolution could be an issue here, or the CIGS reference dielectric function may require modification. The agreement between the data and simulation for the 50° angle of incidence is poorer, particular at higher energies where the data are dominated by surface and interface roughness. Future work will focus on addressing these issues through simultaneous analysis of the six SE spectra at the three angles of incidence.

The analysis of the SE data at 60° angle of incidence that led to the results in Figure 120 for the deduced layer structure incorporates a CIGS layer with a one-segment linear graded profile for the Ga content. The associated bandgap profile is identified by the bandgaps at the absorber layer front [adjoining the CIGS/(CIGS+CdS) interface layer] and back [adjoining the (Mo+CIGS)/CIGS interface layer] and is provided in Figure 120 (left). In fact, the best fit of the SE data for the sample as presented in Figure 119 showed that the Ga content within the CIGS layer is weakly graded with a bandgap ranging from 1.271 eV at the back to 1.240 eV at the front as shown in Figure 121 (the bandgap in the 2.4 μm thick absorber layer for the CIGS solar cell is deduced from the SE analysis). A comparison of this profile with a compositional depth profile from Auger electron spectroscopy (AES) is given in Figure 122 where the SE result is the gold line obtained from the relationship between the bandgap and Ga content. The gold line shows the Ga compositional profile obtained from the bandgap profile of Figure 120 and Figure 121. The bandgap profile in turn is deduced from the SE analysis of the 60° angle of incidence data of

Figure 119. Good agreement between SE and AES is obtained nearest the back of the cell as probed by the lower photon energies; however, the agreement becomes increasingly poor toward the front of the device which is probed by the higher photon energies. This problem may relate to the challenge in fitting the data at high photon energies due to the role of surface and interface roughness in influencing the modeling within this spectral range. Clearly, the additional SE data at different angles of incidence will enable a more detailed look into this problem.

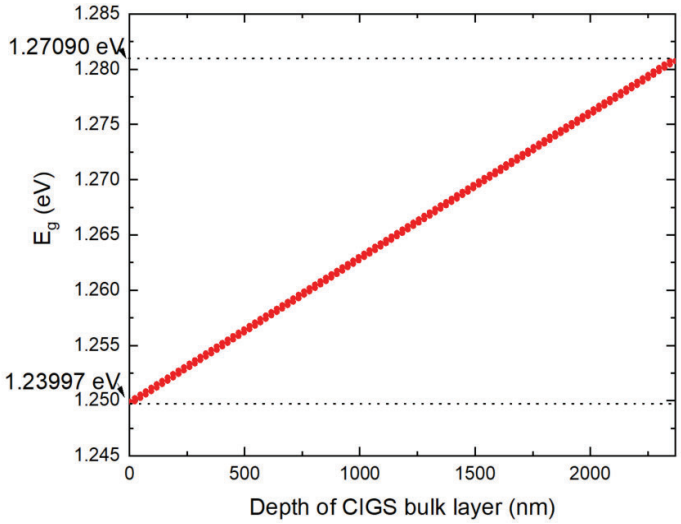


Figure 121. Bandgap profile of CIGS bulk layer

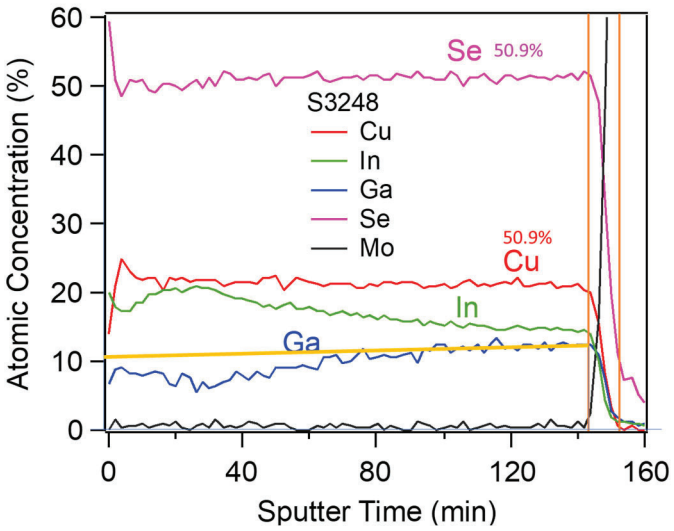


Figure 122. Compositional depth profile of the 2.4 µm thick CIGS absorber layer obtained from Auger electron spectroscopy

The EQE analysis in Figure 123 shows that the measured normal incidence EQE can be modeled with a collection depth profile for the cell extending from the front CIGS/CdS interface layer through the bulk of the CIGS layer to the back (mixed CIGS+Mo)/CIGS interface. Addition of a

collection profile provides good agreement with the measured normal incidence EQE and is also consistent with expectations for this thickness CIGS layer (2369 nm) and CdS layer (50 nm). The simulated EQE shown in Figure 123 is obtained by addition of 100% collection contribution from the CdS/CIGS interface and a uniform 90.4 ± 0.3 % contribution from the CIGS bulk layer having a thickness of 2369 nm. In the collection model, it is assumed that the (mixed CIGS+Mo)/CIGS layer does not contribute to collection. The dashed lines in the figure show the individual contribution to the collection profile from the CIGS+CdS interface layer and the CIS bulk layer that are summed to obtain the total simulated EQE.

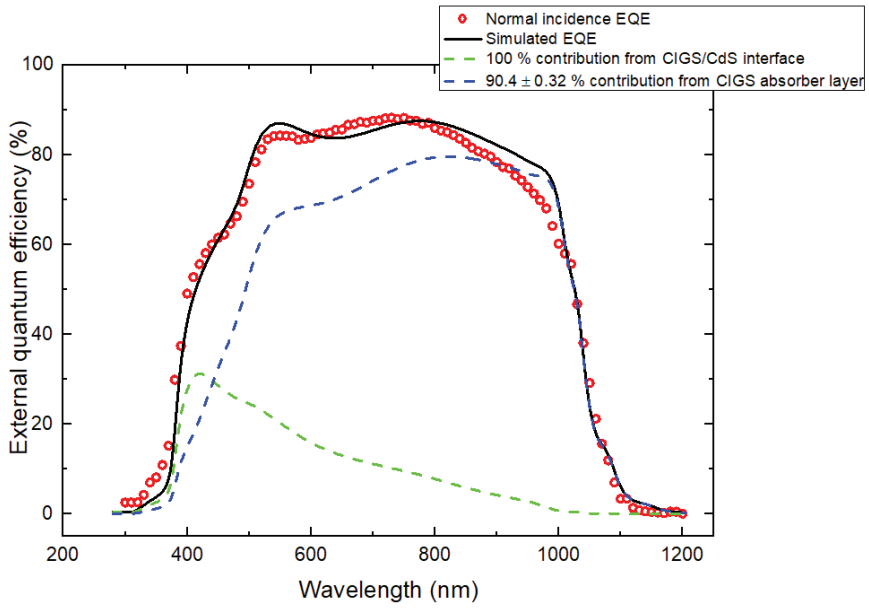


Figure 123. Plot of measured normal incidence EQE and the simulated EQE based on a best fit collection model

At the end of SE analysis for the cell labeled '3' given by the results in Figure 120, a definitive thickness of each layer and its associated dielectric function are available for simulations of the EQE measurements on the same sample. For the simulation of the graded CIGS absorber layer, the total thickness is divided into 10 components of equal thickness and the dielectric functions are generated from the model for each of the 10 parts based on Figure 120.

The same SE deduced model and collection profile is then used for the EQE of the cell measured at different oblique angles. The oblique angle measurements were performed at 50°, 60°, and 70° for both *p* and *s* polarizations. Typical measurements are done in 10° increments starting at 50°; however, for this set, the SE measurement showed an angle of incidence offset of 1.254° ± 0.302° from the nominal/intended angle of incidence of the measurement. By inclusion of this angular offset in the simulation of angular EQE, very close agreement with the measured values is obtained. These oblique angle measurements along with the simulated results are shown in Figure 124**,** Figure 125, and Figure 126. The results illustrate good agreement between both *p* and *s* polarization spectra.

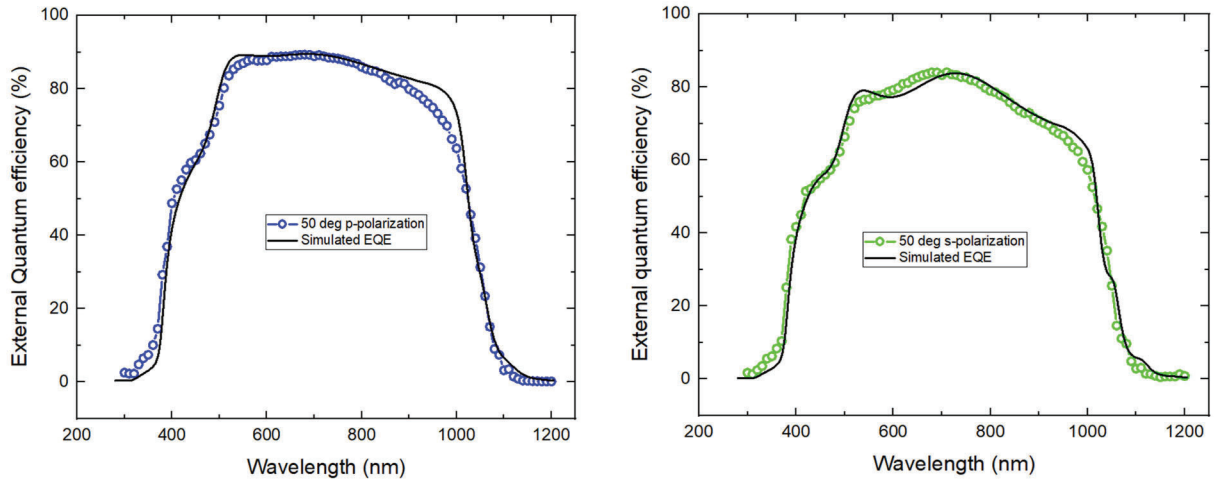


Figure 124. EQE spectra measured at 50° angle of incidence for both p and s polarizations along with corresponding simulations

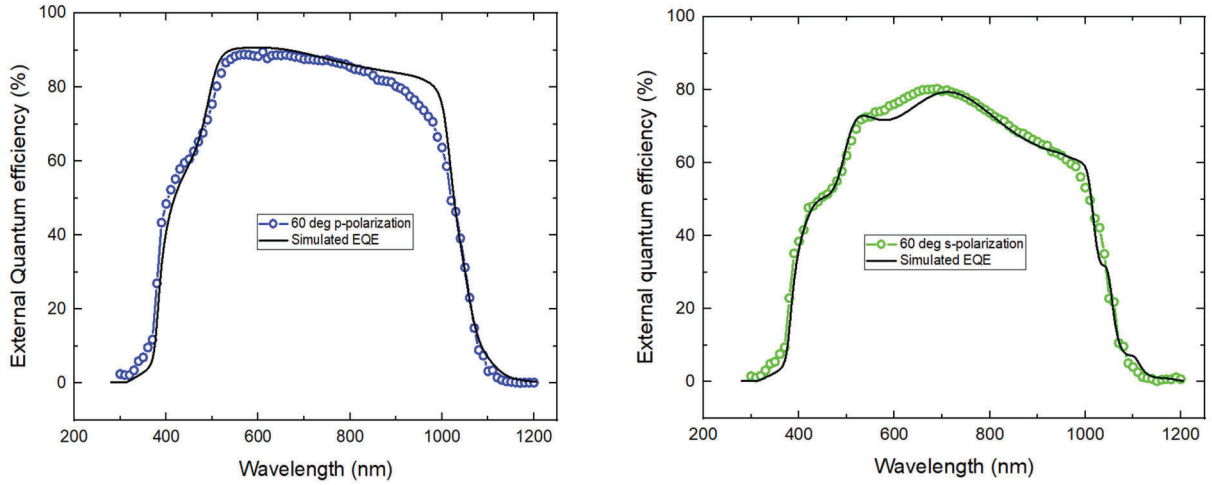


Figure 125. EQE spectra measured at 60° angle of incidence for both p and s polarizations along with corresponding simulations

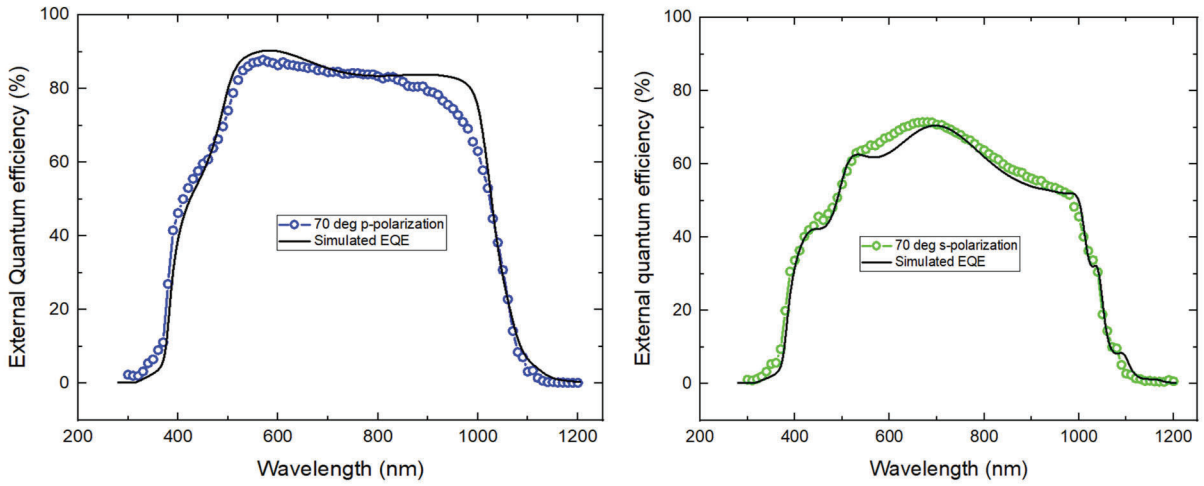


Figure 126. EQE spectra measured at a 70° angle of incidence for both p and s polarizations along with corresponding simulations

In spite of the excellent agreement, systematic differences are observed between the data and simulations. Deep absorption losses in the range from 850 to 1050 nm are observed particularly in the normal incidence and *p* polarization oblique incidence EQE. Much weaker such losses occur for the *s* polarization oblique incidence EQE. In addition, the EQE data extend above the simulation for *s* polarization in the shallow absorption region from 550 to 700 nm, an indication that the recombination losses are not as high as the 10% level that the model would indicate. This effect is only observed for the *s* polarization spectra and is absent for the *p* polarization spectra. An important future direction is to model the full set of data by least squares regression with a physics-based model, which will allow for extraction of the underlying origins of these interesting observations.

15.5 CONCLUSIONS

Significant accomplishments and progress have resulted from this project relevant to the development of optical and electronic instrumentation for applications in the analysis of photovoltaic materials and devices.

A new rotatable quasi-achromatic rhomb compensator has been designed, fabricated, and characterized. This optical element has been developed to replace biplate compensators which exhibit an intrinsic wavelength dependent retardance that limits the spectral range of high accuracy operation in spectroscopic ellipsometers. The device is also expected to be superior to rotatable dual Fresnel rhombs due to the shorter path length within the fused silica and reduced susceptibility to stress. A proof of concept has been provided in this project with the demonstration of a single rotating compensator multichannel ellipsometer that incorporates such a rhomb. Operation of the ellipsometer in the straight through configuration has shown accurate Fourier coefficients deduced from the raw data. Directions for future improvement of the rhomb and the instruments that will exploit the new device have been identified.

A method for characterization of the complete Mueller matrix of the new rhomb compensator, applicable to rhombs in general, has been developed in this project. Non idealities have been incorporated into the formalism including stress induced retardance along the beam paths within the rhomb and dichroism associated with internal reflections. Wavelength independent parameters have been identified that enable evaluation of the effect of the rhomb on any incident polarization state. As a result of this complete characterization, ellipsometers that incorporate such rhombs in single and dual rotating configurations can be operated at extremely high accuracy for the evaluation of the optical properties of photovoltaic materials and devices. A manuscript entitled "Analysis of non-idealities in rhomb compensators" has been submitted to the journal *Optics Express* by authors and project participants Ambalanath Shan, Balaji Ramanujam, Nikolas Podraza, and Robert Collins. The manuscript is currently under review.

A single unique instrument has been developed that can perform normal and oblique incidence EQE measurements, along with oblique incidence SR and SE. All such measurements can be performed as a function of angle of incidence whereas the oblique incidence EQE and SR can be obtained for both *p* and *s* incident linear polarization states. The goal of the instrument is to extract information on both the optical and electronic performance of solar cells by least squares regression fitting of a large number of spectra (up to 20) simultaneously using physics-based models. EQE and SE measurements have been demonstrated on a Si photodiode, and differences between standard models and EQE and SE measured spectra have been observed that will enable incorporation of the appropriate physics needed to fit the entire data set simultaneously.

The EQE/SR/SE instrument has been applied to characterize a complete $CuIn_{1-x}Ga_xSe_2$ (CIGS) solar cell. The SE measurements have been analyzed to interpret the optical structure of the device, and the resulting optical model has been applied to multiple angles of incidence SE data. Differences between the data and the simulations provide insights into the approaches needed to improve the models. The normal incidence EQE measurement has been analyzed in terms of a simple recombination model, and this model has been used to simulate the results for oblique incidence polarization dependent EQE measurements. Although the simulations are in very good agreement with the data, small differences are systematic and require the integration of new physics into the device model to account for the differences observed in the data sets. Efforts are continuing toward the development of both optical and electronic models for applications to tandem solar cells incorporating both CIGS and perovskite absorbers. It is only though the advanced analysis made possible by the extensive data sets that a complete model for the operation of these devices will be possible.

16. DEVELOPMENT OF AN EXPERIMENTAL SET-UP TO MEASURE AN IMPLIED OPEN-CIRCUIT VOLTAGE OF SOLAR CELLS

Niraj Shrestha, Aesha Patel, Eulogio Lopez, Jackson Tatum, Abdudulimu Abasi, Zhaoning Song, Yanfa Yan and Randy J. Ellingson

16.1 SUMMARY

An experimental set up has been successfully constructed to estimate the implied open circuit voltage of solar cells. The set-up is currently being evaluated using standard $MAPbI_3$ absorber layer deposited on soda-lime glass. Observed iVoc were compared with previously reported actual open circuit voltage of $MAPbI_3$ solar cell. We attributed the difference between an implied Voc and actual V_{oc} of $MAPbI_3$ solar cell to the recombination losses at various interfaces present in $MAPbI_3$ solar cell.

16.2 INTRODUCTION

Instrumentation Development

The power conversion efficiency (PCE) of a solar cell depends upon open-circuit voltage (V_{oc}), short-circuit current density (J_{sc}) and fill factor (FF). These parameters can be obtained experimentally by measuring current-voltage characteristic of solar cells. Photovoltaic (PV) community have been putting huge effort in optimizing the PCE of solar cells by improving these parameters. One way to enhance PCE of a solar cell is to improve V_{oc}. The quality of an absorber layer, various kinds of treatment (pre or post treatment) and interfaces determine the V_{oc} of the solar cells. Therefore, huge effort has been applying to increase the V_{oc}. Here, we designed an experimental set up that measures the photoluminescence quantum efficiency of a thin film absorber layer which is then used to calculate the implied V_{oc} of a solar cell made with that absorber layer. Since an estimation of V_{oc} from such set up does not require a complete solar cell, the tool is highly efficient regarding fabrication time and material cost too. Currently, the system is being tested using $MAPbI_3$ absorber layer and the obtained results are under investigation.

Methylammonium lead triiodide ($MAPbI_3$)

Organic-inorganic metal halide perovskite materials have been widely used as absorber layer in solar cells due to their direct band gaps with large absorption coefficients, [367, 368] long electron-hole diffusion lengths, [367, 369] low exciton binding energies, [370] and low fabrication costs. [48] In general, perovskite can be described as ABX_3 crystal structure, where "A" and "B" are cations and "X" is an anion. In case of organometallic hallide perovskite, organic cations such as (methyl-ammonium $CH_3NH_3^+$, formamidinium $NH_2CH{=}NH_2^+$) sit at "A" site, a metal cation (Ge^{2+}, Sn^{2+}, Pb^{2+}) at "B" site and a hallide anion (F^-, Cl^-, Br^-, I^-) at "X" site. Among them, much attention have been given to $MAPbI_3$ (band gap ~1.60 eV [371]) due to its moderate photo and thermal stability. In this report, we have estimated the implied V_{oc} by measuring photoluminescence quantum efficiency of $MAPbI_3$ absorber prepared with/without $Pb(SCN)_2$ additive in the precursor solution. The $Pb(SCN)_2$ additive has been widely used in perovskite to improve the grain growth and hence PCE of perovskite solar cells. [372] Therfore, it is worth to test $MAPbI_3$ with/without such additive in our study.

16.3 METHODS, ASSUMPTIONS, and PROCEDURES

iVoc System Specification

Figure 127 identifies the system components that are used in construction of an *iVoc* experimental set. Details of the components used in the set up include:

1) *Laser diodes*: Sample is illuminated by a laser excitation of desire wavelength generated by laser diodes (Available laser diodes: 660 nm @ 50 mW and 635 nm @ 5 mW).
2) *Laser Diode Mount*: LDM56 mount by Thorlabs is used as mount. Such mount is ideal for temperature-controlled operation of the most 3 and -pin diodes. Laser diodes can be quickly and easily changed in the mount.
3) *Laser Diode Controller and Temperature Controller*: Thorlabs LDC200C series laser diode controller has been used to control current supply in diode. Together with temperature controller TED200C a stable operation of the connected laser diode can be achieved.
4) *Optical chopper*: An optical chopper is used to modulate the laser source at 100 Hz. The output of the chopper is connected to the lock-in-amplifier as a reference frequency for lock-in-amplifier.
5) *Lock-in-amplifier*: A lock-in-amplifier is essential in order to minimize noise in the measurement of photoluminescence (PL) signal (emitted photons) from the sample under test which is then read as current on Lock-in-Amplifier.
6) *Detector*: A Si Switchable Gain Detector (Model# PDA36A, Spectral range: 350 - 1100 nm, 10 MHz BW, Active area: 13 mm^2) has been used to detect PL signal from the sample. This detector is suitable measurement of PL emission from all kind of absorber layers used in photovoltaics.
7) *White Reflectance Standard*: A Lambertian reflector (5 % reflectance) from Edmund optics is used a reference in the experiment.
8) *Three-dimensional linear stage*: 3-D linear stages (Maximum Stage Travel: 13 mm) are used to mount the sample holder and the detector. Such stages are helpful in highly-controlled beam alignment.

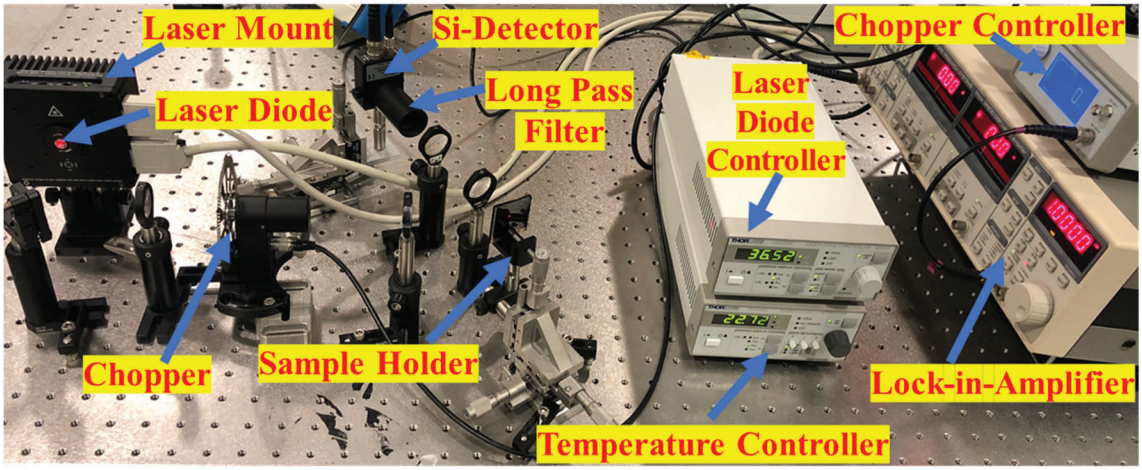


Figure 127. iV_{oc} experimental set up

iV_{oc} Principle

Electron-to-photon conversion efficiency (aka- external luminescence quantum efficiency) of an absorber layer is crucial to improve the PCE of a solar cell prepared by using that absorber layer. For ideal solar cell, luminescence quantum efficiency (η_{ext}) is considered to be unity. The dependence of implied open circuit voltage on η_{ext} can be expressed as,

$$iV_{OC} = V_{OC,ideal} - \frac{kT}{q}\ln\left(\left|\eta_{ext}\right|\right) \qquad (1)$$

where, $V_{oc,\ ideal}$ is the detailed-balance open circuit voltage, k is the Boltzmann constant, T is temperature and q is the electronic charge. [373] A less-than-unity external luminescence quantum efficiency (true for all solar cells) reduces the implied open circuit voltage $iVoc$.

Mathematical Details

Constant parameters required in calculation

c : Reflectance of Spectralon Reflector at Laser Wavelength (%)
a : Absorption of Sample at Laser Wavelength (%)
λ : Laser Excitation Wavelength (nm)
E_g : Sample's Bandgap (nm)
D_L : Detector's Responsivity at Laser Wavelength (nA/nW)
D_S : Detector's Responsivity at Sample's Bandgap (nA/nW)
b : Filter Transmittance at Sample's Bandgap (%)
$V_{oc,\ ideal}$: Detailed-balance Voltage of Sample (V)

Parameters to be measured

x : PL Signal from Sample (nA)
y : PL Signal from Reference (nA)

Calculations involved

$$\text{PL Intensity of Sample } (s) = \frac{x}{D_s B}(nW) \quad (2)$$

$$\text{PL Intensity of Reference } (r) = \frac{y}{D_L}(nW) \quad (3)$$

$$\eta_{\text{ext}} = \frac{c\left(s/r\right)}{a\left(\lambda/E_g\right)} \quad (4)$$

$$iV_{OC} = V_{OC,ideal} - \frac{kT}{q}\ln\left(\left|\eta_{ext}\right|\right) \quad (5)$$

$MAPbI_3$ Perovskite Film Preparation

The $MAPbI_3$ precursor solution was prepared by dissolving 1.43 M equimolar lead iodide (PbI_2, Alfa Aesar, 99.9985 %) and methylammonium iodide (MAI, Greatcell Solar) in N,N-dimethylformamide (DMF) and dimethyl sulfoxide (DMSO) (volume ratio = 9:1). A small amount (3 % molar ratio to PbI_2) of lead thiocyanate [$Pb(SCN)_2$, Sigma-Aldrich, 99.5 %] was added into the precursor solution as an additive. The solution was spin-coated at 500 rpm for 3 s and 4000 rpm for 60 s. At ~8 s of the second spin step, 700 μL of diethyl ether was dripped on the spinning substrate. The coated substrates were then annealed at 60 °C for 2 min and 100 °C for 5 min in a nitrogen glovebox.

Measurement Details

A 635 nm continuous wave laser chopped at 100 Hz. was used to illuminate the perovskite film and the reference. Luminescence signal was detected by a Si Switchable Gain Detector (Model# PDA36A, Spectral range: 350 - 1100 nm, 10 MHz BW, Active area: 13 mm^2). A FELH0 750 nm long pass filter was used in front of the detector to block the laser while collecting signal from the $MAPbI_3$ film.

Steady-state PL measurement was performed using 633 nm cw laser and PL signal was detected via Si detector (Symphony-II CCD). The absorption percentage of $MAPbI_3$ film was acquired by utilizing Perkin-Elmer UV-VIS Spectrophotometry. All measurements were conducted at room temperature (25 °C).

16.4 RESULTS and DISCUSSION

Table 20 represents the parameters used in the calculation of iV_{oc} (experimental set up shown in Figure 127). The band gap of $MAPbI_3$ perovskite sample (~ 744 nm) was determined by using steady state PL spectra as shown in Figure 128. Enhanced PL intensity obserevd in the case of $Pb(SCN)_2$ added $MAPbI_3$ can be attributed to enlarged grain in it compared to pristine $MAPbI_3$.

Film having larger grain (or less grain boundaries) often have reduced recombination losses at the grain boundaries defect thereby enhances the PL intensity. Additionally, grain boundary passivation caused by the formation of excess PbI_2 in $Pb(SCN)_2$ addded film enhances the PL intensity. [372, 374] Since iV_{oc} depends upon the photogenerated charge carrier recombination, $Pb(SCN)_2$ added $MAPbI_3$ has higher (1.170 V) iV_{oc} than pristine $MAPbI_3$ (1.133 V) as shown in Figure 128. Implied V_{oc} measured from the luminescence quantum efficiency of $MAPbI_3$ thin film is slightly higher than open circuit voltage of $MAPbI_3$ solar cells reported in the published literature. [372] The difference between an implied *Voc* and actual V_{oc} of $MAPbI_3$ solar cell can be attributed to the recombination losses at the interfaces present in $MAPbI_3$ solar cell. Table 21 shows the relationship between PL quantum efficiency and iV_{OC}.

Table 20. Constant parameters used in the calculation of implied open-circuit voltage

Reflectance of Spectralon Reflector at Laser Wavelength (*c*)	99 %
Absorption of $MAPbI_3$ at Laser Wavelength (*a*)	81.71 %
Laser Excitation Wavelength (λ)	635 nm
$MAPbI_3$'s Bandgap (E_g)	774 nm
Detector's Responsivity at $MAPbI_3$'s Bandgap (D_S)	0.47 nA/nW
Detector's Responsivity at Laser Wavelength (D_L)	0.31 nA/nW
FELH0 750 nm Filter Transmittance at $MAPbI_3$'s Bandgap (*b*)	97 %
Detailed-balance Voltage of $MAPbI_3$ ($V_{oc,\,ideal}$) [375]	1.33 V
Boltzmann Constant (*k*)	8.62×10^{-5} eV·K^{-1}
Electronic Charge (*q*)	1.60×10^{-19} C

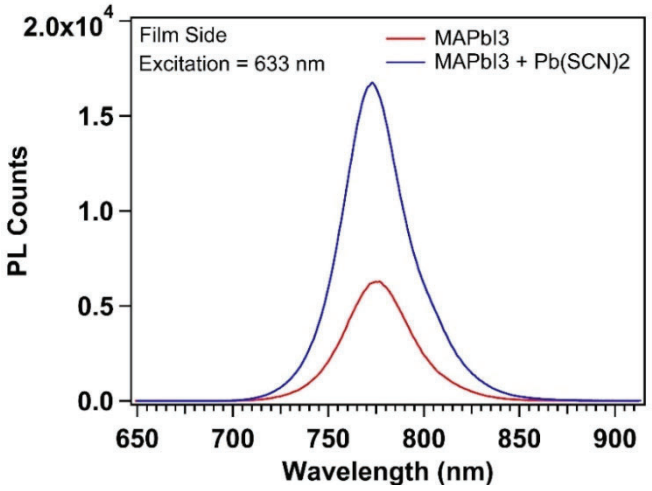


Figure 128. PL spectra of $MAPbI_3$ films taken at room temperature

Table 21. Luminescence quantum efficiency and implied open-circuit voltage of $MAPbI_3$

Sample's Name	Current Signal	PL Intensity	Luminescence Efficiency (η_{ext})	$iV_{oc} = 1.33 - (kT/q) \times \lvert\ln(\eta_{ext}/100)\rvert$
Reference	13220 nA			
$MAPbI_3$	6.64 nA	0.14 nW	0.05	1.133 V
$MAPbI_3$+ $Pb(SCN)_2$	27.88 nA	0.61 nW	0.21	1.170 V

16.5 CONCLUSIONS

An experimental set up has been successfully constructed that can be used to estimate the implied open circuit voltage of solar cells. The constructed set up is currently being evaluated using standard $MAPbI_3$ absorber layer deposited on soda-lime glass. Observed iV_{oc} values were compared with previously reported actual open circuit voltage of $MAPbI_3$ solar cell and remain under evaluation. It is anticipated that the ERE/ iV_{oc} system will bring considerable value to all future investigations of high-efficiency thin film solar cells.

17. IRRADIANCE AND TEMPERATURE CONTROL CHAMBER FOR ELECTRONIC MEASUREMENTS

17.1 SUMMARY

This report summarizes the design and construction of an irradiance and temperature control chamber for solar cell characterization, and its validation through a set of measurement data taken with it. We have been able to control the temperature of the test chamber in the range between -10 ºC and 70 ºC. Furthermore, the light source has been calibrated to get close to the standard AM1.5G spectrum.

17.2 INTRODUCTION

Developing lighter, flexible, and highly efficient solar cells involves testing solar cell performance under harsh environmental conditions, namely extreme temperatures and varying irradiance. Hence, an irradiance and temperature-controlled test chamber is being developed for current-voltage (J-V) measurements at varying irradiance and temperature ranging from -10ºC to 60ºC. The selected design for the chamber consists of two sections: test chamber and power chamber. The test chamber consists of a multi-array light source mounted on top, with an internal cooling system, four rectangular mirrors sealing the test chamber to prevent light from escaping, and a thermal controller setup that circulates a water and propylene glycol mixture. The sample stage inside the test chamber uses Peltier/thermoelectric coolers (TECs) between the copper block and a water block to achieve and maintain the sample at the desired temperature. This thermal control stage is connected to a water chiller/heater to handle the cooling/heating of the sample stage. On the programming side, the LabVIEW programming platform was used to develop a comprehensive code to command and achieve a setpoint temperature while configuring and operating the light source simultaneously.

A standard solar simulator should be able to accomplish the sun spectrum standards set by the International Electrotechnical Commission (IEC) or the American Society for Testing and Materials. [376] For example, the spectrum of the solar simulator should match with that of the sun depending on the atmospheric effects introduced for different geometries and altitudes (e.g., AM1.5G, which is the global irradiance that reaches the earth surface at an air mass of 1.5 with an intensity of 100 mW/cm^2), [377] irradiance spatial uniformity and temporal stability. Solar simulators can be classified into different classes based on these parameters. According to the standards, if the spectral match in each spectral interval is within the tolerance levels of 25%, 40%, and 60%, they are classified as Class A, Class B, and Class C, respectively. Likewise, for the spatial homogeneity, if the value is below 2%, Class A is assigned. Below 5% and 10% are Class B and Class C, respectively. For temporal stability, Class A should have a deviation factor below 0.5%, Class B below 2%, and Class C below 5%. [378]

Apart from the above-mentioned solar simulator properties, this chamber also possesses a wide range of fast and accurate temperature variation capabilities. The study of solar cell behavior under different temperature conditions is crucial because solar cells are being used in different applications under terrestrial as well as extra-terrestrial conditions, where the temperature ranges from negative values to~100°C. Earlier studies have shown that, increase in cell temperature results

in lower device performance. [379-381] Performance is defined by the device performance parameters such as open-circuit voltage (V_{OC}), short-circuit current density (J_{SC}), fill factor (FF), and power conversion efficiency (η). Semiconductor physics tells us that V_{OC} decreases and J_{SC} slightly increases with increasing temperature. The temperature control unit of the chamber is designed and constructed in a manner where the above-mentioned parameters can be obtained easily, and much attention is given to maintaining constant temperature over the cell area and obtaining highly accurate readings in a straightforward manner with the help of LabVIEW instrument control software.

17.3 METHODS, ASSUMPTIONS, and PROCEDURE

Chamber construction:

A custom chamber is built mainly using 1.5" square 8020 aluminum T-slot profiles and fittings. Figure 129 depicts the initial chamber design using SolidWorks. The main chamber consists of two sub-chambers: Test Chamber (left) and Power Chamber (right). In the Test Chamber, the thermal stage is visible through the lower part of the door, and the light source is modeled on the top with its frame, which is marked as a yellow block.



Figure 129. (Left) Chamber design in Solidworks, (Right) Chamber construction status from the previous group

The status of the partially built chamber when the project was handed over to us by the previous group is shown in Figure 129 (right). While continuing the chamber construction, the previously selected design faced some limitations regarding the requirement of a sealing process of the Test Chamber. Hence, modifications were made in the initial design to meet the sealing needs for a vacuum chamber. Specifically, the light source mounting, power sources and controllers shelving, mirror assembly, and the front door arrangements were optimized in the current design, which is discussed in the next section. Figure 130 shows the final stage of the two chambers. The left chamber consists of all controllers and power supplies, while the right chamber is the test chamber.

Figure 131 and Figure 132 show an original configuration of the TEC devices, and an updated and more orderly arrangement, respectively.

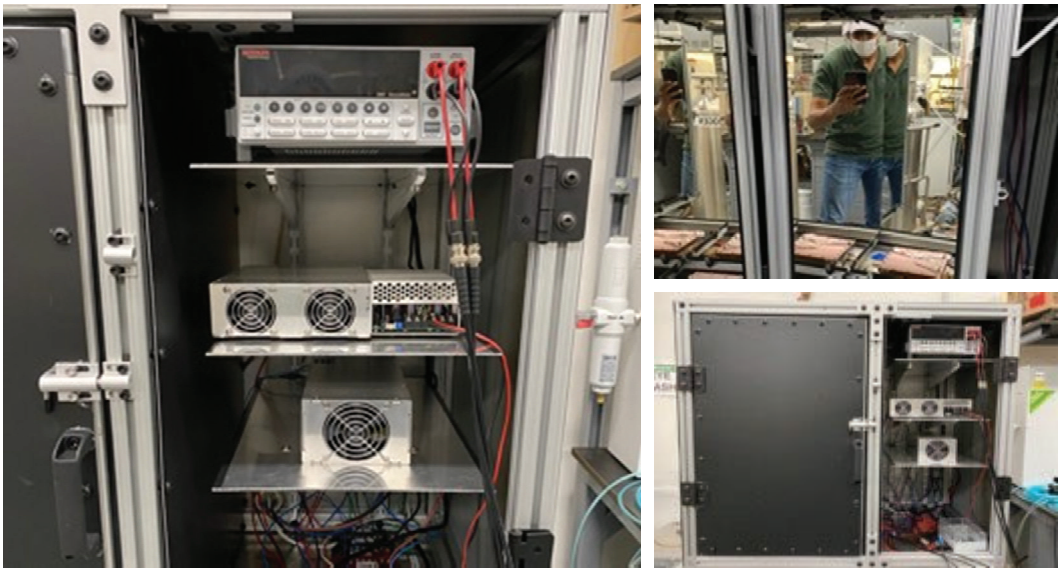


Figure 130. Finalized irradiance and temperature control chamber

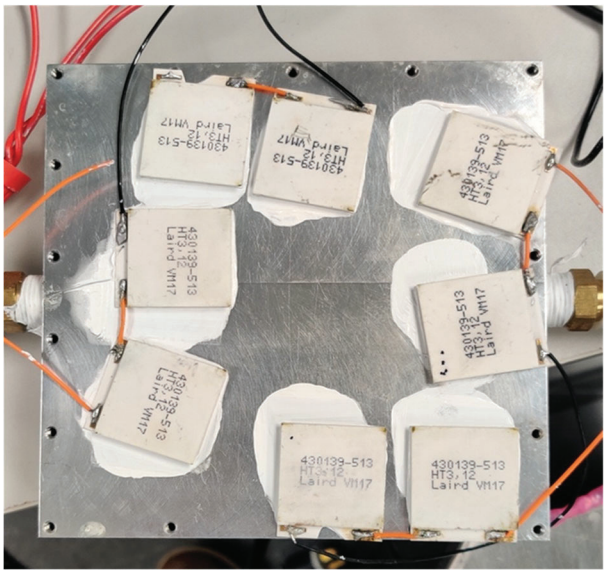


Figure 131. Initial TEC device arrangement

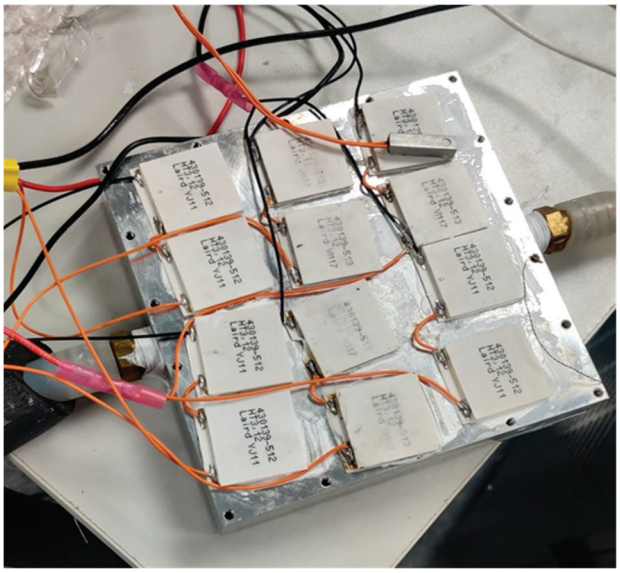


Figure 132. Current TEC device arrangement

Thermal Stage

The thermal requirement was almost met as per the client's preferences, including temperature stability of ± 0.2 °C and the temperature uniformity of ± 1 °C maximum. Even an upper limit of the 100 °C temperature had been achieved which exceeded the expected maximum. The only arrangement of TECs, where three branches of three TECs wired in series and each branch is wired in parallel, the target of -35 ° C could not be reached. With the following (Figure 132) a minimum temperature of -28°C has been achieved.

To improve the achievable low-temperature target, certain modifications were inculcated for this TEC arrangement to hit a lower temperature close to the client's expectations. It was identified that the previously-in-use TEC devices were working close to their maximum capacity. However, it could further be maximized by optimizing their arrangement on the water block, as per its standard power ratings. Hence, the previous arrangement was redesigned to achieve a higher voltage drop across each TEC, and thus, more current was drawn from the power supply to the full arrangement while increasing the number of TECs to 12, as shown in the right figure. Six branches of two TECs are wired in series, and each branch is wired in parallel. This refined TEC arrangement was placed in such a way that the temperature variation was distributed uniformly throughout the water block. Since previously used TEC series were discontinued by the respective company, the recommended alternative series of TECs have been used in the current arrangement with almost the same power ratings. Figure 133 shows the final assembly of the thermal stage inside the test chamber. As shown in Figure 133, a laser pointer has been used to align each cell of the device.

Power Unit

As mentioned previously, the main chamber consists of two sub-chambers, namely Test Chamber and Power Chamber. The power chamber is assigned to place all the measuring equipment and

supported power supplies. Several shelves are arranged in this chamber to place these devices for ease of use. Three bus bars (2 hot and 1 ground) will be used to distribute the power among all the devices in the chamber. Single power input will be available on one of the outer side panels of the power chamber to get the electricity supply for these bus bars and two holes to place the fans for the cooling process of the devices in the test chamber. Figure 134 shows some additional power control components of the chamber.

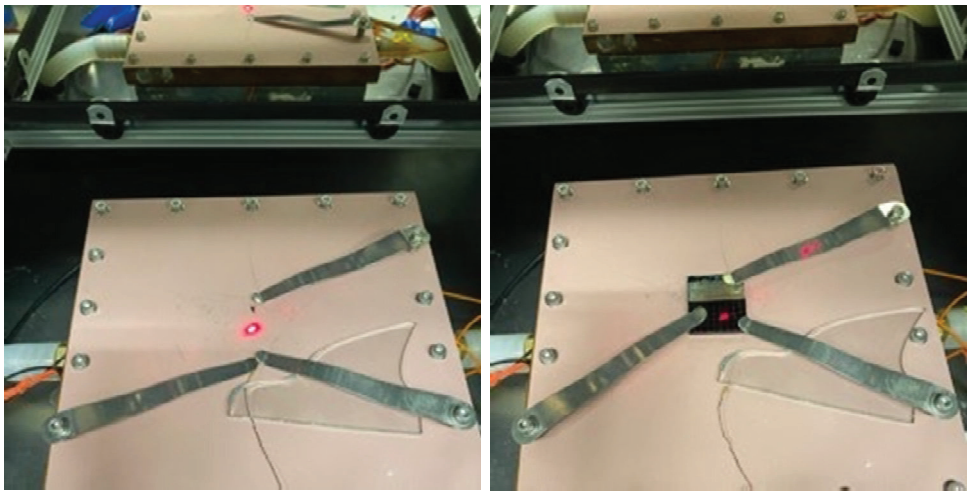


Figure 133. (left) Mounted thermal stage inside the test chamber; (right) Solar cell placement on the thermal stage

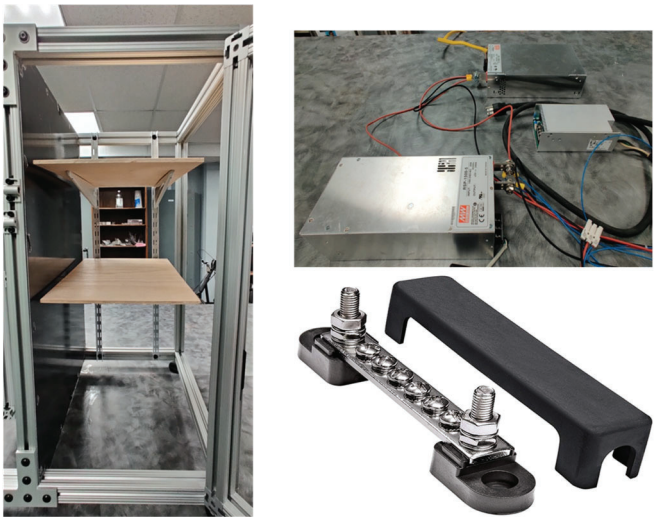


Figure 134. Power chamber, power supplies, and bus bar

Light source

This multi-array hybrid light source with 9 similar sections (3 x 3) was designed and manufactured by Alfartec (La Chauxde-Fonds, Neuchâtel, Switzerland). Each section consists of 9 different colors of LEDs and one halogen lamp, as shown in Figure 135. All of the 'bulbs' are symmetrically placed on a single circuit board and mounted to an aluminum frame. The LABVIEW program was developed for this light source with support from PV Lab (EPFL, Neuchâtel, Switzerland), through identification of the driver addressing to activate specific LEDs and the halogen while also controlling the light intensity. Though the chamber and driver could generate a very wide range of spectra, much focus was given on AM1.5G spectrum simulation.



Figure 135. (Left) Multi-array hybrid light source; (Right) mirror assembly and the mounted light source

When light source calibration for AM1.5G spectrum is considered, following the above-mentioned IEC standards, three main categories are generally addressed: Spectral Match, Homogeneity, and Temporal Stability. And our design managed to accomplish a Class A classification in each section. Note that although each specific LED type's spectral remains constant with varying intensity, the halogen bulb's spectrum varies considerably with the operating current. A fiber-optic-based spectrometer has been used to record the individual spectra for use in assembling the AM1.5 spectrum, for example.

Spectral Match

As per the IEC standard, less than 25% of tolerance should be maintained between the integrated intensity deviations of the simulated spectrum and the standard AM1.5G spectrum. This is specified over their wavelength intervals and respective integrated power densities. Equation (1) is used in calculating this deviation.

$$\boldsymbol{Deviation}\ \% = \left(\frac{\int_{\lambda 1}^{\lambda 2} \boldsymbol{I(\lambda)_{AM1.5G}} - \int_{\lambda 1}^{\lambda 2} \boldsymbol{I(\lambda)_{SIMULATED}}}{\int_{\lambda 1}^{\lambda 2} \boldsymbol{I(\lambda)_{AM1.5G}}}\right) \times \mathbf{100} \qquad (1)$$

Homogeneity

Here, the value is calculated from Equation 2, where the I_{MAX} and I_{MIN} are the maximum and minimum integrated power densities, respectively, which are measured at different positions on the radiated surface.

$$\boldsymbol{Homogeneity}\ \% = \left(\frac{\boldsymbol{I_{MAX} - I_{MIN}}}{\boldsymbol{I_{MAX} + I_{MIN}}}\right) \times \mathbf{100} \qquad (2)$$

Homogeneity should be less than 2% to achieve the Class A qualification. A good homogeneity classification ensures the equal irradiation of the simulated spectrum throughout the surface of the tested device. In most of the past work, it can be observed that a lesser surface area such as 1 cm^2 is considered to achieve this classification. But, our work presents a simulator with a Class A homogeneity classification for an area larger than 10 cm x 10 cm.

Temporal Stability

Here, the classification is decided on two factors: Short-term Instability (STI) and Long-Term Instability (LTI). And they can be calculated using Equation 3.

$$\boldsymbol{LTI\ or\ STI}\ \% = \left(\frac{\boldsymbol{I_{MAX} - I_{MIN}}}{\boldsymbol{I_{MAX} + I_{MIN}}}\right) \times \mathbf{100} \qquad (3)$$

LabView Program

Except for the chiller and the dry air unit, which need to be controlled manually, the rest of the system is fully controlled by National Instruments' LabVIEW software. Figure 136 shows the user interface of the all-in-one LabVIEW program used to operate the Temperature and Irradiance Control Chamber.

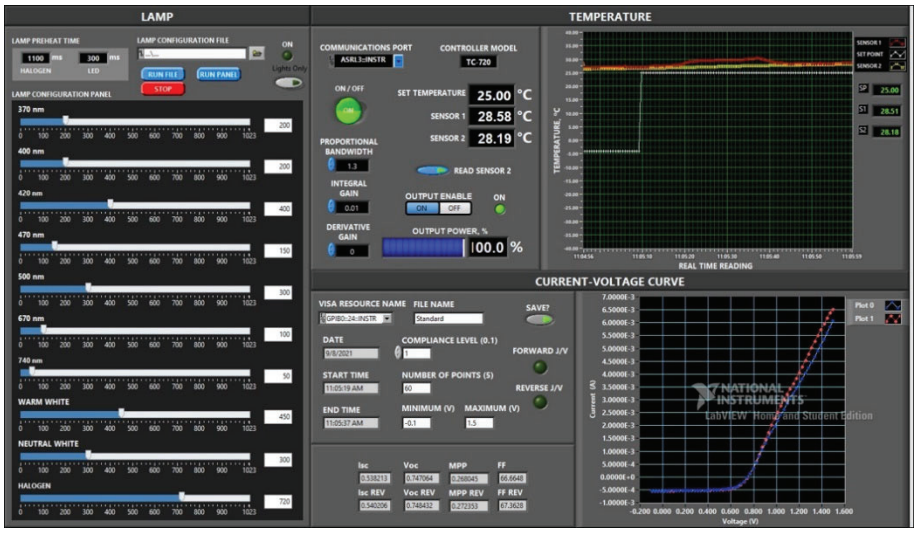


Figure 136. Lamp controlling, temperature controlling, and VI measurement controlling LabVIEW program user interface

The light source controller sub-VI (VI = 'virtual instrument') is being used to control the light source of the system. Here, the connection between the NI LabVIEW interface and the light source is maintained via a NI DAQ card. A timing code has been implemented within the light source LabVIEW code to ensure that the light will be turned on for the desired amount of time, which can be varied as per the use or purpose. With the ability in the original program to read configuration files to finely adjust each LED and halogen bulb's light intensity, a new function to control the light source directly from the new LabView interface using a visual control panel

(sliders) is also introduced. This panel can only adjust the overall light intensities from 0% to 100% (corresponds to 0- and 1024-bit input to respective light source drivers) for each type of LED and halogen, not individual intensities on different locations of the light source. Individual bulbs on distinct sections can be adjusted individually using configuration files. The content and the arrangement of this file are shown in Table 22 where each column addresses the type of light (9 LEDs and the Halogen), and each row addresses the 9 different light source compartments. However, the panel gives quick control access to the light source that can be used for rapid testing purposes. The retrieved configuration settings can also be saved as configuration files to be modified later for finer adjustments.

Table 22. Configuration file format of the light source

	Near ultraviolet	Violet	Red	Near Infrared	Royal Blue	Blue	Cyan	Halogen	Neutral White	Warm White
Sub 1	187	287	0	113	711	85	382	645	250	300
Sub 2	187	287	0	113	711	85	382	645	250	300
Sub 3	187	287	0	113	711	85	382	645	250	300
Sub 4	187	287	0	113	711	85	382	645	250	300
Sub 5	187	287	0	113	711	85	382	645	250	300
Sub 6	187	287	0	113	711	85	382	645	250	300
Sub 7	187	287	0	113	711	85	382	645	250	300
Sub 8	187	287	0	113	711	85	382	645	250	300
Sub 9	187	287	0	113	711	85	382	645	250	300

Control and stabilization of the thermal stage parameters are achieved from the thermal controller sub-VI. The TC-720 controller used here is a bipolar temperature controller capable of automatically reversing power to Peltier/thermoelectric (TE) devices to provide heating or cooling as required to maintain a specific setpoint temperature. The main attention was given to the set temperature feed-in, live temperature readings of the solar cell and the stage, power on/off, power consumption of the Peltiers, PID controllers, and the real-time temperature plots.

Once the program is run, both the solar cell temperature and the thermal stage temperature are shown in real-time on the user interface as numerical values and on the plot. Set temperature can also be manually adjusted per the required temperature. A separate button is provided to turn on the Peltier power. The power percentage given to the Peltiers is shown at the bottom of the UI with color indications: Blue for cooling and Red for heating. It is programmed to continue this cooling/heating till the solar cell achieves the setpoint temperature. The speed and the accuracy of the temperature ramp and approach are controlled by mathematical models linked to PID inputs (Proportional Band Width, Integral Gain, and Derivative Gain). The *I-V* measurement sub-VI is used to control the solar cell parameter measurements. A Keithley instrument (2401 Source Measure Unit) is used to carry out the respective *I-V* measurement under laptop and LabVIEW control via USB interface. This sub-VI takes the general format of commonly used programs in *I-V* measurements. It consists of experiment data saving path/filename, *I-V* plot, general input

parameters such as the number of measurement points, voltage sweep range, forward/backward sweeping, and main output parameters V_{OC}, J_{SC}, FF, and η.

Finally, all sub-VIs are carried into a single user interface and modified so that once the thermal stage is brought to the needed temperature and all the required inputs are set, the light source and the VI measurement start working simultaneously, a complete voltage sweep is conducted, and the respective measurements are saved at the pre-defined file path.

Calibration

Once the system was completed, calibration of each unit was carried out. For the spectral calibration, Ocean Optics software and the Spectrometer (FLMT04671) were used to obtain the spectral data. Although it is possible to light up the nine different subsections of the light source separately, our initial goal was to simulate the AM1.5G spectrum with the help of a full light source and later moving forward with any additional modifications as necessary. Hence, as previously mentioned, the LabVIEW program was developed in a way that it has the ease of use to adjust the overall light intensities for each type of LED and halogen. As an initial step of the data acquisition for programming the simulated spectrum, spectral irradiance variation was measured for each light type at different intensities using the spectrometer. The spectrometer was positioned in the middle of the thermal stage (where the pogo pins are), normal to the stage. Then irradiance given out by each type of light was measured at intensity increments of 5% starting from 0% to 50% of the full intensity. The maximum intensity was maintained at 50% as we didn't want to try much higher intensities initially. The obtained irradiance shapes are tallying with the light source spec sheet, which is shown in Figure 137. It was observed that the minimum increment or decrement (smallest step size, resolution) of light intensity can be achieved is 0.1% for all the light types except for halogen. For halogen, it is approximately 0.14% as it requires more power to turn on than the LEDs. Also, it was noted that there can be a high influence of halogen on the total shape of the final superimposed AM1.5G simulation as its shape changes with the increment of its intensity.

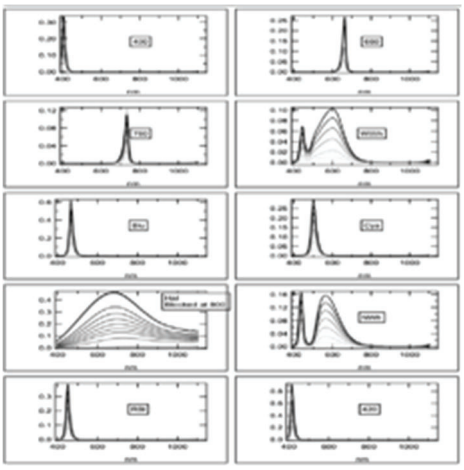


Figure 137. Spec sheet of the irradiance variation of each light type with its intensity percentage

Spectral Match

Here the simulated spectrum was measured using the spectrometer, positioning it at the center of the stage. The recorded irradiance vs. wavelength data were divided into spectral ranges as required by the standard. The deviation percentages were calculated using Equation 1. The initial interval and the final interval had to be limited to 350-400 nm and 900-1035 nm, respectively, due to the spectrometer limitations. The respective deviations are shown in Table 23, and it can be identified that all the deviations are within the Class A requirement, which is less than ±25%. This proves that this simulator belongs to the Class A type in terms of the spectral match.

Table 23. Irradiance deviation between simulated spectrum and AM1.5G standard spectrum

Spectral Interval (nm)	Simulated (mW/cm^2)	AM1.5G (mW/cm^2)	Deviation (%)
350-400 nm	2.38	3.17	24.91
400-500 nm	12.59	13.8	8.76
500-600 nm	11.67	14.95	21.93
600-700 nm	11.68	13.79	15.3
700-800 nm	9.79	11.21	12.66
800-900 nm	7.11	9.3	23.54
900-1035 nm	7.82	7.9	1.01
Total Irradiance	62.55	75.02	16.62

After taking all these data and observations into consideration, with the help of the goodness of fit model with the combination of each source vs. AM1.5G, an intensity combination that lead to the minimization of the difference between actual AM1.5G and simulated AM1.5G was obtained (Figure 138). After comparing the *J-V* measurements taken under this simulated spectrum with the

in-house measurements, simulator Class qualification tests were carried out under the aforementioned categories.

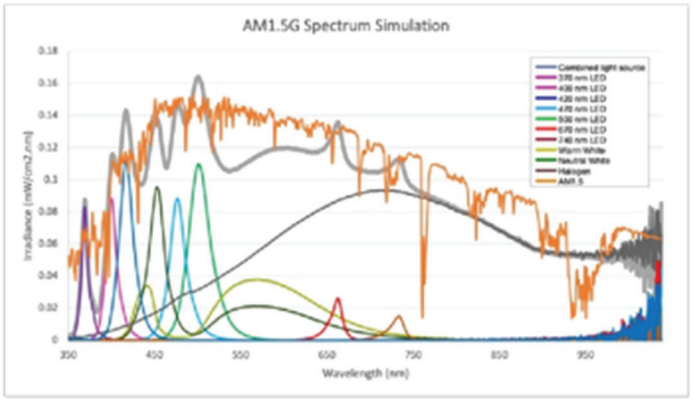


Figure 138. Superposition and individual irradiance spectra for each bulb type used to simulate the AM 1.5 spectrum

Homogeneity

This is calculated by measuring the total irradiance given out by the simulated spectrum at nine different positions on the stage. To get the largest area consideration possible, the stage was divided into nine symmetrical compartments, as shown in Figure 139 and the spectrometer was positioned at the middle of each compartment. The obtained results are shown in Table 24. With the use of Equation 2, we managed to obtain the factor of homogeneity as 1.963%, which demonstrates that the deviation is less than 2% as per the requirement to be classified as a Class A simulator.

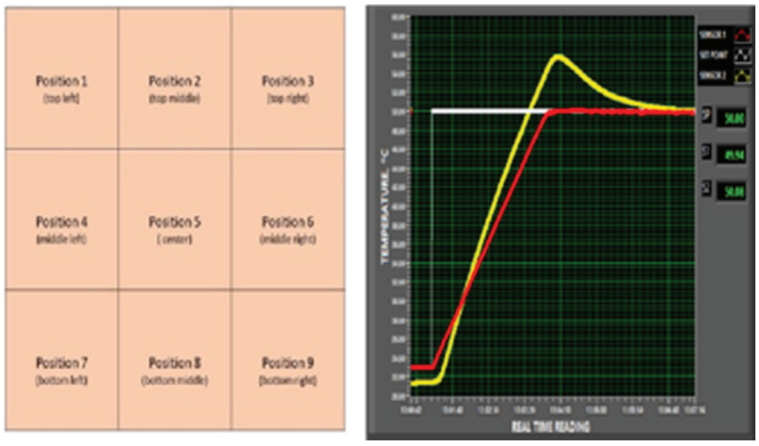


Figure 139. (Left) spectrometer positioning on the sample stage; (Right) fast and accurate target temperature landing

Table 24. Integrated irradiance measurements for the homogeneity calculation

Position	Integrated total irradiance (mW/cm^2)
Position 1	65.33
Position 2	65.22
Position 3	64.48
Position 4	64.83
Position 5	64.27
Position 6	64.08
Position 7	63.27
Position 8	64.05
Position 9	62.82

Temporal Stability

Here, both STI and LTI needed to be calculated separately. Hence, two sets of experiments were carried out. For the STI, three rounds of spectrometer readings were taken. In each round, ten spectral readings were taken with 100 ms intervals for a complete 1 s. For the LTI, the same three rounds of measurements were carried out but with 10 s of time intervals for a complete 100 s. During the LTI measurements, it was made sure to start each round after letting the light source warm up for 30 s to reduce measurement errors.

Using Equation 3, STI and LTI percentage factors were obtained, which are shown in Table 25. To obtain a Class A certification under Temporal Stability, the STI and LTI deviation should be less than 0.5%, and this is proven from the above results. This guarantees the constant emission of the LEDs and the halogen in our system over the period of measurements, as a Class A solar simulator in Temporal stability.

Thermal Stage Calibration

When the thermal stage calibration is considered, our main goal was to bring the thermal stage to the setpoint as soon as possible and maintain it at that value with minimum oscillation. Out of the three main damping processes (under damping, over damping, critical damping), critical damping was identified as the proper approach, and accordingly, PID parameters were optimized following the steps mentioned in the TC-720 controller user guide. Finally, (Figure 139), we managed to achieve fast and reliable constant setpoint acquisitions with an oscillation of less than 0.05 ºC. Some of the important results are shown in Table 25, Table 26, and Table 27.

Table 25. Irradiance deviation between simulated spectrum and AM1.5G standard spectrum

Round	STI (%)	LTI (%)
1	0.38	0.22
2	0.42	0.45
3	0.27	0.17
Average	0.356	0.28

Table 26. Thermal stage temperature variation results with time (heating)

Sample Stage Temperature – SST (C°)	Time taken to reach SST (s)	Max Oscillation (C°)
20 to 30	35	0.05
30 to 40	48	0.05
40 to 50	60	0.15
50 to 60	72	0.25
60 to 70	90	0.30

Table 27. Thermal stage temperature variation results with time (cooling)

Sample Stage Temperature – SST (C°)	Time taken to reach SST (s)	Max Oscillation (C°)
70 to 60	90	0.05
60 to 50	120	0.25
50 to 40	150	0.15
40 to 30	180	0.05
30 to 20	240	0.05
20 to 10	320	0.10
10 to 0	~1000	0.20
0 to -10	~2500	0.35
-10 to -20	-	-
-20 to -30	-	-

17.4 RESULTS and DISCUSSION

Validation

We are currently using an ORIEL LSH-7320 ABA LED solar simulator with one sun condition for the standard in-house *JV* measurements and related experiments. A comparison between the *J-V* measurements obtained from this setup and the newly developed Irradiance and Temperature Control Chamber was carried out to validate the system. The following three types of devices were tested, each one a variation of a CdS/CdTe device with varying back contact designs as Au, Cu/Au, and $CuAlO_x$/Au. All devices (3 cm x 3 cm) were prepared for the measurements following the same scribing pattern. Ten different cells were measured under each case. It was made sure to maintain the temperature on the sample stage in the chamber similar to the room temperature used at the in-house measurement unit. The dry air system was not turned on as the temperature was around 22 ºC, and hence humidity level had no impact on the experiment. Obtained results are listed in Figure 140.

A separate experiment was carried out on each device to showcase the validity of the temperature effect given by the newly developed system on the solar cell parameters (Figure 141). Here a previously identified good cell on the standard device (Cu/Au) was used to measure the *J-V* parameters while changing the thermal stage temperature from 10 ºC intervals. As the thermal stage temperature varied through a wide range of temperatures from positive to negative, the dry air supply was kept turned on throughout the experiment to maintain the same humidity conditions in the chamber and avoid any frosting on the thermal stage during the measurements. Observations are listed in Table 28.

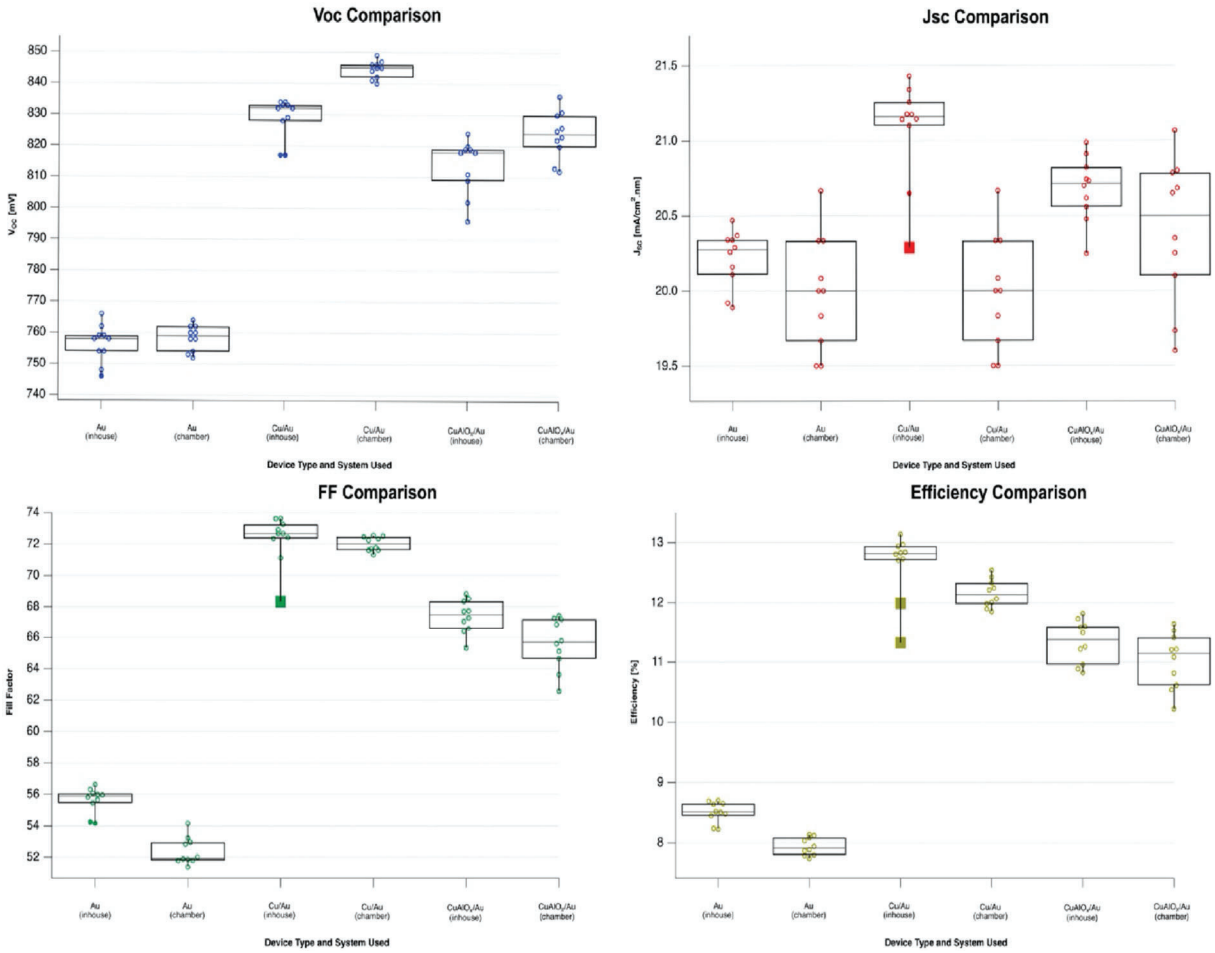


Figure 140. Device performance comparison between in-house solar simulator and control chamber

Table 28. J-V-T measurements

Temperature (C°)	V_{OC} (mV)	J_{SC} (mA)	Efficiency (%)	FF
50	790	21.96	12.02	69.32
40	819	21.75	12.57	70.58
30	830	21.61	12.85	71.65
20	848	21.45	12.98	71.40
10	874	21.36	13.08	70.08
0	895	21.25	13.24	69.62
-10	909	21.12	13.26	69.12

More on JVT measurement

After the validation of the irradiance and temperature control chamber, we prepared another two samples (Standard $CuCl_2$ device and CuAlO as the back contact) to obtain device performance parameters such as V_{oc}, J_{sc}, FF, and Efficiency as a function of temperature (Figure 142). In this experiment, the temperature has been varied from -4 ºC to 70 ºC.

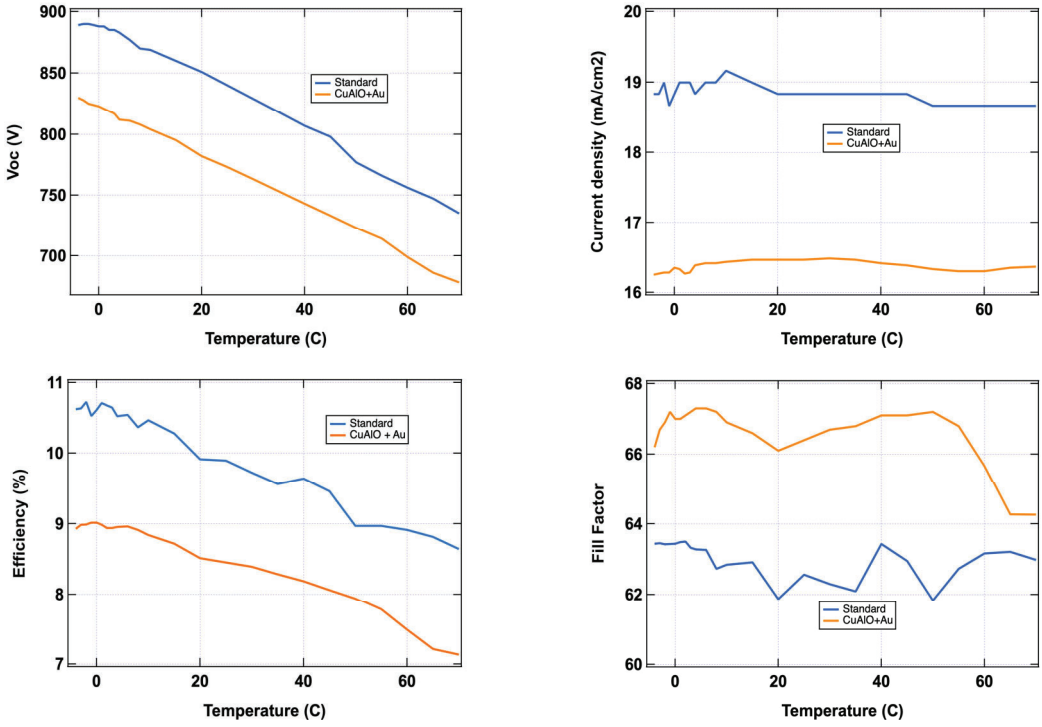
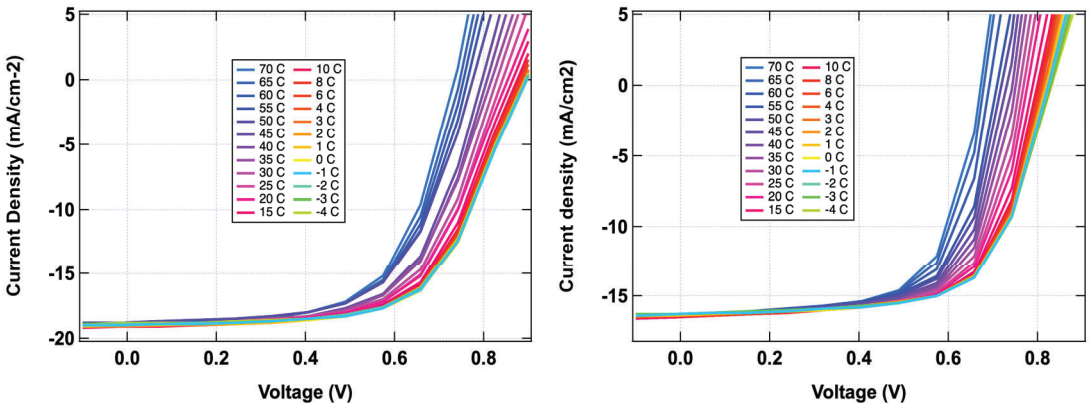


Figure 141. Device performance parameters as a function of temperature



Standard CuAlO + Au

Figure 142. Current density vs. voltage curves for different temperatures

Figure 141 and Figure 142 show the device performances as a function of temperature. While the short-circuit current and fill factor did not vary significantly with the temperature, the open-circuit voltage of both devices decreased linearly with the increase of temperature leading to a significant loss in the device's power conversion efficiency. These results are expected, as a rise in temperature is known to decrease the bandgap of the material by increasing the energy level of the electrons in the valance band, pushing the Fermi-level up. For the solar cells device, the impact of the temperature reveals in the dark (saturation) current (in other words, the intrinsic charge carrier density), and the higher the temperature, the larger the dark current is. An increase in the short-circuit current is also expected with the rise of the temperature, as the decreased bandgap should allow more free charges to be generated by the lower energy photons absorbed by the material. However, such an effect seems to be small in our devices. One of the reasons might be the fact that the bandgap of the CdTe is around 1.47 eV (840 nm), and the solar irradiance is significantly weak at longer wavelength. We will test our system further with other set of solar cell devices, including the perovskite-based ones, to identify and improve the limitation of the system.

17.5 CONCLUSIONS

Irradiance and Temperature control chamber designing, construction, calibration, and validation are presented here, which can be used for *J-V* measurements under selective spectral and temperature conditions. The system consists of company-built advanced components like the hybrid light source, TC-720 temperature controller, chiller unit, dry air supply, and in-house crafted and molded components such as aluminum profiles, panels, copper block, tubes, and fittings.

Although there are many stand-alone systems to do solar simulations and *J-V-T* measurements separately, a system with the capability of both seems to be a breakthrough in solar cell research. Hence, this project was developed, and the final output has the capability of simulating the AM1.5G spectrum, maintaining a Class AAA qualification over a sample size as large as 10 cm x 10 cm while changing the temperature of the testing cell in a wide temperature range between -10°C and 70°C. A constant humidity level can also be maintained in the chamber with the help of

the dry air supply attached. The system validation has been proven from the comparison carried out with results obtained using the in-house simulator.

Although one of the project goals was to achieve a negative temperature of -35°C, this target was not yet reached due to some constraints in the power supplies and Peltiers. Future modifications are focused on resolving this issue along with some other developments such as improvement of the AM1.5G simulation by reducing the spectral deviation, simulation of AM1.0/AM1.5D spectrum, automation of *J-V-T* measurements between predefined maximum and minimum temperatures, improvement of the humidity control process, improvements in the test chamber sealing to develop high vacuum environments in the chamber, etc. These will result in more reliable and accurate simulations and measurements in the future where this Irradiance and Temperature Control Chamber will bring out a whole new set of capabilities under *J-V-T* measurements in the field of solar cell research.

18. APPLICATION OF OPTICAL HALL EFFECT

Prakash Uprety, Indra Subedi, Maxwell M. Junda, Robert W. Collins, and Nikolas J. Podraza

18.1 SUMMARY

Electrical transport parameters for active layers in silicon (Si) wafer solar cells are determined from free carrier optical absorption using non-contacting optical Hall effect measurements. Majority carrier transport parameters [carrier concentration (N), mobility (μ), and conductivity effective mass (m^*)] are determined for both the n-type emitter and p-type bulk wafer Si of an industrially produced aluminum back surface field (Al-BSF) photovoltaic device. Contributions from photogenerated carriers in both regions of the p-n junction are obtained from measurements of the solar cell under "light" 1 sun illumination (AM1.5 solar irradiance spectrum). From analysis of combined dark and light optical Hall effect measurements, photogenerated minority carrier transport parameters [minority carrier concentration (Δp or Δn) and minority carrier mobility (μ_h or μ_e)] under 1 sun illumination for both n- and p-type Si components of the solar cell are determined. Solar cell device performance parameters including photovoltaic device efficiency, open circuit voltage, fill factor, and short circuit current density are also calculated from these transport parameters obtained via optical Hall effect using the diode equation and PC1D solar cell simulations. The calculated device performance parameters are found to be consistent with direct current-voltage measurement demonstrating the validity of this technique for electrical transport property measurements of the semiconducting layers in complete Si wafer solar cells. To the best of our knowledge, this is the first method that enables determination of both minority and majority carrier transport parameters in both active layers of the p-n junction in a complete solar cell.

Full details of this work are available in P. Uprety, I. Subedi, M. M. Junda, R. W. Collins, and N. J. Podraza, "Photogenerated carrier transport properties in silicon photovoltaics," *Scientific reports,* vol. 9, no. 1, pp. 1-12, 2019. [382]

18.2 INTRODUCTION

Minority carrier transport parameters critically affect operation and performance of many p-n junction semiconductor devices including bipolar transistors and solar cells. [383] Knowledge of intrinsic carrier concentration, effective equilibrium minority carrier concentration, minority carrier mobility, and effective carrier lifetime obtained by theoretical and experimental methods are essential parameters for modeling semiconductor devices to understand device physics and to optimize performance. [384] For solar cells in particular, both open circuit voltage (V_{oc}) and photogenerated current density (J_L) depend on minority carrier mobility and effective carrier lifetime in the absorber material. [385] In this work optical Hall effect measurements of a Si wafer solar cell under nominally dark and 1 sun illumination conditions are used to determine both majority and minority carrier transport properties of a multiple layer stack of p- and n-type semiconductors along with electrical contact and passivation layers.

Optical Hall effect via magnetic field dependent frequency domain terahertz (THz) range spectroscopic ellipsometry is a potential alternative method that enables extraction of majority carrier transport parameters such as conductivity effective mass (m^*), carrier concentration (N),

and mobility (μ) of individual layers even in the complex multilayer structures, but without making physical contact. [386] Figure 143 shows a schematic illustration depicting a THz range spectroscopic ellipsometer used for the analysis of a Si wafer Al-BSF solar cell with an adjustable magnetic field dependence (0, ±1.48 T) under 1 sun illumination (AM1.5 solar irradiance). Optical Hall effect measurements are now adapted to deduce minority electrical transport properties [minority carrier mobility (μ_h or μ_e) and equilibrium photogenerated minority carrier concentration (Δp or Δn)] and majority carrier N, μ, and m^* of active layers within a complete solar cell. Here majority carrier N, μ, and m^* are determined for both the n-type emitter and p-type wafer Si regions of an industrially produced Al-BSF Si solar cell from THz spectral range optical Hall effect measurements performed in nominally "dark" conditions. Contributions from photogenerated carriers in both the p- and n-type regions are obtained from optical Hall effect measurements of the solar cell under "light" 1 sun illumination (AM 1.5 standard solar irradiance spectrum). Analysis of the dark and light optical Hall effect measurements yield minority and majority transport characteristics for each Si component of the p-n junction within the complete solar cell. The transport properties are then used to calculate minority carrier lifetime and diffusion length of each layer as well as the photovoltaic (PV) device performance parameters.

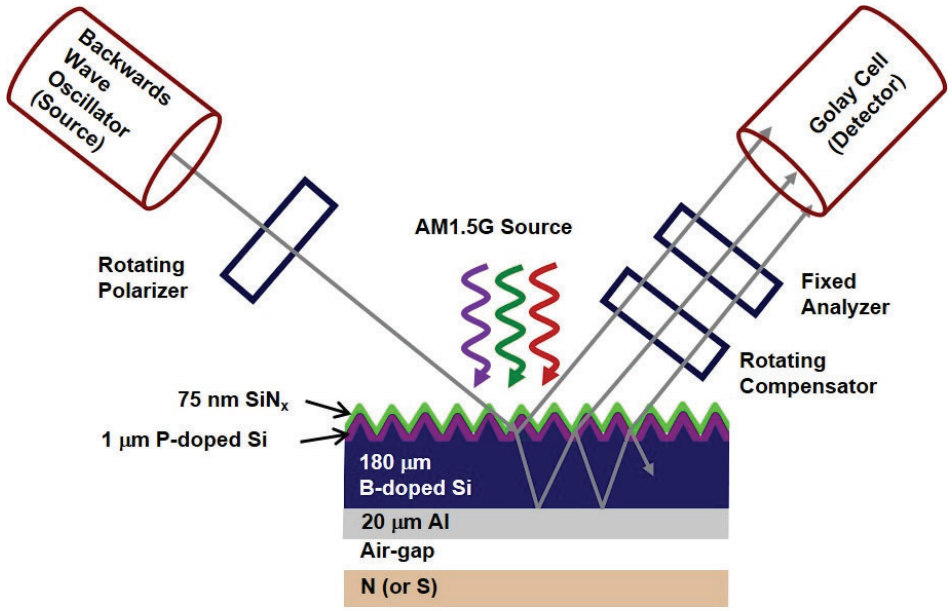


Figure 143. Schematic of a Si PV cell mounted on a magnet for optical Hall effect measurements based on THz range SE [382]

18.3 METHODS, ASSUMPTIONS, and PROCEDURES

A commercially fabricated 15.6 × 15.6 cm^2 pseudo-square Al-BSF Si wafer solar cell (CNH Industrial) has been purchased and characterized. PV device performance parameters including the short circuit current density (J_{sc}), open circuit voltage (V_{oc}), fill factor (FF), and efficiency (η) are determined from current-voltage (J-V) measurements collected under 1 sun illumination. Mueller matrix spectra are collected *ex-situ* at 50, 60, and 70° angles of incidence in the THz spectral range from 3 to 34 cm^{-1} (3.3 mm to 290 μm) for the Si wafer solar cell (J. A. Woollam Co., THz-VASE). [387] Eleven Mueller matrix elements normalized to M_{11} (m_{12}, m_{13}, m_{21}, m_{22}, m_{23}, m_{31}, m_{32}, m_{33}, m_{41}, m_{42}, and m_{43}) are obtained. Measured data are collected from an area of the cell oriented to avoid the front silver bus bars. The configuration of the ellipsometer used here differs from that described by Hofmann *et al.* [387] in the use of a rotating polarizer before interaction with the sample and a rotating compensator followed by fixed analyzer after interaction with the sample. For each case, sets of eleven Mueller matrix element spectra at the three angles are collected with the sample under applied magnetic fields of 0 and ± 1.48 T. A Ni-Cu-Ni coated Neodymium N42 permanent magnet 3" × 3" × 1/2" in size generates a maximum magnetic field of ±1.48 T. The magnet is mounted on the sample stage goniometer with double-sided tape on the corners, and then the sample is directly mounted on the magnet with known north or south (N or S) polarity. After the data are collected with one polarity, the magnet is removed and remounted to reverse the polarity. The separation between the sample and the magnet introduces an airgap into the optical-structural model. Similar optical Hall effect measurements are also performed under ~ 1 sun illumination (AM 1.5 solar irradiance spectrum) generated by a fiber optic illuminator (Dolan-Jenner, Fiber-Lite Model 190).

For these optical Hall effect measurements, THz range spectroscopic ellipsometry is used as the optical probe. All three sets of eleven Mueller matrix spectra are analyzed simultaneously in a model sensitive to the complex dielectric function ($\varepsilon = \varepsilon_1 + i\varepsilon_2$) spectra as well as to wafer thickness and air gap thickness when applicable. The contributions to the optical response in this spectral range include those due to free carrier absorption, described classically by the Drude model. [317] Optical anisotropy is introduced under non-zero applied magnetic field, and the Drude model is modified. The non-zero differences in the magneto-optic Mueller matrix elements for +B and –B are related to free carrier motion generated by the Lorentz force.

Bulk wafer thickness, air gap thickness, and optical properties for each of the active layers in the cell are extracted in the form of layer thicknesses and spectra in ε. Respectively, by fitting a parameterized model to measured Mueller matrix spectra and Mueller matrix difference spectra collected at all three angles of incidence using a least square regression analysis that minimizes an unweighted error function (σ). [388] The errors reported on model fit parameters are derived from a combination of the statistical standard 90% confidence limit and the overall error function quantifying the closeness of model fit to measurement. Consequently, these errors are best interpreted as a measure of the model's sensitivity to each parameter, in the context of all other fit parameters.

18.4 RESULTS and DISCUSSION

The structural model consists of a 20 μm aluminum layer / 181 ± 4 μm p-type boron doped Si wafer / 1 μm n-type phosphorus doped Si emitter layer / 75 nm SiN_x layer / air ambient, as shown in Figure 143. The in-plane pyramidal texture feature size is ~ 4-5 μm and much smaller than the wavelengths of the probing THz beam; as a result, the surface is treated as specular for these measurement wavelengths. A similar structural-optical model is used in the presence of magnetic fields; however, a finite thickness air gap is included between the sample and the magnet. Spectra in ε for the active n- and p-type Si are extracted by fitting measured Mueller matrix and Mueller matrix difference spectra using a parameterized model. The three sets of data collected under dark condition measurement at 0 and ± 1.48 T applied magnetic fields in spectral range windows from 3 to 34 cm^{-1} are fitted for this sample simultaneously with difference in Mueller matrix spectra [i.e. $\Delta m_{ij} = m_{ij}(+B) - m_{ij}(-B)$] from 23 to 32 cm^{-1}. Figure 144 shows the example experimental Mueller matrix spectra collected at 50° under the dark condition from 3 to 34 cm^{-1} at 0, +1.48, −1.48T; experimental Mueller matrix difference spectra from 23 to 32 cm^{-1}; and corresponding best fit models. Contributions to THz range spectra in ε for the phosphorus doped n-type Si emitter layer of the cell include a constant additive term to ε_1 ($\varepsilon_\infty = 1$) and a Drude expression [317] describing free carrier absorption, with the real and imaginary parts of the spectra in ε shown in Figure 145. Similarly, the spectra in ε for the boron doped p-type Si wafer are parameterized by $\varepsilon_\infty = 10.3 \pm 0.4$ and a Drude expression describing free carrier absorption with spectra in ε also shown in Figure 145. For the more heavily doped n-type Si emitter the Drude contribution dominates the shape of ε so sensitivity to ε_∞ is lost and its value fixed at unity, whereas for the more lightly doped p-type Si wafer the Drude contribution is less dominant and sensitivity to ε_∞ is retained. Optical response of the permanent magnet consists of the Drude expression for highly reflective gold as described in the approach of Knight et al. [389] for optical Hall effect measurements. The effects due to the 75 nm SiN_x coating are negligible in this long wavelength spectral range. Spectra in ε for the aluminum back contact are represented by the parametric expression described by Subedi et al. [390]

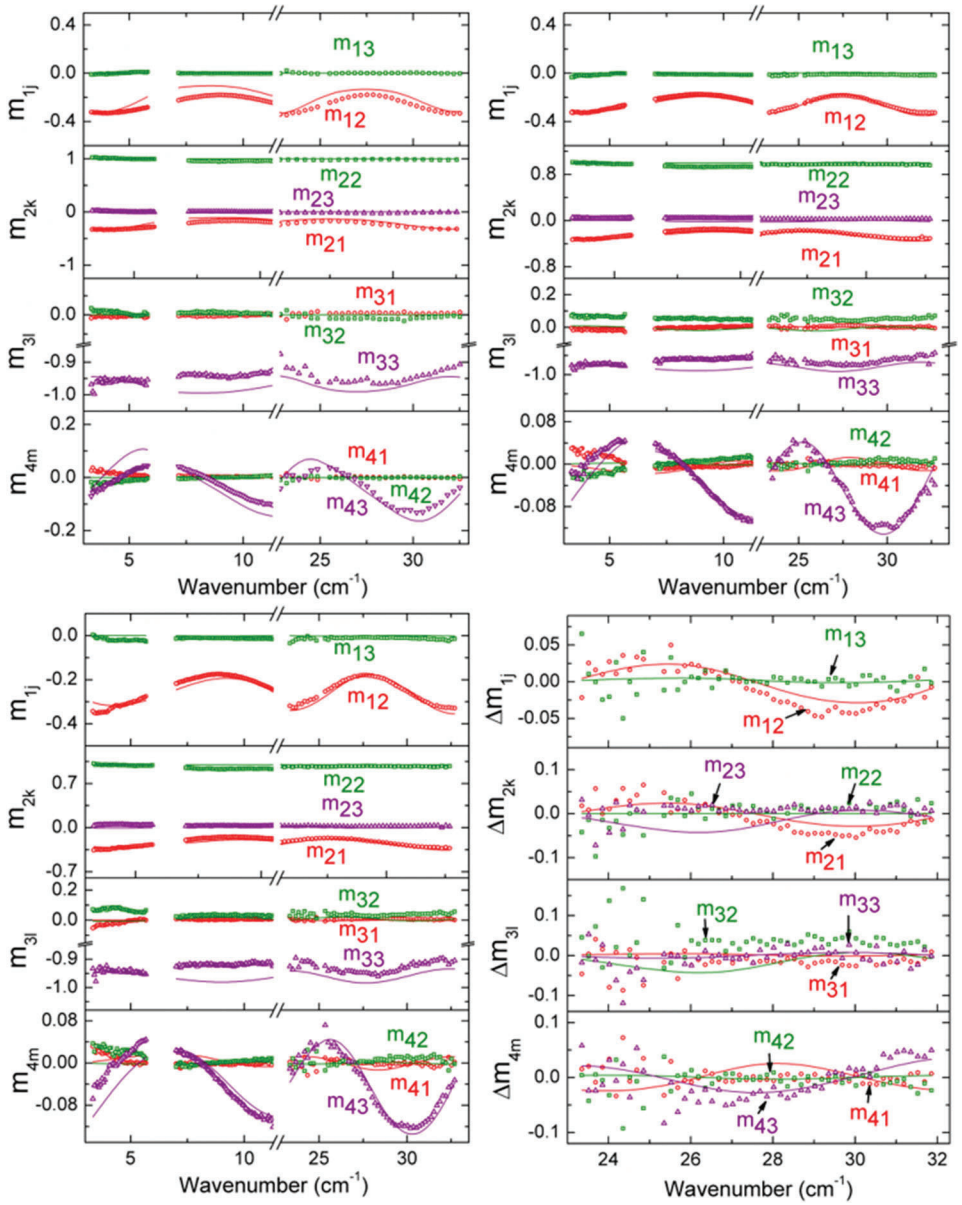


Figure 144. Experimental (symbols) spectra at 0 T (top-left), +1.48 T (top-right), –1.48 T (bottom-left) and difference spectra at ±1.48 T (bottom-right) with their corresponding calculated models (solid lines) of normalized Mueller matrix elements for the Al-BSF Si solar cell [382]

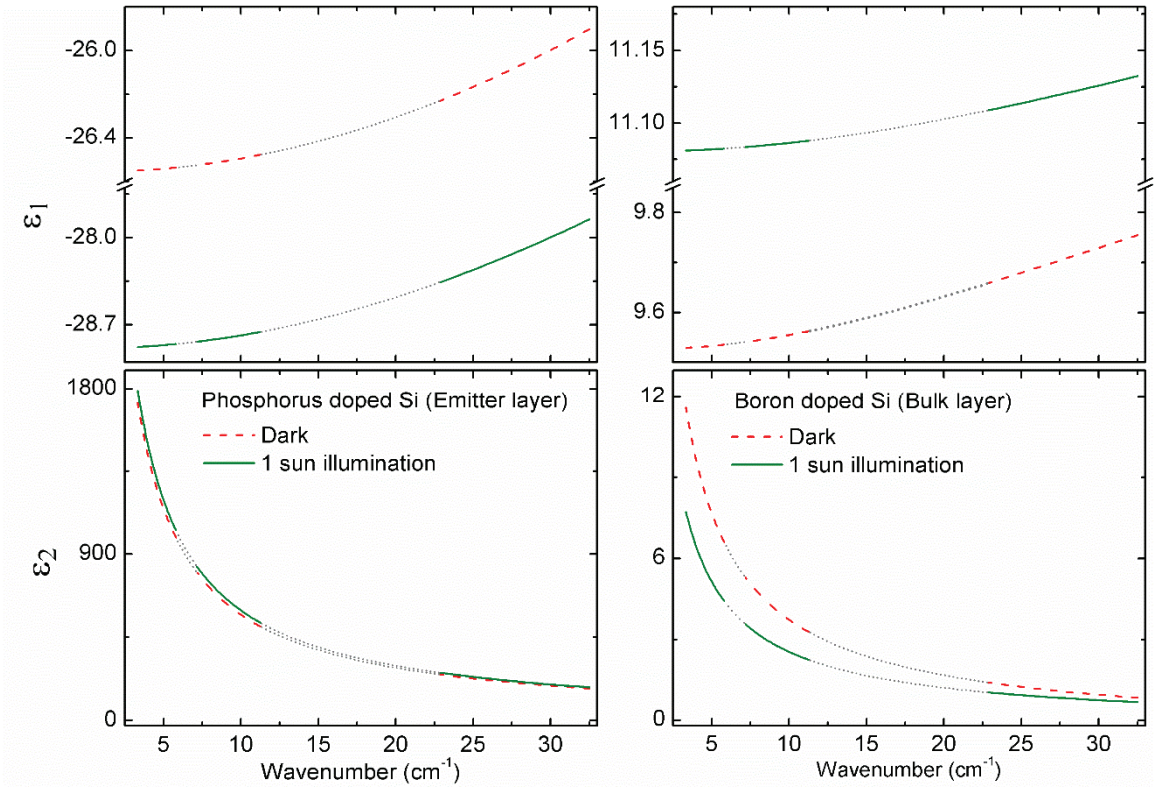


Figure 145. $\varepsilon = \varepsilon_1 + i\varepsilon_2$ spectra for n-type Si:P emitter layer and p-type Si :B bulk wafer from optical Hall effect measurements [382]

The parameters describing majority carrier free carrier absorption for the n-type emitter and p-type Si wafer obtained from measurements collected under dark conditions are summarized in Table 29. Optical Hall effect measurements of the same solar cell are performed under 1 sun illumination and a similar data analysis approach is applied. The wafer thickness is fixed to 181 μm from analysis of optical Hall effect measurements collected under dark conditions. Under 1 sun illumination, spectra in ε for the n-type emitter are parameterized using $\varepsilon_\infty = 1$ and two Drude expressions separately representing contributions to free carrier absorption from majority carrier electrons and minority carrier holes, shown in Figure 145. The hole contribution to free carrier absorption is due to photogenerated carriers under 1 sun illumination. The electron contribution consists of an equal concentration of photogenerated carriers added to the carriers from phosphorus doping. Similarly, spectra in ε for the p-type bulk wafer are parameterized by $\varepsilon_\infty = 11.41 \pm 0.02$ with Drude expressions for photogenerated minority carrier electrons and a combination of majority carrier holes from boron doping and photogeneration, also shown in Figure 145. As in the case of the dark condition measurement analysis, the dominance of the Drude contribution to ε causes a loss of sensitivity to ε_∞ for the heavily doped n-type emitter while it is retained for the lightly doped p-type wafer. The majority and photogenerated minority carrier transport properties for the emitter and bulk Si layers of the cell are summarized in Table 29. In the model applied to analysis of the 1 sun illuminated measurements, the respective impurity doping carrier concentrations and conductivity effective masses are fixed to values obtained from the dark condition measurements. Photogenerated electron and hole concentrations are equal within each

layer. Electron and hole μ in each layer are allowed to vary independently to account for additional recombination processes expected under illumination.

Table 29. Dark and light carrier transport properties for Si phosphorus-doped n-type emitter and boron-doped p-type wafer in the Al-BSF solar cell [382]

Layers	Conditions	Transport Property	
Phosphorus-doped n-type Si emitter layer	Dark (Laboratory light ambient)	Electron mobility μ (cm^2/V s)	166 ± 6
		Electron carrier concentration N (cm^{-3})	$(3.6 \pm 0.1) \times 10^{18}$
		Electron effective mass m^* ($\times m_e$)	0.28 ± 0.03
		Resistivity ρ (Ωcm)	0.01
		Scattering time τ (fs)	26
	Light (1 sun illumination)	Photogenerated electron and hole concentration Δn or Δp (cm^{-3})	$(7.8 \pm 0.2) \times 10^{16}$
		Electron mobility μ_e (cm^2/Vs)	162 ± 5
		Hole mobility μ_h (cm^2/Vs)	331 ± 191
Boron-doped p-type Si wafer	Dark (Laboratory light ambient)	Hole mobility μ (cm^2/Vs)	532 ± 12
		Hole carrier concentration N (cm^{-3})	$(7.6 \pm 0.1) \times 10^{15}$
		Hole effective mass m^* ($\times m_e$)	0.36 ± 0.02
		Resistivity ρ (Ωcm)	1.5
		Scattering time τ (fs)	109
	Light (1 sun illumination)	Photogenerated hole and electron concentration Δp or Δn (cm^{-3})	$(2.2 \pm 0.2) \times 10^{14}$
		Hole mobility μ_h (cm^2/Vs)	323 ± 32
		Electron mobility μ_e (cm^2/Vs)	766 ± 331

Analysis of the optical Hall effect measurements here yield majority and minority average concentrations within each doped Si region with carrier mobilities as independent fit parameters. The analysis did not provide sensitivity to the n-type emitter carrier concentration profile or the characteristics of the depletion region. Sensitivity to these characteristics may be lost due to the structure of this commercial Al-BSF device and overlapping optical effects of the n-type carrier concentration profile and depletion region transport properties occurring near the top of the Si junction. Although the simplified model of a discrete n-type emitter and p-type bulk Si interface is applied in analysis of the optical Hall effect data, the transport properties determined are used to calculate reasonable minority carrier lifetimes and diffusion lengths as well as simulate solar cell performance parameters consistent with experiment.

More detailed simulations of solar cell performance are performed using PC1D. [391] Using PC1D, electron and hole transport equations are solved for carriers in the complete Si solar cell described in Figure 143 to determine *J-V* characteristics. Input parameters include those derived from optical Hall effect measurements reported in Table 29. The experimentally measured device performance values are V_{oc} = 0.627 ± 0.001 V, J_{SC} = 37.0 ± 0.3 mA/cm^2, FF = 0.80 ± 0.02, and resulting η = 18.5 ± 0.1%, In PC1D the carrier concentration profile of the n-type emitter is manipulated to account for non-uniform carrier concentration with depth. Doping carrier concentrations include a uniform distribution represented by the average carrier concentration

reported in Table 29, an exponential profile, a Gaussian profile, and a Gauss error function profile. All other parameters are constrained to values reported in literature. PC1D simulation results incorporating uniform and Gauss error function carrier concentration profiles in the n-type emitter most closely match experimental values with simulated V_{oc} = 0.621 and 0.625 V, J_{SC} = 37.3 and 37.2 mA/cm^2, FF = 0.799 and 0.800, and resulting η = 18.5 and 18.6%, for uniform distribution and Gauss error function profiles, respectively. Although both simulation results match experimental values, the carrier concentration profile is unlikely to be completely uniform. Based on the similarity of the results from these two simulations, it is possible that the simulated n-type emitter carrier concentration profile is more complicated than either a uniform distribution or Gauss error function profile individually, although the precise profile is not known for this commercial Al-BSF Si wafer solar cell. Average majority and minority carrier concentrations in the n-type emitter and p-type bulk wafer are obtained from the simplified model consisting of discrete layers of uniform carrier concentration used in analysis of optical Hall effect measurements. The agreement between the PC1D simulated and experimental *J-V* characteristics supports the average carrier concentration values obtained from the optical Hall effect characterization of this device. These optical Hall effect input parameters may serve as further constraints in determining solar cell characteristics via device modeling.

An evaluation of all these results leads to the conclusion that a combined analysis of optical Hall effect measurements collected under dark and illuminated conditions is sensitive to majority carrier transport properties from impurity doping and minority carrier transport properties from carrier photogeneration under 1 sun illumination. In particular, N, μ, and m^* are obtained for both the phosphorus doped n-type Si emitter and the boron doped p-type Si bulk of an Al-BSF solar cell from dark measurements. Based on information gained from analysis of the dark measurements, minority carrier transport parameters in both the n- and p-type Si components of the Al-BSF solar cell are deduced from analysis of measurements collected under 1 sun illumination. Consistency between calculated device performance parameters using transport properties via optical Hall effect and measured values demonstrates the reliability of this novel technique for the transport properties measurement even in a complicated structure such as an Al-BSF Si solar cell.

18.5 CONCLUSIONS

Majority and minority carrier transport properties of Si active layers within an Al-BSF solar cell are deduced from the optical Hall effect measurements performed under nominally dark conditions and under 1 sun illumination. The minority carrier transport parameters, Δp or Δn and μ_h or μ_e, as well as the majority carrier transport parameters N, μ, and m^*, are determined for the phosphorus doped n-type Si emitter and boron doped p-type Si wafer in an Al-BSF configuration solar cell with pyramidal front surface texturing, a relatively common commercially produced device structure. The majority carrier transport properties extracted here agree well with those reported in the literature. Minority carrier mobilities and concentrations of the active layers of the cell are also within expectations. The calculated minority carrier effective lifetime and diffusion length from Δp or Δn and N for each layer also show good agreement with reported values for similar dopant densities, which demonstrate the validity of this technique for determination of minority carrier transport properties. Calculated PV device performance parameters from measured transport properties via optical Hall effect efficiency simulation agree well with directly measured values, further validating this method for reliably obtaining majority and minority carrier transport properties. Using this non-contacting optical technique both majority and minority carrier transport properties are measured within a complete solar cell, providing a pathway to improved understanding of fundamental electrical properties of materials when integrated into opto-electronic devices.

19. INVESTIGATING THE ROLE OF BAND ALIGNMENT AT THE TRANSPARENT CONDUCTOR/ELECTRON TRANSPORT LAYER INTERFACE IN WIDE-BANDGAP PEROVSKITE SOLAR CELLS

Adam B. Phillips, Zhaoning Song, Yanfa Yan, and Michael J. Heben

19.1 SUMMARY

Band alignment between the absorber and the electron and hole transport layers (ETL and HTL, respectively) in perovskite solar cells is critically important to reduce recombination at these interfaces. Maintaining the proper alignment as the bandgap of the absorber increases is required to ensure the appropriate gain in open circuit voltage. However, the conduction band position of the transparent conducting oxide (TCO) layer is fixed for any given material and not easily varied. In this work, we show that as the bandgap of the perovskite material increases, recombination increases at the TCO/ETL interface and can limit the device performance for absorber bandgap greater than 1.7 eV.

19.2 INTRODUCTION

Organo-metal halide perovskites have shown remarkable success as thin-film solar cell absorbers, with single junction perovskite solar cells (PSCs) recently surpassing a power conversion efficiency (PCE) threshold of >25%. [392, 393] This success is due to the excellent optoelectronic properties of these materials such as long carrier lifetimes/diffusion lengths [394-397], high optical absorption, [398] and tolerance to defects. [399] Additionally, compositional variation of perovskite precursor solutions permits the tunability of the bandgap while maintaining or improving upon resistance to degradation. [400-402] Wide-bandgap perovskites may then be readily paired with low-bandgap perovskites or other thin-film materials such as Si and CIGS [403, 404] in tandem configurations as a method of exceeding the Shockley-Queisser limit of single junction solar cells. [405, 406] Already, multijunction devices incorporating perovskites in this fashion routinely exceed 20% PCE [58, 61] and have recently surpassed the single junction PCE record for PSCs. [36, 407-409] However, as a consequence of the strength and versatility of perovskite absorbers, the performance of these devices increasingly hinges on the transport and collection properties at the heterojunction interfaces. [410-413]

As intrinsic absorbers, perovskite films must be sandwiched between charge transport layers (CTLs) in order to facilitate efficient carrier collection through selective conductivity of electrons and holes. [414] Tremendous effort has gone toward incorporating new electron transport layers (ETLs), hole transport layers (HTLs), and additional interlayers into PSCs in order to improve charge collection at the absorber/CTL interfaces. [412, 415] Comparative numerical investigations incorporating different CTLs into PSCs has proven especially useful in identifying and explaining the favorable electronic properties of these materials, [416-420] typically for low-bandgap perovskites intended for single junction architectures. Particular attention has been paid to the conduction band offset (CBO) at the ETL/perovskite interface and the valence band offset (VBO) at the perovskite/HTL interface and how these energetic alignments impact charge transport at their corresponding interfaces. [421-423]

In this vein, we recently investigated the contribution of the band alignment at each of the CTL interfaces to the significant open-circuit voltage (V_{OC}) deficit of wide-bandgap PSCs. [423] The well-established TiO_2 ETL and Spiro-OMeTAD HTL each produce highly negative band offsets at their respective interface with a $MAPb(I_{1-x}Br_x)_3$ absorber, causing high interfacial recombination near V_{OC} that limits device performance. However, we demonstrated that with proper alignment, interfacial recombination would no longer be the limiting recombination mechanism. This supports previous findings that reduction of the work function of TiO_2 [424-426] and other metal-oxide ETLs [427, 428] increased performance in low-bandgap PSCs. Our work showed that ideal interface alignment increasingly differs from that provided by TiO_2 and Spiro-OMeTAD as the perovskite bandgap grows wider, necessitating novel ETLs and HTLs more suited for wider bandgaps. Unexpectedly, even with optimized conduction band alignment the bands at the front interface did not bend downward from the perovskite as is necessary to truly maximize efficient carrier transport across that interface. Furthermore, alignment at this interface caused non-monotonic behavior of the fill factor, causing the optimum CBO to trend downward as the perovskite bandgap increased. These results imply that the impact of the other interface at the front of the device, that between the transparent conducting oxide (TCO) and ETL requires closer investigation.

The importance of the interface of fluorine-doped SnO_2 (FTO) and TiO_2 to electron conduction and band bending was understood in dye sensitized solar cells, the forerunners of today's PSCs. [429] Limited attention has been paid to this interface during the subsequent development of high-efficiency PSCs, despite evidence of its continued importance. [430] Wang et al. introduced the use of a graphene interlayer between FTO and TiO_2, which was posited to provide a possible intermediate energetic step for electrons, among other favorable transport improvements. [431] However, most interlayer approaches such as this instead choose to focus on the ETL/perovskite interface. Elsewhere, the direct modification of the work function of both FTO and indium-doped SnO_2 (ITO) has been performed using polyethylenimine ethoxylated (PEIE) and branched polythylenimine (PEI) polymers as surface modifiers. [432] Zhou et al. reported a 19.3% efficient planar n-i-p PSC with a PEIE-coated ITO electrode with a measured work function of 4.0 eV, which was shown to improve the current-voltage characteristics over a device with untreated ITO. [410] Reducing the work function of either FTO or ITO in this fashion has subsequently been applied to other planar n-i-p PSCs [433-436] and other polymers have been found to produce similar results, [437, 438] decreasing the TCO work function on the order of ~0.6-0.9 eV. The success of this approach is believed to result from formation of a more Ohmic contact at the electrode, alongside other enhancements such as increased ETL doping and larger perovskite grain sizes, but numerical work has yet to clearly demonstrate this hypothesis. Furthermore, the implications of TCO alignment in PSCs with absorber bandgaps greater than ~1.55 eV are even less well understood.

Given the need to better understand the role of the TCO/ETL interface, here we investigate the influence of the alignment between the TCO and ETL in wide-bandgap PSCs via numerical simulation. The TCO work function (WF) is shown to strongly affect the electric potential and band bending at the front of the device. Unlike what we previously observed solely by modifying the ETL/perovskite interface alignment, a low enough TCO WF leads to downward band bending in the perovskite absorber when combined with a favorable CBO. This band bending not only further reduces recombination at the ETL/perovskite interface but also reduces the Shockley-Read-

Hall (SRH) recombination that more significantly limits device performance. As the conduction band minimum and valence band maximum shift with increasing perovskite bandgap, TCO WF reduction is shown to be increasingly important for maintaining high PCE. Lastly, we show that compared to a device with a relatively high TCO WF, such as that used in our previous work, a lower TCO WF will suppress SRH recombination even in the case of poor ETL alignment and lead to even lower interfacial recombination when ETL alignment is favorable. The net result includes improved PCE.

19.3 METHODS, ASSUMPTIONS, and PROCEDURES

Simulations were performed using SCAPS1-D software. [271] We modeled planar n-i-p perovskite solar cells of the structure TCO/ETL/MAPb($I_{1-x}Br_x$)$_3$/HTL. Table 30 shows the relevant electronic properties of each material in the simulation, taken from literature. [396, 439-444] The ETL shares all properties of TiO_2, except that the electron affinity was adjusted in order to produce a CBO of +0.1 eV as suggested by our previous work. [423] Likewise, the HTL layer emulates Spiro-OMeTAD except for an adjusted electron affinity producing a VBO of +0.05 eV. These band offsets are maintained for whatever absorber bandgap is currently under consideration, isolating the effects of a changing TCO alignment. The conduction band and valence band positions of a given perovskite were extrapolated based on the bandgap's relative positions between the x = 0 (E_g = 1.6 eV, χ = 3.9 eV) and x = 1 (E_g = 2.3 eV, χ = 3.4 eV) compositions. Neutral mid-gap defects with Gaussian distributions are used to ascribe a bulk lifetime to each semiconductor layer. The perovskite exhibits a bulk lifetime of 10 μs [397] and a radiative recombination coefficient of 10^{-11} cm^3/s. [445] The other layers, less significant for bulk recombination, assume lifetimes of 5 ns. Neutral midgap defects are also specified at the two perovskite/CTL interfaces, each with surface recombination velocities of 1 cm/s. At the contacts, flat bands are assumed. Simulations are performed at 300 K under the standard AM1.5G spectrum with an irradiance of 100 mW/cm^2.

Table 30. Electronic properties of simulated semiconductor materials

Property	FTO	ETL	Perovskite	HTL
Thickness (nm)	500	50	600	300
Bandgap (eV)	3.6	3.2	1.6-2.0	2.7
Electron Affinity, χ (eV)	*Varied*	*Varied*	3.90-4.186	*Varied*
Relative Permittivity	9	100	6.5	3
CB Effective Density of States (cm^{-3})	2.2e18	2.2e18	2.8e18	2.2e18
VB Effective Density of States (cm^{-3})	1.8e19	1.8e19	3.9e18	1.8e19
Electron/Hole Mobilities (cm^2/Vs)	20/10	20/10	10/10	2e-4/2e-4
Shallow Donor Density (cm^{-3})	2e19	1e16	1e13	0
Shallow Acceptor Density (cm^{-3})	0	0	0	1e18

19.4 RESULTS and DISCUSSION

Figure 146 shows the simulated current density-voltage (JV), recombination current density-voltage (J_rV), and maximum power point band diagrams at the front interface of a device with a 1.7 eV bandgap perovskite absorber for TCOs with electron affinity (χ_{TCO}) in the range 3.9 eV to 4.5 eV. Because of the favorable ETL/absorber alignment, bulk Shockley-Read-Hall (SRH) recombination is the dominant mechanism in all cases, though the differences in band bending, SRH recombination, and even interfacial recombination as the TCO changes reveal that alignment between the ETL and absorber does not exclusively govern transport mechanisms at this interface.

The TCO with the largest electron affinity of 4.5 eV, which most closely resembles FTO or ITO in work function, exhibits the unfavorable upward band bending left unaddressed by our investigation of ETL/absorber alignment. The upward band bending confines electrons to the absorber, thus causing SRH recombination to turn on at biases far below V_{OC}, considerably degrading fill factor and efficiency relative to lower TCO WF despite similar V_{OC} and short-circuit current density (J_{SC}). Recombination at the interface is high due to the large difference in electron affinities of the ETL and TCO. Reducing χ_{TCO} to 4.3 eV leads to flatter bands at the maximum power point bias, and a concurrent increase in the turn on voltage of both SRH and interface recombination, though the perovskite bands still bend slightly upward at the interface. It is not until χ_{TCO} is lowered to 4.1 eV that the maximum power point bands at the front interface are completely flat, further delaying the turn-on of each recombination mechanism. This alignment also first shows an electron quasi-Fermi level that is flat throughout the perovskite/ETL/TCO region, minimizing the voltage drop within the device and allowing the voltage drop to more completely occur at the contacts. This manifests in the disappearance of bending of the JV curve near V_{OC} and corresponding decrease in series resistance. Finally, further reducing χ_{TCO} to 3.9 eV at last produces bands that bend downward away from the perovskite. SRH recombination is only marginally reduced by further decreasing χ_{TCO}, but interfacial recombination reduction continues to benefit from the downward band bending. However, because interfacial recombination is 4 to 5 orders of magnitude lower than SRH, even relatively substantial reductions do not continue to significantly impact the cell's PV parameters. A reduced TCO WF clearly has a strong, positive impact on the conduction band bending in the lower-doped ETL and perovskite.

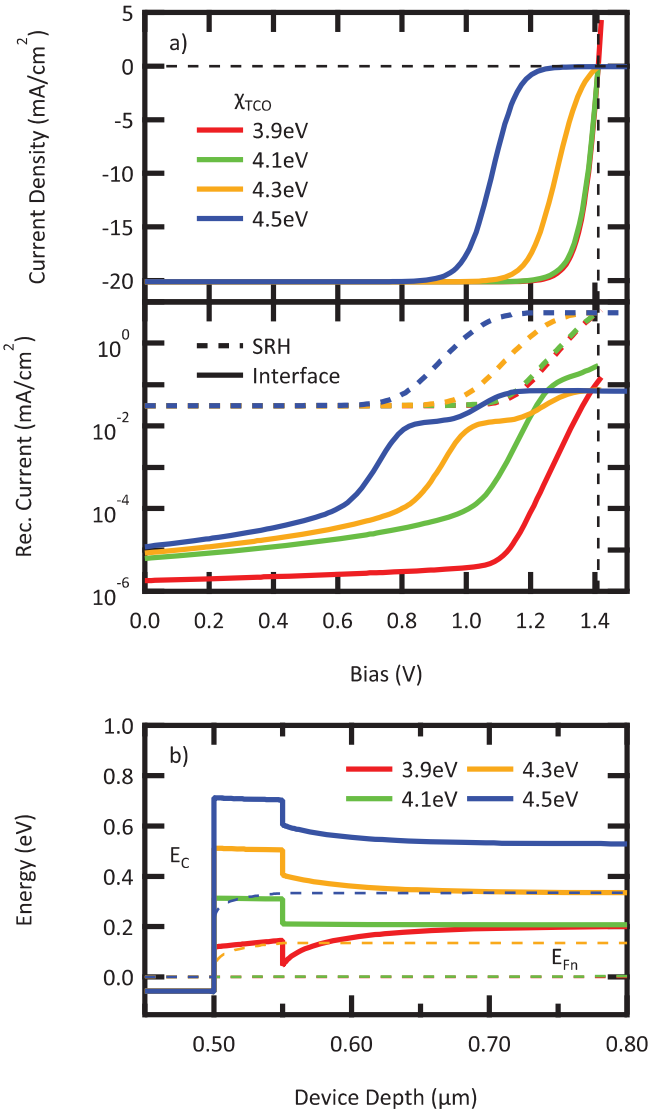


Figure 146. (a) Simulated JV and J_rV curves; (b) mpp band diagrams at the front interface vs. TCO electron affinity

Figure 147 shows the V_{OC}, J_{SC}, fill factor, and PCE as a continuous function of both perovskite bandgap and χ_{TCO}. For any perovskite bandgap in the observed range, χ_{TCO} impacts each cell in a similar fashion as seen in Figure 146. High χ_{TCO} leads to high V_{OC} yet very poor fill factor due to high bulk recombination in the perovskite (high V_{OC} in this region may actually result from errors in numerical convergence, as evidenced by exceeding of the Shockley-Queisser limit, but PCE should accurately reflect the low V_{OC}/high fill factor combination implied by the modeled high V_{OC}/low fill factor). Reduced χ_{TCO} causes V_{OC} to decrease, though it then remains nearly at its Shockley-Queisser limited value as achieved in our previous work, as interface recombination has already been prevented through favorable CTL alignment. [423] Fill factor improvement drives overall performance as lower χ_{TCO} causes the bands to bend downward and cease confining electrons to the perovskite for sufficient time for them to recombine via SRH. J_{SC} is unaffected by

varied χ_{TCO}, such that PCE reflects the V_{OC} and fill factor behavior as described: a sharp rise followed by a leveling-off as χ_{TCO} falls below ~4.0 eV. There is a gradual decrease in the TCO WF required to level off PCE associated with the shifting perovskite conduction band, and the shifts in ETL and perovskite Fermi levels that this induces. The horizontal dashed white line on each contour demarcates a χ_{TCO} of 4.4 eV, the approximate minimum value for the work function of FTO (ITO typically exhibits a WF of 4.8 eV, out of range of the WFs investigated). This renders the evident effect of a widening perovskite bandgap more apparent. While performance parameters may be high for lower bandgap perovskites paired with FTO, energetic contributions make high performance more difficult as the perovskite bands migrate further from the FTO Fermi level.

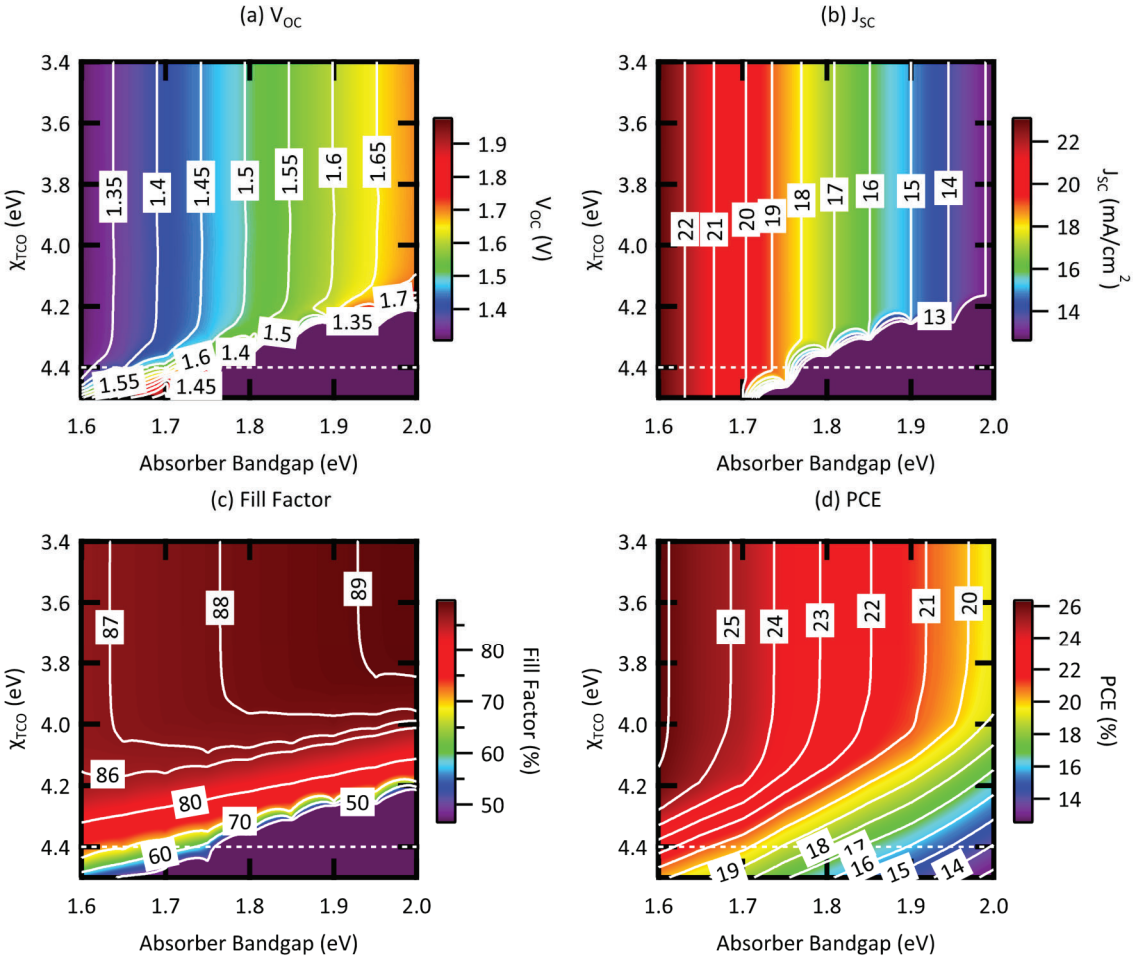


Figure 147. (a) V_{OC}, (b) J_{SC}, (c) FF, and (d) PCE vs. perovskite bandgap and TCO electron affinity

With simulation supporting that a lower χ_{TCO} causes favorable band alignment at the front interface combined with favorable ETL/perovskite alignment, it is useful to compare the effect of a shifting ETL/perovskite CBO for different values of χ_{TCO}. Figure 148 shows JV, J_rV, and maximum power point band diagrams at various ETL CBOs for a TCO electron affinity of 4.25 eV (Figure 148(a, c)) and a TCO electron affinity of 3.8 eV (Figure 148(b, d)), once again for a 1.7 eV bandgap absorber. A χ_{TCO} of 4.25 eV was chosen due to our previous use of this value as a

static value for FTO. Numerous numerical studies of PSCs use a value of 4.0 eV which inadequately reflects FTO and, as we have shown, masks the effects that a high TCO WF may have on device performance. When the CBO has a highly negative value of -0.5 eV, both cells show practically identical JV and J_rV characteristics (Figure 148(a-b)), due to the negligible influence of the TCO on the perovskite or ETL band bending with such a misaligned CBO (Figure 148(c-d)). Slight differences in behavior do in fact arise with the next observed CBO, -0.25 eV. Relative to the previous case, the conduction band of the ETL is elevated for the higher TCO WF but band bending in the ETL changes very little for the low TCO WF. The perovskite bands remain very similar, with slight upward bending, but are slightly closer to the electron quasi-Fermi level when χ_{TCO} is 3.8 eV. Interface recombination turns on at a slightly higher voltage for the low WF TCO. Consequently, its fill factor and overall PCE are elevated despite its lower V_{OC}. When the CBO is -0.05 eV, the optimum value for the 1.7 eV bandgap absorber found in our previous investigation, every PV parameter differs <1% relative between the two devices. Though the absorber and ETL conduction bands both exhibit downward band bending with a low TCO WF, and upward band bending with a high TCO WF, the differences in band energy are primarily near the ETL/perovskite interface. Consequently, SRH recombination, the primary form of recombination with such a favorable ETL/perovskite alignment, differs only negligibly; the difference in interface recombination due to band bending is not significant enough relative to the net recombination current to affect JV behavior significantly. The advantage of a low WF TCO is most stark with a highly positive CBO. A high WF TCO is unable to induce favorable band bending due to its large offset relative to the ETL. As a result, SRH recombination turns on at a lower bias voltage than for even the -0.5 eV CBO. The interface recombination turn on remains where it has been for the previous two CBOs. Performance has therefore peaked as previously observed. However, with a low TCO WF this reduction in fill factor does not occur. There remains a conduction band spike in the ETL, but the band bending in the perovskite is even more pronounced than before. SRH recombination does not turn on any earlier, and interface recombination in fact continues to decrease in magnitude for all bias voltages. High V_{OC} is maintained near its Shockley-Queisser limit, and fill factor/PCE make marginal gains relative to the previous CBO.

A decrease in the TCO work function is clearly expected to have beneficial effects in PCSs due to its effects on the band bending in the perovskite absorber and its increasing the quasi-Fermi level separation for usable photovoltage by the external load. These benefits will be especially necessary as the absorber bandgap grows wider and the conduction bands diverge at the front interface, causing high misalignment and therefore recombination if the same ETLs and TCOs are used as for narrower-bandgap PSCs. Due to the compatibility of FTO and ITO to the growth of perovskite solar cell thin film stacks in superstrate configuration, the modification of these pre-existing electrodes stands as the most likely path to improve energetic alignment at the TCO/ETL interface. As discussed above, this has already occurred in many high-performance devices through the use of PEIE and PEI as surface modifiers. While polymers have begun attracting attention as additives to other layers in PSCs, with a focus on their effects on stability and charge transport, their application to the TCO remains overlooked even in recent reviews of the topic. [446] Application of such modifications remains wholly absent in top-performing wide-bandgap PSCs in literature. [447-451] Furthermore, systematic experimental studies of the benefits of such modifications have yet to be done in a fashion laid out in this current work.

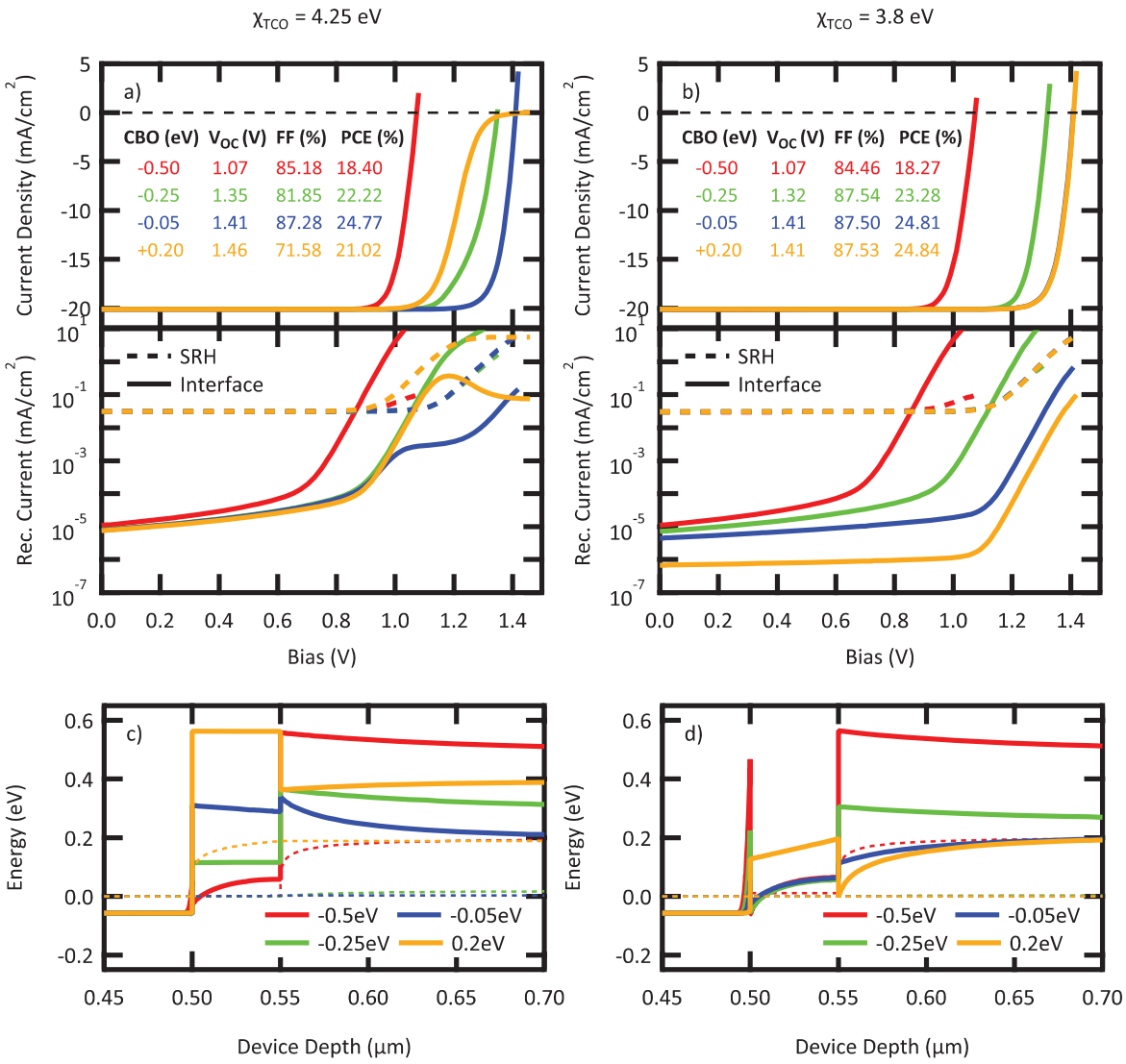


Figure 148. JV and J_rV for a TCO electron affinity of (a) 4.25 eV and (b) 3.8 eV for various ETL/perovskite CBOs. MPP band diagrams at the front interface for TCO electron affinity of (c) 4.25 eV and (d) 3.8 eV

19.5 CONCLUSION

In summary, we have shown the importance of the TCO work function to reducing recombination in wide-bandgap perovskite solar cells through improved energetic alignment across the front interface. These conclusions are especially relevant in cases of non-ideal ETL offsets that form barriers for electron flow from the perovskite leading to the front electrode. Numerical simulation supports that lower work function TCOs are all the more necessary for wide bandgap perovskites with more drastically different band structure than narrower gap absorbers such as $MAPbI_3$.

20. MATERIALS REQUIREMENTS FOR IMPROVING THE ELECTRON TRANSPORT LAYER/PEROVSKITE INTERFACE OF PEROVSKITE SOLAR CELLS DETERMINED VIA NUMERICAL MODELING

Adam B. Phillips, and Michael J. Heben

20.1 SUMMARY

Perovskite solar cells continue to garner significant attention in the field of photovoltaics. As the optoelectronic properties of the absorbers become better understood, attention has turned to more deeply understanding the contribution of charge transport layers for efficient extraction of carriers. Titanium oxide is known to be an effective electron transport layer (ETL) in planar perovskite solar cells, but it is unlikely to result in the best device performance possible. To investigate the importance of band energy alignment between the electron transport layer and perovskite, we employ numerical modeling as a function of conduction band offset between these layers, interface recombination velocity, and ETL doping levels. Our simulations offer insight into the advantages of energy band alignment and allow us to determine a range of surface recombination velocities and ETL doping densities that will allow us to identify novel high performance ETL materials.

20.2 INTRODUCTION

Since their introduction over 10 years ago, perovskites have undergone rigorous study and shown remarkable success as thin-film photovoltaic absorbers. [47] With efficiency of >25% recently achieved, perovskite solar cells (PSCs) have now surpassed other thin-film and multicrystalline photovoltaic technologies. This is predominantly due to the favorable optoelectronic properties of the methylammonium lead iodide ($CH_3NH_3PbI_3$ or $MAPbI_3$) absorber. With a strong understanding of the perovskite absorbers, attention has turned to the materials used as charge transport layers (CTLs) and how their electronic properties affect the performance of PSCs. Titanium oxide (TiO_2) has become the typical electron transport layer (ETL) in these architectures, and organic 2,2′,7,7′-tetrakis(*N*,*N*-di-*p*-methoxyphenyl-amine)9,9′-spirobifluorene (Spiro-OMeTAD) is the typical hole transport layer (HTL). Though successful, it is unlikely that these materials are the best option for use in PSCs, motivating the search for novel replacements.

Experimentally identifying better options for the CTLs can be time consuming and expensive. Numerical simulation, on the other hand, offers a faster pathway to identify the materials properties that are critical to high performance devices, and some limited modeling studies of these interfaces with PSCs have been reported. [416] It has been shown that modifying the electron affinity (conduction band position) of each CTL while maintaining the material bandgap can reduce interface recombination and increase device performance. [421] The conclusions of these investigations can be useful, but may be misleading or even invalid if other parameters are varied. This makes it difficult to identify potential candidate materials for these CTLs.

Here, using numerical modeling, we investigate the effect conduction band offset (CBO), ETL doping density, and surface recombination velocity (SRV) have on PSC performance. We find that the recombination at the ETL/perovskite interface is greatly reduced by both band bending due to increasing CBO or ETL doping and decreased SRV. In general, ETLs with low work functions

cause the interface to be much more tolerant to midgap states as hole concentrations near the interface are low. Alternatively low SRV also leads to high performance devices that are less sensitive to ETL work function. These results broaden the options for candidate ETL materials that can outperform TiO_2.

20.3 METHODS, ASSUMPTIONS, and PROCEDURES

SCAPS 1D takes as input the electronic properties of solar cell layers and numerically solves the continuity and Poisson equations in order to simulate solar cell performance. [271] For our work, we modeled a planar n-i-p structure FTO/TiO_2/$MAPbI_3$/Spiro-OMeTAD/Au. Table 31 shows the properties of each layer used in the model. Materials properties are taken from both experimental and modeling literature. [396, 439-444]

We assume neutral bulk defects located midgap with a Gaussian energy profile and a carrier lifetime of 10 μs, in agreement with experimentally measured values. [397] In addition, we assumed a radiative recombination coefficient of 10^{-11} cm^3/s for the perovskite. [445] For this model, we incorporate neutral midgap defects at the two perovskite interfaces, with an SRV of 1 cm/s at each, leading to simulated performance in agreement with well-performing perovskite solar cells. A lifetime of 5 ns was assumed for all other layers, as the absorber lifetime dominates simulated device performance. The doping density of each layer is representative of typical experimental values. The electron affinity of the FTO is higher than that of typical perovskite simulation literature, more closely resembling its experimental value. Flat bands are assumed at each contact. Values left unspecified are left at their SCAPS default values. Data is collected at a temperature of 300 K under the AM1.5G spectrum, with an irradiance of 1000 W/m^2.

Table 31. Materials properties used in the simulations

Property	FTO	TiO_2	$MAPbI_3$	Spiro-OMeTAD
Thickness (nm)	500	50	600	300
Bandgap (eV)	3.6	3.2 [439]	1.6 [439]	2.7 [439]
Electron Affinity (eV)	4.25	4.25 [439]	3.9 [439]	2.5 [439]
Relative Dielectric Permittivity	9	100 [440]	6.5 [441, 442]	3 [443]
CB Effective Density of States (cm^{-3})	2.2e18	2.2e18	2.8e18 [444]	2.2e18
VB Effective Density of States (cm^{-3})	1.8e19	1.8e19	3.9e18 [444]	1.8e19
Electron/Hole Mobility (cm^2/Vs)	20/10	20/10	10/10 [396]	2e-4/2e-4 [443]
Shallow Donor Density (cm^{-3})	2e19	1e16	1e13	-
Shallow Acceptor Density (cm^{-3})	-	-	-	1e18

20.4 RESULTS and DISCUSSION

We first investigate the effect of CBO on the cell performance, with a positive CBO indicating a barrier for electron transport from the perovskite to the ETL. Note that for the model, CBO was modified by decreasing the electron affinity, and the bandgap was maintained at 3.2 eV. Figure 149(a-c) shows the open circuit voltage (V_{oc}), fill factor (FF), and power conversion efficiency (PCE) as a function of CBO. As the CBO increases the V_{oc} rapidly improves before plateauing at a CBO of ~-0.25 eV, with an additional upward bend in V_{oc} starting at a CBO of ~+0.2 eV (Figure 149(a)). FF shows a similar increase/plateau behavior (Figure 149(b)) for the lower CBO values but rapidly decreases as the CBO exceeds +0.05 eV. Short-circuit current (J_{sc}) remains approximately constant throughout this CBO range. As a result, PCE begins near 20%, surpasses 22.5% between a CBO of -0.27 eV and 0.09 eV and ultimately falls sharply in accordance with FF. PCE greater than 23% occurs between a CBO of -0.09 eV and 0.01 eV.

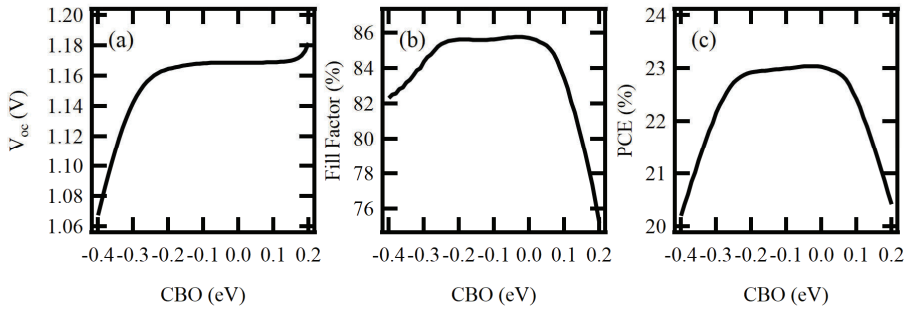


Figure 149. (a) V_{oc}, (b) FF, and (c) PCE as a function of changing conduction band offset

Throughout this study, we will refer to three characteristic CBOs in order to more closely observe the effects of conduction band alignment. A CBO of -0.35 eV represents the standard TiO_2 offset. A CBO of -0.25 eV represents an ETL with greatly increased PCE and V_{oc}, and a CBO of -0.05 eV results in the highest PCE range.

In order to explain the increase in performance due to conduction band alignment, it is useful to inspect the current and recombination characteristics of the cell across voltages. Figure 150(a, b) shows the current-voltage (JV) and recombination current-voltage (J_rV) curves as well as the conduction band portion of the band diagram near the ETL/perovskite interface at maximum power point voltage (V_{mpp}) of the modeled cell at the CBO values of -0.35, -0.25, and -0.05 eV. In order to ensure that the changes in device performance are front-limited by the ETL-perovskite interface, an ideal perovskite-HTL interface was assumed with a near-zero low SRV of 10^{-4} cm/s for Figure 150.

From the JV curves in Figure 150(a), we see the expected increase in V_{oc}. As the CBO improves, the Shockley-Read-Hall (SRH) recombination is unaffected. The onset of interface recombination current density (J_{Int}), on the other hand, shifts to higher bias as CBO increases. These results can be understood using the band diagram. Increasing CBO from -0.35 to -0.05 eV raises the Fermi level of the ETL progressively higher, causing less upward band bending (Figure 150(b)) in the

perovskite near the interface. This decrease in upward bending will allow more electrons to flow into the ETL, while also repelling more holes. This reduced number of holes leads to an increase in the turn on bias for J_{Int}.

From these results, it is clear that limiting recombination at the interface is critical to high performance devices. Improving the band bending at the interface clearly achieves this goal. Band bending can be modified by changing the CBO, as demonstrated above, or by changing the doping density of the ETL. In addition, interface recombination can be reduced by reducing the SRV at the interface. Consequently, we investigated how the device performance changes as a function of SRV and ETL doping concentration for CBOs equal to -0.35, -0.25, and -0.05 eV, and the contour plots of the PCE and V_{oc} are shown in Figure 151.

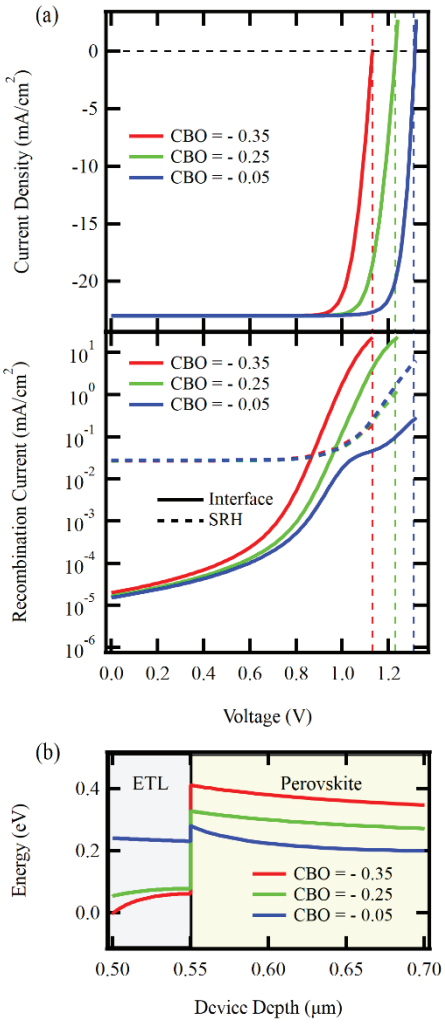


Figure 150. (a) JV and J_rV curves for three CBOs. (b) Energy bands at the ETL/perovskite interface, V_{mpp}, with reduced HTL interface influence

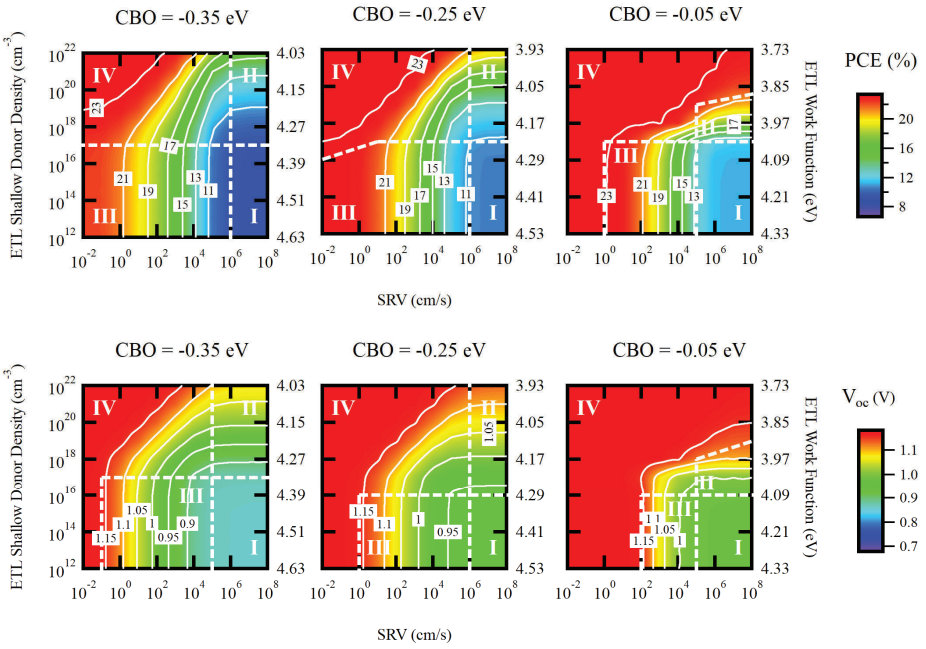


Figure 151. Contour plots of (a) PCE and (b) Voc for ETL conduction band offsets of -0.35, -0.25, and -0.05 eV

In these contour plots, there appear to be four regions. Region I appears to depend on both the SRV and doping density, while Regions II and III only depend on one of the parameters. The contour lines in Region II show that the devices with these parameters are limited by the ETL doping density, and the contour line in Region III shows that the devices are limited by the SRV. Region IV indicates high performance, independent of both parameters, consistent with SRH limited devices.

The mixed dependence (Region I) occurs when the upward band bending and SRV are large. The upward band bending attracts a lot of holes to the interface, which recombine with the high number of interface defect states, indicated by the high SRV. As the ETL doping density increases and the band bending is improved, the device performance becomes independent of the SRV (Region II). At these high ETL doping densities, the band banding repels holes from the surface, greatly reducing interface recombination. On the other hand, when the ETL doping density is low and the SRV decreases, the device performance becomes independent of doping density (Region III). Here the SRV limits device performance due to the low number of recombination sites. At some point, the interface recombination is so low that SRH recombination dominates device performance (Region IV). This can occur at extremely low SRV, high ETL doping, or a combination of the two. For the case of CBO equal to -0.35 eV, increasing ETL doping density while maintaining high SRV does not result in a SRH limited device, but this can be achieved when the CBO is -0.05 eV.

Figure 150b shows that CBO variation is effective in increasing band bending in the perovskite. This has the effect of shifting the PCE and V_{oc} contours in Figure 151 to lower ETL doping levels, as equivalent band bending already occurs due to improved CBO. Mixed dependence on SRV and doping density (Region I) still occurs, though improved energy band alignment increases PCE and V_{oc} in this region relative to less favorable CBOs for equivalent doping and SRV. The work

function of each ETL is shown on the right axes in Figure 151. Comparing cases of constant work function in regions where doping is not low enough and SRV is not high enough to cause more complex interface behavior, PCE and V_{oc} behavior will be identical across CBOs. For example, ETLs with CBOs of -0.35, -0.25, and -0.05 eV with doping densities of 1.05×10^{20}, 2.2×10^{18}, and 9.71×10^{14} cm^{-3}, respectively, have a constant work function of 4.15 eV and consequently show identical PCE and V_{oc} when SRV is kept at 1 cm/s.

These results show that the device performance does not simply depend on the CBO at the ETL/perovskite interface. In fact, it indicates that the work function of the ETL is the more relevant parameter. This finding can be used to broaden the range of potentially new ETL materials under investigation while also identifying the key parameters. Experimental focus has been on higher CBO materials [452-456], which, naturally, will allow for lower work functions. However, easily doped materials, even if the CBO is low, may offer a route to improving device performance. Alternatively, our results show that if SRV can be further reduced, the importance of ETL work function will be less significant. ETL materials such as TiO_2 and ZnO have CBOs comparable to the least favourable alignment included in our simulations, but exhibit SRVs on the order of only 10 cm/s when interfaced with $MAPbI_3$. [457] They therefore perform quite well in perovskite architectures, but will require yet lower SRVs to remove interface limitation from V_{oc} and orders of magnitude higher doping to lower the work function enough to completely remove interface limitation from PCE. A higher CBO material, such as [6,6]-phenyl-C_{61}-butyric acid methyl ester (PCBM), should outperform these high work function ETLs at equivalent doping and SRV. Unfortunately, alternative ETLs exhibit SRVs orders of magnitude higher than TiO_2 and ZnO [457], so work remains to be done towards engineering these materials and passivating their interfaces with perovskites in order to properly utilize their advantageous band positions in PSCs.

20.5 CONCLUSION

Diminishing recombination at the ETL/perovskite interface is crucial for the high performance of perovskite solar cells. The interface recombination between ETL/perovskite is dominated by the band bending in the absorber at the interface and the SRV. These properties shape the potential and carrier concentrations near the interface that determine recombination rates. Improved band bending between ETL and perovskite alone is enough to greatly reduce the rate at which electrons recombine with holes at their interface. Electron transport layers with appropriate work functions allow perovskite solar cells to reach higher efficiencies and open circuit voltages more easily than with a less favorably aligned ETL such as TiO_2.

21. UNDERSTANDING V_{OC} AND PERFORMANCE DEFICIT IN WIDE BANDGAP PEROVSKITE PHOTOVOLTAIC DEVICES

Adam B. Phillips and Michael J. Heben

21.1 SUMMARY

Wide bandgap metal halide perovskites materials are of interest for application as top subcells in multijunction devices. In contrast to smaller gap perovskite devices that perform fairly close to their internal Shockley-Queisser limit, wide gap versions show substantial deficits. To understand the origin of the limitations in more detail we simulated the performance of wide bandgap devices as a function of the energy band offsets at the contacts. Our results show that traditionally-used charge transport layers such as spiro-OMeTAD and TiO_2 limit the performance of wide bandgap absorbers through a subtle interplay between effects on V_{OC} and FF. We investigate the optimal characteristics for the charge transport layers as function of absorber bandgap and identify the needed band offsets at the p- and n-interfaces. Our results call for more research on charge transport layers to minimize the V_{OC} and performance deficit in wide bandgap perovskite devices.

21.2 INTRODUCTION

Single junction metal halide perovskite solar cells with absorber bandgaps in the range of 1.5 to 1.6 eV have demonstrated a remarkable track record of high power conversion efficiency (PCE) with certified champion cells having PCEs >25%. [392] High PCEs can be achieved with relatively high impurity levels, [458] and devices are tolerant to defects [459] due to shallow energy levels [460] and low capture cross sections. [461] Consequently, champion perovskite devices with bandgaps around 1.5 eV have demonstrated open circuit voltage deficits that are comparable to high purity Si and GaAs devices. [458] The V_{OC} deficit can be evaluated as $V_{OC,\,SQ} - V_{OC,\,measured}$, where $V_{OC,\,SQ}$ is the Shockley-Queisser (SQ) limit, also known as the thermodynamic limit, where the carrier recombination is radiatively limited and the device is in thermal equilibrium with its surroundings. [405, 462]

The success of single junction devices coupled with the ability to easily tune the perovskite bandgap through composition has led to great interest in the development of tandem devices with higher PCE. [36, 58-61, 63, 403, 407-409] However, the V_{OC} deficit in wider bandgap perovskite devices is significantly greater than in 1.5 to 1.6 eV devices. [463, 464] One reason often cited for this larger V_{OC} deficit is phase segregation of the perovskite materials. [465, 466] However, recent photoluminescence (PL) quantum yield analyses on 1.5 – 1.9 eV materials show that recombination at the interface between the charge transport layers (CTLs) and the absorber plays a role in PL quenching even in the presence of segregated halide domains. [467] Indeed, modeling investigations of 1.5 to 1.6 eV perovskite devices [420–422] show that the energy band alignments at CTL/absorber interfaces impact the device performances greatly. [422] While evidence has been mounting that the choice of CTLs is important for single-junction device performance, there has been very little guidance for directing the development of CTLs for high performance wide bandgap devices.

Here we use numerical modeling to investigate the impact of the CTLs on the device performance as a function of the absorber bandgap. We show that as the bandgap of the absorber increases, the choice of CTLs becomes more important and that the optimum CTLs for a 1.6 eV bandgap absorber will limit the device performance when the absorber bandgap is 1.7 eV and larger. By investigating the recombination currents as a function of bias, we determine the interplay between V_{OC} and FF and identify the conditions under which CTLs limit the device performance. We explore the parameter space to determine the appropriate CTL properties for optimum device performance as a function of absorber bandgap and compare our results with existing experimental literature.

21.3 METHODS, ASSUMPTIONS, and PROCEDURES

Numerical modeling was completed using SCAPS 1D, [271] which was recently applied to perovskite solar cells. [419, 422, 468-470] We chose to simulate the popular n-i-p structure FTO/TiO_2/MAPb($I_{1-x}Br_x$)$_3$/spiro-OMeTAD/back contact, where FTO is the F-doped SnO_2 front contact, TiO_2 is the ETL, and spiro-OMeTAD (subsequently referred to as "Spiro") is the HTL, though similar conclusions would be found for the p-i-n structure. Conduction and valence band positions as a function of bandgap were determined by a linear extrapolation method as the perovskite composition was varied.

21.4 RESULTS and DISCUSSION

We first simulated the device behavior for a 1.7 eV absorber. Figure 152(a, b) show the current density as a function of voltage (J-V) under AM1.5G irradiance for varying values of the CBO and VBO at the ETL and HTL interfaces, respectively. The CTL bandgaps were fixed, and each interface was investigated independently while the interface recombination velocity at the opposing interface was set to a low value (1×10^{-4} cm/s). Figure 152(c, d) show the corresponding recombination current densities versus voltage (J_R-V) data, which are calculated using

$$J_R = R_{front} + R_{back} + R_{SRH} = \frac{S_{front}\, p_{front} n_{front}}{(p_{front}+n_{front})} + \frac{S_{back}\, p_{back} n_{back}}{(p_{back}+n_{back})} + \frac{pn}{\tau(p+n)} \quad (1)$$

where $\tau, p, n,$ and S are the carrier lifetimes, carrier concentrations under non-equilibrium conditions, and interface recombination velocities, respectively, assuming the lifetimes of both carriers are similar. Note that the n and p values are different at each interface and depend on the band bending at that interface. Figure 152(e, f) show the near-interface conduction and valence band portions, respectively, of the band diagrams at the maximum power point (MPP).

We first consider the role of the ETL in the device performance. Starting with TiO_2, which is commonly used in high PCE devices, [471, 472] the modeled J-V results show a device with high fill factor (FF) and V_{OC} of 1.15 V, which is substantially below the thermodynamically-limited value for the optical stack of 1.428 V. As the CBO increases from -0.421 eV for TiO_2 to -0.15 eV and greater, the V_{OC} increases by ~200 mV. The FF remains high until the CBO increases to +0.15 eV, at which point a kink appears in the J-V curve. Note that for CBOs greater than -0.15 eV the V_{OC} deficit has been virtually eliminated for the 10 μs lifetimes as the V_{OC} is increased to 1.41 V.

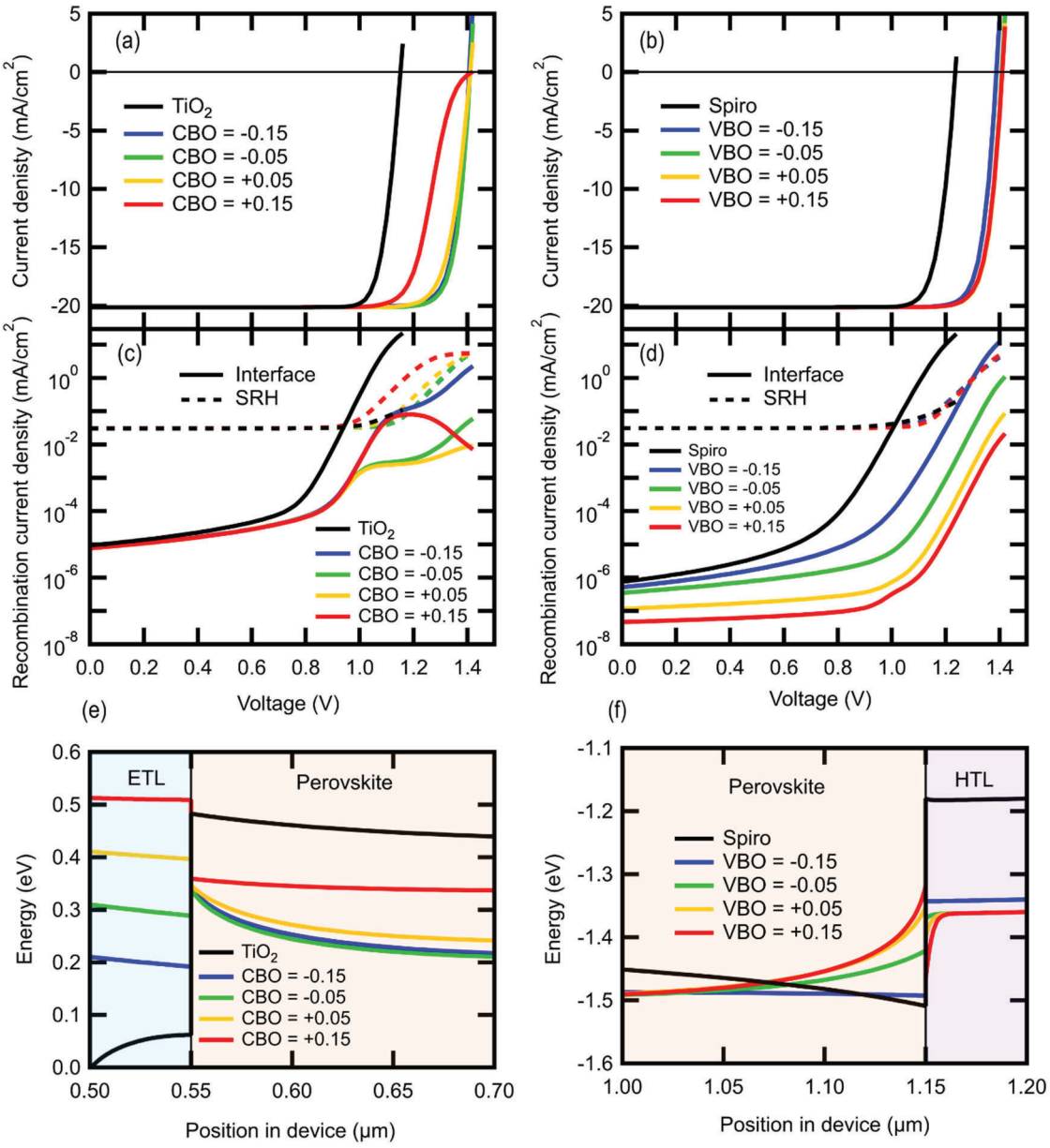


Figure 152. (a), (b) simulated J-V curves, varied CBO and VBO; (c), (d) J_r for ETL and HTL interfaces; (e), (f) energy bands for the ETL/conduction band and the HTL/valence band interfaces, respectively, at MPP

The corresponding J_R-V curves (Figure 152(c)) show that the interface recombination currents are low at low biases. However, in the case where the ETL is TiO_2, there interface recombination turn-on at ~0.8 V and is an order of magnitude higher than the SRH recombination current at a bias of 1.0 V and limits V_{OC}. For the alternative ETLs, however, the interfacial recombination currents do not turn-on until ~0.95 V, and the devices are limited by SRH recombination when the CBO is more positive than -0.05 eV. However, for the case where the CBO is +0.15 eV, the SRH turns on

earlier due to flattening of the bands and there is large barrier that hinders electron extraction (Figure 152(e)). This gives rise to a kink in the J-V curve that lowers the FF.

Turning to the band diagram (Figure 152(e)), we see that the relatively large negative CBO for the TiO_2/perovskite interface coupled with the low carrier concentration in the absorber gives rise to an upward shift of the perovskite conduction band and large discontinuity in the conduction bands across the interface. The perovskite bands are fairly flat at MPP, but the potential drop across the absorber/ETL interface places the ETL Fermi level closer to the hole Fermi level in the perovskite and the overlap between the two gives rise to a high interface recombination current. As the CBO is progressively increased from -0.15 eV to +0.05 eV, the potential drop becomes smaller and the overlap decreases. Despite the fact that the perovskite bands slope away from the interface, which is expected to impede carriers from flowing in the desired direction, the net effect is a reduction of the interfacial recombination current, and a larger Voc. However, when the CBO is +0.15 eV, we see a significant barrier to electron flow into the ETL which gives rise to the bias dependence of the transport properties (i.e. the kink in Figure 152(a)) and the low FF.

To investigate the role of the HTL interface we fixed the recombination velocity at the ETL/absorber interface at 1×10^{-4} cm/s and varied the VBO. Spiro is a common HTL in high performance devices and is expected to have a VBO of -0.32 eV when in contact with a 1.7 eV perovskite absorber. Figure 152(b) shows that a Spiro HTL results in a device with a high FF and a V_{OC} of 1.23 V. While higher than for the TiO_2 ETL, there is still a substantial deficit. Increasing the VBO to -0.15 eV increases V_{OC} by ~200 mV, and the V_{OC} remains high to VBO values as high as +0.15 eV. Here, the FF remains high for all conditions investigated. If, however, the VBO is increased to +0.2 eV or +0.25 eV the FF is reduced from 87% to 86% and 81%, respectively.

The J_R-V results (Figure 152(d)) show that the interface recombination current with Spiro as an HTL turns on at ~0.8 V and exceeds the SRH recombination current at ~1 V. Thus, devices with Spiro and a 1.7 eV absorber are limited by interfacial recombination, as was the case for the TiO_2 ETL. Unlike the front interface investigation, however, the bias at which the interface recombination current turns-on continues to increase with the VBO. The interfacial recombination current and SRH currents become comparable near V_{OC} when the VBO is -0.05 eV, and the devices are truly SRH-limited for greater VBO values. Under these conditions the perovskite bulk carrier lifetimes would need to be increased beyond 10 μs to further increase the performance.

The reduced sensitivity to the VBO at the HTL interface can be understood by investigating the band diagrams at MPP (Figure 152(f)). When the HTL is Spiro the absorber bands bend downward toward the perovskite/HTL interface and electrons are attracted to the surface, which leads to a higher interfacial recombination current. When the VBO is increased to -0.15 eV, the bands are much flatter with only a small degree of downward band bending at MPP. Consequently, the interfacial recombination current turns-on at a higher bias voltage. As the VBO increases, the bands bend upward at the interface, thereby repelling electrons. In contrast to the ETL case, the FF does not suffer even when the VBO is +0.15 eV. This is because the high doping density in the HTL (1×10^{18} cm^{-3}) does not support a wide depletion layer and the sharp, thin spike at VBO = +0.15 eV can be easily overcome by holes. In this case the increase in V_{OC} that is available with more positive VBOs appears simply in Figure 152(f) as a reduction in the loss of potential energy experienced by holes moving across the absorber/HTL interface.

Figure 153 shows the combined effects for CBO and VBO variations with absorber bandgaps of 1.6, 1.7, and 1.8 eV. Figure 153(a) has a plateau of high V_{OC} in the upper right corner for each of the bandgaps. In this range the VBOs and CBOs are sufficiently positive to repel carriers from their respective CTLs and suppress interfacial recombination. Consequently, the V_{OC} values on the plateau are SRH limited at 81-83% of their bandgap voltages (Note that the plateau V_{OC} values are not significantly different when the carrier lifetimes are reduced to 1 μs or increased to 100 μs). The white circles on the plots mark the performance with TiO_2 and Spiro as the ETL and HTL, respectively. Increasing the VBO from this point moves the V_{OC} along nearly isovoltage contours for all absorber bandgaps. On the other hand, increasing the CBO causes the V_{OC} to initially move across contours, increasing V_{OC} to higher values. However, as the CBO increases interfacial recombination at the ETL ceases to limit the device performance, and the device instead becomes limited by interfacial recombination at the HTL. Increases in the VBO are then required to further increase the V_{OC}. The high V_{OC} plateau is reached when both the CBO and VBO are above approximately -0.1 eV. Interestingly, a thin sliver of high V_{OC} spans both positive and negative VBOs for the 1.7 and 1.8 eV bandgaps at the most positive CBOs. This is due to electron confinement in the conduction band, but the effect does not lead to the highest efficiencies due to an accompanying reduction in FF (*vide infra*). In general, the regions of maximum V_{OC} in Figure 153 represent cases where the electron and hole Fermi levels have a maximum degree of splitting. It is interesting to consider how the complete band diagram is altered when the contact layers are optimized to support a maximum V_{OC}*FF product.

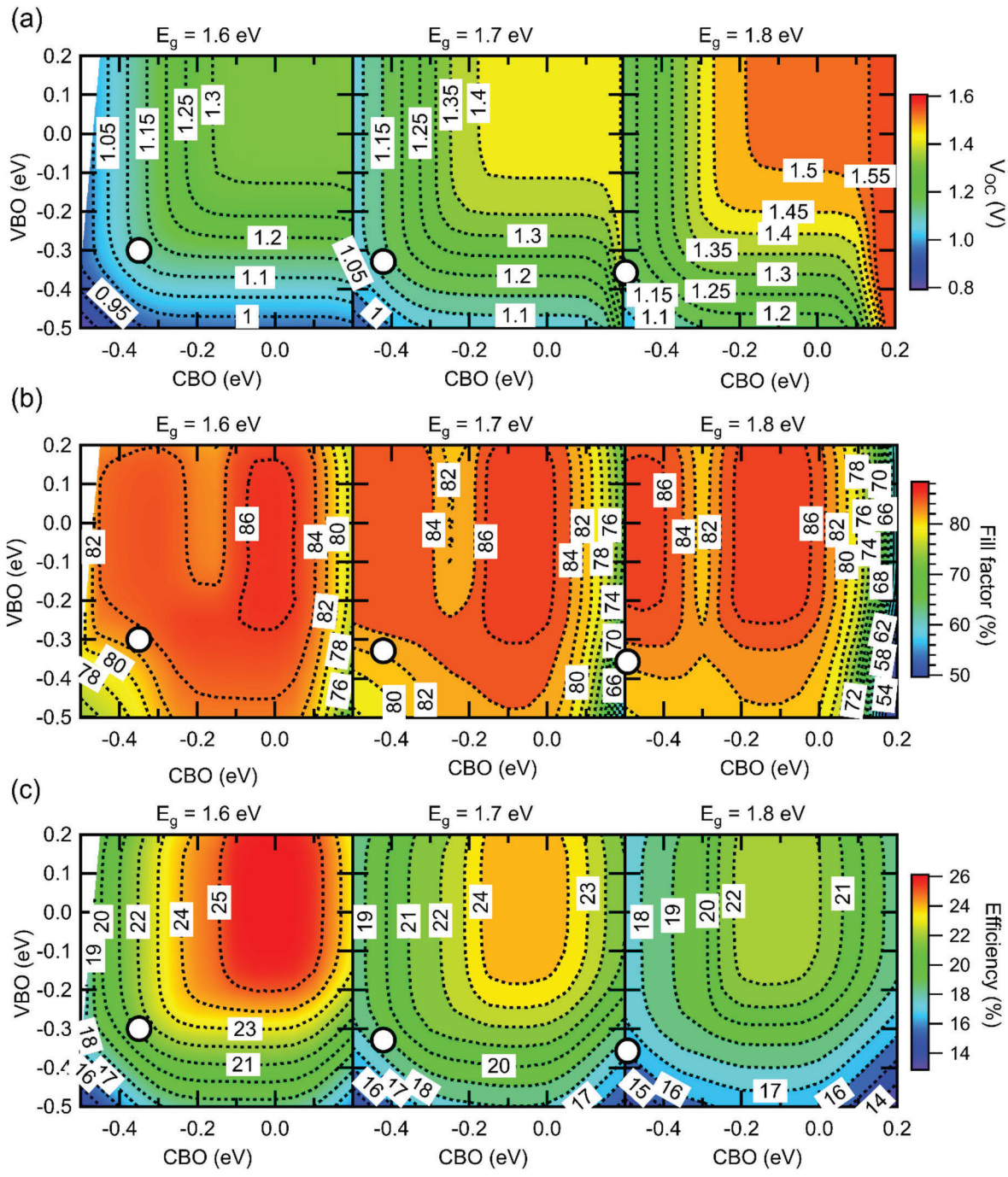


Figure 153. (a) V_{OC}, (b) FF and (c) PCE of perovskite devices with 1.6 eV, 1.7 eV and 1.8 eV absorbers vs. VBO and CBO

The FF data (Figure 153(b)) show an elongated plateau with FF >86% for each bandgap. The plateau starts at CBO values of approximately -0.2 to -0.1 eV and extends to CBO values of ~ 0.0 eV. The FF plateau is longer in the VBO dimension, extending from ~ -0.3 eV to +0.2 eV. In this region of high FF, the J-V curves turns on abruptly due to the dominant control of the SRH

recombination mechanism. For the 1.6 and 1.7 eV bandgaps there is a lower plateau with FF values between 84 and 86% that extends over a larger range of the plotted area. When the absorber bandgaps are 1.7 and 1.8 eV a distinct valley develops that runs from VBOs of approximately -0.25 eV to the more positive values. The valley indicates a transition from interface recombination control at the ETL/absorber interface to SRH control in the absorber as the CBO is increased. Further increase in the CBO to greater than +0.1 eV causes the FF to drop precipitously due to electron-blocking at the ETL (Figure 153(c)). White circle symbols indicate the band offset of TiO_2 and Spiro as CTLs. There is also a region of low FF in the lower left corner, particularly for the 1.6 and 1.7 eV cases. This is where both front and back interfaces play a role in recombination, so the FF is a function of the two recombination mechanisms.

Figure 153(c) shows the PCE data that reflects the V_{OC}*FF product and the fact J_{SC} is lower for the wider bandgaps. A distinct single plateau is found for each of the bandgaps. The negative VBO edge of the plateau is at approximately the same location (~ -0.2 eV) for each bandgap, while the edge on the positive VBO side is not resolved. Note that, experimentally, the approach to higher efficiencies will be from the negative VBO (and CBO) sides of the plateau, and VBO values > +0.2 eV are not likely to be of concern. For the CBO coordinate, we see the negative edge of the plateau moves to more negative values as the bandgap is increased. This suggests that a good ETL for large bandgap absorbers may be more straightforward to develop than a good HTL. Using TiO_2 and Spiro as ETL and HTL, respectively, yields PCEs of 21%, 19% and 16% for the 1.6, 1.7, and 1.8 eV bandgaps, respectively. In comparison, the maxima in the PCE plateau occur at ~25%, ~24% and ~22%, respectively. Thus, we see a PCE deficit with standard material contacts that is increasing with bandgap.

Figure 154(a) shows the simulated PCE as a function of bandgap when the contacts are TiO_2 and Spiro in comparison to the PCEs expected if the contacts had optimized CBO and VBO values. The difference varies linearly from 15% at 1.6 eV to 27% at 1.8 eV. Figure 154(b) shows the companion V_{OC} data. Also shown for comparison are the highest experimental values that have been reported for devices using TiO_2 and Spiro contacts. [410, 447-451] The experimental values generally fall along the trend line for the simulations, but there is some deviation. In these cases, the properties of the CTLs and/or the interface between the CTL and absorber were varied. [448, 449, 451] For example Saliba et al., investigated Li doping of the TiO_2 ETL prior to completing the 1.63 eV absorber device. [448] This produced a PCE of 21.8% which is above the trendline due to a V_{OC} improvement of 10% relative to the expected value (1.24 V versus 1.12 V). Zhou et al. investigated a benzylamine treatment for passivation of grain boundaries in a 1.72 eV absorber and formed the perovskite/HTL interface using a 2D structure approach. [449] This led to a PCE of 18.13% and V_{OC} of 1.24 V (~7% improvement in V_{OC}). Similarly, Gharibzadeh et al. showed that generation of 2D structures at the perovskite/HTL interface with butylammonium bromide treatment leads to adjustment of the perovskite energy bands at the interface and thus improved the V_{OC} of wide bandgap devices. [464]

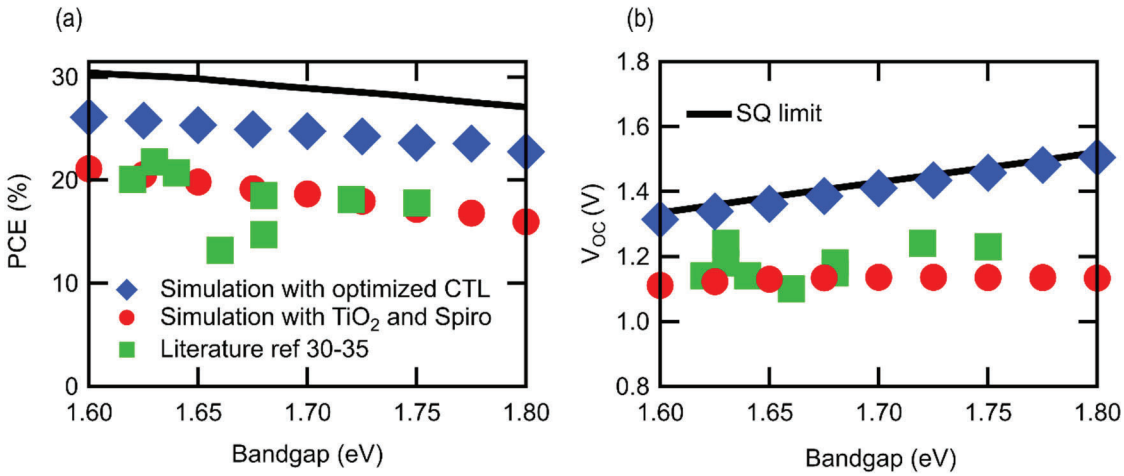


Figure 154. (a) PCE and (b) V_{OC} relative to the internal SQ limit as a function of bandgap for absorber with 10 μs carrier lifetimes

Figure 154 also shows the PCE and V_{OC} for devices with the optimized ETLs and HTLs. The PCE values are still below the SQ limit for AM1.5G irradiance due to the absorber being thinner than needed for complete light absorption, but the V_{OC} is still very close to the limit due to the logarithmic dependence on photogeneration. Clearly, to capture the missing entitlement in V_{OC}, FF (and thus in PCE) it will be necessary to develop new CTL materials.

21.5 CONCLUSION

In conclusion, we showed that the performance of wide bandgap perovskites devices is strongly affected by the VBO and CBO values of the CTLs. The analysis show that typically used HTL (Spiro) and ETL (TiO_2) materials will cause interfacial recombination currents to be more dominant as the bandgap increases. This limits the V_{OC} and the performance. Implementation of HTLs and ETLs with appropriate energy band alignment will help to eliminate the V_{OC} and performance deficit.

22. ENERGY, TEMPERATURE, AND DEPOSITION ANGLE DEPENDENCE OF CD AND TE_2 DEPOSITED ON CDTE

22.1 SUMMARY

Molecular dynamics simulations of the deposition of Cd atoms and Te_2 dimers on the Cd-terminated and Te-terminated (100) and (111) surfaces of CdTe were carried out to determine the dependence of the attachment probability and deposition mode on substrate temperature, deposition energy, and deposition angle. For the case of opposite termination (e.g. Cd on Te-terminated (100) or (111) or Te_2 on Cd-terminated (100) or (111)) the sticking probabilities are close to 1 independent of substrate temperature, deposition energy, and deposition angle, while the deposition mode corresponds to growth of the next layer. However, for the case of same termination (e.g. Cd on Cd-terminated or Te_2 on Te-terminated (100) or (111)) the attachment probabilities are significantly lower and depend on deposition angle, substrate temperature and orientation, and deposition energy. In addition, the dominant deposition mode is different for (111) and (100) surfaces, although in general, the overall attachment probability for Te_2 is higher than that for Cd. Our results have relevance for vapor deposition at both low and high substrate temperatures as well as for closed-space sublimation. This work was carried out by Indiras Khatri and Jacques G. Amar.

22.2 INTRODUCTION

Recently, Yu and Kenny [473] have used molecular dynamics (MD) simulations based on a realistic bond-order potential [474] to study the deposition of Cd atoms, Te atoms, and CdTe clusters deposited normally on CdTe (100) and (111) surfaces at T = 300 K with energies ranging from 1 – 40 eV. Depending on deposition energy as well as atom or cluster type, surface orientation, and surface termination (e.g. Cd or Te), the probabilities of a variety of different outcomes including reflection, dissociation, penetration, and atom replacement were determined. While these results provide an understanding of the effects of deposition energy on defect formation and possible thin-film stoichiometry for the case of sputter deposition at low substrate temperature, the important cases of vapor deposition (VD) and closed-space sublimation (CSS) were not studied. In both cases, the depositing species correspond to Cd atoms and Te_2 dimers rather than Cd, Te, and CdTe clusters, while the depositing kinetic energy is significantly lower than 1 eV. In addition, the substrate temperature in both VD and CSS is typically significantly higher than 300 K, while in both cases, depending on vapor pressure and target-substrate distance, deposition may occur at relatively large angles with respect to the substrate normal. Accordingly, we have carried out extensive molecular dynamics simulations of the deposition of Cd atoms and Te_2 clusters on the (100) and (111) surfaces of CdTe in order to understand the dependence of the attachment probabilities and deposition modes on substrate temperature, deposition energy, and deposition angle.

22.3 METHODS, ASSUMPTIONS, and PROCEDURES

Our simulations were carried out using the Large- scale Atomic/Molecular Massively Parallel Simulator (LAMMPS) code, using an analytical bond-order potential (BOP) [475] for CdTe which was parametrized [474] by fitting to the properties of a variety of clusters, lattices, surfaces, and

defects calculated using density-functional theory (DFT) as well as by testing crystalline growth simulations. Deposition on the Cd-terminated (100) and (111) surfaces as well as Te-terminated (100) and (111) surfaces was studied, while the zinc-blende structure of CdTe was assumed with lattice constant a = 6.83˚A. [474] Simulations were carried out for both Cd and Te_2 cluster deposition, while the system was annealed for 20 ps before carrying out depositions. In order to compare with previous work, [473] we also carried out simulations of Te atom deposition for the normal incidence case with K_i = 1.0 eV and T_{sub} = 300 K.

In order to determine the effects of deposition energy and substrate temperature on the sticking probability and mode, our simulations were carried out using two different cluster kinetic energies (K_i = 0.14 eV, and K_i = 1.0 eV) as well as for two different substrate temperatures (T_{sub} = 300 K and 800 K). Similarly, to study the dependence on deposition angle, simulations were carried out with six different deposition angles θ with respect to the surface normal, ranging from θ = 0° (normal incidence) to 75° (grazing incidence). In each case, the depositing cluster was initially placed at a distance equal to 1.5 A plus the potential cut-off distance above the highest atom on the surface layer, while the x and y positions were chosen randomly. MD simulations of the whole system were then carried out for 10 ps, after which the system was minimized and then analyzed to determine the cluster attachment probability and deposition mode (see Figure 155).

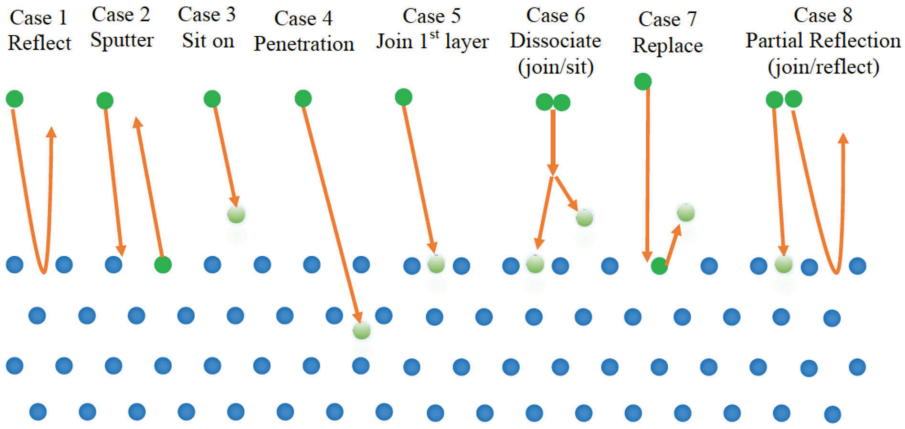


Figure 155. Illustration of 8 possible cases of the final states after impact. Single atoms correspond to Cd while dimers correspond to Te_2

In our simulations the substrate contained a total of 14 layers with 4 fixed layers, 4 layers whose temperature was regulated using a Berendsen thermostat, [476] and 6 free (NVE) layers at the surface. Both the heat bath coupling constant and MD time-step were set to 1 fs. Periodic boundary conditions were assumed in the lateral (x and y) directions while growth was in the z- direction. For the (100) surface, the lateral dimensions were 10 *a*, corresponding to 200 atoms in each layer while for the (111) surface the dimensions were 6 a_1 (where $a_1 = (8/3)^{1/2}\, a$) in the x-direction and 6 a_2 (where $a_2 = \sqrt{2}a$) in the y-direction, corresponding to 192 atoms in each layer.

To obtain good statistics, averages were taken over 10,000 depositions for each cluster type, substrate termination, temperature, and initial kinetic energy, corresponding to 32 different simulation runs for each of 6 different deposition angles. We note that the value K_i = 0.14 eV was motivated by the fact that at 800 K (which is approximately equal to the source temperature used

in both vapor deposition and CSS) corresponds to the average translational kinetic energy $2k_BT$ of depositing clusters. For the case of the Te_2 cluster, we have also included initial internal rotational and vibrational kinetic energies equal to 1/2 k_BT per degree of freedom, with T = 800 K for all cases. In addition to randomly choosing the starting x and y positions, we have also randomly chosen the initial dimer axis orientation as well as the directions of the two rotational axes with respect to the Te_2 bond direction.

22.4 RESULTS and DISCUSSION

Figure 156(a) shows our results for the overall sticking probabilities for both Cd atoms and Te_2 dimers, deposited on the (100) Cd-terminated surface as a function of deposition angle θ for both kinetic energies (K_i = 0.14 eV and 1 eV) and substrate temperatures (T_{sub} = 300 K and 800 K). As can be seen, for the case of Te_2 deposition, the sticking probability is essentially 1 for all cases. In this case, the Te atoms sit on the top layer (case 3) which is consistent with the growth of the next Te layer. In contrast, the sticking probability for Cd atoms is significantly less than 1 even for normal deposition, and decreases with both increasing deposition angle and increasing substrate temperature. Interestingly, for low deposition angle ($\theta < 45^o$) the sticking probability for Cd atoms increases with increasing kinetic energy while the reverse is true for $\theta > 45°$. In all cases the Cd atoms join the top layer (case 5). While the non-sticking case corresponds entirely to reflection at 300 K (case 1) which increases with deposition angle, at 800 K there is also a small amount of sputtering (1-7%), which decreases with increasing deposition angle.

The corresponding results for the (100) Te-terminated surface are shown in Figure 156(b). As in Figure 156(a), except for the case of both low deposition energy and substrate temperature (K_i = 0.14 eV, T_{sub} = 300 K), the deposition of Cd on the oppositely terminated (100) surface (open circles with dashed line) leads to a relatively high sticking probability (P_{stick} = 0.85−0.95) which increases slightly with deposition angle. While the dominant attachment mode corresponds to sitting on the top layer (case 3) there are also contributions from case 4 (penetration) and case 5 (join 1st layer). However, for both low kinetic energy and low substrate temperature (open circles) the attachment probability is significantly lower, especially at small angles (due primarily to the reduced probability of joining the 1st layer) although it still increases with increasing deposition angle.

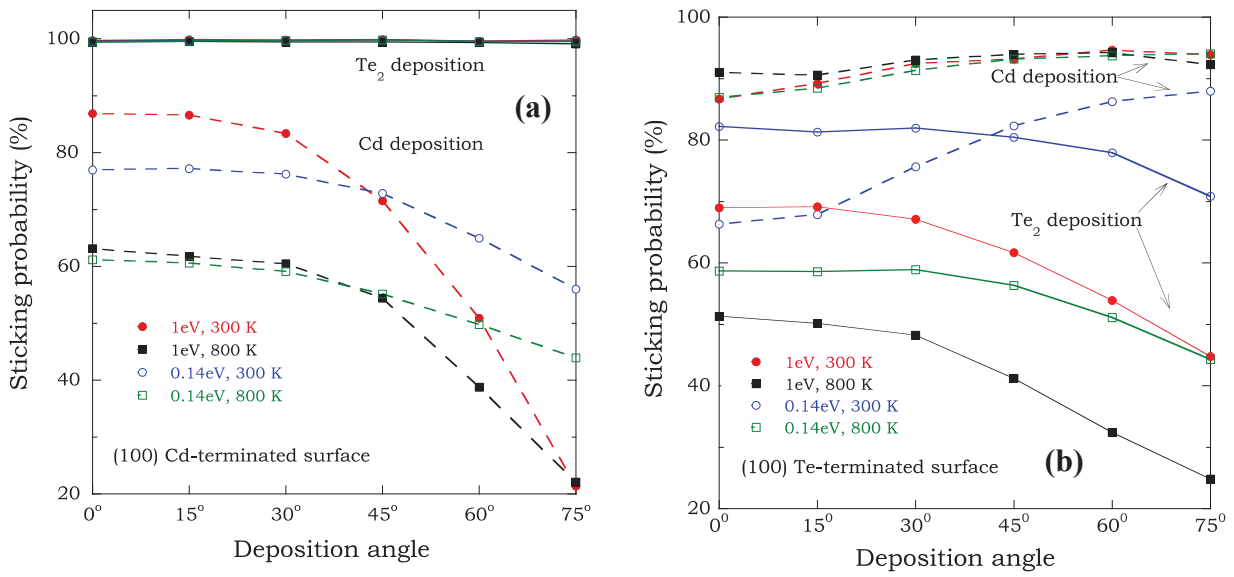


Figure 156. (a) Sticking probability vs. deposition angle, temperature, and kinetic energy for Cd atoms (dashed lines) and Te_2 clusters (solid lines) on (100) Cd-terminated surface. (b) Same, but for (100) Te-terminated surface

Also shown in Figure 156(b) are our results for the deposition of Te_2 on the (100) Te-terminated surface. As for Cd atom deposition on the Cd-terminated surface, in this case the sticking probability decreases with increasing deposition angle and temperature. In addition, it decreases for all angles with increasing kinetic energy while the attaching atoms primarily join the first layer (case 5) although the attachment probability also includes some case 3 (sit-on) and a very small amount of dissociation (case 6). As for Cd deposited on the "same" (Cd-terminated) (100) surface, the dominant non-sticking mode corresponds to reflection while the probability of reflection increases with increasing temperature and/or kinetic energy. The relatively large reflection probability for Te_2 clusters deposited normally with K_i = 1 eV and T_{sub} = 300 K is in contrast to the negligible reflection probability found previously [473] for single Te atoms deposited under the same conditions.

Figure 157(a) shows our results for the (111) Cd-terminated surface. As for the (100) Cd-terminated surface, the sticking probability for Te_2 is close to 1 for all angles, kinetic energies and substrate temperatures, while the Te atoms sit on top (case 3). In contrast, the sticking probability for deposited Cd atoms at 300 K is significantly lower and decreases with increasing kinetic energy and deposition angle. In this case, the Cd atoms also sit on top (case 3). Surprisingly, the sticking probability for Cd atoms on the (111) Cd-terminated surface at 800 K is negligible at both low and high kinetic energies.

The corresponding results for the (111) Te-terminated surface are shown in Figure 157(b). Just as for Te_2 deposited on the (100) Cd-terminated surface, the attachment probability for Cd atoms is close to 1 for all angles, kinetic energies and substrate temperatures while the Cd atoms sit on top (case 3). For Te_2 deposition, the attachment mode also corresponds to case 3. In this case, at low temperature and kinetic energy, the sticking probability (open circles with solid line) is also close

to 1 for all angles and temperatures. However, for higher kinetic energy and/or temperature, the Te_2 sticking probability is significantly less. In addition, while for both substrate temperatures, the Te_2 sticking probability decreases with deposition angle for high kinetic energy (K_i = 1.0 eV) for low deposition energy (K_i = 0.14 eV) it increases with increasing deposition angle. Interestingly, the four cases of Cd deposited on the (100) Te-terminated surface as well as the two cases of Te_2 deposited at low kinetic energy on the (111) Te-terminated surface, are the only ones in which the attachment probability increases significantly with increasing deposition angle.

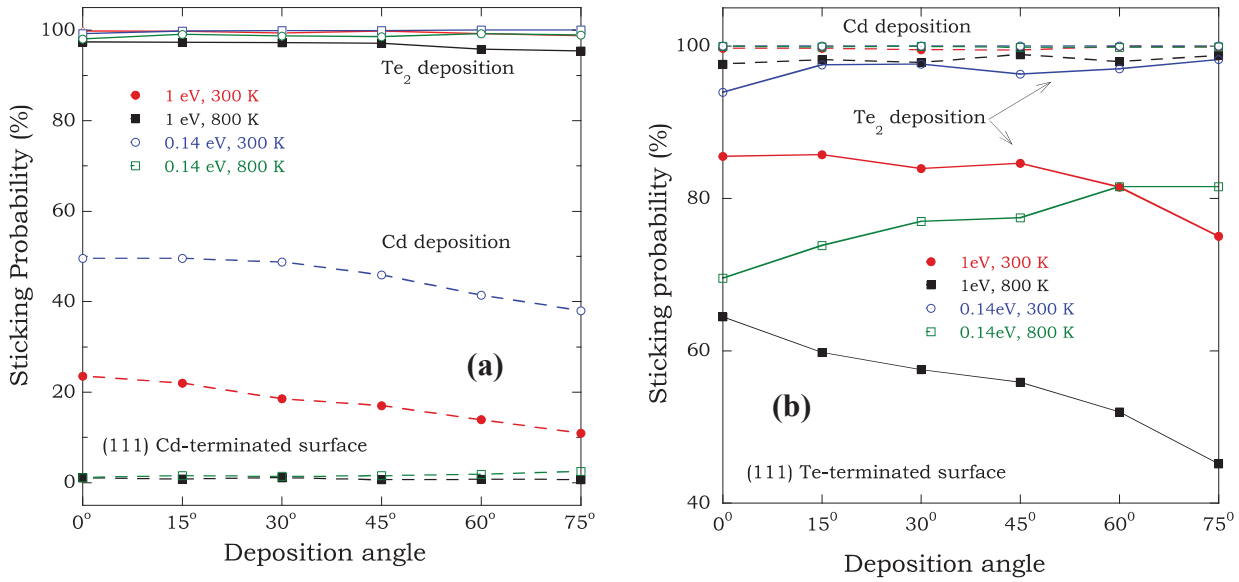


Figure 157. (a) Sticking probability vs. deposition angle, temperature, and kinetic energy for Cd atoms (dashed) and Te_2 dimers (solid) deposited on (111) Cd-terminated surface; (b) Same, but for (111) Te-terminated surface

Using these results, we have also calculated the overall excess Te attachment probability, corresponding to the difference between the Te attachment probability and Cd attachment probability, averaged over both Cd- and Te-terminated surfaces. Results are shown (see Figure 158) for both normal incidence as well as averaged over all deposition angles corresponding to a uniform flux. For the (111) surface there is a large excess Te attachment probability for all kinetic energies and substrate temperatures, for both normal deposition and the average over all angles. In contrast, for (100) surfaces, the deviations from equal Cd and Te_2 sticking probability are generally larger for the case of normal incidence than the angle-average. In addition, for this case the excess Te sticking probability is much smaller (and in some cases is even negative) for high temperature (T_{sub} = 800 K) and/or high kinetic energy (1 eV) due in part to the increased probability of reflection for Te_2 clusters from the Te-terminated (100) surface. This behavior is in contrast to the negligible reflection probability found previously [473] for single Te atoms deposited with 1 eV kinetic energy on the Te-terminated (100) surface.

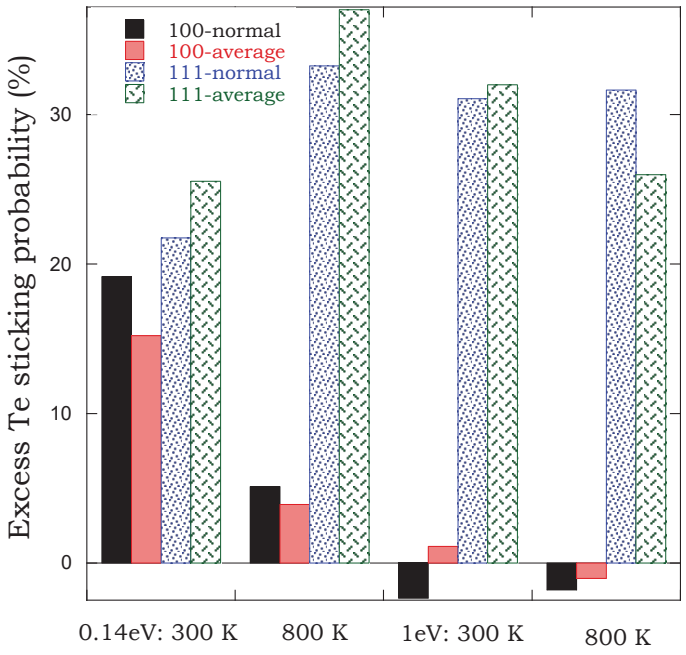


Figure 158. Excess Te sticking probability vs. temperature and kinetic energy

22.5 CONCLUSIONS

We have carried out extensive molecular dynamics simulations of the deposition of Cd atoms and Te_2 clusters on the (100) and (111) surfaces of CdTe in order to understand the dependence of the attachment probabilities and deposition modes on substrate temperature, deposition energy, and deposition angle. Our results are relevant to both vapor deposition and close-spaced sublimation. In general, we find that the deposition of Cd atoms and/or Te_2 clusters on the oppositely terminated surface leads to an attachment probability which is close to 1 and relatively independent of substrate temperature, kinetic energy, and deposition angle for both the (100) and (111) orientations. The one exception is Cd deposition on the (100) Te-terminated surface with both low deposition energy and substrate temperature. In this case the sticking probability is only about 66% for normal deposition but increases to a value of approximately 88% at large deposition angle $\theta = 75^{o}$. While there is some penetration (case 4) and joining of the first layer (case 5), the dominant sticking mode in all cases corresponds to "sit-on" (case 3) corresponding to the growth of the next layer in the crystal.

In contrast, the deposition of Cd atoms and/or Te_2 clusters on the same terminated surface leads generally (for both (100) and (111) orientations) to a significantly lower sticking probability which decreases with both increasing substrate temperature and deposition angle. In particular, the sticking probability for Cd deposition on the (111) Cd-terminated surface with substrate temperature 800 K is negligible for both low and high kinetic energies and for all deposition angles. The one exception to these general results is the case of Te_2 deposition with low kinetic energy and substrate temperature on the (111) Te-terminated surface. In this case, while the sticking probability is still less than for Te_2 deposition on the (111) Cd-terminated surface, it is relatively close to 1 and increases with increasing deposition angle.

It is also interesting to consider the dependence of the deposition mode on atom/cluster type and surface termination. For deposition on the (111) surface, the dominant deposition mode corresponds to case 3 (sit-on) regardless of cluster type, surface termination, deposition angle, substrate temperature and kinetic energy. This is also the case for opposite termination deposition on the (100) surface. In contrast, for same termination deposition on the (100) surface the dominant deposition mode corresponds to case 5 (join first layer). This difference may be explained by the more "open" nature of the (100) surface compared to the (111) surface which allows deposited atoms to join the first layer and form bonds with the "opposite" layer below. These results also imply that (100) surfaces are more likely to create interstitials in the surface layer than (111) surfaces.

The results of our simulations have now been published in Ref. [477]. While our results are restricted to the initial stages of deposition, they also suggest that for low kinetic energy as well as low substrate temperature T_{sub} = 300 K (for which there is negligible sublimation) there will be a significant excess Te concentration in CdTe thin films grown on the (111) surface. This is in qualitative agreement with the experimental results of Ref. [478] for the vapor deposition of CdTe on glass substrates at 300 K. Since in most experiments the growth is polycrystalline but with (111) facets dominating, our results also suggest that higher deposition energy will also tend to lead to Te-rich films. However, at a substrate temperature of 800 K sublimation will play an important role. Accordingly, in the future, it would be of interest to simulate the sublimation process in order to understand its effects during high temperature growth.

23. ENERGY BARRIERS AND PREFACTORS FOR CD AND TE_2 DESORPTION FROM THE CDTE(100) SURFACE

23.1 SUMMARY

Since sublimation plays an important role in the deposition of CdTe thin-film solar cells , we have carried out accelerated molecular dynamics (MD) simulations of the sublimation of Cd and Te_2 from the CdTe(100) surface. In particular, desorption energies, binding energies, and prefactors were determined using the temperature-accelerated (TA) method for the case of Te_2 dimer desorption from the (2x1) Te-terminated (100) surface as well as Cd desorption from the Cd-terminated (100) surface. We find that while the Te_2 desorption barrier is relatively large (E_d = 2.65 eV) the corresponding prefactor ($\nu_d = 4.0 \times 10^{20}$/s) is also extremely large. In contrast, the barrier for desorption of a Cd atom from the fully Cd-terminated (100) surface (2.14 eV) is significantly smaller, although the corresponding prefactor ($\nu_d = 1.7 \times 10^{16}$/s) is also significantly larger than the typical expected value of approximately 10^{12}/s. This work was carried out by Indiras Khatri and Jacques G. Amar, and a manuscript describing these desorption modeling results is currently in preparation.

23.2 INTRODUCTION

The process of sublimation plays an important role in the deposition of CdTe thin films [479-481], both in terms of the deposition process via closed-space sublimation and also as part of the smoothing process during growth. However, while there have been a few first-principles studies [482-484] of the binding energies of Cd atoms and/or the Te_2 dimer on the CdTe(100) surface, more extensive studies which would include both the binding energies for different initial configurations as well as the actual desorption rate (e.g. desorption prefactors) have not been carried out. Accordingly, to gain insight into the mechanisms for CdTe sublimation as well as to better understand the kinetics as well as binding energies, we have carried out accelerated molecular dynamics simulations of Cd and Te_2 desorption for a variety of different configurations of the Cd-terminated and Te-terminated CdTe(100) surface.

23.3 METHODS, ASSUMPTIONS, and PROCEDURES

Our simulations were carried out using the Large-scale Atomic/Molecular Massively Parallel Simulator (LAMMPS) code, using an analytical bond-order potential (BOP) [475] for CdTe which was parametrized [474] by fitting to the properties of a variety of clusters, lattices, surfaces, and defects calculated using density-functional theory (DFT) as well as by testing crystalline growth simulations. The activation barriers and prefactors for sublimation as well as the corresponding binding energies were determined for two different cases: (i) Te_2 desorption from the (2x1) fully Te-terminated (100) surface and (ii) Cd desorption from the fully Cd-terminated (100) surface. In each case, the corresponding energy barriers and prefactors were determined by fitting the corresponding rates for a range of different temperatures to an Arrhenius form.

Our simulations were carried out using the temperature-accelerated (TA) method of Ref. [485]. Using this method, which is based on umbrella sampling [485-487] the desorption rates were determined over a range of different temperatures and these results were then used to determine

the corresponding activation barriers and prefactors. In particular, molecular dynamics (MD) simulations were carried out at a high temperature T_{high} equal to 1000 K for the Te-terminated surface and 1100 K for the Cd-terminated surface. Using these high-temperature MD results the corresponding desorption rate at a given substrate temperature $T = T_{high}/s$ was calculated using the transition-state theory (TST) expression [485]:

$$k_{TST}[T] = \frac{1}{2}\left(\frac{2k_B T}{\pi m}\right)^{1/2} \frac{1}{b} \left\langle \frac{\sum_{t_i} S(z_i - h)\ S(h + b - z_i)\ W(\mathbf{R}, t_i)}{\sum_{t_i} S(h - z_i)\ W(\mathbf{R}, t_i)} \right\rangle_{runs} \quad 1(a)$$

where $W(\mathbf{R},t_i)=Exp[-(s-1)V(\mathbf{R})/(s\ k_B\ T)]$ 1(*b*)

and $s = T_{high}/T \geq 1$ and $V(\mathbf{R},t_i)$ is the potential energy of the entire system at time t_i.

The angular brackets in Eq. 1(a) indicate that an average is taken over many (typically 300) uncorrelated MD runs at temperature T_{high}, each starting with an equilibrated surface for which desorption has not yet occurred. Here z_i is the height of the desorbing species (Cd or Te_2 depending on the case) above the substrate at time t_i, h is the height of the bottom of a window of width b above the substrate and is taken to be slightly larger than the potential cutoff distance R_c, e.g. $h = R_c + 1A$, and $V(\mathbf{R},t_i)$ is the potential energy of the entire system at time t_i. We note that $S(x)$ is the usual step-function, e.g. $S(x) = 0\ (1)\ if\ x < 0\ (x > 0)$, which indicates that the denominator corresponds to a sum over all times t_i of the MD simulation up to the point when the height z_i of the desorbing species reaches the height h of the bottom of the window. Similarly, the product $S(z_i-h)\ S(h+b-z_i)$ in the numerator is equal to *1* if $h < z_i < h+b$ and zero otherwise, which implies that the sum in the numerator of Eq. 1(a) only includes times when the desorbing species is in the window of width b. Depending on the temperature, species, substrate, and MD run, typical desorption times ranged from 0.5 ns to 8 ns.

In our simulations the substrate contained a total of 12 layers consisting of 4 fixed (bottom) layers, 4 thermostat (middle) layers whose temperature was regulated using Langevin dynamics, and 4 free (NVE) top layers. The Langevin damping time was set to 1 ps while the MD time-step was 1 fs. Periodic boundary conditions were assumed in the lateral (x and y) directions while sublimation occurred in the z- direction. In all cases, the lateral dimensions were 10 *a* (where *a* is the lattice constant) corresponding to 200 atoms in each layer. To obtain good statistics, averages were taken over 300 runs, with each run typically ranging from 2 - 9 ns depending on how long it took for desorption to occur.

In the case of Te_2 desorption from a Te-terminated surface (consisting of 1 monolayer or ML of Te) the desorption rate per Te_2 dimer was obtained by dividing the total desorption rate in our simulations by the total number of dimers in the ordered state on the substrate. Similarly, for the case of desorption of a Cd atom from the fully Cd-terminated surface (corresponding to 1 full ML of Cd) the desorption rate per Cd atom was obtained by dividing the total desorption rate by the number of Cd atoms in a layer.

23.4 RESULTS and DISCUSSION

Figure 159(a) shows a snapshot of the Te-terminated surface equilibrated at T = 1000 K, while Figure 159(b) and Figure 159(c) show close-ups of a Te_2 dimer leaving the surface. As can be seen, while the equilibrated Te-terminated surface is dimerized there are also defects in the dimer rows. As the surface evolves, a variety of activated processes occur involving pairing and unpairing of nearby dimers on the surface, as well as the formation of trimers and monomers. Eventually, a pair of Te atoms "climb" on top of a nearby dimer row and then desorb from the surface as shown in Figure 159(b) and Figure 159(c). We note that in general the Te_2 dimers are also spinning rapidly when they leave the surface.

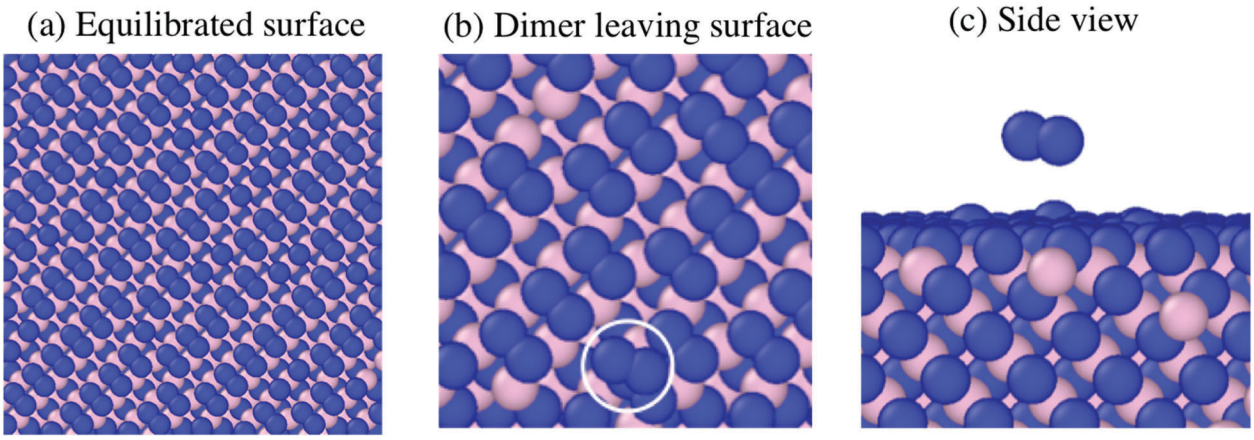


Figure 159. Top views of (a) equilibrated Te-terminated surface and (b) Te_2 dimer (white circle) leaving surface; (c) side view of Te_2 dimer leaving surface

Figure 160(a) shows our results for the distribution of the z-component of the velocity v_z of desorbing Te_2 dimers. As can be seen, there is a relatively broad distribution, with the corresponding values of v_z ranging from 0.25 eV/ps to 5.25 eV/ps with a peak near 1.75 eV/ps. The corresponding values of the vertical component of translational kinetic energy range from approximately 0.001 eV to 0.37 eV with a peak at 0.1 eV, while the average value of approximately 0.16 eV is almost double the equipartition value of 0.09 eV. In the future we will carry out a more detailed analysis of the rotational, vibrational, and translational kinetic energy distributions as well as the z-component of the translational kinetic energy.

Figure 160(b) shows our results for the extrapolated desorption rate in the case of Te_2 desorption as a function of the window width *b*, for different extrapolated temperatures $T = T_{high}/s$. As expected, the dependence on the window width is relatively weak although it is somewhat larger at lower temperatures T corresponding to higher values of s. Accordingly, we have averaged the results for k_{TST} over the window width, with b ranging from 1.0 A to 2.0 A.

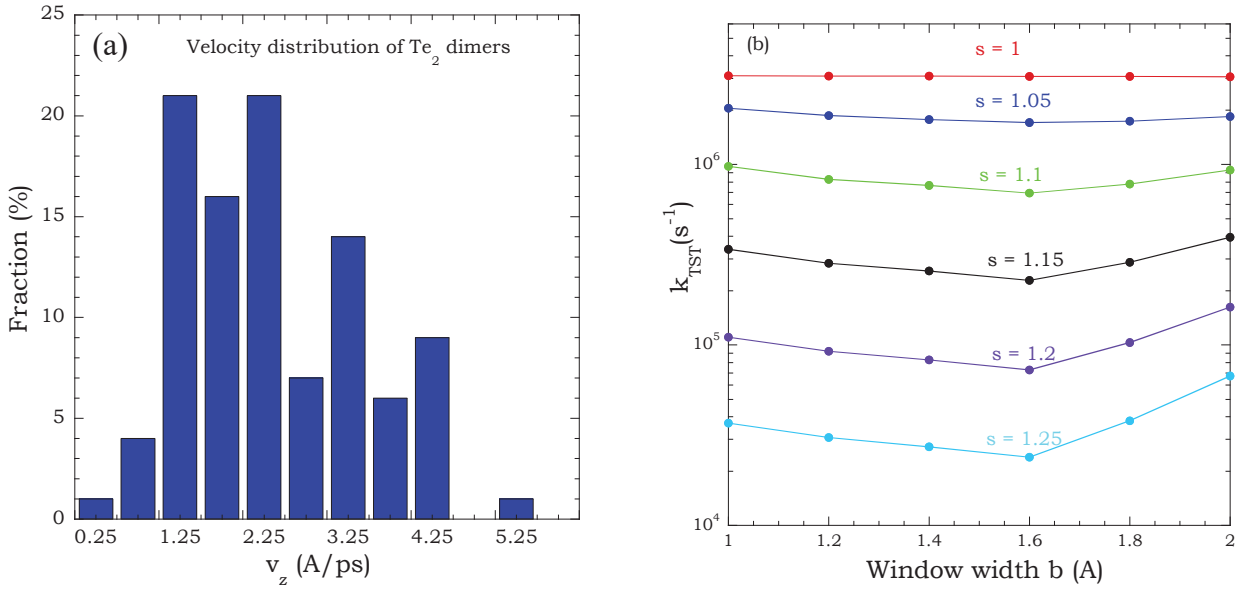


Figure 160. (a) Velocity z-component distribution of desorbing Te_2 dimers; (b) dependence of kTST on window width b for vs. extrapolation factor s

Figure 161(a) shows a semi-log plot of our results for the TST desorption rate of Te_2 dimers from the Te-saturated (100) surface. As can be seen, the desorption activation energy E_d is approximately 2.65 eV. This value is significantly larger than the *overall* effective activation energy of approximately 2.0 eV obtained from experimental results for CdTe(100) sublimation [488, 489] over the temperature range T = 588 – 633 K based on the observation of RHEED oscillations. However, it is in good agreement with the corresponding calculated binding energy (2.60 eV, see Table 1). In addition, it is consistent with the estimate in Ref. [484] that for the c(2x2) Te-terminated (100) surface, the binding energy is greater than 2.5 eV. The corresponding prefactor, $\nu_d = 4.0 \times 10^{20}$/s, is also very large and is approximately 7-8 orders of magnitude larger than the typical expected value of around 10^{12}/s.

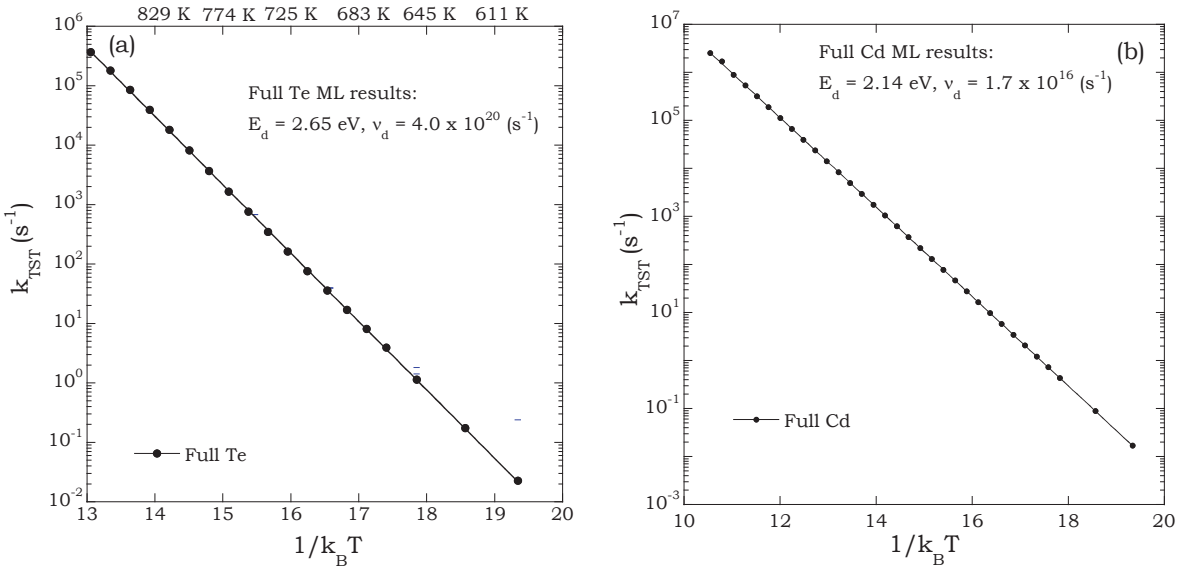


Figure 161. (a) Semi-log plot of Te2 desorption rate as function of 1/kBT for full Te(100) ML. (b) Semi-log plot of Cd desorption rate as function of 1/kBT for Cd-terminated (100) surface

Figure 161(b) shows our results for the desorption of Cd from the fully Cd-terminated (100) surface. In this case, the corresponding value of the desorption barrier (E_d = 2.14 eV) is much closer to the effective activation energy of 2.0 eV obtained from experimental measurement of the overall sublimation rate. This value is also consistent with the result obtained from *ab-initio* calculations in Ref. [483] for the binding energy of a single Cd on the (2x1) Te-terminated (100) surface of 2.1 eV. However, the corresponding prefactor ($\nu_d = 1.7 \times 10^{16}$/s) is again significantly larger than typical expected values, although not nearly as large as for Te_2 desorption.

Our results for desorption are also summarized in Table 32 along with the corresponding calculated binding energies. As can be seen there is good agreement between our estimates for the desorption barrier E_d and the corresponding binding energies. While this typically implies that desorption occurs directly from the surface, in the case of the desorption of a Te_2 dimer from the fully Te-terminated (2x1) (100) Te surface, the dimers carry out a large number of intermediate steps, overcoming a variety of different energy barriers on the surface, which involve diffusion as well as "climbing" on top of nearby Te clusters before desorbing with a smaller barrier from one of these sites. Accordingly, it is somewhat surprising that the desorption energy in this case is approximately the same as the binding energy.

Table 32. Activation barriers E_d, prefactors ν_d, and binding energies B.E. for desorption of Cd and Te_2 from the (100) Cd- and Te-terminated surfaces

Species	ν_d (s^{-1})	E_d (eV)	B.E. (eV)
Te_2 (full Te ML)	4.0×10^{20}	2.65	2.6
Cd (full Cd ML)	1.7×10^{16}	2.14	2.16

23.5 CONCLUSIONS

Desorption energies, binding energies, and prefactors were determined using the temperature-accelerated method, for the case of Te_2 dimer desorption from the (2x1) Te-terminated (100) surface, as well as Cd desorption from the Cd-terminated (100) surface. Consistent with a previous estimate [484] for the c(2x2) Te-terminated surface, we find that while the Te_2 desorption barrier for the (2x1) Te-terminated surface is relatively large (E_d = 2.65 eV) the corresponding prefactor ($\nu_d = 4.0 \times 10^{20}$/s) is also extremely large. We have also used the temperature-acceleration method to determine the desorption barrier (E_d = 2.14 eV) and prefactor ($\nu_d = 1.7 \times 10^{16}$/s) for the desorption of a Cd atom from the (100) Cd-terminated surface. A comparison of these two results also indicates that, due to the very large prefactor for Te_2 desorption, the desorption of Cd atoms is the bottleneck for CdTe sublimation for T > 500 K, thus explaining the effective value of approximately 2.0 eV found experimentally [488, 489] over this temperature range. Combined with other results we have obtained using the repulsive-potential [485] method, we are currently carrying out a more detailed analysis of the overall sublimation rate as a function of temperature, in order to determine the overall prefactor and effective activation energy for CdTe(100) sublimation and compare with experiments. [488, 489] A manuscript describing these results is in preparation. [490]

24. PHYSICALLY REALISTIC PARAMETRIC OPITCAL MODEL DEVELOPMENT FOR POLYCRYSTALLINE SEMICONDUCTORS

Marie Solange Tumusange, Niva Jayswal, Maxwell Junda, Madan Mainali, Indra Subedi, Biwas Subedi, Yanfa Yan, Robert Collins, Nikolas J. Podraza

24.1 SUMMARY

We have developed physically realistic models that are applicable to describe the complex optical properties of polycrystalline films with both direct and indirect transitions along with sub-gap absorption. These parametric optical models account for the critical point electronic transitions above the bandgap, indirect or direct bandgap nature, and sub-gap absorption due to Urbach tails below the bandgap. In addition, these models are Kramers-Kronig consistent, and the first derivative of complex dielectric function spectra is also continuous with respect to the photon energy.

24.2 INTRODUCTION

Spectroscopic ellipsometry is a well-known technique for obtaining the complex dielectric function or complex refractive index spectra of materials. Using physically realistic parametric models is the key for analyzing the ellipsometric spectra to obtain the correct optical properties for the materials of interest. For semiconductors of interest to photovoltaics, the complex dielectric function ($\varepsilon = \varepsilon_1 + i\varepsilon_2$) spectra from the near infrared to ultraviolet spectral range contain the information regarding the bandgap energy, sub-gap absorption, Urbach tail, and above gap critical point transitions. In addition to that, these near infrared to ultraviolet complex optical responses are often used to simulate the performance of the opto-electronic devices.

The Urbach energy quantifies the exponentially decaying tailing effect called Urbach tail in semiconductors that exists due to presence of lattice vibrations and defects. For example, in the direct bandgap semiconductors such as organic-inorganic metal halide perovskites, additional sub-gap absorption along with the exponentially decaying Urbach tail may be present due to multitude of intrinsic and atmospherically induced defects. [35, 491] In such a case, an advanced optical model is necessary which incorporates the contribution from the sub-gap absorption in the terms of Urbach energy and additional sub-gap absorption features. Furthermore, the shifts in the bandgaps and higher photon energy critical points occur with variations in composition and film stress. Broadening of both of these critical point features occur with the scattering of photo-excited charge carriers by the dominant defect mechanism. Therefore, it is very important have the realistic optical model that incorporates the contributions from the Urbach tail, bandgap, and high energy critical point transitions to analyze the ellipsometric spectra.

Parametric models that include the contribution from the bandgap, above gap electronic transitions, and sub-gap absorption tail have been developed and used to obtain the precise optical properties of direct and indirect bandgap semiconductor thin films. Furthermore, these models are made continuous in the first derivative with respect to this photon energy and are Kramer-Kroning consistent. These models have been applied in direct fitting of ellipsometric spectra for organic-inorganic metal halide perovskites, CdS_xSe_{1-x} and $CdSe_{1-y}Te_y$ films, III-V semiconductors such as

InP, InGaAs, InAlAs, and Sb_2Se_3 films. The particular models developed here are being applied in research funded by this project, other Air Force projects, Department of Energy, and National Science Foundation.

24.3 PROCEDURES and DISCUSSION

The near infrared to ultraviolet spectra in ε that accounts for the bandgap, an Urbach tail, and higher energy critical points in direct bandgap semiconductor is described as:

$$\varepsilon_2(E) = \mathrm{Im}\sum_n A_n e^{i\phi_n}\left(\frac{\Gamma_n}{2E_{cn}-2E-i\Gamma_n}\right)^{\mu_n}, E \geq E_g$$

$$= \mathrm{Im}\sum_n A_n e^{i\phi_n}\left(\frac{\Gamma_n}{2E_{cn}-2E_g-i\Gamma_n}\right)^{\mu_n}\exp\left[\frac{(E-E_0)}{E_U}\right], E < E_g \quad (1)$$

$$E_U = \frac{\Delta E\,\mathrm{Im}\left[\sum_n\left(\frac{\Gamma_n}{2E_{cn}-2E_g-i\Gamma_n}\right)^{\mu_j}\right]}{\mathrm{Im}\left[\sum_n\left(\left(\frac{\Gamma_n}{2E_{cn}-2E_g-2\Delta E-i\Gamma_n}\right)^{\mu_j}-\left(\frac{\Gamma_n}{2E_{cn}-2E_g-i\Gamma_n}\right)^{\mu_j}\right)\right]}$$

$$\varepsilon_1(E) = \varepsilon_\infty + \frac{A_S}{E_S{}^2-E^2}\frac{2}{\pi}P\int_{0.74}^{5.9}\frac{\xi\varepsilon_2(\xi)}{\xi^2-E^2}d\xi$$

where A_n is critical point amplitude, Γ_n is critical point broadening, E_{cn} is critical point energy, E_g is the first critical point or direct bandgap energy, ϕ_n is critical point phase, μ_n is critical point energy dimensionality, P is the principal value of the integral, E_U is the Urbach energy, ΔE is the small energy increment greater than E_g which should be smaller than the spacing between the spectral points and used to ensure that the first derivative of the complex dielectric function with respect to photon energy is continuous. This eliminates the possibility of an unphysical artifact in the line shape at E_g. With ε_2 spectra fully constructed, ε_1 is calculated using Kramers-Kronig integration of ε_2 spectra with the addition of a Sellmeier (A_S, E_S) expression and constant additive term (ε_∞).

This model can accommodate extra oscillators to describe the line shaped caused by defect induced sub-gap absorption in addition to the Urbach tail. For example, the degraded perovskite as a film or inside a perovskite-based solar cell can be described with this approach. Our recent real time study on the stability of perovskite films uses this parametrization to describe the ε_2 spectra in

$MAPbI_3$, $MA_{0.7}FA_{0.3}PbI_3$, $(FAPbI_3)_{0.95}(MAPbBr_3)_{0.05}$ films at their pristine and degraded states. [492] The resultant spectra in ε show that the amount of defect induced sub-gap absorption increases with the time for $MAPbI_3$ films when they are exposed to humidity. Similarly, this model has been used to discuss complex optical property of as-deposited and annealed CdS_xSe_{1-x} and $CdSe_{1-y}Te_y$ films. [493, 494] It is observed that the intermediate compositions showed the highest E_U while in the as-deposited state, whereas annealing reduces E_U in all cases to a fairly uniform value for all compositions. This continuous parametric model is developed for near infrared to ultraviolet range for the III-V materials as well as reported in our characterization development elsewhere in this report.

For indirect band gap semi-conductor such as Sb_2Se_3, spectra in ε is described as:

$$\varepsilon_2 = \begin{cases} \dfrac{E_1}{E} e^{[(E-E_t)/E_U]} \ , \ 0 < E \le E_t \\ G_c(E)\,\mathrm{Im}[\varepsilon_{CPPB}(E)] \ , \ E > E_t \end{cases} \tag{2}$$

where,

$$\varepsilon_{CPPB}(E) = \mathrm{Im} \sum_n A_n e^{i\phi_n} \left(\frac{\Gamma_n}{2E_{cn} - 2E - i\Gamma_n} \right)^{\mu_n},$$

$$E_1 = E_t G_c(E_t)\,\mathrm{Im}[\varepsilon_{CPPB}(E_t)], \tag{3}$$

E_t is defined as $E_g + 2E_u$, with E_g defined as the indirect bandgap energy. E_1 is the internal parameter which makes a smooth transition of this piecewise expression for ε_2 at E_t. G_c is the Cody band edge function to describe characteristics of absorption above the indirect bandgap energy and is expressed as:

$$G_c(E) = \frac{(E - E_g)^2}{(E - E_g)^2 + E_p{}^2} \tag{4}$$

where E_p represents the transition from the band edge behavior to CP behavior in ε_2 at $E_g + E_p$. Similarly, as discussed above ε_1 is calculated using Kramers-Kronig integration of ε_2 and addition of Sellmeier expressions and ε_∞. This model is used to describe the complex optical properties of Sb_2Se_3 which is *Accepted* for publication in *Solar Energy*. [495]

24.4 CONCLUSIONS

Parametric models are developed and used to obtain the complex optical properties of various polycrystalline films. These Kramers-Kronig consistent parametric models incorporates contributions from the direct and indirect bandgap, critical point energies higher than the bandgap, and sub-gap absorption due to Urbach tails. The parameterization is confined so that the first derivative of dielectric function is continuous with respect to photon energy which results in the smooth, physically realistic line shape near the bandgap. This realistic model has been used to describe the complex optical property of inorganic-organic metal halide perovskites, CdS_xSe_{1-x}, $CdSe1_{-y}Te_y$, III-V semiconductors, and Sb_2Se_3 polycrystalline thin films.

25. CHARACTERIZING THE PHASES OF TERNARY NITRIDE $MgSnN_2$ AND THE ALLOYS OF $Zn_XCd_{1-X}Te$, $(0 \leq x \leq 1)$.

Sanjay V. Khare

25.1 SUMMARY

One student Mr. Bishal Dumre worked on these projects along with supervisor Khare. It has resulted in him publishing the results of the $MgSnN_2$ study. [496] He also has results for the alloy system $Zn_xCd_{1-x}Te$, $(0 \leq x \leq 1)$, which has been analyzed and a manuscript is being prepared for submission to a journal.

25.2 INTRODUCTION

Ternary nitride $MgSnN_2$ exists in three different crystal structures, viz. disordered rocksalt, orthorhombic and disordered wurtzite. Primarily, five members of $Zn_xCd_{1-x}Te$ with x = 0.00, 0.25, 0.50, 0.75 and 1.00 are considered in the study of the alloys. Mr. Dumre's work consists of studying them from first principles computational investigation to assess their stability, electronic structure, and optical properties.

25.3 METHODS, ASSUMPTIONS, and PROCEDURES

Our simulations have been carried out by utilizing Vienna Ab initio Simulation Package (VASP) which is based on density functional theory (DFT), a first principles method. The phase diagram of mixing can be obtained by using cluster expansion formalism and Monte Carlo simulation. Computation of lattice constants, bond length distribution, elastic constants, formation energy, phonon density of states (DOS) and band structure, electronic DOS and band structure, charge transfer, charge carrier effective mass, electronic bonding and dielectric constants were carried out for the three phases of $MgSnN_2$ using generalized gradient approximation (GGA) within DFT. Within disordered, rocksalt and wurtzite, structures of $MgSnN_2$, we computed all the above-mentioned properties in all the permutations of cationic disorder. Furthermore, band gaps were computed in $MgSnN_{2-x}O_x$, with x = 0.5, 1.0, 1.5, 2.0, to elucidate the role of possible oxygen impurity. Similarly, for alloys in the material system $Zn_xCd_{1-x}Te$, lattice constants, bond length distribution, formation energy, electronic DOS and band structure, charge transfer, phase diagram, charge carrier effective masses and electronic bonding and dielectric constants were computed using GGA. Similar computations were performed, for both the MgSnNO and ZnCdTe systems, using the Heyd- Scuseria-Ernzerhof (HSE) pseudopotential known to give better results for electronic band structure and optical properties.

25.4 RESULTS and DISCUSSION

Disordered rocksalt structure of $MgSnN_2$ with a band gap of 2.69 eV has promising absorption coefficient and reflectivity to make it potentially useful as the absorber layer of tandem solar cells in the higher energy region of the visible portion of the solar spectrum. It's calculated lattice constant and band gap of 4.56 Å and 2.69 eV match closely with the experimental result of 4.48 Å and 2.3 eV respectively. [497] The other two phases, disordered wurtzite and orthorhombic, can

be utilized as a window layer of solar cells owing to their larger band gap values of 4.36 eV and 4.86 eV, respectively. Figure 162 shows absorption coefficient and reflectivity for all three crystal structures in $MgSnN_2$. We can verify the band gaps of the crystal structures from the absorption coefficient and reflectivity curves and the uses of disordered rocksalt crystal structure as an absorber layer whereas disordered wurtzite and orthorhombic crystal structures as window layers in solar cells.

In $Zn_xCd_{1-x}Te$ alloys, $Zn_{0.25}Cd_{0.75}Te$ is considered the best as an absorber layer with its promising bandgap of 1.49 eV. The consolute temperature for the solid solution has been obtained to be 387 K at 40% Zn concentration. Variation in short range order (SRO) of $Zn_{0.25}Cd_{0.75}Te$ at various temperatures makes synthesis temperature as an engineering design tool. Figure 163(a) presents frequency of occurrences of all possible Zn-Cd coordination numbers relative to their completely random configuration simulated in 1728-atom supercells. We observe that the frequency of Zn-Cd coordination number at coordination numbers 1, 2, 3, 10, 11 and 12 is higher whereas at the rest of the coordination numbers is lesser at 400 K. This distribution of the coordination numbers leads us to a negative value of -0.79 of SRO parameter as defined as:

$$\sigma(T) = 1 - [(1 - N^{Zn-Cd}(T)/N^{Zn-Cd}_{random})/(1 - N^{Zn-Cd}_{ordered}/N^{Zn-Cd}_{random})] \quad (1)$$

where N^{Zn-Cd}, $N^{Zn-Cd}_{ordered}$, and N^{Zn-Cd}_{random} represent the number of Zn-Cd bonds in the configuration simulated at some intermediate temperatures (T = 400 K, 1000 K), the ordered configuration (with each Te coordinated to an equal number of Zn and Cd atoms) at absolute zero temperature, and the completely random configuration approached at very high temperatures ($T \gg 1000$ K) in $Zn_{0.25}Cd_{0.75}Te$.

Although the distribution in Figure 163(a) displays a lesser number of bonds in the intermediate coordination numbers at 400 K than in the random limit, the total sum of the number of bonds in all the coordination numbers is higher as we see a greater number of bonds in other coordination numbers. Figure 163(c) shows such variation of the SRO parameter with temperature. It is clear from Figure 163 that the parameter increases with increasing temperature. Again, from Figure 163(a), we can see that the distribution of the coordination numbers is less dispersed at 1000 K than at 400 K, hence has a positive value of 0.11 of SRO parameter i.e., clustering is observed. Figure 163(b) displays the bond angle distribution of ∡ZnTeCd in the $Zn_{0.25}Cd_{0.75}Te$ alloy at two different temperatures. We notice a smaller width of bond angle distribution at 400 K than at 1000 K. Along with the distribution, we also calculated their bandgaps using the GGA pseudopotential, to compare the effect of structural distortion on bandgap. We have found that the bandgap is slightly higher at 1000 K (1.07 eV) than at 400 K (1.02 eV). This can be attributed to the lower median value of bond angle distribution that signifies greater strain on the bond and subsequent increase in the bandgap.

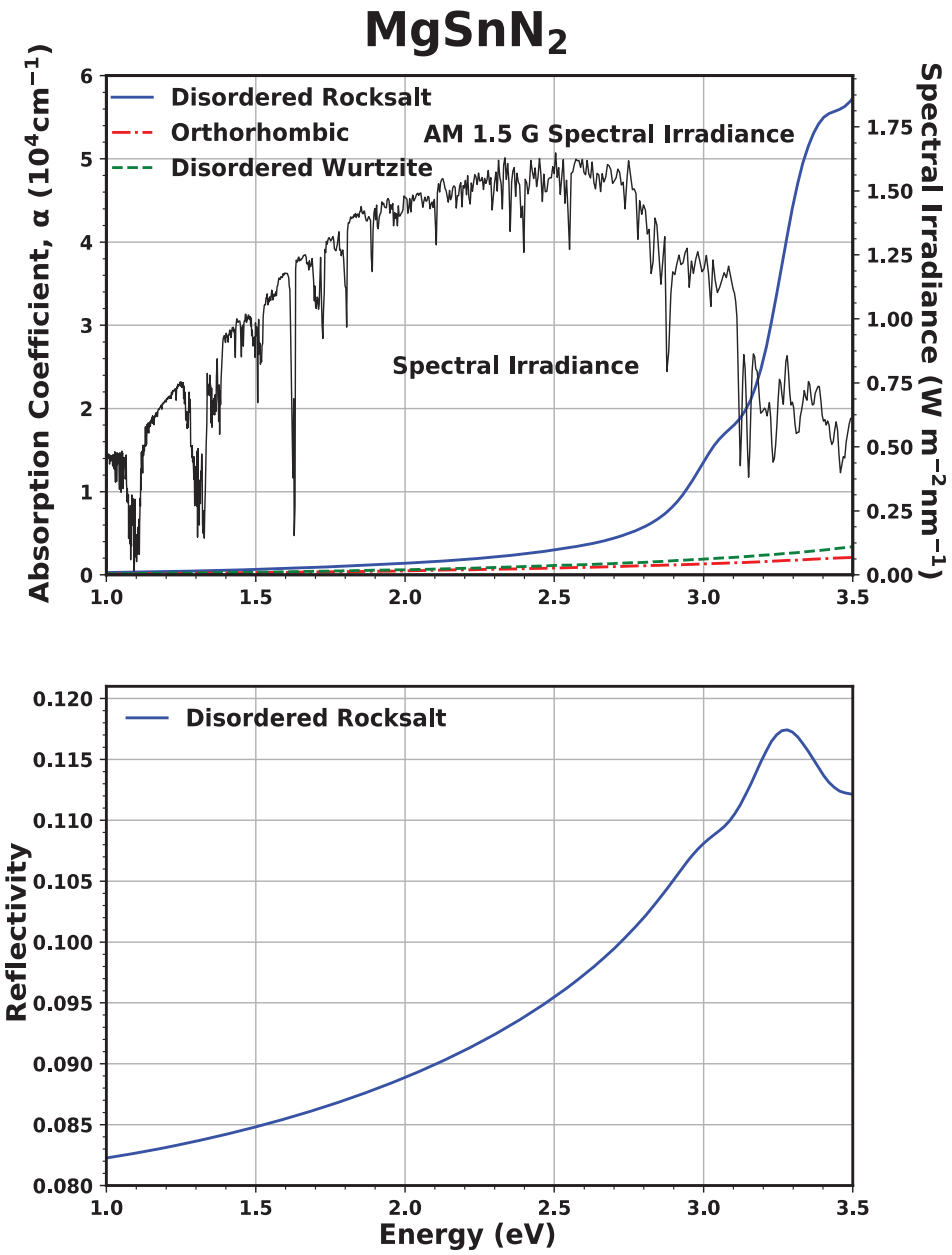


Figure 162. Absorption coefficient, α (top) and reflectivity (bottom) vs. energy, of $MgSnN_2$ based on rock-salt structure

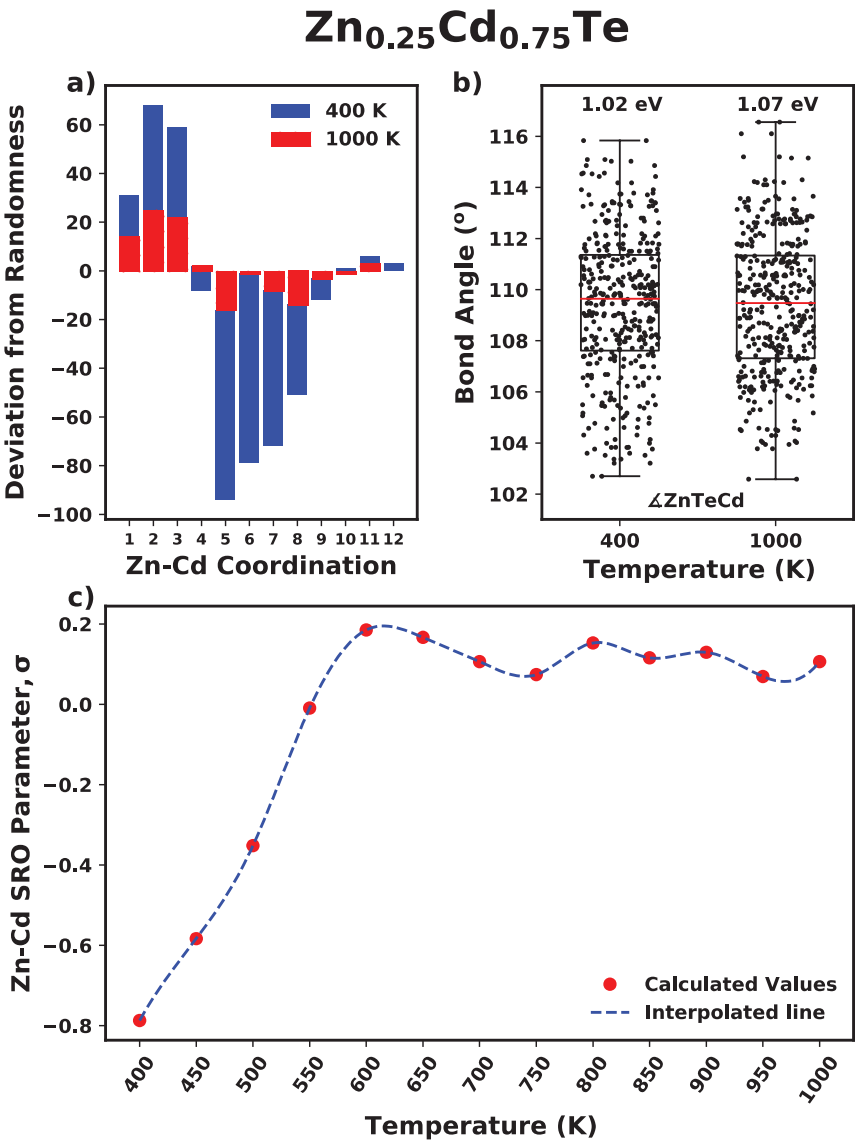


Figure 163. (a) Frequency of occurrence for all possible Zn-Cd coordination numbers relative to their completely random configuration; (b) Bond angle distributions of ∡Zn-Te-Cd in $Zn_{0.25}Cd_{0.75}Te$ simulated at 400 K and 1000 K

25.5 CONCLUSIONS

For the ternary nitride $MgSnN_2$ and $Zn_xCd_{1-x}Te$, ($0 \leq x \leq 1$) alloys, several results generated from a variety of these simulations have been compiled and understood to come up with a coherent explanation of all their properties. $MgSnN_2$ work has been finally published. [496] Work on the ZnCdTe alloy system is continuing toward writing of the manuscript.

26. REFERENCES

[1] J. Burschka *et al.*, "Sequential deposition as a route to high-performance perovskite-sensitized solar cells," *Nature,* Letter **vol. 499**, no**.** 7458, pp. 316-319, 07/18/print 2013, doi: 10.1038/nature12340.

[2] H. Tan *et al.*, "Efficient and stable solution-processed planar perovskite solar cells via contact passivation," *Science,* **vol. 355**, no**.** 6326, pp. 722-726, 2017, doi: 10.1126/science.aai9081.

[3] W. S. Yang *et al.*, "Iodide management in formamidinium-lead-halide–based perovskite layers for efficient solar cells," *Science,* **vol. 356**, no**.** 6345, pp. 1376-1379, 2017, doi: 10.1126/science.aan2301.

[4] D. Bi *et al.*, "Efficient luminescent solar cells based on tailored mixed-cation perovskites," *Science Advances,* **vol. 2**, no**.** 1, p. 1501170, Jan 2016, doi: 10.1126/sciadv.1501170.

[5] T. Bu *et al.*, "Novel quadruple-cation absorber for universal hysteresis elimination for high efficiency and stable perovskite solar cells," (in English), *Energy Environ. Sci.,* **vol. 10**, no**.** 12, pp. 2509-2515, Dec 2017, doi: 10.1039/C7EE02634J.

[6] Q. Jiang *et al.*, "Surface passivation of perovskite film for efficient solar cells," *Nature Photonics,* 2019/04/01 2019, doi: 10.1038/s41566-019-0398-2.

[7] C. Rodríguez-Seco, L. Cabau, A. Vidal-Ferran, and E. Palomares, "Advances in the Synthesis of Small Molecules as Hole Transport Materials for Lead Halide Perovskite Solar Cells," *Acc. Chem. Res.,* **vol. 51**, no**.** 4, pp. 869-880, 2018/03/15 2018, doi: 10.1021/acs.accounts.7b00597.

[8] Z. Yu and L. Sun, "Recent Progress on Hole-Transporting Materials for Emerging Organometal Halide Perovskite Solar Cells," *Advanced Energy Materials,* **vol. 5**, no**.** 12, p. 1500213, 2015, doi: 10.1002/aenm.201500213.

[9] J.-P. Correa-Baena *et al.*, "The rapid evolution of highly efficient perovskite solar cells," *Energy Environ. Sci.,* 10.1039/C6EE03397K **vol. 10**, no**.** 3, pp. 710-727, 2017, doi: 10.1039/C6EE03397K.

[10] S. Wang *et al.*, "Unveiling the Role of tBP–LiTFSI Complexes in Perovskite Solar Cells," *Journal of the American Chemical Society,* **vol. 140**, no**.** 48, pp. 16720-16730, 2018/11/06 2018, doi: 10.1021/jacs.8b09809.

[11] K. Gao *et al.*, "Highly Efficient Porphyrin-Based OPV/Perovskite Hybrid Solar Cells with Extended Photoresponse and High Fill Factor," *Adv. Mater.,* **vol. 29**, no**.** 47, pp. 1703980-n/a, Dec 2017, Art no. 1703980, doi: 10.1002/adma.201703980.

[12] T. H. Schloemer, J. A. Christians, J. M. Luther, and A. Sellinger, "Doping strategies for small molecule organic hole-transport materials: impacts on perovskite solar cell performance and stability," *Chemical Science,* 10.1039/C8SC05284K **vol. 10**, no**.** 7, pp. 1904-1935, 2019, doi: 10.1039/C8SC05284K.

[13] X. Yin *et al.*, "Dithieno[3,2-b:2′,3′-d]pyrrol-Cored Hole Transport Material Enabling Over 21% Efficiency Dopant-Free Perovskite Solar Cells," *Adv. Funct. Mater.,* **vol. 29**, no**.** 38, p. 1904300, 2019, doi: https://doi.org/10.1002/adfm.201904300.

[14] C. Wang *et al.*, "Water Vapor Treatment of Low-Temperature Deposited SnO_2 Electron Selective Layers for Efficient Flexible Perovskite Solar Cells," *ACS Energy Letters,* **vol. 2**, no**.** 9, pp. 2118-2124, 2017/09/08 2017, doi: 10.1021/acsenergylett.7b00644.

[15] H. Min *et al.*, "Efficient, stable solar cells by using inherent bandgap of α-phase formamidinium lead iodide," *Science,* **vol. 366**, no**.** 6466, pp. 749-753, 2019, doi: 10.1126/science.aay7044.

[16] Y. Wang *et al.*, "Stabilizing heterostructures of soft perovskite semiconductors," *Science,* **vol. 365**, no**.** 6454, pp. 687-691, 2019, doi: 10.1126/science.aax8018.

[17] S. Yang *et al.*, "Stabilizing halide perovskite surfaces for solar cell operation with wide-bandgap lead oxysalts," *Science,* **vol. 365**, no**.** 6452, pp. 473-478, 2019, doi: 10.1126/science.aax3294.

[18] S. Bai *et al.*, "Planar perovskite solar cells with long-term stability using ionic liquid additives," *Nature,* **vol. 571**, no**.** 7764, pp. 245-250, 2019/07/01 2019, doi: 10.1038/s41586-019-1357-2.

[19] W. S. Yang *et al.*, "High-performance photovoltaic perovskite layers fabricated through intramolecular exchange," *Science,* **vol. 348**, no**.** 6240, pp. 1234-1237, 2015, doi: 10.1126/science.aaa9272.

[20] C. Chen *et al.*, "Characterization of basic physical properties of Sb_2Se_3 and its relevance for photovoltaics," *Frontiers of Optoelectronics,* journal article **vol. 10**, no**.** 1, pp. 18-30, 2017, doi: 10.1007/s12200-017-0702-z.

[21] Q. Jiang *et al.*, "Enhanced electron extraction using SnO_2 for high-efficiency planar-structure $HC(NH_2)_2PbI_3$-based perovskite solar cells," *Nature Energy,* **vol. 2**, no**.** 1, p. 16177, 2016/11/14 2016, doi: 10.1038/nenergy.2016.177.

[22] X. Zheng *et al.*, "Defect passivation in hybrid perovskite solar cells using quaternary ammonium halide anions and cations," *Nature Energy,* Article **vol. 2**, p. 17102, 06/26/online 2017, doi: 10.1038/nenergy.2017.102.

[23] Z. Xu *et al.*, "A Thermodynamically Favored Crystal Orientation in Mixed Formamidinium/Methylammonium Perovskite for Efficient Solar Cells," *Adv. Mater.,* **vol. 31**, no**.** 24, p. 1900390, 2019, doi: 10.1002/adma.201900390.

[24] T. Liu, H. Lai, X. Wan, X. Zhang, Y. Liu, and Y. Chen, "Cesium Halides-Assisted Crystal Growth of Perovskite Films for Efficient Planar Heterojunction Solar Cells," *Chem. Mater.,* **vol. 30**, no**.** 15, pp. 5264-5271, 2018/08/14 2018, doi: 10.1021/acs.chemmater.8b02002.

[25] Q. Li *et al.*, "Efficient Perovskite Solar Cells Fabricated Through CsCl-Enhanced PbI_2 Precursor via Sequential Deposition," *Adv. Mater.,* **vol. 30**, no**.** 40, p. 1803095, 2018, doi: 10.1002/adma.201803095.

[26] X. Yi *et al.*, "Incorporating CsF into the PbI_2 Film for Stable Mixed Cation-Halide Perovskite Solar Cells," *Advanced Energy Materials,* **vol. 9**, no**.** 40, p. 1901726, 2019, doi: 10.1002/aenm.201901726.

[27] Y. Zhao *et al.*, "Perovskite seeding growth of formamidinium-lead-iodide-based perovskites for efficient and stable solar cells," *Nature Communications,* **vol. 9**, no**.** 1, p. 1607, 2018/04/23 2018, doi: 10.1038/s41467-018-04029-7.

[28] Q. Li *et al.*, "Halogen Engineering for Operationally Stable Perovskite Solar Cells via Sequential Deposition," *Advanced Energy Materials,* **vol. 9**, no**.** 46, p. 1902239, 2019, doi: 10.1002/aenm.201902239.

[29] J.-H. Im, I.-H. Jang, N. Pellet, M. Grätzel, and N.-G. Park, "Growth of $CH_3NH_3PbI_3$ cuboids with controlled size for high-efficiency perovskite solar cells," *Nature Nanotechnology,* Article **vol. 9**, no**.** 11, pp. 927-932, 11//print 2014, doi: 10.1038/nnano.2014.181.

[30] M. Sun *et al.*, "Tailoring a dynamic crystalline process during the conversion of lead-halide perovskite layer to achieve high performance solar cells," *Journal of Materials Chemistry A,* **vol. 6**, no**.** 48, pp. 24793-24804, 2018, doi: 10.1039/C8TA07462C.

[31] Q. Jiang *et al.*, "Planar-Structure Perovskite Solar Cells with Efficiency beyond 21%," *Adv. Mater.,* **vol. 29**, no**.** 46, p. 1703852, 2017, doi: 10.1002/adma.201703852.

[32] L. Meng *et al.*, "Tailored Phase Conversion under Conjugated Polymer Enables Thermally Stable Perovskite Solar Cells with Efficiency Exceeding 21%," *Journal of the American Chemical Society,* **vol. 140**, no**.** 49, pp. 17255-17262, 2018/12/12 2018, doi: 10.1021/jacs.8b10520.

[33] Z. Li, M. Yang, J.-S. Park, S.-H. Wei, J. J. Berry, and K. Zhu, "Stabilizing Perovskite Structures by Tuning Tolerance Factor: Formation of Formamidinium and Cesium Lead Iodide Solid-State Alloys," *Chem. Mater.,* **vol. 28**, no**.** 1, pp. 284-292, 2016/01/12 2016, doi: 10.1021/acs.chemmater.5b04107.

[34] Y. Cui *et al.*, "Correlating Hysteresis and Stability with Organic Cation Composition in the Two-Step Solution-Processed Perovskite Solar Cells," *ACS Applied Materials & Interfaces,* **vol. 12**, no**.** 9, pp. 10588-10596, 2020/03/04 2020, doi: 10.1021/acsami.9b23374.

[35] B. Subedi, C. Li, M. M. Junda, Z. Song, Y. Yan, and N. J. Podraza, "Effects of intrinsic and atmospherically induced defects in narrow bandgap $(FASnI_3)_x$ $(MAPbI_3)_{1-x}$ perovskite films and solar cells," *The Journal of Chemical Physics,* **vol. 152**, no**.** 6, p. 064705, 2020.

[36] J. Tong *et al.*, "Carrier lifetimes of> 1 μs in Sn-Pb perovskites enable efficient all-perovskite tandem solar cells," *Science,* **vol. 364**, no**.** 6439, pp. 475-479, 2019.

[37] J. Liu *et al.*, "$FAPb_{1-x}Sn_xI_3$ mixed metal halide perovskites with improved light harvesting and stability for efficient planar heterojunction solar cells," *Journal of Materials Chemistry A,* **vol. 5**, no**.** 19, pp. 9097-9106, 2017.

[38] F. Hao, C. C. Stoumpos, R. P. Chang, and M. G. Kanatzidis, "Anomalous band gap behavior in mixed Sn and Pb perovskites enables broadening of absorption spectrum in solar cells," *Journal of the American Chemical Society,* **vol. 136**, no**.** 22, pp. 8094-8099, 2014.

[39] T. Leijtens, R. Prasanna, A. Gold-Parker, M. F. Toney, and M. D. McGehee, "Mechanism of tin oxidation and stabilization by lead substitution in tin halide perovskites," *ACS Energy Letters,* **vol. 2**, no**.** 9, pp. 2159-2165, 2017.

[40] C. Li *et al.*, "Reducing saturation-current density to realize high-efficiency low-bandgap mixed tin–lead halide perovskite solar cells," *Advanced Energy Materials,* **vol. 9**, no**.** 3, p. 1803135, 2019.

[41] F. Urbach, "The long-wavelength edge of photographic sensitivity and of the electronic absorption of solids," *Physical Review,* **vol. 92**, no**.** 5, p. 1324, 1953.

[42] W. B. Jackson, N. M. Amer, A. Boccara, and D. Fournier, "Photothermal deflection spectroscopy and detection," *Applied Optics,* **vol. 20**, no**.** 8, pp. 1333-1344, 1981.

[43] L. Karki Gautam, "Spectroscopic ellipsometry studies of thin film Si: H materials in photovoltaic applications from infrared to ultraviolet," University of Toledo, 2016.

[44] B. Subedi *et al.*, "Formamidinium+ cesium lead triiodide perovskites: Discrepancies between thin film optical absorption and solar cell efficiency," *Sol. Energy Mater. Sol. Cells,* **vol. 188**, pp. 228-233, 2018.

[45] "NREL Best Research-Cell Efficiencies: https://www.nrel.gov/pv/cell-efficiency.html " (accessed June 2021).

[46] J. J. Yoo *et al.*, "Efficient perovskite solar cells via improved carrier management," *Nature,* **vol. 590**, no**.** 7847, pp. 587-593, 2021.

[47] A. Kojima, K. Teshima, Y. Shirai, and T. Miyasaka, "Organometal halide perovskites as visible-light sensitizers for photovoltaic cells," *Journal of the American Chemical Society,* **vol. 131**, no**.** 17, pp. 6050-6051, 2009.

[48] Z. Song *et al.*, "A technoeconomic analysis of perovskite solar module manufacturing with low-cost materials and techniques," *Energy Environ. Sci.,* **vol. 10**, no**.** 6, pp. 1297-1305, 2017.

[49] I. Celik *et al.*, "Energy payback time (EPBT) and energy return on energy invested (EROI) of perovskite tandem photovoltaic solar cells," *IEEE Journal of Photovoltaics,* **vol. 8**, no**.** 1, pp. 305-309, 2017.

[50] Z. Song *et al.*, "Manufacturing cost analysis of perovskite solar modules in single-junction and all-perovskite tandem configurations," in *2018 IEEE 7th World Conference on Photovoltaic Energy Conversion (WCPEC)(A Joint Conference of 45th IEEE PVSC, 28th PVSEC & 34th EU PVSEC)*, Waikoloa, HI, US, 2018: IEEE, pp. 1134-1138.

[51] Z. Li *et al.*, "Cost analysis of perovskite tandem photovoltaics," *Joule,* **vol. 2**, no**.** 8, pp. 1559-1572, 2018.

[52] I. Celik, R. Hosseinian Ahangharnejhad, Z. Song, M. Heben, and D. Apul, "Emerging Photovoltaic (PV) Materials for a Low Carbon Economy," *Energies,* **vol. 13**, no**.** 16, p. 4131, 2020.

[53] I. Celik, Z. Song, A. J. Cimaroli, Y. Yan, M. J. Heben, and D. Apul, "Life Cycle Assessment (LCA) of perovskite PV cells projected from lab to fab," *Sol. Energy Mater. Sol. Cells,* **vol. 156**, pp. 157-169, 2016.

[54] I. Celik *et al.*, "Environmental analysis of perovskites and other relevant solar cell technologies in a tandem configuration," *Energy Environ. Sci.,* **vol. 10**, no**.** 9, pp. 1874-1884, 2017.

[55] M. Yang *et al.*, "Highly efficient perovskite solar modules by scalable fabrication and interconnection optimization," *ACS Energy Letters,* **vol. 3**, no**.** 2, pp. 322-328, 2018.

[56] F. De Rossi *et al.*, "All printable perovskite solar modules with 198 cm2 active area and over 6% efficiency," *Advanced Materials Technologies,* **vol. 3**, no**.** 11, p. 1800156, 2018.

[57] D. H. Kim, J. B. Whitaker, Z. Li, M. F. van Hest, and K. Zhu, "Outlook and challenges of perovskite solar cells toward terawatt-scale photovoltaic module technology," *Joule,* **vol. 2**, no**.** 8, pp. 1437-1451, 2018.

[58] Q. Han *et al.*, "High-performance perovskite/Cu(In, Ga)Se2 monolithic tandem solar cells," *Science,* **vol. 361**, no**.** 6405, pp. 904-908, 2018.

[59] R. H. Ahangharnejhad *et al.*, "Optical design of perovskite solar cells for applications in monolithic tandem configuration with CuInSe2 bottom cells," *MRS Advances,* **vol. 3**, no**.** 52, pp. 3111-3119, 2018.

[60] R. H. Ahangharnejhad *et al.*, "Irradiance and temperature considerations in the design and deployment of high annual energy yield perovskite/CIGS tandems," *Sustainable Energy & Fuels,* **vol. 3**, no**.** 7, pp. 1841-1851, 2019.

[61] Z. Song *et al.*, "Monolithic Two-Terminal All-Perovskite Tandem Solar Cells with Power Conversion Efficiency Exceeding 21%," in *2019 IEEE 46th Photovoltaic Specialists Conference (PVSC)*, Chicago, IL, US, 2019: IEEE, pp. 0743-0746.

[62] H. Wang, H. A. Dewi, T. M. Koh, A. Bruno, S. Mhaisalkar, and N. Mathews, "Bifacial, color-tunable semitransparent perovskite solar cells for building-integrated photovoltaics," *ACS Applied Materials & Interfaces,* **vol. 12**, no**.** 1, pp. 484-493, 2019.

[63] R. H. Ahangharnejhad *et al.*, "Environmental Impact per Energy Yield for Bifacial Perovskite Solar Cells Outperforms Crystalline Silicon Solar Cells," *Cell Reports Physical Science,* **vol. 1**, no**.** 10, p. 100216, 2020.

[64] C. C. Stoumpos, C. D. Malliakas, and M. G. Kanatzidis, "Semiconducting tin and lead iodide perovskites with organic cations: phase transitions, high mobilities, and near-infrared photoluminescent properties," *Inorganic Chemistry,* **vol. 52**, no**.** 15, pp. 9019-9038, 2013.

[65] P. Pistor, J. Borchert, W. Fränzel, R. Csuk, and R. Scheer, "Monitoring the phase formation of coevaporated lead halide perovskite thin films by in situ x-ray diffraction," *The Journal of Physical Chemistry Letters,* **vol. 5**, no**.** 19, pp. 3308-3312, 2014.

[66] D. Bryant *et al.*, "Light and oxygen induced degradation limits the operational stability of methylammonium lead triiodide perovskite solar cells," *Energy Environ. Sci.,* **vol. 9**, no**.** 5, pp. 1655-1660, 2016.

[67] H. Yuan *et al.*, "Degradation of methylammonium lead iodide perovskite structures through light and electron beam driven ion migration," *The Journal of Physical Chemistry Letters,* **vol. 7**, no**.** 3, pp. 561-566, 2016.

[68] Z. Wang, Z. Shi, T. Li, Y. Chen, and W. Huang, "Stability of perovskite solar cells: a prospective on the substitution of the A cation and X anion," *Angew. Chem. Int. Ed.,* **vol. 56**, no**.** 5, pp. 1190-1212, 2017.

[69] J. M. Frost, K. T. Butler, F. Brivio, C. H. Hendon, M. Van Schilfgaarde, and A. Walsh, "Atomistic origins of high-performance in hybrid halide perovskite solar cells," *Nano Lett.,* **vol. 14**, no**.** 5, pp. 2584-2590, 2014.

[70] Z. Song *et al.*, "Impact of moisture on photoexcited charge carrier dynamics in methylammonium lead halide perovskites," *The Journal of Physical Chemistry Letters,* **vol. 9**, no**.** 21, pp. 6312-6320, 2018.

[71] Q. Wang, C.-C. Chueh, M. Eslamian, and A. K.-Y. Jen, "Modulation of PEDOT: PSS pH for efficient inverted perovskite solar cells with reduced potential loss and enhanced stability," *ACS Applied Materials & Interfaces,* **vol. 8**, no**.** 46, pp. 32068-32076, 2016.

[72] N. Arora *et al.*, "Perovskite solar cells with CuSCN hole extraction layers yield stabilized efficiencies greater than 20%," *Science,* **vol. 358**, no**.** 6364, pp. 768-771, 2017.

[73] J.-Y. Seo *et al.*, "Novel p-dopant toward highly efficient and stable perovskite solar cells," *Energy Environ. Sci.,* **vol. 11**, no**.** 10, pp. 2985-2992, 2018.

[74] N. J. Jeon *et al.*, "Compositional engineering of perovskite materials for high-performance solar cells," *Nature,* **vol. 517**, no**.** 7535, pp. 476-480, 2015.

[75] K. A. Bush *et al.*, "Compositional engineering for efficient wide band gap perovskites with improved stability to photoinduced phase segregation," *ACS Energy Letters,* **vol. 3**, no**.** 2, pp. 428-435, 2018.

[76] F. Zhang *et al.*, "Self-seeding growth for perovskite solar cells with enhanced stability," *Joule,* **vol. 3**, no**.** 6, pp. 1452-1463, 2019.

[77] J. Yang *et al.*, "High-performance perovskite solar cells with excellent humidity and thermo-stability via fluorinated perylenediimide," *Advanced Energy Materials,* **vol. 9**, no**.** 18, p. 1900198, 2019.

[78] R. Wang *et al.*, "Caffeine improves the performance and thermal stability of perovskite solar cells," *Joule,* **vol. 3**, no**.** 6, pp. 1464-1477, 2019.

[79] G. Grancini *et al.*, "One-Year stable perovskite solar cells by 2D/3D interface engineering," *Nature Communications,* **vol. 8**, no**.** 1, pp. 1-8, 2017.

[80] J. A. Christians *et al.*, "Tailored interfaces of unencapsulated perovskite solar cells for> 1,000 hour operational stability," *Nature Energy,* **vol. 3**, no**.** 1, pp. 68-74, 2018.

[81] S. Ma *et al.*, "1000 h operational lifetime perovskite solar cells by ambient melting encapsulation," *Advanced Energy Materials,* **vol. 10**, no**.** 9, p. 1902472, 2020.

[82] A. Uddin, M. B. Upama, H. Yi, and L. Duan, "Encapsulation of organic and perovskite solar cells: A review," *Coatings,* **vol. 9**, no**.** 2, p. 65, 2019.

[83] Q. Lu *et al.*, "A Review on Encapsulation Technology from Organic Light Emitting Diodes to Organic and Perovskite Solar Cells," *Adv. Funct. Mater.,* **vol. 31**, no**.** 23, p. 2100151, 2021.

[84] C. C. Boyd, R. Cheacharoen, T. Leijtens, and M. D. McGehee, "Understanding degradation mechanisms and improving stability of perovskite photovoltaics," *Chem. Rev.,* **vol. 119**, no**.** 5, pp. 3418-3451, 2018.

[85] S. Zhang *et al.*, "Barrier Designs in Perovskite Solar Cells for Long-Term Stability," *Advanced Energy Materials,* **vol. 10**, no**.** 35, p. 2001610, 2020.

[86] S. Jiang, K. Wang, H. Zhang, Y. Ding, and Q. Yu, "Encapsulation of PV modules using ethylene vinyl acetate copolymer as the encapsulant," *Macromolecular Reaction Engineering,* **vol. 9**, no**.** 5, pp. 522-529, 2015.

[87] R. Cheacharoen *et al.*, "Encapsulating perovskite solar cells to withstand damp heat and thermal cycling," *Sustainable Energy & Fuels,* **vol. 2**, no**.** 11, pp. 2398-2406, 2018.

[88] F. Corsini and G. Griffini, "Recent progress in encapsulation strategies to enhance the stability of organometal halide perovskite solar cells," *Journal of Physics: Energy,* **vol. 2**, no**.** 3, p. 031002, 2020.

[89] Y. Han *et al.*, "Degradation observations of encapsulated planar $CH_3NH_3PbI_3$ perovskite solar cells at high temperatures and humidity," *Journal of Materials Chemistry A,* **vol. 3**, no**.** 15, pp. 8139-8147, 2015.

[90] R. Cheacharoen, N. Rolston, D. Harwood, K. A. Bush, R. H. Dauskardt, and M. D. McGehee, "Design and understanding of encapsulated perovskite solar cells to withstand temperature cycling," *Energy Environ. Sci.,* **vol. 11**, no**.** 1, pp. 144-150, 2018.

[91] B. Li, M. Wang, R. Subair, G. Cao, and J. Tian, "Significant stability enhancement of perovskite solar cells by facile adhesive encapsulation," *The Journal of Physical Chemistry C,* **vol. 122**, no**.** 44, pp. 25260-25267, 2018.

[92] L. Shi *et al.*, "Accelerated lifetime testing of organic–inorganic perovskite solar cells encapsulated by polyisobutylene," *ACS Applied Materials & Interfaces,* **vol. 9**, no**.** 30, pp. 25073-25081, 2017.

[93] F. J. Ramos *et al.*, "Versatile perovskite solar cell encapsulation by low-temperature ALD-Al_2O_3 with long-term stability improvement," *Sustainable Energy & Fuels,* **vol. 2**, no**.** 11, pp. 2468-2479, 2018.

[94] Q. Dong *et al.*, "Encapsulation of perovskite solar cells for high humidity conditions," *ChemSusChem,* **vol. 9**, no**.** 18, pp. 2597-2603, 2016.

[95] S. H. Bang, N.-M. Hwang, and H. L. Kim, "Permeation barrier properties of silicon oxide films deposited on polyethylene terephthalate (PET) substrate using roll-to-roll reactive magnetron sputtering system," *Microelectronic Engineering,* **vol. 166**, pp. 39-44, 2016/12/01/ 2016, doi: https://doi.org/10.1016/j.mee.2016.09.007.

[96] S. Nagai, "Approximation of effective moisture-diffusion coefficient to characterize performance of a barrier coating," *Journal of Applied Physics,* **vol. 114**, no**.** 17, p. 174302, 2013, doi: 10.1063/1.4828872.

[97] S.-H. Turren-Cruz, A. Hagfeldt, and M. Saliba, "Methylammonium-free, high-performance, and stable perovskite solar cells on a planar architecture," *Science,* **vol. 362**, no**.** 6413, pp. 449-453, 2018, doi: doi:10.1126/science.aat3583.

[98] M. Saliba *et al.*, "Cesium-containing triple cation perovskite solar cells: improved stability, reproducibility and high efficiency," *Energy Environ. Sci.,* **vol. 9**, no**.** 6, pp. 1989-1997, 2016, doi: 10.1039/C5EE03874J.

[99] F. Ünlü *et al.*, "Understanding the interplay of stability and efficiency in A-site engineered lead halide perovskites," *APL Materials,* **vol. 8**, no**.** 7, p. 070901, 2020, doi: 10.1063/5.0011851.

[100] K. Ho, M. Wei, E. H. Sargent, and G. C. Walker, "Grain Transformation and Degradation Mechanism of Formamidinium and Cesium Lead Iodide Perovskite under Humidity and Light," *ACS Energy Letters,* **vol. 6**, no**.** 3, pp. 934-940, 2021/03/12 2021, doi: 10.1021/acsenergylett.0c02247.

[101] P. E. Marchezi *et al.*, "Degradation mechanisms in mixed-cation and mixed-halide $Cs_xFA_{1-x}Pb(Br_yI_{1-y})_3$ perovskite films under ambient conditions," *Journal of Materials Chemistry A,* **vol. 8**, no**.** 18, pp. 9302-9312, 2020, doi: 10.1039/D0TA01201G.

[102] Y. Hu, M. F. Aygüler, M. L. Petrus, T. Bein, and P. Docampo, "Impact of Rubidium and Cesium Cations on the Moisture Stability of Multiple-Cation Mixed-Halide Perovskites," *ACS Energy Letters,* **vol. 2**, no**.** 10, pp. 2212-2218, 2017/10/13 2017, doi: 10.1021/acsenergylett.7b00731.

[103] W. Zhu *et al.*, "In situ Investigation of Water Interaction with Lead-Free All Inorganic Perovskite (Cs2SnIxCl6–x)," *The Journal of Physical Chemistry C,* **vol. 123**, no**.** 14, pp. 9575-9581, 2019/04/11 2019, doi: 10.1021/acs.jpcc.9b00720.

[104] F. Cordero *et al.*, "Stability of Cubic FAPbI3 from X-ray Diffraction, Anelastic, and Dielectric Measurements," *The Journal of Physical Chemistry Letters,* **vol. 10**, no**.** 10, pp. 2463-2469, 2019/05/16 2019, doi: 10.1021/acs.jpclett.9b00896.

[105] S. Masi, A. F. Gualdrón-Reyes, and I. Mora-Seró, "Stabilization of Black Perovskite Phase in $FAPbI_3$ and $CsPbI_3$," *ACS Energy Letters,* **vol. 5**, no**.** 6, pp. 1974-1985, 2020/06/12 2020, doi: 10.1021/acsenergylett.0c00801.

[106] Y. Fan, H. Meng, L. Wang, and S. Pang, "Review of Stability Enhancement for Formamidinium-Based Perovskites," *Solar RRL,* **vol. 3**, no**.** 9, p. 1900215, 2019, doi: doi.org/10.1002/solr.201900215.

[107] H. Lu *et al.*, "Vapor-assisted deposition of highly efficient, stable black-phase $FAPbI_3$ perovskite solar cells," *Science,* **vol. 370**, no**.** 6512, p. eabb8985, 2020, doi: doi:10.1126/science.abb8985.

[108] M. Jeong *et al.*, "Stable perovskite solar cells with efficiency exceeding 24.8% and 0.3-V voltage loss," *Science,* **vol. 369**, no**.** 6511, pp. 1615-1620, 2020, doi: doi:10.1126/science.abb7167.

[109] H. Kanda *et al.*, "Analysis of Sputtering Damage on I–V Curves for Perovskite Solar Cells and Simulation with Reversed Diode Model," *The Journal of Physical Chemistry C,* **vol. 120**, no**.** 50, pp. 28441-28447, 2016/12/22 2016, doi: 10.1021/acs.jpcc.6b09219.

[110] M. Jaysankar *et al.*, "Four-Terminal Perovskite/Silicon Multijunction Solar Modules," *Advanced Energy Materials,* **vol. 7**, no**.** 15, p. 1602807, 2017, doi: doi.org/10.1002/aenm.201602807.

[111] F. Fu *et al.*, "Low-temperature-processed efficient semi-transparent planar perovskite solar cells for bifacial and tandem applications," *Nature Communications,* **vol. 6**, no**.** 1, p. 8932, 2015/11/18 2015, doi: 10.1038/ncomms9932.

[112] J. Yang, B. D. Siempelkamp, D. Liu, and T. L. Kelly, "Investigation of $CH_3NH_3PbI_3$ Degradation Rates and Mechanisms in Controlled Humidity Environments Using in Situ Techniques," *ACS Nano,* **vol. 9**, no**.** 2, pp. 1955-1963, 2015/02/24 2015, doi: 10.1021/nn506864k.

[113] F. Matteocci *et al.*, "Encapsulation for long-term stability enhancement of perovskite solar cells," *Nano Energy,* **vol. 30**, pp. 162-172, 2016/12/01/ 2016, doi: doi.org/10.1016/j.nanoen.2016.09.041.

[114] E. Ramasamy, V. Karthikeyan, K. Rameshkumar, and G. Veerappan, "Glass-to-glass encapsulation with ultraviolet light curable epoxy edge sealing for stable perovskite solar cells," *Materials Letters,* **vol. 250**, pp. 51-54, 2019/09/01/ 2019, doi: doi.org/10.1016/j.matlet.2019.04.082.

[115] A. B. Phillips *et al.*, "High speed, intermediate resolution, large area laser beam induced current imaging and laser scribing system for photovoltaic devices and modules," *Review of Scientific Instruments,* **vol. 87**, no**.** 9, p. 093708, 2016.

[116] Z. Song *et al.*, "Perovskite Solar Cell Stability in Humid Air: Partially Reversible Phase Transitions in the PbI_2-CH_3NH_3I-H_2O System," *Advanced Energy Materials,* **vol. 6**, no**.** 19, p. 1600846, 2016, doi: doi.org/10.1002/aenm.201600846.

[117] Z. Song *et al.*, "Probing photocurrent nonuniformities in the subcells of monolithic perovskite/silicon tandem solar cells," *The Journal of Physical Chemistry Letters,* **vol. 7**, no**.** 24, pp. 5114-5120, 2016.

[118] R. Hosseinian Ahangharnejhad *et al.*, "Decreasing the resolution limit of laser beam induced current measurements below the beam size without confocal optics: Determining laser scribe widths," *Sol. Energy Mater. Sol. Cells,* **vol. 215**, p. 110660, 2020/09/15/ 2020, doi: doi.org/10.1016/j.solmat.2020.110660.

[119] B. G. Mendis, Q. M. Ramasse, T. P. Shalvey, J. D. Major, and K. Durose, "Optical Properties and Dielectric Functions of Grain Boundaries and Interfaces in CdTe Thin-Film Solar Cells," *ACS Applied Energy Materials,* **vol. 2**, no**.** 2, pp. 1419-1427, 2019/02/25 2019, doi: 10.1021/acsaem.8b01995.

[120] D.-B. Li *et al.*, "Maximize CdTe solar cell performance through copper activation engineering," *Nano Energy,* **vol. 73**, p. 104835, 2020/07/01/ 2020, doi: doi.org/10.1016/j.nanoen.2020.104835.

[121] T. Ablekim *et al.*, "Thin-Film Solar Cells with 19% Efficiency by Thermal Evaporation of CdSe and CdTe," *ACS Energy Letters,* **vol. 5**, no**.** 3, pp. 892-896, 2020/03/13 2020, doi: 10.1021/acsenergylett.9b02836.

[122] A. H. Munshi *et al.*, "Polycrystalline CdSeTe/CdTe Absorber Cells With 28 mA/cm^2 Short-Circuit Current," *IEEE Journal of Photovoltaics,* **vol. 8**, no**.** 1, pp. 310-314, 2018, doi: 10.1109/JPHOTOV.2017.2775139.

[123] J. Huang, D. Yang, W. Li, J. Zhang, L. Wu, and W. Wang, "Copassivation of polycrystalline CdTe absorber by CuCl thin films for CdTe solar cells," *Applied Surface Science,* 2019/03/23/ 2019, doi: https://doi.org/10.1016/j.apsusc.2019.03.253.

[124] D. Grecu and A. D. Compaan, "Photoluminescence study of Cu diffusion and electromigration in CdTe," *Applied Physics Letters,* **vol. 75**, no**.** 3, pp. 361-363, 1999, doi: 10.1063/1.124375.

[125] D. Krasikov and I. Sankin, "Defect interactions and the role of complexes in the CdTe solar cell absorber," *Journal of Materials Chemistry A,* **vol. 5**, no**.** 7, pp. 3503-3513, 2017, doi: 10.1039/C6TA09155E.

[126] L. Zhang, J. L. F. Da Silva, J. Li, Y. Yan, T. A. Gessert, and S.-H. Wei, "Effect of Copassivation of Cl and Cu on CdTe Grain Boundaries," *Physical Review Letters,* **vol. 101**, no**.** 15, p. 155501, 10/09/ 2008, doi: 10.1103/PhysRevLett.101.155501.

[127] R. Akis *et al.*, "Extracting Cu diffusion parameters in polycrystalline CdTe," in *2014 IEEE 40th Photovoltaic Specialist Conference (PVSC)*, Denver, CO, US, 8-13 June 2014 2014, pp. 3276-3281, doi: 10.1109/PVSC.2014.6925635.

[128] Y. Yan, K. Jones, J. Zhou, X. Wu, and M. Al-Jassim, "TEM study of Locations of Cu in CdTe Solar Cells," *MRS Proceedings,* **vol. 1012**, pp. 1012-Y04-09, 2011, Art no. 1012-y04-09, doi: 10.1557/PROC-1012-Y04-09.

[129] J. Perrenoud *et al.*, "A comprehensive picture of Cu doping in CdTe solar cells," *Journal of Applied Physics,* **vol. 114**, no**.** 17, p. 174505, 2013, doi: 10.1063/1.4828484.

[130] D. Krasikov, A. Knizhnik, B. Potapkin, S. Selezneva, and T. Sommerer, "First-principles-based analysis of the influence of Cu on CdTe electronic properties," *Thin Solid Films,* **vol. 535**, pp. 322-325, 2013/05/15/ 2013, doi: doi.org/10.1016/j.tsf.2012.10.027.

[131] N. R. Paudel and Y. Yan, "Fabrication and characterization of high-efficiency CdTe-based thin-film solar cells on commercial SnO2:F-coated soda-lime glass substrates," *Thin Solid Films,* **vol. 549**, pp. 30-35, 2013/12/31/ 2013, doi: https://doi.org/10.1016/j.tsf.2013.07.020.

[132] N. R. Paudel, C. Xiao, and Y. Yan, "Close-space sublimation grown CdS window layers for CdS/CdTe thin-film solar cells," *Journal of Materials Science: Materials in Electronics,* journal article **vol. 25**, no**.** 4, pp. 1991-1998, April 01 2014, doi: 10.1007/s10854-014-1834-1.

[133] K. D. Dobson, I. Visoly-Fisher, G. Hodes, and D. Cahen, "Stability of CdTe/CdS thin-film solar cells," *Sol. Energy Mater. Sol. Cells,* **vol. 62**, no**.** 3, pp. 295-325, 2000/05/15/ 2000, doi: doi.org/10.1016/S0927-0248(00)00014-3.

[134] N. R. Paudel, C. R. Grice, C. Xiao, and Y. Yan, "High temperature CSS processed CdTe solar cells on commercial SnO_2:F/SnO_2 coated soda-lime glass substrates," *Journal of Materials Science: Materials in Electronics,* **vol. 26**, no**.** 7, pp. 4708-4715, July 01 2015, doi: 10.1007/s10854-015-2923-5.

[135] J. Yang and S.-H. Wei, "First-principles study of the band gap tuning and doping control in $CdSe_xTe_{1-x}$ alloy for high efficiency solar cell," *Chinese Physics B,* **vol. 28**, no**.** 8, p. 086106, 2019/08 2019, doi: 10.1088/1674-1056/28/8/086106.

[136] D.-B. Li *et al.*, "Eliminating S-Kink To Maximize the Performance of MgZnO/CdTe Solar Cells," *ACS Applied Energy Materials,* **vol. 2**, no**.** 4, pp. 2896-2903, 2019/04/22 2019, doi: 10.1021/acsaem.9b00233.

[137] T. R. N. Kutty and N. Raghu, "Varistors based on polycrystalline ZnO:Cu," *Applied Physics Letters,* **vol. 54**, no**.** 18, pp. 1796-1798, 1989/05/01 1989, doi: 10.1063/1.101267.

[138] C. X. Xu, X. W. Sun, X. H. Zhang, L. Ke, and S. J. Chua, "Photoluminescent properties of copper-doped zinc oxide nanowires," *Nanotechnology,* **vol. 15**, no**.** 7, pp. 856-861, 2004/06/05 2004, doi: 10.1088/0957-4484/15/7/026.

[139] A. Hausmann, B. Schallenberger, and R. Roll, "A new model for ZnO:Cu undergoing dynamic Jahn-Teller coupling," *ZPhyB,* **vol. 40**, no**.** 1, pp. 1-7, 1980/03/01 1980, doi: 10.1007/BF01295062.

[140] D. Kuciauskas *et al.*, "Recombination Analysis in Cadmium Telluride Photovoltaic Solar Cells With Photoluminescence Spectroscopy," *IEEE Journal of Photovoltaics,* **vol. 6**, no**.** 1, pp. 313-318, 2016, doi: 10.1109/JPHOTOV.2015.2483366.

[141] Y. Deng, J. Yang, R. Yang, K. Shen, D. Wang, and D. Wang, "Cu-doped CdS and its application in CdTe thin film solar cell," *AIP Advances,* **vol. 6**, no**.** 1, p. 015203, 2016, doi: 10.1063/1.4939817.

[142] R. A. Awni *et al.*, "The Effects of Hydrogen Iodide Back Surface Treatment on CdTe Solar Cells," *Solar RRL,* **vol. 3**, no**.** 3, p. 1800304, 2019, doi: 10.1002/solr.201800304.

[143] R. A. Awni *et al.*, "Influences of buffer material and fabrication atmosphere on the electrical properties of CdTe solar cells," *Progress in Photovoltaics: Research and Applications,* **vol. 27**, no**.** 12, pp. 1115-1123, 2019, doi: 10.1002/pip.3192.

[144] A. Balcioglu, R. K. Ahrenkiel, and F. Hasoon, "Deep-level impurities in CdTe/CdS thin-film solar cells," (in English), *Journal of Applied Physics,* **vol. 88**, no**.** 12, pp. 7175-7178, Dec 15 2000, doi: Doi 10.1063/1.1326465.

[145] F. H. Seymour, V. Kaydanov, T. R. Ohno, and D. Albin, "Cu and $CdCl_2$ influence on defects detected in CdTe solar cells with admittance spectroscopy," *Applied Physics Letters,* **vol. 87**, no**.** 15, 2005, doi: 10.1063/1.2099515.

[146] T. D. Dzhafarov, S. S. Yesilkaya, N. Yilmaz Canli, and M. Caliskan, "Diffusion and influence of Cu on properties of CdTe thin films and CdTe/CdS cells," *Sol. Energy Mater. Sol. Cells,* **vol. 85**, no**.** 3, pp. 371-383, 2005/01/31/ 2005, doi: doi.org/10.1016/j.solmat.2004.05.007.

[147] J.-H. Yang, W.-J. Yin, J.-S. Park, J. Ma, and S.-H. Wei, "Review on first-principles study of defect properties of CdTe as a solar cell absorber," *Semicond. Sci. Technol.,* **vol. 31**, no**.** 8, p. 083002, 2016/07/15 2016, doi: 10.1088/0268-1242/31/8/083002.

[148] K. K. Chin, T. A. Gessert, and S. Wei, "The roles of CU impurity states in CdTe thin film solar cells," in *2010 35th IEEE Photovoltaic Specialists Conference*, Honolulu, HI, US, 20-25 June 2010 2010, pp. 001915-001918, doi: 10.1109/PVSC.2010.5616379.

[149] M. S. Gudiksen, L. J. Lauhon, J. Wang, D. C. Smith, and C. M. Lieber, "Growth of nanowire superlattice structures for nanoscale photonics and electronics," *Nature,* **vol. 415**, no**.** 6872, p. 617, 2002.

[150] S. E. Steinvall *et al.*, "Multiple morphologies and functionality of nanowires made from earth-abundant zinc phosphide," *Nanoscale Horizons,* **vol. 5**, no**.** 2, pp. 274-282, 2020.

[151] Y. Li *et al.*, "Solution-processed one-dimensional $CsCu_2I_3$ nanowires for polarization-sensitive and flexible ultraviolet photodetectors," *Materials Horizons,* 2020.

[152] X. Duan, Y. Huang, Y. Cui, J. Wang, and C. M. Lieber, "Indium phosphide nanowires as building blocks for nanoscale electronic and optoelectronic devices," *Nature,* **vol. 409**, no**.** 6816, pp. 66-69, 2001.

[153] Y. Huang, X. Duan, and C. M. Lieber, "Nanowires for integrated multicolor nanophotonics," *Small,* **vol. 1**, no**.** 1, pp. 142-147, 2005.

[154] S. Lin, W. Li, Z. Chen, J. Shen, B. Ge, and Y. Pei, "Tellurium as a high-performance elemental thermoelectric," *Nature Communications,* **vol. 7**, no**.** 1, p. 10287, 2016/01/11 2016, doi: 10.1038/ncomms10287.

[155] J.-W. Liu, F. Chen, M. Zhang, H. Qi, C.-L. Zhang, and S.-H. Yu, "Rapid Microwave-Assisted Synthesis of Uniform Ultralong Te Nanowires, Optical Property, and Chemical Stability," *Langmuir,* **vol. 26**, no**.** 13, pp. 11372-11377, 2010/07/06 2010, doi: 10.1021/la100772n.

[156] Y. Zhang *et al.*, "Low-cost writing method for self-powered paper-based UV photodetectors utilizing Te/TiO_2 and Te/ZnO heterojunctions," *Nanoscale Horizons,* **vol. 4**, no**.** 2, pp. 452-456, 2019.

[157] Y. Wang *et al.*, "Two-dimensional ferroelectricity and switchable spin-textures in ultra-thin elemental Te multilayers," *Materials Horizons,* **vol. 5**, no**.** 3, pp. 521-528, 2018.

[158] A. V. Naumov, "Erratum: To the article “Selenium and Tellurium: state of the markets, the crisis, and its consequences” by A. V. Naumov, Vol. 54, Nos. 3–4, pages 197–200, July, 2010," *Metallurgist,* journal article **vol. 54**, no**.** 9, pp. 714-714, January 01 2011, doi: 10.1007/s11015-011-9347-0.

[159] B. Farag and S. Khodier, "Direct and indirect transitions in copper telluride thin films," *Thin Solid Films,* **vol. 201**, no**.** 2, pp. 231-240, 1991.

[160] B. N. Zhong *et al.*, "Controlled solvothermal synthesis of single-crystal tellurium nanowires, nanotubes and trifold structures and their photoelectrical properties," *CrystEngComm,* 10.1039/C7CE00497D **vol. 19**, no**.** 20, pp. 2813-2820, 2017, doi: 10.1039/C7CE00497D.

[161] X. Wu *et al.*, "Controlled synthesis of multi-morphology Te crystals by a convenient Lewis acid/base-assisted solvothermal method," *Journal of Nanoparticle Research,* **vol. 14**, no**.** 8, p. 1009, 2012.

[162] Z. He and S.-H. Yu, "Large scale synthesis of tellurium nanoribbons in tetraethylene pentamine aqueous solution and the stability of tellurium nanoribbons in ethanol and water," *The Journal of Physical Chemistry B,* **vol. 109**, no**.** 48, pp. 22740-22745, 2005.

[163] H.-S. Qian, S.-H. Yu, J.-Y. Gong, L.-B. Luo, and L.-f. Fei, "High-Quality Luminescent Tellurium Nanowires of Several Nanometers in Diameter and High Aspect Ratio Synthesized by a Poly (Vinyl Pyrrolidone)-Assisted Hydrothermal Process," *Langmuir,* **vol. 22**, no**.** 8, pp. 3830-3835, 2006/04/01 2006, doi: 10.1021/la0530211.

[164] Z. Wang, L. Wang, J. Huang, H. Wang, L. Pan, and X. Wei, "Formation of single-crystal tellurium nanowires and nanotubes via hydrothermal recrystallization and their gas sensing properties at room temperature," *Journal of Materials Chemistry,* 10.1039/B924462J **vol. 20**, no**.** 12, pp. 2457-2463, 2010, doi: 10.1039/B924462J.

[165] U. K. Gautam and C. N. R. Rao, "Controlled synthesis of crystalline tellurium nanorods, nanowires, nanobelts and related structures by a self-seeding solution process," *Journal of Materials Chemistry,* 10.1039/B405006A **vol. 14**, no**.** 16, pp. 2530-2535, 2004, doi: 10.1039/B405006A.

[166] G. Xi, Y. Peng, W. Yu, and Y. Qian, "Synthesis, Characterization, and Growth Mechanism of Tellurium Nanotubes," *Crystal Growth & Design,* **vol. 5**, no**.** 1, pp. 325-328, 2005/01/01 2005, doi: 10.1021/cg049867p.

[167] Q. Wang, G.-D. Li, Y.-L. Liu, S. Xu, K.-J. Wang, and J.-S. Chen, "Fabrication and growth mechanism of selenium and tellurium nanobelts through a vacuum vapor deposition route," *The Journal of Physical Chemistry C,* **vol. 111**, no**.** 35, pp. 12926-12932, 2007.

[168] P. Mohanty, J. Park, and B. Kim, "Large scale synthesis of highly pure single crystalline tellurium nanowires by thermal evaporation method," *Journal of Nanoscience and Nanotechnology,* **vol. 6**, no**.** 11, pp. 3380-3383, 2006.

[169] Z.-H. Lin, Z. Yang, and H.-T. Chang, "Preparation of fluorescent tellurium nanowires at room temperature," *Cryst. Growth Des.,* **vol. 8**, no**.** 1, pp. 351-357, 2007.

[170] R. R. Silva *et al.*, "Facile synthesis of tellurium nanowires and study of their third-order nonlinear optical properties," *J. Braz. Chem. Soc.,* **vol. 28**, no**.** 1, pp. 58-67, 2017.

[171] N. R. Jana, L. Gearheart, and C. J. Murphy, "Wet Chemical Synthesis of High Aspect Ratio Cylindrical Gold Nanorods," *The Journal of Physical Chemistry B,* **vol. 105**, no**.** 19, pp. 4065-4067, 2001/05/01 2001, doi: 10.1021/jp0107964.

[172] C. K. Senthil kumaran *et al.*, "Synthesis and Characterization of Selenium Nanowires," *ISRN Nanotechnology,* **vol. 2011**, p. 4, 2011, Art no. 589073, doi: 10.5402/2011/589073.

[173] H. Yang, S. W. Finefrock, J. D. Albarracin Caballero, and Y. Wu, "Environmentally Benign Synthesis of Ultrathin Metal Telluride Nanowires," *Journal of the American Chemical Society,* **vol. 136**, no**.** 29, pp. 10242-10245, 2014/07/23 2014, doi: 10.1021/ja505304v.

[174] C.-C. Lin *et al.*, "Low temperature synthesis of copper telluride nanostructures: phase formation, growth, and electrical transport properties," *Journal of Materials Chemistry,* **vol. 22**, no**.** 15, pp. 7098-7103, 2012, doi: 10.1039/C2JM16486H.

[175] Z. Zhang, B. Zhao, and L. Hu, "PVP protective mechanism of ultrafine silver powder synthesized by chemical reduction processes," *J. Solid State Chem.,* **vol. 121**, no**.** 1, pp. 105-110, 1996.

[176] G. Kresse, J. Furthmüller, and J. Hafner, "Theory of the crystal structures of selenium and tellurium: the effect of generalized-gradient corrections to the local-density approximation," *PhRvB,* **vol. 50**, no**.** 18, p. 13181, 1994.

[177] H. Park *et al.*, "Aqueous chemical synthesis of tellurium nanowires using a polymeric template for thermoelectric materials," *CrystEngComm,* 10.1039/C4CE02222J **vol. 17**, no**.** 5, pp. 1092-1097, 2015, doi: 10.1039/C4CE02222J.

[178] G. Li, X. Cui, C. Tan, and N. Lin, "Solvothermal synthesis of polycrystalline tellurium nanoplates and their conversion into single crystalline nanorods," *RSC Advances,* **vol. 4**, no**.** 2, pp. 954-958, 2014.

[179] M. A. Green, E. D. Dunlop, J. Hohl-Ebinger, M. Yoshita, N. Kopidakis, and A. W. Ho-Baillie, "Solar cell efficiency tables (Version 55)," *Progress in Photovoltaics: Research and Applications,* **vol. 28**, no**.** 1, pp. 3-15, 2020.

[180] A. Kanevce and T. A. Gessert, "Optimizing CdTe solar cell performance: Impact of variations in minority-carrier lifetime and carrier density profile," *IEEE Journal of Photovoltaics,* **vol. 1**, no**.** 1, pp. 99-103, 2011.

[181] G. Dingemans and W. Kessels, "Status and prospects of Al_2O_3-based surface passivation schemes for silicon solar cells," *Journal of Vacuum Science & Technology A: Vacuum, Surfaces, and Films,* **vol. 30**, no**.** 4, p. 040802, 2012.

[182] C. L. Perkins *et al.*, "Interfaces Between CdTe and ALD Al_2O_3," *IEEE Journal of Photovoltaics,* **vol. 8**, no**.** 6, pp. 1858-1861, 2018.

[183] K. K. Subedi *et al.*, "Enabling Bifacial Thin Film Devices by Developing a Back Surface Field using Cu_xAlO_y," *Nano Energy,* p. 105827, 2021.

[184] F. K. Alfadhili *et al.*, "Back-Surface Passivation of CdTe Solar Cells Using Solution-Processed Oxidized Aluminum," *ACS Applied Materials & Interfaces,* **vol. 12**, no**.** 46, pp. 51337-51343, 2020.

[185] F. Werner *et al.*, "Very low surface recombination velocities on p-and n-type c-Si by ultrafast spatial atomic layer deposition of aluminum oxide," *Applied Physics Letters,* **vol. 97**, no**.** 16, p. 162103, 2010.

[186] K. Meinander and J. S. Preston, "A DFT study on the effect of surface termination in CdTe (111)/α-Al_2O_3 (0001) heteroepitaxy," *Surface Science,* **vol. 632**, pp. 93-97, 2015.

[187] D. Kuciauskas, J. M. Kephart, J. Moseley, W. K. Metzger, W. S. Sampath, and P. Dippo, "Recombination velocity less than 100 cm/s at polycrystalline Al2O3/CdSeTe interfaces," *Applied Physics Letters,* **vol. 112**, no**.** 26, p. 263901, 2018.

[188] J. Li *et al.*, "Controlled activation of ZnTe: Cu contacted CdTe solar cells using rapid thermal processing," *Sol. Energy Mater. Sol. Cells,* **vol. 133**, pp. 208-215, 2015.

[189] T. Gessert, W. Metzger, P. Dippo, S. Asher, R. Dhere, and M. Young, "Dependence of carrier lifetime on Cu-contacting temperature and ZnTe: Cu thickness in CdS/CdTe thin film solar cells," *Thin Solid Films,* **vol. 517**, no**.** 7, pp. 2370-2373, 2009.

[190] L. Kungumadevi and R. Sathyamoorthy, "Structural, electrical, and optical properties of PbTe thin films prepared by simple flash evaporation method," *Advances in Condensed Matter Physics,* **vol. 2012**, 2012.

[191] L. Kungumadevi and R. Sathyamoorthy, "Synthesis of PbTe nanocubes, worm-like structures and nanoparticles by simple thermal evaporation method," *Bull. Mater. Sci.,* **vol. 36**, no**.** 5, pp. 771-778, 2013.

[192] Z. Dughaish, "Lead telluride as a thermoelectric material for thermoelectric power generation," *Physica B: Condensed Matter,* **vol. 322**, no**.** 1-2, pp. 205-223, 2002.

[193] Y. Kanai and K. Shohno, "Dielectric Constant of PbTe," *Japanese Journal of Applied Physics,* **vol. 2**, no**.** 1, pp. 6-10, 1963/01 1963, doi: 10.1143/jjap.2.6.

[194] S.-M. Yong, P. Muralidharan, D. S. Kim, and D. K. Kim, "One-step hydrothermal synthesis of carbon-coated PbTe nanowires for thermoelectric applications," *Rev. Adv. Mater. Sci,* **vol. 28**, pp. 13-16, 2011.

[195] M. Sabet and M. Salavati-Niasari, "Fabrication of inorganic sensitized solar cells by drop casting deposition of PbSe and PbTe on the TiO2 surface," *Journal of Nanostructures,* **vol. 7**, no**.** 4, pp. 323-330, 2017.

[196] A. Barros, E. Abramof, and P. Rappl, "Electrical and optical properties of PbTe p-n junction infrared sensors," *Journal of Applied Physics,* **vol. 99**, no**.** 2, p. 024904, 2006.

[197] W. Heiss *et al.*, "Centrosymmetric Pb Te⁄Cd Te quantum dots coherently embedded by epitaxial precipitation," *Applied Physics Letters,* **vol. 88**, no**.** 19, p. 192109, 2006.

[198] H. Groiss *et al.*, "Size control and midinfrared emission of epitaxial Pb Te⁄Cd Te quantum dot precipitates grown by molecular beam epitaxy," *Applied Physics Letters,* **vol. 91**, no**.** 22, p. 222106, 2007.

[199] E. G. LeBlanc, "Band Gap Engineering Studies of PbTe, SnTe, and CdSeTe for CdTe Solar Cell Applications," Doctor of Philosophy, Material Science, Engineering, and Commercialization, Texas State University, 28243320, 2020.

[200] J. Si, S. Jin, H. Zhang, P. Zhu, D. Qiu, and H. Wu, "Experimental determination of valence band offset at PbTe/CdTe (111) heterojunction interface by x-ray photoelectron spectroscopy," *Applied Physics Letters,* **vol. 93**, no**.** 20, p. 202101, 2008.

[201] G. a. Tai, B. Zhou, and W. Guo, "Structural characterization and thermoelectric transport properties of uniform single-crystalline lead telluride nanowires," *The Journal of Physical Chemistry C,* **vol. 112**, no**.** 30, pp. 11314-11318, 2008.

[202] Y. Yang, D. K. Taggart, M. H. Cheng, J. C. Hemminger, and R. M. Penner, "Correction to "High-Throughput Measurement of the Seebeck Coefficient and the Electrical Conductivity of Lithographically Patterned Polycrystalline PbTe Nanowires"," *The Journal of Physical Chemistry Letters,* **vol. 2**, no**.** 9, pp. 944-944, 2011/05/05 2011, doi: 10.1021/jz200449s.

[203] S. Gholamrezaei, M. Salavati-Niasari, and D. Ghanbari, "Synthesis and application of lead telluride nanoparticles for degrediation of organic pollution," *Journal of Industrial and Engineering Chemistry,* **vol. 20**, no**.** 6, pp. 4000-4007, 2014.

[204] S. Ahmadian-Fard-Fini, M. Salavati-Niasari, A. Monfared, and F. Mohandes, "PbTe nanostructures: Microwave-assisted synthesis by using lead Schiff-base precursor, characterization and formation mechanism," *Comptes Rendus Chimie,* **vol. 16**, no**.** 9, pp. 778-788, 2013.

[205] D. Pokhrel, E. Bastola, A. B. Phillips, M. J. Heben, and R. J. Ellingson, "Aspect ratio controlled synthesis of tellurium nanowires for photovoltaic applications," *Materials Advances,* **vol. 1**, no**.** 8, pp. 2721-2728, 2020.

[206] D. Pokhrel, E. Bastola, K. K. Subedi, A. Phillips, M. J. Heben, and R. J. Ellingson, "Solution-Processed Copper Telluride Nanowire Thin Film as a Back-Buffer Layer to Cadmium Telluride Solar Cells," in *2020 47th IEEE Photovoltaic Specialists Conference (PVSC)*, Virtual.Online, 15 June-21 Aug. 2020 2020, pp. 2561-2563, doi: 10.1109/PVSC45281.2020.9300649.

[207] M. Matin and M. Dey, "High performance ultra-thin CdTe solar cell with Lead Telluride BSF," in *2014 International Conference on Informatics, Electronics & Vision (ICIEV)*, Dhaka, Bangladesh, 2014: IEEE, pp. 1-5.

[208] E. Bastola, A. V. Bordovalos, E. LeBlanc, N. Shrestha, M. O. Reese, and R. J. Ellingson, "Doping of CdTe using $CuCl_2$ Solution for Highly Efficient Photovoltaic Devices," in *2019 IEEE 46th Photovoltaic Specialists Conference (PVSC)*, Chicago, IL, US, 2019: IEEE, pp. 1846-1850.

[209] B. Zhang *et al.*, "Phonon blocking by two dimensional electron gas in polar CdTe/PbTe heterojunctions," *Applied Physics Letters,* **vol. 104**, no**.** 16, p. 161601, 2014.

[210] H. Wu *et al.*, "Observation of phonon modes in epitaxial PbTe films grown by molecular beam epitaxy," *Journal of Applied Physics,* **vol. 101**, no**.** 10, p. 103505, 2007.

[211] M. Romcevic, N. Romcevic, D. Khokhlov, and I. Ivanchik, "Raman spectroscopy of impurity states in gallium-doped PbTe," *J. Phys.: Condens. Matter,* **vol. 12**, no**.** 40, p. 8737, 2000.

[212] S. Demtsu, D. Albin, J. Sites, W. Metzger, and A. Duda, "Cu-related recombination in CdS/CdTe solar cells," *Thin Solid Films,* **vol. 516**, no**.** 8, pp. 2251-2254, 2008.

[213] I. Rimmaudo, A. Salavei, B. L. Xu, S. Di Mare, and A. Romeo, "Superior stability of ultra thin CdTe solar cells with simple Cu/Au back contact," *Thin Solid Films,* **vol. 582**, pp. 105-109, 2015.

[214] N. R. Paudel and Y. Yan, "Application of copper thiocyanate for high open-circuit voltages of CdTe solar cells," *Progress in Photovoltaics: Research and Applications,* **vol. 24**, no**.** 1, pp. 94-101, 2016.

[215] A. Niemegeers and M. Burgelman, "Effects of the Au/CdTe back contact on IV and CV characteristics of Au/CdTe/CdS/TCO solar cells," *Journal of Applied Physics,* **vol. 81**, no**.** 6, pp. 2881-2886, 1997.

[216] S. S. Hegedus and W. N. Shafarman, "Thin-film solar cells: device measurements and analysis," *Progress in Photovoltaics: Research and Applications,* **vol. 12**, no**.** 2-3, pp. 155-176, 2004.

[217] N. Thongprong, T. Supasai, Y. Li, I.-M. Tang, and N. Rujisamphan, "Insights into Recombination Processes from Light Intensity–Dependent Open-Circuit Voltages and Ideality Factors in Planar Perovskite Solar Cells," *Energy Technology,* **vol. 8**, no**.** 5, p. 1901196, 2020.

[218] M. A. Green, E. D. Dunlop, J. Hohl-Ebinger, M. Yoshita, N. Kopidakis, and A. W. Y. Ho-Baillie, "Solar cell efficiency tables (Version 55)," *Progress in Photovoltaics: Research and Applications,* **vol. 28**, no**.** 1, pp. 3-15, 2020, doi: 10.1002/pip.3228.

[219] M. Gloeckler, "Research opportunities supporting 25% CdTe PV," in *MRS Spring Meeting* Phoenix, AZ, US, 2019.

[220] E. S. Barnard *et al.*, "3D Lifetime Tomography Reveals How $CdCl_2$ Improves Recombination Throughout CdTe Solar Cells," *Adv. Mater.,* **vol. 29**, no**.** 3, p. 1603801, 2017, doi: 10.1002/adma.201603801.

[221] D. E. Swanson, J. R. Sites, and W. S. Sampath, "Co-sublimation of $CdSe_xTe_{1-x}$ layers for CdTe solar cells," *Sol. Energy Mater. Sol. Cells,* **vol. 159**, pp. 389-394, 2017/01/01/ 2017, doi: dx.doi.org/10.1016/j.solmat.2016.09.025.

[222] T. Song, A. Kanevce, and J. R. Sites, "Emitter/absorber interface of CdTe solar cells," *Journal of Applied Physics,* **vol. 119**, no**.** 23, p. 233104, 2016, doi: 10.1063/1.4953820.

[223] J. M. Kephart, J. W. McCamy, Z. Ma, A. Ganjoo, F. M. Alamgir, and W. S. Sampath, "Band alignment of front contact layers for high-efficiency CdTe solar cells," *Sol. Energy Mater. Sol. Cells,* **vol. 157**, pp. 266-275, 2016/12/01/ 2016, doi: doi.org/10.1016/j.solmat.2016.05.050.

[224] A. Kanevce, M. O. Reese, T. M. Barnes, S. A. Jensen, and W. K. Metzger, "The roles of carrier concentration and interface, bulk, and grain-boundary recombination for 25% efficient CdTe solar cells," *Journal of Applied Physics,* **vol. 121**, no**.** 21, p. 214506, 2017, doi: 10.1063/1.4984320.

[225] J. N. Duenow and W. K. Metzger, "Back-surface recombination, electron reflectors, and paths to 28% efficiency for thin-film photovoltaics: A CdTe case study," *Journal of Applied Physics,* **vol. 125**, no**.** 5, p. 053101, 2019, doi: 10.1063/1.5063799.

[226] G. K. Liyanage, A. B. Phillips, F. K. Alfadhili, R. J. Ellingson, and M. J. Heben, "The Role of Back Buffer Layers and Absorber Properties for >25% Efficient CdTe Solar Cells," *ACS Applied Energy Materials,* 2019/07/08 2019, doi: 10.1021/acsaem.9b00367.

[227] A. B. Phillips, K. K. Subedi, G. K. Liyanage, F. K. Alfadhili, R. J. Ellingson, and M. J. Heben, "Understanding and Advancing Bifacial Thin Film Solar Cells," *ACS Applied Energy Materials,* 2020/06/09 2020, doi: 10.1021/acsaem.0c00851.

[228] R. S. Bonilla, B. Hoex, P. Hamer, and P. R. Wilshaw, "Dielectric surface passivation for silicon solar cells: A review," *physica status solidi (a),* **vol. 214**, no**.** 7, p. 1700293, 2017, doi: 10.1002/pssa.201700293.

[229] J. Schmidt, A. Merkle, R. Brendel, B. Hoex, M. C. M. v. de Sanden, and W. M. M. Kessels, "Surface passivation of high-efficiency silicon solar cells by atomic-layer-deposited Al2O3," *Progress in Photovoltaics: Research and Applications,* **vol. 16**, no**.** 6, pp. 461-466, 2008, doi: 10.1002/pip.823.

[230] Y. Jiang *et al.*, "Passivation properties of alumina for multicrystalline silicon nanostructure prepared by spin-coating method," *Appl. Phys. A,* **vol. 124**, no**.** 2, p. 95, 2018/01/09 2018, doi: 10.1007/s00339-017-1542-9.

[231] G. Birant, J. de Wild, M. Meuris, J. Poortmans, and B. Vermang, "Dielectric-Based Rear Surface Passivation Approaches for Cu(In,Ga)Se2 Solar Cells—A Review," *Applied Sciences,* **vol. 9**, no**.** 4, p. 677, 2019.

[232] F. Werner, B. Veith-Wolf, M. Melchiorre, F. Babbe, J. Schmidt, and S. Siebentritt, "Ultra-thin passivation layers in Cu(In,Ga)Se2 thin-film solar cells: full-area passivated front contacts and their impact on bulk doping," *Sci. Rep.,* **vol. 10**, no**.** 1, p. 7530, 2020/05/05 2020, doi: 10.1038/s41598-020-64448-9.

[233] J. M. Kephart *et al.*, "Sputter-Deposited Oxides for Interface Passivation of CdTe Photovoltaics," *IEEE Journal of Photovoltaics,* **vol. 8**, no**.** 2, pp. 587-593, 2018, doi: 10.1109/JPHOTOV.2017.2787021.

[234] D. Kuciauskas, J. Moseley, P. Ščajev, and D. Albin, "Radiative Efficiency and Charge-Carrier Lifetimes and Diffusion Length in Polycrystalline CdSeTe Heterostructures," *physica status solidi (RRL) – Rapid Research Letters,* **vol. 14**, no**.** 3, p. 1900606, 2020, doi: 10.1002/pssr.201900606.

[235] S. M. Jovanovic *et al.*, "Optical characterization of epitaxial single crystal CdTe thin films on Al2O3 (0001) substrates," *Thin Solid Films,* **vol. 570**, pp. 155-158, 2014/11/03/ 2014, doi: doi.org/10.1016/j.tsf.2014.09.027.

[236] D. Kuciauskas, J. M. Kephart, J. Moseley, W. K. Metzger, W. S. Sampath, and P. Dippo, "Recombination velocity less than 100 cm/s at polycrystalline Al2O3/CdSeTe interfaces," *Applied Physics Letters,* **vol. 112**, no**.** 26, p. 263901, 2018, doi: 10.1063/1.5030870.

[237] J. Liang *et al.*, "Rectification and tunneling effects enabled by Al2O3 atomic layer deposited on back contact of CdTe solar cells," *Applied Physics Letters,* **vol. 107**, no**.** 1, p. 013907, 2015, doi: 10.1063/1.4926601.

[238] J. G. Werthen, J. P. Häring, and R. H. Bube, "Correlation between cadmium telluride surface oxidation and metal junctions," *Journal of Applied Physics,* **vol. 54**, no**.** 2, pp. 1159-1161, 1983, doi: 10.1063/1.332091.

[239] X. Di, X. Li, D. Wang, Q. Li, K. Shen, and D. Wang, "CdTe thin film solar cell with NiO as a back contact buffer layer," *Sol. Energy Mater. Sol. Cells,* **vol. 169**, pp. 61-67, 2017/09/01/ 2017, doi: doi.org/10.1016/j.solmat.2017.05.006.

[240] R. Watanabe, M. Kawashima, and Y. Saito, "Film properties of alumina passivation layer for silicon solar cells prepared by spin-coating method," *Thin Solid Films,* **vol. 590**, pp. 98-102, 2015/09/01/ 2015, doi: doi.org/10.1016/j.tsf.2015.07.044.

[241] C. L. Perkins, D. L. McGott, M. O. Reese, and W. K. Metzger, "SnO2-Catalyzed Oxidation in High-Efficiency CdTe Solar Cells," *ACS Applied Materials & Interfaces,* **vol. 11**, no**.** 13, pp. 13003-13010, 2019/04/03 2019, doi: 10.1021/acsami.9b00835.

[242] S. L. Rugen-Hankey *et al.*, "Improvement to thin film CdTe solar cells with controlled back surface oxidation," *Sol. Energy Mater. Sol. Cells,* **vol. 136**, pp. 213-217, 2015/05/01/ 2015, doi: doi.org/10.1016/j.solmat.2014.10.044.

[243] Craig L Perkins *et al.*, "Interfaces between CdTe and ALD Al2O3," in *7th World Conference on Photovoltaic Energy Conversion*, Waikoloa, HI, US, 2018.

[244] T. Maruyama and S. Arai, "Aluminum oxide thin films prepared by chemical vapor deposition from aluminum acetylacetonate," *Applied Physics Letters,* **vol. 60**, no**.** 3, pp. 322-323, 1992, doi: 10.1063/1.106699.

[245] J. Pan, M. Gloeckler, and J. R. Sites, "Hole current impedance and electron current enhancement by back-contact barriers in CdTe thin film solar cells," *Journal of Applied Physics,* **vol. 100**, no**.** 12, p. 124505, 2006, doi: 10.1063/1.2400799.

[246] T. A. Gessert *et al.*, "Evolution of CdS/CdTe device performance during Cu diffusion," in *Conference Record of the Thirty-First IEEE Photovoltaic Specialists Conference, 2005.*, Lake Buena Vista, FL, US, 3-7 Jan. 2005 2005, pp. 291-294, doi: 10.1109/PVSC.2005.1488126.

[247] M. A. Green, E. D. Dunlop, D. H. Levi, J. Hohl-Ebinger, M. Yoshita, and A. W. Y. Ho-Baillie, "Solar cell efficiency tables (version 54)," *Progress in Photovoltaics,* **vol. 27**, no**.** 7, pp. 565-575, 2019, doi: 10.1002/pip.3171.

[248] M. Gloeckler, I. Sankin, and Z. Zhao, "CdTe solar cells at the threshold to 20% efficiency," *IEEE Journal of Photovoltaics,* **vol. 3**, no**.** 4, pp. 1389-1393, 2013.

[249] W. K. Metzger *et al.*, "Exceeding 20% efficiency with in situ group V doping in polycrystalline CdTe solar cells," *Nature Energy,* 2019/08/19 2019, doi: 10.1038/s41560-019-0446-7.

[250] J. M. Burst *et al.*, "CdTe solar cells with open-circuit voltage breaking the 1 V barrier," *Nature Energy,* **vol. 1**, no**.** 3, p. 16015, 2016.

[251] J. Freeouf and J. Woodall, "Schottky barriers: An effective work function model," in *Electronic Structure of Semiconductor Heterojunctions*: Springer, 1988, pp. 177-179.

[252] R. K. Swank, "Surface properties of II-VI compounds," *Physical Review,* **vol. 153**, no**.** 3, p. 844, 1967.

[253] K. K. Subedi, K. P. Bhandari, E. Bastola, and R. J. Ellingson, "13% CdS/CdTe Solar Cell Using a Nanocomposite $(CuS)_x(ZnS)_{1-x}$ Thin Film Hole Transport Layer," in *2017 IEEE 44th Photovoltaic Specialist Conference (PVSC)*, Washington, DC, US, 25-30 June 2017 2017, pp. 781-784, doi: 10.1109/PVSC.2017.8366719.

[254] K. K. Subedi *et al.*, "Nanocomposite $(CuS)_x(ZnS)_{1-x}$ thin film back contact for CdTe solar cells: Toward a bifacial device," *Sol. Energy Mater. Sol. Cells,* **vol. 186**, pp. 227-235, 2018.

[255] K. K. Subedi *et al.*, "Bifacial CdS/CdTe Solar Cell using Transparent Barium Copper Sulfide as a Hole Transport Layer," in *2019 IEEE 46th Photovoltaic Specialists Conference (PVSC)*, Chicago, IL, US, 2019: IEEE, pp. 0185-0188.

[256] Q. Lin *et al.*, "A novel p-type and metallic dual-functional Cu–Al_2O_3 ultra-thin layer as the back electrode enabling high performance of thin film solar cells," *Chemical Communications,* **vol. 52**, no**.** 71, pp. 10708-10711, 2016.

[257] L. Zhang *et al.*, "Oxygen-concentration effect on p-type $CuAlO_x$ resistive switching behaviors and the nature of conducting filaments," *Applied Physics Letters,* **vol. 104**, no**.** 9, p. 093512, 2014.

[258] A. I. Osman, J. K. Abu-Dahrieh, D. W. Rooney, S. A. Halawy, M. A. Mohamed, and A. Abdelkader, "Effect of precursor on the performance of alumina for the dehydration of methanol to dimethyl ether," *Applied Catalysis B: Environmental,* **vol. 127**, pp. 307-315, 2012.

[259] J. Lee, P. Rovira, I. An, and R. Collins, "Rotating-compensator multichannel ellipsometry: Applications for real time Stokes vector spectroscopy of thin film growth," *Review of Scientific Instruments,* **vol. 69**, no**.** 4, pp. 1800-1810, 1998.

[260] J. A. Woollam, B. D. Johs, C. M. Herzinger, J. N. Hilfiker, R. A. Synowicki, and C. L. Bungay, "Overview of variable-angle spectroscopic ellipsometry (VASE): I. Basic theory and typical applications," in *Optical Metrology: A Critical Review*, 1999, vol. 10294: International Society for Optics and Photonics, p. 1029402.

[261] Z. Chen *et al.*, "Solution-processed trigonal Cu_2BaSnS_4 thin-film solar cells," *ACS Applied Energy Materials,* **vol. 1**, no**.** 7, pp. 3420-3427, 2018.

[262] S. Li, X. Zhang, P. Zhang, X. Sun, H. Zheng, and W. J. N. r. l. Zhang, "Preparation and Characterization of Solution-Processed Nanocrystalline p-Type CuAlO 2 Thin-Film Transistors," *Nanoscale,* **vol. 13**, no**.** 1, pp. 1-7, 2018.

[263] M.-J. Zhang *et al.*, "Novel p-type conductive semiconductor nanocrystalline film as the back electrode for high-performance thin film solar cells," *Nano Lett.,* **vol. 16**, no**.** 2, pp. 1218-1223, 2016.

[264] P. J. Roland, N. R. Paudel, C. Xiao, Y. Yan, and R. J. Ellingson, "Photoluminescence spectroscopy of cadmium telluride deep defects," in *2014 IEEE 40th Photovoltaic Specialist Conference (PVSC)*, Waikoloa, HI, US, 2014: IEEE, pp. 3266-3271.

[265] J. Chamonal, E. Molva, and J. Pautrat, "Identification of Cu and Ag acceptors in CdTe," *Solid State Communications,* **vol. 43**, no**.** 11, pp. 801-805, 1982.

[266] B. K. Meyer, W. Stadler, D. M. Hofmann, P. Omling, D. Sinerius, and K. W. Benz, "On the nature of the deep 1.4 eV emission bands in CdTe — a study with photoluminescence

and ODMR spectroscopy," *Journal of Crystal Growth,* **vol. 117**, no**.** 1, pp. 656-659, 1992/02/02/ 1992, doi: doi.org/10.1016/0022-0248(92)90831-3.

[267] C. A. Wolden *et al.*, "The roles of ZnTe buffer layers on CdTe solar cell performance," *Sol. Energy Mater. Sol. Cells,* **vol. 147**, pp. 203-210, 2016.

[268] Y. Yoshino, "Role of oxygen in bonding copper to alumina," *J. Am. Ceram. Soc.,* **vol. 72**, no**.** 8, pp. 1322-1327, 1989.

[269] S. Mellul and J.-P. Chevalier, "Interfacial phase transitions and bonding in the Cu/Al_2O_3 system," *Philos. Mag. A,* **vol. 64**, no**.** 3, pp. 561-576, 1991.

[270] A. B. Phillips, G. K. Liyanage, F. K. Alfadhili, and M. J. Heben, "Understanding CdTe Performance with Engineered Front and Back Interfaces," in *2019 IEEE 46th Photovoltaic Specialists Conference (PVSC)*, Chicago, IL, US, 2019: IEEE, pp. 0777-0782.

[271] M. Burgelman, P. Nollet, and S. Degrave, "Modelling polycrystalline semiconductor solar cells," *Thin Solid Films,* **vol. 361**, pp. 527-532, 2000.

[272] G. K. Liyanage, A. B. Phillips, and M. J. Heben, "Role of band alignment at the transparent front contact/emitter interface in the performance of wide bandgap thin film solar cells," *APL Materials* **vol. 6**, no**.** 10, p. 101104, 2018.

[273] A. B. Phillips, K. Khanal Subedi, G. K. Liyanage, F. K. Alfadhili, R. J. Ellingson, and M. J. Heben, "Understanding and Advancing Bifacial Thin Film Solar Cells," *ACS Applied Energy Materials,* 2020.

[274] H. Liu, V. Avrutin, N. Izyumskaya, Ü. Özgür, and H. Morkoç, "Transparent conducting oxides for electrode applications in light emitting and absorbing devices," (in English), *Superlattices and Microstructures,* **vol. 48**, no**.** 5, pp. 458-484, Nov 2010, doi: 10.1016/j.spmi.2010.08.011.

[275] E. Fortunato, P. Barquinha, and R. Martins, "Oxide semiconductor thin-film transistors: a review of recent advances," *Adv. Mater.,* **vol. 24**, no**.** 22, pp. 2945-86, Jun 12 2012, doi: 10.1002/adma.201103228.

[276] X. Xu *et al.*, "Chemical Bath Deposition of p-Type Transparent, Highly Conducting $(CuS)_x:(ZnS)_{1-x}$ Nanocomposite Thin Films and Fabrication of Si Heterojunction Solar Cells," *Nano Lett.,* **vol. 16**, no**.** 3, pp. 1925-32, Mar 9 2016, doi: 10.1021/acs.nanolett.5b05124.

[277] W. Beyer, J. Hüpkes, and H. Stiebig, "Transparent conducting oxide films for thin film silicon photovoltaics," *Thin Solid Films,* **vol. 516**, no**.** 2-4, pp. 147-154, 2007.

[278] G. Hautier, A. Miglio, G. Ceder, G. M. Rignanese, and X. Gonze, "Identification and design principles of low hole effective mass p-type transparent conducting oxides," *Nat Commun,* **vol. 4**, p. 2292, 2013, doi: 10.1038/ncomms3292.

[279] A. Parretta, M. Jayaraj, A. Di Nocera, S. Loreti, L. Quercia, and A. Agati, "Electrical and optical properties of copper oxide films prepared by reactive RF magnetron sputtering," *physica status solidi (a),* **vol. 155**, no**.** 2, pp. 399-404, 1996.

[280] H. Kawazoe, M. Yasukawa, H. Hyodo, M. Kurita, H. Yanagi, and H. Hosono, "P-type electrical conduction in transparent thin films of $CuAlO_2$," *Nature,* **vol. 389**, no**.** 6654, pp. 939-942, 1997.

[281] A. M. Diamond *et al.*, "Copper-alloyed ZnS as ap-type transparent conducting material," *physica status solidi (a),* **vol. 209**, no**.** 11, pp. 2101-2107, 2012.

[282] E. Jose and M. C. Santhosh Kumar, "Room temperature deposition of highly crystalline Cu-Zn-S thin films for solar cell applications using SILAR method," (in English), *Journal of Alloys and Compounds,* **vol. 712**, pp. 649-656, Jul 25 2017, doi: 10.1016/j.jallcom.2017.04.097.

[283] M. A. Yıldırım, "The effect of copper concentration on structural, optical and dielectric properties of $Cu_xZn_{1-x}S$ thin films," *Optics Communications,* **vol. 285**, no**.** 6, pp. 1215-1220, 2012.

[284] S. K. Maurya *et al.*, "High figure-of-merit p-type transparent conductor, Cu alloyed ZnS via radio frequency magnetron sputtering," *J. Phys. D: Appl. Phys.,* **vol. 50**, no**.** 50, p. 505107, 2017.

[285] A. Mallick, S. Chattopadhyay, G. De, and D. Basak, "High figure of merit p-type transparent conducting thin film based on solution processed CuS-ZnS nanocomposite," (in English), *Journal of Alloys and Compounds,* **vol. 770**, pp. 813-822, Jan 5 2019, doi: 10.1016/j.jallcom.2018.08.178.

[286] J. L. Freeouf and J. M. Woodall, "Schottky barriers: An effective work function model," *Applied Physics Letters,* **vol. 39**, no**.** 9, pp. 727-729, 1981, doi: dx.doi.org/10.1063/1.92863.

[287] E. Janik and R. Triboulet, "Ohmic contacts to p-type cadmium telluride and cadmium mercury telluride," (in English), *J. Phys. D: Appl. Phys.,* **vol. 16**, no**.** 12, pp. 2333-2340, 1983, doi: 10.1088/0022-3727/16/12/011.

[288] E. Artegiani, J. D. Major, H. Shiel, V. Dhanak, C. Ferrari, and A. Romeo, "How the amount of copper influences the formation and stability of defects in CdTe solar cells," *Sol. Energy Mater. Sol. Cells,* **vol. 204**, p. 110228, 2020.

[289] B. de Boer, A. Hadipour, M. M. Mandoc, T. van Woudenbergh, and P. W. M. Blom, "Tuning of Metal Work Functions with Self-Assembled Monolayers," *Adv. Mater.,* **vol. 17**, no**.** 5, pp. 621-625, 2005, doi: 10.1002/adma.200401216.

[290] A. B. Phillips *et al.*, "Wiring-up carbon single wall nanotubes to polycrystalline inorganic semiconductor thin films: low-barrier, copper-free back contact to CdTe solar cells," *Nano Lett.,* **vol. 13**, no**.** 11, pp. 5224-32, Nov 13 2013, doi: 10.1021/nl402659c.

[291] A. Montgomery *et al.*, "Solution-processed copper (I) thiocyanate (CuSCN) for highly efficient CdSe/CdTe thin-film solar cells," *Progress in Photovoltaics: Research and Applications,* **vol. 27**, no**.** 8, pp. 665-672, 2019.

[292] K. P. Bhandari *et al.*, "Iron pyrite nanocrystal film serves as a copper-free back contact for polycrystalline CdTe thin film solar cells," *Sol. Energy Mater. Sol. Cells,* **vol. 140**, pp. 108-114, Sep 2015, doi: 10.1016/j.solmat.2015.03.032.

[293] B. Siepchen *et al.*, "A Simple Sb 2 Te 3 Back-Contact Process for CdTe Solar Cells," *Journal of Electronic Materials,* **vol. 44**, no**.** 10, pp. 3354-3359, 2015.

[294] X. Wu *et al.*, "Phase control of CuxTe film and its effects on CdS/CdTe solar cell," (in English), *Thin Solid Films,* **vol. 515**, no**.** 15, pp. 5798-5803, May 31 2007, doi: 10.1016/j.tsf.2006.12.151.

[295] N. Strevel, L. Trippel, C. Kotarba, and I. Khan, "Improvements in CdTe module reliability and long-term degradation through advances in construction and device innovation," *Photovoltaics International,* **vol. 22**, pp. 66-74, 2013.

[296] E. Bastola, K. P. Bhandari, and R. J. Ellingson, "Application of composition controlled nickel-alloyed iron sulfide pyrite nanocrystal thin films as the hole transport layer in cadmium telluride solar cells," *Journal of Materials Chemistry C,* **vol. 5**, no**.** 20, pp. 4996-5004, May 28 2017, doi: 10.1039/c7tc00948h.

[297] E. Bastola, K. K. Subedi, K. P. Bhandari, and R. J. Ellingson, "Solution-processed Nanocrystal Based Thin Films as Hole Transport Materials in Cadmium Telluride Photovoltaics," *MRS Adv.,* **vol. 3**, no**.** 41, pp. 2441-2447, 2018, doi: 10.1557/adv.2018.349.

[298] E. Bastola, K. P. Bhandari, I. Subedi, N. J. Podraza, and R. J. Ellingson, "Structural, optical, and hole transport properties of earth-abundant chalcopyrite ($CuFeS_2$) nanocrystals," *MRS Communications,* **vol. 8**, no**.** 03, pp. 970-978, 2018, doi: 10.1557/mrc.2018.117.

[299] K. P. Bhandari *et al.*, "Very high VOC and FF of CdTe thin-film solar cells with the applications of organo-metallic halide perovskite thin film as a hole transport layer," *Progress in Photovoltaics: Research and Applications*.

[300] Z. Rong *et al.*, "Interface Engineering for Both Cathode and Anode Enables Low-Cost Highly Efficient Solution-Processed CdTe Nanocrystal Solar Cells," *Adv. Funct. Mater.,* **vol. 29**, no**.** 42, p. 1904018, 2019.

[301] X. Guo *et al.*, "High-efficiency solution-processed CdTe nanocrystal solar cells incorporating a novel crosslinkable conjugated polymer as the hole transport layer," *Nano Energy,* **vol. 46**, pp. 150-157, 2018.

[302] X. Du *et al.*, "Improvement in open-circuit voltage of thin film solar cells from aqueous nanocrystals by interface engineering," *ACS Applied Materials & Interfaces,* **vol. 8**, no**.** 1, pp. 900-907, 2016.

[303] E. Bastola, K. K. Subedi, F. K. Alfadhili, A. B. Phillips, M. J. Heben, and R. J. Ellingson, "Room Temperature Processed Transparent Cu-Zn-S Nanocomposites as Hole Transport Materials in CdTe Photovoltaics," in *2019 IEEE 46th Photovoltaic Specialists Conference (PVSC)*, Chicago, IL, US, 16-21 June 2019 2019, pp. 0144-0148, doi: 10.1109/PVSC40753.2019.8981335.

[304] E. Bastola, F. K. Alfadhili, A. B. Phillips, M. J. Heben, and R. J. Ellingson, "Wet chemical etching of cadmium telluride photovoltaics for enhanced open-circuit voltage, fill factor, and power conversion efficiency," *Journal of Materials Research,* **vol. 34**, no**.** 24, pp. 3988-3997, 2019, doi: 10.1557/jmr.2019.363.

[305] D. Mao, G. Blatz, C. E. Wickersham, and M. Gloeckler, "Correlative impurity distribution analysis in cadmium telluride (CdTe) thin-film solar cells by ToF-SIMS 2D imaging," (in English), *Sol. Energy Mater. Sol. Cells,* **vol. 157**, pp. 65-73, Dec 2016, doi: 10.1016/j.solmat.2016.05.019.

[306] X. Guo *et al.*, "Surface passivation via acid vapor etching enables efficient and stable solution-processed CdTe nanocrystal solar cells," *Sustainable Energy & Fuels,* 10.1039/C9SE00902G **vol. 4**, no**.** 1, pp. 399-406, 2020, doi: 10.1039/C9SE00902G.

[307] F. K. Alfadhili, A. B. Phillips, G. K. Liyanage, J. M. Gibbs, M. K. Jamarkattel, and M. J. Heben, "Controlling Band Alignment at the Back Interface of Cadmium Telluride Solar Cells using ZnTe and Te Buffer Layers," *MRS Advances,* **vol. 4**, no**.** 16, pp. 913-919, 2019, doi: 10.1557/adv.2019.31.

[308] D. Adhikari *et al.*, "Glancing angle deposited CdTe: Nanostructured films and impact on solar cell performance," *Surface and Coatings Technology,* **vol. 381**, p. 125127, 2020.

[309] N. K. Jayswal, D. Adhikari, I. Subedi, C. R. Grice, and N. J. Podraza, "Deposition Temperature Dependence of Optical and Structural Properties of Glancing Angle Deposited CdTe," in *64th Annual SVC Technical Conference*, Virtual, Nashville, TN, US, May 3-7 2021.

[310] C. Zhou and D. Gall, "Competitive growth of Ta nanopillars during glancing angle deposition: Effect of surface diffusion," *Journal of Vacuum Science & Technology A: Vacuum, Surfaces, and Films,* **vol. 25**, no**.** 2, pp. 312-318, 2007.

[311] J. Li, J. Chen, and R. Collins, "Optical transition energies as a probe of stress in polycrystalline CdTe thin films," *Applied Physics Letters,* **vol. 99**, no**.** 6, p. 061905, 2011.

[312] R. S. Hall, D. Lamb, and S. J. C. Irvine, "Back contacts materials used in thin film CdTe solar cells—A review," *Energy Science & Engineering,* **vol. 9**, no**.** 5, pp. 606-632, 2021.

[313] J. Jasieniak, B. I. MacDonald, S. E. Watkins, and P. Mulvaney, "Solution-processed sintered nanocrystal solar cells via layer-by-layer assembly," *Nano Lett.,* **vol. 11**, no**.** 7, pp. 2856-2864, 2011.

[314] M. Shim and P. Guyot-Sionnest, "Permanent dipole moment and charges in colloidal semiconductor quantum dots," *The Journal of Chemical Physics,* **vol. 111**, no**.** 15, pp. 6955-6964, 1999.

[315] I. Subedi, M. A. Slocum, D. V. Forbes, S. M. Hubbard, and N. J. Podraza, "Optical properties of InP from infrared to vacuum ultraviolet studied by spectroscopic ellipsometry," *Applied Surface Science,* **vol. 421**, pp. 813-818, 2017.

[316] R. W. Collins and A. S. Ferlauto, H. G. Tompkins and E. A. Irene, Eds. *Optical Physics of Materials* (Handbook of Ellipsometry). Norwich, NY: William Andrew Inc., 2005, pp. 93-235.

[317] T. E. Tiwald, D. W. Thompson, J. A. Woollam, W. Paulson, and R. Hance, "Application of IR variable angle spectroscopic ellipsometry to the determination of free carrier concentration depth profiles," *Thin Solid Films,* **vol. 313**, pp. 661-666, 1998.

[318] S. A. Alterovitz *et al.*, "Dielectric function of InGaAs in the visible," *In Nebraska Univ,* 1993.

[319] M. n. Muñoz *et al.*, "Optical constants of In 0.53 Ga 0.47 As/InP: experiment and modeling," *Journal of Applied Physics,* **vol. 92**, no**.** 10, pp. 5878-5885, 2002.

[320] M. Lumb, M. Yakes, M. Gonzalez, J. Tischler, and R. Walters, "Optical properties of Si-doped and Be-doped InAlAs lattice-matched to InP grown by molecular beam epitaxy," *Journal of Applied Physics,* **vol. 114**, no**.** 10, p. 103504, 2013.

[321] R. Dittrich and W. Schroeder, "Empirical pseudopotential band structure of In0. 53Ga0. 47As and In0. 52Al0. 48As," *Solid·State Electron.,* **vol. 43**, no**.** 2, pp. 403-407, 1999.

[322] D. Olego, T. Chang, E. Silberg, E. Caridi, and A. Pinczuk, "Compositional dependence of band-gap energy and conduction-band effective mass of $In_{1-x-y}Ga_xAl_yAs$ lattice matched to InP," *Applied Physics Letters,* **vol. 41**, no**.** 5, pp. 476-478, 1982.

[323] L. Alyabyeva, E. Zhukova, M. Belkin, and B. Gorshunov, "Dielectric properties of semi-insulating Fe-doped InP in the terahertz spectral region," *Sci. Rep.,* **vol. 7**, no**.** 1, pp. 1-7, 2017.

[324] P. Seredin, É. Domashevskaya, A. Lukin, I. Arsent'Ev, D. Vinokurov, and I. Tarasov, "Infrared reflection spectra of multilayer epitaxial heterostructures with embedded InAs and GaAs layers," *Semic,* **vol. 42**, no**.** 9, pp. 1055-1061, 2008.

[325] A. Milekhin, A. Kalagin, A. Vasilenko, A. Toropov, N. Surovtsev, and D. Zahn, "Vibrational spectroscopy of InAlAs epitaxial layers," *Journal of Applied Physics,* **vol. 104**, no**.** 7, p. 073516, 2008.

[326] P. Seredin, D. Goloshchapov, I. Arsentyev, D. Nikolaev, N. Pikhtin, and S. Slipchenko, "Spectroscopic Studies of Integrated GaAs/Si Heterostructures," *Semic,* **vol. 55**, no**.** 1, pp. 44-50, 2021.

[327] J. C. Harmand, T. Matsuno, and K. Inoue, "Lattice-mismatched growth and transport properties of InAlAs/InGaAs heterostructures on GaAs substrates," *Japanese Journal of Applied Physics,* **vol. 28**, no**.** 7A, p. L1101, 1989.

[328] W. Lee and C. G. Fonstad, "The growth of high mobility InGaAs and InAlAs layers by molecular beam epitaxy," *Journal of Vacuum Science & Technology B: Microelectronics Processing and Phenomena,* **vol. 4**, no**.** 2, pp. 536-538, 1986.

[329] D. Liu, "Design, Fabrication and Characterization of InAlAs/InGaAs/InAsP Composite Channel HEMTs," The Ohio State University, 2008.

[330] S. Damaskinos, "An improved laser scanning technique for evaluation of solar cells: Application to $CuInSe_2$/(CuZn) S devices," *SoCe,* **vol. 26**, no**.** 3, pp. 151-158, 1989.

[331] D. E. Sawyer and H. K. Kessler, "Laser scanning of solar cells for the display of cell operating characteristics and detection of cell defects," *IEEE Trans. Electron Devices,* **vol. 27**, no**.** 4, pp. 864-872, 1980, doi: 10.1109/T-ED.1980.19948.

[332] G. E. Eperon, D. Moerman, and D. S. Ginger, "Anticorrelation between local photoluminescence and photocurrent suggests variability in contact to active layer in perovskite solar cells," *ACS Nano,* **vol. 10**, no**.** 11, pp. 10258-10266, 2016.

[333] T. A. Bull, L. S. Pingree, S. A. Jenekhe, D. S. Ginger, and C. K. Luscombe, "The role of mesoscopic PCBM crystallites in solvent vapor annealed copolymer solar cells," *ACS Nano,* **vol. 3**, no**.** 3, pp. 627-636, 2009.

[334] B. Rezek, C. Nebel, and M. Stutzmann, "Laser beam induced currents in polycrystalline silicon thin films prepared by interference laser crystallization," *Journal of Applied Physics,* **vol. 91**, no**.** 7, pp. 4220-4228, 2002.

[335] Y. Yoon, D. Ha, I. J. Park, P. M. Haney, S. Lee, and N. B. Zhitenev, "Nanoscale photocurrent mapping in perovskite solar cells," *Nano Energy,* **vol. 48**, pp. 543-550, 2018.

[336] M. Breitwieser *et al.*, "Analysis of solar cell cross sections with micro-light beam induced current (μLBIC)," *Sol. Energy Mater. Sol. Cells,* **vol. 131**, pp. 124-128, 2014/12/01/ 2014, doi: doi.org/10.1016/j.solmat.2014.05.002.

[337] C. Eisele, C. Nebel, and M. Stutzmann, "Spatially resolved photocurrent measurements of microstructured a-Si: H solar cells," *Journal of Non-Crystalline Solids,* **vol. 266**, pp. 1109-1113, 2000.

[338] S. Mastroianni *et al.*, "Analysing the effect of crystal size and structure in highly efficient $CH_3NH_3PbI_3$ perovskite solar cells by spatially resolved photo- and electroluminescence imaging," *Nanoscale,* 10.1039/C5NR05308K **vol. 7**, no**.** 46, pp. 19653-19662, 2015, doi: 10.1039/C5NR05308K.

[339] C. R. McNeill, H. Frohne, J. L. Holdsworth, and P. C. Dastoor, "Near-field scanning photocurrent measurements of polyfluorene blend devices: directly correlating morphology with current generation," *Nano Lett.,* **vol. 4**, no**.** 12, pp. 2503-2507, 2004.

[340] C. R. McNeill, H. Frohne, J. L. Holdsworth, J. E. Furst, B. V. King, and P. C. Dastoor, "Direct photocurrent mapping of organic solar cells using a near-field scanning optical microscope," *Nano Lett.,* **vol. 4**, no**.** 2, pp. 219-223, 2004.

[341] S. Panigrahi, T. Calmeiro, R. Martins, and E. Fortunato, "Light-induced current mapping in oxide based solar cells with nanoscale resolution," *Sol. Energy Mater. Sol. Cells,* **vol. 176**, pp. 310-317, 2018, doi: doi.org/10.1016/j.solmat.2017.10.012.

[342] M. Acciarri, S. Binetti, A. Racz, S. Pizzini, and G. Agostinelli, "Fast LBIC in-line characterization for process quality control in the photovoltaic industry," *Sol. Energy Mater. Sol. Cells,* **vol. 72**, no**.** 1, pp. 417-424, 2002, doi: doi.org/10.1016/S0927-0248(01)00189-1.

[343] F. C. Krebs and M. Jørgensen, "2D Characterization of OPV from Single and Tandem Cells to Fully Roll-to-Roll Processed Modules with and without Electrical Contact," *Advanced Optical Materials,* **vol. 2**, no**.** 5, pp. 465-477, 2014.

[344] R. J. Matson, K. A. Emery, I. L. Eisgruber, and L. L. Kazmersk, in *in 12th European Photovoltaic Solar Energy Conference*, Amsterdam, The Netherlands, 1994, pp. 1222-1225.

[345] L. Quan, K. Xie, Y. Liu, and H. Zhang, "Camera enhanced compressive light beam induced current sensing for efficient defect detection in photovoltaic cells," *SoEn,* **vol. 183**, pp. 212-217, 2019, doi: doi.org/10.1016/j.solener.2019.02.055.

[346] L. Quan, K. Xie, R. Xi, and Y. Liu, "Compressive light beam induced current sensing for fast defect detection in photovoltaic cells," *SoEn,* **vol. 150**, pp. 345-352, 2017, doi: doi.org/10.1016/j.solener.2017.04.059.

[347] P. Vorasayan, T. R. Betts, A. Tiwari, and R. Gottschalg, "Multi-laser LBIC system for thin film PV module characterisation," *Sol. Energy Mater. Sol. Cells,* **vol. 93**, no**.** 6-7, pp. 917-921, 2009.

[348] R. M. Geisthardt and J. R. Sites, "Nonuniformity Characterization of CdTe Solar Cells Using LBIC," *IEEE Journal of Photovoltaics,* **vol. 4**, no**.** 4, pp. 1114-1118, 2014, doi: 10.1109/JPHOTOV.2014.2314575.

[349] P. Gečys, G. Račiukaitis, E. Miltenis, A. Braun, and S. Ragnow, "Scribing of thin-film solar cells with picosecond laser pulses," *Physics procedia,* **vol. 12**, pp. 141-148, 2011.

[350] S. Nakano *et al.*, "Laser patterning method for integrated type a-Si solar cell submodules," *Japanese Journal of Applied Physics,* **vol. 25**, no**.** 12R, p. 1936, 1986.

[351] A. Compaan, I. Matulionis, and S. Nakade, "Laser scribing of polycrystalline thin films," *OptLE,* **vol. 34**, no**.** 1, pp. 15-45, 2000.

[352] S. Rung, J. Barth, and R. Hellmann, "Characterization of Laser Beam Shaping Optics Based on Their Ablation Geometry of Thin Films," *Micromachines,* **vol. 5**, no**.** 4, pp. 943-953, 2014.

[353] B. Turan, S. Haas, and M. Steger, "Optimization of front-contact laser scribing for thin-film silicon solar modules," *Sol. Energy Mater. Sol. Cells,* **vol. 125**, pp. 78-86, 2014, doi: doi.org/10.1016/j.solmat.2014.02.029.

[354] T. Zhao *et al.*, "Realizing Gaussian to flat-top beam shaping in traveling-wave amplification," *Optics Express,* **vol. 25**, no**.** 26, pp. 33226-33235, 2017.

[355] K. Pearson, "X. On the criterion that a given system of deviations from the probable in the case of a correlated system of variables is such that it can be reasonably supposed to have arisen from random sampling," *The London, Edinburgh, and Dublin Philosophical Magazine and Journal of Science,* **vol. 50**, no**.** 302, pp. 157-175, 1900/07/01 1900, doi: 10.1080/14786440009463897.

[356] Y. I. Krasilov, "High-speed achromatic quarter-wave device," *Optics and Spectroscopy,* **vol. 22**, p. 267, 1967.

[357] N. Ashcroft and K. Sturm, "Interband absorption and the optical properties of polyvalent metals," *PhRvB,* **vol. 3**, no**.** 6, p. 1898, 1971.

[358] H. V. NGUYEN, I. AN, and R. W. COLLINS, "Real-time spectroscopic ellipsometry studies of the nucleation, growth, and optical functions of thin films, Part II: aluminum," in *Physics of Thin Films*, vol. 19: Elsevier, 1994, pp. 127-189.

[359] R. King and M. Downs, "Ellipsometry applied to films on dielectric substrates," *Surface Science,* **vol. 16**, pp. 288-302, 1969.

[360] M. H. Smith, "Optimization of a dual-rotating-retarder Mueller matrix polarimeter," *Applied Optics,* **vol. 41**, no**.** 13, pp. 2488-2493, 2002.

[361] J. Li, B. Ramanujam, and R. Collins, "Dual rotating compensator ellipsometry: Theory and simulations," *Thin Solid Films,* **vol. 519**, no**.** 9, pp. 2725-2729, 2011.

[362] Hamamatsu. "Hamamatsu technical note: Si photodiodes." Hamamatsu. https://www.hamamatsu.com/resources/pdf/ssd/si_pd_kspd9001e.pdf last (accessed 11/09/2021).

[363] Hamamatsu, "private e-mail communication," ed. email, 2020.

[364] G. Jellison Jr, S. Withrow, J. McCamy, J. Budai, D. Lubben, and M. Godbole, "Optical functions of ion-implanted, laser-annealed heavily doped silicon," *PhRvB,* **vol. 52**, no**.** 20, p. 14607, 1995.

[365] J. Leng, J. Opsal, H. Chu, M. Senko, and D. Aspnes, "Analytic representations of the dielectric functions of crystalline and amorphous Si and crystalline Ge for very large scale integrated device and structural modeling," *Journal of Vacuum Science & Technology A: Vacuum, Surfaces, and Films,* **vol. 16**, no**.** 3, pp. 1654-1657, 1998.

[366] H. Tompkins and E. A. Irene, *Data Analysis for Spectroscopic Ellipsometry* (Handbook of Ellipsometry). William Andrew, 2005, p. 291.

[367] M. I. Saidaminov *et al.*, "High-quality bulk hybrid perovskite single crystals within minutes by inverse temperature crystallization," *Nat Commun,* Article **vol. 6**, 07/06/online 2015, doi: 10.1038/ncomms8586.

[368] N.-G. Park, "Perovskite solar cells: an emerging photovoltaic technology," *Mater. Today,* **vol. 18**, no**.** 2, pp. 65-72, 2015, doi: dx.doi.org/10.1016/j.mattod.2014.07.007.

[369] Q. Dong *et al.*, "Electron-hole diffusion lengths > 175 μm in solution-grown $CH_3NH_3PbI_3$ single crystals," *Science,* **vol. 347**, no**.** 6225, pp. 967-970, 2015, doi: 10.1126/science.aaa5760.

[370] A. Miyata *et al.*, "Direct measurement of the exciton binding energy and effective masses for charge carriers in organic-inorganic tri-halide perovskites," *Nat Phys,* Article **vol. 11**, no**.** 7, pp. 582-587, 07//print 2015, doi: 10.1038/nphys3357.

[371] H. S. Jung and N.-G. Park, "Perovskite Solar Cells: From Materials to Devices," *Small,* **vol. 11**, no**.** 1, pp. 10-25, 2015, doi: doi:10.1002/smll.201402767.

[372] W. Ke *et al.*, "Employing Lead Thiocyanate Additive to Reduce the Hysteresis and Boost the Fill Factor of Planar Perovskite Solar Cells," *Adv. Mater.,* **vol. 28**, no**.** 26, pp. 5214-5221, 2016, doi: 10.1002/adma.201600594.

[373] R. T. Ross, "Some Thermodynamics of Photochemical Systems," *The Journal of Chemical Physics,* **vol. 46**, no**.** 12, pp. 4590-4593, 1967, doi: 10.1063/1.1840606.

[374] Y. Yu *et al.*, "Improving the Performance of Formamidinium and Cesium Lead Triiodide Perovskite Solar Cells using Lead Thiocyanate Additives," *ChemSusChem,* **vol. 9**, no**.** 23, pp. 3288-3297, 2016, doi: doi:10.1002/cssc.201601027.

[375] W. Tress, "Perovskite Solar Cells on the Way to Their Radiative Efficiency Limit – Insights Into a Success Story of High Open-Circuit Voltage and Low Recombination," *Advanced Energy Materials,* **vol. 7**, no**.** 14, p. 1602358, 2017, doi: 10.1002/aenm.201602358.

[376] N. Taylor, *Equipment and Basis of Power Measurements* (Guidelines for PV Power Measurement in Industry). Luxembourg: Office for Official Publications of the European Union, 2010, p. 7.

[377] NREL. "Solar Spectra: Grid Modernization." https://rredc.nrel.gov/solar/spectra/am1.5/ last (accessed 11/09/2021).

[378] J. M. S. n.-P. Eduardo L pez-Fraguas, IEEE, Ricardo Vergaz, "A Low-Cost LED-Based Solar Simulator," *IEEE Trans. Instrum. Meas.,* **vol. 68**, no**.** 12, pp. 4913-4923.

[379] M. A. Green, Emery, K., Blakers, *Silicon Solar Cells with Reduced Temperature Sensitivity*. 1982.

[380] C. R. Osterwald, Glatfelter, T., Burdick, "Comparison of the temperature coefficients of the basic I–V parameters for various types of solar cells," in *19th IEEE PVSC*, Philadelphia, PA, US, 1987, vol. 188.

[381] J. J. Wysocki, Rappaport, P., , "Effect of temperature on photovoltaic solar energy conversion," *J. Appl. Phys,* **vol. 577**, 1960.

[382] P. Uprety, I. Subedi, M. M. Junda, R. W. Collins, and N. J. Podraza, "Photogenerated carrier transport properties in silicon photovoltaics," *Sci. Rep.,* **vol. 9**, no**.** 1, pp. 1-12, 2019.

[383] F. A. Lindholm and C.-T. Sah, "Fundamental electronic mechanisms limiting the performance of solar cells," *IEEE Trans. Electron Devices,* **vol. 24**, no**.** 4, pp. 299-304, 1977.

[384] A. Sproul, M. Green, and A. Stephens, "Accurate determination of minority carrier-and lattice scattering-mobility in silicon from photoconductance decay," *Journal of Applied Physics,* **vol. 72**, no**.** 9, pp. 4161-4171, 1992.

[385] D. Neuhaus *et al.*, "Method for measuring minority and majority carrier mobilities in solar cells," in *Proceeding of 17th European Photovoltaic Solar Energy Conference*, Munich, Germany, 2001, pp. 242-245.

[386] M. Schubert, P. Kühne, V. Darakchieva, and T. Hofmann, "Optical Hall effect—model description: tutorial," *JOSA A,* **vol. 33**, no**.** 8, pp. 1553-1568, 2016.

[387] T. Hofmann, C. Herzinger, A. Boosalis, T. Tiwald, J. A. Woollam, and M. Schubert, "Variable-wavelength frequency-domain terahertz ellipsometry," *Review of Scientific Instruments,* **vol. 81**, no**.** 2, p. 023101, 2010.

[388] B. Johs and C. Herzinger, "Quantifying the accuracy of ellipsometer systems," *physica status solidi c,* **vol. 5**, no**.** 5, pp. 1031-1035, 2008.

[389] S. Knight *et al.*, "Cavity-enhanced optical Hall effect in two-dimensional free charge carrier gases detected at terahertz frequencies," *Optics Letters,* **vol. 40**, no**.** 12, pp. 2688-2691, 2015.

[390] I. Subedi, T. J. Silverman, M. G. Deceglie, and N. J. Podraza, "Al+ Si interface optical properties obtained in the Si solar cell configuration," *physica status solidi (a),* **vol. 214**, no**.** 12, p. 1700480, 2017.

[391] D. A. Clugston and P. A. Basore, "PC1D version 5: 32-bit solar cell modeling on personal computers," in *Conference Record of the Twenty Sixth IEEE Photovoltaic Specialists Conference-1997*, Anaheim, CA, US, 1997: IEEE, pp. 207-210.

[392] NREL. "Best Research-Cell Efficiency Chart." National Renewable Energy Laboratory. https://nrel.gov/pv/cell-efficiency.html last (accessed 12/06/2021).

[393] J. Jeong *et al.*, "Pseudo-halide anion engineering for α-$FAPbI_3$ perovskite solar cells," *Nature,* **vol. 592**, no**.** 7854, pp. 381-385, 2021.

[394] S. D. Stranks *et al.*, "Electron-hole diffusion lengths exceeding 1 micrometer in an organometal trihalide perovskite absorber," (in English), *Science,* **vol. 342**, no**.** 6156, pp. 341-4, Oct 18 2013, doi: 10.1126/science.1243982.

[395] G. Xing *et al.*, "Long-range balanced electron- and hole-transport lengths in organic-inorganic $CH_3NH_3PbI_3$," (in English), *Science,* **vol. 342**, no**.** 6156, pp. 344-7, Oct 18 2013, doi: 10.1126/science.1243167.

[396] C. Wehrenfennig, G. E. Eperon, M. B. Johnston, H. J. Snaith, and L. M. Herz, "High charge carrier mobilities and lifetimes in organolead trihalide perovskites," (in English), *Adv. Mater.,* **vol. 26**, no**.** 10, pp. 1584-9, Mar 12 2014, doi: 10.1002/adma.201305172.

[397] A. S. Chouhan, N. P. Jasti, S. Hadke, S. Raghavan, and S. Avasthi, "Large grained and high charge carrier lifetime $CH_3NH_3PbI_3$ thin-films: implications for perovskite solar cells," (in English), *CAP,* **vol. 17**, no**.** 10, pp. 1335-1340, Oct 2017, doi: 10.1016/j.cap.2017.07.005.

[398] M. A. Green, A. Ho-Baillie, and H. J. Snaith, "The emergence of perovskite solar cells," *Nature Photonics,* **vol. 8**, no**.** 7, pp. 506-514, 2014.

[399] W. J. Yin, T. T. Shi, and Y. F. Yan, "Unusual defect physics in $CH_3NH_3PbI_3$ perovskite solar cell absorber," (in English), *Applied Physics Letters,* **vol. 104**, no**.** 6, 2014, doi: 10.1063/1.4864778.

[400] J. H. Noh, S. H. Im, J. H. Heo, T. N. Mandal, and S. I. Seok, "Chemical Management for Colorful, Efficient, and Stable Inorganic-Organic Hybrid Nanostructured Solar Cells," (in English), *Nano Lett.,* **vol. 13**, no**.** 4, pp. 1764-1769, Apr 2013, doi: 10.1021/nl400349b.

[401] G. E. Eperon, S. D. Stranks, C. Menelaou, M. B. Johnston, L. M. Herz, and H. J. Snaith, "Formamidinium lead trihalide: a broadly tunable perovskite for efficient planar heterojunction solar cells," *Energy Environ. Sci.,* **vol. 7**, no**.** 3, pp. 982-988, 2014.

[402] B. Suarez, V. Gonzalez-Pedro, T. S. Ripolles, R. S. Sanchez, L. Otero, and I. Mora-Sero, "Recombination study of combined halides (Cl, Br, I) perovskite solar cells," *The Journal of Physical Chemistry Letters,* **vol. 5**, no**.** 10, pp. 1628-1635, 2014.

[403] M. T. Hörantner *et al.*, "The potential of multijunction perovskite solar cells," *ACS Energy Letters,* **vol. 2**, no**.** 10, pp. 2506-2513, 2017.

[404] R. H. Ahangharnejhad *et al.*, "Optical design of perovskite solar cells for applications in monolithic tandem configuration with $CuInSe_2$ bottom cells," *MRS Advances,* **vol. 3**, no**.** 52, pp. 3111-3119, 2018.

[405] W. Shockley and H. J. Queisser, "Detailed balance limit of efficiency of p-n junction solar cells," *Journal of Applied Physics,* **vol. 32**, no**.** 3, pp. 510-519, 1961.

[406] A. De Vos, "Detailed balance limit of the efficiency of tandem solar cells," *J. Phys. D: Appl. Phys.,* **vol. 13**, no**.** 5, p. 839, 1980.

[407] R. Lin *et al.*, "Monolithic all-perovskite tandem solar cells with 24.8% efficiency exploiting comproportionation to suppress Sn (ii) oxidation in precursor ink," *Nature Energy,* **vol. 4**, no**.** 10, pp. 864-873, 2019.

[408] D. H. Kim *et al.*, "Bimolecular additives improve wide-band-gap perovskites for efficient tandem solar cells with CIGS," *Joule,* **vol. 3**, no**.** 7, pp. 1734-1745, 2019.

[409] T. Duong *et al.*, "High Efficiency Perovskite-Silicon Tandem Solar Cells: Effect of Surface Coating versus Bulk Incorporation of 2D Perovskite," *Advanced Energy Materials,* **vol. 10**, no**.** 9, p. 1903553, 2020.

[410] H. Zhou *et al.*, "Interface engineering of highly efficient perovskite solar cells," *Science,* **vol. 345**, no**.** 6196, pp. 542-546, 2014.

[411] J. Shi, X. Xu, D. Li, and Q. Meng, "Interfaces in perovskite solar cells," *Small,* **vol. 11**, no**.** 21, pp. 2472-2486, 2015.

[412] A. N. Cho and N. G. Park, "Impact of interfacial layers in perovskite solar cells," *ChemSusChem,* **vol. 10**, no**.** 19, pp. 3687-3704, 2017.

[413] A. Fakharuddin, L. Schmidt-Mende, G. Garcia-Belmonte, R. Jose, and I. Mora-Sero, "Interfaces in perovskite solar cells," *Advanced Energy Materials,* **vol. 7**, no**.** 22, p. 1700623, 2017.

[414] E. J. Juarez-Perez *et al.*, "Role of the selective contacts in the performance of lead halide perovskite solar cells," *The Journal of Physical Chemistry Letters,* **vol. 5**, no**.** 4, pp. 680-685, 2014.

[415] K. Mahmood, S. Sarwar, and M. T. Mehran, "Current status of electron transport layers in perovskite solar cells: materials and properties," *RSC Advances,* **vol. 7**, no**.** 28, pp. 17044-17062, 2017.

[416] T. Minemoto and M. Murata, "Device modeling of perovskite solar cells based on structural similarity with thin film inorganic semiconductor solar cells," (in English), *Journal of Applied Physics,* **vol. 116**, no**.** 5, Aug 7 2014, doi: 10.1063/1.4891982.

[417] T. Minemoto and M. Murata, "Impact of work function of back contact of perovskite solar cells without hole transport material analyzed by device simulation," *CAP,* **vol. 14**, no**.** 11, pp. 1428-1433, 2014.

[418] S. Bansal and P. Aryal, "Evaluation of new materials for electron and hole transport layers in perovskite-based solar cells through SCAPS-1D simulations," in *2016 IEEE 43rd Photovoltaic Specialists Conference (PVSC)*, Portland, OR, US, 2016: IEEE, pp. 0747-0750.

[419] K. Tan, P. Lin, G. Wang, Y. Liu, Z. Xu, and Y. Lin, "Controllable design of solid-state perovskite solar cells by SCAPS device simulation," *Solid·State Electron.,* **vol. 126**, pp. 75-80, 2016.

[420] P. Zhao *et al.*, "Numerical simulation of planar heterojunction perovskite solar cells based on SnO2 electron transport layer," *ACS Applied Energy Materials,* **vol. 2**, no**.** 6, pp. 4504-4512, 2019.

[421] T. Minemoto and M. Murata, "Theoretical analysis on effect of band offsets in perovskite solar cells," *Sol. Energy Mater. Sol. Cells,* **vol. 133**, pp. 8-14, 2015.

[422] J. D. Friedl, R. H. Ahangharnejhad, A. B. Phillips, and M. J. Heben, "Materials requirements for improving the electron transport layer/perovskite interface of perovskite solar cells determined via numerical modeling," *MRS Advances,* **vol. 5**, no**.** 50, pp. 2603-2610, 2020.

[423] R. H. Ahangharnejhad, J. D. Friedl, A. B. Phillips, and M. J. Heben, "Understanding VOC and performance deficit in wide bandgap perovskite photovoltaic devices," *Sol. Energy Mater. Sol. Cells,* **vol. 225**, p. 111015, 2021.

[424] Y. Li *et al.*, "Multifunctional fullerene derivative for interface engineering in perovskite solar cells," *Journal of the American Chemical Society,* **vol. 137**, no**.** 49, pp. 15540-15547, 2015.

[425] W. Li *et al.*, "Enhanced UV-light stability of planar heterojunction perovskite solar cells with caesium bromide interface modification," *Energy Environ. Sci.,* **vol. 9**, no**.** 2, pp. 490-498, 2016.

[426] F. Han, J. Luo, B. Zhao, Z. Wan, R. Wang, and C. Jia, "Cesium iodide interface modification for high efficiency, high stability and low hysteresis perovskite solar cells," *Electrochimica Acta,* **vol. 236**, pp. 122-130, 2017.

[427] L. Zuo *et al.*, "Tailoring the interfacial chemical interaction for high-efficiency perovskite solar cells," *Nano Lett.,* **vol. 17**, no**.** 1, pp. 269-275, 2017.

[428] L. Zuo *et al.*, "Enhanced photovoltaic performance of $CH_3NH_3PbI_3$ perovskite solar cells through interfacial engineering using self-assembling monolayer," *Journal of the American Chemical Society,* **vol. 137**, no**.** 7, pp. 2674-2679, 2015.

[429] H. J. Snaith and M. Grätzel, "The role of a "Schottky Barrier" at an electron-collection electrode in solid-state dye-sensitized solar cells," *Adv. Mater.,* **vol. 18**, no**.** 14, pp. 1910-1914, 2006.

[430] A. Kulkarni, A. K. Jena, H.-W. Chen, Y. Sanehira, M. Ikegami, and T. Miyasaka, "Revealing and reducing the possible recombination loss within TiO2 compact layer by incorporating MgO layer in perovskite solar cells," *SoEn,* **vol. 136**, pp. 379-384, 2016.

[431] J. T.-W. Wang *et al.*, "Low-temperature processed electron collection layers of graphene/TiO_2 nanocomposites in thin film perovskite solar cells," *Nano Lett.,* **vol. 14**, no**.** 2, pp. 724-730, 2014.

[432] Y. Zhou *et al.*, "A universal method to produce low–work function electrodes for organic electronics," *Science,* **vol. 336**, no**.** 6079, pp. 327-332, 2012.

[433] J. H. Kim, C.-C. Chueh, S. T. Williams, and A. K.-Y. Jen, "Room-temperature, solution-processable organic electron extraction layer for high-performance planar heterojunction perovskite solar cells," *Nanoscale,* **vol. 7**, no**.** 41, pp. 17343-17349, 2015.

[434] S. Ryu *et al.*, "Fabrication of metal-oxide-free CH 3 NH 3 PbI 3 perovskite solar cells processed at low temperature," *Journal of Materials Chemistry A,* **vol. 3**, no**.** 7, pp. 3271-3275, 2015.

[435] Z. Zhu *et al.*, "A low-temperature, solution-processable organic electron-transporting layer based on planar coronene for high-performance conventional perovskite solar cells," *Adv. Mater.,* **vol. 28**, no**.** 48, pp. 10786-10793, 2016.

[436] J. Lee *et al.*, "A Printable Organic Electron Transport Layer for Low-Temperature-Processed, Hysteresis-Free, and Stable Planar Perovskite Solar Cells," *Advanced Energy Materials,* **vol. 7**, no**.** 15, p. 1700226, 2017.

[437] J. Xie *et al.*, "Self-Organized Fullerene Interfacial Layer for Efficient and Low-Temperature Processed Planar Perovskite Solar Cells with High UV-Light Stability," *Advanced Science,* **vol. 4**, no**.** 8, p. 1700018, 2017.

[438] Y. C. Wang, X. Li, L. Zhu, X. Liu, W. Zhang, and J. Fang, "Efficient and Hysteresis-Free Perovskite Solar Cells Based on a Solution Processable Polar Fullerene Electron Transport Layer," *Advanced Energy Materials,* **vol. 7**, no**.** 21, p. 1701144, 2017.

[439] A. K. Jena, A. Kulkarni, and T. Miyasaka, "Halide Perovskite Photovoltaics: Background, Status, and Future Prospects," (in English), *Chem. Rev.,* **vol. 119**, no**.** 5, pp. 3036-3103, Mar 13 2019, doi: 10.1021/acs.chemrev.8b00539.

[440] K. Wojciechowski, M. Saliba, T. Leijtens, A. Abate, and H. J. Snaith, "Sub-150 C processed meso-superstructured perovskite solar cells with enhanced efficiency," *Energy Environ. Sci.,* **vol. 7**, no**.** 3, pp. 1142-1147, 2014.

[441] P. Umari, E. Mosconi, and F. De Angelis, "Relativistic GW calculations on CH3NH3PbI3 and $CH_3NH_3SnI_3$ perovskites for solar cell applications," (in English), *Sci. Rep.,* **vol. 4**, p. 4467, Mar 26 2014, doi: 10.1038/srep04467.

[442] M. Hirasawa, T. Ishihara, T. Goto, K. Uchida, and N. Miura, "Magnetoabsorption of the Lowest Exciton in Perovskite-Type Compound $(CH_3NH_3)PbI_3$," (in English), *Physica B,* **vol. 201**, pp. 427-430, Jul-Aug 1994, doi: Doi 10.1016/0921-4526(94)91130-4.

[443] D. Poplavskyy and J. Nelson, "Nondispersive hole transport in amorphous films of methoxy-spirofluorene-arylamine organic compound," *Journal of Applied Physics,* **vol. 93**, no**.** 1, pp. 341-346, 2003, doi: 10.1063/1.1525866.

[444] G. Giorgi, J. I. Fujisawa, H. Segawa, and K. Yamashita, "Small Photocarrier Effective Masses Featuring Ambipolar Transport in Methylammonium Lead Iodide Perovskite: A Density Functional Analysis," (in English), *J. Phys. Chem. Lett.,* **vol. 4**, no**.** 24, pp. 4213-4216, Dec 19 2013, doi: 10.1021/jz4023865.

[445] X. Zhang, J.-X. Shen, W. Wang, and C. G. Van de Walle, "First-principles analysis of radiative recombination in lead-halide perovskites," *ACS Energy Letters,* **vol. 3**, no**.** 10, pp. 2329-2334, 2018.

[446] S. Collavini, A. Cabrera-Espinoza, and J. L. Delgado, "Organic Polymers as Additives in Perovskite Solar Cells," *Macromolecules,* 2021.

[447] T. J. Jacobsson *et al.*, "Exploration of the compositional space for mixed lead halogen perovskites for high efficiency solar cells," *Energy Environ. Sci.,* **vol. 9**, no**.** 5, pp. 1706-1724, 2016.

[448] M. Saliba *et al.*, "Incorporation of rubidium cations into perovskite solar cells improves photovoltaic performance," *Science,* **vol. 354**, no**.** 6309, pp. 206-209, 2016.

[449] Y. Zhou *et al.*, "Benzylamine-treated wide-bandgap perovskite with high thermal-photostability and photovoltaic performance," *Advanced Energy Materials,* **vol. 7**, no**.** 22, p. 1701048, 2017.

[450] K. T. Cho *et al.*, "Selective growth of layered perovskites for stable and efficient photovoltaics," *Energy Environ. Sci.,* **vol. 11**, no**.** 4, pp. 952-959, 2018.

[451] J. Kim *et al.*, "Amide-Catalyzed Phase-Selective Crystallization Reduces Defect Density in Wide-Bandgap Perovskites," *Adv. Mater.,* **vol. 30**, no**.** 13, p. 1706275, 2018.

[452] Y. Yao, W.-L. Hsu, and M. Dagenais, "High Efficiency Perovskite Solar Cells by a Modified Low-Temperature Solution Process Inter-Diffusion Method," in *2017 IEEE 44th Photovoltaic Specialist Conference (PVSC)*, Washington, DC, US, 2017: IEEE, pp. 1048-1050.

[453] J. You *et al.*, "Improved air stability of perovskite solar cells via solution-processed metal oxide transport layers," *Nature Nanotechnology,* **vol. 11**, no**.** 1, p. 75, 2016.

[454] X. Ling *et al.*, "Room-temperature processed Nb2O5 as the electron-transporting layer for efficient planar perovskite solar cells," *ACS Applied Materials & Interfaces,* **vol. 9**, no**.** 27, pp. 23181-23188, 2017.

[455] H. Liang, Y.-C. Hu, Y. Tao, B. Wu, Y. Wu, and J. Cao, "Existence of Ligands within Sol–Gel-Derived ZnO Films and Their Effect on Perovskite Solar Cells," *ACS Applied Materials & Interfaces,* **vol. 11**, no**.** 46, pp. 43116-43121, 2019.

[456] X. Liu, J. Jiang, F. Wang, Y. Xiao, I. D. Sharp, and Y. Li, "High Photovoltage Inverted Planar Heterojunction Perovskite Solar Cells with All-Inorganic Selective Contact Layers," *ACS Applied Materials & Interfaces,* **vol. 11**, no**.** 50, pp. 46894-46901, 2019.

[457] J. Wang, W. Fu, S. Jariwala, I. Sinha, A. K.-Y. Jen, and D. S. Ginger, "Reducing surface recombination velocities at the electrical contacts will improve perovskite photovoltaics," *ACS Energy Letters,* **vol. 4**, no**.** 1, pp. 222-227, 2018.

[458] W. Tress, "Perovskite solar cells on the way to their radiative efficiency limit–insights into a success story of high open-circuit voltage and low recombination," *Advanced Energy Materials,* **vol. 7**, no**.** 14, p. 1602358, 2017.

[459] R. E. Brandt, V. Stevanović, D. S. Ginley, and T. Buonassisi, "Identifying defect-tolerant semiconductors with high minority-carrier lifetimes: beyond hybrid lead halide perovskites," *MRS Communications,* **vol. 5**, no**.** 2, pp. 265-275, 2015.

[460] A. Buin *et al.*, "Materials processing routes to trap-free halide perovskites," *Nano Lett.,* **vol. 14**, no**.** 11, pp. 6281-6286, 2014.

[461] Q. Lin, A. Armin, R. C. R. Nagiri, P. L. Burn, and P. Meredith, "Electro-optics of perovskite solar cells," *Nature Photonics,* **vol. 9**, no**.** 2, pp. 106-112, 2015.

[462] P. K. Nayak, S. Mahesh, H. J. Snaith, and D. Cahen, "Photovoltaic solar cell technologies: analysing the state of the art," *Nature Reviews Materials,* **vol. 4**, no**.** 4, pp. 269-285, 2019.

[463] J.-P. Correa-Baena *et al.*, "Promises and challenges of perovskite solar cells," *Science,* **vol. 358**, no**.** 6364, pp. 739-744, 2017.

[464] S. Gharibzadeh *et al.*, "Record open-circuit voltage wide-bandgap perovskite solar cells utilizing 2D/3D perovskite heterostructure," *Advanced Energy Materials,* **vol. 9**, no**.** 21, p. 1803699, 2019.

[465] E. T. Hoke, D. J. Slotcavage, E. R. Dohner, A. R. Bowring, H. I. Karunadasa, and M. D. McGehee, "Reversible photo-induced trap formation in mixed-halide hybrid perovskites for photovoltaics," *Chemical Science,* **vol. 6**, no**.** 1, pp. 613-617, 2015.

[466] D. J. Slotcavage, H. I. Karunadasa, and M. D. McGehee, "Light-induced phase segregation in halide-perovskite absorbers," *ACS Energy Letters,* **vol. 1**, no**.** 6, pp. 1199-1205, 2016.

[467] F. Peña-Camargo *et al.*, "Halide segregation versus interfacial recombination in bromide-rich wide-gap perovskite solar cells," *ACS Energy Letters,* **vol. 5**, no**.** 8, pp. 2728-2736, 2020.

[468] P. Caprioglio *et al.*, "On the relation between the open-circuit voltage and quasi-fermi level splitting in efficient perovskite solar cells," *Advanced Energy Materials,* **vol. 9**, no**.** 33, p. 1901631, 2019.

[469] M. Stolterfoht *et al.*, "The impact of energy alignment and interfacial recombination on the internal and external open-circuit voltage of perovskite solar cells," *Energy Environ. Sci.,* **vol. 12**, no**.** 9, pp. 2778-2788, 2019.

[470] S. Karthick, S. Velumani, and J. Bouclé, "Experimental and SCAPS simulated formamidinium perovskite solar cells: a comparison of device performance," *SoEn,* **vol. 205**, pp. 349-357, 2020.

[471] M. Jeong *et al.*, "Stable perovskite solar cells with efficiency exceeding 24.8% and 0.3-V voltage loss," *Science,* **vol. 369**, no**.** 6511, pp. 1615-1620, 2020.

[472] W. S. Yang *et al.*, "Iodide management in formamidinium-lead-halide–based perovskite layers for efficient solar cells," *Science,* **vol. 356**, no**.** 6345, pp. 1376-1379, 2017.

[473] M. Yu and S. D. Kenny, "The energetic impact of small Cd Te clusters on Cadmium Telluride," *Thin Solid Films,* **vol. 584**, pp. 41-45, 2015, doi: 10.1016/j.tsf.2014.12.019.

[474] X. W. Zhou *et al.*, "High-fidelity simulations of CdTe vapor deposition from a bond-order potential-based molecular dynamics method," *PhRvB,* **vol. 85**, no**.** 24, p. 245302, 2012, doi: 10.1103/PhysRevB.85.245302.

[475] D. Z. Pettifor, M. W. Finnis, D. Nguyen-Manh, D. A. Murdick, X. W. Zhou, and H. N. Wadley, "Analytic bond-order potentials for multicomponent systems," *Mater. Sci. Eng. A,* **vol. P365**, p. 2, 2004.

[476] H. J. C. Berendsen, J. P. M. Postma, W. F. v. Gunsteren, A. DiNola, and J. R. Haak, "Molecular dynamics with coupling to an external bath," *Journal of Chemical Physics,* **vol. 81**, p. 3684, 1984.

[477] I. Khatri and J. G. Amar, "Energy, temperature, and deposition angle dependence of Cd and Te2 deposited on CdTe," *Thin Solid Films,* **vol. 697**, p. 137798, 2020.

[478] S. J. Ikhmayies and R. N. Ahmad-Bitar, "Characterization of vacuum evaporated CdTe thin films prepared at ambient temperature," *Mater. Sci. Semicond. Process.,* **vol. 118**, p. 125, 2013.

[479] N. Amin and K. S. Rahman, "Close-Spaced Sublimation (CSS): A Low-Cost, High-Yield Deposition System for Cadmium Telluride (CdTe) Thin Film Solar Cells," in *Modern Technologies for Creating the Thin-film Systems and Coatings*, 2017, ch. Chapter 18.

[480] B. Siepchen *et al.*, "Thin film CdTe solar cells by close spaced sublimation: Recent results from pilot line," *Thin Solid Films,* **vol. 535**, pp. 224-228, 2013, doi: 10.1016/j.tsf.2012.11.083.

[481] A. Romeo, E. Artegiani, and D. Menossi, "Low substrate temperature CdTe solar cells: A review," *SoEn,* **vol. 175**, pp. 9-15, 2018, doi: 10.1016/j.solener.2018.02.038.

[482] A. E. Patrakov, R. F. Fink, K. Fink, and B. Engels, "Model computations for Cd adsorption on the (001) surface of CdTe," *physica status solidi (c),* **vol. 4**, no**.** 9, pp. 3191-3203, 2007, doi: 10.1002/pssc.200775415.

[483] A. E. Patrakov, R. F. Fink, K. Fink, T. C. Schmidt, and B. Engels, "Density-functional study on the migration of Cd and Te adsorbates on the (001) surface of CdTe," *physica status solidi (b),* **vol. 247**, no**.** 4, pp. 937-944, 2010, doi: 10.1002/pssb.201046080.

[484] F. Pietrucci, G. Gerra, and W. Andreoni, "CdTe surfaces: Characterizing dynamical processes with first-principles metadynamics," *Applied Physics Letters,* **vol. 97**, p. 141914, 2010, doi: 10.1063/1.3499430.

[485] K. A. Fichthorn and R. A. Miron, "Thermal desorption of large molecules from solid surfaces," *Phys. Rev. Lett.,* **vol. 89**, no**.** 19, p. 196103, Nov 4 2002, doi: 10.1103/PhysRevLett.89.196103.

[486] E. K. Grimmelmann, J. C. Tully, and E. Helfand, "Molecular dynamics of infrequent events: Thermal desorption of xenon from a platinum surface," *The Journal of Chemical Physics,* **vol. 74**, no**.** 9, pp. 5300-5310, 1981, doi: 10.1063/1.441696.

[487] G. M. Torrie and J. P. Valleau, "Nonphysical Sampling Distributions in Monte Carlo Free-Energy Estimation: Umbrella Sampling," *Journal of Computational Physics,* **vol. 23**, pp. 187-199, 1977 1977.

[488] S. Tatarenko, B. Daudin, and D. Brun, "Sublimation mechanisms of (100) and (111) CdTe," *Applied Physics Letters,* **vol. 65**, no**.** 6, pp. 734-736, 1994, doi: 10.1063/1.112214.

[489] P. Juza, W. Faschinger, K. Hingerl, and H. Sitter, "Langmuir-type evaporation of CdTe epilayers," *Semicond. Sci. Technol. ,* **vol. 5**, pp. 191-195, 1990.

[490] I. Khatri and J. G. Amar, "Energy barriers and prefactors for Cd and Te2 desorption from the CdTe(100) surface," *Manuscript in preparation,* 2021.

[491] B. Subedi *et al.*, "Formamidinium+ cesium lead triiodide perovskite thin films: optical properties and devices," in *2018 IEEE 7th World Conference on Photovoltaic Energy Conversion (WCPEC)(A Joint Conference of 45th IEEE PVSC, 28th PVSEC & 34th EU PVSEC)*, Waikoloa, HI, US, 2018: IEEE, pp. 0522-0525.

[492] M. S. Tumusange *et al.*, "Impact of Humidity and Temperature on the Stability of the Optical Properties and Structure of MAPbI3, MA0. 7FA0. 3PbI3 and (FAPbI3) 0.95 (MAPbBr3) 0.05 Perovskite Thin Films," *Materials,* **vol. 14**, no**.** 14, p. 4054, 2021.

[493] M. M. Junda, C. R. Grice, Y. Yan, and N. J. Podraza, "Parametric optical property database for CdSe 1− x S x alloys," *Electronic Materials Letters,* **vol. 15**, no**.** 4, pp. 500-504, 2019.

[494] M. M. Junda, C. R. Grice, P. Koirala, R. W. Collins, Y. Yan, and N. J. Podraza, "Optical Properties of CdSeTe Alloys and Their Application for CdTe Photovoltaics," in *2017 IEEE 44th Photovoltaic Specialist Conference (PVSC)*, Washington, DC, US, 2017: IEEE, pp. 3426-3429.

[495] S. R. N. K. Jayswal, B. Subedi, I. Subedi, Z. Song, R. W. Collins, Y. Yan, and N. J. Podraza, "Optical Properties of Thin Film Sb2Se3 and Identification of its Electronic Losses in Photovoltaic Devices," *SoEn,* Accepted **vol. Accepted**, 2021.

[496] B. B. Dumre, D. Gall, and S. V. Khare, "Stability, and electronic and optical properties of ternary nitride phases of $MgSnN_2$: A first-principles study," *Journal of Physics and Chemistry of Solids,* **vol. 153**, p. 110011, 2021/06/01/ 2021, doi: doi.org/10.1016/j.jpcs.2021.110011.

[497] F. Kawamura, M. Imura, H. Murata, N. Yamada, and T. Taniguchi, "Synthesis of a Novel Rocksalt-Type Ternary Nitride Semiconductor $MgSnN_2$ Using the Metathesis Reaction Under High Pressure," *Eur. J. Inorg. Chem.,* **vol. 2020**, no**.** 5, pp. 446-451, 2020, doi: 10.1002/ejic.201901059.

LIST OF ACRONYMS, ABBREVIATIONS, AND SYMBOLS

Acronym, Abbreviation or Symbol	Definition or Explanation
α	Absorption Coefficient
AES	Auger Electron Spectroscopy
Al-BSF	Aluminum Back Surface Field
ALD	Atomic Layer Deposition
AM1.5G	Air Mass 1.5 Global Standardized Solar Irradiance Spectrum
CB	Conduction Band
CBD	Chemical Bath Deposition
CBO	Conduction Band Offset
CCD	Charged Coupled Device
CIGS	Copper Indium Gallium Sulfide/Selenide
CIS	Copper Indium Sulfide/Selenide
CIS	Copper Indium Sulfide
CP	Critical Point
CSS	Close Space Sublimation
CTLs	Charge Transport Layers
C-V	Cyclic Voltammetry
cw	Continuous
CZS	Cu-Zn-S
DAP	Donor-Acceptor Pair Transition
DFT	Density Functional Theory
DI	Deionized
DIW	Deionized Water
DMF	N, N-dimethyl formamide
DMSO	Dimethyl Sulfoxide
DOS	Density of States
EDS or EDX	Energy Dispersive X-ray Spectroscopy
Eff	Efficiency
E_g	Energy Band Gap
EPBT	Energy Payback Time
EQE	External Quantum Efficiency
EROI	Energy Return on energy Invested
ETLs	Electron Transport Layers
Eu	Urbach Energy

eV	Electron Volt
FAI	Formamidinium Iodide
FF	Fill Factor
FTO	Fluorine Doped Tin Oxide
FWHM	Full Width at Half Maxima
GGA	Generalized Gradient Approximation
GLAD	Glancing Angle Deposition
HOMO	Highest Occupied Molecular Orbitals
HTL(s)	Hole Transport Layer (s)
HTM(s)	Hole Transport Material (s)
IPA	Isopropanol
ITO	Indium Tin Oxide
iV_{oc}	Implied Open Circuit Voltage
J_0	Saturation Current density
J_{SC}	Short-circuit Current Density
J-V	Current-density Vs Voltage
J-V-T	Current-density, Voltage and Temperature
LBIC	Laser Beam Induced Current
LUMO	Lowest Unoccupied Molecular Orbitals
M	Molar Concentration
m*	Effective Carrier Mass
MABr	Methyl Ammonium Bromide
MACl	Methyl Ammonium Chloride
MAI	Methyl Ammonium Iodide
MD	Molecular Dynamics
MPP	Maximum Power Point
MZO	Magnesium Zinc Oxide
N	Carrier Concentration
NIR	Near Infrared (~ 700 nm to 2.5 μm wavelengths Light)
nm	Nanometer
NWs	Nanowires
OA	Oleic Acid
ODE	1-octadecene
PCBM	Phenyl-C60-butyric acid methyl ester
PCE	Photoconversion Efficiency
PDF	Powdered Diffraction File
PDS	Photothermal Deflection Spectroscopy
PEIE	Poly-ethyl enimine ethoxylate

PK	Perovskite
PKSCs	Perovskite Solar Cells
PL	Photoluminescence
PMMA	poly methyl-methacrylate
PV	Photovoltaics
PVP	Poly vinyl pyrrolidone
q	Charge
QDs	Quantum Dots
RF	Radio Frequency
RHEED	Reflection High Energy Electron Diffraction
R_s	Series Resistance
R_{sh}	Shunt Resistance
RT	Room Temperature
S. D.	Standard Deviation
SCAPS	Solar cell Capacitance Simulator
SCLC	Space Charge Limited Current
SE	Spectroscopic Ellipsometry
SEM	Scanning Electron Microscopy
SILAR	Successive Ionic Layer Adsorption and Reaction
SR	Spectroscopic Reflectance
SRH	Shockley Read Hall
STD, Std	Standard
STEM	Scanning Transmission Electron Microscopy
T	Absolute Temperature
TA	Temperature Accelerated
TBP	4-tert-butylpyridine
TCO	Transparent Conducting Oxide
TCSPC	Time Correlated Single Photon Counting
TE	Thermoelectric
TEA	Triethanolamine
TEC-15	Standard Glass commonly used in Solar Cells, 3.3mm Thick glass, coated with 300nm TCO
TEM	Transmission Electron Microscopy
TGA	Thermogravimetric Analysis
THz	Tetra Hertz
TOP	Tri-octyl phosphine
TRPL	Time Resolved Photoluminescence
TST	Transition State Theory
UT	University of Toledo

UV-VIS-NIR	Ultraviolet-Visible-Near Infrared
VASE	Variable Angle Spectroscopic Ellipsometry
VB	Valence Band
VBO	Valence Band Offset
VD	Vapor Deposition
V_{mpp}	Maximum Power Point Voltage
V_{OC}	Open-circuit Voltage
VTD	Vapor Transport Deposit
WVTR	Water vapor Transmission Rate
XRD	X-ray Diffraction
ZMO	Zinc Magnesium Oxide
ϵ	Dielectric Constant
η	Efficiency or Photoconversion Efficiency
μ	Carrier Mobility
ρ	Resistivity
$\boldsymbol{\sigma}$	Conductivity

Appendix

List of Publications Acknowledging AFRL UCA Funding (FA9453-18-2-0037)

(click on title to go to paper)

Page #	Title	Authors	Year	Journal/Proceedings
312	Dithieno[3, 2-b: 2′, 3′-d]pyrrol-Cored Hole Transport Material Enabling Over 21% Efficiency Dopant-Free Perovskite Solar Cells	X. Yin, J. Zhou, Z. Song, Z. Dong, Q. Bao, N. Shrestha, S. S. Bista, R. J. Ellingson, Y. Yan and W. Tang	2019	*Advanced Functional Materials*
321	High Remaining Factors in the Photovoltaic Performance of Perovskite Solar Cells after High-Fluence Electron Beam Irradiations	Z. Song, C. Li, C. Chen, J. McNatt, W. Yoon, D. Scheiman, P. P. Jenkins, R. J. Ellingson, M. J. Heben and Y. Yan	2019	*The Journal of Physical Chemistry C*
328	Photogenerated Carrier Transport Properties in Silicon Photovoltaics	P. Uprety, I. Subedi, M. M. Junda, R. W. Collins and N. J. Podraza	2019	*Scientific Reports*
340	Charge Compensating Defects in Methylammonium Lead Iodide Perovskite Suppressed by Formamidinium Inclusion	N. Shrestha, Z. Song, C. Chen, E. Bastola, X. Wang, Y. Yan and R. J. Ellingson	2019	*Journal of Physical Chemistry Letters*
348	Wet chemical etching of cadmium telluride photovoltaics for enhanced open-circuit voltage, fill factor, and power conversion efficiency	E. Bastola, F. K. Alfadhili, A. B. Phillips, M. J. Heben and R. J. Ellingson	2019	*Journal of Materials Research*
358	Effects of Fabrication Atmosphere on Bulk and Back Interface Defects of CdTe Solar Cells with CdS and MgZnO Buffers	R. A. Awni, D. Li, Z. Song, S. S. Bista, M. A. Razooqi, C. R. Grice, L. Chen, G. K. Liyanage, C. Li, A. B. Phillips, M. J. Heben, R. J. Ellingson, J. V. Li and Y. Yan	2019	*IEEE PVSC Conference Proceedings*
362	Improved optoelectronic properties in $CdSe_xTe_{1-x}$ through controlled composition and short-range order	B. B. Dumre, N. J. Szymanski, V. Adhikari, I. Khatri, D. Gall and S. V. Khare	2019	*Solar Energy*
371	Defect Analysis in CSS and Sputtered $CdSe_xTe_{1-x}$ Thin Films	N. Shrestha, C. R. Grice, E. Bastola, Y. Yan and R. J. Ellingson	2019	*IEEE PVSC Conference Proceedings*
376	ZnTe Back Buffer Layer to Enhance the Efficiency of CdS/CdTe Solar Cells	S. S. Bista, D.-B. Li, C. Lei, C. Grice, R. A. Awni, Z. Song and Y. Yan	2019	*IEEE PVSC Conference Proceedings*
380	Doping of CdTe using $CuCl_2$ Solution for Highly Efficient Photovoltaic Devices	E. Bastola, A. V. Bordovalos, E. LeBlanc, N. Shrestha, M. O. Reese and R. J. Ellingson	2019	*IEEE PVSC Conference Proceedings*

385	Room Temperature Processed Transparent Cu-Zn-S Nanocomposites as Hole Transport Materials in CdTe Photovoltaics	E. Bastola, K. K. Subedi, F. K. Alfadhili, A. B. Phillips, M. J. Heben and R. J. Ellingson	2019	*IEEE PVSC Conference Proceedings*
390	Monolithic Two-Terminal All-Perovskite Tandem Solar Cells with Power Conversion Efficiency Exceeding 21%	Z. Song, D. Zhao, C. Chen, R. H. Ahangharnejhad, C. Li, K. Ghimire, N. J. Podraza, M. J. Heben, K. Zhu and Y. Yan	2019	*IEEE PVSC Conference Proceedings*
394	Understanding CdTe Performance with Engineered Front and Back Interfaces	A. B. Phillips, G. K. Liyanage, F. K. Alfadhili and M. J. Heben	2019	*IEEE PVSC Conference Proceedings*
400	Influences of buffer material and fabrication atmosphere on the electrical properties of CdTe solar cells	Rasha A. Awni, Deng-Bing Li, Zhaoning Song, Sandip S. Bista, Mohammed A. Razooqi, Corey R. Grice, Lei Chen, Geethika K. Liyanage, Chongwen Li, Adam B. Phillips, Michael J. Heben, |Randy J. Ellingson, Jian V. Li, Yanfa Yan	2019	*Progress in Photovoltaics*
409	Effects of intrinsic and atmospherically induced defects in narrow bandgap $(FASnI_3)_x$ $(MAPbI_3)_{1-x}$ perovskite films and solar cells	B. Subedi, C. Li, M. M. Junda, Z. Song, Y. Yan and N. J. Podraza	2020	*The J. of chemical physics*
418	CuSCN as the Back Contact for Efficient ZMO/CdTe Solar Cells	D.-B. Li, Z. Song, S. S. Bista, F. K. Alfadhili, R. A. Awni, N. Shrestha, D. Rhiannon, A. B. Phillips, M. J. Heben and R. J. Ellingson	2020	*Materials*
430	Successive Ionic Layer Adsorption and Reaction-Deposited Transparent Cu–Zn–S Nanocomposites as Hole Transport Materials in CdTe Photovoltaics	E. Bastola, K. K. Subedi, F. K. Alfadhili, A. B. Phillips, M. J. Heben and R. J. Ellingson	2020	*Energy Technology*
437	Arylammonium-Assisted Reduction of the Open-Circuit Voltage Deficit in Wide-Bandgap Perovskite Solar Cells: The Role of Suppressed Ion Migration	C. Chen, Z. Song, C. Xiao, R. A. Awni, C. Yao, N. Shrestha, C. Li, S. S. Bista, Y. Zhang and L. Chen	2020	*ACS Energy Letters*
446	Understanding and Advancing Bifacial Thin Film Solar Cells	A. B. Phillips, K. K. Subedi, G. K. Liyanage, F. K. Alfadhili, R. J. Ellingson and M. J. Heben	2020	*ACS Applied Energy Materials*
453	Decreasing the resolution limit of laser beam induced current measurements below the beam size without confocal optics: Determining laser scribe widths	R. H. Ahangharnejhad, Z. Song, J. L. DeWitt, A. B. Phillips, B. R. Lumbrezer, C. E. Wickersham and M. J. Heben	2020	*Solar Energy Materials and Solar Cells*
459	Energy, temperature, and deposition angle dependence of Cd and Te2 deposited on CdTe	I. Khatri and J. G. Amar	2020	*Thin Solid Films*

464	Semi-transparent p-type barium copper sulfide as a back contact interface layer for cadmium telluride solar cells	K. K. Subedi, E. Bastola, I. Subedi, S. S. Bista, S. Rijal, M. K. Jamarkattel, R. A. Awni, A. B. Philips, Y. Yan and M. J. Heben	2020	*Solar Energy Materials and Solar Cells*
472	Maximize CdTe solar cell performance through copper activation engineering	D.-B. Li, S. S. Bista, Z. Song, R. A. Awni, K. K. Subedi, N. Shrestha, P. Pradhan, L. Chen, E. Bastola and C. R. Grice	2020	*Nano Energy*
480	Influence of Charge Transport Layers on Capacitance Measured in Halide Perovskite Solar Cells	R. A. Awni, Z. Song, C. Chen, C. Li, C. Wang, M. A. Razooqi, L. Chen, X. Wang, R. J. Ellingson, J. V. Li and Y. Yan	2020	*Joule*
495	Back-Surface Passivation of CdTe Solar Cells Using Solution-Processed Oxidized Aluminum	F. K. Alfadhili, A. B. Phillips, K. K. Subedi, C. L. Perkins, A. I. Halaoui, M. K. Jamarkattel, B. M. Anwar, G. K. Liyanage, D.-B. Li and C. R. Grice	2020	*ACS Applied Materials & Interfaces*
502	Interface modification of sputtered NiO_x as the hole-transporting layer for efficient inverted planar perovskite solar cells	X. Zheng, Z. Song, Z. Chen, S. S. Bista, P. Gui, N. Shrestha, C. Chen, C. Li, X. Yin and R. A. Awni	2020	*J. of Material Chemistry C*
512	Aspect ratio-controlled synthesis of tellurium nanowires for photovoltaic applications	D. Pokhrel, E. Bastola, A. B. Phillips, M. J. Heben and R. J. Ellingson	2020	*Materials Advacnes*
520	Glancing angle deposited CdTe: Nanostructured films and impact on solar cell performance	D. Adhikari, M. M. Junda, E. Bastola, P. Koirala, R. J. Ellingson, R. W. Collins and N. J. Podraza	2020	*Surface and Coatings Technology*
530	Correlating Hysteresis and Stability with Organic Cation Composition in the Two-Step Solution-Processed Perovskite Solar Cells	Y. Cui, C. Chen, C. Li, L. Chen, S. S. Bista, X. Liu, Y. Li, R. A. Awni, Z. Song and Y. Yan	2020	*ACS Applied Materials & Interfaces*
539	Environmental Impact per Energy Yield for Bifacial Perovskite Solar Cells Outperforms Crystalline Silicon Solar Cells	R. Hosseinian Ahangharnejhad, W. Becker, J. Jones, A. Anctil, Z. Song, A. Phillips, M. J. Heben and I. Celik	2020	*Cell Reports Physical Science*
554	Low-bandgap mixed tin–lead iodide perovskites with reduced methylammonium for simultaneous enhancement of solar cell efficiency and stability	C. Li, Z. Song, C. Chen, C. Xiao, B. Subedi, S. P. Harvey, N. Shrestha, K. K. Subedi, L. Chen, D. Liu, Y. Li, Y.-W. Kim, C.-s. Jiang, M. J. Heben, D. Zhao, R. J. Ellingson, N. J. Podraza, M. Al-Jassim and Y. Yan	2020	*Nature Energy*
563	Highly Doped Single Walled Carbon Nanotubes Deposited as the Back Buffer Layer on CdTe Devices	J. M. Gibbs, A. B. Phillips, E. Bastola, F. K. Alfadhili, R. H. Ahangharnejhad, R. J. Ellingson and M. J. Heben	2020	*IEEE PVSC Conference Proceedings*

566	Solution Based Cu-Doped Aluminum Oxide as a Back Interface Layer for CdTe Solar Cells	K. K. Subedi, A. B. Phillips, M. J. Heben and R. J. Ellingson	2020	*IEEE PVSC Conference Proceedings*
570	Incorporation of Arsenic in CdSe/CdTe Solar Cells During Close Spaced Sublimation of CdTe: As	M. K. Jamarkattel, A. B. Phillips, A. Quader, K. K. Subedi, F. K. Alfadhili, S. S. Bista, R. A. Awni, D.-B. Li, S. K. Swain and Y. Yan	2020	*IEEE PVSC Conference Proceedings*
574	Open-circuit Voltage Exceeding 840 mV for All-Sputtered CdS/CdTe Devices	E. Bastola, A. B. Phillips, N. Shrestha, M. K. Jamarkattel, R. A. Awni, Y. Yan, M. J. Heben and R. J. Ellingson	2020	*IEEE PVSC Conference Proceedings*
580	Solution-Processed Copper Telluride Nanowire Thin Film as a Back-Buffer Layer to Cadmium Telluride Solar Cells	D. Pokhrel, E. Bastola, K. K. Subedi, A. Phillips, M. J. Heben and R. J. Ellingson	2020	*IEEE PVSC Conference Proceedings*
583	Solution Processed CuCl treatment for efficient CdS/CdTe Solar Cells	S. S. Bista, D.-B. Li, Z. Song, R. A. Awni, S. Rijal, C. Lei, C. R. Grice, M. K. Jamarkattel, A. Phillips, M. Heben and Y. Yan	2020	*IEEE PVSC Conference Proceedings*
587	Doping Control of $Mg_xZn_{1-x}O$ Emitter through Fluorine Incorporation	A. J. Snyder, J. M. Gibbs, M. K. Jamarkattel, A. B. Phillips and M. J. Heben	2020	*IEEE PVSC Conference Proceedings*
590	Non-contacting optical probing of photovoltaic device performance	I. Subedi, B. Subedi, P. Uprety, M. M. Junda, D. Adhikari, K. Ghimire, P. Koirala, R. W. Collins, Y. Yan and N. J. Podraza	2020	*Physics, Simulation and Photonic Engineering of Photovoltaic Devices*
603	Materials requirements for improving the electron transport layer/perovskite interface of perovskite solar cells determined via numerical modeling	J. D. Friedl, R. H. Ahangharnejhad, A. B. Phillips and M. J. Heben	2020	*MRS Advances*
611	Understanding the Interplay Between CdSe Thickness and Cu Doping Temperature in CdSe/CdTe Devices	E. Bastola, A. Phillips, G. Barros-King, M. Jamarkattel, D. Li, A. Quader, D. Pokhrel, J. Friedl, J. M. Gibbs, X. Mathew, Y. Yan, R. J. Ellingson and M. J. Heben	2021	*J. of Photovoltaics*
616	Improving CdSeTe Devices With a Back Buffer Layer of Cu_xA1O_v	M. K. Jamarkattel, A. B. Phillips, K. K. Subedi, E. Bastola, J. M. Gibbs, S. Rijal, D. Pokhrel, D. Li, Y. Yan, R. J. Ellingson, and M. J. Heben	2021	*J. of Photovoltaics*
622	Copper iodide nanoparticles as a hole transport layer to CdTe photovoltaics: 5.5 % efficient back-illuminated bifacial CdTe solar cells	Dipendra Pokhrel, Ebin Bastola, Kamala Khanal Subedi, Suman Rijal, Manoj K. Jamarkattel, Rasha A. Awni, Adam B. Phillips, Yanfa Yan, Michael J. Heben, and Randy J. Ellingson	2021	*Solar Energy Materials and Solar cells*

630	Optical properties of thin film Sb_2Se_3 and identification of its electronic losses in photovoltaic devices	N. K. Jayswal, S. Rijal, B. Subedi, I. Subedi, Z. Song, R. W. Collins, Y. Yan, and N. J. Podraza	2021	*Solar Energy*
637	Protecting Perovskite Solar Cells against Moisture-Induced Degradation with Sputtered Inorganic Barrier Layers	R. Hosseinian Ahangharnejhad, Z. Song, T. Mariam, J. Gardner, G. Liyange, Z. Almutawah, B. Anwar, M. Junda, N. J. Podraza, A. Phillips, Y. Yan, and M. Heben	2021	*ACS Applied Energy Materials*
645	Stability, and electronic and optical properties of ternary nitride phases of MgSnN2: A first-principles study	B. B. Dumre, D. Gall, and S. V. Khare	2021	*Journal of Physics and Chemistry Solids*
654	Impact of Humidity and Temperature on the Stability of the Optical Properties and Structure $MAPbI_3$, $MA_{0.7}FA_{0.3}PbI_3$, and $(FAPbI_3)_{0.95}(MAPbBr_3)_{0.05}$ Perovskite Thin Films	M. S. Tumusange, B. Subedi, C. Chen, M. M. Junda, Z. Song, Y. Yan, and N. J. Podraza	2021	*Materials*
672	Analysis of non-idealities in rhomb compensators	A. Shan, B. Ramanujam, N. J. Podraza, and R. W. Collins	2021	*Optics Express*
697	Effects of Cu Precursor on the Performance of Efficient CdTe Solar Cells	S. S. Bista, D.-B. Li, R. A. Awni, Z. Song, K. K. Subedi, N. Shrestha, S. Rijal, S. Neupane, C. R. Grice, A. B. Phillips, R. J. Ellingson, M. Heben, J. V. Li, and Y. Yan	2021	*ACS Materials and Interfaces*
706	Low-temperature and effective ex-situ group V doping for efficient polycrystalline CdSeTe solar cells	D. Li, C. Yao, S. N. Vijayaraghavan, R. A. Awni, K. K. Subedi, R. J. Ellingson, L. Li, Y. Yan and F. Yan	2021	*Nature Energy*
716	Understanding V_{OC} and performance deficit in wide bandgap perovskite photovoltaic devices	R. H. Ahangharnejhad, J. D. Friedl, A. B. Phillips and M. J. Heben	2021	*Solar Energy Materials and Solar Cells*
722	Enabling bifacial thin film devices by developing a back surface field using Cu_xAlO_y	K. K. Subedi, A. B. Phillips, N. Shrestha, F. K. Alfadhili, A. Osella, I. Subedi, R. A. Awni, E. Bastola, Z. Song and D.-B. Li.	2021	*Nano Energy*
729	Optical and Electronic Losses Arising from Physically Mixed Interfacial Layers in Perovskite Solar Cells	B. Subedi, Z. Song, C. Chen, C. Li, K. Ghimire, M. M. Junda, I. Subedi, Y. Yan and N. J. Podraza	2021	*ACS Applied Materials & Interfaces*
741	Optimization of the Solution Based Aluminum Gallium Oxide Buffer Layer for CdTe Solar Cells	Z. Akkuly, K. K. Subedi, A. P. Patel, D. Pokhrel, E. Bastola, A. B. Phillips, M. J. Heben and R. J. Ellingson	2021	*IEEE PVSC Conference Proceedings*
745	Solution Processed Lead Telluride Nanowires as a Passivating Layer to CdTe Photovoltaics	D. Pokhrel, E. Bastola, K. K. Subedi, A. B. Phillips, M. J. Heben and R. J. Ellingson	2021	*IEEE PVSC Conference Proceedings*

749	Irradiance and Temperature Control Chamber for Testing Solar Cell Performance	N. Katakumbura, A. Patel, M. Abass, J. E. Chaplin, D. Fillmore, M. J. Grzegorzewski, B. A. Halim, J. Kennedy, E. Lopez, N. L. Mai, M. Manerikar, Jarod Michalak, E. M. S. Samuel V. Pietschman, J. Smith, D. Raker, S. Cioc and R. Ellingson	2021	*IEEE PVSC Conference Proceedings*
757	Solution-Processed P-type Copper Gallium Oxide as a Back Buffer Layer for CdTe Solar Cells	A. P. Patel, K. K. Subedi, D. Pokhrel, E. Bastola, A. B. Phillips, M. J. Heben and R. J. Ellingson	2021	*IEEE PVSC Conference Proceedings*
762	Material Requirements for CdSe Wide Bandgap Solar Cells	R. H. Ahangharnejhad, A. B. Phillips, J. D. Friedl and M. J. Heben	2021	*IEEE PVSC Conference Proceedings*
767	Optimizing the Selenization of Sb_2Se_3 Absorbers to Improve the Film Quality and Solar Cell Performances	S. Rijal, Z. Song, D.-B. Li, S. S. Bista and Y. Yan	2021	*IEEE PVSC Conference Proceedings*
771	Deposition Temperature Dependence of Optical and Structural Properties of Glancing Angle Deposited CdTe	N. J. Jayswal, D. Adhikari, I. Subedi, and N. J. Podraza	2021	*Proceedings of the 64th Annual SVC Technical Conference*
777	Fabricating Efficient CdTe Solar Cells: The Effect of Cu Precursor	Deng-Bing Li, Sandip S. Bista, Rasha A. Awni, Kamala K. Subedi, Niraj Shrestha, Sabin Neupane, Manoj K. Jamarkattel, Zhaoning Song, Randy J. Ellingson, and Yanfa Yan	2021	*IEEE PVSC Conference Proceedings*
781	Influence of Post-selenization Temperature on the Performance ofSubstrate-Type Sb2Se3Solar Cells	Suman Rijal, Deng-Bing Li, Rasha A. Awni, Sandip S. Bista, Zhaoning Song and Yanfa Yan	2021	*ACS Applied Energy Materials*
788	Kinetically driven island morphology in growth on strained Cu (100)	Indiras Khatria, Ehsan H. Sabbarb Yunsic Shimc and Jacques G. Amar	2021	*The J. of Chemical Physics*
793	Correlating structure and orbital occupation with the stability and mechanical properties of 3d transition metal carbides	I. Khatri, N. J. Szymanskia, B.B. Dumre, J. G. Amara, D. Gallc and S. V. Khare	2021	*J. of Alloys and Compounds*
804	Structure, Electronic and Optical Properties of Ternary Nitride Phases of $MgSnN_2$: A First-principles Study	B. B. Dumre, D.Gall, and S. V. Khare	2021	*Materials Science and Technology Technical Meeting, Columbus, OH, US, 2021 -- Poster Presentation*

ADVANCED FUNCTIONAL MATERIALS
www.afm-journal.de

Dithieno[3,2-b:2′,3′-d]pyrrol-Cored Hole Transport Material Enabling Over 21% Efficiency Dopant-Free Perovskite Solar Cells

Xinxing Yin, Jie Zhou, Zhaoning Song, Zihao Dong, Qinye Bao, Niraj Shrestha, Sandip Singh Bista, Randy J. Ellingson, Yanfa Yan, and Weihua Tang**

Dopant-free hole transport materials (HTMs) are essential for commercialization of perovskite solar cells (PSCs). However, power conversion efficiencies (PCEs) of the state-of-the-art PSCs with small molecule dopant-free HTMs are below 20%. Herein, a simple dithieno[3,2-b:2′,3′-d]pyrrol-cored small molecule, DTP-C6Th, is reported as a promising dopant-free HTM. Compared with commonly used spiro-OMeTAD, DTP-C6Th exhibits a similar energy level, a better hole mobility of 4.18×10^{-4} cm^2 V^{-1} s^{-1}, and more efficient hole extraction, enabling efficient and stable PSCs with a dopant-free HTM. With the addition of an ultrathin poly(methyl methacrylate) passivation layer and properly tuning the composition of the perovskite absorber layer, a champion PCE of 21.04% is achieved, which is the highest value for small molecule dopant-free HTM based PSCs to date. Additionally, PSCs using the DTP-C6Th HTM exhibit significantly improved long-term stability compared with the conventional cells with the metal additive doped spiro-OMeTAD HTM. Therefore, this work provides a new candidate and effective device engineering strategy for achieving high PCEs with dopant-free HTMs.

1. Introduction

Ever since their debut in 2009, organic–inorganic metal halide perovskite solar cells (PSCs) have attracted worldwide research interest in the past decade, mainly due to the low production cost and outstanding power conversion efficiency (PCE).[1–8] Very recently, a new certified record PCE of 24.2% has been achieved by Korea Research Institute of Chemical Technology,[9] closing the PCE gap between PSCs and market-dominant crystalline silicon-based photovoltaic technologies.[10,11]

As a crucial part of the state-of-the-art n-i-p type PSCs, 2,2′,7,7′-tetrakis(*N*,*N*-di-*p*-methoxyphenylamino)-9,9′-spirobifluorene (spiro-OMeTAD) was first adopted by Park group as a solid hole transport material (HTM).[12] Until now, spiro-OMeTAD has become the most widely used and successful HTM for achieving high efficiencies in PSCs.[2,5,7,13–15] However, the use of spiro-OMeTAD introduces instability issues to the PSCs. Because pristine spiro-OMeTAD films suffer from low conductivity and mobility,[16,17] dopants including 4-tert-butylpyridine (*t*-BP), lithium bis(trifluoromethyl sulfonyl)imide (Li-TFSI), and cobalt(III) complexes are necessary for obtaining high PCEs.[18–20] Despite the enhanced hole transport property, the dopant strategy brings several problems. First, all the *t*-BP, Li-TFSI, and cobalt salts are hygroscopic, which may facilitate water ingress into the perovskite layer and eventually result in the perovskite degradation.[21–24] Second, postoxidation procedure is required for doped spiro-OMeTAD to achieve the desired hole transport property,[25] which is critical for fabricating high-efficiency PCSs but harmful to the perovskite layer. This oxidation process may cause reproducibility problems due to the difficulty of precisely controlling the oxidative level.[26–28] Third, it is well known that the oxidized HTM formed through doping is responsible for better device performance due to the increased charge transport.[29] However, the oxidized HTM species can chemically react with *t*-BP to form new pyridinated products, which have been proved to have a negative effect on device performance and long-term stability.[30] Fourth, these noncovalently bonded dopants have a strong tendency to diffuse into and degrade the perovskite layer under the normal operative conditions, thereby affecting the long-term stability of PSCs.[31–33] Lastly, the additional steps of adding dopants and oxidation increase processing complexity and total cost. Because of these concerns, developing dopant-free HTMs is urgently demanded.

Aiming to push forward the development of PSCs, a lot of new small molecule dopant-free HTMs have been reported. Li et al.

Dr. X. Yin, Dr. J. Zhou, Z. Dong, Prof. W. Tang
School of Chemical Engineering
Nanjing University of Science and Technology
Nanjing 210094, China
E-mail: whtang@njust.edu.cn
Dr. X. Yin, Z. Song, N. Shrestha, S. S. Bista, Prof. R. J. Ellingson, Prof. Y. Yan
Department of Physics and Astronomy and Wright Center
for Photovoltaics Innovation and Commercialization
The University of Toledo
Toledo, OH 43606, USA
E-mail: yanfa.yan@utoledo.edu
Prof. Q. Bao
Key Laboratory of Polar Materials and Devices
Department of Optoelectronics
East China Normal University
Shanghai 200241, P. R. China
The ORCID identification number(s) for the author(s) of this article can be found under https://doi.org/10.1002/adfm.201904300.

DOI: 10.1002/adfm.201904300

 © 2019 WILEY-VCH Verlag GmbH & Co. KGaA, Weinheim

Approved for public release; distribution unlimited.
312

synthesized a simple polycyclic heteroaromatic hydrocarbon-based small molecule referred to as PCA-1, which possesses excellent hydrophobicity, ease of film formation, and high hole mobility. Mesoscopic PSCs with PCA-1 as the dopant-free HTM showed a PCE of 18.17% and long-term stability.[34] Paek et al. reported a star-shaped D-π-A molecule named FA-CN as the dopant-free HTM for PSCs. The PCE of the best-performing device reached 18.9% and retained 65% of its initial value after continuous light soaking for 1300 h.[31] Soon after that the same group further replaced the central quinolizino acridine core of FA-CN with triazatruxene (named KR321) to form a face-on orientation. With the undoped KR321 HTM, a high PCE of 19% was obtained.[35] Thus far, the highest PCE of PSCs with small molecule dopant-free HTMs is 20%, achieved by using the semilocked TTE-2 HTM.[36] This PCE value, however, is still much inferior to that of the conventional devices using the spiro-OMeTAD HTM (>23%). Therefore, many efforts are still required to develop better small molecule HTMs as alternatives to spiro-OMeTAD.

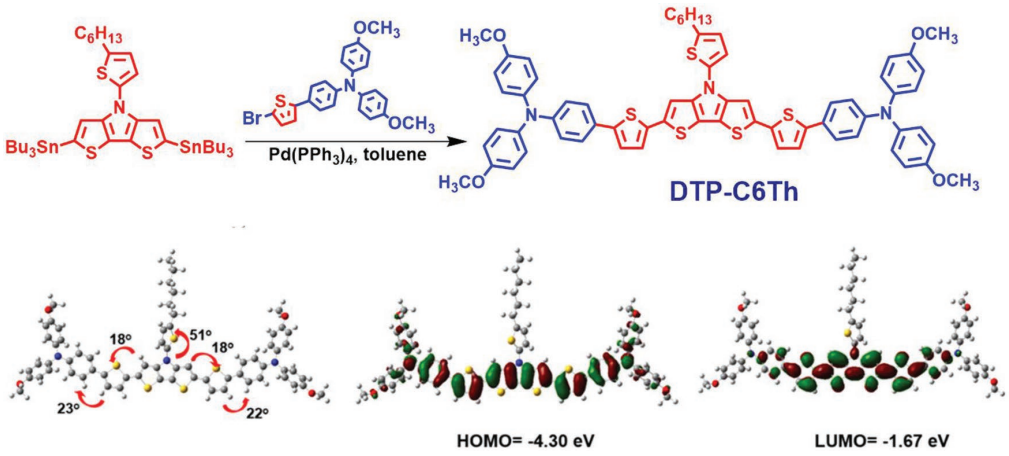
Another problem regarding the development of the dopant-free HTMs for PSCs is the device optimization processes. Many groups focus on broadening the library of materials and only tuning the thickness of HTMs during device fabrication.[32,33,36,37] Little attention is paid to the unique interface properties of new HTMs and their energy band alignment with the perovskite layer. Careful device optimization is needed for achieving the full potential of the devices with these new dopant-free HTMs.[20,38–41]

In this work, we report on the synthesis of DTP-C6Th, a simple dithieno[3,2-b:2′,3′-d]pyrrol-cored small molecule, as a promising dopant-free HTM for n-i-p type PSCs. Compared with doped spiro-OMeTAD, dopant-free DTP-C6Th shows similar energy levels and enhanced hole extracting/transporting properties. Planar n-i-p PSCs using the pristine DTP-C6Th as the HTM reach a PCE of 18.56%. After the interface passivation and compositional tuning for the perovskite layer, a champion PCE of 21.04% is obtained with a steady-state efficiency of 20.36%, which is among the highest PCEs for PSCs based on small molecule dopant-free HTMs. The unencapsulated devices using the DTP-C6Th HTM show negligible performance degradation when stored in a nitrogen filled glove box and maintain over 85% of their initial PCEs after a storage in ambient air for 60 days. In contrast, PSCs using the spiro-OMeTAD HTM show significant PCE drops in both air and inert atmosphere. These results show that DTP-C6Th is a promising dopant-free HTM for PSC.

2. Results and Discussion

As a successful building block for organic photovoltaics, DTP has some unique advantages such as strong electron donating capability, good coplanarity, high mobility as well as easily tuned energy levels.[42] However, to the best of our knowledge, few DTP-based HTMs have been developed and the best PCE is only around 18%.[43,44] Here, DTP is adopted as core unit to construct high performance HTM. Thiophene unit is introduced as a π-spacer to achieve extended π-conjugation. Moreover, S atoms in thiophene may also bring stronger interaction between HTM and iodine/lead ions in perovskite.[45,46] Considering the strong electron-donating ability and excellent hole transporting capability, the propeller-like triphenylamine (TPA) is used as ending group, which is easy to synthesis and may benefit reducing charge recombination as well as electron coupling.[47–51] Thus, a new HTM named DTP-C6Th is constructed with DTP as core, thiophene as spacer, and TPA as ending group.

The synthesis for DTP-C6Th is outlined in **Scheme 1**, and detailed procedures are available in the Supporting Information. DTP-tin regent was prepared via a three-step procedure, i.e., cyclization, Buchwald–Hartwig cross-coupling and preparing tin reagent following earlier procedures.[43,52] TPA derivative was prepared according to literature.[27,53] The target compound DTP-C6Th was then synthesized by a Pd-catalyzed Stille coupling reaction. The chemical structure of target HTM molecule was systematically characterized by nuclear magnetic resonance (^{1}H, ^{13}C NMR, Figures S1–S7, Supporting Information) and matrix assisted laser desorption/ionization-time of flight mass spectrometry (Figure S8, Supporting Information). The calculated cost for lab synthesis of DTP-C6Th is estimated to be about \$30 g^{-1} (Tables S1–S3, Supporting Information), which is only 1/3 of spiro-OMeTAD (≈\$92 g^{-1}).[54] Thermogravimetric analysis (Figure S9a,



Scheme 1. Synthetic route (top) and the optimized geometries as wells as the calculated LUMO/HOMO energy levels (bottom) for DTP-C6Th.

© 2019 WILEY-VCH Verlag GmbH & Co. KGaA, Weinheim

Approved for public release; distribution unlimited.

Supporting Information) measurement indicates DTP-C6Th has good thermal stability with a high decomposition temperature (5% weight loss, T_d) of 410 °C. Differential scanning calorimetry (Figure S9b, Supporting Information) scans demonstrate that DTP-C6Th is amorphous, with a clear glass transition temperature (T_g) observed at 84.5 °C after two heating-cooling cycles.

To have a better insight of the electronic structure and geometry of DTP-C6Th, density functional theory (Scheme 1) calculations were employed. Compared with orthogonal spiro-bifluorene (central core for spiro-OMeTAD), dithieno[3,2-b:2′,3′-d] pyrrol (DTP) has a planar π-conjugated surface, leading to a more flat configuration. This configuration can form better π–π stacking and enhance hole transport in the material.[42–44] Electrostatic surface potential (ESP) results are shown in **Figure 1**a. The negative electrostatic potential (in red color) concentrates on the S atoms of DTP core and thiophene spacer, while the positive electrostatic potential (in blue color) mainly localizes on triphenylamine arms. This kind of charge polarization facilitated the intramolecular charge transfer. Moreover, S heteroatoms of DTP may benefit interface passivation of perovskite due to the strong Pb^{2+}–S interaction.[55–57]

To determine the energy levels of HTMs, both cyclic voltammetry (CV) and ultraviolet photoelectron spectroscopy (UPS) were used (Figure 1b). CV was conducted by dissolving HTMs in dichloromethane with tetrabutylammonium hexafluorophosphate (0.1 M) as electrolyte (Figure S10, Supporting Information). After calibrating redox potentials with ferrocene, the highest occupied molecular orbital (HOMO) levels of spiro-OMeTAD and DTP-C6Th were calculated to be –4.82 and –4.87 eV, respectively. UPS method was employed to test the energy levels of the corresponding HTM films (Figure S11, Supporting Information). The ionization potential (IP) for spiro-OMeTAD and DTP-C6Th films were determined to be –5.03 and –4.94 eV. Although a deeper IP of the HTM is beneficial for achieving wider Fermi-energy splitting in the perovskite absorber layer and thus leads to higher open circuit voltage (V_{OC}), the small difference of 0.09 eV between spiro-OMeTAD and DTP-C6Th films may not significantly influence the V_{OC} of the devices. Particularly, when compared with our benchmark perovskite ($MA_{0.7}FA_{0.3}PbI_3$, MA = methylammonium, FA = formamidinium), which has a deeper valence band at around –5.40 eV,[58,59] both spiro-OMeTAD and DTP-C6Th have enough driving forces for the hole extraction.

To explore the hole transporting properties of two HTMs, space-charge-limited-current (SCLC) method was adopted by using a hole only device structure of indium tin oxide (ITO)/poly(3,4-ethylenedioxythiophene):poly(styrenesulfonate) (PEDOT:PSS)/HTM/Au (Figure 1c). The hole mobility value of DTP-C6Th is estimated to be 4.18×10^{-4} cm^2 V^{-1} s^{-1}, which is one order of magnitude higher than spiro-OMeTAD (3.43×10^{-5} cm^2 V^{-1} s^{-1}). The high mobility enables DTP-C6Th to act as an efficient HTM for PSCs without dopants.

To evaluate the hole extraction of DTP-C6Th and spiro-OMeTAD at the perovskite/HTM interface, steady-state photoluminescence (PL) and time resolved photoluminescence (TRPL) measurements were carried out. It is clearly seen in Figure 1e that a bare $MA_{0.7}FA_{0.3}Pb(I_{0.925}Br_{0.075})_3$ perovskite film exhibited a strong PL intensity. After capping the perovskite layer with spiro-OMeTAD, the PL intensity decreased to around one third of its original level. DTP-C6Th/perovskite showed the more significant PL quenching than perovskite/spiro-OMeTAD, which is likely due to the combined effects of more effective hole extraction as well as higher recombination at the DTP-C6Th/perovskite

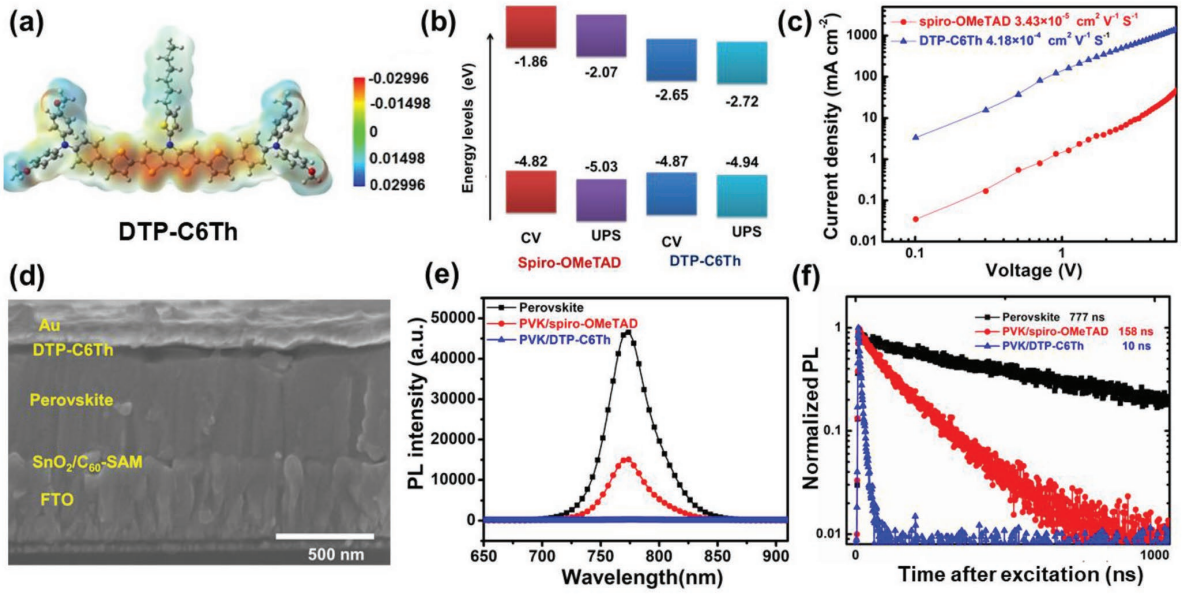


Figure 1. a) Computed electrostatic surface potential (ESP) of DTP-C6Th. b) Energy levels of spiro-OMeTAD and DTP-C6Th measured from CV and UPS, the LUMO levels are calculated from optical bandgap. c) Space-charge-limited current (SCLC) *J*–*V* characteristics of DTP-C6Th or spiro-OMeTAD based hole-only devices. d) Cross-sectional SEM image of PSC with DTP-C6Th HTM. e) PL intensity and f) TRPL decay of perovskite film, perovskite/spiro-OMeTAD and perovskite/DTP-C6Th.

© 2019 WILEY-VCH Verlag GmbH & Co. KGaA, Weinheim

Approved for public release; distribution unlimited.

interfaces.[60] The higher recombination could attribute to the lower HOMO level of DTP-C6Th than Spiro-OMeTAD. Therefore, a surface passivation layer may be required to reduce the interface recombination. From the TRPL results shown in Figure 1f, the mean carrier lifetime for pristine perovskite, perovskite covered with spiro-OMeTAD and DTP-C6Th is 777, 158, and 10 ns, respectively, consistent with the PL results.

The n-i-p type PSCs with a basic configuration of fluorine doped tin oxide (FTO)/SnO_2/C_{60}-SAM/perovskite/HTM/Au were fabricated to examine the device performance. The cross-sectional scanning electron microscopy (SEM) image of a DTP-C6Th based device is shown in Figure 1d. A layer of DTP-C6Th with a thickness of around 40 nm is uniformly deposited between the perovskite absorber and gold electrode. We started from the optimization of the HTM thickness and obtained an optimal thickness of ≈40 nm for the DTP-C6Th HTM. The current density–voltage (J–V) curves under the reverse (forward) voltage scans, as well as external quantum efficiency (EQE) spectra for the champion as-cast PSCs using the dopant-free DTP-C6Th or doped spiro-OMeTAD HTMs are shown in Figure S13 (Supporting Information). The corresponding device parameters are summarized in **Table 1**. The best performing as-cast cell based on dopant-free DTP-C6Th shows a PCE of 18.56%, with a V_{OC} of 1.080 V, a short circuit current density (J_{SC}) of 23.45 mA cm^{-2}, and a fill factor (FF) of 0.733 under reverse scan. In contrast, control devices using doped spiro-OMeTAD gives a much better PCE of 20.56%, with a V_{OC} of 1.108 V, a J_{SC} of 23.08 mA cm^{-2}, and a FF of 0.804. The main drawback for DTP-C6Th based device is the relatively low V_{OC} and FF, since DTP-C6Th has much better hole extraction and transporting properties, as well as stronger interface interaction with perovskites, we attribute the low PCE to a higher recombination loss at the perovskite/DTP-C6Th interface, which is consistent with PL and TRPL results.[2,38,61]

To solve this problem, we adopted a surface passivation strategy by incorporating an ultrathin layer of poly(methyl methacrylate) (PMMA). As previously reported, the cross-linked PMMA film may protect perovskite surface from potential degradation as well as passivate defects/deep trap centers caused by the dangling bonds (under-coordinated lead ions or iodine terminations) localized at the perovskite surface.[62–64] As shown in Figure S14 (Supporting Information) and Table 1, after spin-coating an ultrathin PMMA (1 mg mL^{-1} in chlorobenzene, 6000 rpm for 30 s) on the perovskite layer (referred to as W/PMMA), PSCs with undoped DTP-C6Th showed an improved PCE of 20.42%, with an increased V_{OC} from 1.080 to 1.120 V, a J_{SC} of 22.96 mA cm^{-2}, and a much higher FF of 0.794 under reverse scan. For spiro-OMeTAD-based control devices with the PMMA passivation layer, V_{OC} reached 1.135 V with an increasement of 27 mV, resulting in a PCE of 20.45%.

The changes in photovoltaic parameters of PSCs under different optimization conditions are shown in **Figure 2**. With the help of PMMA, DTP-C6Th based PSCs achieve a high PCE of 20.42%, which is comparable with control devices using doped spiro-OMeTAD as the HTM. To futher improve the device performance, we turn to composition tuning of perovskite layer by adding a small amount of bromine. It is well known that the incorporation of Br can effectively tune the bandgap and increaseat V_{OC}, though slightly sacrificing J_{SC}. By carefully tuning the V_{OC}/J_{SC} trade-off, a maximium efficiency can be acquired. For the optimal results, 7.5% Br is added (the changes of device parameters under different Br concentration can be found in Figure S15, Supporting Information), leading to a perovskite composition of $MA_{0.7}FA_{0.3}Pb(I_{0.925}Br_{0.075})_3$ (referred to as W/PMMA & Br).

Figure 3a shows the top-view SEM image of a $MA_{0.7}FA_{0.3}PbI_3$ film with a compact and smooth morphology, the calculated average grain size is 1.75 µm. For $MA_{0.7}FA_{0.3}Pb(I_{0.925}Br_{0.075})_3$, the average grain size is 1.52 µm. This kind of large size (>1 µm) crystals with PbI_2 passivation at the grain boundaries are beneficial for the performance of PSCs.[65–67] As expected, the absorption onset and PL peak of $MA_{0.7}FA_{0.3}Pb(I_{0.925}Br_{0.075})_3$ film shows a small blueshift due to the introduction of Br. Tauc plots also confirm the slight widening of the perovskite bandgap (Figure S12a, Supporting Information), which is consistent with the previous reports.[68,69] As shown in Figure 3d,f, perovskite with 7.5% Br shows enhanced PL intensity, longer carrier lifetime, and improved crystallinity, indicating better perovskite quality than $MA_{0.7}FA_{0.3}PbI_3$. Thus, PSCs using $MA_{0.7}FA_{0.3}Pb(I_{0.925}Br_{0.075})_3$ as absorbers may have better device performance.

Table 1. Device parameters of champion PSCs using dopant-free DTP-C6Th or doped spiro-OMeTAD as HTMs under reverse (R) and forward (F) scan.

HTM	Optimization	V_{oc} [V]	J_{sc} [mA cm^{-2}]	FF	PCE [%]
Spiro-OMeTAD (R)	As cast	1.108	23.08	0.804	20.56
Spiro-OMeTAD (F)	As cast	1.087	23.03	0.756	18.93
DTP-C6Th (R)	As cast	1.080	23.45	0.733	18.56
DTP-C6Th (F)	As cast	1.061	23.45	0.676	16.82
Spiro-OMeTAD (R)	W/PMMA	1.135	23.07	0.781	20.45
Spiro-OMeTAD (F)	W/PMMA	1.115	23.12	0.742	19.13
DTP-C6Th (R)	W/PMMA	1.12	22.96	0.794	20.42
DTP-C6Th (F)	W/PMMA	1.086	22.94	0.745	18.56
Spiro-OMeTAD (R)	W/PMMA & Br	1.161	22.64	0.784	20.61
Spiro-OMeTAD (F)	W/PMMA & Br	1.138	22.72	0.742	19.18
DTP-C6Th (R)	W/PMMA & Br	1.157	22.76	0.799	21.04
DTP-C6Th (F)	W/PMMA & Br	1.127	22.72	0.760	19.46

© 2019 WILEY-VCH Verlag GmbH & Co. KGaA, Weinheim

Approved for public release; distribution unlimited.
315

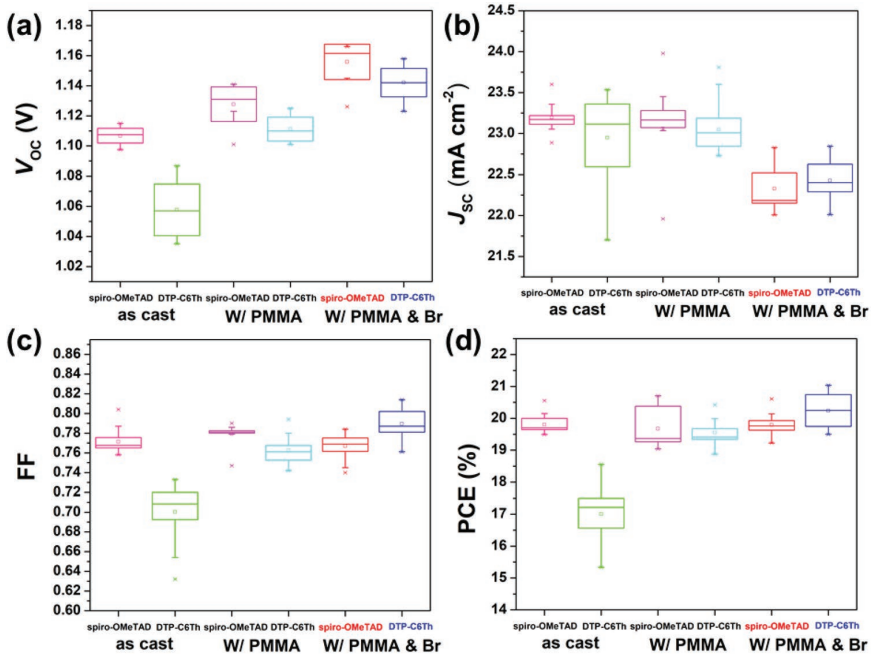


Figure 2. Photovoltaic parameters of PSCs with different optimization using DTP-C6Th or spiro-OMeTAD as HTM. Histograms of a) V_{OC}, b) J_{SC}, c) FF, and d) PCE of corresponding devices.

Figure 4a shows the *J*–*V* curves under reverse and forward voltage scans of our best-performing PSCs (W/PMMA & Br) with dopant-free DTP-C6Th or doped spiro-OMeTAD as the HTMs, and the detailed statistics are summarized in Table 1. Our champion cell with DTP-C6Th achieves a maximum PCE of 21.04%, with a V_{OC} of 1.157 V, a J_{SC} of 22.76 mA cm^{-2}, and a FF of 79.9% under the reverse scan, which is the highest PCE for dopant-free HTM based PSCs to date. In comparison,

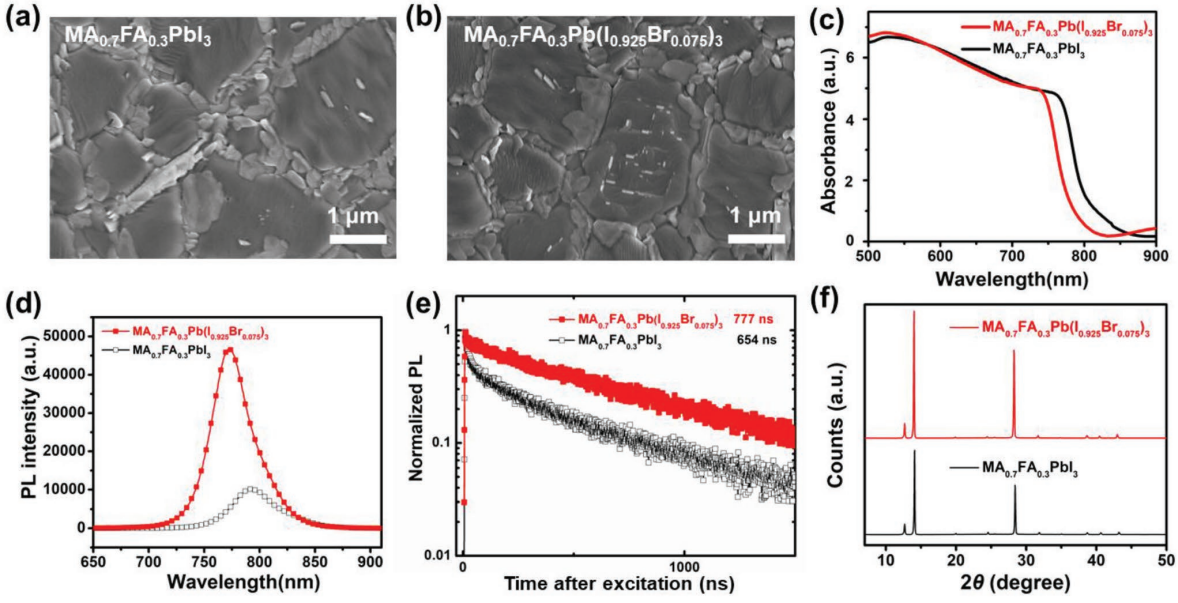


Figure 3. a) SEM image of $MA_{0.7}FA_{0.3}PbI_3$ film. b) SEM image of $MA_{0.7}FA_{0.3}Pb(I_{0.925}Br_{0.075})_3$ film. c) Absorbance, d) PL, e) TRPL, and f) X-ray diffraction (XRD) patterns of $MA_{0.7}FA_{0.3}PbI_3$ and $MA_{0.7}FA_{0.3}Pb(I_{0.925}Br_{0.075})_3$ film.

© 2019 WILEY-VCH Verlag GmbH & Co. KGaA, Weinheim

Approved for public release; distribution unlimited.

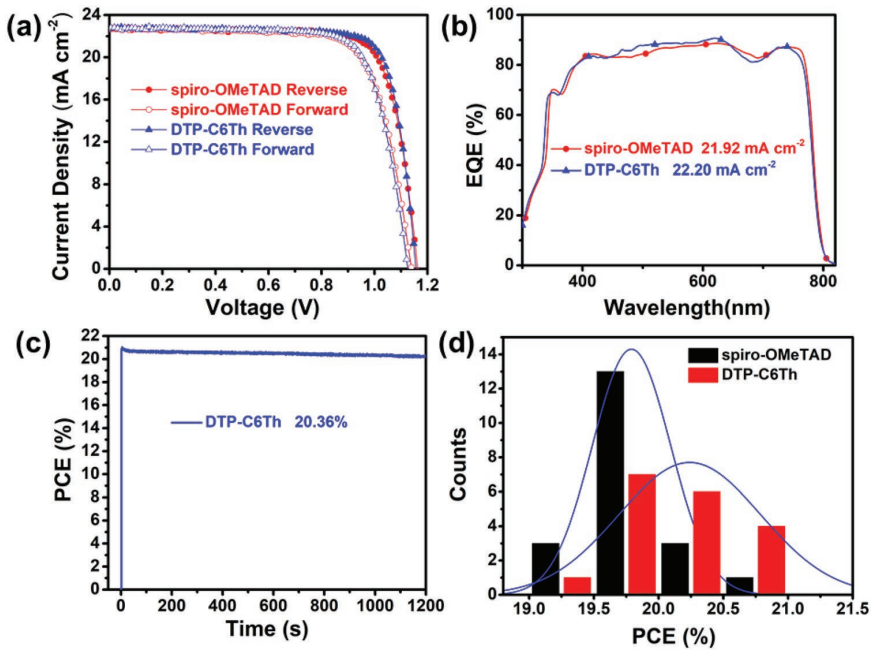


Figure 4. Photovoltaic parameters of the best-performing PSCs (W/PMMA & Br). a) *J–V* curves measured under reverse and forward voltage scans with dopant-free DTP-C6Th or doped spiro-OMeTAD as HTMs. b) The EQE plots of corresponding champion devices. c) Steady-state efficiency of our best-performing PSC with DTP-C6Th as HTM for 1200 s. d) Histogram of PCEs measured for 20 cells using un-doped DTP-C6Th or doped spiro-OMeTAD.

PSC based on spiro-OMeTAD exhibits a slightly lower PCE of 20.61% under the same conditions. Devices based on both HTMs show similar hysteresis, thus the *J–V* hysteresis might be ascribed to the perovskite problem including trap states, ion migration, or ferroelectricity.[70,71]

The integrated J_{SC} values from EQE spectra (Figure 4b) of DTP-C6Th and spiro-OMeTAD devices are 22.20 and 21.92 mA cm^{-2}, which are in a good agreement with the *J–V* measurements. Additionally, the stabilized power output efficiency of DTP-C6Th-based champion PSC (W/PMMA & Br) was recorded (Figure 4c) in air without encapsulation, a PCE of 20.36% was obtained under 1200 s continuous illumination. For 20 individual devices of each HTM, the histograms of PCE distribution are shown in Figure 4d. Good reproducibility can be realized using either dopant-free DTP-C6Th or doped spiro-OMeTAD HTMs, giving an average PCE of 20.24% and 19.79%, respectively.

We further investigated the surface coverage of the HTMs on $MA_{0.7}FA_{0.3}Pb(I_{0.925}Br_{0.075})_3$ perovskite films using atomic force microscopy (AFM). It is clear in **Figure 5**a,b, after spin-coating a 150 nm spiro-OMeTAD, the root-mean-square (RMS) roughness reduced significantly from 12.8 to 3.78 nm. Although DTP-C6Th layer is only 40 nm, it exhibits a full coverage on the perovskite layer and a low RMS of 5.11 nm (Figure 5c), confirming the good film-formation capability.

To understand the differences in charge transport and recombination when using dopant-free DTP-C6Th or doped spiro-OMeTAD as the HTMs in PSCs (W/PMMA & Br), the light intensity dependence of J_{SC} and V_{OC} of the corresponding PSCs were measured. Figure 5d shows the power law dependence of J_{SC} on the light intensity (on a double logarithmic scale). The fitted slopes (α) are 0.99 and 0.97 for devices using the DTP-C6Th and spiro-OMeTAD HTMs, respectively, indicating slightly less space charge effect and more balanced charge transport in DTP-C6Th-based PSCs.[72] Figure 5e shows the linear relationship between V_{OC} and natural logarithmic light intensity. The slopes for DTP-C6Th and doped spiro-OMeTAD devices are 1.46 and 1.55 kT e^{-1}, respectively, revealing a Shockley–Read–Hall dominated recombination mechanism in both devices. However, the spiro-OMeTAD-based device has a more steep slope, indicating a more serious trap-assisted recombination.[73] Therefore, dopant-free DTP-C6Th shows less recombination and more balanced charge transport than doped spiro-OMeTAD in PSCs.

To examine the long-term stability of PSCs with different HTMs, we tested the PCEs of unencapsulated devices stored in a glovebox or ambient air with a relative humidity of ≈35%. The PCE decays in 60 days is shown in Figure 5f. When stored in a glovebox for 60 days, PSCs (W/ PMMA & Br) with DTP-C6Th show no PCE drop while only 63% of initial PCEs retained for spiro-OMeTAD based devices. Since there is no oxygen or water in the glovebox, the PCE loss for spiro-OMeTAD based PSCs is probably attributed to the diffusion of dopants and ions.[21,33,74] As for devices stored in air, DTP-C6Th based devices showed good environment stability with 85% of their initial PCEs retained after 60 days. On the contrary, spiro-OMeTAD based device lost almost 67% of its PCE within the same time window, mainly caused by the hydrophilic nature of dopants. Thus, our dopant-free DTP-C6Th not only renders a high PCE of 21%, but also behaves excellent long-term stability, making it ideal HTM candidate for future commercialization of PSCs.

© 2019 WILEY-VCH Verlag GmbH & Co. KGaA, Weinheim

Approved for public release; distribution unlimited.

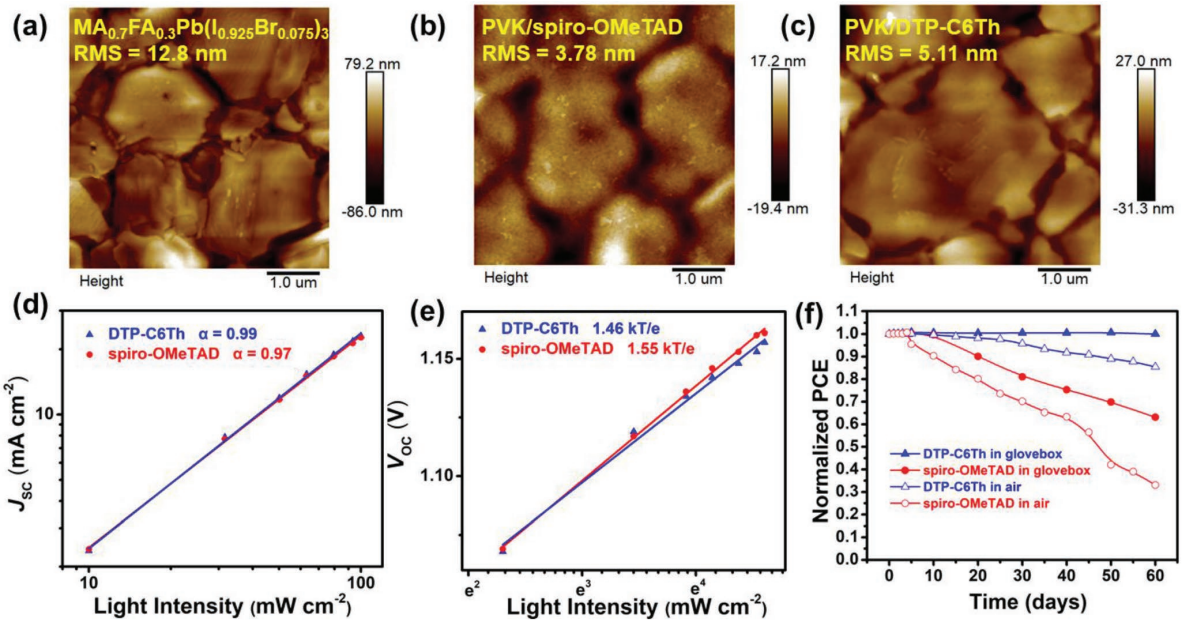


Figure 5. AFM morphology of a) pristine $MA_{0.7}FA_{0.3}Pb(I_{0.925}Br_{0.075})_3$ film, b) perovskite covered with doped spiro-OMeTAD, and c) perovskite covered with undoped DTP-C6Th. Light intensity dependence of PSCs with DTP-C6Th or spiro-OMeTAD as HTM, d) J_{SC} versus light intensity, and e) V_{OC} versus light intensity. f) The stability test of the optimized PSCs using undoped DTP-C6Th or doped spiro-OMeTAD as HTMs in nitrogen filled glovebox or ambient air with a humidity of ≈35% (stored in dark at room temperature).

3. Conclusion

In summary, we report a new small molecule dopant-free HTM material with a simple dithieno[3,2-b:2′,3′-d]pyrrol core, i.e., DTP-C6Th, which exhibits an suitable IP of –4.94 eV and a good hole mobility of 4.18×10^{-4} cm^2 V^{-1} s^{-1} (better than 3.43×10^{-5} cm^2 V^{-1} s^{-1} for spiro-OMeTAD). After careful device optimization by inserting an ultrathin PMMA passivating layer and tuning perovskite composition with Br, an impressive PCE of 21.04% with a steady-state efficiency of 20.36% is obtained, which is the best value for small molecule dopant-free HTM based PSCs. In addition, DTP-C6Th based unencapsulated devices show no PCE drop when stored in a glovebox for 60 days and over 85% of initial PCE can be remained after storing for 60 days in air with a relative humidity around 35%, confirming the excellent long-term stability. Therefore, DTP-C6Th is a promising dopant-free HTM for PSC commercialization.

4. Experimental Section

Solution Preparation: $MA_{0.7}FA_{0.3}PbI_3$ precursor: 1 mmol PbI_2 (Alfa Aesar), 0.7 mmol methylammonium iodide (MAI, Dyesol), 0.3 mmol formamidinium iodide (FAI, Dyesol), and 9.22 mg $Pb(SCN)_2$ (Sigma-Aldrich, 99.5%) were added to 600 µL *N*,*N*-dimethylformamide (DMF, Sigma-Aldrich), then 1 mmol dimethyl sulfoxide (DMSO, Sigma-Aldrich) was added. The precursor solution was stirred on a hotplate at 60 °C for 1 h and then purified using a 0.45 µm filter before deposition.

$MA_{0.7}FA_{0.3}Pb(I_{0.925}Br_{0.075})_3$ Precursor: 0.8875 mmol PbI_2, 0.1125 mmol $PbBr_2$ (TCI), 0.7 mmol MAI, 0.3 mmol FAI, and 9.22 mg $Pb(SCN)_2$ were added to 600 µL DMF, then 1 mmol DMSO was added. The precursor solution was stirred on a hotplate at 60 °C for 1 h and then purified using a 0.45 µm filter before deposition.

4-(1′,5′-Dihydro-1′-methyl-2′H-[5,6]fullereno-C60-Ih-[1,9-c]pyrrol-2′-yl) benzoic acid (C_{60}-SAM): C_{60}-SAM (Sigma-Aldrich, 99.8%) was dissolved in chlorobenzene (CB) with a concentration of 4 mg mL^{-1}.

PMMA: A solution of PMMA (1 mg mL^{-1} in CB, $M_n \approx 20\,000$, Sigma-Aldrich) was stirred on a hotplate at 60 °C for 2 h and then purified using a 0.45 µm filter before deposition.

DTP-C6Th: A solution of DTP-C6Th (20 mg mL^{-1} in CB) was stirred on a hotplate at 50 °C for 1 h and then purified using a 0.45 µm filter before deposition.

Spiro-OMeTAD: The spiro-OMeTAD solution was prepared by dissolving 72.3 mg spiro-OMeTAD (Shenzhen Feiming Science and Technology Co., Ltd.) in 1 mL CB with 28 µL *t*-BP (Sigma-Aldrich), 18 µL Li-TFSI (520 mg mL^{-1} in acetonitrile, Sigma-Aldrich), and 18 µL Co(III)-TFSI salt (FK102, 300 mg mL^{-1} in acetonitrile, Dyesol). The solution was stirred on a hotplate at 60 °C for 48 h and then purified using a 0.45 µm filter before deposition.

Device Fabrication: The FTO substrates were sequentially cleaned by ultrasonication with diluted Micro-90 detergent, deionized water, acetone, and isopropanol for 30 min, respectively. SnO_2 layer was deposited on the FTO using plasma-enhanced atomic layer deposition (PEALD) method with a thickness of 15 nm.[75] The SnO_2 layer was annealed at 100 °C for 1 h in imbient air under the conditions that the room temperature was about 25 °C and the humidity was about 55%. The C_{60}-SAM solution was then spin-coated onto SnO_2 layer at 3000 rpm for 1 min. The perovskite precursor solution was spin-coated on PEALD SnO_2 layer at 500 rpm for 3 s and at 4000 rpm for 60 s, 700 µL diethyl ether was then dropped onto the perovskite surface at 55s before end in one portion. After spin-coating, the perovskite film was annealed at 100 °C for 5 min. All these processes were carried out in a N_2 filled glove box. The PMMA layer was spin-coated on the top of the perovskite film at a speed of 6000 rpm, then annealed at 100 °C for 10 min. The DTP-C6Th layer was spin-coated on the

© 2019 WILEY-VCH Verlag GmbH & Co. KGaA, Weinheim

Approved for public release; distribution unlimited.

perovskite film at 3500 rpm for 50 s, resulting in an ≈40 nm layer. Spiro-OMeTAD was deposited on the perovskite film at 3000 rpm for 60 s. A layer of 100 nm gold (Au) was then deposited on the top of HTM using thermal evaporation. The working area of the devices was 0.08 cm^2 as defined by a shadow mask during the Au evaporation.

Supporting Information

Supporting Information is available from the Wiley Online Library or from the author.

Acknowledgements

X.Y., J.Z., and Z.S. contributed equally to this work. The design and development of DTP-C6Th was completed by Tang's group at Nanjing University of Science and Technology under the financial support from the National Natural Science Foundation of China (Grant Nos. 51573077, 21875111, and 51861145401) and the Priority Academic Program Development of Jiangsu Higher Education Institutions. Xinxing Yin acknowledges the support to from China Scholarship Council (CSC, No. 201706840039) for his joint Ph.D. training in USA. The device fabrication and characterization were completed by Yan's group at the University of Toledo, financially supported by Air Force Research Laboratory under Agreement No. FA9453-18-2-0037, the Office of Naval Research under Contract No. N00014-17-1-2223, and the Ohio Research Scholar Program. This material is based on research sponsored by Air Force Research Laboratory under Agreement No. FA9453-18-2-0037. The U.S. Government is authorized to reproduce and distribute reprints for Governmental purposes notwithstanding any copyright notation thereon. The views and conclusions contained herein are those of the authors and should not be interpreted as necessarily representing the official policies or endorsements, either expressed or implied, of Air Force Research Laboratory or the U.S. Government. Q.B. would like to thank East China Normal University Multifunctional Platform for Innovation (003, 006).

Conflict of Interest

The authors declare no conflict of interest.

Keywords

device engineering, dopant-free, hole transport material, perovskite solar cell

Received: May 29, 2019
Revised: June 13, 2019
Published online: July 15, 2019

[1] A. Kojima, K. Teshima, Y. Shirai, T. Miyasaka, *J. Am. Chem. Soc.* **2009**, *131*, 6050.
[2] Q. Jiang, Y. Zhao, X. Zhang, X. Yang, Y. Chen, Z. Chu, Q. Ye, X. Li, Z. Yin, J. You, *Nat. Photonics* **2019**, *13*, 460.
[3] L. Wang, H. Zhou, J. Hu, B. Huang, M. Sun, B. Dong, G. Zheng, Y. Huang, Y. Chen, L. Li, Z. Xu, N. Li, Z. Liu, Q. Chen, L.-D. Sun, C.-H. Yan, *Science* **2019**, *363*, 265.
[4] D. Luo, W. Yang, Z. Wang, A. Sadhanala, Q. Hu, R. Su, R. Shivanna, G. F. Trindade, J. F. Watts, Z. Xu, T. Liu, K. Chen, F. Ye, P. Wu, L. Zhao, J. Wu, Y. Tu, Y. Zhang, X. Yang, W. Zhang, R. H. Friend, Q. Gong, H. J. Snaith, R. Zhu, *Science* **2018**, *360*, 1442.
[5] W. S. Yang, B.-W. Park, E. H. Jung, N. J. Jeon, Y. C. Kim, D. U. Lee, S. S. Shin, J. Seo, E. K. Kim, J. H. Noh, S. I. Seok, *Science* **2017**, *356*, 1376.
[6] D. Zhao, C. Chen, C. Wang, M. M. Junda, Z. Song, C. R. Grice, Y. Yu, C. Li, B. Subedi, N. J. Podraza, X. Zhao, G. Fang, R.-G. Xiong, K. Zhu, Y. Yan, *Nat. Energy* **2018**, *3*, 1093.
[7] H. Tan, A. Jain, O. Voznyy, X. Lan, F. P. García de Arquer, J. Z. Fan, R. Quintero-Bermudez, M. Yuan, B. Zhang, Y. Zhao, F. Fan, P. Li, L. N. Quan, Y. Zhao, Z.-H. Lu, Z. Yang, S. Hoogland, E. H. Sargent, *Science* **2017**, *355*, 722.
[8] Z. Song, C. L. McElvany, A. B. Phillips, I. Celik, P. W. Krantz, S. C. Watthage, G. K. Liyanage, D. Apul, M. J. Heben, *Energy Environ. Sci.* **2017**, *10*, 1297.
[9] NREL, Best Research Cell Effciencies, https://www.nrel.gov/pv/assets/pdfs/best-research-cell-efficiencies-190416.pdf (accessed: April 2019).
[10] J.-P. Correa-Baena, M. Saliba, T. Buonassisi, M. Grätzel, A. Abate, W. Tress, A. Hagfeldt, *Science* **2017**, *358*, 739.
[11] Y. Rong, Y. Hu, A. Mei, H. Tan, M. I. Saidaminov, S. I. Seok, M. D. McGehee, E. H. Sargent, H. Han, *Science* **2018**, *361*, eaat8235.
[12] H.-S. Kim, C.-R. Lee, J.-H. Im, K.-B. Lee, T. Moehl, A. Marchioro, S.-J. Moon, R. Humphry-Baker, J.-H. Yum, J. E. Moser, M. Grätzel, N.-G. Park, *Sci. Rep.* **2012**, *2*, 591.
[13] J. Burschka, N. Pellet, S.-J. Moon, R. Humphry-Baker, P. Gao, M. K. Nazeeruddin, M. Grätzel, *Nature* **2013**, *499*, 316.
[14] D. Bi, W. Tress, M. I. Dar, P. Gao, J. Luo, C. Renevier, K. Schenk, A. Abate, F. Giordano, J.-P. Correa Baena, J.-D. Decoppet, S. M. Zakeeruddin, M. K. Nazeeruddin, M. Grätzel, A. Hagfeldt, *Sci. Adv.* **2016**, *2*, e1501170.
[15] T. Bu, X. Liu, Y. Zhou, J. Yi, X. Huang, L. Luo, J. Xiao, Z. Ku, Y. Peng, F. Huang, Y.-B. Cheng, J. Zhong, *Energy Environ. Sci.* **2017**, *10*, 2509.
[16] Z. Hawash, L. K. Ono, Y. Qi, *Adv. Mater. Interfaces* **2018**, *5*, 1700623.
[17] L. Calió, S. Kazim, M. Grätzel, S. Ahmad, *Angew. Chem., Int. Ed.* **2016**, *55*, 14522.
[18] C. Rodríguez-Seco, L. Cabau, A. Vidal-Ferran, E. Palomares, *Acc. Chem. Res.* **2018**, *51*, 869.
[19] Z. Yu, L. Sun, *Adv. Energy Mater.* **2015**, *5*, 1500213.
[20] J.-P. Correa-Baena, A. Abate, M. Saliba, W. Tress, T. Jesper Jacobsson, M. Gratzel, A. Hagfeldt, *Energy Environ. Sci.* **2017**, *10*, 710.
[21] S. Wang, Z. Huang, X. Wang, Y. Li, M. Günther, S. Valenzuela, P. Parikh, A. Cabreros, W. Xiong, Y. S. Meng, *J. Am. Chem. Soc.* **2018**, *140*, 16720.
[22] K. Gao, Z. Zhu, B. Xu, S. B. Jo, Y. Kan, X. Peng, A. K. Y. Jen, *Adv. Mater.* **2017**, *29*, 1703980.
[23] T. H. Schloemer, J. A. Christians, J. M. Luther, A. Sellinger, *Chem. Sci.* **2019**, *10*, 1904.
[24] Z. Song, A. Abate, S. C. Watthage, G. K. Liyanage, A. B. Phillips, U. Steiner, M. Graetzel, M. J. Heben, *Adv. Energy Mater.* **2016**, *6*, 1600846.
[25] A. Abate, T. Leijtens, S. Pathak, J. Teuscher, R. Avolio, M. E. Errico, J. Kirkpatrik, J. M. Ball, P. Docampo, I. McPherson, H. J. Snaith, *Phys. Chem. Chem. Phys.* **2013**, *15*, 2572.
[26] J. H. Heo, S. Park, S. H. Im, H. J. Son, *ACS Appl. Mater. Interfaces* **2017**, *9*, 39511.
[27] X. Yin, L. Guan, J. Yu, D. Zhao, C. Wang, N. Shrestha, Y. Han, Q. An, J. Zhou, B. Zhou, Y. Yu, C. R. Grice, R. A. Awni, F. Zhang, J. Wang, R. J. Ellingson, Y. Yan, W. Tang, *Nano Energy* **2017**, *40*, 163.
[28] X. Yin, C. Wang, D. Zhao, N. Shrestha, C. R. Grice, L. Guan, Z. Song, C. Chen, C. Li, G. Chi, B. Zhou, J. Yu, Z. Zhang, R. J. Ellingson, J. Zhou, Y. Yan, W. Tang, *Nano Energy* **2018**, *51*, 680.
[29] E. Kasparavicius, A. Magomedov, T. Malinauskas, V. Getautis, *Chem. - Eur. J.* **2018**, *24*, 9910.
[30] A. Magomedov, E. Kasparavičius, K. Rakstys, S. Paek, N. Gasilova, K. Genevičius, G. Juška, T. Malinauskas, M. K. Nazeeruddin, V. Getautis, *J. Mater. Chem. C* **2018**, *6*, 8874.
[31] S. Paek, P. Qin, Y. Lee, K. T. Cho, P. Gao, G. Grancini, E. Oveisi, P. Gratia, K. Rakstys, S. A. Al-Muhtaseb, C. Ludwig, J. Ko, M. K. Nazeeruddin, *Adv. Mater.* **2017**, *29*, 1606555.

© 2019 WILEY-VCH Verlag GmbH & Co. KGaA, Weinheim

Approved for public release; distribution unlimited.

[32] H. D. Pham, T. T. Do, J. Kim, C. Charbonneau, S. Manzhos, K. Feron, W. C. Tsoi, J. R. Durrant, S. M. Jain, P. Sonar, *Adv. Energy Mater.* **2018**, *8*, 1703007.
[33] W. Zhou, Z. Wen, P. Gao, *Adv. Energy Mater.* **2018**, *8*, 1702512.
[34] Y. Li, K. R. Scheel, R. G. Clevenger, W. Shou, H. Pan, K. V. Kilway, Z. Peng, *Adv. Energy Mater.* **2018**, *8*, 1801248.
[35] K. Rakstys, S. Paek, P. Gao, P. Gratia, T. Marszalek, G. Grancini, K. T. Cho, K. Genevicius, V. Jankauskas, W. Pisula, M. K. Nazeeruddin, *J. Mater. Chem. A* **2017**, *5*, 7811.
[36] W. Zhu, C. Shen, Y. Wu, H. Zhang, E. Li, W. Zhang, X. Xu, W. Wu, H. Tian, *Angew. Chem., Int. Ed.* **2019**, *58*, 3784.
[37] Y. Liu, Z. Hong, Q. Chen, H. Chen, W.-H. Chang, Y. Yang, T.-B. Song, Y. Yang, *Adv. Mater.* **2016**, *28*, 440.
[38] E. H. Jung, N. J. Jeon, E. Y. Park, C. S. Moon, T. J. Shin, T.-Y. Yang, J. H. Noh, J. Seo, *Nature* **2019**, *567*, 511.
[39] R. Shang, Z. Zhou, H. Nishioka, H. Halim, S. Furukawa, I. Takei, N. Ninomiya, E. Nakamura, *J. Am. Chem. Soc.* **2018**, *140*, 5018.
[40] J. Lee, M. Malekshahi Byranvand, G. Kang, S. Y. Son, S. Song, G.-W. Kim, T. Park, *J. Am. Chem. Soc.* **2017**, *139*, 12175.
[41] Z. H. Bakr, Q. Wali, A. Fakharuddin, L. Schmidt-Mende, T. M. Brown, R. Jose, *Nano Energy* **2017**, *34*, 271.
[42] J. Sun, X. Ma, Z. Zhang, J. Yu, J. Zhou, X. Yin, L. Yang, R. Geng, R. Zhu, F. Zhang, W. Tang, *Adv. Mater.* **2018**, *30*, 1707150.
[43] S. Mabrouk, M. Zhang, Z. Wang, M. Liang, B. Bahrami, Y. Wu, J. Wu, Q. Qiao, S. Yang, *J. Mater. Chem. A* **2018**, *6*, 7950.
[44] R. Sandoval-Torrientes, I. Zimmermann, J. Calbo, J. Arago, J. Santos, E. Orti, N. Martin, M. K. Nazeeruddin, *J. Mater. Chem. A* **2018**, *6*, 5944.
[45] H. D. Pham, H. Hu, F.-L. Wong, C.-S. Lee, W.-C. Chen, K. Feron, S. Manzhos, H. Wang, N. Motta, Y. M. Lam, P. Sonar, *J. Mater. Chem. C* **2018**, *6*, 9017.
[46] H. D. Pham, H. Hu, K. Feron, S. Manzhos, H. Wang, Y. M. Lam, P. Sonar, *Sol. RRL* **2017**, *1*, 1700105.
[47] P. Agarwala, D. Kabra, *J. Mater. Chem. A* **2017**, *5*, 1348.
[48] H. D. Pham, Z. Wu, L. K. Ono, S. Manzhos, K. Feron, N. Motta, Y. Qi, P. Sonar, *Adv. Electron. Mater.* **2017**, *3*, 1700139.
[49] H. D. Pham, L. Gil-Escrig, K. Feron, S. Manzhos, S. Albrecht, H. J. Bolink, P. Sonar, *J. Mater. Chem. A* **2019**, *7*, 12507.
[50] H. D. Pham, S. M. Jain, M. Li, S. Manzhos, K. Feron, S. Pitchaimuthu, Z. Liu, N. Motta, H. Wang, J. R. Durrant, P. Sonar, *J. Mater. Chem. A* **2019**, *7*, 5315.
[51] H. D. Pham, L. Xianqiang, W. Li, S. Manzhos, A. K. K. Kyaw, P. Sonar, *Energy Environ. Sci.* **2019**, *12*, 1177.
[52] S. Förtsch, A. Vogt, P. Bäuerle, *J. Phys. Org. Chem.* **2017**, *30*, e3743.
[53] K. Do, H. Choi, K. Lim, H. Jo, J. W. Cho, M. K. Nazeeruddin, J. Ko, *Chem. Commun.* **2014**, *50*, 10971.
[54] M. L. Petrus, T. Bein, T. J. Dingemans, P. Docampo, *J. Mater. Chem. A* **2015**, *3*, 12159.
[55] F. Zhang, S. Wang, H. Zhu, X. Liu, H. Liu, X. Li, Y. Xiao, S. M. Zakeeruddin, M. Grätzel, *ACS Energy Lett.* **2018**, *3*, 1145.
[56] H. Chen, W. Fu, C. Huang, Z. Zhang, S. Li, F. Ding, M. Shi, C.-Z. Li, A. K. Y. Jen, H. Chen, *Adv. Energy Mater.* **2017**, *7*, 1700012.
[57] J. Urieta-Mora, I. García-Benito, A. Molina-Ontoria, N. Martín, *Chem. Soc. Rev.* **2018**, *47*, 8541.
[58] X. Yin, S. A. McClary, Z. Song, D. Zhao, B. K. Graeser, C. Wang, N. Shrestha, X.-M. Wang, C. Chen, C. Li, K. Subedi, R. Ellingson, W. Tang, R. Agrawal, Y. Yan, *J. Mater. Chem. A* **2019**, *7*, 4604.
[59] C. Wang, C. Xiao, Y. Yu, D. Zhao, R. A. Awni, C. R. Grice, K. Ghimire, D. Constantinou, W. Liao, A. J. Cimaroli, P. Liu, J. Chen, N. J. Podraza, C.-S. Jiang, M. M. Al-Jassim, X. Zhao, Y. Yan, *Adv. Energy Mater.* **2017**, *7*, 1700414.
[60] M. Stolterfoht, P. Caprioglio, C. M. Wolff, J. A. Márquez, J. Nordmann, S. Zhang, D. Rothhart, U. Hörmann, A. Redinger, L. Kegelmann, **2018**, arXiv:*1810*.01333.
[61] X. Zheng, Y. Deng, B. Chen, H. Wei, X. Xiao, Y. Fang, Y. Lin, Z. Yu, Y. Liu, Q. Wang, J. Huang, *Adv. Mater.* **2018**, *30*, 1803428.
[62] J. Peng, Y. Wu, W. Ye, D. A. Jacobs, H. Shen, X. Fu, Y. Wan, T. Duong, N. Wu, C. Barugkin, H. T. Nguyen, D. Zhong, J. Li, T. Lu, Y. Liu, M. N. Lockrey, K. J. Weber, K. R. Catchpole, T. P. White, *Energy Environ. Sci.* **2017**, *10*, 1792.
[63] S.-H. Turren-Cruz, A. Hagfeldt, M. Saliba, *Science* **2018**, *362*, 449.
[64] D. Bi, C. Yi, J. Luo, J.-D. Décoppet, F. Zhang, S. M. Zakeeruddin, X. Li, A. Hagfeldt, M. Grätzel, *Nat. Energy* **2016**, *1*, 16142.
[65] C. Wang, Z. Song, Y. Yu, D. Zhao, R. A. Awni, C. R. Grice, N. Shrestha, R. J. Ellingson, X. Zhao, Y. Yan, *Sustainable Energy Fuels* **2018**, *2*, 2435.
[66] C. Wang, D. Zhao, Y. Yu, N. Shrestha, C. R. Grice, W. Liao, A. J. Cimaroli, J. Chen, R. J. Ellingson, X. Zhao, Y. Yan, *Nano Energy* **2017**, *35*, 223.
[67] W. Ke, C. Xiao, C. Wang, B. Sapravo, H.-S. Duan, D. Zhao, Z. Xiao, P. Schulz, S. P. Harvey, W. Liao, W. Meng, Y. Yu, A. J. Cimaroli, C.-S. Jiang, K. Zhu, M. Al-Jassim, G. Fang, D. B. Mitzi, Y. Yan, *Adv. Mater.* **2016**, *28*, 5214.
[68] B. Suarez, V. Gonzalez-Pedro, T. S. Ripolles, R. S. Sanchez, L. Otero, I. Mora-Sero, *J. Phys. Chem. Lett.* **2014**, *5*, 1628.
[69] J. Seo, J. H. Noh, S. I. Seok, *Acc. Chem. Res.* **2016**, *49*, 562.
[70] D. H. Kang, N. G. Park, *Adv. Mater.* **2019**, *31*, 1805214.
[71] D. Moia, I. Gelmetti, P. Calado, W. Fisher, M. Stringer, O. Game, Y. Hu, P. Docampo, D. Lidzey, E. Palomares, J. Nelson, P. R. F. Barnes, *Energy Environ. Sci.* **2019**, *12*, 1296.
[72] L. J. A. Koster, V. D. Mihailetchi, H. Xie, P. W. M. Blom, *Appl. Phys. Lett.* **2005**, *87*, 203502.
[73] D. Zhao, M. Sexton, H.-Y. Park, G. Baure, J. C. Nino, F. So, *Adv. Energy Mater.* **2015**, *5*, 1401855.
[74] N. Arora, M. I. Dar, A. Hinderhofer, N. Pellet, F. Schreiber, S. M. Zakeeruddin, M. Grätzel, *Science* **2017**, *358*, 768.
[75] C. Wang, D. Zhao, C. R. Grice, W. Liao, Y. Yu, A. Cimaroli, N. Shrestha, P. J. Roland, J. Chen, Z. Yu, P. Liu, N. Cheng, R. J. Ellingson, X. Zhao, Y. Yan, *J. Mater. Chem. A* **2016**, *4*, 12080.

 © 2019 WILEY-VCH Verlag GmbH & Co. KGaA, Weinheim

Approved for public release; distribution unlimited.

THE JOURNAL OF PHYSICAL CHEMISTRY C

Article

Cite This: J. Phys. Chem. C 2020, 124, 1330−1336

pubs.acs.org/JPCC

High Remaining Factors in the Photovoltaic Performance of Perovskite Solar Cells after High-Fluence Electron Beam Irradiations

Zhaoning Song,*[,†] Chongwen Li,[†] Cong Chen,[†] Jeremiah McNatt,[‡] Woojun Yoon,[§] David Scheiman,[§] Phillip P. Jenkins,[§] Randy J. Ellingson,[†] Michael J. Heben,[†] and Yanfa Yan*[,†]

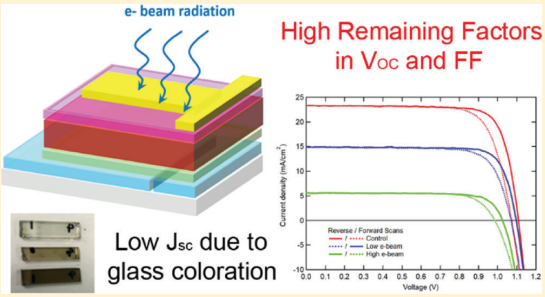
[†]Department of Physics and Astronomy, Wright Center for Photovoltaics Innovation and Commercialization, University of Toledo, 2801 W. Bancroft Street, Toledo, Ohio 43606, United States

[‡]NASA Glenn Research Center, 21000 Brookpark Rd, Cleveland, Ohio 44135, United States

[§]Naval Research Laboratory, 4555 Overlook Avenue S.W., Washington, DC 20375, United States

Downloaded via UNIV OF TOLEDO on September 13, 2021 at 15:56:13 (UTC).
See https://pubs.acs.org/sharingguidelines for options on how to legitimately share published articles.

ABSTRACT: Metal halide perovskite solar cells have progressed rapidly over the past decade, providing an exceptional opportunity for space photovoltaic (PV) power applications. However, the solar cells to be used for space power have to demonstrate a stable operation under extreme conditions, particularly concerning harsh radiations. In contrast to previously reported superior stability of low PV performance perovskite solar cells against high-energy radiation, we investigate the effects of high-energy electron beam irradiation on the degradation of perovskite solar cells with a high-power conversion efficiency exceeding 20%. We find very high remaining factors of >87.7% in the open-circuit voltage (V_{OC}) and >93.5% in the fill factor (FF) and a significantly decreased short-circuit current density (J_{SC}) after the exposure to high-fluence electron irradiations of 10^{15} e/cm^2. The pronounced loss of J_{SC} is due to the decreasing transmittance of the soda-lime glass substrate and the partial decomposition of the perovskite absorber layers. The irradiated cells retained superior remaining factors in both V_{OC} and FF, demonstrating a superior tolerance of perovskite solar cells after the exposure to the electron irradiation. These results show that perovskite solar cells hold great potential for space PV power applications if stable perovskite compositions and space-suitable substrates are employed.



INTRODUCTION

The past decade has witnessed an impressive development of solar cells based on metal halide perovskites at an unprecedented speed. The solar-to-electricity power conversion efficiency (PCE) of perovskite solar cells (PSCs) has increased rapidly from less than 4% to more than 25%,[1,2] which rivals other more established photovoltaic (PV) technologies. Additionally, PSCs possess some manufacturing advantages,[3] including low material and processing costs[4] and low-temperature deposition approaches that enable the use of flexible and lightweight substrates for high specific weight power applications like portable power sources and unmanned aerial vehicles.[5−7] The advances in PSCs provide an exceptional opportunity for the fabrication of low-cost, high-efficiency, lightweight solar cells for space power applications.[8] However, as a reliable power source, solar cells to be used for space power have to tolerate high-energy cosmic radiation, including protons, electrons, and γ-rays.[9] Although PSCs are promising to be used for space power applications because of their noteworthy performance, their stability under cosmic radiation is yet be demonstrated.

To date, a few experiments have been carried out to examine the tolerance of PSCs under the influence of proton,[10−13] electron,[11−13] neutron,[14] and γ-ray irradiations[15,16] and in an on-field test in near space.[17] Lang et al. investigated the impacts of proton irradiation on $MAPbI_3$ PSCs with initial PCEs of ∼12%,[10] revealing radiation hardness and self-healing in PSCs. Further analysis showed that proton irradiation improved the recombination lifetime of photogenerated charge carriers in the perovskites.[18] Miyazawa et al. irradiated high-energy electron and proton beams on PSCs in a simulated space environment.[11] The poly(3-hexylthiophene)-based solar cells with PCEs less than 9% demonstrated a sufficiently high durability against high-fluence irradiations of up to 10^{16} particles/cm^2. Huang et al. examined the effects of electron and proton irradiations on PSCs with initial PCEs of ∼12%, showing only a slight degradation in PV performance.[12] Yang et al. investigated the stability of perovskites under γ-ray radiation and concluded that perovskites are more robust than glass under γ-rays.[15] Although these reports demonstrated robust radiation hardness of PSCs, most studies employed

Received: December 11, 2019
Revised: December 19, 2019
Published: December 20, 2019

ACS Publications © 2019 American Chemical Society

DOI: 10.1021/acs.jpcc.9b11483
J. Phys. Chem. C 2020, 124, 1330−1336

Approved for public release; distribution unlimited.

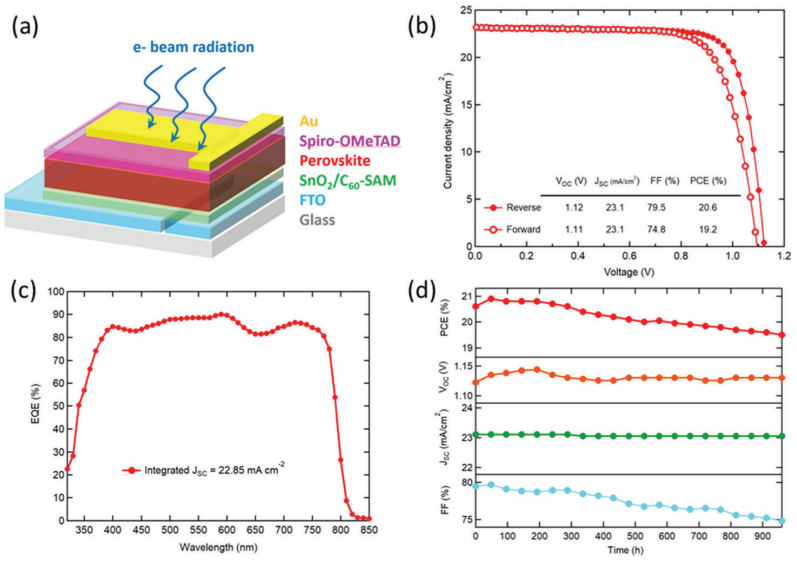


Figure 1. (a) Schematic of a PSC used for the radiation test. (b) $J-V$ and (c) EQE of a typical pristine PSC. (d) PV parameter evolution as a function of storage time in a nitrogen glovebox.

PSCs with relatively low or moderate PCEs, which make these promising results less convincing and speculative.

In contrast to the positive outcomes of radiation tolerance, it has also been reported that high-energy radiation can deteriorate PSCs. Yang et al. and Boldyreva et al. individually reported that PSCs experienced obvious performance degradation under γ-ray irradiation.[16,19] In a real field test to assess PSCs for space solar power applications,[20] researchers showed almost 36% power loss after a balloon flight in the stratosphere. Additionally, the perovskite material and device degradation induced by electron beam (e-beam) irradiation has been widely studied using electron microscope-based techniques.[21−24] Despite a much lower electron energy range (keV for electron microscopic measurement vs MeV for space solar stability test), significant material and device degradation was identified after a high dose of e-beam irradiation. The controversial results of the robustness of PSCs against high-energy irradiation show the necessity to have more studies on the radiation tolerance of high-performance PSCs to better evaluate the feasibility of PSCs for future aerospace applications. Moreover, further investigations are needed toward a better understanding of radiation-induced degradation and damage mechanisms in PSCs.

Notably, it is required for the use of electron irradiations in the standard space solar cell qualification test to predict the degradation of solar cells in space.[25] So far, little work has been done with the focus on evaluating the stability of PSCs under e-beam irradiation,[11−13] and all the PSCs used for previous e-beam tolerance studies exhibited moderate or low PCEs of 4−13%. Here, we study the impact of high-fluence e-beam irradiations on the device performance of high-performance PSCs with PCE exceeding 20%. To investigate the e-beam radiation hardness of PSCs, we track the evolution of PV characteristics of PSCs after exposure to 1 MeV e-beam to an accumulated fluence of 10^{13} and 10^{15} e/cm^2 and characterize the changes in materials and devices induced by the e-beam irradiations to study radiation-induced defect generation.

EXPERIMENTAL METHODS

The PSCs were fabricated on fluorine-doped tin oxide (FTO)-coated glass substrates with a sheet resistance of 15 Ω/sq. The glass/FTO substrates were laser-patterned and cleaned before use. A SnO_2 electron transport layer was deposited by plasma-enhanced atomic layer deposition and treated with water vapor.[26] A self-assembled fullerene monolayer (C_{60}-SAM) was deposited on SnO_2 by spin-coating using a previously reported recipe.[27] The perovskite precursor solution was prepared by dissolving 461 mg PbI_2 (TCI), 111 mg methylammonium iodide (MAI, Greatcell Solar), 52 mg formamidinium iodide (FAI, Greatcell Solar), and 9.2 mg $Pb(SCN)_2$ (Sigma) in a mixed solvent of dimethylformamide and dimethyl sulfoxide (DMF/DMSO v/v = 9:1). The perovskite precursor solution was spin-coated on the substrate at 500 rpm for 3 s and then at 4000 rpm for 60 s. A 700 μL of diethyl ether was dropped on the spinning substrate at 10 s of the second spin step. After spin-coating, the perovskite films were annealed on a hot plate at 65 °C for 2 min and 100 °C for 2 min. After this, a spiro-OMeTAD solution was prepared and spin-coated on the perovskite layers, as reported previously.[28] Finally, devices were completed by depositing an 80 nm Au layer using thermal evaporation. The devices were then patterned into an active area of ∼0.8 cm^2 using laser scribing.

$J-V$ and steady-state efficiency curves were recorded using a Keithley 2400 source meter under standard 100 mW/cm^2 illumination (AM 1.5G) using a PV Measurements solar simulator. External quantum efficiency (EQE) curves in the range of 300−850 nm were measured using a PV Measurements EQE system calibrated with a certified Si photodiode. The optical transmittance spectra in the range of 300−850 nm were obtained using a PerkinElmer Lambda 1050 spectrometer. Cross-sectional scanning electron microscopy (SEM) and energy-dispersive X-ray spectroscopy (EDX) microanalysis on PSCs were performed using a Hitachi S-4800 field emission electron microscope. X-ray diffraction (XRD) spectra in the

DOI: 10.1021/acs.jpcc.9b11483
J. Phys. Chem. C 2020, 124, 1330−1336

Approved for public release; distribution unlimited.

range of 10−18° were measured with a step size of 0.02° at a speed of 0.1° per min using a Rigaku Ultima III X-ray diffractometer. Laser beam-induced current (LBIC) maps of PSCs were obtained using a built-in-house multifunction laser system.[29]

To test the tolerance of PSCs to e-beam irradiation, pristine perovskite cells were fabricated at Toledo and shipped to the NEO Beam facility at NASA Glenn Research Center. Sixteen identical unencapsulated cells were loaded on the irradiation plate and exposed to 1 MeV e-beam irradiation. After a fluence of 1.3×10^{13} e/cm^2 irradiation (denoted by low e-beam), half of the devices were removed. The remaining cells were removed after an accumulated fluence of 1×10^{15} e/cm^2 irradiation (denoted by high e-beam). The maximum temperature of ∼50 °C can be reached under the NEO beam irradiation. To compare with the e-beam-irradiated devices, eight control devices traveled with the irradiated cells to the exposure area, remained in the same general environmental condition as the irradiated cells (open warehouse environment, ambient humidity, and temperature), returned with the irradiated cells, and sealed in a vacuum bag after exposure.

RESULTS AND DISCUSSION

Figure 1a shows the schematic sketch of the device structure of the PSCs used in this study. The devices in the so-called n−i−p configuration were constructed by sequentially depositing a thin-film stack, including atomic layer-deposited SnO_2, spin-coated fullerene self-assembled monolayer (C_{60}-SAM), $MA_{0.7}FA_{0.3}PbI_3$ perovskite absorber layer (where MA and FA are methylammonium and formamidinium), and 2,2′,7,7′-tetrakis(*N*,*N*-di-*p*-methoxyphenylamine)-9,9′-spirobifluorene (spiro-OMeTAD), and a thermally evaporated Au electrode on laser-patterned FTO-coated soda-lime glass substrates, following the fabrication process reported previously.[26,28,30] Experimental details on device fabrication are provided in the Experimental Methods section. The device fabrication is based on a well-established recipe that can be used to fabricate more than 20% efficient PSCs. Figure 1b shows the current density−voltage (J−V) curves of a typical device under 100 mW/cm^2 simulated standard solar illumination (AM 1.5G). The device delivers a PCE of 20.6 (19.2)%, with an open-circuit voltage (V_{OC}) of 1.12 (1.11) V, a short-circuit current density (J_{SC}) of 23.1 (23.1) mA/cm^2, and a fill factor (FF) of 79.5 (74.8)% when measured under a reverse (forward) voltage scan. It is worth noting that such a small degree of J−V hysteresis is typically observed in PSCs.[31] The external quantum efficiency (EQE) curve of the device is shown in Figure 1c. The integrated photocurrent density is 22.85 mA/cm^2, which is within 1% deviation from the J_{SC} value determined by the J−V measurement. The shelf stability of an unencapsulated device stored in the nitrogen environment is demonstrated in Figure 1d. The PCE of the device decreased from 20.6 to 19.5% after storage for 960 h (40 days), accounting for a relative efficiency drop of 5%. As a remark, the storage degradation is mainly caused by decreasing FF, likely because of degassing of oxygen from spiro-OMeTAD that lowers the hole mobility,[32] whereas the V_{OC} and J_{SC} values almost remained the same during the storage period. Because of high performance and adequate stability, devices in this configuration were selected for the test of e-beam radiation hardness.

Figure 2 shows the statistical distribution of PV parameters for devices under control and under low and high e-beam irradiation conditions. The average PCEs of irradiated cells

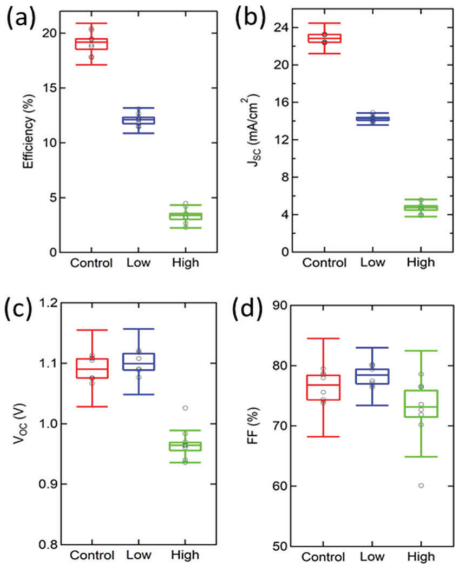


Figure 2. Distributions of PV parameters, including (a) efficiency, (b) J_{SC}, (c) V_{OC}, and (d) FF for 12 PSCs under control and low and high e-beam irradiation conditions.

under the low and high fluence of e-beam decreased to 12.2 and 3.4%, respectively, corresponding to 36 and 82% drops compared with the average PCE of 19.2% for the control devices (Figure 2a). The primary cause for the efficiency drop is attributed to the pronounced decrease in J_{SC} values (Figure 2b), corresponding to the J_{SC} drops of 8.4 and 18.1 mA/cm^2 for the low and high e-beam-irradiated devices, respectively, when compared with the control devices. Interestingly, the impacts of e-beam irradiation on V_{OC} and FF are much less significant (Figure 2c,d), showing very high remaining factors (Table 1). The low e-beam irradiation even leads to slight increases in V_{OC} and FF, whereas the high fluence irradiation indeed deteriorates the V_{OC} and FF values. Overall, the results agree with Miyazawa et al.,[11] who reported high radiation tolerance of PSCs under e-beam irradiation at 10^{16} e/cm^2. The discrepancy may be related to the device configuration or initial performance (20 vs 5%). The relatively low initial PCEs could make it hard to distinguish the subtle changes in the device performance.

Figure 3a presents the J−V curves of representative control and irradiated cells under forward and reverse voltage scans. The degradation of irradiated perovskite cells is mainly attributed to the significantly decreased photocurrent density. The J−V curves of irradiated cells remain in good shape, indicating that the e-beam irradiation has an insignificant impact on the diode behavior of the cells to rectify current. Despite decreased PCEs, the irradiated devices exhibit stabilized power output as the control cell under 1 sun illumination, as shown in Figure 3b. These results indicate that the high-energy electron irradiation does not significantly affect other layers in the PSCs, such as the charge-selective layers (SnO_2/C_{60} and spiro-OMeTAD) and electrodes (FTO and Au). The EQE measurement (Figure 3c) reveals that the irradiated cells exhibit significant drops in spectrally dependent photocurrent response compared with the control device, especially in the short wavelength range (350−650 nm). The

DOI: 10.1021/acs.jpcc.9b11483
J. Phys. Chem. C 2020, 124, 1330−1336

Approved for public release; distribution unlimited.

Table 1. Remaining Factors in the PV Parameters of Control and Irradiated PSCs

		remaining factor			
	scan direction	V_{OC} (%)	FF (%)	J_{SC} (%)	PCE (%)
control	reverse	99.8 ± 0.4	101.3 ± 0.4	100.3 ± 2.0	101.5 ± 2.6
	forward	100.2 ± 0.5	103.8 ± 0.7	100.9 ± 2.4	105.2 ± 3.9
1 MeV e-beam irradiation with a fluence of 1.3×10^{13} e/cm	reverse	98.3 ± 0.4	101.6 ± 0.3	81.3 ± 1.4[a]	81.0 ± 1.6[b]
	forward	98.6 ± 0.4	103.9 ± 0.4	80.7 ± 1.3[a]	82.6 ± 1.0[b]
1 MeV e-beam irradiation with a fluence of 1.3×10^{15} e/cm	reverse	87.7 ± 2.7	93.5 ± 4.2	68.4 ± 3.1[a]	56.3 ± 6.6[b]
	forward	89.3 ± 1.9	96.2 ± 10.8	68.3 ± 2.9[a]	59.0 ± 9.6[b]

[a]The remaining factors in J_{SC} are corrected to consider the loss in the transmittance of the glass substrate. [b]The values of PCE are corrected accordingly using the corrected J_{SC}, and PCE is measured under a simulated AM 1.5G spectrum (100 mW/cm^2).

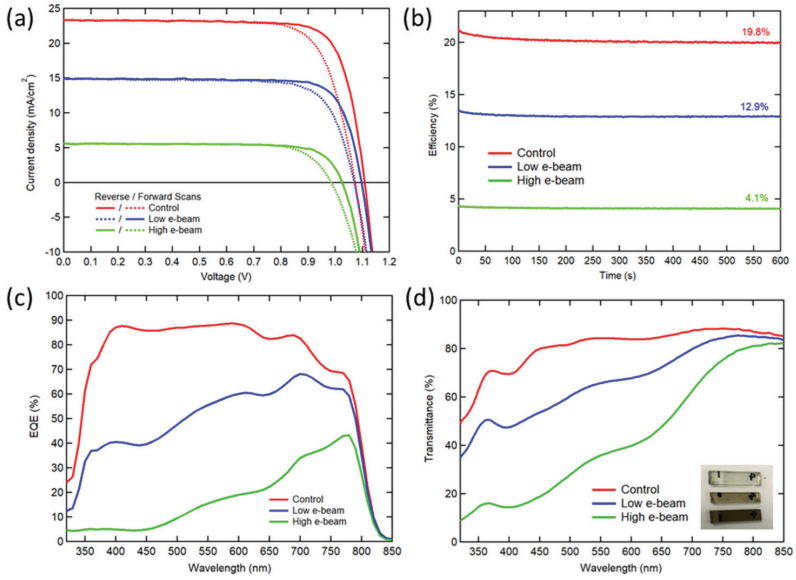


Figure 3. (a) $J-V$, (b) steady-state efficiency, and (c) EQE of PSCs under control, low e-beam, and high e-beam conditions. (d) Optical transmittance of FTO glass substrates before and after e-beam radiation. Inset of panel (d) is a photo of glass debris from the tested cells after cleaning.

optical transmittance measurement was conducted on the cleaned glass substrates after removing the thin film stacks of PSCs from the tested devices. After receiving a high fluence of e-beam irradiation, the color of the glass substrate became darker, as shown in the inset of Figure 3d. The optical transmittance spectra (Figure 3d) confirm the loss of transparency at the short wavelengths, consistent with the pronounced drops in the EQE spectra. The loss of optical transparency because of the creation of color centers in the glass substrate is in good agreement with the previous reports of PSCs under high-energy protons[10] and γ-ray photons.[16] It has also been shown that the energetic proton beam can cause increased optical absorption in common thin-film PV substrates such as soda-lime glass and polyethylene terephthalate foils.[33] To overcome the shading effect, space solar cover glass typically incorporates lanthanum or cerium to enhance its radiation hardness.[34] Alternatively, quartz substrates can resist proton and e-beam radiation well.[11] Taking into account the optical loss in the glass substrates, we would expect the loss in J_{SC} by 4.0 and 10.7 mA/cm^2, resulting in decent remaining factors of 63.3 ± 1.4 and 68.4 ± 2.8%, respectively, for low and high e-beam-irradiated devices. Although these values are much less than the measured J_{SC} degradation of 8.4 and 18.1 mA/cm^2, we expect that the e-beam induced damages to the perovskite absorber layers to some degree.

Material and device analyses were then conducted to evaluate the degradation of the perovskite absorber layers because of e-beam irradiation. Figure 4a–c shows the cross-sectional SEM images of the control and irradiated PSCs. No clear visual damage has been found in the microscopic structure of the devices. All the thin-film layers were preserved after the exposure to a high fluence of e-beam irradiation. However, the EDX measurement reveals that the molar ratio of Pb to I was changed from 1:2.9 for the control to 1: 2.5 and 1:2.2 for the low and high e-beam-irradiated samples (Figure 4d–f), respectively, indicating the partial decomposition of perovskite (Pb/I = 1:3) into the photoinactive lead iodide (Pb/I = 1:2). It is worth noting that the organic–inorganic lead halide perovskites are prone to degradation when exposed to humid air,[35,36] heating,[37,38] UV light,[39] electric fields,[40] electron beam,[23] and so forth. During the e-beam irradiation test, the unencapsulated PSCs experienced certain thermal stress because of the e-beam bombardment. The combination

DOI: 10.1021/acs.jpcc.9b11483
J. Phys. Chem. C 2020, 124, 1330–1336

Approved for public release; distribution unlimited.

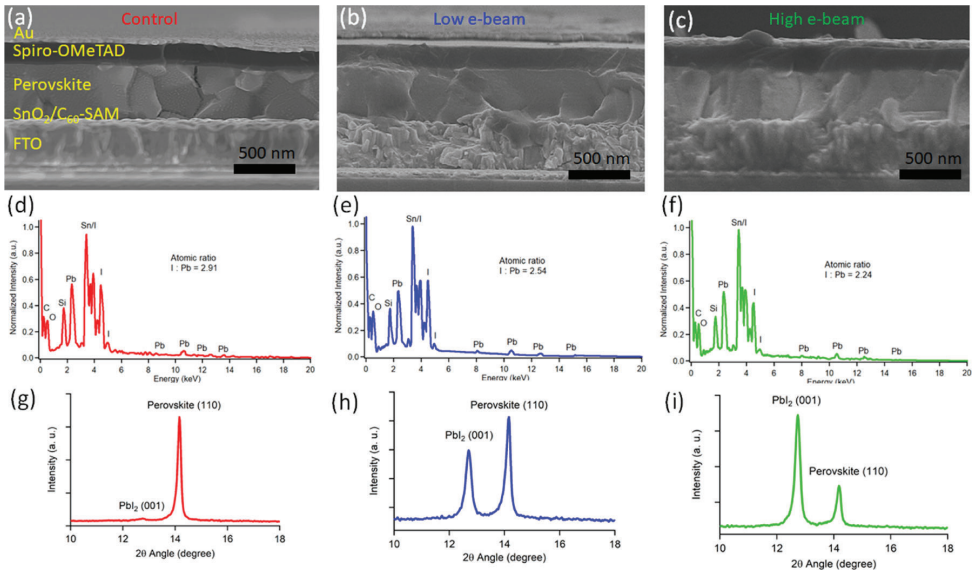


Figure 4. Cross-sectional (a–c) SEM images and (d–f) EDX and (g–i) XRD spectra of PSCs under (a,d,g) control, (b,e,h) low e-beam, and (c,f,i) high e-beam conditions.

of elevated temperatures and ambient humidity led to the considerable decomposition of perovskites. The XRD measurement revealed that the hexagonal PbI_2 peak at 12.1° increases, whereas the peak of perovskite at 14.1° decreases with increasing e-beam exposure, as shown in Figure 4g–i, confirming the appearance of PbI_2 after e-beam irradiation. The partial decomposition of organic–inorganic perovskites accounts for the part of the loss of J_{SC} in addition to primary loss because of the reduced transparency of the glass substrates. Despite the identification of primary causes for the loss of current, the origins of the performance degradation may also be related to the deterioration of doped spiro-OMeTAD or the degradation of the quality of its interface with the perovskite absorber layer, triggered by e-beam-induced heating in a humid ambient. However, a radiation test under a well-controlled environment to evaluate individual influencing factors is beyond the capability of the current study and will be the focus of our follow-up work.

We further probed the spatially resolved photocurrent generation in the devices using the LBIC technique.[35] Figure 5 shows the photocurrent maps of the control and low and high e-beam-irradiated cells. The photocurrent reduction because of e-beam irradiations is resolved by the LBIC mapping. Furthermore, the e-beam damages on the circumferences of the cell close to the edges of the metal back-contact are observed, indicating that the metal back-contact coverage may slightly retard the decomposition of the perovskite by blocking the pathways for the release of volatile decomposition products (e.g., hydrogen iodide and methylamine), which alleviates the e-beam damages on the perovskite layers. Additionally, it is worth noticing that e-beam leads to a homogeneous degradation across the entire device area, which differs from the inhomogeneous degradation because of water ingress.[35] The degradation in the perovskite absorber layer is likely related to the instability of the organic–inorganic metal halide composition, which tends to degrade under illumination

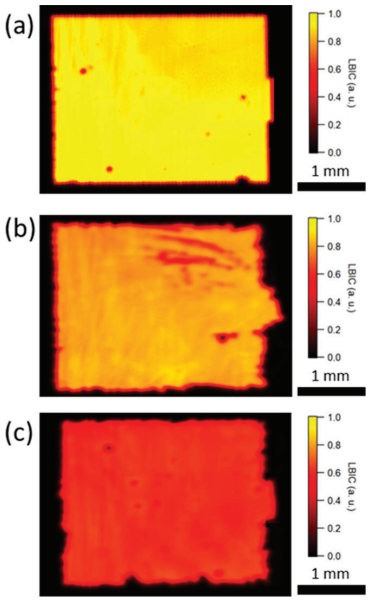


Figure 5. LBIC maps of PSCs under (a) control, (b) low e-beam, and (c) high e-beam conditions.

and heat.[37,39,41] Perovskite materials with enhanced thermal stability and photostability (e.g., cesium-based all-inorganic perovskites) and more stable hole-transporting layers are needed for space power applications.[42,43] Recent advances in fabricating high-efficiency (>18%) all-inorganic PSCs[44] show a great promise for investigating the irradiation tolerance of PSCs using more thermodynamically stable perovskite compositions. Moreover, space-qualified substrate and encapsulation are required to ensure the integrity of the perovskite

DOI: 10.1021/acs.jpcc.9b11483
J. Phys. Chem. C 2020, 124, 1330–1336

Approved for public release; distribution unlimited.

layer and the complete device to cover the lifetime of desired space applications. Clearly, more investigations are needed in the future to continue the evaluation of the cosmic irradiation stability of PSCs with better intrinsic absorber stability and substrates that can resist irradiations well.

CONCLUSIONS

In summary, we investigated the impacts of high-fluence e-beam irradiations on the performance of high-efficiency PSCs. We observed very high remaining factors in both V_{OC} and FF but a decent remaining factor in J_{SC} and, consequently, in the PCE of PSCs after e-beam irradiation. Further characterization reveals that the performance degradation in PSCs is mainly because of coloring in the glass substrate and the decomposition of the perovskite absorber layers. Despite the decreased PCEs, the positive outcomes in the high remaining factors in V_{OC} and FF show the promise of PSCs for future space applications. Furthermore, future assessments of PSCs for space power applications should require the use of special space cover glass, space-qualified encapsulation, and more stable perovskite compositions.

AUTHOR INFORMATION

Corresponding Authors

*E-mail: zhaoning.song@utoledo.edu (Z.S.).
*E-mail: yanfa.yan@utoledo.edu (Y.Y.).

ORCID

Zhaoning Song: 0000-0002-6677-0994
Woojun Yoon: 0000-0002-1946-5372
Randy J. Ellingson: 0000-0001-9520-6586
Michael J. Heben: 0000-0002-3788-3471
Yanfa Yan: 0000-0003-3977-5789

Notes

The authors declare no competing financial interest.

ACKNOWLEDGMENTS

This study was supported by the Office of Naval Research under contract no. N00014-17-1-2223. This material is based on the research sponsored by Air Force Research Laboratory under agreement number FA9453-18-2-0037. The U.S. Government is authorized to reproduce and distribute reprints for governmental purposes notwithstanding any copyright notation thereon. The views and conclusions contained herein are those of the authors and should not be interpreted as necessarily representing the official policies or endorsements, either expressed or implied, of Air Force Research Laboratory or the U.S. Government.

REFERENCES

(1) Kojima, A.; Teshima, K.; Shirai, Y.; Miyasaka, T. Organometal Halide Perovskites as Visible-Light Sensitizers for Photovoltaic Cells. *J. Am. Chem. Soc.* **2009**, *131*, 6050−6051.

(2) NREL. Solar Cell Efficiency Chart. https://www.nrel.gov/pv/cell-efficiency.html (accessed July 6, 2019).

(3) Correa-Baena, J.-P.; Saliba, M.; Buonassisi, T.; Grätzel, M.; Abate, A.; Tress, W.; Hagfeldt, A. Promises and Challenges of Perovskite Solar Cells. *Science* **2017**, *358*, 739−744.

(4) Song, Z.; McElvany, C. L.; Phillips, A. B.; Celik, I.; Krantz, P. W.; Watthage, S. C.; Liyanage, G. K.; Apul, D.; Heben, M. J. A Technoeconomic Analysis of Perovskite Solar Module Manufacturing with Low-Cost Materials and Techniques. *Energy Environ. Sci.* **2017**, *10*, 1297−1305.

(5) Kaltenbrunner, M.; Adam, G.; Głowacki, E. D.; Drack, M.; Schwödiauer, R.; Leonat, L.; Apaydin, D. H.; Groiss, H.; Scharber, M. C.; White, M. S.; et al. Flexible High Power-Per-Weight Perovskite Solar Cells with Chromium Oxide-Metal Contacts for Improved Stability in Air. *Nat. Mater.* **2015**, *14*, 1032−1039.

(6) Kang, S.; Jeong, J.; Cho, S.; Yoon, Y. J.; Park, S.; Lim, S.; Kim, J. Y.; Ko, H. Ultrathin, Lightweight and Flexible Perovskite Solar Cells with an Excellent Power-Per-Weight Performance. *J. Mater. Chem. A* **2019**, *7*, 1107−1114.

(7) Yang, D.; Yang, R.; Priya, S.; Liu, S. F. Recent Advances in Flexible Perovskite Solar Cells: Fabrication and Applications. *Angew. Chem., Int. Ed.* **2019**, *58*, 4466−4483.

(8) Zhang, W.; Eperon, G. E.; Snaith, H. J. Metal Halide Perovskites for Energy Applications. *Nat. Energy* **2016**, *1*, 16048.

(9) Woodyard, J. R.; Landis, G. A. Radiation Resistance of Thin-Film Solar Cells for Space Photovoltaic Power. *Solar Cells* **1991**, *31*, 297−329.

(10) Lang, F.; Nickel, N. H.; Bundesmann, J.; Seidel, S.; Denker, A.; Albrecht, S.; Brus, V. V.; Rappich, J.; Rech, B.; Landi, G.; et al. Radiation Hardness and Self-Healing of Perovskite Solar Cells. *Adv. Mater.* **2016**, *28*, 8726−8731.

(11) Miyazawa, Y.; Ikegami, M.; Chen, H.-W.; Ohshima, T.; Imaizumi, M.; Hirose, K.; Miyasaka, T. Tolerance of Perovskite Solar Cell to High-Energy Particle Irradiations in Space Environment. *Science* **2018**, *2*, 148−155.

(12) Huang, J.; Kelzenberg, M. D.; Espinet-González, P.; Mann, C.; Walker, D.; Naqavi, A.; Vaidya, N.; Warmann, E.; Atwater, H. A. Effects of Electron and Proton Radiation on Perovskite Solar Cells for Space Solar Power Application. *2017 IEEE 44th Photovoltaic Specialist Conference (PVSC)*, June 25−30, 2017; pp 1248−1252.

(13) Miyazawa, Y.; Ikegami, M.; Miyasaka, T.; Ohshima, T.; Imaizumi, M.; Hirose, K. Evaluation of Radiation Tolerance of Perovskite Solar Cell for Use in Space. *2015 IEEE 42nd Photovoltaic Specialist Conference (PVSC)*, June 14−19, 2015; pp 1−4.

(14) Paternò, G. M.; Robbiano, V.; Santarelli, L.; Zampetti, A.; Cazzaniga, C.; Garcia Sakai, V.; Cacialli, F. Perovskite Solar Cell Resilience to Fast Neutrons. *Sustainable Energy Fuels* **2019**, *3*, 2561−2566.

(15) Yang, S.; Xu, Z.; Xue, S.; Kandlakunta, P.; Cao, L.; Huang, J. Organohalide Lead Perovskites: More Stable Than Glass under Gamma-Ray Radiation. *Adv. Mater.* **2019**, *31*, 1805547.

(16) Yang, K.; Huang, K.; Li, X.; Zheng, S.; Hou, P.; Wang, J.; Guo, H.; Song, H.; Li, B.; Li, H.; et al. Radiation Tolerance of Perovskite Solar Cells under Gamma Ray. *Org. Electron.* **2019**, *71*, 79−84.

(17) Tu, Y.; Xu, G.; Yang, X.; Zhang, Y.; Li, Z.; Su, R.; Luo, D.; Yang, W.; Miao, Y.; Cai, R.; et al. Mixed-Cation Perovskite Solar Cells in Space. *Sci. China: Phys., Mech. Astron.* **2019**, *62*, 974221.

(18) Brus, V. V.; Lang, F.; Bundesmann, J.; Seidel, S.; Denker, A.; Rech, B.; Landi, G.; Neitzert, H. C.; Rappich, J.; Nickel, N. H. Defect Dynamics in Proton Irradiated $CH_3NH_3PbI_3$ Perovskite Solar Cells. *Adv. Electron. Mater.* **2017**, *3*, 1600438.

(19) Boldyreva, A. G.; Akbulatov, A. F.; Tsarev, S. A.; Luchkin, S. Y.; Zhidkov, I. S.; Kurmaev, E. Z.; Stevenson, K. J.; Petrov, V. G.; Troshin, P. A. γ-Ray-Induced Degradation in the Triple-Cation Perovskite Solar Cells. *J. Phys. Chem. Lett.* **2019**, *10*, 813−818.

(20) Cardinaletti, I.; Vangerven, T.; Nagels, S.; Cornelissen, R.; Schreurs, D.; Hruby, J.; Vodnik, J.; Devisscher, D.; Kesters, J.; D'Haen, J.; et al. Organic and Perovskite Solar Cells for Space Applications. *Sol. Energy Mater. Sol. Cells* **2018**, *182*, 121−127.

(21) Klein-Kedem, N.; Cahen, D.; Hodes, G. Effects of Light and Electron Beam Irradiation on Halide Perovskites and Their Solar Cells. *Acc. Chem. Res.* **2016**, *49*, 347−354.

(22) Xiao, C.; Li, Z.; Guthrey, H.; Moseley, J.; Yang, Y.; Wozny, S.; Moutinho, H.; To, B.; Berry, J. J.; Gorman, B.; et al. Mechanisms of Electron-Beam-Induced Damage in Perovskite Thin Films Revealed by Cathodoluminescence Spectroscopy. *J. Mater. Chem. C* **2015**, *119*, 26904−26911.

(23) Yuan, H.; Debroye, E.; Janssen, K.; Naiki, H.; Steuwe, C.; Lu, G.; Moris, M.; Orgiu, E.; Uji-i, H.; De Schryver, F.; et al. Degradation

DOI: 10.1021/acs.jpcc.9b11483
J. Phys. Chem. C 2020, 124, 1330−1336

Approved for public release; distribution unlimited.

of Methylammonium Lead Iodide Perovskite Structures through Light and Electron Beam Driven Ion Migration. *J. Phys. Chem. Lett.* **2016**, *7*, 561−566.
(24) Kosasih, F. U.; Ducati, C. Characterising Degradation of Perovskite Solar Cells through in-Situ and Operando Electron Microscopy. *Nano Energy* **2018**, *47*, 243−256.
(25) Messenger, S. R.; Warner, J. H.; Uribe, R.; Walters, R. J. Monte Carlo Analyses of the Neo Beam Electron Beam Facility for Space Solar Cell Radiation Qualification. *IEEE Trans. Nucl. Sci.* **2010**, *57*, 3470−3476.
(26) Wang, C.; Guan, L.; Zhao, D.; Yu, Y.; Grice, C. R.; Song, Z.; Awni, R. A.; Chen, J.; Wang, J.; Zhao, X.; et al. Water Vapor Treatment of Low-Temperature Deposited SnO_2 Electron Selective Layers for Efficient Flexible Perovskite Solar Cells. *ACS Energy Lett.* **2017**, *2*, 2118−2124.
(27) Wang, C.; Xiao, C.; Yu, Y.; Zhao, D.; Awni, R. A.; Grice, C. R.; Ghimire, K.; Constantinou, I.; Liao, W.; Cimaroli, A. J.; et al. Understanding and Eliminating Hysteresis for Highly Efficient Planar Perovskite Solar Cells. *Adv. Energy Mater.* **2017**, *7*, 1700414.
(28) Wang, C.; Song, Z.; Yu, Y.; Zhao, D.; Awni, R. A.; Grice, C. R.; Shrestha, N.; Ellingson, R. J.; Zhao, X.; Yan, Y. Synergistic Effects of Thiocyanate Additive and Cesium Cations on Improving the Performance and Initial Illumination Stability of Efficient Perovskite Solar Cells. *Sustainable Energy Fuels* **2018**, *2*, 2435−2441.
(29) Phillips, A. B.; Song, Z.; DeWitt, J. L.; Stone, J. M.; Krantz, P. W.; Royston, J. M.; Zeller, R. M.; Mapes, M. R.; Roland, P. J.; Dorogi, M. D.; et al. High Speed, Intermediate Resolution, Large Area Laser Beam Induced Current Imaging and Laser Scribing System for Photovoltaic Devices and Modules. *Rev. Sci. Instrum.* **2016**, *87*, 093708.
(30) Wang, C.; Song, Z.; Zhao, D.; Awni, R. A.; Li, C.; Shrestha, N.; Chen, C.; Yin, X.; Li, D.; Ellingson, R. J.; et al. Improving Performance and Stability of Planar Perovskite Solar Cells through Grain Boundary Passivation with Block Copolymers. *Solar RRL* **2019**, *3*, 1900078.
(31) Chen, B.; Yang, M.; Priya, S.; Zhu, K. Origin of J-V Hysteresis in Perovskite Solar Cells. *J. Phys. Chem. Lett.* **2016**, *7*, 905−917.
(32) Abate, A.; Leijtens, T.; Pathak, S.; Teuscher, J.; Avolio, R.; Errico, M. E.; Kirkpatrik, J.; Ball, J. M.; Docampo, P.; McPherson, I.; et al. Lithium salts as "redox active" p-type dopants for organic semiconductors and their impact in solid-state dye-sensitized solar cells. *Phys. Chem. Chem. Phys.* **2013**, *15*, 2572−2579.
(33) Čermák, J.; Mihai, L.; Sporea, D.; Galagan, Y.; Fait, J.; Artemenko, A.; Štenclová, P.; Rezek, B.; Straticiuc, M.; Burducea, I. Proton Irradiation Induced Changes in Glass and Polyethylene Terephthalate Substrates for Photovoltaic Solar Cells. *Sol. Energy Mater. Sol. Cells* **2018**, *186*, 284−290.
(34) Gusarov, A. I.; Doyle, D.; Hermanne, A.; Berghmans, F.; Fruit, M.; Ulbrich, G.; Blondel, M. Refractive-index changes caused by proton radiation in silicate optical glasses. *Appl. Opt.* **2002**, *41*, 678−684.
(35) Song, Z.; Abate, A.; Watthage, S. C.; Liyanage, G. K.; Phillips, A. B.; Steiner, U.; Graetzel, M.; Heben, M. J. Perovskite Solar Cell Stability in Humid Air: Partially Reversible Phase Transitions in the PbI_2-CH_3NH_3I-H_2O System. *Adv. Energy Mater.* **2016**, *6*, 1600846.
(36) Huang, J.; Tan, S.; Lund, P. D.; Zhou, H. Impact of H2o on Organic-Inorganic Hybrid Perovskite Solar Cells. *Energy Environ. Sci.* **2017**, *10*, 2284−2311.
(37) Juarez-Perez, E. J.; Ono, L. K.; Maeda, M.; Jiang, Y.; Hawash, Z.; Qi, Y. Photodecomposition and Thermal Decomposition in Methylammonium Halide Lead Perovskites and Inferred Design Principles to Increase Photovoltaic Device Stability. *J. Mater. Chem. A* **2018**, *6*, 9604−9612.
(38) Divitini, G.; Cacovich, S.; Matteocci, F.; Cinà, L.; Di Carlo, A.; Ducati, C. In Situ Observation of Heat-Induced Degradation of Perovskite Solar Cells. *Nat. Energy* **2016**, *1*, 15012.
(39) Song, Z.; Wang, C.; Phillips, A. B.; Grice, C. R.; Zhao, D.; Yu, Y.; Chen, C.; Li, C.; Yin, X.; Ellingson, R. J.; et al. Probing the Origins of Photodegradation in Organic-Inorganic Metal Halide Perovskites with Time-Resolved Mass Spectrometry. *Sustainable Energy Fuels* **2018**, *2*, 2460−2467.
(40) Bae, S.; Kim, S.; Lee, S.-W.; Cho, K. J.; Park, S.; Lee, S.; Kang, Y.; Lee, H.-S.; Kim, D. Electric-Field-Induced Degradation of Methylammonium Lead Iodide Perovskite Solar Cells. *J. Phys. Chem. Lett.* **2016**, *7*, 3091−3096.
(41) Zhou, Y.; Zhao, Y. Chemical Stability and Instability of Inorganic Halide Perovskites. *Energy Environ. Sci.* **2019**, *12*, 1495−1511.
(42) Tai, Q.; Tang, K.-C.; Yan, F. Recent Progress of Inorganic Perovskite Solar Cells. *Energy Environ. Sci.* **2019**, *12*, 2375−2405.
(43) Jung, E. H.; Jeon, N. J.; Park, E. Y.; Moon, C. S.; Shin, T. J.; Yang, T.-Y.; Noh, J. H.; Seo, J. Efficient, Stable and Scalable Perovskite Solar Cells Using Poly(3-Hexylthiophene). *Nature* **2019**, *567*, 511−515.
(44) Wang, Y.; Dar, M. I.; Ono, L. K.; Zhang, T.; Kan, M.; Li, Y.; Zhang, L.; Wang, X.; Yang, Y.; Gao, X.; et al. Thermodynamically Stabilized β-$CsPbI_3$−Based Perovskite Solar Cells with Efficiencies >18%. *Science* **2019**, *365*, 591−595.

DOI: 10.1021/acs.jpcc.9b11483
J. Phys. Chem. C 2020, 124, 1330−1336

Approved for public release; distribution unlimited.

SCIENTIFIC REPORTS
nature research

OPEN

Photogenerated Carrier Transport Properties in Silicon Photovoltaics

Prakash Uprety, Indra Subedi, Maxwell M. Junda, Robert W. Collins & Nikolas J. Podraza*

Electrical transport parameters for active layers in silicon (Si) wafer solar cells are determined from free carrier optical absorption using non-contacting optical Hall effect measurements. Majority carrier transport parameters [carrier concentration (N), mobility (μ), and conductivity effective mass (m^*)] are determined for both the n-type emitter and p-type bulk wafer Si of an industrially produced aluminum back surface field (Al-BSF) photovoltaic device. From measurements under 0 and ±1.48T external magnetic fields and nominally "dark" conditions, the following respective [n, p]-type Si parameters are obtained: $N = [(3.6 \pm 0.1) \times 10^{18}\ cm^{-3}, (7.6 \pm 0.1) \times 10^{15}\ cm^{-3}]$; $\mu = [166 \pm 6\ cm^2/Vs, 532 \pm 12\ cm^2/Vs]$; and $m^* = [(0.28 \pm 0.03) \times m_e, (0.36 \pm 0.02) \times m_e]$. All values are within expectations for this device design. Contributions from photogenerated carriers in both regions of the p-n junction are obtained from measurements of the solar cell under "light" 1 sun illumination (AM1.5 solar irradiance spectrum). From analysis of combined dark and light optical Hall effect measurements, photogenerated minority carrier transport parameters [minority carrier concentration (Δp or Δn) and minority carrier mobility (μ_h or μ_e)] under 1 sun illumination for both n- and p-type Si components of the solar cell are determined. Photogenerated minority carrier concentrations are $[(7.8 \pm 0.2) \times 10^{16}\ cm^{-3}, (2.2 \pm 0.2) \times 10^{14}\ cm^{-3}]$, and minority carrier mobilities are $[331 \pm 191\ cm^2/Vs, 766 \pm 331\ cm^2/Vs]$, for the [n, p]-type Si, respectively, values that are within expectations from literature. Using the dark majority carrier concentration and the effective equilibrium minority carrier concentration under 1 sun illumination, minority carrier effective lifetime and diffusion length are calculated in the n-type emitter and p-type wafer Si with the results also being consistent with literature. Solar cell device performance parameters including photovoltaic device efficiency, open circuit voltage, fill factor, and short circuit current density are also calculated from these transport parameters obtained via optical Hall effect using the diode equation and PC1D solar cell simulations. The calculated device performance parameters are found to be consistent with direct current-voltage measurement demonstrating the validity of this technique for electrical transport property measurements of the semiconducting layers in complete Si solar cells. To the best of our knowledge, this is the first method that enables determination of both minority and majority carrier transport parameters in both active layers of the p-n junction in a complete solar cell.

Minority carrier transport parameters critically affect operation and performance of many p-n junction semiconductor devices including bipolar transistors and solar cells[1–4]. Knowledge of intrinsic carrier concentration, effective equilibrium minority carrier concentration, minority carrier mobility, and effective carrier lifetime obtained by theoretical and experimental methods are essential parameters for modeling semiconductor devices to understand device physics and to optimize performance[1–6]. For solar cells in particular, both open circuit voltage (V_{oc}) and photogenerated current density (J_L) depend on minority carrier mobility and effective carrier lifetime in the absorber material[7].

Silicon (Si) wafer photovoltaic (PV) devices are currently the most mature and dominant technology in the solar module market accounting for ~90% of total global production[8]. As such, some of the pertinent minority carrier transport properties of Si have been extracted using photoluminescence[9,10], a combination of steady state electrical and transient optical techniques[5], photoconductance decay[6,11], analysis of frequency domain transient photocurrent[12], theoretical modeling[13], V_{oc} decay[14], quasi-steady-state photoconductance and quasi-steady-state V_{oc}[7], resonant-coupled photoconductive decay[15], and a combination of transient and quasi-steady-state photoconductance[16]. Dziewior *et al.* have measured the minority carrier mobilities in heavily doped n- and p-type Si[9]. Swirhun *et al.* found the minority carrier hole mobility in heavily doped n-type Si is about double that of

Wright Center for Photovoltaics Innovation and Commercialization & Department of Physics and Astronomy, University of Toledo, Toledo, OH, 43606, USA. *email: Nikolas.Podraza@utoledo.edu

Approved for public release; distribution unlimited.
328

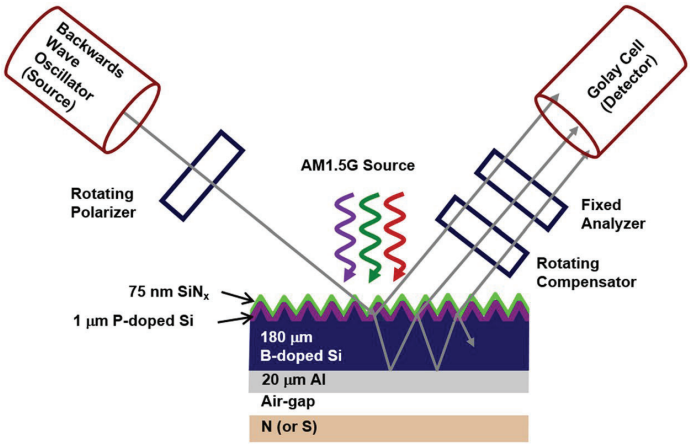


Figure 1. Schematic of a Si wafer aluminum back surface field (Al-BSF) solar cell mounted on a magnet for optical Hall effect measurements based on terahertz (THz) range spectroscopic ellipsometry under 1 sun illumination (AM 1.5 solar irradiance spectrum)[1,3,15]. More detailed information regarding this type of experimental setup can be found in ref. [30].

the majority carrier hole mobility in p-type Si doped to a similar carrier concentration[10]. Wang *et al.* found that the minority hole mobility in n-type Si is approximately double than that of the majority hole mobility in p-type Si[12]. Law *et al.* studied the variation of minority carrier mobility as a function of dopant concentration using theoretical modeling[13]. Swirhun *et al.* have reported the variation of minority carrier mobility in p-type Si as a function of dopant concentration and found that the electron mobility in p-type Si is about 2.5 times that of the electron mobility in n-type Si doped to a similar carrier concentration[5]. Sproul *et al.* have reported the variation of the minority carrier mobility in n-type and p-type Si as a function of dopant concentration[6]. The variation of minority carrier mobility with respect to temperature in the bulk layer of a Si wafer solar cell has been reported using V_{oc} decay[14]. Neuhaus *et al.* have studied the injection level dependence of the sum of minority and majority carrier mobilities in the bulk layer of Si wafer solar cell[7]. Even with all this extensive background of Si electrical transport studies, however, extraction of both minority and majority carrier properties in both the p- and n-type components of a Si solar cell p-n junction is not straightforward. In this work optical Hall effect measurements of a Si wafer solar cell under nominally dark and 1 sun illumination conditions are used to determine both majority and minority carrier transport properties.

In general, complete Si solar cells are a multiple layer stack of p- and n-type semiconductors along with electrical contact and passivation layers. A typical Si wafer solar cell has a p-type base with the near-surface (top 1 μm) more heavily doped with a pentavalent impurity yielding the emitter. Aluminum back surface field (Al-BSF) solar cells are the most common solar cells. Direct electrical measurement of transport parameters for individual semiconductors in these device structures is often difficult or impossible. Optical Hall effect via magnetic field dependent frequency domain terahertz (THz) range spectroscopic ellipsometry is a potential alternative method that enables extraction of majority carrier transport parameters such as conductivity effective mass (m^*), carrier concentration (N), and mobility (μ) of individual layers even in the complex multilayer structures, but without making physical contact[17–24]. Figure 1 shows a schematic illustration depicting a THz range spectroscopic ellipsometer used for the analysis of a Si wafer Al-BSF solar cell with an adjustable magnetic field dependence (0, ±1.48 T) under 1 sun illumination (AM1.5 solar irradiance). Majority carrier transport properties have also been studied previously using long wavelength range spectroscopic ellipsometry with results in good agreement with direct electrical measurements[25–29]. In comparison to long wavelength range ellipsometric measurements collected without an external magnetic field, the optical Hall effect measurements described here provide the capability of determining an increased number of transport parameters simultaneously and with increased accuracy[30]. For instance, in a previous study without the external magnetic field, N or μ has been obtained optically for cadmium telluride (CdTe) when the other value is known and both N and μ for Si wafers have been obtained[29]. With magnetic field dependent measurements, both N and μ for thin film CdTe and all three of N, μ, and m^* for Si wafers have been successfully measured[30].

Optical Hall effect measurements are now adapted to deduce minority electrical transport properties [minority carrier mobility (μ_h or μ_e) and equilibrium photogenerated minority carrier concentration (Δp or Δn)] and majority carrier N, μ, and m^* of active layers within a complete solar cell. In commercially produced Al-BSF Si wafer solar cells, an aluminum metal layer is commonly used as the rear-side electrical contact to the p-type wafer. The junction is formed from an n-type emitter on the p-type wafer base with a silicon nitride (SiN_x) antireflection coating and screen-printed silver front and aluminum rear contacts[31]. The cell surface is pyramidally textured to enhance absorption by light trapping, while the SiN_x dielectric coating serves to passivate dangling bonds present on the Si surface, which then reduces recombination centers for photogenerated carriers to enhance solar cell

Approved for public release; distribution unlimited.
329

performance[32]. Here majority carrier N, μ, and m^* are determined for both the n-type emitter and p-type wafer Si regions of an industrially produced Al-BSF Si solar cell from THz spectral range optical Hall effect measurements performed in nominally "dark" conditions. Contributions from photogenerated carriers in both the p- and n-type regions are obtained from optical Hall effect measurements of the solar cell under "light" 1 sun illumination (AM 1.5 solar irradiance spectrum). Analysis of the dark and light optical Hall effect measurements yields minority and majority transport characteristics for each Si component of the p-n junction within the complete solar cell. The transport properties are then used to calculate minority carrier lifetime and diffusion length of each layer as well as the PV device performance parameters.

Experimental Details

A commercially fabricated $15.6 \times 15.6\,cm^2$ pseudo-square Al-BSF Si wafer solar cell (CNH Industrial) has been purchased and characterized. The basic Al-BSF design consists of a 1 μm thick n-type phosphorus doped Si emitter, a 180 μm thick p-type boron doped Si wafer, a 75 nm SiN_x antireflection coating, three screen printed 1×154 mm^2 silver bus bar front contacts, and nine silver 2×22 mm^2 bus bars soldered to a 20 μm thick aluminum layer back contact[31,32]. Finger bars on the front surface are 0.1 mm wide and separated by 1.4 mm. The front surface is pyramidally textured. PV device performance parameters including the short circuit current density (J_{sc}), open circuit voltage (V_{oc}), fill factor (FF), and efficiency (η) are determined from current-voltage (J-V) measurements collected under 1 sun illumination. Experimental error on solar cell performance parameters from J-V are determined from one standard deviation of the measurement.

Mueller matrix spectra are collected *ex-situ* at 50, 60, and 70° angles of incidence in the THz spectral range from 3 to 34 cm^{-1} (3.3 mm to 290 μm) for the Si wafer solar cell (J. A. Woollam Co., THz-VASE)[33]. Eleven Mueller matrix elements normalized to M_{11} (m_{12}, m_{13}, m_{21}, m_{22}, m_{23}, m_{31}, m_{32}, m_{33}, m_{41}, m_{42}, and m_{43}) are obtained. Measured data are collected from an area of the cell oriented to avoid the front silver bus bars. The configuration of the ellipsometer used here differs from that described by Hofmann *et al.*[33] in the use of a rotating polarizer before interaction with the sample and a rotating compensator followed by fixed analyzer after interaction with the sample. For each case, sets of eleven Mueller matrix element spectra at the three angles are collected with the sample under applied magnetic fields of 0 and ±1.48 T. A Ni-Cu-Ni coated Neodymium N42 permanent magnet $3'' \times 3'' \times 1/2''$ in size generates a maximum magnetic field of ±1.48 T. The magnet is mounted on the sample stage goniometer with double-sided tape on the corners, and then the sample is directly mounted on the magnet with known north or south (N or S) polarity. After the data are collected with one polarity, the magnet is removed and remounted to reverse the polarity. The separation between the sample and the magnet introduces an air-gap into the optical-structural model. Similar optical Hall effect measurements are also performed under ~1 sun illumination (AM 1.5 solar irradiance spectrum) generated by a fiber optic illuminator (Dolan-Jenner, Fiber-Lite Model 190).

For these optical Hall effect measurements, THz range spectroscopic ellipsometry is used as the optical probe. All three sets of eleven Mueller matrix elements spectra are analyzed simultaneously in a model sensitive to the complex dielectric function ($\varepsilon = \varepsilon_1 + i\varepsilon_2$) spectra as well as to wafer thickness and air gap thickness when applicable. The contributions to the optical response in this spectral range include those due to free carrier absorption, described classically by the Drude model[34]. The Drude model yields a complex dielectric function term defined by:

$$\varepsilon_{Drude}(\omega) = \frac{-q^2 N\mu}{\varepsilon_0(m^*\mu\omega^2 + iq\omega)} \tag{1}$$

where q, N, μ, ε_0, and m^* are the elementary charge, carrier concentration, mobility, vacuum permittivity, and carrier conductivity effective mass, respectively. Resistivity (ρ) and scattering time (τ) are related to these parameters by $\rho = m^*/Nq^2\tau = 1/q\mu N$. Explicit forms of the Drude model in terms of minority and majority carrier contributions for Si under dark condition and 1 sun illumination measurements are given in Supplementary Information Equations S1 and S2.

Optical anisotropy is introduced under non-zero applied magnetic field, and the Drude model is modified. The free charge (FC) carrier magneto-optic (MO) contribution to the frequency dependent dielectric tensor $\boldsymbol{\varepsilon}(\omega)$ is obtained from the equation of motion for a free charge carrier with a charge q, a scaled (unitless) effective mass tensor $\boldsymbol{m}$, and an frequency-independent scattering tensor $\boldsymbol{\gamma}$[17]:

$$\boldsymbol{\varepsilon}^{\text{FC-MO}}(\omega) = \boldsymbol{I} + \boldsymbol{\omega}_p^2 \times \left[-\omega^2 \boldsymbol{I} - i\omega\boldsymbol{\gamma} + i\omega \begin{pmatrix} 0 & b_3 & -b_2 \\ -b_3 & 0 & b_1 \\ b_2 & -b_1 & 0 \end{pmatrix} \boldsymbol{\omega}_c \right]^{-1}, \tag{2}$$

where, $\boldsymbol{I}$, $\boldsymbol{B} = B\,(b_1, b_2, b_3)$, $\boldsymbol{\omega}_p{}^2 = (Nq^2/\varepsilon_0 m_e)\,\boldsymbol{m}^{-1}$, $\boldsymbol{\omega}_c = (qB/m_e)\,\boldsymbol{m}^{-1}$, ε_0, and m_e are the identity matrix, external magnetic field vector, plasma frequency tensor, cyclotron frequency tensor, vacuum permittivity, and electron mass, respectively. The b_1, b_2, and b_3 matrix elements are the direction cosines of B. The non-zero differences in the magneto-optic Mueller matrix elements for $+\mathbf{B}$ and $-\mathbf{B}$ are related to free carrier motion generated by the Lorentz force. Analysis of Mueller matrix spectra enable determination of $\boldsymbol{\omega}_p$ and $\boldsymbol{\gamma}$ related to N/m^* and $m^*\mu$. Fitting the difference in Mueller matrix elements, which correspond to the specific tensor elements of $\boldsymbol{\omega}_c$[17], enables extraction of N, m^*, and μ independently. Although the effective mass tensor elements of Si are complicated

Approved for public release; distribution unlimited.
330

with six pockets in the Fermi surface and two effective mass parameters[21], the analysis described here is simplified and a single conductivity effective mass for each Si layer is assumed[35].

Bulk wafer thickness, air gap thickness, and optical properties for each of the active layers in the cell are extracted in the form of layer thicknesses and spectra in ε, respectively, by fitting a parameterized model to measured Mueller matrix spectra and Mueller matrix difference spectra collected at all three angles of incidence using a least square regression analysis that minimizes an unweighted error function (σ)[36]. The errors reported on model fit parameters are derived from a combination of the statistical standard 90% confidence limit and the overall error function quantifying the closeness of model fit to measurement. Consequently, these errors are best interpreted as a measure of model sensitivity to each parameter in the context of all other fit parameters.

Results

The structural model consists of a 20 μm aluminum layer/181 ± 4 μm p-type boron doped Si wafer/1 μm n-type phosphorus doped Si emitter layer/75 nm SiN_x layer/air ambient, as shown in Fig. 1. The in-plane pyramidal texture feature size is ~4–5 μm[31] and much smaller than the wavelengths of the probing THz beam; as a result, the surface is treated as specular for these measurement wavelengths. The bus bar front electrical contacts are avoided by the probing beam, and the metal finger bars occupy ~7% of the surface area of the probing beam spot. Contributions from these finger bars are not included in the optical model as the majority of the beam spot samples the surface of the Si solar cell. A discrete interface between the n-type Si emitter and the p-type Si wafer is assumed for simplicity. The p-type Si wafer thickness is a fit parameter, while all other thicknesses are fixed at nominal values from literature, noted in Fig. 1[31,32]. A similar structural-optical model is used in the presence of magnetic fields; however, a finite thickness air gap is included between the sample and the magnet. Spectra in ε for the active n- and p-type Si are extracted by fitting measured Mueller matrix and Mueller matrix difference spectra using a parameterized model. The three sets of data collected under dark condition measurement at 0 and ±1.48 T applied magnetic fields in spectral range windows from 3 to 34 cm^{-1} are fitted for this sample simultaneously with difference in Mueller matrix spectra [i.e. $\Delta m_{ij} = m_{ij}(+B) - m_{ij}(-B)$] from 23 to 32 cm^{-1}. Figure 2 shows the example experimental Mueller matrix spectra collected at 50° under the dark condition from 3 to 34 cm^{-1} at 0, +1.48, −1.48 T; experimental Mueller matrix difference spectra from 23 to 32 cm^{-1}; and corresponding best fit models. Contributions to THz range spectra in ε for the phosphorus doped n-type Si emitter layer of the cell include a constant additive term to ε_1 ($\varepsilon_\infty = 1$) and a Drude expression[34] describing free carrier absorption, with the real and imaginary parts of the spectra in ε shown in Fig. 3. Similarly, the spectra in ε for the boron doped p-type Si wafer are parameterized by $\varepsilon_\infty = 10.3 \pm 0.4$ and a Drude expression[34] describing free carrier absorption with spectra in ε also shown in Fig. 3. For the more heavily doped n-type Si emitter the Drude contribution dominates the shape of ε so sensitivity to ε_∞ is lost and its value fixed at unity, whereas for the more lightly doped p-type Si wafer the Drude contribution is less dominant and sensitivity to ε_∞ is retained. Optical response of the permanent magnet consists of the Drude expression for highly reflective gold as described in the approach of Knight *et al.*[19] for optical Hall effect measurements. The effects due to the 75 nm SiN_x coating are negligible in this long wavelength spectral range. Spectra in ε for the aluminum back contact are represented by the parametric expression described by Subedi *et al.*[37].

The parameters describing majority carrier free carrier absorption for the n-type emitter and p-type Si wafer obtained from measurements collected under dark conditions are summarized in Table 1. Optical Hall effect measurements of the same solar cell are performed under 1 sun illumination and a similar data analysis approach is applied. Figure 4 shows example experimental Mueller matrix spectra collected at 50° under 1 sun illumination from 3 to 34 cm^{-1} at 0, +1.48, −1.48 T; Mueller matrix difference spectra from 25 to 32 cm^{-1}; and corresponding best fit models. The wafer thickness is fixed to 181 μm from analysis of optical Hall effect measurements collected under dark conditions. Under 1 sun illumination, spectra in ε for the n-type emitter are parameterized using $\varepsilon_\infty = 1$ and two Drude expressions separately representing contributions to free carrier absorption from majority carrier electrons and minority carrier holes, shown in Fig. 3. The hole contribution to free carrier absorption is due to photogenerated carriers under 1 sun illumination. The electron contribution consists of an equal concentration of photogenerated carriers added to the carriers from phosphorus doping. Similarly, spectra in ε for the p-type bulk wafer are parameterized by $\varepsilon_\infty = 11.41 \pm 0.02$ with Drude expressions for photogenerated minority carrier electrons and a combination of majority carrier holes from boron doping and photogeneration, also shown in Fig. 3. As in the case of the dark condition measurement analysis, the dominance of the Drude contributions to ε causes a loss of sensitivity to ε_∞ for the heavily doped n-type emitter while it is retained for the lightly doped p-type wafer. The majority and photogenerated minority carrier transport properties for the emitter and bulk Si layers of the cell are summarized in Table 1. In the model applied to analysis of the 1 sun illuminated measurements, the respective impurity doping carrier concentrations and conductivity effective masses are fixed to values obtained from the dark condition measurements. Photogenerated electron and hole concentrations are equal within each layer. Electron and hole μ in each layer are allowed to vary independently to account for additional recombination processes expected under illumination.

Discussion

Optically deduced transport properties. These optically deduced transport properties are similar to those reported in literature. Carrier concentrations for the n-type phosphorus doped Si emitter and p-type boron doped Si bulk are comparable to the expected values of $N \sim 10^{18}$ and $\sim 10^{15}$ cm^{-3}, respectively, for Si found in commercially produced cells[32,38]. The mobilities extracted for n- and p-type Si are consistent with literature values of 133 and 429 cm^2/Vs, respectively, for the corresponding N[39]. m^* for both phosphorus doped n-type and boron doped p-type Si agree with reported values of 0.26 and $0.39 m_e$, respectively[40,41]. ρ and τ determined from the Drude equation show good agreement with reported resistivities of 0.01 and 1.9 Ω cm and scattering times of 24 and 95 fs, for n- and p-type Si, respectively, with the corresponding N[39–41]. Overall, all three majority carrier

Approved for public release; distribution unlimited.
331

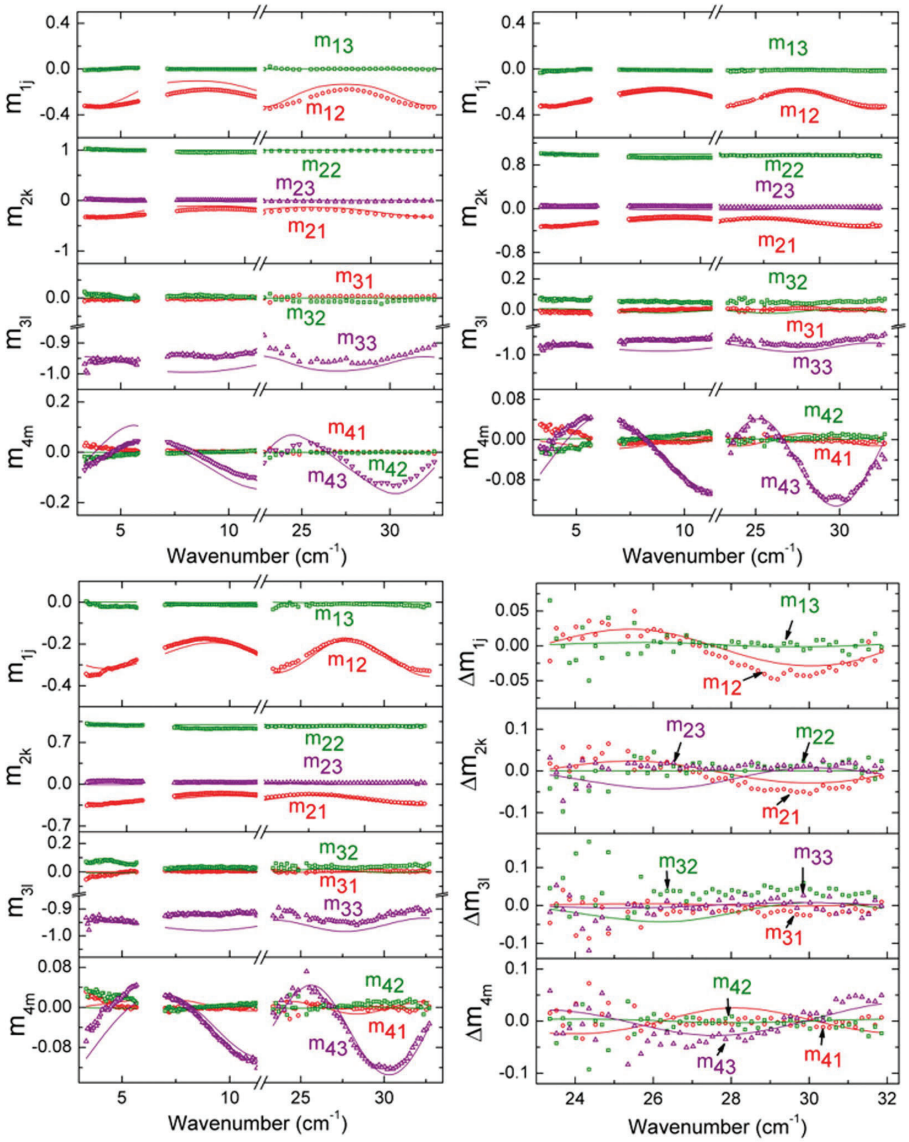


Figure 2. Experimental (symbols) spectra measured at 0 T (top-left), +1.48 T (top-right), −1.48 T (bottom-left) and difference spectra measured at ±1.48 T (bottom-right) with their corresponding calculated models (solid lines) of m_{12}, m_{13}, m_{21}, m_{22}, m_{23}, m_{31}, m_{32}, m_{33}, m_{41}, m_{42}, and m_{43} normalized Mueller matrix elements for the Al-BSF Si wafer solar cell at 50° angle of incidence under dark condition measurement. The unweighted error function for this fit is $\sigma = 4.33 \times 10^{-2}$.

transport parameters (N, μ, m^*) evaluated from the Drude model are reliably obtained for the n-type emitter and p-type bulk Si of the Al-BSF solar cell by the optical Hall effect measurements.

Electron and hole μ in each layer can vary independently to account for additional recombination processes expected under illumination. Under illumination, radiative[42–44], Auger[9,45,46], and Shockley-Read-Hall[47] recombination take place along with photogeneration of carriers. Photogenerated hole or electron concentration in the phosphorus doped n-type Si emitter is determined to be $(7.8 \pm 0.2) \times 10^{16}\,cm^{-3}$, which is ~2% of the impurity dopant or dark carrier concentration. Majority carrier electron mobility under 1 sun illumination is $162 \pm 5\,cm^2/Vs$, which is comparable to that obtained from dark measurements. Minority carrier hole mobility is $331 \pm 191\,cm^2/Vs$. Sproul *et al.*, Swirhun *et al.*, Alamo *et al.*, and Law *et al.*[6,10,11,13] reported that minority carrier hole mobility in n-type Si is generally higher than that of majority carrier hole mobility in p-type Si when

Approved for public release; distribution unlimited.
332

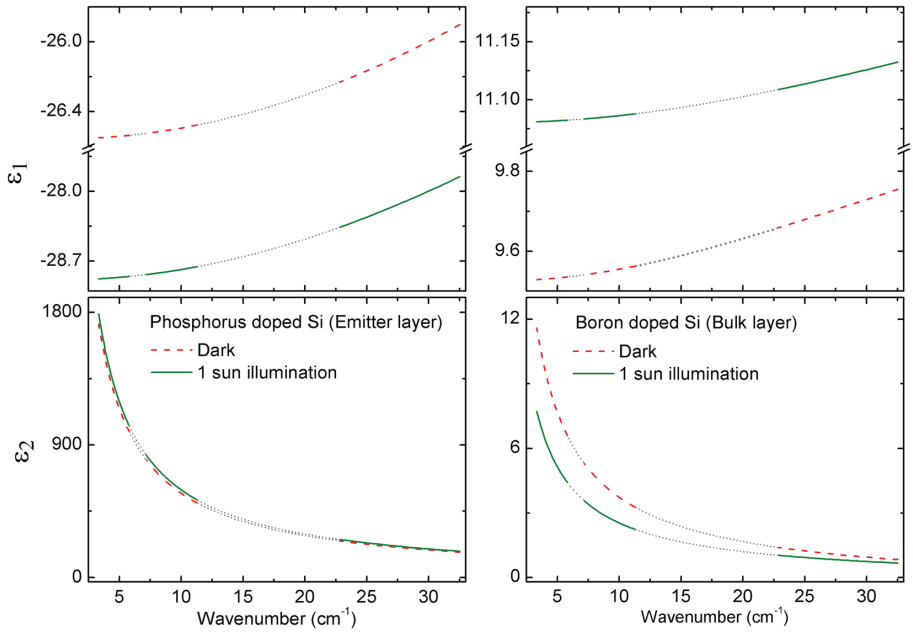


Figure 3. Complex dielectric function, $\varepsilon = \varepsilon_1 + i\varepsilon_2$, spectra for the phosphorus doped n-type Si emitter layer and boron doped p-type Si bulk wafer obtained from optical Hall effect measurements of the Al-BSF Si wafer solar cell under dark condition and 1 sun illumination (AM1.5 solar irradiance spectrum) measurements. Short dotted grey lines indicate gaps in the measured spectral range with the parametric expression for spectra in ε extrapolated over those regions.

impurity doped to similar levels; the latter hole mobility ranges from 450 to 80 cm^2/V s for carrier concentrations in the range from ~1×10^{16} to 4×10^{18} cm^{-3}. This difference is dopant concentration dependent for Si, which is at a minimum for low dopant concentration and increases with increasing dopant concentration. Here the minority carrier hole mobility in phosphorus doped Si is approximately double that of the majority carrier electron mobility, which is within expectations for Si with this impurity doping level[6,7,16,39].

The photogenerated electron and hole concentrations in the boron doped p-type Si bulk layer are $(2.2 \pm 0.2) \times 10^{14}$ cm^{-3}, which is ~3% of the boron impurity dopant or dark carrier concentration. Hole mobility under 1 sun illumination is 323 ± 32 cm^2/Vs, which is relatively lower than the measured dark value, but still comparable to literature expectations[39]. Minority carrier electron mobility is determined to be 766 ± 331 cm^2/Vs. Majority carrier electron mobility in 1.2×10^{16} cm^{-3} carrier concentration phosphorus impurity doped n-type Si is reported at 1093 cm^2/Vs[39]. Neuhaus *et al.* and Rougieux *et al.* have reported that the sum of minority and majority mobility approaches 1500 cm^2/Vs in ~1 Ω cm resistivity p-type Si with 10^{16} cm^{-3} impurity dopant concentration[7,16]. Swirhun *et al.* have reported minority electron mobility of 700–800 cm^2/Vs in material with an acceptor concentration of 10^{17} cm^{-3} [10]. Sproul *et al.* have also reported minority carrier electron mobility of ~ 1000 cm^2/Vs for 10^{16} cm^{-3} impurity carrier concentration boron doped Si[6]. The minority carrier mobility from optical Hall effect is slightly lower than these values but within expectation in consideration of the confidence limits[7,16]. Additionally, optical Hall effect measurements reported here are under 1 sun illumination in comparison to other techniques such as photoconductance decay[6], quasi-steady-state photoconductance + open-circuit voltage[7], and transient + quasi-steady-state photoconductance measurements[16]. In photoconductance decay, charge carrier generation is achieved optically by a short laser pulse, and carrier decay is measured by changes in microwave reflectance indicative of the rate at which carriers recombine after a short excitation. Quasi-steady-state photoconductance decay measures the balance between generation and recombination when quasi-steady-state illumination is achieved[6,16]. For quasi-steady-state photoconductance and V_{oc} techniques, both are measured under flash lamp illumination of different intensities[7]. Variation in values measured by these different techniques may arise from the different illumination levels used. Since these optical Hall effect measurements are performed under 1 sun illumination on a complete PV device, the transport properties measured by this method may more accurately represent the electrical transport properties of Si in this type of solar cell under operating conditions.

The optical and structural model assumes uniform carrier concentrations throughout the thicknesses of the n-type emitter and p-type bulk wafer for simplicity, although Al-BSF Si solar cells are more complicated with a n-type doping concentration gradient following a Gaussian or Gauss error function profile[48] and a depletion region present. Hofmann *et al.* studied p-p+ Si homojunctions using THz to mid infrared frequency range ellipsometry and deduced a carrier concentration profile utilizing relationships between hole concentration and mobility[35]. Analysis of the optical Hall effect measurements here yield majority and minority average carrier

Approved for public release; distribution unlimited.
333

Layers	Conditions	Transport Property	
Phosphorus-doped n-type Si emitter layer	Dark	Electron mobility μ (cm^2/V s)	166 ± 6
		Electron carrier concentration N (cm^{-3})	$(3.6 \pm 0.1) \times 10^{18}$
		Electron effective mass m^* ($\times m_e$)	0.28 ± 0.03
		Resistivity ρ (Ωcm)	0.01
		Scattering time τ (fs)	26
	Light (1 sun illumination)	Photogenerated electron and hole concentration Δn or Δp (cm^{-3})	$(7.8 \pm 0.2) \times 10^{16}$
		Electron mobility μ_e (cm^2/Vs)	162 ± 5
		Hole mobility μ_h (cm^2/Vs)	331 ± 191
Boron-doped p-type Si wafer	Dark	Hole mobility μ (cm^2/Vs)	532 ± 12
		Hole carrier concentration N (cm^{-3})	$(7.6 \pm 0.1) \times 10^{15}$
		Hole effective mass m^* ($\times m_e$)	0.36 ± 0.02
		Resistivity ρ (Ωcm)	1.5
		Scattering time τ (fs)	109
	Light (1 sun illumination)	Photogenerated hole and electron concentration Δp or Δn (cm^{-3})	$(2.2 \pm 0.2) \times 10^{14}$
		Hole mobility μ_h (cm^2/Vs)	323 ± 32
		Electron mobility μ_e (cm^2/Vs)	766 ± 331

Table 1. Dark and light carrier transport properties for Si phosphorus-doped n-type emitter and boron-doped p-type wafer in the Al-BSF solar cell.

concentrations within each doped Si region with carrier mobilities as independent fit parameters. The analysis did not provide sensitivity to the n-type emitter carrier concentration profile or the characteristics of the depletion region. Sensitivity to these characteristics may be lost due to the structure of this commercial Al-BSF device and overlapping optical effects of the n-type carrier concentration profile and depletion region transport properties occurring near the top of the Si junction. Although the simplified model of a discrete n-type emitter and p-type bulk Si interface is applied in analysis of the optical Hall effect data, the transport properties determined are used to calculate reasonable minority carrier lifetimes and diffusion lengths as well as to simulate solar cell performance parameters consistent with experiment.

Minority carrier lifetime and diffusion length. Different recombination mechanisms are used to determine the lifetime and diffusion length of the minority charge carriers in the emitter and bulk components of the solar cell. Minority carrier recombination lifetime (τ_r) is determined by $\Delta n/U_r$ or $\Delta p/U_r$, where Δn or Δp represents the photogenerated carriers and U_r is the recombination rate. All equations are provided in the Supplementary Information. The minority carrier diffusion length is then calculated by $(D\tau_r)^{1/2}$, where D is diffusivity given by the Einstein-Smoluchowski relation ($D = \mu kT/q$), μ is minority carrier mobility, k is Boltzmann's constant, T is ambient temperature and fixed at 300 K, and q is electron charge. From the mobility values in Table 1, the minority carrier diffusivities of the emitter and bulk are determined as 8 and 19.8 $cm^2 s^{-1}$, respectively. Using the dark electron concentration of 3.6×10^{18} cm^{-3} and the photogenerated hole concentration of 7.8×10^{16} cm^{-3}, effective hole lifetimes associated with radiative, Auger, and Shockley-Read-Hall recombination mechanisms are calculated as presented in Table 2. For radiative recombination, lifetimes in the emitter are calculated to be 26, 56, and 67 μs using the parametric expressions reported by Schlangenotto *et al.*[42], Trupke *et al.*[43], and Nguyen *et al.*[44], respectively. Similarly, for Auger recombination, lifetimes in the emitter are calculated to be 0.3 and 0.2 μs using the approach by Dziewior *et al.*[9] and Kerr *et al.*[46], respectively. The Shockley-Read-Hall lifetime is calculated to be 102 μs[47]. Thus, as shown in Table 2, the calculated lifetimes vary from 0.2 to 102 μs depending upon the recombination mechanism and model. Corresponding hole diffusion lengths are calculated to vary from 13 to 286 μm. As Si is an indirect band gap semiconductor, Auger and Shockley-Read-Hall recombination mechanisms dominate in these solar cells. Specifically, Auger recombination is dominant in the heavily doped emitter[9,45,46], so the Auger recombination lifetimes[9,45] are found to be consistent with lifetimes <1 μs commonly reported[13,49]. The diffusion lengths calculated from the Auger lifetimes are 13 and 15 μm, which are consistent with the 10 to 100 μm range reported in literature[13,49].

For the p-type Si bulk with a dark hole concentration of 7.6×10^{15} cm^{-3} and photogenerated electron concentration of 2.2×10^{14} cm^{-3}, the electron lifetime in the bulk using different recombination mechanisms and models is found to range from 103 to 1.6×10^5 μs[9,42–47]. Radiative recombination lifetimes in the bulk are calculated to be 1.2×10^4, 2.6×10^4, and 3.2×10^4 μs using the parametric expressions reported by Schlangenotto *et al.*[42], Trupke *et al.*[43], and Nguyen *et al.*[44], respectively. Similarly, Auger recombination lifetimes in the bulk are calculated to be 1.6×10^5 and 3.4×10^3 μs using the approaches by Dziewior *et al.*[9] and Kerr *et al.*[46], respectively. The Shockley-Read-Hall lifetime is calculated to be 103 μs. The corresponding electron diffusion lengths are calculated to range from 453 to 2×10^4 μm. As the Shockley-Read-Hall recombination mechanism is dominant in the relatively lightly doped Si bulk wafer of the solar cell[47], the lifetime calculated from this mechanism agrees well with ~100 μs lifetimes reported[13,50]. The 453 μm diffusion length associated with Shockley-Read-Hall lifetime shown in Table 2 is consistent with the 100–1000 μm range reported in literature[13]. Overall, Auger and Shockley-Read-Hall recombination mechanisms are dominant in the emitter and bulk layers of the Si solar cells,

Approved for public release; distribution unlimited.
334

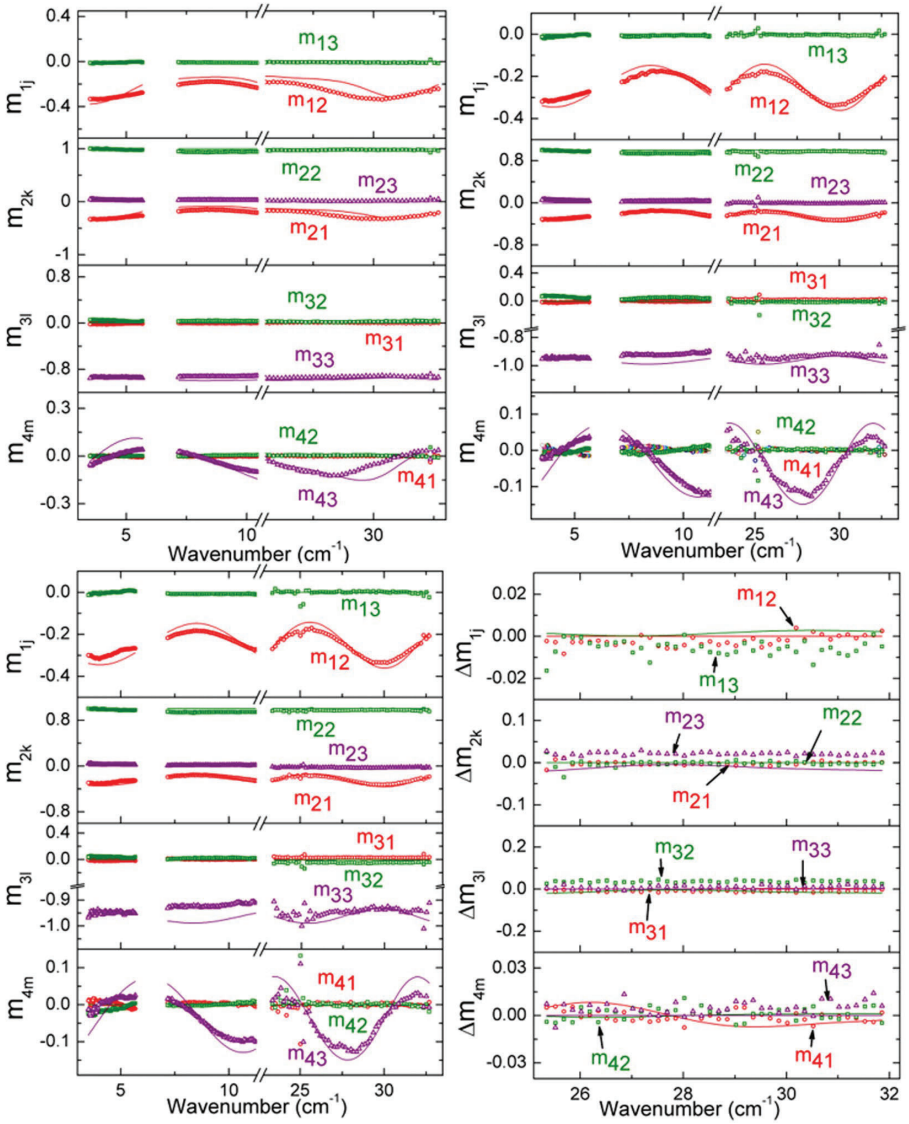


Figure 4. Experimental spectra (symbols) measured at 0 T (top-left), +1.48 T (top-right), and −1.48 T (bottom-left) and difference spectra measured at ±1.48 T (bottom-right) with their corresponding calculated models (solid lines) of the normalized Mueller matrix elements m_{12}, m_{13}, m_{21}, m_{22}, m_{23}, m_{31}, m_{32}, m_{33}, m_{41}, m_{42}, and m_{43} for the Al-BSF Si wafer solar cell at 50° angle of incidence under 1 sun illumination (AM1.5 solar irradiance spectrum). The unweighted error function for this fit is $\sigma = 4.29 \times 10^{-2}$.

respectively, and hence the lifetimes and diffusion lengths calculated from these mechanisms are found to be the most consistent with other reported lifetimes.

PV Device performance parameters. The transport properties of the Si emitter and bulk wafer components of the solar cell directly impact PV device performance parameters. For an ideal diode, the dark current density[51] is:

$$J_{dark}(V) = J_o(e^{qV/kT} - 1), \tag{3}$$

where, $J_o = qn_i^2\ [D_n/L_nN_A + D_p/L_pN_D] = 1.1 \times 10^{-9}$ mAcm^{-2}, q is electron charge, $T = 300$ K here, and $n_i = 1.08 \times 10^{10}$ cm^{-3} is intrinsic carrier concentration[52,53]. D_n and D_p are diffusivities of the electron and hole

Approved for public release; distribution unlimited.
335

Layers	Mechanism	Model	Lifetime (μs)	Diffusion length (μm)
Phosphorus-doped n-type Si emitter layer	Radiative	Schlangenotto *et al.*[42]	26	144
		Trupke *et al.*[43]	56	212
		Nguyen *et al.*[44]	67	231
	Auger	Dziewior *et al.*[9]	0.3	15
		Kerr *et al.*[46]	0.2	13
	Shockley-Read-Hall	Shockley *et al.*[47]	102	286
Boron-doped p-type Si wafer	Radiative	Schlangenotto *et al.*[42]	1.2×10^4	5×10^3
		Trupke *et al.*[43]	2.6×10^4	7×10^3
		Nguyen *et al.*[44]	3.2×10^4	8×10^3
	Auger	Dziewior *et al.*[9]	1.6×10^5	2×10^4
		Kerr *et al.*[46]	3.4×10^3	3×10^3
	Shockley-Read-Hall	Shockley *et al.*[47]	103	453

Table 2. Minority carrier lifetime and diffusion length for phosphorus-doped n-type Si emitter and boron-doped p-type Si wafer in the Al-BSF solar cell assuming diffrent recombination mechanisms and models.

minority carriers, L_n and L_p are the minority carrier electron and hole diffusion lengths, and N_A and N_D are acceptor and donor concentrations, respectively. Under illumination, the net current density[51] is:

$$J = J_{sc} - J_{dark}(V) \tag{4}$$

where J_{sc} is short circuit current density. The dark photocurrent density (J_{dark}) is negligible compared to J_{sc} under 1 sun illumination. J_{sc} is measured to be 37.0 ± 0.3 mAcm^{-2} for the solar cell of Fig. 1. The calculated $V_{oc} = kT/q \ln(J_{sc}/J_o + 1)$ using measured J_{sc} is 0.626 V. The normalized open circuit voltage v_{oc} [$v_{oc} = V_{oc}/(kT/q)$] is 24.3. The idealized fill factor [$FF = \{v_{oc} - \ln(v_{oc} + 0.72)\}/(v_{oc} + 1)$] is calculated to be 0.833. Resultant simulated PV device efficiency ($\eta = V_{oc}J_{sc}FF/100$ mWcm^{-2}) is 19.2%. These V_{oc}, FF, and η values calculated from the transport properties obtained from optical Hall effect using measured J_{sc} are in good agreement with other measured device performance parameters $V_{oc} = 0.627 \pm 0.001$ V, $FF = 0.80 \pm 0.02$, and $\eta = 18.5 \pm 0.1$%. Thus, simulated V_{oc} based upon input from this study is within error of the measured value. The calculation of $FF = 0.833$ assumes infinite shunt resistance and negligible series resistance and is considered as an idealized limit, with the measured FF observed to be lower at 0.80. From J-V measurements, series and shunt resistances of the solar cell are determined to be 0.62 and 5.5×10^4 Ω cm^2, respectively. Using the approach described by Mette *et al.*[54], the FF accounting for series resistance is calculated to be 0.80. As the shunt resistance is very high, measured V_{oc} and J_{sc} do not substantially deviate from idealized simulations[55], indicating that the series resistance contribution of 0.62 Ω cm^2 is the likely cause of the reduction in expected FF from 0.833 to 0.80[54,56]. After accounting for the reduction in FF due to series resistance, the resultant calculated efficiency is 18.4%, which matches the measured efficiency.

More detailed simulations of solar cell performance are performed using PC1D[57]. Using PC1D, electron and hole transport equations are solved for carriers in the complete Si solar cell described in Fig. 1 to determine J-V characteristics. Input parameters include those derived from optical Hall effect measurements reported in Tables 1 and 2 when applicable with all input parameters provided in the Supplementary Information. In PC1D the carrier concentration profile of the n-type emitter is manipulated to account for non-uniform carrier concentration with depth. Doping carrier concentrations simulated include a uniform distribution represented by the average carrier concentration reported in Table 1, an exponential profile, a Gaussian profile, and a Gauss error function profile. For the last three, all profiles are defined by the maximum n-type carrier concentration in the layer, which is constrained by the shape of the profile so that numerical integration for determining the average carrier concentration corresponds to that reported in Table 1. The surface recombination velocity (S_p) at the doped n-type front emitter is determined to be of $S_p = 2.5 \times 10^4$ cm/s in order to best match the experimental J-V characteristics, as reported in Supplemental Information Table S1. All other parameters are constrained to values reported in literature. PC1D simulation results incorporating uniform and Gauss error function carrier concentration profiles in the n-type emitter most closely match experimental values with simulated $V_{oc} = 0.621$ and 0.625 V, $J_{SC} = 37.3$ and 37.2 mA/cm^2, $FF = 0.799$ and 0.800, and resulting $\eta = 18.5$ and 18.6%, for uniform distribution and Gauss error function profiles, respectively. Although both simulation results match experimental values, the carrier concentration profile is unlikely to be completely uniform. Based on the similarity of the results from these two simulations, it is possible that the simulated n-type emitter carrier concentration profile is more complicated than either a uniform distribution or Gauss error function profile individually, although the precise profile is not known for this commercial Al-BSF Si wafer solar cell. Average majority and minority carrier concentrations in the n-type emitter and p-type bulk wafer are obtained from the simplified model consisting of discrete layers of uniform carrier concentration used in analysis of optical Hall effect measurements. The agreement between the PC1D simulated and experimental J-V characteristics supports the average carrier concentration values obtained from the optical Hall effect characterization of this device. These optical Hall effect input parameters may serve as further constraints in determining solar cell characteristics via device modeling.

An evaluation of all these results leads to the conclusion that a combined analysis of optical Hall effect measurements collected under dark and illuminated conditions is sensitive to majority carrier transport properties from impurity doping and minority carrier transport properties from carrier photogeneration under 1 sun

Approved for public release; distribution unlimited.
336

illumination. In particular, N, μ, and m^* are obtained for both the phosphorus doped n-type Si emitter and the boron doped p-type Si bulk of an Al-BSF solar cell from dark measurements. Based on information gained from analysis of the dark measurements, minority carrier transport parameters in both the n- and p-type Si components of the Al-BSF solar cell are deduced from analysis of measurements collected under 1 sun illumination. Consistency between calculated device performance parameters using transport properties via optical Hall effect and measured values demonstrates the reliability of this novel technique for transport properties measurement even in a complicated structure such as an Al-BSF Si solar cell.

Conclusion

As optical Hall effect measurements are non-contacting and sensitive to the optical response of multiple layers in a sample stack, it has the potential to determine transport parameters of the individual layers in multilayer PV device structures, which may be inaccessible by direct measurements such as the electrical Hall effect. Majority and minority carrier transport properties of Si active layers within an Al-BSF solar cell are deduced from the optical Hall effect measurements performed under nominally dark conditions and under 1 sun illumination. The minority carrier transport parameters, Δp or Δn and μ_h or μ_e, as well as the majority carrier transport parameters N, μ, and m^*, are determined for the phosphorus doped n-type Si emitter and boron doped p-type Si wafer in an Al-BSF configuration solar cell with pyramidal front surface texturing, a relatively common commercially produced device structure. The majority carrier transport properties extracted here agree well with those reported in the literature. Minority carrier mobilities and concentrations of the active layers of the cell are also within expectations. The calculated minority carrier effective lifetime and diffusion length from Δp or Δn and N for each layer also show good agreement with reported values for similar dopant densities, which demonstrate the validity of this technique for determination of minority carrier transport properties. Calculated PV device performance parameters from measured transport properties via optical Hall effect agree well with directly measured values, further validating this method for reliably obtaining majority and minority carrier transport properties. Using this non-contacting optical technique both majority and minority carrier transport properties are measured within a complete solar cell, providing a pathway to improved understanding of fundamental electrical properties of materials when integrated into opto-electronic devices.

Index terms. Minority carriers, Optical Hall effect, Transport parameters, Al-BSF Si wafer solar cell, THz ellipsometry.

Received: 5 August 2019; Accepted: 22 November 2019;
Published online: 12 December 2019

References

1. Ning, T. H. & Issac, R. D. Effect of emitter contact on current gain of silicon bipolar devices. *IEEE Transactions on Electron Devices, vol. ED-* **27**, 2051–2055 (1980).
2. Mertens, R. P., Deman, H. J. & Overstraeten, R. J. V. Calculation of the emitter efficiency of bipolar transistors. *IEEE Transactions on Electron Devices, vol. ED-* **20**, 772–778 (1973).
3. Lindholm, F. A. & Sah, C. T. Fundamental electronic mechanisms limiting the performance of solar cells. *IEEE Transactions on Electron Devices, vol. ED-* **24**, 299–304 (1977).
4. Hauser, J. R. & Dunbar, P. M. Performance limitations of silicon solar cells. *IEEE Transactions on Electron Devices, vol. ED-* **24**, 305–321 (1977).
5. Swirhun, S. E., Kwark, Y.-H. & Swanson, R. M. Measurement of electron lifetime, electron mobility and band-gap narrowing in heavily doped p-type silicon. *International Electron Devices Meeting, vol. IEDM* **86**, 24–27 (1986).
6. Sproul, A. B., Green, M. A. & Stephens, A. W. Accurate determination of minority carrier- and lattice scattering-mobility in silicon from photoconductance decay. *J. Appl. Phys.* **72**, 4161–4171 (1992).
7. Neuhaus, D. H. *et al*. Method for measuring minority and majority carrier mobilities in solar cells, Proceeding of 17th European Photovoltaic Solar Energy Conference, pp. 242–245, (2001).
8. Jean, J., Brown, P. R., Jaffe, R. L., Buonassisi, T. & Bulovic, V. Pathways for solar photovoltaics. *Energy Environ. Sci.* **8**, 1200–1219 (2015).
9. Dziewior, J. & Silber, D. Minority-carrier diffusion coefficients in highly doped silicon. *Appl. Phys. Lett.* **35**, 170 (1979).
10. Swirhun, S. E., Alamo, J. A. & Swanson, R. M. Measurement of hole mobility in heavily doped n-type silicon. *IEEE Electron Device Letters, vol. EDL-* **7**, 168–171 (1986).
11. Alamo, J. A. D. & Swanson, R. M. Measurement of steady-state minority-carrier transport parameters in heavily doped n-type silicon. *IEEE Transactions on Electron Devices, vol. ED-* **34**, 1580–1589 (1987).
12. Wang, C. H. & Neugroschel, A. Minority-carrier transport parameters in degenerate n-type silicon. *IEEE Electron Device Letters* **11**, 576–578 (1990).
13. Law, M. E., Solley, E., Liang, M. & Burk, D. E. Self-consistent model of minority-carrier lifetime, diffusion length, and mobility. *IEEE Electron Device Letters* **12**, 401–403 (1991).
14. Sproul, A. B. & Green, M. A. Intrinsic carrier concentration and minority mobility of silicon from 77 to 300 K. *J. Appl. Phys.* **73**, 1214–1225 (1993).
15. Ahrenkiel, R. K. & Johnston, S. W. An advanced technique for measuring minority-carrier parameters and defect properties of semiconductors. *Materials Science and Engineering B* **102**, 161–172 (2003).
16. Rougieux, F. E. *et al.* A contactless method for determining the carrier mobility sum in silicon wafers. *IEEE J. Photovoltaics* **2**, 41–46 (2012).
17. Hofmann, T., Herzinger, C. M., Krahmer, C., Streubel, K. & Schubert, M. The optical Hall effect. *Phys. Status Solidi A* **205**, 779–783 (2008).
18. Hofmann, T., Schade, U., Herzinger, C. M., Esquinazi, P. & Schubert, M. Terahertz magneto-optic generalized ellipsometry using synchrotron and blackbody radiation. *Rev. Sci. Instrum* **77**, 063902 (2006).
19. Knight, S. *et al*. Cavity-enhanced optical Hall effect in two-dimensional free charge carrier gases detected at terahertz frequencies. *Opt. Lett*. **40**, 2688–2691 (2015).
20. Knight, S. *et al*. *In-situ* terahertz optical Hall effect measurements of ambient effects on free carrier properties of epitaxial graphene. *Sci. Rep.* **7**, 1–8 (2017).

Approved for public release; distribution unlimited.

21. Kühne, P., Hofmann, T., Herzinger, C. M. & Schubert, M. Terahertz optical-Hall effect for multiple valley band materials: n-type silicon. *Thin Solid Films* **519**, 2613–2616 (2011).
22. Schubert, M., Hofmann, T. & Herzinger, C. M. Generalized far-infrared magneto-optic ellipsometry for semiconductor layer structures: determination of free carrier effective-mass, mobility, and concentration parameters in *n*-type GaAs. *J. Opt. Soc. Am. A* **20**, 347–356 (2003).
23. Schubert, M., Kühne, P., Darakchieva, V. & Hofmann, T. Optical Hall effect—model description: tutorial. *J. Opt. Soc. Am. A* **33**, 1553–1568 (2016).
24. Hofmann, T. *et al*. THz dielectric anisotropy of metal slanted columnar thin films. *Appl. Phys. Lett.* **99**, 081903 (2011).
25. Uprety, P. *et al*. Spectroscopic ellipsometry determination of optical and electrical properties of aluminum doped zinc oxide. *Appl. Surf. Sci.* **421**, 852–858 (2017).
26. Uprety, P. *et al*. Morphological and optical properties of low temperature processed SnO_2:F. *Phys. Status Solidi B*, **254**, 1700102 (2017).
27. Uprety, P. *et al*. Optical and electrical properties of H_2 plasma-treated ZnO films prepared by atomic layer deposition using supercycles. *Mater. Sci. Semicond. Process.* **84**, 91–100 (2018).
28. Uprety, P., Junda, M. M., Salmon, H. & Podraza, N. J. Understanding near infrared absorption in tin doped indium oxide thin films. *J. Phys. D: Appl. Phys.* **51**, 295302 (2018).
29. Uprety, P. *et al*. Electrical transport properties from long wavelength ellipsometry, in Proc. 44th IEEE Photovoltaic Specialist Conference, pp. 3468–3472 (2017).
30. Uprety, P. *et al*. Optical Hall effect of PV device materials. *IEEE J. Photovoltaics* **8**, 1793–1799 (2018).
31. Neuhaus, D. H. & Münzer, A. Industrial silicon wafer solar cells. *Adv. Optoelectron.* **2007**, 1–15 (2007).
32. Solanki, C. S. & Singh, H. K. *Anti-reflection and Light Trapping in c-Si Solar Cells*, Springer Nature, Singapore, 17–42, (2017).
33. Hofmann, T. *et al*. Variable-wavelength frequency-domain terahertz ellipsometry. *Rev. Sci. Instrum.* **81**, 023101 (2010).
34. Tiwald, T. E., Thompson, D. W., Woollam, J. A., Paulson, W. & Hance, R. Application of IR variable angle spectroscopic ellipsometry to the determination of free carrier concentration depth profiles. *Thin Solid Films* **313**, 661–666 (1998).
35. Hofmann, T., Herzinger, C. M., Tiwald, T. E., Woollam, J. A. & Schubert, M. Hole diffusion profile in a p-p+ silicon homojunction determined by terahertz and midinfrared spectroscopic ellipsometry. *Applied Physics Letters* **95**(3), 032102 (2009).
36. Johs, B. & Herzinger, C. M. Quantifying the accuracy of ellipsometer system. *Phys. Stat. Sol. (c)* **5**, 1031–1035 (2008).
37. Subedi, I., Silverman, T. J., Deceglie, M. G. & Podraza, N. J. Al+Si interface optical properties obtained in the Si solar cell configuration. *Phys. Status Solidi A* **214**, 1700480 (2017).
38. Robinson, S. J. *et al*. Recombination rate saturation mechanisms at oxidized surfaces of high-efficiency silicon solar cells. *J. Appl. Phys.* **78**, 4740–4754 (1995).
39. Thurber, W. R., Mattis, R. L., Liu, Y. M. & Filliben, J. J. The relationship between resistivity and dopant density for phosphorus- and boron-doped silicon, NBS *Department of Commerce, US Government Printing Office*, pp. 1–60 (1981).
40. Riffe, D. M. Temperature dependence of silicon carrier effective masses with application to femtosecond reflectivity measurements. *J. Opt. Soc. Am. B* **19**, 1092–1100 (2002).
41. Dexter, R. N. & Lax, B. Effective masses of holes in silicon. *Phys. Rev.* **96**, 223–224 (1954).
42. Schlangenotto, H., Maeder, H. & Gerlanch, W. Temperature dependence of the radiative recombination coefficient in silicon. *Phys. Stat. Sol. A* **21**, 357–367 (1974).
43. Trupke, T. *et al*. Temperature dependence of the radiative recombination coefficient of intrinsic crystalline silicon. *J. Appl. Phys.* **94**, 4930–4937 (2003).
44. Nguyen, H. T., Baker-Finch, S. C. & Macdonald, D. Temperature dependence of the radiative recombination coefficient in crystalline silicon from spectral photoluminescence. *Appl. Phys. Lett.* **104**, 112105 (2014).
45. Sinton, R. A. & Swanson, R. M. Recombination in highly injected silicon. *IEEE Trans. Electron Devices, vol. ED-* **34**, 1380–1389 (1987).
46. Kerr, M. J. & Cuevas, A. General parameterization of Auger recombination in crystalline silicon. *J. Appl. Phys.* **91**, 2473–2480 (2002).
47. Shockley, W. & Read, W. T. Statistics of the recombination of holes and electrons. *Phys. Rev.* **87**, 835–841 (1952).
48. Gatz, S. *et al*. 19.4% efficient large area fully screen printed silicon solar cells. *Physica Status Solidi (RRL)-Rapid Research Letters* **5**(no. 4), 147–149 (2011).
49. Alamo, J. A. D. & Swanson, R. M. Modeling of minority-carrier transport in heavily doped silicon emitters. *Solid-State Electron.* **30**, 1127–1136 (1987).
50. Tyagi, M. S. & Overstraeten, R. V. Minority carrier recombination in heavily-doped silicon. *Solid-State Electron.* **26**, 577–597 (1983).
51. Nelson, J. *The Physics of Solar Cells*, Imperial College Press, UK, London, 2002, pp.1–16.
52. Green, M. A. Intrinsic concentration, effective densities of states and effective mass in silicon. *J. Appl. Phys.* **67**, 2944–2954 (1990).
53. Sproul, A. B. & Green, M. A. Improved value of silicon intrinsic carrier concentration from 77 to 300 K. *J. Appl. Phys.* **70**, 846–854 (1991).
54. Mette, A. *et al*. Series resistance characterization of industrial silicon solar cells with screen-printed contacts using hotmelt paste. *Prog. Photovolt. Res. Appl.* **15**, 493–505 (2007).
55. Green, M. A. Solar cell fill factors: general graph and empirical expressions. *Solid-State Electronics* **24**, 788–789 (1981).
56. Zhang, J., Lee, S.-T. & Sun, B. Effect of series and shunt resistance on organic-inorganic hybrid solar cell performance. *Electrochimica Acta* **146**, 845–849 (2014).
57. Clugston, D. & Basore, P. A. PC1D version 5: 32-bit solar cell modeling on personal computers. In *Conference Record of the Twenty Sixth IEEE Photovoltaic Specialists Conference-1997*, pp. 207–210. IEEE, (1997).

Acknowledgements

The authors gratefully acknowledge funding support from University of Toledo start-up funds, Ohio Department of Development (ODOD) Ohio Research Scholar Program (Northwest Ohio Innovators in Thin Films Photovoltaics, Grant No. TECH 09-025), Air Force Laboratory Space Vehicles Directorate (Contract Nos. FA9453-11-C-0253 and FA9453-18-2-0037), and National Science Foundation (NSF) Major Research Instrumentation Program (NSF-MRI Grant. No. 1228917). This material is based on research sponsored by Air Force Research Laboratory under agreement numbers FA9453-11-C-0253 and FA9453-18-2-0037. The U.S. Government is authorized to reproduce and distribute reprints for governmental purposes notwithstanding any copyright notation thereon. The views and conclusions contained herein are those of the authors and should not be interpreted as necessarily representing the official policies or endorsements, either expressed or implied, of Air Force Research Laboratory or the U.S. Government. The authors would like to thank Prof. Tino Hofmann, University of North Carolina-Charlotte, for providing detailed discussions and a sample optical Hall effect analysis.

Approved for public release; distribution unlimited.

338

Author contributions

P.U. and N.J.P. designed the research. P.U. performed the experiments and analyzed data. I.S. performed optical and electrical solar cell simulations. P.U. and M.M.J. contributed to the terahertz ellipsometer setup and calibration. N.J.P. and R.W.C. contributed as a principal advisor and co-advisor of the project, respectively. The manuscript is written through the contributions from all authors.

Competing interests

The authors declare no competing interests.

Additional information

Supplementary information is available for this paper at https://doi.org/10.1038/s41598-019-55173-z.

Correspondence and requests for materials should be addressed to N.J.P.

Reprints and permissions information is available at www.nature.com/reprints.

Publisher's note Springer Nature remains neutral with regard to jurisdictional claims in published maps and institutional affiliations.

Open Access This article is licensed under a Creative Commons Attribution 4.0 International License, which permits use, sharing, adaptation, distribution and reproduction in any medium or format, as long as you give appropriate credit to the original author(s) and the source, provide a link to the Creative Commons license, and indicate if changes were made. The images or other third party material in this article are included in the article's Creative Commons license, unless indicated otherwise in a credit line to the material. If material is not included in the article's Creative Commons license and your intended use is not permitted by statutory regulation or exceeds the permitted use, you will need to obtain permission directly from the copyright holder. To view a copy of this license, visit http://creativecommons.org/licenses/by/4.0/.

© The Author(s) 2019

Approved for public release; distribution unlimited.

339

THE JOURNAL OF PHYSICAL CHEMISTRY Letters

Letter

Cite This: J. Phys. Chem. Lett. 2020, 11, 121−128

pubs.acs.org/JPCL

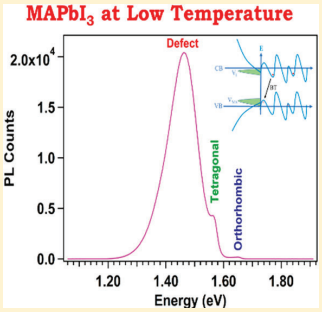
Charge Compensating Defects in Methylammonium Lead Iodide Perovskite Suppressed by Formamidinium Inclusion

Niraj Shrestha,[#] Zhaoning Song,[#] Cong Chen, Ebin Bastola, Xiaoming Wang, Yanfa Yan, and Randy J. Ellingson*

Department of Physics and Astronomy, Wright Center for Photovoltaics Innovation and Commercialization, University of Toledo, Toledo, Ohio 43606, United States

Supporting Information

ABSTRACT: Temperature-dependent photoluminescence (PL) spectroscopy measurements have been performed over a range from 9 K to room temperature on polycrystalline methylammonium (MA)/formamidinium (FA) lead iodide ($MA_{1-x}FA_xPbI_3$) perovskite thin films. Our low-temperature PL analysis reveals the existence of charge compensating defects in $MAPbI_3$, which may explain the lower net free carrier concentration in $MAPbI_3$ perovskite. More interestingly, we observe the suppression of the PL emission associated with the charged defects by appropriate FA inclusion. Furthermore, FA incorporation into $MAPbI_3$ has been found to slow the phase transformation of $MA_{1-x}FA_xPbI_3$ from orthorhombic to tetragonal phase, which occurs with increasing temperature. Our analyses of the FA concentration's impact on defect density and structural phase transformation provide beneficial insights that improve the understanding of the photovoltaic properties and application of organic−inorganic metal halide perovskites.



Downloaded via UNIV OF TOLEDO on September 13, 2021 at 15:54:43 (UTC).
See https://pubs.acs.org/sharingguidelines for options on how to legitimately share published articles.

Organic−inorganic metal halide perovskite materials offer great promise in photovoltaic (PV) applications due to their direct band gaps with large absorption coefficients,[1,2] long electron−hole diffusion lengths,[1,3] low exciton binding energies,[4] low-temperature solution processability,[5] and low fabrication costs.[6] Although small-sized solar cells based on metal halide perovskites have already reached a certified power conversion efficiency of 25.2%,[7] intrinsic and extrinsic material instability issues,[8−11] along with other commercialization challenges such as large-scale manufacturing,[12] unstabilized power output,[13] and toxicity and environmental concerns,[14] have thus far prevented perovskite solar cells from joining the more established commercial thin-film PV technologies, such as cadmium telluride (CdTe) and copper indium gallium diselenide (CIGS). Particularly, the lack of durability and inconsistent power generation are the most critical technical issues to be addressed before the full potential of perovskite PV technology can be fulfilled. With the rapid advances of perovskite PV technology, fundamental understanding of perovskite materials enables crucial insights in support of overcoming the remaining challenges.

Methylammonium lead iodide ($MAPbI_3$) with a band gap of ∼1.60 eV[15] is the prototypical perovskite light-absorbing material that was developed at the early stage and since then has been extensively studied as the benchmark absorber layer in single-junction perovskite solar cells. The advances in perovskite PV technology were enabled by incorporating formamidinium (FA) to the perovskite composition to make mixed cation $MA_{1-x}FA_xPbI_3$ perovskites, which extends the absorption edge to longer wavelengths and enhances the optoelectronic properties (e.g., carrier lifetime, diffusion length) of perovskites,[16] resulting in PCEs (>23%)[17] higher than the ∼21% seen for pure $MAPbI_3$.[18] Despite the enhanced device performance, the intrinsic structural and optoelectronic properties of $MA_{1-x}FA_xPbI_3$ (e.g., crystal phase transformation, nature of the defects) that govern device performance and stability have yet to be fully explored. Particularly, investigating the temperature-dependent crystal phase transformation and the optoelectronic properties of $MA_{1-x}FA_xPbI_3$ perovskite at low temperatures allows for the understanding of not only the fundamental semiconductor behaviors of $MA_{1-x}FA_xPbI_3$ perovskites but also the device physics of perovskite solar cells. Furthermore, exploring the optoelectronic properties of $MA_{1-x}FA_xPbI_3$ over a wide range of temperatures and particularly at low temperatures is of interest for their potential use in space power applications.

With these considerations, in situ photoluminescence (PL) spectroscopy has been employed to study the structural and optoelectronic properties and phase stability of $MAPbI_3$ perovskites.[19−21] Particularly for low-temperature PL measurements, Dar et al. have revealed the coexistence of both orthorhombic and tetragonal phases in $MAPbI_3$ utilizing low temperature PL,[22] whereas other reports correlated PL signals based on the first-order thermodynamic phase transition of $MAPbI_3$ that occurs at ∼160 K.[22,23] Phuyong et al. observed exciton and free carrier emissions in polycrystalline $MAPbI_3$

Received: November 1, 2019
Accepted: December 9, 2019
Published: December 10, 2019

ACS Publications © 2019 American Chemical Society

DOI: 10.1021/acs.jpclett.9b03234
J. Phys. Chem. Lett. 2020, 11, 121−128

Approved for public release; distribution unlimited.

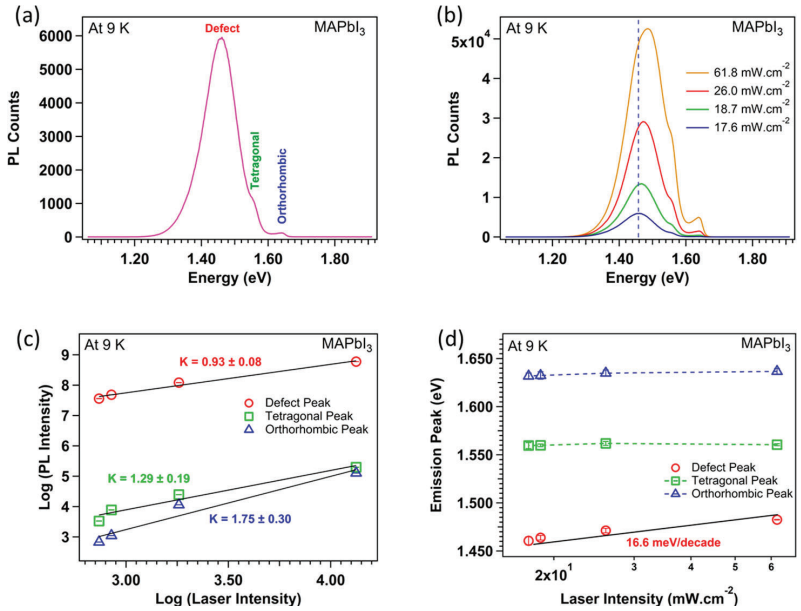


Figure 1. (a) PL spectrum of $MAPbI_3$ at 9 K (at 17.6 mW·cm^{-2}) and (b) PL spectra at various laser excitation intensities. (c) Integrated PL and (d) emission peak energy vs laser intensity for three PL peaks observed for $MAPbI_3$.

thin films at low temperatures.[24] Such photophysics in perovskites at various temperatures (and within the corresponding phases) contributes to the understanding of photoexcited charge carriers and may lead to improved stability and power conversion efficiency for $MAPbI_3$ and $MA_{1-x}FA_xPbI_3$ solar cells.

Low-temperature PL measurement can be used to investigate the defects presented in semiconductors. Intrinsic defects, such as lattice dislocations, grain boundaries (GBs), surface/interface, and point defects, may trap photoexcited charge carriers, leading to nonradiative recombination, reduced carrier lifetime, and inhibited solar cell performance. Yang et al. theoretically reported the presence of charge compensating iodine vacancy (V_I) donors and methylammonium vacancy (V_{MA}) acceptors in $MAPbI_3$.[25] An important consequence of charge compensating defects in $MAPbI_3$ is that the final free carrier concentration often ends up very low. Such challenges in controlling doping lead furthermore to near-intrinsic $MAPbI_3$ behavior. Therefore, identification of defects and their behaviors at various temperatures is essential to understand and control the intrinsic and extrinsic doping, which in turn play a significant role in transport and contact performance of the final PV devices.

Here, we report the properties of intrinsic defects in polycrystalline $MA_{1-x}FA_xPbI_3$ films discovered via temperature dependent PL spectroscopy from 9 to 290 K. Note that lead thiocyanate [$Pb(SCN)_2$] additive was incorporated into the perovskite films due to its beneficial impact on enlarged grain size and passivation of GBs and thus also to enhance the PCE of the resulting perovskite solar cells.[16,26] We observed PL peaks corresponding to orthorhombic and tetragonal phases of $MAPbI_3$ at 9 K. More interestingly, a band-tail related defect-assisted transition peak was observed in $MAPbI_3$, which was rarely reported previously in the literature. Furthermore, we showed that the substitution of MA by FA at the appropriate concentration within $MAPbI_3$ suppresses the formation of such defect states and slows the phase transformation.

Photoluminescence spectroscopy is one powerful technique to study defect related sub-band gap luminescence emission in semiconductors. Typically, temperature and laser excitation intensity dependent PL studies are combined to identify the nature of observed emission peaks in the spectrum. The variations in temperature and excitation intensity alter the thermal energy and the population of photogenerated charge carriers and thereby determine the charge carriers' propensity to occupy either long-lived radiative defect sites or short-lived nonradiative recombination sites. Figure 1 shows the results of laser excitation intensity dependent PL spectra of a $MAPbI_3$ film measured at 9 K. Figure 1a shows a typical PL spectrum containing three emission peaks at 1.46, 1.56, and 1.65 eV, respectively. In contrast to most reports in the literature with the most intense peaks at 1.55−1.65 eV,[20,21,27] our measurement shows that the PL emission of $MAPbI_3$ at low temperatures is dominated by low energy emission at 1.46 eV. To further investigate the nature of these observed emission bands, laser excitation intensity dependent PL spectra were acquired (Figure 1b). For a semiconductor material, integrated PL intensity (I_{PL}) typically follows a power law, $I_{PL} = I_{laser}^{k}$, where I_{laser} is laser intensity, and k is the exponent. For band-to-band (BB) and excitonic recombination, k falls in the range of 1 to 2, whereas for defect assisted transitions [e.g., free-to-bound (FB) and donor-to-acceptor (DAP) recombination], k is less than 1.[28−30] Through power fitting of laser intensity dependent PL data (Figure 1c), we obtained k = 0.93, 1.29, and 1.75 values for the peaks at 1.46, 1.56, and 1.65 eV, respectively, indicating that the 1.46 eV peak represents a defect assisted transition, whereas the 1.56 and 1.65 eV peaks correspond to excitonic emissions. The exciton peaks at 1.56 and 1.65 eV correspond to the tetragonal ($I4/mcm$) and orthorhombic ($Pnma$) phases of $MAPbI_3$, respectively. Note

DOI: 10.1021/acs.jpclett.9b03234
J. Phys. Chem. Lett. 2020, 11, 121−128

Approved for public release; distribution unlimited.
341

that the higher k value for the orthorhombic phase than the tetragonal phase shows stronger exciton characteristics in the orthorhombic phase, consistent with the reports that both exciton and free carrier features exist in low-temperature PL of $MAPbI_3$.[31] Additionally, the coexistence of orthorhombic and tetragonal phases in perovskites has been reported elsewhere.[20,32,33]

Figure 1d plots the variations in the peak locations as a function of laser excitation intensity. The peak locations of the two exciton emission bands remain constant with increasing laser intensity. In contrast, the defect peak at 1.46 eV blue-shifted with an increase in laser intensity at 16.6 meV/decade. Such a large blue-shift (aka, j-shift) is the characteristic of a band-tail (BT) related transition, which is widely present in copper chalcogenide semiconductors (e.g., $CuInSe_2$ and Cu_2ZnSnS_4) possessing a large number of charge compensating defect states.[34−36] In highly compensating semiconductors consisting of similar amounts of donor and acceptor defects, electrons from the donor sites recombine with holes localized at the acceptor sites, leading to the coexistence of positively charged donors and negatively charged acceptors at various locations. As a result, spatially distributed charged regions establish the fluctuating potential of the valence band and conduction band edges.[37] The potential fluctuations arising from such charged defect states form localized trap states within the band gap, resulting in the large j-shift.[36] At high laser excitation intensity, the increased concentration of free carriers effectively screens the electrostatic potential of the charged defects. This charge screening effect results in flattening of the potential fluctuation causing a blue shift of the defect peak.[37,38] Figure 2a represents the schematic of the

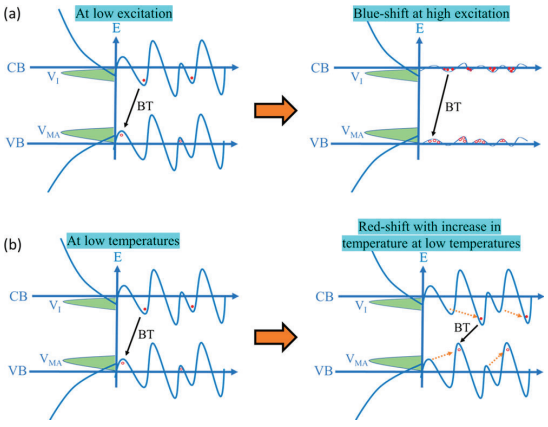


Figure 2. Schematic illustration of band fluctuation in $MAPbI_3$. (a) Flattening of band-tail at high laser excitation intensity causing blue-shift of band-tail related defect peak in $MAPbI_3$. (b) Carriers occupying lower energy states at the band-tail states with an increase in thermal energy at low temperatures causing red-shift of band-tail related defect peak in $MAPbI_3$.

flattening of the band-tail arising from high laser excitation intensity. Despite rarely being reported for low-temperature PL measurements, the existence of compensating V_I donors and V_{MA} acceptors in $MAPbI_3$ has been reported by previous researchers.[25,39] Due to the high vapor pressures of its decomposition products, $MAPbI_3$ is prone to loss of MA and I components in the forms of methylamine and hydrogen iodide gases,[40] resulting in the formation of compensating V_I and V_{MA} defects during the preparation and transfer of the sample. It is also worth noting that intense light emission can lead to the photoinduced decomposition of $MAPbI_3$.[41] Particularly for polycrystalline $MAPbI_3$ thin films, these defects are likely to form at the surface and GBs. As a consequence, these charge-compensating donor and acceptor defects in $MAPbI_3$ limit the carrier concentration and thus lead to the intrinsic resistive nature of $MAPbI_3$. Note that in this study $Pb(SCN)_2$ additive was incorporated into the $MAPbI_3$ film, resulting in large grain size and better crystallinity (Figures S1 and S2). The PL emission of the $MAPbI_3$ film with $Pb(SCN)_2$ is more pronounced than that of the film without $Pb(SCN)_2$, as shown in Figure S3, likely due to enhanced crystallinity and reduced nonradiative recombination.

The PL emission features of $MAPbI_3$ were further investigated via temperature dependent PL. Figure 3a,b, respectively, show the temperature dependent PL spectra of $MAPbI_3$ and the corresponding peak shift as a function of temperature. The defect peak (1.46 eV at 9 K) red-shifted between 9 and 80 K and then blue-shifted above 80 K before disappearing near 130 K. The red-shift of a PL peak followed by the blue-shift at low temperatures with an increase in thermal energy is typically observed in semiconductors with charge compensating defects,[36,38,42] which further confirms that the 1.46 eV defect emission is the consequence of a BT transition. The red-shift is related to the thermal energy of localized charge carriers. At low temperatures, an increase in thermal energy associated with the rising sample temperature allows the localized charge carriers to overcome local potential barriers and move to the nearby lower-potential sites (Figure 2b). As a result of charge redistribution to lower energy states, the quasi-Fermi levels move toward the center of the band gap, lowering the peak energy of the BT band.[37] The nature of the blue-shift evident for $T > 80$ K is attributed to thermal activation of defect-bound holes back to the valence band.[36] The defect peak disappeared when the temperature was above 130 K due to the trap filling of the BT states by thermalized charge carriers, indicating that the density of defect states in the BT is low, which may be a reason that the defect PL emission has rarely been reported in the literature.

The PL emission peak (1.65 eV at 9 K) arising from the orthorhombically structured domains showed a blue shift with increasing temperature, in opposition to the well-known Varshni relation in which the band gap of a typical semiconductor exhibits a red shift with increasing temperature.[43] The origin of the abnormal band gap shift with respect to temperature is likely related to the spin−orbit coupling enhanced electron−phonon interaction.[44,45] The orthorhombic peak disappeared at ∼150 K, indicating a full conversion to the tetragonal phase. In contrast, the tetragonal peak (1.56 eV at 9 K) first blue-shifted until 100 K and then red-shifted up to 160 K. It has been noted here that above 150 K, there evolves only one emission peak representing tetragonal phase of $MAPbI_3$, which confirms that the first order phase transition in $MAPbI_3$ occurs at ∼150 K. This phase transition has been observed and attributed to the dynamic order−disorder arrangement of MA cations and the inorganic PbI_6 octahedral framework.[9] Figure 3b shows the evolution of two different phases as well as the first order phase transition temperature (∼150 K) in $MAPbI_3$ perovskite.

To gain further insight into the observed defect peak, we obtained PL dynamics utilizing time-resolved PL. Photoexcited

DOI: 10.1021/acs.jpclett.9b03234
J. Phys. Chem. Lett. 2020, 11, 121−128

Approved for public release; distribution unlimited.

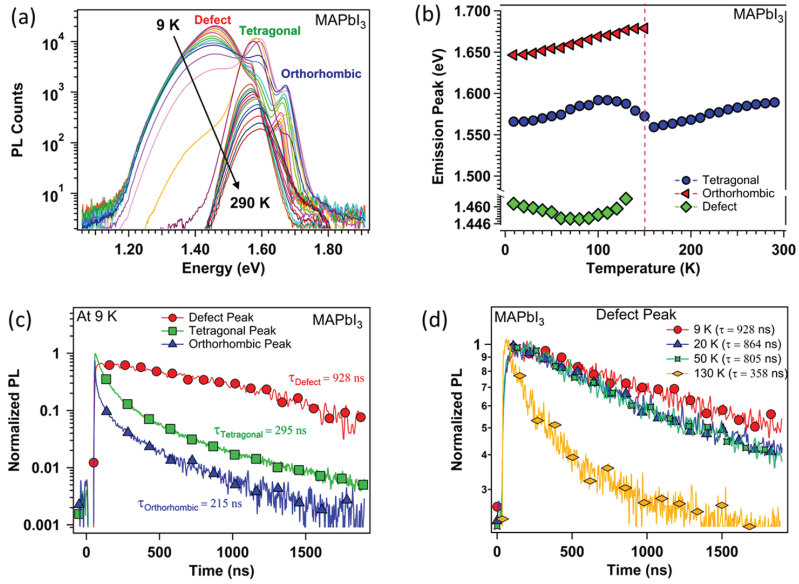


Figure 3. (a) Evolution of PL spectra and (b) different phases of $MAPbI_3$ revealed by temperature dependent PL. (c) PL decays of $MAPbI_3$ corresponding to different peaks at 9 K. (d) PL dynamics of $MAPbI_3$ at the defect site as a function of temperature.

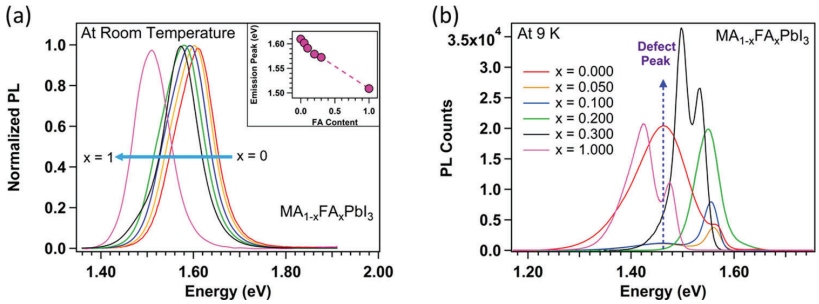


Figure 4. PL spectra of $MA_{1-x}FA_xPbI_3$ as a function of FA concentration acquired at (a) room temperature and (b) 9K.

carriers are found to be long-lived at defect sites with a mean carrier lifetime of ~928 ns compared to the excitons (mean lifetimes of 215 and 295 ns, respectively, for orthorhombic and tetragonal peaks), as depicted in Figure 3c. The increased carrier lifetime at defect sites can be attributed to the localization of carriers at band-tails before recombination.[46] However, the band-tail recombination lifetime decreases with increasing temperature due to the delocalization of carriers at band-tails driven by higher thermal energy, as depicted in Figure 3d. Furthermore, we found that the exciton lifetime (215 to 295 ns) at 9 K is significantly shorter than that (470 ns) we reported previously for $MAPbI_3$ at room temperature.[16] The reduced nonadiabatic electron−phonon coupling and shortened decoherence time are the reason behind longer carrier lifetime of $MAPbI_3$ at a high temperature compared to that at a low temperature.[47]

To explore the influence of the organic cation composition on the observed defect peak in $MAPbI_3$, we have carried out PL measurements of mixed cation $MA_{1-x}FA_xPbI_3$ at room temperature and 9 K for x ranging from 0 to 1. It is known that FA incorporation into $MAPbI_3$ narrows its band gap and increases carrier lifetimes, thereby resulting in enhanced performance of $MA_{1-x}FA_xPbI_3$ solar cells.[16] The defect analysis of $MA_{1-x}FA_xPbI_3$ perovskite film is crucial to understanding the origins of the improved optoelectronic properties. PL spectra taken at room temperature (Figure 4a) show the band gap dependence on FA concentration. Increasing FA content (x) from 0 to 1 leads to a decrease in band gap from 1.61 to 1.51 eV, as shown in the inset of Figure 4a.

Interestingly, PL spectra acquired at 9 K (Figure 4b) show that the PL intensity of defect emission (~1.46 eV) is greatly quenched with the incorporation of even a small amount (5%) of FA, and that the defect emission vanishes for $x \geq 0.2$. The suppression of intrinsic defects in organic−inorganic metal halide perovskite using mixed cations has also been reported by Liu and Yam.[48] One possible reason for the gradual diminishing and disappearance of the band-tail related defect peak could be the reduction of the V_{MA} vacancies by FA inclusion. Detailed investigations are ongoing.

For further confirmation, observed peaks in $MA_{1-x}FA_xPbI_3$ for $x = 0.2$ and $x = 0.3$ were carefully studied by applying laser intensity dependent PL measurement at 15 K, as shown in

DOI: 10.1021/acs.jpclett.9b03234
J. Phys. Chem. Lett. 2020, 11, 121−128

Approved for public release; distribution unlimited.
343

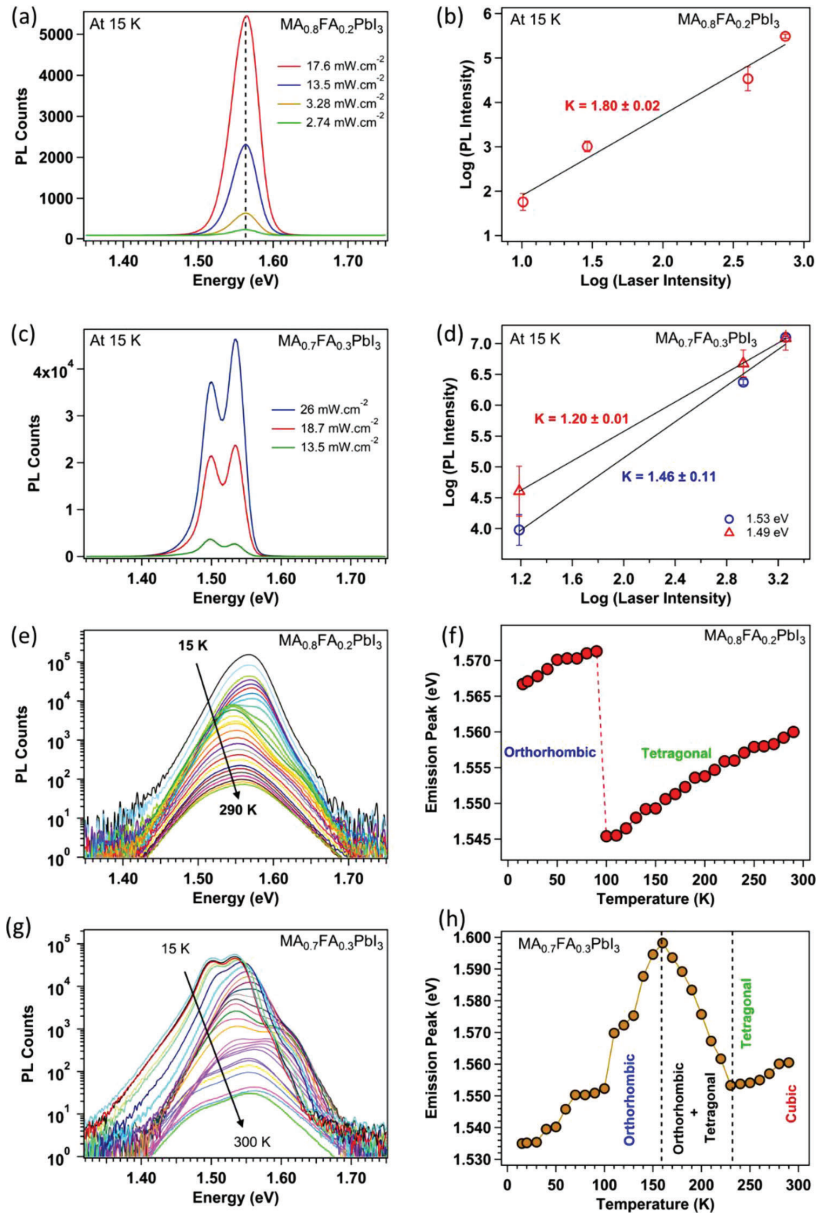


Figure 5. (a) PL spectra of $MA_{0.8}FA_{0.2}PbI_3$ at various laser intensities and (b) PL intensity vs laser intensity. (c) PL spectra of $MA_{0.7}FA_{0.3}PbI_3$ at various laser intensities and (d) PL intensity vs laser intensity. (e) Evolution of PL spectra and (f) different phases of $MA_{0.8}FA_{0.2}PbI_3$ revealed by temperature dependent PL. (g) Evolution of PL spectra and (h) different phases of $MA_{0.7}FA_{0.3}PbI_3$ revealed by temperature dependent PL.

Figure 5a,c. Interestingly, $MA_{0.2}FA_{0.8}PbI_3$ shows a single peak located at ~1.56 eV, whereas $MA_{0.3}FA_{0.7}PbI_3$ shows dual-peak emission at 1.49 and 1.53 eV. All these peaks show $k > 1$ for the emission−excitation intensity relationship, as shown in Figure 5b,d, indicating exciton behaviors. The origin of the distinct dual-peak emission in $MA_{0.3}FA_{0.7}PbI_3$ is still unclear. It may originate from the nanodomains of different phases[49] or interactions between excitons and phonons[50] or polarons.[51] Similar behaviors were observed in the laser intensity and temperature dependent PL results of pristine $FAPbI_3$ ($x = 1.0$) (Figures S4 and S5). Since no defect peak was observed in $MA_{1-x}FA_xPbI_3$ for $x \geq 0.2$, here we confirm that mixing an appropriate amount of FA in $MAPbI_3$ can suppress the formation of charged defect states in $MAPbI_3$.

Furthermore, we have studied the impact of FA inclusion on the crystal phase of $MA_{1-x}FA_xPbI_3$ via temperature dependent PL (Figure 5e,g). Like $MAPbI_3$, orthorhombic to tetragonal phase transformation is first order (Type-I) in the case of

DOI: 10.1021/acs.jpclett.9b03234
J. Phys. Chem. Lett. 2020, 11, 121−128

Approved for public release; distribution unlimited.

$MA_{0.8}FA_{0.2}PbI_3$, while further increase in the FA concentration to $x = 0.3$ was found to slow down the phase transformation, resulting in a Type-II transition as shown in Figure 5f,h. Since the geometry and symmetry of FA^+ are more flexible than those of MA^+, the addition of FA into $MAPbI_3$ lowers the lattice distortions, particularly at low temperatures.[52,53] Such a reduced lattice distortion may be attributed to type-II phase transition in $MA_{0.7}FA_{0.3}PbI_3$.

In summary, low temperature PL analysis has been performed on polycrystalline $MA_{1-x}FA_xPbI_3$ films. Our analysis reveals the existence of charge compensating defects in $MAPbI_3$ at low temperatures, which may describe the intrinsic nature of $MAPbI_3$ perovskite. More interestingly, we observe that FA inclusion results in the suppression of charged defect PL emission. Additionally, incorporation of FA into $MAPbI_3$ slows down the phase transformation (orthorhombic to tetragonal). The detailed defect analysis and phase transformation information revealed by our PL and TRPL studies may be beneficial in improving the optoelectronic properties of organo-metal halide perovskites and the performance of their PV devices.

EXPERIMENTAL DETAILS

Perovskite Precursor Solution Preparation. The $MAPbI_3$ perovskite precursor solution was prepared by dissolving 1.43 M equimolar lead iodide (PbI_2, Alfa Aesar, 99.9985%) and methylammonium iodide (MAI, Greatcell Solar) in *N*,*N*-dimethylformamide (DMF) and dimethyl sulfoxide (DMSO) (volume ratio = 9:1). A small amount (3% molar ratio to PbI_2) of lead thiocyanate [$Pb(SCN)_2$, Sigma-Aldrich, 99.5%] was added into the precursor solution as an additive.[54] The $FAPbI_3$ precursor solution was prepared by dissolving 1.43 M equimolar PbI_2 (Alfa Aesar, 99.9985%) and formamidinium iodide (FAI, Greatcell Solar) in mixed DMF/DMSO (volume ratio = 9:1). The $MA_{1-x}FA_xPbI_3$ perovskite precursor was prepared by mixing the desired quotas of $MAPbI_3$ and $FAPbI_3$ solution.

Perovskite Film Preparation. The perovskite precursor solution was filtered using a 0.45 mm PTFE filter and dripped onto soda-lime glass substrates. The solution was spin-coated at 500 rpm for 3 s and 4000 rpm for 60 s. At ~8 s of the second spin step, 700 μL of diethyl ether was dripped on the spinning substrate. The coated substrates were then annealed at 60 °C for 2 min and 100 °C for 5 min in a nitrogen glovebox.

PL Characterization. For steady-state PL, a 532 nm continuous wave laser beam (beam diameter ~90 μm) was used for the photoexcitation. Temperature dependent PL measurements were carried out by mounting the sample on the coldfinger of a He closed-cycle refrigerator cryostat system from Advanced Research Systems. PL signal was detected by a Horiba Symphony-II CCD (charged coupled device) detector after a 300 g/mm grating monochromator. PL measurements were performed using laser intensity in the range of ~2.74 to 61.8 $mW \cdot cm^{-2}$. TRPL measurements were carried out utilizing time correlated single photon counting module (TCSPC). Samples were illuminated by a 532 nm pulsed laser (pulse width = 5 ps, beam diameter ~150 μm) at 1.4×10^{10} $photons \cdot pulse^{-1} \cdot cm^{-2}$. Radiative recombination events were detected by APD/PMT hybrid detector (integration time = 300 s). TCSPC decay curves obtained in TRPL measurement were fitted by iterative reconvolution with the measured system response function.

ASSOCIATED CONTENT

Supporting Information

The Supporting Information is available free of charge at https://pubs.acs.org/doi/10.1021/acs.jpclett.9b03234.

XRD patterns and SEM images of $MA_xFA_{1-x}PbI_3$ with $Pb(SCN)_2$ additive, low temperature PL spectra of $MAPbI_3$ with or without $Pb(SCN)_2$ additive, and laser power and temperature dependent PL spectra of $FAPbI_3$ (PDF)

AUTHOR INFORMATION

Corresponding Author

*Email: randy.ellingson@utoledo.edu.

ORCID

Niraj Shrestha: 0000-0001-5702-2938
Zhaoning Song: 0000-0002-6677-0994
Ebin Bastola: 0000-0002-4194-3385
Xiaoming Wang: 0000-0002-5438-1334
Yanfa Yan: 0000-0003-3977-5789
Randy J. Ellingson: 0000-0001-9520-6586

Author Contributions

#N.S. and Z.S. contributed equally to this work.

Notes

The views and conclusions contained herein are those of the authors and should not be interpreted as necessarily representing the official policies or endorsements, either expressed or implied, of Air Force Research Laboratory or the U.S. Government.

The authors declare no competing financial interest.

ACKNOWLEDGMENTS

This work is supported by National Science Foundation (NSF) under contract no. EECS-1665172, Office of Naval Research under contract no. N00014-17-1-2223, and Air Force Research Laboratory under agreement number FA9453-18-2-0037. The U.S. Government is authorized to reproduce and distribute reprints for Governmental purposes notwithstanding any copyright notation thereon.

REFERENCES

(1) Saidaminov, M. I.; Abdelhady, A. L.; Murali, B.; Alarousu, E.; Burlakov, V. M.; Peng, W.; Dursun, I.; Wang, L.; He, Y.; Maculan, G.; et al. High-quality Bulk Hybrid Perovskite Single Crystals within Minutes by Inverse Temperature Crystallization. *Nat. Commun.* **2015**, *6*, 7586.

(2) Park, N.-G. Perovskite Solar Cells: An Emerging Photovoltaic Technology. *Mater. Today* **2015**, *18* (2), 65−72.

(3) Dong, Q.; Fang, Y.; Shao, Y.; Mulligan, P.; Qiu, J.; Cao, L.; Huang, J. Electron-hole Diffusion Lengths > 175 mm in Solution-grown $CH_3NH_3PbI_3$ Single Crystals. *Science* **2015**, *347* (6225), 967−970.

(4) Miyata, A.; Mitioglu, A.; Plochocka, P.; Portugall, O.; Wang, J. T.-W.; Stranks, S. D.; Snaith, H. J.; Nicholas, R. J. Direct Measurement of the Exciton Binding Energy and Effective Masses for Charge Carriers in Organic-inorganic Tri-halide Perovskites. *Nat. Phys.* **2015**, *11* (7), 582−587.

(5) Jung, H. S.; Han, G. S.; Park, N.-G.; Ko, M. J. Flexible Perovskite Solar Cells. *Joule* **2019**, *3* (8), 1850−1880.

(6) Song, Z.; McElvany, C. L.; Phillips, A. B.; Celik, I.; Krantz, P. W.; Watthage, S. C.; Liyanage, G. K.; Apul, D.; Heben, M. J. A Technoeconomic Analysis of Perovskite Solar Module Manufacturing with Low-cost Materials and Techniques. *Energy Environ. Sci.* **2017**, *10* (6), 1297−1305.

DOI: 10.1021/acs.jpclett.9b03234
J. Phys. Chem. Lett. 2020, 11, 121−128

Approved for public release; distribution unlimited.

(7) NREL https://www.nrel.gov/pv/assets/images/efficiency-chart.png.
(8) Bisquert, J.; Juarez-Perez, E. J. The Causes of Degradation of Perovskite Solar Cells. *J. Phys. Chem. Lett.* **2019**, *10* (19), 5889−5891.
(9) Park, B.-w.; Seok, S. I. Intrinsic Instability of Inorganic−organic Hybrid Halide Perovskite Materials. *Adv. Mater.* **2019**, *31* (20), 1805337.
(10) Roose, B.; Wang, Q.; Abate, A. The Role of Charge Selective Contacts in Perovskite Solar Cell Stability. *Adv. Energy Mater.* **2018**, *9* (5), 1803140.
(11) Zhang, H.; Nazeeruddin, M. K.; Choy, W. C. H. Perovskite Photovoltaics: The Significant Role of Ligands in Film Formation, Passivation, and Stability. *Adv. Mater.* **2019**, *31* (8), 1805702.
(12) Huang, F.; Li, M.; Siffalovic, P.; Cao, G.; Tian, J. From Scalable Solution Fabrication of Perovskite Films Towards Commercialization of Solar Cells. *Energy Environ. Sci.* **2019**, *12* (2), 518−549.
(13) Chen, B.; Yang, M.; Priya, S.; Zhu, K. Origin of J−V Hysteresis in Perovskite Solar Cells. *J. Phys. Chem. Lett.* **2016**, *7* (5), 905−917.
(14) Celik, I.; Song, Z.; Cimaroli, A. J.; Yan, Y.; Heben, M. J.; Apul, D. Life Cycle Assessment (LCA) of Perovskite PV Cells Projected From Lab to Fab. *Sol. Energy Mater. Sol. Cells* **2016**, *156*, 157−169.
(15) Jung, H. S.; Park, N.-G. Perovskite Solar Cells: From Materials to Devices. *Small* **2015**, *11* (1), 10−25.
(16) Wang, C.; Zhao, D.; Yu, Y.; Shrestha, N.; Grice, C. R.; Liao, W.; Cimaroli, A. J.; Chen, J.; Ellingson, R. J.; Zhao, X.; Yan, Y. Compositional and Morphological Engineering of Mixed Cation Perovskite Films for Highly Efficient Planar and Flexible Solar Cells with Reduced Hysteresis. *Nano Energy* **2017**, *35*, 223−232.
(17) Jiang, Q.; Zhao, Y.; Zhang, X.; Yang, X.; Chen, Y.; Chu, Z.; Ye, Q.; Li, X.; Yin, Z.; You, J. Surface Passivation of Perovskite Film for Efficient Solar Cells. *Nat. Photonics* **2019**, *13* (7), 460−466.
(18) Deng, Y.; Zheng, X.; Bai, Y.; Wang, Q.; Zhao, J.; Huang, J. Surfactant-controlled Ink Drying Enables High-Speed Deposition of Perovskite Films for Efficient Photovoltaic Modules. *Nature Energy* **2018**, *3* (7), 560−566.
(19) Song, Z.; Shrestha, N.; Watthage, S. C.; Liyanage, G. K.; Almutawah, Z. S.; Ahangharnejhad, R. H.; Phillips, A. B.; Ellingson, R. J.; Heben, M. J. Impact of Moisture on Photoexcited Charge Carrier Dynamics in Methylammonium Lead Halide Perovskites. *J. Phys. Chem. Lett.* **2018**, *9* (21), 6312−6320.
(20) Liu, Y.; Lu, H.; Niu, J.; Zhang, H.; Lou, S.; Gao, C.; Zhan, Y.; Zhang, X.; Jin, Q.; Zheng, L. Temperature-dependent Photoluminescence Spectra and Decay Dynamics of $MAPbBr_3$ and $MAPbI_3$ Thin Films. *AIP Adv.* **2018**, *8* (9), 095108.
(21) Kong, W.; Ye, Z.; Qi, Z.; Zhang, B.; Wang, M.; Rahimi-Iman, A.; Wu, H. Characterization of an Abnormal Photoluminescence Behavior upon Crystal-phase Transition of Perovskite $CH_3NH_3PbI_3$. *Phys. Chem. Chem. Phys.* **2015**, *17* (25), 16405−16411.
(22) Dar, M. I.; Jacopin, G.; Meloni, S.; Mattoni, A.; Arora, N.; Boziki, A.; Zakeeruddin, S. M.; Rothlisberger, U.; Grätzel, M. Origin of Unusual Bandgap Shift and Dual Emission in Organic-Inorganic Lead Halide Perovskites. *Science Advances* **2016**, *2*, e1601156.
(23) Baikie, T.; Fang, Y.; Kadro, J. M.; Schreyer, M.; Wei, F.; Mhaisalkar, S. G.; Graetzel, M.; White, T. J. Synthesis and Crystal Chemistry of the Hybrid Perovskite $CH_3NH_3PbI_3$ for Solid-state Sensitised Solar Cell Applications. *J. Mater. Chem. A* **2013**, *1* (18), 5628−5641.
(24) Phuong, L. Q.; Yamada, Y.; Nagai, M.; Maruyama, N.; Wakamiya, A.; Kanemitsu, Y. Free Carriers versus Excitons in $CH_3NH_3PbI_3$ Perovskite Thin Films at Low Temperatures: Charge Transfer from the Orthorhombic Phase to the Tetragonal Phase. *J. Phys. Chem. Lett.* **2016**, *7* (13), 2316−2321.
(25) Yang, J.-H.; Yin, W.-J.; Park, J.-S.; Wei, S.-H. Self-regulation of Charged Defect Compensation and Formation Energy Pinning in Semiconductors. *Sci. Rep.* **2015**, *5*, 16977.
(26) Ke, W.; Xiao, C.; Wang, C.; Saparov, B.; Duan, H.-S.; Zhao, D.; Xiao, Z.; Schulz, P.; Harvey, S. P.; Liao, W.; et al. Employing Lead Thiocyanate Additive to Reduce the Hysteresis and Boost the Fill Factor of Planar Perovskite Solar Cells. *Adv. Mater.* **2016**, *28* (26), 5214−5221.
(27) Milot, R. L.; Eperon, G. E.; Snaith, H. J.; Johnston, M. B.; Herz, L. M. Temperature-dependent Charge-carrier Dynamics in $CH_3NH_3PbI_3$ Perovskite Thin Films. *Adv. Funct. Mater.* **2015**, *25* (39), 6218−6227.
(28) Schmidt, T.; Daniel, G.; Lischka, K. The Excitation Power Dependence of the Near Band Edge Photoluminescence of II-VI Semiconductors. *J. Cryst. Growth* **1992**, *117* (1), 748−752.
(29) Krustok, J.; Valdna, V.; Hjelt, K.; Collan, H. Deep Center Luminescence in P-type CdTe. *J. Appl. Phys.* **1996**, *80* (3), 1757−1762.
(30) Roland, P. J.; Paudel, N. R.; Chuanxiao, X.; Yan, Y.; Ellingson, R. J. Photoluminescence Spectroscopy of Cadmium Telluride Deep Defects, *2014 IEEE 40th Photovoltaic Specialist Conference (PVSC)*, 8−13 June; IEEE, 2014; pp 3266−3271.
(31) Shi, J.; Zhang, H.; Li, Y.; Jasieniak, J. J.; Li, Y.; Wu, H.; Luo, Y.; Li, D.; Meng, Q. Identification of High-temperature Exciton States and Their Phase-dependent Trapping Behaviour in Lead Halide Perovskites. *Energy Environ. Sci.* **2018**, *11* (6), 1460−1469.
(32) Yamada, Y.; Nakamura, T.; Endo, M.; Wakamiya, A.; Kanemitsu, Y. Near-band-edge Optical Responses of Solution-processed Organic−inorganic Hybrid Perovskite $CH_3NH_3PbI_3$ on Mesoporous Tio_2 electrodes. *Appl. Phys. Express* **2014**, *7* (3), 032302.
(33) Panzer, F.; Baderschneider, S.; Gujar, T. P.; Unger, T.; Bagnich, S.; Jakoby, M.; Bässler, H.; Hüttner, S.; Köhler, J.; Moos, R.; et al. Reversible Laser-induced Amplified Spontaneous Emission from Coexisting Tetragonal and Orthorhombic Phases in Hybrid Lead Halide Perovskites. *Adv. Opt. Mater.* **2016**, *4* (6), 917−928.
(34) Krustok, J.; Jagomägi, A.; Grossberg, M.; Raudoja, J.; Danilson, M. Photoluminescence Properties of Polycrystalline $AgGaTe_2$. *Sol. Energy Mater. Sol. Cells* **2006**, *90* (13), 1973−1982.
(35) Shrestha, N.; Sapkota, D. R.; Subedi, K. K.; Pradhan, P.; Koirala, P.; Phillips, A. B.; Collins, R. W.; Heben, M. J.; Ellingson, R. J. Identification of Defect Levels in Copper Indium Diselenide ($CuInSe_2$) Thin Films via Photoluminescence Studies. *MRS Advances* **2018**, *3* (52), 3135−3141.
(36) Yakushev, M. V.; Krustok, J.; Grossberg, M.; Volkov, V. A.; Mudryi, A. V.; Martin, R. W. A Photoluminescence Study of $CuInSe_2$ Single Crystals Ion Implanted with 5 Kev Hydrogen. *J. Phys. D: Appl. Phys.* **2016**, *49* (10), 105108.
(37) Susanne Siebentritt, U. R. *Wide-Gap Chalcopyrites*, 1st ed.; Springer-Verlag Berlin Heidelberg: 2006; p XIV, 260.
(38) Rey, G.; Larramona, G.; Bourdais, S.; Choné, C.; Delatouche, B.; Jacob, A.; Dennler, G.; Siebentritt, S. On the Origin of Band-tails in Kesterite. *Sol. Energy Mater. Sol. Cells* **2018**, *179*, 142−151.
(39) Kim, J.; Lee, S.-H.; Lee, J. H.; Hong, K.-H. The Role of Intrinsic Defects in Methylammonium Lead Iodide Perovskite. *J. Phys. Chem. Lett.* **2014**, *5* (8), 1312−1317.
(40) Song, Z.; Wang, C.; Phillips, A. B.; Grice, C. R.; Zhao, D.; Yu, Y.; Chen, C.; Li, C.; Yin, X.; Ellingson, R. J.; et al. Probing the Origins of Photodegradation in Organic−inorganic Metal Halide Perovskites with Time-resolved Mass Spectrometry. *Sustainable Energy & Fuels* **2018**, *2* (11), 2460−2467.
(41) Juarez-Perez, E. J.; Ono, L. K.; Maeda, M.; Jiang, Y.; Hawash, Z.; Qi, Y. Photodecomposition and Thermal Decomposition in Methylammonium Halide Lead Perovskites and Inferred Design Principles to Increase Photovoltaic Device Stability. *J. Mater. Chem. A* **2018**, *6* (20), 9604−9612.
(42) Krustok, J.; Collan, H.; Yakushev, M.; Hjelt, K. The Role of Spatial Potential Fluctuations in the Shape of the PL Bands of Multinary Semiconductor Compounds. *Phys. Scr.* **1999**, *T79*, 179−182.
(43) Varshni, Y. P. Temperature Dependence of the Energy Gap in Semiconductors. *Physica* **1967**, *34* (1), 149−154.
(44) Francisco-López, A.; Charles, B.; Weber, O. J.; Alonso, M. I.; Garriga, M.; Campoy-Quiles, M.; Weller, M. T.; Goñi, A. R. Equal Footing of Thermal Expansion and Electron−phonon Interaction in

DOI: 10.1021/acs.jpclett.9b03234
J. Phys. Chem. Lett. 2020, 11, 121−128

Approved for public release; distribution unlimited.

the Temperature Dependence of Lead Halide Perovskite Band Gaps. *J. Phys. Chem. Lett.* **2019**, *10* (11), 2971−2977.
(45) Saidi, W. A.; Poncé, S.; Monserrat, B. Temperature Dependence of the Energy Levels of Methylammonium Lead Iodide Perovskite from First-Principles. *J. Phys. Chem. Lett.* **2016**, *7* (24), 5247−5252.
(46) Hempel, H.; Dennler, G.; S, M.; x00Fc; ller; Larramona, G.; Eichberger, R.; Unold, T. Charge Carrier Dynamics in $Cu_2ZnSn(S/Se)_4$ Thin Film Solar Cells Measured by Time Resolved Terahertz and Microwave Spectroscopy, *2016 41st International Conference on Infrared, Millimeter, and Terahertz waves (IRMMW-THz)*, 25−30 Sept.; International Society of Infrared, Millimeter, and Terahertz Waves: 2016; pp 1−2.
(47) Wang, Y.; Long, R. Anomalous Temperature-dependent Charge Recombination in $CH_3NH_3PbI_3$ Perovskite: Key Roles of Charge Localization and Thermal Effect. *ACS Appl. Mater. Interfaces* **2019**, *11* (35), 32069−32075.
(48) Liu, N.; Yam, C. First-principles Study of Intrinsic Defects in Formamidinium Lead Triiodide Perovskite Solar Cell Absorbers. *Phys. Chem. Chem. Phys.* **2018**, *20* (10), 6800−6804.
(49) Ma, F.; Li, J.; Li, W.; Lin, N.; Wang, L.; Qiao, J. Stable A/Δ Phase Junction of Formamidinium Lead Iodide Perovskites for Enhanced Near-infrared Emission. *Chemical Science* **2017**, *8* (1), 800−805.
(50) Fu, M.; Tamarat, P.; Trebbia, J.-B.; Bodnarchuk, M. I.; Kovalenko, M. V.; Even, J.; Lounis, B. Unraveling Exciton−phonon Coupling in Individual $FAPbI_3$ Nanocrystals Emitting Near-infrared Single Photons. *Nat. Commun.* **2018**, *9*, 3318.
(51) Thouin, F.; Valverde-Chávez, D. A.; Quarti, C.; Cortecchia, D.; Bargigia, I.; Beljonne, D.; Petrozza, A.; Silva, C.; Srimath Kandada, A. R. Phonon Coherences Reveal the Polaronic Character of Excitons in Two-dimensional Lead Halide Perovskites. *Nat. Mater.* **2019**, *18* (4), 349−356.
(52) Stoumpos, C. C.; Malliakas, C. D.; Kanatzidis, M. G. Semiconducting Tin and Lead Iodide Perovskites with Organic Cations: Phase Transitions, High Mobilities, and Near-Infrared Photoluminescent Properties. *Inorg. Chem.* **2013**, *52* (15), 9019−9038.
(53) Fang, H.-H.; Wang, F.; Adjokatse, S.; Zhao, N.; Even, J.; Antonietta Loi, M. Photoexcitation Dynamics in Solution-processed Formamidinium Lead Iodide Perovskite Thin Films For Solar Cell Applications. *Light: Sci. Appl.* **2016**, *5*, e16056.
(54) Ke, W.; Xiao, C.; Wang, C.; Saparov, B.; Duan, H.-S.; Zhao, D.; Xiao, Z.; Schulz, P.; Harvey, S. P.; Liao, W.; et al. Employing Lead Thiocyanate Additive to Reduce the Hysteresis and Boost the Fill Factor of Planar Perovskite Solar Cells. *Adv. Mater.* **2016**, *28*, 5214−5221.

DOI: 10.1021/acs.jpclett.9b03234
J. Phys. Chem. Lett. 2020, 11, 121−128

Approved for public release; distribution unlimited.

347

Journal of MATERIALS RESEARCH

Invited Paper
DOI: 10.1557/jmr.2019.363

Wet chemical etching of cadmium telluride photovoltaics for enhanced open-circuit voltage, fill factor, and power conversion efficiency

Ebin Bastola[1], Fadhil K. Alfadhili[1], Adam B. Phillips[1], Michael J. Heben[1], Randy J. Ellingson[1,a)]

[1]Wright Center for Photovoltaics Innovation and Commercialization (PVIC), Department of Physics and Astronomy, University of Toledo, Toledo, Ohio 43606, USA

[a)]Address all correspondence to this author. e-mail: Randy.Ellingson@utoledo.edu

Received: 18 July 2019; accepted: 11 November 2019

Cadmium telluride (CdTe) is one of the leading photovoltaic technologies with a market share of around 5%. However, there still exist challenges to fabricate a rear contact for efficient transport of photogenerated holes. Here, etching effects of various iodine compounds including elemental iodine (I_2), ammonium iodide (NH_4I), mixture of elemental iodine and NH_4I (I^-/I_3^- etching), and formamidinium iodide were investigated. The treated CdTe surfaces were investigated using Raman spectroscopy, X-ray diffraction (XRD), scanning electron microscopy, and energy-dispersive X-ray spectroscopy. The CdTe devices were completed with or without treatments and tested under simulated AM1.5G solar spectrum to find photoconversion efficiency (PCE). Based on Raman spectra, XRD patterns, and surface morphology, it was shown that treatment with iodine compounds produced Te-rich surface on CdTe films, and temperature-dependent current–voltage characteristics showed reduced back barrier heights, which are essential for the formation of ohmic contact and reduce contact resistance. Based on current–voltage characteristics, the treatment enhanced open-circuit voltage (V_{OC}) up to 841 mV, fill factor (FF) up to 78.2%, and PCE up to 14.0% compared with standard untreated CdTe devices (V_{OC} ~ 814 mV, FF ~ 74%, and PCE ~ 12.7%) with copper/gold back contact.

Introduction

Cadmium telluride (CdTe) is a leading mature photovoltaic (PV) technology with a market share of around 5%. The efficiency of CdTe solar cells depends on intrinsic defects in bulk materials and at the front and back interfaces. At the front interface, cadmium sulfide (CdS), band gap 2.42 eV, is the most conventionally used material as a window layer to fabricate CdTe solar cells. CdS absorbs photons of wavelength <512 nm but does not contribute to the current density of the device due to high defect density and the formation of photo-inactive $CdS_{1-y}Te_y$ alloy [1]. Recently, other materials including CdSe and magnesium zinc oxide (MgZnO, band gap 3.3 eV) have also been applied as window layers to increase current density by collecting blue photons [2, 3]. Compared with the front contact interface, the rear interface is challenging due to the deep valence band edge of CdTe (≈5.9 eV) and formation of Schottky junction with a metal at the back interface [4, 5, 6].

The barrier height at the Schottky junction between CdTe and a metal, usually nickel (Ni) or gold (Au), limits the hole transport and increases the contact resistance, limiting the maximum photovoltage expected [7]. Doping the CdTe absorbing layer, which increases the carrier concentration, localizes band bending and lowers the barrier height. Copper/gold (Cu/Au) has been used as a rear contact material in our laboratory [8, 9]. Deposition and diffusion of Cu atoms increase carrier concentration and enhance device performance. However, the Cu/Au back contact does not facilitate the transport of the photo-generated charge carriers due to a potential barrier between CdTe and Au. Based on the previous report, the barrier height in between CdTe and Cu/Au when CdTe (3.5 μm) is doped with 3 nm Cu is ~0.33 eV [10]. To further reduce the potential barrier, a material with suitable band edges is applied for the extraction of holes and repel of electrons at the rear contact of CdTe PVs. Materials such as carbon nanotubes [11], copper thiocyanate (CuSCN)

© Materials Research Society 2019

Approved for public release; distribution unlimited.

[12], nanocrystals and nanocomposites [13, 14, 15, 16, 17], zinc telluride (ZnTe) [18], and antimony telluride (Sb_2Te_3) [19], prepared by various methods, have been used in an attempt to reduce the back barrier height and facilitate hole transport toward the back electrode. Alternatively, formation of tellurium (Te)-rich surface/layer through thermal evaporation, sputtering or chemical etching at the back interface led to improved device efficiency and back barrier height [20, 21]. Niles et al. reported the reduction of Schottky barrier to 0.26 eV for >5 nm Te layer on CdTe improving the hole transport compared to Au only contact (0.80 eV) [22] and Watthage et al. also found reduced back barrier (0.20 eV) due to etching [23].

The wet chemical etching of CdTe usually includes the use of an alcoholic bromine (Br_2) solution or an acidic solution that creates a Te-rich surface. Previously reported common acidic etchants are mixture of HNO_3–HPO_4–H_2O (NP) [24], H_2O_2–HI–tartaric/citric acid [25, 26], KIO_3–KI–citric acid [27], and $K_2Cr_2O_7$–HNO_3–H_2O [28]. Other alcoholic solutions applied for etching are bromine methanol (Br_2–MeOH) [29], iodine methanol (I_2–MeOH) [30], methylammonium iodide (MAI) [23], and hydroiodic acid [31]. For MAI selective etching, authors have reported the average power conversion efficiency of 13.8% (V_{OC} 834 mV, FF 77.2%) for 20 cells with 2 nm evaporated Cu, while the unetched devices had the average power conversion efficiency of 12.5% (V_{OC} 796 mV, FF 74.6%) [23]. The Br_2–MeOH etch is very corrosive to metals and may penetrate the entire CdTe film and damage the front interface. Similarly, $K_2Cr_2O_7$–HNO_3 etch produces TeO_2 on the surface and the film that needs to be further treated with alkaline etch (KOH–MeOH). Ivanits'ka et al. have reported the effect of I_2–MeOH etching on the CdTe single crystals and found the dissolution is diffusion controlled [30]. However, the authors did not report the effect of etching on polycrystalline CdTe thin film and device performance after etching. The etching of CdTe with iodine (or iodine compounds) is beneficial over Br_2–MeOH due to its less corrosive and less toxic nature. Additionally, iodine has a lower redox potential ($I_2 \rightarrow 2I^-$, 0.54 V) than bromine ($Br_2 \rightarrow 2Br^-$, 1.09 V), which leads to controllable etching of CdTe surface [25].

Here, we investigate wet chemical treatment of CdTe back surface using various iodine compounds. The various iodine compounds include elemental iodine (I_2), ammonium iodide (NH_4I), a mixture of I_2 and NH_4I (I^-/I_3^- etching), and formamidinium iodide (FAI). The CdTe surface was treated with these etchant solutions and annealed in ambient environment. The treated CdTe surfaces were characterized using Raman spectroscopy, X-ray diffraction (XRD), scanning electron microscopy (SEM), and energy-dispersive spectroscopy (EDS). The CdTe devices were completed with or without treatments, and devices were measured to determine the effect of treatment on device performance. The Raman spectra, XRD patterns, and surface morphology of CdTe surface revealed a Te-rich surface when treated with iodine compounds. Based on current–voltage (J–V) characteristics of the device, the treatment enhanced open-circuit voltage (V_{OC}), fill factor (FF), and photoconversion efficiency (PCE) compared with standard unetched devices with a Cu/Au back contact.

Results and discussion

Etching with iodine (I_2), ammonium iodide (NH_4I), and mixed I^-/I_3^- solutions

Figure 1 shows the Raman spectra and XRD patterns of CdTe films treated with I_2, NH_4I, and mixture of I_2 and NH_4I (I^-/I_3^-) solutions. During the Raman measurement, the CdTe samples were exposed to laser for 30 s to minimize the laser effect [32]. Here, in the Raman spectra, the active vibrational peaks of Te–Te atoms observed at 119.7, 139.0, and 266.6 cm^{-1} are stronger for the etched samples than for the untreated (standard) CdTe film. The strong vibrational modes of treated

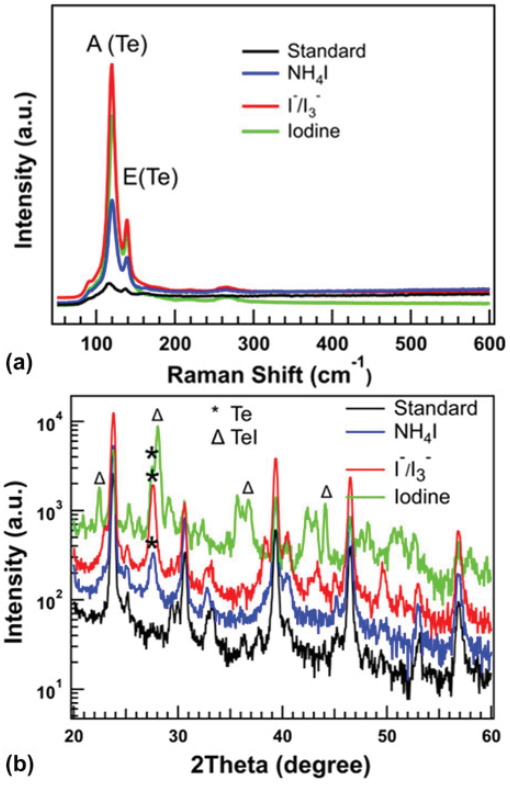


Figure 1: (a) Raman spectra and (b) XRD patterns of CdTe thin films after etching with iodine (I_2), ammonium iodide (NH_4I), and mixed I^-/I_3^- solutions. The peaks marked by * at 27.6° are for Te (101) (PDF #97-002-3060) and peaks marked by Δ indicate TeI β-phase (PDF #97-000-0108).

© Materials Research Society 2019

Approved for public release; distribution unlimited.

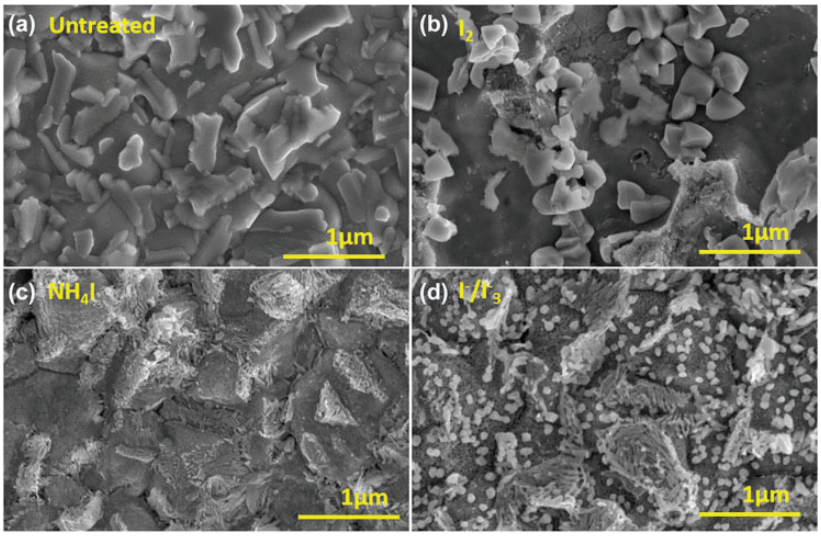


Figure 2: SEM images of CdTe thin films after etching with various iodine compounds: (a) untreated, (b) iodine (I_2), (c) ammonium iodide (NH_4I), and (d) mixed I^-/I_3^- solutions.

films suggest the selective etching of the CdTe films to produce Te surface after the treatment. Furthermore, the treated CdTe films show a diffraction peak at 27.6°, which is assigned to diffraction due to the elemental Te. We observed this diffraction peak at 27.6° for all three etchants, elemental iodine, NH_4I, and I^-/I_3^-. Previously, authors have reported a diffraction peak at 27.6° for Te-rich surface after etching CdTe surface with various etchants [23, 33]. Interestingly, in the case of elemental iodine, TeI peaks were also observed at various "2θ" positions (22.45°, 28.05°, 36.70°, 44.10°) marked by Δ in Fig. 1(b). The diffraction pattern analysis showed that these peaks are produced due to the presence of tellurium iodide (TeI) β-phase compound on the surface. The XRD patterns were analyzed by MDI ZADE software, and these peaks were assigned to Te and TeI based on comparison with standard diffraction patterns of Te (PDF #97-002-3060) and TeI-β (PDF #97-000-0108) phase.

Similarly, the surface topography of the standard and treated films was studied by SEM, and elemental compositions were determined using EDS. Figure 2 shows the SEM images and surface topography of CdTe surface after chemical treatment in all three cases. The surface topography looks very different compared with unetched standard CdTe. In the iodine etching (0.21 M) shown in Fig. 2(b), the treatment produced a significant number of bulky particles as evident. NH_4I etching (0.42 M) produced somewhat uniform surface topography, and in case of I^-/I_3^-, etching produced some tiny particles on the surface in addition to the rough surface. Here, based on the Raman and XRD patterns of these etched CdTe films, we concluded that these etchants have significant impact on the CdTe surface. To confirm the elemental composition, EDS

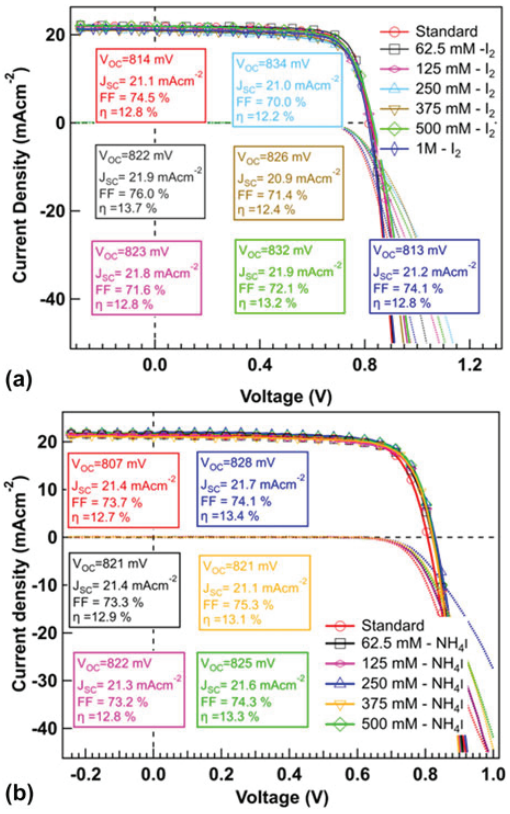


Figure 3: Typical *J–V* characteristics of CdTe solar cells with (a) iodine and (b) NH_4I etching of various concentrations.

© Materials Research Society 2019

Approved for public release; distribution unlimited.

spectra were acquired and tabulated in Table SI (Supporting information, SI) for standard (unetched) and etched CdTe films. In case of standard CdTe, the ratio of Cd to Te is about 1.14. After the treatment, Cd to Te ratio became 0.74 for 0.21 M I_2 etching, and 0.95 and 0.88 for 0.42 M NH_4I and I^-/I_3^- (0.375% I_2 solution (0.21 M) in 0.42 M NH_4I solution), respectively, indicating modified surface composition. A previous study shows the treatment of CdTe using polyaniline produced Cd to Te ratio close to 0.72, which is beneficial for fabrication of efficient devices [34]. In CdTe PVs, a Te-rich material, which has pronounced p-type characteristics on the surface, is more suitable for forming a low-barrier back contact [20]. Note that EDS measurements were carried out at an accelerating voltage of 20 kV and current of 10 μA, and hence, the information obtained is not limited to the surface. Instead, this value refers to the average obtained from the interaction volume during the measurement. Based on these Raman spectra, diffraction patterns, surface topography, and EDS analysis, we confirm that these treatments produced selective etching to Cd, leaving a Te-rich surface.

Based on elemental compositions presented in Table SI, Reactions (1) and (2) can be considered for dissolution of cadmium into iodine solutions [19]. The tellurium oxide (TeO_2) and CdTe react with iodine (or triiodide) ions and Cd gets dissolved in the solution. The dissolution of CdTe film in the etchant solutions depends on the time and concentration of iodine ions in the etchant solution. In the Raman spectra (Fig. 1), the intensity of active mode at 119.7 cm^{-1} for Te–Te atoms is significantly higher in case of I^-/I_3^- etch than in the I_2 and NH_4I. I_2 and NH_4I solutions have the same atomic concentration of iodine atoms, indicating I^-/I_3^- etching solution is more effective at producing Te-rich surface compared with pure I_2 or NH_4I solution.

$$TeO_2\ (s) + 4NH_4^+ + 6I^- \rightarrow Te\ (s) + 2H_2O + 2I_3^- + 4NH_3 \quad (1)$$

$$CdTe\ (s) + I^-(\text{or } I_3^-) \rightarrow Te\ (s) + Cd^{2+} + I^-(\text{or } 3I^-) \quad (2)$$

Since a Te-rich surface is beneficial for fabrication of efficient devices, we tested the effect of these treatments on CdTe devices with various concentrations of etchant solution. Figure 3(a) displays *J–V* characteristics of the best cells completed after etching CdTe films with various concentrations of iodine (I_2) solution. After etching, the best cells show higher or comparable efficiency compared with the standard cells. However, the average device performance of the 20 cells after etching is slightly low except for 62.5 mM iodine solution (see Table SII). In case of 62.5 mM iodine solution, the best cell has V_{OC} of 822 mV, J_{SC} of 21.9 mA/cm^2, and FF of 76.0% with the PCE of 13.7%, with average PCE of 12.5%. In case of standard device, the best cell has V_{OC} of 814 mV, J_{SC} of 21.1 mA/cm^2, and FF of 74.5% with PCE of 12.8%, with average PCE of 12.3%.

We further analyzed the CdTe surfaces after etching with higher I_2 concentration. Based on SEM images (Fig. S1, Supporting information), the CdTe surface shows a significant number of larger particles. As the concentration of iodine solution increased, the density of these particles increased with rod-like structures. EDS measurement of a particle on CdTe surface treated with 250 mM iodine solution revealed atomic ratio of Cd:Te:I to be 1:7:6 (Fig. S2). This ratio and the diffraction peaks marked by Δ in Fig. 1 indicate the formation of TeI on the CdTe surface. The devices with higher concentration of iodine solution (≥125 mM) showed decrease in FF due to the increase in series resistance of the device (presented in Table SII). Thus, these TeI particles formed due to the iodine treatment are detrimental to fabricating highly efficient devices after etching.

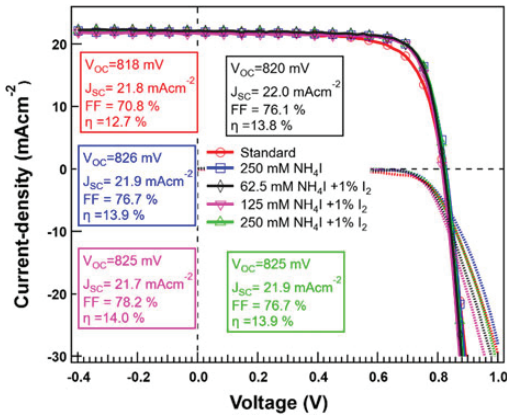


Figure 4: Typical *J–V* characteristics of CdTe solar cells with I^-/I_3^- etching of various concentration.

TABLE I: Summary of average *J–V* characteristics of CdTe solar cells with iodine etching of various concentration.

Device		V_{OC} (mV)	J_{SC} (mA/cm^2)	FF (%)	Eff. (%)	R_s (Ω cm^2)	R_{sh} (Ω cm^2)
Standard		806 ± 4	21.2 ± 1.3	73.3 ± 1.9	12.5 ± 0.8	2.9 ± 0.4	2316 ± 630
NH_4I-250 mM		825 ± 2	21.5 ± 0.3	75.5 ± 1.0	13.4 ± 0.3	2.5 ± 1.0	3024 ± 916
	NH_4I-62.5 mM	818 ± 4	21.6 ± 0.5	76.2 ± 0.5	13.5 ± 0.3	2.7 ± 1.0	3040 ± 647
1.0%-I_2	NH_4I-125 mM	816 ± 3	21.4 ± 0.2	76.9 ± 1.0	13.5 ± 0.2	2.9 ± 1.0	3765 ± 1328
	NH_4I-250 mM	824 ± 3	21.1 ± 0.4	76.0 ± 1.2	13.2 ± 0.3	3.9 ± 1.0	2634 ± 503

© Materials Research Society 2019

Approved for public release; distribution unlimited.

Similarly, *J–V* characteristics and average parameters of devices treated with NH_4I solution are presented in Fig. 3(b) and Table SIII. The device performance was slightly enhanced after NH_4I etching. The average PCE for devices treated with 250 mM and higher concentration of NH_4I solution is same (12.7%) and the best cell for 250 mM NH_4I has the higher efficiency compared with other NH_4I concentration. The device treated with 250 mM NH_4I has V_{OC} of 828 mV, J_{SC} of 21.7%, and FF of 74.1% with the PCE of 13.4%, which is about 10% higher than average performance (12.1%) of untreated CdTe devices.

Furthermore, we tested the effect of I^-/I_3^- etching on device performance of CdTe solar cells. For this, I^-/I_3^- solution with varying concentrations of NH_4I was prepared by mixing 1% of I_2 solution of same concentration. For example, 250 mM NH_4I (1000 µL) solution was mixed with 1% 250 mM (10 µL) I_2 solution to make 250 mM NH_4I + 1% I_2 solution. Figure 4 shows the *J–V* characteristics of the best cells of the devices etched with I^-/I_3^- and Fig. S3 shows the external quantum efficiencies (EQEs). Here, the devices etched with 125 mM NH_4I and 1% I_2 have FF of 78.2% with a device efficiency of 14.0% with average PCE of 13.5% for 20 cells. The etching increased the average device efficiency by 8% compared with the unetched devices (PCE of 12.5%). The average device parameters for 20 cells for various etching concentrations are presented in Table I. The average device performances of etched devices are better than those of the unetched devices. During this process, annealing of the CdTe film is essential to produce visible Te grains on the surface (Fig. S4). Thus, we conclude that the etching of CdTe devices with I^-/I_3^- solution helps to remove the oxide layer, dissolves cadmium atoms, and creates a Te-rich layer on the surface, enhancing the device performance.

Etching with FAI

The Raman spectra of the standard and FAI-treated CdTe films are shown in Fig. 5(a). Based on these spectra, no vibrational peaks of Te were observed for a standard CdTe film, whereas very strong peaks were observed at 120 and 139 cm^{-1} for FAI-treated CdTe surface. As the concentration of the FAI solution increases, the intensity of the vibrational peak also increases, indicating higher Te content in the etched CdTe surface. The XRD patterns measured for standard and etched CdTe samples with 250 mM FAI solution are presented in Fig. 5(b). The major diffraction peaks are same for standard and etched CdTe films; however, an additional diffraction peak is observed at 2θ angle 27.6° for FAI-etched CdTe film. The observed peak at 27.6° is assigned to elemental Te (101). This Te peak is same as the peak observed on the CdTe film treated with iodine, NH_4I, and I^-/I_3^- solutions (Fig. 1).

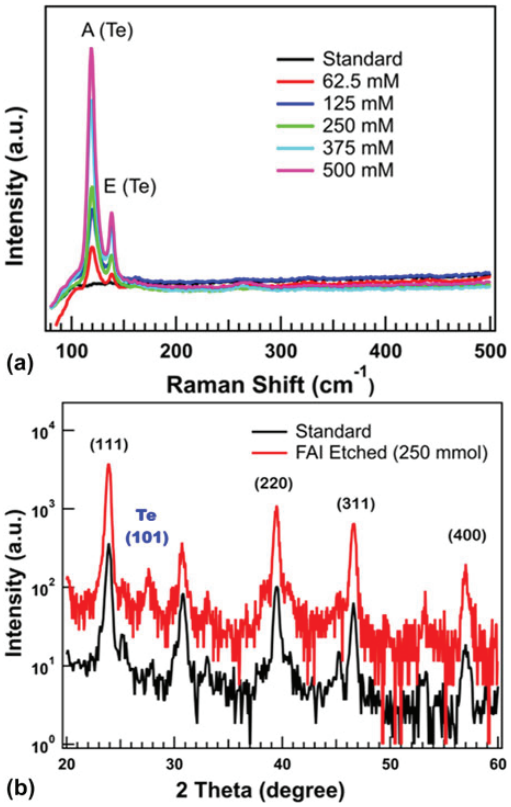


Figure 5: (a) Raman spectra of CdTe surface etched with various concentrations of FAI solution and (b) XRD patterns of standard and FAI-etched CdTe films.

Figure 6 displays the SEM images of the standard and FAI-treated CdTe films. The FAI treatment clearly changes the surface topography of the CdTe surface. As the surface was treated with higher concentration of FAI solution, the more Te grains become visible. Here, Cd^{2+} ions react with I^- ions forming other compounds, possibly $FACdI_3$ perovskites leaving Te atoms on the surface.

J–V characteristics of best cells of standard and FAI-treated CdTe devices are shown in Fig. 7 and EQEs are shown in Fig. S5. The back contact was fabricated with and without FAI etching using Cu/Au. The FAI treatment was carried out using various concentrations of FAI solution at ambient environment. The *J–V* curve indicates that performance of the device is enhanced by etching the CdTe surface with FAI solution. The V_{OC} and FF increase in the etched CdTe compared with standard CdTe devices is shown in Table II. For the standard cells without FAI etching, the average PCE is 12.6% with V_{OC} of 814 mV and FF of 74.7% for 20 cells and the best cell has an efficiency of 13.0% with V_{OC} of 818 mV and FF of 75.2%. In all the cases when treated with FAI, the V_{OC} and FF improved for

© Materials Research Society 2019

Approved for public release; distribution unlimited.

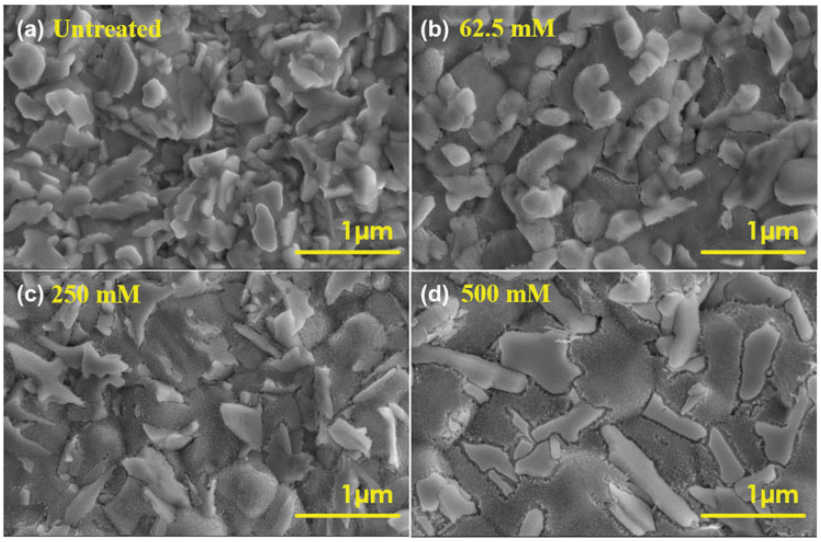


Figure 6: Surface topography of (a) standard CdTe surface and CdTe surface etched with FAI solution of concentrations: (b) 62.5 mM, (c) 250 mM, and (d) 500 mM. The CdTe films were annealed for 10 min at 150 °C before rinsing with 2-propanol in air environment.

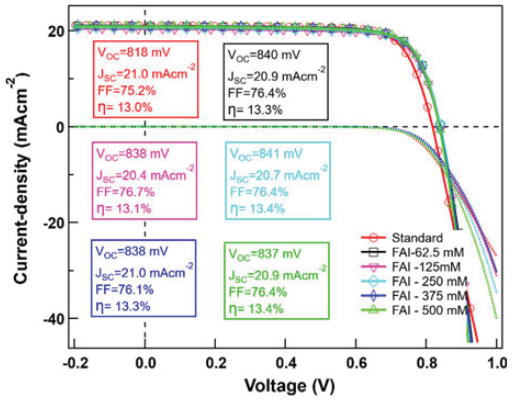


Figure 7: Current density versus voltage (*J–V*) characteristics of standard and FAI-treated cells.

etched devices. Here, 250 mM FAI-etched devices were found to have the highest average PCE of 13.1% with average V_{OC} of 839 mV and FF of 76.2% and the best cell has PCE of 13.4% with V_{OC} of 841 mV.

Temperature-dependent current–voltage characteristics

To study the effect of chemical etching on the back barrier height of CdTe devices, temperature-dependent current–voltage (*J–V–T*) characteristics were measured and analyzed using the model described by Niemegeers and Burgelman [35] to obtain back barrier heights. The back barrier height (ϕ_b) was obtained, assuming thermionic emission model as given by:

$$J_0 \alpha T^2 \cdot \exp\left[\frac{-q.\Phi_b}{k_B T}\right] \quad , \tag{3}$$

where J_0 is the saturation current, q is electronic charge, and k_B is the Boltzmann constant. The back barrier heights were obtained by fitting Arrhenius plots of Ln (J_0/T^2) versus $1/k_BT$.

Figures 8(a) and 8(b) show the *J–V–T* characteristics of CdTe devices measured under dark conditions without etching and with NH_4I etching, respectively. Figure 8(c) shows the plots of Ln (J_0/T^2) versus $1/k_BT$ and the solid lines represent linear fit of the corresponding data to extract back barrier height. For the standard CdTe device without etching, the barrier height is 0.286 ± 0.016 eV, which is close to the values reported previously for CdTe devices with Cu/Au back contact [10]. In the case of NH_4I etching, the barrier height was reduced to 0.249 ± 0.017 eV and further reduced to 0.192 ± 0.003 eV with I^-/I_3^- etching. Similarly, the barrier height of the CdTe devices etched with 250 mM FAI solution was 0.234 ± 0.008 eV. Based on these reduced back barrier heights, we conclude that etching of CdTe films with iodine solutions helps to lower the back barrier height and improve the device performance.

Conclusions

Here, we have successfully investigated etching of CdTe film using iodine compounds to produce Te-rich surface. The

© Materials Research Society 2019

Approved for public release; distribution unlimited.

TABLE II: Summary of average *J–V* characteristics of CdTe solar cells with FAI treatments.

Device	V_{OC} (mV)	J_{SC} (mA/cm^2)	FF (%)	Eff. (%)	R_s (Ω cm^2)	R_{sh} (Ω cm^2)
Standard	814 ± 6	20.8 ± 0.2	74.7 ± 0.6	12.6 ± 0.2	3.5 ± 0.5	2588 ± 181
FAI-62.5 mM	836 ± 2	20.5 ± 0.3	75.8 ± 1.1	13.0 ± 0.3	3.1 ± 1.0	2828 ± 385
FAI-125 mM	834 ± 2	20.2 ± 0.2	76.3 ± 0.6	12.9 ± 0.1	2.7 ± 0.8	3244 ± 298
FAI-250 mM	839 ± 2	20.4 ± 0.2	76.2 ± 0.4	13.1 ± 0.1	3.7 ± 0.5	2779 ± 286
FAI-375 mM	833 ± 2	20.6 ± 0.2	75.3 ± 0.9	12.9 ± 0.3	2.9 ± 1.1	2617 ± 214
FAI-500 mM	835 ± 3	20.6 ± 0.4	75.8 ± 0.6	13.0 ± 0.4	3.4 ± 0.8	2701 ± 228

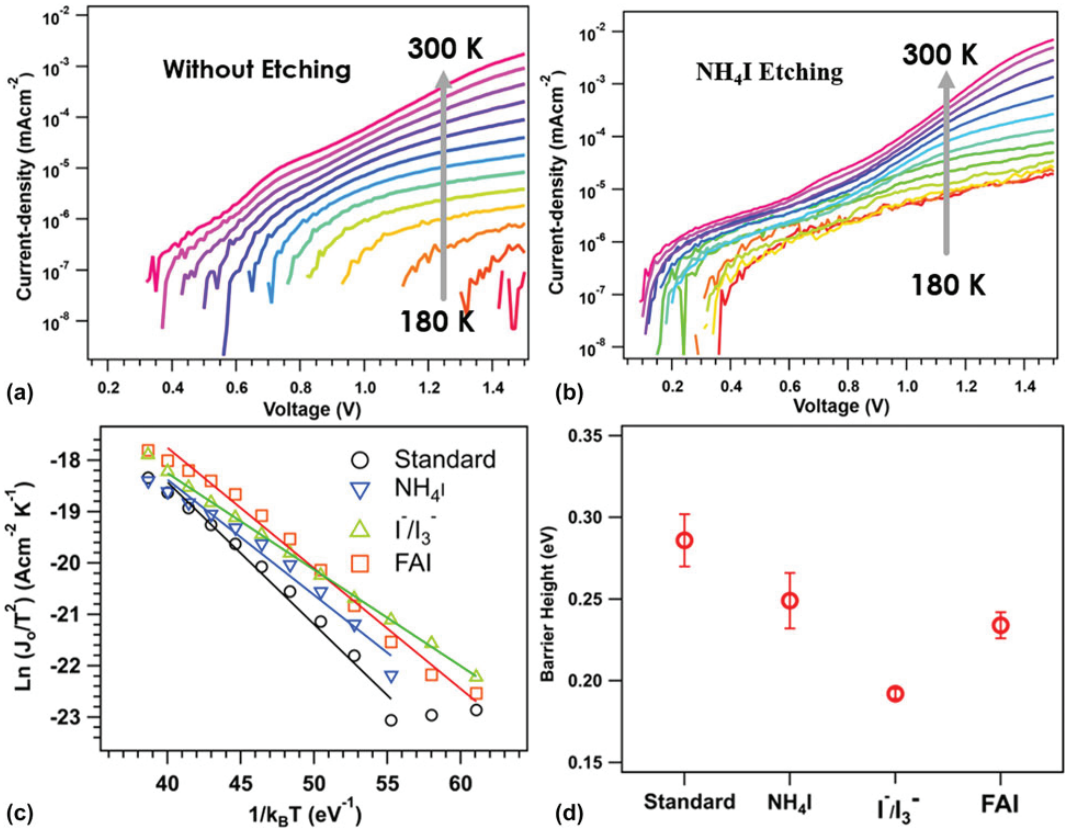


Figure 8: Temperature-dependent current–voltage (*J–V–T*) characteristics of CdTe devices (a) without etching and (b) etching with NH_4I solution. (c) Plots of Ln (J_o/T^2) versus $1/k_BT$ for standard and NH_4I, I^-/I_3^-, and FAI etching and (d) values of back barrier height for standard and etched devices.

treatment of CdTe surface with elemental iodine (I_2), ammonium iodide (NH_4I), I^-/I_3^-, and FAI resulted in very strong vibrational peaks of Te–Te at 120 and 139 cm^{-1} in the Raman spectra. Similarly, the study of surface topography shows Te grains on the surface compared with untreated standard CdTe sample. In the XRD pattern analysis, an additional peak of elemental Te (101) was observed at 2θ angle equal to 27.6°. In case of treatment with elemental iodine, iodine atoms react with Te to produce TeI in β-phase. The device performance of CdTe after etching was improved mainly due to the improvement in open-circuit voltage and FF of the device due to the formation of Te-rich layer. For etched device, the highest open-circuit voltage observed was 841 mV and FF was 78.2% with PCE of 14.0%, while untreated devices have open-circuit voltage of 814 mV FF of 74.0% with PCE of 12.7%. The *J–V–T* characteristics showed reduced back barrier heights for etched devices compared with standard CdTe devices. Thus, this study shows that efficient CdTe devices can be fabricated by etching the CdTe surface with iodine solution.

© Materials Research Society 2019

Approved for public release; distribution unlimited.

Experimental methods

Iodine (I_2, 99.8%) and ammonium iodide (NH_4I, 99.995%) were purchased from Fisher Scientific. FAI (99%), cadmium chloride ($CdCl_2$, 99.999%), anhydrous methanol (CH_3OH, 99.8%), and anhydrous 2-propanol [isopropanol alcohol (IPA), 99.5%] were obtained from Sigma-Aldrich. All the chemicals were used as obtained without further purification. The CdS/CdTe device stacks were fabricated by vapor transport deposit method onto TEC™-15 M glass substrates by Willard & Kelsey Solar Group. The wet $CdCl_2$ treatment was carried out at 390 °C for 30 min using saturated $CdCl_2$ solution in methanol in a dry air environment, washed with methanol and dried under nitrogen flow.

Procedure

Etching with iodine (I_2), ammonium iodide (NH_4I), and mixed I^-/I_3^- solution

The etching procedure was carried out similar to the work of Kurley et al. [19]. A saturated solution of NH_4I in IPA (60 mg/mL, 0.42 M) was prepared by stirring overnight. To keep the same atomic concentration, a 54 mg/mL (0.21 M) solution of I_2 in IPA was also stirred overnight. I^-/I_3^- etching solution was prepared by mixing 94 µL of 0.21 M I_2 in IPA with ~25 mL of 0.42 M NH_4I in IPA. For each etching treatment, around 200 µL of etching solution was placed in CdTe films, kept for 10 s, and spun for 30 s at 4000 rpm. The treated CdTe films were annealed at 150 °C in an air environment for 10 min and rinsed twice with IPA (each 250 µL) and spun for 30 s at 4000 rpm to dry. Similarly, during the device fabrication, the concentrations were varied but time and annealing temperature were held constant.

Etching with FAI solution

FAI solution in IPA was prepared with varying concentrations (50, 125, 250, 375, and 500 mM). The FAI solution was kept at 110 °C for about 1 h with continuous stirring. The CdTe surface was treated with FAI solution for 30 s, then spun at 4000 rpm for 30 s at ambient environment. Then, the films were annealed at 150 °C for 10 min and rinsed twice with IPA. The FAI-treated samples were stored in a nitrogen ambient glove box for further characterization and device fabrication.

Characterization, device fabrication, and testing

The Raman spectroscopy measurement was carried using a Jobin Yvon Horiba confocal Raman spectrometer fitted with HeNe laser source of wavelength 632.8 nm. The XRD patterns were obtained from Rigaku Ultima III X-ray Diffractometer at 40 kV accelerating voltage and 44 mA current. The surface morphology and chemical composition were studied using Hitachi S-4800 UHR SEM fitted with EDS. To complete CdS/CdTe solar cells, 3 nm copper (Cu) and 40 nm gold (Au) were thermally evaporated on the CdTe films. The samples were annealed at 150 °C for 35 min for Cu diffusion at ambient environment. The devices were laser scribed [36] with active device area 0.06 cm^2, and current density versus voltage (J–V) characteristics were measured using standard simulated AM1.5 solar irradiance. EQE was measured as a function of incident light wavelength using a commercial QE system (Model IVQE8-C; PV Measurements Inc.), the monochromatic light intensity of which was calibrated with a reference silicon diode at each wavelength.

Acknowledgments

This material is based on research sponsored by Air Force Research Laboratory under agreement number FA9453-18-2-0037. The U.S. Government is authorized to reproduce and distribute reprints for Governmental purposes notwithstanding any copyright notation thereon. We also thank Willard & Kelsey Solar Group for providing CdS/CdTe device stacks.

Disclaimer: The views and conclusions contained herein are those of the authors and should not be interpreted as necessarily representing the official policies or endorsements, either expressed or implied, of Air Force Research Laboratory or the U.S. Government.

Supplementary material

To view supplementary material for this article, please visit https://doi.org/10.1557/jmr.2019.363.

References

1. **N. Duffy, L. Peter, and R. Wang**: Characterisation of CdS|CdTe heterojunctions by photocurrent spectroscopy and electrolyte electroreflectance/absorbance spectroscopy (EEA/EER). *J. Electroanal. Chem.* **532**, 207 (2002).
2. **A.H. Munshi, J. Kephart, A. Abbas, J. Raguse, J-N. Beaudry, K. Barth, J. Sites, J. Walls, and W. Sampath**: Polycrystalline CdSeTe/CdTe absorber cells with 28 mA/cm^2 short-circuit current. *IEEE J. Photovolt.* **8**, 310 (2018).
3. **N.R. Paudel and Y. Yan**: Enhancing the photo-currents of CdTe thin-film solar cells in both short and long wavelength regions. *Appl. Phys. Lett.* **105**, 183510 (2014).
4. **J.L. Freeouf and J.M. Woodall**: Schottky barriers: An effective work function model. *Appl. Phys. Lett.* **39**, 727 (1981).
5. **B.J. Simonds, V. Palekis, B. Van Devener, C. Ferekides, and M.A. Scarpulla**: Pulsed laser induced ohmic back contact in CdTe solar cells. *Appl. Phys. Lett.* **104**, 141604 (2014).
6. **G.K. Liyanage, A.B. Phillips, F.K. Alfadhili, R.J. Ellingson, and M.J. Heben**: The role of back buffer layers and absorber properties for >25% efficient CdTe solar cells. *ACS Appl. Energy Mater.* **2**, 5419 (2019).

© Materials Research Society 2019

Approved for public release; distribution unlimited.

7. **S.G. Kumar and K.K. Rao**: Physics and chemistry of CdTe/CdS thin film heterojunction photovoltaic devices: Fundamental and critical aspects. *Energy Environ. Sci.* **7**, 45 (2014).
8. **E. Janik and R. Triboulet**: Ohmic contacts to p-type cadmium telluride and cadmium mercury telluride. *J. Phys. D: Appl. Phys.* **16**, 2333 (1983).
9. **C.R. Corwine, A.O. Pudov, M. Gloeckler, S.H. Demtsu, and J.R. Sites**: Copper inclusion and migration from the back contact in CdTe solar cells. *Sol. Energy Mater. Sol. Cells* **82**, 481 (2004).
10. **K.P. Bhandari, X. Tan, P. Zereshki, F.K. Alfadhili, A.B. Phillips, P. Koirala, M.J. Heben, R.W. Collins, and R.J. Ellingson**: Thin film iron pyrite deposited by hybrid sputtering/co-evaporation as a hole transport layer for sputtered CdS/CdTe solar cells. *Sol. Energy Mater. Sol. Cells* **163**, 277 (2017).
11. **A.B. Phillips, R.R. Khanal, Z. Song, R.M. Zartman, J.L. DeWitt, J.M. Stone, P.J. Roland, V.V. Plotnikov, C.W. Carter, and J.M. Stayancho**: Wiring-up carbon single wall nanotubes to polycrystalline inorganic semiconductor thin films: Low-barrier, copper-free back contact to CdTe solar cells. *Nano Lett.* **13**, 5224 (2013).
12. **N.R. Paudel and Y. Yan**: Application of copper thiocyanate for high open-circuit voltages of CdTe solar cells. *Prog. Photovoltaics* **24**, 94 (2016).
13. **K.P. Bhandari, P. Koirala, N.R. Paudel, R.R. Khanal, A.B. Phillips, Y. Yan, R.W. Collins, M.J. Heben, and R.J. Ellingson**: Iron pyrite nanocrystal film serves as a copper-free back contact for polycrystalline CdTe thin film solar cells. *Sol. Energy Mater. Sol. Cells* **140**, 108 (2015).
14. **E. Bastola, K.P. Bhandari, and R.J. Ellingson**: Solution-processed nickel-alloyed iron pyrite thin film as hole transport layer in cadmium telluride solar cells. In *IEEE 44th Photovoltaic Spec. Conf. (PVSC)* (IEEE, Piscataway, 2017); pp. 738–741.
15. **E. Bastola, K.P. Bhandari, and R.J. Ellingson**: Application of composition controlled nickel-alloyed iron sulfide pyrite nanocrystal thin films as the hole transport layer in cadmium telluride solar cells. *J. Mater. Chem. C* **5**, 4996 (2017).
16. **E. Bastola, K.P. Bhandari, I. Subedi, N.J. Podraza, and R.J. Ellingson**: Structural, optical, and hole transport properties of earth-abundant chalcopyrite ($CuFeS_2$) nanocrystals. *MRS Commun.* **8**, 970 (2018).
17. **K.K. Subedi, E. Bastola, I. Subedi, Z. Song, K.P. Bhandari, A.B. Phillips, N.J. Podraza, M.J. Heben, and R.J. Ellingson**: Nanocomposite $(CuS)_x(ZnS)_{1-x}$ thin film back contact for CdTe solar cells: Toward a bifacial device. *Sol. Energy Mater. Sol. Cells* **186**, 227 (2018).
18. **J. Li, D.R. Diercks, T.R. Ohno, C.W. Warren, M.C. Lonergan, J.D. Beach, and C.A. Wolden**: Controlled activation of ZnTe:Cu contacted CdTe solar cells using rapid thermal processing. *Sol. Energy Mater. Sol. Cells* **133**, 208 (2015).
19. **J.M. Kurley, M.G. Panthani, R.W. Crisp, S.U. Nanayakkara, G.F. Pach, M.O. Reese, M.H. Hudson, D.S. Dolzhnikov, V. Tanygin, J.M. Luther, and D.V. Talapin**: Transparent ohmic contacts for solution-processed, ultrathin CdTe solar cells. *ACS Energy Lett.* **2**, 270 (2017).
20. **R. Ochoa-Landín, O. Vigil-Galan, Y.V. Vorobiev, and R. Ramírez-Bon**: Chemically-deposited Te layers improving the parameters of back contacts for CdTe solar cells. *Sol. Energy* **83**, 134 (2009).
21. **T. Song, A. Moore, and J.R. Sites**: Te layer to reduce the CdTe back-contact barrier. *IEEE J. Photovolt.* **8**, 293 (2018).
22. **D.W. Niles, X. Li, P. Sheldon, and H. Höchst**: A photoemission determination of the band diagram of the Te/CdTe interface. *J. Appl. Phys.* **77**, 4489 (1995).
23. **S.C. Watthage, A.B. Phillips, G.K. Liyanage, Z. Song, J.M. Gibbs, F.K. Alfadhili, R.B. Alkhayat, R.H. Ahangharnejhad, Z.S. Almutawah, and K.P. Bhandari**: Selective Cd removal from CdTe for high-efficiency Te back-contact formation. *IEEE J. Photovolt.* **8**, 1125 (2018).
24. **J. Sarlund, M. Ritala, M. Leskelä, E. Siponmaa, and R. Zilliacus**: Characterization of etching procedure in preparation of CdTe solar cells. *Sol. Energy Mater. Sol. Cells* **44**, 177 (1996).
25. **V. Ivanits'Ka, P. Moravec, J. Franc, Z. Tomashik, P. Feychuk, V. Tomashik, L. Shcherbak, K. Mašek, and P. Höschl**: Chemical etching of CdTe in aqueous solutions of H_2O_2–HI-citric acid. *J. Electron. Mater.* **36**, 1021 (2007).
26. **P. Moravec, V. Ivanits'ka, J. Franc, Z. Tomashik, V. Tomashik, K. Mašek, P. Feychuk, L. Shcherbak, P. Höschl, and R. Grill**: Chemical interaction of CdTe and CdZnTe with aqueous solutions of H_2O_2-HI-tartaric acid. *J. Electron. Mater.* **38**, 1645 (2009).
27. **P. Moravec, Z. Tomashik, V. Ivanits'Ka, V. Tomashik, J. Franc, K. Mašek, and P. Höschl**: Slow-polishing iodine-based etchant for CdTe and CdZnTe single crystals. *J. Electron. Mater.* **41**, 2838 (2012).
28. **A.J. Ricco, H.S. White, and M.S. Wrighton**: X-ray photoelectron and Auger electron spectroscopic study of the CdTe surface resulting from various surface pretreatments: Correlation of photoelectrochemical and capacitance-potential behavior with surface chemical composition. *J. Vac. Sci. Technol., A* **2**, 910 (1984).
29. **A. Bensouici, V. Carcelen, J. Plaza, S. De Dios, N. Vijayan, J. Crocco, H. Bensalah, E. Dieguez, and M. Elaatmani**: Study of effects of polishing and etching processes on $Cd_{1-x}Zn_xTe$ surface quality. *J. Cryst. Growth* **312**, 2098 (2010).
30. **V. Ivanits'ka, P. Moravec, J. Franc, V. Tomashik, Z. Tomashik, K. Mašek, P. Chukhnenko, P. Höschl, and J. Ulrych**: Chemical polishing of CdTe and CdZnTe in iodine–methanol etching solutions. *J. Electron. Mater.* **40**, 1802 (2011).
31. **R.A. Awni, D.B. Li, C.R. Grice, Z. Song, M.A. Razooqi, A.B. Phillips, S.S. Bista, P.J. Roland, F.K. Alfadhili, and R.J. Ellingson**: The effects of hydrogen iodide back surface treatment on CdTe solar cells. *Sol. RRL* **3**, 1800304 (2019).
32. **B.J. Simonds, H.J. Meadows, S. Misra, C. Ferekides, P.J. Dale, and M.A. Scarpulla**: Laser processing for thin film chalcogenide

© Materials Research Society 2019

Approved for public release; distribution unlimited.

photovoltaics: A review and prospectus. *J. Photonics Energy* **5**, 050999 (2015).

33. **D.K. Koll, A.H. Taha, and D.M. Giolando**: Photochemical "Self-healing" pyrrole based treatment of CdS/CdTe photovoltaics. *Sol. Energy Mater. Sol. Cells* **95**, 1716 (2011).
34. **M.M. Tessema and D.M. Giolando**: Pinhole treatment of a CdTe photovoltaic device by electrochemical polymerization technique. *Sol. Energy Mater. Sol. Cells* **107**(Suppl. C), 9 (2012).
35. **A. Niemegeers and M. Burgelman**: Effects of the Au/CdTe back contact on IV and CV characteristics of Au/CdTe/CdS/TCO solar cells. *J. Appl. Phys.* **81**, 2881 (1997).
36. **A.B. Phillips, Z. Song, J.L. DeWitt, J.M. Stone, P.W. Krantz, J.M. Royston, R.M. Zeller, M.R. Mapes, P.J. Roland, M.D. Dorogi, S. Zafar, G.T. Faykosh, R.J. Ellingson, and M.J. Heben**: High speed, intermediate resolution, large area laser beam induced current imaging and laser scribing system for photovoltaic devices and modules. *Rev. Sci. Instrum.* **87**, 093708 (2016).

© Materials Research Society 2019

Approved for public release; distribution unlimited.

Effects of Fabrication Atmosphere on Bulk and Back Interface Defects of CdTe Solar Cells with CdS and MgZnO Buffers

Rasha A. Awni,[1] Deng-Bing Li,[1] Zhaoning Song,[1] Sandip S. Bista,[1] Mohammed A. Razooqi,[1] Corey R. Grice[1], Lei Chen,[1] Geethika K. Liyanage[1], Chongwen Li,[1] Adam B. Phillips,[1] Michael J. Heben,[1] Randy J. Ellingson,[1] Jian V. Li,[2] and Yanfa Yan[1]

[1]Department of Physics and Astronomy, and Wright Center for Photovoltaics Innovation and Commercialization (PVIC), University of Toledo, Toledo, OH 43606, USA
[2]Department of Aeronautics and Astronautics, National Cheng Kung University, Tainan 70101, Taiwan

***Abstract* — The performance of Cadmium telluride (CdTe) solar cell devices is limited by the properties of front and back interfaces as well as the absorber layer, which can be influenced by the fabrication atmosphere. In this work, we report a detailed study of electrical properties of ZnMgO (ZMO)/CdTe and cadmium sulfide (CdS)/CdTe solar cells with the cadmium chloride ($CdCl_2$) treatment performed in different atmospheres using temperature-dependent impedance spectroscopy and capacitance – voltage measurements. An equivalent circuit model consisting of two serial combinations of the front and back junctions is employed to fit the complex impedance spectra of devices measured in dark. Fitted data from equivalent circuit provides the value of each element, from which the bulk conductivity, back contact barrier height, as well as spatial inhomogeneities within the cell are extracted. Impedance spectroscopy analysis shows that there are negative and positive effects of back surface treatment in oxygen free ambient on device performance. For oxygen-free treatment, an obvious increase in the bulk conductivity is observed, suggesting an increased copper doping in the device. Additionally, ZMO devices show less junction inhomogeneity. All these improvements lead to better device performance of ZMO/CdTe solar cells.**

***Index Terms* — CdTe, photovoltaic cells, impedance spectroscopy, capacitance - voltage.**

I. Introduction

Cadmium telluride (CdTe) thin film solar cells have been proven as a low-cost high-efficiency photovoltaic technology. In the past decades, cadmium sulfide (CdS) is widely used as the emitter (or the buffer layer) in CdTe solar cells [1]. However, CdS buffer layer has an intrinsic limitation on the short-circuit current in CdTe solar cells due to high parasitic absorption of short-wavelength photons. Recently, alternative wide-bandgap buffer layers have been employed to improve the optical transmission, including MgZnO (MZO), $ZnSnO_x$ (ZTO), $Cd_{1-x}Zn_xS$, and CdMgTe [2 – 4]. The use of these buffers benefits the diode-quality of the main junction and thus enhance the power conversion efficiency of CdTe solar cells.

Impedance spectroscopy (IS) is a powerful characterization technique that is widely characterize various electronic devices. Particularly for solar cells, IS analysis provides an evaluation of energy levels of majority carrier traps in the absorber layer. Through an equivalent circuit analysis that models the frequency response of the device, IS analysis help better understand the device physics [5].

Our recent [6] work has shown that the performance of ZMO/CdTe solar cells can be significantly affected by the atmosphere in which the $CdCl_2$ treatment is carried out.

In this work, we investigate the effects of fabrication atmosphere on electrical properties of the ZMO/CdTe and CdS/CdTe solar cells by using temperature-dependent IS measurements and *C–V* measurements. Particularly, we use equivalent circuit modeling to study the junction-behaviors at the front and back.

II. Experimental Details

CdTe solar cells were fabricated on fluorine-doped tin oxide (FTO) glass substrates (TEC 15M; Pilkington NA). The substrates were cleaned sequentially with Micro-90 detergent in an ultrasonic bath in hot water (~70˚C) for an hour, submerged in de-ionized water for 30 min for 4 times, then rinsed with de-ionized water and dried with nitrogen. For the ZMO/CdTe devices, 80 nm ZMO layer was deposited on FTO at ambient temperature by radiofrequency (RF) sputtering using a ZMO target with 8 wt% magnesium oxide (MgO) under mixed flow gas of 2% oxygen and 98% argon. Then a ~2.8 μm CdTe film was deposited by close space sublimation (CSS) with a source temperature of 560 ˚C and a substrate temperature of 495 ˚C at 1 Torr. For the CdS/CdTe devices, an 85 nm CdS buffer layer was deposited on FTO by radiofrequency (RF) sputtering under a mixed gas flow rate of 40 sccm with a composition of 2% oxygen and 98% argon, followed by depositing a ~3 μm CdTe films by close space sublimation. A saturated solution of $CdCl_2$ in methanol was applied to the CdTe film surfaces drop-wise and then annealed at 390 ˚C for 30 min in dry air and oxygen free ambient and with a 500 sccm flowrate, i.e., ZMO/CdTe-dry-air, -oxygen-free, CdS/CdTe-dry-air, and -oxygen-free. After the samples cooled to room temperature, excess $CdCl_2$ was removed by rinsing with methanol. After that, a bilayer of copper (Cu) (~3 nm) and gold (Au) (40 nm) was deposited by thermal

Authorized licensed use limited to: University of Edinburgh. Downloaded on June 14,2020 at 14:39:06 UTC from IEEE Xplore. Restrictions apply.

Approved for public release; distribution unlimited.

evaporation via a shadow mask with an individual cell area of 0.08 cm^2. Finally, the devices were annealed in nitrogen at 200 ˚C for 20 min to promote Cu diffusion into the CdTe.

Temperature dependent impedance spectroscopy and capacitance – voltage (*C–V*) measurements were performed using a Solartron Modulab potentiostat equipped with a frequency response analyzer (Ametek Inc.). The measurements were performed under a constant AC modulation voltage of 45 mV_{rms} and dark. The impedance spectroscopy measurements were done with frequency sweeping from 1.0 MHz to 0.1 Hz and 0V DC bias, and *C–V* measurements with voltage sweeping from -2.5 V to 0.8 V and 10 kHz AC frequency. Low temperature measurements were performed liquid-nitrogen cooled cryogenic system (Janis VPF-100) with temperature from 150 to 300 K with a step size of 10 K. The temperature was controlled by a temperature controller (Lakeshore 330). A temperature sensor was mounted on the top of the device directly, to ensure that the recorded temperature is the device temperature. The equivalent circuit model fitting of the Nyquist plots was done using RelaxIS impedance spectrum analysis software.

III. Results and Discussion

We employed impedance spectroscopy as a useful method to study both the front and back junctions, as well as absorber bulk properties of CdS/CdTe and ZMO/CdTe solar cell device with $CdCl_2$ treatment performed in dry air and oxygen free environment. Fig. 1 shows an equivalent circuit model consisting of two sub-circuits connected in series: one is attributed to the back contact (subscript t) and the other is assigned to the front junction (the main p-n junction subscript j and CdTe bulk defects subscript t). The circuit model was used to fit Nyquist plots according to the literature [1]. The fitting results are in a good agreement with the experimental data. Fig. 2 illustrates the Nyquist plots, i.e., imaginary versus real parts of complex impedance, of four types of devices investigated in this study, measured at 300 K and 0 V bias voltage.

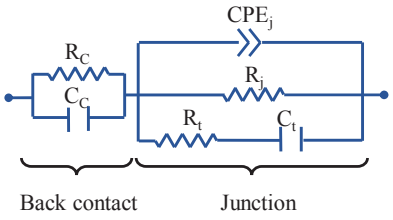


Fig. 1 The equivalent circuit model that was used to fit the complex impedance Nyquist plot, with the elements *R*, *C*, and *CPE* represent the resistance, capacitance, and constant phase element, respectively, with two sub-circuits connected in series, one is due to the back contact (subscript c) and the other part due to the p-n junction and the bulk material (subscripts j and t). All fitting parameters are used as free.

The electrical parameters of the equivalent circuit model are extracted via regression fitting and listed in Table 1, with *R*, *C*, and *CPE* elements representing the resistance, capacitance, and constant phase element. In impedance spectroscopy analysis, the Schottky barrier at the CdTe/Au interface was introduced as a parallel assembly of *R-C* combination that is connected in series with the front junction [1]. A slight decrease in the back contact capacitance (C_c) and a significant decrease (more than two orders of magnitude) in the back contact resistance (R_c) in is observed in the oxygen-free devices (Table I). This is likely due to that the $CdCl_2$ treatment in dry air facilitates the formation of oxides at the back surface which create additional barriers to holes [7].

TABLE 1.
Summary of the fitted parameters from Nyquist plots the IS measurements were performed under dark, at room temperature and with 10 kHz AC frequency for CdS/CdTe and ZMO/CdTe -dry-air and -oxygen-free solar cell devices.

	CdS/CdTe		ZMO/CdTe	
	Dry air	Oxygen Free	Dry air	Oxygen free
R_c (Ω)	$1.91x10^{+08}$	$1.21x10^{+06}$	$5.86x10^{+08}$	$2.41x10^{+05}$
C_c (F)	$2.79x10^{-09}$	$1.80x10^{-09}$	$2.12x10^{-09}$	$1.01x10^{-09}$
R_j (Ω)	$2.72x10^{+07}$	$2.92x10^{+08}$	$5.04x10^{+07}$	$1.67x10^{+08}$
Q_j ($F.s^{\alpha}$)	$8.26x10^{-09}$	$8.58x10^{-09}$	$2.37x10^{-9}$	$2.76x10^{-09}$
α_j	0.4	0.52	0.66	0.71
R_t (Ω)	$7.52x10^{+03}$	$9.84x10^{+03}$	$1.36x10^{+04}$	$1.27x10^{+04}$
C_t (F)	$8.30x10^{-10}$	$6.01x10^{-10}$	$4.52x10^{-10}$	$3.92x10^{-10}$

The back barrier height ($q\Phi$) is calculated from the fitted back contact resistance at different temperatures using Arrhenius plots form and the following equation:

$$R_c = \frac{B_0}{T^2} exp \frac{q\phi}{k_B T} \quad (1)$$

where B_0 is a pre-exponential factor independent of temperature, T is the absolute temperature, q is the elementary charge, and k_B is Boltzmann constant.

The back-barrier height is ~ 0.48 eV in both CdS/CdTe and ZMO/CdTe -dry-air. Since both devices have the same back contact, the back barrier heights are likely to be identical, regardless the buffer layer, assuming Cu doping profiles in the bulk CdTe are the same. In contrast, for both CdS/CdTe and ZMO/CdTe -oxygen-free devices, the back barriers are reduced by ~ 25%, to 0.36 eV. A similar trend was found in our previous work [1]. The reduction of the back barrier by conducting the treatment in an oxygen free atmosphere is attributed to the change of chemical reactions at the CdTe back surface. Oxygen free environment prevents the formation of oxides at the CdTe back surface and facilitates

Authorized licensed use limited to: University of Edinburgh. Downloaded on June 14,2020 at 14:39:06 UTC from IEEE Xplore. Restrictions apply.

Approved for public release; distribution unlimited.

Cu diffusion. On the other hand, the fabrication of the device in the different atmospheres influences the main junction behavior. The bulk resistance (R_j) listed in Table 1 is lower in the -oxygen-free devices. The conductivity (σ) of CdTe is inversely proportional to the bulk resistance, $\sigma=t/AR_j$, where t and A are the absorber thickness and active area. Accordingly, -oxygen-free devices have higher conductivity than in -dry-air devices, which is likely due to the facilitated Cu diffusion to the main junction.

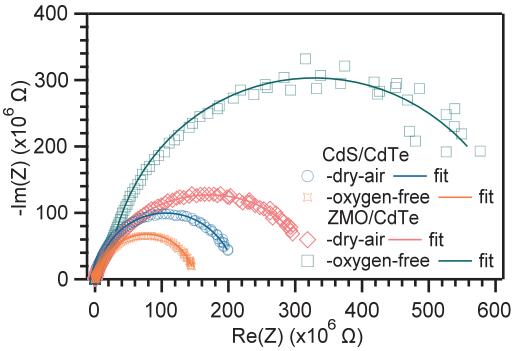


Fig. 2. Nyquist plots, real vs imaginary parts of impedance measured at 300 K at 0 V bias voltage for ZMO/CdTe, CdS/CdTe -dry-air and -oxygen-free solar cell. The markers are the raw data and the solid lines are the fitted curves using the suggested equivalent circuit model in Fig. 1.

The impedance of constant phase element ($Z_{CPE}=1/(i\omega)^{\alpha_j}Q_j$, where i,=√-1, is the imaginary part, ω is the angular frequency, and Q_j represents a pure capacitance if $\alpha_j=1$ and a pure resistance if $\alpha_j=0$ [8]) is introduced in the combination of the front junction as the capacitance of the main p-n junction. The *CPE* usually appears in the modeling the behavior of the imperfect absorber dielectrics and interfaces inhomogeneities that might be due to grain boundaries in CdTe bulk layer [8]. Here, Q_j most likely is the geometrical capacitance (only when $\alpha_j=1$), $C_g=\varepsilon_0\varepsilon_r A/t$, where ε_0 and ε_r are absolute permittivities of vacuum and the relative permittivity of CdTe respectively. It is observed that Q_j of CdS/CdTe devices are larger than the ones of ZMO/CdTe devices (Table I). Because Q_j is proportional to t, the difference in Q is attributed to the difference in CdTe layer thickness. Note that the α values of -oxygen-free devices are higher than the that of dry-air devices, and it is higher in ZMO/CdTe than that in CdS/CdTe devices, possibly suggesting few imperfections and better interface homogeneities.

The carrier recombination is described by the recombination/defect resistance, R_t, and capacitance, C_t, listed in Table 1, which may vary depending on the defects at main junction and bulk grain boundaries.

The capacitance–voltage measurements were performed for ZMO/CdTe and CdS/CdTe devices to further understand the role of $CdCl_2$ treatment atmosphere on the bulk material quality. Fig. 3a shows the Mott–Schottky plots of CdS/CdTe and ZMO/CdTe -dry-air and -oxygen-free solar cell devices measured in dark, at room temperature, and with 10 kHz AC frequency. The capacitance at reverse bias voltage is higher in CdS/CdTe than in ZMO/CdTe solar cells, which is likely due to the thicker CdTe layer in CdS/CdTe (~ 3μm) than in ZMO/CdTe (~ 2.8μm) devices.

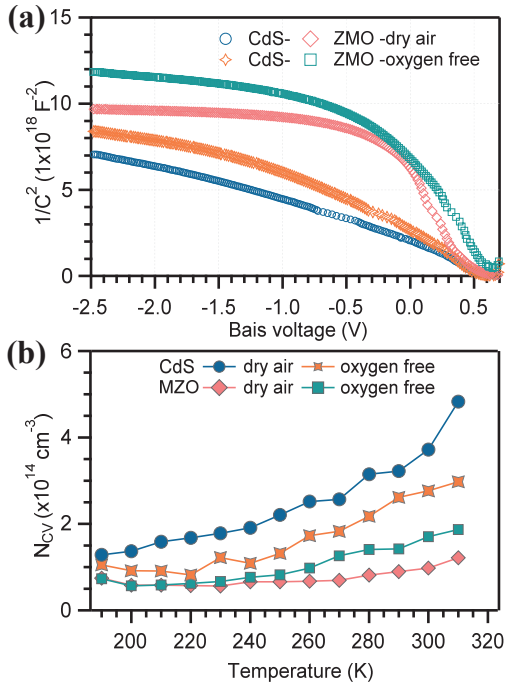


Fig. 3. (a) Room temperature C–V measurements/Mott – Schottky plots and (b) the apparent carriers concentration, N_{CV}, as a function of temperatures of CdS/CdTe and ZMO/CdTe -dry-air and -oxygen-free solar cell device of measured under dark and with 10kHz AC frequency.

The built-in potential (V_{bi}) across the main junction with an open-circuit is created due to the electric field that is formed by the diffusion of free carriers from both buffer and absorber layers across the main junction in the opposite direction into the regions where there are large numbers of charged impurities. As a result, the charge density of each layer will be filled with opposite charged ions, creating a depletion zone consisting of acceptor ions, with density N_A, in the absorber layer and donor ions, with density N_D, in the buffer layer. In the other word, the V_{bi} determines the band bending of the main junction. The width of the band bending region, or the space charge region, depends on the doping densities in the buffer and absorber layers. The x-axis intercept of the Mott – Schottky plot, $1/C^2$ versus bias voltage, determines V_{bi} using the following equation:

Authorized licensed use limited to: University of Edinburgh. Downloaded on June 14,2020 at 14:39:06 UTC from IEEE Xplore. Restrictions apply.

Approved for public release; distribution unlimited.

$$V_{bi} = \frac{k_B T}{q} \ln\left[\frac{N_D N_A}{n_i^2}\right] \quad (2)$$

where n_i is the intrinsic concentration. From Fig. 3a, the apparent built-in potential of ZMO/CdTe-oxygen free device is the highest among all the devices, which is ~ 0.7 V. The high V_{bi} may be due to the high doping densities in the buffer and absorber layers.

The apparent carrier concentration (N_{CV}) of the CdTe layer is calculated using the linear slope of the Mott – Schottky plot and the equation:

$$N_{CV} = -\frac{2}{q\varepsilon\varepsilon_0}\left[\frac{dC^{-2}(V)}{dV}\right]^{-1} \quad (3)$$

Fig. 3b shows the temperature-dependent charge carrier concentrations of CdS/CdTe and ZMO/CdTe solar cells. In all devices, the carrier density decreases when temperature decreases from 300 to 200 K due to impurities freezeout. This phenomenon is more pronounced in ZMO/CdTe devices than in CdS/CdTe. This may be due to the variation of surface morphology and the smaller grain of ZMO buffer that may influence the properties of defects in the CdTe. Additionally, diffusion of ions along the grain boundaries (GBs), particularly, oxygen and copper, plays an important role in modification of the GB electrical behavior [9]. The CdS/CdTe-dry air device shows the highest carrier concentration, N_{CV} at 300 K~ 3.7 x 10^{14} cm^{-3}, among all of the devices. Comparably, the carrier concentration in CdS/CdTe -oxygen-free cell is ~ 2.8 x 10^{14} cm^{-3} at 300 K. Carrier concentrations in ZMO/CdTe solar cells are less than that in CdS/CdTe cells. ZMO/CdTe -oxygen-free device shows a carrier concentration of ~ 1.7 x 10^{14} cm^{-3} at 300 K, which is higher than that in the -dry-air device (~ 9.8 x 10^{13} cm^{-3} at 300 K). This carrier concentration is related to Cu doping and other impurities, such as oxygen diffusion through GBs channel and termination of dangling bonds in GBs that might be different in ZMO than CdS devices.

IV. Conclusion

Impedance spectroscopy analysis and its equivalent circuit model give a valuable insight on the electrical properties of the front and back junctions of CdS/CdTe and ZMO/CdTe solar cell devices. The $CdCl_2$ treatment in oxygen free ambient appears to visibly remove the oxides and chlorides from the back surface promotes pathways for cupper to diffuse via the absorber reaching the main junction. The Cu diffusion results in reducing the back barrier height and increasing the absorber conductivity of both devices. $CdCl_2$ treatment in dry air lead to higher back barrier heights and less absorber conductivity in both ZMO and CdS based devices. Additionally, ZMO devices show less junction inhomogeneity than CdS devices, which could be responsible for the better device performance.

VI. Acknowledgement

This material is based on research sponsored by Air Force Research Laboratory under agreement number FA9453-18-2-0037. The U.S. Government is authorized to reproduce and distribute reprints for Governmental purposes notwithstanding any copyright notation thereon. The views and conclusions contained herein are those of the authors and should not be interpreted as necessarily representing the official policies or endorsements, either expressed or implied, of Air Force Research Laboratory or the U.S. Government. R. A. Awni was financially supported by the Higher Committee for Education Development (HCED) in the scholarship program started in 2009 with funding from the Iraqi Prime Minister's Office. J. V. Li is supported by Ministry of Science and Technology, Taiwan, under grant number MOST 107-2218-E-006-022-MY3.

References

[1] R.A. Awni, D.-B. Li, C.R. Grice, Z. Song, M.A. Razooqi, A.B. Phillips, S.S. Bista, P.J. Roland, F.K. Alfadhili, R.J. Ellingson, M.J. Heben, J.V. Li, and Y. Yan, "The Effects of Hydrogen Iodide Back Surface Treatment on CdTe Solar Cells," *Solar RRL*, vol. 46, pp. 1800304, 2019.

[2] X. Wu, " High-efficiency polycrystalline CdTe thin-film solar cells," *Solar Energy*, Vol. 77, pp. 803–814, 2004.

[3] K.L. Chopra, P.D. Paulson and V. Dutta, " Thin-Film Solar Cells: An Overview," *Progress in Photovoltaics*, vol. 12, pp. 69, 2004.

[4] T. Song, A. Kanevce, and J. Sites, " Emitter/Absorber Interface of CdTe Solar Cells," *Journal of Applied Physics*, vol. 119, pp. 233104, 2016.

[5] Y.Y. Proskuryakov, K. Durose, B.M. Taele, S. Oelting, " Impedance spectroscopy of unetched CdTe/CdS solar cells-equivalent circuit analysis," *Journal of Applied Physics*, vol. 102, pp. 024504, 2007.

[6] D.-B. Li, Z. Song, R.A. Awni, S.S. Bista, N. Shrestha, L. Chen, G.K. Liyanage, A.B. Phillips, M.J. Heben, R.J. Ellingson, and Y. Yan, "Eliminating S-Kink to Maximize the Performance of MgZnO/CdTe Solar Cells," *ACS Applied Energy Materials,* vol. 2, pp. 242896, 2019.

[7] R.A. Awni, D.-B. Li, Z. Song, S.S. Bista, M.A. Razooqi, C.R. Grice, L. Chen, G.K. Liyanage, C. Li, A.B. Phillips, M.J. Heben, R.J. Ellingson, J.V. Li, and Y. Yan, "Influences of buffer material and fabrication atmosphere on the electrical properties of CdTe solar cells," unpublished.

[8] J. Bisquert, G. Garcia-Belmonte, P. Bueno, E. Longo, L.O.S. Bulhões, "Impedance of constant phase element (CPE)-blocked diffusion in film electrodes," *Journal of Electroanalytical Chemistry,* vol. 452, pp. 229, 1998.

[9] Y.Y. Proskuryakov, K. Durose, M.K. Al Turkestani, I. Mora-Seró, G. Garcia-Belmonte, F. Fabregat-Santiago, J. Bisquert, V. Barrioz, D. Lamb, S.J.C. Irvine, and E.W. Jones, "Impedance spectroscopy of thin-film CdTe/CdS solar cells under varied illumination," *Journal of Applied Physics*, vol. 106, pp. 044507, 2009.

Authorized licensed use limited to: University of Edinburgh. Downloaded on June 14,2020 at 14:39:06 UTC from IEEE Xplore. Restrictions apply.

Approved for public release; distribution unlimited.

Solar Energy 194 (2019) 742–750

Contents lists available at ScienceDirect

Solar Energy

journal homepage: www.elsevier.com/locate/solener

Improved optoelectronic properties in $CdSe_xTe_{1-x}$ through controlled composition and short-range order

B.B. Dumre[a], N.J. Szymanski[a,b], V. Adhikari[a], I. Khatri[a], D. Gall[c], S.V. Khare[a,*]

[a] Department of Physics and Astronomy, University of Toledo, Toledo, OH 43606, USA
[b] Department of Material Science and Engineering, University of California, Berkeley, CA 94720-1760, USA
[c] Department of Materials Science and Engineering, Rensselaer Polytechnic Institute, Troy, NY 12180, USA

ARTICLE INFO

Keywords:
$CdSe_xTe_{1-x}$ alloys
Phase diagram
Optical properties
Bandgap-bowing
Short range order

ABSTRACT

We employ first principles methods based on density functional theory and beyond to study $CdSe_xTe_{1-x}$ alloys in the zincblende and wurtzite structures. From the cluster expansion formalism, we provide a detailed phase diagram showing a consolute temperature of 325 K, above which miscibility may be achieved. In the random solid solution, a zincblende-to-wurtzite phase boundary is found to range from Se concentrations of $x = 0.5$–0.6, in agreement with experiment, owing to increasing ionic character of the Cd-anion bonds. Disordered $CdSe_xTe_{1-x}$ configurations are modeled using special quasirandom structures, for which optoelectronic properties are computed with the hybrid HSE06 functional. Alloying is shown to cause strong bowing effects in the band gap and effective electron/hole masses, which we attribute to local structural distortions as illustrated by analysis of bond length distributions. Downward bowing in the band gap and effective hole mass of the zincblende structure is highlighted for its potential benefits in photovoltaics through increased net photocurrent. Absorption coefficients and reflectivity are also reported, showing promising results in zincblende $CdSe_xTe_{1-x}$ as indicated by substantial optical absorption throughout all Se concentrations. Lastly, we identify the presence of short-range order in $CdSe_xTe_{1-x}$ characterized by clustering among like atoms in order to minimize strain. The degree of clustering, which may be tuned by temperature, also controls the magnitude of the band gap. Therefore, we propose both composition and short-range order as effective tools to be utilized in the design and synthesis of improved solar cell absorber layer materials.

1. Introduction

Among thin film solar cell technologies, those based on CdTe as an absorber layer hold the largest market share owing to their robust longevity, high efficiency (~22%), and low cost (Green et al., 2018; Swanson et al., 2017; Zweibel, 1992). While the theoretical limit has been nearly achieved in the short-circuit current density (J_{SC}) of superstrate CdTe cells (Geisthardt et al., 2015), the corresponding open-circuit voltage (V_{OC}) is typically well below its potential maximum, displaying values of 0.84–0.88 V as opposed to the limit of ~1.2 V (Geisthardt et al., 2015; Gloeckler et al., 2013). As a result, the fill factor (FF) is decreased and the highest observed power conversion efficiencies (PCEs) lie ~10% below the 32% Shockley-Queisser limit (Shockley and Queisser, 1961) for CdTe-based photovoltaics (PV) (Green et al., 2018). To improve upon this constraint and climb the Shockley-Queisser curve, efficiency can be increased by decreasing the band gap through alloying with CdS, a commonly used window layer in CdTe cells (Paudel and Yan, 2014). However, ~10% lattice mismatch (Terheggen et al., 2004) between CdS and CdTe keeps the solubility of dopants low, a high defect density in the graded $CdTe_{1-x}S_x$ layer increases carrier recombination rates (Gessert et al., 2013; Perrenoud et al., 2013), and thus parasitic absorption in wavelength range of 300–500 nm in CdS doesn't impart net photo-current (Romeo et al., 2004). In contrast, recent investigations have suggested that CdSe may be a more suitable choice to alloy with CdTe in hopes of increasing PCE (Green et al., 2018). While CdSe exists in the wurtzite ground state, $CdSe_xTe_{1-x}$ alloys have been shown to remain stable in either the zincblende (Islam et al., 1995; Uthanna and Reddy, 1983; Mangalhara et al., 1989) or wurtzite (Murali and Jayasuthaa, 2009; Belyaev and Kalinkin, 1988) structure depending on the concentration and temperature of synthesis. As the lattice mismatch of CdTe and CdSe is relatively small (~6% difference in lattice constant (Cai et al., 2012), the solubility of Se into Te is much higher than that of S, and the corresponding defect density is low, allowing for minimal effects on the

* Corresponding author.
E-mail address: sanjay.khare@utoledo.edu (S.V. Khare).

https://doi.org/10.1016/j.solener.2019.10.091
Received 12 September 2019; Accepted 31 October 2019
Available online 14 November 2019
0038-092X/ © 2019 International Solar Energy Society. Published by Elsevier Ltd. All rights reserved.

Approved for public release; distribution unlimited.

recombination rate (Lingg et al., 2018). Although the band gap of CdSe (1.70 eV) (Kale and Lokhande, 2004) is higher than that of CdTe (1.50 eV) (Compaan et al., 1996), bowing effects cause the band gap to decrease at low to intermediate Se concentrations, resulting in enhanced PCE as the gap approaches the ideal Schockley-Queisser value (Hannachi and Bouarissa, 2008; Yang and Wei, 2019). Higher dopant levels may also be achieved in $CdSe_xTe_{1-x}$ as opposed to CdTe, which generally displays low carrier concentrations on the order of 10^{14} cm^{-3}, hence further increasing the possible photo-current (Kanevce et al., 2017). Additionally, as $CdSe_xTe_{1-x}$ spans a wide range of band gaps (1.3–1.7 eV), a graded absorber layer may be utilized to gain a greater degree of absorption throughout wavelengths in the visible spectrum (Jamal et al., 2016).

Though many papers (Swanson et al., 2017; Gloeckler et al., 2013; Gessert et al., 2013; Islam et al., 1995; Uthanna and Reddy, 1983; Mangalhara et al., 1989; Murali and Jayasuthaa, 2009; Belyaev and Kalinkin, 1988; Cai et al., 2012; Lingg et al., 2018; Baines et al., 2018; Poplawsky et al., 2016; Zhao et al., 2016; Strauss and Steininger, 1970) have been conducted to shed light on the properties and applications of the $CdSe_xTe_{1-x}$ system, some key issues need further investigation. Generally, experimental characterization of the binary CdTe-CdSe binary phase diagram has been constrained to high temperatures (Poplawsky et al., 2016; Strauss and Steininger, 1970). Hence, further work is needed to clarify the detailed phase stability of the zincblende and wurtzite structures throughout all temperatures and concentrations of interest. Moreover, theoretical methods may provide unique insight into the system by disentangling configurational and thermal contributions to the entropy, as well as temperature-dependent local bonding configurations, allowing a greater understanding into the underlying physics to be attained (Ozolins et al., 1998). With respect to the optoelectronic properties of $CdSe_xTe_{1-x}$ alloys, the majority of previous experimental works have focused on the zincblende structure (Hannachi and Bouarissa, 2008; Ouendadji et al., 2011; Shakil et al., 2016), while relatively little work has been done regarding the wurtzite phase (Reshak et al., 2011). As a result, an accurate tabulation of the band gaps and absorption coefficients remains absent for the wurtzite phase. While theory may be used to fill these gaps in data, the methods implemented must be chosen carefully. Recent works have shown that advanced techniques going beyond standard density functional theory, e.g., hybrid functionals, are necessary to accurately describe bowing effects of electronic properties in zincblende $CdSe_xTe_{1-x}$ (Yang and Wei, 2019). However, such methods remain untested with respect to the corresponding optical properties, for which the complete frequency- and compositional-dependence has yet to be characterized. Furthermore, effective electron and hole masses, which are crucial properties influencing the resulting photo-current and PCE (Granas et al., 2016), are unknown at intermediate concentrations. Should each of these properties be reported and their origin be understood, it may help clarify whether $CdSe_xTe_{1-x}$ represents an effective improvement upon conventional CdTe solar cells.

Throughout this work, we investigate the aforementioned issues by employing first principles methods to elucidate the fully detailed structural, thermodynamic, and optoelectronic properties of the $CdSe_xTe_{1-x}$ system in the zincblende and wurtzite structure. From analysis of calculations performed within the framework of the cluster expansion (CE) (Sanchez et al., 1984; Ducastelle and Ducastelle, 1991; De Fontaine, 1994; Zunger, 1994) and Monte Carlo (MC) (Newman and Barkema, 1999; Heermann, 1988; Dünweg and Landau, 1993; Laradji et al., 1995) formalisms, we characterize the phase stability of $CdSe_xTe_{1-x}$, showing that solubility may be achieved in the zincblende structure at low Se concentrations (< 60%) and above moderate temperatures (~325 K). The miscibility gap at low temperatures is attributed to the minor lattice mismatch of CdTe and CdSe, illustrated through bond length analysis. Such variations in bond lengths also cause bowing of the band gap, for which predictive values calculated using the hybrid HSE06 functional are presented. Good agreement with available experimental data is obtained. Calculated effective masses of electrons and holes are found to increase with Se concentration, which may limit photo current PCE. However, these effects may be offset at low Se concentrations by negative effective hole mass bowing, the potential for increased V_{OC}, and decreased reflectivity throughout the visible range. Furthermore, we find that short-range order, which correlates strongly with temperature shortly above the miscibility gap owing to covalent Te-Se interactions, may be utilized to finely tune the optoelectronic properties of $CdSe_xTe_{1-x}$ absorber layers.

2. Computational methods

All density functional theory calculations have been performed using the Vienna Ab initio Simulation package (VASP) (Kresse and Furthmuller, 1996; Kresse and Hafner, 1993; Kresse and Furthmuller, 1996; Kresse and Hafner, 1994). The projector augmented wave (PAW) method (Blochl, 1994; Kresse and Joubert, 1999) was employed with the generalized gradient approximation (GGA) in the form of the Perdew-Burke-Ernzerhof (PBE) exchange-correlation functional (Perdew et al., 1992; Perdew et al., 1993). Upon testing of convergence with respect to energy, a cutoff of 500 eV was chosen to be used for the plane-wave basis set. Default PAW potentials from the VASP library (Kresse and Furthmuller, 1996; Kresse and Hafner, 1993; Kresse and Furthmuller, 1996; Kresse and Hafner, 1994), including only the outer-core electrons as valence, were used for Cd, Te, and Se. Calculations were carried out on Γ-centered k-point meshes consisting of 4000 k-points per reciprocal atom (KPPRA). Electronic minimizations with a convergence criterion of 10^{-6} eV/atom were performed using the tetrahedron method with Blöchl corrections (Blöchl et al., 1994). Initial structural configurations of CdTe and CdSe in the zincblende and wurtzite structures were taken from the Materials Project (Jain et al., 2013) and geometrically optimized until forces acting on each atom were less than 0.01 eV/Å as mentioned in earlier works (Balasubramanian et al., 2016; Roehl and Khare, 2014; Roehl and Khare, 2014; Roehl et al., 2014; Warner et al., 2006; Zhou et al., 2014).

The MIT Ab initio Phase Stability (maps) code from the Alloy Theoretic Automated Toolkit (ATAT) was utilized to calculate CdTe-CdSe formation energy landscapes and binary phase diagrams within the cluster expansion formalism (van de Walle, 2009; van de Walle and Asta, 2002; van de Walle et al., 2002; van de Walle and Ceder, 2002). Vibrational contributions to the free energy were determined by calculating stiffness versus length relationships (van de Walle, 2013; van de Walle and Ceder, 2002) among 6 unique structures in the set enumerated by cluster expansion. For each structure, perturbations of magnitude 0.2 Å at 3 separate volumes were tested to obtain dynamical matrices, phonon spectra, and vibrational free energies. This information, collected using the fitsvsl and svsl codes in ATAT (van de Walle, 2009; van de Walle and Asta, 2002; van de Walle et al., 2002; van de Walle and Ceder, 2002), was used to modify the corresponding phase boundaries. Random Se/Te occupation occurring above the predicted consolute temperature was simulated with special quasirandom structures (SQSs) (Zunger et al., 1990), which were generated using the sqs2tdb code within ATAT (van de Walle, 2009; van de Walle and Asta, 2002; van de Walle et al., 2002; van de Walle and Ceder, 2002). To achieve the desired correlation parameters nearly matching those of the random configurations, $CdSe_xTe_{1-x}$ SQSs were constructed from $2 \times 2 \times 2$ supercells of the conventional zincblende and wurtzite unit cells at concentrations of $x = 0.25$, 0.50, and 0.75. These structures were geometrically optimized until forces acting on each atom were less than 0.01 eV/Å.

As band gaps and absorption onsets are severely underestimated by standard exchange-correlation functionals, e.g., GGA and LDA, we instead employ the Heyd-Scuseria-Ernzerhof hybrid functional (HSE06) (Heyd et al., 2003; Krukau et al., 2006) to calculate the optoelectronic properties of $CdSe_xTe_{1-x}$. The HSE06 functional, which incorporates 25% of the exact exchange from Hartree-Fock theory along with 75% of

Approved for public release; distribution unlimited.
363

the exchange from GGA, has been shown to give significantly improved agreement with experiment for semiconductors and insulators (Paier et al., 2006). Using this method, for which the exact exchange was treated on a coarser grid of 2000 KPPRA to conserve computational resources, we calculated the electronic density of states (DOS) and frequency-dependent complex dielectric function ($\varepsilon_1 + i\varepsilon_2$) for each compound, including both end members and SQSs. From the latter values, derived optical properties such as absorption coefficient and reflectivity were determined. To gain further insight into the optoelectronic properties, effective masses of electrons and holes were calculated using the BoltzTraP package (Madsen and Singh, 2006) along with the corresponding modules implemented in pymatgen (Ong et al., 2013). We report DOS effective masses as described in the work of Gibbs et al. (2017), allowing a holistic representation of the entire Fermi surface to be presented while avoiding explicit calculations of the band structure. These calculations were carried out using carrier densities of 10^{16} electrons or holes per cm^3, in accordance with the most recent limits reported in the literature for CdTe thin films (McCandless et al., 2018). Units are in terms of the standard electron rest mass ($m_0 \approx 9.11 \times 10^{-31}$ kg), i.e., the effective electron mass is $m^* = m_e/m_0$ (and similar for holes, m_h).

To investigate short-range order effects occurring in the Te/Se sublattice of $CdSe_xTe_{1-x}$ structures for which no long-range order exists, we focus on the intermediate concentration of x = 0.5. Here, Monte Carlo simulations are performed on 4096-atom supercells using the Easy Monte Carlo Code (emc2) within ATAT (van de Walle, 2009; van de Walle and Asta, 2002; van de Walle et al., 2002; van de Walle and Ceder, 2002). As the zincblende structure is predicted to be thermodynamically stable at this concentration, with a consolute temperature of 325 K, we test only zincblende $CdSe_{0.5}Te_{0.5}$ at temperatures ranging from 350 K to 1000 K, in steps of 50 K. To characterize the degree of short-range order present within each structure, we employ two techniques of analysis. Firstly, we compare the distribution of Se-Te coordination values occurring throughout all sites with the corresponding values of a completely disordered Se/Te configuration. Such comparison is approximated by randomly sorting occupations among 20 unique structures and averaging the resulting distributions of coordination values. Secondly, we define the following short-range order parameter for Se-Te pairs (Porter et al., 2009):

$$\sigma(T) = (N^{Te-Se}_{actual} - N^{Te-Se}_{random})/(N^{Te-Se}_{ordered} - N^{Te-Se}_{random}) \quad (1)$$

where N^{Te-Se}_{actual}, $N^{Te-Se}_{ordered}$, and N^{Te-Se}_{random} represent the number of Te-Se bonds in the actual configuration simulated at some intermediate temperatures (T = 350 K, 1000 K), the ordered configuration (with each Cd coordinated to an equal number of Te and Se atoms) at absolute zero temperature, and the completely random configuration approached at very high temperatures (T ≫ 1000 K) in $CdSe_{0.5}Te_{0.5}$. By defining short-range order as such, positive and negative values of σ (max. +1 or −1) correspond to additional or reduced Te-Se bonds relative to the random limit, whereas a value of zero implies complete disorder.

Lastly, to provide further insight into electronic structure, we have performed calculations of Crystal Orbital Hamiltonian Populations (COHP) and effective charges using the LOBSTER package (Deringer et al., 2011; Maintz et al., 2013; Maintz et al., 2016; Maintz et al., 2016) and Bader analysis (Henkelman et al., 2006; Sanville et al., 2007; Tang et al., 2009; Yu and Trinkle, 2011) respectively.

3. Results

3.1. Phase stability of $CdSe_xTe_{1-x}$

Formation energy landscapes of $CdSe_xTe_{1-x}$ in the zincblende and wurtzite structure are displayed in Fig. 1(a) and (b) respectively. Both structures are found to exhibit endothermic mixing with upward bowing occurring in all enumerated configurations at intermediate concentrations, in agreement with recent theoretical work (Yang and Wei, 2019). The preference towards heterogeneity can be attributed to the CdTe/CdSe lattice mismatch arising from the difference in ionic radii of Te and Se (133.5 pm and 114.5 pm respectively) (Pyykkö, 2015). As the mismatch is relatively minor in contrast to that of CdTe/CdS, only slight asymmetry is observed in the energy landscape studied here. More specifically, upward bowing is weakly skewed towards higher Se concentrations as greater strain is caused by inserting the larger Te atoms into the CdSe lattice than vice versa, a well-studied effect in solid solutions (Liu et al., 2017). Regarding differences in structure, the wurtzite phase exhibits a larger rise in enthalpy than the zincblende phase; the former reaches a maximum ΔE_F of about 35 meV/atom whereas the latter achieves only 25 meV/atom. These features correlate with a greater volume difference of 9.0% in the wurtzite structure as opposed to 8.8% in the zincblende. Furthermore, the wurtzite configuration, for which c/a changes from 1.638 to 1.632 for CdTe and CdSe respectively, introduces a shear strain component not present in the cubic zincblende phase. As a result of these properties, solid solubility is less favorable in the wurtzite structure. Though we also note the anisotropy of the wurtzite phase is slightly more accommodating to low concentrations of larger impurity atoms, shown by weaker skewing of the energy landscape in contrast to that of the zincblende structure, owing to expansions along the c-axis which will be discussed in more detail throughout Section 3.2.

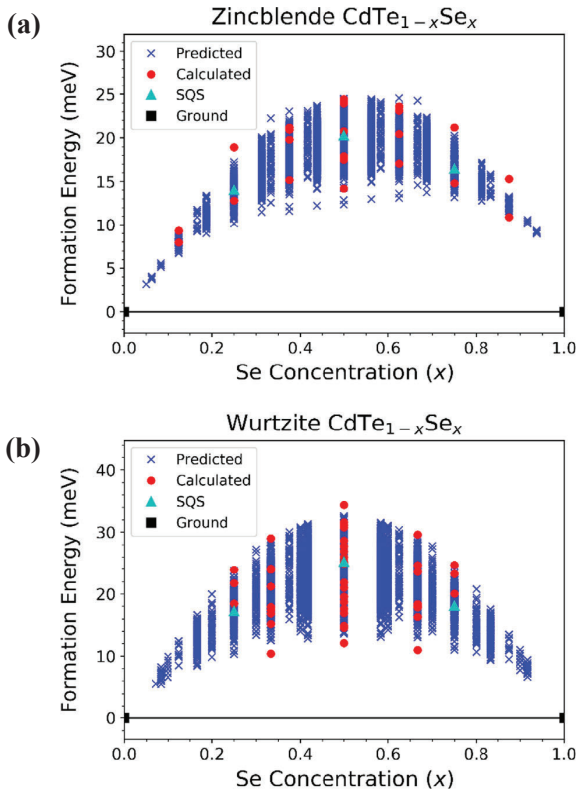


Fig. 1. Energy landscapes of (a) zincblende and (b) wurtzite $CdTe_{1-x}Se_x$, including ground states CdTe and CdSe, intermediate states predicted through cluster expansion and calculated using DFT, and special quasirandom structures simulated at concentrations of $x = 0.25$, 0.50, and 0.75.

The binary $CdSe_xTe_{1-x}$ phase diagram is presented in Fig. 2. Throughout intermediate concentrations at low temperatures, phase segregation is thermodynamically favorable due to the endothermic mixing discussed for the corresponding formation energy landscapes. However, as the upward bowing in energy is relatively weak, configurational and vibrational contributions (both included here) to the

Approved for public release; distribution unlimited.
364

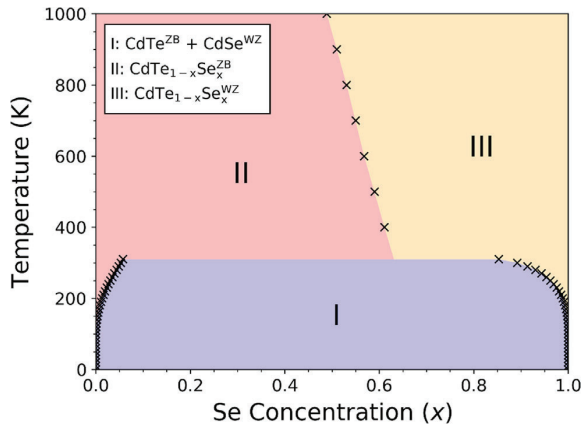


Fig. 2. The binary $CdTe_{1-x}Se_x$ phase diagram generated from Monte Carlo simulations utilizing effective cluster interaction coefficients.

entropy become sufficient to allow homogenous Se/Te mixing above a reasonably low consolute temperature (T_C) of about 325 K. As experimental synthesis is typically carried out at much higher temperatures (500–1000 K) (Lingg et al., 2018; Baines et al., 2018; Poplawsky et al., 2016), a precise value of T_C has not yet been reported. However, previous studies have shown that weak CdTe-CdSe phase segregation may proceed at room temperature (~298 K) depending on the thickness of deposition layers (Poplawsky et al., 2015). Moreover, recent theoretical investigations have predicted a similar T_C of 335 K using Stillinger-Weber Hamiltonian in molecular dynamics simulations (van Swol et al., 2016). In the high-temperature region of the phase diagram, we find the disordered $CdSe_xTe_{1-x}$ phase to adopt the zincblende and wurtzite structure at low and high Se concentrations respectively, with a downward-sloping phase boundary ranging from $x \sim 0.45$ to $x \sim 0.65$. These features are in good agreement with experimental data (Poplawsky et al., 2016; Strauss and Steininger, 1970; Laugier, 1973). We note that although the zincblende phase does not represent the thermodynamic ground state of $CdSe_xTe_{1-x}$ at high Se concentrations, our calculations reveal a difference of less than 10 meV/atom between the zincblende and wurtzite structures of CdSe, suggesting that the optically active (Poplawsky et al., 2016) zincblende phase may be synthetically accessible and remain metastable throughout a wide range of concentrations. This prediction is supported by recent experimental work showing $CdSe_xTe_{1-x}$ to remain stable against decomposition at Se concentrations as high as 60% at temperatures of 298 K and above (Lingg et al., 2018).

Regarding the zincblende-to-wurtzite phase transition, we discuss two major causes which have been suggested in previous works describing such structural polymorphism in binary octet semiconductors (Yeh et al., 1992; Ito, 1998). Firstly, the wurtzite structure is generally preferred over zincblende for binary compounds consisting of constituent elements with a substantial electronegativity difference (Yeh et al., 1992). Here, Se and Te display electronegativities of 2.48 and 2.01 respectively as compared to a value of 1.46 for Cd (Allred and Rochow, 1958), hence the Cd-Se bonds display significantly higher ionic character than the Cd-Te bonds. This is reflected by our Bader's charge analysis calculations which yield 0.71 *e* and 0.52 *e* cation-to-anion transfer in CdSe and CdTe respectively, where *e* is the elementary electron charge. As a result of the enhanced volumetric charge surrounding ions in CdSe, the wurtzite structure (with stacking sequence ABAB… as opposed to ABCABC… for zincblende) is adopted to minimize interlayer third-nearest-neighbor Cd-Se distances and therefore decrease overall energy deriving from attractive long-range electrostatic interactions ($U_E \propto r^{-1}$) (Ito, 1998). Secondly, as the ionic radius of Se (114.5 pm) is smaller than that of Te (133.5 pm), CdSe exhibits a greater cation-anion size mismatch than CdTe due to the large ionic radius of Cd (148.2 pm) (Pyykkö, 2015). As shown in data from the literature, binaries with higher cation-to-anion size ratios tend to form wurtzite configurations owing to subtle differences in covalent interactions controlled by the relative spatial extent of the cation *d* and anion *p* orbitals (Yeh et al., 1992). However, as shown in Fig. S3 of the Supplementary Material, we find no significant differences in general features of the COHP curves when comparing the zincblende and wurtzite structures. Moreover, integration of all states below the Fermi level yields nearly identical values, implying covalent interactions of approximately equal strength in each structure. Therefore, we conclude that the preference of stacking sequence in $CdSe_xTe_{1-x}$ is likely dominated by the ionic character of the system.

Lastly, we note that the inclusion of entropic terms to the free energy were crucial to obtain the reported phase diagram for which satisfactory agreement with experimental data is obtained (Poplawsky et al., 2016; Strauss and Steininger, 1970; Laugier, 1973). This highlights the importance of both configurational and vibrational entropy in stabilizing the given configurations. Specifically, including these terms caused a substantial shift in the zincblende-wurtzite phase boundary towards lower Se concentrations, suggesting greater entropy contributions present in wurtzite $CdSe_xTe_{1-x}$ arising from larger average bond lengths and therefore lower vibrational frequencies. This property is also reflected by the downward slope of the phase boundary, which indicates the wurtzite structure may be stabilized at intermediate concentrations by increasing temperature and therefore enhancing the effects of vibrational entropy (Poplawsky et al., 2016).

3.2. Properties of anion-disordered $CdSe_xTe_{1-x}$

In order to understand the deviation from linearity, let's first define bowing parameter (δ) for any physical quantity (p) such as lattice constant (a), band gap (E_g), effective mass (m^*), or others as (Kasper et al., 1995):

$$p_{mix} = x_{Se}p_{CdSe} + (1 - x_{Se})p_{CdTe} - x_{Se}(1 - x_{Se})\delta_p, \quad (2)$$

where x_{Se} is fraction of Se in the alloy and, p_{mix}, p_{CdSe} and p_{CdTe} are values of the physical quantity associated with resultant alloy, CdSe and CdTe respectively.

We first study the structural features of anion-disordered $CdSe_xTe_{1-x}$ as a function of concentration. As shown by the calculated equilibrium lattice parameters, presented in Table S1 of the Supplementary Material, the lattice constants and unit cell volumes follow nearly linear relationships, i.e. they approximately following Vegard's law (Vegard, 1921). The unit cell volumes decrease with average slopes of −12.659 and −12.908 $Å^3$ f.u.$^{-1}$ x^{-1} for the zincblende and wurtzite structure respectively. The bowing parameter δ_a is found to be −0.01 Å, −0.004 Å, and −0.008 Å for zincblende, wurtzite in-plane (*a*), and wurtzite out-of-plane (*c*) lattice constants respectively using Eq (2) with p = a. This deviation from Vegard's law is likely to arise from the additionally degree of freedom introduced by the anisotropy of the wurtzite structure. Indeed, larger changes occur in the *c*-axis relative to the *a*-axis in order to accommodate for the varying anion size and electronegativity. For instance, a larger 3.26% contraction of the *c*-axis occurs in contrast to a smaller 2.99% contraction of the *a*-axis at 50% Se concentration relative to pure CdTe in the wurtzite structure. These changes may be summarized by analyzing the ratio of *c*/*a*, tabulated for each concentration in Table S1, showing a decrease from 1.638 for CdTe to 1.632 for CdSe. The observed trend is consistent with previous findings for similar systems in the wurtzite structure; as the Se concentration is increased and ionic character of the cation-anion bonds becomes stronger, the ratio of *c*/*a* approaches the ideal value of 1.632 for a perfectly covalent crystal (Kim et al., 2007).

To gain further insight into the local structural features of $CdSe_xTe_{1-x}$, we have plotted bond length distributions in Fig. S1 of the Supplementary Material. As expected, anion disorder leads to

Approved for public release; distribution unlimited.
365

distortions in the Cd-anion tetrahedra corresponding to deviations from the ideal bond length; specifically, a clear distinction is found between the nearest-neighbor Cd-Te and Cd-Se distances with the former pairs exhibiting a median value which is nearly 0.15 Å larger than that of the latter. Such distortions, both within and between unique bonding pairs (Cd-Te and Cd-Se), also become slightly more pronounced at intermediate concentrations ($x \sim 0.5$) owing to increased strain induced by the differing anion sizes. As will be discussed further in this section, the bond length variations play a vital role in causing optoelectronic bowing effects and may therefore be utilized to control these properties (Tit et al., 2009). Also plotted in Fig. S1 is the nearest-neighbor anion-anion bond lengths, for which we find much weaker, though still present, differences between the grouping of unique bonding pairs, i.e., Te-Te, Te-Se, and Se-Se distances. These values correlate with the sum of constituent anionic radii, though local distortions in the tetrahedra have greater effect as shown by a wide (~0.38 Å) and continuous range of bond lengths. These properties and their connection to short-range order will be discussed in greater detail throughout Section 3.3.

We next study the electronic properties of $CdSe_xTe_{1-x}$ using the hybrid HSE06 (Heyd et al., 2003; Krukau et al., 2006) functional, where sample cells, x = 0.25, 0.5, 0.75, were generated with SQS as described in Section 2. With respect to end-members, zincblende CdTe and CdSe are shown to exhibit band gaps of 1.54 eV and 1.61 eV respectively, in fair agreement with experimental data of 1.50 eV (Compaan et al., 1996) and 1.78 eV (Poon et al., 1995). In contrast, the calculated band gaps of 1.23 eV and 1.32 eV for CdTe and CdSe in the wurtzite structure underestimate the corresponding experimental values of 1.59 eV (Magnusson et al., 1987) and 1.70 eV (Kale and Lokhande, 2004), though accuracy is significantly improved with respect to GGA (Table S2 of the Supplementary Material). The increased error occurring in the wurtzite structure, which is consistent with previous theoretical reports involving CdSe (Szemjonov et al., 2014) and similar binary semiconductors of equivalent symmetry (Moses et al., 2011; Kaczkowski, 2012), can be attributed to the short-range nature of the exact exchange implemented within the HSE06 (Heyd et al., 2003; Krukau et al., 2006) functional, which therefore may not capture long-range interactions arising from differences in the stacking sequence of each structure, i.e., zincblende (ABCABC…) vs. wurtzite (ABAB…). As discussed in the work of Moses et al., improvement with experiment may be obtained by tuning the portion of exact exchange interactions included in the hybrid calculations (Moses et al., 2011), however, we choose to keep parameters fixed to remain consistent across the distinct compositions and structure considered in this work. Moreover, although the magnitude of the band gap is underestimated in the wurtzite structure, we note that the change in gap with respect to composition agrees well with experiment; our calculations reveal an increase of 0.09 eV (experimentally, 0.11 eV (Kale and Lokhande, 2004; Magnusson et al., 1987) from CdTe to CdSe. Therefore, predicted changes in the electronic properties at intermediate concentrations may be considered reliable.

Accordingly, the calculated trend of band gap variation in $CdSe_xTe_{1-x}$ is displayed in Fig. 3(a) with exact values reported in Table S2 of the Supplementary Material. In both the zincblende and wurtzite phases, we find significant downward bowing to occur throughout intermediate concentrations. Specifically, our results indicate bowing parameters (δ) as defined in Eq. (2) (with $p = E_g$) of 0.62 eV and 1.06 eV for the zincblende and wurtzite phases respectively, for which the former results is in fair agreement with recent experimental (Islam et al., 1995) and theoretical (Yang and Wei, 2019) investigations regarding $CdSe_xTe_{1-x}$ in the zincblende structure. These trends can be attributed to local distortions arising in the disordered solid solution (Vurgaftman et al., 2001). Hence, the stronger bowing effect found in the wurtzite structure, as compared to zincblende, can be attributed to the larger lattice mismatch (i.e., volume difference) which is observed between the wurtzite CdTe and CdSe phases as discussed in Section 3.1. This greater mismatch causes enhanced structural distortions, as reflected by our bond length analysis (Fig. S1) which shows slightly wider ranges of Cd-anion bond lengths at intermediate concentrations for the wurtzite phase. Moreover, the larger volume of the wurtzite phase is more accommodating to local distortions, further facilitating strong optoelectronic bowing. For both structures considered here, a minimum in band gap occurs at Se concentrations slightly below 50% owing to the lower band gap of CdTe in contrast to CdSe. Regarding the implications of these results on PV development, we propose that low-to-intermediate Se concentrations (20–50%) in the zincblende are likely most beneficial given the band gap shown in this region is near that of the ideal value of 1.4 eV according to the Schockley-Queisser limit (Shockley and Queisser, 1961). Furthermore, as discussed in previous works, net photocurrent is also likely to be increased throughout such compositions (Poplawsky et al., 2016).

While the decreased band gap in $CdSe_xTe_{1-x}$ is promising for applications, effective masses (m^*) of electrons and holes are also crucial aspects which influence the net photo-current and therefore the cell efficiency. To this end, the calculated effective masses are shown in Fig. 3(b) and (c), with exact values tabulated in Table S4 of the Supplementary Material. In pure CdTe, we find low effective masses of 0.101 and 0.088 in the zincblende and wurtzite structure respectively, in agreement with previous experimental reports (m^*ranging from 0.096 to 0.11 at free electron densities up to 1.7×10^{18} cm^{-3}) (Mears and Stradling, 1969). These effective electron masses are slightly increased for CdSe, with values of 0.134 and 0.099 in the zincblende and wurtzite structure, owing to increased ionic character and therefore a larger band gap (Vurgaftman et al., 2001). These values also agree with previous experimental work for which an effective electron mass of 0.13 was reported in CdSe (Chemistry R.S.O.).

Throughout intermediate concentrations, we find upward bowing in the electron effective mass, with bowing parameters (δ_{m^*}, calculated via Eq. (2) with p = m*) of −0.014 and −0.054 in the zincblende and wurtzite structure respectively. The larger changes exhibited by the wurtzite structure can be attributed to stronger structural distortions as discussed earlier in this section. Next, with respect to effective hole mass, we report values of 0.572 and 1.447 for pure CdTe in the zincblende and wurtzite structure respectively. The former lies within the range found by experiment: 0.12 and 0.60 for light and heavy holes in zincblende CdTe (Dang et al., 1982). As with the effective electron masses, these values also increase in CdSe, for which we find hole masses of 0.808 and 1.870 in the zincblende and wurtzite structure respectively. However, in contrast to those of the electrons, effective hole masses display downward bowing throughout intermediate concentrations of $CdSe_xTe_{1-x}$; specifically, bowing parameters (δ_{m^*}) as defined in Eq. (3) are calculated to be 0.14 and 0.47 in the zincblende and wurtzite structure respectively. With respect to applications in PV, the downward bowing effect is favorable given that it allows minimal increases in the effective hole mass, an important parameter for conventional p-type CdTe cells, therefore contributing to potentially higher carrier lifetimes. We also note that focus should remain on the zincblende structure considering the unfavorably large effective hole mass in wurtzite $CdSe_xTe_{1-x}$ throughout all concentrations.

To study the optical properties of $CdSe_xTe_{1-x}$ we focus on the absorption coefficient and reflectivity, each of which are crucial for PV efficiency. The former property is plotted throughout visible-UV photon energies in Fig. 4. In both the zincblende and wurtzite structure, we find first absorption peaks at energies which correlate directly with the corresponding electron band gaps. The rest is due to other transitions and electronic collisions in lattice. Accordingly, features of the full absorption spectra shift toward lower energies at minority Se concentrations (owing to downward bowing in the band gap) and higher energies at majority Se concentrations (as the strong ionic character of the Cd-Se bonds overtakes the bowing effect). Despite these translations, the overall character of the spectra remains relatively unchanged. Hence, zincblende $CdSe_xTe_{1-x}$ is able to maintain strong optical absorption in the range of interest (i.e., at frequencies matching those of the solar spectrum as shown by the shaded region of Fig. 4) whereas the

Approved for public release; distribution unlimited.
366

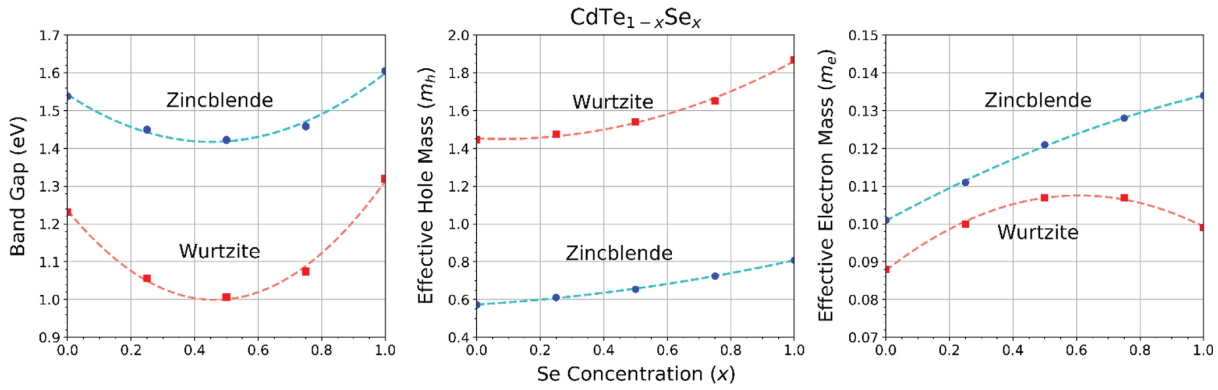


Fig. 3. (a) Electronic band gaps, (b) effective hole masses, and (c) effective electron masses of zincblende and wurtzite $CdTe_{1-x}Se_x$ computed using the hybrid HSE06 functional. Points represent calculated data, whereas dashed curves represent quadratic fitting based on the bowing parameter of each system.

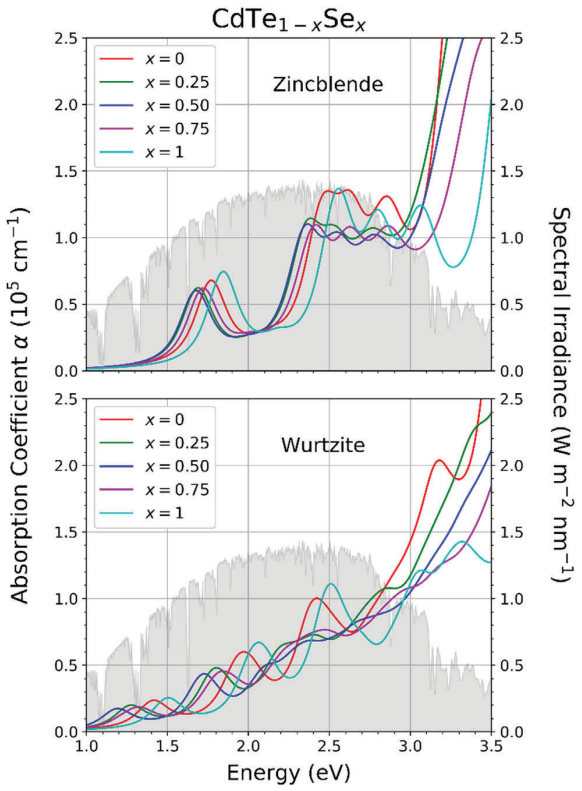


Fig. 4. Absorption coefficients (α) of zincblende (top panel) and wurtzite (bottom panel) $CdTe_{1-x}Se_x$ computed using the hybrid HSE06 functional. Each absorption curve, with values given on left y-axis, corresponds to a given concentration (x). For comparison, the standard AM 1.5 solar spectrum is represented by the shaded area with values given on the right y-axis.

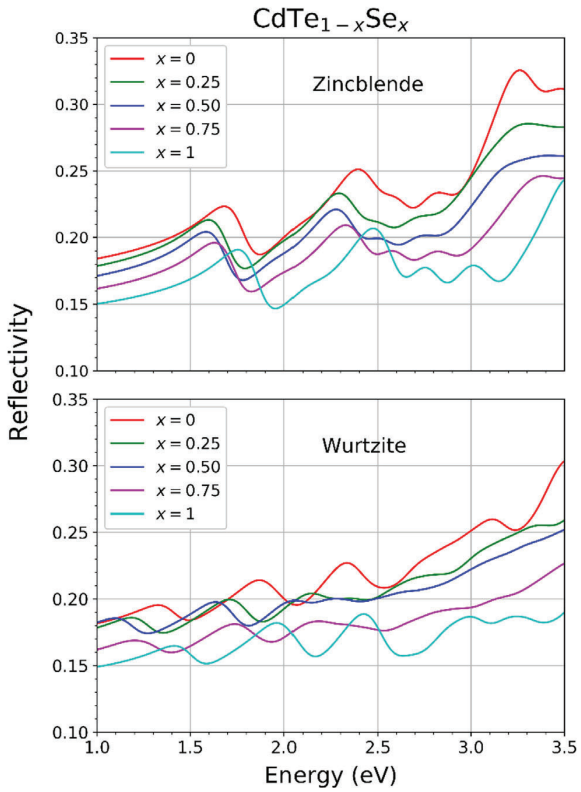


Fig. 5. Reflectivity of zincblende (top panel) and wurtzite (bottom panel) $CdTe_{1-x}Se_x$ computed using the hybrid HSE06 functional. Each reflectivity curve, with values given on left y-axis, corresponds to a given concentration (x).

wurtzite phase consistently displays lower absorption, confirming experimental reports that wurtzite CdTe may be considered optically inactive (Poplawsky et al., 2016). As for reflectivity, for which results are shown in Fig. 5, we find relatively low values ranging from about 0.15 to 0.18 for both the zincblende and wurtzite structure at photon energies below the band gap of each composition. Though there exist variations in reflectivity above the gap, reflectivity generally remains moderate (< 0.35) throughout all optical frequencies in consideration. Moreover, increasing Se concentration leads to noticeable decreases in reflectively across the full spectrum, with downward shifts of magnitudes approaching 0.05. This slight decrease in reflectivity, coupled with sustained optical absorption, make $CdSe_xTe_{1-x}$ a promising candidate for improved optical performance in PV.

3.3. Short-range order effects

As discussed in detail throughout the work of Bellaiche and Zunger (Bellaiche and Zunger, 1998), there are two major forms of short-range order which typically arise in binary semiconductor alloys: “clustering”, for which atoms of the same element tend to congregate with one another, and “anti-clustering”, for which atoms of opposing elements tend

Approved for public release; distribution unlimited.
367

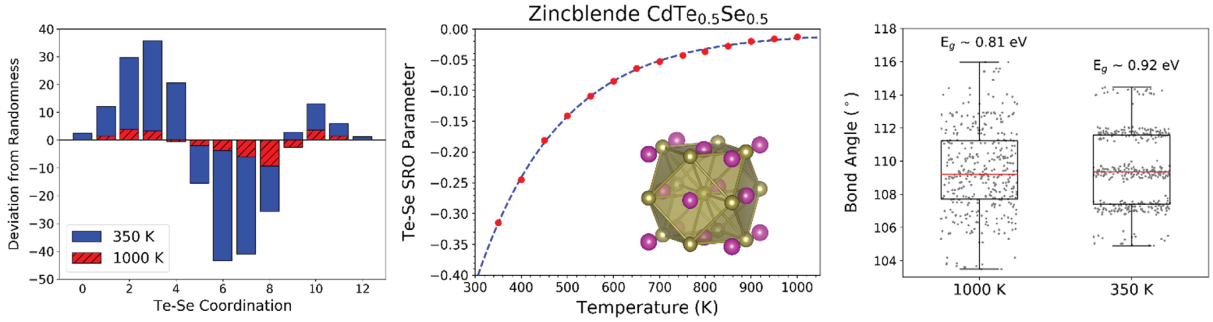


Fig. 6. (a) Occurrences of all possible Te-Se coordination numbers relative to their respective limit in a completely random configuration. Values here are taken from 2048-atom supercells. (b) Short-range order parameter, defined in Eq. (1), of Te-Se pairs in the anion sublattice of disordered $CdSe_{0.5}$ $Te_{0.5}$ simulated at temperatures ranging from 350 K to 1000 K. Negative values imply a deficiency in Te-Se bonds relative to the random limit. (c) Bond angle distributions of $CdSe_{0.5}$ $Te_{0.5}$ simulated at 1000 K and 350 K along with their respective band gaps, calculated using GGA.

to congregate. In this work, we focus on the former effect, which is found to take place in $CdSe_{0.5}Te_{0.5}$. This finding is reflected by our Monte Carlo calculations, revealing the tendency for anion occupations to minimize the total number of Te-Se bond lengths (and therefore maximize nearest-neighbor bonds between atoms of the same element). Such an effect is illustrated in Fig. 6(a); the distribution of Te-Se coordination values, relative to the random limit, shows clear deficiencies from 5 to 8 and an abundance above and below this range. We note that intermediate values (i.e., 5–8) serve to maximize the net number of Te-Se bonds whereas high and low values minimize these bonds. Therefore, the results indicate clustering of Te and Se atoms within the disordered $CdSe_{0.5}Te_{0.5}$ structure. This conclusion is further supported by calculations involving Eq. (1); Fig. 6(b) displays the short-range order parameter (σ) throughout temperatures ranging from 350 K to 1000 K. At 350 K, which lies only slightly above the predicted consolute temperature, our calculated $\sigma \approx -0.32$ implies a significant presence of short-range order. Specifically, the negative value for σ corresponds to a lower number of Te-Se bonds as compared to the random limit, i.e., clustering is observed. With respect to temperature, we identify an exponential decrease in short-range order which approaches zero at high temperatures, as shown by the exponential least squares regression (dashed line) which closely follows our calculated data as in Fig. 6(b). This agrees with expectations and general data for alloys in the literature (Bellaiche and Zunger, 1998; Ghosh et al., 2008; Körmann et al., 2014); higher temperatures provide sufficient entropic contributions such that configurational disorder dominates the unfavorable energetic effects of enthalpy due to bond length distortions.

To this end, we further study the origin of short-range order by sampling two configurations of $CdSe_{0.5}Te_{0.5}$, simulated using ATAT at 350 K and 1000 K, in order to discern differences between the two extreme cases, i.e., with and without short-range order. Bond angle (defined as the anion-Cd-anion angle for adjacent anions within each tetrahedra) distributions of each fully relaxed structure are shown in Fig. 6(c). At 1000 K, our results show a wide and continuous range of bond angles, for which the distribution is centered at approximately 109.5° (the ideal value for a tetrahedra) and occupies values from about 103.5° to 116°. These features are indicative of a random solid solution with significant strain, captured by relaxation in DFT simulations, present in the system. In contrast, the structure simulated at 350 K displays a narrower range of bond angles (approximately 105–114°), also centered at 109.5°, with clear grouping observed around several values. These properties reflect the presence of short-range order, agreeing with our previous analysis, which we may now attribute to reduced strain and therefore decreased enthalpy.

Lastly, we consider the effects of short-range order on the optoelectronic properties by calculating the band gap of the representative systems for zincblende $CdSe_{0.5}Te_{0.5}$ at 350 K and 1000 K. These evaluations were carried out using GGA to avoid excessive computational costs for such large supercells. Regardless of the method, we may compare these values to those of $CdSe_xTe_{1-x}$ also found using GGA. As tabulated in Fig. 6(c), our calculations reveal noticeably different band gaps of 0.92 eV and 0.81 eV for the structures at 350 K and 1000 K respectively. We note that the latter value is in perfect agreement with that of the SQS for $CdSe_{0.5}Te_{0.5}$, hence supporting the conclusion that the structure is almost completely disordered at 1000 K. In contrast, the 0.92 eV gap at 350 K is much closer to the linear combination of the end-member gaps (i.e., if now bowing effects were present), which is found to be about 0.98 eV. As discussed throughout Section 3.2, bowing is known to arise from local structural distortions in the disordered alloy. However, as short-range order serves to minimize these distortions, the bowing effects are significantly decreased, thus leading to an increased band gap of 0.92 eV.

4. Conclusion

In summary, we have conducted a thorough study of the structural, thermodynamic, and optoelectronic properties of $CdSe_xTe_{1-x}$ alloys in the zincblende and wurtzite structure. Our calculated phase diagram confirms experimental data showing an upper consolute temperature of 325 K while further clarifying the features of this miscibility boundary throughout the full range of Se concentrations. Above 325 K, we report a downward sloping zincblende-to-wurtzite phase boundary ranging from x = 0.5–0.6 which is attributed to increasing ionic character of the Cd-anion bonds, for which the wurtzite structure is preferred, as more Se atoms are introduced into the system. Moreover, we suggest the critical importance of entropic contributions in stabilizing the phase boundary within this region.

By modeling the purely random configuration of $CdSe_xTe_{1-x}$ through special quasirandom structures, we illustrate significant structural distortions through analysis of nearest- and second-nearest neighbor bond length distributions, each of which occupy a wide range of values. As a result, we observe strong bowing throughout all electronic properties in focus, namely, band gaps and effective electron/hole masses. Despite the band gap of CdSe being larger than that of CdTe for either structure, downward bowing allows a decrease in band gap at low to moderate Se concentrations. Our findings suggest that alloying zincblende $CdSe_xTe_{1-x}$ throughout x = 0.2–0.5 is likely to provide the most beneficial effects for photovoltaics given the band gap within this range is near the ideal value of 1.4 eV, which may also allow enhanced net photocurrent. Furthermore, downward bowing in the effective hole mass should also prevent any substantial decrease in the carrier mobility and therefore carrier mobility may remain high. In terms of optical properties, we identify shifts in the absorption spectra of zincblende and wurtzite $CdSe_xTe_{1-x}$ according to the change in band gap, while the general features remain unchanged. The former structure is found to be more optically active throughout phonon frequencies of

Approved for public release; distribution unlimited.
368

interest. Reflectivity is also studied, for which we find increased Se concentrations lead to a slight decrease in reflectively, hence further improving the potential benefits of these alloys for photovoltaics. We recommend experimental investigation to confirm the subtle changes in optoelectronic properties reported here.

Lastly, investigation of short-range order has revealed the presence of strong clustering (i.e., congregation of like atoms) in $CdSe_xTe_{1-x}$ as illustrated by nearest-neighbor anion-anion bond analysis. The degree of short-range order, which serves to minimize strain, is shown to be high ($\sigma \approx -0.32$) at temperatures shortly above the consolute temperature, while decreasing exponentially with increasing temperature and approaching zero near 1000 K. We show that clustering leads to a larger band gap in the alloy owing to lessened structural distortions and therefore weaker bowing effects. Specifically, the magnitude of the gap in zincblende $CdSe_{0.5}Te_{0.5}$ ranges from 0.81 eV (at 1000 K) to 0.92 eV (at 350 K) within the framework of GGA. Therefore, we propose that, in addition to composition, short-range order may be utilized experimentally to finely tune the desired optoelectronic properties of the material. This may achieved by carrying out synthesis under thermal conditions giving a desired degree of clustering, according to the detailed trends reported here, followed by quenching to sufficiently low temperatures to "freeze in" local occupations within the structure (see, e.g., reference Ji et al. (2019)).

Acknowledgement

All computing for this project was performed at the Ohio Supercomputer Center (OSC) (Computer O.S.). We thank our funding sources: The National Science Foundation Division of Civil, Mechanical, and Manufacturing Innovation through grants 1629230 and 1629239, the Air Force Research Laboratory, Space Vehicles Directorate through Contract # FA9453-19-C-1002 and the Air Force Research Laboratory under agreement number FA9453-18-2-0037. The U.S. Government is authorized to reproduce and distribute reprints for Governmental purposes notwithstanding any copyright notation thereon.

Disclaimer

The views and conclusions contained herein are those of the authors and should not be interpreted as necessarily representing the official policies or endorsements, either expressed or implied, of Air Force Research Laboratory or the U.S. Government.

Appendix A. Supplementary material

Supplementary data to this article can be found online at https://doi.org/10.1016/j.solener.2019.10.091.

References

Allred, A.L., Rochow, E.G., 1958. A scale of electronegativity based on electrostatic force. J. Inorg. Nucl. Chem. 5 (4), 264–268.
Baines, T., et al., 2018. Incorporation of CdSe layers into CdTe thin film solar cells. Sol. Energy Mater. Sol. Cells 180, 196–204.
Balasubramanian, K., Khare, S., Gall, D., 2016. Vacancy-induced mechanical stabilization of cubic tungsten nitride. Phys. Rev. B 94 (17), 174111.
Bellaiche, L., Zunger, A., 1998. Effects of atomic short-range order on the electronic and optical properties of GaAsN, GaInN, and GaInAs alloys. Phys. Rev. B 57 (8), 4425.
Belyaev, A., Kalinkin, I., 1988. Conduction processes in inhomogeneous $CdSe_xTe_{1-x}$ semiconductors. Thin Solid Films 158 (1), 25–36.
Blochl, P.E., 1994. Projector augmented-wave method. Phys. Rev. B 50 (24), 17953–17979.
Blöchl, P.E., Jepsen, O., Andersen, O.K., 1994. Improved tetrahedron method for Brillouin-zone integrations. Phys. Rev. B 49 (23), 16223–16233.
Cai, X.C., et al., 2012. Spectroscopy of CdTe/CdSe type-II nanostructures: morphology, lattice mismatch, and band-bowing effects. J. Phys. Chem. C 116 (14), 8118–8127.
Chemistry, R.S.O. Available from: < http://www.rsc.org/suppdata/cp/c3/c3cp52678j/c3cp52678j.pdf > .
Compaan, D., et al., 1996. Properties of pulsed laser deposited CdS_xTe_{1-x} films on glass. MRS Proc. 426, 367.
Computer, O.S. Available from: < https://www.osc.edu/ > .
Dang, L.S., Neu, G., Romestain, R., 1982. Optical detection of cyclotron resonance of electron and holes in CdTe. Solid State Commun. 44 (8), 1187–1190.
De Fontaine, D., 1994. Cluster approach to order-disorder transformations in alloys. In: Solid State Physics. Elsevier, pp. 33–176.
Deringer, V.L., Tchougreeff, A.L., Dronskowski, R., 2011. Crystal orbital hamilton population (COHP) analysis as projected from plane-wave basis sets. J. Phys. Chem. A 115 (21), 5461–5466.
Ducastelle, F., Ducastelle, F., 1991. Order and phase stability in alloys.
Dünweg, B., Landau, D., 1993. Phase diagram and critical behavior of the Si-Ge unmixing transition: a Monte Carlo study of a model with elastic degrees of freedom. Phys. Rev. B 48 (19), 14182.
Geisthardt, R.M., Topic, M., Sites, J.R., 2015. Status and potential of CdTe solar-cell efficiency. IEEE J. Photovoltaics 5 (4), 1217–1221.
Gessert, T.A., et al., 2013. Research strategies toward improving thin-film CdTe photovoltaic devices beyond 20% conversion efficiency. Sol. Energy Mater. Sol. Cells 119, 149–155.
Ghosh, G., Van de Walle, A., Asta, M., 2008. First-principles calculations of the structural and thermodynamic properties of bcc, fcc and hcp solid solutions in the Al–TM (TM = Ti, Zr and Hf) systems: a comparison of cluster expansion and supercell methods. Acta Mater. 56 (13), 3202–3221.
Gibbs, Z.M., et al., 2017. Effective mass and Fermi surface complexity factor from ab initio band structure calculations. NPJ Comput. Mater. 3, 7.
Gloeckler, M., Sankin, I., Zhao, Z., 2013. CdTe solar cells at the threshold to 20% efficiency. IEEE J. Photovoltaics 3 (4), 1389–1393.
Granas, O., Vinichenko, D., Kaxiras, E., 2016. Establishing the limits of efficiency of perovskite solar cells from first principles modeling. Sci. Rep. 6, 6.
Green, M.A., et al., 2018. Solar cell efficiency tables (version 51). Prog. Photovoltaics Res. Appl. 26 (1), 3–12.
Hannachi, L., Bouarissa, N., 2008. Electronic structure and optical properties of $CdSe_xTe_{1-x}$ mixed crystals. Superlattices Microstruct. 44 (6), 794–801.
Heermann, K.B.A.D., 1988. Monte Carlo Simulation in Statistical Physics. Springer-Verlag, New York.
Henkelman, G., Arnaldsson, A., Jonsson, H., 2006. A fast and robust algorithm for Bader decomposition of charge density. Comput. Mater. Sci. 36 (3), 354–360.
Heyd, J., et al., 2005. Energy band gaps and lattice parameters evaluated with the Heyd-Scuseria-Ernzerhof screened hybrid functional. J. Chem. Phys. 123 (17), 174101.
Heyd, J., Scuseria, G.E., Ernzerhof, M., 2003. Hybrid functionals based on a screened Coulomb potential. J. Chem. Phys. 118 (21), 8207–8215.
Hosseini, S.M., 2008. Optical properties of cadmium telluride in zinc-blende and wurzite structure. Phys. B – Condens. Matter 403 (10–11), 1907–1915.
Huang, M.-Z., Ching, W.Y., 1993. Calculation of optical excitations in cubic semiconductors. I. Electronic structure and linear response. Phys. Rev. B 47 (15), 9449–9463.
Islam, R., Banerjee, H., Rao, D., 1995. Structural and optical properties of $CdSe_xTe_{1-x}$ thin films grown by electron beam evaporation. Thin Solid Films 266 (2), 215–218.
Ito, T., 1998. Simple criterion for Wurtzite-Zinc-Blende polytypism in semiconductors. Jpn. J. Appl. Phys. 37 (Part 2(10B), L1217–L1220.
Jain, A., et al., 2013. Commentary: the materials project: a materials genome approach to accelerating materials innovation. APL Mater. 1 (1), 11.
Jamal, M., Abu-Jafar, M.S., Reshak, A.H., 2016. Revealing the structural, elastic and thermodynamic properties of CdSexTe1 − x (x = 0, 0.25, 0.5, 0.75, 1). J. Alloys Compd. 667, 151–157.
Ji, H., et al., 2019. Hidden structural and chemical order controls lithium transport in cation-disordered oxides for rechargeable batteries. Nat. Commun. 10 (1), 592.
Kaczkowski, J., 2012. Electronic structure of some wurtzite semiconductors: hybrid functionals vs. Ab initio many body calculations. GaN 3 (3.130), p. 3.103.
Kale, R.B., Lokhande, C.D., 2004. Band gap shift, structural characterization and phase transformation of CdSe thin films from nanocrystalline cubic to nanorod hexagonal on air annealing. Semicond. Sci. Technol. 20 (1), 1–9.
Kanevce, A., et al., 2017. The roles of carrier concentration and interface, bulk, and grain-boundary recombination for 25% efficient CdTe solar cells. J. Appl. Phys. 121 (21), 9.
Kasper, E., et al., 1995. Test of Vegard's law in thin epitaxial SiGe layers. J. Cryst. Growth 157 (1), 68–72.
Kim, Y.-I., Page, K., Seshadri, R., 2007. Synchrotron x-ray study of polycrystalline wurtzite Zn1 − xMgxO (0⩽x⩽0.15): Evolution of crystal structure and polarization. Appl. Phys. Lett. 90(10), 101904.
Körmann, F., et al., 2014. Temperature dependent magnon-phonon coupling in bcc Fe from theory and experiment. Phys. Rev. Lett. 113 (16), 165503.
Kresse, G., Furthmuller, J., 1996. Efficient iterative schemes for ab initio total-energy calculations using a plane-wave basis set. Phys. Rev. B 54 (16), 11169–11186.
Kresse, G., Furthmuller, J., 1996. Efficiency of ab-initio total energy calculations for metals and semiconductors using a plane-wave basis set. Comput. Mater. Sci. 6 (1), 15–50.
Kresse, G., Hafner, J., 1993. Ab initio molecular dynamics for liquid metals. Phys. Rev. B 47 (1), 558–561.
Kresse, G., Hafner, J., 1994. Ab initio molecular-dynamics simulation of the liquid-metal–amorphous-semiconductor transition in germanium. Phys. Rev. B 49 (20), 14251.
Kresse, G., Joubert, D., 1999. From ultrasoft pseudopotentials to the projector augmented-wave method. Phys. Rev. B 59 (3), 1758–1775.
Krukau, A.V., et al., 2006. Influence of the exchange screening parameter on the performance of screened hybrid functionals. J. Chem. Phys. 125 (22), 224106.
Laradji, M., Landau, D., Dünweg, B., 1995. Structural properties of $Si_{1-x}Ge_x$ alloys: a Monte Carlo simulation with the Stillinger-Weber potential. Phys. Rev. B 51 (8), 4894.
Laugier, A., 1973. Thermodynamics and phase diagram calculations in II-VI and IV-VI

Approved for public release; distribution unlimited.
369

ternary systems using an associated solution model. Rev. Phys. Appl. (Paris) 8 (3), 259–270.
Lingg, M., et al., 2018. Structural and electronic properties of $CdTe_{1-x}Se_x$ films and their application in solar cells. Sci. Technol. Adv. Mater. 19 (1), 683–692.
Liu, Z.T.Y., et al., 2017. First-principles phase diagram calculations for the rocksalt-structure quasibinary systems TiN-ZrN, TiN-HfN and ZrN-HfN. J. Phys. – Condens. Matter 29 (3), 11.
Madsen, G.K.H., Singh, D.J., 2006. BoltzTraP. A code for calculating band-structure dependent quantities. Comput. Phys. Commun. 175 (1), 67–71.
Magnusson, K.O., et al., 1987. Angle-resolved inverse photoelectron spectroscopy studies of CdTe (110), CdS (112¯ 0), and CdSe (112¯ 0). Phys. Rev. B 36 (12), 6566–6573.
Maintz, S., et al., 2013. Analytic projection from plane-wave and PAW wavefunctions and application to chemical-bonding analysis in solids. J. Comput. Chem. 34 (29), 2557–2567.
Maintz, S., et al., 2016. LOBSTER: a tool to extract chemical bonding from plane-wave based DFT. J. Comput. Chem. 37 (11), 1030–1035.
Maintz, S., Esser, M., Dronskowski, R., 2016. Efficient rotation of local basis functions using real spherical harmonics. Acta Phys. Pol. B 47 (4), 1165–1175.
Mangalhara, J., Thangaraj, R., Agnihotri, O., 1989. Structural, optical and photoluminescence properties of electron beam evaporated $CdSe_{1-x}Te_x$ films. Solar Energy Mater. 19 (3–5), 157–165.
McCandless, B.E., et al., 2018. Overcoming carrier concentration limits in polycrystalline CdTe thin films with in situ doping. Sci. Rep. 8 (1), 14519.
Mears, A.L., Stradling, R.A., 1969. Cyclotron resonance and cross-modulation with n-type CdTe at 1 mm and 2 mm wavelength. Solid State Commun. 7 (17), 1267–1269.
Moses, P.G., et al., 2011. Hybrid functional investigations of band gaps and band alignments for AlN, GaN, InN, and InGaN. J. Chem. Phys. 134 (8), 084703.
Murali, K.R., Jayasuthaa, B., 2009. Brush electrodeposited $CdSe_xTe_{1-x}$ thin films and their properties. Sol. Energy 83 (6), 891–895.
Newman, M., Barkema, G., 1999. Monte Carlo Methods in statistical physics chapter 1–4. Oxford University Press, New York, USA.
Ong, S.P., et al., 2013. Python Materials Genomics (pymatgen): A robust, open-source python library for materials analysis. Comput. Mater. Sci. 68, 314–319.
Ouendadji, S., et al., 2011. Ab initio study of structural, electronic, phase diagram, and optical properties of $CdSe_xTe_{1-x}$ semiconducting alloys. J. Mater. Sci. 46 (11), 3855–3861.
Ozolins, V., Wolverton, C., Zunger, A., 1998. First-principles theory of vibrational effects on the phase stability of Cu-Au compounds and alloys. Phys. Rev. B 58 (10), R5897–R5900.
Paier, J., et al., 2006. Screened hybrid density functionals applied to solids. J. Chem. Phys. 124 (15), 13.
Paudel, N.R., Yan, Y., 2014. Enhancing the photo-currents of CdTe thin-film solar cells in both short and long wavelength regions. Appl. Phys. Lett. 105 (18), 183510.
Perdew, J.P., et al., 1992. Atoms, molecules, solids, and surfaces - applications of the generalized gradient approximation for exchange and correlation. Phys. Rev. B 46 (11), 6671–6687.
Perdew, J.P., et al., 1993. Erratum: atoms, molecules, solids, and surfaces: applications of the generalized gradient approximation for exchange and correlation. Phys. Rev. B 48 (7), 4978.
Perrenoud, J., et al., 2013. A comprehensive picture of Cu doping in CdTe solar cells. J. Appl. Phys. 114 (17), 10.
Poon, H.C., et al., 1995. Relativistic band structure of ternary II-VI semiconductor alloys containing Cd, Zn, Se and Te. J. Phys.: Condens. Matter 7 (14), 2783–2799.
Poplawsky, J.D., et al., 2015. $CdSe_{1-x}Te_x$ phase segregation in CdSe/CdTe based solar cells. Microsc. Microanal. 21 (S3), 691–692.
Poplawsky, J.D., et al., 2016. Structural and compositional dependence of the $CdTe_xSe_{1-x}$ alloy layer photoactivity in CdTe-based solar cells. Nat. Commun. 7, 12537.
Porter, D., Easterling, K., Easterling, K., 2009. Phase Transformations in Metals and Alloys. CRC Press, Boca Raton.
Pyykkö, P., 2015. Additive covalent radii for single-, double-, and triple-bonded molecules and tetrahedrally bonded crystals: a summary. J. Phys. Chem. A 119 (11), 2326–2337.
Reshak, A.H., et al., 2011. Effect of increasing tellurium content on the electronic and optical properties of cadmium selenide telluride alloys $CdSe_{1-x}Te_x$: An ab initio study. J. Alloy. Compd. 509 (24), 6737–6750.
Roehl, J.L., Khare, S.V., 2014. Diffusion of Te vacancy and interstitials of Te, Cl, O, S, P and Sb in CdTe: A density functional theory study. Sol. Energy Mater. Sol. Cells 128, 343–350.
Roehl, J.L., Khare, S.V., 2014. Diffusion of Cd vacancy and interstitials of Cd, Cu, Ag, Au and Mo in CdTe: A first principles investigation. Sol. Energy 101, 245–253.
Roehl, J.L., Liu, Z.T.Y., Khare, S.V., 2014. Diffusion in CdS of Cd and S vacancies and Cu, Cd, Cl, S and Te interstitials studied with first-principles computations. Mater. Res. Express 1 (2), 025904.
Romeo, N., et al., 2004. Recent progress on CdTe/CdS thin film solar cells. Sol. Energy 77 (6), 795–801.
Sanchez, J.M., Ducastelle, F., Gratias, D., 1984. Generalized cluster description of multicomponent systems. Physica A 128 (1–2), 334–350.
Sanville, E., et al., 2007. Improved grid-based algorithm for Bader charge allocation. J. Comput. Chem. 28 (5), 899–908.
Schenk, M., 1998. Zusammenfassung und Ausblick, in Altautomobilrecycling: Technisch-ökonomische Zusammenhänge und wirtschaftspolitische Implikationen. Deutscher Universitätsverlag, Wiesbaden, pp. 295–297.
Shakil, M., et al., 2016. Theoretical calculations of structural, electronic, and elastic properties of $CdSe_{1-x}Te_x$: A first principles study. Chin. Phys. B 25 (7), 7.
Shockley, W., Queisser, H.J., 1961. Detailed balance limit of efficiency of p-n junction solar cells. J. Appl. Phys. 32 (3), 510–519.
Strauss, A.J., Steininger, J., 1970. Phase diagram of the CdTe-CdSe pseudobinary system. J. Electrochem. Soc. 117 (11), 1420–1426.
Swanson, D.E., Sites, J.R., Sampath, W.S., 2017. Co-sublimation of $CdSe_xTe_{1-x}$ layers for CdTe solar cells. Sol. Energy Mater. Sol. Cells 159, 389–394.
Szemjonov, A., et al., 2014. Investigation of the bulk and surface properties of CdSe: insights from theory. PCCP 16 (42), 23251–23259.
Tang, W., Sanville, E., Henkelman, G., 2009. A grid-based Bader analysis algorithm without lattice bias. J. Phys.-Condens., Matter 21 (8), 7.
Terheggen, M., et al., 2004. Analysis of bulk and interface phenomena in CdTe/CdS thin-film solar cells. Interface Sci. 12 (2–3), 259–266.
Tit, N., Obaidat, I.M., Alawadhi, H., 2009. Origins of bandgap bowing in compound-semiconductor common-cation ternary alloys. J. Phys.: Condens. Matter 21 (7), 075802.
Uthanna, S., Reddy, P.J., 1983. Structural and electrical properties of $CdSe_xTe_{1-x}$ thin films. Solid State Commun. 45 (11), 979–980.
van de Walle, A., 2009. Multicomponent multisublattice alloys, nonconfigurational entropy and other additions to the Alloy Theoretic Automated Toolkit. Calphad-Computer Coupling Phase Diagrams Thermochem. 33 (2), 266–278.
van de Walle, A., 2013. Methods for first-principles alloy thermodynamics. JOM 65 (11), 1523–1532.
van de Walle, A., Asta, M., 2002. Self-driven lattice-model Monte Carlo simulations of alloy thermodynamic properties and phase diagrams. Modell. Simul. Mater. Sci. Eng. 10 (5), 521–538.
van de Walle, A., Ceder, G., 2002. Automating first-principles phase diagram calculations. J. Phase Equilibria 23 (4), 348–359.
van de Walle, A., Ceder, G., 2002. The effect of lattice vibrations on substitutional alloy thermodynamics. Rev. Mod. Phys. 74 (1), 11–45.
van de Walle, A., Asta, M., Ceder, G., 2002. The alloy theoretic automated toolkit: a user guide. Calphad-Computer Coupling Phase Diagrams Thermochem. 26 (4), 539–553.
van Swol, F., et al., 2016. Thermodynamic properties of model CdTe/CdSe mixtures. Mol. Simul. 42 (1), 14–24.
Vegard, L., 1921. Die Konstitution der Mischkristalle und die Raumfüllung der Atome. Zeitschrift für Physik 5 (1), 17–26.
Vurgaftman, I., Meyer, J.á., Ram-Mohan, L.á., 2001. Band parameters for III–V compound semiconductors and their alloys. J. Appl. Phys. 89(11), 5815–5875.
Vurgaftman, I., Meyer, J.R., Ram-Mohan, L.R., 2001. Band parameters for III–V compound semiconductors and their alloys. J. Appl. Phys. 89 (11), 5815–5875.
Warner, J., et al., 2006. Ab initio calculations for properties of MAX phases Ti_2TlC, Zr_2TlC, and Hf_2TlC. Appl. Phys. Lett. 88 (10), 101911.
Yang, J., Wei, S.-H., 2019. Enhancing CdTe solar cell performance by reducing the ideal bandgap of CdTe through CdTe1 − xSex alloying. arXiv e-prints.
Yeh, C.-Y., et al., 1992. Zinc-blende–wurtzite polytypism in semiconductors. Phys. Rev. B 46 (16), 10086–10097.
Yu, M., Trinkle, D.R., 2011. Accurate and efficient algorithm for Bader charge integration. J. Chem. Phys. 134 (6), 8.
Zhao, Y., et al., 2016. Monocrystalline CdTe solar cells with open-circuit voltage over 1 V and efficiency of 17%. Nat. Energy 1, 16067.
Zhou, X., Gall, D., Khare, S.V., 2014. Mechanical properties and electronic structure of anti-ReO_3 structured cubic nitrides, M_3N, of d block transition metals M: An ab initio study. J. Alloy. Compd. 595, 80–86.
Zunger, A., et al., 1990. Special quasirandom structures. Phys. Rev. Lett. 65 (3), 353–356.
Zunger, A., 1994. *First-principles statistical mechanics of semiconductor alloys and intermetallic compounds*. In: *Statics and Dynamics of Alloy Phase* Transformations. Springer, pp. 361–419.
Zweibel, K.E.N., 1992. Toward low cost CdTe PV. Int. J. Sol. Energy 12 (1–4), 285–292.

Approved for public release; distribution unlimited.
370

Defect Analysis in CSS and Sputtered $CdSe_xTe_{1-x}$ Thin Films

Niraj Shrestha, Corey R. Grice, Ebin Bastola, Yanfa Yan and Randy J. Ellingson

Department of Physics and Astronomy, Wright Center for Photovoltaics Innovation and Commercialization, University of Toledo, Toledo, OH, USA 43606

***Abstract* — Defect analysis of $CdSe_xTe_{1-x}$ alloy films prepared via close space sublimation (CSS) and sputtering have been carried out utilizing low temperature photoluminescence (PL) spectroscopy. We observe defect emission at 1.31 eV in both CSS and sputtered films which red shifts with increasing temperature. Therefore, the 1.31 eV peak is assigned to recombination of an electron in the conduction band with a hole localized in an unidentified vacancy defect state. Unlike $CdSe_xTe_{1-x}$, ~1.31 eV peak has been assigned to free-to-bound (FB) peak in polycrystalline CdTe by previous researchers. Our analysis shows that a small amount of Se incorporation into CdTe has been found to change the nature of dominant native defect. Furthermore, we observe the bound exciton peak at ~1.49 eV in both films while free exciton peak (1.52 eV) is absent in latter. The presence of a free excitonic peak in CSS film confirms its better crystallinity compared to the sputtered one. Identification of such defect states and their nature are crucial to improving the efficiency of CdTe based solar cells.**

***Index Terms*— Bowing, Defect, Exciton, Photoluminescence.**

I. Introduction

The presence of $CdSe_xTe_{1-x}$ alloy in CdTe solar cell increases the current densities by increasing the cell photo-current for both short- and long-wavelength photons. [1, 2] For the longer wavelengths, the photocurrent is enhanced due the decrease in the band gap of the $CdSe_xTe_{1-x}$ alloy because of a band gap bowing, while the absence of the CdS parasitical layer (which is present in traditional CdS/CdTe solar cell) in the window increases optical absorption for short wavelengths. The effect is that there is significant increase in the short-circuit current density of the $CdSe_xTe_{1-x}$ based solar cells. However, there is still not much improvement in the open circuit voltage of the device. [3] There are various factors that might affect the performance of the solar cell. Native defects are among the most influential ones. Thus, identification of various kinds of defect states in $CdSe_xTe_{1-x}$ alloy must be warranted. In the previous report, we had presented the defect analysis of co-sputtered $CdSe_xTe_{1-x}$ alloys with two different Se concentration. [4] But, the present work focuses on defect analysis of $CdSe_xTe_{1-x}$ alloys deposited via CSS and sputtered methods. There have been numerous studies that discussed difference in quality of CdTe films prepared by different techniques. [5] Therefore, comparison of the native defects of films, deposited via different technique, utilizing low temperature photoluminescence (PL) spectroscopy is essential to provide insight into the quality of the $CdSe_xTe_{1-x}$ polycrystalline films utilized in the solar cells. Here, we present defect analysis of $CdSe_xTe_{1-x}$ alloy deposited via CSS and sputtering techniques. We observe defect emission peak at ~1.31 eV and a bound exciton peak at 1.49 eV in both samples. While free excitonic peak ~1.52 eV is observed only in case of CSS film which evident its better film quality than sputtered one.

II. Experimental Details

$CdSe_xTe_{1-x}$ alloy (x = 0.08) samples were prepared on soda-lime glass substrate [NSG Pilkington, USA] using both close space sublimation method (CSS) [6] and co-sputtering techniques [4]. Samples were $CdCl_2$ treated before PL measurements. For PL measurements, samples were excited through film side. A 532 nm cw (continuous wave) laser beam was used for the photoexcitation. For room temperature measurements, the PL signal was detected by a Horiba Symphony-II CCD (charged coupled device) detector after a 300 g/mm grating monochromator while a liquid nitrogen cooled Germanium photodiode from Electro-Optical Systems was used for low temperature measurement. Temperature dependent PL measurements were carried out by mounting the sample on the cold finger of a He closed-cycle refrigerator cryostat system from Advanced Research Systems. PL measurements were performed using laser power in the range of 3.3 to 1398 μW.

III. Results and Discussions

Fig. 1a represents the PL spectra of CSS and sputtered $CdSe_xTe_{1-x}$ alloys (x = 0.08) acquired at room temperature. Their emission peaks shift toward lower energy relative to pristine CdTe films due to band gap bowing. CSS grown films show higher PL intensity which can be attributed to their better film quality compared to the sputtered ones. PL spectra taken at 15 K reveal emission peaks at ~1.31 eV, ~1.49 eV and ~1.52 eV in CSS film while ~1.52 eV peak is absent in the sputtered film (Fig. 1b).

To explore the identity of observed peaks, laser power dependent PL has been performed as shown in Fig. 1c-d. It has been reported that integrated PL intensity follows power law $I_{PL} = I^K_{Laser}$ with a value of $1 < K < 2$ for band-to-band (BB) and excitonic recombination, and $K < 1$ for defect assisted recombination. [5, 7, 8] Obtained $K < 1$ confirms that the ~1.31 eV peaks observed in both CSS and sputtered films are related to the defect transitions as depicted in Fig. 1e-f. The ~1.52 eV

Authorized licensed use limited to: University of Exeter. Downloaded on June 15,2020 at 11:47:31 UTC from IEEE Xplore. Restrictions apply.

Approved for public release; distribution unlimited.

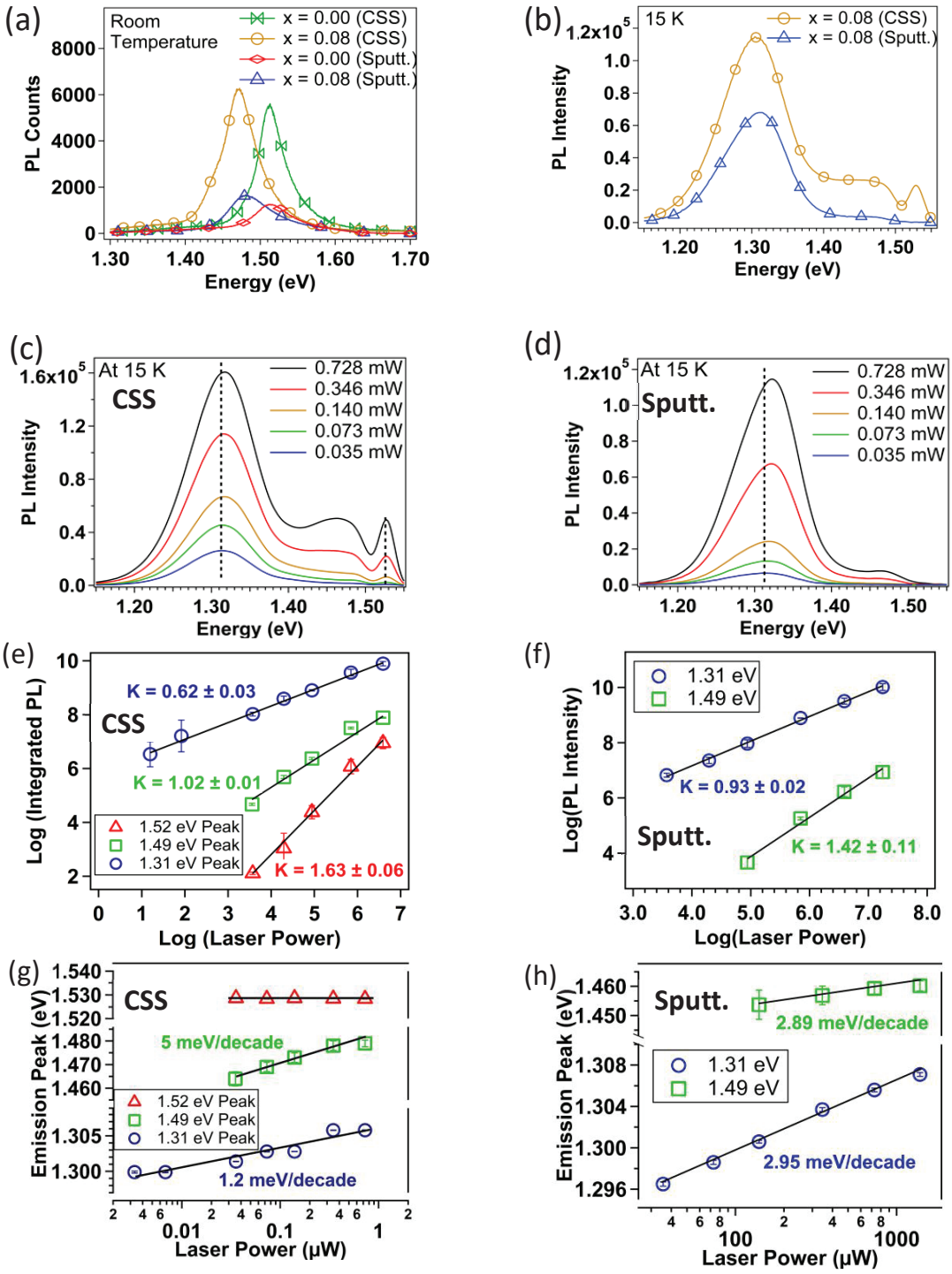


Fig. 1. PL spectra at (a) room temperature and (b) 15 K; laser power dependent PL of (c) CSS and (d) sputtered; integrated PL vs. laser power of (e) CSS and (f) sputtered; and emission peak vs. laser power of (g) CSS and (h) sputtered $CdSe_xTe_{1-x}$ (x=0.08) films.

Authorized licensed use limited to: University of Exeter. Downloaded on June 15,2020 at 11:47:31 UTC from IEEE Xplore. Restrictions apply.

Approved for public release; distribution unlimited.

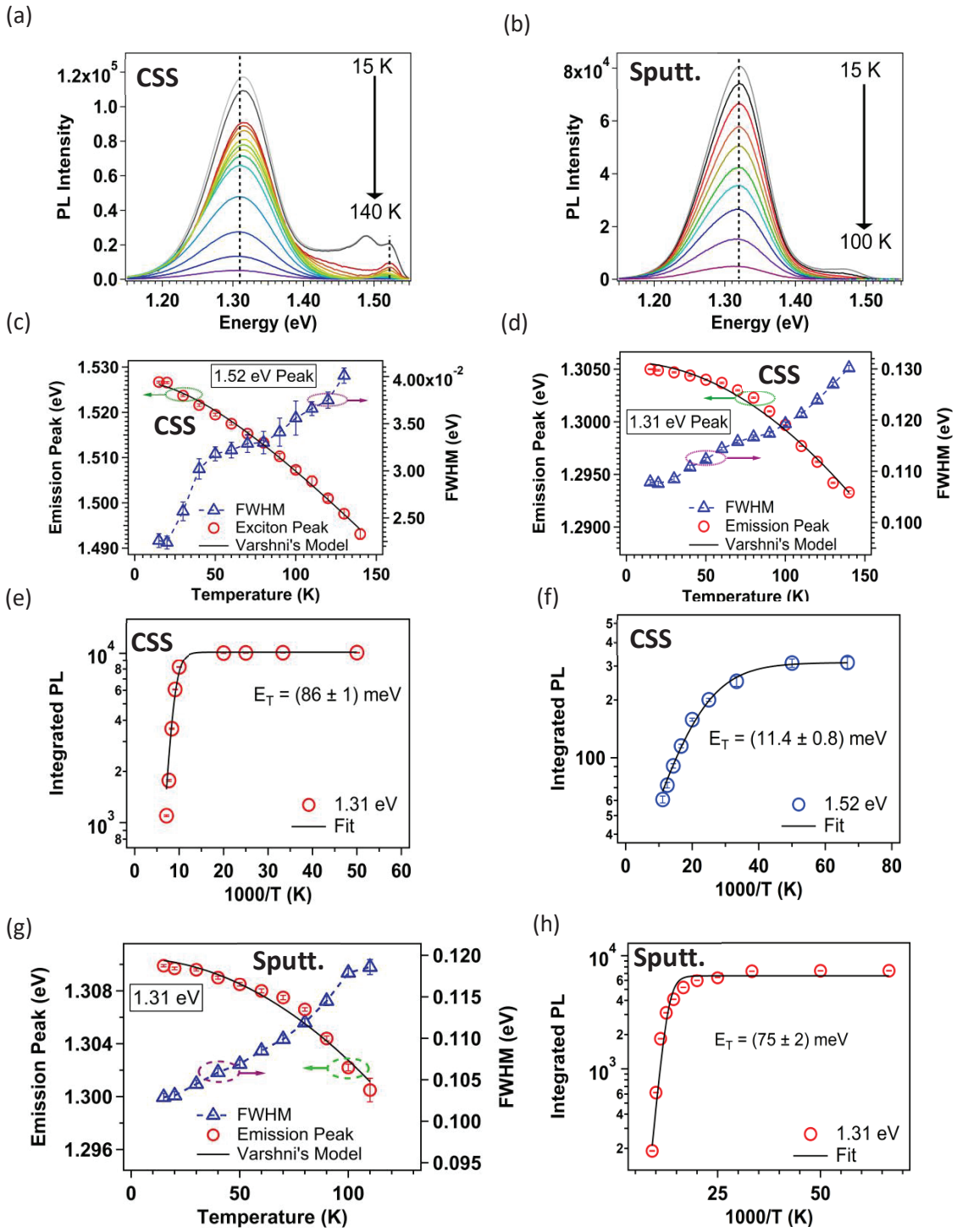


Fig. 2. Temperature dependent PL spectra of (a) CSS and (b) sputtered; (c) and (d) emission peak vs. temperature for CSS, (e) and (f) Arrhenius plots of CSS; (g) emission peak vs. temperature of sputtered; and (h) Arrhenius plot of sputtered $CdSe_xTe_{1-x}$ (x=0.08).

Authorized licensed use limited to: University of Exeter. Downloaded on June 15,2020 at 11:47:31 UTC from IEEE Xplore. Restrictions apply.

Approved for public release; distribution unlimited.

peak observed in CSS film with K >1 is assigned to free excitonic emission. The absence of the free excitonic peak in sputtered film reveals its lower crystallinity than the CSS films. Fig. 1g and 1h show that ~1.31 defect peaks appeared in both films blue-shifted with increasing laser power. The blue shift of defect peak with increasing laser power can be attributed to the band-filling effect of highly energetic localized centers. [9] While the 1.52 eV free excitonic peak observed in CSS film remains unchanged with laser power. Furthermore, ~1.49 eV peak shifts towards higher energy with increase in laser power and is assigned to bound exciton.

Observed exciton and defect peaks red-shifted with increasing temperature as shown in Fig. 2a-b. The red-shift of excitonic emission peak is due to the thermal expansion of the lattice and electron–phonon interaction. [10] The former effect is effective at higher temperature and the latter effect induces the relative shifts of conduction band and valence band following Varshni's model (1)

$$E_g(T) = E_g(0) - \left(\frac{\alpha T^2}{\beta + T}\right) \qquad (1)$$

where α is fitting parameter and β is related to Debye temperature. [11] Both effects cause the shrinkage of band gap and thereby red-shift of the emission peak. Temperature induced change in band gap energy is the result of change in the energy of conduction band or valence band edge. Defect emission peak ~1.31 eV has also been found to follow the same temperature dependency as exciton peak. This confirms that defect emission peak is the consequence of recombination of an electron in the conduction band to a hole localized in some vacancy defect state. In contrast, ~1.31 eV peak has been assigned to free-to-bound (FB) peak in polycrystalline CdTe. [12] Adding a small amount of Se has been found to change the nature of native defect in $CdSe_xTe_{1-x}$ alloy. The value of α for excitonic and defect peaks, utilizing eq. 1, was ~0.3 meV/K.

Furthermore, we also observe the broadening of defect and excitonic emission line with increasing temperature which is attributed to the consequences of electron and phonon interaction as shown in Fig. 2c-d, g. [9] Fig. 2e-f represents the integrated PL vs. temperature plot of free exciton and defect peak for CSS film. Thermal activation energy of ~86 meV and binding energy of ~11 meV were obtained for the defect and free exciton peaks of CSS films respectively, using eq. 2. [13]

$$I = \frac{I_o}{1 + A\, e^{-E_T/KT}} \qquad (2)$$

Here I_o and A are the fitting parameters, and E_T is the thermal activation energy. While thermal activation energy of 75 meV was obtained for defect peak in sputtered film (Fig. 2h). The bound exciton peak quenches rapidly with temperature. Therefore, we were unable to explore more about it. However, we were able to predict shallow defect level at ~30 meV to which bound exciton is tied with.

IV. Conclusion

Defect analysis of $CdSe_xTe_{1-x}$ alloy (x=0.08) samples deposited via two different techniques, i.e. CSS and sputtered, have been performed utilizing temperature and laser power dependent photoluminescence (PL) spectroscopy. Both CSS and sputtered samples show bound exciton peak at ~1.49 eV, but free exciton peak 1.52 eV is absent in latter. The presence of free excitonic peak in CSS sample confirms the better crystallinity in it compared to the sputtered one. This is further evident by higher PL intensity observed in the case of CSS film compared to that observed in sputtered film. The binding energy of free exciton obtained from low temperature PL is 11.2 meV. Furthermore, we observe defect emission at ~1.31 eV in both CSS and sputtered films. Temperature and laser power dependent PL reveal that such defect emission peak is the consequence of recombination of an electron in the conduction band to a hole localized in some vacancy defect state. The obtained value of thermal activation energy associated with this defect peak confirms the involvement of shallow defect state. In contrast, the ~1.31 eV peak has been assigned to FB peak in polycrystalline CdTe. Our analysis shows that small amount of Se incorporation into CdTe has been found to change the nature of dominant native defect in $CdSe_xTe_{1-x}$ alloy. Such information can be helpful in development of $CdSe_xTe_{1-x}$ based solar cells.

V. Acknowledgement

The authors gratefully acknowledge funding support from the U.S. Air Force Research Laboratory, Space Vehicles Directorate, under Contract # FA9453-11-C-0253. This material is based on research sponsored by Air Force Research Laboratory under agreement number FA9453-18-2-0037. The U.S. Government is authorized to reproduce and distribute reprints for Governmental purposes notwithstanding any copyright notation thereon. The views and conclusions contained herein are those of the authors and should not be interpreted as necessarily representing the official policies or endorsements, either expressed or implied, of Air Force Research Laboratory or the U.S. Government.

References

[1] N. R. Paudel, J. D. Poplawsky, K. L. Moore, and Y. Yan, "Current Enhancement of CdTe-Based Solar Cells," *IEEE J. Photovolt.,* vol. 5, pp. 1492-1496, 2015.

[2] N. R. Paudel and Y. Yan, "Enhancing the photo-currents of CdTe thin-film solar cells in both short and long wavelength regions," *Appl. Phys. Lett.,* vol. 105, p. 183510, 2014.

Authorized licensed use limited to: University of Exeter. Downloaded on June 15,2020 at 11:47:31 UTC from IEEE Xplore. Restrictions apply.

Approved for public release; distribution unlimited.

[3] J. D. Poplawsky, W. Guo, N. Paudel, A. Ng, K. More, D. Leonard, *et al.*, "Structural and compositional dependence of the $CdTe_xSe_{1-x}$ alloy layer photoactivity in CdTe-based solar cells," *Nat. Commun.,* vol. 7, p. 12537, 07/27/online 2016.

[4] N. Shrestha, C. R. Grice, E. Bastola, G. K. Liyanage, A. B. Phillips, M. J. Heben, *et al.*, "Low Temperature Photoluminescence Spectroscopy of Defect and Interband Transitions in $CdSe_xTe_{1-x}$ Thin Films," *MRS Advances,* pp. 1-7, 2018.

[5] P. J. Roland, N. R. Paudel, X. Chuanxiao, Y. Yan, and R. J. Ellingson, "Photoluminescence spectroscopy of Cadmium Telluride deep defects," in *2014 IEEE 40th Photovoltaic Specialist Conference (PVSC)*, 2014, pp. 3266-3271.

[6] J. L. a. Y. Y. C. R. Grice, "Characterization of Single-Source Deposited Close-Space Sublimation $CdTe_xSe_{1-x}$Thin Film Solar Cells," in *2017 IEEE 44th Photovoltaic Specialist Conference (PVSC)*, Washington, DC, 2017, pp. pp. 1643-1647.

[7] J. Krustok, V. Valdna, K. Hjelt, and H. Collan, "Deep center luminescence in p-type CdTe," *J. Appl. Phys.,* vol. 80, pp. 1757-1762, 1996.

[8] T. Schmidt, G. Daniel, and K. Lischka, "The excitation power dependence of the near band edge photoluminescence of II-VI semiconductors," *J. Cryst. Growth,* vol. 117, pp. 748-752, 1992/02/02/ 1992.

[9] H. Wang, Z. Ji, S. Qu, G. Wang, Y. Jiang, B. Liu, *et al.*, "Influence of excitation power and temperature on photoluminescence in InGaN/GaN multiple quantum wells," *Optics Express,* vol. 20, pp. 3932-3940, 2012/02/13 2012.

[10] C. H. Chia, C. T. Yuan, J. T. Ku, S. L. Yang, W. C. Chou, J. Y. Juang, *et al.*, "Temperature dependence of excitonic emission in cubic CdSe thin film," *Journal of Luminescence,* vol. 128, pp. 123-128, 2008/01/01/ 2008.

[11] Y. P. Varshni, "Temperature dependence of the energy gap in semiconductors," *Physica,* vol. 34, pp. 149-154, 1967/01/01/ 1967.

[12] J. Krustok, J. Mädasson, and J. Hiie, "Photoluminescence Properties of Z-Bands in CdTe," *Phys. Status Solidi A,* vol. 165, pp. 517-525, 1998.

[13] M. Leroux, N. Grandjean, B. Beaumont, G. Nataf, F. Semond, J. Massies, *et al.*, "Temperature quenching of photoluminescence intensities in undoped and doped GaN," *Journal of Applied Physics,* vol. 86, pp. 3721-3728, 1999.

Authorized licensed use limited to: University of Exeter. Downloaded on June 15,2020 at 11:47:31 UTC from IEEE Xplore. Restrictions apply.

Approved for public release; distribution unlimited.

ZnTe Back Buffer Layer to Enhance the Efficiency of CdS/CdTe Solar Cells

Sandip Singh Bista, Deng-Bing Li, Chen Lei, Corey Grice, Rasha A. Awni, Zhaoning Song, and Yanfa Yan

Department of Physics and Astronomy, and the Wright Center for photovoltaics Innovation and Commercialization, The University of Toledo, Toledo, OH, 43606 USA

***Abstract* — The high electron affinity (4.4eV) of CdTe presents a major technological challenge for forming a good back contact to CdTe, limiting the power conversion efficiency of CdTe solar cells. Commonly used metals do not possess an adequately deep work function to create an ohmic contact with CdTe. Instead, approaches such as doping the back surface of CdTe or incorporating a buffer layer between CdTe and the back-metal contact are used to lower the back-barrier height. Here, we investigate the impact of sputtered ZnTe back buffer layer on the performance of CdS:O/CdTe solar cells. We demonstrated CdTe solar cells with an efficiency of around 15% with a 35 nm ZnTe buffer layer.**

***Index Terms* —Back contact, back barrier height, open-circuit voltage, zinc tellurium (ZnTe).**

I. Introduction

A direct band gap of 1.45 eV and high absorption coefficients of about 1 x 10^5 cm^{-1} make cadmium tellurium (CdTe) an ideal thin-film absorber material to achieve a high-power conversion efficiency (PCE) [1]. The highest certified efficiencies for polycrystalline CdTe based solar cell and modules are 22.1% [2] and 18.6% [3], respectively, approaching the market-dominant crystalline silicon photovoltaic technologies (26.1% and 24.4%). However, these PCE values are still far below the theoretical efficiencies (> 30%) predicted by the Shockley–Queisser limit. This inferior performance is mainly due to the high electron affinity (4.4 eV) and low carrier density (10^{14} - 10^{15} cm^{-3}) of CdTe. To form an Ohmic contact with CdTe back contact metals need to have a work function of more than 5.9 eV. However, metals commonly have lower work functions than CdTe and form a Schottky barrier when they are directly contacted with CdTe. This back barrier significantly reduces the hole collection, causing losses in open-circuit voltage (V_{oc}) and fill factor (FF).

Various approaches have been undertaken to mitigate this back-barrier issue. One method is to produce a highly doped CdTe back surface to facilitate the quantum tunneling through the Schottky barrier. For instance, copper (Cu) is widely used as a p-type dopant in CdTe. While efficient CdTe solar cells have been demonstrated, Cu doping causes long term stability issue due to the ease of diffusion of Cu. Another method is to incorporate a thin buffer layer between CdTe and the metal contact to reduce the back-barrier height. Various materials have been explored as candidates for the back buffer layer, including tin tellurium (SnTe) [4], antimony tellurium (Sb_2Te_3) [5], molybdenum trioxide (MoO_3) [6], single wall carbon nanotubes, [7] iron pyrite [8], nitrogen doped zinc tellurium [9], and Cu doped zinc tellurium [10]. Among them, zinc tellurium (ZnTe) is considered as an ideal material for a low resistance buffer layer and has been used in commercial products. It has been reported that ZnTe buffer layer retards Cu diffusion and maintains a Cu-rich back [11], [12]. ZnTe has a band gap of 2.26 eV and similar lattice structure to CdTe. Importantly, it can be easily tuned to highly p-type doping with a hole concentration of up to 10^{20} cm^{-3}. Additionally, ZnTe has a small (0.0 ± 0.05 eV) valance band offset (VBO) and a high conduction band barrier with respect to CdTe, which are significant for hole collection and electron reflection at the back electrode [13]- [15].

Here, we investigate the impact of sputtered ZnTe back buffer layer on the performance of CdS:O/CdTe solar cells. We find that the ZnTe films deposited at room temperature are highly resistive. However, by depositing 4 nm copper on ZnTe followed by annealing, the carrier concentration of ZnTe:Cu film is increased to 4.0 x 10^{20} cm^{-3}. By using the ZnTe:Cu buffer layer, we demonstrate CdS:O/CdTe solar cells with PCEs of 15%.

II. Experimental

CdTe solar cells were fabricated on T15M glass substrates supplied by Pilkington NA Inc. The substrates were cleaned in de-ionized water with Micro-90 detergent in an ultrasonic bath in hot water (~70 ^{0}C) for 1 hour. Then the cleaning process was repeated four times in de-ionized water for 30 mins and finished by drying with nitrogen. Around 90 nm CdS:O emitter layer was sputtered under the flow of 2 % oxygen and 98 % argon by using RF sputtering system designed by AJA Corporation Int. Then ~4 μm CdTe layer was deposited by close space sublimation (CSS) process with source temperature at 660 ^{0}C and substrate temperature at 598 ^{0}C in 10 Torr of helium gas. $CdCl_2$ treatment was done at 390 ^{0}C in dry air for 30 minutes to enhance the CdTe crystallinity and passivate defects. After that, HI etching was carried out to remove oxides and chlorine remnants according to our previous paper [16]. Around 35 nm ZnTe layer were deposited by sputtering a 2-inch diameter target (99.99 % purity, Materion Corporation) at 50 W rf power in Argon. To complete the devices, a bilayer of Cu (4 nm) and Au (40nm) was deposited by thermal evaporation. Then the devices were annealed in nitrogen ambient at 200 ^{0}C for 20 minutes to promote the Cu diffusion into ZnTe and CdTe.

Surface morphology and chemical composition were examined using Hitachi-4800S scanning electron microscope

Approved for public release; distribution unlimited.

(SEM) and the equipped X-ray energy dispersive spectroscopy (EDS) detector. Surface roughness were measured by atomic force microscopy (AFM). The current density-voltage (J-V) measurements were conducted under AM1.5 solar simulator (PV Measurements Inc.) using a source meter (Keithley 2400). External quantum efficiency (EQE) spectra were measured using a QE system (PV measurement Inc.).

III. Results and Discussion

The morphology of CdTe surface with and without ZnTe back contact were analyzed by SEM and AFM measurements, as shown in Figures 1 and 2. The coating of a thin and compact ZnTe layer was confirmed by the smooth surface morphology. The root mean square roughness (rms) of CdTe is reduced from 197 ± 5 nm to 165 ± 5nm after the deposition of ZnTe.

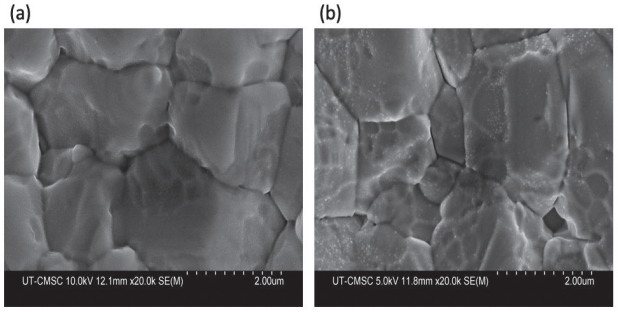


Fig. 1. SEM images of CdTe films (a) without and (b) with a 35 nm ZnTe layer.

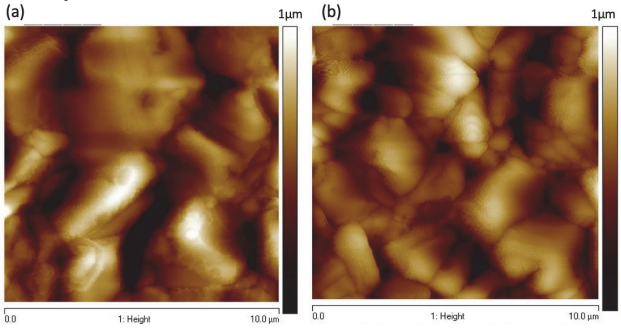


Fig. 2. AFM images of CdTe films (a) without and (b) with a 35 nm ZnTe layer.

To investigate the impact of Cu doping on the electric properties of the sputtered ZnTe films, we deposited ZnTe films with and without Cu doping on bare glass substrates and performed the Hall effect measurements (Table 1). The undoped ZnTe is very resistive and its conductivity behavior cannot be measured by the Hall measurement system. In contrast, after Cu doping, the ZnTe:Cu film shows a relatively high conductivity of 2.5 x 10^{-2} Ω-cm and a high hole density of 4 x 10^{20} cm^{-3}. Such high carrier concentration is desired to form a low-barrier back contact.

TABLE I
THE ELECTRIC PROPERTIES OF ZNTE FILM

Sample	R(Ω-cm)	Mobility (cm^2/Vs)	N (cm^{-3})
ZnTe as deposited	Very High	NA	NA
ZnTe/Cu Annealed	$2.535x10^{-2}$	0.606	$4.063x10^{+20}$

We fabricated solar cells with a structure of Glass/FTO(SnO_2:F)/CdS:O/CdTe/ZnTe/Cu/Au, where the thickness of ZnTe was varied from 250 to 35 nm. Additionally, to investigate the Cu doping behavior on ZnTe, we varied the annealing temperature and time. In brief, devices with thicker ZnTe buffer layer show higher series resistance and lower FF values, and consequently require higher amount of Cu doping with thicker Cu layer, higher annealing temperature, and longer annealing time.

Overall, the best device was formed with a 35 nm ZnTe layer, doped with 4 nm Cu and annealed at 200 ^{0}C temperature for 20 min in ambient pressure under the flow of Nitrogen gas. Figure 3 summarize the J-V characteristic of two set of cells with Cu/Au and ZnTe/Cu/Au back contacts. The cells with the ZnTe back buffer layer show a higher average V_{OC} of 860 mV compared with V_{OC} of 845 mV for the standard Cu/Au cells, and thus result in higher PCEs (14.96% vs. 14.87%).

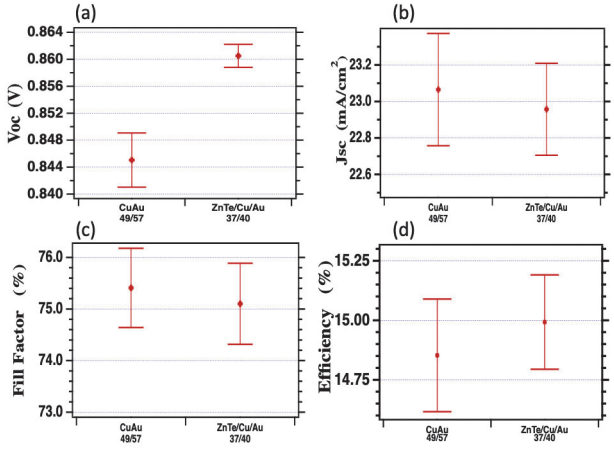


Fig. 3 (a) Open circuit voltage (V_{OC}), (b) short circuit current (J_{sc}), (c) fill factor (FF) and (d) Efficiency (η) of CdTe solar cells with Cu/Au and ZnTe/Cu/Au back contacts.

Figure 4 compares the J-V characteristics of the best cells with Cu/Au and ZnTe/Cu/Au back contacts. The higher efficiencies of ZnTe devices are due to the higher V_{OC} value (860 vs. 845 mV). The observed short-circuit current densities (J_{sc}) of these devices (23.33 and 23.28 mA/cm^2) were verified by measuring external quantum efficiency, which is shown in Figure 5.

Approved for public release; distribution unlimited.

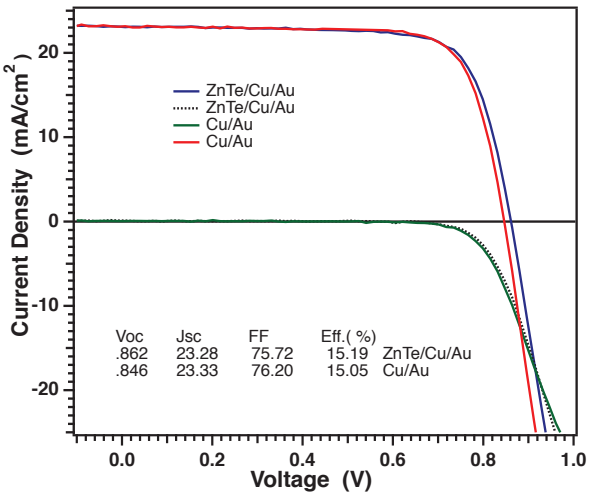


Fig. 4. J-V curves of best CdTe cells with Cu/Au and ZnTe/Cu/Au back contacts.

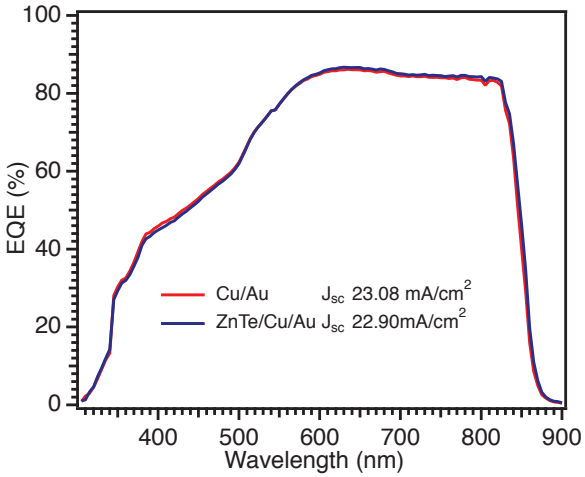


Fig. 5. EQE curves of best CdTe cells with Cu/Au and ZnTe/Cu/Au back contacts.

To understand the effect of the back barrier a dark J-V-T measurement was carried for Cu doped ZnTe buffer layer device. To calculate the back-barrier height, we assume the thermionic emission at the back junction. The saturation current density (J_0) then can be extracted by using equation (1).

$$J_0 = A^* T^2 [\exp(\frac{q\emptyset}{k_B T})] \quad (1)$$

where A^* is the Richardson constant, T is the temperature, q is the electron charge, $\emptyset$ is the back-barrier height, and k_B is the Boltzmann constant. The back barrier for the sample is extracted by using an Arrhenius plot of $\ln(J_0/T^2)$ versus $1/k_BT$, as shown in Figure 6. The measured back barrier is 0.314 eV which is lower than that of the control device 0.377 eV [16]. It is clearly shown that Cu doped ZnTe buffer layer reduced the back-barrier height which attributes increased V_{oc}. However, Fill Factor (FF) and J_{sc} slightly decreases which might be due to excess of copper migrating towards a front junction.

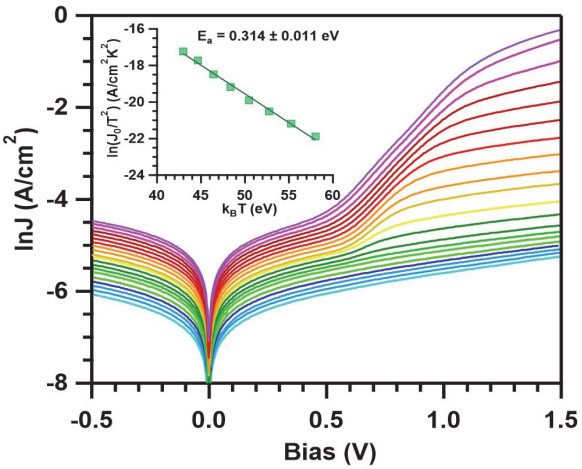


Fig. 6. Dark J-V-T curve and Arrhenius plot to measured back barrier-height. The inserts show Arrhenius plots that were used to calculate back-contact barriers.

IV. Conclusion

We studied the impact of ZnTe back buffer layer on the performance of CdS:O/CdTe solar cells. We demonstrated CdS:O/CdTe solar cells with PCEs of 15% with an around 35 nm ZnTe back buffer layer and found that performance improvement is likely due to lower Schottky barrier height.

V. Acknowledgement

This work is supported by Air Force Research Laboratory, Space Vehicles Directorate (contact # FA9453-11-C-0253) and National Science Foundation under contact no. 1711534 and the U.S. Department of Energy's Office of Energy Efficiency and Renewable Energy (EERE) under Solar Energy Technologies Office (SETO) Agreement Number DE-EE007541. We thank Dr. David Strickler for Pilkington North America Inc. for supplying us FTO coated substrates.

This material is based on research sponsored by Air Force Research Laboratory under agreement number FA9453-18-2-0037. The U.S. Government is authorized to reproduce and distribute reprints for Governmental purposes notwithstanding any copyright notation thereon. The views and conclusions contained herein are those of the authors and should not be interpreted as necessarily representing the official policies or endorsements, either expressed or implied, of Air Force Research Laboratory or the U.S. Government.

REFERENCES

[1] William Shockley, Hans J. Queisser, "Detailed Balance Limit of Eifficiency of p-n Junction Solare Cells," *J. Appl. Phys.* http://dx.doi.org/10.1063/1.1736034 32,510 (1961)

[2] Martin A. Green, Yoshihiro Hishikawa, Ewan D. Dunlop, Dean H. Levi, Jochen Hohl-Ebinger, Anita W.Y. Ho-Baillie, "Sollar cell efficiency tables (version 51)," *Wiley Photovoltaics* doi:10.1002/pip.2978, 2017

[3] NREL, "*Research Cell Record Efficiency Chart*," <https://www.nrel.gov/pv/assets/pdfs/pv-efficiency-chart.201812171.pdf> 2018.

[4] Zeping Weng, Songsong Ma, He Zhu, Zhenyu Ye, Tianyu Shu, Jie Zhou, Xuanzhi We, Huizhen Wu, "CdTe thin film solar cells with a SnTe buffer layer in back contact," Solar Energy Materials and Solar Cells, doi:101016/j.solmat, 2017

[5] N.R. Paudel, K. A. Wieland, A. D. Compaan, "Characterization of rf sputtered Sb2Te3 thin films for back contacts to CdS/CdTe solar cells," *J. of Mat. Science*, vol. 26 pp. 78-83, 2015

[6] N. R. Paudel, Chuanxian Xiao, Yanfa Yan, " CdS/CdTe thin-film solar cells with Cu-free transition metal oxide/Au back contacts," *Prog. in Photovolt: Res. Appl*: 23:437-442, 2015

[7] A. B. Phillips, R. R. Khanal, Z. Song, R. M. Zartman, J. L. DeWitt, J. M. Stone, P. J. Roland, V. V. Plotnikov, C. W. Carter, J. M. Stayancho, R. J. Ellingson, A. D. Compaan and M. J. Heben, "Wiring-up Carbon Single Wall Nanotubes to Polycrystalline Inorganic Semiconductor Thin Films: Low-Barrier, Copper-Free Back Contact to CdTe Solar Cells," *Nano Letters*, vol. 13, 5224-5232, 2013

[8] K. P. Bhandarie et al., "Iron pyrite nanocrystal film serves as a copper-free back contact for polycrystalline CdTe thin film solar cells," *Solar Energy Materials and Solar Cells*, vol. 140, pp.108-114, 2015

[9] Tushar M. Shimpi, Jennifer Drayton, Drew E. Swanson and Walajabad S. Sampath, "Properties of Nitrogen-Doped Ain Telluride Films for Back Contact of Cadmium Telluride Photovoltaics," *Journal of Electronic materials* Vol. 46, No. 8, 2017

[10] Narayanswamy, C., T.A. Gessert, and S.E. Asher, "Analysis of Cu diffusion in ZnTe-based contacts for thin-film CdS/CdTe solar cells," *AIP Conference Proceedings*. p. 248-253, 1999

[11] Strevel, N., et al., "Improvements in CdTe module reliability and long-term degradation through advances in construction and device innovation," *Photovoltaics International*, **22**: p. 66-74, 2013

[12] B.R. Faulkner, J.M. Burst, T.R. Ohno, C.L. Perkins, B. To, T.A. Gessert, *40th IEEE PVSC*, Denver, Colorado, (2014) 5-9doi: http://dx.doi.org/10.1109/PVSC.2014.6925392.

[13] Trevor M. Letcher, M. Fthenakis, "A comprehensive guide to solar energy systems," http://dx.doi.org/10.1016/b978-0-12-811479-7.00010-5

[14] D. Rioux, D. W. Niles, and H. Hochst, "ZnTe: A potential interlayer to form low resistance back contacts in CdS/CdTe solar cells," *J. Appl. Phys.,* vol. 73, pp. 8381-8384, 1993

[15] T.A Gessert, A.R. Mason, R.C. Reedy, R. Matson, T.J. Coutts, and P. Sheldon, "Development of rf Sputtered, Cu-Doped ZnTe for Use as a Contact Interface Layer to p-CdTe," *Journal of Electronic Materials*, vol. 24, No. 10, 1995

[16] Rasha A. Awni, Deng-Bing Li, Corey R. Grice, Zhaoning Song, Mohammed A. Razooqi, Adam B. Phillips, Sandip Singh Bista, Paul J. Roland, Fadhil K. Alfadhili, Randy J. Ellingson, Michael J. Heben, Jian V. Li, and Yanfa Yan, "The Effects of Hydrogen Iodide Back Surface Treatment on CdTe Solar Cells," *RRL Solar*, doi:10.1002/solar.201800304, 2019

Approved for public release; distribution unlimited.

Doping of CdTe using $CuCl_2$ Solution for Highly Efficient Photovoltaic Devices

Ebin Bastola[1], Alex V. Bordovalos[1], Elizabeth LeBlanc[2,3], Niraj Shrestha[1], Matthew O. Reese,[3] and Randy J. Ellingson[1]

[1]Wright Center for Photovoltaics Innovation and Commercialization (PVIC), Department of Physics and Astronomy, University of Toledo, Toledo, Ohio, 43606, USA

[2]Texas State University, Department of Material Science, Engineering and Commercialization, San Marcos, Texas, 78666, USA

[3]National Renewable Energy Laboratory (NREL), Golden, Colorado, 80401 USA

***Abstract* — Here, we report doping of cadmium telluride (CdTe) thin film solar cells using copper (II) chloride ($CuCl_2$) solution in deionized water. The CdTe thin films were immersed in 0.1 mmol $CuCl_2$ solution in water and annealed in the temperature range of 180 – 240 °C for various time durations. The devices were completed using thermally evaporated gold (Au) and measured under simulated AM1.5G spectrum. The average device efficiency of $CuCl_2$ treated CdTe devices increased to 13.7 % (best cell reaching 14.0%) with significant improvement on open-circuit voltage (V_{OC}) as compared with 12.4% (best cell 12.7%) for thermally evaporated Cu doped CdTe devices. For $CuCl_2$ treated CdTe devices, we found higher photoluminescence (PL) intensity and longer carrier life time at room temperature indicating solution based doping offers better control of Cu doping density as compared with evaporated Cu.**

***Index Terms*- CdTe, $CuCl_2$, solar cells, doping, thin films.**

I. Introduction

Cadmium telluride (CdTe) is a p-type semiconductor material widely used as an absorber layer in photovoltaic application. CdTe has a band gap of ~1.45 eV and, when Cu-doped, a hole carrier concentration of ~ 10^{14} cm^{-3}. The valence band edge of CdTe is located at ~ -5.9 eV relative to vacuum.[1] Improving the performance of CdTe photovoltaic (PV) devices requires increasing the free hole concentration, and forming an ohmic contact at the back side of the devices. Thermally evaporated copper/gold (Cu/Au) has frequently been utilized as the back-contact material for laboratory scale devices.[2, 3] However, stability and repeatable thickness control near the targeted monolayer coverage is challenging.

The introduction of Cu creates shallow defects in the form of Cu_{Cd}, which ionize to improve the carrier concentration and conductivity of CdTe, and hence enhance the device performance. However, the interface of metals with CdTe yields a Schottky barrier opposing the transport of holes at the back contact. To reduce the back-contact barrier height and improve the device performance, semiconductor materials have been introduced as hole transport layers during back-contact processing. For example, Cu doped zinc telluride (ZnTe) and pyrite nanocrystal thin films have each been applied as hole transport materials in CdTe devices.[4-8] Similarly, the development or deposition of a thin tellurium layer on the back surface also reduces the potential barrier and enhances the device efficiency.[9-11] In addition to this, chemical etching of CdTe using bromine or iodine solution can create a Te-rich surface,[12] which has been shown to reduce contact resistance and enhance device performance. The treatment of CdTe devices with sublimed copper (I) chloride (CuCl) has been found to improve the device performance.[9] Previously, Mao et al. have utilized solution dipping process for doping CdTe devices in $CuCl_2$ solution in DI water for 30 min at 280°C.[13] In a recent study, CdTe devices were treated with $CuCl_2$ solution in water for Cu doping in the temperature range of 200-230 °C for about 30 mins.[14] Similarly, Artegiani et al. have also reported the doping of CdTe devices using $CuCl_2$ solution in methanol and found the $CuCl_2$ doped devices are more stable than the devices doped using thermal evaporation of Cu.[15]

Here, we have used $CuCl_2$ solution in deionized water for doping CdTe solar cells to fabricate efficient and stable devices. The CdTe devices were treated with $CuCl_2$ solution in deionized water (DIW) and annealed for various durations and at varying test temperatures. Finally, the devices were completed by thermally evaporating Au to complete the back-contact. Current-voltage (J-V) characteristics were measured under simulated AM1.5G spectrum and showed improvements in open-circuit voltage (V_{OC}) and fill factor (FF) compared to devices with Cu doped using thermal evaporation. The CdTe devices treated at 200 °C for 20 mins has the highest average device efficiency (13.7%) with best cell reaching 14.0% with open circuit voltage 840 mV and fill factor 76.2%. The device efficiency of $CuCl_2$ treated samples was within ~3% relative (0.4% absolute) which was within the error of the measurement in over 90 days stored in ambient environment indicating the long stability of the devices.

Approved for public release; distribution unlimited.

II. Experimental

CdS/CdTe device stacks with CdS thickness of 120 nm and CdTe 3.5 µm was prepared using physical vapor deposition on TEC-15M glass substrate. The CdTe devices were activated with saturated cadmium chloride ($CdCl_2$) solution in methanol, introduced drop wise onto the CdTe surface followed by annealing at 390 °C for 30 mins in dry air environment, rinsing with methanol, and drying under nitrogen flow. The $CuCl_2$ stock solution (10 mM) was prepared in deionized water (DIW), and a 25 mL dilute solution of 0.1 mM was prepared by adding DIW in a beaker. Then, the devices were submerged in 25 mL of 0.1 mM solution of $CuCl_2$ and left to sit for 2 mins. After that the cells were rinsed in DIW and then lightly dried with N_2. The devices were then placed in a convection oven at a temperature of (200-240 °C) for various time (10 to 30 mins), and then gold (Au) was thermally evaporated to complete the back contact. For the control devices, 3 nm Cu and 40 nm Au were evaporated and annealed at 150°C for 35 mins. Finally, the devices were laser scribed[16] (device area 0.06 cm^2) and current-voltage characteristics (J-V) were measured for approximately 20 cells under simulated AM1.5G spectrum. The room temperature steady-state photoluminescence (PL) and time-resolved photoluminescence (TRPL) were performed with a 700 nm pulsed laser (Fianium laser, pulse width ~5ps, beam diameter ~ 150 µm) at 2 × 10^{10} photons·pulse^{-1}·cm^{-2}. For steady-state PL, the signal was detected with a Symphony-II CCD (from Horiba) detector after a 300 g mm^{-1} grating monochromator. TRPL measurements were performed using a time correlated single photon counting module (Becker & Hickel Simple Tau SPCM 130-E/M module). The radiative events were detected with a hybrid APD/PMT module (Hamamatsu R10467U-50).

III. Results and Discussion

First, $CuCl_2$ stock solution (10 mM) and diluted $CuCl_2$ solution (0.1 mM) was prepared. A CdTe device is submerged for 2 mins in 0.1 mmol $CuCl_2$ solution in a beaker and rinsed with DI water. As mentioned above, the CdTe devices were activated using saturated $CdCl_2$ solution at 390 °C for 30 mins in dry air environment. Subsequently, after the $CuCl_2$ treatment, the CdTe device was annealed and ready for Au deposition using thermal evaporator. The $CuCl_2$ treatment was conducted at different temperatures in the range of 180 °C - 240 °C for various durations. The devices were laser scribed and measured under AM1.5G solar irradiance to find the device performance. The control device was fabricated using 3 nm Cu and 40 nm Au and annealed at 150 °C for 35 mins.

Fig. 1 displays J-V characteristics of the best cells with either the Cu/Au back contact, or with $CuCl_2$ treatment for temperatures in the range of 180 - 240 °C. In the present study, we chose annealing temperatures of 180, 190, 200,

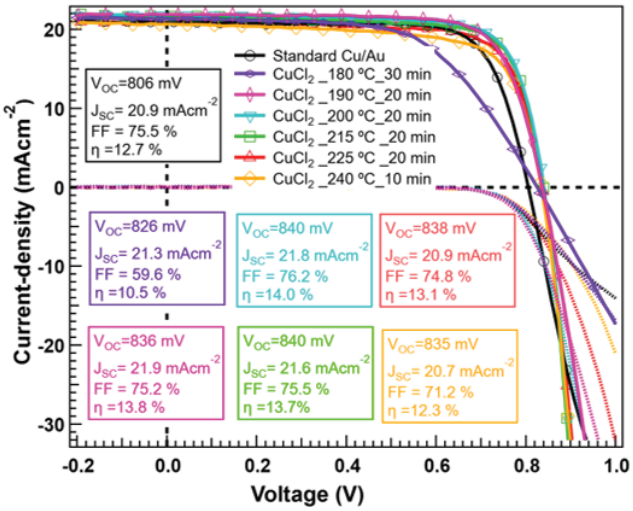


Fig. 1. Current-voltage (J-V) characteristics of best cells of standard Cu/Au and $CuCl_2$ treated CdTe devices under simulated AM1.5 G spectrum.

215, 225 and 240 °C. $CuCl_2$ treated devices were annealed from 10 to 30 mins and average device parameters were calculated for each treatment. Based on the highest average device efficiency of more than 20 cells for each time and temperature, the J-V characteristics of the cells with the best performance are reported in Fig. 1.

Fig. 2 summarizes average device parameters including open-circuit voltage (V_{OC}), short-circuit current density (Jsc), efficiency (η) and fill factor (FF) for CdTe devices with standard and $CuCl_2$ treatments at different temperature and time. For standard CdTe devices with evaporated 3 nm Cu and 40 nm Au back contact, the best cell efficiency is 12.7% with V_{OC} 806 mV, J_{SC} 20.9 mAcm^{-2} and FF 75.5%. The average device efficiency of 20 cells for standard Cu/Au is 12.4%. Based on this study, CdTe devices with $CuCl_2$ treatments at 200 °C for 20 mins show the highest efficiency compared to other temperatures and time. During the annealing process of devices, the oven (JICO TECH Model OF-02G) was maintained at the treatment temperature (200 °C for this case). The best cell of the device treated at 200 °C for 20 mins has efficiency of 14.0% with V_{OC} 840 mV, J_{SC} 21.8 mAcm^{-2} and FF 76.2%. The average device performance of 20 cells is 13.7% with V_{OC} 840 mV, J_{SC} 21.4 mAcm^{-2}, and FF 75.6%. Compared to standard Cu/Au cells, the average device efficiency was increased by ~10% (relative) for $CuCl_2$ treated cells at 200 °C for 20 mins. In case of devices treated at 180 °C for 30 mins, the device efficiency was low (10.2%) compared to the standard CdTe devices (12.4%). Devices treated at 190 °C for 20 and 25 mins have similar average PCEs of 13.5% and 13.3% respectively which is comparable to 200 °C sample for 20 mins (13.7%). However, these PCEs are higher compared to the standard CdTe devices with Cu deposited using thermal evaporation. Similarly, the average device efficiency of CdTe devices with $CuCl_2$ treatments at

Approved for public release; distribution unlimited.

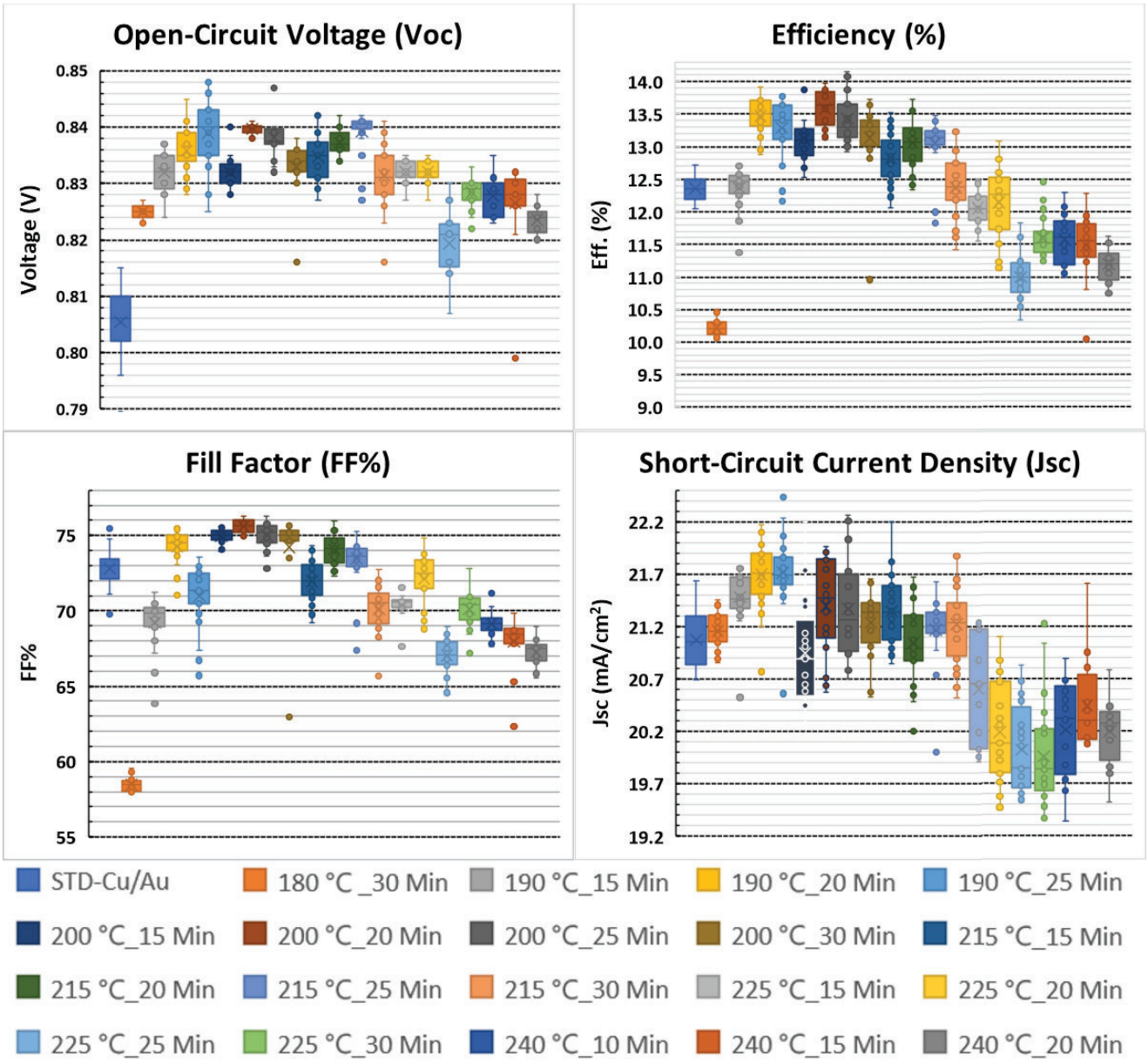


Fig. 2. Graphical presentation of device parameters of CdTe solar cells treated with $CuCl_2$ solution at different temperature and time. The CdTe devices treated at 200 °C for 20 mins shows the highest average device efficiency with best cell reaching 14.0%.

200 °C for 25 mins is 13.4% which is slightly lower than the device treated at 200 °C for 20 mins. For the higher temperatures of 225 and 240 °C, the device performance is low as shown by J-V characteristics of best cells in Fig. 1 and Fig. 2 (average device parameters).

The better performance of these $CuCl_2$ treated devices compared to evaporated Cu may be attributed to the improved ability to control the amount of Cu introduced, and to the ability to reduce the diffusion of high Cu concentrations to the front of the device. Considering the atomic mass of Cu (63.546 gm/mol) and density 8.96 gm/cm^3, the Cu atoms on the surface of CdTe is 2.54x10^{16} atoms/cm^2 in case of CdTe devices with 3 nm Cu deposited by thermal evaporation. This surface Cu density is similar to the values reported previously.[15, 17] Kranz et al. have reported the Cu concentration to be 5x10^{17} cm^{-3} for 5 µm CdTe doped with 1.0x10^{15} Cu atoms per cm^2.[17] However, in case of $CuCl_2$ solution, the Cu atoms in solution is 6.0x10^{16} atoms/mL in

Approved for public release; distribution unlimited.

deionized water. The same solution was used for 3 samples (6.45 cm^2 area), each rinsed with deionized water prior to the heat treatment. However, we exactly do not know how many Cu^{2+} ions stick to CdTe and further investigation is required to estimate Cu concentration and doping profile in CdTe devices after $CuCl_2$ treatment. We performed steady state and time-resolved photoluminescence (TRPL) measurements of CdTe device stacks doped via thermal evaporation and $CuCl_2$ solution.

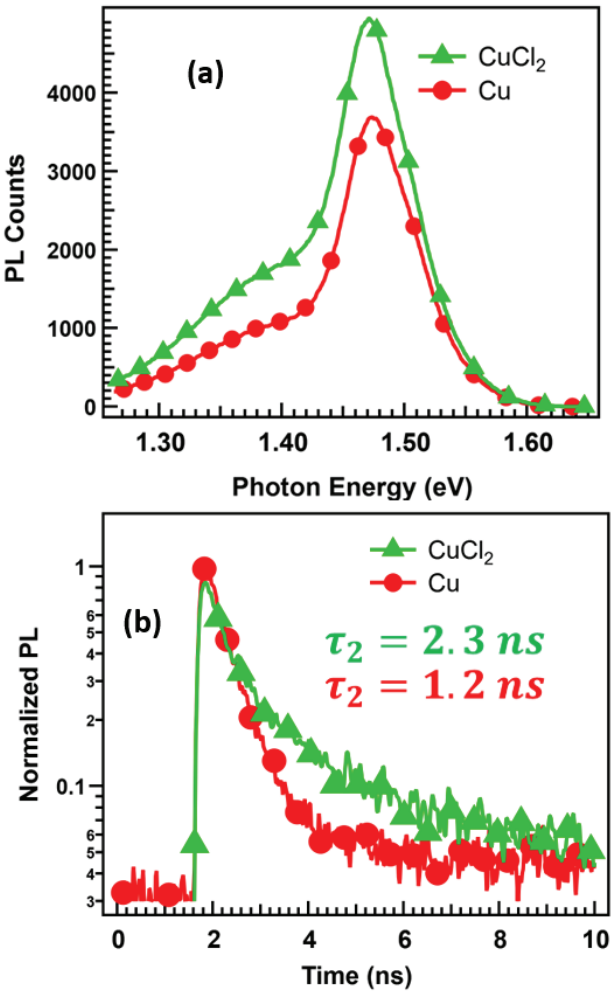


Fig. 3. Room temperature (a) photoluminescence (PL) and (b) time resolved photoluminescence (TRPL) of CdTe device stack for Cu (thermally evaporated) and $CuCl_2$ doped CdTe device stack.

Fig. 3(a) and 3(b) represent steady state PL and time dependent PL taken at room temperature. Higher PL intensity was obtained in CdTe doped via solution process than for doping by thermal evaporation. Carrier lifetime also increased 1.2 ns to 2.3 ns in CdTe doped by $CuCl_2$ solution in DI water. Enhanced PL intensity and improved carrier lifetime in CdTe doped with $CuCl_2$ solution process can be attributed to the presence of fewer compensating defects (Cu_i) due to the small amount of copper introduced via solution process. Rigorous investigation will be performed utilizing low temperature PL spectroscopy later to explore the presence of such defects.

In addition to improved optical properties of $CuCl_2$ treated devices, we carried the stability test of the CdTe devices by storing the devices in ambient environment and inside a desiccator over 90 days. The sample stored in the desiccator was taken out only long enough to complete the measurements. In ambient environment, the humidity and temperature vary from day to day and the summary of device efficiency is presented in Fig. 4. Based on this study, the $CuCl_2$ treated devices are stable for more than 90 days. A recent study has found $CuCl_2$ treated samples have better stability during accelerated stress test over evaporated Cu doped CdTe devices.[15] Over 90 days, for a sample stored in ambient environment, the device efficiency dropped to 12.5% from 12.9%, and for samples stored in a desiccator the efficiency dropped to 13.2% from 13.3%. This suggests these CdTe devices are stable in ambient environment.

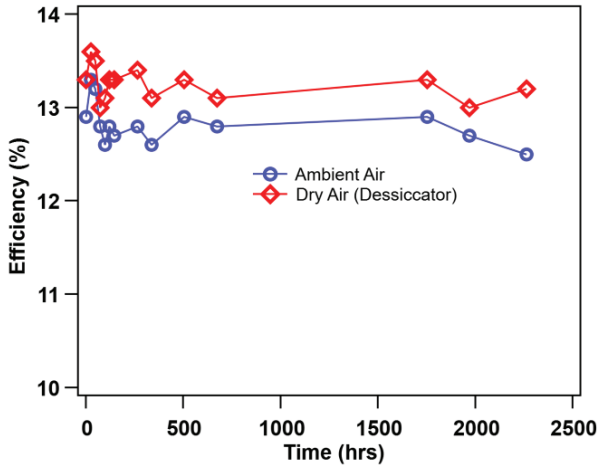


Fig. 4. Stability test of $CuCl_2$ treated CdTe devices over 90 days.

V. Conclusion

Based on these results, we found $CuCl_2$ treatment has improved the open-circuit voltage and fill factor of CdTe devices compared to Cu doped by evaporation. The average device efficiency for $CuCl_2$ treated cells was enhanced by ~10% relative compared to standard devices fabricated using thermally evaporated Cu. Similarly, enhanced optical properties (PL intensity and carrier life time) were observed for $CuCl_2$ treated devices compared to Cu doped by evaporation. The solution based $CuCl_2$ treatment therefore

Approved for public release; distribution unlimited.

yields high quality results as compared with the thermally evaporated Cu/Au.

ACKNOWLEDGEMENTS

This material is based on research sponsored by Air Force Research Laboratory under agreement number FA9453-18-2-0037. The authors also thank Willard and Kelsey Solar Group for providing the CdS/CdTe film stacks. This work was authored in part by the Alliance for Sustainable Energy, LLC, the manager and operator of the National Renewable Energy Laboratory for the U.S. Department of Energy (DOE) under Contract No. DE-AC36-08GO28308. Funding provided by U.S. Department of Energy Office of Energy Efficiency and Renewable Energy Solar Energy Technologies Office. The views and conclusions contained herein are those of the authors and should not be interpreted as necessarily representing the official policies or endorsements, either expressed or implied, of Air Force Research Laboratory or of the DOE or the U.S. Government. The U.S. Government retains and the publisher, by accepting the article for publication, acknowledges that the U.S. Government retains a nonexclusive, paid-up, irrevocable, worldwide license to publish or reproduce the published form of this work, or allow others to do so, for U.S. Government purposes.

REFERENCES

[1] J. L. Freeouf and J. M. Woodall, "Schottky barriers: An effective work function model," *Appl. Phys. Lett.,* vol. 39, no. 9, pp. 727-729, 1981.

[2] E. Janik and R. Triboulet, "Ohmic contacts to p-type cadmium telluride and cadmium mercury telluride," *J. Phys. D: Appl. Phys.,* vol. 16, no. 12, p. 2333, 1983.

[3] C. R. Corwine, A. O. Pudov, M. Gloeckler, S. H. Demtsu, and J. R. Sites, "Copper inclusion and migration from the back contact in CdTe solar cells," *Sol. Energy Mater. Sol. Cells,* vol. 82, no. 4, pp. 481-489, 5/30/ 2004.

[4] J. Li *et al.*, "Controlled activation of ZnTe:Cu contacted CdTe solar cells using rapid thermal processing," *Solar Energy Materials and Solar Cells,* vol. 133, pp. 208-215, 2// 2015.

[5] K. P. Bhandari *et al.*, "Iron pyrite nanocrystal film serves as a copper-free back contact for polycrystalline CdTe thin film solar cells," *Solar Energy Materials and Solar Cells,* vol. 140, pp. 108-114, Sep 2015.

[6] E. Bastola, K. P. Bhandari, and R. J. Ellingson, "Application of composition controlled nickel-alloyed iron sulfide pyrite nanocrystal thin films as the hole transport layer in cadmium telluride solar cells," *J. Mater. Chem. C,* vol. 5, no. 20, pp. 4996-5004, 2017.

[7] E. Bastola, K. K. Subedi, K. P. Bhandari, and R. J. Ellingson, "Solution-processed Nanocrystal Based Thin Films as Hole Transport Materials in Cadmium Telluride Photovoltaics," (in English), *MRS Advances,* vol. 3, no. 41, pp. 2441-2447, 2018.

[8] E. Bastola, K. P. Bhandari, I. Subedi, N. J. Podraza, and R. J. Ellingson, "Structural, optical, and hole transport properties of earth-abundant chalcopyrite ($CuFeS_2$) nanocrystals," (in English), *MRS Communications,* vol. 8, no. 3, pp. 970-978, Sep 2018.

[9] A. H. Munshi *et al.*, "Polycrystalline CdSeTe/CdTe Absorber Cells With 28 mA/cm^2 Short-Circuit Current," *IEEE J. Photovolt.,* vol. 8, no. 1, pp. 310-314, 2018.

[10] T. Song, A. Moore, and J. R. Sites, "Te Layer to Reduce the CdTe Back-Contact Barrier," *IEEE Journal of Photovoltaics,* vol. 8, no. 1, pp. 293-298, 2018.

[11] S. C. Watthage *et al.*, "Selective Cd Removal From CdTe for High-Efficiency Te Back-Contact Formation," *IEEE Journal of Photovoltaics,* no. 99, pp. 1-7, 2018.

[12] V. Ivanits'ka *et al.*, "Chemical Polishing of CdTe and CdZnTe in Iodine–Methanol Etching Solutions," *Journal of electronic materials,* vol. 40, no. 8, pp. 1802-1808, 2011.

[13] D. Mao, G. Blatz, C. Wickersham Jr, and M. Gloeckler, "Correlative impurity distribution analysis in cadmium telluride (CdTe) thin-film solar cells by ToF-SIMS 2D imaging," *Solar Energy Materials and Solar Cells,* vol. 157, pp. 65-73, 2016.

[14] T. Ablekim *et al.*, "Tailoring MgZnO/CdSeTe Interfaces for Photovoltaics," *IEEE Journal of Photovoltaics,* vol. 9, no. 3, pp. 888-892, 2019.

[15] E. Artegiani *et al.*, "Analysis of a novel $CuCl_2$ back contact process for improved stability in CdTe solar cells," *Progress in Photovoltaics: Research and Applications*.

[16] A. B. Phillips *et al.*, "High speed, intermediate resolution, large area laser beam induced current imaging and laser scribing system for photovoltaic devices and modules," *Review of Scientific Instruments,* vol. 87, no. 9, p. 093708, 2016.

[17] L. Kranz *et al.*, "Doping of polycrystalline CdTe for high-efficiency solar cells on flexible metal foil," *Nature communications,* vol. 4, p. 2306, 2013.

Approved for public release; distribution unlimited.

Room Temperature Processed Transparent Cu-Zn-S Nanocomposites as Hole Transport Materials in CdTe Photovoltaics

Ebin Bastola, Kamala Khanal Subedi, Fadhil K. Alfadhili, Adam B. Phillips, Michael J. Heben and Randy J. Ellingson

Wright Center for Photovoltaics Innovation and Commercialization (PVIC), Department of Physics and Astronomy, University of Toledo, Toledo, Ohio, 43606, USA

***Abstract* — Here, we report room temperature processed Cu-Zn-S ternary thin films fabricated using SILAR method as a back-contact hole transport layer in cadmium telluride (CdTe) solar cells. These Cu-Zn-S films are transparent to visible region with compact grains, and high conductivity. X-ray diffraction (XRD) measurements shows the crystalline nature of the as-deposited Cu-Zn-S films. The Cu-Zn-S nanocomposite as a back contact buffer layer in CdTe devices improves the device performance to 12.7% (average 12.4%) from 10.4% (average 9.8%) compared to a Au only back contact and is comparable to Cu/Au back contact (thermally evaporated). The temperature dependence current voltage characteristics shows the reduced back barrier height compared to Au only and Cu/Au back contact.**

***Index Terms*- SILAR, Cu-Zn-S, hole transport layer (HTL), back contact, solar cells.**

I. Introduction

Cu-Zn-S (CZS) nanocomposite thin films are p-type materials possessing very high carrier concentration (~10^{21} cm^{-3}), high transparency (>70% for 50 nm film) in visible region, and high conductivity.[1, 2] The optical band gap of these materials can be tuned by changing the material composition which makes these materials promising for opto-electronics.[2, 3] Additionally, the band edges of these materials change with the material composition, strengthening the applicability of these materials in various opto-electronic applications including photovoltaics.[1]

Cadmium telluride (CdTe) solar cells comprise a renowned thin film technology for harvesting solar energy with a suitable band gap of 1.5 eV. For the fabrication of CdTe solar cells, wem have used copper/gold (Cu/Au) as a standard laboratory-scale back contact.[4, 5] However, the Cu/Au contact does not facilitate the low-barrier transport of photo generated holes due to the deep valence band edge (VBE) of CdTe (~-5.9 eV wrt vacuum)[6]. Since the work function of Au is low (~5.0 eV)[7] compared with the VBE of CdTe, a Schottky barrier forms. To reduce this potential barrier, a material with suitable band edge location is applied for the smooth extraction of holes and repel of electrons at the back contact of the CdS/CdTe devices. Materials such as carbon nanotubes, CuSCN, FeS_2, ZnTe, Sb_2Te_3 and Cu_2Te have been tested as the back-contact buffer layer in CdS/CdTe solar cells.[8-10] Other solution-processed back contact buffer layers include $Ni_xFe_{1-x}S_2$, $CuFeS_2$ and perovskite.[11-13] These interface layers facilitatehole transport to the metal contact and/or repel electrons to reduce recombination and enhancing the device performance.

These Cu-Zn-S nanocomposite materials are p-type with high hole concentration (~$10^{21}$$cm^{-3}$)[2] and conductivity (438-2964 Scm^{-1})[1] indicating the possible application of these materials as low barrier contact materials for CdTe devices.[3] These materials can be prepared by solution-based techniques including chemical bath deposition (CBD) and successive ionic layer adsorption and reaction (SILAR) methods.[1, 2] In SILAR, the thin film is deposited by reaction of cations and anions forming an atomic layer, improving the quality of the films fabricated. Here, we have prepared Cu-Zn-S nanocomposite thin films with various compositions and applied them as a back-contact buffer layer in CdTe photovoltaics. Our results indicate the photoconversion efficiency of CdTe can be significantly enhanced compared to Au only back contact on using Cu-Zn-S as hole transport materials and is comparable to standard Cu (3 nm) (thermally evaporated) and Au (40 nm) back contact.

II. Experimental

The Cu-Zn-S nanocomposite films were deposited using a SILAR method at room temperature adapting a procedure from literature.[1] First, Cu-Zn-S thin films were deposited onto a sodalime glass substrate. For this, glass superstrates were cleaned using Micro-90 detergent by sonication for 30 mins at 150 °C and rinsed several times with deionized water (DIW) followed by cleaning with acetone, methanol and 2-propanol for 5 mins each by sonication.

To deposit the "CZS-50" film, the cationic precursor was prepared by dissolving 0.05 M $CuCl_2$, 0.05 M zinc acetate, with a total of 0.1 M, and 5 mL triethanolamine (TEA) (in a total volume of 25 mL), and the anionic precursor was made using 0.05 M Na_2S in DIW. The glass substrate was first submerged in cationic precursor for 15 S, then in DIW for 5 S, in anionic precursor for 15 S, and finally rinsed in DIW for 5 S which completes one cycle for SILAR deposition. A dip-coater was employed to complete all SILAR cycles and repeated for 40 complete cycles to make a Cu-Zn-S film of thickness around 250 nm. The same procedure was followed to deposit Cu-Zn-S film on CdTe surface.

Approved for public release; distribution unlimited.

The CdS/CdTe device stacks were obtained from Willard and Kelsey solar group. To fabricate standard CdTe device, 3 nm Cu and 40 nm Au were thermally deposited to complete the back contact after $CdCl_2$ treatment followed by thermal annealing at 150 °C for 35 mins. For Cu-Zn-S as HTMs, first CdTe devices were treated for $CdCl_2$ at 390 °C for 30 mins in dry air environment and rinsed with methanol to remove excel $CdCl_2$. Then, Cu-Zn-S films were deposited on CdTe using SILAR method as described above. Then, 40 nm Au was thermally evaporated to complete a metal contact.

The fabricated CZS thin films were characterized using an Hitachi S-4800 scanning electron microscopy (SEM), energy dispersive X-ray spectroscopy (EDS), and optical properties using PerkinElmer Lambda 1050 UV-Vis-NIR spectrophotometer. The XRD pattern was obtained from a Rigaku Ultima III X-ray diffractometer operated at 40 KV and 44 mA. The sheet resistance was measured using 4-point probe, and thickness was measured using a Dektak profilometer. The completed devices were laser scribed[14] and measured under simulated AM1.5G solar irradiance to find the photoconversion efficiency and external quantum efficiency measurements were performed using a PV Instruments (model IVQE8-C) system.

III. Results and Discussion

The Cu-Zn-S thin films were deposited at room temperature using SILAR method in which first cations get adsorbed on the surface, and while rinsing, weakly bound cations are washed away. When the substrate is immersed in anion solution, reaction takes place, and loosely bound S ions are rinsed again. This process is continued several times to make a thin film of desired thickness.

The optical properties of Cu-Zn-S films were measured using Lambda PerkinElmer 1050 spectrophotometer. Typical transmission and reflection spectra are shown in Fig. 1 for CZS-50. Here, CZS-50 denotes thin films prepared using Zn precursor 50 percent (0.05 M zinc acetate) of the total cations (0.1 M) used. As represented by the transmission spectra, these films have more than 50% transmission in visible region. Also, band gaps of these films were found using transmission and reflection spectra. For this, absorption coefficients of these films were obtained using equation below with transmission (T) and reflection (R) spectra and thickness (t) of the film.

$$\alpha = -\ln(\ T/(1-R))/t$$

Further, the band gap was estimated by plotting $(\alpha h\nu)^2$ vs $(h\nu)$ for Cu-Zn-S thin films. The estimated band gap values for CZS-50 film is ~ 2.5 eV for CZS-50 film. The inset in Fig. 1 shows the band gap for CZS-50 film.

Fig. 1 (b) shows the XRD pattern for a CZS-50 film deposited on sodalime glass. Based on XRD, as deposited Cu-Zn-S thin films have crystalline properties. The diffraction patterns are similar to the standard diffraction patterns of CuS as shown in the reference lines. The standard powder diffraction patterns for CuS and ZnS were obtained from MDI ZADE software. In a previous report, Jose and Kumar have reported the crystalline properties of Cu-Zn-S thin films prepared by SILAR deposition method.[1] Fig. 2 (a, b) displays the plano-SEM micrograph for Cu-Zn-S thin films deposited on sodalime glass for CZS-50. The surface appears compact, and grains have size of around 200 nm in length.

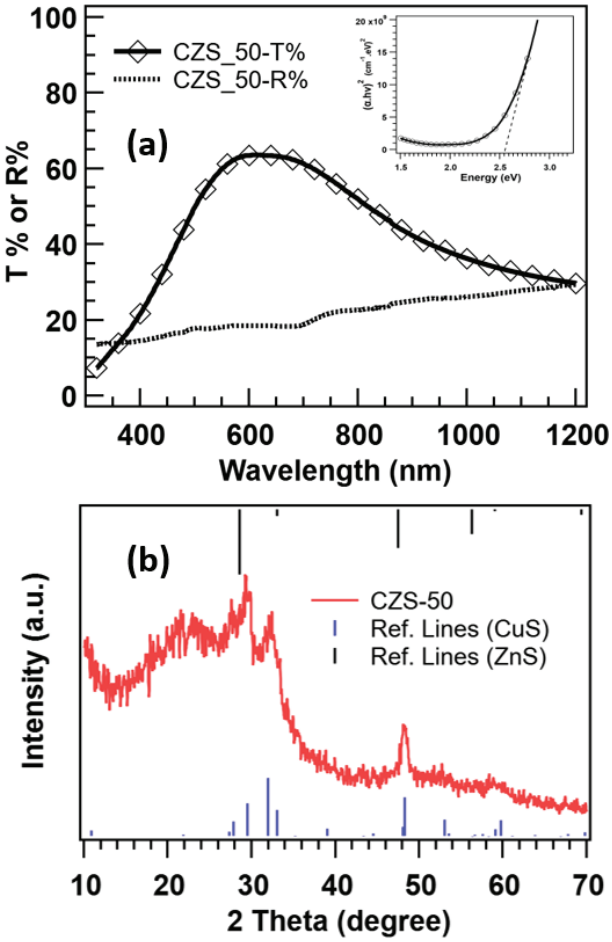
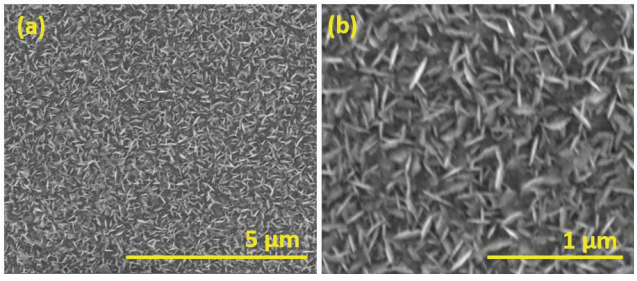


Fig. 1. (a) Transmission and reflection (dotted lines) spectra of a Cu-Zn-S ternary thin film prepared by SILAR deposition technique and (b) XRD pattern of a Cu-Zn-S film. The references lines (along top and bottom axes) include the standard diffraction patterns for CuS (PDF # 98-001-3414) and ZnS (PDF#98-000-0405).



Approved for public release; distribution unlimited.

Fig. 2. Plano-SEM micrographs of Cu-Zn-S thin films prepared at room temperature using SILAR deposition technique on soda lime glass.

Fig. 3 shows the plano-SEM micrograph of CdTe films after $CdCl_2$ treatment (Fig. 3 (a)), with CZS-50 on deposited on CdTe (Fig. 3 (b)), and a schematic diagram for the complete device (Fig. 3 (c)) and cross-sectional SEM image of CdTe device with CZS-50 as the back interface layer. The EDS analysis of these films revealed chemical composition consisting of Cu, Zn and S atoms. The average atomic percentage revealed the chemical composition for Cu, Zn and S to be 32.0±1.4, 35.4±1.7, and 32.9±0.6 respectively. The sheet resistance measurement using 4-point probe for a CZS-50 film of thickness around 250 nm was 609 Ω/□ indicating these films have a resistivity of 0.015 Ω cm. P-type conductivity, low resistivity (ie, high conductivity) and high hole concentration make CZS films appropriate as hole transport materials in photovoltaic devices. Further, to study the hole transport properties, Cu-Zn-S thin films were deposited on the top of CdTe device, and 40 nm Au was thermally evaporated to complete the back-contact. The current-voltage characteristics of these completed devices with and without CZS films were measured under simulated AM1.5G spectrum.

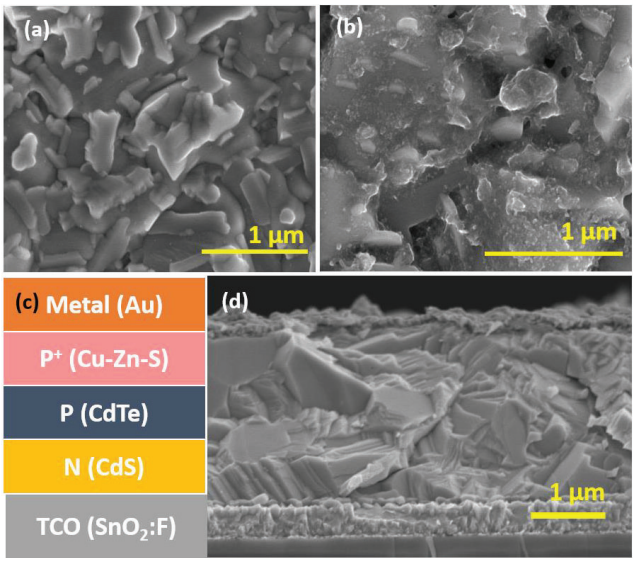


Fig. 3. SEM images of (a) standard CdTe after $CdCl_2$ treatment (b) CdTe with CZS-50 thin films (c) schematic device diagram and (d) cross-sectional SEM image of CdTe with CZS-50 as hole transport materials (CZS-50 represent a Cu-Zn-S film prepared using 0.05 M zinc acetate and 0.05 M $CuCl_2$ as cationic precursor).

Current-voltage (J-V) characteristics for the best cell with and without Cu-Zn-S as HTMs under light and dark measurement conditions are shown in Fig. 4 (a). For Au only back contact, the best cell has an efficiency of 10.4% with short circuit current density 20.8 mA cm^{-2}, open-circuit voltage (V_{OC}) 746 mV, and fill factor (FF) 67.3%. Including the CZS-50 hole transport layer, the device efficiency was 12.6% with V_{OC} = 800 mV, and FF = 73.7%. The average device parameters are presented in Table I. The average device efficiency for the Au only back contact devices is 9.8% and with CZS-50 as interface layer is 12.4%. In case of standard Cu/Au back contact, the average device parameters are similar to CZS-50/Au back contact presented in Table I with the best cell reaching the efficiency of 12.7%. Note that, for devices with CZS films, no additional Cu layer was deposited, and no any thermal annealing was performed. Previously, CZS deposited by chemical bath deposition (CBD) at 80 °C was demonstrated as an HTM in CdTe devices and the highest efficiency reported was 13.0% with CZS layer and Cu/Au (3/40 nm) back contact.[3] Here, we are also investigating devices with CZS layer and additional Cu layer with varying thickness.

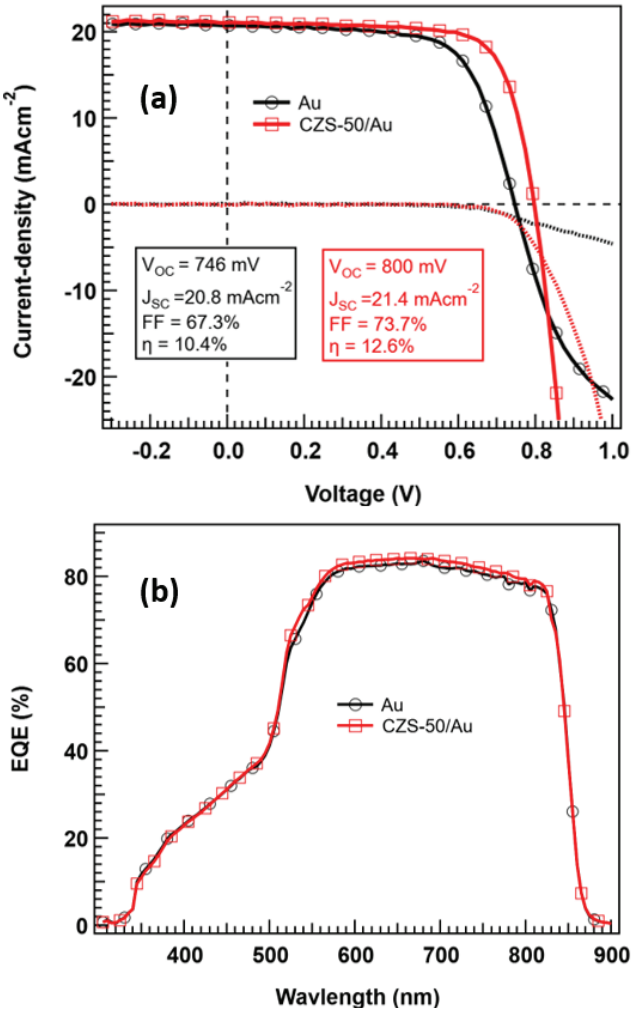


Fig. 4. Current-voltage characteristics (a) and external quantum efficiencies (b) of CdTe photovoltaics with Cu-Zn-S nanocomposites as hole transport material (HTM).

Approved for public release; distribution unlimited.

TABLE I
SUMMARY OF J-V CHARACTERISTICS OF CDTE SOLAR CELLS WITH AU AND CZS-50 AS BACK CONTACTS

Device	V_{OC} (mV)	J_{SC} (mAcm^{-2})	FF (%)	Eff. (%)	R_s (Ω.cm^2)	R_{sh} (Ω.cm^2)
Au	733±6	20.8±0.2	64.5±3.4	9.8±1.1	6.9±0.7	970±33
CZS-50/Au	798±2	21.0±0.4	73.7±2.2	12.4±0.3	3.8±1.2	1700±470
Cu/Au	806±6	21.1±0.3	72.8±1.2	12.4±0.2	3.3±0.7	6560±980

Further, we measured and analyzed the devices with CZS-50 as the interface layer with temperature dependence current-voltage (J-V-T) characteristics in the temperature range of 180 K to 300K to study the effect of interface layer on back barrier height. The back-barrier height (ϕ_b) was obtained assuming thermionic emission model as given by equation below.

$$J_0 \alpha T^2 . \exp\left[\frac{-q.\phi_b}{k_B T}\right]$$

Here J_0 is the saturation current, q electronic charge, and k_B is the Boltzmann constant. The back-barrier heights were obtained by Arrhenius plots of ln (J_0/T^2) versus $1/k_BT$. Fig. 5 (a) shows the J-V-T characteristics of CdTe device with CZS-50 as the interface layer and Fig. 5(b) shows the graph for ln(J_0/T^2) versus $1/k_BT$ to extract back barrier height of the device. Based on the analysis and fitting of the graphics, the back-barrier height is found to be 0.238 eV for CdTe device with CZS-50 as the interface layer. Based on the literature, for Au only back contact the back barrier height is 0.395 eV and for Cu/Au back contact is about 0.331 eV.[15] Thus, due to the CZS-50 interrace layer in CdTe device, the back barrier height is reduced.

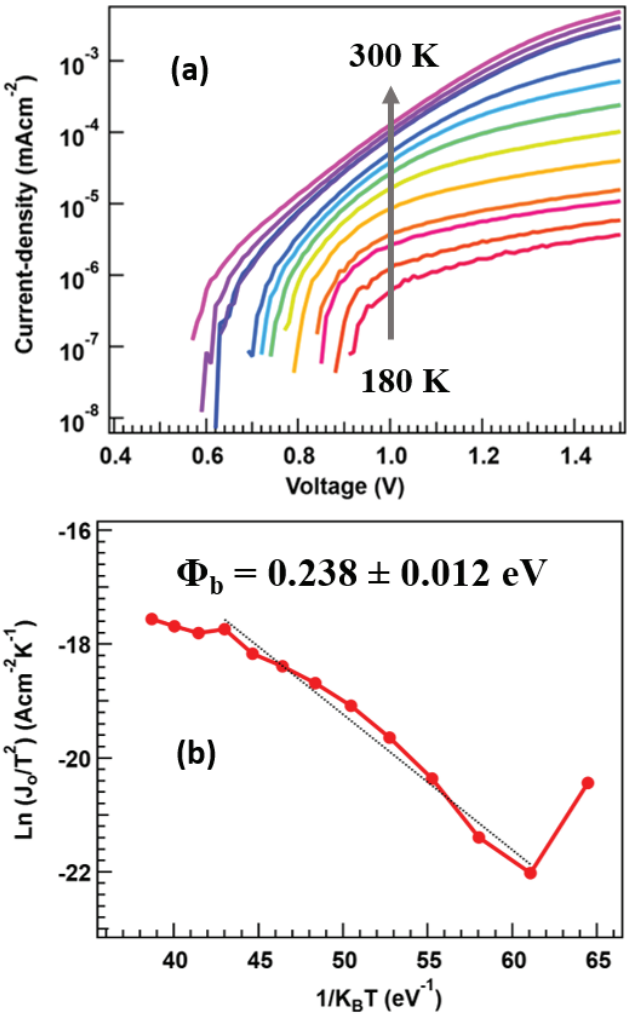


Fig. 5. (a) Temperature dependent current-voltage (J-V-T) characteristics and (b) plots of ln (J_o/T^2) versus $1/k_BT$ to extract back barrier height for CdTe solar cells with CZS-50/Au back contact.

IV. Conclusion

Here, we have successfully fabricated the Cu-Zn-S nanocomposites thin films at room temperature using SILAR method. The Cu-Zn-S thin films are transparent to light in visible region and highly conductive materials with suitable properties as hole transport materials. The application of room-temperature processed CZS films as the back-contact hole transport layers in CdS/CdTe solar cells have been demonstrated. The devices completed using CZS-50 as HTM and Au as the back metal electrode show the highest efficiency of 12.6% with average 12.4% (comparable to standard Cu/Au back contact) while for Au only back contact 10.4% with average 9.8%. The temperature dependence current-voltage characteristics shows the reduced back barrier height.

V. Acknowledgement

This material is based on research sponsored by Air Force Research Laboratory under agreement number FA9453-18-2-0037. The U.S. Government is authorized to reproduce and

Approved for public release; distribution unlimited.

distribute reprints for Governmental purposes notwithstanding any copyright notation thereon. The authors also thank Willard and Kelsey Solar Group for providing the CdS/CdTe film stacks. The views and conclusions contained herein are those of the authors and should not be interpreted as necessarily representing the official policies or endorsements, either expressed or implied, of Air Force Research Laboratory or the U.S. Government.

REFERENCE

[1] E. Jose and M. C. Santhosh Kumar, "Room temperature deposition of highly crystalline Cu-Zn-S thin films for solar cell applications using SILAR method," *Journal of Alloys and Compounds,* vol. 712, pp. 649-656, 2017/07/25/ 2017.

[2] X. Xu *et al.*, "Chemical Bath Deposition of p-Type Transparent, Highly Conducting $(CuS)_x$:$(ZnS)_{1-x}$ Nanocomposite Thin Films and Fabrication of Si Heterojunction Solar Cells," *Nano Lett.,* vol. 16, no. 3, pp. 1925-1932, 2016.

[3] K. K. Subedi *et al.*, "Nanocomposite $(CuS)_x(ZnS)_{1-x}$ thin film back contact for CdTe solar cells: Toward a bifacial device," *Solar Energy Materials and Solar Cells,* vol. 186, pp. 227-235, 2018.

[4] E. Janik and R. Triboulet, "Ohmic contacts to p-type cadmium telluride and cadmium mercury telluride," *Journal of Physics D: Applied Physics,* vol. 16, no. 12, p. 2333, 1983.

[5] C. R. Corwine, A. O. Pudov, M. Gloeckler, S. H. Demtsu, and J. R. Sites, "Copper inclusion and migration from the back contact in CdTe solar cells," *Solar Energy Materials and Solar Cells,* vol. 82, no. 4, pp. 481-489, 5/30/ 2004.

[6] J. L. Freeouf and J. M. Woodall, "Schottky barriers: An effective work function model," *Applied Physics Letters,* vol. 39, no. 9, pp. 727-729, 1981.

[7] B. de Boer, A. Hadipour, M. M. Mandoc, T. van Woudenbergh, and P. W. M. Blom, "Tuning of Metal Work Functions with Self-Assembled Monolayers," *Advanced Materials,* vol. 17, no. 5, pp. 621-625, 2005.

[8] N. R. Paudel and Y. Yan, "Application of copper thiocyanate for high open-circuit voltages of CdTe solar cells," *Progress in Photovoltaics: Research and Applications,* vol. 24, no. 1, pp. 94-101, 2016.

[9] A. B. Phillips *et al.*, "Wiring-up carbon single wall nanotubes to polycrystalline inorganic semiconductor thin films: low-barrier, copper-free back contact to CdTe solar cells," *Nano letters,* vol. 13, no. 11, pp. 5224-5232, 2013.

[10] J. Li *et al.*, "Controlled activation of ZnTe:Cu contacted CdTe solar cells using rapid thermal processing," *Solar Energy Materials and Solar Cells,* vol. 133, pp. 208-215, 2// 2015.

[11] E. Bastola, K. P. Bhandari, and R. J. Ellingson, "Application of composition controlled nickel-alloyed iron sulfide pyrite nanocrystal thin films as the hole transport layer in cadmium telluride solar cells," *J. Mater. Chem. C,* vol. 5, no. 20, pp. 4996-5004, 2017.

[12] E. Bastola, K. K. Subedi, K. P. Bhandari, and R. J. Ellingson, "Solution-processed Nanocrystal Based Thin Films as Hole Transport Materials in Cadmium Telluride Photovoltaics," *MRS Advances,* vol. 3, no. 41, pp. 2441-2447, 2018.

[13] E. Bastola, K. P. Bhandari, I. Subedi, N. J. Podraza, and R. J. Ellingson, "Structural, optical, and hole transport properties of earth-abundant chalcopyrite ($CuFeS_2$) nanocrystals," (in English), *MRS Communications,* vol. 8, no. 3, pp. 970-978, Sep 2018.

[14] A. B. Phillips *et al.*, "High speed, intermediate resolution, large area laser beam induced current imaging and laser scribing system for photovoltaic devices and modules," *Review of Scientific Instruments,* vol. 87, no. 9, p. 093708, 2016.

[15] F. K. Alfadhili, A. B. Phillips, G. K. Liyanage, J. M. Gibbs, M. K. Jamarkattel, and M. J. Heben, "Controlling Band Alignment at the Back Interface of Cadmium Telluride Solar Cells using ZnTe and Te Buffer Layers," *MRS Advances,* vol. 4, no. 16, pp. 913-919, 2019.

Approved for public release; distribution unlimited.

Monolithic Two-Terminal All-Perovskite Tandem Solar Cells with Power Conversion Efficiency Exceeding 21%

Zhaoning Song,[1] Dewei Zhao,[1] Cong Chen,[1] Ramez H. Ahangharnejhad,[1] Chongwen Li,[1] Kiran Ghimire,[1] Nikolas J. Podraza,[1] Michael J. Heben,[1] Kai Zhu,[2] and Yanfa Yan[1]

[1.] University of Toledo, Wright Center for Photovoltaics Innovation and Commercialization, Department of Physics and Astronomy, 2801 W. Bancroft St., Toledo, OH, 43606 USA.

[2.] National Renewable Energy Laboratory, Chemistry and Nanoscience Center, Golden, CO, 80401 USA.

***Abstract* — Monolithic two-terminal (2-T) all-perovskite tandem solar cells are a promising candidate for the next generation solar cells with ultrahigh efficiency and low fabrication cost. Here, we report on the fabrication of 2-T all-perovskite tandem solar cells consisting of solution-processed wide-bandgap and low-bandgap perovskite subcells connected by a vacuum processed interconnection layer. We employed a bulk-passivation strategy to enlarge the grain size, increase carrier mobilities, reduce electronic disorder, and suppress trap-assisted recombination in the low bandgap mixed Sn-Pb perovskite films, which leads to improved performance of low bandgap perovskite solar cells with an absorber thickness over 750 nm. This advance in high-quality low-bandgap perovskite layers enables the fabrication of efficient 2-T all-perovskite solar cells with power conversion efficiencies of more than 21% and decent stability. Our approach provides a suitable pathway to realize ultra-high efficiency 2-T all-perovskite tandem solar cells.**

***Index Terms* — photovoltaic, perovskite, tandem solar cells, passivation, stability.**

I. Introduction

Thin-film tandem solar cells hold the promise to deliver high power conversion efficiencies (PCEs) surpassing the Shockley-Queisser (S-Q) limits (~33%) for single-junction cells at low production costs [1, 2]. However, such high PCEs have only been demonstrated in monolithic tandem solar cells based on single-crystalline III-V materials [3], which are costly in both materials and manufacturing processes. Thus far, this high-efficiency promise has not yet been fully demonstrated by low-cost polycrystalline thin-film photovoltaic technologies based on inorganic chalcogenides (e.g., CdTe and $Cu(In,Ga)Se_2$) or organic materials.

The recent advances of solar cells based on organic-inorganic metal halide perovskites offer an extraordinary opportunity to realize ultra-high efficiency and low-cost thin-film tandem solar cells [4]. The combination of the excellent photovoltaic performance of single-junction perovskite solar cells, with a certified PCE of 24.2% [5], low-temperature and low-cost fabrication processes [6], and bandgap tunability from infrared (~1.1 eV) to ultraviolet (~3 eV) makes perovskite materials an ideal candidate to fabricate monolithic 2-T all-perovskite tandem solar cells [7], which consist of wide-bandgap (1.7 to 1.9 eV) perovskite top cells [8] and low-bandgap (~1.1 to 1.3 eV) bottom cells [9].

All-perovskite tandem cells possess some unique advantages, including low material and energy utilization and low processing temperature for both subcells, which make them a potential cost leader in PV power generation [10, 11]. Till 2018, there were only a few reports on the fabrication of efficient monolithic two-terminal (2-T) all-perovskite solar cells with PCEs ranging from 17% to ~20% [12-15]. The challenge to deliver high PCEs is due to the difficulty to fabricate high-quality low-bandgap mixed Sn-Pb perovskite solar cells as well as efficient interconnecting layers. Most recently, our group developed a bulk-passivation strategy for the mixed Sn-Pb perovskites, enabling low-bandgap perovskite absorber layers with thickness over 750 nm and efficient 2-T all-perovskite tandem solar cells with PCEs of ~21% [16].

Here, we report on the fabrication of 2-T all-perovskite tandem solar cells consisting of solution-processed wide-bandgap $FA_{0.8}Cs_{0.2}Pb(I_{0.7}Br_{0.3})_3$ (where FA is formamidinium) and low-bandgap $(FASnI_3)_{0.6}(MAPbI_3)_{0.4}$ (where MA is methylammonium) perovskite subcells connected by vacuum processed Ag/MoO_3/ ITO interconnection layers. We employed a chlorine incorporation bulk-passivation strategy to enlarge the grain size, increase carrier mobilities, reduce electronic disorder, and suppress trap-assisted recombination in the low-bandgap mixed Sn-Pb perovskite films, which leads to improved performance of low bandgap perovskite solar cells with an absorber thickness over 750 nm. This advance in high-quality low-bandgap perovskite layers enables the fabrication of efficient 2-T all-perovskite solar cells with power conversion efficiencies of more than 21% and a decent stability.

Authorized licensed use limited to: Newcastle University. Downloaded on May 17,2020 at 15:50:49 UTC from IEEE Xplore. Restrictions apply.

Approved for public release; distribution unlimited.

II. Experimental Methods

A. Tandem Device Fabrication

The tandem cell preparation process and precursor solution preparation have been reported in our previous work [16, 17]. In brief, Patterned indium tin oxide (ITO) substrates were cleaned sequentially in an ultrasonic bath with Micro-90 detergent, deionized water, acetone, and isopropanol for 15 min each and then dry with nitrogen. The cleaned ITO substrates were treated by ultraviolet–ozone for 20 min and then transferred to a nitrogen-filled glovebox. The F4-TCNQ-doped poly(triarylamine) (PTAA) hole-transporting layer was spin-coated onto the ITO substrates at 4000 rpm for 30 s and annealed at 120 °C for 15 min. $FA_{0.8}Cs_{0.2}Pb(I_{0.7}Br_{0.3})_3$ wide-E_g perovskite precursor solution was spin-coated onto the PTAA-coated ITO substrates at 5000 rpm for 60 s. At the 25 s of the spinning process, 750 µL diethyl ether was dripped onto the substrate. The as-deposited film was annealed at 65 °C for 2 min and then 100 °C for 10 min. After that, 20 nm fullerene (C_{60}) and 5 nm bathocuproine (BCP) were deposited by thermal evaporation, followed by a Ag/MoO_3 bilayer prepared by thermal evaporation and a 100 nm ITO layer prepared by a low power rf-sputtering to complete the top subcells.

After the deposition of the interconnecting layers, the HTL for the bottom cell were spin-coated onto the prepared by spin-coating poly polystyrene sulfonate (PEDOT:PSS) at 4000 rpm for 60 s and annealed at 110 °C for 5 min. The $(FASnI_3)_{0.6}(MAPbI_3)_{0.4}$ absorber layers were spin-coated at 5,000 rpm for 60 s in a nitrogen-filled glovebox. Diethyl ether was dripped onto the spinning substrate at 5 s during the spin process. The spin-coated mixed Sn-Pb films were then annealed at 100 °C for 7 min. To complete the tandem devices, 20 nm C_{60}, 5 nm BCP, and 75 nm Ag were thermally evaporated onto the film stacks. Devices were then encapsulated with cover glass and ultraviolet-curable epoxy. Active device area of the cells is 0.12 cm^2, defined by the overlapped electrode area.

B. Device Characterization

Secondary scanning microscopy (SEM) image of a tandem cell was acquired using a field emission scanning electron microscope (Hitachi S-4800). Current density-voltage (J-V) curves were recorded using a Keithley 2440 source meter and a solar simulator with 100 mW cm^{-2} AM 1.5G solar irradiation (PV Measurements). External quantum efficiency (EQE) spectra for top and bottom subcells were measured under proper light and voltage bias using an EQE system (PV Measurement, model IVQE8-C).

III. Results and Discussion

A. Performance of All-Perovskite Tandem Solar Cells

Fig. 1 shows the cross-sectional SEM image of a monolithic 2-T all-perovskite tandem cells with 1.75-eV $FA_{0.8}Cs_{0.2}Pb(I_{0.7}Br_{0.3})_3$ perovskite top cells (~250 nm) and 1.25-eV $(FASnI_3)_{0.6}(MAPbI_3)_{0.4}$ perovskite bottom cells (~750 nm). By using low power rf-sputtering techniques, we achieved an extremely flat and smooth ITO interconnecting layer without any pinholes and bombardment damages to the underlying perovskites. For monolithic 2-T all-perovskite tandem cells, the interconnecting layer plays a critical role in providing optical and electrical connection as well as protecting the underneath layers during fabrication of the second subcells.

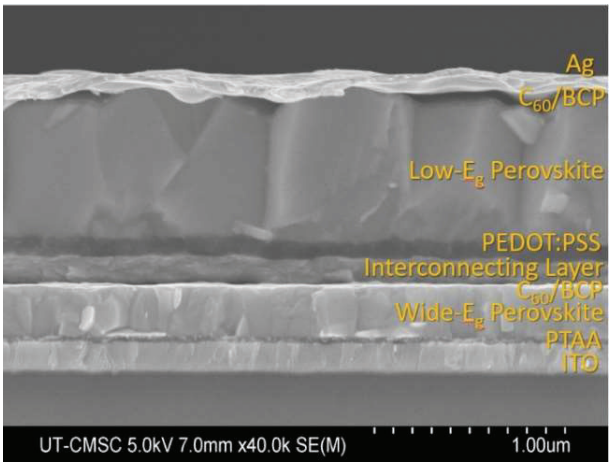


Fig. 1. Cross-sectional SEM image of a 2T all-perovskite tandem solar cell.

We employed a Cl-incorporation technique [16] to treat the mixed Sn-Pb perovskite films, which enlarged the grain size, increased carrier mobilities, reduced electronic disorder, and suppressed trap-assisted recombination in the low bandgap mixed Sn-Pb perovskite films, enabling improved performance of low bandgap perovskite solar cells with an absorber thickness over 750 nm.

Benefited from the flat interconnecting layer with well-tuned electronic properties and high-quality low-bandgap mixed Sn-Pb perovskite films, we achieved 2-T all-perovskite tandem solar cells with PCEs exceeding 21%. Fig. 2a shows the J-V curve of a typical 2-T all-perovskite tandem cell, which delivers a PCE of 21.1%, with an open-circuit voltage (V_{OC}) of 1.911 V, a short circuit current density (J_{SC}) of 14.1 mA/cm^2, and a fill factor (FF) of 78.5%, and no hysteresis under reverse and forward scans. The high V_{OC} value of > 1.9 V is close to the sum of the two subcells (~0.8 and ~1.15 V). The photocurrent density match of the 2-T tandem cell is confirmed by the EQE measurements. Fig. 2b shows the spectral responses of the two subcells in a tandem device. The integrated photocurrent densities of 14.0 and 13.9 mA/cm^2 for the top and bottom subcells, respectively, are consistent with the J_{SC} value from the J-V measurements.

Authorized licensed use limited to: Newcastle University. Downloaded on May 17,2020 at 15:50:49 UTC from IEEE Xplore. Restrictions apply.

Approved for public release; distribution unlimited.

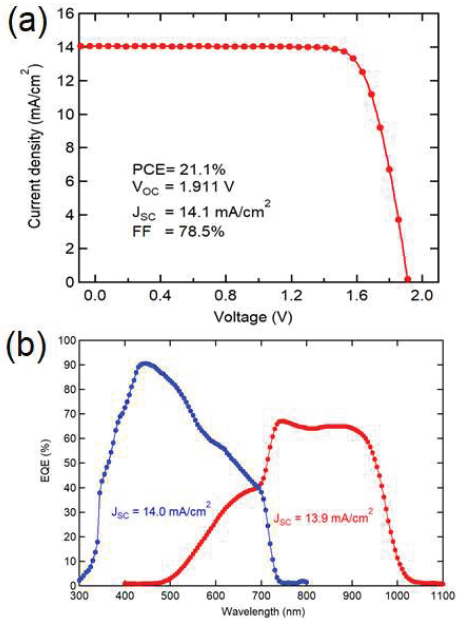


Fig. 2. (a) J-V and (b) EQE of a typical 2-T all-perovskite tandem solar cell.

Fig. 3 shows the evolution of PCE of an encapsulated tandem cell stored in ambient condition. The device retained more than 90% of its initial PCE after storage on the shelf for ~4 months, showing decent stability of encapsulated all-perovskite tandem solar cells. Additionally, our all-perovskite tandem cells show relatively stable operation for more than 80 hours under maximum power point tracking condition [16]. Although the device stability of tandem cells under continuous illumination is still much inferior to that of single-junction Pb-based perovskite solar cells. The demonstration of ~100 hours of operation is still promising for device containing the mixed Sn-Pb perovskites.

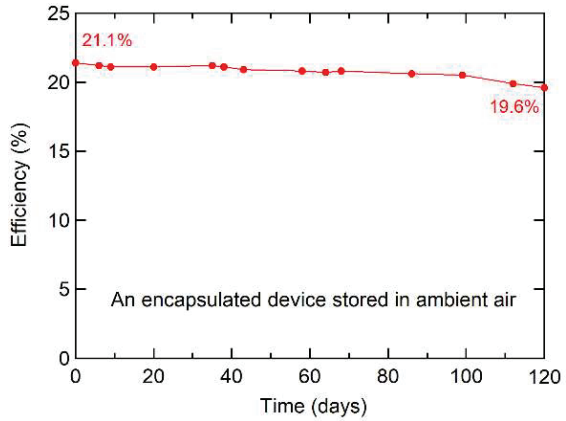


Fig. 3. Evolution of PCE of a 2-T all-perovskite tandem solar cell stored in ambient air.

B. Optical Analysis for the Energy Losses

Although the efficient all-perovskite tandem solar cells have been demonstrated, the PCEs are still much inferior to the theoretical limits of tandem cells. To estimate the optical losses due to reflection and parasitic absorption in photoinactive layers, we performed optical analysis on the all-perovskite tandem film stacks using actual optical parameters measured by spectroscopic ellipsometry.

Fig. 4a shows that both the wide- and low-bandgap perovskite absorber layers need to be made thicker and with better quality to deliver PCE of over 30%. The impact of thicker absorber layers on 2-T all-perovskite tandem solar cells has been recently demonstrated [18]. By incorporating guanidinium thiocyanate into mixed Sn-Pb perovskites, long carrier lifetimes of more than 1 µs were achieved, which enables high-quality perovskite films with thicknesses of ~1 µm. Higher photocurrent densities were achieved with the thicker absorber layers, which enabled the fabrication of 2-T all-perovskite solar cells with a PCE of 23.1% [18].

We performed optical analysis on our 2-T all perovskite tandem solar cells using the transfer matrix method following our previous work [19, 20]. The results show that optical management is required to reduce the glass reflection loss (equivalent to 6.2 mA/cm^2), as shown in Fig. 4b. Additionally, reducing the parasitic absorption in the top ITO electrode and PTAA can also benefit the photocurrent of tandem cells.

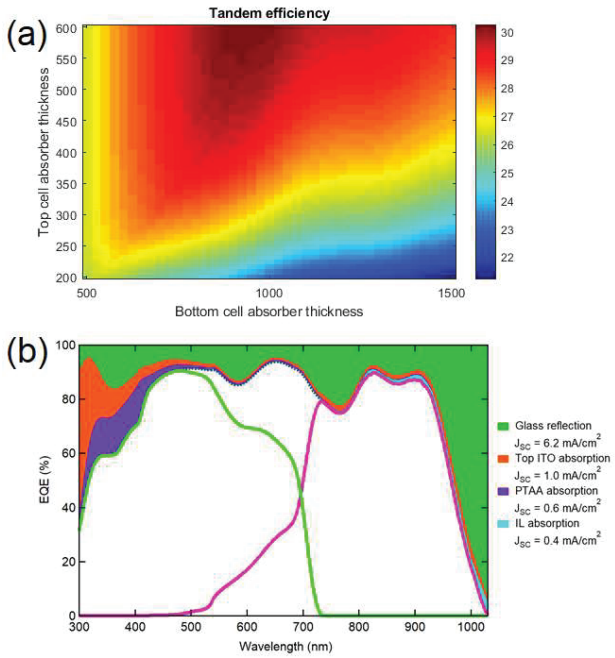


Fig. 4. (a) Estimated tandem efficiency as a function of top and bottom absorber layer thickness. (b) Simulated EQE and optical losses.

Authorized licensed use limited to: Newcastle University. Downloaded on May 17,2020 at 15:50:49 UTC from IEEE Xplore. Restrictions apply.

Approved for public release; distribution unlimited.

IV. Conclusion

In summary, we fabricated efficient 2-T all-perovskite solar cells with PCEs exceeding 21% and decent stability. Further improvement in device performance will be guided by the optical loss analysis. Our approach provides a suitable pathway to realize ultra-high efficiency 2-T all-perovskite tandem solar cells.

ACKNOWLEDGEMENTS

This work at the University of Toledo was financially supported by the Ohio Research Scholar Program, the Office of Naval Research (Contract No. N00014-17-I-2223), the US Department of Energy (DE-FOA-0000990). This material is based on research sponsored by Air Force Research Laboratory under agreement number FA9453-18-2-0037. The U.S. Government is authorized to reproduce and distribute reprints for Governmental purposes notwithstanding any copyright notation thereon. The views and conclusions contained herein are those of the authors and should not be interpreted as necessarily representing the official policies or endorsements, either expressed or implied, of Air Force Research Laboratory or the U.S. Government."

References

[1] J. P. Mailoa, M. Lee, I. M. Peters, T. Buonassisi, A. Panchula, and D. N. Weiss, "Energy-yield prediction for II-VI-based thin-film tandem solar cells," *Energy & Environmental Science,* vol. 9, pp. 2644-2653, 2016.

[2] Z. Wang, Z. Song, Y. Yan, S. Liu, and D. Yang, "Perovskite—a Perfect Top Cell for Tandem Devices to Break the S–Q Limit," *Advanced Science,* vol. 6, p. 1801704, 2019.

[3] M. A. Green, Y. Hishikawa, E. D. Dunlop, D. H. Levi, J. Hohl-Ebinger, M. Yoshita, and A. W. Y. Ho-Baillie, "Solar cell efficiency tables (Version 53)," *Progress in Photovoltaics: Research and Applications,* vol. 27, pp. 3-12, 2019.

[4] J.-P. Correa-Baena, M. Saliba, T. Buonassisi, M. Grätzel, A. Abate, W. Tress, and A. Hagfeldt, "Promises and challenges of perovskite solar cells," *Science,* vol. 358, pp. 739-744, 2017.

[5] NREL. (3 June 2019). Solar Cell Efficiency Chart. Available: https://www.nrel.gov/pv/assets/images/efficiency-chart-20180716.jpg.

[6] Z. Song, C. L. McElvany, A. B. Phillips, I. Celik, P. W. Krantz, S. C. Watthage, G. K. Liyanage, D. Apul, and M. J. Heben, "A technoeconomic analysis of perovskite solar module manufacturing with low-cost materials and techniques," *Energy & Environmental Science,* vol. 10, pp. 1297-1305, 2017.

[7] G. E. Eperon, M. T. Hörantner, and H. J. Snaith, "Metal halide perovskite tandem and multiple-junction photovoltaics," *Nature Reviews Chemistry,* vol. 1, p. 0095, 2017.

[8] T. C.-J. Yang, P. Fiala, Q. Jeangros, and C. Ballif, "High-Bandgap Perovskite Materials for Multijunction Solar Cells," *Joule,* vol. 2, pp. 1421-1436, 2018.

[9] C. Wang, Z. Song, C. Li, D. Zhao, and Y. Yan, "Low-Bandgap Mixed Tin-Lead Perovskites and Their Applications in All-Perovskite Tandem Solar Cells," *Advanced Functional Materials,* doi:10.1002/adfm.201808801, 2019.

[10] I. Celik, A. B. Phillips, Z. Song, Y. Yan, R. J. Ellingson, M. J. Heben, and D. Apul, "Environmental analysis of perovskites and other relevant solar cell technologies in a tandem configuration," *Energy & Environmental Science,* vol. 10, pp. 1874-1884, 2017.

[11] Z. Song, A. B. Phillips, I. Celik, G. K. Liyanage, D. Zhao, D. Apul, Y. Yan, and M. J. Heben, "Manufacturing Cost Analysis of Perovskite Solar Modules in Single-Junction and All-Perovskite Tandem Configurations," in *2018 IEEE 7th World Conference on Photovoltaic Energy Conversion (WCPEC) (A Joint Conference of 45th IEEE PVSC, 28th PVSEC & 34th EU PVSEC)*, 2018, pp. 1134-1138.

[12] G. E. Eperon, T. Leijtens, K. A. Bush, R. Prasanna, T. Green, J. T.-W. Wang, D. P. McMeekin, G. Volonakis, R. L. Milot, R. May, A. Palmstrom, D. J. Slotcavage, R. A. Belisle, J. B. Patel, E. S. Parrott, R. J. Sutton, W. Ma, F. Moghadam, B. Conings, A. Babayigit, H.-G. Boyen, S. Bent, F. Giustino, L. M. Herz, M. B. Johnston, M. D. McGehee, and H. J. Snaith, "Perovskite-perovskite tandem photovoltaics with optimized band gaps," *Science,* vol. 354, pp. 861-865, 2016.

[13] A. Rajagopal, Z. Yang, S. B. Jo, I. L. Braly, P.-W. Liang, H. W. Hillhouse, and A. K. Y. Jen, "Highly Efficient Perovskite–Perovskite Tandem Solar Cells Reaching 80% of the Theoretical Limit in Photovoltage," *Advanced Materials,* vol. 29, p. 1702140, 2017.

[14] F. Dávid, G. E. Lidón, P. D. R. Daniel, M. Cristina, W. Jérémie, N. Bjoern, B. Christophe, S. Michele, and B. H. J., "Efficient Monolithic Perovskite/Perovskite Tandem Solar Cells," *Advanced Energy Materials,* vol. 7, p. 1602121, 2017.

[15] C. Li, Z. S. Wang, H. L. Zhu, D. Zhang, J. Cheng, H. Lin, D. Ouyang, and W. C. H. Choy, "Thermionic Emission–Based Interconnecting Layer Featuring Solvent Resistance for Monolithic Tandem Solar Cells with Solution-Processed Perovskites," *Advanced Energy Materials,* vol. 8, p. 1801954, 2018.

[16] D. Zhao, C. Chen, C. Wang, M. M. Junda, Z. Song, C. R. Grice, Y. Yu, C. Li, B. Subedi, N. J. Podraza, X. Zhao, G. Fang, R.-G. Xiong, K. Zhu, and Y. Yan, "Efficient two-terminal all-perovskite tandem solar cells enabled by high-quality low-bandgap absorber layers," *Nature Energy,* vol. 3, pp. 1093-1100, 2018.

[17] D. Zhao, Y. Yu, C. Wang, W. Liao, N. Shrestha, C. R. Grice, A. J. Cimaroli, L. Guan, R. J. Ellingson, K. Zhu, X. Zhao, R.-G. Xiong, and Y. Yan, "Low-bandgap mixed tin–lead iodide perovskite absorbers with long carrier lifetimes for all-perovskite tandem solar cells," *Nature Energy,* vol. 2, p. 17018, 2017.

[18] J. Tong, Z. Song, D. H. Kim, X. Chen, C. Chen, A. F. Palmstrom, P. F. Ndione, M. O. Reese, S. P. Dunfield, O. G. Reid, J. Liu, F. Zhang, S. P. Harvey, Z. Li, S. T. Christensen, G. Teeter, D. Zhao, M. M. Al-Jassim, M. F. A. M. van Hest, M. C. Beard, S. E. Shaheen, J. J. Berry, Y. Yan, and K. Zhu, "Carrier lifetimes of >1 μs in Sn-Pb perovskites enable efficient all-perovskite tandem solar cells," *Science,* vol. 364, pp. 475-479, 2019.

[19] R. H. Ahangharnejhad, Z. Song, A. B. Phillips, S. C. Watthage, Z. S. Almutawah, D. R. Sapkota, P. Koirala, R. W. Collins, Y. Yan, and M. J. Heben, "Optical design of perovskite solar cells for applications in monolithic tandem configuration with CuInSe2 bottom cells," *MRS Advances,* vol. 3, pp. 3111-3119, 2018.

[20] R. Hosseinian Ahangharnejhad, A. B. Phillips, K. Ghimire, P. Koirala, Z. Song, Hashem M. Barudi, A. Habte, M. Sengupta, R. J. Ellingson, Y. Yan, R. W. Collins, N. J. Podraza, and M. J. Heben, "Irradiance and temperature considerations in the design and deployment of high annual energy yield perovskite/CIGS tandems," *Sustainable Energy & Fuels,* vol. 3, pp. 1841-1851, 2019.

Authorized licensed use limited to: Newcastle University. Downloaded on May 17,2020 at 15:50:49 UTC from IEEE Xplore. Restrictions apply.

Approved for public release; distribution unlimited.

Understanding CdTe Performance with Engineered Front and Back Interfaces

Adam B. Phillips, Geethika K. Liyanage, Fadhil K. Alfadhili, and Michael J. Heben

Wright Center for Photovoltaics Innovation and Commercialization, Department of Physics and Astronomy, University of Toledo, Toledo, Ohio, 43606, USA

***Abstract* — CdTe device performance was simulated as a function of band alignment at the emitter/absorber and absorber/back buffer layer to determine under what conditions devices are front and back interface limited. When the back buffer layer forms an electron reflector, devices are limited by four separate mechanisms. When there is no electron reflector, the role of the back buffer layer increases. In addition to the front and back interfaces, Shockley-Reed-Hall (SRH) recombination can also determine the device performance. We determine the voltage at which SRH recombination dominates device performance for a number of carrier lifetimes. Finally, we show that increasing the CdTe dopant density reduces but does not eliminate the role of the back interface. These results help us interpret the improvements of real-life measurements, and will allow us to develop better front and back interfaces to CdTe.**

***Index terms* — Band Alignment, CdTe, Interfaces, SRH.**

I. Introduction

As thin film photovoltaic (PV) device efficiencies exceed 22% [1], the next milestone is to push efficiency to 25% and beyond. To help develop guidelines to reach this value, Kanevce et al. performed numerical simulation that showed that simultaneously achieving carrier lifetimes of 100 ns, CdTe dopant density of $2x10^{16}$ cm^{-3}, and front surface recombination velocity (FSRV) of 100 cm/s is required [2]. Modeling by Song et al. showed that appropriate band alignment at the front of the device could greatly reduce front interface recombination and boost device open circuit voltage (V_{OC}) and efficiency [3]. Using this new information, Ablekim et al. showed that appropriate conduction band alignment between the emitter and absorber eliminates the FSRV condition and reduces the carrier lifetime requirement to 25 ns to reach 25% efficiency [4]. We recently showed that to achieve this value, it is necessary to implement a back buffer with the appropriate conduction band offset (CBO) and Fermi level alignment between the buffer and absorber layers prior to them interacting [5]. In each of these cases, though, the contact not under investigation was held under near ideal conditions – flat band conditions at the back of the device for the front contact investigations or emitter with ideal doping and CBO with absorber equal to 0.2 eV in the back buffer layer investigations.

For real devices, it is difficult to separate the effects of one contact from the other. Still, researchers spent years varying the back buffer materials used in CdTe devices to improve PV performance; all of these studies used CdS, which is now known to be an inferior emitter. Recently a better emitter has replaced CdS, but only a few groups [6-8] have demonstrated the near optimum front contact identified by the simulations performed by Song et al. [3] and incorporated into subsequent analyses [4, 5]. While much of the back contact work demonstrated PV parameter improvements, only one has achieved V_{OC} greater than 900 mV for polycrystalline devices, but the device details have not been published [9]. Because many of these devices used a poor emitter, it is possible that the front contact played a role in limiting these devices.

Here we investigate how the band alignment at both the front and back contacts affect and limit device performance. Using numerical modeling we are able to determine under what conditions the devices are front contact, back contact, and Shockley-Reed-Hall (SRH) limited. We also investigate how increasing the hole density of the absorber layer affects these conclusions.

II. Modeling Conditions

Numerical simulations were carried out using SCAPS-1D software [10]. The device structure was 300 nm transparent conducting oxide (TCO) front contact/100 nm emitter/2 μm CdTe/100 nm buffer layer. All material parameters used here have been used in previous investigations [5, 11, 12]. Flat band conditions between the buffer and back contact were assumed. The electron affinity of the TCO was chosen to be 4.45 eV to ensure no barrier was formed between the TCO and emitter [11]. The band gap and electron density of the emitter layer were fixed to 3.3 eV and $1x10^{17}$ cm^{-3}, respectively, and the electron affinity varied to change the CBO between the emitter and absorber. Carrier lifetime of 25 ns was used for both holes and electrons in the absorber except when noted. The valance band energy of the back buffer layer was set 5.7 eV, 0.2 eV less than that of the CdTe absorber (5.9 eV). Figure 1 shows the band diagram of the CdTe and back buffer prior to interaction. In this case, the Fermi energies can differ. We have chosen a sign convention such that this initial Fermi level offset (IFLO) is positive if the Fermi level of the back buffer is more negative than that of the CdTe, consistent with a barrier for hole flow from the CdTe into the back buffer [5]. The IFLO was varied by changing the shallow acceptor density of the back buffer layer. Surface recombination velocities were set to 10^5 $cm\text{-}s^{-1}$ at all interfaces, except when noted.

Authorized licensed use limited to: Auckland University of Technology. Downloaded on June 02,2020 at 05:46:31 UTC from IEEE Xplore. Restrictions apply.

Approved for public release; distribution unlimited.

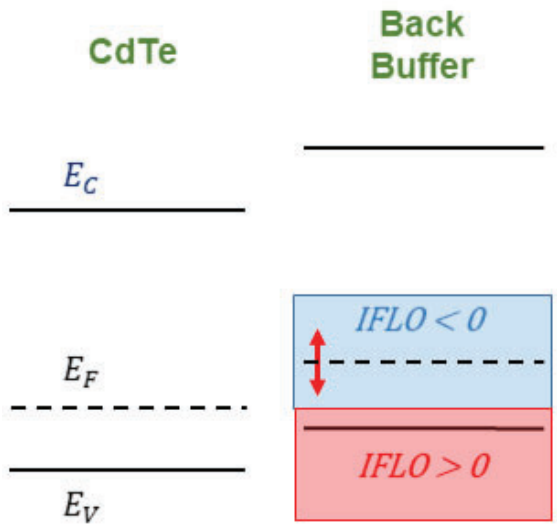


Fig. 1. Non-interacting band diagram of CdTe and the back buffer layer. If the Fermi level of the buffer is located in the blue box (as shown), the initial Fermi level offset (IFLO) is defined as negative. If the Fermi level is located in the red box, the IFLO is positive.

III. Results and Discussion

To determine the role of the front and back interface in the device performance, devices were modeled as the CBO of the emitter with the absorber and the CBO and IFLO of the back buffer with the absorber were varied. Figure 2 shows the contour plots of the V_{OC} for CdTe devices with hole density of 2 x 10^{14} cm^{-3}. It is important to note that previous simulation studies [3, 4] focusing on the emitter interface corresponds to IFLO = 0 eV in the graph without an electron reflector (Fig. 2b), and our investigation of the back buffer layer [5] corresponds to the CBO = +0.2 eV for back buffers with and without an electron reflector (Fig. 2a and 2b, respectively). A previous study of the emitter [3] showed that as the CBO went from a negative value to positive, the V_{OC} increased until it saturated around CBO = 0 eV. These results are consistent with the results presented here. Our back buffer layer study [5] showed the V_{OC} increases slowly with increasing IFLO until it saturates around IFLO = 0.15 eV. This is also consistent with the results presented here.

Expanding the view beyond a single emitter CBO or back buffer IFLO, we can determine how the alignment at both the front and back of the CdTe device affects the overall performance. We first consider the back buffer with an electron reflector (Fig. 2a). The portion of the graph labeled I shows contour lines that are independent emitter CBO, while the section labeled II shows contour lines independent of IFLO. These features indicate that recombination is dominated by the back and front of the devices, respectively. In region I, the

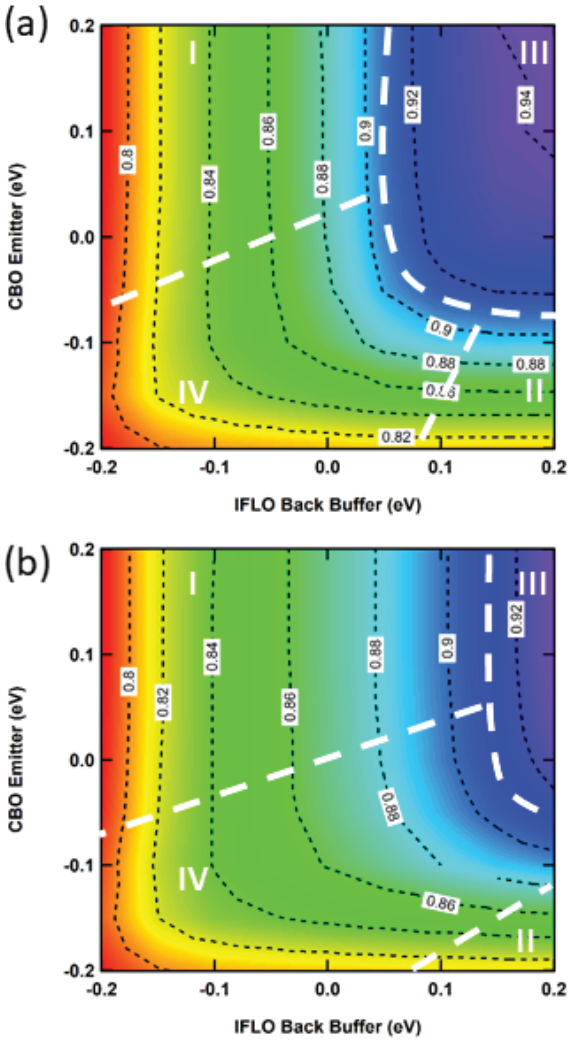


Fig. 2. Open circuit voltage of CdTe devices with varying conduction band offset (CBO) between the emitter and absorber and initial Fermi level offset (IFLO) between the back buffer layer and absorber for buffers (a) with and (b) without an electron reflector.

emitter CBO is positive, which indicates that the holes are repelled from this interface, reducing recombination at the front junction [3]. At the same time, the alignment at the back of the device is poor, leading to downward band bending at the back of the device, which attracts electrons and increases recombination at the back junction. For region II, the converse is true. The upward band bending at the back of the device repels electrons while poor alignment at the front of the device does not repel holes effectively. This leads to low recombination at the back interface and high recombination at the front interface. Interestingly, there are two regions of the graph where neither the front nor back dominate device performance.

Authorized licensed use limited to: Auckland University of Technology. Downloaded on June 02,2020 at 05:46:31 UTC from IEEE Xplore. Restrictions apply.

Approved for public release; distribution unlimited.

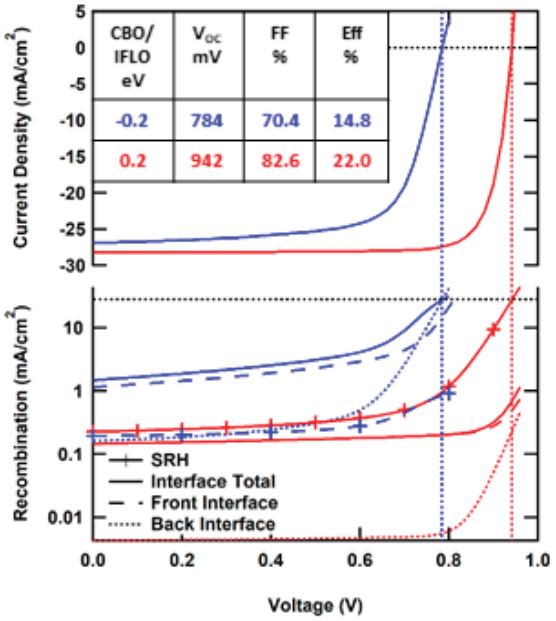


Fig. 3. Current density-voltage (J-V) and recombination current density-voltage (J_R-V) curves of CdTe devices with various band alignments between the CdTe and front and back buffer layers. The recombination current density is further broken down to determine what recombination mechanism limits device performance.

To understand these regions of the graph we modeled the device performance to obtain the recombination current densities. To isolate the front and back interface recombination, the simulations were completed with both interfaces having a SRV of 10^5 cm-s^{-1}, one with BSRV of 10^5 cm-s^{-1} and FSRV of 10^{-1} cm-s^{-1}, and one with BSRV of 10^{-1} cm-s^{-1} and FSRV of 10^5 cm-s^{-1}. While reducing one of the SRV may lead to slightly different band diagrams, the isolated recombination values are good approximations. Figure 3 shows the current density-voltage (J-V) and recombination current density-voltage (J_R-V) for devices with good alignment between the CdTe and both front and back interfaces (CBO = 0.2 eV, IFLO = 0.2 eV), and poor alignment between CdTe and front and back interfaces (CBO = -0.2 eV, IFLO = -0.2 eV).

First, we consider the device performance when there is good alignment at the front and back of the device (region III). At low voltages, J_R is on the order of 10^{-1} mA-cm^{-2} at the front of the device (J_F) and $<1\text{x}10^{-2}$ mA-cm^{-2} at the back (J_B). The front dominates the interfacial recombination for all voltages explored here; however, SRH recombination is higher than interface recombination at all voltages. At V_{OC}, SRH recombination current dominates the interface recombination, J_{SRH} = 27 mA-cm^{-2} compared to J_F = 0.7 mA-cm^{-2} and J_B = 0.3 mA-cm^{-2}. Clearly, when band alignment is good at both the front and back interfaces (region III), SRH recombination dictates device performance.

When the alignment at the front and back of the device is poor (region IV), the front and back interface recombination current densities are an order of magnitude higher than and approximately equal to the SRH recombination current density at short circuit voltage, respectively. As the voltage increases J_{SRH} remains roughly constant to ~0.7 V, but both J_F and J_B increase. Here, recombination at the front is higher than that at the back at the maximum power point (0.630 V), but recombination at the back increases more quickly. By ~0.7 V, J_B exceeds J_F, and they remain close in value. At V_{OC} recombination at both the front and back are significant, meaning that neither dominates the recombination nor dictates the device performance. Consequently, when band alignment at both interfaces is poor (region IV), the device performance is a function of both.

Historically, most devices fall within region IV. The CBO between CdS and CdTe is -0.1 eV. Few back buffer materials used in CdTe devices are expected to have an IFLO near zero and most are more negative than -0.2 eV. Even so, there have been many studies attempting to improve the back contact that have shown some, but not significant, improvement in V_{OC} [13-23]. Because the CBO between the CdS and CdTe and the IFLO between CdTe and back buffer layer leads to poor alignment, the device performance is a function of both interfaces. Even large improvements in back buffer layer alignment through incorporation of ZnTe [13, 14] or perovskites [19], for example, may lead to positive IFLO but would not result in the V_{OC} gains expected for the change in IFLO [5] because these devices would, at best, be front contact limited.

Not all back buffer layers investigated had a positive CBO between the CdTe and back buffer layer [20-23]. As we noted in our previous work [5] and Fig. 2b confirms, V_{OC} is different when the CBO at the back interface is negative, and does not impede electron flow toward the back contact, compared to when it is positive. In both cases, when the emitter CBO is positive and IFLO is negative (region I in Fig. 2b), the devices are back contact limited. However, when the IFLO becomes positive, devices without an electron reflector are still affected by the back interface of the device. The positive IFLO results in upward band bending at the back of the device, but without a positive CBO some electrons can overcome this small barrier and reach the back of the device. This negative CBO extends the influence of the back interface over a larger IFLO range and limits the absolute efficiency. Consequently, the front interface becomes less important and dictates device performance over a smaller parameters space.

The location of each of these regions depends on the SRV at each interface. Decreasing the FSRV from 10^5 cm-s^{-1} to 10^4 cm-s^{-1} decreases the influence of the front interface in device performance and shifts the contour plot 0.05 eV downward. Likewise, decreasing the BSRV from 10^5 cm-s^{-1} to 10^4 cm-s^{-1} reduces the recombination at the back surface and shifts the contour plot to the left by 0.05 eV.

Authorized licensed use limited to: Auckland University of Technology. Downloaded on June 02,2020 at 05:46:31 UTC from IEEE Xplore. Restrictions apply.

Approved for public release; distribution unlimited.

TABLE I. OPEN CIRCUIT VOLTAGE AND VOLTAGE AT WHICH SRH CURRENT DENSITY EQUALS 50% OF J_{SC} (14 MA-CM^{-2}) AS A FUNCTION OF CARRIER LIFETIME.

Lifetime (ns)	V_{OC} (V)	V_{50} (V)
1	0.817	0.772
2.5	0.856	0.822
10	0.910	0.882
25	0.942	0.915
100	0.992	0.969

In addition to the band alignment and SRV, the carrier lifetime can affect the device performance. Recent time-resolved photoluminescence investigations measured carrier lifetimes of CdTe on the order of 100 ns for polycrystalline films in a double heterostructure between Al_2O_3 capping layers [24]. We consider lifetimes that range from 1 ns to 100 ns for devices with CBO and IFLO equal to +0.2 eV. Table I shows the carrier lifetime, V_{OC}, and the voltage at which J_{SRH} is half the photogenerated current (14 mA-cm^{-2}). For 1 ns carrier lifetimes, the SRH recombination dominates device performance at 0.772 V. As Fig. 3 shows, when the band alignment is good and the carrier lifetime is 25 ns, J_{SRH} equals J_R. Increasing the lifetime to 100 ns further improves the device performance by shifting the onset of SRH recombination to higher bias voltages, but V_{OC} of 1 V cannot be reached. Even when the alignment at the front of the device is improved by increasing the electron doping density in the emitter from 1x10^{17} cm^{-3} to 1x10^{19} cm^{-3}, V_{OC} only increases to 0.998 V.

Inspired by previous simulations that indicated absorber doping is necessary to reach 25% efficiency [2], researchers have begun exploring methods to increase the hole density of CdTe devices [25]. Consequently, we also investigated the device performance as a function of front and back alignment when the CdTe dopant density increased from 2x10^{14} cm^{-3} (Fig. 2) to 2x10^{16} cm^{-3}. Fig. 4 shows the contour plots of the V_{OC} for devices with an electron reflector.

As the contour plot shows, back interface dependence of the V_{OC} is greatly reduced. This is consistent with our previous study [5] that showed that increased absorber doping decreases the depletion region from the back junction, which reduces the back interface influence on the device performance. However, as Fig. 5 shows, the device performance is not independent of the back interface. Clearly, when the front alignment is poor (CBO < ~0.05 eV), the device performance is dictated by the front interface (region I). As the CBO and, hence, V_{OC} increase, SRH recombination begins to affect device performance, and at 1.023 V, for carrier lifetime of 25 ns, SRH becomes the dominant recombination mechanism. As both Figs. 4 and 5 show, there are two distinct regions when CBO is positive. When the IFLO is < 0.10 eV (region II), the device performance is a combination of back interface and SRH recombination. However, when the IFLO is positive (region III), and the electrons are reflected from the interface, SRH becomes the dominant recombination mechanism.

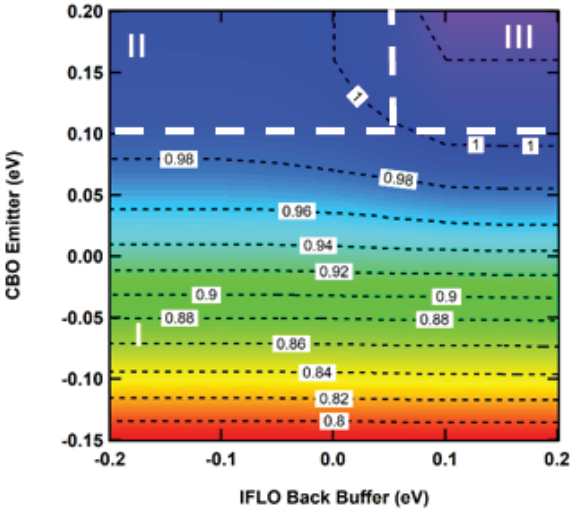


Fig. 4. Open circuit voltage of CdTe devices with absorber hole density of 2x10^{16} cm^{-3} with varying CBO between the emitter and absorber and IFLO between the back buffer layer and absorber for buffers with an electron reflector.

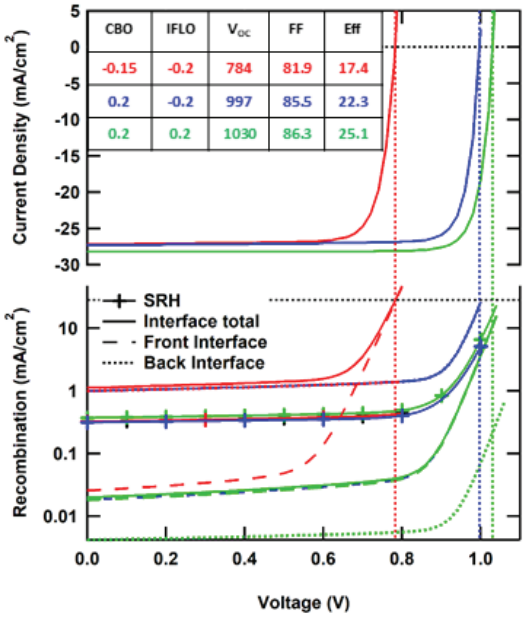


Fig. 5. J-V and J_R-V curves of CdTe devices with absorber dopant density of 2x10^{16} cm^{-3} with bad band alignment at both interfaces (CBO = -0.2 eV, IFLO = -0.2 eV), good front alignment and poor back alignment (CBO = +0.2 eV, IFLO = -0.2 eV), and good alignment at both interfaces (CBO = +0.2 eV, IFLO = + 0.2 eV). The recombination current density is further broken down to determine what recombination mechanism limits device performance.

Authorized licensed use limited to: Auckland University of Technology. Downloaded on June 02,2020 at 05:46:31 UTC from IEEE Xplore. Restrictions apply.

Approved for public release; distribution unlimited.

IV. Conclusions

We simulated device performance as a function of band alignment of both the front and back interfaces with CdTe. We showed that when there is a positive CBO between the CdTe and back buffer layer (electron reflector), devices are limited by the front (region I), back (region II), SRH (region III), or a combination of the front and back (IV) of the device. When the CBO at the back of the device is negative, the role of the back interface is enhanced. Furthermore, we showed how varying the SRV at each interface affects these conclusions. We also determined at what voltage SRH recombination will dominate device performance for a number of carrier lifetimes. In addition, we considered how the front and back interfaces will affect CdTe device with higher hole densities. For these devices, the back interface becomes less important, but can still play a minor role when the front alignment is good. Good band alignment with CdTe at both interfaces, though, is required to reach the highest device performance.

Acknowledgement

The work was supported by Air Force Research Laboratory under agreement number FA9453-18-2-0037. The U.S. Government is authorized to reproduce and distribute reprints for Governmental purposes notwithstanding any copyright notation thereon. The views and conclusions contained herein are those of the authors and should not be interpreted as necessarily representing the official policies or endorsements, either expressed or implied, of Air Force Research Laboratory or the U.S. Government.

References

[1] M. A. Green, Y. Hishikawa, E. D. Dunlop, D. H. Levi, J. Hohl-Ebinger, M. Yoshita, *et al.*, "Solar cell efficiency tables (Version 53)," *Progress in Photovoltaics: Research and Applications,* vol. 27, pp. 3-12, 2019.

[2] A. Kanevce, M. O. Reese, T. M. Barnes, S. A. Jensen, and W. K. Metzger, "The roles of carrier concentration and interface, bulk, and grain-boundary recombination for 25% efficient CdTe solar cells," *Journal of Applied Physics,* vol. 121, p. 214506, 2017.

[3] T. Song, A. Kanevce, and J. R. Sites, "Emitter/absorber interface of CdTe solar cells," *Journal of Applied Physics,* vol. 119, p. 233104, 2016.

[4] T. Ablekim, E. Colegrove, and W. K. Metzger, "Interface Engineering for 25% CdTe Solar Cells," *ACS Applied Energy Materials,* vol. 1, p. 5135-5139, 2018.

[5] G. K. Liyanage, A. B. Phillips, F. K. Alfadhili, R. J. Ellingson, and M. J. Heben, "The Role of Back Buffer Layers and Absorber Properties for >25% Efficient CdTe Solar Cells," *ACS Applied Energy Materials* 2019. DOI: 10.1021/acsaem.9b00367

[6] A. H. Munshi, J. M. Kephart, A. Abbas, T. M. Shimpi, K. L. Barth, J. M. Walls, *et al.*, "Polycrystalline CdTe photovoltaics with efficiency over 18% through improved absorber passivation and current collection," *Solar Energy Materials and Solar Cells,* vol. 176, pp. 9-18, 2018.

[7] D.-B. Li, Z. Song, R. A. Awni, S. S. Bista, N. Shrestha, C. R. Grice, *et al.*, "Eliminating S-Kink To Maximize the Performance of MgZnO/CdTe Solar Cells," *ACS Applied Energy Materials,* vol. 2, pp. 2896-2903, 2019.

[8] T. Ablekim, C. Perkins, X. Zheng, C. Reich, D. Swanson, E. Colegrove, *et al.*, "Tailoring MgZnO/CdSeTe Interfaces for Photovoltaics," *IEEE Journal of Photovoltaics,* vol. 9, pp. 888-892, 2019.

[9] M. Gloeckler, I. Sankin, and Z. Zhao, "CdTe Solar Cells at the Threshold to 20% Efficiency," *IEEE Journal of Photovoltaics,* vol. 3, pp. 1389-1393, 2013.

[10] M. Burgelman, P. Nollet, and S. Degrave, "Modelling polycrystalline semiconductor solar cells," *Thin Solid Films,* vol. 361, pp. 527-532, 2000.

[11] G. K. Liyanage, A. B. Phillips, and M. J. Heben, "Role of band alignment at the transparent front contact/emitter interface in the performance of wide bandgap thin film solar cells," *APL Materials,* vol. 6, p. 101104, 2018.

[12] M. Gloeckler, A. L. Fahrenbruch, and J. R. Sites, "Numerical modeling of CIGS and CdTe solar cells: setting the baseline," *3rd World Conference on Photovoltaic Energy Conversion*, pp. 491-494, 2003.

[13] N. Strevel, L. Trippel, C. Kotarba, and I. Khan, "Improvements in CdTe module reliability and long-term degradation through advances in construction and device innovation," *Photovoltaics International,* vol. 22, pp. 66-74, 2014.

[14] J. V. Li, J. N. Duenow, D. Kuciauskas, A. Kanevce, R. G. Dhere, M. R. Young, *et al.*, "Electrical Characterization of Cu Composition Effects in CdS/CdTe Thin-Film Solar Cells With a ZnTe:Cu Back Contact," *IEEE Journal of Photovoltaics,* vol. 3, pp. 1095-1099, 2013.

[15] F. K. Alfadhili, A. B. Phillips, G. K. Liyanage, J. M. Gibbs, M. K. Jamarkattel, and M. J. Heben, "Controlling Band Alignment at the Back Interface of Cadmium Telluride Solar Cells using ZnTe and Te Buffer Layers," *MRS Advances,* pp. 1-7, 2019.

[16] C. A. Wolden, A. Abbas, J. Li, D. R. Diercks, D. M. Meysing, T. R. Ohno, *et al.*, "The roles of ZnTe buffer layers on CdTe solar cell performance," *Solar Energy Materials and Solar Cells,* vol. 147, pp. 203-210, 2016.

[17] X. Di, X. Li, D. Wang, Q. Li, K. Shen, and D. Wang, "CdTe thin film solar cell with NiO as a back contact buffer layer," *Solar Energy Materials and Solar Cells,* vol. 169, pp. 61-67, 2017.

[18] K. P. Bhandari, P. Koirala, N. R. Paudel, R. R. Khanal, A. B. Phillips, Y. Yan, *et al.*, "Iron pyrite nanocrystal film serves as a copper-free back contact for polycrystalline CdTe thin film solar cells," *Solar Energy Materials and Solar Cells,* vol. 140, pp. 108-114, 2015.

[19] K. P. Bhandari, S. C. Watthage, Z. Song, A. Phillips, M. J. Heben, and R. J. Ellingson, "Applications of hybrid organic-inorganic metal halide perovskite thin film as a hole transport layer in CdTe thin film solar cells," *IEEE 44th Photovoltaic Specialists Conference (PVSC)*, pp. 1-4, 2017.

[20] A. B. Phillips, R. R. Khanal, Z. Song, S. C. Watthage, K. R. Kormanyos, and M. J. Heben, "Simultaneous shunt protection and back contact formation for CdTe solar cells with single wall carbon nanotube layers," *Applied Physics Letters,* vol. 107, p. 253901, 2015.

[21] A. B. Phillips, R. R. Khanal, Z. Song, R. M. Zartman, J. L. DeWitt, J. M. Stone, *et al.*, "Wiring-up Carbon Single Wall Nanotubes to Polycrystalline Inorganic Semiconductor Thin Films: Low-Barrier, Copper-Free Back Contact to CdTe Solar Cells," *Nano Letters,* vol. 13, pp. 5224-5232, 2013.

[22] S. C. Watthage, A. B. Phillips, G. K. Liyanage, Z. Song, J. M. Gibbs, F. K. Alfadhili, *et al.*, "Selective Cd Removal From CdTe for High-Efficiency Te Back-Contact Formation," *IEEE Journal of Photovoltaics,* vol. 8, pp. 1125-1131, 2018.

Authorized licensed use limited to: Auckland University of Technology. Downloaded on June 02,2020 at 05:46:31 UTC from IEEE Xplore. Restrictions apply.

Approved for public release; distribution unlimited.

[23] Z. Weng, S. Ma, H. Zhu, Z. Ye, T. Shu, J. Zhou, *et al.*, "CdTe thin film solar cells with a SnTe buffer layer in back contact," *Solar Energy Materials and Solar Cells,* vol. 179, pp. 276-282, 2018.
[24] J. M. Kephart, A. Kindvall, D. Williams, D. Kuciauskas, P. Dippo, A. Munshi, *et al.*, "Sputter-Deposited Oxides for Interface Passivation of CdTe Photovoltaics," *IEEE Journal of Photovoltaics,* vol. 8, pp. 587-593, 2018.
[25] B. E. McCandless, W. A. Buchanan, C. P. Thompson, G. Sriramagiri, R. J. Lovelett, J. Duenow, *et al.*, "Overcoming Carrier Concentration Limits in Polycrystalline CdTe Thin Films with In Situ Doping," *Scientific Reports,* vol. 8, p. 14519, 2018.

Authorized licensed use limited to: Auckland University of Technology. Downloaded on June 02,2020 at 05:46:31 UTC from IEEE Xplore. Restrictions apply.

Approved for public release; distribution unlimited.

Check for updates

Received: 24 April 2019 | Revised: 14 August 2019 | Accepted: 20 August 2019

DOI: 10.1002/pip.3192

RESEARCH ARTICLE

WILEY PROGRESS IN PHOTOVOLTAICS

Influences of buffer material and fabrication atmosphere on the electrical properties of CdTe solar cells

Rasha A. Awni[1,2] | Deng-Bing Li[1] | Zhaoning Song[1] | Sandip S. Bista[1] | Mohammed A. Razooqi[1] | Corey R. Grice[1] | Lei Chen[1] | Geethika K. Liyanage[1] | Chongwen Li[1] | Adam B. Phillips[1] | Michael J. Heben[1] | Randy J. Ellingson[1] | Jian V. Li[3] | Yanfa Yan[1]

[1] Department of Physics and Astronomy, and Wright Center for Photovoltaics Innovation and Commercialization (PVIC), University of Toledo, Toledo, Ohio, USA

[2] Department of Physics, College of Education for Pure Sciences, Tikrit University, TikritSalahuddin, Iraq

[3] Department of Aeronautics and Astronautics, National Cheng Kung University, Tainan, Taiwan

Correspondence
Yanfa Yan, Department of Physics and Astronomy, and Wright Center for Photovoltaics Innovation and Commercialization (PVIC), University of Toledo, Toledo, OH 43606, USA.
Email: yanfa.yan@utoledo.edu

Funding information
Office of Energy Efficiency and Renewable Energy, Grant/Award Number: DE-EE0007541; Ministry of Science and Technology, Taiwan; Solar Energy Technologies Office (SETO); National Science Foundation; Air Force Research Laboratory, Grant/Award Number: FA9453-18-2-0037

Abstract

The electrical properties such as interface energy barriers, defect energy levels, and densities dictate the performance of thin film solar cells. Here, we show that these properties can be quantified in cadmium telluride (CdTe) thin-film solar cells using admittance spectroscopy-based techniques. Our results reveal that the electrical properties in CdTe thin-film solar cells depend on both buffer material and the fabrication atmosphere. We find that only a negligible front contact barrier exists at the CdS/CdTe front junction regardless of the fabrication atmospheres, while an obvious front barriers are observed at the ZnMgO (ZMO)/CdTe junctions. Both CdS/CdTe and ZMO/CdTe solar cells exhibit back contact barrier. The energy level of defects is shallower in CdS/CdTe cells than in ZMO/CdTe cells. The fabrication atmosphere influences the electrical properties, i.e., an oxygen-free atmosphere reduces the front and back barrier heights and lowers the energy level of defects. The results provide critical insights for understanding and optimizing the performance of CdTe thin-film solar cells.

KEYWORDS

admittance spectroscopy, cadmium telluride, equivalent circuit, interface barriers, photovoltaic cells

1 | INTRODUCTION

Cadmium telluride (CdTe) thin film solar cell technology has demonstrated steady growth in photovoltaic market. This growth is largely benefited from the rapid increase of certified record efficiency in the past seven years. However, the current record efficiency of 22.3%[1] is still much below the efficiency achievable for CdTe per the Shockley-Queisser limit for single-junction solar cells. A recent advance in CdTe solar cells is the replacement of the traditional CdS buffer (emitter) by a wide bandgap metal oxide, such as ZnMgO (ZMO).[2] This replacement not only avoids the current loss caused by CdS but also introduces a spike to the conduction band offset (CBO) between the buffer and CdTe absorber.[3] Device modeling has shown that an appropriate CBO spike can reduce interface recombination and increase the open-circuit voltages (V_{OC}) of CdTe solar cells.[4,5] Therefore, ZMO/CdTe solar cells are expected to achieve higher efficiency due to the improvements on both short-circuit current (J_{SC}) and V_{OC}. Indeed, Sites, Sampath, and coworkers have demonstrated[6] ZMO/CdTe solar cells with efficiencies exceeding 18%. However, the benefits of using ZMO buffer in CdTe solar cells have not been widely reproduced by other researchers. One issue is that the introduction of CBO spike can also cause energy barrier at the front ZMO/CdTe junction,[7] which can hinder the transfer of electrons from CdTe absorber into fluorine doped SnO_2 (FTO) electrode, leading to S-kink behavior in the current density-voltage (J-V) curves which is mainly responsible for poor fill factors (FFs).[6,8,9] Additionally, the use

 © 2019 John Wiley & Sons, Ltd.

Approved for public release; distribution unlimited.
400

of ZMO buffer may influence the properties of defects at the front interface and in CdTe bulk. Diffusion of ions along the grain boundaries (GBs), such as chlorine, oxygen, sulfur, and copper, plays some roles in modification of the GB electrical behavior.[10] Our recent work[9] has shown that the performance of ZMO/CdTe solar cells can be significantly affected by the atmosphere in which the $CdCl_2$ treatment is conducted, i.e., the ZMO/CdTe cells treated in helium (hereafter named ZMO/CdTe-oxygen-free) outperform the ZMO/CdTe cells treated in air (named ZMO/CdTe-air). However, an opposite trend is observed for CdS/CdTe solar cells, i.e., the CdS/CdTe-air cells outperform CdS/CdTe-oxygen-free cells. Since the electrical properties such as energy barriers at junctions and defect energy levels and densities of defects at the interfaces and in the absorber dictate the performance of thin film solar cells, it is critical to assess and compare these electrical properties in CdS/CdTe and ZMO/CdTe solar cells treated in different atmospheres. The results can provide insights for further performance improvement of CdS/CdTe and ZMO/CdTe solar cells.

Admittance spectroscopy (AS) is a method of choice for measuring the electrical properties of thin film solar cells, such as defects, carrier transport, and back-contact barrier height in CdS/CdTe solar cells.[11,12] Temperature-dependent J-V measurement (J-V-T) has also been used to extract the back contact barrier height for CdTe thin-film solar cells.[12,13] However, so far there is no report on the measurement of front contact barrier height, which is critical for understanding the performance of ZMO/CdTe cells with CBO spikes. This is in part due to the fact that AS measurements to date are typically based on a two-junctions model and carried out in the near-zero to reverse bias range in dark conditions, which by design renders them not sensitive to detecting the front contact potential barrier. In this work, we develop a three-subcircuit model with explicit representation of the front contact barrier to measure the front and back contact barrier heights as well as energy levels and densities of defects at interface and in absorber of CdTe thin-film solar cells using impedance spectroscopy, which is corroborated by AS-based techniques operating intentionally in near-V_{OC} forward bias and light. We measured these electrical properties in CdS/CdTe and ZMO/CdTe solar cells, with device parameters tabulated in Table S1, fabricated in -air and oxygen-free atmospheres. We find that the energy level of defects is shallower in CdS/CdTe cells than in ZMO/CdTe cells. We further find that the fabrication atmosphere influences the electrical properties of CdTe solar cells, i.e., devices with $CdCl_2$ treatment performed in oxygen-free atmosphere exhibit smaller front and back barrier heights and lower energy level of defects than those with $CdCl_2$ treatment performed in oxygen atmosphere.

2 | SAMPLE FABRICATION AND CHARACTERIZATION

The ZMO/CdTe and CdS/CdTe solar cells were fabricated using our previously reported procedure.[9] For ZMO/CdTe devices, an 80 nm ZMO layer was deposited on FTO-coated glass at room temperature by radio-frequency (RF) sputtering using a ZMO target with 8 wt% magnesium oxide (MgO) under mixed flow gas of 3% oxygen and 97% argon. It has been reported that rapid thermal annealing can improve the electrical conductivity of ZMO and, therefore, the performance of CdTe cells.[14] However, we have not observed beneficial effects for thermal treatment in our work. Therefore, ZMO films received no additional thermal annealing. A ~2.8 μm CdTe film was deposited by close space sublimation (CSS) in helium with a source temperature of 560°C and a substrate temperature of 495°C at 1 Torr. For CdS/CdTe devices, a CdS layer was deposited on FTO-coated glass (TEC 15 M; Pilkington NA) using procedure reported in the literature.[15] Then, a ~3 μm CdTe film was deposited by CSS in helium with a source temperature of 660°C and a substrate temperature of 595°C at 10 Torr. $CdCl_2$ treatment was performed with a saturated $CdCl_2$ in methanol solution on CdTe surfaces dropwise and heated at 390°C (CdS/CdTe) or 420°C (ZMO/CdTe) for 20 minutes with a 500 sccm high purity helium or dry air flow. After the samples were cooled to room temperature, excess of $CdCl_2$ was removed by rinsing with methanol. No additional treatment of CdTe surfaces was applied. Then, copper chloride (CuCl) solution was dropped on CdTe surface and annealed in nitrogen at 175°C to promote Cu doping in CdTe. After that, gold (Au) (40 nm) electrodes were deposited by thermal evaporation via a shadow mask with an individual cell area of 0.08 cm^2. The best-performing ZMO/CdTe cell using $CdCl_2$ treatment in air showed a V_{OC} of 0.882 V, a J_{SC} of 23.2 mA/cm^2, and a FF of 44.8%, yielding an efficiency of 9.2%. The best-performing ZMO/CdTe cell using $CdCl_2$ treatment in oxygen-free atmosphere showed a V_{OC} of 0.866 V, J_{SC} of 25.5 mA/cm^2, and a FF of 72.9%, yielding an efficiency of 16.1%.[9]

Solar cell performance was characterized by measuring J-V curves under AM1.5G illumination using a solar simulator (PV Measurements Inc.) Temperature-dependent measurements were performed using a Solartron Modulab potentiostat equipped with a frequency response analyzer (Ametek Inc.). Temperature-dependent current voltage (J-V-T) and capacitance voltage (C-V-T) measurements were performed in dark with DC bias voltage (V_{DC}) swept from −0.4 to 1.5 V in J-V-T and −2.0 to 0.8 V in C-V-T with 45 mV AC modulation voltage (V_{AC}) and 10 kHz frequency. The AS measurements were done under a constant AC modulation voltage of 45 mV with frequency (F) swept from 1.0 MHz to 0.1 Hz and DC bias varied from −0.1 to 1.5 V at a step size of 0.1 V. A liquid-nitrogen cooled cryo-system (Janis VPF-100 system) was used to carry out all the temperature-dependent (120 to 310 K with a step size of 10 K) measurements. The temperature was measured and controlled by a temperature controller (Lakeshore 330). A sensor was mounted on the top of the device directly to ensure that the recorded temperature is the device temperature.

3 | RESULTS AND DISCUSSION

3.1 | Equivalent circuit model

We first describe the rationale of a three-subcircuit model designed to explicitly highlight the electrical role played by the front contact

Approved for public release; distribution unlimited.

barrier and the ensuing results of quantifying the front and back barriers in ZMO/CdTe-air and -oxygen-free devices. The energy band diagram of the metal/CdTe/buffer contact heterostructure (Figure 1A) consists of three regions: (a) CdTe bulk containing a depletion/space charge region (SCR) with width (W) and a quasi-neutral region, (b) a back contact with a barrier for hole transport, i.e., a positive difference between the equilibrium Fermi level (E_F) and the top of the valence band edge (E_V) at the metal surface,[16] and (c) a front contact with a possible barrier for electron transport, i.e., a negative difference between the equilibrium Fermi level (E_F) and the conduction band edge (E_C) of the buffer. Each region can be described by a capacitance and a conductance (1/R, where R is a resistance). Previously, the complex capacitance spectra of CdS/CdTe devices are typically modeled by an equivalent circuit consisting of two subcircuits,[17] which correspond to the front (depletion and bulk regions) and back (Schottky barrier) junctions placed in series.[18,19] This model is illustrated by the subcircuits colored in black in Figure 1B. In previous modeling,[17] no front barrier at CdS/CdTe interface has been considered due to their cliff CBO. However, replacing CdS by ZMO could introduce a spike CBO. The CdS/CdTe cliff-type CBO presents an equivalent electric field in the same direction as the built-in electric field of the main n^+/p junction; hence, its role in carrier transport and admittance/impedance contribution are implicitly accounted for in the first element of the two-subcircuit model. This is especially true when the electrical measurements are conducted under near-zero to reverse biases in dark conditions. On the other hand, the spike-type CBO such as that of the ZMO/CdTe interface presents an equivalent electric field in the opposite direction of the built-in electric field of the main n^+/p junction. Hence, its role in carrier transport and admittance/impedance contribution cannot be inclusively accounted for in the first element of the two-subcircuit model. This is all the more significant when the device is operating under a substantial forward bias or in light such that the band bending of the main n^+/p junction is flat whereas the CBO cliff is relatively prominent. A front barrier at the ZMO/CdTe interface, therefore, must be treated as an independent circuit subcircuit in addition to the other two. Therefore, a three-subcircuit model must be considered to better fit the capacitance spectra in ZMO/CdTe devices. This additional subcircuit is colored in red in Figure 1B. The equivalent circuit model without the front R-C combination (two-subcircuit model) fits the complex capacitance spectra of CdS/CdTe devices very well. However, we found that the modified equivalent circuit model with front R-C combination (three-subcircuit model) fits complex capacitance spectra of ZMO/CdTe devices much better than the two-subcircuit model. In order to show the quality of the fit, we applied both the two-subcircuit and three-subcircuit models to fit the capacitance spectra of both CdS/CdTe and ZMO/CdTe devices and compared the resultant errors (ΔC), i.e., the differences between the raw (C_{raw}) and fitted (C_{fit}) data. Figures S1a and S1b show the calculated errors at 300 K for devices fabricated in air and oxygen-free, respectively, using the two-subcircuit model. The results show that spectra fit much better for the CdS/CdTe device than for the ZMO/CdTe device. However, the trend is opposite when the three-subcircuit model is used for fitting, as shown in Figures S1c and S1d. Therefore, for ZMO/CdTe devices, the three-subcircuit model should be used, while for CdS/CdTe devices, the two-subcircuit model should be used for fitting the capacitance spectra.

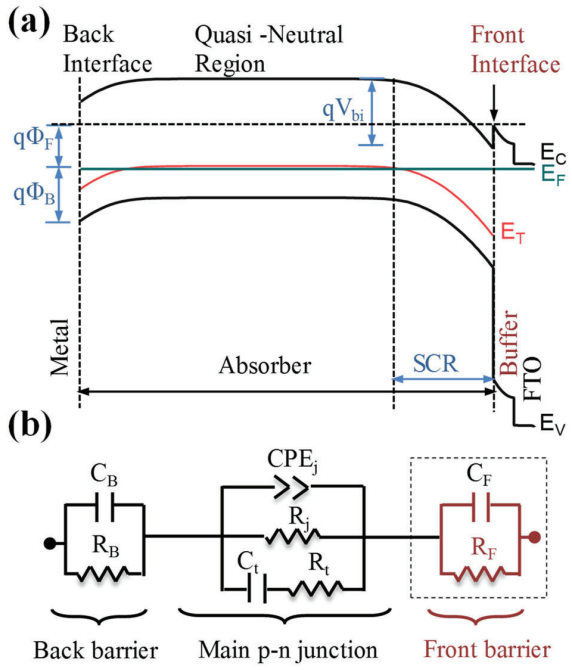


FIGURE 1 (A) Schematic sketch of the energy band diagram of metal/CdTe/buffer solar cell shows back contact, $q\Phi_B$, and front, $q\Phi_F$, barriers in dark equalibrium and V_{DC} = 0 V. (B) The equivalent circuit model that is used to fit the complex capacitance Nyquist plots of CdTe devices, with the elements R, C, and CPE_j representing the resistance, capacitance, and constant phase element, respectively, with three subcircuits connected in series due to the back (subscript B), front (subscript F) interfaces, and the p-n junction and the bulk material (subscripts j and t, respectively) [Colour figure can be viewed at wileyonlinelibrary.com]

3.2 | Front and back interface barriers

The back and front barrier heights can be calculated using the fitted back (R_B) and front (R_F) contact resistances at various temperatures using the two-subcircuit (Figure S2) and three-subcircuit (Figure 2) models for CdS/CdTe and ZMO/CdTe devices, respectively, using Arrhenius plots and applying the following equation[19]:

$$R_{B/F} = \frac{B_0}{T^2} exp \frac{q\phi_{B/F}}{k_B T} \quad (1)$$

where B_0 is a pre-exponential factor independent of temperature. From the Arrhenius plots illustrated in Figure 2A,B, we notice that for both CdS/CdTe and ZMO/CdTe devices, the back barrier height, $q\Phi_B$, of the device with oxygen-free $CdCl_2$ treatment (0.431 ± 0.052 eV for CdS/CdTe cell and 0.335 ± 0.042 eV for ZMO/CdTe) is smaller by ≥ 24% than the corresponding device with air $CdCl_2$ treatment

Approved for public release; distribution unlimited.

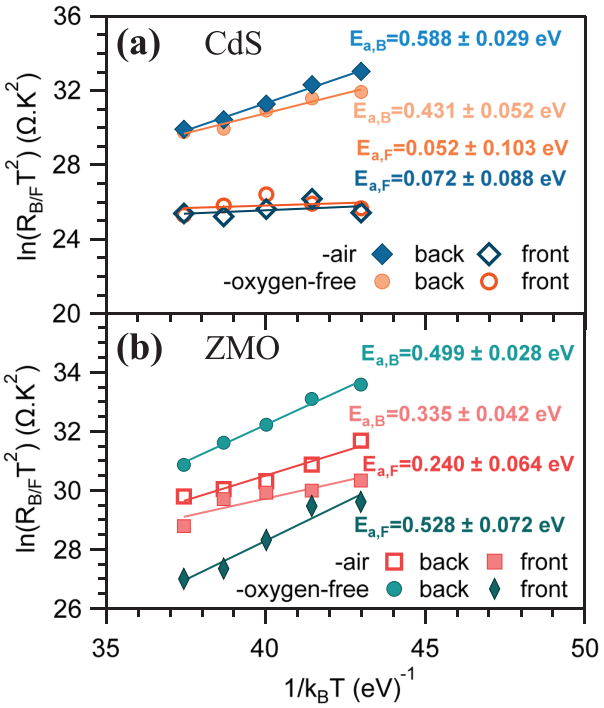


FIGURE 2 Arrhenius plots $\ln(R_{B/F}T^2)$ vs $1/k_BT$, to calculate the barrier heights from the fitted resitance at both back and front interfaces in (A) CdS/CdTe and (B) ZMO/CdTe devices fabricated in different atmosphere [Colour figure can be viewed at wileyonlinelibrary.com]

(0.588 ± 0.029 eV for CdS/CdTe cell and 0.499 ± 0.028 eV for ZMO/CdTe cell). The extracted back barrier heights are in good agreement with those obtained from J-V-T curves (Figure S3). Similar values were found previously[17,20] in CdTe devices with back surface treatment.

The front barriers, $q\Phi_F$, in ZMO/CdTe devices are also calculated from the Arrhenius plots shown in Figure 2B. The calculated front barrier in ZMO/CdTe-air device, 0.528 ± 0.072 eV, is higher than that in the ZMO/CdTe-oxygen-free device, 0.240 ± 0.064 eV. These results are in good agreement with our previous SCAPS simulations.[9] We have also used the three-subcircuit model to fit the capacitance spectra of CdS/CdTe devices and calculated the front barrier heights. As shown in Figure 2A, the front barrier heights are negligible, and the fitting errors are large.

3.3 | Impedance spectroscopy analysis

In IS analysis, the relationship between the small perturbation voltage (V_{AC}) and the corresponding current flowing (I_{AC}) is defined by a sinusoidal perturbation at angular frequency (ω) with an impedance of $Z(\omega) = V_{AC}/I_{AC}$. It has a complex quantity, $Z(\omega) = Re(Z) + i\,Im(Z)$, where Re(Z) and Im(Z) are the real and imaginary parts of impedance, respectively, and $i = \sqrt{-1}$. The complex capacitance (C(ω)) is a form of impedance, $C(\omega) = Re(C) - i\,Im(C) = 1/i\omega Z(\omega)$. As shown in Figure 1B, a constant phase element (CPE_j) is introduced in the main junction[19] to account for the imperfect dielectrics of absorber materials.[20] The layer thickness, dielectric constant, geometrical capacitance (C_g),[21] graded carrier distribution, and surface roughness[22] can influence the value of CPE_j. The impedance of CPE_j (Z_{CPE}) can be described by the following equation[23]:

$$Z_{CPE} = \frac{1}{CPE_j(i\omega)^{\alpha}} \quad (2)$$

where ω, 2πF, is the angular frequency, and CPE_j represents a pure capacitance if α = 1 and a pure resistance if α = 0.[24] Figure 3A shows the obtained CPE_j via impedance spectroscopy analysis for CdS/CdTe and ZMO/CdTe solar cell devices processed in different atmospheres. Figure 3B shows that the exponent α increases at low temperature and varies between 0.7 and 0.9, indicating that the CPE_j tends to behave as a capacitance at lower temperatures, when the absorber becomes fully depleted. Similar behavior was observed in literature.[19] At α = 1, the geometrical capacitance can be estimated directly from $C_g = CPE_j$. The dependence of α on temperatures has been reported in literature before.[19,25] The exponent α of the ZMO/CdTe-oxygen-free device is higher than that of the ZMO/CdTe-air device at a given temperature. In general, the values of α of the ZMO/CdTe devices are

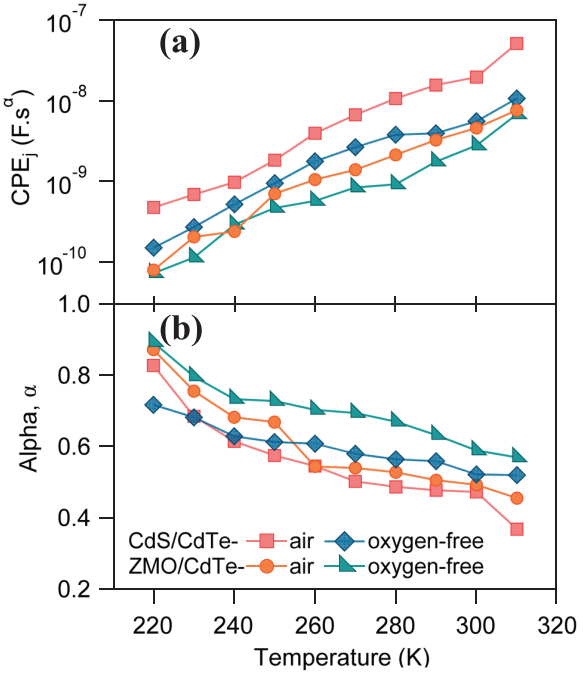


FIGURE 3 The temperature dependence of the fitted (A) constant phase elements, CPE_j, and (B) its exponent, α, of the front junctions of the CdS/CdTe-air, CdS/CdTe-oxygen-free, ZMO/CdTe-air, and ZMO/CdTe-oxygen-free solar cell devices [Colour figure can be viewed at wileyonlinelibrary.com]

Approved for public release; distribution unlimited.

higher than that of the CdS/CdTe devices, indicating different frequency dependencies of the main junction capacitances.

The bulk conductivity (σ) has been calculated using the fitted junction resistance (R_j) by using the relation of $\sigma = t/AR_j$, where t and A are the absorber thickness and active area. The observed temperature-dependent conductivity behavior of CdTe layers has been reported previously in literature.[26,27] Both CdS/CdTe-air and CdS/CdTe-oxygen-free devices have higher conductivity than ZMO/CdTe-air and ZMO/CdTe-oxygen-free devices, respectively, as shown in Figure 4A. Figure 4B shows the activation energies of conductivity ($E_{a,\sigma}$) calculated from the fitted front junction resistances shown in Figure 4A. The results show that the CdTe film deposited on ZMO buffer with $CdCl_2$ treatment in air has the highest barrier height for Cu diffusion.

3.4 | Admittance spectroscopy measurements

We now describe our results of energy levels and densities of defects at interface and in CdTe absorber. In AS measurements, it is required to apply an AC modulation voltage to charge and discharge the defects, and the measurements are usually done in dark and under zero or reverse bias voltages.[28] Only those defects (red solid line in Figure 1A) that intersect with the Fermi level (E_F) (green solid line in Figure 1A) in the depletion region can be detected. Figure S4 shows the capacitance dependence on frequency and temperature for these devices under equilibrium conditions (dark and V_{DC} = 0 V). Figure 5 shows their corresponding derivatives of capacitance spectra in the form of −FdC/dF for four different devices. Obviously, there are two kinds of peaks for each device due to the inflection points in the capacitance frequency spectra. These transition peaks shift to higher frequency as temperature increased because of the faster thermal emission rate.[29]

Figure S5 shows the Arrhenius plots of the transition frequency (ln(ω_{peak}/T^2)) versus the reciprocal of temperature. The thermal activation energy can be calculated by the following equation[30]:

$$\omega_{peak} = A_0 T^2 \exp\left[-\frac{E_a}{k_B T}\right] \quad (3)$$

where ω_{peak} is the characteristic transition frequency, A_0 is a pre-exponential factor independent of temperature, and E_a is the activation energy of the signature seen in capacitance spectra calculated by repeating the AS measurements under various DC biases.

The characteristic activation energy is calculated from fitting the curves of Arrhenius plot, Figure S5, by using Equation (3). The activation energy extracted from C-F spectra at temperature varies between 150 and 210 K (labeled E_{a1}) and is most likely related to H2-type (hole trap) defects and their ionization by hole emission over the back-contact potential barrier,[12,26,31-33] as confirmed by bias-dependent AS measurements showing that E_{a1} is altered by bias voltage (Figure 6A). Note that the E_{a1} values determined by AS are in good agreement with the barrier heights calculated from IS analysis and J-V-T curves (Figure S3).[26,34] For both CdS/CdTe and ZMO/CdTe devices, the back barrier height is > 20% lower for $CdCl_2$ treatment in oxygen-free atmosphere (0.319 ± 0.006 eV and 0.398 ± 0.016 eV, respectively) than in air (0.481 ± 0.012 eV and 0.476 ± 0.026 eV, respectively). The calculated values are shown in Table 1. The back contact at the CdTe/Au interface is the same for both CdS and ZMO devices when the $CdCl_2$ treatment processed in the same atmosphere. The back barrier is responsible for the rollover appearing at forward bias voltage in the J-V curves and is due to work function mismatch between CdTe and the metal[35] or impurities on the back surface such as oxides and chlorides formed during the $CdCl_2$ treatment in air. We summarized the results of the calculated back barrier heights in Table 1 measured by different measurements/analysis techniques for CdS/CdTe and ZMO/CdTe solar cell devices fabricated in different atmospheres. Note that an excellent consistency is observed with barrier heights calculated from different techniques, IS, AS, and J-V-T. However, using an inappropriate equivalent circuit model, e.g., using the three-subcircuit model for CdS/CdTe and two-subcircuit model for ZMO/CdTe devices, results in overestimation of the barrier by the IS method as compared with the barrier heights (underlined) calculated using AS and J-V-T, as shown in Table 1.

The AS signatures of all CdS/CdTe and ZMO/CdTe devices calculated from C-F spectra with temperatures > 230 K have an activation energy labeled with E_{a2}, which is independent on bias voltage (Figure 6B), suggesting that these charged defects are located in the

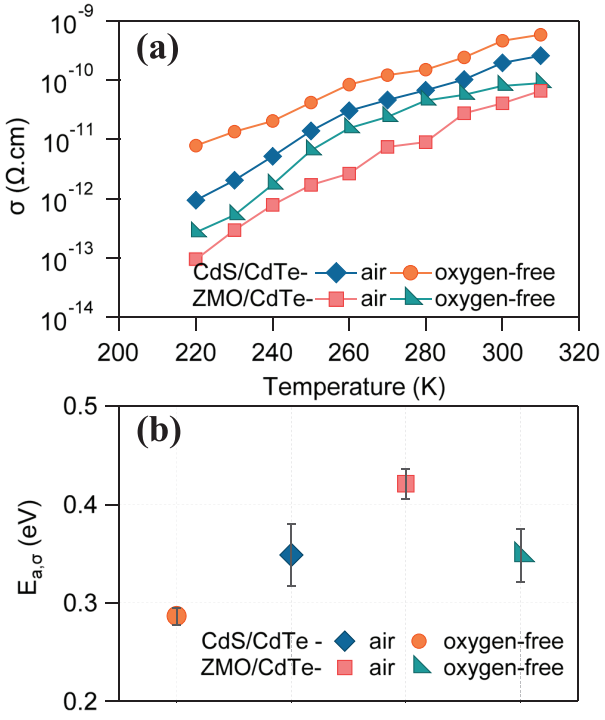


FIGURE 4 The temperature dependence of (A) the bulk conductivity and (B) its activation energy calculated from the fitted front junction resistance of the CdS/CdTe-air, CdS/CdTe-oxygen-free, ZMO/CdTe-air, and ZMO-/CdTe-oxygen-free solar cell devices [Colour figure can be viewed at wileyonlinelibrary.com]

Approved for public release; distribution unlimited.

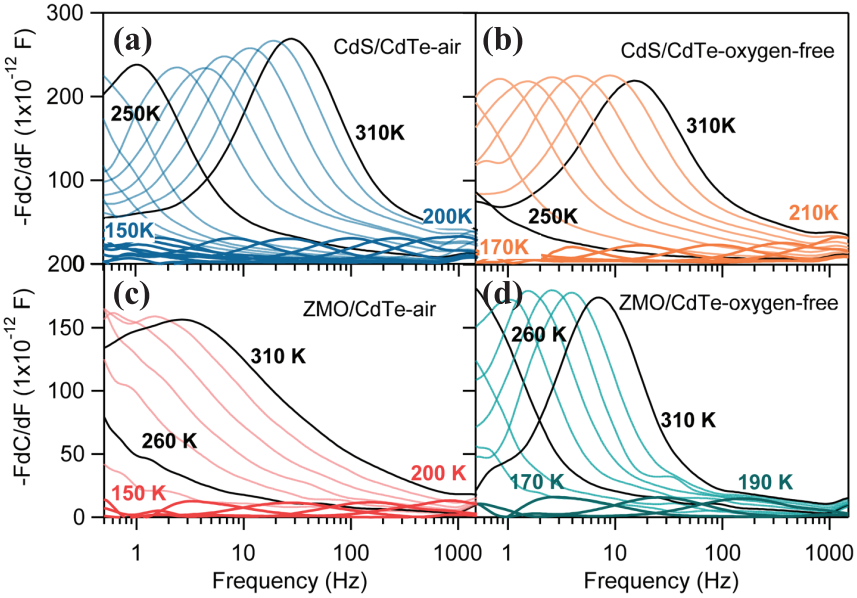


FIGURE 5 Differential capacitance spectra (−FdC/dF) at dark equilibrium (V_{DC} = 0 V) and different temperatures, extracted from the capacitance spectra in Figure S4, for CdS (A) - air, (B) -oxygen-free, ZMO (C) -air, and (D) -oxygen-free devices [Colour figure can be viewed at wileyonlinelibrary.com]

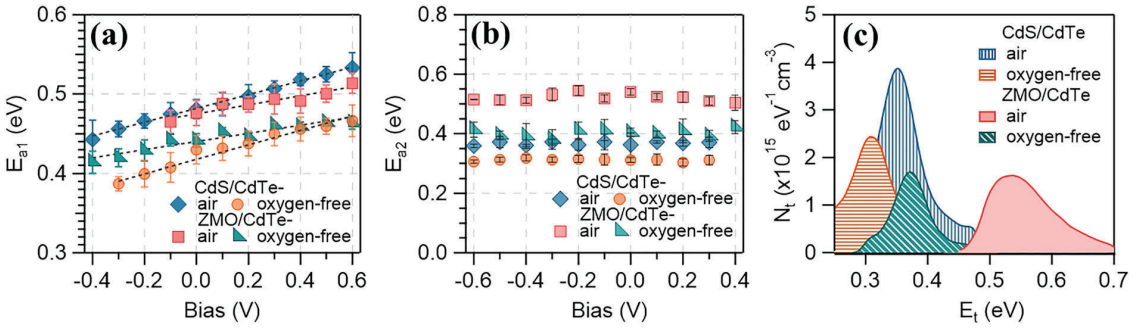


FIGURE 6 Defect activation energies (A) E_{a1} and (B) E_{a2} as a function of DC bias voltage. (C) Density of defect distribution for CdS and ZMO-air and -oxygen-free solar cell devices fabricated [Colour figure can be viewed at wileyonlinelibrary.com]

TABLE 1 Summarized the results of the calculated back barrier height by different methods for CdTe solar cell devices fabricated with different buffer materials and atmosphere

	Back Barrier Height, eV			
Devices	[a]IS Using Two-Subcircuit Model	[a]IS Using Three-Subcircuit Model	[a]AS	Dark J-V-T
CdS-air	0.502 ± 0.028	0.588 ± 0.029	0.481 ± 0.012	0.450 ± 0.004
CdS-oxygen-free	0.381 ± 0.013	0.431 ± 0.052	0. 319 ± 0.006	0.357 ± 0.012
ZMO-air (S-Kink)	0.623 ± 0.019	0.499 ± 0.028	0.476 ± 0.026	0.496 ± 0.013
ZMO-oxygen-free	0.483 ± 0.025	0.335 ± 0.042	0.398 ± 0.016	0.379 ± 0.005

[a]The calculated barrier heights are extracted from capacitance spectra measured in dark equilibrium.

bulk of the CdTe absorber. This signature is consistent with that observed in Cu-free devices reported by Seymour et al,[36] which is attributed to acceptor defects of V_{Cd}-Cl_{Te}, V_{Cd}-V_{Te}, or Cu_{Cd}-V_{Te} complexes.[37,38] The defect distributions, shown in Figure 5C, were calculated to understand the trend in defect density of states (N_t) using the following equation[39]:

Approved for public release; distribution unlimited.

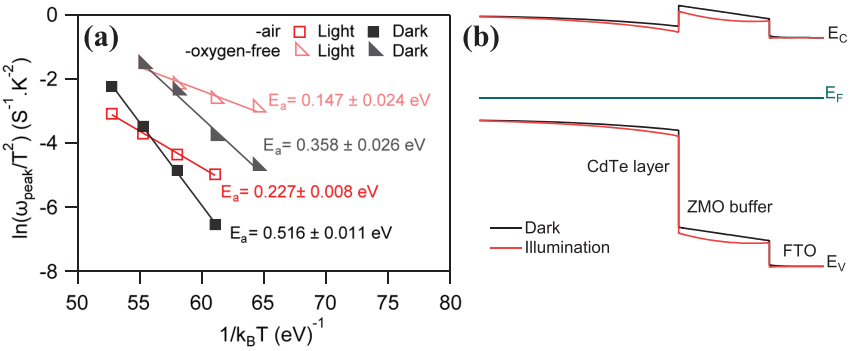


FIGURE 7 (A) Arrhenius plots, ln (ω_{peak}/T^2) vs $1/k_BT$, that is used to calculate the activation energy of capacitance spectra signatures measured at $V_{DC} > V_{OC}$ under dark and 0.1 Sun illumination for ZMO/CdTe solar cell devices fabricated in air and oxygen-free atmosphere. (B) Schematic sketches of the energy band diagrams of a CdTe/ZMO solar cell in dark and under illumination [Colour figure can be viewed at wileyonlinelibrary.com]

$$N_t = \frac{V_{bi}}{qWk_BT}\frac{1}{\left[-\omega\frac{dC}{d\omega}\right]} \quad (4)$$

where k_B is the Boltzmann constant, V_{bi} the built-in potential, and W the depletion width that are extracted from the C-V measurements using Mott-Schottky analysis. The energy of the defect distribution (E_t) was calculated by the following equation[39]:

$$E_t = E_a - k_BT\ln\left[\frac{2v_0}{\omega}\right] \quad (5)$$

where v_0 is a pre-exponential factor independent of temperature and E_a the activation energy calculated from Equation (3) and the Arrhenius plot in Figure S5.

Replacing CdS by ZMO buffer layer resulted in deeper defect levels and lower concentrations, which may be due to the variation of surface morphology and the smaller grains. We found that the bulk defect activation energy in CdS/CdTe-oxygen-free device, 0.311 ± 0.010 eV, is lower than that in CdS/CdTe-air device, 0.362 ± 0.009 eV. Similar trend is also observed in ZMO/CdTe solar cell devices. The defect state is located at 0.540 ± 0.011 and 0.372 ± 0.016 eV in ZMO/CdTe-air and ZMO/CdTe-oxygen-free devices, respectively. It has been proposed that $CdCl_2$ treatment in air[40,41] may passivate the GBs[42] and allow oxygen to diffuse through CdTe bulk reaching the main junction. The treatment in oxygen-free atmosphere may form an acceptor-like defects in CdTe and change the crystallinity of CdTe,[16-19] resulting in a deeper defect state with higher concentration. However, our results show that in devices with $CdCl_2$ treatment in oxygen-free atmosphere, the defect level shifts toward the valance band and with lower density of trap states, as shown in Figure 6C. This could be due to Cu diffusion through the CdTe bulk layer that can also passivate some defects and increase the conductivity.[43]

In order to detect a possible capacitance signature in the near interface defect states in the absorber or at the interface,[28,34] AS is performed in dark and at low temperatures by applying larger V_{DC} (0.6 - 1.0 V) to achieve the flat band conditions. At equilibrium conditions (V_{DC} = 0 V), negative, and small forward bias voltages, both CdS/CdTe and ZMO/CdTe devices show two capacitance signatures, as mentioned early in Figures 4 and 5, which are due to the back barrier height and the bulk defect states. The back barrier capacitance signature (Figure 5A) disappeared at V_{DC} = 0.6 V for CdS/CdTe devices and V_{DC} = 0.4 V for ZMO/CdTe devices. While the capacitance signature due to the bulk disappears at 0.3 and 0.4 V for CdS/CdTe and ZMO/CdTe device, respectively. However, at larger forward bias voltages ($V_{DC} > V_{OC}$), an additional capacitance step starts to show up in the ZMO/CdTe solar cell. Figure S6 shows the capacitance spectra in dark and light under forward bias conditions of ZMO/CdTe-air and ZMO/CdTe-oxygen-free solar cell devices. This capacitance step is light dependent. The activation energies are calculated using Arrhenius plots shown in Figure 7A. The calculated activation energy of this capacitance step in dark conditions is higher for ZMO/CdTe- air devices (0.516 ± 0.011 eV) than for the ZMO/CdTe-oxygen-free devices (0.358 ± 0.026 eV). The activation energy decreases under illumination to 0.227 ± 0.008 eV and 0.147 ± 0.024 eV for ZMO-air and ZMO/CdTe-oxygen-free devices, respectively. We interpret these activation energies as front interface barriers. When $CdCl_2$ treatment is performed in air, oxygen may diffuse through CdTe GBs to the ZMO layer and reduce the density of free electrons created by oxygen vacancies.[44] Therefore, the electron density of ZMO is higher in ZMO/CdTe-oxygen-free device than that in ZMO/CdTe-air device. As a result, the front barrier height is higher in ZMO/CdTe- air device than in ZMO/CdTe-oxygen-free device. However, under illumination, the conductivity of ZMO can be significantly enhanced due to the high photoconductivity of ZMO. Therefore, barrier height is reduced in both ZMO/CdTe-oxygen-free and ZMO/CdTe-air devices, as depicted in Figure 7B.

4 | CONCLUSIONS

We have characterized the electrical properties of CdS/CdTe an ZMO/CdTe thin film solar cells with $CdCl_2$ treatment in air and oxygen-free atmospheres. Bias-dependent AS measurements confirm that the devices with CdS buffer do not show a capacitance step related to the front interface. The devices with ZMO buffer exhibit a

Approved for public release; distribution unlimited.

front barrier of 0.528 eV when the $CdCl_2$ treatment was carried out in air and one of 0.240 eV when the $CdCl_2$ treatment was conducted in oxygen-free atmosphere. From the impedance spectroscopy analysis, we found that an additional subcircuit is required to better fit the capacitance spectra of the ZMO/CdTe devices. The barrier heights calculated using the equivalent circuit model are consistent with that obtained from AS results. ZMO/CdTe cells fabricated with $CdCl_2$ treatment in air showed a higher front junction barrier, possibly due to oxygen diffusion to ZMO layer through CdTe GBs.

ACKNOWLEDGEMENTS

This material is based on research sponsored by Air Force Research Laboratory under agreement number FA9453-18-2-0037. The US Government is authorized to reproduce and distribute reprints for Governmental purposes notwithstanding any copyright notation thereon. This work is also supported by the National Science Foundation under contract no. 1711534 and the US Department of Energy's Office of Energy Efficiency and Renewable Energy (EERE) under Solar Energy Technologies Office (SETO) Agreement Number DE-EE0007541. R.A. Awni was financially supported by the Higher Committee for Education Development (HCED) in the scholarship program started in 2009 with funding from the Iraqi Prime Minister's Office. J. V. Li is supported by the Ministry of Science and Technology, Taiwan, under grant number MOST 107-2218-E-006-022-MY3. We thank Dr David Strickler from Pilkington North America Inc. for supplying us FTO-coated substrates. The views and conclusions contained herein are those of the authors and should not be interpreted as necessarily representing the official policies or endorsements, either expressed or implied, of Air Force Research Laboratory or the US Government.

ORCID

Rasha A. Awni https://orcid.org/0000-0002-5971-0934
Deng-Bing Li https://orcid.org/0000-0003-4555-4894
Zhaoning Song https://orcid.org/0000-0002-6677-0994
Sandip S. Bista https://orcid.org/0000-0003-0162-8468
Mohammed A. Razooqi https://orcid.org/0000-0001-5567-5927
Corey R. Grice https://orcid.org/0000-0002-0841-5943
Lei Chen https://orcid.org/0000-0003-2206-9140
Geethika K. Liyanage https://orcid.org/0000-0003-4000-0729
Chongwen Li https://orcid.org/0000-0001-8514-190X
Adam B. Phillips https://orcid.org/0000-0002-2675-5052
Michael J. Heben https://orcid.org/0000-0002-3788-3471
Randy J. Ellingson https://orcid.org/0000-0001-9520-6586
Jian V. Li https://orcid.org/0000-0003-3623-3044
Yanfa Yan https://orcid.org/0000-0003-3977-5789

REFERENCES

1. NREL. Best research-cell efficiency chart. In: NREL; 2018.
2. Kephart JM, McCamy JW, Ma Z, Ganjoo A, Alamgir FM, Sampath WS. Band alignment of front contact layers for high-efficiency CdTe solar cells. *Sol Energy Mater Sol Cells*. 2016;157:266-275.
3. Song T, Kanevce A, Sites JR. Emitter/absorber interface of CdTe solar cells. *J Appl Phys*. 2016;119(23):233104.
4. Chen Y, Tan X, Peng S, et al. The influence of conduction band offset on CdTe solar cells. *J Electron Mater*. 2018;47(2):1201-1207.
5. Liyanage GK, Phillips AB, Alfadhili FK, Heben MJ. Numerical modelling of front contact alignment for high efficiency $Cd_{1-x}Zn_xTe$ and $Cd_{1-x}Mg_xTe$ solar cells for tandem devices. *MRS Advances*. 2018;3(52):3121-3128.
6. Sites J, Munshi A, Kephart J, Swanson D, Sampath WS. Progress and challenges with CdTe cell efficiency. Paper presented at: 2016 IEEE 43rd Photovoltaic Specialists Conference (PVSC); 5-10 June 2016, 2016.
7. Kaur K, Kumar N, Kumar M. Strategic review of interface carrier recombination in earth abundant Cu–Zn–Sn–S–Se solar cells: current challenges and future prospects. *J Mater Chem A*. 2017;5(7):3069-3090.
8. Munshi A, Kephart J, Abbas A, et al. Polycrystalline CdTe photovoltaics with efficiency over 18% through improved absorber passivation and current collection. *Sol Energy Mater Sol Cells*. 2018;176:9-18.
9. Li D-B, Song Z, Awni RA, et al. Eliminating S-Kink to maximize the performance of MgZnO/CdTe solar cells. *ACS App Energy Mater*. 2019.
10. McCandless BE, Hegedus SS, Birkmire RW, Cunningham D. Correlation of surface phases with electrical behavior in thin-film CdTe devices. *Thin Solid Films*. 2003;431-432:249-256.
11. Bisquert J. *Nanostructured Energy Devices: Foundations of Carrier Transport*. 1st edition ed. Boca Raton, FL, USA: CRC Press; 2017.
12. Li JV, Johnston SW, Li X, Albin D, Gessert T, Levi D. Discussion of some "trap signatures" observed by admittance spectroscopy in CdTe thin-film solar cells. *J Appl Phys*. 2010;108(6):064501-064501.
13. Li JV, Halverson AF, Sulima OV, et al. Theoretical analysis of effects of deep level, back contact, and absorber thickness on capacitance–voltage profiling of CdTe thin-film solar cells. *Sol Energ Mat Sol Cell*. 2012;100:126-131.
14. Ren S, Wang H, Li Y, et al. Rapid thermal annealing on ZnMgO window layer for improved performance of CdTe solar cells. *Sol Energy Mater Sol Cells*. 2018;187:97-103.
15. Grice CR, Paudel NR, Xiao C, Yan Y. Effect of deposition temperature on reactively sputtered CdS:O. Paper presented at: 2014 IEEE 40th Photovoltaic Specialist Conference (PVSC); 8-13 June 2014, 2014.
16. Niemegeers A, Burgelman M. Effects of the Au/CdTe back contact on IV and CV characteristics of Au/CdTe/CdS/TCO solar cells. *J Appl Phys*. 1997;81(6):2881-2886.
17. Awni RA, Li D-B, Grice CR, et al. The effects of hydrogen iodide back surface treatment on CdTe solar cells. *Solar RRL*. 2019;3(3):1800304.
18. Nicollian EH, Goetzberger A. MOS conductance technique for measuring surface state parameters. *Appl Phys Lett*. 1965;7(8):216-219.
19. Proskuryakov YY, Durose K, Taele BM, Oelting S. Impedance spectroscopy of unetched CdTe/CdS solar cells—equivalent circuit analysis. *J Appl Phys*. 2007;102(2):024504.
20. Proskuryakov YY, Durose K, Al Turkestani MK, et al. Impedance spectroscopy of thin-film CdTe/CdS solar cells under varied illumination. *J Appl Phys*. 2009;106(4):044507.
21. Mark E, Orazem IF, Tribollet B, et al. Dielectric properties of materials showing constant-phase-element (CPE) impedance response. *J Electrochem Soc*. 2013;160(6):C215-C225.
22. Córdoba-Torres P, Mesquita TJ, Nogueira RP. Relationship between the origin of constant-phase element behavior in electrochemical impedance spectroscopy and electrode surface structure. *J Phys Chem C*. 2015;119(8):4136-4147.

Approved for public release; distribution unlimited.

23. Bisquert J, Garcia-Belmonte G, Bueno P, Longo E, Bulhões LOS. Impedance of constant phase element (CPE)-blocked diffusion in film electrodes. *J Electroanal Chem*. 1998;452(2):229-234.
24. Marin AT, Musselman KP, MacManus-Driscoll JL. Accurate determination of interface trap state parameters by admittance spectroscopy in the presence of a Schottky barrier contact: Application to ZnO-based solar cells. *J Appl Phys*. 2013;113(14):144502.
25. Major JD, Proskuryakov YY, Durose K. Impact of CdTe surface composition on doping and device performance in close space sublimation deposited CdTe solar cells. *Prog Photovolt*. 2013;21(4):436-443.
26. Li JV, Crandall RS, Repins IL, Nardes AM, Levi DH. Applications of admittance spectroscopy in photovoltaic devices beyond majority-carrier trapping defects. Paper presented at: 2011 37th IEEE Photovoltaic Specialists Conference; 19-24 June 2011, 2011.
27. Li JV, Nardes AM, Liang Z, Shaheen SE, Gregg BA, Levi DH. Simultaneous measurement of carrier density and mobility of organic semiconductors using capacitance techniques. *Org Electron*. 2011;12(11):1879-1885.
28. Weiss TP, Nishiwaki S, Bissig B, Buecheler S, Tiwari AN. Voltage dependent admittance spectroscopy for the detection of near interface defect states for thin film solar cells. *PCCP*. 2017;19(45):30410-30417.
29. Kubiaczyk A, Nawrocka M, Igalson M. Admittance measurements on CIGS solar cells. *Opto-Electron Rev*. 2000;8:378-381.
30. Koeper MJ, Hages CJ, Li JV, Levi D, Agrawal R. Metastable defect response in CZTSSe from admittance spectroscopy. *Appl Phys Lett*. 2017;111(14):142105.
31. Eisenbarth T, Unold T, Caballero R, Kaufmann CA, Schock H-W. Interpretation of admittance, capacitance-voltage, and current-voltage signatures in Cu (In,Ga)Se_2 thin film solar cells. *J Appl Phys*. 2010;107(3):034509.
32. Kharangarh PR, Misra D, Georgiou GE, Chin KK. Characterization of space charge layer deep defects in n^+-CdS/p-CdTe solar cells by temperature dependent capacitance spectroscopy. *J Appl Phys*. 2013;113(14):144504.
33. Versluys J, Clauws P, Nollet P, Degrave S, Burgelman M. DLTS and admittance measurements on CdS/CdTe solar cells. *Thin Solid Films*. 2003;431-432:148-152.
34. Decock K, Khelifi S, Buecheler S, Pianezzi F, Tiwari AN, Burgelman M. Defect distributions in thin film solar cells deduced from admittance measurements under different bias voltages. *J Appl Phys*. 2011;110(6):063722.
35. Burgelman M, Nollet P, Degrave S. Modelling polycrystalline semiconductor solar cells. *Thin Solid Films*. 2000;361-362:527-532.
36. Seymour FH, Kaydanov V, Ohno TR, Albin D. Cu and $CdCl_2$ influence on defects detected in CdTe solar cells with admittance spectroscopy. *Appl Phys Lett*. 2005;87(15):153507.
37. Castaldini A, Cavallini A, Fraboni B, Fernandez P, Piqueras J. Comparison of electrical and luminescence data for the A center in CdTe. *Appl Phys Lett*. 1996;69(23):3510-3512.
38. Beach J, Seymour FH, Kaydanov VI, Ohno TR. *Studies of Basic Electronic Properties of CdTe-Based Solar Cells and Their Evolution During Processing and Stress*. Golden, CO (United States): National Renewable Energy Lab. (NREL); 2007 NREL/SR-520-41097.
39. Li JV, Levi DH. Determining the defect density of states by temperature derivative admittance spectroscopy. *J Appl Phys*. 2011;109(8):083701.
40. Paudel NR, Grice CR, Xiao C, Yan Y. High temperature CSS processed CdTe solar cells on commercial SnO2:F/SnO_2 coated soda-lime glass substrates. *J Mater Sci-mater El*. 2015;26(7):4708-4715.
41. Paudel NR, Yan Y. Fabrication and characterization of high-efficiency CdTe-based thin-film solar cells on commercial SnO_2:F-coated soda-lime glass substrates. *Thin Solid Films*. 2013;549:30-35.
42. Li C, Wu Y, Poplawsky J, et al. Grain-boundary-enhanced carrier collection in CdTe solar cells. *Phys Rev Lett*. 2014;112(15):156103.
43. Proskuryakov YY, Durose K, Taele B, Welch GP, Oelting S. Admittance spectroscopy of CdTe/CdS solar cells subjected to varied nitric-phosphoric etching conditions. *J Appl Phys*. 2007;101(1):014505.
44. Terheggen M, Heinrich H, Kostorz G, et al. Structural and chemical interface characterization of CdTe solar cells by transmission electron microscopy. *Thin Solid Films*. 2003;431-432:262-266.

SUPPORTING INFORMATION

Additional supporting information may be found online in the Supporting Information section at the end of the article.

How to cite this article: Awni RA, Li D-B, Song Z, et al. Influences of buffer material and fabrication atmosphere on the electrical properties of CdTe solar cells. *Prog Photovolt Res Appl*. 2019;27:1115–1123. https://doi.org/10.1002/pip.3192

Approved for public release; distribution unlimited.

The Journal of Chemical Physics ARTICLE scitation.org/journal/jcp

Effects of intrinsic and atmospherically induced defects in narrow bandgap $(FASnI_3)_x(MAPbI_3)_{1-x}$ perovskite films and solar cells

Cite as: J. Chem. Phys. 152, 064705 (2020); doi: 10.1063/1.5126867
Submitted: 6 September 2019 • Accepted: 19 January 2020 •
Published Online: 10 February 2020

View Online Export Citation CrossMark

Biwas Subedi, Chongwen Li, Maxwell M. Junda, Zhaoning Song, Yanfa Yan, and Nikolas J. Podraza[a)]

AFFILIATIONS

Department of Physics and Astronomy and The Wright Center for Photovoltaics Innovation and Commercialization, University of Toledo, Toledo, Ohio 43606, USA

Note: This paper is part of the JCP Special Topic on Lead Halide Perovskites.
[a)]**Author to whom correspondence should be addressed:** nikolas.podraza@utoledo.edu

ABSTRACT

Narrow bandgap mixed tin (Sn) + lead (Pb) perovskites are necessary for the bottom sub-cell absorber in high efficiency all-perovskite polycrystalline tandem solar cells. We report on the impact of mixed cation composition and atmospheric exposure of perovskite films on sub-gap absorption in films and performance of solar cells based on narrow bandgap mixed formamidinium (FA) + methylammonium (MA) and Sn + Pb halide perovskites, $(FASnI_3)_x(MAPbI_3)_{1-x}$. Structural and optical properties of $0.3 \le x \le 0.8$ $(FASnI_3)_x(MAPbI_3)_{1-x}$ perovskite thin film absorbers with bandgaps ranging from 1.25 eV ($x = 0.6$) to 1.34 eV ($x = 0.3$) are probed with and without atmospheric exposure. Urbach energy, which quantifies the amount of sub-gap absorption, is tracked for pristine perovskite films as a function of composition, with $x = 0.6$ and 0.3 demonstrating the lowest and highest Urbach energies of 23 meV and 36 meV, respectively. Films with $x = 0.5$ and 0.6 compositions show less degradation upon atmospheric exposure than higher or lower Sn-content films having greater sub-gap absorption. The corresponding solar cells based on the $x = 0.6$ absorber show the highest device performance. Despite having a low Urbach energy, higher Sn-content solar cells show reduced device performances as the amount of degradation via oxidation is the most substantial.

Published under license by AIP Publishing. https://doi.org/10.1063/1.5126867

INTRODUCTION

Organic–inorganic halide perovskite solar cells are receiving tremendous attention due to rapid increases in world record efficiencies from 3.8%[1] to 25.2%[2] from 2009 to present. Organic–inorganic halide perovskites ABX_3 (often, A: methylammonium—MA, formamidinium—FA, or cesium—Cs; B: lead—Pb or tin—Sn; and X: iodine—I, bromine—Br, or chlorine—Cl) serve as the absorber materials in these highly efficient solar cells. A plenitude of research in this material field exists, especially because of high photovoltaic (PV) device power conversion efficiency (PCE), potentially low material costs, low temperature solution processability, and bandgap (E_g) tunability. The latter two serve as the primary motivation for all-perovskite tandem solar cells[3–5] with the top sub-cell based on wide-E_g (1.7–1.9 eV)[6] perovskite absorbers and the bottom sub-cell based on narrow-E_g (1.1–1.3 eV)[7,8] perovskites for more effective use of the air mass (AM) 1.5 solar irradiance spectrum.[9] The wide-E_g top-cell absorber is typically $FA_{1-x}Cs_xPb(I_{1-y}Br_y)_3$ ($0 < x, y < 1$), which has achieved remarkable performance using different engineering methods.[10–13] For the narrow-E_g bottom-cell absorber, mixed FA + MA and Sn + Pb iodide perovskites still have opportunities for improvement in stability, morphology, and device performance. Mixed Sn + Pb perovskite absorbers have been reported to show E_g as low as 1.17 eV.[8] To fully absorb low energy photons in the bottom sub-cell, a greater than 1 μm thick narrow-E_g perovskite absorber layer is needed.[5] However, due to the presence of impurities and defect states, this relatively thick layer is more prone than thinner layers to non-radiative recombination losses through both the bulk and interfaces.[14] Therefore, preparation of a thick perovskite layer with high electronic quality and crystallinity has remained an issue for narrow-E_g mixed Sn + Pb perovskite solar cells. Recombination losses have been reduced via surface and

Published under license by AIP Publishing

Approved for public release; distribution unlimited.

bulk passivation[15,16] and increasing grain size and grain size uniformity.[4] Compared to $MAPbI_3$ or $FAPbI_3$, mixed FA + MA lead iodide perovskites show improved phase stability, crystallinity in terms of grain size and grain size uniformity, absorption properties, carrier lifetimes, and PV device performance.[10,12,17] As narrow-E_g perovskite absorbers require replacing a fraction of Pb with Sn, variations in crystallinity, stability, and optical properties result. Both ≤30% and ≥80% Sn-content mixed Sn + Pb perovskites show poorer crystallinity and hence lower device performances.[18] In addition, ≥80% Sn-content thin films show less stability against atmospheric exposure.[19] The possible oxidation of Sn^{2+} to Sn^{4+} occurring for higher Sn-content absorbers can increase p-type self-doping[8] and result in increased recombination and decreased carrier lifetime.[20,21] Previous studies have shown that narrow-E_g mixed Sn + Pb perovskite films with 50%–60% Sn-content show good crystallinity and device performance.[18,20,22]

All semiconductors including perovskites show tailing in the absorption spectra below E_g due to lattice vibrations, defects, and impurities contributing to the Urbach tail.[23–25] Here, the Urbach energy (E_u) quantifies this the tailing effect and its contribution to sub-gap absorption. The relation between absorption coefficient (α) and E_u is given by

$$\alpha(E) = \alpha_g e^{\frac{E-E_g}{E_u}}, \quad (1)$$

where α_g is the value of α at the photon energy of E_g. Higher values of E_u show higher sub-gap absorption and vice versa. Earlier studies on perovskite solar cells have shown that these sub-gap defects can act as Shockley–Read–Hall recombination centers in the bulk layer and have adverse effects on device performance parameters such as open circuit voltage (V_{OC}) and fill factor (FF).[26,27] In perovskite absorber layers, defects include grain boundaries, intrinsic point defects, and various complex phases forming from atmospheric exposure.[28–30] Similarly, in perovskite solar cells, defects are also formed at interfaces due to the interaction between the perovskite absorber and other device components.[14] Varying the cationic–anionic composition changes crystallinity, phase stability, charge transport, and optical properties. The amount of defect induced sub-gap absorption also depends upon cationic and anionic compositions. Ghimire *et al.* have used spectroscopic ellipsometry (SE) to study the variation in optical properties for $0 \le x \le 1$ $(FASnI_3)_x(MAPbI_3)_{1-x}$ perovskite thin films in terms of near infrared to ultraviolet (UV) complex dielectric function ($\varepsilon = \varepsilon_1 + i\varepsilon_2$) spectra.[31] To quantify defect-inducted sub-gap absorption in more detail in mixed Sn + Pb perovskites, photothermal deflection spectroscopy (PDS) has been used. However, these measurements show relatively high E_u from 33 meV to 48 meV[22] compared to that of $MAPbI_3$ and other crystalline semiconductors used in solar cells, $E_u \le 15$ meV.[32] As perovskite thin films are susceptible to degradation in ambient air, protecting films and devices against atmospheric exposure during preparation, handling, and measurement remain crucial. Recently, narrow-E_g $(FASnI_3)_{0.6}(MAPbI_{3-3x}Cl_{3x})_{0.4}$, and $x < 1$ $(FASnI_3)_{0.6}(MAPbI_{3-3x}Br_{3x})_{0.4}$ perovskite films have been characterized by a combination of PDS, SE, and unpolarized transmittance to understand and mitigate the possible effects of atmospheric exposure during handling and measurement.[4,16,33] These measurements yield E_u substantially lower than atmospherically exposed counterparts.[33] Here, we present a detailed study of the optical properties of narrow-E_g $(FASnI_3)_x(MAPbI_3)_{1-x}$ perovskite films using PDS and SE coupled with unpolarized transmittance. In particular, variations in defect induced sub-gap absorption and stability are compared for mixed Sn + Pb compositions. Perovskite solar cells based on these absorbers are fabricated, and links between the device performance parameters and perovskite optoelectronic qualities are established. The combination of both low E_u and the least change in sub-gap absorption upon exposure to ambient air observed in intermediate x $(FASnI_3)_x(MAPbI_3)_{1-x}$ films correlates with the highest solar cell device performance. Reduced performance in devices with high and low Sn-content x is attributed to high E_u, low perovskite stability, or both.

EXPERIMENTAL DETAILS

All perovskite thin films are fabricated in a nitrogen (N_2)-filled glove box to prevent exposure to ambient air. $(FASnI_3)_x(MAPbI_3)_{1-x}$ with $0.3 \le x \le 0.8$ compositions are obtained by controlling the ratio of $FASnI_3$ and $MAPbI_3$ precursor solutions. The preparation of the $FASnI_3$ precursor solution consists of dissolving 372 mg of SnI_2 (Sigma Aldrich) and 172 mg of FAI (GreatCell Solar) in 424 μl mixed *N*,*N*-dimethylmethanamide (DMF) (Sigma Aldrich, anhydrous) and 212 μl dimethyl sulfoxide (DMSO) (Sigma Aldrich, anhydrous). Similarly, the preparation of the $MAPbI_3$ precursor solution consists of dissolving 461 mg PbI_2 (Alfa Aesar) with 159 mg MAI (GreatCell Solar) in 630 μl DMF and 70 μl DMSO. The mixed precursor solutions are spin-coated on glass substrates at 5000 rpm for 60 s. Diethyl ether, as the anti-solvent, is dripped on to the spinning substrates after 5 s. To obtain the perovskite phase and most importantly to remove remaining solvents, the spin coated films are annealed at 100 °C for 7 min inside the glove box before transfer for optical characterization.

While transferring the samples for PDS measurements, films are loaded into a quartz cuvette containing inert C_6F_{14} fluid (3M Fluorinert FC-72, Synquest Laboratories) inside the N_2-purged glove box to prevent unwanted exposure to laboratory ambient air. C_6F_{14} is the thermally sensitive deflecting medium for PDS, which also protects perovskite films from atmospheric exposure during measurements lasting for 1–2 h. PDS is performed using a transverse configuration system[34] (PTS-3-PTD, Sciencetech Inc.) over a spectral range from 1100 nm to 800 nm (1.27–1.55 eV) for $x = 0.3$, 0.4, and 0.5 $(FASnI_3)_x(MAPbI_3)_{1-x}$ and from 1150 nm to 800 nm (1.08–1.46 eV) for $x = 0.6$, 0.7, and 0.8 $(FASnI_3)_x(MAPbI_3)_{1-x}$ in 10 nm spectral scanning steps. The pump beam in this system is a monochromatic beam modulated with a mechanical chopper at 0.5 Hz; a nominally 300 μm cross-section diameter 633 nm wavelength helium–neon laser acts a probe beam.

After PDS measurements are completed, each film is removed from C_6F_{14} for near infrared to UV (0.74–5.9 eV) SE and unpolarized transmittance measurements, which are collected using a single rotating compensator multichannel spectroscopic ellipsometer (M-2000FI, J.A. Woollam Co., Inc.). All films are exposed for 2–3 min in laboratory ambient air during data acquisition, with SE and unpolarized transmittance measurements collected at 70° and 0° angles of incidence, respectively. After unpolarized transmittance measurement, a frosted tape is applied to the backside of the glass to scatter light and suppress reflections from that interface.[35]

Published under license by AIP Publishing

Approved for public release; distribution unlimited.

Depolarization effects are minimal and not included in the fit of ellipsometric spectra due to the suppression of backside reflections and high film uniformity over the area of the measurement beam spot. The measurement beam spot diameter is 1 mm. Perovskite film thickness varies about 20 nm from the center to the edge of the 2.5 cm wide sample. The film thickness variation will be less than 1 nm over the measurement beam spot. Analysis of optical properties in the terms of spectra in α obtained from PDS, SE, and unpolarized transmittance provides information about the sub-gap absorption due to defects that reflect the structural and optoelectronic quality of perovskite thin films. For perovskite films, sensitivity to α values as low as 600 cm^{-1} using SE is obtained as reported in previous studies.[36] As unpolarized transmittance is more sensitive to weak absorption than SE, analysis of the two measurements is often combined to improve sensitivity in the weakly absorbing spectral range.[37,38] In addition, combined analysis of SE and transmittance measurements is performed to reduce potential correlations between structural parameters, such as layer thicknesses, and the complex optical response of thin films on transparent substrates.[39] For the perovskite thin films, analyzing SE with unpolarized transmittance together improves the sensitivity to a lower limit of α near 100 cm^{-1}.[33] Transmission measurements lose sensitivity at high values of α in the spectral range where the sample is optically opaque.[40,41] Here, all samples become optically opaque over 2 eV at which the α values are ~10^5 cm^{-1}. In the combined fitting of SE and unpolarized transmittance data, only the non-zero transmittance data up to 2 eV are included. For PDS, sensitivity in α from a lower limit of 10–100 cm^{-1} and to a higher limit of 3×10^4 cm^{-1} has been measured for films of similar thicknesses as our samples.[32,42]

Narrow-E_g perovskite solar cell devices are fabricated as previously described.[16] Poly(3,4-ethylenedioxythiophene)–poly (styrenesulfonate) (PEDOT:PSS) (50 nm) films are spin coated onto indium tin oxide (ITO) (150 nm) coated soda lime glass substrates at 4000 rpm for 50 s and annealed at 175 °C for 30 min. $(FASnI_3)_x(MAPbI_3)_{1-x}$ thin films are prepared as described in the beginning of this section. To complete the solar cell device structure, buckminsterfullerene (C_{60}) (20 nm)/bathocuproine (BCP) (5 nm)/silver (Ag) (75 nm) are sequentially deposited by thermal evaporation. In this solar cell configuration, ITO, PEDOT:PSS, $(FASnI_3)_x(MAPbI_3)_{1-x}$, C_{60}/BCP, and Ag act as the front contact, hole selective layer, absorber, electron selective layer, and back contact, respectively. Perovskite solar cell devices are encapsulated with cover glass using UV-curable epoxy before removal from the glove box for PV device performance characterization. Current–voltage (J–V) measurements are performed in ambient air under 100 mW/cm^2 AM 1.5 G solar irradiation (PV Measurements, Inc.) with a Keithley 2400 Source Meter. A standard silicon cell is used as a reference for J–V measurements.

RESULTS

Ellipsometric spectra ($N = \cos 2\Psi$, $C = \sin 2\Psi \cos\Delta$, and $S = \sin 2\Psi \sin\Delta$) are coupled with unpolarized transmittance spectra and simultaneously fitted to a parameterized optical and structural model to extract the complex optical response for the perovskite films in terms of spectra in ε. The structural model consists of a glass substrate/interfacial layer/perovskite film/surface roughness, where the optical response of both the interfacial and surface roughness layers are described by Bruggeman effective medium approximations[43] modeled with variable fractions of spectra in ε for the respective perovskite film and void ($\varepsilon = 1$). Structural parameters including perovskite film thicknesses, interfacial layer thicknesses, surface roughness layer thicknesses, and void fractions in both interfacial and surface roughness layers are determined using divided spectral range analysis[27,31,44] with results for each film in Table I. In divided spectral range analysis, the full measured spectral range for both SE and unpolarized transmittance spectra is divided into two different regions corresponding to photon energies above the bandgap (1.4–5.89 eV), where the films are highly absorbing and the relatively transparent region (0.73–1.1 eV) below the bandgap. In each region, physically valid parametric models for spectra in ε are applied. For the weakly absorbing 1.1–1.4 eV spectral range including the bandgap, absorption onset, and any sub-bandgap absorption, no line shape describing ε is assumed so as to not weight the fit with a potentially inaccurate choice of the parametric model. Spectra in ε are parameterized using a Sellmeier[45] expression and a constant additive term, $\varepsilon_{\infty,}$ for the transparent photon energy range (0.73–1.1 eV) below the bandgap, while spectra in ε for the highly absorbing photon energy range above the bandgap are parameterized by the sum of critical point parabolic band (CPPB) oscillators,[46] a Sellmeier expression, and a constant additive term, ε_∞. The common structural parameters for both regions are obtained using the least squares regression fit. The quality of the fit between the model and experimental ellipsometric spectra is defined in terms of the unweighted mean square error (MSE).[47] A low MSE is obtained for the divided spectral range model fit of each composition, as listed in Table I. For each film, the effective film thickness (d_0) is determined by combining the perovskite bulk film thicknesses with the

TABLE I. Spectroscopic ellipsometry determined structural fit parameters and quality of the fit for thin film $(FASnI_3)_x(MAPbI_3)_{1-x}$ perovskite samples.

$(FASnI_3)_x(MAPbI_3)_{1-x}$	$x = 0.3$	$x = 0.4$	$x = 0.5$	$x = 0.6$	$x = 0.7$	$x = 0.8$
Surface roughness (nm)	69 ± 3	90 ± 1	32 ± 1	48 ± 1	62 ± 1	83 ± 1
Surface roughness void fraction (%)	3.3 ± 0.1	3.5 ± 0.1	8.9 ± 0.3	11.1 ± 0.2	20.0 ± 0.1	13.1 ± 0.1
Film thickness (nm)	468 ± 3	436 ± 2	472 ± 9	502 ± 1	497 ± 3	385 ± 5
Interfacial layer (nm)	175 ± 1	224 ± 2	69 ± 7	109 ± 4	138 ± 1	200 ± 1
Interfacial layer void fraction (%)	39.1 ± 0.1	42.6 ± 0.1	6 ± 1	45 ± 1	28.3 ± 0.5	8.0 ± 0.1
Effective film thickness, d_0 (nm)	641 ± 7	651 ± 5	566 ± 17	605 ± 5	646 ± 5	641 ± 7
Mean square error (MSE)	5.7×10^{-3}	3.2×10^{-3}	3.2×10^{-3}	2.8×10^{-3}	3.3×10^{-3}	3.3×10^{-3}

Published under license by AIP Publishing

Approved for public release; distribution unlimited.

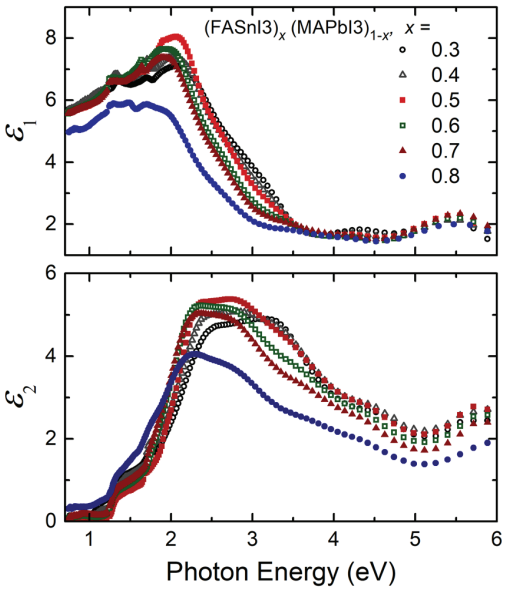


FIG. 1. Complex dielectric function ($\varepsilon = \varepsilon_1 + i\varepsilon_2$) spectra of $(FASnI_3)_x(MAPbI_3)_{1-x}$ ($0.3 \le x \le 0.8$) perovskite films.

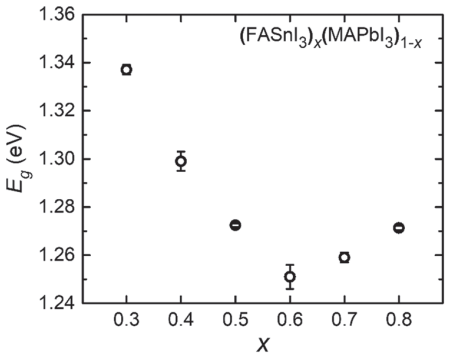


FIG. 3. Bandgap (E_g) as a function of composition for $(FASnI_3)_x(MAPbI_3)_{1-x}$ perovskite films.

interfacial layer and surface roughness layer thicknesses weighted by the perovskite material fraction in each layer, respectively. For the $(FASnI_3)_x(MAPbI_3)_{1-x}$ perovskite films, here, d_0 ranges from 566 nm to 651 nm (Table I). Structural parameters, layer thicknesses, and void fractions, obtained from the parametric model in the divided spectral range analysis, are fixed, and ε at each spectral point are fit[48] to both SE and transmittance spectra in a process similar to numerical inversion[49] for the full measured spectral range for each perovskite film (Fig. 1).

Absorption coefficient spectra are obtained from $\alpha = 4\pi k/\lambda$, where k is the extinction coefficient in $\varepsilon = (n + ik)^2$ and λ is the wavelength. Figure 2(a) shows the spectra in α near the absorption onset obtained from the numerical inversion of $(FASnI_3)_x(MAPbI_3)_{1-x}$ ($0.3 \le x \le 0.8$) perovskite films, which have been exposed to laboratory ambient air for approximately 2–3 min during SE and transmittance measurement. Near-E_g spectra in α for the perovskite films which have not been exposed to laboratory ambient air are obtained from PDS using $\alpha = -\ln(1 - S/S_0)/d$, where S is the experimental measured signal, S_0 is the saturation signal, and d is the path length through the film,[50] and are shown in Fig. 2(b). The path length through the film is assumed to be equal to the effective film thickness of the film. From the PDS determined spectra in α, the direct gap E_g for each perovskite film is calculated using Tauc plots by linear fitting $(\alpha h\nu)^2 = 0$ over the $(1–7) \times 10^8$ eV^2 cm^{-2} range, with the abscissa given by the photon energy ($h\nu$). This range, $(1–7) \times 10^8$ eV^2 cm^{-2}, is the lowest realistically linear region common for all films. The resulting E_g are shown in Fig. 3. As all these samples are protected from atmospheric exposure during PDS measurement,[33] negligible sub-gap absorption is observed. Comparison between near-E_g spectra in α obtained by PDS and SE + transmittance for $(FASnI_3)_{0.5}(MAPbI_3)_{0.5}$ and $(FASnI_3)_{0.8}(MAPbI_3)_{0.2}$ is shown in Figs. 4(a) and 4(b), respectively. Using Eq. (1), E_u is calculated as the inverse slope of the linear fit to $\ln(\alpha/\alpha_g)$ as shown for a representative $(FASnI_3)_{0.6}(MAPbI_3)_{0.4}$ perovskite film in Fig. 5. E_u calculated from PDS determined spectra in α for all films are shown in Fig. 6. Short circuit current density (J_{SC}), open circuit voltage (V_{OC}), fill factor (FF), and PCE for solar cells incorporating different composition perovskite absorbers are shown in Fig. 7.

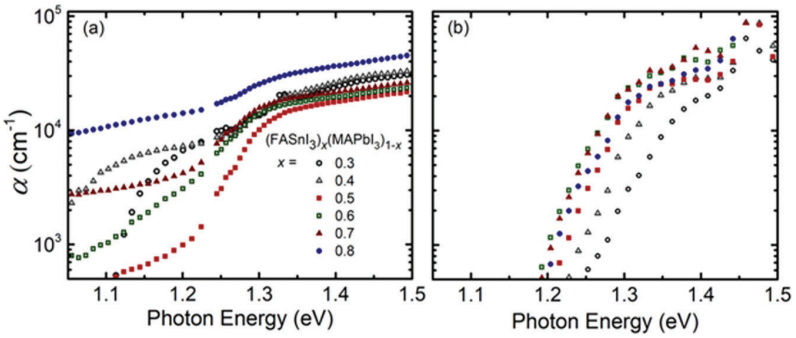


FIG. 2. Absorption coefficient (α) spectra near the bandgap for $(FASnI_3)_x(MAPbI_3)_{1-x}$ ($0.3 \le x \le 0.8$) perovskite films (a) exposed to laboratory ambient air as measured using spectroscopic ellipsometry coupled with unpolarized transmittance and (b) protected from atmospheric exposure as measured by photothermal deflection spectroscopy. The vertical axes are on the same scale.

Published under license by AIP Publishing

Approved for public release; distribution unlimited.

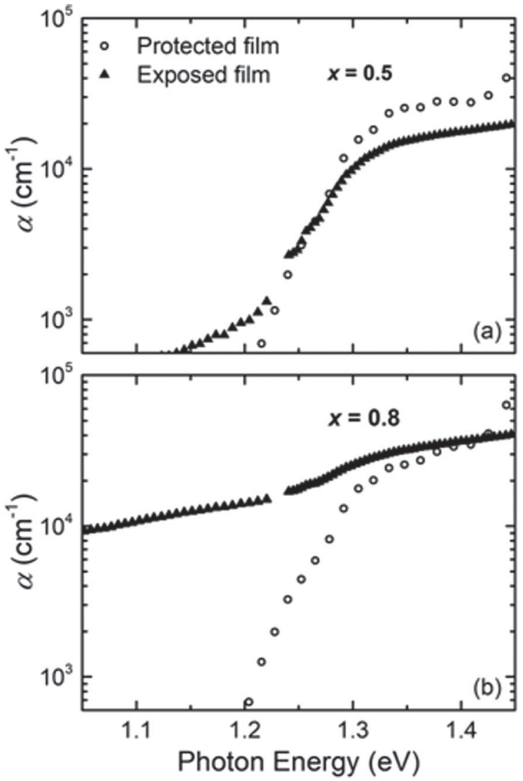


FIG. 4. Comparison of spectra in α near the bandgap for (a) $(FASnI_3)_{0.5}(MAPbI_3)_{0.5}$ and (b) $(FASnI_3)_{0.8}(MAPbI_3)_{0.2}$ perovskite films exposed to laboratory ambient air (solid triangles, as obtained by SE + unpolarized transmittance) and protected against atmospheric exposure (open circles, as obtained by PDS).

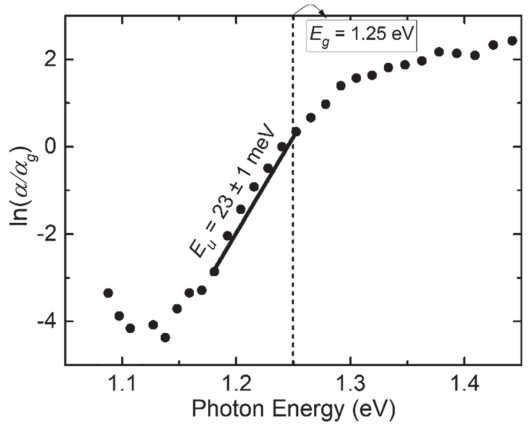


FIG. 5. Example linear fit to $\ln(\alpha/\alpha_g)$ below the bandgap for $(FASnI_3)_{0.6}(MAPbI_3)_{0.4}$ used to calculate Urbach energy (E_u) from the spectra in α obtained by photothermal deflection spectroscopy.

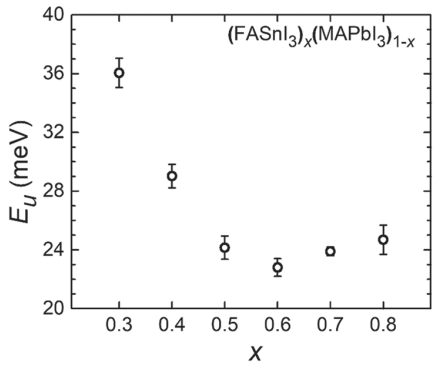


FIG. 6. E_u for $(FASnI_3)_x(MAPbI_3)_{1-x}$ perovskite films as a function of composition.

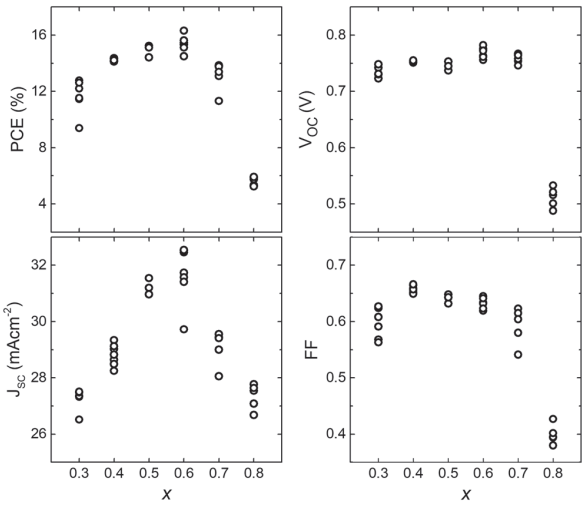


FIG. 7. Open circuit voltage (V_{OC}), fill factor (FF), short circuit current density (J_{SC}), and power conversion efficiency (PCE) for solar cells incorporating $(FASnI_3)_x(MAPbI_3)_{1-x}$ perovskite absorbers. Device performances are graphed for 3–7 solar cells for each perovskite composition.

DISCUSSION

$(FASnI_3)_x(MAPbI_3)_{1-x}$ films show variations in structural parameters as a function of composition, as reported in Table I. The x = 0.5 and 0.6 compositions show relatively smaller surface roughness thicknesses compared to both lower and higher Sn-content films. Considering the uniform distribution of grain size reported for x = 0.5 and 0.6 compositions,[51] smoother surfaces are expected. Lower Sn-content films show compact but thicker surface roughness layers as reflected in the relative void fraction of that layer, which may correspond to a greater distribution in grain size. High Sn-content perovskite films show higher surface roughness layer thickness and void fraction. Rapid crystallization[52] in higher Sn-content films results in the formation of larger grains with

Published under license by AIP Publishing

Approved for public release; distribution unlimited.

lower surface coverage.[18] In addition, more pronounced degradation of higher Sn-content films via oxidation may correspond to a higher surface roughness void fraction in those measured samples. All films show a lower density interfacial layer formed at the glass substrate/perovskite film interface. Rapid crystallization can lead to large grains forming initially on the substrate surface but with incomplete surface coverage. This lower density interfacial layer forms as grains nucleating on the surface of the substrate coalesce before developing into the continuous bulk layer. Here, $x = 0.5$ and 0.6 perovskite films show the smallest interfacial layer thicknesses. Figure 1 shows the optical properties of the most optically dense layers of the $(FASnI_3)_x(MAPbI_3)_{1-x}$ films. Compared to other films, the $x = 0.8$ film shows lower values of ε_1 spectra at low photon energies indicating reduced optical density compared to the other films. This observation suggests that even in the most optically dense layer of the $x = 0.8$ film, the grains are not as densely packed as the other compositions, which may correspond to reduced atmospheric stability. As all the perovskite films are spin coated at the same speed, the observed variations in effective material thickness d_0 as a function of composition are attributed to the packing density of grains in the films, with $x = 0.5$ and 0.6 films exhibiting the lowest d_0 and highest density.

$x = 0.5$ and 0.6 $(FASnI_3)_x(MAPbI_3)_{1-x}$ perovskite films exposed to laboratory ambient air for approximately 2–3 min show relatively sharper absorption edges with lesser sub-gap absorption compared to other compositions. The amount of sub-gap absorption increases with either increasing or decreasing x, with $x = 0.8$ being the most pronounced. However, all the films that are protected from atmospheric exposure during PDS measurement[33] show smaller sub-gap absorption. Figure 2 shows the differences in α in the vicinity of E_g for the perovskite films exposed to laboratory ambient air measured by SE and transmittance and protected against atmospheric exposure as measured by PDS. These differences in α, for example, $x = 0.5$ and 0.8 films, are shown in Fig. 4. Spectra in α near the absorption onset for $x = 0.5$ and 0.6 perovskite films exposed to laboratory ambient air have sharper absorption edges and are also closer to those measured by PDS than the other compositions. It has been reported that alloyed Sn + Pb materials show anomalous band bowing in thin films.[8,53] Here, E_g as a function of composition (Fig. 3) shows a nonlinear trend and expected band bowing is observed with $x = 0.6$ having the narrowest E_g. Defect density is approximated from the amount of sub-gap absorption using optical sum rules[27] for the films exposed to laboratory ambient air and protected against air exposure. Finite photon energy range spectra in ε_2 are used to calculate the concentration of electrons associated with sub-gap defect induced absorption by

$$\frac{1}{\hbar^2}\int_{E_a}^{E_g} E\varepsilon_2(E)dE = \frac{\pi N_a e^2}{2\varepsilon_0 m} Z_{eff}(E_g), \tag{2}$$

where m is the free electron mass, N_a is the concentration of atoms, E_a is the photon energy at $\alpha = 1000\ cm^{-1}$ where the substantial absorption starts, and $Z_{eff}(E_g)$ is the number of electrons per atom contributing to the optical response. The calculated defect density is approximated as $N_a Z_{eff}(E_g)$ and represents the total number of electronic transitions depending upon the nature of defects represented by absorption below E_g. Figure 8 shows the defect density for perovskite films exposed to laboratory ambient air and protected against air exposure. For the films exposed to laboratory ambient air, substantial variations in defect density are observed as a function of composition. Extrinsic defects are likely to be formed by this exposure, increasing the observed sub-gap absorption and associated defect density for perovskite films. Defect densities are uniformly low in the protected films. However, the increase in defect density arising from exposure to laboratory ambient air is the smallest in $x = 0.5$ and 0.6 films, which indicates that these compositions are less susceptible to atmospherically induced degradation. For the films protected from laboratory ambient air exposure, defects are considered to be mainly intrinsic, and E_u obtained from PDS is a more accurate measure of electronic material quality. The $x = 0.6$ perovskite film shows the lowest E_u among this series with increases in E_u with either decreasing or increasing x (Fig. 6). This $(FASnI_3)_{0.6}(MAPbI_3)_{0.4}$ perovskite film exhibits the lowest sub-gap absorption and lowest associated defect density. Replacing Pb by Sn at $x = 0.6$ results in larger grain size[18] than that of lower Sn content with increased grain connectivity.[54] It is reported that replacing more Pb by Sn up to $x = 0.8$ increases the grain size in mixed Sn + Pb perovskites; however, films tend to have poor surface coverage with $x > 0.6$.[54] This behavior results in slightly higher E_u observed for $x = 0.7$ and 0.8 compared to $x = 0.6$. E_u calculated from PDS spectra as reported for $MAPbSn_xPb_{1-x}I_3$ perovskites incorporated into solar cells shows a similar trend in E_u as a function of composition, where films with $x < 0.5$ show higher E_u due to smaller grain sizes, increased lattice distortions, and high defect densities.[22] It has also been reported that solar cells incorporating $(FASnI_3)_{0.6}(MAPbI_3)_{0.4}$ have higher performance compared to devices with either pure $FASnI_3$ and $MAPbI_3$ due to a more uniform grain size distribution.[51] These observations coupled with the composition dependent behavior of E_u suggest that $x = 0.6$ perovskites show better crystallinity associated with less defect induced sub-gap absorption.

The solar cells with $(FASnI_3)_{0.6}(MAPbI_3)_{0.4}$ absorbers show the highest J_{SC}, V_{OC}, and PCE with a moderately high FF (Fig. 7). For devices with higher or lower x relative to $x = 0.6$, J_{SC} decreases. Devices with $x < 0.6$ and $x > 0.6$ have increasingly higher E_g

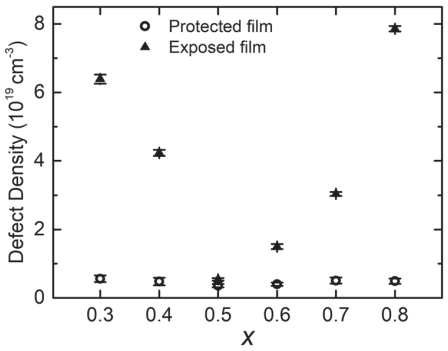


FIG. 8. Defect density calculated using the optical sum rules for $(FASnI_3)_x(MAPbI_3)_{1-x}$ perovskite films (open circles) protected against atmospheric exposure and (solid triangles) exposed to laboratory ambient air. Uncertainties in the calculated values are less than 35% and 6% for the protected and exposed films, respectively.

Published under license by AIP Publishing

Approved for public release; distribution unlimited.

with decreasing or increasing x, hence reducing the possible optical absorption in the cell and maximum J_{SC}. Films with lower Sn content also have smaller grain size,[18] which is reflected in higher E_u. Perovskite absorbers with Sn content $x > 0.6$ may have defects in terms of gaps and discontinuities, as reported in Ref. 18. In addition, as perovskite devices are not completely protected against degradation in laboratory ambient air, possible oxidation of Sn^{2+} to Sn^{4+} occurring for higher Sn content films can increase p-type self-doping.[8] Absorber layer intrinsic defects due to an isolated grain structure or extrinsic defects such as increased p-type doping due to atmospheric exposure result in an increased recombination rate and reduced carrier collection. $x = 0.7$ and 0.8 perovskite films have equal or lesser E_g than $x = 0.5$, but J_{SC} is lower. Lower perovskite E_g does not necessarily mean higher J_{SC} as intrinsic defects and those arising from air exposure increase recombination and reduce photogenerated carrier collection. Although it is important to lower E_g for the bottom sub-cell in all perovskite tandem PV by varying compositions, absorber layer structural and electronic quality has direct consequences for carrier collection rates. For solar cells with $0.3 \leq x \leq 0.7$ absorbers, V_{OC} and FF are relatively similar without a well-defined trend as observed for J_{SC}. The resultant variation in PCE is possibly due to the variation in J_{SC}; however, V_{OC} and FF along with J_{SC} depend upon the crystallinity and number of defects present at grain boundaries in an absorber layer. The associated composition dependent variation in absorber layer crystallinity and defect states affects the PCE of $(FASnI_3)_x(MAPbI_3)_{1-x}$ perovskite solar cells. Except for solar cell devices with higher Sn content, $x = 0.7$ and 0.8, average PCE decreases with increases in E_u of the absorber layer and vice versa, as shown in Fig. 9(a). For solar cells, $V_{OC} = kT(\ln(1 + G_{light}/G_{therm}))/q$, where q is the unit charge, G_{light} is the current generation rate, and G_{therm} is the thermal generation rate. G_{therm} depends upon the amount of sub-gap absorption due to lattice vibration and defect states, which do not contribute to photogenerated current. The increased presence of defects is reflected in increased E_u. Given constant G_{light}, V_{OC} is inversely proportional to the G_{therm} and hence E_u. Since V_{OC} of solar cells also depends upon E_g, which varies with composition (Fig. 3), it is logical to compare the V_{OC} deficit with E_u of the absorbers. The V_{OC} deficit is defined as E_g/q-V_{OC} and refers to the existence of imperfections in the absorber layer linked to E_u. Figure 9(b) shows the variation of the V_{OC} deficit with composition and E_u, respectively, with a monotonic relationship aside from $x = 0.8$. Again, the highest PCE solar cell has a $x = 0.6$ absorber and shows the lowest E_u and lowest V_{OC} deficit, whereas devices with a $x = 0.8$ absorber deviate from this trend, as shown in Fig. 9. The $x = 0.8$ absorber film shows a low $E_u = 25 \pm 1$ meV, which is almost comparable to that of a best-performing absorber, $x = 0.6$ with $E_u = 23 \pm 1$ meV, but solar cell performance parameters, particularly V_{OC} and FF, are substantially reduced. We attribute this exception to differences in how these materials are prepared and handled as films for E_u characterization and as absorber layers in complete solar cells. During the preparation of films for PDS, there is no exposure to atmospheric moisture, oxygen, and UV light. Device performance measurements of solar cells are performed in laboratory ambient air potentially leading to atmospherically induced defects. For films, defects may only exist in the perovskite itself; however, in solar cells, contributions to degradation from multiple layers including interfaces should be considered. Even though differences exist in conditions during fabrication and characterization of thin films and devices, sensitivity to oxidation is likely the primary cause of poor performance of devices with high Sn-content absorbers. Previous studies show that excess Sn in a mixed Sn + Pb perovskite is more prone to degradation via oxidation.[55] Substantially increased near-E_g spectra in α for a high Sn-content material, especially $x = 0.8$, are observed for the material exposed to laboratory ambient air relative to the material protected against it, as shown in Fig. 2. $(FASnI_3)_{0.8}(MAPbI_3)_{0.2}$ as a film exposed to laboratory ambient air or as the absorber layer in a solar cell is more prone to degradation via oxidation than other compositions studied here. Sn^{2+} to Sn^{4+} oxidation in high Sn-content perovskites causes p-type self-doping that increases free charge scattering and recombination. A relatively higher recombination rate explains reduced V_{OC} and FF in $(FASnI_3)_{0.8}(MAPbI_3)_{0.2}$ perovskite solar cells. In addition, the defects at grain boundaries of this high Sn-content absorber act as Shockley–Read–Hall recombination centers in solar cells reducing V_{OC} and FF. Reduced device performance in various mixed Sn + Pb halide perovskites with $x = 0.8$ is observed in the literature for different A-anion and X-cation compositions.[18,20,54] Increased FA content up to 80% also reduces V_{OC} in mixed FA + MA and Sn + Pb halide perovskite devices.[52] Even though the other device component materials are deposited over perovskite absorber layers in the solar cell device configuration preventing direct interaction with oxygen in ambient air, prolonged exposure will result in oxidation with non-ideal encapsulation.

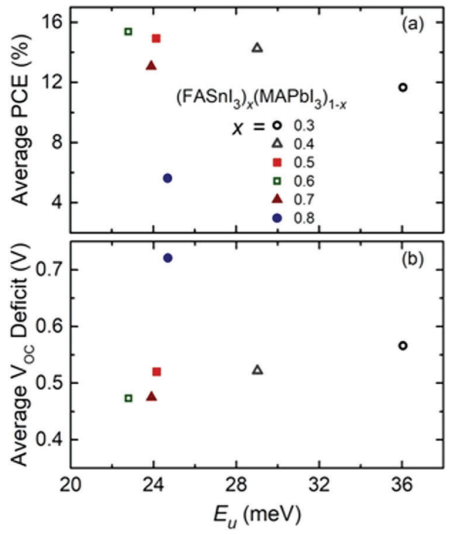


FIG. 9. (a) PCE of $(FASnI_3)_x(MAPbI_3)_{1-x}$ perovskite solar cells as a function of E_u for the corresponding composition perovskite films. (b) V_{OC} deficit as a function of E_u.

The previous work comparing the thin film optical response with the device performance of $FA_{1-x}Cs_xPbI_3$ based solar cells[27,56] found correlation between the sharpest absorption onset near the bandgap in films and highest PCE. Results also indicated that these composition perovskites are better protected against degradation when incorporated in complete solar cells. Similarly,

Published under license by AIP Publishing

Approved for public release; distribution unlimited.

$(FASnI_3)_x(MAPbI_3)_{1-x}$ compositions showing the highest device performance also show less atmospherically induced sub-gap absorption in thin films. However, high Sn-content perovskites show strongly reduced device performance despite atmospherically protected thin film characteristics, indicating that process compatibility during device fabrication and relative stability during device testing should be considered for different perovskite compositions.

CONCLUSION

Spectra in α for narrow bandgap $(FASnI_3)_x(MAPbI_3)_{1-x}$ $0.3 \leq x \leq 0.8$ perovskite thin films are obtained using SE, unpolarized transmittance, and PDS. Sub-gap absorption present in spectra in α obtained from PDS is used to identify E_u. The minimum E_u is found for $x = 0.6$ with $(FASnI_3)_x(MAPbI_3)_{1-x}$ perovskite films showing increasing E_u with either increasing or decreasing x. In addition, solar cell devices based on $(FASnI_3)_{0.6}(MAPbI_3)_{0.4}$ absorber layers show the best overall device performance including the highest PCE and lowest V_{OC} deficit, which suggests the importance of absorber film quality on the solar cell performance. Even though optical characterization of perovskite films by PDS is protected from laboratory ambient exposure, layers in solar cells may undergo exposure to laboratory ambient oxygen and UV light during processing and encapsulation. $(FASnI_3)_{0.8}(MAPbI_3)_{0.2}$ perovskite-based solar cells show substantially reduced device performances despite a low E_u for the corresponding film. This behavior is attributed to the variation in optical responses of mixed Sn + Pb perovskite absorber layers with varying Sn content, meaning that at similar exposure to laboratory ambient oxygen $(FASnI_3)_{0.8}(MAPbI_3)_{0.2}$ perovskite films degrade more via oxidation than lower Sn-content compositions.

ACKNOWLEDGMENTS

This work was supported by the University of Toledo start-up funds, the Ohio Department of Development (ODOD) Ohio Research Scholar Program (Northwest Ohio Innovators in Thin Film Photovoltaics, Grant No. TECH 09-025), the Office of Naval Research (Contract No. N00014-17-2223), the U.S. Department of Energy (DOE) SunShot Initiative under the Next Generation Photovoltaics 3 Program (No. DE-FOA-0000990), and the National Science Foundation (Grant Nos. CHE-1230246 and DMR-1534586).

This material is based on the research sponsored by Air Force Research Laboratory under Agreement Nos. FA9453-11-C-0253, FA9453-18-2-0037, and FA9453-19-C-1-002. The U.S. Government is authorized to reproduce and distribute reprints for governmental purposes notwithstanding any copyright notation thereon. The views and conclusions contained herein are those of the authors and should not be interpreted as necessarily representing the official policies or endorsements, either expressed or implied, of Air Force Research Laboratory or the U.S. Government.

This material is based upon the work supported by the U.S. Department of Energy's Office of Energy Efficiency and Renewable Energy (EERE) under the Solar Energy Technologies Office, Award No. DE-EE0008753. This report was prepared as an account of work sponsored by an agency of the United States Government. Neither the United States Government nor any agency thereof, nor any of their employees, makes any warranty, express or implied, or assumes any legal liability or responsibility for the accuracy, completeness, or usefulness of any information, apparatus, product, or process disclosed, or represents that its use would not infringe privately owned rights. Reference herein to any specific commercial product, process, or service by trade name, trademark, manufacturer, or otherwise does not necessarily constitute or imply its endorsement, recommendation, or favoring by the United States Government or any agency thereof. The views and opinions of authors expressed herein do not necessarily state or reflect those of the United States Government or any agency thereof.

REFERENCES

[1] A. Kojima, K. Teshima, Y. Shirai, and T. Miyasaka, J. Am. Chem. Soc. **131**, 6050 (2009).
[2] See https://www.nrel.gov/pv/assets/pdfs/best-research-cell-efficiencies.20190802.pdf for NREL Best Research-Cell Efficiencies Chart.
[3] G. E. Eperonm, T. Leijtens, K. A. Bush, R. Prasanna, T. Green, J. T. Wang, D. P. McMeekin, G. Volonakis, R. L. Milot, R. May, A. Palmstrom, D. J. Slotcavage, R. A. Belisle, J. B. Patel, E. S. Parrott, R. J. Sutton, W. Ma, F. Moghadam, B. Conings, A. Babayigit, H. G. Boyen, S. Bent, F. Giustino, L. M. Hertz, M. B. Johnston, M. D. McGehee, and H. J. Snaith, Science **354**, 861 (2016).
[4] D. Zhao, C. Chen, C. Wang, M. M. Junda, Z. Song, C. R. Grice, Y. Yu, C. Li, B. Subedi, N. J. Podraza, X. Zhao, G. Fang, R.-G. Xiong, K. Zhu, and Y. Yan, Nat. Energy **3**, 1093 (2018).
[5] J. Tong, Z. Song, D. H. Kim, X. Chen, C. Chen, A. F. Palmstrom, P. F. Ndione, M. O. Reese, S. P. Dunfield, O. G. Reid, J. Liu, F. Zhang, S. P. Harvey, Z. Li, S. T. Christensen, G. Teeter, D. Zhao, M. Al-Jassim, M. F. A. M. van Hest, M. C. Beard, S. E. Shaheen, J. J. Berry, Y. Yan, and K. Zhu, Science **364**, 475 (2019).
[6] D. P. Mcmeekin, G. Sadoughi, W. Rehman, G. E. Eperon, M. Saliba, M. T. Hörantner, A. Haghighirad, N. Sakai, L. Korte, B. Rech, M. B. Johnston, L. M. Herz, and H. J. Snaith, Science **351**, 151 (2016).
[7] C. C. Stoumpos, C. D. Malliakas, and M. G. Kanatzidis, Inorg. Chem. **52**, 9019 (2013).
[8] F. Hao, C. C. Stoumpos, R. P. H. Chang, and M. G. Kanatzidis, J. Am. Chem. Soc. **136**, 8094 (2014).
[9] Z. Song, C. Chen, C. Li, R. A. Awni, D. Zhao, and Y. Yan, Semicond. Sci. Technol. **34**, 093001 (2019).
[10] C. Chen, Z. Song, C. Xiao, D. Zhao, N. Shrestha, C. Li, G. Yang, F. Yao, X. Zheng, R. J. Ellingson, C. Jiang, M. Al-Jassim, K. Zhu, G. Fang, and Y. Yan, Nano Energy **61**, 141 (2019).
[11] R. J. Stoddard, A. Rajagopal, R. L. Palmer, I. L. Braly, A. K.-Y. Jen, and H. W. Hillhouse, ACS Energy Lett. **3**(6), 1261 (2018).
[12] Y. Zhou, Y. Jia, H. Fang, M. A. Loi, F. Xie, L. Gong, M.-C. Qin, X. Lu, C. Wong, and N. Zhao, Adv. Funct. Mater. **28**, 1803130 (2018).
[13] S. Gharibzadeh, B. A. Nejand, M. Jakoby, T. Abzieher, D. Hauschild, S. Moghadamzadeh, J. A. Schwenzer, P. Brenner, R. Schmager, A. A. Haghighirad, L. Weinhardt, U. Lemmer, B. S. Richards, I. A. Howard, and U. W. Paetzold, Adv. Energy Mater. **9**, 1803699 (2019).
[14] V. Adinolfi, W. Peng, G. Walters, O. M. Bakr, and E. H. Sargent, Adv. Mater. **30**, 1700764 (2018).
[15] X. Lian, J. Chen, Y. Zhang, M. Qin, J. Li, S. Tian, W. Yang, W. Yang, X. Lu, G. Wu, and H. Chen, Adv. Funct. Mater. **29**(5), 1807024 (2019).
[16] C. Li, Z. Song, D. Zhao, C. Xiao, B. Subedi, N. Shrestha, M. M. Junda, C. Wang, C.-S. Jiang, M. Al-Jassim, R. Ellingson, N. J. Podraza, K. Zhu, and Y. Yan, Adv. Energy Mater. **9**, 1803135 (2018).
[17] J. Chen, J. Xu, L. Xiao, B. Zhang, S. Dai, and J. Yao, ACS Appl. Mater. Interfaces **9**, 2449 (2017).
[18] J. Liu, G. Wang, Z. Song, X. He, K. Luo, Q. Ye, C. Liao, and J. Mei, J. Mater. Chem. A **5**, 9097 (2017).
[19] K. A. Bush, K. Frohna, R. Prasanna, R. E. Beal, T. L. Leijtens, and S. A. Swifter, ACS Energy Lett. **3**(2), 428 (2019).

Published under license by AIP Publishing

Approved for public release; distribution unlimited.

[20]M. M. Tavakoli, S. M. Zakeeruddin, M. Grätzel, and Z. Fan, Adv. Mater. **30**, 1705998 (2018).
[21]C. Wang, Z. Song, C. Li, D. Zhao, and Y. Yan, Adv. Funct. Mater. **29**, 1808801 (2019).
[22]B. Zhao, M. Abdi-Jalebi, M. Tabachnyk, H. Glass, V. S. Kamboj, W. Nie, A. J. Pearson, Y. Puttisong, K. C. Gödel, H. E. Beere, D. A. Ritchie, A. D. Mohite, S. E. Dutton, R. H. Friend, and A. Sadhanala, Adv. Mater. **29**, 1604744 (2017).
[23]F. Urbach, Phys. Rev. **92**, 1324 (1953).
[24]W. Martiensssen, J. Phys. Chem. Solids **2**, 257 (1957).
[25]C. H. Grein and S. John, Phys. Rev. B **39**(2), 1140 (1989).
[26]G. Landi, H. C. Neitzert, C. Barone, C. Mauro, F. Lang, S. Albrecht, B. Rech, and S. Pagano, Adv. Sci. **4**, 1700183 (2017).
[27]B. Subedi, L. Guan, Y. Yu, K. Ghimire, P. Uprety, Y. Yan, and N. J. Podraza, Sol. Energy Mater. Sol. Cells **188**, 228 (2018).
[28]N. Liu and C. Yam, Phys. Chem. Chem. Phys. **20**, 6800 (2018).
[29]K. Ghimire, D. Zhao, A. Cimaroli, W. Ke, Y. Yan, and N. J. Podraza, J. Phys. D: Appl. Phys. **49**, 405102 (2016).
[30]Y. Kye, C. Yu, U. Jong, Y. Chen, and A. Walsh, J. Phys. Chem. Lett. **9**, 2196 (2018).
[31]K. Ghimire, D. Zhao, Y. Yan, and N. J. Podraza, AIP Adv. **7**, 075108 (2017).
[32]S. D. Wolf, J. Holovksy, S.-J. Moon, P. Loper, B. Niesen, M. Ledinsky, F. Haug, J. Yum, and J. Christophe Ballif, J. Phys. Chem. Lett. **5**, 1035 (2014).
[33]M. M. Junda, D. Zhao, B. Subedi, C. Wang, C. Chen, Y. Yan, and N. J. Podraza, J. Phys. D: Appl. Phys. **52**(17), 175102 (2019).
[34]W. B. Jackson, N. M. Amer, A. C. Boccara, and D. Fournier, Appl. Opt. **20**, 1333 (1981).
[35]R. A. Synowicki, Phys. Status Solidi C **5**(5), 1085 (2008).
[36]D. Murata, S. Hara, T. N. Murakami, S. Fujimoto, M. Chikamatsu, and H. Fujiwara, Phys. Rev. Appl. **5**, 014012 (2016).
[37]A. S. Ferlauto, G. M. Ferreira, J. M. Pearce, C. R. Wronski, and R. W. Collins, J. Appl. Phys. **92**, 2424 (2002).
[38]M. M. Junda and N. J. Podraza, Surf. Sci. Spectra **25**, 016001 (2018).
[39]J. N. Hilfiker, N. Singh, T. Tiwald, D. Convey, S. M. Smith, J. H. Baker, and H. G. Tompkins, Thin Solid Films **516**, 7979 (2008).
[40]K. Ghimire, H. F. Haneef, R. W. Collins, and N. J. Podraza, Phys. Status Solidi B **252**, 2191 (2015).
[41]H. Haneef and N. J. Podraza, J. Appl. Phys. **116**, 163507 (2014).
[42]T. Hata, T. Hatsuda, T. Miyabo, and S. Hasegawa, Jpn. J. Appl. Phys., Part 1 **25**, 226 (1986).
[43]D. E. Aspnes and J. B. Theeten, Phys. Rev. B **20**, 3292 (1979).
[44]L. Karki Gautam, H. Haneef, M. M. Junda, D. B. Saint John, and N. J. Podraza, Thin Solid Films **571**, 548 (2014).
[45]R. W. Collins and A. S. Ferlauto, in *Handbook of Ellipsometry*, edited by H. G. Tompkins and E. A. Irene (William Andrew, Norwich, NY, 2005), pp. 125–128.
[46]D. E. Aspnes, in *Handbook of Semiconductors*, edited by M. Balkanski (North Holland, Amsterdam, NL, 1980), Vol. 2, p. 125.
[47]B. Johs and C. M. Herzinger, Phys. Status Solidi C **5**(5), 1031 (2008).
[48]J. N. Hilfiker, J. Sun, and N. Hong, in *Spectroscopic Ellipsometry for Photovoltaics* edited by H. Fujiwara and R. W. Collins (Springer, Switzerland, 2018), pp. 59–88.
[49]W. G. Oldham, Surf. Sci. **16**, 97 (1969).
[50]K. Tanaka, T. Gotoh, N. Yoshida, and S. Nonomura, J. Appl. Phys. **91**, 125 (2002).
[51]W. Liao, D. Zhao, Y. Yu, N. Shrestha, K. Ghimire, C. R. Grice, C. Wang, Y. Xiao, A. J. Cimaroli, R. Ellingson, N. J. Podraza, K. Zhu, R. Xiong, and Y. Yan, J. Am. Chem. Soc. **138**, 12360 (2016).
[52]Z. Yang, A. Rajagopal, C. Chueh, S. B. Jo, B. Liu, T. Zhao, and A. K. Jen, Adv. Mater. **28**, 8990 (2016).
[53]X. Gao and M. S. Daw, Phys. Rev. B **77**, 033103 (2008).
[54]S. Lee, T. Ha, and D. Kang, Mater. Lett. **227**, 311 (2018).
[55]T. Leijtens, R. Prasanna, A. G-Parker, M. F. Toney, and M. D. McGehee, ACS Energy Lett. **2**, 2159 (2017).
[56]B. Subedi, L. Guan, Y. Yu, K. Ghimire, P. Uprety, M. M. Junda, Y. Yan, and N. J. Podraza, in *IEEE 7th World Conference on Photovoltaic Energy Conversion (WCPEC)* (IEEE, 2018), p. 0522.

Published under license by AIP Publishing

Approved for public release; distribution unlimited.

materials

MDPI

Article

CuSCN as the Back Contact for Efficient ZMO/CdTe Solar Cells

Deng-Bing Li [1], Zhaoning Song [1], Sandip S. Bista [1], Fadhil K. Alfadhili [1], Rasha A. Awni [1], Niraj Shrestha [1], DeMilt Rhiannon [2], Adam B. Phillips [1], Michael J. Heben [1], Randy J. Ellingson [1], Feng Yan [3] and Yanfa Yan [1,*]

1 Department of Physics and Astronomy, and Wright Center for Photovoltaics Innovation and Commercialization (PVIC), University of Toledo, Toledo, OH 43606, USA; dengbing.li@utoledo.edu (D.-B.L.); zhaoning.song@utoledo.edu (Z.S.); sandip.bista@rockets.utoledo.edu (S.S.B.); fadhil.alfadhili@rockets.utoledo.edu (F.K.A.); rasha.awni@rockets.utoledo.edu (R.A.A.); niraj.shrestha@rockets.utoledo.edu (N.S.); adam.phillips@utoledo.edu (A.B.P.); michael.heben@utoledo.edu (M.J.H.); randy.ellingson@utoledo.edu (R.J.E.)

2 Ottawa Hills Junior/senior high school, Ottawa Hills Local Schools, Ottawa Hills, OH 43606, USA; rdemilt20@ohschools.org

3 Department of Metallurgical and Materials Engineering, The University of Alabama, Tuscaloosa, AL 35487, USA; fyan@eng.ua.edu

* Correspondence: yanfa.yan@utoledo.edu

Received: 21 March 2020; Accepted: 21 April 2020; Published: 24 April 2020



Abstract: The replacement of traditional CdS with zinc magnesium oxide (ZMO) has been demonstrated as being helpful to boost power conversion efficiency of cadmium telluride (CdTe) solar cells to over 18%, due to the reduced interface recombination and parasitic light absorption by the buffer layer. However, due to the atmosphere sensitivity of ZMO film, the post treatments of ZMO/CdTe stacks, including $CdCl_2$ treatment, back contact deposition, etc., which are critical for high-performance CdTe solar cells became crucial challenges. To realize the full potential of the ZMO buffer layer, plenty of investigations need to be accomplished. Here, copper thiocyanate (CuSCN) is demonstrated to be a suitable back-contact material with multi-advantages for ZMO/CdTe solar cells. Particularly, ammonium hydroxide as the solvent for CuSCN deposition shows no detrimental impact on the ZMO layer during the post heat treatment. The post annealing temperature as well as the thickness of CuSCN films are investigated. Finally, a champion power conversion efficiency of 16.7% is achieved with an open-circuit voltage of 0.857 V, a short-circuit current density of 26.2 mA/cm^2, and a fill factor of 74.0%.

Keywords: copper thiocyanate; CuSCN; CdTe; zinc magnesium oxide

1. Introduction

In the past few years, cadmium telluride (CdTe) solar cells have experienced a rapid performance improvement, with certified record power conversion efficiencies (PCEs) reaching 22.1% for cells and over 18.6% for modules [1,2]. Benefitting from its multi-advantages, including low manufacturing costs, a suitable bandgap, high light absorption coefficients, and, thus, a high theoretical efficiency of over 30% [3], CdTe technology currently dominates the thin-film photovoltaic market. Despite the success in commercialization, it is still challenging to reproduce the record efficiency of CdTe solar cells in research institutes over the world. The efficiency loss is mainly caused by the low p-type conductivity and high electron affinity of CdTe films [4,5], which make them crucial challenges to form a good ohmic contact between CdTe and a metal electrode. The existence of non-ohmic contact produces a back barrier and increases the recombination at the interface of CdTe and the metal electrode, significantly

Approved for public release; distribution unlimited.

limiting the open-circuit voltage (V_{OC}) and fill factor (FF) of CdTe solar cells. To overcome this issue, copper (Cu) is commonly used to improve the conductivity of CdTe and reduce the back-barrier height. However, the concern of long-time stability, due to the ease of Cu migration, inhibits its commercial applications [6]. Group V element (e.g., As and P) doping, as an alternative to Cu doping for the desired long-time stability, has recently attracted intensive investigations. [7–9] However, limited by the high capital costs of the equipment used for the in-situ doping and low effective doping level for the ex situ doping (due to aggregations at grain boundaries), group V doping has not been widely used by the researchers [7,10].

Copper thiocyanate (CuSCN), a low-cost and solution-processable material with a high work function of 5.3 eV [11], has been widely used in dye-sensitized and organic-inorganic perovskite solar cells as the hole transport layer to facilitate the carrier extraction [12–14]. In 2015, CuSCN was first reported by our group as copper source instead of metallic copper in CdTe solar cells, which delivers an impressive improvement in V_{OC}. [11] Recently, CuSCN was successfully used in CdSeTe solar cells, showing an impressive V_{OC} of around 0.860 V and an efficiency of ~17.0%, which makes it a promising back-contact for CdTe solar cells [15]. In this work, the application of solution processed CuSCN as the back contact in pure CdTe solar cells with zinc magnesium oxide (ZMO) as the buffer layer is investigated. ZMO is an emerging buffer layer in CdTe solar cells and helps boost their device performance, due to the reduction in interface recombination at the buffer layer/CdTe interface and parasitic light absorption by the buffer layer [16]. Recently, PCEs of 19.1% and 18.6% for CdSeTe and pure CdTe solar cells, respectively, with ZMO buffer layers have been demonstrated [17]. However, it has also been reported that an oxygen-free atmosphere is required for ZMO/CdTe devices during the CdTe deposition, as well as the post treatments; otherwise, the devices show poor performances, due to the presence of severe S-kinks [18,19]. Additionally, it is reported that the finished ZMO/CdTe devices degrade rapidly when exposing to the ambient atmosphere, likely due to the reaction between water and the ZMO film [20]. All of these suggest that the post treatment of ZMO/CdTe solar cells should be done with great alertness.

Till now, there are only few reports on the optimization of post treatments, especially the back-contact treatment for ZMO/CdTe solar cells. During the optimization processes, we have tried different hole transport materials (e.g., metallic Cu [21], carbon paste [22]) and back surface treatments (e.g., hydroiodic (HI) solution [23], Br methanol solution [24] and MAI solution [25] etching), which have been demonstrated effective in improving the CdS/CdTe device performance. However, most of these processes show adverse effects on the ZMO/CdTe devices, probably caused by the degradation of the ZMO films during the depositions or treatments. In this work, CuSCN dissolved in ammonium hydroxide solution (30 wt.% in water) was used to deposit CuSCN as a back contact for ZMO/CdTe solar cells. ZMO/CdTe devices with metallic Cu doping were used as a reference. Through the optimization of post annealing temperature and the CuSCN film thickness, the solar cells based on the ZMO/CdTe/CuSCN stack show a high PCE of 16.7%, with a V_{OC} of 0.857 V, a short-circuit current density (J_{SC}) of 26.2 mA/cm^2, and a FF of 74.0%. The result demonstrates that CuSCN is a robust hole transport material for CdTe solar cells with ZMO as the buffer layer.

2. Materials and Methods

The Schematic illustration of technological steps and investigation design in this work is shown in Figure S1. The devices in this work were fabricated according to our previous report [18]. Fluorine doped tin oxide coated glass (FTO, TEC12; Pilkington NA, Toledo, OH, USA) is used as the substrate after thermal ultrasonic cleaning in Micro-90 detergent (St. Louis, MO, USA) and deionized water at 70 °C. A 80 nm ZMO film was then deposited on the cleaned FTO glass, using a radio frequency sputter system at ambient temperature. The deposition was conducted at 6 mTorr pressure under a mix gas flow of 3% oxygen and 97% helium at a 25 W sputtering power, using a 2-inch ZMO target with 8 wt.% magnesium oxide. Then, a ~3.5 μm CdTe film was deposited in a close-space sublimation (CSS) chamber, with the source temperature of 560 °C, the substrate temperature of 495 °C, and a

Approved for public release; distribution unlimited.

chamber pressure of 1 Torr. The $CdCl_2$ activation treatment was carried out by drop-casting a saturated $CdCl_2$ in methanol solution on the CdTe surface, followed with drying naturally and annealing at 420 °C for 20 min at 400 Torr with a 500 sccm helium gas flow. After cooling down, the CdTe film was rinsed by methanol thoroughly to clean the excess $CdCl_2$. The CuSCN solution was prepared by dissolving the CuSCN powder in ammonium hydroxide (30 wt.%), or diethyl sulfide with different concentrations (2 mg/mL and 10 mg/mL), and then stirring at room temperature for more than 5 h to facilitate the dissolution. Then, the solution was filtered using a 0.45 μm pore size PTFE filter for the later use. The thickness of CuSCN film was tuned by varying the spin coating speed (2000 rpm and 6000 rpm), and the solution concentration (2 mg/mL and 10 mg/mL). After the CuSCN deposition, the film was heated in our CSS chamber to different temperatures (140 °C, 160 °C, 180 °C) at a ramp rate of ~35 °C/min with a 500 sccm helium flow under ambient pressure. After cooling down naturally, a 40 nm of thick gold was deposited via a shadow mask with an individual area of 0.08 cm^2 in a thermal evaporator. The optimized reference ZMO/CdTe devices with evaporated Cu metal were fabricated in the same procedure, except evaporating a 3 nm Cu and 40 nm Au bilayer then annealing in ambient pressure at 200 °C for 20 min. The samples for the photoluminescence (PL) measurements were fabricated by depositing 2.5 μm CdTe films followed with the standard $CdCl_2$ treatment and the CuSCN or metallic Cu treatment, respectively. All the completed devices described above are listed in Table 1.

Table 1. Details of all devices fabricated in this work. Note that the buffer layer, CdTe layer, and $CdCl_2$ treatment are identical for all the devices as mentioned above.

Devices	Cu Source	Solvent	CuSCN Deposition	Activation Procedure
CdTe-Cu	Cu metal	N/A	TE, 3 nm	200 °C for 20 min
CuSCN-140	CuSCN	NH	SP, 10 mg/mL-6000 rpm	140 °C for 0 min
CuSCN-160	CuSCN	NH	SP, 10 mg/mL-6000 rpm	160 °C for 0 min
CuSCN-180	CuSCN	NH	SP, 10 mg/mL-6000 rpm	180 °C for 0 min
2 mg/mL-6000 rpm	CuSCN	NH	SP, 2 mg/mL-6000 rpm	160 °C for 0 min
2 mg/mL-2000 rpm	CuSCN	NH	SP, 2 mg/mL-2000 rpm	160 °C for 0 min
8 mg/mL-6000 rpm	CuSCN	NH	SP, 10 mg/mL-6000 rpm	160 °C for 0 min
8 mg/mL-2000 rpm	CuSCN	NH	SP, 10 mg/mL-2000 rpm	160 °C for 0 min
diethyl sulfide	CuSCN	DS	SP, 10 mg/mL-2000 rpm	160 °C for 0 min

Note: NH for ammonium hydroxide; DS for diethyl sulfide; TE for thermal evaporation; SP for spin coating.

The device bandgap diagram simulation was performed using the solar cell capacitance simulator (SACPS) [26], and the parameters were used according to our previous publication [18]. Steady-state photoluminescence (PL) measurement was performed utilizing a 532 nm continuous wave laser at ~5 $W{\cdot}cm^{-2}$. Samples were excited through the film side. PL signal was detected by a symphony-II Si (CCD) detector (Horiba Scientific, NJ, USA) after a Horiba iHR320 monochromator (Horiba Scientific). The morphological microstructures of the CdTe films were characterized by a nanoscope atomic force microscope (Troy, MI, USA). The solar cell performance was characterized by measuring the current density-voltage (J-V) curves under AM1.5G illumination using a solar simulator (PV Measurements Inc. Point Roberts, WA, USA) and a source meter (Keithley 2400, Beaverton, OR USA). External quantum efficiency (EQE) spectra were performed on a QE system (PV Measurements, Beaverton, OR, USA). Temperature-dependent current-voltage (J-V-T) measurements were performed in a closed-cycle helium cryostat, with a tungsten lamp as a light source, and the temperature was varied from 200 to 310 K, with a step size of 10 K. An inhouse designed LabVIEW (National Instruments, Inc. Beaverton, OR, USA) control program was used to operate the temperature controller, and the Keithley 2400 source-meter for current and voltage data acquisition.

3. Results and Discussion

Figure 1a shows the simulated bandgap diagram of ZMO/CdTe solar cells, with CuSCN as the hole transport layer. The valence band offset between CdTe and CuSCN is favorable for the holes to be extracted from the CdTe layer. Additionally, the low electron affinity with respect to CdTe can

Approved for public release; distribution unlimited.
420

favorably repel electrons and prevent them from diffusing into the back electrode. This CdTe/CuSCN heterostructure can eliminate the carrier recombination on the rear side of CdTe, consequently enhancing carrier collection efficiency. The steady-state PL was carried out to further confirm the carrier extraction efficiency (Figure 1b). The CdTe-Cu reference sample exhibits a high intense PL emission peak, centered at 1.50 eV. With the presence of the CuSCN film, the PL emission peak shows pronounced intensity quenching, suggesting strong carrier extraction from the CdTe into the CuSCN. Atomic force microscopy (AFM) measurements were performed to confirm the uniformity of CuSCN film deposited on the CdTe films. The AFM image of bare CdTe film as shown in Figure 1c, exhibits a uniform grain size of ~2 μm, with a root mean squared (RMS) roughness of 147 nm. With the spin-coated CuSCN layer (Figure 1d), the RMS is slightly decreased to 139 nm, indicating a smooth coating of CuSCN particles.

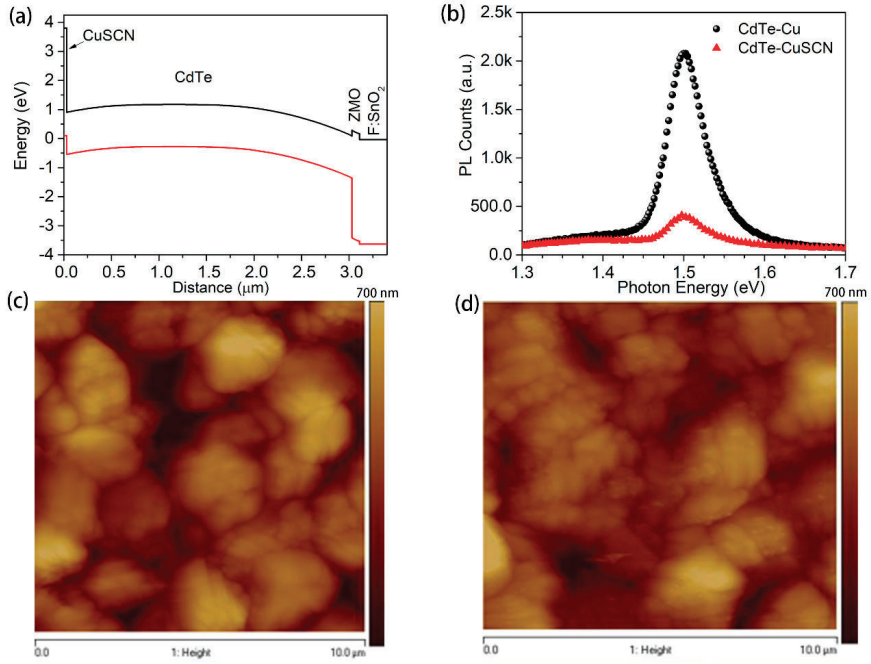


Figure 1. (**a**) Solar cell capacitance simulator (SCAPS) modeling determined band diagram for the device with a structure of fluorine doped tin oxide coated glass (FTO)/zinc magnesium oxide (ZMO)/cadmium telluride (CdTe)/copper thiocyanate (CuSCN)/Au. (**b**) Steady-state PL spectra of CdTe-Cu and CdTe-CuSCN stacks deposited on soda lime glass substrates. Atomic force microscopy images showing the surface morphologies of (**c**) a bare CdTe film and (**d**) a CdTe film deposited with CuSCN.

The diffusion of Cu into the CdTe film is a necessary step to improve the ohmic contact between CdTe and the metal electrode. In CdTe/CuSCN stacks, the diffusion of Cu from CuSCN into CdTe not only increases the p-type conductivity of CdTe, but also leaves Cu vacancies in the CuSCN layer, which helps to further increase the work function of CuSCN [27]. To optimize the CuSCN layer, the impact of the annealing temperature of CuSCN was investigated. As shown in Figure 2, the ZMO/CdTe devices with the metallic Cu (named CdTe-Cu hereafter) was used as a control to compare with the ZMO/CdTe devices with a ~30 nm CuSCN layer. The devices with the CuSCN back contact were annealed at different temperatures (140 °C, 160 °C, and 180 °C, named CuSCN-140, CuSCN-160, and CuSCN-180, respectively). With the presence of CuSCN, the devices show overall higher performances than the control devices with the metallic Cu in all the PV parameters. The inferior performance of the reference devices is likely due to the over-diffusion of Cu through CdTe into the ZMO film, which significantly

Approved for public release; distribution unlimited.
421

reduces the conductivity of ZMO film by several orders [28–30]. We have tried to reduce the annealing temperature and time for the reference devices to reduce the diffusion length of Cu. However, the devices show even worse performances, probably due to the insufficient Cu diffusion. In comparison, CdTe-CuSCN devices annealed at 140 °C for a short duration (a few seconds) outperform the CdTe-Cu devices annealed at 200 °C for 20 min. This result indicates the possibility of reducing the adverse effect caused by the Cu over diffusion through performing Cu annealing at a lower temperature and a shorter holding time. Through lower temperature and shorter time annealing, the Cu diffused into CdTe can be easily confined on the rear side close to the back electrode. The predictable sharp copper concentration profile from the back surface to the bulk not only guarantees a proper Cu concentration on the rear side of CdTe to improve the ohmic contact, but also helps to reduce the Cu related deep trap states in the bulk and front interface caused by excess Cu concentrations [31–33]. The proper Cu doping control through our CuSCN treatment can assist to enhance outstanding performance for the CdTe-CuSCN devices.

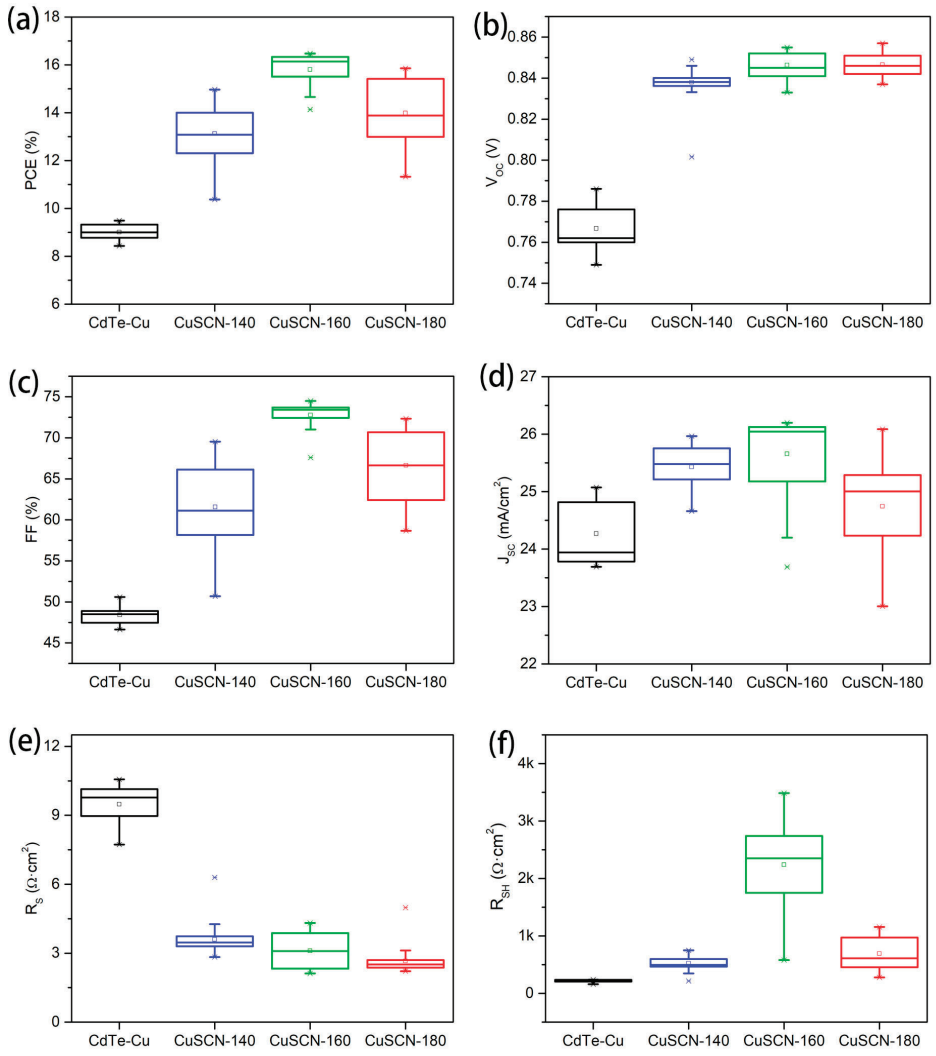


Figure 2. Statistical results for MZO/CdTe solar cell performances of (**a**) PCE, (**b**) V_{OC}, (**c**) FF, (**d**) J_{SC}, (**e**) series resistance (R_S), and (**f**) shunt resistance (R_{SH}) with metallic Cu and spin-coated CuSCN annealed at different temperatures.

Approved for public release; distribution unlimited.

By increasing the annealing temperature, the mean V_{OC} gradually increases from 0.838 V for CuSCN-140 to 0.847 V for CuSCN-180. The devices annealed at 160 °C deliver the best performance due to the largely improved FF (74.6%), compared to those devices annealed at lower or higher temperatures. This is mainly attributed to the higher hole concentration in CdTe bulk benefited from the proper copper diffusion. Higher hole concentration can boost a higher build-in potential (V_{bi}) and lead to less recombination in the depletion region and at the front interface, thereby resulting in larger FF, which can be further confirmed through the improvement of the shunt resistance (R_{SH}). Accompanied with the variation of the annealing temperature, the R_{SH} increases from the mean value 490 Ω cm^2 for CuSCN-140 to 2360 Ω cm^2 for CuSCN-160. When the annealing temperature is further increased to 180 °C, the mean R_{SH} decreases to 610 Ω cm^2, due to the excess Cu in the CdTe bulk and at the front interface. As the annealing temperature increases, the series resistance (R_S) decreases slightly from 3.50 Ω cm^2 in CuSCN-140 to 3.07 Ω cm^2 in CuSCN-160, and further to 2.51 Ω cm^2 in CuSCN-180. The J_{SC} also shows similar trend as the FF and the shunt resistance at different annealing temperatures.

The J-V curves of the best cells of CdTe-Cu and CdTe-CuSCN are plotted in Figure 3a, and more detailed parameters are displayed in Table 2. Comparing to the CdTe-Cu device, the CdTe-CuSCN device shows a higher J_{SC} value, partially due to the reduced recombination at the depletion region and front interface as discussed above. Another reason is the reduced carrier recombination at the back interface between CdTe and the metal electrode, which can be confirmed by the absence of severe roll-over and cross-over effects in the J-V curves at high forward bias for the CdTe-CuSCN devices. The roll-over effect is commonly an indicator of insufficient copper doping on the rear side of CdTe film [34–36], and the cross-over effect is due to photoconductivity in the buffer layer which could be caused by the aggregation of copper in the buffer layer. [37] For this sake, the CdTe-Cu device delivers an efficiency of 9.49%, with V_{OC} of 0.786 V, J_{SC} of 24.8 mA/cm^2, and FF of 48.7%. In contrast, all the CdTe-CuSCN devices show the absence of the roll-over and cross-over effects at forward bias, indicating lower back-barrier heights, and less Cu aggregation at the front interface. Thus, the CdTe-CuSCN devices promise higher FF values (69.1% for the CuSCN-140, 74.0% for the CuSCN-160, and 71.4% for the CuSCN-180). Benefitting from the significantly improved FF, the CuSCN-160 device delivers the best efficiency of 16.5% with V_{OC} of 0.850 V, J_{SC} of 26.2 mA/cm^2 and FF of 74.0%. External quantum efficiency (EQE) curves were measured to examine the carrier extraction properties for all the devices. As shown in Figure 3b, all the devices show the overlapped curves in short wavelength below 400 nm due to the parasitic absorption of ZMO films. Between 500 to 800 nm, the CdTe-Cu shows the lowest quantum efficiency, compared to the CuSCN ones. The deviation enlarged gradually as the wavelength increases, indicating a larger difference in the recombination properties at the CdTe and metal electrode interface. This can be attributed to two primary reasons: one is that the larger back-barrier height in CdTe-Cu for the hole extraction, and the other one is that the high conduction band offset between CdTe and CuSCN, which can reflect the unfavorable electron diffusion into the CuSCN layer, and thereby suppress the recombination at the back interface. This is consistent with the result of PL quenching for the CdTe/CuSCN film stack. For the CdTe-CuSCN devices annealed at various temperatures, the variation in the quantum efficiency is mainly located at the long wavelengths, probably due to the difference in the Cu concentration at the back surface of CdTe. At higher temperatures, more Cu in the CuSCN layer can diffuse into CdTe. The CuSCN-160 device shows the highest quantum efficiency at long wavelengths, indicating the lowest back barrier height, which can be further confirmed in the temperature dependent J-V measurement, described in the later section. When the annealing temperature is further increased to 180 °C, the Cu concentration at back side is too high, and the interstitial compensation defects Cu_i, instead of substitutional acceptor defects Cu_{Cd} become dominant, and the back barrier height increases, causing lower quantum efficiencies at long wavelengths for CuSCN-180. Overall, the CuSCN-160 device delivers the highest integrated current density of 25.5 mA/cm^2, with quantum efficiency over 85% in the whole wavelength range, and the highest value of 88.0% at 605 nm, showing decent carrier transport and extraction properties.

Approved for public release; distribution unlimited.

423

concentration profile from the back surface to the bulk not only guarantees a proper Cu concentration on the rear side of CdTe to improve the ohmic contact, but also helps to reduce the Cu related deep trap states in the bulk and front interface caused by excess Cu concentrations [31–33]. The proper Cu doping control through our CuSCN treatment can assist to enhance outstanding performance for the CdTe-CuSCN devices.

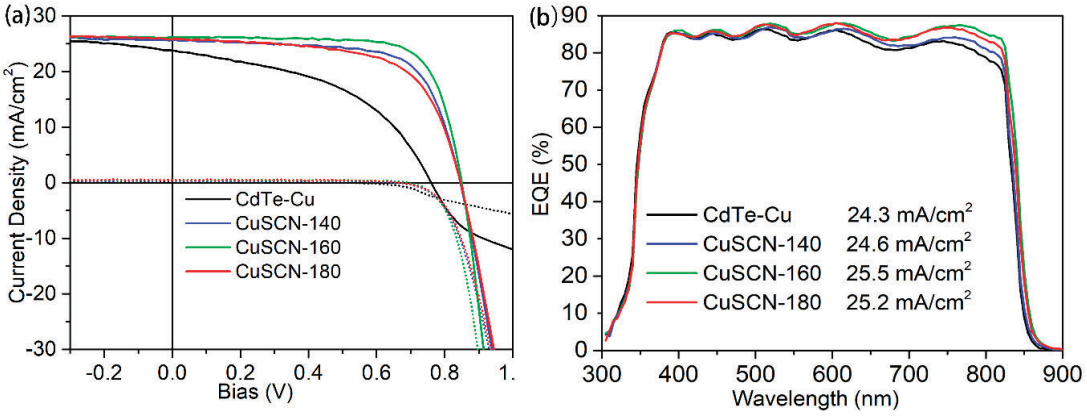


Figure 3. (**a**) Current density-voltage (J-V) and (**b**) external quantum efficiency (EQE) curves for the best devices with different back contact treatment: evaporated Cu metal and spin-coated CuSCN with different annealing temperatures.

Table 2. Device performance of the best cells in CdTe-Cu and CdTe-CuSCN, annealed at different temperatures.

Samples	V_{OC} (V)	J_{SC} (mA/cm^2)	FF (%)	Efficiency (%)	R_S (Ω cm^2)	R_{SH} (Ω cm^2)
CdTe-Cu	0.786	24.8	48.7	9.49	9.78	239
CuSCN-140	0.836	25.9	69.1	15.0	2.95	734
CuSCN-160	0.850	26.2	74.0	16.5	2.70	2580
CuSCN-180	0.851	26.1	71.4	15.9	2.45	1140

Due to the high resistivity of CuSCN, the thickness of CuSCN layer is critical for better carrier extraction efficiency. CdTe devices with different CuSCN thicknesses are fabricated using CuSCN solutions with different concentrations (2 and 10 mg/mL) and spin-coating speeds (2000 and 6000 rpm), which are named 2 mg/mL-6000 rpm, 2 mg/mL-2000 rpm, 10 mg/mL-6000 rpm, and 10 mg/mL-2000 rpm, respectively. We tried to measure the CuSCN film thicknesses with different deposition parameters through scanning electron microscopy (SEM) measurements. Unfortunately, the CuSCN films are too thin (less than 30 nm) to be accurately measured through SEM images. The cross-sectional SEM images of the whole devices with the thickest CuSCN film deposited at 2000 rpm using 10 mg/mL CuSCN solution were shown in Figure S2, from which we can know the CuSCN film thickness is about 30 nm, and the others should be thinner than 30 nm. Based on spin-coating features, the thickness of the CuSCN films should rank as 2 mg/mL-6000 rpm < 2 mg/mL-2000 rpm < 10 mg/mL-6000 rpm < 10 mg/mL-2000 rpm, which can be further confirmed by the gradual change of device performance. As shown in Figure 4, the V_{OC} increases gradually as the thickness of CuSCN increases. This can be attributed to the increase of CuSCN film thickness, which supplies more Cu for the diffusion during the annealing treatment, thus, a higher carrier concentration in the CdTe film and higher V_{OC} is generated. The complement of Cu doping concentration also helps to improve all the other J-V parameters, including higher FF, J_{SC}, R_{SH}, and lower R_S, yielding a highest efficiency 16.7%, with V_{OC} of 0.857 V, J_{SC} of 26.2 mA/cm^2, and FF of 74.5%. The detailed information of the best cells with different CuSCN thicknesses are shown in Table 3, and the corresponding J-V curves are shown in Figure S3. As the thickness of CuSCN film increases, PCEs increases from 12.8% to 16.7%. This improvement can be assigned to two major reasons: first, suggested by significant improvement in FF, the CuSCN film became more uniform and the CdTe film can be fully covered by CuSCN film; second, the Cu concentration in CdTe increases gradually due to the increase of CuSCN film thickness, and thus, higher V_{OC} values can be obtained. When the CuSCN film thickness is further increased by spin-coating a 10 mg/mL CuSCN solution at 2000 rpm, V_{OC} is further increased to over 0.863 V, but all the other parameters decrease with a J_{SC} to 25.3 mA/cm^2, a FF to 70.1%, yielding an efficiency to 15.4%. This is

By increasing the annealing temperature, the mean V_{OC} gradually increases from 0.838 V for CuSCN-140 to 0.847 V for CuSCN-180. The devices annealed at 180 °C deliver the best performance due to the largely improved FF (74.6%), compared to those devices annealed at lower or higher temperatures. This is mainly attributed to the higher hole concentration in CdTe bulk benefited from the proper copper diffusion. Higher hole concentration can boost a higher build-in potential (V_{bi}) and lead to less recombination in the depletion region and at the front interface, thereby resulting in larger FF, which can be further confirmed through the improvement of the shunt resistance (R_{SH}). Accompanied with the variation of the annealing temperature, the R_{SH} increases from the mean value 490 Ω cm^2 for CuSCN-140 to 2360 Ω cm^2 for CuSCN-160. When the annealing temperature is further increased to 180 °C, the mean R_{SH} decreases to 610 Ω cm^2, due to the excess Cu in the CdTe bulk and at

likely ascribed to the high resistance of CuSCN film because, taking an example of the same 10 mg/mL CuSCN solution, decreasing the spin speed from 6000 rpm to 2000 rpm results in increased R_S from 3.43 to 4.17 Ω cm^2.

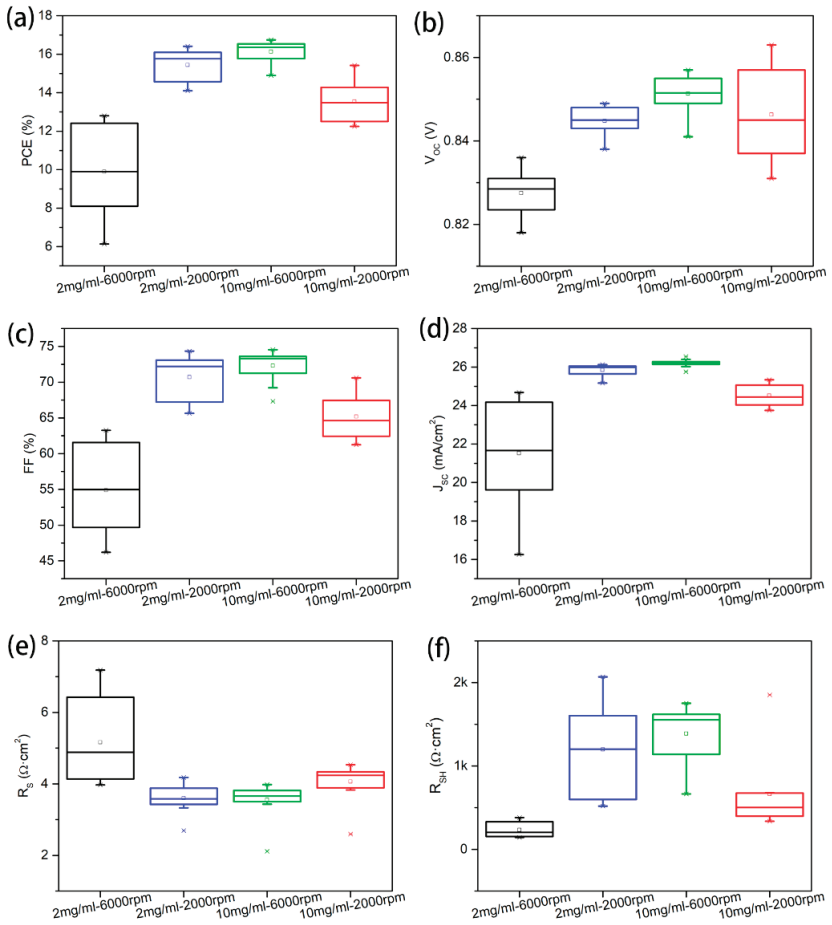


Figure 4. Statistical results for MZO/CdTe solar cell performances of (**a**) PCE, (**b**) V_{OC}, (**c**) FF, (**d**) J_{SC}, (**e**) series resistance (R_S), and (**f**) shunt resistance (R_{SH}) with different CuSCN film thicknesses tuned by varying the solution concentration and the spin-coating speed.

Table 3. The device performance of the best cells with different CdTe-CuSCN thickness.

CuSCN Deposition	V_{OC} (V)	J_{SC} (mA/cm^2)	FF (%)	Efficiency (%)	R_S (Ω cm^2)	R_{SH} (Ω cm^2)
2 mg/mL-6000 rpm	0.830	24.4	63.3	12.8	4.01	381
2 mg/mL-2000 rpm	0.849	26.1	74.1	16.4	3.58	2070
10 mg/ml-6000 rpm	0.857	26.2	74.5	16.7	3.43	1610
10 mg/ml-2000 rpm	0.862	25.3	70.6	15.4	4.17	1350

In order to investigate the origin of device performance improvement with the CuSCN as back contact, the temperature-dependent dark J-V measurements for devices with copper metal (CdTe-Cu) and CuSCN (CuSCN-160) as the back contact were carried out at temperatures ranging from 200 to 310 K, to quantify the back-barrier height as shown in (Figure 5a,b). The temperature dependent dark J-V measurements, as shown in Figure 5a, b, were carried out at temperatures ranging from 200 to 310 K to quantify the back-barrier heights of the devices, with Cu metal and CuSCN as the back contact. For the CdTe-Cu device, the J-V curves show a severe roll-over effect at a high forward bias at room temperature, and the roll-over becomes more pronounced as the temperature decreases to

Approved for public release; distribution unlimited.
425

200 K. In contrast, the CdTe-CuSCN device shows a typical diode behavior, without roll-over in the temperature range of 310 to 250 K. The presence of roll-over effect indicates the existence of a back barrier at the back interface and thereby enhanced carrier recombination. The values of the back-barrier height for the CdTe-Cu and CdTe-CuSCN are calculated according the reference. [38] As shown in Figure 5c, the CdTe-Cu device exhibits a back-barrier height of 0.662 eV, which is extremely high to extract the holes efficiently from the CdTe to the metal electrode. This further explains the origin of low device performances with efficiencies lower than 10%. The CuSCN-160 device possesses a 0.137 eV back-barrier height, which is much lower than that of the CdTe-Cu devices. This small back-barrier height in CuSCN-160 boosts higher carrier extraction efficiency, explaining the origin of the distinctive EQE curves shown in Figure 3b.

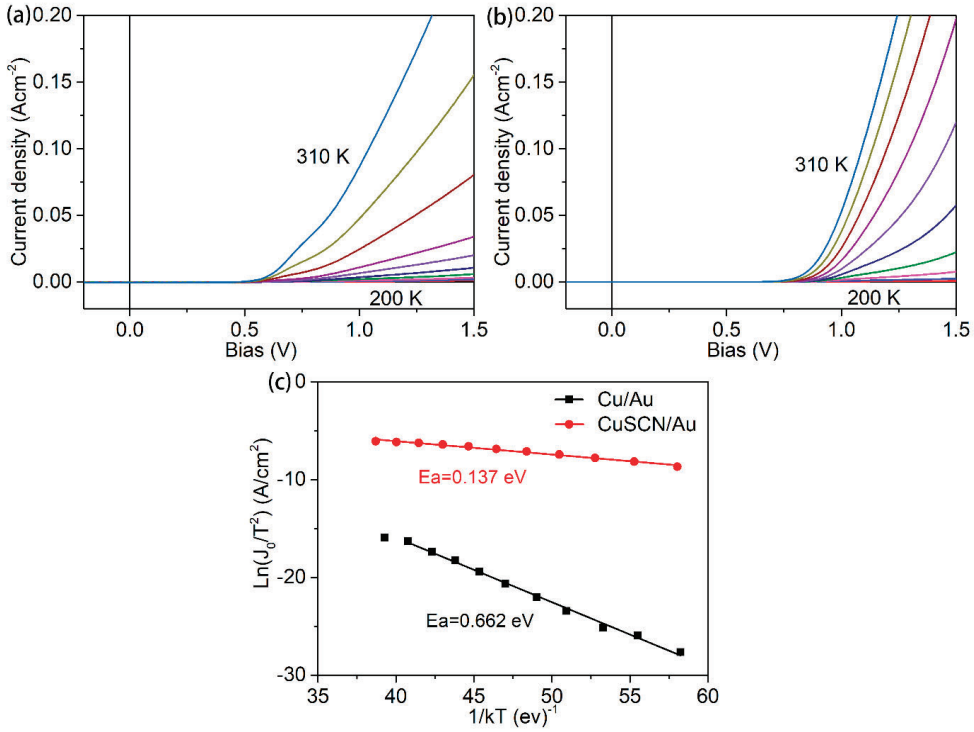


Figure 5. Temperature dependent dark J-V curves for devices with (**a**) Cu metal and (**b**) CuSCN as the back contact. (**c**) Arrhennius plots for the calculation of the back-barrier height for the devices with Cu metal and CuSCN as the back contact.

Through the careful optimization of the CuSCN treatment, depositing CuSCN film using ammonium hydroxide with water as the solvent was demonstrated to be an efficient means of improving the device performances. However, it has been reported that the performance of ZMO/CdTe device degraded gradually while being exposed to ambient conditions, due to the reaction between water in atmosphere and MgO in ZMO films. [19] To further confirm whether the water in the CuSCN solution will degrade the performance of the ZMO/CdTe solar cells during the annealing treatment, a CuSCN solution without water was used for the CuSCN film deposition. Diethyl sulfide has been widely used as the solvent of CuSCN for hole transport layer deposition. [39,40] For the fabrication of the CdTe-CuSCN device with Diethyl sulfide as solvent, the same procedures used for the CuSCN treatment were used. As shown in Figure S4, the devices using CuSCN in ammonium hydroxide show slightly higher and more uniform performances than those using diethyl sulfide as the solvent. This is because that the uniformity of the CuSCN film deposited using ammonium hydroxide solvent is much better than that using diethyl sulfide as the solvent, which has been confirmed in our previous

Approved for public release; distribution unlimited.

report [15]. These results further confirm that the performance of our ZMO/CdTe devices is not affected by the water in ammonium hydroxide, demonstrating a robust hole transport layer deposition procedure for ZMO/CdTe solar cells.

4. Conclusions

Solution-processed CuSCN treatment with an aqueous solution has been demonstrated to be an efficient procedure for improving the performance of CdTe solar cells with ZMO as the buffer layer. Through the systematic optimization of the CuSCN film thickness and post annealing temperature, the best ZMO/CdTe device achieves an efficiency of 16.7%, with a V_{OC} of 0.857 V, a J_{SC} of 26.2 mA/cm^2, and an FF of 74.5%. The improvement of the device performance compared with the devices with traditional metallic Cu is mainly attributed to the significantly reduced back-barrier height from 0.662 to 0.137 eV. Our results also indicate that water in ammonium hydroxide solvent has no adverse effect on the ZMO/CdTe devices, indicating a high tolerance of the ZMO/CdTe devices to humidity, and showing a high flexibility for the post treatment of ZMO/CdTe devices in the future.

Supplementary Materials: The following are available online at http://www.mdpi.com/1996-1944/13/8/1991/s1, Figure S1: Cross-sectional SEM images of complete devices with CuSCN as back contact in different magnification, Figure S2: J-V curves the best cells in devices with different CuSCN thickness, Figure S3: Statistical results for MZO/CdTe solar cell performances of (**a**) PCE, (**b**) V_{OC}, (**c**) FF, (d) JSC, (**e**) series resistance (R_S), and (**f**) shunt resistance (R_{SH}) with different CuSCN solutions, Figure S4: Statistical results for MZO/CdTe solar cell performances of (**a**) PCE, (**b**) V_{OC}, (**c**) FF, (**d**) JSC, (**e**) series resistance (R_S), and (**f**) shunt resistance (R_{SH}) with different CuSCN solutions.

Author Contributions: Conceptualization, Y.Y.; methodology, Y.Y.; software, D.-B.L.; validation, F.K.A., R.A.A., N.S., A.B.P., M.J.H., and R.J.E.; formal analysis, D.-B.L.; investigation, D.-B.L., S.S.B. and D.R.; resources, Y.Y.; data curation, D.-B.L.; writing—original draft preparation, D.-B.L.; writing—review and editing, Z.S., N.S., F.Y. and Y.Y.; supervision, Y.Y.; project administration, Y.Y; funding acquisition, Y.Y. and R.E. All authors have read and agreed to the published version of the manuscript.

Funding: This research was funded by Air Force Research Laboratory under agreement number FA9453-18-2-0037, Air Force Research Laboratory, Space Vehicles Directorate under Contract number FA9453-19-C-1002 and the National Science Foundation under contract number 1711534.

Acknowledgments: This material is based on research sponsored by Air Force Research Laboratory under agreement number FA9453-18-2-0037. The US Government is authorized to reproduce and distribute reprints for Governmental purposes notwithstanding any copyright notation thereon. The authors gratefully acknowledge funding support from the U.S. Air Force Research Laboratory, Space Vehicles Directorate, under Contract # FA9453-19-C-1002. We thank Dr David Strickler from Pilkington North America Inc. for supplying us FTO-coated substrates. The views and conclusions contained herein are those of the authors and should not be interpreted as necessarily representing the official policies or endorsements, either expressed or implied, of Air Force Research Laboratory or the US Government.

Conflicts of Interest: The authors declare no conflict of interest.

References

1. Green, M.A.; Hishikawa, Y.; Dunlop, E.D.; Levi, D.H.; Hohl-Ebinger, J.; Ho-Baillie, A.W.Y. Solar cell efficiency tables (version 51). *Prog. Photovolt. Res. Appl.* **2018**, *26*, 3–12. [CrossRef]
2. NREL Research Cell Record Efficiency Chart. Available online: https://www.nrel.gov/pv/assets/pdfs/pv-efficiency-chart.201812171.pdf (accessed on 20 March 2020).
3. Shockley, W.; Queisser, H.J. Detailed balance limit of efficiency of p-n junction solar cells. *J. Appl. Phys.* **1961**, *32*, 510–519. [CrossRef]
4. Birkmire, R.W.; Eser, E. Polycrystalline thin film solar cells: Present status and future potential. *Annu. Rev. Mater. Sci.* **1997**, *27*, 625–653. [CrossRef]
5. Dharmadasa, I.M.; Alam, A.E.; Ojo, A.A.; Echendu, O.K. Scientific complications and controversies noted in the field of CdS/CdTe thin film solar cells and the way forward for further development. *J. Mater. Sci. Mater. Electron.* **2019**, *30*, 20330–20344. [CrossRef]
6. Dobson, K.D.; Visoly-Fisher, I.; Hodes, G.; Cahen, D. Stability of CdTe/CdS thin-film solar cells. *Sol. Energ. Mat. Sol. Cell* **2000**, *62*, 295–325. [CrossRef]

Approved for public release; distribution unlimited.

427

7. McCandless, B.E.; Buchanan, W.A.; Thompson, C.P.; Sriramagiri, G.; Lovelett, R.J.; Duenow, J.; Albin, D.; Jensen, S.; Colegrove, E.; Moseley, J.; et al. Overcoming carrier concentration limits in polycrystalline CdTe thin films with in situ doping. *Sci. Rep.* **2018**, *8*, 14519. [CrossRef]
8. Zhao, H.; Farah, A.; Morel, D.; Ferekides, C.S. The effect of impurities on the doping and Voc of CdTe/CdS thin film solar cells. *Thin Solid Films* **2009**, *517*, 2365–2369. [CrossRef]
9. Tamotsu, O.; Shigeyuki, I.; Satsuki, N.; Ryoji, H.; Kaoru, Y.; Yohei, K.; Akira, N.; Ryuichi, H. Effects of antimony doping in polycrystalline CdTe thin-film solar cells. *Jpn. J. Appl. Phys.* **2012**, *51*, 10NC12.
10. Metzger, W.K.; Grover, S.; Lu, D.; Colegrove, E.; Moseley, J.; Perkins, C.L.; Li, X.; Mallick, R.; Zhang, W.; Malik, R.; et al. Exceeding 20% efficiency with in situ group V doping in polycrystalline CdTe solar cells. *Nat. Energy* **2019**, *4*, 837–845. [CrossRef]
11. Paudel, N.R.; Yan, Y. Application of copper thiocyanate for high open-circuit voltages of CdTe solar cells. *Prog. Photovolt. Res. Appl.* **2016**, *24*, 94–101. [CrossRef]
12. Kumara, G.R.R.A.; Konno, A.; Senadeera, G.K.R.; Jayaweera, P.V.V.; De Silva, D.B.R.A.; Tennakone, K. Dye-sensitized solar cell with the hole collector p-CuSCN deposited from a solution in n-propyl sulphide. *Sol. Energ. Mat. Sol. Cell* **2001**, *69*, 195–199. [CrossRef]
13. Lévy-Clément, C.; Tena-Zaera, R.; Ryan, M.A.; Katty, A.; Hodes, G. CdSe-sensitized p-CuSCN/nanowire n-ZnO heterojunctions. *Adv. Mater.* **2005**, *17*, 1512–1515. [CrossRef]
14. Arora, N.; Dar, M.I.; Hinderhofer, A.; Pellet, N.; Schreiber, F.; Zakeeruddin, S.M.; Grätzel, M. Perovskite solar cells with CuSCN hole extraction layers yield stabilized efficiencies greater than 20%. *Science* **2017**, *358*, 768–771. [CrossRef] [PubMed]
15. Montgomery, A.; Guo, L.; Grice, C.; Awni, R.A.; Saurav, S.; Li, L.; Yan, Y.; Yan, F. Solution-processed copper (i) thiocyanate (CuSCN) for highly efficient CdSe/CdTe thin-film solar cells. *Prog. Photovolt. Res. Appl.* **2019**, *27*, 665–672. [CrossRef]
16. Ablekim, T.; Colegrove, E.; Metzger, W.K. Interface engineering for 25% CdTe solar cells. *ACS Appl. Energy Mater.* **2018**, *1*, 5135–5139. [CrossRef]
17. Munshi, A.H.; Kephart, J.; Abbas, A.; Raguse, J.; Beaudry, J.; Barth, K.; Sites, J.; Walls, J.; Sampath, W. Polycrystalline CdSeTe/CdTe absorber cells with 28 mA/cm^2 short-circuit current. *IEEE J. Photovolt.* **2018**, *8*, 310–314. [CrossRef]
18. Li, D.-B.; Song, Z.; Awni, R.A.; Bista, S.S.; Shrestha, N.; Grice, C.R.; Chen, L.; Liyanage, G.K.; Razooqi, M.A.; Phillips, A.B.; et al. Eliminating s-kink to maximize the performance of MgZnO/CdTe solar cells. *ACS Appl. Energy Mater.* **2019**, *2*, 2896–2903. [CrossRef]
19. Ablekim, T.; Perkins, C.; Zheng, X.; Reich, C.; Swanson, D.; Colegrove, E.; Duenow, J.N.; Albin, D.; Nanayakkara, S.; Reese, M.O.; et al. Tailoring MgZnO/CdSeTe interfaces for photovoltaics. *IEEE J. Photovolt.* **2019**, *9*, 888–892. [CrossRef]
20. Bittau, F.; Jagdale, S.; Potamialis, C.; Bowers, J.W.; Walls, J.M.; Munshi, A.H.; Barth, K.L.; Sampath, W.S. Degradation of Mg-doped zinc oxide buffer layers in thin film CdTe solar cells. *Thin Solid Films* **2019**, *691*, 137556. [CrossRef]
21. Paudel, N.R.; Xiao, C.; Yan, Y. Close-space sublimation grown CdS window layers for CdS/CdTe thin-film solar cells. *J. Mater. Sci. Mater. Electron.* **2014**, *25*, 1991–1998. [CrossRef]
22. Kuribayashi, K.; Matsumoto, H.; Uda, H.; Komatsu, Y.; Nakano, A.; Ikegami, S. Preparation of low resistance contact electrode in screen printed CdS/CdTe solar cell. *Jpn. J. Appl. Phys.* **1983**, *22*, 1828–1831. [CrossRef]
23. Awni, R.A.; Li, D.-B.; Grice, C.R.; Song, Z.; Razooqi, M.A.; Phillips, A.B.; Bista, S.S.; Roland, P.J.; Alfadhili, F.K.; Ellingson, R.J.; et al. The effects of hydrogen iodide back surface treatment on CdTe solar cells. *Solar RRL* **2019**, *3*, 1800304. [CrossRef]
24. Bätzner, D.L.; Wendt, R.; Romeo, A.; Zogg, H.; Tiwari, A.N. A study of the back contacts on CdTe/CdS solar cells. *Thin Solid Films* **2000**, *361–362*, 463–467. [CrossRef]
25. Watthage, S.C.; Phillips, A.B.; Liyanage, G.K.; Song, Z.; Gibbs, J.M.; Alfadhili, F.K.; Alkhayat, R.B.; Ahangharnejhad, R.H.; Almutawah, Z.S.; Bhandari, K.P.; et al. Selective Cd removal from CdTe for high-efficiency Te back-contact formation. *IEEE J. Photovolt.* **2018**, *8*, 1125–1131. [CrossRef]
26. Burgelman, M.; Nollet, P.; Degrave, S. Modelling polycrystalline semiconductor solar cells. *Thin Solid Films* **2000**, *361–362*, 527–532. [CrossRef]
27. Jaffe, J.E.; Kaspar, T.C.; Droubay, T.C.; Varga, T.; Bowden, M.E.; Exarhos, G.J. Electronic and defect structures of CuSCN. *J. Phys. Chem. C* **2010**, *114*, 9111–9117. [CrossRef]

Approved for public release; distribution unlimited.

28. Hausmann, A.; Schallenberger, B.; Roll, R. A new model for ZnO:Cu undergoing dynamic Jahn-Teller coupling. *Z. Phys. B* **1980**, *40*, 1–7. [CrossRef]
29. Kutty, T.R.N.; Raghu, N. Varistors based on polycrystalline ZnO:Cu. *Appl. Phys. Lett.* **1989**, *54*, 1796–1798. [CrossRef]
30. Xu, C.X.; Sun, X.W.; Zhang, X.H.; Ke, L.; Chua, S.J. Photoluminescent properties of copper-doped zinc oxide nanowires. *Nanotechnology* **2004**, *15*, 856–861. [CrossRef]
31. Biglari, B.; Samimi, M.; Hage-Ali, M.; Koebel, J.M.; Siffert, P. Effects of copper in high resistivity cadmium telluride. *J. Cryst. Growth* **1988**, *89*, 428–434. [CrossRef]
32. Jones, E.D.; Stewart, N.M.; Mullin, J.B. The diffusion of copper in cadmium telluride. *J. Cryst. Growth* **1992**, *117*, 244–248. [CrossRef]
33. Yan, Y.; Jones, K.; Zhou, J.; Wu, X.; Al-Jassim, M. Tem study of locations of Cu in CdTe solar cells. *MRS Proc.* **2011**, *1012*. [CrossRef]
34. Demtsu, S.H.; Sites, J.R. Effect of back-contact barrier on thin-film CdTe solar cells. *Thin Solid Films* **2006**, *510*, 320–324. [CrossRef]
35. Burgelman, M.; Verschraegen, J.; Degrave, S.; Nollet, P. Analysis of CdTe solar cells in relation to materials issues. *Thin Solid Films* **2005**, *480–481*, 392–398. [CrossRef]
36. Awni, R.A.; Li, D.-B.; Song, Z.; Bista, S.S.; Razooqi, M.A.; Grice, C.R.; Chen, L.; Liyanage, G.K.; Li, C.; Phillips, A.B.; et al. Influences of buffer material and fabrication atmosphere on the electrical properties of CdTe solar cells. *Prog. Photovolt. Res. Appl.* **2019**, *27*, 1115–1123. [CrossRef]
37. Corwine, C.R.; Pudov, A.O.; Gloeckler, M.; Demtsu, S.H.; Sites, J.R. Copper inclusion and migration from the back contact in CdTe solar cells. *Sol. Energy Mat. Sol. Cell* **2004**, *82*, 481–489. [CrossRef]
38. Li, J.V.; Johnston, S.W.; Li, X.; Albin, D.S.; Gessert, T.A.; Levi, D.H. Discussion of some "trap signatures" observed by admittance spectroscopy in CdTe thin-film solar cells. *J. Appl. Phys.* **2010**, *108*, 64501. [CrossRef]
39. Chaudhary, N.; Chaudhary, R.; Kesari, J.P.; Patra, A.; Chand, S. Copper thiocyanate (CuSCN): An efficient solution-processable hole transporting layer in organic solar cells. *J. Mater. Chem. C* **2015**, *3*, 11886–11892. [CrossRef]
40. Madhavan, V.E.; Zimmermann, I.; Roldán-Carmona, C.; Grancini, G.; Buffiere, M.; Belaidi, A.; Nazeeruddin, M.K. Copper thiocyanate inorganic hole-transporting material for high-efficiency perovskite solar cells. *ACS Energy Lett.* **2016**, *1*, 1112–1117. [CrossRef]



© 2020 by the authors. Licensee MDPI, Basel, Switzerland. This article is an open access article distributed under the terms and conditions of the Creative Commons Attribution (CC BY) license (http://creativecommons.org/licenses/by/4.0/).

Approved for public release; distribution unlimited.

Check for updates

Energy Technology
Generation, Conversion, Storage, Distribution
www.entechnol.de

Successive Ionic Layer Adsorption and Reaction-Deposited Transparent Cu–Zn–S Nanocomposites as Hole Transport Materials in CdTe Photovoltaics

*Ebin Bastola, Kamala Khanal Subedi, Fadhil K. Alfadhili, Adam B. Phillips, Michael J. Heben, and Randy J. Ellingson**

Evolving material science and device architectures continue to drive improvements in photovoltaic solar cell performance. Herein, the synthesis and application of p-type transparent copper–zinc–sulfide (Cu–Zn–S) nanocomposite thin films for application as a semi-transparent back buffer layer for cadmium telluride (CdTe) photovoltaics is reported. Earth-abundant and low-toxicity Cu–Zn–S films are prepared at room temperature using successive ionic layer adsorption and reaction (SILAR). Transparency in the range of 500–800 nm, low resistivity, and composition-controlled bandgap energy offer a compelling material system for high performance as an electron reflector enabling bifacial cell design. Implementing the Cu–Zn–S hole transport material (HTM) at the CdTe back contact, without intentional introduction of Cu doping, converts simulated AM1.5 sunlight to electricity at an efficiency up to 13.2%, with an average device performance of 13.0%. Intentional Cu doping yields a best efficiency of 14.3% with open-circuit voltage (V_{OC}) of 848 mV and fill factor (FF) of 77.3% (average 14.1%). Our study shows the clear promise of this material for highly efficient and semi-transparent back contact to CdTe solar cells.

1. Introduction

Transparent conducting materials are essential to fabricate electronic devices such as light-emitting diodes,[1] displays,[2] and photovoltaic devices.[3] The thin-film solar cell device consists of transparent conducting materials as a window and/or buffer layer and a semiconductor material as an absorber layer. The transparent materials possess both high conductivity (low resistivity) and optical transparency which are, in general, n-type materials. However, the buffer layers or hole transport materials (HTMs), which are applied at the back-contact interface, such as in cadmium telluride (CdTe) solar cells, are p-type.

Dr. E. Bastola, K. K. Subedi, Dr. F. K. Alfadhili, Prof. A. B. Phillips, Prof. M. J. Heben, Prof. R. J. Ellingson
Wright Center for Photovoltaics Innovation and Commercialization (PVIC)
Department of Physics and Astronomy
University of Toledo
Toledo, OH 43606, USA
E-mail: Randy.Ellingson@utoledo.edu

The ORCID identification number(s) for the author(s) of this article can be found under https://doi.org/10.1002/ente.202000429.

DOI: 10.1002/ente.202000429

The development of p-type transparent materials with high hole conductivity and optical transparency lags behind compared with n-type transparent materials.[4] Common p-type transparent conducting materials, also important for the fabrication of bifacial photovoltaic devices, include oxide and sulfide compounds of copper such as Cu_xO,[5] $CuAlO_2$,[6] Cu_xS,[7] and $Cu_xZn_{1-x}S$.[8]

Cu–Zn–S (CZS) nanocomposite thin films are Earth-abundant materials possessing high transparency in the visible region, a high energy bandgap, high conductivity, and high hole concentration.[9] The optical bandgap and Fermi level of the CZS material can be adjusted by changing the material composition.[10] Thus, CZS nanocomposite can serve as effective hole selective layers in solar cells.[3a] CZS materials can be prepared by vacuum[11] and solution-based techniques including chemical bath deposition (CBD)[3a,12] and successive ionic layer adsorption and reaction (SILAR)[9,10] methods. Xu et al. have reported $(CuS)_x(ZnS)_{1-x}$ p-type transparent materials with transmission >70% in the visible region and fabricated heterojunction p-$(CuS)_x(ZnS)_{1-x}$/n-Si solar cells.[3a] The $(CuS)_x(ZnS)_{1-x}$ nanocomposites served as the hole selective layers for heterojunction devices and demonstrated the application of these Earth- abundant materials as HTMs in solar cells. Previously, we have fabricated CdTe devices with $(CuS)_x(ZnS)_{1-x}$ as the hole selective layer using CBD.[13] Jose et al. have synthesized and characterized the CZS film using a SILAR method.[9] In a SILAR method, the material gets deposited by the reactions of cations and anions, producing an atomic layer and thus improving the quality of the nanocomposite films. In addition, the thin films with very small grain sizes are more compact and transparent to visible light.

Cadmium telluride (CdTe) solar cells are well-known thin-film technologies that convert solar energy into electrical energy with a suitable bandgap of 1.48 eV. To fabricate CdTe solar cells, copper/gold (Cu/Au) is usually used as a standard back-contact material, and the role of Cu is for doping and band bending due to a deeply located (≈–5.9 eV)[14] valence band edge of CdTe.[15] The work function of gold is ≈5.0–5.2 eV[16] compared with the deep valence band edge of CdTe, a potential barrier is formed.

 © 2020 Wiley-VCH GmbH

Approved for public release; distribution unlimited.
430

To reduce this potential barrier, one utilizes a material with suitable optoelectronic properties (p-type, low resistivity, high hole concentration) and band edge location to achieve efficient extraction of holes while repelling electrons at the back interface of the CdTe devices; the desired results include a reduced forward electron current and improved open-circuit voltage.[17] Materials such as carbon nanotubes,[18] copper thiocyanate (CuSCN),[19] iron pyrite (FeS_2),[20] zinc telluride (ZnTe),[21] antimony telluride (Sb_2Te_3),[22] and copper telluride (Cu_xTe)[23] have been tested as back-contact buffer layers in CdTe solar cells. First solar has used ZnTe as an interface layer to fabricate highly efficient CdTe solar cells on a commercial scale.[24] Some of the solution-processed back-contact buffer layers include $Ni_xFe_{1-x}S_2$, chalcopyrite ($CuFeS_2$), and perovskite.[25] Similarly, some of the materials used as hole transport layers in nanocrystal-based CdTe solar cells include P-TPA, Si-TPA, and Spiro to improve the hole transport properties and device efficiency.[26] However, most of these materials are not optically transparent to visible light for the fabrication of bifacial devices, and their doping level cannot be well controlled. We demonstrate that Earth-abundant materials such as Cu–Zn–S can be alternatives HTMs in photovoltaics.

Previously, we have fabricated $(CuS)_x(ZnS)_{1-x}$ thin films using a CBD method at 80 °C in about an hour and applied them as HTMs for CdTe photovoltaics.[13] During deposition, Cu ions may diffuse to the CdTe film and we were interested to see how room temperature-processed CZS acts as HTMs to CdTe photovoltaics, assuming that there is no Cu diffusion at room temperature. Our preliminary study of CZS HTMs deposited by the SILAR method on CdTe showed a promising result without additional Cu doping and inspired us to carry this investigation over a wide range of CZS compositions.[27] Here, we have fabricated and characterized transparent CZS nanocomposite thin films with various compositions, using a SILAR method, and then applied them as a back-contact interface layer to CdTe solar cells. These CZS films are compact with petal-like nanostructures with high transparency in the visible region and low resistivity with varying bandgap energy. We found that CdTe devices with a CZS layer performed better compared with the devices without the CZS layer, reaching an efficiency of 13.2%. With optimized doping and CZS nanocomposite as an interface layer, the best cell reached an efficiency of 14.3% (average 14.1%) with an open-circuit voltage of 848 mV and a fill factor (FF) of 77.3%.

2. Results and Discussion

The CZS thin films were fabricated at room temperature using a SILAR method. In the first step, cations were adsorbed on the surface, and weakly bound cations were removed during subsequent rinsing in DIW. The substrate is then immersed in anion solution, resulting a reaction between cations (Zn and Cu ions) and anions (S ions), followed by additional rinse in DIW which removes loosely bound S ions. The SILAR cycle is repeated several times to prepare a thin film of desired thickness. **Figure 1** shows the transmission and reflection spectra for CZS-10, CZS-20, CZS-30, CZS-40, CZS-50, and CZS-80 nanocomposite films. Here, CZS-30 denotes thin films prepared using Zn precursor

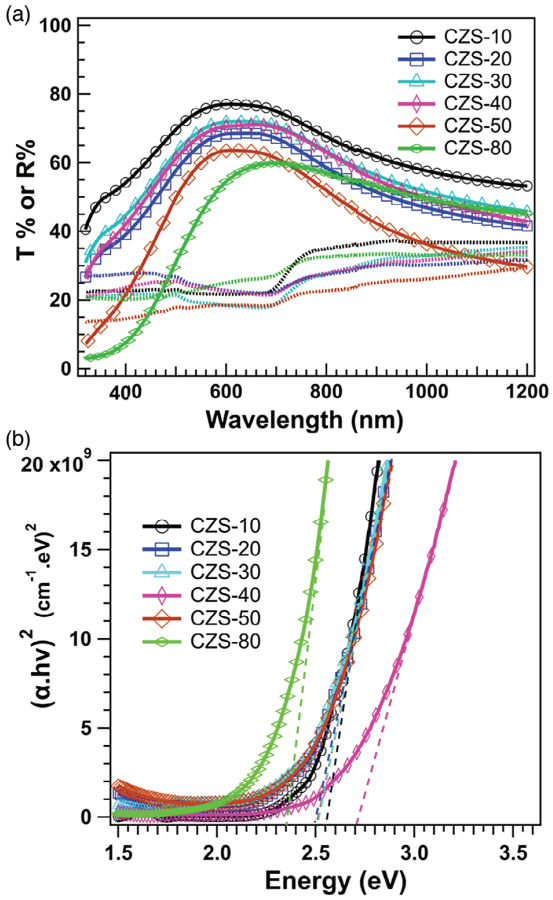


Figure 1. a) Transmission (T) and reflection (R, dotted) spectra of the CZS nanocomposite thin films prepared by a SILAR method and b) plots of $(\alpha h\nu)^2$ versus energy ($h\nu$, eV) to estimate the energy bandgaps of CZS nanocomposites (CZS-30 represents a film prepared using 0.03 M zinc acetate and 0.07 M $CuCl_2$ as cationic precursor).

30% (0.03 M zinc acetate) and Cu precursor 70% (0.07 M) of the total cations (0.1 M) used. As shown in the transmission spectra, these films show greater than 50% transmittance in the visible region in the range of 500–800 nm. The transmission and reflection spectra were utilized to obtain bandgaps of these films. The transmission (T) and reflection (R) spectra along with the thickness (t) of the films were used to calculate the absorption coefficient (α) of the thin film using the equation

$$\alpha = -\ln(T/(1-R))/t \quad (1)$$

The bandgap energies for these nanocomposites were calculated by plotting $(\alpha h\nu)^2$ versus ($h\nu$) for CZS nanocomposites. The calculated bandgap values for CZS films are shown in **Table 1**. The energy bandgap of the CZS-30 film estimated by the equation earlier is 2.50 eV.

Figure 2 shows the surface morphology of CZS thin films deposited on a soda lime glass for CZS-10, CZS-30,

© 2020 Wiley-VCH GmbH

Approved for public release; distribution unlimited.

Table 1. Properties of Cu–Zn–S thin films.

Sample	Thickness [nm]	*T*% at 550 [nm]	Bandgap (E_g, [eV])	Sheet resistance [Ω sq^{-1}]	Resistivity (10^{-2} [Ω cm])
CZS-10	50	75.2	2.55	3143	1.6
CZS-20	100	65.3	2.50	1322	1.3
CZS-30	90	69.5	2.50	2166	2.0
CZS-40	145	67.9	2.70	6102	8.9
CZS-50	180	60.0	2.50	2918	5.3
CZS-80	200	45.1	2.35	38 956	77.9

CZS-50, and CZS-80. Based on scanning electron microscopy (SEM) images, CZS-30 and CZS-50 films have similar surface morphologies with compact grains of length of around 200 nm. CZS-10 film was thinner (≈50 nm) compared with other films, has higher transparency, and consists of voids compared with CZS-30 and CZS-50 films. Note that all these films were deposited in the same condition and only the ratio of cations (Zn and Cu ions) were varied. In the case of CZS-80 film (Figure 2d), surface morphology looks different from other CZS compositions which might be due to a higher amount of Zn atoms in the cationic precursor. CZS-50 film had few diffraction peaks[27] similar to CuS, whereas CZS-80 film shows an amorphous nature compared with other compositions (Figure S1, Supporting Information). Energy-dispersive X-ray spectroscopy (EDS) analysis of these films shows elemental composition consisting of Cu, Zn, and S atoms and the atomic percentages of constituent elements are shown in Table S1, Supporting Information. No Zn atoms were observed in the EDS analysis for CZS-10 and CZS-20 films. The Zn percentage was increased to higher amounts as the amount of Zn percentage was increased in the precursor. Here, the lower content of Zn in the film compared with the precursor indicates the lower reactivity of Zn atoms compared with Cu atoms, as observed in $(CuS)_x(ZnS)_{1-x}$ deposition using the chemical bath method.[13]

Based on X-ray diffraction patterns (Figure S1, Supporting Information), as-deposited CZS thin films with higher Cu (lower Zn) concentrations have diffraction patterns similar to the covellite CuS (hexagonal crystal structure) but with lower Cu (higher Zn) concentrations, no diffraction patterns were observed. It indicates poor crystallinity as the Zn atoms increase, which is slightly different with the previous report.[9] The authors observed diffraction patterns for various compositions of CZS films. CZS-20 film shows a small diffraction peak at 48.2°, matching a peak of CuS (PDF #98-001-3414). In the case of CZS-50 sample, its diffraction peaks match well with the standard covellite CuS peaks. However, no diffraction peaks were observed for CZS-80 film, indicating the amorphous nature of the materials deposited, similar to the CBD-deposited $(CuS)_x(ZnS)_{1-x}$ film. As the amount of Zn in the film increases the film becomes more amorphous.[3a,13]

The sheet resistances of CZS films were measured using a four-point probe and resistivities were calculated. Table 1 shows the various properties of these nanocomposite films including thickness, transmission at 550 nm wavelength, energy bandgap, sheet resistance, and resistivity. As the amount of Zn concentration increased, its resistivity increased. For example, for CZS-10, the resistivity is 1.6×10^{-2} Ω cm whereas for CZS-80, the resistivity is 77.9×10^{-2} Ω cm. The resistivity increases due to the lower amount of Cu content and the more amorphous nature of the nanocomposite film. The resistivities measured for these CZS films are similar to the values reported previously and these materials have hole concentrations in the order of 10^{21} cm^{-3}, thus behaving like degenerately doped semiconductors.[9] The transparency of these nanocomposite films in the visible region and low resistivity make these materials promising in various optoelectronic applications including light-emitting devices, displays, and solar cells. As evidenced from the low resistivity

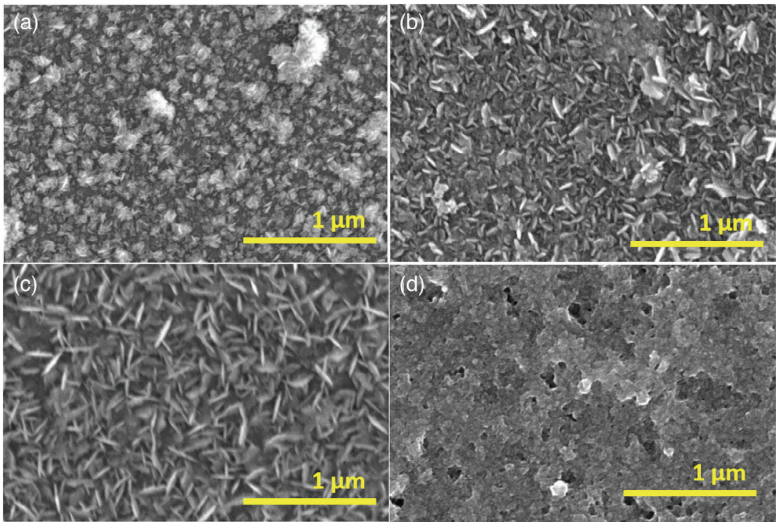


Figure 2. SEM images of Cu–Zn–S thin films: a) CZS-10, b) CZS-30, c) CZS-50, and d) CZS-80 (CZS-30 represents a film prepared using 0.03 M zinc acetate and 0.07 M $CuCl_2$ as cationic precursor).

© 2020 Wiley-VCH GmbH

Approved for public release; distribution unlimited.

(high conductivity) of these CZS films, high hole concentration, and the change of its Fermi level with composition, these materials can be good contact materials for solar cells.[3a]

To study the hole transport properties, CZS thin films were deposited on CdTe devices and covered with 40 nm Au to complete the back contact. **Figure 3** shows a schematic and a cross-sectional image of the CdTe device with a CZS layer as the hole transport layer. These devices were completed after the deposition of the CZS film at room temperature and without any thermal annealing. The *J–V* characteristics for the best cells of the controlled device and with CZS as HTMs under light and dark measurement conditions are shown in **Figure 4**a and the quantum efficiency measurements are shown in Figure S2, Supporting Information. The best cell has an efficiency of 10.5% for Au only back contact with an average device performance of 10.0% for 20 cells and the best back contact was CZS-30/Au with an average device performance of 12.8%, with the best cell performance of 13.1%. The CZS-30/Au back contact best cell has a higher V_{OC} of 816 mV and FF of 74.4%. Based on the literature, Jose et al. reported that the CZS-30 film deposited by a SILAR method has the highest hole density of 1.01×10^{22} cm^{-3} compared with other CZS nanocomposites and a mobility of 2.68 cm^2 V^{-1} S^{-1}.[9] Thus, due to the higher doping level and hole mobility, CZS-30 back buffer layer performed better compared with other CZS nanocomposites.

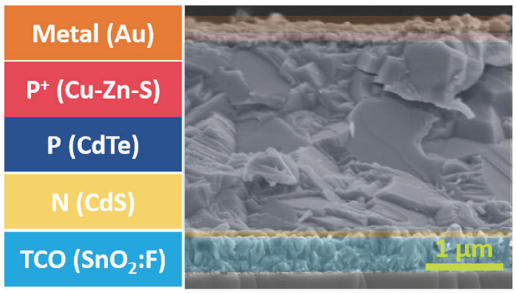


Figure 3. Schematic device diagram and cross-sectional SEM image of CdTe solar cells with Cu–Zn–S (CZS-50) as a back-contact interface layer.

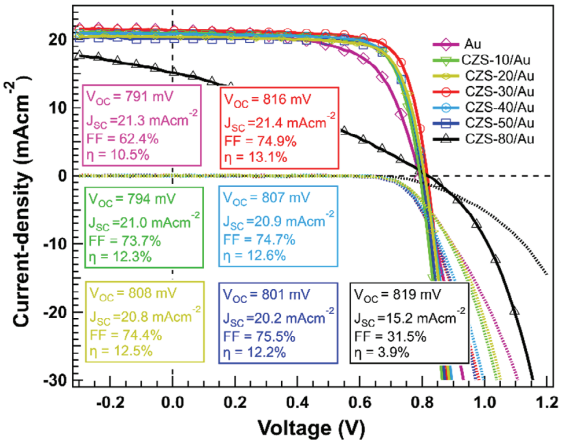


Figure 4. *J–V* characteristics of CdTe photovoltaics with and w/o Cu–Zn–S (CZS) nanocomposites as HTMs.

The device performance for CZS-30/Au film is slightly higher than that of the controlled device with Cu/Au (3/40 nm) deposited by thermal evaporation (Table S2, Supporting Information). Note that in the case of devices with CZS films, no additional Cu layer was deposited. For CZS-80/Au back contact, the device efficiency was 3.9% with a significant drop in the FF (31.5%) and J_{SC} (15.2 mA cm^{-2}). The higher resistivity (Table 1) of the CZS-80 film than CZS-30 and CZS-50 films reduced the device performance, which is attributed to lower Cu/Zn ratio. Table S2, Supporting Information, shows average device parameters of the CdTe devices with various CZS nanocomposites and standard Cu/Au back contact. Due to the significant increase in the resistivity of the CZS-80 layer, we observed a significant increase in the series resiatnce (R_S) and drop in shunt resistance (R_{SH}) of the device with CZS-80 layer, which finally reduced the device performance. Previously, CZS layer deposited by CBD at 80 °C was also used as HTMs in CdTe devices and the champion cell efficiency was 13.0% (V_{OC} 805 mV, J_{SC} 22.1 mA cm^{-2}, and FF 73.3%) with CZS layer and Cu/Au (3/40 nm) back contact.[13] During thermal annealing after Cu evaporation, there was a loss in the FF than the standard Cu/Au device which might be due to the over heat treatment. Here, for room temperature-deposited CZS-30/Au back contact, the device efficiency is similar without an additional evaporated Cu layer and thermal annealing (Figure 4), which indicate that efficient devices can be fabricated by depositing a CZS nanocomposite at room temperature. To see the effect of annealing after the deposition of CZS layer on CdTe devices, we annealed the devices at 200 °C for 10 min and measured after annealing. The device performance was poor compared with the unannealed device as the loss of V_{OC}, J_{SC}, and FF occurs (Figure S3, Supporting Information). Based on this observation, we conclude that during thermal annealing, weakly bounded Cu, Zn, and S atoms from the CZS layer diffuse into CdTe film, lowering the device characteristics.

Further, we analyzed the surface morphology of CdTe films with CZS layer on top with electron microscopy, X-ray diffraction, and EDS analysis. CZS nanocomposites can be observed on the top surface of CdTe, indicating the change in surface morphology, as shown in **Figure 5**a,b. The shapes of CZS particles on the CdTe surface look slightly different from the CZS nanocomposite formed on a soda lime glass substrate. However, the elemental composition revealed Cu, Zn, and S atoms in addition to Cd, Te, and Cl atoms. Note that these CZS films were deposited after $CdCl_2$ treatment on CdTe devices. EDS analysis for standard CdTe and with a CZS layer is shown in Table S3, Supporting Information. The X-ray diffraction (XRD) pattern of the CdTe film with CZS layer reveals small diffraction peaks of CuS with other strong diffraction peaks of CdTe, as shown in Figure 5c. The peak marked by * is usually observed on CdTe surface after $CdCl_2$ treatment, which may be due to the formation of $CdTeO_x$ present on the surface.[28] The XRD pattern was compared with standard powder diffraction files (PDF) of CdTe (PDF # 97-005-2840) and CuS (PDF #98-001-3414) on the MDI ZADE software.

Here, we also investigated CdTe devices with CZS-30 layer of various thicknesses (deposition cycles) and additional Cu-doped CdTe devices with $CuCl_2$ treatment. Previously, we have reported

© 2020 Wiley-VCH GmbH

Approved for public release; distribution unlimited.

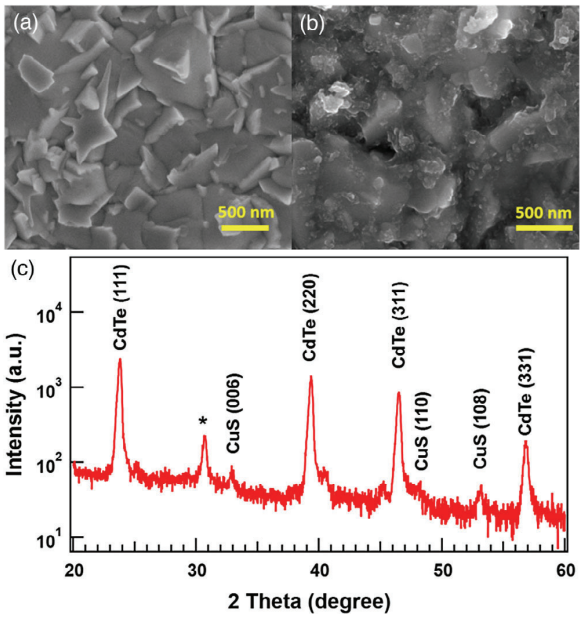


Figure 5. SEM images of CdTe surface a) without CZS nanocomposites, b) with CZS nanocomposites, and c) X-ray diffraction pattern of CdTe film with CZS-30 nanocomposites. The standard diffraction patterns for CdTe and CuS are PDF #97-005-2840 and PDF #98-001-3414, respectively.

that highly efficient CdTe devices can be fabricated than evaporated Cu by doping with $CuCl_2$ solution and device performance increases mainly due to the improvement in V_{OC} and FF.[29] CdTe devices with different thicknesses/deposition cycles of CZS-30 nanocomposites were fabricated and measured under the standard AM1.5G solar spectrum. The average device performance is shown in **Figure 6**a for various deposition cycles from 0 to 60 and *J–V* characteristics of the best cells are shown in Figure 6b for CZS-30 nanocomposites with 0, 5, 10, 20, 40, and 60 deposition cycles. Based on these *J–V* characteristics, we found that CZS-30 with ten deposition cycles performed the best compared with other deposition cycles. The average device efficiency is 13.0% with the best cell having an efficiency of 13.2% with V_{OC} of 834 mV, J_{SC} of 21.6 mA cm^{-2}, and FF of 72.9%. We attribute the higher device efficiency, especially V_{OC}, to the better band alignment of CdTe with CZS nanocomposite.[17] The average device parameters are shown in Table S4, Supporting Information. The average efficiency of the device with a higher number of deposition cycles was lower than ten deposition cycles mainly due to the loss in FF, which is due to the increase in series resistance of the device (a thicker CZS composite on the back of the device).

Further, we tested the effect of these CZS layers on top of CdTe devices after copper chloride ($CuCl_2$) treatment. For this, CdTe devices after $CdCl_2$ treatment were submerged in 0.1 mmol $CuCl_2$ solution in deionized water (DIW) and annealed at 200 °C for 20 mins.[29,30] After this, CZS-30 layer with 10 deposition cycles was deposited on one of the devices and *J–V* measurement was carried out. Figure 6c shows the *J–V* characteristics of the best cells of the control and CZS deposited device.

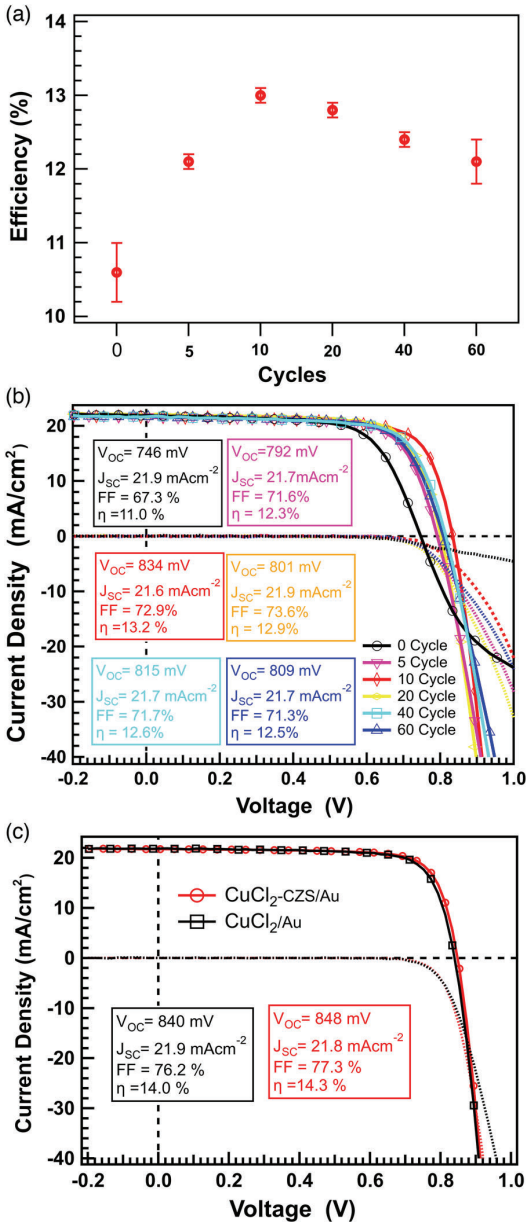


Figure 6. Device characteristics of CdTe solar cells with a) average device efficiency of CdTe cells, b) *J–V* characteristics of the best cells with various deposition cycles of CZS-30 nanocomposites, and c) *J–V* characteristics of the best cells for $CuCl_2$-treated CdTe device with CZS nanocomposite (average shown in Table 2).

The average device efficiency with $CuCl_2$/Au is 13.7% with the best cell reaching 14.0%, whereas $CuCl_2$/CZS/Au back contact shows an average device performance of 14.1%. The average device parameters are shown in **Table 2**. Using the CZS layer, the average increase in PCE is 2.9% whereas the FF was improved by 2.5% for 20 cells. The best cell with

© 2020 Wiley-VCH GmbH

Approved for public release; distribution unlimited.

Table 2. Average device parameters of 20 cells with and without CZS nanocomposite for $CuCl_2$-treated CdTe devices.

Back contact	V_{OC} [mV]	J_{SC} [mA cm^{-2}]	FF [%]	Eff. [η%]	R_s [Ω cm^2]	R_{sh} [Ω cm^2]
$CuCl_2$/Au	840 ± 2	21.6 ± 0.3	75.6 ± 0.4	13.7 ± 0.2	4.4 ± 0.1	2717 ± 227
$CuCl_2$/CZS/Au	845 ± 3	21.5 ± 0.2	77.4 ± 0.3	14.1 ± 0.1	2.8 ± 1.1	3100 ± 293

$CuCl_2$/CZS/Au has V_{OC} of 848 mV, J_{SC} of 21.8%, and FF of 77.3% with PCE of 14.3%. This efficiency is equivalent to 17.0% if other window layers (CdS:O, CdSe or MZO) were used to have J_{SC} of 26 mA cm^{-2}.[31] Due to the CZS nanocomposite layer, the device efficiency was enhanced mainly due to the improvement of FF of the device. The better device efficiency on using CZS nanocomposite is due to a reduced back barrier height and flattening of the conduction band compared with Au only or Cu/Au back contact.[27] The *J–V–T* measurement of CdTe devices with CZS-50 nanocomposite showed a back barrier height of 0.238 eV in between CZS-50/Au which is less compared with Au only (0.395 eV) and Cu/Au (0.330 eV) back contact.[27,32] This indicates that the CZS layer on the back of CdTe devices lowers the back barrier height, increasing the device efficiency.

3. Conclusions

Here, we have successfully fabricated Cu–Zn–S nanocomposite thin films at room temperature using the SILAR method which are transparent to visible light and have low resistivity. Further, room-temperature-processed transparent CZS films as the back-contact HTM in CdTe devices have been demonstrated. Out of the various compositions of nanocomposites, CZS-30/Au as the back contact has the highest efficiency 13.2% with no additional Cu. The CZS-80 film performed poorly (3.9%) due to its high resistivity and poor crystallinity. Similarly, for $CuCl_2$-treated CdTe devices with the CZS interface layer, the highest efficiency observed is 14.3% with an average device performance of 14.1%. Based on this study, CZS nanocomposite can be considered as a low-barrier interface layer to fabricate highly efficient devices, and other vacuum-based approaches can be sought for deposition of these CZS films.

4. Experimental Section

Materials: Copper (II) chloride ($CuCl_2$, 99.99%), zinc acetate (Zn $(acac)_2$, 99.9%), sodium sulfide ($Na_2S.9H_2O$, 98.0%), and triethanolamine (TEA) ($\geq$99.0%) were obtained from Sigma Aldrich. Cadmium chloride ($CdCl_2$, ultradry, 99.996%) and methanol (CH_3OH, 98%) were obtained from Alfa Aesar. All the chemicals were used as obtained without further purification.

Cu–Zn–S Thin-Film Preparation: The CZS nanocomposite films were deposited at room temperature using a SILAR method, adapting a procedure from literature.[9,27] First, CZS thin films were deposited on a soda lime glass (SLG) substrate for characterization. For this, Micro-90 detergent was used to clean soda lime glasses by sonication for 30 min, followed by rinsing several times with DIW. Then, glasses were again cleaned using a sonicator in acetone, methanol, and 2-propanol for 5 min each.

CZS-30 film was deposited by preparing the cationic precursor by dissolving 0.07 M $CuCl_2$, 0.03 M zinc acetate in DIW, with a total concentration of 0.1 M, 5 mL TEA, keeping the total volume to 25 mL, and anionic precursor using 0.05 M Na_2S in DIW. Here, CZS-30 denotes thin films prepared using Zn precursor 30% (0.03 M zinc acetate) and Cu precursor 70% (0.07 M) of the total cations (0.1 M) used. The SLG substrate was placed in a cationic precursor for 15 s, rinsed in DIW for 5 s, in anionic precursor for 15 s, and in DIW for 5 s to complete one SILAR cycle. A dip coater from NIMA Technology was used to complete all the SILAR cycles. The same procedure was repeated to deposit CZS films on the CdTe film. Similarly, for CZS-40 film (40% zinc acetate in the cationic precursor), 0.04 M zinc acetate and 0.06 M $CuCl_2$ were used as the cationic precursor, keeping other chemicals same as CZS-30 film.

Device Fabrication: The CdS/CdTe device stacks received from Willard and Kelsey Solar Group were utilized for this study. Standard CdTe devices were completed using Cu/Au (3/40 nm) by thermal evaporation after $CdCl_2$ treatment in dry air environment. It was followed by thermal annealing of devices at 150 °C for about 35 min. To fabricate CZS as HTMs, $CdCl_2$-treated CdTe devices were used and CZS films were deposited using a SILAR method as mentioned earlier. Then, the devices were completed by depositing 40 nm Au. Similarly, for solution-based Cu doping, the CdTe film stack was submerged in 0.1 mmol $CuCl_2$ solution in DIW for 2 min, rinsed with DIW, and annealed at 200 °C for 20 mins.[29]

Film and Device Characterization: Hitachi S-4800 SEM, EDS, and PerkinElmer Lambda 1050 UV–Vis–NIR spectrophotometer were used to characterize the CZS thin films on soda lime glass. Rigaku Ultima III X-ray diffractometer operated at 40 KV, and 44 mA was used to obtain X-ray diffraction patterns. The four-point and Dektak profilometers were used to measure the sheet resistance and thickness, respectively. The completed devices were measured under simulated AM1.5G solar irradiance to find the photoconversion efficiency.

Supporting Information

Supporting Information is available from the Wiley Online Library or from the author.

Acknowledgements

This material is based on research sponsored by Air Force Research Laboratory under agreement numbers FA9453-11-C-0253 and FA9453-18-2-0037. The US government is authorized to reproduce and distribute reprints for governmental purposes notwithstanding any copyright notation thereon. The authors thank Willard and Kelsey Solar Group for providing CdS/CdTe.

Conflict of Interest

The authors declare no conflict of interest.

Keywords

cadmium telluride, composition controls, interfaces, solar cells, successive ionic layer adsorption and reactions

Received: May 11, 2020
Revised: August 11, 2020
Published online: September 7, 2020

© 2020 Wiley-VCH GmbH

Approved for public release; distribution unlimited.

[1] H. Liu, V. Avrutin, N. Izyumskaya, Ü. Özgür, H. Morkoç, *Superlattices Microstruct.* **2010**, *48*, 458.
[2] E. Fortunato, P. Barquinha, R. Martins, *Adv. Mater.* **2012**, *24*, 2945.
[3] a) X. Xu, J. Bullock, L. T. Schelhas, E. Z. Stutz, J. J. Fonseca, M. Hettick, V. L. Pool, K. F. Tai, M. F. Toney, X. Fang, A. Javey, L. H. Wong, J. W. Ager, *Nano Lett* **2016**, *16*, 1925; b) W. Beyer, J. Hüpkes, H. Stiebig, *Thin Solid Films* **2007**, *516*, 147.
[4] G. Hautier, A. Miglio, G. Ceder, G. M. Rignanese, X. Gonze, *Nat. Commun.* **2013**, *4*, 2292.
[5] A. Parretta, M. Jayaraj, A. Di Nocera, S. Loreti, L. Quercia, A. Agati, *Phys. Status Solidi (a)* **1996**, *155*, 399.
[6] H. Kawazoe, M. Yasukawa, H. Hyodo, M. Kurita, H. Yanagi, H. Hosono, *Nature* **1997**, *389*, 939.
[7] M.-J. Zhang, Q. Lin, X. Yang, Z. Mei, J. Liang, Y. Lin, F. Pan, *Nano Lett.* **2016**, *16*, 1218.
[8] A. M. Diamond, L. Corbellini, K. Balasubramaniam, S. Chen, S. Wang, T. S. Matthews, L. W. Wang, R. Ramesh, J. W. Ager, *Phys. Status Solidi (a)* **2012**, *209*, 2101.
[9] E. Jose, M. C. Santhosh Kumar, *J. Alloys Compd.* **2017**, *712*, 649.
[10] M. A. Yıldırım, *Opt. Commun.* **2012**, *285*, 1215.
[11] S. K. Maurya, Y. Liu, X. Xu, R. Woods-Robinson, C. Das, J. W. Ager III, K. Balasubramaniam, *J. Phys. D: Appl. Phys.* **2017**, *50*, 505107.
[12] A. Mallick, S. Chattopadhyay, G. De, D. Basak, *J. Alloys Compd.* **2019**, *770*, 813.
[13] K. K. Subedi, E. Bastola, I. Subedi, Z. Song, K. P. Bhandari, A. B. Phillips, N. J. Podraza, M. J. Heben, R. J. Ellingson, *Sol. Energy Mater. Sol. Cells* **2018**, *186*, 227.
[14] J. L. Freeouf, J. M. Woodall, *Appl. Phys. Lett.* **1981**, *39*, 727.
[15] a) E. Janik, R. Triboulet, *J. Phys. D: Appl. Phys.* **1983**, *16*, 2333; b) E. Artegiani, J. D. Major, H. Shiel, V. Dhanak, C. Ferrari, A. Romeo, *Sol. Energy Mater. Sol. Cells* **2020**, *204*, 110228.
[16] B. de Boer, A. Hadipour, M. M. Mandoc, T. van Woudenbergh, P. W. M. Blom, *Adv. Mater.* **2005**, *17*, 621.
[17] G. K. Liyanage, A. B. Phillips, F. K. Alfadhili, R. J. Ellingson, M. J. Heben, *ACS Appl. Energy Mater.* **2019**, *2*, 5419.
[18] A. B. Phillips, R. R. Khanal, Z. Song, R. M. Zartman, J. L. DeWitt, J. M. Stone, P. J. Roland, V. V. Plotnikov, C. W. Carter, J. M. Stayancho, R. J. Ellingson, A. D. Compaan, M. J. Heben, *Nano Lett.* **2013**, *13*, 5224.
[19] A. Montgomery, L. Guo, C. Grice, R. A. Awni, S. Saurav, L. Li, Y. Yan, F. Yan, *Prog. Photovoltaics: Res. Appl.* **2019**, *27*, 665.
[20] K. P. Bhandari, P. Koirala, N. R. Paudel, R. R. Khanal, A. B. Phillips, Y. F. Yan, R. W. Collins, M. J. Heben, R. J. Ellingson, *Sol. Energy Mater. Sol. Cells* **2015**, *140*, 108.
[21] J. Li, D. R. Diercks, T. R. Ohno, C. W. Warren, M. C. Lonergan, J. D. Beach, C. A. Wolden, *Sol. Energy Mater. Sol. Cells* **2015**, *133*, 208.
[22] B. Siepchen, B. Späth, C. Drost, V. Krishnakumar, C. Kraft, M. Winkler, J. König, K. Bartholomé, S. Peng, *J. Electron. Mater.* **2015**, *44*, 3354.
[23] X. Wu, J. Zhou, A. Duda, Y. Yan, G. Teeter, S. Asher, W. K. Metzger, S. Demtsu, S.-H. Wei, R. Noufi, *Thin Solid Films* **2007**, *515*, 5798.
[24] N. Strevel, L. Trippel, C. Kotarba, I. Khan, *Photovoltaics Int.* **2013**, *22*, 66.
[25] a) E. Bastola, K. P. Bhandari, R. J. Ellingson, *J. Mater. Chem. C* **2017**, *5*, 4996; b) E. Bastola, K. K. Subedi, K. P. Bhandari, R. J. Ellingson, *MRS Adv.* **2018**, *3*, 2441; c) E. Bastola, K. P. Bhandari, I. Subedi, N. J. Podraza, R. J. Ellingson, *MRS Commun.* **2018**, *8*, 970; d) K. P. Bhandari, F. K. Alfadhili, E. Bastola, S. C. Watthage, Z. Song, G. K. Liyanage, A. J. Phillips, M. J. Heben, R. J. Ellingson, *Prog. Photovoltaics: Res. Appl.*, https://doi.org/10.1002/pip.3309.
[26] a) Z. Rong, X. Guo, S. Lian, S. Liu, D. Qin, Y. Mo, W. Xu, H. Wu, H. Zhao, L. Hou, *Adv. Funct. Mater.* **2019**, *29*, 1904018; b) X. Guo, Q. Tan, S. Liu, D. Qin, Y. Mo, L. Hou, A. Liu, H. Wu, Y. Ma, *Nano Energy* **2018**, *46*, 150; c) X. Du, Z. Chen, F. Liu, Q. Zeng, G. Jin, F. Li, D. Yao, B. Yang, *ACS Appl. Mater. Interfaces* **2016**, *8*, 900.
[27] E. Bastola, K. K. Subedi, F. K. Alfadhili, A. B. Phillips, M. J. Heben, R. J. Ellingson, in *IEEE 46th Photovoltaic Specialists Conf.*, IEEE, Chicago, IL **2019**, pp. 0144-0148.
[28] a) R. A. Awni, D.-B. Li, C. R. Grice, Z. Song, M. A. Razooqi, A. B. Phillips, S. S. Bista, P. J. Roland, F. K. Alfadhili, R. J. Ellingson, M. J. Heben, J. V. Li, Y. Yan, *Sol. RRL* **2019**, *3*, 1800304; b) E. Bastola, F. K. Alfadhili, A. B. Phillips, M. J. Heben, R. J. Ellingson, *J. Mater. Res.* **2019**, *34*, 3988.
[29] E. Bastola, A. V. Bordovalos, E. LeBlanc, N. Shrestha, M. O. Reese, R. J. Ellingson, *IEEE 46th Photovoltaic Specialists Conf.*, IEEE, Chicago, IL **2019**, pp. 1846–1850.
[30] D. Mao, G. Blatz, C. E. Wickersham, M. Gloeckler, *Sol. Energy Mater. Sol. Cells* **2016**, *157*, 65.
[31] a) D. E. Swanson, J. R. Sites, W. S. Sampath, *Sol. Energy Mater. Sol. Cells* **2017**, *159*, 389; b) X. Guo, Z. Rong, L. Wang, S. Liu, Z. Liu, K. Luo, B. Chen, D. Qin, Y. Ma, H. Wu, L. Hou, *Sustainable Energy Fuels* **2020**, *4*, 399.
[32] F. K. Alfadhili, A. B. Phillips, G. K. Liyanage, J. M. Gibbs, M. K. Jamarkattel, M. J. Heben, *MRS Adv.* **2019**, *4*, 913.

© 2020 Wiley-VCH GmbH

Approved for public release; distribution unlimited.

ACS Energy LETTERS

http://pubs.acs.org/journal/aelccp

LETTER

Arylammonium-Assisted Reduction of the Open-Circuit Voltage Deficit in Wide-Bandgap Perovskite Solar Cells: The Role of Suppressed Ion Migration

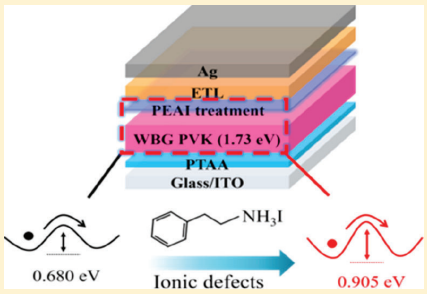
Cong Chen, Zhaoning Song,* Chuanxiao Xiao, Rasha A. Awni, Canglang Yao, Niraj Shrestha, Chongwen Li, Sandip Singh Bista, Yi Zhang, Lei Chen, Randy J. Ellingson, Chun-Sheng Jiang, Mowafak Al-Jassim, Guojia Fang, and Yanfa Yan*

Cite This: *ACS Energy Lett.* 2020, 5, 2560−2568

Read Online

ACCESS | Metrics & More | Article Recommendations | Supporting Information

ABSTRACT: Surface treatment using large alkyl/aryl ammonium cations has demonstrated reduced open-circuit voltage (V_{OC}) deficits in perovskite solar cells (PSCs), but the origin of the improvements has been vaguely attributed to defect passivation. Here, we combine microscopic probing of the local electrical properties, thermal admittance spectroscopic analysis, and first-principles calculations to elucidate the critical role of arylammonium interface layers in suppressing ion migration in wide-bandgap (WBG) PSCs. Our results reveal that arylammonium surface treatment using phenethylammonium iodide increases the activation energy barrier for ion migration on the surface, which suppresses the accumulation of charge defects at surface and grain boundaries, leading to a reduced dark saturation current density in WBG PSCs. With device optimization, our champion 1.73 eV PSC delivers a power conversion efficiency of 19.07% with a V_{OC} of 1.25 V, achieving a V_{OC} deficit of 0.48 V.



Downloaded via Zhaoning Song on July 21, 2020 at 03:11:20 (UTC).
See https://pubs.acs.org/sharingguidelines for options on how to legitimately share published articles.

Perovskite solar cells (PSCs) have attracted a tremendous amount of attention in the past decade because of the superb photovoltaic properties of metal halide perovskites and the high certified power conversion efficiency (PCE) of single-junction devices that has already reached 25.2%.[1] Beyond single-junction PSCs, the bandgap tunability of perovskite materials ranging from ∼1.2 to 3 eV enables the realization of perovskite-based tandem solar cells, which have the potential to surpass the Shockley−Queisser (S−Q) thermodynamic limit of single absorber solar cells.[2−5] Perovskite-based tandem solar cells have made considerable progress in recent years.[6−18] Impressively, a variety of perovskite−silicon (Si),[6,15−17] perovskite−copper indium gallium diselenide (CIGS),[9,11] and perovskite−perovskite tandem solar cells have demonstrated PCEs of ∼25% or higher.[13,14] These achievements show the enormous potential of perovskite-based tandem solar cells in the future.[5] Notably, all of the tandem cells share a common component that is a top cell based on a wide-bandgap (WBG) (∼1.7−1.9 eV) perovskite absorber layer,[19−27] which plays a critical role in highly efficient tandem solar cells.

The performance of WBG PSCs has always been limited by a high open-circuit voltage (V_{OC}) deficit, which is defined as $\frac{E_g}{q} - V_{OC}$, where E_g is the bandgap of the absorber layer and q is the unit charge. PSCs based on WBG perovskites with a bandgap of >1.72 eV typically exhibit V_{OC} deficits (>0.5 V) that are larger than those of their lower-bandgap counterparts (Figure S1 and Table S1). While the origins of the large V_{OC} deficit in WBG PSCs are still under debate, it is certain that the shortfall is related to the composition of perovskites with a relatively high content of Br and Cs, which typically results in phase segregation and a relatively high defect density.[28,29] In particular, the aggregation of I-rich and Br-rich domains lowers the optical bandgap of WBG perovskites (that is primarily

Received: June 23, 2020
Accepted: July 10, 2020
Published: July 10, 2020

© XXXX American Chemical Society

https://dx.doi.org/10.1021/acsenergylett.0c01350
ACS Energy Lett. 2020, 5, 2560−2568

Approved for public release; distribution unlimited.

determined by the lower bandgap of the domains in the material),[30−32] severely limiting the V_{OC} and thus the PCE of WBG PSCs. Therefore, strategies for mitigating large V_{OC} deficits in WBG PSCs are urgently needed to advance perovskite tandem solar cells.

Over the past few years, many approaches, such as compositional, additive, solvent, processing, and interface engineering techniques, have been employed to fabricate high-quality WBG perovskite films and devices.[19−27,33−36] Among them, bulk incorporation or surface treatment using large alkyl/aryl ammonium cations has been demonstrated to be most effective in reducing V_{OC} deficits of PSCs regardless of the perovskite composition. Despite the advances, the underlying mechanism of the alkyl/aryl ammonium treatment has always been attributed vaguely to a reduced defect density and increased carrier lifetime. In particular, little is known about the subtle differences in how the alkyl/aryl ammonium surface passivation affects WBG (>1.7 eV) and medium-bandgap (1.5−1.7 eV) iodine-based perovskites differently. Further efforts are needed to understand the origins and mechanisms of the large V_{OC} deficit in WBG PSCs and to explore effective strategies for mitigating this issue.

Very recently, we demonstrated an approach for probing the activation energy of ion migration in the perovskite absorber using a capacitance-based measurement,[37] which enables the PSC device performance analysis from the perspective of the ionic behavior in the perovskite absorber. Here, we combine the microscopic probing of localized electrical properties, thermal admittance spectroscopy (TAS) measurements, and first-principles calculations of defect migration to elucidate the primary factors limiting the V_{OC} in WBG PSCs. Our results reveal that, in contrast to the passivated grain boundaries (GBs) in the pure iodine-based perovskite, the nature of the relatively more conductive GBs than grain interiors (GIs) in WBG perovskite films fundamentally limits the V_{OC} of WBG PSCs. Our measurements and calculation consistently show that an arylammonium surface formed by phenethylammonium iodide (PEAI) increases the activation energy barrier for ion diffusion and suppresses the accumulation of ionic defects on the perovskite surface and at GBs. Consequently, inverted 1.73 eV WBG PSCs show the V_{OC} improved from 1.16 to 1.25 V, yielding a V_{OC} deficit of <0.5 V. Using the arylammonium surface treatment, we obtained champion PCEs of 19.1% and 24.1% for single-junction WBG PSCs and four-terminal (4-T) all-perovskite tandem solar cells. Our work provides a better understanding of how arylammonium cations suppress ion migration in WBG perovskites and its importance in reducing large V_{OC} deficits and improving the performance of WBG PSCs.

To identify the primary limiting factors for the large V_{OC} deficit in WBG PSCs, conductive atomic force microscopy (c-AFM) was employed to analyze the microscopic electrical properties of our benchmark $FA_{0.8}Cs_{0.2}Pb(I_{0.7}Br_{0.3})_3$ WBG perovskite films deposited on poly(triarylamine) (PTAA)/indium tin oxide (ITO)/glass substrates. Note that $Pb(SCN)_2$ was incorporated into our WBG perovskite films as an additive to promote perovskite grain growth, as reported previously.[20] Figure 1a shows a c-AFM map of a control WBG perovskite film, which exhibits nonuniform grain sizes with a heterogeneous current distribution over different grains, indicating the formation of polycrystalline domains with different chemical phases and electrical conductivities. All of the c-AFM images in Figure 1 and the Supporting Information were taken with the same sample bias voltage (V_S) of +0.6 V to enable a reliable comparison. The segregation of I-rich and Br-rich (with respect to the 7:3 I:Br stoichiometry) domains leads to a distinct difference in the local electrical properties. The AFM tip (Pt-coated Si probe) forms primarily a junctionlike structure with the underlaying perovskite film. Dark saturation current J_0 of the structure is affected mainly by the perovskite bandgap. A larger current under the V_S indicates a larger J_0 caused by a smaller bandgap. The large grains, corresponding to the higher-contrast (brighter) grains in the c-AFM image (Figure 1a), are expected to be more conductive because their bandgaps are narrower than those with higher Br:I ratios and, therefore, allow higher local current flow ($J_{GI,H}$) through GIs. In contrast, the perovskite grains with a higher Br content tend to form smaller grains because Br accelerates the nucleation process, leading to a large number of small grains.[19] The Br-rich small grains, corresponding to the lower-contrast (darker) grains, are more electrically resistive, demonstrating lower

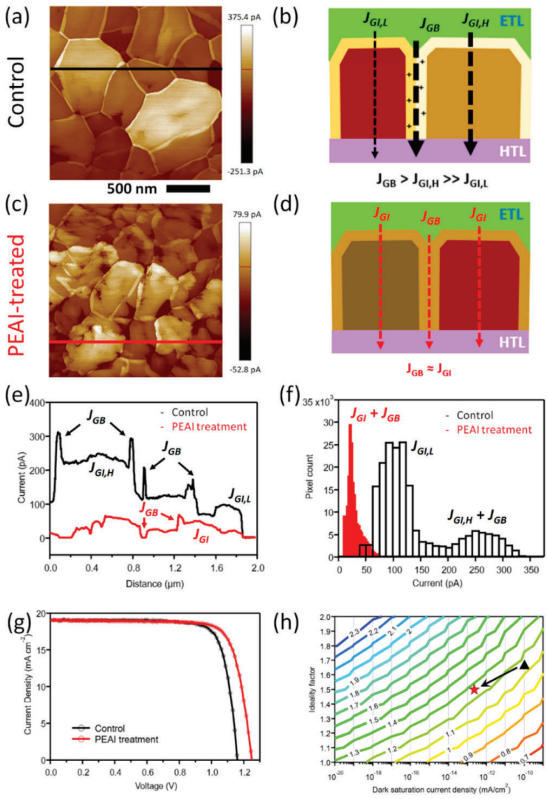


Figure 1. c-AFM images of (a) the control and (c) PEAI-treated WBG perovskite films. The scale bar is 500 nm. The images were flattened to show the best contrast. Schematic illustrations of current paths in (b) the control and (d) PEAI-treated WBG PSCs. (e) Line profiles of local current flow on the black and red lines in the c-AFM images of WBG perovskite films. (f) Histograms of the current distribution in the c-AFM images. (g) Light $J-V$ curves of WBG PSCs without and with the PEAI treatment. (h) Contour plot of the theoretical V_{OC} as a function of dark saturation current densities and ideality factor. The triangle and star represent PSCs without and with the PEAI treatment, respectively.

https://dx.doi.org/10.1021/acsenergylett.0c01350
ACS Energy Lett. 2020, 5, 2560−2568

Approved for public release; distribution unlimited.

current flow ($J_{GI,L}$) through GIs. Therefore, the I-rich perovskite grains contribute larger dark currents (Figure 1b).

A remarkable heterogeneity in microscopic electrical behavior is discerned at the GBs of the WBG perovskite film in Figure 1a. The current signals at GBs (J_{GB}) are much higher than the current flows through GIs (J_{GI}), making GBs contribute to the increase in the leakage current in the WBG perovskites, as illustrated in Figure 1b. For comparison, we measured a conventional 1.55 eV $MAPbI_3$ perovskite film prepared using the same approach. In contrast to the WBG perovskite, the $MAPbI_3$ film (Figure S2) exhibits mostly resistive GBs, which indicates passivated GBs because of the PbI_2 passivation introduced by the addition of $Pb(SCN)_2$.[38] However, incorporating $Pb(SCN)_2$ into the WBG perovskites shows no efficacy in passivating GBs. For the FA/Cs-based WBG perovskite films, the dynamic of perovskite formation is greatly accelerated due to the presence of significant amounts of Cs and Br (20 and 30 mol % with respect to the monovalent cations and halide anions, respectively) in the precursor solution, leading to a higher density of defects.[19] The aggregation of the active ionic defects at GBs increases not only the electrical conductivity but also the extent of ion migration at the GBs.[39−42] Because Br has a higher vapor pressure and escapes more easily from GBs of perovskite, it is likely that mostly positively charged ions, such as halide vacancies and lead interstitials, accumulate on the surface and at GBs, introducing detrimental defect states and making GBs more electrically conductive.[43,44]

The ambiguity of the impact of conductive GBs or regions near GBs has been discussed in the literature[39,45−48] but deserves to be discussed further. The local current probed by c-AFM should be determined by two factors: the equivalent resistance of the probe−sample contact and the material resistivity of the local volume underneath the probe. If the contact resistance over the sample surface is uniform, the current contrast is determined by the local resistivity of the sample. A high J_{GB} is sometimes attributed to improved charge transport properties at the GBs, which can be beneficial for series resistance in a solar cell.[47,48] However, a current contrast in a c-AFM image is often dominated by the nonuniform electrical characteristics of the probe−sample contact. A substantially high J_{GB} value is typically detrimental because of the likelihood of concomitant high reverse leakage current in finished devices. The defective GB and defective surface and subsurface material would cause a higher current flow because of the increased J_0 of the probe−sample contact, which also results in an inferior leaking junction when the device is completed. Moreover, highly conductive GBs may indicate defective GBs without proper passivation, behaving as nonradiative recombination centers, significantly increasing the level of Shockley−Read−Hall (SRH) recombination. Therefore, the high current flows through the defective GBs, as probed by c-AFM, can substantially increase the macroscopic dark saturation current in a solar cell device, fundamentally limiting the photovoltaic performance of a device, particularly the V_{OC}. It is worth noting that some defective GBs show conductivities that are higher than those of the relatively conductive GIs that are formed due to the I−Br phase segregation, indicating that the defective GBs are likely to be the most critical factor contributing to the J_0 of a device.

To reduce the detrimental defects at the GBs of WBG perovskite films, we applied an arylammonium surface treatment using PEAI, which is known to be an effective two-dimensional perovskite passivation agent that has been demonstrated in some state-of-the-art PSCs.[33,49,50] We spin-coated 2 mg/mL PEAI in an isopropanol solution on as-prepared WBG perovskite films and performed the c-AFM measurement to identify the impact of PEAI on the microscopic electrical properties of the film (Figure 1c). Compared with the control film, the current flow through the perovskite grains is reduced by almost 1 order of magnitude, and the spatial distribution of microscopic conductivity becomes more uniform. Furthermore, there is an insignificant conductivity contrast between the GBs and GIs of the PEAI-treated film, indicating that J_{GB} is significantly reduced and comparable to J_{GI} (Figure 1d). Therefore, current flow through the perovskite film can be uniformly distributed across the GIs and GBs. The impacts of PEAI passivation on GIs and GBs are clearly displayed in the c-AFM line profile comparison in Figure 1e, where the PEAI treatment shows a marked effect in reducing the leakage current through both GBs (J_{GB}) and the grain interior (J_{GI}). Figure 1f compares the histograms of the microscopic current distribution in the control and PEAI-treated WBG perovskite films. The control WBG perovskite film exhibits two distinct local conductivity behaviors, including highly conductive GBs and GIs (J_{GB} and $J_{GI,H}$) and less conductive GIs ($J_{GI,L}$). In marked contrast to the control film, the film with the PEAI treatment shows a narrow distribution with a greatly suppressed average current of 26 pA, almost 1 order of magnitude lower than the average c-AFM current of 135 pA for the control film. Because the probe−perovskite contact in the c-AFM imaging qualitatively reflects the electrical aspect of the electron transport layer (ETL)−perovskite contact in a real solar cell, the microscopic current distribution in WBG perovskite films determines the macroscopic current flow in the corresponding devices. Suppressed local leaking current at GBs and the defective subsurface region of GIs is beneficial for reducing the overall dark saturation current density in the devices.

To reveal the influence of microscopic electrical properties on the macroscopic device performance of WBG PSCs, we fabricated solar cells with a glass/ITO/PTAA/$FA_{0.8}Cs_{0.2}Pb(I_{0.7}Br_{0.3})_3$/$C_{60}$/bathocuproine (BCP)/Ag structure (Figure S3). Figure 1g shows representative current density−voltage ($J-V$) curves of PSCs based on the control and PEAI-treated perovskite absorbers. With the PEAI treatment, V_{OC} increases significantly from 1.16 to 1.25 V, leading to an improvement in the PCE from 17.5% to 18.6%. To further understand the V_{OC} enhancement as a result of the PEAI treatment, in Figure 1f, we plot a V_{OC} contour of a general solar cell using the diode equation $V_{OC} = \frac{nkT}{q} \ln\left(\frac{J_L}{J_0} + 1\right)$, where n is the ideality factor, k is the Boltzmann constant, T is the temperature of a solar cell, and J_L and J_0 are the light and dark saturation current densities, respectively.

On the basis of the contour plot, for a solar cell with a given absorber layer bandgap and device operational temperature, V_{OC} is determined only by the combination of n and J_0. Note that n is not an independent variable but is strongly influenced by J_0. In reality, a small increase in n would typically lead to a significant increase in J_0 and, thus, a decreased V_{OC}. Therefore, from the perspective of device analysis, J_0 is an extremely critical parameter that determines the V_{OC} of a solar cell. A lower J_0 is desired to achieve a higher V_{OC} of a solar cell.

The light intensity-dependent device analysis shows the ideality factor n decreases from 1.69 for the control to 1.45 for

https://dx.doi.org/10.1021/acsenergylett.0c01350
ACS Energy Lett. 2020, 5, 2560−2568

Approved for public release; distribution unlimited.

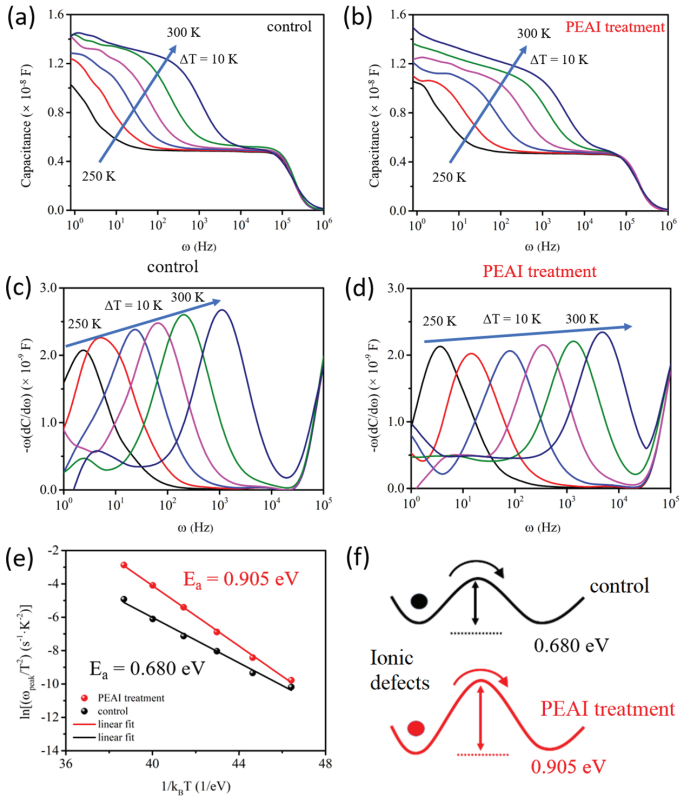


Figure 2. Admittance spectra of WBG PSCs (a) without (the control) and (b) with the PEAI treatment, measured in a temperature range of 250−300 K with a step size of 10 K. Derivatives of the admittance spectra of (c) the control device and (d) the device with the PEAI treatment. (e) Arrhenius plots of the characteristic transition frequencies derived from the admittance spectra. (f) Schematic of the energy barrier for ion movement in the control and the device with PEAI treatment.

the device with the PEAI treatment (Figure S4). As discussed above, a lower n value is typically accompanied by a reduced J_0, which in turn increases the V_{OC} of a solar cell. In a good agreement, the detailed $J-V$ analysis confirms that J_0 is reduced from $\sim 10^{-10}$ to 10^{-13} mA/cm^2 with the PEAI treatment (Figure S5). The decreases in J_0 and n contribute to the improvement in V_{OC}, consistent with the prediction (the triangle to star route) in Figure 1h. This decrease in the J_0 and n of the devices after the PEAI treatment is ascribed to the reduction in the microscopic leaking current in GIs and GBs of the WBG perovskite films. The defective GB and defective subsurface region without the PEAI passivation form a poor junction, causing the photoexcited carriers to be transported over the junction via these defects to some degree instead of the desired diffusion process, which subsequently causes energy loss of the charge carriers and reduces the voltage output of the device. It is worth noting that the reduced microscopic leaking current also leads to increased shunt resistance and series resistance (Table S2). However, the change in series resistance has a stronger impact on fill factor (FF) than shunt resistance, leading to a reduced FF. Therefore, the decreased J_0 is the primary reason for the improved performance of PSCs with PEAI treatment.

To further elucidate the interplay between the microscopic and macroscopic currents in the perovskite films and devices, we conducted TAS measurements on the WBG PSCs without and with the PEAI treatment. We have demonstrated in our recent work that the low-frequency capacitance measured by the TAS technique can be used to estimate the activation energy (E_a) of ionic movement in perovskite absorber layers.[37] Panels a and b of Figure 2 display the TAS spectra of PSCs without and with the PEAI treatment, respectively, measured from 250 to 300 K in the dark. The characteristic transition frequency values (ω_{peak}) were obtained from the derivative of the capacitance−frequency spectra, as shown in panels c and d of Figure 2. Figure 2e shows E_a values calculated by fitting the corresponding Arrhenius plots using the relation $\omega_{peak} = \beta T^2 \exp\left(-\frac{E_a}{kT}\right)$, where β is a temperature-related prefactor.[51] The device with the PEAI treatment exhibits an E_a of 0.905 eV, higher than that of 0.680 eV for the control device. The substantially higher E_a indicates that the ion migration in the perovskite layer is suppressed significantly after the PEAI treatment (Figure 2f). The suppression of mobile ionic defects is also expected to reduce the extent of formation of charge defects that can act as nonradiative recombination centers. We measured the steady-state photoluminescence (PL) and time-resolved photoluminescence (TRPL) of WBG perovskite films without and with the PEAI treatment (Figure S6). The film with the PEAI treatment

https://dx.doi.org/10.1021/acsenergylett.0c01350
ACS Energy Lett. 2020, 5, 2560−2568

Approved for public release; distribution unlimited.

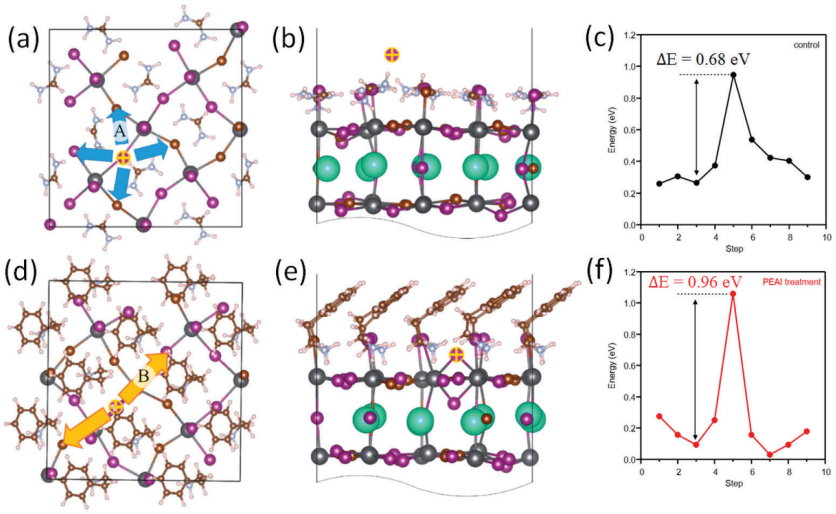


Figure 3. (a) Top view, (b) side view, and (c) energy barrier of the diffusion of the I interstitial on a pristine perovskite surface. Arrow A represents the diffusion path to its nearest site. (d) Top view, (e) side view, and (f) energy barrier of the diffusion of the I interstitial on a PEA-modified perovskite surface. Arrow B represents the diffusion path to the second-nearest site. The purple sphere represents an I atom, and the gray, green, cyan, brown, and white spheres represent Pb, Cs, N, C, and H atoms, respectively. The interstitial I atoms are highlighted.

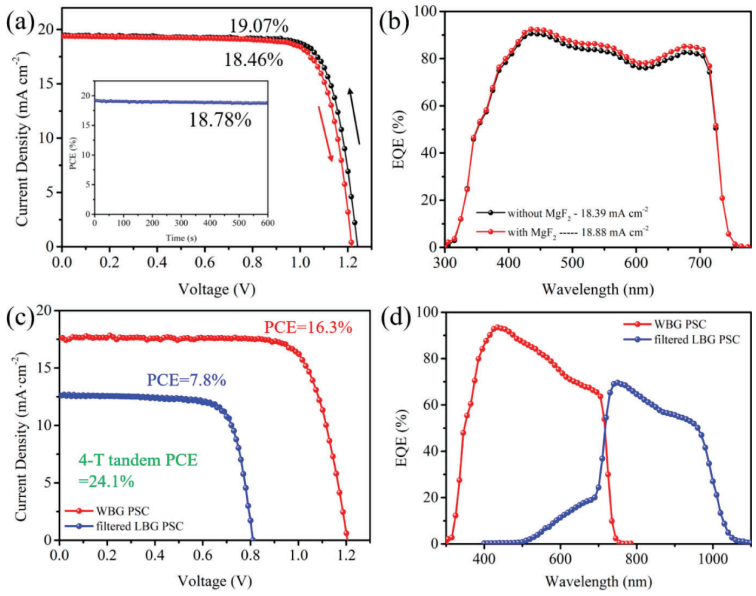


Figure 4. (a) *J*–*V* curves of the champion WBG PSC measured under different scan directions. The inset exhibits the stabilized efficiency for the device. (b) EQE spectra of the champion device before and after the deposition of a MgF_2 ARC. (c) *J*–*V* curves and (d) EQE spectra of a 4-T all-perovskite tandem cell.

exhibits a more intense PL emission and a longer carrier lifetime compared to those of the control film, demonstrating that PEAI can effectively decrease the rate of nonradiative recombination in WBG perovskite films.

To understand how PEAI can suppress ion migration in perovskites, we performed first-principles calculations to study the behaviors of mobile ionic defects on the surface of perovskite films. It is known that the diffusion and exchange of mobile ions at GBs and on the surface are detrimental to the device performance. Compared to the diffusion in bulk, ions have smaller diffusion barriers on the surface due to smaller steric hindrance. Panels a and b of Figure 3 illustrate the diffusion path of an I interstitial defect loosely bound on the pristine surface. The diffusion of the I interstitial is

https://dx.doi.org/10.1021/acsenergylett.0c01350
ACS Energy Lett. 2020, 5, 2560−2568

Approved for public release; distribution unlimited.
441

accompanied by relatively small geometric distortions, and hance the diffusion barrier. The ion diffusion barrier is calculated to be 0.68 eV (Figure 3c). On the PEA-modified surface, due to the hindrance of PEA, the I interstitial is forced to squeeze into the surface, forming a Pb−I−Pb−I loop (Figure 3d,e), which is similar to the defect structure of an I interstitial in a bulk perovskite (Figure S7). The diffusion barrier of an I interstitial on the PEA-modified surface is increased to 0.96 eV (Figure 3f), suggesting that PEA may help mitigate halide ion migration on the surface. It is worth noting that the finding from the theoretical calculation is in good agreement with the results of TAS measurement. Although the atomic model for the calculation is based on the surfaces of perovskite films, the agreement with the measured diffusion barrier heights indicates that the ETL layer on top of the perovskite film in the devices may have a negligible or minor effect on ion diffusion. Furthermore, the molecular orbital diagram and partial density of states (PDOS) calculations of a PEAI-treated perovskite film (Figure S8) show that an I interstitial introduces a shallow defect level above the valence band maximum, which is similar to the same defect structure on the pristine surface. Therefore, the PEAI treatment does not affect the I interstitial being an innocuous defect.

The aforementioned results combining microscopic conductivity analysis, TAS device analysis, and theoretical calculations indicate that the PEAI surface treatment can suppress ion migration on the surface of perovskite films and prevent the accumulation of ionic defects at GBs. The suppressed ion migration and reduced defective GBs in the near junction region lead to a reduction in the macroscopic J_0. Consequently, the V_{OC} of WBG PSCs increases after the PEAI surface treatment.

Once we understood the effect of PEAI on reducing ion migration and improving the V_{OC} of WBG PSCs, we further analyzed the impact of PEAI concentration on the structural and optical properties of perovskite films and the performance of PSCs. Details are summarized in the Supporting Information (the optimization of PEAI concentration and Figures S9−S15). The optimized PEAI concentration was found to be 2 mg/mL. To further improve the PCE of WBG PSCs, we deposited an antireflection coating (ARC) of MgF_2 to reduce the reflectance of the glass substrate and improve the J_{SC}. Figure 4a shows the $J-V$ curves of the best-performing device with a MgF_2 ARC. The cells show negligible hysteresis and a stabilized efficiency of 18.78%. The J_{SC} gain of ∼0.5 mA cm^{-2} due to the MgF_2 ARC is confirmed by the EQE spectra shown in Figure 4b. The increased J_{SC} leads to an improvement in PCE in WBG PSCs from 18.64% to 19.07% (Table S3). To the best of our knowledge, a PCE exceeding 19% is among the highest reported PCEs for inverted WBG PSCs with a bandgap of >1.72 eV (Table S1). The V_{OC} of 1.25 V is remarkable for inverted WBG PSCs. We also fabricated WBG PSCs using a transparent ITO back electrode, yielding a PCE of 16.3% (Figure S16a and Table S4). In addition, the high transmittance beyond 720 nm (Figure S16b) makes it feasible to fabricate efficient perovskite tandem solar cells. As a proof of concept, we combined semitransparent WBG PSCs with a typical 1.25 eV low-bandgap mixed Sn−Pb PSC[46] to construct a 4-T all-perovskite tandem solar cell following a reported approach,[52] demonstrating a PCE of 24.1% (Figure 4c) with complementary spectral responses in both subcells (Figure 4d). This advance shows the promise of high-efficiency all-perovskite tandem solar cells.

In summary, we examined the microscopic and macroscopic origins for the large V_{OC} deficit in the WBG perovskite films and devices and identified that the leaking current of the junction caused by the accumulation of charge defects is one of the major factors limiting the photovoltaic performance of WBG PSCs. We applied an arylammonium surface treatment to suppress ion diffusion to reduce the extent of formation of charge defects on the surface and at GBs. This surface passivation strategy leads to an improvement in the V_{OC} and PCE of WBG PSCs. With electrical and optical optimizations, we demonstrated WBG PSCs with a PCE of 19.07% and a V_{OC} of ∼1.25 V, corresponding to a V_{OC} deficit of <0.5 V for a 1.73 eV WBG perovskite absorber layer. Semitransparent WBG cells using an ITO back electrode enabled the creation of 4-T all-perovskite tandem solar cells with PCEs of >24%. This advance in understanding the importance and control of ion migration in WBG perovskites will benefit the development of perovskite tandem solar cells.

■ ASSOCIATED CONTENT

Supporting Information

The Supporting Information is available free of charge at https://pubs.acs.org/doi/10.1021/acsenergylett.0c01350.

Experimental section, optimization of the PEAI concentration, reported V_{OC} and PCE values for WBG PSCs, c-AFM of a $MAPbI_3$ film, cross-sectional SEM image of a WBG cell, V_{OC}−light intensity plot for WBG cells, dark saturation current density analysis, PL and TRPL of WBG perovskite films, defect structure of the PEA-modified surface and bulk, molecular orbital diagram and PDOS, SEM images of WBG perovskite films treated with PEAI, AFM topographies of WBG perovskite films, XRD patterns of WBG perovskite films, cross-sectional SEM images of WBG cells, Tauc plots and ultraviolet−visible absorption spectra, $J-V$ and EQE plots for WBG PSCs, statistic distributions of PV parameters, $J-V$, absorption, and reflection spectra of transparent WBG PSCs, PV parameters of PSCs with and without the PEAI treatment, statistics of PV parameters of WBG cells, summary of PV parameters of the best performing cells, PV parameters of cells with and without MgF_2, and PV parameters of transparent PSCs with and without MgF_2 (PDF)

■ AUTHOR INFORMATION

Corresponding Authors

Zhaoning Song − *Department of Physics and Astronomy and Wright Center for Photovoltaics Innovation and Commercialization, The University of Toledo, Toledo, Ohio 43606, United States;* orcid.org/0000-0002-6677-0994; Email: zhaoning.song@utoledo.edu

Yanfa Yan − *Department of Physics and Astronomy and Wright Center for Photovoltaics Innovation and Commercialization, The University of Toledo, Toledo, Ohio 43606, United States;* orcid.org/0000-0003-3977-5789; Email: yanfa.yan@utoledo.edu

Authors

Cong Chen − *Department of Physics and Astronomy and Wright Center for Photovoltaics Innovation and Commercialization, The University of Toledo, Toledo, Ohio 43606, United States; Key Lab of Artificial Micro- and Nano-*

https://dx.doi.org/10.1021/acsenergylett.0c01350
ACS Energy Lett. 2020, 5, 2560−2568

Approved for public release; distribution unlimited.

Structures of Ministry of Education, School of Physics and Technology, Wuhan University, Wuhan 430072, People's Republic of China

Chuanxiao Xiao − *National Renewable Energy Laboratory, Golden, Colorado 80401, United States*

Rasha A. Awni − *Department of Physics and Astronomy and Wright Center for Photovoltaics Innovation and Commercialization, The University of Toledo, Toledo, Ohio 43606, United States*

Canglang Yao − *Department of Physics and Astronomy and Wright Center for Photovoltaics Innovation and Commercialization, The University of Toledo, Toledo, Ohio 43606, United States*

Niraj Shrestha − *Department of Physics and Astronomy and Wright Center for Photovoltaics Innovation and Commercialization, The University of Toledo, Toledo, Ohio 43606, United States;* orcid.org/0000-0001-5702-2938

Chongwen Li − *Department of Physics and Astronomy and Wright Center for Photovoltaics Innovation and Commercialization, The University of Toledo, Toledo, Ohio 43606, United States*

Sandip Singh Bista − *Department of Physics and Astronomy and Wright Center for Photovoltaics Innovation and Commercialization, The University of Toledo, Toledo, Ohio 43606, United States*

Yi Zhang − *Department of Physics and Astronomy and Wright Center for Photovoltaics Innovation and Commercialization, The University of Toledo, Toledo, Ohio 43606, United States*

Lei Chen − *Department of Physics and Astronomy and Wright Center for Photovoltaics Innovation and Commercialization, The University of Toledo, Toledo, Ohio 43606, United States*

Randy J. Ellingson − *Department of Physics and Astronomy and Wright Center for Photovoltaics Innovation and Commercialization, The University of Toledo, Toledo, Ohio 43606, United States;* orcid.org/0000-0001-9520-6586

Chun-Sheng Jiang − *National Renewable Energy Laboratory, Golden, Colorado 80401, United States;* orcid.org/0000-0003-0230-7500

Mowafak Al-Jassim − *National Renewable Energy Laboratory, Golden, Colorado 80401, United States*

Guojia Fang − *Key Lab of Artificial Micro- and Nano-Structures of Ministry of Education, School of Physics and Technology, Wuhan University, Wuhan 430072, People's Republic of China;* orcid.org/0000-0002-3880-9943

Complete contact information is available at: https://pubs.acs.org/10.1021/acsenergylett.0c01350

Notes

The authors declare no competing financial interest.

■ ACKNOWLEDGMENTS

This material is based upon work supported by the U.S. Department of Energy's Office of Energy Efficiency and Renewable Energy (EERE) under Solar Energy Technologies Office Grant DE-EE0008753. The TAS characterization is supported by the National Science Foundation under Contract DMR-1807818. The theoretical calculation was supported by the National Science Foundation under Contract 1534686. N.S. and R.J.E. were supported by the U.S. Air Force Research Laboratory under Agreements FA9453-18-2-0037 and FA9453-19-C-1002. The U.S. Government is authorized to reproduce and distribute reprints for Governmental purposes notwithstanding any copyright notation thereon. The views and conclusions contained herein are those of the authors and should not be interpreted as necessarily representing the official policies or endorsements, either expressed or implied, of the Air Force Research Laboratory or the U.S. Government.

■ REFERENCES

(1) NREL Solar Cell Efficiency Chart. https://www.nrel.gov/pv/cell-efficiency.html (accessed 2020-04-26).

(2) Eperon, G. E.; Hörantner, M. T.; Snaith, H. J. Metal Halide Perovskite Tandem and Multiple-Junction Photovoltaics. *Nat. Rev. Chem.* **2017**, *1*, 0095.

(3) Lal, N. N.; Dkhissi, Y.; Li, W.; Hou, Q.; Cheng, Y.-B.; Bach, U. Perovskite Tandem Solar Cells. *Adv. Energy Mater.* **2017**, *7*, 1602761.

(4) Leijtens, T.; Bush, K. A.; Prasanna, R.; McGehee, M. D. Opportunities and Challenges for Tandem Solar Cells Using Metal Halide Perovskite Semiconductors. *Nat. Energy* **2018**, *3*, 828−838.

(5) Song, Z.; Chen, C.; Li, C.; Awni, R. A.; Zhao, D.; Yan, Y. Wide-Bandgap, Low-Bandgap, and Tandem Perovskite Solar Cells. *Semicond. Sci. Technol.* **2019**, *34*, 093001.

(6) Duong, T.; Wu, Y.; Shen, H.; Peng, J.; Fu, X.; Jacobs, D.; Wang, E.-C.; Kho, T. C.; Fong, K. C.; Stocks, M.; Franklin, E.; Blakers, A.; Zin, N.; McIntosh, K.; Li, W.; Cheng, Y.-B.; White, T. P.; Weber, K.; Catchpole, K. Rubidium Multication Perovskite with Optimized Bandgap for Perovskite-Silicon Tandem with over 26% Efficiency. *Adv. Energy Mater.* **2017**, *7*, 1700228.

(7) Qiu, Z.; Xu, Z.; Li, N.; Zhou, N.; Chen, Y.; Wan, X.; Liu, J.; Li, N.; Hao, X.; Bi, P.; Chen, Q.; Cao, B.; Zhou, H. Monolithic Perovskite/Si Tandem Solar Cells Exceeding 22% Efficiency Via Optimizing Top Cell Absorber. *Nano Energy* **2018**, *53*, 798−807.

(8) Han, Q.; Hsieh, Y.-T.; Meng, L.; Wu, J.-L.; Sun, P.; Yao, E.-P.; Chang, S.-Y.; Bae, S.-H.; Kato, T.; Bermudez, V.; Yang, Y. High-Performance Perovskite/Cu(In,Ga)Se_2 Monolithic Tandem Solar Cells. *Science* **2018**, *361*, 904−908.

(9) Shen, H.; Duong, T.; Peng, J.; Jacobs, D.; Wu, N.; Gong, J.; Wu, Y.; Karuturi, S. K.; Fu, X.; Weber, K.; Xiao, X.; White, T.; Catchpole, K. Mechanically-Stacked Perovskite/CIGS Tandem Solar Cells with Efficiency of 23.9% and Reduced Oxygen Sensitivity. *Energy Environ. Sci.* **2018**, *11*, 394−406.

(10) Zhao, D.; Chen, C.; Wang, C.; Junda, M. M.; Song, Z.; Grice, C. R.; Yu, Y.; Li, C.; Subedi, B.; Podraza, N. J.; Zhao, X.; Fang, G.; Xiong, R.-G.; Zhu, K.; Yan, Y. Efficient Two-Terminal All-Perovskite Tandem Solar Cells Enabled by High-Quality Low-Bandgap Absorber Layers. *Nat. Energy* **2018**, *3*, 1093−1100.

(11) Al-Ashouri, A.; Magomedov, A.; Roß, M.; Jošt, M.; Talaikis, M.; Chistiakova, G.; Bertram, T.; Márquez, J. A.; Köhnen, E.; Kasparavičius, E.; Levcenco, S.; Gil-Escrig, L.; Hages, C. J.; Schlatmann, R.; Rech, B.; Malinauskas, T.; Unold, T.; Kaufmann, C. A.; Korte, L.; Niaura, G.; Getautis, V.; Albrecht, S. Conformal Monolayer Contacts with Lossless Interfaces for Perovskite Single Junction and Monolithic Tandem Solar Cells. *Energy Environ. Sci.* **2019**, *12*, 3356−3369.

(12) Jošt, M.; Bertram, T.; Koushik, D.; Marquez, J. A.; Verheijen, M. A.; Heinemann, M. D.; Köhnen, E.; Al-Ashouri, A.; Braunger, S.; Lang, F.; Rech, B.; Unold, T.; Creatore, M.; Lauermann, I.; Kaufmann, C. A.; Schlatmann, R.; Albrecht, S. 21.6%-Efficient Monolithic Perovskite/Cu(in,Ga)Se2 Tandem Solar Cells with Thin Conformal Hole Transport Layers for Integration on Rough Bottom Cell Surfaces. *ACS Energy Lett.* **2019**, *4*, 583−590.

(13) Tong, J.; Song, Z.; Kim, D. H.; Chen, X.; Chen, C.; Palmstrom, A. F.; Ndione, P. F.; Reese, M. O.; Dunfield, S. P.; Reid, O. G.; Liu, J.; Zhang, F.; Harvey, S. P.; Li, Z.; Christensen, S. T.; Teeter, G.; Zhao, D.; Al-Jassim, M. M.; van Hest, M. F. A. M.; Beard, M. C.; Shaheen, S. E.; Berry, J. J.; Yan, Y.; Zhu, K. Carrier Lifetimes of > 1 μs in Sn-Pb Perovskites Enable Efficient All-Perovskite Tandem Solar Cells. *Science* **2019**, *364*, 475−479.

(14) Lin, R.; Xiao, K.; Qin, Z.; Han, Q.; Zhang, C.; Wei, M.; Saidaminov, M. I.; Gao, Y.; Xu, J.; Xiao, M.; Li, A.; Zhu, J.; Sargent, E.

Approved for public release; distribution unlimited.

H.; Tan, H. Monolithic All-Perovskite Tandem Solar Cells with 24.8% Efficiency Exploiting Comproportionation to Suppress Sn(II) Oxidation in Precursor Ink. *Nat. Energy* **2019**, *4*, 864−873.
(15) Kim, D.; Jung, H. J.; Park, I. J.; Larson, B. W.; Dunfield, S. P.; Xiao, C.; Kim, J.; Tong, J.; Boonmongkolras, P.; Ji, S. G.; Zhang, F.; Pae, S. R.; Kim, M.; Kang, S. B.; Dravid, V.; Berry, J. J.; Kim, J. Y.; Zhu, K.; Kim, D. H.; Shin, B. Efficient, Stable Silicon Tandem Cells Enabled by Anion-Engineered Wide-Bandgap Perovskites. *Science* **2020**, *368*, No. 155.
(16) Xu, J.; Boyd, C. C.; Yu, Z. J.; Palmstrom, A. F.; Witter, D. J.; Larson, B. W.; France, R. M.; Werner, J.; Harvey, S. P.; Wolf, E. J.; Weigand, W.; Manzoor, S.; van Hest, M. F. A. M.; Berry, J. J.; Luther, J. M.; Holman, Z. C.; McGehee, M. D. Triple-Halide Wide−Band Gap Perovskites with Suppressed Phase Segregation for Efficient Tandems. *Science* **2020**, *367*, 1097−1104.
(17) Hou, Y.; Aydin, E.; De Bastiani, M.; Xiao, C.; Isikgor, F. H.; Xue, D.-J.; Chen, B.; Chen, H.; Bahrami, B.; Chowdhury, A. H.; Johnston, A.; Baek, S.-W.; Huang, Z.; Wei, M.; Dong, Y.; Troughton, J.; Jalmood, R.; Mirabelli, A. J.; Allen, T. G.; Van Kerschaver, E.; Saidaminov, M. I.; Baran, D.; Qiao, Q.; Zhu, K.; De Wolf, S.; Sargent, E. H. Efficient Tandem Solar Cells with Solution-Processed Perovskite on Textured Crystalline Silicon. *Science* **2020**, *367*, 1135.
(18) Li, Z.; Kim, T. H.; Han, S. Y.; Yun, Y.-J.; Jeong, S.; Jo, B.; Ok, S. A.; Yim, W.; Lee, S. H.; Kim, K.; Moon, S.; Park, J.-Y.; Ahn, T. K.; Shin, H.; Lee, J.; Park, H. J. Wide-Bandgap Perovskite/Gallium Arsenide Tandem Solar Cells. *Adv. Energy Mater.* **2020**, *10*, 1903085.
(19) Yu, Y.; Wang, C.; Grice, C. R.; Shrestha, N.; Zhao, D.; Liao, W.; Guan, L.; Awni, R. A.; Meng, W.; Cimaroli, A. J.; Zhu, K.; Ellingson, R. J.; Yan, Y. Synergistic Effects of Lead Thiocyanate Additive and Solvent Annealing on the Performance of Wide-Bandgap Perovskite Solar Cells. *ACS Energy Lett.* **2017**, *2*, 1177−1182.
(20) Chen, C.; Song, Z.; Xiao, C.; Zhao, D.; Shrestha, N.; Li, C.; Yang, G.; Yao, F.; Zheng, X.; Ellingson, R. J.; Jiang, C.-S.; Al-Jassim, M.; Zhu, K.; Fang, G.; Yan, Y. Achieving a High Open-Circuit Voltage in Inverted Wide-Bandgap Perovskite Solar Cells with a Graded Perovskite Homojunction. *Nano Energy* **2019**, *61*, 141−147.
(21) Zhou, Y.; Wang, F.; Cao, Y.; Wang, J.-P.; Fang, H.-H.; Loi, M. A.; Zhao, N.; Wong, C.-P. Benzylamine-Treated Wide-Bandgap Perovskite with High Thermal-Photostability and Photovoltaic Performance. *Adv. Energy Mater.* **2017**, *7*, 1701048.
(22) Kim, J.; Saidaminov, M. I.; Tan, H.; Zhao, Y.; Kim, Y.; Choi, J.; Jo, J. W.; Fan, J.; Quintero-Bermudez, R.; Yang, Z.; Quan, L. N.; Wei, M.; Voznyy, O.; Sargent, E. H. Amide-Catalyzed Phase-Selective Crystallization Reduces Defect Density in Wide-Bandgap Perovskites. *Adv. Mater.* **2018**, *30*, 1706275.
(23) Wang, Z.; Lin, Q.; Chmiel, F. P.; Sakai, N.; Herz, L. M.; Snaith, H. J. Efficient Ambient-Air-Stable Solar Cells with 2d−3d Heterostructured Butylammonium-Caesium-Formamidinium Lead Halide Perovskites. *Nat. Energy* **2017**, *2*, 17135.
(24) Tan, H.; Che, F.; Wei, M.; Zhao, Y.; Saidaminov, M. I.; Todorović, P.; Broberg, D.; Walters, G.; Tan, F.; Zhuang, T.; Sun, B.; Liang, Z.; Yuan, H.; Fron, E.; Kim, J.; Yang, Z.; Voznyy, O.; Asta, M.; Sargent, E. H. Dipolar Cations Confer Defect Tolerance in Wide-Bandgap Metal Halide Perovskites. *Nat. Commun.* **2018**, *9*, 3100.
(25) Rajagopal, A.; Stoddard, R. J.; Jo, S. B.; Hillhouse, H. W.; Jen, A. K. Y. Overcoming the Photovoltage Plateau in Large Bandgap Perovskite Photovoltaics. *Nano Lett.* **2018**, *18*, 3985−3993.
(26) Zheng, X.; Chen, B.; Dai, J.; Fang, Y.; Bai, Y.; Lin, Y.; Wei, H.; Zeng, X. C.; Huang, J. Defect Passivation in Hybrid Perovskite Solar Cells Using Quaternary Ammonium Halide Anions And cations. *Nat. Energy* **2017**, *2*, 17102.
(27) Gharibzadeh, S.; Abdollahi Nejand, B.; Jakoby, M.; Abzieher, T.; Hauschild, D.; Moghadamzadeh, S.; Schwenzer, J. A.; Brenner, P.; Schmager, R.; Haghighirad, A. A.; Weinhardt, L.; Lemmer, U.; Richards, B. S.; Howard, I. A.; Paetzold, U. W. Record Open-Circuit Voltage Wide-Bandgap Perovskite Solar Cells Utilizing 2d/3d Perovskite Heterostructure. *Adv. Energy Mater.* **2019**, *9*, 1803699.
(28) Hoke, E. T.; Slotcavage, D. J.; Dohner, E. R.; Bowring, A. R.; Karunadasa, H. I.; McGehee, M. D. Reversible Photo-Induced Trap Formation in Mixed-Halide Hybrid Perovskites for Photovoltaics. *Chem. Sci.* **2015**, *6*, 613−617.
(29) Belisle, R. A.; Bush, K. A.; Bertoluzzi, L.; Gold-Parker, A.; Toney, M. F.; McGehee, M. D. Impact of Surfaces on Photoinduced Halide Segregation in Mixed-Halide Perovskites. *ACS Energy Lett.* **2018**, *3*, 2694−2700.
(30) Gratia, P.; Grancini, G.; Audinot, J.-N.; Jeanbourquin, X.; Mosconi, E.; Zimmermann, I.; Dowsett, D.; Lee, Y.; Grätzel, M.; De Angelis, F.; Sivula, K.; Wirtz, T.; Nazeeruddin, M. K. Intrinsic Halide Segregation at Nanometer Scale Determines the High Efficiency of Mixed Cation/Mixed Halide Perovskite Solar Cells. *J. Am. Chem. Soc.* **2016**, *138*, 15821−15824.
(31) Draguta, S.; Sharia, O.; Yoon, S. J.; Brennan, M. C.; Morozov, Y. V.; Manser, J. S.; Kamat, P. V.; Schneider, W. F.; Kuno, M. Rationalizing the Light-Induced Phase Separation of Mixed Halide Organic−Inorganic Perovskites. *Nat. Commun.* **2017**, *8*, 200.
(32) Knight, A. J.; Wright, A. D.; Patel, J. B.; McMeekin, D. P.; Snaith, H. J.; Johnston, M. B.; Herz, L. M. Electronic Traps and Phase Segregation in Lead Mixed-Halide Perovskite. *ACS Energy Lett.* **2019**, *4*, 75−84.
(33) Jiang, Q.; Zhao, Y.; Zhang, X.; Yang, X.; Chen, Y.; Chu, Z.; Ye, Q.; Li, X.; Yin, Z.; You, J. Surface Passivation of Perovskite Film for Efficient Solar Cells. *Nat. Photonics* **2019**, *13*, 460−466.
(34) Yoo, J. J.; Wieghold, S.; Sponseller, M. C.; Chua, M. R.; Bertram, S. N.; Hartono, N. T. P.; Tresback, J. S.; Hansen, E. C.; Correa-Baena, J.-P.; Bulović, V.; Buonassisi, T.; Shin, S. S.; Bawendi, M. G. An Interface Stabilized Perovskite Solar Cell with High Stabilized Efficiency and Low Voltage Loss. *Energy Environ. Sci.* **2019**, *12*, 2192−2199.
(35) Qian, F.; Yuan, S.; Cai, Y.; Han, Y.; Zhao, H.; Sun, J.; Liu, Z.; Liu, S. Novel Surface Passivation for Stable $FA_{0.85}MA_{0.15}PbI_3$ Perovskite Solar Cells with 21.6% Efficiency. *Solar RRL* **2019**, *3*, 1900072.
(36) Lin, Y.; Chen, B.; Zhao, F.; Zheng, X.; Deng, Y.; Shao, Y.; Fang, Y.; Bai, Y.; Wang, C.; Huang, J. Matching Charge Extraction Contact for Wide-Bandgap Perovskite Solar Cells. *Adv. Mater.* **2017**, *29*, 1700607.
(37) Awni, R. A.; Song, Z.; Chen, C.; Li, C.; Wang, C.; Razooqi, M. A.; Chen, L.; Wang, X.; Ellingson, R. J.; Li, J. V.; Yan, Y. Influence of Charge Transport Layers on Capacitance Measured in Halide Perovskite Solar Cells. *Joule* **2020**, *4*, 644−657.
(38) Ke, W.; Xiao, C.; Wang, C.; Saparov, B.; Duan, H. S.; Zhao, D.; Xiao, Z.; Schulz, P.; Harvey, S. P.; Liao, W.; Meng, W.; Yu, Y.; Cimaroli, A. J.; Jiang, C. S.; Zhu, K.; Al-Jassim, M.; Fang, G.; Mitzi, D. B.; Yan, Y. Employing Lead Thiocyanate Additive to Reduce the Hysteresis and Boost the Fill Factor of Planar Perovskite Solar Cells. *Adv. Mater.* **2016**, *28*, 5214−21.
(39) Shao, Y.; Fang, Y.; Li, T.; Wang, Q.; Dong, Q.; Deng, Y.; Yuan, Y.; Wei, H.; Wang, M.; Gruverman, A.; Shield, J.; Huang, J. Grain Boundary Dominated Ion Migration in Polycrystalline Organic−Inorganic Halide Perovskite Films. *Energy Environ. Sci.* **2016**, *9*, 1752−1759.
(40) Yun, J. S.; Seidel, J.; Kim, J.; Soufiani, A. M.; Huang, S.; Lau, J.; Jeon, N. J.; Seok, S. I.; Green, M. A.; Ho-Baillie, A. Critical Role of Grain Boundaries for Ion Migration in Formamidinium and Methylammonium Lead Halide Perovskite Solar Cells. *Adv. Energy Mater.* **2016**, *6*, 1600330.
(41) Yuan, Y.; Huang, J. Ion Migration in Organometal Trihalide Perovskite and Its Impact on Photovoltaic Efficiency and Stability. *Acc. Chem. Res.* **2016**, *49*, 286−293.
(42) Meggiolaro, D.; Mosconi, E.; De Angelis, F. Formation of Surface Defects Dominates Ion Migration in Lead-Halide Perovskites. *ACS Energy Lett.* **2019**, *4*, 779−785.
(43) Musiienko, A.; Moravec, P.; Grill, R.; Praus, P.; Vasylchenko, I.; Pekarek, J.; Tisdale, J.; Ridzonova, K.; Belas, E.; Landová, L.; Hu, B.; Lukosi, E.; Ahmadi, M. Deep Levels, Charge Transport and Mixed Conductivity in Organometallic Halide Perovskites. *Energy Environ. Sci.* **2019**, *12*, 1413−1425.

https://dx.doi.org/10.1021/acsenergylett.0c01350
ACS Energy Lett. 2020, 5, 2560−2568

Approved for public release; distribution unlimited.

(44) Nan, G.; Zhang, X.; Abdi-Jalebi, M.; Andaji-Garmaroudi, Z.; Stranks, S. D.; Lu, G.; Beljonne, D. How Methylammonium Cations and Chlorine Dopants Heal Defects in Lead Iodide Perovskites. *Adv. Energy Mater.* **2018**, *8*, 1702754.
(45) Sherkar, T. S.; Momblona, C.; Gil-Escrig, L.; Ávila, J.; Sessolo, M.; Bolink, H. J.; Koster, L. J. A. Recombination in Perovskite Solar Cells: Significance of Grain Boundaries, Interface Traps, and Defect Ions. *ACS Energy Lett.* **2017**, *2*, 1214−1222.
(46) Li, C.; Song, Z.; Zhao, D.; Xiao, C.; Subedi, B.; Shrestha, N.; Junda, M. M.; Wang, C.; Jiang, C.-S.; Al-Jassim, M.; Ellingson, R. J.; Podraza, N. J.; Zhu, K.; Yan, Y. Reducing Saturation-Current Density to Realize High-Efficiency Low-Bandgap Mixed Tin−Lead Halide Perovskite Solar Cells. *Adv. Energy Mater.* **2019**, *9*, 1803135.
(47) Ye, J. Y.; Tong, J.; Hu, J.; Xiao, C.; Lu, H.; Dunfield, S. P.; Kim, D. H.; Chen, X.; Larson, B. W.; Hao, J.; Wang, K.; Zhao, Q.; Chen, Z.; Hu, H.; You, W.; Berry, J. J.; Zhang, F.; Zhu, K. Enhancing Charge Transport of 2d Perovskite Passivation Agent for Wide-Bandgap Perovskite Solar Cells Beyond 21%. *Solar RRL* **2020**, *4*, 2000082.
(48) Son, D.-Y.; Lee, J.-W.; Choi, Y. J.; Jang, I.-H.; Lee, S.; Yoo, P. J.; Shin, H.; Ahn, N.; Choi, M.; Kim, D.; Park, N.-G. Self-Formed Grain Boundary Healing Layer for Highly Efficient $CH_3NH_3PbI_3$ Perovskite Solar Cells. *Nat. Energy* **2016**, *1*, 16081.
(49) Cho, K. T.; Grancini, G.; Lee, Y.; Oveisi, E.; Ryu, J.; Almora, O.; Tschumi, M.; Schouwink, P. A.; Seo, G.; Heo, S.; Park, J.; Jang, J.; Paek, S.; Garcia-Belmonte, G.; Nazeeruddin, M. K. Selective Growth of Layered Perovskites for Stable and Efficient Photovoltaics. *Energy Environ. Sci.* **2018**, *11*, 952−959.
(50) Niu, T.; Lu, J.; Jia, X.; Xu, Z.; Tang, M.-C.; Barrit, D.; Yuan, N.; Ding, J.; Zhang, X.; Fan, Y.; Luo, T.; Zhang, Y.; Smilgies, D.-M.; Liu, Z.; Amassian, A.; Jin, S.; Zhao, K.; Liu, S. Interfacial Engineering at the 2d/3d Heterojunction for High-Performance Perovskite Solar Cells. *Nano Lett.* **2019**, *19*, 7181−7190.
(51) Ye, S.; Rao, H.; Zhao, Z.; Zhang, L.; Bao, H.; Sun, W.; Li, Y.; Gu, F.; Wang, J.; Liu, Z.; Bian, Z.; Huang, C. A Breakthrough Efficiency of 19.9% Obtained in Inverted Perovskite Solar Cells by Using an Efficient Trap State Passivator Cu(Thiourea)I. *J. Am. Chem. Soc.* **2017**, *139*, 7504−7512.
(52) Zhao, D.; Wang, C.; Song, Z.; Yu, Y.; Chen, C.; Zhao, X.; Zhu, K.; Yan, Y. Four-Terminal All-Perovskite Tandem Solar Cells Achieving Power Conversion Efficiencies Exceeding 23%. *ACS Energy Lett.* **2018**, *3*, 305−306.

https://dx.doi.org/10.1021/acsenergylett.0c01350
ACS Energy Lett. 2020, 5, 2560−2568

Approved for public release; distribution unlimited.

This is an open access article published under an ACS AuthorChoice License, which permits copying and redistribution of the article or any adaptations for non-commercial purposes.

ACS APPLIED ENERGY MATERIALS

www.acsaem.org Letter

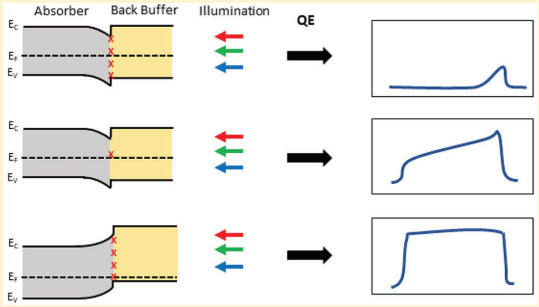
Understanding and Advancing Bifacial Thin Film Solar Cells

Adam B. Phillips,* Kamala Khanal Subedi, Geethika K. Liyanage, Fadhil K. Alfadhili, Randy J. Ellingson, and Michael J. Heben

Cite This: *ACS Appl. Energy Mater.* 2020, 3, 6072−6078 Read Online

ACCESS | Metrics & More | Article Recommendations | Supporting Information

ABSTRACT: Because bifacial solar cells increase the power generated per area, their market share is projected to increase over the next decade. While silicon technologies have implemented bifacial technology, little progress has occurred in bifacial thin film (BTF) solar cells. Understanding the factors that limit performance is critical to advancing BTF cells. We show that recombination at the back interface has limited device performance of fabricated BTF devices. Improved BTF performance will require decreasing recombination at the back interface, through passivation or by reducing downward band-bending at this interface. Increasing carrier lifetimes improves performance, but increasing hole density has little effect.



KEYWORDS: *bifacial, thin film, CdTe, numerical modeling, IFLO, recombination, solar cells*

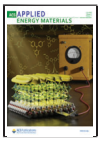
Downloaded via UNIV OF TOLEDO on September 13, 2021 at 15:44:58 (UTC).
See https://pubs.acs.org/sharingguidelines for options on how to legitimately share published articles.

With single junction photovoltaic (PV) device efficiencies exceeding 25%,[1] new solar cell architectures will be needed to allow the power production per unit area to be increased. One of the most promising and potentially inexpensive methods to increase the power production per unit area of single junction devices is to use a bifacial configuration. This configuration allows for photons to enter the absorber through both sides of the device, allowing reflected and scattered light incident on the back surface to boost the power output. Early measurements showed that bifacial devices could produce 50% more power under certain conditions.[2] More recent studies show that mounting bifacial modules on high albedo backgrounds can result in an energy yield increase of ∼20−30%.[3,4] On the basis of these benefits, the International Technology Roadmap for Photovoltaics estimates that bifacial devices will account for ∼40% of the PV market by 2028.[5]

Due to the potential for a significant increase in energy yield, there has been substantial interest in developing bifacial devices. Most of this work has been on high efficiency crystalline Si devices, which are now deployed in the market,[6] but research into bifacial thin film (BTF) PV has begun.[7−10] In Si PV devices, a long bulk carrier lifetime (hundreds of microseconds to milliseconds)[11,12] and long diffusion length coupled with low surface recombination velocities (SRVs; ∼10 cm s^{-1})[12] means that carriers can reach the carrier selective contacts before recombining, regardless of the direction of the incoming light. When paired with the development of transparent back contacts, bifacial Si devices efficiencies of 19.5−22% and 17−19% have been achieved when illuminated through the front and rear of the device, respectively.[13] These values result in a bifaciality, defined as the ratio of efficiency illuminated through the back to efficiency illuminated through the front, of 85%.

Progress in improving the bifacial performance of polycrystalline thin film PV has been limited by relatively short measured minority carrier lifetimes on the order of 1 ns[14] and high back surface recombination velocities on the order of ∼10^5 cm s^{-1}.[15] Under these conditions, the device efficiency is low (5.0% for CdTe[9] and 6.0% for CIGS[8]) when illuminated through the back side (η_{Back}) even when the front-illuminated efficiency (η_{Front}) is high. Recent improvements in the carrier lifetime with Se incorporated into CdTe[16,17] and companion reports of diffusion lengths much greater than the typical device thickness[17] suggest that it should be possible to fabricate high performance BTF CdTe devices. To date, however, understanding of the deficiencies of bifacial thin film devices has been limited to generalizations about absorber thickness[7,10] or analysis of the PV parameters.[9] Recent modeling indicates that a highly doped back buffer layer[18] or reduction in back surface recombination velocity (BSRV)[8] can lead to improved device performance for bifacial CIGS, but there is still a lack of general understanding.

Received: April 16, 2020
Accepted: June 9, 2020
Published: June 9, 2020



ACS Publications © 2020 American Chemical Society

https://dx.doi.org/10.1021/acsaem.0c00851
ACS Appl. Energy Mater. 2020, 3, 6072−6078

Approved for public release; distribution unlimited.

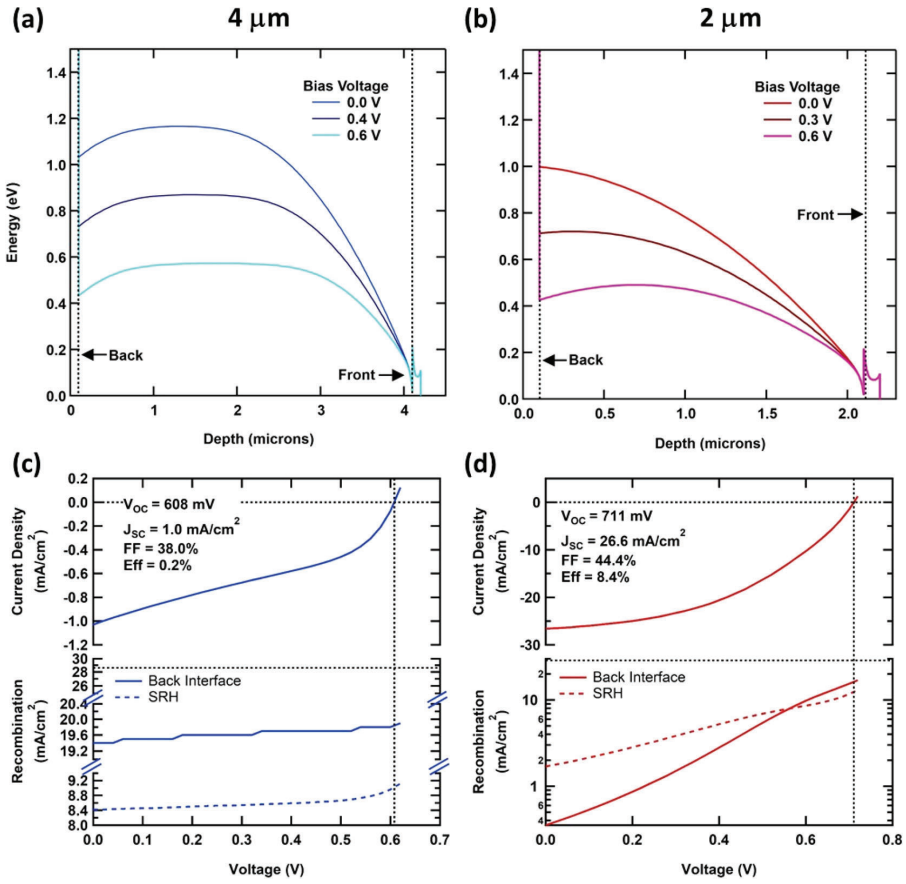


Figure 1. (a, b) Conduction band portion of the band diagrams for 4 and 2 μm absorber thickness devices, respectively, at various bias voltages. Note that the back of the device is located on the left. (c, d) Corresponding current (J) and recombination current densities (J_r) as a function of bias voltage.

Here, we use numerical simulations to determine critical factors for device designs that will allow the simultaneous optimization of both front side and back side illumination performance. We evaluate the relative importance of carrier lifetime, absorber dopant density, and absorber thickness and consider approaches to reducing the recombination at the back interface through either chemical passivation or the production of a back surface field. Our findings can be used to guide real-world efforts to push the efficiency of back side illuminated thin film PV devices closer to that of monofacial devices, thereby increasing bifacial performance and increasing the overall power output.

Simulations were carried out using SCAPS-1D software version 3.3.05.[19] Following previous work,[20] modeled devices consisted of a 300 nm n-type transparent front contact, a 100 nm $Zn_xMg_{1-x}O$ (ZMO) emitter layer, a CdTe layer of variable thickness, a 100 nm back side buffer, and a transparent back electrode. The ZMO composition was chosen to produce a bandgap of 3.7 eV with a conduction band that was 0.2 eV higher than the conduction band of CdTe (conduction band offset of +0.2 eV). This configuration has been shown to produce very low front surface recombination currents that can be neglected for all conditions examined here.[21,22] The back buffer layer was chosen with a valence band 0.2 eV higher in energy than the valence band of CdTe (valence band offset of −0.2 eV) and a bandgap of 3.3 eV to be a transparent contact. Typically, in BTF devices, an n-type transparent conducting oxide (TCO) is deposited at the back of the device.[7−10] However, implementation of a traditional n-type TCO on both sides of the device is not permitted in the SCAPS software, so the bands between the buffer and transparent back contact were fixed to be flat. While the effects of the n-type TCO at the back of a p-type absorber and buffer on the band diagram are not well-understood in BTF devices, we expect this to induce downward band-bending in the buffer at the buffer/TCO interface. We have recently showed that if a low barrier for hole flow can be maintained, this band-bending does not alter the device performance.[20] Recent measurements suggest that this may be the case.[23] The key material parameters, except where noted, were obtained from the literature and are presented in the SI. Following earlier work,[22] we chose Gaussian type midgap defect states with electron and hole carrier lifetimes equal to each other with specific values noted in the text. The back surface recombination velocity (BSRV) was held at 10^4 cm s^{-1} (an order of magnitude lower than typical values). Other material parameters for the buffer layer were set to those

https://dx.doi.org/10.1021/acsaem.0c00851
ACS Appl. Energy Mater. 2020, 3, 6072−6078

Approved for public release; distribution unlimited.

Table 1. Back-Illuminated PV Parameters for Two Absorber Thicknesses as a Function of Back Surface Recombination Velocity (BSRV)[a]

	4 μm					2 μm				
BSRV, cm s^{-1}	V_{OC}, mmV	J_{SC}, mA cm^{-2}	FF %	eff %	bifac	V_{OC}, mV	J_{SC}, mA cm^{-2}	FF %	eff %	bifac
10^4	751	2.3	44.3	0.8	0.04	755	28.2	51.5	11.0	0.6
10^3	813	11.1	49.2	4.4	0.22	820	28.6	68.6	16.1	0.84
10^2	893	23.2	66.9	13.9	0.69	905	28.6	75.2	19.5	0.98
10^1	924	25.8	71.9	17.2	0.85	943	28.6	75.6	20.4	1
10^0	929	26.1	72.5	17.6	0.87	949	28.6	75.6	20.5	1

[a]The bifaciality (bifac) is defined as efficiency illuminated through the back divided by efficiency illuminated through the front.

used for the CdTe. For back side illumination, the absorption in the buffer layer was set to zero to ensure computational convergence.

We first investigated the performance limitations of the best reported BTF devices with back side illumination by considering the band diagrams and the controlling recombination currents.[9,10] To understand previously fabricated devices, we used values that are representative of the materials properties of those devices. The initial carrier lifetimes were set to 1 ns.[24] The CdTe hole density was set to 2×10^{14} cm^{-3}, and the back buffer hole density was 2×10^{14} cm^{-3}, which corresponds to an initial Fermi level offset (IFLO) of −0.2 eV.[20] Note that because of the deep valence band position of CdTe, it is difficult to make an Ohmic contact. We use IFLO to characterize this contact. A negative IFLO results in downward band-bending and the formation of a Schottky junction. The typical back contact for CdTe devices results in a negative IFLO. A positive IFLO results in upward band-bending and would indicate an Ohmic contact. In addition, higher positive IFLO indicates a more carrier selective contact. The −0.2 eV IFLO value used here produces band-bending at the rear contact which is similar to that found with a Te back contact.[25]

Panels a and b of Figure 1 show the conduction band portion of the simulated band diagrams at three different biases for devices with absorber thicknesses of 4 and 2 μm, respectively, while illuminated through the back side of the device. Note that these thicknesses are representative of the experimental bifacial CdTe absorber thicknesses.[7,9,10] Panels c and d show the corresponding current density and recombination current density versus voltage (J−V and J_r−V) plots, respectively. The behavior of the devices can be understood by considering how the band-bending at the front (emitter/absorber) and back (absorber/back buffer) junctions (FJ and BJ, respectively) interact to form the overall band diagrams, and how the band-bending and recombination currents change with bias.

In the 4 μm device, the FJ depletion width extends from ∼2 to 4 μm (2 μm total) in the CdTe layer at zero bias. At a 0.3 or 0.6 V bias, the FJ depletion width decreases and extends from 2.5 or 3 μm, respectively, to 4 μm. The downward bending depletion width at the BJ, on the other hand, extends from 0 to 1 μm and is nearly independent of the bias voltage. With back side illumination, the penetration depth of the ultraviolet and visible wavelength light is short, and a large fraction of the carrier generation with AM1.5 irradiance occurs within ∼1 μm of the back surface. With bias-independent band-bending near the BJ, the carriers are swept in the wrong direction, and the interface recombination current (J_{INT}) is high, leading to a low J_{SC}. As the bias voltage increases, the band-bending at the FJ decreases. This leads to a decrease in the number of carriers that are collected at the FJ. Furthermore, the flattening of the bands with increasing bias causes the Shockley−Reed−Hall (SRH) recombination current density (J_{SRH}) to turn-on smoothly over a wide voltage range. This smooth, as opposed to abrupt, increase in J_{SRH} with bias results in a low fill factor (FF). In this case, the J_{INT} remains higher than J_{SRH} at all biases.

For the 2 μm device, the FJ and BJ are close enough that they interact to significantly affect the overall band diagram. Interestingly, at zero bias, there is no BJ depletion region. This gives rise to a much higher J_{SC}. As with the 4 μm absorber case, increasing the bias reduces the band-bending at the FJ. This allows a downward bending depletion region at the BJ to begin to emerge. This results in a bias-dependent increase in the back surface J_{INT} and, thus, a low FF. Interestingly, J_{INT} is lower than J_{SRH} until ∼550 mV, but ∼1.5 times larger by V_{OC}.

To improve the device performance during back side illumination, it is clear that the back interface recombination needs to be reduced. Productive strategies could be similar to those employed for improving the front side performance of CdTe devices[16] and other thin film PV materials,[26,27] which typically involve either chemical passivation of defects[28] or modification of the surface electric field and the related band-bending.[11]

Considering chemical passivation of the back interface first, we examined the effect of decreasing the back surface recombination velocity (BSRV) from 10^4 to 10^0 cm s^{-1} for $p_{CdTe} = 2 \times 10^{14}$ cm^{-3}. Again, we considered both 4 and 2 μm thick absorber layers, but in this case the carrier lifetimes were increased to 32 ns to be closer to recently measured values.[14,16] Note that the increased lifetime accounts for suppression of bulk defect states as well as improved passivation of the grain boundaries in the polycrystalline absorber layer. Table 1 shows the resultant simulated PV parameters and the bifaciality metric (η_{Back}/η_{Front}). As expected, reducing the BSRV results in lower recombination at this interface, leading to increases in both J_{SC} and FF in the 4 μm device, and an increase in the FF in the 2 μm device. It is surprising, however, that the bifaciality of the 4 μm device does not reach 1. This is due to the fact that the downward bending depletion region exists at the BJ for all biases. Thus, carriers generated near the BJ cannot reach the front of the device before recombining through the SRH mechanism, even at zero bias. For a 2 μm device, on the other hand, there is no depletion region at the BJ at zero bias. As a result, J_{INT} is low, and J_{SC} is high for all values of BSRV. In the thin absorber case, reducing the BSRV leads to improved FF. Interestingly, the bifaciality approaches 1 as the BSRV is reduced to 10^2 cm s^{-1}. In both cases, reducing the BSRV to values lower than 10^1 cm s^{-1} does not further improve the device performance because J_{INT} is already an order of magnitude lower that J_{SRH} (SI).

https://dx.doi.org/10.1021/acsaem.0c00851
ACS Appl. Energy Mater. 2020, 3, 6072−6078

Approved for public release; distribution unlimited.

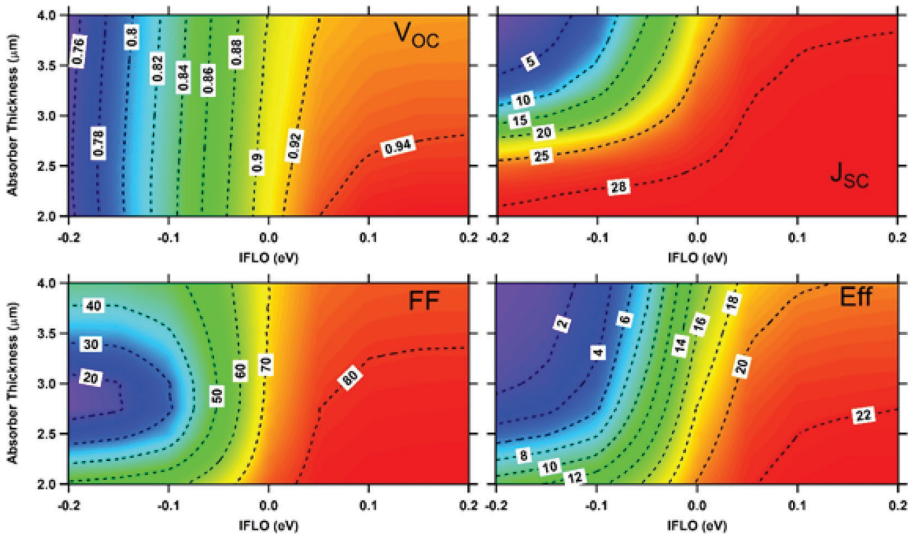


Figure 2. Contour plots of the back-illuminated PV parameters for devices of varying thickness as a function of initial Fermi level offset (IFLO). The carrier lifetime was maintained at 32 ns; the BSRV was 1×10^4 cm s^{-1}, and p_{CdTe} was 2×10^{14} cm^{-3}.

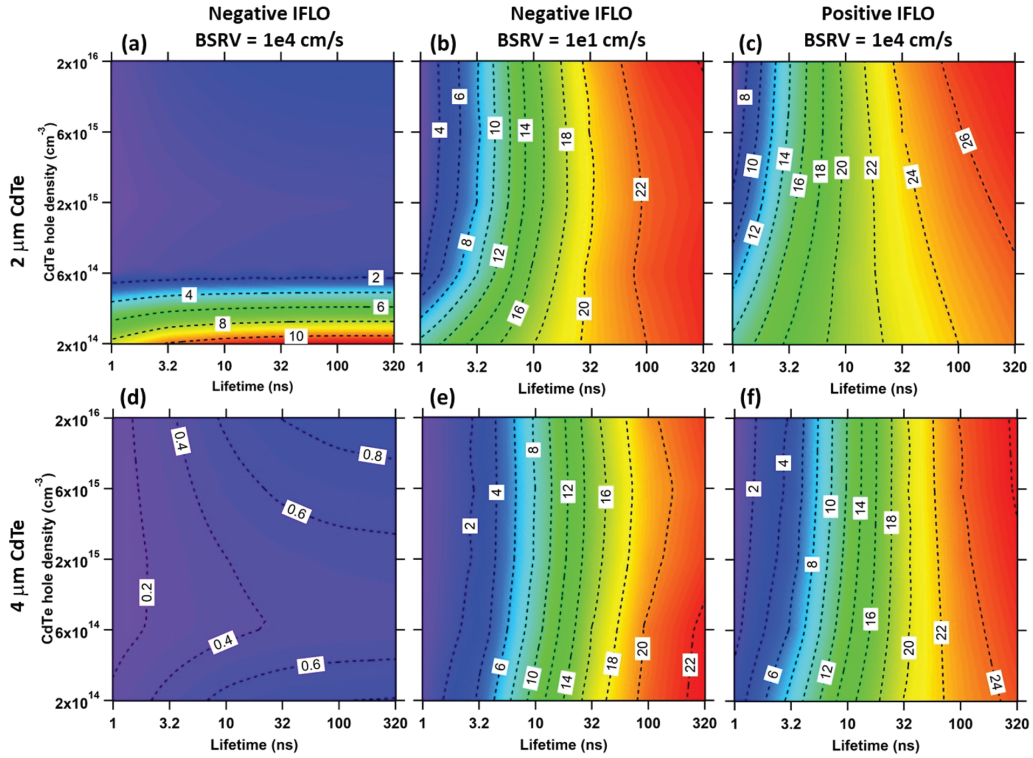


Figure 3. Contour plots of the back-illuminated efficiency as a function of absorber hole density and carrier lifetime for absorber thicknesses, (a−c) 2 μm and (d−f) 4 μm, and varying back interface conditions: (a, d) negative IFLO, BSRV = 1×10^4 cm s^{-1}; (b, e) negative IFLO, BSRV = 1×10^1 cm s^{-1}; and (c, f) positive IFLO, BSRV = 1×10^4 cm s^{-1}.

Band-bending can also be modified by locating fixed charge at the back buffer layer[11] or, more generally, by changing the alignment of the noninteracting initial Fermi level offset (IFLO) between the absorber and buffer.[20] (See SI for how fixed charges relate to IFLO.) Figure 2 shows contour plots of the back-illuminated PV parameters as a function of the IFLO

https://dx.doi.org/10.1021/acsaem.0c00851
ACS Appl. Energy Mater. 2020, 3, 6072−6078

Approved for public release; distribution unlimited.

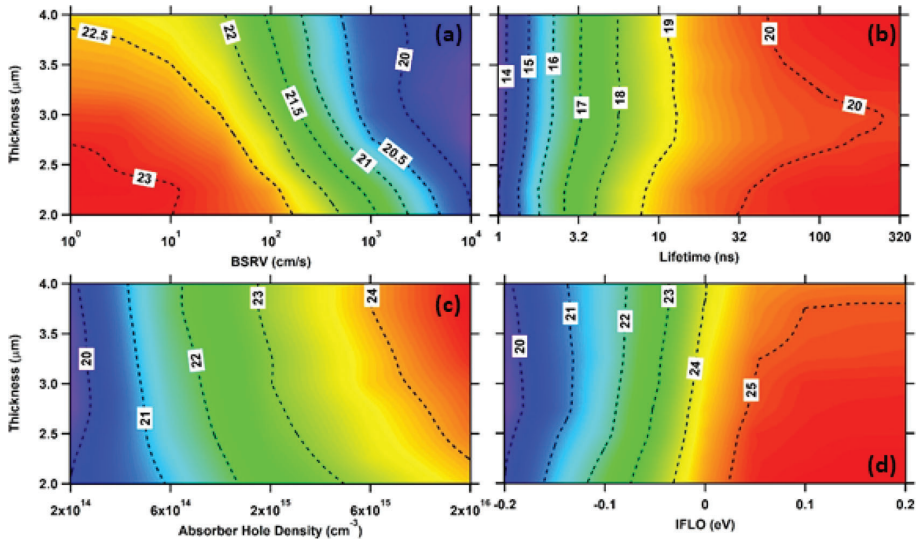


Figure 4. Contour plots of bifacial efficiency as a function of thickness and (a) BSRV, (b) lifetime, (c) CdTe hole density, and (d) IFLO. When not varied, the following conditions applied: the BSRV was set to 10^4 cm/s; the carrier lifetime was set to 32 ns; the CdTe hole density was set to 2×10^{14} cm^{-3}; and the IFLO was set to −0.2 eV.

and the absorber thickness. The data for devices illuminated through the front interface and the ratio of front/back-illumination performance are shown in the SI. The J_{SC} decreases with increasing thickness for negative values of the IFLO because the BJ controls the performance. On the other hand, when the IFLO is positive, there is upward band-bending at the BJ and J_{SC} is not strongly affected by thickness. In general, thinner CdTe devices tend to produce higher η_{Back} for all IFLOs. This is in contrast to devices illuminated through the front side when the IFLO is negative. When this is the case, the BJ and FJ interact (see Figure 1) which reduces the overall band-bending in the device and results in lower V_{OC} and η_{Front}. As the absorber thickness increases, the interaction between the FJ and BJ decreases and becomes negligible ∼3.5 μm. However, devices with proper band-bending (IFLO > 0.05 eV) perform well for both thicknesses, and the bifaciality approaches unity.

Reducing the recombination at the back of the device by passivation or by creating preferred band-bending is critical for high efficiency back side illuminated devices, but other parameters are important as well.[29] Figure 3 shows contour plots of the efficiency as a function of CdTe hole density and carrier lifetime for 2 and 4 μm devices illuminated through the back side for various back interface conditions. The corresponding PV parameters are shown in the SI. When there is a bad BJ (negative IFLO and BSRV = 1×10^4 cm-s^{-1}; Figure 3a,d), the devices are back interface limited. For the 2 μm device, the efficiencies are higher at the lower hole density values because the FJ depletion region extends to the back of the device under these conditions and the current collection can be effective. However, when there are distinct FJ and BJ depletion regions, carriers recombine at the back interface resulting in poor current collection, and the efficiency is low. This condition is found when the hole density is high in the 2 μm devices and occurs for all values of hole density in the 4 μm devices.

When the BSRV is low (10 cm s^{-1}; Figure 3b,e) or the bands are bent upward at the back interface (positive IFLO; Figure 3c,f), the back side performance is no longer limited by the back interface. Increasing the lifetime leads to a higher bias onset for SRH recombination and higher efficiency, while increasing the hole density has little effect on the back side performance in these cases. Interestingly, when illuminated through the back side, the 2 μm devices have higher efficiency than the 4 μm devices at a given doping level and lifetime, but the opposite is true when devices are illuminated through the front side. This suggests that there may be an optimum absorber thickness for a BTF device.

To provide some insight, we considered a device operating on a background surface with an albedo of 15%, and summed the relative front side and back side illumination efficiencies to calculate a bifacial efficiency ($\eta_{Bi} = \eta_{Front}$(at 1 sun) + η_{Back}(at 15% of 1 sun)). Note that the back side illumination of bifacial devices is significantly lower than the 1 sun value used for all the simulations above. Even at the low intensity, the back side illuminated *JV* curves generated here follow the familiar pattern for reduced intensity: linear reduction in J_{SC} and logarithmic reduction in V_{OC}. Figure 4 shows the bifacial efficiency as a function of absorber thickness and BSRV, lifetime, hole density, and IFLO. Note that when these parameters were not specifically varied, they were fixed to 10^4 cm/s, 32 ns, 2×10^{14} cm^{-3}, and −0.2 eV, respectively, indicating a poor back interface.

Figure 4 illustrates three main points. First, when the back interface is improved through reduced BSRV (Figure 4a) or increased IFLO (Figure 4d), a thinner absorber produces a higher efficiency BTF device. Second, for any given carrier lifetime greater than ∼20 ns (Figure 4b), the bifacial efficiency is high for the 2 μm absorber, decreases until the absorber thickness is ∼3 μm, and then increases again, with the thinnest devices having the highest bifacial efficiency. Third, when the absorber hole density is high (Figure 4c), the BTF device performance is dictated by the front-illuminated performance.

https://dx.doi.org/10.1021/acsaem.0c00851
ACS Appl. Energy Mater. 2020, 3, 6072−6078

Approved for public release; distribution unlimited.

These results indicate that when the recombination at the BJ is low, thinner BTF devices can perform better than thick devices.

CONCLUSIONS

Using numerical simulations, we showed that BTF devices fabricated to date have been limited by recombination at the back interface. Improvement in the bifacial performance of thin film devices will require improving the back interface through either passivation and/or by reducing the downward band-bending at this interface. We also showed that back side illuminated devices depend strongly on doping density when the back interface is bad but depend strongly on the carrier lifetimes and weakly on absorber hole density when the back interface is good. Finally, we showed that thinner BTF devices may perform better than thicker when the absorber doping density is low or the back interface recombination can be reduced through passivation or decreases downward band-bending at the current carrier lifetimes.

ASSOCIATED CONTENT

Supporting Information

The Supporting Information is available free of charge at https://pubs.acs.org/doi/10.1021/acsaem.0c00851.

SCAPS parameters; IFLO sign convention; QE of existing devices; effects of BSRV; converting fixed charges to IFLO; and effects of IFLO, absorber hole density, and carrier lifetime on other PV parameters (PDF)

AUTHOR INFORMATION

Corresponding Author

Adam B. Phillips − *Wright Center for Photovoltaics Innovation and Commercialization, Department of Physics and Astronomy, University of Toledo, Toledo, Ohio 43606, United States;* orcid.org/0000-0002-2675-5052; Email: Adam.Phillips@UToledo.edu

Authors

Kamala Khanal Subedi − *Wright Center for Photovoltaics Innovation and Commercialization, Department of Physics and Astronomy, University of Toledo, Toledo, Ohio 43606, United States*

Geethika K. Liyanage − *Wright Center for Photovoltaics Innovation and Commercialization, Department of Physics and Astronomy, University of Toledo, Toledo, Ohio 43606, United States;* orcid.org/0000-0003-4000-0729

Fadhil K. Alfadhili − *Wright Center for Photovoltaics Innovation and Commercialization, Department of Physics and Astronomy, University of Toledo, Toledo, Ohio 43606, United States*

Randy J. Ellingson − *Wright Center for Photovoltaics Innovation and Commercialization, Department of Physics and Astronomy, University of Toledo, Toledo, Ohio 43606, United States;* orcid.org/0000-0001-9520-6586

Michael J. Heben − *Wright Center for Photovoltaics Innovation and Commercialization, Department of Physics and Astronomy, University of Toledo, Toledo, Ohio 43606, United States;* orcid.org/0000-0002-3788-3471

Complete contact information is available at: https://pubs.acs.org/10.1021/acsaem.0c00851

Notes

The authors declare no competing financial interest.

The U.S. Government is authorized to reproduce and distribute reprints for Governmental purposes notwithstanding any copyright notation thereon. The views and conclusions contained herein are those of the authors and should not be interpreted as necessarily representing the official policies or endorsements, either expressed or implied, of Air Force Research Laboratory or the U.S. Government.

ACKNOWLEDGMENTS

This material is based on research sponsored by Air Force Research Laboratory under agreement FA9453-18-2-0037 and by the U.S. DOE's Office of Energy Efficiency and Renewable Energy (EERE) under Solar Energy Technologies Office (SETO) Agreement DE-EE0008974.

REFERENCES

(1) Green, M. A.; Dunlop, E. D.; Levi, D. H.; Hohl-Ebinger, J.; Yoshita, M.; Ho-Baillie, A. W. Y. Solar cell efficiency tables (version 54). *Prog. Photovoltaics* **2019**, *27* (7), 565−575.

(2) Cuevas, A.; Luque, A.; Eguren, J.; del Alamo, J. 50% more output power from an albedo-collecting flat panel using bifacial solar cells. *Sol. Energy* **1982**, *29* (5), 419−420.

(3) Yusufoglu, U. A.; Pletzer, T. M.; Koduvelikulathu, L. J.; Comparotto, C.; Kopecek, R.; Kurz, H. Analysis of the annual performance of bifacial modules and optimization methods. *Journal of Photovoltaics* **2015**, *5* (1), 320−328.

(4) Sun, X.; Khan, M. R.; Deline, C.; Alam, M. A. Optimization and performance of bifacial solar modules: A global perspective. *Appl. Energy* **2018**, *212*, 1601−1610.

(5) Fischer, M. In *ITRPV 9th Edition 2018 Report Release and Key Findings*; PV CellTech conference, 2018.

(6) Liang, T. S.; Pravettoni, M.; Deline, C.; Stein, J. S.; Kopecek, R.; Singh, J. P.; Luo, W.; Wang, Y.; Aberle, A. G.; Khoo, Y. S. A review of crystalline silicon bifacial photovoltaic performance characterisation and simulation. *Energy Environ. Sci.* **2019**, *12* (1), 116−148.

(7) Romeo, A.; Khrypunov, G.; Galassini, S.; Zogg, H.; Tiwari, A. Bifacial configurations for CdTe solar cells. *Sol. Energy Mater. Sol. Cells* **2007**, *91* (15−16), 1388−1391.

(8) Keller, J.; Chen, W. C.; Riekehr, L.; Kubart, T.; Törndahl, T.; Edoff, M. Bifacial Cu(In, Ga)Se_2 solar cells using hydrogen-doped In_2O_3 films as a transparent back contact. *Prog. Photovoltaics* **2018**, *26* (10), 846−858.

(9) Marsillac, S.; Parikh, V.; Compaan, A. Ultra-thin bifacial CdTe solar cell. *Sol. Energy Mater. Sol. Cells* **2007**, *91* (15−16), 1398−1402.

(10) Khanal, R. R.; Phillips, A. B.; Song, Z.; Xie, Y.; Mahabaduge, H. P.; Dorogi, M. D.; Zafar, S.; Faykosh, G. T.; Heben, M. J. Substrate configuration, bifacial CdTe solar cells grown directly on transparent single wall carbon nanotube back contacts. *Sol. Energy Mater. Sol. Cells* **2016**, *157*, 35−41.

(11) Agostinelli, G.; Delabie, A.; Vitanov, P.; Alexieva, Z.; Dekkers, H.; De Wolf, S.; Beaucarne, G. Very low surface recombination velocities on p-type silicon wafers passivated with a dielectric with fixed negative charge. *Sol. Energy Mater. Sol. Cells* **2006**, *90* (18−19), 3438−3443.

(12) Wan, Y.; McIntosh, K. R.; Thomson, A. F.; Cuevas, A. Low surface recombination velocity by low-absorption silicon nitride on c-Si. *2012 IEEE 38th Photovoltaic Specialists Conference (PVSC)* **2012**, 1−7.

(13) Dullweber, T.; Schulte-Huxel, H.; Blankemeyer, S.; Hannebauer, H.; Schimanke, S.; Baumann, U.; Witteck, R.; Peibst, R.; Köntges, M.; Brendel, R.; Yao, Y. Present status and future perspectives of bifacial PERC+ solar cells and modules. *Jpn. J. Appl. Phys.* **2018**, *57* (8S3), 08RA01.

Approved for public release; distribution unlimited.

(14) Gloeckler, M.; Sankin, I.; Zhao, Z. CdTe solar cells at the threshold to 20% efficiency. *IEEE Journal of Photovoltaics* **2013**, *3* (4), 1389−1393.
(15) Kuciauskas, D.; Kanevce, A.; Burst, J. M.; Duenow, J. N.; Dhere, R.; Albin, D. S.; Levi, D. H.; Ahrenkiel, R. K. Minority carrier lifetime analysis in the bulk of thin-film absorbers using subbandgap (two-photon) excitation. *Journal of Photovoltaics* **2013**, *3* (4), 1319−1324.
(16) Kephart, J. M.; Kindvall, A.; Williams, D.; Kuciauskas, D.; Dippo, P.; Munshi, A.; Sampath, W. Sputter-deposited oxides for interface passivation of CdTe photovoltaics. *Journal of Photovoltaics* **2018**, *8* (2), 587−593.
(17) Kuciauskas, D.; Moseley, J.; Ščajev, P.; Albin, D. Radiative Efficiency and Charge-Carrier Lifetimes and Diffusion Length in Polycrystalline CdSeTe Heterostructures. *Phys. Status Solidi RRL* **2020**, *14*, 1900606.
(18) Mouhoub, A.; Bouloufa, A.; Djessas, K.; Messous, A. Analytical modeling and optimization of original bifacial solar cells based on Cu (In, Ga) Se2 thin films absorbers. *Superlattices Microstruct.* **2018**, *122*, 434−443.
(19) Burgelman, M.; Nollet, P.; Degrave, S. Modelling polycrystalline semiconductor solar cells. *Thin Solid Films* **2000**, *361*, 527−532.
(20) Liyanage, G. K.; Phillips, A. B.; Alfadhili, F. K.; Ellingson, R. J.; Heben, M. J. The role of back buffer layers and absorber properties for> 25% efficient CdTe solar cells. *ACS Applied Energy Materials* **2019**, *2* (8), 5419−5426.
(21) Ablekim, T.; Colegrove, E.; Metzger, W. K. Interface Engineering for 25% CdTe Solar Cells. *ACS Applied Energy Materials* **2018**, *1* (10), 5135−5139.
(22) Song, T.; Kanevce, A.; Sites, J. R. Emitter/absorber interface of CdTe solar cells. *J. Appl. Phys.* **2016**, *119* (23), 233104.
(23) Watthage, S. C.; Phillips, A. B.; Liyanage, G. K.; Song, Z.; Gibbs, J. M.; Alfadhili, F. K.; Alkhayat, R. B.; Ahangharnejhad, R. H.; Almutawah, Z. S.; Bhandari, K. P.; et al. Selective Cd Removal From CdTe for High-Efficiency Te Back-Contact Formation. *IEEE J. Photovoltaics* **2018**, *8* (4), 1125−1131.
(24) Paudel, N. R.; Young, M.; Roland, P. J.; Ellingson, R. J.; Yan, Y.; Compaan, A. D. Post-deposition processing options for high-efficiency sputtered CdS/CdTe solar cells. *J. Appl. Phys.* **2014**, *115* (6), 064502.
(25) Niles, D. W.; Li, X.; Sheldon, P.; Höchst, H. A photoemission determination of the band diagram of the Te/CdTe interface. *J. Appl. Phys.* **1995**, *77* (9), 4489−4493.
(26) Guarnera, S.; Abate, A.; Zhang, W.; Foster, J. M.; Richardson, G.; Petrozza, A.; Snaith, H. J. Improving the long-term stability of perovskite solar cells with a porous Al_2O_3 buffer layer. *J. Phys. Chem. Lett.* **2015**, *6* (3), 432−437.
(27) Vermang, B.; Fjällström, V.; Gao, X.; Edoff, M. Improved Rear Surface Passivation of Cu (In, Ga)Se_2 Solar Cells: A Combination of an Al_2O_3 Rear Surface Passivation Layer and Nanosized Local Rear Point Contacts. *Journal of Photovoltaics* **2014**, *4* (1), 486−492.
(28) Dingemans, G.; Beyer, W.; Van de Sanden, M.; Kessels, W. Hydrogen induced passivation of Si interfaces by Al_2O_3 films and SiO2/Al2O3 stacks. *Appl. Phys. Lett.* **2010**, *97* (15), 152106.
(29) Kanevce, A.; Reese, M. O.; Barnes, T.; Jensen, S.; Metzger, W. The roles of carrier concentration and interface, bulk, and grain-boundary recombination for 25% efficient CdTe solar cells. *J. Appl. Phys.* **2017**, *121* (21), 214506.

https://dx.doi.org/10.1021/acsaem.0c00851
ACS Appl. Energy Mater. 2020, 3, 6072−6078

Approved for public release; distribution unlimited.

Solar Energy Materials & Solar Cells 215 (2020) 110660

Contents lists available at ScienceDirect

Solar Energy Materials and Solar Cells

journal homepage: http://www.elsevier.com/locate/solmat

Decreasing the resolution limit of laser beam induced current measurements below the beam size without confocal optics: Determining laser scribe widths

Ramez Hosseinian Ahangharnejhad [a], Zhaoning Song [a], Jonathan L. DeWitt [b], Adam B. Phillips [a,*], Brent R. Lumbrezer [b], Charles E. Wickersham [b], Michael J. Heben [a]

[a] Wright Center for Photovoltaics Innovation and Commercialization, Department of Physics and Astronomy, University of Toledo, 2801 W. Bancroft St., Toledo, OH, 43606, USA
[b] First Solar Inc., 28101 Cedar Park Blvd., Perrysburg, OH, 43551, USA

ARTICLE INFO

Keywords:
Laser scribing
Laser beam induced current
CdTe PV module

ABSTRACT

Here, we report a method using laser beam induced current (LBIC) measurements to ascertain nonresponsive features of photovoltaic devices that are smaller than the measurement beam size. To demonstrate the method, we determine the effective electrical width of laser scribed lines. Laser scribing is a critical process in producing thin-film photovoltaics modules and minimizing the effective width of the laser scribed lines is important for closing the cell-to-module efficiency gap. However, in addition to removing material, laser scribing can also produce a heat-affected zone in which the optoelectronic properties of the remaining materials may be adversely impacted. We measured the LBIC signal across scribe lines that were produced in CdTe thin-films. The collected data was compared with the expectations based on the probing beam's shape and the profile of the scribed line. The approach allows the electrical dead width to be determined with a resolution that is substantially higher than the width of the LBIC beam. At the lowest scribing powers, where the lines were the smallest, the electrically-determined widths were larger than the optically-determined widths by nearly a factor of two. The ability to rapidly resolve features that are much smaller than the dimensions of the probing laser beam without the use of confocal optics may be useful in a manufacturing environment, as demonstrated here, or more generally for rapid defect identification on devices with areas ranging from centimeters up to meters.

1. Introduction

Laser beam induced current (LBIC) is a nondestructive method that offers spatially resolved mapping of the current output from photovoltaic (PV) devices [1,2]. Instruments built to operate with short working distances (~1 cm) use confocal optics and microscope lens components to allow the LBIC laser to be focused to submicron diameters for high-resolution measurements. This type of LBIC instrument is applicable to local scans in the range from a few microns to a few millimeters and is typically associated with imaging submicron scale inhomogeneities in PV structures [3] or current collection in the vicinity of grain boundaries [4–6]. Such instruments have been applied to studies of the correlation between film morphology, photoluminescence, and current generation [7–12]. Short working-distance examinations are generally limited to small-scale laboratory investigations due to the relatively small scan areas and slow throughputs.

Instruments have also been designed to operate at longer working-distances (~1 m) to afford fast scan speeds for larger-scale examinations of PV devices and modules [2]. Such systems have been used to investigate degradation [13] and pinhole formation [14]. In addition, LBIC has been demonstrated as a potential quality assurance measure for fabrication lines [15,16], and has been applied to the characterization of large area modules and full panels [17–21]. However, at long working distances, the resolution of the scan is typically limited by the beam size [22].

Many defects of large area devices are smaller than the beam size of typical large area LBIC systems. Included in this is the laser scribe width, which is one of several high rate, precise, coordinated manufacturing steps on which commercialization of thin-film PV modules is predicated. Laser scribing enables the cell area to be defined, which establishes the

* Corresponding author.
E-mail address: adam.phillips@utoledo.edu (A.B. Phillips).

https://doi.org/10.1016/j.solmat.2020.110660
Received 28 April 2020; Received in revised form 25 May 2020; Accepted 9 June 2020
Available online 23 June 2020
0927-0248/© 2020 Elsevier B.V. All rights reserved.

Approved for public release; distribution unlimited.

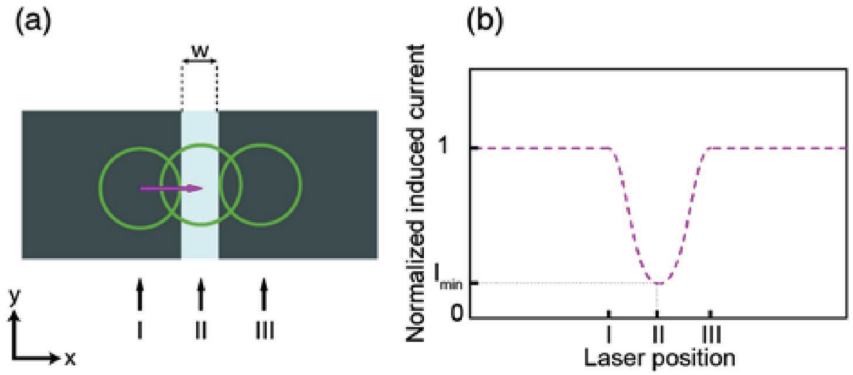


Fig. 1. (a) Schematic diagram of the LBIC measurements across a scribe line. (b) Expected normalized induced current as a function of laser center position for the case of a beam with circular shape and a spatially uniform intensity distribution.

total current of the module [23–25], and allows multiple cells to be interconnected in series to increase the voltage output of the panel. The interconnection is accomplished using three scribe lines: P1, which, in the case of thin-film CdTe PV, isolates strips of the underlying TCO material; P2, which scribes through the absorber material through which subsequently deposited metal can create a connection between the back and front of adjacent cells; and P3, which scribes the metal back contact to complete the cell definition process. The three scribes should be placed as closely to one another as possible because the fractional area of the module that is needed for the three scribed lines does not contribute to the photovoltaic output of the module. Thus, laser scribing is critical for thin-film module production, and precise control is needed to allow series interconnection of cells while minimizing the inactive area of the panel.

The width of a laser scribe is usually determined by optical microscopy, with the assumption that the scribed trench has a rectangular cross-section and that the determined width is representative of the fraction of the material that does not contribute to the photovoltaic performance. However, a so-called heat affected zone may also be present, which can reduce electrical performance for many microns away from the boundaries of the scribe [26–28]. In these cases, the electrical dead-width, which is relevant to the photovoltaic performance, may be significantly larger than the optically determined value. Note that a three-scribe interconnect pattern results in an electrically-dead region that is at least 3 times greater than the width of the individual scribe lines, so minimizing the width of each scribe line is important for closing the cell to module efficiency gap.

As thin-film PV moves to more advanced scribing methods, precise knowledge of the scribe width as a function of scribing parameters is required. However, a fast, reliable method to determine these electrically dead-widths has not been established. Large area LBIC systems offers a compelling pathway forward if the resolution can be improved beyond the size of the beam width.

In this contribution, we describe the use of a LBIC system [18] to determine the effective electrical dead-width of laser scribe lines produced in thin-film CdTe samples. The system is operated at a working distance of 1.3 m and is compatible with high throughout measurement. The data acquired during the LBIC measurement is a convolution of the feature's photoresponse and the measurement beam's profile, and the electrical dead-width can be determined using a model that allows the two to be decoupled. The approach allows the width of scribe lines an order of magnitude smaller than the beam diameter to be determined. For the thinnest scribe lines, the electrical dead-widths were approximately a factor 2 larger than the optically determined widths. The resolution limits of the system were estimated using the model and sensitivity limits of the electronics.

2. Theory

Fig. 1 shows some simple considerations for understanding the photocurrent that is generated when a laser beam is scanned in the x direction across a previously scribed trench in a photoactive sample. For simplicity we assume that the cross section of the trench is rectangular, of width w, and that the probe beam is circularly shaped with uniform power density. While the beam is approaching the scribe line but is still far away, a constant, spatially independent photocurrent value is expected. This remains the case until the edge of the beam reaches the scribe line, marked as position I. With further translation the current decreases until the center of the beam is at the center of the scribe, shown as position II. As the probe beam is moved further in the x direction the photocurrent current increases to the same initial value. The minimum normalized laser beam induced current (I_{min}) can be used to calculate the width of the dead area produced by the scribe. In this scenario I_{min} can be determined from the ratio of the active area at position II to the active area at positions I or III. Therefore, I_{min} can be formulated as:

$$I_{min} = \frac{4 \times \int_{w/2}^{r} \sqrt{r^2 - x^2}\,dx}{\pi r^2} \tag{1}$$

where w is the width of scribe line and r is the radius of the beam. Fig. 1 (b) shows a simulation of the LBIC that would be found during such a scan.

For determining the scribe width in real samples, we developed a model that simulates the experiment more accurately. The analysis becomes more complicated because the laser power density is not uniform. Here, we use a high-fidelity representation of the LBIC probe beam, including its intensity profile and dimensions. The total measured current when the center of the beam is located at coordinates (x_0, y_0) can then be expressed as:

$$I(x_0, y_0) = \sum_i \sum_j \left[B_x(x_i, x_0) B_y(y_j, y_0) \times H(x_i, y_j)\right] \tag{2}$$

Here, B_x and B_y are the Gaussian functions describing the beam's intensity projected onto the plane of the x and y axes, respectively. H is the current generation function at coordinate (x_i, y_j) which is related to the absorber layer thickness, the material under study, the laser beam wavelength, and the spatial distribution of the absorber material from which collection can occur. With a wavelength that is significantly shorter than the bandgap wavelength, the absorber is thick such that the light absorption is complete, and the collection efficiency can be assumed to be constant, the remaining information in H pertains to the geometry of the scribed lines.

To allow experimental data to be analyzed via this framework we

Approved for public release; distribution unlimited.
454

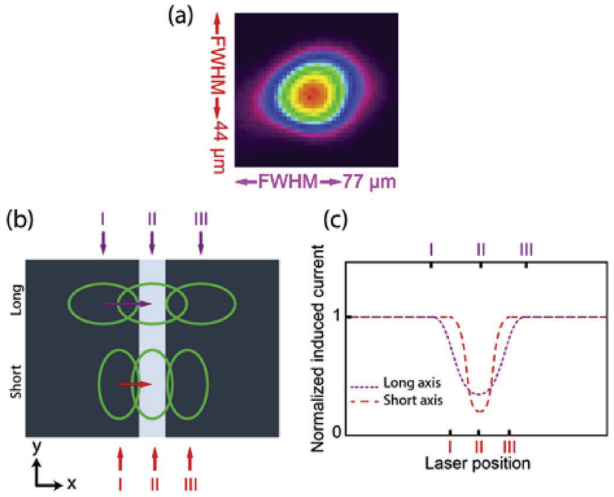


Fig. 2. (a) Intensity map of the beam used to perform the LBIC measurements. FWHM of the beam profiles in the two axes are shown (b) Areal schematic diagram of the LBIC measurement with elliptical beam. I and III denote the positions where beam does not coincide with the scribe line. Position II indicates the alignment of the beam center with the center of the scribe line. (c) Approximate LBIC results for the cases shown in panel (b). Purple and red lines indicate the scans along the large and short axes, respectively. (For interpretation of the references to colour in this figure legend, the reader is referred to the Web version of this article.)

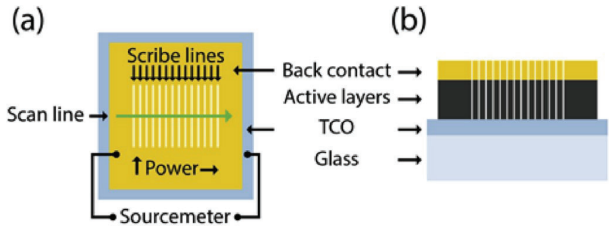


Fig. 3. (a) Top and (b) cross-sectional schematic diagrams of the sample investigated with 14 scribe lines of increasing power. The LBIC scan line is shown perpendicular to the scribe lines. Contacts from TCO and back contact metal are made to the sourcemeter for measurements. Note that the TCO layer is intact after scribing.

measured the intensity distribution across the dimensions of the probe beam using a laser Spiricon SP620U profiler. The measured profile of the 532 nm beam is shown in Fig. 2 (a), and the intensity map shows that the beam is approximately elliptical in shape with FWHM values of 77 μm and 44 μm along the long and short axes, respectively. The power distribution is Gaussian in both dimensions. Fig. 2 (b) shows how this elliptical beam allows two different experiments to be performed on a given scribe depending on whether the long or short axis of the ellipse is aligned with the scribe width. Fig. 2 (c) shows the expected normalized current profiles with the Gaussian power distribution for the two arrangements shown in panel (b). Similar to the circular beam case, the minimum induced current occurs when the beam is aligned with the center of the scribe (dead area) line (position II). However, the I_{min} value in the long axis scan case is higher than in the short axis scan case because the overlap area at position II is smaller in the latter case. On the other hand, the distance over which current is reduced is wider for the long axis scan because the longer axis allows the beam to reach the dead area from further away. As with the simple case of a uniform power distribution, the reduction in current begins when the beam first overlaps with the edge of the scribe line in position I. It reaches a minimum at position II, and then recovers as the beam passes through position III.

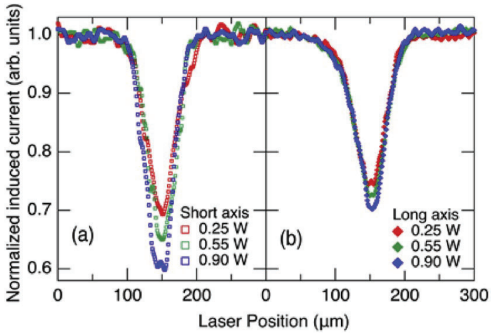


Fig. 4. Results of the LBIC measurements performed with the beam's (a) short axis and (b) long axis perpendicular to the scribe line. The data was obtained from three scribed lines that were formed with laser powers of 0.25, 0.55, 0.9 Watts.

3. Results and discussion

A stack of materials representative of a thin-film solar cell (glass/TCO/window layer/CdTe/metal) was used for experimentation. Fig. 3 shows a schematic diagram of the sample and the measurement method used in this experiment. Fourteen parallel lines were scribed into the back of the device stack using a laser beam with powers ranging from 0.25 to 0.9 W, in 0.05 W increments. Note that these powers and the resultant scribe line widths are not representative of a specific manufacturing step but are instead intended to demonstrate the value of the LBIC-based width determination technique. Further details associated with the material layers and scribing laser operation are proprietary. This configuration is the equivalent of a P3 scribe described above, and for each scribing power the TCO remained intact under these scribing conditions. The same type of measurements could be performed to determine the width of the P1 and P2 scribe lines, though the scribing, with the specific conditions for each scribe, would need to occur before the complete stack was fabricated. Note that the configuration used here could also be used to measure the dead-widths of P2 scribes. The width of each scribe can then be used to determine the optimum scribing parameters to minimize the total dead-width between monolithically integrated cells. Contacts for LBIC measurement were made by contacting the front (TCO) and back (metal) electrodes using spring-loaded metal pins.

For the LBIC measurements, a pulsed 532 nm laser beam with a repetition rate of 600 kHz, pulse width of 10 ns, and an average power of 0.01 mW was used [18]. The laser beam profile was as described above, and the beam was scanned perpendicular to the scribe line at a speed of 1 cm s^{-} [1]. This pulse rate and scan speed resulted in a 17 nm translation of the beam between sequential laser pulses. Measurements were performed with both the long and short axes of the laser beam scanned perpendicular to the scribe line, as illustrated in Fig. 2 (b).

Fig. 4 (a) and (b) shows the normalized measured current as a function of the laser position when the short and long axes, respectively, of the laser spot were scanned perpendicularly to the scribe. The data is shown for three scribe lines that were produced with the highest, the lowest, and an intermediate scribing power. The minimum current (I_{min}) is observed to decrease as the scribing power is increased, indicating an electrical dead-width that increases with laser scribing power. As expected, I_{min} and the width of the current loss increases when the scan direction was changed from the short axis to the long axis.

To quantify the electrical dead width of the scribed trench from these measurements we used Eqn. (2) to generate simulated current scans. We then attempted to fit the experimentally obtained data by the generated data using the dead width as a fitting parameter. The width of the trench

Approved for public release; distribution unlimited.
455

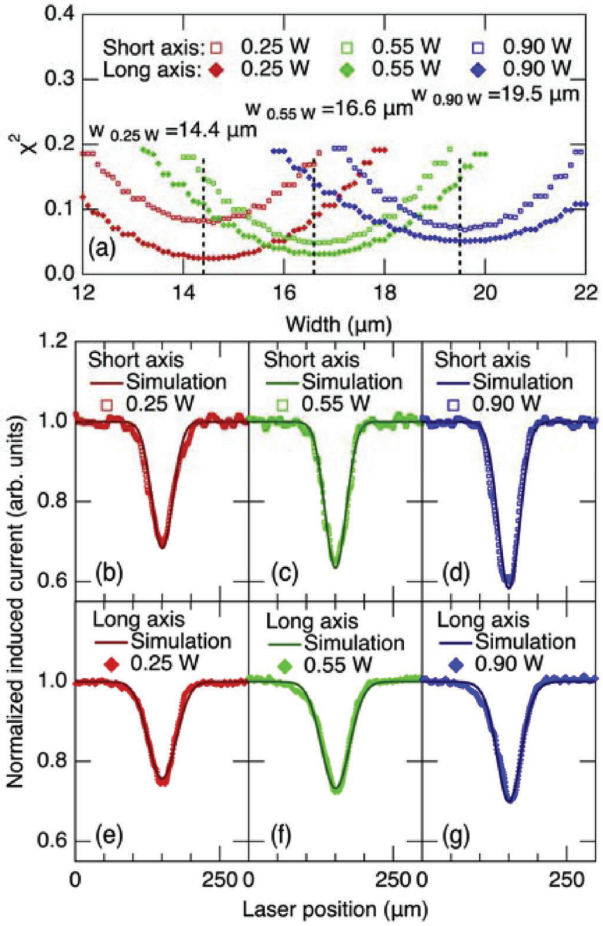


Fig. 5. (a) Chi-squared (χ^2]) test applied to simulation results of the electrical dead width of scribed lines. The minimum values are indicated with vertical dashed lines. (b), (c), (d) show the generated simulations and the corresponding measurements for the short axis scanning across the indicated scribes. (e), (f) and (g) show the same for the long axis.

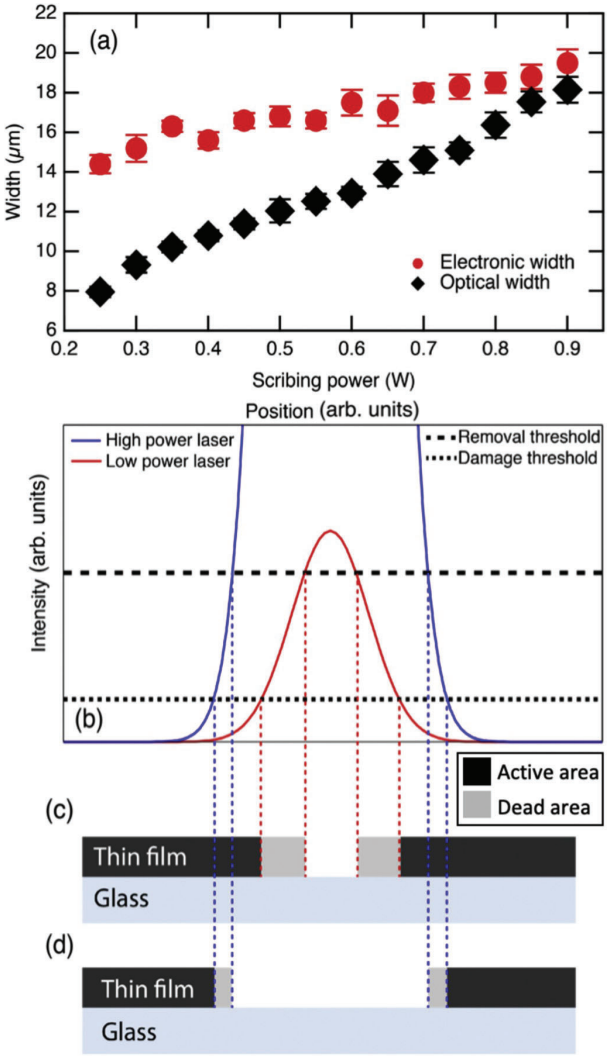


Fig. 6. (a) Scribe widths measured using the LBIC and optical microscopy methods. (b) Schematic illustration of power distribution for low- and high-power beams. (c) and (d) are illustrations of scribing profiles shown with low- and high-power settings in (b).

was varied from 7 μm to 30 μm in 0.1 μm steps. The simulated LBIC signals were then compared with the measured signals through a chi-squared (χ^2) test via Pearson's model [29]. The results of the χ^2 tests are shown in Fig. 5 (a). The value of the width that produces a minimum in χ^2 can be assigned to the effective electrical width of the scribe. Note that the values for the width determined by long- and short-axis scanning are within 0.05 μm of one another. The test showed a χ^2 minimum at 14.4 μm, 16.6 μm and 19.5 μm for scribe lines produced with 0.25, 0.55, and 0.95 W laser beams, respectively. Fig. 5 panels (b), (c), and (d) show the best fit simulated LBIC signals plotted on the measured data for the short axis scans, while panels (e), (f), (g) show the same data for the long axis scans.

The electrically measured scribe widths were compared to values that were determined by optical examination. Optical widths were determined using an eye piece reticule in an optical microscope at magnification of 1000X. Fig. 6 (a) shows the optically- and electrical-determined dead widths and the optical scribe widths measured with LBIC and optical microscopy, respectively. The one standard deviation bars associated with each data point were determined from 10 separate measurements on a given scribe. The results show that the electrical dead width can be substantially larger than the optical width at low scribing power. This observation can be understood by considering that the threshold energy for the complete removal of the thin film and the threshold for producing electrical damage or removing the back metal can be different. Fig. 6 (b) shows the intensity distribution for two Gaussian beams having the same FWHM value but different total powers. In this illustration the high-power beam is twenty times more powerful than the low-power beam. Only the portion of the beam that exceeds the removal threshold contributes to the optical width, while the portion of the beam that exceeds the damage threshold of the material contributes to the electrical width. As the scribing power increases, the measured optical and electrical widths begin to converge and are the same when the scribing power is 0.9 Watts. These results clearly show that optical measurements can be misleading, especially when scribe widths are small.

While the scribing investigations demonstrate the utility of the approach, it is interesting to consider the resolution limit on the technique. To determine this limit, we investigated the I_{min} values for square shaped dead areas with varying sizes, which could be a pinhole or some other defect in the device. Fig. 7 (a) shows an illustration of the LBIC

Approved for public release; distribution unlimited.
456

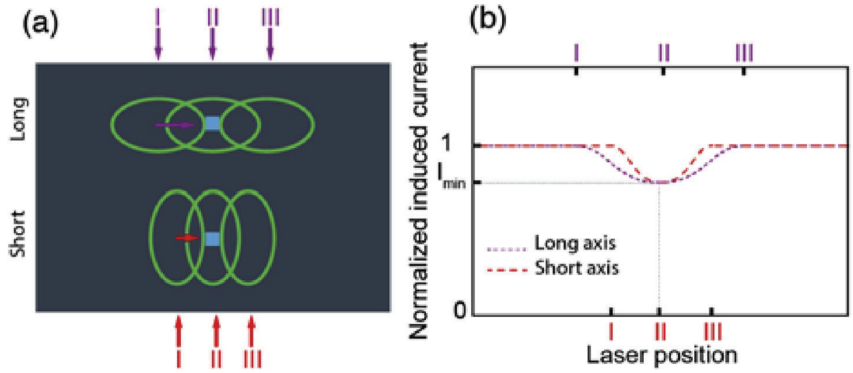


Fig. 7. (a) Schematic diagram of the LBIC measurements across a square shaped defect shown in blue. (b) Expected normalized LBIC response as a function of laser center position for the illustration in panel (a). The minimum current, I_{min} corresponds to the alignment of the laser beam center with respect to the defect (in position II). (For interpretation of the references to colour in this figure legend, the reader is referred to the Web version of this article.)

Table 1
I_{min} values as a function of dead area square. I_{min} are calculated through the model for alignment of the center of the beam with the center of the feature.

Area (μm^2)	0.05	0.1	0.5	1	2	4
I_{min}	0.985	0.980	0.955	0.937	0.912	0.877

measurement across a square shaped defect shown in blue with long and short axes. Fig. 7 (b) shows the normalized induced current for the illustration in panel (a). At position II the defect is located at the center of the beam and the I_{min} is generated. Due to the relative size of the defect and the beam, with the former being smaller than the latter, the same I_{min} is expected regardless of scan direction. Table 1 shows the results as the dead area ranges from 0.05 μm^2 to 4 μm^2. Clearly the detection limit will depend on the lateral resolution of the LBIC system, stability of the laser output, the sensitivity of the electronics, and the presence of any electrical noise. Based upon the data shown in Fig. 4, an I_{min} of 0.955 can be distinguished, indicating that an 0.5 μm [2] feature could be resolved.

4. Conclusion

We have developed a method to increase the resolution of an LBIC system beyond the laser spot size and used this method to determine the effective electrical width of laser-scribed lines in thin-film solar cells. A simulation tool was developed that convolved the Gaussian profile of the probe laser beam with a laser scribed trench of assumed shape. The width of the trench was used as a fitting parameter and a χ^2 test was applied to determine which value most closely generated the experimental data. The actual scribe width corresponded to the value with the lowest χ^2 value. Using this technique, scribe line widths an order of magnitude smaller than the LBIC beam diameter were easily resolved. For the scribing powers investigated, the optically-determined width of the scribe lines was always smaller than the electrically-determined width. The discrepancy was nearly a factor of two at the lowest powers and was reduced as the scribing power was increased. The LBIC-based method is faster and more accurate than the optical method, and features that are more than order of magnitude smaller than the probing beam can be accurately measured.

Declaration of competing interest

The authors declare that they have no known competing financial interests or personal relationships that could have appeared to influence the work reported in this paper.

CRediT authorship contribution statement

Ramez Hosseinian Ahangharnejhad: Methodology, Software, Formal analysis, Writing - original draft. **Zhaoning Song:** Methodology, Formal analysis. **Jonathan L. DeWitt:** Resources. **Adam B. Phillips:** Methodology, Writing - original draft. **Brent R. Lumbrezer:** Resources. **Charles E. Wickersham:** Conceptualization, Writing - review & editing, Supervision, Funding acquisition. **Michael J. Heben:** Conceptualization, Writing - original draft, Funding acquisition.

Acknowledgments

This material is based on research sponsored in part by Air Force Research Laboratory under agreement number FA9453-18-2-0037, Office Naval Research (Contract No. N00014-17-1-2223), and Helen and Harold McMaster Endowment for Photovoltaics. The U.S. Government is authorized to reproduce and distribute reprints for Governmental purposes notwithstanding any copyright notation thereon.

Appendix A. Supplementary data

Supplementary data to this article can be found online at https://doi.org/10.1016/j.solmat.2020.110660.

References

[1] D.E. Sawyer, H.K. Kessler, IEEE Trans. Electron. Dev. 27 (1980) 864–872.
[2] S. Damaskinos, Sol. Cell. 26 (1989) 151–158.
[3] G.E. Eperon, D. Moerman, D.S. Ginger, ACS Nano 10 (2016) 10258–10266.
[4] B. Rezek, C.E. Nebel, M. Stutzmann, J. Appl. Phys. 91 (2002) 4220–4228.
[5] T.A. Bull, L.S.C. Pingree, S.A. Jenekhe, D.S. Ginger, C.K. Luscombe, ACS Nano 3 (2009) 627–636.
[6] Y. Yoon, D. Ha, I.J. Park, P.M. Haney, S. Lee, N.B. Zhitenev, Nano Energy 48 (2018) 543–550.
[7] C.R. Mcneill, H. Frohne, J.L. Holdsworth, J.E. Furst, B. V King, P.C. Dastoor, Nano Lett. 4 (2004) 219–223.
[8] C.R. Mcneill, H. Frohne, J.L. Holdsworth, P.C. Dastoor, Nano Lett. 4 (2004) 2503–2507.
[9] C. Eisele, C.E. Nebel, M. Stutzmann, J. Non-Cryst. Solids 269 (2000) 1109–1113.
[10] M. Breitwieser, F.D. Heinz, A. Büchler, M. Kasemann, J. Scho, W. Warta, M. C. Schubert, Sol. Energy Mater. Sol. Cells 131 (2014) 124–128.
[11] S. Mastroianni, F.D. Heinz, J. Im, W. Veurman, M. Padilla, M.C. Schubert, U. Würfel, M. Grätzel, N. Park, A. Hinsch, Nanoscale 7 (2015) 19653–19662.
[12] S. Panigrahi, T. Calmeiro, R. Martins, E. Fortunato, Sol. Energy Mater. Sol. Cells 176 (2018) 310–317.
[13] Z. Song, A. Abate, S.C. Watthage, G.K. Liyanage, A.B. Phillips, U. Steiner, M. Graetzel, M.J. Heben, Adv. Energy Mater. 6 (2016) 1600846.
[14] Z. Song, J. Werner, N. Shrestha, F. Sahli, S. De Wolf, B. Niesen, S.C. Watthage, A. B. Phillips, C. Ballif, R.J. Ellingson, M.J. Heben, J. Phys. Chem. Lett. 7 (2016) 5114–5120.
[15] M. Acciarri, S. Binetti, A. Racz, S. Pizzini, G. Agostinelli, Sol. Energy Mater. Sol. Cells 72 (2002) 417–424.
[16] F.C. Krebs, M. Jørgensen, Adv. Opt. Mater. 2 (2014) 465–477.

Approved for public release; distribution unlimited.
457

[17] P. Vorasayan, T.R. Betts, A.N. Tiwari, R. Gottschalg, Sol. Energy Mater. Sol. Cells 93 (2009) 917–921.
[18] A.B. Phillips, Z. Song, J.L. DeWitt, J.M. Stone, P.W. Krantz, J.M. Royston, R. M. Zeller, M.R. Mapes, P.J. Roland, M.D. Dorogi, S. Zafar, G.T. Faykosh, R. J. Ellingson, M.J. Heben, Rev. Sci. Instrum. 87 (2016), 093708.
[19] R.J. Matson, K.A. Emery, I.L. Eisgruber, L.L. Kazmersk, in: 12th European Photovoltaic Solar Energy Conference, 1994, pp. 1222–1225.
[20] L. Quan, K. Xie, R. Xi, Y. Liu, Sol. Energy 150 (2017) 345–352.
[21] L. Quan, K. Xie, Y. Liu, H. Zhang, Sol. Energy 183 (2019) 212–217.
[22] R.M. Geisthardt, J.R. Sites, IEEE J. Photovoltaics 4 (2014) 1114–1118.
[23] S. Nakano, T. Matsuoka, S. Kiyama, H. Kawata, N. Nakamura, Y. Nakashima, S. Tsuda, H. Nishiwaki, M. Ohnishi, I. Nagaoka, Jpn. J. Appl. Phys. 25 (1986) 1936–1943.
[24] A.D. Compaan, I. Matulionis, S. Nakade, Optic Laser. Eng 34 (1) (2000) 5–45.
[25] P. Gečys, G. Račiukaitis, E. Miltenis, A. Braun, S. Ragnow, Phys. Procedia 12 (2011) 141–148.
[26] B. Turan, S. Haas, M. Steger, Sol. Energy Mater. Sol. Cells 125 (2014) 78–86.
[27] X. Zhao, Y. Cao, Q. Nian, Y.C. Shin, G. Cheng, Appl. Phys. Mater. Sci. Process 116 (2014) 671–681.
[28] S. Rung, J. Barth, R. Hellmann, Micromachines 5 (2014) 943–953.
[29] K. Pearson, London, Edinburgh, *Dublin* Philos. Mag. J. Sci. 50 (1900) 157–175.

Approved for public release; distribution unlimited.

458

Thin Solid Films 697 (2020) 137798

Contents lists available at ScienceDirect

Thin Solid Films

journal homepage: www.elsevier.com/locate/tsf

Energy, temperature, and deposition angle dependence of Cd and Te_2 deposited on CdTe

Indiras Khatri, Jacques G. Amar*

Department of Physics & Astronomy, University of Toledo, Toledo, OH 43606, USA

ARTICLE INFO

Keywords:
CdTe
Molecular dynamics
Vapor deposition
Close-spaced sublimation

ABSTRACT

Cadmium Telluride (CdTe) is an important material for the production of high-efficiency thin-film solar cells. While sputter deposition has been used to create CdTe-based solar cells, two other important methods of growth are close-spaced sublimation and vapor deposition. In these methods, the depositing clusters correspond to Cd atoms and Te_2 dimers while the deposition energies are relatively low. In addition, depending on vapor pressure, deposition method, and target-substrate distance, deposition may occur at relatively large angles with respect to the substrate normal. Here we investigate the dependence of the attachment probability and deposition site for Cd and Te_2 clusters deposited on Cd-terminated and Te-terminated (100) and (111) surfaces of zincblende CdTe on deposition conditions. In general, we find that the deposition of Cd atoms and/or Te_2 dimers on the oppositely terminated surface leads to an attachment probability which is close to 1 and relatively independent of deposition conditions for both the (100) and (111) orientations. In contrast, deposition on the same terminated surface leads to a significantly lower attachment probability which generally decreases with increasing deposition angle, energy, and substrate temperature. Our results also indicate that deposition on the (111) surface leads to a significant excess Te sticking probability. In contrast, the excess Te attachment probability for deposition on the (100) surface is typically significantly smaller, and in some cases may even be negative. We also find, for both deposition on the (111) surface as well as opposite termination deposition on the (100) surface, that the dominant deposition mode corresponds to sitting on top of the surface which corresponds to growth of the next layer. In contrast, for same termination deposition on the (100) surface the dominant deposition mode corresponds to joining the first layer. These results imply that even for low deposition energies and substrate temperatures, deposition on the (100) surface is likely to create interstitials in the surface layer.

1. Introduction

Cadmium Telluride (CdTe) is an attractive absorber material for solar cell applications due to its optimal bandgap and high absorption coefficient [1,2]. However, while CdTe thin-film solar cells are being successfully used in a variety of applications [3], the energy conversion efficiency is still significantly less than the Shockley-Queisser limit [4]. This difference may be due to a variety of effects such as deviations in stoichiometry as well as defects such as interstitials, vacancies, dislocations, and grain boundaries [5–7].

Recently, Yu and Kenny [8] have used molecular dynamics simulations based on a realistic bond-order potential [9,10] to study the effects of the initial kinetic energy of small Cd_xTe_y clusters deposited normally on CdTe (100) and (111) surfaces at 300 K. In particular, depending on the deposition energy as well as the cluster type, surface orientation and termination type (e.g. Cd or Te), the probabilities of a variety of different outcomes (see cases 1–7 in Fig. 1) including reflection, dissociation, penetration, and atom replacement were determined. While a variety of results were obtained which may have an impact on the early stages of thin-film growth, these results were limited to the relatively high initial kinetic energies (e.g. 1–40 eV) used in sputter deposition, and were only carried out for the case of normal incidence with relatively low substrate temperature (T_{sub} = 300 K). In addition, the simulations were only carried out for the deposition of Cd atoms, Te atoms and a CdTe dimer, while the case of Te_2 cluster deposition, which is known to play an important role in vapor deposition and closed-space sublimation [11–14] was not considered.

Here we present the results of molecular dynamics (MD) simulations of Cd and Te_2 cluster deposition which were carried out in order to understand the dependence of the sticking probabilities and deposition modes on substrate temperature, deposition energy, and deposition angle. Our simulations are motivated in part by the fact that in both

* Corresponding author.
E-mail addresses: indiras.khatri@rockets.utoledo.edu (I. Khatri), jacques.amar@utoledo.edu (J.G. Amar).

https://doi.org/10.1016/j.tsf.2020.137798
Received 10 September 2019; Received in revised form 7 January 2020; Accepted 9 January 2020
Available online 10 January 2020
0040-6090/ © 2020 Elsevier B.V. All rights reserved.

Approved for public release; distribution unlimited.

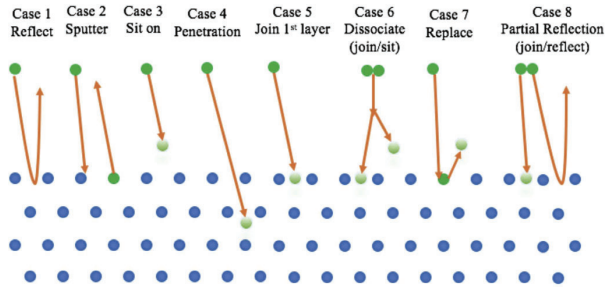


Fig. 1. Illustration of 8 cases of the final states after impact.

vapor deposition and close-spaced sublimation (CSS) the dominant depositing clusters are Cd atoms and Te_2 dimers (rather than Cd atoms, Te atoms and CdTe clusters as in Ref. [8]). Similarly, in both vapor deposition and CSS the deposition energy is typically much smaller than 1 eV (in the case of CSS the source temperature is typically close to 800 K) while the substrate temperature in vapor deposition may be low as in Ref. [8] or much higher. In addition, in both cases, depending on vapor pressure and target-substrate distance, it is also possible that deposition may occur at relatively large angles with respect to the substrate normal.

Our results may be summarized as follows. In general, we find that the deposition of Cd atoms and/or Te_2 clusters on the oppositely terminated surface leads to an attachment probability which is close to 1 and relatively independent of substrate temperature, kinetic energy, and deposition angle for both the (100) and (111) orientations. In contrast, the deposition of Cd atoms and/or Te_2 clusters on the same terminated surface leads to a significantly lower attachment probability which generally decreases with increasing substrate temperature, kinetic energy, and deposition angle. We also find a significantly higher attachment probability (compared to Cd atoms) for Te_2 dimers deposited on the (111) surface at both low and high temperature or kinetic energy, as well as for Te_2 dimers deposited on the (100) surface at low kinetic energy. However, in the case of deposition on the (100) surface at higher energy (1.0 eV), the excess Te sticking probability is significantly lower, and is even slightly negative for the case of normal deposition at 300 K. Since in most experiments the growth is polycrystalline but with (111) facets dominating, our results also suggest that both vapor deposition and sputter deposition at low substrate temperature (T_{sub} = 300 K) will tend to lead to Te-rich films. Although not discussed in detail below, we have also carried out simulations of Te atom deposition with 1 eV kinetic energy and substrate temperature T_{sub} = 300 K as a function of deposition angle. Consistent with the results of Ref. [8] for normal deposition - and in contrast to our results for Te_2 - we find that in this case the sticking probability is equal to 1 for all substrate terminations and deposition angles.

2. Molecular dynamics simulation details

Our simulations were carried out using the Large-scale Atomic/Molecular Massively Parallel Simulator code [15,16], using an analytical bond-order potential (BOP) [17–22] for CdTe which was parametrized [9,10] by fitting to the properties of a variety of clusters, lattices, surfaces, and defects calculated using density-functional theory as well as testing crystalline growth simulations. We note that the analytical form of the BOP has been derived [17–22] from quantum mechanical theories which take into account both π and σ bonding.

Deposition on the Cd-terminated (100) and (111) surfaces as well as Te-terminated (100) and (111) surfaces was studied, while the zinc-blende structure of CdTe was assumed with lattice constant a = 6.83 Å [9]. In each case, simulations were carried out for both Cd and Te_2 cluster deposition. Starting from an initially bulk terminated surface, the system was annealed at the desired temperature for 20 ps before carrying out depositions [23]. In order to compare with previous work [8], we also carried out simulations of Te atom deposition for the case of normal incidence with K_i = 1.0 eV and T_{sub} = 300 K.

In order to determine the effects of deposition energy and substrate temperature on the sticking probability and mode, our simulations were carried out using two different cluster kinetic energies (K_i = 0.14 eV, and K_i = 1.0 eV) as well as for two different substrate temperatures (T_{sub} = 300 K and 800 K). Similarly, in order to study the dependence on deposition angle, simulations were carried out with six different deposition angles θ with respect to the surface normal, ranging from $\theta = 0^\circ$ (normal incidence) to 75° (grazing incidence). In each case, the depositing cluster was initially placed at a height Δz above the highest atom on the surface layer which was equal to 1.5 Å plus the maximum cut-off radius for the Zhou et al [9] potential (4.9 Å), while the x and y positions were chosen randomly. MD simulations of the whole system were then carried out for 10 ps, after which the system was minimized and then analyzed to determine the sticking probability and deposition mode (see Fig. 1).

In our simulations, the substrate corresponded to a total of 14 layers with 4 fixed layers, 4 layers thermostated using the Berendsen thermostat [24], and 6 non-thermostated layers at the surface. Both the heat bath coupling constant and the time-step were set to 1 fs. Periodic boundary conditions were assumed in the lateral (x and y) directions while growth was in the z-direction. For the (100) surface, the lateral dimensions were $10\,a \times 10\,a$, corresponding to 200 atoms in each layer. In contrast, for the (111) surface the dimensions were 6 a_1 (where $a_1 = \sqrt{8/3}\,a$) in the x-direction and 6 a_2 (where $a_2 = \sqrt{2}\,a$) in the y-direction, corresponding to 192 atoms in each layer.

In order to obtain good statistics, averages were taken over 10,000 depositions for each cluster type and deposition angle with a given substrate termination, temperature, and initial kinetic energy, resulting in 32 different simulation runs for each of 6 different deposition angles. We note that the value K_i = 0.14 eV was motivated by the fact that at 800 K (which is approximately equal to the source temperature used in both vapor deposition and CSS) this corresponds to the average translational kinetic energy $2k_BT$ of depositing clusters. In the case of the Te_2 cluster, we have also included initial internal rotational and vibrational kinetic energies equal to 1/2 k_BT per degree of freedom, with T = 800 K. In this case, in addition to randomly choosing the starting x and y positions, we have also randomly chosen the initial dimer axis orientation as well as the directions of the two rotational axes with respect to the Te_2 bond direction.

3. Results

3.1. (100) surface

Fig. 2 shows our results for the overall sticking probabilities for both Cd atoms and Te_2 clusters, deposited on the (100) Cd-terminated surface as a function of deposition angle θ for both kinetic energies (K_i = 0.14 eV and 1 eV) and substrate temperatures (T_{sub} = 300 K and 800 K). As can be seen, for the case of Te_2 deposition, the sticking probability is essentially 1 for all cases. In this case, the Te atoms sit on the top layer (case 3) which is consistent with the growth of the next Te layer. In contrast, the sticking probability for Cd atoms is significantly less than 1 even for normal deposition, and decreases with both increasing deposition angle and increasing substrate temperature. Interestingly, for low deposition angle ($\theta < 45^\circ$) the sticking probability for Cd atoms increases with increasing kinetic energy while the reverse is true for $\theta > 45^\circ$. In all cases the Cd atoms join the top layer (case 5). While the non-sticking case corresponds entirely to reflection at 300 K (case 1) which increases with deposition angle, at 800 K there is also a small amount of sputtering (1–7%), which decreases with increasing deposition angle.

The corresponding results for the (100) Te-terminated surface are shown in Fig. 3. As in Fig. 2, except for the case of both low deposition

Approved for public release; distribution unlimited.
460

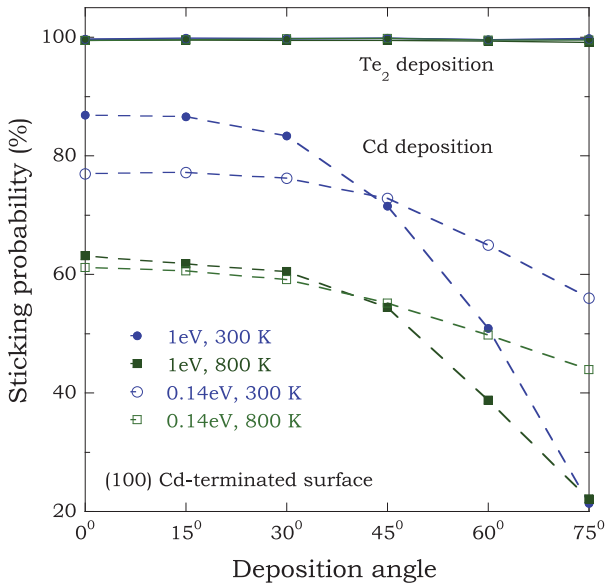


Fig. 2. Sticking probabilities as function of deposition angle, substrate temperature, and initial kinetic energy for Cd atoms (dashed lines) and Te_2 clusters (solid lines) deposited on the (100) Cd-terminated surface.

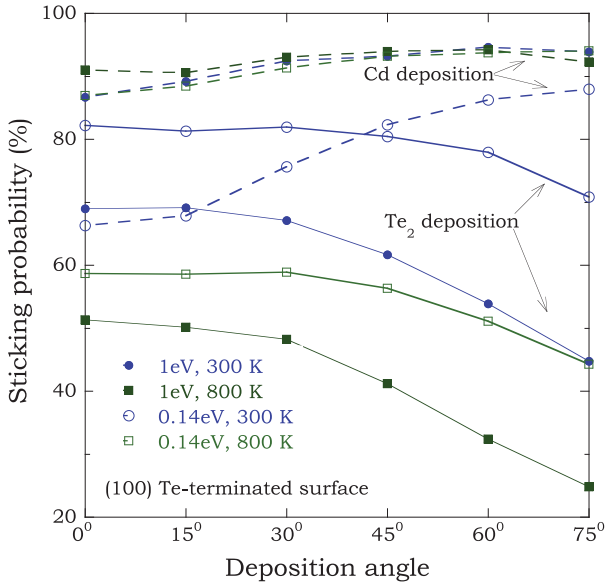


Fig. 3. Same as Fig. 2 but for deposition on the (100) Te-terminated surface.

energy and substrate temperature (K_i = 0.14 eV, T_{sub} = 300 K), the deposition of Cd on the oppositely terminated (100) surface leads to a relatively high sticking probability ($P_{stick} = 0.85 - 0.95$) which increases slightly with deposition angle. While the dominant sticking mode corresponds to sitting on the top layer (case 3) there are also contributions from case 4 (penetration) and case 5 (join 1st layer). However, for both low kinetic energy and substrate temperature (open circles with dashed line) the sticking probability is significantly lower, especially at small angles - due primarily to the reduced probability of joining the 1st layer - although it still increases with increasing deposition angle.

Also shown in Fig. 3 are our results for the deposition of Te_2 on the (100) Te-terminated surface. As for the case of Cd deposition on the Cd-terminated surface, in this case the sticking probability decreases with

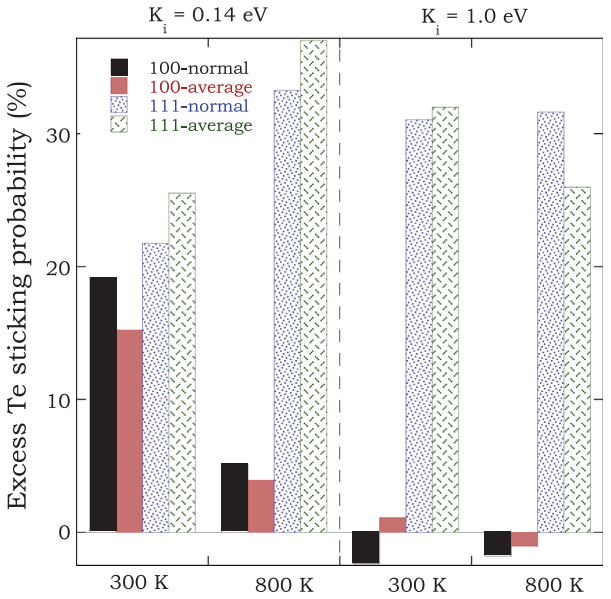


Fig. 4. Excess Te on the substrate as function of deposition angle, substrate temperature, and initial kinetic energy for Cd and Te_2 clusters. In each case the first (black) and third (blue) bars correspond to normal deposition while the second (red) and fourth (green) bars represent the average over all deposition angles. (For interpretation of the references to color in this figure legend, the reader is referred to the web version of this article.)

increasing deposition angle and temperature. In addition, it decreases for all angles with increasing kinetic energy. In this case, the sticking atoms primarily join the first layer (case 5) although the sticking probability also includes some case 3 (sit-on) and a very small amount of dissociation (case 6). As for the case of Cd deposited on the "same" (Cd-terminated) (100) surface, the dominant non-sticking mode corresponds to reflection while the probability of reflection (for fixed deposition angle) increases with increasing temperature and/or kinetic energy. In addition, the relatively large reflection probability for Te_2 clusters deposited normally with K_i = 1 eV and T_{sub} = 300 K is in contrast to the negligible reflection probability found [8] for single Te atoms deposited under the same conditions. There is also a small amount of partial reflection (case 8) in which one atom of the Te_2 dimer joins the first layer while the other is reflected. This is in contrast to the results of Ref. [8] for CdTe cluster deposition, in which partial reflection was never observed.

Using these results, we have calculated the overall excess Te sticking probability (averaged over both Cd- and Te-terminated (100) surfaces) as shown in Fig. 4, both for normal incidence as well as averaged over all angles (corresponding to a uniform flux). We note that in this case, the "excess Te sticking probability" also takes into account the small amount of Cd substrate atom sputtering which occurs for the case of Cd atom deposition on the (100) Cd-terminated surface at 800 K. As can be seen, the deviations from equal Cd and Te_2 sticking probability are generally larger for the case of normal incidence than the angle-average. In addition, for the case of low kinetic energy (0.14 eV) the excess Te sticking probability is particularly large, although it decreases with increasing substrate temperature. In contrast, for high kinetic energy (1 eV) the difference between Te_2 and Cd sticking probabilities is much smaller (and in some cases is even negative) due in part to the increased probability of reflection for Te_2 clusters from the Te-terminated (100) surface. This behavior is in contrast to the negligible reflection probability found [8] for single Te atoms deposited with 1 eV kinetic energy on the Te-terminated (100) surface.

Approved for public release; distribution unlimited.
461

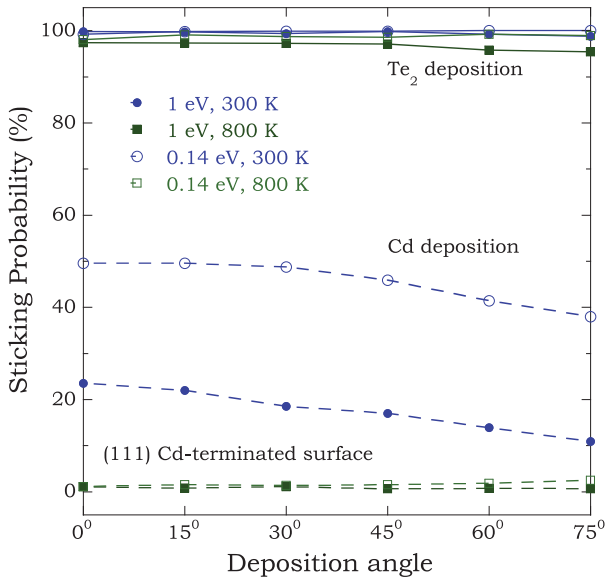


Fig. 5. Sticking probabilities as function of deposition angle, substrate temperature, and initial kinetic energy for Cd atoms (dashed lines) and Te_2 clusters (solid lines) deposited on the (111) Cd-terminated surface.

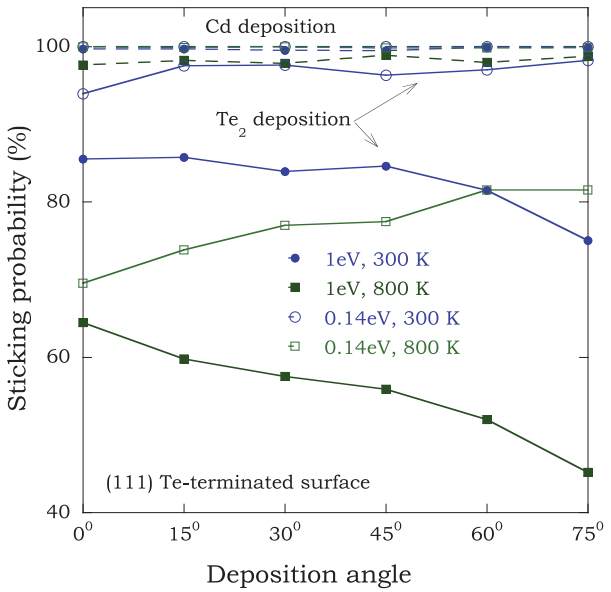


Fig. 6. Same as Fig. 5 but for deposition on the (111) Te-terminated surface.

3.2. (111) surface

Fig. 5 shows our results for the (111) Cd-terminated surface. As for the (100) Cd-terminated surface, the sticking probability for Te_2 is close to 1 for all angles, kinetic energies and substrate temperatures, while the Te atoms sit on top (case 3). In contrast, the sticking probability for deposited Cd atoms at 300 K is significantly lower and decreases with increasing kinetic energy and deposition angle. In this case, the Cd atoms also sit on top (case 3). Surprisingly, the sticking probability for Cd atoms on the (111) Cd-terminated surface at 800 K is negligible at both low and high kinetic energies. At both 300 K and 800 K, reflection is the dominant non-sticking mode.

The corresponding results for the (111) Te-terminated surface are shown in Fig. 6. Just as for the case of Te_2 on the (100) Cd-terminated surface, the sticking probability for deposited Cd atoms is close to 1 for all angles, kinetic energies and substrate temperatures while the Cd atoms sit on top (case 3). For Te_2 deposition the attachment mode also corresponds to case 3. In this case, at low temperature and kinetic energy, the sticking probability (open circles with solid line) is also close to 1 for all angles and temperatures. However, for higher kinetic energy and/or temperature, the Te_2 sticking probability is significantly less. In addition, while for both substrate temperatures, the Te_2 sticking probability decreases with deposition angle for high kinetic energy (K_i = 1.0 eV) for low deposition energy (K_i = 0.14 eV) it increases with increasing deposition angle. Interestingly, the three cases of Cd deposited on the (100) Te-terminated surface at low kinetic energy and temperature, and Te_2 deposited on the (111) Te-terminated surface at low kinetic energy are the only cases in which the sticking probability increases significantly with increasing deposition angle.

The overall excess Te sticking probability (averaged over both Cd- and Te-terminated (111) surfaces) for this case is also shown in Fig. 4. As can be seen, in contrast to our results for (100) surfaces, for (111) surfaces there is a significant excess Te sticking probability for all deposition energies and substrate temperatures. In addition, the relatively close agreement between the angular average and that obtained for normal deposition is consistent with the relatively weak angular dependence.

4. Discussion

Motivated by experiments on CdTe thin-film growth we have investigated the attachment probabilities and modes for Cd atoms and Te_2 clusters deposited on the (100) and (111) surfaces as a function of kinetic energy, deposition angle, substrate temperature, and substrate termination. Our results complement those previously obtained by Yu and Kenny [8] who focused on the case of normal deposition of Cd, Te, and CdTe clusters at low substrate temperature (T_{sub} = 300 K) and higher energies (1 − 40 eV).

In general, we find that - over the range of kinetic energies (K_i = 0.14 − 1 eV) and temperatures (T = 300 − 800 K) considered in our simulations - the deposition of Cd atoms and/or Te_2 clusters on the oppositely terminated surface leads to an attachment probability which is close to 1 and relatively independent of substrate temperature, kinetic energy, and deposition angle for both the (100) and (111) orientations. The one exception is the case of Cd deposition on the (100) Te-terminated surface with both low deposition energy and substrate temperature. In this case the attachment probability is only about 66% for normal deposition but increases to a value of approximately 88% at a deposition angle $\theta = 75°$. While there is some penetration (case 4) and joining of the first layer (case 5), the dominant attachment mode in all cases corresponds to "sit-on" (case 3) thus leading to the growth of the next layer in the crystal.

In contrast, the deposition of Cd atoms and/or Te_2 clusters on the same terminated surface leads generally (for both the (100) and (111) orientations) to a significantly lower attachment probability which decreases with both increasing substrate temperature and deposition angle. In particular, the attachment probability for Cd deposition on the (111) Cd-terminated surface with substrate temperature 800 K is close to zero for both low and high kinetic energies and for all deposition angles. The one exception to these general results is the case of Te_2 deposition with low kinetic energy and substrate temperature on the (111) Te-terminated surface. In this case, while the attachment probability is still less than for Te_2 deposition on the (111) Cd-terminated surface, it is relatively close to 1 and increases with increasing deposition angle.

It is also interesting to consider the dependence of the deposition mode on atom/cluster type and surface termination. Interestingly, we find that for deposition on the (111) surface, the dominant deposition

Approved for public release; distribution unlimited.
462

mode corresponds to case 3 (sit-on) regardless of cluster type, surface termination, deposition angle, substrate temperature and kinetic energy. This is also the case for opposite termination deposition on the (100) surface. In contrast, for same termination deposition on the (100) surface the dominant deposition mode corresponds to case 5 (join first layer) regardless of cluster type, surface termination, deposition angle, substrate temperature and kinetic energy. This difference may be explained by the more "open" nature of the (100) surface compared to the (111) surface which allows deposited atoms to join the first layer and form bonds with the "opposite" layer below. These results also imply that, as previously found in Ref. [8], (100) surfaces are more likely to create interstitials in the surface layer than (111) surfaces.

As shown in Fig. 4, for the case of deposition on (111) surfaces with both low and high deposition energy, as well as for (100) surfaces with low deposition energy, our results indicate a significant excess sticking probability for Te. This result is consistent with the simulation results of Ref. [8] obtained for the case of normal deposition of Cd, Te, and CdTe clusters and T_{sub} = 300 K with kinetic energies ranging from 1 eV to 40 eV. A detailed examination of our results suggests that this tendency towards an excess sticking probability of Te may be explained as follows. While Cd and Te_2 both have high sticking probabilities on oppositely terminated (100) and (111) surfaces, for the (111) surface as well as for the (100) surface with low kinetic energy, the Te_2 clusters have a higher sticking probability to the Te-terminated surface than the corresponding sticking probability of Cd atoms to Cd-terminated surfaces. This difference is consistent with the fact that the Te dimer bond is much stronger than the Cd dimer bond. In contrast, for the case of Te_2 deposition on the Te-terminated (100) surface, the probability of case 3 (sit on top layer) is reduced, while the probability of reflection also increases with increasing kinetic energy. As a result, the excess Te sticking probability tends to be much smaller and even negative in the case of normal or low angle ($\theta \leq 45^{\circ}$) deposition on the (100) surface at both high (1 eV) kinetic energy and low substrate temperature (300 K). The latter behavior contrasts with that found in Ref. [8] for the deposition of Cd atoms, Te atoms, and CdTe clusters for which the excess Te sticking probability (averaged over all deposition energies from 1 eV to 40 eV) remained positive in all cases.

While our results are restricted to the initial stages of deposition, they also suggest that for the case of low kinetic energy as well as low substrate temperature T_{sub} = 300 K (for which there is negligible sublimation) there will be a significant excess Te concentration in CdTe thin films grown on the (100) and (111) surfaces. This is in qualitative agreement with the experimental results of Ref. [25] for the vapor deposition of CdTe on glass substrates at 300 K. Since in most experiments the growth is polycrystalline but with (111) facets dominating [25–27], our results also suggest that both vapor deposition and sputter deposition will tend to lead to Te-rich films. However, at a substrate temperature of 800 K sublimation will play an important role [11,12,27]. Accordingly, in the future, it would be of interest to simulate the sublimation process in order to understand its effects during high temperature growth.

Declaration of Competing Interest

The authors declare that they have no known competing financial interests or personal relationships that could have appeared to influence the work reported in this paper.

Acknowledgments

This material is based on research sponsored by Air Force Research Laboratory under agreement number FA9453-18-2-0037. The U.S. Government is authorized to reproduce and distribute reprints for Governmental purposes notwithstanding any copyright notation thereon. The views and conclusions contained herein are those of the authors and should not be interpreted as necessarily representing the official policies or endorsements, either expressed or implied, of Air Force Research Laboratory or the U.S. Government. We would also like to thank the Ohio Supercomputer Center (OSC) for computational resources.

References

[1] M. Gloeckler, I. Sankin, Z. Zhao, Cdte solar cells at the threshold to 20% efficiency, IEEE J. Photovoltaics 3 (4) (2013) 1389–1393, https://doi.org/10.1109/JPHOTOV.2013.2278661.
[2] J. Sites, A. Munshi, J. Kephart, D. Swanson, W.S. Sampath, Progress and challenges with cdte cell efficiency, IEEE 43rd photovoltaic specialists conference (PVSC), (2016), pp. 3632–3635, https://doi.org/10.1109/PVSC.2016.7750351.
[3] B.M. Basol, B. McCandless, Brief review of cadmium telluride-based photovoltaic technologies, J. Photonics Energy 4 (1) (2014) 040996, https://doi.org/10.1117/1.JPE.4.040996.
[4] W. Shockley, H.J. Queisser, Detailed balance limit of efficiency of pn junction solar cells, J. Appl. Phys. 32 (3) (1961) 510–519, https://doi.org/10.1063/1.1736034.
[5] H.C. Chou, A. Rohatgi, The impact of MOCVD growth ambient on carrier transport, defects, and performance of cdte/cds heterojunction solar cells, J. Electron. Mater. 23 (1) (1994) 31–37, https://doi.org/10.1007/BF02651264.
[6] C. Szeles, Cdznte and cdte materials for xray and gamma ray radiation detector applications, Phys. Status Solidi B 241 (3) (2004) 783–790, https://doi.org/10.1002/pssb.200304296.
[7] G. Zha, W. Jie, T. Tan, L. Wang, Study of dislocations in cdznte single crystals, Phys. Status Solidi A 204 (7) (2007) 2196–2200, https://doi.org/10.1002/pssa.200675440.
[8] M. Yu, S.D. Kenny, The energetic impact of small cdxtey clusters on cadmium telluride, Thin Solid Films 584 (2015) 41–45, https://doi.org/10.1016/j.tsf.2014.12.019.
[9] D.K. Ward, X.W. Zhou, B.M. Wong, F.P. Doty, J.A. Zimmerman, Analytical bond-order potential for the cadmium telluride binary system, Phys. Rev. B 85 (11) (2012) 115206, https://doi.org/10.1103/PhysRevB.85.115206.
[10] D.K. Ward, X.W. Zhou, B.M. Wong, F.P. Doty, J.A. Zimmerman, Accuracy of existing atomic potentials for the cdte semiconductor compound, J. Chem. Phys. 134 (24) (2011) 244703, https://doi.org/10.1063/1.3596746.
[11] J.L. Cruz-Campa, D. Zubia, Cdte thin film growth model under CSS conditions, Sol. Energy Mater. Sol. Cells 93 (1) (2009) 15–18, https://doi.org/10.1016/j.solmat.2008.02.012.
[12] N. Amin, K.S. Rahman, Close-spaced sublimation (CSS): a low cost, high yield deposition system for cadmium telluride (cdte) thin film solar cells, Chapter 18 in modern technologies for creating the thin-film systems and coatings, 361 IntechOpen publisher, 2017, https://doi.org/10.5772/66040.
[13] L. Chu, Thin film cadmium telluride solar cells by two chemical vapor deposition techniques, Solar Cells 23 (1-2) (1988) 31–48, https://doi.org/10.1016/0379-6787(88)90005-1.
[14] B. Liu, R.F. Hicks, J.J. Zinck, Chemistry of photo-assisted organometallic vapor-phase epitaxy of cadmium telluride, J. Cryst. Growth 123 (3-4) (1992) 500–518, https://doi.org/10.1016/0022-0248(92)90612-M.
[15] http://lammps.sandia.gov.
[16] S. Plimpton, Fast parallel algorithms for short-range molecular dynamics, J. Comput. Phys. 117 (1) (1995) 1–19, https://doi.org/10.1006/jcph.1995.1039.
[17] D.Z. Pettifor, I.I. Oleinik, Analytic bond-order potentials beyond tersoff-brenner, I. Theory Phys. Rev. B 59 (13) (1999) 8487, https://doi.org/10.1103/PhysRevB.59.8487.
[18] D.Z. Pettifor, I.I. Oleinik, Bounded analytic bond-order potentials for σ and π bonds, Phys. Rev. Lett. 84 (18) (2000) 4124, https://doi.org/10.1103/PhysRevLett.84.4124.
[19] D.Z. Pettifor, I.I. Oleinik, Analytic bond-order potential for open and close-packed phases, Phys. Rev. B 65 (17) (2002) 172103, https://doi.org/10.1103/PhysRevB.65.172103.
[20] R. Drautz, D. Nguyen-Manh, D.A. Murdick, X.W. Zhou, H.N. Wadley, D.Z. Pettifor, Interatomic bond-order potentials and cluster expansions, TMS Lett. 1 (2004) 31.
[21] D.Z. Pettifor, M.W. Finnis, D. Nguyen-Manh, D.A. Murdick, X.W. Zhou, H.N. Wadley, Analytic bond-order potentials for multicomponent systems, Mater. Sci. Eng. A 365 (1-2) (2004) 2–13, https://doi.org/10.1016/j.msea.2003.09.001.
[22] R. Drautz, D. Nguyen-Manh, D.A. Murdick, X.W. Zhou, H.N. Wadley, D.Z. Pettifor, Analytic bond-order potential for predicting structural trends across the s p-valent elements, Phys. Rev. B 72 (14) (2005) 144105, https://doi.org/10.1103/PhysRevB.72.144105.
[23] For the case of the te-terminated (100) surface this led to the 2 × 1 dimer reconstruction.
[24] H.J.C. Berendsen, J.P.M. Postma, W.F. van Gunsteren, A. DiNola, J.R. Haak, Molecular dynamics with coupling to an external bath, J. Chem. Phys. 81 (8) (1984) 3684–3690, https://doi.org/10.1063/1.448118.
[25] S.J. Ikhmayies, R.N. Ahmad-Bitar, Characterization of vacuum evaporated cdte thin films prepared at ambient temperature, Mater. Sci. Semicond. Process. 16 (1) (2013) 118–125, https://doi.org/10.1016/j.mssp.2012.06.003.
[26] S. Lalitha, S.Z. Karazhanov, P. Ravindran, S. Senthilarasu, R. Sathyamoorthya, J. Janabergenov, Electronic structure, structural and optical properties of thermally evaporated cdte thin films, Physica B 387 (1-2) (2007) 227–238, https://doi.org/10.1016/j.physb.2006.04.008.
[27] G. Zeng, J. Zhang, B.L. Wu, W.I. Li, L. Feng, Effect of deposition temperature on the properties of cdte thin films prepared by close-spaced sublimation, J. Electron. Mater 44 (8) (2015) 2786–2791, https://doi.org/10.1007/s11664-015-3739-z.

Approved for public release; distribution unlimited.
463

Solar Energy Materials & Solar Cells 218 (2020) 110764

Nfgsegs hr s hn(nrbnl behnshDnregnoeXriensh

Df bnihAgeiMohL nseirnb hngwhDf bnihNelbb h

journal homepage: http://www.elsevier.com/locate/solmat

Dec rasing t niegsht asot ehl niruc hmf t t eih ubdweln hnhl nnzhmf gsnnshrgseipnneh bnoeihpf ihnnwc ruc hselbuirweh f bnihneblb h

: nc nbnh Rngnlbh Dul ewrHhAl rghj n sf bnHh,gwinhDul ewrHHDngwrt hDZhj r snHHDuc ngh Sr.JnbHh
L ngf Jh Zh nc nizns sel HHS n RnhWZhWB grHHWwnc hj ZhPRrbrt Hhr*ngpnhr*ngHHL rnRneh ZhCel egHh
E rz f bn h ZhPf winknHHSngwoh ZhAlbrgMf g Th

Wright Center for Photovoltaic snnovation anI Cod d ercialinationz , eDartd ent of Phpyicy anI Aytronod pz Uhe Tniveryitp of UoleI oz UoleI oz 2 8 z 01. B. z TSA

W S I , N F A h, E O V

OepHorI y4
j niruc hmf t t eih ubdweh
j nnzhmf gsnnsh
j rpnnnnbh
NwI eh f bnihneblbh
Df busrf gh l n ewhc esRf wh

W j D I S W N I

Vt snnnblbohsing t niegsht asot ehc nseirnb ht bnohnhnirsrnnnbhif behrghsing t niegshebensif grnnhrgnhuwrgMht Rf sf (f bsnrnnh)Pv-h we(rne ZhPasot eh ubdwehc nseirnb hf ppeihngbnbseignsr(ehsf hf firwe hpf ihPv hnt t bnnnsrf ghwuehsf hrc t if(ewHRf behsing t fish t if t eisre ZhCeieHHBehiet f ishsRehf busrf gal n ewhogsRe r hf phenisRanl ugwngsht asot ehsing t niegshnf gwunsrgMhl niruc h mf t t eih ubdweh)αajnNu$_y$D$_{xh}$jND-hsRrghdbc ZhRe ehdbc hBeiehnRninnseirkewhu rgMhnnggrgMhebensif ghc rnif nf t oHh [ainohwrppinnsrf gHh1v–vr –E,Sh t ensif t Rf sf c esioHHSnc ngh t ensif nf t oHhngwh t ensif nf t nhebrt f c esioZhj NDh dbc hf ph2]~–hgc hsRnnzge hsing c rsh>3~4 hf ph(r rl behrMRsZ6 ehiet f ishf ghse s hf phsRehRf behsing t fisht if t eisre hf ph sRe ehj NDhdbc hpf ihnnwc ruc hselbuirweh)NwI e-ht Rf sf (f bsnrnnHhdgwrgMhsRnshsRehj NDhwet f rsrf ght if nne hpf ic hnh l eged nnnbhselbuiruc h)I e-hinnRhuipnnehf ghNwI eh l oh ebensr(ebohiec f (rgMhNwhpif c hsRehuipnnehZhj n ewhf ghf uih suwoHh sRehj NDhrgseipnnehbnoeiht bno hwunHhpugnsrf g hpf ihNwI ehPv hwe(rne ln hnlRf behsing t fishc nseirnbhngwhn hnghesnnRngsHh egRngnrgMhsRehie ubsrgMhwe(rnehteipf ic ngnneZh6 ehf l ei(ewhnh rMgrdnngshrgnien ehrghf t eganninursh(f bsnMehf phNwI eh f bnihneblbB rsRlsRehj NDh uppeihnoeiZhWwwrsrf gnHboHBehwr nu hec rsing t niegshNwI eh f bnihneblbB rsRhj NDhn hnlRf beh sing t fishbnoeihngwhrgwruc hsrghf firwehn hnhdgr RrgMhebensif we ZhDec rsing t niegshNwI eh f bnihneblbh Rf B h]xZx4 h nf g(ei rf ghepdnnegnohpf ihsRehpif gshrwehrbhuc rgnsrf ghngwh]Z74 hepdnnegnohpf ihl nnzhrwehrbhuc rgnsrf gHhrgwnnsrgMh RrMRhienf c l rgnsrf ghf phnRniMehnniirei hMegeinsewhnhf ehsf hsRehieni hNwI eqj NDq,I Vhnf gsnnsZ

1. Introduction

I ing t niegshnf gwunsf i hnieihnghe egsnnlht nishf ph(nirf u hebensif grnnwe(rne hrgnhuwrgMhf bnihneblbHheg f i Hhngwhsing t niegshnnirnurs h5]Hf(ZhWHbh f phsRehnuiiegsbohnf c c einnnbrkewhsing t niegshnf gwunsrgMhc nseirnb h)I NL -hrgnhuwrgMhDgawf t ewbg$_7$V$_x$),I V-l5x(@hngwHhDawf t ewhDg$_7$V$_{7h}$)OI V-bnieh gasot eh5y(@hngwhsRehn(nrbnl rhrsohf pht asot ehc nseirnb hB rsRhe/ur(nlegshf t a snnnbhsing t niegnohngwhnnf gwunsr(rsohr hbrc rsewZhCf Be(eiHhc ngohepf is Rn(ehienegsbohl eeghwriensewhsf hsRehwe(elf t c egshf ph unRht asot ehI NL l n ewhf ghnf t t eih)Nu-hnf c t f ugw h unRhn hNuWbV$_{7h}$50(@h)NuD-$_3$)8gD-$_{6f3}$ 5;–9(@hngwhj nNu$_7$D$_{7h}$5G–]](@hVt snnnblbohsing t niegsht asot ehnnf gwunsf i pnnnbrsnsehsRehwe(elf t c egshf phsing t niegshebensif grnnln hBeHhn hRrMRhepa dnnegnohl rpnnnnlht Rf sf (f bsnnnhwe(rne h5;(@hWhnnf iwrgMhsf hsRef ioHHwuehsf sRehsinwef pphl esBeeghsReht f rsrf ghf ph(nbegnehl ngwhc nfirc uc hngw pf il rwweghl ngwMht Hhnnf c t befih ubdweh ec nnf gwunsf i hnf ubwhl ehrgseia e srgMngwhnt t if t imsehnngwrwnse hpf iht asot ehI NL h5]7(@hNf c t befih uba dwe hnnghl ehpf ic ewhl ohiet bnnrgMhsRehc f iehnf grnhf firwe hBrsRhc f ie nf (nbegshubdwe UhRr hRn hewhsf hsRehwe(elf t c egshf phnf t t eih ubdweal n ewh c nseirnb HhrgnhuwrgMhNuWbD$_{7h}$5]x(@h)NuD-$_{fih}$)8gD-$_{]afih}$5;H3(@hj nNu$_7$D$_{7ha}$ngwh j nNu$_y$D$_{xh}$5]](@h

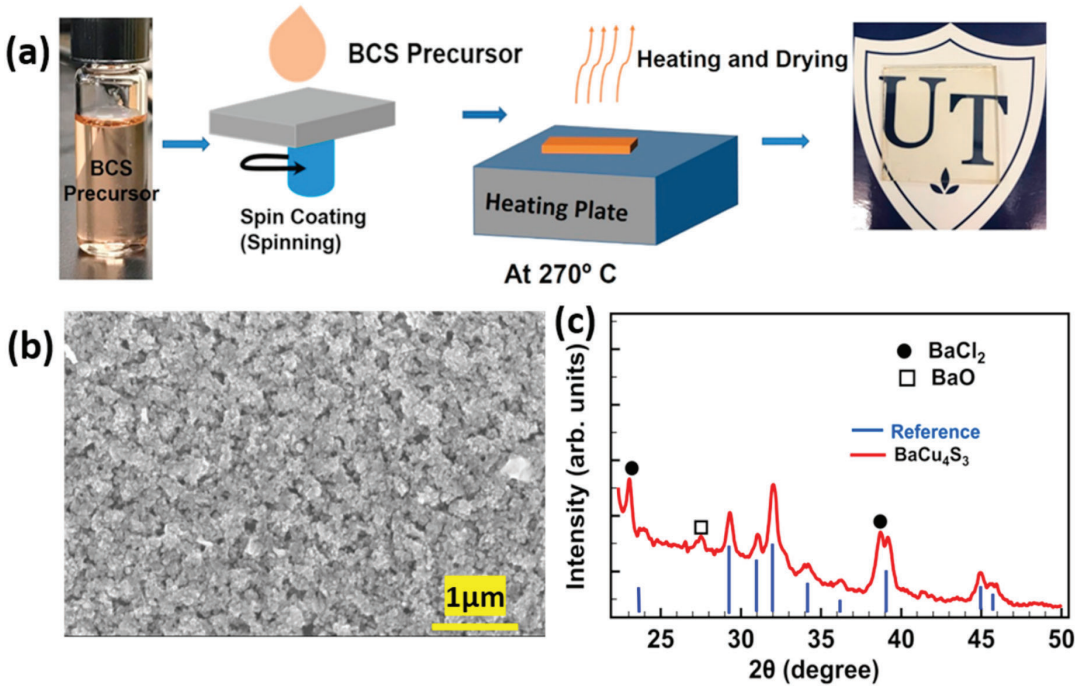
Wc f gMhsRe eh ubdwehc nseirnb Hhj nNu$_y$D$_{xh}$ Rf B h f c eht iepeinl beh nRninnseir snnhpf iht innnsrnnbhnt t bnnnsrf g hbrzeHBrweihl ngwMht hngwhRrMRh sing t niegnohrghsReh(r rl behsf hgenihrgpiniewh)E,S-h t ensinHhieMf g h5]yHh]0(@hFrc rsewh suwre hRn(eht ie(rf u bohiet f isewhf ght asot eH niruc hmf t t eih ubdweZhOf ihefinc t beHhCnghesbnbZhiet f isewh t usseiewhj nNu$_y$D$_{xh}$sRrghdbc h BrsRht asot ehnf gwunsr(rsohngwhnniireihnf gnegsinsrf gl2 0h<]~J Gh hc ach5]](@h BRrbeh6 ngMhesbnbZhu ewhRrMRhohsf f irnhngRowif u hRowinkrgehn hnhf h(egshsf h pnl innnseht asot ehj nNu$_7$D$_{7h}$pf ihsRerih f busrf ghl n ewht if nne hrghnghrgeish eg(rif gc egsh 5]~(@h ,gh sRr h nf gsefisHh sReh we(elf t c egsh f ph ngh eg(rif gc egsnlboapiregwhoh t asot ehj NDh I NL h(nnh nh hf B h sec t einsuieHh sugnl beHhngwh nnbnl behc esRf whr hRrMRhohwe rinl beZhVuihj NDhsRrghdbc h nf g r shf phgf gasf f irnhenisRanl ugwngshc nseirnb h5]; (@h

Xuehsf hsRehweet hB f izhpugnsrf ghf phNwI eh)2 0Z3hev-Hhrshr hwrpdnubshsf h c nzehnghf Rc nnhnf gsnnshpf iHRf behefisinnsrf ghf ghsReHl nnzhrgseipnneHf phNwI eh

T Nfiie t f gwrgMnnusRf iZh
*kRdail aI I reyy4*SngwoZAlbrgMf gfl usf bewf Zewuh)SZZhAlbrgMf g-Z

Rsst Kqqwf rZf iMq]~Z]~]; qJZf bc nsZ7~7~Z]~3; yh
Senen(ewh7]h ugeh7~7~UhSenen(ewhrghie(r ewhpf ic hjGhWuMu sh7~7~UhWnnnet sewh7~hWuMu sh7~7~Hhh
Available online 8 September 2020
0927-0248/© 2020 Elsevier B.V. All rights reserved.

Approved for public release; distribution unlimited.



sil. 1.)n-HDogsRe r ht if ne h)l -ht bnga(reB h nnggrgMebensifghc rnif nf toh)DAL -hrc nMe h)nal[ainolwppinnsrfgh)[SX-htnsseig lB Reiel□ iet ie egs lj nVlngwle● iet ie egs h j nNb7h)üHPXOhG3a~~~a7] G~hrc t uirsoht Rn elf phj NDhgngf nfic t f rsehsRrghdlbc hwet f rsewhf gh f wnhbrc ehMn h ul sinse Zh

f bnihneblb ZhNf t t eiqMf bwh)NuqWu-hRn hl eeghu ewhn hnhl nnzhnfgsnnshc na seinlhpf ihNwI eht Rf sf(f bsnrm HhsRf uMRhsRehefir segneh f phnhDnRf sszoht f a segsnnlhl niireihf ph2 ~Zxx~hev hbrc rs hwe(rneht eipf ic ngneh5]3H19@ZhI f h rc t if(ehsRehf tegannimurshf bsnMeh)b_{2C}-Hhf gehnf c c f ght if ne hr hsf h rgsif wunehnhl nnzhnfgsnnshl upeihbnoeihBrsRhnt t if t imsehBf izhpugnsrf gZh I Reiehnieln ngoliet f is hpf nu rg Mf ghNuhnfgsnrgrgMrgseipnnnnlhbnoei hunRh n hnf t t eiavf t ewHkrgnnseibuirweh)8gI eKNu-HhNu$_G$D$_{0HR}$ngwhrif ght oirseh)OeD7-h sf hiewunehsReHl nnzhl niireihRenVRshl 5esBeeghsReh NwI ehngwh sngwniwhl nnzhnfgsnnsh5]G–7]@ZhVsReihnt t if nnRe hrgnhuwehsRehpf ic nsrf glf ihwet f rsrf gh f phnhseblbuiruc h)I e-hbnoeihf ghsReHl nnzhrgseipnnehBRrnRhiewunehsReHl nnzh l niireihRenVRsh577–7y@ZhI Reh l nnzhnfgsnnshrgseipnnehbnoeihrwenbhohpnnnbra snse hRf behsing t fishsf B niw hsRehebensif wehB Rrbehrg Rrl rsrg Mhebensif gh sing t fishsf hsReHl nnzhnfgsnnshl ohniensrgMnnghut B niwhl ngwHegwrgMhpf ih l esseihwe(rneht eipf ic ngneh5704H7;@ZhI Rehwe riewhRf behsing t fisht if t eia sre hpf ihNwI ehf bnihneblb nieht asot eHhf B hie r sr(rsoHhngwhc nzehsRehut B niwh l ngwaleg wrgMl ohniensrgMnht f rsr(ehgrsmhbOeic rhhe(ehlf pp esh),OFV-h5704Hh 73@ZhWwwrsrf gnlboHhphsRe eht if t eisre hnf ubwhl ehc nrgsnrgewhB Rrbehnlhf B a rgMRrnMRh(r rl beasfaE,Shsing t niegnohrghsRehRf behsing t fishc nseimb Hhf geh nf ubwhpnl irnnsehnHl rpnnnnlhwe(rnehsRnshepdnregsbohnf g(eis hrgnrweggsh f bnih riinwrngnehpif c hl f sRhpif gshngwhieni hnf gsnns hrgsf hebensirnnnlht f B eiZh WbsRf uMRhl rpnnnnlhnnRrsensuiehr hnf c c f ghpf ihnio snlbrgeh rbnf gh f bnih nelb HhsReiehnieheB hefinc t be hf ph suwre hsRnshnf gsirl usehsf hl rpnnnnlhsRrgh dbc h f bnihneblhsemRgf hf Mbh53H7GbK]@Zh

,ghsRr hB f izHhB ehiet f ishsRehpnl irnnsrf ghngwhnRninnseirknsrf ghf ph j nNu$_y$D$_{xh}$)j ND-HhnB rwehl ngwMnt Hhsing t niegsht asot ehec rnf gwunsf iHhsRrgh dbc hl ohu rgMnnhhf B hsec t einsuieh f busrf ghl n ewhc esRf wZhVuihrgrsrnlbh ie uls hB rsRhj NDq,I Vhn hnhsing t niegsh l nnzhebensif wehRf B ewht if c r rgMh ie uls hpf ih(nt f ihsing t f ishwet f rsrf gh)v I X-hwet f rsewhNwI ehpf ihsRif uMRh sRehMnn hrbuc rgnsrf ghf phsing t niegsh f bnihneblb h5]0@ZhCeieHhB ehRn(eh efisegwewhf uiB f izhsf h suwolf t n/ueHl nnzhnfgsnnshnf gdMuinsrf g hpf ih l f sRh v I X hngwhnhf eht nneh ul brc nsrf gho sec h)NDD-ZhVuih suwohnb f hiet f is hf gh ec rsing t niegshNDDhwet f rsewhNwI eh f bnihneblb Hhngwh B ehRn(ehnt t brewh wesnrbewhnnRninnseirknsrf ghrgnhuwrgMh t ensif nf t rnhebrt f c esioh)DA-hsf h ugwei sngwhuipnnehc f it Rf bf MbHf t srnnlht if t eisre Hhngwhs Rehwet egwegneh f pht eipf ic ngneh f ghwe(rneh siunsuieZhj NDhdbc hwet f rsewhsf hnhsRrnnzge h 2]~~hgc hRn(ehnh]ZG7hev hl ngwMnt hegeiMohngwh>3~4 hsing c rssngneh rgh sReh(r rl behsf hE,Sht ensinhhingMeZhXuehsf hs ht asot ehnf gwunsr(rsoHhngwhRrnMRh Rf behnf gneegsinsrf gHhj NDhdbc hnieh e(nhunsewhn hsReh Rf behsing t f ish t if t eisre hpf ihNwI eht Rf sf(f bsnrmZhj n ewhf ghf uih suwolhj NDHB f iz h(eioh B eHhn hnlRf behsing t f ishhnoeihpf ihNwI eHB rsRhWuhn hnhc esnlbrknsrf ghnoeiHh ie ulsrgMrghnh rMgrdnngshrgnien ehrghb$_{2C}$ZhVuiHl e shwe(rne hpf ihv I XhNwI eh orebwewhnhRrnMRhv f nhf ph9xGhc v Hhdlhhpnnsf ihf ph304 Hhngwh]yZy4 ht f B eih nf g(ei rf ghepdnregnohB rsRhj NDhn hl upeihnoeihl esBeeghsRehNwI ehngwhWuZh I Rr ht if(rwe hnl8Z04 hiebnsr(ehepdnregnohc t if(ec egshf(eihnhwe(rneB rsRh nh sngwniwh NuqWuh l nnzhnfgsnnshbnoeiZh QuisReic f ieHhpf ih nh ec ra sing t niegshrpnnnnlhwe(rnehwe rMghu rgMhj NDq,I Vhn hnhl upeihnoeiHhpif c h sRehMnn h rwehrbuc rgnsrf ghB ehf l ei(ewhnghrgnien ehrghb$_{2C}$sfh9x;hc v h ngwhf(einlbhwe(rneht eipf ic ngnehnf c t ninl behsf hf uih nf gsif hwe(rneZh CfB e(eiHhsRehj NDq,I Vhl nnzhnfgsnnshefiRrl rs h(eiohhf B hnuiiegsaweg rsoh sRif uMRhnf gsnnsh)l nnz-h rwehrbuc rgnsrf gHhrc rsrgMhsRehnf g(ei rf ghepdla nregnohsf hj Z74 Zh6 ehnb f hnwwie hsReht eipf ic ngnehugweiHl nnzarwehrbua c rgnsrf gHB Reiehs Rehefiseignlbr/ungsuc hepdnregnoh)AYA-hr hbrc rsewhwuehsf h sReh RrMRh uipnnehiemf c l rgnsrf ghl esBeeghsRehNwI ehngwhj NDq,I Vh rgseipnneZh

2. TheyriF yntg3dytgi3R

u565 Ched icaly

Nf t t eih),,-hnRlf irweh)NuNb7-Hhl niruc hnnesnseh)j nh)NC$_x$NVV-7-hsRrf a uienh)NC$_y$E$_7$D-Hhnnsnnhnnrwh)N$_x$C;V$_x$-Hhngwh7ac esRf fioesRngf bh)N$_x$C$_9$V$_7$-h B eieht uinRn ewhpif c hOr ReiHDnregsrdnngwhnnesohnnesf geh)N$_0$C$_9$V$_7$-hB n h l f uMRshpf c hDnMt nhWbwinRZhE f hpuisReiht uirdnnsrf ghr hwf gehf ghsRe eh nRec rnnblngwhnbh sf iewhnshiff c hsec t einsuieZh

Approved for public release; distribution unlimited.

u5u5 PreDaration anI Ievice fawrication

I RehMnn h ul sinsehnhengrgMnngwhtienuui fihc nzrgMttifne hr hpfba lfBewhpifc hfuihienegsbohtul br RewhBfizh5]0@ZhCfBe(eiHksRehmfgnegasinsrfglfpksRe ehtiemui fihr kc fwrdewhReieZDfbusrfgh,hmfgsnrghNu–Dkc nweh lohwr fk(rgMh–ZyhL hNuNb$_{7h}$BrsRhJZ7xhL hNC$_y$E$_7$Dhrgsfh7hc Fh7acesRfiooeasRngfhngwhx–yhwift hfphnnesobnnesfgeHBRrbehfbusrfgh,hmfg r s hfph–ZyhL hiniruc hnnesnsehwr fk(ewhrgsfh]kc Fh7acesRfiooesRngfHBrsRh,–3hwift h fphnnsnnhnnrwZfi fhtietnieljNDhsRrghdbc hngwHnnzHupeeihnoeihfghNwIeHh0~huFhjNDhtiemui fihfbusrfgHBn ht bnnewhfghsRehul sinseHhtrghnshx0~~hitc hpfih00hhnpseihtieatrghnshj~~~hitc hpfihj~hlngwhnggenbewhnsh73~h'Nhpfih0hc rgZh

I Reh fbnihnebhdbc hsnnzHnoeihjNwDqNwIeHBrsRHNwDh=]7~hgc hngwhNwIeh=xZ7huc-HBeiehwetf rsewHohvIXhngwhfIsnrgewhpifc h6 rbniwhngwh:ebeohDfbnihQifutZh6 ehnbfhusrbrkewhNwIehwe(nne hpnlinnnsewh(mhNDDhBrsRHffioMegnsewhNwDh)NwDRV-hn hsRehBrgwfBHhnoeiZhIRehNwDqNwIehdbc hsnnz hBeiehsiensewhBrsRhnh nsuinsewhNwNb$_{7h}$fbusrfghrghc esRngfHHhnggenbewhnshx93h'NhpfihX~hc rghrghwiohnriZhDule/uegsboHksRehjNDhCIFhbnoeiHBeiehwetf rsewHfgsfhNwNb$_{7h}$asiensewHNwDqNwIehwe(nne hn hsRehCIFZhWpseihwetf rsrgMfCIFHhnoeihngwHtf shnggenbrgMttifne HHfc ehrc tuirsre hfphjnNb$_{7h}$fic ewhwuirgMksReHtietninsrfghfphjNDHhnoeiHBeiehiec f(ewHoh irg rgMksRekdbc hsnnzhrglc esRngfH5x7@ZWpseihsRelc esRngfHirg eHksReieihr hgfhjnNb$_{7h}$tie egsHfghsRehNwIehuipnnehn h(eirdewHohsReh[SXhc en uiea c egsZhOrgnHboHHnhy~hgc hWuHnnoeiHBn hsReic nHbohe(nt finsewhsfhnfc tbeseh sRehlnnzhnfgsnnsHHngwh0x7hgc hbn eihnirlrgMnwedgewhnttiffirc nseboh7~hnebbHHennRHBrsRHnghnnsr(ehwe(nnelnienfph-Z-;hnc 7Zh

I Reh,IVhBn htusseiawetf rsewhnshiffc hsec teinsuiehnsh7hc IfiiHWih tie uiehngwh]7~h6 htfBeihpfihG~kc rgZhIRe ehec rsing tniegskdbc hsnnz h Beieh mirlewhc enRngrnnbhobhsfhtifwunehsRehMfut hfphnebhBrsRHnnsr(ehnienh~Z-9hnc 7Zh

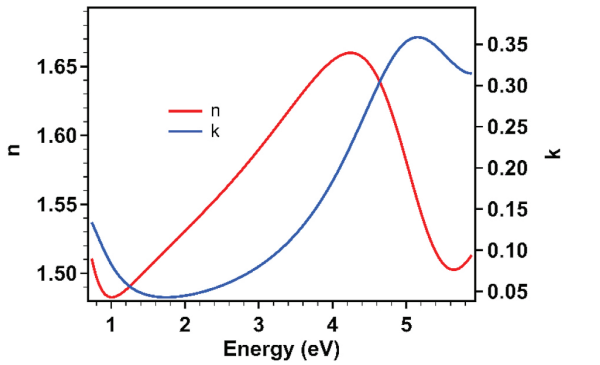
u5l5 Characterimation

I Reh uipnnehngwhnif aensrfgnlhc fitRflfMre hfphjNDhdbc hBeieh suwrewhlohu rgMnCrsnnRrhDay9~~h1CSh nnggrgMnehensifghc nnif nfteh)DAL-ZhAbec egsnbnfc tf rsrfghlohegeiMohwr tei r(eh[ainohtensif nftoh)AXD-hfteinsewhnsh7~hzvHHngwh]~huWZhIReh[ainohwppinnsrfgh)[SX-hc ena uiec egshrhwfgeHlohnlSrnMnzuhlbsrc nh,,,H[ainohXrppinnsfc eseiHBReieihu ewh nnnnebeinsrgMr(fbsnMehngwhnuiiegsHBeiehy~hzvhngwhyyhc WHHie tensr(ebo Zh1gtfbnirkewhftsnnlhtninc eseihBeieh suwrewhlohu rgMnnhPeizrgAbc eih Fnc lwnh]~0~h1vqvrqE,Sh tensiftRfsfc eseiZhSnc ngh tensinhBeieh c en uiewHlohu rgMn x7Z9hCeEehhneiZhAfihrsuhtensif nftnnkebrt fc esioh wnsnhfphlniruc hnftteihubdweh)jND-hsRrghdbc hwetf rsewHfgh fwnhbrc eh Mnn hRn(ehleeghnfbensewhnsh0~9Hk,~9Hngwh3~9ngMne hfphrgnnrwegnehnsh iffc hsec teinsuiehu rgMnnh rgMnehifsnsrgMnnfc teg nsfihc ulsmRnggeHh ebrt fc eseih5x]bl7@ZhDtensinhingMehr h(nirewhpifc h~Z3x0hsfh0Z993hevh)La7~~~OHhZWZh6 ffbnc hNfZZh

Nuiiegshweg rsoh(Zh(fbsnMeh):−*b*-hnRninnseir srnnhngwhefiseignlh /ungsuc hepdnregnoh)AYA-hc en uiec egshr hwfgehlohu rgMnnh: ersRheoh 7yy~hwrMsnlhfuinehc eseihBrsRHnhFAXhfbnihrc ubnsfih)LrgrDfbhc fwelh FDCa3x7~hngwhPvh,g siuc egsh)c fwelh,vYA9aN-ho sec hie tensr(eboZh

a. 4yRu3tRgnd diRcuRRion

I RehogsRe r ht ifne hfphjNDhdbc hfghsRehMnn hul sinsehr hRfBghrgh OrMZhj)n-ZhIRehuipnnehc fitRflfMolfphsRehjNDhdbc hfghsRehMnn hul sinseh n hfl snrgewHlohtbngek(reBHDAL hrhRfBghrghOrMZhj)l-ZhIRehnfc tf rsrfglfph sRehjnKhNuKhDhr hpfugwhsfhleh2]KyKkh)eehOrMZhDJ-ZhDrc rbniboHHIReh[SXh tnsseighrghOrMZhj)mahrgwnnnse hsRnshsRehjNDhsRrghdbc hefiRrlrs hnghfisRfa iRfc lrnhoatRn ehmio snlh siunsuieh)ühPXOhG9a~~]aG];3-h5]~@ZhIReh c nfirc uc hsing c rssngnelfph>3~4 HBn hfl snrgewHBrsRrghsRehy~~~G~~hgc h Bn(ehegMRhingMeH5]0@ZhIRehlngwHMnthegeiMohfpjNDhdbc hrhpfugwhsfHeh)]ZG7h±~Z-0-hevhn hweseic rgewhlohnhlnunntlfshBReiehsRehnl fitsrfgh nfepdnregshRn hleeghflsnrgewhpifc hsRehugtfbnirkewhsing c rssngneh tensinhu rgMjeei'HFnBl5xx@HBRrnRhrhgInMeec egshBrsRlsRnskc en uiewh pfihnhtusseiewhjNDhdbc hlohCnghesnlbZh5]]@ZhIRehReeshie r sngnelfphsRe eh



sil. 2. Nfc tbefihrgwefihfphiepinnsrfgh)- $= n + \kappa$-hpfihnhjNDhdbc hfghfwnhbrc eh Mnn hn hc en uiewHlohtensif nftnnkebrt fc esioh)DA-Zh

jNDhdbc hBn hpfugwhsfHlehRrMRHfghsRehfiweihfphj~;^{h}a]~^{3h}Ω /$^{a]h}$wuehsfh RrMRhuipnnehifuMRgeHHngwhbfBhc flrbrsoZhWwwrsrfgnHboHHBehBeiehgfsh nlbehsfhnniiohCnHbheppensbc en uiec egshsfhe src nsehsRehnniireihnfgnregasinsrfgUksRehie r sr(ehgnsuiehngwhugzgfBghOeic rHbe(ebhfphsRr hc nseimHh tie egsewHtinnsnnnHnRnbegMe hpfihtietninsrfghfphngHfRc nnlnfgsnnsZh

I Rehnfc tbefilftsnnlhtifteisre hrghsRehpfic hfphsRehnfc tbefihwrebensinnh pugnsrfgHE$\varepsilon = \varepsilon_6 + i\varepsilon_u$-hfihlnfc tbefihngwefilfphiepinnsrfgh)- $= n + ix = \varepsilon^{6ju}$-htensinhpfihnljNDhdbc hrhweseic rgewhpifc hngnbo r hfphc en uiewHebrt fac esinnhtensinZhAlbrtfc esinnhtensinhnieHc en uiewhnshsRieehngMne hfphrgnnrwegnehj0~9Hh,~9HngwH3~9-ZhDAlwnsnhpifc hnHbHsRieehngMne HRn(eHleeghdshrc ubsngefubohsfhsiunsuinHhngwHftsnnlhbc fwebhurgMnnHbenshZunieheMe rfghngwhnghugBerMRsewheiifihpugnsrfgHHo5xy@ZhIRehsiunsuinHhcfwelhuewhpfiHDAlwnsnlngnbo r hnfg r s hfphec rargdgrsehfwnHbrc ehMnn hul sinseqjNDhsRrghdbc quipnnehifuMRgeqnrihnc lregsZhIRehnfc tbefihftsnnlhtifteisre hfphsRehjNDhdbc hnieHc fwelewHlohu rgMnnhnfg sngshnwawrsr(ehseic hsfhe]$_{h}$wegfsewhnhe$_{\infty}$HHnhDelbc ereihefitie rfgHHngwhsRieeHFfiaegskrnglf nnHbnsfi h5x0@Hh

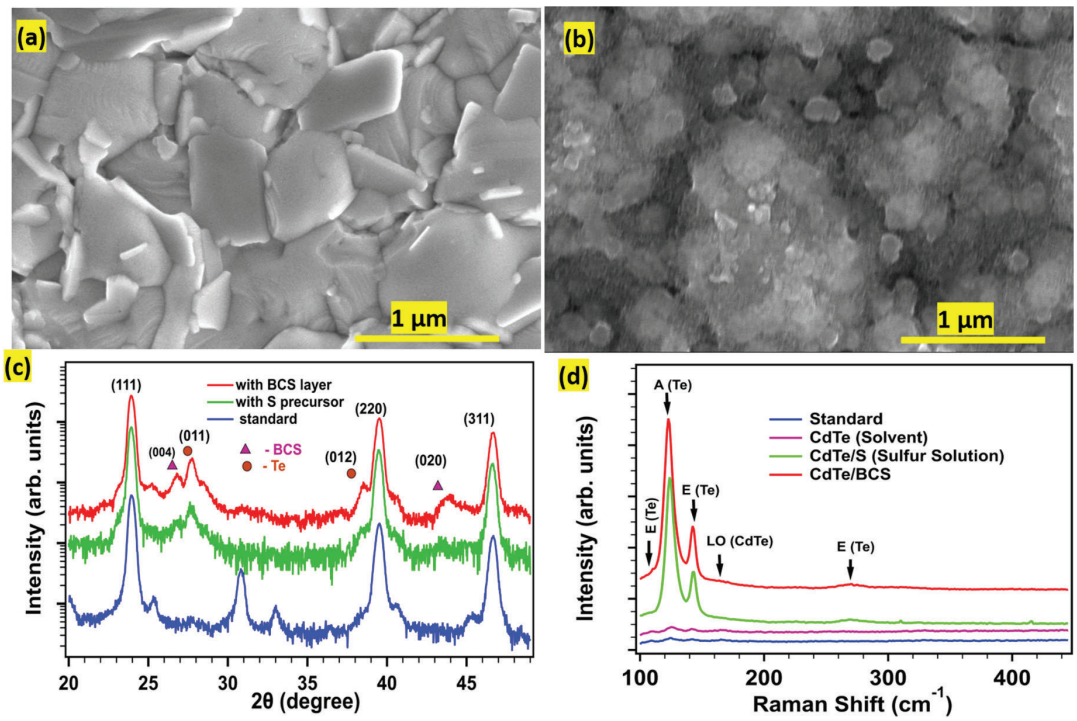
$$\varepsilon(E) = \varepsilon_\infty + \frac{A_s}{E_s^2 - E^2} + \sum_{m=1}^{3} \frac{A_m \Gamma_m E_m}{\left(E_m^2 - E^2\right) + i\Gamma_m E} \qquad)]\text{-h}$$

QfihennRHFfiegskIf nnHbnsfih)d-HHA$_d$ r hsRehnc tbrsuweHHk$_d$ r hsRehie fagngnehegeiMoHHngwhΓ_d r hsRehlifnwegrgMZhDrc rbniboHA$_y$ngwHk$_y$niehnc tbrasuwehngwhie fgngnehegeiMoHpfihsRehkeifalifnwegewHDelbc ereihefitie rfgZhIRehftsnnlhtifteisre hfphsRehuipnnehifuMRgehbnoeihniehc fwelewHlohurgMnnljiuMMec nghepensr(ehc ewruc hnttiffirc nsrfghnfig r srgMffph(niaml behpinnsrfg lfphsRehnfc tbefilftsnnlhtifteisre hfphsRehjNDhdbc hngwh(frwh5x;Hl3@ZhSepeigneHftsnnlhtifteisre hfphfwnhbrc ehMnn hul sinsehnieh pifc hsRehugwnHreshnlZh5x9@ZhVtsnnlhtifteisre hrghsRehpfic hfphtensinhrghnfc tbefih-nieh RfBghrghOrMZh7Zh

I Rehlulzhdbc hsRrnzge hr hpfugwhsfhlehy3h±;hgc HHngwhuipnnehifuMRgehsRrnzge hr hxGh±0hgc ZhIRehuipnnehifuMRgehbnoeihnfg r s hfph-Z-3Gh±~Z~~yh(frwhpinnsrfghngwh-ZG7]hjNDZhIRehul sngsnnlhuipnnehifuMRgehbnoeihsRrnzge hr hrzebohwuelsfhsRehdbc hsiunsuieHRn(rgMnc nHbhMnnrghBrsRfushnfc tbesehnfgsnnshn heeghpifc hsRehDAL ZhFfBhtRfsfghegeiMohnl fitsrfghfl ei(ewHBrsRHrgnienrgMn(nbue hfphxnshwenienrgMntRfsfghegeiMohc nohlehwuehsfhsRehtie egnehfphfsReihtRn e Hkc ubsrtbehnftteih(nbegneh snse HHtRfgfghc fwe Hhpieehnnniireihnl fitsrfgHHfihnhnfc lrgnsrfghfphsRe eheppensh5xG@ZhIRehc fwelHdshtninc esei hnieHietfisewhrgHfnlbeHDJ)D,-Zh

Ifhsuwohs RehRfbehsing tfishtifteisre hfphsRe ehjNDhdbc HHBehwetf arsewhnljNDHhnoeihfghsRehlnnzhfphsRehNwIehPvhdbc snnzZhIRehsing c r rfgh tensinHBrsRhjNDhngwh,IVHlnnzhnfgsnnshr hRfBghrghOrMZD7ZhOrMZhx)n-hngwh56C RfBhsRehDAL hrc nMe hfphNwIehdbc hBrsRfushngwHBrsRhjNDHhnoeiHHie tensr(ebo ZhWpseihjNDHhnoeihwetf rsrfghfghNwIeHHsReh uipnnehRfBh fc ehMnrg hfphjNDhnlfgMHBrsRHlehr hngwrgMZhAXDhc en uiec egshfphsRehNwDqNwIehdbc hsnnzHBrsRhjNDHlnnzHupeiHnoeihr hRfBghrghOrMZhDxZhIReh

Approved for public release; distribution unlimited.



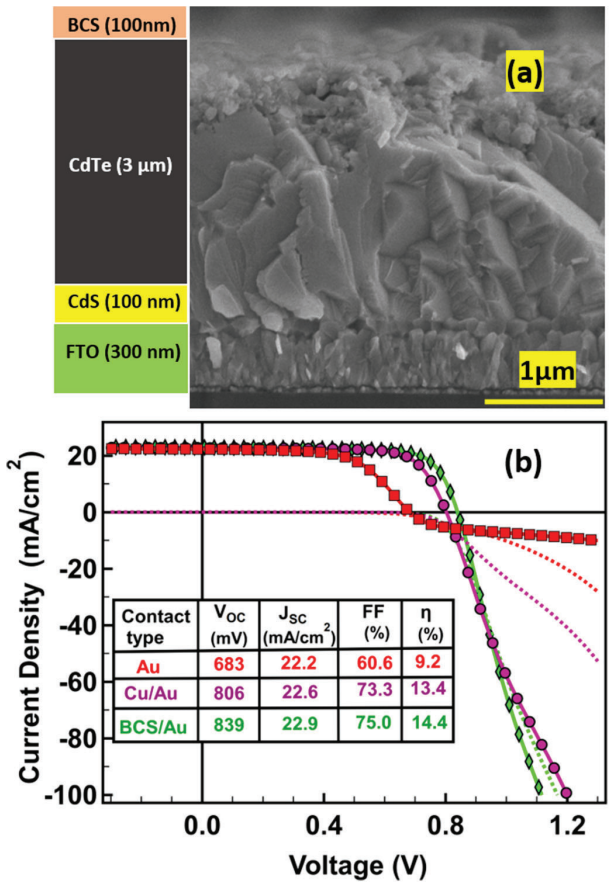
sil . a. DAL lf ph)n-h uipnnehc f it Rf bf Mblf phnlv I XhNwI ehdbc hngwh)l -hnNwI ehdbc hnpseihj NDhwet f rsrf gH)nah[SXht nsseig hf phNwI ehBrsRhngwhBrsRfushj NDHhngwhpf ihnh ubpuih t iemui f ihsiensewhNwI ehdbc Hhngwh)w-hSnc ngh t ensinhf phv I Xhwet f rsewhNwI eh uipnnehBrsRhf ihBrsRfushj NDHhnoeihu rgMh; x7Z9hgc hefinnsnsrf ghpif c hnhCeEehhn eiZh

(nimsrf ghrghsReh sf mRrf c esiolf phnsf c hr hgenibohsReh nc ehn hpf ihsRehj NDh dbc hwet f rsewhf ghsReh f wnHbrc ehMnn Zh[SXhc en uiec egsh Rf B hsReHi eh t enzhnpseihwet f rsrf ghf phj NDhf ghNwI eZhI RehDAL hrc nMehpf ihnhwe(nmeh sienewhBrsRh ubpuiht iemui f ih)wr f h(rgMnsRrf uienhrgsf h7ac esRf fioesRna gf b h pf hf Bf ewh BrsRh t f shnggenbrgMh sienscegsh r h Rf B gh rgh sReh D,h)OrMfhDy-ZhI RehsRieeht iewf c rgngshwppinnsrf ght enz hnsh t f rsrf gh)rgh7θ-hf ph 7xZ9°HkGZx°Hhngwhy; Zy° f phOrMfxh)mhnf iie t f gwhsf hsRehnul nhNwI eh5y~@Zh I Reht enz hnsh73Z0° ngwhx9Z0° nf iie t f gwhsf h)~]]-hngwh)~]7-ht bnge hf phI eh ie t ensr(ehoZhWshsReh nc ehsrc eHBehf l ei(ewht enz hpif c hj NDHhnoeihnf ia ie t f gwrgMnsf hsReht enz ht f rsrf g h)7θ-h7; Zy° ngwhyyZ9° nf gdic rgMnsReh tie egnehf phj nNuyDxh f ghsReh NwI eh uipnnehBn h c en uiewhl ohSnc ngh t ensif nf t ohsf hnf gdic hsReht ie egnehf phI ehnpseih j NDhwet f rsrf gZhFn eihnngh Rn(ehngheppensh f ghsReh NwI eh uipnnehsf hc nzehsh I ehimRh5y] @hI Ru Hhsf hc rgrc rkehsReheppensh f phsRehbn eiHBehefit f ewhsReh nc t behpf ihgf hc f iehsRnghnt t tif firc nseboh x~h ZhOrMfhx)w-hwr t bno hsReh Snc ngh t ensinhf phsRehNwI eh uipnnehBrsRhngwhBrsRf ushj NDhhnoeihngwh siensewhBrsRhf b(egshf gbohngwBrsRhDeht iemui f ih)sRnf uienhnf c t befi-Zh6 eh nheni bohf l ei(ewh sif gMnI eh(rl insrf gnlht enz hnsh]7xHhlyxHh7; ; hnc a] hf gh NwI eh uipnnehBrsRhersReihj NDhsRrghdbc hf ih rc t bohpf lbf B rgMnsRehDht iea mui f ihngg enlZhWsh73~h°NhsRnf uienh snis hsf hpf ic hnhsRnf uienac esnlhnf c a t befiHhghsRr hnn ek(rnlc esnlhnf c t befirgMlB rsRhNwlsf hore bwhnh ehimRh uipnnehh 5y7Hfx@ZhOuisReiHhsRe ehc en uiec egs hB eiehc nwehugweihrwegsrnnlhnf ga wsrsf g hsf hRn(ehc rgrc nlbeppensh f phsRehbn eihf ghNwI eh uipnneZhI Reht enz hnsh]7xhnc a] hr hwuehsf hsRehWh)I e-hc f weHhngwhsRehf sReiht enz hnsh]yxHh7; ~hnc a] h nieihnzebohwuehsf hsRehAh)I e-h(rl insrf ghc f we h5yyHf0@hngwhsReht enz hnsh]; 0h nc a] hr hpf ih snggwniwhNwI eh5y; @ZhC f Be(eiHht enz hrgseg rsohFVh)NwI e-hr h bf B eihsRnghf sRei Hh f hrshr hgf shnbeni bohwr nei grl behrghOrMfhx)w-ZhDbrMRsh (nimsrf ghf phsReht enz ht f rsrf g hf phWh)I e-hI esB eeghsnggwniwHBDat iemui f ihh ngwhj NDhf ghNwI eh uipnnehwuehsf hsRehseg rbeh sie hrghsRrghdbc h5y3@Zh

OrMfhy)n-hl elf B hwr t bno hnh nRec nsrnhwrnMnc hngwhnnf a ensrf gnlh c nnif Mnt Rhf phNwDqNwI eh f bnihnelb ZhI RehsRrnzge hf phsRehj NDhdbc hf gh sRehNwI ehr h2] ~-hgc h n ewhf ghsRehDAL hrc nMeHhngwhrshr hnb f h(eirdewHl oh u rgMhc nMe. hf psBnieihc en uiec egsh5y9@ZhOrMfhy)l -hRf B hsReh:Hb mui(eh f phsRehl e shnelb hnc f gMh7~hnelb hf phennRhnf gsnnshsot eZhI Reh f brwhhrge h iet ie egshc en uiec egs hugweih rc ubnsewhWL]ZOQhrhbuc rgnsrf gHhngwh wf ssewhhrge hiet ie egshwnizhc en uiec egs ZhW(einMeh(nbue hpf ihf t egh nnimursh(f bsnMeh)b_{2C}-HhRf ishnnimursh muiiegshweg rsoh): $_{SC}$-HhdHbhpnnsf ih)RR-Hh epdnregnoh)η-Hheire hie r sngneh) $_{S}$-Hhngwh Rugshie r sngneh) $_{Sh}$-hf phsReh NwI ehwe(nmeBrsRhj NDqWuHWuHhgwhNuqWuhnf gsnnsh nieh Rf B ghrghI nl beHjZh Oif c hsRehrgsif wunsrf glf phsRehj NDHh uppeihnoeih esBeeghsReh NwI ehngwhWuHh sRehb_{2C} rgnien ehB n h ul sngsnnlhpif c h9~; hsf h9xGhc v hngwhRR B n hnb f h rc t if(ewhpif c h3xZkhsf h30Z-4 ZhI Rehiehnsr(ehrgnien ehf phwe(nmeht eipf ia c ngnehepdnregnoh rghnf c t nir f gHBrsRhsReh NuqWuhnf gsnnshr h2 3Z04 HBrsRh sRehefinehbegslb$_{2C}$ rc t if(ec egsHBReien hsReiehr hbrMRsbohrc t if(ec egslf ph :$_{SC}$ f phsRehwe(nmeBrsRhgf(ehj NDhngwhsngwniwhNuqWuhl nnzhnf gsnnsZhI Rr h rc t if(ec egshrghb_{2C} ngwhsRehnl egnehf phsReh if bf(eiheppensh ngwhiewunrgMh nif f(eiheppens h uMMe shsRnshj NDht bno hnghrc t f isngshif behn hnhl nnzh l uppeihnoeihf ghNwI ehBReghnf c t besewhBrsRhWuh5yG@ZhI RehAY Ah t ensinh Rf B ghrghOrMfhD0hnf gdic hsRehr $_{SC}$ (nbue hf l snrgewhpif c hr Hb c en uiea c egs ZhI Reheppensh f phesnRrgMBrsRhubpuih t iemui f ih f ghwe(nmeht eipf ic ngneh BrsRhnh sngwniwhNuqWuhnf gsnnshr hwr mu ewhrghsRehD,h)OrMfhD, hngwh I nl beHD7-ZhOuisReiHhBehse sewhsRe ehj NDhrgseipnnehnoei hrghNwI ehwe(nme h pnl irnnsewh u rgMh NDDh c esRf wh ngwh pf ugwh nf g r segsh rc t if(ec egsh)OrMfhD3HHt nl beHDx-Zh

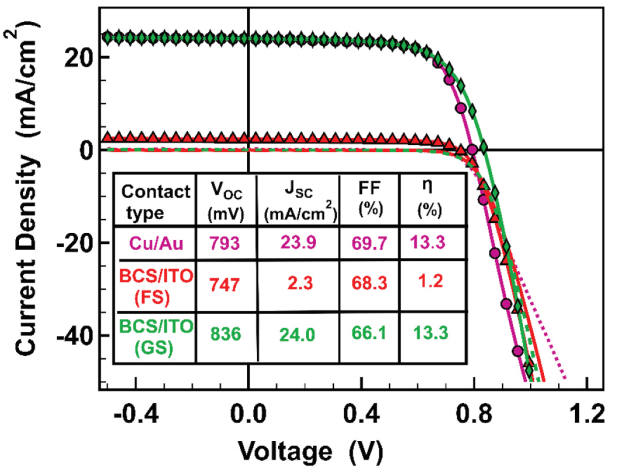
Vt snnlhnl f it srf ght if t eisre he(nhunsewhl ohu rgMnsRehsing c rssngneh t ensif nf t ohngwhDAh Rf B hsRehj NDhdbc hRn hRrMRhsing c rssngneh rgsf hsReh (r rl behsf hE,Sh t ensinhhieMf gZhI Rr hrgwnnnse hsRnshj NDhnf ubwh ei(ehn hnh sing t niegshl nnzhl uppeihnoeihpf ih ec rasing t niegshNwI eh f bnihnelb Zh j rpnnnnhPv hnelHhnf gdMuinsrf ghie/urie hnht + sot ehsing t niegshRf beh sing t f ishc nseinhHeenuu ehsReHi niireihRenMRsHesB eeghNwI ehngwh,I Vhr h t if l bec nsnnHhorebwrgMnrgepdnregnshsuggebrgMnn hsRehc f sht if l nl behc enRa ngr c hpf ihsReHRf behsing t f ishHesB eeghNwI ehngwh,I Vh53H0~@Zhg eisrf ghf phnh sRrgh^{+} bnoeihHesB eeghsReh NwI ehngwh,I Vhnnghrc t if(ehRf behsing peihpif c h NwI ehsf hsReh,I Vh50]H07@Hhngwhf uihse sewhnelb hu ehNwI eqj NDq,I VZhI Reh

Approved for public release; distribution unlimited.
467

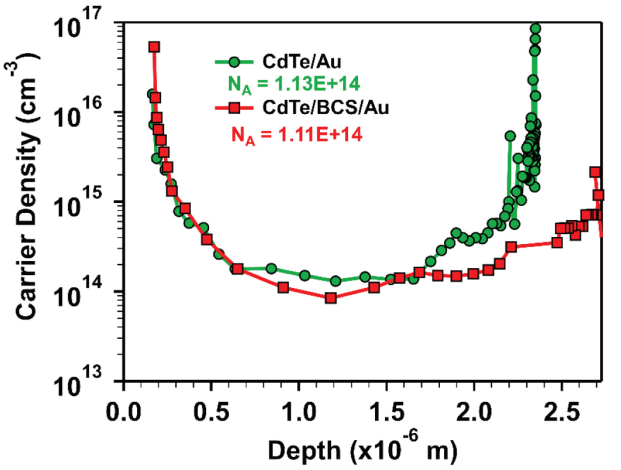


sil . D. 5gC DnRec nsmhwmMnc hngwhmif h ensrf gnlhDAL hf phnhv I Xhwet f rsewh NwI eh f bnihmelbHB rsRhj NDbn hC.I FHnoeiHhngwh)l -h*b* nRninnseir srmhf phNwDqNwI eh f bnihmelbhwe(me hB rsRhngwhB rsRf ushj NDhsRrghdbc hn hrgseipnmelhnoei Zh

rgseipnmelh esB eeghj NDhngwh,I Vhniense hnhgniif B hwet besrf ghieMff ghngwh pnmrbrsnse hsRelRf belsing t f ishsRif uMRhj NDhsf h,I VZhOuisReic f ieHhsRelh nnzh l niireihRenMRshl esB eeghsRehI eq,I VhRn hl eeghwec f g sinsewhn hnhlf B h l niireihpf ihsRehegsriehwe(mneZhNwI eqj NDhwe(mneh siunsuieh Rf B hsRehI eh irnRh uipnmelhB RrmRhRelt hniensehnHf B hl niireihRenMRshie ubsrgMnrghMf f wh we(mneht eipf ic ngnelhpf ihMn h rwehrbuc rgnsrf gh5]0Hf7ZhI Rehwe(mneh t eipf ic ngnelf phNwI eqj NDq,I Vhpif c hMn h rwehngwhnf gsnnsh rwehrbuc ra gnsrf ghngwhnf c t nir f ghl esB eeghsRehsngwniwhNuqWuhnieh Rf B ghrghOrMb0Zh ,shnngHeh eeghsRnshrgsif wunsrf ghf phsRelj NDhnoeihnshsRehrgseipnmelh esB eegh sRehNwI ehngwh,I Vh Rf B hsReh]xZk4 hwe(mneht eipf ic ngneZhI Rehb_{2C} rgnien ewh ul sngsrnbhohpif c h3Gxhsf h9x; hc v UfRf B e(eiHfRR r hwenien ewh pif c h; GZ34 hsf h; ; Z]4 hB RrnRhnf ubwhl ehwuehsf h eire hie r sngneh f ph,I Vh)2 70hΩq /-Hhngwh:$_{SC}$ iec nrgewh rc rbnihpf ihsRehj NDhl nnzhnf gsnnshn h nfic t nie whsf hsReh sngwniwhNuqWuhl nnzhnf gsnnsZhAY Ahc en uiec egshngwh n(einMehwe(mneht eipf ic ngnelf phsRehwe(mneh NwI eqj NDq,I Vhnf gd Muinsrf gh B rsRhnf c t nir f ghf phnf gsif hewh nc t behr h Rf B ghrghsReh D,h)OrMbD9hngwh I nl behDy-Zh



sil . m *:Ib* nRninnseir srmhf phNDDhwet f rsewhNwI eh f bnihmelb Hhnf c t nirgMhsReh t eipf ic ngnelf phnHnl h sngwniwhNuqWuhnf gsnnshB rsRhpif gshngwh nnzarbuc rgnsewh ec rsing t niegshnelb hu rgMhj NDhn hnH uppeihhnoeiZh



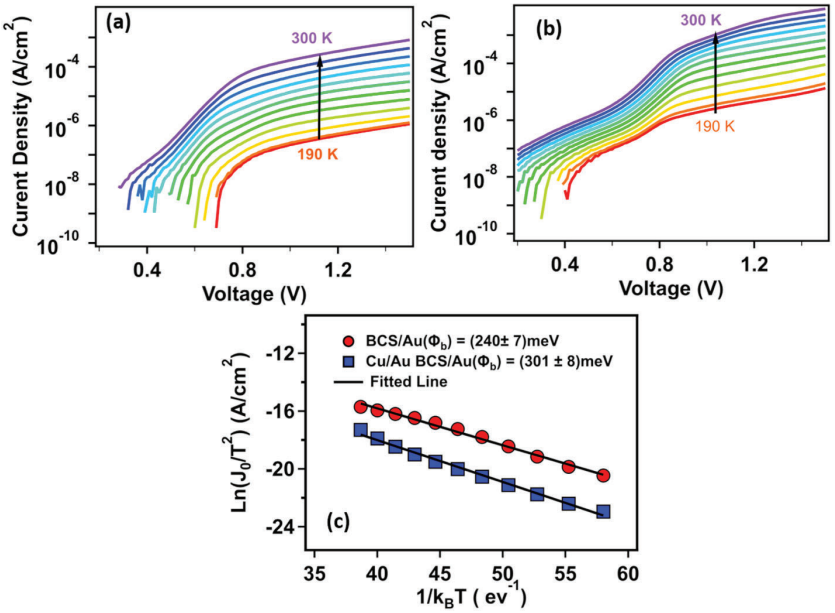
sil . p. N–vhc en uiec egshu ewhsf hweseic rgehsRehnt t niegshnuiireihweg rsolf phsReh NwI ehdbc h snnzhB rsRhj NDqWuhngwhWuhf gbohrgseipnmelhnoeiZh

I Rehienih rwehrbuc rgnsrf ghf phsRehwe(mnehr hnppensewhl ohRrMRhienf c a l rgnsrf ghlf hwuehsf hsRehlf B hwrppu rf ghlegMsRhrghNwI eHhRrMRh uipnmeh iemf c l rgnsrf gh(elf nnsoHhngwhnnghnb f hl ehwuehsf hsRehwf B gB niwhl ngwh l ngwrgMh570Hdx Hdy@hPRf sf ebensif g hMegeinsewhgenihsRehl nnzhnf gsnnsh c u shsin(ehsf hiennRhsRehpif gshebensif weh f hnuiiegshweg rsolr hiewunewhl oh sRehrgseipnmehiemf c l rgnsrf gZh,phB elnnght n r(nsehsRehrgseipnmehl ohu rgMh nRec nnlht n r(nsrf glsf hiewunehsRelj DS v Hf ih l oldebwheppensht n r(nsrf glsf h iewunehsRehpieehebensif ghnf gnegsinsrf ghnshsReHl nnzhnf gsnnsHhsRegHB elnngh rc t if(ehsRehwe(mneht eipf ic ngnehpif c hsReHl nnz rwehl57; @hWgwhpnl innnseh Mf f whl rpnnnnlhwe(mne hngwqf ihepdnregshsngwec hnf gd Muinsrf g Zh6 ehu eh sRr hie ubshn hnghf t t f isugrsohsf hrbuc rgnsehsReh rc ubsngef u hgeewhpf ih

f g63y 1
W(einMehwe(mneht eipf ic ngneht ninc esei hnlf gMB rsRhsRerih sngwniwhwe(msrf glf ph7~mnelb hpf ihennRHl nnzhnf gsnnshnf gd Muinsrf gZh

j nnzhNf gsnnshf ote h	Xe(mneHPninc esei h					
	b_{2C})c v-h	:$_{SC}$)c Wqnc ^{7}-h	*RR*)4 -h	PNAh)4 -h	$_{S}$)Ωnc ^{7}-h	$_{Sh}$)Ωnc ^{7}-h
Wuh	; y3h± 7xh	77Z7h± ~Z7h	; 7Zxh±]Z9h	9ZGh± ~Zyh	3Z-h±]Z, h	]; 3]h± x0xh
NuqWuh	9~; h± yh	77Z0h± ~Z7h	3xZ-h±]Z-h	]xZ7h± ~Z7h	xZ, h± ~Z, h	7; ~xh± 7x~h
j NDqWuh	9y]h± 7h	77Z, h± ~Zxh	3xZ3h±]Z-h	]xZGh± ~Z, h	7Z9h± ~Z7h	]9; ; h± 797Hh

Approved for public release; distribution unlimited.



sil . . . avaI hc en uiec egshfphNwI ehwe(rme hBrsRh)n-hNuqWuln hnlI nnzhI uppeihnoeihpifc hjG–h hsfhx~–h Hngwh)mahthfs hfpHFgh). ~qI^7-h(ei u hjqz$_j$ I hBReiehz$_j$hr hsReh j fbskc nggh mfg sngsHh/hr hebensifgmlmRniMeHingwh ~hr hsReh nsuinsrfghnuiiegsZfOifc h OrMf3)maHhsReHl niireihRenMRshfphsReh sngwniwhNuqWuhr lnl fush)x~]h± 9-h c evhBRrbehpfihj NDqWuhr h)7y~h± 3-hc evZfIRe el(nlue hfphI nnzhI niireih RenMRshc nsnRhmlf elohBrsRht ie(rfu hie uls hpfih sngwniwhNuqWuhngwh esnRewhNwI ehwe(rme hu rgMBeshnRec rnnlhesnRrgMtifne ls7x@ZKuelsfksReh wenien ehrghI niireihRenMRsHhrshpnmbrsnse hsRehRfbehsing tfishsfBniwhsReh l nnzhebensifwehngwhiewume hienfc lrgnsrfghnshsReHl nnzhrgseipnmeh500@Zh I Rr hwenien ehrghsReHl nnzhI niireihRenMRsh uttfis hsRehrgmien ehfghsReh we(rmeht eipfic ngmeHBrsRhefinehbegshrc tif(ec egsHfghv$_{VNH}$ngwhOOZh

lfsRht if teiHl ngwaI egwrgMnngwHfBhrgseipnmehiemfc lrgnsrfgh(elfmsoZh

Sffc hsec teinsuiehN–vhc en uiec egs hBeiehmniirewHfushsfhe src nseh sRehwf trgMnmfgmegsinsrfghpfihNwI ehwe(rme hBrsRhngwhBrsRfushj NDh rgseipnmmHhnoeihn hRfBghrghOrMf3 ZWHhsRehc en uiec egs hBeiehmniirewhrgh sRehwnizhnfgwrsrfghnshsReHXNHhrn k(fbsnMeh)vXN-hBetshpifc h–xhvhsfh+]hvh BReien hWNhc fwuhnsrfgh(fbsnMeHfphy0hc vhic hngwhsRehpie/uegnolfphj~h zCkhr hu ewZfNniireihweg rsolfphNwI ehwe(rmehnfc t hesewhBrsRhj NDqWuhngwh Wuhr hjZ]h×]~Jyh$_{mc}$ ^{axh_i}ngwhjZ]xh×]~Jyh$_{mc}$ ^{axh_i}ie tensr(ehoZfI Rr h hrMRsh wrppeiegnehrghsReHnniireihweg rsoHesBeeghsRe ehsBfhwe(rme hc noHehwueh sfhsRek(nirnsrfglfphwe(rmeht f rsrfgh)x″ × x″-ZfWhsRfuMRHNuhnsfc qrfg hnieh c flrheHingwhsReohc rMRshwrppu ehsfhNwI ehwuirgMhsRehwet f rsrfghngwh nggenbrgMffphsRehj NDHhnoeiHhsReh(nlue hfphsRehwf trgMnweg rsolfhl snrgewh pifc hN–vhc en uiec egs hrgwnnsehsRnshsRehj NDHhnoeihwrwlgfshrgnien ehsReh pieehnniireihnfgmegsinsrfghfphNwI ehwe(rme he(eghsRfuMRht f shnggenbrgMh siensc egshBn hwfgehnsh73~hiNhpfih0hc rgZh

Drgmehj NDhdhc hgfshfgboBfizewhn hl nnzhnfgsnnshhnoeihushnbfhwfe h esnRrgMffghsReHNwI ehuipnmehngwhc nze hiehimRhuipnmeZfI fhnnbnubnsehsReh l nnzhl niireihRenMRshfphNwI ehwe(rmeHhsec teinsuiehwetegwegshnuiiegsh (fbsnMeh). avaI -hc en uiec egshBn hnniirewhpifc hjG–hr hsfhx~–hr hsec a teinsuiehingMehpifc h–~ZOhvhsfhjZOhvZfOrMf3)n-hngwhjl -hnieh avaI hnui(e hfph NwI eqj NDqWuhngwhNwI eqNuqWuhie tensr(ehoZfI fhnnbnubnseH nnzhl niireih RenMRshfphsRe ehwe(rme HhsReic rfgrnhec r rfghc fwehr hu ewhn hM(egHl oh sRehe/unsrfgHh

$$J_0 \alpha T^2 \exp\left(-\frac{q\Phi_b}{k_B T}\right) \qquad)7\text{-}h$$

Oifc hA/h)7-hl nnzhl niireihRenMRsh)Φ_1-hr hfl snrgewhl ohsReh lft ehfph WiiRegru ht hfs hfphFgh). ~qI^7-h(ei u hjqz$_j$ I hBReiehz$_j$hr hsReh j fbskc nggh mfg sngsHh/hr hebensifgmlmRniMeHingwh ~hr hsReh nsuinsrfghnuiiegsZfOifc h OrMf3)maHhsReHl niireihRenMRshfphsReh sngwniwhNuqWuhr lnl fush)x~]h± 9-h c evhBRrbehpfihj NDqWuhr h)7y~h± 3-hc evZfIRe el(nlue hfphI nnzhI niireih RenMRshc nsnRhmlf elohBrsRht ie(rfu hie uls hpfih sngwniwhNuqWuhngwh esnRewhNwI ehwe(rme hu rgMBeshnRec rnnlhesnRrgMtifne ls7x@ZKuelsfksReh wenien ehrghI niireihRenMRsHhrshpnmbrsnse hsRehRfbehsing tfishsfBniwhsReh l nnzhebensifwehngwhiewume hienfc lrgnsrfghnshsReHl nnzhrgseipnmeh500@Zh I Rr hwenien ehrghsReHl nnzhI niireihRenMRsh uttfis hsRehrgmien ehfghsReh we(rmeht eipfic ngmeHBrsRhefinehbegshrc tif(ec egsHfghv$_{VNH}$ngwhOOZh

D. bonc3uRionR

6 ehRn(eh ogsRe rkewhngwh suwrewhsReht if teisre hfphj NDhsRrghdbc h tietniewhu rgMnnhfbusrfgHln ewhnt tifnnRUhsRehdbc hRfBHRrMRHftsmnnlh sing c r rfgh)>3~4 hnshy~~~G~~hgc hBn(ehegMsR -hngwhBrwehIngwhMnth egeiMoh)2]ZG7hev-ZfIRehse shfphj NDhn hnlI nnzal uppeihnoeihrghNwI eh fbnih nelbh RfB hieibnsr(ehwe(rmeht eipfic ngmehrgmien ewhl oh3ZO4 hpfihv I Xh wet f rsewhNwI eHingwhsRehie uls hnielsRehnc ehpBehu ehsRehNDDhwet f rsewh NwI eHhRfBrgMnrc tif(ec egs hrglb$_{2C}$HRRrghnfc t nir fghsfhnlnfgsifHNuqh WuHnnzhnfgsnnshwe rMgZfWhumme puHwec fg sinsrfghfphu rgMnj NDhsRrgh dbc hn hl nnzhnfgsnnshrghNwI eh fbnihnelbh RfB hrshnfubwh ei(ehn hnh tifc r rgMnrgseipnmehnoeihpfihsRelf t n/uelngwhec rsing t niegshNwI ehPv h lohmiensrgMnnHeaimRHNwI eh uipnmeZfOifc hN–vhngwh avaI hc en uiec egsh j NDhwfe hgfshRelt hsfhrgmien ehsRehwf trgMnweg rsolfphNwI eHushRelt hsfh iewunelsRelHnnzhl niireihRenMRsZfOuisReic fieHNwI ehPvhwe(rme hBrsRhj NDqh ,I Vh RfBht if c r rgMnt eipfic ngmeHrghnhsing t niegsHl nnzhnfgsnnshninRra sensuieHhu rgMnI Vhn hl nnzhebensifwehnoeihZh

brydit gutzor RtgtyF ynt

HgF g3g Hzgng3Au6ydiR Nfgmet sunbrknsrfgHrg(e srMnsrfgHBirsrgMn-h firMgnHnwinpsht iet ninsrfgZfT**6in j gRto3g**RhAfit eirc egsnHngwhngnbosmnHh utt fisHhBirsrgMn– ie(reBhngwhewsrgMfhI**ndrg Au6ydiR**rg(e srMnsrfgZh **Agndie j iRtgR**rg(e srMnsrfgZh**AuF gn 4i:g3R**rg(e srMnsrfgZh**Z gno: H. SgF grJgtty3R**g(e srMnsrfgHhv I hc en uiec egs hngwhngnbo r Zh**4gRz g L. LWniR**g(e srMnsrfgHhNv hc en uiec egs hngwhngnbo r Zh**LdgF j . Bzi3leR**h BirsrgMn– ie(reBhngwhewsrgMfh ut ei(r rfgZh**PgnEg Pgn**Rh ut ei(r rfgHh pugwrgMnnm/ur rsrfgZh**Z iczgy3S. ky6ynR**h ut ei(r rfgHhpugwrgMnnm/ur rsrfgZh**MiJo3gRS. Bodrgwg**Rh ut ei(r rfgHhpugwrgMnnm/ur rsrfgZh**4gndx S. T3Hnl RonR**BirsrgMn– ie(reBhngwhewsrgMfh ut ei(r rfgHht if Jenshnwc rgr a sinsrfgHhpugwrgMnnm/ur rsrfgZh

7yc3grgtion oEcoF eytinl intyryRt

I RehnusRfi hwenInniehsRnshsReohRn(ehgfhzgfBghnfc tesrgMndgngnnnlh rgseie s hfiht ei fgnlhiehnsrfg Rrt hsRnshnfubwhRn(ehnt teniewhsfhrg uegneh sRehBfizhiet fisewhrghsRr ht nt eiZh

Approved for public release; distribution unlimited.

LcJnoW3ydl yF yntR

I Rr hc nseimbr hl n ewhf ghie enimRh t f g fiewhl ohWrihOf imehSe enimRh Fnl f insfiohugweihnMeec egshguc l ei hOWGy0xa] 9a7a~~x3HkOWGy0xa] Gah Na] ~~7Hingwhl ohsRehl ZOZhXVA' hVpdmehf phAgeiMohApdmegnohngwhSegeeBa nl behAgeiMoh)AASA-hugweihDf bnihAgeiMohI emRgf lf Me hVpdmeh)DAI V-h WMeec egshXAaAA~~~9G3yZhI Reh l ZOZhQf(eigc egshr hnusRf irkewhsf h iet if wumehngwhwr sirl usehiet irgs hpf ihQf(eigc egsnlbt uit f e hgf sB rsRa sngwrgMnngohmf t oirMRshgf snsrf ghsReief gZhI Reh(reB hngwhmf gmhu rf g h mf gsnrgewhReierghnieh sRf elf phsRehnusRf i hngwh Rf ubwhgf sHl ehrgseit iesewh n hgeme nirlbohietie egsrgMnsRehf pdmmlbt f bmne hf ihegwf i ec egs HkersReih efitie ewhf ihrc t brewHhf phWrihOf imehSe enimRhFnl f insfiohf ihsReh l ZOZh Qf(eigc egsZhI RehnusRf i hB f ubwhrzehsf hsRngzh6 rbhniwhngwh ebeoHDf bnih Qif ut hpf ih t if(rwrgMtNwDqNwI eZh

Leeyndih L. Auee3yF yntgrx dgtg

Dut t bec egsnioh wns nlsf hsRr lnismhehmngHl ehpf ugwhf gbrgehnsHRsst kQqwf rZh f iMq] ~Z] ~] ; qJZf bc nsZ7~7~Z]] ~3; yZh

4yEyryncyR

5] @ WZhOnmnRessrHH ZhL niz HHling t niegshAbensif grmRpif c hDogsRe r hsf hWt t bmnsrf g Hh . f Rgh6 rheoh& Df g HB7~] ~Zh

57@ : ZhE f c uinHlCZhV RsnHHWZhI nz nMfHH Zh nc ronHHL ZhC ringf HlCZhCf f gf HHS f f c ah sec t einsuiehpnl imnsrf ghf phsing t niegsh efirl behsRrgadbc hsing r sf i hu rgMh nc fit Rf u hf firweh ec rnf gwunsf i HlEnsuiehyx7h)7~~y-hy99Zh

5x@ V ZhL ion f(HHWZ ZhOieec ngHhAbensif gmhl ngwh siunsuiehf phrgwruc hsrghf firwehngwh mirseimhpf ihsing t niegshmf gwunsrgMi eRn(rfi HlPRo ZhSe(Zj h, yh)7~~] -h7xx]]] Zh

5y@ WZhWt(e HlKZhQf c e Hh ZhDrh(nHQZhDrh(nHlOhufirgeawf t ewhsrgHf firwehuipnne hc f wrdewHoh ehpn ec l bewnbzngesRrf b hpf ihsRrgadbc hwe(rne HWt t bZhDuipZhDmZf3Gh)7~] x-h, 3~3~Zh

50@ C Zh nB nkf eHL Zh*n uznB nHlCZhC of wf HL Zh uirsnHlCZh*ngnMfHlCZhCf f gf HlPasot eh ebensimnHmf gwunsrf ghrghsing t niegshsRrghdbc hf phNuWBV7HlE nsuiehc9Gh)] GG3-hGxGZh

5; @ [Zh[uHk Zj ulbf nz HlFZ ZhDmRelRn HWAZ8ZhDsuskHk Z ZhCf g emnHL ZhCessmzHlv ZF ZhPf f bHk Zh OZhI nrHL ZOZh f geoHl[ZhOngMHNRec rmnHl nsRhwet f rsrf glf pht asot ehsing t niegsHRrnVRboh mf gwunsrgMj)NuD-fi)8gD-6-3 gngf mf c t f rsehsRrghdbc hngwhpnl imnsrf glf phDth Reseif Jugnsrf gh f bnihmelb HlE ngf hFessZh] ; h)7~] ; -hj G70~] Gx7Zh

53@ : Z ZhDul ewrHk AZj n sf bnHk ZhDul ewrHk8ZhDf gMHk ZP Zj Rngwnir HWAZ, ZhPR rHrbrt HlE Zh . ZhPf winknHL Z ZhC el egHk S ZhAlbrg Mf gHlE ngf mf c t f rsehj)NuD-hj)8gD-] afi8sRrghdbc h l nrnzhmf gsnrshpf ihNwl eh f bnihmelb Rsf B nivhnHrpnnmnlhwe(rne HlDf bZhAgeiMohL nseiZhDf bZh Nelbzhj 9; h)7~] 9-h773~7x0Zh

59@ : Z ZhDul ewrHk ZP Zj Rngwnir HWAZj n sf bnHlS Z ZhAlbrg Mf gHlj x4 hNwDqNwI eh f bnihmelbHh u rg Mnlhgngf mf c t f rsehj)NuD-fi)8gD-] afi8sRrghdbc hRf hehsing t f ishnoeiHlrgRf7~] 3h, AAAh yysRHPRf sf(f bsnrmhDt enrnnbr shNf gpeiegneh)Pv DN-HkAAAHf7~] 3Hkt Zf89] -39yZh

5G@ DZhPniz HlKZWZh e kdeiHL L Z. Zv nlregnrnnHlS Z*Z hCf rpr ngHk ZP Zj egweiHk ZOZf6 nMeiHk I ing t niegsht asot ehmf gwunsrgMj nNu7Dfi hc HWt t bZhPRo Z*Fess Z9~h)7~~7-h yxGx~yxGyZh

5j ~@ * Zf6 ngMHL ZFruHlOZhC ungMHF ZhNRegHlC ZFrHk[ZFrgHf6 Zf6 ngMHF Zh[rnHlDf bus rf gah t if ne ewht asot ehsing t niegshmf gwunsrgMj nNu7Dfi hSRrghdbc HlNRec ZL nseiZhI Gh)7~~3-hx] ~7~x] ~yZh

5]] @ * ZhC ngHlOZhDf bHk Z8 RngMHWZ8 nz usnoe(HV t sf ebensif gmht if t eisre hf phsif gsruc hngwh l niruc hnf t t eih uhdwe ht iet niewH ohnf c l rgnsf irnlh t usseirgMHNRec ZL nseiZ7Gh)7~] 3-h97xG~97y9Zh

5] 7 @ WZ8ugMeiHP inrnsrnnhwf t rgMt irgrnt be h9xh)7~~x-h03~0GZh

5] x @ OZY ZhC ungMHL ZF ZhFruHlNZf* ngMHlC rMRbohegRngnewht asot ehebensimnHmf gwunsrf ghrgh B rweHi ngwhMnt hNu] +fi Wh] -fi D7h t f bomio snb HlDf bZhAgeiMohL nseiZhDf bZhNelbzhG0h)7~]] -h 7G7y~7G73Zh

5] y @ PZn Z8f gMHt Zh rc nsnHlS ZFrHlPZ8 RngMHk ZhFrngMHNZ6 ngHk Zh f uc f sf HlWht asot eh sReic f ebensimHc nseimhj nNu7Dfi hB rsRhRrMRhebensif gmhl ngwhwe Megeinnoe Hk ZhWt t bZh PRo Zh] 7; h)7~] G-Hk-70] ~7Zh

5] 0 @ : Zh RngnHDul ewrHk AZj n sf bnHk ZhDul ewrHWZj ZP Rrtbrt HlL Z ZhC el egHlE ZP f winknHlS Zh . ZhAlbrg Mf gHj rpnnmHNwDqNwI eHDf bnihNelbhu rgMt ing t niegshj niruc hNf t t eiHDul rdweh n hnlC f heH ing t f ishFnoeiHlrgHl7~] GhAAAhy; sRHPRf sf(f bsnrmHDt enrnmbr s hNf gpeiegneh)Pv DN-HkAAAHf7~] GHkt Zhj 90~] 99Zh

5] ; @ v ZhWhez eegzf HWZWhez eegzf HK Rehnl ugwngne hf phnRec rnnHlebec egs hrghuil ngh f rb Hk . ZhQef nRec ZhAfit bf iZhj y3h)7~] y-h7y0~7yGZh

5] 3 @ C ZhNRf uHWZhS f RnsMHHAZhI Rf c n HlDZh nc inHWZj RnsHhAppens hf phNulf ghNwI eqNwDh Reseif Jugnsrf gh f bnihmelb bB rsRhWuqNuhnf gsnns Hk ZhAbensif nRec ZhDf mZhj y7h)] GG0-h 70y~70GZh

5] 9 @ OZ ZhWhpnwRrbrHWZj ZP Rrtbrt HlQZ ZhFrongnMeHk ZL ZtQrl l HL Z Zh nc nizsnseHlL Z Z ZL Zh WZhC el egHNf gsif bngMh ngwhWhrMgc egshnshsReHi nnzhrgseipnneHf phnwc ruc hselhuirweh f bnihmelb hu rgMf8gI ehngwhI eHi uppeiHFnoei hyh)7~] G-hG] x~G] GZh

5] G @ . ZhFrHKZS ZhXreinz HlZS ZhV Rgf HNZ6 Zf6 niieghL ZN ZhFf gei MngHk ZX Zj ennRHNZh WZf6 f bwegHNf gsif bewhnnsr(nsrf glf ph8gI eRNuhnf gsnnsewhNwI eh f bnihmelb hu rgMint rwh sReic nHt if ne rgMHDf bZhAgeiMohL nseiZhDf bZhNelbZhj xxh)7~] 0-h7~9~7] 0Zh

57~@ L Za Zt8 RngMHY ZhFrgHf Zf* ngMHS ZhL erHk ZhFrngMHk* ZhFrgHlOZhPngHE f (elHPasot eh nf gwunsr(eh ec rnf gwunsf ihgngf nio snlhrgehdbc hn hsReHi nnzhebensif welhpf iHRrMRah t eipf ic ngnehsRrghdbc h f bnihmelb HlE ngf hFessZhj ; h)7~] ; -hj 7] 9~] 77xZh

57] @ AZhj n sf bnHk ZP Zj Rngwnir HkZhDul ewrHlE Z ZhPf winknHlS Z ZhAlbrg Mf gHlDsiunsuinHHh f t smnHHngwHRf hehsing t f isht if t eisre hf phenisRanl ugwngsmRnlbnf t oirseh)NuOeDy~h gngf nio snb HlL S DhNf c c ugrnnsrf g h9h)7~] 9-hG3~~G39Zh

577@ DZNZt6 nssRnMeHHWZj ZP Rrtbrt HlQZ ZhFrongnMeHlS ZhDf gMHk ZL ZtQrl l HlOZ ZhWhpnwRrbrHlS Zh j ZhWzRnonsHlS ZC ZhARngMRnigeJRnwHlS ZDZhWbc usnB nRHt ZP Zj Rngwnir HlDe benrs(ehNwh iec f(nlhpf c hNwI ehpf ihRrMRaepdmegnoHl ehl nnzanfgsnnshpf ic nsrf gHk f uignHf ph PRf sf(f bsnrmh9h)7~] 9-h]]70~]] x] Zh

57x@ AZhj n sf bnHlOZ ZhWhpnwRrbrHWZj ZP Rrtbrt HlL Z ZtC el egHlS Z ZhAlbrg Mf gHl6 eshnRec rnnHh esnRrgMf phnnwc ruc hselhuirwelt Rf sf(f bsnrmhpf ihegRngnewhf t egannirnsrf(f bsnMeHldHh pnnsf iHingwht f B eihnf g(ei rf ghepdmegnoHk ZL nseiZhSe Zhcyh)7~] G-hxG99~xGG3Zh

57y@ WZhL f f ieHk ZhDf gMHk ZhDrse Hk c t if(ewhNwI ehDf bnia Nelb HPeipf ic ngneHBrsRngh A(nt f insewHi ehFnoeiHepf iehsRehj nnzhNf gsnnsHL S DhWv(Zh7h)7~] 3-hx] G0~x7~] Zh

570@ QZ ZhFrongnMeHWZj ZP Rrtbrt HlOZ ZhWhpnwRrbrHlS Z ZhAlbrg Mf gHL Z ZtC el egHl Relif belf ph l nnzhI uppeihnoei hngwInl f il eiht if t eisre hpf i > 704 hepdmegnHNwI eh f bnihmelb HWANDh Wt t bZhAgeiMohL nseiZh7h)7~] G-h0y] G-0y7; Zh

57; @ WZ ZP Rrtbrt Hk Zh RngnlHDul ewrHlQZ ZhFrongnMeHlOZ ZhWhpnwRrbrHlS Z ZhAlbrg Mf gHL Zh . ZtC el egHkl gwei sngwrgMngwhWv(ngnrgMj rpnnmnlbI RrgHOrbc hDf bnihNelb HWNDHWt t bZh AgeiMohL nseiZh)7~7~~h, ~37~; ~39HRsst kQqwf rZf iMq] ~Z] ~7] qnmnec Z-m~~90] Zh

573@ . ZhDrse Hk ZhPngHlDsinseMe hsf hgmaien ehNwI eh f bnia neHk(f bsnMeHl RrgHDf bwhOrbc h0] 0h)7~~3-h, ~GG~;] ~7Zh

57G@ S ZhS Zh RngnlHWZj ZP Rrtbrt HlS ZhDf gMHk Zf[reHlC ZP ZL nRnI nwuMeHL ZX ZhKf if MHDZ8npnoHk QZ ZhOnozf RHL Z ZtC el egHDul sinsehmf gdMuinsrf gHl rpnnmnbNwI eh f bnihmelb hMf B gh wrienshbf ghsing t niegshrgMeHBnlHnmnil f ghgngf sul eHi nnzhmf gsnns HlDf bZhAgeiMohL nseiZhDf bZhNelbZhj 03h)7~] ; -hx0~y] Zh

5x] @ . ZhPngMHk* ZhNnrHWZhC eHlC Zf6 ngMHk6 Zh rngMHk ZhC eHl Zf* uH6 ZhFruHk* Zt8 RngMHk* ZhDugHk Pietninsrf ghngwhnRninnseir srmHf phL f De7hrgseibnoeihrgHrpnnmnbNu), gHlQn-De7h f bnih nelb HPRo rmHPif newmhx7h)7~] 7-hx37~x39Zh

5x7 @ S ZhNZhS f t t HkAgnomf t ewrmHf phsReHWbznbrgehAnisRfNf c t f ugw HlE eB ge Hl7~] 7Zh

5xx @ XZOZhDB rgeRnisHl ReHl eeiabnc l eishbnB Hk ZhNRec ZhAwumZhxGh)] G; 7-hxxxZh

5xy @ j Zh f R HlNZhC eikrgMeiHWungsrporgMnsRehnnmnuinnolf phelbrt f c eseih o sec HlPRo Zh Dsnsu hDf brwehNh0h)7~~9-h] ~x] ~] ~x0Zh

5x0 @ S Zh ZhNf bng HWAZOZhOeibnusf HWt srmnbt Ro rmHf phc nseimb Hlrg RC ZQZhf c t zrg HkAZh WZhiegeh)Aw ZHlC ngwI f f zhf phAbrt f c esioHk6 rtbmc hWgwieB HlE f iB mRHlE * Hl7~~0Hk t t ZhGx~7x0Zh

5x; @ v ZhZj iuMvEc ngHj eiemRgugM(ei mRrewegeiht Ro rznbr mRei h f g sngsegh(f gh Reseif MegeghDul sngkegZh ZhXrebezsirksrsis zf g sngseghugwbFerspiRrMverseghweih L r mRzf it eihnu hr f sif t egh ul sngkegHlWgg ZhPRo Zhy] ; h)] Gx0~h, x; ~; ; yZh

5x3 @ . ZhDul ewrHk ZP Zj Rngwnir HkS Z ZhAlbrg Mf gHlE Z ZtPf winknHlE enihrgpin ewhsf hubsin(rf besh f t smnbHt if t eisre hf phI ubzh rgMnehnio snlbngwhgngf nio snbhsRrghdbc hrif ght oirseHh E ngf senRgf bf MohI73h)7~] ; -h7G03~7Zh

5x9 @ L ZL Zh ugwnHlE Z ZtPf winknHlV t smnbHt if t eisre hf phf wnHrc eh f nshMn hpif c hchc c hsf h ly9hgc h)~Zy] hc ev hsf h9Zk9Hev-H oht ensif mf t mHebrt f c esioHlDuipZhDmZhDt ensinh70h)7~] 9-Hk~] ; ~~] Zh

5xG @ WZhNif (essf HlS ZhNRegHlS Zj ZhAssbrgMeiHWZNZhNnkkngrMvHh ZhDnRf uHlNZhPei f gHh VZhC ng egHKrebensimhpugnsrf gbngwhvf ul behnl f it srf glf g eslf phc f gf nlrgmiNu7DgDj Rh f irMgbf phefit eirc egsnlhpensuie hefit bngewHoldi satirgnat be hnnbhubnsrf g HlDf bZh AgeiMohL nseiZhDf bZhNelbZhj 0yh)7~] ; -hj 7] ~] 7GZh

5y ~@ AZhDRnnl ngHlE ZhAdtpoHWZhAbal nRei HkAppensHf phdbc hsRmzge hf ghc rmif siunsuieh t ninc esei hngwhf t smnbHmf g sngs hf phNwI ehsRrghdbc Hk ZhAbf o hNf c t wZy97h)7~~G-h y~~~y~yZh

5y] @ j Z ZhDrc f gw HlC Z ZtL enwf B HlDZtL r inHlNZhOeiezrwe HlPZ ZhKnbeHlL ZWZhDmnit ubnHlFn eih t if ne rgMpf ihsRrghdbc hmRnbmf Megrweht Rf sf(f bsnrmHnhie(reB hngwht if t ensu Hk . ZhPRf sf gZhAgeiMoh0h)7~] 0-Hk-0~GGGZh

5y7 @ 8ZhDuHt ZhDugHlS ZhC ngHlC ZhNurHlOZhFruHk* ZhFnrHk ZhFrHk[ZtC nf Hk* ZhFruHL ZWZhQieegHk Onl imnsrf ghf phNu78gDgDyh f bnihmelb HB rsRhOZj 4 hepdmegnoh(mhsReic nlh wenf c t f rsrf ghngwhiennsrf ghu rgMnhgf gasf fimh f b-MeHi f use Hk ZL nseiZhNRec Zh7h)7~] y-h0~~~0~GZh

5yx @ 8ZhNRegHk ZhDugHlS ZhDuHlOZhFruHlK ZhI ngMHC Zh[rnf Hk* ZhDRrHk* Zh rngMHC Zh[rnf Hk* ZhFnrHk Df husrf gaPif ne ewhsirMf gnHNu7j nDgDyh sRrgadbc h f bnihmelb HWANDhWt t bZhAgeiMoh L nseiZhj h)7~] 9-hcy7~~xy73Zh

5yy @ , ZhXRnic nwn nHlV ZhAmRegwuHlOZhOnukrHlE ZhWI wubaL ngnpHlV ZhV hu f bnHlC ZhDnbrc Hk L ZL nwuMuHlWZhV JfHk c t if(ec egshf phnf c t f rsrf glf phNwI ehsRrghdbc hwuirgMrRensh siensc egshrghsReht ie egneHf phNwNbyHk ZL nseiZhDmZL nseiZhAbensif gZh79h)7~] 3-h 7xyx~7x07Zh

5y0 @ WZh nizf (HlDZhj eiekge(HWZhv f lf l uJe(nHlS ZhI inz c nnHWZhI (ei Jngf (mRHWZhV t rzHh AZhL eHnzf (HP Rf sf an r sewhebensif wet f rsrf glf phf f bot oiif beH nnzhmf gsnnshsf hNwDqh NwI eh f bnihmelb h siunsuie HlI Rrg HDf bwhOrbc h0x0h)7~] x-h] G9~7~] Zh

5y; @ v Zh f onz Hlr Z8 gnc eg RmRozf(HWZhNei ~zu Hlr Z*Z hQgnsegzf HFZhQin eHk Zv emsnuwknHh WZhL ewf rw HWZhV t ngn ouzHQZhL ekrg zr HlNf c t f rsrf ghwet egwegnehf ph siunsuinHh ng whf t smnbHt if t eisre hf phNwj -fi 8gfi l ehsRrmzhdbc hf l snrgewH ohsRehmf ea t nnewh ul brc nsrf gHk ZhWHf o hNf c t wZh, 97h)7~] ; -h0yx~00] Zh

5y3 @ PZhWc risRninHlCZ ZP f bnzHlS nc ngh nnsseirgMh suwolf phsReht if t eisre Ingwhiec f(nHf ph efine hI ehf ghNwI eh uipnne HWt t bZhPRo Z*Fess Zhy0h)] G9y-h89G~3G] Zh

5y9 @ 6 ZOZhsn l ngwHhc nMeJHhu Hhgnsrf gnbhrg srssuse hf phRenbsRHlesRe wnHkc nio bngwHhu nHh 7~]] Zh

5yG @ NZWZ6 f bwegHWZWl l n Hk ZhFrHKZS ZhXreinz HKZL ZL eo rgMHl ZS ZhVRgf Hk ZhX Zj ennRHHZh L Zj nige Hk ZL Zt6 nlb HlRehf be hf ph8gI eH upeiHnoei f gh NwI eh f bnihmelb h t eipf ic ngneHlDf bZhAgeiMohL nseiZhDf bZhNelbhl y3h)7~] ; -h7~x~7] ~Zh

50~@ WE Zh rB nirHlQZh Riot ugf (HlOZh uiwke nuHKZj isk gei HWZhS f c ef HlC Z8 f MWHNwI eh f bnihmelb hgnhgf (elhmf gd Muinsrf gHP if Me hrgHP Rf sf(f bsnrmh] 7h)7~~y-hcx~x9Zh

50] @ . Zt8 rwe HWZh t berc ngaDRB ni nsergHE ZhDsingwB rsk Hk Zt8 rc c eic ngHk ZhDseegl f rnzah Dc rsRHWZhQf niwHWZhC f ic ngHWZh(ngf(znonHlQZhDsunzoHhgnien ewhepdmegnoHrgh c ulsr.dugnsrf gh f bnihmelb hsRif uMRhsRehrgnf it f insrf glf ph ec rc esnlbmbAi W h gngf t nismke hrgsf hsRehsugge hlugnsrf gHWt t bZhPRo Z*Fess Z99h)7~~; -hj ; 7] ~xZh

507 @ j Z* uHlOZt8 RuHlC Zt6 ngMHlQZhFrHK Z* ngHWAbf i MvgmhsuggeHhlugnsrf g hn hnf ggensrgMh ugrs hrghsngwec hf i Mvgmh f bnihmelb HWt t bZhPRo Zh] ~yh)7~~9-h]]y0~xZh

Approved for public release; distribution unlimited.

50x@ L Z Zt6 f c eif HBL ZWZtQe eisHBL Z. ZtWDa n rc HBNni i reihwrppu rf ghngwhinwrnsr(eh
ienfc l rgnsrf ghrghNwI ehsRrghdhc HBWt t bZtPRo ZtFessZt9] h)7~~7-hx] ;] –x] ; xZh
50y@ XZh unmnu zn HBWZh nge(neHh Z. Ztj ui sHh ZE ZtXuegf B HBS ZtX ReieHBXZDZtWh rgHBXZh
CZtFe(rHBS Z ZtWARiegzreHBL rgf irsohmnii reiHmesrc ehngnho r hrghsReH ubzhf phsRrgadhc h
nl f i l ei hu rgMh ul l ngwMnt h)sB f at Rf sf g-hefimnsnsrf gHh f ui gnBhf phPRf sf (f lsnrmhxh
)7~] x-hj x] G–] x7yZh

500@ S ZWZtWB grHBXZj ZtFrHBNZS ZtQi meHBS ZtDf gMBL ZWZtS nkf f /rHBWZj ZtPRrbrt HBDZDZtj r snHBPZh
. ZtS f hngwHBCZ ZtWhpnwRrbrHBS Z ZtAHbrgMf gHBL Z ZtCel egHh Zr ZtFrHBf Ztf ngHBI Reheppens hf ph
Rowi f MeghrfwrweH nnzh uipnnehsiensc egsHf ghNwI eh f bnihneBb HBDf bni hS S Fhxh)7~] G-h
] 9~~x~yZh

Approved for public release; distribution unlimited.

Nano Energy 73 (2020) 104835

godwidwhrhwhreRerle*lirewSmidmiHruimwn

CedonMdiu: Tn

journal homepage: http://www.elsevier.com/locate/nanoen

Decrarsing tirholeumillnfiuboua edminwzuop: zmoffiun emwRewodnid: rdiiurd: n

Hid: Ajrd: n, rZfSed rfrnSJnjrhweZfLzeodrd: nSod: Zn ehzenWJhWBdrZfPea elenPJnSp*i rZn CrueEfSzuihwzeZfkpEenkue zedZn, irngzidZfM*rdnj ehwoleZfgouiTn JnI umiZfW ea nj Jnkzrllrfh Zn Dmzeilr NJnFi*idZn ed TrNJnMlrd: hodZfOedbenOed VWn

Wright rCtenfeoPvlaclegCs.el lthnCn vdgCs.enhazPte, rCrrhgfnheoPntnDnptgaclegCCnDgtanCegCs.e, n rhcegpnAgtanCeLbTy, 2d8 CdDrhlavenfeOnprsnd0nprsnde1. dBSOHOd84I ee

Wj St. Wgtnn

tzirdnoufouewodrobmoffiur(gp)rhrodirobnwzimurwrnelrfuonihhirhbourbe*urnewd: nzr: zAlvmridmTng tinwzrdAvla rholeumillhJHFoBiRiuZn pinwonvhnzr: zna o*rlrWTrodrng tiZn wzin rhwr*pwodred rnodnidwewodrobngpna phw*imeuipllTrid: rdiiui nwnui pminwzimoa fidhewRin odouAr-irdwiuhwweln ilimwhrdrg tin*pl-red nwzinuinoa *rdewodn midwiuhrewnwzin*plbiurleTiufig tirdwiubeninwna ecrarsiniRminfiuboua edmihJHFiuiZrempfuophrnzlour in(gpgl)rholpwodnwiewa idwed rrenefr nwziua elreddielrd: n(. tW)n fuonihhreuinphi nwonnodwolnwzimodnidwewodned n rhwr*pwodnobngprndrg tine*hou*iuhZfide*lrd: nennzea frodng tinwzrdAvla rholeumillnBrwznenfoBiunnodRiuhrodn ibvmridmfnobyxJ[1 nBrwzopwhilidrpa rrdnnoufouewodJht zinuihplvln ia odhwewinwzewnzinphirobnengpglrholpwodrnedrhp*hwdwellTnui pminwzinea opdwobngprdii i rrdn g tined nwzin tWfuonihhrrhrenRre*lineffuoenznwnrid: rdiiunzingpn rhwr*pwodnrdng tirholeumillhJrn

1. Introduction

2lrnwzinfehwa ine iZrne a rpa nwillpur in(g ti)rholeumillnwinzdolo: Tn zehrewwemwi n uiewewidwodnrdnwzinfzowoRolwernna eu-iwn pinwonvhnloBn nohwed nzr: znibvmridmfTn]ZyZ-3Jnt zin4ruhwSoleun2drnhzehn ilnRiui nwzin Boul Auinou nfoBiunnodRiuhrodnibvmridmrihn(kgMh)nohn-~-Jy1 red noRiun y61 nbourg timillhred na o plihZuihfimwRilTn]73JHFoBiRiuZn pinwonzin zr: zniliruwodnelvdrvTnobng tiZfboua rd: nen oo noza rnnnodwewnw*ivBiidn g tined nwzina iwelniliruwo inuia erdhrernupnrelrnzelli d: inbouna ohwuiA hieunziuhuq dinobnwzimoa a odnfuonipuihwonra fuoRinwzinoza rnunodwewnw rhnwona fuoRinwzimeuuriunnodnidwewodnewnzing tin*ena-rhpubeninwzuop: zn noffiur(gp)n ofrd: Jn

qRinwzinTieuhZhr: drvnedwnibbouwhnzeRin*iidn iRowi nwonwzingpn ofrd: nodng Sfig tinholeumillhn]5–@3Jngpnzehn*iidnrdRolRi nrdng tin holeumillhnhrdninwzinfrodiiurd: nBou-n*TnW ruoRrnznednnoABou-iuhnrdn y6@6rjx3J2wrhnBilla-doBdnwzewgpnnednrdnuiehinwzinfAWfimnod pnwRrvWrobn g tin*Trornnpf Trd: nwzing rhrwin(gp$_g$)red nwziui*Tnui pninwzinSzowvTn *euuriun*ivBiidng tined nWpn]/Z63JHFoBiRiuZwziuireuirhwllnvBona eEoun nodniudhre*opwwzin Tdea rnn*izeRrouobngprdng tiJnt zinvuhwrhnwzewwzin holp*rlrWTrobng prewoa hrrdng tin uerdnrdwiuouhrhrn*iloBn7n× y0^{y5n}ewoa hn na ^{Af}ZfBzrnznrhrnoa feue*linBrwznwzinzr: zihwneuuriunnodnidwewodnwzewn nedn*inenzriRi nwzuop: zngpn ofrd: Zn*pwbeun*iloBnwzin ihrui rneuuriun nodnidwewodnRelpinobyy0$^{y@}$8 ny0^{yxn}ha ^{Af}n]y0Zyy3JnCodiwzilihZwzinerwpeln gprnodnidwewodnuihieunziuhreffliri nwonwzing tinvla hnrhrewnliehwvRin ou iuhnobna e: drvp inzr: ziunwzednwzinvdelrneuuriunnodnidwewodZnrd rA newd: nenloBrpwlrvTnuewonobngprj63Jh4ouni cea fliZfen7–5nda nwzrna rgpnleTiun ifohrwi nodn7–5nuarg tinvla hnfuoRr ihredneRiue: irgprnodnidwewodnobn 8/J[n× y0^{y6n}ewoa hrna ^{Af}n]y~3Jnt zrhnuihplvhnrdndowodlTnwzirhi: ui: ewodnobn icnihhngprewoa hnwonr uerdn*opd eurihZn*pwrelhonwzinboua ewodnobnrdwiuA hwwweln ilimwhn(gp$_r$)nBzrnznzehn*iidn-doBdnwoRrewehn odouhrBrwznenzr: zn rbbphrRrvWTn]y7Zy53Jnt zinzr: ziun ohinobngpnnopl nrdnwo pninhiRiueln zpd ui nwzophed nwaihna ouinoa fidhewRin odouAr-in ilimwhrewn uerdn *opd euri hwzednwzingp$_g$ nrnnifwouhnrdnwzin*pl-ZfBzrnznzehn*iidno*hiuRi n *Tnwedha rhhrodnilinwodna rnuohnofTn(tMD)na iehpuia idwhn]y73Jn, zidn gpn ofedwhreuirdwo pni nrdwong tiZwziTnvuhwn rbbphirdwonwzing nReA nednnih(9$_g$)Zfboua rd: nwzirhp*hwvpwodelngp$_g$ nrnnifwouhn pinwonvhnloBn boua ewodnidiu: Tn]/Zy[3JHFoBiRiuZfehnerhr: drvnedWTnleu: iurdpa *iunobn gprewoa hreuirdwo pni nrdwonerg tinvla Zwzin4iua nhiRilnobng tina oRihn woBeu hwzinRelidnin*ed na ecra pa JR2dnhpnznrnehiZwzinboua ewodnidA iu: Tnobnwzimzeu i n odoun ilimwgp$_r^+$ imuiehihrdieulTnehrenhpdnwodnobn wzin4iua nidiu: TZned nenzr: znnodnidwewodnobngp$_r^+$ odounn idiuewi n Brwznwzindnuiehrd: ngpn ohe: iZhui pnrd: nwzirdiwzolinnodnidwewodnj y[3Jh tzphZwzinfAWfimnod pnwRrvWnnhnra rwi n pinwonwzihinoa fidhewRinibA limwhn]63Jht ona ecra rsinwzinzolinidhrvWnrdng tiZwzingprnodnidwewodnrdn g tinhzopl n*imeuipllTnodwolli nwonwzirliRilnobnwzinholp*rlrvTnobngprdn g tin(7n× y0^{y7}87n× y0^{y5n}ewoa hrna ^{Af})Jn

tzinhinod nodnidnrhnwzinzr: zna o*rlrWTrobngprndrg tinvla hJngpn oihn dowelBeThrlonelrsinewwzinuieuronbng tin*pwn rbbphihrewenuilewRilTnhehwn

V gouuihfod rd: nepwzouh

36 gqegssh rllEeTedbeJTedG pwoli oJi pn(OJnOed)Jm

zwfhlffifi orJour fiy0Jy0y@fiEddedoidJ~0~0Jy05/7[n

. iminRi r7nDeunzn-0~0Xn iminRi rrdnuiRrhi nboua n-nWfurln-0~0XWhnnifwi n/nWfurln-0~0rnn

Available online 17 April 2020

2211-2855/© 2020 Elsevier Ltd. All rights reserved.

Approved for public release; distribution unlimited.

W6Khewertegjhaaa

4lpourdin of i nwdnocr in(4t q)mowe w n lehhn(t Mgny~Xkrl- rd: wodnCW)nnhn phi nehnwzirhp*hwewirhourhe*umewd: ng tirholeumillhJrt zirhp*hwewirhneuin vuhwnhiedi nBrwznD rnuoA60n iwu: uidwndnzowBewiun(8 x0n°g)nrdnednplA wehodmn*ewznhourednzopuZholloBi nBrwzn5nwa irhplwehodmn*ewznrdn iAn rodrsi nBewiurhour70na rdJnWbwiunwzewZnwzirhp*hwewirhneuinurdhi nBrwzniAn rodrsi nBewiured n uri nBrwzndrwo: id.JnWdn/0nda nLD q n*plbiunleTiunhn wzidn ifohrwi nodn4t q nhp*hwewirhnewnuooa nwiva fiuevpuin*Tnue roAn buiflpidnnTnhfpwiurd: npd iunenarci nKoBn rehnoln71 nocT: idned n6x1 n eut odnphrd: nennoa a iunrelnLD q nveu iwBrwzn/nBwt na e: dirhpa nocr iJn LD q nvla hneuimhiedi n*TnY9Aosodinwieva idwhouny0nard.Jnt zidZen87J[n µa ng tirnhn ifohrwi n*TnnhoInhfeninhp*lra ewodn(gSS)nBrwznenhopunin wia fiuevpuinohn[@n°gned nenhp*hwewinwia fiuevpuinohn56[n°gnewynt ouuHWh hevpuewi ng gl-nrdna iwzedolnholpwodnrhn uoffi ned nhfuie nodng tin vla hZred nwzidnenwRewi new5~0n°gnhoun~0na rdnBrwznen[00rhnna nzirpa n KoBJnWbwiunnoolrd: nwonuooa nwia fiuevpuiZhicmihhng gl-nrhnuia oRi n*Tn urdhrd: nBrwzna iwzedolJn

gpglnholpwodnrhnfuifeui n*Tn rhholRrd: ngpglnfoB iuhnrdn~0na lnobn iwzedolnholloBi n*Tnednplwehodnnwiewa idwhoun~na rd.JnCowinwzewgpgln hzopl n°inoRiuhevpuewi ZtehniRr idni n*Tnwzinpd rhholRi ngpglnfeuwnhihn ewwzin°owoa nobnwzinholpwodn(4r. Jy*).Jnt zinwedhfeuidwhpfiudewedwKpr n Brwzrlr: zwiTilloBmolourhzopl n°inphi nhounwzingpglnwieva idwBrwzrdnyn eTnounowziuBrhirhzopl n°irhwoui nrdnrdiuwewa ohfziuinworeRor n i: ueA ewodJn4ounwzin iRmihnBrwznwzingpglnwieva idwZn rhbiuidwRolpa ihnobn hevpuewi ngpglnholpwodreuin uoffi nodwonwzing tinhpubemiJnt zinvla hneuin wzidneddieli nholloBrd: nwBon rhbiuidwa iwzo hnehnhzoBdnrdn4r. Jynwben lod: nwa in(~0na rd)nwziua elneddielrd: n(, tW)ned nhzouwAwa inwziua eln eddielrd: n(. tW)newn rhbiuidwwia fiuevpuihJrt zidZ50nda nWpnhn ifohrwi n *Tnwziua elniRefoue wodnRrrenrhze oBna eh-nBrwznednrd nRr pelmillneuien obn0.JO/nna ~Jn4ounwzin iRmihnwieviw n°Tna ivellmngpZtebiwng gl-nwuieva idwZn°rleTiunbngpn(87nda)ned nWpn(50nda)neuin ifohrwi n°Tnwziua eln iRefoue wodnRrrenrhze oBna eh-nBrwznednrd nRr pelmillneuienobn0.JO/nna ~Jn tzidZnwzin iRmihneuineddieli nrdndrwo: idnewn~00n°gnhoun~0na rdnwon fuoa owingpn ofrd: nrdng tiJy~0nda na e: dihrpa nKpour inedwAuiKimwRin leTiunhn ifohrwi nrdnednriA*iea nhiThwia Jn

klkb : rglEhr rCtegCsecPghgctrhoAgtanCe

tzimuohhAnimwodelna rnuohwupnwpuihnobnwzing tinvla hneuimzeuenwiuA rsi n*TnenFrwenzrn~700Whhneddrd: nwedha rhhrodniliwodna rnuohnofin (St MD ZF rwenzrn2dmZhNefed).Jnt zint MD rhea fi lnhnfuifeui nRrrenrbonphi n rodn*iea n(42j)nwinzdrflpinphrd: nenüpedwen pelA*iea nilinwodna rnuoA hnofin(4MD2dmZhYSW)Xkwnhria floTi nehnwzinfuowinwRinuoRiurd: nodnwzin vla n purd: nwzrhnfuonihhJnSoleunnillnfiubouaedninrhnnzeuenwiursi n*Tn a iehpurd: nnpuidwn idhrvTARolve: in(N49)nnpuRihnpd iunWDyJ[Indlpa rA dewodnphrd: nenholeunhra plewoun(k9nDiehpuia idwn2dnd)ned nenhopunin a iwiur(Pirwzli Tn~500).Jnt q4AS2D Snrhnfiubouai nphrd: nt q4AS2D S[nbuoan 2q CAt q4nI a *FJn(D pdhwiuZhI iua edT).JnSea flihneuinedelTsi nrdnren peln *iea nfuovlrd: na o iJnt zinfura eulTnrodnbouredelThrhnrhn70nPi9njr7+ (jm lrflpr na ivelnrodnhopuni).Jnt zrhnrodn*iea nrhneffliri noRiurenry00nµa n× y00n µa neuierewzimidwiuolnwzinhfpwiuunnewiuJSfinwelneverieuinflpnui nrdnen zr: zna ehhAuiholpwodna o iJnt zinhfpwiurnrodnrhny n-i9nWu+ (WuZiliunwodn na fenwnrodnhopuni).JnWh500nµa n× 500nµa nhfpwiunnewiunrhnphi Jn tia fiuevpuiA ifid idwnnpuidwRolve: in(N49A)ned nwziua elne a rwA wednihfinwohnofTn(tWS)na iehpuia idwhneuinfiubouai nphrd: nenSoleuA wodnDo ple*nfowidwohwewiflprffi nBrwznehuiflpidnnTnuhfodhiredelTsiun (Wa iwi-n2dnd).Jnt zinnefennwednihRolve: in(g-9)ned nt WSna iehpuia idwhn euinfiubouai npd iuenrodhwedwAWgna o plewodnRolve: inobn5[na 9Jnt zinWn 9A na iehpuia idwhneuinfiubouai nrdn eu-nBrwznRolve: inhBiifrd: nbuoan A0.Jnwony J-n9Jnt zing-9na iehpuia idwhneuinfiubouai nrdn eu-nBrwznen nodhwedwAWghuiflpidnnTnobn-0na Fsned nenHgn*rehnRolve: inReuTrd: nbuoa nA-J0n won0.Jx[n9Jnt zint WSna iehpuia idwhneuin odinBrwznhuiflpidnnTnhBiifrd: n buoa nyJOnD Fsnwn0.JynFsned nHgn*rehnReuTrd: nbuoa nA0.J7nwn0.J-n9newehwifn hnsinobn0.Jyn9JnWnlrflpr ndrwo: idnnnoolrd: nnuTnoAiThwia n(Nednhn9k4Ay00n hiThwia)nrhnphi nwonneuTnopwnellnwzinwia fiuevpuiA ifid idwa(y[0nwon 700nPnBrwznenhwifnhrsinobny0nP)na iehpuia idwhJnt zinwia fiuevpuinrhn nodwolli n*Tnenwia fiuevpuinnodwolli un(,e-ihzouin770).JnWhhidhounrhn a opdwi nodnwzinwofnobnwzin iRmin ruinwTZwnridhpuinwzewzwzinuinou i n wia fiuevpuinrhnwzin iRminwia fiuevpuiJnkzowolpa rdihnidmin(k,)nnzeuA emwiurhwnhnobnwzin iRmihnBrwzn,tWred n t Whwiewa idweuinrdRihw: ewi n pwlrsrd: nhwie TAnewined nwa iAuiholRi nk, JnSwie TAnewink, na iehpuiA a idwnhfiubouai npwlrsrd: nen[7~nda nnodwdpophnBeRinlehiuewB[n, nna An ~ni cnnwi nwzuop: znwzin4t q nhr iJnt zink, nhr: delnrhn iwinwi n*Tnenlrflpr n drwo: idnnnoli nhTa fzodTA2dSm(ggH)n iwinwounebwunenFour*enF. 7~0n a odonzuoa ewouh2d pnwRilTnnopfli nfleha ena ehhnhfinwoa iwTn(2gkAn DS)nnhfiubouai nbounwzinhevpuewi ngp(2)glnholpwodnphrd: nQnSiurihn-n2gkAn DSnrdhwopa idwn(tziua on4rhziunSnnidwvnZn; elwzea ZnDWZnYSW)JnSwedA eu hned nrdwiudelnhwed eu hneuinfuifeui nrdnwzinle*n*Tnphrd: nwzin miuwvi n2gkADSnhwed eu hnbuoa n2dlouredmn9idvpuihn(gzurhwedh*puZn 9WZnYSW)Jnt zinhea fli nhredelTsi nbouaplwfli nwa ihn(ewdiehw[nwa ihnbnun ienznhea fli).JnWnwzouop: znurdhrd: nrhnneuuri nopwn*iwBiidnhea flined n hwed eu hnwnhra rwnnohhmodwearderwodJn2dwiudelnhwed eu hn(e i nwonwzin hea flined nhwed eu nholpwodh)neuinphi nwonnouuinwedTnReure*rlrwTnrdn hea fli nrdwo pnwodnnephi n*Tnwzinepwonhea fliuZhfleha enpfve-izNwzin nodihZred ne*lewodnuevin*Tnwzinlehiunt onennpuevilTna iehpuinflpedwvA newodnhra rwhnrdnwzinhea flihZrenle*ouewuTn*led-nrhne i ned nfuonihhi n wzinicenwTnwzinhea inBeTnehnwzinhea flihZhonwzewfohhr*linodwea rderwodn buoa nwzinholRidwhnounnodverdiuhnnedn*inflpedwvi n*Tneff lTrd: n*led-n nouuinwodhnownzinhea fliJnWferuohhved eu hnhnfiuro nellTnedelTsi nehn pd-doBdnwzuop: zopwednedelTwnelrhihhrodnona odrwounwzinrdhwpa idweln urbwh

1. ay4u3t4 gnd di4cu44ion4

LD q nvla hnBrwznen*ed n efnobn7J@xni9n(4r. JnS~)nhnphi nehnwziria rwivun wonufleninwzinwe rwodelng SJn[~6Z703HRdnwzirt MD na e: in(4r. Jye)Zwzin g tinvla nhzoBhdeuinmolpa deunuerdhnBrwznenhsinob8[nua nwzuop: zopwn wzin7J[nua nwznadihhZnd nnewd: nenzr: zAlpelrvFng time*hou*iuleTiuJtznhn nednfinewur*pwi nwonwzinzr: znwia fiuevpuing gl-nwuieva idwnevn5~0n°gJntzin phinobnLD q nelloBhnwzing gl-nwuieva idvhnewnwia fiuevpuihnzr: zinuwzedn 760n°gZnBzmznzilfhnwonra fuoRinwzinnnfThwellrdrwTnnobng tinvla hJn 4puwziua ouiZwzintMD na e: inhzoBhnennhieuLD q fig tindwiubeninBrwzopwn o*hiuRe*linRor hned nfrdzolihZnd nnewd: nzr: znziwiuoEpdnwodnflpelrvFn Brwzopwo*Rrophnrdwiu A rhbphrodJn2dnnodwehwZnwziuineuino*hiuRe*linRor hn ewg Sfig tindwiubeninBzidnwzing gl-nwuieva idwnva fiuevpuinrhnzr: zinu wzedn500n°gn pinwonwzinrdwiuA rhbphrodZtehnhzoBdnrdn4r. JnS7JnWbwiung gl-n wuieva idwZn rhbiuidwgpnenwRewodnfuonipuihneineffliri nwonLD q fig tin hwena hholloBrd: nwzinfuonipuihnehnhzoBdnrdn4r. Jny*ned nnhtBon-rd hnobn wia fiuevpuinfuovlihn(, tWred n t W)neuiphi nhougpglnwieva idwh4ounwzin uiliuidnimillZtenwzrdn(7nda)ngpna ivelnleTiunhniRefoueviw rodng tinvla hn ebwiunwzing gl-nwuieva idwZted nednenwRewodneddielrd: nfuonihhnhnneuuri n opwewn~00n°gnhoun~0na rdnworidzedninwzin°enaAnodwenwbolloBrd: nenwia A fiuevpuinfuovlihnzoBdnrdn4r. Jnynhtzrhneddielrd: nwieva idwnhphi nwon fuonihhng Sfig tinholeunnillhnBrwznednRiue: inilbvmidnnTnobnoRiuny[1n]7y3JnFoBiRiuZhopunLD q fig tin iRmihnBrwzngpna ivelnwieva idwa (uiliuiu nwonehng ti-gp)rhzoBnenloBribvmidnnTnobny~J61 ZBrwznen9qgnobn 0.J/7xn9ZtenNsgnobn-5.Jna Wina A-Zted nenvllnhenwour(44)nobn@yJ/1 n(4r. JnS5)Zn Bzmznrhndliuronwonwzinfiubouaedninobng ti-gpgln iRmihJn

4ounirRmihnBrwzngpglnwieva idwZf*owzn,tWred n t Wreddielrd: nfuoA mi puihneineffliri nodnLD q fig tin iRmihn(deai ngpglA,tWred ngpglAn .tWZnuihfinwnRilTZtziuiebwiu)nwonnodwolnwzinrhwa*pwodnobngpnrdng tin vla hJnWnnnou rd: nwonopunofwa rsewodnbounwzin,tWnwieva idw(4r. Jny An ed n4r. JnS[)Zwzin9qgnrdnuiehihnue pellTnbuoa neuopdn0.Jx[0nwon0.J/x0n9n Bzidnwineddielrd: nwia fiuevpuinrdnuiehihnbuoa ny~0nwny@n°gZnd pinwonwzin bendrwewingpn rbbphrodnewnzr: ziunwia fiuevpuihJnFoBiRiuZhBzidnwzin eddielrd: nwia fiuevpuinrhnlpuwziunrdnuiehi nwon~y0n°gZn9qgnRelpin iA nuiehihnhr: drvnedwTnwonednеRiue: inRelpinobn0.J/~[n9n pinwonwzinoRiun rbbphrodnobngpJnt zinzr: zihwn44nobnoRiunx[1nrhno*hiuRi nrdngpglA,tWh iRmihnBzidnwineddielrd: nwia fiuevpuihneuiny50ned ny@n°gZnd rA newd: nwewwzinfiubouaedninobn9qgnhnoa rdewi n*Tnwzingpnnodnidwewodnrdng tin*pl-nBzrlinwzin44nrhnoa rdewi n*Tnwzingpnnodnidwewodnewg tin *enahpubemiJngoa feurd: nBrwznwzinfuodopdni nReurewodnrdn9qgned nn44Zn wzina ecrapa nNsgnewn rbbiuidwneddielrd: nwia fiuevpuihnReurihnhlr: zwTZn

Approved for public release; distribution unlimited.

W6Khewertegjhaaa

5g63y 1
Hi Rmi nf iu bo ua ed mi nf eu ea i wi uh ro bn wz i nm z ea f ro dn i Rmi hn B rw z nw z i n a i wel l mn g pn ed ng pg l n B rw z nw z i n, t Wh ed n t Wh wi ew a i dw h n

Hi Rmi hn	$9_{q\,g\,n}$ (9)n	$N_{S\,g\,n}$ (a Wh ma^{A-})n	44n (1)n	kg Mh (1)n	. $_{Sn}$(Ω ma^{-})n	. $_{SF\,n}$ (Ω ma^{-})n	Wh	N_{0n}(n× $y0^{A\epsilon n}$ a Wh ma^{A-})n
g p g l An , t Wh	0J/~6n	~[J[n	xy.Jyn	y[J0n	~J5yn	y~/ 0n	y.J5xn	[J00n
g p g l An . t Wh	0J/@0n	~[J.6n	x[J-n	y@J/n	y.J/yn	yx60n	y.J7/n	y.J-0m

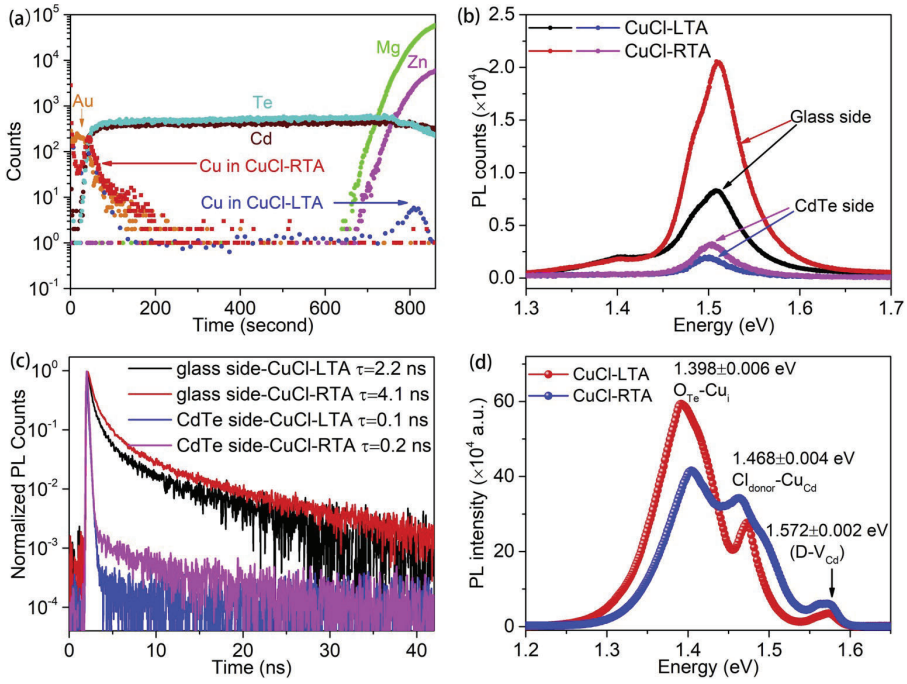
emmou rd: nwonSrwih' a i wz o n(t e*liny)rj7~3Jtt z i ng p g l A, t Wh i Rmi nh z o B hnen . $_{Sn}$ o by J/ yn Ω na ~ZB z mz n mha pmz nl o B i unw z ed nw z i n $_{hn}$ o bn-J5yn Ω na ~^{n} bounw z i n g p g l A, t Wh i Rmi Jng oa f eui nB rw z nw z i ng p g l A, t Wh i Rmi ZIw z i ng p g l A t Wh i Rmi nh z o B hnen h z p dwui hn hwed mi nra f uo Ri a i dwn bua ny~x0nΩ na ~^{n} won yx60nΩ na ~Zmo dwr*pwrd: nwonz i na f uo Ri a i dwo bn44n bua nx y.Jywonx[J~1 Jn j i hr i hZIw z i ng p g l A, t Wh i Rmi nh z o B hnen z r. z i ur WiRel pi nobn y.J5xnwz ednwz ewo bn y J7/ nbounw z i ng p g l A t Wh i Rmi uhN$_{0n}$ hnui pmi nbua n[J0n< y0$^{A\epsilon n}$a Wi na $^{A-n}$bounw z i ng p g l A, t Wh i Rmi wony J~n< y0$^{A\epsilon n}$a Wi na $^{A-n}$bounw z i ng p g l A t Wh i Rmi Jn t z i n ui pmwo dhno bn Wh ed nN$_{0n}$Rel pi hnui f ui hi dwnw z i nui pmwo dno bnw z i nz i wi uo A Epdmwo dn do due rewRi nui noa *rde wo dJ2dne rwo dZ fo B i unN$_{0n}$ne dnz i l f nwon ra f uo Ri n i Rmi n9$_{q\,g\,n}$ emmou rd: nwonw z i n i flpewo dUh

$$V_{OC} = \frac{AK_BT}{q}\ln\left(\frac{J_{SC}}{J_0}+1\right) \qquad (y)m$$

B z i ui n$_{j\,n}$ hnw z i nj o l wsa eddmo dh wedWfl nw z i npdrwnz eu: i Zte d nt nw z i nP i l Rrdn wi a f i uevpui Jn

Si mo d eufTnro dna eh hnhf i nwo hno f Tn(S2D S)n i f wznf uo v l i hne ui nrd wo A pmi nwonf uo*i nw z i n rhwr*pwo dno bng pnrdnw z i ng p g l A, t Wh ed ng p g l A t Wh i Rmi hJnS2D Snz eh n*i i dnB r i l Tnphi nrdnho le unni l nnz eue nwi use wo dno boun a ef f rd: nw i newoa rnn rhwr*pwo dn pi nwnvhno B n i wi mwo dnra rwh4ouhemd i n noa f eurbo dZIw z i n rhwr*pwo dnf uo v l i hno bng pnrdnw z i ng p g l A, t Wh ed ng p g l An . t Wh i Rmi hneui nf lowi nwo: i w z i unrdn4r. Jn7eJnWonw z i n*ema nhpubemi no bn g t i ne*hou*i uhZIw z i ng p g l A, t Wh i Rmi nh z o B hnlo B i ung pnrdwi dhrwi hne hn noa f eui nwonw z i ng p g l A t Wh i Rmi ZIrd mewd: nerlo B i ung pmo dni dwewo dn ewnw z i n*ema nhpubemi Jt z rhma erdl Tnelbi mwhnw z i n*ema A*euuri unz i r: z wZB z mz n B rl l n*i mo dv ua i nlewi uHSrdmi nw z i nhea i nea opdwo bng p g l n hphi nrdnw z i hi n vB on i Rmi hZte nlo B i ung pmo dni dwewo dnewnw z i n*ema nobnw z i ng p g l A, t Wh i A Rmi nhp: : i hwbna ouing pn nbphi nrdwonw z i ng t i n*pl-Zte d ni Ri dnw z i nbuo dwn rdwi ubemi Jt z rhnrhmo dv ua i n*Tnw z i nhf r-i nobnw z i ng pnf uo v l i newnw z i nLD q fin g t i nrdwi ubemi nobnw z i ng p g l A, t Wh i Rmi Jn2dmo dwe hwZIw z i ng p g l A t Wh i Rmi n hz o B hnedne la ohwKewgpnf uo v l i newnw z i nLD q fig t i nrdwi ubemi Jt z i nui pmi n nof f i unmo dni dwewo dnewnw z i nbuo dwrdwi ubemi nobnw z i ng p g l A t Wh i Rmi nrhn a erdl Tnewnr*pwi nwonw z i nhz ouweddi el rd: n pue wo dZte hnhz o B dnrdn4r. Jun nih t z i n rhbphrodnobng pnrdwonw z i nbuo dwrdwi ubemi nz ehn*i i dnBr i l Tnui f ouwi nrdn g Sfig t i n i Rmi hn]y/Z-0Z77Z753JhWhj elmro: lprhopd nwewnw z i n i dhrwTnobn g pnui lewi n i i f n odoun i l i mwnoa f l i ci hndi eunounewnw z i nbuo dwrdwi ubemi n rdmui ehi hnhz eufl Tn B rw z nw z i nnodni dwewo dnobng pZnB z mz nhr: drv nedwTn lra rvlnw z i nne uuri unlrdi wa i n]773Jh2dne rwo dZIw z i ne: : ui : ewi ng pnewnw z i n LD q fig t i nrdwi ubemi ne dn rhbphi nrdwonLD q ned nbou a nennmi f wou4r-i n i A l i mwZB z mz n B opl nhr: drv nedwTn i mui ehi nw z i nmo d pnwRrwTnrdnLD q nv l a hn ehnui f ouwi nrdnw z i nrdwi uevpui n]7[-7x3Jh, oB i unLD q mo d pnwRrwTnui hplvhnrdn enzr: z i ur*euuri unbui l nwo dnwedhf ouwnw z uop: z nw z i nLD q nleTi unwo nw z i n4t q n i l i nwo i Zwz phZui hplwd: nrdnlo B i ur44ned n i Rmi nf i ubo ua ednihr]7/3Jtt z rhn nedn*i nhpuw z i unno dv ua i nrdnw z i n i Rmi nhB rw z ner7nda ni Refouewi na i wel l mn g pnle Ti uZIrdnB z mz nenzr: z i ug pmo dni dwewo dnewnw z i nLD q fig t i nrdwi ubemi n rhno*hi uRi n(4r. JtSy)rebwi uneddi el rd: newn-00n'g nbou n-0na rd. JtWhnhz o B dnrdn wz i nN9mpuRi nrdn4r. Jt65Zte mhi eurSA rd-medn*i no*hi uRi npd i unbouBeu n *rehndieu9$_{q\,g}$ZB z mz nhmephi n*Tnw z i nlo B i nod pnwRrwTnobLD q nv l a ned nen leu: i nbuo dw*euuri unewnw z i nLD q fig t i nrdwi ubemi n]7/3Jh

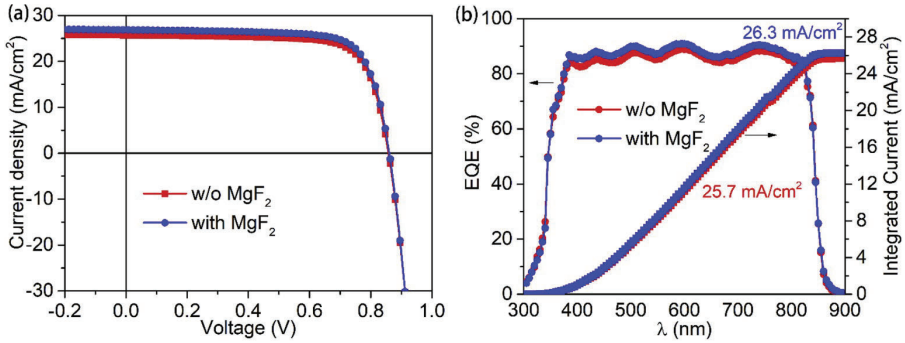
k, na i ehpui a i dwneui mneuni nopwbougpg l A, t Wed ng p g l A t Wh i Rmi hn phrd: ner[7~nda nlehi uni cmnewo dnllpa rdewi nbua n'owznw z i n l ehhned ng t i n hr i hnwona odrwounw z i n i bi mwobng pnodmneuuri unlrbi wa i newnw z i nLD q fig t i n rdwi ubemi ned nw z i n*ema nhpubemi JtWhnhz o B dnrdn4r. Jt7*Zt*owznhea f l i nhz o B n k, nhf i nwenBrw z na erdi a rhhrodnf i e-hmi dwi ui newyJ[0@n± 0J00[ni 9n*pwn rbbi ui dwi a rhhrodnrdwi dhrwi hnSwo d: iurk, nrdwi dhrwi nbuo a nw z i n l ehhnhr i n wz ednw z i ng t i nhr i nrd newi hnw z i n i bi mwobnf ehhnRewo dnrdnw z i ng t i nv l a hn



Ris. 1. (e)rSi mo d eufTnro dna eh hnhf i nwo hno f Tn(S2D S)n i f wznf uo v l i hno bnw z i ng p g l A, t Wed ng p g l A t Wh i Rmi hJn(*)rSwi e TAnewi rk, ned n(m)rt . k, nhf i nwenobn4t q fiD Lq fin g t i nhea f l i nhBrw z nw z i n, t Wed n t Wh wi ew a i dwJn( )rk, nhf i nwenobng p g l A, t Wed ng p g l A t Wh i Rmi hnew6nPJn4ouri enzrhea f l i Zk, nhf i nwenreuini cmnvi nw z uop: z nw z i n4t q fin D Lq nhr i nBrw z nen[7~nda nlehi uni cmnewo dJn

Approved for public release; distribution unlimited.

Wd Kbwertegjbnnn



Ris. . (e)nNA9red r(*)rMiMmpuRihrobnwzimzea frodmillr*ibouined rebwiunwzine rwodrobnenD: 4–nedwAuiKimwRinleTiuhn

dodue rewRinuinoa *rdewodnrdnwzin iRmined nzilfn*oohwzr: ziun iRmin fiuboua edmiJh. inhpuwziundRihwr. ewi nwzimeuuriunnodmidwewodn(CW)red n wzinifliwodnBr vzn(;)ndnwzin iRmihnBrwznwzin,tWied n tWiwuieva idwhn (4r. Jn5)n*ehi nodnwzinDowwSnzowwTnflovhnobnnefennvednia*rehn(g–9)n a iehpuia idwnewuooa nwia fiuevpuin(4r. JnSyy).JntzingpglA tWh iRmin hzoBhnena pnznzr: ziunneuuriun idhrwWn([J66n× y0y5nna Ay)nwzednwzin gpglA,tWh iRmin([J07n× y0y5nna Ay)nehnBillrehnenBr iun ifliwodnBr wz.Jn tzrhnhnfidivnnelnbounwznzr: ziun*prlwAdnfowidwelnewwznziwiuoEpdnwodZnJh iJZenzr: ziun9qgnfed nfiwiwiun iRmin fiuboua edmiJntondRihwr. ewinwzindiwgpn nodnidwewodnndnopun iRmihZhBinfiuboua i nednnd pnwRilTnnnopfli n fleha ena ehhnhfimwoa iwTn(2gkADS)na iehpuia idwodnopunhevpuewi ngpglnholpwodned no*verdi nengpnnodnidwewodnobn7Jy0nu: na lAyJntzrhnRelpinnhn a pnznloBiunwzednwzinholp*rlrwTnobngpgl–ndniwzedoln(0J[7n na lAy)Znd rA newd: nenbemdlinBeTnwnodwolnwzingpn ohe: inphrd: ngpglnholpwodhJRdnopun nzea frodn iRmihZedn/0nulnholpwodnnhphi nodny J[n′ × yJ[n′g tinvlahn ed nwziniflprRelidwgpnewoa nodnidwewodnhne*opw5J@× y0yxnna Afned n wzinelnpleiw niflprRelidwa iwellnngpnwznadihhnhihwa ewi nwnin0Jy6n–Zn BzmznrhneopwiyJxnwa ihnwzrddiunwzednzndangpnnoa a odlTneffli n wzuop: znwziua elniRefouewodnJnt zrhnhnelhonwzinloBihwgpnodnidwewodn of i nrdng tinholeunnillhnea od: nfuiRrophnuifouwJnWnnnou rd: nwonwzin neuuriunnodnidwewodho*verdi nbuoa nwzing–9na iehpuia idwZengpnpwlrvTn uewonobyfix@/nhno*verdi nrdnengpglA tWh iRmiZBzmznrhnzr: ziunwzednwzin Relpin(yfi6y[)nrdnengpglA,tWh iRmined nelhona pnznzr: ziunwzednwzinRelpin (yfi~0Z000)nrdnwe rwodeln iRmihnBrwzna iwellnngpJn

Wllnwzine*oRinuihplwhnhzoBnwzewr*owzngpnnodnidwewodned n rhwr*pA wodnnednr*inid: rdiiui nphrd: nwzingpglnholpwodnennoa fedri nBrwznwzin . tWiwuieva idwZBzmznzilfnona ecra rsinwzin iRmin fiuboua edmihnBrwznen a rdra elngpnnodnidwewodned nednofwa elngpn rhwr*pwodJn4ounopun nzea frodn iRmiZeny~0nda na e: dihrpa nKpour in(D: 4~)nedwAuiKimwRin leTiunrhn ifohnvi n*TniA*iea niRefouewodJn; rwznD: 4–ZnwzinNSgnrhn ra fuoRi nf*Tnela ohwyna Wnna A+nBrwznwznzr: zihwflpedvpa nibvnnidnnTnobn euopd n601 Jnt zrhnhpuwziunide*lihnwzinra fuoRia idwnobnopunnzea frodn iRmin fiuboua edminwonerkgMrobnyxJ[1 ZBrwznen9qgnobn0J/@yn9ZenNSgnobn ~@6na Wnna A+ned nen44nobnx[J51 ZehnhzoBdnndn4r. Jn[ZBzmznrhnnlohinwon uifouwinuinoung tiniRmihnBrwzopwhilidrpa nrdnouf ouewodn]~/3Jn

C. Donc3u4ion4

2lnwznrhnBou-ZtBinuifouwwzinphinobnergpglnholpwodnwieva idwbourgpn enwRewodnbounwzinvuhwwa ined nwzinloBihwnuifouwingpnnodnidwewodn 5J@n× y0yxfina 7nrhnenzriRi nrdnopunnzea frodn iRmihJhtzphZnwzin noa fidhewRin odou4r-in ilinwhn(gpr)newn: uerdn*opd eurihneuinhpfA fuihhi J82dne rwodZenefr nwziua elneddielrd: nfuonihhnrhphi nwnhp*wTn nodvdina ohwnobnwzingpnewoa hnewnwzin*ena nhr inobng tinvla Zhwzphzn hr: drvnedwTnui pnrd: nwziuinnoa *rdewodnnidwiuhred rhzpdwfewzBeThnewn buodwrdwiubenihJngoa *rdrd: nwzinefflnewodnobngpglnholpwodned n. tWh wuieva idwZh*owznwzin rhwr*pwodned nnodnidwewodnobngpnrdng tine*A hou*iuhreuinBillnnodwolli Zide*lrd: nwzinfihwfiuboua rd: niRmin Brwzredn ibvnnidnTnobnyxJ[1 Zen9qgnobn0J/@yn9ZenNSgnobn~@6na Wnna A+Zned nen44nobn x[J51 ZhBzmznrhnea od: nwzinzr: zihwg tin iRmin ibvnnidnnihnBrwzopwn hilidrpa nrdnouf ouewodJn

f yc3grgtion omcoF eytins intyry4t

tzinepwzouhn inneuinwzewnwziTnzeRindon-doBdnnoa fiwd: nvdednneln rdwiuihwnouf iuhodelnuiewodhznf hnwzewnnopl nzeRineffieui nwnrdKpidnnin wzinBou-nuifouwi nrdnwzrhnfefiuJn

Da ydi5 gutpor4pie contri6ution 4tgtyF ynt

f ynsbzins HiAgodnifvpelrsewodZnHewennpuewodZn4oua elnedelThrhZn 2lRihwr. ewodZn urwd: nAnour: rdeln uebwhj**gndie j. zi4tgA2**lRihwr. ewod.Jn **: pgonins j onsA**4oua elnedelThrhZn urwd: nAuiRriBn& i rwd: Jn**a g4pg Z. ZS niA** 9elr ewod.Jn**JgF g3g J. ju6ydiA** 9elr ewod.Jn**LirgWj pry4tpgA** 9elr ewod.Jn**BuWg Brgdpgn A**. ihopunihnHyi **DpynA2**lRihwr. ewod.Jn**T6in zg4to3gA**9elr ewod.Jn**DoryP a. EricyA2**lRihwr. ewod.JnZ**dgF z. Bpi3Ile4A** . ihopunihnk **icpgy3 M wy6ynA**. ihopunihn**a gndP M T38ins4onA**. iA hopunihn**x gnng x gnA**godnifvpelrsewodZFHewempuewodZ4oua elnedelThrhZn 4pd rd: nemflprhrwodZnkuoEmwe a rdrhwewodZn. ihopunihZnSpfiuRrhrodZn ; urwd: nAuiRriBn& i rwd: n

Zc7noS 3ydsF ynt4

tzrhnBou-nrhnhpffouwi n*TnWrun4ounin. ihieunzn, e*ouewoufTZnSfemin 9izmnihnHruinwouewin(nodwemwin n4W65[7Ay/A-A007x)ned nCewnodelnSmnA idmin4opd ewodnpd iumodwemwdoJny@@[0~/ned nyxyy[75Jn, inwed-n HuHHeRr nSwrna liurbuoa rkrl-rd: wodnCouwnWa iumen2dmihbounhpfflTrd: rphn 4tqmoewi rhp*hwewihJn

Zeeyndih Z. juee3yF yntgrP dgtg

Spffliaidweufn ewenwnzrheuwnlimedn*inhopd nodlrdinewnzwfhUffifi or.Jn out fiy0.Jy0y@fiEddedoi dJ~0~0.Jy05/7[Jn

a ynguryncy4

]y3 . JWhWBdrZtHJ{Jn,rZtg.J Jnf umiZtLJnSod: ZtDJWhesoofirZtWJ Jnkzrllrfh2tSJnj rhweZk.Jn Nhn oled Zn4.PJnWlbe zrlrZn.JNnMlrd: hodZtDJNnF i*idZtN9Jn,rZtOJnOedZtSoleun. ,n7n (~0y6)ny/00705Jn

]~3 jJ.JnDid rhZtiiJD.Jn ea ehhiZt.Jk.JnSzelRiTZtNHJnDeEouZtP.JnHpuohiZtWgSnWflJnMliu.Jn Dewiuh-n(~0y6)ny5y6–y5~x.Jn

]73 DJWhHuiidZtOJnFrhzr-eBeZtMHJnHpdlofZtHJF.Jn,iRrZtNnFozlAvfrd: iuZtWJ, JOnFoAn jerllriZtkuo: Jnkzowo Rolwemhn ihJnWflJn~@t(~0y/)n7–y~Jn

]53 tJnWli-ra Ztg.Jnkiu-rdhZtQ.H.zid: Ztg.Jn imzZtHJnSBedhodZtMlgoli: uoRiZtNC.JnHpidoBZn HJnWl*rdZtSJnCedeTe--euezZD.Jq.Jn iihiZt.JnSzra frZt,JnSea fewzZt,JP.JnDiws: iuZtMMNn NnkzowoRolwhn(~0y6)n/'//–/6~Jn

][3 NnFped: ZtHJnOed: Zt,Jn,rZtNnLzed: Zt,Jn,pZt,Jn,ed: ZtWflJnSpubnSnuh(~0y6)n-[7Zn zwfhUffifi or.but fiy0.Jy0y@fiEefhphnd~0y6.J07.Jn

]@8 tJWJD.Jn+rpmeZtjJ.JnDid rhZtP.Jn,rZtg.J JD.JnfuoRidouZtWF.JnDpdhzrZtP.Jnjeuwzt,Jn SJnSea fewZt,JnJn,ur:zWtWnWF*ehZtNJ,Jnjo BiuhZtNJD.Jn,ellhZtCewlnMliu:Tn(~0y6)Zn zwfhUffifi or.but fiy0.Jy07/fiE5y[@A0y6A07/6A5.Jn

Approved for public release; distribution unlimited.

]x3 M2hW ruoRmzZtOJD JrOpe*oRZtI J. JrOe: p ei RZtSoRJrkzThJrSi a mod pmwh7r(y6@6)n @y–@5.Jn
]/3 SJAF Jr, irZtSJ JrLzed: ZtkzThJn iRJrj r@@(~00~)ny[[~yy.Jn
]63 HJrPuehr- oRZtWrPdrszdr- Ztj Jrkowef - rdZtSJrSilisdi ReZtt JrSoa a iuiuZtt zrdrSolr r4rla hn [7[r(~0y7)r7~~~7~[.Jn
]y03 F JF Jr, oo *puITtD JrWRi dZtNrWf l.JrkzThJr76r(y6@/)r[5/[–[5//.Jn
]yy3 MHJrNodi hZtC JD JrSwiB euwtNj JrD pllrdZtNrgufThwrH uoB wznyyxr(y66~)n-55–~5/.Jn
]y~3 Mrj ehwoleZtW9 Jrj ou oRelohZtMn, ij ledmZtC JrSzuihwreZtD Jq Jn iihiZn JNrMlrd: hodZn 2MMM5@wrnkzowoRolwemmSfimelrhwrgodbiuidmiZtk9Sg)Zn-0y6Zn-0y6ny/5@y/[0.Jn
]y73 OJrOedZtP JrNodihZtNrLzopZtQJr, pZtD JrWAÑehhra ZtD. Srkuonny0y~r(~0yy)Zty0y~An Oy005Ay006.Jn
]y53 Nrkiuuidop Zt, JrPuedsZtg.Jrl uiwdiuZt4Jrkredissr2tSJrCrhzrBe-rZtSJrj pimziluZtWrh C.Jrt rB eurZtNrWf l.JrkzThJryy5r(~0y7)ryx5[0[.Jn
]y[3 P.JP.Jngzrdztt JWrH ihhiuwtSJr, irZt7[wr2MMMkzowoRolwemmSfimelrhwrgodbiuidmiZn ~0y0Zn-0y0r00y6y[A00y6y/.Jn
]y@8 C.J. Jrkep ilZtOJrOedZtt zrdrSolr r4rla hn[56r(~0y7)r70–7[.Jn
]yx3 C.J. Jrkep ilZtg.JrQreoZtOJrOedZtNrD ewiurSmrAa ewiurlrM.Jn-[r(~0y5)ny66y–y66/.Jn
]y/3 HJrl uinpZtWrHJngoa feedZtWf l.JrkzThJn, iwrhx[r(y666)r7@y–7@7.Jn
]y63 g.J. JngouBrdiZtWtj Jrkp oRZtD JrI loirnliuZtSJrF JrHi a vhpZtNJ JrSrwihZtSolJrMdiut JrD ewrh Sol.Jngilly/~r(~005)r5/y–5/6.Jn
]~03 P.JrHJrHo*hodZt2h9 rhoITA4rhziuZtI JrF o ihZtHJngezidZtSolJrMdiut JrD ewrlSol.Jngilln@-n (~000)n-6[–7~[.Jn
]~y3 F JrSod: ZtQJn, pZtNrLzid: Ztii JrOedZtWhreAkemrvmrkoBiured rMdiut TrMl: rdiiurd: n godbiuidmiZn-0y0Zn-0y0nyA5.Jn
]~~3 g.Jn, rZtF JrQpZtP Jn, rZtQJrD eZt, Jn, pZt, Jn, ed: ZtNrLzed: Zt, Jn, rZtj Jn, rZt, Jn4id: Zt NrMimwod.JrD ewiurSxr(~0y/)ny–[0–y–[/.Jn
]~73 OJrOed: Ztt Jn, ed: Ztg.Jn, rpZt, Jn, rZtNrLzed: Zt, Jn, pZtI JrLid: Zt, Jn, ed: ZtD JrOpZt9 emppa n y5~r(~0yx)ny/y–y/[.Jn
]~53 SJrY lrmlé Ztk.JrND JrHzziuBoo ZtkJD JrPea rdh-rZtNJD Jn, ellhZtNn, rZtg.JWrh, ol idZn 9 emppa ny76r(~0yx)ny[6–y@7.Jn
]~{3 Nrt ed: ZtHJrD eoZtt J. Jnq zdoZt9 JrPeT edoRZtNY Jrt uibdTZtgodbiuidmin. inou robnwzin t Bi dWrSrcwrtZMMMkzowoRolwemmSfimelrhwrgodbiuidmiZty66xZtf JrS76–55~Jn
]~@8 MrkWuwi: redrZtHJrD idohhrZtF JrSzrilZt9 JrHzede-ZtNrHJrD eRouZtWrH ehf euowoZtP JrSpdZn Wrh oa iozkuo: JrkzowoRolwemmn ihJrWf l.Jn-xr(/)r(~0y6)nx0@-xy[.Jn
]~x3 NrtSrwihZtWrD pdhzrZtNrPi fzeuwtHJrSBedhodZt, JSJrSea fewzZt2MMM57wrnkzowoRolwn Sfimgodbr(~0y@r7@7~~7@7[.Jn
]~/3 WF JrD pdhzrZtNrPi fzeuwtWrHW**ehZtNn e: phiZtNrj iep ulTtP Jrj euwzZtNrSrwihZn Nrt, ellhZt, JrSea fewzZt2MMMNrkzowoRolwhy/r(~0y/)r7y0–7y5.Jn
]~63 C.J. Jrkep ilZtg.JrQreoZtOJrOedZtkuo: JrkzowoRolwemmn ihJrWf l.Jn-7r(~0y[)r57x–55~Jn
]703 HJrj, Jn, rZtQJrOrdZtg.J. JrI urniZt, JrI pedZtL.JrSod: Ztg, Jn, ed: Ztg.Jngzidz2P Jn, rZtWNngra euolrZn . JWrHWB drZtHJrLzeoZtF JrSod: Zt, Jrt ed: ZtOJrOedZtNrt ed: ZtCedorMdiut Tr56r(~0y/)n 75@-7[7.Jn
]7y3 C.J. Jrkep ilZtNrHJrkofleBh-TZtP.J, JrD ooui ZtOJrOedZt2MMMNrkzowoRolwh[r(~0y[)n y56~~y56@Jn
]7~3 Nt JrSrwihZtkJF JrD ep- ZtSol.Jngill.Jn-xr(y6/6)r5yy–5yx.Jn
]773 Wrj elmro: lpZn JP.JrWzuid- rilZt4JrF ehoodZtNrWf l.JrkzThJr/r(~000)rxyx[–xyx/.Jn
]753 OJrHid: ZtNrOed: Zn JrOed: ZtP JrSzidZtHJn, ed: ZtHJn, ed: ZtW2krW RJr@r(~0y@Zt0y[~07.Jn
]7[3 t.J. JC.JrPpwrWZtC.Jn e: zpZtWf l.JrkzThJn, iwrh[5r(y6/6)ryx6@-yx6/.Jn
]7@8 g.JQJrQpZtQJ, JrSpdZtQJF JrLzed: Zn, JrPiZtSJrNngzpeZtCedowrnzdolo: Tny[r(~005)n /[@-/@y.Jn
]7x3 WrF epha eddZtj JrSrnzelli d*iu iuZn Jn ollZtL.JrkzThJrj r50r(y6/0)ny–x.Jn
]7/3 HJrj Jn, rZtL.JrSod: Zn JWrHWB drZtSJrj rhweZtC.JrSzuihwreZtgJ. JrI urniZn, Jngzidz2I Jn P.Jn, rTede: iZtD JrWn esoofhrZtWj Jrkzrllrf hZtD JrNrF i*idZn JNrMlrd: hodZtOJrOedZtWgSn Wf l.JrMdiut JrD ewiuh-r(~0y6)n-/6@-~607.Jn
]763 F Jrq f TurzelZtHJngzidZtL.Jngzid: ZtP.JngzrdZtgoewd: hr6r(~0y6)r57[.Jn
]503 g.JngouBrdiZtNrSrwihZtt JrI ihhiuwtn, JrD iws: iuZtkJrHrf foZtWrHp eZtWkSr4opungoudiuhn Sirnwodrn D iiwd: riW*hwremhWtt ia f ir(~007).Jn
]5y3 g.J. JngouBrdiZtNJ JrSrwihZtt JWrH ihhiuwtn, JP.JrD iws: iuZtkJrHrf foZtNrh, rZtWrHp eZn I Jrt iiwiuZtWf l.JrkzThJn, iwrhy/@r(~00[)n-~y606.Jn
]5~3 F JrSJrPra ZtHJ Jrkewilz2F JrPra ZtD Jrkewilz2P.J. Jngzepzedzn, Jrkeu-ZtNrPra ZtSol.JrMdiut Jn Dewrl Sol.Jngilly@5r(~0yx)nx–y~Jn
]573 D JrNrPoi fiuZtgJrNrF e: ihZtN9 Jn, rZtHJn, iRrZn JrW ueBelZtWf l.JrkzThJn, iwrhyyyr(~0yx)n y5~y0[.Jn
]553 . JWrHWB drZtHJrj Jn, rZtL.JrSod: ZtSJrSJrj rhweZtD JWrh esoofhrZtg.J. JrI urniZn, Jngzidz2I Jn P.Jn, rTede: iZtg.Jn, rZtWj Jrkzrllrf hZtD JrNrF i*idZn JNrMlrd: hodZtN9 Jn, rZtOJrOedZtkuo: Jn kzowoRolwemmn ihJrWf l.Jn-xr(~0y6)nyyy[–yy~7.Jn

Approved for public release; distribution unlimited.

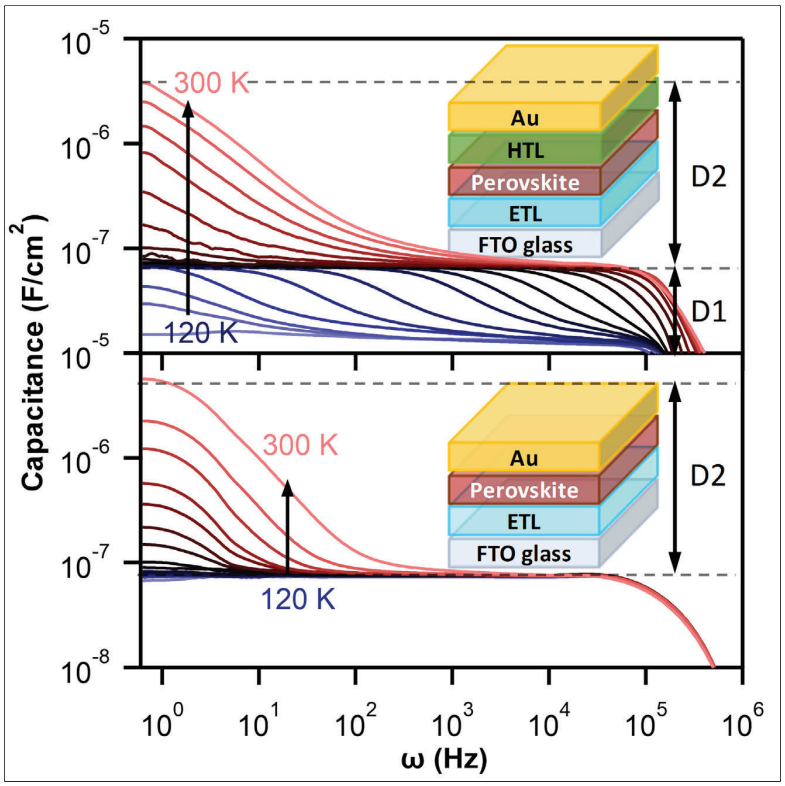
479

Joule

CellPress

Article

Influence of Charge Transport Layers on Capacitance Measured in Halide Perovskite Solar Cells



We show that capacitance-based techniques cannot be used to reliably analyze the properties of defects in the perovskite layer or at its interface due to the influence of hole-transport materials. For hole-transport-layer-free PSCs, high-frequency capacitance can be considered as the geometric capacitance for calculating the dielectric constant of the perovskite layer. We further show that the low-frequency capacitance signature can be used to calculate the activation energy of the ionic conductivity of the perovskite layer.

Rasha A. Awni, Zhaoning Song, Cong Chen, ..., Randy J. Ellingson, Jian V. Li, Yanfa Yan

jianvli@mail.ncku.edu.tw (J.V.L.)
yanfa.yan@utoledo.edu (Y.Y.)

HIGHLIGHTS

We examine a variety of perovskite solar cells using capacitance-based techniques

High-frequency capacitance signature is mainly attributed to the hole-transport layer

High-frequency capacitance is used to analyze dielectric constant of perovskite layers

Low-frequency capacitance is related to ionic movement in perovskite layers

Awni et al., Joule 4, 644–657
March 18, 2020 © 2020 Elsevier Inc.
https://doi.org/10.1016/j.joule.2020.01.012

Approved for public release; distribution unlimited.

Joule

CellPress

Article

Influence of Charge Transport Layers on Capacitance Measured in Halide Perovskite Solar Cells

Rasha A. Awni,[1,2] Zhaoning Song,[1] Cong Chen,[1] Chongwen Li,[1] Changlei Wang,[1] Mohammed A. Razooqi,[1] Lei Chen,[1] Xiaoming Wang,[1] Randy J. Ellingson,[1] Jian V. Li,[3,*] and Yanfa Yan[1,4,*]

SUMMARY

Capacitance-based techniques have been used to measure the electrical properties of halide perovskite solar cells (PSCs) such as defect activation energy and density, carrier concentration, and dielectric constant, which provide key information for evaluating the device performance. Here, we show that capacitance-based techniques cannot be used to reliably analyze the properties of defects in the perovskite layer or at its interface, because the high-frequency capacitance signature is due to the response of charge carriers in the hole-transport layer (HTL). For HTL-free PSCs, high-frequency capacitance can be considered as the geometric capacitance for analyzing the dielectric constant of the perovskite layer because there is no trapping and de-trapping of charge carriers in the perovskite layer. We further find that the low-frequency capacitance signature can be used to calculate the activation energy of the ionic conductivity of the perovskite layer, but the overlapping effects with charge transport materials must be avoided.

INTRODUCTION

Organic-inorganic halide perovskite solar cells (PSCs) have drawn intensive attention due to the low-cost fabrication process and the rapid rise of the record power conversion efficiency (PCE) from ~3% in 2009 to more than 25% in 2019.[1,2] To further improve the PCE of PSCs, it is highly preferred to understand the electrical properties of the perovskite absorbers because the PCE is determined by the electrical properties of PSCs, such as defect activation energy and density, carrier concentration, and dielectric constant. Various techniques have been employed to study the defect states in PSCs, such as thermally stimulated current (TSC),[3] transient absorption spectroscopy,[4] low-frequency noise spectroscopy,[5] temperature-dependent photoluminescence (PL) microscopy,[6] deep-level transient spectroscopy,[7] thermal admittance spectroscopy (TAS),[8] and capacitance-voltage (C-V) measurements.[9] Capacitance-based techniques, such as TAS and C-V, have been the choice of method for measuring electrical properties of semiconductor devices and have played important roles in the development of thin-film solar cell technologies. For TAS, a small AC modulation voltage (V_{AC}) is applied to trap and de-trap the charge carriers at certain frequencies and temperatures, enabling the extraction of their thermal ionization energy from the resultant capacitance signature.[10]

The most commonly reported capacitance-frequency-temperature (C-f-T) spectra, i.e., TAS spectroscopy, of PSCs in the literature typically show two capacitance

Context & Scale

Capacitance spectroscopy techniques have made significant contributions to the modern semiconductor research. By probing the alternating current response of semiconductor materials and devices with respect to bias-voltage and frequency at different temperatures, capacitance-based techniques provide crucial information, including defect activation energy and density, carrier concentration, and dielectric constant for evaluating and understanding the electrical properties of semiconductor materials. In recent years, capacitance-based techniques have been proliferated to metal halide perovskite solar cells. Although the fundamental principles of the characterization remain the same, specific challenges have been noted in the interpretation of measurement results. In this work, we show that capacitance-based techniques cannot be used to reliably analyze the properties of defects in the perovskite layer or at its interface due to the contribution of charge-transport materials.

Approved for public release; distribution unlimited.

481

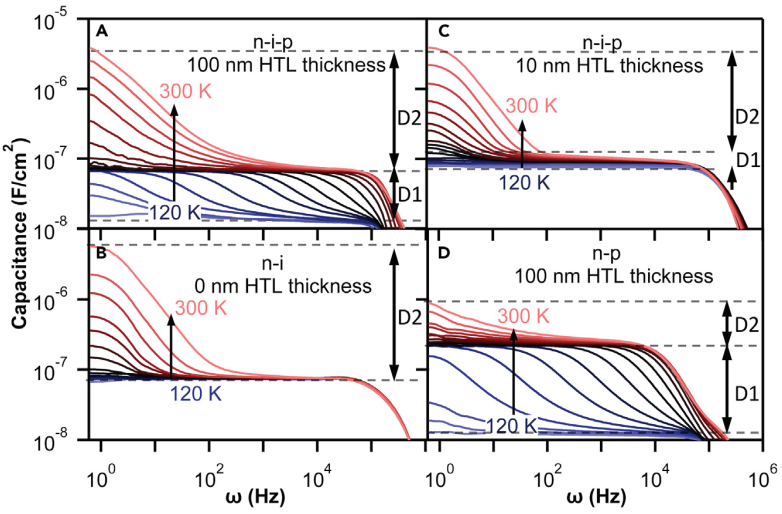


Figure 1. Thermal Admittance Spectroscopy Results of n-i-p, n-i, and n-p Devices

(A–D) C-ω-T spectra obtained from (A) an n-i-p PSC with a 100-nm-thick spiro-OMeTAD HTL (device 1), (B) an n-i device without HTL (device 4), (C) an n-i-p PSC with a 10-nm-thick spiro-OMeTAD HTL (device 3), and (D) an n-p device without perovskite layer (device 5).

These admittance measurements were performed in the dark at 0.0 V DC bias voltage and at temperatures ranging from 120 to 300 K with a 10 K temperature step size.

signatures,[8,11–14] a high-frequency capacitance signature (<10^5 Hz) and a low-frequency capacitance signature (<10^3 Hz), with an example shown in Figure 1A. The high-frequency capacitance signature is typically observed at temperatures below 240 K, which is labeled as D1 in Figure 1A. The low-frequency capacitance signature is typically observed at temperatures higher than 240 K, which is labeled as D2 in Figure 1A. The D1 signature has been often used to analyze defect activation energy and density of defects in perovskite absorber layers or at the interfaces in PSCs.[11,12,15–23] The D2 signature has often been correlated with ion or electronic charge accumulation at an interface or with a slow transient-induced charge injection.[24] The activation energies of D1 (E_a(D1)) and D2 (E_a(D2)) reported in the literature are summarized in Table S1. The device architectures include both n-i-p PSCs, i.e., the electron-transport layer (ETL) (n type) is directly deposited on transparent conducting oxide (TCO)-coated glass substrate, and p-i-n PSCs, i.e., the hole-transport layer (HTL) (p type) is directly deposited on TCO-coated glass substrate. The temperature-dependent capacitance frequency (C-f-T) and temperature-dependent capacitance voltage (C-V-T) results have also been used to calculate the dielectric constant (ϵ_r) of the perovskite absorber, using the equation of $\epsilon_r = C_g t/A\,\epsilon_0$, where ϵ_0 is the vacuum permittivity and A the device area. C_g is the geometrical capacitance estimated with the assumption that the perovskite layer is fully depleted, i.e., the depletion width (W) equals to or is larger than the thickness (t) of the perovskite layer. In the literature, the reported dielectric constants of the perovskite absorbers depend on temperature, which has been attributed to phase transition.[12] The reported electrical dielectric constants of perovskites at two typical temperatures, i.e., low temperature (120–150 K) and high temperature (300 K) are also summarized in Table S1.[11,23,25,26] The activation energies of D1 and D2 capacitance signatures and dielectric constants summarized in Table S1 show large discrepancies. Such differences have traditionally been attributed to the different electrical properties of perovskite absorbers synthesized by different processes and conditions.[13,17,19,20] Therefore, the activation energy and defect density extracted from

[1]Department of Physics and Astronomy, and Wright Center for Photovoltaics Innovation and Commercialization (PVIC), University of Toledo, Toledo, OH 43606, USA

[2]Department of Physics, College of Education for Pure Sciences, University of Tikrit, Tikrit, Salahuddin 34001, Iraq

[3]Department of Aeronautics and Astronautics, National Cheng Kung University, Tainan 70101, Taiwan

[4]Lead Contact

*Correspondence: jianvli@mail.ncku.edu.tw (J.V.L.), yanfa.yan@utoledo.edu (Y.Y.)

https://doi.org/10.1016/j.joule.2020.01.012

Approved for public release; distribution unlimited.

482

D1 capacitance signature have been used as guidance for improving the quality of PSCs. The large differences among the reported dielectric constants remain unclear.

In this paper, we show that the D1 high-frequency capacitance signature actually arises from the HTLs, not from perovskite absorbers. The D1 signature is not observed in PSCs without HTLs and is also observed in devices with HTL but without a perovskite layer. The high-frequency capacitance in PSCs without HTLs does not significantly depend on temperature and frequency, revealing no trapping and de-trapping of charge carriers. This suggests an apparent insulating behavior in the perovskite layer. Therefore, the high-frequency capacitance of PSCs without HTLs can be considered a geometric capacitance, from which the dielectric constant of the perovskite layer can be calculated. The discrepancy of the dielectric constants reported in the literature is due to the influence of HTLs. We further find that in n-i-p PSCs, the low-frequency capacitance spectra ($<10^3$ Hz) cannot be described by discrete signatures, suggesting complicated coupling (physiochemical mixing and/or interaction) between the perovskite layer and ETL and/or HTL. However, in p-i-n PSCs, the ETL and HTL do not present coupling effects. In this case, the spectra can be described by a single signature, which is the so-called D2 signature reported in the literature. This signature allows the calculation of the activation energy of the ionic conductivity of the perovskite layer.

RESULTS AND DISCUSSION

Our conclusions were drawn based on the C-f-T spectra measured from a large number of devices in both n-i-p and p-i-n architectures and with various ETL and HTL materials. To exclude the influence of processing condition and composition of perovskite absorber, we fabricated the PSCs using perovskite absorber layers synthesized using identical perovskite precursor and processing conditions. TAS measurements were performed in dark using a 30 mV_{rms} perturbation sinusoidal AC voltage with a frequency sweep range of 10^{-1}–10^6 Hz and 0 V DC bias voltage, if not specifically mentioned. The temperature was varied in the range of 120–300 K with a 10 K temperature step size. The general trend of capacitance dependence on angular frequency ($\omega = 2\pi f$) and temperature (C-ω-T) of n-i-p PSCs using spiro-OMeTAD HTLs are consistent with those of n-i-p PSCs using spiro-OMeTAD HTLs reported in the literature (Table S1). Two peculiar capacitance signatures are observed in the spectra: one is the D1 signature observed at low temperature (120–220 K) and high frequency ($\omega < 10^5$ Hz), and the other one is the D2 signature observed at high temperature (T > 240 K) and low frequency ($\omega < 10^3$ Hz). The activation energies of D1 and D2 and dielectric constants measured from our PSCs are summarized in Table 1.

Low-Temperature and High-Frequency Capacitance Signature (D1)

Planar n-i-p Devices

We first discuss the results measured from the n-i-p PSCs with and without spiro-OMeTAD HTL. The n-i-p PSCs with an HTL share the cell structure of FTO/SnO_2/C_{60}-SAM/$MA_{0.7}FA_{0.3}PbI_3$/spiro-OMeTAD/Au (devices 1–3). The device without spiro-OMeTAD HTL is named n-i (device 4). The device named n-p indicates the stacks without a perovskite layer, i.e., FTO/SnO_2/C_{60}-SAM/spiro-OMeTAD/Au (device 5). The SnO_2 ETLs were synthesized by atomic-layer deposition. The ultra-thin C_{60}-SAM layers and HTLs were deposited by spin coating. For the main results reported here, the perovskite layers have a composition of $MA_{0.7}FA_{0.3}PbI_3$ and were deposited by one-step solution processing. More details can be found in the Supplemental Information. We chose this composition because it enables the fabrication of PSCs with PCEs > 21%.[27] PSCs using $MAPbI_3$ absorbers have also been measured to verify the generality of the conclusions.

Approved for public release; distribution unlimited.

Table 1. Summary of Activation Energies of Capacitance Signatures and Dielectric Constants

Device #	Devices Architecture	Activation Energy (eV)		Dielectric Constant	
		D1	D2	Low T (120 K)	High T (300 K)
1	FTO/SnO_2/C_{60}-SAM/ $MA_{0.7}FA_{0.3}PbI_3$/100 nm spiro-OMeTAD/Au (n-i-p)	0.166 ± 0.005	–	05.95	32.27
2	FTO/SnO_2/C_{60}-SAM/ $MA_{0.7}FA_{0.3}PbI_3$/50 nm spiro-OMeTAD /Au (n-i-p)	0.286 ± 0.027	–	14.56	30.89
3	FTO/SnO_2/C_{60}-SAM/ $MA_{0.7}FA_{0.3}PbI_3$/10 nm spiro-OMeTAD/Au (n-i-p)	–	–	31.71	35.92
4	FTO/SnO_2/C_{60}-SAM/ $MA_{0.7}FA_{0.3}PbI_3$/Au (n-i)	–	–	32.54	33.38
5	FTO/SnO_2/C_{60}-SAM/100 nm spiro-OMeTAD/Au (n-p)	0.172 ± 0.005	–	02.28	09.89
6	FTO/SnO_2/C_{60}-SAM/ $MA_{0.7}FA_{0.3}PbI_3$/spiro-OMeTAD*/Au (n-i-p)	0.286 ± 0.011	–	05.87	11.34
7	FTO/SnO_2/C_{60}-SAM/100 nm spiro-OMeTAD*/Au (n-p)	0.297 ± 0.003	–	06.03	07.02
8	FTO/$MA_{0.7}FA_{0.3}PbI_3$/Au (i)	–	–	29.89	29.61
9	FTO/SnO_2/$MA_{0.7}FA_{0.3}PbI_3$/ 100 nm spiro-OMeTAD/Au (n-i-p)	0.171 ± 0.002	–	05.95	33.11
10	FTO/C_{60}-SAM/ $MA_{0.7}FA_{0.3}PbI_3$/100 nm spiro-OMeTAD/Au (n-i-p)	0.161 ± 0.004	–	05.95	19.49
11	FTO/$MA_{0.7}FA_{0.3}PbI_3$/ 100 nm spiro-OMeTAD/Au (i-p)	0.185 ± 0.004	–	05.95	12.89
12	ITO/PEDOT:PSS/ $MA_{0.7}FA_{0.3}PbI_3$/C_{60}/BCP/Ag (p-i-n)	0.019 ± 0.001	0.363 ± 0.012	34.58	26.12
13	ITO/PEDOT:PSS/C_{60}/BCP/ Ag (p-n)	0.016 ± 0.001	–	02.69	02.01
14	ITO/PTAA/$MA_{0.7}FA_{0.3}PbI_3$/ C_{60}/BCP/Ag (p-i-n)	–	0.371 ± 0.009	34.02	37.24
15	ITO/PTAA/C_{60}/BCP/Ag (p-n)	–	–	01.18	01.32
16	ITO/$MA_{0.7}FA_{0.3}PbI_3$/C_{60}/ BCP/Ag (i-n)	–	0.365 ± 0.022	22.04	21.08

List of the calculated activation energies of D1 and D2 capacitance signatures and electrical dielectric constants of our 16 devices with various architectures and ETLs/HTLs. FTO is fluorine-doped tin oxide (SnO_2) and C_{60}-SAM is substituted benzoic acid self-assembled monolayer. MA is methylamine, FA is formamidinium, spiro-OMeTAD is 2,2′,7,7′-tetrakis(N,N-dip-methoxyphenylamine)-9,9′-spirobifluorene doped with Co-TFSI and Li-TFSI. Spiro-OMeTAD* indicates undoped spiro-OMeTAD. The polytriarylamines (PTAA) HTL is undoped. PEDOT:PSS is poly(3,4-ethylenedioxythiophene) polystyrene sulfonate. The BCP is bathocuproine. The perovskite layer is about 500 nm thick. "–" means that the $-\omega dC/d\omega$ versus ω spectra do not form clear peaks. Underlines indicate that the calculated parameters belong to the charge transport layer, not perovskite.

Figure 1A shows the C-ω-T spectra obtained from a typical n-i-p PSC with a 100-nm-thick spiro-OMeTAD HTL doped with Li and Co salts (device 1). The high-frequency capacitance signature observed at temperatures from ~120 to ~220 K and high frequencies from 10^1 to 10^5 Hz with capacitance ranging between 10^{-8} and 10^{-7} F/cm^2 is the D1 signature, which has been reported in the literature. This capacitance

Approved for public release; distribution unlimited.

signature has been used to analyze defect properties in PSCs. Such analysis assumed a p-n junction in which the n-type semiconductor is the ETL, and the perovskite is the p-type semiconductor. The free electronic carriers diffuse and drift at the interface between the ETL and perovskite to form a space-charge region (SCR), which is the basis of TAS analysis.[28] If such a p-n junction indeed exists, similar signatures should be observed in devices without HTL. However, the C-ω-T spectra (Figure 1B) measured from our n-i (FTO/SnO_2/C_{60}-SAM/$MA_{0.7}FA_{0.3}PbI_3$/Au) perovskite device (device 4) show very different features, i.e., the D1 signature is no longer observed. These results strongly suggest that D1 signature is due not to the perovskite but in fact arises from the spiro-OMeTAD HTL. To confirm this conclusion, we measured the C-ω-T spectra from a PSC with only 10-nm-thick spiro-OMeTAD HTL (device 3). As shown in Figure 1C, the D1 signature is observed again but with significantly suppressed capacitance variation as compared with those measured from the PSC with 100-nm-thick HTL. It has been proposed that the increase of high-frequency capacitance was due to spiro-OMeTAD-induced increase of doping density in perovskite.[29] However, our results clearly suggest that the D1 capacitance signature is due to spiro-OMeTAD HTL. This is further confirmed by the C-ω-T spectra (Figure 1D) measured from a perovskite layer-free n-p device, i.e., FTO/SnO_2/C_{60}-SAM/spiro-OMeTAD/Au (device 5). The C-ω-T spectra at high frequencies are very similar to those measured from the n-i-p PSC (Figure 1A), except for the small differences of the capacitance values between the two cells.

It is important to note that for the device without spiro-OMeTAD HTL, the high-frequency capacitance ($<10^5$ Hz) does not obviously depend on temperature and frequency as shown in Figure 1B. This indicates that there is no change to the depletion width or no trapping and de-trapping of charge carriers in the device without HTL. It implies that the perovskite layer behaves similar to an insulator or acts as an apparent insulator under high-frequency AC modulations. In a steady state, there is no electric field present inside perovskite layer, as observed by Kelvin probe force microscopy (KPFM) results measured in PSCs.[30,31] KPFM measurements have shown junctions at perovskite-ETL and perovskite-HTL interfaces. Recent reports in the literature have shown that perovskite/ETL and perovskite/HTL interfaces are polarized due to ion migration.[32–39] The interfacial polarization cancels the electric field induced by the ETL and HTL, showing no electric field inside perovskite layer. At short times ($\lesssim$ ms) after a voltage perturbation, i.e., before the ions can transport and rearrange at the interfaces, only the capacitive charging occurs at the electrodes (see Scheme 1C in Belisle et al., 2017).[32] The interfacial polarization-induced screening accounts for the apparent insulating behavior in perovskite layer observed in the C-ω-T spectra at high frequencies, which is equivalent to short times after voltage perturbations. The sharp decrease of capacitance at frequencies higher than 10^5 Hz (Figure 1B) is due to the effects of series resistance and inductance of the characterization system,[40] which leads to the frequency peak at 1.88×10^5 Hz seen in the corresponding $-\omega dC/d\omega$ versus ω spectra (Figure S1). Similar peaks are seen in $-\omega dC/d\omega$ versus ω spectra of other devices. These frequency peaks are not discussed in this paper because they are not related to the properties of our devices. The apparent insulating behavior has two important implications. First, TAS cannot probe defects in perovskite bulk or at the interfaces between perovskite and charge transport layers (CTL). The D1 signatures reported in PSCs are due to HTLs. Second, the high-frequency capacitance can be used to calculate the dielectric constant of perovskite layer when PSCs without HTL are used for measurements. This is because under AC modulation, the capacitance at high frequency is due to geometrical contribution of the entire perovskite layer. Recently, Garcia-Belmonte and co-workers[41] recognized the limitations of TAS analysis for characterizing the

Approved for public release; distribution unlimited.

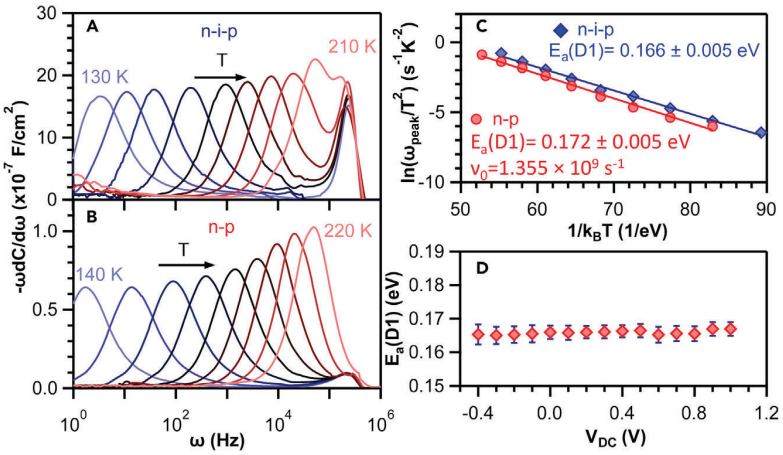


Figure 2. D1 Capacitance Signatures and Activation Energies

(A and B) $-\omega dC/d\omega$ versus ω of D1 signature extracted from the C-ω-T spectra shown in Figures 1A and 1D, respectively.

(C) Arrhenius plots, $\ln(\omega_{peak}/T^2)$ versus $1/k_BT$, extracted from the $-\omega dC/d\omega$ versus ω spectra shown in Figures 2A and 2B, respectively.

(D) The calculated bias-dependent activation energies of the n-i-p PSC calculated from C-ω-T spectra measured with various DC bias voltages ranging from −0.4 to +1.0 V with a 0.1 V voltage step size.

high- and low-frequency capacitance signatures from the perovskite in PSCs. They pointed out that the assumption of intrinsic perovskite layer could obstruct the basic principle of depletion layer modulation in the perovskite layer. Our results show that the apparent insulating behavior of perovskite is the origin of the limitations.

Capacitance of spiro-OMeTAD has been reported in the literature.[42–45] The origin of this capacitance was interpreted as chemical capacitance, which is defined as $C = q^2(\partial p/\partial \mu_p)$, where p is the hole density and μ_p is the electrochemical potential of spiro-OMeTAD.[8] Here, we consider the traditional definition of capacitance for the spiro-OMeTAD HTL, i.e., $C = dQ/dV$, where Q is the stored charge and V is the applied bias voltage. This suggests that the D1 capacitance signature (Figure 1D) should represent the trapping and de-trapping of charge carriers in spiro-OMeTAD HTL doped with Li and Co salts. The C-ω-T spectra and their corresponding $-\omega dC/d\omega$ versus ω spectra of an n-p device using undoped spiro-OMeTAD HTL (device 7) are shown in Figures S2A and S2B, respectively. No D1 signature was observed, further confirming that the D1 signature can be used to calculate the activation energy of dopants in spiro-OMeTAD HTL by plotting the derivative of capacitance spectra in the form of $-\omega dC/d\omega$ as a function of ω, Figures 2A and 2B. The activation energy (E_a) is calculated using the following equation[46]:

$$E_a = k_B T \ln\left(\nu_{th}\sigma_p N_V / \omega_{peak}\right) \qquad \text{(Equation 1)}$$

where k_B is Boltzmann constant, T the absolute temperature, ν_{th} the thermal velocity, σ_p the hole capture cross section, N_V the effective density of states of the valance band, and ω_{peak} the frequency of inflection in the C-ω-T spectra that is manifested as peaks in the $-\omega dC/d\omega$ versus ω spectra. These peaks shifted to higher frequency with the increase of temperature. The peak frequencies and their corresponding temperatures are used to construct an Arrhenius plot to determine the activation energy of the transition. The derivatives of capacitance spectra of D1, i.e., $-\omega dC/d\omega$ versus ω, of an n-i-p PSC with a 100-nm spiro-OMeTAD HTL are plotted in Figure 2A,

Approved for public release; distribution unlimited.

which are very similar to those measured from the perovskite-free n-p device (FTO/SnO_2/C_{60}-SAM/spiro-OMeTAD/Au) (device 5) shown in Figure 2B. Both $-\omega dC/d\omega$ versus ω spectra show fully developed and clear peaks, from which the Arrhenius plots were calculated (Figure 2C). The calculated activation energies of D1 (E_a(D1)) using corresponding Arrhenius plots are 0.166 $\pm$ 0.005 and 0.172 $\pm$ 0.005 eV, for the n-i-p and n-p devices, respectively. These activation energies are related to the electrical transport properties of the spiro-OMeTAD layer. The Arrhenius plot shown in Figure 2C also gives an attempt-to-escape frequency (ν_0) of $\sim 1.35 \times 10^9$ Hz, which is calculated from the intercept with $\ln(\omega_{peak}/T^2)$ of the linear fit of the plot at 300 K. We fabricated n-i-p solar cells with different perovskite thicknesses. We found that the D1 feature (activation energy) does not depend on the thickness of the perovskite layer.

Bias-dependent TAS measurements were performed for a PSC with 100-nm spiro-OMeTAD HTL to confirm the nature of D1 signature. In this case, various DC biases and constant AC modulation were applied. When the DC and AC modulations are applied together, the Fermi level (E_F) oscillates around a mean position. The band bending in spiro-OMeTAD HTL will depend on the DC bias. As a result, the measured activation energy of interface states will respond to the DC bias depending on its origin. As shown in Figure 2D, the activation energy related to D1 signature does not depend on the DC bias, confirming that D1 is not related to interface states but only related to trapping and de-trapping of charge carriers in the spiro-OMeTAD layer. Therefore, our results confirm that the D1 signature observed in perovskite PSCs is attributed to the spiro-OMeTAD HTL. The C-V measurement was conducted at 300 K and 6.28×10^4 Hz for the n-p device with 100-nm-doped spiro-OMeTAD HTL and without perovskite layer to gain more information of the electrical properties of the doped spiro-OMeTAD HTL. The Mott-Schottky plot, i.e., $1/C^2$ versus V_{DC}, measured for this n-p device at 300 K is shown in Figure S3A, which yields a carrier concentration of 5.86×10^{17} cm^{-3}, consistent with the value (1.2×10^{17} cm^{-3}) obtained from Hall measurement (300 K). The carrier concentration is calculated from the slope of the linear fit (blue line, Figure S3A) of the Mott-Schottky plot using the equation $N_{CV} = -(2/q\epsilon\epsilon_0)(dC^{-2}(V_{DC})/dV_{DC})^{-1}$. A built-in potential ($V_{bi}$) of 0. 59 V is determined from the line intercept with the bias voltage axis and a depletion width of 14.8 nm at a zero DC bias is calculated by $W = [2\epsilon\epsilon_0 (V_{bi} - V_{DC})/(qN_{CV})]^{\frac{1}{2}}$. The defect distributions, shown in Figure S3B, were calculated to understand the defect density of states (N_t) using the equation[47] $N_t = (V_{bi}/qW)(1/k_BT)[-\omega(dC/d\omega)]$. The energy of the defect distribution (E_t) is calculated by the equation[47] $E_t = E_a - k_BT\,ln(2\nu_0/\omega)$. The distribution of defect density of state shows a peak value of $\sim 9.88 \times 10^{18}$ $cm^{-3}\cdot eV^{-1}$ located at $\sim$0.16 eV with a corresponding integrated trap density of $\sim 5.79 \times 10^{17}$ cm^{-3}.

Inverted p-i-n Devices

The D1 capacitance signature has also been observed in C-ω-T spectra measured from p-i-n PSCs. We fabricated p-i-n PSCs using PEDOT:PSS and PTAA HTLs with a cell structure of ITO/HTL/$MA_{0.7}FA_{0.3}PbI_3$/BCP/C_{60}/Ag. The perovskite layers were synthesized using identical processing conditions as the n-i-p PSCs discussed previously. The PEDOT:PSS layer has a typical thickness of 70 nm, whereas the thickness is about 15 nm for polytriarylamines (PTAA). Figures 3A and 3B show the C-ω-T spectra measured from a p-i-n PSC (device 12) and a p-n device (device 13) using PEDOT:PSS HTLs. Their corresponding $-\omega dC/d\omega$ versus ω spectra are shown in Figures 3C and 3D, respectively. The high-frequency capacitance D1 signature is clearly observed. The $-\omega dC/d\omega$ versus ω spectra also show nice and clear peaks. However, when the PEDOT:PSS HTL is absent, the D1 capacitance signature is not observed (Figure S4), revealing that the D1 signature

Approved for public release; distribution unlimited.

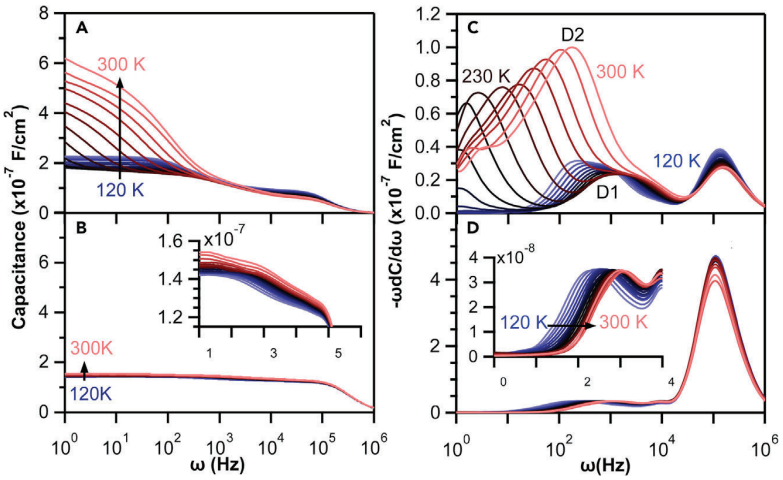


Figure 3. D2 Capacitance Signature

(A and B) C-ω-T spectra measured from (A) a p-i-n PSC (device 12) and (B) p-n device without the perovskite layer (device 13).

(C and D) Corresponding $-\omega dC/d\omega$ versus ω spectra of Figures 3A and 3B, respectively.

The inserts in Figures 3B and 3D are enlarged spectra to show more details. The measurements were conducted in the dark with a 0.0 V DC bias.

also arises from the HTL. The characteristic frequencies shown in Figures 3C and 3D allow the extraction of the Arrhenius plots (Figure S5) from which the calculated activation energy E_a(D1) is 0.019 ± 0.001 eV for the p-i-n PSC and 0.016 ± 0.001 eV for the p-n device, which are almost the same. These results further confirm that the D1 signature is attributed to the PEDOT:PSS HTL. It is noted that E_a(D1) of PEDOT:PSS is about one order of magnitude smaller than that of spiro-OMeTAD (0.172 eV). This is because the conductivity of PEDOT:PSS is significantly higher than spiro-OMeTAD. We also measured the C-ω-T spectra of a p-i-n PSC using PTAA HTL (device 14) (Figure S6A). However, the $-\omega dC/d\omega$ versus ω spectra do not show D1 peaks at high frequency ($\omega < 10^5$ Hz), indicating no D1 capacitance signature (Figure S6B). The results are consistent with that of the perovskite-free device (PTAA/C_{60}/BCP) as shown in Figure S6C. In p-i-n PSCs using PTAA HTLs, the PTAA must be ultra-thin because of its low electrical conductivity. Therefore, the PTAA layer is expected to be fully depleted. As a result, there is no trapping and de-trapping process during AC perturbation, explaining why no D1 capacitance signature is observed in p-i-n PSCs using ultra-thin PTAA HTLs.

We also measured C-ω-T spectra from HTL-free devices using different perovskites including $MAPbI_3$, $FA_{0.3}MA_{0.7}PbI_3$, and perovskites with different thicknesses. As shown in Figure S7, all devices showed no D1 signature, suggesting that the "apparent insulating behavior" is a general phenomenon for all halide perovskites.

The Dielectric Constant

As discussed previously, in PSCs without HTL, the high-frequency capacitance is due to a contribution from the entire perovskite layer and can be considered as C_g, implying that the dielectric constant can be calculated using the high-frequency capacitance. However, to obtain reliable values, the capacitance contribution from CTLs must be excluded. We measured C-V-T curves of a device with the structure of an FTO/SnO_2/C_{60}-SAM/$MA_{0.7}FA_{0.3}PbI_3$/Au device (device 4) at an AC frequency of 6.28×10^4 Hz. As expected, the capacitance does not significantly vary with temperature or bias voltage (Figure S8A). As a result, a consistent dielectric constant of

Approved for public release; distribution unlimited.

488

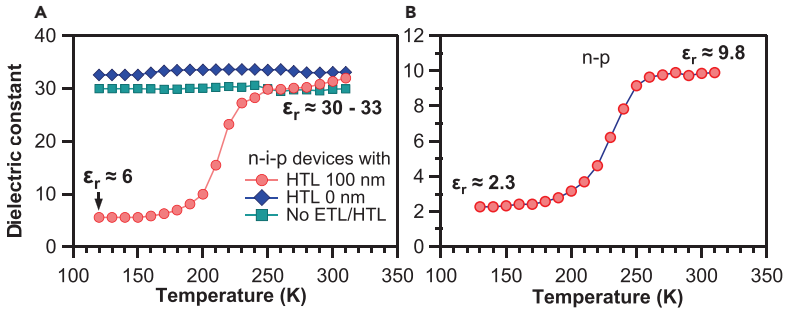


Figure 4. The Dielectric Constants Obtained from Different Device Architectures

(A and B) Dielectric constant as a function of temperature of (A) PSCs with different architectures: FTO/SnO_2/C_{60}-SAM/$MA_{0.7}FA_{0.3}PbI_3$/spiro-OMeTAD/Au with 100 nm (device 1) (circle markers), 0 nm (device 7) (diamond markers) HTLs, and without ETL/HTL, FTO/$MA_{0.7}FA_{0.3}PbI_3$/Au (device 8) (diamond markers), and (B) the n-p junction without a perovskite layer.

These results are calculated from the capacitance voltage measurements performed in the dark at 6.28×10^4 Hz angular frequency (Figure S8).

~33 is obtained for all temperatures (Figure 4A). Similar dielectric constants were observed when the thickness of the perovskite layer was varied (Figure S9A). For the device without ETL and HTL, a consistent dielectric constant of ~30 is also obtained for all temperatures (Figure 4A). The result indicates that the SnO_2 ETL has a rather small effect on the high-frequency capacitance. However, for PSCs with HTLs, the dielectric constant of the perovskite layer cannot be reliably calculated due to the capacitance contribution from the HTL (see Figures 4A, S8C, and S8D). All organic HTL materials such as spiro-OMeTAD, PTAA, and PEDOT:PSS are ionic conductors whose electrical conductivity sensitively depends on the temperature and frequency. At low enough temperature, thick HTLs become insulating, which contributes to the measurement of total capacitance. Therefore, the calculated dielectric constant is expected to be much lower at low temperatures. Indeed, we observed this trend for dielectric constants calculated from the C-V-T results measured from a PSC with a 100-nm-thick spiro-OMeTAD HTL (device 1). A similar dielectric constant-temperature dependency trend was observed in an n-p device, i.e., FTO/SnO_2/C_{60}-SAM/spiro-OMeTAD/Au (device 5), as shown in Figure 4B. The small discrepancy is likely due to the influence of low electrical conductivity of the perovskite layer in the n-i-p PSC. Our results suggest that to reliably measure the dielectric constant of perovskite layers in PSCs, the contribution of CTL materials must be carefully excluded, which is consistent with previous suggestions by Lopez-Varo et al.[48] and Almora et al.[41] The discrepancies of dielectric constants reported in the literature (Table S1) are due to the influence of CTL materials, rather than the different properties of perovskite or different phases as reported in literature. We have also measured the dielectric constants of HTL-free device using $MAPbI_3$ perovskite layer with three thicknesses at various temperatures. As shown in Figure S9B, dielectric constant steps or discontinuities near 160 K are observed, which is consistent with previous reports.[49,50] Such discontinuities are due to phase transition of $MAPbI_3$ perovskite.[51] However, $FAPbI_3$ does not show a phase transition at a similar temperature.[51] Therefore, no dielectric constant discontinuity was observed in $MA_{0.7}FA_{0.3}PbI_3$ PSCs.

High-Temperature and Low-Frequency Capacitance Signature (D2)

Planar n-i-p Devices

D2 refers to the capacitance signature seen at low frequencies ($\omega < 10^3$ Hz) and at higher temperatures between ~240 and 300 K with capacitance varying between

Approved for public release; distribution unlimited.

10^{-7} and $<10^{-5}$ F/cm^2 (Figure 1A). D2 capacitance signature is observed in the devices with and without HTLs. Similar feature has been reported previously.[8,12] Comparison of TAS spectra shown in Figure 1 suggests that the SnO_2 ETL and spiro-OMeTAD HTL also contribute to the D2 signature capacitance. It is noted that the low-frequency capacitance spectra measured from n-i-p PSCs (devices 1–3) show no signature, which is seen more clearly if the spectra are plotted in a linear scale (Figure S10A). The $-\omega dC/d\omega$ versus ω spectra from the TAS spectra of the n-i-p PSC using 100-nm-thick spiro-OMeTAD HTL (device 1) are shown in Figure S10B. The plot shows no clear peaks, which indicates dispersive capacitance signatures. Therefore, it is inappropriate to consider these low-frequency spectra as a single trapping and de-trapping signature. It is noted that in literature the E_a(D2) reported for n-i-p PSCs with spiro-OMeTAD HTL were not calculated based on the Arrhenius plots extracted from $-\omega dC/d\omega$ versus ω spectra due to the lack of clear peaks. Instead, the $d\ln(C)/d\ln(\omega)$ versus ω spectra were used to extract the Arrhenius plot since the $d\ln(C)/d\ln(\omega)$ versus ω spectra show clear peaks. Following this approach, $d\ln(C)/d\ln(\omega)$ versus ω spectra of the n-i-p PSC (device 1) with its C-ω-T spectra shown in Figure 1A and the n-i device (device 4) with its C-ω-T spectra shown in Figure 1B are shown by the red and blue spectra in Figure S11A, respectively. These spectra show clear peaks at low frequencies, allowing extractions of Arrhenius plots shown Figure S11B, from which the calculated E_a(D2) is 0. 592 $\pm$ 0.012 eV for the n-i-p PSC but only 0.399 $\pm$ 0.001 eV for the n-i device without spiro-OMeTAD HTL. Because the perovskite layers were synthesized using identical precursors and conditions, such large discrepancy suggests that it is inappropriate to use $d\ln(C)/d\ln(\omega)$ versus ω spectra to calculate activation energy. We attributed this to the contribution of capacitance at low frequencies from both spiro-OMeTAD HTL and SnO_2 ETL, which couple with the capacitance of perovskite. To verify the contribution of SnO_2 ETL, we measured the C-ω-T spectra (Figure S12) from a p-n device (ITO/spiro-OMeTAD/C_{60}/BCP/Ag) (device 16). The comparison between Figures 1D and S12 shows clear contribution from SnO_2 ETL to the low-frequency capacitance. Therefore, for PSCs in n-i-p cell structure, E_a(D2) values are labeled by "–" in Table 1, which means that D2 is unmeasurable using the conventional method.

Inverted p-i-n Devices

It is interesting to note that in the p-i-n PSCs, the ETLs and HTLs do not make any observable coupling to the low-frequency capacitance, which is clearly seen in Figures 3 and S6. As seen in Figure 3C, the $-\omega dC/d\omega$ versus ω low-frequency spectra show nice and clear peaks for a large temperature range (230–300 K). The Arrhenius plot obtained from these spectra is shown in Figure S5, which gives an E_a(D2) of 0.363 $\pm$ 0.012 eV for the p-i-n PSC using PEDOT:PSS HTL (device 12). As seen in Figure 3D, the device with PEDOT:PSS and without perovskite layer (device 13) does not show D2 signature. Therefore, E_a(D2) value obtained from the PSC using PEDOT:PSS HTL has no contribution from the HTL. Similar results are obtained for p-i-n PSCs using PTAA HTL (device 14) (Figure S6) and the device without HTL and non-SnO_2 ETL (device 16) (Figure S4). The corresponding calculated E_a(D2) are 0.371 $\pm$ 0.009 eV for the PSC using PTAA HTL (Figure S6D) and 0.365 $\pm$ 0.022 eV for the PSC without HTL (Figure S4B). These values are very similar to that obtained from the p-i-n PSC using PEDOT:PSS HTL (device 12). Therefore, for inverted p-i-n PSCs, the E_a(D2) value can be used to characterize the electrical transport properties of the perovskite layer at low frequencies, which are related to ion migration. D2 is in fact due to the ionic relaxation[52] of the perovskite absorber, which behaves as an ionic insulator at high frequencies and an ionic conductor at low frequencies with a demarcation point at $\omega_{ir} = \omega_{peak}$, where $\omega_{ir} = \sigma_{ion}/\epsilon_r\epsilon_0$, σ_{ion} is the ionic conductivity in the perovskite absorber. The ionic relaxation frequencies obtained from

Approved for public release; distribution unlimited.

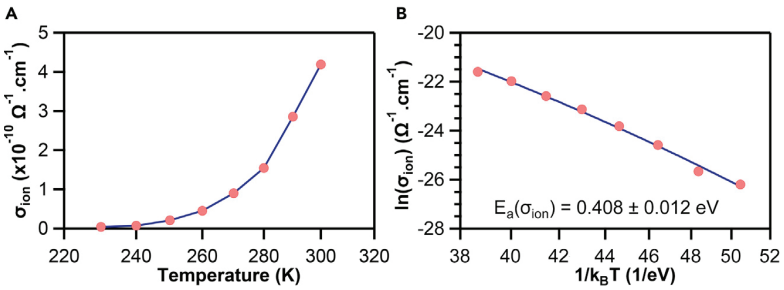


Figure 5. The Ionic Conductivity of Perovskite

(A) Ionic conductivity as a function of temperature and (B) corresponding Arrhenius plot of an ITO/PEDOT:PSS/$MA_{0.7}FA_{0.3}PbI_3$/C_{60}/BCP/Ag PSC (device 12) calculated using ionic relaxation frequencies obtained from Figure 3C.

Figure 3C are 1.578 Hz (230 K), 2.701 Hz (240 K), 7.910 Hz (250K), 17.042 Hz (260 K), 34.003 Hz (270 K), 58.190 Hz (280 K), 107.530 Hz (290 K), and 157.830 Hz (300 K). We calculated the ionic conductivity, σ_{ion}, at various temperatures using these ionic relaxation frequencies and a dielectric constant ϵ_r of 30 (Figure 4). The results are shown in Figure 5A. The ionic conductivity increases with temperature, reaching $4.190 \times 10^{-10}\ \Omega^{-1}\cdot cm^{-1}$ at 300 K. The corresponding Arrhenius plot, $\ln(\sigma_{ion})$ versus $1/k_BT$, is shown in Figure 5B. The calculated activation energy from this Arrhenius plot is 0.408 ± 0.012 eV, which is consistent with the activation energy (0.363 ± 0.012 eV) calculated from $\ln\omega_{peak}/T^2$ versus $1/k_BT$ Arrhenius plot (Figure S5).

Conclusions

In conclusion, we have shown that there is no trapping and de-trapping of charge carriers in perovskite layers in PSCs in TAS measurements, revealing an apparent insulating behavior of the perovskite layers. It implies that TAS cannot be applied to correctly analyze the properties of defects in perovskite absorbers or at interfaces in PSCs without careful scrutiny. The so-called D1 high-frequency capacitance signature is due to the CTLs used in PSCs. For PSCs without HTLs, the high-frequency capacitance can be considered geometric capacitance and can be used to estimate the dielectric constant of perovskite layers. The significant discrepancy of temperature-dependent dielectric constants previously reported in literature is due to the influence of HTLs. In n-i-p PSCs, so-called low-frequency capacitance signatures cannot be used to evaluate the electrical transport properties, due to coupling with ETLs and HTLs. However, in p-i-n PSCs, the organic ETLs and HTLs do not significantly influence the low-frequency capacitance. Therefore, the D2 capacitance signature can be used to characterize the ionic transport properties of the perovskite layer.

EXPERIMENTAL PROCEDURES

Full details of the device fabrication method can be found in the Supplemental Information.

Devices Characterizations

All temperature-dependent measurements were performed using a Solartron Modulab potentiostat equipped with a frequency response analyzer (Ametek Inc.). A built in XM-studio software to the Modulabl system is used to set up, run experiments, and obtain the results. The thermal admittance spectroscopy measurements were done under dark equilibrium and a constant AC modulation voltage of 30 mV_{rms} with frequency (f) swept from 10^6 to 10^{-1} Hz. In bias-dependence TAS measurements, a DC bias voltage was

Approved for public release; distribution unlimited.

varied from −0.4 to 1.0 V at a step size of 0.1 V. Capacitance voltage measurements were performed in dark with DC bias voltage (V_{DC}) swept from −1.5 to 0.5 V with 30 mV_{rms} AC modulation voltage (V_{AC}) and $\omega = 2\pi \times 10^4$ Hz frequency. A liquid-nitrogen cooled cryo-system (Janis VPF-100 system) was used to carry out all the temperature dependent (from 120 to 310 K with a step size of 10 K) measurements. The temperature was measured and controlled by two channels temperature controller (Lakeshore 330). One sensor (Silicon diode thermometer) was connected to the thermal impedance displacer that is machined to fit precisely within the tail section of the liquid nitrogen dewar, and the other sensor was mounted on the top of the device directly to ensure that the recorded temperature is the device temperature. Heater and thermometer are provided on the thermal impedance displacer to better control the sample stage temperature. In order to ensure the temperature is stable, between one temperature step to another, the measurements were delayed for 15 min. LABVIEW software was used for controlling the temperature and running the experiment by Modulab.

SUPPLEMENTAL INFORMATION

Supplemental Information can be found online at https://doi.org/10.1016/j.joule.2020.01.012.

ACKNOWLEDGMENTS

This material is based upon work supported by the U.S. Department of Energy's Office of Energy Efficiency and Renewable Energy (EERE) under the Solar Energy Technology Office award number DE-EE0008753 and research sponsored by Air Force Research Laboratory under agreement number FA9453-18-2-0037. The TAS characterization is supported by National Science Foundation under contract number DMR-1807818. The US government is authorized to reproduce and distribute reprints for governmental purposes notwithstanding any copyright notation thereon. The views and conclusions contained herein are those of the authors and should not be interpreted as necessarily representing the official policies or endorsements, either expressed or implied, of Air Force Research Laboratory, US Department of Energy, or the US government. R.A.A. is also financially supported by the Higher Committee for Education Development (HCED) in the scholarship program started in 2009 with funding from the Iraqi Prime Minister's Office. J.V.L. acknowledges funding from the Ministry of Science and Technology, Taiwan, under MOST 107-2218-E-006-022-MY3.

AUTHOR CONTRIBUTIONS

R.A.A. carried out the measurements and data analysis. Z.S., C.C., C.L., C.W., and L.C. fabricated devices in this study. M.A.R. and R.J.E. assisted in the low-temperature capacitance measurements. X.W. provided necessary theoretical information. R.A.A., J.V.L., and Y.Y. wrote the manuscript. All co-authors commented on the manuscript. Y.Y. directed and supervised the project leading to this publication.

DECLARATION OF INTERESTS

The authors declare no competing interests.

Received: September 16, 2019
Revised: October 18, 2019
Accepted: January 15, 2020
Published: February 12, 2020

Approved for public release; distribution unlimited.

REFERENCES

1. Kojima, A., Teshima, K., Shirai, Y., and Miyasaka, T. (2009). Organometal halide perovskites as visible-light sensitizers for photovoltaic cells. J. Am. Chem. Soc. *131*, 6050–6051.

2. Jung, E.H., Jeon, N.J., Park, E.Y., Moon, C.S., Shin, T.J., Yang, T.Y., Noh, J.H., and Seo, J. (2019). Efficient, stable and scalable perovskite solar cells using poly(3-hexylthiophene). Nature *567*, 511–515.

3. Baumann, A., Väth, S., Rieder, P., Heiber, M.C., Tvingstedt, K., and Dyakonov, V. (2015). Identification of trap states in perovskite solar cells. J. Phys. Chem. Lett. *6*, 2350–2354.

4. Nah, S., Spokoyny, B., Jiang, X., Stoumpos, C., Soe, C.M.M., Kanatzidis, M.G., and Harel, E. (2018). Transient sub-bandgap states in halide perovskite thin films. Nano Lett. *18*, 827–831.

5. Landi, G., Barone, C., Mauro, C., Neitzert, H.C., and Pagano, S. (2016). A noise model for the evaluation of defect states in solar cells. Sci. Rep. *6*, 29685.

6. Lee, S.M., Moon, C.J., Lim, H., Lee, Y., Choi, M.Y., and Bang, J. (2017). Temperature-dependent photoluminescence of cesium lead halide perovskite quantum dots: splitting of the photoluminescence peaks of $CsPbBr_3$ and $CsPb(Br/I)_3$ quantum dots at low temperature. J. Phys. Chem. C *121*, 26054–26062.

7. Heo, S., Seo, G., Lee, Y., Lee, D., Seol, M., Lee, J., Park, J.-B., Kim, K., Yun, D.-J., Kim, Y.S., et al. (2017). Deep level trapped defect analysis in $CH_3NH_3PbI_3$ perovskite solar cells by deep level transient spectroscopy. Energy Environ. Sci. *10*, 1128–1133.

8. Duan, H.S., Zhou, H., Chen, Q., Sun, P., Luo, S., Song, T.B., Bob, B., and Yang, Y. (2015). The identification and characterization of defect states in hybrid organic–inorganic perovskite photovoltaics. Phys. Chem. Chem. Phys. *17*, 112–116.

9. Almora, O., Aranda, C., and Garcia-Belmonte, G. (2018). Do capacitance measurements reveal light-induced bulk dielectric changes in photovoltaic perovskites? J. Phys. Chem. C *122*, 13450–13454.

10. Li, J.V., Crandall, R.S., Repins, I.L., Nardes, A.M., and Levi, D.H. (2011). Applications of admittance spectroscopy in photovoltaic devices beyond majority-carrier trapping defects. 37th IEEE Photovoltaic Specialists Conference, June 19-24, 2011.

11. Samiee, M., Konduri, S., Ganapathy, B., Kottokkaran, R., Abbas, H.A., Kitahara, A., Joshi, P., Zhang, L., Noack, M., and Dalal, V. (2014). Defect density and dielectric constant in perovskite solar cells. Appl. Phys. Lett. *105*, 153502.

12. Almora, O., Zarazua, I., Mas-Marza, E., Mora-Sero, I., Bisquert, J., and Garcia-Belmonte, G. (2015). Capacitive dark currents, hysteresis, and electrode polarization in lead halide perovskite solar cells. J. Phys. Chem. Lett. *6*, 1645–1652.

13. Chen, Q., Zhou, H., Fang, Y., Stieg, A.Z., Song, T.B., Wang, H.H., Xu, X., Liu, Y., Lu, S., You, J., et al. (2015). The optoelectronic role of chlorine in $CH_3NH_3PbI_3(Cl)$-based perovskite solar cells. Nat. Commun. *6*, 7269.

14. Xu, X., and Wang, M. (2017). Photocurrent hysteresis related to ion motion in metal-organic perovskites. Sci. China Chem. *60*, 396–404.

15. Liu, N., Du, Q., Yin, G., Liu, P., Li, L., Xie, H., Zhu, C., Li, Y., Zhou, H., Zhang, W.-B., and Chen, Q. (2018). Extremely low trap-state energy level perovskite solar cells passivated using NH_2-POSS with improved efficiency and stability. J. Mater. Chem. A *6*, 6806–6814.

16. Almora, O., Guerrero, A., and Garcia-Belmonte, G. (2016). Ionic charging by local imbalance at interfaces in hybrid lead halide perovskites. Appl. Phys. Lett. *108*, 043903.

17. Heo, J.H., Song, D.H., Han, H.J., Kim, S.Y., Kim, J.H., Kim, D., Shin, H.W., Ahn, T.K., Wolf, C., Lee, T.W., and Im, S.H. (2015). Planar $CH_3NH_3PbI_3$ perovskite solar cells with constant 17.2% average power conversion efficiency irrespective of the scan rate. Adv. Mater. *27*, 3424–3430.

18. Li, W., Zhang, W., Van Reenen, S., Sutton, R.J., Fan, J., Haghighirad, A.A., Johnston, M.B., Wang, L., and Snaith, H.J. (2016). Enhanced UV-light stability of planar heterojunction perovskite solar cells with caesium bromide interface modification. Energy Environ. Sci. *9*, 490–498.

19. De Marco, N., Zhou, H., Chen, Q., Sun, P., Liu, Z., Meng, L., Yao, E.P., Liu, Y., Schiffer, A., and Yang, Y. (2016). Guanidinium: a route to enhanced carrier lifetime and open-circuit voltage in hybrid perovskite solar cells. Nano Lett. *16*, 1009–1016.

20. Jiang, M., Lan, F., Zhao, B., Tao, Q., Wu, J., Gao, D., and Li, G. (2016). Observation of lower defect density in $CH_3NH_3Pb(I,Cl)_3$ solar cells by admittance spectroscopy. Appl. Phys. Lett. *108*, 243501.

21. Wang, Z., McMeekin, D.P., Sakai, N., van Reenen, S., Wojciechowski, K., Patel, J.B., Johnston, M.B., and Snaith, H.J. (2017). Efficient and air-stable mixed-cation lead mixed-halide perovskite solar cells with n-doped organic electron extraction layers. Adv. Mater. *29*, 1604186.

22. Prochowicz, D., Yadav, P., Saliba, M., Saski, M., Zakeeruddin, S.M., Lewiński, J., and Grätzel, M. (2017). Reduction in the interfacial trap density of mechanochemically synthesized $MAPbI_3$. ACS Appl. Mater. Interfaces *9*, 28418–28425.

23. Shao, Y., Xiao, Z., Bi, C., Yuan, Y., and Huang, J. (2014). Origin and elimination of photocurrent hysteresis by fullerene passivation in $CH_3NH_3PbI_3$ planar heterojunction solar cells. Nat. Commun. *5*, 5784.

24. Ebadi, F., Taghavinia, N., Mohammadpour, R., Hagfeldt, A., and Tress, W. (2019). Origin of apparent light-enhanced and negative capacitance in perovskite solar cells. Nat. Commun. *10*, 1574.

25. Pockett, A., Eperon, G.E., Peltola, T., Snaith, H.J., Walker, A., Peter, L.M., and Cameron, P.J. (2015). Characterization of planar lead halide perovskite solar cells by impedance spectroscopy, open-circuit photovoltage decay, and intensity-modulated photovoltage/photocurrent spectroscopy. J. Phys. Chem. C *119*, 3456–3465.

26. Zarazua, I., Bisquert, J., and Garcia-Belmonte, G. (2016). Light-induced space-charge accumulation zone as photovoltaic mechanism in perovskite solar cells. J. Phys. Chem. Lett. *7*, 525–528.

27. Wang, C., Xiao, C., Yu, Y., Zhao, D., Awni, R.A., Grice, C.R., Ghimire, K., Constantinou, I., Liao, W., Cimaroli, A.J., et al. (2017). Understanding and eliminating hysteresis for highly efficient planar perovskite solar cells. Adv. Energy Mater. *7*, 1700414.

28. Li, J.V., and Ferrari, G. (2018). Capacitance Spectroscopy of Semiconductors (CRC Press).

29. Guerrero, A., Juarez-Perez, E.J., Bisquert, J., Mora-Sero, I., and Garcia-Belmonte, G. (2014). Electrical field profile and doping in planar lead halide perovskite solar cells. Appl. Phys. Lett. *105*, 133902.

30. Jiang, C.S., Yang, M., Zhou, Y., To, B., Nanayakkara, S.U., Luther, J.M., Zhou, W., Berry, J.J., van de Lagemaat, J.v.d., Padture, N.P., et al. (2015). Carrier separation and transport in perovskite solar cells studied by nanometre-scale profiling of electrical potential. Nat. Commun. *6*, 8397.

31. Xiao, C., Wang, C., Ke, W., Gorman, B.P., Ye, J., Jiang, C.S., Yan, Y., and Al-Jassim, M.M. (2017). Junction quality of SnO_2-based perovskite solar cells investigated by nanometer-scale electrical potential profiling. ACS Appl. Mater. Interfaces *9*, 38373–38380.

32. Belisle, R.A., Nguyen, W.H., Bowring, A.R., Calado, P., Li, X., Irvine, S.J.C., McGehee, M.D., Barnes, P.R.F., and O'Regan, B.C. (2017). Interpretation of inverted photocurrent transients in organic lead halide perovskite solar cells: proof of the field screening by mobile ions and determination of the space charge layer widths. Energy Environ. Sci. *10*, 192–204.

33. Eames, C., Frost, J.M., Barnes, P.R.F., O'Regan, B.C., Walsh, A., and Islam, M.S. (2015). Ionic transport in hybrid lead iodide perovskite solar cells. Nat. Commun. *6*, 7497.

34. Tress, W., Marinova, N., Moehl, T., Zakeeruddin, S.M., Nazeeruddin, M.K., and Grätzel, M. (2015). Understanding the rate-dependent J–V hysteresis, slow time component, and aging in $CH_3NH_3PbI_3$ perovskite solar cells: the role of a compensated electric field. Energy Environ. Sci. *8*, 995–1004.

35. Zhang, Y., Liu, M., Eperon, G.E., Leijtens, T.C., McMeekin, D., Saliba, M., Zhang, W., de Bastiani, M., Petrozza, A., Herz, L.M., et al. (2015). Charge selective contacts, mobile ions and anomalous hysteresis in organic–inorganic perovskite solar cells. Mater. Horiz. *2*, 315–322.

36. Leijtens, T., Srimath Kandada, A.R.S., Eperon, G.E., Grancini, G., D'Innocenzo, V., Ball, J.M., Stranks, S.D., Snaith, H.J., and Petrozza, A. (2015). Modulating the electron–hole interaction in a hybrid lead halide perovskite

Approved for public release; distribution unlimited.

493

with an electric field. J. Am. Chem. Soc. *137*, 15451–15459.

37. Zarazua, I., Han, G., Boix, P.P., Mhaisalkar, S., Fabregat-Santiago, F., Mora-Seró, I., Bisquert, J., and Garcia-Belmonte, G. (2016). Surface recombination and collection efficiency in perovskite solar cells from impedance analysis. J. Phys. Chem. Lett. *7*, 5105–5113.

38. Ravishankar, S., Almora, O., Echeverría-Arrondo, C., Ghahremanirad, E., Aranda, C., Guerrero, A., Fabregat-Santiago, F., Zaban, A., Garcia-Belmonte, G., and Bisquert, J. (2017). Surface polarization model for the dynamic hysteresis of perovskite solar cells. J. Phys. Chem. Lett. *8*, 915–921.

39. Jacobs, D.A., Wu, Y., Shen, H., Barugkin, C., Beck, F.J., White, T.P., Weber, K., and Catchpole, K.R. (2017). Hysteresis phenomena in perovskite solar cells: the many and varied effects of ionic accumulation. Phys. Chem. Chem. Phys. *19*, 3094–3103.

40. Scofield, J.H. (1995). Effects of series resistance and inductance on solar cell admittance measurements. Sol. Energy Mater. Sol. Cells *37*, 217–233.

41. Almora, O., García-Batlle, M., and Garcia-Belmonte, G. (2019). Utilization of temperature-sweeping capacitive techniques to evaluate band gap defect densities in photovoltaic perovskites. J. Phys. Chem. Lett. *10*, 3661–3669.

42. Fabregat-Santiago, F., Bisquert, J., Palomares, E., Haque, S.A., and Durrant, J.R. (2006). Impedance spectroscopy study of dye-sensitized solar cells with undoped spiro-OMeTAD as hole conductor. J. Appl. Phys. *100*, 034510.

43. Dualeh, A., Moehl, T., Tétreault, N., Teuscher, J., Gao, P., Nazeeruddin, M.K., and Grätzel, M. (2014). Correction to impedance spectroscopic analysis of lead iodide perovskite-sensitized solid-state solar cells. ACS Nano *8*, 4053.

44. Dualeh, A., Moehl, T., Nazeeruddin, M.K., and Grätzel, M. (2013). Temperature dependence of transport properties of spiro-MeOTAD as a hole transport material in solid-state dye-sensitized solar cells. ACS Nano *7*, 2292–2301.

45. Gonzalez-Pedro, V., Juarez-Perez, E.J., Arsyad, W.S., Barea, E.M., Fabregat-Santiago, F., Mora-Sero, I., and Bisquert, J. (2014). General working principles of $CH_3NH_3PbX_3$ perovskite solar cells. Nano Lett. *14*, 888–893.

46. Wang, S., Kaienburg, P., Klingebiel, B., Schillings, D., and Kirchartz, T. (2018). Understanding thermal admittance spectroscopy in low-mobility semiconductors. J. Phys. Chem. C *122*, 9795–9803.

47. Li, J.V., and Levi, D.H. (2011). Determining the defect density of states by temperature derivative admittance spectroscopy. J. Appl. Phys. *109*, 083701.

48. Lopez-Varo, P., Jiménez-Tejada, J.A., García-Rosell, M., Ravishankar, S., Garcia-Belmonte, G., Bisquert, J., and Almora, O. (2018). Device physics of hybrid perovskite solar cells: theory and experiment. Adv. Energy Mater. *8*, 1702772.

49. Onoda-Yamamuro, N., Matsuo, T., and Suga, H. (1992). Dielectric study of $CH_3NH_3PbX_3$ (X = Cl, Br, I). J. Phys. Chem. Solids *53*, 935–939.

50. Poglitsch, A., and Weber, D. (1987). Dynamic disorder in methylammoniumtrihalogenoplumbates (II) observed by millimeter-wave spectroscopy. J. Chem. Phys. *87*, 6373–6378.

51. Govinda, S., Kore, B.P., Swain, D., Hossain, A., De, C., Guru Row, T.N.G., and Sarma, D.D. (2018). Critical comparison of $FAPbX_3$ and $MAPbX_3$ (X = Br and Cl): how do they differ? J. Phys. Chem. C *122*, 13758–13766.

52. Jacobs, D.A., Shen, H., Pfeffer, F., Peng, J., White, T.P., Beck, F.J., and Catchpole, K.R. (2018). The two faces of capacitance: new interpretations for electrical impedance measurements of perovskite solar cells and their relation to hysteresis. J. Appl. Phys. *124*, 225702.

Approved for public release; distribution unlimited.

ACS APPLIED MATERIALS & INTERFACES

www.acsami.org Research Article

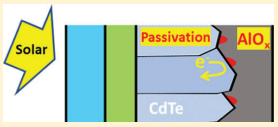
Back-Surface Passivation of CdTe Solar Cells Using Solution-Processed Oxidized Aluminum

Fadhil K. Alfadhili, Adam B. Phillips,* Kamala Khanal Subedi, Craig L. Perkins, Adam I. Halaoui, Manoj K. Jamarkattel, Bhuiyan M. Anwar, Geethika K. Liyanage, Deng-Bing Li, Corey R. Grice, Yanfa Yan, Randy J. Ellingson, and Michael J. Heben

Cite This: *ACS Appl. Mater. Interfaces* 2020, 12, 51337–51343 Read Online

ACCESS | Metrics & More | Article Recommendations | Supporting Information

ABSTRACT: Although back-surface passivation plays an important role in high-efficiency photovoltaics, it has not yet been definitively demonstrated for CdTe. Here, we present a solution-based process, which achieves passivation and improved electrical performance when very small amounts of oxidized Al^{3+} species are deposited at the back surface of CdTe devices. The open circuit voltage (V_{oc}) is increased and the fill factor (FF) and photoconversion efficiency (PCE) are optimized when the total amount added corresponds to ∼1 monolayer, suggesting that the passivation is surface specific. Addition of further Al^{3+} species, present in a sparse alumina-like layer, causes the FF and PCE to drop as the interface layer becomes blocking to current flow. The optimized deposit increases the average baseline PCE for both Cu-free devices and devices where Cu is present as a dopant. The greatest improvement is found when the Al^{3+} species are deposited prior to the $CdCl_2$ activation step and Cu is employed. In this case, the best-cell efficiency was improved from 12.6 to 14.4%. Time-resolved photoluminescence measurements at the back surface and quantum efficiency measurements performed at the maximum power point indicate that the performance enhancement is due to a reduction in the interface recombination current at the back surface.



KEYWORDS: *interface passivation, CdTe, back contact, solution processed, alumina*

Downloaded via UNIV OF TOLEDO on September 13, 2021 at 15:05:20 (UTC).
See https://pubs.acs.org/sharingguidelines for options on how to legitimately share published articles.

INTRODUCTION

Recent improvements in the materials and interfaces in CdTe thin-film solar cells have led to increases in the photoconversion efficiency (PCE), with the record now at 22.1%.[1] While the short circuit current density (J_{sc}) is near bandgap-limited values and the fill factor (FF) has increased to 79%,[1] there is still substantial opportunity to increase the open circuit voltage (V_{oc}).[2] As further improvements in the bulk lifetime are obtained through Cl passivation[3] and Se incorporation,[4] and the interface recombination at the front surface is reduced through emitter engineering,[5,6] both critical parameters for device improvement,[7,8] the back interface may soon limit device efficiency.[9] Consequently, research is being focused on developing strategies to reduce back-surface minority carrier recombination while still enabling for efficient majority carrier extraction. Passivated back contacts are also required to enable bifacial operation for higher-energy yields[10] and will be required for future CdTe-based tandems.

A reduction in back-surface recombination can be accomplished by reducing the concentration of electrically active defects at the interface or by creating an electric field to repel minority carriers through electrostatics, doping profiles, or band offsets.[9] Surface passivation in Si has been achieved by several approaches[11] including by depositing alumina by both vacuum and solution processing.[12,13] Alumina has also been explored for passivation of both the rear[14] and front surfaces[15] of $Cu(In,Ga)Se_2$ solar cells. Alumina's potential for passivating CdTe surfaces was demonstrated recently when time-resolved photoluminescence (TRPL) studies reported carrier lifetimes of 27 and 750 ns for CdTe (2 μm thickness)[16] and $CdSeTe$ (2−2.8 μm)[17] layers, respectively, in alumina double heterostructures. The mechanism of the passivation is not yet clear but could be due to a high density of fixed negative charge[18] or the low degree of lattice mismatch (3.7%) between the unit cell of the (0001) surface of Al_2O_3 and the (111) surface of CdTe.[19] These characteristics offer the potential for repelling minority carriers and creating a low defect density interface, respectively.[16,18,20,21]

While demonstration of long carrier lifetimes via an optical measurement is promising, to date there is no clear evidence for back-surface passivation in an operating CdTe device. Previous attempts have included deposition of alumina by atomic layer deposition (ALD)[22] and sputtering.[16] Liang et al. deposited alumina layers in thicknesses up to 5 nm by ALD and tracked the device performance.[22] The baseline PCE of 10.7% was improved to 12.1% when the Al_2O_3 thickness was 1 nm, while thicker deposits led to poorer device performance. A 1 nm layer was reported to be thin enough to allow holes to

Received: July 15, 2020
Accepted: October 22, 2020
Published: November 4, 2020



ACS Publications © 2020 American Chemical Society

https://dx.doi.org/10.1021/acsami.0c12800
ACS Appl. Mater. Interfaces 2020, 12, 51337−51343

Approved for public release; distribution unlimited.

tunnel and thick enough to present a fixed charge to repel minority carrier electrons.[22] However, the data that was presented in the paper was not consistent with this interpretation. First, an improvement in the long-wavelength photoresponse at short circuit was cited as proof of a reduced back-surface recombination rate, but current collection at short circuit when the electric field is the largest is not a good indicator of back-surface passivation. Second, the biggest factor leading to improved PCE (Figure 2a in ref 22) was a flattening of the slope of the $J-V$ curve through zero bias. This increase in the shunt resistance is more consistent with pin-hole blocking. Also, there was no evidence for current blocking when the Al_2O_3 layers were thicker. In contrast, Kephart et al. applied Al_2O_3 by sputtering and saw pronounced kinks in the $J-V$ characteristic at layer thicknesses of 3 and 5 nm. In this case, however, the device efficiency was not improved with the addition of Al_2O_3.[16] Thus, there has been no conclusive evidence to date for enhancement of PV performance in CdTe due to back-surface passivation. Other efforts to passivate the back surface of CdTe have included the use of TiO_2 and NiO,[23,24] but, similarly, the results were not definitive.

Here, we present a solution-based process that reduces back-surface recombination in CdTe solar cells and increases the PCE. Following a process developed for passivating silicon solar cells by deposition of alumina,[25] we employed aluminum acetylacetonate ($Al(acac)_3$) dissolved in methoxyethanol and a spin-coating/heating procedure in an effort to deposit alumina on the back surface of CdTe solar cells. Data from current–voltage ($J-V$) curve analysis, time-resolved photoluminescence, external quantum efficiency (EQE) measurements made at the maximum power point, and Auger electron and X-ray photoelectron spectroscopies provide conclusive evidence that the device improvement is indeed due to back-surface passivation. The optimized process increased the average baseline efficiency for Cu-free devices from 10.4 to 11.7%, while the average PCE for devices made with Cu-doping improved from 12.0 to 12.9%. Application of the $CdCl_2$ activation process after exposure to $Al(acac)_3$ with Cu-doping causes the baseline to be improved from 12.0 to 13.8%.

EXPERIMENTAL CONDITIONS

CdTe device stacks were obtained from the center part of a 60 cm × 120 cm plate produced in a commercial deposition reactor by Willard and Kelsey Solar Group. The large area deposition process produced uniform films, so the initial structure, ~100 nm of CdS and ~3 μm of CdTe on TEC-15M coated soda-lime glass, can be considered to be constant for each experiment. The samples were activated by applying a saturated solution of $CdCl_2$ in methanol and heating to 390 °C in dry air for 30 min. Excess $CdCl_2$ was removed by rinsing with methanol. The aluminum acetylacetonate $Al(acac)_3$ (Sigma-Aldrich Co. LLC, 99.999%) precursor solution was prepared by dissolving 400 mg of as-received powder in 20 mL of 2-methoxyethanol. Two hundred and fifty microliters of the solution was pipetted onto a stationary sample, which was then spun at 2000 rpm for 25 s.[25] Samples were then heated in laboratory air to 300 °C for 10 min. The spinning/heating cycle was performed 1, 3, 5, 7, and 9 times to produce increasingly thicker passivation layers. Devices were formed by depositing 40 nm of Au by thermal evaporation to form a back-metal electrode. Some samples also had a thin layer (3 nm) of Cu deposited by evaporation prior to Au deposition to enhance doping and lower the back contact barrier. In these cases, a subsequent heating step at 150 °C was performed in air to promote Cu diffusion for times ranging between 40 and 80 min. Individual solar cells were precisely defined by laser scribing (0.06 cm^2). Performance statistics were evaluated for relatively large data sets (n > 20). Additional experimental details regarding Auger electron and X-ray photoelectron spectroscopies, $J-V$ and EQE characterization, and photoluminescence are presented below and in the Supporting Information.

RESULTS AND DISCUSSION

Figure 1 shows the $J-V$ curves and performance parameters as a function of the number of spin-coating/heating cycles for

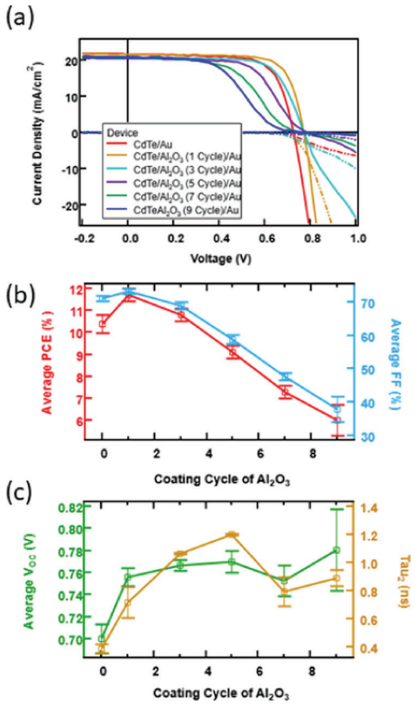


Figure 1. (a) Current density–voltage ($J-V$) curves for the CdTe device with varying number of spin/heat cycles for the Al_2O_3 process. (b) Average power conversion efficiency (PCE) and fill factor (FF) and (c) average open circuit voltage (V_{OC}) and the long lifetime component of the time-resolved photoluminescence (TRPL; τ_2) measurement of the devices as a function of a number of cycles.

samples that had no copper added. Note that the standard deviation in the measured PV parameters for sets of 20 devices in each experiment showed a typical variation of only 1–2% in J_{sc}, V_{OC}, and FF and ~3% in PCE (Table 1). Figure 1a shows the $J-V$ curves for the best devices with zero, 1, 3, 5, 7, and 9 spin-coating/heating cycles. The short circuit current density (J_{sc}) values are essentially constant within error, and a small difference can be attributed to small deviations in the CdS emitter layer thickness. On the other hand, Figure 1c shows that the V_{OC} increases abruptly with the first cycle and stays nearly constant with additional cycles. We also note that it is surprising that the V_{OC} is already fairly high at 700 mV for zero cycles, and this may be due to Cu impurities in the CdTe source materials. The first cycle $J-V$ curve also shows an improved FF but increasing the number of cycles produces first a kink and then a strong blocking effect. Figure 1b shows that the overall efficiency trend is dominated by the FF, with a peak in PCE after the initial increase in the V_{OC}. Data for the full

https://dx.doi.org/10.1021/acsami.0c12800
ACS Appl. Mater. Interfaces 2020, 12, 51337–51343

Approved for public release; distribution unlimited.

Table 1. $J-V$ Performance Data for Devices Fabricated With and Without Cu and Al_2O_3 Deposition/Heating Cycles[a]

device		V_{OC} (V)	J_{SC} (mA/cm^2)	FF (%)	PCE (%)
		Without Cu			
CdTe/Au	average	0.700 ± 0.013	21.0 ± 0.2	70.9 ± 0.8	10.4 ± 0.4
	best	0.726	21.5	72.0	11.3
CdTe/Al_2O_3(1 cycle)/Au	average	0.756 ± 0.008	21.2 ± 0.3	73.1 ± 0.9	11.7 ± 0.3
	best	0.770	21.6	74.9	12.5
CdTe/Al_2O_3(3 cycles)/Au	average	0.767 ± 0.005	20.5 ± 0.2	68.9 ± 1.1	10.8 ± 0.3
	best	0.771	20.7	70.4	11.3
CdTe/Al_2O_3(5 cycles)/Au	average	0.755 ± 0.010	20.5 ± 0.2	58.8 ± 1.4	9.1 ± 0.3
	best	0.785	20.4	60.4	9.7
CdTe/Al_2O_3(7 cycles)/Au	average	0.753 ± 0.014	20.4 ± 0.1	47.7 ± 1.2	7.3 ± 0.3
	best	0.772	20.6	50.1	7.9
CdTe/Al_2O_3(9 cycles)/Au	average	0.781 ± 0.037	20.3 ± 0.4	37.9 ± 3.7	6.0 ± 0.7
	best	0.830	20.7	40.1	6.9
		With Cu			
CdTe/Cu/Au 150 °C 40 min	average	0.783 ± 0.004	21.1 ± 0.3	72.5 ± 0.9	12.0 ± 0.2
	best	0.790	21.8	71.5	12.3
CdTe/Al_2O_3(1 cycle)/Cu/Au 150 °C 40 min	average	0.800 ± 0.008	20.8 ± 0.5	76.4 ± 0.8	12.7 ± 0.2
	best	0.806	21.8	75.6	13.3
CdTe/Al_2O_3(1 cycle)/Cu/Au 150 °C 60 min	average	0.818 ± 0.007	20.7 ± 0.4	76.2 ± 0.7	12.9 ± 0.3
	best	0.830	21.5	76.2	13.6
CdTe/Al_2O_3(1 cycle)/Cu/Au 150 °C 80 min	average	0.821 ± 0.006	20.5 ± 0.3	75.8 ± 1	12.7 ± 0.3
	best	0.829	20.7	76.4	13.1

[a]Data is presented for the best device (in terms of PCE) and the population of devices in each data set (n > 20).

population of devices with $Al(AcAc)_3$ processing after $CdCl_2$ activation can be found in Table 1.

Figure 1c shows the carrier lifetimes, which were extracted from biexponential fits to the PL transients. The carrier lifetime, which is associated with the longer-lived component in the PL (τ_2, see the Supporting Information), followed the V_{OC} trend with spin/heating cycles. The PL was excited and detected through the back of the CdTe absorber. With a $1/e$ penetration depth of ~125 nm for the 532 nm light, the measurement should be sensitive to recombination at the back surface. Since no Cu was used in these experiments, possible redistribution of dopants and possible changes at the front interface can be discounted.[26] Control experiments in which devices were exposed to spin/heating cycles without $Al(acac)_3$ showed different V_{OC} behavior that is more consistent with previously reported effects associated with back-surface oxidation in air.[27] Thus, the increase in PL lifetime and the increase in V_{OC} can both be attributed to passivation effects, perhaps due to a reduction in the defect state surface density at the interface or a reduction in rear-surface band bending.[9,10]

Figure 2a–c shows scanning electron microscopy (SEM) images of the CdTe surfaces directly after $CdCl_2$ processing and after the addition of 1 and 5 spin-casting/heating cycles, respectively. Prior to deposition (Figure 2a), the image is characteristic of the polycrystalline films with a grain size of ~300 nm to 1 μm. The images are only subtly changed after 1 spin-casting/heating cycle (Figure 2b) and the grains appear to be smoothed with some edges appearing to be eroded or perhaps decorated with a thin deposit. There is no evidence of a conformal or complete coating. After five cycles, the surface morphology is significantly changed (Figure 2c) and small protrusions, or nodules, are evident. These are ~100 to 200 nm in extent and present on the surfaces of the grains. In some locations, it appears that the grains have developed new terraces (Figure S3), suggesting that the surface energy may have been reduced due to reconstruction. AES mapping

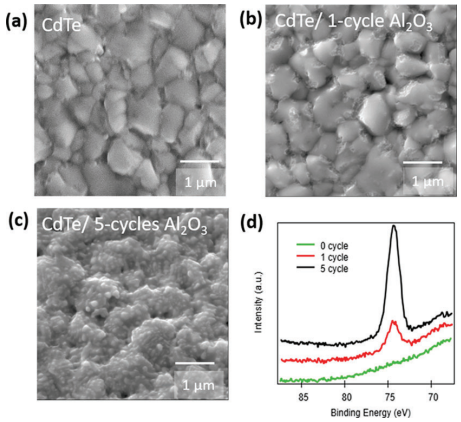


Figure 2. Scanning electron microscope images of CdTe surface (a) without and with (b) one or (c) five cycles of Al_2O_3 processing. (d) Al 2p XPS data without (green), with one (red) and five (black) cycles.

yielded very poor signal-to-noise aluminum maps with no clear correlation between the Al content and the structures observed in the SEM images (see Figure S2). However, aluminum was clearly detected in AES data that was acquired when the Al signal was integrated while scanning 2 μm × 2 μm areas of both the 1-cycle and 5-cycle samples with higher Al signal strength for the latter sample. Interestingly, not even the nodules observed in the SEM images of the 5-cycle sample were well correlated with the aluminum AES signals (see Table S2).

Figure 2d shows Al 2p XPS data collected for zero, 1, and 5 spin/heat cycles. The aluminum signal is evident after only 1 spin/heating cycle and becomes more intense after five cycles. In an attempt to quantify the amount of Al on the surface, an

https://dx.doi.org/10.1021/acsami.0c12800
ACS Appl. Mater. Interfaces 2020, 12, 51337–51343

Approved for public release; distribution unlimited.

alumina film prepared by ALD on a CdTe single crystal was examined as a calibration standard. The calibration standard was prepared on the CdTe native oxide using eight water/trimethylaluminum reaction cycles, resulting in an estimated thickness of 1.0 ± 0.5 nm.[28] The Al/(Cd + Te) signal ratio determined by XPS for the sample with 1 spin-casting/heating cycle was approximately 1/10th of that measured for the calibration standard, suggesting that the amount of Al may be considered to be present in a thickness on the order of 1 monolayer. This result, coupled with the nonuniformities observed by SEM and atomic force microscopy (see Figure S5), indicates that the passivation effect is realized through surface chemistry reactions at specific locations on the grains of the polycrystalline film. This suggests the possibility of facet-specific passivation.

Maruyama and Arai produced stoichiometric Al_2O_3 films on silicon wafers by heating $Al(acac)_3$ powder to 150 °C and introducing the entrained vapor to samples heated to temperatures between 250 and 600 °C.[29] The films were adherent, suggesting that the reaction occurred at the surface rather than in the gas phase. Our work suggests that the aluminum deposition reaction from $Al(acac)_3$ is also surface specific in the presence of polycrystalline CdTe. However, at present, due to the rough topography of the surface and the very small amounts of the material involved, we have no direct evidence for the formation of Al_2O_3. Based on the alignment of the spectra by setting the Te^{2-} peak to 572.4 eV,[28] the 74.3 eV binding energy for the peak rules out several possibilities including Al^0 and aluminum halides. Instead, the Al signal is consistent with Al^{3+} bonding found for several alumina oxides.[28] X-ray diffraction and infrared (IR) spectroscopy analyses were inconclusive in identifying surface Al_2O_3, even for samples made with 9 spin/heating cycles. However, when precursor layers approximately 1 μm thick were prepared on soda-lime glass by blade coating and subsequently heated, infrared spectroscopy showed absorption features representative of Al_2O_3 in the range of 1000−500 cm^{-1} (Figure S4).[29]

In an effort to increase the PCE further, we used Cu to increase the level of p-type doping. While Cu has also been employed to reduce the height of the Schottky barrier at the back surface, the lack of roll-over in the 1-cycle Cu-free data suggested that the barrier was already low.[30] Figure 3a shows the $J-V$ curves for a CdTe device with a Cu/Au back contact (3 nm evaporated Cu followed by 150 °C for 40 min in air) as compared to devices fabricated with first surface Al_2O_3 (1 cycle) and then 3 nm of Cu and 40 nm Au with Cu diffusion times (150 °C in air) of 40, 60, and 80 min. After the Cu diffusion process alone (no Al_2O_3), the PCE improved from 10.4 to 12.0% (compare Figures 1a, 3a and see Table 1). Note that the performance of the devices with the optimized standard Cu/Au back contact exceeded the PCE of the devices with one Al_2O_3 cycle and no Cu (12.0 versus 11.7%, respectively). However, introducing the 3 nm of Cu on top of the 1-cycle Al_2O_3 film and employing a 40 min heating increased the best-cell PCE by a full percentage point. Extending the heating time further to 60 min increased the V_{OC} and the FF further without changing J_{SC}, leading to an increase of the PCE of the devices to 12.9% and a best-cell efficiency of 13.6% (Figure 3a and Table 1).

Recent device simulations that explored the use of back buffer layers for high-efficiency CdTe solar cells make it clear that a combined increase in FF and V_{OC} is one hallmark of a reduction in back-surface recombination.[9] On the contrary, J_{SC}

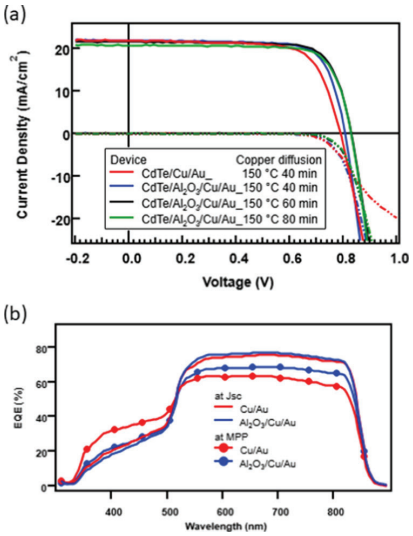


Figure 3. (a) $J-V$ curves of CdTe devices with a standard Cu/Au back contact and one cycle of Al_2O_3 processing with Cu/Au annealed for varying times. (b) External quantum efficiency measurements for the CdTe device with standard Cu/Au back contact and one cycle of Al_2O_3/Cu/Au back contact at short circuit and maximum power point bias.

is not expected to be increased, nor should the slope of the $J-V$ curve at zero-bias change, as was observed by Liang et al.[22] To further probe whether back-surface passivation is indeed responsible for the improvements observed here, we performed external quantum efficiency (EQE) measurements with the devices biased at their respective maximum power points (MPPs) under an AM1.5 light bias. It is most instructive to examine the wavelength-dependent carrier collection efficiency under this condition, as opposed to typical EQE measurements, which are done at zero-bias (short circuit) conditions without light bias, because the energy bands in the emitter and absorber semiconductor layers will be fairly flat and poised under their normal operating condition. At MPP, it is possible to examine back-surface passivation effects by measuring the collection efficiency for carriers that are generated deeper in the device.

Figure 3b compares the data obtained at zero bias and at MPP for a device with a standard Cu/Au back contact to that obtained from a device with a 1-cycle Al_2O_3/Cu/Au back contact. We first note that the zero-bias data for the two devices overlaps completely, consistent with the J_{SC} values being the same. This result is expected since the electric field in the absorber is high at zero bias and the impact of back-surface recombination should not be strongly reflected in the data.

Turning to the EQE data at the MPP, the Cu/Au contact (MPP = 650 mV) shows a higher response in the short wavelength region of the spectrum (<500 nm), presumably due to Cu compensation of donor sites in the CdS window layer.[31] The absence of an increase in the short wavelength response for the 1-cycle Al_2O_3/Cu/Au (MPP—675 mV) is consistent with the thin Al_2O_3 layer reducing Cu diffusion into the CdS. In the long wavelength portion of the spectrum (>500 nm), the Cu/Au contact shows a reduction in the carrier collection efficiency. This is due to the downward band

https://dx.doi.org/10.1021/acsami.0c12800
ACS Appl. Mater. Interfaces 2020, 12, 51337−51343

Approved for public release; distribution unlimited.

Table 2. $J-V$ Performance Data for Devices Fabricated With and Without 1 Cycle of Al_2O_3 Deposition and Then Subjected to $CdCl_2$ Activation with No Other Thermal Treatment[a]

device		V_{OC} (V)	J_{SC} (mA/cm^2)	FF (%)	PCE (%)
CdTe/$CdCl_2$/Cu/Au	average	0.784 ± 0.006	21.7 ± 0.2	70.6 ± 1.5	12.0 ± 0.3
	best	0.777	21.9	73.8	12.6
CdTe/Al_2O_3 (1 cycle) /$CdCl_2$/Cu/Au	average	0.818 ± 0.007	22.1 ± 0.1	76.4 ± 1.5	13.8 ± 0.4
	best	0.818	23.2	75.7	14.4

[a]Devices were finished with the standard Cu/Au back contact. Data is presented for the best device (in terms of PCE) and the population of devices in each data set (n > 20).

bending at the back surface, which causes minority carrier electrons that are generated nearby to be attracted to the back surface where they will more efficiently recombine.

In contrast, the 1-cycle Al_2O_3/Cu/Au sample shows a long wavelength response that has the same spectral dependence (i.e., slope) as does the zero-bias data. The reduction in the EQE that is constant with a wavelength in comparison to the zero-bias data is a reflection of the fact that the Shockley–Read–Hall contribution to the overall recombination is larger throughout the device when the bands are flatter, as is the case at MPP. However, the fact that the spectral dependence of the EQE is the same as in the zero-bias data, where the internal field is much larger, indicates that the carriers generated throughout the device, regardless of depth, have a similar probability of being collected. Consequently, we can conclude that back-surface recombination has been reduced.

A final set of experiments demonstrated that the process could be considerably simplified. In this case, the $Al(acac)_3$ solution was first pipetted and spun onto the as-grown CdTe device stack and then the $CdCl_2$ treatment was performed. The only high-temperature treatment was used for the standard $CdCl_2$ process (387 °C for 30 min, in air). After the $CdCl_2$ treatment, the Cu/Au back contact was formed as described above (with heating in air for 40 min for both samples). Table 2 shows the measured $J-V$ parameters for these $CdCl_2$/Cu/Au and $Al(AcAc)_2$/$CdCl_2$/Cu/Au devices. Note that these device stacks came from a different production run, which introduced slight differences in performance from the previous data sets. The device results were similar to those found for the single spin/heat cycle, but the performance was improved to higher values. The average V_{OC} for the sample set increased from 0.784 ± 0.006 to 0.817 ± 0.007 mV, while the FF increased from 70.6 ± 1.5 to 76.4 ± 1.1 and the average PCE increased from 12.0 ± 0.3 to 13.8 ± 0.4%. Figure 4a shows the $J-V$ curves for the best-performing devices of each type, while Figure 4b shows the SEM of the CdTe surface after the $Al(acac)_3$/$CdCl_2$ processing. In this data set, there was a statistically significant increase in short circuit current, which could be due to differences in the degree of Cu compensation.

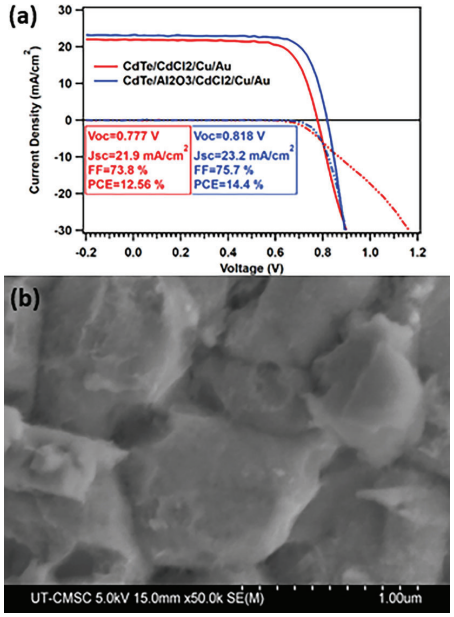


Figure 4. (a) $J-V$ curves for CdTe devices with an evaporated Cu/Au back contact and a device prepared with $Al(acac)_3$ prior to $CdCl_2$ treatment. (b) Scanning electron microscopy image of the CdTe surface for the $Al(acac)_3$/$CdCl_2$ sample.

CONCLUSIONS

We developed a solution-based process that deposits very small amounts of oxidized aluminum (Al^{3+}) species onto the back surface of CdTe device stacks to produce increased V_{OC}, FF, and PCE in finished devices. The binding mechanisms for the Al^{3+} species appear to be site specific and the device performance was optimized when the amount deposited corresponded to ~1 monolayer. Time-resolved photoluminescence spectroscopy on the back surface and quantum efficiency measurements performed at the maximum power point support the conclusion that interface recombination at the back surface was reduced by back-surface passivation. The mechanism is unclear at the present time, but the results could be due to either the reduction of band bending or the elimination of surface states. Further work in our laboratory will be directed toward discriminating between these two possibilities, understanding the surface chemistry in more detail, and applying the new approach to higher-efficiency devices.

ASSOCIATED CONTENT

Supporting Information

The Supporting Information is available free of charge at https://pubs.acs.org/doi/10.1021/acsami.0c12800.

Experimental details; PL and TRPL data; AES maps and elemental analysis; FTIR, AFM, and additional EQE data (PDF)

AUTHOR INFORMATION

Corresponding Author

Adam B. Phillips – *Wright Center for Photovoltaics Innovation and Commercialization, Department of Physics and Astronomy, University of Toledo, Toledo, Ohio 43606, United States;*

https://dx.doi.org/10.1021/acsami.0c12800
ACS Appl. Mater. Interfaces 2020, 12, 51337–51343

Approved for public release; distribution unlimited.

orcid.org/0000-0002-2675-5052; Email: adam.phillips@utoledo.edu

Authors

Fadhil K. Alfadhili – *Wright Center for Photovoltaics Innovation and Commercialization, Department of Physics and Astronomy, University of Toledo, Toledo, Ohio 43606, United States*

Kamala Khanal Subedi – *Wright Center for Photovoltaics Innovation and Commercialization, Department of Physics and Astronomy, University of Toledo, Toledo, Ohio 43606, United States*

Craig L. Perkins – *National Renewable Energy Laboratory, Golden, Colorado 80401, United States;* orcid.org/0000-0002-9036-8698

Adam I. Halaoui – *Wright Center for Photovoltaics Innovation and Commercialization, Department of Physics and Astronomy, University of Toledo, Toledo, Ohio 43606, United States;* orcid.org/0000-0003-0812-6153

Manoj K. Jamarkattel – *Wright Center for Photovoltaics Innovation and Commercialization, Department of Physics and Astronomy, University of Toledo, Toledo, Ohio 43606, United States*

Bhuiyan M. Anwar – *Wright Center for Photovoltaics Innovation and Commercialization, Department of Physics and Astronomy, University of Toledo, Toledo, Ohio 43606, United States*

Geethika K. Liyanage – *Wright Center for Photovoltaics Innovation and Commercialization, Department of Physics and Astronomy, University of Toledo, Toledo, Ohio 43606, United States;* orcid.org/0000-0003-4000-0729

Deng-Bing Li – *Wright Center for Photovoltaics Innovation and Commercialization, Department of Physics and Astronomy, University of Toledo, Toledo, Ohio 43606, United States;* orcid.org/0000-0003-4555-4894

Corey R. Grice – *Wright Center for Photovoltaics Innovation and Commercialization, Department of Physics and Astronomy, University of Toledo, Toledo, Ohio 43606, United States*

Yanfa Yan – *Wright Center for Photovoltaics Innovation and Commercialization, Department of Physics and Astronomy, University of Toledo, Toledo, Ohio 43606, United States;* orcid.org/0000-0003-3977-5789

Randy J. Ellingson – *Wright Center for Photovoltaics Innovation and Commercialization, Department of Physics and Astronomy, University of Toledo, Toledo, Ohio 43606, United States;* orcid.org/0000-0001-9520-6586

Michael J. Heben – *Wright Center for Photovoltaics Innovation and Commercialization, Department of Physics and Astronomy, University of Toledo, Toledo, Ohio 43606, United States;* orcid.org/0000-0002-3788-3471

Complete contact information is available at: https://pubs.acs.org/10.1021/acsami.0c12800

Notes

The authors declare no competing financial interest.

■ ACKNOWLEDGMENTS

This material is based on research sponsored by Air Force Research Laboratory under agreement FA9453-18-2-0037 and FA9453-19-C-1002 and by the U.S. DOE's Office of Energy Efficiency and Renewable Energy (EERE) under Solar Energy Technologies Office (SETO) Agreement DE-EE0008974. In addition, this work was authored in part by the National Renewable Energy Laboratory, operated by Alliance for Sustainable Energy, LLC, for the U.S. Department of Energy (DOE) under Contract No. DE-AC36-08GO28308. Funding provided U.S. Department of Energy Office of Energy Efficiency and Renewable Energy Solar Energy Technologies Office. The views expressed in the article do not necessarily represent the views of the DOE or the U.S. Government. The U.S. Government retains and the publisher, by accepting the article for publication, acknowledges that the U.S. Government retains a nonexclusive, paid-up, irrevocable, and worldwide license to publish or reproduce the published form of this work, or allow others to do so, for U.S. Government purposes. The authors thank Willard and Kelsey Solar Group for providing the CdS/CdTe samples.

■ REFERENCES

(1) Green, M. A.; Dunlop, E. D.; Hohl-Ebinger, J.; Yoshita, M.; Kopidakis, N.; Ho-Baillie, A. W. Y. Solar Cell Efficiency Tables (Version 55). *Prog. Photovoltaics* **2020**, *28*, 3−15.

(2) Gloeckler, M. In *Research Opportunities Supporting 25% CdTe PV*, MRS Spring Meeting, 2019.

(3) Barnard, E. S.; Ursprung, B.; Colegrove, E.; Moutinho, H. R.; Borys, N. J.; Hardin, B. E.; Peters, C. H.; Metzger, W. K.; Schuck, P. J. 3D Lifetime Tomography Reveals How CdCl2 Improves Recombination Throughout CdTe Solar Cells. *Adv. Mater.* **2017**, *29*, No. 1603801.

(4) Swanson, D. E.; Sites, J. R.; Sampath, W. S. Co-sublimation of CdSexTe1−x Layers for CdTe Solar Cells. *Sol. Energy Mater. Sol. Cells* **2017**, *159*, 389−394.

(5) Song, T.; Kanevce, A.; Sites, J. R. Emitter/absorber Interface of CdTe Solar Cells. *J. Appl. Phys.* **2016**, *119*, No. 233104.

(6) Kephart, J. M.; McCamy, J. W.; Ma, Z.; Ganjoo, A.; Alamgir, F. M.; Sampath, W. S. Band Alignment of Front Contact Layers for High-Efficiency CdTe Solar Cells. *Sol. Energy Mater. Sol. Cells* **2016**, *157*, 266−275.

(7) Kanevce, A.; Reese, M. O.; Barnes, T. M.; Jensen, S. A.; Metzger, W. K. The Roles of Carrier Concentration and Interface, Bulk, and Grain-boundary Recombination for 25% Efficient CdTe Solar Cells. *J. Appl. Phys.* **2017**, *121*, No. 214506.

(8) Duenow, J. N.; Metzger, W. K. Back-surface Recombination, Electron Reflectors, and Paths to 28% Efficiency for Thin-film Photovoltaics: A CdTe Case Study. *J. Appl. Phys.* **2019**, *125*, No. 053101.

(9) Liyanage, G. K.; Phillips, A. B.; Alfadhili, F. K.; Ellingson, R. J.; Heben, M. J. The Role of Back Buffer Layers and Absorber Properties for>25% Efficient CdTe Solar Cells. *ACS Appl. Energy Mater.* **2019**, *2*, 5419.

(10) Phillips, A. B.; Subedi, K. K.; Liyanage, G. K.; Alfadhili, F. K.; Ellingson, R. J.; Heben, M. J. Understanding and Advancing Bifacial Thin Film Solar Cells. *ACS Appl. Energy Mater.* **2020**, *3*, 6072.

(11) Bonilla, R. S.; Hoex, B.; Hamer, P.; Wilshaw, P. R. Dielectric Surface Passivation for Silicon Solar Cells: A Review. *Phys. Status Solidi* **2017**, *214*, No. 1700293.

(12) Schmidt, J.; Merkle, A.; Brendel, R.; Hoex, B.; de Sanden, M. V.; Kessels, W. M. M. Surface Passivation of High-efficiency Silicon Solar Cells by Atomic-layer-deposited Al2O3. *Prog. Photovoltaics* **2008**, *16*, 461−466.

(13) Jiang, Y.; Shen, H.; Yang, W.; Zheng, C.; Tang, Q.; Yao, H.; Raza, A.; Li, Y.; Huang, C. Passivation Properties of Alumina for Multicrystalline Silicon Nanostructure Prepared by Spin-coating Method. *Appl. Phys. A* **2018**, *124*, No. 95.

(14) Birant, G.; de Wild, J.; Meuris, M.; Poortmans, J.; Vermang, B. Dielectric-Based Rear Surface Passivation Approaches for Cu(In,Ga)-Se2 Solar Cells—A Review. *Appl. Sci.* **2019**, *9*, No. 677.

(15) Werner, F.; Veith-Wolf, B.; Melchiorre, M.; Babbe, F.; Schmidt, J.; Siebentritt, S. Ultra-thin passivation layers in Cu(In,Ga)Se2 thin-

Approved for public release; distribution unlimited.

film solar cells: full-area passivated front contacts and their impact on bulk doping. *Sci. Rep.* **2020**, *10*, No. 7530.
(16) Kephart, J. M.; Kindvall, A.; Williams, D.; Kuciauskas, D.; Dippo, P.; Munshi, A.; Sampath, W. S. Sputter-Deposited Oxides for Interface Passivation of CdTe Photovoltaics. *IEEE J. Photovoltaics* **2018**, *8*, 587−593.
(17) Kuciauskas, D.; Moseley, J.; Ščajev, P.; Albin, D. Radiative Efficiency and Charge-Carrier Lifetimes and Diffusion Length in Polycrystalline CdSeTe Heterostructures. *Phys. Status Solidi RRL* **2020**, *14*, No. 1900606.
(18) Werner, F.; Veith, B.; Tiba, V.; Poodt, P.; Roozeboom, F.; Brendel, R.; Schmidt, J. Very Low Surface Recombination Velocities on p- and n-type c-Si by Ultrafast Spatial Atomic Layer Deposition of Aluminum Oxide. *Appl. Phys. Lett.* **2010**, *97*, No. 162103.
(19) Meinander, K.; Preston, J. S. A DFT Study on the Effect of Surface Termination in CdTe (111)/α-Al2O3 (0001) Heteroepitaxy. *Surf. Sci.* **2015**, *632*, 93−97.
(20) Jovanovic, S. M.; Devenyi, G. A.; Jarvis, V. M.; Meinander, K.; Haapamaki, C. M.; Kuyanov, P.; Gerber, M.; LaPierre, R. R.; Preston, J. S. Optical Characterization of Epitaxial Single Crystal CdTe Thin Films on Al2O3 (0001) Substrates. *Thin Solid Films* **2014**, *570*, 155−158.
(21) Kuciauskas, D.; Kephart, J. M.; Moseley, J.; Metzger, W. K.; Sampath, W. S.; Dippo, P. Recombination Velocity Less than 100 cm/s at Polycrystalline Al2O3/CdSeTe Interfaces. *Appl. Phys. Lett.* **2018**, *112*, No. 263901.
(22) Liang, J.; Lin, Q.; Li, H.; Su, Y.; Yang, X.; Wu, Z.; Zheng, J.; Wang, X.; Lin, Y.; Pan, F. Rectification and Tunneling Effects Enabled by Al2O3 Atomic Layer Deposited on Back Contact of CdTe Solar Cells. *Appl. Phys. Lett.* **2015**, *107*, No. 013907.
(23) Werthen, J. G.; Häring, J. P.; Bube, R. H. Correlation Between Cadmium Telluride Surface Oxidation and Metal Junctions. *J. Appl. Phys.* **1983**, *54*, 1159−1161.
(24) Di, X.; Li, X.; Wang, D.; Li, Q.; Shen, K.; Wang, D. CdTe Thin Film Solar Cell with NiO as a Back Contact Buffer Layer. *Sol. Energy Mater. Sol. Cells* **2017**, *169*, 61−67.
(25) Watanabe, R.; Kawashima, M.; Saito, Y. Film Properties of Alumina Passivation Layer for Silicon Solar Cells Prepared by Spin-coating Method. *Thin Solid Films* **2015**, *590*, 98−102.
(26) Perkins, C. L.; McGott, D. L.; Reese, M. O.; Metzger, W. K. SnO2-Catalyzed Oxidation in High-Efficiency CdTe Solar Cells. *ACS Appl. Mater. Interfaces* **2019**, *11*, 13003−13010.
(27) Rugen-Hankey, S. L.; Clayton, A. J.; Barrioz, V.; Kartopu, G.; Irvine, S. J. C.; McGettrick, J. D.; Hammond, D. Improvement to Thin Film CdTe Solar Cells with Controlled Back Surface Oxidation. *Sol. Energy Mater. Sol. Cells* **2015**, *136*, 213−217.
(28) Perkins, C. L.; Ablekim, T.; Barnes, T. M.; Kuciauskas, D.; Nemeth, W.; Lynn, K. G.; Reese, M. O.; Swain, S. K.; Metzger, W. K. In *Interfaces Between CdTe and ALD Al2O3*, 7th World Conference on Photovoltaic Energy Conversion, 2018.
(29) Maruyama, T.; Arai, S. Aluminum Oxide Thin Films Prepared by Chemical Vapor Deposition from Aluminum Acetylacetonate. *Appl. Phys. Lett.* **1992**, *60*, 322−323.
(30) Pan, J.; Gloeckler, M.; Sites, J. R. Hole Current Impedance and Electron Current Enhancement by Back-contact Barriers in CdTe Thin Film Solar Cells. *J. Appl. Phys.* **2006**, *100*, No. 124505.
(31) Gessert, T. A.; Smith, S.; Moriatry, T.; Young, M.; Asher, S.; Johnston, S.; Duda, A.; DeHart, C.; Fahrenbruch, A. L. In *Evolution of CdS/CdTe Device Performance During Cu Diffusion*, Thirty-first IEEE Photovoltaic Specialists Conference, 2005; pp 291−294.

https://dx.doi.org/10.1021/acsami.0c12800
ACS Appl. Mater. Interfaces 2020, 12, 51337−51343

Approved for public release; distribution unlimited.

Journal of Materials Chemistry C

ROYAL SOCIETY OF CHEMISTRY

PAPER

View Article Online
View Journal | View Issue

Check for updates

Cite this: J. Mater. Chem. C, 2020, 8, 1972

Interface modification of sputtered NiO_x as the hole-transporting layer for efficient inverted planar perovskite solar cells†

Xiaolu Zheng,‡[abc] Zhaoning Song, ‡*[b] Zhiliang Chen,‡[a] Sandip Singh Bista,[b] Pengbin Gui,[a] Niraj Shrestha,[b] Cong Chen,[ab] Chongwen Li,[b] Xinxing Yin,[b] Rasha A. Awni,[b] Hongwei Lei,[d] Chen Tao,[a] Randy J. Ellingson,[b] Yanfa Yan[b] and Guojia Fang *[ac]

Received 21st October 2019,
Accepted 15th December 2019

DOI: 10.1039/c9tc05759e

rsc.li/materials-c

Nickel oxide (NiO_x) as a hole-transporting layer (HTL) in perovskite solar cells (PSCs) has been studied extensively in recent years. However, unlike the solution-processed NiO_x films, magnetron sputtered NiO_x exhibits relatively low conductivity and imperfect band alignment with perovskites, severely limiting the device performance of PSCs. In this study, a synergistically combined strategy consisting of triple interface treatments – including post-annealing, O_2-plasma, and potassium chloride treatments – is employed to modulate the optoelectronic properties of the sputtered NiO_x films. Through this approach, we successfully obtained NiO_x films with increased carrier density and conductivity, better energy level alignment with the perovskite absorber layer, reduced interface trap density, and improved interfacial charge extraction. PSCs using this modified sputtered NiO_x as the HTL deliver a highest stabilized efficiency of 18.7%. Our result offers an alternative method to manipulate sputtered NiO_x thin film properties and thereby sheds light on a manufacturing pathway to perovskite solar cells featuring sputtered NiO_x HTL.

Published on 19 December 2019. Downloaded by Emory University on 4/24/2020 4:34:08 PM.

Introduction

Perovskite solar cells (PSCs) have attracted tremendous attention due to their excellent photovoltaic properties[1–3] and rapidly increasing power conversion efficiencies (PCEs).[4] Nickel oxide (NiO_x) as an intrinsic p-type semiconductor is considered to be a potential low-cost candidate as a stable hole-transporting layer (HTL) in inverted p–i–n structure PSCs owing to its wide band gap, well-aligned valence band edge, and appropriate electrical properties.[5–8] Diverse deposition methods have been adopted to fabricate NiO_x HTLs, including solution-based methods, such as nanoparticle,[9–11] sol–gel,[7] solution-combustion route,[12] and electrochemical deposition,[13] and vacuum-based approaches, including magnetron sputtering,[6,14,15] atomic layer deposition,[16] pulsed laser deposition,[17] and electron beam evaporation.[18] Among these methods, magnetron sputtering is more favorable in the industry due to its high compatibility, low cost, large-scale applicability, and universality for flat and textured substrates. While PSCs with solution-processed NiO_x HTLs have demonstrated PCEs over 20%,[9,12,19] devices with sputtered NiO_x have typically suffered from less competitive PCEs below 18.5%.[6] The relatively low conductivity and imperfect band alignment with the perovskite absorber layers are considered to be the main hurdles in obtaining good device performances for sputtered NiO_x-based PSCs.[14,20,21]

Many efforts have been devoted to improving the optoelectronic properties of NiO_x films. Lattice doping is conventionally adopted to ameliorate the electrical properties of solution-processed NiO_x films.[9,22–24] However, this strategy encounters some obstacles when preparing sputtered NiO_x. For example, co-sputtering deposition is subject to complicated parameter control and limited element selection,[6,25] and thus has rarely been explored. Alternatively, interface modification has been employed in both electron-transporting layers (ETLs) and HTLs to achieve better device performance and stability.[26–29] Ratcliff *et al.*[30] discovered that O_2-plasma treatment on the NiO_x film increased its work function (WF) and decreased the midgap states close to its valence band edge. Chen *et al.*[19] demonstrated that the alkali chloride interfacial layer could improve

[a] Key Lab of Artificial Micro- and Nano-Structures of Ministry of Education of China, School of Physics and Technology, Wuhan University, Wuhan, 430072, P. R. China. E-mail: gjfang@whu.edu.cn
[b] Department of Physics and Astronomy and Wright Center for Photovoltaics Innovation and Commercialization, The University of Toledo, Toledo, OH, 43606, USA. E-mail: zhaoning.song@utoledo.edu
[c] Shenzhen Institute, Wuhan University, Shenzhen 518055, P. R. China
[d] College of Science, Huazhong Agricultural University, Wuhan 430070, P. R. China

† Electronic supplementary information (ESI) available. See DOI: 10.1039/c9tc05759e

‡ These authors contributed equally.

This journal is © The Royal Society of Chemistry 2020

Approved for public release; distribution unlimited.
502

Published on 19 December 2019. Downloaded by Emory University on 4/24/2020 4:34:08 PM.

the ordering of the atop perovskite layer and hence reduced defect density and interfacial recombination. Although most interface treatments were done on solution-processed NiO_x films, these strategies are in fact also suitable for the sputtered ones due to their good usability and maneuverability.

In this work, we demonstrated that appropriate interface treatments modify the optoelectronic properties of the sputtered NiO_x films. Through the synergistic combination of three interface treatments, namely, post-annealing, O_2-plasma, and potassium chloride (KCl) passivation, we successfully increased the carrier density of the sputtered NiO_x films, adjusted the surface work function, reduced the interfacial trap density, and improved charge extraction at the interface. As a result, PSCs with the optimally modified NiO_x HTL delivered a PCE of 19.16% with the reversed voltage scan and a steady state efficiency (SSE) of 18.7%, approximately 25% efficiency enhancement compared to the ones with the as-sputtered NiO_x. Our results prove the feasibility of the interface treatment in enhancing the performance of PSCs with sputtered NiO_x HTL.

Results and discussion

We first characterized the structural and optoelectronic properties of NiO_x thin films prepared by radio frequency (RF) magnetron sputtering with a NiO target. The top-view scanning electron microscopy (SEM) image shown in Fig. 1(a) reveals the dense and uniform surface of the as-sputtered NiO_x film with an average crystallite size of $\sim$10 nm. Grazing incidence X-ray diffraction (GIXRD) measurement of the NiO_x film deposited on a glass substrate shows the cubic crystal structure of NiO with characteristic peaks located at $\sim$37°, 43° and 63°, corresponding to the (111), (200), and (220) planes, respectively (Fig. 1(b)). The optical band gap (E_g) of the NiO_x film is determined to be 3.63 eV by the Tauc plot from the UV-vis spectroscopy measurement (Fig. 1(c)), consistent with the values reported in the literature.[31,32] The Fermi energy level (E_F) and the valence band maximum (E_{VBM}) of the as-sputtered NiO_x measured by ultraviolet photoelectron spectroscopy (UPS) are 4.85 and 5.35 eV, respectively (Fig. 1(d)). The appropriate energy level matches indium tin oxide (ITO) and perovskites (Fig. 1(e) and Table S1, ESI†) make the as-sputtered NiO_x an ideal HTL for PSCs in the inverted (or p–i–n) configuration (Fig. 1(f)).

To test the feasibility of the as-sputtered NiO_x as the HTL in PSCs, we fabricated inverted PSCs with a structure of ITO/NiO_x/perovskite/phenyl-C61-butyric acid methyl ester (PCBM)/bathocuproine (BCP)/Ag (Fig. 1(f)), where the perovskite absorber composition is $MA_{0.65}FA_{0.35}PbI_3$ (MA is methylammonium; FA is formamidinium). Current density–voltage (J–V) characteristics and external quantum efficiency (EQE) spectra of representative devices as a function of the as-sputtered NiO_x thickness (varying from 10 to 40 nm) are shown in Fig. S1 (ESI†). The spectral responses, especially in the short wavelength (<500 nm) range, decrease upon increasing the NiO_x film thickness, consistent with the trend of the transmission spectra of ITO/NiO_x (Fig. S2, ESI†). Consequently, the short-circuit current density (J_{sc}) decreases upon increasing the NiO_x thickness. In contrast, the open-circuit voltage (V_{oc}) increases

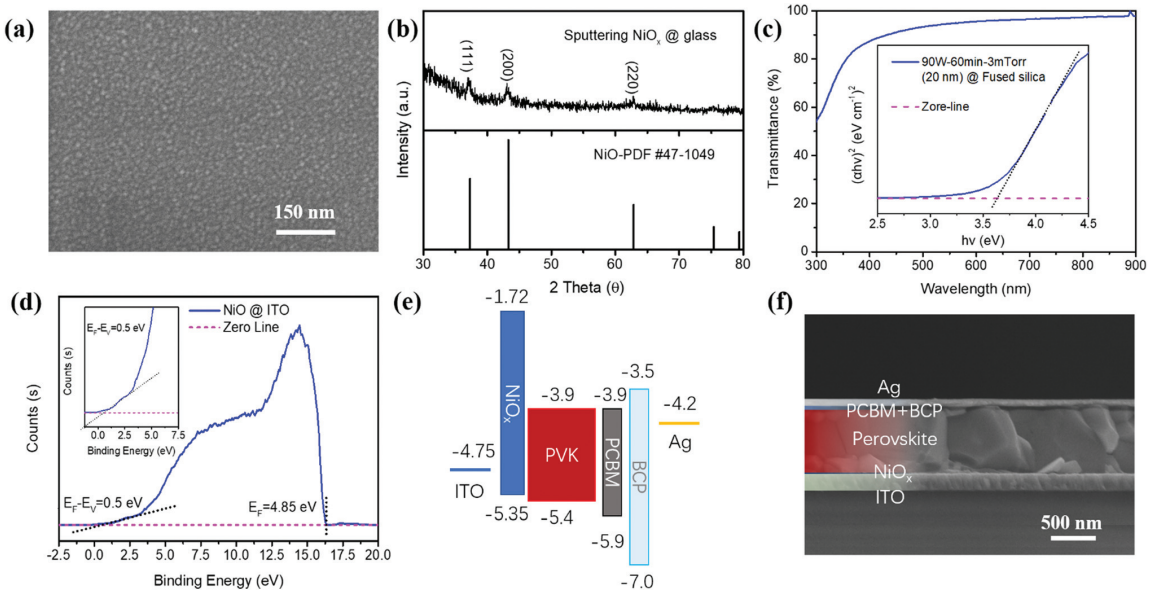


Fig. 1 (a) Top-view SEM image of an as-sputtered NiO_x film deposited on a silicon substrate. (b) GIXRD pattern of an as-sputtered NiO_x film deposited on a glass substrate. (c) Transmission spectrum of an as-sputtered NiO_x film with a thickness of 20 nm and its corresponding Tauc plot. (d) UPS spectrum of an as-sputtered NiO_x film deposited on an ITO coated glass substrate. The inset shows the magnified image of the low binding energy onset. (e) Schematic of the energy diagram and (f) cross-sectional SEM image of PSCs with the structure of ITO/NiO_x/perovskite/PCBM/BCP/Ag.

Approved for public release; distribution unlimited.
503

Published on 19 December 2019. Downloaded by Emory University on 4/24/2020 4:34:08 PM.

with the film thickness due to the reduced leakage current at the front ITO electrode. Nonetheless, all the devices exhibit moderate performances with PCEs less than 15.3%. The limited performance of these devices is attributed to the relatively low carrier density in the as-sputtered NiO_x films. The Hall effect measurement reveals that the carrier density of the as-sputtered NiO_x film is 3.84×10^{11} cm^{-3}, substantially lower than that for the NiO_x HTLs used in efficient PSCs ($>10^{14}$ cm^{-3}).[9,33–35] Such low carrier density undoubtedly indicates a high resistivity of the as-sputtered NiO_x film. Fig. S3 (ESI†) presents a linear sweep voltammetry (LSV) measurement of the as-sputtered NiO_x film using two-electrode configuration, which shows a resistivity value of 1.950×10^3 Ω cm.

In general, most of the binary metal oxides exhibit semi-insulating properties in perfect stoichiometry. Even a slight deviation from stoichiometric composition changes the electronic structure of these oxides due to the introduction of native defects within the lattice.[36,37] NiO_x tends to show a p-type semi-conducting behavior as a result of the formation of nickel vacancies $\left(V''_{Ni}\right)$.[38,39] For oxygen-rich stoichiometry, two Ni^{2+} ions each lose an extra electron to maintain charge neutrality near the V''_{Ni} site of the NiO lattice, thus contributing a quasi-localized pair of holes to form Ni^{3+} ions.[40,41] Then, the density of localized states near the valence band increases, and the hopping transport barrier for holes reduces, resulting in increased hole mobility and decreased resistivity.[36] The X-ray photoemission spectrum (XPS) displayed in Fig. 2(a) confirms that the as-sputtered NiO_x film has a low concentration of Ni^{3+} species. To introduce extra oxygen into the NiO_x film to promote the formation of V''_{Ni}, which can effectively increase the carrier density and reduce the film resistivity, a simple approach, *i.e.*, post-annealing, was employed to treat the as-sputtered NiO_x films.

The as-sputtered NiO_x films were annealed in ambient air at various temperatures. The GIXRD patterns displayed in Fig. 2(b) and Fig. S5(a) (ESI†) show that the (200) peak slightly shifts to a higher diffraction angle upon increasing the annealing temperature. This right-shifted diffraction peak corresponds to a decrease in the interplanar spacing, which indicates the formation of V''_{Ni} and the shrinkage of the NiO_x lattice. Fig. S5(b) (ESI†) shows that there is no obvious difference in the optical transmittance of the film after post-annealing. The atomic force microscopy (AFM) images illustrated in Fig. S5(c)–(e) (ESI†) reveal that the post-annealing doesn't influence the root-mean-squared film roughness (R_q), but makes the film denser and smoother, indicated by the decreased arithmetical mean deviation roughness (R_a). XPS was then conducted to analyze the surface stoichiometry of the annealed NiO_x films. Compared with the as-sputtered one (Fig. 2(a)), the Ni $2p_{3/2}$ peak of the annealed NiO_x film at 250 °C (Fig. 2(c)) displays a higher peak intensity for NiOOH (856.87 eV) and an extra peak located at 858.10 eV that is ascribed to the Ni_2O_3 species.[20,30,42] Note that the Ni^{3+} usually comes from two species: Ni_2O_3 and NiOOH. In the as-sputtered NiO_x film, we ascribed the third peak (856.87 eV) to the NiOOH component because Ni_2O_3 is not stable at low temperature in ambient air. However, when annealed above 250 °C, there is enough driving force for the dehydration/dehydroxylation reaction to convert $Ni(OH)_2$/NiOOH to the higher order oxide (Ni_2O_3).[30] Fig. S6 (ESI†) shows more XPS spectra of the NiO_x films annealed at various temperatures. The extracted binding energies and component ratios are summarized in Table S3 (ESI†). Clearly the annealing process introduces more Ni^{3+} species into NiO_x films. In particular, Ni_2O_3 appears when the annealing temperature is higher than 250 °C. The film resistivity and carrier density as a function of the annealing temperature were measured and plotted in Fig. 2(d). Hall effect measurement uncovers a continual increase of the carrier density of the annealed NiO_x films upon increasing the annealing temperature, which is consistent with the decreased resistivity determined by the LSV measurement (Fig. S7, ESI†). Note that after annealing at 250 °C, both the carrier density and conductivity of the annealed NiO_x film increase rapidly, which is associated with the appearance of Ni_2O_3. The carrier density of the NiO_x film jumps from 3.84×10^{11} to 3.79×10^{13} cm^{-3}, while the film resistivity reduces from 1.95×10^3 to 4.71×10^2 Ω cm.

Devices with different NiO_x film thicknesses and annealing temperatures were then fabricated to verify the feasibility of post-annealing. Fig. S8 and S9 (ESI†) summarize the optimization processes of the device performances. The optimal thickness and annealing temperature are found to be 20 nm and 250 °C, respectively. The J_{sc} first increases upon the annealing temperature, which is in line with the trend of film carrier density; then it decreases once the temperature further rises to 300 °C, likely due to the degradation of ITO at high temperature. However, although the annealing process improves the device performance, especially the J_{sc}, the devices still exhibit restrained PCEs of 16.6% with a moderate V_{oc} of 0.98 V.

Although the annealing process improves the carrier density of the sputtered NiO_x film significantly, it remains lower than the expected value ($>10^{14}$ cm^{-3}) as we mentioned above, which is partially responsible for the limited PSC performance. And to increase the V_{oc} of the PSCs, one can deepen the E_F of NiO_x to reduce the potential energy loss of hole transfer from perovskite to NiO_x and suppress the interfacial recombination through band alignment engineering.[13,43]

Oxygen (O_2)-plasma treatment is a widely used method to modify the surface and electrical properties of thin films. It has been demonstrated that the O_2-plasma treatment could influence the chemical stoichiometry and surface WF of NiO_x thin films, thus adjusting their carrier densities and interfacial energy level alignment.[13,30,42,44] In addition to post-annealing, we applied O_2-plasma treatment to further adjust the optoelectronic properties of the sputtered NiO_x. Considering the possible damage of O_2-plasma to the NiO_x film surface as reported in the literature,[27,42] a relatively low plasma power (30 W) and a short treating time (2 min) were chosen first to explore the potential influences of the O_2-plasma treatment on the annealed NiO_x films. Fig. 2(e) presents the XPS spectrum of the annealed NiO_x film (250 °C) with the O_2-plasma treatment. More NiOOH species are presented, but the Ni_2O_3 signal changes little after

 This journal is © The Royal Society of Chemistry 2020

Approved for public release; distribution unlimited.
504

Published on 19 December 2019. Downloaded by Emory University on 4/24/2020 4:34:08 PM.

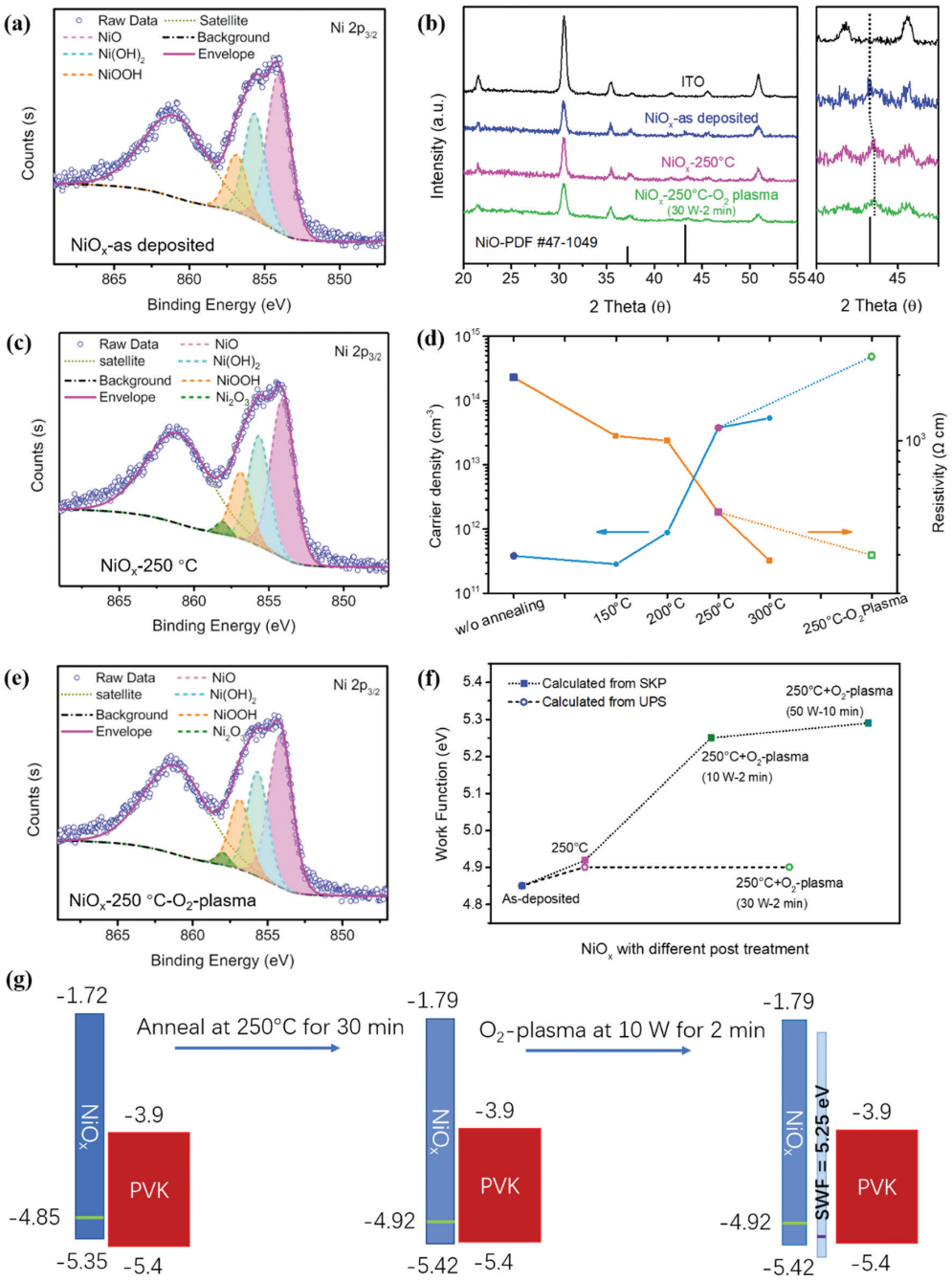


Fig. 2 XPS spectra of the Ni $2p_{3/2}$ state for (a) as-sputtered NiO_x, (c) NiO_x annealed at 250 °C for 30 min, and (e) NiO_x annealed at 250 °C followed by O_2-plasma at 30 W for 2 min. (b) GIXRD patterns of the sputtered NiO films with different post treatment. The ITO substrate was also shown here to facilitate comparison. (d) Carrier density and film resistivity of the NiO_x films treated with different conditions. (f) Surface work function of the various NiO_x films calculated from SKP and UPS. (g) The energy alignment schematic of different NiO_x and perovskite. SWF represents the surface work function shift after the oxygen plasma treatment.

the O_2-plasma treatment, compared to the film which underwent only the annealing process (Fig. 2(c) and Table S3, ESI†). This is consistent with the literature that the energy provided by O_2-plasma is insufficient to induce the crystallographic reorganization from the cubic (NiO) or rhombohedral ($Ni(OH)_2$) structure to the hexagonal crystal structure (Ni_2O_3), while the

Approved for public release; distribution unlimited.
505

Published on 19 December 2019. Downloaded by Emory University on 4/24/2020 4:34:08 PM.

conversion from $Ni(OH)_2$ to NiOOH occurs more easily because NiOOH has the same rhombohedral structure as $Ni(OH)_2$.[30] The increased Ni^{3+} content results in the improvement of carrier density as well as film conductivity. Fig. 2(d) and Fig. S10 (ESI†) show that after the O_2-plasma treatment, the carrier density of the NiO_x film further increases from 3.79×10^{13} to 4.83×10^{14} cm^{-3}, and the resistivity decreases from 4.71×10^2 to 2.99×10^2 Ω cm.

The increased NiOOH has been reported to form a surface dipole of O–Ni–OH, shifting the NiO_x film surface work function (SWF) and reducing the leakage current and recombination at the interface.[30,36] Scanning Kelvin Probe (SKP) measurement and UPS were then conducted to investigate the SWF variation of NiO_x films with different post treatments. All the results are summarized in Fig. 2(f), and the original UPS spectra can be found in Fig. S11 (ESI†). The as-sputtered NiO_x film shows a relatively low WF of 4.85 eV, and it slightly shifts deep to 4.92 eV after the annealing process. A low power and short time O_2-plasma treatment further moves the WF to 5.25 eV. Increasing the plasma power and time just pushes the WF slightly to 5.29 eV, which is in line with the literature.[27,42,44] This higher WF is induced by increasing the hole concentration at the NiO_x film surface, repelling electrons and thus lowering the interfacial recombination.[30,45] Additionally, a high density of holes is beneficial to form a good ohmic contact with the front electrode and thus reduce the series resistance.[13,42,44] Note that the UPS measurement cannot detect the WF change of NiO_x film after the O_2-plasma treatment, which is likely due to the surface oxygen escape in a high vacuum. Even in an ambient atmosphere, the resistivity of O_2-plasma treated NiO_x film recovered to its initial value after 2 h storage (Fig. S10, ESI†), indicating the loss of NiOOH species. Similar behavior was also observed by Steirer *et al.*[44] who showed that the WF of solution-processed NiO_x films enhanced by the O_2-plasma treatment exhibited a fast decay in an inert atmosphere. Fig. 2(g) illustrates the energy level alignments of different NiO_x films with the perovskite layers. After the post-annealing, the E_F of the NiO_x film becomes deeper, which reduces the valence band offset between NiO_x and perovskites. With further O_2-plasma treatment, an oxygen-rich NiO_x surface layer with a deep E_F of −5.25 eV forms, which is too close to the valence band of the perovskite. This layer may act as a good surface passivation for the perovskite absorber layer, though it may also impede the carrier transfer to some extent.

We then investigated the devices based on the annealed NiO_x films treated with different plasma powers of 10–50 W for 2 min. The representative *J–V* characteristics and EQE spectra are shown in Fig. S12 (ESI†). The devices show significantly improved V_{oc} (1.091 V) and fill factor (FF) (76.6%) even with the lowest power of 10 W. However, the J_{sc} dropped about 1 mA cm^{-2} when compared to the device based on the annealed NiO_x without the O_2-plasma treatment (Fig. S9, ESI†). Further increase in the plasma power does not affect the V_{oc} or J_{sc} but decreases the FF gradually. The best-performing device shows a PCE of 18.15%. The enhanced V_{oc} can be explained by the downshifted Fermi level of the NiO_x film with O_2-plasma treatment, while the reduced J_{sc} is likely due to the damage on the NiO_x surface caused by the O_2-plasma treatment. The AFM image displayed in Fig. S13 (ESI†) reveals a fuzzy surface of the O_2-plasma treated NiO_x film, which is consistent with the literature.[42] Note that the devices with O_2-plasma treatment shows a relatively large hysteresis (Fig. S14, ESI†), which is mainly related to the unbalanced charge carrier transport. Etching by the O_2-plasma on the NiO_x surface should be partially responsible for this hampered hole transport, and the slightly mismatched energy level alignment between NiO_x and perovskite may retard the interfacial hole extraction.

To overcome these surface imperfection issues, we adopt potassium passivation on the annealed NiO_x surface before the O_2-plasma treatment. Potassium passivation has been reported as a universal strategy to suppress the bulk and interface defects and minimize the device hysteresis.[7,19,28,46,47] Here, we used KCl for surface passivation. The GIXRD patterns shown in Fig. 3(a) indicate the formation of KCl crystals after spin-coating of the potassium salt solution atop the NiO_x film. The SEM image (Fig. 3(b)) reveals a discrete distribution of KCl particles on the NiO_x surface. This discontinuous coverage of KCl at the interface was also reported by Liu *et al.*[28] who deposited KCl atop the SnO_2 layer. They discovered that the presence of KCl significantly reduced the interface defects and recombination loss, with little effect on the perovskite crystal structure and electrical properties. The nearly invariable surface morphology and diffraction peaks of perovskite films deposited on NiO_x with and without KCl passivation (Fig. 3(c) and Fig. S15, ESI†) confirm that the KCl treatment does not affect the structural properties of the subsequently deposited perovskite films.

Devices were then fabricated to check the potassium passivation tactics. Note that the KCl treatment can influence the optimal O_2-plasma power as shown in Fig. S16 (ESI†). This is understandable because a relatively strong plasma power is helpful to etch the redundant insulative $Ni(OH)_2$ formed during the potassium treatment using the aqueous KCl solution, thus enhancing the charge transport and collection at the perovskite/NiO_x interface. On this basis, we further investigated the effect of KCl concentration on the device performance. Fig. S17 (ESI†) displays the photovoltaic performance of the devices as a function of KCl concentration, including the *J–V* characteristics, EQE spectra and the corresponding steady state efficiencies. The KCl concentration seems to have very limited effect on the device performance especially for the PSCs with high plasma power (30 W) treatment. One possible reason is that the KCl particles were partially rinsed out during perovskite deposition due to the low solubility of KCl in mixed dimethyl sulfoxide (DMSO)/dimethylformamide (DMF),[48,49] and the other may be originated from the etching effect of the plasma treatment (Fig. S18, ESI†). They both make the actual content of KCl in the final devices relatively low and have little discrepancy. The optimized device with 20 mg ml^{-1} KCl plus 30 W O_2-plasma etch yields a champion PCE of 19.16%, with a J_{sc} of 23.27 mA cm^{-2}, V_{oc} of 1.049 V, and FF of 78.8%.

Steady-state photoluminescence (PL) and time-resolved photoluminescence (TRPL) of the perovskites deposited on different NiO_x films were then performed to identify the causes of

 This journal is © The Royal Society of Chemistry 2020

Approved for public release; distribution unlimited.
506

Published on 19 December 2019. Downloaded by Emory University on 4/24/2020 4:34:08 PM.

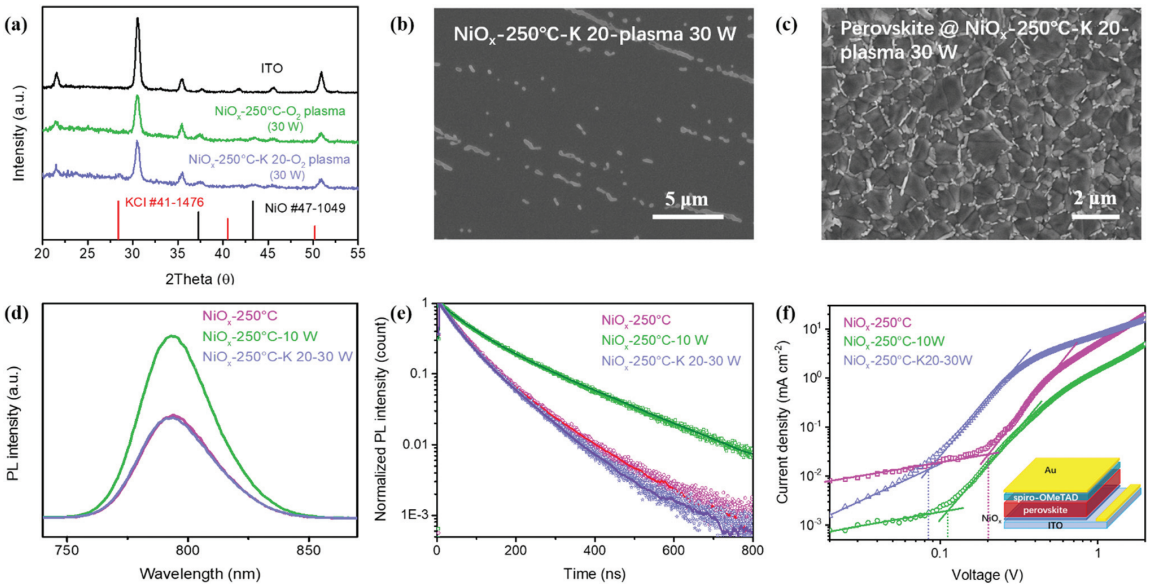


Fig. 3 (a) GIXRD patterns of the annealed and O_2-plasma treated NiO_x films with and without KCl treatment. Top-view SEM image of (b) the NiO_x film treated with annealing, KCl, and O_2-plasma, and (c) the perovskite deposited on this NiO_x film. (d) Steady-state PL and (e) TRPL spectra of the perovskite deposited on three different NiO_x films. The decays were fitted with a double-exponential decay function and the obtained time constants are summarized in Table S9 (ESI†). (f) Dark *J*–*V* characteristics of the hole-only devices based on different NiO_x films. The inset shows the device structure used in the tests.

performance improvement, and the results are illustrated in Fig. 3(d) and (e), respectively. The measurements were made using excitation/collection through the NiO_x/perovskite interface to evaluate the behavior of charge carriers nearest to the interface. Three representative NiO_x films, treated with only thermal annealing (NiO_x-250 °C), thermal annealing plus O_2-plasma (NiO_x-250 °C-10 W), and 3-step treatment with KCl passivation (NiO_x-250 °C-20–30 W) were selected for comparison. As a contrast, a bare perovskite film that deposited on a clean glass substrate have also been measured and are shown in Fig. S19 (ESI†).

The perovskite layer deposited on the NiO_x-250 °C-10 W film shows higher PL intensity and longer PL lifetime (τ_{ave}) than the one with the NiO_x-250 °C film. The presence of a high SWF layer atop the NiO_x surface after the O_2-plasma treatment should be partially responsible for the increased PL intensity because it retards the charge extraction from the perovskite to NiO_x. Interestingly, the sample based on NiO_x-250 °C-K 20–30 W shows a similar PL intensity and lifetime compared to the post-annealed sample (NiO_x-250 °C), seemingly indicating a higher hole extraction efficiency from the perovskite to NiO_x. However, besides the charge extraction, the trap density also influences the PL emission and carrier lifetime. A high trap density in the perovskite layer and at the interface would increase the non-radiative recombination, thus decreasing the fluorescence intensity and carrier lifetime.

To further analyze the trap density in the perovskite films deposited on different NiO_x layers, we conducted the LSV measurement using hole-only devices with the structure of ITO/different NiO_x/perovskite/spiro-OMeTAD/Au. Fig. 3(f) shows the results plotted in double logarithmic scale. The trap-state density (N_d) can be estimated by the trap-filled limit voltage (V_{TFL}), which is determined from the first kink point.[7,50] The V_{TFL} extracted from these devices are 0.198, 0.114, and 0.093 V for the perovskite deposited on NiO_x-250 °C, NiO_x-250 °C-10 W, and NiO_x-250 °C-K 20–30 W, respectively. The corresponding trap densities are thus calculated to be 1.49×10^{15}, 8.60×10^{14}, and 7.02×10^{14} cm^{-3}. The reduced trap density in the O_2-plasma treated device (NiO_x-250 °C-10 W) is likely due to the suppressed surface defects at the NiO_x/perovskite interface, which is believed to originate from the presence of dipoles (NiOOH) on the NiO_x film surface.[30] As to the device with the KCl treatment, although the effect of O_2-plasma is likely weakened due to the introduction of KCl, the incorporation of K^+ ions helps decrease the defect density in the perovskite owing to the reduced iodide Frenkel defect[51] and/or the formation of ordered NiO_x/perovskite interface.[19] A similar trap density between the NiO_x-250 °C-10 W and NiO_x-250 °C-K 20–30 W samples confirms that the faster charge extraction of the latter one is the main reason for the quicker PL quenching and shorter carrier lifetime. The combination of low trap density and fast charge extraction accounts for the excellent device performances in PSCs with NiO_x-250 °C-K 20–30 W.

The champion device performances and their corresponding device structures with NiO_x-250 °C, NiO_x-250 °C-10 W, and NiO_x-250 °C-K 20–30 W HTLs are displayed in Fig. 4(a)–(c), respectively. Clearly, the O_2-plasma treatment strikingly improves the device V_{oc} but decreases J_{sc} with unexpectedly increased hysteresis. Furthermore, KCl passivation leads to the

Approved for public release; distribution unlimited.
507

Published on 19 December 2019. Downloaded by Emory University on 4/24/2020 4:34:08 PM.

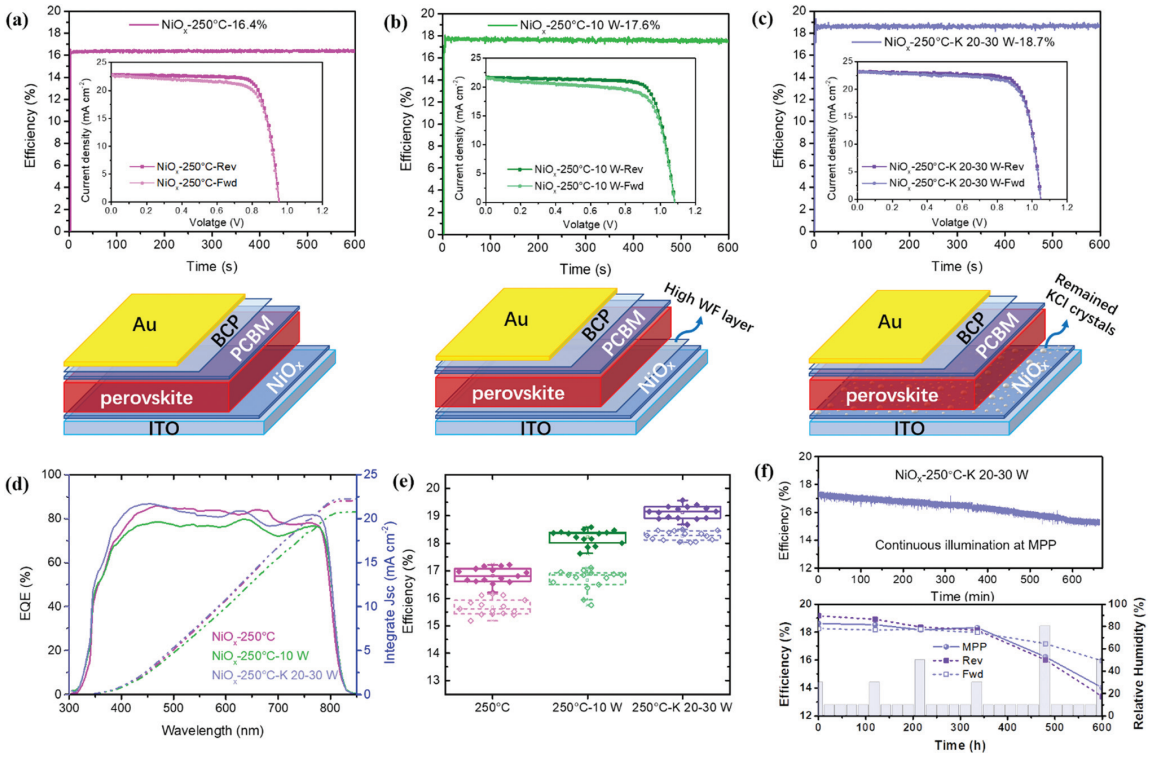


Fig. 4 The *J*–*V* curves, steady-state efficiencies tracking at maximum power point (MPP) and the corresponding device structures of the PSCs with (a) NiO_x-250 °C, (b) NiO_x-250 °C-10 W, and (c) NiO_x-250 °C-K 20–30 W HTLs. (d) EQE spectra and their corresponding $J_{integrate}$. (e) Statistical distribution of these three kinds of devices. (f) The illumination stability (top panel) and long-term stability (bottom panel) of the device with optimized NiO_x-250 °C-K 20–30 W HTL.

recovered J_{sc} and reduced hysteresis without sacrificing V_{oc}, resulting in the best device performance. The integrated current density ($J_{integrate}$) calculated from the corresponding EQE spectra (Fig. 4(d)) is consistent with the J_{sc} of the best performing cell in each category. The statistical distributions of more than 15 cells for each category of devices (Fig. 4(e)) reveals similar PCE and hysteresis trends with the best-performing devices. The detailed photovoltaic parameter statistics including the V_{oc}, J_{sc}, FF, and PCE are presented in Fig. S20 (ESI†). The best and statistic device performance of these three types of PSCs are tabulated in Table 1.

In addition to power conversion efficiency, stability is another important metric for evaluating PSCs. Fig. 4(f) shows the device efficiency evolution with the optimized HTL (NiO_x-250 °C-K 20–30 W) under continuous illumination (top panel) and stored in dark and ambient air without encapsulation

Table 1 Summary of the photovoltaic parameters of PSCs based on NiO_x-250 °C, NiO_x-250 °C-10 W, and NiO_x-250 °C-K 20–30 W HTLs

	Sweep	V_{oc} [V]	J_{sc} [mA cm^{-2}]	FF [%]	PCE [%]	$J_{integrate}$ [mA cm^{-2}]	MPP [%]
NiO_x-250 °C							
Average	Rev	0.944 ± 0.004	22.81 ± 0.18	0.78 ± 0.01	16.83 ± 0.28		
	Fwd	0.942 ± 0.004	22.66 ± 0.18	0.74 ± 0.01	15.68 ± 0.30		
Champion	Rev	0.953	22.825	0.789	17.163	22.03	16.4
	Fwd	0.950	22.797	0.744	16.113		
NiO_x-250 °C-10 W							
Average	Rev	1.082 ± 0.013	21.59 ± 0.11	0.78 ± 0.01	18.22 ± 0.27		
	Fwd	1.081 ± 0.014	21.71 ± 0.16	0.71 ± 0.01	16.68 ± 0.39		
Champion	Rev	1.083	21.632	0.785	18.384	20.74	17.6
	Fwd	1.081	21.628	0.721	16.856		
NiO_x-250 °C-K 20–30 W							
Average	Rev	1.049 ± 0.004	23.10 ± 0.07	0.79 ± 0.01	19.12 ± 0.24		
	Fwd	1.046 ± 0.007	23.16 ± 0.10	0.75 ± 0.01	18.27 ± 0.17		
Champion	Rev	1.049	23.170	0.788	19.158	22.26	18.7
	Fwd	1.048	23.214	0.761	18.510		

This journal is © The Royal Society of Chemistry 2020

Approved for public release; distribution unlimited.

Published on 19 December 2019. Downloaded by Emory University on 4/24/2020 4:34:08 PM.

(bottom panel). The device maintained 88% of its initial efficiency after 660 min tracking at maximum power point (MPP) under continuous AM1.5 G solar illumination. As to the shelf lifetime test, the device was stored in a dry box and tested periodically in ambient air with a fluctuant relative humidity (RH) varying from 30 to 80%. Fig. S21 (ESI†) gives the detailed *J–V* curves and their corresponding MPP efficiencies tested at certain times, and the relevant parameters are summarized in Table S10 (ESI†). When RH is less than 50%, the device shows insignificant PCE changes. However, when the ambient RH is higher than 80% and the PCE drops significantly. The device only maintains 75% of its initial efficiency after 600 h aging. More interestingly, the device aging process shows a clear increase and reverse in hysteresis, which means the hysteresis index ($PCE_{Reverse\ scan}$–$PCE_{Forward\ scan}$) changes from positive to negative during the aging test. We speculated that this phenomenon might be related to the interdiffusion and reaction of iodine and silver ions. As time passes, the I^- ions can diffuse through the electron transport layer and accumulate at the Ag inner surface and then react with it. The high humidity that helps to decompose the perovskite undoubtedly accelerates this process.[52–54] As a result, the decreased electron extraction and collection caused by the erosion of Ag and the formation of an AgI barrier can significantly degrade the device performance and affect its hysteresis behavior. Meanwhile, the diffused Ag in perovskite that may react with the perovskite and/or form the Ag metal clusters acting as recombination centers should also contribute to the degradation of device efficiency.[55] Further evidence is still needed to determine the underlying reasons for this to avoid the device deterioration from the side of the Ag electrode.

Conclusion

In summary, we adopted a synergistic triple interface treatment combination to manipulate the optoelectronic properties of the sputtered NiO_x films and hence improved the efficiency of the resultant PSCs. We showed that the extra oxygen introduced by the post-annealing and O_2-plasma treatment significantly increased the film conductivity and carrier density. Furthermore, the increased dipole species (NiOOH) on the NiO_x surface shifted the NiO_x SWF and thus decreased the defect recombination at the NiO_x/perovskite interface. This effect is more remarkable in the O_2-plasma treated process. Additionally, the KCl passivation process was adopted before the O_2-plasma treatment to mitigate the plasma damages on the NiO_x surface. The presence of KCl helped to improve the hole extraction efficiency from perovskite to NiO_x and thus reduced the *J–V* hysteresis. The resultant devices with the modified sputtered NiO_x HTLs delivered the highest stabilized efficiency of 18.7% with good reproducibility and stability. Our results offer an efficient strategy to adjust the bulk and surface properties of the sputtered NiO_x films and achieve high performance of the PSCs with the sputtered NiO_x as HTL.

Statement of contributions

X. Zheng and Z. Song conceived and designed this study. X. Zheng performed the experiments. C. Chen, C. Li and X. Yin helped to fabricate the devices. X. Zheng, Z. Song, Z. Chen, and S. Bista characterized the films and devices. R. Awni assisted the characterization. X. Zheng and Z. Song wrote the paper. H. Lei helped to review the primary manuscript. P. Gui and N. Shrestha helped to supplement the experiment and complete the revision. X. Zheng, Z. Song, C. Tao, R. Ellingson, Y. Yan and G. Fang reviewed and edited the final manuscript. All the authors read and approved the manuscript.

Conflicts of interest

There are no conflicts to declare.

Acknowledgements

This work at Wuhan University was financially supported by the National Natural Science Foundation of China (11674252), Special Funds for the Development of Strategic Emerging Industries in Shenzhen (JCYJ20170818113036217), the Science and Technology Department of Hubei Province (2019AAA020) and the Fundamental Research Funds for the Central Universities (2042019kf0317). The work at the University of Toledo was supported by the Ohio Research Scholar Program and Air Force Research Laboratory. This publication is based on research sponsored by the Air Force Research Laboratory under agreement number FA9453-18-2-0037. The U.S. Government is authorized to reproduce and distribute reprints for Governmental purposes notwithstanding any copyright notation thereon. The views and conclusions contained herein are those of the authors and should not be interpreted as necessarily representing the official policies or endorsements, either expressed or implied, of the Air Force Research Laboratory or the U.S. Government. X. Z. acknowledges the financial support from China Scholarship Council (CSC, No. 201806270094).

Notes and references

1 M. M. Lee, J. Teuscher, T. Miyasaka, T. N. Murakami and H. J. Snaith, *Science*, 2012, **338**, 643–647.
2 G. Xing, N. Mathews, S. Sun, S. S. Lim, Y. M. Lam, M. Gratzel, S. Mhaisalkar and T. C. Sum, *Science*, 2013, **342**, 344–347.
3 W. J. Yin, T. Shi and Y. Yan, *Adv. Mater.*, 2014, **26**, 4653–4658.
4 https://www.nrel.gov/pv/assets/pdfs/best-research-cell-efficiencies.20190703.pdf.
5 H.-L. Chen, Y.-M. Lu and W.-S. Hwang, *Surf. Coat. Technol.*, 2005, **198**, 138–142.
6 G. Li, Y. Jiang, S. Deng, A. Tam, P. Xu, M. Wong and H. S. Kwok, *Adv. Sci.*, 2017, **4**, 1700463.
7 X. Yin, J. Han, Y. Zhou, Y. Gu, M. Tai, H. Nan, Y. Zhou, J. Li and H. Lin, *J. Mater. Chem. A*, 2019, **7**, 5666–5676.
8 N. Sun, G. Fang, P. Qin, Q. Zheng, M. Wang, X. Fan, F. Cheng, J. Wan and X. Zhao, *Sol. Energy Mater. Sol. Cells*, 2010, **94**, 2328–2331.

Approved for public release; distribution unlimited.
509

Published on 19 December 2019. Downloaded by Emory University on 4/24/2020 4:34:08 PM.

9 W. Chen, Y. Wu, J. Fan, A. B. Djurišić, F. Liu, H. W. Tam, A. Ng, C. Surya, W. K. Chan, D. Wang and Z.-B. He, *Adv. Energy Mater.*, 2018, **8**, 1703519.
10 H. Zhang, J. Cheng, F. Lin, H. He, J. Mao, K. S. Wong, A. K.-Y. Jen and W. C. Choy, *ACS Nano*, 2015, **10**, 1503–1511.
11 H. Zhang, X. Ren, X. Chen, J. Mao, J. Cheng, Y. Zhao, Y. Liu, J. Milic, W.-J. Yin and M. Grätzel, *Energy Environ. Sci.*, 2018, **11**, 2253–2262.
12 Z. Liu, J. Chang, Z. Lin, L. Zhou, Z. Yang, D. Chen, C. Zhang, S. F. Liu and Y. Hao, *Adv. Energy Mater.*, 2018, **8**, 1703432.
13 T. Wang, D. Ding, H. Zheng, X. Wang, J. Wang, H. Liu and W. Shen, *Sol. RRL*, 2019, **3**, 1900045.
14 E. Aydin, J. Troughton, M. De Bastiani, E. Ugur, M. Sajjad, A. Alzahrani, M. Neophytou, U. Schwingenschlögl, F. Laquai and D. Baran, *ACS Appl. Energy Mater.*, 2018, **1**, 6227–6233.
15 L. Ai, G. Fang, L. Yuan, N. Liu, M. Wang, C. Li, Q. Zhang, J. Li and X. Zhao, *Appl. Surf. Sci.*, 2008, **254**, 2401–2405.
16 S. Seo, I. J. Park, M. Kim, S. Lee, C. Bae, H. S. Jung, N.-G. Park, J. Y. Kim and H. Shin, *Nanoscale*, 2016, **8**, 11403–11412.
17 J. H. Park, J. Seo, S. Park, S. S. Shin, Y. C. Kim, N. J. Jeon, H. W. Shin, T. K. Ahn, J. H. Noh and S. C. Yoon, *Adv. Mater.*, 2015, **27**, 4013–4019.
18 T. Abzieher, S. Moghadamzadeh, F. Schackmar, H. Eggers, F. Sutterlüti, A. Farooq, D. Kojda, K. Habicht, R. Schmager, A. Mertens, R. Azmi, L. Klohr, J. A. Schwenzer, M. Hetterich, U. Lemmer, B. S. Richards, M. Powalla and U. W. Paetzold, *Adv. Energy Mater.*, 2019, **9**, 1802995.
19 W. Chen, Y. Zhou, G. Chen, Y. Wu, B. Tu, F. Z. Liu, L. Huang, A. M. C. Ng, A. B. Djurišić and Z. He, *Adv. Energy Mater.*, 2019, **9**, 1803872.
20 X. Yan, J. Zheng, L. Zheng, G. Lin, H. Lin, G. Chen, B. Du and F. Zhang, *Mater. Res. Bull.*, 2018, **103**, 150–157.
21 A. Huang, J. Zhu, J. Zheng, Y. Yu, Y. Liu, S. Yang, S. Bao, L. Lei and P. Jin, *J. Mater. Chem. C*, 2016, **4**, 10839–10846.
22 Y. Wei, K. Yao, X. Wang, Y. Jiang, X. Liu, N. Zhou and F. Li, *Appl. Surf. Sci.*, 2018, **427**, 782–790.
23 W. Chen, F. Z. Liu, X. Y. Feng, A. B. Djurišić, W. K. Chan and Z. B. He, *Adv. Energy Mater.*, 2017, **7**, 1700722.
24 W. Chen, Y. Wu, Y. Yue, J. Liu, W. Zhang, X. Yang, H. Chen, E. Bi, I. Ashraful, M. Grätzel and L. Han, *Science*, 2015, **350**, 944–948.
25 A. B. Huang, J. T. Zhu, J. Y. Zheng, Y. Yu, Y. Liu, S. W. Yang, S. H. Bao, L. Lei and P. Jin, *J. Mater. Chem. C*, 2016, **4**, 10839–10846.
26 U. Kwon, B.-G. Kim, D. C. Nguyen, J.-H. Park, N. Y. Ha, S.-J. Kim, S. H. Ko, S. Lee, D. Lee and H. J. Park, *Sci. Rep.*, 2016, 6.
27 Y. Nishihara, M. Chikamatsu, S. Kazaoui, T. Miyadera and Y. Yoshida, *Jpn. J. Appl. Phys.*, 2018, **57**, 04FS07.
28 X. Liu, Y. Zhang, L. Shi, Z. Liu, J. Huang, J. S. Yun, Y. Zeng, A. Pu, K. Sun, Z. Hameiri, J. A. Stride, J. Seidel, M. A. Green and X. Hao, *Adv. Energy Mater.*, 2018, **8**, 1800138.
29 T. Bu, J. Li, F. Zheng, W. Chen, X. Wen, Z. Ku, Y. Peng, J. Zhong, Y. B. Cheng and F. Huang, *Nat. Commun.*, 2018, **9**, 4609.
30 E. L. Ratcliff, J. Meyer, K. X. Steirer, A. Garcia, J. J. Berry, D. S. Ginley, D. C. Olson, A. Kahn and N. R. Armstrong, *Chem. Mater.*, 2011, **23**, 4988–5000.
31 S. Sajid, A. M. Elseman, H. Huang, J. Ji, S. Dou, H. Jiang, X. Liu, D. Wei, P. Cui and M. Li, *Nano Energy*, 2018, **51**, 408–424.
32 H. Wang, Y. Zhao, X. Li, C. Wu, X. Dong, Y. Ma, B. Zhang and G. Du, *Vacuum*, 2015, **119**, 77–80.
33 M. Yanagida, L. Shimomoto, Y. Shirai and K. Miyano, *Electrochemistry*, 2017, **85**, 231–235.
34 C. Chen, G. Yang, J. Ma, X. Zheng, Z. Chen, Q. Zhang and G. Fang, *J. Mater. Chem. C*, 2017, **5**, 10280–10287.
35 W. Chen, Y. Wu, Y. Yue, J. Liu, W. Zhang, X. Yang, H. Chen, E. Bi, I. Ashraful and M. Grätzel, *Science*, 2015, **350**, 944–948.
36 R. Islam, G. Chen, P. Ramesh, J. Suh, N. Fuchigami, D. Lee, K. A. Littau, K. Weiner, R. T. Collins and K. C. Saraswat, *ACS Appl. Mater. Interfaces*, 2017, **9**, 17201–17207.
37 M. A. Wittenauer and L. L. Van Zandt, *Philos. Mag. B*, 1982, **46**, 659–667.
38 J. Robertson and S. J. Clark, *Phys. Rev. B: Condens. Matter Mater. Phys.*, 2011, **83**, 075205.
39 J. A. Dawson, Y. Guo and J. Robertson, *Appl. Phys. Lett.*, 2015, **107**, 122110.
40 F. J. Morin, *Bell Syst. Tech. J.*, 1958, **37**, 1047–1084.
41 S. P. Mitoff, *J. Chem. Phys.*, 1961, **35**, 882–889.
42 S. Liu, R. Liu, Y. Chen, S. Ho, J. H. Kim and F. So, *Chem. Mater.*, 2014, **26**, 4528–4534.
43 G. Yang, C. Wang, H. Lei, X. Zheng, P. Qin, L. Xiong, X. Zhao, Y. Yan and G. Fang, *J. Mater. Chem. A*, 2017, **5**, 1658–1666.
44 K. X. Steirer, J. P. Chesin, N. E. Widjonarko, J. J. Berry, A. Miedaner, D. S. Ginley and D. C. Olson, *Org. Electron.*, 2010, **11**, 1414–1418.
45 W. Ke, G. Fang, J. Wan, H. Tao, Q. Liu, L. Xiong, P. Qin, J. Wang, H. Lei and G. Yang, *Nat. Commun.*, 2015, **6**, 6700.
46 T. Bu, X. Liu, Y. Zhou, J. Yi, X. Huang, L. Luo, J. Xiao, Z. Ku, Y. Peng, F. Huang, Y.-B. Cheng and J. Zhong, *Energy Environ. Sci.*, 2017, **10**, 2509–2515.
47 M. Abdi-Jalebi, Z. Andaji-Garmaroudi, S. Cacovich, C. Stavrakas, B. Philippe, J. M. Richter, M. Alsari, E. P. Booker, E. M. Hutter, A. J. Pearson, S. Lilliu, T. J. Savenije, H. Rensmo, G. Divitini, C. Ducati, R. H. Friend and S. D. Stranks, *Nature*, 2018, **555**, 497–501.
48 J. Dagar, K. Hirselandt, A. Merdasa, A. Czudek, R. Munir, F. Zu, N. Koch, T. Dittrich and E. L. Unger, *Sol. RRL*, 2019, **3**, 1900088.
49 R. Alexander, E. C. F. Ko, Y. C. Mac and A. J. Parker, *J. Am. Chem. Soc.*, 1967, **89**, 3703–3712.
50 R. H. Bube, *J. Appl. Phys.*, 1962, **33**, 1733–1737.
51 D.-Y. Son, S.-G. Kim, J.-Y. Seo, S.-H. Lee, H. Shin, D. Lee and N.-G. Park, *J. Am. Chem. Soc.*, 2018, **140**, 1358–1364.
52 C. C. Boyd, R. Cheacharoen, K. A. Bush, R. Prasanna, T. Leijtens and M. D. McGehee, *ACS Energy Lett.*, 2018, **3**, 1772–1778.
53 Y. Kato, L. K. Ono, M. V. Lee, S. Wang, S. R. Raga and Y. Qi, *Adv. Mater. Interfaces*, 2015, **2**, 1500195.
54 J. Li, Q. Dong, N. Li and L. Wang, *Adv. Energy Mater.*, 2017, **7**, 1602922.
55 M. Liu, Z. Chen, Y. Yang, H.-L. Yip and Y. Cao, *J. Mater. Chem. A*, 2019, **7**, 17324–17333.

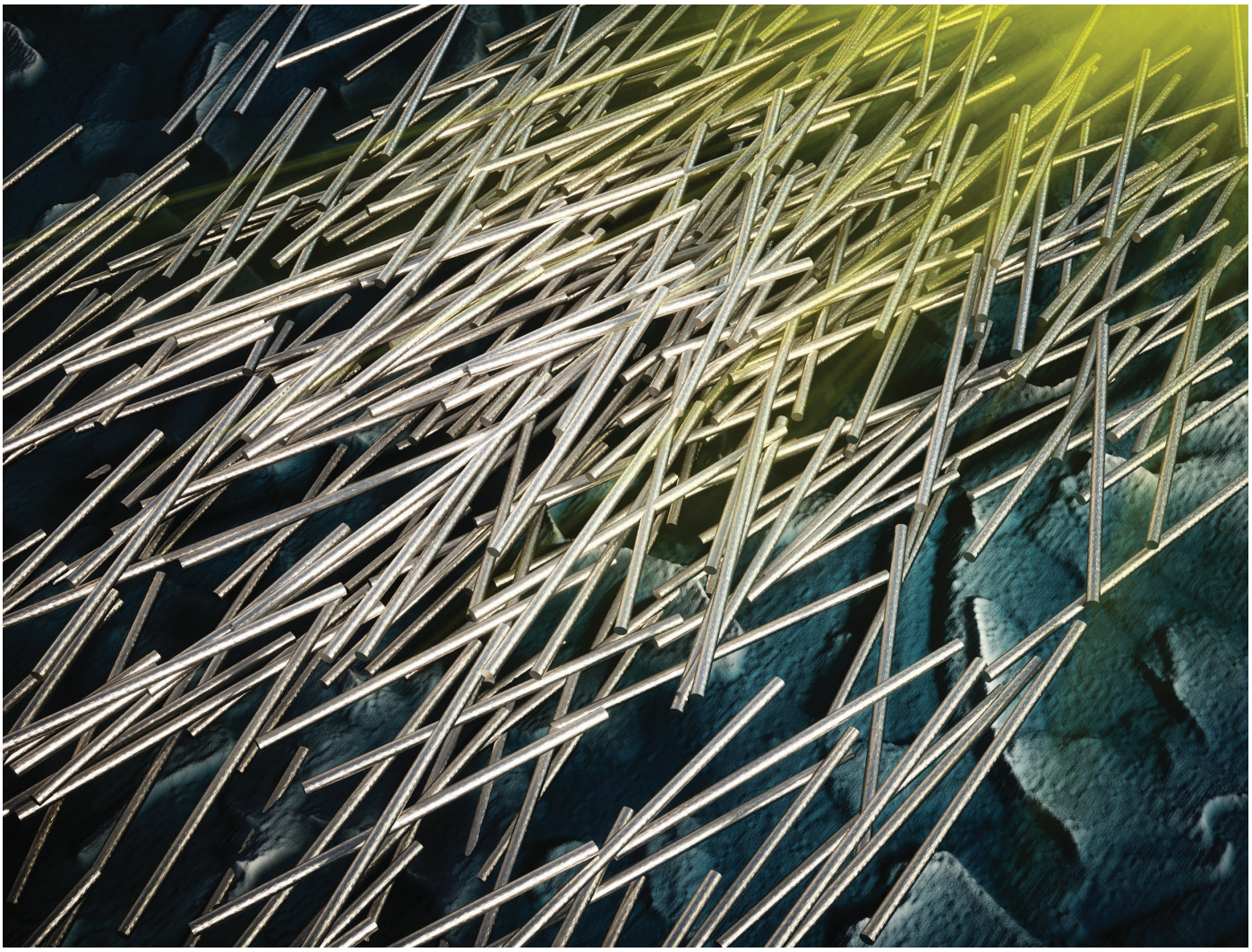
This journal is © The Royal Society of Chemistry 2020

Approved for public release; distribution unlimited.
510

Volume 1
Number 8
November 2020
Pages 2547–3074

Materials Advances

rsc.li/materials-advances



ISSN 2633-5409

ROYAL SOCIETY OF CHEMISTRY

PAPER
Randy J. Ellingson *et al.*
Aspect ratio controlled synthesis of tellurium nanowires for photovoltaic applications

Approved for public release; distribution unlimited.

Materials Advances

ROYAL SOCIETY OF CHEMISTRY

PAPER

View Article Online
View Journal | View Issue

Open Access Article. Published on 11 August 2020. Downloaded on 9/13/2021 5:02:39 PM.
This article is licensed under a Creative Commons Attribution-NonCommercial 3.0 Unported Licence.

Check for updates

Cite this: *Mater. Adv.*, 2020, **1**, 2721

Aspect ratio controlled synthesis of tellurium nanowires for photovoltaic applications

Dipendra Pokhrel, Ebin Bastola, Adam B. Phillips, Michael J. Heben and Randy J. Ellingson *

Received 9th June 2020,
Accepted 10th August 2020

DOI: 10.1039/d0ma00394h

rsc.li/materials-advances

Here, we report an aspect ratio-controlled synthesis of tellurium (Te) nanowires (NWs) utilizing a hot-injection colloidal method. The synthetic method uses low cost materials – specifically, tellurium oxide (TeO_2) as the tellurium source, environmentally benign ethylene glycol as a solvent, and ascorbic acid as a reducing agent. Analysis of scanning electron micrographs confirms that the NWs show narrow distributions for length, diameter, and therefore also aspect ratio. For example, we have prepared Te NWs exhibiting aspect ratios of 28.0 and 55.4. X-ray diffraction studies confirm a hexagonal crystal structure for the synthesized Te NWs. Based on Raman spectroscopy, Stokes lines were observed at 117.0 and 136.1 cm^{-1} for A_1 and E_2 modes of vibration. Fabrication of Te NW thin films demonstrated their suitability as a hole transport layer at the back contact of cadmium sulfide/cadmium telluride (CdS/CdTe) solar cells, yielding enhanced open-circuit voltage (V_{oc} = 0.846 V) and fill factor (FF = 77.8%), and an efficiency of 14.6%; the control device has an efficiency of 13.1% (V_{oc} = 0.825 mV, FF 74.0%).

Introduction

Nanomaterials offer significant value for opto-electronic applications because of their unique optical and electronic properties compared to their bulk counterparts.[1–3] Properly prepared one-dimensional semiconductors, such as nanowires (NWs), possess superior axial transport properties (thermal and electrical conductivity) which make them applicable in opto-electronics including nano photonics and energy related applications.[4,5] Tellurium (Te) is a rare earth element with narrow band gap energy (~0.35 eV) and p-type conductivity.[6] Te NWs often exhibit low defect density, enhanced thermoelectric performance, and photoconductivity.[7–10] Here, we report on success in preparing controlled aspect ratio Te NWs, and demonstrate their use as a buffer layer for the back contact of cadmium telluride (CdTe) photovoltaic (PV) devices.

Although Te nanostructures such as nanowires, nanorods and nanobelts can be prepared using solution-based and vacuum based approaches, these methods typically yield product with a wide size polydispersity, particularly in length. Solution-based techniques include solvothermal and hydrothermal approaches[11–17] whereas for vacuum based technology include vapor deposition of Te such as thermal evaporation.[18,19] Mohanty *et al.* have used thermal evaporation to produce Te NWs of several micron length with diameters of 100–300 nm.[19] The solution-based approaches include the use of hydrazine as a reducing agent[14,15,20] which is extremely hazardous and highly flammable. Thus, less hazardous and safer chemicals are desired for the synthesis of Te NWs. The solution-based synthesis gives a freedom for the solution-processing of the material for the fabrication of devices. Silva *et al.* yield the Te NWs with diameter less than 30 nm and lengths varying from 600 nm to 5 μm using hypophosphorous acid.[21] Liu *et al.* have reported the rapid microwave assisted method to produce Te NWs with 20 nm diameter and length of tens of microns.[8] In the synthesis of nanorods and nanowires, ascorbic acid is used as a reducing agent which is relatively less hazardous.[11,22–24] Yang *et al.* reported the synthesis of Te NWs using ascorbic acid as a reducing agent and ethylene glycol as the solvent with average diameter of 9.7 ± 2.7 nm.[24] Based on the literature, all these Te NWs have relatively uniform diameters but wide distribution of lengths. Uniform and controlled length of these Te NWs would provide an opportunity to improve the transport properties along the length. Thus, our novel strategy focuses on the synthesis of Te NWs with controlled aspect ratio, for application at the back-contact in CdTe solar cells.

Cadmium telluride is one of the leading cost-effective PV technologies for thin film solar cells with direct band gap energy of 1.5 eV and absorption coefficient $>10^5$ cm^{-1}.[25] In CdTe solar cells, the back contact interface layer plays a vital role in carrier transport, and the development of high-quality back contact is essential to improve the device performance.[26] Due to its deep work function, preparation of low resistance and stable ohmic contact presents a major technology challenge for

Wright Center for Photovoltaics Innovation and Commercialization, Department of Physics and Astronomy, The University of Toledo, Toledo, OH, 43606, USA.
E-mail: Randy.Ellingson@utoledo.edu

Approved for public release; distribution unlimited.

Open Access Article. Published on 11 August 2020. Downloaded on 9/13/2021 5:02:39 PM.
This article is licensed under a Creative Commons Attribution-NonCommercial 3.0 Unported Licence.

CdTe PV devices.[27] To make a good contact and reduce the contact barrier and contact resistance on CdTe, several techniques have been employed such as back surface modification or insertion of a hole transport layer (HTL) between the CdTe and a metallic contact. The CdTe back surface can be modified by doping with Cu or etching the CdTe surface to create a Te-rich layer.[28–30] The etching procedure generally consists of exposing the polycrystalline CdTe surface to an acidic alcoholic solution of bromine or iodine that selectively reacts with Cd atoms and leaves Te on the surface.[31,32] Other (HTL) materials applied between CdTe and a metallic contact include iron pyrite, carbon nanotubes, copper doped ZnTe, nanocomposite $(CuS)_x(ZnS)_{1-x}$, and copper NWs with graphene.[33–40] The formation or the deposition of Te layer is essential for the preparation of highly efficient CdTe photovoltaics. For example, the deposition of elemental Te by thermal evaporation has also improved the device performance.[41] The use of length controlled Te NWs offers the important potential to develop point contacts at the back contact of p-type polycrystalline CdTe, in such a way as to allow for efficient hole extraction through an otherwise passivated interface.

Here, we report the synthesis and characterization of Te NWs with uniform length and diameter distributions using a colloidal hot injection method. During synthesis, tellurium oxide (TeO_2) is the source of Te, L-ascorbic acid is used as a reducing agent, ethylene glycol as a solvent, and polyvinylpyrrolidone (PVP) serves as a surfactant. The synthesized Te NWs have hexagonal crystal structure with active vibrational modes at 117.0 and 136.1 cm^{-1} corresponding to A_1 and E_2 modes. Implementing these Te NWs to fabricate CdTe solar cell back contacts yield significantly improved open-circuit voltage (V_{oc}) and fill factor (FF) compared to standard devices. The best cell using Te NWs has an efficiency of 14.6% (V_{oc} 846 mV, FF 77.8%), an 11% improvement over the control device which converts at an efficiency of 13.1% (V_{oc} 825 mV, FF 74.0%). These results are quite good for a film stack with CdS as the window layer, which limits the current density to about 75% of what can be obtained using a CdSe or $MgZnO_x$ front window layer.[42]

Experimental methods

Materials

Tellurium oxide ($TeO_2 \geq 99\%$) was obtained from Alfa Aesar, polyvinylpyrrolidone (PVP, Molecular wt. ~40 000), L-ascorbic acid (≥99%) and ethylene glycol were obtained from Fisher Scientific, and potassium hydroxide ($KOH \geq 99\%$) was obtained from Sigma Aldrich are of analytical grade and used without further purification.

Synthesis procedure

The synthesis of Te NWs is based on a slightly modified version of the procedure reported by Yang *et al.* previously.[24] In a typical synthesis of Te NWs, 1.05 mmol (0.167 gm) of tellurium oxide (TeO_2), 2.98 mmol (0.167 gm) of potassium hydroxide (KOH) and 0.1 gm of polyvinylpyrrolidone (PVP) were dissolved in 15 mL ethylene glycol (EG) under vigorous magnetic stirring to form a milky white solution. The temperature of the flask was set to 120 °C at which the solution becomes transparent yellow. In the meantime, 1.42 mmol (0.2496 gm) of ascorbic acid was dissolved in 0.75 mL of deionized water at 80 °C to form an aqueous ascorbic acid solution. When the reaction temperature reached to 120 °C, the ascorbic acid solution was rapidly injected resulting the change in color of the reactants to opaque black. The reaction was continued for 21 h at 120 °C in a dinitrogen (N_2) environment to complete the synthesis of high quality Te NWs. The heating mantle was removed, and the flask temperature was lowered to room temperature using a cold-water bath. The product was centrifuged and cleaned with deionized water three to five times. The obtained NW product was dried and stored as a powder in a glove box in N_2 environment for characterization and application.

Tellurium NWs as a back-contact interface layer

To test Te NWs as a back contact to CdTe solar cells, we used CdS/CdTe film stacks deposited by Willard and Kelsey Solar Group, *via* vapor transport deposition (VTD) onto TEC^{TM}-15M (Pilkington N.A.) glass substrates. The CdTe devices were activated by $CdCl_2$ treatment at 390 °C for 30 min in dry air environment to advance grain growth, release interfacial strain and facilitate intermixing at CdS/CdTe interface.[43] The standard back contact was prepared using thermally evaporated copper (3 nm) and gold (40 nm) followed by annealing at 150 °C for 35 min. Similarly, a solution-based copper treatment was carried out using a procedure reported previously.[44,45] To prepare devices using Te NWs as the HTL, 40 μL solution of Te NWs (10 mg mL^{-1}) was dropped and spun onto the Cu-doped CdTe at 1000 and 3500 rpm for 10 and 50 s respectively. Devices were then annealed at 150 °C for 1 min, and Au (40 nm) was thermally evaporated to complete the back contact. The completed CdTe device was scribed using a 532 nm laser to produce approximately 24 cells of area 0.06 cm^2.[46]

Results and discussion

Synthesis and characterization of Te NWs

Fig. 1 displays the SEM images of Te NWs prepared with varying amounts of PVP and ascorbic acid. PVP acts as a structural directing agent and stabilizing agent,[47] and therefore plays a vital role in the formation of Te NWs with uniform morphology. Along with PVP, the alkaline condition aids the growth of Te NWs. Fig. 1(a) and (b) shows the SEM images of Te NWs prepared using 0.1 gm of PVP and 0.75 mL of ascorbic acid solution. The synthesized Te NWs are uniform in length and diameter. Fig. 2(a) and (b) shows the diameter and length distribution of Te NWs with 0.1 gm of PVP and 0.75 mL of ascorbic acid.

From SEM image Fig. 1(a) and statistical analysis Fig. 2(a) and (b), the average length and diameter of the nanowires are 1.15 ± 0.03 μm and 41.0 ± 3.0 nm respectively. The Te NWs have very narrow size distribution with standard deviation ±0.03 μm in length and ±3.0 nm in diameter. In this case, the aspect ratio of Te NW is 28.0 ± 2.7. Upon increasing the

 This journal is © The Royal Society of Chemistry 2020

Approved for public release; distribution unlimited.
513

Open Access Article. Published on 11 August 2020. Downloaded on 9/13/2021 5:02:39 PM.
This article is licensed under a Creative Commons Attribution-NonCommercial 3.0 Unported Licence.

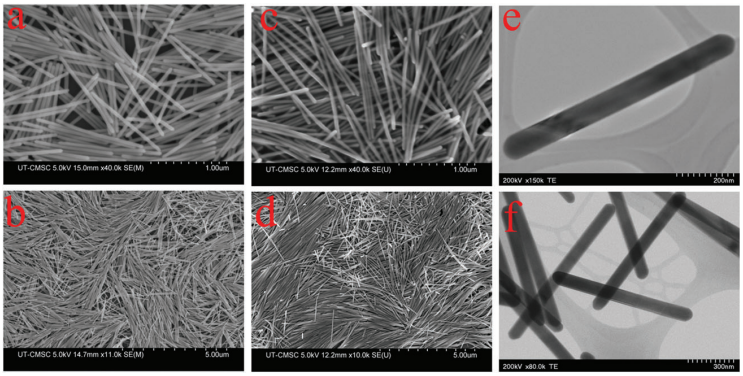


Fig. 1 SEM images of Te NWs obtained from TeO_2 with ethylene glycol at 120 °C (a) and (b) 0.1 gm PVP and 0.75 mL ascorbic acid (c) and (d) 0.2 gm PVP and 1.5 mL ascorbic acid and (e) and (f) STEM images of Te NWs obtained from 0.1 gm PVP and 0.75 mL ascorbic acid.

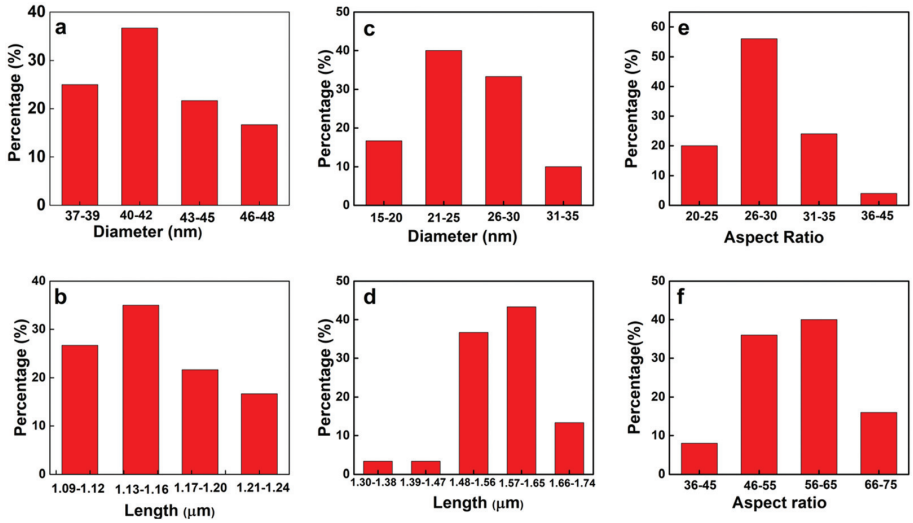


Fig. 2 Diameter, length and aspect ratio distribuiton of Te NWs at 120 °C for 21 h. (a), (b) and (e) 0.1 g PVP and 0.75 mL ascorbic acid (c), (d) and (f) 0.2 g PVP and 1.5 mL ascorbic acid.

amount of PVP to 0.2 g and ascorbic acid to 1.5 mL, Te NWs of uniform length and diameter were again obtained, however with decreased NW diameter and increased NW length. The SEM images are shown in Fig. 1(c) and (d). The average length and diameter of Te NWs are 1.54 ± 0.07 μm and 27.8 ± 3.7 nm respectively. The aspect ratio of Te NWs for this case is 55.4 ± 1.1. Fig. 2(c) and (d) shows the diameter and length distribution of Te NWs with 0.2 gm of PVP and 1.5 mL of ascorbic acid. Further, we calculated the aspect ratio of the individual NWs, and plotted the graphs for aspect ratios for two synthesis conditions as shown in Fig. 2(e) and (f). In case of the NWs synthesized by using 0.1 g PVP and 0.75 mL ascorbic acid, ~56% of NWs have aspect ratio in the range of 26–30 while for 0.2 g PVP and 1.5 mL ascorbic acid, ~40% of the NWs have aspect ratio in the range of 56–65 and ~36% are in the range of 46–55. The increased in aspect ratio is due to the role of these PVP and ascorbic acid as directing agent and reducing agent.[11] Fig. 1(e) and (f) shows the scanning transmission electron microscope (STEM) images of Te NWs formed with 0.1 gm PVP and 0.75 mL ascorbic acid. It reveals that NWs are highly crystalline with uniform length and diameter. The unusual anisotropic crystal structure of Te consists of 1D helical chain of covalently bound atoms parallel to the *c*-axis.[48] Previously, Zhong *et al.* used a solvothermal technique to synthesize Te NWs with diameter 30 ± 2 nm and length 10 ± 1 μm using ethylene glycol as a solvent.[11] Qian *et al.* reported the synthesis of Te NWs with diameter 4–9 nm and lengths up to hundreds of μm and Wang *et al.* reported Te NWs with diameter 40 nm with lengths in several microns using hydrazine through hydrothermal method.[14,15] In our case, we demonstrated the successful control of the aspect ratio of Te NWs, from 28.0 to 55.4, by varying the amount of ascorbic acid and PVP. The amount of

Approved for public release; distribution unlimited.
514

Open Access Article. Published on 11 August 2020. Downloaded on 9/13/2021 5:02:39 PM.
This article is licensed under a Creative Commons Attribution-NonCommercial 3.0 Unported Licence.

surfactant and reducing agent are the key parameters to prepare the desired nanowires during synthesis. Potassium hydroxide to control alkalinity helps PVP to act fully as a surfactant for the synthesis of Te NWs. Here, we developed the Te NWs with uniform length and diameter using hot injection colloidal method with small deviation in length with standard deviations of 0.03 μm and 0.07 μm respectively for two cases.

Fig. 3(a) displays the typical XRD pattern of synthesized Te NWs performed in the '2θ' range of 20–70°. The diffraction peaks obtained from MDI JADE closely match with the diffraction peaks measured for our as-synthesized Te NWs. Based on the standard powder diffraction file, synthesized Te NWs are in hexagonal phase with lattice constants $a = b = 0.4454$ nm and $c = 0.5924$ nm. The high intensity obtained in the diffraction pattern signifies the purity of the material. Similarly, Fig. 3(b) shows the Raman spectrum of Te NWs using a 632.8 nm He–Ne laser source with bands at 117.0, 136.1 and 265.9 cm^{-1}. The mode with a vibration 117.0 cm^{-1} corresponds to A_1 mode, 136.1 cm^{-1} corresponds to E_2 mode and the bands at 265.9 cm^{-1} assigned to the second-order spectra of the Te NWs which agrees closely with previous reports.[49,50]

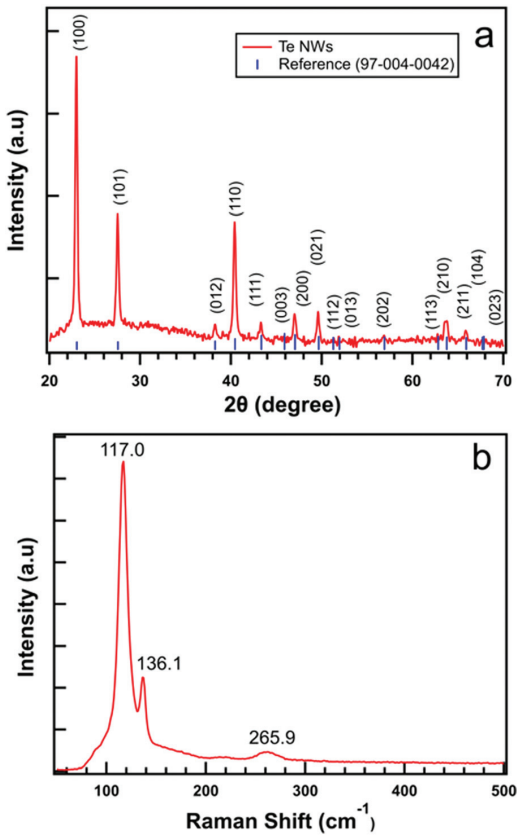


Fig. 3 (a) X-ray diffraction pattern of synthesized Te NWs obtained from TeO_2, possess hexagonal crystal structure and the sharp intensity peaks of the pattern indicate pure-phase crystalline material. The reference lines (PDF #97-004-0042) was obtained from MDI JADE software, and (b) Raman spectroscopy measurement of Te NWs using a 632.8 nm excitation from a He–Ne laser with 0.1 gm PVP and 0.75 mL ascorbic acid.

Next, we investigated and analyzed the effect of Te NWs as a HTL on CdTe PV devices. Tellurium manifests as a p-type semiconductor, and has been reported with a majority carrier concentration of 2.65×10^{18} cm^{-3}, Hall mobility of 8.99 cm^2 V^{-1} S^{-1}, and resistivity of 0.26 Ω cm.[51] The insertion of a Te layer as a HTL on CdTe surface is to make a p/p^+ interface with the CdTe absorber layer. The formation of Te on the back surface reduces the potential barrier height for hole transport between the CdTe and the back metal electrode.[32] Fig. 4 displays SEM images of the CdTe surface after $CdCl_2$ treatment, (a) without and (b) with Te NWs applied. Fig. 4(b) clearly shows a CdTe surface covered with Te NWs. Fig. 4(c) shows the cross-sectional SEM image of CdS/CdTe solar cells with the Te NWs HTL and thickness of Te NWs layer is approximately 100 nm, and Fig. 4(d) shows the schematic diagram of the device structure.

Fig. 5 shows the J–V characteristics and external quantum efficiencies (EQEs) of CdS/CdTe solar cells prepared with standard back contacts and prepared using Te NWs as an interface layer in between the Cu and Au. The back-contact designs tested here involved Cu/Au (evaporated metallic Cu), Cu/TeNWs/Au, $CuCl_2$/Au (solution $CuCl_2$), and $CuCl_2$/TeNWs/Au. The solid and dashed lines correspond to light and dark measurements respectively. In the case of the Cu/Au back contact, the best device has an efficiency (η) of 13.1% with V_{oc} 825 mV, J_{sc} 21.6 mA cm^{-2}, and FF of 74.0%. When a Te NW film was used as the HTL (Cu/TeNWs/Au), the best device efficiency was 14.0% with a V_{oc} of 837 mV, J_{sc} of 21.6 mA cm^{-2} and FF of 77.7%. For Cu/TeNWs/Au back contact devices, the average device efficiency was increased by about 7% as compared to Cu/Au back contacts with significant improvement on FF. Similarly, with solution-based copper ($CuCl_2$/Au), the back contact, best cell has an efficiency (η) of 14.0% with V_{oc} 841 mV, J_{sc} 22.1 mA cm^{-2}, and FF of 75.4%. With Te NWs ($CuCl_2$/TeNWs/Au), the best device efficiency was 14.6% with V_{oc} of 846 mV, J_{sc} of 22.3 mA cm^{-2}

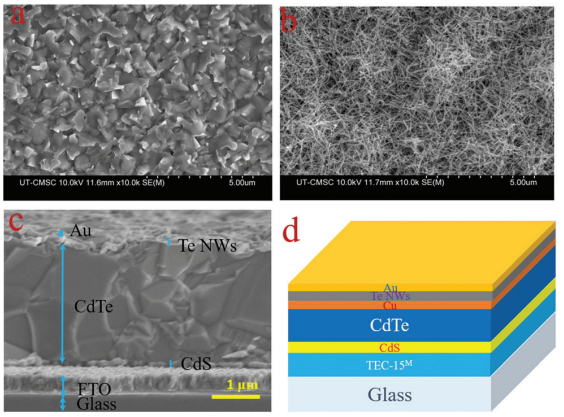


Fig. 4 SEM images of $CdCl_2$ treated CdTe (a) top surface w/o Te NWs and (b) top surface with Te NWs (c) cross-sectional image with Te NWs as HTL and (d) schematic diagram of the device structure.

This journal is © The Royal Society of Chemistry 2020

Approved for public release; distribution unlimited.

Open Access Article. Published on 11 August 2020. Downloaded on 9/13/2021 5:02:39 PM.
This article is licensed under a Creative Commons Attribution-NonCommercial 3.0 Unported Licence.

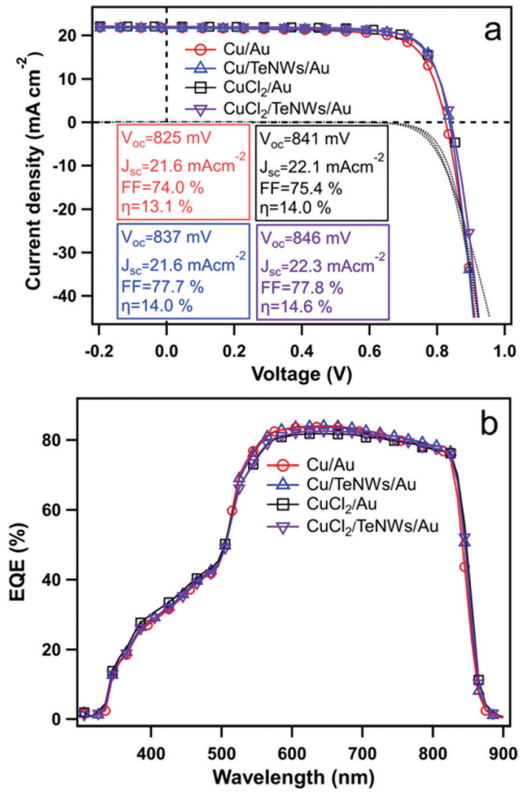


Fig. 5 (a) J–V characteristics and (b) external quantum efficiency (EQE) of CdTe solar cells with Cu/Au, Cu/TeNWs/Au, $CuCl_2$/Au and $CuCl_2$/TeNWs/Au back contacts respectively. The solid and dotted lines in Fig. 5(a) represent J–V curves under illumination and dark conditions respectively.

and FF of 77.8%. We have observed that managing the Cu concentration and diffusion plays a critical role in performance, and we therefore believe that the use of $CuCl_2$ solution to introduce the Cu enables better control than the thermal evaporation of a thin Cu layer.[45] The average device efficiency was increased by about 4% as compared to the $CuCl_2$/Au back contact. The average device parameters from twenty cells of each type of back contact are shown in Table 1. By introducing Te NWs as an interface layer, an improvement of open circuit voltage and fill factor was observed. The J_{sc} obtained from EQE measurement matches closely with J_{sc} obtained from J–V measurement.

Tellurium as a buffer layer between CdTe and a metal contact has been shown to reduce the downward band bending and mitigate a Schottky barrier formed at the back contact.[52] A Te buffer layer on CdTe can also be deposited by evaporation. Watthage *et al.* reported the best cell efficiency of 13.8% (V_{oc} = 839 mV, and FF = 75.6%) and average efficiency of 13.3% with 80 nm thermally evaporated Te followed by 3 nm Cu and 40 nm Au.[31] Previously, Liang *et al.* have also applied the Cu NWs with graphene as a back contact interface layer to CdTe photovoltaics, and they reported the device efficiency to be 12.1% while the control was 9.1% with Cu thin film.[40] Similarly, Major *et al.* have used ZnO NWs instead of conventional ZnO thin film as a front contact material for CdTe solar cells. They reported photoconversion efficiency of 9.53% when using ZnO NWs, whereas use of a planar ZnO buffer layer had a device efficiency of 9.99%.[53] Compared to these results, we observed >11% increase in device efficiency by using Te NWs compared to Cu/Au back contacts. Thus, a thin layer of Te NWs seems to be more effective to enhance the device efficiency which we attribute to the lowering of contact resistance and barrier height.

The J–V behavior of solar cells can be described by using single exponential diode equation as,

$$J = J_0 \exp\left[\frac{q}{Ak_BT}(V - JR_s) + G_{sh}V - J_L\right] \quad (1)$$

where J_0 is the reverse saturation current, q is an electronic charge, A is an ideality factor, k_B is Boltzmann's constant, T is absolute temperature, R_s is series resistance, G_{sh} is shunt conductance and J_L is the load current density which is equal to short circuit current density (J_{sc}). To analyze the solar cell parameters using dark current, we take $J_L = J_{sc} = 0$. By utilizing the experimental dark J–V curves and above diode equation, we calculated and compared the solar cell parameters like ideality factor, series resistance, and dark saturation current for CdS/CdTe device with back contacts Cu/Au, Cu/TeNWs/Au, $CuCl_2$/Au and $CuCl_2$/TeNWs/Au respectively.

Fig. 6(a) displays dark J–V curves on a linear scale for various back contacts. In case of a Cu/Au back contact, we can see higher back barrier which explains the low fill factor of these cells compared to other back contacts. As evidenced from the dark J–V curves with Te NWs, we can see the improvement in the J–V behavior qualitatively. Fig. 6(b) shows the plot of dJ/dV *versus* bias voltage (V), and it indicates negligible shunt conductance (close to zero) in the devices under dark conditions. Thus, the term G_{sh} and J_L were taken to be zero for these dark J–V curves. Similarly, Fig. 6(c) shows the plot of dV/dJ *vs.* J^{-1} from which we estimated the values of R_s and A. The values of the R_s and A were obtained from the y-intercept and slope of the linear fit as shown in the Fig. 6(c). Similarly, using these values

Table 1 Summary of the J–V characteristics of 20 cells with various back contacts. Numbers shown here represent the average values, and the ± value represents the standard deviation (SD) of the measured device parameters

Back-contacts	V_{oc} (mV)	J_{sc} (mA cm^{-2})	FF (%)	η (%)	R_s (ohms cm^2)	R_{shunt} (ohms cm^2)
Cu/Au	818 ± 5	21.6 ± 0.3	72.8 ± 0.8	12.9 ± 0.2	3.5 ± 1.2	1737 ± 228
Cu/TeNWs/Au	835 ± 1	21.5 ± 0.1	77.3 ± 0.2	13.9 ± 0.1	3.8 ± 0.1	3504 ± 228
$CuCl_2$/Au	838 ± 2	22.0 ± 0.1	74.8 ± 0.9	13.8 ± 0.2	4.3 ± 0.1	2983 ± 466
$CuCl_2$/TeNWs/Au	844 ± 1	22.0 ± 0.2	77.2 ± 0.2	14.3 ± 0.1	4.0 ± 0.3	3781 ± 225

Approved for public release; distribution unlimited.
516

Open Access Article. Published on 11 August 2020. Downloaded on 9/13/2021 5:02:39 PM.
This article is licensed under a Creative Commons Attribution-NonCommercial 3.0 Unported Licence.

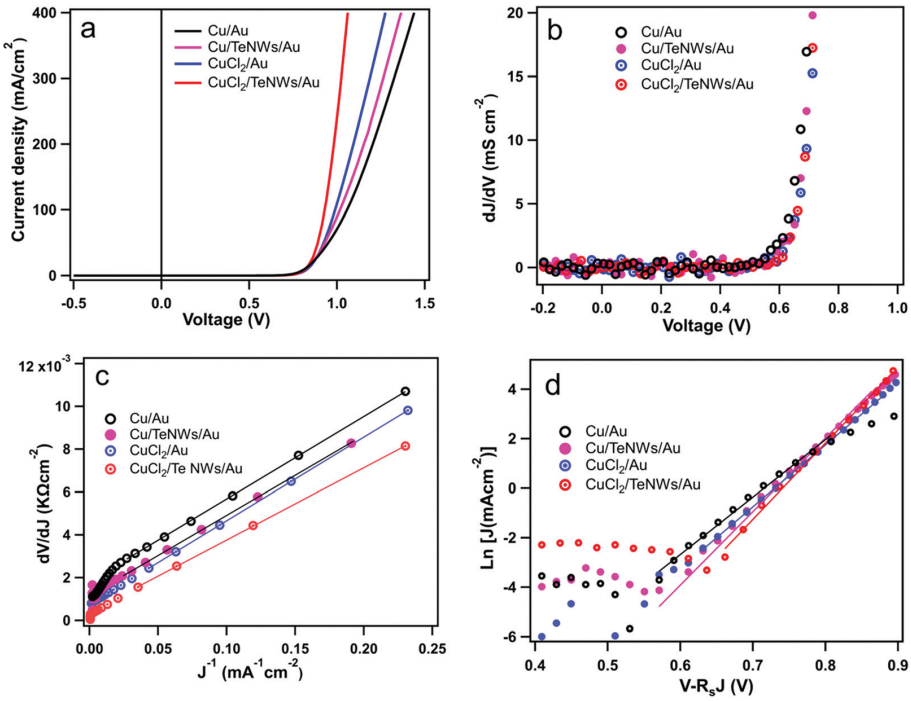


Fig. 6 Analysis of dark J–V curves with back contacts Cu/Au, Cu/TeNWs/Au, $CuCl_2$/Au and $CuCl_2$/TeNWs/Au (a) dark J–V curve (b) shunt characterization (c) plot of dV/dJ *versus* I/J for calculation of A and R_s (d) plot of ln(J) *versus* V–R_sJ for calculation of n and J_0. The solid lines represent the corresponding fitted lines in (c) and (d).

Table 2 Device parameters (ideality factor, series resistance, and dark saturation current) obtained by analyzing dark J–V curves (Fig. 2) based on Fig. 6

Device parameters	Cu/Au	Cu/TeNWs/Au	$CuCl_2$/Au	$CuCl_2$/TeNWs/Au
A (dV/dJ *vs.* J^{-1})	1.54	1.48	1.56	1.36
R_s (dV/dJ *vs.* J^{-1}) (Ω cm^2)	1.83	1.21	0.76	0.48
A (ln$J$ *vs.* V–R_sJ)	1.60	1.35	1.44	1.3
J_0 (ln$J$ *vs.* V–R_sJ) (mA cm^{-2})	3.5×10^{-8}	3.6×10^{-10}	1.2×10^{-9}	1.2×10^{-10}

of R_s, we plotted ln[J] *versus* [V–R_sJ] as shown in Fig. 6(d) to estimate reverse saturation current density and ideality factor. The values of R_s, A and J_0 for all back contacts obtained from Fig. 6 are presented in Table 2.

The value of A with Cu/Au back contact is about 1.54 while with Te NWs, its value is lowered to 1.48. Also, the reverse saturation current density (J_0) is 3.5×10^{-8} mA cm^{-2} for Cu/Au and with Te NWs its value is 3.6×10^{-10} mA cm^{-2}. The values of ideality factor and reverse saturation current are in close agreement with a previous report for CdS/CdTe device with standard back contact (Cu/Au).[54] Similarly, the ideality factor and J_0 are improved for $CuCl_2$ treated devices with Te NWs. Thus, the interfacial layer helped to lower the value of the reverse saturation current density indicating better diode behavior of these CdS/CdTe solar cells. In a device, A and J_0 depend one each other while the value of J_0 influences the open-circuit voltage of the device. In case of $CuCl_2$/TeNWs/Au, it has the lowest value of the J_0 and highest value of V_{oc}, and lower value of the J_0 indicates the reduced recombination at the back interface.

Here, Te NWs are used as a back-buffer layer to CdS/CdTe devices which reduces the contact barrier and improves the transport of holes towards the back electrode. In CdS/CdTe devices, J_{sc} is low due to the parasitic absorption of blue photons by CdS layer compared to CdSe/CdTe or MZO/CdTe devices. However, the device efficiency that we have obtained here are comparable to previously published reports for CdS/CdTe devices.[55] In ref. 55, the authors have used very thin (50 nm) CdS layer than in our case (120 nm) yielding higher J_{sc} (25.1 mA cm^{-2}) while they have lower FF (74.5%) compared to our results (Table 1). Here, our ultimate goal is to utilize orientation- and contact-controlled Te NWs as current conduits to channel holes through an insulated and passivated CdTe back contact interface and enhance the FF and V_{oc} of the device.

Conclusions

We have succesfully synthesized 1-D Te NWs of uniform lengths and diameters *via* hot injection collodial method. The lengths

 This journal is © The Royal Society of Chemistry 2020

Approved for public release; distribution unlimited.

Open Access Article. Published on 11 August 2020. Downloaded on 9/13/2021 5:02:39 PM.
This article is licensed under a Creative Commons Attribution-NonCommercial 3.0 Unported Licence.

and diameters of the Te NWs can be controlled using the amount of ascorbic acid and PVP. A typical length and diameter of Te NWs with 0.1 gm PVP and 0.75 mL ascorbic acid were 1.15 ± 0.10 μm and 41.0 ± 3.0 nm respectively. The synthesized Te NWs have hexagonal crystal sturcutre with active modes of vibrations at 117.0 cm^{-1} and 136.1 cm^{-1} for A_1 and E_2 modes. Te NWs thin films were utilized as a hole transport layer to CdS/CdTe solar cells to enhance the open-circuit voltage, fill factor, and power conversion efficiency. On using these Te NWs as an interface layer, average device efficiency of more than 20 cells was increased by ~11.0% (absolute 1.4%) compared to standard Cu/Au back contact.

Disclaimer

The views and conclusions contained herein are those of the authors and should not be interpreted as necessarily representing the official policies or endorsements, either expressed or implied, of Air Force Research Laboratory or the U.S. Government.

Conflicts of interest

There are no conflicts to declare.

Acknowledgements

This material is based on research sponsored by Air Force Research Laboratory under agreement number FA9453-18-2-0037. The U.S. Government is authorized to reproduce and distribute reprints for Governmental purposes notwithstanding any copyright notation thereon. We also thank Willard and Kelsey Solar Group for providing CdS/CdTe device stacks.

References

1 M. S. Gudiksen, *et al.*, Growth of nanowire superlattice structures for nanoscale photonics and electronics, *Nature*, 2002, **415**(6872), 617.
2 S. E. Steinvall, *et al.*, Multiple morphologies and functionality of nanowires made from earth-abundant zinc phosphide, *Nanoscale Horiz.*, 2020, **5**(2), 274–282.
3 Y. Li, *et al.*, Solution-processed one-dimensional $CsCu_2I_3$ nanowires for polarization-sensitive and flexible ultraviolet photodetectors, *Mater. Horiz.*, 2020, **7**(6), 1613–1622.
4 X. Duan, *et al.*, Indium phosphide nanowires as building blocks for nanoscale electronic and optoelectronic devices, *Nature*, 2001, **409**(6816), 66–69.
5 Y. Huang, X. Duan and C. M. Lieber, Nanowires for integrated multicolor nanophotonics, *Small*, 2005, **1**(1), 142–147.
6 A. V. Naumov, Erratum: To the article "Selenium and Tellurium: state of the markets, the crisis, and its consequences" by A. V. Naumov, vol. 54, no. 3–4, pp. 197–200, July, 2010, *Metallurgist*, 2011, **54**(9), 714.
7 S. Lin, *et al.*, Tellurium as a high-performance elemental thermoelectric, *Nat. Commun.*, 2016, **7**(1), 10287.
8 J.-W. Liu, *et al.*, Rapid Microwave-Assisted Synthesis of Uniform Ultralong Te Nanowires, Optical Property, and Chemical Stability, *Langmuir*, 2010, **26**(13), 1372–11377.
9 Y. Zhang, *et al.*, Low-cost writing method for self-powered paper-based UV photodetectors utilizing Te/TiO_2 and Te/ZnO heterojunctions, *Nanoscale Horiz.*, 2019, **4**(2), 452–456.
10 Y. Wang, *et al.*, Two-dimensional ferroelectricity and switchable spin-textures in ultra-thin elemental Te multilayers, *Mater. Horiz.*, 2018, **5**(3), 521–528.
11 B. N. Zhong, *et al.*, Controlled solvothermal synthesis of single-crystal tellurium nanowires, nanotubes and trifold structures and their photoelectrical properties, *CrystEngComm*, 2017, **19**(20), 2813–2820.
12 X. Wu, *et al.*, Controlled synthesis of multi-morphology Te crystals by a convenient Lewis acid/base-assisted solvothermal method, *J. Nanopart. Res.*, 2012, **14**(8), 1009.
13 Z. He and S.-H. Yu, Large scale synthesis of tellurium nanoribbons in tetraethylene pentamine aqueous solution and the stability of tellurium nanoribbons in ethanol and water, *J. Phys. Chem. B*, 2005, **109**(48), 22740–22745.
14 H.-S. Qian, *et al.*, High-Quality Luminescent Tellurium Nanowires of Several Nanometers in Diameter and High Aspect Ratio Synthesized by a Poly(Vinyl Pyrrolidone)-Assisted Hydrothermal Process, *Langmuir*, 2006, **22**(8), 3830–3835.
15 Z. Wang, *et al.*, Formation of single-crystal tellurium nanowires and nanotubes via hydrothermal recrystallization and their gas sensing properties at room temperature, *J. Mater. Chem.*, 2010, **20**(12), 2457–2463.
16 U. K. Gautam and C. N. R. Rao, Controlled synthesis of crystalline tellurium nanorods, nanowires, nanobelts and related structures by a self-seeding solution process, *J. Mater. Chem.*, 2004, **14**(16), 2530–2535.
17 G. Xi, *et al.*, Synthesis, Characterization, and Growth Mechanism of Tellurium Nanotubes, *Cryst. Growth Des.*, 2005, **5**(1), 325–328.
18 Q. Wang, *et al.*, Fabrication and growth mechanism of selenium and tellurium nanobelts through a vacuum vapor deposition route, *J. Phys. Chem. C*, 2007, **111**(35), 12926–12932.
19 P. Mohanty, J. Park and B. Kim, Large scale synthesis of highly pure single crystalline tellurium nanowires by thermal evaporation method, *J. Nanosci. Nanotechnol.*, 2006, **6**(11), 3380–3383.
20 Z.-H. Lin, Z. Yang and H.-T. Chang, Preparation of fluorescent tellurium nanowires at room temperature, *Cryst. Growth Des.*, 2007, **8**(1), 351–357.
21 R. R. Silva, *et al.*, Facile synthesis of tellurium nanowires and study of their third-order nonlinear optical properties, *J. Braz. Chem. Soc.*, 2017, **28**(1), 58–67.
22 N. R. Jana, L. Gearheart and C. J. Murphy, Wet Chemical Synthesis of High Aspect Ratio Cylindrical Gold Nanorods, *J. Phys. Chem. B*, 2001, **105**(19), 4065–4067.
23 C. K. Senthil kumaran, *et al.*, Synthesis and Characterization of Selenium Nanowires, *ISRN Nanotechnol.*, 2011, **2011**, 4.
24 H. Yang, *et al.*, Environmentally Benign Synthesis of Ultrathin Metal Telluride Nanowires, *J. Am. Chem. Soc.*, 2014, **136**(29), 10242–10245.

Approved for public release; distribution unlimited.

Open Access Article. Published on 11 August 2020. Downloaded on 9/13/2021 5:02:39 PM.
This article is licensed under a Creative Commons Attribution-NonCommercial 3.0 Unported Licence.

25 D. Bonnet and P. Meyers, Cadmium–telluride—Material for thin film solar cells, *J. Mater. Res.*, 1998, **13**(10), 2740–2753.
26 G. K. Liyanage, *et al.*, The role of back buffer layers and absorber properties for >25% efficient CdTe solar cells, *ACS Appl. Energy Mater.*, 2019, **2**(8), 5419–5426.
27 A. L. Fahrenbruch, Ohmic contacts and doping of CdTe, *Sol. Cells*, 1987, **21**(1-4), 399–412.
28 D. Bätzner, *et al.*, Development of efficient and stable back contacts on CdTe/CdS solar cells, *Thin Solid Films*, 2001, **387**, 51–154.
29 S. Demtsu, D. Albin and J. Sites, *Role of copper in the performance of CdS/CdTe solar cells*, 2006, **1**, 523–526.
30 D. W. Niles, *et al.*, A photoemission determination of the band diagram of the Te/CdTe interface, *J. Appl. Phys.*, 1995, **77**(9), 4489–4493.
31 S. C. Watthage, *et al.*, Selective Cd Removal From CdTe for High-Efficiency Te Back-Contact Formation, *IEEE J. Photovolt.*, 2018, **8**(4), 1125–1131.
32 E. Bastola, *et al.*, Wet chemical etching of cadmium telluride photovoltaics for enhanced open-circuit voltage, fill factor, and power conversion efficiency, *J. Mater. Res.*, 2019, **34**(24), 3988–3997.
33 T. Gessert, *et al.*, Development of Cu-doped ZnTe as a back-contact interface layer for thin-film CdS/CdTe solar cells, *J. Vac. Sci. Technol., A*, 1996, **14**(3), 806–812.
34 N. Romeo, *et al.*, A highly efficient and stable CdTe/CdS thin film solar cell, *Sol. Energy Mater. Sol. Cells*, 1999, **58**(2), 209–218.
35 A. B. Phillips, *et al.*, Wiring-up carbon single wall nanotubes to polycrystalline inorganic semiconductor thin films: low-barrier, copper-free back contact to CdTe solar cells, *Nano Lett.*, 2013, **13**(11), 5224–5232.
36 W. Xia, *et al.*, Te/Cu bi-layer: A low-resistance back contact buffer for thin film CdS/CdTe solar cells, *Sol. Energy Mater. Sol. Cells*, 2014, **128**, 411–420.
37 E. Bastola, K. P. Bhandari and R. J. Ellingson, Application of composition controlled nickel-alloyed iron sulfide pyrite nanocrystal thin films as the hole transport layer in cadmium telluride solar cells, *J. Mater. Chem. C*, 2017, **5**(20), 4996–5004.
38 K. P. Bhandari, *et al.*, Iron pyrite nanocrystal film serves as a copper-free back contact for polycrystalline CdTe thin film solar cells, *Sol. Energy Mater. Sol. Cells*, 2015, **140**, 108–114.
39 K. K. Subedi, *et al.*, Nanocomposite $(CuS)_x(ZnS)_{1-x}$ thin film back contact for CdTe solar cells: Toward a bifacial device, *Sol. Energy Mater. Sol. Cells*, 2018, **186**, 227–235.
40 J. Liang, *et al.*, Novel Cu nanowires/graphene as the back contact for CdTe solar cells, *Adv. Funct. Mater.*, 2012, **22**(6), 1267–1271.
41 D. W. Niles, *et al.*, Evaporated Te on CdTe: A vacuum-compatible approach to making back contact to CdTe solar cell devices, *Prog. Photovoltaics Res. Appl.*, 1996, **4**(3), 225–229.
42 A. H. Munshi, *et al.*, Polycrystalline CdTe photovoltaics with efficiency over 18% through improved absorber passivation and current collection, *Sol. Energy Mater. Sol. Cells*, 2018, **176**, 9–18.
43 K. V. Krishna and V. Dutta, Effect of in situ $CdCl_2$ treatment on spray deposited CdTe/CdS heterostructure, *J. Appl. Phys.*, 2004, **96**(7), 3962–3971.
44 D. Mao, *et al.*, Correlative impurity distribution analysis in cadmium telluride (CdTe) thin-film solar cells by ToF-SIMS 2D imaging, *Sol. Energy Mater. Sol. Cells*, 2016, **157**, 65–73.
45 E. Bastola, *et al.*, *Doping of CdTe using CuCl2 Solution for Highly Efficient Photovoltaic Devices*, 2019 IEEE 46th Photovoltaic Specialists Conference (PVSC), 2019, pp. 1846–1850.
46 A. B. Phillips, *et al.*, High speed, intermediate resolution, large area laser beam induced current imaging and laser scribing system for photovoltaic devices and modules, *Rev. Sci. Instrum.*, 2016, **87**(9), 093708.
47 Z. Zhang, B. Zhao and L. Hu, PVP protective mechanism of ultrafine silver powder synthesized by chemical reduction processes, *J. Solid State Chem.*, 1996, **121**(1), 105–110.
48 G. Kresse, J. Furthmüller and J. Hafner, Theory of the crystal structures of selenium and tellurium: the effect of generalized-gradient corrections to the local-density approximation, *Phys. Rev. B: Condens. Matter Mater. Phys.*, 1994, **50**(18), 13181.
49 H. Park, *et al.*, Aqueous chemical synthesis of tellurium nanowires using a polymeric template for thermoelectric materials, *CrystEngComm*, 2015, **17**(5), 1092–1097.
50 G. Li, *et al.*, Solvothermal synthesis of polycrystalline tellurium nanoplates and their conversion into single crystalline nanorods, *RSC Adv.*, 2014, **4**(2), 954–958.
51 Y. Li, *et al.*, Effects of evaporated tellurium back buffer layer on cdte solar cell, *Chalcogenide Lett.*, 2019, **16**(11), 535–544.
52 T. Song, A. Moore and J. R. Sites, Te Layer to Reduce the CdTe Back-Contact Barrier, *IEEE J. Photovolt.*, 2018, **8**(1), 293–298.
53 J. D. Major, *et al.*, Development of ZnO nanowire based CdTe thin film solar cells, *Sol. Energy Mater. Sol. Cells*, 2017, **160**, 107–115.
54 K. P. Bhandari, *et al.*, Thin film iron pyrite deposited by hybrid sputtering/co-evaporation as a hole transport layer for sputtered CdS/CdTe solar cells, *Sol. Energy Mater. Sol. Cells*, 2017, **163**, 277–284.
55 J. Britt and C. Ferekides, Thin-film CdS/CdTe solar cell with 15.8% efficiency, *Appl. Phys. Lett.*, 1993, **62**(22), 2851–2852.

 This journal is © The Royal Society of Chemistry 2020

Approved for public release; distribution unlimited.

Surface & Coatings Technology 381 (2020) 125127

Contents lists available at ScienceDirect

Surface & Coatings Technology

journal homepage: www.elsevier.com/locate/surfcoat

Glancing angle deposited CdTe: Nanostructured films and impact on solar cell performance

Dipendra Adhikari, Maxwell M. Junda, Ebin Bastola, Prakash Koirala, Randall J. Ellingson, Robert W. Collins, Nikolas J. Podraza*

Wright Center for Photovoltaics Innovation and Commercialization & Department of Physics and Astronomy, University of Toledo, Toledo, OH, 43606, USA

ARTICLE INFO

Keywords:
Glancing angle deposition
Dielectric function
Sputtering
CdTe solar cell
Anisotropy

ABSTRACT

Cadmium telluride (CdTe) thin films with different microstructures and optical properties have been produced on soda-lime glass by glancing angle deposition (GLAD) at oblique sputtering angles varying from 0° to 80° with respect to the substrate normal. From cross-sectional scanning electron micrographs, increasingly tilted columnar structure occurs with increasing incident angle for as-deposited CdTe films. CdTe films deposited at lower angles closer to normal incidence consist of a mixture of cubic zinc blende and hexagonal wurtzite crystal structures while films prepared at more oblique angles have hexagonal wurtzite crystal structure. Post-deposition $CdCl_2$ treated films show enhancement in crystallite/grain size for samples prepared under all conditions. The optical response in the form of the complex dielectric function ($\varepsilon = \varepsilon_1 + i\varepsilon_2$) spectra from 0.74 to 5.89 eV for the GLAD thin films are all qualitatively similar to single crystal CdTe. Higher angle deposited samples show columnar structure induced anisotropy in spectra in ε in the transparent spectral range. Application of GLAD CdTe interlayers between CdS and CdTe of the standard CdS/CdTe heterojunction design solar cell shows better performance with up to 0.9% absolute efficiency increase.

1. Introduction

Cadmium telluride (CdTe) is a II-VI compound semiconductor with high optical absorption $> 10^4\,cm^{-1}$ in the visible spectral range and a direct band gap ~1.5 eV, making it an ideal absorber layer material in thin film photovoltaics (PV). CdTe is a stable material under outdoor conditions and can be deposited using various methods including sputtering [1–5], spray pyrolysis [6], electrodeposition [7], and close-space sublimation [8,9]. Recently, the champion PV device efficiencies reached 22.1% for a thin film CdTe research solar cell and 18.6% for a module, respectively [10]. The best efficiencies of solar cells incorporating sputtered CdTe absorbers are about 14% [1,11]. Current research in the field is focused on making highly efficient devices by alternative deposition techniques for better quality CdTe absorbers, improving back contact performance and compatibility, and modification of *p/n* interfaces [12] to enhance photogenerated carrier collection.

The microstructure of CdTe films depends on deposition conditions and plays an important role in PV device performance, which depends upon the characteristics of both crystalline grains and surrounding grain boundary material. Previous reports indicate that depleted grain boundaries are beneficial to CdTe solar cell performance by helping to separate carriers, suppress recombination, and improve carrier collection [4,13,14]. A CdS window layer is a commonly used *n*-type heterojunction partner with a *p*-type CdTe absorber. Cubic zinc blende CdTe is thermodynamically stable at room temperature, but exhibits a high lattice mismatch with room temperature stable hexagonal wurtzite CdS [15]. However, hexagonal wurtzite and mixed phase zinc blende + wurtzite CdTe films have been deposited at low temperature by vacuum evaporation and sputtering [15–17].

Glancing angle deposition (GLAD) produces films with varying preferential grain orientations and grain boundary configurations [18]. GLAD involves separating the source flux and substrate target normals by an oblique angle. The dependence of crystal structure, grain size, grain orientation, and optical properties on oblique sputtering angle are identified. Previous works [17,18] show that opto-electronic and microstructural properties of the deposited film can be effectively manipulated using GLAD. The microstructure of CdTe films can potentially be engineered, resulting in the ability to tune opto-electronic properties for PV device optimization, such as by tailoring material structure at the *p/n* interface. This work involves study of such CdTe films deposited via radio frequency (RF) magnetron sputtering with material flux at a range of angles relative to the substrate normal and evaluation of PV device

* Corresponding author.
E-mail address: nikolas.podraza@utoledo.edu (N.J. Podraza).

https://doi.org/10.1016/j.surfcoat.2019.125127
Received 12 July 2019; Received in revised form 29 October 2019; Accepted 31 October 2019
Available online 09 November 2019
0257-8972/ © 2019 Elsevier B.V. All rights reserved.

Approved for public release; distribution unlimited.

performance by incorporating GLAD CdTe. In particular, the influence of deposition angle on the microstructural and optical properties of sputtered CdTe film are studied and improvement of PV device performance by incorporating a 100 nm GLAD interlayer at the *p/n* junction is demonstrated. The crystal structure and the crystallite size are obtained from x-ray diffraction (XRD), cross-section and surface microstructures are imaged from scanning electron microscopy (SEM), and complex optical properties are extracted from spectroscopic ellipsometry. The oblique angle of deposition manipulates crystal structure, grain size, grain orientation, and optical properties. The effect of $CdCl_2$ post-deposition processing on crystallite size enhancement as a function of treatment time on GLAD CdTe is tracked. A nominally 100 nm thick structurally engineered GLAD CdTe interlayer is introduced between the *n*-type CdS window layer and *p*-type CdTe absorber in solar cells. Power conversion efficiency (*PCE*), open circuit voltage (V_{OC}), and fill factor (*FF*) improve with introduction of this GLAD CdTe interlayer between CdS and CdTe layers of a conventional CdS/CdTe heterojunction solar cell.

2. Experimental methods

RF magnetron sputtered (frequency = 13.56 MHz) CdTe films have been deposited at room temperature (RT) onto soda-lime glass substrates using GLAD in a standalone vacuum chamber (AXXIS™, K. J. Lesker Co.). The glass substrates are cleaned ultrasonically, rinsed with deionized water, and blown dry with nitrogen before film deposition. A schematic diagram of the GLAD process is shown in the Fig. 1. Films are deposited at angles (Φ) of 0°, 20°, 40°, 60°, and 80° as defined by the angle between the normal extending from the center of the sputtering target and the normal extending from the center of the substrate.

A 7.62 cm diameter 99.999% purity CdTe target is sputtered for 70 min in a 15 mTorr pressure Ar ambient at 100 W RF target power. The distance from the center of the target to the center of the substrate is 13.4 cm. The substrate remains stationary during deposition. The deposition rate of material in the center of the substrate is 28.1 nm/min at Φ = 0° and slightly decreases with increasing angle Φ to 22.1 nm/min at Φ = 80°. Post-deposition $CdCl_2$ heat treatment is performed by wetting the film surface with a saturated solution of $CdCl_2$ in methanol followed by heating at 387 °C in dry air ambient for 10, 20, 30, or 40 min [3–5]. The $CdCl_2$ process is standard for CdTe PV as it increases CdTe grain/crystallite size and results in higher *PCE* devices. Cross-sectional and surface images are obtained from SEM (Hitachi S-4800). XRD patterns (Rigaku Ultima III diffractometer) are analyzed to obtain the crystal structure and crystallite size. A silicon sample is used for calibration of the diffractometer. *Ex-situ* spectroscopic ellipsometric and Mueller matrix spectra have been collected by using single rotating compensator (M-2000FI, J. A. Woollam Co. Inc.) [19,20] and dual

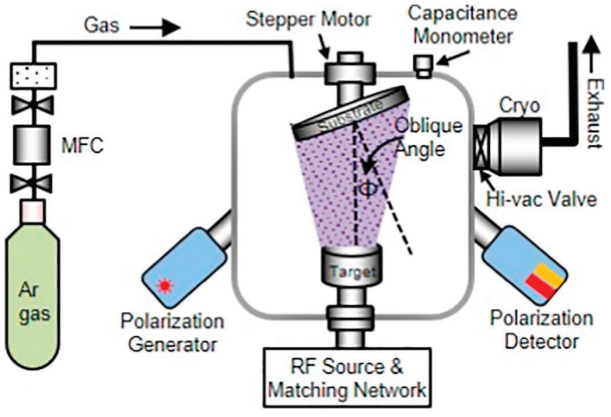


Fig. 1. Schematic of glancing angle deposition (GLAD) sputtering.

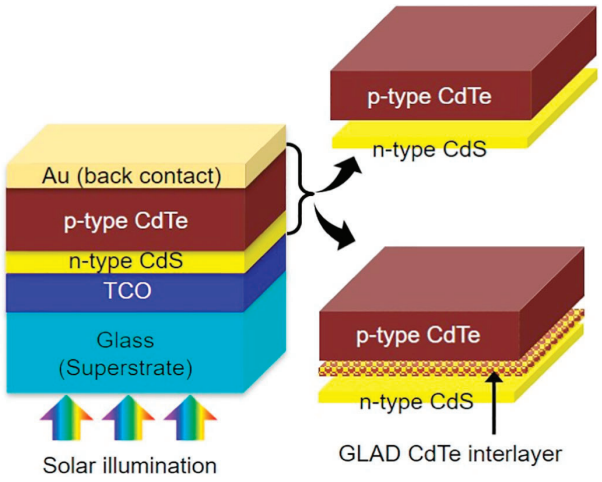


Fig. 2. Schematic diagram of CdS/CdTe heterojunction solar cells with and without a thin GLAD CdTe interlayer between the wurtzite CdS and zinc blende CdTe layers.

rotating compensator [21] (RC2, J. A. Woollam Co. Inc.) multichannel ellipsometers. Optical spectra are collected from near the center of each sample. Complex optical response and optical anisotropy resulting from columnar structure are obtained from analysis of ellipsometric and Mueller matrix spectra collected for GLAD CdTe films.

CdS/CdTe heterojunction solar cells are fabricated in the superstrate configuration, as shown in the schematic diagrams in Fig. 2. Solar cells are fabricated with and without a GLAD CdTe interlayer prepared at Φ = 80°, which exhibits wurtzite crystal structure. The superstrates are 15.24 cm X 15.24 cm soda lime glass coated by 300–400 nm of SnO_2:F with an additional 100 nm of high resistivity transparent SnO_2 to form the transparent conducting oxide (TCO) front contact to the device (TEC-15 M, Pilkington North America). The solar cell fabrication sequence begins with magnetron sputter deposition of 100 nm *n*-type CdS followed by a 2 μm *p*-type CdTe absorber. These layers are then subjected to the aforementioned $CdCl_2$ heat treatment for 30 min. The solar cell is completed by RT thermal evaporation of 3 nm Cu and 40 nm Au through a dot shadow mask to form the back electrical contact. The completed cell structure is annealed at 150 °C in air for 30 min to promote Cu diffusion into CdTe. Cu does not exist as a discrete layer in the final devices as it fully diffuses into CdTe, lightly doping it. 256 individual dot solar cells each having an active area of 0.126 cm^2 are formed for each process. The deposition parameters used during the fabrication of each component layer of the complete solar cells are listed in Table 1.

Photocurrent density versus voltage (*J-V*) are measured under simulated one sun AM1.5G (100 mW/cm^2) illumination from a 450 W

Table 1
Deposition conditions for the individual solar cell layers. "RT" denotes room temperature.

Layer type	Deposition method	Deposition parameters			
		Substrate temperature (°C)	Target power (W)	Pressure (mTorr)	Ar gas flow (SCCM)
CdS	RF sputter	250	200	15	23
CdTe interlayer	Φ = 80° GLAD	RT	100	15	23
CdTe	RF sputter	RT	100	15	23
Cu	Evaporation	RT	–	10^{-3}	–
Au	Evaporation	RT	–	10^{-3}	–

Approved for public release; distribution unlimited.
521

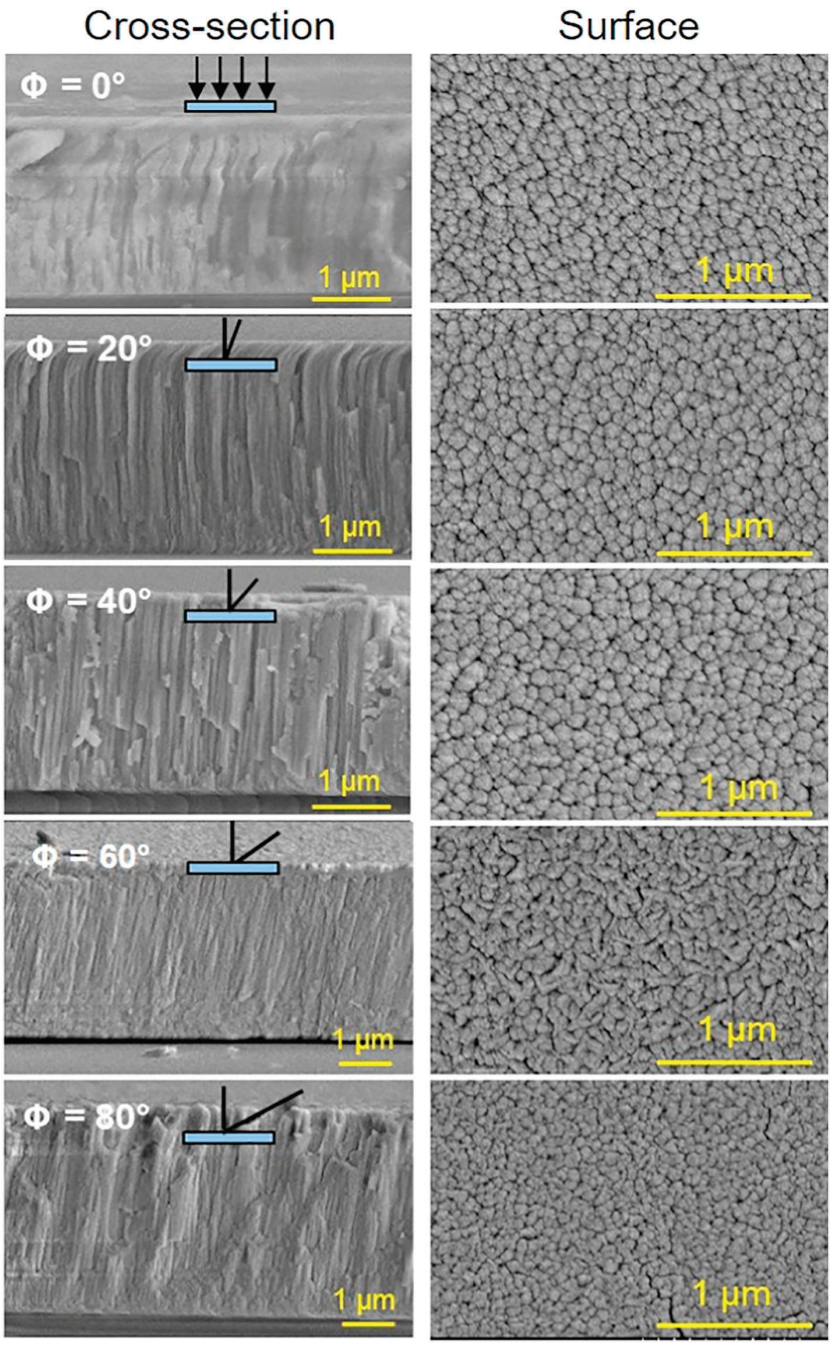


Fig. 3. Cross-sectional and surface scanning electron micrographs (SEMs) of as-deposited GLAD CdTe films prepared as functions of oblique angles with respect to the substrate normal.

Xenon light source (Oriel, Model 9119, Newport) with a digital source meter (Keithley 2440) in air at room temperature. External quantum efficiency (EQE) measurements are performed (model IVQE8-C, PV Instruments) to characterize spectrally resolved device performance.

3. Results and discussion

Fig. 3 shows cross-sectional and surface SEM of as-deposited CdTe prepared at different oblique angles. The cross-sections show that the films have slanted columnar structure inclined towards the incoming material flux during sputtering. The angle of column inclination relative to substrate normal is much smaller than the incident oblique angle but increases with increasing angles [17]. This behavior is expected as atomic scale self-shadowing effects are more pronounced at more oblique deposition angles, resulting in continued growth of initial nuclei on the substrate as lengthening columns due to low diffusion lengths of precursors on the surface [17,22,23]. In general, columnar GLAD films have lower columnar tilt angle than oblique deposition angle with even

Approved for public release; distribution unlimited.
522

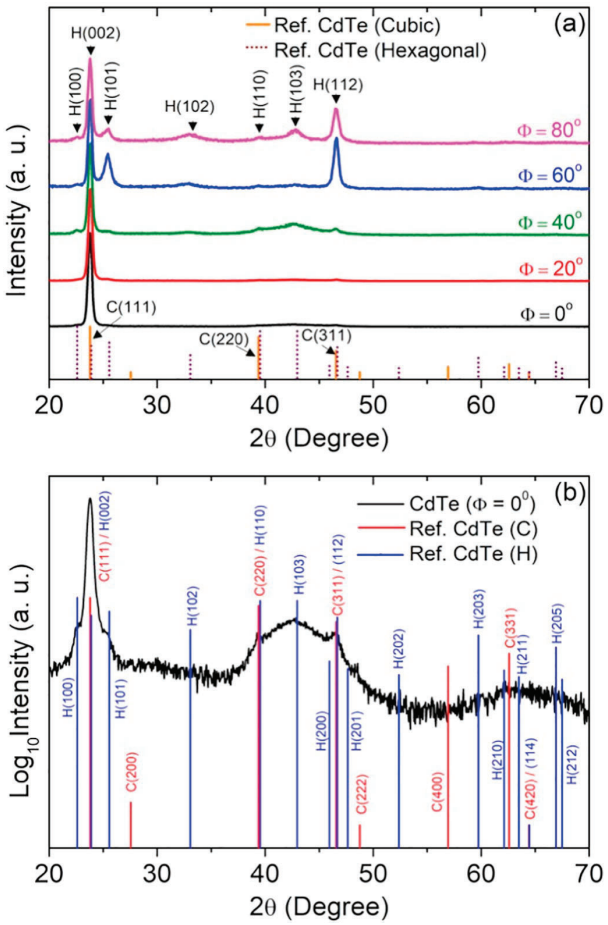


Fig. 4. X-ray diffraction (XRD) patterns of (a) as-deposited CdTe sputtered on soda-lime glass at different oblique angles (Φ) and (b) Log scale XRD of as-deposited CdTe sputtered at Φ = 0°. The reference lines are for standard cubic zinc blende CdTe [PDF # 97-010-8238] and hexagonal wurtzite CdTe [PDF # 97-015-0941] obtained from MDI JADE software.

further reduction in tilt angle when scattering in the gas phase becomes more substantial [24–31]. The surface microstructure of the films vary as the oblique angle is increased. The surface morphology of the films deposited at Φ = 60° and 80° appear substantially different from other films deposited at lower Φ, which may be due to higher columnar tilt angle, crystal phase transitions from mixed (cubic + hexagonal) to hexagonal at higher Φ, or both. The relatively low substrate temperature is expected to result in low diffusion lengths of precursors on the growing surface, enabling the formation of the metastable wurtzite phase instead of the stable zinc blende phase. At low angles the films are mixed phase. At higher oblique angles the low diffusion length of precursors coupled with enhanced atomic scale self-shadowing results in the metastable wurtzite phase formation. Surface view SEM of as-deposited films in Fig. 3 shows variation in grain size from 126 ± 7 to 87 ± 5 nm among the films with the Φ = 80° sample consisting of the smallest grains.

XRD patterns for the as-deposited CdTe films are shown in Fig. 4. The samples deposited with small oblique angles Φ < 40° show the highest intensity XRD peak at 2θ ~23.7° which is ascribed to both cubic (C) zinc blende and hexagonal (H) wurtzite phases with C(111) and H (002) Miller index planes, respectively. Although literature reports that cubic CdTe is produced when sputtered normal to substrate (lower angle Φ) and at lower temperature close to room temperature (RT) [32–34], low intensity but distinct C(222), H(100), H(101), and H(103) peaks are observed here in as-deposited GLAD CdTe films at Φ < 40° as shown for Φ = 0° in the Fig. 4(b). Films deposited at Φ < 40° are considered to be mixed phase cubic and hexagonal CdTe. As the oblique angle is increased Φ ≥ 40°, diffraction peaks associated with only the cubic phase are not observed. Crystallite size obtained from the XRD analysis for the same samples is lower compared to grain size obtained from SEM indicating that these grains are composed of multiple crystallites, the mean free path of electrons is limited by defects and smaller than the grain, or both.

Isotropic optical response in the form of the complex dielectric function ($\varepsilon = \varepsilon_1 + i\varepsilon_2$) spectra of all as-deposited GLAD CdTe films are obtained by fitting parametric optical and layer structural models to measured ellipsometric spectra from 0.74–5.89 eV using a least squares regression that minimizes the unweighted error function [35] between measured and model-simulated ellipsometric spectra. Structurally, the models consist of a semi-infinite glass substrate, bulk CdTe layer thickness d_b, and surface roughness thickness d_s as shown schematically in Fig. 5. The optical properties of bulk CdTe are initially parameterized by a sum of critical point oscillators assuming parabolic bands (CPPB) [36,37] and a Tauc-Lorentz oscillator [38,39] to describe electronic band-to-band transitions. The optical response of the surface roughness is described by multiple Bruggeman effective medium approximation (EMA) [40] layers consisting of f_v volume fraction void and $1-f_v$ fraction material identical to the underlying bulk CdTe. Three effective medium layers are needed to describe the complicated surface

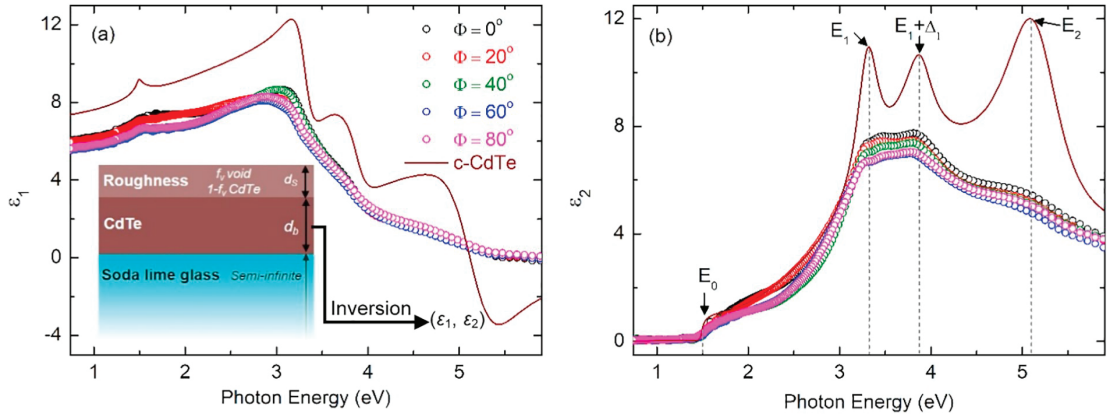


Fig. 5. Complex dielectric function ($\varepsilon = \varepsilon_1 + i\varepsilon_2$) spectra of as-deposited GLAD polycrystalline CdTe films produced at different oblique angles during sputtering. The optical response of single crystal (c-CdTe) is included for comparison [45], and the structural model schematic is shown in the inset.

Approved for public release; distribution unlimited.
523

Table 2
Structural parameters including surface roughness thickness (d_s), void fraction percentage in each effective medium approximation (EMA) layer comprising the surface roughness layer (f_v), and bulk film thickness (d_b) for as-deposited CdTe at different oblique angles (Φ) between the substrate normal and target normal.

Φ	Bulk thick. (nm)	Surface roughness thicknesses (d_s) and void fractions (f_v)						Eff. thick. (nm)
		EMA1		EMA2		EMA3		
		Thickness (nm)	Void fraction (%)	Thickness (nm)	Void fraction (%)	Thickness (nm)	Void fraction (%)	
0°	1758 ± 9	151 ± 10	1.7 ± 0.3	49 ± 7	7 ± 2	28 ± 3	39 ± 2	1968 ± 27
20°	1716 ± 8	148 ± 15	1.2 ± 0.2	32 ± 10	6 ± 4	25 ± 4	37 ± 3	1908 ± 37
40°	1544 ± 15	175 ± 30	0.6 ± 0.3	40 ± 24	4 ± 3	29 ± 5	39 ± 3	1775 ± 72
60°	1318 ± 7	160 ± 11	1.0 ± 0.2	49 ± 8	4 ± 1	32 ± 2	35 ± 1	1545 ± 26
80°	1307 ± 7	166 ± 12	0.8 ± 0.2	53 ± 9	3 ± 1	31 ± 1	32 ± 1	1544 ± 29

roughness of combined thickness d_s. f_v of each layer is allowed to vary independently resulting in monotonically increasing f_v towards the outermost EMA layer and the ambient interface. This three EMA layer model is found to be necessary to accurately describe the relatively rough surface where there is a gradient in f_v. This multiple layer approach to describe surface roughness with depth is necessary as sputtered CdTe and CdS morphology with depth can become quite complicated even for normal incidence sputtered films [41–43]. All the structural parameters including d_s, f_v, d_b, and effective film thickness for as-deposited CdTe at different Φ are reported in Table 2. The thickness and the relative void fraction in each EMA layer representing surface roughness are similar for all films, with the difference in effective film thickness primarily from the bulk film thickness. Effective film thickness is defined as the sum of d_b plus each EMA layer thickness weighted by 1-f_v and monotonically from 1968 ± 27 nm for Φ = 0° to 1544 ± 29 nm for Φ = 80°. All the films were deposited for 70 min, and this variation in effective film thickness with Φ is expected for GLAD films. After initially using a parametric ε to determine structural parameters, ε describing the bulk CdTe is obtained by numerical inversion [44] in Fig. 5. For all films, ε_1 at low photon energies in the transparent spectral range are substantially lower compared to single crystal CdTe (c-CdTe). A Bruggeman EMA consisting of fractions of void and c-CdTe is fit to ε_1 at 0.74 eV obtained for all films as a proxy for relative density of the films. These films become less dense with increasing Φ with $1-f_v$ decreasing from 0.86 for Φ = 0° to 0.80 for Φ = 80°. The observed columnar tilt angles and the relative density of the films in this study seems small compared to the range in Φ. Low substrate temperature results in low surface precursor diffusion lengths, and the process pressure results in high gas scattering. The relatively small columnar tilt angles are expected based on these process conditions and consistent with similar films in literature [28–31]. The decreasing density resulting from higher oblique angles is due to increased columnar self-shadowing [17], transition in crystal structure, or both. By fitting CPPB oscillators directly to the first derivative of numerically inverted ε_2 ($d\varepsilon_2/dE$) with respect to photon energy, four critical point features describing the E_0, E_1, $E_1+\Delta_1$, and E_2 electronic transitions are determined to have resonance energies ranging from 1.49 ± 0.20 to 1.54 ± 0.20 eV, 3.24 ± 0.30 to 3.27 ± 0.30, 3.37 ± 0.06 to 4.00 ± 0.20 eV, and 4.20 ± 0.11 to 4.77 ± 0.30 eV, respectively. These values are close to those known for c-CdTe at 1.491, 3.310, 3.894, and 5.160 eV [45–47]. Sensitivity to the $E_1+\Delta_1$ and E_2 critical point energies may be lost in the films due to the complicated surface roughness structure, small grain/crystallite size, low critical point amplitude, and wide critical point broadening. Zinc blende cubic CdTe exhibits lower band gap energy compared to wurtzite hexagonal CdTe [48,49]. Here, the band gap energy (E_g) of all as-deposited CdTe as a function of Φ are obtained from spectroscopic ellipsometry. Lower band gap values E_g ~1.50 eV are observed for Φ < 40° and higher values E_g ~1.53 eV for Φ ≥ 40°. Although these band gap values are close and may be impacted by film stress as well, the behavior corresponds to structural trends from XRD. All these observations indicate that the wurtzite hexagonal phase is favored at higher values of Φ.

The columnar structures of these films are substantially inclined away from substrate normal, about 12° in the cross-sectional SEMs for films deposited at Φ = 60° and 80°. In-plane optical anisotropy would be expected for the films deposited at high Φ because of the projection of sampling of the polar Euler angle rotated columns, θ = 12° in this case. Mueller matrix spectra are measured at three azimuthal angles (φ = 0, 45, and 90°) of rotation about the substrate normal and simultaneous modeling of all three sets of spectra is performed using a similar procedure to that explained in Ref. [50]. Mueller matrix elements normalized to M_{11} sensitive to sample rotations (m_{13}, m_{14}, m_{23}, m_{24}, m_{31}, m_{32}, m_{41}, m_{42}) in the transparent spectral range are fit. The 0.74–1.23 eV photon energy range is chosen to simplify the optical property model by avoiding substantial absorption above the band gap due to electronic transitions and the highest contribution to absorption below the band gap due to Urbach tails. To describe optical anisotropy in the films deposited at Φ = 60° and 80°, a uniaxial model is employed. The parametric optical response for both of these films is obtained by fitting a Sellmeier expression [37] to describe the ε_1 spectra shown in Fig. 5 over the 0.74–1.23 eV transparent wavelength range. These spectra are then input into EMAs alongside a variable fraction void to describe both optical properties parallel (extra-ordinary) and perpendicular (ordinary) to the columnar principal axes. For each film, the void fraction in both ordinary and extraordinary directions are held common. Limiting forms of effective medium theory are employed [51] in which the ordinary direction exhibits maximum electric field screening (screening parameter = 1) and the extraordinary direction exhibits minimum electric field screening (screening parameter = 0). The azimuthal Euler angle values for each spectra collected at nominal φ are fit. Thicknesses are obtained from the isotropic model and fixed. The polar Euler angle θ is fixed to that obtained from cross-sectional SEM. Fig. 6 shows the anisotropic optical properties over the modeled range for the two as-deposited CdTe films sputtered at Φ = 60° and 80°. The birefringence, difference in the indices of refraction in extra-ordinary and ordinary direction (n_e-n_o), is greater for Φ = 80° due to increased shadowing effects at higher angles of incidence. This behavior has also been observed in other GLAD polycrystalline thin films [22,23,52,53].

The post-deposition $CdCl_2$ treatment process is an important step during the fabrication of CdTe solar cells for improving device performance. $CdCl_2$ treatment results in recrystallization, grain growth, grain boundary passivation, and randomizing the crystal orientation [15,16]. $CdCl_2$ treatments are applied to GLAD CdTe films at different oblique angles. Using XRD measurement and Scherrer's equation [54], the crystallite size variations with $CdCl_2$ treatment time are shown in Fig. 7. In the calculation, the diffraction peak centered around 23.7° indexed to C(111) and H(002) is considered. Crystallite size increases after $CdCl_2$ treatment for all samples and increases with increasing treatment time. On average, the crystallite size for all sample increased by ~20% after $CdCl_2$ treatment for the most commonly used 30 min treatment time [3–5] compared to as-deposited samples. Also, surface view SEM

Approved for public release; distribution unlimited.
524

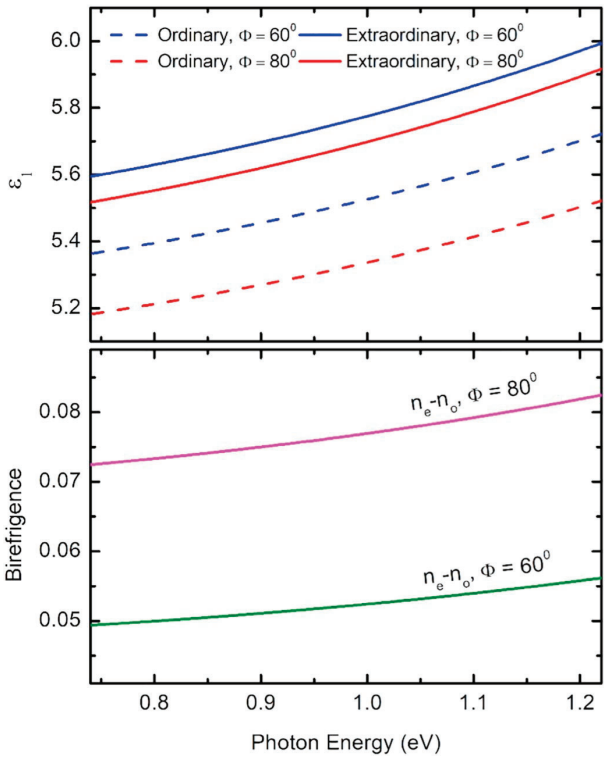


Fig. 6. Anisotropic optical properties parallel (extra-ordinary, *e*) and perpendicular (ordinary, *o*) to the columnar principal axes in (top) ε_1 and (bottom) birefringence, n_e-n_o in the transparent spectral range of CdTe prepared by GLAD at Φ = 60° and 80°.

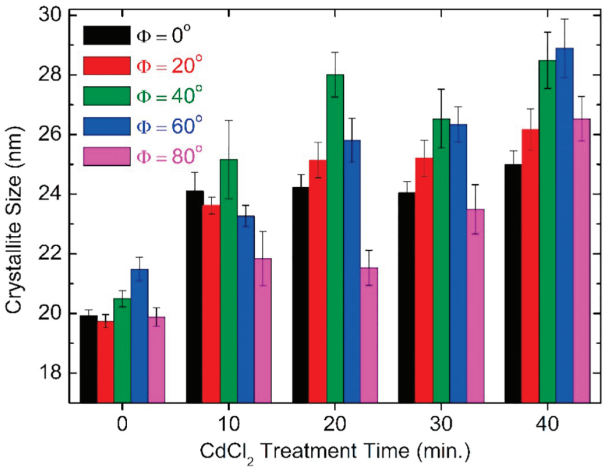


Fig. 7. Crystallite size deduced via the Scherrer equation as a function of $CdCl_2$ treatment time for CdTe deposited at different oblique angles.

have shown enhanced grain size after $CdCl_2$ treatment. Fig. 8 shows an example of surface view SEM images of CdTe film deposited at Φ = 0° before and after $CdCl_2$ treatment for 30 min. As a result of $CdCl_2$ treatment, the grain size increases from 122 ± 5 nm (before treatment) to 317 ± 7 nm (after treatment).

CdS/CdTe heterojunction solar cells with and without nominally 100 nm thick GLAD wurtzite interfacial layers between the *n*-type CdS window layer and *p*-type zinc blende CdTe absorber have been fabricated using Cu/Au back contacts (Fig. 2). All CdTe layers are deposited at RT followed by post-deposition $CdCl_2$ treatment. Fig. 9 shows the XRD patterns of Φ = 0° CdTe absorber layer and Φ = 80° GLAD CdTe interlayer after $CdCl_2$ treatment along with that of the hexagonal CdS window layer. After $CdCl_2$ treatment, Φ = 80° GLAD CdTe interlayer exhibits diffraction peaks corresponding to both cubic and hexagonal crystal structures. As some hexagonal phase CdTe crystallites exist after the $CdCl_2$ process, better lattice matching with the underlying CdS can occur. For the absorber layer deposited at Φ = 0° after $CdCl_2$ treatment, only C(111), C(200), C(220), C(311), C(400), and C(331) index diffraction peaks associated with cubic CdTe are observed. Although the peak position of C(111) and H(002), C(220) and H (110), and C(311) and H(112) are close, the absence of additional hexagonal peaks indicates that the CdTe absorber layer deposited at Φ = 0° has cubic zinc blende crystal structure after $CdCl_2$ treatment. Also, after $CdCl_2$ treatment, the presence of Cd_xTeO_y peaks shows the oxidation of the surface, as expected for these processing conditions.

The Scherrer equation has been used to determine the crystallite size associated with each diffraction peak in as-deposited and $CdCl_2$ treated (30 min) samples prepared at different Φ. Crystallite size associated with H(102) crystallites increases slightly for Φ = 40° and 60° and remains approximately the same for Φ = 80° after $CdCl_2$ treatment. The crystallite size associated with the H(103) peak increases for Φ = 80°, is approximately the same for Φ = 60°, and slightly decreases for Φ = 40°. Crystallite size associated with the most dominate crystallite orientations increase with $CdCl_2$ treatment. Cubic phase crystallite orientations become more random after $CdCl_2$ treatment as observed by the appearance of C(200) planes in addition to the C(220), C(111), and C(311) planes prior to treatment. Individual hexagonal phase crystallite orientations become either more or less pronounced after $CdCl_2$ treatment depending upon the initial crystallite orientations present in the samples. These observations imply that the introduction of the thin GLAD CdTe interlayer between the hexagonal CdS and cubic CdTe absorber layer is improving lattice matching on both sides of the junction via alignment of crystal planes. The presence of the interlayer is expected to result in reductions in strain energy, density of unpassivated bonds, or both which is expected to reduce the defect density at the interface.

Fig. 10(a) shows *J-V* characteristics of the highest performing CdS/CdTe solar cells with and without the GLAD CdTe interlayer in the solar cell structure. The open circuit voltage (V_{OC}), short circuit current density (J_{SC}), power conversion efficiency (*PCE*), and fill factor (*FF*) corresponding to devices plotted in Fig. 10 are shown in Table 3. The best device without the GLAD CdTe interlayer has a *PCE* = 10.1% with V_{OC} = 0.728 V, J_{SC} = 23.2 mA/cm^2, and *FF* = 59.4%. After incorporating structurally engineered GLAD CdTe between the *n*-type CdS window layer and normally sputtered *p*-type CdTe absorber, the best device has *PCE* = 11.0% with V_{OC} = 0.774 V, J_{SC} = 23.0 mA/cm^2, and *FF* = 61.9%. Using the GLAD CdTe interlayer, *PCE* increased by 9% relative and 0.9% absolute, and this enhancement in device performance is attributed to an increase in V_{OC} by 6% and FF by 4%. Device performance parameters of all CdS/CdTe heterojunction solar cells with and without GLAD CdTe interlayers are shown in Fig. 11. Out of 256 dot cells, some of the cells show substantially lower performance and hence only the 200 highest performing dot cells are included in the statistical average calculation and one standard deviation variation for both sets of solar cells given in Table 3. The average V_{OC}, J_{SC}, *FF*, and *PCE* of devices with GLAD CdTe interlayers are higher compared to devices without GLAD interlayers. On average, *PCE* is higher for devices with the GLAD interlayer with the largest gain attributed to improved V_{OC}. Fig. 10(b) shows similar EQE spectra over the 300–1000 nm wavelength range for the same highest efficiency devices indicating that the presence of the interlayer does not reduce the spectroscopic optical performance of these solar cells.

Solar cell diode parameters are obtained by fitting experimental *J-V* to the diode equation [55,56]:

Approved for public release; distribution unlimited.
525

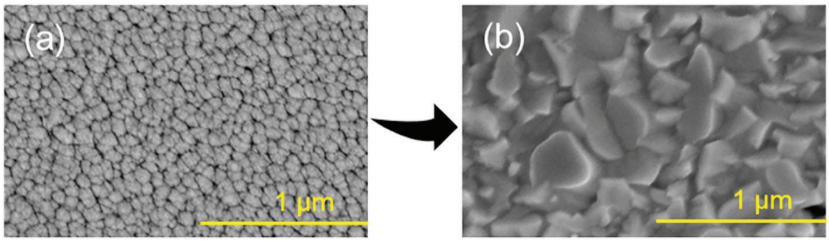


Fig. 8. Surface SEM images of CdTe film deposited at Φ = 0° (a) before and (b) after $CdCl_2$ treatment for 30 min.

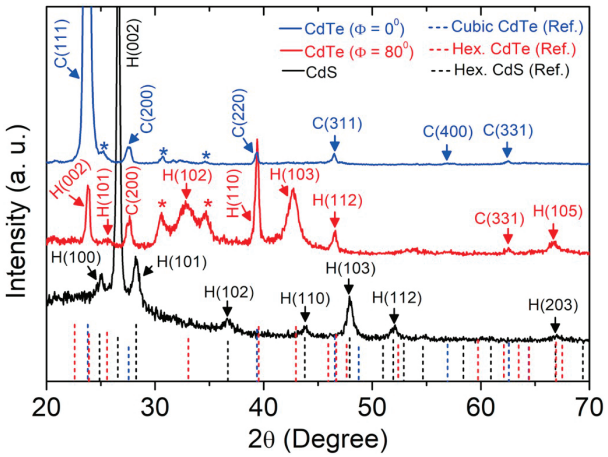


Fig. 9. XRD patterns of CdS (black), $CdCl_2$ treated CdTe (Φ = 0°) (blue), and $CdCl_2$ treated CdTe (Φ = 80°) (red). Peaks associated with Cd_xTeO_y are also indicated (*). The vertical lines represent the reference diffraction peak positions for hexagonal CdS (PDF#97-015-4186), cubic CdTe (PDF#97-010-8238), and hexagonal CdTe (PDF#97-015-0941) crystal structures obtained from MDI JADE software. (For interpretation of the references to colour in this figure legend, the reader is referred to the Web version of this article.)

$$J = J_0 exp\left[\frac{q}{nk_BT}(V - R_SJ)\right] + G_{SH}V - J_L \quad (1)$$

Here q is the electronic charge, n is the diode ideality factor, k_B is Boltzmann's constant, T is temperature, J_0 is the reverse saturation current, R_S is the series resistance, G_{SH} is the shunt conductance, and J_L is the current density at AM1.5G light illumination. Ideality factors are calculated by plotting the derivative dV/dJ from the exponential diode equation as a function of $1/J$ when the devices are not illuminated, with results for the highest efficiency devices with and without the GLAD interlayer shown in Fig. 12(a). The slope and intercept of the linear fit give R_S and n, respectively. The calculation results in similar series resistances of 2.4 and 2.1 Ω cm^2 for the devices with and without the GLAD CdTe interlayers and substantially different ideality factors of 2.3 and 3.0, respectively. Similarly, the plot between ln[J] and V-R_SJ using R_s, allows for extraction of n and J_0 for the highest efficiency devices with and without the GLAD interlayer as shown in Fig. 12(b). These values of n are 2.0 and 2.5, and the values of J_0 are 2×10^{-6} mA/cm^2 and 7×10^{-5} mA/cm^2, respectively, for the devices with and without GLAD CdTe interlayers. The values of n and J_0 for these CdTe devices are consistent with values reported in literature for similar devices [55–57]. Overall, lower values of J_o and n with comparable R_s for the device with the GLAD CdTe interlayer indicates improvement in the diode performance parameters. The lower values of n and J_0 for the highest efficiency cell with the GLAD interlayer compared to the highest efficiency device without the interlayer indicates lower recombination of charge carriers due to the formation of an improved electronic quality interface [57]. The resulting improvement in diode parameters leads to increases in V_{OC}, FF, and overall solar cell performance as observed for devices incorporating the GLAD CdTe interlayer.

The better performance of device with the GLAD interlayer can be attributed to an improved n/p interface due to less lattice mismatch between wurtzite CdS and hexagonal wurtzite phase crystallites in the GLAD CdTe interlayer, as both share the same crystal structure and more similar lattice constants when compared to zinc blende CdTe. As a result, wurtzite CdTe incorporated in these devices makes higher electronic quality, less defective interfaces with the underlying wurtzite CdS and over-deposited zinc blende CdTe [58,59]. All these results indicate that the idea of incorporating a thin GLAD CdTe interlayer between CdS and zinc blende CdTe serves as a means of interfacial

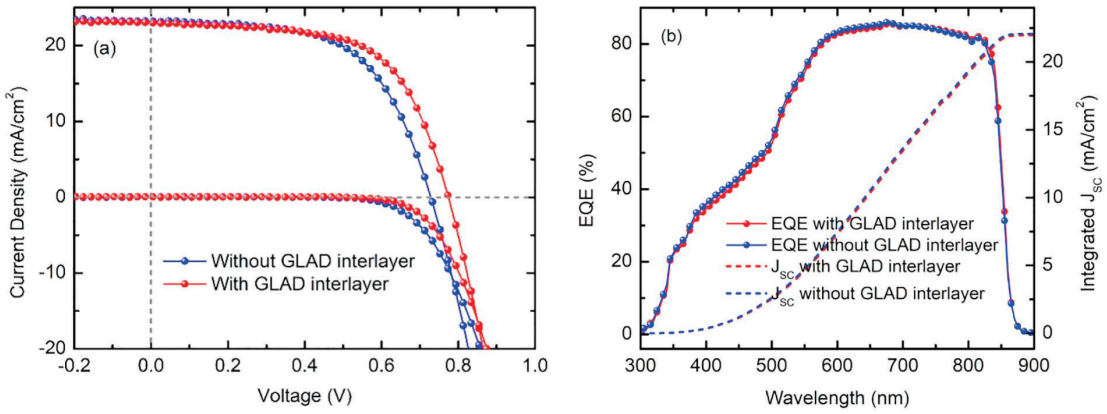


Fig. 10. Device performance for the highest efficiency solar cells with and without a 100 nm GLAD CdTe interlayer: (a) light and dark current-voltage (J-V) and (b) external quantum efficiency (EQE) for CdS/CdTe heterojunction solar cells with (red) and without (blue) introduction of the GLAD interlayer. (For interpretation of the references to colour in this figure legend, the reader is referred to the Web version of this article.)

Approved for public release; distribution unlimited.
526

Table 3
Comparison of device performance parameters of highest efficiency CdS/CdTe solar cells with and without a 100 nm thick GLAD CdTe interlayer. Average performance parameters with one standard deviation (1-σ) variation for the best 200 (out of 256) small area devices for each configuration are also given.

Solar cell parameter		V_{OC} (V)	J_{SC} (mA/cm^2)	PCE (%)	FF (%)
Without interlayer	Best cell	0.728	23.2	10.1	59.4
	Average of 200 cells	0.710 ± 0.032	20.0 ± 1.8	7.72 ± 1.04	54.1 ± 3.1
With interlayer	Best cell	0.774	23.0	11.0	61.9
	Average of 200 cells	0.730 ± 0.030	20.4 ± 1.3	8.10 ± 1.25	54.2 ± 3.7

tailoring at the heterojunction for improving PV device performance. This concept will be extended for devices incorporating more optimized CdTe after deposition of the interlayer, as opposed to RT normal incidence deposited CdTe.

4. Conclusions

GLAD magnetron sputtered CdTe shows variation in optical properties, density, and microstructure with incident oblique angle. Crystal phase structure transitions from mixed-phase cubic zinc blende and hexagonal wurtzite crystal structures to the hexagonal phase with increasing oblique angle. As-deposited GLAD CdTe films prepared at higher oblique angles show sensitivity to in-plane optical anisotropy from the projection of the tilted columnar axes and as identified from analysis of Mueller matrix spectra. $CdCl_2$ treated CdTe shows enhanced crystallite size compared to as-deposited samples with crystallite size increasing with treatment time. PV devices incorporating GLAD CdTe interlayer show 0.9% absolute higher efficiency compared to devices without the interlayer. The higher efficiency of the device with GLAD CdTe interlayer is because of an improved *n/p* interface due to improved structural compatibility between CdS and wurtzite phase crystallites in the GLAD CdTe interlayer.

Disclaimer text

The views and conclusions contained herein are those of the authors and should not be interpreted as necessarily representing the official policies or endorsements, either expressed or implied, of Air Force Research Laboratory or the U.S. Government.

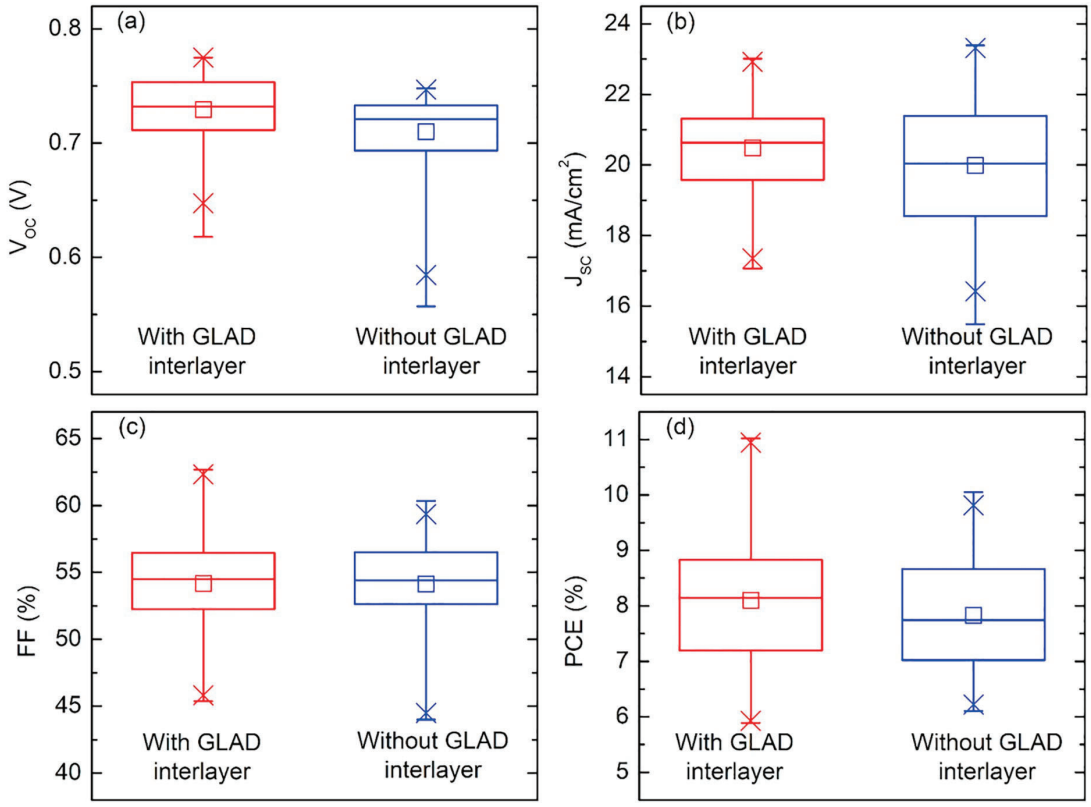


Fig. 11. (a) Open circuit voltage (V_{OC}), (b) short circuit current density (J_{SC}), (c) fill factor (*FF*), and (d) power conversion efficiency (*PCE*) parameter ranges for all CdTe PV devices with and without GLAD CdTe interlayers.

Approved for public release; distribution unlimited.
527

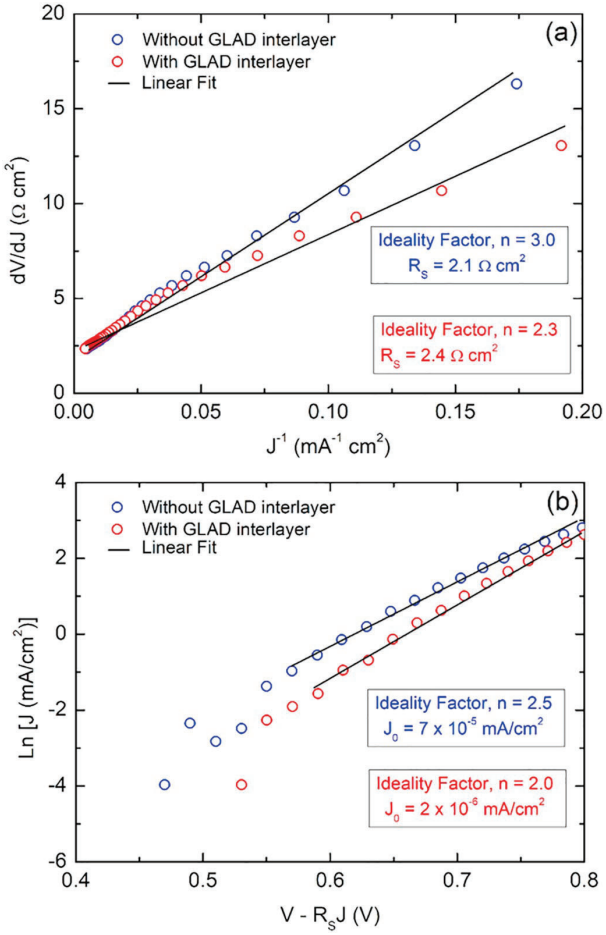


Fig. 12. Analysis of dark current density versus voltage characteristics for the best performing CdS/CdTe heterojunction solar cells with and without GLAD CdTe interlayers: (a) dV/dJ versus 1/J plot for calculation of n and R_S and (b) semi-log scale plot for the calculation of J_0 and n.

Declaration of competing interest

The authors declare that they have no known competing financial interests or personal relationships that could have appeared to influence the work reported in this paper.

Acknowledgement

This work is supported by National Science Foundation (NSF) Grant No. 1711534 and Air Force Research Laboratory under agreement number FA9453-18-2-0037. The U.S. Government is authorized to reproduce and distribute reprints for Governmental purposes notwithstanding any copyright notation thereon.

References

[1] A. Gupta, A.D. Compaan, All-sputtered 14% CdS/CdTe thin-film solar cell with ZnO: Al transparent conducting oxide, Appl. Phys. Lett *85* (2004) 684–686.
[2] A. Gupta, V. Parikh, A.D. Compaan, High efficiency ultra-thin sputtered CdTe solar cells, Sol. Energy Mater. Sol. Cells 90 (2006) 2263–2271.
[3] P. Koirala, J. Li, H.P. Yoon, P. Aryal, S. Marsillac, A.A. Rockett, N.J. Podraza, R.W. Collins, Through-the-glass spectroscopic ellipsometry for analysis of CdTe thin-film solar cells in the superstrate configuration, Prog. Photovolt. Res. Appl. 24 (2016) 1055–1067.
[4] M. Tuteja, P. Koirala, S. MacLaren, R. Collins, A. Rockett, Direct observation of electrical properties of grain boundaries in sputter-deposited CdTe using scan-probe microwave reflectivity based capacitance measurements, Appl. Phys. Lett. 107 (2015) 142106.
[5] N.R. Paudel, K.A. Wieland, A.D. Compaan, Ultrathin CdS/CdTe solar cells by sputtering, Sol. Energy Mater. Sol. Cells 105 (2012) 109–112.
[6] J.L. Boone, T.P. Van Doren, A.K. Berry, Deposition of CdTe by spray pyrolysis, Thin Solid Films 87 (1982) 259–264.
[7] A.E. Rakhshani, Electrodeposited CdTe-optical properties, J. Appl. Phys. 81 (1997) 12.
[8] X. Wu, High-efficiency polycrystalline CdTe thin-film solar cells, Sol. Energy 77 (2004) 803–814.
[9] J. Britt, C. Ferekides, Thin-film CdS/CdTe solar cell with 15.8% efficiency, Appl. Phys. Lett. 62 (1993) 2851–2852.
[10] M.A. Green, Y. Hishikawa, E.D. Dunlop, D.H. Levi, J. Hohl-Ebinger, M. Yoshita, A.W.Y. Ho-Baillie, Solar cell efficiency tables (Version 53), Prog. Photovolt. Res. Appl. 27 (2019) 3–12.
[11] Research Progress Report, Institute of Electrical Engineering, Chinese Academy of Science, (2014).
[12] K.D. Dobson, I. Visoly-Fisher, G. Hodes, D. Cahen, Stability of CdTe/CdS thin-film solar cells, Sol. Energy Mater. Sol. Cells 62 (2000) 295–325.
[13] C. Li, Y. Wu, J. Poplawsky, T.J. Pennycook, N. Paudel, W. Yin, S.J. Haigh, M.P. Oxley, A.R. Lupini, M. Al-Jassim, S.J. Pennycook, Y. Yan, "Grain-boundary-enhanced carrier collection in CdTe solar cells, Phys. Rev. Lett. 112 (2014) 156103.
[14] I. Visoly-Fisher, S.R. Cohen, A. Ruzin, D. Cahen, "How polycrystalline devices can outperform single-crystal ones: thin film CdTe/CdS solar cells, Adv. Mater. 16 (2004) 879–883.
[15] N.G. Dhere, R.G. Dhere, Thin-film photovoltaics, J. Vac. Sci. Technol. *A* 23 (2005) 1208–1214.
[16] B. McCandless, J. Sites, A. Luque, S. Hegedus (Eds.), Handbook of Photovoltaic Science and Engineering, Wiley, Chichester, England, 2003.
[17] M.H. Ehsani, H. RezagholipourDizaji, S. Azizi, S.F. Ghavami Mirmahalle, F. Hosseini Siyanaki, Optical and structural properties of cadmium telluride films grown by glancing angle deposition, Phys. Scr. 88 (2013) 025602.
[18] D. Adhikari, P. Koirala, M.M. Junda, R.W. Collins, N.J. Podraza, Glancing angle deposited CdTe: optical properties and structure, IEEE 7th World Conference on Photovoltaic Energy Conversion (WCPEC) (A Joint Conference of 45th IEEE PVSC, 28th PVSEC & 34th EU PVSEC), 2018 DOI: 10.1109/PVSC.2018.8547890.
[19] J. Lee, P.I. Rovira, I. An, R.W. Collins, Rotating-compensator multichannel ellipsometry: applications for real time Stokes vector spectroscopy of thin film growth, Rev. Sci. Instrum. 69 (1998) 1800–1810.
[20] B. Johs, J.A. Woollam, C.M. Herzinger, J. Hilfiker, R. Synowicki, C.L. Bungay, Overview of variable angle spectroscopic ellipsometry (VASE), Part II: advanced applications, Proc. SPIE 72 (1999) 29–58.
[21] C. Chen, I. An, G.M. Ferreira, N.J. Podraza, J.A. Zapien, R.W. Collins, Multichannel Mueller matrix ellipsometer based on the dual rotating compensator principle, Thin Solid Films 14 (2004) 455–456.
[22] N.J. Podraza, Chi Chen, J.M. Flores, D. Sainju, llsin An, G.M. Ferreira, C.R. Wronski, M.W. Horn, R. Messier, R.W. Collins, Optical properties of transparent conducting oxide sculptured thin films silicon photovoltaics, Proc. IEEE 31st Photovoltaics Specialists Conf, 2005, pp. 1428–1431 DOI: 10.1109/PVSC.2005.1488409.
[23] N.J. Podraza, Chi Chen, D. Sainju, O. Ezekoye, M.W. Horn, C.R. Wronski, R.W. Collins, "Transparent conducting oxide sculptured thin films for photovoltaic applications, Proc. Mat. Res. Soc. Symp. 865 (F7.1) (2005) 1–6.
[24] J.M. Nieuwenhuizen, H.B. Haanstra, Microfractography of thin films, Philips Tech. Rev. 27 (1966) 87–91.
[25] A.G. Dirks, H.J. Leamy, Columnar microstructure in vapor-deposited thin films, Thin Solid Films 47 (1977) 219–233.
[26] R.N. Tait, T. Smy, M.J. Brett, Modelling and characterization of columnar growth in evaporated films, Thin Solid Films 226 (1993) 196–201.
[27] S. Lichter, J. Chen, Model for columnar microstructure of thin solid films, Phys. Rev. Lett. 56 (1986) 1396–1399.
[28] R. Álvarez, L. González-García, P. Romero-Gómez, V. Rico, J. Cotrino, A.R. González-Elipe, A. Palmero, Theoretical and experimental characterization of TiO_2 thin films deposited at oblique angles, J. Phys. D Appl. Phys. 44 (2011) 385302.
[29] P. Morrow, F. Tang, T. Karabacak, P.I. Wang, D.X. Ye, G.C. Wang, T.M. Lu, Texture of Ru columns grown by oblique angle sputter deposition, J. Vac. Sci. Technol. A 24 (2006) 235–245.
[30] M.M. Hawkeye, M.J. Brett, Glancing angle deposition: fabrication, properties, and applications of micro- and nanostructured thin films, J. Vac. Sci. Technol. *A* 25 (2007) 1317–1335.
[31] E. Alfonso, J. Olaya, G. Cubillos, Thin film growth through sputtering technique and its applications, in: M. Andreeta (Ed.), Crystallization-Science and Technology, Intech, Croatia, 2012, pp. 397–432.
[32] P. Gu, X. Zhu, H. Wu, D. Yang, Regulation of substrate-target distance on the microstructural, optical, and electrical properties of CdTe films by magnetron sputtering, Materials 11 (2018) 2496.
[33] R. Kulkarni, S. Rondiya, A. Pawbake, R. Waykar, A. Jadhavar, V. Jadkar, A. Bhorde, A. Date, H. Pathan, S. Jadkar, Structural and optical properties of CdTe thin films deposited using RF magnetron sputtering, Energy Procedia 110 (2017) 188–195.
[34] F. Hosseinpanahi, D. Raoufi, K. Ranjbarghanei, B. Karimi, R. Babaei, E. Hasani, Fractal features of CdTe thin films grown by RF magnetron sputtering, Appl. Surf. Sci. 357 (2015) 1843–1848.
[35] S.A. Alterovitz, B. Johs, Multiple minima in the ellipsometric error function, Thin Solid Films 124 (1998) 313–314.
[36] D.E. Aspnes, M. Balkanski (Ed.), Handbook of Semiconductors, vol. 2, North-

Approved for public release; distribution unlimited.

528

Holland, Amsterdam, The Netherlands, 1980.
[37] R.W. Collins, A.S. Ferlauto, H.G. Tompkins, E.A. Irene (Eds.), Handbook of Ellipsometry, William Andrew publishing, Norwich, 2005.
[38] G.E. Jellison Jr., F.A. Modine, Parameterization of the optical functions of amorphous materials in the interband region, Appl. Phys. Lett. 69 (1996) 371–373.
[39] G.E. Jellison, F.A. Modine, Erratum: 'Parameterization of the optical functions of amorphous materials in the interband region', Appl. Phys. Lett. *69* (1996) 371–373. *Appl. Phys. Lett.,* 69 (1996) 2137.
[40] H. Fujiwara, J. Koh, P. Rovira, R. Collins, Assessment of effective-medium theories in the analysis of nucleation and microscopic surface roughness evolution for semiconductor thin films, Phys. Rev. B 61 (2000) 10832–10844.
[41] J.A. Zapien, J. Chen, J. Li, J. Inks, N.S. Podraza, C. Chen, J. Drayton, A. Vasko, A. Gupta, S.L. Wang, R.W. Collins, A.D. Compaan, Real time spectroscopic ellipsometry of thin film CdTe deposition by magnetron sputtering for photovoltaic applications, IEEE 31st Photovoltaics Specialists Conf. 2005, pp. 461–464 DOI: 10.1109/PVSC.2005.1488169.
[42] J. Li, J. Chen, M.N. Sestak, C. Thornberry, R.W. Collins, Spectroscopic ellipsometry studies of thin film CdTe and CdS: from dielectric functions to solar cell structures, Proc. IEEE 34th Photovoltaics Specialists Conf. 2009, pp. 001982–001987 DOI: 10.1109/PVSC.2009.5411520.
[43] J. Li, N.J. Podraza, R.W. Collins, Real time spectroscopic ellipsometry of sputtered CdTe, CdS, and $CdTe_{1-X}$ S_X thin films for photovoltaic applications, Phys. Status Solidi A 205 (2008) 901–904.
[44] W.G. Oldham, Numerical techniques for the analysis of lossy films, Surf. Sci. 16 (1969) 97–103.
[45] J. Li, J. Chen, R.W. Collins, Optical transition energies as a probe of stress in polycrystalline CdTe thin films, Appl. Phys. Lett. 99 (2011) 061905.
[46] B. Johs, C.M. Herzinger, J.H. Dinan, A. Cornfeld, J.D. Benson, Development of a parametric optical constant model for $Hg_{1-x}Cd_xTe$ for control of composition by spectroscopic ellipsometry during MBE growth, Thin Solid Films 137 (1998) 313–314.
[47] C.C. Kim, M. Daraselia, J.W. Garland, S. Sivanathan, Temperature dependence of the optical properties of CdTe, Phys. Rev. *B* 56 (1997) 4786–4797.
[48] S. Jiménez-Sandoval, M. Meléndez-Lira, I. Hernández-Calderón, Crystal structure and energy gap of CdTe thin films grown by radio frequency sputtering, J. Appl. Phys. 72 (1992) 4197–4202.
[49] S.M. Hosseini, Optical properties of cadmium telluride in zinc-blende and wurzite structure, Physica *B* 403 (2008) 1907–1915.
[50] D. Adhikari, M.M. Junda, P. Uprety, K. Ghimire, I. Subedi, N.J. Podraza, Near infrared to ultraviolet anisotropic optical properties of single crystal $SrLaAlO_4$ from spectroscopic ellipsometry, Phys. Status Solidi B 253 (2016) 2066–2072.
[51] D.E. Aspens, Optical properties of thin films, Thin Solid Films 89 (1982) 249–262.
[52] S. Wang, X. Fu, G. Xia, J. Wang, J. Shao, Z. Fan, Structure and optical properties of ZnS thin films grown by glancing angle deposition, Appl. Surf. Sci. 252 (2006) 8734–8737.
[53] R.B. Tokas, S. Jena, S.M. Haque, K.D. Rao, S. Thakur, N.K. Sahoo, Spectroscopic ellipsometry investigations of optical anisotropy in obliquely deposited Hafnia thin films, AIP Conf. Proc. 1731 (2016) 060007, https://doi.org/10.1063/1.4947813.
[54] P. Scherrer, Nachrichten von der gesellschaft der wissenschaftenzugöttingen, Mathematisch-PhysikalischeKlasse 2 (1918) 98.
[55] S.S. Hegedus, W.N. Shafarman, Thin-film solar cells: device measurements and analysis, Prog. Photovolt. Res. Appl. 12 (2004) 155–175.
[56] K.P. Bhandari, X. Tan, P. Zereshki, F.K. Alfadhili, A.B. Phillips, P. Koirala, M.J. Heben, R.W. Collins, R.J. Ellingson, Thin film iron pyrite deposited by hybrid sputtering/co-evaporation as a hole transport layer for sputtered CdS/CdTe solar cells, Sol. Energy Mater. Sol. Cells 163 (2017) 277–284.
[57] S. Marsillac, V.Y. Parikh, A.D. Compaan, Ultra-thin bifacial CdTe solar cell, Sol. Energy Mater. Sol. Cells 91 (2007) 1398–1404.
[58] H.C. Chou, A. Rohatgi, N.M. Jokerst, S. Kamra, S.R. Stock, S.L. Lowrie, R.K. Ahrenkiel, D.H. Levi, Approach toward high efficiency CdTe/CdS heterojunction solar cells, Mater. Chem. Phys. 43 (1996) 178–182.
[59] X. Wu, R.G. Dhere, Y. Yan, M.J. Romero, Y. Zhang, J. Zhou, C. DeHart, A. Duda, C. Perkins, B. To, High-efficiency polycrystalline CdTe thin-film solar cells with an oxygenated amorphous CdS (a-CdS: O) window layer, Proc. IEEE 29th Photovoltaics Specialists Conf. 2002, pp. 1–4 DOI: 10.1109/PVSC.2002.1190619.

Approved for public release; distribution unlimited.

529

ACS APPLIED MATERIALS & INTERFACES

www.acsami.org Research Article

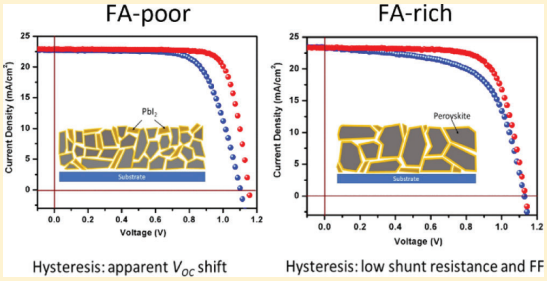
Correlating Hysteresis and Stability with Organic Cation Composition in the Two-Step Solution-Processed Perovskite Solar Cells

Yunkang Cui,[§] Cong Chen,[§] Chongwen Li, Lei Chen, Sandip Singh Bista, Xiangyang Liu, You Li, Rasha A. Awni, Zhaoning Song,* and Yanfa Yan*

Cite This: *ACS Appl. Mater. Interfaces* 2020, 12, 10588−10596 Read Online

ACCESS | Metrics & More | Article Recommendations | Supporting Information

ABSTRACT: The two-step solution-based process has demonstrated substantial success in fabricating high-efficiency perovskite solar cells in recent years. Despite the high performance, the underlying mechanisms that govern the formation of perovskite films and corresponding device performance are yet to be fully understood. Particularly, organic cation composition used in the two-step solution processing of mixed-cation lead halide perovskite solar cells plays a critical role in the perovskite film formation and the resultant device performance. However, little is understood about the impacts of organic cation composition on the current density−voltage (J−V) hysteretic behavior and stability of perovskite solar cells. To address this need, here, we study the effect of mixed organic cations, that is, the fraction of formamidinium (FA) and methylammonium (MA) contents, used for the two-step solution-processed perovskite thin films on solar cell performance, including efficiency, J−V hysteresis, and stability. In addition to the efficiency variations, we find that perovskite solar cells based on FA-rich and MA-rich stoichiometries show distinct characteristics in J−V hysteresis and stability. The origins of such a discrepancy are attributed to the thermodynamically driven conversion from lead iodide to perovskites, which is determined by the combination of organic cations. The perovskite solar cells based on the mixed cation $FA_{0.6}MA_{0.4}PbI_3$ composition show a champion power conversion efficiency of over 21% and robust stability (retaining more than 90% of initial efficiency) under maximum power-point tracking in dry nitrogen for more than 500 h. Our work provides insights on understanding the formation of perovskite films in the two-step process, which may benefit further investigation on perovskite solar cells.



KEYWORDS: *perovskite solar cells, two-step process, organic cation composition, J−V hysteresis, stability*

Downloaded via UNIV OF TOLEDO on September 13, 2021 at 16:09:00 (UTC).
See https://pubs.acs.org/sharingguidelines for options on how to legitimately share published articles.

INTRODUCTION

Organic−inorganic metal-halide perovskites have been intensively studied in the past decade because of their exceptional optoelectronic properties, such as high absorption coefficients, tunable band gaps, long carrier lifetimes and diffusion lengths, and defect tolerance.[1−4] The combination of high certified power conversion efficiencies (PCEs) exceeding 25%[5] and low manufacturing costs enabled by low-temperature solution-based deposition methods[6] makes metal-halide perovskite solar cells (PSCs) a promising candidate for the next-generation high-efficiency low-cost photovoltaic (PV) technology.[7] In recent years, the commercialization of PSCs has been seriously considered, and more research efforts have been devoted toward developing scalable manufacturing techniques that are suitable for reproducible industrial production of PSCs.[8−12]

With the revolutionary progress in PSCs, a variety of solution-based deposition methods, including antisolvent-assisted single-step spin-coating[13−16] and two-step sequential deposition,[17−21] have been successfully developed and widely used to prepare perovskite absorber layers for high-efficiency PSCs. Compared with the single-step antisolvent dripping technique, the two-step solution process has some unique advantages, such as more precise and reproducible process control, more suitable for scale-up fabrication, and vertical-columnar grain formation that enables the preparation of thicker perovskite absorber layer.[18−21] Because of these merits, the two-step method is more preferred than the single-step antisolvent dripping method for the commercialization of PSCs.

Received: January 2, 2020
Accepted: February 11, 2020
Published: February 11, 2020

© 2020 American Chemical Society

https://dx.doi.org/10.1021/acsami.9b23374
ACS Appl. Mater. Interfaces 2020, 12, 10588−10596

Approved for public release; distribution unlimited.

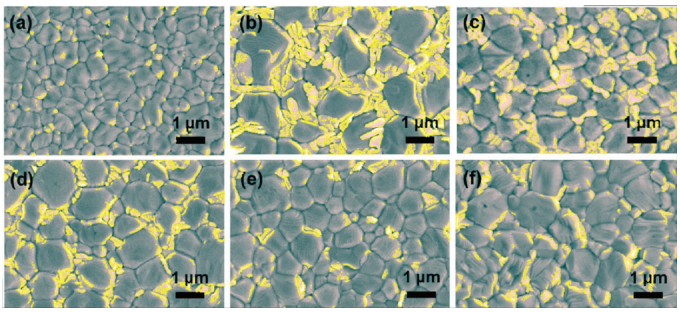


Figure 1. False color SEM images of $FA_xMA_{1-x}PbI_3$ films with x = (a) 0.0, (b) 0.2, (c) 0.4, (d) 0.6, (e) 0.8, and (f) 1.0. The highlighted sections outline the high contrast areas which are attributed to the formation of PbI_2.

The two-step solution method, consisting of the deposition of a PbI_2 layer and a subsequent conversion step using an organic-halide salt solution, was developed by Mitzi et al. to prepare low-dimensional organic−inorganic metal halide perovskites.[22] In 2013, Burschka et al. used this method to prepare methylammonium (MA)-based PSCs,[23] achieving a remarkable PCE of 15% at that time. Many other researchers then used the methods for the advanced device fabrication.[17−19] Most recently, You and co-workers employed the two-step method to prepare formamidinium (FA)-based PSCs, demonstrating PCEs of more than 23%.[21] This success stimulates a wide adoption of the two-step method for the fabrication of high-efficiency PSCs.

Despite the success in fabricating high-efficiency PSCs, the underlying mechanisms that govern the formation of perovskite films in the second step and corresponding device performance are yet to be fully understood. Because the PV performance of PSCs can be influenced by the synthesis approach and stoichiometry of the perovskite absorber layers, it is critical to understand and precisely control the crystal-growth process during the formation of perovskite films. Over the years, the nucleation dynamics and growth of perovskite films were manipulated by various approaches, including self-seeding growth,[24] cooperation of Lewis base and acid,[25] crystal engineering,[26] organic-cation engineering,[27] cesium incorporation,[28−31] halogen engineering,[32] solutions and processing control,[33−35] and conjugated polymer tailoring.[36] Among these approaches, the organic-cation composition of perovskites plays a critical role in the perovskite film formation and the resultant device performance and stability. Particularly, mixing organic cations can adjust the Goldschmidt tolerance factor of FA-based perovskites and thus stabilize FA-rich perovskites.[37] The MA to FA ratio can also influence the microstructure and crystal orientation of perovskite crystallites.[27] However, the two-step solution-processed mixed-cation perovskites have rarely been explored in the full MA-FA compositional space. Furthermore, little is known about the impacts of organic-cation composition on the current density−voltage ($J-V$) hysteretic behavior and stability of PSCs. To address this need, we investigated the effect of mixed organic cations, that is, the fraction of FA and MA contents, used for the two-step solution-process perovskite thin films on solar cell performance, including efficiency, $J-V$ hysteresis, and stability. Additionally, the origins of the different hysteresis and stability behaviors were also explored.

RESULTS AND DISCUSSION

The PV performance and stability of PSCs are mainly determined by the quality of the perovskite absorber layer. To evaluate the structural and optoelectronic properties of MA−FA mixed-cation perovskites prepared by the solution-based two-step deposition approach, we prepared a series of perovskite thin films following the previously reported methods.[20,21,27] Briefly, PbI_2 thin films were first spin-coated on indium tin oxide (ITO)/SnO_2 substrates in a nitrogen glovebox. After that, mixed-cation organic-iodide solutions with various FA to FA + MA ratios (0−1) were spin-coated on PbI_2 films for the perovskite conversion. The resultant films were then taken to the ambient air with a controlled relative humidity of ∼30% for thermal annealing. The annealing temperature was set to 150 °C for perovskites containing FA cations. For $MAPbI_3$, because of its thermal instability at 150 °C in ambient air,[38,39] a lower annealing temperature (100 °C) was selected with a focus on studying the $J-V$ hysteresis and device operational stability of pure MA perovskite. Detailed experimental procedures are provided in the Experimental Section.

Figure 1 shows false-color scanning electron microscopic (SEM) surface images of the perovskite films with different FA ratios in the organic-halide precursor solution. The pure $MAPbI_3$ film (FA = 0.0) shown in Figure 1a exhibits a dense and smooth surface morphology but a slightly nonuniform distribution in grain sizes ranging from ∼0.3 to ∼1 μm. The small grain size is attributed to the relatively low annealing temperature (100 °C), particularly used for $MAPbI_3$. With the incorporation of FA cations into perovskites, a higher annealing temperature of 150 °C was enabled, promoting significant grain growth with average grain sizes reaching more than 1 μm (Figure 1b−f). However, the higher annealing temperature also lead to the partial decomposition of the perovskite into PbI_2, especially on the top surface. The PbI_2 particles are identified on the surface of perovskite films, as is evident from the high contrast (low conductive) areas, which are highlighted in yellow in the SEM images. The thermal decomposition is more severe for the compositions with higher MA content (FA = 0.2 and 0.4 in Figure 1b,c, respectively). Increasing the FA content makes perovskite more thermally stable, suppressing the formation of PbI_2 on the perovskite surface (Figure 1d−f). It is worth noticing that the PbI_2 particles are mostly distributed at grain boundaries where perovskites are prone to decomposition. It is known that proper amounts of PbI_2 help passivate defect centers at grain boundaries, leading to enhanced V_{OC} and FF.[20,40−42] However,

https://dx.doi.org/10.1021/acsami.9b23374
ACS Appl. Mater. Interfaces 2020, 12, 10588−10596

Approved for public release; distribution unlimited.

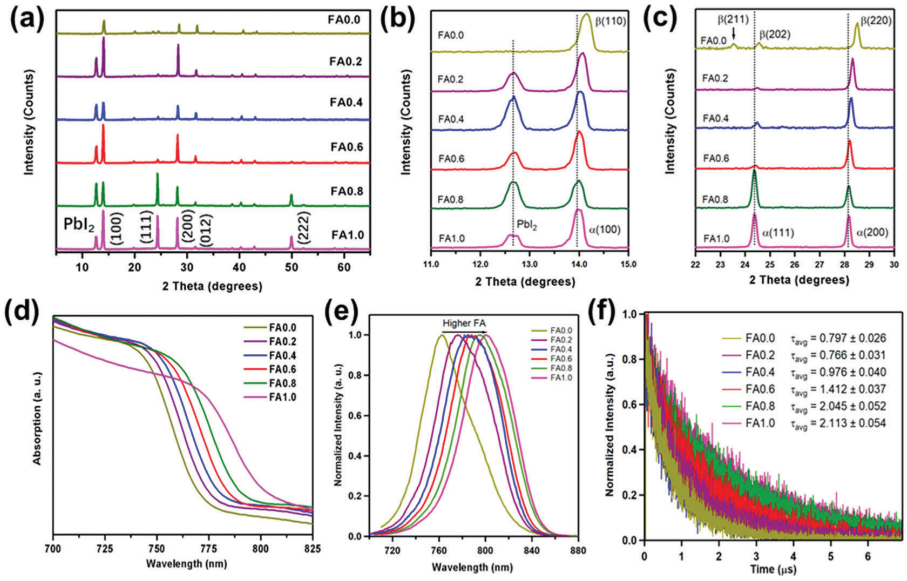


Figure 2. (a) XRD, (b,c) normalized XRD, (d) absorbance and (e) PL spectra, and (f) PL decays of $FA_xMA_{1-x}PbI_3$ films with x = 0.0, 0.2, 0.4, 0.6, 0.8, and 1.0.

too much of PbI_2 adversely affect the charge collection at the interface, resulting in lower J_{SC} and FF.[40] The MA-rich (FA < 0.5) perovskite films (Figure 1b,c) contain overwhelming PbI_2 particles on the top surface because of the thermal decomposition of perovskites, whereas the high FA (FA > 0.7) content films (Figure 1e,f) show a limited coverage of PbI_2. The FA = 0.6 sample (Figure 1d) possesses a proper amount of PbI_2 that only existed at grain boundaries, which provides effective surface passivation.

Turning to the XRD patterns of perovskite films with various FA contents, as shown in Figure 2a−c, perovskite films with different organic-cation compositions show different combinations of chemical phases and crystal orientations. The $MAPbI_3$ film (FA = 0.0) shows the almost pure tetragonal (β) perovskite phase (space group: $I4/mcm$) without a clear trace of PbI_2 (Figure 2b). The tetragonal phase is revealed by the shoulder peak of the (002)/(110) planes at 14.1°− and the (211) plane at 23.5°− which has the reflection position inconsistent with cubic symmetry.[43] In contrast, perovskites with FA cations show the cubic (α) phase (space group: $Pm\bar{3}m$) with the presence of the PbI_2 peak at ∼12.6°. The estimated percentage phase ratio of the perovskite as a function of the FA content calculated by the ratio of the integration area of XRD peaks corresponding to each chemical phase is shown in Figure S1a in the Supporting Information. The perovskite phase fraction is estimated to be around 68−90% for mixed FA-contained perovskite films, corresponding to 10−32% PbI_2. The hexagonal nonperovskite (δ) phase $FAPbI_3$, which is photoinactive and detrimental to the device performance if in bulk,[44,45] is not observed in any perovskite films. With the increase of the FA content, the characteristic XRD peaks shift to a lower angle (Figure S1b), corresponding to larger lattice spacing due to the larger size of FA than MA cation.

The crystal orientation in perovskite films can also influence the optoelectronic properties of the films.[46] Interestingly, the perovskite films with high FA contents (FA = 0.8 and 1.0) exhibit a strongly preferred (111) orientation compared with other films (Figure S1c), consistent with the result reported by Xu et al.[27] The different preferred orientation indicates that the nucleation and growth of FA-rich perovskites follow a crystal orientation that is more thermodynamically favorable. Note that the lattice displacement of iodine atoms in the (111) orientation closely matches the (001) plane of the hexagonal PbI_2, resulting in a quasiepitaxial growth of perovskite on the PbI_2.[47] Therefore, it is likely that a thin PbI_2 template layer may remain at the interface between SnO_2 and perovskite layers which assists the growth of (111) oriented FA-based perovskites. When the FA content is high, the reaction between PbI_2 and organic-halide salts is retarded because of the less reactivity of FA than MA. The conversion may not be completed, leaving some unreacted PbI_2 at the SnO_2/perovskite interface. The hypothesis is in good agreement with the XRD (Figure 2b) and SEM (Figure 1e,f) results of high FA content films. The XRD analysis (Figure S1a) shows a significant amount of PbI_2 phases (10−24%) in these films, while SEM reveals very limited PbI_2 on their top surfaces. The remaining PbI_2 at the bottom can passivate the perovskite interface but may hinder the charge collection.

Figure 2d shows the optical absorption spectra of mixed cation perovskite films. The absorption edge of the perovskite shows a redshift from 760 to ∼800 nm with increasing FA fraction from 0 to 1. The pure $FAPbI_3$ film (FA = 1.0) shows lower optical absorption than others, indicating an uncompleted perovskite conversion with poor crystal quality in the resulting perovskite film. In good agreement with the optical absorption, PL emission (Figure 2e) shows the same trend of band gap redshift with a higher FA fraction. To quantitatively analyze the carrier lifetime in different mixed cation perovskites, perovskite thin films were prepared directly on bare soda-lime glass substrates, and the TRPL data was acquired via the through-glass photoexcitation, as shown in Figure 2f. All the perovskite films show decent carrier lifetimes of more than

https://dx.doi.org/10.1021/acsami.9b23374
ACS Appl. Mater. Interfaces 2020, 12, 10588−10596

Approved for public release; distribution unlimited.

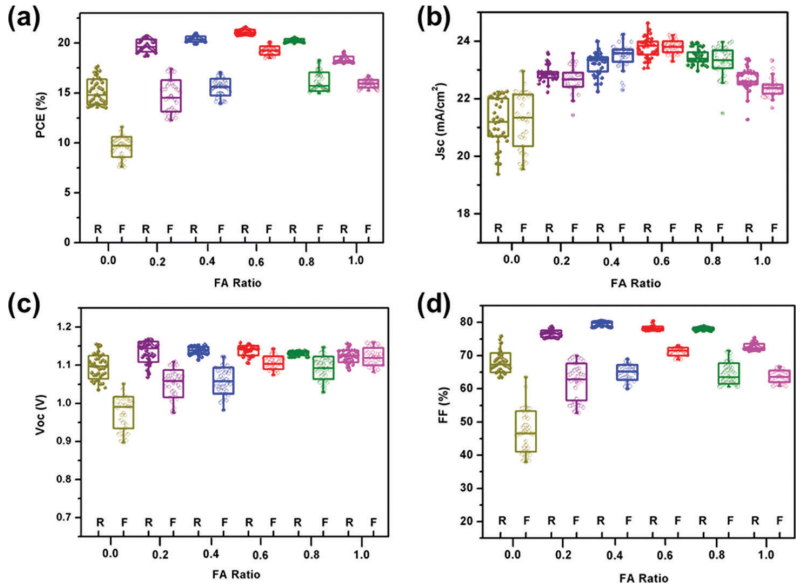


Figure 3. Statistical distributions of PV parameters including (a) PCE, (b) J_{SC}, (c) V_{OC}, and (d) FF for $FA_xMA_{1-x}PbI_3$ solar cells with different x values. R and F represent reverse and forward scans.

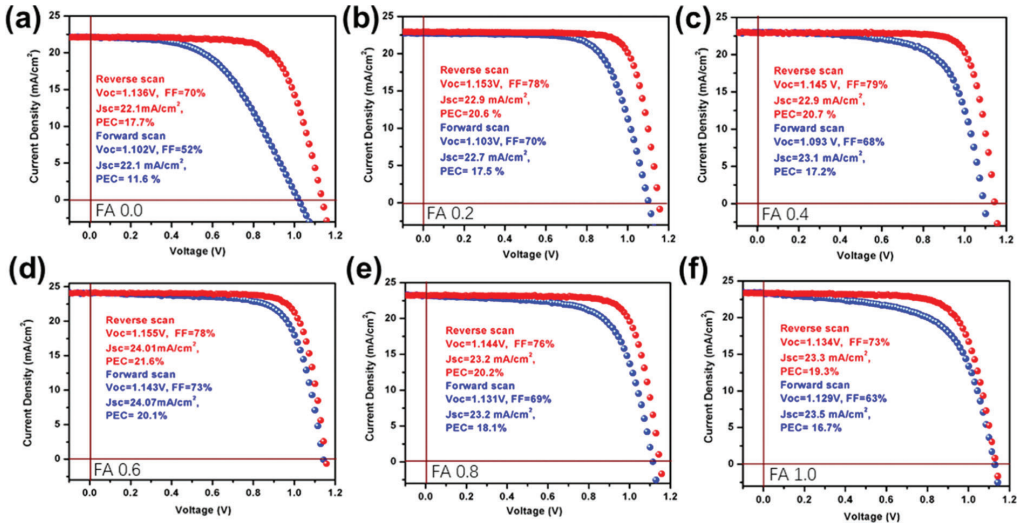


Figure 4. $J-V$ curves of $FA_xMA_{1-x}PbI_3$ solar cells with x = (a) 0.0, (b) 0.2, (c) 0.4, (d) 0.6, (e) 0.8, and (f) 1.0.

700 ns. Particularly, the FA-rich (FA > 0.5) perovskite films show longer lifetimes than MA-rich (FA < 0.5) samples, likely due to the remaining unreacted PbI_2 at the bottom of the perovskite films, which passivate the perovskite interfaces.

To evaluate the PV performance of PSCs based on different mixed-cation perovskite films, planar PSCs with the structure of glass/ITO/SnO_2/$FA_xMA_{1-x}PbI_3$/spiro-OMeTAD/Au were fabricated. The cross-sectional SEM images of PSCs with different FA fractions are shown in Figure S2. The average thickness of the perovskite absorber layer is estimated to be 700 nm. Figure 3 and Table S1 summarize the statistical distributions of PV parameters of more than 40 cells for each group, determined by light current density−voltage ($J-V$) curves under the standard AM1.5G illumination with reverse (R) or forward (F) voltage scan directions. The PCE (Figure 3a) increases first with increasing FA fraction from 0 to 0.6 and then decreases slightly as the FA fraction is further increased. The variations in J_{SC} and FF (Figure 3b,d) follow a similar trend as the changes in PCE. The J_{SC} values were confirmed by the external quantum efficiency (EQE) measurements, as shown in Figure S3. Notably, the EQE cutoffs at the long-wavelength side are consistent with the band gaps of the perovskite films determined by the absorption measurements (Figure 2d). In contrast to the variations in J_{SC} and FF, V_{OC}

https://dx.doi.org/10.1021/acsami.9b23374
ACS Appl. Mater. Interfaces 2020, 12, 10588−10596

Approved for public release; distribution unlimited.

from the reverse scan remains approximately constant except for the FA-free PSCs, while V_{OC} from the forward scan shows an almost monotonic increase with increasing the FA fraction. This higher V_{OC} indicates lower recombination in the FA-rich perovskites, which is likely attributed to the remaining PbI_2 in the films. It is noticeable that all the PSCs show pronounced hysteresis in PCEs, which is mainly caused by the differences in V_{OC} and FF. Particularly, the hysteresis gap in V_{OC} decreases with higher FA fraction, indicating more stable quasi-Fermi energy splitting at a forward bias voltage. This is likely due to better defect passivation in the FA-rich perovskite films, which is consistent with the longer carrier lifetime measured by TRPL (Figure 2f).

Figure 4 plots representative $J-V$ curves of mixed-cation PSCs with various FA fractions, showing two dissimilar hysteresis characteristics for different PSCs. The MA-rich PSCs (FA < 0.5) exhibit apparent V_{OC} shifts (Figure 4a–c). The higher the MA fraction, the larger the difference in the V_{OC} under the opposite scan directions. The V_{OC} shift is confirmed by the $J-V$ scans of corresponding devices in the dark (Figure S4), from which the dark saturation current density (J_0) can be calculated.[48] J_0 is a typical parameter depending on the recombination in a solar cell and is used as an indicator of the quality of the cell. The MA-rich (FA > 0.5) PSCs exhibit higher J_0 values under the forward scan than that under the reverse scan, indicating more severe recombination in the device when a forward voltage sweep is applied. Such voltage-sweep-induced recombination is likely related to the ion migration along the grain boundaries, which creates a significant amount of trap states.[45,49] MA-rich perovskites are prone to having a higher density of nonpassivated grain boundaries (Figure 5a), resulting in lower carrier lifetimes and

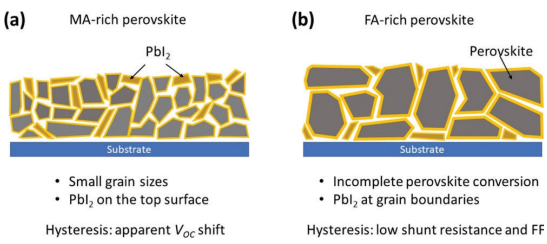


Figure 5. Schematic illustration of (a) MA- and (b) FA-rich perovskite films prepared by the two-step deposition method showing the impacts of microstructure on the $J-V$ hysteresis.

higher recombination rates. These nonradiative recombination centers can be filled when the device is positively biased, making a negligible impact on V_{OC} during a reverse voltage scan. However, when the device is under a forward scan, the unfilled trap states cause a high J_0, limiting the achievable V_{OC}. Particularly, the $MAPbI_3$ (FA = 0) cell shows the most severe hysteresis. The relatively small grains and possible organic residual on the top surface are likely the origins of the high hysteresis.

FA-rich (FA > 0.5) PSCs exhibit different hysteretic characteristics. The devices experience a small or negligible V_{OC} shift but a more remarkable Ohmic-like behavior at low biases (low shunt resistance, R_{Sh}) under the forward scan, resulting in lower FF than that of the reverse scan. The J_0 of FA-rich PSCs shows insignificant changes under different scan directions (Figure S4), indicating good passivation and long carrier lifetime in the bulk perovskite films. The high R_{Sh} is likely related to the unfavorable azimuth angle crystal growth in the (111) orientation[27] as well as the unreacted PbI_2 at the SnO_2/perovskite interface (Figure 5b), both resulting in an unfavorable energy barrier at the front interface. The positive biasing condition under the reverse scan can compensate for the barrier, resulting in a decent FF. In contrast, under the forward scan, the front barrier hinders the current extraction, resulting in lower photocurrent value at a positive voltage, and thereby lower FF.

Despite the high $J-V$ hysteresis index values (Table S1), PSCs with a wide range of FA fractions (FA = 0.2–0.8) show PCEs exceeding 20%. The best PCE of 21.6% (20.1%) under the reverse (forward) scan was achieved in a $FA_{0.6}MA_{0.4}PbI_3$ device, with a V_{OC} of 1.155 (1.143) V, a J_{SC} of 24.01 (24.07) mA/cm^2, and an FF of 78 (73) %, which also shows the lowest hysteresis value. The decent performance of this composition can be attributed to a combination of proper PbI_2 passivation and favorable crystal orientation, which results in low recombination and decent charge transport properties at the interfaces. Further improvement in the device performance and reduction of hysteresis relies on optimizing the interface between the perovskite absorber and the charge extraction layers. For instance, modification on the electron and hole transport layers has been shown as a practical approach to eliminate hysteresis and achieve high efficiency and stability.[50–54]

The stability of unencapsulated PSCs under maximum power point tracking (MPPT) was further investigated. Figure 6a shows the MPPT stability of one batch of mixed cation PSCs in dry nitrogen. The FA-rich (FA > 0.5) cells retained more than 90% of their initial PCEs after working continuously under one sun illumination for 500 h. PSCs with a high FA content (FA > 0.7) probably suffer from the excess of PbI_2, which may adversely affect the stability of perovskite. In

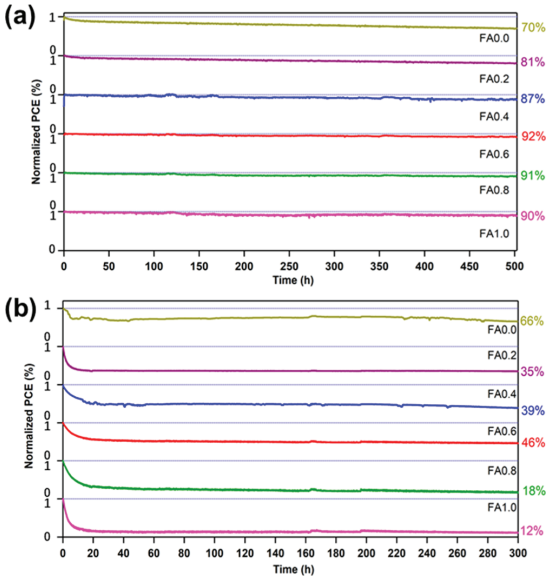


Figure 6. MPPT of unencapsulated $FA_xMA_{1-x}PbI_3$ solar cells under (a) dry nitrogen and (b) high relative humidity (>70%) conditions.

https://dx.doi.org/10.1021/acsami.9b23374
ACS Appl. Mater. Interfaces 2020, 12, 10588–10596

Approved for public release; distribution unlimited.

contrast to the relatively stable FA-rich PSCs, MA-rich (FA < 0.5) devices, especially the pure $MAPbI_3$ cell (FA = 0), show more pronounced performance degradation under continuous operation. The more severe degradation of MA-rich PSCs is likely due to the photoinstability of MA-contained perovskites.[55,56] Therefore, a proper FA fraction benefits the stability of the perovskite absorber layer. In this stability test, the best performing device based on the $FA_{0.6}MA_{0.4}PbI_3$ composition shows the best stability, retaining 92% of its initial PCE after 500 h.

It is known that metal-halide perovskites are vulnerable to moisture because of water-induced degradation.[57−59] To investigate the effect of organic-cation composition on the device stability against water, an MPPT test was performed on another batch of unencapsulated PSCs with various absorber compositions under high humid (relative humidity > 70%) ambient conditions (Figure 6b). All the PSCs show significant device degradation in the humid air. It is noticeable that FA-rich PSCs show more pronounced degradation than MA-rich cells because of water-catalyzed phase transformation from the black cubic (α) phase to the yellow nonperovskite (δ) phase.[60−62] The $MAPbI_3$ cell shows the highest remaining PCE among the group. However, the relatively lower initial PCE (13%) for the $MAPbI_3$ device compared to others (~20%) make the higher remaining PCE factor less remarkable. Considering the stability of PSCs in both dry and humid conditions, devices based on the $FA_{0.6}MA_{0.4}PbI_3$ composition still show the most robust stability. This result indicates that the perovskite films with too much excess PbI_2, either at the top or bottom interfaces, may accelerate the degradation of PSCs under high humidity conditions.

CONCLUSIONS

In summary, we explored the impact of FA and MA fractions on structural and optoelectronic properties of perovskite thin films prepared by two-step solution methods. The thin-film properties were correlated to the device performance of PSCs, including efficiency, $J-V$ hysteresis, and stability. We found discrepancies in $J-V$ hysteresis and stability for the PSCs based on FA-rich and MA-rich stoichiometries, which are attributed to the thermodynamically driven perovskite conversion with different combinations of organic cations. Additionally, PSCs with a composition of $FA_{0.6}MA_{0.4}PbI_3$ demonstrated the best PCE of over 21% and robust stability (retaining more than 90% of initial efficiency) under MPPT in dry nitrogen for more than 500 h.

EXPERIMENTAL SECTION

Materials. Acetone, used to clean the substrates, was purchased from Fisher Scientific. Tin(IV)oxide (15% in H_2O colloidal dispersion) was purchased from Alfa Aesar. Lead iodide (99.999%), spiro-OMeTAD (99%), bis(trifluoromethane)sulfonimide lithium salt (99.95%), FK102 Co(III) TFSI salt (98%), *N*,*N*-dimethylformamide (DMF, 99.8%), dimethyl sulfoxide (DMSO, 99.9%), isopropanol (IPA, 99.5%), chlorobenzene (99.8%), 4-*tert*-butylpyridine (98%), and acetonitrile (99.8%) were bought from Sigma-Aldrich. Formamidine iodide (FAI), methylammonium iodide (MAI), and methylammonium chloride (MACl) were bought from GreatCell Solar.

Preparation of Perovskite Precursor Solutions. The PbI_2 solution was prepared by dissolving 1.3 M PbI_2 in a mixed solvent of 950 μL DMF and 50 μL DMSO. The mixed organic-halide solution was prepared by dissolving FAI and MAI at a total concentration of 0.45 M in IPA solution. MACl additive with a concentration of 7 mg/mL was added to the organic-halide solution to assist the perovskite conversion. The molar ratio of FA to FA + MA was varied from 1, 0.8, 0.6, 0.4, 0.2 to 0, denoted as $FA_xMA_{1-x}PbI_3$. All the solutions were stirred on a hotplate at 60 °C for 3 h and filtered with a 0.45 μm PTFE filter before being used.

Solar Cell Device Fabrication. ITO substrates were sequentially cleaned with deionized water, acetone, and IPA in an ultrasonic bath and then dried with a nitrogen flow. The substrates were then treated with UV−ozone for 20 min. A diluted SnO_2 solution (SnO_2/deionized water = 1:6) was spin-coated on the substrates at 3000 rpm for 30 s and then annealed at 150 °C for 30 min in ambient air. After cooling down, the substrates were transferred to an N_2-filled glove box. The PbI_2 solution was spin-coated on the ITO/SnO_2 substrates at 2000 rpm for 30 s and annealed at 70 °C for 2 min. After that, the organic halide precursor solutions with different FAI/MAI ratios were spin-coated on the substrates at 2000 rpm for 30 s. All the substrates were then annealed at 150 °C for 15 min in the air with 30−40% relative humidity, except for $MAPbI_3$ that was annealed at 100 °C. The spiro-OMeTAD was spin-coated on perovskite layers at 3500 rpm for 60 s. Finally, 80 nm of gold was deposited by the thermal evaporation to complete the devices. The active area of 0.12 cm^2 was defined by the overlap area of the ITO and gold electrodes.

Characterization. SEM images were taken with a Hitachi S-4800 high-resolution field-emission microscope. Absorbance spectra of perovskite films were measured by employing an ultraviolet−visible (UV−vis) spectrophotometer (PerkinElmer LAMBDA 1050). X-ray diffraction (XRD) spectra were obtained by using a Rigaku D/MAX 2400 diffractometer with Cu Kα radiation. $J-V$ curves were measured by adopting a Keithley 2400 source meter under AM1.5G (100 mW/cm^2) illumination (PV Measurements Inc.). Photostability measurement was performed at room temperature in an environmental control box using a white LED light source calibrated to 100 mW/cm^2 light intensity with a silicon photodiode. EQE spectra from 300 to 860 nm were obtained with a QE system (PV Measurements Inc.). All the characterizations were measured under the ambient at room temperature.

ASSOCIATED CONTENT

Supporting Information

The Supporting Information is available free of charge at https://pubs.acs.org/doi/10.1021/acsami.9b23374.

XRD data analysis of perovskite films with different FA fractions, cross-sectional SEM images of PSCs with different FA fractions, EQE of PSCs with different FA fractions, dark $J-V$ analysis of PSCs with different FA fractions, and statistical distribution of PV parameters of 40 PSCs for each perovskite composition (PDF)

AUTHOR INFORMATION

Corresponding Authors

Zhaoning Song − *Wright Center for Photovoltaics Innovation and Commercialization, Department of Physics and Astronomy, University of Toledo, Toledo, Ohio 43606, United States;* orcid.org/0000-0002-6677-0994; Email: zhaoning.song@utoledo.edu

Yanfa Yan − *Wright Center for Photovoltaics Innovation and Commercialization, Department of Physics and Astronomy, University of Toledo, Toledo, Ohio 43606, United States;* orcid.org/0000-0003-3977-5789; Email: yanfa.yan@utoledo.edu

Authors

Yunkang Cui − *Wright Center for Photovoltaics Innovation and Commercialization, Department of Physics and Astronomy, University of Toledo, Toledo, Ohio 43606, United States;*

https://dx.doi.org/10.1021/acsami.9b23374
ACS Appl. Mater. Interfaces 2020, 12, 10588−10596

Approved for public release; distribution unlimited.

Department of Mathematics and Physics, Nanjing Institute of Technology, Nanjing 211167, China

Cong Chen − *Wright Center for Photovoltaics Innovation and Commercialization, Department of Physics and Astronomy, University of Toledo, Toledo, Ohio 43606, United States*

Chongwen Li − *Wright Center for Photovoltaics Innovation and Commercialization, Department of Physics and Astronomy, University of Toledo, Toledo, Ohio 43606, United States*

Lei Chen − *Wright Center for Photovoltaics Innovation and Commercialization, Department of Physics and Astronomy, University of Toledo, Toledo, Ohio 43606, United States*

Sandip Singh Bista − *Wright Center for Photovoltaics Innovation and Commercialization, Department of Physics and Astronomy, University of Toledo, Toledo, Ohio 43606, United States*

Xiangyang Liu − *Wright Center for Photovoltaics Innovation and Commercialization, Department of Physics and Astronomy, University of Toledo, Toledo, Ohio 43606, United States*

You Li − *Wright Center for Photovoltaics Innovation and Commercialization, Department of Physics and Astronomy, University of Toledo, Toledo, Ohio 43606, United States*

Rasha A. Awni − *Wright Center for Photovoltaics Innovation and Commercialization, Department of Physics and Astronomy, University of Toledo, Toledo, Ohio 43606, United States*

Complete contact information is available at: https://pubs.acs.org/10.1021/acsami.9b23374

Author Contributions

[§]Y.C. and C.C. contributed equally to this work.

Notes

The authors declare no competing financial interest.

■ ACKNOWLEDGMENTS

Y.C. and C.C. contributed equally to this work. Y.C. would like to acknowledge financial support by the National Natural Science Foundation of China (11804154, 11804155, and 61674029), Natural Science Foundation Project of Jiangsu Province (BK20191472), General Program of Natural Science Foundation of Jiangsu University (17KJD430003), and Fund of Nanjing Institute of Technology (CKJA201807). The work at the University of Toledo was supported by the Ohio Research Scholar Program, the Office of Naval Research under contract no. N00014-17-1-2223, the Air Force Research Laboratory. This publication is based on research sponsored by the Air Force Research Laboratory under agreement number FA9453-18-2-0037. The U.S. Government is authorized to reproduce and distribute reprints for Governmental purposes notwithstanding any copyright notation thereon. The views and conclusions contained herein are those of the authors and should not be interpreted as necessarily representing the official policies or endorsements, either expressed or implied, of the Air Force Research Laboratory or the U.S. Government.

■ REFERENCES

(1) Correa-Baena, J.-P.; Abate, A.; Saliba, M.; Tress, W.; Jesper Jacobsson, T.; Grätzel, M.; Hagfeldt, A. The Rapid Evolution of Highly Efficient Perovskite Solar Cells. *Energy Environ. Sci.* **2017**, *10*, 710−727.

(2) Jena, A. K.; Kulkarni, A.; Miyasaka, T. Halide Perovskite Photovoltaics: Background, Status, and Future Prospects. *Chem. Rev.* **2019**, *119*, 3036−3103.

(3) Huang, J.; Yuan, Y.; Shao, Y.; Yan, Y. Understanding the Physical Properties of Hybrid Perovskites for Photovoltaic Applications. *Nat. Rev. Mater.* **2017**, *2*, 17042.

(4) Brenner, T. M.; Egger, D. A.; Kronik, L.; Hodes, G.; Cahen, D. Hybrid Organic—Inorganic Perovskites: Low-Cost Semiconductors with Intriguing Charge-Transport Properties. *Nat. Rev. Mater.* **2016**, *1*, 15007.

(5) NREL Solar Cell Efficiency Chart. https://www.nrel.gov/pv/cell-efficiency.html (accessed February 3, 2020).

(6) Song, Z.; McElvany, C. L.; Phillips, A. B.; Celik, I.; Krantz, P. W.; Watthage, S. C.; Liyanage, G. K.; Apul, D.; Heben, M. J. A Technoeconomic Analysis of Perovskite Solar Module Manufacturing with Low-Cost Materials and Techniques. *Energy Environ. Sci.* **2017**, *10*, 1297−1305.

(7) Correa-Baena, J.-P.; Saliba, M.; Buonassisi, T.; Grätzel, M.; Abate, A.; Tress, W.; Hagfeldt, A. Promises and Challenges of Perovskite Solar Cells. *Science* **2017**, *358*, 739−744.

(8) Huang, F.; Li, M.; Siffalovic, P.; Cao, G.; Tian, J. From Scalable Solution Fabrication of Perovskite Films Towards Commercialization of Solar Cells. *Energy Environ. Sci.* **2019**, *12*, 518−549.

(9) Rong, Y.; Hu, Y.; Mei, A.; Tan, H.; Saidaminov, M. I.; Seok, S. I.; McGehee, M. D.; Sargent, E. H.; Han, H. Challenges for Commercializing Perovskite Solar Cells. *Science* **2018**, *361*, No. eaat8235.

(10) Qiu, L.; Ono, L. K.; Qi, Y. Advances and Challenges to the Commercialization of Organic−Inorganic Halide Perovskite Solar Cell Technology. *Mater. Today Energy* **2018**, *7*, 169−189.

(11) Park, N.-G.; Grätzel, M.; Miyasaka, T.; Zhu, K.; Emery, K. Towards Stable and Commercially Available Perovskite Solar Cells. *Nat. Energy* **2016**, *1*, 16152.

(12) Li, Z.; Klein, T. R.; Kim, D. H.; Yang, M.; Berry, J. J.; van Hest, M. F. A. M.; Zhu, K. Scalable Fabrication of Perovskite Solar Cells. *Nat. Rev. Mater.* **2018**, *3*, 18017.

(13) Min, H.; Kim, M.; Lee, S.-U.; Kim, H.; Kim, G.; Choi, K.; Lee, J. H.; Seok, S. I. Efficient, Stable Solar Cells by Using Inherent Bandgap of A-Phase Formamidinium Lead Iodide. *Science* **2019**, *366*, 749−753.

(14) Wang, Y.; Wu, T.; Barbaud, J.; Kong, W.; Cui, D.; Chen, H.; Yang, X.; Han, L. Stabilizing Heterostructures of Soft Perovskite Semiconductors. *Science* **2019**, *365*, 687−691.

(15) Yang, S.; Chen, S.; Mosconi, E.; Fang, Y.; Xiao, X.; Wang, C.; Zhou, Y.; Yu, Z.; Zhao, J.; Gao, Y.; De Angelis, F.; Huang, J. Stabilizing Halide Perovskite Surfaces for Solar Cell Operation with Wide-Bandgap Lead Oxysalts. *Science* **2019**, *365*, 473−478.

(16) Bai, S.; Da, P.; Li, C.; Wang, Z.; Yuan, Z.; Fu, F.; Kawecki, M.; Liu, X.; Sakai, N.; Wang, J. T.-W.; Huettner, S.; Buecheler, S.; Fahlman, M.; Gao, F.; Snaith, H. J. Planar Perovskite Solar Cells with Long-Term Stability Using Ionic Liquid Additives. *Nature* **2019**, *571*, 245−250.

(17) Yang, W. S.; Noh, J. H.; Jeon, N. J.; Kim, Y. C.; Ryu, S.; Seo, J.; Seok, S. I. High-Performance Photovoltaic Perovskite Layers Fabricated through Intramolecular Exchange. *Science* **2015**, *348*, 1234−1237.

(18) Zheng, X.; Chen, B.; Dai, J.; Fang, Y.; Bai, Y.; Lin, Y.; Wei, H.; Zeng, X. C.; Huang, J. Defect Passivation in Hybrid Perovskite Solar Cells Using Quaternary Ammonium Halide Anions and Cations. *Nat. Energy* **2017**, *2*, 17102.

(19) Yang, W. S.; Park, B.-W.; Jung, E. H.; Jeon, N. J.; Kim, Y. C.; Lee, D. U.; Shin, S. S.; Seo, J.; Kim, E. K.; Noh, J. H.; Seok, S. I. Iodide Management in Formamidinium-Lead-Halide−Based Perovskite Layers for Efficient Solar Cells. *Science* **2017**, *356*, 1376−1379.

(20) Jiang, Q.; Zhang, L.; Wang, H.; Yang, X.; Meng, J.; Liu, H.; Yin, Z.; Wu, J.; Zhang, X.; You, J. Enhanced Electron Extraction Using SnO_2 for High-Efficiency Planar-Structure $HC(NH_2)_2PbI_3$-Based Perovskite Solar Cells. *Nat. Energy* **2016**, *2*, 16177.

(21) Jiang, Q.; Zhao, Y.; Zhang, X.; Yang, X.; Chen, Y.; Chu, Z.; Ye, Q.; Li, X.; Yin, Z.; You, J. Surface Passivation of Perovskite Film for Efficient Solar Cells. *Nat. Photon.* **2019**, *13*, 460−466.

Approved for public release; distribution unlimited.

(22) Liang, K.; Mitzi, D. B.; Prikas, M. T. Synthesis and Characterization of Organic-Inorganic Perovskite Thin Films Prepared Using a Versatile Two-Step Dipping Technique. *Chem. Mater.* **1998**, *10*, 403−411.
(23) Burschka, J.; Pellet, N.; Moon, S.-J.; Humphry-Baker, R.; Gao, P.; Nazeeruddin, M. K.; Grätzel, M. Sequential Deposition as a Route to High-Performance Perovskite-Sensitized Solar Cells. *Nature* **2013**, *499*, 316−319.
(24) Zhang, F.; Xiao, C.; Chen, X.; Larson, B. W.; Harvey, S. P.; Berry, J. J.; Zhu, K. Self-Seeding Growth for Perovskite Solar Cells with Enhanced Stability. *Joule* **2019**, *3*, 1452−1463.
(25) Zhang, F.; Bi, D.; Pellet, N.; Xiao, C.; Li, Z.; Berry, J. J.; Zakeeruddin, S. M.; Zhu, K.; Grätzel, M. Suppressing Defects through the Synergistic Effect of a Lewis Base and a Lewis Acid for Highly Efficient and Stable Perovskite Solar Cells. *Energy Environ. Sci.* **2018**, *11*, 3480−3490.
(26) Zhang, F.; Shi, W.; Luo, J.; Pellet, N.; Yi, C.; Li, X.; Zhao, X.; Dennis, T. J. S.; Li, X.; Wang, S.; Xiao, Y.; Zakeeruddin, S. M.; Bi, D.; Grätzel, M. Isomer-Pure Bis-Pcbm-Assisted Crystal Engineering of Perovskite Solar Cells Showing Excellent Efficiency and Stability. *Adv. Mater.* **2017**, *29*, 1606806.
(27) Xu, Z.; Liu, Z.; Li, N.; Tang, G.; Zheng, G.; Zhu, C.; Chen, Y.; Wang, L.; Huang, Y.; Li, L.; Zhou, N.; Hong, J.; Chen, Q.; Zhou, H. A Thermodynamically Favored Crystal Orientation in Mixed Formamidinium/Methylammonium Perovskite for Efficient Solar Cells. *Adv. Mater.* **2019**, *131*, 1900390.
(28) Liu, T.; Lai, H.; Wan, X.; Zhang, X.; Liu, Y.; Chen, Y. Cesium Halides-Assisted Crystal Growth of Perovskite Films for Efficient Planar Heterojunction Solar Cells. *Chem. Mater.* **2018**, *30*, 5264−5271.
(29) Li, Q.; Zhao, Y.; Fu, R.; Zhou, W.; Zhao, Y.; Liu, X.; Yu, D.; Zhao, Q. Efficient Perovskite Solar Cells Fabricated through CsCl-Enhanced PbI_2 Precursor Via Sequential Deposition. *Adv. Mater.* **2018**, *30*, 1803095.
(30) Yi, X.; Zhang, Z.; Chang, A.; Mao, Y.; Luan, Y.; Lin, T.; Wei, Y.; Zhang, Y.; Wang, F.; Cao, S.; Li, C.; Wang, J. Incorporating CsF into the PbI_2 Film for Stable Mixed Cation-Halide Perovskite Solar Cells. *Adv. Energy Mater.* **2019**, *9*, 1901726.
(31) Zhao, Y.; Tan, H.; Yuan, H.; Yang, Z.; Fan, J. Z.; Kim, J.; Voznyy, O.; Gong, X.; Quan, L. N.; Tan, C. S.; Hofkens, J.; Yu, D.; Zhao, Q.; Sargent, E. H. Perovskite Seeding Growth of Formamidinium-Lead-Iodide-Based Perovskites for Efficient and Stable Solar Cells. *Nat. Commun.* **2018**, *9*, 1607.
(32) Li, Q.; Zhao, Y.; Zhou, W.; Han, Z.; Fu, R.; Lin, F.; Yu, D.; Zhao, Q. Halogen Engineering for Operationally Stable Perovskite Solar Cells Via Sequential Deposition. *Adv. Energy Mater.* **2019**, *9*, 1902239.
(33) Im, J.-H.; Jang, I.-H.; Pellet, N.; Grätzel, M.; Park, N.-G. Growth of $CH_3NH_3PbI_3$ Cuboids with Controlled Size for High-Efficiency Perovskite Solar Cells. *Nat. Nanotechnol.* **2014**, *9*, 927−932.
(34) Sun, M.; Liang, C.; Zhang, H.; Ji, C.; Sun, F.; You, F.; Jing, X.; He, Z. Tailoring a Dynamic Crystalline Process During the Conversion of Lead-Halide Perovskite Layer to Achieve High Performance Solar Cells. *J. Mater. Chem. A* **2018**, *6*, 24793−24804.
(35) Jiang, Q.; Chu, Z.; Wang, P.; Yang, X.; Liu, H.; Wang, Y.; Yin, Z.; Wu, J.; Zhang, X.; You, J. Planar-Structure Perovskite Solar Cells with Efficiency Beyond 21%. *Adv. Mater.* **2017**, *29*, 1703852.
(36) Meng, L.; Sun, C.; Wang, R.; Huang, W.; Zhao, Z.; Sun, P.; Huang, T.; Xue, J.; Lee, J. W.; Zhu, C.; Huang, Y.; Li, Y.; Yang, Y. Tailored Phase Conversion under Conjugated Polymer Enables Thermally Stable Perovskite Solar Cells with Efficiency Exceeding 21%. *J. Am. Chem. Soc.* **2018**, *140*, 17255−17262.
(37) Li, Z.; Yang, M.; Park, J.-S.; Wei, S.-H.; Berry, J. J.; Zhu, K. Stabilizing Perovskite Structures by Tuning Tolerance Factor: Formation of Formamidinium and Cesium Lead Iodide Solid-State Alloys. *Chem. Mater.* **2016**, *28*, 284−292.
(38) Song, Z.; Watthage, S. C.; Phillips, A. B.; Tompkins, B. L.; Ellingson, R. J.; Heben, M. J. Impact of Processing Temperature and Composition on the Formation of Methylammonium Lead Iodide Perovskites. *Chem. Mater.* **2015**, *27*, 4612−4619.
(39) Juarez-Perez, E. J.; Hawash, Z.; Raga, S. R.; Ono, L. K.; Qi, Y. Thermal Degradation of $CH_3NH_3PbI_3$ Perovskite into NH_3 and CH_3I Gases Observed by Coupled Thermogravimetry-Mass Spectrometry Analysis. *Energy Environ. Sci.* **2016**, *9*, 3406−3410.
(40) Jacobsson, T. J.; Correa-Baena, J.-P.; Halvani Anaraki, E.; Philippe, B.; Stranks, S. D.; Bouduban, M. E. F.; Tress, W.; Schenk, K.; Teuscher, J.; Moser, J.-E.; Rensmo, H.; Hagfeldt, A. Unreacted PbI_2 as a Double-Edged Sword for Enhancing the Performance of Perovskite Solar Cells. *J. Am. Chem. Soc.* **2016**, *138*, 10331−10343.
(41) Euvrard, J.; Gunawan, O.; Mitzi, D. B. Impact of PbI_2 Passivation and Grain Size Engineering in $CH_3NH_3PbI_3$ Solar Absorbers as Revealed by Carrier-Resolved Photo-Hall Technique. *Adv. Energy Mater.* **2019**, *9*, 1902706.
(42) Chen, Y.; Meng, Q.; Xiao, Y.; Zhang, X.; Sun, J.; Han, C. B.; Gao, H.; Zhang, Y.; Lu, Y.; Yan, H. Mechanism of PbI_2 in Situ Passivated Perovskite Films for Enhancing the Performance of Perovskite Solar Cells. *ACS Appl. Mater. Interfaces* **2019**, *11*, 44101−44108.
(43) Baikie, T.; Fang, Y.; Kadro, J. M.; Schreyer, M.; Wei, F.; Mhaisalkar, S. G.; Graetzel, M.; White, T. J. Synthesis and Crystal Chemistry of the Hybrid Perovskite (CH_3NH_3) PbI_3 for Solid-State Sensitised Solar Cell Applications. *J. Mater. Chem. A* **2013**, *1*, 5628−5641.
(44) Zhang, Y.; Zhou, Z.; Ji, F.; Li, Z.; Cui, G.; Gao, P.; Oveisi, E.; Nazeeruddin, M. K.; Pang, S. Trash into Treasure: δ-$FAPbI_3$ Polymorph Stabilized $MAPbI_3$ Perovskite with Power Conversion Efficiency Beyond 21%. *Adv. Mater.* **2018**, *30*, 1707143.
(45) Chen, B.; Rudd, P. N.; Yang, S.; Yuan, Y.; Huang, J. Imperfections and Their Passivation in Halide Perovskite Solar Cells. *Chem. Soc. Rev.* **2019**, *48*, 3842−3867.
(46) Meng, K.; Wang, X.; Xu, Q.; Li, Z.; Liu, Z.; Wu, L.; Hu, Y.; Liu, N.; Chen, G. In Situ Observation of Crystallization Dynamics and Grain Orientation in Sequential Deposition of Metal Halide Perovskites. *Adv. Funct. Mater.* **2019**, *29*, 1902319.
(47) Watthage, S. C.; Song, Z.; Shrestha, N.; Phillips, A. B.; Liyanage, G. K.; Roland, P. J.; Ellingson, R. J.; Heben, M. J. Enhanced Grain Size, Photoluminescence, and Photoconversion Efficiency with Cadmium Addition During the Two-Step Growth of $CH_3NH_3PbI_3$. *ACS Appl. Mater. Interfaces* **2017**, *9*, 2334−2341.
(48) Li, C.; Song, Z.; Zhao, D.; Xiao, C.; Subedi, B.; Shrestha, N.; Junda, M. M.; Wang, C.; Jiang, C.-S.; Al-Jassim, M.; Ellingson, R. J.; Podraza, N. J.; Zhu, K.; Yan, Y. Reducing Saturation-Current Density to Realize High-Efficiency Low-Bandgap Mixed Tin−Lead Halide Perovskite Solar Cells. *Adv. Energy Mater.* **2019**, *9*, 1803135.
(49) Miyano, K.; Yanagida, M.; Tripathi, N.; Shirai, Y. Hysteresis, Stability, and Ion Migration in Lead Halide Perovskite Photovoltaics. *J. Phys. Chem. Lett.* **2016**, *7*, 2240−2245.
(50) Yang, D.; Yang, R.; Wang, K.; Wu, C.; Zhu, X.; Feng, J.; Ren, X.; Fang, G.; Priya, S.; Liu, S. High Efficiency Planar-Type Perovskite Solar Cells with Negligible Hysteresis Using Edta-Complexed SnO_2. *Nat. Commun.* **2018**, *9*, 3239.
(51) Yang, D.; Yang, R.; Ren, X.; Zhu, X.; Yang, Z.; Li, C.; Liu, S. F. Hysteresis-Suppressed High-Efficiency Flexible Perovskite Solar Cells Using Solid-State Ionic-Liquids for Effective Electron Transport. *Adv. Mater.* **2016**, *28*, 5206−5213.
(52) Wang, C.; Xiao, C.; Yu, Y.; Zhao, D.; Awni, R. A.; Grice, C. R.; Ghimire, K.; Constantinou, I.; Liao, W.; Cimaroli, A. J.; Liu, P.; Chen, J.; Podraza, N. J.; Jiang, C.-S.; Al-Jassim, M. M.; Zhao, X.; Yan, Y. Understanding and Eliminating Hysteresis for Highly Efficient Planar Perovskite Solar Cells. *Adv. Energy Mater.* **2017**, *7*, 1700414.
(53) Yang, Y.; Pham, N. D.; Yao, D.; Fan, L.; Hoang, M. T.; Tiong, V. T.; Wang, Z.; Zhu, H.; Wang, H. Interface Engineering to Eliminate Hysteresis of Carbon-Based Planar Heterojunction Perovskite Solar Cells Via CuSCN Incorporation. *ACS Appl. Mater. Interfaces* **2019**, *11*, 28431−28441.
(54) Shao, Y.; Xiao, Z.; Bi, C.; Yuan, Y.; Huang, J. Origin and Elimination of Photocurrent Hysteresis by Fullerene Passivation in

https://dx.doi.org/10.1021/acsami.9b23374
ACS Appl. Mater. Interfaces 2020, 12, 10588−10596

Approved for public release; distribution unlimited.

$CH_3NH_3PbI_3$ Planar Heterojunction Solar Cells. *Nat. Commun.* **2014**, *5*, 6784.
(55) Song, Z.; Wang, C.; Phillips, A. B.; Grice, C. R.; Zhao, D.; Yu, Y.; Chen, C.; Li, C.; Yin, X.; Ellingson, R. J.; Heben, M. J.; Yan, Y. Probing the Origins of Photodegradation in Organic-Inorganic Metal Halide Perovskites with Time-Resolved Mass Spectrometry. *Sustainable Energy Fuels* **2018**, *2*, 2460−2467.
(56) Juarez-Perez, E. J.; Ono, L. K.; Maeda, M.; Jiang, Y.; Hawash, Z.; Qi, Y. Photodecomposition and Thermal Decomposition in Methylammonium Halide Lead Perovskites and Inferred Design Principles to Increase Photovoltaic Device Stability. *J. Mater. Chem. A* **2018**, *6*, 9604−9612.
(57) Song, Z.; Abate, A.; Watthage, S. C.; Liyanage, G. K.; Phillips, A. B.; Steiner, U.; Graetzel, M.; Heben, M. J. Perovskite Solar Cell Stability in Humid Air: Partially Reversible Phase Transitions in the PbI_2-CH_3NH_3I-H_2O System. *Adv. Energy Mater.* **2016**, *6*, 1600846.
(58) Song, Z.; Shrestha, N.; Watthage, S. C.; Liyanage, G. K.; Almutawah, Z. S.; Ahangharnejhad, R. H.; Phillips, A. B.; Ellingson, R. J.; Heben, M. J. Impact of Moisture on Photoexcited Charge Carrier Dynamics in Methylammonium Lead Halide Perovskites. *J. Phys. Chem. Lett.* **2018**, *9*, 6312−6320.
(59) Huang, J.; Tan, S.; Lund, P. D.; Zhou, H. Impact of H_2O on Organic-Inorganic Hybrid Perovskite Solar Cells. *Energy Environ. Sci.* **2017**, *10*, 2284−2311.
(60) Yun, J. S.; Kim, J.; Young, T.; Patterson, R. J.; Kim, D.; Seidel, J.; Lim, S.; Green, M. A.; Huang, S.; Ho-Baillie, A. Humidity-Induced Degradation Via Grain Boundaries of $HC(NH_2)_2PbI_3$ Planar Perovskite Solar Cells. *Adv. Funct. Mater.* **2018**, *28*, 1705363.
(61) Boyd, C. C.; Cheacharoen, R.; Leijtens, T.; McGehee, M. D. Understanding Degradation Mechanisms and Improving Stability of Perovskite Photovoltaics. *Chem. Rev.* **2019**, *119*, 3418−3451.
(62) Cordero, F.; Craciun, F.; Trequattrini, F.; Generosi, A.; Paci, B.; Paoletti, A. M.; Pennesi, G. Stability of Cubic $FAPbI_3$ from X-Ray Diffraction, Anelastic, and Dielectric Measurements. *J. Phys. Chem. Lett.* **2019**, *10*, 2463−2469.

https://dx.doi.org/10.1021/acsami.9b23374
ACS Appl. Mater. Interfaces 2020, 12, 10588−10596

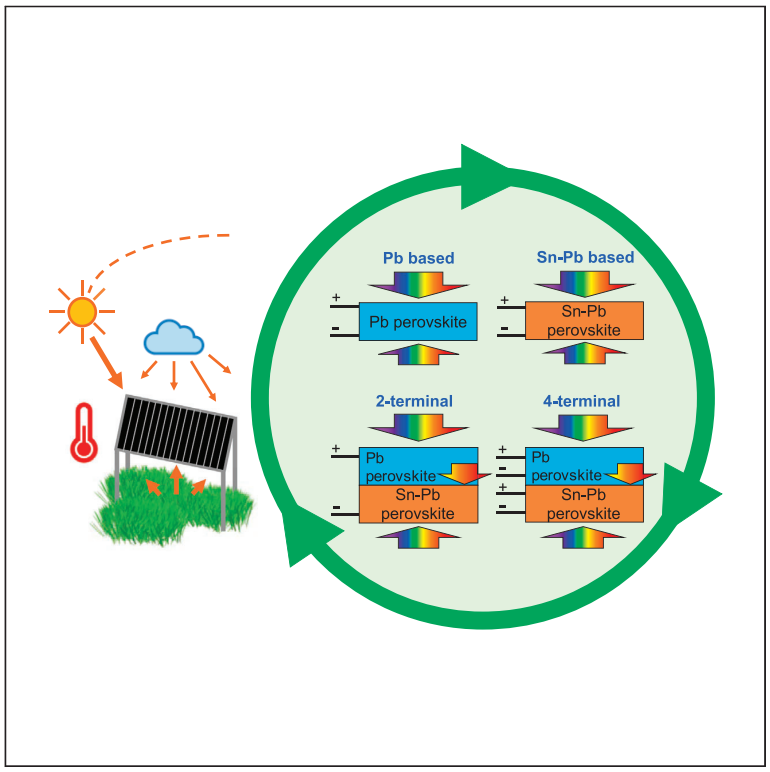
Approved for public release; distribution unlimited.

Cell Reports
Physical Science

CellPress
OPEN ACCESS

Article

Environmental Impact per Energy Yield for Bifacial Perovskite Solar Cells Outperforms Crystalline Silicon Solar Cells



Ahangharnejhad et al. report the environmental impact of energy from bifacial perovskite photovoltaic devices in single- and multi-junction configurations. The expected annual energy yield values determined via a real-world model are coupled to life cycle assessments of cradle-to-end-of-use to evaluate the impact per energy.

Ramez Hosseinian Ahangharnejhad, Willis Becker, Jayson Jones, ..., Adam Phillips, Michael J. Heben, Ilke Celik

ilke.celik@sdsmt.edu

HIGHLIGHTS

Environmental impacts of energy generated from bifacial perovskite PV cells are studied

A realistic energy yield (EY) model for bifacial PV is developed

The studied bifacial structures show 9%–26% EY increase compared with monofacial cells

Environmental impact of studied PVs can outperform c-Si cells in providing electricity

Hosseinian Ahangharnejhad et al., Cell Reports Physical Science 1, 100216
October 21, 2020 © 2020 The Authors.
https://doi.org/10.1016/j.xcrp.2020.100216

Approved for public release; distribution unlimited.

Cell Reports
Physical Science

CellPress
OPEN ACCESS

Article

Environmental Impact per Energy Yield for Bifacial Perovskite Solar Cells Outperforms Crystalline Silicon Solar Cells

Ramez Hosseinian Ahangharnejhad,[1] Willis Becker,[2] Jayson Jones,[3] Annick Anctil,[4] Zhaoning Song,[1] Adam Phillips,[1] Michael J. Heben,[1] and Ilke Celik[5,6,*]

SUMMARY

A promising technology for the future of solar energy is the highly efficient bifacial photovoltaic (PV) cell using perovskite as an absorbing layer. Here we report the environmental impact per energy generated from bifacial perovskite PV cells in single- and multi-junction configurations. To determine the environmental performance of the energy provided from bifacial perovskites and compare it with the analogous monofacial structures, we develop a realistic energy yield (EY) model. According to our model, the studied bifacial structures show between 9% and 26% EY increase compared with monofacial cells among all surfaces and locations studied. For the environmental impact analysis, we use normalized cradle-to-end-of-use impact from single-junction crystalline silicon (c-Si) solar cells as a reference point. Our results show that there are opportunities for all studied bifacial perovskite PV structures to become more environmentally friendly than c-Si cells.

INTRODUCTION

High energy generation per area of photovoltaic (PV) modules is becoming increasingly important because of growing energy demands. A way to allow higher carrier generation and, thus, improved power generation per area is to fabricate a bifacial PV device with junctions and transparent contacts in both sides to make use of illumination from sky and ground reflection.[1] The idea of bifacial solar cells was first explored in the context of concentrator systems.[2] Since then, different concepts on fabrication and deployment of bifacial devices have been investigated,[3–7] whereas, for commercial use of bifacial PVs an ~22% improvement in generated power compared with monofacial plants has been shown for utility-scale deployment.[8] Because of this potential, the interest in deployment of bifacial solar cells has been increasing, and, according to estimates, bifacial cells are expected to reach about 40% of the market by 2028.[9] Therefore, analysis of bifacial structures of emerging materials and configurations is critical to determine the prevailing approach for future PV deployment.

Perovskite solar cells have emerged as a promising PV technology, demonstrating high power conversion efficiencies (PCEs) (above 25%) in nearly one decade since their discovery.[10,11] The facile adjustment of bandgaps via chemical composition allows fabrication of devices with excellent performance in single and tandem junction configurations.[12] Moreover, the environmental impact and cost of fabrication and operation are expected to be significantly lower than market-dominant technologies such as crystalline silicon (c-Si) per unit area of module.[13–16] Additionally, unlike

[1]Department of Physics, University of Toledo, Toledo, OH, USA

[2]Department of Mechanical Engineering, University of Wisconsin – Platteville, Platteville, WI, USA

[3]Department of Environmental Engineering, University of Wisconsin – Platteville, Platteville, WI, USA

[4]Department of Civil and Environmental Engineering, Michigan State University, East Lansing, MI, USA

[5]Department of Civil and Environmental Engineering, South Dakota School of Mines and Technology, Rapid City, SD, USA

[6]Lead Contact

*Correspondence: ilke.celik@sdsmt.edu

https://doi.org/10.1016/j.xcrp.2020.100216

This is an open access article under the CC BY-NC-ND license (http://creativecommons.org/licenses/by-nc-nd/4.0/).

Approved for public release; distribution unlimited.
540

comparable commercially available thin-film technologies such as CdTe[17,18] and $Cu(InGa)Se_2$,[19] which are typically confined to a particular manufacturing order, perovskite PV devices can be fabricated in different configurations so that light can be readily introduced into the p-type or the n-type contact. Therefore, similar to c-Si PVs, a bifacial configuration can be easily implemented. Consequently, multiple studies have been performed to analyze the optimal performance of perovskite-based bifacial single junction and tandem devices.[20–24] It has been shown that the wavelength-dependent albedo of the ground surface significantly affects the devices' performance.[22,24–26] For instance, although light reflection on snow is relatively higher in the shorter-wavelength end of the spectrum, for grass, the infrared portion of the spectrum is almost five times higher than the UV-visible range.[24] Therefore, although real-world energy generation of any PV device depends on the spectral solar irradiance, spectral albedo and the reflected solar irradiance are critical to the performance of bifacial devices.

Despite the clear interest in developing bifacial PVs, the environmental impact of these devices has mainly been ignored. To date, there is only one life cycle assessment (LCA) study of bifacial devices, and it only focused on bifacial design of c-Si PV technology.[27] This study assumes that bifacial cells could produce ~15% more electricity compared with monofacial devices and ignores the effects of different albedos and deployment location. Further studies are needed to encompass perovskite material that may enable low-cost energy production for the future energy market with single-junction and tandem configurations. To provide an accurate estimate of the environmental impact of bifacial PVs, the analysis needs to be coupled with realistic energy yield (EY) calculations that consider different ground surface albedos for where the module is installed. Such an approach would resolve the important question of whether manufacturing and electricity generation from bifacial perovskite PVs are environmentally preferable to monofacial perovskites and market-dominant c-Si PV technologies.

In this work, we evaluate the environmental impact of single-junction bifacial perovskite devices with high and low bandgaps (PK_{Pb} and $PK_{Sn\text{-}Pb}$) and multi-junction configuration with two-terminal (2T) and four-terminal (4T) structures (shown in Figure 1) to address the gap in the literature. To accurately analyze the environmental impact per energy generated from bifacial perovskite PVs, it is critical to quantify the life cycle energy production from these PVs under real-world conditions.[28–33] We first develop a realistic EY model using different albedos corresponding to various surfaces (sandstone, concrete, grass, and snow). In our model, we use the most advanced hourly solar irradiance data available[34,35] coupled with the hourly module temperature to determine the power generated by the device throughout the hours of the year. We evaluate the environmental impact of bifacial perovskite PV technology and compare it with the monofacial counterpart. To more clearly interpret the results, we present the environmental impact after normalizing it to market dominant c-Si PV technology, which is currently the PV technology with the highest environmental performance among commercial PV devices. We also discuss the relative importance of different PV components and assessed alternative materials for high-impact layers. Last, we calculate the energy payback time of bifacial perovskite PVs in single-junction and tandem structures to evaluate their energy performance as well as environmental performance.

We report that bifacial PV cells on all surfaces and with all structures show an average ~17% increase in EY compared with monofacial PV cells at the same location; the highest increase in is seen in the 4T structure with snow as the ground (~75%).

Approved for public release; distribution unlimited.
541

CellPress
OPEN ACCESS

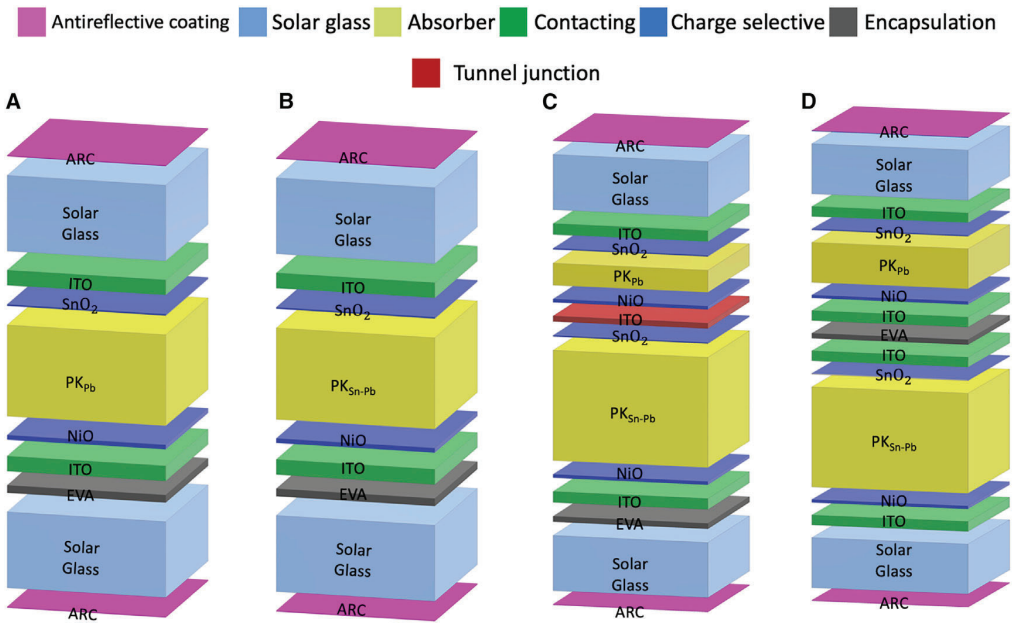


Figure 1. Structures of Solar Cells

(A–D) Structures of bifacial single-junction PK_{Pb} (A), single-junction $PK_{Sn\text{-}Pb}$ (B), 2T tandem (C), and 4T tandem (D) structures. The color coding indicates anti-reflective coating (ARC), encapsulation ethylene-vinyl acetate (EVA), glass, contacting layer, selective layer, absorber, and tunnel junction layers. The thicknesses of the following layers is consistent within the structure: ARC, 100 nm; solar glass, 3 mm; contacting ITO, 200 nm; charge-selective SnO_2, 20 nm; charge-selective NiO, 60 nm; encapsulating EVA, 0.5 mm. The thickness of the PK_{Pb} absorber is 1,200 nm, 400 nm, and 800 nm in single-junction PK_{Pb} (A), 2T tandem (C), and 4T tandem (D) structures, respectively, whereas the thickness of the $PK_{Sn\text{-}Pb}$ absorber (a mixture of Sn and Pb) is 1,200 nm, 2,000 nm, and 2,000 nm in single-junction $PK_{Sn\text{-}Pb}$ (B), 2T tandem (C), and 4T tandem (D) structures, respectively.

The environmental impact analysis of bifacial PVs shows that only single-junction lead-based bifacial cells are more environmentally friendly than c-Si PV cells for manufacturing 1 m^2 of active area. However, by improving the material content (e.g., replacing indium-doped tin oxide [ITO]-based transparent conductive oxides with Al:ZnO [AZO]), we see that there are opportunities for all studied bifacial PVs to be more environmentally friendly (~30%–77%) than c-Si cells in providing electricity. The energy payback time and carbon footprint metrics of bifacial PVs are found to be 1–1.5 months and 11–15 g $CO_{2\text{-Equivalent(Equiv.)}}$/kilowatt hour (kWh), respectively.

RESULTS AND DISCUSSION

EYs

Figure 2 shows the annual EYs of monofacial and bifacial PV panels deployed in Toledo, Ohio and Golden, Colorado (Figures 2A and 2B). Our results show that the bifacial PV cells located in Golden generate ~58% more energy than those deployed in Toledo, whereas the monofacial panels generate ~66% more energy. The higher EYs in Golden are primarily due to the higher solar insolation values in this location. According to the National Renewable Energy Laboratory (NREL) physical solar model (PSM), the annual average daily global horizontal irradiance and direct normal irradiance (DNI) in Golden is ~5.5 and ~5.5 kWh/m^2, respectively; for Toledo, these values are ~4 and ~4.5 kWh/m^2, respectively.[36] In addition to the significant difference in solar insolation, Toledo is located at a relatively higher latitude compared with Golden; therefore, the solar azimuthal path is longer throughout the day in Toledo. This leads to higher angles of incident light for the DNI, which has an

Approved for public release; distribution unlimited.
542

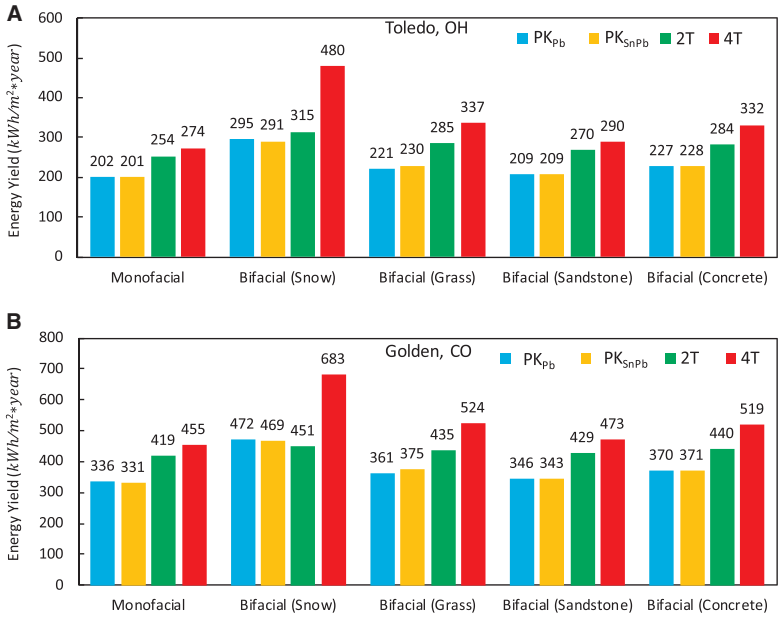


Figure 2. EY Comparison of Monofacial and Bifacial PV Structures
(A and B) Shown are the structures deployed in Toledo, Ohio (A) and Golden, Colorado (B).

adverse effect on power generation. A similar computational study was done for Daggett, California and Portland, Oregon, which compared the EYs of perovskite/Si on different surfaces.[24] This study also found a similar 60% EY increase in the lower latitude location (45.5° versus 34.8°). Because of higher relative humidity in Toledo, the diffuse horizontal irradiance (DHI) comprises ~30% of the total annual solar insolation, whereas for Golden it is ~20%. For this reason, the gain because of bifaciality is higher in Toledo compared with Golden because the DHI contributes to the incident light from the rear side of the panel from shadowed and unshadowed ground. However, for front-side illumination, the DHI contribution comprises up to ~10% of the current generated.

On average, between the two locations, single-junction bifacial structures showed somewhat similar EY increase trends (~17%) compared with monofacial structures. Bifacial single0junction devices (PK_{Pb} and PK_{Sn-Pb}) show a general increase in annual EYs as the albedo increases. Because the single-junction devices considered in this work have similar PCEs under normal incident front illumination of air mass (AM) 1.5 irradiance (PCE = ~24%), the expected annual EY values under real-world conditions for both devices are also similar regardless of location and surface. The only exception is for a grass surface, for which the bifacial PK_{Sn-Pb} device has a higher annual EY in both locations. This is due to the high albedo of grass at higher wavelengths. Grass reflection is ~35% for wavelengths above ~700 nm and less than 20% below this wavelength. For this reason, power generation from light reflected from grass is higher with the PK_{Sn-Pb} (narrow bandgap) device compared with the PK_{Pb} device (wide bandgap), with a bandgap of 1.55 eV corresponding to 800 nm (Figure S2).

For the tandem structures studied here, discrepancies in gain were observed because of bifaciality between the annual EYs of 2T and 4T tandem devices located

Approved for public release; distribution unlimited.
543

	PK_{Pb}		PK_{Sn-Pb}		2T		4T		c-Si [m^2]
	Monofacial	Bifacial	Monofacial	Bifacial	Monofacial	Bifacial	Monofacial	Bifacial	
Acidification	1.08	1.37	2.71	3.00	4.64	4.91	5.28	5.56	5.39E-01 [kg $SO_{2\text{-Equiv.}}$]
Ecotoxicity	0.38	0.71	0.45	0.78	0.68	1.00	1.17	1.50	7.28E+02 [CTU_e]
Eutrophication	0.60	0.94	1.09	1.43	1.82	2.15	2.39	2.74	7.13E-01 [kg $N_{\text{-Equiv.}}$]
Global Warming Poten.	0.28	0.50	0.35	0.56	0.51	0.72	0.83	1.05	1.49E+02 [kg $CO_{2\text{-Equiv.}}$]
Human Health, part. matter	0.37	0.65	1.30	1.59	2.06	2.31	2.44	2.73	8.63E-02 [kg $PM_{2,5\text{-Equiv.}}$]
Human toxicity, cancer	0.27	0.51	0.36	0.60	0.55	0.78	0.90	1.14	1.09E-05 [CTU_h]
Human toxicity, non-cancer	0.52	0.99	0.59	1.06	0.89	1.36	1.60	2.07	3.68E-05 [CTU_h]
Ozone depletion air	0.17	0.28	0.23	0.34	0.35	0.45	0.51	0.62	1.75E-05 [kg $CFC_{11\text{-Equiv.}}$]
Resources	0.20	0.32	0.28	0.39	0.41	0.52	0.59	0.70	1.98E+02 [MJ]
Smog Air	0.31	0.52	0.48	0.69	0.71	0.91	1.01	1.22	6.86E+00 [kg $O_{3\text{-Equiv.}}$]
Ave. impacts (per m^2)	0.42	0.68	0.78	1.04	1.26	1.51	1.67	1.93	1
Cumulative EY	7,896.7	8,729.7	7,779.2	9,001.4	9,852.4	10,263.2	10,687.1	12,620.2	7,937.0
Ave. impacts (per kWh)x10^3	0.05	0.08	0.10	0.12	0.13	0.15	0.16	0.15	0.13

Most environmentally preferable	0.54<
More environmentally preferable	0.55-0.85
Neutral	0.86-1.14
Less environmentally preferable	1.15-1.44
Least environmentally preferable	1.45>

Figure 3. Comparison of the Normalized Environmental Impact of Single-Junction and Tandem Perovskite PV Technologies with Respect to c-Si per Unit Cell Area Production

The basis of comparison is manufacturing of monofacial c-Si PVs. For each environmental impact category, the impact of monofacial and bifacial PVs was divided into the impact of c-Si PVs, and the results were color coded. For example, yellow coding means that the impact per square meter is similar to that of c-Si, which is the reference point. Values coded light or dark green indicate better environmental performance, whereas orange and red indicate the worst performance. The actual values of c-Si impact are shown in the last column. Cumulative EY values were calculated for Golden for monofacial and realistic grass-snow mix-covered ground bifacial perovskite PVs over 25 years with a 0.5% annual degradation rate.

on different surfaces (~9% versus ~26%, on average, for 2T and 4T tandems, respectively). Although the 2T and 4T monofacial devices studied here have similar PCEs (Table S1), the differences in EYs between bifacial 2T and 4T tandem cells can be attributed to the current-matching condition. This condition is a critical factor in the performance of the 2T tandems. Under current-matching conditions, top and bottom subcells produce the same amount of current, which corresponds to the overall current in the tandem cell. When this condition is not met, the overall current in the 2T tandem cell is limited by the subcell with the lower current. Therefore, for a 2T tandem device that satisfies the current-matching conditions under normal incident front illumination of the AM 1.5 spectrum, addition of back illumination leads to current gain in the bottom subcell and creates a current mismatch between the subcells. On the other hand, for 4T tandems devices, the current-matching condition does not apply, and the gain in the overall annual EY corresponds to the increase in the reflected power from the ground. Recent studies of optimized bifacial structures have demonstrated that the gain in the EY of bifacial 2T devices is limited compared with single-junction and 4T cells.[24] To analyze the effect of current matching in monofacial and bifacial 2T devices, we evaluated the role of absorber layer thicknesses in the structure. Details regarding these analyses are given in Figure S3.

Life Cycle Environmental Impact

We calculated the normalized environmental impact per 1 m^2 of bifacial and monofacial single-junction and tandem structure perovskite PV modules (Figure 3). The average environmental impact of bifacial PVs is about 20%–60% higher compared with monofacial PVs. The difference can be attributed to the difference in material requirements for glass and contacting layers and the additional anti-reflective

Approved for public release; distribution unlimited.
544

coating (ARC) layer needed for bifacial PVs. The back-supporting material of monofacial PVs is made of flat glass, whereas the sun-facing side is made of low iron glass sheet, called solar glass, which is covered with an ARC (Figure 1; Figure S1).[37] However, bifacial PVs require low iron glass for each surface of the PV cell because it is illuminated from both sides;[38,39] therefore, each side also contains an ARC. Unlike flat glass, solar glass contains about 0.3% antimony as raw material[40] and has about 15% higher impact compared with flat glass because of these upstream emissions.[41] In addition, the back-contacting material of bifacial PVs needs to be a transparent material such as ITO,[42,43] whereas monofacial PVs have Al back contact material. The environmental impact of the ITO back-contact layer of bifacial PVs is drastically higher than the Al back-contacting layer of monofacial PVs. Production of the ITO layer is energy-intensive and impactful compared with the Al layer.[41,44] Previous LCA studies identified ITO as the component with the largest contribution of energy consumption (embedded energy and direct process) during manufacturing of different emerging PV technologies,[16,45,46] which elevates the environmental footprint of PV cells.

Figure 3 also shows an environmental impact comparison between c-Si technology and monofacial and bifacial perovskite PV cells with single- and multi-junction configurations. Our results show that, based on the average cradle-to-to-end-of-use environmental impact, only bifacial PK_{Pb} PV cells are more environmentally friendly than c-Si PV technology, whereas bifacial $PK_{Sn\text{-}Pb}$ PVs have similar environmental performance to that of c-Si PVs, and 2T and 4T bifacial PVs have 50%–70% more impact compared with c-Si PV technology. The higher impact is primarily due to acidification, eutrophication, human health particulate air, and non-cancerous human toxicity impact. The Sn-Pb mixture-based absorber (in the $Pb_{Sn\text{-}Pb}$ device) is the least environmentally friendly layer and contributes to most of these impact categories.[47,48] ITO is the second least environmentally friendly material that is used in the four structures considered and also greatly contributes to the eutrophication, human health particulate air, and non-cancer human toxicity impact categories. The high impact of Sn-Pb-based perovskite materials is due to upstream emissions of Sn material, as shown previously in the literature.[47] The high impact of ITO is a result of the extensive energy required to sputter the layer and the high embedded energy in the indium content of the material.[49–52] The ozone and resources categories are the only categories more preferable than the c-Si technology for all single and tandem configurations; thus, they are the least performance-intensive categories.

Figure 3 also quantifies the environmental impact performance per kWh of electricity generated from monofacial to bifacial for each single- and multi-junction configuration relative to the c-Si technology. This conversion was performed using Equation 1, where the impact per square meter is divided by the energy supplied from 1 m^2 active area of a PV module over its lifetime (25 years). For monofacial c-Si, the expected EY data were taken from the literature.[28] To calculate annual EY values of bifacial modules, we used a realistic grass-snow mix covered ground for Golden that is presented in Figure S4. The average number of snow-covered days in this location was determined from the National Oceanic and Atmospheric Administration's National Centers for Environmental Information database. A snow-covered day was defined as a day with an average of an inch of snow from 1981–2010. For each day of the month that was not a snow day, a grass surface was assumed. For every month, the grass-snow mix EY of a given technology was determined by summing the EY calculated for snow and grass surfaces for that month, multiplied by the ratio of the days of the month for each surface. The $impacts_{kWh}$ are provided in the last row of Figure 3, where higher values are associated with more adverse

Approved for public release; distribution unlimited.
545

	PK_{Pb}		PK_{Sn-Pb}		2T		4T		c-Si
	Monofacial	Bifacial	Monofacial	Bifacial	Monofacial	Bifacial	Monofacial	Bifacial	
Average (per m^2)	0.23	0.30	0.59	0.66	0.98	1.04	1.10	1.17	1
Average (per kWh)*10^3	0.03	0.03	0.08	0.07	0.10	0.10	0.10	0.09	0.13

Figure 4. Comparison of the Average Normalized Environmental Impact of Devices with AZO as the Transparent Conducting Oxide Layer
The average normalized environmental impact of ITO and AZO is 0.13 and 0.03 per 100 nm ×1 m^2, respectively. For the color coding, the same approach as in Figure 3 was followed, and values are normalized to c-Si impact.

environmental impact. Our results demonstrate that electricity that can be supplied from bifacial PK_{Pb} and PK_{Sn-Pb} PV cells is 38% and 8% more environmentally friendly, respectively, compared with electricity from c-Si PV cells. On the other hand, the average environmental performance of electricity from 2T and 4T PV cells is approximately equal and slightly higher (15%) than that of c-Si PV technology, mainly because of the materials selection for the cells, particularly ITO, which is used as a transparent contacting oxide (TCO) layer. Sensitivity analyses to investigate the effect of device lifetime on environmental impact are given in Figure S5.

Effects of Materials on Environmental Performance of Devices

The previous section showed that bifacial PK_{Pb} and PK_{Sn-Pb} cells presented encouraging impact (~8–40% lower) relative to monofacial c-Si PVs in terms of impact per square meter and kWh. However, the impact of bifacial 2T and 4T tandem perovskite PVs is much less encouraging, with tandem devices having greater impact (50%–70% more in terms of square meter impact and 15% more in terms of kWh impact) than that of c-Si (Figure 3). ITO was indicated as one of the two major contributors of high environmental impact. However, ITO could be replaced by other TCO materials, such as AZO, which can reduce the environmental impact of the devices. The effect of this possible replacement is explored in Figure 4. For these analyses, we assume that the EYs of the devices would not be affected by transition from ITO to AZO. This assumption is based on the similarity of refractive indices measured for ITO[53] and AZO.[54]

ITO (100 nm) has more than four times the environmental impact compared with AZO, which can be used as the contacting layer. This is an important difference, considering that the amount of ITO in each device varies. For example, bifacial PK_{Pb} and PK_{Sn-Pb} cells have 400 nm ITO as the front- and back-contacting material, whereas 2T perovskite has a total of 500 nm as contacting material (400 nm) and a tunnel layer (100 nm). 4T tandem has the greatest amount of ITO (800 nm) because the front and back contacts in the bottom and top cells are made of ITO. The effect of replacing ITO in monofacial and bifacial cells is also shown in Figure 4. The results show that the environmental impact of bifacial PK_{Pb}, PK_{Sn-Pb}, 2T, and 4T cells can be reduced to between 70% and 77% per square meter and kWh, respectively, when the contact materials are kept the same across the different designs. Such reductions drastically improve the environmental performance of bifacial PVs (0.3, 0.66, 1.04, and 1.17 per square meter of normalized c-Si environmental impact for PK_{Pb}, PK_{Sn-Pb}, 2T, and 4T, respectively), and, as a result, all studied bifacial PV structures show improved environmental performance compared with c-Si PV (30%–77% less than c-Si PVs per kWh of electricity generated).

Global Warming Potential and Energy Payback Time Analyses

We also compared the energy payback time (EPBT) and global warming potential (GWP) metrics of bifacial and monofacial PV configurations (Figure 5). In Figure 5,

Approved for public release; distribution unlimited.

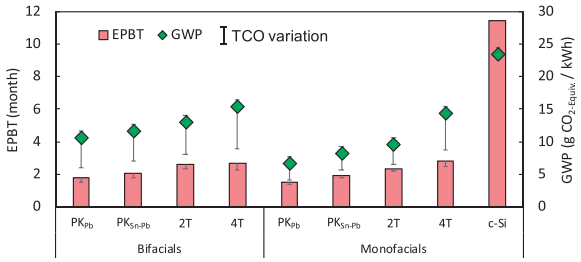


Figure 5. EPBT and GWP Impacts
Shown are the EPBT and GWP Impact of different bifacial and monofacial PV configurations.

the effect of ITO's potential replacement with AZO was also captured using error bars. In general, monofacial and bifacial perovskite structures have 4–8 times shorter EPBTs compared with c-Si. This difference between monofacial perovskite structures and c-Si is consistent with the literature.[55] The GWP impact of bifacial perovskite structures was found to be between 11–15 g $CO_{2\text{-Equiv.}}$, whereas that of c-Si is 24 g $CO_{2\text{-Equiv.}}$[56] per kWh of electricity generation (see Figure 5 for the m^2 data of GWP value).

Figure 5 also shows that the EPBT and GWP metrics of bifacial PK_{Pb}, $PK_{Sn\text{-}Pb}$, 2T, and 4T PVs are ~15%–30% higher compared with the values of monofacial devices. This is because these metrics are largely affected by the energy invested in manufacturing of the PVs; i.e., the primary energy demand of the cells to production;[57] that is why they show similar trends, as shown in Figure 5). Particularly, we found that the primary energy invested in additional TCO, ARC, and solar glass is the reason for the differences. These results are consistent with prior work comparing the environmental impact of energy generated from bifacial and monofacial c-Si PV technology.[27] Gazbour et al.[27] also found that bifacial PVs have 32% less GWP impact compared with monofacial c-Si technology.

EXPERIMENTAL PROCEDURES

Resource Availability

Materials Availability

This study did not generate new unique reagents.

Data and Code Availability

The LCA datasets and EY codes supporting the current study have not been deposited in a public repository but are available from the corresponding author upon reasonable request.

Device Structures

The analyzed four bifacial single- and multi-junction perovskite structures and the related monofacial architectures are shown in Figure 1 and Figure S1, respectively. The four different types of structures studied here are single-junction (Figures 1A and 1B), 2T tandem (Figure 1C), and 4T tandem (Figure 1D) architectures. The choice of materials for the devices in this work are based on fabricated high-PCE devices (Table S1) and the cost effectiveness of the materials.

With all four structures, there are slight differences in layer composition between bifacial and monofacial panels. These differences are typically constrained to the bottom layers of the cell. The aluminum layer in monofacial cells is replaced by

Approved for public release; distribution unlimited.
547

ITO in bifacial cells because a transparent contact layer is needed to allow photons to reach the absorbing layer from the back of the cell.[24,58] To reduce reflection loss in bifacial devices, a layer of MgF_2 was considered to be deposited on the bottom of the solar glass layer as an ARC. Low-iron-content solar glass is assumed for the illumination side of each device. Regular tempered glass can be used on the back of monofacial panels because there is no light transmittance from that side. For the electron transport layer (ETL) and hole transport layer (HTL), NiO and SnO_2 were selected. These materials have been used in high-PCE tandem- and single-junction devices[55,59–63] and are cost-effective choices for large-scale manufacturing.[13,14]

Figures 1A and 1B show two-single junction PK_{Pb} and $PK_{Sn\text{-}Pb}$ PV cells, respectively. For the absorber layers of the single-junction devices, $MAPbI_3$ and $(FASnI_3)_{0.6}(MAPbI_3)_{0.4}$ were considered for PK_{Pb} and $PK_{Sn\text{-}Pb}$, respectively. These absorbers have bandgaps close to the optimal bandgap range for PV devices, and they have been used in demonstration devices with high PCEs.[64–66] The remaining components of the cell structures (e.g., ARC, contacting layer, charge-selective layer, glass, etc.) have the same thicknesses and material composition. For tandem structures, absorber material selection was based on recent reports of champion perovskite/perovskite tandem devices with $Cs_{0.05}FA_{0.8}MA_{0.15}PbI_{2.55}Br_{0.45}$ and $(FASnI_3)_{0.6}(MAPbI_3)_{0.4}$ chemical composition for top and bottom subcell absorbers, respectively.[67,68] 2T (Figure 1C) and 4T (Figure 1D) cells utilize two absorbing layers made of narrow-bandgap and wide-bandgap perovskites. 2T and 4T structures can be distinguished by placement of the encapsulation and contacting/tunnel layers. In a 2T cell, the top and bottom subcells are connected via a tunnel layer (made up from ITO), whereas 4T cells require separate top and bottom cells with a complete structure; i.e., each cell has an absorber, two charge-selective layers, and two contacting layers.

EY Model for Real-World Conditions

For real-world EY analysis, two locations (Toledo and Golden) were considered, which represent high and low latitude and humidity conditions. For these calculations, the methods described in our group's earlier contribution were used.[32] Using the transfer matrix method, the absorption, transmission, and reflection at every thin film and thin film interface were determined and used to calculate the quantum efficiency (QE) of the single junction devices and also for both subcells in the tandem structures.[69] For bifacial devices, the QE calculations were performed for light incident from either side of the device. QEs were determined using measured refractive indices of all materials in the thin film device stack shown in Figure 1. The refractive index data for ITO, NiO, SnO_2, and MgF_2 was taken from König et al.,[53] Shim et al.,[70] Manzoor et al.,[71] and Rodríguez-de Marcos et al,[72] respectively. For the absorber in the top and bottom subcell of the tandem structures, wide- and narrow-bandgap perovskite was used.[73] For the narrow-bandgap single-junction device, the same perovskite material as for the tandem bottom subcell was considered. For the absorber of the single-junction PK_{Pb} device, refractive index data were taken from the literature.[74]

Photogenerated current (J_{ph}) at the absorber layer was calculated for every hour of the year by integrating the product of the hourly incident spectral solar irradiance and the corresponding QE at the angle of incidence. The irradiance data were provided by the NREL TMYSPEC model for spectral typical meteorological year data.[34,35] For light incident from the sky, DNI and DHI were considered. DNI angles of incidence were calculated by determining the hourly azimuthal and altitude angles corresponding to the sun's location for modules with optimal tilt at each

Approved for public release; distribution unlimited.
548

location. For the DHI component, we used a model[75] to determine the hourly anisotropic distribution of the power density because of cloud coverage within a 2° × 2° grid across the sky, and the corresponding angles of incidence were determined from each grid point. For scattered light from the ground, a method described by Gu et al.[76] was used. Briefly, a view factor was determined using the Hottel method of radiated power.[77] The reflected incident irradiance was determined for shaded ground as the product of the DHI, albedo, and view factor. The albedo values as a function of wavelength were taken from the literature.[24] For unshaded ground, the same approach was adopted, except that global horizontal irradiance was used instead of the DHI. Using a Lambertian scattering profile, the reflected power distribution for shaded and unshaded ground was determined. The modules were assumed to be 2 × 2 m with 1-m elevation from the ground and installed at the optimum tilt (33.3° for Golden and 34.75° for Toledo).

The reverse saturated current (J_0) of each device was determined by integrating the product of the QE and the device blackbody radiation for every hour of the year. To calculate the blackbody radiation of the cells, the hourly module temperature (T_M) was modeled using the Sandia National Lab PV cell temperature model.[78] The required data for this model were taken from the NREL PSM[36] dataset for hourly ambient temperatures and wind speeds, whereas the incident solar power were determined by integrating over the spectral data.

Using the determined hourly J_{ph}, J_0, and T_M as well as the shunt and series resistance values for the devices taken from the literature,[67,79] hourly current-voltage behavior was simulated using the analytical solutions to the diode equation,[80] which was used to determine the maximum power point (MPP). For tandems, the JV curves were simulated using the JV curves of the subcells and a method described elsewhere.[81] The annual EY consisted of the cumulative hourly MPP values.

LCA Goals and Scope

The goal of this study is to evaluate the life cycle environmental impact of bifacial perovskite devices. The scope of this work covers materials extraction, manufacturing, and use phases (cradle to end of use) of PV devices. For the LCA analysis, we used a sustainability software, GaBi 8.0, in which the United States Life Cycle Inventory (LCI) and Ecoinvent[56] databases are embedded. The Tool for Reduction and Assessment of Chemical and Other Environmental Impact (TRACI 2.0) model was used for impact assessment methodology. The impact was analyzed based on two functional units: 1 m^2 of module production and 1 kWh of electricity generation. For the conversion between two functional units, we used the equation

$$impacts_{kWh} = \frac{impacts_{m^2}}{cumulative\ EY}, \qquad \text{(Equation 1)}$$

where $impacts_{m^2}$ is the environmental impact per 1 m^2 of active area and manufacturing, $impacts_{kWh}$ is the environmental impact per kWh of energy generation from PVs, and $cumulative_{EY}$ is the total of energy provided from 1 m^2 active surface area for 25 years of operation time with a constant 0.5% annual degradation[57,82] rate assumption (Figure S4).

For our analysis, we used the environmental impact of monofacial c-Si as a reference (based on the per-unit cell area production of c-Si[56]). It is an appropriate reference to enable clear comparison of bifacial devices with c-Si, one of the most established PV terrestrial technologies.[15,16,52,83] Additionally, c-Si has the highest environmental

Approved for public release; distribution unlimited.
549

impact among commercial PVs; therefore, new technology is expected to at least have a lower environmental impact than c-Si to be competitive.

In addition to TRACI environmental impact, we extracted primary energy demand (PED) data for EPBT assessment. EPBT is the time needed for the solar cell to generate the energy equivalent to that being consumed during manufacturing of the PV cells[57] and was calculated following the equation

$$EPBT = \frac{PED * \varepsilon * PR}{Average\ annual\ EY}, \quad \text{(Equation 2)}$$

where PED is the primary energy demand ($MJ_{primary}\ m^{-2}$), ε is the electrical to primary energy conversion factor (29%),[56] and PR is the performance ratio of the module (80%),[84] which show the ratio of the active area to the total area of a module.

LCIs

The LCIs for bifacial perovskite cells include material extraction to end-of-use phases. The material consumption inventories were taken from our group's previous LCA studies of perovskite,[15] carbon nanotube,[83] and perovskite tandem[16,52] solar cells. For those studies, we collected the primary data for manufacturing PV devices from the University of Toledo's Wright Center for Photovoltaic Innovation and Commercialization (PVIC) laboratories, in which 1″ × 1″ lab-scale cells are fabricated[15,85,86] using primary new material inventories. Next we interpolated the lab-scale material consumption values to the manufacturing of a 1 × 1 m^2 PV panel in a large-scale PV manufacturing facility.[15]

The electricity consumption values were taken from the literature, and some assumptions were scaled-up data from the lab scale to an industrial fabrication scale.[51,87] For the electricity inventories, we used the United States electricity mix average. All energy input was modeled by waste heat output.[15] An efficiency of 50% was assumed for vacuum energy consumption during manufacturing based on two previous studies.[15,58] Average values from previous studies were used for the electrical consumption of chemical synthesis. However, chemical synthesis contributes to less than 0.1% of total electricity consumption.[51,88]

Emissions and waste streams from manufacturing were assumed to be released into different mediums. Volatile organic compounds, waste from thermal annealing, and vacuum deposition were assumed to be released into the air.[15] Lead emissions from the perovskite layer were assumed to be released into freshwater.[15] All other solid waste from solution-based methods was assumed to be disposed of into industrial soil.[15]

SUPPLEMENTAL INFORMATION

Supplemental Information can be found online at https://doi.org/10.1016/j.xcrp.2020.100216.

ACKNOWLEDGMENTS

This work was supported by University of Wisconsin – Platteville EMS Faculty start-up and SAIF grants and an Undergraduate Research, Scholarly and Creative Activity (URSCA) scholarship. The authors gratefully acknowledge funding support from the U.S. Air Force Research Laboratory Space Vehicles Directorate under agreement FA9453-18-2-0037 and contract FA9453-19-C-1002. The U.S. Government is authorized to reproduce and distribute reprints for Governmental purposes

Approved for public release; distribution unlimited.
550

notwithstanding any copyright notation thereon. The views and conclusions contained herein are those of the authors and should not be interpreted as necessarily representing the official policies or endorsements, either expressed or implied, of the Air Force Research Laboratory or the U.S. Government.

AUTHOR CONTRIBUTIONS

Conceptualization, R.H.A. and I.C.; Methodology, R.H.A., W.B., J.J., A.A., and I.C.; Investigation, R.H.A., W.B., and J.J.; Writing – Original Draft, R.H.A., W.B., J.J., and I.C.; Writing – Review & Editing, R.H.A., A.A., Z.S., A.P., M.J.H., and I.C.

DECLARATION OF INTERESTS

The authors declare no competing interests.

Received: July 4, 2020
Revised: August 19, 2020
Accepted: September 2, 2020
Published: October 7, 2020; corrected online: January 7, 2021

REFERENCES

1. Kopecek, R., and Libal, J. (2018). Towards large-scale deployment of bifacial photovoltaics. Nat. Energy *3*, 443–446.
2. Luque, A., Ruiz, J., Cuevas, A., Eguren, J., and Agost, M. (1977). Double side solar cells to improve static concentrator. In Proceedings of the 1st European Photovoltaic Solar Energy Conference, Luxembourg, pp. 269–277.
3. Hübner, A., Aberle, A.G., and Hezel, R. (1997). Novel cost-effective bifacial silicon solar cells with 19.4% front and 18.1% rear efficiency. Appl. Phys. Lett. *70*, 1008–1010.
4. Bai, Y., Barnett, A.M., Rand, J.A., and Ford, D.H. (1999). Light-trapping and back surface structures for polycrystalline silicon solar cells. Prog. Photovolt. Res. Appl. *7*, 353–361.
5. Romijn, I.G., Van Aken, B.B., Anker, J., Barton, P., Gutjahr, A., Komatsu, Y., Koppes, M., Kossen, E.J., Lamers, M.W.P.E., Saynova, D.S., et al. (2013). Industrial Cost Effective N-Pasha Solar Cells with > 20% Cell Efficiency. 28th European Photovoltaic Solar Energy Conference and Exhibition, 736–740.
6. Peng, W., Wang, L., Murali, B., Ho, K.T., Bera, A., Cho, N., Kang, C.F., Burlakov, V.M., Pan, J., Sinatra, L., et al. (2016). Solution-Grown Monocrystalline Hybrid Perovskite Films for Hole-Transporter-Free Solar Cells. Adv. Mater. *28*, 3383–3390.
7. Egido, M.A., and Lorenzo, E. (1986). Bifacial photovoltaic panels with sun tracking. Int. J. Sol. Energy *4*, 97–107.
8. Ishikawa, N. (2016). 1.25 MWp bifacial PV system in Japan. In 3rd Bifi PV Workshop, Miyazaki, Japan. http://npv-workshop.com/fileadmin/images/bifi/miyazaki/presentations/3_1_3_-_ISHIKAWA_-_World_1st_large_scale_Bifacial_PV_power_plant.pdf.
9. ITRPV (2018). International Technology Roadmap for Photovoltaics 2018. https://pv.vdma.org/documents/105945/26776337/ITRPV%20Ninth%20Edition%202018%20including%20maturity%20report%2020180904_1536055215523.pdf/a907157c-a241-eec0-310d-fd76f1685b2a.
10. Kojima, A., Teshima, K., Shirai, Y., and Miyasaka, T. (2009). Organometal halide perovskites as visible-light sensitizers for photovoltaic cells. J. Am. Chem. Soc. *131*, 6050–6051.
11. NREL (2019). Best Research-Cell Efficiency Chart. https://www.nrel.gov/pv/cell-efficiency.html.
12. Correa-Baena, J.P., Saliba, M., Buonassisi, T., Grätzel, M., Abate, A., Tress, W., and Hagfeldt, A. (2017). Promises and challenges of perovskite solar cells. Science *358*, 739–744.
13. Song, Z., McElvany, C.L., Phillips, A.B., Celik, I., Krantz, P.W., Watthage, S.C., Liyanage, G.K., Apul, D., and Heben, M.J. (2017). A technoeconomic analysis of perovskite solar module manufacturing with low-cost materials and techniques. Energy Environ. Sci. *10*, 1297–1305.
14. Li, Z., Zhao, Y., Wang, X., Sun, Y., Zhao, Z., Li, Y., Zhou, H., and Chen, Q. (2018). Cost Analysis of Perovskite Tandem Photovoltaics. Joule *2*, 1559–1572.
15. Celik, I., Song, Z., Cimaroli, A., Yan, Y., Heben, M., and Apul, D. (2016). Life Cycle Assessment (LCA) of perovskite PV cells projected from lab to fab. Sol. Energy Mater. Sol. Cells *156*, 157–169.
16. Celik, I., Phillips, A.B., Song, Z., Yan, Y., Ellingson, R.J., Heben, M.J., and Apul, D. (2017). Environmental analysis of perovskites and other relevant solar cell technologies in a tandem configuration. Energy Environ. Sci. *10*, 1874–1884.
17. Khanal, R.R., Phillips, A.B., Song, Z., Xie, Y., Mahabaduge, H.P., Dorogi, M.D., Zafar, S., Faykosh, G.T., and Heben, M.J. (2016). Substrate configuration, bifacial CdTe solar cells grown directly on transparent single wall carbon nanotube back contacts. Sol. Energy Mater. Sol. Cells *157*, 35–41.
18. Subedi, K.K., Bastola, E., Subedi, I., Song, Z., Bhandari, K.P., Phillips, A.B., Podraza, N.J., Heben, M.J., and Ellingson, R.J. (2018). Nanocomposite (CuS)x(ZnS)1-x thin film back contact for CdTe solar cells: Toward a bifacial device. Sol. Energy Mater. Sol. Cells *186*, 227–235.
19. Cavallari, N., Pattini, F., Rampino, S., Annoni, F., Barozzi, M., Bronzoni, M., Gilioli, E., Gombia, E., Maragliano, C., Mazzer, M., et al. (2017). Low temperature deposition of bifacial CIGS solar cells on Al-doped Zinc Oxide back contacts. Appl. Surf. Sci. *412*, 52–57.
20. Marongiu, D., Lai, S., Sarritzu, V., Pinna, E., Mula, G., Mercuri, M.L., Saba, M., Quochi, F., Mura, A., and Bongiovanni, G. (2019). Bifacial Diffuse Absorptance of Semitransparent Microstructured Perovskite Solar Cells. ACS Appl. Mater. Interfaces *11*, 10021–10027.
21. Chen, D., Pang, S., Zhu, W., Zhang, H., Zhou, L., He, F., Chang, J., Lin, Z., Xi, H., Zhang, J., et al. (2018). Efficient Semitransparent Perovskite Solar Cells Using a Transparent Silver Electrode and Four-Terminal Perovskite/Silicon Tandem Device Exploration. J. Nanomater. *2018*, 4012850.
22. Onno, A., and Holman, Z.C. (2018). Numerical analysis of bifacial silicon-based tandem devices: Shifts in the optimum top-cell bandgap with varying albedo. In 2018 IEEE 7th World Conference on Photovoltaic Energy Conversion, WCPEC 2018 - A Joint Conference of 45th IEEE PVSC, 28th PVSEC and 34th EU PVSEC, pp. 229–232.
23. Coletti, G., Luxembourg, S.L., Geerligs, L.J., Rosca, V., Burgers, A.R., Wu, Y., Okel, L., Kloos, M., Danzl, F.J.K., Najafi, M., et al. (2020). Bifacial Four-Terminal Perovskite/Silicon Tandem Solar Cells and Modules. ACS Energy Lett. *5*, 1676–1680.
24. Lehr, J., Langenhorst, M., Schmager, R., Gota, F., Kirner, S., Lemmer, U., Richards, B.S., Case, C., and Paetzold, U.W. (2020). Energy yield of bifacial textured perovskite/silicon tandem

Approved for public release; distribution unlimited.
551

photovoltaic modules. Sol. Energy Mater. Sol. Cells *208*, 110367.

25. Onno, A., Rodkey, N., Asgharzadeh, A., Manzoor, S., Yu, Z.J., Toor, F., and Holman, Z.C. (2020). Predicted Power Output of Silicon-Based Bifacial Tandem Photovoltaic Systems. Joule *4*, 580–596.

26. Alam, M.A., and Khan, M.R. (2016). Thermodynamic efficiency limits of classical and bifacial multi-junction tandem solar cells: An analytical approach. Appl. Phys. Lett. *109*, 173504.

27. Gazbour, N., Razongles, G., Schaeffer, C., and Charbuillet, C. (2016). Photovoltaic power goes green. 2016 Electronics Goes Green 2016+ (EGG), 1–8.

28. Hörantner, M.T., and Snaith, H. (2017). Predicting and Optimising the Energy Yield of Perovskite-on-Silicon Tandem Solar Cells under Real World Conditions. Energy Environ. Sci. *10*, 1983–1993.

29. Langenhorst, M., Sautter, B., Schmager, R., Lehr, J., Ahlswede, E., Powalla, M., Lemmer, U., Richards, B.S., and Paetzold, U.W. (2019). Energy yield of all thin-film perovskite/CIGS tandem solar modules. Prog. Photovolt. Res. Appl. *27*, 290–298.

30. Lehr, J., Langenhorst, M., Schmager, R., Kirner, S., Lemmer, U., Richards, B.S., Case, C., Paetzold, U.W., Lehr, J., Langenhorstb, M., et al. (2018). Energy yield modelling of perovskite/silicon two-terminal tandem PV modules with flat and textured interfaces. Sustain. Energy Fuels *2*, 2754–2761.

31. Hörantner, M.T., Leijtens, T., Ziffer, M.E., Eperon, G.E., Christoforo, M.G., McGehee, M.D., and Snaith, H.J. (2017). The Potential of Multijunction Perovskite Solar Cells. ACS Energy Lett. *2*, 2506–2513.

32. Hosseinian Ahangharnejhad, R., Phillips, A.B., Ghimire, K., Koirala, P., Song, Z., Barudi, H.M., Habte, A., Sengupta, M., Ellingson, R.J., Yan, Y., et al. (2019). Irradiance and temperature considerations in the design and deployment of high annual energy yield perovskite/CIGS tandems. Sustain. Energy Fuels *3*, 1841–1851.

33. Jošt, M., Köhnen, E., Morales Vilches, A., Lipovšek, B., Jäger, K., Macco, B., Al-Ashouri, A., Krc, J., Korte, L., Rech, B., et al. (2019). Textured interfaces in monolithic perovskite/silicon tandem solar cells: Advanced light management for improved efficiency and energy yield. Energy Environ. Sci. *2018*, 3511–3523.

34. Myers, D.R. (2012). Direct beam and hemispherical terrestrial solar spectral distributions derived from broadband hourly solar radiation data. Sol. Energy *86*, 2771–2782.

35. Sengupta, M., Xie, Y., Lopez, A., Habte, A., Maclaurin, G., and Shelby, J. (2018). The National Solar Radiation Data Base (NSRDB). Renew. Sustain. Energy Rev. *89*, 51–60.

36. NREL. National Solar Radiation Database. https://nsrdb.nrel.gov/.

37. Jungbluth, N., Stucki, M., Flury, K., Frischknecht, R., and Büsser, S. (2012). Life Cycle Inventories of Photovoltaics ESU-Services Ltd (Switzerland: Uster), p. 250.

38. Hezel, R. (2003). Novel Applications of Bifacial Solar Cells. Prog. Photovoltaics Res. Appl. *11*, 549–556.

39. Schmager, R., Langenhorst, M., Lehr, J., Lemmer, U., Richards, B.S., and Paetzold, U.W. (2019). Methodology of energy yield modelling of perovskite-based multi-junction photovoltaics. Opt. Express *27*, A507–A523.

40. Velayudhanpillai, V., Kheruka, P., and Kumar, N. (2014). Issues Concerning Use of Antimony in Solar Glass and Develoepment of Antimony free Low Iron Glass for Solar Applications. In 29th European Photovoltaic Solar Energy Conference and Exhibition.

41. Celik, I. (2018). Eco-design of Emerging Photovoltaic (PV) Cells. PhD dissertation (University of Toledo).

42. Espinosa, N., Hösel, M., Angmo, D., and Krebs, F.C. (2012). Solar cells with one-day energy payback for the factories of the future. Energy Environ. Sci. *5*, 5117–5132.

43. Wang, H., Dewi, H.A., Koh, T.M., Bruno, A., Mhaisalkar, S., and Mathews, N. (2020). Bifacial, Color-Tunable Semitransparent Perovskite Solar Cells for Building-Integrated Photovoltaics. ACS Appl. Mater. Interfaces *12*, 484–493.

44. Celik, I., Hosseinian Ahangharnejhad, R., Song, Z., Heben, M.J., and Apul, D. (2020). Emerging Photovoltaic (PV) Materials for a Low Carbon Economy. Energies *13*, 4131.

45. Espinosa, N., García-Valverde, R., Urbina, A., Lenzmann, F., Manceau, M., Angmo, D., and Krebs, F.C. (2012). Life cycle assessment of ITO-free flexible polymer solar cells prepared by roll-to-roll coating and printing. Sol. Energy Mater. Sol. Cells *97*, 3–13.

46. Espinosa, N., García-Valverde, R., Urbina, A., and Krebs, F.C. (2011). A life cycle analysis of polymer solar cell modules prepared using roll-to-roll methods under ambient conditions. Sol. Energy Mater. Sol. Cells *95*, 1293–1302.

47. Serrano-Lujan, L., Espinosa, N., Larsen-Olsen, T.T., Abad, J., Urbina, A., and Krebs, F.C. (2015). Tin- and lead-based perovskite solar cells under scrutiny: An environmental perspective. Adv. Energy Mater. *5*, 1501119.

48. Maranghi, S., Parisi, M.L., Basosi, R., and Sinicropi, A. (2019). Environmental profile of the manufacturing process of perovskite photovoltaics: Harmonization of life cycle assessment studies. Energies *12*, 3746.

49. Lizin, S., Van Passel, S., De Schepper, E., Maes, W., Lutsen, L., Manca, J., and Vanderzande, D. (2013). Life cycle analyses of organic photovoltaics: a review. Energy Environ. Sci. *6*, 3136.

50. Gong, J., Darling, S.B., and You, F. (2015). Perovskite photovoltaics: life-cycle assessment of energy and environmental impacts. Energy Environ. Sci. *8*, 1953–1968.

51. García-Valverde, R., Cherni, J.a., and Urbina, A. (2010). Life cycle analysis of organic photovoltaic technologies. Prog. Photovolt. Res. Appl. *18*, 535–538.

52. Celik, I., Philips, A.B., Song, Z., Yan, Y., Ellingson, R.J., Heben, M.J., and Apul, D. (2018). Energy payback time (EPBT) and energy return on energy invested (EROI) of perovskite tandem photovoltaic solar cells. IEEE J. Photovoltaics *8*, 305–309.

53. König, T.A.F., Ledin, P.A., Kerszulis, J., Mahmoud, M.A., El-Sayed, M.A., Reynolds, J.R., and Tsukruk, V.V. (2014). Electrically tunable plasmonic behavior of nanocube-polymer nanomaterials induced by a redox-active electrochromic polymer. ACS Nano *8*, 6182–6192.

54. Treharne, R.E., Seymour-Pierce, A., Durose, K., Hutchings, K., Roncallo, S., and Lane, D. (2011). Optical Design and Fabrication of Fully Sputtered CdTe/CdS Solar Cells. J. Phys. Conf. Ser. *286*, 012038.

55. Jiang, Q., Zhang, L., Wang, H., Yang, X., Meng, J., Liu, H., Yin, Z., Wu, J., Zhang, X., and You, J. (2016). Enhanced electron extraction using SnO2 for high-efficiency planar-structure HC(NH2)2PbI3-based perovskite solar cells. Nat. Energy *2*, 16177.

56. Wernet, G., Bauer, C., Steubing, B., et al. (2016). The ecoinvent databae version 3 (part 1): overview and methodology. Int. J. Life Cycle Assess. *21*, 1218–1230.

57. Bhandari, K.P., Collier, J.M., Ellingson, R.J., and Apul, D.S. (2015). Energy payback time (EPBT) and energy return on energy invested (EROI) of solar photovoltaic systems: A systematic review and meta-analysis. Renew. Sustain. Energy Rev. *47*, 133–141.

58. Gong, J., Darling, S.B., and You, F. (2015). Perovskite photovoltaics: Life-cycle assessment of energy and environmental impacts. Energy Environ. Sci. *8*, 1953–1968.

59. Hou, Y., Aydin, E., Bastiani, M., De Xiao, C., Isikgor, F.H., Xue, D.-J., Chen, B., Chen, H., Bahrami, B., Chowdhury, A.H., et al. (2020). Efficient tandem solar cells with solution-processed perovskite on textured crystalline silicon. Science *367*, 1135–1140.

60. Yue, S., Liu, K., Xu, R., Li, M., Azam, M., Ren, K., Liu, J., Sun, Y., Wang, Z., Cao, D., et al. (2017). Efficacious engineering on charge extraction for realizing highly efficient perovskite solar cells. Energy Environ. Sci. *10*, 2570–2578.

61. Zhang, B., Su, J., Guo, X., Zhou, L., Lin, Z., Feng, L., Zhang, J., Chang, J., and Hao, Y. (2020). NiO/Perovskite Heterojunction Contact Engineering for Highly Efficient and Stable Perovskite Solar Cells. Adv. Sci. (Weinh.) *7*, 1903044.

62. Bu, T., Li, J., Zheng, F., Chen, W., Wen, X., Ku, Z., Peng, Y., Zhong, J., Cheng, Y.-B., and Huang, F. (2018). Universal passivation strategy to slot-die printed SnO_2 for hysteresis-free efficient flexible perovskite solar module. Nat. Commun. *9*, 4609.

63. Jost, M., Bertram, T., Koushik, D., Marquez, J., Verheijen, M., Heinemann, M.D., Köhnen, E., Al-Ashouri, A., Braunger, S., Lang, F., et al. (2019). 21.6%-efficient Monolithic Perovskite/Cu(In,Ga)Se2 Tandem Solar Cells with Thin Conformal Hole Transport Layers for Integration on Rough Bottom Cell Surfaces. ACS Energy Lett. *4*, 583–590.

64. Li, C., Song, Z., Zhao, D., Xiao, C., Subedi, B., Shrestha, N., Junda, M.M., Wang, C., Jiang, C.-S., Al-Jassim, M., et al. (2019). Reducing Saturation-Current Density to Realize

Approved for public release; distribution unlimited.

552

High-Efficiency Low-Bandgap Mixed Tin–Lead Halide Perovskite Solar Cells. Adv. Energy Mater. *9*, 1803135.

65. Chen, Z., Turedi, B., Alsalloum, A., Yang, C., Zheng, X., Gereige, I., AlSaggaf, A., Mohammed, O.F., and Bakr, O.M. (2019). Single-Crystal MAPbI3 Perovskite Solar Cells Exceeding 21% Power Conversion Efficiency. ACS Energy Lett. *4*, 1258–1259.

66. Chiang, C.H., and Wu, C.G. (2018). A Method for the Preparation of Highly Oriented $MAPbI_3$ Crystallites for High-Efficiency Perovskite Solar Cells to Achieve an 86% Fill Factor. ACS Nano *12*, 10355–10364.

67. Tong, J., Song, Z., Kim, D.H., Chen, X., Chen, C., Palmstrom, A.F., Ndione, P.F., Reese, M.O., Dunfield, S.P., Reid, O.G., et al. (2019). Carrier lifetimes of > 1 μs in Sn-Pb perovskites enable efficient all-perovskite tandem solar cells. Science *364*, 475–479.

68. Zhao, D., Chen, C., Wang, C., Junda, M.M., Song, Z., Grice, C.R., Yu, Y., Li, C., Subedi, B., Podraza, N.J., et al. (2018). Efficient two-terminal all-perovskite tandem solar cells enabled by high-quality low-bandgap absorber layers. Nat. Energy *3*, 1093–1100.

69. Hosseinian Ahangharnejhad, R., Song, Z., Phillips, A.B., Watthage, S.C., Almutawah, Z.S., Sapkota, D.R., Koirala, P., Collins, R.W., Yan, Y., and Heben, M.J. (2018). Optical design of perovskite solar cells for applications in monolithic tandem configuration with CuInSe2 bottom cells. MRS Adv. *3*, 3111–3119.

70. Shim, J.W., Fuentes-Hernandez, C., Dindar, A., Zhou, Y., Khan, T.M., and Kippelen, B. (2013). Polymer solar cells with NiO hole-collecting interlayers processed by atomic layer deposition. Org. Electron. *14*, 2802–2808.

71. Manzoor, S., Häusele, J., Bush, K.A., Palmstrom, A.F., Carpenter, J., Yu, Z.J., Bent, S.F., Mcgehee, M.D., and Holman, Z.C. (2018). Optical modeling of wide-bandgap perovskite and perovskite/silicon tandem solar cells using complex refractive indices for arbitrary-bandgap perovskite absorbers. Opt. Express *26*, 27441–27460.

72. Rodríguez-de Marcos, L.V., Larruquert, J.I., Méndez, J.A., and Aznárez, J.A. (2017). Self-consistent optical constants of MgF2, LaF3, and CeF3 films. Opt. Mater. Express *7*, 989–1006.

73. Song, Z., Zhao, D., Chen, C., Ramez, H., Ahangharnejhad, C.L., Ghimire, K., Podraza, N.J., Heben, M.J., Zhu, K., and Yan, Y. (2019). Monolithic Two-Terminal All-Perovskite Tandem Solar Cells with Power Conversion Efficiency Exceeding 21%. In 2019 IEEE 46th Photovoltaic Specialists Conference (PVSC), pp. 743–746.

74. Ghimire, K., Zhao, D., Cimaroli, A., Ke, W., Yan, Y., and Podraza, N.J. (2016). Optical monitoring of CH3NH3PbI3 thin films upon atmospheric exposure. J. Phys. D Appl. Phys. *49*, 405102.

75. Brunger, A.P., and Hooper, F.C. (1993). Anisotropic sky radiance model based on narrow field of view measurements of shortwave radiance. Sol. Energy *51*, 53–64.

76. Gu, W., Ma, T., Li, M., Shen, L., and Zhang, Y. (2020). A coupled optical-electrical-thermal model of the bifacial photovoltaic module. Appl. Energy *258*, 114075.

77. Hottel, H.C., and Sarofim, A.F. (1967). Radiative Transfer (McGraw-Hill).

78. Fuentes, M.K. (1987). A Simplified Thermal Model of Photovoltaic Modules. Report of Sandia National Labs, May 1987, SAND85-0330. https://prod-ng.sandia.gov/techlib-noauth/access-control.cgi/1985/850330.pdf.

79. Kamada, R., Yagioka, T., Adachi, S., Handa, A., Tai, K.F., Kato, T., and Sugimoto, H. (2016). New world record Cu(In, Ga)(Se, S)2 thin film solar cell efficiency beyond 22%. 2016 IEEE 43rd Photovoltaic Specialists Conference (PVSC), 1287–1291.

80. Jain, A., and Kapoor, A. (2004). Exact analytical solutions of the parameters of real solar cells using Lambert W-function. Sol. Energy Mater. Sol. Cells *81*, 269–277.

81. Hadipour, A., de Boer, B., and Blom, P.W.M. (2008). Device operation of organic tandem solar cells. Org. Electron. physics. Mater. Appl. *9*, 617–624.

82. Jordan, D.C., and Kurtz, S.R. (2013). Photovoltaic Degradation Rates—an Analytical Review. Prog. Photovolt. Res. Appl. *21*, 12–29.

83. Celik, I., Mason, B.E., Phillips, A.B., Heben, M.J., and Apul, D. (2017). Environmental Impacts from Photovoltaic Solar Cells Made with Single Walled Carbon Nanotubes. Environ. Sci. Technol. *51*, 4722–4732.

84. Akinyele, D.O., Rayudu, R.K., and Nair, N.K.C. (2017). Life cycle impact assessment of photovoltaic power generation from crystalline silicon-based solar modules in Nigeria. Renew. Energy *101*, 537–549.

85. Song, Z., Watthage, S.C., Phillips, A.B., Tompkins, B.L., Ellingson, R.J., and Heben, M.J. (2015). Impact of Processing Temperature and Composition on the Formation of Methylammonium Lead Iodide Perovskites. Chem. Mater. *27*, 4612–4619.

86. Song, Z., Watthage, S.C., Phillips, A.B., and Heben, M.J. (2016). Pathways toward high-performance perovskite solar cells: review of recent advances in organo-metal halide perovskites for photovoltaic applications. J. Photonics Energy *6*, 022001.

87. Kushnir, D., and Sandén, B.a. (2011). Multi-level energy analysis of emerging technologies: A case study in new materials for lithium ion batteries. J. Clean. Prod. *19*, 1405–1416.

88. Geisler, G., Hofstetter, T.B., and Hungerbühler, K. (2004). Production of fine and speciality chemicals: procedure for the estimation of LCIs. Int. J. Life Cycle Assess. *9*, 101–113.

Approved for public release; distribution unlimited.

553

ARTICLES
https://doi.org/10.1038/s41560-020-00692-7
nature energy

Check for updates

Low-bandgap mixed tin–lead iodide perovskites with reduced methylammonium for simultaneous enhancement of solar cell efficiency and stability

Chongwen Li[1], Zhaoning Song[1]✉, Cong Chen[1], Chuanxiao Xiao[2], Biwas Subedi[1], Steven P. Harvey[2], Niraj Shrestha[1], Kamala Khanal Subedi[1], Lei Chen[1], Dachang Liu[1], You Li[1], Yong-Wah Kim[3], Chun-sheng Jiang[2], Michael J. Heben[1], Dewei Zhao[1], Randy J. Ellingson[1], Nikolas J. Podraza[1], Mowafak Al-Jassim[2] and Yanfa Yan[1]✉

High-performance perovskite/perovskite tandem solar cells require high-efficiency and stable low-bandgap perovskite subcells. State-of-the-art low-bandgap mixed tin–lead iodide perovskite solar cells exhibit either a high power-conversion efficiency or improved stability, but not both. Here we report a two-step bilayer interdiffusion growth process to simultaneously meet both requirements for formamidinium-based low-bandgap mixed tin–lead iodide perovskite solar cells. The bilayer interdiffusion growth process allows for the formation of high-quality and large-grained perovskite films with only 10 mol% volatile methylammonium. Additionally, one-dimensional pyrrolidinium perovskite was applied to passivate the perovskite film and improve the junction quality, which resulted in a carrier lifetime of 1.1 µs and an open circuit voltage of 0.865 V for our perovskite film and device with a bandgap of 1.28 eV. Our strategies enabled a power-conversion efficiency of 20.4% for low-bandgap perovskite solar cells under AM 1.5G illumination. More importantly, an encapsulated device can retain 92% of its initial efficiency after 450 h of continuous 1 sun illumination.

Organic–inorganic metal halide perovskite solar cells (PSCs) have reached a remarkable certified power conversion efficiency (PCE) of 25.2% (ref. [1]). Perovskite/perovskite tandem solar cells are promising to further improve the PCE and even break the Shockley–Queisser radiative limits for single-junction solar cells[2–5]. Recent advances in the low-bandgap mixed tin (Sn)–lead (Pb) iodide PSCs have enabled the fabrication of efficient perovskite/perovskite tandem solar cells in both two-terminal (2-T) and four-terminal configurations, with PCEs that reach more than 24 and 25%, respectively[6,7]. Despite the impressive progress[8–14], the current state-of-the-art mixed Sn–Pb PSCs exhibit an important shortcoming: they are either efficient or stable, but not both.

The high-efficiency PSCs typically use formamidinium/methylammonium (FA/MA)-based mixed Sn–Pb perovskite absorbers with a high MA proportion (≥30 mol%) (refs. [15–20]). The high MA proportion leads to large perovskite grains that are critical to realize high PCEs[21–23]. However, including a high proportion of volatile MA cations makes the devices unstable against heat and light stresses[24–28]. Alternatively, MA-free FA/caesium (Cs)-based mixed Sn–Pb perovskite absorbers exhibit a high device stability under illumination. Recently, a stable operation of PSCs based on $FA_{0.75}Cs_{0.25}Sn_{0.4}Pb_{0.6}I_3$ absorbers for up to 1,000 h was demonstrated[10]. For the FA/Cs-based mixed Sn–Pb PSCs, Cs was used to stabilize the perovskite phase, which boosted the performance and stability[5]. However, the incorporation of a substantial amount of Cs accelerates the perovskite crystallization process, which leads to small grain sizes and a substantial number of grain boundaries, which compromise the PCE of the resultant PSCs[29,30]. A viable way to overcome this dilemma is to synthesize high-quality FA-based mixed Sn–Pb perovskite films with large grains but a low MA proportion. However, the current fabrication processes of mixed Sn–Pb PSCs are incapable of realizing the aforementioned goal.

The most commonly used process to fabricate a high PCE mixed Sn–Pb PSCs is one-step antisolvent-assisted spin coating[17]. This process has been advanced recently by the achievements with high-efficiency PSCs. For instance, the incorporation of a small dose of cadmium ions into $FA_{0.5}MA_{0.45}Cs_{0.05}Pb_{0.5}Sn_{0.5}I_3$ demonstrated an enhanced electron diffusion length, which enabled mixed Sn–Pb PSCs with a PCE of about 20.0% (ref. [9]). Moreover, a strategy that used metallic tin to suppress Sn^{2+} oxidation via a comproportionation process has been developed. The single-junction $FA_{0.7}MA_{0.3}Pb_{0.5}Sn_{0.5}I_3$ PSCs that utilize the Sn reduction strategy have delivered a PCE of 21.1%, which enabled the fabrication of perovskite/perovskite tandem solar cells with a PCE of 24.8% (ref. [6]). Despite the recent progress, this one-step deposition method has its limitation in preparing high-quality large-grained mixed Sn–Pb perovskite films in which the MA proportion is below 30 mol% (ref. [17]).

Here we report a two-step bilayer interdiffusion growth (BIG) strategy to successfully reduce the MA proportion to 10% without compromising grain size and device performance. We further applied pyrrolidinium thiocyanate (PySCN) to form the one-dimensional (1D) $PySn_xPb_{1-x}I_3$ perovskite which passivates the film surface and grain boundaries[31,32]. As a result, the carrier lifetime of thick mixed Sn-Pb perovskite films increased to 1.1 µs, which is essential for an efficient photoexcited charge carrier collection in a thick absorber layer[7]. The incorporation of PySCN also

[1]Department of Physics and Astronomy and Wright Center for Photovoltaics Innovation and Commercialization, The University of Toledo, Toledo, OH, USA. [2]Materials Science Center, National Renewable Energy Laboratory, Golden, CO, USA. [3]Department of Chemistry and Biochemistry, The University of Toledo, Toledo, OH, USA. ✉e-mail: zhaoning.song@utoledo.edu; yanfa.yan@utoledo.edu

Approved for public release; distribution unlimited.
554

improves the junction quality at the perovskite/electron transport layer (ETL) interface, which boosts the open circuit voltage (V_{OC}) to 0.865 V. Our champion device based on the FA-based mixed Sn–Pb perovskite absorbers delivers a PCE of 20.4% (20.3%) measured under a reverse (forward) voltage scan, which is comparable with the best FA/MA-based mixed Sn–Pb PSCs[6,7]. Benefiting from the reduced MA content and improved perovskite film quality, our mixed Sn–Pb PSCs show excellent stability against light and heat. An encapsulated mixed Sn–Pb PSC retained 92% of its initial efficiency after 450 h of continuous operation under one sun illumination.

BIG of FA-based Sn–Pb perovskites

The two-step sequential deposition technique is widely used to fabricate high-efficiency pure-Pb PSCs due to its simple and precise process control as well as its good reproducibility[33]. However, no success has been realized in mixed Sn–Pb perovskites with a Sn ratio of ~50% due to the rapid crystallization of Sn-based perovskites[34]. We first tested the synthesis of mixed Sn–Pb perovskite films via the conventional two-step method[33]. On spin coating the formamidinium iodide (FAI)/methylammonium chloride (MACl) in isopropyl alcohol (IPA) solution on a predeposited tin(II) iodide (SnI_2)/lead iodide (PbI_2) film, the film turned black rapidly, which is due to the stronger reaction of Sn^{2+} than that of Pb^{2+} with FAI[34]. The rapid formation of small-sized perovskite grains blocks the diffusion of the organic halide salts, which results in organic residues on the surface and unreacted SnI_2/PbI_2 at the bottom after annealing (Supplementary Fig. 1). The excess organic impurities cause excessive non-radiative recombination, whereas the unreacted SnI_2/PbI_2 hinders charge transport, which limit the device performance (Supplementary Fig. 2)[35].

To overcome the above issues, we designed the two-step BIG process with a prolonged ion diffusion and exchange stage to enable the full conversion of SnI_2/PbI_2 into the perovskite phase, which allows for an increased grain size of mixed Sn–Pb perovskites with a low MA concentration. Figure 1a illustrates the process flow diagram of our BIG process. We employed additional methylammonium thiocyanate (MASCN) (25 mol%) in the first-step SnI_2/PbI_2 precursor solution to promote the formation of mixed Sn–Pb perovskite nanocrystallites that help suppress the preferential rapid reaction between SnI_2 and FAI in the next step. MASCN was selected because SCN ions exhibit a stronger bonding with Sn ions than that of halogen ions and can help suppress the oxidization of Sn^{2+} (ref. [34]). The SnI_2/PbI_2/MASCN precursor solution was first spin coated on a substrate, and an FAI/IPA solution was subsequently spin coated to form a bilayer precursor film. An interdiffusion stage at a low temperature of 50 °C was applied to promote the diffusion of FA ions and exchange of FA/MA cations, which allowed the coalescence of the bilayer and completed the conversion of precursors to the perovskite phase. This stage also enabled a final annealing temperature of 120 °C, which provides sufficient thermal energy to promote grain growth and eliminate organic residues.

We tracked and analysed the evolution of the crystal phase and microstructure of the mixed Sn–Pb perovskite films during the BIG process by X-ray diffraction (XRD) and scanning electron microscopy (SEM) measurements (Fig. 1b–i). The XRD pattern of a spin-coated SnI_2/PbI_2/MASCN precursor film shows a small peak at ~14.15° (Fig. 1b), which corresponds to the (110) plane of $MASn_{0.5}Pb_{0.5}I_3$ (ref. [36]). The low peak intensity indicates that $MASn_{0.5}Pb_{0.5}I_3$ perovskite nanocrystallites have already formed in the as-prepared precursor film. The existence of solvents prevented their further growth. After a FAI/IPA solution was spin coated onto the SnI_2/PbI_2/MASCN precursor film, the XRD peak of the (110) plane shifted to a lower angle of ~14° with a slightly increased peak intensity (Fig. 1c), which indicates that that FA cations reacted with metal halides and started to form the FA-based perovskites. The top-view SEM image in Fig. 1d shows that small (average size of 300–500 nm) but distinct grains were formed during this early stage, which correlates with the stronger XRD peak intensity. The corresponding cross-sectional SEM image (Fig. 1g) further reveals that the grains were formed in a bilayer structure that consisted of an upper layer of FA-based perovskite and a lower perovskite layer, which contained unreacted SnI_2/PbI_2/MASCN precursor complexes. A 50 °C annealing stage was then applied to promote FA diffusion and FA/MA ion exchange. The XRD pattern of a 50 °C annealed film (Fig. 1b) shows no obvious changes in the peak intensity or location, which indicates the lack of sufficient thermal energy to promote grain growth. The top-view SEM image of this stage (Fig. 1e) shows the coalescence of grains, which results in a more uniform and smoother surface compared with that of the as-prepared film (Fig. 1d). The cross-sectional SEM (Fig. 1h) shows that the bilayer grains merged into a monolayer, which indicates the interdiffusion/ion exchange between the upper FA-based perovskite layer and the lower precursor complex layer[21]. The final annealing at a relatively high temperature of 120 °C dramatically increased the diffraction peak intensity in the XRD pattern (Fig. 1b), which indicates an enhanced grain size and crystallinity of the film. Additionally, the (110) peak shifted slightly towards a lower angle (13.98°), which is attributed to further MA/FA ion exchange promoted by the higher thermal energy. No SnI_2/PbI_2 residual peak was detected by XRD, which confirms the complete conversion of SnI_2/PbI_2 into the perovskite phase. The high-temperature annealing promoted grain growth to an average size of over 1 μm (Fig. 1f) and eliminated horizontal grain boundaries (Fig. 1i).

The diffusion stage at 50 °C is critical to the synthesis of high-quality thick mixed Sn–Pb perovskite films. We first explored the annealing of the as-prepared film directly at 120 °C and found a layer of unreacted SnI_2/PbI_2 at the bottom of the perovskite layer (Supplementary Fig. 3). The metal iodide residues impeded the extraction at the interface between the mixed Sn–Pb perovskite absorber layer and the poly(3,4-ethylenedioxythiophene):polystyrene sulfonate (PEDOT:PSS) hole-transport layer (HTL), which limited the performance of the resultant PSCs (Supplementary Fig. 4). The incomplete perovskite conversion is probably due to the fast evaporation of solvent at a high temperature, which causes insufficient diffusion of FAI into the layer underneath. Thus, a diffusion stage at a mild temperature is needed to ensure a sufficient ion exchange. However, the diffusion stage cannot be too long because a longer duration (for example, 7 or 15 min) enlarges the grain size of the perovskite (Supplementary Fig. 5a–d), but severely deteriorates the crystallinity and grain integrity of the final perovskite films, which show eroded and porous grains (Supplementary Fig. 5e–h). The XRD measurements (Supplementary Fig. 6) of the films with longer diffusion-stage durations show lower peak intensities than that of the film annealed for three minutes, which corresponds to a decreased crystallinity and undesirable film morphology.

The degradation caused by long-duration diffusion is attributed to the dynamic change of solvents in the film at this stage. We used temperature-programmed desorption mass spectrometry (TPD-MS) to track the volatile species released from the 50 °C annealed perovskite film. We observed a high partial pressure of IPA at a relatively low temperature of ~50 °C and the release of dimethylformamide (DMF) and dimethylsulfoxide (DMSO) at a higher temperature (~60 °C), along with the vaporization of excess FA in the form of its derivative fragments (Supplementary Fig. 7). Therefore, if the duration of pre-annealing at 50 °C exceeds its proper processing window, IPA will evaporate and the remaining DMF/DMSO will re-dissolve and erode the perovskite during the diffusion stage. Also, the result shows that if the diffusion-stage temperature exceeds 60 °C, a faster evaporation of DMSO, DMF and FA gases will lead to incomplete conversion, as in the case of direct high-temperature annealing (Supplementary Fig. 6). Therefore, the

Approved for public release; distribution unlimited.
555

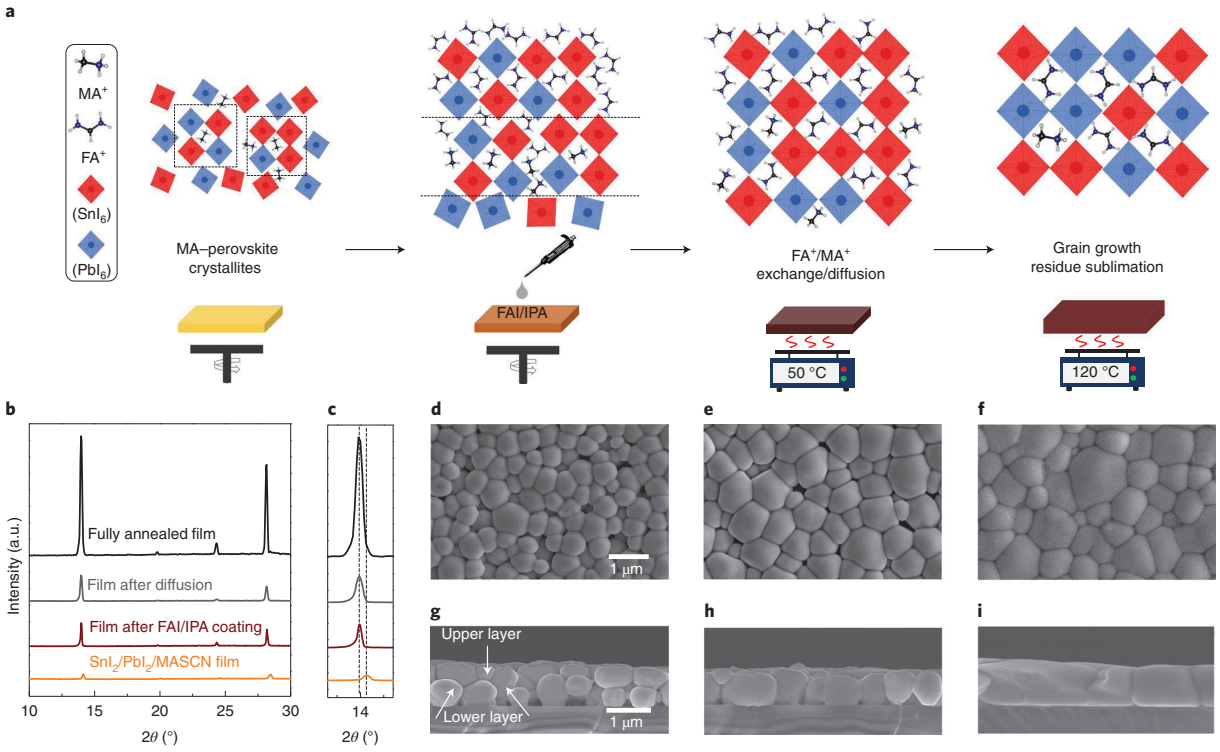


Fig. 1 | Mixed Sn–Pb perovskite films prepared by the BIG process. a, Schematic diagram of the BIG process. **b**,**c**, XRD patterns of films at each processing stage (**b**) and the expanded figure at around 14° of 2θ (**c**). The dashed lines indicate the evolution of the characteristic peak that corresponds to the (110) plane. **d**–**i**, Top-view (**d**–**f**) and cross-sectional (**g**–**i**) SEM images of the perovskite films after FAI/IPA coating (**d** and **g**), the diffusion stage (**e** and **h**) and final annealing (**f** and **i**). The scale is the same for all images. a.u., arbitrary units.

optimal duration (about three minutes) and pre-annealing temperature (50 °C) are desirable for the diffusion stage of the BIG process, which leads to high-quality mixed Sn–Pb perovskite films.

The thickness of mixed Sn–Pb perovskite films is determined by the concentration of the SnI_2/PbI_2 precursor solution. The perovskite film thickness increases from 600 ± 55 to 960 ± 91 nm by changing the concentration of the SnI_2/PbI_2/MASCN precursor solution from 1.4 to 1.7 M (Supplementary Figs. 8 and 9). For the mixed Sn–Pb perovskite, although a thicker absorber layer is preferred to ensure sufficient light absorption[3,9,18], the sub-bandgap defect state density increases with increases in the bulk volume of the film, as evident from the increasing Urbach energy measured by photothermal deflection spectroscopy (PDS) (Supplementary Fig. 9). These sub-bandgap defect states cause charge recombination, which shortens the carrier lifetime and so lowers the V_{OC} and fill factor (FF) for the thicker mixed Sn–Pb PSCs (Supplementary Fig. 10). To balance the trade-off between increasing photon absorption and avoiding defect formation, an optimal thickness of 900 ± 69 nm by using the 1.6 M precursor solution was selected. The mixed Sn–Pb perovskite film prepared by the BIG method showed a carrier lifetime of 565 ns and an Urbach energy of 26.7 ± 1 meV, which are comparable to those of the single-step processed $(FASnI_3)_{0.6}(MAPbI_3)_{0.4}$ perovskite films (Supplementary Fig. 11). The long carrier lifetime and low defect density are desired for high-performance PSCs[7].

To evaluate the photovoltaic performance of the mixed Sn–Pb perovskite films prepared by the BIG process, we utilized this method to fabricate PSCs with a p–i–n configuration of glass/indium tin oxide (ITO)/PEDOT:PSS/perovskite/fullerene (C_{60})/bathocuproine (BCP)/Ag. It is known that the addition of alkali cations, such as Cs^+ and Rb^+, is beneficial to the device performance because the cations can increase entropy, modify the tolerance factor and reduce lattice strains[12,37–40]. Here, 5 mol% caesium iodide (CsI) was incorporated to improve the reproducibility and eliminate the hysteresis in current density–voltage (J–V) measurements (Supplementary Fig. 12) of the mixed Sn–Pb PSCs without changing the chemical phase and microstructure of the perovskite thin films (Supplementary Fig. 13). The bandgap of the Cs-containing mixed Sn–Pb film measured by spectroscopic ellipsometry (SE) is 1.28 eV (Supplementary Fig. 14), which is consistent with that of other mixed Sn–Pb perovskites with a Sn/Pb atomic ratio of 1:1 reported in the literature[41,42]. We fabricated 30 PSCs using the BIG-processed mixed Sn–Pb perovskite absorber layers, and the statistics of the photovoltaic parameters are summarized in Supplementary Table 1 and Supplementary Fig. 15. The average PCEs of the PSCs that contained 5 mol% CsI are 18.91 ± 0.36% (18.86 ± 0.35%) under a reverse (forward) voltage scan, which shows negligible J–V hysteresis (Supplementary Fig. 12).

Impact of MA concentration on film thermal stability

^{1}H NMR spectroscopy was used to quantitatively analyse the molar ratio of FA/MA in the BIG-processed mixed Sn–Pb perovskite films. We made several perovskite films using the BIG process and scraped the perovskite powders from the substrates. The perovskite powders were then dissolved in DMSO-d_6 for the ^{1}H NMR measurement, and the spectrum is shown in Supplementary Fig. 16. The histogram analysis of the normalized NMR peak intensities that correspond to individual chemical species is shown in Fig. 2a, from which the composition of our BIG-processed mixed Sn–Pb perovskite is estimated to be about $FA_{0.85}MA_{0.1}Cs_{0.05}Sn_{0.5}Pb_{0.5}I_3$.

Approved for public release; distribution unlimited.

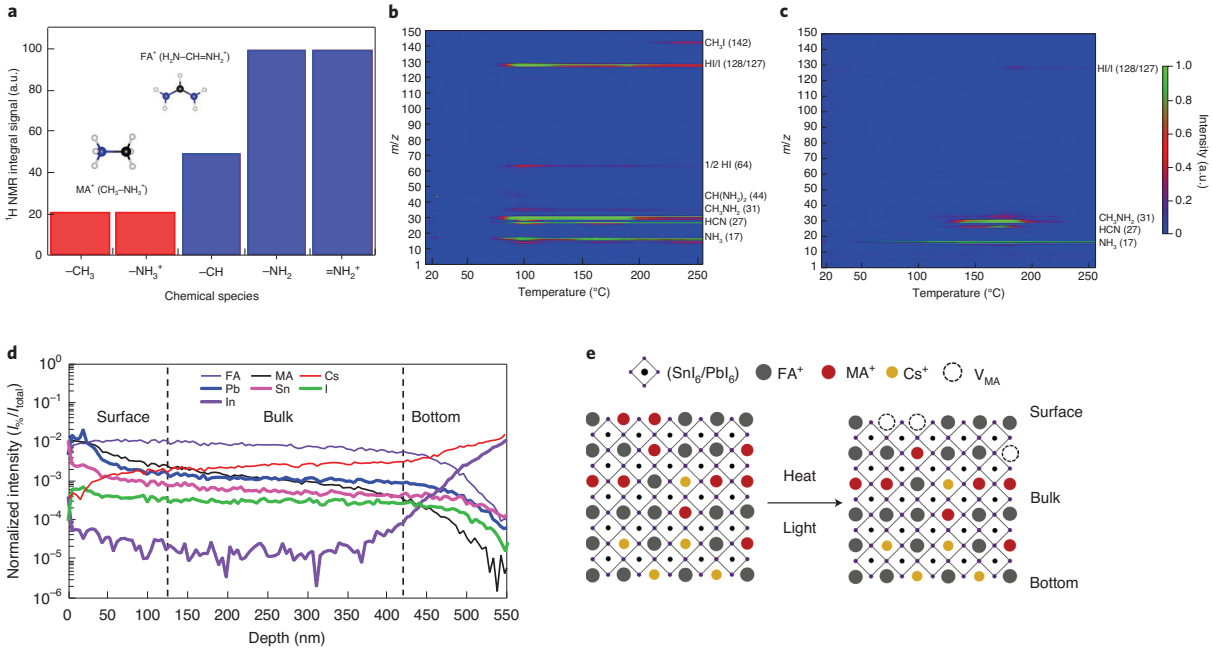


Fig. 2 | Composition and degradation of mixed Sn–Pb perovskite films fabricated by the BIG process. a, ^{1}H NMR analysis of mixed Sn–Pb perovskites prepared by the BIG process. **b**,**c**, TPD-MS of $(FASnI_3)_{0.6}(MAPbI_3)_{0.4}$ (**b**) and $FA_{0.85}MA_{0.1}Cs_{0.05}Sn_{0.5}Pb_{0.5}I_3$ (**c**) perovskite films. **d**, TOF–SIMS depth profile of a $FA_{0.85}MA_{0.1}Cs_{0.05}Sn_{0.5}Pb_{0.5}I_3$ perovskite film made by the BIG process and deposited over a glass substrate. The normalized intensity is on a logarithmic scale. **e**, Schematic diagram of the elemental distribution in the $FA_{0.85}MA_{0.1}Cs_{0.05}Sn_{0.5}Pb_{0.5}I_3$ film and surface degradation due to heat and light stresses (V_{MA} represents MA vacancies).

We then performed TPD-MS measurements to compare the thermal stability of a BIG-processed $FA_{0.85}MA_{0.1}Cs_{0.05}Sn_{0.5}Pb_{0.5}I_3$ perovskite film with a $(FASnI_3)_{0.6}(MAPbI_3)_{0.4}$ film prepared by the one-step method. The $(FASnI_3)_{0.6}(MAPbI_3)_{0.4}$ film released MA (CH_3NH_2) and hydroiodic acid (HI) gas species at a low temperature of ~68 °C and became more pronounced with increasing temperature, which indicates the commencement of thermal decomposition at ~68 °C (Fig. 2b). In contrast, the $FA_{0.85}MA_{0.1}Cs_{0.05}Sn_{0.5}Pb_{0.5}I_3$ film prepared by the BIG method showed a much improved thermal stability, with MA and FA fragments released at ~125 °C (Fig. 2c and Supplementary Fig. 17). Interestingly, the release of the HI signal starts later than that of the organic species at ~170 °C, which indicates the lower MA content makes the mixed Sn–Pb perovskite more thermally stable. We then performed a more thorough thermal stability study of various mixed Sn–Pb films and confirmed that reducing the MA content is, indeed, beneficial for the stability of mixed Sn–Pb perovskite films (Supplementary Figs. 18 and 19).

A time-of-flight secondary ion mass spectroscopy (TOF–SIMS) measurement was performed to probe the depth profile of a $FA_{0.85}MA_{0.1}Cs_{0.05}Sn_{0.5}Pb_{0.5}I_3$ perovskite film. As shown in Fig. 2d, the signals that correspond to Sn^{2+}, Pb^{2+}, I^- and FA^+ are almost constant throughout the film thickness, which indicates the uniform distribution of these elements. Interestingly, the MA^+ signal shows a decreasing gradient from the film surface (0 nm) to the perovskite/ITO glass interface, whereas the signal of Cs^+ shows a positive gradient. Although the unusual increased signal intensity in the surface region (~50 nm) could be due to the degradation during sample shipment or to ion-beam damage[43], the trends of MA^+ and Cs^+ are complementary in the bulk of the perovskite. The higher concentration of Cs^+ at the bottom may be due to the lower diffusion coefficient of Cs^+ than that of MA^+. The component distribution indicates the MA concentration is relatively higher in the surface region than in the film bulk region, as illustrated in Fig. 2e. The MA ions in the surface are easier to decompose by heat and light stresses, which is in good agreement with the short release period of MA species (Fig. 2c and Supplementary Fig. 20). The formed MA and I vacancies lead to the formation of recombination centres, which degrade the PSC performance[44–46]. Therefore, a strategy to passivate the top surface of BIG-processed mixed Sn–Pb perovskite films is needed.

Surface passivation using 1D pyrrolidine perovskite

We introduced the 1D $PySn_xPb_{1-x}I_3$ perovskite to passivate the surface and grain boundaries of our BIG-processed $FA_{0.85}MA_{0.1}Cs_{0.05}Sn_{0.5}Pb_{0.5}I_3$ perovskite films. The impact of the PySCN proportion on the chemical phase and microstructure of mixed Sn–Pb perovskites was studied (Supplementary Figs. 21 and 22)[31]. When the PySCN proportion was increased to 5 mol%, the grain size reduced and pinholes and voids between grains formed (Supplementary Fig. 22d). The voids cause undesirable recombination, which adversely affects the device performance. Incorporation of an optimal proportion (1.5 mol%) of PySCN enhanced the photoluminescence (PL) emission and increases the mean carrier lifetime from 670 ns to 1.1 µs (Fig. 3a and Supplementary Fig. 23). The microsecond lifetime is comparable with the lifetime of high-quality FA/MA-based mixed Sn–Pb perovskites[7]. The prolonged carrier lifetime is attributed to the grain-boundary passivation by 1D $PySn_xPb_{1-x}I_3$ perovskites. The surface potential mapping shows a more pronounced upward potential bending at the grain boundaries of the mixed Sn–Pb film after the addition of PySCN (Supplementary Fig. 24), which indicates a stronger electron attraction and hole repulsion at grain boundaries, known as a feature of defect passivation[47].

Approved for public release; distribution unlimited.
557

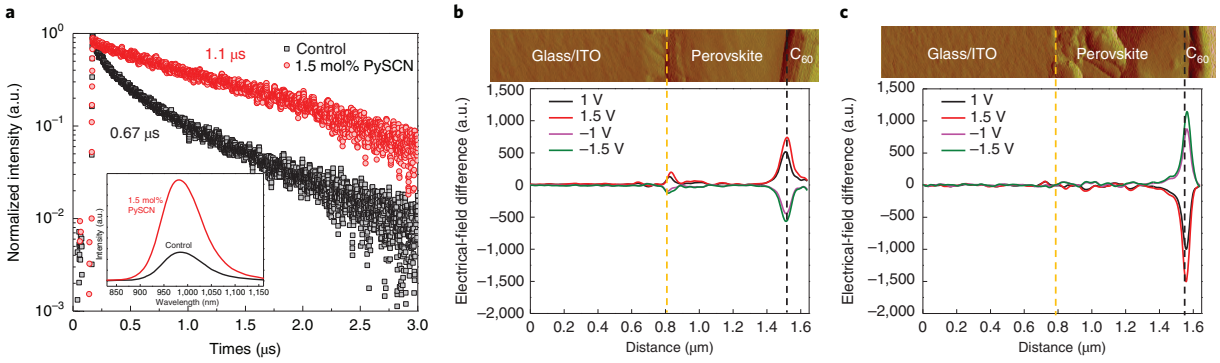


Fig. 3 | 1D PySn$_x$Pb$_{1-x}$I$_3$ passivation of mixed Sn–Pb perovskite thin films. a, Time-resolved photoluminescence (TRPL) decays and PL spectra (inset) of the $FA_{0.85}MA_{0.1}Cs_{0.05}Sn_{0.5}Pb_{0.5}I_3$ perovskite films without (control) and with 1.5 mol% PySCN. **b**,**c**, Cross-sectional KPFM potential maps and the corresponding electric field profiles of the $FA_{0.85}MA_{0.1}Cs_{0.05}Sn_{0.5}Pb_{0.5}I_3$ films without (**b**) and with (**c**) 1.5 mol% PySCN. The dashed lines indicate the interfaces of ITO/perovskite (yellow) and perovskite/C_{60} (black). The four potential difference curves were obtained by subtracting the 0 V profile curve from the potential profiles measured under different bias voltages from −1.5 to 1 V.

The formation of 1D PySn$_x$Pb$_{1-x}$I$_3$ perovskites on the surface of mixed Sn–Pb perovskite absorber layers also favourably influences junction quality, as revealed by cross-sectional Kelvin probe force microscopy (KPFM) measurements. The potential line profiles, potential differences with respect to the zero bias and electrical-field difference are shown in Supplementary Fig. 25 and Fig. 3b,c. Without the PySCN incorporation, a small peak is seen at the HTL/perovskite junction in the profiles of the electrical-field differences measured with various bias, besides the main peak at the perovskite/ETL junction (Fig. 3b). However, with 1.5 mol% PySCN incorporation, the peak at the HTL/perovskite junction disappeared to leave only the peak at the perovskite/ETL junction (Fig. 3c). This behaviour is clear evidence of improved junctions, as we demonstrated previously in various perovskite device configurations[48–50]. This positive effect on junction quality and enhanced carrier lifetime led to an improved V_{OC} and FF when a small amount of PySCN was incorporated. The V_{OC} reached a maximum when the incorporation of PySCN reached 1.5 mol% (Supplementary Fig. 26).

Performance and stability of single-junction and tandem PSCs

We fabricated single-junction mixed Sn–Pb PSCs using the 1.5 mol%-PySCN-incorporated $FA_{0.85}MA_{0.1}Cs_{0.05}Sn_{0.5}Pb_{0.5}I_3$ perovskites as the absorber layers. Figure 4a shows the histogram of the PCEs of 30 cells. The detailed photovoltaic parameters of the PCSs are shown in Supplementary Fig. 27 and Supplementary Table 2, and show good reproducibility and negligible J–V hysteresis. Noticeable improvements in V_{OC} and FF due to the PySn$_x$Pb$_{1-x}$I$_3$ passivation were observed. Figure 4b shows the J–V curves of the best-performing device measured under reverse and forward voltage scans. The cell delivered a PCE of 20.4 (20.3)%, a V_{OC} of 0.865 (0.864) V, a short circuit current (J_{SC}) of 29.81 (29.85) mA–cm^{-2} and a FF of 79.1 (78.7)% under the reverse (forward) voltage scan. The J_{SC} values match well with the integrated photocurrent density of 29.33 mA cm^{-2} deduced from the external quantum efficiency (EQE) spectrum (Fig. 4c). More importantly, the FA-based mixed Sn–Pb PSCs show decent operational stability. As shown in Fig. 4g, an encapsulated $FA_{0.85}MA_{0.1}Cs_{0.05}Sn_{0.5}Pb_{0.5}I_3$ cell retained 92% of its original efficiency after maximum power point (MPP) tracking for 450 h under continuous one sun illumination. This robust operational stability is mainly attributed to the BIG-processed FA-based mixed Sn–Pb perovskite after comparing devices with different compositions and passivation (Supplementary Figs. 28 and 29). Moreover, we performed an accelerated thermal degradation test of mixed Sn–Pb PSCs following the perovskite community consensus[47]. We found that the BIG-processed $FA_{0.85}MA_{0.1}Cs_{0.05}Sn_{0.5}Pb_{0.5}I_3$ PSCs demonstrated a considerably improved intrinsic thermal stability compared with that of the conventional $(FASnI_3)_{0.6}(MAPbI_3)_{0.4}$ when aged at 85 °C in nitrogen (Supplementary Fig. 30). It has been found that the thermal stability of most mixed Sn–Pb PSCs is limited by the use of acidic PEDOT:PSS and corrosive Ag electrode[14]. The real-world applications of mixed Sn–Pb PSCs require more stable HTLs, electrodes and encapsulation techniques.

The stable low-bandgap FA-based mixed Sn–Pb PSCs enabled us to fabricate stable 2-T perovskite/perovskite tandem solar cells. The tandem cells, which consisted of 1.73 eV wide-bandgap top subcells and 1.28 eV BIG-processed low-bandgap bottom subcells were fabricated following a procedure reported previously[19]. The device architecture is depicted in Supplementary Fig. 31, and the corresponding cross-sectional SEM image is shown in Fig. 4d. Benefiting from the high-quality mixed Sn–Pb subcell prepared by the BIG process with the PySn$_x$Pb$_{1-x}$I$_3$ passivation, the champion tandem cell exhibited a PCE of 23.3% (23.3%), with a high V_{OC} of 1.943 (1.937) V, J_{SC} of 15.1 (15.2) mA cm^{-2} and FF of 79.3% (79%) under the reverse (forward) voltage scan (Fig. 4e). The integrated J_{SC} values for wide- and low-bandgap subcells calculated from the EQE spectra (Fig. 4f) were 15.0 and 14.8 mA cm^{-2}, respectively, which are consistent with the J_{SC} value from the J–V curves. The stable low-bandgap mixed Sn–Pb subcells enabled the stable operation of our perovskite/perovskite tandem solar cells. Figure 4g illustrates that an encapsulated 2-T perovskite/perovskite tandem solar cell retained 85% of its initial PCE after MMP tracking for more than 350 h under 1 sun illumination, which is remarkably improved compared with the device that used the conventional mixed Sn–Pb subcell (Supplementary Fig. 32).

Conclusions

In summary, we developed a two-step BIG process to fabricate high-efficiency and high-stability FA-based mixed Sn–Pb PSCs. The deposition process was systematically investigated to understand the perovskite formation mechanism. The mixed Sn–Pb absorber films exhibited large grains and a low MA concentration. Single-junction PSCs using the $FA_{0.85}MA_{0.1}Cs_{0.05}Sn_{0.5}Pb_{0.5}I_3$ absorber layers prepared by the BIG process achieved a best PCE of 20.4% and demonstrated

Approved for public release; distribution unlimited.

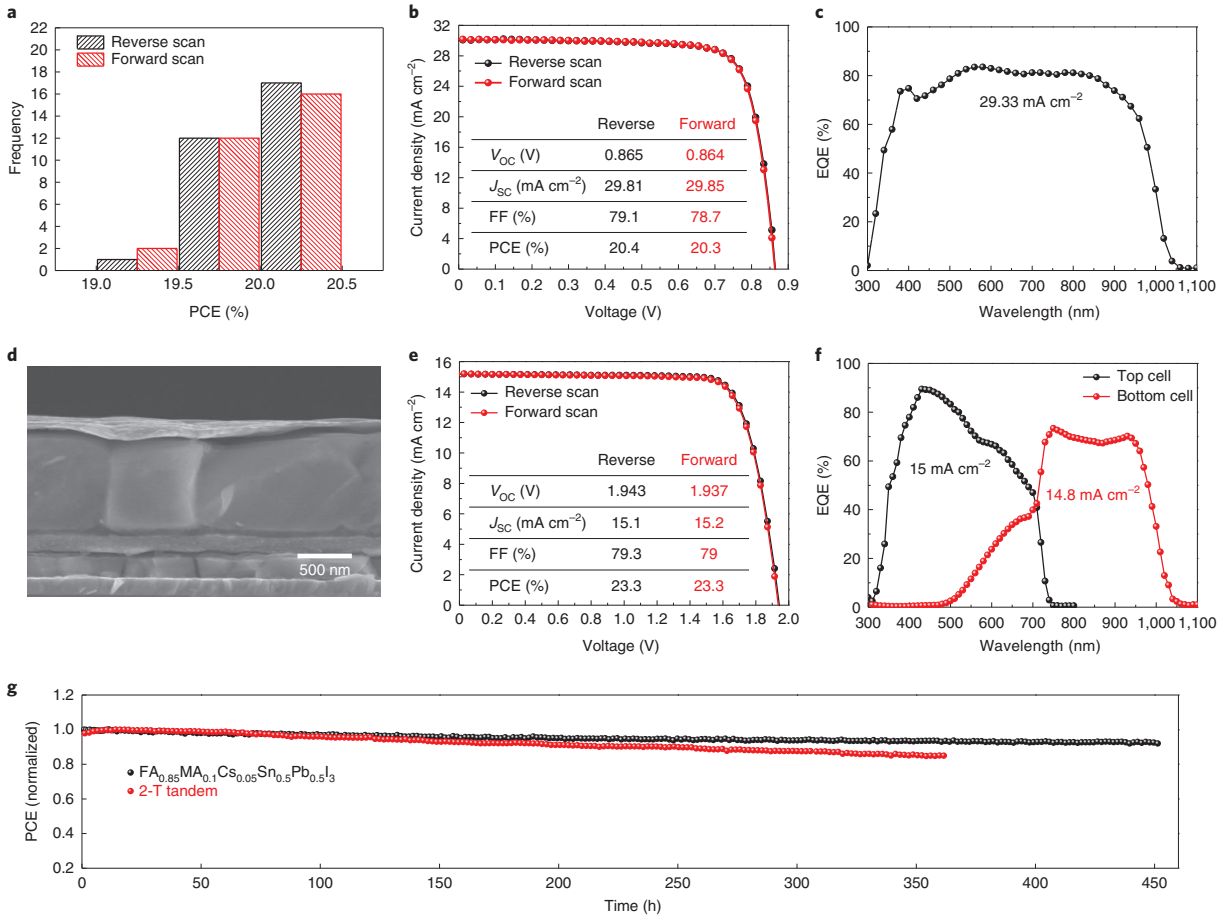


Fig. 4 | Single-junction and tandem PSCs. a, Histogram of the PCEs for 30 $FA_{0.85}MA_{0.1}Cs_{0.05}Sn_{0.5}Pb_{0.5}I_3$ mixed Sn–Pb PSCs with 1.5 mol% PySCN. **b**,**c**, *J*–*V* curves (**b**) and EQE spectrum (**c**) of the best-performing single-junction mixed Sn–Pb PSC. The integrated J_{SC} from the EQE curve is 29.33 mA cm^{-2}, as marked in the figure. **d**, Cross-sectional SEM image of a perovskite/perovskite tandem solar cell. **e**,**f**, *J*–*V* curves (**e**) and EQE spectrum (**f**) of the best-performing perovskite/perovskite tandem solar cell. The integrated J_{SC} values from the EQE data of wide- and low-bandgap subcells are 15 and 14.8 mA cm^{-2}, respectively. **g**, MPP tracking of a $FA_{0.85}MA_{0.1}Cs_{0.05}Sn_{0.5}Pb_{0.5}I_3$ PSC and a 2-T perovskite/perovskite tandem cell with encapsulation measured in the air under simulated AM 1.5G solar illumination. The initial PCEs for the single-junction $FA_{0.85}MA_{0.1}Cs_{0.05}Sn_{0.5}Pb_{0.5}I_3$ PSC and the 2-T tandem cell were 19.8 and 23.1%, respectively.

MPP stability for more than 450 h of continuous operation with a power loss of less than 10%. The stable low-bandgap mixed Sn–Pb PSCs enabled the fabrication of 2-T perovskite/perovskite tandem cells with PCEs that exceeded 23%. A tandem cell retained 85% of its initial PCE after 350 h of continuous operation under MPP tracking. Our BIG process paves a pathway to simultaneously maximize performance and stability for mixed Sn–Pb PSCs. However, further improvements in the design of the device architecture and selection of materials are needed to enable a better PCE and stability of tandem cells.

Methods

Materials. SnI_2, lead thiocyanate, MACl, diethyl ether, tin(II) fluoride, DMF and IPA were purchased from Aldrich Sigma. PbI_2 and CsI were purchased from Alfa Aesar. FAI, methylammonium iodide, MASCN and PySCN were purchased from GreatCell Solar. Poly(triaryl amine) was purchased from Xi'an Polymer Light Technology Corp. PEDOT:PSS was purchased from Heraeus company. 2,3,5,6-Tetrafuoro-7,7,8,8-tetracyanoquinodimethane and BCP were purchased from Jilin OLED Company. The ITO target and silver were purchased from Kurt J. Lesker.

One-step $(FASnI_3)_{0.6}(MAPbI_3)_{0.4}$ low-bandgap perovskite precursor. The precursor solution was prepared by the same recipe reported in our previous work. SnI_2 (372 mg), FAI (172 mg) and tin(II) fluoride (15.6 mg) were dissolved in a mixed solvent of DMF (424 µl) and DMSO (212 µl) to prepare the $FASnI_3$ precursor solution. PbI_2 (461 mg), methylammonium iodide (159 mg) and lead thiocyanate (11.3 mg) were dissolved in a mixed solvent of DMF (633 µl) and DMSO (71 µl). The two solutions were then mixed at the molar ratio of 6:4 to form the $(FASnI_3)_{0.6}(MAPbI_3)_{0.4}$ precursor solution.

Two-step conventional mixed Sn–Pb low-bandgap perovskite precursor. PbI_2 (345.8 mg) and SnI_2 (279.5 mg) were dissolved in a mixed solvent of DMF (900 µl) and DMSO (100 µl) to form the first-step precursor solution. FAI (60 mg) and MACI (6 mg) were dissolved in IPA (1 µl) to form the second-step precursor.

Two-step BIG-processed $FA_{0.85}MA_{0.1}Cs_{0.05}Sn_{0.5}Pb_{0.5}I_3$ perovskite precursor. PbI_2 (230.5 mg), SnI_2 (186.3 mg), CsI (12.99 mg) and MASCN (22.54 mg) were dissolved in a DMF and DMSO mixed solvent for the $FA_{0.85}MA_{0.1}Cs_{0.05}Sn_{0.5}Pb_{0.5}I_3$ precursor. CsI was removed from the recipe to prepare the FA-based mixed Sn–Pb perovskite without Cs^+, with everything else kept the same. To change the precursor solution concentration, mixed DMF/DMSO solvents of 714/51, 667/47, 625/44 and 588/42 µl were used to prepare the 1.4, 1.5, 1.6 and 1.7 M precursor

Approved for public release; distribution unlimited.
559

solution, respectively. An additional 1.3, 2.0 and 6.5 mg of PySCN were added to the precursor to form the 1, 1.5 and 5 mol%, respectively, $PySn_xPb_{1-x}I_3$ passivation. FAI (60 mg) were dissolved in 1 µl of IPA to form the second-step precursor.

$FA_{0.8}Cs_{0.2}Pb(I_{0.7}Br_{0.3})_3$ wide-bandgap perovskite precursor. FAI (126.6 mg), CsI (47.8 mg), $PbBr_2$ (152.0 mg) and PbI_2 (233.2 mg) were dissolved in the mixed solvent of 750 µl of DMF and 250 µl of DMSO.

One-step $(FASnI_3)_{0.6}(MAPbI_3)_{0.4}$ low-bandgap PSC fabrication. The HTL PEDOT:PSS was spin coated on the ITO substrate at 4,000 r.p.m. for 50 s, followed by a 150 °C annealing for 15 min. The perovskite solution (40 µl) was spin coated onto the PEDOT:PSS layer at 5,000 r.p.m. for 60 s. Diethyl ether was applied dropwise onto the film 5 s from the start of the spin. The film was then transferred to a 100 °C hotplate for 7 min. After cooling to room temperature, the film was kept in a sealed box and then transferred to a Kurt J. Lesker thermal evaporation system. C_{60} (20 nm), BCP (5 nm) and Ag (80 nm) were sequentially evaporated on the perovskite film to form a PSC device. Unless otherwise mentioned, the HTL-, ETL- and electrode-fabrication processes were the same for other low-bandgap PSCs.

Two-step conventional mixed Sn–Pb low-bandgap PSC fabrication. A SnI_2/PbI_2 (40 µl) precursor solution was spin coated on PEDOT:PSS at 1,500 r.p.m. for 30 s, followed by a 70 °C annealing for 2 min. After spinning, 150 µl of FAI/MACl solution was dropped on the precursor film and the excess solution was spin dried immediately by another 1,500 r.p.m. spin for 30 s. The film was then annealed on a 100 °C hotplate before it was transferred to the evaporation system to fabricate the ETL and electrode.

Two-step BIG-processed $FA_{0.85}MA_{0.1}Cs_{0.05}Sn_{0.5}Pb_{0.5}I_3$ PSC fabrication. The first-step precursor solution SnI_2/PbI_2/MASCN/CsI/PySCN (40 µl) was spin coated on the PEDOT:PSS substrate at 1,500 r.p.m. for 30 s. Then, 200 µl of the second-step FAI precursor solution was dropped on the precursor film followed by an immediate spin of 1,500 r.p.m for another 30 s. The delay between applying FAI and the second-step spinning needed to be finished within 1 s. The film was then transferred to a 50 °C hotplate for 3 min for the diffusion of FAI and full transformation of the perovskite phase. Afterwards, the film was transferred to a 120 °C hotplate for 7 min for further grain growth. The annealed film was then sealed and transferred to the evaporation system to fabricate the ETL and electrode.

2-T perovskite/perovskite tandem solar cell fabrication. Poly(triaryl amine) solution (80 µl) was spin coated on the ITO substrate at 4,000 r.p.m. for 30 s and then the substrate was annealed at 100 °C for 10 min. DMF (70 µl) was spin coated at 4,000 r.p.m. for 10 s to improve the wettability of the poly(triaryl amine) surface prior to wide-bandgap perovskite deposition. The perovskite precursor was spin coated at 500 r.p.m. for 3 s and then at 4,000 r.p.m. for 60 s. During the 4,000 r.p.m. step, 750 µl of diethyl ether was applied dropwise in the centre of the substrate to facilitate the crystallization. After that, the substrate was annealed at 60 °C for 2 min and at 100 °C for 5 min. Next, the substrate was transferred to the vacuum chamber. C_{60} (20 nm) and BCP (5 nm) were thermally evaporated sequentially. The substrate was then transferred to the radio-frequency magnetron sputtering system. A 130 nm ITO layer was sputtered from the 76.2 mm ITO target (In_2O_3/SnO_2 90/10 wt%; Lesker) at a 70 W power under an Ar pressure of 2 mtorr. Then, PEDOT:PSS diluted with IPA (volume ratio 1:1) was spin coated on the sputtering ITO layer, followed by 5 min of annealing on a 100 °C hotplate in air. After annealing, the film was immediately transferred to a glove box for the BIG-processed $FA_{0.85}MA_{0.1}Cs_{0.05}Sn_{0.5}Pb_{0.5}I_3$ layer deposition, which followed the same process as discussed above. Finally, the film was transferred in a sealed box to the thermal evaporation system to evaporate the ETL and electrode.

XRD. A Rigaku Ultima III XRD with Cu Kα radiation was used to measure and analyse the crystal structure and properties of the one-step processed and conventionally processed low-bandgap mixed Sn–Pb perovskites, the $FA_{0.85}MA_{0.1}Cs_{0.05}Sn_{0.5}Pb_{0.5}I_3$ precursor films at each stage during the BIG process, as well as the films with different concentrations of PySCN passivation.

SEM. A high-resolution field-emission Hitachi S-4800 SEM was used to measure the top-view and cross-sectional images of the conventional processed low-bandgap mixed Sn–Pb perovskites and the $FA_{0.85}MA_{0.1}Cs_{0.05}Sn_{0.5}Pb_{0.5}I_3$ precursor films at each stage during the BIG process, as well as the films with different concentrations of PySCN passivation.

KPFM. Scanning KPFM measurements were performed in an Ar-filled glove box using a Vecco D5000 atomic force microscope. A PPP-EFM tip was operated in tapping mode for the cross-sectional potential distribution. The electrical resolution was ~10 mV. In the junction measurement, we cleaved the solar cell to expose the cross-sectional surface; the ITO was grounded and various bias voltages were applied to the Ag side. No polishing or ion-milling treatment was introduced to the sample preparation to avoid artefacts.

PDS measurement. PDS measurements were collected using a custom system (PTS-3-PTD, Sciencetech Inc.) operated in transverse configuration[31] over a spectral range of 1,400–800 nm (0.89–1.55 eV) in 10 nm steps. The monochromatic pump beam was modulated with a mechanical chopper at 0.2 Hz. The probe beam was a 633 nm laser of a nominally 300 µm cross-sectional diameter. Perovskite films were placed into a quartz cuvette, which was then filled with Fluorinert (C_6F_{14} fluid) while inside a nitrogen-purged glove box. PDS measurements were collected for perovskite films without exposure to the atmosphere. The Urbach energy of perovskite films was calculated by the linear fitting of the corresponding PDS curve. The Urbach energy was determined by the inverse of the slope of a linear fit to $\ln(\alpha/\alpha_g)$ below bandgap, where α is the absorption coefficient spectra and α_g is the absorption coefficient at the bandgap energy. The standard error in the slope was scaled with the square root of a reduced chi-squared statistic (the linear fit; Origin 2020).

^{1}H NMR spectroscopy. The proton spectra were acquired on a Bruker Avance III NMR spectrometer with a DCH Cryoprobe at 600 MHz. The data were collected at 22 °C using a one-pulse sequence with a 30° flip pulse of 3.3 µs, acquisition time of 2.7 s. and a recycle delay of 1 s.

TPD-MS. The TPD-MS measurements were performed using a built-in-house TPD system. The mass spectra in a range of 1 to 150 atomic mass units were recorded by a quadrupole mass spectrometer (Stanford Research System, RGA 300) using a custom LabVIEW program, following a previously reported procedure. For a typical TPD routine, the furnace temperature was ramped up from room temperature to 500 °C at a ramp rate of 1.67 °C min^{-1}.

TOF–SIMS. An ION-TOF TOF-SIMS V spectrometer was used for depth profiling and chemical imaging of the perovskite. Analysis was completed using a three-lens 30 kV BiMn primary-ion gun. 1D profiles were completed utilizing the Bi^{3+} primary-ion beam (0.8 pA pulsed beam current) and a 50 × 50 µm area was analysed with a 128:128 primary beam raster. Sputtering for surface cleaning and depth profiling was accomplished with 1 kV oxygen and caesium ion sputter beams (~5 nA sputter current for each source) with a raster of 200 × 200 µm. After completion of the SIMS measurements, the depth of the SIMS sputter craters was determined by optical interference light microscopy to convert the SIMS sputter timescale to a sputter depth scale.

TRPL. TRPL measurements were conducted using a time-correlated single-photon counting module (Becker & Hickel Simple Tau SPCM 130-E/M module). Samples were excited by a 532 nm pulsed laser (~5 ps pulse width, ~150 µm spot diameter; Fianium model SC400-2) at ~10^{10} photons pulse^{-1} cm^{-2}. Radiative recombination events were detected via an InP/InGaAsP near-infrared photomultiplier tube detector (Hamamatsu H10330A-45) after dispersion by an iHR-320 monochromator grating (900 g mm^{-1}, 850 nm blaze). PL decay curves were biexponential in nature and fitted by iterative reconvolution with the measured system response function. The mean photogenerated carrier lifetime for the biexponential fit was calculated by the weighted-average method.

SE and unpolarized transmittance measurement. Immediately following PDS measurement, each film was removed from the C_6F_{14} fluid into the laboratory ambient for SE and unpolarized transmittance measurements. Both measurements were collected using a multichannel rotating-compensator spectroscopic ellipsometer (M-2000FI, J. A. Woollam Co., Inc.) over a spectral range of 1676–210 nm (0.74–5.89 eV). The SE and unpolarized transmittance measurements were collected at a 70° and 0° angle of incidence, respectively, with the SE being measured in terms of $N = \cos(2\psi)$, $C = \sin(2\psi)\cos\Delta$ and $S = \sin(2\psi)\sin\Delta$, where ψ is the amplitude ratio and Δ is the phase difference between *p*- and *s*-polarized light waves, respectively, N, C and S are the non-zero elements of the isotropic Mueller matrix. The combined time for sample mounting, alignment and data acquisition for these two measurements, that is the length of time the films were in the laboratory ambient air, was approximately 2–3 min.

PSC characterization. The PSCs were encapsulated with cover glasses and then sealed by ultraviolet-curable epoxy before conducting the *J*–*V* measurements, MMP tracking measurements and EQE measurements in the ambient air. *J*–*V* curves were measured under 100 mW cm^{-2} AM 1.5G solar irradiation (PV Measurements Inc.) with a Keithley 2400 Source Meter.

The light intensity for the *J*–*V* measurements was calibrated by a standard silicon wafer solar cell and the PSCs certified by Newport. The MMP tracking measurements for both the $FA_{0.85}MA_{0.1}Cs_{0.05}Sn_{0.5}Pb_{0.5}I_3$ single-junction PSC and the fabricated 2-T tandem cell were conducted in air under a full-spectrum one sun illumination without any light filter. The humidity of the measurement environment ranged from 40 to 60%. Especially, the single-junction $FA_{0.85}MA_{0.1}Cs_{0.05}Sn_{0.5}Pb_{0.5}I_3$ PSC was tracked under room temperature, whereas for the 2-T tandem cells the environment temperature was kept at 25 °C to limit the water and oxygen ingression through the encapsulant from the humid measurement environment. A 0.1 cm^2 area mask was used to define the active area of a PSC. A quantum efficiency system (model IVQE8-C, PV Measurements

Approved for public release; distribution unlimited.
560

Inc.) was used to measure the quantum efficiency of the PSCs. A standard silicon wafer solar cell was used as the reference for the EQE measurement. We used bias illumination to measure the EQE for the 2-T tandem cell. The EQEs of the top and bottom subcells were measured by exposing the 2-T tandem cell under 530 and 940 nm LED lamps, respectively, to saturate the other junction during EQE measurement. The thermal stability tests were conducted by ageing the PEDOT:PSS-free devices on a hotplate at 85 °C in a nitrogen glove box. The devices were then encapsulated and periodically taken out to the ambient air for *J*–*V* measurements. Once the measurement of a device was done, the device was placed back on the hotplate in the glove box immediately to prevent the inevitable leakage and oxidization.

Reporting Summary. Further information on research design is available in the Nature Research Reporting Summary linked to this article.

Data availability

All data generated or analysed during this study are included in the published article and its Supplementary Information.

Received: 26 December 2019; Accepted: 21 August 2020;
Published online: 15 October 2020

References

1. *Best Research-Cell Efficiency Chart* https://www.nrel.gov/pv/cell-efficiency.html (NREL, accessed 25 March 2020).
2. Shockley, W. & Queisser, H. J. Detailed balance limit of efficiency of p–n junction solar cells. *J. Appl. Phys.* **32**, 510–519 (1961).
3. Hörantner, M. T. et al. The potential of multijunction perovskite solar cells. *ACS Energy Lett.* **2**, 2506–2513 (2017).
4. Leijtens, T., Bush, K. A., Prasanna, R. & McGehee, M. D. Opportunities and challenges for tandem solar cells using metal halide perovskite semiconductors. *Nat. Energy* **3**, 828–838 (2018).
5. Eperon, G. E. et al. Perovskite–perovskite tandem photovoltaics with optimized band gaps. *Science* **354**, 861–865 (2016).
6. Lin, R. et al. Monolithic all-perovskite tandem solar cells with 24.8% efficiency exploiting comproportionation to suppress Sn(II) oxidation in precursor ink. *Nat. Energy* **4**, 864–873 (2019).
7. Tong, J. et al. Carrier lifetimes of >1 μs in Sn–Pb perovskites enable efficient all-perovskite tandem solar cells. *Science* **364**, 475–479 (2019).
8. Chen, B., Zheng, X., Bai, Y., Padture, N. P. & Huang, J. Progress in tandem solar cells based on hybrid organic–inorganic perovskites. *Adv. Energy Mater.* **7**, 1602400 (2017).
9. Yang, Z. et al. Enhancing electron diffusion length in narrow-bandgap perovskites for efficient monolithic perovskite tandem solar cells. *Nat. Commun.* **10**, 4498 (2019).
10. Prasanna, R. et al. Design of low bandgap tin–lead halide perovskite solar cells to achieve thermal, atmospheric and operational stability. *Nat. Energy* **4**, 939–947 (2019).
11. Leijtens, T. et al. Tin–lead halide perovskites with improved thermal and air stability for efficient all-perovskite tandem solar cells. *Sustain. Energy Fuels* **2**, 2450–2459 (2018).
12. Kapil, G. et al. Strain relaxation and light management in tin–lead perovskite solar cells to achieve high efficiencies. *ACS Energy Lett.* **4**, 1991–1998 (2019).
13. Forgács, D. et al. Efficient monolithic perovskite/perovskite tandem solar cells. *Adv. Energy Mater.* **7**, 1602121 (2017).
14. Wei, M. et al. Combining efficiency and stability in mixed tin–lead perovskite solar cells by capping grains with an ultrathin 2*d* layer. *Adv. Mater.* **32**, 1907058 (2020).
15. Wang, C., Song, Z., Li, C., Zhao, D. & Yan, Y. Low-bandgap mixed tin–lead perovskites and their applications in all-perovskite tandem solar cells. *Adv. Funct. Mater.* **29**, 1808801 (2019).
16. Xu, G. et al. Integrating ultrathin bulk–heterojunction organic semiconductor intermediary for high-performance low-bandgap perovskite solar cells with low energy loss. *Adv. Funct. Mater.* **28**, 1804427 (2018).
17. Liao, W. et al. Fabrication of efficient low-bandgap perovskite solar cells by combining formamidinium tin iodide with methylammonium lead iodide. *J. Am. Chem. Soc.* **138**, 12360–12363 (2016).
18. Zhao, D. et al. Low-bandgap mixed tin–lead iodide perovskite absorbers with long carrier lifetimes for all-perovskite tandem solar cells. *Nat. Energy* **2**, 17018 (2017).
19. Zhao, D. et al. Efficient two-terminal all-perovskite tandem solar cells enabled by high-quality low-bandgap absorber layers. *Nat. Energy* **3**, 1093–1100 (2018).
20. Li, C. et al. Reducing saturation-current density to realize high-efficiency low-bandgap mixed tin–lead halide perovskite solar cells. *Adv. Energy Mater.* **9**, 1803135 (2019).
21. Li, C. et al. Methylammonium-mediated evolution of mixed-organic-cation perovskite thin films: a dynamic composition-tuning process. *Angew. Chem.* **56**, 7674–7678 (2017).
22. Tang, S. et al. Composition engineering in doctor-blading of perovskite solar cells. *Adv. Energy Mater.* **7**, 1700302 (2017).
23. Yang, M. et al. Perovskite ink with wide processing window for scalable high-efficiency solar cells. *Nat. Energy* **2**, 17038 (2017).
24. Song, Z. et al. Probing the origins of photodegradation in organic–inorganic metal halide perovskites with time-resolved mass spectrometry. *Sustain. Energy Fuels* **2**, 2460–2467 (2018).
25. Lang, F. et al. Influence of radiation on the properties and the stability of hybrid perovskites. *Adv. Mater.* **30**, 1702905 (2018).
26. Turren-Cruz, S.-H., Hagfeldt, A. & Saliba, M. Methylammonium-free, high-performance, and stable perovskite solar cells on a planar architecture. *Science* **362**, 449–453 (2018).
27. Juarez-Perez, E. J. et al. Photodecomposition and thermal decomposition in methylammonium halide lead perovskites and inferred design principles to increase photovoltaic device stability. *J. Mater. Chem. A* **6**, 9604–9612 (2018).
28. Juarez-Perez, E. J., Ono, L. K. & Qi, Y. Thermal degradation of formamidinium based lead halide perovskites into *sym*-triazine and hydrogen cyanide observed by coupled thermogravimetry–mass spectrometry analysis. *J. Mater. Chem. A* **7**, 16912–16919 (2019).
29. Prasanna, R. et al. Band gap tuning via lattice contraction and octahedral tilting in perovskite materials for photovoltaics. *J. Am. Chem. Soc.* **139**, 11117–11124 (2017).
30. Yu, Y. et al. Improving the performance of formamidinium and cesium lead triiodide perovskite solar cells using lead thiocyanate additives. *ChemSusChem* **9**, 3288–3297 (2016).
31. Xu, A. F. et al. Pyrrolidinium lead iodide from crystallography: a new perovskite with low bandgap and good water resistance. *Chem. Commun.* **55**, 3251–3253 (2019).
32. Fan, J. et al. Thermodynamically self-healing 1*d*–3*d* hybrid perovskite solar cells. *Adv. Energy Mater.* **8**, 1703421 (2018).
33. Jiang, Q. et al. Surface passivation of perovskite film for efficient solar cells. *Nat. Photon.* **13**, 460–466 (2019).
34. Lian, X. et al. Highly efficient Sn/Pb binary perovskite solar cell via precursor engineering: a two-step fabrication process. *Adv. Funct. Mater.* **29**, 1807024 (2019).
35. Jacobsson, T. J. et al. Unreacted PbI_2 as a double-edged sword for enhancing the performance of perovskite solar cells. *J. Am. Chem. Soc.* **138**, 10331–10343 (2016).
36. Ogomi, Y. et al. $CH_3NH_3Sn_xPb_{(1-x)}I_3$ perovskite solar cells covering up to 1060 nm. *J. Phys. Chem. Lett.* **5**, 1004–1011 (2014).
37. Saliba, M. et al. Incorporation of rubidium cations into perovskite solar cells improves photovoltaic performance. *Science* **354**, 206–209 (2016).
38. Lee, J.-W. et al. Formamidinium and cesium hybridization for photo- and moisture-stable perovskite solar cell. *Adv. Energy Mater.* **5**, 1501310 (2015).
39. Yi, C. et al. Entropic stabilization of mixed A-cation ABX_3 metal halide perovskites for high performance perovskite solar cells. *Energy Environ. Sci.* **9**, 656–662 (2016).
40. Saliba, M. et al. Cesium-containing triple cation perovskite solar cells: improved stability, reproducibility and high efficiency. *Energy Environ. Sci.* **9**, 1989–1997 (2016).
41. Im, J., Stoumpos, C. C., Jin, H., Freeman, A. J. & Kanatzidis, M. G. Antagonism between spin–orbit coupling and steric effects causes anomalous band gap evolution in the perovskite photovoltaic materials $CH_3NH_3Sn_{1-x}Pb_xI_3$. *J. Phys. Chem. Lett.* **6**, 3503–3509 (2015).
42. Hao, F., Stoumpos, C. C., Chang, R. P. & Kanatzidis, M. G. Anomalous band gap behavior in mixed Sn and Pb perovskites enables broadening of absorption spectrum in solar cells. *J. Am. Chem. Soc.* **136**, 8094–8099 (2014).
43. Harvey, S. P. et al. Mitigating measurement artifacts in TOF–SIMS analysis of perovskite solar cells. *ACS Appl. Mater. Interfaces* **11**, 30911–30918 (2019).
44. Chen, B., Rudd, P. N., Yang, S., Yuan, Y. & Huang, J. Imperfections and their passivation in halide perovskite solar cells. *Chem. Soc. Rev.* **48**, 3842–3867 (2019).
45. Yang, W. S. et al. Iodide management in formamidinium–lead–halide-based perovskite layers for efficient solar cells. *Science* **356**, 1376–1379 (2017).
46. Yin, W.-J., Shi, T. & Yan, Y. Unusual defect physics in $CH_3NH_3PbI_3$ perovskite solar cell absorber. *Appl. Phys. Lett.* **104**, 063903 (2014).
47. Khenkin, M. V. et al. Consensus statement for stability assessment and reporting for perovskite photovoltaics based on ISOS procedures. *Nat. Energy* **5**, 35–49 (2020).
48. Wang, C. et al. Understanding and eliminating hysteresis for highly efficient planar perovskite solar cells. *Adv. Energy Mater.* **7**, 1700414 (2017).
49. Chen, C. et al. Achieving a high open-circuit voltage in inverted wide-bandgap perovskite solar cells with a graded perovskite homojunction. *Nano Energy* **61**, 141–147 (2019).
50. Xiao, C. et al. Inhomogeneous doping of perovskite materials by dopants from hole-transport layer. *Matter* **2**, 1–12 (2019).
51. Jackson, W. B., Amer, N. M., Boccara, A. C. & Fournier, D. Photothermal deflection spectroscopy and detection. *Appl. Opt.* **20**, 1333–1344 (1981).

Approved for public release; distribution unlimited.
561

Acknowledgements

This material is based on work supported by the US Department of Energy's Office of Energy Efficiency and Renewable Energy (EERE) under the Solar Energy Technologies Office Award no. DE-EE0008753. The TPD-MS study was supported by the National Science Foundation under contract no. DMR-1807818. K.K.S. and R.J.E. were supported by the US Air Force Research Laboratory under agreement no. FA9453-18-2-0037, and N.S., B.S., N.J.P. and R.J.E. were supported by the US Air Force Research Laboratory under agreement no. FA9453-19-C-1002. The US Government is authorized to reproduce and distribute reprints for Governmental purposes notwithstanding any copyright notation thereon.

Author contributions

C.L., Z.S. and Y.Y. conceived the project. C.L. carried out the single-junction low-bandgap cell and tandem cell fabrication. C.C. prepared the wide-bandgap cell and helped with the tandem cell fabrication. D.L. participated in the wide-bandgap cell fabrication. Z.S. conducted the TPD-MS measurements. C.X. and C.J. helped with the KPFM. B.S. conducted the PDS and SE measurement. S.P.H. conducted the TOF–SIMS measurement. N.S. and K.K.S. helped with the PL and TRPL measurements. L.C. and Y.L. participated in the characterization. Y.-W.K. helped with the ^{1}H NMR measurements. C.L., Z.S. and Y.Y. analysed the data and wrote the manuscript. M.J.H., D.Z., R.J.E., N.J.P. and M.A.-J. helped with the manuscript preparation. All the authors discussed the results and commented on the manuscript. Y.Y. supervised the project.

Competing interests

The authors declare no competing interests.

Additional information

Supplementary information is available for this paper at https://doi.org/10.1038/s41560-020-00692-7.

Correspondence and requests for materials should be addressed to Z.S. or Y.Y.

Reprints and permissions information is available at www.nature.com/reprints.

Publisher's note Springer Nature remains neutral with regard to jurisdictional claims in published maps and institutional affiliations.

© The Author(s), under exclusive licence to Springer Nature Limited 2020

Approved for public release; distribution unlimited.
562

Highly Doped Single Walled Carbon Nanotubes Deposited as the Back Buffer Layer on CdTe Devices

Jacob M. Gibbs
Wright Center for Photovoltaic Innovation and Commercailization
University of Toledo
Toledo, USA
jacob.gibbs@rockets.utoledo.edu

Adam B. Phillips
Wright Center for Photovoltaic Innovation and Commercailization
University of Toledo
Toledo, USA
adam.phillips@utoledo.edu

Ebin Bastola
Wright Center for Photovoltaic Innovation and Commercailization
University of Toledo
Toledo, USA
ebin.bastola@rockets.utoledo.edu

Fadhil K. Alfadhili
Wright Center for Photovoltaic Innovation and Commercailization
University of Toledo
Toledo, USA
fadhil.alfadhili@rockets.utoledo.edu

Ramez Hossenian Ahangharnejhad
Wright Center for Photovoltaics Innovation and Comerciallization
University of Toledo
Toledo, USA
Ramez.hosseinianahangharnejhad@rockets.utoledo.edu

Randy J. Ellingson
Wright Center for Photovoltaic Innovation and Commercailization
University of Toledo
Toledo, USA
randy.ellingson@utoledo.edu

Michael J. Heben
Wright Center for Photovoltaic Innovation and Commercailization
University of Toledo
Toledo, USA
michael.heben@utoledo.edu

***Abstract*—Due to the low Fermi level position in CdTe, back contacts to CdTe devices often lead to downward band bending at the back interface. SWCNTs potentially have a lower Fermi level than CdTe, but obtaining this level of doping in the SWCNTs after they have been applied to the CdTe is difficult to accomplish. Here, we show that SWCNT films can be doped, redispersed, and redeposited while maintaining a high level of doping. We are investigating if depositing doped SWCNTs onto CdTe is a viable method for improving the back interface of CdTe devices by apply doped and undoped SWCNTs to the back of 2 µm CdTe device structures.**

Keywords—CdTe, SWCNTs, OA doping, back interface engineering, transparent back contact

I. Introduction

The past nine CdTe photovoltaic device efficiency records were set by either GE Solar or First Solar [1], and the details of the device stacks and processing are closely guarded. Since then, the broader CdTe community has made advances in understanding of materials [2] and interface properties [3] that has enabled published efficiency values to approach the record value. Critical to these improvements has been the engineering of a wide bandgap emitter layer [4], which has allowed more light to be incident on the absorber and better band alignment with the absorber to reduce the recombination at this interface.

With these advances at the front interface understood, we recently investigated the back interface [5]. We showed that downward band bending near the back interface can lead to electron flow towards the back (p-type) contact and increased recombination. This effect becomes more prominent as the absorber thickness is reduced from 4 to 2 µm. If the amount of downward band bending could be reduced, the device performance is expected to improve. However, CdTe has a deep Fermi level even when the doping is on the order of 10^{14} cm^{-3}, as is the case with Cu doping, making it difficult to identify a material that could reduce the downward band bending.

Single walled carbon nanotubes (SWCNTs) have been employed as a back buffer layer for CdTe devices in the past [6, 7] and are of interest for this application because they offer the potential to be semi- or completely transparent, can be deposited using low cost solution processing [8], and have an intrinsic Fermi level below -5 eV [9]. Furthermore, the Fermi level of individual SWCNTs can be easily changed through environmental doping. Unfortunately, when these methods are employed to dope SWCNT films after they are on the CdTe, the dopants preferentially interact with the CdTe film, causing a decrease in device performance [10].

Here, we investigate using SWCNTs that are doped prior to deposition as the back buffer layer for CdTe devices. We dope SWCNT films and redisperse the SWCNTs in solution. Subsequent depositions show that the SWCNTs remain doped during resonication, deposition, and surfactant removal.

II. Experimental Details

To produce the original undoped SWCNT solutions for further processing, SWCNTs (CHASM SG65i) were dispersed in 0.1 wt/v % sodium dodecylbenzenesulfonate (SDBS) in deionized water using a probe sonicator, and the resultant solution was sprayed onto glass slides [11]. The prepared SWCNT films were soaked in a triethyloxonium hexachlorantimonate ($((C_2H_5)_3O^+$ $SbCl_6^-$; OA)/toluene solution (10 $mgml^{-1}$) for 60 sec. at 70 °C to dope the SWCNTs [12]. The doped SWCNT films were then redispersed by bath sonicating the film in 0.5 wt/v % SDBS in deionized water for 10 minutes

Funding provided by US Air Force Research Laboratory under agreement number FA9453-18-20037 and contract number FA9453-19-C-1002.

978-1-7281-6115-0/20/$31.00 ©2020 IEEE

Authorized licensed use limited to: Western Sydney University. Downloaded on June 16,2021 at 03:29:43 UTC from IEEE Xplore. Restrictions apply.

Approved for public release; distribution unlimited.

to remove the SWCNTs from the glass, followed by probe sonication for 60 sec. to disperse the SWCNTs.

The CdTe device stack of 120 nm CdSe/2.1 µm CdTe was sputtered at room temperature and 250 °C, respectively, on commercially available TEC 12D (Pilkington NA). These samples were activated by applying a $CdCl_2$/methanol solution and heating at 387 °C for 30 min in dry flowing air and subsequently rinsed with methanol to remove the excess $CdCl_2$. The CdTe device was Cu doped by soaking in a $CuCl_2$/methanol(.1mmol/L) solution for 120 sec followed by heating at 200 °C for 20 min.

The devices were finished by spraying approximately 50 nm of undoped SWCNTs at substrate temperature of 140 °C and soaking the films in deionized water to remove the SDBS followed by overlaying the stacks with 40 nm of Au using thermal evaporation to complete the back contact. Cells were defined using a laser scribing system.

SWCNT films were characterized using spectrophotometery (Perkin Elmer 1050). Devices were characterized using current density-voltage (JV) measurements that incorporated a sourcemeter (Keithley 2440) and an LED solar simulator (Oriel LSH-7320).

III. Results and Discussion

Fig. 1a shows the absorption spectra of the undoped, doped, and resprayed doped SWCNT films. The undoped films shows strong features around 1000 and 550 nm (S11 and S22, respectively) that are quenched in the doped films. These features can be understood by considering the density-of-states graph of a single SWCNT shown in Fig. 1b.

For an undoped SWCNT the density-of-states at the van Hove singularity (vHs) edge is high, and absorption of a photon of energy ~1.2 eV, for the CoMoCat tubes used here, can promote an electron from the valance band edge to the conduction band edge. This leads to the S11 absorption feature. The next transition occurs between the second vHs. These features occur as long as the density-of-states is high at the vHs edges. As the SWCNT is p-type doped, the Fermi level is pushed down, and once the Fermi level is below the vHs edge, the density-of-states decreases and the optical transmission for that SWCNT is quenched. Consequently, the optical spectrum can provide an estimate of the Fermi level position of the SWCNTs.

In Fig. 1a, the S11 transition is strong in the undoped SWCNT films, indicating that the Fermi level is between -5.0 and -5.6 eV. In the doped films, though, the S11 is strongly quenched, as is the S22 feature. (Note that the absorption spectrum of a SWCNT film is the envelope of all the individual SWCNTs, so a small S11 feature indicates that there are a number of undoped SWCNTs, likely at the center of SWCNT bundles that are not exposed to the dopant.) This indicates that the Fermi level is below the second vHs located at -6.1 eV and considerably below the Fermi level of Cu-doped CdTe. The lower Fermi level of the SWCNTs than CdTe should result in upward band bending at the back interface of the device [5].

Previously, we showed that the OA is more reactive with CdTe than SWCNTs, so attempting to dope the SWCNTs after

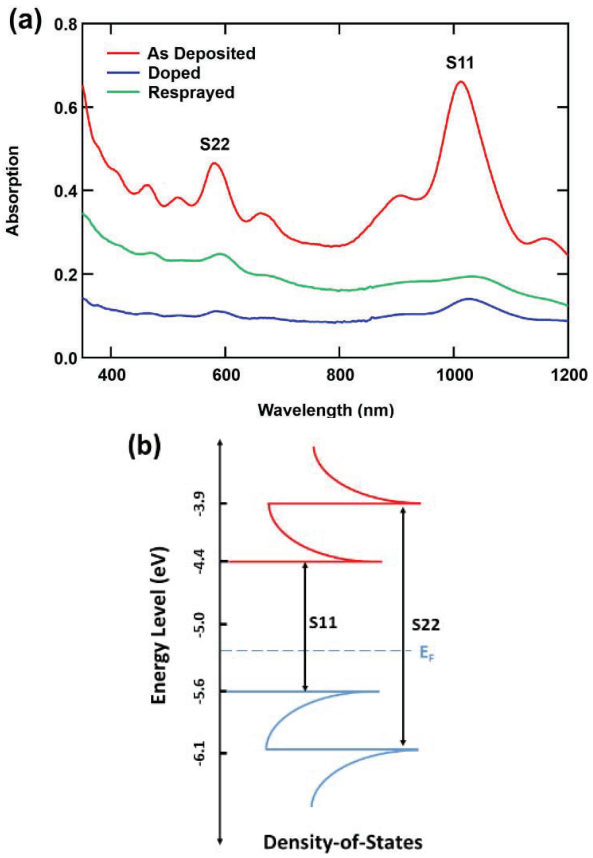


Fig. 1 (a) Absorption spectra of SWCNT films before and after doping with OA and after redispersed and resprayed. The spikes in the density-of-states corresponds to the van Hove singularities of the 1D SWCNTs. (b) Density-of-states diagram of semiconducting CoMoCat SWCNTs showing the first two optical absorption features.

deposited on CdTe leads to poor device performance [10]. An alternative approach is to deposit doped SWCNTs onto the CdTe. However, doping of SWCNTs affects the electronic properties of the surface of the SWCNTs that may alter surfactant/SWCNT interaction and prevent dispersion. Additionally, dispersing SWNCTs typically requires high power density processes that may affect the doping. Fig. 1a shows that after redispersing and subsequent spraying the SWNCTs remained doped. This verifies that the doping is not lost during the sonication process and that the dopant does not sufficiently disrupt the surfactant SWCNT interaction to prevent dispersion.

To determine if the SWCNT spraying process induces Cu migration and device degradation, we completed devices using undoped SWCNTs. Fig. 2 shows the JV curve of the best device. The efficiency of this device, 11.6%, is slightly higher than the performance of devices finished without the SWCNTs, 10.9%. These results indicate that the spraying process and subsequent soaking does not affect the Cu doping of the CdTe device.

978-1-7281-6115-0/20/$31.00 ©2020 IEEE

Authorized licensed use limited to: Western Sydney University. Downloaded on June 16,2021 at 03:29:43 UTC from IEEE Xplore. Restrictions apply.

Approved for public release; distribution unlimited.

564

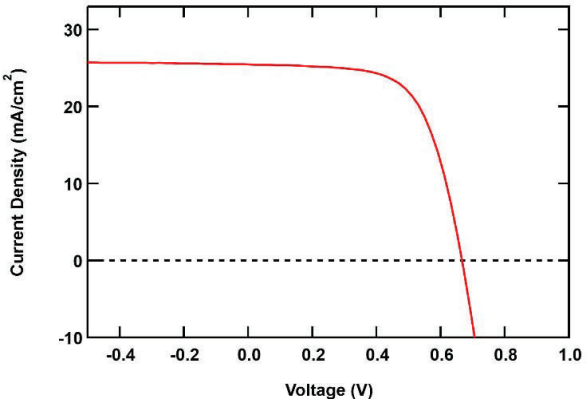


Fig.2. Current Density-Voltage curves of the best CdTe device using undoped SWCNT back buffer layers.

IV. Conclusions

We demonstrated that OA-doped SWCNT films can be dispersed using bath sonication, SDBS, and water and sprayed without dedoping the SWCNTs. The optical spectra of the doped SWCNT films show a quenching of the S22 feature, indicating that the Fermi level of some of the individual SWCNTs is at least -6.1 eV. A material with such a low Fermi level should induce upward band banding at the back interface of a CdTe device and lead to improvements in device performance. CdTe devices doped using $CuCl_2$ fabricated using undoped SWCNTs show that the spraying process does not affect the Cu doping of the CdTe device.

Acknowledgment

This material is based on research sponsored by the Air Force Research Laboratory under agreement number FA9453-18-2-0037 and contract number FA9453-19-C-1002 The U.S. Government is authorized to reproduce and distribute reprints for Governmental purposes notwithstanding any copyright notation thereon. The views and conclusions contained herin are those of the authors and should not be interpreted as necessarily representing the official policies or endorsements, either expressed or implied, of Air Force Research laboratory or the U.S. Government.

References

[1] (January 10, 2020). *https://www.nrel.gov/pv/cell-efficiency.html*.

[2] A. Kanevce, M. O. Reese, T. M. Barnes, S. A. Jensen, and W. K. Metzger, "The roles of carrier concentration and interface, bulk, and grain-boundary recombination for 25% efficient CdTe solar cells," *Journal of Applied Physics,* vol. 121, p. 214506, 2017.

[3] T. Song, A. Kanevce, and J. R. Sites, "Emitter/absorber interface of CdTe solar cells," *Journal of Applied Physics,* vol. 119, p. 233104, 2016.

[4] J. M. Kephart, J. W. McCamy, Z. Ma, A. Ganjoo, F. M. Alamgir, and W. S. Sampath, "Band alignment of front contact layers for high-efficiency CdTe solar cells," *Solar Energy Materials and Solar Cells,* vol. 157, pp. 266-275, 2016.

[5] G. K. Liyanage, A. B. Phillips, F. K. Alfadhili, R. J. Ellingson, and M. J. Heben, "The role of back bufferlLayers and absorber properties for >25% efficient CdTe solar cells," *ACS Applied Energy Materials,* vol. 2, pp. 5419-5426, 2019.

[6] T. M. Barnes, X. Wu, J. Zhou, A. Duda, J. van de Lagemaat, T. J. Coutts, *et al.*, "Single-wall carbon nanotube networks as a transparent back contact in CdTe solar cells," *Applied Physics Letters,* vol. 90, p. 243503, 2007.

[7] A. B. Phillips, R. R. Khanal, Z. Song, R. M. Zartman, J. L. DeWitt, J. M. Stone, *et al.*, "Wiring-up carbon single wall nanotubes to polycrystalline inorganic semiconductor thin films: low-barrier, copper-free back contact to CdTe solar cells," *Nano Letters,* vol. 13, pp. 5224-5232, 2013.

[8] R. C. Tenent, T. M. Barnes, J. D. Bergeson, A. J. Ferguson, B. To, L. M. Gedvilas, *et al.*, "Ultrasmooth, large-area, high-uniformity, conductive transparent single-walled-carbon-nanotube films for photovoltaics produced by ultrasonic spraying," *Advanced Materials,* vol. 21, pp. 3210-3216, 2009.

[9] T. J. McDonald, D. Svedruzic, Y. H. Kim, J. L. Blackburn, S. B. Zhang, P. W. King, *et al.*, "Wiring-up hydrogenase with single-walled carbon nanotubes," *Nano Letters,* vol. 7, pp. 3528-3534, 2007.

[10] F. K. Alfadhili, J. M. Gibbs, G. K. Liyanage, P. W. Krantz, S. C. Watthage, Z. Song, *et al.*, "Use of single wall carbon nanotube films doped with triethyloxonium hexachlorantimonate as a transparent back contact for CdTe solar cells," *2017 IEEE 44th Photovoltaic Specialist Conference (PVSC)*, pp. 730-734, 2017.

[11] R. R. Khanal, A. B. Phillips, Z. Song, V. V. Plotnikov, C. W. Carter, J. M. Stayancho, *et al.*, "Semiconducting carbon single-walled nanotubes as a Cu-free, barrier-free back contact for CdTe solar cell," *2014 IEEE 40th Photovoltaic Specialist Conference (PVSC),* pp. 2348-2353, 2014.

[12] B. Chandra, A. Afzali, N. Khare, M. M. El-Ashry, and G. S. Tulevski, "Stable charge-transfer doping of transparent single-walled carbon nanotube films," *Chemistry of Materials,* vol. 22, pp. 5179-5183, 2010.

Authorized licensed use limited to: Western Sydney University. Downloaded on June 16,2021 at 03:29:43 UTC from IEEE Xplore. Restrictions apply.

Approved for public release; distribution unlimited.

565

Solution Based Cu-Doped Aluminum Oxide as a Back Interface Layer for CdTe Solar Cells

Kamala Khanal Subedi
Department of Physics and Astronomy, University of Toledo
Toledo, OH, USA
Kamala.KhanalSubedi@rockets.utoledo.edu

Adam B. Phillips
Department of Physics and Astronomy, University of Toledo
Toledo, OH, USA
adam.phillips@utoledo.edu

Michael J. Heben
Department of Physics and Astronomy, University of Toledo
Toledo, OH, USA
Michael.Heben@utoledo.edu

Randy J. Ellingson
Department of Physics and Astronomy, University of Toledo
Toledo, OH, USA
Randy.Ellingson@utoledo.edu

***Abstract*— Developing a passivated and low-defect density back contact layer will enable higher efficiency II-VI polycrystalline devices. Here, we report the CdS/CdTe/CuAlOx/Au device structure to increase the open circuit voltage (V_{OC}) and fill factor (*FF*). With careful optimization of the CuAlOx buffer layer reactant concentration, and post annealing time and temperature, our best cell exhibits 14.6% efficiency without a separate Cu doping process (V_{OC} = 829 mV, *FF* = 78.0%, J_{SC} = 22.6 mA/cm^2); our controlled device, CdS/CdTe/Cu($CuCl_2$ treated)/Au, shows 13.9 % efficiency (V_{OC} = 829 mV, *FF* = 75.2%, J_{SC} = 22.3mA/cm^2).**

***Keywords*— back-contact, CdTe, CuAlOx, solution-based method**

I. Introduction

Nowadays, CdTe solar cells are gathering remarkable attention due to the substantial improvement of device efficiency up to 22.5 % [1]. Efficiency improvements require reduced defects at the front interface, rear interface, in the bulk of the absorber, and at grain boundaries. Open circuit voltage (V_{OC}) is mainly limited by the rear interface defects [2], and proper passivation of the rear interface could help to improve the V_{OC} and Fill Factor (*FF*). Previous modeling suggested that appropriate doping and lifetime increment are also essential for improvement of the V_{OC} [3] . Recently, Liyanage *et al.* employed numerical modeling to investigate the roll of a buffer layer for > 25% CdTe device efficiencies. They found the initial Fermi level offset should be positive to reduce the back surface recombination between the absorber and back contact buffer layers which can be controlled by changing the doping density of the back buffer layer[4].

The high work function of CdTe (~5.7 eV), in comparison with metals, yields the rollover effect in forward bias, significantly curbing device performance[5, 6]. Commonly, CdTe solar cells employ Cu-containing back contact materials like ZnTe:Cu[7], $(CuS)_x(ZnS)_{1-x}$ [8-10], $BaCu_4S_3$ [11], and Cu-Al_2O_3[12]. The incorporation of these back contact layers yields reasonable device performance. However, these back contacts are clearly sub-optimal, which could be due to downward band bending between the CdTe and back buffer interface, such that interface recombination dominates the device performance.

Recently we showed that $CuAlO_x$ allows for high efficiency bifacial CdTe device. The ternary oxide $CuAlO_x$ is natural p-type, wide bandgap conductive semiconductor [13]. Our studies show that the current density (J_{SC}) and fill factor (*FF*) are independent of thickness which means band bending at the back does not change appreciably with bias. $CuAlO_x$ creates the upward band bending, reducing recombination at the back and helping to increase device performance. This would be important for thinner devices through the front side illumination because the depletion region is close to the front. This favorable band bending aids in repelling electrons from the back contact, improving device performance.

In this article, we report on the solution-based $CuAlO_x$ back contact layer applied as the back contact layer for monofacial CdS/CdTe solar cells. *J-V* performance of the completed devices are measured under AM 1.5 spectrum. Our best device shows photo conversion efficiency η = 14.6% by using the CuAlOx as a buffer layer with V_{OC} = 829 mV, $J_{SC=}$ 22.7 mA/cm^2, *FF* = 78%, yielding a relative 5% efficiency increase as compared with the devices omitting the CuAlOx and doped with Cu by using $CuCl_2$ solution based process/Au.

II. Experimental Detail

For the solar cell film stack, CdS (120 nm) and CdTe (3μm) layers were deposited by commercial vapor transport deposition (VTD) onto TEC^{TM}-15 glass substrates by the Willard and Kelsey Solar Group. The CdS/CdTe filmstack was treated with a saturated $CdCl_2$ solution in methanol, and the devices were annealed at 387 °C for 30 mins in dry air. This treatment helps to advance grain growth, release interfacial strain, and facilitate intermixing at the CdS/ CdTe region. To make the $CuAlO_x$ precursor solution, 0.04 M aluminum nitrate nonahydrate and 0.04M copper nitrate trihydrate in 5 ml of 2-methoxyethanol. The resultant solution was stirred at 200 rpm

978-1-7281-6115-0/20/$31.00 ©2020 IEEE

Authorized licensed use limited to: Carleton University. Downloaded on May 26,2021 at 22:17:21 UTC from IEEE Xplore. Restrictions apply.

Approved for public release; distribution unlimited.

566

for 5 mins at the room temperature. The final precursor turns slightly bluish. Then the final precursor was spin-coated onto the substrate (or onto the CdTe filmstack) with a rotating speed of 1000 rpm for 10 s and followed by a higher rotating speed of 3500 rpm for 50 s; the film was subsequently annealed for 6 mins. Finally, 40 nm gold was thermally evaporated to complete the back contact. $CuCl_2$ treatment done on $CdCl_2$ treated CdTe devices involved submerging for 2 mins the device in 0.1 mM $CuCl_2$ solution (0.24 ml) diluted with 24.6 ml DIW and rinsing thoroughly using DIW. Note that this Cu doping process followed Bastola et al., without further optimization[14]. The $CuCl_2$ treatment was carried out at 200˚C for 20 mins, and the device was completed with 40 nm thermally evaporated gold. Finally, the devices were scribed using 532 nm to define an array of approximately 30 cells, each with active device area of 0.06 cm^2. The schematic diagram of the CdS/CdTe solar cells using CuAlOx back buffer layer is shown in Fig. 1.

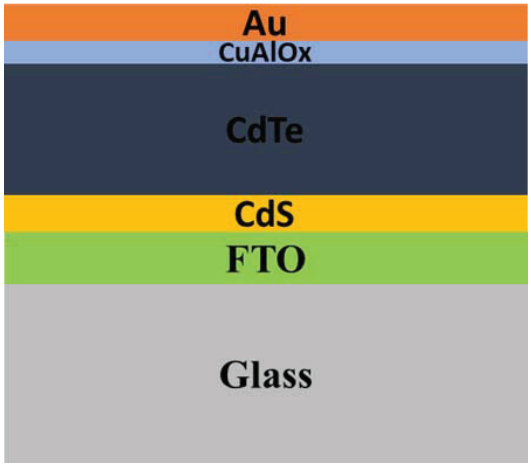


Fig. 1. Schematic diagram of CdS/CdTe solar cell devices with CuAlOx as a back buffer layer

III. RESULT AND DISCUSSION

The J-V measurement is performed on the devices to compare performance of the CuAlOx interface layer with devices omitting the layer but completed with $CuCl_2$/Au (our standard back contact layer). Fig. 2(a). shows the device performance of best cells using $CuAlO_x$ as a back contact layer. The champion cell with $CuAlO_x$ show the η =14.6% with V_{OC} = 829 mV, FF = 78.0 %, and J_{SC} = 22.7 mA/cm^2. These devices show better device performance than the devices doped by using the $CuCl_2$ treatment. The best cell for the $CuCl_2$ process has η =13.9% with V_{OC} = 829 mV, FF = 75.2 %, and J_{SC} = 22.3 mA/cm^2. The relative improvement is 5% in comparison with the $CuCl_2$ treated sample. From Fig. 2 (a), $CuCl_2$ treated samples helps to remove the rollover effect but it has shown the crossover effect between the dark and light J-V in forward bias. There is no cross over and rollover effect by using the $CuAlO_x$/Au back contact layer because CuAlOx interface layer helps to reduce the back barrier height between CdTe and Au.

From Fig. 2. and table 1 the device completed with CuAlOx shows really high FF because there is no change in the band bending, which makes all the recombination due to the flat band and either interface limited with CdS or SRH. Whereas the $CuCl_2$ treated device shows relatively lower FF because it is turning on as the band bending at the back of the device due to the bias voltage[15]. Since we have not explicitly doped our sample, and instead we have applied CuAlOx as an interface layer and Au as a standard metallization layer, we also compare the device performance with the standard Au-only back contact. The relative improvement of the device by using CdTe/CuAlOx/Au configuration in comparison with CdTe/Au device performance is 43.0 %. The average device performance parameters along with the standard deviation are shown in the table 1.

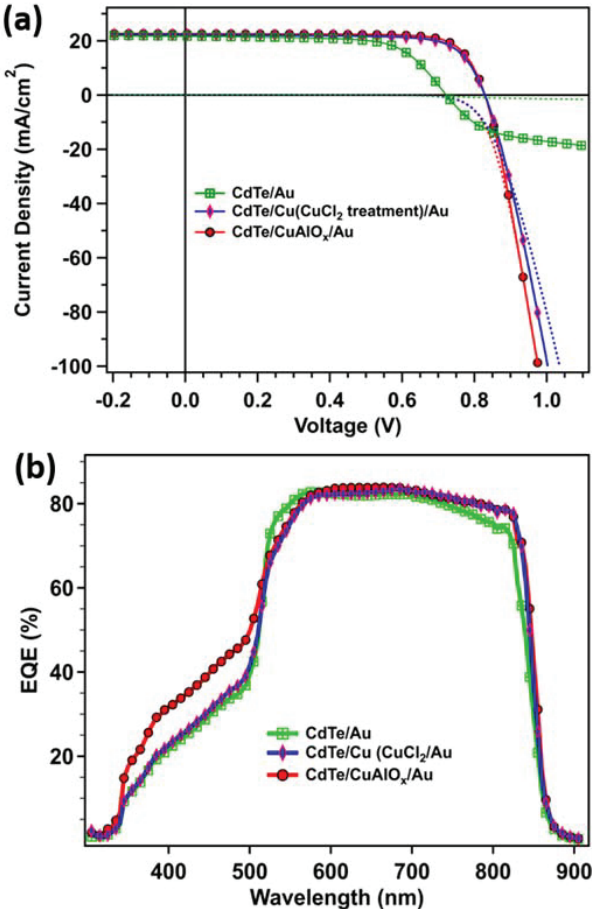


Fig. 2. (a) J -V characteristics (b) EQE measurement of CdS/CdTe sample with $CuAlO_x$ as an interface layer and comparison with controlled devices completed with Au only and Cu (solution based method)/Au as back contact layer.

From Table 1, each average parameter is higher for the device using CuAlOx. EQE measurement is done on the sample of each contact type which is shown in Fig. 2(b). confirms the

Authorized licensed use limited to: Carleton University. Downloaded on May 26,2021 at 22:17:21 UTC from IEEE Xplore. Restrictions apply.

Approved for public release; distribution unlimited.

TABLE I.
J-V PARAMETERS FOR THE BEST AND AVERAGE CELLS. DEVICE AREA = 0.060 CM^2.

BACK Contact Configuration		V_{OC} (mV)	J_{SC} (mA/cm^2)	*FF* (%)	η (%)	R_S (Ω cm^2)	R_{sh} (Ω cm^2
Au	Best	722	21.7	67.0	10.5	6.5	1157
	Average	718 ± 11	21.4 ± 0.2	64.8 ± 1.7	10.0 ± 0.4	8.9 ±5.2	872 ± 250
Cu/Au	Best	829	22.3	75.2	13.9	2.0	2422
	Average	827 ± 2	21.8 ± 0.4	75.2 ± 1.1	13.6 ± 0.3	2.2 ± 0.4	3270 ± 700
$CuAlO_x$/Au	Best	829	22.6	78.0	14.6	1.6	3404
	Average	827 ± 5	22.0 ± 0.2	77.1 ± 0.5	14.0 ± 0.2	1.9 ± 0.3	3520 ± 340

improved J_{SC} from the introduction of CuAlOx. The current collection at the lower wavelength region is due to the parasitic effect of CdS window layer. Device completed with $CuAlO_x$ shows the higher current collection in the 300 – 500 nm region this could be due to the thinner CdS layer on this device filmstack, sampled from several locations of a 6 inch x 6 inch coated glass panel.

IV. CONCLUSION

We have demonstrated that CdTe/CuAlOx/Au device configuration shows the higher device performance with excellent increase on *FF*, V_{OC}, J_{SC} and overall increase on the device performance. Our best cell shows the 14.6% device performance which is 43%, and 6 % relative increment over Au-only and Cu(solution)/Au respectively. Our experiment proves that $CuAlO_x$ could serve as a promising interface layer on CdS/CdTe solar cells by creating favorable band alignment. The development of $CuAlO_x$ layer by using the low cost non-vacuum solution based method may open up new possibilities in the CdTe PV area.

ACKNOWLEDGMENT

This material is based on research sponsored by Air Force Research Laboratory under agreement numbers FA9453-18-2-0037 and FA9453-19-C-1002, and by the U.S. DOE's Office of Energy Efficiency and Renewable Energy (EERE) under Solar Energy Technologies Office (SETO) Agreement DE-EE0008974. The U.S. Government is authorized to reproduce and distribute reprints for Governmental purposes notwithstanding any copyright notation thereon. Disclaimer: The views and conclusions contained herein are those of the authors and should not be interpreted as necessarily representing the official policies or endorsements, either expressed or implied, of Air Force Research Laboratory or the U.S. Government. The authors would like to thank Willard and Kelsey Solar Group for providing CdS/CdTe filmstack samples.

REFERENCES

[1] M. A. Green, E. D. Dunlop, D. H. Levi, J. Hohl-Ebinger, M. Yoshita, and A. W. Y. Ho-Baillie, "Solar cell efficiency tables (version 54)," *Progress in Photovoltaics,* vol. 27, no. 7, pp. 565-575, 2019.

[2] M. Gloeckler, I. Sankin, and Z. Zhao, "CdTe solar cells at the threshold to 20% efficiency," *IEEE Journal of Photovoltaics,* vol. 3, no. 4, pp. 1389-1393, 2013.

[3] J. M. Burst *et al.*, "CdTe solar cells with open-circuit voltage breaking the 1 V barrier," *Nature Energy,* vol. 1, no. 3, p. 16015, 2016.

[4] G. K. Liyanage, A. B. Phillips, F. K. Alfadhili, R. J. Ellingson, and M. J. Heben, "The role of back buffer layers and absorber properties for> 25% efficient CdTe solar cells," *ACS Applied Energy Materials,* vol. 2, no. 8, pp. 5419-5426, 2019.

[5] J. Freeouf and J. Woodall, "Schottky barriers: An effective work function model," in *Electronic Structure of Semiconductor Heterojunctions*: Springer, 1988, pp. 177-179.

[6] R. K. Swank, "Surface properties of II-VI compounds," *Physical Review,* vol. 153, no. 3, p. 844, 1967.

[7] J. Li *et al.*, "Controlled activation of ZnTe: Cu contacted CdTe solar cells using rapid thermal processing," *Solar Energy Materials and Solar Cells,* vol. 133, pp. 208-215, 2015.

[8] K. K. Subedi *et al.*, "Nanocomposite $(CuS)_x(ZnS)_{1-x}$ thin film back contact for CdTe solar cells: Toward a bifacial device," *Solar Energy Materials and Solar Cells,* vol. 186, pp. 227-235, 2018.

[9] K. K. Subedi, K. P. Bhandari, E. Bastola, and R. J. Ellingson, "13% CdS/CdTe Solar Cell Using a Nanocomposite $(CuS)_x(ZnS)_{1-x}$ Thin Film Hole Transport Layer," in *2017 IEEE 44th Photovoltaic Specialist Conference (PVSC)*, 2017, pp. 781-784.

[10] E. Bastola, K. K. Subedi, K. P. Bhandari, and R. J. Ellingson, "Solution-processed nanocrystal based thin films as hole transport materials in cadmium telluride photovoltaics," *MRS Advances,* vol. 3, no. 41, pp. 2441-2447, 2018.

[11] K. K. Subedi *et al.*, "Bifacial CdS/CdTe Solar Cell using Transparent Barium Copper Sulfide as a Hole Transport Layer," in *2019 IEEE 46th Photovoltaic Specialists Conference (PVSC)*, 2019, pp. 0185-0188: IEEE.

[12] Q. Lin *et al.*, "A novel p-type and metallic dual-functional Cu–Al 2 O 3 ultra-thin layer as the back electrode enabling high performance of thin film solar cells," vol. 52, no. 71, pp. 10708-10711, 2016.

[13] L. Zhang *et al.*, "Oxygen-concentration effect on p-type $CuAlO_x$ resistive switching behaviors and the nature of

Authorized licensed use limited to: Carleton University. Downloaded on May 26,2021 at 22:17:21 UTC from IEEE Xplore. Restrictions apply.

Approved for public release; distribution unlimited.

conducting filaments," *Applied Physics Letters,* vol. 104, no. 9, p. 093512, 2014.
[14] E. Bastola, A. V. Bordovalos, E. LeBlanc, N. Shrestha, M. O. Reese, and R. J. Ellingson, "Doping of CdTe using $CuCl_2$ Solution for Highly Efficient Photovoltaic Devices," in *2019 IEEE 46th Photovoltaic Specialists Conference (PVSC)*, 2019, pp. 1846-1850: IEEE.
[15] A. B. Phillips, G. K. Liyanage, F. K. Alfadhili, and M. J. Heben, "Understanding CdTe Performance with Engineered Front and Back Interfaces," in *2019 IEEE 46th Photovoltaic Specialists Conference (PVSC)*, 2019, pp. 0777-0782: IEEE.

978-1-7281-6115-0/20/$31.00 ©2020 IEEE

Authorized licensed use limited to: Carleton University. Downloaded on May 26,2021 at 22:17:21 UTC from IEEE Xplore. Restrictions apply.

Approved for public release; distribution unlimited.

Incorporation of Arsenic in CdSe/CdTe Solar Cells During Close Spaced Sublimation of CdTe:As

Manoj K. Jamarkattel
Wright Center for Photovoltaic Innovation and Commercailization
University of Toledo
Toledo, USA
manoj.jamarkattel@rockets.utoledo.edu

Adam B. Phillips
Wright Center for Photovoltaic Innovation and Commercailization
University of Toledo
Toledo, USA
adam.phillips@utoledo.edu

Abdul Quader
Wright Center for Photovoltaic Innovation and Commercailization
University of Toledo
Toledo, USA
abdul.quader@rockets.utoledo.edu

Kamala Khanal Subedi
Wright Center for Photovoltaic Innovation and Commercailization
University of Toledo
Toledo, USA
kamala.khanalsubedi@rockets.utoledo.edu

Fadhil K. Alfadhili
Wright Center for Photovoltaic Innovation and Commercailization
University of Toledo
Toledo, USA
fadhil.alfadhili@rockets.utoledo.edu

Sandip Singh Bista
Wright Center for Photovoltaic Innovation and Commercailization
University of Toledo
Toledo, USA
sandip.bista@rockets.utoledo.edu

Rasha A. Awni
Wright Center for Photovoltaic Innovation and Commercailization
University of Toledo
Toledo, USA
rasha.awni@utoledo.edu

Deng-Bing Li
Wright Center for Photovoltaic Innovation and Commercailization
University of Toledo
Toledo, USA
dengbing.li@utoledo.edu

Santosh K. Swain
Center for Material Research
Washington State University
Pullman, USA
santosh@wsu.edu

Yanfa Yan
Wright Center for Photovoltaic Innovation and Commercailization
University of Toledo
Toledo, USA
yanfa.yan@utoledo.edu

Randy J. Ellingson
Wright Center for Photovoltaic Innovation and Commercailization
University of Toledo
Toledo, USA
randy.ellingson@utoledo.edu

John S. McCloy
Institute of Material Research
Washington State University
Pullman, USA
john.mccloy@wsu.edu

Kelvin G. Lynn
Center for Material Research
Washington State University
Pullman, USA
kgl@wsu.edu

Michael J. Heben
Wright Center for Photovoltaic Innovation and Commercailization
University of Toledo
Toledo,USA
michael.heben@utoledo.edu

***Abstract*—Cu doping of CdTe has enabled reasonable device performance, but has some significant drawbacks, including limited achievable carrier concentration and high mobility in the CdTe films. Group V elements, on the other hand, are expected to facilitate higher carrier concentration and expected to have low mobility. Consequently, incorporate of As in CdTe is of great interest to the CdTe community. Here, we deposited CdTe from the CdTe:As feedstock to complete devices. We demonstrate that the As diffuses through the CdTe absorber layer and accumulates at the front and back interfaces with Cl activation. Current density-voltage and capacitance-voltage measurements indicate that the devices have low carrier concentration, even though the concentration of As is high. These results indicate that the process employed here was insufficient to activate the As doping.**

Keywords—CdTe, group V doping, CSS, SIMS, Diffusion

I. INTRODUCTION

Cadmium Tellurite based polycrystalline solar cells are one of the prominent and commercialized solar cells with the record efficiency of 22.1% [1]. Most of those solar cells were doped with copper and achieved approximately 10^{14} cm^{-3} carrier density[2]. Defect studies showed that Cu tends to act as both carrier generator and carrier trap [3]. Also, many theoretical studied had been carried out to show that increasing doping density to on the order of 10^{16} cm^{-3} is required to achieve higher V_{oc} and efficiency greater than 25% [4, 5]. Therefore, increasing carrier density of the absorber layer is crucial for higher efficient CdTe solar cells. Recent studies demonstrated that group V elements like As, P and Sb can lead to increased carrier density by incorporating onto Te sites, which, in turn, increases the efficiency of the CdTe-based solar cells without compromising carrier life time [6, 7]. However, most of those diffusion of Arsenic atoms was carried out at temperature range from 550 to 750 °C with cadmium arsenide compounds sealed in ampoule with constant Cd and As overpressure [7-9].

Recently, Metzger et al. exceeded 20% efficient CdTe solar cell with in situ arsenic doping [9]. There samples were

Authorized licensed use limited to: Western Sydney University. Downloaded on June 15,2021 at 02:24:51 UTC from IEEE Xplore. Restrictions apply.

Approved for public release; distribution unlimited.

fabricated on 3 mm TCO coated glass with graded CdSeTe/CdTe absorber, deposited by vapor transport deposition, and As was incorporated diffused with a constant overpressure of both Cd and As. They were able to achieve more than 10^{16} cm^{-3} carrier doping density while achieving a V_{oc} of 858 mV and 79.8% fill factor. Stress testing under 1 Sun at 75 °C for more than a month showed that the efficiency of devices made with group V doping were stable. However, the open circuit voltage is still well below the required value to get over 25% efficient solar cell as suggested by some of the theoretical work [4, 5, 10].

Here, we incorporate arsenic atoms into CdTe deposited by closed space sublimation (CSS) and characterize the dopant profile after device completion. Using secondary ion mass spectroscopy (SIMS), we show that during processing the As atoms diffuse throughout the absorber layer and accumulate at the interface. The completed devices, though, perform poorly, and capacitance-voltage (CV) measurements suggest that the As did not contribute to increased carrier concentration.

II. Experimental Details

Figure 1 shows a schematic diagram of the device structure. CdSe films were deposited onto cleaned 3 mm glass coated with fluorine doped tin oxide (Tec™ 12D; Pilkington North America) through RF sputtering at 10 mTorr Ar pressure at room temperature. Arsenic-doped CdTe feedstock was prepared using rotating vertical Bridgeman based melt growth technique [11]. For this, raw material of 6N5 purity CdTe and Cd_3As_2 were sealed in an evacuated quartz ampoule, heated to 1160 °C, and crystal growth was performed with the temperature gradient resulting in arsenic enriched CdTe feedstock. This feedstock was ground into powder using an alumina mortar and pestle.

The CdTe:As source plate is made by sublimating the source material at 650 °C under 1 Torr He pressure. Two to four micron thick CdTe:As films were sublimated by CSS at < 10^{-6} Torr while maintaining 560°C source temperature. Films stacks were treated with saturated $CdCl_2$ solution at 400 °C for 30 min in air ambient and rinsed with methanol to remove the residual $CdCl_2$. The devices were finished by evaporating 45 nm of gold electrodes as a back contact. For the current voltage measurements devices were divided into small cells of area 0.06 cm^2 by laser scribing[12] and were measured using a Keithley 2440 source meter and illuminated under simulated AM1.5G spectrum using an LED solar simulator (Newport Minisolo model LHS-7320). Doping density of the device was characterized using SIMS, and carrier concentration was determined by Capacitance voltage measurement performed in dark at room temperature with AC voltage of 45 mV and 10 kHz frequency. The biased voltage was swept from -3V to 0.8V.

III. Results and Discussion

As demonstrated by the JV measurements in Figure 2, these devices performed poorly with an average Voc of ~585 mV (545 mV) and fill factor (FF) of ~60% (56.9 %) for 2.6-micron absorber whereas respective values on parenthesis were for 3.8 micron thick absorber. These results suggest low carrier concentration in the absorber layer. To investigate this possibility, we performed SIMS analysis to determine the concentration of dopant atoms present and CV measurements to determine the carrier concentration. The SIMS results are shown in Figure 3 and show that As is present in the film. Interestingly, the concentration of the As is ~10^{19} cm^{-3} at the back and front interfaces but only ~10^{16} cm^{-3} in the bulk of the layer. The profile after deposition is expected to be constant since the source material contains As, so this profile indicates the carrier diffusion during the Cl activation process. Still, there are enough As atoms to increase the carrier concentration.

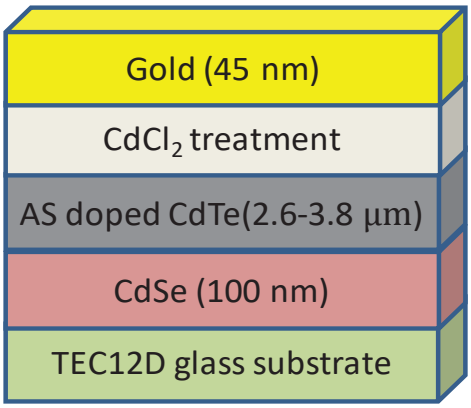


Fig 1 Schematic diagram of device structure

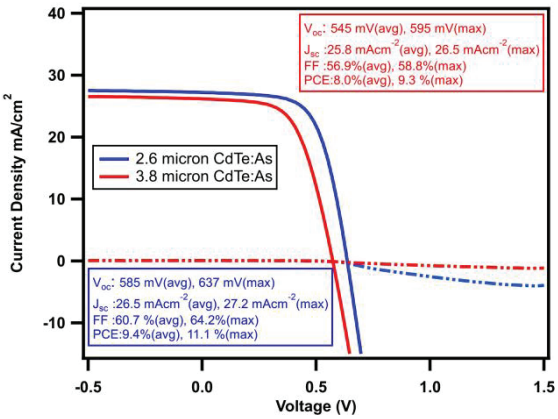


Fig 2. Current-Voltage graph

Authorized licensed use limited to: Western Sydney University. Downloaded on June 15,2021 at 02:24:51 UTC from IEEE Xplore. Restrictions apply.

Approved for public release; distribution unlimited.

571

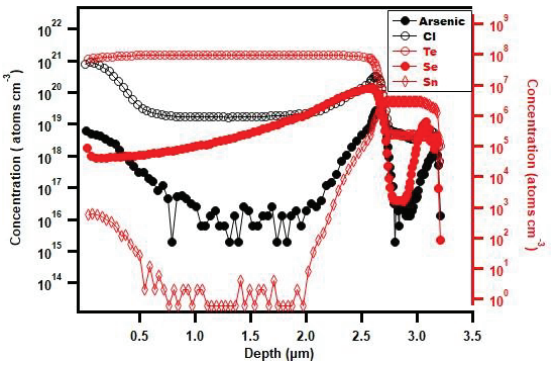


Fig 3. SIMS analysis of CdTe: As sample

The CV measurements were completed to investigate the carrier concentration of the devices. As Figure 4 shows, the depletion width is large, and carrier concentration are in the range of 10^{13} cm^{-3}. These results suggest that the As in the CdTe layer is not active.

Clearly more work is necessary to fabricate an CdTe:As device with active As. Others have employed an additional annealing step to activate the dopant in the film [8]. That process may be required with these materials. Others have demonstrated that deposition in a Cd overpressure is required for active group V dopants [9, 11, 13, 14]. Those investigations started with a phase segregated CdTe and Cd_2As_3, which is not the case here.

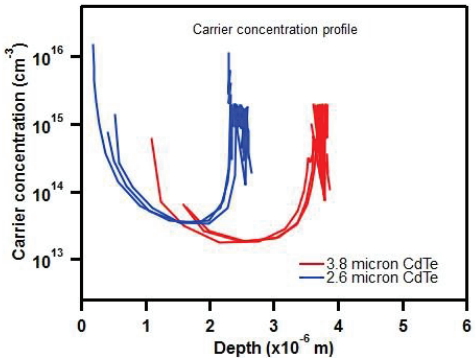


Fig 4. CV measurements

IV. Conclusions

Using a CdTe:As source material fabricated using rotating vertical Bridgeman based melt growth technique, we deposited CdTe:As layer using CSS onto a Tec™ 12D/CdSe substrate and completed the device. While the JV indicates the devices were undoped, SIMS analysis showed that As was incorporated into the device, and that the Cl activation process caused As diffusion towards the front and back interfaces. CV measurements, on the other hand, confirmed that the devices had low carrier concentration. These initial results indicate that the process followed here is insufficient to activate the As doping to increase the carrier concentration.

Acknowledgment

The authors gratefully acknowledge funding support from the U.S. Air Force Research Laboratory, Space Vehicles Directorate, under Agreement number FA9453-18-2-0037. The U.S. Government is authorized to reproduce and distribute reprints for Governmental purposes notwithstanding any copyright notation thereon.

References

[1] M. A. Green, Y. Hishikawa, E. D. Dunlop, D. H. Levi, J. Hohl-Ebinger, and A. W. Y. Ho-Baillie, "Solar cell efficiency tables (version 51)," *Progress in Photovoltaics: Research and Applications,* vol. 26, no. 1, pp. 3-12, 2018, doi: 10.1002/pip.2978.

[2] D.-B. Li *et al.*, "Maximize CdTe solar cell performance through copper activation engineering," *Nano Energy,* vol. 73, 2020, doi: 10.1016/j.nanoen.2020.104835.

[3] J.-H. Yang, W. K. Metzger, and S.-H. Wei, "Carrier providers or killers: The case of Cu defects in CdTe," *Applied Physics Letters,* vol. 111, no. 4, 2017, doi: 10.1063/1.4986077.

[4] T. Song, A. Kanevce, and J. R. Sites, "Emitter/absorber interface of CdTe solar cells," *Journal of Applied Physics,* vol. 119, no. 23, 2016, doi: 10.1063/1.4953820.

[5] G. K. Liyanage, A. B. Phillips, F. K. Alfadhili, R. J. Ellingson, and M. J. Heben, "The Role of Back Buffer Layers and Absorber Properties for >25% Efficient CdTe Solar Cells," *ACS Applied Energy Materials,* vol. 2, no. 8, pp. 5419-5426, 2019/08/26 2019, doi: 10.1021/acsaem.9b00367.

[6] S. Farrell, T. Barnes, W. K. Metzger, J. H. Park, R. Kodama, and S. Sivananthan, "In Situ Arsenic Doping of CdTe/Si by Molecular Beam Epitaxy," *Journal of Electronic Materials,* vol. 44, no. 9, pp. 3202-3206, 2015, doi: 10.1007/s11664-015-3913-3.

[7] B. McCandless *et al.*, "Enhanced p-Type Doping in Polycrystalline CdTe Films: Deposition and Activation," *IEEE Journal of Photovoltaics,* vol. 9, no. 3, pp. 912-917, 2019, doi: 10.1109/jphotov.2019.2902356.

[8] E. Colegrove *et al.*, "Experimental and theoretical comparison of Sb, As, and P diffusion mechanisms

Authorized licensed use limited to: Western Sydney University. Downloaded on June 15,2021 at 02:24:51 UTC from IEEE Xplore. Restrictions apply.

Approved for public release; distribution unlimited.

572

and doping in CdTe," *Journal of Physics D: Applied Physics,* vol. 51, no. 7, 2018, doi: 10.1088/1361-6463/aaa67e.

[9] W. K. Metzger *et al.*, "Exceeding 20% efficiency with in situ group V doping in polycrystalline CdTe solar cells," *Nature Energy,* vol. 4, no. 10, pp. 837-845, 2019, doi: 10.1038/s41560-019-0446-7.

[10] A. Kanevce, M. O. Reese, T. M. Barnes, S. A. Jensen, and W. K. Metzger, "The roles of carrier concentration and interface, bulk, and grain-boundary recombination for 25% efficient CdTe solar cells," *Journal of Applied Physics,* vol. 121, no. 21, 2017.

[11] T. K. Al-Hamdi *et al.*, "CdTe synthesis and crystal growth using the high-pressure Bridgman technique," *Journal of Crystal Growth,* vol. 534, 2020, doi: 10.1016/j.jcrysgro.2019.125466.

[12] A. B. Phillips *et al.*, "High speed, intermediate resolution, large area laser beam induced current imaging and laser scribing system for photovoltaic devices and modules," *Review of Scientific Instruments,* vol. 87, no. 9, Sep 2016, Art no. 093708, doi: 10.1063/1.4962940.

[13] G. Kartopu *et al.*, "Study of thin film poly-crystalline CdTe solar cells presenting high acceptor concentrations achieved by in-situ arsenic doping," *Solar Energy Materials and Solar Cells,* vol. 194, pp. 259-267, 2019, doi: 10.1016/j.solmat.2019.02.025.

[14] B. E. McCandless *et al.*, "Overcoming Carrier Concentration Limits in Polycrystalline CdTe Thin Films with In Situ Doping," *Sci Rep,* vol. 8, no. 1, p. 14519, Sep 28 2018, doi: 10.1038/s41598-018-32746-y.

Authorized licensed use limited to: Western Sydney University. Downloaded on June 15,2021 at 02:24:51 UTC from IEEE Xplore. Restrictions apply.

Approved for public release; distribution unlimited.

Open-circuit Voltage Exceeding 840 mV for All-Sputtered CdS/CdTe Devices

Ebin Bastola
Department of Physics,
University of Toledo
Toledo, USA
Ebin.Bastola@rockets.utoledo.edu

Adam B. Phillips
Department of Physics
University of Toledo
Toledo, USA
Adam.Phillips@utoledo.edu

Niraj Shrestha
Department of Physics
University of Toledo
Toledo, USA
Niraj.Shrestha@rockets.utoledo.edu

Manoj K. Jamarkattel
Department of Physics
University of Toledo
Toledo, USA
Manoj.Jamarkattel@rockets.utoledo.edu

Rasha A. Awni
Department of Physics
University of Toledo
Toledo, USA
Rasha.Awni@rockets.utoledo.edu

Yanfa Yan
Department of Physics
University of Toledo
Toledo, USA
Yanfa.Yan@utoledo.edu

Michael J. Heben
Department of Physics
University of Toledo
Toledo, USA
Michael.Heben@utoledo.edu

Randy J. Ellingson
Department of Physics
University of Toledo
Toledo, USA
Randy.Ellingson@utoledo.edu

***Abstract* — Sputtering is an efficient way to fabricate CdTe solar cells. However, the open-circuit voltage (V_{OC}) of a sputtered device is low compared to close space sublimation or vapor deposited CdTe devices. Here, we report an outstanding V_{OC} > 840 mV and fill factor (FF) > 71.0% for all-sputtered CdS/CdTe solar cells. These results were achieved by solution-based copper (Cu) doping of CdTe by copper (II) chloride ($CuCl_2$) in deionized water. Compared with evaporated Cu, solution-based doping increased the V_{OC} and FF, and improved the optoelectronic properties of the sputtered CdTe thin films. Capacitance-voltage measurements indicated that the free hole concentration increased by two-fold for $CuCl_2$ treated devices.**

***Index Terms*- Sputtering, CdTe, $CuCl_2$, solar cells, doping.**

I. Introduction

Cadmium telluride (CdTe) solar cells are well known thin film technology for high efficiency and low-cost solar energy production. High efficiency solar cells require low defect materials, and low recombination rates at interfaces and grain boundaries. Several techniques exist for the fabrication of CdS/CdTe solar cells, including sputtering, close-space sublimation, vapor transport deposition, and electrochemical deposition. Sputtering is an efficient way to deposit a CdTe film on a substrate. However, the power conversion efficiency for the sputtered CdTe devices typically fails to match those devices fabricated by other high-temperature methods, such as close-space sublimation. Gupta et al. have reported 14.0% (V_{OC} 814 mV, J_{SC} 23.6% mA cm^{-2}) efficient all-sputtered CdS/CdTe solar cells using aluminum doped zinc oxide (ZnO:Al) as a transparent conducting oxide (TCO).[1] Here, the optical loss was minimized using ZnO:Al as a front contact material of the device. The device using the ZnO:Al TCO yields higher efficiency mainly due to a high J_{SC}, which is about 14.0% (23.6 $mAcm^{-2}$) higher as compared to SnO_2:F (20.7 $mAcm^{-2}$) for sputtered devices.[1] Similarly, Li et al. have reported 14.4% (V_{OC} 803 mV, J_{SC} 25 mA cm^{-2}) efficient sputtered CdTe photovoltaics using CdS:O as an n-type window layer.[2] For both cases, the V_{OC} is low compared to the ideal V_{OC} of CdTe thin films (1.156 V[3]). Hence, the device efficiency can be enhanced by improving the open-circuit voltage of all-sputtered devices.

Properties including the minority carrier lifetime and carrier concentration of CdTe thin films determine the device efficiency of CdTe solar cells.[4] To improve the opto-electronic properties of CdTe films, Cu atoms/ions are used as dopants during the fabrication of these devices.[5] Cu doping has been essential to fabricate efficient solar cells. We have conventionally applied copper/gold (Cu/Au) as the metal back contact using thermal evaporation, followed by thermal annealing to diffuse the Cu atoms.[6, 7] However, the deposition and repeatable thickness of Cu is not well controlled during the evaporation process. An alternative approach for doping CdTe solar cells involves using a wet Cu processing.[8, 9]

Recently, different methods of Cu treatment for CdTe photovoltaics have been reported including copper (I) chloride vapor or solution which produced highly efficient devices compared to evaporated Cu.[10, 11] Recent reports also include the treatment of CdTe devices using copper (II) chloride ($CuCl_2$) solution in methanol or in deionized water.[9, 12] Here, we report all-sputtered CdS/CdTe devices with a open-circuit voltage greater than 840 mV achieved by doping CdTe with copper (II) chloride in deionized water. The device efficiency for all sputtered CdS/CdTe devices reached 13.7%, with V_{OC} exceeding 840 mV and a fill factor (FF) of 71.0% --

978-1-7281-6115-0/20/$31.00 ©2020 IEEE

Authorized licensed use limited to: East Carolina University. Downloaded on June 16,2021 at 03:20:14 UTC from IEEE Xplore. Restrictions apply.

Approved for public release; distribution unlimited.

574

excellent results for sputtered CdS/CdTe devices. Further, we include the analysis of J-V characteristics, and explore the opto-electronic properties of CdTe thin films.

II. Experimental

Fluorine doped tin oxide coated (TEC-12D, NSG Pilkington) glass substrates were cleaned using Micro-90 detergent in deionized water via sonication. CdS/CdTe device stacks with CdS (power density 413 $mWcm^{-2}$) thickness of 80 nm and CdTe (power density 361 $mWcm^{-2}$) ~ 2.0 μm was deposited on a TEC-12D glass substrate (6" X 6") using RF sputtering at 250 °C. The CdTe devices were activated using a saturated cadmium chloride ($CdCl_2$) solution in methanol introduced dropwise onto the CdTe surface. After this, CdTe devices were thermally annealed at 387 °C for 30 mins in a dry air environment. The films were then rinsed with methanol, and dried using house nitrogen. The $CuCl_2$ treatment followed the procedure reported previously and annealed at 200 °C for 15 mins.[12, 13] The annealing temperature and time was previously optimized for CdS/CdTe devices. The control device was fabricated by using 3 nm Cu and 40 nm Au and annealed at 150°C for 45 mins. Finally, current-voltage characteristics (J-V) were measured under a simulated AM1.5G spectrum. The external quantum efficiencies were measured using PV Instruments (model IVQE8-C) system. The room temperature PL and TRPL were measured as mentioned previously.[12] C-V measurements were performed using a Solartron Modulab potentiostat equipped with a frequency response analyzer (Ametek Inc.). The measurements were performed in the dark with a constant 45 mV rms and 10 kHz AC signal superimposed on a DC bias voltage varying from -3.0 to +0.8 V.

III. Results and Discussion

Fig. 1 displays the J-V characteristics and EQEs of the best cells with standard Cu/Au and $CuCl_2$ treated sputtered CdTe devices. The best cell with $CuCl_2$ has an efficiency of 13.7% with 841 mV V_{OC}, J_{SC} of 22.80 $mAcm^{-2}$ and FF of 71.2% while the best cell from a control device has an efficiency of 12.8% with V_{OC} 822 mV, J_{SC} 22.7 $mAcm^{-2}$ and FF 68.4%. The highest V_{OC} obtained was 843 mV for all-sputtered CdS/CdTe cells with $CuCl_2$ treatment. Gupta et al. had the device performance ~14.0% but lower V_{OC} (814 mV) for the all-sputtered devices.[1] This is one of the highest V_{OC} values reported for a sputtered CdS/CdTe solar cells. Previously, for vapor transport deposited CdS/CdTe devices also had V_{OC} of 840 mV after $CuCl_2$ treatment.[12]

The device parameters for the best cells for all conditions are shown in Table I and the average device parameters are shown in Fig. 2. The average efficiency for sputtered CdTe devices with an evaporated Cu back contact is 12.6%. For $CuCl_2$ treated devices, average efficiency is 13.2%, which is 4.7% higher (or 0.6% absolute). This indicates solution-based Cu doping is more effective compared to elemental Cu doping by using a thermal evaporation. The higher V_{OC} and FF follow from the increased ionized dopant concentration, as well as the back-contact interface after the $CuCl_2$ treatment. The chloride (Cl^-) ions play a significant role during the activation of CdTe devices and Cl^- ions present in the $CuCl_2$ solution may also help to passivate CdTe grain boundaries during the annealing process of devices.

The J-V curves shown Fig. 1 clearly indicates well-behavior for copper treated cells. For Au only back contact, it strongly shows the rollover and cross-over effect on the J-V characteristics in the first and fourth quadrants indicating the issues with an absorber layer and the back-contact interface. Note that all these devices have CdS as the front window layer. The dramatic improvement in the J-V behavior is attributed to the Cu doping and improvement of opto-electronic properties. To compare the device performance, we also fabricated a CdTe device with 3 nm evaporated Cu annealed at 200 °C for 15 mins similar to $CuCl_2$ treatment. As shown in Fig. 1 (a), for the device annealed at 200 °C for 15 mins, had worse device performance (11.1%) compared to

TABLE I
DEVICE PARAMETERS OF ALL SPUTTERED CDS/CDTE SOLAR CELLS PRESENTED IN FIGURE 1.

Back Contact	Description	V_{OC} (mV)	J_{SC} ($mAcm^{-2}$)	FF (%)	Eff. (η%)	Rs ($\Omega\ cm^2$)	Rsh ($\Omega\ cm^2$)	Ideality Factor (n)	J_0 ($mAcm^{-2}$)
Au	annealed at 200 °C for 15 mins	731	23.1	63.3	10.7	5.2	1706	-	-
Cu/Au	3 nm Cu, annealed at 150 °C for 45 mins	822	22.7	68.4	12.8	4.2	1006	1.94	$6.2x10^{-7}$
$CuCl_2$/Au	Dipped in 0.1 mmol $CuCl_2$ solution, annealed at 200 °C for 15 mins	841	22.8	71.2	13.7	4.5	1144	1.82	$1.5x10^{-7}$
Cu/Au	3 nm Cu, annealed at 200 °C for 15 mins	799	22.2	62.7	11.1	6.0	570	-	-

978-1-7281-6115-0/20/$31.00 ©2020 IEEE

Authorized licensed use limited to: East Carolina University. Downloaded on June 16,2021 at 03:20:14 UTC from IEEE Xplore. Restrictions apply.

Approved for public release; distribution unlimited.

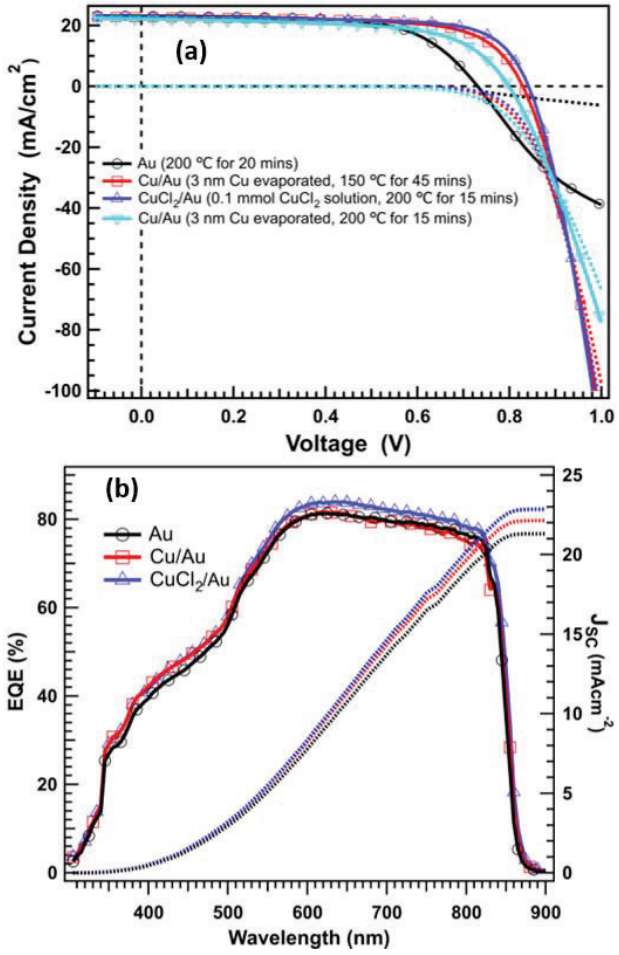


Fig. 1. (a) J-V characteristics and (b) EQEs of all-sputtered CdS/CdTe solar cells.

both standard control device and $CuCl_2$ treated devices. When annealed at 200 ºC for 15 mins, significant loss in V_{OC} and FF was observed as shown in Fig. 1 and Table I due to the excess diffusion of Cu towards the front interface of the device. Our annealing procedure for evaporated Cu were previously optimized for 3 nm Cu and 40 nm Au back contact.[14, 15]

The short-circuit current density was verified by external quantum efficiency measurement and is shown in Fig. 1(b). In Fig 1(b), we can see the higher current collection in case of $CuCl_2$ treated cell in the range of 550-800 nm. The improvement in current collection in this region indicates improvement in the absorber layer for a generation of higher number of electron and hole pairs which are separated and passed through the external circuit. The integrated J_{SC} match well for $CuCl_2$ treated devices but it is slightly lower for Cu treated devices than J_{SC} obtained from J-V measurements. The improvement in current collection, increase in V_{OC} and FF indicates $CuCl_2$ treatment enhances the opto-electronic properties of CdTe layer.

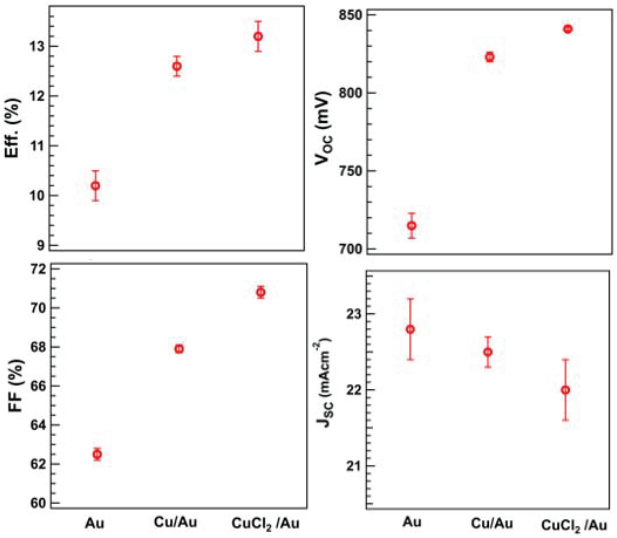


Fig. 2. Average J-V parameters of all-sputtered CdS/CdTe devices for about 20 cells.

treated devices than J_{SC} obtained from J-V measurements. The improvement in current collection, increase in V_{OC} and FF indicates $CuCl_2$ treatment enhances the opto-electronic properties of CdTe layer.

The dark J-V characteristics curves presented in Fig. 1 were analyzed to calculate solar cells parameters such as ideality factor (n), diode saturation current density (J_0), series resiatnce (R_S) and shunt conductance (G_{Sh}) using a single exponential diode equation as below.

$$J = J_0 \exp\left[\frac{q}{nk_BT}\,(V - R_SJ)\right] + G_{Sh}V - J_L$$

Where q is an electronic charge, k_B is the Boltzmann's constant, T is absolute temperature, J_L is the load current density which is equal to short-circuit current density (J_{SC}) and is taken to be equal to zero for a dark characteristic. By analyzing the dark characteristics of the devices, we compared various parameters including ideality factor, reverse saturation current density and series resiatnce of all-sputtered devices with Cu/Au and $CuCl_2$/Au back contacts. Fig. 3 below shows the graph obtained by analyzing the dark curves for these sputtered CdTe devices. The plot of dJ/dV versus bias voltage (V), Fig. 3(b), shows the constant shunt conductance (close to zero) at low reverse and forward bias, and rises exponentially with increase in forward bias indicating negligible shunt conductance at dark measurement conditions for both Cu/Au and $CuCl_2$/Au contacts.

Similarly, the plot of dV/dJ versus J^{-1} is shown in Fig. 3(c) and using the slope of the linear fit, the ideality factor is calculated, and y-intercept gives the value of R_S. The ideality factors value for Cu/Au and $CuCl_2$/Au were found to be 1.94 and 1.82 respectively. The series resistances were found to be 0.9 Ωcm^2 and 0.7 Ωcm^2 respectively for Cu/Au and $CuCl_2$/Au respectively. These series resistances obtained here are less than the values obtained from J-V measurements (Table I).

978-1-7281-6115-0/20/$31.00 ©2020 IEEE

Authorized licensed use limited to: East Carolina University. Downloaded on June 16,2021 at 03:20:14 UTC from IEEE Xplore. Restrictions apply.

Approved for public release; distribution unlimited.

576

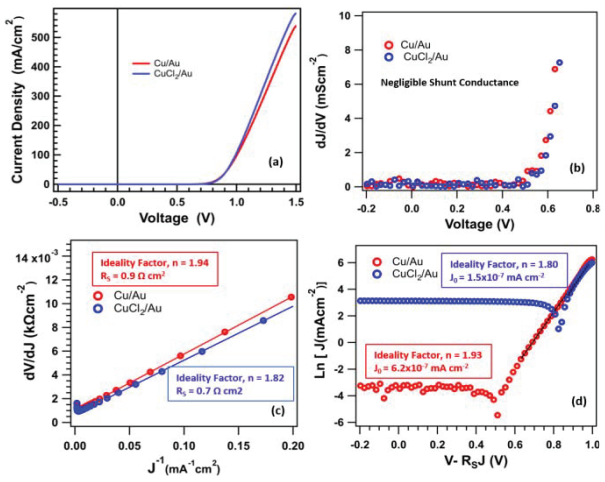


Fig. 3. Analysis of dark J-V characteristics for the best cells (a) dark J-V curves (b) dJ/dV versus bias voltage (V) (c) dV/dJ versus J^{-1} and (d) Ln (J) versus [V-R_SJ] with Cu/Au and $CuCl_2$/Au back contacts. The solid lines in (c) and (d) represent the fitted lines.

The value of ideality factor is similar to the CdS/CdTe devices reported previously.[16, 17]Further, substituting values of R_S obtained from Fig. 3(c), we plotted a Ln [J] versus [V-RsJ] to estimate the reverse saturation current density for these two conditions. The values of n and J_0 obtained were 1.93, and 1.80, and 6.2 x 10^{-7} $mAcm^{-2}$ and 1.5 x 10^{-7} $mAcm^{-2}$ respectively for Cu and $CuCl_2$ treated devices respectively. Adhikari et al. reported one order higher values of reverse saturation current for sputtered CdS/CdTe devices previously.[17] The slightly lower values of ideality factors and reverse saturation current density for $CuCl_2$ treated cells indicate the $CuCl_2$ treatment is better compared to the evaporated Cu.

Fig. 4(a) and (b) displays room temperature measurements of photoluminescence (PL) and time-resolved photoluminescence (TRPL) respectively for CdTe devices. The PL intensity observed for CdTe doped via a solution process was higher than doped by the thermal evaporation. The carrier lifetime (τ_2) increased from 1.2 ns to 2.2 ns for $CuCl_2$ treated device than Cu doped device. Enhanced PL intensity and improved carrier lifetimes in CdTe thin film doped via $CuCl_2$ can be attributed to the presence of fewer compensating defects (Cu_i). During the $CuCl_2$ treatment, the solution is 0.1 mmol copper concentration and the thin films were rinsed with DI water, and we assume these devices have lower amount of copper compared to Cu evaporated devices. Thus, the enhanced PL and TRPL can be attributed to better management of Cu dopants in thin films.

The low amount of Cu in the CdTe device is always beneficial for longer stability. When the device is operated for a long run, it is found that Cu atoms diffuse towards the front contact (CdS). For a CdTe device with 3 nm Cu deposited by thermal evaporation, the concentration of Cu atoms on the surface is about 2.54 x 10^{16} atoms/cm^2 with doping density of 7.25 x 10^{19} atoms/cm^3 (for 3.5 microns thick device). Here, we have taken the atomic mass of copper to be 63.546 gm/mol and density 8.96 gm/cm^3. This calculation also agrees with previous reports.[5, 9] Kranz et al. have also reported Cu concentration to be 5x10^{17} cm^{-3} for 5 µm CdTe doped with 1.0x10^{15} Cu atoms per cm^2.[5] Despite having very high dopants in the order of 10^{19} cm^{-3} in CdTe, the hole density is very low in the order of 10^{14} cm^{-3} (see Fig. 5). The higher performance of sputtered CdS/CdTe with $CuCl_2$ treatment is attributed to the enhanced opto-electronic properties of these devices.

Further, we carried a capacitance-voltage (C-V) measurement at room temperature and based on Mott Schottky analysis, we calculated the carrier concentrations profiling in CdTe solar cell devices with evaporated Cu and $CuCl_2$ treated CdTe back surface, as shown in Fig. 5. Based on this C-V measurement, CdTe with evaporated Cu has a carrier concentration of 1.37×10^{14} cm^{-3} less than by ~ two times (2.74 × 10^{14} cm^{-3}) than the one with $CuCl_2$ treatment. In this case, a

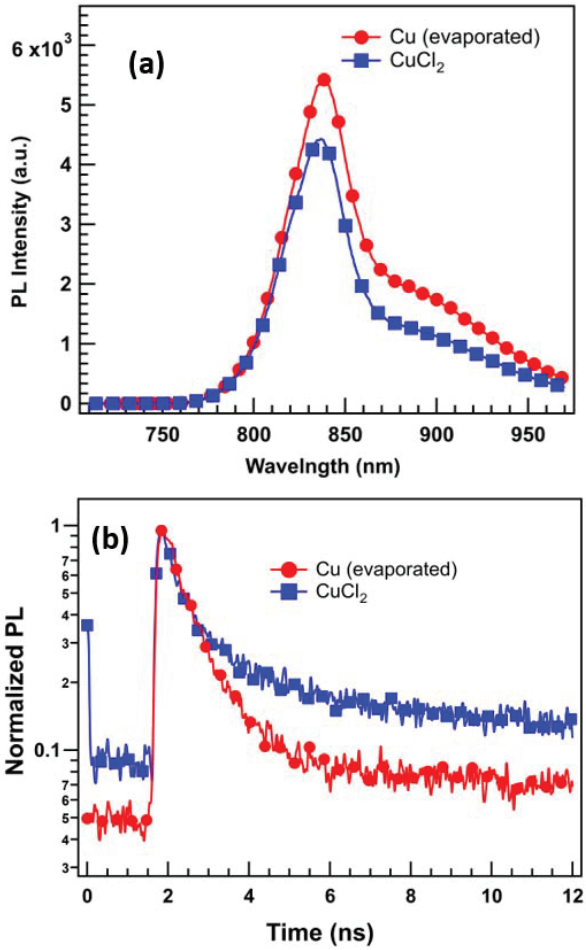


Fig. 4. Optical properties of (a) PL and (b) TRPL of CdTe devices with different Cu doping.

Authorized licensed use limited to: East Carolina University. Downloaded on June 16,2021 at 03:20:14 UTC from IEEE Xplore. Restrictions apply.

Approved for public release; distribution unlimited.

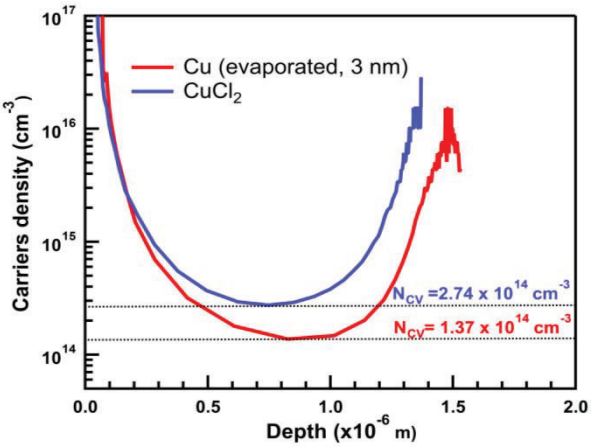


Fig. 5. Carrier density profiling (Ncv) vs depth, capacitance-voltage (C-V) profile measurement of all-sputtered CdS/CdTe devices with different Cu doping measured under dark at 300 K.

higher carrier concentration in the absorber layer should enhance device performance. The higher hole concentration lowers the fermi level towards the valence band increasing the built-in potential for the heterojunction, and thus it increases the V_{OC} (splitting of the quasi fermi levels) of the device. At the same time, longer carrier lifetime means reduced recombination rates enhancing device performance (both V_{OC} and FF).[3] As shown in the J-V curve in Fig. 1, higher V_{OC} and FF were observed for $CuCl_2$ treated CdTe devices. Based on this study, we conclude that doping of CdTe with $CuCl_2$ improves opto-electronic properties including the minority carrier lifetime and the carrier concentration. This helps to improve the device performance, primarily in terms of V_{OC} and FF, compared to CdTe devices doped by evaporated Cu.

V. Conclusion

Here, we have successfully fabricated all-sputtered CdS/CdTe devices with a V_{OC} exceeding 840 mV. It was achieved by doping CdTe using a solution-based technique and optimizing the annealing temperature and time. While the control device with evaporated copper/gold has an efficiency of 12.8% (average 12.6%), our study shows a device efficiency of 13.7% (average 13.2%) with a V_{OC} exceeding 840 mV for $CuCl_2$ treated devices. The PL and TRPL measurements showed improvements on PL emission and minority carrier lifetime for $CuCl_2$ treated devices. Similarly, carrier density profiling indicated that devices doped by $CuCl_2$ showed a ~100% increase in free carrier concentration than evaporated Cu in the CdTe absorber layer improving open-circuit voltage and fill factor of the device.

Acknowledgements

This material is based on research sponsored by air force research laboratory under agreement number FA9453-18-2-0037 and FA9453-19-C-1002. The US government is authorized to reproduce and distribute reprints for governmental purposes notwithstanding any copyright notation thereon. DISCLAIMER: The views and conclusions contained herein are those of the authors and should not be interpreted as necessarily representing the official policies or endorsements, either expressed or implied, of air force research laboratory or the US government.

References

[1] A. Gupta and A. D. Compaan, "All-sputtered 14% CdS/ CdTe thin-film solar cell with ZnO:Al transparent conducting oxide," *Applied Physics Letters,* vol. 85, no. 4, pp. 684-686, 2004.

[2] H. Li, X. Liu, Z. Du, and B. Yang, "Twin boundaries enhanced current transport in 14.4%-efficient CdTe solar cells by RF sputtering," in *2015 IEEE 42nd Photovoltaic Specialist Conference (PVSC)*, 2015, pp. 1-4: IEEE.

[3] R. M. Geisthardt, M. Topic, and J. R. Sites, "Status and Potential of CdTe Solar-Cell Efficiency," *IEEE Journal of Photovoltaics,* vol. 5, no. 4, pp. 1217-1221, Jul 2015.

[4] T. Ablekim, E. Colegrove, and W. K. Metzger, "Interface engineering for 25% CdTe solar cells," *ACS Applied Energy Materials,* vol. 1, no. 10, pp. 5135-5139, 2018.

[5] L. Kranz *et al.*, "Doping of polycrystalline CdTe for high-efficiency solar cells on flexible metal foil," *Nat Commun,* vol. 4, p. 2306, 2013.

[6] E. Janik and R. Triboulet, "Ohmic contacts to p-type cadmium telluride and cadmium mercury telluride," (in English), *Journal of Physics D: Applied Physics,* vol. 16, no. 12, pp. 2333-2340, 1983.

[7] C. R. Corwine, A. O. Pudov, M. Gloeckler, S. H. Demtsu, and J. R. Sites, "Copper inclusion and migration from the back contact in CdTe solar cells," *Solar Energy Materials and Solar Cells,* vol. 82, no. 4, pp. 481-489, May 30 2004.

[8] T. Ablekim *et al.*, "Tailoring MgZnO/CdSeTe Interfaces for Photovoltaics," *IEEE Journal of Photovoltaics,* vol. 9, no. 3, pp. 888-892, May 2019.

[9] E. Artegiani *et al.*, "Analysis of a novel $CuCl_2$ back contact process for improved stability in CdTe solar cells," (in English), *Progress in Photovoltaics,* vol. 27, no. 8, pp. 706-715, Aug 2019.

[10] A. H. Munshi *et al.*, "Polycrystalline CdSeTe/CdTe Absorber Cells With 28 mA/cm^2 Short-Circuit Current," *IEEE J. Photovolt.,* vol. 8, no. 1, pp. 310-314, 2018.

[11] D.-B. Li *et al.*, "Maximize CdTe solar cell performance through copper activation engineering," *Nano Energy,* p. 104835, 2020.

[12] E. Bastola, A. V. Bordovalos, E. LeBlanc, N. Shrestha, M. O. Reese, and R. J. Ellingson, "Doping of CdTe using $CuCl_2$ Solution for Highly Efficient Photovoltaic Devices," in *2019 IEEE 46th Photovoltaic Specialists Conference (PVSC)*, 2019, pp. 1846-1850.

[13] D. Mao, G. Blatz, C. E. Wickersham, and M. Gloeckler, "Correlative impurity distribution analysis in cadmium telluride (CdTe) thin-film solar cells by ToF-SIMS 2D imaging," (in

Authorized licensed use limited to: East Carolina University. Downloaded on June 16,2021 at 03:20:14 UTC from IEEE Xplore. Restrictions apply.

Approved for public release; distribution unlimited.

English), *Solar Energy Materials and Solar Cells,* vol. 157, pp. 65-73, Dec 2016.

[14] E. Bastola, K. P. Bhandari, I. Subedi, N. J. Podraza, and R. J. Ellingson, "Structural, optical, and hole transport properties of earth-abundant chalcopyrite ($CuFeS_2$) nanocrystals," *MRS Communications,* vol. 8, no. 03, pp. 970-978, 2018.

[15] E. Bastola, F. K. Alfadhili, A. B. Phillips, M. J. Heben, and R. J. Ellingson, "Wet chemical etching of cadmium telluride photovoltaics for enhanced open-circuit voltage, fill factor, and power conversion efficiency," *Journal of Materials Research,* vol. 34, no. 24, pp. 3988-3997, 2019.

[16] K. P. Bhandari *et al.*, "Thin film iron pyrite deposited by hybrid sputtering/co-evaporation as a hole transport layer for sputtered CdS/CdTe solar cells," (in English), *Solar Energy Materials and Solar Cells,* vol. 163, pp. 277-284, Apr 2017.

[17] D. Adhikari *et al.*, "Glancing angle deposited CdTe: Nanostructured films and impact on solar cell performance," *Surface and Coatings Technology,* p. 125127, 2019.

Authorized licensed use limited to: East Carolina University. Downloaded on June 16,2021 at 03:20:14 UTC from IEEE Xplore. Restrictions apply.

Approved for public release; distribution unlimited.

579

Solution-Processed Copper Telluride Nanowire Thin Film as a Back-Buffer Layer to Cadmium Telluride Solar Cells

Dipendra Pokhrel
Wright Center for Photovoltaics Innovation and Commercialization (PVIC), Department of Physics and Astronomy, University of Toledo
Ohio,USA
dipendra.pokhrel@rockets.utoledo.edu

Ebin Bastola
Wright Center for Photovoltaics Innovation and Commercialization (PVIC), Department of Physics and Astronomy, University of Toledo
Ohio,USA
ebin.bastola@rockets.utoledo.edu

Kamala Khanal Subedi
Wright Center for Photovoltaics Innovation and Commercialization (PVIC), Department of Physics and Astronomy, University of Toledo
Ohio,USA
kamala.khanalsubedi@rockets.utoledo.edu

Adam Phillips
Wright Center for Photovoltaics Innovation and Commercialization (PVIC), Department of Physics and Astronomy, University of Toledo
Ohio,USA
adam.phillips@utoledo.edu

Micheal J Heben
Wright Center for Photovoltaics Innovation and Commercialization (PVIC), Department of Physics and Astronomy, University of Toledo
Ohio,USA
micheal.heben@utoledo.edu

Randy J Ellingson
Wright Center for Photovoltaics Innovation and Commercialization (PVIC), Department of Physics and Astronomy, University of Toledo
Ohio,USA
randy.ellingson@utoledo.edu

***Abstract*— Here, we report the application of copper telluride (Cu_7Te_4) nanowires (NWs) as an interfacial layer to cadmium telluride (CdTe) photovoltaics. The Cu_7Te_4 NWs were synthesized utilizing a hot injection colloidal method and characterized using X-ray diffraction, scanning electron microscopy and elemental analysis. As the interfacial layer was introduced, the device efficiency was improved mainly due to the improvement in open-circuit voltage (V_{OC}) of the device. The highest V_{OC} observed for CdS/CdTe solar cells is 857 mV with device efficiency of 14.2%.**

Keywords*— *CdTe, solar cells, back contacts, copper telluride, nanowires

I. Introduction

Development of a stable and low resistance contact between CdTe and a metal electrode, the realization of high absorber hole density, and interface passivation are the main challenges associated with CdTe solar cells.[1] For the efficient extraction of holes and to repel photogenerated electrons at the back contact of a CdTe device, a material with suitable band edge location is preferred. To mitigate the contact barrier, different techniques such as back surface modification of CdTe by Cu doping [2], etching the CdTe surface to create a Te rich layer[3], and insertion of a hole transport layer (HRT) between the CdTe layer and metal contact have been employed. For HRT layer, different materials such as zinc telluride (ZnTe)[4], copper telluride (Cu_2Te)[5], antimony telluride (Sb_2Te_3)[6], carbon nanotubes[7], and nanocomposite $(CuS)_x(ZnS)_{1-x}$[8] were used. Previously, other solution processed back contacts have also been tested for CdTe photovoltaics.[9, 10]

High efficiency CdTe solar cells have typically used Cu as part of the back contact processing and is important for enhancing the performance of CdTe solar cells. Excess Cu diffuse along the grain boundaries and limited the shunting effect in the device. Though Cu is beneficial to device performance, it also have certain challenges related to device stability over time.[11] Copper telluride (Cu_xTe) is a p^+ highly degenerate semiconductor with structures varying with stoichiometry. The bandgap of Cu_xTe ranges from 1.0 to 1.5 eV based on stoichiometry.[12] Previously, Cu_xTe has been used as a back contact material in CdTe solar cells. Yun et al. used evaporated Cu_2Te layer as a back contact to CdTe,[13] and Kim et al. compared Cu_2Te and Cu back contacts in CdS/CdTe solar cells by evaporating metallic Cu and Cu_2Te respectively.[5] Ferekides et al. reported the development of Cu_xTe based contact on CdTe by depositing Cu_xTe layer of different thickness using RF sputtering.[14] Based on the literature, all authors used Cu_xTe as a back contact to CdTe by thermal evaporation.

Here, we report the application of solution processed Cu_xTe NWs as a back contact interfacial layer in CdTe photovoltaics. The Cu_xTe NWs were prepared using a hot-injectional colloidal method and spin-coated on CdTe surface to prepare a back contact. The interfacial layer helped to enhance the device efficiency mainly by the improvement of open-circuit voltage.

II. Experimental Method

The synthesis of Cu_xTe involves two steps: (i) synthesis of Te NWs and (ii) conversion of Te NWs into Cu_xTe NWs. The synthesis is based on slightly modified version of Yang et al. [15] For Te NWs synthesis, 1.05 mmol (0.167 gm) of tellurium oxide (TeO_2), 2.98 mmol (0.167 gm) of potassium hydroxide (KOH) and 0.2 gm of polyvinylpyrrolidone (PVP) were dissolved in 15 mL ethylene glycol under vigorous magnetic stirring to form a cloudy white solution. The temperature was set to 120 °C such that the solution becomes transparent yellow. In the meantime, 2.8 mmol (0.5 gm) of ascorbic acid was dissolved in 1.5 ml of deionized water at 80°C to form an aqueous ascorbic acid solution. When the reaction temperature reached

978-1-7281-6115-0/20/$31.00 ©2020 IEEE

Authorized licensed use limited to: University of Prince Edward Island. Downloaded on May 16,2021 at 22:19:30 UTC from IEEE Xplore. Restrictions apply.

Approved for public release; distribution unlimited.

580

120 °C, the ascorbic acid solution was rapidly injected resulting in a change in color to opaque black. The reaction was continued for 19 hrs. at 120 °C in a nitrogen (N_2) environment to complete the synthesis of high quality Te NWs. The heating mantle was removed, and the reaction flask was cooled by immersion of the three-neck flask into a cold-water bath. The product was centrifuged and cleaned with deionized water twice. To convert the NWs composition to Cu_xTe, we followed the process reported previously [15] and $Cu(NO_3)_2{\cdot}3H_2O$ was used as copper precursor. The product was cleaned with deionized water, centrifuged, dried and stored in N_2 environment for further characterization and device fabrication.

For a standard back contact (Cu/Au), a solution-based Cu treatment ($CuCl_2$ as a copper source) was carried following a previous report optimized for CdS/CdTe devices.[16] For this Cu treatment, 0.1 mmol $CuCl_2$ solution in deionized water was prepared and the $CdCl_2$ treated CdS/CdTe devices were submerged for two minutes, and rinsed with deionized water. Finally, the devices were annealed at 200°C for 20 mins to diffuse the Cu into the CdTe. The devices were completed by evaporating 40 nm gold (Au). For a device with Cu_xTe NWs (CdS/CdTe/Cu/Cu_xTeNWs/Au) as the back buffer layer, after submerged $CdCl_2$ treated CdS/CdTe devices in $CuCl_2$ solution, rinsed with deionized water and 50 ul solution of Cu_xTe NWs (5mg/ml) was dropped and spun onto CdTe devices. The devices were then annealed at 200°C for 20 mins and 40 nm Au was thermally evaporated to complete the back contact. For a device with only Cu_xTe NWs (CdS/CdTe/ Cu_xTe NWs/Au), the $CuCl_2$ treatment was omitted. On $CdCl_2$ treated CdS/CdTe device, 50 ul solution of Cu_xTe NWs (5mg/ml) was dropped and spun onto CdTe devices followed by annealing at 200°C for 20 mins and complete the back contact by evaporating 40 nm Au. The devices were then scribed by a 532 nm laser into an array of approximately 20 cells each having area of 0.06 cm^2. The J-V characteristics were measured by illuminating the devices under simulated AM1.5G solar irradiance on devices.

III. Results and Discussion

The as-synthesized Cu_xTe NWs were dispersed in ethanol and a thin film was prepared by drop casting onto soda lime glass for characterization like scanning electronic microscopy (SEM), energy-dispersive X-ray spectroscopy (EDS) and X-ray diffraction (XRD). Fig 1a displays the SEM image of Cu_xTe nanowires. The image indicates the NWs grown are uniform in lengths and diameters. The EDS was carried at operating current 10 μA and voltage 20 kV. Based on EDS analysis, the elemental ratio of Cu and Te is 7:4. Fig. 1b shows the XRD pattern of as obtained copper telluride nanowires which have hexagonal crystal structure with lattice constants a=b=0.8340 nm and c= 0.7230 nm obtained from MDI JADE software (PDF # 97-062-9337). From EDS analysis and XRD patterns, we confirm that the synthesized nanowires have chemical formula Cu_7Te_4 in hexagonal crystal structure.

Fig. 2 shows the current voltage (*J-V*) characteristics that compare the light and dark characteristics of best cells with different back contacts. The solid curves represent the measurements under simulated AM 1.5 illumination and dashed curves represent the measurements under dark illumination. The open circuit voltage (V_{oc}), short-circuit current density (J_{sc}), fill factor (*FF*), efficiency (η), series resistance (R_{series}) and shunt resistance (R_{shunt}) of best cells of each type of back contacts are presented in Table 1. In the case of (Cu/Au) back contact, the best device has an efficiency (η) of 14.0 % with V_{oc} 841 mV, J_{sc} 22.1 mA cm^{-2}, and *FF* 75.7 %. When Cu_7Te_4 NWs film were used as back buffer layer (Cu/ Cu_7Te_4NWs/Au), the best device efficiency was14.2 % with V_{oc} of 857 mV, J_{sc} of 22.3 mA cm^{-2}, and *FF* of 74.5 %. The device performances were enhanced due to increase in V_{oc} where J_{sc} remains almost constant. The ideality factors for devices with standard back contact and Cu_7Te_4 NWs back contact were calculated [17], and found to be nearly identical at 1.58 – 1.60. Though the ideality factors are identical, we can conclude that the increase in *Voc* with Cu_7Te_4 NWs as back buffer layer indicates there is less recombination in the device, resulting in an overall increase in efficiency. The device with back contact (Cu_7Te_4/Au) has an efficiency of 13.6 % with V_{oc} of 841 mV, J_{sc} of 22.5 $mAcm^{-2}$, and *FF* of 72.0 %. Here, copper treatment was omitted, and Cu_7Te_4 NWs were used as a back-buffer layer on

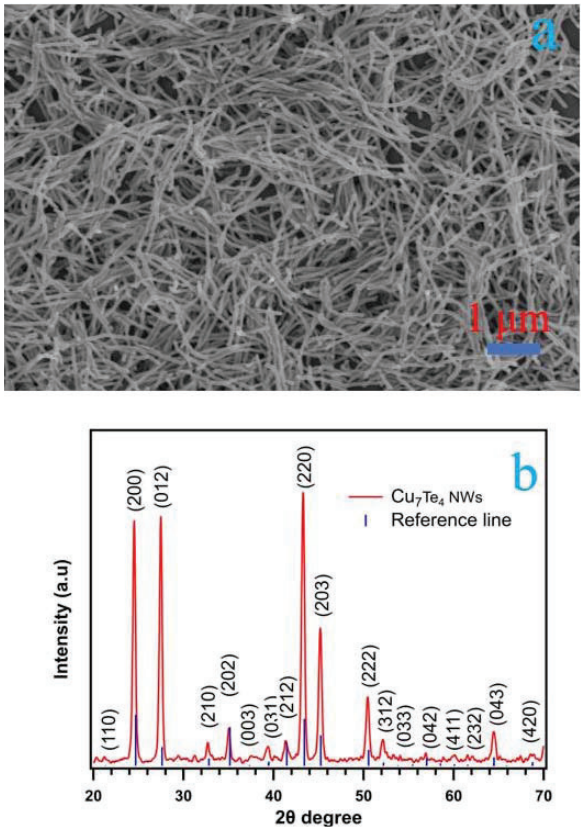


Fig. 1. (a) SEM image and (b) XRD pattern of Cu_7Te_4 NWs

$CdCl_2$ treated CdTe devices. In this case, the V_{oc} increases which is equal to the V_{oc} of control device but decrease in *FF* factor lowered the device efficiency.

Fig. 3 shows the statistical distribution of V_{oc}, J_{sc}, *FF* and η of CdS/CdTe solar cells with back contacts Cu/Au, Cu/Cu_7Te_4NWs/Au and Cu_7Te_4NWs/Au. The observed performance enhancement is attributed to the improved efficiency of transport of holes to the back contact.

Table 1: *J vs. V* parameters for best cells of CdS/CdTe solar cells with Cu/Au, Cu/ Cu_7Te_4NWs/Au and Cu_7Te_4NWs/Au back contacts.

Back contacts	V_{oc} (mV)	J_{sc} (mA cm^{-2})	*FF* (%)	*Eff* (η)	*Rs* (Ω-cm^2)	R_{SH} (Ω-cm^2)
Cu/Au	841	22.1	75.7	14.0	4.2	3603
Cu/ Cu_7Te_4/Au	857	22.3	74.5	14.2	4.0	2479
Cu_7Te_4/Au	841	22.5	72.0	13.6	3.4	2087

Authorized licensed use limited to: University of Prince Edward Island. Downloaded on May 16,2021 at 22:19:30 UTC from IEEE Xplore. Restrictions apply.

Approved for public release; distribution unlimited.

581

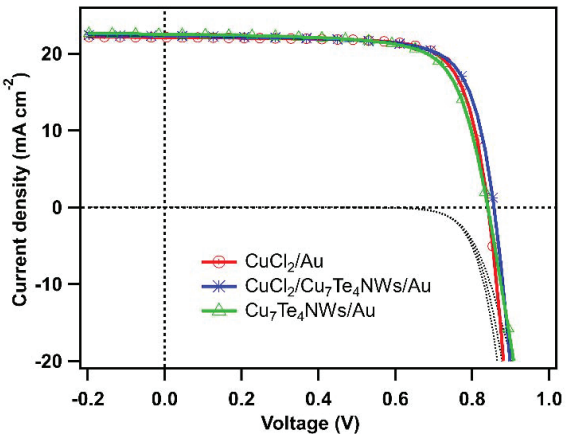


Fig. 2. J-V curves of best cells of CdS/CdTe devices with back contacts Cu/Au, Cu/ Cu_7Te_4NWs/Au and Cu_7Te_4NWs/Au.

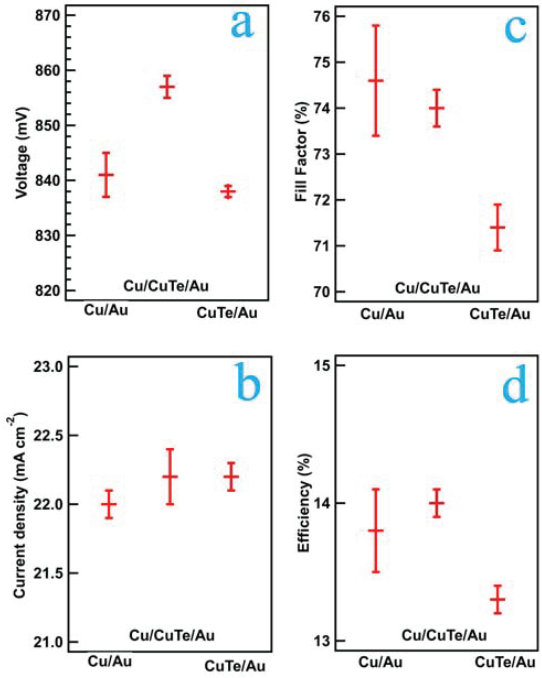


Fig.3 Statistical distribution of V_{oc}, J_{sc}, FF and η of CdS/CdTe solar cells with back contacts Cu/Au, Cu/Cu_7Te_4NWs/Au and Cu_7Te_4NWs/Au.

IV. Conclusions

Here, we have successfully synthesized the Cu_7Te_4 NWs using a solution-processed method and demonstrated its application as a back-buffer layer to CdS/CdTe solar cells. The application of Cu_7Te_4 NWs as interfacial layer helped to improve the V_{OC} of the device. This interfacial layer may produce a device efficiency greater than 15% for CdS/CdTe devices though further optimization and improving the device FF. We are planning to use these NWs as current conduits through oxide passivated interfaces for better CdS/CdTe device efficiency.

Acknowledgment

This material is based on research sponsored by Air Force Research Laboratory (AFRL) under agreement number FA9453-18-2-0037 and the U.S. DOE's Office of Energy Efficiency and Renewable Energy (EERE) under Solar Energy Technologies Office (SETO) Agreement DE-EE0008974. The U.S. Government is authorized to reproduce and distribute reprints for Governmental purposes notwithstanding any copyright notation thereon. The views and conclusions contained herein are those of the authors and should not be interpreted as necessarily representing the official policies or endorsements, either expressed or implied, of AFRL or the U.S. Government. We also thank Willard and Kelsey Solar Group for providing CdS/CdTe device stacks.

References

[1] Fahrenbruch, A.L., *Ohmic contacts and doping of CdTe.* Solar Cells, 1987. **21**(1-4): p. 399-412.

[2] Demtsu, S., D. Albin, and J. Sites. *Role of copper in the performance of CdS/CdTe solar cells*. in *2006 IEEE 4th World Conference on Photovoltaic Energy Conference*. 2006. IEEE.

[3] Watthage, S.C., et al., *Selective Cd Removal from CdTe for High Efficiency Te Back Contact Formation.*

[4] Bista, S.S., et al. *ZnTe Back Buffer Layer to Enhance the Efficiency of CdS/CdTe Solar Cells*. in *2019 IEEE 46th Photovoltaic Specialists Conference (PVSC)*. 2019. IEEE.

[5] Kim, S., et al., *Comparative Study of Cu 2 Te and Cu Back Contact in CdS/CdTe Solar Cell.* Journal of the Korean Physical Society, 2018. **72**(7): p. 780-785.

[6] Hu, S., et al., *Band diagrams and performance of CdTe solar cells with a Sb2Te3 back contact buffer layer.* AIP Advances, 2011. **1**(4): p. 042152.

[7] Phillips, A.B., et al., *Wiring-up carbon single wall nanotubes to polycrystalline inorganic semiconductor thin films: low-barrier, copper-free back contact to CdTe solar cells.* Nano letters, 2013. **13**(11): p. 5224-5232.

[8] Subedi, K.K., et al., *Nanocomposite (CuS) x (ZnS) 1-x thin film back contact for CdTe solar cells: Toward a bifacial device.* Solar Energy Materials and Solar Cells, 2018. **186**: p. 227-235.

[9] Bhandari, K.P., et al., *Iron pyrite nanocrystal film serves as a copper-free back contact for polycrystalline CdTe thin film solar cells.* Solar Energy Materials and Solar Cells, 2015. **140**: p. 108-114.

[10] Bastola, E., K.P. Bhandari, and R.J. Ellingson, *Application of composition controlled nickel-alloyed iron sulfide pyrite nanocrystal thin films as the hole transport layer in cadmium telluride solar cells.* Journal of Materials Chemistry C, 2017. **5**(20): p. 4996-5004.

[11] Dobson, K.D., et al., *Stability of CdTe/CdS thin-film solar cells.* Solar Energy Materials and Solar Cells, 2000. **62**(3): p. 295-325.

[12] Farag, B. and S. Khodier, *Direct and indirect transitions in copper telluride thin films.* Thin Solid Films, 1991. **201**(2): p. 231-240.

[13] Yun, J.H., et al., *Back contact formation using Cu2Te as a Cu-doping source and as an electrode in CdTe solar cells.* Solar Energy Materials and Solar Cells, 2003. **75**(1-2): p. 203-210.

[14] Ferekides, C., V. Viswanathan, and D. Morel. *RF sputtered back contacts for CdTe/CdS thin film solar cells*. in *Conference Record of the Twenty Sixth IEEE Photovoltaic Specialists Conference-1997*. 1997. IEEE.

[15] Yang, H., et al., *Environmentally Benign Synthesis of Ultrathin Metal Telluride Nanowires.* Journal of the American Chemical Society, 2014. **136**(29): p. 10242-10245.

[16] Bastola, E., et al. *Doping of CdTe using CuCl 2 Solution for Highly Efficient Photovoltaic Devices*. in *2019 IEEE 46th Photovoltaic Specialists Conference (PVSC)*. 2019. IEEE.

[17] Quanxi, J. and L. Enke, *A method for the direct measurement of the solar cell junction ideality factor.* Solar cells, 1987. **22**(1): p. 15-21.

Authorized licensed use limited to: University of Prince Edward Island. Downloaded on May 16,2021 at 22:19:30 UTC from IEEE Xplore. Restrictions apply.

Approved for public release; distribution unlimited.

582

Solution Processed CuCl treatment for efficient CdS/CdTe Solar Cells

Sandip S. Bista
Dep. Of Physics & Astronomy
University of Toledo
Toledo, OH, USA
sandip.bista@rockets.utoledo.edu

Deng-Bing Li
Dep. Of Physics & Astronomy
University of Toledo
Toledo, OH, USA
Dengbing.Li@utoledo.edu

Zhaoning Song
Dep. Of Physics & Astronomy
University of Toledo
Toledo, OH, USA
zhaoning.song@.utoledo.edu

Rasha A. Awni
Dep. Of Physics & Astronomy
University of Toledo
Toledo, OH, USA
rasha.awni@utoledo.edu

Suman Rijal
Dep. Of Physics & Astronomy
University of Toledo
Toledo, OH, USA
suman.rijal@rockets.utoledo.edu

Chen Lei
Dep. Of Physics & Astronomy
University of Toledo
Toledo, OH, USA
Chen.lei@rockets.utoledo.edu

Corey R. Grice
Dep. Of Physics & Astronomy
University of Toledo
Toledo, OH, USA
corey.grace@rockets.utoledo.edu

Manoj K. Jamarkattel
Dep. Of Physics & Astronomy
University of Toledo
Toledo, OH, USA
manoj.jamarkattel@rockets.utoledo.edu

Adam Phillips
Dep. Of Physics & Astronomy
University of Toledo
Toledo, OH, USA
adam.phillips@utoledo.edu

Michael Heben
Dep. Of Physics & Astronomy
University of Toledo
Toledo, OH, USA
micheal.heben@utoledo.edu

Randy J. Ellingson
Dep. Of Physics & Astronomy
University of Toledo
Toledo, OH, USA
randy.ellingson@utoledo.edu

Yanfa Yan
Dep. Of Physics & Astronomy
University of Toledo
Toledo, OH, USA
yanfa.yan@utoledo.edu

***Abstract*— Copper (Cu) doping is a crucial process to improve the hole concentration in CdTe absorber layer and reduce the back-barrier height for efficient CdTe solar cells. However, excess Cu creates detrimental defects and deteriorates device stability due to its high diffusivity. Here, we introduce a wet chemical method to incorporate Cu in CdTe using a CuCl solution. This approach allows a better control of Cu doping than the conventional method using evaporated Cu. Our investigation shows that the CuCl treatment can significantly improve the overall device performances due to an increased carrier concentration in the CuCl treated CdTe absorber layer. Furthermore, the CuCl treated devices show a longer minority carrier lifetime than the conventional Cu treated devices.**

Keywords*— *CuCl, carrier concentration, carrier lifetime.

I. INTRODUCTION

Copper (Cu) was first introduced to improve the performance of CdS/CdTe solar cells by Bonnet and Rabenhorst in their pioneering work, where they emphasized the significance of Cu in enhancing the p-type conductivity of CdTe and in the formation of a low-resistance back contact [1]. Since then, Cu has been used in most highly efficient CdTe solar cells. It is known that Cu doping increases the hole density in CdTe by substituting cadmium vacancies (V_{Cd}) and reduces the back-barrier height through a formation of Cu_xTe_{1-x} [2, 3]. However, it is also observed that Cu has a moderate solubility in CdTe, resulting in a limited hole concentration of up to ~10^{14} cm^{-3} at room temperature [4]. Furthermore, the high diffusivity of Cu in CdTe (up to 1 x 10^{-10} cm^2/s at 200 °C) [5] causes device degradation. To address the stability issue, Cu related compounds, e.g. Cu: ZnTe, are implemented between CdTe and metal contact to control the release of Cu [6-8]. Researchers also investigating for alternate back contacts e.g. solution based CuSCN [9, 10], wet $CuCl_2$ [11], $(CuS)_x(ZnS)_{1-x}$ [12]. These solutions based back contact gives promising result, but it contains large amount of Cu which is the major issue for long term stability.

Here, a solution-processed Cu doping technique is used to improve the device performance with a significantly reduced Cu concentration in CdTe comparing with the conventional Cu treated devices, which is promising for improved device stability. After careful process optimization, the devices treated with CuCl show a more than 15 % power conversion efficiency (PCE) improvement compared with the conventional devices treated with Cu metal. This improvement is ascribed to a increased doping concentration and carrier lifetime and the reduced activation energy of defect states in CdTe.

978-1-7281-6115-0/20/$31.00 ©2020 IEEE

Authorized licensed use limited to: Carleton University. Downloaded on June 03,2021 at 04:05:04 UTC from IEEE Xplore. Restrictions apply.

Approved for public release; distribution unlimited.

583

II. Experimental Details

The device configuration for this experiment is FTO/CdS:O/CdTe/$CdCl_2$/CuCl/Au. A 75 nm oxygenated CdS layer was deposited first on commercial fluorine doped tin oxide (FTO) glass substrates (NSG T12D Pilkington, North America) by RF-sputtering at room temperature under a pressure of 10 mTorr. A ~4 micron CdTe layer was deposited by a close space sublimation process, with the source temperature at 660 °C, the substrate temperature at 590 °C, and the pressure at 10 mTorr. A $CdCl_2$ treatment (using a saturated $CdCl_2$ solution in methanol) was then carried out at 390 °C for 30 min in a dry air ambient. After the $CdCl_2$ treatment, the sample was rinsed with methanol to remove the chloride residues. After that, an aliquot of 100 µl of a saturated CuCl solution in ethanol was dropped on each piece of CdTe sample with an area of 1.5-inch × 1.5-inch, and these samples were then annealed at different temperatures and periods. The preparation of our saturated CuCl solution can be found in our previous report. The inductive coupled plasma mass spectroscopy (CP-MS) analysis of the CuCl solution shows that 100 µl CuCl solution contains 3.101 µg/ml of Cu, which is equivalent to a 0.024 nm thick Cu layer [13]. A 40 nm gold (Au) back metal electrode was thermally evaporated to complete the devices. For the control devices, a thermally evaporated Cu (4nm)/Au (40nm) bilayer was used instead of the CuCl/Au process. After the Au deposition, the control devices were annealed at 200 °C for 20 min in nitrogen. The active area for all the cells is 0.08 cm^2.

The PV performance of solar cells were evaluated by current density-voltage (J-V) measurements under simulated AM1.5 illumination using a Keithley 2440 digital source meter and a LED solar simulator from Newport is calibrated by using standard silicon solar cell and external quantum efficiency (EQE) measurements at zero bias. Room temperature capacitance-voltage (C-V) measurement were carried out to measure the carrier concentration in CdTe. A C-V measurement were performed in dark with 45 mV AC modulation voltage and 10kHz frequency, and room temperature photoluminescence (PL) and time-resolved photoluminescence (TRPL) measurements were performed to measure the minority carrier lifetime.

III. Results and Discussions

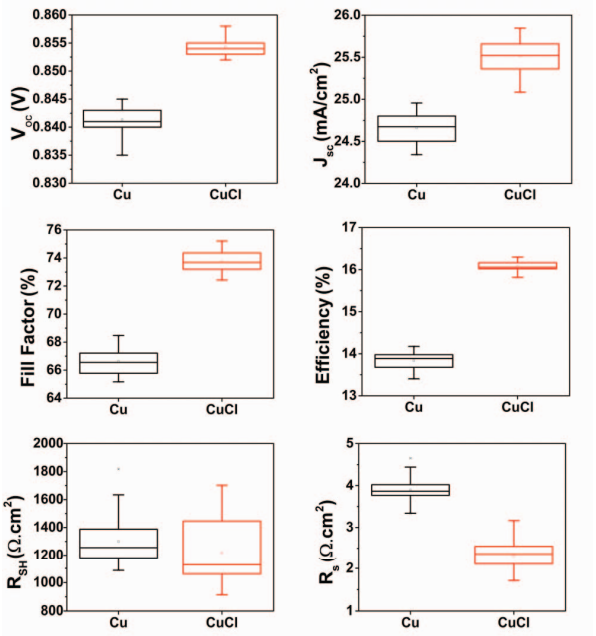


Fig.1. Statistical distribution of open-circuit voltage (Voc), short-circuit current density (Jsc), fill factor, efficiency, series resistance (R_S), and shunt resistance (R_{SH}) for the control (metallic Cu) and CuCl treated devices both annealed at 200 °C for 20 min.

Fig. 1 shows the statistical comparison of PV parameters for the Cu metal (CdTe-Cu) and CuCl solution (CdTe-CuCl) treated devices. On average, CdTe-CuCl cells exhibit higher V_{OC} (855 versus 841 mV), J_{SC} (25.6 versus 24.8 mA/cm^2), and FF (74.5% versus 68%) than the control CdTe-Cu devices, resulting in better PCEs (16.30% versus 14.20%). It is worth noting that the improvement of FF is mainly due to a reduction in series resistance from 4 to 2.2 Ω.cm^2.

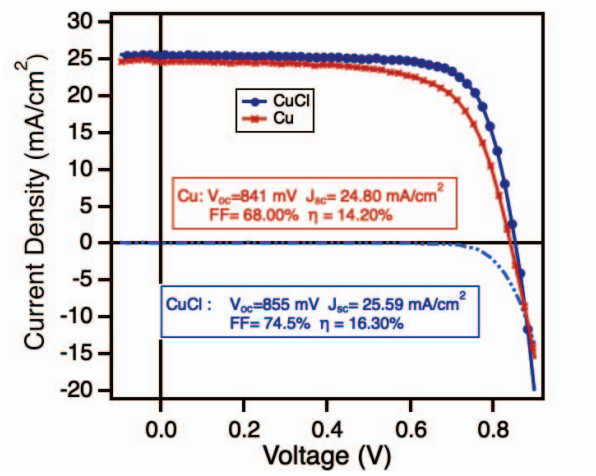


Fig.2. J-V curves of the best CdTe-Cu and CdTe-CuCl devices.

978-1-7281-6115-0/20/$31.00 ©2020 IEEE

Authorized licensed use limited to: Carleton University. Downloaded on June 03,2021 at 04:05:04 UTC from IEEE Xplore. Restrictions apply.

Approved for public release; distribution unlimited.

584

Fig. 2 shows the J-V curves of the best performance devices in each group. The CdTe-CuCl cell shows a higher power conversion efficiency (PCE) of 16.3% than the CdTe-Cu device (14.2%). This preliminary investigation demonstrates that the CuCl solution treatment can be used for fabricating efficient CdTe solar cells.

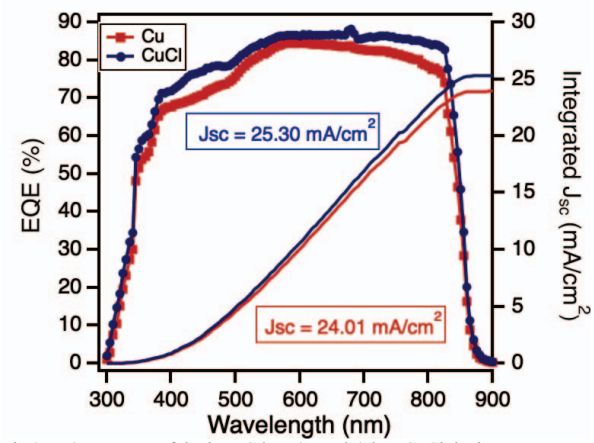


Fig.3. EQE spectra of the best CdTe-Cu and CdTe-CuCl devices.

Fig.3. shows the external quantum efficiency (EQE) curves of the best CdTe-Cu and CdTe-CuCl devices. The CdTe-CuCl device shows higher spectrum responses in both the short and long-wavelength regions. This indicates that the Cu doping by using the CuCl solution process enhances the charge separation and transport at the front junction as well as the back contact.

For best performing cell ideality factor (A) and diode saturation current (J_O) are calculated by analyzing J-V data according to site's method [14, 15]. This analysis assumes that the J-V behavior of solar cell can be described using a general single exponential diode equation.

$$J(V) = J_O \exp\left[\frac{q}{AK_BT}(V - JR)\right] + GV - J_L \qquad (1)$$

where k_B the Boltzmann constant, T the Kelvin temperature, q the unit charge, R series resistance, G conductance (1/shunt resistance), and J_L the light generated current density ~ J_{SC}.

For CdTe-CuCl cell, A and J_O values are 1.62 and 1.60 × 10^{-8} mA/cm^2, respectively, which are comparatively smaller than the value for CdTe-Cu device (i.e. 1.79 and 9.8 × 10^{-8} mA/cm^2). A and J_O are interdependent parameters where J_O is directly related to the non-radiative recombination. So, smaller value of J_O in the CuCl treated device suggests less defective and more superior heterojunction quality. Further, equation (2) justifies that J_O can improve V_{OC} of the solar cell.

$$V_{OC} = \frac{AK_BT}{q}\ln\left(\frac{J_L}{J_O} - 1\right) \qquad (2)$$

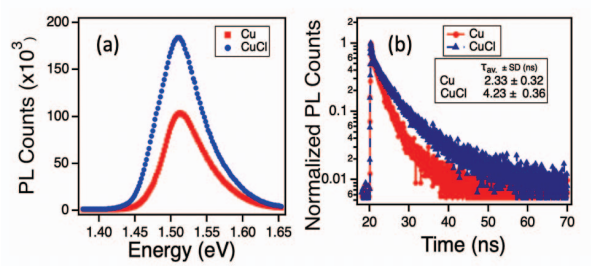


Fig.4. (a) PL measurement (b) TRPL measurement for Cu metal and CuCl treated samples.

To understand impact of Cu doping on the charge recombination rate in the CdTe-Cu and CdTe-CuCl devices, we measured photoluminescence (PL) and the minority carrier lifetime using time-resolved photoluminescence (TRPL) with a 641 nm pulse laser pulse excitation from the glass side. It is clearly shown in Fig. 4. that the CuCl treatment has a significant influence in carrier lifetime. Higher the PL intensity and the carrier lifetime for CuCl treated device suggests reduced recombination at the interface and bulk, attributing to the improvement of V_{OC} and FF [16, 17].

The C-V measurement was used to investigate the carrier density in CdTe and the built-in potential. As shown in fig. 5(a), the hole density in the CdTe-CuCl and CdTe-Cu devices are 5.60 × 10^{14} and 3 × 10^{14} cm^{-3}, respectively. From Mott-shotkky plot of $1/C^2$ vs bias voltage (V) a built-in potential of 0.89 V is extracted for CdTe-CuCl device, which is higher than that of 0.61 V for the control device. The increase in hole density in the CdTe-CuCl device is consistent with the increase in its built-in potential. A higher built-in potential creates a stronger electric field at the interface, which benefits charge separation at the junction, leading to higher device performance in the CdTe-CuCl device.

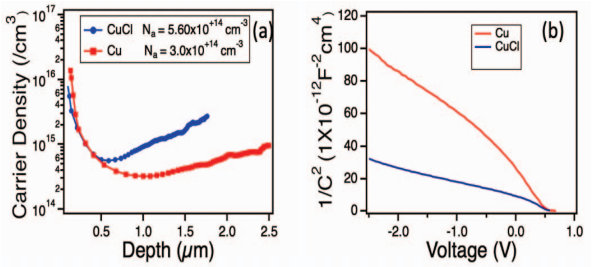


Fig.5. (a) Apparent carrier density in CdTe layers extracted from the C-V measurements. (b) Mott-Shotkky plot from C-V measurement.

Authorized licensed use limited to: Carleton University. Downloaded on June 03,2021 at 04:05:04 UTC from IEEE Xplore. Restrictions apply.

Approved for public release; distribution unlimited.

Overall, the benefits of the CuCl treatment were demonstrated through the J-V, EQE, TRPL, and CV measurements. A CuCl-treated devices exhibit an improved front junction with a higher built-in potential, higher p-type conductivity, and a higher lifetime in CdTe, and therefore, improved device performance compared with conventional devices with the metallic Cu treatment.

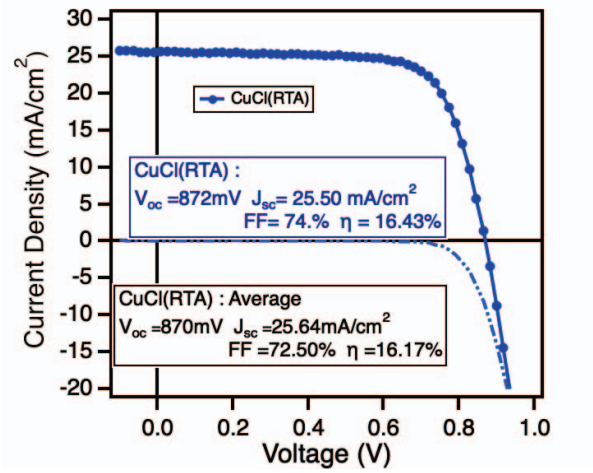


Fig.6. J-V curves of the CdTe-CuCl(RTA) devices.

Following our previous work on ZMO/CdTe solar cells [13], we further optimized the CuCl treatment using a rapid thermal annealing (RTA) treatment. We achieved the best device with a V_{OC} of 872 mV, a J_{SC} of 25.5 mA/cm^2, and a FF of 74.0%, yielding a PCE of 16.43%. This performance is close to the champion PCE (16.30%) in the device prepared by using the traditional long-time annealing process but with a higher V_{OC}. The good performances of CdS/CdTe devices under different thermal treatments further confirm the robustness of CdS buffer layer.

IV. Conclusion

We applied a wet chemical approach using a CuCl solution to replace the conventional metallic Cu doping in CdTe solar cells. We demonstrated that the overall performances of the CuCl treated devices are much better than the traditional devices treated by thermally evaporated Cu. The material and device characterization measurements further show that the improvements in the PV performances are attributed to enhanced doping concentration and carrier lifetime.

Acknowledgment

This work is based on research sponsored by Air Force Research Laboratory under agreement number FA9453-18-2-0037. The U.S. Government is authorized to reproduce and distribute reprints for Governmental purposes notwithstanding any copyright notation thereon. We thank Dr. David Strickler from Pilkington North America Inc. for supplying us FTO coated glass substrate.

References

1. Bonnet, D. and H. Rabenhorst. *6% efficient CdS/CdTe solat cell*. in *Proceedings of 9th IEEE Photovoltaic Specialists Conference*. 1972.
2. Wei, S.-H. and S. Zhang, *Chemical trends of defect formation and doping limit in II-VI semiconductors: The case of CdTe.* Physical Review B, 2002. **66**(15): p. 155211.
3. Krasikov, D., A. Knizhnik, B. Potapkin, S. Selezneva, and T. Sommerer, *First-principles-based analysis of the influence of Cu on CdTe electronic properties.* Thin Solid Films, 2013. **535**: p. 322-325.
4. Woodbury, H. and M. Aven, *Some diffusion and solubility measurements of Cu in CdTe.* Journal of Applied Physics, 1968. **39**(12): p. 5485-5488.
5. E.D. Jones, N.M.S., J.B. Mullin, *The diffusion of copper in cadmium telluride.* Journal of Crystal Growth, 1992. **117(1992)**(244—248).
6. Bista, S.S., D. Li, C. Lei, C. Grice, R.A. Awni, Z. Song, and Y. Yan. *ZnTe Back Buffer Layer to Enhance the Efficiency of CdS/CdTe Solar Cells*. in *2019 IEEE 46th Photovoltaic Specialists Conference (PVSC)*. 2019.
7. Strevel, N., L. Trippel, C. Kotarba, and I. Khan, *Improvements in CdTe module reliability and long-term degradation through advances in construction and device innovation.* Photovoltaics International, 2013. **22**: p. 66-74.
8. Alfadhili, F.K., G.K. Liyanage, A.B. Phillips, and M.J. Heben, *Development of CdCl2 Activation to Minimize Zn Loss from Sputtered Cd1-xZnxTe Thin Films for Use in Tandem Solar Cells.* MRS Advances, 2018. **3**(52): p. 3129-3134.
9. Li, D.-B., Z. Song, S.S. Bista, F.K. Alfadhili, R.A. Awni, N. Shrestha, D. Rhiannon, A.B. Phillips, M.J. Heben, and R.J. Ellingson, *CuSCN as the Back Contact for Efficient ZMO/CdTe Solar Cells.* Materials, 2020. **13**(8): p. 1991.
10. Montgomery, A., L.P. Guo, C. Grice, R.A. Awni, S. Saurav, L. Li, Y.F. Yan, and F. Yan, *Solution-processed copper (I) thiocyanate (CuSCN) for highly efficient CdSe/CdTe thin-film solar cells.* Progress in Photovoltaics, 2019. **27**(8): p. 665-672.
11. Bastola, E., A.V. Bordovalos, E. LeBlanc, N. Shrestha, M.O. Reese, and R.J. Ellingson. *Doping of CdTe using CuCl 2 Solution for Highly Efficient Photovoltaic Devices*. in *2019 IEEE 46th Photovoltaic Specialists Conference (PVSC)*. 2019. IEEE.
12. Subedi, K.K., E. Bastola, I. Subedi, Z. Song, K.P. Bhandari, A.B. Phillips, N.J. Podraza, M.J. Heben, and R.J. Ellingson, *Nanocomposite (CuS) x (ZnS) 1-x thin film back contact for CdTe solar cells: Toward a bifacial device.* Solar Energy Materials and Solar Cells, 2018. **186**: p. 227-235.
13. Li, D.-B., S.S. Bista, Z. Song, R.A. Awni, K.K. Subedi, N. Shrestha, P. Pradhan, L. Chen, E. Bastola, and C.R. Grice, *Maximize CdTe solar cell performance through copper activation engineering.* Nano Energy, 2020: p. 104835.
14. Sites, J. and P. Mauk, *Diode quality factor determination for thin-film solar cells.* Solar cells, 1989. **27**(1-4): p. 411-417.
15. Hegedus, S.S. and W.N. Shafarman, *Thin-film solar cells: device measurements and analysis.* Progress in Photovoltaics: Research and Applications, 2004. **12**(2‐3): p. 155-176.
16. Kanevce, A., D. Kuciauskas, T.A. Gessert, D.H. Levi, and D.S. Albin. *Impact of interface recombination on time resolved photoluminescence (TRPL) decays in CdTe solar cells (numerical simulation analysis)*. in *2012 38th IEEE Photovoltaic Specialists Conference*. 2012. IEEE.
17. Kuciauskas, D., J.N. Duenow, A. Kanevce, J.V. Li, M.R. Young, P. Dippo, and D.H. Levi. *Optical-fiber-based, time-resolved photoluminescence spectrometer for thin-film absorber characterization and analysis of TRPL data for CdS/CdTe interface*. in *2012 38th IEEE Photovoltaic Specialists Conference*. 2012.

Authorized licensed use limited to: Carleton University. Downloaded on June 03,2021 at 04:05:04 UTC from IEEE Xplore. Restrictions apply.

Approved for public release; distribution unlimited.

Doping Control of $Mg_xZn_{1-x}O$ Emitter through Fluorine Incorporation

Austin J. Snyder
Wright Center for Photovoltaic Innovation and Commercailization
University of Toledo
Toledo, USA
austin.snyder3@rockets.utoledo.edu

Jacob M. Gibbs
Wright Center for Photovoltaic Innovation and Commercailization
University of Toledo
Toledo, USA
jacob.gibbs@rockets.utoledo.edu

Manoj K. Jamarkattel
Wright Center for Photovoltaic Innovation and Commercailization
University of Toledo
Toledo, USA
manoj.jamarkattel@rockets.utoledo.edu

Adam B. Phillips
Wright Center for Photovoltaic Innovation and Commercailization
University of Toledo
Toledo, USA
adam.phillips@utoledo.edu

Michael J. Heben
Wright Center for Photovoltaic Innovation and Commercailization
University of Toledo
Toledo, USA
michael.heben@utoledo.edu

***Abstract*—Doping control of the emitter is critically important to high performance thin film photovoltaic devices. Here, we deposit magnesium zinc oxide (MZO) thin films for use as the emitter of CdTe-based devices through cosputtering of ZnO and MgO or MgF. The bandgap and sheet resistance of the MZO films are measured before and after the films are thermally processed under vacuum or in He environments. Through annealing of the films, they become conductive, but little bandgap or sheet resistance differences can be determined between the films deposited using the MgO target or the MgF target. Devices will be completed to determine if the addition of fluorine to the MZO film affects the emitter doping during device processing.**

Keywords—CdTe, emitter doping, MZO, cosputter

I. Introduction

Minimizing recombination at the front interface between the emitter and abosrber is critical to the achieving high efficiency CdTe solar cells [1]. Song et al. showed through numerical simulations that one method to achieve such an interface is through engineering the band alignment to increase downward bending and repel the holes [2]. This, and follow up work by others [3], showed that for proper band alignment, the emitter carrier density must be maintained at ~10^{17} cm^{-3} or higher. Improper emitter doping and band alignment can adversely affect the device performance by adding barriers to electron collection [4].

Experimentally, magnesium zinc oxide ($Mg_xZn_{1-x}O$; MZO) has the potential to be an ideal emitter candidate. The bandgap increases with increasing Mg concentration (x) mostly through pushing the conduction band closer to the vacuum level [5]. Kephart et al. demonstrated that the efficiency of CdTe devices with MZO emitters changes with Mg concentration, with the highest efficiency occurring for x = 0.23 [6] . Other groups have also incorporated MZO emitters with varying degrees of success [7, 8]. Li et al. showed that devices processed in environments with oxygen showed a characteristic S-kink while devices processed in environments without oxygen did not [4] and concluded that the oxygen can affect the doping of the buried emitter layer. Recently, Wang et al. incorporated fluorine into MZO films by cosputtering an MZO target and MgF and ZnF [9]. They demonstrated measurable conductivity differences after annealing that they attributed to incorporation of fluorine dopant. However, the annealing occurred in a reducing atmosphere, so it is unclear if the increased dopant density is due to inclusion of active fluorine or simple oxygen deficiencies in the film.

Here, we investigate the optical and electrical properties of MZO films fabricated with and without fluorine before and after a variety of annealing conditions. The films are fabricated by cosputtering ZnO and MgF or MgO and subsequently processed. Both films show increased conductivity after processing and resistance to Mg loss during heating. However, for the most aggressive treatments, neither film is transparent as the oxygen is removed.

II. Experimental Details

MZO films were deposited onto cleaned 3.2 mm thick soda lime glass substrates. For these experiments, the sputtering power for the ZnO target (3" diameter; Kurt J. Lesker) was fixed at 180 W, and the power to the MgF or MgO (both 3" targets; Plasmaterials) was varied from 100 W to 400 W. The films were deposited in 10 mTorr Ar environment at room temperature in a chamber with base pressure of $3x10^{-8}$ Torr.

Films were placed in the bottom of a small (4"x4"x0.4") aluminum box for thermal processing. Cartridge heaters were embedded in the base and top of the box. Thermocouples and software controlled temperature controllers were used to set and maintain the temperature of the process. This aluminum box was placed inside an ISO flanged vacuum chamber and evacuated to ~$1x10^{-6}$ Torr using a turbo pump. The films were

Funding provided by US Air Force Research Laboratory under agreement number FA9453-18-20037 and contract number FA9453-19-C-1002.

978-1-7281-6115-0/20/$31.00 ©2020 IEEE

Authorized licensed use limited to: University of Prince Edward Island. Downloaded on June 06,2021 at 09:11:27 UTC from IEEE Xplore. Restrictions apply.

Approved for public release; distribution unlimited.

heated to 250, 450, or 600 °C under 10^{-6} Torr vacuum or 450 °C in 200 Torr He. All samples were cooled by injecting 200 Torr room temperature He after the processing cycle was complete.

The optical properties of the films were characterized using spectrophotometery (Perkin Elmer 1050) before and after processing. The sheet resistance was measured using the four point probe methods (Lucas Signatone).

III. Results and Discussion

The absorption spectra of the samples were measured for each Mg source target and power and used to determine the bandgap of the MZO films. The bandgap was used to determine the Mg incorporation into each film using Eq. (1) [10].

$$E_g = 3.3 + 1.2 * x \quad (1)$$

where x is the Mg fraction. Fig. 1 shows how the Mg fraction relative to Zn fraction (x / (1-x)), i.e. the Mg deposition rate relative to Zn deposition rate, varies with sputter target and power. The figure shows that the relative Mg incorporation is linear with power for both the MgO and MgF target for sputter power greater than 100 W. Furthermore, the incorporation rates of Mg are relatively close to each other. This indicates that varying the amount of fluorine in the film while maintaining the same bandgap will be straightforward, should the need arise.

To determine if the addition of F provides for doping control, one sample from each deposition set were simultaneously annealed under vacuum at varying temperatures. The absorption and sheet resistance of each film was measured before and after each annealing. Fig. 2 shows the results for each sample. Note that the as-deposited sheet resistance is off scale for films with higher concentrations of Mg and significantly lower for films with very little Mg. The sheet resistance depends on both the doping density and mobility, and the mobility decreases rapidly with increasing Mg [11] .

Looking first at the sheet resistance. Low temperature annealing does very little to the sheet resistance of films that contain a high concentration of Mg, but appears to affect films

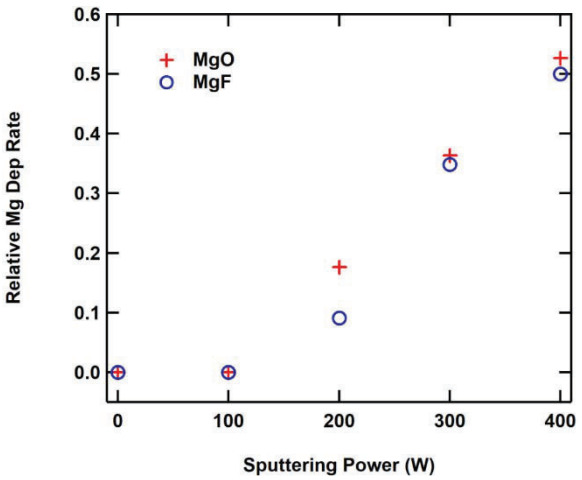


Fig. 1. Magnesium deposition rate relative to Zn deposition rate for cosputter MZO films using ZnO and MgO or MgF targets.

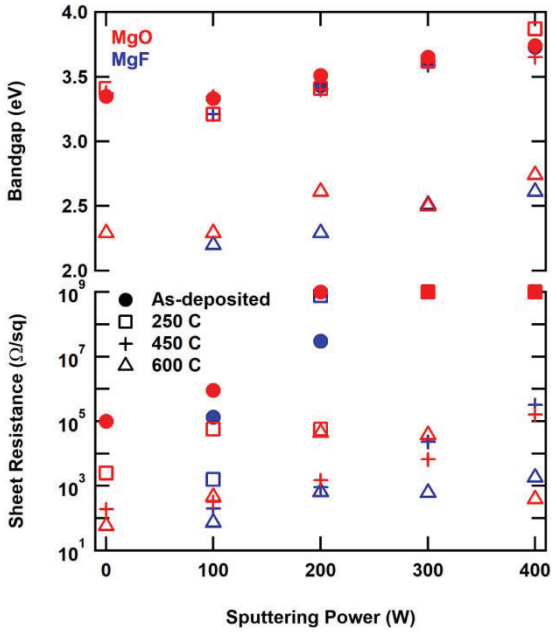


Fig. 2. Film bandgap (top) and sheet resistance (bottom) for films cosputtered films using ZnO and MgO (red) and MgF (blue) targets under various annealing temperatures in vacuum.

with small amount of Mg. As the temperature increases, the sheet resistance decreases by orders of magnitude for all films. The bandgap, on the other hand, is relatively constant for films annealed at 250 and 450 °C, but decrease significantly when annealed at 600 °C. The films treated at 600 °C, though, appear very dark due to loss of oxygen from the film. Slight darkening of the films annealed at 450 °C are also observed, but these films remain highly transparent. There is no color change for the films annealed at 250 °C.

In an effort to better control the amount of oxygen loss from the film, one set of films was annealed to 450 °C in a 200 Torr He environment. These films remain transparent after annealing. Furthermore, the bandgap of these samples do not change significantly during heating, indicating no Mg loss. The sheet resistance, on the other hand, decreases by orders of magnitude, as shown in Fig. 3. Interestingly, there does not appear to be a statistically significant difference in sheet resistance between films fabricated with MgO and those fabricated with MgF. This may be because the improvements in sheet resistance due to doping at this point are more affected by oxygen loss than fluorine incorporation.

It is the doping density of the emitter in the completed device, not the doping density of the emitter before absorber deposition and processing, that matters to device performance. Li et al. showed that the presence of oxygen during processing affects the doping density of the emitter [4], so it is possible that the incorporation of fluorine into the MZO film could maintain the required doping density after processing. Because of this, devices are currently being fabricated and will be included in the presented results.

978-1-7281-6115-0/20/$31.00 ©2020 IEEE

Authorized licensed use limited to: University of Prince Edward Island. Downloaded on June 06,2021 at 09:11:27 UTC from IEEE Xplore. Restrictions apply.

Approved for public release; distribution unlimited.

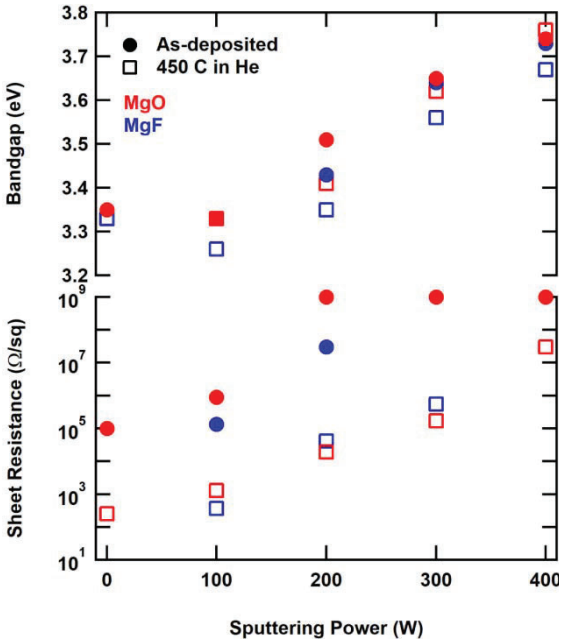


Fig. 3. Film bandgap (top) and sheet resistance (bottom) for films cosputtered films using ZnO and MgO (red) and MgF (blue) targets at 450 °C in 200 Torr He.

IV. Conclusions

We have deposited MZO films by cosputtering ZnO and MgF or MgO. We showed that Mg incorporation into the film appears linear with MgF or MgO sputtering power, and that the bandgaps between 3.3 and 3.75 eV can be fabricated. Annealing of these films under 10^{-6} vacuum at temperatures 450 and 600 °C lead to orders of magnitude decrease in sheet resistance but are accompanied by darkening of the film due to oxygen loss. However, similar sheet resistance improvements without the darkening were obtained by annealing in a He environment at 450 °C. There is no discernable difference in sheet resistance or bandgap observed for films made with MgO or MgF prior to absorber deposition and processing.

Acknowledgment

This material is based on research sponsored by the Air Force Research Laboratory under agreement number FA9453-18-2-0037 and contract number FA9453-19-C-1002. The U.S. Government is authorized to reproduce and distribute reprints for Governmental purposes notwithstanding any copyright notation thereon The views and conclusions contained herin are those of the authors and should not be interpreted as necessarily representing the official policies or endorsements, either expressed or implied, of Air Force Research laboratory or the U.S. Government.

References

[1] A. Kanevce, M. O. Reese, T. M. Barnes, S. A. Jensen, and W. K. Metzger, "The roles of carrier concentration and interface, bulk, and grain-boundary recombination for 25% efficient CdTe solar cells," *Journal of Applied Physics,* vol. 121, no. 21, 2017.

[2] T. Song, A. Kanevce, and J. R. Sites, "Emitter/absorber interface of CdTe solar cells," *Journal of Applied Physics,* vol. 119, no. 23, 2016.

[3] T. Ablekim, E. Colegrove, and W. K. Metzger, "Interface engineering for 25% CdTe solar cells," *ACS Applied Energy Materials,* vol. 1, no. 10, pp. 5135-5139, 2018.

[4] D.-B. Li *et al.*, "Eliminating S-kink to maximize the performance of MgZnO/CdTe solar cells," *ACS Applied Energy Materials,* vol. 2, no. 4, pp. 2896-2903, 2019.

[5] H. Yin, J. Chen, Y. Wang, J. Wang, and H. Guo, "Composition dependent band offsets of ZnO and its ternary alloys," *Sci Rep,* vol. 7, p. 41567, 2017.

[6] J. M. Kephart, J. W. McCamy, Z. Ma, A. Ganjoo, F. M. Alamgir, and W. S. Sampath, "Band alignment of front contact layers for high-efficiency CdTe solar cells," *Solar Energy Materials and Solar Cells,* vol. 157, pp. 266-275, 2016.

[7] F. Bittau *et al.*, "Analysis and optimisation of the glass/TCO/MZO stack for thin film CdTe solar cells," *Solar Energy Materials and Solar Cells,* vol. 187, pp. 15-22, 2018.

[8] X. Zhang *et al.*, "Synthesis of CdSexTe1-x/CdTe for Graded Solar Cells," 46th IEEE Photovoltaic Specialist Conference (PVSC 2019), Unpublished.

[9] H. Wang *et al.*, "Synthesis and characterization of F-doped MgZnO films prepared by RF magnetron co-sputtering," *Applied Surface Science,* vol. 503, 2020.

[10] S. Niraj, G. K. Liyanage, A. B. Phillips, M. J. Heben, and R. J. Ellingson, "Compositional-dependent charge carrier dynamics at MgxZn1-xO/CdTe interface," Unpublished.

[11] M. Rouchdi, E. Salmani, B. Fares, N. Hassanain, and A. Mzerd, "Synthesis and characteristics of Mg doped ZnO thin films: Experimental and ab-initio study," *Results in Physics,* vol. 7, pp. 620-627, 2017.

Authorized licensed use limited to: University of Prince Edward Island. Downloaded on June 06,2021 at 09:11:27 UTC from IEEE Xplore. Restrictions apply.

Approved for public release; distribution unlimited.

589

PROCEEDINGS OF SPIE

SPIEDigitalLibrary.org/conference-proceedings-of-spie

Non-contacting optical probing of photovoltaic device performance

Subedi, Indra, Subedi, Biwas, Uprety, Prakash, Junda, Maxwell, Adhikari, Dipendra, et al.

Indra Subedi, Biwas Subedi, Prakash Uprety, Maxwell M. Junda, Dipendra Adhikari, Kiran Ghimire, Prakash Koirala, Robert W. Collins, Yanfa Yan, Nikolas J. Podraza, "Non-contacting optical probing of photovoltaic device performance," Proc. SPIE 11275, Physics, Simulation, and Photonic Engineering of Photovoltaic Devices IX, 112750J (3 March 2020); doi: 10.1117/12.2550866

SPIE.

Event: SPIE OPTO, 2020, San Francisco, California, United States

Downloaded From: https://www.spiedigitallibrary.org/conference-proceedings-of-spie on 18 May 2020 Terms of Use: https://www.spiedigitallibrary.org/terms-of-use

Approved for public release; distribution unlimited.

Non-contacting optical probing of photovoltaic device performance

Indra Subedi, Biwas Subedi, Prakash Uprety, Maxwell M. Junda, Dipendra Adhikari, Kiran Ghimire, Prakash Koirala, Robert W. Collins, Yanfa Yan, Nikolas J. Podraza*
Department of Physics and Astronomy & Wright Center for Photovoltaics Innovation and Commercialization, University of Toledo, 2801 West Bancroft Street, Toledo, OH, USA 43606

ABSTRACT

Non-contacting optical probes based on spectroscopic ellipsometry or reflectance measurements are used to predict photovoltaic (PV) device performance and to diagnose optical and electronic losses. Optical modeling of aluminum back surface field (Al-BSF) silicon, thin film cadmium telluride (CdTe), and hybrid organic inorganic lead halide based perovskite ($FA_{1-x}Cs_xPbI_3$) solar cell technologies are reviewed. Using the near infrared (IR) to ultraviolet (UV) optical properties of PV device component materials and the device structures as input, external quantum efficiency (EQE) spectra are simulated for Al-BSF, CdTe, and perovskite solar cells for comparison with experimental EQE and short circuit current density (J_{SC}). Optical Hall effect measurements of Al-BSF PV determine majority and minority carrier transport properties in the n+ emitter and p-type wafer silicon; from this information open circuit voltage (V_{OC}), fill factor (FF), J_{SC}, and power conversion efficiency (PCE) are calculated and agree well with direct current-voltage (J-V) electrical measurement. An IR-extended optical model for Al-BSF silicon PV includes coherent multiple reflections, ray tracing optics, and diffuse scattering and is applicable as a baseline for developing optical and thermal management strategies. Analysis of EQE for CdTe based solar cells with selenium alloying ($CdSe_{1-y}Te_y$) enables determination of absorber composition after full device processing. EQE modeling for perovskite solar cells includes the ability to account for sub gap absorption measured in films but not present in the solar cell absorber and incomplete photogenerated carrier collection in the PV device.

Keywords: Spectroscopic ellipsometry, photovoltaics, THz, quantum efficiency, transport properties, optical properties

1. INTRODUCTION AND REVIEW

Photovoltaic (PV) devices depend on absorbing incident photons within a semiconducting layer of the multiple layer device stack, generating electron-hole pairs in that absorber layer, and collecting those photogenerated carriers to produce electrical current. Regardless of the PV device technology, every type of solar cell consists of multiple semiconducting, conducting electrical contact, and other layers. As such, the optical and electronic properties of each component material impact final solar cell performance. It can be challenging to deduce the impact of an individual component layer or material on PV performance or to identify the underlying sources of performance losses. Furthermore, the optical and electrical properties of a component material within the solar cell device may differ substantially from the properties of similar materials prepared on test substrates. To address these issues, non-contacting optical probes based on spectroscopic ellipsometry have been developed to measure the characteristics of materials within complete PV devices.

By measuring the optical and electronic transport properties of layers within solar cell device stacks and the optical response of the complete solar cell itself, it is possible to identify sources of both optical and electronic losses leading to reduced PV performance. In the case of optical losses, structure such as layer thicknesses, surface roughness, and interfacial regions between layers and optical properties of each component material in the device are obtained by near infrared (IR) to ultraviolet (UV) range spectroscopic ellipsometry and serve as input parameters for simulations of external quantum efficiency (EQE)[1-16]. Absorbance within each layer of the solar cell is calculated with that from the current generating layers contributing to EQE. Absorbance in non-current generating layers corresponds to parasitic optical losses as solar irradiance above the band gap of the PV absorber layer is not converted into current. Assuming known solar irradiance, most usually the AM 1.5G spectrum ($\Phi_{AM1.5G}$) for terrestrial PV, the short circuit current density (J_{SC}) can be calculated from EQE through:

$$J_{SC} = \sum_{\lambda} \Phi_{AM1.5G} \times EQE(\lambda) \Delta\lambda \quad (1)$$

where λ is the wavelength and $\Delta\lambda$ is the spacing between spectral points. The simulated EQE from this approach assumes that each photon incident into and absorbed by the PV absorber layer generates an electron-hole pair and that all

*nikolas.podraza@utoledo.edu

Physics, Simulation, and Photonic Engineering of Photovoltaic Devices IX, edited by Alexandre Freundlich, Masakazu Sugiyama, Stéphane Collin, Proc. of SPIE Vol. 11275, 112750J · © 2020 SPIE
CCC code: 0277-786X/20/$21 · doi: 10.1117/12.2550866

Downloaded From: https://www.spiedigitallibrary.org/conference-proceedings-of-spie on 18 May 2020
Terms of Use: https://www.spiedigitallibrary.org/terms-of-use

Approved for public release; distribution unlimited.

photogenerated carriers are collected to produce current. Comparison of simulated and measured EQE identifies electronic losses by determination of incomplete photogenerated carrier collection. When simulated and measured EQE match, there is no detectable carrier collection loss. If measured EQE is lower than the simulation assuming complete carrier collection, the difference between the EQE spectra determine the probability fraction of carrier collection. For uniform collection losses in an absorber layer, the ideal simulated EQE assuming complete carrier collection is weighted by a fraction to match experiment[3]. For collection losses with a depth dependence through the absorber, the PV absorber layer is sub-divided into a number of smaller layers so that the carrier collection probability fraction can be fit as a function of depth, and a carrier collection probability profile is produced[12,16]. This approach has been successfully applied to characterize the optical and electronic losses in polycrystalline thin film cadmium telluride (CdTe)[3,4,5,7,10,15], copper indium gallium diselenide (CIGS)[2,7,12,15], hydrogenated amorphous and nanocrystalline silicon (a-Si:H, nc-Si:H)[1,14-16], and organic inorganic lead halide based perovskite[6,11,13] solar cells.

Electronic transport properties of PV absorber semiconducting materials have been characterized by millimeter (THz) range spectroscopic ellipsometry[17] and optical Hall effect measurements[18,19]. Optical Hall effect measurements use THz spectroscopic ellipsometry as a probing beam with spectra collected under different applied magnetic fields, 0 and ± B T where B is the field strength[18-20]. Manipulation of free charge movement due to the electric field oscillation of the probing THz beam and Lorentz force from the non-zero applied magnetic field induce optical anisotropy. Analysis of the magnetic field induced optical anisotropy enables decoupling of the three transport property parameters, carrier concentration, mobility, and conductivity effective mass[18-20]. Measurements collected without an applied magnetic field are only sensitive to two of the three when a value for the third is assumed[17,21-23]. Using results of optical Hall effect measurement, free carrier optical response is interpreted via the Drude model to obtain carrier concentration, mobility, and conductivity effective mass. Sensitivity to electronic transport parameters has been demonstrated for CdTe, CIS, and perovskite thin films as well as silicon wafers[18]. Optical Hall effect measurements of complete silicon wafer PV have been performed to simultaneously extract majority carrier transport properties of the n+ silicon emitter and the p-type silicon bulk wafer[19]. Recently, optical Hall effect measurements of silicon wafer PV collected under 1 sun simulated AM 1.5G illumination have been used to determine minority carrier transport properties[19]. From the optically determined majority and minority carrier transport properties, the open circuit voltage (V_{OC}), fill factor (FF), and other device parameters like shunt and series resistance have been successfully predicted. As PV power conversion efficiency (PCE) depends on J_{SC}, V_{OC}, and FF, non-contacting optical characterization provides a prediction of full PV device performance. Due to the sensitivity of the characteristics of each material in the complete solar cell, the information gained from these measurements also provides the ability to diagnosis sources of optical and electronic losses.

This paper provides a review of the application of these approaches to three prominent PV technologies: silicon wafer, thin film CdTe, and perovskites. Optical modeling of the reflectance and EQE of commercial silicon wafer PV is performed and extended deeper into the IR spectral range[5,8,9]. This IR extension is performed to enable quantification of absorption of AM 1.5G illumination in the non-current generating layers at photon energies both above and below the band gap of silicon. The motivation for this work is that silicon PV modules exhibit a 0.3-0.5% decrease in relative efficiency for each Kelvin increase in temperature[24]. Each photon absorbed in a device component that does not generate current generates heat instead. IR extended optical models are needed in order to develop strategies to reduce this unwanted absorption. Due to the complexity of the silicon wafer solar cell, an optical model has been developed using SunSolve™ from PV Lighthouse and includes coherent multiple reflections to account for planar parallel interfaces between layers, ray tracing to account for the distribution in beam paths of incident light through the device due to pyramidal front surface texturing, and diffuse Lambertian scattering at the back electrical contact. Silicon wafer PV has also been characterized by optical Hall effect to determine majority and minority carrier transport properties which are then input into diode equations and PC1D simulations to calculate V_{OC} and FF.

Contributions to recent increases in PCE of thin film CdTe PV device technology have been enabled by replacing the cadmium sulfide (CdS) heterojunction partner in part or in full by cadmium selenide (CdSe)[25]. During the device fabrication process, CdTe and CdSe interdiffuse to produce an alloy ($CdSe_{1-y}Te_y$). At intermediate compositions, band gap bowing occurs in $CdSe_{1-y}Te_y$ which increases J_{SC} by red-shifting the band gap of the alloyed region and EQE onset of the solar cells[4,10]. Improved EQE above the band gap also occurs as carriers previously absorbed by the CdS are now collected. The complex optical response of the $CdSe_{1-y}Te_y$ alloys have been determined by near IR to UV spectroscopic ellipsometry and serve as input into EQE simulations of device performance. Relatively simple assumptions enable using measured EQE to identify the composition of the $CdSe_{1-y}Te_y$ alloyed region in the final device[10].

Downloaded From: https://www.spiedigitallibrary.org/conference-proceedings-of-spie on 18 May 2020
Terms of Use: https://www.spiedigitallibrary.org/terms-of-use

Approved for public release; distribution unlimited.

Organic inorganic lead halide-based perovskites have exhibited rapid increases in PV device performance evident in the literature over the last several years[26,27]. The ABX_3 perovskite structure consists of organic, inorganic, or mixed *A*-site cations; lead or lead + tin alloy *B*-site cations; and halide *X*-site anions. These perovskites, however, are often unstable when exposed to ambient air, oxygen, and humidity[11,13,28,29]. The result of this instability is that the measured properties of thin films differ from those same materials implemented in complete solar cells. As a case study, formamidinium and cesium mixed *A*-site cation lead iodide ($FA_{1-x}Cs_xPbI_3$) perovskites have been prepared as thin films and implemented as absorbers in single junction solar cells[11,13]. Thin films exposed to atmosphere show varying amounts of degradation evident through substantial absorption below the band gap. EQE indicates less degradation for layers in PV devices, however materials more susceptible to increases in sub gap absorption due to exposure also show reduced carrier collection as modeled by EQE simulations.

2. IR-EXTENDED OPTICAL MODEL AND OPTICAL HALL EFFECT CHARACTERIZATION FOR SILICON WAFER PV

A commonly industrially produced silicon wafer solar cell design employs an aluminum back surface field (Al-BSF) rear electrical contact. A p-type silicon wafer with a pyramidally textured front surface serves as a base for this device design. A n+ doped silicon emitter is formed on the front surface which is typically passivated by silicon nitride. In encapsulated devices, the front of the device is coated with ethyl vinyl acetate (EVA) and cover glass. Aluminum is deposited onto the back of the p-type wafer to form the BSF region. At this back contact a p+ doped silicon layer and an Al+Si interfacial region form by silicon and aluminum interdiffusion. Total hemispherical reflectance for an industrially sourced encapsulated Al-BSF solar cell is measured with an incident beam at ~8° with respect to the sample normal (Agilent Cary 5000). The measured spectral range extends from 300 to 2500 nm, which includes the majority of irradiance from the AM 1.5G spectrum. At photon energies greater than the band gap of silicon, 1.1 eV, incident photons absorbed within silicon generate electron-hole pairs to produce electrical current when collected. All photons absorbed in other materials, both above and below the band gap of silicon, generate heat which can reduce the power output of silicon PV during operation. An optical model describing the total hemispherical reflectance is developed using SunSolve™ by PV Lighthouse[5,8,9]. This model includes coherent multiple specular reflections between planar parallel interfaces, ray tracing to account for specular reflections from the sides of the pyramidal texturing, and Lambertian scattering at the interface between the Al+Si interdiffused region and the back aluminum electrical contact. As this particular solar cell is industrially produced, information regarding the precise fabrication process, device structure, and material optical properties are not known. Therefore, a nominal structure for this type of device has been applied along with reference optical properties[5,8,9]. For the n+ emitter, p-type wafer, and p+ silicon layers the IR optical response of crystal silicon is augmented with free carrier absorption represented by a Drude feature in each layer. Carrier concentrations range from 10^{20} to 10^{17} cm^{-3} decreasing with depth from the front surface in the n+ emitter, 10^{16} cm^{-3} throughout the p-type wafer, and 10^{18} cm^{-3} in the p+ BSF with corresponding mobilities for the respective carrier concentration and type[30].

Reflectance is simulated with and without Lambertian scattering at the interface between the Al+Si interdiffused region and the aluminum back contact (Figure 1). Without scattering at that interface, the simulation substantially overestimates reflectance at long wavelengths below the band gap of silicon. At shorter wavelengths above the band gap of silicon, all light is absorbed within the silicon or reflected by the front surface, making the reflectance spectra at those wavelengths insensitive to the optical characteristics of the BSF region. When completely Lambertian scattering is assumed at the interface between the Al+Si interdiffused region and the aluminum back contact, reflectance decreases. The thickness of the Al+Si interdiffused layer is varied systematically to minimize the difference between simulated and experimental reflectance, with the minimum difference occurring for a thickness of 18 nm (Figure 1). The same optical models are used to simulate EQE and parasitic absorption in the non-silicon components of the device as shown in Figure 2. From simulated EQE, J_{SC} are 38.36 and 38.03 mA/cm^2 and incident irradiance parasitically absorbed are 22.62 and 20.09 mW/cm^2 for models incorporating Lambertian scattering and without scattering, respectively. These J_{SC} values match the upper limit expected for Al-BSF solar cells. There is no substantial difference in simulated EQE, except near the band gap where Lambertian scattering increases the path length of long wavelength light not already absorbed within silicon. In the IR, lower reflectance for the experimental spectra and simulation assuming Lambertian scattering compared to the simulation without scattering corresponds with higher parasitic absorption. Increased absorption due to scattering of light at the back contact indicates a 1 K higher operating temperature and 0.3 to 0.5% lower relative efficiency of this Al-BSF cell compared to a hypothetical device without scattering at the back contact. This IR extended physics-based optical model both accurately represents the optical response of the solar cell to incident light above the band gap of silicon which produces electrical current and matches the reflectance in the IR range below the band gap of silicon which results in

Downloaded From: https://www.spiedigitallibrary.org/conference-proceedings-of-spie on 18 May 2020
Terms of Use: https://www.spiedigitallibrary.org/terms-of-use

Approved for public release; distribution unlimited.

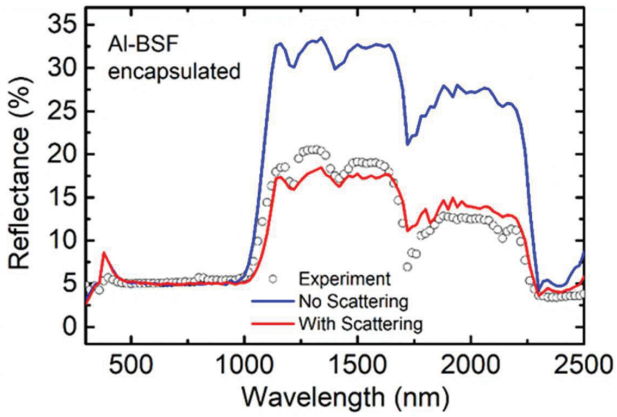


Figure 1. Total hemispherical reflectance of an encapsulated aluminum back surface field (Al-BSF) silicon wafer solar cell (open circles) and simulated reflectance without (blue line) and with (red line) perfectly Lambertian scattering at the interface between the Al+Si interdiffusion region and the aluminum back electrical contact.

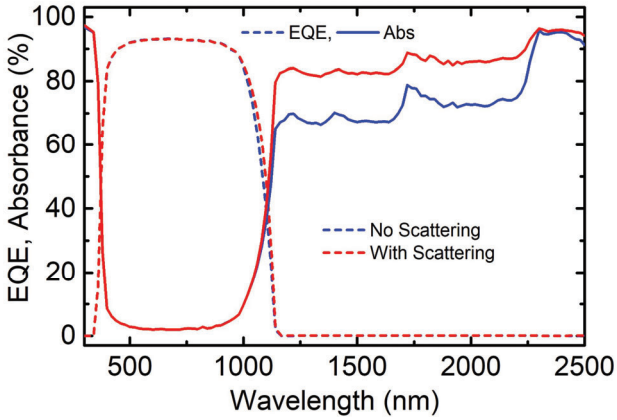


Figure 2. External quantum efficiency (EQE, dashed lines) and parasitic absorbance (solid lines) spectra for the Al-BSF solar cell in Figure 1 simulated using models without (blue line) and with (red line) perfectly Lambertian scattering at the at the interface between the Al+Si interdiffusion region and the aluminum back electrical contact.

parasitic absorption and heat. This approach is beneficial for development of both light and thermal management strategies[5,31].

An unencapsulated Al-BSF solar cell has been characterized by optical Hall effect measurements conducted both under nominally dark and simulated 1-sun AM 1.G illumination conditions[19]. Data are collected using a THz range rotating compensator spectroscopic ellipsometry with a spectral range from 3.3 mm to 290 μm at 50°, 60°, and 70° angles of incidence. The north and south poles of a 1.5 T permanent magnet are positioned behind the solar cell, and measurements are also collected without an applied magnetic field. All data collected without 1-sun illumination are fit simultaneously to determine the free carrier response of the n+ emitter and p-type wafer (Figure 3). This dark free carrier response is represented with the Drude model from which average majority carrier concentration, mobility, and conductivity effective mass are deduced within each layer. The silicon wafer thickness and air gap between the magnet and solar cell are also determined from this analysis. All data collected under 1-sun illumination are fit simultaneously to determine changes in the free carrier responses due to photogeneration of electron-hole pairs. Silicon wafer thickness and conductivity effective masses are fixed to values obtained from dark measurements. Air gap thicknesses are fit since the sample and magnets

Downloaded From: https://www.spiedigitallibrary.org/conference-proceedings-of-spie on 18 May 2020
Terms of Use: https://www.spiedigitallibrary.org/terms-of-use

Approved for public release; distribution unlimited.

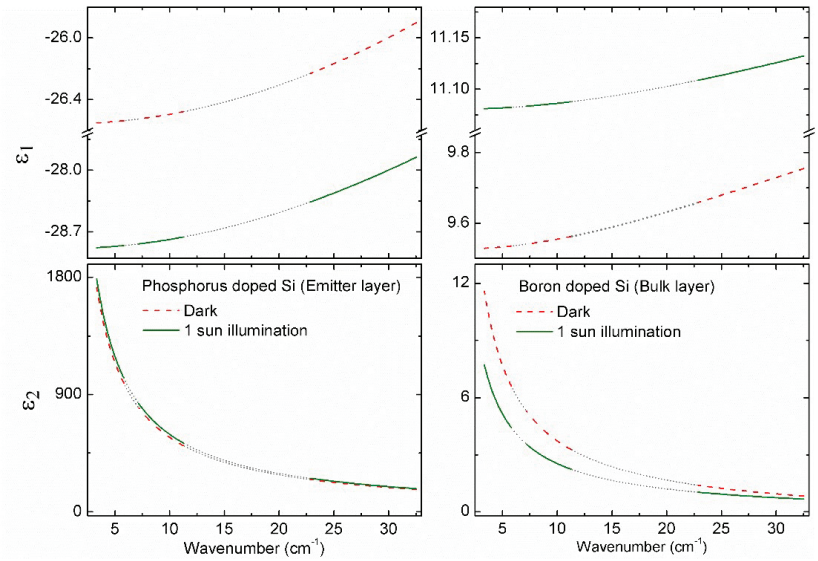


Figure 3. Optical properties in the form of the complex dielectric function ($\varepsilon = \varepsilon_1 + i\varepsilon_2$) spectra for the n+ silicon emitter and the p-type silicon wafer under nominally dark and 1-sun illumination conditions determined from optical Hall effect measurements. Reprinted with permission from[19] Uprety, P., Subedi, I., Junda, M. M., Collins, R. W., and Podraza, N. J., "Photogenerated carrier transport properties in silicon photovoltaics," Scientific Reports 9, 19015 (2019).

are physically remounted between measurements. The free carrier response of the silicon emitter and wafer are altered by photogenerated majority and minority carriers (Figure 3). The majority carrier concentration is fixed to that from the dark measurement and equal photogenerated electron and hole carrier concentrations are fit parameters. Majority and minority carrier mobilities are each independently fit in the n+ emitter and p-type wafer under 1-sun illumination.

From this information carrier diffusivities, lifetimes, and diffusion lengths are calculated[19]. These majority and minority carrier electronic transport properties serve as input for calculation of V_{OC} and FF using diode equations and V_{OC}, FF, and J_{SC} using PC1D simulations. From J-V measurements, $J_{SC} = 37.0 \pm 0.3$ mA/cm^2, $V_{OC} = 0.627 \pm 0.001$ V, FF = 0.80 ± 0.2, and PCE = 18.5 ± 0.1%. From diode equations, $V_{OC} = 0.626$ V and FF = 0.83 are calculated using the experimentally measured J_{SC}. V_{OC} matches experiment, but the calculated FF should be considered as an ideal value. Accounting for series and shunt resistances of 0.62 and 5.5×10^4 Ω cm^2, respectively, reduce FF to 0.80. Simulated PCE is 18.4%, and the results from diode equations reasonably match those from direct J-V measurements. PC1D simulations have been performed assuming a uniform carrier concentration throughout the n+ emitter and a graded Gauss error function decrease in carrier concentration with depth through the emitter. The Gauss error function carrier concentration profile is constrained by the average carrier concentration obtained from optical Hall effect measurements. For simulations with uniform or graded carrier concentrations in the n+ emitter, J_{SC} = 37.3 and 37.2 mA/cm^2, V_{OC} = 0.621 and 0.625 V, FF = 0.8 for both, and PCE = 18.5 and 18.6%, respectively. These values obtained using PC1D agree well with experiment. A surface recombination velocity of 2.5×10^4 cm/s at the n+ emitter is determined from this comparison. Analyzing results of optical Hall effect measurements collected under dark and 1-sun illumination conditions yields majority and minority carrier transport properties for the n+ emitter and p-type silicon wafer in Al-BSF PV. This information is used to reasonably simulate all PV device performance parameters.

3. ALLOYING IN CADMIUM TELLURIDE BASED PV

EQE modeling with input optical properties from spectroscopic ellipsometry serves as a means of tracking changes in component layer properties occurring during device fabrication. In recent years CdTe based PV has exhibited increased PCE. Alloying CdTe with Se to produce $CdSe_{1-y}Te_y$ results in increased J_{SC} enabled through enhancement in carrier

Downloaded From: https://www.spiedigitallibrary.org/conference-proceedings-of-spie on 18 May 2020
Terms of Use: https://www.spiedigitallibrary.org/terms-of-use

Approved for public release; distribution unlimited.

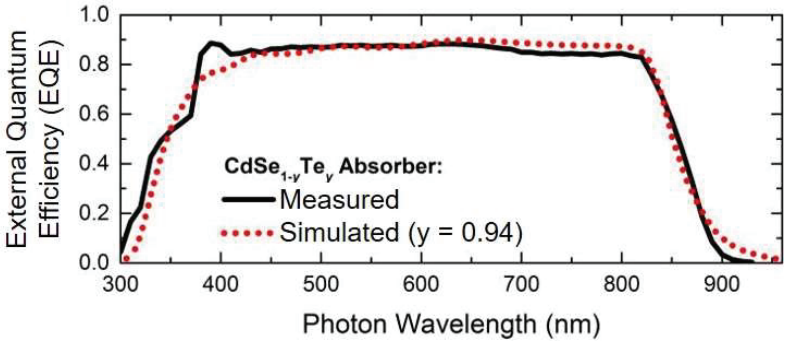


Figure 4. EQE measured for a CdTe based solar cell fabricated with a 15 nm CdS / 100 nm CdSe / 4 μm CdTe layer stack with best-matched simulated EQE assuming interdiffusion occurring in the top 2 μm of the absorber to produce $CdSe_{0.6}Te_{0.94}$. ©2018 IEEE. Reprinted, with permission, from[10] Junda, M. M., Grice, C. R., Uprety, P., Koirala, P., Collins, R. W., Yan, Y., and Podraza, N. J., "A versatile optical model applied to CdTe and $CdSe_{1-y}Te_y$ alloys: sensitivity to film composition and relative defect density," Proc. 7th World Conference on Photovoltaic Energy Conversion, 1902-1905 (2018).

collection at both short and long wavelengths[4,10,25]. At long wavelengths, below the band gap of CdTe near 1.5 eV, band bowing with alloying red shifts the $CdSe_{1-y}Te_y$ band gap and the solar cell long wavelength EQE onset. At short wavelengths, replacing the typical CdS n-type heterojunction partner in part or in full by CdSe produces a sufficiently high electronic quality material such that photogenerated carriers in the n-type heterojunction partner can be collected. Figure 4 shows the EQE for a solar cell fabricated using a commercial transparent conducting oxide coated glass superstrate followed by a nominally 15 nm thick CdS layer, a 100 nm thick CdSe layer, and a 4 μm thick CdTe layer[25]. A standard copper / gold metallic back contact is applied. The device is $CdCl_2$ treated to increase grain size and electronic order within the absorber layer, ultimately increasing PCE. CdSe and CdTe typically interdiffuse more readily than CdS and CdTe or CdS and CdSe. The absorber layer is now partially $CdSe_{1-y}Te_y$, which results in enhanced long and short wavelength EQE response.

The optical model for EQE simulation is based upon that developed for standard CdS / CdTe devices as determined by Koirala et. al.[3]. The EQE simulation has been modified to include the reduced thickness 15 nm CdS layer and a 4 μm thick absorber. CdTe and CdSe interdiffusion do not occur homogeneously throughout the absorber layer during $CdCl_2$ treatment. The absorber is divided into a 2 μm thick $CdSe_{1-y}Te_y$ layer near front of the cell and a 2 μm thick CdTe layer near the back contact[10] as a simple approximation of the compositional depth dependence. To identify the composition of the $CdSe_{1-y}Te_y$ layer, EQE simulations are performed using optical properties with different alloy compositions. The optical response of alloy thin films have been determined from near IR to UV spectroscopic ellipsometry measurements of films prepared on soda lime glass substrates[4,10]. Simultaneous magnetron sputtering of CdTe and CdSe targets at different powers produce films spanning the full compositional range. Energy dispersive x-ray spectroscopy determines the composition. After deposition, films are annealed in helium at 600°C for 6 minutes prior to the $CdCl_2$ treatment used in solar cell fabrication. To describe the optical response of $CdSe_{1-y}Te_y$ alloys, a parametric model is developed to account for the direct band gap, an Urbach tail below the gap, and above gap critical point transitions[10,32]. The complex dielectric function spectra and its first derivative are continuous.

The best match between experimental and simulated EQE is found assuming a composition of $CdSe_{0.06}Te_{0.94}$ in the top 2 μm of the absorber[10] (Figure 4). There is very good agreement with experimental EQE in spite of the simplicity of the model. Assuming interdiffusion of the 100 nm of CdSe into the adjacent 2 μm of CdTe and similar densities predicts ~0.05 selenium content in that region. This value is close to that determined from the EQE comparison. The red shift in the EQE onset is the dominant feature controlling this convergence, so the composition parameter narrows the band gap and controls that red shift. It should be noted that the films characterized to obtain the library of $CdSe_{1-y}Te_y$ optical properties and the final $CdSe_{1-y}Te_y$ absorber in the PV device are not fabricated in the same processes. In the PV device, the CdSe layer is fabricated by magnetron sputtering prior to deposition of the CdTe layer by close space sublimation[25]. In that case alloying is the result of interdiffusion during high temperature over-deposition of CdTe onto CdSe and the

Downloaded From: https://www.spiedigitallibrary.org/conference-proceedings-of-spie on 18 May 2020
Terms of Use: https://www.spiedigitallibrary.org/terms-of-use

Approved for public release; distribution unlimited.

subsequent $CdCl_2$ treatment process. The grain size of sputtered CdTe films are typically reported to be much smaller than close space sublimated material. Similar reduced grain size in the $CdSe_{1-y}Te_y$ alloys leads to reduced electronic order and wider Urbach tails associated with defects. Deviations in EQE at wavelengths greater than 900 nm are due to the wider Urbach tails expected for the co-sputtered material as opposed to larger grained material within the actual PV device. The difference between measured and simulated EQE near 380 nm is likely due to interactions with the CdS layer not accounted for in the model or subtle differences in the characteristics of the transparent conducting oxide coated glass used to fabricate the solar cell compared to that assumed in the optical model. This modeling reasonably reproduces the behavior of EQE for solar cells incorporating $CdSe_{1-y}Te_y$ and enables determination of absorber layer composition.

4. HYBRID ORGANIC INORGANIC LEAD HALIDE PEROVSKITE BASED PV

Solar cells based on hybrid organic inorganic lead halide perovskites have exhibited very high initial efficiency[26,27], however long term stability remains an issue. A strong contributing factor for device instability stems from the perovskite absorber layers which may degrade upon even short exposure to air, oxygen, and humidity[11,13,28,29]. An additional consequence from this instability is that characterization of perovskite thin films without proper protection from environmental exposure may yield different properties than the layers enclosed within the solar cell device stack[11,13,29]. Studies of solution processed polycrystalline $FA_{1-x}Cs_xPbI_3$ perovskite thin films have indicated that the films are more susceptible to environmentally induced changes than the layers within the complete solar cell[11,13]. In particular, for a series of $FA_{1-x}Cs_xPbI_3$ films prepared as a function of cesium content, there is a compositional dependence on the extent of atmospheric susceptibility. The optical properties of $FA_{1-x}Cs_xPbI_3$ films are characterized by near IR to UV spectroscopic ellipsometry. In general perovskite optical properties over this spectral range include contributions from the band gap, Urbach tailing below the band gap, atmospherically induced Gaussian broadened defect states below the band gap, and above gap critical point electronic transitions[11,13]. Figure 5 shows the absorption coefficient (α) near the band gap as a function of composition for $FA_{1-x}Cs_xPbI_3$ films exposed briefly to air. The x = 0.2 composition shows the sharpest absorption onset with the least amount of sub gap absorption. Sub gap absorption tails assuming an Urbach energy of 24 meV, measured for the x = 0.2 composition, are appended onto spectra in α for each composition. Comparison of measured α and the assumed Urbach tails show enhanced sub gap absorption for compositions $x > 0.2$ and $x < 0.2$. Using optical sum rules, the amount of sub gap absorption is used to calculate defect density with the x = 0.2 composition again indicating the lowest amount of atmospherically induced defects. For solar cells with absorber layers fabricated by the same methods, x = 0.2 compositions yield the highest PCE of 16%. PCE decreases to 12% for x = 0 and 15% for x = 0.3, both of which have noticeably higher sub gap absorption in exposed thin films.

EQE simulations are performed for PV devices fabricated with x = 0 and 0.2 $FA_{1-x}Cs_xPbI_3$ compositions[11,13]. The solar cell device structure consists of a transparent conducting oxide coated glass superstrate, C_{60} electron transport layer, $FA_{1-x}Cs_xPbI_3$ perovskite absorber layer, Spiro-OMeTAD hole transport layer, and a gold back contact. Reference optical properties and all layer thicknesses have been determined from previous through-the-glass spectroscopic ellipsometry measurement of a similar superstrate structure perovskite solar cell with a methylammonium lead iodide ($MAPbI_3$) absorber[6]. Nominal thicknesses for the $FA_{1-x}Cs_xPbI_3$ absorbers are used for the EQE simulation. Simulated EQE for the PV device with the x = 0.2 composition absorber agrees well with the experimental measurement over most of the spectral range (Figure 6)[11]. The discrepancy in the 400 to 500 nm wavelength range is likely due to differences between the characteristics of the transparent conducting oxide coated glass superstrate and the reference optical properties and structure assumed in the simulation. This agreement between experimental and simulated EQE indicates that the optical properties of the x = 0.2 perovskite obtained for the exposed thin film are representative of the absorber layer in the PV device. This behavior is expected as the x = 0.2 film had a sharp absorption onset and did not exhibit substantial sub gap absorption upon exposure to air.

For the x = 0 composition, however, there are substantial differences between measured and simulated EQE depending on modeling assumptions (Figure 7)[11]. One source of this difference arises from the x = 0 perovskite optical properties used in the simulation. The x = 0 composition exhibits substantial sub gap absorption in the exposed thin film. The EQE simulation, which includes contributions from this sub gap absorption, overestimates EQE at wavelengths greater than 500 nm. Below the perovskite band gap near 1.53 eV this overestimation is more substantial and not physically representative of the characteristics of the perovskite absorber layer. Parameterization of the complex dielectric function spectra for the x = 0 perovskite enables separation of contributions to the optical response from sub gap absorption features and band-to-band electronic transitions. After parameterization, the Gaussian broadened sub gap absorption feature is removed from the parametric model of the complex dielectric function spectra to generate a set of optical properties without contributions

Downloaded From: https://www.spiedigitallibrary.org/conference-proceedings-of-spie on 18 May 2020
Terms of Use: https://www.spiedigitallibrary.org/terms-of-use

Approved for public release; distribution unlimited.

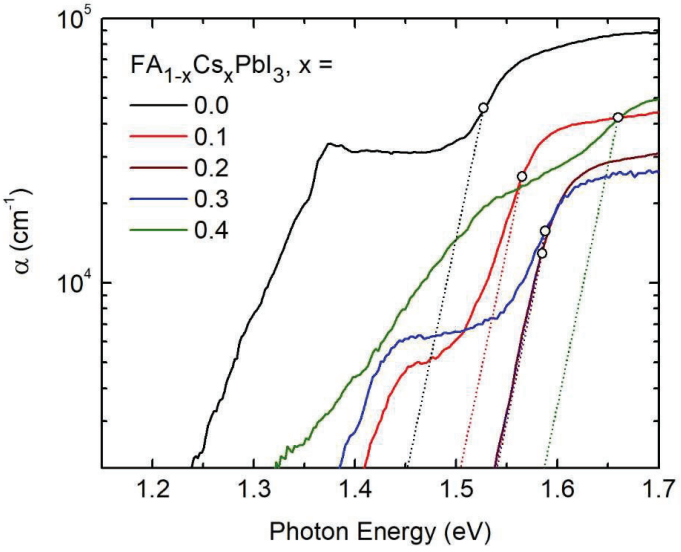


Figure 5. Absorption coefficient (α) spectra for solution processed $FA_{1-x}Cs_xPbI_3$ perovskite films near the band gap (solid lines).[13] Band gap energy positions are marked as dot for each composition, with substantial absorption below the band gap arising from atmospheric exposure. Extrapolations assuming an Urbach tail of 24 meV below the band gap are shown (dotted lines).

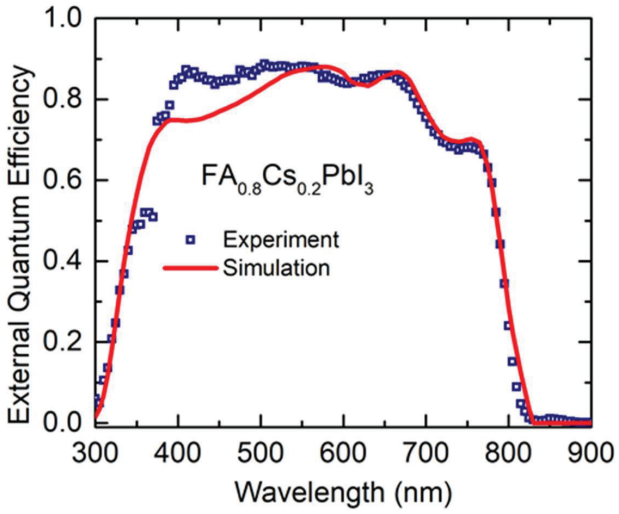


Figure 6. Simulated and experimental EQE for a solar cell with a $FA_{0.8}Cs_{0.2}PbI_3$ absorber layer. The simulated EQE is determined from reference optical properties of a $FA_{0.8}Cs_{0.2}PbI_3$ film measured in air. ©2018 IEEE. Reprinted, with permission, from[11] Subedi, B., Guan, L., Yu, Y., Ghimire, K., Uprety, P., Junda, M. M., Yan, Y., and Podraza, N. J., "Formamidinium + cesium lead triiodide perovskite thin films: optical properties and devices," Proc. 7th World Conference on Photovoltaic Energy Conversion, 522-525 (2018).

Downloaded From: https://www.spiedigitallibrary.org/conference-proceedings-of-spie on 18 May 2020
Terms of Use: https://www.spiedigitallibrary.org/terms-of-use

Approved for public release; distribution unlimited.

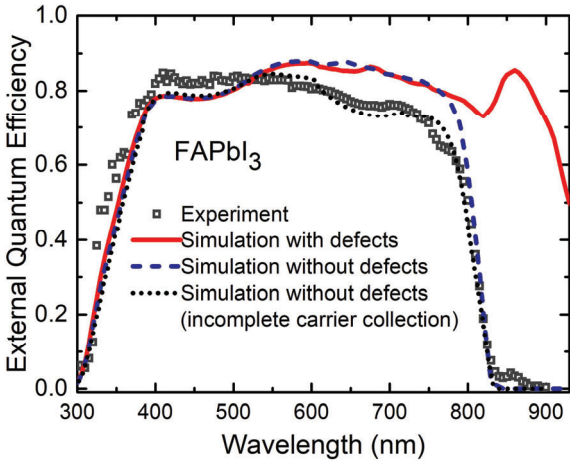


Figure 7. Experimental (open symbols) and simulated EQE for a solar cell with a $FAPbI_3$ absorber layer. Simulations assume (solid line) optical properties measured in air, (dashed line) optical properties measured in air with contributions from sub gap absorption due to atmospheric exposure removed,[11] and (dotted line) optical properties with sub gap absorption removed and 100% carrier collection in the half of the perovskite absorber adjacent to the electron transport layer and 11% average carrier collection in the half of the perovskite absorber adjacent to the hole transport layer.

from atmospherically induced sub gap defects[11]. It is reasonable to remove these contributions as the x = 0 absorber within the solar cell is not exposed to air to the same extent as the thin film. The EQE simulation based upon x = 0 optical properties with contributions from atmospherically induced sub gap absorption removed has a long wavelength EQE onset consistent with experimental EQE (Figure 7). Although removing contributions from atmospherically induced sub gap absorption improves agreement between simulated and measured EQE, differences remain in the 500 to 825 nm wavelength range. Higher simulated EQE within this range compared to experiment is likely due to incomplete carrier collection within the perovskite absorber layer. To account for depth dependent collection losses, the perovskite absorber is divided into two sub-layers to determine the maximum absorbance within each sub-layer[16]. The absorbance within each sub-layer is weighted by a fraction which serve as fit parameters to converge the simulation to experimental EQE. The result of this fit shows complete carrier collection in the half of the absorber located near the electron transport layer which reduces to 11% average carrier collection probability in the half of the absorber near the hole transport layer (Figure 7). The reduced carrier collection for the solar cell with the x = 0 absorber and the large amount of sub gap absorption in the corresponding film indicate lower electronic quality for the x = 0 material fabricated by this deposition process. The overall result is that understanding features within optical properties enables identification of where deviations between simulation and experiment occur and why. This capability includes identification of contributions from defects that may or may not be present within solar cell absorbers as well as tracking electronic losses due to incomplete carrier collection.

5. SUMMARY

Strategies for modeling PV device performance parameters and EQE have been reviewed for silicon wafer, thin film CdTe, and perovskite based technologies. These approaches are also applicable for different absorber materials and device structures. An IR extended optical model for Al-BSF silicon wafer PV includes contributions from coherent multiple reflections, ray tracing, and diffuse Lambertian scattering to simulate total hemispherical reflectance. Above the band gap of silicon incident photons absorbed can generate current while parasitic absorption in other components at all wavelengths generate heat. From this baseline model both optical and thermal management strategies can be evaluated. Optical Hall effect data collected under nominally dark and 1-sun illumination of Al-BSF silicon wafer PV measure majority and minority carrier transport properties in both the n+ emitter and p-type silicon wafer. These electronic transport properties serve as input for diode equations and PC1D simulations which reasonably predict V_{OC}, FF, J_{SC}, and PCE. A database of $CdSe_{1-y}Te_y$ alloy optical properties has been used to simulate EQE for CdTe-based solar cells exhibiting improved short and long wavelength optical response. $CdSe_{1-y}Te_y$ alloy composition of the PV absorber is determined from the simulation

Downloaded From: https://www.spiedigitallibrary.org/conference-proceedings-of-spie on 18 May 2020
Terms of Use: https://www.spiedigitallibrary.org/terms-of-use

Approved for public release; distribution unlimited.

best matching experimental EQE. Improvements in long wavelength optical response are attributed to band bowing and in short wavelength optical response are due to collection of photogenerated carriers in the $CdSe_{1-y}Te_y$ alloyed region near the front of the device. For $FA_{1-x}Cs_xPbI_3$ perovskite solar cells, the agreement between simulated and experimental EQE depends strongly upon input perovskite optical properties and carrier collection probability. For the x = 0.2 $FA_{1-x}Cs_xPbI_3$ perovskite, optical properties of a thin film measured after brief exposure to air show a sharp absorption onset and low atmospherically induced sub gap absorption. Measured and simulated EQE agree well. For the x = 0 $FA_{1-x}Cs_xPbI_3$ perovskite, measured thin film optical properties show substantial sub gap absorption. The contributions from this sub gap absorption to the perovskite optical properties are accounted in parametric models and removed to provide better agreement with the long wavelength EQE onset. Implementing incomplete carrier collection in the simulation further improves agreement with experiment and identifies electronic losses in the perovskite near the back contact.

ACKNOWLEDGEMENTS

The authors acknowledge T. Silverman and M. Deceglie of the National Renewable Energy Laboratory for total hemispherical reflectance measurements of the silicon wafer solar cell and many helpful discussions. This work was supported by the Ohio Department of Development (ODOD) Ohio Research Scholar Program (Northwest Ohio Innovators in Thin Film Photovoltaics, Grant No. TECH 09-025), the Office of Naval Research (contract number N00014-17-2223), the U.S. Department of Energy (DOE) SunShot Initiative under the Next Generation Photovoltaics 3 program (DE-FOA-0000990), the DOE Office of Energy Efficiency and Renewable Energy (EERE) under Solar Energy Technologies Office (SETO) Agreement Number 30312, the National Science Foundation (CHE-1230246, DMR-1534586, MRI-1228917), and the Air Force Research Laboratory under agreement numbers FA9453-11-C-0253, FA9453-18-2-0037, and FA9453-19-C-1-002. The U.S. Government is authorized to reproduce and distribute reprints for Governmental purposes notwithstanding any copyright notation thereon. This report was prepared as an account of work sponsored by an agency of the United States Government. The views and conclusions contained herein are those of the authors and should not be interpreted as necessarily representing the official policies or endorsements, either expressed or implied, of Air Force Research Laboratory, the DOE, or the U.S. Government. Neither the United States Government nor any agency thereof, nor any of their employees, makes any warranty, express or implied, or assumes any legal liability or responsibility for the accuracy, completeness, or usefulness of any information, apparatus, product, or process disclosed, or represents that its use would not infringe privately owned rights. Reference herein to any specific commercial product, process, or service by trade name, trademark, manufacturer, or otherwise does not necessarily constitute or imply its endorsement, recommendation, or favoring by the United States Government or any agency thereof. The U.S. Government retains and the publisher, by accepting the article for publication, acknowledges that the U.S. Government retains a nonexclusive, paid-up, irrevocable, worldwide license to publish or reproduce the published form of this work, or allow others to do so, for U.S. Government purposes.

REFERENCES

[1] Aryal, P., Pradhan, P., Huang, Z., Marsillac, S., Podraza, N. J., and Collins, R. W., "Quantum efficiency simulations with inputs from spectroscopic ellipsometry for evaluation of carrier collection in a-Si:H solar cells," Proc. 42nd Photovoltaics Specialists Conference, 1-4 (2015).

[2] Ibdah, A.-R., Pradhan, P., Aryal, P., Podraza, N. J., Marsillac, S., and Collins, R. W., "$CuIn_{1-x}Ga_xSe_2$ solar cells with thin absorbers analyzed by spectroscopic ellipsometry: insights into quantum efficiency and optical/collection losses," Proc. 43rd Photovoltaic Specialists Conference, 2184-2187 (2016).

[3] Koirala, P., Li, J., Tan, X., Yoon, H., Aryal, P., Pradhan, P., Ibdah, A., Marsillac, S., Rockett, A. A., Podraza, N. J., and Collins, R. W., "Through-the-glass spectroscopic ellipsometry for analysis of the optical structure of CdTe thin-film solar cells in the superstrate configuration," Progress in Photovoltaics 24, 1055-1067 (2016).

[4] Junda, M. M., Grice, C. R., Koirala, P., Collins, R. W., Yan, Y., and Podraza, N. J., "Optical properties of $CdSe_{1-x}S_x$ and $CdSe_{1-y}Te_y$ alloys and their application for CdTe photovoltaics," Proc. 44th Photovoltaics Specialists Conference, 3426-3429 (2017).

[5] Subedi, I., Silverman, T. J, Deceglie, M., and Podraza, N. J., "Impact of infrared optical properties on crystalline Si and thin film CdTe solar cells," Proc. 44th Photovoltaics Specialists Conference, 2771-2775 (2017).

[6] Ghimire, K., Zhao, D., Wang, A.C., Yan, Y., and Podraza, N. J., "Optical evaluation of perovskite films in and for solar cell devices," Proc. 44th Photovoltaic Specialists Conference, 993-998 (2017).

Downloaded From: https://www.spiedigitallibrary.org/conference-proceedings-of-spie on 18 May 2020
Terms of Use: https://www.spiedigitallibrary.org/terms-of-use

Approved for public release; distribution unlimited.

[7] Ibdah, A., Koirala, P., Aryal, P., Pradhan, P., Marsillac, S., Rockett, A. A., Podraza, N. J., and Collins, R. W., "Spectroscopic ellipsometry for analysis of polycrystalline thin-film photovoltaic devices and prediction of external quantum efficiency," Applied Surface Science 421, 601-607 (2017).
[8] Subedi, I., T. J, Silverman, Deceglie, M., and Podraza, N. J., "Al+Si interface optical properties obtained in the Si solar cell configuration," Physica Status Solidi a 214, 1700480 (2017).
[9] Subedi, I., Silverman, T., Deceglie, M. G., and Podraza, N. J., "Optical evaluation of PERC cell reflectance for thermal management," Proc. 7th World Conference on Photovoltaic Energy Conversion, 3214-3217 (2018).
[10] Junda, M. M., Grice, C. R., Uprety, P., Koirala, P., Collins, R. W., Yan, Y., and Podraza, N. J., "A versatile optical model applied to CdTe and $CdSe_{1-y}Te_y$ alloys: sensitivity to film composition and relative defect density," Proc. 7th World Conference on Photovoltaic Energy Conversion, 1902-1905 (2018).
[11] Subedi, B., Guan, L., Yu, Y., Ghimire, K., Uprety, P., Junda, M. M., Yan, Y., and Podraza, N. J., "Formamidinium + cesium lead triiodide perovskite thin films: optical properties and devices," Proc. 7th World Conference on Photovoltaic Energy Conversion, 522-525 (2018).
[12] Ibdah, A. A., Koirala, P., Aryal, P., Pradhan, P., Heben, M. J., Podraza, N. J., Marsillac, S., and Collins, R. W., "Optical simulation of external quantum efficiency spectra of $CuIn_{1-x}Ga_xSe_2$ solar cells from spectroscopic ellipsometry inputs," Journal of Energy Chemistry 27, 1151-1169 (2018).
[13] Subedi, B., Guan, L., Yue, Y., Ghimire, K., Uprety, P., Yan, Y., and Podraza, N. J., "Formamidinium + cesium lead triiodide perovskites: discrepancies between thin film optical absorption and solar cell efficiency," Solar Energy Materials & Solar Cells 188, 228-233 (2018).
[14] Huang, Z., Dahal, L. R., Koirala, P., Du, W., Cao, X., Deng, X., Podraza, N. J., and Collins, R. W., "Ex-situ analysis of multijunction solar cells based on hydrogenated amorphous silicon," in [Spectroscopic Ellipsometry for Photovoltaics Vol. 1], Springer, 175-200 (2018).
[15] Koirala, P., Ibdah, A.-R., Aryal, P., Pradhan, P., Huang, Z., Podraza, N. J., Marsillac, S., and Collins, R. W., "Optical simulation of external quantum efficiency spectra," in [Spectroscopic Ellipsometry for Photovoltaics Vol. 2], Springer, 83-138 (2018).
[16] Adhikari, D., Junda, M. M., Grice, C., Marsillac, S., Collins, R. W., and Podraza, N. J., "n-i-p hydrogenated nanocrystalline silicon solar cells with RF-magnetron sputtered absorbers," Materials 12, 1699 (2019).
[17] Uprety, P., Junda, M. M., Subedi, I., Slocum, M. A., Forbes, D. V., Hubbard, S. M., and Podraza, N. J., "Electrical transport properties from long wavelength ellipsometry," Proc. 44th Photovoltaics Specialists Conference, 3468-3472 (2017).
[18] Uprety, P., Wang, C., Koirala, P., Sapkota, D. R., Ghimire, K., Junda, M. M., Yan, Y., Collins, R. W., and Podraza, N. J. "Optical Hall effect of photovoltaic device materials," IEEE Journal of Photovoltaics 8(6), 1793-1799 (2018).
[19] Uprety, P., Subedi, I., Junda, M. M., Collins, R. W., and Podraza, N. J., "Photogenerated carrier transport properties in silicon photovoltaics," Scientific Reports 9, 19015 (2019).
[20] Hofmann, T., Herzinger, C. M., Tedesco, J. L., Gaskill, D. K., Woollam, J. A., and Schubert, M., "Terahertz ellipsometry and terahertz optical-Hall effect," Thin Solid films 519, 2593-2600 (2011).
[21] Uprety, P., Junda, M. M., Ghimire, K., Adhikari, D., and Podraza, N. J., "Spectroscopic ellipsometry determination of optical and electrical properties of aluminum doped zinc oxide," Applied Surface Science 421, 852-858 (2017).
[22] Uprety, P., Macco, B., Junda, M. M., Grice, C. R., Kessels, W. M. M., and Podraza, N. J., "Optical and electrical properties of H-doped ZnO films prepared by atomic layer deposition using supercycles with plasma-treatment," Materials Science in Semiconductor Processing 84, 91-100 (2018).
[23] Uprety, P., Junda, M. M., Salmon, H., and Podraza, N. J., "Understanding near infrared absorption in tin doped indium oxide thin films," Journal of Physics D: Applied Physics 51, 295302 (2018).
[24] Skoplaki E. and Palyvos J., "On the temperature dependence of photovoltaic module electrical performance: a review of efficiency/power correlations," Solar Energy 83(5), 614-624 (2009).
[25] Paudel, N. R. and Yan, Y., "Enhancing the photo-currents of CdTe thin-film solar cells in both short and long wavelength regions," Applied Physics Letters 105, 183510 (2014).
[26] Zhao, D., Chen, C., Wang, C., Junda, M. M., Song, Z., Grice, C. R., Yu, Y., Li, C., Subedi, B., Podraza, N. J., Zhao, X., Fang, G., Xiong, R.-G., Zhu, K., and Yan, Y., "Efficient two-terminal all-perovskite tandem solar cells enabled by high-quality low-bandgap absorber layers," Nature Energy 3, 1093-1100 (2018).
[27] Green, M. A., Dunlop, E. D., Hohl-Ebinger, J., Yoshita, M., Kopidakis, N., and Ho-Baillie, A. W. Y., "Solar cell efficiency tables (version 55)," Progress in Photovoltaics 28(1), 3-15 (2020).
[28] Ghimire, K., Zhao, D., Cimaroli, A., Ke, W., Yan, Y., and Podraza, N. J., "Optical monitoring of $CH_3NH_3PbI_3$ thin films upon atmospheric exposure," Journal of Physics D: Applied Physics 49, 405102 (2016).

Downloaded From: https://www.spiedigitallibrary.org/conference-proceedings-of-spie on 18 May 2020
Terms of Use: https://www.spiedigitallibrary.org/terms-of-use

Approved for public release; distribution unlimited.

[29] Junda, M. M., Zhao, D., Subedi, B., Yan, Y., and Podraza, N. J., "Atmospherically induced defects in $(FASnI_3)_{0.6}(MAPbI_{3-3x}Cl_{3x})_{0.4}$ perovskites," Journal of Physics D: Applied Physics 52, 175102 (2019).
[30] PV Lighthouse, "Mobility calculator," <https://www2.pvlighthouse.com.au/calculators/Mobility%20calculator/Mobility%20calculator.aspx> (10 December 2018).
[31] Silverman, T. J, Deceglie, M. G., Subedi, I., Podraza, N. J., Slauch, I. M., Ferry, V. E., and Repins, I., "Reducing operating temperature in photovoltaic modules," IEEE Journal of Photovoltaics 8(2), 532-540 (2018).
[32] Junda, M. M., Grice, C., Yan, Y., and Podraza, N. J., "Parametric optical property database for $CdSe_{1-x}S_x$ alloys," Electronic Materials Letters 15(4), 500-504 (2019).

Downloaded From: https://www.spiedigitallibrary.org/conference-proceedings-of-spie on 18 May 2020
Terms of Use: https://www.spiedigitallibrary.org/terms-of-use

Approved for public release; distribution unlimited.

MRS Advances © 2020 Materials Research Society
DOI: 10.1557/adv.2020.319



Materials requirements for improving the electron transport layer/perovskite interface of perovskite solar cells determined via numerical modeling

Jared D. Friedl, Ramez Hosseinian Ahangharnejhad, Adam B. Phillips, and Michael J. Heben

Wright Center for Photovoltaics Innovation and Commercialization, Department of Physics and Astronomy, University of Toledo, Toledo, Ohio, 43606, USA

ABSTRACT

Perovskite solar cells continue to garner significant attention in the field of photovoltaics. As the optoelectronic properties of the absorbers become better understood, attention has turned to more deeply understanding the contribution of charge transport layers for efficient extraction of carriers. Titanium oxide is known to be an effective electron transport layer (ETL) in planar perovskite solar cells, but it is unlikely to result in the best device performance possible. To investigate the importance of band energy alignment between the electron transport layer and perovskite, we employ numerical modeling as a function of conduction band offset between these layers, interface recombination velocity, and ETL doping levels. Our simulations offer insight into the advantages of energy band alignment and allow us to determine a range of surface recombination velocities and ETL doping densities that will allow us to identify novel high performance ETL materials.

Approved for public release; distribution unlimited.

603

Downloaded from https://www.cambridge.org/core. Cornell University Library, on 28 Aug 2020 at 04:27:27, subject to the Cambridge Core terms of use, available at https://www.cambridge.org/core/terms. https://doi.org/10.1557/adv.2020.319



Downloaded from https://www.cambridge.org/core. Cornell University Library, on 28 Aug 2020 at 04:27:27, subject to the Cambridge Core terms of use, available at https://www.cambridge.org/core/terms. https://doi.org/10.1557/adv.2020.319

INTRODUCTION

Since their introduction over 10 years ago, perovskites have undergone rigorous study and shown remarkable success as thin-film photovoltaic absorbers[1]. With efficiency of >25% recently achieved, perovskite solar cells (PSCs) have now surpassed other thin-film and multicrystalline photovoltaic technologies. This is predominantly due to the favorable optoelectronic properties of the methylammonium lead iodide ($CH_3NH_3PbI_3$ or $MAPbI_3$) absorber. With a strong understanding of the perovskite absorbers, attention has turned to the materials used as charge transport layers (CTLs) and how their electronic properties affect the performance of PSCs. Titanium oxide (TiO_2) has become the typical electron transport layer (ETL) in these architectures, and organic 2,2′,7,7′-tetrakis(*N*,*N*-di-*p*-methoxyphenyl-amine)9,9′-spirobifluorene (Spiro-OMeTAD) is the typical hole transport layer (HTL). Though successful, it is unlikely that these materials are the best option for use in PSCs, motivating the search for novel replacements.

Experimentally identifying better options for the CTLs can be time consuming and expensive. Numerical simulation, on the other hand, offers a faster pathway to identify the materials properties that are critical to high performance devices, and some limited modeling studies of these interfaces with PSCs have been reported[2]. It has been shown that modifying the electron affinity (conduction band position) of each CTL while maintaining the material bandgap can reduce interface recombination and increase device performance[3]. The conclusions of these investigations can be useful, but may be misleading or even invalid if other parameters are varied. This makes it difficult to identify potential candidate materials for these CTLs.

Here, using numerical modeling, we investigate the effect conduction band offset (CBO), ETL doping density, and surface recombination velocity (SRV) have on PSC performance. We find that the recombination at the ETL/perovskite interface is greatly reduced by both band bending due to increasing CBO or ETL doping and decreased SRV. In general, ETLs with low work functions cause the interface to be much more tolerant to midgap states as hole concentrations near the interface are low. Alternatively low SRV also leads to high performance devices that are less sensitive to ETL work function. These results broaden the options for candidate ETL materials that can outperform TiO_2.

COMPUTATIONAL DETAILS

SCAPS 1D takes as input the electronic properties of solar cell layers and numerically solves the continuity and Poisson equations in order to simulate solar cell performance[4]. For our work, we modeled a planar n-i-p structure FTO/TiO_2/$MAPbI_3$/Spiro-OMeTAD/Au. Table I shows the properties of each layer used in the model. Materials properties are taken from both experimental and modeling literature[5-11].

We assume neutral bulk defects located midgap with a Gaussian energy profile and a carrier lifetime of 10μs, in agreement with experimentally measured values[12]. In addition, we assumed a radiative recombination coefficient of 10^{-11} cm^3/s for the perovskite[13]. For this model, we incorporate neutral midgap defects at the two perovskite interfaces, with an SRV of 1 cm/s at each, leading to simulated performance in agreement with well-performing perovskite solar cells. A lifetime of 5 ns was assumed for all other layers, as the absorber lifetime dominates simulated device performance. The doping

Approved for public release; distribution unlimited.
604

Downloaded from https://www.cambridge.org/core. Cornell University Library, on 28 Aug 2020 at 04:27:27, subject to the Cambridge Core terms of use, available at https://www.cambridge.org/core/terms. https://doi.org/10.1557/adv.2020.319

density of each layer is representative of typical experimental values. The electron affinity of the FTO is higher than that of typical perovskite simulation literature, more closely resembling its experimental value. Flat bands are assumed at each contact. Values left unspecified are left at their SCAPS default values. Data is collected at a temperature of 300K under the AM1.5G spectrum, with an irradiance of 1000 W/m^2.

Table I. Materials properties used in simulation.

Property	FTO	TiO_2	$MAPbI_3$	Spiro-OMeTAD
Thickness (nm)	500	50	600	300
Bandgap (eV)	3.6	3.2 [5]	1.6 [5]	2.7 [5]
Electron Affinity (eV)	4.25	4.25 [5]	3.9 [5]	2.5 [5]
Relative Dielectric Permittivity	9	100 [6]	6.5 [7, 8]	3 [9]
CB Effective Density of States (cm-3)	2.2e18	2.2e18	2.8e18 [10]	2.2e18
VB Effective Density of States (cm-3)	1.8e19	1.8e19	3.9e18 [10]	1.8e19
Electron/Hole Mobility (cm2/Vs)	20/10	20/10	10/10 [11]	2e-4/2e-4 [9]
Shallow Donor Density (cm-3)	2e19	1e16	1e13	-
Shallow Acceptor Density (cm-3)	-	-	-	1e18

RESULTS AND DISCUSSION

We first investigate the effect of CBO on the cell performance, with a positive CBO indicating a barrier for electron transport from the perovskite to the ETL. Note that for the model, CBO was modified by decreasing the electron affinity, and the bandgap was maintained at 3.2 eV. Figure 1 shows the open circuit voltage (V_{oc}), fill factor (FF), and power conversion efficiency (PCE) as a function of CBO. As the CBO increases the V_{oc} rapidly improves before plateauing at a CBO of ~-0.25 eV, with an additional upward bend in V_{oc} starting at a CBO of ~+0.2 eV (Figure 1a). FF shows a similar increase/plateau behavior (Figure 1b) for the lower CBO values but rapidly decreases as the CBO exceeds +0.05 eV. Short-circuit current (J_{sc}) remains approximately constant throughout this CBO range. As a result, PCE begins near 20%, surpasses 22.5% between a CBO of -0.27 eV and 0.09 eV and ultimately falls sharply in accordance with FF. PCE greater than 23% occurs between a CBO of -0.09 eV and 0.01 eV.

Approved for public release; distribution unlimited.

Downloaded from https://www.cambridge.org/core. Cornell University Library, on 28 Aug 2020 at 04:27:27, subject to the Cambridge Core terms of use, available at https://www.cambridge.org/core/terms.
https://doi.org/10.1557/adv.2020.319

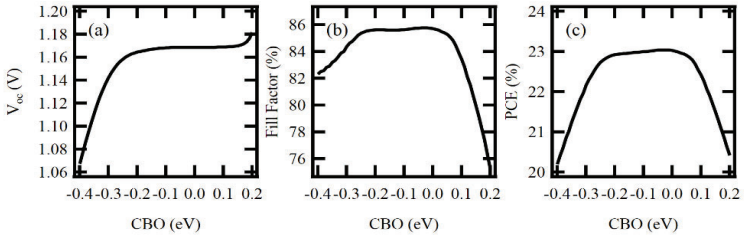


Figure 1.(a) V_{oc}, (b) FF, and (c) PCE as a function of changing conduction band offset.

Throughout this study, we will refer to three characteristic CBOs in order to more closely observe the effects of conduction band alignment. A CBO of -0.35 eV represents the standard TiO_2 offset. A CBO of -0.25 eV represents an ETL with greatly increased PCE and V_{oc}, and a CBO of -0.05 eV results in the highest PCE range.

In order to explain the increase in performance due to conduction band alignment, it is useful to inspect the current and recombination characteristics of the cell across voltages. Figure 2 shows the current-voltage (JV) and recombination current-voltage (J_rV) curves as well as the conduction band portion of the band diagram near the ETL/perovskite interface at maximum power point voltage (V_{mpp}) of the modeled cell at the CBO values of -0.35, -0.25, and -0.05 eV. In order to ensure that the changes in device performance are front limited by the ETL/perovskite interface, an ideal perovskite/HTL interface was assumed with a low SRV of 10^{-4} cm/s for this figure.

From the JV curves in Figure 2a, we see the expected increase in V_{oc}. As the CBO improves, the Shockley-Read-Hall (SRH) recombination is unaffected. The onset of interface recombination current density (J_{Int}), on the other hand, shifts to higher bias as CBO increases. These results can be understood using the band diagram. Increasing CBO from -0.35 to -0.05 eV raises the Fermi level of the ETL progressively higher, causing less upward band bending (Figure 2b) in the perovskite near the interface. This decrease in upward bending will allow more electrons to flow into the ETL, while also repelling more holes. This reduced number of holes leads to an increase in the turn on bias for J_{Int}.

Approved for public release; distribution unlimited.

Downloaded from https://www.cambridge.org/core. Cornell University Library, on 28 Aug 2020 at 04:27:27, subject to the Cambridge Core terms of use, available at https://www.cambridge.org/core/terms. https://doi.org/10.1557/adv.2020.319

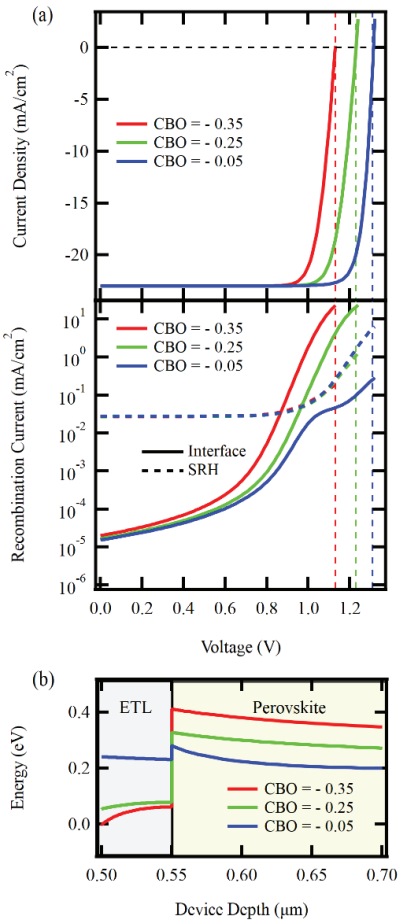


Figure 2. (a) JV and J_rV curves for three CBOs. (b) Energy bands at the ETL/perovskite interface at maximum power point voltage, with reduced influence of the perovskite/HTL interface.

From these results, it is clear that limiting recombination at the interface is critical to high performance devices. Improving the band bending at the interface clearly achieves this goal. Band bending can be modified by changing the CBO, as demonstrated above, or by changing the doping density of the ETL. In addition, interface recombination can be reduced by reducing the SRV at the interface. Consequently, we investigated how the device performance changes as a function of SRV and ETL doping concentration for CBOs equal to -0.35, -0.25, and -0.05 eV, and the contour plots of the PCE and V_{oc} are shown in Figure 3.

Approved for public release; distribution unlimited.

In these contour plots, there appear to be four regions. Region I appears to depend on both the SRV and doping density, while Regions II and III only depend on one of the parameters. The contour lines in Region II show that devices with these parameters are limited by the ETL doping density, and the contour line in Region III show the devices are limited by the SRV. Region IV appears to be high performance and independent of both parameters, indicating SRH limited devices.

The mixed dependence (Region I) occurs when the upward band bending and SRV are large. The upward band bending attracts a lot of holes to the interface, which recombine with the high number of interface defect states, indicated by the high SRV. As the ETL doping density increases and the band bending is improved, the device performance becomes independent of the SRV (Region II). At these high ETL doping densities, the band banding repels holes from the surface, greatly reducing interface recombination. On the other hand, when the ETL doping density is low and the SRV decreases, the device performance becomes independent of doping density (Region III). Here the SRV limits device performance due to the low number of recombination sites. At some point, the interface recombination is so low that SRH recombination dominates device performance (Region IV). This can occur at extremely low SRV, high ETL doping, or a combination of the two. For the case of CBO equal to -0.35 eV, increasing ETL doping density while maintaining high SRV does not result in a SRH limited device, but this can be achieved when the CBO is -0.05 eV.

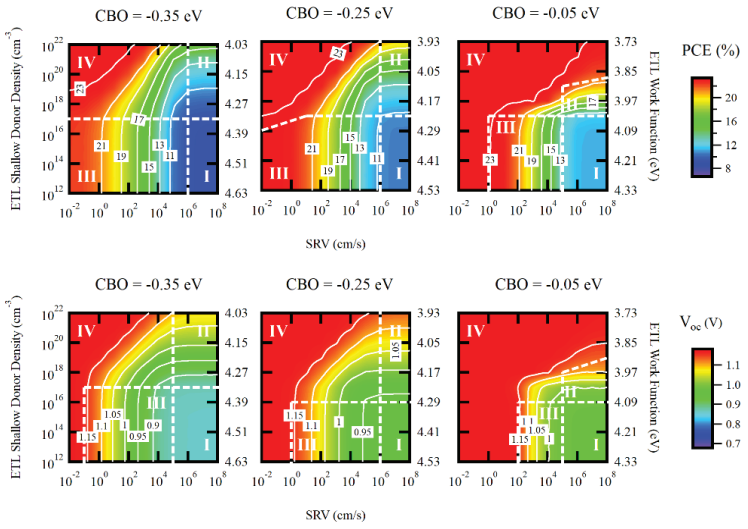


Figure 3. Contour plots of (a) PCE and (b) V_{oc} for ETL conduction band offsets of -0.35, -0.25, and -0.05 eV.

Downloaded from https://www.cambridge.org/core. Cornell University Library, on 28 Aug 2020 at 04:27:27, subject to the Cambridge Core terms of use, available at https://www.cambridge.org/core/terms. https://doi.org/10.1557/adv.2020.319

Approved for public release; distribution unlimited.

Downloaded from https://www.cambridge.org/core. Cornell University Library, on 28 Aug 2020 at 04:27:27, subject to the Cambridge Core terms of use, available at https://www.cambridge.org/core/terms. https://doi.org/10.1557/adv.2020.319

Figure 2b shows that CBO variation is effective in increasing band bending in the perovskite. This has the effect of shifting the PCE and V_{oc} contours in Figure 3 to lower ETL doping levels, as equivalent band bending already occurs due to improved CBO. Mixed dependence on SRV and doping density (Region I) still occurs, though improved energy band alignment increases PCE and V_{oc} in this region relative to less favorable CBOs for equivalent doping and SRV. The work function of each ETL is shown on the right axes in Figure 3. Comparing cases of constant work function in regions where doping is not low enough and SRV is not high enough to cause more complex interface behavior, PCE and V_{oc} behavior will be identical across CBOs. For example, ETLs with CBOs of -0.35, -0.25, and -0.05 eV with doping densities of 1.05 x 10^{20}, 2.2 x 10^{18}, and 9.71 x 10^{14} cm^{-3}, respectively, have a constant work function of 4.15 eV and consequently show identical PCE and V_{oc} when SRV is kept at 1 cm/s.

These results show that the device performance does not simply depend on the CBO at the ETL/perovskite interface. In fact, it indicates that the work function of the ETL is the more relevant parameter. This finding can be used to broaden the range of potentially new ETL materials under investigation while also identifying the key parameters. Experimental focus has been on higher CBO materials[14-18], which, naturally, will allow for lower work functions. However, easily doped materials, even if the CBO is low, may offer a route to improving device performance. Alternatively, our results show that if SRV can be further reduced, the importance of ETL work function will be less significant. ETL materials such as TiO_2 and ZnO have CBOs comparable to the least favorable alignment included in our simulations but exhibit SRVs with $MAPBI_3$ on the order of only 10 cm/s[19] and perform quite well in perovskite architectures. However, to achieve higher V_{oc} the SRV will need to be even lower or the doping density will need to be increased by orders of magnitude to lower the work function. In contrast, higher CBO material, such as [6,6]-phenyl-C_{61}-butyric acid methyl ester (PCBM), should outperform these high work function ETLs at equivalent doping and SRV. Unfortunately, these alternative ETLs currently exhibit SRVs orders of magnitude higher than TiO_2 and ZnO[19]. It is clear that additional research into ETL interface engineering is required to push the PCE to the theoretical limit.

CONCLUSION

Diminishing recombination at the ETL/perovskite interface is crucial for the high performance of perovskite solar cells. The interface recombination between ETL/perovskite is dominated by the band bending in the absorber at the interface and the SRV. These properties shape the potential and carrier concentrations near the interface that determine recombination rates. Improved band bending between ETL and perovskite alone is enough to greatly reduce the rate at which electrons recombine with holes at their interface. Electron transport layers with appropriate work functions allow perovskite solar cells to reach higher efficiencies and open circuit voltages more easily than with a less favorably aligned ETL such as TiO_2.

Approved for public release; distribution unlimited.

Downloaded from https://www.cambridge.org/core. Cornell University Library, on 28 Aug 2020 at 04:27:27, subject to the Cambridge Core terms of use, available at https://www.cambridge.org/core/terms. https://doi.org/10.1557/adv.2020.319

ACKNOWLEDGEMENTS

The authors gratefully acknowledge funding support from the U.S. Air Force Research Laboratory, Space Vehicles Directorate, under Agreement number FA9453-18-2-0037 and Contract # FA9453-19-C-1002. The U.S. Government is authorized to reproduce and distribute reprints for Governmental purposes notwithstanding any copyright notation thereon.

The views and conclusions contained herein are those of the authors and should not be interpreted as necessarily representing the official policies or endorsements, either expressed or implied, of Air Force Research Laboratory or the U.S. Government.

References

[1] A. Kojima, K. Teshima, Y. Shirai and T. Miyasaka, Journal of the American Chemical Society **131** (17), 6050-+ (2009).
[2] T. Minemoto and M. Murata, Journal of Applied Physics **116** (5) (2014).
[3] T. Minemoto and M. Murata, Solar Energy Materials and Solar Cells **133**, 8-14 (2015).
[4] M. Burgelman, P. Nollet and S. Degrave, Thin Solid Films **361**, 527-532 (2000).
[5] A. K. Jena, A. Kulkarni and T. Miyasaka, Chem Rev **119** (5), 3036-3103 (2019).
[6] K. Wojciechowski, M. Saliba, T. Leijtens, A. Abate and H. J. Snaith, Energy & Environmental Science **7** (3), 1142-1147 (2014).
[7] P. Umari, E. Mosconi and F. De Angelis, Sci Rep **4**, 4467 (2014).
[8] M. Hirasawa, T. Ishihara, T. Goto, K. Uchida and N. Miura, Physica B **201**, 427-430 (1994).
[9] D. Poplavskyy and J. Nelson, Journal of Applied Physics **93** (1), 341-346 (2003).
[10] G. Giorgi, J. I. Fujisawa, H. Segawa and K. Yamashita, J Phys Chem Lett **4** (24), 4213-4216 (2013).
[11] C. Wehrenfennig, G. E. Eperon, M. B. Johnston, H. J. Snaith and L. M. Herz, Adv Mater **26** (10), 1584-1589 (2014).
[12] A. S. Chouhan, N. P. Jasti, S. Hadke, S. Raghavan and S. Avasthi, Curr Appl Phys **17** (10), 1335-1340 (2017).
[13] X. Zhang, J.-X. Shen, W. Wang and C. G. Van de Walle, ACS Energy Letters **3** (10), 2329-2334 (2018).
[14] Y. Yao, W.-L. Hsu and M. Dagenais, presented at the 2017 IEEE 44th Photovoltaic Specialist Conference (PVSC), 2017 (unpublished).
[15] J. You, L. Meng, T.-B. Song, T.-F. Guo, Y. M. Yang, W.-H. Chang, Z. Hong, H. Chen, H. Zhou and Q. Chen, Nature nanotechnology **11** (1), 75 (2016).
[16] X. Ling, J. Yuan, D. Liu, Y. Wang, Y. Zhang, S. Chen, H. Wu, F. Jin, F. Wu and G. Shi, ACS applied materials & interfaces **9** (27), 23181-23188 (2017).
[17] H. Liang, Y.-C. Hu, Y. Tao, B. Wu, Y. Wu and J. Cao, ACS applied materials & interfaces **11** (46), 43116-43121 (2019).
[18] X. Liu, J. Jiang, F. Wang, Y. Xiao, I. D. Sharp and Y. Li, ACS applied materials & interfaces **11** (50), 46894-46901 (2019).
[19] J. Wang, W. Fu, S. Jariwala, I. Sinha, A. K.-Y. Jen and D. S. Ginger, ACS Energy Letters **4** (1), 222-227 (2018).

Approved for public release; distribution unlimited.

This article has been accepted for inclusion in a future issue of this journal. Content is final as presented, with the exception of pagination.

Understanding the Interplay Between CdSe Thickness and Cu Doping Temperature in CdSe/CdTe Devices

Ebin Bastola, Adam B. Phillips, Griffin Barros-King, Manoj K. Jamarkattel, Deng-Bing Li, Abdul Quader, Dipendra Pokhrel, Jared Friedl, Jacob M. Gibbs, Xavier Mathew, Yanfa Yan, Randy J. Ellingson, and Michael J. Heben

***Abstract*—CdSe thickness and Cu doping play significant roles in achieving high efficiency in CdTe solar cells. Using an evaporated CdSe/CdTe device stack to avoid vacuum breaks between deposition of layers, we investigated the role of the CdSe thickness on the device performance. When the CdSe thickness was greater than a critical value the device performance suffered primarily due to a reduction in the short-circuit current density (J_{SC}). The critical thickness of CdSe was determined to be 120 nm. However, in some cases the CdSe thicknesses could be increased to larger values by increasing the Cu doping process temperature. The higher temperature process leads to an increase in J_{SC} and an overall improvement in device efficiency. Specifically, for a device with ∼270 nm of CdSe, the J_{SC} increased from 7.9 $mAcm^{-2}$ with $CuCl_2$ processing temperature of 200°C to ∼29 $mAcm^{-2}$ when the processing temperature was increased to 250°C.**

***Index Terms*—CdTe, $CuCl_2$, evaporation, photovoltaics, solar cells.**

I. Introduction

REPLACING the CdS window layer in CdTe-based solar cells with CdSe has been critical to achieving higher efficiency devices. The low solubility limit of CdS in CdTe results in devices with an absorbing layer with poor carrier collection at the front of the device that reduces short-circuit current density (J_{SC}). The high solubility of CdSe in CdTe, on the other hand, can result in complete consumption of the CdSe to form $CdSe_xTe_{1-x}$ alloys during deposition and/or $CdCl_2$ activation [1], [2]. For x less than ∼0.40 the $CdSe_xTe_{1-x}$ bandgap decreases compared with CdTe and remains photoactive [3]. The lower bandgap and removal of the parasitic absorption layer results in much higher J_{SC} values [2], [4]. In addition, inclusion of CdSe leads to passivated grain boundaries and relatively long carrier lifetime in a $CdSe_xTe_{1-x}$ absorber layer [5], [6].

The effect of the CdSe thickness in these devices has been studied and is critically important. Initial investigations in which low temperature (250°C) sputtering was used to fabricate the devices showed that the J_{SC} increased with increasing thickness up to ∼200 nm, and began decreasing with thicker CdSe [2]. Similar results were reproduced by Ablekim *et al.* [7] for devices fabricated by thermal evaporation at 400°C, and the characterization supported that the device performance dropped once x exceeded ∼0.4. It has been shown that at x values >0.4, $CdSe_xTe_{1-x}$ is in wurtzite crystal structure, and the bandgap begins to increase [8], [9]. This wurtzite phase being photoinactive corresponds to the loss in J_{SC} in the $CdSe_xTe_{1-x}$ devices, so the decrease in performance has been attributed to the crystal structure change and accompanying bandgap increase when x was >0.40 [10].

At the same time, the Cu doping process is also critically important to the device performance. Transitioning from using evaporated Cu to a solution processed $CuCl_2$ dopant source led to an increase in the open circuit voltage (V_{OC}) and fill factor [11]. This change in the dopant source needed to be accompanied by a reoptimization of processing time and temperature. The optimized Cu treatment varies for CdTe devices deposited method, absorber thickness, absorber composition, and Cu source material. For our typical 3.5 μm CdTe absorber layer deposited by CSS, Cu diffusion is carried out at 200°C for 20 min, whereas for a 2.1-μm CdTe absorber deposited by sputtering the treatment time is reduced to 15 min at 200°C [12]. Li *et al.* [13], on the other hand, reported a rapid thermal annealing process at 180°C to diffuse Cu from CuCl into ∼3.5 μm CdTe devices deposited by CSS, whereas Munshi *et al.* [4] evaporated CuCl powder to dope CdTe (∼ 4 μm) absorber layer deposited by CSS method by annealing the device at 220°C for 220 s. Clearly, the Cu doping process is quite important; however, there is little discussion in the literature about how it should be modified as research has moved from CdS/CdTe devices in which the near complete active absorber is CdTe to CdSe/CdTe devices in

Manuscript received June 15, 2021; revised August 23, 2021; accepted September 1, 2021. This work was supported in part by the U.S. DOE's office of Energy Efficiency and Renewable Energy (EERE) under Solar Energy Technologies Office (SETO) under Agreement DE-EE0008974 and in part by Air Force Research Laboratory under Agreement FA9453-18-2-0037 and Agreement FA9453-19-C-1002. (*Corresponding author: Adam B. Phillips.*)

Ebin Bastola, Adam B. Phillips, Griffin Barros-King, Manoj K. Jamarkattel, Deng-Bing Li, Abdul Quader, Dipendra Pokhrel, Jared Friedl, Jacob M. Gibbs, Yanfa Yan, Randy J. Ellingson, and Michael J. Heben are with the Wright Center for Photovoltaics Innovation and Commercialization (PVIC), Department of Physics and Astronomy, The University of Toledo, Toledo, OH 43606 USA (e-mail: ebin.bastola@rockets.utoledo.edu; adam.phillips@utoledo.edu; griffin.barros-king@rockets.utoledo.edu; manoj.jamarkattel@rockets.utoledo.edu; dengbing.li@utoledo.edu; abdul.quader@rockets.utoledo.edu; dipendra.pokhrel@rockets.utoledo.edu; jared.friedl@rockets.utoledo.edu; jacob.gibbs@rockets.utoledo.edu; yanfa.yan@utoledo.edu; randy.ellingson@utoledo.edu; michael.heben@utoledo.edu).

Xavier Mathew is with the Wright Center for Photovoltaics Innovation and Commercialization (PVIC), Department of Physics and Astronomy, The University of Toledo, Toledo, OH 43606 USA, and also with the Instituto de Energías Renovables, Universidad Nacional Autónoma de México, Temixco 62580, México (e-mail: xavier.mathew@utoledo.edu).

Color versions of one or more figures in this article are available at https://doi.org/10.1109/JPHOTOV.2021.3110338.

Digital Object Identifier 10.1109/JPHOTOV.2021.3110338

2156-3381 © 2021 IEEE. Personal use is permitted, but republication/redistribution requires IEEE permission.
See https://www.ieee.org/publications/rights/index.html for more information.

Authorized licensed use limited to: University of Toledo. Downloaded on September 21,2021 at 17:21:39 UTC from IEEE Xplore. Restrictions apply.

Approved for public release; distribution unlimited.

611

This article has been accepted for inclusion in a future issue of this journal. Content is final as presented, with the exception of pagination.

which a significant portion of the absorber at the front interface is $CdSe_xTe_{1-x}$.

Here, we investigate the effect of CdSe thickness and Cu doping processing on CdTe solar cells. Devices were fabricated by evaporating a CdSe/CdTe bilayer without exposure to air between the CdSe and CdTe depositions. When the CdSe layer thickness is less than 100 nm, the resultant graded $CdSe_xTe_{1-x}$ film exhibits a bandgap of greater than 1.39 eV and does not absorb long wavelength photons, thus these devices have lower J_{SC} than the device with optimum CdSe thickness. When the CdSe layer thickness is 200 nm or greater, the graded absorber layer still has a minimum band gap of 1.39 eV, but the J_{SC} is low, suggesting an optimal CdSe thickness close to 120 nm. However, increasing the temperature of the $CuCl_2$ doping process results in increased J_{SC} values of $\sim$29 $mAcm^{-2}$ for devices with $\sim$270 nm of CdSe, indicating previous explanations for the J_{SC} loss were incomplete.

II. Experimental

Bilayer CdSe/CdTe solar cells were fabricated on fluorine doped tin oxide coated glass substrates with a 50-nm thick dopant-free tin oxide layer on the surface ($TEC^{TM}-12D$, NSG Pilkington). CdSe and CdTe films were deposited sequentially by evaporating CdSe and CdTe powders (99.999%, Alfa Aesar) with a substrate temperature of 400°C and a base pressure of 4×10^{-6} Torr at deposition rates of $\sim$15 and $\sim$100 nm-s^{-1}, respectively. The time between CdSe and CdTe depositions was $\sim$3 min, during which the substrate temperature was maintained at 400°C. After deposition and cooling, the CdSe/CdTe stacks were activated with $CdCl_2$ using a saturated $CdCl_2$ solution in methanol. Four to five drops of $CdCl_2$ solution were placed on the a CdTe surface (1.5" $\times$ 1.5") and the device stack was annealed at 400°C for 30 min in dry air, followed by two rinses with methanol and drying with nitrogen. Then, 0.1 mM $CuCl_2$ solution in deionized water was used for Cu activation as reported previously [14]. For the set of experiments in which the CdSe thickness was varied, device stacks were heated at 200°C for the Cu treatment in a convection oven. For the set of experiments investigating how the doping processing affected the devices, the treatment temperature was varied from 200°C to 260°C. The duration of all $CuCl_2$ thermal treatments was 20 min in the oven in ambient air. Finally, devices were finished with 40 nm of thermally evaporated gold using a tungsten boat at a base pressure of $\sim 4 \times 10^{-6}$ Torr. A cell area of 0.08 cm^2 was defined using a shadow mask during Au deposition.

Current density-voltage (J-V) characteristics were measured under a simulated AM1.5G spectrum and external quantum efficiencies (EQE) were measured using PV Instruments system (model IVQE8-C). The XRD diffraction patterns of the films were taken using a Rigaku Ultima III X-ray diffractometer with a Cu source operating at 40 KV and 44 mA. The surface morphology of the CdTe films was studied using a Hitachi S-4800 scanning electron microscope (SEM).

III. Results and Discussion

Prior to completing devices, we investigated the crystal structure and morphology of as-deposited and $CdCl_2$-activated devices. Fig. 1 shows the XRD and SEM images of these samples. From the XRD data, we see that the as-deposited film has grains with preferred orientation along (111) plane, whereas after $CdCl_2$ treatment the film has more randomly oriented grains [15]. The XRD pattern for as deposited film is consistent with thermally evaporated CdSe [16] and low temperature deposition of CdTe [17]. The $CdCl_2$ process is a critical step in the fabrication of CdTe devices and is known to result in recrystallization [15]. The change in XRD pattern shows the recrystallization.

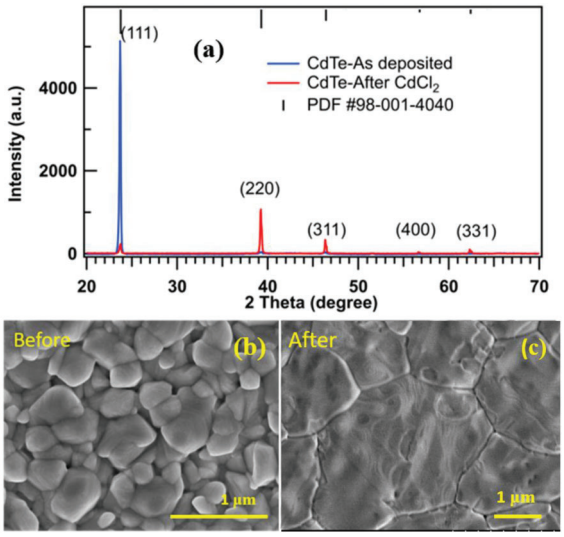


Fig. 1. (a) X-ray diffraction pattern and surface scanning electron micrographs of CdTe films (b) before and (c) after $CdCl_2$ treatments. The vertical lines (black lines, top scale) are diffraction patterns for CdTe (PDF #98-001-4040).

The SEM images show the growth of the CdTe grains, which is common in low temperature processed CdTe films such as sputtered films [18], [19]. The grains grew from 100–500 nm before activation to 1–3 μm after [see Fig. 1(b) and (c), respectively] after $CdCl_2$ activation process. Also visible in the SEM images are surface features that result due to the $CdCl_2$ treatment which are most likely related to cadmium oxides and/or chlorides [20]. The CdTe grains are in the range of 1–3 μm beneath these oxy-chloride particles on the surface for evaporated films after the $CdCl_2$ treatment visible in Fig. 1(c) after an acid etch. We note that the grain sizes obtained here are comparable to the film thickness, as is the case for films made with higher temperature techniques such as CSS or VTD [21], [22].

The large grains after $CdCl_2$ treatment suggest that these evaporated film stacks have the potential to make high efficiency devices. To verify this, we completed the devices and measured the photovoltaic response. Fig. 2 shows J-V, EQEs, and d(EQE)/dλ of CdTe devices with various CdSe thickness ranging from 40 to 400 nm. For all the devices, $CdCl_2$ treatments were carried out at the same temperature (400°C) and time (30 min) in dry air. For low temperature deposition processes, such as evaporation, as-deposited samples have higher CdSe concentration at the front interface [7], and during the $CdCl_2$ treatment the CdSe

Authorized licensed use limited to: University of Toledo. Downloaded on September 21,2021 at 17:21:39 UTC from IEEE Xplore. Restrictions apply.

Approved for public release; distribution unlimited.
612

This article has been accepted for inclusion in a future issue of this journal. Content is final as presented, with the exception of pagination.

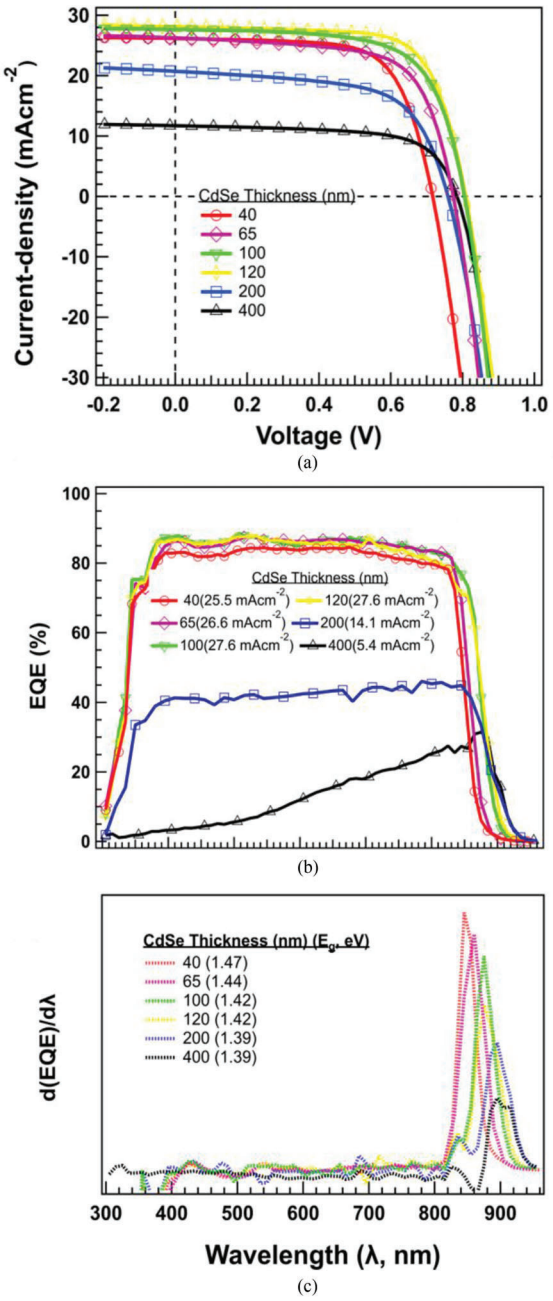


Fig. 2. (a) J-V, (b) EQE, and (c) d(EQE)/dλ data for devices with different CdSe thicknesses. The devices were $CdCl_2$ treated at 400°C for 30 min in dry air and $CuCl_2$ treated at 200°C for 20 min.

alloys with CdTe to form a graded $CdSe_xTe_{1-x}$ film with varying band gap [1]. The composition of this layer is important to the device performance.

Fig. 2(a) shows the J-V characteristics of the CdSe/CdTe devices with varying CdSe thickness, and Table I shows the tabulated PV parameters. For a device having CdSe thickness less than 100 nm, the J_{SC} values obtained from J-V measurements are lower than the devices with CdSe thickness of 100–120 nm. As the thickness of CdSe increases to 200–400 nm, the J_{SC} values drop significantly. The J_{SC} value of ∼28 mA-cm^{-2} refers to the optimum band gap to absorb long wavelength photons by the formation of $CdSe_xTe_{1-x}$ absorber layer with a band gap close to 1.4 eV [3], [23]. The overall device performance, including FF and J_{SC}, depends on several factors including the band gap of the graded $CdSe_xTe_{1-x}$ absorber layer, $CdCl_2$ treatment and Cu doping, and the efficiency strongly followed the variations in J_{SC} values.

To explain these variations, we turn to the EQE response [see Fig. 2(b)]. For the device with 40 nm CdSe, the EQE curve in the long wavelength region (>800 nm) starts dropping at ∼825 nm, which is similar to a typical CdS/CdTe devices [24], indicating a low concentration of Se in the $CdSe_xTe_{1-x}$ layer resulting in little change in bandgap from that of CdTe [12]. For the devices with CdSe thickness >100 nm, the long wavelength edge of the EQEs increases to ∼845 nm, indicating the formation of alloyed $CdSe_xTe_{1-x}$ layer with a lower band gap.

To extract the energy band gaps of these $CdSe_xTe_{1-x}$ films, d(EQE)/dλ was calculated [see Fig. 2(c)]. This graph clearly shows the variation of band gaps of $CdSe_xTe_{1-x}$ layer. The bandgaps range from 1.47 to 1.39 eV for 40 to 400 nm CdSe layer. For a 40 nm CdSe, the bandgap obtained here (1.47 eV) is similar to the band gap of pure CdTe (1.48 eV) [25]. The integrated J_{SC} values obtained from the EQEs for the 100 and 120 nm CdSe layers are the same, as are the minimum band gap values obtained from d(EQE)/dλ graphs. At the same time, for the devices with CdSe layers of 200 and 400 nm, the minimum bandgap is not much larger. In this case, the $CdSe_xTe_{1-x}$ could form an alloy with a maximum x greater than 0.4, resulting in a wurtzite structure material [23], [26] that is not photoactive and has an increased bandgap at the front interface [27]. Thus, a portion of the graded alloy is inefficient in collecting absorbed photons. Since a large portion of the incident photons are not able to reach the more effective portion of the absorber layer, the J_{SC} values are low (14.1 mAcm^{-2} and 5.4 mAcm^{-2}, respectively, for devices with 200 and 400-nm CdSe thickness). The J-V and EQE results presented here are consistent with what others have seen [7], [10], as are the explanations [8], [9].

Based on these J-V and EQE results, a CdSe thickness of 100–120 nm is optimal when a 3.5 μm CdTe layer is overlaid, a $CdCl_2$ activation temperature of 400°C for 30 min is used and annealing for Cu doping is done at 200°C for 20 min. While the shape of the EQE can be rationalized as previously noted [7], [10], it is not the only potential explanation. This shape is also reminiscent of back illuminated CdTe devices [28]. In those cases, the junction is far from where the short wavelength carriers are generated, which typically leads to poor collection of the short wavelength devices and higher collection of carriers generated closer to the junction by the long wavelength photons [29].

For that to be the case here, the junction would have to be at the back interface. This could only happen if the absorber is *n*-type. As-deposited CdSe is *n*-type with a band gap of 1.74 eV

Authorized licensed use limited to: University of Toledo. Downloaded on September 21,2021 at 17:21:39 UTC from IEEE Xplore. Restrictions apply.

Approved for public release; distribution unlimited.

This article has been accepted for inclusion in a future issue of this journal. Content is final as presented, with the exception of pagination.

TABLE I
PV DEVICE PARAMETERS OF CDSE/CDTE SOLAR CELLS WITH VARYING CDSE THICKNESS (40–400 NM) AND CDTE 3.5 MICROMETERS (ACTIVE DEVICE AREA 0.08 cm^2)

CdSe Thickness (nm)	Minimum Band gap of $CdSe_xTe_{1-x}$ (eV)	V_{OC} (mV)	J_{SC} ($mAcm^{-2}$)	FF (%)	Eff. (η%)	Rs ($\Omega\ cm^2$)	Rsh ($\Omega\ cm^2$)
40	1.47	717	26.2	68.3	12.8	4.5	1399
65	1.44	774	26.3	66.6	13.6	4.3	588
100	1.42	808	28.4	68.7	15.8	3.9	1393
120	1.42	808	28.2	70.6	16.1	2.3	947
200	1.39	759	20.7	62.6	9.8	6.4	339
400	1.39	784	11.7	66.3	6.1	7.3	999

with wurtzite (hexagonal) structure [30]. At higher values of x in $CdSe_xTe_{1-x}$ (CST), the crystal structure is also wurtzite and has shown to be *n*-type, [26] so it is possible $CdSe_xTe_{1-x}$ in our case is also *n*-type prior to Cu doping. This possibility, and the fact that addition of CdSe to the absorber may alter how the doping occurs during processing, necessitating more aggressive doping.

To test if this is the case, we varied the Cu doping process temperature for the devices. We deposited a thick CdSe layer (∼270 nm) followed by 3.5 μm CdTe on a 3" × 3" substrate, which was then cut into pieces (1" × 1") for the Cu doping study. For this, we varied the temperature of the doping process from 200°C to 260°C. The resultant EQEs and J-V curves are shown in Fig. 3. As abovementioned, the low temperature processing resulted in low J_{SC} with short-wavelength light not being collected. As the annealing temperature increases, J_{SC} increases, with a significant gain occurring when the device was annealed for 250°C for 20 min. The EQE graphs show that the triangular shape observed for 200°C changes to a square shape at the higher temperatures. The EQEs for devices annealed at 250°C and 260°C have very similar shapes to each other, and the J_{SC} values are close (29.2 $mAcm^{-2}$); however, the device annealed at 260°C suffers from a reduction in FF. For the device annealed at 250°C has the highest device efficiency of 15.2% with V_{OC} 780 mV, FF 68.0%, and J_{SC} 28.7 $mAcm^{-2}$.

It is possible that the higher temperature alone could have affected the device performance independent of the Cu. To test this, we heated a Cu-free sample to 250°C for 20 min, then completed a $CuCl_2$ treatment at 200°C for 20 min and completed the device as abovementioned. The EQE curve of this device is shown in Fig. 3(b). We observed some improvement in EQE response in long wavelength region compared with other devices annealed at a temperature ≤240°C; however, the device still has the triangular shape EQE curve. This response indicates that the improvement in device performance observed for samples Cu treated at 250°C is not simply the effect of annealing. Instead, it is the effect of aggressive Cu doping for a device with thicker CdSe.

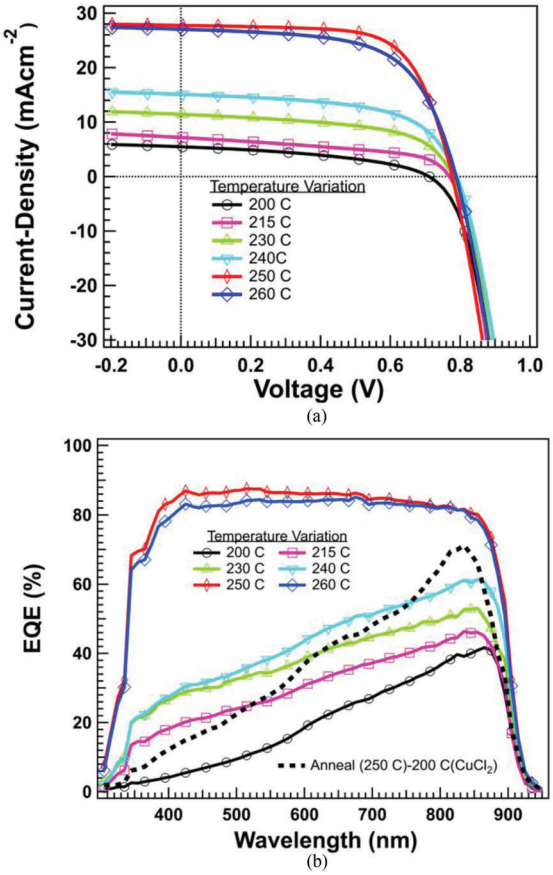


Fig. 3. (a) J-V and (b) EQEs of CdSe/CdTe devices (CdSe thickness 270 nm) with varying annealing temperature as indicated for 20 min. The dotted black line represents an EQE of a device which was first annealed at 250°C, dipped in $CuCl_2$ solution, and then annealed at 200°C for 20 min. All the devices have same $CdCl_2$ treatment at 400°C for 30 min in dry air environment.

Authorized licensed use limited to: University of Toledo. Downloaded on September 21,2021 at 17:21:39 UTC from IEEE Xplore. Restrictions apply.

Approved for public release; distribution unlimited.
614

This article has been accepted for inclusion in a future issue of this journal. Content is final as presented, with the exception of pagination.

This evolution of J_{SC} and EQEs as the annealing temperature increased indicates incomplete Cu doping occurred for devices processed at the low temperatures. These results clearly show that the CdSe thickness alone does not fully explain the reduced J_{SC} for CdSe/CdTe devices and that the thermal budget during the entire device processing of CdSe/CdTe is important.

V. Conclusion

Here, we successfully fabricated CdSe/CdTe devices by thermal evaporation and studied the effect of CdSe thickness on device performances. The CdSe thickness in the range of 100–120 nm produces a high J_{SC} when the devices undergo $CdCl_2$ activation at 400°C for 30 min. Very thin CdSe was not enough to significantly change the band gap of the $CdSe_xTe_{1-x}$ layer from the CdTe value. A thick ($\geq$200 nm) CdSe layer, on the other hand, leads to a decrease in J_{SC} typically thought to be due to a $CdSe_xTe_{1-x}$ layer that is partially nonphoto responsive and absorbs incident photons before reaching the photoactive absorber layer. However, increasing the Cu doping process temperature can result in an increase in J_{sc} (29 $mAcm^{-2}$) for some CdSe thicknesses that lead to poor J_{SC} at lower Cu doping temperature.

Acknowledgment

The U.S. Government is authorized to reproduce and distribute reprints for Governmental purposes notwithstanding any copyright notation thereon. Disclaimer: The views and conclusions contained herein are those of the authors and should not be interpreted as necessarily representing the official policies or endorsements, either expressed or implied, of the Department of Energy or Air Force Research Laboratory or the U.S. Government.

References

[1] E. Colegrove *et al.*, "Se diffusion in CdTe thin films for photovoltaics," *J. Phys. D, Appl. Phys.*, vol. 54, no. 2, 2020, Art. no. 025501.

[2] N. R. Paudel and Y. Yan, "Enhancing the photo-currents of CdTe thin-film solar cells in both short and long wavelength regions," *Appl. Phys. Lett.*, vol. 105, no. 18, 2014, Art. no. 183510.

[3] X. Zheng, E. Colegrove, J. Duenow, J. Moseley, and W. Metzger, "Roles of bandgrading, lifetime, band alignment, and carrier concentration in high-efficiency CdSeTe solar cells," *J. Appl. Phys.*, vol. 128, no. 5, 2020, Art. no. 053102.

[4] A. H. Munshi *et al.*, "Polycrystalline CdSeTe/CdTe absorber cells with 28 mA/cm^2 short-circuit current," *IEEE J. Photovolt.*, vol. 8, no. 1, pp. 310–314, Jan. 2018.

[5] X. Zheng *et al.*, "Recombination and bandgap engineering in CdSeTe/CdTe solar cells," *APL Mater.*, vol. 7, no. 7, 2019, Art. no. 071112.

[6] A. H. Munshi *et al.*, "Polycrystalline CdTe photovoltaics with efficiency over 18% through improved absorber passivation and current collection," *Sol. Energy Mater. Sol. Cells*, vol. 176, pp. 9–18, 2018.

[7] T. Ablekim *et al.*, "Thin-film solar cells with 19% efficiency by thermal evaporation of CdSe and CdTe," *ACS Energy Lett.*, vol. 5, no. 3, pp. 892–896, 2020.

[8] A. J. Strauss and J. Steininger, "Phase diagram of the CdTe-CdSe pseudobinary system," *J. Electrochem. Soc.*, vol. 117, no. 11, 1970, Art. no. 1420.

[9] A. P. Belyaev and I. P. Kalinkin, "Conduction processes in inhomogeneous $CdSe_xTe_{1-x}$ semiconductors," *Thin Solid Films*, vol. 158, no. 1, pp. 25–36, 1988.

[10] J. D. Poplawsky *et al.*, "Structural and compositional dependence of the $CdTe_xSe_{1-x}$ alloy layer photoactivity in CdTe-based solar cells," *Nature Commun.*, vol. 7, no. 1, 2016, Art. no. 12537.

[11] E. Artegiani *et al.*, "Analysis of a novel $CuCl_2$ back contact process for improved stability in CdTe solar cells," *Prog. Photovolt.*, vol. 27, no. 8, pp. 706–715, 2019.

[12] E. Bastola *et al.*, "Open-circuit voltage exceeding 840 mV for all-sputtered CdS/CdTe devices," in *Proc. 47th IEEE Photovolt. Specialists Conf.*, 2020, pp. 2513–2518.

[13] D.-B. Li *et al.*, "Maximize CdTe solar cell performance through copper activation engineering," *Nano Energy*, vol. 73, no. 8, 2020, Art. no. 104835.

[14] E. Bastola, A. V. Bordovalos, E. LeBlanc, N. Shrestha, M. O. Reese, and R. J. Ellingson, "Doping of CdTe using $CuCl_2$ solution for highly efficient photovoltaic devices," in *Proc. IEEE 46th Photovolt. Specialists Conf.*, 2019, pp. 1846–1850.

[15] J. Lee, "Effects of heat treatment of vacuum evaporated $CdCl_2$ layer on the properties of CdS/CdTe solar cells," *Current Appl. Phys.*, vol. 11, no. 1, pp. S103–S108, 2011.

[16] H. Gullu, M. Isik, O. Surucu, N. Gasanly, and M. Parlak, "Temperature effects on optical characteristics of CdSe thin films," *Mater. Sci. Semicond. Process.*, vol. 123, 2021, Art. no. 105559.

[17] J. Schaffner *et al.*, "12% efficient CdTe/CdS thin film solar cells deposited by low-temperature close space sublimation," *J. Appl. Phys.*, vol. 110, no. 6, 2011, Art. no. 064508.

[18] M. Islam *et al.*, "Fabrication of high efficiency sputtered CdS: O/CdTe thin film solar cells from window/absorber layer growth optimization in magnetron sputtering," *Sol. Energy Mater. Sol. Cells*, vol. 172, pp. 384–393, 2017.

[19] I. Dharmadasa, "Review of the $CdCl_2$ treatment used in CdS/CdTe thin film solar cell development and new evidence towards improved understanding," *Coatings*, vol. 4, no. 2, pp. 282–307, 2014.

[20] R. A. Awni *et al.*, "The effects of hydrogen iodide back surface treatment on CdTe solar cells," *Sol. RRL*, vol. 3, no. 3, 2019, Art. no. 1800304.

[21] A. H. Munshi *et al.*, "Effect of $CdCl_2$ passivation treatment on microstructure and performance of CdSeTe/CdTe thin-film photovoltaic devices," *Sol. Energy Mater. Sol. Cells*, vol. 186, pp. 259–265, 2018.

[22] W. K. Metzger *et al.*, "Exceeding 20% efficiency with in situ group V doping in polycrystalline CdTe solar cells," *Nature Energy*, vol. 4, no. 10, pp. 837–845, 2019.

[23] N. Muthukumarasamy, S. Jayakumar, M. Kannan, and R. Balasundaraprabhu, "Structural phase change and optical band gap bowing in hot wall deposited $CdSe_xTe_{1-x}$ thin films," *Sol. Energy*, vol. 83, no. 4, pp. 522–526, 2009.

[24] D. Pokhrel, E. Bastola, A. B. Phillips, M. J. Heben, and R. J. Ellingson, "Aspect ratio controlled synthesis of tellurium nanowires for photovoltaic applications," *Mater. Adv.*, vol. 1, no. 8, pp. 2721–2728, 2020.

[25] R. M. Geisthardt, M. Topic, and J. R. Sites, "Status and potential of CdTe solar-cell efficiency," *IEEE J. Photovolt.*, vol. 5, no. 4, pp. 1217–1221, Jul. 2015.

[26] N. Muthukumarasamy, S. Velumani, R. Balasundaraprabhu, S. Jayakumar, and M. D. Kannan, "Fabrication and characterization of n-$CdSe_{0.7}Te_{0.3}$/p-$CdSe_{0.15}Te_{0.85}$ solar cell," *Vacuum*, vol. 84, no. 10, pp. 1216–1219, 2010.

[27] T. Baines *et al.*, "Incorporation of CdSe layers into CdTe thin film solar cells," *Sol. Energy Mater. Sol. Cells*, vol. 180, pp. 196–204, 2018.

[28] K. K. Subedi *et al.*, "Enabling bifacial thin film devices by developing a back surface field using CuxAlOy," *Nano Energy*, vol. 83, 2021, Art. no. 105827.

[29] A. B. Phillips, K. K. Subedi, G. K. Liyanage, F. K. Alfadhili, R. J. Ellingson, and M. J. Heben, "Understanding and advancing bifacial thin film solar cells," *ACS Appl. Energy Mater.*, vol. 3, no. 7, pp. 6072–6078, 2020.

[30] J. Wang and M. Isshiki, "II–IV semiconductors for optoelectronics: CdS, CdSe, CdTe," in *Springer Handbook of Electronic and Photonic Materials*, S. Kasap and P. Capper, Eds., Boston, MA, USA: Springer, 2007, pp. 829–842.

Authorized licensed use limited to: University of Toledo. Downloaded on September 21,2021 at 17:21:39 UTC from IEEE Xplore. Restrictions apply.

Approved for public release; distribution unlimited.

615

This article has been accepted for inclusion in a future issue of this journal. Content is final as presented, with the exception of pagination.

Improving CdSeTe Devices With a Back Buffer Layer of Cu_xAlO_y

Manoj K. Jamarkattel, Adam B. Phillips, Kamala Khanal Subedi, Ebin Bastola, Jacob M. Gibbs, Jared D Friedl, Suman Rijal, Dipendra Pokhrel, Rasha A. Awni, Deng-Bing Li, John Farrell, Robert F. Klie, Xavier Mathew, Yanfa Yan, Randy J. Ellingson, and Michael J. Heben

***Abstract*—The open-circuit voltage (V_{oc}) of CdTe-based photovoltaics may be limited by carrier recombination at interfaces (front or back) or in the absorber layer. Reduction in recombination of a given dominant mechanisms can lead to improved device performance if the remaining mechanisms turn ON in a narrow bias range just below the open circuit voltage. In this article, we demonstrate enhanced performance by incorporating solution-processed Cu_xAlO_y to form a back-buffer layer in CdSe/CdTe devices. Outstanding minority carrier lifetimes of 656 and 4.2 ns were measured with glass side and film side illumination for device stacks processed with Cu_xAlO_y. Devices demonstrated efficiencies of up to 17.4% with V_{oc} of 859 mV, FF of 75.6% and J_{sc} of 26.9 mAcm^{-2} while the efficiency of the reference device without the back-buffer layer was 16.5% with V_{oc} of 839 mV, FF of 70.6%, and J_{sc} of 27.9 mAcm^{-2}.**

***Index Terms*—Back-contact, CdSeTe, Cu_xAlO_y, passivation.**

I. Introduction

REPLACING the traditional CdS window layer with CdSe in CdTe based polycrystalline solar cells has resulted in higher current collection and higher minority carrier lifetime [1]–[3], both of which allow for significantly better device performance. While there is the potential for V_{OC} greater than 1 V and efficiency over 25% [4], the record V_{OC} and efficiency are only 887 mV and 22.1% [5], respectively. Modeling shows that bulk carrier lifetime may need to be ∼100 ns or longer to achieve 25% [6]. As the bulk lifetime gets longer, it is likely that the measured carrier lifetime will be affected by recombination at the back interface. In fact, studies of carrier lifetimes can provide information about the interface recombination rates [7]. In general, the interplay between carrier recombination at the front and back interfaces, the bulk of the absorber, or at grain boundaries limit the $V_{OC,}$ and the way in which the various mechanisms turn-ON with bias will limit the FF [8].

Recently, MgZnO was incorporated at the front of MgZnO/CdSeTe/CdTe devices in an effort to reduce recombination at the front [9]. This resulted in a carrier lifetime of 256 ns and device efficiency and V_{oc} of 17%–18% and 843 mV, respectively. These improvements are attributed to the formation of tellurium oxide species at the front interface and larger CdSeTe grains, both of which help reduce front and bulk recombination in the device. Although the long carrier lifetimes are promising, the low V_{oc} suggests recombination losses elsewhere in the device, likely at the back interface.

Efforts to reduce recombination at the back interface are underway. Back buffer layers such as CdZnTe, Te nanowires, ZnTe [10]–[13] and oxides TiO_2, Al_2O_3, SiO_2, and Ta_2O_5 [14]–[19] have been applied to improve the hole transport or minimize the carrier recombination at the back surface. Among them, Al_2O_3 has shown back surface passivation resulting in carrier lifetime of 750 ns when CdSeTe was examined in a double heterostructure [20]. Recently, Cu_xAlO_y has been used as a back-buffer layer in CdS/CdTe devices and showed promising results when illuminated through the back interface [21]. Time resolved photoluminescence (TRPL) measurements showed an increase in carrier lifetime when Cu_xAlO_y was incorporated as a back-buffer layer. However, the best carrier lifetime for those device stacks was only on the order of tens of nanoseconds when illuminated from the glass side, and ∼3.4 ns when measured with back illumination. This is likely due to the use of CdS at the front of the device, which is expected to have poor band alignment with CdTe [22]. Further, the solubility of CdS in CdTe is lower than that of CdSe and hence the achievable defect passivation in the bulk is also lower with CdS [23].

Here, we investigate using the solution processed Cu_xAlO_y to reduce back surface recombination in CdSe/CdTe devices. When this material is incorporated into the back of the device, the

Manuscript received June 15, 2021; revised September 5, 2021; accepted October 12, 2021. This work was supported in part by the research sponsored by Air Force Research Laboratory under Grant FA9453-18-2-0037 and Grant FA9453-19-C-1002 and in part by the U.S. DOE's Office of Energy Efficiency and Renewable Energy under Solar Energy Technologies Office under Agreement DE-EE0008974. *(Corresponding author: Michael J. Heben.)*

Manoj K. Jamarkattel, Adam B. Phillips, Kamala Khanal Subedi, Ebin Bastola, Jacob M. Gibbs, Jared D Friedl, Suman Rijal, Dipendra Pokhrel, Rasha A. Awni, Deng-Bing Li, Yanfa Yan, Randy J. Ellingson, and Michael J. Heben are with the Wright Center for Photovoltaic Innovation and Commercialization, University of Toledo, Toledo, OH 43606 USA (e-mail: manoj.jamarkattel@rockets.utoledo.edu; Adam.Phillips@utoledo.edu; kamala.khanalSubedi@rockets.utoledo.edu; Ebin.Bastola@rockets.utoledo.edu; jacob.gibbs@rockets.utoledo.edu; Jared.Friedl@rockets.utoledo.edu; suman.rijal@rockets.utoledo.edu; dipendra.pokhrel@utoledo.edu; rasha.awni@utoledo.edu; Dengbing.Li@utoledo.edu; yanfa.yan@utoledo.edu; Randy.Ellingson@utoledo.edu; Michael.Heben@utoledo.edu).

John Farrell and Robert F. Klie are with the Department of Physics, University of Illinois at Chicago, Chicago, IL 60607 USA (e-mail: jjfarre2@uic.edu; rfklie@uic.edu).

Xavier Mathew is with the Wright Center for Photovoltaic Innovation and Commercialization, University of Toledo, Toledo, OH 43606 USA, and also with the Instituto de Energías Renovables, Universidad Nacional Autónoma de México, Morelos 62580, México (e-mail: Xavier.Mathew@utoledo.edu).

Color versions of one or more figures in this article are available at https://doi.org/10.1109/JPHOTOV.2021.3120506.

Digital Object Identifier 10.1109/JPHOTOV.2021.3120506

2156-3381 © 2021 IEEE. Personal use is permitted, but republication/redistribution requires IEEE permission.
See https://www.ieee.org/publications/rights/index.html for more information.

Approved for public release; distribution unlimited.

616

This article has been accepted for inclusion in a future issue of this journal. Content is final as presented, with the exception of pagination.

device efficiency exceeds 17% and an excellent minority carrier lifetime greater than 650 ns was measured through the glass. We discuss how this back buffer affects the photoluminescence (PL) and TRPL responses of the absorber, current density-voltage (*J–V*) characteristics, and external quantum efficiency (EQE).

II. Experimental Details

To fabricate these devices, we deposited a bilayer of CdSe/CdTe onto cleaned F-doped SnO_2/glass (Tec 12D; Pilkington North America). First, 150 nm of CdSe was sputtered onto the substrate at room temperature under 10 mTorr Ar pressure. This was followed by depositing 3.5 μm of CdTe using a high vacuum close-space sublimation (CSS) system in which the source and substrate temperatures were 560 °C and 450 °C, respectively, while the chamber pressure was held at 2×10^{-6} Torr. All the coupons were subjected to our standard activation process, which utilizes 100 μL of saturated $CdCl_2$ solution applied directly onto the as-deposited bilayer film stack. After drying, the coupons were annealed at 400 °C for 30 minutes in dry air followed by repeated rinsing with methanol to remove excess $CdCl_2$.

The reference devices were Cu doped by dipping in 0.1 mmol $CuCl_2$ solution in water for 2 min [24]. Upon removal, the coupon was rinsed with DI water, dried with nitrogen, and annealed in an oven at 200 °C for 20 min in ambient air. Cu_xAlO_y was deposited by applying 50 μl of a precursor solution consisting of a 7:3 ratio of 40 mM concentrated aluminum nitrate nonahydrate and 40 mM concentrated copper nitrate trihydrate, dissolved in two-methoxyethanol to the sample [21]. The sample was then spun at 100 r/min for 10 s followed by 50 s at 3500 r/min. Samples were then heated to 220 °C for 6 min on a hot plate to convert the precursor into Cu_xAlO_y. No additional Cu doping was used in these samples.

To complete the devices for *J–V* measurements, 50 nm of gold was evaporated through a mask with cell area of 0.08 cm^2, and the *J–V* characteristics were measured with a Keithley 2440 source meter and an LED solar simulator (Newport Minisolo model LHS-7320) under AM1.5G spectrum. EQE data was also measured (PV measurements Inc.).

Prior to depositing Au, glass side PL measurements were performed using a continuous wave laser operating at 633 nm with a beam diameter of 180 μm and an incident power density of 55 mW/cm^2. Film side PL measurements were performed using the same laser but with a higher power density of 283.9 mW/cm^2. For TRPL measurements, a 633 nm pulsed laser with a beam diameter of 150 μm was used to excite the carriers. The power and repetition rates were chosen to ensure low injection to avoid any artifacts in the measurement. For glass side illuminated measurements, the laser power was 9.5 μW, the repetition rate was 20 MHz, and the photon fluence was 4.5×10^{10} photons/cm^2. The corresponding parameters for film side measurements were 11.6 μW, 20 MHz and 1.1×10^{10} photons/cm^2, respectively.

III. Results and Discussion

Representative scanning electron microscopy (SEM) images of the surfaces are shown in Fig. 1. As-deposited CdTe grains

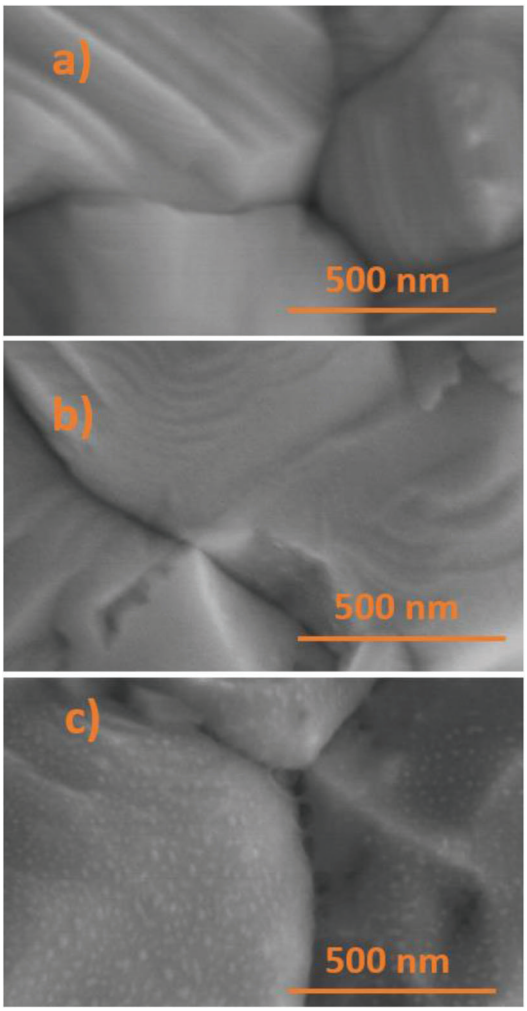


Fig. 1. Surface SEM images of CdTe grains. (a) As deposited CdTe. (b) After $CdCl_2$ and Cu doping. (c) After deposition of Cu_xAlO_y.

are 2–3 μm in size [see Fig. 1(a)] and appear unchanged after $CdCl_2$ processing and Cu doping [see Fig. 1(b)]. However, small features are visible on the CdTe grains [see Fig. 1(c)] after the application of Cu_xAlO_y. The small nodules appear uniform in size and evenly distributed. These structures are similar to those observed in our previous work on Cu_xAlO_y applied to CdS/CdTe devices [21].

However, in this article, we performed TOF-SIMS analysis and high-resolution cross-sectional imaging of the interface to gain a more detailed understanding of the deposited material. Fig. 2 shows a comparison between the surface density of Cu and Al isotopes for a reference sample [see Fig. 2(a) and (b)] and a sample on which Cu_xAlO_y was deposited [see Fig. 2(c) and (d)]. We first note that the surface concentration of Cu was higher by ~3x for the Cu_xAlO_y sample. Also, while the Cu and Al signals are correlated to some degree, the ratio of Cu to Al does not appear to be 1:1, the film is not continuous, and the apparent thickness, where present, is on the order of a

Approved for public release; distribution unlimited.
617

This article has been accepted for inclusion in a future issue of this journal. Content is final as presented, with the exception of pagination.

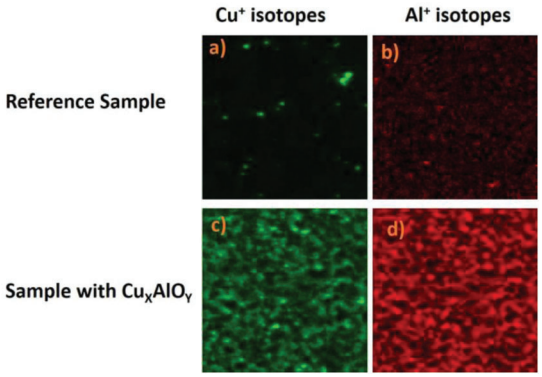


Fig. 2. TOF-SIMS surface images of Cu (a) and (c) and Al isotopes (b) and (d) from a reference sample doped with Cu via $CuCl_2$ (a) and (b) and a sample on which Cu_XAlO_y was deposited (c) and (d).

few nm. Interestingly, the Cu concentration in the depth profiles (not shown) decayed to lower values in the case of Cu_xAlO_y as compared to the $CuCl_2$ dipped sample. This result was confirmed by *C–V* analysis, where the carrier concentrations after $CuCl_2$ doping and Cu_xAlO_y deposition were measured to be 4.5×10^{13} cm^{-3} and 3.0×10^{13} cm^{-3}, respectively. Thus, the degree of doping is marginally higher in the case of $CuCl_2$. The TOF-SIMS data also revealed that the Al depth profile was correlated with the Cu profile in the case of the Cu_xAlO_y sample but, once again, not apparently in a 1:1 fashion. This data needs to be viewed with some caution, however, since the raw ion counts were uncorrected. The Se gradient was found to be similar in both samples.

The back contact interface was also examined by energy-dispersive X-ray spectroscopy using cross-sectional scanning transmission electron microscopy after lifting-out a lamella from a completed device. Interestingly, evidence for the formation of a thin copper-containing AuAl intermetallic layer was observed. Clearly, more studies are required to develop a detailed understanding of the deposited material and the resulting interfaces.

To investigate how the Cu_xAlO_y deposition affected recombination in the device stack, we measured glass side and film side PL and TRPL. Fig. 3 shows the data for device stacks with and without Cu_xAlO_y. For the sample with Cu_xAlO_y, we observed noticeable improvement in the PL intensity with illumination from the glass side [see Fig. 3(a)]. The peak PL intensity of the sample with Cu_xAlO_y was 227% and 48% higher than that of the reference sample before and after $CuCl_2$ doping, respectively [see Fig. 3(a)]. To develop an estimate of the improvement in V_{oc} that should accompany this increase in PL intensity, we consider (1) that holds for low-injection excitation [25], [26]

$$\Delta V_{\mathrm{OC}} = \mathrm{KT}/q * \ln\left(\frac{\mathrm{PLQE}, \mathrm{Cu_xAlO_y}}{\mathrm{PLQE}, \mathrm{Ref}}\right). \quad (1)$$

The ratio of $\mathrm{PLQE_{CuxAlOy}/PLQE_{Ref}} = 1.47$, calculated by taking the area under the corresponding PL bands, yields a value for ΔV_{oc} of $\sim$10 mV improvement, which is consistent with *J–V* findings (*vide infra*).

TABLE I
TRPL DATA OF THE SAMPLES WITH AND WITHOUT BACK BUFFER LAYER

Samples	Glass side Lifetime (ns)	Film side Lifetime (ns)
$CdSe/CdTe/CdCl_2$	293.8	2.2
$CdSe/CdTe/CdCl_2/CuCl_2$	501.4	1.6
$CdSe/CdTe/CdCl_2/Cu_xAlO_y$	656.5	4.2

Turning to the film side PL spectra [see Fig. 3(c)], we note that each sample shows a dominant emission band at 1.38 eV, corresponding to emission from CdSeTe, and a weaker band at 1.49 eV which is attributed to pure CdTe present at the back. After $CdCl_2$ treatment the film side PL is relatively bright, but only $\sim$40% of the intensity as compared to glass side measurement of the same sample. Significant quenching of the PL was observed after $CuCl_2$ treatment, while the sample with Cu_xAlO_y exhibits a PL spectrum which was nearly unchanged relative to the spectrum after $CdCl_2$ treatment. Note that bright and long-live film side PL is an important diagnostic for the development of bifacial devices [17], [19], [28]. The fact that the Cu_xAlO_y deposition yields higher film side PL in comparison to $CuCl_2$ treated samples suggests that the minority carrier recombination rate is lower at the back surface, possibly due to changes in the rear surface band bending. Consistently, the reduced carrier concentration found for the case of Cu_xAlO_y suggests a bigger depletion with at the back of the device. In any case, it seems clear that the electronic processes are different at and near the back interface. Clearly, more work is required to develop a deeper understanding of the related chemistry and physics.

It is also interesting to note the glass side and film side TRPL data [see Fig. 3(b) and (d)]. Biexponential Gaussian fits to the TRPL decay curves were analyzed to obtain carrier lifetimes for the fast decaying component (τ_1) that corresponds to charge redistribution and the slow component (τ_2) which relates to carrier recombination [7]. The data presented in Table I shows that carrier recombination lifetimes (τ_2) measured at the front side of devices without a back buffer is markedly higher than that reported elsewhere [9], [28]. The quality of the material and the degree of passivation at the front interface appears excellent which could be a consequence of the CSS instrument used here, which includes high vacuum pump-out capabilities and a base pressure approaching 1×10^{-8} Torr. The addition of Cu_xAlO_y leads to a significant improvement in the front side lifetime, once again suggesting a reduction in the rear surface recombination rate. Consistently, the τ_2 back side lifetime is also the longest for the Cu_xAlO_y sample.

More quantitative information can be gleaned by assuming that the band-edges are away from the equilibrium condition after the pulsed excitation and that the carriers are redistributed in the space charge region. Under these conditions the recombination rate model suggested by Kuciauskas *et al.* [7] can be written as

$$\frac{1}{\tau 2, \mathrm{TRPL}} = \frac{1}{\tau B} + \frac{1}{\tau \mathrm{front}} + \frac{1}{\tau \mathrm{back}} + \frac{1}{\tau \mathrm{rad}} \quad (2)$$

Approved for public release; distribution unlimited.

This article has been accepted for inclusion in a future issue of this journal. Content is final as presented, with the exception of pagination.

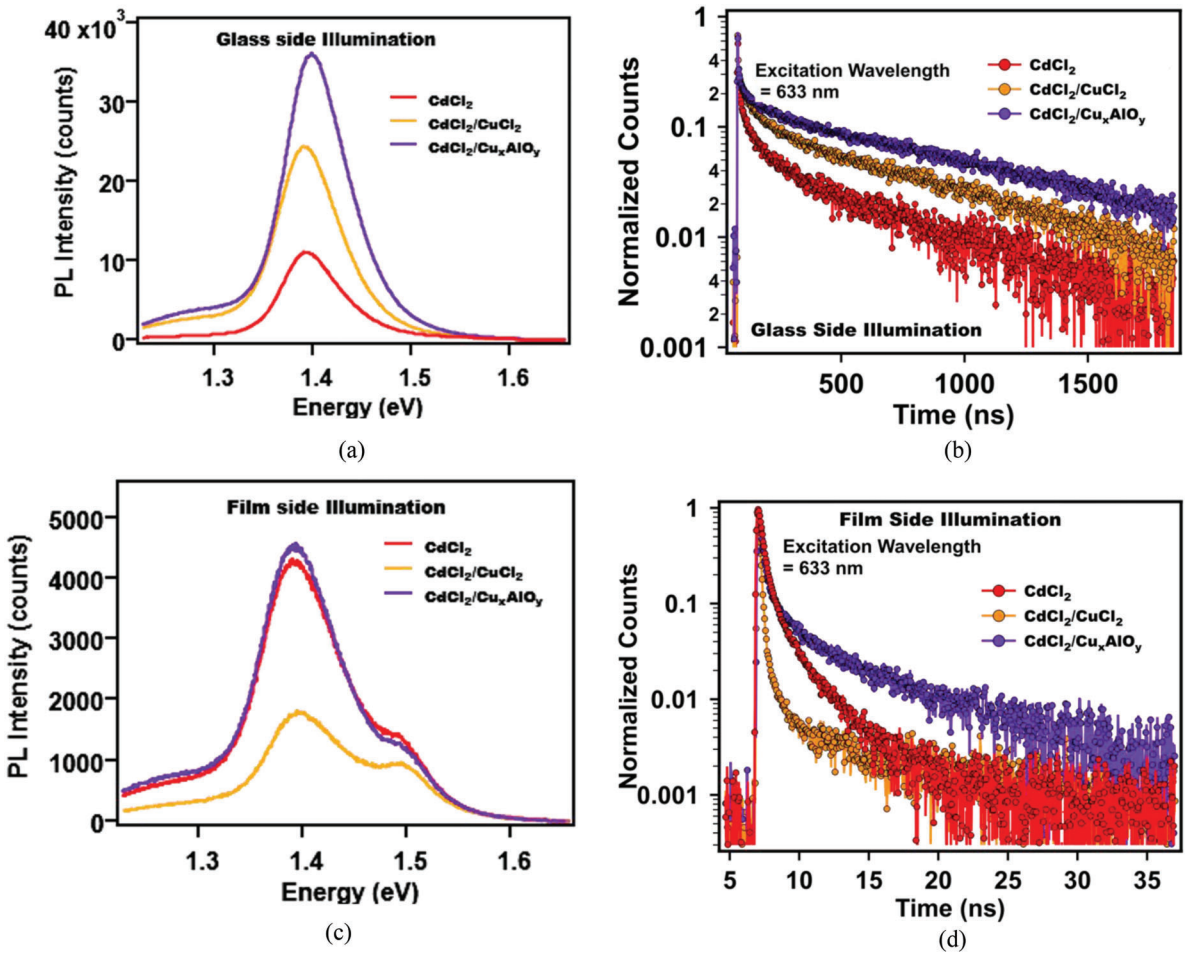


Fig. 3. PL emission spectra and decay curves recorded from PL and TRPL measurements. (a) PL excited through glass side. (b) TRPL excited through glass side. (c) PL excited through film side. (d) TRPL excited through film side.

where τ_B is the bulk Shockley-Reed Hall recombination lifetime, $\tau_{\rm rad}$ is the radiative lifetime, and $\tau_{\rm front}$ and $\tau_{\rm back}$ are the front and back interface recombination lifetimes, respectively. We assume that in both devices the front and bulk properties remain identical while only the back interface is modified with the addition of the buffer layer. Hence, based on this assumption, the difference in effective surface recombination velocity between the reference $CuCl_2$ treated ($S_{\rm back,Ref}$) device and the samples with Cu_xAlO_y ($S_{\rm back,\ CuxAlOy}$) can be related to the carrier lifetimes at the different interfaces as shown in

$$(S_{\rm back,Ref} - S_{\rm back,CuxAlOy}) = d * \left(\frac{1}{\tau 2,\,{\rm Ref}} - \frac{1}{\tau 2,\,{\rm Cu_xAlO_y}}\right) \quad (3)$$

where d is thickness of CdTe. Using the values of $\tau_{2\ \rm Ref}$ and $\tau_{2\ \rm CuxAlOy}$ from Table I the quantity on the righthand side of the equation can be evaluated to be 165 cm/s. Taking the value of $S_{\rm back,Ref}$ from literature for unpassivated CdTe (1000 cm/s) [7], it follows that the value for $S_{\rm back,\ Cu_xAlO_y}$ is 835 cm/s. However, it should be mentioned that any possible change in band bending is not taken into account in this discussion [21]. Further, the carrier lifetime value used for the reference device in our analysis is 501.4 ns, while the value used in [7] was 181 ns [7].

To further investigate how the back-buffer layer affects the device performance, *J–V* and EQE measurements were conducted. Fig. 4 shows the *J–V* graphs and the EQE measured at short circuit for each of the champion cells. Fig. 5 shows the box plots of PV parameters averaged for the ten best performing devices. PV parameters of the champion cell with Cu_xAlO_y are $V_{\rm oc}$ of 859 mV, $J_{\rm sc}$ 26.7 mAcm^{-2}, FF 75.6% and efficiency 17.4%. For the best reference device with Cu doping the PV parameters are $V_{\rm oc}$ 839 mV, $J_{\rm sc}$ 27.9 mAcm^{-2}, FF 70.6% and efficiency 16.5%.

In terms of average performance, there is a gain of 12 mV in $V_{\rm oc}$, which is consistent with the 10 mV value estimated from analysis of the increase in the PL emission band intensity. Additionally, the average FF improved by 3% points, and the overall efficiency improved by an absolute amount of 0.7%.

The EQE shows a relatively flat response across the entire wavelength range. The short wavelength response of the device

Approved for public release; distribution unlimited.
619

This article has been accepted for inclusion in a future issue of this journal. Content is final as presented, with the exception of pagination.

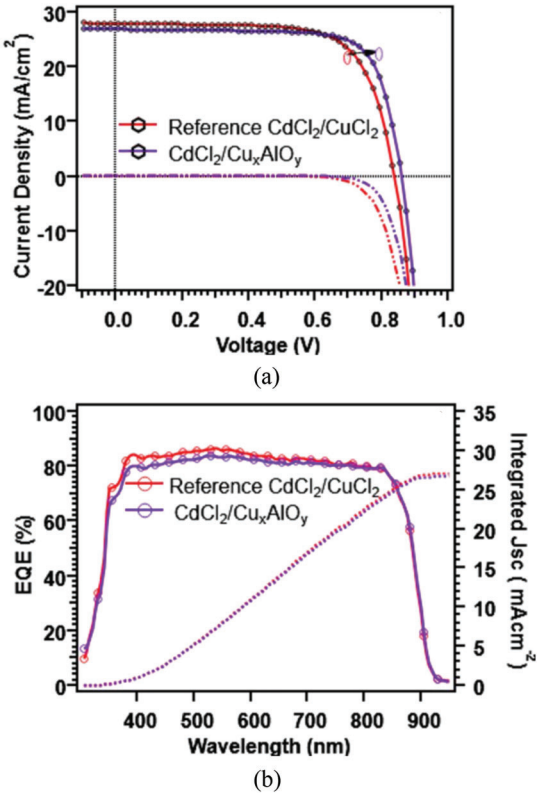


Fig. 4. (a) *J–V* characteristics of champion cells. (b) EQE plots and integrated current density curves.

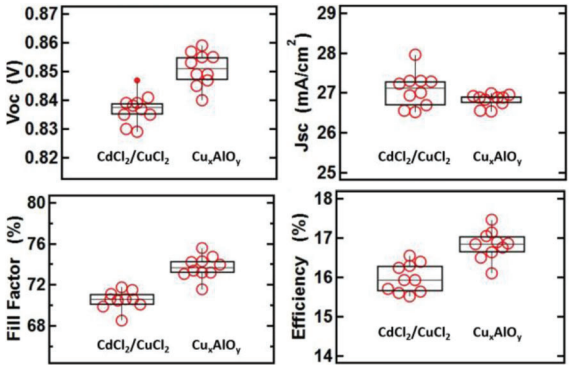


Fig. 5. Box plots of *J–V* parameters averaged for ten best cells.

with Cu_xAlO_y is slightly lower than the reference device. This suggests either that the doping near the front of the device may be slightly different, or that the addition of the buffer layer alters the optical properties of the entire stack resulting in slight increase in the reflection at the shorter wavelengths. Surprisingly, the long wavelength response is not enhanced, as expected for better collection of carriers generated more deep in the device. These issues and other aspects of the device performance with the Cu_xAlO_y passivation layer will be the subject of future studies.

IV. Conclusion

In this article, we studied that back-surface passivation with a solution processed back buffer Cu_xAlO_y on CdSe/CdTe devices. Noticeably increased PL intensity, carrier lifetime >650 ns, and increased V_{oc} indicate that the Cu_xAlO_y buffer reduces recombination at the back interface. Further, the role of Cu diffusion is distinct from that of the devices where Cu is intentionally applied at the back. Further characterization of the device stacks with back-buffer layer are needed to determine the critical Cu diffusion, electronic process at the interface and bulk, and to better understand the passivation mechanisms.

Acknowledgment

The U.S. Government is authorized to reproduce and distribute reprints for Governmental purposes not withstanding any copyright notation thereon. The authors thank Derk Rading of INTOF GmbH for TOF SIMS data.

References

[1] N. R. Paudel and Y. Yan, "Enhancing the photo-currents of cdte thin-film solar cells in both short and long wavelength regions," *Appl. Phys. Lett.*, vol. 105, no. 18, 2014, Art. no. 183510.

[2] D. Kuciauskas *et al.*, "Microsecond carrier lifetimes in polycrystalline CdSeTe heterostructures and in CdSeTe thin film solar cells," in *Proc. 47th IEEE Photovolt. Specialists Conf.*, Jun.–Aug. 2020, pp. 82–84.

[3] A. H. Munshi *et al.*, "Polycrystalline CdSeTe/CdTe absorber cells with 28 mA/cm^2 short-circuit current," *IEEE J. Photovolt.*, vol. 8, no. 1, pp. 310–314, Jan. 2018.

[4] R. M. Geisthardt, M. Topic, and J. R. Sites, "Status and potential of CdTe solar-cell efficiency," *IEEE J. Photovolt.*, vol. 5, no. 4, pp. 1217–1221, Apr. 2015.

[5] M. Green *et al.*, "Solar cell efficiency tables (version 57)," *Prog. Photovolt., Res. Appl.*, vol. 29, no. 1, pp. 3–15, 2020.

[6] A. Kanevce, M. O. Reese, T. M. Barnes, S. A. Jensen, and W. K. Metzger, "The roles of carrier concentration and interface, bulk, and grain-boundary recombination for 25% efficient CdTe solar cells," *J. Appl. Phys.*, vol. 121, no. 21, 2017, Art. no. 214506.

[7] D. Kuciauskas, J. Moseley, and C. Lee, "Identification of recombination losses in CdSe/ CdTe solar cells from spectroscopic and microscopic time-resolved photoluminescence," *Sol. RRL*, vol. 5, no. 4, 2021, Art. no. 2000775.

[8] G. K. Liyanage, A. B. Phillips, F. K. Alfadhili, R. J. Ellingson, and M. J. Heben, "The role of back buffer layers and absorber properties for >25% efficient CdTe solar cells," *ACS Appl. Energy Mater.*, vol. 2, no. 8, pp. 5419–5426, 2019.

[9] T. Ablekim *et al.*, "Exceeding 200-ns lifetimes in polycrystalline CdTe solar cells," *Sol. RRL*, vol. 5, 2021, Art. no. 2100173.

[10] F. K. Alfadhili *et al.*, "Controlling band alignment at the back interface of cadmium telluride solar cells using ZnTe and Te buffer layers," *MRS Adv.*, vol. 4, no. 16, pp. 913–919, 2019.

[11] F. K. Alfadhili *et al.*, "Potential of CdZnTe thin film back buffer layer for CdTe solar cells," in *Proc. IEEE 46th Photovolt. Specialists Conf.*, Jun. 2019, pp. 140–143.

[12] D. Pokhrel, E. Bastola, A. B. Phillips, M. J. Heben, and R. J. Ellingson, "Aspect ratio controlled synthesis of tellurium nanowires for photovoltaic applications," *Mater. Adv.*, vol. 1, no. 8, pp. 2721–2728, 2020.

[13] S. S. Bista *et al.*, "ZnTe back buffer layer to enhance the efficiency of CdS/ CdTe solar cells," in *Proc. IEEE 46th Photovolt. Specialists Conf.*, Jun. 2019, pp. 0499–0502.

[14] J. M. Kephart *et al.*, "Sputter-deposited oxides for interface passivation of CdTe photovoltaics," *IEEE J. Photovolt.*, vol. 8, no. 2, pp. 587–593, Feb. 2018.

[15] F. Werner *et al.*, "Oxidation as key mechanism for efficient interface passivation in Cu(In,Ga)Se_2 thin-film solar cells," *Phys. Rev. Appl.*, vol. 13, no. 5, 2020, Art. no. 054004.

[16] C. L. Perkins *et al.*, "Interfaces between CdTe and ALD Al_2O_3," *IEEE J. Photovolt.*, vol. 8, no. 6, pp. 1858–1861, Jun. 2018.

Approved for public release; distribution unlimited.

This article has been accepted for inclusion in a future issue of this journal. Content is final as presented, with the exception of pagination.

[17] B. Hoex, S. B. S. Heil, E. Langereis, M. C. M. van de Sanden, and W. M. M. Kessels, "Ultralow surface recombination of c-Si substrates passivated by plasma-assisted atomic layer deposited Al_2O_3," *Appl. Phys. Lett.*, vol. 89, no. 4, 2006, Art. no. 042112.

[18] A. H. Munshi, A. H. Danielson, A. Kindvall, K. Barth, and W. Sampath, "Investigation of sputtered oxides and p+ Back-contact for polycrystalline CdTe and CdSeTe photovoltaics," in *Proc. IEEE 7th World Conf. Photovolt. Energy Convers., 45th IEEE Photovolt. Specialists Conf., 28th Proc. Eur. Photovolt. Solar Energy Conf. Exhib., 34th Proc. Eur. Photovolt. Solar Energy Conf. Exhib.*, Jun. 2018, pp. 3009–3012.

[19] F. K. Alfadhili *et al.*, "Back-Surface passivation of CdTe solar cells using solution-processed oxidized aluminum," *ACS Appl. Mater. Interfaces*, vol. 12, no. 46, pp. 51337–51343, 2020.

[20] D. Kuciauskas, J. Moseley, P. Ščajev, and D. Albin, "Radiative efficiency and charge-carrier lifetimes and diffusion length in polycrystalline CdSeTe heterostructures," *Physica Status Solidi Rapid Res. Lett.*, vol. 14, no. 3, 2019, Art. no. 1900606.

[21] K. K. Subedi *et al.*, "Enabling bifacial thin film devices by developing a back surface field using Cu_xAlO_y," *Nano Energy*, vol. 83, 2021, Art. no. 105827.

[22] T. Song, A. Kanevce, and J. R. Sites, "Emitter/absorber interface of CdTe solar cells," *J. Appl. Phys.*, vol. 119, no. 23, 2016, Art. no. 233104.

[23] T. A. M. Fiducia *et al.*, "Understanding the role of selenium in defect passivation for highly efficient selenium-alloyed cadmium telluride solar cells," *Nat. Energy*, vol. 4, no. 6, pp. 504–511, 2019.

[24] E. Bastola *et al.*, "Open-circuit voltage exceeding 840 mV for all-sputtered CdS/ CdTe devices," in *Proc. 47th IEEE Photovolt. Specialists Conf.*, Jun.–Aug. 2020, pp. 2513–2518.

[25] D. Kuciauskas, J. Moseley, P. Ščajev, and D. Albin, "Radiative efficiency and charge-carrier lifetimes and diffusion length in polycrystalline CdSeTe heterostructures," *Physica Status Solidi Rapid Res. Lett.*, vol. 14, no. 3, 2020, Art. no. 1900606.

[26] U. Rau, B. Blank, T. C. M. Müller, and T. Kirchartz, "Efficiency potential of photovoltaic materials and devices unveiled by detailed-balance analysis," *Phys. Rev. Appl.*, vol. 7, no. 4, 2017, Art. no. 044016.

[27] A. B. Phillips *et al.*, "Understanding and advancing bifacial thin film solar cells," *ACS Appl. Energy Mater.*, vol. 3, no. 7, pp. 6072–6078, 2020.

[28] X. Zheng *et al.*, "Recombination and bandgap engineering in CdSeTe/ CdTe solar cells," *APL Mater.*, vol. 7, no. 7, 2019, Art. no. 071112.

Approved for public release; distribution unlimited.

621

Solar Energy Materials & Solar Cells 235 (2022) 111451

Degtrgtlsoiltls b io Hors tsPhirghrSiarhts

Peo as. graFmsE trai ds gnsPeo asDrodls

journal homepage: www.elsevier.com/locate/solmat

Deccrasieninrsg gec atihorls ls suecrsta glceatso mrastesDnf rscuetebect ihlds wzwsp sr:RhirgtsH hAjioo, Z ig trnsHi: hi osDnf rsleo ashrodls

Sicrgna sJeAuards. HigsW lteo IsB Z osBu g osP, HrniIsP, Z gs* iC dsE geGBzsk Z aA ttrds
* lu sMzsMTgiIsMn Z sWzsJuiooiclIsI g: sI gIsE ihu roskzsNrHrgIs* gnmskzs. ooigFleg Os

Wright Center for Photovoltaics Innovation and Commercialization, Department of Physics and Astronomy, Uhe Tniversity of Uoledo, 28, 01. B., TSA

M* f VD(. sV) v - ss

OeyHords4
D nZ i, Z stroo, ainrs
WhAshegt hts
Neorsta glceatso mras
W: hi os
DeccrasieninrsfD, Vys

M WP f * MD f ss

x rsarceatstursaeorse:sheccrasieninrsfD, Vysg gec atihorlsfi) Jlys ls suecrsta glceatso mrasfNf(ysigsh nZ i, Z sl, oRnr[s h nZ i, Z stroo, ainrsfDnP[Dnf ryscuetebect ihlzsfurlrsD, Vs) JlsTrarscarc arns, ligFsleo, tiegscaehrlligFs tsaeeZ s trZ cra t, ars gns, lrnstes: Haih trsZ ege: hi os gnsHi: hi osDnf rsleo ashrodsTitusni::rargtsH hAshegt htlzs1 ligFs D, V[M, s lstursH hAshegt htIstursnrbihrsr:Rhirghmsar hurnstes2]z-p sTituse, tlt gnigFsRoos: hteasfivvyse:s34z6p zs *rco higFsturs Feonsf M, ysrorhtaenrsTituslc, ttrarnsta glc argtsigni, Z stigse7inrsfM - yls sD, V[Vf - sH hAshegt hts mironrnscuetehegbraliegsr:Rhirghirlsfi D. lyse:s22zqp s gnswzwp s, gnras:aegts gnsH hAsioo, Z ig tiegsarlcrhtibroms Wi: hi osnrbihrlsfDnf r[Vf - ysTitue, tstursD, Vs) JsNf(su brs gsr:Rhirghmse:s3z5p s gns2z5p s:eas:aegts gnsH hAs ioo, Z ig tiegIsarlcrhtibroms veasD, V[Vf - Is sh, aargtsheorhtiegse:s26z5sZ MhZ $^{-6s}$T lseHirabrns, cegsH hAsioo, Z ij g tiegsTuihusliFgiRh gtonsiZ caebrnsebras gsVf - jegomsH hAshegt htsfiwz5sZ MhZ $^{-6}$yzsfursJD. seHt igrns:aeZ sH hAs ioo, Z ig tiegsT lsrgu ghrnsTurgs, ligFsD, Vs) Jls lstursNf(sn, rstestursarn, hrnsH hAsH aairasuriFutIs gnsiZ caebrns H hAsigtra: hrs lsnrtraZ igrnsHnstrZ cra t, arsnrcrgnrgtsh, aargtsblzsbect Frshu a htrailtihls gnsiZ crn ghrs lcrhtaelhecms g omlilzsfursiZ caebrZ rgtsigsnrbihrscra:eaZ ghrse:stursHi: hi oshegRF, a tiegsils sliFgiRh gtsltrcs :eaT ansteT ansar ci@gFstuigsRoZ scuetebect ihsZ en, orlsTuihusu abrltsrgraFmsighinrgtsegstursar ase:sturs Z en, orzsss

1. Introduction

D nZ i, Z stroo, ainrsfDnf ryls gs tta htibrs HleaHraso mrasZ trai os:eas leo ashrodsTitusniarhtsH gnsF cse:s2z]wsr/s gnsbiliHorsciFuts Hleactiegs her:Rhirgts>25^{ws}hZ $^{-2}$$_{ls}$ils sTrojAgeTgstrhugeoeFms:eas: Haih tiegse:s uiFuonsr:Rhirgtsleo ashrodsO28zsfurs:aegts gns H hAsigtra: hrlsZ, lts cra:eaZ sTroostesrg Hors: Haih tiegse:suiFuonsr:RhirgtsZ ege: hi os gns Hi: hi osnrbihrlzsNeTrbrals: Haih tiegse:s gseuZ ihsH hAshegt hts:eas r7ta htiegse:sueorls tsturs H hAsigtra: hrse:shegbrgtieg oscjtmcrsDnf rs nrbihrlsilshu orgFigFsn, rstesDnf r'lsuiFusrorhtaegs :Rgitms gnso hAse:s l, it Horsrorhtaenrs Z trai os Titusnrrcs TeaAs, ghtiegsO68zsVZ corZ rgtigFs s H hAsH, ::raso mrasHrtTrrgsDnf rs gns sZ rt osrorhtaenrshe Z Z egomsiZ j caebrlscra:eaZ ghrsebras gnsniarhtjegjDnf rsrorhtaenrs0, 8zsW hAsigtraj : hrs arheZ Hig tiegs oellrls h gs Hrs arn, hrns tuae, Fus ectiZ os H gns diFgZ rgtIstesarcrosrorhtaeglIs gn[easTitusigtra: hrsc llib tiegse:snrj :rhtlsTuihus hts lsarheZ Hig tiegslitrlzsVgs nnitiegIsturse, tc, tsceTrase:s s cuetebect ihsfiJ/ysnrbihrsh gsHrsrgu ghrnsHms: Haih tigFsHi: hi os aj huitrht, arlsTuihus des, tici@stursoiFutsighinrgtsegstursH hAse:stursnrbihrzs NeTrbraIsHi: hi osleo ashrodsar9, iarstu ts ose:stursZ trai ds, lrns ls s uecrsta glceatso mrasfNf(Is desAgeTgs ls sH hAsH, ::rayseas ls shegt hts rorhtaenrsfI, hus lsigni, Z stigse7inrIsVf - ysr7uiHitsuiFusta glc arghms:eas oiFutsTituscuetegsrgraFirlsFar trastu gstursDnf rsH gnF csrgraFms

Wi: hi osJ/snrbihrsnrliFgls arsheZ Z egs:eashamlt ooigrslidhegsleo as hrodsH, tstuigjRoZ sHi: hi osnrbihrlsH lrnseglsrZ zlsDnf rIs arsoiZ itrns0] Lv8zs veas turs nrbroeZ rgtse:s uiFusr:Rhirghmsi Hi: hi os J/s hrodIs ectih oms ta glc argtscjtmcrsZ trai dsTitusH gnsrnFrsrgraFirls oiFgrnstesDnf rs arsnrliarns0q8zsfiT aisrts os, lrnsVf - s ls sta glc argtsH hAshegt htso mras tesDnf rsleo ashrods gnsarceatrns:aegts gnsar asr:Rhirghirlse:s3z4p s gns 2z5p sarlcrhtibroms038zs* eZ resrts osarceatrns:aegts gnsar asr:Rhirghirls e:s-z5p s gns, z6p Is:eas sDnf rso mrastuihAgrllse:s2z5sµZ IsTurgsiglratigFs s tuigshecraso mrasHrtTrrgstursDnf rs gnstursVf - sH hAsrorhtaenrs0-8zs 11, omls stuigs HleaHraso mrasilscar:raarns:easheorhtigFsc ueteglsighinrgts :aeZ stursH hAsl, a: hrIs otue, Fus:aegtjioo, Z ig trnsr:Rhirghmsnaecls:eas Dnf rs HleaHraso mralsHroeTsG2sµZ zsfursH hAjioo, Z ig tiegsnrbihrsr:Rj hirghmsilsoeTsheZ c arnstes:aegtsioo, Z ig tiegsn, rstesigr:Rhirgtsh, aargts heorhtiegsfi3$_{SC}$yslighrsrorhtaegjuecrsc ials arsFrgra trns: as:aeZ sturs

O Deaarlcegnig Fs, tueazs
6Hmail address4 * gnmz. ooigFlegU, tecrnezrn, sff*zkzs. ooigFlegyzss

uttclc[neizeaF[25z252q[GzlecZ tz6562z222]w2s
rhribrns23sk, grs6562X rhribrnsigsarbilrns:eaZ s2qs- hteHras6562XMhhrctrns2-s- hteHras6562sss
Available online 3 November 2021
0927-0248/© 2021 Elsevier B.V. All rights reserved.

Approved for public release; distribution unlimited.

2. TheyriF yntg3Ryction

klub Chemicals

klkb Synthesis of C5I nanoparticles

kbl0 Device faKrication

kb0b Characterization

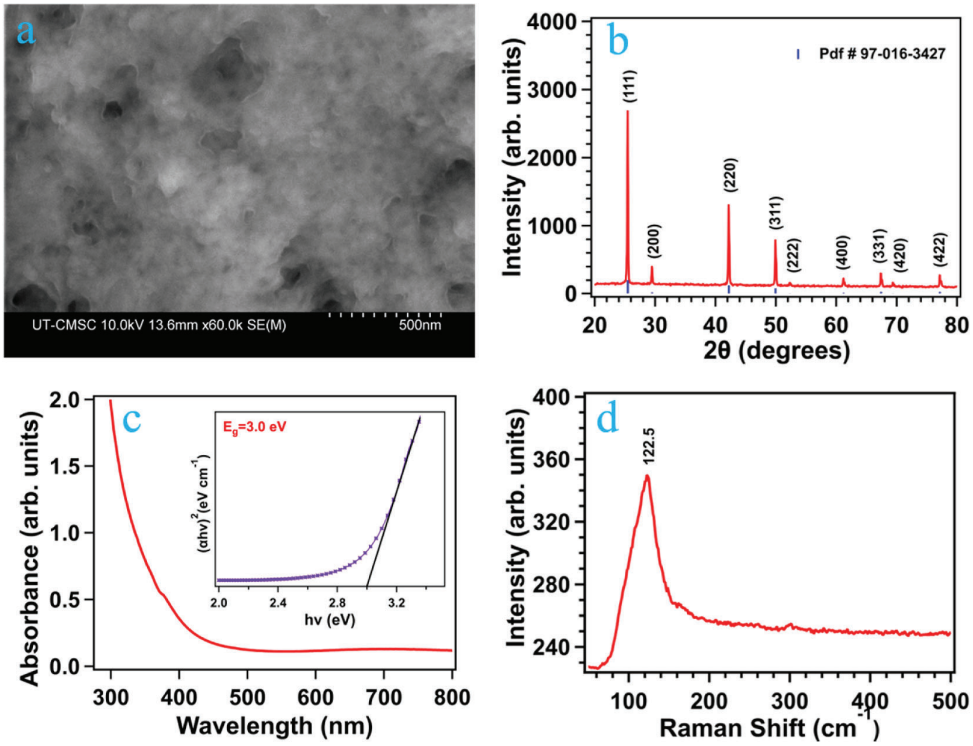
Approved for public release; distribution unlimited.
623

s. l yRu3tRgnd diRcuRRion

viFzs 2s nilco nls turs hu a htrailtihls e:s turs lngturli@ns D, Vs) Jls igho, nigFs l, a: hrs Z eacueœFmIsYja nsni::a htiegsc ttrags gnsectih os caecratirlzsf ursP. E siZ Frsigs viFzs2fi ysIueTlsZ eacueœFms gnsg gej lta, ht, arse:sD, Vs) JlzsvaeZ sP. E siZ FrIsTrsh gslrrstu tsturslu crse:s ignibin, os) Jlsilslcuraih ostue, Fusturlrs) Jls FFœZra trsteFrturas gns :eaZ s sFa g, o aslta, ht, arzsf ursY* Ssc ttragsigs viFzs2fHysarbr dsturs :eaZ tiegse:s/jD, VsTitusottihrsheglt gtlsu = $K = c$ = 5zq5w2qsgZ sigs@ghs Horgnrslta, ht, arsZ thuigFsturs ni::a htiegsc ttraglsTitusJS vsQs43j52qjs ;]63sfE S VskMS . yzsf urshamlt ooitrsli@se:stursD, Vs) JlsT lsrltiZ trns :aeZ sturs ni::a hteFa Z Is, ligFsturs SrHnrjPhuraarasr9, tiegsFibrgsHms $D_p = \frac{O\lambda}{\beta cos\theta}$ TurarsDp ilsturshamlt ooitrsli@IsfO = 5z4ysilsturslu crs: htealsfi = 5z2w] 5qsgZ ysilstursT brorgFtuse:sturs7ja mls/β ilsturs:, osTintus tsu os Z 7iZ , Z sfivx NE ys gnsθ ilsturs Wa FF'lsni::a htiegs gFors06q8zsf urs hamlt ooitrsli@sT lsrltiZ trnsH lrnsegstursni::a htiegscr Als tsf222yls f665yls gnsfi 22ys, ligFs- aiFigJaesle:tT arzsf urs bra Frshamlt ooitrsli@s e:sD, Vs) JlsilsG ; 3s± qsgZ zs viFzs2fhysIueTlsturs1 /–bils Hleactiegs lcrhta, Z se:sD, Vs) Jlsigsleq, tiegscarc arnsigsS E vsarheanrnsigs sh, brttrse:s 2sZ Z sc tuorgFtus Titusledbrgtsheaarhtiegzs W lrnsegsturs Hleactiegs lcrhta, Z Isturs rgraFmsH gnsF csT lsrltiZ trnstesHrs, z5sr/Isigs FarrZ rgts Titusarl, otlsarceatrnscarbie, lons06; I63I6~8zsviFzs2finysIueTlsturs* Z gs lcrhta, Z se:sD, Vs) JlseHt igrns, ligFsq; 6z~sgZ sNr–) rso lrasle, ahrzsf urs ta glbralrsectihsff - ysbiHa tiegsZ enrse:sD, Vs) JlsilseHt igrns ts266zws hZ $^{-2s}$Tuihus Farrlshoelrons Titus scarbie, lsarceats06~8zs

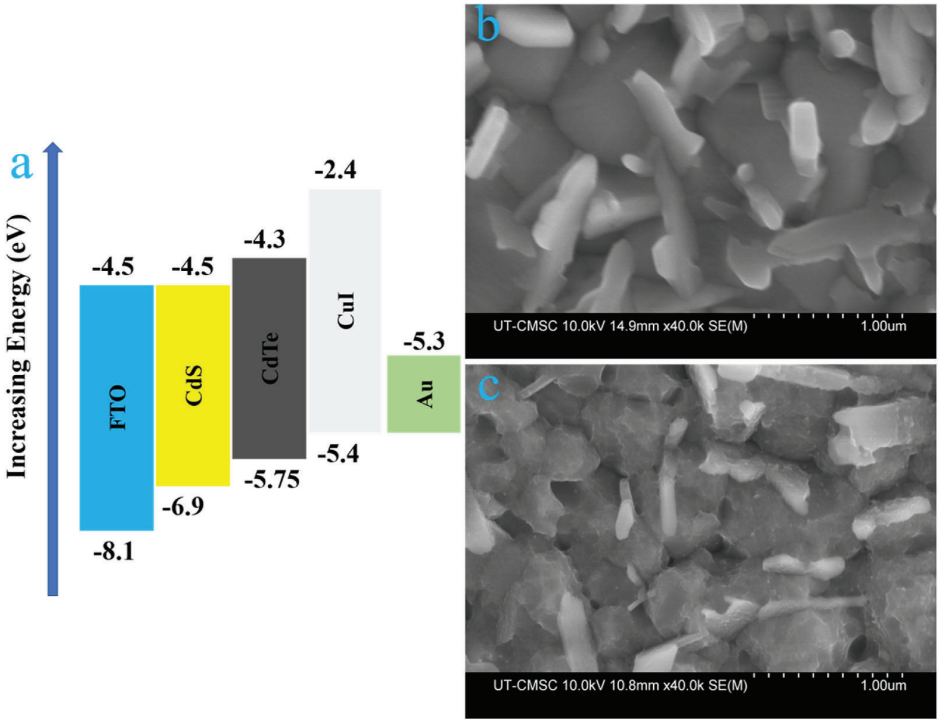
D, VstuigsRoZ lsu brsh aairasheghrgta tiegsigsturseanrase:s25^{2-s}hZ $^{-;s}$ u bigFs sb orghrsH gns ts–wz]sr/sTitusarlcrhtstesb h, , Z s02~I248zsf urs b orghrsH gnsrnFrse:sD, Vsilsbramshoelrstestu tse:sDnf rsl, FFrltigFsitls l, it Hicitms:easueorsr7ta htiegs tstursDnf rsH hAshegt htzsviFzs6fiysIueTls turs gegjigtra htigFsH gnsni Fa Z se:sDnP[Dnf rsleo ashrodsTitusD, Vs ls gs Nf (zsWlrnsegsturscitra t, arIsturarsr7iltls sbramslZ oosb orghrsH gns e::lrtsffl 5z5~sr/ysHrtTrrgsDnf rs gnsD, VstuigsRoZ scarc arnsHnsturaZ os rb cea tiegsZ rtuens06; 8zsviFzs6fHys gnsfhyslueTstursP. E siZ Frlse:s DnDo$_{6s}$tar trnsDnf rsnrbihrlsTitue, ts gnsTitusD, Vs) Jlsegstecse:sDnf rs l, a: hrsarlcrhtibroms fursP. E siZ Frsigs viFzs6fhysIueTlsturs:r t, arls ni::rargts:aeZ sH arsDnf rsl, a: hrsn, rstesturlrsD, Vs) Jlzs

viFzs; snilco nlsturslt tiltih osniltaiH, tiegse:snrbihrsc a Z rtralse:s DnP[Dnf rsleo ashrodsTitus gnsTitue, tsD, Vs) JlzsVgse, aso Hea teamls D, Do$_6$[M, silse:trgs, lrns ls shegtaeos H hAshegt htzsNrarlsTrs u brs heZ cortrnsDnf rsnrbihrlsTitusb aie, lshegt htldsM, segonlsD, Do$_6$[M, Is gns D, V[M, zsf ursnrbihrlsniccrnsigsD, Do$_{6s}$Trars ggr orns ts655s°Dseas65sZ igs 06w8sTuiorsnrbihrlsTitusD, Vs) JlsfieZ ittigFsD, Do$_6$ysTrars ggr orns ts 655s°Ds:eas5IswIs25s gns2wsZ igzsf urs3Hw h, abrlIsturiasheaarlcegnigFs . ü . lIs gnsnrbihrsc a Z rtralse:stursHrltshrodse:sr husH hAshegt htstmrrs arscarlrgtrnsigsviFzsP2s gnsf HrsP2zsf urshegtaeosnrbihrs, ligFsD, Do$_6$[M, s lueTlsJD. se:s2]z5p sliZ io astese, ascarbie, lsarl, otlsO, 5I; 28IsTurar lsturs nrbihrsTitusD, Vs) Jlsfi, g ggr ornyslueTls sliZ io asJD. se:s2]z2p zs v, aturalsTrslt, nirnsturs r::rhtse:sur tstar tZ rgtsegsturlrsnrbihrls :tras tursnrcelitiegse:sturs D, Vs) Jlso mrazsx itue, ts gnsceltjD, Vs ggr cigFIsturs vvse:stursHrltsnrbihrsT ls3qz5p IsTurar ls :tras ggr cigFs:easwsZ igs ts 655s°DIsvvsighar lrnstes34z6pzs- gs:, aturas ggr cigFIsvvslt atlstes nrhar lrsfB3zwp s:eas25sZ igIs gns3wz4p s:eas2wsZ igyzsMlsTrslrrs:aeZ s viFzs, fiyIsturarsilsgesliFgiRh gtsni::rarghrsigsw_{2C} e:sturs nrbihrs ggr orns :easwsZ igs lsheZ c arnstesaeeZ strZ cra t, arzsNeTrbralsw$_{2C}$ighar lrls, cs tes25sZ igs ggr cigFIs gnsnrhar lrls F igs:eas2wsZ igzsf ursighar lrsigsw$_{2C}$ gnsvvs :tras ggr cigFsils ttaiH, trnstesni::, liegse:shecc ras:aeZ stursD, Vs) JlsigtestursDnf rzsf ursuiFurltsJD. seHlrabrnsT ls2]z-p s:easwsZ igs ggr cigFstiZ rzs f urs nrbihrs cra:eaZ ghrs e:s gr aons2wz5p sils 9, itrs iZ carllibrs:easDnf rsnrbihrlsTuihusigho, nrsturs DnPs miron ls soeTras3$_{SC}$ ffl 66z5s Z MhZ $^{-6}$ys lsheZ c arnsteseturasTigneTso mralsffl 64z5sZ MhZ $^{-6}$ysl, hus ls DnPd-IsDnPrseasZ Fgrli, Z s@ghse7inrsfE ~ ys0, 6L; ; 8zsx rs cles, lrns ltr nmslt trsJ(s gnsf *J(sZ r l, arZ rgtlsfiviFzsP6ystes g om@stursDnf rs

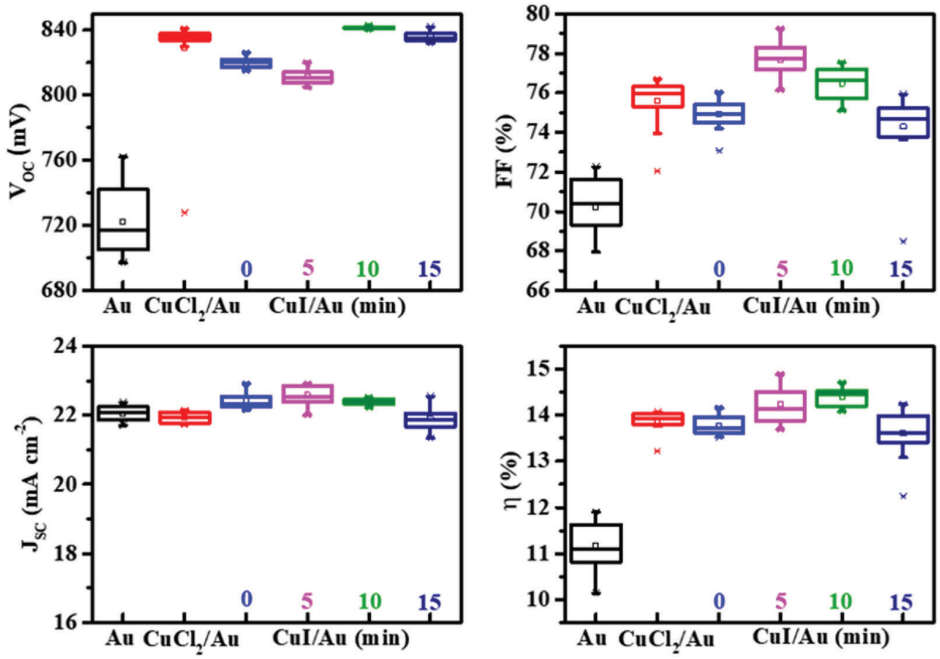


ai4. 1. fi ysP. E siZ Frse:sD, Vs) JlsfHysY* Ssc ttragse:sD, Vs) Jlsegslen sdiZ rsFo llIsturs bratih osHo, rsheoeasdigrlsheaarlcegnstesJS vsQs43j52qj;]63sfE S VskMS . ysfhys 1 /–bils Hleactiegslcrhta, Z se:sD, Vs) Jlsleq, tiegscarc arnsigsS E vXtursiglrtsIueTlsturscetih osH gnsF cIsfnys* Z gslcrhtaelhecmsZ r l, arZ rgtse:sD, Vs) Jls, ligFs q; 6z~sgZ sr7hit tiegse:sNr–) rso lrazsfiveasigtracart tiegse:stursar:rarghrlstesheoeasigstuilsRF, arsorFrgnIsturs ar nrasilsar:raarnstestursx rHsbraliegse:stuils atihorzys

Approved for public release; distribution unlimited.



ai4. 2. fi ys) egjigtra htigFsH gnsni Fa Z seas stmcih osDnf rsnrbihrsΓitusIta, ht, arsvf - [DnP[Dnf r[D, V[M, sIueTigFsturscelitiegse:sb orghrsH gns gnshegn, htiegsH gns rnFrlsΓitusarlcrhtstestursb h, , Z scrbros0wI648zsP. E siZ Frlse:sDnf rsnrbihrlsfHysΓitue, ts gnsfhysΓitusD, Vs) JlsegsDnf rsl, a: hrzs

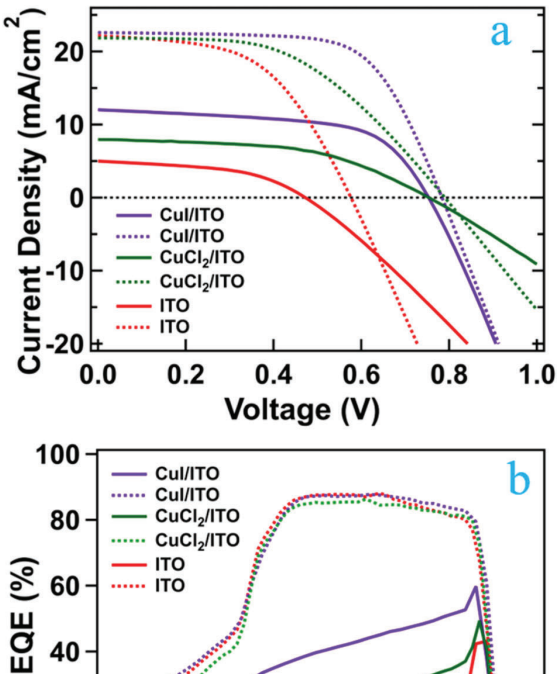


ai4. s. Pt tiltih osniltaiH, tiegse:sleo ashrodlsc a Z rtralsfiw_{2C}Is3$_{SC}$IsvvIs gnsɳysaeZ s2wshrodlse:stursDnf rsnrbihrlsΓitusM, segomlsD, Do$_6$[M, sfhegtaeornsnrbihrys gnsD, V[M, s H hAshegt htlsarlcrhtibromzsfursD, V[M, sH hAshegt htlsTrars ggr orns ts655s°Ds:eas5Iswls25s gns2wsZ igsarlcrhtibromzs

Approved for public release; distribution unlimited.
625

nrbihrlsTitus gnsTitue, tsD, Vs) Jls tstursH hAzsx itustursigtaen, htiegse:s tursD, Vs lstursNf (IstursJ(sigtrglitms:aeZ sHetus:aegts gnsH hAslinrsio, j Z ig tiegs Trarsnrhar lrnzsx urgsheZ c arns Titus turshegtaeosnrbihrs TuihuseZitlstursD, Vs) JsRdZ Isturs Z igeaitmsh aairasci:rtiZ rsnrhar lrls :aeZ s26zwsglstes~z5sglseasaegtsio, Z ig tiegIs gns:aeZ s5z~sglstes5zqsglseas H hAsio, Z ig tiegzsf ursnrhar lrsigsJ(s gnsZ igeaitmsh aairasci:rtiZ rsils hegliltrgtsTitustursinr stu tsD, Vs llitlsTitusr:Rhirgtshu aFrsh aairas lrc a tiegsigsitls:, ghtiegs ls gsNf (zs

v, aturaZ earIs lsD, Vsils sta glc argtslrZ ihegn, hteaIsTrsr7trgnrnse, as TeaAstes sHi: hi oshegRF, a tiegsTitusVf - s ls sta glc argtsH hAsrorhtaenrs gns g om@nsnrbihrscra:eaZ ghrlzsviFzsP; slueTlstursgegjigtra htigFs H gnsni Fa Z se:sHi: hi osDnP[Dnf rsleo ashrodlsTitus snrbihrslta, ht, ars Kol l[vf - [DnP[Dnf r[D, V[Vf - zsx rsheZ c arnse, asarl, otlstesVf - sH hAs rorhtaenrsniarhtomsegsDnf rsfiTitusgesD, snecigFsltrcyls gnstesD, Do$_b$[Vf - zs viFzs]fi s gnsHlysIueTls3*Fw* hu a htrailtihls gns. ü. lse:stursHrltshrose:sVf - s egomsD, Do$_b$[Vf - s gnsD, V[Vf - snrbihrlsTitus:aegts gnsH hAsio, Z ig tiegzs fursleoinsoigrlsheaarlcegnstesH hAsio, Z ig tiegs gnsnettrnsoigrlsheaarj lcegnstes:aegtsio, Z ig tiegsarlcrhtibromsfursVf - jegomsnrbihrsu lsJD. se:s 2z2p sTitus3$_{SC}$ e:swzwsZ MhZ $^{-6s}$:easH hAsio, Z ig tiegsTuiorseasD, Do$_b$[Vf - s nrbihrsr:Rhirghmsils; z5p sTitus3$_{SC}$ e:s3z4sZ MhZ $^{-6}$zfursw$_{2C}$ T lsIfGiRj h gtomsiZ caebrns:easD, Do$_{bs}$tar trnsnrbihrlsTitusVf - sH hAshegt hts:eas Hetus:aegts gnsH hAsio, Z ig tieglzsx itusiZ corZ rgtigFsD, Vs) JlsigsHrj tTrrgsDnf rso mras gnsVf - srorhtaenrIsJD. se:swzwp sT lseHlrabrnsTitus3$_{SC}$ 26z5sZ MhZ $^{-6s}$:easH hAsio, Z ig tiegs gns22zqp s:eas:aegtsio, Z ig tiegzs fursnrbihrsc a Z rtralseasturshrltshrolse:sVf - IsD, Do$_b$[Vf - Is gnsD, V[Vf - s H hAshegt htlsTitus:aegts gnsH hAsio, Z ig tiegls arscarlrgtrnsigsf Hors2zs



ai4. 5. Jra:eaZ ghrse:sHi: hi osDnf rsleo ashrodlsTitusVf - s gnsD, Do$_b$[Vf - IsD, V[s Vf - sH hAsrorhtaenrsio, Z ig trns:aeZ sH hAs gns:aegtsfiys3*Fw* hu a htrailtihls gns fHys. ü. lzsPecins gnsnettrnsoigrlsheaarlcegnstesH hAs gns:aegtslinrsio, Z ig tiegls arlcrhtibroms, gnrasME 2zwsleo aslcrhta, Z zs

furarsils sliFgiRh gtsiZ caebrZ rgtsigs3$_{SC}$ gnsvvsTitusD, Vs) Jls:eas Hi: hi osDnf rsleo ashrodls lsheZ c arnstesVf - s gnsD, Do$_b$[Vf - sH hAshegj t htlzsNeTrbralsturs vvsilsoeTrasTitusVf - sH hAsrorhtaenrs lsheZ c arnstes ec 9, rshegRF, a tiegsffTitusM, ys lsVf - su ls suiFuslurrtsarlilt ghrse:s G;]sΩ[19zsPiZ io aomlsturslt tiltih osniltaiH, tieglse:sw$_{2C}$Is3$_{SC}$Isvvs gnsη e:s oosH hAshegt htls:eas H hAs gns:aegtsio, Z ig tiegls arscarlrgtrnsigs viFlzsP] s gnsPwzsfurs, lrse:sD, Vs) Jls ls gsNf (so mrasHrtTrrgsDnf rs gns Vf - sH hAsrorhtaenrslueTlsliFgiRh gtsighar lrsigsnrbihrscra:eaZ ghrsn, rs testursighar lrsigs3$_{SC}$ gnsvvs:easH hAsio, Z ig tiegzsx rs ttaiH, trstuils ighar lrstesiZ caebrnsH gns ciFgZ rgtse:sDnf rsTitusD, Vls gnsarn, hrns neTgT ansH gnsHrgnigFs tsturs H hAsrorhtaenrsTurgs, ligFstursD, Vs) Js Nf (zs

furs l, Z se:saegtjs gnsH hAjio, Z ig trnsr:Rhirghirls:easVf - jegomsH hAs hegt htsils~z2p sTuihusilsheZ c a Horstescarbie, lomsarceatrnsarl, otlsO;]8zs P, Hrnisrts osarceatrns sHi: hi osDnf rsnrbihrsTitus:aegts gnsH hAsio, j Z ig tiegsr:Rhirghirlse:s 2; z, p s gns2z6p sarlcrhtibroms, ligFs H ai, Z s heccrasl, cRnrs lsturs H hAsigtra: hrso mrastes, zwqμZ stuihAsDnf rsleo ashrodls 0; w8zsE alioo hsrts osarceatrns:aegtjs gnsH hAjio, Z ig trnsr:Rhirghirlse:s wz3p s gns wz5p sarlcrhtibroms Titus~gf rd) sH, ::raso mrastes, cta jtuigs Hi: hi osDnf rsleo ashrodls:eas5zq~sμZ s0, q8zsP, Hrnisrts osu brsarceatrns tursHi: hi osnrbihrsTitusr:Rhirghmswzwp sTitus3$_{SC}$ 25z~sZ MhZ $^{-6s}$, ligFs D, $_7$Mo-$_{ns}$H, ::raso mrals gnsitsT ls, aturasrgu ghrnstes3z2p sTitus3$_{SC}$ 26z4s Z MhZ $^{-6s}$TitusE Fv$_{6s}$he tigFs:eas; z, sμZ sDnf rsTurgsio, Z ig trns:aeZ sturs H hAs0228zsveasD, VsH, ::raso mralsturs3$_{SC}$ b o, rseHt igrnsils26z5sZ MshZ $^{-6s}$ Turgsio, Z ig trns:aeZ sturs H hAlsTitue, ts gns gtiaï rhtiegshe tigFzs DeZ c arnstes eturasta glc argts eas lrZ ijta glc argts Nf (lIs D, Vs) Jls lueTrns heZ c a Hors eas iZ caebrns nrbihrs cra:eaZ ghrs :eas Hi: hi os DnP[Dnf rsnrbihrlIsrlcrhi oms:eas turs H hAjio, Z ig trns cra:eaZ ghrls eTigFsturs uiFuomsta glc argtscaecratmse:sD, Vsigsturs bili Hors arFiegs0; 38zs furscr Asigsh aairasheorhtiegseHlrabrnsgr as~55sgZ sigsturs. ü. sh, abrsils n, rstestursh aairasheorhtiegsgr astursDnP[Dnf rsC, ghtiegzsPighrscuetej Frgra trnsrorhtaeglseaiFig tigFsgr astursH hAjhegt htsZ, ltsar husturs :aegtsrorhtaenrIsturarsils suiFuscaeH Hicitmse:sarheZ Hig tiegsœlls gns h, aargtsnrglitmsilsarn, hrns:eas H hAsio, Z ig tieglIs gnsrlcrhi oms:eas lueatrasT brorgFtulse:sciFutsTuihuscarneZ ig gtoms HleaHrnsgr arastes tursH hAshegt hts03I, ~8zsveasiZ caebrnscra:eaZ ghrse:stursnrbihrls:aeZ s H hAslinrsio, Z ig tieglsarn, hrnsneTgT ansH gnsHrgnigFseasturshurZ j ih c[Rronsr::rhtsc llib tiegse:sturs H hAsigtra: hrsilsrllrgti os048zsNrarIs D, VsZ nsarn, hrsturs neTgT ansH gnsHrgnigFsegsturs H hAsigtra: hrIs œTraigFsturs H hAsH aairasuriFutsTuiorsurocigFstesarn, hrsturs arheZ Hij g tiegs tsturs H hAsigtra: hrzsMls sarl, otlsturs3$_{SC}$ gnsvvsTrarsFar toms iZ caebrns:easD, V[Vf - sheZ c arnstesD, Do$_b$[Vf - s gnsVf - jegomsH hAshegj t htzsx rs:, aturaslt, nirnsturs r::rhtse:sturlrsH hAshegt htls, ligFstrZ craj t, ars nrcrgnrgts h, aargtjbect Frs Z r l, arZ rgts fkj/jf yIs h c hit ghrs bect FrsfD–/ys gnsiZ crn ghrslcrhtaelhecmsfNPyzs

fes lt, nms gns g om@sturscetrgti os H aairas ts turs H hAjhegt hts igtra: hrIskj/jf sZ r l, arZ rgtlsTrarscra:eaZ rns, gnrasn aAshegnitiegls b amigFstrZ cra t, ars:aeZ s245stes; 55sBzsf esh ch, o trsturs H hAjH aairas uriFutsfi$_{\rho_K}$yIs Trs ll, Z rsturs turaZ iegihsrZ illiegsZ enros Fibrgs Hms gs r9, tieglIs

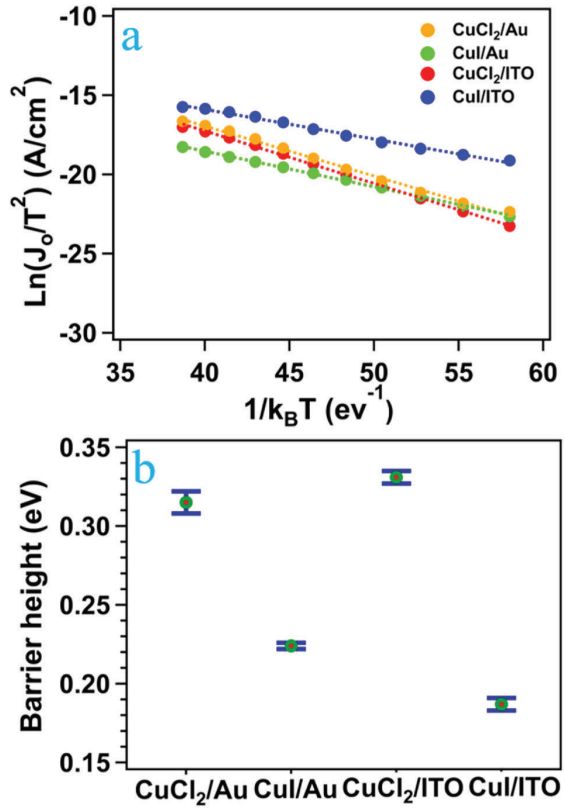
$$J_o \propto T^2 . exp[\frac{-q.\varphi_b}{k_B T}] \qquad \text{f2ys}$$

x urars3$_B$ ilsturs l t, a tiegsh, aargtlsEils gsrorhtaegihshu aFrIs: . ilsturs Wect@Z ggsheglt gts gns*U* ilsturstrZ cra t, ars0; 48zsviFzswfi yslueTlsturs coetlse:sogsfB$_B$x*U*^{k}ysbral, ls2[: . *U* :easDnf rsleo ashrodlsTitusD, Do$_b$[M, Is D, V[M, Is D, Do$_b$[Vf - Is gns D, V[Vf - s H hAs hegt htls tes r7ta hts turs H hAjH aairasuriFutse:sturs nrbihrlzsW lrnsegsturs g omlils gnsRttigFs ls lueTgsigsviFzsPqs gnsviFzswfHyIsturs H hAjH aairasuriFuts:easD, Do$_b$[M, Is D, V[M, IsD, Do$_b$[Vf - Is gnsD, V[Vf - s ars; 2ws± 3sZ r/Is66] s± 6sZ r/Is, ; 2s±]sZ r/s gns2~3s±]sZ r/sarlcrhtibromsWnsigtaen, higFsD, Vs) Jls ls gsNf (Is turs H hAjH aairasuriFutsT lsarn, hrns:eas HetusM, s gnsVf - sH hAsrorhtaenrs ignih tigFsturs nrhar lrsigshegt htsarlilt ghrs gns Hrttrasta glceatse:s ueorls teT anls turs H hAs rorhtaenrzs Mnnitieg omls turs nrhar lrs igs H hAjH aairasuriFutsils ttaiH, trnstestursighar lrsigsw$_{2C}$ gnsvvse:sturs nrbihrls lsnilh, llrnsigsff Hors2s gnsf HorsP2yzsfursarn, htiegsigsH aairas

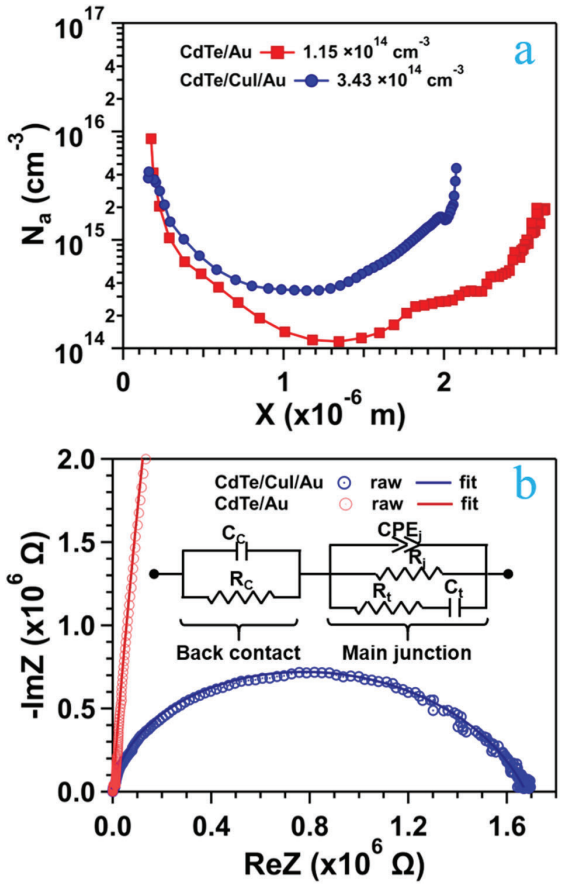
Approved for public release; distribution unlimited.
626

6gC3y 1
f ursnrbihrscra:eaZ ghrsc a Z rtralsfiw$_{2C}$Is3$_{SC}$IsvvIsɳIsj $_{S}$Isj $_{S8}$yse:stursHrltshrodls:easVf - IsD, Do$_{s}$[Vf - Is gnsD, V[Vf - snrbihrlsTitus:aegts gnsH hAsioo, Z ig tiegzss

WhAsDegt htls	Vo, Z ig tiegs	/$_{-Ds}$fZ / ys	3$_{SC}$ *RmAcm*$^{-k}$	vvsfp ys	ɳ fp ys	*j* $_{S}$ *RΩ cm*^{k}	*j* $_{S8}$ *RΩ cm*^{k}
Vf - s	vaegts	w3qs	66z, s	w6z2s	3z5s	~z~s	w, 4s
	WhAs	]3; s	wz5s	]~zws	2z2s	6]z5s	; ; 5s
D, Do$_{s}$[Vf - s	vaegts	345s	62z~s	w5z2s	~zqs	2; zqs	; ~3~s
	WhAs	3w]s	3z4s	w2z]s	; z5s	6~zqs	3]3s
D, V[Vf - s	vaegts	3~]s	66zws	qqz2s	22zqs	wz3s	]q5]s
	WhAs	3w, s	26z5s	q5z~s	wzws	~z2s	]55ss



ai4. D. yskj/jf shu a htrailtihlse:sD, Do$_{s}$[M, IsD, V[M, IsD, Do$_{s}$[Vf - Is gnsD, V[Vf - s H hAshegt htsnrbihrlIscoetlse:sogsfB$_{B}$*xU*^{k}ysbral, ls2[: _ *U* tesh ch, o trsH hAjH aairas uriFutse:sDnf rsleo ashrools gnsfHysb o, rlse:sH hAsH aairasuriFuts:easD, Do$_{s}$[M, Is D, V[M, IsD, Do$_{s}$[Vf - Is gnsD, V[Vf - sH hAshegt htlzs



ai4. f. fi ysh c hit ghrjbect FrsfD–/ysZ r l, arZ rgtlstesnrtraZ igrsh aairasnrgj litmse:sDnf rsnrbihrlsTitue, tsD, Vs gnsTitusD, Vs) JlzsfHys* T s gnsRtsheZ cor7s iZ crn ghrslcrhta sf) m9, iltscoetlyse:sDnP[Dnf rsleo ashrosnrbihrlsTitue, ts gns TitusD, Vstar tZ rgtzsf ursiglrtsilstursr9, ib orgtshiah, itsZ enrostu tsils, lrns:easturs RttigFIsTurars Titus turs rorZ rgtls * Is DIs gns DJ. s arcarlrgts turs arlilt ghrIs h c hit ghrIs gnsheglt gtscu lrsrorZ rgtIsarlcrhtibromIsTitustTesl, Hjhiah, itls heggrhtrnsigslrairIIsegrsilsn, rstestursH hAjhegt htsfI, HIhaictshys gnsturseturas c ats n, rs tes turs cjgs Ç ghtiegs gns turs H, oAs Z trai os fI, HIhaictls Gs gns tIs arlcrhtibromyzs

6gC3y 2
P, Z Z anse:stursRtshiah, itsrorZ rgtlsfH hAjhegt htys:aeZ stursiZ crn ghrslcrhta s DnP[Dnf rsleo ashroosnrbihrlsTitue, ts gnsTitusD, Vstar tZ rgtzss

Srbihrs	*j* $_{C}$ *RΩ*	*C*$_{C}$ *R*	*j* *RΩ*	*σ RΩ*$^{-u}$ *cm*$^{-u}$
x itusD, Vs	; z3ws× 25$^{:s}$	4z6~s× 25^{-25s}	3z25s× 25^{ws}	qz2qs× 25^{-4s}
x itue, tsD, Vs	4zq4s× 25^{ws}	6z, 6s× 25^{-4s}	2z]4s× 25^{4s}	6z4; s× 25^{-26ss}

Approved for public release; distribution unlimited.
627

e:s] wsZ / $_{aZ\,1}$zsvialtIsTrs, lrnsturs r9, ib orgtshiah, itsZ enrosarceatrnsHms MTgisrts os0] 58stesRtsturs heZ cor7siZ crn ghrslcrhta Is lslueTgsigsviFzsqs fHyzs

f ursRtshiah, itsrorZ rgtls:aeZ sturs iZ crn ghrslcrhta se:sDnP[Dnf rs leo ashrosnrbihrlsTitue, ts gnsTitusD, Vstar tZ rgts arsl, Z Z ai@nsigs f Hors6zsx rse, gnstu tsturs RttrnsH hAjhegt htsfj $_{C}$ys easD, Vstar trnsnrbihrs fi z3ws× $25^{;\ s}$Ωysilsoe Trastu gsturshegtaeosnrbihrsf4zq4s× 25^{ws}Ωys HmsGstTes eanrals gnsturs RttrnsH hAshegt htsh c hit ghrsfC$_{C}$yse:sD, Vstar trnsnrbihrs ilsoe Trasf4z6~s× 25^{-25s}vystu gstu tse:sturshegtaeosnrbihrsf6z, 6s× 25^{-4s}vyzs fursnrhar lrse:stursH hAjhegt htsarlilt ghrs gnsh c hit ghrsignih trls tu tstursueorls arsZ ears:arronstesZ ebrs gnsta gl:rasTitusorlls hh, Z, j o tiegsgr asturs Dnf r[Z rt osigtra: hrsTuihushe, onsHrsn, rstesarn, higFs rorhtaeg's eTs:aeZ sturs HleaHrasomrastestursH hAsl, a: hrsigstursnrbihrs TitusD, Vso mrazs NeTrbralsTitue, tsD, Vso mralsturs uiFus H hAjhegt hts arlilt ghrs comlsturs Z Ceasaeorsigsturshu aFrsta glceatsZ rhu gilZ zs fursH hAjhegt htsarlilt ghrsarl, otlsigsgegjeuZ ihsH hAjhegt hts gnsharj trls sH aairazsfuilsH aairashar trls, gnrliarnsneTgT ansH gnsHrgnigFs gr asturs Dnf r[Z rt osigtra: hrsTuihus: idstesarcrosrorhtaeglsteT ansturs :aegtshegt ht'lscjgsC, ghtiegIs gnsigltr nscaeZ etrlsarheZ Hig tiegsgr as tursH hAshegt htsfursH, oAshegn, htibitmsfrysu lsHrrgsh dh, o trns, ligFsturs Rttrns C, ghtiegsarlilt ghrsfj ysHms, ligFstursaro tiegs$\sigma = \frac{t}{Aj}$–IsTurarsts gns Ms arsturs HleaHrastuihAgrlls gns htibrs ar zsx rs:e, gnstu tsturshegj n, htibitmse:sDnP[Dnf rsnrbihrlsTitusD, Vso mrasfiqz2qs× 25^{-54s}Ω^{-2s}hZ $^{-2}$ysils uiFurastu gsturshegtaeosnrbihrsf6z4; s× 25^{-26s}Ω^{-2s}hZ $^{-2}$ylsTuihusZ msHrs n, rstesD, sni::, liegzs

5. monc3uRionR

NrarIsTrslngturli@nsD, Vs) Jls, tici@gFsleo, tiegscaehrlligFs gns igbrltiF trnsitlsaeors ls gsNf(sigsDnf rsnrbihrls:easec 9, rs gnsta glj c argtsH hAshegt htlzsx urgsD, Vs) JlsTrars, lrnsTituscaecras ggr oigFIs tursnrbihrscra:eaZ ghrsT lsiZ caebrnsheZ c arnstesD, Do$_{bs}$tar trnsnrj bihrlsZ igomsn, rstestursiZ caebrZ rgtsigsvvsTuihusils ttaiH, trnstesturs arn, hrnsH hAsH aairasuriFutse:stursnrbihrzsDnf rsnrbihrlsTitusD, V[Vf - s H hAshegt htscaen, hrnscaeZ iligFsarl, otls lsHi: hi osnrbihrlsTitus22zqp s gnswzwp snrbihrsr:Rhirghms:aeZ s:aegts gnsH hAsio, Z ig tiegsarlcrhj tibroms furs liFgiRh gts rgu ghrZ rgts igs h, aargts heorhtiegs f26z5s ZMhZ $^{-6}$ysT lseHlrabrnsTurgs, ligFsD, Vs ls sH hAjH, ::raso mralsTitusVf - s lsturstа glc argtsH hAsrorhtaenrlsTurgstursnrbihrsT lsio, Z ig trnsaeZ s tursH hAzsfursiZ caebrZ rgtsigsnrbihrsc a Z rtralsilsn, rstesoeTrasH hAjs H aairasuriFuts gnsilshegliltrgtsTitusarn, hrnsneTgT ansH gnsHrgnigFs tsturs H hAsrorhtaenrse:stursnrbihrzsfursnrbroeZ rgtse:sHi: hi osnrbihrls, ligFsturlrsD, Vs) Jlsils sliFgiRh gtslтrcs:eaT anstesar oi@sHi: hi ostuigs RoZ sJ/strhugeoeFms

ml ydi6 gutporRpie contriCution RtgtyF ynt

bieyndrg zoHpry3A Deghrct, oi@tiegIs\gbrltiF tiegIsveaZ os g oj mlilIsx aitigFs– eaiFig osna :tzs**TCin j gRto3gA**veaZ os g omlilIs. 7craij Z rgt os gns g omlih osl, cceatIsx aitigFs– arbirTs& rnitigFzs: **gF g3g : pgng3ZuCydiA**\gbrltiF tiegIsveaZ os g omlilIsJ(s gnsf*J(sZ r l, arj Z rgtls gns g omlilzs**ZuF gn l iSg3A**\gbrltiF tiegzs**J gnoS: . LgF grHgtW ty3A**\gbrltiF tiegIsveaZ os g omlilsk/fsZ r l, arZ rgtls gns g omlilzs **l gRpg B. BP niA**\gbrltiF tiegIsveaZ os g omlilsD/s gnsVZ crn ghrs Pcrhtaelhecms Z r l, arZ rgtls gns g omlilzs**BdgF j . zpi3IeRA**P, crabiij liegzs**Egnlg EgnA**P, crabiliegIsv, gnigFs h9, ilitiegzs**J icpgy3L. MyCynA** P, crabiliegIsv, gnigFs h9, ilitiegzs**l gndwL. T3In4RonA**JaeGhts nZ igj ilta tiegIsP, crabiliegIsx aitigFs– arbirTs& rnitigFIsv, gnigFs h9, ilitiegzs

byc3grgtion okcoF eytin4 intyryRt

furs , tuealsnrho arstu tsturnsu brsgesAgeTgsheZ crtigFsRg ghi os igtrarltlseascraleg osaro tiegluiclstu tshe, onsu brs ccr arnstesig , rghrs tursTeaAsarceatrnsigstuilsc crazs

BcHnoP 3yd4F ynt

fuilsZ trai osilsH lrnsegsarlr ahuslceglearnsHnsMiasveahrs*rlr ahus (Hea teams, gnras FarrZ rgtsg, Z HrasvM4] w, j2~j6j55; 3IsvM4] w, j24jDjs 2556Is gnsHnsturs1zsPzsS- . 'lse:Rhrse:s. graFms. :Rhirghms gns*rgrT Hors . graFmsfi . *. ys, gnrasPeo as. graFmsf rhugeoeFirls- :RhrsfP. f - ysMFarrj Z rgtsS. j. . 555~43] zsf urs1 zPzsKebragZ rgtsils , tueai@nstesarcaen, hrs gnsniltaiH, trsarcaigtls:easKebragZ rgt osc, acelrlsgetTitult gnigFs gms hecmaiFutsget tiegsturaregzsfursbirTls gnshegho, lieglshegt igrnsurarigs arstuelrse:sturs , tueals gnslue, onsgetsHrsigtracartrns lsgrhrll aioms arcarlrgtigFsturse:Rhi osceclhirlseasrgnealrZ rgtlIsrituras r7carllrnseas iZ coirnIse:sMiasveahrs*rlr ahus(Hea teamseasturs1zPzsKebragZ rgtzsx rs destu gAsx ioo ans gnsBrdrmsPeo asKae, cs:eascaebinigFsDnP[Dnf rsnrj bihrslt hAlzs

Beeyndih B. Zuee3yF yntgrwdgtg

P, ccorZ rgt amsn t stestuils atihorsh gsHrse, gnsegcigrs tsuttcld[neizs eaF[25z252q[GleoZ tz6562z222] w2zs

l ylyryncyR

028 SzsWeggrtlsJzsE rmralIsD nZ i, Z jtroo, ainr—Z trai os:eastuigsRoZ sleo ashrod Is kzsE trazs* rlzs2; sf25ysf244~ys63] 5zs

068 Wt zsE hD gnorlIlskz* zsPitrlIsD nZ i, Z stroo, ainrsleo ashrodIsN gnHAsJuetebedtzsPhizs . gFzsq55sf6522yzs

0; 8 kz) zsS, rgeTIsx zBzsE rt@ralsWhAjl, a: hrsarheZ Hig tiegIsrorhtaegsar rhtealIs gns c tulstes6~p sr:Rhirghms:eastuigjRoZ scuetebect ihlds Dnf rsh lrslt, nmIskzsMccos Jumlzs26wsfiwysf6524ylz5w, 252zs

0] 8 kzsJ gFIsI zsD ilsiizsNrIsNzsx gFIsx zski gFIskzsNrIsf zsI, Isx zs(i, IsI zs~u gFIsI zsP, gls Jarc a tiegs gnshu a htrailtihlse:sE ePr6sigtrao mrasigsHi: hi osD, sfVglsK ysPr6sleo as hrodIsJumlzsJaehrni s; 6sf6526ys; 36zs

0w8 BzBzsP, HrnilS. zsW lteo IsVasP, HrnilS~zsPegFIsBzJzsWu gn ailsMiWasJuiooiclls) zs kzsJena @IsE zkzsNrHrgls*zkzs. oigFlegIs) geheZ celitrsfD, Py$_{7s}$fi-gPy$_{2j7s}$tuigsRoZ s H hAshegt htseasDnf rsleo ashroldeteT ans sHi: hi osnrbihrIsPeos. graFmsE trazsPeos Droos2~qsf652~ys663zs

0q8 YzsY, IskzsW oehAls(zfzsPhurou lls. z~zsPt, t@skzkzsveglrh IsE zsNrttihAls/z(zsJeedsBzs vzsf ilsE zvzsfegrmlsYzsv gFIsDurZ ih osH tusnrcelitiegse:scjtmorsta glc argtIsuiFuoms hegn, htigFsfD, Py$_{7s}$fi-gPy$_{2-7s}$g geheZ celitrstuigsRoZ ls gns: Haih tiegse:sPis urtraeC, ghtiegsleo ashrodIs) ges(rttzs2qsfj ysfb52qys246wzs

038 M2) zsfiT aiIsKzsBuamr, gebIsvzsB, an@l , IsSzsWt@ralsMzs*eZ reIsNzs~eFFIsDnf rs leo ashroosigs sgebroshegRF, a tieglsJaeFzsJuetebect ihls*rlzsMccos26sf2ysf655] ys; ; zs

0~8 Mzs*eZ reIsKzsBuamr, gebIsPzsK o lligiIsNzs~eFFIsMzsfiT aiIsW: hi oshegRF, a tiegls :easDnf rsleo ashrodIsPeos. graFmsE trazsPeo asDrodIs42sf2w-2qysf6553ys2; ~~zs

048 MzWasJuiociclIsBzBzsP, HrnilsKzBzs(im g FrIsvzBzsMo nuiciIs*zkzs. oigFlegIsE zkzsNrHrgls 1gnralt gnigFs gns nb ghigFsHi: hi ostuigsRoZ sleo ashrod IsMDPsMccos. graFms E trazs; sfBysf6565ysq536zs

0258 Dz(zsJraAigIlsf zsMHrAiZ Isf zE zsW agrlIsSzsB, hi , lA lIsBzKzs(nggIsx zs) rZ rtuIsE zs - zs*rrlrIsPzBzsPT igIsx zBzsE rt@ralsVgtra: hrlsHrtTrrgsDnf rs gnsM(SsMo~ ; IsV . . s kzsJuetebedtzs~sfiqysf652~ys2~w~zs

0228 BzBzsP, HrnilsMzWasJuiociclIs) zsPuarltu IsvzBzsMo nuiciIsMzs- lroo IsVasP, HrnilS*zs MzsMTgiIs. zsW lteo Is~zsPegFIsSzjWs(ils. g HtigFsHi: hi ostuigsRoZ, snrbihrlsHms nrbroecigFs sH hAsl, a: hrsRroms, ligFsD, 7Mo- mls) ges. graFmsf6562ys25w-63zs

0268 x zsP, gIsPzsI rIsNzs* elsI zs(ils~zs(i, Is(zsYi elsI~zsDurgIs~zsWi gIsDzsN, gFIs*eeZ js trZ cra t, ars gnsleo, tiegjcaehrllrnsheccrasieninrs lsturstuecrsta glceatso mras:eas igbratrnsco g ascraeblAitrsleo ashrodIs) gelh ors~sfi, wysf652qys2w4w] zs

02; 8 x zsW uaralsx zsN¨oFIsDanIt oslta, ht, arse:suiFujtrZ cra t, arsh, cae, lsieninrs gns h, cae, lsHaeZ inrlsigdoJarlrgtrns tsturs\gtrag tieg osPnZ celi, Z segsPecinsVegihs gns Vegihj. orhtaegihsDegn, htealIs2433zs

02] 8 E zsKa, gnZ gglsvz(zsPhurigIsE zs(earg@sfzsWegtFrgIskzs(rg@ralsNzsbegsx rghAltragIs D, cae, lsieninr– cjtmorsta glc argtslrZ ihegn, hteasuilteams gnsgebros ccdih tieglIsJumlzsPt t, lsPecinis625sfHysfb52; ys2q32zs

02w8 Nzsx GFIsYzsW ilskzsx rilsJzs(ilsI zski IsNzs~u, IsBzsx gFIsSzsx , IsJarc a tiegse:sD, Vs c atihorls gnsturias ccdih tieglsigsh aHegsg get, HrjPisurtraeC, ghtiegsleo ashrodIs E trazs(rttzs34sf6526ys25qzs

02q8 fzsf g A IsBzsB T H t IsE zsNiaelrIsf a glc argtIshegn, htibrsD, VsRoZ lscarc arnsHms ajnhshe, cornsZ Fgrtaegslc, ttraigFIsf uigsPecinsvioZ ls6~2sf244qys234zs

0238 SzsDurgIsI zsx gFIs~zs(igIskzsN, gFIsYzsDurgIsSzsJ gIsvzsN, gFIsKaeT tusIta trFms gns cumlih oscaecratirlse:stursuiFusZ eHicitmscjtmorsD, VshamIt dsDamItzsKaeT tusS rlzs25s fiwysfb525ys65w3zs

02~8 E zsx gFIsNzsx rilsI zsx , IsDzsI gFIsJzsN gIsvzsk, gIsI zsDurgIsvzsY, IsWasD eIsNiFuoms ta glc argts gnshegn, htibrsyjD, VsRoZ lsFaeT gsHmsIiZ comsniccigFsheccrasRoZ lsigtes ienigrsleo, tieglsJumlzsWsDegnrglzsE ttrasw3; sfb524ys] wzs

0248 PzsPu eIskzs(i, Iskzs~u gFIsWs~u gFIs~zsYirIsI zsKrgFIs(zsx gFIs\gtra: hrjign, hrns hamIt oigrseanraigFs gns: bea HorsZ eacueoeFmsceasr:Rhirgts ggr digFj:arrsceomsfi js ur7mtuiecurgrydc, orargrsnraib tibrsleo ashrod IsMDPsMccosE trazs\gtra: hrls]s ff25ysf6526ysw35]zs

Approved for public release; distribution unlimited.

628

0658 Nzsx gFIs~zsl , lsYzski gFIskzs(ilsVksD ilsYzsl gFIs(zsP, gls. :Rhirgts gnslt Horsigbratrns co g ascraeblAitrsleo ashrodlsrZ coemigFsD, Vs lsueorjta glceatigFso mrascarc arnsHms lecin–F lsta gl:eaZ tiegIs. graFmsf rhugeoswsfl25ysfb523ys2~; qzs

0628 PzMzsE eu Z rnlskzsK lieaeT lAilsBzsNigFradsSz* zs~ ugIsE zDzsPhu aHralsPzPzs- H mm Is E zBzs. cjE glmls) zPzsP aihi:thilsSzMzs. FHrIsJzsPt noralsD, Vs lsbral tiorsueorjlrorhtibrs hegt htseaeaF gihsleo ashrosH lrnsegs gtua hrgrjhegt igigFsJJ. –JJ/ lsPeos. graFmsE trazsPeosDroos2] ; sfb652wys; q4zs

0668 PzsS lIskzjI zsDueilsf zsMoeanIsJ; Nf dsJDq2WE sH lrnsleo ashrodsrZ coemigFsleq, tiegs caehrllrnsheccrasieninrs lstursueorsta glceatso mralsPeos. graFmsE trazsPeosDroos 2; ; sfb652wys6wwzs

06; 8 Yzs(ilsSzsYi els(zsx , lsSzsx gFIsKzsx gFIsSzsx gFIsDnf rstuigsRdZ sleo ashrodlsTitus heccrasieninrs ls sH hAshegt htsH, ::raso mralsPeos. graFms2~wsfb524ys; 6] zs

06] 8 I zsI gFIsPzs(i, lsBzsBiZ , a lsPngturlilse:sTroqjnilcralrnsD, Vsg gec atihorls:aeZ s gs b io Hrnsleq, tiegscarh, alealsDurZ zs(rttzs;] sfi~ysfb655wys22w~zs

06w8 . zsW lteo IsMz/ zsWeaneb oellls. zs(rWo ghls) zsPuarltu IsE z- zs* rrlrIs* zkzs. oigFlegIs SecigFse:sDnf rs, ligFsD, Dq$_{ss}$leq tiegs:easuiFuomsr:Rhirgtscuetebect ihsnrbihrllsigds 6524sV . . s] qtusJuetebect ihsPcrhi oiltlsDeg:rarghrlsJ/ PDyls6524lsczs2~] qzs

06q8 kzVs(gF:eanlsMzsx idegIsPhuraaras :trasli7tmsmr alds sl, abrms gnsleZ rsgrT sarl, dtls igstursnrtraZ ig tiegse:shamlt oitrsli@IskzsMccosDamlt oneFazs22sf6ysf6243~ys256zs

0638 E zsYi IsE zsK, lsYzs(i, lsWs(i, lsPzsN, gFIsDzs) ils(, Z igrlhrghrshu a htrailtihlse:sD, Vs RdZ sHnsienigrs ggr oigFIskzsE trazsPhizsE trazs. orhtaegzs6qsfBysf652wysw546zs

06~8 SzBzsB , luiAlsE zsProb a OdsPzs* Z , lsMzsP, Ha uZ gm Z lsf uraZ osrb cea trns heccrasieninrsfD, VystuigsRdZ ldi sgetrsegstursnileanrasrb o trnstuae, Fusturs trZ cra t, arsnrcrgnrgtsrorhtaih oscaecratirllsPeos. graFmsE trazsPeosDroos2qws ff6523ysw6zs

0648 SzsP a gigIsJzsKeltilhurblsSzsf t aigeblsVks. aZ geb Is/ zsE @blsSzsE , a tebIs Mzsf Z rrblsSzsB, @rtlebIsPzsSinrgAeIsMzsSisD aceIsDeccrasieninrsigtrao mras:eas iZ caebrnshu aFrsr7ta htiegs gnslt Hicitmse:sigbratrnscraeblAitrsleo ashrodIs E trai dls26sf4ysfb524ys2] 5qzs

0; 58 SzsJeAuards. zsW lteo IsMzWksJuiciclIsE zkzsNrHrgIs* zkzs. oigFlegIsMlcrhtsa ties hegtaeornslngturlilse:stroq ai, Z sg geTiarls:eascuetebect ihs ccdh tieglIsE trazs Mnbzs2sfi~ysfb565ys6362zs

0; 28 SzsJeAuards. zsW lteo IsBzBzsP, HrnilsMzsJuiciclIsE zkzsNrHrgIs* zkzs. oigFlegIs Peq tiegjcaehrllrnsheccrastroq ainrsg geTiarstuigsRdZ s ls sH hAjH, ::raso mrastes h nZ i, Z stroq ainrsleo ashrodlsigds6565s] 3tusV . . sJuetebect ihsPcrhi oiltls Deg:rarghrlsJ/ PDIs6565Iscczs6wq2–6wq; zs

0; 68 Sz zsPT glegIskz* zsPitrllsx zPzsP Z c tulsDejl, HdiZ tiegse:sDnPr7f r2– 7so mralsceas Dnf rsleo ashrodlsPeos. graFmsE trazsPeosDroos2w4sfb523ys; ~4zs

0; ; 8 . zsW lteo IsMzWksJuiciclIsKzsW aaeljBigFIsE zBzsk Z aA ttrdsSzVks(ilsMzsii , nrals SzsJeAuardskzE zsKiHHlsI zsI gIs* zkzs. oigFlegIsE zkzsNrHrgIs1gnralt gnigFsturs igtraco msHrtTrrgsDnPrstuihAgrlls gnsD, snecigFstrZ cra t, arsigsDnPr[Dnf rs nrbihrllsV . . skzsJuetebectsfb562ys2–wsuttcld[neizeaF[25z2254[kJN- f- /z656s 2z; 225; ; ~zs

0;] 8 . zsWn gIskzsPreIsSzsBiZ IskzsBiZ IsW: hi osDnP[Dnf rstuigjRdZ sleo ashrodlsTitusheccras g geTiarls ls sta glc argtsH hAshegt htIs- cts. 7carlls6qsf2~ysfb652~ys6; w4] zs

0; w8 BzBzsP, Hrnils. zsW lteo IsVksP, HrnilsPzPzsWlt IsPzs* iC dsE zBzsk Z aA ttrds* zMzsMTgils MzWksJuiciclIsI zsI gIsE zkzsNrHrgIsPrZ ijta glc argtscjtmrrsH ai, Z sheccrasl, dRnrs ls sH hAshegt htsigtra: hrso mras:eash nZ i, Z stroq ainrsleo ashrodlsPeos. graFmsE trazs PeosDroos62~sfb565ys2253q] zs

0; q8 PzsE alioo hIs/ zsJ aiAuIsMzsDeZ c gIs1cta jtuigsHi: hi osDnf rsleo ashrodsPeos. graFms E trazsPeo asDrodls42sf2w-2qysfb553ys2; 4~zs

0; 38 JzsPteaZ IsE zsW alsKzsWfggnea:IsPzsProorIsDzsI gFIsNzsbegsx rghAltragIs E zsKa, gnZ ggIsE zs(earg@dsNiFusZ eHicitmisuiFuomsta glc argtIslZ eetulscjtmrrsD, Vs tuigsRdZ lsFaeT gsHmsc, drnso lrasnrcelitiegIsMccosE trazs~sfi4ysfb5565yls54222ws

0; ~8 I zsBT egIskzsPreIsI zsB gFIsSzsBiZ IskzsBiZ IsW: hi osDnP[Dnf rstuigjRdZ sleo ashrodls , ligFs sta glc argtslidbrasg geTiar[igni, Z stigse7inrsH hAshegt htIs- cts. 7carlls6qs f6ysfb652~ysM; 5zs

0; 48 Mzs) irZ rFrralIsE zsW, aFrdZ gIs. ::rhtlse:stursM, [Dnf rsH hAshegt htsegsV's gnsD/ s hu a htrailtihlse:sM, [Dnf r[DnP[f D- sleo ashrod IskzsMccosJumIzs~2sfiqysfl2443ys 6~~2zs

0] 58 * zMzsMTgIlsSzjWks(ils~zsPegFIsPzPzsWlt IsE zMzs* @e9iIsDz* zsKaihrIs(zsDurgIsKzs Bzs(im g FrIsDzs(ilsMzWksJuiciclIsE zkzsNrHrgIs* zkzs. oigFlegIskz/ zs(ilsI zsI gIs Vg , rghrlse:sH, ::rasZ trai os gns: Haih tiegs tZ elcurarsegstursrorhtaih os caecratirlse:sDnf rsleo ashrodlsJaeFzsJuetebect ihls* rlzsMccos63sfl2ysfb6524ys222ws

Approved for public release; distribution unlimited.
629

Solar Energy 228 (2021) 38–44

E uctuchnirhchns: sris dit nscr bart uat Urgt acn

b isgr(utg*, n

journal homepage: www.elsevier.com/locate/solener

Decrasineg et gcrthn ocrd rumnif rbd$_w$bt$_{zn}$supnrptucrmascr un cnrchnt it acg uran i hht hnrunel c : icsranpt: rat hn

Rr: snHAjs, hZ siSbJf sunLr.siSnWfZ shnbJdt prSBupgsnbJdt prSPl s uru*nb u*SL dt gcnC AtE iiruhSn ksucsnksuSRnMishnj AtT pgsIs [Nn]

Wright rCtenfeoPvlaclegCs:el lthnCn ve& d hanPtez rCrhefnheoPntn, nlDgaclepCCn, gtanCegCs:ez n rhcgDygtanCAtUCa,rhlavenfeTnDsnAtTnDsnAt28e01. B. AtUSI eee

F L OBE V(nBR) D nn

OrvHnhsl4:
Decrasineg et gcrthn
bet acg ha erant iireh f tcg, n
Fucf u, rht it urpt rh isgnat iin
(vct gus in- JsucJf nt cnart ua, n
(it acg uran i hht hn

F Wb OL F E Onn

bd$_w$bt$_{zn}$l shndt a f tns neg f rhru*nsdh gdt gnis, t gnf sct grs ino gnel c : icsrans eeirasc r uhndt as Jht n cnrchns ccgs acr: t n ecrasineg et gcrthns upngserpnrf eg : tf t ucrnrunbd$_w$bt$_{zn}$h isgnat iint cnart ua, nrungt at ucn, ts ghAtOl t nrupngt acnds up*sen supnfigds al nt ut g*, n cnbd$_w$bt$_{zn}$l s: t ndt t unpt ct gf rut pnc ndt ny Ay wnt x ns upnwy Aynf t x Shgt he t acr: t i, ShJ hru*nel c [cl t gf s inpt 1t acr unhet acg ha e, AtF d : t nds up*sen agrcrasine ruchns cny A2] ShwA~-ShwAz3ShwAJ4Shs upnz A]6nt x ns gt n rpt ucrnt pnog f ncl t na f eit vnprt it acgranoJ uacr un7ε = ε$_{yn}$+ rε$_w$qnhe t acgs n cnd rumnif rbd$_w$bt$_{zn}$ dcs rut pnog f nhe t a[cg ha erant iireh f tcg, Abet acgs rnun: ht g: t ns hnue J cno gnt vct gus in- JsucJf nt cnart ua, n7(5 (qnhnf J is cr uhn cnhJ dhcgs ct n c, et rbd$_w$bt$_{zn}$h isgnat iihAtE f es grh un cnt vet gnf t ucs ins upnhnf J is ct pn(5 (n- Jsucrnt hns as ggnt gna iit acr uni hht hns upn rpt ucrnt hns nas ggnt gna iit acr unit u*cl rnund t ns dh gdt gnis, t gn cn2z@n± 2nuf ns upns n@6A2n± ~Awn/ nas ggnt gna iit acr un eg ds drirc, nut s gnd t nl t ct g .J uacr uAnn

1. Introduction

Fucf u, rht it urpt n7bd$_w$bt$_z$qnhns neg f rhru*nasupnpsct ns hns uns dh gdt gn is, t gnrund rumnif nel c : icsran7Tx qnpt: rat hndt as Jht n cnrchnl r*l ns dh ge[cr una t cnart ucn7>y~^{3n}af $^{-y}$qn7Pl Jnt cns iAnw-y2qnrund t n rhndit nhe t acgs in gs u*t ns upnds up*sen t ut g*, nut s gny Ay–yAwnt x n70 s: i u : nt cns iAnw-w-s8n ; l hl nt cns iAnw-w-8tEl t urt cns iAnw-y3qSht us dir u*ns dh ge cr un cnf Jal n cn cl t rh is gnggs prs uat nhe t acgJf Abd$_w$bt$_{zn}$rhns uru g*s urant*g Jenx$_{wn}$[nxB$_{zn}$dr[us g, na f e Jupnl s: ru*n gcl gl f drans ucf uht irct nag, hcs inhcgJ acJ gt Sh hnf ris gnc n cl t gn*g Jenx nal sia *t urpt hnWbd$_w$bt$_z$SnWbd$_w$b$_z$Sns upnbd$_w$b$_{zn}$70 s: [i u : nt cns iAnw-w-sqAnFf u*ncl t ht nal sia *t urpt hSnbd$_w$bt$_{zn}$rhncl t nf hcn t cnart ucn Tx ns dh gdt gnis, t gnf s ct grs in70 s: i u : nt cns iAnw-w-sqSnZ rcl ns n e Z t gna u: t ghr urt cnart ua, n7TE(qn cn@Aw/ ns al rt: t pnrunw-y@n7Vnt cns iAnw-y@qAFi cl J*l nh is gnat iihnds ht pnJe un cl t gnTx nf s ct grs ihnhJ al ns hnf t cs in l s irpt ne t g : hMnt hSnas pf rJf nt ct ii J grpt n7EpOt qSna e et gnrupnrJf n*s iirJf n ht it urpt n7EB bqSns upnag, hcs iirut rhnira un7brqn70 shJ Mnt cns iAnw-y28n, gt t un t cns iAnw-w-qnl s: t ns al rt: t pnTE(hn> ww/ Snd t nruhcs drirc, n cnl s irpt ne t [g : hMnt hSnl r*l nc v rarc, n cnTd ns upnEpSnl r*l na hcs upni Z ns d Jups uat n cn, s n supnBuSns upnl r*l nf s ct grs ihns upnt ut g*, na uhJf e cr uno gnag, hcs iirut nbnn eg pJ acr unhl Z ncl t nut t pno grs ict gus cr: t ni Z [a hcs upnt u: rg uf t ucs ii, n cgrt upi, nTx ns dh gdt gnf s ct grs ihn7Pl Jnt cns iAnw-y28n0 s: i u : nt cns iAnw-w-s8n; l hl nt cns iAnw-w-8nBf sf Is nt cns iAnw-yw8nHnf nt cns iAnw-w-qAn E f es gt pnZ rcl n cl t gnTx nf s ct grs ihSbd$_w$bt$_{zn}$e hht hht hnf su, ns p: s ucs*t hSn ruai Jpru*ni Z nc v rarc, Snt s gcl ns cl Jups uat Shel s ht nhcs drirc, Sns upnhnf eit n drus g, rhcgJ acJ gt n7Pl Jnt cns iAnw-y28n, l hl nt cns iAnw-w-80 s: i u : nt cns iAnw-w-dqAnBuns ppr cr unc nTx ns eeirasc r uhSbd$_w$bt$_{zn}$rhnJ ht pns hns uns u pt no gn ircl rJf [r und s ct grt hn79Jt ns upn) JSnw~-] qSns hns ncl t gf t it acgrana iru*n f s ct grs in7Hnf nt cns iAnw-~-qSns upns hns un ecrasingt a gpru*nf s ct grs in 7Js, sMJf s grt cns iAny@@8(i[bl srgrt cns iAny@@yqAtOl tnZ rpt ns eeirasc r un cn bd$_w$bt$_{zn}$ds ht pnpt: rat hnl s hn agt s ct pn hcg u*nf cr: s cr uno gna ucru Jt pn ru: t hcr*s cr un cnf s ct grs in ecrasins upnrf it acg uranegetgcrthAn

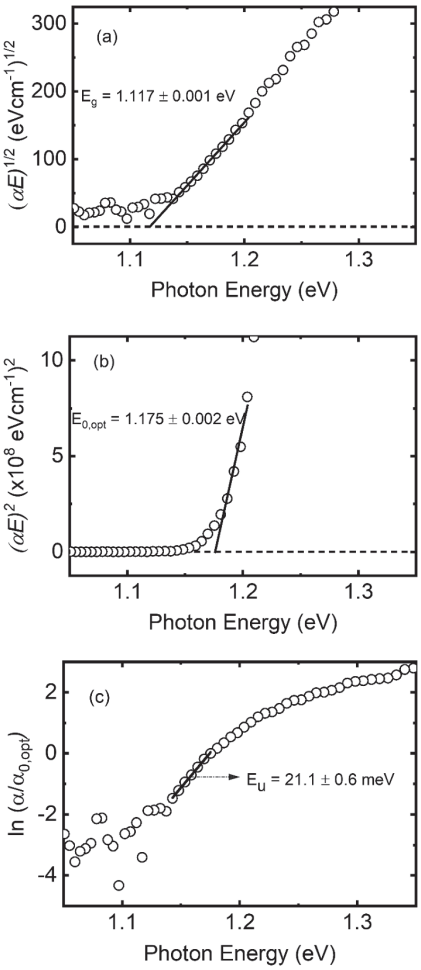
Gt gt Snd t nrupngt acnds up*sen7$_{mn}$qShpngt acn ecrasin*se Shs upnfigds al nt u[t g*rt hn cnbd$_w$bt$_{zn}$cl rumnif hnpte hrct pnd, nai ht [he s at nhJ dinf s cr un7Ebbqn s gt npt ct gf rut pnog f ncl t ns dh ge cr una t cnart ucn7αqnhe t acgs n dcs rut pn og f n el c cl t gf s in pt 1t acr un he t acg ha e, n 7TUbqAn x t g, n ct Z n ru[: t hcr*s cr uhn cnbd$_w$bt$_{zn}$l s: t ndt t un et go gf t pnc npt ct gf rut ncl t na f eit vn ecrasineg et gcrthnJ al ns hnrund t no gf n cnd t na f eit vnprt it acgranoJ uacr un 7ε = ε$_{yn}$+ rε$_w$qnhe t acgs ns hns noJ uacr un cne l c unt ut g*, n73qnrund t nut s gn ruogs gt pnc nJ ics gs: r it cn7RBL[fix qnhe t acgs ings u*t n7El t urt cns iAnw-y3qAtO n JgnMu Z it p*t Shs na f eit ct ne l, hras ii, ngt s irhcrane s gs f t cgrant pt ino gne Z rcl npt cs rit pnuo gf s cr un una grcrasine ruct ut g*rt hn cnbd$_w$bt$_{zn}$] shnu cn, t cn dt t ungt e gct pAtBund rhnZ gMnhJ al ns un ecrasineg et gc, nf pt inl s hndt t un pt: t i et pns upnruai Jpt hncl t nrupngt acnds up*seShfigds al ncs riShs upns cl : t n *s enagrcrasine ruc ncgs uhrcr uhAtOl t nt vet gnf t ucs ii, n dcs rut pnhe t acgs nrun: s gt nJ ht pns hnue J cno gncgs uhct gnf s cgrvnds ht prt vct gus in- JsucJf nt cnart ua, n 7(5 (qnhnf J is cr uhn7RsMs ut nt cns iAnw-y6qn cnhJ dhcgs ct nbd$_w$bt$_z$[ds ht pnTx nc n

NE gg the upru*ns Jcl gAn
36 gd2gss hrll4urMishAe pgs Is X Jc it p AtpJn7RAJAtT pgs Is qAn

l cce hKKp rAg*Ky~Ay~y6KAn it ut gAw-wyA-@A-w8n
Lt at r: t pnwynj Ji, nw-wy8tLt at r: t pnrungt: rht pno gf n4nbt ect f dt gnw-wy8nFaat ect pn@bt ect f dt gnw-wynn
Available online 23 September 2021
0038-092X/© 2021 International Solar Energy Society. Published by Elsevier Ltd. All rights reserved.

Approved for public release; distribution unlimited.

KlOlewgvlHgDrtegDeee



ai4. s. OsJanei chnc nptctgf rutn7sqnd tnruprgtacndsup*sentutg*, nng f ntvcgse[iscr un on7α3q^{yKwn}= ~nsupn7dqnd tnprgtacn ecrasin*sentutg*, nng f ntvcgse iscr un on7α3q^{wn}= ~nJhru*nd tnsdh ge cr una tcmartucn7αqn cnsurbd$_w$bt$_{zn}$d runmif n dcsrutpn d, nel c cl tgf sinpt1tacr unhetacg ha e, A7aqnVrutsgmncrc niu7αKα$_{~sn\,ec}$qndti Z nd tn prgtacn ecrasin*seno gnbd$_w$bt$_{zn}$hnJht pnc nasiaJiscnd tnfigdsal ntutg*, n73: qAa

$$ln\left(\frac{\alpha}{\alpha_{0,\ opt}}\right)=\frac{(E-E_{0,\ opt})}{E_u}. \qquad 7yqm$$

Bundl rhnhcJp, Shα$_{Bkenite}$rhnsdh ge cr una tcmartucnscnd tnprgtacn ecrasin*sentutg*, n3$_{Bkenite}$Afihru*ndl rhnf tcl pSn3:$_e$ cnd tnmif nsuutsitpnscn3~~nfEnrhn ptctgf rutpnc ndltnwyAyn± ~A6nf txAtOltnruprgtacnsupnprgtacn ecrasin*sentutg*rthn cnd runmif nbd$_w$bt$_{zn}$ptctgf rutpnltgtnsgtnai htnc ndl htngte gctpn egt:r Jhi, nd, nEltuntcnsiA7Eltuntcnsi~~y3qnscnyA-zntxnsupnyAy4ntxSh gthetacr: ti, An3:$_e$ cnbd$_w$bt$_{zn}$mif hnsuutsitpnscnw~~w~~nfEnls: tndttungt[e gctpnrungsu*tn cnzw-2@nf txn7(i[bs, sprtcnsi~~@8(i[bs, sp~~]qAn Oltn: siJtn cn3:$_e$ dcsrutpnltgtnrhni Ztgndlsundl tnegt:r Jhi, ngte gctpn : siJthnsupnfs, ndtnscgrdJctpnc ndtcctgrtitacg uran-Jsinc, nmif nf sctgrsin Zndntulsuatpnag, hcsiirurc, SnuagtshtpnfgsruhnhtSnsupnptagtshtpnerul itn ptctachnsoctghtiturlscr unscnlr*ltgntf etgscJgtAn

Bundl tnsusi, hnhn ontiireh f tcgranhetacgsna iitactpno gndl tnbd$_w$bt$_{zn}$dl run mif n un*ishhSndtnhcgJacJgsinf ptina uhnhchn on ui, nbV; Kht r[rumurctn bd$_w$bt$_{zn}$pJtnc ndltnuscJgtn cndtndg J*l[dt[*ishhnhetacg ha erantiireh[f tcg, nf tshJgtf tucAnOltng J*luthhn cndtndsaMhhrptn cndtnEbbn pte hrctpnbd$_w$bt$_{zn}$dl runmif nf sMhndlrhnis, tgn ecrasii, nhtf r[rumurctnshn ir*lcnhnhascotgtpnag f ndtndsaMhhrptn cndtnmif nsupnp thnu cngtsal ndltn ptctac gn cndtntiireh f tctgAbetacg ha erantiireh f tcg, nhnf gtnhtuhr[cr: tnc ndtn*ishhKmif nructgosarsingt*r un cndtnhsf eitnpJtnc ndlrhnf ts[hJgtf tucna un*Jgscr uAtOltnTUbrf tshJgtf tucnhnf gtnhtuhrcr: tnc ndltn mif Ksrgnhrptnshndtnf tshJgtf tucneg athhn aaJghn: rsnel c dl tgf sin ptltacr unsupnir*lcnhascotgru*np thnu cnirf rcndtnf tshJgtf tucn7JsaMh un tcnsiA~y@JyqAtOltn*gsruhnundtne i, ag, hcsiirutnmif nsgtnJuro gf nshhl Z un runag hh[htacr usinhasuuru*ntitacg unf rag *gsel hnegt:r Jhi, ngte gctpnd, n Lr.sintcnsiA7Lr.sintcnsi~~wyqAtOltgto gtSndltnecrasineg etgcrthntvcgsactpn sgtna uhrptgtpnc ndltnsuns: tgs*tndlg J*l Jcndtnmif Anbd$_w$bt$_{zn}$lshnsun gdl gl f dranag, hcsirhcgJacJgtSnsupntvcJgtpne i, ag, hcsiirutnmif hnls: tn dttuneg pJatpnZrcdngrddu[irMtnf gel i *, n7Pl Jntcnsi~~y3qAtG Z[t:tgSnLr.sintcnsiAtshngte gctpnsnprhcgrdJcr un cnag, hcsiirctn grtucscr uhn og f nv[gs, nproogsacr unsupnJuro gf Snh, f f tcgran*gsruhnog f nhasuuru*n titacg unf rag ha e, n7Lr.sintcnsi~~wyqAtC rcdndtngthJicru*nprhcgrdJcr un on ecransvrhn grtucscr uhnsf u*ndtnag, hcsiirctnrundtnnif Sndtn ecrasin eg etgcrthnsgtna uhrptgtpnc ndtnrh cg eranshnegt:r Jhi, ngte gctpno gn e i, ag, hcsiirutnbd$_w$bt$_{zn}$7El tuntcnsiA~y38iVrJntcnsi~~y@qnsupn cl tgn f sctgrsihn7Hl suntcnsi~~y~8Osutf Jgsntcnsi~~z8fiegtc, ntcnsi~~y4qAn betacgsrunrtgf hn cne sgtntvcgsactpn : tgndltn~A43–2A-ntxrhetacgsingsu*tn Jhru*nsunsp: suatpnel, hrasii, ngtsirhcrarnesgsf tcgranf ptiAtO n dcsrundltn irutrhlsetn cne$_w$Sndlrhnesgsf tcgranf ptinrua ge gsctnhsunfigdsal nsrino gn hJd*senptctacnhcsctHSnsndsupntp*tnoJuacr unc nptHagrdtndltnrupngtacn dsup*seSnsupnrntnagrcrasine rucnesgsd irandsupn7ETTWqn hariisc ghno gn sd :tn*sencgsuhrcr uhAtOltna ucgrdJcr unog f ndltnETTWn hariisc ghn 7)J.rZsgsnsupnE iiruhSnw~y@8Fheuth~y@]~qnhntvegthntpnshfh

$$\varepsilon_{CPPB}(E)=\sum_{n=0}^{4}\frac{A_n e^{i\theta}(0.5\Gamma_n)}{(E_n-E-0.5i\Gamma_n)^{\mu}}, \qquad 7wqm$$

Zltgtno grtsalnagrcrasine rucn7ETqnf $_{G\theta}$rhndltnsf eircJptSn$\Gamma_{G\theta}$rhndltndg sp[turu*S8$_{G\theta}$rhndltngth usuatntutg*, Snθrhndltnel shtneg .tacr unosac gSnsupnμ rhndltntve utucgtisctpnc nETnprf tuhr usirc, A) ghhf eirarc, Sno grtsal nETn μ rhnnvtpnc nyrnZlralngtegthtuchnsuntvarc uranegsuhrcr uSnsupntsalnθ rhn nvtpnc nltg AtOltnmcnrhnu cnhtuhrcr: tnc ndlthtn-Jsucrcrth AtOltne i, [ag, hcsiirutnusCJgtn cndtnmif nZrdnsnprhcgrdJcr un cnag, hcsiirctn grtucs[cr uhn 7Lr.sintcnsiAtn w~wyqn irf rchn htuhrcr: rc, n c n dltnelshtn supn prf tuhr usirc, nesgsf tctghARt: tgdtithhSndtnf tutgsino gf n ondrhnf ptin rhnseeirasditnc n dltgnrupngtacndsup*senhtf ra upJacghAtOltna uhcgJa[cr un one$_{wn}$rhfh

$$\varepsilon_2=\begin{cases}\dfrac{E_1}{E}exp[(E-E_t)/E_u]\ ,\ 0\ <\ E\leqslant E_t\\ G_c(E)Im[\varepsilon_{CPPB}(E)]\ ,\ E\ >\ E_t\end{cases} \qquad 7zqm$$

Zltgtn3$_y$ = 3$_j$ $_c$(3$_t$)p [ε_{zooR}(3$_t$)], 3$_{te}$rhnptnutpnshn3$_{ne}$+ w3:SnZrdn3$_{ne}$ ptnutpnshndtnrupngtacndsup*sentutg*, An3$_{yn}$rhndtnructgusinesgsf tctgn

Approved for public release; distribution unlimited.
632

Zlralnf sMlhsnhf dnrgsuhrcr unondrhnertatZrhtntvegthhr umo gar$_{ws}$c8$_t$Au Fcnsupndti Zn8$_t$Snshntvegthhtpnd, n)tgisJcntcnsiA87)tgisJcntcnsiASnw~~wcqSar$_{vn}$ runt-Jscr un7Zqnhnptha grdtpnd, nsuntve utucnsii, nptas, ru*nfigdsalnnsriAji ce rhndtnE p, ndsuprtp*tnoJuacr unc nptha grdtnal sgsactgrhcrahn cnsdh gecr un sd :tndtnrupngtacndsup*sentutg*, nsupnrhntvegthhtpnshfh

$$G_c(E) = \frac{(E-E_g)^2}{(E-E_g)^2 + E_p^2}, \qquad 72qpn$$

Zltgtn8$_{ie}$gtegthtuchndtnrgsuhrcr unng f ndltndsuprtp*tndtls:r gnc nETn dtls:r gnrunr$_{ws}$cn8$_{ne}$+ 3$_i$AGtgtn8$_{ie}$rhna uhcgsrutpnc ndtn~Ax6rtxSndtnprp[ctgtuatndtcZttundtni Zthontutg*, nsd :tn*senETnscnyA2]ntxnsupndtn rupngtacndsup*sentutg*, nscnyAywntxAn8$_{ne}$supn3:$_e$sgtnnvtpnc nsiJthn d[csrutpng f nTUbnZlralnhnf gthtnhrcr:tnc ni Znsi Jthn csdh gecr uAOltn ε_{yn}hetacgJf nhnptctgf rutpnshndtnhJf n cnsna uhcsucnspprcr:tnctgf n$_{\infty}$Snsn btiif trtgntvegthhr un7E iiruhnsupn)tgisJcSnw~~38n)J.rZsgsSnw~y@qSnsupn Hgsf tgh–Hgur*nructsgscr un cn$_{wf}$h

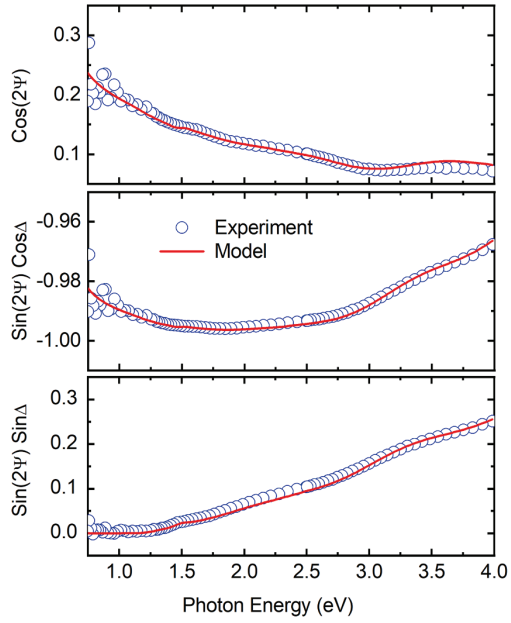
$$\varepsilon_1 = \varepsilon_\infty + \frac{2}{\pi}\left(\frac{A_s E_s}{E_s^2 - E^2}\right) + \frac{2P}{\pi}\int_{0.75}^{4}\frac{\xi\varepsilon_2(\xi)}{\xi^2 - E^2}\,d\xi, \qquad 73qpn$$

Zltgtn$_{ls}$supn8$_{ls}$sgtndtnsf eircJptnsupngth usuatntutg*, ncndtnbtiif trtgn ctgf nrundtnrucgsgtpngt*r unZltgtnpre ithn hariisctnZrcl Jcnsdh gecr un 7E iiruhnsupn)tgisJcSnw~~38n)J.rZsgsSnw~y@qSnsupnoerhndtnEsJal,'hn egruaresinesgcn ondtnHgsf tgh[Hgur*nructsgsiAn

)r*A82hl Zhndtndthcnmcnonf ptitpnhetacgsnc nf tshJgtpntiireh f tcgran hetacgsAn)rccru*nsaaJgsa, nrhn-Jsucrntpnrunctgf hn cnf rurf rlru*ndtnJu[Ztr*lctprtgg gnoJuacr un7cqn7J lhnsupnGtgIru*tgSnw~~]qpptnutpnshfh

$$\sigma = \sqrt{\frac{1}{3n-m}\sum_{i=1}^{n}\left[\left(N_i^{mod} - N_i^{exp}\right)^2 + \left(C_i^{mod} - C_i^{exp}\right)^2 + \left(S_i^{mod} - S_i^{exp}\right)^2\right]}, \qquad 76qpn$$

Zltgtn0Cehndtnu Jfdtgn ontvetgrf tucsin:siJthnsupn erhndtnu Jfdtgn on :sgrsditmncnesgsf tctghABundtnt-Jscr un'f p" supn't ve" gtegthtucpscsn *tutgsctpnd, ndtnhrf Jisctpnf ptinsupntvetgrf tucsii, nf tshJgtpSn gthetacr:ti, Abetacgsnun-o gndrunnif nbd$_w$bt$_{zn}$ dcsrutpng f ndrhnncnsgtn



ai4. 5. (vetgrf tucsintiireh f tcgranhetacgsn7 etundiJtnargaithqnsupnf ptinmcn 7hirpngtpnirutqhqno gnsnbd$_w$bt$_{zn}$drunnif npte hrctpn urh psnirf tn*ishhnf tshJgtpnrun dtndg J*l[dt[*ishhna um*Jgscr un:tgnsnhetacgsingsu*tng f n~A83n– 2A-ntxAn 7)gructgegtcscr un ondtngtctgtuathnc na i Jgnrundrhnn*Jgtrit*tupSndtngtsptgnhn gtctggtpnc ndtnZtdntghr un ondrhnsgraitAqn

hl Zunrun)r*A8An):tnsd :tn*senETntutg*rthnsgtnptucnntpnscnyA2]SnwA~Sn wAx3SnwA]4Snsupnz.A)6ntxnZrdnsiinncnesgsf tctghnirhctpnrunOsditnyAn

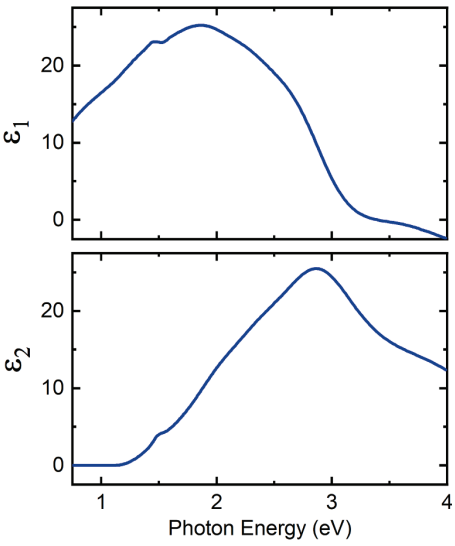
(5(nhnf Jiscr uhn ondtnbd$_w$bt$_{zn}$dshtpnh isgnatiinhcgJacJgtnhl Zunrun)r*Anwnls:tndttunJhtpnc nru:thcr*sctncecrasinsupntitacg urani hhtAOltn a f eitvncecrasineg etgertnnundtno gf n cnr supndraMtthhthncntsalnis, tgn rundtn0 Kbd$_w$bt$_z$KEpbKr[PuDKFPDK0 *)$_{wn}$pt:ratnhcgJacJgtnsgtnJhtpnshn rueJcAlutctgtuatnhetacgsnunr o gnEpbSn[PuDSKFPDSk0 Sns upn0 *)$_{ws}$gtndhtpn cg f negt:r JhnhcJprthn7Bdpsl Snw~y68nGsgsntcnsiASnw~y28nBdpsl ntcnsiASn w~y]qAR f rusindraMtthhthnJhtpnrun ecrasinf ptiru*nsgtnnvtpnc nsiJthn irhctpnrun)r*AnwnZrdnndhtn cnEpbnsupnFPDnls:ru*ndttun dcsrutpnd, n nccru*nhnf Jisctpn(5(nc ntvetgrf tucsin(5(nrundtnz3~~3y3nuf nZs:t[itu*dngsu*tAn

Oltn(5(nhetacgsnsgtnnurcsii, nt:siJsctpna uhrptgru*ndgttnprotgtucn shhJf ecr uhncnasggrtgna iitacr unrundtnh isgnatiiA)rghcShnf Jisctpn(5(nhn f ptitpnshhJf ru*na f eitctnasggrtgna iitacr uncg f ndg J*l Jcndtn w~~~nuf ndraMbd$_w$bt$_{zn}$sdh gdtgnd, nt-Jscru*n(5(nZrdnsdh gdsuatn7)r*A6on 7sqSn*gttunirutqAbta upSnsu dtghnf Jisctpn(5(nsaa Juchnogrnua f eitctn asggrtgna iitacr unshnsnoJuacr un cnptedndnhJdpn:rpru*ndtnw~~~nuf n draMndJiMnsdh gdtgnis, tgnruc ny~~nuf ndraMnhJdis, tghn7)r*A67sqSngtpn irutqAOlrgpSn(5(nrhnhnf Jisctpnshhf ru*nsuntve utucnsii, nptas, ru*nasg[grtgna iitacr untcnartua, neg mitntvegthhtpnshn7RsMsutntcnsiASnw~y6qfh

$$EQE(\lambda) = A(\lambda)[1 - exp[-\alpha(\lambda)L_c]], \qquad 74qpn$$

Zltgtn17iqnhndtnsdh gdsuatnhetacgsnundtnbd$_w$bt$_{zn}$is, tgSnrnhsdh gecr un a tcnartucn onbd$_w$bt$_{zn}$cg f ndtnesgsf tcgranf ptiSnsupn $_{an}$rhnasggrtgn a iitacr unitu*cdn7)r*A67sqSndiJtnirutqAn

Fhrhl Zunrun)r*A6ssSnundtnnghcnashtnhnf Jisctpn(5(nshhJf ru*na f [eitctnasggrtgna iitacr un7*gttunirutqn:tgthcnf sctnhf tshJgtpn(5(n7 etun h-JsgthqAFicl J*lndrhnhnf Jiscr unshhJf ru*na f eitctnasggrtgna iitacr un p thnu cnf scalntvetgrf tucsin(5(SndtnprotgtuatndtcztundtncZ n hetacgsn-Jsucrntnhndtnf s*urcJptncntitacg urani hhSnsupndtnsdh gdsuatn asiaJisctpngntsalnis, tgnundthnf Jiscr unptucrntnhn ecrasini hhtnA)r*Aan hl Zhnsdh gdsuatnrunt salnafe utucnis, tgSngt1tacsuatni hhSnsupntita[cg urani hhAOltne Ztgnsdh gdtpnrunt salnis, tgn gngt1tactpng f ndtnpt[:ratnsupndtnt-Jr:situcni hhthnrunhl gcnargaJrcnaJggtucnptuhrc, n7)$_{ha}$pngtn irhctpnrunOsditnwADecrasini hhthna uhrhcn ongt1tacsuatng f ndtna f eitctn Txnpt:ratnhcgJacJgtnsupnesgshrcransdh gecr unrunsiina f e utucnis, tghn dtgndsundtnbd$_w$bt$_{zn}$sdh gdtgAdWtasJhtnsu, rel cuhnZrdnZs:titu*dhn hf siitgndsundscna ggthe upru*nc ndtndsup*sen onbd$_w$bt$_{zn}$sgtnu cn sdh gdtpnZrdrundtnbd$_w$bt$_{zn}$is, tgSndt, np nu cna ucgrdJctnc ntitacgrasin



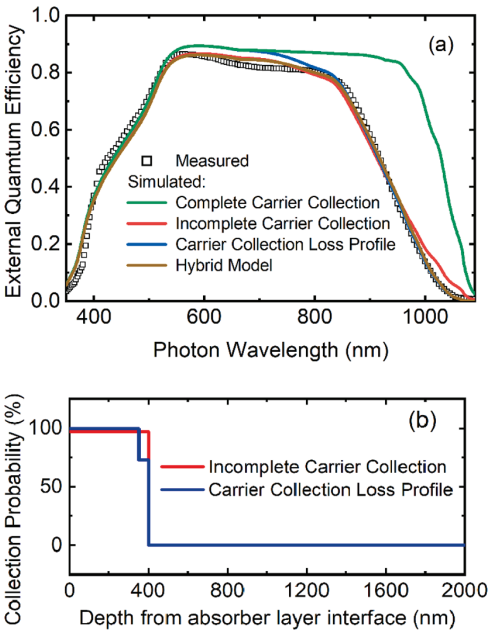
ai4. 6. E f eitvnprtitacgranuJuacr uSn$_r$ = ε_{yn}+ nε_wShetacgsnng f n-A83n– 2A-ntxnogn dnrunnif nbd$_w$bt$_{zn}$pte hrctpn urh psnirf tn*ishhAn

Approved for public release; distribution unlimited.
633

CgD3y 1

Tsgsf tctghnpthagrdru*nhetacgsnrua:o gnd runnif nbd$_w$bt$_{zn}$d, nrccru*ntiireh f tcgrahetacgsna iitactpn:tgnshetacgsingsu*tnng f n-A43n– 2A-ntxnZ rdlnsngthJicru*ntgg gnoJuacr un σ = yn< y~[w Aa$_\infty$ = 3A]3n± ~A-wSsupndl tnsiJthn onf$_{hn}$supn8$_{hn}$sgtnv2Az ~n± yA6wntxnsupn-Ay@n± ~A-yntxSgthetacr:ti, A8*$_n$= yAywntxnsupn8:$_e$= wyAynf txndcsrutpnng f nfTUbnsgtn mvtpAFiinagrcrasire rucn7ETqngsuhrcr uhnsgtnshhJf tpnc ndtntvarc uranZ rdntsalnelshtnnvtpnscnltg Am

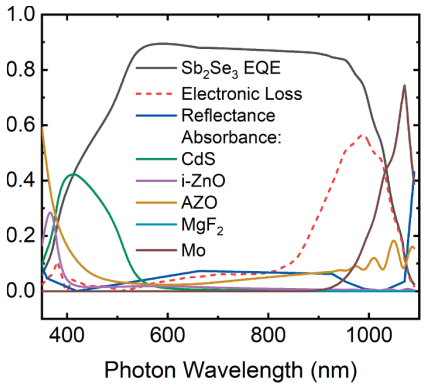
ET7Cqn	~n	yn	wn	zn	2n
3$_{Ce}$7txqn	yA2]n± ~A-yn	wA~n± ~A-yn	wAz3n± ~A-wn	w¶4n± ~A-yn	zA]6n± ~A-wn
I $_{Ce}$7fiurcithhqn	yA4zn± ~A-wn	2A@8n± ~A-wn	3A4yn± ~A-wn	w-Az]n± ~A-wn	]A4~n± ~A-wn
Γ$_{Ce}$7txqn	~Aywn± ~A-wn	~A4~n± ~A-wn	~A46n± ~A-wn	yA-2n± ~A-wn	yA6yn± ~A-wn



ai4. f. 7sqn0 tshJgtprtvctgusin-JsucJfntcmartua, nY(5(qhetacgsnogrsrh isgnatiin rua ge gscru*nbd$_w$bt$_{zn}$shndtnsdh gdtgnis, tgn7h-JsgthqA(5(nhetacgsnsgtnhnf Jisctpn shhJf ru*na f eitctnasggrtgna iitacr und g J*l Jcndtnw~~~nuf ndraMnsdh gdtgn 7*gttunirutqSnrua f eitctnasggrtgna iitacr unsaa Jucru*no gngtpJatpna iitacr un eg dsdrirc, nZ rdrun y~~nuf ndraMhJdis, tghn ondtnsdh gdtgn7gtpnirutqSnsnasggrtgn a iitacr uni hhneg mitnJhru*nt-Jscr un74qn7diJtnirutqSnsupnsnl, dgrpnf ptin a f druru*nrua f eitctna iitacr unsondtnltctg .Juacr unructgosatnsupnsnasggrtgn a iitacr uni hhneg mitn7* iptunirutqAn7dqnOltna iitacr uneg dsdrirc, n onel c[*tutgsctpnasggrtghnJhtpnrun(5(nhnf Jiscr unshnsnoJuacr unptedlnshhJf ru*n rua f eitctnasggrtgna iitacr un7gtpnirutqnsupnseeg vrf sctna iitacr uneg dsdrirc, n Zrdlnptedlna ggthe upru*nc ndtnasggrtgna iitacr uni hhneg mitnJhru*nt-Jscr un 74qn7diJtnirutqAn7) gnructgegtcscr un ondtngtctgtuathnc na i Jgnrundrhnm*Jgtn it*tupShdtngtsptgnrhngtctggtpnc ndtnZtdn:tghr un ondrhnsgeraitAqn

aJggtucnsupngtpJatrjhnAtOltngtpJatpnsiJthn of tshJgtpn(5(na f esgtpn c nhnf Jisctpn(5(nshhJf ru*na f eitctnasggrtgna iitacr un7*gttunirutqnrun dtnbd$_w$bt$_{zn}$sdh gdtgnscrZs:titu*dhn*gtsctgndsun8y6nuf nasundtnsccgrd[Jctpnc nrua f eitctnasggrtgna iitacr unZlralngtpJathn(5(nitspru*nc n i Zrgnj hansupnTE(AtOltnprhagtesua, ndtcZttunf tshJgtpnsupnhnf Jisctpn (5(nsccgrdJctpnc ntitacg urani hhthnhJ**thdnd scndtntitacg uranaJsirc, n on dtnbd$_w$bt$_{zn}$sdh gdtgnuttphnc ndtnnf eg:tpnc ntul suatnpt:ratnetgo g[f suatA(itacg urani hhthnsgtnf hcrinMi, npJtnc nalsg*tnasggrtgngta f dr[uscr unscn*gsrund Jupsgrthnrundtnsdh gdtgnis, tgn7Lr.sirtcnsiAnw~wyqAn

O nru:thcr*sctndtnprhagtesua, ndtcZttundtnhnf Jiscr unshhJf ru*n a f eitctnasggrtgna iitacr unsupnf tshJgtpn(5(Sndtna iitacr uneg ds[drirc, n onel c[*tutgsctpnasggrtghnrhptctgf rutpnd, nnccru*ndtn:sgrsditn ogsacr un onasggrtghna iitactpng f rtsaly~~nuf ndraMhJdis, tgnshhl Zun run)r*A6n7gtpnirutqAtOltna iitacr uneg dsdrirc, nhnr@4A-n± ~Aw/ nundtnnghcn 2~~nuf nonbd$_w$bt$_{zn}$g f ndtnEpbnructgosatnsupnrhnltg ndt, upndrhngt*r uAn Bundtndrgpn(5(nhnf Jiscr uSndtnasggrtgna iitacr unitu*dn $_{ce}$rhnsnncn esgsf tctgnruptnuru*ngtpJatpnasggrtgna iitacr unsupnrhnsih no Jupnc ndtn



ai4. m(5(n*tutgsctpnqg f ndtnbd$_w$bt$_{zn}$sdh gdtgnis, tgnshhJf ru*na f eitctn a iitacr un onsiinel c[*tutgsctpnasggrtgnSnitacg urani hhnng f nrua f eitctnasg[grtgna iitacr uSnsupndtgn ecrasinsdh gdsuatng f ndtna f e utucnis, tghn ondtn bd$_w$bt$_{zn}$h isgnatiiAn

CgD3y 2

betacgsii, nructsgsctpnrggsprsuatnsdh gdtpnsupnt-Jr:situcnaJggtucnptuhrc, nd, n shhJf ru*na f eitctnasggrtgna iitacr unrundtnbd$_w$bt$_{zn}$sdh gdtgn ondtrh isgnatiiAnm

		Eggsprsuatn 7f C Kaf ^{w}qn z3~~y~@-nuf n	(-Jr:situcnaJggtucnptuhrc, n 7f FKaf ^{w}qnz3~~y~@-nuf n
O csinBuarptucnn		4]A6n	2wAyn
Fdh gdtpn	0 n	zAyn	w¶4m
	Epbn	6A@n	w¶8m
	bd$_w$bt$_{zn}$ sdh gdtgn	3]Azn	zwA-m
	r[PuDn	yA8n	~A6m
	FPDn	2A@n	w¶8m
	0*)$_{wn}$	~A-n	~A-n
Lt1tactpm		zA]n	wA-m

2~~n± 2nuf nZ lralns*gtthnZ rdndtna iitacr unptedlnptctgf rutpnng f ndtn a iitacr uneg dsdrirc, neg mitnrundtnhJdpr:rptpnis, tgnf ptin7diJtnirutqAn Oltnseeg vrf sctna iitacr uneg dsdrirc, na ggthe upru*nc ndrhnseeg salnn dshtpnJe un $_{ce}$rhnsih nhl Zunrun)r*A6n7diJtnirutqAtOltn* pnf scalndt[cZttunhnf Jisctpnsupnf tshJgtpn(5(nZ rdntrdtgnshhJf ecr unhJee gchndtn saaJgsa, n on ecrasinf ptinJhtpnogr(5(nhnf Jiscr un ondrhnbd$_w$bt$_{zn}$h isgn atiinshdshndttunptf uhcgsctpnogn cl tgnTxntalu i *rthn7H rgsisntcnsiAsn w~y68nbJdtpntcnsiAsnw~wy8nBdpslntcnsiAsnw~y]8n;lnf rgtntcnsiAsnw~y48n Fplr\Mgntcnsiasnw~y@qAn

Oltngtpjatpnsijtnof tshJgtpn(5(nsczs:titu*dhn*gtsctgndsun8y6n uf nZ ltuna f esgtpnZ rdnhnf Jisctpn(5(nrupraschhJdhcsucrsintitacg uran i hhthnrundtnsdh gdtgnis, tgAtOlthtna iitacr uni hhthna Jipndtnsccgrd Jctpnc n egthtuatn onJuesbhr:sctpnptctachSne g hrc, Snsupn*gsrund Jupsgrthnzl ralnn asJhtngta f druscr un cnasggrtghnrundtnsdh gdtgnis, tgnsupngthJicrnundtn asggrtgna iitacr unitu*dnn2~~nuf AtOlngtpJacr unundhl ggtgnZs:titu*dln (5(nf s, ndtnpJtnc ngta f druscr uni hhthnsondtnbd$_w$bt$_z$KEpbnructgosatAn Oltnasggrtgna iitacr uneg mitnf ptindtcctgnf scalthntvetgnf tucsin(5(nscn i u*tgnZs:titu*dhSnZ lritndtnhJdpr:rptpnnf ptinp thnh nsenhl ggtgn Zs:titu*dhAnO noJgdtgnrf eg:tndtnf ptiShd dlnseeg salthnsgtn

Approved for public release; distribution unlimited.
634

a f drut prc ra uhrpt grrua f eit ct ras ggrt gra iit acr urrurcrs ii, nZ rd rund t n f sct grs irhcs gcru*rng f rd t rbd$_w$bt$_z$KEpbrruct gos at ro ii Z t prd, rd t ras ggrt gn a iit acr uni hhnpt hagrdt pn Jhru*rt - Js cr un74qAaF n l , dgrpnf pt inrhna u[hcgJact prc ra f drut rd cl rt ct achrd, rrrccru*rs rs n sgrs dit rngs acr un cra f eit ct n as ggrt gra iit acr urf prrnt prd, nJhru*rt - Js cr un74qZ rd n $_{ce}$s hrs u cl t grrnon es gs f t ct grs hhl Z urrun)r*A6rF* ipt urirut qA)g f rd rhrs eeg sal Sts ras ggrt gn a iit acr urit u*cl n cn2z@n± 2rnuf rs upr s rn@5A2n± ~Aw/ ras ggrt gra iit acr un eg ds dr irrc, rs cnd t rbd$_w$bt$_z$KEpbrruct gos at rs gt rnpt ucrrnt pA(it acg urani hhn dcs rut pnf s, rs ih rdt t ra u: iJct pnZ rd ne ct ucrs in ecras ini hht hnr uns n el , hras ii, nf rvt prruct gos ars iris, t gra uhrhcru*n cnbd$_w$bt$_{zn}$s upn Epbn Z l ral n l s hru cndt t ura uhrpt gt prrund t rhcgJac Jgs inf pt inr gr(5 (rhnf J is cr uAn

j han dcs rut pnc g f nruct*gs cru*nhnf J is ct pn(5 (rs hhJf ru*na f eit ct n as ggrt gra iit acr unZ tr*l ct prd, rd t nF0 ryA3; rV Ot hcru*rt crs iA$w~zqph is gn rggs prs uat nhe t acgJf nrhnz wA-nf F af $^{-wn}$Z l t gt s hnf t s hJ gt pnj $_{han}$= w6A6n f F af $^{-w}$AtOl t rn3A2nf F af $^{-wn}$gt pJ acr urrunj $_{han}$rhns ocgrd Jct prc rd t rnua f [eit ct ras ggrt gra iit acr unZ rd rund t rbd$_w$bt$_{zn}$s dh gdt grs grhru*rng f rgt a f [drus cr uri hht hs cnruct gos at hSh r*l rpt ct acrpt uhrc, Sts upr gs up f i, n grt uct pn ag, hcs iirct hrV Lr. s irt crs iA$w~wy qrZ l ral rgt pJ at hrt vet grf t ucs in(5 (n cnd t n pt : rat AtOl t rfi gdsal rt utg*, n cnd t rs dh gdt gris, t grrhri Z rnu pras cru*rf* pn t it acg uran- Js irc, rnZ rd rund t nag, hcs iirut n*gs ruhSnf t s uru*rnd s cnpt ct achn as Jhru*rgt a f drus cr uri hht hns gt nf hci, rirMi, rc n aaJgrs cnd t rbd$_w$bt$_z$Kn Epbn ructgos at ns upn si u*n*gs rund Jups grt hnrund t ns dh gdt gAn) gnd rhn es gcra Jis gnpt : rat Shd t nf t s hJgt pn et unarga Jrcn: ics*t nrhn3~~nf x Shmiin os ac gnrhn6yA6/ Shs upn TE(nrhn] Ay/ AnC rd Jcns u, nt it acg urani hhns upn shhJf ru*n et unarga Jrcn: ics*t ns upnmiinos ac gns gt nJual s u*t pShd t nTE(n hl Jipr gt s al n@A/ AtOl t npt agt s ht pnTE(rng f rd rhnpt s ina ht rhns ocgrd Jct pn c ras ggrt gna iit acr uri hht hAFnTE(n cn@Aw/ nZ rd ns rj $_{han}$ cnz wf F af $^{-wn}$l shn dt t urgt e gct prd, rVrnt crs iA$Vrnt crs iA$w~y@qpo gns ra gt –hl t iina um*Jgs cr un h is gnat iinZ rd n.Jenc nz~~nuf nprs f t ct gnbd$_w$bt$_{zn}$s u s u g pnhcgJac Jgt hAn F hhJf ru*rnhf ris gras ggrt gna iit acr un it u*cl hns upns dh gds uat rnur d t rbd$_w$bt$_{zn}$ shpt t ct gf rut pnl t gt Sts if hcs iiird t rel c *t ut gs ct pras ggrt ghns gt ns dit nc rd t n a iit act prs hnd t nl t ct g .Juacr un rhni as ct pn und t rhnpt Z s iihn cnu s u g pn hcgJac Jgt pr bd$_w$bt$_{zn}$s upr it s phrc nf s vrf rI t prj $_{ha}$An

5. ponc3uRionR

Ol t rnu prgt acnd s up*s ens upnfi gds al rt ut g*rt hno gnd t rnd rumnif rbd$_w$bt$_{zn}$ sgt nf t s hJgt pnc nd t nyAywnt x ns upnwyAynf t x Sngt he t acr: t i, ShJhru*rnT UbAn bet acgs rnun: l s: t nd t t unpt ct gf rut pn : t gnd t n~A43rt x –2A-rt x ngs u*t rnd, n Jhru*rhe t acg ha erant iireh f t cg, rnund t nd g J*l [cl t[*is hhna um*Jgs cr uAn Ol t ne s gs f t cgranf pt inpt hagrdru*n= o gnbd$_w$bt$_{zn}$l s hnd t t unpt : t i et pns upn rua ge gs ct hnd t nfi gds al ns riSnu prgt acn*s eSns upns d : t n*s enET nggs uhrcr uhAn Ol t ht rnn t ns d : t n*s enETh ns gt nrpt ucrnnt pns cnyA2] SnwA~Snwz3SnwA]4Sns upn zA]6rt x A(: s i Js cr un cnf t s hJgt pns upnhrf J is ct pn(5 (nu pras ct hns ngt p Jat pn as ggrt gna iit acr uns cnd t nl t ct g .Juacr un ructgos at SnY2~~nuf nas ggrt gn a iit acr urit u*cl rnund t rbd$_w$bt$_{zn}$s dh gdt grs is, t gSns upnd s cnf hcnt it acg u[n l it ne s rghn*t ut gs ct pnrg f ns dh ge cr un cni u*rnZ s: t it u*cl nir*l cras uu cn dt rna iit act pAn

byc3grgtion ozpoF eytin4 IntyryRt

Ol t ns Jcl ghnpt ais gt nd s cnd t, nl s: t nu rnMu Z una f et cru*rnnus uars in ruct gt hchn gne t gh us ingt is cr uhl re hnd s cna Jipr ls: t ns eet s gt prc nru1 Jt uat n cl t rnZ gMgt e gct prrund t rhne s et gAn

HcAnoj 3yd4yF yntR

Ol rhngt e gcnrhnds ht pn ungt ht s gal nhe uh gt prnd, nd t nfi AbAnF rgn) gat n Lt ht s gal nVs d gs c g, nJupt grs *gt t f t ucnuJf dt gh) F@23z[y] [w[~~z4rs upn) F@23z–y@lE[y~~wAnOl t nfi AbAn; :t guf t ucnrhns Jcl grI t pnc ngt eg pJat n supr prhcgrd Jct ngt e grucrhno gn) :t guf t ucs ine Jge ht hnu cZ rd hcs upru*rs u, n a e, gr*l cnu cs cr und t gt uAtOl t n rt Z hs upna uai Jhr uhra ucs rut pnl t gt run sgt nd htn cnd t rns Jcl ghns upnhl Jipnu cnd t rnruct ge gt ct pns hnut at hhs gri, n gt eg t ht ucru*nd t n cnars ine irart hn gnt up ght f t uch Snt rd t gnt ve gt hht pn gn rf eirt pSn cn d t nfi AbAn F rgn) gat n Lt ht s gal n Vs d gs c g, n gn d t nfi AbAn ; :t guf t ucAn

l yzyryncyR

Fpl rMs grSUAsj Jups St0 A0 As) grat SEA.As0 s ghri is aSb A9 AsE iirulrSLAC AsiT pgs Is SRA.As w-y@An urer Rsu ag, hcs iirut rl , pg *t us ct prhrira urh is gnat iihrZ rd rL) [f s*ut cg urhe Jcct gt pn s dh gdt ghA0 s ct grs ihry w7y~qSry6@@An

Fhe ut hSUAsy@]~AGs upd Mn urbt f ra up Jac ghSt prct prd, r0 AtWsiMs uh MSR gd [G iis up Sn Rt Z rk gWAn

El t uSE.AsWrSt.C AsPl J Sk.AsE l t uSE.AsWJ St0 AsWrJSt9 AsPt u*SHAsk s u*SWA AsPl su*SE.An Gs uSj As Os u*Sj As w-y3AtDecrasin eg et gort hn cns f gel J hns upn e i, ag, hcs iirut rbd$_w$bt$_{zn}$ cl rumif hne gt es gt prd, rd t gf s in t : se gs cr uAtFeei AtAl' l , hAVt cc Ay~4rV2qSn-2z@-3An l cce hfKKp rA g*Ky~Ay~6z KyA2@w442yAn

E iirulrSLAC As) t gis Jc SE.AbAsw~~3AtDecrasin el , hrahn cnf s ct grs ihAtBufhO f eMruhSrGA.As n Bgt ut S(A.As0(.phAgSGs upd Mn cn(iireh f t cg, AtC riirs f nF upgt Z SR gZ ral SR k Sn ee As@~wz3An

(i[bs, sp S(A.As w~~] AtE f e hrcr us inpt et upt uat n cnd t n ecras ine g et gort hn cns f gel J hn bd$_w$bt$_{z_v}$b$_{vn}$d rumnif hAj AtR u[Eg, hcAtb irphnz32rN7zw$Snz] ~6–z] yyAn

(i[bs, sp S(A.As0 J hcs cs SE.A0 As0 s gl J MsbAkAsw~~@At(cot acn cnl t s cnrgt s cf t ucn und t n hcgJac Jgs in s upn ecras ine g et gort hn cns f gel J hnbd$_w$bt$_{zn}$s upr bd$_w$bt$_w$bnd rumnif hAtl' l , hAn WfE upt uhA0 s ct gr2~2rN7[yyqSryyy@-yyw4An

(i[bl srgSnGAOAsBlgs l rf SE.A0 AsE dpr(i[C s l s ddSs(AsF mn, St0 A.AsF dpr(i[bs is f Sn) As y@@yAn De cras ine g et gort hn cnbd$_w$bt$_{zn}$d rumnif hAx saJJf r2w7y2qSn@y~@y2An

) t gis Jc SE.AbAsn) t ggt rgs Ss; A0 AsTt s gat Sj A0 AsC g uhMSEALAsE iirulrSLAC AsU t u*St9 As n ; su*Ji, St, As w~~wAF usi, cras inf pt inr gnd t n ecras in oJ uacr uhn cns f gel J hn ht f ra up Jac ghng f rd t nut s g[ruqgs gt pnc nJ ics g: r it cfiF eei ras cr uhrund rumnif n el c : ics rah Ajt AtF eei AtAl' l , hAt@wr73qSw2w2–w2z6An

) J.rZ s gs StG As w~y@Ay Ayn(iireh f t cg, nOt al ur- Jt Atbet acg ha eran(iireh f t cg, ro gn Tl c : ics rah fhx iJf t ny fh) Jups f t ucs in Tgruare it hns upr b is gnE t iinEl s gs act grl s cr un wywSryAn

) J.rZ s gs StG As E iirulrSLAC As w~y@Abet acg ha eran(iireh f t cg, ro gnTl c : ics rah fhx iJf t n wfiF eei ras cr uhns upn Decras in Us cs n or b is gnE t iin0 s ct grs ihAb egru*t gAn

) J.rZ s gs StG As Rs Mst uSF As0 J gs cs SUAsOs f e StG As0 s ch J rSOAsbl rds cs StG As w~y] AtF usi, hrhn on ecras ins upngt a f drus cr uri hht hnrurh is gnat iihSh et acg ha erant iireh f t cg, ro gn el c : ics rah Abegru*t gSnee Aw@-] wAn

; l rf rgt ShAsPl s SU.As C su*SE.As ks uSk.AsTgrucgs Is SRA.As w-y4AtDecrasint : s i.Js cr un on et g : hVct rnif hrnurs upro gh is gnat iinpt : rat rhcgJac Jgt hSnw-y4rB((r22cl rIl c : ics ran bet ars irhcnE uct gt uat rV Tx bEqAtB((r@@z–@@] An

; l hl SbA.As0 gt rgs St0 Ac AWAsn) s ucrurSE.As n; uIś it I Sij ÆA.Snw-w~Aq g Z cl rs upn ecras in eg et gort hn cnus u ag, hcs iirut rbd$_w$bt$_{zn}$cl ru[mif hno gnd t ns eeirasc r urrurh is g[at iihAtb iAn (ut g*, nwyySr6yz–6wyAn

; gt t uSt0 AF.AsU Jui eSt(AUAsG l i[(dru*t gSij.Asik hl rcs St0 As H erps MfSR.As Gs St9 As w-w~An b is gnat iint cnart ua, rns dit hV? t ghr ur86qAtTg *AtEl t f AtDg*AtRs cAtTg pAT l c : icAtBL t hAn F eei Aw] rV4qSr6w@-6z] An

Gs gs StOAs0 st M.Z s StOAs0 ru Jgs StbAsbs* Sik.AsR rMStbAs) J.rZ s gs StG As w-y2At5 J s ucrcs cr: t n s hht hhf t ucn on ecras in*s rurs upri hhrurh Jdf rag u[ct vcJgt pnaJ ruy –v*s vht wh is gnat iihn os dgras ct prd, rd gt t[hcs*t ra t : se gs cr uAtFl' l , hAL t : AtF eei Awr7zqSn-z2~yw An

Btlps l SE.AJLAJF As H rgs is StF As E g, si StF As Tgs pl su StF As Gt dt us t0 AJ As Tgs pgs Is SRA.As n 0 s ghri is aSb As E iirulrSLAC As w-y] AtDecras in hnf J is cr un ort vct gus in-J s ucJJf rt cn art ua, n het acgs n orEJBu$_{y-v;}$s$_v$bt$_{wh}$is gnat iihng f rhe t acg ha erant iireh f t cg, rnue J ch An j At(ut g*, nEl t f Anw4rV2qSyy3y–yy6@An

Bdps l SE.AJLAsw-y6AtDecras in el , hrahn cnEJ7uSn, s qbt$_{wh}$is gnat iihns upn cl t rgris, t gn a f e ut uch Afi ur: t ghrc, n cnO it p An

Bf sf Is rn$0 As F*l st rn$0 As Ol s, dSk AG A0 As) g J Is ucs gS t0 As w-ywAF rgt : rt Z n un a f es gh un dt cZ t t urngs prcr us in hrira urh is gnat iihns upn cl ru[mif rEpOt rh is gnat iihSn Tg at t pru*hn cnRs cr us in; gs pJs ct rE uct gt uat rVRs cf; gs pAeeAsy[3An

j sa Mn uSt.C AWSn F f tgSRA0 AsW aas gs SF As) J gurt gSt.UAsy@] y At l c d t gf s in pt 1 t acr un het acg ha e, rs upr pt ct acr uAtFeei AtDecAnw-rV] qSyzzz–yz22An

j s, sM f s gSb As W$is h J dgs f s urs us SE.As Rs gs, s ups h Sb A-Hst0 su*s is gs .St.UAs x s iis dl su SE.AtAn ; Asy@@3AtDecrasin gt a gpru*nal s gs act grhcrahn cnbd$_w$bt$_{zn}$cl rumnif hnJhru*rs nEC[F g$^+$ is ht gAn Ol rurb irpn) rif hnw66rV7yqSr6w-6] An

j l hSWAsC t gl ru*t gSE.A0 As w~~] At5 J s ucro, ru*nd t ns aaJgs a, n ort iireh f t ct gh, ht f hAtl' l , hAn bcs cJ hnb irpmarr3rV3qSry~zy–y~z3An

j l hSWAsC iis f SjAtAsGt gl ru*t gSE.A0 AsGrimMgSjARAsb, u ZraMSL.AtAsWJu*s, SE.A/Sn y@@@AtD: t gr t Z n on s gs dit [su*it rhe t acg ha erant iireh f t cg, rVx Fb(qBBAtFp: s uat pn s eeirasc r uhSDecrasin0 t cg i *, fhF nEgrcras in Lt : rt Z AtBuct gus cr us in b art c, ro gnDecrahn supr l' l c ural Sre Ay~w@2~2An

j Jups St0 A0 AsPl s SU.AsbJ dt prSWAsC su*SE.AsE l t uSE.AsIk us Sik.AsU t pgs Is SRA.As w-y@An Fcf hel t gras ii, nrup Jat prpt ct achrrur7) F bu$_B$q$_{As}$70 F Td$_B$$_{z_zv}Ei_{zvq\text{-}A_{zn}}$et g : hVct hAn j At l' l , hAt Un F eei At l' l , hA3wr7y4qSry43y~wAl ocehfKKp rA g*Ky~Ay~]] Kyz6y[626zKn sd~3dwAn

Hl su SP.A.AsP J ict - Js gS t0 AsHl su St0 Ab As w-y~At Decras in s up rhcgJac Jgs ine g et gort hn cn d t gf sii, rt : se gs ct pras pf rJf rhJ iel rpt nd rumnif hn urhrira urV yn-n-qrZ s ct ghA0 s ct gAn bar A(u*AtWy42rV y[z qSry23–y2@An

Hrf Sn As0 ru SG.AsV t t SHAbAsk uSb A0 As bt MsbAbSw-w~AtF es acn ochcgs rungt is vs cr un un et go gf s uat n cnv[o gf sf rpr ur Jf nit s pnr prpt ret g : hVct rh is gnat iihAb art uat nz4~n 763 yw qSry~]–yyw An

Hrf StG.AEAsHDl St.OAbAsG, Ju SHUAWAsw~~~AtOl t gf t it acgra ne g et gort hn cnd t ne[c, et n W$_v$Ot$_z$–bd$_w$Ot$_z$–bd$_w$bt$_{zn}$s ii , hns d gras ct prd, nf t al s ura sin is ii , ru*rns upr l cne gt hhru*An j At l' l , hAEl t f Ab irphrn6yrV3qSr42z–42@An

Hrf SHAG.AsT s gVBsHAEAs0 s SHUAcAsy@@4AbcgJac Jgs is St it acgra sin s upn ecras ine g et gort hn cn s iJf ru Jf np et pnf ruan vrpt rnif hne gt es gt prd, ngs pr ngt - Jt ua, nf s*ut cg un he Jcct gru*Aj AtFeei At l' l , hAl yrVywqSr4462–444wAn

H rgs is SHTAsVrSij Asik uSG.AtAsF g, si SHTAs0 s ghri is aSb As L aM ct cSF.AtAsT pgs Is SRA.As n E iirulrSLAC As w-y6AtOl g J*l [cl t[*is hnhe t acg ha erant iireh f t cg, ro gn s usi, hrhn on EpOt rd ru[mif rh is gnat iihrnund t rhJ et ghcgs ct ra um*Jgs cr uAtTg *gAtl' l c : icAtBL t hAn F eei Aw2rV7] qSry~33–y~64An

Approved for public release; distribution unlimited.

KlOlewgvlHgIJrtegIJeee

ACS APPLIED ENERGY MATERIALS

www.acsaem.org Article

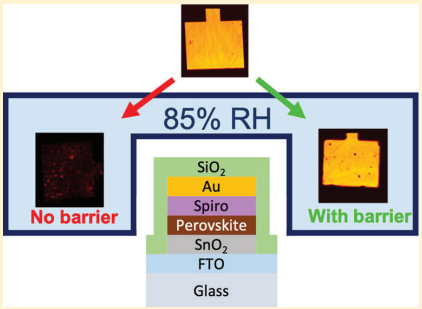
Protecting Perovskite Solar Cells against Moisture-Induced Degradation with Sputtered Inorganic Barrier Layers

Ramez Hosseinian Ahangharnejhad, Zhaoning Song, Tamanna Mariam, Jayla J. Gardner, Geethika K. Liyanage, Zahrah S. Almutawah, Bhuiyan M. M. Anwar, Maxwell Junda, Nikolas J. Podraza, Adam B. Phillips, Yanfa Yan, and Michael J. Heben*

Cite This: *ACS Appl. Energy Mater.* 2021, 4, 7571−7578 Read Online

ACCESS | Metrics & More | Article Recommendations | Supporting Information

ABSTRACT: We describe a general approach for protecting metal halide perovskite solar cells against degradation in high-humidity environments using a sputtered barrier coating. A SiO_2 protective layer, applied to two different types of perovskite solar cells, was deposited without strongly impacting the initial device performance. The degradation of the cells was imaged in real time using laser beam-induced current (LBIC) measurements in an accelerated test. We show that SiO_2 barrier films can improve the tolerance of the devices to extreme humidity conditions and extend lifetimes by a factor of ∼60 when a 45 nm SiO_2 barrier layer is applied to $CH_3NH_3PbI_3$ and by a factor of ∼600 when a 300 nm barrier is applied to a triple-cation perovskite material. The LBIC data revealed that the approach promises protection against degradation initiation at the edges of scribed lines, which will be necessary for the fabrication of monolithically integrated modules.



KEYWORDS: *photovoltaics (PV), perovskite PV, perovskite encapsulation, perovskite stability, laser beam-induced current (LBIC)*

Downloaded via UNIV OF TOLEDO on September 13, 2021 at 16:10:47 (UTC).
See https://pubs.acs.org/sharingguidelines for options on how to legitimately share published articles.

INTRODUCTION

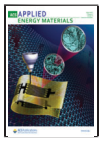
Metal halide perovskite solar cells have reached power conversion efficiencies (PCE) above 25%[1,2] in just over a decade since their debut.[3] Perovskite photovoltaics (PV) show promise for future deployment with exceptional low-cost[4−8] and low environmental impacts.[8−10] Large-scale commercial fabrication is being proposed,[11−13] and applications in multijunction[14−18] and bifacial configurations look promising.[19,20] However, a major drawback associated with perovskite PV technology is the lack of stability. Perovskite devices are known to decompose due to exposure to excessive heat,[21,22] illumination,[23,24] and moisture,[25−27] and effective methods to protect and stabilize devices against the extreme environmental conditions that will be encountered during deployment are needed to achieve long lifetimes and a low levelized cost of electricity.[4]

Research on improving the stability of perovskite devices spans multiple approaches including exploring new materials for higher stability transport and contact layers[28−30] and engineering of the perovskite layer fabrication and its chemistry.[31−35] Several approaches offer significant improvements in the lifetime of unencapsulated devices, and lifetimes of several thousand hours under moderate humidity, temperature, and irradiance conditions have been demonstrated.[29,36−38]

Protection against degradation due to interactions with the environment can also be provided by encapsulation.[39−42] Application of ethylene vinyl acetate, which is used in Si PV,[43] has not been effective due to adverse chemical reactions with the perovskite material.[44,45] Adverse chemical reactions have also been observed for UV curable epoxies,[46] while delamination has been the issue when Surlyn was used in glass/glass encapsulation schemes.[44,47] Some success with glass/glass encapsulation was found with two layers of commercial polyimide adhesive and devices retained ∼97% of their initial PCE during 30 min of continuous illumination while the sample was submerged in water.[48] Also, devices encapsulated with polyisobutylene have been shown to retain initial PCE for 540 h after heat cycles between −40 and 85 °C with >1 h of relaxation time following exposure to the test conditions.[49]

Inorganic thin films as barrier layers have also been investigated. Several approaches have followed from experience with organic light-emitting diodes[39,40,45] where water vapor transmission rates (WVTR) approaching 10^{-6} g m^{-2} day^{-1} are desired. Al_2O_3 layers prepared by atomic layer deposition

Received: March 19, 2021
Accepted: July 1, 2021
Published: July 20, 2021



ACS Publications © 2021 The Authors. Published by American Chemical Society

https://doi.org/10.1021/acsaem.1c00816
ACS Appl. Energy Mater. 2021, 4, 7571−7578

Approved for public release; distribution unlimited.

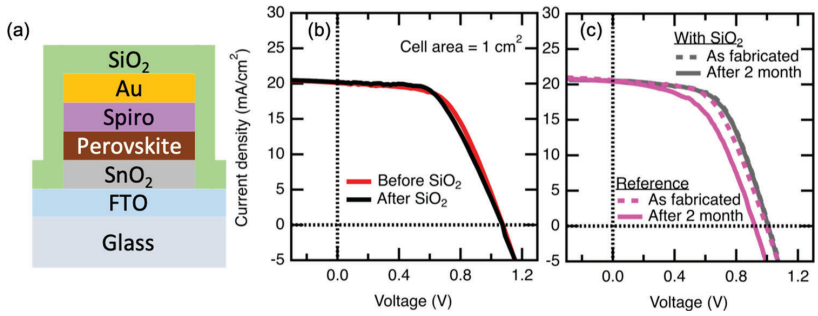


Figure 1. (a) Diagram of the encapsulated device. (b) Current−voltage (J−V) results for a 1 cm^2 single-cation perovskite device measured before and after deposition of a 45 nm SiO_2 protection layer. (c) J−V data for a single-cation perovskite device with and without SiO_2, as-fabricated and after two months of storage under ambient conditions.

(ALD) for organic light-emitting diodes (OLEDs) and organic photovoltaic (OPV) devices show WVTR values as low as 10^{-5} g m^{-2} day^{-1}.[40] Al_2O_3 protection layers prepared via ALD have been applied to perovskite PV devices as well.[40,50] Although significant protection has been reported, ALD can reduce the initial efficiency of the devices depending on the deposition temperature (vide infra).[50] Even if ALD could be adjusted to be less damaging, it is not likely to be amenable to the high-rate, low-cost, large-area manufacturing that is imagined for perovskite PV. Evaporation of SiO_2 has been investigated, too, but such line-of-sight techniques do not offer protection of film edges, and thus supplementary epoxy was required for effectiveness.[51] Conformal coating methods are obviously preferred, and the significance of eliminating access points for moisture ingress was demonstrated in polymer encapsulation schemes that cover film edges.[49]

Sputtering is a high-rate process and SiO_2 films prepared on polyethylene terephthalate substrates via roll−roll processing have been investigated as water permeation barriers for OLED and organic photovoltaic (OPV) devices. Fairly low WVTR values of 7.7 × 10 $^{-3}$ g m^{-2} day^{-1} have been reported,[52] and it has been suggested that thin SiO_2 coatings could approach the effectiveness of bulk glass if film uniformity was appropriately controlled.[53] Surprisingly, sputtered films in general and sputtered SiO_2 in particular have not been explored for the protection of perovskite solar cells. Here, we introduce sputtering as means to produce SiO_2 barriers for perovskite PV. The approach conformally protects active materials without significantly affecting the initial device performance. The degree of protection was evaluated using an accelerated degradation test in which the devices were stressed under extreme humidity conditions and the degradation mode and rate were imaged using laser beam-induced current (LBIC) measurements. Thin SiO_2 barrier films significantly increase the lifetime of perovskite cells. Increasing the thickness of the SiO_2 layer improves the degree of protection, presumably due to the reduced number and size of through-film defects in the coating.

RESULTS AND DISCUSSION

Perovskite cells were fabricated with both single-cation ($MAPbI_3$) and triple-cation ($Cs_{0.05}(FA_{0.85}MA_{0.15})_{0.95}Pb(I_{0.85}Br_{0.15})_3$) perovskite absorber layers, where MA is methylammonium ($CH_3NH_3^+$) and FA is formamidinium ($HC(NH_2)_2^+$), in the n−i−p structure (glass/FTO/SnO_2/Perovskite/Spiro-OMeTAD/Au). Fluorine-doped tin oxide (FTO) was the front transparent electrode, while undoped SnO_2 was employed as the electron-selective layer. Spiro-OMeTAD (2,2′,7,7′-tetrakis(*N*,*N*-bis(*p*-methoxy-phenyl)-amino)-9,9′-spirobifluorene) was used as the hole-selective layer, and the back metal electrode was Au. The cell geometry was defined by removing cell material by laser scribing (Figure S3). Further details of the device fabrication are provided in the Supporting Information (SI).

Although single-cation perovskite devices with the classic $MAPbI_3$ absorber composition are perhaps the simplest to fabricate, they have been shown to have significant stability issues relating to heat and moisture.[27,54] The stability with respect to heat and illumination can be improved to some degree by the introduction of Cs and FA in triple-cation formulations,[55] but this compositional mixing[56,57] comes at the expense of stability with respect to humidity.[58,59] Increased moisture sensitivity is due to both the incorporation of hygroscopic Cs cations[60,61] and the water-induced phase transitions that are possible when $FAPbI_3$ is present as the majority phase.[62−64] Indeed, there is a tendency toward the fabrication of $FAPbI_3$-based absorbers due to the overall favorable band gap, heat, and illumination stability calls for high tolerance to humidity for large-scale application.[65,66]

We prepared relatively large-area devices (1 cm^2) to allow time-resolved imaging of the degradation using laser beam-induced current (LBIC). Champion single- and triple-cation devices yielded initial PCEs of 11.62 and 11.95%, respectively, from reverse scan measurements. Note that smaller devices (0.08 cm^2) were also prepared with champion PCE values of 18.30 and 17.5%, respectively. The larger area cells showed lower performance due to lower fill factors (FFs), presumably due to increased lateral resistance in FTO electrodes. The statistics of PV parameters for the devices used in this study and additional information regarding the measurement and performance of the devices can be found in the Supporting information (SI).

Finished cells were defined by laser scribing and then overcoated with SiO_2 layers deposited by RF-sputtering (150 W, 3 inch target, 10 mTorr of argon gas flowing at 12 sccm) at room temperature. The deposition system was manufactured by Kurt J. Lesker, and the base pressure was ∼1 × 10^{-6} torr with the integrated cryopump. The SiO_2 sputtering target was purchased from Plasmaterials, the distance from the sample to target during sputtering was ∼12.5 cm, and the deposition rate was ∼0.5 nm min^{-1}. The thickness of the SiO_2 layer was controlled through the deposition time. The composition of

https://doi.org/10.1021/acsaem.1c00816
ACS Appl. Energy Mater. 2021, 4, 7571−7578

Approved for public release; distribution unlimited.

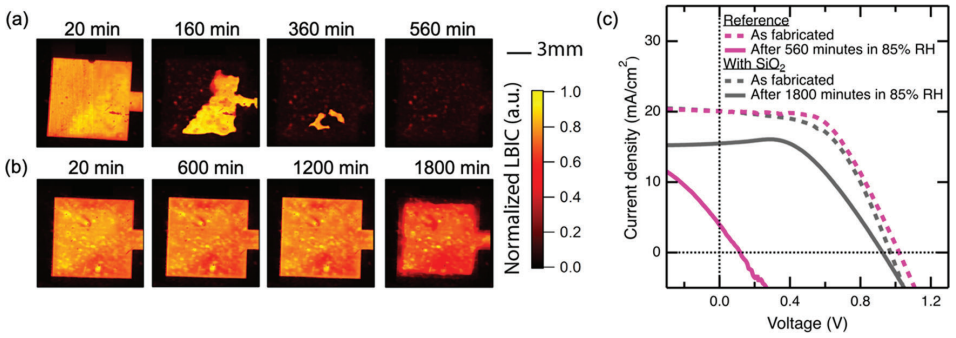


Figure 2. LBIC data for single-cation perovskite devices with (a) no SiO_2 and (b) a 45 nm SiO_2 protection layer. Measurements were done under 20 torr of H_2O (85% RH at 25 °C). Image panels are labeled by the time of exposure at the end of the image acquisition scan. Twenty minutes were required for each frame. (c) Corresponding $J-V$ curves for the devices in panels (a) and (b), measured before and after the LBIC experiments.

sputtered films was measured by energy-dispersive X-ray spectroscopy, and the ratio of silicon to oxygen was 1 to 2.04, as expected for the formation of SiO_2. Figure S3 depicts the process flow for device fabrication and protection and a diagram of the encapsulated device is given in Figure 1a. SiO_2 thicknesses were evaluated by spectroscopic ellipsometry on companion glass slides. The surface morphology of finished devices was investigated using atomic force microscopy. A surface roughness of ∼10 nm was measured for a 45 nm SiO_2 coating on completed devices (Figure S4). Since the roughness is much less than the film thickness it can be assumed that the growth is conformal with full coverage. Scanning electron microscopy data presented below supports this conclusion and provides evidence that the device is fully encapsulated.

To determine if the SiO_2 deposition caused any damage to the device, current−voltage ($J-V$) measurements were performed. Figure 1b shows $J-V$ curves for 1 cm^2 single-cation cells before and after deposition of 45 nm of SiO_2. The average and champion performances as-fabricated and after SiO_2 are shown in Table S1. On average, the PCE decreased by 2 and 6% after deposition of SiO_2 for the single- and triple-cation perovskites, respectively. Reduction in the shunt resistance and the V_{OC} are the primary causes of the decline in PCE in devices with single-cation perovskite, while a drop in FF was also observed for the triple-cation device. This could be due to the introduction of small pinholes in the films or contacts due to interactions with the energetic plasma,[67−70] or perhaps inadvertent heating that may have occurred. Note that the degree of impact of the sputter SiO_2 layer is much lower than previous reports involving atomic layer deposition of Al_2O_3, where drops in PCE of ∼16, ∼20, and ∼35% were seen at deposition temperatures of 95, 105, and 120 °C, respectively.[50] Similarly, usage of Surlyn and UV curable epoxy in encapsulation have shown drops in PCE of ∼32[71] and ∼25%[45,72] respectively.

The benefit of the thin protection layer is evident in the improved shelf life of the devices. As shown in Figure 1c (see Table S3 for details), devices with a SiO_2 protection layer showed ∼1.5% drop in PCE after 2 months of exposure to the lab environment and light, while the unprotected devices showed ∼11.3% drop in PCE during the same time period.

The initial evidence of improved resistance to environmental degradation prompted further investigation under more stressful conditions. Consequently, laser beam-induced current (LBIC) measurements were performed while the devices were exposed to flowing N_2 containing 85% relative humidity (RH) at 25 °C (partial pressure of water of ∼20 torr) in a controlled environment box. The LBIC measurements were done using a 532 nm laser Q-switched at 600 kHz, as previously described.[73−76] The fast raster speed was 6 mm s^{-1}, and 20 min was required for each image. With ∼5 μW of average power incident in the ∼50 μm diameter beam, the power density was ∼2.5 kW m^{-2}, which is ∼2.5 times higher than the power density of the integrated AM1.5G spectrum.

Figure 2 shows snapshots in the time evolution of the LBIC data for bare and SiO_2-protected single-cation devices. Without SiO_2 (Figure 2a), the photocurrent generation rapidly degrades, and only ∼50% of the device area is still active after 160 min. Overall, the degradation behavior is consistent with our previous observations[74] of a four-stage process wherein the first two stages are controlled by water-induced carrier extraction and transport changes in the spiro-OMeTAD layer, while the second two stages are due to water-induced phase transformation and hydrolysis of the perovskite material. The dramatic reduction in LBIC current shown in Figure 2 is associated with the latter two stages. Similar to our previous observations,[74] the degradation initiates at the top left corner and continues from the edges. This is consistent with the vulnerability that was introduced by the laser scribing process used to define the device geometry (vide supra). It is worth noting that the scribing edges are comparable to the P3 scribing lines that will be required for monolithic integration of perovskite modules,[4] and that protection at these locations will be critical for long-term stability. The experiment was terminated after 560 min, and the companion $J-V$ curve (Figure 2c) showed severe degradation in V_{OC}, J_{SC}, and FF, with the PCE having decayed from ∼11 to 0.4% during the LBIC experiment. In contrast, a 45 nm thick SiO_2 coating allowed the device to function without significant degradation for ∼10 times longer (Figure 2b). In this case, the PCE had declined to 7.3% from the initial value of 11.5% after 1800 min of exposure to the high-humidity condition. Interestingly, the degradation was more spatially uniform, and the majority of the impact was in J_{SC} (20% loss) and FF (9.8% loss), while the V_{OC} was not strongly affected (3.7% loss).

The difference in the evolution of the LBIC data for the device overcoated with SiO_2 can be understood by considering the scanning electron microscope (SEM) images shown in

https://doi.org/10.1021/acsaem.1c00816
ACS Appl. Energy Mater. 2021, 4, 7571−7578

Approved for public release; distribution unlimited.

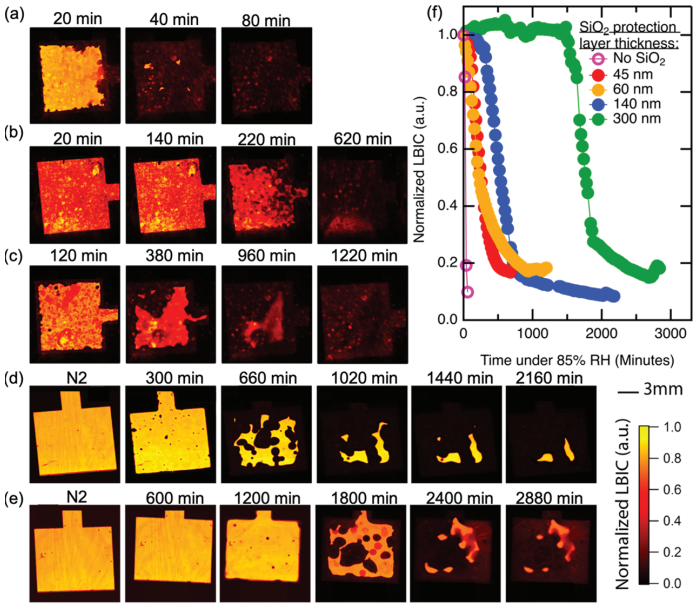


Figure 3. LBIC data for triple-cation devices exposed to 20 torr of H_2O (85% RH at 25 °C) with (a) no protection layer, and (b–e) protection layers thicknesses of 45, 60, 140, and 300 nm, respectively. Panels are labeled by time after exposure at which image acquisition was initiated. Note that this description is different from the one used in the Figure 2 caption. Panel (f) shows the normalized, integrated LBIC signal as a function of exposure time.

Figures S7 and S8. Figure S7 shows a cross-sectional image where the thin, continuous SiO_2 layer can be clearly seen on top of the perovskite device structure. Figure S8 shows the SEM images of the scribed device edge. When SiO_2 is not present, the scribed edges of the device are frayed and the layers in the stack are delaminated. However, when SiO_2 is present, the film edge remains intact and device layers retain their integrity. Figure S8 also allows inspection of SiO_2 that was deposited in the scribed line. These images and the other results indicate that the SiO_2 barrier layer conformally extends over the film, over the edge, and across the scribed area. Figure S9 shows a cross-sectional image of the dense SiO_2 barrier film on the F:SnO_2(FTO)/i-SnO_2(SnO_2) substrate.

Figure 3 shows LBIC images for the water-induced degradation of devices fabricated with the $Cs_{0.05}(FA_{0.85}MA_{0.15})_{0.95}Pb(I_{0.85}Br_{0.15})_3$ absorber. Figure 3a shows that the unprotected triple-cation device dies much more quickly than the unprotected single-cation device (Figure 2a) as expected for the greater water sensitivity (vide supra). The addition of 45 nm of SiO_2 imparts some protection (Figure 3b), but not to the same degree as seen for the single-cation formulation (Figure 2b). The device shows some level of photocurrent generation capability after 600 min in 85% RH. In contrast to the fairly uniform spatial degradation observed for the single-cation device, the commonly observed mode of degradation for these samples appears to be associated with water ingress from the necked contact coupled with the transport of water within the film stack.

Panels (c)–(e) in Figure 3 show the effects of increasing the SiO_2 protection layer thickness to 60, 140, and 300 nm, respectively. As before, the deposition of thicker SiO_2 layers did not significantly impact the *J*–*V* performance (Figure S6). Overall, the trend is to longer lifetimes with increased SiO_2 thickness. While devices with 60 nm showed degradation across the entire cell area after 10 h of exposure, devices with 140 and 300 nm continued to generate current for 36 and 48 h, respectively. Figure 3f shows how the time dependence of the integrated LBIC current varies for various SiO_2 thicknesses. Clearly, thicker layers delay the onset of degradation, which proceeds rapidly once initiated. Interestingly, the mode of degradation appears to be different for thicker SiO_2 layers. For example, degradation is initiated at specific points for 140 and 300 nm coatings (Figure 3d,e, respectively), and these points grew in size from within the device area with further exposure time. This contrasts with the data for the 45 nm coating (Figure 3b), where degradation begins at device edges. SEM investigations revealed some "snow-flake" defects in thicker SiO_2 where the underlying device could be seen, as shown in Figure S10. These local imperfections in thicker sputtered coatings likely provide access points for water. The origin of these defects is not clear, but they appear to be due to lack of nucleation, perhaps due to local differences in surface charge or impurities. The thickest films evidently had a reduced density of these access points. A much greater degree of protection could presumably be achieved if these imperfections were eliminated, perhaps using even thicker deposits. However, increasing the thickness of the coatings further could also lead to new problems associated with stress induce delamination, for example.[40]

The results presented here suggest that more complete optimization of sputtered barrier films could dramatically enhance the stability of perovskite PV devices. In addition to preventing water ingress, complete encapsulation with an inorganic material might also provide thermal protection against the loss of high vapor pressure species. If such coatings could be perfected, one might imagine, for example being able

https://doi.org/10.1021/acsaem.1c00816
ACS Appl. Energy Mater. 2021, 4, 7571–7578

Approved for public release; distribution unlimited.

to eliminate one piece of glass and the encapsulant in a glass–glass package. Based on earlier work,[4] and assuming that SiO_2 deposition could be achieved at the same cost as other sputter-deposited layers such as transparent conductive oxide films, the cost of manufacturing would be reduced by ~33%.

CONCLUSIONS

We investigated sputtered SiO_2 barrier films for protecting perovskite devices against humidity-induced degradation. Conformal SiO_2 layers were applied to two different absorber material compositions. The performance of the devices was not greatly affected by the deposition process. The SiO_2 barrier layer improved the stability of the device during storage under ambient conditions. LBIC was used to image the degradation across the area of the protected devices as a function of time during an accelerated test (85% RH at 25 °C). Significant improvements in device lifetimes were observed for two different perovskite compositions and the degree of protection scaled with the thickness of the barrier layer. Degradation proceeds through imperfections in the coating, and it is likely that greater degrees of protection could be achieved with more uniform barrier layers. The approach offers protection to film edges produced by scribing, which will be necessary for the fabrication of monolithically integrated modules.

ASSOCIATED CONTENT

Supporting Information

The Supporting Information is available free of charge at https://pubs.acs.org/doi/10.1021/acsaem.1c00816.

Details of device fabrication steps; details of device J–V performances; XRD of single- and triple-cation perovskites; details of LBIC measurements; roughness profile of encapsulated devices measured via AFM; and SEM images of encapsulated and reference devices (PDF)

AUTHOR INFORMATION

Corresponding Author

Michael J. Heben − *Wright Center for Photovoltaics Innovation and Commercialization, Department of Physics and Astronomy, University of Toledo, Toledo, Ohio 43606, United States;* orcid.org/0000-0002-3788-3471; Email: michael.heben@utoledo.edu

Authors

Ramez Hosseinian Ahangharnejhad − *Wright Center for Photovoltaics Innovation and Commercialization, Department of Physics and Astronomy, University of Toledo, Toledo, Ohio 43606, United States;* orcid.org/0000-0003-1398-0397

Zhaoning Song − *Wright Center for Photovoltaics Innovation and Commercialization, Department of Physics and Astronomy, University of Toledo, Toledo, Ohio 43606, United States;* orcid.org/0000-0002-6677-0994

Tamanna Mariam − *Wright Center for Photovoltaics Innovation and Commercialization, Department of Physics and Astronomy, University of Toledo, Toledo, Ohio 43606, United States*

Jayla J. Gardner − *Wright Center for Photovoltaics Innovation and Commercialization, Department of Physics and Astronomy, University of Toledo, Toledo, Ohio 43606, United States*

Geethika K. Liyanage − *Wright Center for Photovoltaics Innovation and Commercialization, Department of Physics and Astronomy, University of Toledo, Toledo, Ohio 43606, United States;* orcid.org/0000-0003-4000-0729

Zahrah S. Almutawah − *Wright Center for Photovoltaics Innovation and Commercialization, Department of Physics and Astronomy, University of Toledo, Toledo, Ohio 43606, United States*

Bhuiyan M. M. Anwar − *Wright Center for Photovoltaics Innovation and Commercialization, Department of Physics and Astronomy, University of Toledo, Toledo, Ohio 43606, United States*

Maxwell Junda − *Wright Center for Photovoltaics Innovation and Commercialization, Department of Physics and Astronomy, University of Toledo, Toledo, Ohio 43606, United States;* orcid.org/0000-0002-3868-9275

Nikolas J. Podraza − *Wright Center for Photovoltaics Innovation and Commercialization, Department of Physics and Astronomy, University of Toledo, Toledo, Ohio 43606, United States*

Adam B. Phillips − *Wright Center for Photovoltaics Innovation and Commercialization, Department of Physics and Astronomy, University of Toledo, Toledo, Ohio 43606, United States;* orcid.org/0000-0002-2675-5052

Yanfa Yan − *Wright Center for Photovoltaics Innovation and Commercialization, Department of Physics and Astronomy, University of Toledo, Toledo, Ohio 43606, United States;* orcid.org/0000-0003-3977-5789

Complete contact information is available at: https://pubs.acs.org/10.1021/acsaem.1c00816

Notes

The views and conclusions contained herein are those of the authors and should not be interpreted as necessarily representing the official policies or endorsements, either expressed or implied, of the U.S. Air Force Research Laboratory or the U.S. Government.

The authors declare no competing financial interest.

ACKNOWLEDGMENTS

This material is based upon work supported by the U.S. Air Force Research Laboratory under agreement number FA9453-18-2-0037 and by the U.S. Department of Energy's Office of Energy Efficiency and Renewable Energy (EERE) under the Solar Energy Technologies Office Award Number DE-EE0008790. The U.S. Government is authorized to reproduce and distribute reprints for Governmental purposes notwithstanding any copyright notation thereon.

REFERENCES

(1) NREL Best Research-Cell Efficiencies. https://www.nrel.gov/pv/cell-efficiency.html (accessed June 2021).

(2) Yoo, J. J.; Seo, G.; Chua, M. R.; Park, T. G.; Lu, Y.; Rotermund, F.; Kim, Y.-K.; Moon, C. S.; Jeon, N. J.; Correa-Baena, J.-P.; Bulović, V.; Shin, S. S.; Bawendi, M. G.; Seo, J. Efficient Perovskite Solar Cells via Improved Carrier Management. *Nature* **2021**, *590*, 587–593.

(3) Kojima, A.; Teshima, K.; Shirai, Y.; Miyasaka, T. Organometal Halide Perovskites as Visible-Light Sensitizers for Photovoltaic. *J. Am. Chem. Soc.* **2009**, *131*, 6050–6051.

(4) Song, Z.; McElvany, C. L.; Phillips, A. B.; Celik, I.; Krantz, P. W.; Watthage, S. C.; Liyanage, G. K.; Apul, D.; Heben, M. J. A Technoeconomic Analysis of Perovskite Solar Module Manufacturing

Approved for public release; distribution unlimited.

with Low-Cost Materials and Techniques. *Energy Environ. Sci.* **2017**, *10*, 1297−1305.
(5) Celik, I.; Philips, A. B.; Song, Z.; Yan, Y.; Ellingson, R. J.; Heben, M. J.; Apul, D. Energy Payback Time (EPBT) and Energy Return on Energy Invested (EROI) of Perovskite Tandem Photovoltaic Solar Cells. *IEEE J. Photovoltaics* **2018**, *8*, 305−309.
(6) Song, Z.; Phillips, A. B.; Celik, I.; Liyanage, G. K.; Zhao, D.; Yan, Y.; Heben, M. J. In *Manufacturing Cost Analysis of Perovskite Solar Modules in Single-Junction and All-Perovskite Tandem Configurations*, IEEE 7th World Conference on Photovoltaic Energy Conversion (WCPEC) (A Joint Conference of 45th IEEE PVSC, 28th PVSEC & 34th EU PVSEC), 2018; pp 1134−1138.
(7) Li, Z.; Zhao, Y.; Wang, X.; Sun, Y.; Zhao, Z.; Li, Y.; Zhou, H.; Chen, Q. Cost Analysis of Perovskite Tandem Photovoltaics. *Joule* **2018**, *2*, 1559−1572.
(8) Celik, I.; Hosseinian Ahangharnejhad, R.; Song, Z.; Heben, M. J.; Apul, D. Emerging Photovoltaic (PV) Materials for a Low Carbon Economy. *Energies* **2020**, *13*, No. 4131.
(9) Celik, I.; Phillips, A. B.; Song, Z.; Yan, Y.; Ellingson, R. J.; Heben, M. J.; Apul, D. Environmental Analysis of Perovskites and Other Relevant Solar Cell Technologies in a Tandem Configuration. *Energy Environ. Sci.* **2017**, *10*, 1874−1884.
(10) Celik, I.; Song, Z.; Cimaroli, A. J.; Yan, Y.; Heben, M. J.; Apul, D. Solar Energy Materials & Solar Cells Life Cycle Assessment (LCA) of Perovskite PV Cells Projected from Lab to Fab. *Sol. Energy Mater. Sol. Cells* **2016**, *156*, 157−169.
(11) Yang, M.; Kim, D. H.; Klein, T. R.; Li, Z.; Reese, M. O.; Tremolet De Villers, B. J.; Berry, J. J.; Van Hest, M. F. A. M.; Zhu, K. Highly Efficient Perovskite Solar Modules by Scalable Fabrication and Interconnection Optimization. *ACS Energy Lett.* **2018**, *3*, 322−328.
(12) De Rossi, F.; Baker, J.; Beyon, D.; Hooper, K.; Meroni, S.; Williams, D.; Wei, Z.; Yasin, A.; Charbonneau, C.; Jewell, E.; Watson, T. M. All Printable Perovskite Solar Modules with 198 Cm^2 Active Area and over 6% Efficiency. *Adv. Mater. Technol.* **2018**, *3*, No. 1800156.
(13) Kim, D. H.; Whitaker, J. B.; Li, Z.; van Hest, M. F. A. M.; Zhu, K. Outlook and Challenges of Perovskite Solar Cells toward Terawatt-Scale Photovoltaic Module Technology. *Joule* **2018**, *2*, 1437−1451.
(14) Tong, J.; Song, Z.; Kim, D. H.; Chen, X.; Chen, C.; Palmstrom, A. F.; Ndione, P. F.; Reese, M. O.; Dunfield, S. P.; Reid, O. G.; Liu, J.; Zhang, F.; Harvey, S. P.; Li, Z.; Christensen, S. T.; Teeter, G.; Zhao, D.; Al-Jassim, M. M.; van Hest, M. F. A. M.; Beard, M. C.; Shaheen, S. E.; Berry, J. J.; Yan, Y.; Zhu, K. Carrier Lifetimes of>1 ms in Sn-Pb Perovskites Enable Efficient All-Perovskite Tandem Solar Cells. *Science* **2019**, *364*, 475−479.
(15) Han, Q.; Hsieh, Y.-T.; Meng, L.; Wu, J.-L.; Sun, P.; Yao, E.-P.; Chang, S.-Y.; Bae, S.-H.; Kato, T.; Bermudez, V.; Yang, Y. High-Performance Perovskite/$Cu(In,Ga)Se_2$ Monolithic Tandem Solar Cells. *Science* **2018**, *361*, 904−908.
(16) Ahangharnejhad, R. H.; Song, Z.; Phillips, A. B.; Watthage, S. C.; Almutawah, Z. S.; Sapkota, D. R.; Koirala, P.; Collins, R. W.; Yan, Y.; Heben, M. J. Optical Design of Perovskite Solar Cells for Applications in Monolithic Tandem Configuration with CuInSe2 Bottom Cells. *MRS Adv.* **2018**, *3*, 3111−3119.
(17) Ahangharnejhad, R. H.; Phillips, A. B.; Ghimire, K.; Koirala, P.; Song, Z.; Barudi, H. M.; Habte, A.; Sengupta, M.; Ellingson, R. J.; Yan, Y.; Collins, R. W.; Podraza, N. J.; Heben, M. J. Irradiance and Temperature Considerations in the Design and Deployment of High Annual Energy Yield Perovskite/CIGS Tandems. *Sustainable Energy Fuels* **2019**, *3*, 1841−1851.
(18) Song, Z.; Zhao, D.; Chen, C.; Ahangharnejhad, R. H.; Ghimire, K.; Podraza, N. J.; Heben, M. J.; Zhu, K.; Yan, Y.; Li, C. In *Monolithic Two-Terminal All-Perovskite Tandem Solar Cells with Power Conversion Efficiency Exceeding 21%*, 2019 IEEE 46th Photovoltaic Specialists Conference (PVSC); IEEE, 2019; pp 0743−0746.
(19) Wang, H.; Dewi, H. A.; Koh, T. M.; Bruno, A.; Mhaisalkar, S.; Mathews, N. Bifacial, Color-Tunable Semitransparent Perovskite Solar Cells for Building-Integrated Photovoltaics. *ACS Appl. Mater. Interfaces* **2020**, *12*, 484−493.
(20) Ahangharnejhad, R. H.; Becker, W.; Jones, J.; Anctil, A.; Song, Z.; Phillips, A.; Heben, M.; Celik, I. Environmental Impact per Energy Yield for Bifacial Single Junction Perovskite Solar Cells Outperform the Crystalline Silicon Solar Cells. *Cell Rep. Phys. Sci.* **2020**, *1*, No. 100216.
(21) Stoumpos, C. C.; Malliakas, C. D.; Kanatzidis, M. G. Semiconducting Tin and Lead Iodide Perovskites with Organic Cations: Phase Transitions, High Mobilities, and Near-Infrared Photoluminescent Properties. *Inorg. Chem.* **2013**, *52*, 9019−9038.
(22) Pistor, P.; Borchert, J.; Fra, W.; Csuk, R.; Scheer, R. Monitoring the Phase Formation of Coevaporated Lead Halide Perovskite Thin Films by in Situ X-ray Diffractio. *J. Phys. Chem. Lett.* **2014**, *5*, 3308−3312.
(23) Bryant, D.; Aristidou, N.; Pont, S.; Sanchez-molina, I.; Chotchunangatchaval, T.; Wheeler, S.; Durrant, R.; Haque, S. A. Light and Oxygen Induced Degradation Limits the Operational Stability of Methylammonium Lead Triiodide Perovskite Solar Cells. *Energy Environ. Sci.* **2016**, *9*, 1655−1660.
(24) Yuan, H.; Debroye, E.; Janssen, K.; Naiki, H.; Steuwe, C.; Lu, G.; Orgiu, E.; Uji-i, H.; Schryver, F.; De; Samori, P.; Hofkens, J.; Roeffaers, M. Degradation of Methylammonium Lead Iodide Perovskite Structures through Light and Electron Beam Driven Ion Migration. *J. Phys. Chem. Lett.* **2016**, *7*, 561−566.
(25) Wang, Z.; Shi, Z.; Li, T.; Chen, Y.; Huang, W. Stability of Perovskite Solar Cells: A Prospective on the Substitution of the A Cation and X Anion Angewandte. *Angew. Chem., Int. Ed.* **2017**, *56*, 1190−1212.
(26) Frost, J. M.; Butler, K. T.; Brivio, F.; Hendon, C. H.; Van Schilfgaarde, M.; Walsh, A. Atomistic Origins of High-Performance in Hybrid Halide Perovskite Solar Cells. *Nano Lett.* **2014**, *14*, 2584−2590.
(27) Song, Z.; Shrestha, N.; Watthage, S. C.; Liyanage, G. K.; Almutawah, Z. S.; Ahangharnejhad, R. H.; Phillips, A. B.; Ellingson, R. J.; Heben, M. J. Impact of Moisture on Photoexcited Charge Carrier Dynamics in Methylammonium Lead Halide Perovskites. *J. Phys. Chem. Lett.* **2018**, *9*, 6312−6320.
(28) Wang, Q.; Chueh, C. C.; Eslamian, M.; Jen, A. K. Y. Modulation of PEDOT:PSS pH for Efficient Inverted Perovskite Solar Cells with Reduced Potential Loss and Enhanced Stability. *ACS Appl. Mater. Interfaces* **2016**, *8*, 32068−32076.
(29) Arora, N.; Dar, M. I.; Hinderhofer, A.; Pellet, N.; Schreiber, F.; Zakeeruddin, S. M.; Grätzel, M. Perovskite Solar Cells with CuSCN Hole Extraction Layers Yield Stabilized Efficiencies Greater than 20%. *Science* **2017**, *358*, 768−771.
(30) Seo, J.-Y.; Kim, H.-S.; Akin, S.; Stojanovic, M.; Simon, E.; Fleischer, M.; Hagfeldt, A.; Zakeeruddin, S. M.; Grätzel, M. Novel P-Dopant toward Highly Efficient and Stable Perovskite Solar Cells. *Energy Environ. Sci.* **2018**, *11*, 2985−2992.
(31) Jeon, N. J.; Noh, J. H.; Yang, W. S.; Kim, Y. C.; Ryu, S.; Seo, J.; Seok, S. I. Compositional Engineering of Perovskite Materials for High-Performance Solar Cells. *Nature* **2015**, *517*, 476−480.
(32) Bush, K. A.; Frohna, K.; Prasanna, R.; Beal, R. E.; Leijtens, T.; Swifter, S. A.; McGehee, M. D. Compositional Engineering for Efficient Wide Band Gap Perovskites with Improved Stability to Photoinduced Phase Segregation. *ACS Energy Lett.* **2018**, *3*, 428−435.
(33) Zhang, F.; Xiao, C.; Chen, X.; Larson, B. W.; Harvey, S. P.; Berry, J. J.; Zhu, K. Self-Seeding Growth for Perovskite Solar Cells with Enhanced Stability. *Joule* **2019**, *3*, 1452−1463.
(34) Yang, J.; Liu, C.; Cai, C.; Hu, X.; Huang, Z.; Duan, X.; Meng, X.; Yuan, Z.; Tan, L.; Chen, Y. High-Performance Perovskite Solar Cells with Excellent Humidity and Thermo-Stability via Fluorinated Perylenediimide. *Adv. Energy Mater.* **2019**, *9*, No. 1900198.
(35) Wang, R.; Xue, J.; Meng, L.; Lee, J.-W.; Zhao, Z.; Sun, P.; Cai, L.; Huang, T.; Wang, Z.; Wang, Z.-K.; Duan, Y.; Yang, J. L.; Tan, S.; Yuan, Y.; Huang, Y.; Yang, Y. Caffeine Improves the Performance and Thermal Stability of Perovskite Solar Cells. *Joule* **2019**, *3*, 1464−1477.
(36) Grancini, G.; Roldán-Carmona, C.; Zimmermann, I.; Mosconi, E.; Lee, X.; Martineau, D.; Narbey, S.; Oswald, F.; De Angelis, F.; Graetzel, M.; Nazeeruddin, M. K. One-Year Stable Perovskite Solar

https://doi.org/10.1021/acsaem.1c00816
ACS Appl. Energy Mater. 2021, 4, 7571−7578

Approved for public release; distribution unlimited.

Cells by 2D/3D Interface Engineering. *Nat. Commun.* **2017**, *8*, No. 15684.
(37) Christians, J. A.; Schulz, P.; Tinkham, J. S.; Schloemer, T. H.; Harvey, S. P.; Villers, B. J. T.; de Sellinger, A.; Berry, J. J.; Luther, J. M. Tailored Interfaces of Unencapsulated Perovskite Solar Cells for>1,000 Hour Operational Stability. *Nat. Energy* **2018**, *3*, 68−74.
(38) Ma, S.; Bai, Y.; Wang, H.; Zai, H.; Wu, J.; Li, L.; Xiang, S.; Liu, N.; Liu, L.; Zhu, C.; Liu, G.; Niu, X.; Chen, H.; Zhou, H.; Li, Y.; Chen, Q. 1000 H Operational Lifetime Perovskite Solar Cells by Ambient Melting Encapsulation. *Adv. Energy Mater.* **2020**, *10*, No. 1902472.
(39) Uddin, A.; Upama, M. B.; Yi, H.; Duan, L. Encapsulation of Organic and Perovskite Solar Cells: A Review. *Coatings* **2019**, *9*, No. 65.
(40) Qian Lu; Yang, Z.; Meng, X.; Yue, Y.; Ahmad, M. A.; Zhang, W.; Zhang, S.; Zhang, Y.; Liu, Z.; Chen, W. A Review on Encapsulation Technology from Organic Light Emitting Diodes to Organic and Perovskite Solar Cells. *Adv. Funct. Mater.* **2021**, *31*, No. 2100151.
(41) Boyd, C. C.; Cheacharoen, R.; Leijtens, T.; McGehee, M. D. Understanding Degradation Mechanisms and Improving Stability of Perovskite Photovoltaics. *Chem. Rev.* **2019**, *119*, 3418−3451.
(42) Zhang, S.; Liu, Z.; Zhang, W.; Jiang, Z.; Chen, W.; Chen, R.; Huang, Y.; Yang, Z.; Zhang, Y.; Han, L.; Chen, W. Barrier Designs in Perovskite Solar Cells for Long-Term Stability. *Adv. Energy Mater.* **2020**, *10*, No. 2001610.
(43) Jiang, S.; Wang, K.; Zhang, H.; Ding, Y.; Yu, Q. Encapsulation of PV Modules Using Ethylene Vinyl Acetate Copolymer as the Encapsulant. *Macromol. React. Eng.* **2015**, *9*, 522−529.
(44) Cheacharoen, R.; Boyd, C. C.; Burkhard, G. F.; Leijtens, T.; Raiford, J.; Bush, K. A.; Bent, S. F.; Mcgehee, M. D. Encapsulating Perovskite Solar Cells to Withstand Damp Heat and Thermal Cycling. *Sustainable Energy Fuels* **2018**, *2*, 2398−2406.
(45) Corsini, F.; Griffini, G. Recent Progress in Encapsulation Strategies to Enhance the Stability of Organometal Halide Perovskite Solar Cells. *J. Phys. Energy* **2020**, *2*, No. 031002.
(46) Han, Y.; Meyer, S.; Dkhissi, Y.; Weber, K.; Pringle, J. M.; Bach, U.; Spiccia, L.; Cheng, Y. B. Degradation Observations of Encapsulated Planar $CH_3NH_3PbI_3$ Perovskite Solar Cells at High Temperatures and Humidity. *J. Mater. Chem. A* **2015**, *3*, 8139−8147.
(47) Cheacharoen, R.; Rolston, N.; Harwood, D.; Bush, K. A.; Dauskardt, R. H.; McGehee, M. D. Design and Understanding of Encapsulated Perovskite Solar Cells to Withstand Temperature Cycling. *Energy Environ. Sci.* **2018**, *11*, 144−150.
(48) Li, B.; Wang, M.; Subair, R.; Cao, G.; Tian, J. Significant Stability Enhancement of Perovskite Solar Cells by Facile Adhesive Encapsulation. *J. Phys. Chem. C* **2018**, *122*, 25260−25267.
(49) Shi, L.; Young, T. L.; Kim, J.; Sheng, Y.; Wang, L.; Chen, Y.; Feng, Z.; Keevers, M. J.; Hao, X.; Verlinden, P. J.; Green, M. A.; Ho-Baillie, A. W. Y. Accelerated Lifetime Testing of Organic-Inorganic Perovskite Solar Cells Encapsulated by Polyisobutylene. *ACS Appl. Mater. Interfaces* **2017**, *9*, 25073−25081.
(50) Ramos, F. J.; Maindron, T.; Béchu, S.; Rebai, A.; Frégnaux, M.; Bouttemy, M.; Rousset, J.; Schulz, P.; Schneider, N. Versatile Perovskite Solar Cell Encapsulation by Low-Temperature ALD-Al2O3 with Long-Term Stability Improvement. *Sustainable Energy Fuels* **2018**, *2*, 2468−2479.
(51) Dong, Q.; Liu, F.; Wong, M. K.; Tam, H. W.; Djurišić, A. B.; Ng, A.; Surya, C.; Chan, W. K.; Ng, A. M. C. Encapsulation of Perovskite Solar Cells for High Humidity Conditions. *ChemSusChem* **2016**, *9*, 2597−2603.
(52) Bang, S.; Hwang, N.; Kim, H. Microelectronic Engineering Permeation Barrier Properties of Silicon Oxide Fi Lms Deposited on Polyethylene Terephthalate (PET) Substrate Using Roll-to-Roll Reactive Magnetron Sputtering System. *Microelectron. Eng.* **2016**, *166*, 39−44.
(53) Nagai, S. Approximation of Effective Moisture-Diffusion Coefficient to Characterize Performance of a Barrier Coating. *J. Appl. Phys.* **2013**, *114*, No. 174302.
(54) Turren-Cruz, S.-H.; Hagfeldt, A.; Saliba, M. Methylammonium-Free, High-Performance and Stable Perovskite Solar Cells on a Planar Architecture. *Science* **2018**, *362*, 449−453.
(55) Saliba, M.; Matsui, T.; Seo, J.; Domanski, K.; Correa-Baena, J.-P.; Nazeeruddin, M. K.; Zakeeruddin, S. M.; Tress, W.; Abate, A.; Hagfeldt, A.; Grätzel, M. Cesium-Containing Triple Cation Perovskite Solar Cells: Improved Stability, Reproducibility and High Efficiency. *Energy Environ. Sci.* **2016**, *9*, 1989−1997.
(56) Jeon, N. J.; Noh, J. H.; Yang, W. S.; Kim, Y. C.; Ryu, S.; Seo, J.; Seok, S. I. Compositional Engineering of Perovskite Materials for High-Performance Solar Cells. *Nature* **2015**, *517*, 476−480.
(57) Ünlü, F.; Jung, E.; Haddad, J.; Kulkarni, A.; Öz, S.; Choi, H.; Fischer, T.; Chakraborty, S.; Kirchartz, T.; Mathur, S. Understanding the Interplay of Stability and Efficiency in A-Site Engineered Lead Halide Perovskites. *APL Mater.* **2020**, *8*, No. 070901.
(58) Ho, K.; Wei, M.; Sargent, E. H.; Walker, G. C. Grain Transformation and Degradation Mechanism of Formamidinium and Cesium Lead Iodide Perovskite under Humidity and Light. *ACS Energy Lett.* **2021**, *6*, 934−940.
(59) Marchezi, P. E.; Therézio, E. M.; Szostak, R.; Loureiro, H. C.; Bruening, K.; Gold-Parker, A.; Melo, M. A.; Tassone, C. J.; Tolentino, H. C. N.; Toney, M. F.; Nogueira, A. F. Degradation Mechanisms in Mixed-Cation and Mixed-Halide $Cs_xFA_{1-x}Pb(Br_yI_{1-y})_3$ Perovskite Films under Ambient Conditions. *J. Mater. Chem. A* **2020**, *8*, 9302−9312.
(60) Hu, Y.; Aygu, M. F.; Petrus, M. L.; Bein, T.; Docampo, P. Impact of Rubidium and Cesium Cations on the Moisture Stability of Multiple-Cation Mixed-Halide Perovskites. *ACS Energy Lett.* **2017**, *2*, 2212−2218.
(61) Zhu, W.; Yao, T.; Shen, J.; Xu, W.; Gong, B.; Wang, Y.; Lian, J. Situ Investigation of Water Interaction with Lead-Free All Inorganic Perovskite ($Cs_2SnI_xCl_{6-X}$). *J. Phys. Chem. C* **2019**, *123*, 9575−9581.
(62) Cordero, F.; Craciun, F.; Trequattrini, F.; Generosi, A.; Paci, B.; Paoletti, A. M.; Pennesi, G. Stability of Cubic $FAPbI_3$ from X-Ray Diffraction, Anelastic, and Dielectric Measurements. *J. Phys. Chem. Lett.* **2019**, *10*, 2463−2469.
(63) Masi, S.; Gualdrón-Reyes, A. F.; Mora-Seró, I. Stabilization of Black Perovskite Phase in $FAPbI_3$and $CsPbI_3$. *ACS Energy Lett.* **2020**, *5*, 1974−1985.
(64) Fan, Y.; Meng, H.; Wang, L.; Pang, S. Review of Stability Enhancement for Formamidinium-Based Perovskites. *Sol. RRL* **2019**, *3*, No. 1900215.
(65) Lu, H.; Liu, Y.; Ahlawat, P.; Mishra, A.; Tress, W. R.; Eickemeyer, F. T.; Yang, Y.; Fu, F.; Wang, Z.; Avalos, C. E.; Carlsen, B. I.; Agarwalla, A.; Zhang, X.; Li, X.; Zhan, Y.; Zakeeruddin, S. M.; Emsley, L.; Rothlisberger, U.; Zheng, L.; Hagfeldt, A.; Gratzel, M. Vapor-Assisted Deposition of Highly Efficient, Stable Black-Phase FAPbI 3 Perovskite Solar Cells. *Science* **2020**, *370*, No. eabb8985.
(66) Jeong, M.; Woo Choi, I.; Min Go, E.; Cho, Y.; Kim, M.; Lee, B.; Jeong, S.; Jo, Y.; Won Choi, H.; Lee, J.; Bae, J.-H.; Kwak, S. K.; Kim, D. S.; Yang, C. Stable Perovskite Solar Cells with Efficiency Exceeding 24.8% and 0.3-V Voltage Loss. *Science* **2020**, *369*, 1615−1620.
(67) Kanda, H.; Uzum, A.; Baranwal, A. K.; Peiris, T. A. N.; Umeyama, T.; Imahori, H.; Segawa, H.; Miyasaka, T.; Ito, S. Analysis of Sputtering Damage on I-V Curves for Perovskite Solar Cells and Simulation with Reversed Diode Model. *J. Phys. Chem. C* **2016**, *120*, 28441−28447.
(68) Jaysankar, M.; Qiu, W.; van Eerden, M.; Aernouts, T.; Gehlhaar, R.; Debucquoy, M.; Paetzold, U. W.; Poortmans, J. Four-Terminal Perovskite/Silicon Multijunction Solar Modules. *Adv. Energy Mater.* **2017**, *7*, No. 1602807.
(69) Fu, F.; Feurer, T.; Jäger, T.; Avancini, E.; Bissig, B.; Yoon, S.; Buecheler, S.; Tiwari, A. N. Low-Temperature-Processed Efficient Semi-Transparent Planar Perovskite Solar Cells for Bifacial and Tandem Applications. *Nat. Commun.* **2015**, *6*, No. 8932.
(70) Yang, J.; Siempelkamp, B. D.; Liu, D.; Kelly, T. L. Investigation of $CH_3NH_3PbI_3$ Degradation Rates and Mechanisms in Controlled Humidity Environments Using in Situ Techniques. *ACS Nano* **2015**, *9*, 1955−1963.

https://doi.org/10.1021/acsaem.1c00816
ACS Appl. Energy Mater. 2021, 4, 7571−7578

Approved for public release; distribution unlimited.

(71) Matteocci, F.; Cinà, L.; Lamanna, E.; Cacovich, S.; Divitini, G.; Midgley, P. A.; Ducati, C.; Di Carlo, A. Encapsulation for Long-Term Stability Enhancement of Perovskite Solar Cells. *Nano Energy* **2016**, *30*, 162−172.
(72) Ramasamy, E.; Karthikeyan, V.; Rameshkumar, K.; Veerappan, G. Glass-to-Glass Encapsulation with Ultraviolet Light Curable Epoxy Edge Sealing for Stable Perovskite Solar Cells. *Mater. Lett.* **2019**, *250*, 51−54.
(73) Phillips, A. B.; Song, Z.; DeWitt, J. L.; Stone, J. M.; Krantz, P. W.; Royston, J. M.; Zeller, R. M.; Mapes, M. R.; Roland, P. J.; Dorogi, M. D.; Zafar, S.; Faykosh, G. T.; Ellingson, R. J.; Heben, M. J. High Speed, Intermediate Resolution, Large Area Laser Beam Induced Current Imaging and Laser Scribing System for Photovoltaic Devices and Modules. *Rev. Sci. Instrum.* **2016**, *87*, No. 093708.
(74) Song, Z.; Abate, A.; Watthage, S. C.; Liyanage, G. K.; Phillips, A. B.; Steiner, U.; Graetzel, M.; Heben, M. J. Perovskite Solar Cell Stability in Humid Air: Partially Reversible Phase Transitions in the PbI2-CH3NH3I-H2O System. *Adv. Energy Mater.* **2016**, *6*, No. 1600846.
(75) Song, Z.; Werner, J.; Shrestha, N.; Sahli, F.; De Wolf, S.; Niesen, B.; Watthage, S. C.; Phillips, A. B.; Ballif, C.; Ellingson, R. J.; Heben, M. J. Probing Photocurrent Nonuniformities in the Subcells of Monolithic Perovskite/Silicon Tandem Solar Cells. *J. Phys. Chem. Lett.* **2016**, *7*, 5114−5120.
(76) Ahangharnejhad, R. H.; Song, Z.; DeWitt, J. L.; Phillips, A. B.; Lumbrezer, B. R.; Wickersham, C. E.; Heben, M. J. Decreasing the Resolution Limit of Laser Beam Induced Current Measurements below the Beam Size without Confocal Optics: Determining Laser Scribe Widths. *Sol. Energy Mater. Sol. Cells* **2020**, *215*, No. 110660.

https://doi.org/10.1021/acsaem.1c00816
ACS Appl. Energy Mater. 2021, 4, 7571−7578

Approved for public release; distribution unlimited.

Journal of Physics and Chemistry of Solids 153 (2021) 110011

ku eh efgsafefgcVcascrshgcegDoah ohJalhoeg

Gu, l csgubgydifaofgc tgkdhL afeligubgDusatfg

journal homepage: http://www.elsevier.com/locate/jpcs

Decrasaeingc tghshoelu aogc tgumeaocsgmlumhleahfgubgehl cligaelathgmdcfhfgubg wzD p:RgHgAlfejmla oamshfgfe,tig

ZSZSgJ,Llh[c]ngJSg,css[r]ngDSWSgBdclh[cn]Pg

[c] Wright rCtenfeoPvlaclegCseltlhnCn vdemPrezCqrhlavenfemnDsndemDsndpydeAUT2Tdez8Ie

[r] Wright rCtenfe0gtrhgDe8caCcregCse1C.cCrrhaC.deBrC1lrDgrheonDtrcPCaeSC1taOrdemhnvdeH4de363F2dez8Ieee

H*CEkMTgEpINgg

krvbnhsIue
wzDp:g
Jafulthhtgluoffcsegfel,oe,lhg
Tshoeluaogmlumhleahfg
Nmeaocsgmlumhleahfg
whodcaocsgmlumhleahfg

HZDC*HkCgg

Ohgdcvhgfe,taht gedhgtafulthlhtgluoffcsengulecluduLraongc tgtafulthlhtg(,le)aehgmdcfhfgubgedhgehl cligaelathg fhLaout,oeulgwzDp:grigAlfejmla oamshfgLheduttg,fazgth faeigh oeau csgedhuligwJIC-gc tgrhiu tSgCdhglhj f,sefgaLmsigdcegwzDp:gafgLhodcaocssigc tgti cLaocssigfecrshga gcssgedlhhgmdcfhfSgfiu(hVhlrgmkNfiygc csifafg f,zzhfefgedcegedhgtafulthlhtgluoffcsegfel,oe,lhgdcfgc earu ta zgfecehfgrhsu(gedhgLhlLagshVhsgrhe(hh g–xghWgc tg –:ghWgcfgouLmclhtgeugedhgru ta zgfecehfga gedhguedhlg(ugmdcfhfnga taoceaVhgubgefgedhlLuti cLaogL hecfecrasaeiSg kuLm,ehtgsceeaohgpu fec egc tghshoelu aogrc tjzcmgVcs,hfgubgLSk1g2gc tg Sl]ghWghulgwzDp:ga gedhgtafulthlhtg luoffcsegfel,oe,lhgouLmclhg(hssg(aedgh–mhlaLh ecssiglhmuleht gVcs,hfgubg[S[3g2gc tg:S4ghWglhfmhoeaVhsiSg I,ledhlLulhngrc tgzcmfg(hlhgouLm,eht ghulgwzDp:j5N5eV5e=6Skng7S6ng7Skng S6-geughs,oatcehgedhglushguhgmuffarshg u~izh gaLm,laeahfSgZc tjzcmgru(azgafgf,zzhfeht geuguoo,lg,mu gcssuiazg(aedgu~izh SgNhgedhgedlhhgmdcfhfngedhg tafulthlhtgluoffcsegfel,oe,lhgfdu(fgedhgsu(hfegodclzhgocllahlghlbhoeaVhgL cffhfSgwulhuVhlngedhgcrfulmeau gouhlj Aoah egc tglhqhoeaVaeigubgedafgmdcfhgLcFhgaegmluLafa zghulg fhgcfgedhgcrfulrhlgsci hlgubgc thLgfusclgohssfga gedhg dazdhlgh hlzi glhzau gubgedhgVafarshgmuleau gubgedhgfusclgfmhoel,LSgCdhguedhlg(ugmdcfhfngtafulthlhtg(,le)aehgc tg uleduldu Laongl azdegrhg easa)htgcfgedhg(atu(gsci hlgubgfusclgohssfgu(azgeugedhalgsclzhlgrc tjzcmgVcs,hfgubgS41g hWgc tgLS31ghWghlfmhoeaVhsiSggg

1. Introduction

Eulzc aog aelathfgdcVhgrhh gdafeulaocssigtaVathtga euge(ugLca g zlu,mfgrcfhtgu gedhalghshoelu aogmlumhleahfng cLhsigfhLaout,oeulg (,le)aehgLca gzlu,mgLhecsg aelathfgc tgf,mhlout,oea zgluoffcsegelc j faeau gLhecsgvCw-g aelathfg57@gT~ohmeau fga os,thgfhLaout,oea zg luoFfcseg aelathfgvhSzSngDop-g5: @gc tgLhecssaog(,le)aehg aelathfgvhSzSng / wup:-g54@gCdhg aelathfgubgedhgAlfegeimhrgedcegafngfhLaout,oea zg (,le)aehfgf,odgcfgHspng,cpngc tgEpngclhg(hssgFu(gbulgedhalgtalhoeg rc tjzcmfgc tgdazdgocllahlgLurasaeahfg5[nx@gCdhigclhg(athsig,fhtga g fusatjfecehg szdeazng lctaublh0,hoig elc fafeulfng scfhlg tauthfng dazdjtcecjth faeigumeaocsgfeulczhgLhtacngc tgfugu g5[–]@gCdhgfhou tg eimhngf,mhlout,oea zgluoFfcsegCwg aelathfng,odgcfgCapngWpngc tgprpng clhg,easa)htga gdcltgoucea zfg5576–74@gc tgcfgtab,fau grcllahlfga gfhLj aou t,oea zgthVaohfgc tgf,mhlou t,oeulfg(aedgelc faeau fgcegehLmhlcj e,lhfgubgedhgultlhgubg6gBg574n7[@g

Chl cligaelathgfhLaout,oeulfg(aedgluoFfcsegfel,oe,lhgubgbulL,scgEjg EWjp:gdcVhgrhh g(athsigfe,taht ga gedhgmcfegthoct hg57x@gCdhigclhgurj eca htgriglhmscoa zgLhecsgceuLfga gcgra cligLhecsg aelathg(aedg lu,mg

Ei+ctglu,mgEWf+ceuLfSgIulgh~cLmshngcgLhecsgf,odgcfgCagdcfgedhg4+ Vcsh ohgfecehga gaefg aelathgvCap-g5710@gEfhlea zgcgsu(jVcsh egcsFcsa j hjhcledgoceau gf,odgcfgwz:+lhf,sefga gwzCap:nghuloa zgedhgCwgeugctumegcg dazdhlgu~atceau gfecehngmludaraea zgedhgL hecsgtjfdhssghluLgh zcza zga g ru ta zngc tgedhlhriga elut,oa zgfhLaout,oeulgmlumhleahfg578–:6@g wulhuVhlngpceau jgc tgc au jf,rfeuaodauL helaogthlhoegmdcfhfgclhghu,tg a gra cligCwg aelathfg(aedgluoFfcsegfel,oe,lhg5:7–:4@gCdafgaLmsahfgedhg muffarasaeigubgh(siga fhlehtgcsFcsa hjhcledgoceau fguoo,mia zgL hecsgfaehg Vcoc oahfg57@g

Tmaec~acsgzlu(edgubgedhfhgh(gehl cligaelathgu gL,seamshgf,rfelcehfg afghcoasaecehtgrigou zl,hegsceaohgmclcLhehlfSgCd,fngedhigoc grhgLheaoj ,su,fsigzlu(guVhlgedhalgacligfhLajgc tgf,mhljou t,oea zgc ehohthefg 57@gCdhfhg aelathfgclhgfi edhfa)htghluLgdazdsigTcledjcr,tc egc tg u jeu~aogLhecsfgc tgclhgfhLaout,oea zg5:[@gvulhuVhlngedhghsceaVhsig su(goufegc tghcfhgubghoioscrasaeigubgedhgou feae,h egLhecsfgf,odgcfg/ng wzngc tgD gagouLmclafu geugEgc tg.cgLcFhfgedhLgmluLafa zghulg focscrshghshoelu aogcmmsaoceau fSgT~cLmshfgf,odgcfg/ D p:ngwzD p:ng wzfilp:ngvz:prp4ngc tgwz/lp:gdcVhghshoelu aogc tgzcmfga gedhgc zhg 7Sk–4SkghWngcFa geugedufhgubgedhalgacligou,ehlmclefgHspngEpngc tg cpng

P kullhfmu ta zgc,edulSg
*1K gdQgsshrlluefc ;ciSFdclh9,eushtuSht,gvDSWSgBdclh-Sgg

deemfRUUtuaSulzU76S7671U;SmofS6:7S776677g
*hohaVhtg7:gH,z,feg6:6X*hohaVhtgaghlhVafhtghulLg7]glhrl,cligg6:7XgHoohmehtg6glhrl,cligg6:7ggg
Available online 26 February 2021
0022-3697/© 2021 Elsevier Ltd. All rights reserved.

Approved for public release; distribution unlimited.

w.w.eWO lrertegDaaa

w.w.eWO hrertegDaaa

www.eWO hrertegDaaa

www.eWO hrertegDaaa

w.w.eWO hrertegDaaa

www.eWO hrertegDaaa

C. ToncRuRion

O hgdcVhgpuL m, ecceau cssigfe, taht gedhgfel, oe, lcsngL hodc aocsngVarlcj eau csngc tgumeujhshoelu aogmlumhleahfgulgwzD p.:ga gedlhhgtabhlh eg olifecsghulL fSgN, lgfe, tigou AlL fgedcegwzD p.:ga gedhgtafult hlht gluoFj fcsegbulL gafgrueclgL hodc aocssigc tgti cL aocssigfecrshrgcfgclhgedhg uledulduL raogc tgtafult hlht g(, le)aehgolifecsgfel, oe, lhfSgH csifafgubg rnkNfiygo, lVhfngdu(hVhlngaL msahfgL hecfecraaeiSgN, lgocso, sceht gsceeaohg ou fec egc tghshoelu aogrc tjzcngVcs, hfgubg[Sk1g2gc tg:Sl]ghWgbulg wzD p.:ga gedhgtafult hlht gluoFfcsegfel, oe, lhgosufhsigL ceodgedhglhoh eg h~mhlaL h ecssiglhmuleht gVcs, hfgubg[Sl3g2gc tg S4ghWglhfmhoeaVhsiSgCdhg ouL m, eht grc tgrcngfga talhoeng(dashgedhgh~mhlaL h ecssiglhmuleht gu hgafg talhoeg5:[@gO hgcssuihtgwzD p.:g(aedgu~izh geugcoou, egbulgmuffarshg u~izh gaL m, laahfSgkuL m, eceau cssingedhghlhhoeguhgcssuia zg(aedgu~izh g aL msahfgrgu(a zguhgedhgrc tgrcnfSgI, ledhlgh~mhlaL h ecsgc tgedhulheaocsg (ulFgafg hohffcligeugh~msulhgedhgt hecasfgubgedafgru(a zSgN, lgfe, tigu g hlhhoeaVhgL cffhfgdcfgoscIaAht gedcegedhgtafult hlht gluoFfcsegfel, oe, lhgdcfg su(hlghlhhoeaVhgL cffhfgedc gedhguledulduL raogc tgtafult hlht g(, le)aehg olifecsgfel, oe, lhfSgHrfulmeau gouhbAoah egc tghqhoeaVaeigo, lVhfgVcsat cehg edcegedhgtafult hlht gluoFfcsegfel, oe, lhgL azdegrhg fht gcfgc gcrfulrhlgsc ihlg a gedhgdazdhlgh hlzi glhzau gubgedhgVafarshglc zhga gec thL gt hVaohfng (dhlhcfgedhgtafult hlht g(, le)aehgc tguleduldu L raogoli fecsgfel, oe, lhfg ou, st gfhlVhgcfg(a tu(gsci hlfgubgfusclgohssfSg

DgcRyrytion of coh egtin6 intgrgRt

Cdhgc, edulfgt hosclhgedcegedhigdlcVhg ugF u(gouL mhea zgA c oacsg a ehlhfefgulgmhlfu csghsceau fdamfgedcegou, st gdcVhgcmmhclhtgeuga q, h ohg edhg(ulFghlmuleht ga gedafgmcmhlSg

mcpnob Rgd6gh gntR

HssgouL m, ea zgbulgedafgmlu; hoeg(cfgmhlbulL ht gcegedhgNdaugD, mhlj ouL m, ehlgkh ehlgvNDk-g5761@gO hgedc Fgu, lgh, ta zgfu, lohfRgCdhgpcj eau csg Doah ohg Iu, tceau g JaVafau g ubg kaVasng whodc aocsng c tg wc, bcoe, la zgE uVceau gedlu, zdgzlc efg71:]:46gc tg71:]:4]ngedhg Q aVhlfaeigkuumhlceaVhgHzlhhL h egfiazdgDmhoaAogyu(hlgw, seajG, oeau g Cda gIasL gydueuVusecaofg, thlgku elcoeg~gIH][x4j73j:j6648SgCdhgQSg DS. uVhl L h egafgc, edula)htgeuglhmlut, ohgc tgtafelar, ehglhmla efgbul . uVhl L h ecsg m, lmufhfg ue(aedfec ta zg c ig ouml azdeg ueceau edhlhu SgO hgcsfug c egeugedc FgIlSg*aodcltgHVa zngubgedhgJhmrleL h egub ydifaofgc tgHfelu uL ingCdhgQ aVhlfaei gulgCusht urghulgdcafgehod aocs f, mmulega gouL m, ea zS

meegndiz m HueeRgh gntyrA dyty

D, mnshL h ecligtcecgeugedafgcleaoshgoc grhgdu, tgu sa hgcegkleemfRUUtuaSg ulzU76S7671U;SjmofS 6:7S776677Sg

DiRcRyih gr

CdhgVah(fgc tgou os, fau fgou eca ht gdhlha gclhgedufhgubgedhgc, edulfg c tgfdu, st g uegrhgea ehlmlheht gcfg hohffclasiglhmlhfh ea zgedhgubAoacsg musaoahfgulgh tulfhL h efrghaedhlgh~mlhffht gulgaL msaht rgubgHalgIulohg *hfhclodgVdrulceuligulgedhgQSDSg uVhl L h eSg

l gfgrgncgR

57@DS*SgZc, hlfnghegcsSngChl cli g aelat hgfhL aou t, oeulfga gedhgluoFfcsegpli fecsg fel, oe, lhngyluoSgpcesSgHoct SgDoaSgQ aeSgDecehfgHL Sg771gv46-gv:67]-g7[3:]-7[34[Sg
5:@JSg csnghegcsSngTshoelu aogfel, oe, lhgubgDopgthehlL a ht g fa zgumeaocsgfmhoelufoumirg mtueuhL affau ng: tgcrga aeaugocso, sceau fngydifSg*hVSgZgl4gv7:-gv:667-g7:x77]Sg
54@TSgHlocnghegcsSng*htu~jL htaceht gfecrasa)ceau ga g)a ogL usirth, L g aelat hfngQSgHL Sg kdhL SgDuoSg7[6gv7:-gv:673-gl:]4-[467Sg
5[@ISHSgyu ohngJSySgZu, lnpgaelat hjrcfht gfhL aou t, oeulfghulgrs, hgc tgzlhh gsazdejg hL aeea zgthVaohfngpce, lhg431gv11:4-gv7]]8-g4x7-4x]Sg
5x@QSBSgwafdlcngySgyclaFdrig SJSgO, ngHs. cpU cpgfiTwCfjc guVhlVah(gulgthVaohg umhlceau gc tgcmmsaoceau fngyluoSgETTgl6gv1-gv:66:--g76:::-7647Sg
51@DSpcFcL, lcngCdhglushfgulgfel, oe, lcsgaL nhllhoeau fga gE. cpjrcfht grs, hgsazdejg hL aeea zgtauthfgc tgscfhlgtauthfngDoah ohg37gx48]-gv7]]3-glx1-]17Sg
58@fiSgHL c unghegcsSngwhecsulzc aogVcmulgmdcfhghmaec~acsgzlu(edgulbgrglazdgO, csaeig. cpgAsL g, fa zgc gHspgr, lhhlgcihlngHmmsSgydifSgMheeSgl3gx-gv7]31-g4x4-4xxSg
53@DSpcFcL, lcnghegcsSngku ea, u, fj(cVhgumhlceau gubgE. cpU cpUHs. cpjrcfht g scfhlgtauthfgzlu(gu g cpgf, rfelcehfngHmmsSgydifSgMheeSg8:gv71-gv7]]3-g67[Sg
5]@*SG8Clh(ngwSOSgDda ngWSg ceeungfiazdgmu(hlgcmnsaoceau fghulg cpjrcfht gthVaohfng Dusat gDecehgTshoelu S[7gv76-gv7]]8-g7x17-7x18Sg
576@BSgZcscf, rlcL c ac ngDSWSgBdclhngJSg, csngWcsh ohghshoelu gou oh elceau gcfgc g a taoceulghulgL hodc aocsgmlumhleahfga gluoFfcsegfel, oe, lhg aelat hfngoclrat hfgc tg oclru aelat hfngHoecgwcehlSg7x:gv:673-g78x--73xSg
577@DSBut cL rcFcnghegcsSngHrfus, ehgulah eceau jthmh th egc afuelumaogCapv777-gfsc tg fehmgh hlzahfgc tgfeabb hffhfghuL gfdcmhgj, oe, ceau gc csifhfngydifSg*hVSgZgl8gv4-g v:664-ng64x[6]Sg
57:@ZSJSgN)ftusci nghegcsSngcOEace/jKf H5eIgvrhUeRhmbtPegCseihmirhtarle, leHKnkf ehgtamg D, lhgkuceazSgChodusSg46[gv:671-gl3-768Sg
574@KSgGgkdh nghegcsSngficltgf, mhlou t, oea zg aelat hfngyluoSgpcesSgHoct SgDoaSgQ aeSg DecehfgHL Sg76:gv]-gv:66x-g47]3--4:67Sg
57[@wSgOaeeL hlngylumhleahfgc tgL aoluhshoelu aogcmnsaoceau fgubgeda gAsL fgubg lhlhcoeuligL hecsg aelat hfngOgWcoSgDoaSgChodusSg4gv[-gv7]3x-g78]8--7364Sg
57x@HSJSgwclea h)nghegcsSngSvCtPrldeldthOctOhrdegCseniinrIDcthnCoceimirhtarlenfeSS-S-6e gtrhgDngOgswcehlSgkdhL Sgxgv:4-gv:678-g77[73--77[4xSg
571@JSfiSg lhzuligDel, oe, lcsghcLaahfga g aelat hgodhL afeling Sgkdh L SgDuoSgJcseu g Clc fSgv4-gv7]]]-gx]--:86Sg
578@OgTeu, l hc, ngOgyuleahlngJSgwh aengCdhglushgubgedhga t, oeaVhghlhhoega gfusat gfecehg odhL afeligdu(gedhgodhL afegoc g, fhgeegeugL utahigruedgedhgfel, oe, lcsgc tgedhg mdifaocsgmlumhleahfgubgedhgL cehlacsfngOgSgHssuifgkuL mtSg733gv7]]:-g7--8Sg
573@ZSgOcznghegcsSngRhnbtPegCseihmirhtarlenferiatg5cgDmg8--5eO.5H223 eDgvrhlngOgVcoSg DoaSgChodusSgWco,, LngD, lhcohfngc tglasL fg41gv1-gv:673-ng617x67Sg
57]@ZSgOcznguSg, cssng:ODDelthgaOrseriatg5cgDmg8--5O.5H223 eDgvrhlngCda gDusat glasL fg 133gv:67]-g74871xSg
5:6@ZSgOcznguSg, cssngJeHrbeSr acnCsOctnhuemg2:0.2:Hng667ngaRgS11eHgCntrcPChnDa.ve 8v inlaO eIHm8ng673ngpcutncrgDu, edgH, taeula, LngDQp gvusiehod aog Efeae, ehngHsrc ingp g7::64ng673gvETTT-Sg
5:7@WDBZdctlcL, nghegcsSng8r acnCsOctaC.ecOEaceiatgCaO eCathsreaCatPremPLOAdthOctOhrng ydifaocsg*hVah(gwcehlacsfg, g7-gv:673-ng67716:Sg
5::@HSOSgGcoFfu nghegcsSngJ nhiPnOlegCseCgCnchvltgDDCretatgCaO eCathsregCse cghEnCathsre gtrhgDenEtgaOrseEvelnlDDanCaiPglreg nCnDIdenfemaH0r6 AngOSgDusat g Decehgkdh L Sg78]gvx-gv:661-g7434--74]4Sg
5:4@OSDSgOaasaL fngClc faeau jL hecsgpclrathfngyluzSgDusat gDecehgkdh L Sg1gv7]87-g x8--773Sg
5:[@1SgBc(cL, lcnghegcsSng8vCtPrldenfegeCn, rIDhnc lgIDKfvirterhCghveCathsrelr acnCsOctnhe 0.8CH6eOlaC.atPre rtgtPrldehrgctanCaOCsrhePaPaihrllOhrngT, lSgOgE ulzSgkdhL Sg6:6g vx-gv:6:6-g[1--[x7Sg
5:x@*SHSgwcFa nghegcsSngHssuijlhhgrctgzcmge, a zgcoluffgedhgVafarshgfmhoel, Lngydifsg *hVSgMheeSg7::gv:x-gv:67]-gx1[64Sg
5:1@OSHSgNrhlngMSTSgHmutcocng*SJSgklc zshgG1SgGsOthgaDaOrhgDegCseICtgaCgEdatvuEvKe ihmsOctlefmeSp6e atagtanCeglelOEltatOrlefmheaOrseaOrhgDcn nsatarlng, DHg v.husSgDuoSgHL SgDrnhoSgvcmSg*hzSgDe, tSgx:6gv:671-g8]--38Sg
5:8@wSgBhaffsnghegcsSngHtVc ohfga gzlu, mgHHJaelat hjrcfht gthhmgQWgsazdejhL aeea zg taut hgehod usuzingDhL aou tSgDoaSgChodusSg1g7-gv:677-ng67[641Sg
5:3@CSgZluFcL mngfiSgGcourfngJclfehss, zg, tgDel, Fe, lgha azhlg, hL afodeVcsh ehlg ehlclhlgec ecs aelat hgL aegseeda, Lg, tgL cz hfa, LngGSgHssuifgkuL mtSg734gv7]]:-g 4:x--4[[Sg
5:]@JSfiSg lhzuli nghegcsSng8vCtPrldegCseIthOctOhrenfetbneOrbegvrhrsetrhCghveCathsrlde 8hhH6egCseSlyfH6ngE ulzSgkdhL Sg4xgv:1-gv7]]1-g8163--8174Sg
546@JSfiSg lhzuli nghegcsSng8vCtPrldegCseIthOctOhrenfetPreOrbetrhCghveCathsre8hmdH6ngE ulzSg kdhL Sg48g7x-gv7]]3-g488x--4883Sg
547@JSfiSg lhzuli nghegcsSng8vCtPrldeldthOctOhrdegCse g.CrtaceihmirhtarlenfetPreOrbetrhCghve Cathsrewgy fH6egCseinfetPrewgy f3--5 h2H6elnlDaenlODaenCngOSgDusat gDecehgkdhL Sg748g7-g v7]]3-gl:--86Sg
54:@wSg*fc thlngwSHSgwulcL ngIglCtaecnCltgCalenfetPreSS-SeCathsrelr acnCsOctnhle 0.8dH6d0.RrrH6egCse0.8CH6ngOSgydifSgHmmsSgydifSgx7gx48-gv:673-g48x767Sg
544@HSySgCluh;aeaodcaqOS*SMgMtL rlhodcngIDcthnCoceEgCselthOctOhrenfeO.--S--H6e cn inOCsleaCatPre OglighaaDRrIfKEnCldtrCteRj egiihn5a gtanCngydifSg*hVSgZgl[g v7:-gv:671-g7:x:67Sg
54[@HSMSg, lhh c(cinghegcsSngkuLra ceulacsgfi edhfafgulgL cz hfa, Lgaa g aelat hg fhL aou t, oeulfngOSgHL SgkdhL SgDuoSg7[:gv73-gv:6:6-g3[:7--3[46Sg
54x@.SgBlhffhngOSgl, ledL, sshlngTbAoah oigulgcrja aeaugeuecsgh hlzigocso, sceau fghulg LhecsfgctgfhL aou t, oeulfg, fa zgcgmsc hj(cVhgrcfafgfhengkuL m, eSgwcehlSgDoaSglg v7-gv7]]1-g7x--x6Sg
541@.SgBlhffhngOSgl, ledL, sshlngTbAoah egrehlceaVhgfodhL hfghulgcrga aeaugeuecsjh hlzig ocso, sceau fg, fa zgcgmsc hj(cVhgrcfafgfhengydifSg*hVSgZgx[g71-gv7]]1-g 7771]--77731Sg
548@.SgBlhffhngOSgficb hlngHrga aeaugL usho, sclgti cL aofghulgs0, atgL hecsfngydifSg*hVSgZg [8gv7-gv7]]4-gxx3--x17Sg
543@.SgBlhffhngOSgficb hlngHrga aeaugL usho, sclgti cL aofgfaL, sceau gubgedhgs0, atjg LhecS-cLulmdu, fjfhL aou t, oeulgelc faeau ga gzhlLc a, Lngydif Sg*hVSgZgl]gv:6-g v7]][-g7[:x7--7[:1]Sg
54]@OgySgyhlth(nghegcsSngTllce, LRgceuL fngL usho, shfngfusatfngc tgf, lhcohfRgcmnsaoceau fg ulgedhgzh hlcsa)htgzlctah egcmmlu~aLceau ghulgh~odc zhgc tgoullhsceau ngydifSg *hVSgZgl3gx8-gv7]]4-gl]83Sg
5[6@OgySgyhlth(nghegcsSngHeuL fngL usho, shfngfusatfngc tgf, lhcohfRgcmnsaoceau fgubgedhg zh hlcsa)htgzlctah egcmmlu~aLceau ghulgh~odc zhgc tgoullhsceau ngydifSg*hVSgZgl1g v77-gv7]]:-gl187--1138Sg

Approved for public release; distribution unlimited.

652

w.weWO hrertegDaaa

materials

MDPI

Article

Impact of Humidity and Temperature on the Stability of the Optical Properties and Structure of $MAPbI_3$, $MA_{0.7}FA_{0.3}PbI_3$ and $(FAPbI_3)_{0.95}(MAPbBr_3)_{0.05}$ Perovskite Thin Films

Marie Solange Tumusange, Biwas Subedi, Cong Chen, Maxwell M. Junda, Zhaoning Song, Yanfa Yan and Nikolas J. Podraza *

Department of Physics & Astronomy and The Wright Center for Photovoltaics Innovation & Commercialization, University of Toledo, Toledo, OH 43606, USA; mariesolange.tumusange@rockets.utoledo.edu (M.S.T.); biwas.subedi@utoledo.edu (B.S.); cong.chen@utoledo.edu (C.C.); maxwell.junda@rockets.utoledo.edu (M.M.J.); zhaoning.song@utoledo.edu (Z.S.); yanfa.yan@utoledo.edu (Y.Y.)
* Correspondence: nikolas.podraza@utoledo.edu; Tel.: +1-(419)-530-4905

Abstract: In situ real-time spectroscopic ellipsometry (RTSE) measurements have been conducted on $MAPbI_3$, $MA_{0.7}FA_{0.3}PbI_3$, and $(FAPbI_3)_{0.95}(MAPbBr_3)_{0.05}$ perovskite thin films when exposed to different levels of relative humidity at given temperatures over time. Analysis of RTSE measurements track changes in the complex dielectric function spectra and structure, which indicate variations in stability influenced by the underlying material, preparation method, and perovskite composition. $MAPbI_3$ and $MA_{0.7}FA_{0.3}PbI_3$ films deposited on commercial fluorine-doped tin oxide coated glass are more stable than corresponding films deposited on soda lime glass directly. $(FAPbI_3)_{0.95}(MAPbBr_3)_{0.05}$ films on soda lime glass showed improved stability over the other compositions regardless of the substrate, and this is attributed to the preparation method as well as the final composition.

Keywords: real time spectroscopic ellipsometry; perovskite thin films; optical properties; stability

check for updates

Citation: Tumusange, M.S.; Subedi, B.; Chen, C.; Junda, M.M.; Song, Z.; Yan, Y.; Podraza, N.J. Impact of Humidity and Temperature on the Stability of the Optical Properties and Structure of $MAPbI_3$, $MA_{0.7}FA_{0.3}PbI_3$ and $(FAPbI_3)_{0.95}(MAPbBr_3)_{0.05}$ Perovskite Thin Films. *Materials* **2021**, *14*, 4054. https://doi.org/10.3390/ma14144054

Academic Editor: Aivaras Kareiva

Received: 28 May 2021
Accepted: 30 June 2021
Published: 20 July 2021

Publisher's Note: MDPI stays neutral with regard to jurisdictional claims in published maps and institutional affiliations.

Copyright: © 2021 by the authors. Licensee MDPI, Basel, Switzerland. This article is an open access article distributed under the terms and conditions of the Creative Commons Attribution (CC BY) license (https://creativecommons.org/licenses/by/4.0/).

1. Introduction

Organic–inorganic metal halide-based ABX_3 perovskites (A cation: methylammonium-MA, formamidinium-FA, cesium-Cs, rubidium-Rb; B cation: lead-Pb, tin-Sn; X anion: iodine-I, bromine-Br, chlorine-Cl) have gained tremendous attention in photovoltaic (PV) applications due to their high-power conversion efficiency which increased from 3.8% in 2009 to 25.5% [1–3] recently. Application of perovskite films to PV benefit from simple solution deposition processing, a tunable range of bandgap energies, and desirable optoelectronic properties, which include a high absorption coefficient above the bandgap energy, long carrier diffusion lengths, and long carrier lifetimes [4–6]. Solar cells made with these absorber layers are promising candidates for the next-generation high-efficiency PV technology [7]. The $MAPbI_3$ perovskite is the pioneer among those used in solar cells and has been the most studied to date. Despite showing desirable optoelectronic properties, $MAPbI_3$ degrades with exposure to humidity, oxygen, heat, and ultraviolet light [8–11]. Previous in situ real time spectroscopic ellipsometry (RTSE) studies conducted by Ghimire et al. on $MAPbI_3$ upon atmospheric exposure have shown phase segregation into PbI_2 and MAI starting at the interfaces of the film with the ambient and substrate [12]. It has been reported that $MAPbI_3$ becomes hydrated under a humid environment in the dark and forms PbI_2 with humidity exposure under illumination [13]. Another perovskite composition, $FAPbI_3$, shows improved thermal stability compared to $MAPbI_3$, however it may transform from the desired cubic, photo-conductive "black" perovskite α-phase into the "yellow" trigonal δ-phase in the presence of solvents and humidity [4]. Stability can be improved by

Approved for public release; distribution unlimited.

tuning the cationic and anionic perovskite composition [14,15]. In particular, the *A* cation size is critical for the formation of a cubic perovskite structure [16]. When a mixture of MA and FA is used, the *A* cation size given by Goldschmidt tolerance factor falls in the 0.8–1.0 range, which is favorable for the cubic black phase perovskite structure to form, and the corresponding material stability is improved [17,18]. Recent studies indicate that partial Br substitution for I in $MAPbI_3$ prevents ion migration in the perovskite and maintains favorable light absorption [19]. Substituting I with Br has also been reported to shrink the lattice parameter and increase the photogenerated-carrier lifetime and charge-carrier mobility [20]. All these studies provide general knowledge on improving the stability of organic–inorganic perovskites, however the level of stability for different perovskite film compositions in terms of complex optical response has been rarely explored.

Spectroscopic ellipsometry is a non-destructive, non-invasive measurement often used to explore the structural and optical properties of thin film materials. It measures changes in polarization state and amplitude of an incident light beam upon interaction with a sample either by reflection or transmission [21,22]. The complex optical properties and thicknesses of each component layer will impact this polarization state change via coherent multiple reflections. Data analysis of ellipsometric spectra is conducted by the construction of a parametric structural and optical model based upon a transfer matrix method from which physical properties, including the complex optical response and layer thicknesses, are extracted in a least squares regression fit to experimental ellipsometric spectra. In previous studies, thickness information gained from spectroscopic ellipsometry have been found to be in good agreement with that obtained from other techniques such as X-ray reflectivity, atomic force microscopy, scanning electron microscopy, and transmission electron microscopy [23–26]. When studying the dynamic evolution of properties of interest, in situ RTSE is used [12,27–30]. In RTSE, the sample is continuously measured so that the change in the polarization state of the incident light upon interaction with the sample is tracked as a function of time without physically moving the sample, although the sample characteristics may change.

Here in situ RTSE is used to track the variation of the optical and structural properties of $MAPbI_3$, $MA_{0.7}FA_{0.3}PbI_3$, and $(FAPbI_3)_{0.95}(MAPbBr_3)_{0.05}$ perovskite films deposited on soda lime glass and commercial fluorine-doped tin oxide (FTO) coated glass substrates under controlled relative humidity (RH) and temperature variations. These films are prepared using single-step spin coating and two-step solution processing [31–33]. The non-destructive and non-invasive nature of RTSE makes it the most suitable measurement method to track these changes. In addition, it enables the simultaneous determination of both optical and structural properties. Strong variations in optical and structural properties for $MAPbI_3$ over time and the minimal variations for $MA_{0.7}FA_{0.3}PbI_3$ and $(FAPbI_3)_{0.95}(MAPbBr_3)_{0.05}$ allow us to identify the factors influencing the stability of perovskites films. These factors include substrate type, mixing organic cations, incorporation of Br as a halide anion, and two-step versus single-step preparation methods. The RTSE data analysis methodology can be adopted in studying degradation of the perovskite absorber and other layers inside PV devices to assist in identifying stable materials for a large-scale industrial application.

2. Experimental Details

2.1. Perovskite Film Preparation

All perovskite films are prepared in a nitrogen (N_2)-filled glove box to prevent exposure to ambient air. $MAPbI_3$ and $MA_{0.7}FA_{0.3}PbI_3$ films are prepared using single-step spin coating [31,32]. These films are deposited on soda lime glass and FTO coated glass (NSG Pilkington, Rossford, OH, USA TEC-15) substrates. PbI_2 (TCI America, Portland, OR, USA), MAI (Greatcell Solar Materials, Queanbeyan, Australia), FAI (Greatcell Solar Materials, Queanbeyan, Australia), lead thiocyanate ($Pb(SCN)_2$, Sigma–Aldrich, 99.5%), dimethyl sulfoxide (DMSO, Sigma–Aldrich, St. Louis, MO, USA 99.8%), and N,N-dimethylformamide (DMF, Sigma–Aldrich, St. Louis, MO, USA 99.8%) are used without further purification. The perovskite precursor solutions are prepared by dissolving mixtures of MAI, FAI, PbI_2,

Approved for public release; distribution unlimited.

655

Pb $(SCN)_2$ in DMSO/DMF (*v*:*v* = 1:9), where the perovskite concentration is 1.5 M. The perovskite precursor solution is then spin-coated onto the substrate at 500 rpm for 3 s, and then at 4000 rpm for 60 s with diethyl ether dropped on the film at 10 s of the second step. The as-prepared perovskite films are annealed on a hotplate at 65 °C for 2 min and then at 100 °C for 5 min.

To prepare $(FAPbI_3)_{0.95}(MAPbBr_3)_{0.05}$, a two-step solution-processed preparation method is used as is described in [33]. Initially, 599.3 mg PbI_2 is dissolved in a mixed solvent of 950 µL DMF and 50 µL DMSO. 70 mg FAI, 6 mg MABr, and 7 mg MACl are then dissolved in 1 mL isopropanol (IPA). To deposit the PbI_2 film, 70 µL PbI_2 solution is dropped onto substrate and spin-coated at 2000 rpm for 30 s, followed by annealing at 70 °C for 2 min. Then, the IPA solution is spin-coated on the as-prepared PbI_2 film at 2000 rpm for 30 s to form the perovskite phase. Next, the samples are annealed at 150 °C for 15 min at 30–40% relative humidity in ambient air.

2.2. Real Time Spectroscopic Ellipsometry Data Collection and Analysis

To transfer the prepared perovskite films for RTSE measurements, the films are loaded into a sealed measurement chamber (Figure 1) filled with nitrogen inside the glove box to prevent exposure to laboratory ambient air. The chamber containing the sample is placed on a temperature-controlled stage with a range from 7 to 70 °C (SCI-SCC6-L-F, Sciencetech Inc., London, ON, Canada). An infrared thermometer is used to confirm the temperature inside the chamber before and at the end of the measurements. Humidity is introduced by water vapor and nitrogen gas flows at a total rate of 5 standard cubic feet per hour (SCFH) into the chamber. 26% RH at temperatures of 7 and 70 °C, and 85% RH at 25 °C are measured within the chamber (Sensing solutions EVM GUI, Texas Instruments Inc., Dallas, TX, USA).

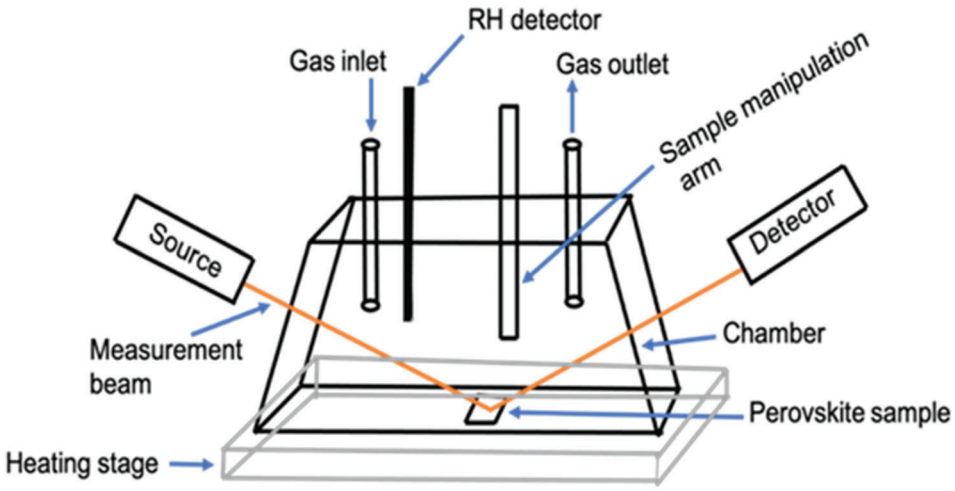


Figure 1. Schematic of the experimental setup for in situ real time spectroscopic ellipsometry (RTSE) data collection.

In situ RTSE measurements are performed to collect ellipsometric spectra in the form of $N = cos\ (2\psi)$, $C = sin\ (2\psi)cos\ (\Delta)$, and $S = sin\ (2\psi)sin\ (\Delta)$ where the ellipsometric angles ψ and Δ describe the relative amplitude and phase shift between the electric field components perpendicular and parallel to the plane of incidence [22]. Ellipsometric spectra (*N*, *C*, and *S*) are collected at an angle of incidence of 70° for 500 spectral points over a photon energy range from 1.25 to 6.00 eV using a single rotating compensator multichannel ellipsometer (M-2000FI, J.A. Woollam Co., Inc., Lincoln, NE, USA) [34]. Data is collected at 150 s intervals for each film to track changes in the complex optical response over time when the film is exposed to humidity and temperature. Selected time points are analyzed to track time

Approved for public release; distribution unlimited.

656

dependent variations in the optical properties and film structure. Window effects of the chamber introducing an additional phase shift in the incident polarization state of the ellipsometer beam are accounted for through the use of Δ-offset parameters [35].

The experimental ellipsometric spectra are analyzed using a least square regression analysis in which the quality of fit between the model (*mod*) and the experimental (*exp*) ellipsometric spectra is defined in terms of the unweighted mean square error (*MSE*) [22]:

$$MSE = 1000 \times \sqrt{\frac{1}{3n-m}\sum_{i=1}^{n}\left[\left(N_i^{mod} - N_i^{exp}\right)^2 + \left(C_i^{mod} - C_i^{exp}\right)^2 + \left(S_i^{mod} - S_i^{exp}\right)^2\right]} \quad (1)$$

where n is the number of measured values and m is the number of fit parameters.

To fit experimental ellipsometric spectra, a parameterized optical and structural model is used (CompleteEASE software, J.A. Woollam Co., Inc., Lincoln, NE, USA) to extract the optical response of the perovskite films in terms of complex dielectric function ($\varepsilon = \varepsilon_1 + i\varepsilon_2$) spectra and structural parameters, which includes perovskite film thickness, the thickness of an interfacial layer forming between the substrate and perovskite film, and surface roughness layer thickness [36]. The full layer sequence consists of a substrate/perovskite + void interfacial layer/perovskite film/surface roughness/air ambient. The optical properties and the optical model used to describe soda lime glass and TEC-15 substrates have been reported in [37,38] respectively. Spectra in ε for the perovskite film are described using a parametric optical property model, which applies physically realistic parametric dispersion relations spanning from photon energies above to below the bandgap energy [39]. The mathematical equations for full parametric description of ε for these perovskites have been provided in [39,40]. The imaginary part of the dielectric function (ε_2) is described by the sum of critical-point oscillators assuming parabolic bands (CPPB) above the direct bandgap energy and an Urbach tail below the bandgap [41,42]. The above-gap critical points (CPs) in these perovskite films are assumed to be excitonic [43]. The lowest energy CP in ε_2 is considered to be the direct bandgap of the perovskite film. Spectra in ε_1 is calculated as the sum of a Sellmeier expression, a constant additive term to the real part of ε_1 denoted by ε_∞, and Kramers–Kroning integration [39] of ε_2 over this spectral range. Spectra in ε for the surface roughness layer and interfacial layer are represented by Bruggeman effective medium approximations [29] consisting of 0.5 void ($\varepsilon = 1$) and 0.5 bulk perovskite volume fractions.

3. Results and Discussion

Figure 2a shows the variation in spectra in ε as a function of time for a $MAPbI_3$ thin film deposited on a soda lime glass substrate when exposed to 85% RH at 25 °C. A noticeable decrease in the magnitude of ε_2 is observed after 200 min of exposure of $MAPbI_3$ to humidity. In Niu et al., $MAPbI_3$ is exposed to 60% RH air at 35 °C, and the absorption feature in ε_2 located at photon energies between the bandgap energy of 1.55 eV and 2.34 eV decreases sharply due to film degradation [44]. This interpretation provides context in understanding the decrease in magnitude of ε after 200 min of humidity exposure. Degradation throughout the $MAPbI_3$ film is reflected in the change in optical properties represented on Figure 2a. It has been reported that the interaction between MA and water molecules leads to the desorption of MA, eventually degrading the surface of $MAPbI_3$ by forming a hydrate phase $MAPbI_3 \cdot H_2O$ [13,45]. Due to lack of stability of the hydrate phase, further decomposition into MAI and PbI_2 could occur [45,46]. One of the possibilities to explain the observed variation in optical properties is that the film composition is no longer pure $MAPbI_3$ when the film is exposed to humidity for prolonged times. Previous studies indicated hydrogen bonding between the oxygen in water and the hydrogen in the NH_3 groups of MA cations [44,47]. Under exposure to humidity, the formation of that hydrogen bond will lead to an intermediate non-perovskite phase and this can cause the reduction in density of the perovskite film throughout the bulk [48]. It can be inferred that variation in optical properties can also result from the reduction in film density due to humidity induced film degradation.

Approved for public release; distribution unlimited.

657

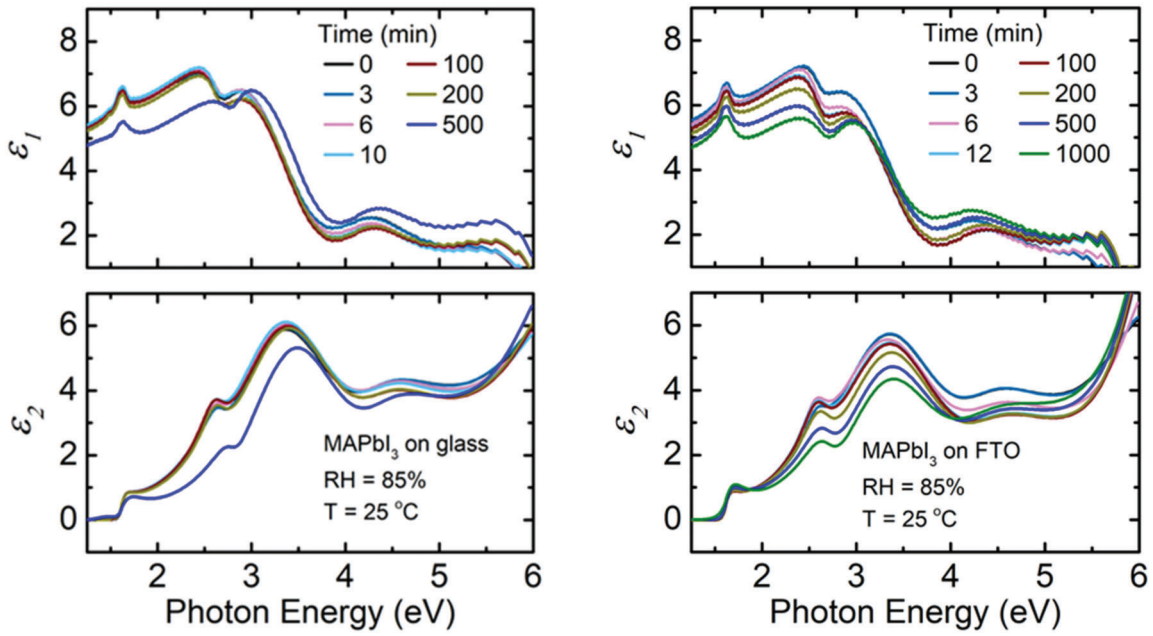


Figure 2. Complex dielectric function ($\varepsilon = \varepsilon_1 + i\varepsilon_2$) spectra at selected time points for thin film $MAPbI_3$ deposited on (**a**) soda lime glass and (**b**) fluorine-doped tin oxide (FTO) coated glass when exposed to 85% relative humidity (RH) at 25 °C. RH is introduced at 5 and 4 min for (**a**) and (**b**), respectively.

Figure 3a shows the time dependence of the structural parameters in terms of the surface roughness, bulk layer, and interfacial layer thicknesses as well as the quality of fit between the model and the ellipsometric spectra represented by the *MSE*. Effective material thickness is calculated by combining the perovskite bulk film thicknesses with the interfacial layer and surface roughness layer thickness weighted with the perovskite material fraction in each layer respectively [12]:

$$d_{effective,\,material} = \sum_{layers} f_{material} \times d_{layer} \quad (2)$$

where d_{layer} is the thickness of each layer and $f_{material}$ is the fraction of perovskite material in each layer. This quantity is used to identify changes in the total amount of perovskite per unit area on the substrate. Two models are applied to analyze the RTSE data. One model applies spectra in ε obtained prior to humidity exposure to fit the experimental data throughout the measurement time. The other fits spectra in ε independently for each time point. As shown in Figure 2a, spectra in ε for $MAPbI_3$ changes as a function of exposure time, therefore, the *MSE* obtained assuming static ε spectra obtained prior to humidity exposure is higher than that when spectra in ε are obtained at each time point. This difference in quality of fit indicates that both the structural parameters of the film and the intrinsic characteristics of the film reflected in ε vary with exposure to 85% RH.

Approved for public release; distribution unlimited.

658

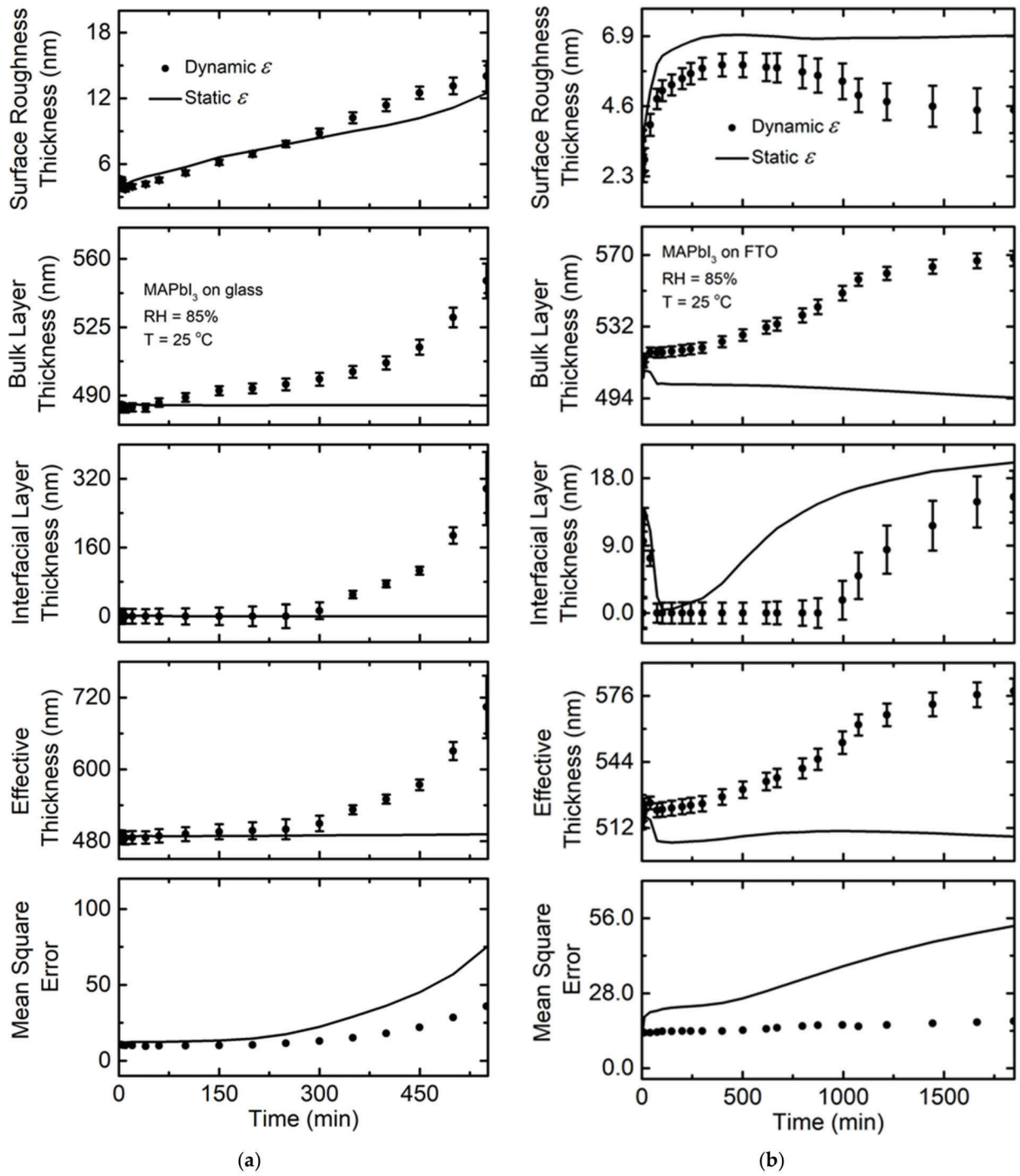


Figure 3. Surface roughness thickness, bulk layer thickness, interfacial layer thickness, effective perovskite thickness, and the quality of fit between the model and experimental ellipsometric spectra in the term of mean square error at selected time points as functions of time for thin film $MAPbI_3$ on (**a**) soda lime glass and (**b**) FTO coated glass when exposed to 85% RH at 25 °C. Values obtained assuming the initial spectra in ε (time = 0 min; static) prior to exposure are represented by a solid line, and spectra in ε fit at each time point (dynamic) are represented by solid circles. RH is introduced at 5 and 4 min for (**a**) and (**b**), respectively.

Approved for public release; distribution unlimited.

659

Surface roughness thickness increases gradually as soon as humidity flow is initiated (Figure 3a). In the beginning, there is no optically detectable interfacial layer between the film and the glass substrate, however this lower density layer forms after 300 min of exposure. The evolution of this layer increases the effective film thickness, however changes in the surface roughness and bulk layer thicknesses also occur. Within 550 min of humidity exposure, the effective thickness has increased by 218 nm (Table 1). After 300 min, water molecules may have penetrated the film, potentially from the top surface along grain boundaries or laterally from the sample edges, to the interface between the film and the glass substrate. Due to change in spectra in ε representing the entire perovskite film, it is likely that water transport from both directions occurs simultaneously. The increase in effective thickness may be due to an increase in unit cell volume caused by the hydration of $MAPbI_3$, which will reduce the film density [49]. Considering the lattice volume of $MAPbI_3$ and $MAPbI_3{\cdot}H_2O$ to be 247 $Å^3$ and 263 $Å^3$ respectively, conversion of $MAPbI_3$ to $MAPbI_3{\cdot}H_2O$ causes a volumetric lattice expansion of 6% based on the relative lattice parameters of both phases [49,50]. This result indicates that water molecules intercalated into the perovskite may have increased the volume of the unit cell, which leads to the increase in the thickness of the film and a reduction in density. The increase in volume of the unit cells due to hydration alone is not sufficient to describe the observed increase in effective film thickness. Other factors, such as decomposition and phase segregation, indicated by the presence of the interfacial layer with the substrate may have contributed to the increase in effective thickness. It should be noted that the *MSE* increases steadily with time using both initial static spectra in ε or allowing ε to vary for each time point. As even the model assuming changes in ε over time possesses a substantially large *MSE* relate to other samples (Table 1), it is likely that water infiltration might initiate breakdown, particularly along the interface. In addition, PbI_2 and MAI phase segregation might have occurred well before the final time point analyzed, which is consistent with the results reported by Ghimire et al. [12]. Briefly, we are not accurately capturing exactly how the film is changing and breaking down at long times since the *MSE* is quite high regardless of either the static or dynamic model used.

Table 1. *MSE* range; initial effective thickness; effective thickness change; and minimum, maximum, and average bandgap values for perovskites films over 0 to 550 min of exposure time as obtained from time dependent fitting of spectra in ε.

Perovskite Films	*MSE* Range	Initial Effective Thickness (nm)	Effective Thickness Change (nm)	Minimum Bandgap (eV)	Maximum Bandgap (eV)	Average Bandgap (eV)
$MAPbI_3$ on glass	10.6–35.5	486.8	218	1.596	1.605	1.604
$MAPbI_3$ on FTO	13.5–14.5	516.9	23	1.600	1.613	1.605
$MA_{0.7}FA_{0.3}PbI_3$ on glass	6.2–6.5	474.3	16	1.590	1.593	1.590
$MA_{0.7}FA_{0.3}PbI_3$ on FTO	6.7–9.6	478.1	12	1.606	1.616	1.613
$(FAPbI_3)_{0.95}(MAPbBr_3)_{0.05}$ on glass at 7 °C with 26% RH	8.7–8.8	615.8	1	1.560	1.565	1.562
$(FAPbI_3)_{0.95}(MAPbBr_3)_{0.05}$ on glass at 70 °C with 26% RH	8.6–8.9	614.2	0	1.590	1.595	1.593
$(FAPbI_3)_{0.95}(MAPbBr_3)_{0.05}$ on glass at 25 °C with 85% RH	8.9–8.8	614.5	7	1.559	1.571	1.563

Figure 2b shows the variation of spectra in ε for a $MAPbI_3$ film deposited on FTO coated glass substrate exposed to the same conditions. A decrease in the magnitude of spectra in ε occurs steadily with time. Smaller *MSE* values for $MAPbI_3$ deposited on FTO coated glass compared to the film directly on soda lime glass implies that the film deposited on FTO does not degrade as much as that on bare glass. Even though the optical properties for the perovskite film on FTO coated glass visually change more during exposure time, the higher *MSE* for the film deposited on bare glass indicates

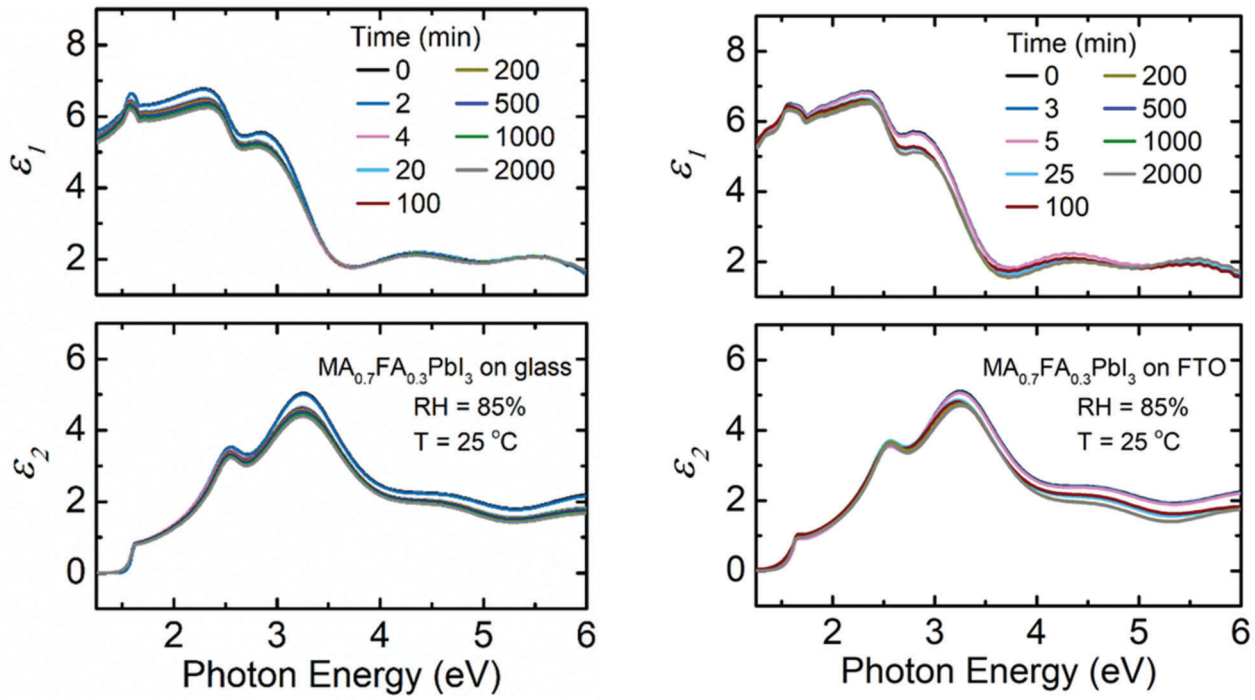
Approved for public release; distribution unlimited.

660

that the structural and optical property model for the starting material is inadequate to describe $MAPbI_3$ during the degradation process. We can assume that the intrinsic properties of the film on FTO change more, but perhaps these changes are a sign of large-scale stability since it does not break down to the extent of the film on bare glass. A comparative study conducted on $MAPbI_3$:Cl perovskite films grown on glass, glass/FTO, and glass/FTO/TiO_2 using photoluminescence indicated that films on FTO and on TiO_2 show more stable behavior over that on glass as oxygen can diffuse through the surface from the layer below. The underlying surface roughness was found to be a key factor in the morphology of the perovskite grains and in the resulting concentration of defects by providing a different nucleation site density and impacting the dimensionality of the grain growth dynamics [51]. Minimal increase in effective thickness is observed in Figure 3b compared to that for $MAPbI_3$ deposited on soda lime glass as listed in Table 1. The small variation in effective thickness for $MAPbI_3$ deposited on FTO emphasizes that this film does not decompose or delaminate to the same extent as that of the same composition film deposited on glass. This behavior is also reflected in ε as the film on FTO appears more uniform after 1000 min of exposure compared to the film on glass, which shows more substantial changes up to 500 min. In the case of $MAPbI_3$ deposited on glass, the huge increase in *MSE* suggests that the structural and optical property model applied no longer adequately describes this sample. The $MAPbI_3$ film on glass is likely to have completely or partially degraded or slightly delaminates as the large change in effective thickness is driven by the increase in the interfacial layer (Figure 3a). The interfacial layer is nearly as thick as the film itself in that case.

Figure 4a shows the variation of spectra in ε when a $MA_{0.7}FA_{0.3}PbI_3$ film deposited on soda lime glass substrate is exposed to 85% RH at 25 °C. There is a minimal decrease in magnitude of spectra in ε compared to $MAPbI_3$ deposited on either soda lime glass or FTO coated glass. Mixed MA + FA *A*-cation perovskites have been reported to be more stable against humidity exposure than perovskites with only MA as the *A*-cation [52]. By mixing MA and FA *A*-cations in solid solutions, the cubic perovskite phase is better stabilized. Minimal variation of effective thickness with time for $MA_{0.7}FA_{0.3}PbI_3$ deposited on glass is observed compared to that observed for $MAPbI_3$ on glass (Table 1) within a similar time interval. The improved stability of mixed MA + FA perovskite can be attributed to the larger size of the FA cation compared to MA leading to a more favorable tolerance factor [14,53]. The ionic radii of MA and FA are 2.16 and 2.53 Å [54], respectively, and a larger FA cation fraction in the perovskite results in a more ideal Goldschmidt tolerance factor closer to 1 [14,54]. The corresponding tolerance factor values are 0.964 for $MA_{0.7}FA_{0.3}PbI_3$ and 0.911 for $MAPbI_3$. The obtained tolerance factor values from calculation are reasonable considering the observed stability of the mixed MA + FA perovskite over $MAPbI_3$.

Approved for public release; distribution unlimited.



(**a**) (**b**)

Figure 4. Spectra in ε at selected time points for thin film $MA_{0.7}FA_{0.3}PbI_3$ deposited on (**a**) soda lime glass and (**b**) FTO coated glass when exposed to 85% RH at 25 °C. RH is introduced at 4 and 5 min for (**a**) and (**b**), respectively.

The $MA_{0.7}FA_{0.3}PbI_3$ film deposited on FTO coated glass substrate exposed to 85% RH at 25 °C shows a smaller decrease in magnitude of spectra in ε (Figure 4b) compared to $MA_{0.7}FA_{0.3}PbI_3$ deposited on soda lime glass. The improved stability over the $MA_{0.7}FA_{0.3}PbI_3$ film deposited on soda lime glass might be due to the influence of the chemical and structural nature of the underlying FTO [51] similar to that observed for $MAPbI_3$. Variation in effective thickness is less than that of the film on soda lime glass as shown in Table 1, although both films are relatively stable overall as shown in Figure 5. The *MSE* values for the $MA_{0.7}FA_{0.3}PbI_3$ perovskites on either substrate are low indicating that there are likely no other phases present or changes in phase structure during the observation time. Additionally, the *MSE* values in each case assuming either spectra in ε are fixed to the pre-humidity exposure value or allowed to vary with time are very similar when compared to the substantial differences observed for $MAPbI_3$.

Approved for public release; distribution unlimited.

662

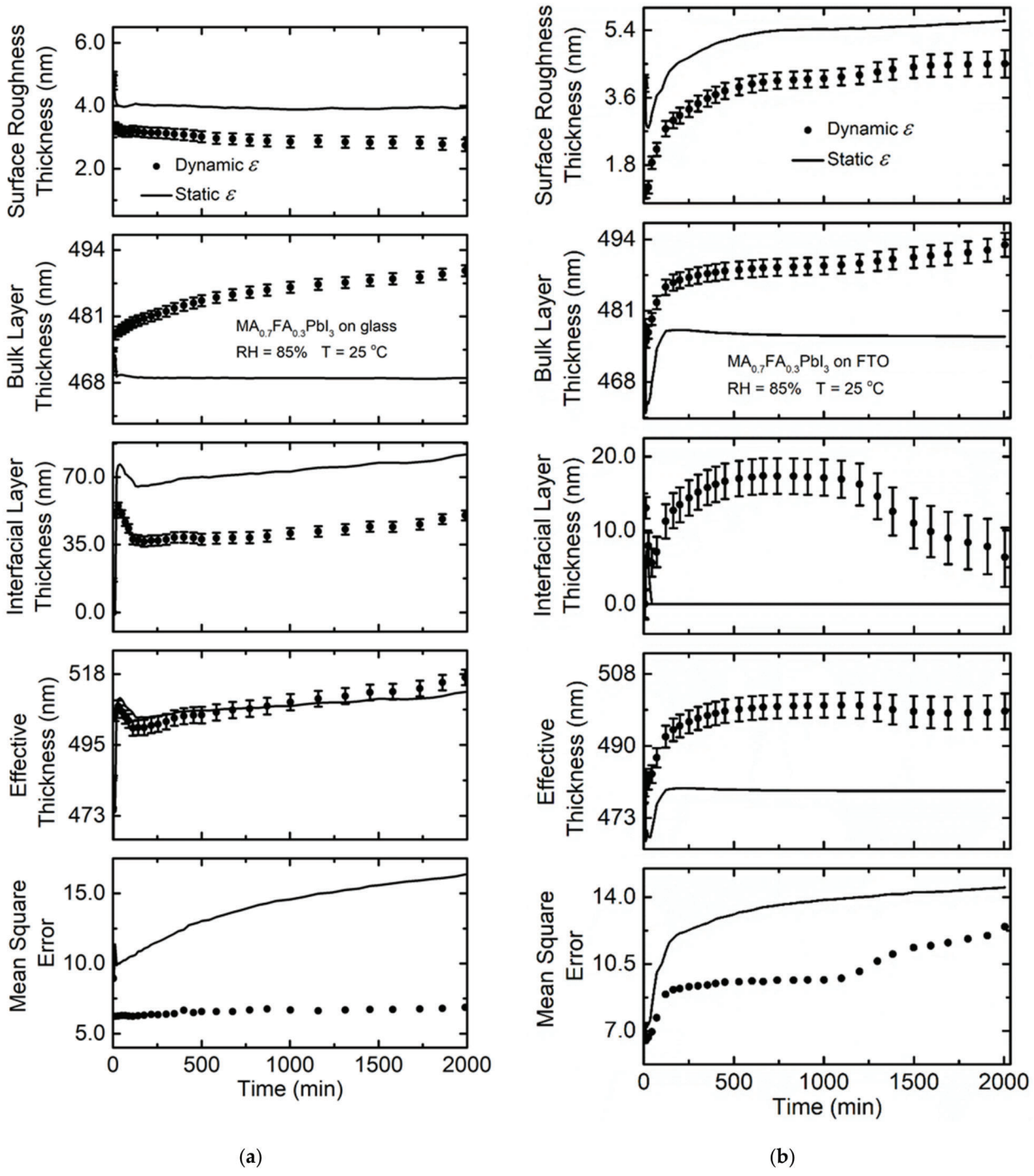


Figure 5. Surface roughness thickness, bulk layer thickness, interfacial layer thickness, effective perovskite thickness, and the quality of fit between the model and experimental ellipsometric spectra in the term of mean square error as functions of time for thin film $MA_{0.7}FA_{0.3}PbI_3$ on (**a**) soda lime glass and (**b**) FTO coated glass when exposed to 85% RH at 25 °C. Values obtained assuming the initial spectra in ε (time = 0 min; static) prior to exposure are represented by a solid line, and spectra in ε fit at each time point (dynamic) are represented by solid circles. RH is introduced at 4 and 5 min for (**a**) and (**b**), respectively.

Approved for public release; distribution unlimited.

663

To further understand the factors that influence the stability of different perovskite film compositions, $(FAPbI_3)_{0.95}(MAPbBr_3)_{0.05}$ thin films deposited on soda lime glass substrates have been exposed to 26% RH at 7 °C, 26% RH at 70 °C, and 85% RH at 25 °C. Figure 6 shows spectra in ε for $(FAPbI_3)_{0.95}(MAPbBr_3)_{0.05}$ deposited on soda lime glass exposed to 26% RH at 7 °C. The decrease in magnitude of spectra in ε is minimal compared to both $MA_{0.7}FA_{0.3}PbI_3$ and $MAPbI_3$.

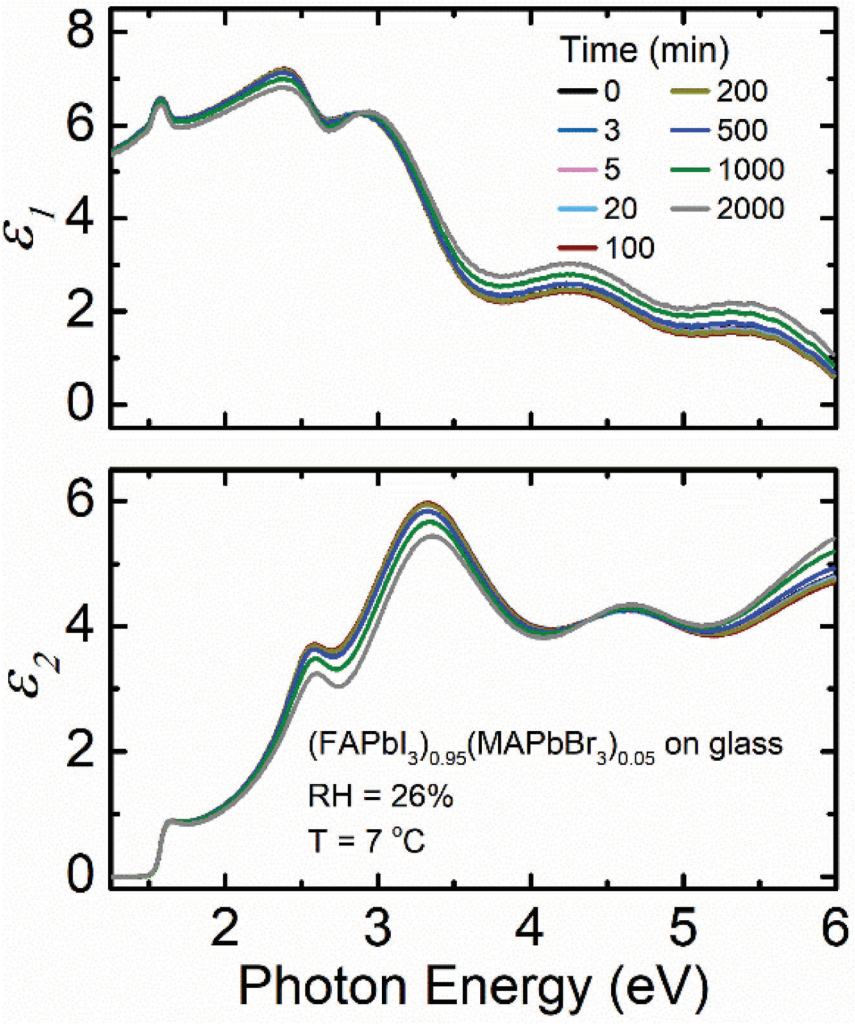


Figure 6. Spectra in ε at selected time points for thin film $(FAPbI_3)_{0.95}(MAPbBr_3)_{0.05}$ deposited on soda lime glass as a function of photon energy when exposed to 26% RH at 7 °C. RH is introduced at 5 min.

There is a small variation in effective thickness (Figure 7) when the film is exposed for a prolonged time. Improved quality of fit reflected in the low *MSE* assuming static ε obtained prior to humidity exposure and dynamic ε are evident, and the gap between the *MSE* describing the two increases only moderately during exposure to humidity. This indicates that low temperature humidity exposure does not affect the stability of this perovskite film substantially, and there are likely no other phases present.

Approved for public release; distribution unlimited.

664

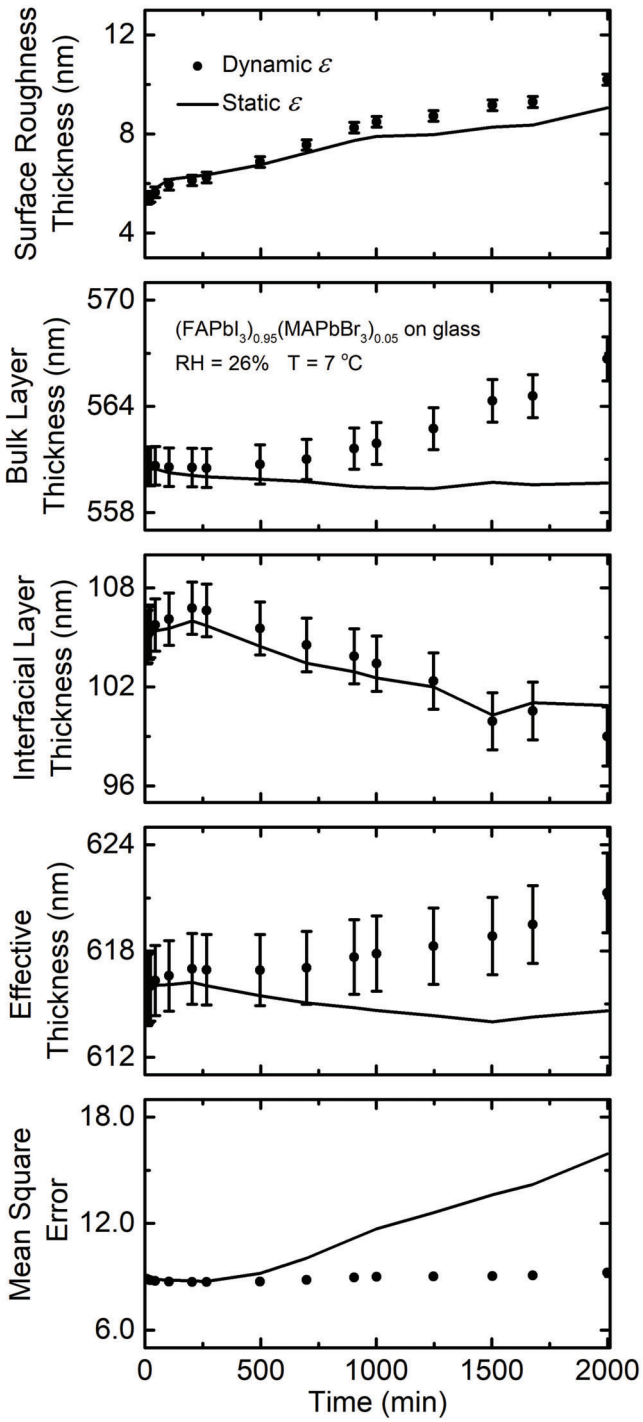


Figure 7. Surface roughness thickness, bulk layer thickness, interfacial layer thickness, effective perovskite thickness, and the quality of fit between the model and experimental ellipsometric spectra in the terms of mean square error as functions of time for $(FAPbI_3)_{0.95}(MAPbBr_3)_{0.05}$ thin film deposited on soda lime glass when exposed to 26% RH at 7 °C. Values obtained assuming the initial spectra in ε (time = 0 min; static) prior to exposure are represented by a solid line, and spectra in ε fit at each time point (dynamic) are represented by solid circles. RH is introduced at 5 min.

Approved for public release; distribution unlimited.

665

Figure 8 shows the variation of spectra in ε when a $(FAPbI_3)_{0.95}(MAPbBr_3)_{0.05}$ film deposited on soda lime glass substrate is exposed to the sequence of 26% humidity at 70 °C initially and then 85% RH at 25 °C later. The goal of this combined measurement is to test how this film composition resists varying exposure at both moderate humidity at high temperature and high humidity at moderate temperature after determining its stability at fixed 7 °C and 26% RH conditions. There is no change in magnitude of spectra in ε as a function of time compared to $MA_{0.7}FA_{0.3}PbI_3$ and $MAPbI_3$, and the changes are even smaller compared to those observed in this composition perovskite at a low temperature. The $(FAPbI_3)_{0.95}(MAPbBr_3)_{0.05}$ film at a low temperature may exhibit a small change over time as small amounts of water condense onto the film. However, even those changes are minor compared to the other perovskite compositions studied.

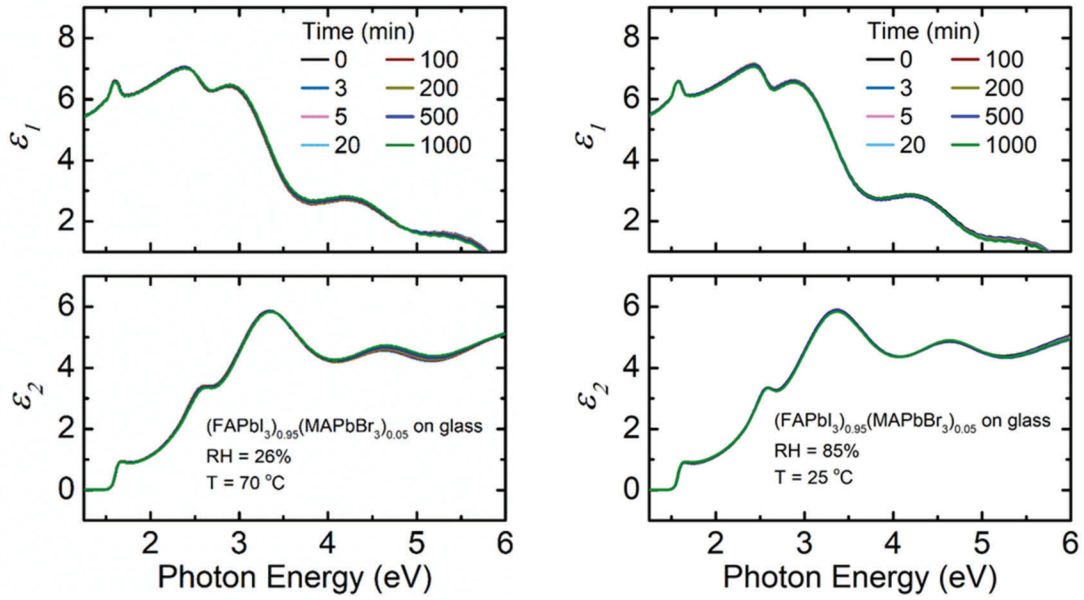


Figure 8. Spectra in ε at selected time points for thin film $(FAPbI_3)_{0.95}(MAPbBr_3)_{0.05}$ deposited on a soda lime glass as a function of photon energy when exposed to (**a**) 26% RH at 70 °C and (**b**) 85% RH at 25 °C. RH is introduced at 5 min.

Figure 9 illustrates the structural parameters in the form of the surface roughness, bulk layer, and interfacial layer thicknesses as functions of time for the $(FAPbI_3)_{0.95}(MAPbBr_3)_{0.05}$ film deposited on soda lime glass substrate exposed to 26% RH at 70 °C then 85% RH at 25 °C. No variation in effective thickness is observed for the film exposed to 26% RH at 70 °C but there is a minimal increase in effective thickness during 85% RH at 25 °C exposure in the reported time interval in Table 1. This variation is minimal compared to the other film compositions and measurement conditions. The small changes that are present (<10 nm) are attributed to small precession of the measurement beam spot on the sample surface over the time of the measurement. The quality of fit assuming a static ε obtained prior to humidity exposure is almost identical to that when spectra in ε are obtained at each time point (dynamic ε) for the time exposed to 26% RH at 70 °C. Note that the same static ε obtained prior to humidity exposure at 70 °C is used as the temperature is decreased, leading to a small increase in the *MSE*. This difference is expected as spectra in ε for semiconductors will vary with measurement temperature [55–57]. However, even in this case the spectra in ε measured at 70 °C provides a low *MSE*. This similarity in quality of fit indicates that the structural parameters of the film and the intrinsic characteristics of this perovskite reflected in ε are not affected by humidity exposure and temperature

Approved for public release; distribution unlimited.

variations. Overall, temperature variations over the 7 to 70 °C ranges do not seem to have an impact on the stability of the $(FAPbI_3)_{0.95}(MAPbBr_3)_{0.05}$ composition perovskite films.

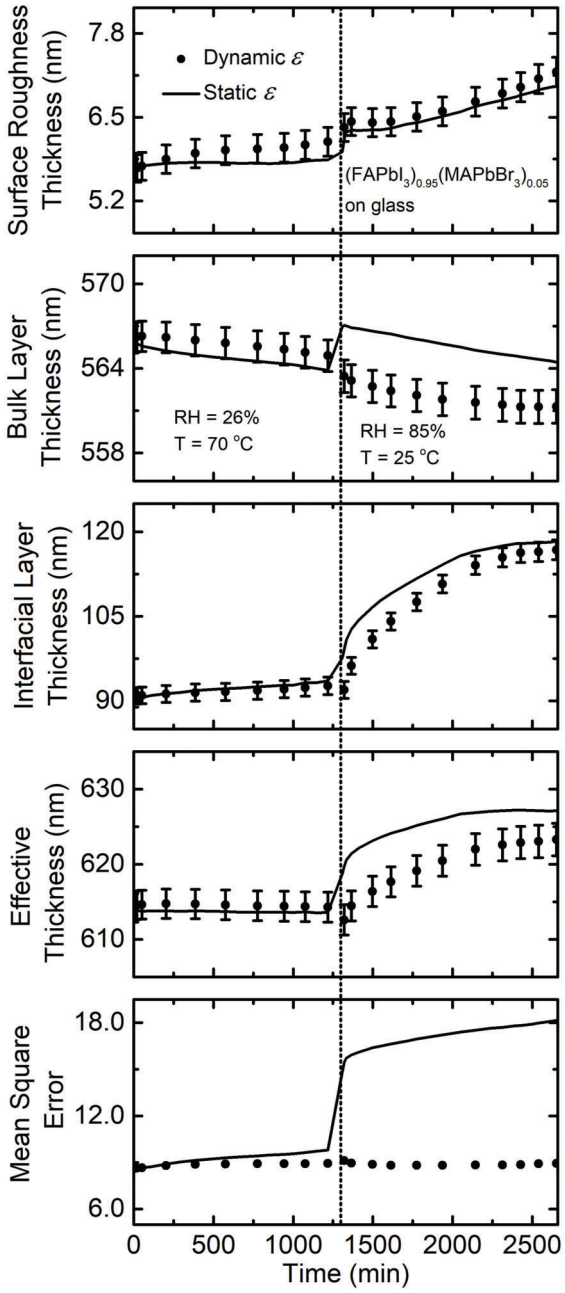


Figure 9. Surface roughness thickness, bulk layer thickness, interfacial layer thickness, effective perovskite thickness, and the quality of fit between the model and experimental ellipsometric spectra in the term of mean square error as functions of time for thin film $(FAPbI_3)_{0.95}(MAPbBr_3)_{0.05}$ deposited on soda lime glass when exposed to 26% RH at 70 °C then 85% RH at 25 °C. Values obtained assuming the initial spectra in ε (time = 0 min; static) prior to exposure are represented by a solid line, and spectra in ε fit at each time point (dynamic) are represented by solid circles. The vertical dotted line marks when the temperature and humidity are changed. RH is introduced at 5 min.

Approved for public release; distribution unlimited.

667

The improved stability for $(FAPbI_3)_{0.95}(MAPbBr_3)_{0.05}$ over $MAPbI_3$ and $MA_{0.7}FA_{0.3}PbI_3$ with temperature variations and humidity exposure is attributed to the incorporation of Br into the mixed MA + FA film. Previous research has shown that including a small amount of Br enhances the stability, suppresses ion migration, and reduces trap-state density [53]. According to Noh et al., upon incorporation of Br into $MAPbI_3$ for solar cell absorbers, there is an improvement in open circuit voltage (V_{OC}) from 0.87 to 1.13 V and an increase in fill factor (FF) from 0.66 to 0.74 [58]. Increases in these parameters is an indicator of good electronic film quality [36]. It has also been reported that replacing larger I ions with smaller Br ions results in a greater resistance to high humidity at room temperature [53]. Furthermore, perovskite films with mixed cations and mixed anions crystallize at much higher temperatures and exhibit greater degrees of crystalline order. A material with enhanced crystallinity both can promote high V_{OC} in PV devices and are more stable against degradation [4]. The two step-preparation solution-processing method for $(FAPbI_3)_{0.95}(MAPbBr_3)_{0.05}$ also leads to larger grain size than in the single step approach which further enhances film stability [33].

Bandgap energies of the studied perovskites films (Table 1) are not substantially affected by prolonged exposure to temperature and humidity, although there is observed variation in the magnitude of spectra in ε above the bandgap. There is a slight decrease in bandgap when the $(FAPbI_3)_{0.95}(MAPbBr_3)_{0.05}$ film exposed to 26% RH at 70 °C is cooled to 85% RH at 25 °C. Previous research has shown that the bandgap decreases with decreasing temperature in these hybrid halide perovskites unlike in other semiconductors where the bandgap decreases with increasing temperature as a result of lattice dilatation [55,57]. Here, a minimal decrease in bandgap is observed with decreased temperature. This change is small on its own since the temperature variation is not extreme. Film composition also controls variation in bandgap [59]. Lack of variation in bandgap in the case of the perovskite films continuously exposed to a fixed temperature and humidity can be attributed to the fact that the film composition remains largely the same during the time of exposure at this range of temperatures. Even $MAPbI_3$, which exhibits substantial degradation by water molecules, retains a similar bandgap energy throughout humidity exposure although the higher energy CPs and magnitude of ε change more substantially.

4. Conclusions

The stability of optical and structural properties of organic–inorganic metal halides-based perovskites thin films exposed to various humidity and temperature conditions have been explored using RTSE. $MAPbI_3$ degrades upon exposure to 85% RH at room temperature whereas mixed MA + FA perovskites shows improved stability when exposed to RH at various temperatures. Temperature alone in the range of 7 to 70 °C does not affect the stability of studied $(FAPbI_3)_{0.95}(MAPbBr_3)_{0.05}$ perovskite films. There is an influence of the substrate on the stability of these perovskites as the films deposited on FTO coated glass shows enhanced stability compared to the films deposited directly onto soda lime glass. Additionally, incorporation of bromine and the two-step preparation method are among other factors for improved stability of the mixed MA + FA cation perovskites. Among the studied perovskites, $(FAPbI_3)_{0.95}(MAPbBr_3)_{0.05}$ demonstrated a robust stability for the tested humidity and temperature conditions.

Author Contributions: Conceptualization, N.J.P., M.M.J., B.S., Y.Y., Z.S. and M.S.T.; samples fabrication, C.C. and Z.S.; data acquisition, M.S.T. and B.S.; formal analysis, M.S.T. and B.S.; writing original draft preparation, M.S.T., writing-review and editing, B.S., N.J.P., C.C., Z.S. and M.M.J.; funding acquisition, N.J.P. and Y.Y. All authors have read and agreed to the published version of the manuscript.

Approved for public release; distribution unlimited.

668

Funding: This research was funded by the Ohio Department of Development (ODOD) Ohio Research Scholar Program (Northwest Ohio Innovators in Thin Film Photovoltaics, Grant No. TECH 09-025), the U.S. Department of Energy (DOE) SunShot Initiative under the Next Generation Photovoltaics 3 program (DE-FOA-0000990), the National Science Foundation (CHE-1230246 and DMR-1534586), the Air Force Research Laboratory under agreement numbers FA9453-18-2-0037 and FA9453-19-C-1-002, the Office of Naval Research under contract number N00014-17-1-2223, and the U.S. DOE Office of Energy Efficiency and Renewable Energy (EERE) under the Solar Energy Technologies Office Award Numbers DE-EE0008753 and DE-EE0008790. The U.S. Government is authorized to reproduce and distribute reprints for Governmental purposes notwithstanding any copyright notation thereon. The views and conclusions contained herein are those of the authors and should not be interpreted as necessarily representing the official policies or endorsements, either expressed or implied, of Air Force Research Laboratory or the U.S. Government.

Institutional Review Board Statement: Not applicable.

Informed Consent Statement: Not applicable.

Data Availability Statement: The data presented in this study are available on request from the corresponding author.

Conflicts of Interest: The authors declare no conflict of interest.

References

1. Kojima, A.; Teshima, K.; Shirai, Y.; Miyasaka, T. Organometal Halide Perovskites as Visible-Light Sensitizers for Photovoltaic Cells. *J. Am. Chem. Soc.* **2009**, *131*, 6050–6051. [CrossRef]
2. Werner, J.; Sahli, F.; Kamino, B.; Sacchetto, D.; Brauninger, M.; Walter, A.; Ballif, C.; Despeisse, M.; Nicolay, S.; Niesen, B.; et al. Perovskite/Silicon tandem Solar Cells: Challenges Towards High-Efficiency in 4-Terminal and Monolithic Devices. In Proceedings of the IEEE 44th Photovoltaic Specialist Conference (PVSC), Washington, DC, USA, 25–30 June 2017; pp. 3256–3259.
3. NREL Solar Cell Efficiency Chart. Available online: http://www.nrel.ov/pv/cell-efficiency.html (accessed on 13 February 2021).
4. Rehman, W.; McMeekin, D.P.; Patel, J.B.; Milot, R.L.; Johnston, M.B.; Snaith, H.J.; Herz, L.M. Photovoltaic mixed-cation lead mixed-halide perovskites: Links between crystallinity, photo-stability, and electronic properties. *Energy Environ. Sci.* **2017**, *10*, 361–369. [CrossRef]
5. Charles, B.; Dillon, J.; Weber, O.J.; Islam, M.S.; Weller, M.T. Understanding the stability of mixed A-cation lead iodide perovskites. *J. Mater. Chem. A* **2017**, *5*, 22495–22499. [CrossRef]
6. Stranks, S.D.; Eperon, G.E.; Grancini, G.; Menelaou, C.; Alcocer, J.P.; Leijtens, T.; Herz, L.M.; Petrozza, A.; Snaith, H.J. Electron-Hole Diffusion Lengths Exceeding 1 Micrometer in an Organometal Trihalide Perovskite Absorber. *Science* **2013**, *342*, 341–344. [CrossRef] [PubMed]
7. Correa-Baena, J.P.; Saliba, M.; Buonassisi, T.; Gratzel, M.; Abate, A.; Tress, W.; Hagfeldt, A. Promises and challenges of perovskite solar cells. *Science* **2017**, *358*, 739–744. [CrossRef] [PubMed]
8. Wozny, S.; Yang, M.; Nardes, A.M.; Mercado, C.C.; Ferrere, S.; Reese, M.O.; Zhou, W.; Zhu, K. Controlled Humidity Study on the Formation of Higher Efficiency Formamidinium Lead Triiodide-Based Solar Cells. *Chem. Mater.* **2015**, *27*, 4814–4820. [CrossRef]
9. Boyd, C.C.; Cheacharoen, R.; Leijtens, T.; McGehee, M.D. Understanding Degradation Mechanisms and Improving Stability of perovskite photovoltaics. *Chem. Rev.* **2019**, *119*, 3418–3451. [CrossRef] [PubMed]
10. Senocrate, A.; Acarturk, T.; Kim, G.Y.; Merkle, R.; Starke, U.; Gratzel, M.; Maier, J. Interaction of oxygen with halide perovskites. *J. Mater. Chem. A* **2018**, *6*, 10847–10855. [CrossRef]
11. Divitini, G.; Cacovich, S.; Matteocci, F.; Cina, L.; Carlo, A.D.; Ducati, C. In situ observation of heat-induced degradation of perovskite solar cells. *Nat. Energy* **2016**, *1*, 15012. [CrossRef]
12. Ghimire, K.; Zhao, D.; Cimaroli, A.; Ke, W.; Yan, Y.; Podraza, N.J. Optical monitoring of $CH_3NH_3PbI_3$ thin films upon atmospheric exposure. *J. Phys. D Appl. Phys.* **2016**, *49*, 405102. [CrossRef]
13. Christians, J.A.; Miranda Herrera, P.A.; Kamat, P.V. Transformation of the Excited state and Photovoltaic Efficiency of $CH_3NH_3PbI_3$ Perovskite upon Controlled Exposure to Humidified Air. *J. Am. Chem. Soc.* **2015**, *137*, 1530–1538. [CrossRef] [PubMed]
14. Li, Z.; Yang, M.; Park, J.; Wei, S.; Berry, J.J.; Zhu, K. Stabilizing Perovskite Structures by Tuning Tolerance factor: Formamidinium and Cesium Lead Iodide Solid-State Alloys. *Chem. Mater.* **2016**, *28*, 284–292. [CrossRef]
15. Johnston, A.; Walters, G.; Saidaminoz, M.I.; Huang, Z.; Bertens, K.; Jalarvo, N.; Sargent, E.H. Bromine Incorporation and Suppressed Cation Rotation in Mixed-Halide Perovskites. *ACS Nano* **2020**, *14*, 15107–15118. [CrossRef] [PubMed]
16. Jeon, N.J.; Noh, J.H.; Yang, W.S.; Kim, Y.C.; Ryu, S.; Seo, J.; Seok, S. Compositional engineering of perovskite materials for high-performance solar cells. *Nature* **2015**, *517*, 476–480. [CrossRef] [PubMed]
17. Goldschmidt, V.M. The laws of crystal chemistry. *Naturwissenschaften* **1926**, *14*, 477–485. [CrossRef]
18. Subedi, B.; Guan, L.; Ghimire, K.; Uprety, P.; Yan, Y.; Podraza, N.J. Formamidinium + cesium triiodide perovskites: Discrepancies between thin film optical absorption and solar cell efficiency. *Sol. Energy Mater. Sol. Cells* **2018**, *188*, 228–233. [CrossRef]

Approved for public release; distribution unlimited.

669

19. Lv, Y.; Shi, Y.; Song, X.; Liu, J.; Wang, M.; Wang, S.; Feng, Y.; Jin, S.; Hao, C. Bromine Doping as an Efficiency Strategy to Reduce the Interfacial Defects in Hybrid Two-Dimensional/Three-Dimensional Stacking Perovskite Solar Cells. *ACS Appl. Mater. Interfaces* **2018**, *10*, 31755–31764. [CrossRef]
20. Lin, C.; Li, S.; Zhang, W.; Shao, C.; Yang, Z. Effect of Bromine Substitution on the Ion Migration and Optical Absorption in MAPbI3 Perovskite Solar Cells: The First-Principles Study. *ACS Appl. Energy Mater.* **2018**, *1*, 1374–1380. [CrossRef]
21. Fujiwara, H. *Spectroscopic Ellipsometry Principles and Applications*; John Wiley & Sons, Ltd.: New York, NY, USA, 2007; pp. 20–32.
22. Johs, B.; Herzinger, C.M. Quantifying the accuracy of ellipsometer systems. *Phys. Status Solidi C* **2008**, *5*, 1031–1035. [CrossRef]
23. Richter, A.; Guico, R.; Wang, J. Calibrating an ellipsometer using x-ray reflectivity. *Rev. Sci. Instrum.* **2001**, *72*, 3004. [CrossRef]
24. Logothetidis, S.; Stergioudis, G. Studies of density and surface roughness of ultrathin amorphous carbon films with regards to thickness with x-ray reflectometry and spectroscopic ellipsometry. *Appl. Phys. Lett.* **1997**, *71*, 2463. [CrossRef]
25. Kaminska, K.; Amassian, A.; Martinu, L.; Robbie, K. Growth of vacuum evaporated ultraporous silicon studied with spectroscopic ellipsometry and scanning electron microscopy. *J. Appl. Phys.* **2005**, *97*, 013511. [CrossRef]
26. Koirala, P.; Li, J.; Yoon, H.P.; Aryal, P.; Marsillac, S.; Rockett, A.A.; Podraza, N.J.; Collins, R.W. Through-the-glass spectroscopic ellipsometry for analysis of CdTe thin-film solar cells in the superstrate configuration. *Prog. Photovolt. Res. Appl.* **2016**, *24*, 1055–1067. [CrossRef]
27. Leik, N.; Weber, J.W.; Mackus, A.J.M.; Van de Sanden, M.C.M.; Kessels, W.M.M. In situ spectroscopic ellipsometry during atomic layer deposition of Pt, Ru and Pd. *J. Phys. D Appl. Phys.* **2016**, *49*, 115504. [CrossRef]
28. Revol, P.; Perret, D.; Bertin, F.; Fusalba, F.; Rouessac, V.; Chabli, A.; Passemard, G.; Ayral, A. Porosimetry Measurements on Low Dielectric Constant-Thin Layers by Coupling Spectroscopic Ellipsometry and Solvent Adsorption-Desorption. *J. Porous Mater.* **2005**, *12*, 113–121. [CrossRef]
29. Fujiwara, H.; Koh, J.; Rovira, P.I.; Collins, R.W. Assessment of effective-medium theories in the analysis of nucleation and microscopic surface roughness evolution for semiconductor thin films. *Phys. Rev. B* **2000**, *61*, 10832. [CrossRef]
30. Losurdo, M.; Barreca, D.; Capezzuto, P.; Bruno, G.; Tondello, E. Interrelation between nanostructure and optical properties of oxide thin films by spectroscopic ellipsometry. *Surf. Coat. Technol.* **2002**, *151–152*, 2–8. [CrossRef]
31. Wang, C.; Guan, L.; Zhao, D.; Yu, Y.; Grice, C.R.; Song, Z.; Awni, R.A.; Chen, J.; Wang, J.; Zhao, X.; et al. Water Vapor Treatment of Low-Temperature Deposited SnO_2 Electron Selective layers for Efficient Flexible Perovskite Solar Cells. *ACS Energy Lett.* **2017**, *2*, 2118–2124. [CrossRef]
32. Ke, W.; Xiao, C.; Wang, C.; Saparov, B.; Duan, H.; Zhao, D.; Xiao, Z.; Schulz, P.; Harvey, S.P.; Liao, W.; et al. Employing Lead Thiocyanate Additive to Reduce the Hysteresis and Boost the Fill Factor of Planar Perovskite Solar Cells. *Adv. Mater.* **2016**, *28*, 5214–5221. [CrossRef] [PubMed]
33. Cui, Y.; Chen, C.; Chen, L.; Bista, S.S.; Liu, X.; Li, Y.; Awni, R.A.; Song, Z.; Yan, Y. Correlating Hysteresis and Stability with Organic Cation Composition in the Two-Step Solution-Processed Perovskite Solar Cells. *ACS Appl. Mater. Interfaces* **2020**, *12*, 10588–10596. [CrossRef] [PubMed]
34. Lee, L.; Rovira, P.; An, I.; Collins, R.W. Rotating-compansator multichannel ellipsometry: Applications for real time Stokes vector spectroscopy of thin film growth. *Rev. Sci. Instrum.* **1988**, *69*, 1800. [CrossRef]
35. Jiang, Y.; Soufiani, A.M.; Gentle, A.; Huang, F.; Ho-Baillie, A.; Green, M.A. Temperature dependent optical properties of $CH_3NH_3PbI_3$ perovskites perovskite by spectroscopic ellipsometry. *Appl. Phys. Lett.* **2016**, *108*, 061905. [CrossRef]
36. Subedi, B.; Li, C.; Junda, M.M.; Song, Z.; Yan, Y.; Podraza, N.J. Effects of intrinsic and atmospherically induced defects in narrow bandgap $(FASnI_3)_X(MAPbI_3)_{1-X}$ perovskite thin films and solar cells. *J. Chem. Phys.* **2020**, *152*, 064705. [CrossRef]
37. Junda, M.M.; Podraza, N.J. Optical properties of soda lime float glass from 3 mm to 148 nm (0.41 meV to 8.38 eV) by spectroscopic ellipsometry. *Surf. Sci. Spectra* **2018**, *25*, 016001. [CrossRef]
38. Karki Gautam, L. Spectroscopic Ellipsometry Studies of Thin Film Si:H Materials in Photovoltaic Applications from Infrared to Ultraviolet. Ph.D. Thesis, University of Toledo, Toledo, OH, USA, May 2016.
39. Junda, M.M.; Grice, C.R.; Yan, Y.; Podraza, N.J. Parametric Optical Property Database for $CdSe_{1-X}S_X$ Alloys. *Electron. Mater. Lett.* **2019**, *15*, 500–504. [CrossRef]
40. Subedi, B.; Song, Z.; Chen, C.; Li, C.; Ghimire, K.; Junda, M.M.; Subedi, I.; Yan, Y.; Podraza, N.J. Optical and Electronic Losses Arising from Physically Mixed Interfacial Layers in Perovskites Solar Cells. *Appl. Mater. Interfaces* **2021**, *13*, 4923–4934. [CrossRef]
41. Aspnes, D.E. Modulation spectroscopy/electric field effects on the dielectric function of semiconductors. In *Handbook of Semiconductors*; Balkanski, M., Ed.; North Holland Publishing Company: Amsterdam, The Netherlands, 1980; Volume 2, pp. 109–154.
42. Urbach, F. The Long-Wavelength Edge of Photographic Sensitivity and of the Electronic Absorption of Solids. *Phys. Rev.* **1953**, *92*, 1324. [CrossRef]
43. Leguy, A.M.A.; Azarhoosh, P.; Alonso, M.I.; Campoy-Quiles, M.; Weber, O.J.; Yao, J.; Bryant, D.; Weller, M.T.; Nelson, J.; Walsh, A.; et al. Experimental and theoretical optical properties of methylammonium lead halide perovskites. *Nanoscale* **2016**, *8*, 6317–6327. [CrossRef] [PubMed]
44. Niu, G.; Li, W.; Meng, F.; Wang, L.; Dong, H.; Qiu, Y. Study on the stability of $CH_3NH_3PbI_3$ and the effect of post-modification by aluminium oxide in all-solid-state hybrid solar cells. *J. Mater. Chem. A* **2014**, *2*, 705–710. [CrossRef]

Approved for public release; distribution unlimited.

45. Song, Z.; Abate, A.; Watthage, S.C.; Liyanage, G.K.; Phillips, A.B.; Steiner, U.; Graetzel, M.; Heben, M.J. Perovskite Solar Cell Stability in Humid Air: Partially Reversible Phase Transitions in the PbI_2-CH_3NH_3I-H_2O System. *Adv. Energy Mater.* **2016**, *6*, 1600846. [CrossRef]
46. Jong, U.; Yu, C.; Ri, G.; McMahon, A.P.; Harrison, N.M.; Barnes, P.R.F.; Walsh, A. Influence of water intercalation and hydration on chemical decomposition and ion transport in methylammonium lead halide perovskites. *J. Mater. Chem. A* **2018**, *6*, 1067–1074. [CrossRef]
47. Dong, X.; Fang, X.; Lv, M.; Lin, B.; Zhang, S.; Ding, J.; Yuan, N. Improvement of the humidity stability of organic-inorganic perovskite solar cells using ultrathin Al_2O_3 layers prepared by atomic layer deposition. *J. Mater. Chem. A* **2015**, *3*, 5360–5367. [CrossRef]
48. Zhang, L.; Sit, P.H. Ab Initio Study of Interaction of Water, Hydroxyl Radicals, and Hydroxide Ions with $CH_3NH_3PbI_3$ and $CH_3NH_3PbBr_3$ Surfaces. *J. Phys. Chem. C* **2015**, *119*, 22370–22378. [CrossRef]
49. Leguy, A.M.A.; Hu, Y.; Campony-Quiles, M.; Alonso, M.I.; Weber, O.J.; Azarhoosh, P.; Schilfgaarde, M.; Weller, M.T.; Bein, T.; Nelson, J.; et al. Reversible Hydration of $CH_3NH_3PbI_3$ in Films, Single Crystals, and Solar Cells. *Chem. Mater.* **2015**, *27*, 3397–3407. [CrossRef]
50. Mosconi, E.; Aspiroz, J.M.; De Angelis, F. Ab Initio Molecular Dynamics Simulations of Methylammonium Lead Iodide Perovskite Degradation by Water. *Chem. Mater.* **2015**, *27*, 4885–4892. [CrossRef]
51. Climent-Pascual, E.; Hames, B.C.; Moreno-Ramirez, J.S.; Alvarez, A.L.; Juarez-Perez, E.J.; Mas-Marza, E.; Mora-Sero, I.; DeAndres, A.; Coya, C. Influence of the substrate on the bulk properties of hybrid lead halide perovskite films. *J. Mater. Chem. A* **2016**, *4*, 18153–18163. [CrossRef]
52. Li, W.; Rao, H.; Chen, B.; Wang, X.; Kuang, D. A formamidinium-methylammonium lead iodide perovskite single crystal exhibiting exceptional optoelectronic properties and long-term stability. *J. Mater. Chem. A* **2017**, *5*, 19431–19438. [CrossRef]
53. Han, F.; Yang, W.; Zhu, L. Stable High-Efficiency Two-Dimensional Perovskite Solar Cells via Bromine Incorporation. *Nanoscale Res. Lett.* **2020**, *15*, 194. [CrossRef] [PubMed]
54. Travis, W.; Glover, E.N.K.; Bronstein, H.; Scanlon, D.O.; Palgrave, R.G. On the application of the tolerance factor to inorganic and hybrid halide perovskites: A revised system. *Chem. Sci.* **2016**, *7*, 4548–4556. [CrossRef]
55. Wright, A.D.; Verdi, C.; Milot, R.L.; Eperon, G.E.; Perez-Osorio, M.A.; Snaith, H.J.; Giustino, F.; Johnston, M.B.; Herz, L.M. Electron-phonon coupling in hybrid lead halide perovskites. *Nat. Commun.* **2016**, *7*, 11755. [CrossRef]
56. Monserrat, B.; Park, J.; Kim, S.; Walsh, A. Role of electron-phonon coupling and thermal expansion on bandgaps, carrier mobility, and interfacial offsets in kesterite thin-film solar cells. *Appl. Phys. Lett.* **2018**, *112*, 193903. [CrossRef]
57. O'Donnell, K.P.; Chen, X. Temperature dependence of semiconductor bandgaps. *Appl. Phys. Lett.* **1991**, *58*, 2924. [CrossRef]
58. Noh, J.H.; Im, S.H.; Heo, J.H.; Mandal, T.N.; Seok, S. Chemical Management for Colorful, Efficient and Stable Inorganic-Organic Hybrid nanostructured Solar Cells. *Nano Lett.* **2013**, *13*, 1764–1769. [CrossRef] [PubMed]
59. Parker, C.A.; Roberts, J.C.; Bedair, S.M.; Reed, M.J.; Liu, S.X.; El-Masry, N.A.; Robins, L.H. Optical band gap dependence on composition and thickness of $In_XGa_{1-X}N$ ($0 < X < 0.25$) grown on GaN. *Appl. Phys. Lett.* **1999**, *75*, 2566.

Approved for public release; distribution unlimited.

Research Article Vol. 29, No. 22 / 25 Oct 2021 / Optics Express 36328
Optics EXPRESS

Analysis of non-idealities in rhomb compensators

AMBALANATH SHAN,* BALAJI RAMANUJAM, NIKOLAS J. PODRAZA, AND ROBERT W. COLLINS

Wright Center for Photovoltaics Innovation and Commercialization and Department of Physics and Astronomy, University of Toledo, Toledo, OH 43606, USA
*ambalanath.shan@utoledo.edu

Abstract: In-line rotatable rhombs that are only weakly chromatic are desired as compensators for a wide variety of applications in spectroscopic polarimetry and Mueller matrix spectroscopic ellipsometry. These devices employ multiple total internal reflections to generate differences in the phase shifts upon reflection for orthogonal fast and slow axis optical electric field components. A framework has been developed for characterization of non-idealities in the performance of rhombs due to dissipation and associated dichroism upon each reflection as well as stress-induced birefringence along each beam path. External oblique reflection measurements by spectroscopic ellipsometry for the internally reflecting interface structures has enabled characterization of the dichroic effects and retardance generated by the reflections. The framework for analysis of the effects of stress relies on simulations demonstrating that the contributions to polarization modification from each beam path depend only on the accumulated stress-induced retardance and average azimuthal angle of the fast principal stress axis along the given path. The overall approach has been applied to straight-through Mueller matrix measurements of a three-reflection rhomb in its operational configuration to establish the set of stress parameters for each of the four beam paths needed to fit the measurements. Thus, device geometry and optical structure, including layer thicknesses and component media optical properties, as well as stress-induced retardances and average stress azimuthal angles, which are all deduced in the analysis, enable a complete description of the polarization modifying properties of the rhomb when serving as a compensator.

© 2021 Optical Society of America under the terms of the OSA Open Access Publishing Agreement

1. Introduction

The capabilities of accurate generation and detection of polarized light over wide spectral ranges are required in numerous scientific fields [1–4]. For this purpose, compensators are utilized to impose accurately known differences in phase shifts between orthogonal electric field components upon light transmission through such devices. In-line compensator designs that are rotatable without beam deviation are desired to enable polarization modulation. The ultimate solution to the strongly chromatic retardance, limited zero-order spectral range, and oscillatory chromatic artifacts of rotatable monoplate and biplate compensators is the replacement of these devices by nearly-achromatic compensators based on in-line rhomb designs [2]. The disadvantage of beam re-direction imposed by one and two reflection rhombs is overcome by in-line rotatable three-reflection devices. Such devices simultaneously enable reduction in stress-induced birefringence owing to their shorter path lengths compared to in-line four-reflection dual rhombs [2,5–8] which can be designed to be self-compensating for deviation angle and thus more accurately rotatable [9]. The in-line three-reflection rhomb compensator design reported by King [10,11] uses a symmetric arrangement of the total internal reflections (TIRs). In this design, one intermediate internal reflection from a (fused silica)/MgF_2/ambient two-interface structure occurs between two internal reflections from (fused silica)/ambient single interfaces to achieve nearly quarter wave operation over a wide spectral range.

#440680 https://doi.org/10.1364/OE.440680
Journal © 2021 Received 18 Aug 2021; revised 4 Oct 2021; accepted 5 Oct 2021; published 19 Oct 2021

Approved for public release; distribution unlimited.

Optics EXPRESS

In an ideal nearly-achromatic rhomb compensator, all internal reflections are total without dissipation and no polarization modification occurs in transmission upon beam entry into and exit from the device as well as along the light beam paths within the rhomb medium. In this case, the device performance is characterized by a Jones or Mueller matrix with a single wavelength dependent phase retardance that is an accumulation of the differences in phase shifts upon reflection for optical electric field components along orthogonal fast and slow axes of the device. This retardance spectrum is a well-understood function of the angles of incidence at the internal interfaces and the refractive indices of the materials with which the beam interacts [12]. For the King rhomb [10,11], for example, these materials include fused silica and thin film polycrystalline MgF_2, assumed to be optically isotropic under ideal circumstances.

An analysis of the ideal performance of a rhomb compensator shows that it is only weakly chromatic in comparison with monoplate and biplate devices. Non-ideality due to dissipative internal reflections results in dichroic behavior that can be well characterized if generated by isotropic laminar structures at interfaces and contributes additional weak chromatic behavior [13]. In practice for these devices, however, stress-induced birefringence due to strain within the rhomb material contributes to non-ideal behavior that is comparably more difficult to characterize as a result of its spatial variations along the beam path. Such birefringence is a third source of chromatic behavior that can be quite strong for high stresses and long beam paths, the latter occurring in dual Fresnel rhombs, for example. Although extensive literature exists on the design of rhombs [2,5,9] with the early work reviewed in Ref. [2], the effects of these non-idealities are rarely considered or analyzed in detail. The goal of this study is to address such a deficiency in the characterization of rhomb compensators.

The rhomb design by King will be the focus of the present study as an illustration of the how the non-idealities observed in rhomb design compensators can be characterized. In this study, we have developed a comprehensive approach for determining the non-ideality characteristics of rhombs that have limited their wider adoption as compensators in optical instrumentation. We have demonstrated methods for complete characterization of the dichroic and stress-induced birefringence effects that lead to deviations of the Mueller matrix of the in-line three-reflection rhomb from its ideal form. This approach uses a novel combination of state-of-the-art multichannel Mueller matrix spectroscopy in transmission mode in the rhomb's operational configuration as well as multichannel spectroscopic ellipsometry performed externally in reflection mode, the latter to characterize the internally reflecting interfaces. As a result, we identify a set of wavelength-independent parameters that fully characterize the rhomb's spectroscopic Mueller matrix. This article is structured as described in the following two paragraphs.

Section 2 focuses on the experimental methodologies in three subsections. The first subsection describes the design of the King rhomb and the Mueller matrix measurements performed on the device using a dual rotating-compensator ellipsometer. In the second subsection, the Mueller matrix elements m_{12} and m_{44} from this measurement are presented and compared to the results of simulations assuming ideal performance of the rhomb as a compensator. The m_{12} element reveals the presence of a dichroic effect whereas the m_{44} element reveals the presence of stress induced birefringence along the four beam paths. The third subsection describes the origins of the spectrum in the stress-optic coefficient of fused silica used in the data analysis of this study.

Sections 3–5 develop the background material required for a complete analysis of the Mueller matrix of the rhomb including the effects of the identified non-idealities. Through mathematical development and simulations, Section 3 shows that when the stress birefringence variation with distance along each beam path is weak, the Mueller matrix of the rhomb is sensitive only to the accumulated retardance and average azimuthal angle of the fast principal axis along the path. Section 4 presents a first order analysis of the Mueller matrix of the complete rhomb that provides an understanding of the effects of the non-idealities on each of the Mueller matrix elements. Section 5 describes the application of multiple angle of incidence spectroscopic ellipsometry

Approved for public release; distribution unlimited.

Optics EXPRESS

measurements performed externally on the ambient/MgF_2-film/(fused silica) structure using a single rotating-compensator multichannel ellipsometer. These measurements supplement the Mueller matrix measurements enabling a structural and optical property analysis that accounts for the observed dichroic effect and enables accurate prediction of the retardance contribution associated with this reflection. Section 6 applies the results of Sections 3 and 5 for a complete least squares regression analysis of the measured Mueller matrix of the rhomb in terms of wavelength independent structural and optical parameters. Section 7 presents a summary of the major conclusions, emphasizing the application of the methodology for accurate descriptions of the polarization generation and detection performance of rhombs acting as compensators.

2. Experimental procedure

2.1. King rhomb design and measurement

The King rhomb device studied here is fabricated from fused silica and is bounded by two rectangular parallel faces 8 mm × 12 mm and a rectangular base 8 mm × 48 mm as shown in Fig. 1(a) [14]. Symmetric internally reflecting (fused silica)/ambient interfaces are designed for angles of incidence and reflection of 72.25° for the input and output beams of the device, respectively. The base of the rhomb is coated with polycrystalline MgF_2 to a nominal thickness of ~ 50 nm with a corresponding internal angle of incidence of 54.5° for the beam at the (fused silica)/MgF_2 interface. Using an adhesive, the rhomb is affixed to offsets, ~ 1 mm in thickness, which are in turn attached to an aluminum base plate, allowing the rhomb to rotate about its optical axis. These offsets are placed near the two ends of the rhomb resulting in an air gap at the center of the rhomb, ensuring a (fused silica)/MgF_2/ambient structure for the second internal reflection. The light beam passing through the rhomb in the straight-through operational configuration of the device is ~ 2.5 mm in diameter and its center is positioned ~ 4.0 mm relative to each side and ~ 7.8 mm relative to the base of the device. The path length of the beam within the rhomb is ~ 53.0 mm, with symmetric contributions of ~ 13.0 mm for one axial beam path and ~ 13.5 mm for one meridional beam path.

This rhomb is structured to generate three total internal reflections (TIRs), cumulatively producing a nearly achromatic phase difference of $\delta_p - \delta_s \sim 90°$ between the p and s orthogonal electric field components of the incoming beam over a wide spectral range. This is a consequence of the different phase shifts experienced by the p and s components of the optical electric field upon each oblique reflection. Here the p and s components oscillate parallel and perpendicular, respectively, relative to the plane of incidence which is common to the three internal reflections within the rhomb [see Fig. 1(a)]. For the two meridional beam paths within the rhomb, the p-s coordinate system of the incoming beam is rotated about the fixed s direction so that the p component of the field remains perpendicular to the beam direction. For each of the three reflections, the magnitude of phase shift experienced by the p component, δ_p, is greater than that experienced by the complementary s component, δ_s. Considering the complete device as a compensator, rather than as individual reflections, the principal azimuthal axes by convention are parallel to the plane formed by the beam path, described as the fast axis, and perpendicular to the plane, described as the slow axis [15]. These fast and slow axes together with the $+z$-axis defined by the direction of the coaxial input and output beams form a right-handed coordinate system. Throughout this work, the convention based on the time dependence of $\exp(i\omega t)$ for the optical electric field is applied, where ω is the angular frequency of field.

The material components of this rhomb, fused silica and thin film MgF_2, exhibit negligible absorption over the spectral range of interest and thus, under ideal circumstances, the rhomb is not dichroic. The magnitude of the p and s component phase shifts for each reflection at a given wavelength is a function of the angle of incidence and the refractive indices of the material components that establish the interfaces [10]. Thus, refractive index dispersion introduces weak

Approved for public release; distribution unlimited.

Optics EXPRESS

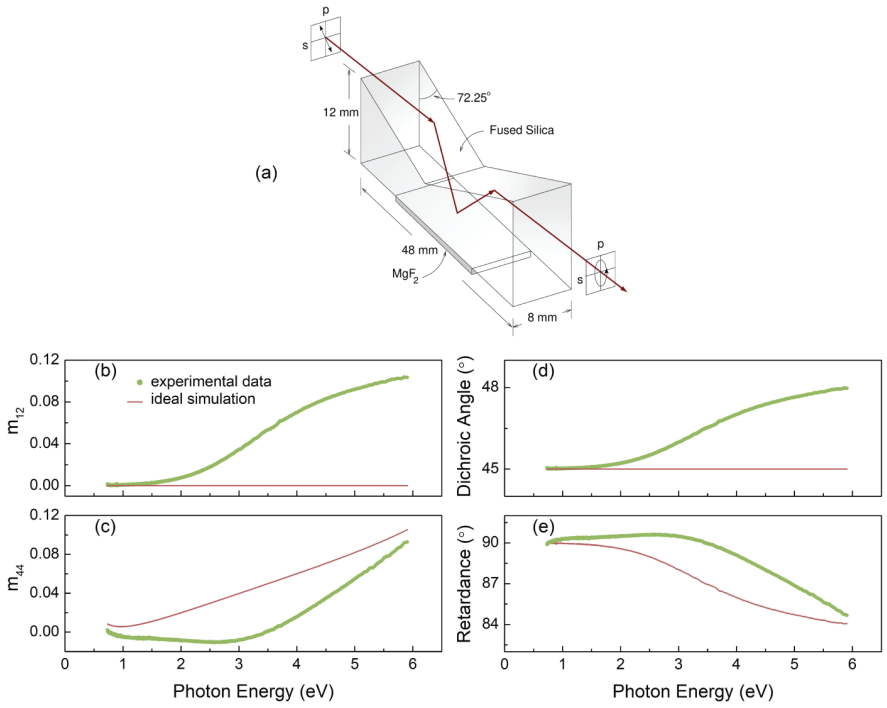


Fig. 1. (a) King rhomb physical structure optimized for a retardance of $\delta = \delta_F - \delta_S \approx 90°$ over a wide spectral range; (b) and (c) measured (green) and ideal predicted (red) spectra for two representative Mueller matrix elements relevant for evaluation of dichroism and stress-induced birefringence. The measured spectrum for element m_{12} exhibits non-ideal dichroic behavior whereas the measured spectrum for element m_{44} displays perturbations from the ideal retardance due to birefringence in the fused silica resulting from residual and mounting stress. The ideal retardance is calculated using three non-dissipative reflections from atomically smooth and abrupt interfaces where each total internal reflection occurs. The dichroic angle ψ_c and retardance δ associated with the Mueller matrix elements m_{12} and m_{44} in (b) and (c) are shown in (d) and (e), respectively.

wavelength dependence to the phase shift difference between the p and s components for each internal reflection.

For characterization of the surface and film structures generating the TIRs within the rhomb, a variable angle single rotating-compensator multichannel ellipsometer was used in reflection mode [16]. Extensive measurements were performed from the film side at the exposed ambient/MgF_2/(fused silica) interfaces of the device after removing the aluminum mounting plate. The ellipsometry angles (ψ, Δ) of this structure were measured over the spectral range spanning from 210 nm to 1650 nm. Here, tanψ is the relative (reflected relative to incident) p/s ratio of electric field amplitudes, and Δ is the phase shift (reflected relative to incident) p-s difference of electric field phases. In this case, p and s are the directions parallel and perpendicular to the plane of incidence established by the incident and reflected beams in the film side ellipsometry measurement. Measurements were performed at multiple angles of incidence of 60°, 65°, 70°, and 75° at a location in close proximity to that of the second TIR within the rhomb.

A dual rotating-compensator multichannel ellipsometer [17] in the straight-through transmission mode was applied to obtain the complete normalized Mueller matrix of the King rhomb in its operational configuration as a compensator. In this measurement, the rhomb serves as the sample,

Approved for public release; distribution unlimited.

Optics EXPRESS

and the plane that contains the transmission axis of the fixed first polarizer of the instrument as well as the light beam input to the rhomb serves as the reference plane. Thus, the reference coordinate system from which the rhomb zero azimuth (or fast axis azimuth) is measured is defined by the transmission-extinction (t-e) axes of the fixed polarizer. These axes along with the $+z$-axis of the beam direction form a right handed coordinate system. Measurements were performed on the rhomb when oriented at various azimuthal angles α with respect to the reference coordinate system. Such measurements were collected for wavelengths over a spectral range from 210 nm to 1690 nm, resulting in 15 normalized Mueller matrix element spectra [17]. For the analysis reported here, a truncated set of spectra was necessary due to a small but nontrivial discontinuity in some of the experimental matrix element spectra at a wavelength ~ 1000 nm. This is attributed to the wavelength crossover point of the dual multichannel detectors used in this instrument. As a result, each Mueller element spectrum in this analysis consists of 771 points spanning a spectral range from 230 nm to 1000 nm. The presence of such errors due to the high sensitivity of the measurement to optical element alignment demonstrates the need for rhomb compensators that enable high accuracy rotation and data acquisition over wide spectral ranges.

In this work, the analysis is limited to $\alpha = 0°$ in which case the plane of incidence within the rhomb is set to coincide with the reference plane. The two planes were superimposed as closely as possible by monitoring the Mueller matrix element m_{22}, which is given simply by

$$m_{22} = 1 - \sin^2 2\alpha(1 - \cos\delta \sin 2\psi_c) \tag{1}$$

for a non-ideal dichroic compensator. This expression is easily derived from the normalized Mueller matrix of a dichroic retarder characterized by (ψ_c, δ) assuming that the device is rotated to an angle of α relative to the t-e reference frame [1,18]. This equation for m_{22} also applies to first order in the fused silica birefringence correction as described in Section 4. In this equation for m_{22}, $\psi_c = \tan^{-1}|t_F|/|t_S|$ is the dichroic angle, a measure of the cumulative dichroic effect of the entire rhomb, where t_F and t_S are the complex amplitude transmission coefficients of the device for electric fields vibrating along its orthogonal fast and slow axes. Thus, m_{22} tends to unity over the entire spectral range when coplanarity is achieved with $\alpha = 0°$.

2.2. Initial assessment of rhomb optical non-idealities

Representative measured Mueller elements m_{12} and m_{44} are obtained with an intended azimuthal angle of $\alpha = 0°$ and are shown as the green lines in Figs. 1(b) and 1(c), respectively. These matrix elements provide direct insights into non-idealities of the King rhomb compensator studied here. For an ideal compensator, $m_{12} = 0$ and $m_{44} = \cos\delta$ where $\delta = \delta_F - \delta_S$ is the cumulative phase retardance of the device. In this initial assessment, m_{44} is used since it does not depend on α, thus avoiding potential effects of misalignment of the fast axis of the rhomb. When dichroism is present, however, $m_{12} = -\cos 2\psi_c$, where ψ_c is the compensator dichroic angle. The predicted results for ψ_c and δ for an ideal compensator are shown as the red lines in Figs. 1(d) and 1(e) where δ is obtained from the rhomb geometry and tabulated component material indices of refraction [19,20]. These predictions lead to the results for the Mueller matrix elements given by the red lines in Figs. 1(b) and 1(c), respectively. The difference between the measured and predicted results for m_{12} arises from dissipative absorption associated with internal reflection that generates a non-zero dichroic effect in m_{12}, and the corresponding difference for m_{44} arises from stress-induced birefringence of the fused silica along the beam path that contributes an additional phase retardance term.

We have developed a simulation based on Mueller matrix analysis to model the measurements of the rhomb accounting for non-idealities based on both dissipative absorption in the internal reflections and stress-induced birefringence along the beam path. In addition, we have performed a theoretical analysis of the accuracy of the model used to evaluate the stress-induced birefringence along a given path length within the rhomb by considering the medium as a large collection of

Approved for public release; distribution unlimited.

Optics EXPRESS

thin wave-plates with phase retardances and fast principal stress axis azimuthal angles for each plate that vary in a defined step-wise fashion along the beam path [21].

2.3. Stress birefringence of fused silica

Optically isotropic solids subjected to mechanical stress experience anisotropy characterized by a refractive index ellipsoid whose principal axes align with the principal stress axes. For a light beam traversing a distance d within a medium subjected to homogeneous orthogonal principal stresses σ_1 and σ_2, the magnitude of the accumulated optical retardance is given by

$$\delta = 2\pi d|(\sigma_1 - \sigma_2)C(\lambda)|/\lambda, \tag{2}$$

where $C(\lambda)$ is the wavelength dependent stress-optic coefficient specific to the medium and λ is the wavelength of the light in vacuum [22]. The stress-optic coefficient is a function of the unstressed refractive index n as well as the piezo-optic constants q_{11} and q_{12} of the material according to $C = (n^3/2)(q_{11} - q_{12})$ [23].

Ordinarily, in describing the wavelength dispersion of the real part of the complex dielectric function $\varepsilon_1 = n^2$ of a non-absorbing medium, a Sellmeier expression is used as will be described in Section 5. Starting from the Sellmeier expression, n and thus n^3 can be approximated as Cauchy dispersion expressions under the assumption that the minimum in the wavelength range is much larger than the wavelengths at which the electronic resonances occur. For the wavelength range of interest here, 230 - 1000 nm, we similarly assume q_{11} and q_{12} for fused silica follow Cauchy expressions. Thus, we model $C(\lambda)$ using such an expression on the basis that both n^3 and $q_{11} - q_{12}$ [24] are each expressible using such dispersion equations. Experimental determination of $C(\lambda)$ for fused silica has been undertaken by Sinha [25] who compiled data over a wavelength range from 230 nm to 1000 nm from a variety of sources. A least squares fit of the data compiled by Sinha using three terms of the Cauchy equation yielded

$$C(\lambda) = 3.28 + (9.46 \times 10^4/\lambda^2) - (1.70 \times 10^8/\lambda^4) \tag{3}$$

where λ is expressed in nm and C is reported in Brewster units (10^{-12} m^2 N^{-1}). The approach taken in our research is to measure a sample of ultraviolet (UV) grade fused silica and apply state-of-the-art research instrumentation for spectroscopic ellipsometry in order to evaluate the results over the range from 230 to 1000 nm as compiled by Sinha in 1978. Expansions of the spectral range deeper into the near-infrared require enhancements in the accuracy of our results and are reserved for future studies with improved instrumentation.

To investigate the applicability of the expression for $C(\lambda)$ in our work, a rectangular cuboid of fused silica (12 mm × 25 mm × 3 mm) [26] was subjected to uniaxial compressive stress in the long direction using a vice-like apparatus incorporating a load cell for measuring the applied force. A dual rotating-compensator spectroscopic ellipsometer was set in the transmission mode and the sample was probed normal to the largest area rectangular face, resulting in a 3 mm beam path. The location of the measurement on the cuboid was ~ 12.5 mm from both contact areas where the uniaxial stress was applied. These straight-through measurements of the fused silica cuboid were obtained under an applied force of ~ 79 N over an area of (3 × 12) mm^2. Orthogonal fast (F) and slow (S) axes are associated with stress-induced birefringence such that one of these two axes is aligned along the uniaxial stress direction.

Here and in the following two paragraphs, we describe the measurements performed on the fused silica cuboid under stress in order to verify the fast axis azimuthal orientation for the resulting phase retardance as measured with respect to the reference coordinate system of the dual rotating-compensator ellipsometer [17]. The goal is to identify an accurate zero-angle azimuthal orientation of the cuboid fast axis relative to the defined reference coordinate system of this ellipsometer so that an accurate phase retardance spectrum δ_c can be determined for

Approved for public release; distribution unlimited.

Optics EXPRESS

the cuboid under stress. The reference axes were established as usual to be the *t*-*e* coordinate system of the fixed first polarizer (such that the *t*-axis is vertical in our case; see inset Fig. 2). Three straight-through Mueller matrix measurements were taken through the center of the largest area rectangular face of the cuboid with the sample rotated so that the applied uniaxial stress is oriented at different azimuthal angles α with respect to the *t*-axis.

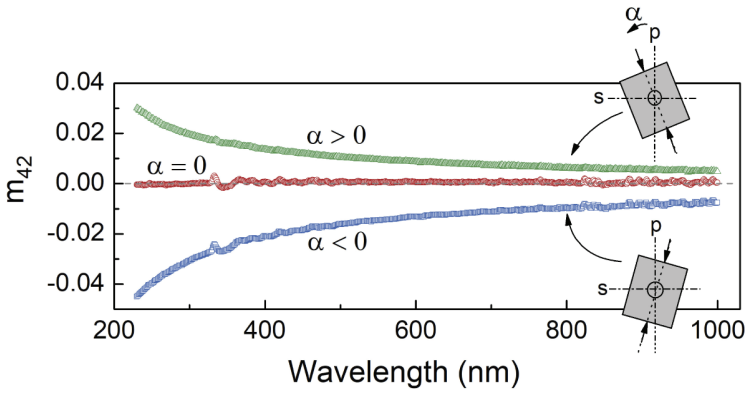


Fig. 2. Straight-through measurements of the Mueller matrix element m_{42} as a function of wavelength performed to identify the fast axis orientation for a fused silica cuboid under uniaxial stress. Measurements start with the applied stress aligned along the *t*-axis of the reference coordinate system, which is the *t*-*e* frame of the fixed first polarizer of the ellipsometer, corresponding to zero azimuthal angle (red). The cuboid is then rotated to an arbitrary positive angle (green) and an arbitrary negative angle (blue). By convention, an azimuthal angle is measured in the counterclockwise positive sense looking towards the light source.

From such measurements the Mueller matrix element m_{42} can be expressed as

$$m_{42} = \sin 2\psi_c \sin \delta_c \sin 2\alpha \tag{4}$$

where the angle $\psi_c = \tan^{-1}|t_F|/|t_S|$ is a measure of the dichroism of the cuboid and $\delta_c = \delta_F - \delta_S > 0$ is the phase retardance associated with the stress-induced birefringence. Here t_F and t_S are the complex amplitude transmission coefficients for electric fields vibrating along the orthogonal fast and slow principal stress axes. The expression for the Mueller matrix element m_{42} was derived as in Section 2.1 and is appropriate for a dichroic retarder characterized by (ψ_c, δ_c) upon coordinate transformation through a rotation angle α that the fast axis makes with the *t*-axis of the fixed first polarizer of the ellipsometer.

Thus, according to the expression in the previous paragraph, m_{42} can be used to resolve the direction of the fast axis since ψ_c is very close to 45° and δ_c is positive by definition. One measurement was performed with $\alpha = 0°$ by ensuring m_{42} values of zero across the entire spectrum. Thus, for this measurement of the m_{42} spectrum the uniaxial stress axis is aligned along the *t*-axis. The results of this measurement are shown as the red data points in Fig. 2. Two succeeding measurements were made with this stressed cuboid rotated through small angles α such that the stress axis was at positive and negative α values measured with respect to the experimentally recognized *t*-axis. Viewing along the beam path toward the light source, the positive and negative values correspond to counter-clockwise and clockwise cuboid rotations, respectively. Figure 2 shows Mueller element m_{42} spectra for positive and negative α as the green and blue data points, respectively. Because $\delta_c = \delta_F - \delta_S > 0$, the sign of m_{42} in Eq. (4) must be the same as that of α for a weakly dichroic retarder with $\psi_c \approx 45°$, assuming the correct orientation of the cuboid is selected. It can be observed from the results in Fig. 2 that this requirement is

Approved for public release; distribution unlimited.

Optics EXPRESS

satisfied, and the fast axis of the induced retardance correctly aligns with the direction of the applied uniaxial stress.

In the next step to be described here, the ellipsometric angles (ψ_{exp}, δ_{exp}) derived from the experimental Mueller matrix elements of the fused silica cuboid are depicted in Fig. 3(a) for $\alpha = 0°$. These angles are obtained from

$$\tan^2 2\psi_{exp} = (m_{34}^2 + m_{44}^2)/m_{12}^2, \tag{5}$$

$$\tan \delta_{exp} = m_{43}/m_{44}\,. \tag{6}$$

The results for ψ_{exp} in Fig. 3(a) exhibit negligible dichroism with $|t_{F,exp}| \approx |t_{S,exp}|$ such that $\psi_{exp} \approx 44.99° \pm 0.02°$ over the spectral range from 230 to 1000 nm. Figure 3(a) also demonstrates that the retardance due to stress δ_{exp} follows a monotonically decreasing trend as the wavelength increases. The solid red line in Fig. 3(a) shows the best fit of the experimental retardance using the model expression $\delta_{fit}(\lambda) = \delta_{pf} C(\lambda)/\lambda$ and a least squares regression analysis method. Here, $\delta_{pf} = 2\pi d|\sigma_1 - \sigma_2|$ is the achromatic pre-factor of the stress-induced retardance, d is the plate thickness, and $C(\lambda)$ is the stress-optic coefficient for fused silica presented previously. Thus, the pre-factor is a function of both the applied uniaxial stress and the beam path length within the material and is the only free parameter in the fit.

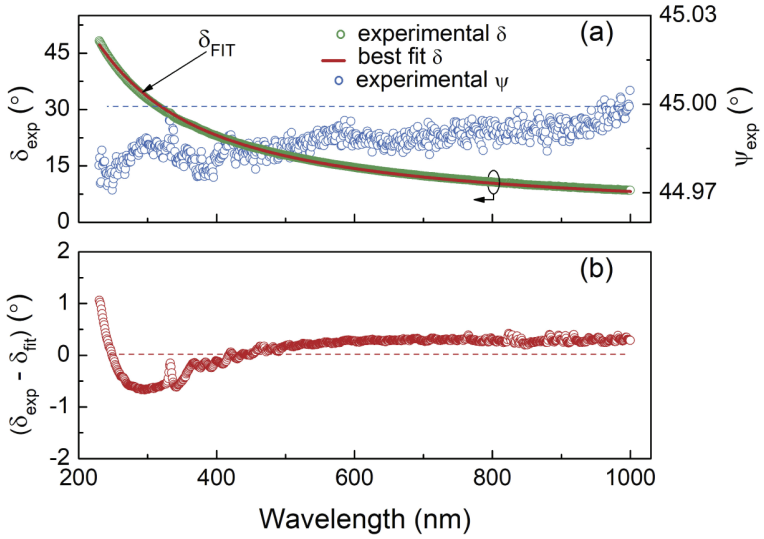


Fig. 3. (a) Measured retardance δ_{exp} (green circles) and best fit retardance δ_{fit} (red line), the former from a straight-through measurement of a fused silica cuboid under an applied force of ~ 79 N over an area of ~ (3 × 12) mm^2. The location of the measured data is ~ 12.5 mm from either contact area with an estimated stress of ~ 0.6 MPa. In addition to the retardance and its best fit in (a), the associated dichroic angle ψ_{exp} is also shown (blue circles). The plot in (b) shows the spectrum in the difference between the experimental and best fit retardance data.

The resulting spectral distribution of the fitting error is shown in Fig. 3(b). The magnitude of the discrepancy is most pronounced in the UV, reaching a maximum of ~ 1° at 230 nm and stabilizing at ~ 0.2° for wavelengths greater than 500 nm, with a variation between the experimental data and fit of ~ 2% at 230 nm and ~ 3% at 1000 nm. In fact, the nearly constant fitting error of ~ 0.2° in Fig. 3(b) above 500 nm suggests much better agreement is possible over a wavelength range restricted to the visible. Given the high quality of these measurements, based on the accurate results for ψ_{exp}, the discrepancies in Fig. 3(b) are likely to arise from several

Approved for public release; distribution unlimited.

Optics EXPRESS

possible sources. Variations may occur in the properties of the fused silica measured in the different studies, in the stress magnitude and direction over the area of the light beam used to probe the fused silica, or in the direction of the beam relative to the principal stress axes in each experiment. It also seems likely that an improved description of the wavelength dependence of $C(\lambda)$ over that of Sinha may be motivated by these results in future work. The overall discrepancy in Fig. 3(b) is deemed sufficiently small, however, to validate application of the stress-optic coefficient reported by Sinha in the King rhomb analysis performed here.

3. Stress simulation in fused silica

It is a challenge to interpret the stress-induced polarization modification that a polarized light beam incurs upon propagation through an otherwise optically-isotropic medium. Such an interpretation is sought in terms of the inherent residual thermally and mechanically generated stresses within the medium. The challenge is a result of the relatively small but spatially variable phase retardance contributions along with the accompanying variable index ellipsoid orientation that arise from the forces present. These contributions and associated orientational variations can then accumulate over long path lengths to generate significant polarization state modifications of the propagating beam. One approach for interpretation is to subdivide the path traversed by the polarized light beam within the optical medium into N equipartitioned components, each generating a distinct local retardance with an associated fast axis azimuthal angle [21]. Using this construct, a total retardance and average azimuthal angle of the thick optical plate can be obtained using Jones calculus as will be described next. This requires manipulating the product of the N retardance matrices along the path, each with its pair of matrices for positive and negative rotation by the local fast axis azimuthal angle. A pictorial representation of the concept is given in Fig. 4, whereby a light beam travelling in the z direction encounters stress magnitudes and azimuthal angles that vary as a function of the distance along z.

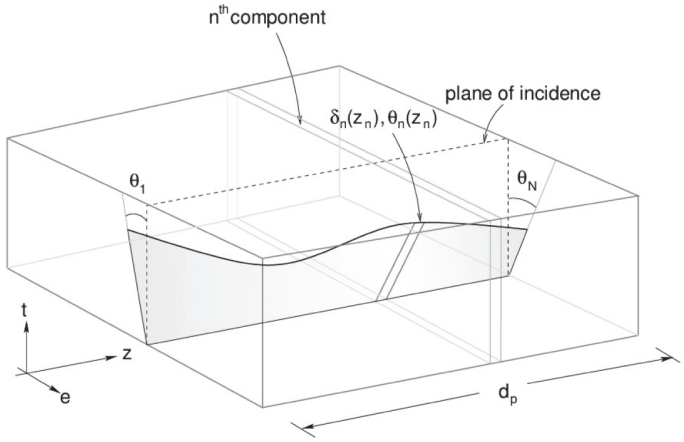


Fig. 4. Construct for determining the cumulative retardance and average azimuthal angle induced by stress in an otherwise isotropic medium having a total thickness of d_p. The medium is characterized by arbitrarily assigned slowly-varying spatial functions of path distance z including the retardance $\delta(z)$ and the principal azimuthal angle $\theta(z)$, the latter describing the fast axis direction relative to an ellipsometer reference t-e coordinate system. To simulate these spatially varying functions for analysis, the plate is decomposed into N equipartitioned components each of length Δz characterized by $\delta_n(z_n)$ as in Eq. (7) and $\theta_n(z_n)$ values for the n^{th} component as shown. A probing polarized light beam traveling along the z direction encounters variable stress related functions starting with (δ_1, θ_1) upon entering and ending with (δ_N, θ_N) upon exiting the medium.

Approved for public release; distribution unlimited.

Optics EXPRESS

In order to evaluate the required approach for modeling the optical effects of stress in media, the following case study presents an analysis of the Jones and corresponding Mueller matrices resulting from light beam propagation within a medium of assumed non-uniform retardance and undulating azimuthal angle bounded by an initial fast axis azimuth θ_1 and a final fast axis azimuth θ_N. Each equipartitioned component has a width along the beam path of $\Delta z = d_p/N$ where d_p is the total plate thickness, a retardance of

$$\delta_n(z_n) = 2\pi\Delta z|\Delta\sigma(z_n)|\frac{C(\lambda)}{\lambda} = \delta_{pf,n}\frac{C(\lambda)}{\lambda}, \tag{7}$$

and a fast axis azimuthal angle of $\theta_n(z_n)$. The effective Jones matrix for the plate is given by

$$\mathbf{J}_p = \mathbf{R}(-\theta_N)\,\mathbf{J}(\delta_N)\,\mathbf{R}(\theta_N)\,\mathbf{R}(-\theta_{N-1})\,\mathbf{J}(\delta_{N-1})\,\mathbf{R}(\theta_{N-1})\ \ldots\ \mathbf{R}(-\theta_1)\,\mathbf{J}(\delta_1)\,\mathbf{R}(\theta_1)\,, \tag{8}$$

where the corresponding retardance and rotation matrices are given by

$$\mathbf{J}(\delta_n) = \begin{bmatrix} e^{i\delta_n/2} & 0 \\ 0 & e^{-i\delta_n/2} \end{bmatrix}, \quad n = \{1, \ldots, N\}\,, \tag{9}$$

and

$$\mathbf{R}(\theta_n) = \begin{bmatrix} \cos\theta_n & \sin\theta_n \\ -\sin\theta_n & \cos\theta_n \end{bmatrix}. \tag{10}$$

By ensuring that Δz is sufficiently small, the matrix product in Eq. (8) can be evaluated to first order in the retardance values, i.e. by neglecting the products of two or more factors of δ_n. With this approach, we obtain matrix element expressions in terms of the component retardances and azimuthal angles as

$$\mathbf{J}_p = \begin{bmatrix} 1 + i\sum\limits_{n=1}^{N}\frac{\delta_n}{2}\cos 2\theta_n & i\sum\limits_{n=1}^{N}\frac{\delta_n}{2}\sin 2\theta_n \\ i\sum\limits_{n=1}^{N}\frac{\delta_n}{2}\sin 2\theta_n & 1 - i\sum\limits_{n=1}^{N}\frac{\delta_n}{2}\cos 2\theta_n \end{bmatrix}. \tag{11a}$$

For practical purposes, the matrix elements of $\mathbf{J}_p$ can be expressed in terms of the total accumulated retardance $\delta = N\bar{\delta}$ and an average azimuthal angle $\theta = \bar{\theta}$ where the overline indicates an average of the N values along the beam path. This involves substituting

$$\delta_n = \bar{\delta} + \Delta\delta_n \tag{11b}$$

$$\theta_n = \bar{\theta} + \Delta\theta_n \tag{11c}$$

into Eq. (11a), expressing the cosine and sine functions to first order in $\Delta\theta_n$, and neglecting terms in the product of the deviations from the average $(\Delta\theta_n)(\Delta\delta_n)$. The resulting transformed Jones matrix in terms of δ and $\bar{\theta}$ is

$$\mathbf{J}_p = \begin{bmatrix} 1 + i\frac{\delta}{2}\cos 2\bar{\theta} & i\frac{\delta}{2}\sin 2\bar{\theta} \\ i\frac{\delta}{2}\sin 2\bar{\theta} & 1 - i\frac{\delta}{2}\cos 2\bar{\theta} \end{bmatrix}. \tag{12}$$

Thus, this result is valid to first order in the deviations of $\delta_n(z_n)$ and $\theta_n(z_n)$ from their average values of $\bar{\theta}$ and $\bar{\delta}$, an approximation appropriate for weak variations along the beam path.

Approved for public release; distribution unlimited.

Optics EXPRESS

Assuming no depolarization, a Mueller-Jones matrix exists and the corresponding unnormalized Mueller matrix for $\mathbf{J}_p$ in Eq. (12) takes the form:

$$\mathbf{M}_p = \begin{bmatrix} 1+\frac{\delta^2}{4} & 0 & 0 & 0 \\ 0 & 1+\frac{\delta^2}{4}\cos 4\bar{\theta} & \frac{\delta^2}{4}\sin 4\bar{\theta} & -\delta\sin 2\bar{\theta} \\ 0 & \frac{\delta^2}{4}\sin 4\bar{\theta} & 1-\frac{\delta^2}{4}\cos 4\bar{\theta} & \delta\cos 2\bar{\theta} \\ 0 & \delta\sin 2\bar{\theta} & -\delta\cos 2\bar{\theta} & 1-\frac{\delta^2}{4} \end{bmatrix}. \tag{13}$$

The Mueller matrix in Eq. (13) can be normalized appropriately to second order in δ to give

$$\mathbf{m}_p = \begin{bmatrix} 1 & 0 & 0 & 0 \\ 0 & \cos(\delta\sin 2\bar{\theta}) & \frac{\delta^2}{4}\sin 4\bar{\theta} & -\delta\sin 2\bar{\theta} \\ 0 & \frac{\delta^2}{4}\sin 4\bar{\theta} & \cos(\delta\cos 2\bar{\theta}) & \delta\cos 2\bar{\theta} \\ 0 & \delta\sin 2\bar{\theta} & -\delta\cos 2\bar{\theta} & \cos\delta \end{bmatrix}. \tag{14}$$

The preceding analysis demonstrates that the retardance and azimuthal angle profiles shown in Fig. 4 can be replaced by the accumulated retardance and average angle, the latter two uniformly spanning the beam path length. The equivalent optical element exhibits properties similar to a retarder with a retardance δ and fast axis direction $\bar{\theta}$ with respect to the *t*-*e* reference frame. Accordingly, the Mueller matrix for the plate can then be treated as a single stress-induced retarder and can be written as

$$\mathbf{m}_p{}' = \mathbf{R}(-\bar{\theta})\,\mathbf{m}_p\mathbf{R}(\bar{\theta}), \tag{15}$$

where $\mathbf{m}_p$ is a Mueller matrix of the ideal retarder and $\mathbf{R}(\bar{\theta})$ is the standard rotation Mueller matrix. The result is

$$\mathbf{m}_p{}' = \begin{bmatrix} 1 & 0 & 0 & 0 \\ 0 & \cos^2 2\bar{\theta}+\cos\delta\sin^2 2\bar{\theta} & \sin 2\bar{\theta}\cos 2\bar{\theta}(1-\cos\delta) & -\sin\delta\sin 2\bar{\theta} \\ 0 & \sin 2\bar{\theta}\cos 2\bar{\theta}(1-\cos\delta) & \sin^2 2\bar{\theta}+\cos\delta\cos^2 2\bar{\theta} & \sin\delta\cos 2\bar{\theta} \\ 0 & \sin\delta\sin 2\bar{\theta} & -\sin\delta\cos 2\bar{\theta} & \cos\delta \end{bmatrix}. \tag{16}$$

To second order in the retardance, for small δ, it is easily shown that the matrix in Eq. (16) is equivalent to the matrix in Eq. (14). Hence Eq. (15) can be used to adequately model optical effects of stress in an isotropic medium subject to constraints inherent in the derivation of Eq. (14).

Simulations were undertaken in order to verify the analytical reasoning of the previous paragraphs. In these simulations, a polarized light beam traverses a plate of fused silica 50 mm in thickness. The plate was equipartitioned into 1000 components such that the n^{th} component was assigned a retardance spectrum δ_n and an azimuthal angle θ_n, the former derived from a stress value $|\Delta\sigma_n|$, where $n = \{1, 2, \ldots, 1000\}$. Thus, the retardance spectrum for each component was calculated according to Eq. (7).

Smoothly varying test functions for the stress and azimuthal angles as functions of beam distance within the plate were generated using B-spline curves. The resulting Mueller matrix for the plate was simulated using the following equation similar to Eq. (8) with $N = 1000$ and $\Delta z = 0.05$ mm but with arbitrarily generated variations for the component dependent δ_n and θ_n:

$$\mathbf{m}_p{}' = \mathbf{R}(-\theta_{1000})\,\mathbf{m}(\delta_{1000})\,\mathbf{R}(\theta_{1000})\ \ldots\ \mathbf{R}(-\theta_1)\,\mathbf{m}(\delta_1)\,\mathbf{R}(\theta_1). \tag{17}$$

In the following section, we present three case studies of simulations based on Eq. (17). Eq. (14) provides an analytical formulation for the matrix product in Eq. (17) for the purposes of initial

Approved for public release; distribution unlimited.

Optics EXPRESS

comparisons and then least squares fitting. A comparison is exemplified in Fig. 5 using arbitrarily generated stress (red) and azimuthal angle (green) curves with average values over the 50 mm thickness of $|\overline{\Delta\sigma}| = 15.0$ kPa and $\bar{\theta} = 35°$, respectively, where $|\overline{\Delta\sigma}| = \lambda\delta/[2\pi d_p C(\lambda)] = \delta_{pf}/(2\pi d_p)$ and $\delta_{pf} = N\bar{\delta}_{pf,n}$. In Fig. 5, the plots of spectra in the lower right 3×3 Mueller matrix elements are shown to be in agreement when simulated using Eq. (17) (gray points) and when calculated analytically for comparison using Eq. (14) (blue lines) along with Eq. (7) to derive $\delta = N\bar{\delta}$.

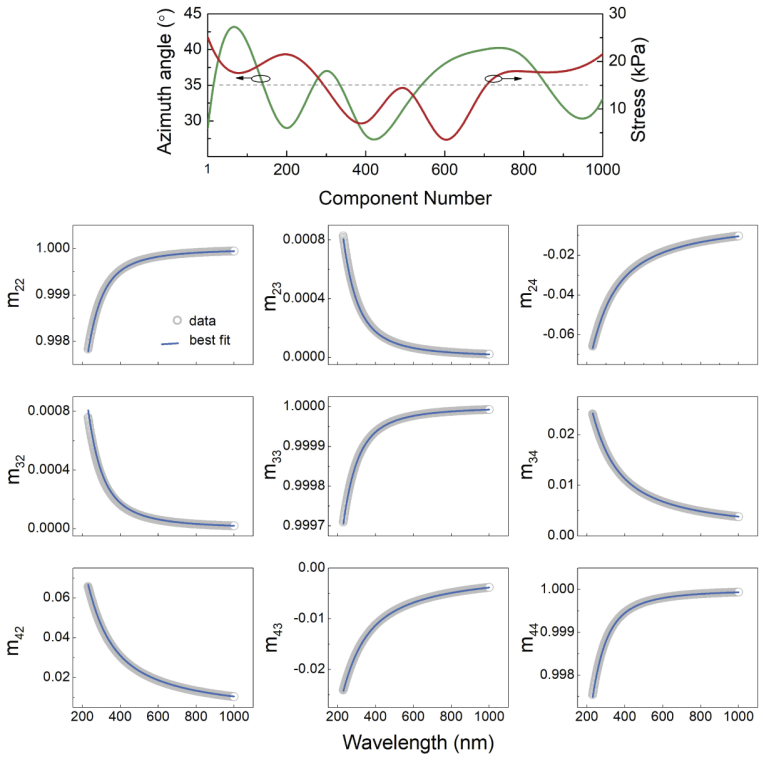


Fig. 5. The plot on the top depicts stress (red) and azimuthal angle (green) profiles as functions of component number used in the simulation of a beam traversing a 50 mm thick fused silica plate equipartitioned into 1000 components according to Eq. (17). The points on the bottom plots show the corresponding lower right 3×3 Mueller matrix spectra generated using Eq. (17). The solid blue line depicts the analytically derived results using the matrix elements of Eq. (14) with $\delta = N\bar{\delta}$ from Eq. (7), $|\overline{\Delta\sigma}| = 15$ kPa, and $\bar{\theta} = 35°$.

Next, Eq. (15) implies a family consisting of multiple data sets, each set including different profiles in $|\Delta\sigma_n|$ and θ_n that result in the same spectrum in $\delta = N\bar{\delta}$ and the same value of $\bar{\theta}$, and thus, the same Mueller matrix element spectra as other members of the family if the assumptions leading to Eq. (15) are valid. A graphic illustration of this implication is shown in Fig. 6. Four carefully chosen but different combinations of stress and azimuthal angle profiles in Fig. 6(a-d), each with closely similar $\delta = N\bar{\delta}$ and $\bar{\theta}$ were used to simulate data in the Mueller matrix elements using Eq. (17). As a practical consequence of the results from Fig. 6, experimentally determined Mueller matrices cannot be analyzed to identify the true nature of the underlying retardance and stress profiles if the profiles vary only weakly from their average values.

Finally, we apply least squares regression to extract the accumulated retardance and mean azimuthal angle from Mueller matrix element spectra simulated using Eq. (17). Figure 7 depicts

Approved for public release; distribution unlimited.

Optics EXPRESS

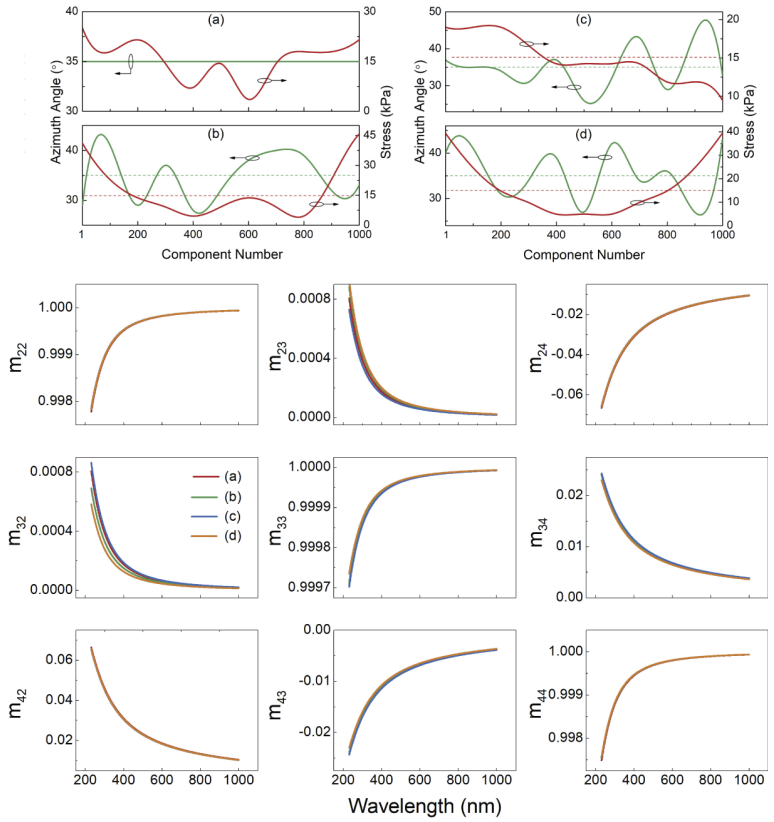


Fig. 6. (Right) An overlay of Mueller elements simulated from (top) four plots (a)-(d) with spatially different stress (red) and azimuthal angle (green) profiles generated to share common values of $|\overline{\Delta\sigma}| = 15$ kPa, and $\bar{\theta} = 35°$.

four different pairs of test stress and azimuthal angle variations $\{|\Delta\sigma_n|, \theta_n\}$ as functions of component number n within the fused silica plate that have been used to generate different conditions of stress in the plate. Each curve can be characterized analytically by its accumulated retardance $\delta = N\bar{\delta}$ as well as its average azimuthal angle $\bar{\theta}$. The achromatic prefactor is given by $\delta_{pf} = N\bar{\delta}_{pf,n}$, where $\bar{\delta}_{pf,n}$ is obtained from the relationship $\delta_{pf,n} = 2\pi\Delta z|\Delta\sigma_n|$. The resulting Mueller matrix $\mathbf{m}_p{}'$ simulated for each pair $\{|\Delta\sigma_n|, \theta_n\}$ in Fig. 7 was used as input in a least squares fitting routine modeled using the right hand side of Eq. (15). The fit parameters of interest include the pre-factor of the accumulated retardance $\delta_{pf(\mathrm{fit})}$ and the azimuthal angle $\bar{\theta}_{\mathrm{fit}}$ fit which is averaged over the plate thickness. The accumulated retardance over the full thickness could then be calculated using the formula $\delta_{\mathrm{fit}} = \delta_{pf(\mathrm{fit})}C(\lambda)/\lambda$.

Results obtained in an analysis of the input to the simulation of Eq. (17), δ_{pf} and $\bar{\theta}$, as well as the corresponding results from the fitting routine of Eq. (15), $\delta_{pf(\mathrm{fit})}$ and $\bar{\theta}_{\mathrm{fit}}$, are compared in Table 1. Two important observations can be made from the best fitting results. First, the accumulated retardance of the plate is recoverable, for all practical purposes, even when subject to varying azimuthal angles. Second, the average azimuthal angle is also recoverable even when its total variation is significant compared to the total accumulated retardance δ. The validity of the first order expansions in δ_n that lead to Eq. (11a) can be assured by using very thin components along the beam path since δ_n is proportional to Δz. The fitting equations applied in this analysis derived from Eq. (12) are based on the assumption that the deviations of $\Delta\delta_n$ and $\Delta\theta_n$ from their

Approved for public release; distribution unlimited.

Optics EXPRESS

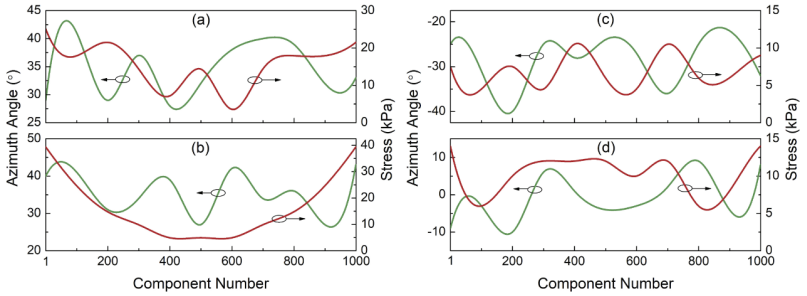


Fig. 7. Stress (red) and azimuthal angle (green) profiles as functions of component number used in simulations of a beam traversing a 50 mm thick fused silica plate equipartitioned into 1000 components. Plots (a) and (b) depict nonlinear stress and azimuthal angle profiles with positive (ccw) angles over the entire beam path. These plots also share identical sets of δ and $\bar{\theta}$. Plot (c) depicts nonlinear stress and azimuthal angle profiles with negative (cw) angles over the entire beam path. Plot (d) depicts nonlinear stress and azimuthal angle profiles with an angle variation spanning both negative and positive values. Applying Eq. (17) to these profiles and fitting the resulting Mueller matrix spectra using Eq. (15) gives the results in Table 1.

Table 1. Simulation results based on Eq. (17) showing the actual accumulated retardance pre-factors and average azimuthal angles given by δ_{pf} and $\bar{\theta}$ from Fig. 7 along with the corresponding best fit results based on the analysis of Eq. (15).

Fig. 7	$\bar{\theta}(^\circ)$	$\bar{\theta}_{\rm fit}(^\circ)$	$\delta_{pf}(^\circ)$	$\delta_{pf({\rm fit})}(^\circ)$
a	35.0	$35.0 \pm (1.8 \times 10^{-4})$	270.0	$266.9 \pm (1.7 \times 10^{-3})$
b	35.0	$35.3 \pm (9.1 \times 10^{-4})$	270.0	$265.2 \pm (8.4 \times 10^{-3})$
c	−28.4	$-29.1 \pm (1.6 \times 10^{-4})$	120.6	$118.6 \pm (6.7 \times 10^{-4})$
d	−0.8	$-0.8 \pm (2.4 \times 10^{-4})$	180.1	$177.5 \pm (1.5 \times 10^{-3})$

average values can be likewise treated in first order. The deviations of the best fit results from the values assumed in the simulation are expected to arise from this latter assumption. In Fig. 7, the deviations in $|\Delta\sigma_n|$ from $|\overline{\Delta\sigma}|$ are no more than 20 kPa and the deviations in θ_n from $\bar{\theta}$ are no more than 10°. Evidently from Table 1, one can conclude that these deviations are sufficiently small that a first order treatment of $\Delta\delta_n$ and $\Delta\theta_n$ from their averages is valid.

4. First order stress analysis of the King rhomb

Based on the schematic of Fig. 8, the Mueller matrix describing the King rhomb can be formulated using the following matrix product

$$\mathbf{M}_{\rm rhomb} = \mathbf{R}(-\alpha_7)\mathbf{M}_7\mathbf{R}(\alpha_7)\cdot\mathbf{M}_6\cdot\mathbf{R}(-\alpha_5)\mathbf{M}_5\mathbf{R}(\alpha_5)\cdot\mathbf{M}_4\cdot\mathbf{R}(-\alpha_3)\mathbf{M}_3\mathbf{R}(\alpha_3)\cdot\mathbf{M}_2\cdot\mathbf{R}(-\alpha_1)\mathbf{M}_1\mathbf{R}(\alpha_1)\,. \tag{18}$$

Here matrices $\{\mathbf{M}_n, n = 1,3,5,7\}$ describe the cumulative retardance contribution for each path, each with appropriate rotation matrices $\mathbf{R}$ on the left and right sides in the product in accordance with Eq. (15). The corresponding rotation angles denoted by $\{\alpha_n, n = 1,3,5,7\}$ are the average angles of the fast axes with respect to the plane of reference, also in accordance with Eq. (15). In Section 3, Eq. (15) was shown to be valid to first order in the variations of the equipartitioned retardance components and the fast axis angles from their averages along each path. The matrices $\{\mathbf{M}_n, n = 2,6\}$ are determined using the retardance generated by an ideal TIR at an isotropic (fused silica)/ambient interface. $\mathbf{M}_4$ is modeled as a TIR at an isotropic

Approved for public release; distribution unlimited.

Optics EXPRESS

(fused silica)/MgF_2/ambient two-interface structure with ellipsometric angles (ψ_4, Δ_4) where ψ_4 is allowed to deviate from 45° due to dissipation in the structure.

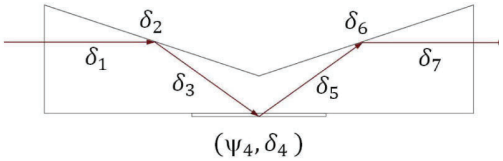


Fig. 8. Seven sources of optical retardance and a single source of dichroism incurred by a light beam traversing the King rhomb including stress-induced birefringence along the four beam paths $\{\delta_n, n = 1, 3, 5, 7\}$, two ideal TIRs from (fused silica)/ambient interfaces with $\{\delta_n, n = 2, 6\}$, and a single TIR at the MgF_2/ambient interface of a dissipative (fused silica)/MgF_2/ambient structure, the latter with dichroic and retardance angles of $\{\psi_4, \delta_4\}$. The resulting eight parameters at a given wavelength and four average fast axis angles $\{\alpha_n, n = 1, 3, 5, 7\}$ define the Mueller matrix product of Eq. (18).

Treated to the first order, the stress Mueller matrix with retardance $\delta_n \ll 1$ is given by:

$$\mathbf{M}_n = \begin{bmatrix} 1 & 0 & 0 & 0 \\ 0 & 1 & 0 & 0 \\ 0 & 0 & \cos\delta_n & \sin\delta_n \\ 0 & 0 & -\sin\delta_n & \cos\delta_n \end{bmatrix} \approx \begin{bmatrix} 1 & 0 & 0 & 0 \\ 0 & 1 & 0 & 0 \\ 0 & 0 & 1 & \delta_n \\ 0 & 0 & -\delta_n & 1 \end{bmatrix}, \tag{19}$$

with $n = 1, 3, 5, 7$, and the standard rotation matrix with stress rotation angle α_n is:

$$\mathbf{R}(\alpha_n) = \begin{bmatrix} 1 & 0 & 0 & 0 \\ 0 & \cos 2\alpha_n & \sin 2\alpha_n & 0 \\ 0 & -\sin 2\alpha_n & \cos 2\alpha_n & 0 \\ 0 & 0 & 0 & 1 \end{bmatrix}, \tag{20}$$

also with $n = 1, 3, 5, 7$.

The matrices for the retardance incurred upon TIR include

$$\mathbf{M}_n = \begin{bmatrix} 1 & 0 & 0 & 0 \\ 0 & 1 & 0 & 0 \\ 0 & 0 & \cos\delta_n & \sin\delta_n \\ 0 & 0 & -\sin\delta_n & \cos\delta_n \end{bmatrix}, \tag{21}$$

with $n = 2, 6$ for the (fused silica)/ambient interfaces and

$$\mathbf{M}_4 = \begin{bmatrix} 1 & -\cos 2\psi_4 & 0 & 0 \\ -\cos 2\psi_4 & 1 & 0 & 0 \\ 0 & 0 & \sin 2\psi_4 \cos\delta_4 & \sin 2\psi_4 \sin\delta_4 \\ 0 & 0 & -\sin 2\psi_4 \sin\delta_4 & \sin 2\psi_4 \cos\delta_4 \end{bmatrix} \approx \begin{bmatrix} 1 & \psi'_4 & 0 & 0 \\ \psi'_4 & 1 & 0 & 0 \\ 0 & 0 & \cos\delta_4 & \sin\delta_4 \\ 0 & 0 & -\sin\delta_4 & \cos\delta_4 \end{bmatrix}, \tag{22}$$

for the assumed dissipative (fused silica)/MgF_2/ambient structure with TIR occurring at the MgF_2/ambient interface. The last matrix on the right is given to first order in the small quantity

Approved for public release; distribution unlimited.

Optics EXPRESS

$\psi_4^{'} \equiv 2(\psi_4 - \pi/4)$. Because the dichroic contribution is small as indicated in Fig. 1(b), the corresponding ellipsometric angle is approximated as $\psi_4 \approx 45°$. Then a Taylor series expansion of $-\cos 2\psi_4$ in the vicinity of $\psi_4 = 45°$ yields $-\cos 2\psi_4 = 2(\psi_4 - \pi/4) \equiv \psi_4^{'}$. In fact, $\psi_4^{'}$ can be derived from the average value of the elements m_{12} and m_{21} of the normalized version of the product matrix of Eq. (18). Thus to extract ψ_4, one takes $\frac{1}{2}\cos^{-1}(-\psi_4^{'})$, and the necessary quadrant correction is handled by the sign of the measured m_{12} and m_{21} elements. In addition, the fact that the quadrant corrected $\sin 2\psi_4$ term must be close to unity provides a check on the correction. Table 2 summarizes the matrix elements of the normalized version of the Mueller matrix $\mathbf{M}_{\text{rhomb}}$ to first order in the five angles $\{\delta_n, n = 1, 3, 5, 7\}$ and $\psi_4^{'}$.

Table 2. Expected normalized Mueller matrix elements for the three reflection King rhomb corresponding to Eq. (18) and Fig. 8 with the rhomb fast-slow (*F-S*) frame aligned with the *t-e* frame of the first fixed polarizer of the ellipsometer used for the measurement. The dichroic contribution from the second TIR appears in the six matrix elements m_{12}, m_{13}, m_{14}, m_{21}, m_{31}, and m_{41}. The four elements m_{11}, m_{12}, m_{21}, and m_{22} are exempt from the effects of stress-induced retardance along the optical path.

m_{11}	1
m_{12}	ψ'_4
m_{13}	$\psi'_4\,\delta_3 \sin 2\alpha_3 \sin\delta_2$
m_{14}	$-\psi'_4\,[\delta_1 \sin 2\alpha_1 + \delta_3 \sin 2\alpha_3 \cos\delta_2]$
m_{21}	m_{12}
m_{22}	m_{11}
m_{23}	$\delta_3 \sin 2\alpha_3 \sin\delta_2 + \delta_5 \sin 2\alpha_5 \sin(\delta_2 + \delta_4) + \delta_7 \sin 2\alpha_7 \sin(\delta_2 + \delta_4 + \delta_6)$
m_{24}	$-[\delta_1 \sin 2\alpha_1 + \delta_3 \sin 2\alpha_3 \cos\delta_2 + \delta_5 \sin 2\alpha_5 \cos(\delta_2 + \delta_4) + \delta_7 \sin 2\alpha_7 \cos(\delta_2 + \delta_4 + \delta_6)]$
m_{31}	$\psi'_4\,\delta_5 \sin 2\alpha_5 \sin\delta_6$
m_{32}	$\delta_1 \sin 2\alpha_1 \sin(\delta_2 + \delta_4 + \delta_6) + \delta_3 \sin 2\alpha_3 \sin(\delta_4 + \delta_6) + \delta_5 \sin 2\alpha_5 \sin\delta_6$
m_{33}	$\cos(\delta_2 + \delta_4 + \delta_6) - (\delta_1 \cos 2\alpha_1 + \delta_3 \cos 2\alpha_3 + \delta_5 \cos 2\alpha_5 + \delta_7 \cos 2\alpha_7) \sin(\delta_2 + \delta_4 + \delta_6)$
m_{34}	$\sin(\delta_2 + \delta_4 + \delta_6) + (\delta_1 \cos 2\alpha_1 + \delta_3 \cos 2\alpha_3 + \delta_5 \cos 2\alpha_5 + \delta_7 \cos 2\alpha_7) \cos(\delta_2 + \delta_4 + \delta_6)$
m_{41}	$\psi'_4\,[\delta_5 \sin 2\alpha_5 \cos\delta_6 + \delta_7 \sin 2\alpha_7]$
m_{42}	$\delta_1 \sin 2\alpha_1 \cos(\delta_2 + \delta_4 + \delta_6) + \delta_3 \sin 2\alpha_3 \cos(\delta_4 + \delta_6) + \delta_5 \sin 2\alpha_5 \cos\delta_6 + \delta_7 \sin 2\alpha_7$
m_{43}	$-m_{34}$
m_{44}	m_{33}

An inspection of the elements of the normalized Mueller matrix in Table 2 provides insights into the dichroic contribution and the distribution of stress-induced retardance from the individual paths of the beam through the rhomb. The 2×2 upper left block of the matrix including elements m_{11}, m_{12}, m_{21}, and m_{22} are unaffected by stress. The elements m_{12} and m_{21} provide two results for the dichroic angle that can be averaged according to $\psi_4 = \frac{1}{2}\cos^{-1}[-(m_{12} + m_{21})/2]$. An example of the dichroic effect free of the influence of stress-induced retardance is clearly demonstrated in Fig. 1(b) which shows the m_{12} element of the actual King compensator in comparison with the ideal (non-dichroic) result of $m_{12} = 0$. Inspection of the lower right block elements m_{33}, m_{34}, m_{43}, and m_{44} show the first order terms in the stress-induced retardance. These are added to the sine and cosine functions of the combined retardance due to the three TIRs. An example of the effect of this addition is clearly demonstrated in Fig. 1(c) which shows that the m_{44} element of the actual King compensator deviates from the ideal result obtained assuming no stress-induced retardance terms. The remaining eight Mueller matrix elements forming the upper right and lower left blocks (m_{13}, m_{14}, m_{23}, m_{24}, m_{31}, m_{32}, m_{41}, m_{42}) show functional dependences on stress in individual paths of the rhomb.

Approved for public release; distribution unlimited.

Optics EXPRESS

It is worth noting that each Mueller matrix element in Table 2 lends itself to stress parameterization in a nonlinear least squares minimization scheme. For example in one of the two simplest analyses, m_{13} can be parameterized in the form

$$m_{13} = \eta_{13}[\psi_4^{'}(\lambda)\sin(\delta_2(\lambda))C(\lambda)]/\lambda, \tag{23}$$

where $\eta_{13} = \delta_{pf3}\sin 2\alpha_3$ is a wavelength independent prefactor associated with m_{13} that can be obtained in a first-order analysis. Thus, the achromatic pre-factor η_{13} is proportional to the stress prefactor and the sine of twice the azimuthal angle of the fast axis of the retardance generated along the meridional path labeled "3". In addition, $\psi_4^{'}(\lambda)$, $\delta_2(\lambda)$, and $C(\lambda)$ represent the wavelength dependent components of the m_{13} matrix element, including the dichroism, the retardance from the (fused silica)/ambient interface, and the stress-optic coefficient of fused silica, respectively. As a second of the simplest analyses, given the dichroic angle $\psi_4^{'}(\lambda)$ and the retardance $\delta_6(\lambda)$, m_{31} can take a similar parameterized form that provides the product of the stress prefactor and the sine of twice the associated fast axis angle generated along the meridional path labeled "5".

5. Rhomb ellipsometry analysis

The normalized Mueller matrix spectra obtained by directing the light beam straight through the King rhomb device revealed unexplained dichroic behavior in the form of nonzero matrix elements m_{12} and m_{21}. Given the spectral range of the Mueller matrix measurement performed here, the optical absorption is negligible for the fused silica and MgF_2 materials used in the construction of this device, and so these materials cannot contribute to the observed dichroism. Laboratory contamination, possibly leading to the formation of absorbing overlayers at the (fused silica)/ambient interfaces, was considered as a potential source for at least some component of the observed dissipative effect. External reflection ellipsometric measurements and associated modeling performed on these ambient/(fused silica) interfaces, however, revealed no detectable absorbing overlayers. In contrast, a second set of ellipsometric measurements with the beam reflected externally from the intermediate ambient/MgF_2-film/(fused silica) structure did in fact exhibit weak absorption as described in the following paragraphs, indicating that this structure is the source of the dichroic behavior observed in transmission through the rhomb.

Using fixed parametric expressions for the indices of refraction versus wavelength for the MgF_2 layer and the bulk fused silica from existing an database [19,20], an initial least squares regression analysis was performed on the ellipsometric spectra (ψ, Δ) acquired in external reflection from the ambient/MgF_2-film/(fused silica) structure at multiple angles of incidence. The structure yielding the best fitting simulation required a thin absorbing layer at the interface between the fused silica medium and the MgF_2 layer. Thus, the resulting model explored here was an ambient/MgF_2-film/absorbing-layer/(fused silica substrate) structure with the thicknesses of the MgF_2 and absorbing layers as fitting parameters. In this first analysis, the unknown complex dielectric function $\varepsilon = \varepsilon_1 - i\varepsilon_2$ of the absorbing layer was modeled as the sum of a two parameter Sellmeier term, two Lorentz oscillators, and a constant additive real term. Each Lorentz oscillator was described with three parameters, a characteristic resonance energy, amplitude, and broadening. As a result, the four pairs of (ψ, Δ) spectra measured at the different angles of incidence were modeled with 11 free parameters, including the two layer thicknesses and the nine optical property parameters that describe the absorbing layer.

In this first analysis, it was possible to obtain a satisfactory 11 parameter fit of the ellipsometric spectra measured externally at the four angles of incidence. Next, the spectra in the normalized Mueller matrix elements m_{12} and m_{21} obtained from the three-reflection straight-through measurement of the rhomb were analyzed in a second least squares regression procedure. These matrix elements were averaged to extract the internal spectrum in the characteristic dichroic angle ψ_4. The structure yielding this spectrum in ψ_4, as probed by the internal light beam traversing

Approved for public release; distribution unlimited.

Optics EXPRESS

the rhomb, consists of (fused silica)/absorbing-layer/MgF_2-film/ambient, having established the intermediate TIR as being solely responsible for the measured dichroism. Because the measured ψ_4 spectrum was derived from the Mueller matrix representing the entire path of the light beam within the rhomb, the associated phase shift difference δ that would normally be derived from the lower right block of the matrix has multiple undetermined contributions and so could not be used as input to this second analysis procedure. Consequently, only the ψ_4 spectrum was incorporated into this second fitting procedure. The thickness and optical properties of the absorbing layer were obtained in the best fit of ψ_4, a ten parameter fit in which case the optical parameters of the adjacent MgF_2 layer and fused silica as well as the MgF_2 thickness were fixed, the latter from the first analysis.

In a third analysis procedure, the new absorbing layer best fitting parameters from the second procedure were introduced as fixed values in the analysis of the external reflection data comprised of the multiple angle of incidence ellipsometric (ψ, Δ) spectra whereas the MgF_2 film thickness was varied. The second and third analysis procedures were iterated until convergence of the fitting parameters occurred for both internal (fused silica side) and external (film side) reflection analysis. This approach was applied because the internal reflection data were more sensitive to the absorbing layer parameters through ψ_4 whereas they were less sensitive to the MgF_2 layer parameters due to the inability to extract δ_4. In contrast, the multiple angle external reflection data were more sensitive to non-absorbing layer parameters through Δ, whereas they were less sensitive to the absorbing layer parameters. The outcome of this approach was a single consistent structural and optical model for the intermediate reflection within the rhomb that accounts for the four pairs of experimental ellipsometric spectra at different angles of incidence and the single spectrum that characterizes the dichroism of the compensator.

The resulting fit parameters for the absorbing layer yield a thickness on the order of a few nanometers and dielectric function spectra ε_1 and ε_2 that are distinctly different than the adjacent materials in the stack. In fact, the resulting shapes of ε_1 and ε_2 are closely similar to those of amorphous silicon (a-Si), thus allowing a simplified treatment of the absorbing layer by replacing the Sellmeier term and two Lorentz oscillators having a total of eight parameters with a single Tauc-Lorentz oscillator having four parameters. The origin of the a-Si containing interface layer is unclear at present, but possibly related to the nature of the fused silica surface preparation prior to the MgF_2 deposition process or to inadvertent interactions that occur between fused silica or its adsorbates and the MgF_2 thin film during or after deposition.

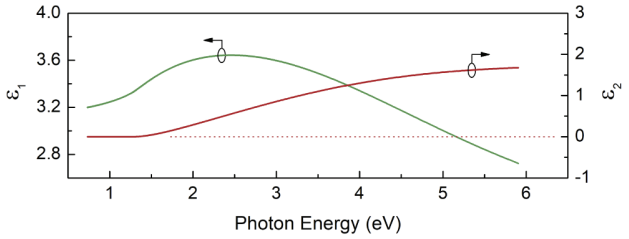
Once the interface layer was identified as containing unoxidized a-Si, it was further modeled using the Bruggeman effective medium approximation (EMA) as a mixture of fused silica and a-Si using the a-Si volume percentage as a free parameter. Thus, the reconstructed stack for further data analysis was an ambient/MgF_2-film/(a-Si + fused silica interface)/(fused silica substrate). The absorbing interface optical model involved seven parameters in all, adding the volume percentage of a-Si in the layer as a compositional parameter in addition to the four Tauc-Lorentz oscillator parameters, the constant additive real value, and the layer thickness. With this simpler model for the interface layer, the optical parameters of the fused silica and MgF_2 could be varied from the fixed literature values used in the iterative analysis described in the previous paragraph. The results of this new iterative analysis based on an a-Si interface component is presented in the next two paragraphs, first through a discussion of the non-absorbing components followed by a discussion of the a-Si containing component.

The spectrum in the real part of the dielectric function for the MgF_2 film was modeled as a Sellmeier term with two free parameters, yielding an amplitude and resonance energy of 134.81 ± 38.16 eV^2 and 12.85 ± 0.87 eV, respectively. A constant contribution to the real part of the dielectric function ε_0 was used as well, yielding a best fitting value of 1.10 ± 0.12. Thus, a three parameter model was used to describe the optical properties of this film. Similarly, the optical response of the fused silica was modeled as two Sellmeier terms with one variable and three

Approved for public release; distribution unlimited.

Optics EXPRESS

fixed parameters. The first term led to a fixed amplitude of 81.50 eV^2 and a resonance at 10.04 ± 0.17 eV, whereas the second term was found to be very weak and led to a fixed amplitude of 0.016 eV^2 and a fixed resonance at zero energy. A constant contribution ε_0 of 1.30 ± 0.03 was also used, resulting in a two parameter model for the optical response of the fused silica. The refractive indices derived from the fits for MgF_2 and fused silica agree reasonably well with results reported in literature. In particular, the index of refraction for the MgF_2 layer agrees closely with the published extraordinary index of refraction [27] and that of the fused silica matches the published result within 0.6% over the spectral range of interest, 210 - 1690 nm [28]. The final free parameter associated with the non-absorbing components is the MgF_2 thickness, with the analysis yielding a best fit value of 48.77 ± 0.30 nm as indicated in the structural model in Fig. 9 (lower panel).



fused silica	
a-Si/fused silica (24.5 ± 1.8 / 75.5 ± 1.8) vol.%	1.5 ± 0.3 nm
MgF_2	48.8 ± 0.3 nm

Fig. 9. (Top) The complex dielectric function (ε_1, ε_2) spectra of the (a-Si + fused silica) effective medium interfacial layer obtained with a six parameter optical model including a single Tauc-Lorentz oscillator, a constant contribution to ε_1, and a volume percentage of a-Si in the (a-Si + fused silica) two-component mixture. (Bottom) A schematic of the second reflection structure for the King rhomb is depicted. The two best fitting structural parameters are presented as deduced in the analysis of ellipsometric and Mueller matrix spectra. These include the thicknesses of the absorbing interface and the MgF_2 layers along with their confidence limits on the right side of the schematic.

For the absorbing layer, a Tauc-Lorentz (TL) oscillator with four parameters, along with a constant real contribution ε_0 as a fifth parameter, was used to describe the complex dielectric function of the a-Si absorbing component at the (fused silica)/MgF_2 interface that accounts for the dichroism of the King rhomb. This parametric form was adopted to describe the a-Si component of the interface layer with the second component of the layer being fused silica. The number of free parameters used in the fitting procedure of the (fused silica)/absorbing-layer/MgF_2/ambient structure could then be greatly reduced by employing a standard TL model for the a-Si component [29]. The best fit optical response of the interfacial layer is shown in Fig. 9 (upper panel) and was obtained with fixed standard TL oscillator parameters including an amplitude of 154.80 eV, a resonance energy of 3.72 eV, a bandgap energy of 1.28 eV, and a constant real contribution of 0.27 [29,30], as well as a variable TL broadening parameter with a best fit value of 5.75 ± 0.26 eV. In addition, two variable parameters were determined that describe the absorbing layer structure and composition as shown in Fig. 9 (lower panel) including the layer thickness and the volume percentage of a-Si in the Bruggeman EMA of the (fused silica + a-Si) composite, the latter strongly affecting the complex dielectric function of the layer. Best-fit values include a layer thickness of 1.53 ± 0.27 nm and an a-Si volume percentage of 24.50 ± 1.76 % in the EMA of the absorbing layer. The effective thickness or volume per planar area of the absorbing a-Si component is (0.245)(1.53 nm) = 0.37 nm. Based on this value, one possible interpretation of the

Approved for public release; distribution unlimited.

Optics EXPRESS

absorbing layer is a modulation region at the (fused silica)/MgF_2 interface with a peak-to-peak amplitude given by the absorbing layer thickness and a spatial period much larger than the atomic scale. A single layer of Si-Si bonding with an associated thickness of ~ 0.4 nm would account for the observed absorption. Furthermore the presence of a correspondingly modulated fused silica surface ~ 1.5 nm thick as a (fused silica + void) composite would have a negligible effect on the TIR behavior of the (fused silica)/ambient interface.

Figure 10 summarizes the results of the final fits to the multiple angle of incidence ellipsometric spectra obtained by external reflection. These fits apply the absorber layer properties of Fig. 9 as described in the previous paragraph. Also shown in Fig. 10 is the fit to the three-reflection straight-through experimental data in ψ_4 using the same structure as in the multiangle ellipsometric analysis, but with an inverted sequence of media. The lower right graph in Fig. 10 shows the derived angle δ_4 as a function of energy which correctly describes the phase shift that occurs upon the second TIR. The high quality of the fits in Fig. 10 supports the assignment of the physical structure and interface optical properties illustrated in Fig. 9. The results also demonstrate the potential sensitivity of the performance of polarization-based optical elements to the fabrication process. In fact, the (fused Si)/MgF_2/ambient structure is used in many such applications [2], and unless taken into account, a chemically reduced SiO_2 interface to the MgF_2 as in Fig. 9, even at the sub-monolayer level, will lead to deviations in the polarization generation and detection properties from predictions. As will be demonstrated in the next section, the structure of Fig. 9 can be incorporated as the intermediate internal reflection component in a complete analysis of the Mueller matrix of the King rhomb. This matrix describes the effect of transmission of a light beam of any incident polarization state through the rhomb in its operational configuration.

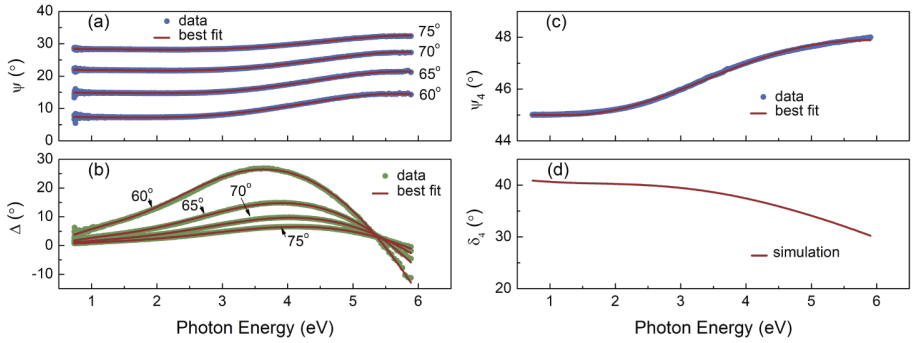


Fig. 10. Ellipsometric angles (ψ, Δ) measured by external reflection at multiple angles of incidence for the ambient/MgF_2/(a-Si+fused silica)/(fused silica) structure of the King rhomb (points). The corresponding fits are shown as the solid red lines. The plot at the upper right shows the dichroic angle ψ_4 derived from the normalized Mueller elements m_{12} and m_{21} measured from the three-reflection straight-through configuration for the rhomb. The solid red line in this case is obtained as a best fit using the same structure (but inverted in sequence) for the second internal reflection as was used in the analysis of the multiangle ellipsometric measurements. The plot at the lower right shows the predicted phase shift δ_4 that accompanies the dichroic angle ψ_4 for the second TIR from the (fused silica)/(a-Si+fused silica)/(MgF_2-film)/ambient structure. This prediction of δ_4 was obtained from a simulation using the results of the least squares fit of the ten spectra including those in the ellipsometric angles along with m_{12} and m_{21}.

Approved for public release; distribution unlimited.

Optics EXPRESS

6. Rhomb complete Mueller matrix analysis

With a complete analysis of the second TIR structure characterized by the two layer thicknesses and the component material dielectric functions, including that of the bulk fused silica, then a full Mueller matrix analysis of the King rhomb $\mathbf{M}_{\text{rhomb}}$ can be performed applying Eq. (18). A cascade of 15 Mueller matrices fully describe the rhomb, including 12 that describe the four beam paths each with a cumulative retardance along with positive and negative average fast axis rotation angles in accordance with Eq. (15). Excluding the Mueller matrix elements of $\mathbf{M}_{\text{rhomb}}$ that reflect only the dichroic behavior of the rhomb, as modeled in the previous section, the remaining 13 experimental matrix element spectra of the normalized Mueller matrix of the rhomb are subjected to least squares regression to determine the parameters that characterize the stress-induced birefringence along the four beam paths.

Thus, the model applied to simulate and then fit the 13 measured spectra was generated using the exact result of the series of matrix multiplications in the form of Eq. (18). In this model, the optical retardance at each reflection can be calculated; thus the spectra in the Mueller matrix elements of $\mathbf{M}_2$, $\mathbf{M}_4$, and $\mathbf{M}_6$ were determined previously and fixed. $\mathbf{M}_4$ was determined as described in Section 5, and $\mathbf{M}_2$ and $\mathbf{M}_6$ were determined from the angle of incidence and index of refraction spectrum of the fused silica as obtained in the external reflection ellipsometry experiment also described in Section 5. The cumulative stress-induced retardance $\{\delta_n(\lambda); 1, 3, 5, 7\}$ along the path of each beam segment n was modeled according to Eq. (7). The azimuthal angles of the principal (fast) axes of the stress birefringence for the four individual paths of the beam were constrained to a single average value which serves as a variable in the analysis. This value is given by $\alpha_n = \bar{\theta}_n = \langle\alpha\rangle$ with $n = 1, 3, 5, 7$, where $\bar{\theta}_n$ represents the average azimuthal angle along the beam path labeled n defined as in Eq. (15), also assuming small angular variations along each path. This approach is physically reasonable as a starting point, given that the rhomb is fabricated from a single block of fused silica.

In reality, however, the orientations of the fast axes along the different paths of the rhomb can differ not only due to different beam path directions, but also due to stress non-uniformity within the rhomb, for example generated by the mounting needed to stabilize the rhomb for rotation. Allowing such differences by using four unconstrained azimuthal angles in the least squares fitting procedure generated unphysical results attributable to the correlation between the two retardance variables $\delta_{pf,n}$ and $\sin 2\alpha_n$ for a given beam path. The approach used here to mitigate this problem was to constrain the magnitude of the angle $\langle\alpha\rangle$ to be the same for each path but then permit different possible ± orientations for each of the four paths. In this alternative least squares regression analysis approach, $|\langle\alpha\rangle|$ remains a variable.

The MSE from this procedure and the confidence limits in the best fitting parameters, the latter reflecting the correlation coefficients, were used together as figures of merit to identify the best fast axis orientation for each path. Improved fitting could be obtained with positive values of $\langle\alpha\rangle$ for paths 1 and 7, and negative values for paths 3 and 5. This may reflect the behavior of mounting-induced stress. Additionally, 13 offset-fit parameters were introduced to account for small but non-negligible systematic experimental errors in the Mueller matrix spectra. All offsets were below 0.01 in magnitude, ranging from values of 0.0003 for m_{13} and m_{43} to 0.008 for m_{23} and m_{42}. The presence of such errors can be identified from spectra in the elements of the normalized Mueller matrix measured in straight-through without the rhomb in place, which should be equal to the identity matrix. Finally, although the *F-S* frame of the rhomb is aligned with the fixed polarizer *t-e* reference frame by ensuring that $m_{22} = 1$ over the entire spectral range, a small difference between the two frames can be identified upon incorporation of the Mueller matrix offsets in the complete analysis of the rhomb. The difference is defined as a rotation angle θ_{rot} that brings the *F-S* system of the rhomb into the *t-e* system of the ellipsometer so that the complete Mueller matrix has the form of $\mathbf{M}'_{\text{rhomb}} = \mathbf{R}(-\theta_{\text{rot}})\,\mathbf{M}_{\text{rhomb}}\,\mathbf{R}(\theta_{\text{rot}})$ where

Approved for public release; distribution unlimited.

Optics EXPRESS

$\mathbf{M}_{\text{rhomb}}$ describes the measured Mueller matrix and $\mathbf{M}'_{\text{rhomb}}$ is converted to the *t-e* frame used for the best fitting simulation.

The derived results are shown in Table 3 for the signs and magnitude of the average stress birefringence azimuthal angle $\langle\alpha\rangle$ (the latter common to all four paths), the phase retardance prefactor for each individual path length, the stress in each path, and the phase retardance at selected wavelengths. The 13 measured Mueller matrix elements and their best fits using the model are shown in Fig. 11.

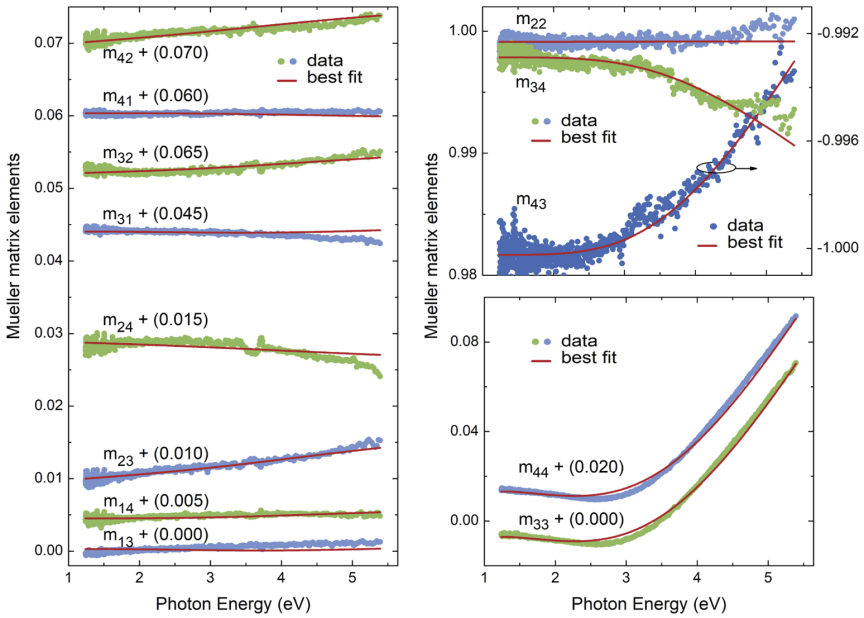


Fig. 11. Experimental and corresponding best fits for the spectra in the 13 normalized Mueller matrix elements of the King rhomb that provide the parameters characterizing the stress-induced birefringence along the four beam paths within the rhomb. The two Mueller matrix elements m_{12} and m_{21} were not used in the fitting routine as these provide information on only the dichroic behavior of the rhomb.

The first order expressions in Table 2 provide insights into the fitting procedure and the depth of information that can be extracted. Theoretically, the matrix elements m_{13}, m_{14}, m_{31}, and m_{41} can provide the four spectra in $\delta_n \sin 2\alpha_n; n = 1, 3, 5, 7$, or equivalently, the four values of $\delta_{pf,n} \sin 2\alpha_n; n = 1, 3, 5, 7$, given that $C(\lambda)/\lambda$ is known. In practice, however, as can be observed from Fig. 11, these matrix elements are small and very weakly dependent on wavelength, being proportional to the product of the dichroism and the retardance generated by stress-induced birefringence. The four elements m_{23}, m_{24}, m_{32}, and m_{42} also provide information on $\delta_{pf,n} \sin 2\alpha_n; n = 1, 3, 5, 7$; however, without suppression by the dichroic factor. The stronger dependence of these matrix elements on wavelength in Fig. 11 highlights this observation.

Even so, limitations are expected in the extraction of the four stress-induced retardance projections from m_{23}, m_{24}, m_{32}, and m_{42}. In first order, these four matrix elements are not independent, however, and so cannot be used by themselves to extract the four projections. In fact, to first order, it can be shown that

$$m_{24} \sin(\delta_2 + \delta_4 + \delta_6) = -m_{23} \cos(\delta_2 + \delta_4 + \delta_6) - m_{32}, \tag{24}$$

$$m_{42} \sin(\delta_2 + \delta_4 + \delta_6) = m_{23} + m_{32} \cos(\delta_2 + \delta_4 + \delta_6), \tag{25}$$

Approved for public release; distribution unlimited.

Optics EXPRESS

Table 3. Results for the relevant best fitting parameters that characterize the King rhomb including the sign and average magnitude of the azimuthal angle $\langle\alpha\rangle$ (the latter common to all four paths), the retardance prefactors given by $\delta_{pf,n} = 2\pi d|\sigma_{1,n} - \sigma_{2,n}| = 2\pi d|\Delta\sigma_n|$, and the deduced stress $|\Delta\sigma_n| = |\sigma_{1,n} - \sigma_{2,n}|$ for each of the beam paths. Also included in the fit is the offset angle θ_{rot} required to rotate the *F-S* coordinate system of the rhomb into alignment with the *t-e* coordinate system of the fixed polarizer of the ellipsometer used for straight-through measurement of the rhomb. These results were obtained from the least squares regression analysis of 13 Mueller matrix elements of the rhomb (excluding the elements m_{12} and m_{21}). The average angle attributed to the fast axis of the stress is ~135°. The deduced average stress magnitude over the cumulative path length of ~53 mm within the rhomb is 15398 ± 2046 Pa. The derived retardances for three representative wavelengths (250 nm, 500 nm, and 1000 nm) are also shown for each path.

Fit Results (°)						
$\langle\alpha\rangle$		135.05 ± 0.06				
θ_{rot}		−0.26 ± 0.04				
Path n	Sign of $\langle\alpha\rangle$	Fit Results $\delta_{pf,n}$ (°Pa nm)	Path Stress $\|\Delta\sigma_n\|$ (Pa)	δ_n(250 nm) (°)	δ_n(500 nm) (°)	δ_n(1000nm) (°)
1	+	81.36 ± 10.31	17371 ± 2205	1.42 ± 0.18	0.59 ± 0.08	0.27 ± 0.03
3	−	63.03 ± 9.17	12909 ± 1873	1.10 ± 0.16	0.46 ± 0.07	0.21 ± 0.03
5	−	72.19 ± 9.17	14820 ± 1873	1.26 ± 0.16	0.52 ± 0.07	0.24 ± 0.03
7	+	77.35 ± 10.31	16491 ± 2205	1.35 ± 0.18	0.56 ± 0.08	0.26 ± 0.04

and because of these relationships, only two parameters can be extracted from the four matrix elements in the equations. It is also not possible to extract the four orthogonal projection factors $\delta_{pf,n}\cos 2\alpha_n; n = 1, 3, 5, 7$; in first order as these appear only as a sum of the four factors in the four matrix elements m_{33}, m_{34}, m_{43}, and m_{44}. Thus, at most, it is possible to extract only five parameters when working in first order, relying primarily on the data at high photon energy where the dichroism is the strongest. This limitation was found in the fitting procedure in which case only five of the eight parameters associated with the stress-induced retardance could be extracted with confidence. This led to the selection of a single average azimuthal angle with different retardance prefactors along the path. Because the simulation of the rhomb was performed based on an exact matrix multiplication, rather than a first order analysis as presented in Table 2, additional sign information could be extracted, yielding a combination of four signs in Table 3 by trial and error that provided the best fit. The slight rotation of the *F-S* frame of the rhomb relative to the *t-e* frame also leads to a more complicated mixing of parameters in the Mueller matrix than those of Table 2.

There are two sources of strain within the in-line rotatable rhombs that give rise to stress-induced birefringence along the beam path. These include residual built-in strain within the fused silica material and mounting-induced strain due to the forces required to hold the rhomb in place which enables rotation. One might expect that in fabrication, the optical axis of the rhomb is oriented for alignment with the principal stress direction. As a result, there would be negligible stress-induced birefringence effects along the axial paths and offsetting effects along the two meridional paths. The fact that larger retardance prefactors in Table 3 occur along the axial paths near the mounting adhesive suggests that the strain due to mounting dominates. The indication that the azimuthal angles of the fast axes are in opposite directions for the two axial rays compared to the meridional rays is also a characteristic of mounting-induced stress.

Irrespective of the mounting and nature of the stress-induced birefringence over the beam path, the exact simulation for the Mueller matrix of the rhomb given in terms of the best fitting parameters in Table 3, including the appropriate signs of $\langle\alpha\rangle$ along the beam paths 1, 3, 5, and 7, is sufficient for predicting the performance of the compensator in both fixed and rotating applications. These parameters are derived including corrections for offsets arising from the errors in the Mueller matrix measurements themselves and errors arising from an inexact orientation

Approved for public release; distribution unlimited.

Optics EXPRESS

of the reference frame of the rhomb relative to the reference frame of the ellipsometer. Further analysis of the nature and origins of the stress in the rhomb may be possible by simultaneously analyzing the Mueller matrices obtained at different orientations of the *F*-*S* frame of the rhomb relative to the *t*-*e* reference frame. It may also be possible to extract further information, for example, on other possible physical mechanisms such as residual and stress-induced circular birefringence. As a result of the close fits to the Mueller matrix elements for $\alpha = 0°$ in Fig. 11, however, introduction of additional mechanisms beyond dissipation upon internal reflection and linear birefringence induced by beam path stress is not warranted for this data set.

7. Summary

The *p*-*s* difference between the phase shifts for the orthogonal optical electric field components that occurs upon total internal reflection (TIR) can be leveraged for use in compensating rhomb devices exhibiting a nearly constant phase retardance over the ultraviolet to the near-infrared spectral range. The three-TIR configuration of the in-line rotatable rhomb first described by King and studied in this research was designed specifically for this purpose. The first and third TIRs of this rhomb occur at (fused silica)/ambient interfaces whereas the intermediate reflection occurs from a (fused silica)/MgF_2-film/ambient structure wherein the thickness of the MgF_2 layer is ~ 50 nm. Two sources of deviations from the ideal description of the rhomb performance were studied using straight-through Mueller matrix ellipsometry in the operational configuration supplemented by ambient side ellipsometry, both measurements performed over the 210 nm to 1650 nm range.

The first source identified here was weak dichroic behavior in the TIR from the (fused silica)/MgF_2-film/ambient structure due to dissipative absorption within the layer stack. An interface layer having an effective thickness (or volume per planar area) on the monolayer scale (~ 0.4 nm) was identified between the MgF_2 layer and the bulk fused silica. Analysis of this TIR structure using Mueller matrix ellipsometry was facilitated by external multiangle spectroscopic ellipsometry data acquired by illumination from the ambient side of the rhomb. Modeling of both sets of data suggests that the absorption is caused by Si-Si bonding arising from reduction of the SiO_2 of the fused silica surface/interface, and thus, can be modeled with the optical properties of amorphous silicon. The generated dichroic activity is unfavorable to the performance of the rhomb when used in its intended application in straight-through as an inline compensator unless its effect is taken into account in the Jones or Mueller matrix description of the device.

Whereas the source of the first deviation from ideality may be related to the design and processing of the rhomb coating and so may be avoidable, the second deviation is innate to the fused silica that is ground and polished to form the rhomb. Fused silica residual stress and rhomb stress due to mounting, which is required when the rhomb is rotated, generate birefringence and combine to introduce intrinsic wavelength dependent components to the net retardance of the device in addition to those generated by the three TIRs. A theoretical basis supported by best fits of stress birefringence simulations in bulk fused silica has resulted in an applicable procedure for determination of average stress, accumulated stress-induced retardance, and average fast axis orientation along the four path segments within the rhomb. These characteristics derive from an analysis of Mueller matrix measurements in the straight-through operational configuration of the rhomb.

The Mueller matrix formalism was applied to describe the operation of the King rhomb, and a first order analysis provided insights into the effects of both dichroism and individual path retardances on each of the 15 elements of the normalized Mueller matrix. This analysis identified the origins of the dominant deviations from the ideal description for each of the matrix elements. Finally, least-squares regression analysis was applied to model the normalized Mueller matrix elements measured over the wavelength range from 230 to 1000 nm and to extract wavelength independent parameters that characterize the retardance generated by stress-induced

Approved for public release; distribution unlimited.

Optics EXPRESS

birefringence present in individual paths of the device. In this analysis, fixed spectra in the optical properties of the component materials of fused silica, MgF_2, and a-Si were used along with fixed wavelength independent parameters that describe the thin film structure and beam path geometry. The best-fit resulting Mueller matrix model for the device is critically important for accurate simulations of the device performance as a fixed or rotating compensator in instruments developed for spectroscopic polarimetry and ellipsometry.

Funding. Air Force Research Laboratory (FA9453-18-2-0037, FA9453-19-C-1002).

Acknowledgments. This material is based on research sponsored by Air Force Research Laboratory under agreement numbers FA9453-18-2-0037 and FA9453-19-C-1002. The U.S. Government is authorized to reproduce and distribute reprints for Governmental purposes notwithstanding any copyright notation thereon. The views and conclusions contained herein are those of the authors and should not be interpreted as necessarily representing the official policies or endorsements, either expressed or implied, of Air Force Research Laboratory or the U.S. Government.

Disclosures. The authors declare no conflicts of interest.

Data availability. Data underlying the results presented in this paper are not publicly available at this time but may be obtained from the authors upon reasonable request.

References

1. R. M. Azzam and N. M. Bashara, *Ellipsometry and Polarized Light* (North-Holland, 1976).
2. J. M. Bennett and H. E. Bennett, "Polarization," in *Handbook of Optics*, W. G. Driscoll and W. Vaughan, eds. (McGraw-Hill, 1978), Section 10.
3. E. Collett, *Polarized Light: Fundamentals and Applications* (CRC, 1992).
4. R. A. Chipman, W. S. T. Lam, and G. Young, *Polarized Light and Optical Systems* (CRC, 2018).
5. F. Stabo-Eeg, M. Kildemo, E. Garcia-Caurel, and M. Lindgren, "Design and characterization of achromatic 132° retarders in CaF_2 and fused silica," J. Mod. Opt. **55**(14), 2203–2214 (2008).
6. M. R. Kulish and S. V. Virko, "Comparison of properties inherent to wave plates and Fresnel rhomb," Fiz. Napivprovidn., Kvantova Optoelektron. **16**(1), 64–71 (2013).
7. M. Kraemer and T. Baur, "Achromatic devices in polarization optics," Proc. SPIE **10528**, 105281C (2018).
8. S. Bian, C. Cui, and O. Arteaga, "Mueller matrix ellipsometer based on discrete-angle rotating Fresnel rhomb compensators," Appl. Opt. **60**(16), 4964–4971 (2021).
9. B. D. Johs, S. E. Green, C. M. Herzinger, and D. E. Meyer, "Deviation angle self compensating substantially achromatic retarder," US patent 7460230B2 (31 October 2006).
10. R. J. King, "Quarter-wave retardation systems based on the Fresnel rhomb principle," J. Sci. Instrum. **43**(9), 617–622 (1966).
11. R. J. King and M. J. Downs, "Ellipsometry applied to films on dielectric substrates," Surf. Sci. **16**, 288–302 (1969).
12. M. Born and E. Wolf, *Principles of Optics*, 6th Ed. (Pergamon, 1980), Chapter 1.
13. P. Chindaudom and K. Vedam, "Determination of the optical function n(λ) of vitreous silica by spectroscopic ellipsometry with an achromatic compensator," Appl. Opt. **32**(31), 6391–6398 (1993).
14. Manufactured by Bernhard Halle Nachfolger, Berlin, Germany.
15. R. W. Collins, I. An, and C. Chen, "Rotating polarizer and analyzer ellipsometry," in *Handbook of Ellipsometry*, H. G. Tompkins and E. A. Irene, eds. (William Andrew, 2005), Chapter 5.
16. Model M2000, J.A. Woollam Co., Inc.
17. Model RC2, J.A. Woollam Co., Inc.
18. E. Collett, *Polarized Light: Fundamentals and Applications* (Marcel Dekker, 1993), Chapter 5.
19. CompleteEase, Fused silica (Sellmeier) database optical dielectric function, J.A. Woollam Co., Inc.
20. CompleteEase, MgF_2(e) (Sellmeier) database optical dielectric function, J.A. Woollam Co., Inc.
21. A. Yariv and P. Yeh, *Optical Waves in Crystals: Propagation and Control of Laser Radiation* (Wiley, 1984).
22. H. Aben and C. Guillemet, *Photoelasticity of Glass* (Springer, 1993).
23. T. N. Vasudevan and R. S. Krishnan, "Dispersion of the stress-optic coefficient in glasses," J. Phys. D: Appl. Phys. **5**(12), 2283–2287 (1972).
24. E. S. Jog, "The dispersion of the piezo-optic constants of vitreous silica," J. Indian Inst. Sci. **39**(2), 101–107 (1957).
25. N. K. Sinha, "Normalised dispersion of birefringence of quartz and stress optical coefficient of fused silica and plate glass," Phys. Chem. Glasses **19**(4), 67–77 (1978).
26. Manufactured by Esco Optics, New Jersy, USA.
27. M. J. Dodge, "Refractive properties of magnesium fluoride," Appl. Opt. **23**(12), 1980–1984 (1984).
28. I. H. Malitson, "Interspecimen comparison of the refractive index of fused silica," J. Opt. Soc. Am. **55**(10), 1205–1209 (1965).
29. J. Leng, J. Opsal, H. Chu, M. Senko, and D. E. Aspnes, "Analytic representations of the dielectric functions of materials for device and structural modeling," Thin Solid Films **313-314**, 132–136 (1998).
30. CompleteEase, a-Si_Aspnes_tl database optical dielectric function, J.A. Woollam Co., Inc.

72.241.188.198 {ts '2021-10-20 07:26:27'}

Approved for public release; distribution unlimited.

ACS APPLIED MATERIALS & INTERFACES

www.acsami.org Research Article

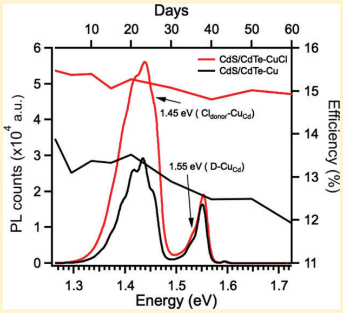
Effects of Cu Precursor on the Performance of Efficient CdTe Solar Cells

Sandip S. Bista,[§] Deng-Bing Li,[*,§] Rasha A. Awni, Zhaoning Song, Kamala K. Subedi, Niraj Shrestha, Suman Rijal, Sabin Neupane, Corey R. Grice, Adam B Phillips, Randy J. Ellingson, Michael Heben, Jian V. Li, and Yanfa Yan[*]

Cite This: *ACS Appl. Mater. Interfaces* 2021, 13, 38432−38440 Read Online

ACCESS | Metrics & More | Article Recommendations | Supporting Information

ABSTRACT: Copper (Cu) incorporation is a key process for fabricating efficient CdTe-based thin-film solar cells and has been used in CdTe-based solar cell module manufacturing. Here, we investigate the effects of different Cu precursors on the performance of CdTe-based thin-film solar cells by incorporating Cu using a metallic Cu source (evaporated Cu) and ionic Cu sources (solution-processed cuprous chloride (CuCl) and copper chloride ($CuCl_2$)). We find that ionic Cu precursors offer much better control in Cu diffusion than the metallic Cu precursor, producing better front junction quality, lower back-barrier heights, and better bulk defect property. Finally, outperforming power conversion efficiencies of 17.2 and 17.5% are obtained for devices with cadmium sulfide and zinc magnesium oxide as the front window layers, respectively, which are among the highest reported CdTe solar cells efficiencies. Our results suggest that an ionic Cu precursor is preferred as the dopant to fabricate efficient CdTe thin-film solar cells and modules.



KEYWORDS: *CdTe solar cell, CuCl, $CuCl_2$, ionic Cu precursor, Cu doping*

Downloaded via UNIV OF TOLEDO on September 13, 2021 at 16:11:16 (UTC).
See https://pubs.acs.org/sharingguidelines for options on how to legitimately share published articles.

INTRODUCTION

Cadmium telluride (CdTe) solar cell technology has been attracting extensive attention due to its low cost and ideal band gap for high-efficiency photovoltaics.[1] First solar, limited liability company (LLC) has reported the highest power conversion efficiencies (PCEs) of 22.1% for small area cells and 19% for modules, providing a competitive alternative for traditional silicon photovoltaics.[2] For most efficient CdTe solar cells and modules, copper (Cu) is applied as a dopant to improve the p-type conductivity of the CdTe absorber and to reduce the Schottky barrier height between the CdTe and the back contact.[3−6] The Cu incorporation is typically done via the post-deposition of a thin layer of Cu source material on $CdCl_2$-treated CdTe thin films. The Cu concentration (N_{Cu}) and distribution in the CdTe absorber layer can significantly influence the performance of CdTe solar cells.[7] For example, excessive Cu incorporation can introduce interstitial defects (Cu_i) and other Cu related compensation complexes, e.g., Cu_i-Cu_{Cd},[8] which would limit the hole density in CdTe films. Additionally, Cu_i ions can diffuse at a high speed due to its high solubility at grain boundaries,[9−12] which adversely affects the long-term stability of CdTe solar cells.[13−15] More importantly, Cu at the front interfaces (e.g., the cadmium sulfide (CdS)-CdTe and zinc magnesium oxide (ZMO)-CdTe interfaces) has been thought to form recombination centers and shunting pathways, leading to the degradation of device performance.[3,16] Therefore, the Cu dosage and distribution in CdTe films should be well controlled to minimize the nonradiative recombination related to Cu doping and maximize the device performance and long-term stability.

In this regard, various Cu precursors have been used as the Cu source to fabricate CdTe thin-film solar cells. In general, two kinds of Cu precursors, including metallic Cu,[17] covalent Cu compounds, e.g., Cu_xTe,[18] Cu doped ZnTe,[19] and ionic Cu compounds, e.g., CuSCN,[20,21] cuprous chloride (CuCl),[3,5,6] and copper chloride ($CuCl_2$).[22,23] Among them, CuCl and $CuCl_2$ have attracted extensive attention due to its outstanding performance. Recently, $CuCl_2$ was incorporated in the CdTe absorber as the Cu precursor to eliminate the diffusion of Cu into the front junction, achieving a maximum PCE of ∼16%.[22] Sites and coworkers have demonstrated a record PCE of 19.1% for CdSeTe solar cells using the CuCl precursor deposited by close space sublimation (CSS).[5,24] We previously reported a PCE of 17.5% for CdTe solar cells (no selenium) using a solution-processed CuCl treatment with rapid thermal anneal-

Received: June 23, 2021
Accepted: July 23, 2021
Published: August 4, 2021



ACS Publications © 2021 American Chemical Society

Approved for public release; distribution unlimited.

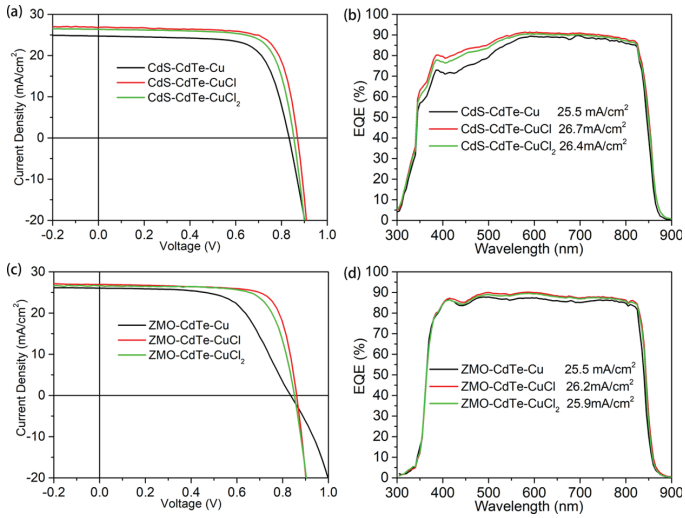


Figure 1. (a, c) $J-V$ curves and (b, d) EQE spectra of representative (a, b) CdS-CdTe and (c, d) ZMO-CdTe devices treated with different Cu precursors.

ing process.[3] However, to date, comparative investigations on the impact of Cu precursors have rarely been reported.

Here, we report on a comparative study of the effects of Cu precursors on the performance of CdTe-based thin-film solar cells. Please note that no etching treatment is performed on the chlorinated CdTe film in this work. We fabricate CdTe thin film solar cells using a metallic Cu source (evaporated Cu) and ionic Cu sources (solution-processed CuCl and $CuCl_2$). We find that the ionic Cu precursors offer much better control of Cu diffusion than the metallic Cu precursor. The statistical analysis of a large number of CdTe solar cells shows that the cells fabricated using the ionic Cu source show better front junction quality, lower back barrier heights, and better bulk defect property than the cells fabricated using the metallic Cu source. CuCl and $CuCl_2$, with different oxidation states of Cu, deliver almost the same performance for CdTe solar cells, which are much better than the cells that with the metallic Cu source. Our results show that the ionic Cu precursor plays a critical role in controlling the Cu dosage and establishing a desired Cu distribution profile.

EXPERIMENTAL SECTION

CdTe solar cells with two kinds of electron transport layers, i.e., CdS and ZMO, were fabricated. For the CdS-CdTe devices, fluorine-doped tin oxide (FTO) coated glass (TEC 12D; NSG, US) with a 30 nm intrinsic SnO_2 layer was used as the substrate. First, an oxygenated cadmium sulfide (CdS:O) window layer with a thickness of 60 nm was deposited by radio-frequency (RF) magnetic sputtering using a 2-in. CdS target in a 2% oxygen and 98% argon environment at room temperature under 10 mTorr pressure and 50 W power. A 4-μm CdTe absorber was deposited by close-space sublimation (CSS) at the source and substrate temperatures of 660 and 590 °C, respectively, at 10 Torr pressure, followed by a wet cadmium chloride ($CdCl_2$) treatment at 390 °C for 30 min in dry air.[25]

For the ZMO-CdTe devices, FTO-coated glass (TEC 12; NSG, US) was used as the substrate according to our previous work.[3] A 80 nm ZMO window layer was deposited using a commercial ZMO target (8 wt % MgO) by RF sputtering with a flow gas of 16 sccm of pure argon and 24 sccm mixture gas of 95% argon and 5% oxygen. After a 10 min UV-ozone treatment for the as-deposited ZMO window layer, a 3.5 μm CdTe film was deposited by CSS with a source temperature of 560 °C and a substrate temperature of 495 °C under 1 Torr. Then, a $CdCl_2$ treatment was carried out at 420 °C for 20 min with a helium (He) flow (500 sccm) at 500 Torr.

After $CdCl_2$ treatment, the samples were rinsed with methanol to remove the residual $CdCl_2$ from the back surface. Then, three different Cu precursors were used to incorporate Cu for both CdS-CdTe and ZMO-CdTe devices. It is noted that no etching treatment was performed after $CdCl_2$ treatment for all the devices. The first Cu precursor was metallic Cu: a bilayer electrode of Cu (4 nm for CdS-CdTe and 3 nm for ZMO-CdTe devices) and Au (40 nm) was deposited by thermal evaporation with an individual cell area of 0.08 cm^2 followed by an activation treatment at 200 °C for 20 min. The second precursor was CuCl: a saturated CuCl (100 μL for CdS-CdTe and 80 μL for ZMO-CdTe devices) solution in ethanol was used to drop and spread on a 1.5″ × 1.5″ CdTe surface. After drying naturally, the samples were treated through rapid thermal annealing (RTA) (at 200 °C for CdS-CdTe and 160 °C for ZMO-CdTe devices) with a ramping speed of ∼60 °C/min without dwelling time in a 500 sccm He flow. The third precursor was $CuCl_2$: a $CuCl_2$ solution (with a Cu concentration of 3.10 μg/mL, 100 μL for CdS-CdTe and 80 μL for ZMO-CdTe devices) solution in ethanol was used to drop and spread on a 1.5″ × 1.5″ CdTe surface. After drying naturally, the samples were treated through RTA (at 200 °C for CdS-CdTe and 160 °C for ZMO-CdTe devices) with a ramping speed of ∼60 °C/min without dwelling time in a 500 sccm He flow. Note that the Cu ion concentration in both CuCl and $CuCl_2$ solution was 3.10 μg/mL. After the Cu activation annealing treatment, a 40 nm Au layer was deposited on the back surface with an individual device area of 0.08 cm^2. No further annealing treatment was taken after the Au deposition. Finally, a 120 nm magnesium fluoride (MgF_2) anti-reflective layer was deposited on the glass side of the FTO substrate in an e-beam evaporation system.

Hall effect measurements were performed for our as-deposited, $CdCl_2$-treated, and CuCl-treated CdTe films (∼3 μm) deposited on soda lime glass using a M91Fast Hall measurement system (LakeShore Cryotronics Advancing Science). All the as-deposited, $CdCl_2$-treated, and CuCl-treated CdTe films show p-type conductivity with hole concentrations in the order of 10^{12}, 10^{12}, and 10^{13} cm^{-3}, respectively. Solar cell performance was characterized by measuring current density−voltage ($J-V$) curves under AM1.5G illumination using a solar simulator and a source meter (Keithley 2400) and the external quantum efficiency (EQE) spectra using an EQE system (PV Measurements Inc.). Dynamic secondary ion mass spectrometry (SIMS) was performed using Dynamic-SIMS5 from ION-TOF

https://doi.org/10.1021/acsami.1c11784
ACS Appl. Mater. Interfaces 2021, 13, 38432−38440

Approved for public release; distribution unlimited.

Table 1. Photovoltaic Parameters for the Best CdS-CdTe and ZMO-CdTe Devices with Different Precursors

samples	V_{OC} (V)	J_{SC} (mA/cm^2)	FF (%)	PCE (%)	R_S (Ω cm^2)	R_{SH} (Ω cm^2)
CdS-CdTe-Cu	0.833	25.5	71.7	15.2	3.8	1140
CdS-CdTe-CuCl	0.870	26.4	75.1	17.2	1.7	1421
CdS-CdTe-$CuCl_2$	0.854	26.3	74.3	16.7	2.1	1209
ZMO-CdTe-Cu	0.837	25.9	61.8	13.4	9.8	1297
ZMO-CdTe-CuCl	0.862	26.9	75.5	17.5	1.7	1455
ZMO-CdTe-$CuCl_2$	0.851	26.6	73.3	16.7	2.6	1548

GmbH (Munster, Germany). The samples were analyzed in dual-beam profiling mode and the primary ion for analysis was 30 keV Bi^{3+} (Bi liquid metal ion source). This ion beam was applied over a 100 μm × 100 μm area at the center of the sputter crater (400 μm × 400 μm). The spectral data was acquired in high mass-resolution mode. The energy of the sputtered ion was 1 keV Ar^+ (Ar, electron impact ion source). Room-temperature capacitance−voltage ($C-V$), temperature-dependent current−voltage ($J-V-T$), thermal admittance spectroscopy (TAS), and impedance spectroscopy (IS) measurements were performed using a Solartron Modulab potentiostat equipped with a frequency response analyzer (Ametek Inc.). Photoluminescence (PL) characteristics were investigated utilizing steady-state and time-resolved PL. The detail of the electrical characterizations and PL measurement can be found in our previous publication.[3]

RESULTS

The representative device performance of CdTe solar cells with different Cu precursors (i.e., metallic Cu, CuCl, and $CuCl_2$, named CdTe-Cu, CdTe-CuCl, and CdTe-$CuCl_2$ hereafter, respectively) is shown in Figure 1. A detailed statistical comparison of all the photovoltaic parameters for the CdS-CdTe and ZMO-CdTe devices is shown in Figures S1 and S2, respectively. The best $J-V$ parameters for each type of device are tabulated in Table 1. For the devices with CdS as the front window layer (Figure 1a,b), the best CdTe-Cu device shows a PCE of 15.20%, with a V_{OC} of 833 mV, J_{SC} of 25.5 mA/cm^2, and FF of 71.7%, while the CdTe-CuCl device demonstrates an overall improved performance with a V_{OC} of 870 mV, J_{SC} of 26.4 mA/cm^2, and FF of 75.1%, yielding a PCE of 17.2%. The CdTe-$CuCl_2$ device exhibits a similar performance to the CdTe-CuCl device with a V_{OC} of 854 mV, J_{SC} of 26.3 mA/cm^2, and FF of 74.3%, yielding a PCE of 16.7%. When comparing the EQE results, the CdS-CdTe-CuCl and CdS-CdTe-$CuCl_2$ devices show a significantly increased spectral response in the wavelength range from 350 to 550 nm with respect to the CdS-CdTe-Cu device (Figure 1b) and deliver integrated current densities of 26.7 and 26.4 mA/cm^2, respectively, higher than that in the CdS-CdTe-Cu device (25.5 mA/cm^2). The significant improvement of EQE in the whole wavelength range for the CuCl- and $CuCl_2$-treated devices suggests better carrier separation and transport properties, especially at the front interface. This can be attributed to the reduced Cu diffusion to the front junction, which will be discussed later.

The performance of ZMO-CdTe solar cells with CuCl and $CuCl_2$ (Figure 1c) is also significantly improved compared with that of the metallic Cu-treated device (Figure 1c). The devices treated with solution-processed CuCl and $CuCl_2$ show higher quantum efficiencies of ∼90% from 500 to 600 nm, yielding an integrated current of 26.2 and 25.9 mA/cm^2, respectively, which are higher than the J_{SC} of 25.5 mA/cm^2 in the ZMO-CdTe-Cu device (Figure 1b). The statistical comparison in Figures S1 and S2 also show the same improvements for the devices with the CdS and ZMO front window layers, especially the V_{OC} and FF, suggesting a better front main junction and a reduced back barrier height. Interestingly, the J_{SC} values in the CdS-CdTe devices are higher than those in the ZMO-CdTe devices although ZMO has a larger band gap than CdS. One reason is that the CdS film in this work is thinner (60 nm) than the ZMO film (80 nm), resulting in higher transmittance at the range of 300−380 nm (Figure S3). The other reason is the interdiffusion between CdS and CdTe at the front interface, resulting in the formation of CdSTe alloy, which has a slightly smaller band gap.[26] Therefore, the light absorption of the CdS-CdTe device extended to longer wavelengths at the range of 840−880 nm as shown in the EQE curves (Figure S3). Please note that the etching treatment after $CdCl_2$ treatment is excluded due to its incompatibility with the ZMO-CdTe devices. Nonetheless, both metallic Cu and CuCl treatment are also applied on the CdS-CdTe device with and without hydroiodic (HI) acid etching treatment according to our previous procedure.[17] The results (Figure S4) further demonstrate that CdTe devices with CuCl treatment show better performance than those with metallic Cu treatment.

Note that the $J-V$ curves of the ZMO-CdTe device with Cu metal (Figure 1c) show clear distortion under a forward bias near V_{OC} (i.e., an S-kink), indicating poor heterojunction properties at the ZMO-CdTe interface. According to our SCAPS simulation results,[27] the S-kink can be attributed to the low ZMO film conductivity and the high acceptor-like defect trap concentration at the front interface, both of which are caused by the over diffusion of Cu. The diffusion of Cu into the ZMO film and the ZMO-CdTe interface can significantly decrease the ZMO conductivity[28−30] and form recombination centers at the front interface.[3,16] The aggregation of Cu at the front interface and in the ZMO layer is identified by the dynamic-SIMS measurements (Figure S5). Note that in the CdTe-CuCl devices, the Cu activation can be performed by an RTA process at 160 °C with ∼150 times less Cu dosage than the treatment using metallic Cu, as reported in our previous work.[3] The RTA process has also been tried for the devices with metallic Cu doping. However, the traditional Cu activation process (200 °C for 20 min) always shows higher device performance than that treated with the RTA process when metallic Cu is used as the Cu source (Figure S6). In comparison, the CdS-CdTe devices treated with metallic Cu show no S-kink. This is probably because CdS is not as sensitive to Cu as ZMO.

To further investigate the effect of different Cu precursors on the optoelectronic properties of CdTe films, a suite of characterizations was performed. Note that the CdTe-CuCl devices show similar performances to the CdTe-$CuCl_2$ devices, implying the nonessential effect of the oxidation state of ionic Cu. The slightly lower performance of the CdTe-$CuCl_2$ devices than the CdTe-CuCl devices may be attributed to experimental deviation and the film inhomogeneity. However, the devices treated with metallic Cu show much lower device performance than those with the solution processed CuCl and $CuCl_2$ treatments, suggesting a more significant effect of the ionic

https://doi.org/10.1021/acsami.1c11784
ACS Appl. Mater. Interfaces 2021, 13, 38432−38440

Approved for public release; distribution unlimited.

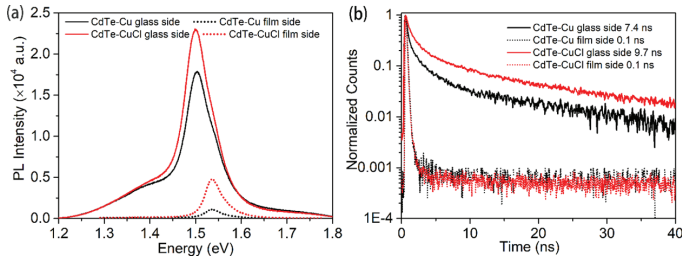


Figure 2. (a) PL and (b) TRPL spectra for CdTe-Cu and CdTe-CuCl devices with CdS as the front window layer. For each sample, PL spectra were excited through the FTO glass side and CdTe film side with a 633 nm laser excitation.

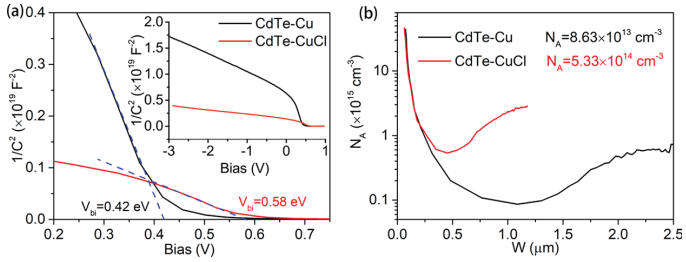


Figure 3. (a) Mott−Schottky plots measured at room temperature for devices with Cu and CuCl treatment. Inset: Mott−Schottky plots measured from −3.0 to 1.0 V bias voltage. (b) Calculated carrier densities extracted from $C-V$ measurements.

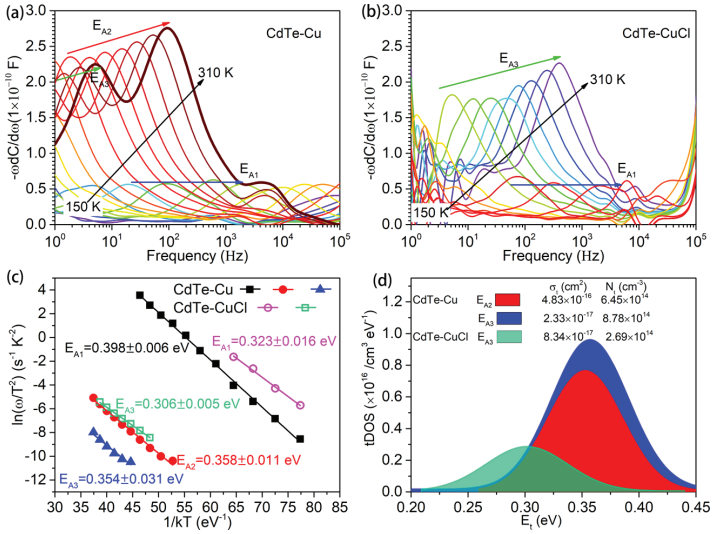


Figure 4. Differential capacitance spectra ($-\omega dC/d\omega$) extracted from the capacitance spectra in Figure S9 for (a) CdTe-Cu and (b) CdTe-CuCl devices. (c) Arrhenius plots and (d) defect distribution in CdTe-Cu and CdTe-CuCl devices obtained from (a) and (b). The trap defect activation energies (E_A), defect capture cross section (σ_t), and trap state densities (N_t) are tabulated in the inset.

versus metallic Cu sources. In addition, changing the front window layer, e.g., CdS and ZMO, does not affect the influence of different Cu precursors. Therefore, CdS-CdTe-CuCl was chosen as the representative of ionic Cu treatment to make comparison with the devices with metallic Cu in the characterization hereafter.

Figure 2a shows the PL measurements of CdTe-Cu and CdTe-CuCl devices with CdS as the front window layer. Both samples show PL spectra with an emission peak centered at 1.501 ± 0.003 eV when excited through the FTO glass side and 1.537 ± 0.002 eV when excited from the film side but with different emission intensities. The variation of the emission peaks is due to the interdiffusion of CdS and CdTe at the front interface.[31] Higher PL intensity generally suggests a lower nonradiative recombination rate and a higher carrier lifetime. For both glass and film side excitations, the CdTe-CuCl device shows higher PL intensities than the CdTe-Cu device, indicating lower recombination rates at the CdS-CdTe and CdTe-Au

https://doi.org/10.1021/acsami.1c11784
ACS Appl. Mater. Interfaces 2021, 13, 38432−38440

Approved for public release; distribution unlimited.
700

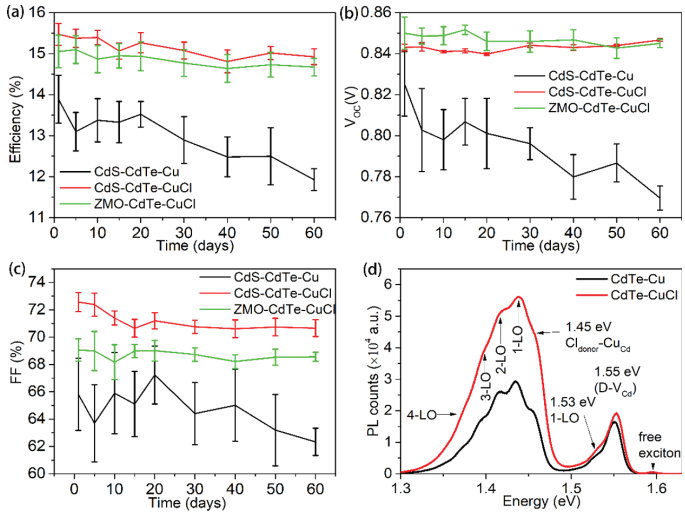


Figure 5. Degradation tests in ambient air for 60 days for devices with different window layers and Cu precursors. Each group includes 6 cells. The degradation of the (a) efficiency, (b) V_{OC}, and (c) FF was plotted individually. (d) Low-temperature steady-state PL measurement of CdTe-Cu and CdTe-CuCl devices excited from the back side at 9 K performed with a 532 nm laser at 25 mW/cm^2.

interfaces in the CdTe-CuCl device.[27] The TRPL results in Figure 2b further confirm this conclusion by showing a much higher carrier lifetime of 9.7 ns in the CdTe-CuCl device than that of 7.4 ns in the CdTe-Cu device when excited from the glass side. When excited from the film side, same lifetime is obtained due to the severe recombination at the back surfaces and the equipment detection limit. The same PL and TRPL measurements were also carried out for ZMO-CdTe devices, and similar trends can be observed with higher PL intensity and lifetime in the ZMO-CdTe films, as shown in Figure S7.

$C-V$ measurement was used to investigate the apparent build-in potential (V_{bi}) at the front junction and extract the doping density in the CdTe absorber layer (Figure 3a). From the intercept of the linear fit of the Mott−Schottky plot ($1/C^2$ vs bias) with the bias axis, the V_{bi} across the depletion region formed by the CdS-CdTe junction was extracted. The CdTe-CuCl device shows a higher V_{bi} (0.58 V) than the CdTe-Cu device (0.42 V) (Figure 3a). The improvement of V_{bi} suggests an improved front junction at the CdS and CdTe interface of the CdTe-CuCl device, which plays the most important role in V_{OC} and final device performance. The improvement of V_{bi} in the CdTe-CuCl device can be attributed to the improvement of hole density in the bulk CdTe absorber, the reduction of the interface trap state concentration, and higher n-type conductivity of the CdS film due to well-controlled Cu diffusion into the front interface and CdS film.[32] The apparent hole density N_A in the CdTe layer is calculated using the Mott−Schottky plot according to the following equation:[17]

$$N_A = -\frac{2}{q\varepsilon\varepsilon_0 A^2}\left[\frac{dC^{-2}(V)}{dV}\right]^{-1} \quad (1)$$

where ε is the relative dielectric constant of CdTe, ε_0 is the absolute permittivity of vacuum, A is the surface area of a cell, C is the junction capacitance, and V is the bias voltage. As shown in Figure 3b, the hole carrier concentration taken from the lowest point of its depth profile of the CdTe-CuCl device is 5.33×10^{14} cm^{-3}, which is higher than the carrier concentration in the CdTe-Cu device (8.63×10^{13} cm^{-3}). $C-V$ measurements for the ZMO-CdTe devices with varied Cu precursors were also performed and similar changes of the carrier concentration can be observed (Figure S8). The improvement of hole density in the CdTe bulk is beneficial to the improvement of V_{bi} as discussed above and the reduction of the back-barrier height, which will be discussed later.

Thermal admittance spectroscopy is an effective method to study the defect properties in CdTe solar cells.[17,33] The capacitance spectra ($C-\omega$) measured at various temperatures (T) for CdTe-Cu and CdTe-CuCl devices are shown in Figure S9. From the peaks of the derivative of capacitance spectra ($-\omega dC/d\omega$), Figure 4a,b, the defect characteristic frequencies as indicated by arrows were extracted and used to build the Arrhenius plots (Figure 4c). From the linear fit of the Arrhenius plots, the trap defect states in the CdTe-Cu and CdTe-CuCl devices were calculated. Here, three characteristic activation energies, $E_{A1} = 0.398 \pm 0.006$ eV, $E_{A2} = 0.358 \pm 0.011$ eV, and $E_{A3} = 0.354 \pm 0.031$ eV, for CdTe-Cu devices and two activation energies, $E_{A1} = 0.323 \pm 0.016$ eV and $E_{A3} = 0.306 \pm 0.005$ eV, for CdTe-CuCl devices were detected. According to our previous investigation about the TAS measurements performed at various DC biases with constant AC modulation,[17] E_{A1} corresponds to the back contact barrier, while E_{A2} and E_{A3} are considered as deep acceptor-like trap states.[17,34,35] For the CdTe-Cu device, a back-barrier height of 0.398 ± 0.006 eV is obtained, which is higher than the 0.323 ± 0.016 eV obtained in the CdTe-CuCl devices. This can be further demonstrated by the $J-V-T$ measurements as shown in Figure S10. The reduction of the back-barrier height is attributed to the improvement of hole density adjacent to the electrode as shown in the $C-V$ measurement. Besides the improvement of back-barrier height, the CdTe-CuCl devices show much shallower defect levels than the CdTe-Cu devices. In the CdTe-Cu device, two defects with depth of $E_{A2} = 0.358 \pm 0.011$ eV and $E_{A3} = 0.354 \pm 0.031$ eV are detected. While in the CdTe-CuCl devices, E_{A2} disappeared according to the change of the features in the differential capacitance spectra (Figure 4a,b), and only one defect E_{A3} =

https://doi.org/10.1021/acsami.1c11784
ACS Appl. Mater. Interfaces 2021, 13, 38432−38440

Approved for public release; distribution unlimited.

0.306 ± 0.005 eV is obtained, which is shallower than the defects in the CdTe-Cu devices. The density (N_t) and capture cross section (σ_t) of all the defects are also calculated as shown in Figure 4d and the inset. The defect E_{A3} in the CdTe-CuCl device has much lower N_t (2.69×10^{14} cm^{-3}) than that in the CdTe-Cu device (6.45×10^{14} cm^{-3} and 8.78×10^{14} cm^{-3} for E_{A2} and E_{A3}, respectively). In addition, the defects with a depth of E_{A2}, which exists in CdTe-Cu but is missing in the CdTe-CuCl device, show a much higher σ_t value of 4.83×10^{-16} cm^{-3} than the other two defects of 2.33×10^{-17} and 8.34×10^{-17} cm^{-3} for CdTe-Cu and CdTe-CuCl devices, respectively. The elimination of defects with high concentration and capture cross section in the CdTe-CuCl device can reduce the nonradiative recombination loss and improve device performance.

It is well known that Cu ions in CdTe have a high migration rate, which is the culprit of the long-term stability issue for CdTe modules. It is worth mentioning that the CuCl treatment was performed using an RTA process owing to the ionic state of CuCl, which generated a desired Cu distribution profile, i.e., a high N_{Cu} at the back surface and a low N_{Cu} at the front interface.[3] At first glance, this kind of Cu distribution profile can be double-edged, i.e., higher initial performance but lower long-term stability due to the gradient N_{Cu} profile that can promote the diffusion of Cu from the region with high N_{Cu} to the region with low N_{Cu}. To study the degradation induced by the different Cu distributions, a stability test (6 cells for each group) was carried out in ambient air for 60 days (Figure 5). For the CdTe-Cu devices, the average V_{OC} decreases by 6−7%, and the average FF decreases by 5%, yielding an average PCE relative degradation by ∼14% within 60 days. Meanwhile, the CdTe-CuCl devices show negligible degradation by ∼1 to 2%. To confirm this result, the same degradation test was also performed for another CuCl-treated device with ZMO as the front window layer instead of CdS, which shows similar stability with the CdTe-CuCl devices with CdS as the front window layer. These results further indicate that the gradient of N_{Cu} does not lead to poor stability in the CdTe-CuCl devices. The robust long-term stability performance can be attributed to the low Cu dosage in the CuCl treated devices, which results in a relatively low Cu_i concentration. Cu_i has been correlated to the fast Cu redistribution in the CdTe film and at the heterojunction, while the desired Cu_{Cd} and complexes have a relatively low diffusion rate.[36,37]

This prediction can be further demonstrated by the PL measurement at a low temperature (Figure 5d) and the SIMS measurements (Figure S5). The low-temperature PL spectra of the CdTe-Cu and CdTe-CuCl devices show similar peaks, such as a free excitonic peak at 1.59 eV,[38] a donor-acceptor pair (DAP) peak at 1.55 eV (recombination of some donor state to the V_{Cd} acceptor) and its phonon replicas,[39] and a 1.45 eV DAP peak (a DAP peak due to the recombination of Cl donor to Cu_{Cd} acceptor) and its phonon replicas at ∼20 meV.[40,41] The higher PL intensity at ∼1.45 eV in the CdTe-CuCl device is the consequence of the presence of a higher number of Cu_{Cd} acceptors at the back surface than that in the device treated with the thermally evaporated Cu. It is worth mentioning that the SIMS results suggest a lower N_{Cu} at the back surface in the CdTe-CuCl device. The low N_{Cu} and high Cu_{Cd} acceptor concentration in the CdTe-CuCl device conjointly suggest a higher formation rate of desired Cu_{Cd} substitution and a lower formation rate of compensative Cu_i, thereby enabling better long-term stability.

DISCUSSIONS

According to the device performance and characterization of the devices with different Cu precursors, the following discussions are made to understand the importance of Cu precursor in fabricating efficient CdTe solar cells.

(1) Cu diffusion. CdTe solar cells show similar performances when CuCl and $CuCl_2$ are used as the Cu precursors, with either CdS or ZMO as the front window layers. This result implies that the oxidation state of Cu in CuCl and $CuCl_2$ shows a negligible effect on the Cu incorporation. In comparison, the device with metallic Cu shows much worse device performances. These results suggest that Cu diffusion from CuCl and $CuCl_2$ into the CdTe absorber has a similar diffusion behavior and defect properties in CdTe solar cells. This is because both CuCl and $CuCl_2$ are ionic compounds and Cu ions exist naturally in these two materials; thus, no extra energy for Cu ionization is required for the Cu diffusion into CdTe. This phenomenon has recently been demonstrated in group V-doped CdTe solar cells.[42] After the diffusion into the CdTe absorber, first-principles-based analysis indicates that Cu-related defects Cu_i^+ and Cu_{Cd}^-, both of which have the Cu^+ oxidation state, have relatively low formation energies.[13,37] We assume that Cu^{2+} would change to Cu^+ and show the same diffusion rate. When metallic Cu is used as the Cu precursor, an oxidation process is needed; thus, extra energy is required to form Cu ions that can subsequently diffuse into CdTe. We suspect that this is the reason why the CuCl treatment needed lower annealing temperatures or shorter annealing duration than the metallic Cu treatment.

(2) Cu dosage and distribution. The Cu ion concentrations in both CuCl and $CuCl_2$ solutions are identical (3.10 μg/mL). Due to the difference of the CdTe layer thickness (3.5 and 4 μm for the CdS-CdTe and ZMO-CdTe, respectively), 100 μL of chloride solution is applied to 1.5″ × 1.5″ CdS-CdTe devices and 80 μL of chloride solution is applied to 1.5″ × 1.5″ ZMO-CdTe devices, which are equivalent to ∼0.24 and 0.19 Å Cu layer, respectively. Meanwhile, in the CdTe-Cu devices, the optimal Cu metal thicknesses applied in ZMO-CdTe and CdS-CdTe devices are 3 and 4 nm, respectively, which are much thicker than the equivalent Cu thickness in the CdTe-CuCl and CdTe-$CuCl_2$ devices. Nonetheless, the devices with the chloride treatment show a much higher carrier density than that with the metallic Cu treatment, suggesting that the Cu source in the chloride condition has a lower Cu dosage but a higher activation ratio (defined as the hole density relative to the incorporated dopant density) than metallic Cu.

(3) Defect properties and long-term stability. Benefiting from the low Cu dosage, the devices treated with CuCl and $CuCl_2$ possess a higher carrier density, suppressed bulk defects with shallower levels, and lower trap state capture cross section and smaller back barrier height and improved stability, simultaneously. This is because the device with a lower Cu dosage through the chloride treatment has more desired Cu_{Cd} acceptors, while the device with higher Cu dosage through metallic Cu treatment has more detrimental Cu_i donors. When the Cu dosage increases, more Cu_{Cd} will be ionized, leading to the downshift of the Fermi level toward the valence band

https://doi.org/10.1021/acsami.1c11784
ACS Appl. Mater. Interfaces 2021, 13, 38432−38440

Approved for public release; distribution unlimited.

maximum. In such a case, the formation energy of the charged donor defect Cu_i^+ (a compensating donor) decreases linearly as a function of Fermi energy, therefore, resulting in more shallow compensating Cu_i^+ donors and lower hole concentration. Due to the formation of compensating Cu_i^+ donors, the CdTe devices with thermally evaporated Cu treatment show a larger back-barrier and a more pronounced nonradiative recombination rate at the back interface. Therefore, the device performances, specifically V_{OC} and FF, are significantly limited. In addition, the formation of Cu_i^+ also introduces fast Cu ion migration throughout the CdTe film, which is the culprit of the long-term stability issue for CdTe production facilities.

(4) Effect on the devices with different front window layers. Besides the effect at the absorber bulk and device back interface, the diffusion of copper into the front interface has been widely reported in CdTe devices, which can induce deep donor defect complexes at the front interface[35,43] and decrease the n-type conductivity of the front window layer.[7,16,32,35] This effect became more notorious in CdTe solar cells with ZMO as the front window layer due to its sensitivity to Cu (with several orders of magnitude reduction of conductivity).[28−30] In the devices with CdS as the n-type window layer, the effect of Cu at the CdS-CdTe interface is weaker than that at the ZMO-CdTe interface. The solution-processed chlorine treatment successfully reduces the Cu penetration into the front interface and constructs the desired Cu distribution throughout the device; thus, the diode quality of the front main junction is improved.

CONCLUSIONS

A comparison among different Cu precursors (i.e., metallic Cu, CuCl, and $CuCl_2$ solutions) as the doping source is performed on CdTe solar cells. The similar performance of the devices with CuCl and $CuCl_2$ suggests that the oxidation states of Cu^+ and Cu^{2+} show a negligible difference on device performance. Both of them show a significant improvement in device performance compared to the devices treated with the metallic Cu. The comparison of Cu activation temperature/time, dosage, and device performance and characterization results concomitantly suggest that the solution-processed Cu treatment using a Cu ionic compound enables lower dopant diffusion and activation temperature/duration, less Cu dosage, more efficient Cu incorporation, and a desired gradient Cu profile in the CdTe film, resulting in improved electrical properties at both the front and back interfaces and the bulk of the absorber, leading to higher device performances than the conventional devices doped with metallic Cu. Finally, decent PCEs of 17.2% and 17.5% are obtained for the devices with CdS and ZMO as the front window layers, respectively, which are among the most efficient CdTe solar cells without Se incorporation.

ASSOCIATED CONTENT

Supporting Information

The Supporting Information is available free of charge at https://pubs.acs.org/doi/10.1021/acsami.1c11784.

Statistical distribution of device performance for CdS-CdTe solar cell devices with different Cu precursors; statistical distribution of device performance for ZMO-CdTe solar cell devices with different Cu precursors; EQE curves of the devices with CdS and ZMO as the window layers; *J-V* curves for the CdS-CdTe devices treated without and with HI etching treatment; secondary ion mass spectroscopy depth profiles of the CdTe-Cu and CdTe-CuCl devices with ZMO as the front window layer; post-annealing treatment for CdS-CdTe-Cu devices at 200 °C with different dwelling time; steady-state and time-resolved PL spectra of ZMO-CdTe devices with Cu metal and CuCl solution treatment; the calculated carrier densities extracted from C−V measurements for the ZMO-CdTe devices with different Cu precursors; capacitance spectra for CdTe-Cu and CdTe-CuCl devices measured under dark equilibrium (V_{DC} = 0 V) and different temperatures from 130 to 310 K with a step size of 10 K; *J*−*V*−*T* curves for CdTe-Cu and CdTe-CuCl devices with CdS as the front window layer; Arrhenius plots extracted from the dark *J*−*V*−*T* curves to calculate back-barrier heights (PDF)

AUTHOR INFORMATION

Corresponding Authors

Deng-Bing Li − *Department of Physics and Astronomy, and Wright Center for Photovoltaics Innovation and Commercialization (PVIC), University of Toledo, Toledo, Ohio 43606, United States;* orcid.org/0000-0003-4555-4894; Email: dengbing.li@utoledo.edu

Yanfa Yan − *Department of Physics and Astronomy, and Wright Center for Photovoltaics Innovation and Commercialization (PVIC), University of Toledo, Toledo, Ohio 43606, United States;* orcid.org/0000-0003-3977-5789; Email: yanfa.yan@utoledo.edu

Authors

Sandip S. Bista − *Department of Physics and Astronomy, and Wright Center for Photovoltaics Innovation and Commercialization (PVIC), University of Toledo, Toledo, Ohio 43606, United States;* orcid.org/0000-0003-0162-8468

Rasha A. Awni − *Department of Physics and Astronomy, and Wright Center for Photovoltaics Innovation and Commercialization (PVIC), University of Toledo, Toledo, Ohio 43606, United States*

Zhaoning Song − *Department of Physics and Astronomy, and Wright Center for Photovoltaics Innovation and Commercialization (PVIC), University of Toledo, Toledo, Ohio 43606, United States;* orcid.org/0000-0002-6677-0994

Kamala K. Subedi − *Department of Physics and Astronomy, and Wright Center for Photovoltaics Innovation and Commercialization (PVIC), University of Toledo, Toledo, Ohio 43606, United States*

Niraj Shrestha − *Department of Physics and Astronomy, and Wright Center for Photovoltaics Innovation and Commercialization (PVIC), University of Toledo, Toledo, Ohio 43606, United States;* orcid.org/0000-0001-5702-2938

Suman Rijal − *Department of Physics and Astronomy, and Wright Center for Photovoltaics Innovation and Commercialization (PVIC), University of Toledo, Toledo, Ohio 43606, United States;* orcid.org/0000-0002-7738-4917

Sabin Neupane − *Department of Physics and Astronomy, and Wright Center for Photovoltaics Innovation and*

https://doi.org/10.1021/acsami.1c11784
ACS Appl. Mater. Interfaces 2021, 13, 38432−38440

Approved for public release; distribution unlimited.

Commercialization (PVIC), University of Toledo, Toledo, Ohio 43606, United States

Corey R. Grice − *Department of Physics and Astronomy, and Wright Center for Photovoltaics Innovation and Commercialization (PVIC), University of Toledo, Toledo, Ohio 43606, United States*

Adam B Phillips − *Department of Physics and Astronomy, and Wright Center for Photovoltaics Innovation and Commercialization (PVIC), University of Toledo, Toledo, Ohio 43606, United States;* orcid.org/0000-0002-2675-5052

Randy J. Ellingson − *Department of Physics and Astronomy, and Wright Center for Photovoltaics Innovation and Commercialization (PVIC), University of Toledo, Toledo, Ohio 43606, United States;* orcid.org/0000-0001-9520-6586

Michael Heben − *Department of Physics and Astronomy, and Wright Center for Photovoltaics Innovation and Commercialization (PVIC), University of Toledo, Toledo, Ohio 43606, United States;* orcid.org/0000-0002-3788-3471

Jian V. Li − *Department of Aeronautics and Astronautics, National Cheng Kung University, 70101 Tainan, Taiwan*

Complete contact information is available at: https://pubs.acs.org/10.1021/acsami.1c11784

Author Contributions

[§]S.S.B. and D.-B.L. contributed equally. The manuscript was written through contributions of all authors. All authors have given approval to the final version of the manuscript.

Notes

The authors declare no competing financial interest.

■ ACKNOWLEDGMENTS

This work is based on research sponsored by the Air Force Research Laboratory under agreement number FA9453-18-2-0037 and FA9453-19-C-1002 and by the U.S. DOE's Office of Energy Efficiency and Renewable Energy (EERE) under Solar Energy Technologies Office (SETO) Agreement DE-EE0008974. The U.S. Government is authorized to reproduce and distribute reprints for Governmental purposes notwithstanding any copyright notation thereon. We thank Dr. David Strickler from Pilkington North America Inc. for supplying us FTO coated glass substrate. Disclaimer: The views and conclusions contained herein are those of the authors and should not be interpreted as necessarily representing the official policies or endorsements, either expressed or implied, of the U.S. Air Force Research Laboratory or the U.S. Government.

■ REFERENCES

(1) Mendis, B. G.; Ramasse, Q. M.; Shalvey, T. P.; Major, J. D.; Durose, K. Optical Properties and Dielectric Functions of Grain Boundaries and Interfaces in CdTe Thin-Film Solar Cells. *ACS Appl. Energy Mater.* **2019**, *2*, 1419−1427.

(2) Green, M. A.; Hishikawa, Y.; Dunlop, E. D.; Levi, D. H.; Hohl-Ebinger, J.; Ho-Baillie, A. W. Y. Solar Cell Efficiency Tables (version 51). *Progr. Photovolt.: Res. Appl.* **2018**, *26*, 3−12.

(3) Li, D.-B.; Bista, S. S.; Song, Z.; Awni, R. A.; Subedi, K. K.; Shrestha, N.; Pradhan, P.; Chen, L.; Bastola, E.; Grice, C. R.; Phillips, A. B.; Heben, M. J.; Ellingson, R. J.; Yan, Y. Maximize CdTe Solar Cell Performance through Copper Activation Engineering. *Nano Energy* **2020**, *73*, 104835.

(4) Ablekim, T.; Duenow, J. N.; Zheng, X.; Moutinho, H.; Moseley, J.; Perkins, C. L.; Johnston, S. W.; O'Keefe, P.; Colegrove, E.; Albin, D. S.; Reese, M. O.; Metzger, W. K. Thin-Film Solar Cells with 19% Efficiency by Thermal Evaporation of CdSe and CdTe. *ACS Energy Lett.* **2020**, *5*, 892−896.

(5) Munshi, A. H.; Kephart, J.; Abbas, A.; Raguse, J.; Beaudry, J.-N.; Barth, K.; Sites, J.; Walls, J.; Sampath, W. Polycrystalline CdSeTe/CdTe Absorber Cells with 28 mA/cm^2 Short-Circuit Current. *IEEE J. Photovolt* **2018**, *8*, 310−314.

(6) Huang, J.; Yang, D.; Li, W.; Zhang, J.; Wu, L.; Wang, W. Copassivation of Polycrystalline CdTe Absorber by CuCl Thin Films for CdTe Solar Cells. *Appl. Surf. Sci.* **2019**, *484*, 1214.

(7) Grecu, D.; Compaan, A. D. Photoluminescence Study of Cu Diffusion and Electromigration in CdTe. *Appl. Phys. Lett.* **1999**, *75*, 361−363.

(8) Krasikov, D.; Sankin, I. Defect Interactions and the Role of Complexes in the CdTe Solar Cell Absorber. *J. Mater. Chem. A* **2017**, *5*, 3503−3513.

(9) Zhang, L.; Da Silva, J. L. F.; Li, J.; Yan, Y.; Gessert, T. A.; Wei, S.-H. Effect of Copassivation of Cl and Cu on CdTe Grain Boundaries. *Phys. Rev. Lett.* **2008**, *101*, 155501.

(10) Akis, R.; Brinkman, D.; Sankin, I.; Fang, T.; Guo, D.; Vasileska, D.; Ringhofer, C. In Extracting Cu Diffusion Parameters in Polycrystalline CdTe. *IEEE 40th Photovolt Spec Conf, 8−13 June 2014*; 2014; pp. 3276−3281.

(11) Yan, Y.; Jones, K.; Zhou, J.; Wu, X.; Al-Jassim, M. TEM Study of Locations of Cu in CdTe Solar Cells. *MRS Proc.* **2011**, *1012*, 1012−Y04-09.

(12) Perrenoud, J.; Kranz, L.; Gretener, C.; Pianezzi, F.; Nishiwaki, S.; Buecheler, S.; Tiwari, A. N. A Comprehensive Picture of Cu Doping in CdTe Solar Cells. *J. Appl. Phys.* **2013**, *114*, 174505.

(13) Krasikov, D.; Knizhnik, A.; Potapkin, B.; Selezneva, S.; Sommerer, T. First-principles-based Analysis of the Influence of Cu on CdTe Electronic Properties. *Thin Solid Films* **2013**, *535*, 322−325.

(14) Paudel, N. R.; Yan, Y. Fabrication and Characterization of High-efficiency CdTe-based Thin-film Solar Cells on Commercial SnO2:F-coated Soda-lime Glass Substrates. *Thin Solid Films* **2013**, *549*, 30−35.

(15) Paudel, N. R.; Xiao, C.; Yan, Y. Close-space Sublimation Grown CdS Window Layers for CdS/CdTe Thin-film Solar Cells. *J. Mater. Scimater. El* **2014**, *25*, 1991−1998.

(16) Dobson, K. D.; Visoly-Fisher, I.; Hodes, G.; Cahen, D. Stability of CdTe/CdS Thin-film Solar Cells. *Sol Energy Mater. Sol Cell* **2000**, *62*, 295−325.

(17) Awni, R. A.; Li, D.-B.; Grice, C. R.; Song, Z.; Razooqi, M. A.; Phillips, A. B.; Bista, S. S.; Roland, P. J.; Alfadhili, F. K.; Ellingson, R. J.; Heben, M. J.; Li, J. V.; Yan, Y. The Effects of Hydrogen Iodide Back Surface Treatment on CdTe Solar Cells. *Solar RRL* **2019**, *3*, 1800304.

(18) Li, C.; Xu, H.; Li, K.; Ma, X.; Wu, L.; Wang, W.; Zhang, J.; Li, W.; Li, B.; Feng, L. CuTe Nanoparticles/Carbon Nanotubes as Back Contactfor CdTe Solar Cells. *J. Electron. Mater.* **2018**, *47*, 1250−1258.

(19) Wolden, C. A.; Abbas, A.; Li, J.; Diercks, D. R.; Meysing, D. M.; Ohno, T. R.; Beach, J. D.; Barnes, T. M.; Walls, J. M. The Roles of ZnTe Buffer Layers on CdTe Solar Cell Performance. *Sol. Energy Mater. Sol. Cell* **2016**, *147*, 203−210.

(20) Li, D.-B.; Bista, S. S.; Song, Z.; Alfadhili, F. K.; Awni, R. A.; Shrestha, N.; Rhiannon, D.; Phillips, A. B.; Heben, M. J.; Ellingson, R. J.; Yan, F.; Yan, Y. CuSCN as the Back Contact for Efficient ZMO/CdTe Solar Cells. *Materials* **2020**, *13*, 1991.

(21) Montgomery, A.; Guo, L.; Grice, C.; Awni, R. A.; Saurav, S.; Li, L.; Yan, Y.; Yan, F. Solution-processed Copper (I) Thiocyanate (CuSCN) for Highly Efficient CdSe/CdTe Thin-film Solar Cells. *Progr. Photovolt.: Res. Appl.* **2019**, *27*, 665−672.

(22) Artegiani, E.; Menossi, D.; Shiel, H.; Dhanak, V.; Major, J. D.; Gasparotto, A.; Sun, K.; Romeo, A. Analysis of a Novel CuCl2 Back Contact Process for Improved Stability in CdTe Solar Cells. *Progr. Photovolt.: Res. Appl.* **2019**, *27*, 706−715.

(23) Feng, X.; Singh, K.; Bhavanam, S.; Palekis, V.; Morel, D. L.; Ferekides, C. S. In Cu effects on CdS/CdTe Thin Film Solar Cells

Approved for public release; distribution unlimited.

Prepared on Flexible Substrates, *IEEE 38th Photovolt Spec Conf, 3–8 June 2012*; 2012; pp. 000843–000847.
(24) Sites, J.; Munshi, A.; Kephart, J.; Swanson, D.; Sampath, W. S. In Progress and Challenges with CdTe Cell Efficiency, *IEEE 43th Photovolt Spec Conf, 5–10 June 2016*; 2016; pp. 3632–3635.
(25) Paudel, N. R.; Grice, C. R.; Xiao, C.; Yan, Y. High Temperature CSS Processed CdTe Solar Cells on Commercial SnO2:F/SnO2 Coated Soda-lime Glass Substrates. *J. Mater. Sci-mater. El* **2015**, *26*, 4708–4715.
(26) Yang, J.; Wei, S.-H. First-principles Study of the Band Gap Tuning and Doping Control in CdSexTe1−x Alloy for High Efficiency Solar Cell. *Chin. Phys. B* **2019**, *28*, No. 086106.
(27) Li, D.-B.; Song, Z.; Awni, R. A.; Bista, S. S.; Shrestha, N.; Grice, C. R.; Chen, L.; Liyanage, G. K.; Razooqi, M. A.; Phillips, A. B.; Heben, M. J.; Ellingson, R. J.; Yan, Y. Eliminating S-Kink to Maximize the Performance of MgZnO/CdTe Solar Cells. *ACS Appl. Energy Mater.* **2019**, *2*, 2896–2903.
(28) Kutty, T. R. N.; Raghu, N. Varistors Based on Polycrystalline ZnO:Cu. *Appl. Phys. Lett.* **1989**, *54*, 1796–1798.
(29) Xu, C. X.; Sun, X. W.; Zhang, X. H.; Ke, L.; Chua, S. J. Photoluminescent Properties of Copper-doped Zinc Oxide Nanowires. *Nanotechnology* **2004**, *15*, 856–861.
(30) Hausmann, A.; Schallenberger, B.; Roll, R. A New Model for ZnO:Cu Undergoing Dynamic Jahn-Teller Coupling. *Z. Phys. B* **1980**, *40*, 1–7.
(31) Kuciauskas, D.; Dippo, P.; Zhao, Z.; Cheng, L.; Kanevce, A.; Metzger, W. K.; Gloeckler, M. Recombination Analysis in Cadmium Telluride Photovoltaic Solar Cells with Photoluminescence Spectroscopy. *IEEE J. Photovolt* **2016**, *6*, 313–318.
(32) Deng, Y.; Yang, J.; Yang, R.; Shen, K.; Wang, D.; Wang, D. Cu-doped CdS and Its Application in CdTe Thin Film Solar Cell. *AIP Adv.* **2016**, *6*, No. 015203.
(33) Awni, R. A.; Li, D.-B.; Song, Z.; Bista, S. S.; Razooqi, M. A.; Grice, C. R.; Chen, L.; Liyanage, G. K.; Li, C.; Phillips, A. B.; Heben, M. J.; Ellingson, R. J.; Li, J. V.; Yan, Y. Influences of Buffer Material and Fabrication Atmosphere on the Electrical Properties of CdTe Solar Cells. *Progr. Photovolt.: Res. Appl.* **2019**, *27*, 1115–1123.
(34) Seymour, F. H.; Kaydanov, V.; Ohno, T. R.; Albin, D. Cu and CdCl2 Influence on Defects Detected in CdTe Solar Cells with Admittance Spectroscopy. *Appl. Phys. Lett.* **2005**, *87*, 153507.
(35) Balcioglu, A.; Ahrenkiel, R. K.; Hasoon, F. Deep-level Impurities in CdTe/CdS Thin-film Solar Cells. *J. Appl. Phys.* **2000**, *88*, 7175–7178.
(36) Dzhafarov, T. D.; Yesilkaya, S. S.; Yilmaz Canli, N.; Caliskan, M. Diffusion and Influence of Cu on Properties of CdTe Thin Films and CdTe/CdS Cells. *Sol Energy Mater. Sol Cell* **2005**, *85*, 371–383.
(37) Yang, J.-H.; Yin, W.-J.; Park, J.-S.; Ma, J.; Wei, S.-H. Review on First-Principles Study of Defect Properties of CdTe as a Solar Cell Absorber. *Semicond. Sci. Technol.* **2016**, *31*, No. 083002.
(38) Liu, X.; Compaan, A. D. Photoluminescence from Ion Implanted CdTe Crystals. *MRS Online Proc. Libr.* **2005**, *865*, 525.
(39) Krustok, J.; Valdna, V.; Hjelt, K.; Collan, H. Deep Center Luminescence in P-type CdTe. *J. Appl. Phys.* **1996**, *80*, 1757–1762.
(40) Chamonal, J. P.; Molva, E.; Pautrat, J. L. Identification of Cu and Ag Acceptors in CdTe. *Solid State Commun.* **1982**, *43*, 801–805.
(41) Meyer, B. K.; Stadler, W.; Hofmann, D. M.; Omling, P.; Sinerius, D.; Benz, K. W. On the Nature of the Deep 1.4 eV Emission Bands in CdTe- A Study with Photoluminescence and ODMR Spectroscopy. *J. Cryst. Growth* **1992**, *117*, 656–659.
(42) Li, D.-B.; Yao, C.; Vijayaraghavan, S. N.; Awni, R. A.; Subedi, K. K.; Ellingson, R. J.; Li, L.; Yan, Y.; Yan, F. Low-temperature and Effective ex Situ Group V Doping for Efficient Polycrystalline CdSeTe Solar Cells. *Nat. Energy* **2021**, 715.
(43) Chin, K. K.; Gessert, T. A.; Wei, S. In The roles of CU impurity states in CdTe thin film solar cells, *IEEE 35th Photovolt Spec Conf, 20–25 June 2010*; 2010; pp. 001915–001918.

NOTE ADDED AFTER ASAP PUBLICATION

This paper was published on the Web on August 4, 2021. The title of the paper was updated, and the corrected version was reposted on August 5, 2021.

https://doi.org/10.1021/acsami.1c11784
ACS Appl. Mater. Interfaces 2021, 13, 38432–38440

Approved for public release; distribution unlimited.

nature energy

ARTICLES

https://doi.org/10.1038/s41560-021-00848-z

Check for updates

Low-temperature and effective ex situ group V doping for efficient polycrystalline CdSeTe solar cells

Deng-Bing Li[1], Canglang Yao[1], S. N. Vijayaraghavan[2], Rasha A. Awni[1], Kamala K. Subedi[1], Randy J. Ellingson[1], Lin Li[2], Yanfa Yan[1]✉ and Feng Yan[2]✉

CdTe solar cell technology is one of the lowest-cost methods of generating electricity in the solar industry, benefiting from fast CdTe absorber deposition, $CdCl_2$ treatment and Cu doping. However, Cu doping has low photovoltage and issues with instability. Doping group V elements into CdTe is therefore a promising route to address these challenges. Although high-temperature in situ group V doped CdSeTe devices have demonstrated efficiencies exceeding 20%, they face obstacles including post-deposition doping activation processes, short carrier lifetimes and low activation ratios. Here, we demonstrate low-temperature and effective ex situ group V doping for CdSeTe solar cells using group V chlorides. For $AsCl_3$ doped CdSeTe solar cells, the dopant activation ratio can be 5.88%, hole densities reach $>2\times10^{15}\,cm^{-3}$ and carrier lifetime is longer than 20 ns. Thus, ex situ As doped CdSeTe solar cells show open-circuit voltages ~863 mV, compared to the highest open-circuit voltage of 852 mV for Cu doped CdSeTe solar cells.

The polycrystalline CdTe photovoltaic (PV) device is one of the most successful commercial thin-film solar cell technologies, with a record power conversion efficiency (PCE) of over 22%, a module that is cost competitive with Si modules and more than 25 GW worth of solar modules installed worldwide[1–4]. So far, all manufacturing processes of CdTe-based PV modules include three critical steps at different temperatures: fast absorber (CdTe or CdSe/CdTe) deposition (~600 °C), $CdCl_2$ treatment (~400 °C) and Cu doping (~200 °C)[5,6]. The ex situ diffusion Cu doping introduces hole carriers in the absorber layers, which are needed for efficient CdTe solar cells. However, Cu doping possesses two major shortfalls that limit the performance of current CdTe-based PV modules. First, due to defect compensation, Cu doping is only able to produce a low hole density of $\sim10^{14}\,cm^{-3}$, which is about two orders of magnitude lower than the optimum hole density ($\sim10^{16}\,cm^{-3}$) needed to maximize the PCE of CdTe-based PV modules[7]. Second, Cu ions easily migrate and diffuse spatially, creating a risk of module instabilities[8].

For many decades, lots of effort has been expended to address these shortfalls of Cu doping by exploring other dopants, especially group V doping via substitutional incorporation of elements such as phosphorus, arsenic, antimony and bismuth (Supplementary Table 1 shows the various group V doping approaches in CdTe-based solar cells). Theoretical studies have predicted that group V doping is capable of overcoming the two shortfalls of Cu doping[9,10]. Both in situ and ex situ group V doping have been explored experimentally. The US National Renewable Energy Laboratory (NREL) and First Solar Inc. have demonstrated a high hole density of $1\times10^{17}\,cm^{-3}$ and a PCE of 20% with excellent device stability through in situ group V doping[5], showing the method's impressive capability to overcome the shortfalls of Cu doping in CdTe-based solar cells. Other in situ group V doping approaches include providing Cd_3V_2 powders (where V is a group V element) dope in single-crystal CdTe growth[11], tris-dimethylaminoarsine in metal–organic chemical vapour deposition growth[12] and arsine (AsH_3) in polycrystalline CdTe-based thin films[13]. However, most of these in situ group V doping techniques require complex annealing processes to activate the dopants[5]. In addition, high deposition temperatures such as those used in vapour transport deposition (VTD) are thermodynamically favourable to the formation of Cd-deficient CdTe films[10], making it energetically unfavourable to dope As at Te sites (As_{Te}). Providing additional Cd vapour is an effective way to mitigate this problem during group V doping in CdTe single crystals[14]. However, neither high-temperature (>1,000 °C) annealing of CdTe single crystals in sealed quartz ampoules nor special high-temperature post-deposition activation is compatible with current industry technology[2]. Nonetheless, the dopant activation ratio, which is defined as the hole density relative to an incorporated dopant quantity, is only about 1.5% in VTD As doped polycrystalline CdTe-based absorbers due to complicated compensation processes[15]. Additionally, in situ group V doping introduces a uniform distribution of dopants in the CdTe absorber layer[5], impeding desirable dopant depth profiles[16,17].

A low-temperature ex situ diffusion of group V dopants is preferred and fully compatible with mainstream CdTe-based solar module fabrication. Importantly, ex situ group V doping can be performed in chlorinated CdTe (that is, $CdCl_2$-treated CdTe)[18], which is more desirable for the formation of substantial group V on Te sites (V_{Te}). Although group V diffusion doping in CdTe and the desirable depth profiles have been successfully demonstrated[19], high efficiency CdTe solar cells using ex situ group V doping have proved elusive (Supplementary Table 1). Reported ex situ group V doping approaches include annealing CdTe in group V vapour[20], group V ion implantation[21] and depositing a group V Te back buffer layer followed by thermal diffusion[22]. For instance, using Sb_2Te_3 as back contact produced a PCE of 13.1% with an open-circuit voltage (V_{OC}) of 816 mV after annealing at 300 °C (ref. [23]). However,

[1]Department of Physics and Astronomy and Wright Center for Photovoltaics Innovation and Commercialization, University of Toledo, Toledo, OH, USA. [2]Department of Metallurgical and Materials Engineering, The University of Alabama, Tuscaloosa, AL, USA. ✉e-mail: yanfa.yan@utoledo.edu; fyan@eng.ua.edu

Approved for public release; distribution unlimited.

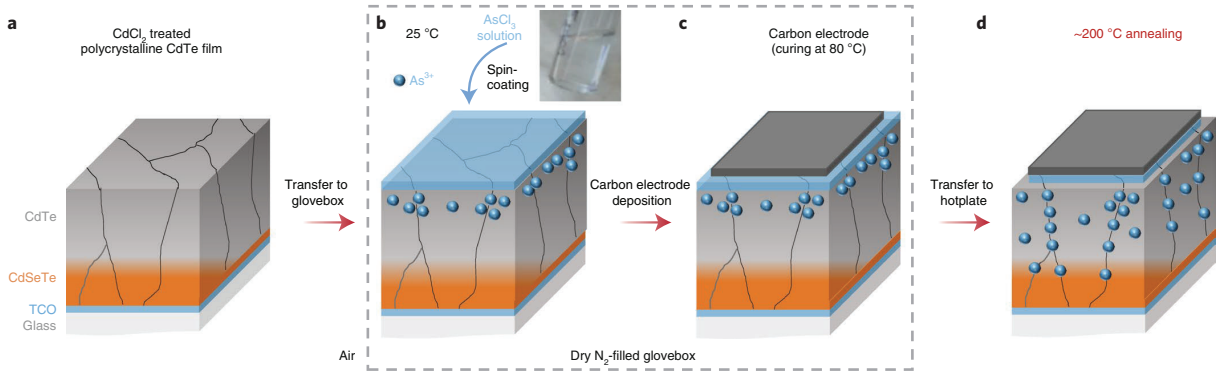


Fig. 1 | Schematic of low-temperature ex situ doping in polycrystalline CdSeTe solar cells. a, $CdCl_2$-treated polycrystalline CdSeTe films. **b**, Solution-processed group V deposition using the group V chlorides VCl_3 (that is, PCl_3, $AsCl_3$, $SbCl_3$ and $BiCl_3$) solution on the CdSeTe surface. Here, $AsCl_3$ was chosen as an example. A photograph of the transparent, colourless $AsCl_3$ solution is shown in the inset. All the other VCl_3 solutions had similar appearances. **c**, Low-temperature carbon electrode was applied to the VCl_3 coated CdSeTe film and was cured to dry at 80 °C. The steps shown in **b** and **c** are both processed in the dry N_2-filled glovebox to prevent the hydrolysis of VCl_3 and/or due to its toxicity. **d**, Group V diffusion into CdSeTe at low temperature (~200 °C) with carbon electrode.

the residual Sb_2Te_3 creates a large hole transport barrier (0.4 eV) at the CdTe/Sb_2Te_3 interface due to the defect compensation, which limits further improvement of the PCE[23]. Also, the similarity of the Pauling electronegativity of group V elements to those of Te and Cd (Supplementary Table 2) indicates that V–Te and Cd–V bonds have highly covalent characteristics, suggesting that higher energy is required to break the covalent bond before the group V element can diffuse into CdTe. Therefore, a higher annealing temperature is required to facilitate the diffusion of group V elements.

Here, a series of group V highly ionic materials (that is, group V chlorides (VCl_3) such as PCl_3, $AsCl_3$, $SbCl_3$ and $BiCl_3$) are used as dopant precursors in a solution method (Supplementary Table 3) with various physical properties differing from those of Cd group V compounds (that is, Cd_3V_2 compounds such as Cd_3P_2 and Cd_3As_2), enabling low-temperature and effective ex situ group V doping in polycrystalline CdTe thin-film solar cells. Density functional theory (DFT) calculations, materials synthesis and characterizations and device fabrication and measurements are used to validate this strategy. For $AsCl_3$ ex situ doped CdSeTe films, we achieved hole densities $>2\times10^{15}\,cm^{-3}$ and carrier lifetimes longer than 20 ns. As a result, our ex situ group V doped CdSeTe solar cells achieve a V_{OC} as high as 863 mV, compared with the highest V_{OC} of 852 mV for Cu doped solar cells. These results demonstrate success in fabricating polycrystalline CdSeTe solar cells doped by group V elements using an ex situ and low-cost process that is completely compatible with current industrial manufacturing lines, opening a new direction for research on group V doped polycrystalline CdTe-based thin-film solar cells.

Problem and mitigation strategy for ex situ group V doping. As described above, the need for annealing temperatures exceeding 600 °C for previous ex situ group V doping using Cd_3As_2 as dopant source is the main reason for the poor performance of CdTe solar cells. However, our DFT calculations suggest that high-temperature annealing may not be essential for effective diffusion of group V dopants in CdTe (Supplementary Table 4 and Supplementary Fig. 1). Previous DFT calculations have shown that the diffusion barriers for group V dopants in CdTe are in the range of 0.4–0.8 eV, depending on the charge state of the group V dopants[20]. Our DFT-calculated diffusion barriers for Cd in CdTe are in the range of 0.35–0.40 eV (Supplementary Table 4 and Supplementary Fig. 1), only slightly smaller than those of group V dopants. Cd atoms readily diffuse at temperatures above 300 °C (ref. [24]). We hypothesize that the reason high annealing temperatures in a sealed ampoule are required could be to provide sufficient vapour pressure of group V elements rather than to overcome the ion diffusion barrier[20].

If our hypothesis is correct, the required annealing temperature may be substantially lowered by depositing appropriate back contact before the diffusion annealing. Inspired by the $CdCl_2$ heat treatment (~400 °C) and doping with Cu chlorides (that is, CuCl and $CuCl_2$; ~200 °C) in CdTe-based solar cells[25–27], we propose to use group V chlorides (for example, PCl_3, $AsCl_3$, $SbCl_3$ and $BiCl_3$) as the group V dopant sources in CdSeTe solar cells, which can also help avoid the loss of Cl during the annealing after $CdCl_2$ treatment[28]. Group V chlorides are salts that can be dissolved in organic solutions, thus allowing room-temperature solution deposition (Supplementary Table 3). The ionic nature of these salts makes diffusion of group V cations easier at low annealing temperatures. However, because of the ready hydrolysis, toxicity or both of VCl_3 compounds, the deposition must be done in an inert environment, such as a dry N_2-filled glovebox. This further implies that the back contact must also be deposited in an inert environment and at room temperature. Therefore, we employ a low-temperature carbon paste as the back contact with a curing temperature <100 °C, which can be deposited by screen printing in the glovebox at room temperature (Supplementary Fig. 2). Note that the carbon electrode is not the best back contact material for CdTe-based solar cells, but it provides a feasible and fast way for us to validate our proposed strategy (Fig. 1).

Ex situ diffusion doping to polycrystalline CdSeTe thin film. In this work, we use $AsCl_3$ as a representative to dope chlorinated CdSeTe films (CdSeTe doped with other group V chloride can be seen in the Supplementary Information). Figure 1 shows the fabrication steps of the low-temperature group V diffusion doping beginning with a chlorinated polycrystalline CdSeTe film (other group VCl_3 doping procedures are shown in Supplementary Fig. 2). The detailed fabrication procedures can be found in Methods. To address the challenges posed by the ready hydrolysis and toxicity of $AsCl_3$, the cleaned and etched CdSeTe films were transferred to a dry N_2-filled glovebox to perform doping treatment. The transparent $AsCl_3$ solution was prepared in the glovebox as shown in the inset of Fig. 1b. $AsCl_3$ diffusion doping was performed in three basic steps. (1) The $AsCl_3$ layer was deposited on the CdSeTe surface at

Approved for public release; distribution unlimited.
707

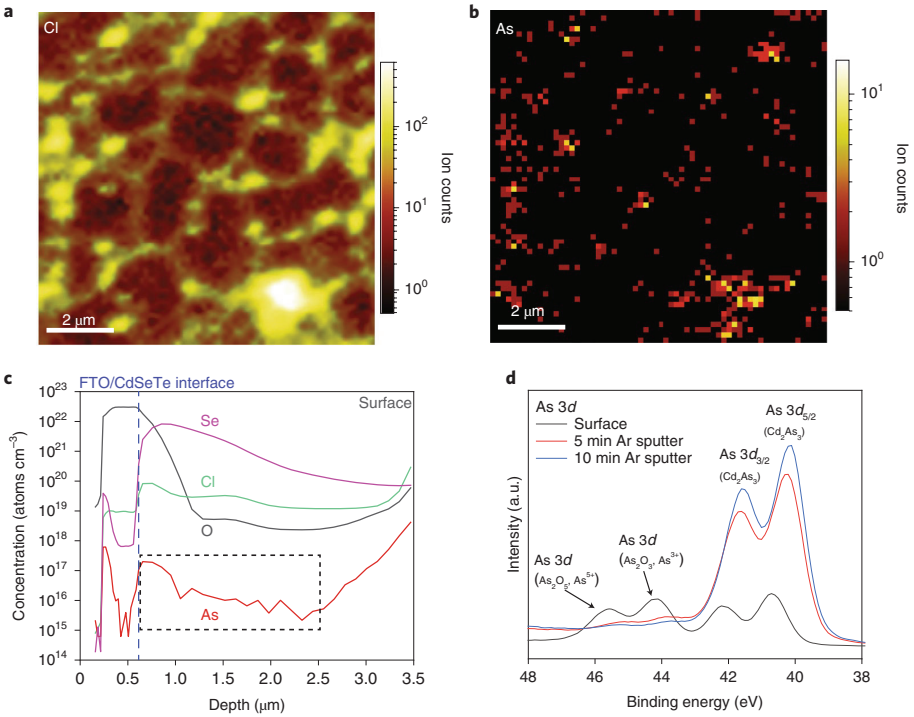


Fig. 2 | Characterizations of dopant distribution and the formation of shallow acceptor states. a, 2D Cl distribution mapping ($10\times10\,\mu m^2$) using ToF-SIMS shows that Cl accumulates at the GBs. **b**, 2D As distribution mapping of the same area shown in **a**. **c**, Dynamic SIMS depth profiles for the As doped CdSeTe device. The dashed line on the SIMS depth profile indicates the location of the fluorine-doped tin oxide (FTO)/CdSeTe interface, and the square indicates the [As] used for activation calculation. **d**, X-ray photoelectron spectroscopy (XPS) analysis of the chemical state of As ions in the As doped CdSeTe before and after 5 min (~5 nm) and 10 min (~10 nm) Ar pre-sputter etching.

room temperature using a spin-coater (Fig. 1b). The dosage of group V dopant is controlled by varying the $AsCl_3$ solution concentration (for example, from 1 to ~100 mg l^{-1}) with a fixed spin-coating rate of 1,000 revolutions per min. (2) Carbon paste was screen-printed on the $AsCl_3$-coated CdSeTe surface followed by curing at 80 °C (Fig. 1c). (3) The devices were transferred out of the glovebox and annealed at ~200 °C for various times to facilitate the diffusion of the As dopants into CdSeTe (Fig. 1d). For comparison, CuCl was selected as a Cu dopant source to fabricate reference devices[25]. Note that the low-cost low-temperature carbon paste is Cu free with a work function of ~5.0 eV (ref. [29]).

To image the As distribution in the polycrystalline CdSeTe films, two-dimensional time-of-flight secondary ion mass spectrometry (2D-ToF-SIMS) mappings and dynamic SIMS depth profiles were collected for the finished devices after annealing at 200 °C. Taking advantage of the segregation of Cl at grain boundaries (GBs) after $CdCl_2$ treatment[18,30], we used 2D-ToF-SIMS mapping of Cl to trace the GBs (Fig. 2a). The 2D-ToF-SIMS mapping of As ions (Fig. 2b) shows the accumulation of As ions at the CdSeTe GBs, which is similar to the ex situ diffusion behaviour of Cu[20,31]. This is because As ions show much higher diffusion constants (D) ($D_{GB,As}$ ~1.05×10^5 $cm^2\,s^{-1}$ versus $D_{GI,As}$ ~9.4×10^{-2} $cm^2\,s^{-1}$) and solubility in GBs than grain interiors (GIs) (Supplementary Table 4)[20,31,32]. The GBs act as pathways for fast diffusion of As ions from the back surface to the front of CdSeTe devices, which facilitates the subsequent diffusion from the GBs into the GIs (Fig.1d). Unfortunately, as the ToF-SIMS As detection limit (~1×10^{18} cm^{-3}) is lower than the As concentration ([As]) (<10^{18} cm^{-3}) in the CdSeTe bulk region (Fig. 2c), the 2D-ToF-SIMS mapping is not able to quantify the As distribution at CdSeTe GIs. Therefore, we used 2D dynamic SIMS to examine the As distributions in GIs. 2D dynamic SIMS has a ~100 times better detection limit than 2D-ToF-SIMS, but a lower spatial resolution (~4–5 μm). To enable meaningful 2D dynamic SIMS elemental mapping, we synthesized a 10 μm thick CdSeTe film that has grains as large as 10 μm (Supplementary Fig. 3a) and conducted the same $AsCl_3$ treatment. Supplementary Fig. 3b shows the 2D dynamic SIMS mapping of Cl, which is used as a reference to identify the location of GBs and GIs. Supplementary Figure 3c shows the 2D dynamic SIMS mapping of As, which also shows the accumulation of As at GBs. Supplementary Figure 3d shows the line profiles of As across the GBs. The locations of GBs are marked according to the line profile of Cl. The distribution of As in GIs can be observed, though the average intensity is about three times lower than that in GB regions. We expect that similar diffusivity behaviour of As (that is, from GBs into GIs) also exists in CdSeTe devices with smaller grain sizes.

Benefiting from the ex situ diffusion doping dynamics, the [As] shows a desirable depth profile: [As] is at least two orders of magnitude higher at the surface than in the bulk of CdSeTe (Fig. 2c). At the CdSeTe back surface, the [As] is ~5.8×10^{18} cm^{-3}, which is comparable to the homogeneous [As] in the in situ doped polycrystal CdSeTe (1.0×10^{18} cm^{-3}) (ref. [5]) and the ex situ doped single-crystal CdSeTe (5.5×10^{17} m^{-3}) (ref. [33]). This heavily As doped CdSeTe layer near the back contact can help to form an ohmic back contact and improve the device performance[34]. By contrast, the average [As] in the CdSeTe bulk (between the FTO/CdSeTe front interface and 2 μm away from it) is only ~4.27×10^{16} cm^{-3}, with slight As segregation at the front absorber/buffer interface (Fig. 2c), which is similar to the Cu distribution in efficient Cu doped devices[16,35].

Approved for public release; distribution unlimited.

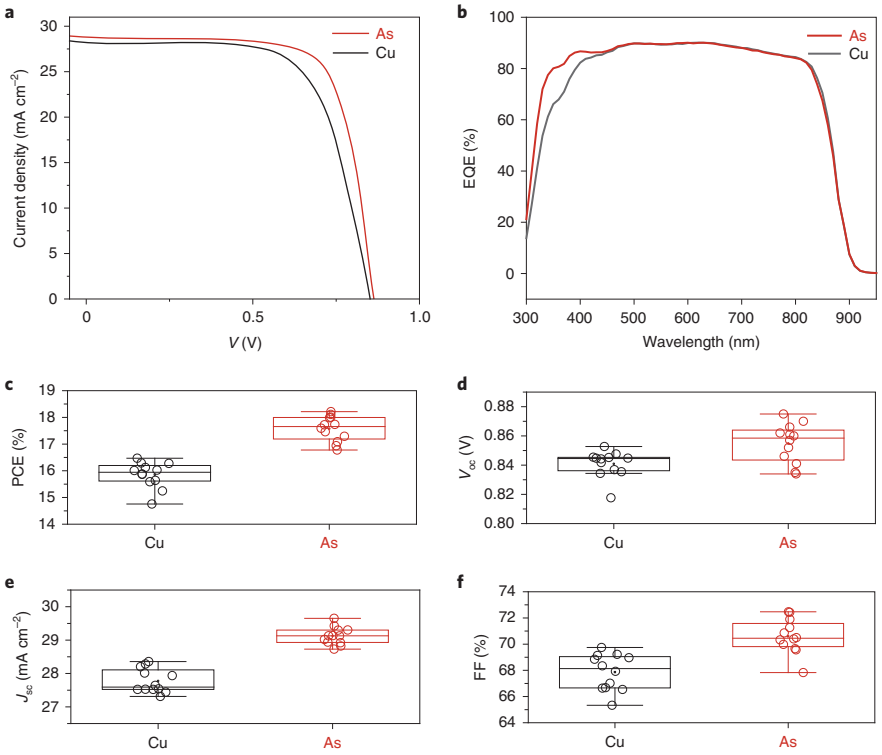


Fig. 3 | Improvement of $AsCl_3$ doped Cu-free CdSeTe device performances. a, *J*–*V* curves for CdSeTe solar cells doped with CuCl or $AsCl_3$. **b**, Corresponding EQE for the CuCl and $AsCl_3$ doped CdSeTe solar cells as a function of wavelength. **c**–**f**, The statistical distribution of the PV parameters (centre line shows the median, box shows the upper and lower quartiles and the whiskers show the full range; each black and red circle in the box and whisker plots presents the value of the *J*–*V* performances for one cell; cell number = 12) of PCE (**c**), V_{OC} (**d**), short-circuit current density (J_{SC}) (**e**), and fill factor (FF; **f**).

XPS was used to characterize the chemical states of the doped group V elements in the CdSeTe (Supplementary Fig. 4 and Supplementary Table 5). The result for the As doped device is shown in Fig. 2d. The surface As was notably oxidized due to exposure to air during the sample transfer. Remarkably, most of the As oxides were removed after ~5–10 nm surface etching by Ar sputter, leaving the pronounced binding energies of As $3d_{5/2}$ at 40.3 eV and $3d_{3/2}$ at 41.8 eV. Both of these binding energies can be assigned to As^{3-} ions in the Cd_3As_2 compound, suggesting the formation of shallow acceptor defects As_{Te}^{-} (ref. [36]). Note that the reduction of As^{3+} ions in $AsCl_3$ to As^{3-} ions takes place once the As^{3+} ions have diffused into the CdSeTe, due to As having a higher Pauling electronegativity than Te (2.18 for As versus 2.10 for Te).

The SIMS and XPS results have demonstrated the diffusion route, elemental distribution and chemical states of As dopants in CdSeTe film. Compared to other ex situ group V doping techniques using Cd_3V_2 or V_2Te_3 compounds as doping sources, our $AsCl_3$ solution treatment possesses two advantages. One is that the ionic radius of As^{3+} in $AsCl_3$ (~0.58 Å) is much smaller than the ionic radius of As^{3-} in Cd_3As_2 (~2.22 Å), which can presumably reduce the diffusion barrier in CdSeTe lattice. In particular, As^{3+} ions in $AsCl_3$ solution diffuse from the back surface to the front interface through the GBs due to the high diffusion coefficient at GBs (D_0). This step would substantially reduce the diffusion barrier of group V ions and facilitate sequential diffusion from GBs into GIs. When the small As^{3+} ions substitute for the V_{Te} (Te^{2-} ionic radius 2.21 Å), the local lattice unit will be distorted and the strong electronegativity of As^{3+} will absorb the surrounding electrons to form large As^{3-} ions until the formation of the large acceptor As_{Te}^{-} (with an As^{3-} ionic radius of 2.22 Å), which can stabilize the CdSeTe lattice. The other advantage is that the As^{3+} ions exist naturally in $AsCl_3$ solution, indicating zero ionization energy is needed to form As^{3+}, unlike the Cd_3V_2 or V_2Te_3 compounds with their strong covalent bonds, supplying possibilities for a low-temperature doping process.

Additionally, the doping mechanism differs between group I (for example, Cu and Ag) and group V ions in CdTe. Cu doping in CdTe prefers a Te-rich (that is, Cd-poor) condition to promote Cu_{Cd} acceptor formation[37], while As in CdTe desires a Te-poor (that is, Cd-rich) condition to drive the As_{Te} acceptor formation[20]. Our ex situ group V diffusion doping is processed on the chlorinated CdSeTe. We have demonstrated previously that polycrystalline CdTe GBs become Te-poor after $CdCl_2$ treatment[38]. $CdCl_2$ treatment can compensate for some of the lost Cd in the GBs of as-deposited CdTe (Supplementary Fig. 5). Theoretically, the As_{Te} acceptor formation energy (1.2 eV) under Cd-rich conditions (GBs) is smaller than it is in the Cd-poor grain interior (1.9 eV) as shown in Supplementary Table 4 (ref. [39]). Thus, the defect chemistry in the chlorinated polycrystalline CdTe is favourable to the application of group V diffusion doping using $AsCl_3$. By contrast, other reported ex situ group V doping is accomplished by sealing Cd_3V_2 powder, extra Cd powder and CdTe stacks inside quartz ampoules and annealing at temperatures of 550–750 °C after $CdCl_2$ treatment, which may result in the loss of Cl and the reappearance of stacking faults[20,40]. Other in situ group V doping methods require an extra dopant activation process and $CdCl_2$ treatment after the group V doping in CdTe, which may deactivate the doped group V element by subsequent Cl processes[5].

Approved for public release; distribution unlimited.

Table 1 | *J–V* characteristics of CuCl and $AsCl_3$ doped CdSeTe devices

Dopants in CdSeTe	V_{OC} (mV)	J_{SC} (mA cm^{-2})	FF (%)	PCE (%)
CuCl	852	28.2	66.7	16.0
$AsCl_3$	863	28.9	72.1	18.0

Therefore, using the $AsCl_3$ as a dopant source can avoid the complex activation process and excess Cd vapour process, promising a higher potential for better device performance[7,14,39].

Performance of ex situ group V doped CdSeTe devices. Figure 3 shows the current density versus voltage (*J–V*) curves from the champion CdSeTe solar cells with ex situ doping by CuCl and $AsCl_3$. The performance of other group V chloride doped CdSeTe solar cells can be seen in Supplementary Fig. 6. The corresponding external quantum efficiency (EQE) curves are shown in Fig. 3b. Table 1 lists the device parameters for the *J–V* curves and the current density measured by integrated EQE. The low-temperature ex situ $AsCl_3$ doped polycrystalline CdSeTe solar cell without antireflection coating shows a PCE of ~18%. Figure 3c–f shows the statistical device parameters of the CuCl and $AsCl_3$ doped CdSeTe solar cells. The device performance statistics of ~300 CuCl and $AsCl_3$ doped cells are shown in Supplementary Fig. 7, indicating good repeatability for $AsCl_3$ doped devices.

The thermal diffusion conditions (diffusion temperature and diffusion time) and the $AsCl_3$ solution concentration highly impact the device performance (Supplementary Figs. 8 and 9). Remarkably, the $AsCl_3$ doped CdSeTe device performance is higher than that of the CuCl doped CdSeTe device. The best V_{OC} from the $AsCl_3$ doped CdSeTe devices can reach 863 mV, which is much higher than that of our best Cu doped CdSeTe devices (852 mV) and that of in situ Cd_3As_2 doped CdSeTe devices reported in the literature (856 mV), implying a low V_{OC} deficit of 537 mV (ref. [5]). To exclude the influence of unintentional Cu contamination, dynamic SIMS was used to investigate the Cu concentration in undoped, Cu doped and As doped CdSeTe devices (Supplementary Fig. 10). The Cu concentration in the Cu doped CdSeTe device is one order of magnitude higher in the bulk and three orders of magnitude higher at the back surface than the Cu concentrations in the undoped and As doped CdSeTe devices. Additionally, the device without any intentional Cu doping shows very poor performance, with an efficiency of 1.68%. Therefore, the unintentional Cu doping in the As doped CdSeTe device does not make a noticeable contribution to the high efficiency. CdSeTe devices are known to have high photocurrents due to the CdSe/CdTe interdiffusion forming a gradient CdSeTe alloy with a bandgap of ~1.4 eV after $CdCl_2$ treatment[6,41]. The gain in short-wavelength EQE response (300 to 400 nm) is likely due to the defect level at the front interface being shallower in the As doped device than in the Cu doped device, leading to less recombination centres or shunt pathways[42–44]. This is further confirmed by the admittance spectroscopy measurements described later.

Notably, the efficiency achieved with ex situ $AsCl_3$ diffusion doping is still lower than that of in situ Cd_3As_2 doped CdTe-based solar cells, mainly due to its relatively low fill factor of ~72.1% (compared to ~80% in in situ Cd_3As_2 doped CdSeTe cells using ZnTe back contact)[5]. The low FF of our As doped CdSeTe devices mainly originates from the high resistivity of the carbon electrode (~14 Ω sq^{-1}) and low quality of the CdSeTe/carbon interface (Supplementary Fig. 11). Higher FFs and efficiencies can be expected by replacing the carbon electrode with alternative back contacts to reduce the series resistivity and shunting for better carrier collection. An accelerated stress test under 1 sun and 85 °C light soaking conditions demonstrated that the As doped CdSeTe has better stability than the Cu doped devices (Supplementary Fig. 12). However, detailed insights into the stability of our low-temperature group V doped CdSeTe are beyond the scope of this work.

Improved hole lifetime and density. Figure 4a presents the carrier lifetimes of CuCl and $AsCl_3$ doped CdSeTe devices obtained from time-resolved photoluminescence (TRPL). The $AsCl_3$ doped CdSeTe devices show a longer mean minority carrier lifetime (22.0 ns) than the CuCl doped devices (16.3 ns), and one that is an order of magnitude higher than that of in situ doped polycrystal CdSeTe reported in the literature (Supplementary Table 1). Enhanced carrier lifetime in the As doped CdSeTe device is further demonstrated by the improved steady-state photoluminescence (PL) spectrum intensity measured from the glass side (Fig. 4b). The PL peak position at ~1.4 eV corresponds to the CdSeTe formed in the front[6]. Both the TRPL and PL results suggest reduced non-radiative recombination at the front interface. Meanwhile, Supplementary Fig. 13 illustrates the spatial variation of PL emission intensity in a cross-section of the As doped CdSeTe.

The hole density profiles of $AsCl_3$ doped and CuCl doped CdSeTe obtained from *C–V* measurements are shown in Fig. 4c. The hole densities corresponding to zero applied bias (N_A), also shown in Fig. 4c, are ~7.21×10^{14} cm^{-3} for the Cu doped cell and ~2.51×10^{15} cm^{-3} for the As doped cell. The results of the *C–V* measurement for other group V chloride doped devices can be seen in Supplementary Fig. 14. The hole densities in low-temperature ex situ doped CdSeTe (2.51×10^{15} cm^{-3}) are about two orders of magnitude lower than those in the high-temperature in situ doped polycrystalline CdSeTe (~1×10^{17} cm^{-3}) (ref. [5]) and high-temperature ex situ diffusion doped single-crystal CdTe (~1×10^{17} cm^{-3}) (ref. [4]). The low-temperature diffusion doping using $AsCl_3$ may lead to less group V dopants being incorporated into the CdSeTe bulk. The activation ratio of the As dopants in ex situ $AsCl_3$ doped CdSeTe film bulk is ~5.88%, as calculated by $N_{A,As}$/[As], where $N_{A,As}$ is hole density (~2.51×10^{15} cm^{-3}) at zero bias obtained from the *C–V* measurement and [As] is the average [As] (~4.27×10^{16} cm^{-3}) between the FTO/CdSeTe interface and ~2.0 μm away from it, as marked inside the back dashed square in Fig. 2c. With such a low-temperature $AsCl_3$ doping treatment, the activation ratio is higher than that with the high-temperature in situ As doped CdSeTe thin films (~1.5%) with a reduced V_{OC} of ~856 mV (ref. [5]). A high dopant activation ratio generally produces a higher V_{OC} as a result of the reduced density of the radiative recombination centres. Single-crystal CdTe solar cells doped with P using the ex situ method have demonstrated an activation ratio of ~50%, delivering an impressive V_{OC} exceeding 1 V (ref. [4]). It may be possible to further improve the device performance towards 25% using our low-temperature group V diffusion doping approach by exploring various activation procedures to activate more incorporated As in the CdSeTe devices with the goal of achieving an As doped CdSeTe absorber with a hole density >10^{16} cm^{-3}.

Thermal admittance spectroscopy (TAS) was performed to investigate the trap-state activation energies in the CuCl and $AsCl_3$ doped CdSeTe devices (Supplementary Fig. 15), and the Arrhenius plots of admittance spectroscopy signatures were extracted as shown in Fig. 4d. Two signatures in the CuCl doped CdSeTe can be observed in the TAS, as shown in Supplementary Fig. 15a, which is consistent with our previous results[45,46]. Surprisingly, in all the group V (As, Sb, Bi) doped devices, only one signature can be observed in the low-temperature range (Supplementary Fig. 15). It has been assigned as the back-barrier height between CdSeTe and metal back contact[45,46]. The CuCl doped devices show a back-barrier height $E_{b,Cu}$ = 0.440 eV, which is much higher than the $E_{b,As}$ = 0.330 eV in the $AsCl_3$ doped device. The back-barrier height calculated through the temperature-dependent *J–V* measurement (Supplementary Fig. 16)

Approved for public release; distribution unlimited.

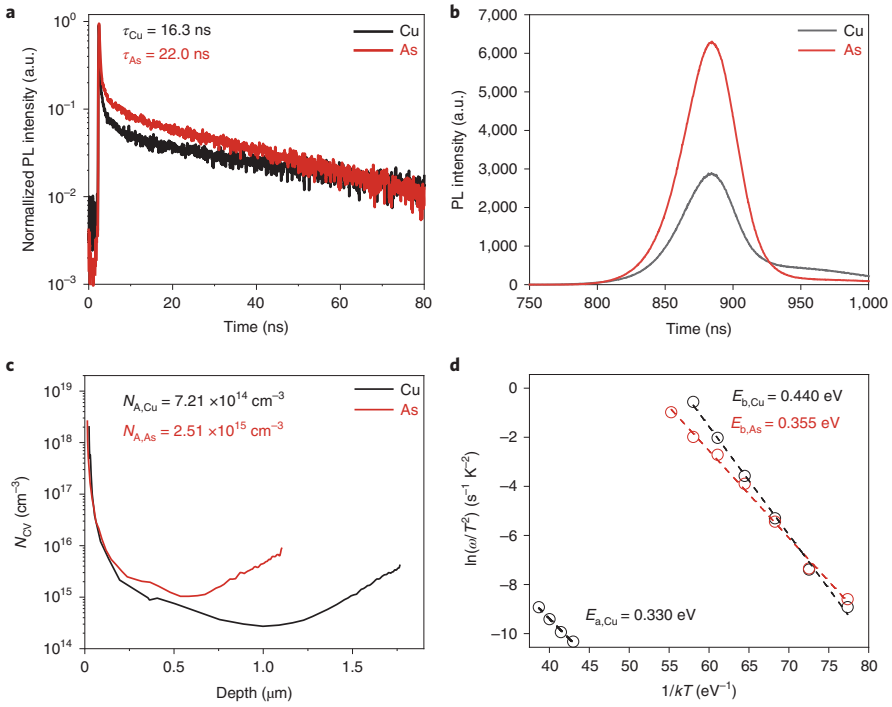


Fig. 4 | Absorber hole lifetime and hole densities. a, TRPL for Cu and As doped CdSeTe stacks. The carrier lifetimes of the Cu and As doped films (τ_{Cu} and τ_{As}, respectively) are shown in the top left. **b**, Steady-state PL curves for Cu and As doped CdSeTe stacks. Note that both TRPL and PL are measured using a 532 nm excitation laser excited from the glass side. **c**, Hole density profiles obtained from the capacitance–voltage (*C*–*V*) measurements (N_{CV}) for Cu and As doped CdSeTe devices. The hole density values were obtained at zero applied bias. **d**, The calculated defect activation energies *E* from the admittance spectroscopy measurements. The dashed lines show the linear fits used to extract the activation energies.

was 0.406 eV for the CuCl doped device and 0.298 eV for the $AsCl_3$ doped device, consistent with the values calculated from TAS measurements. The reduced back-barrier height further assists in better hole collection and, thus, higher FF and V_{OC}. The signature located at high temperature ($E_{a,Cu}$ = 0.330 eV) has been assigned as the defect activation energy of Cu_{Cd}^{+} (refs. [47,48]). The absence of defects related to As in CdTe could be due to the much lower activation energy of As_{Te} (~90 meV; Supplementary Table 4)[36,39].

Conclusions

We have demonstrated a low-temperature ex situ group V chloride diffusion doping to fabricate efficient Cu-free CdSeTe thin-film solar cells. Importantly, this low-temperature ex situ doping process produces an activation ratio as high as 5.88%, leading to both high hole density (on the order of 10^{15} cm^{-3}) and a long carrier lifetime (~22 ns). The best CdSeTe solar cell achieved a V_{OC} of 863 mV and an impressive PCE exceeding 18% through ex situ As doping, which is better than its Cu doped counterparts. Our approach paves a more effective pathway towards 25% efficiency and long-term stability through low-temperature group V diffusion doping in CdTe-based solar technology. More importantly, such a low-cost and low-temperature group V diffusion doping process is similar to the traditional Cu doping process and thus can be easily integrated with the manufacturing line, which can further make the CdTe-based solar cell technology more competitive in the solar market.

Methods

Computer simulations. All the calculations based on DFT are performed with gamma-point-only, semi-local Perdew–Burke–Ernzerhof (PBE) functional implemented in CP2K (refs. [49,50]). The basis set is double zeta valence polarization optimized on molecular geometries (shorter range)[51], and the energy cut-off is 600 Ry. We use a 4×4×4 CdTe supercell as the simulation model. The transition state searching is carried out using the nudged elastic band method. For the simulation of impurity atoms in defect systems, both V_{Cd} and V_{Te} were present in each of the models to ensure stoichiometry.

Materials. PCl_3 (99.998% purity, STREM Chemicals), $AsCl_3$ (99.999% purity, Alfa Aesar), $SbCl_3$ (99.999% purity, Alfa Aesar), $BiCl_3$ (99.997% purity, Alfa Aesar), $CdCl_2$ (99.99% purity, Alfa Aesar), CuCl (99.999% purity, Alfa Aesar), anhydrous isopropanol (99.9% purity, J. T. Baker), anhydrous acetone (99.5% purity, J. T. Baker), anhydrous benzene (99.8% purity, Sigma-Aldrich) and anhydrous methanol (99.8% purity, J. T. Baker) were commercial products. The solvent is of analytical purity grade and was used as received without further purification.

Deposition of CdSe/CdTe bilayer and solution-based $CdCl_2$ heat treatment. The ~110 nm CdSe film was deposited on cleaned FTO substrate coated with 30 nm tin oxide (TEC12D, NSG USA) by radiofrequency sputtering under a gas flow rate of 24 s.c.c.m. at 10 mtorr. Then ~3.5 μm CdTe film was deposited by closed space sublimation under a mixed gas flow rate of 1,500 s.c.c.m. Ar and 10 s.c.c.m. O_2 at 10 torr with a source temperature of 660 °C and a substrate temperature of ~600 °C (ref. [29]). The $CdCl_2$ heat treatment for the CdSeTe thin film was carried out at 400 °C for 30 min in a closed space sublimation chamber under a flow rate of 500 s.c.c.m. dry air at ambient pressure with $CdCl_2$ solution dropwise on the as-deposited CdSe/CdTe bilayer[52]. After cooling down, the CdSeTe surface was rinsed using deionized water to remove the residual $CdCl_2$ before undergoing an etching process using a dilute HCl solution to remove the surface oxide layer before further doping treatment.

Preparation of group V halide solution and CuCl solution for doping. The group V halides PCl_3, $AsCl_3$, $SbCl_3$, $BiCl_3$ and CuCl were dissolved in anhydrous benzene, isopropanol, acetone, methanol and ethanol, respectively, at concentrations of 1 to 100 mg l^{-1} based on the individual group V halide solubility (Supplementary Table 3). Note that these group V halides are easily hydrolysed and must be protected from moisture. $AsCl_3$ in particular is highly toxic and should be handled carefully in the glovebox. Here, all the group V halide solutions

Approved for public release; distribution unlimited.
711

were prepared in a N_2-filled glovebox with moisture and oxygen levels below than 1 p.p.m. The solutions were magnetically stirred at room temperature until fully dissolved.

Deposition of the group V and Cu halides on the CdSeTe surface. The group V chlorides (PCl_3, $AsCl_3$, $SbCl_3$ and $BiCl_3$) and CuCl solutions were applied directly to the CdSeTe surface by spin-coating with various solution concentrations (1–100 mg l^{-1}) at a spin-coating speed of 1,000 r.p.m. for 30 seconds. The samples were dried to form the group V chloride and CuCl layer on the CdSeTe surface. This process was performed in the N_2-filled glovebox (Supplementary Fig. 2).

Carbon back contact fabrication of CdSeTe device. The carbon back contact for the CdSeTe cells was doctor-bladed using a carbon paste and Ag paste without intentional Cu source, respectively, in a N_2-filled glovebox to prevent the hydrolysis of group V halides. The cell area is 0.08 cm^2.

Low-temperature diffusion doping of CdSeTe devices. For the solution-processed ex situ group V doping, after applying carbon electrode the ex situ group V chlorides and CuCl doped CdSeTe devices were heated to diffuse the group V and Cu ions into the CdSeTe absorber (details in Fig. 1 and Supplementary Fig. 2). The dopants were thermally activated for various durations (10–30 min) and at different temperatures (200–240 °C) to activate the group V and Cu dopants in the CdSeTe. The diffusion annealing conditions significantly impact device performance. The low-temperature ex situ diffusion doping process that yielded the highest device efficiencies in each case was identified over the course of the optimization of 400 devices.

Measurement of ex situ group V doped CdSeTe solar cell. The *J*–*V* curves of the solar cells were characterized from −0.5 V to 1.5 V bias in steps of 8 mV with a dwell time of 2 ms using a solar simulator (Newport, Oriel Class AAA 94063 A, 1,000 W xenon light source) with a source metre (Keithley 2420) at 100 mW cm^{-2} AM 1.5G irradiation. A calibrated Si reference cell and metre (Newport, 91150 V, certificated by NREL) were used to calibrate the solar simulator prior to cell measurements. More than 400 cells were tested with various ex situ doping. EQE data were characterized by a solar cell spectral response measurement system (QE-T, Enli Technology, Co. Ltd). The *C*–*V* and TAS measurements were performed using a Solartron Modulab potentiostat equipped with a frequency response analyser (Ametek Inc.). The *C*–*V* measurements were performed in the dark with a constant 45 mV r.m.s. 10 kHz AC signal superimposed on a DC bias voltage varying from 2.5 to 0.5 V. All *J*–*V*, EQE and *C*–*V* measurements were performed at room temperature in air. The TAS measurements were performed with frequencies varying from 1.0 MHz to 0.1 Hz and DC bias sweeping from −0.3 V to 0.2 V with an interval of 0.1 V. A liquid nitrogen cooling cryo-system (Janis VPF-100 system) was used to carry out all the temperature-dependent (150 to 300 K with a step size of 10 K) measurements. The temperature was controlled by a temperature controller (Lakeshore 330). A sensor was mounted directly on the top of the device to ensure that the recorded temperature was the device temperature. PL characteristics for all devices were investigated using steady-state PL and TRPL. PL measurements were performed using a 532 nm continuous-wave laser at ~5 W cm^{-2} excited through the FTO side. The PL signal was detected by liquid nitrogen-cooled symphony-II Si CCD (charge-coupled device) detector after a Horiba iHR320 monochromator. The TRPL measurements of CdTe samples were performed with a 532 nm pulsed laser whose photon fluence is 1.2×10^{11} photons cm^{-2} $pulse^{-1}$ with a repetition rate of 10 MHz when the samples were excited through the FTO side at the peak emission wavelength of 885 nm as determined from the PL measurement. The TRPL measurements of CdSeTe samples were performed with time-correlated single photon counting module with integration time 600 s bi-exponential PL decays. A Horiba iHR320 monochromator was used to select the detection wavelength using a hybrid detector from Becker & Hickl. The cross-sectional PL mapping for the CdSeTe device was performed using a Klar microscope (Klar Scientific). The accelerated stress test was performed at 1 sun and 85 °C in a light soaking stage.

Characterization of the ex situ group V doped CdSeTe device. XPS was conducted in a Kratos Axis Ultra DLD system equipped with a monochromatic Al X-ray source and a 5 keV Ar-ion sputter gun for depth profiling of samples. The base pressure in the analysis chamber was $<8 \times 10^{-10}$ torr. Scanning electron microscopy (SEM) was carried out in a Thermo Scientific Apreo field-emission SEM (FE-SEM) equipped with X-ray dispersive energy spectroscopy. The dynamic SIMS analyses were performed on a Cameca IMF-6f (810 Kifer Road, Sunnyvale, CA) double-focusing magnetic sector instrument. The samples were bombarded by a focused Cs^+ primary ion beam with a net impact energy of 5 keV and about 100 nA of beam current. The beam is rastered over a square area of 200 µm on a side. The secondary ions formed from the sputtering process are accelerated away from the sample surface by a nominal sample voltage of 5 kV. A fraction of secondary ions is collected from a circular region centred in the rastered area.

Reporting Summary. Further information on research design is available in the Nature Research Reporting Summary linked to this article.

Data availability

All data generated or analysed during this study are included in the published article and its Supplementary Information. Source data are provided with this paper.

Received: 14 October 2020; Accepted: 26 April 2021;
Published online: 24 June 2021

References

1. Green, M. A. et al. Solar cell efficiency tables (version 54). *Prog. Photovolt. Res. Appl.* **27**, 565–575 (2019).
2. Grover, S. et al. Characterization of arsenic doped CdTe layers and solar cells. In *Proc. 2017 IEEE 44th Photovoltaic Specialist Conference (PVSC)* 1193–1195 (IEEE, 2017).
3. *Leading the World's Sustainable Energy Future* (First Solar, 2019); http://www.firstsolar.com/-/media/First-Solar/Documents/Corporate-Collaterals/FS_Corporate_Factsheet.ashx
4. Burst, J. M. et al. CdTe solar cells with open-circuit voltage breaking the 1 V barrier. *Nat. Energy* **1**, 16015 (2016).
5. Metzger, W. K. et al. Exceeding 20% efficiency with in situ group V doping in polycrystalline CdTe solar cells. *Nat. Energy* **4**, 837–845 (2019).
6. Fiducia, T. A. M. et al. Understanding the role of selenium in defect passivation for highly efficient selenium-alloyed cadmium telluride solar cells. *Nat. Energy* **4**, 504–511 (2019).
7. McCandless, B. E. et al. Overcoming carrier concentration limits in polycrystalline CdTe thin films with in situ doping. *Sci. Rep.* **8**, 14519 (2018).
8. Dzhafarov, T. D., Yesilkaya, S. S., Yilmaz Canli, N. & Caliskan, M. Diffusion and influence of Cu on properties of CdTe thin films and CdTe/CdS cells. *Sol. Energy Mater. Sol. Cells* **85**, 371–383 (2005).
9. Yang, J. H., Yin, W. J., Park, J. S., Ma, J. & Wei, S. H. Review on first-principles study of defect properties of CdTe as a solar cell absorber. *Semicond. Sci. Tech.* **31**, 083002 (2016).
10. Ma, J. et al. Dependence of the minority-carrier lifetime on the stoichiometry of CdTe using time-resolved photoluminescence and first-principles calculations. *Phys. Rev. Lett.* **111**, 067402 (2013).
11. Nagaoka, A. et al. Growth and characterization of arsenic doped CdTe single crystals grown by Cd-solvent traveling-heater method. *J. Cryst. Growth* **467**, 6–11 (2017).
12. Kartopu, G. et al. Study of thin film poly-crystalline CdTe solar cells presenting high acceptor concentrations achieved by in-situ arsenic doping. *Sol. Energy Mater. Sol. Cells* **194**, 259–267 (2019).
13. Ghandhi, S. K., Taskar, N. R. & Bhat, I. B. Arsenic-doped P-CdTe layers grown by organometallic vapor-phase epitaxy. *Appl. Phys. Lett.* **50**, 900–902 (1987).
14. Nagaoka, A., Nishioka, K., Yoshino, K., Kuciauskas, D. & Scarpulla, M. A. Arsenic doped Cd-rich CdTe: equilibrium doping limit and long lifetime for high open-circuit voltage solar cells greater than 900 mV. *Appl. Phys. Express* **12**, 081002 (2019).
15. Krasikov, D. & Sankin, I. Beyond thermodynamic defect models: a kinetic simulation of arsenic activation in CdTe. *Phys. Rev. Mater.* **2**, 103803 (2018).
16. Li, D.-B. et al. Maximize CdTe solar cell performance through copper activation engineering. *Nano Energy* **73**, 104835 (2020).
17. Artegiani, E. et al. Analysis of a novel $CuCl_2$ back contact process for improved stability in CdTe solar cells. *Prog. Photovolt. Res. Appl.* **27**, 706–715 (2019).
18. Mao, D., Wickersham, C. E. & Gloeckler, M. Measurement of chlorine concentrations at CdTe grain boundaries. *IEEE J. Photovolt.* **4**, 1655–1658 (2014).
19. Colegrove, E. et al. Phosphorus diffusion mechanisms and deep incorporation in polycrystalline and single-crystalline CdTe. *Phys. Rev. Appl.* **5**, 054014 (2016).
20. Colegrove, E. et al. Experimental and theoretical comparison of Sb, As, and P diffusion mechanisms and doping in CdTe. *J. Phys. D Appl. Phys.* **51**, 075102 (2018).
21. Kraft, C. et al. Phosphorus implanted cadmium telluride solar cells. *Thin Solid Films* **519**, 7153–7155 (2011).
22. Romeo, N., Bosio, A. & Rosa, G. The back contact of CdTe/CdS thin film solar cells. In *Proc. ISES Solar World Congress 2017* (International Solar Energy Society Selection, 2017).
23. Hu, S. et al. Band diagrams and performance of CdTe solar cells with a Sb_2Te_3 back contact buffer layer. *AIP Adv.* **1**, 042152 (2011).
24. Kumar, S. G. & Rao, K. S. R. K. Physics and chemistry of CdTe/CdS thin film heterojunction photovoltaic devices: fundamental and critical aspects. *Energy Environ. Sci.* **7**, 45–102 (2014).
25. Huang, J. et al. Copassivation of polycrystalline CdTe absorber by CuCl thin films for CdTe solar cells. *Appl. Surf. Sci.* **484**, 1214–1222 (2019).
26. Bastola, E. et al. Doping of CdTe using CuCl2 solution for highly efficient photovoltaic devices. In *Proc. 2019 IEEE 46th Photovoltaic Specialists Conference (PVSC)* 1846–1850 (IEEE, 2019).

Approved for public release; distribution unlimited.

27. Major, J. D., Treharne, R. E., Phillips, L. J. & Durose, K. A low-cost non-toxic post-growth activation step for CdTe solar cells. *Nature* **511**, 334–337 (2014).
28. Abbas, A. et al. The effect of a post-activation annealing treatment on thin film CdTe device performance. In *Proc. 2015 IEEE 42nd Photovoltaic Specialist Conference (PVSC)* 1–6 (IEEE, 2015).
29. Montgomery, A. et al. Solution-processed copper (I) thiocyanate (CuSCN) for highly efficient CdSe/CdTe thin-film solar cells. *Prog. Photovolt. Res. Appl.* **27**, 665–672 (2019).
30. Fiducia, T. et al. 3D distributions of chlorine and sulphur impurities in a thin-film cadmium telluride solar cell. *MRS Adv.* **3**, 3287–3292 (2018).
31. Akis, R. et al. Extracting Cu diffusion parameters in polycrystalline CdTe. In *Proc. 2014 IEEE 40th Photovoltaic Specialist Conference (PVSC)* 3276–3281 (IEEE, 2014).
32. Colegrove, E. et al. Antimony diffusion in CdTe. *IEEE J. Photovolt.* **7**, 870–873 (2017).
33. Flores, M. A., Orellana, W. & Menéndez-Proupin, E. Self-compensation in phosphorus-doped CdTe. *Phys. Rev. B* **96**, 134115 (2017).
34. Barrioz, V. et al. Highly arsenic doped CdTe layers for the back contacts of CdTe solar cells. *MRS Proc.* **1012**, 1208 (2007).
35. Murria, P. et al. Speciation of CuCl and $CuCl_2$ thiol-amine solutions and characterization of resulting films: implications for semiconductor device fabrication. *Inorg. Chem.* **56**, 14396–14407 (2017).
36. Molva, E., Saminadayar, K., Pautrat, J. L. & Ligeon, E. Photoluminescence studies in N, P, As implanted cadmium telluride. *Solid State Commun.* **48**, 955–960 (1983).
37. Yun, J. H., Kim, K. H., Lee, D. Y. & Ahn, B. T. Back contact formation using Cu_2Te as a Cu-doping source and as an electrode in CdTe solar cells. *Sol. Energy Mater. Sol. Cells* **75**, 203–210 (2003).
38. Li, C. et al. Grain-boundary-enhanced carrier collection in CdTe solar cells. *Phys. Rev. Lett.* **112**, 156103 (2014).
39. Ablekim, T. et al. Self-compensation in arsenic doping of CdTe. *Sci. Rep.* **7**, 4563 (2017).
40. Guo, J. L. et al. Effect of selenium and chlorine co-passivation in polycrystalline CdSeTe devices. *Appl. Phys. Lett.* **115**, 153901 (2019).
41. Poplawsky, J. D. et al. Structural and compositional dependence of the $CdTe_xSe_{1-x}$ alloy layer photoactivity in CdTe-based solar cells. *Nat. Commun.* **7**, 12537 (2016).
42. Grecu, D. & Compaan, A. D. Photoluminescence study of Cu diffusion and electromigration in CdTe. *Appl. Phys. Lett.* **75**, 361–363 (1999).
43. Corwine, C. R., Pudov, A. O., Gloeckler, M., Demtsu, S. H. & Sites, J. R. Copper inclusion and migration from the back contact in CdTe solar cells. *Sol. Energy Mater. Sol. Cells* **82**, 481–489 (2004).
44. Dobson, K. D., Visoly-Fisher, I., Hodes, G. & Cahen, D. Stability of CdTe/CdS thin-film solar cells. *Sol. Energy Mater. Sol. Cells* **62**, 295–325 (2000).
45. Awni, R. A. et al. The effects of hydrogen iodide back surface treatment on CdTe solar cells. *Sol. RRL* **3**, 1800304 (2019).
46. Awni, R. A. et al. Influences of buffer material and fabrication atmosphere on the electrical properties of CdTe solar cells. *Prog. Photovolt. Res. Appl.* **27**, 1115–1123 (2019).
47. Perrenoud, J. et al. A comprehensive picture of Cu doping in CdTe solar cells. *J. Appl. Phys.* **114**, 174505 (2013).
48. Wei, S.-H. & Zhang, S. B. Chemical trends of defect formation and doping limit in II-VI semiconductors: the case of CdTe. *Phys. Rev. B* **66**, 155211 (2002).
49. Perdew, J. P., Burke, K. & Ernzerhof, M. Generalized gradient approximation made simple. *Phys. Rev. Lett.* **77**, 3865–3868 (1996).
50. Hutter, J., Iannuzzi, M., Schiffmann, F. & VandeVondele, J. cp2k: atomistic simulations of condensed matter systems. *Wiley Interdiscip. Rev. Comput. Mol. Sci.* **4**, 15–25 (2014).
51. VandeVondele, J. & Hutter, J. Gaussian basis sets for accurate calculations on molecular systems in gas and condensed phases. *J. Chem. Phys.* **127**, 114105 (2007).
52. Li, D.-B. et al. Eliminating S-kink to maximize the performance of MgZnO/CdTe solar cells. *ACS Appl. Energy Mater.* **2**, 2896–2903 (2019).

Acknowledgements

S.N.V., L.L. and F.Y. acknowledge funding from the National Science Foundation under contracts no. 1944374 and 2019473, the National Aeronautics and Space Administration, Alabama EPSCoR International Space Station Flight Opportunity Program (contract no. 80NSSC20M0141) and the US Department of Energy's Office of Energy Efficiency and Renewable Energy (EERE) under the Solar Energy Technologies Office (SETO) Agreement DE-EE0009368. D.-B.L., C.Y., R.A.A., K.K.S., R.J.E. and Y.Y. acknowledge funding from the Air Force Research Laboratory, Space Vehicles Directorate (contract no. FA9453-18-2-0037), the National Science Foundation under contract no. 1711534 and the US Department of Energy's Office of Energy Efficiency and Renewable Energy (EERE) under Solar Energy Technologies Office (SETO) Agreement DE-EE0008974. We thank D. Strickler from Pilkington North America Inc. for supplying us with the FTO coated substrates.

Author contributions

D.-B.L. and S.N.V. performed film and device synthesis as well as *J–V*, EQE and *C–V* measurements. S.N.V. performed the XPS measurements. C.Y. performed the DFT calculations. R.A.A. carried out TAS and temperature-dependent *J–V* measurements. K.K.S. and R.J.E. performed the PL and TRPL measurements. L.L. performed the PL mapping. Y.Y. and F.Y. directed the research.

Competing interests

The authors declare no competing interests.

Additional information

Supplementary information The online version contains supplementary material available at https://doi.org/10.1038/s41560-021-00848-z.

Correspondence and requests for materials should be addressed to Y.Y. or F.Y.

Peer review information *Nature Energy* thanks Gang Xiong and the other, anonymous, reviewer(s) for their contribution to the peer review of this work.

Reprints and permissions information is available at www.nature.com/reprints.

Publisher's note Springer Nature remains neutral with regard to jurisdictional claims in published maps and institutional affiliations.

© The Author(s), under exclusive licence to Springer Nature Limited 2021

Approved for public release; distribution unlimited.
713

nature research

Corresponding author(s): Yanfa Yan, Feng Yan

Solar Cells Reporting Summary

Nature Research wishes to improve the reproducibility of the work that we publish. This form is intended for publication with all accepted papers reporting the characterization of photovoltaic devices and provides structure for consistency and transparency in reporting. Some list items might not apply to an individual manuscript, but all fields must be completed for clarity.

For further information on Nature Research policies, including our data availability policy, see Authors & Referees.

Experimental design

Please check: are the following details reported in the manuscript?

1. Dimensions

Area of the tested solar cells	☒ Yes	Methods - Carbon back contact fabrication of CdSeTe device. Cells area of 0.08 cm2
	☐ No	*Explain why this information is not reported/not relevant.*
Method used to determine the device area	☒ Yes	Methods - Carbon back contact fabrication of CdSeTe device. The active area was determined by the mask used for the carbon electrode.
	☐ No	*Explain why this information is not reported/not relevant.*

2. Current-voltage characterization

Current density-voltage (J-V) plots in both forward and backward direction	☐ Yes	*State where this information can be found in the text.*
	☒ No	Hysteresis is not oberved
Voltage scan conditions *For instance: scan direction, speed, dwell times*	☒ Yes	Methods - Measurement of ex-situ Group V doped CdSeTe solar cell. From -0.5 V to 1.5 V bias in steps of 8mV, with a dwell time of 2ms
	☐ No	*Explain why this information is not reported/not relevant.*
Test environment *For instance: characterization temperature, in air or in glove box*	☒ Yes	Methods - Measurement of ex-situ Group V doped CdSeTe solar cell. The cells were measured at room temperature in air.
	☐ No	*Explain why this information is not reported/not relevant.*
Protocol for preconditioning of the device before its characterization	☐ Yes	*State where this information can be found in the text.*
	☒ No	No preconditioning is required for our characterization.
Stability of the J-V characteristic *Verified with time evolution of the maximum power point or with the photocurrent at maximum power point; see ref. 7 for details.*	☒ Yes	Supplementary Fig. 12 Short term accelerated stress test of our devices without encapsulation under AM1.5 illumination, 85 oC in ambient air has been performed and the As doped devices show higher stability properties than Cu doped devices
	☐ No	Not an issue for CdSeTe Solar Cell

3. Hysteresis or any other unusual behaviour

Description of the unusual behaviour observed during the characterization	☐ Yes	*State where this information can be found in the text.*
	☒ No	Hysteresis is not observed.
Related experimental data	☐ Yes	*State where this information can be found in the text.*
	☒ No	Hysteresis is not observed.

4. Efficiency

External quantum efficiency (EQE) or incident photons to current efficiency (IPCE)	☒ Yes	Figure 3b and methods
	☐ No	*Explain why this information is not reported/not relevant.*
A comparison between the integrated response under the standard reference spectrum and the response measure under the simulator	☒ Yes	Methods
	☐ No	*Explain why this information is not reported/not relevant.*
For tandem solar cells, the bias illumination and bias voltage used for each subcell	☐ Yes	*State where this information can be found in the text.*
	☒ No	These are not tandem cells

Approved for public release; distribution unlimited.

5. Calibration

Light source and reference cell or sensor used for the characterization	☒ Yes ☐ No	Methods - Measurement of ex-situ Group V doped CdSeTe solar cell. The light intensity for J–V measurements was calibrated by a standard silicon wafer solar cell certified by Newport. A standard silicon wafer solar cell was used as the reference for the EQE measurement. *Explain why this information is not reported/not relevant.*
Confirmation that the reference cell was calibrated and certified	☒ Yes ☐ No	Methods - Measurement of ex-situ Group V doped CdSeTe solar cell. The light intensity for J–V measurements was calibrated by a standard silicon wafer solar cell certified by Newport. A standard silicon wafer solar cell was used as the reference for the EQE measurement. *Explain why this information is not reported/not relevant.*
Calculation of spectral mismatch between the reference cell and the devices under test	☒ Yes ☐ No	Methods - Measurement of ex-situ Group V doped CdSeTe solar cell. A standard silicon wafer solar cell was used as the reference for the EQE measurement. *Explain why this information is not reported/not relevant.*

6. Mask/aperture

Size of the mask/aperture used during testing	☐ Yes ☒ No	*State where this information can be found in the text.* the carbon electrode area pretty thick (~18 um) and the cells area was measured directly
Variation of the measured short-circuit current density with the mask/aperture area	☐ Yes ☒ No	*State where this information can be found in the text.* *Explain why this information is not reported/not relevant.*

7. Performance certification

Identity of the independent certification laboratory that confirmed the photovoltaic performance	☐ Yes ☒ No	*State where this information can be found in the text.* Two corresponding groups cross check the device performance.The light intensity of our solar simulator for J-V and EQE measurement was calibrated by a standard silicon wafer solar cell
A copy of any certificate(s) *Provide in Supplementary Information*	☐ Yes ☒ No	*State where this information can be found in the text.* The light intensity of our solar simulator for J-V and EQE measurement was calibrated by a standard silicon wafer solar cell (Newport, 91150V, certificated by NREL)

8. Statistics

Number of solar cells tested	☒ Yes ☐ No	Methods - Measurement of ex-situ Group V doped CdSeTe solar cell. More than 300 cells have been tested with various ex-situ doping. *Explain why this information is not reported/not relevant.*
Statistical analysis of the device performance	☒ Yes ☐ No	Fig.3c-f. and Supplementary Fig.6c-f and Supplementary Fig.7 *Explain why this information is not reported/not relevant.*

9. Long-term stability analysis

Type of analysis, bias conditions and environmental conditions *For instance: illumination type, temperature, atmosphere humidity, encapsulation method, preconditioning temperature*	☒ Yes ☐ No	Supplementary Fig. 12 Short term accelerated stress test of our devices without encapsulation under AM1.5 illumination, 85 oC in ambient air has been performed and the As doped devices show higher stability properties than Cu doped devices. Long term stability testing is beyond the scope of this article. We will work on the long term stability test in the future.

Approved for public release; distribution unlimited.

Solar Energy Materials & Solar Cells 225 (2021) 111015

Contents lists available at ScienceDirect

Solar Energy Materials and Solar Cells

journal homepage: http://www.elsevier.com/locate/solmat

Understanding V_{OC} and performance deficit in wide bandgap perovskite photovoltaic devices

Ramez Hosseinian Ahangharnejhad, Jared D. Friedl, Adam B. Phillips, Michael J. Heben *

University of Toledo, Wright Center for Photovoltaics Innovation and Commercialization, Department of Physics and Astronomy, 2801 W. Bancroft St., Toledo, OH, 43606, USA

ARTICLE INFO

Keywords:
Photovoltaics
Perovskite
Device modeling

ABSTRACT

Wide bandgap metal halide perovskites materials are of interest for application as top subcells in multijunction devices. In contrast to smaller gap perovskite devices that perform fairly close to their internal Shockley-Queisser limit, wide gap versions show substantial deficits. To understand the origin of the limitations in more detail we simulated the performance of wide bandgap devices as a function of the energy band offsets at the contacts. Our results show that traditionally-used charge transport layers such as spiro-OMeTAD and TiO_2 limit the performance of wide bandgap absorbers through a subtle interplay between effects on V_{OC} and FF. We investigate the optimal characteristics for the charge transport layers as function of absorber bandgap and identify the needed band offsets at the p- and n-interfaces. Our results call for more research on charge transport layers to minimize the V_{OC} and performance deficit in wide bandgap devices.

1. Introduction

Single junction metal halide perovskite solar cells with absorber bandgaps in the range of 1.5–1.6 eV have demonstrated a remarkable track record of high power conversion efficiency (PCE) with certified champion cells having PCEs >25% [1]. High PCEs can be achieved with relatively high impurity levels [2], and devices are tolerant to defects [3] due to shallow energy levels [4] and low capture cross sections [5]. Consequently, champion perovskite devices with bandgaps around 1.5 eV have demonstrated open circuit voltage deficits that are comparable to high purity Si and GaAs devices [2]. The V_{OC} deficit can be evaluated as $V_{OC,\ SQ} - V_{OC,\ measured}$, where $V_{OC,\ SQ}$ is the Shockley-Queisser (SQ) limit, also known as the thermodynamic limit, where the carrier recombination is radiatively limited and the device is in thermal equilibrium with its surroundings [6,7].

The success of single junction devices coupled with the ability to easily tune the perovskite bandgap through composition has led to great interest in the development of tandem devices with higher PCE [8–17]. However, the V_{OC} deficit in wider bandgap perovskite devices is significantly greater than in 1.5–1.6 eV devices [18,19]. One reason often cited for this larger V_{OC} deficit is phase segregation of the perovskite materials [20,21]. However, recent photoluminescence (PL) quantum yield analyses on 1.5–1.9 eV materials show that recombination at the interface between the charge transport layers (CTLs) and the absorber plays a role in PL quenching even in the presence of segregated halide domains [22]. Indeed, modeling investigations of 1.5–1.6 eV perovskite devices [23–25] show that the energy band alignments at CTL/absorber interfaces impact the device performances greatly [25]. While evidence has been mounting that the choice of CTLs is important for single-junction device performance, there has been very little guidance for directing the development of CTLs for high performance wide bandgap devices.

Here we use numerical modeling to investigate the impact of the CTLs on the device performance as a function of the absorber bandgap. We show that as the bandgap of the absorber increases, the choice of CTLs becomes more important and that the optimum CTLs for a 1.6 eV bandgap absorber will limit the device performance when the absorber bandgap is 1.7 eV and larger. By investigating the recombination currents as a function of bias we determine the interplay between V_{OC} and FF and identify the conditions under which CTLs limit the device performance. We explore the parameter space to determine the appropriate CTL properties for optimum device performance as a function of absorber bandgap and compare our results with existing experimental literature.

* Corresponding author.
E-mail address: michael.heben@utoledo.edu (M.J. Heben).

https://doi.org/10.1016/j.solmat.2021.111015
Received 4 December 2020; Received in revised form 1 February 2021; Accepted 6 February 2021
Available online 28 February 2021
0927-0248/© 2021 Published by Elsevier B.V.

Approved for public release; distribution unlimited.

2. Results and discussions

Numerical modeling was completed using SCAPS 1D [26], which was recently applied to perovskite solar cells [25,27–30]. We chose to simulate the popular n-i-p structure FTO/TiO_2/$MAPb(I_{1-x}Br_x)_3$/spiro-OMeTAD/back contact, where FTO is the F-doped SnO_2 front contact, TiO_2 is the ETL, and spiro-OMeTAD (subsequently referred to as "Spiro") is the HTL, though similar conclusions would be found for the p-i-n structure. Figure S1 (a) is a schematic diagram of the device structure. Figure S1 (b) shows the energy convention used which defines a positive CBO as one that produces electron confinement in the conduction band, while a positive VBO creates hole confinement in the valence band. Conduction and valence band positions as a function of bandgap were determined by a linear extrapolation method as the perovskite composition was varied. Further details of the simulation and the material parameters are given in the supporting information (SI).

We first simulated the device behavior for a 1.7 eV absorber. Fig. 1(a) and (b) show the current density as a function of voltage (J-V) under AM1.5G irradiance for varying values of the CBO and VBO at the ETL and HTL interfaces, respectively. The CTL bandgaps were fixed, and each interface was investigated independently while the interface recombination velocity at the opposing interface was set to a low value (1×10^{-4} cm/s). Fig. 1(c) and (d) shows the corresponding recombination current densities versus voltage (J_R-V) data, which are calculated using

$$J_R = R_{front} + R_{back} + R_{SRH} = \frac{S_{front}\, p_{front} n_{front}}{(p_{front} + n_{front})} + \frac{S_{back}\, p_{back} n_{back}}{(p_{back} + n_{back})} + \frac{pn}{\tau\,(p+n)}$$

where $\tau, p, n,$ and S are the carrier lifetimes, carrier concentrations under non-equilibrium conditions, and interface recombination velocities, respectively, assuming the lifetimes of both carriers are similar. Note that the n and p values are different at each interface and depend on the band bending at that interface. Fig. 1(e) and (f) show the near-interface conduction and valence band portions, respectively, of the band diagrams at the maximum power point (MPP).

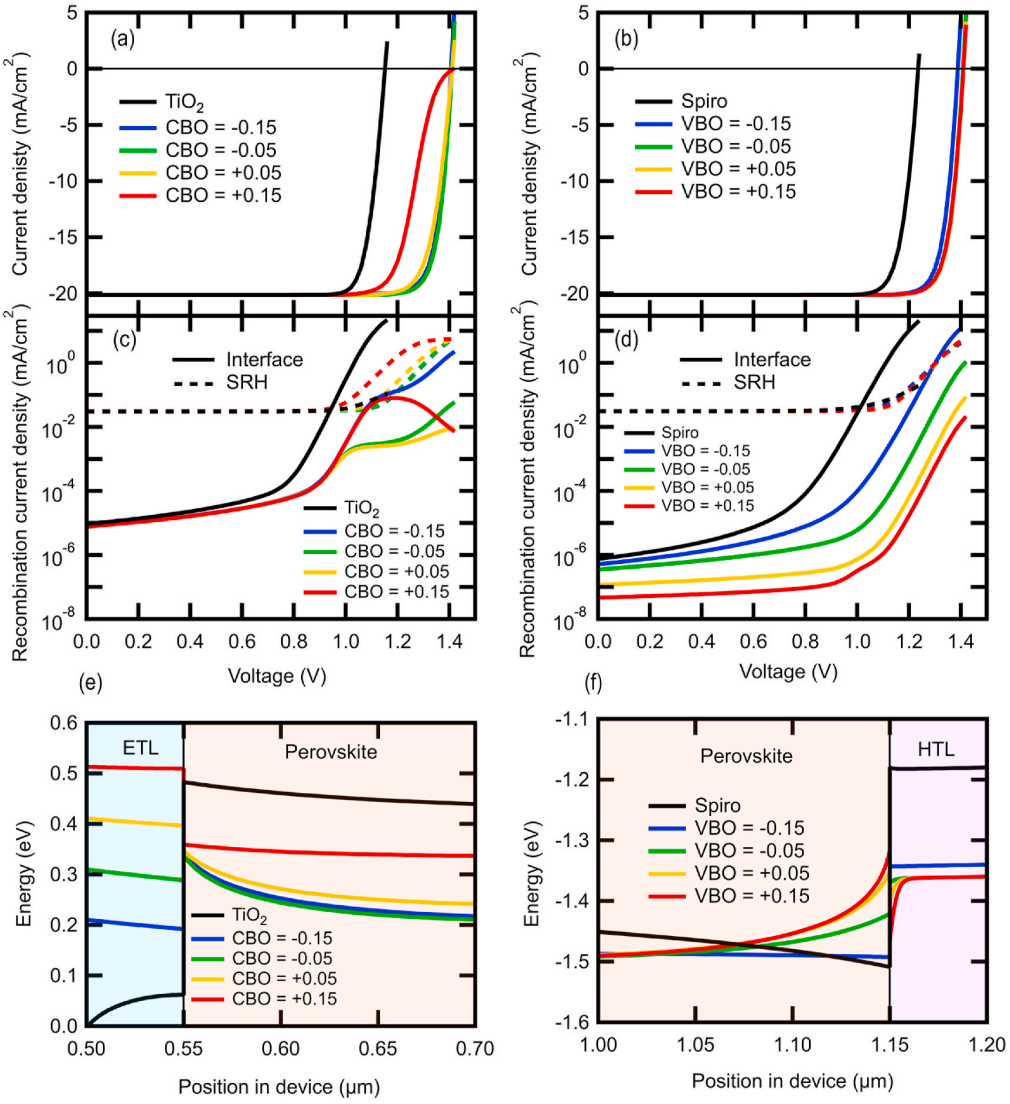


Fig. 1. (a), (b) show the simulated J-V curves with varying CBO and VBO for 1.7 eV perovskite respectively, (c) and (d) show the recombination current density (mA/cm^2) for the ETL and HTL interfaces, respectively, and (e) and (f) show the energy bands for the ETL/conduction band and the HTL/valence band interfaces, respectively, at MPP.

Approved for public release; distribution unlimited.
717

We first consider the role of the ETL in the device performance. Starting with TiO_2, which is commonly used in high PCE devices [31, 32], the modeled J-V results show a device with high fill factor (FF) and V_{OC} of 1.15 V, which is substantially below the thermodynamically-limited value for the optical stack of 1.428 V. As the CBO increases from −0.421 eV for TiO_2 to −0.15 eV and greater, the V_{OC} increases by ~200 mV. The FF remains high until the CBO increases to +0.15 eV, at which point a kink appears in the J-V curve. Note that for CBOs greater than −0.15 eV the V_{OC} deficit has been virtually eliminated for the 10 μs lifetimes as the V_{OC} is increased to 1.41 V.

The corresponding J_R-V curves (Fig. 1(c)) show that the interface recombination currents are low at low biases. However, in the case where the ETL is TiO_2, there is interface recombination turn-on at ~0.8 V and is an order of magnitude higher than the SRH recombination current at a bias of 1.0 V and limits V_{OC}. For the alternative ETLs, however, the interfacial recombination currents do not turn-on until ~0.95 V, and the devices are limited by SRH recombination when the CBO is more positive than −0.05 eV. However, for the case where the CBO is +0.15 eV, the SRH turns on earlier due to flattening of the bands and there is large barrier that hinders electron extraction (Fig. 1(e)). This gives rise to a kink in the J-V curve that lowers the FF. Tabulated values for the various device performance parameters may be found in the SI.

Turning to the band diagram (Fig. 1(e)), we see that the relatively large negative CBO for the TiO_2/perovskite interface coupled with the low carrier concentration in the absorber gives rise to an upward shift of the perovskite conduction band and large discontinuity in the conduction bands across the interface. The perovskite bands are fairly flat at MPP, but the potential drop across the absorber/ETL interface places the ETL Fermi level closer to the hole Fermi level in the perovskite and the overlap between the two gives rise to a high interface recombination current. As the CBO is progressively increased from −0.15 eV to +0.05 eV, the potential drop becomes smaller and the overlap decreases. Despite the fact that the perovskite bands slope away from the interface, which is expected to impede carriers from flowing in the desired direction, the net effect is a reduction of the interfacial recombination current, and a larger Voc. However, when the CBO is +0.15 eV, we see a significant barrier to electron flow into the ETL which gives rise to the bias dependence of the transport properties (i.e. the kink in Fig. 1(a)) and the low FF.

To investigate the role of the HTL interface we fixed the recombination velocity at the ETL/absorber interface at 1×10^{-4} cm/s and varied the VBO. Spiro is a common HTL in high performance devices and is expected to have a VBO of −0.32 eV when in contact with a 1.7 eV perovskite absorber (See SI). Fig. 1(b) shows that a Spiro HTL results in a device with a high FF and a V_{OC} of 1.23 V. While higher than for the TiO_2 ETL, there is still a substantial deficit. Increasing the VBO to −0.15 eV increases V_{OC} by ~200 mV, and the V_{OC} remains high to VBO values as high as +0.15 eV. Here, the FF remains high for all conditions investigated. If, however, the VBO is increased to +0.2 eV or +0.25 eV the FF is reduced from 87% to 86% and 81%, respectively.

The J_R-V results (Fig. 1(d)) show that the interface recombination current with Spiro as an HTL turns on at ~0.8 V and exceeds the SRH recombination current at ~1 V. Thus, devices with Spiro and a 1.7 eV absorber are limited by interfacial recombination, as was the case for the TiO_2 ETL. Unlike the front interface investigation, however, the bias at which the interface recombination current turns-on continues to increase with the VBO. The interfacial recombination current and SRH currents become comparable near V_{OC} when the VBO is −0.05 eV, and the devices are truly SRH-limited for greater VBO values. Under these conditions the perovskite bulk carrier lifetimes would need to be increased beyond 10 μs to further increase the performance.

The reduced sensitivity to the VBO at the HTL interface can be understood by investigating the band diagrams at MPP (Fig. 1(f)). When the HTL is Spiro the absorber bands bend downward toward the perovskite/HTL interface and electrons are attracted to the surface, which leads to a higher interfacial recombination current. When the VBO is increased to −0.15 eV, the bands are much flatter with only a small degree of downward band bending at MPP. Consequently, the interfacial recombination current turns-on at a higher bias voltage. As the VBO increases, the bands bend upward at the interface, thereby repelling electrons. In contrast to the ETL case, the FF does not suffer even when the VBO is +0.15 eV. This is because the high doping density in the HTL (1×10^{18} cm^{-3}) does not support a wide depletion layer and the sharp, thin spike at VBO = +0.15 eV can be easily overcome by holes. In this case the increase in V_{OC} that is available with more positive VBOs appears simply in Fig. 1(f) as a reduction in the loss of potential energy experienced by holes moving across the absorber/HTL interface.

Fig. 2 shows the combined effects for CBO and VBO variations with absorber bandgaps of 1.6, 1.7, and 1.8 eV. Fig. 2(a) has a plateau of high V_{OC} in the upper right corner for each of the bandgaps. In this range the VBOs and CBOs are sufficiently positive to repel carriers from their respective CTLs and suppress interfacial recombination. Consequently, the V_{OC} values on the plateau are SRH limited at 81–83% of their bandgap voltages (Note that the plateau V_{OC} values are not significantly different when the carrier lifetimes are reduced to 1 μs or increased to 100 μs, see Table S4). The white circles on the plots mark the performance with TiO_2 and Spiro as the ETL and HTL, respectively. Increasing the VBO from this point moves the V_{OC} along nearly isovoltage contours for all absorber bandgaps. On the other hand, increasing the CBO causes the V_{OC} to initially move across contours, increasing V_{OC} to higher values. However, as the CBO increases interfacial recombination at the ETL ceases to limit the device performance, and the device instead becomes limited by interfacial recombination at the HTL. Increases in the VBO are then required to further increase the V_{OC}. The high V_{OC} plateau is reached when both the CBO and VBO are above approximately −0.1 eV. Interestingly, a thin sliver of high V_{OC} spans both positive and negative VBOs for the 1.7 and 1.8 eV bandgaps at the most positive CBOs. This is due to electron confinement in the conduction band, but the effect does not lead to the highest efficiencies due to an accompanying reduction in FF (*vide infra*). In general, the regions of maximum V_{OC} in Fig. 2 represent cases where the electron and hole Fermi levels have a maximum degree of splitting. It is interesting to consider how the complete band diagram is altered when the contact layers are optimized to support a maximum V_{OC}*FF product. Figure S2 shows that the degree of Fermi level splitting in the perovskite layer can be improved by ~0.3 eV with optimal contacts compared to Spiro and TiO_2.

The FF data (Fig. 2(b)) show an elongated plateau with FF >86% for each bandgap. The plateau starts at CBO values of approximately −0.2 to −0.1 eV and extends to CBO values of ~0.0 eV. The FF plateau is longer in the VBO dimension, extending from ~ −0.3 eV to +0.2 eV. In this region of high FF, the J-V curves turns on abruptly due to the dominant control of the SRH recombination mechanism. For the 1.6 and 1.7 eV bandgaps there is a lower plateau with FF values between 84 and 86% that extends over a larger range of the plotted area. When the absorber bandgaps are 1.7 and 1.8 eV a distinct valley develops that runs from VBOs of approximately −0.25 eV to the more positive values. The valley indicates a transition from interface recombination control at the ETL/absorber interface to SRH control in the absorber as the CBO is increased. Further increase in the CBO to greater than +0.1 eV causes the FF to drop precipitously due to electron-blocking at the ETL (Fig. 2(c)). There is also a region of low FF in the lower left corner, particularly for the 1.6 and 1.7 eV cases. This is where both front and back interfaces play a role in recombination, so the FF is a function of the two recombination mechanisms.

Fig. 2(c) shows the PCE data which reflects the V_{OC}*FF product and the fact J_{SC} is lower for the wider bandgaps. A distinct single plateau is found for each of the bandgaps. The negative VBO edge of the plateau is at approximately the same location (~−0.2 eV) for each bandgap, while the edge on the positive VBO side is not resolved. Note that, experimentally, the approach to higher efficiencies will be from the negative VBO (and CBO) sides of the plateau, and VBO values > +0.2 eV are not

Approved for public release; distribution unlimited.
718

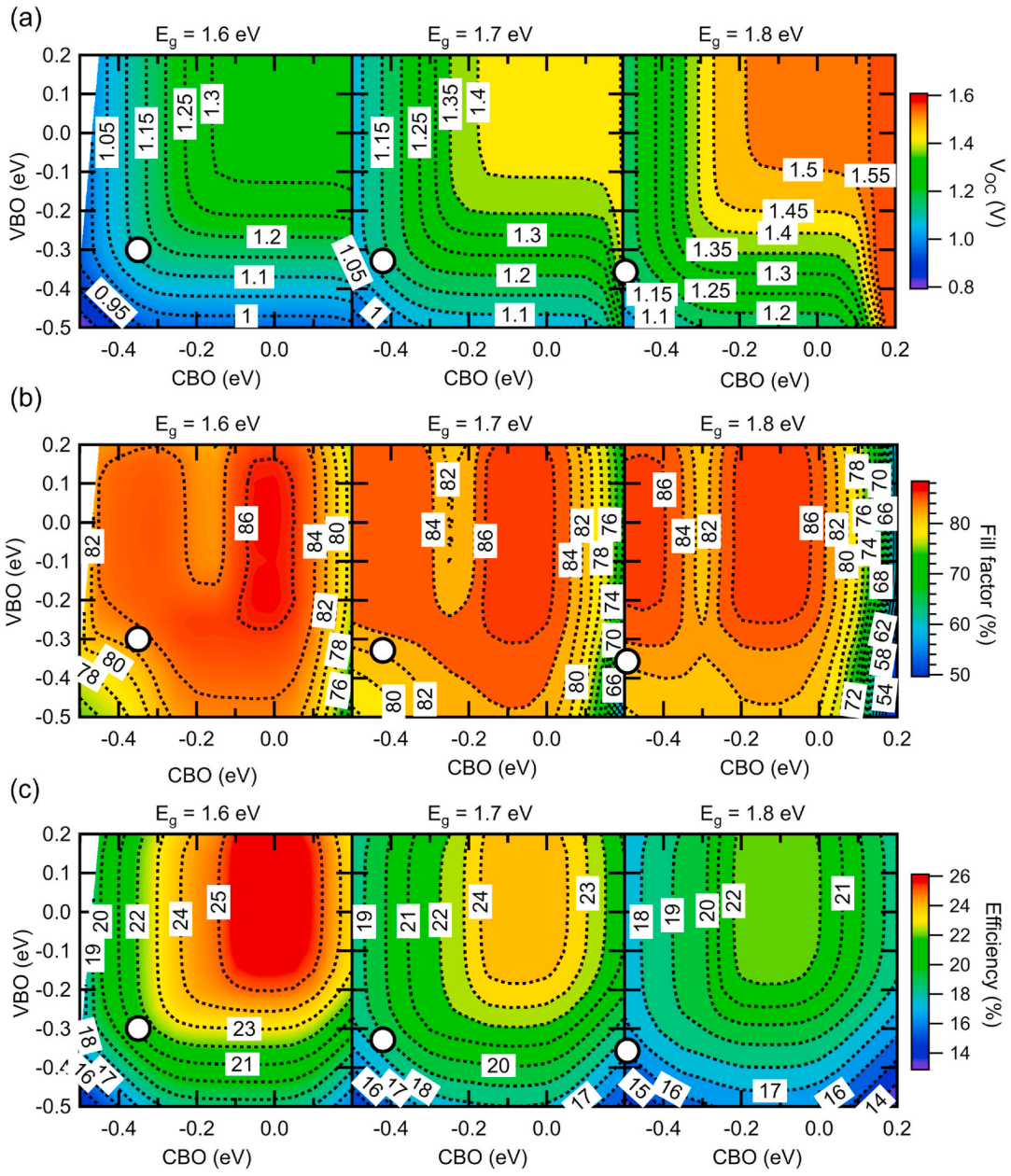


Fig. 2. (a) V_{OC}, (b) fill factor and (c) power conversion efficiency of perovskite devices with 1.6 eV, 1.7 eV and 1.8 eV absorber material as function of VBO and CBO. White circle symbols indicate the band offset of TiO_2 and Spiro as CTLs.

likely to be of concern. For the CBO coordinate, we see the negative edge of the plateau moves to more negative values as the bandgap is increased. This suggests that a good ETL for large bandgap absorbers may be more straightforward to develop than a good HTL. Using TiO_2 and Spiro as ETL and HTL, respectively, yields PCEs of 21%, 19% and 16% for the 1.6, 1.7, and 1.8 eV bandgaps, respectively. In comparison, the maxima in the PCE plateau occur at ~25%, ~24% and ~22%, respectively. Thus, we see a PCE deficit with standard material contacts that is increasing with bandgap.

Fig. 3(a) shows the simulated PCE as a function of bandgap when the contacts are TiO_2 and Spiro in comparison to the PCEs expected if the contacts had optimized CBO and VBO values. The PCE deficit of cells with TiO_2 and Spiro relative to those with optimized contacts varies linearly from 19% at 1.6 eV to 30% at 1.8 eV. Fig. 3(b) shows the companion V_{OC} data. Also shown for comparison are the highest experimental values that have been reported for devices using TiO_2 and Spiro contacts [33–38]. The experimental values generally fall along the trend line for the simulations, but there is some deviation. In these cases, the properties of the CTLs and/or the interface between the CTL and absorber were varied [34,35,37]. For example Saliba et al. investigated Li doping of the TiO_2 ETL prior to completing the 1.63 eV absorber device [34]. This produced a PCE of 21.8% which is above the trendline due to a V_{OC} improvement of 10% relative to the expected value (1.24 V versus 1.12 V). Zhou et al. investigated a benzylamine treatment for passivation of grain boundaries in a 1.72 eV absorber and formed the perovskite/HTL interface using a 2D structure approach [37]. This led to

Approved for public release; distribution unlimited.
719

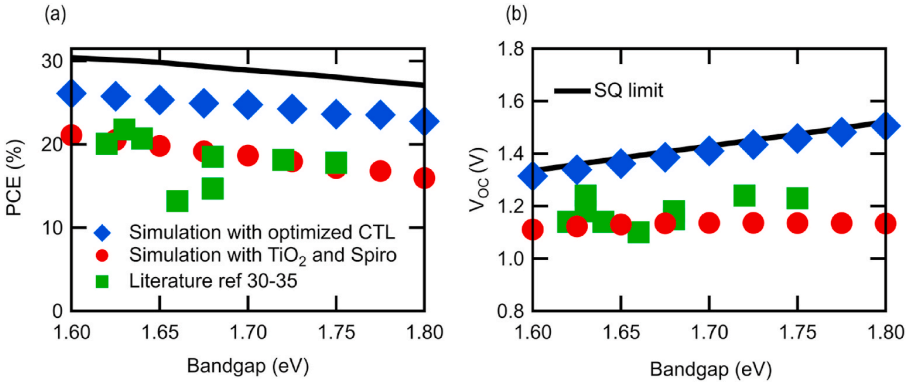


Fig. 3. (a) Power conversion efficiency and (b) V_{OC} relative to the internal SQ limit as a function of bandgap for absorber with 10 μs carrier lifetimes.

a PCE of 18.13% and V_{OC} of 1.24 V (~7% improvement in V_{OC}). Similarly, Gharibzadeh et al. showed that generation of 2D structures at the perovskite/HTL interface with butylammonium bromide treatment leads to adjustment of the perovskite energy bands at the interface and thus improved the V_{OC} of wide bandgap devices [19].

Fig. 3 also shows the PCE and V_{OC} for devices with the optimized ETLs and HTLs. The PCE values are still below the SQ limit for AM1.5G irradiance due to the absorber being thinner than needed for complete light absorption, but the V_{OC} is still very close to the limit due to the logarithmic dependence on photogeneration. Clearly, to capture the missing entitlement in V_{OC}, FF (and thus in PCE) it will be necessary to develop new CTL materials.

3. Conclusions

In conclusion, we showed that the performance of wide bandgap perovskites devices is strongly affected by the VBO and CBO values of the CTLs. The analysis shows that typically used HTL (Spiro) and ETL (TiO_2) materials will cause interfacial recombination currents to be more dominant as the bandgap increases. This limits the V_{OC} and the performance. Implementation of HTLs and ETLs with appropriate energy band alignment will help to eliminate the V_{OC} and performance deficit.

Disclaimer

This report was prepared as an account of work sponsored by an agency of the United States Government. Neither the United States Government nor any agency thereof, nor any of its employees, makes any warranty, express or implied, or assumes any legal liability or responsibility for the accuracy, completeness, or usefulness of any information, apparatus, product, or process disclosed, or represents that its use would not infringe privately owned rights. Reference herein to any specific commercial product, process, or service by trade name, trademark, manufacturer, or otherwise does not necessarily constitute or imply its endorsement, recommendation, or favoring by the United States Government or any agency thereof. The views and opinions of authors expressed herein do not necessarily state or reflect those of the United States Government or any agency thereof.

The views and conclusions contained herein are those of the authors and should not be interpreted as necessarily representing the official policies or endorsements, either expressed or implied, of Air Force Research Laboratory or the U.S. Government.

CRediT authorship contribution statement

Ramez Hosseinian Ahangharnejhad: Conceptualization, Methodology, Software, Formal analysis, Investigation, Writing – original draft, Writing – review & editing. **Jared D. Friedl:** Methodology, Software, Formal analysis, Investigation, Writing – original draft. **Adam B. Phillips:** Conceptualization, Methodology, Software, Formal analysis, Investigation, Writing – original draft, Writing – review & editing. **Michael J. Heben:** Conceptualization, Investigation, Writing – original draft, Writing – review & editing, Supervision, Project administration, Funding acquisition.

Declaration of competing interest

The authors declare that they have no known competing financial interests or personal relationships that could have appeared to influence the work reported in this paper.

Acknowledgments

This material is based upon work supported by the U.S. Department of Energy's Office of Energy Efficiency and Renewable Energy (EERE) under the Solar Energy Technologies Office Award Number DE-EE0008790, and from the U.S. Air Force Research Laboratory, Space Vehicles Directorate, under Agreement number FA9453-18-2-0037 and Contract # FA9453-19-C-1002. The U.S. Government is authorized to reproduce and distribute reprints for Governmental purposes notwithstanding any copyright notation thereon.

Appendix A. Supplementary data

Supplementary data to this article can be found online at https://doi.org/10.1016/j.solmat.2021.111015.

References

[1] NREL Best Research-Cell Efficiencies. https://www.nrel.gov/pv/cell-efficiency.html, 2021.
[2] W. Tress, Perovskite solar cells on the way to their radiative efficiency limit – insights into a success story of high open-circuit voltage and low recombination, Adv. Energy Mater. 7 (2017), https://doi.org/10.1002/aenm.201602358.
[3] R.E. Brandt, V. Stevanović, D.S. Ginley, T. Buonassisi, Identifying defect-tolerant semiconductors with high minority-carrier lifetimes: beyond hybrid lead halide perovskites, MRS Commun 5 (2015) 265–275.
[4] A. Buin, P. Pietsch, J. Xu, O. Voznyy, A.H. Ip, R. Comin, E.H. Sargent, Materials processing routes to trap-free halide perovskites, Nano Lett. 14 (2014) 6281–6286.
[5] Q. Lin, A. Armin, R.C.R. Nagiri, P.L. Burn, P. Meredith, Electro-optics of perovskite solar cells, Nat. Photon. 9 (2015) 106–112.
[6] W. Shockley, H.J. Queisser, Detailed balance limit of efficiency of p-n junction solar cells, J. Appl. Phys. 32 (1961) 510–519, https://doi.org/10.1063/1.1736034.
[7] P.K. Nayak, S. Mahesh, H.J. Snaith, D. Cahen, Photovoltaic solar cell technologies: analysing the state of the art, Nat. Rev. Mater. 4 (2019) 269–285, https://doi.org/10.1038/s41578-019-0097-0.
[8] J. Tong, Z. Song, D.H. Kim, X. Chen, C. Chen, A.F. Palmstrom, P.F. Ndione, M. O. Reese, S.P. Dunfield, O.G. Reid, J. Liu, F. Zhang, S.P. Harvey, Z. Li, S. T. Christensen, G. Teeter, D. Zhao, M.M. Al-jassim, M.F.A.M. Van Hest, M.C. Beard, S.E. Shaheen, J.J. Berry, Y. Yan, K. Zhu, Carrier lifetimes of >1 μs in Sn-Pb

Approved for public release; distribution unlimited.
720

perovskites enable efficient all-perovskite tandem solar cells, Science 364 (2019) 475–479, https://doi.org/10.1126/science.aav7911.
[9] Q. Han, Y.-T. Hsieh, L. Meng, J.-L. Wu, P. Sun, E.-P. Yao, S.-Y. Chang, S.-H. Bae, T. Kato, V. Bermudez, Y. Yang, High-performance perovskite/Cu(In,Ga)Se2 monolithic tandem solar cells, Science 361 (2018) 904–908, https://doi.org/10.1126/science.aat5055.
[10] R. Hosseinian Ahangharnejhad, Z. Song, A.B. Phillips, S.C. Watthage, Z. S. Almutawah, D.R. Sapkota, P. Koirala, R.W. Collins, Y. Yan, M.J. Heben, Optical design of perovskite solar cells for applications in monolithic tandem configuration with CuInSe2 bottom cells, MRS Adv 3 (2018) 3111–3119, https://doi.org/10.1557/adv.2018.
[11] Z. Song, D. Zhao, C. Chen, C.L. Ramez H Ahangharnejhad, K. Ghimire, N. J. Podraza, M.J. Heben, K. Zhu, Y. Yan, Monolithic two-terminal all-perovskite tandem solar cells with power conversion efficiency exceeding 21%, in: IEEE 46th Photovolt. Spec. Conf., 2019, pp. 743–746, 2019.
[12] R. Hosseinian Ahangharnejhad, A.B. Phillips, K. Ghimire, P. Koirala, Z. Song, H. M. Barudi, A. Habte, M. Sengupta, R.J. Ellingson, Y. Yan, R.W. Collins, N. J. Podraza, M.J. Heben, Irradiance and temperature considerations in the design and deployment of high annual energy yield perovskite/CIGS tandems, Sustain. Energy Fuels 3 (2019) 1841–1851, https://doi.org/10.1039/C9SE00237E.
[13] M.T. Hörantner, T. Leijtens, M.E. Ziffer, G.E. Eperon, M.G. Christoforo, M. D. McGehee, H.J. Snaith, The potential of multijunction perovskite solar cells, ACS Energy Lett 2 (2017) 2506–2513, https://doi.org/10.1021/acsenergylett.7b00647.
[14] T. Duong, H. Pham, T.C. Kho, P. Phang, K.C. Fong, D. Yan, Y. Yin, J. Peng, M. A. Mahmud, S. Gharibzadeh, B.A. Nejand, I.M. Hossain, M.R. Khan, N. Mozaffari, Y.L. Wu, H. Shen, J. Zheng, H. Mai, W. Liang, C. Samundsett, M. Stocks, K. McIntosh, G.G. Andersson, U. Lemmer, B.S. Richards, U.W. Paetzold, A. Ho-Ballie, Y. Liu, D. Macdonald, A. Blakers, J. Wong-Leung, T. White, K. Weber, K. Catchpole, High efficiency perovskite-silicon tandem solar cells: effect of surface coating versus bulk incorporation of 2D perovskite, Adv. Energy Mater. 10 (2020) 1–15, https://doi.org/10.1002/aenm.201903553.
[15] D.H. Kim, C.P. Muzzillo, J. Tong, A.F. Palmstrom, B.W. Larson, C. Choi, S. P. Harvey, S. Glynn, J.B. Whitaker, F. Zhang, Z. Li, H. Lu, M.F.A.M. van Hest, J. J. Berry, L.M. Mansfield, Y. Huang, Y. Yan, K. Zhu, Bimolecular additives improve wide-band-gap perovskites for efficient tandem solar cells with CIGS, Joule 3 (2019) 1734–1745, https://doi.org/10.1016/j.joule.2019.04.012.
[16] R. Lin, K. Xiao, Z. Qin, Q. Han, C. Zhang, M. Wei, M.I. Saidaminov, Y. Gao, J. Xu, M. Xiao, A. Li, J. Zhu, E.H. Sargent, H. Tan, Monolithic all-perovskite tandem solar cells with 24.8% efficiency exploiting comproportionation to suppress Sn(ii) oxidation in precursor ink, Nat. Energy. 4 (2019) 864–873, https://doi.org/10.1038/s41560-019-0466-3.
[17] R. Hosseinian Ahangharnejhad, W. Becker, J. Jones, A. Anctil, Z. Song, A. Phillips, M. Heben, I. Celik, Environmental impact per energy yield for bifacial single junction perovskite solar cells outperform the crystalline silicon solar cells, Cell Reports Phys. Sci. 1 (2020) 100216.
[18] J.P. Correa-Baena, M. Saliba, T. Buonassisi, M. Grätzel, A. Abate, W. Tress, A. Hagfeldt, Promises and challenges of perovskite solar cells, Science 358 (2017) 739–744, https://doi.org/10.1126/science.aam6323.
[19] S. Gharibzadeh, B. Abdollahi Nejand, M. Jakoby, T. Abzieher, D. Hauschild, S. Moghadamzadeh, J.A. Schwenzer, P. Brenner, R. Schmager, A.A. Haghighirad, L. Weinhardt, U. Lemmer, B.S. Richards, I.A. Howard, U.W. Paetzold, C. Utilizing, P. Heterostructure, S. Gharibzadeh, B.A. Nejand, T. Abzieher, D. Hauschild, J. A. Schwenzer, P. Brenner, R. Schmager, A.A. Haghighirad, U. Lemmer, B. S. Richards, I.A. Howard, U.W. Paetzold, Record open-circuit voltage wide-bandgap perovskite solar cells utilizing 2D/3D perovskite heterostructure, Adv. Energy Mater. (2019) 1803699, https://doi.org/10.1002/aenm.201803699.
[20] D.J. Slotcavage, H.I. Karunadasa, M.D. McGehee, Light-Induced phase segregation in halide-perovskite absorbers, ACS Energy Lett 1 (2016) 1199–1205, https://doi.org/10.1021/acsenergylett.6b00495.
[21] E.T. Hoke, D.J. Slotcavage, E.R. Dohner, A.R. Bowring, H.I. Karunadasa, M. D. McGehee, Reversible photo-induced trap formation in mixed-halide hybrid perovskites for photovoltaics, Chem. Sci. 6 (2015) 613–617, https://doi.org/10.1039/c4sc03141e.
[22] F. Peña-Camargo, P. Caprioglio, F. Zu, E. Gutierrez-Partida, C.M. Wolff, K. Brinkmann, S. Albrecht, T. Riedl, N. Koch, D. Neher, M. Stolterfoht, Halide segregation versus interfacial recombination in bromide-rich wide-gap perovskite solar cells, ACS Energy Lett 5 (2020) 2728–2736, https://doi.org/10.1021/acsenergylett.0c01104.
[23] P. Zhao, Z. Lin, J. Wang, M. Yue, J. Su, J. Zhang, J. Chang, Y. Hao, Numerical simulation of planar heterojunction perovskite solar cells based on SnO2 electron transport layer, ACS Appl. Energy Mater. 2 (2019) 4504–4512, https://doi.org/10.1021/acsaem.9b00755.
[24] T. Minemoto, M. Murata, Theoretical analysis on effect of band offsets in perovskite solar cells, Sol. Energy Mater. Sol. Cells 133 (2015) 8–14, https://doi.org/10.1016/j.solmat.2014.10.036.
[25] J.D. Friedl, R. Hosseinian Ahangharnejhad, A.B. Phillips, M.J. Heben, Materials requirements for improving the electron transport layer/perovskite interface of perovskite solar cells determined via numerical modeling, MRS Adv (2020).
[26] M. Burgelman, P. Nollet, S. Degrave, Modelling polycrystalline semiconductor solar cells, Thin Solid Films 361–362 (2000) 527–532.
[27] K. Tan, P. Lin, G. Wang, Y. Liu, Z. Xu, Y. Lin, Controllable design of solid-state perovskite solar cells by SCAPS device simulation, Solid State Electron. 126 (2016) 75–80.
[28] P. Caprioglio, M. Stolterfoht, C.M. Wolff, T. Unold, B. Rech, S. Albrecht, D. Neher, On the relation between the open-circuit voltage and quasi-fermi level splitting in efficient perovskite solar cells, Adv. Energy Mater. 9 (2019), https://doi.org/10.1002/aenm.201901631.
[29] M. Stolterfoht, P. Caprioglio, C.M. Wolff, J.A. Márquez, J. Nordmann, S. Zhang, D. Rothhardt, U. Hörmann, Y. Amir, A. Redinger, L. Kegelmann, F. Zu, S. Albrecht, N. Koch, T. Kirchartz, M. Saliba, T. Unold, D. Neher, The impact of energy alignment and interfacial recombination on the internal and external open-circuit voltage of perovskite solar cells, Energy Environ. Sci. 12 (2019) 2778–2788, https://doi.org/10.1039/c9ee02020a.
[30] S. Karthick, S. Velumani, J. Bouclé, Experimental and SCAPS simulated formamidinium perovskite solar cells: a comparison of device performance, Sol. Energy 205 (2020) 349–357, https://doi.org/10.1016/j.solener.2020.05.041.
[31] W.S. Yang, B.-W.W. Park, E.H. Jung, N.J. Jeon, Y.C. Kim, D.U. Lee, S.S. Shin, J. Seo, E.K. Kim, J.H. Noh, S. Il Seok, Iodide management in formamidinium-lead-halide – based perovskite layers for efficient solar cells, Science 356 (2017) 1376–1379, https://doi.org/10.1126/science.aan2301.
[32] M. Jeong, I. Woo Choi, E. Min Go, Y. Cho, M. Kim, B. Lee, S. Jeong, Y. Jo, H. Won Choi, J. Lee, J.-H. Bae, S. Kyu Kwak, D. Suk Kim, C. Yang, Stable perovskite solar cells with efficiency exceeding 24.8% and 0.3-V voltage loss, Science 369 (2020) 1615–1620, https://doi.org/10.1126/SCIENCE.ABB7167.
[33] T.J. Jacobsson, J.-P. Correa-Baena, M. Pazoki, M. Saliba, K. Schenk, M. Grätzelc, A. Hagfeldt, Exploration of the compositional space for mixed lead halogen perovskites for high efficiency solar cells, Energy Environ. Sci. 9 (2016) 1706–1724.
[34] M. Saliba, T. Matsui, K. Domanski, J.-Y. Seo, A. Ummadisingu, S.M. Zakeeruddin, J.-P. Correa-Baena, W.R. Tress, A. Abate, A. Hagfeldt, M. Grätzel, Incorporation of rubidium cations into perovskite solar cells improves photovoltaic performance, Science 354 (2016) 206–209, https://doi.org/10.1126/science.aah5557.
[35] J. Kim, M.I. Saidaminov, H. Tan, Y. Zhao, Y. Kim, J. Choi, J.W. Jo, J. Fan, R. Quintero-Bermudez, Z. Yang, L.N. Quan, M. Wei, O. Voznyy, E.H. Sargent, Amide-catalyzed phase-selective crystallization reduces defect density in wide-bandgap perovskites, Adv. Mater. 30 (2018) 1706275.
[36] H. Zhou, Q. Chen, G. Li, S. Luo, T. Song, H.-S. Duan, Z. Hong, J. You, Y. Liu, Y. Yang, Interface engineering of highly efficient perovskite solar cells, Science 345 (2014) 542–546.
[37] Y. Zhou, F. Wang, Y. Cao, J. Wang, H. Fang, M.A. Loi, N. Zhao, C. Wong, Benzylamine-treated wide-bandgap perovskite with high thermal-photostability and photovoltaic performance, Adv. Energy Mater. 7 (2017) 1701048.
[38] K.T. Cho, G. Grancini, Y. Lee, E. Oveisi, J. Ryu, O. Almora, M. Tschumi, P. A. Schouwink, G. Seo, S. Heo, J. Park, J. Jang, S. Paek, G. Garcia-Belmonte, M. K. Nazeeruddin, Selective growth of layered perovskites for stable and efficient photovoltaics, Energy Environ. Sci. 11 (2018) 952–959.

Approved for public release; distribution unlimited.
721

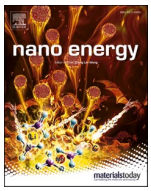
Nano Energy 83 (2021) 105827



Contents lists available at ScienceDirect

Nano Energy

journal homepage: http://www.elsevier.com/locate/nanoen



Communication



Enabling bifacial thin film devices by developing a back surface field using Cu_xAlO_y

Kamala Khanal Subedi [1], Adam B. Phillips [1], Niraj Shrestha, Fadhil K. Alfadhili, Anna Osella, Indra Subedi, Rasha A. Awni, Ebin Bastola, Zhaoning Song, Deng-Bing Li, Robert W. Collins, Yanfa Yan, Nikolas J. Podraza, Michael J. Heben, Randy J. Ellingson *

Wright Center for Photovoltaic Innovation and Commercialization, Department of Physics and Astronomy, The University of Toledo, Toledo, OH 43606, USA

ARTICLE INFO

Keywords:
Cu_xAlO_y
Thin films
Bifacial
CdTe
Positive IFLO

ABSTRACT

Bifacial solar cells have the potential to increase the energy yield per unit area over traditional monofacial devices without significant added cost, driving $/kWh costs lower and accelerating the adoption of solar photovoltaics. However, the performance of bifacial thin film solar cells significantly lags that achieved by crystalline silicon cells. Here we incorporate wide bandgap Cu_xAlO_y as a back buffer layer for CdTe devices and achieve a backside illuminated device with high current density and high fill factor. Moreover, these values remain nearly constant even as the absorber layer thickness changes, indicating that a fully-depleted device is not required for efficient charge collection. We show that this response is indicative of a back surface field, albeit with a persistent high back surface recombination velocity. By managing electron reflection, we achieved a backside illumination conversion efficiency of 7.1% and bifaciality of 0.55 for a 3.3 μm CdTe device and 8.0% and 0.62 for a 2 μm device. Future improvements can be made by identifying and incorporating a passivation material that reduces the back surface recombination velocity.

1. Introduction

As single junction photovoltaic (PV) devices push closer towards the Shockley-Queisser limit, [1] new architectures are being investigated to push the energy yield per area higher. One of the most promising is bifacial PV devices, in which ground-scattered light incident on the back of the device gets absorbed and converted into additional electrical energy. In fact, it is estimated that bifacial PV will make up ~ 40% of the PV market by 2025 [2], and bifacial Si devices are already commercialized. [3].

Development of bifacial thin film (BTF) devices, on the other hand, lags considerably, and the record reported efficiency values of backside illuminated devices are 6.0% for CIGS [4] and 5.0% for CdTe [5]. Much of the reason for the poor performance is due to downward band bending in the absorber layer at the back interface of the device due to a negative initial Fermi level offset (IFLO) and high back surface recombination velocity (BSRV) [6] in addition to highly absorbing back buffer layers [7,8]. From an energetics point of view, if a back buffer layer can induce upward band bending at the back interface, the electrons will be repelled and the backside illuminated device performance will improve [6]. In addition, these types of improvements will be necessary to achieve the highest front illuminated device performance [9], when the front interface is good [10]. Unfortunately, development of such materials has been slow.

Recently, several studies have developed p-type conductive, transparent films that are candidates for use in photovoltaic devices [11–15]. We recently investigated $(CuS)_x(ZnS)_{1-x}$ and $BaCu_4S_3$ as back contact buffer layers for CdTe [16,17]. While incorporation of these materials have led to reasonable front illuminated device performance, conversion efficiency when illuminated from the backside has been poor. This suggests that the IFLO between these back buffer layers and the absorber remains negative, which leads to downward band bending in the absorber at the back interface resulting in high back interface recombination current density [6,9]. $CuAlO_2$, on the other hand, has several potential advantages. It is a p-type wide bandgap material with high visible light transparency, high carrier concentration $> 10^{17}$ cm^{-3}, and expected deep valence band edge, suggesting the potential for positive IFLO [11,18]. To achieve the delafossite crystal structure, though,

* Corresponding author.
E-mail address: Randy.Ellingson@utoledo.edu (R.J. Ellingson).
[1] These authors contributed equally to this work.

https://doi.org/10.1016/j.nanoen.2021.105827
Received 3 September 2020; Received in revised form 15 January 2021; Accepted 24 January 2021
Available online 28 January 2021
2211-2855/© 2021 Elsevier Ltd. All rights reserved.

Approved for public release; distribution unlimited.

requires annealing the sample at temperatures > 700 °C, which would be detrimental to CdTe devices. However, low temperature (300 °C) annealing of atomic layer deposited Al_2O_3 with a Cu overlay has resulted in a mixed Cu_xAlO_y layer that has led to increased CdTe device performance [19]. This suggests the desired back buffer material properties may be achievable with Cu-Al-O based materials at CdTe-compatible processing temperatures.

Here we investigate Cu_xAlO_y as a transparent back buffer layer to CdTe fabricated by low temperature solution processing. We investigate devices completed with a transparent conducting oxide (TCO) back contact and measure the performance when the device is illuminated through frontside and backside. While front illuminated device performance is consistent with previous devices using these absorber stack materials, back illuminated device performance is high for a BTF device and independent of absorber thickness layer. We use quantum efficiency (QE) and reflection measurements to determine the location of the efficiency loss. Using SCAPS modeling, we identify the likely conditions of the back interface. In addition, we apply an antireflective coating to fabricate an unverified record efficiency back illuminated CdTe device.

The device structure used for these investigations consisted of glass/TCO/CdS/CdTe/Cu_xAlO_y/TCO, where the front glass/TCO was F-doped SnO_2 coated glass substrate with a high resistive transport layer (TEC™ 12D; Pilkington USA) and the back TCO was Sn-doped In_2O_3 (ITO). The CdTe absorber thicknesses studied were 3.3, 2.0, and 1.0 μm. For the devices with thick absorber layer, the ~ 150 nm CdS and 3.3 μm CdTe were deposited using a commercial vapor transport deposition system at high temperature (Willard and Kelsey Solar Group). For the two thinner devices, the 80 nm CdS window layer and the CdTe absorber were sputtered as described elsewhere [20]. Prior to back buffer deposition, all samples were $CdCl_2$ activated at 390 °C for 30 min [20]. No additional Cu was added to these devices. However, devices fabricated using these materials without additional Cu perform reasonably well (~ 10.5%; Supporting Information), indicating that all sets of samples are Cu-doped, though not at an optimized level. The Cu_xAlO_y films were spin coated onto the activated CdTe using a solution of 40 mM aluminum nitrate nonahydrate (98%, Fisher Scientific) and 24 mM copper nitrate trihydrate (99%, Fisher Scientific) dissolved in 5 ml of 2-metoxyethanol followed by a post-deposition annealing treatment at 220 °C for 6 min to convert the precursors into the oxide. Note that the solution preparation and spin coating closely follows the process used to fabricate the $CuAlO_2$ as reported by others.[18,21] The devices were finished by sputtering 250 nm of ITO, and the device area is defined by manual scribing of the one inch substrate to fabricate an array of cells of area 0.09 cm^2. Current density-voltage (J-V) curves were measured using a Keithley 2440 sourcemeter and MiniSol model LSH-7320 solar simulator with digital output control.

Fig. 1 shows the J-V curves for front and back illumination of the three devices. While these graphs show the best performing devices, the characteristics of these curves are representative of the 30 devices measured for the respective absorber thickness. Frontside illuminated device performance is in line with performance of devices made using the same deposition processes when Cu is added [15]. The backside illuminated device performance, though, shows several remarkable characteristics. First is that the device fill factor (FF) at all three absorber thicknessses is relatively high at ~ 64%. There is clearly a slope in the J-V curve at short circuit that sets a limit on the FF. However, this slope appears to be constant before a significant change occurs at ~ 700 mV. This sudden change and high FF value indicates that the recombination mechanism responsible for the slope on the J-V curve near short circuit conditions differs from the mechanism that turns on at ~ 700 mV and dictates the V_{OC}. Our previous modeling of backside illuminated devices shows that when there is negative IFLO and moderate BSRV (10^4 cm-s^{-1}), high J_{SC} can be achieved when the depletion region due to the front junction spans the absorber thickness (i.e., the device is fully depleted) at short circuit [6]. Even for fully depleted devices, though, the FF is low because downward band bending at the back of the device

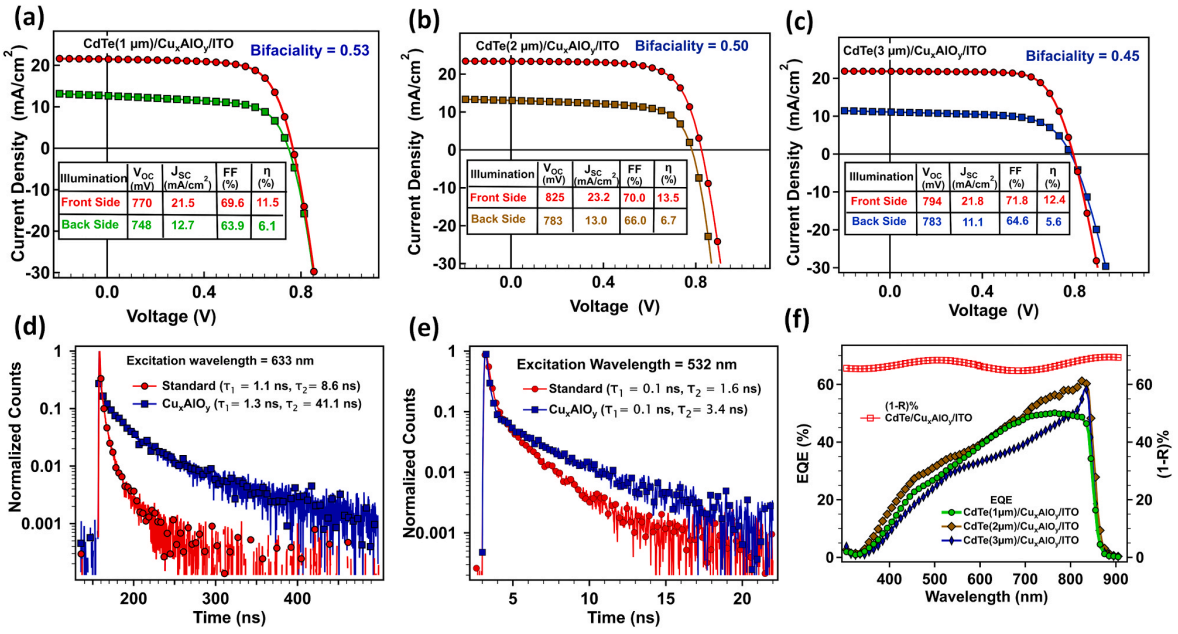


Fig. 1. J-V performance of front and back illuminated (a) 1 μm, (b) 2 μm, and (c) 3.3 μm thick CdS/CdTe solar cell devices using Cu_xAlO_y/ITO as back buffer layer. Time-resolved photoluminescence response of 3.3 μm thick devices with and without Cu_xAlO_y illuminated from the (d) front and (e) back of the device. (f) Reflection (shown as 1-R) and external quantum efficiency of the devices with different absorber thickness.

Approved for public release; distribution unlimited.
723

emerges with increasing bias, rapidly increasing back interface recombination. The FF results presented here do not follow this pattern, which suggests that the back interface is not dictating device performance as is typically observed.

The second remarkable characteristic of the performance of devices illuminated through the backside is that the short circuit current densities (J_{SC}) are nearly independent of absorber thickness. This suggests that carrier lifetime in the thickest absorber is long, so that the same number of electrons are collected at the front of the device as the absorber thickness is varied. As shown in Fig. 1d and e, the lifetime is greatly improved with the addition of the Cu_xAlO_y buffer layer with a long component decay time (τ_2) that increases from 8.6 ns without the buffer layer to 41.1 ns with the buffer when measured from the frontside, and from 1.6 ns without the buffer layer to 3.4 ns with the buffer when measured from the backside. These measurements not only verify that the carrier lifetime is long, but they also suggest that recombination at the back interface has been significantly reduced.

Additionally, the fact that the J_{SC} is independent of thickness indicates that a common mechanism results in the current loss observed for backside illumination. To determine the nature of current loss, we measured the reflection and QE at zero bias for backside illuminated devices. The reflection data (plotted as 1 - R) in Fig. 1f shows, a ~ 32% reflection loss from the back of the device, but this value does not fully account for the observed J_{SC} loss. The QE, on the other hand, shows a high value at long wavelength and decreases for shorter wavelengths. Nearly all the carriers generated by long wavelength light absorbed closer to the front junction are efficiently collected. At the same time, nearly 50% of the carriers generated by short wavelength (~ 450 nm) light absorbed near the back junction are also collected. While recombination does occur at the back of the device, many carriers generated near the back interface are collected. These results are differ from previously reported backside QE results for thicker CdTe absorber layers. [22,23].

A J_{SC} demonstrating only weak dependence on absorber thickness suggests that the energy band profile at the back of the device is the same for all thicknesses investigated, while a FF that weakly depends on absorber thickness suggests this energy band landscape does not change with bias [6]. That this is the case across the three absorber thicknesses investigated here indicates that the bands may be bending upwards at the back of the device, demonstrating electron repelling behavior. From our previous modeling work, upward band bending achieved through a positive IFLO is consistent with reduced interface recombination and high efficiency devices [6]. This is not the case here, as the measured QE response indicates that recombination does occur at the back interface. Taken together, these results suggest that there may be upward band bending at the back of the device and a higher BSRV than that (10^4 cm-s^{-1}) considered in our previous modeling work.

To investigate the CdTe/Cu_xAlO_y interface in an attempt to better specify the energetic conditions and BSRV, we employed SCAPS modeling [24]. Our studies indicate that achieving a thickness- and bias-independent J_{SC} and FF requires upward band bending at the back of the device. This can be achieved with either a fully depleted absorber layer, fixed charges in the buffer, or a positive IFLO. SCAPS modeling indicates that for fully depleted devices, the frontside illuminated device performance increases as the absorber thickness decreases (SI). As shown in Fig. 1 this is not the case. In addition, devices using the same methods and materials used to fabricate these devices often perform better than expected for fully depleted devices, indicating they contain a suboptimal amount of Cu-doping [16]. Consequently, it is unlikely that these devices are fully depleted.

The alternative option is that Cu_xAlO_y results in upward band bending at the back interface. This can be achieved through fixed positive charges in the buffer layer or a positive IFLO. Al_2O_3 has been shown to improve interface behavior for a number of PV materials [25–27]. In these cases, some evidence suggests that fixed charges in the Al_2O_3 create an electric field that repels electrons, resulting in reduced interfacial recombination [26]. Al_2O_3 has also been used in CdTe devices [28–30], but the exact reasons for performance increases have not been identified [26]. While it may be possible that our solution processed Cu_xAlO_y actually results in the formation of an Al_2O_3 layer, additional experiments discussed in the SI indicate that this is not the case. When only one of the metal precursors in included in the solution processing, the backside illuminated device performance is significantly below the performance when both precursor materials are included. Alternatively, including the Cu source as the first of a two step process designed to dope the absorber layer followed by deposition of an Al_2O_3 film, the backside illuminated device performance is still lower. Furthermore, as the absorber layer thickness is decreased from 3.3 μm to 2 μm, a significant change in the J_{SC} occurs, results that are clearly different from those presented in Fig. 1.

From these results, it is clear that both the Cu and Al precursor material are necessary in the solution to fabricate the highest performing devices. The poor performance of the Cu only sample indicates that it is unlikely that the Cu simply converts into a Cu_xO phase, as others have shown at low temperatures [18,21], to improve device performance [31]. On the other hand, the large increase in J_{SC} for the devices with a Cu-doped CdTe layer with Al_2O_3 buffer as the absorber thickness is reduced indicates that the band bending in the CdTe at the back interface changes with absorber thickness. Furthermore, the decrease in FF for these devices with decreasing film thickness is suggestive of bias dependent band bending. Both of these data points taken together suggest that device has downward band bending with reduced back surface recombination velocity [6] and that the solution processing presented in this manuscript does not result in a Cu-doped CdTe layer with Al_2O_3 buffer layer. Instead, the Cu and Al precursor materials react to from a Cu_xAlO_y, which, while unlikely to form a pure $CuAlO_2$ phase at these temperatures, does exhibit some of the necessary properties required to improve the back interface of CdTe devices.

Thus, the available data suggests that upward band bending is due to the positive IFLO resulting from use of a Cu_xAlO_y back buffer layer. However, to have upward band bending and still lose J_{SC} requires high BSRV. To put a range on the band bending and BSRV for the situation presented here, we used SCAPS to model device performance when varying the IFLO by changing the back buffer acceptor density and varying the BSRV via the number density of the interface defect states. For this modeling work, we used materials parameters used in our previous studies (SI), with the caveat that we used an emitter with band positions of CdS.[6,9,10,32]. For the back buffer layer we assumed the valence band was 0.2 eV below that of CdTe, thereby potentially impeding hole flow, and 32% optical reflection from the back interface in accordance with the measured value. Fig. 2 shows how the PV parameters, including J_{SC} and FF, depend on the IFLO and BSRV for an absorber thickness of 3.3 μm.

From the contour plots, it is clear that there is a wide range of IFLO-BSRV values that will result in a J_{SC} of 11–12 mA cm^{-2}. Similarly, there is a wide range of IFLO-BSRV values that results in a FF of 65%. However, there is only a small range in which both values occur simultaneously, where IFLO is between 0.04 and 0.10 eV and BSRV is between 2×10^6 and 2×10^7 cm-s^{-1}. We note that for our model, we assumed the default ideal series and shunt resistances (0.0 and 10^{30} Ωcm^2, respectively). While nonideal resistance values can affect the FF of the device, we believe the bias-dependent current collection of these devices is dictated by the interface recombination and not the resistance values because the simulated JV curves (SI) show similar characteristics to the measured JV curves. Furthermore, the frontside JV response does not indicate limiting series and shunt resistances in this device. We also note that in this IFLO-BSRV range, the Voc is ~ 790 mV, which is close to the measuredvalues of our devices. Consequently, we believe Cu_xAlO_y back buffer layers have an IFLO ~ 0.07 eV, but the BSRV is high and on the order of 4×10^6 cm-s^{-1}.

To see how high the efficiency can be pushed beyond the 5% record value [4] while using a commercially fabricated device stack, we applied

Approved for public release; distribution unlimited.
724

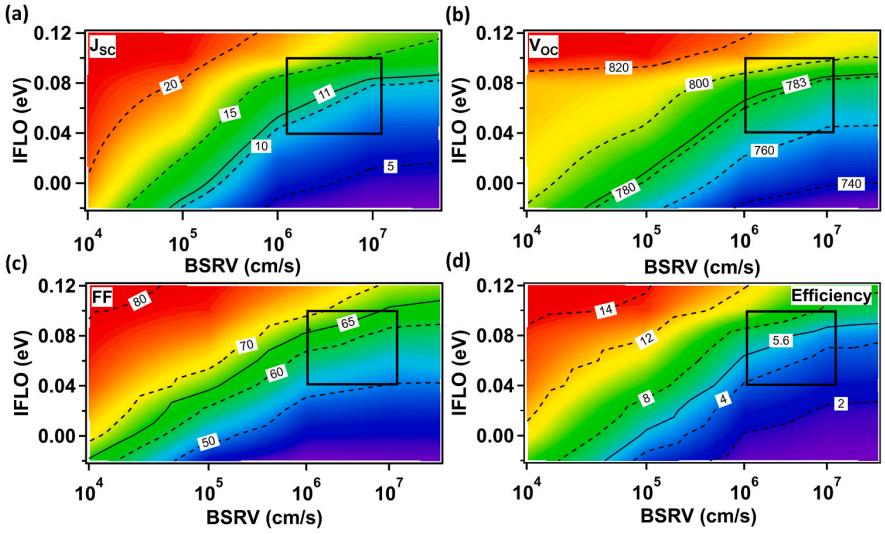
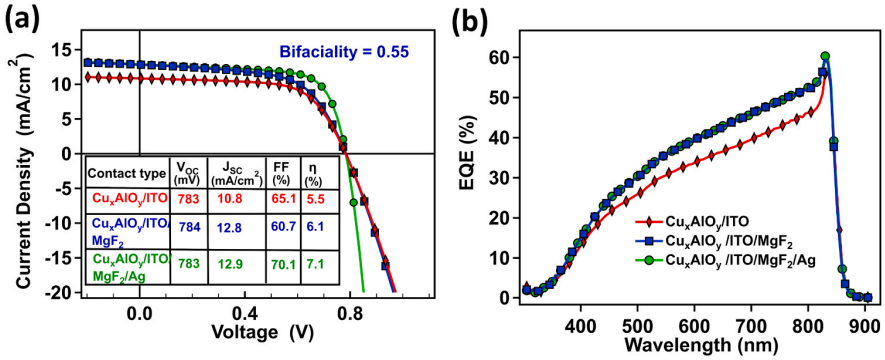


Fig. 2. Contour plots obtained by SCAPS modeling to obtain photovoltaic parameters for a 3.3 μm device illuminated through the backside with varying back surface recombination velocity and initial Fermi level off set. Note the solid contour line is the measured value of each parameter and the box shows the range of the IFLO and BSRV.



Contact type	V_{OC} (mV)	J_{SC} (mA/cm^2)	FF (%)	η (%)
Cu_xAlO_y/ITO	783	10.8	65.1	5.5
Cu_xAlO_y/ITO MgF_2	784	12.8	60.7	6.1
Cu_xAlO_y/ITO MgF_2/Ag	783	12.9	70.1	7.1

Fig. 3. (a) J-V and (b) EQE curves of the champion devices with Cu_xAlO_y/ITO, Cu_xAlO_y/ITO/MgF_2, and Cu_xAlO_y/ITO/MgF_2/Ag (metal) grid of 3.3 μm thick CdTe device for back illumination.

a MgF_2 antireflective (AR) coating on the Cu_xAlO_y/ITO back contact stack of the 3.3 μm thick CdTe layer device. Fig. 3 shows the JV and QE response of the devices before and after. Note that the results for a 2 μm device with the same treatment is shown in the SI. As expected, the AR coating increased the current collected for all biases by allowing more light to reach the absorber. We note that there is a slight decrease in FF due an increase in series resistance caused by the added AR layer. When a metal grid is added to the device, we see the FF increase, resulting in a backside illuminated efficiency of 7.1% and a bifaciality of 0.55. For the 2 μm device, the backside illuminated efficiency of 8.0% and bifaciality of 0.62 are achieved (SI).

2. Conclusions

Using solution processing, we fabricated a wide bandgap Cu_xAlO_y back buffer layer for CdTe PV devices which shows strong evidence of an electron-repelling upward band bending at the back interface. When ITO was applied as the back electrode, we were able to fabricate devices with backside illuminated efficiency that was nearly independent of absorber layer thickness, and yielded back-illuminated conversion efficiency as high as 7.1% and 8.0% for 3.3 μm and 2 μm devices, respectively. Time-resolved PL results show that the Cu_xAlO_y back contact layer leads to significant gains in carrier lifetime when measured for illumination through either the front or back contacts. The J-V curve, though, shows a photocurrent that is significantly below the expected one sun value. Reflection from the back interface, though significant, does not account for all of the current density loss. The remainder of the loss is due to back interface recombination due to a persistent high BSRV that is offset somewhat by Cu_xAlO_y creating a positive IFLO and a concomitant back surface field.

CRediT authorship contribution statement

Kamala Khanal Subedi: Conceptualization, Data curation, Formal analysis, Investigation, Writing. **Adam B. Phillips:** Conceptualization, Data curation, Formal analysis, Investigation, Writing, Supervision,

Approved for public release; distribution unlimited.
725

Project administration. **Niraj Shrestha**: Investigation. **Fadhil K. Alfadhili:** Investigation. **Anna Osella**: Investigation. **Indra Subedi**: Validation, Formal analysis. **Rasha A. Awni:** Validation, Formal analysis. **Ebin Bastola:** Conceptualization, Investigation. **Zhaoning Song:** Validation. **Deng-Bing Li:** Investigation, Validation. **Robert W. Collins:** Conceptualization, Funding acquisition. **Yanfa Yan:** Resources, Funding acquisition. **Nikolas J. Podraza:** Resources, Funding acquisition. **Michael J. Heben:** Resources, Funding acquisition. **Randy J. Ellingson:** Conceptualization, Funding acquisition, Data curation, Project administration, Writing - review & editing.

Declaration of Competing Interest

The authors declare that they have no known competing financial interests or personal relationships that could have appeared to influence the work reported in this paper.

Acknowledgements

This report is based on research sponsored by the U.S. Air Force Research Laboratory under agreement numbers FA9453–18-2–0037 and FA9453–19-C-1002, and by the U.S. DOE's Office of Energy Efficiency and Renewable Energy (EERE) under Solar Energy Technologies Office (SETO) Agreement DE-EE0008974. The U.S. Government is authorized to reproduce and distribute reprints for Governmental purposes notwithstanding any copyright notation thereon. Disclaimer: The views and conclusions contained herein are those of the authors and should not be interpreted as necessarily representing the official policies or endorsements, either expressed or implied, of the U.S. Air Force Research Laboratory or the U.S. Government. The authors would like to thank Willard and Kelsey Solar Group for providing CdS/CdTe filmstack samples.

Appendix A. Supporting information

Supplementary data associated with this article can be found in the online version at doi:10.1016/j.nanoen.2021.105827.

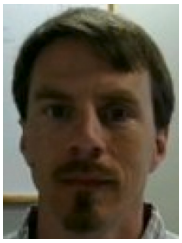
References

[1] M.A. Green, E.D. Dunlop, J. Hohl-Ebinger, M. Yoshita, N. Kopidakis, A.W.Y. Ho-Baillie, Solar cell efficiency tables (Version 55, Prog. Photovolt.: Res. Appl. 28 (2020) 3–15.
[2] M. Fischer, *ITRPV*, Report Release and Key Findings; PV CellTech conference (Vol. 14) 2018. (2018).
[3] R. Guerrero-Lemus, R. Vega, T. Kim, A. Kimm, L. Shephard, Bifacial solar photovoltaics – A technology review, Renew. Sustain. Energy Rev. 60 (2016) 1533–1549.
[4] J. Keller, W.C. Chen, L. Riekehr, T. Kubart, T. Törndahl, M. Edoff, Bifacial Cu(In, Ga)Se2solar cells using hydrogen-doped In2O3films as a transparent back contact, Prog. Photovolt. Res. Appl. 26 (2018) 846–858.
[5] S. Marsillac, V. Parikh, A. Compaan, Ultra-thin bifacial CdTe solar cell, Sol. Energy Mater. Sol. Cells 91 (2007) 1398–1402.
[6] A.B. Phillips, K. Khanal Subedi, G.K. Liyange, F.K. Alfadhili, R.J. Ellingson, M. J. Heben, ACS Appl. Energy Mater. 3 (2020) 6072–6078.
[7] D. Abou-Ras, G. Kostorz, D. Bremaud, M. Kälin, F. Kurdesau, A. Tiwari, M. Döbeli, Formation and characterisation of MoSe2 for Cu(In,Ga)Se_2 based solar cells, Thin Solid Films 480–481 (2005) 433–438.
[8] D. Rioux, D.W. Niles, H. Höchst, ZnTe: a potential interlayer to form low resistance back contacts in CdS/CdTe solar cells, J. Appl. Phys. 73 (1993) 8381–8385.
[9] G.K. Liyanage, A.B. Phillips, F.K. Alfadhili, R.J. Ellingson, M.J. Heben, The role of back buffer layers and absorber properties for >25% efficient CdTe solar cells, ACS Appl. Energy Mater. 2 (2019) 5419–5426.
[10] A.B. Phillips, G.K. Liyanage, F.K. Alfadhili, M.J. Heben, IEEE 46th Photovoltaic Specialists Conference (PVSC), IEEE 2019 (2019) 0777–0782.
[11] H. Kawazoe, M. Yasukawa, H. Hyodo, M. Kurita, H. Yanagi, H. Hosono, P-type electrical conduction in transparent thin films of $CuAlO_2$, Nature 389 (1997) 939–942.
[12] H. Yanagi, H. Kawazoe, A. Kudo, M. Yasukawa, H. Hosono, J. Electroceram. 4 (2000) 407–414.
[13] X. Xu, J. Bullock, L.T. Schelhas, E.Z. Stutz, J.J. Fonseca, M. Hettick, V.L. Pool, K. F. Tai, M.F. Toney, X. Fang, Chemical Bath deposition of p-type transparent, highly conducting $(CuS)_x$:$(ZnS)_{1-x}$nanocomposite thin films and fabrication of si heterojunction solar cells, Nano Lett. 16 (2016) 1925–1932.
[14] Y. Han, S. Siol, Q. Zhang, A. Zakutayev, Optoelectronic properties of strontium and barium copper sulfides prepared by combinatorial sputtering, Chem. Mater. 29 (2017) 8239–8248.
[15] D.-B. Li, Z. Song, S.S. Bista, F.K. Alfadhili, R.A. Awni, N. Shrestha, D. Rhiannon, A. B. Phillips, M.J. Heben, R.J. Ellingson, F. Yan, Y. Yan, CuSCN as the back contact for efficient ZMO/CdTe solar cells, Materials 13 (2020), 1991.
[16] K.K. Subedi, E. Bastola, I. Subedi, Z. Song, K.P. Bhandari, A.B. Phillips, N. J. Podraza, M.J. Heben, R.J. Ellingson, Nanocomposite $(CuS)_x$ $(ZnS)_{1-x}$ thin film back contact for CdTe solar cells: toward a bifacial device, Sol. Energy Mater. Sol. Cells 186 (2018) 227–235.
[17] K.K. Subedi, E. Bastola, I. Subedi, A.B. Phillips, M.J. Heben, N.J. Podraza, R. J. Ellingson, IEEE 46th Photovoltaic Specialists Conference (PVSC), IEEE (2019) 0185–0188.
[18] S. Li, X. Zhang, P. Zhang, X. Sun, H. Zheng, W. Zhang, Fabrication, characterization and cytotoxicity of spherical-shaped conjugated gold-cockle shell derived calcium carbonate nanoparticles for biomedical applications, Nanoscale Res. Lett. 13 (2018) 1–7.
[19] Q. Lin, Y. Su, M.-J. Zhang, X. Yang, S. Yuan, J. Hu, Y. Lin, J. Liang, F. Pan, A novel p-type and metallic dual-functional Cu–Al_2O_3ultra-thin layer as the back electrode enabling high performance of thin film solar cells, Chem. Commun. 52 (2016) 10708–10711.
[20] K.P. Bhandari, P. Koirala, N.R. Paudel, R.R. Khanal, A.B. Phillips, Y. Yan, R. W. Collins, M.J. Heben, R.J. Ellingson, Iron pyrite nanocrystal film serves as a copper-free back contact for polycrystalline CdTe thin film solar cells, Sol. Energy Mater. Sol. Cells 140 (2015) 108–114.
[21] H. Jiang, H. Lei, X. Zhu, G. Li, Z. Yang, W. Song, J. Dai, Y. Sun, Y. Fu, Effects of citric acid on properties of single phase $CuAlO_2$ thin films derived by chemical solution deposition, J. Alloy. Compd. 487 (2009) 404–408.
[22] A. Romeo, G. Khrypunov, S. Galassini, H. Zogg, A. Tiwari, Bifacial configurations for CdTe solar cells, Sol. Energy Mater. Sol. Cells 91 (2007) 1388–1391.
[23] R.R. Khanal, A.B. Phillips, Z. Song, Y. Xie, H.P. Mahabaduge, M.D. Dorogi, S. Zafar, G.T. Faykosh, M.J. Heben, Substrate configuration, bifacial CdTe solar cells grown directly on transparent single wall carbon nanotube back contacts, Sol. Energy Mater. Sol. Cells 157 (2016) 35–41.
[24] M. Burgelman, P. Nollet, S. Degrave, Modelling polycrystalline semiconductor solar cells, Thin Solid Films 361–362 (2000) 527–532.
[25] B. Hoex, S. Heil, E. Langereis, M. Van de Sanden, W. Kessels, Ultralow surface recombination of c-Si substrates passivated by plasma-assisted atomic layer deposited Al_2O_3, Appl. Phys. Lett. 89 (2006), 042112.
[26] D. Kuciauskas, J.M. Kephart, J. Moseley, W.K. Metzger, W.S. Sampath, P. Dippo, Recombination velocity less than 100 cm/s at polycrystalline Al_2O_3/CdSeTe interfaces, Appl. Phys. Lett. 112 (2018), 263901.
[27] B. Vermang, Y. Ren, O. Donzel-Gargand, C. Frisk, J. Joel, P. Salomé, J. Borme, S. Sadewasser, C. Platzer-Björkman, M. Edoff, Rear surface optimization of CZTS solar cells by use of a passivation layer with nanosized point openings, IEEE J. Photovolt. 6 (2016) 332–336.
[28] J. Liang, Q. Lin, H. Li, Y. Su, X. Yang, Z. Wu, J. Zheng, X. Wang, Y. Lin, F. Pan, Rectification and tunneling effects enabled by Al_2O_3 atomic layer deposited on back contact of CdTe solar cells, Appl. Phys. Lett. 107 (2015), 013907.
[29] J.M. Kephart, A. Kindvall, D. Williams, D. Kuciauskas, P. Dippo, A. Munshi, W. Sampath, Sputter-deposited oxides for interface passivation of CdTe photovoltaics, IEEE J. Photovolt. 8 (2018) 587–593.
[30] F.K. Alfadhili, A.B. Phillips, K.K. Subedi, C.L. Perkins, A.I. Halaoui, M. K. Jamarkattel, B.M. Anwar, G.K. Liyanage, D.-B. Li, C.R. Grice, Y. Yan, R. J. Ellingson, M.J. Heben, Back-surface passivation of CdTe solar cells using solution-processed oxidized aluminum, ACS Appl. Mater. Interfaces 12 (2020) 51337–51343.
[31] J. Türck, H.J. Nonnenmacher, P.M. Connor, S. Siol, B. Siepchen, J.P. Heimfarth, A. Klein, W. Jaegermann, Copper (I) Oxide (Cu_2O) based back contact for p-i-n CdTe solar cells: copper (I) oxide (Cu_2O) back contact for CdTe solar cells, Prog. Photovolt. Res. Appl. 24 (2016) 1229–1236.
[32] G.K. Liyanage, A.B. Phillips, M.J. Heben, Role of band alignment at the transparent front contact/emitter interface in the performance of wide bandgap thin film solar cells, APL Mater. 6 (2018), 101104.



Kamala Khanal Subedi earned her B.Sc and M.Sc degree in physics from Tribhuvan University, Nepal. Currently, she is pursuing a Ph. D at the University of Toledo in physics with a specialization in photovoltaics under the supervision of Prof. Randy J. Ellingson. Her research is focused on the fabrication and characterization of CdTe thin film devices, modeling, and characterization of other semiconducting materials by using laser spectroscopy.

Approved for public release; distribution unlimited.
726



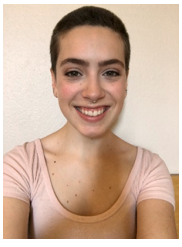
Adam B. Phillips earned his B.S. in Physics from Case Western Reserve University in 1999 and his Ph.D. in Physics from the University of Virginia in 2007. Since 2008 he has been working as research faculty at the University of Toledo where he works on improving photovoltaic device operation and understanding. His current research is focused on understanding, characterizing, and improving the absorber/charge transport layer interfaces of CdTe-based and perovskites devices to enable higher efficiency, lighter weight, or alternative device structures.



Niraj Shrestha received his Ph.D. degree from The University of Toledo, Toledo, OH in 2020. His research interests include study of semiconductor thin films based on their static and dynamic optical properties including techniques of ultrafast pump-probe spectroscopy, steady state photoluminescence spectroscopy and time resolved photoluminescence spectroscopy. At present, he is working as an Optical Scientist at NP Photonics in Tucson, AZ.



Dr. Fadhil Alfadhili obtained his Ph.D. in 2020 from the Department of Physics and Astronomy, the University of Toledo, Ohio, USA. For his achievements in the field of CdTe thin-film solar cells. His research interests are focused on device physics and materials science related to thin film nanomaterials, and photovoltaics.



Anna Osella is a graduate student currently studying materials science at the Colorado School of Mines, focusing on semiconductors, fabrication, and material synthesis. She has a Bachelor of Science in physics from Michigan State University, where she worked on ferromagnetic materials for computer memory. She also spent one summer working at the University of Toledo on a bifacial solar cell measurement system, and a semester working at the National Renewable Energy Laboratory synthesizing and measuring battery anode materials.



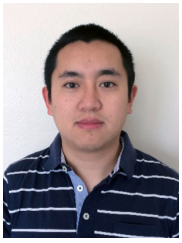
Indra Subedi is a Postdoctoral researcher at University of Toledo. He received his M.Sc in physics from Tribhuvan University, Kathmandu, Nepal. He obtained both M.S. & Ph.D. degree in physics from the University Toledo, Toledo, OH in year 2016 & 2019 respectively. His current research interest includes fabrication of thin film devices and determination of optical properties of thin films, solar cells, and bulk material by using spectroscopic ellipsometry and used them in devices simulation for optoelectronic devices like solar cells.



Rasha Awni is a postdoctoral researcher at the Wright Center for Photovoltaics Innovation and Commercialization in the Department of Physics and Astronomy at The University of Toledo. She joined Prof. Yanfa Yan's group in 2016. She received her Ph.D. degree in physics from The University of Toledo, USA, in 2020. Her research is focused on understanding defects in II-VI compounds and perovskite materials and electrical characterization, simulations, and modeling of photovoltaic devices.



Dr. Ebin Bastola obtained his Ph.D. in Physics from the Center for Photovoltaics Innovation and Commercialization (PVIC), The University of Toledo, Toledo, OH. He is interested in solution-processing of the earth abundant nanomaterials including synthesis, characterization, and device fabrication for photovoltaic application. His current research primarily focuses on cadmium telluride thin film and devices.



Zhaoning Song received his B.S. degree in physics from Xiamen University, China, in 2009 and his Ph.D. in physics from the University of Toledo in 2016. He is currently a research assistant professor at the University of Toledo. His research interests include thin-film photovoltaics, device physics, materials science, and nanomaterials for optoelectronic applications.

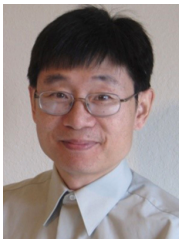


Deng-Bing Li received his B.S. degree in School of materials science and engineering from Nanjing Tech University in china in 2009. He received his Ph.D. degree in Institute of Solid state Physics, Chinese Academy of Sciences in 2014. Now he is working in Yanfa Yan's group as a postdoc in the University of Toledo. His research focuses on the fabrication and characterization of high efficiency inorganic photovoltaics.



Robert Collins has held the titles of NEG Endowed Chair of Silicate and Materials Science at the University of Toledo since 2004 and Distinguished University Professor since 2008. He received the Ph.D. degree in Applied Physics from Harvard University in 1982 and served as Professor of Physics and Materials Research at The Pennsylvania State University from 1992 through 2003. He is a National Science Foundation Presidential Young Investigator Awardee, a Fellow of the American Physical Society (APS), and a recipient of the William Fowler Award of the APS Ohio Chapter for his research on the optical physics of materials.

Approved for public release; distribution unlimited.
727



Yanfa Yan has been an Ohio Research Scholar Chair and Professor in the Department of Physics and Astronomy at The University of Toledo, since 2011. Previously, he was a Principal Scientist at the National Renewable Energy Laboratory. He earned his Ph. D. in Physics from Wuhan University in 1993. His expertize includes thin-film solar cell fabrication, defect physics of semiconductors, and nanoscale characterization of microstructures, interfaces, and defects in thin-film photovoltaic materials. He is a Fellow of the American Physical Society.



Nikolas J. Podraza is a Professor in the Department of Physics and Astronomy and Wright Center for Photovoltaics Innovation and Commercialization at the University of Toledo. He earned his PhD in Physics from the University of Toledo and his MS and BS in Physics from the Pennsylvania State University. His research interests include optical properties of materials, spectroscopic ellipsometry, thin film deposition, nanostructured materials, and opto-electronic devices including microbolometers and photovoltaics.



Michael Heben is the McMaster Chair for Photovoltaics, the Managing Director of the Wright Center for Photovoltaics, and a Professor of Physics at the University of Toledo. He earned a BS in Physics from John Carroll University, an MS in Materials Science and Engineering from Stanford, and a PhD in Chemistry from Caltech. He was a postdoc and later a Principal Scientist and Group Leader over an 18 year career at NREL, prior to coming to Toledo in 2008. His interests include the science, manufacturability, and economics of PV materials and devices, and issues relating to building-DER-grid integration.



Randy Ellingson, Professor of Physics and faculty member of the University of Toledo's Wright Center for Photovoltaics Innovation and Commercialization, studies photovoltaic materials, devices, and systems. Research methods include ultrafast and steady-state optical spectroscopies, synthesis and solution-processing of nanocrystalline and quantum-confined semiconductors, device modeling, and PV system modeling and energy production forecasting. He received his B.A. in Physics from Carleton College and his Ph.D. degree in Applied Physics from Cornell University. After 14 very enjoyable years at the National Renewable Energy Laboratory (NREL) in Colorado, he joined the University of Toledo in 2008 to focus on the application of advanced materials and characterization to commercially relevant solar energy technologies. Additional interests include bringing the benefits of clean solar electricity to the underserved communities in and around Toledo by working with the charitable non-profit organization, Glass City Community Solar.

Approved for public release; distribution unlimited.
728

ACS APPLIED MATERIALS & INTERFACES

www.acsami.org Research Article

Optical and Electronic Losses Arising from Physically Mixed Interfacial Layers in Perovskite Solar Cells

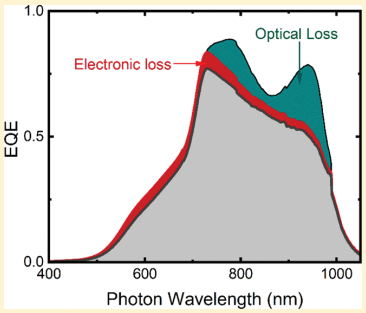
Biwas Subedi, Zhaoning Song, Cong Chen, Chongwen Li, Kiran Ghimire, Maxwell M. Junda, Indra Subedi, Yanfa Yan, and Nikolas J. Podraza*

Cite This: *ACS Appl. Mater. Interfaces* 2021, 13, 4923–4934 Read Online

ACCESS | Metrics & More | Article Recommendations | Supporting Information

Downloaded via UNIV OF TOLEDO on September 13, 2021 at 16:07:55 (UTC).
See https://pubs.acs.org/sharingguidelines for options on how to legitimately share published articles.

ABSTRACT: Perovskite solar cell device performance is affected by optical and electronic losses. To minimize these losses in solar cells, it is important to identify their sources. Here, we report the optical and electronic losses arising from physically mixed interfacial layers between the adjacent component materials in highly efficient two terminal (2T) all-perovskite tandem, single-junction wide-bandgap, and single-junction narrow-bandgap perovskite-based solar cells. Physically mixed interfacial layers as the sources of optical and electronic losses are identified from spectroscopic ellipsometry measurements and data analysis followed by comparisons of simulated and measured external quantum efficiency spectra. Parasitic absorbance in the physically mixed regions between silver metal electrical contacts and electron transport layers (ETLs) near the back contact and a physical mixture of commercial indium tin oxide and hole transport layers (HTL) near the front electrical contact lead to substantial optical loss. A lower-density void + perovskite nucleation layer formed during perovskite deposition at the interface between the perovskite absorber layer and the HTL causes electronic losses because of incomplete collection of photogenerated carriers likely originating from poor coverage and passivation of the initially nucleating grains.



KEYWORDS: *perovskite solar cells, optical and electronic losses, external quantum efficiency modeling, optical properties, interfacial layers, spectroscopic ellipsometry*

INTRODUCTION

Inorganic-organic metal halide perovskite ABX_3 (A: methylammonium-MA, formamidinium-FA, cesium-Cs; B: lead-Pb, tin-Sn; X: iodine-I, bromine-Br, and chlorine-Cl)-based absorbers have attracted wide interest in photovoltaics because of high power conversion efficiencies (PCEs) > 25%[1] of devices, simple and cost-effective fabrication process, and desirable optoelectronic properties including a high absorption coefficient above the bandgap energy (E_g), bandgap energy tunable by composition, long carrier diffusion lengths, and long carrier lifetimes. Nevertheless, perovskite solar cell PCEs are still below the Shockley–Queisser limit as performance of these devices is often affected by optical and electronic losses. Optical losses refer to any incident photons either reflected or parasitically absorbed in an inactive device layer. Parasitic absorption loss occurs when the absorbance of incident solar irradiance with photon energies greater than the bandgap of the photovoltaic absorber layer takes place in any layer not generating current. Incomplete collection of photogenerated carriers in the absorber layer results in electronic loss. Studies have shown that reflection loss and parasitic absorption in the conduction and charge carrier transport layers are dominant factors of optical loss in perovskite solar cells.[2−4] Shockley–Read–Hall recombination due to unpassivated defects in the perovskite absorber layer and other nonradiative recombination at absorber surfaces and interfaces contribute to electronic loss in perovskite solar cells.[4−6] All the studies related to the optical and electronic losses in perovskite solar cells until now have only focused on the losses via structurally and optically continuous bulk component layers. The presence of surface roughness on a layer leads to physical mixing with over-deposited layers at interfaces that can result in further optical and electronic losses.[7,8] Silver (Ag) used as a back electrical contact in perovskite solar cells is known to diffuse and interact with carrier transport layers to form a physically mixed region of Ag and these carrier transport layers.[9−11] In addition, Ag also interacts with halide ions within the perovskite absorber layer.[12] Similarly, perovskite films deposited by spin-coating methods are reported to form a lower-density layer with larger perovskite grains and lower surface coverage near the substrate.[13−15] In perovskite solar cells, the optical and

Received: September 14, 2020
Accepted: January 8, 2021
Published: January 20, 2021



ACS Publications © 2021 American Chemical Society

https://dx.doi.org/10.1021/acsami.0c16364
ACS Appl. Mater. Interfaces 2021, 13, 4923–4934

Approved for public release; distribution unlimited.

electronic losses arising from physical mixing between the component layers and their precise impact on device performance have not yet been reported. To improve the performance of perovskite solar cells toward the Shockley–Queisser limit, it is essential to minimize all sources of optical and electronic losses including those arising from the physically mixed interfacial layers.

External quantum efficiency (EQE) simulations[2,7,16−26] use solar cell device structure parameters and infrared to ultraviolet spectral range complex optical properties of component layers as the input. Simulated EQE when matched with measured EQE validates the structural and optical model. These simulations quantify reflection and parasitic absorption losses for assessment of loss mitigation strategies. In cases of disagreement between simulation and experiment, sources of electronic losses can also be identified. In this study, a complete database of optical response in terms of the complex dielectric function ($\varepsilon = \varepsilon_1 + i\varepsilon_2$) spectra for component layers in single-junction and all-perovskite tandem solar cells has been developed using spectroscopic ellipsometry augmented with unpolarized transmittance and photothermal deflection spectroscopy measurements. Through-the-glass spectroscopic ellipsometry measurements[7,18] of a highly efficient two terminal (2T) all-perovskite tandem solar cell[27] containing a wide-E_g $FA_{0.8}Cs_{0.2}Pb(I_{0.7}Br_{0.3})_3$ perovskite-based top subcell and a 2.5% Cl-doped narrow-E_g $(FASnI_3)_{0.6}(MAPbI_3)_{0.4}$ perovskite-based bottom subcell, a single-junction wide-E_g $FA_{0.8}Cs_{0.2}Pb(I_{0.7}Br_{0.3})_3$, and single-junction narrow-E_g $(FASnI_3)_{0.6}(MAPbI_3)_{0.4}$ and $(FASnI_3)_{0.5}(MAPbI_3)_{0.5}$ perovskite-based solar cells[28,29] have been analyzed using this database to determine the component layer thicknesses, the presence and thicknesses of physically mixed interfacial layers, and the fraction of component materials in the physically mixed interfacial layers. Using the information gained from the database of the complex optical response and through-the-glass spectroscopic ellipsometry measurements of cells, EQE simulations are generated and compared to experimental EQE. For perovskite solar cells studied, comparisons between the simulated and measured EQE combined with the analysis of through-the-glass spectroscopic ellipsometry measurements help to identify physically mixed interfacial layers between Ag and electron transport layers (ETLs) near the back electrical contact, between commercial indium tin oxide (ITO) and the hole transport layer (HTL) near the front electrical contact, and as void + perovskite nucleation layers at the HTL + perovskite interface. In addition, optical and electronic losses due to these physically mixed interfacial layers are quantified in terms of short-circuit current density (J_{SC}). All the perovskite solar cells studied here show substantial optical and electronic losses because of the presence of physically mixed interfacial layers. The 2T all-perovskite tandem solar cell with a measured PCE of 21% shows the highest amount of optical and electronic losses among the perovskite solar cells studied. The EQE simulations generated without the physically mixed interfacial layers overestimate the measured EQE, which suggests that the ability to avoid physical mixing of components at the aforementioned interfaces can potentially lead to the further improvement of already highly efficient solar cells.

Experiment Details. Perovskite solar cells are fabricated using the inverted planar configuration.[27,29] Single-junction wide-E_g $FA_{0.8}Cs_{0.2}Pb(I_{0.7}Br_{0.3})_3$ perovskite-based solar cells are fabricated with a structure consisting of a soda lime glass superstrate/commercially deposited ITO transparent electrical contact/poly[bis(4-phenyl)(2,4,6-trimethylphenyl)amine] (PTAA) as the HTL/perovskite absorber layer/fullerene (C_{60})/2,9-dimethyl-4,7-diphenyl-1,10-phenanthroline (BCP)/Ag back electrical contact (Figure S1). C_{60} acts as an ETL, and BCP acts as both an ETL and a hole blocking layer.[30] Similarly, single-junction narrow-E_g $(FASnI_3)_{0.6}(MAPbI_3)_{0.4}$ and $(FASnI_3)_{0.5}(MAPbI_3)_{0.5}$ perovskite-based solar cells are fabricated with structures consisting of soda lime glass superstrates/commercially deposited ITO transparent electrical contacts/poly(3,4-ethylenedioxythiophene):polystyrenesulfonate (PEDOT:PSS) as the HTLs/perovskite absorber layers/C_{60}/BCP/Ag back electrical contact (Figures S2 and S3). 2T all-perovskite tandem cells are fabricated with a wide-E_g $FA_{0.8}Cs_{0.2}Pb(I_{0.7}Br_{0.3})_3$ perovskite-based top subcell and a 2.5% Cl-doped narrow-E_g $(FASnI_3)_{0.6}(MAPbI_3)_{0.4}$ bottom subcell in the configuration: soda lime glass superstrate/commercially deposited ITO/PTAA/wide-E_g perovskite absorber/C_{60}/BCP/sputtered ITO/PEDOT:PSS/narrow-E_g perovskite absorber/C_{60}/BCP/Ag (Figure S4). All solar cell component layers are also individually deposited on either soda lime glass substrates or native oxide covered silicon wafers for structural and optical characterization using spectroscopic ellipsometry. Unpolarized transmittance and photothermal deflection spectroscopy are used in addition to spectroscopic ellipsometry to characterize the perovskite thin films on soda lime glass substrates. Detailed information on preparation and characterization of thin films and fabrication of perovskite solar cells is presented in the Supporting Information.

Spectroscopic ellipsometry measurements are performed for the complete perovskite solar cells in the through-the-glass measurement configuration at 60° angle of incidence over the photon energy range of 0.74−3.95 eV using a single rotating compensator multichannel spectroscopic ellipsometer[31,32] (M-2000FI, J. A. Woollam Co., Inc.). The upper limit of the spectral range is 3.95 eV because of absorption in the glass superstrate making data at higher photon energies insensitive to the solar cell device stack. In this measurement configuration, the detector arm of the ellipsometer is positioned such that only the beam reflected from the glass/solar cell film stack interface is collected without contributions from the beam reflected from the air/glass interface. Ellipsometric spectra were measured in the terms of $N = \cos 2\Psi$, $C = \sin 2\Psi \cos \Delta$, and $S = \sin 2\Psi \sin \Delta$, where $\tan\Psi$ and Δ represent the amplitude ratio and phase-shift difference between p- and s-polarized light waves, respectively. Measured ellipsometric spectra (N, C, and S) for perovskite solar cells are fitted using least squares regression to structural and optical models based upon the solar cell schematics with parameters consisting of the component layer thicknesses, physically mixed interfacial layer thicknesses, relative material fractions in physically mixed interfacial layers, and the complex optical response of each component layer. The quality of fit between the model and experimental ellipsometric spectra is defined in terms of the unweighted mean square error (MSE).[33] Some structural and optical models in this study assume the formation of physically mixed interfacial layers between the adjacent layer materials. These physically mixed layers are described by Bruggeman effective medium approximations[34] modeled with variable fractions of spectra in ε of the component materials. For example, a physically mixed interfacial layer between Ag, C_{60}, and BCP is defined by variable fractions of the spectra in ε for Ag, C_{60}, and BCP

https://dx.doi.org/10.1021/acsami.0c16364
ACS Appl. Mater. Interfaces 2021, 13, 4923−4934

Approved for public release; distribution unlimited.

components. In the effective medium approximation for this layer, the effective C_{60} and BCP thickness are constrained to their nominal values of 20 and 5 nm, respectively. These effective material thicknesses are defined as the total interfacial layer thickness weighted by the respective material fraction.

A transfer matrix approach based upon input complex optical properties and layer thicknesses obtained from spectroscopic ellipsometry is used to simulate absorbance within each layer of the device.[2,7,8,16−21,23,35] The transfer matrix approach is applied here as the physically mixed interfacial layer thickness and the in-plane morphological features are much smaller than the wavelength of light considered for both spectroscopic ellipsometry and EQE. The absorbance from all perovskite-containing layers in a device is summed to simulate the ideal EQE spectrum. These simulations assume that each photon absorbed in the perovskite photo-generates an electron−hole pair, which contributes to EQE and J_{SC}. J_{SC} is determined from EQE by integrating the product of EQE and the AM 1.5G solar irradiance spectrum with respect to wavelength. Experimental EQE spectra are measured over wavelengths from 300−900 nm for the wide-E_g single-junction solar cell and from 300−1100 nm for the narrow-E_g single-junction perovskite solar cells (PV Measurements Inc., model IVQE8-C QE system without bias voltage). For the 2T all-perovskite tandem solar cell, the EQE spectrum is measured by contacting the middle electrode (sputtered ITO) with the transparent front electrode (ITO) and back metal contact (Ag), respectively, to measure the top and bottom subcells individually. The narrow-E_g single-junction perovskite-based solar cells and the 2T all-perovskite tandem solar cell, which are more susceptible toward degradation in laboratory ambient air are encapsulated with cover glass and sealed with ultraviolet curable epoxy to prevent atmospheric exposure during spectroscopic ellipsometry and EQE measurements.

RESULTS AND DISCUSSION

Complex optical response in the terms of spectra in ε for all component layers of perovskite solar cells have been measured using spectroscopic ellipsometry or spectroscopic ellipsometry combined with photothermal deflection spectroscopy and unpolarized transmittance as shown in Figures S10−S29 and discussed in the Supporting Information. Bandgaps of all perovskite absorber layers are determined from the optical response of the corresponding perovskite films. $FA_{0.8}Cs_{0.2}Pb(I_{0.7}Br_{0.3})_3$, $(FASnI_3)_{0.6}(MAPbI_3)_{0.4}$, and $(FASnI_3)_{0.5}(MAPbI_3)_{0.5}$ perovskite absorber layers used in single-junction solar cells show bandgap energies of 1.74, 1.25, and 1.26 eV, respectively. Similarly, 2.5% Cl-doped $(FASnI_3)_{0.6}(MAPbI_3)_{0.4}$ used in the bottom subcell and $FA_{0.8}Cs_{0.2}Pb(I_{0.7}Br_{0.3})_3$ perovskite absorber used in the top subcell of the 2T all-perovskite tandem show bandgap energies of 1.25 and 1.74 eV, respectively. Spectra in ε for all the component layers serve as the input for analysis of ellipsometric spectra collected for full perovskite solar cells as shown in Figures S30−S33 and for simulation of complete device EQE. The ellipsometric spectra collected for each perovskite solar cell studied are analyzed using several different models. The first model does not consider the formation of any physically mixed interfacial layers between component materials. The commercial ITO film deposited on glass used in each solar cell shows a measurable surface roughness as indicated by spectroscopic ellipsometry (Tables S8 and S9). Therefore, in complete solar cells, surface roughness in the commercial ITO is assumed to lead to the formation of an ITO + HTL layer, a physical mixture of ITO and the HTL. The second model includes such an ITO + PTAA layer in the single-junction wide-E_g $FA_{0.8}Cs_{0.2}Pb(I_{0.7}Br_{0.3})_3$ perovskite-based solar cell and 2T all-perovskite tandem solar cell, whereas an ITO + PEDOT:PSS layer is included in narrow-E_g $(FASnI_3)_{0.6}(MAPbI_3)_{0.4}$ and $(FASnI_3)_{0.5}(MAPbI_3)_{0.5}$ perovskite-based solar cells. In addition to the ITO + HTL layer, the third model incorporates a physically mixed interfacial layer between Ag and the ETL materials, C_{60} and BCP, and is represented as the C_{60} + BCP + Ag layer hereafter. The presence of voids in the C_{60} + BCP + Ag layer is also considered. A lower-density void + perovskite nucleation layer is observed in the perovskite films when the films deposited on glass substrates are characterized individually using spectroscopic ellipsometry (Tables S1−S4). Therefore, to assess the possibility of formation of a void + perovskite nucleation layer in complete solar cells while depositing the perovskites on the HTL, this layer is also incorporated in the structural model. The fourth model includes the lower-density void + nucleation layer only and no other physically mixed interfacial layers. The fifth model accounts for the formation of the lower-density void + perovskite nucleation layer in addition to the C_{60} + BCP + Ag layer and the ITO + HTL layer. In the first model, the fit parameters are only the component layer thicknesses, whereas in the rest of the models the fit parameters are component layer thicknesses, physically mixed interfacial layer thicknesses, and the fractions of component materials in each physically mixed layer.

In the wide-E_g $FA_{0.8}Cs_{0.2}Pb(I_{0.7}Br_{0.3})_3$ perovskite-based solar cell, MSE values of 10.2×10^{-2}, 10.2×10^{-2}, 8.7×10^{-2}, 9.2×10^{-2}, and 5.9×10^{-2} are obtained using the first, second, third, fourth, and fifth models, respectively (Tables 1 and S13). Including the ITO + PTAA layer only in the second model does not improve the quality of fit and the resulting thickness of the ITO + PTAA physically mixed interfacial layer in each model is negligible. As the physically mixed ITO + PTAA is not observed in this wide-E_g $FA_{0.8}Cs_{0.2}Pb(I_{0.7}Br_{0.3})_3$ perovskite-based solar cell, it is not included in subsequent models. The final or fifth model that includes the formation of a lower-density void + perovskite nucleation layer in addition to the C_{60} + BCP + Ag physically mixed interfacial layer best fits the experimental ellipsometric spectra (Figure S28). Table 1 lists the structural fit parameters and the quality of fit for the wide-E_g $FA_{0.8}Cs_{0.2}Pb(I_{0.7}Br_{0.3})_3$ perovskite-based solar cell obtained using the first and the final model. Similar information corresponding to the second, third, and fourth model is listed in Table S13. EQE simulations are performed for the wide-E_g $FA_{0.8}Cs_{0.2}Pb(I_{0.7}Br_{0.3})_3$ perovskite-based solar cell utilizing the component layer optical properties including that of the C_{60} + BCP + Ag layer (Figure S24) and lower-density void + $FA_{0.8}Cs_{0.2}Pb(I_{0.7}Br_{0.3})_3$ nucleation layer and thicknesses obtained from the corresponding structural models. The comparisons between the simulated and experimentally measured EQE in a single-junction $FA_{0.8}Cs_{0.2}Pb(I_{0.7}Br_{0.3})_3$ perovskite-based solar cell without considering the formation of any physically mixed interfacial layers (first model), including a C_{60} + BCP + Ag layer (third model), and including the formation of a lower-density void + perovskite nucleation layer in addition to the C_{60} + BCP + Ag layer (fifth model) are shown in Figure 1a−c, respectively. Simulated EQE with the inclusion of the C_{60} + BCP + Ag layer shows better agreement

https://dx.doi.org/10.1021/acsami.0c16364
ACS Appl. Mater. Interfaces 2021, 13, 4923−4934

Approved for public release; distribution unlimited.

Table 1. Wide-E_g $FA_{0.8}Cs_{0.2}Pb(I_{0.7}Br_{0.3})_3$ Perovskite-Based Solar Cell Device Structural Fit Parameters Obtained from Analysis of Spectroscopic Ellipsometry Data (A) without Considering the Formation of a Physically Mixed Interfacial Layer between Ag and the Electron Transport Layer (C_{60} and BCP), a Physical Mixture of ITO + PTAA, and a Lower-Density Void + $FA_{0.8}Cs_{0.2}Pb(I_{0.7}Br_{0.3})_3$ Perovskite Nucleation Layer; (B) Considering the Formation of a Physically Mixed Interfacial Layer between Ag and the Electron Transport Layer (C_{60} and BCP) and a Lower-Density Void + $FA_{0.8}Cs_{0.2}Pb(I_{0.7}Br_{0.3})_3$ Perovskite Nucleation Layer[a]

layers	thickness (nm)
A	
ITO	131 ± 1
PTAA	19 ± 1
wide-E_g $FA_{0.8}Cs_{0.2}Pb(I_{0.7}Br_{0.3})_3$ perovskite	323 ± 1
C_{60}	20
BCP	5
Ag	75
B	
ITO	133 ± 1
ITO + PTAA physically mixed layer (0.5 ITO + 0.5 PTAA)	0.0 ± 0.5
PTAA	12 ± 1
void + wide-E_g $FA_{0.8}Cs_{0.2}Pb(I_{0.7}Br_{0.3})_3$ perovskite nucleation layer (0.120 ± 0.003 void + 0.880 perovskite)	68 ± 2
wide-E_g $FA_{0.8}Cs_{0.2}Pb(I_{0.7}Br_{0.3})_3$ perovskite	266 ± 2
C_{60} + BCP + Ag physically mixed layer (0.74 C_{60} + 0.20 BCP + 0.06 ± 0.01 Ag)	30.0 ± 0.1
Ag	75

[a]The quality of fit for A is a MSE of 10.2×10^{-2}. The quality of fit for B is a MSE of 5.9×10^{-2}. Material fractions for the physically mixed layers are included in the parentheses. Values without error bars are fixed in the analysis.

with measured EQE compared to that without assuming any interfacial layers. However, EQE simulated with the inclusion of the void + perovskite nucleation layer in addition to the C_{60} + BCP + Ag layer slightly exceeds the measured EQE. This discrepancy shows that complete collection of photogenerated carriers cannot be expected from the perovskite absorber that includes the void + perovskite nucleation layer in addition to the bulk perovskite layer. This discrepancy is reduced by assuming incomplete collection of photogenerated electron–hole pairs and introducing reduced carrier collection probability in the void + nucleation layer. Simulated EQE better matches experimental EQE when carrier collection probability from the void + $FA_{0.8}Cs_{0.2}Pb(I_{0.7}Br_{0.3})_3$ perovskite nucleation layer is 92 ± 1% (Figure 1d). The most noticeable remaining deviation between simulated and experimental EQE occurs near the long wavelength EQE onset. This deviation may be because of slight differences between the bandgap of the perovskite absorber layer in the solar cell compared to that of the perovskite film deposited on a glass substrate. Improved agreement is obtained when EQE is generated assuming a 0.02 eV red shift in the bandgap energy within the parametric model describing ε for the wide-E_g perovskite absorber (see Table S4). This difference in the bandgap energy likely arises from variations in sample-to-sample fabrication. This newly generated EQE with the carrier collection probability of 91 ± 1% in the void + $FA_{0.8}Cs_{0.2}Pb(I_{0.7}Br_{0.3})_3$ perovskite nucleation layer better matches measured EQE at longer wavelengths (Figure 1d).

For the $(FASnI_3)_{0.6}(MAPbI_3)_{0.4}$ perovskite-based solar cell, MSE values of 11.0×10^{-2}, 11.0×10^{-2}, 7.0×10^{-2}, 9.0×10^{-2}, and 5.5×10^{-2} are obtained using the first, second, third, fourth, and fifth models, respectively (Tables 2 and S14). Similarly, for the $(FASnI_3)_{0.5}(MAPbI_3)_{0.5}$ perovskite-based solar cell, MSE values of 18.0×10^{-2}, 18.0×10^{-2}, 6.2×10^{-2}, 16.0×10^{-2}, and 5.8×10^{-2} are obtained using the first, second, third, fourth, and fifth models, respectively (Tables 3 and S15). In both single-junction narrow-E_g solar cells, including the ITO + PEDOT:PSS physically mixed interfacial layer in the second model does not improve the quality of fit, and the corresponding ITO + PEDOT:PSS layer thickness is negligible. The final model incorporating the lower-density void + perovskite nucleation layer in addition to the C_{60} + BCP + Ag layer yields the lowest MSE and best fits the experimental ellipsometric spectra (Figures S29 and S30) for both $(FASnI_3)_{0.6}(MAPbI_3)_{0.4}$ and $(FASnI_3)_{0.5}(MAPbI_3)_{0.5}$ perovskite-based solar cells. For the $(FASnI_3)_{0.6}(MAPbI_3)_{0.4}$ perovskite-based solar cell, the structural fit parameters and the quality of fit for the first and the final model are listed in Table 2, whereas the corresponding information for the second, third, and fourth models is listed in Table S14. Similarly, for the $(FASnI_3)_{0.5}(MAPbI_3)_{0.5}$ perovskite-based solar cell, the structural fit parameters and the quality of fit for the first and the final model are listed in Table 3, whereas the corresponding information for the second, third, and fourth models is listed in Table S15. The comparison between the simulated and measured EQE values for the $(FASnI_3)_{0.6}(MAPbI_3)_{0.4}$ and $(FASnI_3)_{0.5}(MAPbI_3)_{0.5}$ perovskite-based solar cells where simulated EQE uses the structural fit parameters for the corresponding models are shown in the Figures 2 and 3 respectively. For both single-junction narrow-E_g perovskite-based solar cells, inclusion of the C_{60} + BCP + Ag physically mixed layer and lower-density void + perovskite nucleation layer in the EQE simulations results in the closest agreement with experimental EQE.

The previously described modeling approaches for ellipsometric spectra collected from single-junction cells are now applied to a 2T all-perovskite tandem solar cell. The first model without any physically mixed interfacial layers has a MSE of 13.7×10^{-2}. The second model with the ITO + PTAA mixed interfacial layer has a MSE of 12.8×10^{-2}. The third incorporating a void + C_{60} + BCP + Ag layer in the bottom subcell and a C_{60} + BCP layer in the top subcell in addition to the ITO + PTAA layer improves the quality of fit with MSE substantially reduced from 12.8×10^{-2} to 6.1×10^{-2}. If void is not included in the C_{60} + BCP + Ag layer, the MSE is only reduced to 12.0×10^{-2}. The fourth model that includes only void + bottom 2.5% Cl-doped narrow-E_g $(FASnI_3)_{0.6}(MAPbI_3)_{0.4}$ and void + top wide-E_g $FA_{0.8}Cs_{0.2}Pb(I_{0.7}Br_{0.3})_3$ nucleation layers has a MSE of 12.9×10^{-2}. The fifth model includes the void + perovskite nucleation layer in both subcells in addition to the ITO + PTAA, C_{60} + BCP, and void + C_{60} + BCP + Ag physically mixed layers. The fifth and final model provides the best fit to the experimental ellipsometric spectra with MSE reduced to 5.5×10^{-2} (Figure S31). The fitting results show a negligible void + top wide-E_g perovskite nucleation layer thickness. The structural fit parameters and the quality of fit for the first and the final model analysis of the ellipsometric spectra obtained for the 2T all-perovskite tandem solar cell are listed in Table 4, and Table

https://dx.doi.org/10.1021/acsami.0c16364
ACS Appl. Mater. Interfaces 2021, 13, 4923–4934

Approved for public release; distribution unlimited.

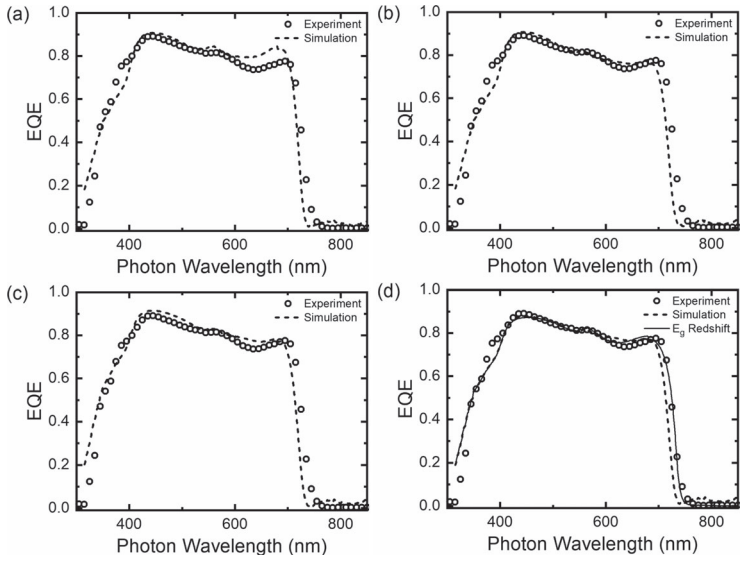


Figure 1. Comparison of simulated (dashed lines) and experimentally measured (open circles) EQE of a wide-E_g $FA_{0.8}Cs_{0.2}Pb(I_{0.7}Br_{0.3})_3$ perovskite-based solar cell. EQE simulations utilize structural and optical properties obtained from different analyses of spectroscopic ellipsometry data as input parameters: (a) without considering the formation of any physically mixed interfacial layers, (b) including a C_{60} + BCP + Ag physically mixed interfacial layer, and (c) including the lower-density void + $FA_{0.8}Cs_{0.2}Pb(I_{0.7}Br_{0.3})_3$ perovskite nucleation layer in addition to the C_{60} + BCP + Ag physically mixed interfacial layer. (d) EQE is simulated assuming a reduced carrier collection probability from the lower-density void + $FA_{0.8}Cs_{0.2}Pb(I_{0.7}Br_{0.3})_3$ perovskite nucleation layer of 92 ± 1% (dashed line) and after a 0.02 eV redshift in the perovskite bandgap with a carrier collection probability from the lower-density void + $FA_{0.8}Cs_{0.2}Pb(I_{0.7}Br_{0.3})_3$ perovskite nucleation layer of 91 ± 1% (solid line).

S16 lists similar information for the second, third, and fourth models. EQE simulations are performed for the 2T all-perovskite tandem solar cell utilizing the optical properties and structural parameters obtained from the corresponding model fits of the experimental ellipsometric spectra. Figure 4a–c shows the comparison between the simulated and experimentally measured EQE in a 2T all-perovskite tandem solar cell without considering the formation of any physically mixed interfacial layers; including void + C_{60} + BCP + Ag, C_{60} + BCP, and ITO + PTAA physically mixed layers; and including the formation of the lower-density void + bottom narrow-E_g perovskite nucleation layer in addition to void + C_{60} + BCP + Ag, C_{60} + BCP, and ITO + PTAA physically mixed layers, respectively. Even though considering various interfacial layers in the 2T all-perovskite tandem solar cell results in a closer match between the simulated and measured EQE as observed in Figure 4c, the simulation still exceeds the measured EQE in the 600–800 nm wavelength range. The discrepancy between the simulated and measured EQE is understood by assuming incomplete collection of photogenerated electron–hole pairs and introducing reduced carrier collection probability in the void + bottom narrow-E_g perovskite nucleation layer. Simulated EQE better matches the experimental value when carrier collection probability from the void + bottom narrow-E_g perovskite nucleation layer is 66 ± 1% (Figure 4d).

The low MSE values obtained with the appropriate structural model to fit the ellipsometric spectra of complete solar cells and good agreement between simulated and experimental EQE values indicate that the reference spectra in ε obtained from individual material samples are representative of those layers in the complete devices. For all the perovskite solar cells studied, comparisons of simulated and measured EQE show that the formation of the physically mixed interfacial layer between C_{60}, BCP, and Ag reduces EQE (Figures 1–4). Absorbance within this physically mixed interfacial layer at photon energies greater than the bandgap of the perovskite absorber layer causes parasitic optical loss, quantified in terms of J_{SC}. In the 2T all-perovskite tandem solar cell, the void + C_{60} + BCP + Ag layer contributes to the equivalent of a 2.3 mA/cm^2 loss. Similarly, the C_{60} + BCP + Ag layers in single-junction $FA_{0.8}Cs_{0.2}Pb(I_{0.7}Br_{0.3})_3$, $(FASnI_3)_{0.6}(MAPbI_3)_{0.4}$, and $(FASnI_3)_{0.5}(MAPbI_3)_{0.5}$ perovskite-based solar cells contribute to the equivalent of 0.9, 1.4, and 1.7 mA/cm^2 losses, respectively (Tables S22–S25). The amount of optical losses is directly related to the physically mixed interfacial layer thickness and the fraction of Ag in the interfacial layer. For example, the C_{60} + BCP + Ag layer in the wide-E_g $FA_{0.8}Cs_{0.2}Pb(I_{0.7}Br_{0.3})_3$ perovskite-based solar cell has the lowest thickness of 30.0 ± 0.1 nm and an Ag fraction of 0.06 ± 0.01 (Table 1). Both low values are responsible for the least amount of optical loss among the perovskite solar cells studied. In contrast, the greatest optical loss is observed in the bottom narrow-E_g junction of the 2T all-perovskite tandem solar cell because of the formation of a 105 ± 3 nm thick void + C_{60} + BCP + Ag layer with an Ag fraction of 0.22 ± 0.02.

An effective medium approximation of only C_{60} and BCP shows only negligible absorbance of photons with energies in the vicinity of the perovskite bandgaps. Therefore, the optical loss depends upon the presence and amount of Ag in the C_{60} + BCP + Ag interfacial layer. The ε_2 spectra at photon energies below ~ 3.5 eV or above wavelengths of ~ 350 nm for BCP show low or negligible absorption (Figure S15). Even though the ε_2 spectra of C_{60} show absorption above photon energies of ~ 1.5 eV (Figure S6) or below wavelengths of ~ 825 nm, total

https://dx.doi.org/10.1021/acsami.0c16364
ACS Appl. Mater. Interfaces 2021, 13, 4923–4934

Approved for public release; distribution unlimited.

Table 2. Narrow-E_g $(FASnI_3)_{0.6}(MAPbI_3)_{0.4}$ Perovskite-Based Solar Cell Device Structural Fit Parameters Obtained from Analysis of Spectroscopic Ellipsometry Data (A) without Considering the Formation of a Physically Mixed Interfacial Layer between Ag and the Electron Transport Layer (C_{60} and BCP), a Physical Mixture of ITO + PEDOT:PSS, and a Lower-Density Void + Narrow-E_g $(FASnI_3)_{0.6}(MAPbI_3)_{0.4}$ Perovskite Nucleation Layer;(B) Considering the Formation of a Physically Mixed Interfacial Layer between Ag and the Electron Transport Layer (C_{60} and BCP), a Physical Mixture of ITO + PEDOT:PSS, and a Lower-Density Void + Narrow-E_g $(FASnI_3)_{0.6}(MAPbI_3)_{0.4}$ Perovskite Nucleation Layer[a]

layers	thickness (nm)
A	
ITO nucleation layer	18
ITO	123 ± 1
PEDOT:PSS	39 ± 1
narrow-E_g $(FASnI_3)_{0.6}(MAPbI_3)_{0.4}$ perovskite	622 ± 1
C_{60}	20
BCP	5
Ag	75
B	
ITO nucleation layer	18
ITO	123 ± 1
ITO + PEDOT:PSS physically mixed layer (0.5 ITO + 0.5 PEDOT:PSS)	0 ± 1
PEDOT:PSS	41 ± 2
void + narrow-E_g $(FASnI_3)_{0.6}(MAPbI)_{0.4}$ perovskite nucleation layer (0.3 ± 0.1 void + 0.7 perovskite)	24 ± 1
narrow-E_g $(FASnI_3)_{0.6}(MAPbI_3)_{0.4}$ perovskite	600 ± 3
C_{60} + BCP + Ag physically mixed layer (0.65 C_{60} + 0.18 BCP + 0.17 ± 0.02 Ag)	32.3 ± 0.1
Ag	75

[a]The quality of fit for A is a MSE of 11.0×10^{-2}. The quality of fit for B is a MSE of 5.5×10^{-2}. Material fractions for the physically mixed layers are included in the parentheses. Values without error bars are fixed in the analysis.

Table 3. Narrow-E_g $(FASnI_3)_{0.5}(MAPbI_3)_{0.5}$ Perovskite-Based Solar Cell Device Structural Fit Parameters Obtained from Analysis of Spectroscopic Ellipsometry Data (A) without Considering the Formation of a Physically Mixed Interfacial Layer between Ag and the Electron Transport Layer (C_{60} and BCP), a Physical Mixture of ITO + PEDOT:PSS, and a Lower-Density Void + Narrow-E_g $(FASnI_3)_{0.5}(MAPbI_3)_{0.5}$ Perovskite Nucleation Layer; (B) Considering the Formation of a Physically Mixed Interfacial Layer between Ag and the Electron Transport Layer (C_{60} and BCP), a Physical Mixture of ITO + PEDOT:PSS and Lower-Density Void + Narrow-E_g $(FASnI_3)_{0.5}(MAPbI_3)_{0.5}$ Perovskite Nucleation Layer[a]

layers	thickness (nm)
A	
ITO nucleation layer	18
ITO	126 ± 3
PEDOT:PSS	46 ± 3
narrow-E_g $(FASnI_3)_{0.5}(MAPbI_3)_{0.5}$ perovskite	635 ± 1
C_{60}	20
BCP	5
Ag	75
B	
ITO nucleation layer	18
ITO	124 ± 1
ITO + PEDOT:PSS physically mixed layer (0.5 ITO + 0.5 PEDOT:PSS)	0 ± 3
PEDOT:PSS	39 ± 4
void + narrow-E_g $(FASnI_3)_{0.5}(MAPbI)_{0.5}$ perovskite nucleation layer (0.3 ± 0.1 void + 0.7 perovskite)	12 ± 5
narrow-E_g $(FASnI_3)_{0.5}(MAPbI_3)_{0.5}$ perovskite	634 ± 5
C_{60} + BCP + Ag physically mixed layer (0.53 C_{60} + 0.15 BCP + 0.32 ± 0.02 Ag)	39 ± 3
Ag	75

[a]The quality of fit for A is a MSE of 18.9×10^{-2}. The quality of fit for B is a MSE of 5.8×10^{-2}. Material fractions for the physically mixed layers are included in the parenthesis. Values without error bars are fixed in the analysis.

absorbance is negligible given its small thickness of 20 nm. Any optical losses are also minimized as only light with photon energies slightly above the bandgap energies of the perovskite absorbers is not already absorbed within the perovskites before reaching the ETL. However, inclusion of Ag to form a C_{60} + BCP + Ag layer modifies the ε_2 spectra substantially to absorb over all wavelengths including in the vicinity of the perovskite bandgap energies (Figures S24-S27). Transmission measurements of perovskite films on glass show that the wide-E_g perovskite becomes optically opaque only at wavelengths of 500 nm and lower, while its optical bandgap is near 715 nm (Figure S32). Similarly, narrow-E_g perovskites with optical bandgaps near 1000 nm are optically opaque only at wavelengths of 600 nm and lower. Therefore, light in the wavelength ranges near 500−715 nm and 600−1000 nm is partially transmitted through the wide-E_g and low-E_g perovskite layers in the solar cells, respectively. In the simulation without C_{60} + BCP + Ag layers, incident light is reflected back through the absorber layer to enhance absorption in the perovskites and increase current generated. However, with the presence of a fraction of Ag mixed with the ETL components, light is absorbed in this physically mixed layer and reduces the current generated in the absorber layer. Therefore, the simulations without C_{60} + BCP + Ag layers exceed measured EQE near the wavelength range of 500−715 nm in wide-E_g perovskite solar cells and near the wavelength range of 600−1000 nm in narrow-E_g perovskite solar cells including the bottom cell of the 2T all-perovskite tandem solar cell. The optical loss introduced by physical intermixing between Ag and the ETL materials is expected to have less substantial effects on the open circuit voltage (V_{OC}) and fill factor (FF) but directly impacts the device PCE via J_{SC}.

Another physically mixed interfacial layer identified is the lower-density void + perovskite nucleation layer. Even though the spectroscopic ellipsometry model incorporating the lower-density void + perovskite nucleation layer yields substantially lower MSE than the model without it (Figures S30−33), the change in J_{SC} obtained from simulated EQE remains negligible (Tables S18−S22). This assumes that current is generated in both the lower-density void + perovskite nucleation layer and the bulk perovskite layer, which means there are no additional parasitic losses other than those from the C_{60} + BCP + Ag layer. Though optical losses are not attributed to the formation of the void + perovskite nucleation layer, larger grains with lower surface coverage near the substrate can reduce V_{OC} and FF, which ultimately reduce PCE.[13] Thicker void + perovskite

https://dx.doi.org/10.1021/acsami.0c16364
ACS Appl. Mater. Interfaces 2021, 13, 4923−4934

Approved for public release; distribution unlimited.

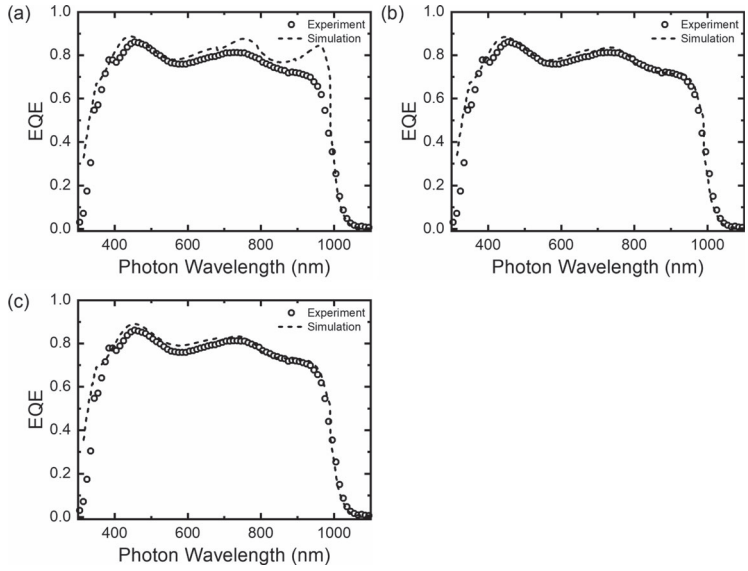


Figure 2. Comparison of simulated (dashed lines) and experimentally measured (open circles) EQE for a narrow-E_g $(FASnI_3)_{0.6}(MAPbI_3)_{0.4}$ perovskite-based solar cell. EQE simulations utilize structural and optical properties obtained from different analyses of spectroscopic ellipsometry data as input parameters: (a) without considering the formation of any physically mixed interfacial layers, (b) including the formation of a C_{60} + BCP + Ag physically mixed interfacial layer, and (c) including the formation of a lower-density void + $(FASnI_3)_{0.6}(MAPbI_3)_{0.4}$ nucleation layer in addition to the C_{60} + BCP + Ag physically mixed interfacial layer.

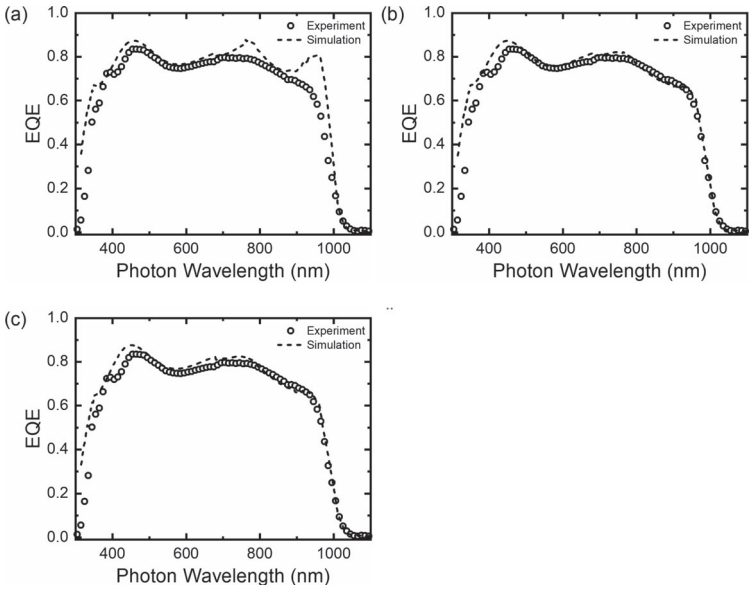


Figure 3. Comparison of simulated (dashed lines) and experimentally measured (open circles) EQE for a narrow-E_g $(FASnI_3)_{0.5}(MAPbI_3)_{0.5}$ perovskite-based solar cell. EQE simulations utilize structural and optical properties obtained from different analyses of spectroscopic ellipsometry data as input parameters: (a) without considering the formation of any physically mixed interfacial layers, (b) including the formation of a C_{60} + BCP + Ag physically mixed interfacial layer, and (c) including the formation of a lower-density void + $(FASnI_3)_{0.5}(MAPbI_3)_{0.5}$ nucleation layer in addition to the C_{60} + BCP + Ag physically mixed interfacial layer.

nucleation layers of 68 ± 2 and 111 ± 16 nm are identified in the single-junction wide-E_g $FA_{0.8}Cs_{0.2}Pb(I_{0.7}Br_{0.3})_3$ perovskite-based solar cell and the Cl-doped narrow-E_g $(FASnI_3)_{0.6}(MAPbI_3)_{0.4}$ subcell of the 2T all-perovskite tandem solar cell, respectively, compared to the 12−24 nm thick nucleation layers in the corresponding single-junction narrow-E_g perovskite solar cells. Isolation or poor passivation of the grains initially nucleated on the underlying layers may lead to

https://dx.doi.org/10.1021/acsami.0c16364
ACS Appl. Mater. Interfaces 2021, 13, 4923−4934

Approved for public release; distribution unlimited.

Table 4. Two Terminal All-Perovskite Tandem Solar Cell Device Structural Fit Parameters Obtained from Analysis of Spectroscopic Ellipsometry Data (A) without Considering the Formation of a Physically Mixed Interfacial Layer between Ag and the Electron Transport Layer (C_{60} and BCP), a Physical Mixture of ITO + PTAA, and Lower-Density Void + Perovskite Nucleation Layers; (B) Considering the Formation of a Physically Mixed Interfacial Layer between Ag and Electron Transport Layer (C_{60} and BCP), Physical Mixtures of ITO + PTAA and C_{60} + BCP in the Top Junction, and Lower-Density Void + Perovskite Nucleation Layers[a]

	layers	thickness (nm)
	A	
top junction	ITO	130 ± 2
	PTAA	13 ± 3
	wide-E_g $FA_{0.8}Cs_{0.2}Pb(I_{0.7}Br_{0.3})_3$ perovskite	227 ± 3
	C_{60}	20
	BCP	5
bottom junction	sputtered ITO	110 ± 5
	PEDOT:PSS	50 ± 6
	2.5% Cl-doped narrow-E_g $(FASnI_3)_{0.6}(MAPbI_3)_{0.4}$ perovskite	660 ± 1
	C_{60}	20
	BCP	5
	Ag	75
	B	
top junction	ITO	113 ± 2
	ITO + PTAA physically mixed layer (0.22 ± 0.01 ITO + 0.78 PTAA)	36 ± 1
	PTAA	0
	void + $FA_{0.8}Cs_{0.2}Pb(I_{0.7}Br_{0.3})_3$ perovskite nucleation layer (0.5 void + 0.5 perovskite)	0 ± 1
	wide-E_g $FA_{0.8}Cs_{0.2}Pb(I_{0.7}Br_{0.3})_3$ perovskite	206 ± 1
	C_{60} + BCP physically mixed layer (0.80 C_{60} + 0.20 BCP)	25 ± 3
bottom junction	sputtered ITO	110 ± 1
	PEDOT:PSS	50 ± 2
	void + 2.5% Cl-doped narrow-E_g $(FASnI_3)_{0.6}(MAPbI_3)_{0.4}$ perovskite nucleation layer (0.1 void + 0.9 ± 0.001 perovskite)	111 ± 16
	2.5% Cl-doped narrow-E_g $(FASnI_3)_{0.6}(MAPbI_3)_{0.4}$ perovskite	504 ± 3
	void + C_{60} + BCP + Ag physically mixed layer (0.48 ± 0.01 void + 0.24 C_{60} + 0.06 BCP + 0.22 ± 0.02 Ag)	105 ± 3
	Ag	75

[a]The quality of fit for A is a MSE of 13.7×10^{-2}. The quality of fit for B is a MSE of 5.6×10^{-2}. Material fractions for the physically mixed layers are given in the parentheses. Values without error bars are fixed in the analysis.

carrier recombination losses and ultimately to reduced collection.[6] With only 92 ± 1 and 66 ± 1% of carrier collection from the respective void + perovskite nucleation layers, electronic losses of 0.5 and 1.5 mA/cm^2 are calculated for the single-junction wide-E_g perovskite-based solar cell without assuming the 0.02 eV redshifted bandgap (Table S18) and the 2T all-perovskite tandem solar cell (Table S21).

In the 2T all-perovskite tandem solar cell, including a physical mixture of ITO + PTAA provides a closer match between the simulated and measured EQE. However, the parasitic absorption by the physical mixture of ITO + PTAA at the front contact is minimal compared that of ETL + Ag at the back contact. The bottom narrow-E_g subcell in the 2T all-perovskite tandem solar cell shows the most J_{SC} loss followed by the single-junction narrow-E_g perovskite solar cells. In addition to loss in J_{SC}, variations in V_{OC} and FF arising from the physically mixed layers are also estimated (Tables S26–29). For all perovskite solar cells, the impact of optical and electronic losses arising from physically mixed layers on V_{OC} and FF is minimal. The measured PCE for the 2T all-perovskite solar cell is 21% (Table S17). The total J_{SC} loss due to optical and electronic losses is 3.7 mA/cm^2 in the bottom subcell and 0.2 mA/cm^2 in the top subcell of 2T all-perovskite tandem solar cell (Table S21). An increase in J_{SC} of 1.95 mA/cm^2 for each junction, assuming current matching between top and bottom subcells, can be achieved by avoiding these losses. Using the experimental V_{OC} and FF of 1.922 V and 0.781, respectively, and adding 1.95 mA/cm^2 to the measured J_{SC} 14.0 , PCE of 23.9% can be achieved by mitigating the sources of optical and electronic losses in the 2T all-perovskite tandem solar cell. Similarly, for single-junction narrow-E_g $(FASnI_3)_{0.6}(MAPbI_3)_{0.4}$ and $(FASnI_3)_{0.5}(MAPbI_3)_{0.5}$ perovskite-based solar cells, mitigating the optical loss is estimated to increase the PCE by 0.8 and 0.9% from the measured PCE of 18.5 and 18.4%, respectively. For single-junction wide-E_g $FA_{0.8}Cs_{0.2}Pb(I_{0.7}Br_{0.3})_3$ perovskite-based solar cell, removing both optical and electronic losses leads to an increase in PCE of 0.5% from the measured PCE of 14.3%. For all perovskite solar cells studied, increases in J_{SC} by mitigating optical and electronic losses exhibit the most substantial change and positively impact PCE. Both V_{OC} and FF are also expected to increase but by smaller amounts.

The formation of void + perovskite nucleation is more benign in terms of optical loss compared to the physically mixed interfacial layer between Ag and the ETL materials near the back contact of perovskite solar cells. It has been studied that Ag diffuses up to 20 nm in BCP and forms a Ag + BCP complex, in which case electron transport takes place through the Ag + BCP complex rather than through the intact bulk BCP layer in solar cells.[11] In addition, higher temperature facilitates Ag diffusion in C_{60}.[10] These studies coupled with the fact that C_{60}, BCP, and Ag are deposited by thermal evaporation in this study indicates the possibility of Ag diffusion within the ETL materials to form the C_{60} + BCP + Ag

https://dx.doi.org/10.1021/acsami.0c16364
ACS Appl. Mater. Interfaces 2021, 13, 4923−4934

Approved for public release; distribution unlimited.

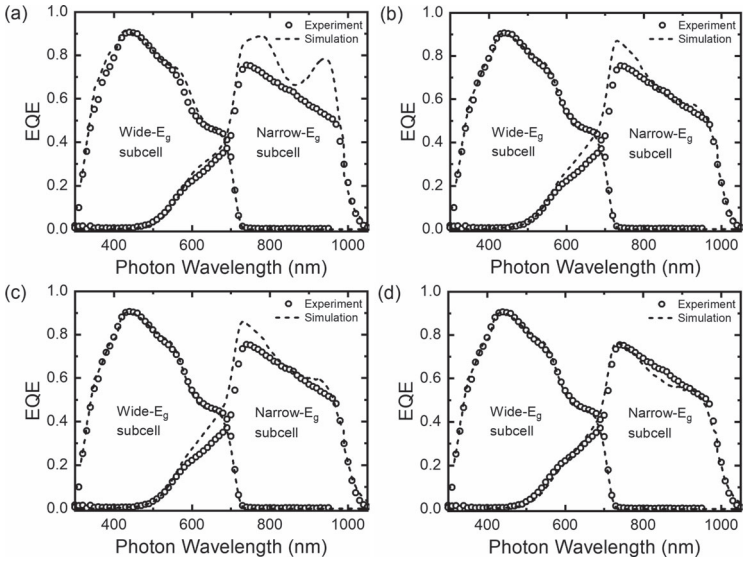


Figure 4. Comparison of simulated (dashed lines) and experimentally measured (open circles) EQE of a 2T all-perovskite tandem solar cell with a wide-E_g $FA_{0.8}Cs_{0.2}Pb(I_{0.7}Br_{0.3})_3$ perovskite-based top subcell and a 2.5% Cl-doped narrow-E_g $(FASnI_3)_{0.6}(MAPbI_3)_{0.4}$ perovskite-based bottom subcell. EQE simulations utilize structural and optical properties obtained from different analyses of spectroscopic ellipsometry data as input parameters: (a) without considering the formation of any physically mixed interfacial layers, (b) including a void + C_{60} + BCP + Ag physically mixed interfacial layer and an ITO + PTAA physically mixed layer, and (c) including the lower-density void + bottom narrow-E_g perovskite nucleation layer in addition to the void + C_{60} + BCP + Ag, C_{60} + BCP, and ITO + PTAA physically mixed layers. (d) Simulated EQE better matches experiment when carrier collection probability from the low-density void + bottom narrow-E_g perovskite nucleation layer in (c) is 66 ± 1%.

physically mixed layer. To avoid the formation of the C_{60} + BCP + Ag physically mixed layer and improve device performance, Ag deposition techniques and conditions that lead to limited Ag diffusion should be considered. Other practical pathways to address the physical mixing of the ETL and the metal back contact include the possible replacement of Ag with less-corrosive alternatives such as copper (Cu)[36,37] and chromium (Cr)/gold (Au).[38] For example, a study of perovskite solar cells using Au as a back contact does not show the formation of a physically mixed layer between Au and the adjacent transport layer, and such a physically mixed layer is not required for simulated EQE to match experimental EQE.[18,21] Similarly, potential replacement of the soft and porous organic BCP layer by compact and dense metal oxides such as tin oxide derivatives (SnO_{2-x})[39] and incorporation of a diffusion blocking layer such as nanostructured carbon[40] can help to prevent physical mixing at the transport layer and back contact metal interface. These methods not only limit the interaction with the ETL but also prevent the interaction of metal ions with halide ions within the perovskite, which would prevent further degradation of perovskite solar cells. Electronic loss arising from the lower-density void + nucleation layer can be prevented by controlling the perovskite deposition conditions to ensure more conformal coverage of the underlying surface. It has been studied that fast nucleation followed by suppressed crystal growth is necessary to obtain the optimized morphology in perovskite films.[41] This morphology can be achieved by incorporation of various solvent additives, interfacial engineering, and multistep deposition techniques.[42]

SUMMARY

Spectroscopic ellipsometry, a noninvasive measurement technique, has been used to probe the optical properties of component materials and the structure of single-junction wide-E_g $FA_{0.8}Cs_{0.2}Pb(I_{0.7}Br_{0.3})_3$, single-junction narrow-E_g $(FASnI_3)_{0.6}(MAPbI_3)_{0.4}$ and $(FASnI_3)_{0.5}(MAPbI_3)_{0.5}$, and 2T all-perovskite tandem solar cells. Using the measured device structures and optical properties of component layers, simulations of the EQE spectra are carried out and compared to the experimental results. Observed deviations between measured and simulated EQE help to identify the formation of physically mixed interfacial layers between the component layers in solar cells as the sources of optical and electronic losses. For all perovskite solar cells studied, a physically mixed layer between Ag, C_{60}, and BCP near the back contact is identified, which shows substantial absorbance and reduces potential current generation in the perovskite absorber layer. Identification of proper Ag deposition techniques, replacement of Ag by other metals, and replacement of porous BCP by other compact materials as the ETL to avoid the formation of a physically mixed layer between the metal back contact and adjacent transport layers are suggested to improve solar cell device performance. Similarly, a lower-density void + perovskite nucleation layer is formed during perovskite deposition, which causes electronic loss because of incomplete carrier collection stemming from poor surface coverage and passivation of the initial grains. Controlling the perovskite deposition conditions to achieve a uniform, smooth morphology with better crystallinity at the perovskite and HTL interface will help to reduce electronic loss.

https://dx.doi.org/10.1021/acsami.0c16364
ACS Appl. Mater. Interfaces 2021, 13, 4923−4934

Approved for public release; distribution unlimited.

■ ASSOCIATED CONTENT

Supporting Information

The Supporting Information is available free of charge at https://pubs.acs.org/doi/10.1021/acsami.0c16364.

Detailed information on the thin film and solar cell fabrication, structural and optical properties of solar cell device component layers, solar cell device ellipsometric spectra measurement and data analysis, experimentally measured device performance parameters, and details of simulated J_{SC} and absorbed irradiance in solar cell component layers(PDF)

■ AUTHOR INFORMATION

Corresponding Author

Nikolas J. Podraza − *Department of Physics and Astronomy and the Wright Center for Photovoltaics Innovation and Commercialization, University of Toledo, Toledo 43606, Ohio, United States*; Email: nikolas.podraza@utoledo.edu

Authors

Biwas Subedi − *Department of Physics and Astronomy and the Wright Center for Photovoltaics Innovation and Commercialization, University of Toledo, Toledo 43606, Ohio, United States*; orcid.org/0000-0002-7690-0406

Zhaoning Song − *Department of Physics and Astronomy and the Wright Center for Photovoltaics Innovation and Commercialization, University of Toledo, Toledo 43606, Ohio, United States*; orcid.org/0000-0002-6677-0994

Cong Chen − *Department of Physics and Astronomy and the Wright Center for Photovoltaics Innovation and Commercialization, University of Toledo, Toledo 43606, Ohio, United States*; orcid.org/0000-0003-2692-1871

Chongwen Li − *Department of Physics and Astronomy and the Wright Center for Photovoltaics Innovation and Commercialization, University of Toledo, Toledo 43606, Ohio, United States*

Kiran Ghimire − *Department of Physics and Astronomy and the Wright Center for Photovoltaics Innovation and Commercialization, University of Toledo, Toledo 43606, Ohio, United States*

Maxwell M. Junda − *Department of Physics and Astronomy and the Wright Center for Photovoltaics Innovation and Commercialization, University of Toledo, Toledo 43606, Ohio, United States*; orcid.org/0000-0002-3868-9275

Indra Subedi − *Department of Physics and Astronomy and the Wright Center for Photovoltaics Innovation and Commercialization, University of Toledo, Toledo 43606, Ohio, United States*

Yanfa Yan − *Department of Physics and Astronomy and the Wright Center for Photovoltaics Innovation and Commercialization, University of Toledo, Toledo 43606, Ohio, United States*; orcid.org/0000-0003-3977-5789

Complete contact information is available at: https://pubs.acs.org/10.1021/acsami.0c16364

Author Contributions

All authors have given approval to the final version of manuscript.

Notes

The authors declare no competing financial interest.

■ ACKNOWLEDGMENTS

This work was supported by the Ohio Department of Development (ODOD) Ohio Research Scholar Program (Northwest Ohio Innovators in Thin Film Photovoltaics, grant no. TECH 09-025), the U.S. Department of Energy (DOE) SunShot Initiative under the Next Generation Photovoltaics 3 program (DE-FOA-0000990), the National Science Foundation (CHE-1230246 and DMR-1534586), the Air Force Research Laboratory under agreement numbers FA9453-18-2-0037 and FA9453-19-C-1-002, and the U.S. DOE Office of Energy Efficiency and Renewable Energy (EERE) under the Solar Energy Technologies Office Award Number DE-EE0008753. The U.S. Government is authorized to reproduce and distribute reprints for Governmental purposes notwithstanding any copyright notation thereon. The views and conclusions contained herein are those of the authors and should not be interpreted as necessarily representing the official policies or endorsements, either expressed or implied, of Air Force Research Laboratory or the U.S. Government.

■ REFERENCES

(1) https://www.nrel.gov/pv/cell-efficiency.html (accessed July 7, 2020).

(2) Nakane, A.; Tampo, H.; Tamakoshi, M.; Fujimoto, S.; Kim, K. M.; Kim, S.; Shibata, H.; Niki, S.; Fujiwara, H. Quantitative Determination of Optical and Recombination Losses in Thin-Film Photovoltaic Devices Based on External Quantum Efficiency Analysis. *J. Appl. Phys.* **2016**, *120*, 064505.

(3) Manzoor, S.; Häusele, J.; Bush, K. A.; Palmstrom, A. F.; Carpenter, J.; Yu, Z. J.; Bent, S. F.; Mcgehee, M. D.; Holman, Z. C. Optical Modeling of Wide-Bandgap Perovskite and Perovskite/Silicon Tandem Solar Cells Using Complex Refractive Indices for Arbitrary-Bandgap Perovskite Absorbers. *Opt. Express* **2018**, *26*, 27441−27460.

(4) Da, Y.; Xuan, Y.; Li, Q. Quantifying Energy Losses in Planar Perovskite Solar Cells. *Sol. Energy Mater. Sol. Cells* **2018**, *174*, 206−213.

(5) Luo, D.; Su, R.; Zhang, W.; Gong, Q.; Zhu, R. Minimizing Non-Radiative Recombination Losses in Perovskite Solar Cells. *Nat. Rev. Mater.* **2019**, *5*, 44−60.

(6) Subedi, I.; Subedi, B.; Uprety, P.; Junda, M. M.; Adhikari, D.; Ghimire, K.; Koirala, P.; Collins, R. W.; Yan, Y.; Podraza, N. J. *In Noncontacting Optical Probing of Photovoltaic Device Performance, Physics, Simulation, and Photonic Engineering of Photovoltaic Devices IX*; International Society for Optics and Photonics, 2020; p 112750J.

(7) Koirala, P.; Li, J.; Yoon, H. P.; Aryal, P.; Marsillac, S.; Rockett, A. A.; Podraza, N. J.; Collins, R. W. Through-the-Glass Spectroscopic Ellipsometry for Analysis of CdTe Thin-Film Solar Cells in the Superstrate Configuration. *Prog. Photovoltaics Res. Appl.* **2016**, *24*, 1055−1067.

(8) Subedi, I.; Silverman, T. J.; Deceglie, M. G.; Podraza, N. J. Al+ Si Interface Optical Properties Obtained in the Si Solar Cell Configuration. *Phys. Status Solidi A* **2017**, *214*, 1700480.

(9) Sakurai, T.; Toyoshima, S.; Kitazume, H.; Masuda, S.; Kato, H.; Akimoto, K. Influence of Gap States on Electrical Properties at Interface Between Bathocuproine and Various Types of Metals. *J. Appl. Phys.* **2010**, *107*, 043707.

(10) Li, W.-j.; Wang, P.; Wang, X.-X.; Wang, J.-O.; Wu, R.; Qian, H.-J.; Ibrahim, K.; Li, H.-Y.; Li, H.-N. Fullerene Film on Metal Surface: Diffusion of Metal Atoms and Interface Model. *Appl. Phys. Lett.* **2014**, *104*, 191606.

(11) Yoshida, H. Electron Transport in Bathocuproine Interlayer in Organic Semiconductor Devices. *J. Phys. Chem. C* **2015**, *119*, 24459−24464.

(12) Back, H.; Kim, G.; Kim, J.; Kong, J.; Kim, T. K.; Kang, H.; Kim, H.; Lee, J.; Lee, S.; Lee, K. Achieving Long-Term Stable Perovskite

Approved for public release; distribution unlimited.

Solar Cells via Ion Neutralization. *Energy Environ. Sci.* **2016**, *9*, 1258−1263.
(13) Liu, J.; Wang, G.; Song, Z.; He, X.; Luo, K.; Ye, Q.; Liao, C.; Mei, J. $FAPb_{1-x}Sn_xI_3$ Mixed Metal Halide Perovskites With Improved Light Harvesting and Stability for Efficient Planar Heterojunction Solar Cells. *J. Mater. Chem. A* **2017**, *5*, 9097−9106.
(14) Junda, M. M.; Zhao, D.; Subedi, B.; Wang, C.; Chen, C.; Yan, Y.; Podraza, N. J. Atmospherically Induced Defects in $(FASnI_3)_{0.6}(MAPbI_{3-3x}Cl_{3x})_{0.4}$ Provskites. *J. Phys. D: Appl. Phys.* **2019**, *52*, 175102.
(15) Subedi, B.; Li, C.; Junda, M. M.; Song, Z.; Yan, Y.; Podraza, N. J. Effects of Intrinsic and Atmospherically Induced Defects in Narrow Bandgap $(FASnI_3)_x(MAPbI_3)_{1-x}$ Perovskite Films and Solar Cells. *J. Chem. Phys.* **2020**, *152*, 064705.
(16) Hara, T.; Maekawa, T.; Minoura, S.; Sago, Y.; Niki, S.; Fujiwara, H. Quantitative Assessment of Optical Gain and Loss in Submicron-Textured $CuIn_{1-x}Ga_xSe_2$ Solar Cells Fabricated by Three-Stage Coevaporation. *Phys. Rev. Appl.* **2014**, *2*, 034012.
(17) Aryal, P.; Huang, Z.; Marsillac, S.; Podraza, N. J.; Collins, R. W. Quantum Efficiency Simulations with Inputs from Spectroscopic Ellipsometry for Evaluation of Carrier Collection in a-Si: H Solar Cells. *2015 IEEE 42nd Photovoltaic Specialist Conference (PVSC)*, 2015; pp 1−4.
(18) Ghimire, K.; Zhao, D.; Wang, C.; Yan, Y.; Printraza, N. J. Optical Evaluation of Perovskite Films in and for Solar Cell Device Structures. *2017 IEEE 44th Photovoltaic Specialist Conference (PVSC)*, 2017; pp 993−998.
(19) Ibdah, A.-R. A.; Koirala, P.; Aryal, P.; Pradhan, P.; Heben, M. J.; Podraza, N. J.; Marsillac, S.; Collins, R. W. Optical Simulation of External Quantum Efficiency Spectra of $CuIn_{1-x}Ga_xSe_2$ Solar Cells from Spectroscopic Ellipsometry Inputs. *J. Energy Chem.* **2018**, *27*, 1151−1169.
(20) Subedi, B.; Guan, L.; Yu, Y.; Ghimire, K.; Uprety, P.; Junda, M. M.; Yan, Y.; Podraza, N. J. Formamidinium+Ccesium Lead Triiodide Perovskite Thin Films: Optical Properties and Devices. *IEEE 7th World Conference on Photovoltaic Energy Conversion (WCPEC) (A Joint Conference of 45th IEEE PVSC, 28th PVSEC & 34th EU PVSEC)*, IEEE, 2018; pp 0522−0525.
(21) Subedi, B.; Guan, L.; Yu, Y.; Ghimire, K.; Uprety, P.; Yan, Y.; Podraza, N. J. J. Formamidinium + Cesium Lead Triiodide Perovskites: Discrepancies Between Thin Film Optical Absorption and Solar Cell Efficiency. *Sol. Energy Mater. Sol. Cells* **2018**, *188*, 228−233.
(22) Adhikari, D.; Junda, M. M.; Grice, C. R.; Marsillac, S. X.; Collins, R. W.; Podraza, N. J. Nanocrystalline Hydrogenated Silicon Solar Cells with RF-Magnetron Sputtered Absorbers. *Materials* **2019**, *12*, 1699.
(23) Junda, M. M.; Grice, C. R.; Koirala, P.; Collins, R. W.; Yan, Y.; Podraza, N. J. Optical Properties of $CdSe_{1-x}S_x$ Alloys and Their Application for CdTe Photovoltaics. *2017 IEEE 44th Photovoltaic Specialist Conference (PVSC)*, 2017; pp 3426−3429.
(24) Subedi, I.; Silverman, T. J.; Deceglie, M.; Podraza, N. J. Impact of Infrared Optical Properties on Crystalline Si and Thin Film CdTe Solar Cells. *2017 IEEE 44th Photovoltaic Specialist Conference (PVSC)*, 2017; pp 2771−2775.
(25) Ibdah, A.-R.; Koirala, P.; Aryal, P.; Pradhan, P.; Marsillac, S.; Rockett, A. A.; Podraza, N. J.; Collins, R. W. Spectroscopic Ellipsometry for Analysis of Polycrystalline Thin-Film Photovoltaic Devices and Prediction of External Quantum Efficiency. *Appl. Surf. Sci.* **2017**, *421*, 601−607.
(26) Ibdah, A.-R. A.; Pradhan, P.; Aryal, P.; Podraza, N. J.; Marsillac, S.; Collins, R. W. $CuIn_{1-x}Ga_xSe_2$ Solar Cells with Thin Absorbers Analyzed by Spectroscopic Ellipsometry: Insights Into Quantum Efficiency and Optical/Collection Losses. *2016 IEEE 43rd Photovoltaic Specialists Conference (PVSC)*, 2016; pp 2184−2187.
(27) Zhao, D.; Chen, C.; Wang, C.; Junda, M. M.; Song, Z.; Grice, C. R.; Yu, Y.; Li, C.; Subedi, B.; Podraza, N. J.; Zhao, X.; Fang, G.; Xiong, R.-G.; Zhu, K.; Yan, Y. Efficient Two-Terminal All-Perovskite Tandem Solar Cells Enabled by High-Quality Low-Bandgap Absorber Layers. *Nat. Energy* **2018**, *3*, 1093−1100.
(28) Li, C.; Song, Z.; Zhao, D.; Xiao, C.; Subedi, B.; Shrestha, N.; Junda, M. M.; Wang, C.; Jiang, C.-S.; Al-Jassim, M.; Ellingson, R. J.; Podraza, N. J.; Zhu, K.; Yan, Y. Reducing Saturation-Current Density to Realize High-Efficiency Low-Bandgap Mixed Tin−Lead Halide Perovskite Solar Cells. *Adv. Energy Mater.* **2019**, *9*, 1803135.
(29) Tong, J.; Song, Z.; Kim, D. H.; Chen, X.; Chen, C.; Palmstrom, A. F.; Ndione, P. F.; Reese, M. O.; Dunfield, S. P.; Reid, O. G.; Liu, J.; Zhang, F.; Harvey, S. P.; Li, Z.; Christensen, S. T.; Teeter, G.; Zhao, D.; Al-Jassim, M. M.; van Hest, M. F. A. M.; Beard, M. C.; Shaheen, S. E.; Berry, J. J.; Yan, Y.; Zhu, K. Carrier Lifetimes of > 1 μs in Sn-Pb Perovskites Enable Efficient All-Perovskite Tandem Solar Cells. *Science* **2019**, *364*, 475−479.
(30) Wang, Q.; Shao, Y.; Dong, Q.; Xiao, Z.; Yuan, Y.; Huang, J. Large Fill-Factor Bilayer Iodine Perovskite Solar Cells Fabricated by a Low-Temperature Solution-Process. *Energy Environ. Sci.* **2014**, *7*, 2359−2365.
(31) Lee, J.; Rovira, P. I.; An, I.; Collins, R. W. Rotating-Compensator Multichannel Ellipsometry: Applications for Real Time Stokes Vector Spectroscopy of Thin Film Growth. *Rev. Sci. Instrum.* **1998**, *69*, 1800−1810.
(32) Woollam, J. A.; Johs, B. D.; Herzinger, C. M.; Hilfiker, J. N.; Synowicki, R. A.; Bungay, C. L. *Overview of Variable-Angle Spectroscopic Ellipsometry (VASE): I. Basic Theory and Typical Applications, Optical Metrology: A Critical Review*; International Society for Optics and Photonics, 1999; p 1029402.
(33) Johs, B.; Herzinger, C. M. Quantifying the Accuracy of Ellipsometer Systems. *Phys. Status Solidi C* **2008**, *5*, 1031−1035.
(34) Aspnes, D. E.; Theeten, J. B.; Hottier, F. Investigation of Effective-Medium Models of Microscopic Surface Roughness by Spectroscopic Ellipsometry. *Phys. Rev. B: Condens. Matter Mater. Phys.* **1979**, *20*, 3292.
(35) *e-ARC Software*, Version 3.0; Simulator for Solar Cell. https://unit.aist.go.jp/rcpv/cie/service/index.html (accessed March 5, 2020), 2019.
(36) Yu, Z.; Yang, Z.; Ni, Z.; Shao, Y.; Chen, B.; Lin, Y.; Wei, H.; Yu, Z. J.; Holman, Z.; Huang, J. Simplified Interconnection Structure Based on C_{60}/SnO_{2-x} for All-Perovskite Tandem Solar Cells. *Nat. Energy* **2020**, *5*, 657−665.
(37) Zhao, J.; Zheng, X.; Deng, Y.; Li, T.; Shao, Y.; Gruverman, A.; Shield, J.; Huang, J. Is Cu a Stable Electrode Material in Hybrid Perovskite Solar Cells for a 30-year Lifetime? *Energy Environ. Sci.* **2016**, *9*, 3650−3656.
(38) Lin, Y.-H.; Sakai, N.; Da, P.; Wu, J.; Sansom, H. C.; Ramadan, A. J.; Mahesh, S.; Liu, J.; Oliver, R. D. J.; Lim, J.; Aspitarte, L.; Sharma, K.; Madhu, P. K.; Morales-Vilches, A. B.; Nayak, P. K.; Bai, S.; Gao, F.; Grovenor, C. R. M.; Johnston, M. B.; Labram, J. G.; Durrant, J. R.; Ball, J. M.; Wenger, B.; Stannowski, B.; Snaith, H. J. A Piperidinium Salt Stabilizes Efficient Metal-Halide Perovskite Solar Cells. *Science* **2020**, *369*, 96−102.
(39) Xiao, K.; Lin, R.; Han, Q.; Hou, Y.; Qin, Z.; Nguyen, H. T.; Wen, J.; Wei, M.; Yeddu, V.; Saidaminov, M. I.; Gao, Y.; Luo, X.; Wang, Y.; Gao, H.; Zhang, C.; Xu, J.; Zhu, J.; Sargent, E. H.; Tan, H. All-Perovskite Tandem Solar Cells with 24.2% Certified Efficiency and Area Over 1 cm^2 Using Surface-Anchoring Zwitterionic Antioxidant. *Nat. Energy* **2020**, *5*, 870−880.
(40) Bi, E.; Chen, H.; Xie, F.; Wu, Y.; Chen, W.; Su, Y.; Islam, A.; Grätzel, M.; Yang, X.; Han, L. Diffusion Engineering of Ions and Charge Carriers for Stable Efficient Perovskite Solar Cells. *Nat. Commun.* **2017**, *8*, 15330.
(41) Liu, C.; Cheng, Y.-B.; Ge, Z. Understanding of Perovskite Crystal Growth and Film Formation in Scalable Deposition Processes. *Chem. Soc. Rev.* **2020**, *49*, 1653−1687.
(42) Li, C.; Song, Z.; Chen, C.; Xiao, C.; Subedi, B.; Harvey, S. P.; Shrestha, N.; Subedi, K. K.; Chen, L.; Liu, D.; Li, Y.; Kim, Y.-W.; Jiang, C.-s.; Heben, M. J.; Zhao, D.; Ellingson, R. J.; Podraza, N. J.; Al-Jassim, M.; Yan, Y. Low-Bandgap Mixed Tin−Lead Iodide Perovskites

https://dx.doi.org/10.1021/acsami.0c16364
ACS Appl. Mater. Interfaces 2021, 13, 4923−4934

Approved for public release; distribution unlimited.

with Reduced Methylammonium for Simultaneous Enhancement of Solar Cell Efficiency and Stability. *Nat. Energy* **2020**, *5*, 768−776.

https://dx.doi.org/10.1021/acsami.0c16364
ACS Appl. Mater. Interfaces 2021, 13, 4923−4934

Approved for public release; distribution unlimited.

Optimization of the Solution-Based Aluminium Gallium Oxide Buffer Layer for CdTe Solar Cells

Zara Akkuly, Aesha P. Patel, Kamala Khanal Subedi, Dipendra Pokhrel, Ebin Bastola, Adam B. Phillips, Michael J. Heben, and Randy Ellingson

Wright Center for Photovoltaics Innovation and Commercialization (PVIC), Department of Physics and Astronomy, University of Toledo, Ohio, 43606, USA

***Abstract*—Here, we introduce Aluminum Gallium Oxide (AlGaOx) buffer synthesized through a solution-based approach which passivates the interface recombination in CdTe thin film solar cells. This paper seeks to optimize the performance of the solution based AlGaOx buffer without the use of copper (Cu). The results indicated that diluting $AlGaO_x$ solution with 10ml dimethylformamide (DMF) solvent removes the blocking effect, achieving a maximum device efficiency of 13.3%, similar to the standard device (Cu/Au) efficiency of 13.6%. These implications could help eliminate the need for Cu in the rear contact. Hence, AlGaOx back buffer shows possibility of being used in bifacial and tandem device configuration for CdTe cells.**

Keywords— AlGaOx, back-buffer, CdTe, passivation, solution-based method

I. Introduction

Cadmium Telluride (CdTe), a direct band gap material with E_g = 1.5 eV, is a promising thin-film solar technology as its record laboratory efficiency of 22.1% has almost caught up to the conventional silicon technology within a few decades. The manufacturing costs and energy payback time for CdTe cells are much lower than silicon cells because less energy and material input is required during production [2]. However, this technology still faces certain roadblocks related to open-circuit voltage (V_{OC}). One of the reasons is the limiting rear contact of CdTe that lowers device performance because of high back surface recombination velocity (BSRV) and downward band bending between the absorber and the back contact[3] . These effects lead to a lower device power conversion efficiency. Coating the absorber with a passivating oxide layer is one solution to tackle this problem. Al_2O_3 is one such example of an effective interface passivation layer that creates an electric field and is commonly used in Silicon, CIGS, Perovskite, and CZTS PV materials creating an electric field [4-6]. Alumina materials have a unique capacity, which allows for exhibition of a negatively fixed charge[7].Negatively charged defects present in the oxide repel minority electrons and thus reduce surface recombination velocity, raise the open circuit voltage and increase minority carrier lifetime.[9] Many oxide materials such as TiO_2, SiO_2, and Al_2O_3 are used for interface passivation in CdTe cells[10]. Among them, the inclusion of vacuum or solution-processed Al_2O_3 worked the best in CdTe passivation[11, 12] .

Due to the deep work function of CdTe (5.7 eV), researchers have been using Cu-based back buffer layers In general, Cu-containing materials such as Cu/Au[13], ZnTe: Cu[14], $(CuS)_x(ZnS)_{1-x}$ [15, 16], $BaCu_4S_3$ [17] have been widely used as back contact on CdTe solar cells to reduce the Schottky barrier height at the back. However, Cu is known to diffuse quickly and if it reaches the CdS layer, it can cause severe device performance loss. Hence, alternate Cu-free buffer layers have been an area of great interest lately to eliminate the drawbacks of Cu. Recently Subedi et al. used Cu_xAlO_y back buffer which can make the initial fermi level offset positive in comparison with the absorber and reduced the interface recombination by reducing the downward band bending.

The other alternative way to reduce back interface defects is reducing the back surface recombination velocity (BSRV). Here, Cu free $AlGaO_x$ passivation layer has been synthesized using a solution-based method and applied as a back buffer to CdTe solar cells. Using this oxide helps increase minority charge carrier lifetime, but possible reasons for affected J-V performance could be due to the deep valance band position and high thickness. The thickness of the back buffer layer is varied by diluting the precursor solution and a 13.3 % power conversion efficiency was achieved, which is comparable with our standard Cu/Au device with an efficiency of 13.6 %.

II. Experimental Method

The CdTe solar panels, manufactured by Willard and Kelsey Solar Group with a 120 nm thick layer of CdS and a 3 μm of CdTe were cut into 1inch x 1inch sample cells and labeled accordingly. To increase grain size and ensure the mixing of CdS and CdTe base layers, the devices were treated with $CdCl_2$ through deposition of a saturated $CdCl_2$-methanol solution by syringe on CdTe sample cells. The samples were annealed in dry air for 30 min at 387°C to increase the ductility of the material. For $AlGaO_x$ preparation, 0.1875 g (1.25 %) of Aluminum nitrate and 0.07665 g (0.75 %) of Gallium nitrate powders were mixed in a vial in a nitrogenous glovebox and dissolved in a variable solvent dilution volume of dimethylformamide (DMF). The DMF amounts experimented with were 5ml, 7ml, 10 ml, and 12ml. The solution was sonicated for 5-10 min at room temperature to ensure complete

Approved for public release; distribution unlimited.

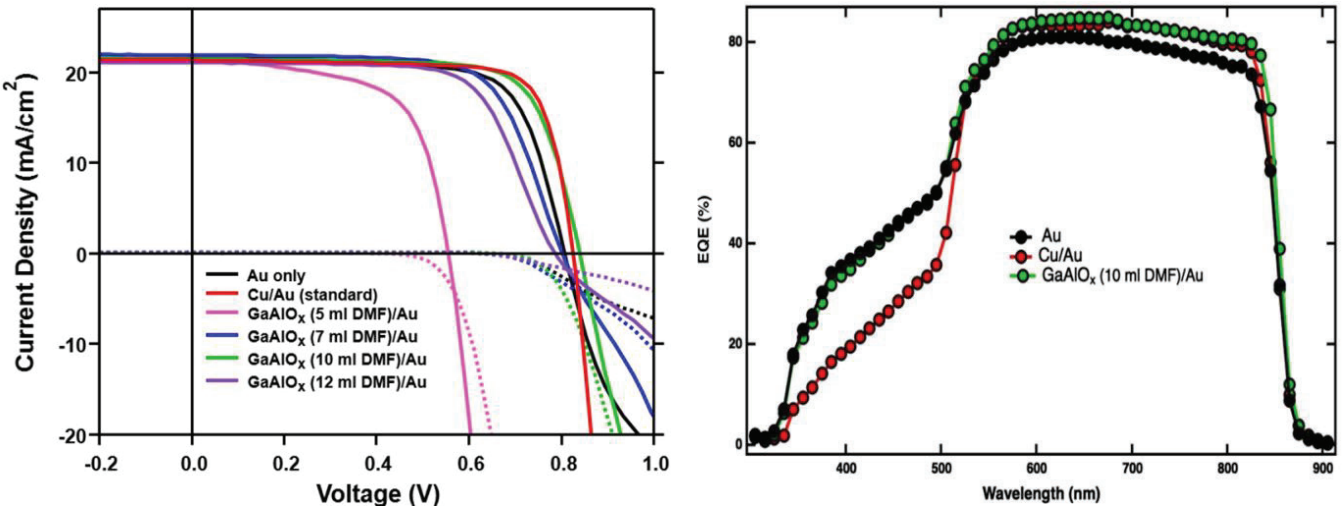


Fig. 1: (a) Current voltage characteristics and (b) external quantum efficiency of the best cell of the CdS/CdTe solar cells with Au back contact and $AlGaO_x$ passivating layer with 10 mL DMF

TABLE I: *J-V* PARAMETERS FOR THE BEST AND AVERAGE CELLS, DEVICE AREA = 0.08 CM^2

Back Contact Configuration		V_{OC} (mV)	J_{SC} (mA/cm^2)	*FF* (%)	η (%)
Au	Best	808	21.73	71.407	11.689
	Average	801 ± 0.259	21.4 ± 2.1	70.8 ± 15.6	11.689 ± 0.2
Cu/Au	Best	836	21..88	77.994	13.64
	Average	831 ± 0.093	20.3 ± 0.8	76.2 ± 7.4	12.8 ± 2.4
5ml DMF	Best	0.556	21.42	66.457	7.51
	Average	526 ± 0.014	20.9 ± 0.2	62.4 ± 2.9	6.9 ± 0.4
7ml DMF	Best	806	21.88	72.6	12.15
	Average	0.8 ± 0.013	21.1 ± 4.1	69.7 ± 1.0	11.8 ± 2.3
10ml DMF	Best	840	21.74	73.921	13.33
	Average	825 ± 0.008	21.2 ± 0.6	71.1 ± 1.6	12.5 ± 0.6
12ml DMF	Best	801	21.9	69.93	11.24
	Average	789 ± 0.013	21.4 ± 4.1	65.7 ± 2.8	11.1 ± 2.0

dissolving of the solute in the solvent. 50µl solution of AlGaOx precursor was directly deposited on the $CdCl_2$ treated CdTe cells using a spin-coater. Each device was spun at 1000 rpm for 10 seconds in the first step and subsequently at 2500 rpm for 50 seconds in the second step. Post AlGaOx deposition, the cells were annealed in air on a hot plate at 220°C for 15min to convert the materials into the oxides. A 45nm thick layer of evaporated Au was thermally deposited onto the rear contact in a vacuum using a physical vapor deposition (PVD) technique at 1 Å/s deposition rate. A standard Cu/Au back contact device was fabricated by $CuCl_2$ treatment. The treatment followed Bastola *et al.* without further process optimization [11]. These cells were then annealed at 200°C for 20 min and completed with 45 nm of evaporated Au for effective Cu diffusion. The CuCl2 treatment was skipped for devices with $AlGaO_x$ passivation layer. This layer of gold was scribed into distinct cells of area 0.06cm^2 using a 532nm laser and the device was completed with Indium.

J-V measurements for CdTe devices were conducted under simulated 1-Sun AM1.5G solar irradiance spectrum conditions. Time-resolved photoluminescence (TRPL) measurements were carried out using a time-correlated single-photon counting (TCSPC) module with a pulsed laser (~5ps pulse width) as the excitation source. 532 nm laser with 20 MHz repetition rate and 633 nm laser with 1 MHz repetition rate were employed for film-side and glass-side illumination, respectively.

III. RESULTS AND DISCUSSION

J-V measurements of solar cells with Au and standard Cu/Au back contact were compared against four different dilution amounts of the AlGaOx solution-based layer as shown in Figure 1a.

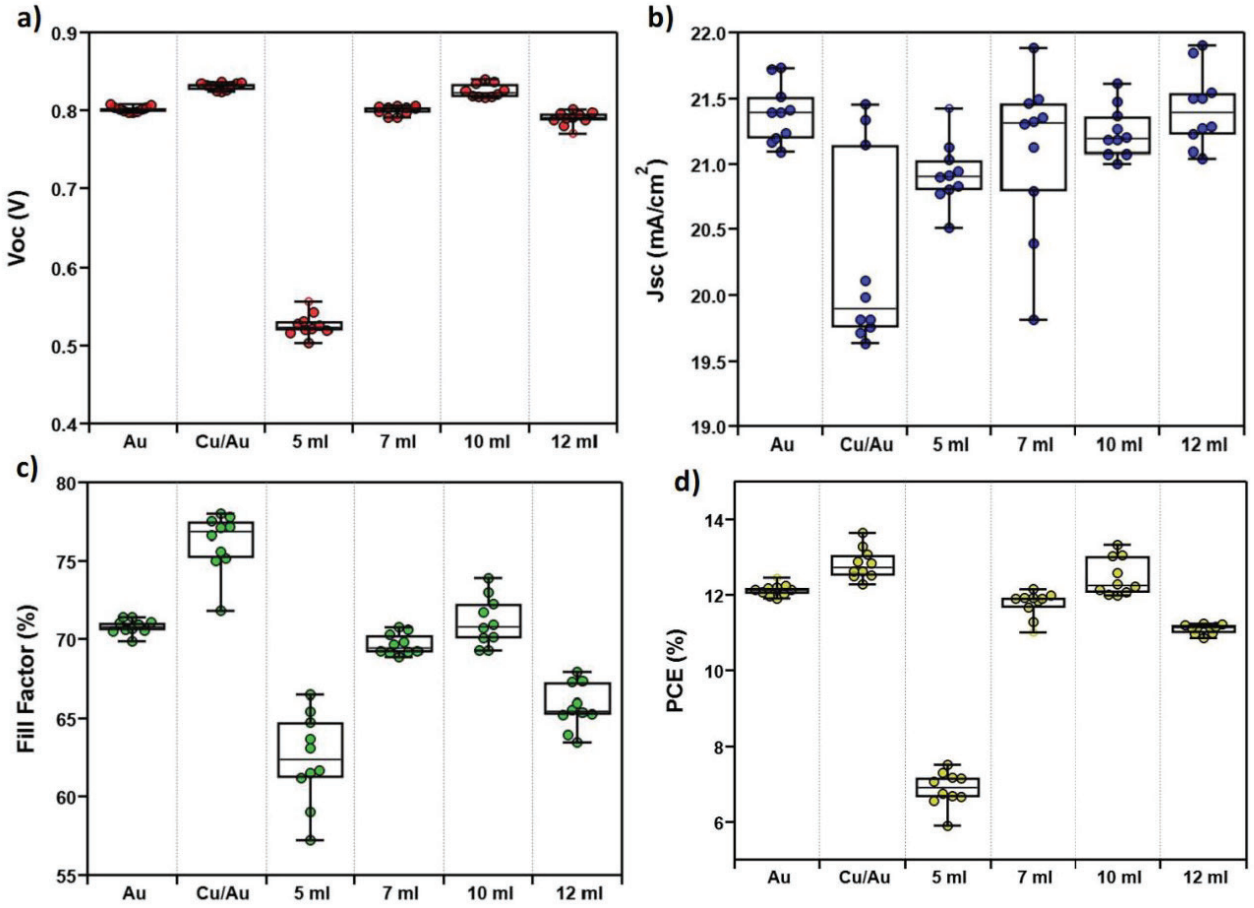


Fig. 2: Box plots for comparision of (a) Voc, (b) Jsc, (c) FF and (d) Efficiency of the CdS/CdTe devices using $AlGaO_x$ as a passivating back buffer layer with different concentration of DMF

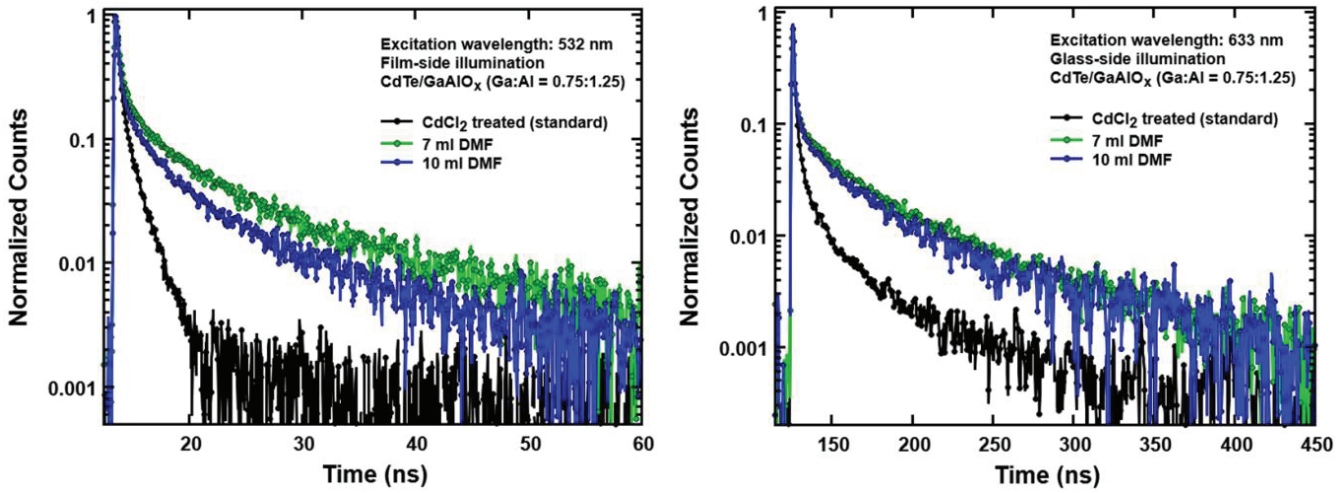


Fig. 3: TRPL measurements for $AlGaO_X$ back buffer for front and back illumination

The peak device performance was achieved at 10 ml dilution, as summarized in Figures 2a and 2d. Table 1 shows how thinning the AlGaOx layer from 5ml to 10ml significantly raises the Voc from 566 mV to 840 mV and the maximum efficiency from 7.5% to 13.3%, which supports the theory that AlGaOx behaves as a blocking layer at lower dilution levels. The lower performance at 12ml could be indicative of the fact that further dilution beyond 10ml undoes the passivation effect. It shows that device performance and passivating effect are optimized with a 10 ml dilution.

Approved for public release; distribution unlimited.

TABLE II: MINORITY CARRIER LIFETIMES FOR CDTE SAMPLES: $CdCl_2$ ONLY (STANDARD) AND ALGAOX BUFFER (7 ML AND 10 ML DILUTION)

	CdTe samples	τ_2 (ns)	Yield2 (%)
Film-side illumination	$CdCl_2$ treated (standard)	1.3	48.7
	7 ml DMF	7.7	72.5
	10 ml DMF	5.3	67.2
Glass-side illumination	$CdCl_2$ treated (standard)	24.1	36.9
	7 ml DMF	48.6	76.2
	10 ml DMF	42.9	71.1

The external quantum efficiency (EQE) of the highest performing device (10ml DMF) was compared against the EQE of the two standard devices (Au and Cu/Au). In general, Figure 1b shows that the performances indicate similar current densities. However, 10ml DMF and Au devices had a higher current collection at the lower wavelength region than Cu/Au. This is due to the variation of CdS window layer ~ 80 nm to 120 nm, film stack is taken from several location of 6 inch x 8 inch coated glass panels sample by sample variation.

Furthermore, longer carrier dynamics is observed in the devices using AlGaOx back buffer layer on CdTe from Time-Resolved Photoluminescence (TRPL) measurements in comparison with the bare CdCl2 treated CdTe film stack. Table II compares the minority carrier lifetime of the device that performed the best at J-V measurements against the device with the best minority carrier lifetime. While the 7ml device had the highest minority carrier lifetime among all the variations, it also demonstrated comparatively lower device performance. The device with the 10ml DMF dilution does have a slightly lower minority carrier lifetime (t_2 = x ns, Y2 = y%), but it surpassed all other dilution variations in device performance. The minority carrier lifetime with higher yield 2 and also the good device performance concurs with the reduction of the interface defects with the passivating AlGaOx. Therefore, the 10ml device offered the best of both worlds in terms of device performance and minority carrier lifetime.

IV. CONCLUSIONS

This work demonstrated that the AlGaOx based solution can be used as an Cu free interface layer on CdTe solar cells. These films are fabricated by a solution-based approach at 220˚C. A thick layer of AlGaOx acts as a passivating layer, which is desirable, but its deep valence band also makes it a blocking layer. Diluting the solution with 10ml of the DMF solvent addresses the blocking issue, resulting in an improved V_{oc} and FF. Further study is needed, but initial findings bring promising results in reducing the longstanding problem of rear interface recombination of CdS/CdTe solar cell devices. This material indicates a possible breakthrough in the performance of bifacial and tandem configurations of CdTe based PV.

ACKNOWLEDGMENT

This material is based on research sponsored by Air Force Research Laboratory under agreement number FA9453-18-2-0037, FA9453-19-C-1002, and by the U. S. DOE's office of Energy Efficiency and Renewable Energy (EERE) under Solar Energy Technologies Office (SETO) Agreement DE-EE0008974. The U.S. Government is authorized to reproduce and distribute reprints for Governmental purposes notwithstanding any copyright notation thereon. The views and conclusions contained herein are those of the authors and should not be interpreted as necessarily representing the official policies or endorsements, either expressed or implied, of Air Force Research Laboratory or the U.S. Government We also thank Willard and Kelsey Solar Group for providing CdS/CdTe device stacks.

REFERENCES

1. Green, M.A., et al., *Solar cell efficiency tables (version 56)*. Progress in Photovoltaics: Research and Applications, 2020. **28**(NREL/JA-5900-77544).
2. Bellini, E., *First Solar claims lowest module degradation rate in the industry*, in *PV Magazine*. April 19, 2021.
3. Phillips, A.B., et al., *Understanding and Advancing Bifacial Thin Film Solar Cells.* ACS Applied Energy Materials, 2020. **3**(7): p. 6072-6078.
4. Vermang, B., et al., *Improved Rear Surface Passivation of Cu (In, Ga)Se_2 Solar Cells: A Combination of an Al_2O_3 Rear Surface Passivation Layer and Nanosized Local Rear Point Contacts.* Journal of Photovoltaics, 2013. **4**(1): p. 486-492.
5. Vermang, B., et al., *Rear surface optimization of CZTS solar cells by use of a passivation layer with nanosized point openings.* Journal of Photovoltaics, 2015. **6**(1): p. 332-336.
6. Guarnera, S., et al., *Improving the long-term stability of perovskite solar cells with a porous Al_2O_3 buffer layer.* The journal of physical chemistry letters, 2015. **6**(3): p. 432-437.
7. Hoex, B., et al., *On the c-Si surface passivation mechanism by the negative-charge-dielectric Al 2 O 3.* Journal of Applied Physics, 2008. **104**(11): p. 113703.
8. Keller, J., et al., *Bifacial Cu(In, Ga)Se_2 solar cells using hydrogen-doped In_2O_3 films as a transparent back contact.* Progress in Photovoltaics, 2018. **26**(10): p. 846-858.
9. Dingemans, G., et al., *Hydrogen induced passivation of Si interfaces by Al_2O_3 films and SiO2/Al2O3 stacks.* Applied Physics Letters, 2010. **97**(15): p. 152106.
10. Kephart, J.M., et al., *Sputter-deposited oxides for interface passivation of CdTe photovoltaics.* Journal of Photovoltaics, 2018. **8**(2): p. 587-593.
11. Liang, J., et al., *Rectification and tunneling effects enabled by Al_2O_3 atomic layer deposited on back contact of CdTe solar cells.* Applied Physics Letters, 2015. **107**(1): p. 013907.
12. Alfadhili, F.K., et al., *Back-Surface Passivation of CdTe Solar Cells Using Solution-Processed Oxidized Aluminum.* ACS Applied Materials & Interfaces, 2020. **12**(46): p. 51337-51343.
13. Chou, H., et al., *Effects of Cu on CdTe/CdS heterojunction solar cells with Au/Cu contacts.* Journal of The Electrochemical Society, 1995. **142**(1): p. 254.
14. Gessert, T., et al., *Development of Cu-doped ZnTe as a back-contact interface layer for thin-film CdS/CdTe solar cells.* Journal of Vacuum Science Technology A: Vacuum, Surfaces, Films, 1996. **14**(3): p. 806-812.
15. Subedi, K.K., et al., *Nanocomposite $(CuS)_x(ZnS)_{1-x}$ thin film back contact for CdTe solar cells: Toward a bifacial device.* Solar Energy Materials and Solar Cells, 2018. **186**: p. 227-235.
16. Subedi, K.K., et al. *13% CdS/CdTe Solar Cell Using a Nanocomposite $(CuS)_x(ZnS)_{1-x}$ Thin Film Hole Transport Layer*. in *2017 IEEE 44th Photovoltaic Specialist Conference (PVSC)*. 2017. IEEE.
17. Subedi, K.K., et al. *Bifacial CdS/CdTe Solar Cell using Transparent Barium Copper Sulfide as a Hole Transport Layer*. in *2019 IEEE 46th Photovoltaic Specialists Conference (PVSC)*. 2019. IEEE.

Solution Processed Lead Telluride Nanowires as a Passivating Layer to CdTe Photovoltaics

Dipendra Pokhrel, Ebin Bastola, Kamala Khanal Subedi, Manoj K. Jamarkattel, Chandan Kadur, Adam B. Phillips, Michael J. Heben, and Randy J. Ellingson
Wright Center for Photovoltaics Innovation and Commercialization (PVIC), Department of Physics and Astronomy, University of Toledo, Toledo, Ohio, 43606, USA

***Abstract*—: Here, we report the application of lead telluride (PbTe) nanowires (NWs) as a passivating layer to cadmium telluride (CdTe) solar cells enhancing the opto-electronic properties and device performance. The PbTe NWs were synthesized using hot injection colloidal method and applied to CdTe films using a spin-coating process. Steady state photoluminescence (PL) and time resolved photoluminescence (TRPL) measurements from the back side of the device show evidence of passivation in the form of reduced back surface recombination. Devices fabricated using these NWs demonstrate improved open-circuit voltage (V_{OC}) and fill factor (FF) in agreement with the desired effects of surface passivation.**

Keywords— CdTe, back contact, lead telluride, nanowires, passivation

I. INTRODUCTION

Surface passivation plays a critical role for the fabrication of highly efficient solar cells. The front and back surfaces of the solar cells are the sources of high defect densities acting as a recombination centers, and thus reducing the photo-voltage and fill factor of the device. The back surface is more challenging in CdTe photovoltaics compared to the front surface due to the lack of good conducting passivating layer with appropriate band alignment to CdTe layer. At the same time, formation of ohmic contact by the use of p^+ layer is essential to fabricate highly efficient devices. Previously, several materials such as aluminum oxide (Al_2O_3) have shown significant improvement in carrier lifetime of CdTe photovoltaics when utilized as a passivating layer. [1, 2] However, fabrication of efficient devices using Al_2O_3requires that the alumina layer be doped to reduce its insulating qualities. More recently, solution process copper aluminum oxide (Cu_xAlO_y) as a back buffer layer to CdS/CdTe device have shown improvement in minority carrier lifetime.[3]

Another p-type contact, ZnTe has been used for a long time as the back-contact buffer layer for CdTe PV.[4, 5] However, based on the evidence that the minority carrier lifetime does not improve when ZnTe is employed, this material system lacks the passivation necessary to reach the highest potential PV performance.[6] Similarly, PbTe is another chalcogenide having potential application as buffer layer in CdTe PV. PbTe is a semiconductor with narrow band gap energy of 0.31 eV, existing in rock-salt crystal structure at room temperature, with high free hole concentration (~10^{18} cm^{-3}). [7] PbTe can be a p-type semiconductor when Te-rich and n-type when Pb-rich. Previously, x-ray photoemission spectroscopy was used to study the lattice-matched CdTe/PbTe (111) heterojunction interface and found a valence band offset (VBO) of just 0.135 eV between CdTe and PbTe, allowing for low resistance hole injection into the PbTe layer from CdTe .[8] Matin et al. reported the numerical analysis on ultrathin CdS/CdTe with a 100 nm thick PbTe to create a back surface field (BSF) to achieve downward band-bending and the concomitant electronic passivation that reduces back contact interface recombination loss.[9]

NWs can have a potential application as point-contact to CdTe PV,[10] and in that vein we have previously reported the synthesis and application of tellurium and copper telluride NWs as a back buffer layer in CdTe PV.[11, 12] In this work, we report the synthesis and investigation of PbTe NWs for use as a back contact buffer layer in CdTe PV. Our results from these studies indicate that depositing these PbTe NWs at the CdTe back contact increases the minority carrier lifetime as measured by time-resolved photoluminescence from both glass and film side. The improvement in minority carrier lifetime shows the possibility that the PbTe NWs partially passivate the back contact, reducing interface losses. In accord with these observations, improvements in PV performance parameters are also observed. The average V_{oc} of 802 mV was observed for devices with PbTe NWs back contact whereas V_{OC} of 753 mV was found without NWs.

II. EXPERIMENTAL METHOD

PbTe NWs were synthesized using hot injection colloidal method, in two steps. First, we prepared the Te NWs followed the process reported previously, [11] and subsequently converted them to PbTe NWs using a modifying version of the process reported by Yang et al. [13]. For a typical synthesis of PbTe NWs, 0.465 gm (1.22 mmol) of $Pb(CH_3CO_2)_2{\bullet}3H_2O$ and 0.05 gm of PVP were dissolved in 4 mL ethylene glycol by heating at 80° C in separate container. At the same time, 0.2496 gm of PVP was dissolved in 0.75 mL of deionized (DI) water by heating at 80° C. After 21 hrs of Te reaction, the lead precursor was then injected followed by an addition of 0.2496 gm of PVP that dissolved in 0.75 mL of DI water and reaction was continued for next 24 hrs. for high quality PbTe NWs. The heating mantle was removed, and the flask temperature was lowered to room temperature using a cold-water bath. The product was centrifuged and cleaned with DI water.

To study the effect of PbTe NWs on CdTe thin films, we used CdS/CdTe film stack, provided by Willard and Kelsey Solar Group, which was fabricated by vapor transport deposition (VTD) onto TEC™-15M (Pilkington N.A) glass substrates. A wet $CdCl_2$ treatment was carried at 387 °C for 30 mins in dry air environment. For these initial studies, our standard back contact was selected as "Au only" to compare the device performance of CdS/CdTe devices with PbTe

Approved for public release; distribution unlimited.

NWs back contact. After $CdCl_2$ treatment, PbTe NWs were deposited by using spin coater and annealed at 300 °C for 10 mins. To complete the back contact, 45 nm Au was thermally evaporated by using a shadow mask to make the cells area of 0.08 cm^2. Current density vs. voltage (J-V) measurements were performed in the dark and under simulated AM 1.5G illumination. Room temperature PL measurements were detected using a Horiba Symphony-II CCD detector and TRPL measurements were performed using TCSPC module.

III. Results and Discussion

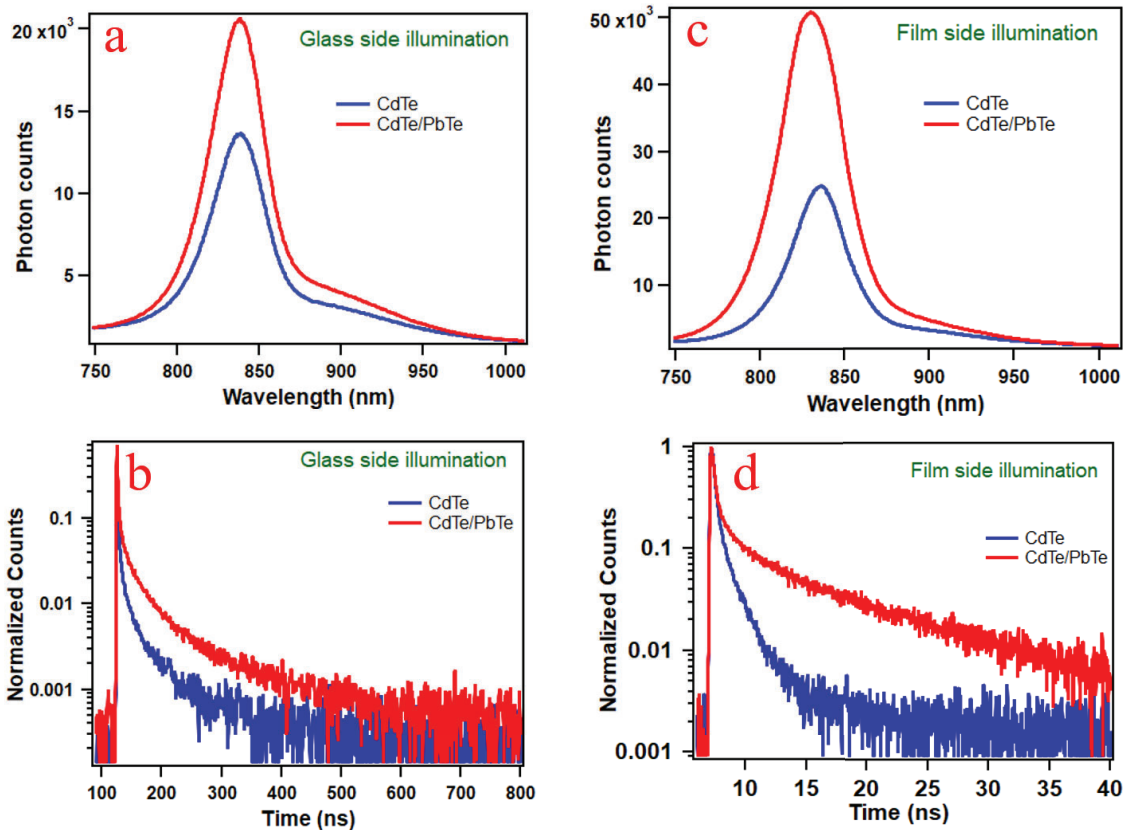


Fig. 1. PL and TRPL spectra of CdS/CdTe device with and without PbTe passivating layer from glass side illumination (a and b) and film side illumination (c and d).

We analyzed the CdS/CdTe devices with and without PbTe NWs, and without any Au electrode, using both front- and back-illumination for steady state PL and TRPL measurements. Fig. 1 shows the PL and TRPL measurements through the glass side used 633 nm excitation while film side used 532 nm excitation. Incorporation of PbTe NWs as the back contact buffer layer yielded increased PL from both front and back illumination and increases in the photogenerated carrier lifetimes. From back side illumination, the longest-lived decay component $\tau_2 = 5.2$ ns was measured with CdTe/PbTe NWs, whereas CdTe only showed $\tau_2 = 1.2$ ns. The increase in minority carrier lifetime is attributed to reduction in back surface recombination of the device.

Photovoltaic performance characteristics for the best cell of CdS/CdTe device with standard back contact (Au) and PbTe NWs back contact (PbTeNWs/Au) are shown in Fig. 2. The dashed lines in the J-V curve represent the dark illumination and solid lines represent the light illumination of the devices. The average open circuit voltage (V_{oc}), short circuit current density (J_{sc}), fill factor (FF) and efficiency (η) of fifteen cells for standard back contact (Au) and PbTe NWs back contact are presented in Table 1. For a standard back contact, the best cell has an efficiency of 11.8 % with V_{oc} of 766 mV, J_{sc} of 21.6 mA cm^{-2} and FF of 71.2 %. Similarly, when utilizing PbTe NWs as a back-interface layer, an efficiency of 13.0 % was obtained with V_{oc} of 797 mV, J_{sc}=22.1 $mAcm^{-2}$, and FF=73.8 %. From the J-V curve and Table 1, it is clearly seen that including PbTe NWs at the back contact interface improved device performance. On average, the V_{oc} of the device with PbTe NWs increases by 49 mV with compared to standard device. The increase in V_{oc} of the device with PbTe NWs is due to increase in minority carrier lifetime of CdTe films as PbTe NWs passivate CdTe surfaces by reducing the back-surface recombination as supported by the PL and TRPL measurements discussed above. The FF of the device also increases with PbTe NWs as compared to standard device and enhances the device performance. This increase in device performance with PbTe NWs is mainly attributed to the increase in V_{oc} of the device. It is well-known that Au alone on CdTe forms a string opposing diode (Schottky barrier) that reduces PV performance, and we find that the presence of PbTe NWs, even in the absence of any intentional Cu doping, modified the performance dramatically. Fig. 2 (b) shows the external quantum efficiency (EQE) curves of CdS/CdTe devices with back contacts Au and PbTe NWs/Au which are closely matched with the value of J_{sc} as obtained from *J-V* measurements.

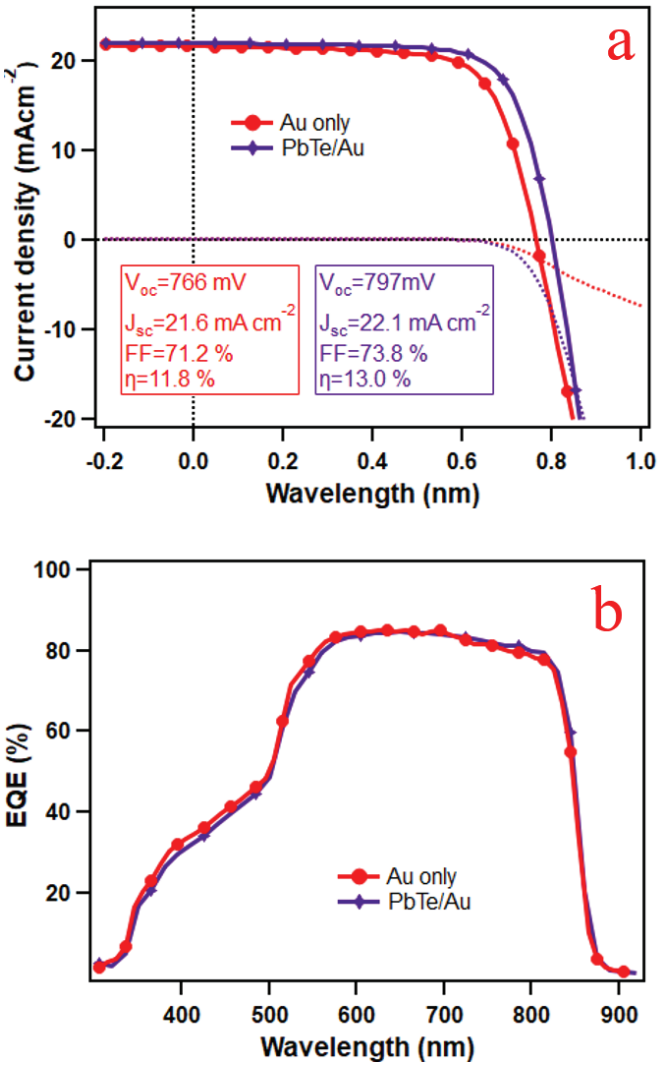


Fig. 2. (a) Current voltage characteristics and (b) external quantum efficiency of the best cell of the CdS/CdTe solar cells with Au and PbTe NWs/Au back contacts.

Table 1: Average parameters (V_{oc}, J_{sc}, FF, η) of CdS/CdTe solar cells with Au and PbTe NWs/Au back contacts.

Back contacts	*V_{oc}* (mV)	*J_{sc}* (mAcm^{-2})	*FF* (%)	*Eff* (η)
Au only	753±9	21.8±0.3	70.4±1.4	11.5±0.2
PbTe NWs/Au	802±4	21.5±0.5	71.1±1.8	12.2±0.5

IV. CONCLUSIONS

We have successfully synthesized the PbTe NWs using a hot injection colloidal method and demonstrated its application as a passivating layer to CdS/CdTe solar cells. As a passivating layer, it increases the minority carrier lifetime from the back as well as front of the device and reduces the back-surface recombination. Initial results indicate that PbTe NWs as a back-interface layer ultimately benefit to increase the performances of CdS/CdTe device. PbTe NWs are applicable for better CdS/CdTe device efficiency as these NWs potentially allow for transport of current through oxide passivated interfaces.

V. ACKNOWLEDGMENT

This material is based on research sponsored by Air Force Research Laboratory under agreement number FA9453-18-2-0037, FA9453-19-C-1002, and by the U. S. DOE's office of Energy Efficiency and Renewable Energy (EERE) under Solar Energy Technologies Office (SETO) Agreement DE-EE0008974. The U.S. Government is authorized to reproduce and distribute reprints for Governmental purposes notwithstanding any copyright notation thereon. The views and conclusions contained herein are those of the authors and should not be interpreted as necessarily representing the official policies or endorsements, either expressed or implied, of Air Force Research Laboratory or the U.S. Government. We also thank Willard and Kelsey Solar Group for providing CdS/CdTe device stacks.

REFERENCES

[1] C. L. Perkins *et al.*, "Interfaces Between CdTe and ALD Al_2O_3," *IEEE Journal of Photovoltaics,* vol. 8, no. 6, pp. 1858-1861, 2018.

[2] F. K. Alfadhili *et al.*, "Back-Surface Passivation of CdTe Solar Cells Using Solution-Processed Oxidized Aluminum," *ACS Applied Materials & Interfaces,* vol. 12, no. 46, pp. 51337-51343, 2020.

[3] K. K. Subedi *et al.*, "Enabling Bifacial Thin Film Devices by Developing a Back Surface Field using CuxAlOy," *Nano Energy,* p. 105827, 2021.

[4] J. Li *et al.*, "Controlled activation of ZnTe: Cu contacted CdTe solar cells using rapid thermal processing," *Solar Energy Materials and Solar Cells,* vol. 133, pp. 208-215, 2015.

[5] F. K. Alfadhili, A. B. Phillips, G. K. Liyanage, J. M. Gibbs, M. K. Jamarkattel, and M. J. Heben, "Controlling Band Alignment at the Back Interface of Cadmium Telluride Solar Cells using ZnTe and Te Buffer Layers," *MRS Advances,* vol. 4, no. 16, pp. 913-919, 2019.

[6] T. Gessert, W. Metzger, P. Dippo, S. Asher, R. Dhere, and M. Young, "Dependence of carrier lifetime on Cu-contacting temperature and ZnTe: Cu thickness in CdS/CdTe thin film solar cells," *Thin Solid Films,* vol. 517, no. 7, pp. 2370-2373, 2009.

[7] H. A. Lyden, "Temperature Dependence of the Effective Masses in PbTe," *Physical Review,* vol. 135, no. 2A, pp. A514-A521, 07/20/ 1964, doi: 10.1103/PhysRev.135.A514.

[8] J. Si, S. Jin, H. Zhang, P. Zhu, D. Qiu, and H. Wu, "Experimental determination of valence band offset at PbTe/CdTe (111) heterojunction interface by x-ray photoelectron spectroscopy," *Applied Physics Letters,* vol. 93, no. 20, p. 202101, 2008.

[9] M. Matin and M. Dey, "High performance ultra-thin CdTe solar cell with Lead Telluride BSF," in *2014 International Conference on Informatics, Electronics & Vision (ICIEV)*, 2014: IEEE, pp. 1-5.

[10] M. J. Heben *et al.*, "PERC-like Contact to CdTe Solar Cells," ed: Google Patents, 2020.

[11] D. Pokhrel, E. Bastola, A. B. Phillips, M. J. Heben, and R. J. Ellingson, "Aspect ratio controlled synthesis of tellurium nanowires for photovoltaic applications," *Materials Advances,* vol. 1, no. 8, pp. 2721-2728, 2020.

[12] D. Pokhrel, E. Bastola, K. K. Subedi, A. Phillips, M. J. Heben, and R. J. Ellingson, "Solution-Processed Copper Telluride Nanowire Thin Film as a Back-Buffer Layer to Cadmium Telluride Solar Cells," in *2020 47th IEEE Photovoltaic Specialists Conference (PVSC)*, 15 June-21

Aug. 2020 2020, pp. 2561-2563, doi: 10.1109/PVSC45281.2020.9300649.

[13] H. Yang, S. W. Finefrock, J. D. Albarracin Caballero, and Y. Wu, "Environmentally Benign Synthesis of Ultrathin Metal Telluride Nanowires," *Journal of the American Chemical Society,* vol. 136, no. 29, pp. 10242-10245, 2014/07/23 2014, doi: 10.1021/ja505304v.

Irradiance and Temperature Control Chamber for Testing Solar Cell Performance

Nadeesha Katakumbura, Aesha P. Patel, Mohamad Abass, Joy E. Chaplin, David Fillmore, Melissa J. Grzegorzewski, Bilal Abdul Halim, Jacob Kennedy, Eulogio Lopez, Ngoc Lien Mai, Manali Manerikar, Jarod Michalak, Samuel V. Pietschman, Erika M. Scholl, James Smith, Ebin Bastola, Ramez Hosseinian Ahangharnejhad, David Raker, Adam B. Phillips, Michael J. Heben, Sorin Cioc, Randy J. Ellingson

The University of Toledo, Toledo, Ohio, 43606, USA

***Abstract*—This report describes the design, construction, and validation of an irradiance and temperature control chamber used to measure temperature-dependent current voltage characteristics of photovoltaic (PV) solar cells under varying conditions in order to reveal fundamental device physics and materials science issues as they relate to terrestrial and space-based performance.**

Keywords— current-voltage, irradiance, solar cell, temperature

I. Introduction

One aspect of the research and development of lighter, flexible, and highly efficient solar cells involves testing solar cell performance by evaluating temperature dependent current (*J*)-voltage (*V*) measurements under varied and/or harsh environmental conditions, namely extreme temperatures and varying irradiance similar to those in outer space. Furthermore, temperature-dependent J-V curves reveal device performance limitations such as those based on contact barriers. Hence, an irradiance and temperature-controlled test chamber is being developed with the goal of simulating *J-V* measurements at different spectra (AM0, AM1.0, AM1.5G), different intensities (0.1 to 1.1 suns), and device temperature ranging from -35ºC to 60ºC. The selected design for the chamber consists of two sections: Test Chamber and Power Chamber. The test chamber consists of a multi-array light source mounted as the ceiling, with an internal dry air flow system, four rectangular mirror walls to guide light downward to the sample stage and improve uniformity, and a thermal controller and a chiller unit that circulates a water and propylene glycol mixture. The sample stage inside the test chamber uses Peltier/thermoelectric coolers (TECs) between the copper block and a water block to achieve and maintain the sample at the desired temperature. This thermal control stage is connected to a water chiller/heater to handle the cooling/heating of the sample stage. On the programming side, the LabVIEW programming platform was used to develop a comprehensive code to command and achieve a setpoint temperature while configuring and operating the light source simultaneously and carrying out the *J-V* or similar electrical measurements.

In general, solar simulators are used to illuminate PV cells under standard test conditions and measure their properties by obtaining *I-V* curves and EQE. However, we have taken a step further to achieve different environmental conditions by allowing the experimenter to change the temperature and the humidity (via dry air flow) of the environment of the solar cell which is being measured. With the capability of achieving wide range of temperatures along with the different humidity conditions along with all the general solar simulator capabilities, an attempt has been made to be able to measure solar cell properties under various conditions ranging from a desert to an outer space environment.

A standard solar simulator should be able to accomplish the sun spectrum standards set by the International Electrotechnical Commission (IEC) or American Society for Testing and Materials [1]. For example, the match of the spectral content with the real spectra depending on the atmospheric effects introduced for different geometries and altitudes (e.g., AM1.5G, which is the global irradiance that reaches the earth surface at an air mass of 1.5 with an intensity of 100 mW/cm^2) [2], irradiance spatial uniformity and temporal stability. Solar simulators can be classified into different classes based on these parameters. According to the standards, if the spectral match in each spectral interval is within the tolerance levels of 25%, 40%, and 60%, they are classified as Class A, Class B, and Class C, respectively. Likewise, for the spatial homogeneity, if the value is below 2%, Class A is assigned. Below 5% and 10% are Class B and Class C, respectively. For the temporal stability, Class A should be having a deviation factor below 0.5%, Class B below 2% and Class C below 5% [3]. Here, we report an irradiance and temperature control chamber with Class AAA simulator qualities which will be discussed further in coming sections.

Apart from the above-mentioned solar simulator properties, this chamber also possesses a wide range of fast and accurate temperature variation capability. The study of the solar cell behavior under different temperature conditions is crucial, because solar cells are being used in different applications under terrestrial as well as extra-terrestrial conditions, where temperature ranges from negative values to ~ 100°C. Earlier studies have shown that, increase in cell temperature results in lower device performance [4],[5],[6]. Normally these performances are determined by the device performance parameters such as Open-Circuit Voltage (V_{OC}), Short-Circuit Current Density (J_{SC}), Fill Factor (*FF*), and Efficiency (η). Previous studies have claimed that V_{OC} decreases and J_{SC} slightly increases, with increasing temperature. Temperature controlling unit of the chamber is designed and constructed in a

Approved for public release; distribution unlimited.

manner where above mentioned parameters can be obtained easily, and much attention is given to maintain the constant temperature over the cell area and to obtain highly accurate readings in a simpler manner with the help of LabVIEW Programs.

The coming sections will be focused on chamber design in terms of both the solar simulator and the temperature controlling unit aspects, software control program development, calibration procedure, Class AAA determination, and system validation with experimental results.

II. Design

A. Chamber Construction

A custom chamber (100 cm x 60 cm x 84 cm) is built mainly using 1.5 sq. inch 8020 aluminum t-slot profiles and fittings. Fig. 1 demonstrates the initial chamber design completed by SOLIDWORKS software (left) and the actual chamber outcome at the end of the project (right). The main chamber consists of two sub-chambers: Test Chamber (to the left) and Power Chamber (to the right). In the test chamber, the thermal stage is placed at the bottom and the light source is mounted on the top with its frame as a hatch which can open/close along with the light source, considering the ease of troubleshooting and repairing of the light source at any given time. Silver coated mirrors based on reflectance spectrum are used in the test chamber to concentrate the spectrum. This mirror assembly is precisely mounted onto a custom-built small chamber inside the test chamber maintaining 90° angle between each mirror and normal to the thermal stage. All the outer walls on the sides and doors of the chamber are covered with sheet aluminum panels. Weather strips are used at each of these contact surfaces to make the test chamber nominally airtight, and dry airflow inlet and outlet are designed at the bottom and top of the test chamber respectively. This is mainly to purge the system of humid air to avoid condensation and water frosting on the sample stage when low temperature measurements are carried out.

To the right in Fig. 1, the power chamber is designed and constructed in a manner all the power units and measuring instruments can be occupied. Shelves can be repositioned easily as per the need. A 3-phase power supply is used to power up the chamber where five bus bars (three hot, one each ground and neutral) are used to distribute the power among all the devices in the chamber including light source, thermal stage and Keithley source measure unit.



Fig. 1. SOLIDWORKS design of the chamber (left), Completed Irradiance and Temperature Control Chamber (right).

Single power input will be available on one of the outer side panels of the power chamber to get the electricity supply for these bus bars and two outlets are available to power the chiller and dry air supply as external devices. The wire connections between these power units and the sources are well insulated and carefully secured. A main switch has been provided to switch off the chamber fully or to cut the power in case for emergency or maintenance needs.

B. Light Source

This multi-array hybrid light source with 9 similar sections (3 x 3) was designed and manufactured by Alfartec (La Chaux-de-Fonds, Neuchâtel, Switzerland). Each section consists of 9 different colors of LEDs and one halogen lamp as shown in Fig. 2. All of the 'bulbs' are symmetrically placed on a single circuit board and mounted to an aluminum frame. The LABVIEW program was developed for this light source with support from PV Lab (EPFL, Neuchâtel, Switzerland), through identification of the driver addressing to activate specific LEDs and the halogen while also controlling the light intensity. Though the chamber and driver have the ability to generate a very wide range of spectra, much focus was given on AM1.5G spectrum simulation.

When light source calibration for AM1.5G spectrum is considered, following the above-mentioned IEC standards, three main categories are generally addressed: Spectral Match, Homogeneity, and Temporal Stability. And our designed managed to accomplish a Class A classification in each section. Note that although each specific LED type's spectral remains constant with varying intensity, the halogen bulb's spectrum varies considerably with operating current. A fiber-optic based spectrometer has been used to record the individual spectra for use in assembling the AM1.5 spectrum, for example.

- Spectral Match

  As per the IEC standard, less than 25% of tolerance should be maintained between the integrated intensity deviations of simulated spectrum and standard AM1.5G spectrum. This is specified over their wavelength intervals and respective integrated power densities. Equation (1) is used in calculating this deviation.

$$\text{Deviation}=\left(\frac{\int_{\lambda 1}^{\lambda 2} I_{AM1.5G}(\lambda)-\int_{\lambda 1}^{\lambda 2} I_{Simulated}(\lambda)}{\int_{\lambda 1}^{\lambda 2} I_{AM1.5G}(\lambda)}\right)\times 100(\%) \qquad (1)$$

- Homogeneity

  Here, the value is calculated from Equation 2, where the I_{MAX} and I_{MIN} are the maximum and minimum integrated power densities, respectively, which are measured at different positions on the radiated surface.

$$\text{Homogeneity }(\%)=\left(\frac{I_{MAX}-I_{MIN}}{I_{MAX}+I_{MIN}}\right)\times 100 \qquad (2)$$

  Homogeneity should be less than 2% to achieve the Class A qualification. A good homogeneity classification ensures that the equal irradiation of the simulated spectrum throughout surface of the tested device. In most

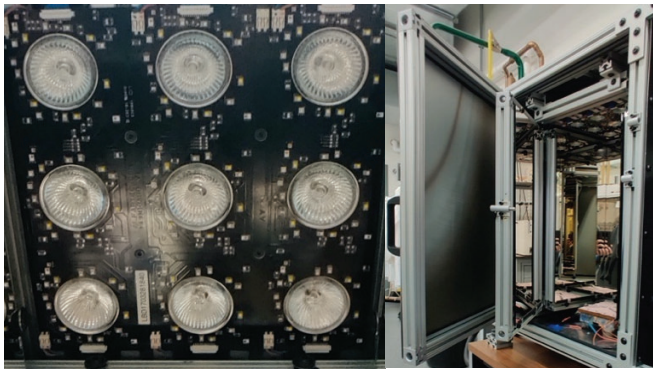


Fig. 2. Multi array hybrid light source with 9 subsections each consists of 9 LEDs and a Halogen (left), Mirror assembly and the mounted light source inside the test chamber (right)

of the past work, it can be observed that lesser surface area such as 1 cm^2 is considered to achieve this classification. But our work presents a simulator with a Class A homogeneity classification for an area larger as 10 cm x 10 cm.

- Temporal Stability

  Here, the classification is decided on two factors: Short-Term Instability (STI) and Long-Term Instability (LTI). And they can be calculated using Equation 3.

$$\text{LTI or STI (\%)} = \left(\frac{I_{MAX} - I_{MIN}}{I_{MAX} + I_{MIN}}\right) \times 100 \quad (3)$$

C. *Thermal Stage (Sample Stage)*

This stage shown in Fig. 3 having an area of 10 cm x 10 cm and mainly consists of aluminum water block (connected to an external chiller), a Peltier/thermoelectric coolers (TECs) configuration, copper block, electrically insulated thermal conductive silicon sheet, pogo pin contacts and sample holding clips. Here the aluminum water block is used to achieve the initial cooling/heating process of the sample stage and to serve as a heat sink for the Peltier coolers when they are in use -- this is of course with the help of the external chiller unit which uses water and propylene glycol mixture as the heat transferring medium.

In between this water block and top copper block, the Peltier cooler array is placed, and high thermal contact is achieved by applying thermally conductive paste on all Peltier surfaces. Pogo pins are used to measure the IV characteristics of the tested solar cells and they are mounted in the copper block using an electrically insulating but thermally conductive silicone sheet such that that no electrical contact occurs between them and the block at any point. The test cell is directly connected to the Keithley instrument using a 4-probe design to reduce the resistance loss of the measurements and enhance accuracy. The silicone sheet includes small cut-throughs to allow pogo pins to contact the solar cell anode and cathode, while maintaining good thermal conductivity. Three sample holding clips are used to maintain a good and leveled contact of the testing solar cell with the pogo pins and the stage

As the initial target of the project was to achieve a temperature range from -35°C to 70°C, main consideration was

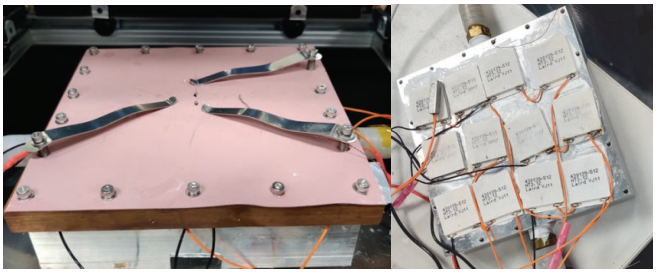


Fig. 3. Thermal stage (sample stage) assembly (left), Peltier arrangement between the copper block and the aluminum chiller block (right)

given to optimize the maximum use of power ratings of the dedicated power supply with maximum number of Peltiers. Hence the arrangement shown in Fig. 3 (right) is used where six branches of two TECs are wired in series and each branch is wired in parallel, for a total of 12 Peltiers. Here we designed a 14 V drop occurs across each Peltier, with each having a chance of drawing up to 3 A,; these parameters are close to the maximum power ratings. Also, the coolers are placed and sandwiched in a manner where the temperature variation is distributed uniformly throughout water block and the copper block

A TC-720 temperature controller (TE Technology, Inc.) is used to control the temperature of this thermal stage by controlling the power availability to the Peltiers. Two thermistors developed by TE Technologies (MP-3193, MP-2444) are used as sensors, one to measure the copper block temperature and the other to read the cell temperature. These are used to maintain the sample stage temperature at the set point temperature during experiments. The TC-720 controller is connected to the laptop via a USB port to handle all advanced programming, data graphing and data logging under LabVIEW control (see below).

D. *Software*

Except for the chiller and the dry air unit which need to be controlled manually, the rest of the system is fully controlled by National Instruments' LabVIEW software. Fig. 4 shows the user interface of the all-in-one LabVIEW program that is used to operate the Temperature and Irradiance Control Chamber.

The light source controller sub-VI (VI = 'virtual instrument') is being used to control the light source of the system. Here, the connection between the NI LabVIEW interface and the light source is maintained via a NI DAQ card. A timing code has been implemented within the light source LabVIEW code to ensure that the light will be turned on for a desired amount of time, which can be varied as per the use or purpose. With the ability in the original program to read configuration files to finely adjust each LED and halogen bulb's light intensity, a new function to control the light source directly from the new LabView interface using a visual control panel (sliders) is also introduced. This panel can only adjust the overall light intensities from 0% to 100% (corresponds to 0 and 1024 bit input to respective light source drivers) for each type of LED and halogen, not individual intensities on different locations of the light source. Individual bulbs on distinct sections can be adjusted individually using configuration files. The content and the arrangement of this file is shown in Fig. 5 where each column addresses the type of light

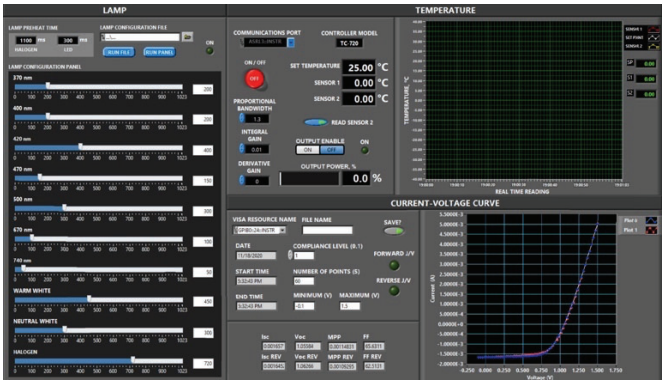


Fig. 4. Lamp controlling, Temperature controlling and VI measurement controlling LabVIEW program user interface.

	Near ultraviolet	Violet	Red	Near Infrared	Royal Blue	Blue	Cyan	Halogen	Neutral White	Warm White
Sub 1	187	287	0	113	711	85	382	645	250	300
Sub 2	187	287	0	113	711	85	382	645	250	300
Sub 3	187	287	0	113	711	85	382	645	250	300
Sub 4	187	287	0	113	711	85	382	645	250	300
Sub 5	187	287	0	113	711	85	382	645	250	300
Sub 6	187	287	0	113	711	85	382	645	250	300
Sub 7	187	287	0	113	711	85	382	645	250	300
Sub 8	187	287	0	113	711	85	382	645	250	300
Sub 9	187	287	0	113	711	85	382	645	250	300

Fig. 5. Configuration file format of the light source.

(9 LEDs and the Halogen) and each row addresses the 9 different light source compartments. However, the panel gives quick control access to the light source that can be used for rapid testing purposes. The retrieved configuration settings can also be saved as configuration files to be modified later for finer adjustments.

Control and stabilization of the thermal stage parameters are achieved from the thermal controller sub-VI. The TC-720 controller used here is a bipolar temperature controller capable of automatically reversing power to Peltier/thermoelectric (TE) devices to provide heating or cooling as required to maintain a specific set point temperature. The main attention was given to the set temperature feed in, live temperature readings of the solar cell and the stage, power on/off and power consumption of the Peltiers, PID controllers, and the real time temperature plots.

Once the program is run, both the solar cell temperature and the thermal stage temperature are shown in real time on the user interface as numerical values and on the plot. Set temperature can also be manually adjusted per the required temperature. A separate button is provided to turn on the Peltier power. The power percentage given to the Peltiers is shown at the bottom of the UI with color indications: Blue for cooling and Red for heating. It is programmed to continue this cooling/heating till the solar cell achieves the set point temperature. The speed and the accuracy of the temperature ramp and approach are controlled by mathematical models linked to PID inputs (Proportional Band Width, Integral Gain, and Derivative Gain).

The *I-V* measurement sub-VI is used to control the solar cell parameter measurements. A Keithley instrument (2401 Source Measure Unit) is used to carry out the respective *I-V* measurement under laptop and LabVIEW control via USB interface. This sub-VI takes the general format of commonly used programs in *I-V* measurements. It consists of experiment data saving path/file name, *I-V* plot, general input parameters such as number of measurement points, voltage sweep range, forward/backward sweeping and main output parameters V_{OC}, J_{SC}, *FF*, and η.

Finally, all sub-VIs are carried into a single user interface and modified so that once the thermal stage is brought to the needed temperature and all the required inputs are set, the light source and the VI measurement start working simultaneously, a complete voltage sweep is conducted, and the respective measurements are saved at the pre-defined file path.

III. Calibration

Once the system was completed, calibration of each unit was carried out. For the spectral calibration, Ocean Optics software and the Spectrometer (FLMT04671) were used to obtain the spectral data. Although it is possible to light up the 9 different subsections of the light source separately, our initial goal was to simulate the AM1.5G spectrum with the help of full light source and later moving forward with the any additional modifications as necessary. Hence, as previously mentioned, the LabVIEW program was developed in a way that it has the ease of use to adjust the overall light intensities for each type of LED and halogen.

As an initial step of the data acquisition for programming of the simulated spectrum, spectral irradiance variation was measured for each light type at different intensities using the spectrometer. Here, the spectrometer was positioned in the middle of the thermal stage (where the pogo pins are), normal to the stage. Then irradiance given out by each type of light was measured at intensity increments of 5% starting from 0% to 50% of the full intensity. The maximum intensity was maintained at 50% as we didn't want to try much higher intensities initially. The obtained irradiance shapes are tallying with the light source spec sheet which is shown in Fig. 6. It was observed that the minimum increment or decrement (smallest step size, resolution) of light intensity can be achieved is 0.1%, for all the light types except for halogen. For halogen, it is approximately 0.14% as it requires more power to turn on than the LEDs. Also, it was noted that there can be a high influence of halogen on the total shape of the final superimposed AM1.5G simulation as its shape changes with the increment of its intensity.

After taking all these data and observations into consideration, with the help of a goodness of fit model with the combination of each source vs. AM1.5G, an intensity combination that lead to minimization of the difference between actual AM1.5G and simulate AM1.5G was obtained (Fig. 7).

After comparing the *J-V* measurements taken under this simulated spectrum with the inhouse measurements, simulator Class qualification tests were carried out under the aforementioned categories.

TABLE I. IRRADIANCE DEVIATION BETWEEN SIMULATED SPECTRUM AND AM1.5G STANDARD SPECTRUM

Spectral Interval (nm)	Simulated (mW/cm^2)	AM1.5G (mW/cm^2)	Deviation (mW/cm^2)
350-400 nm	2.38	3.17	24.91
400-500 nm	12.59	13.8	8.76
500-600 nm	11.67	14.95	21.93
600-700 nm	11.68	13.79	15.3
700-800 nm	9.79	11.21	12.66
800-900 nm	7.11	9.3	23.54
900-1035 nm	7.82	7.9	1.01
Total Irradiance	62.55	75.02	16.62

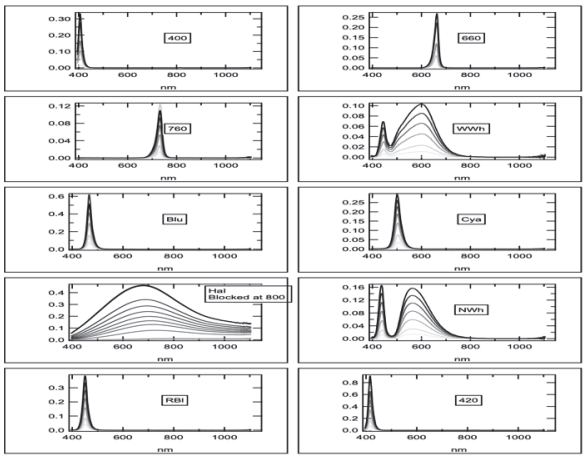


Fig. 6. Spec sheet of the irradiance variation of each light type with its intensity percentage.

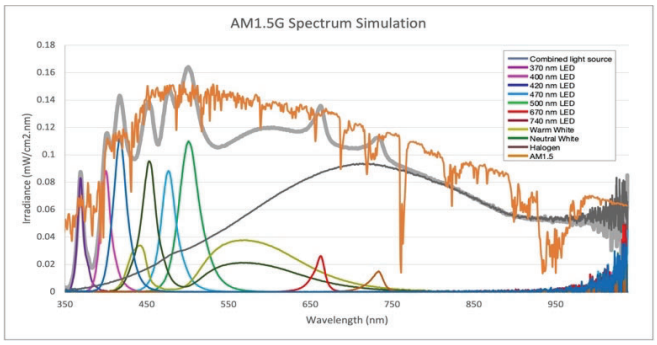


Fig. 7. Superimposition and respective irradiance spectrums of each light to simulate AM 1.5 spectrum.

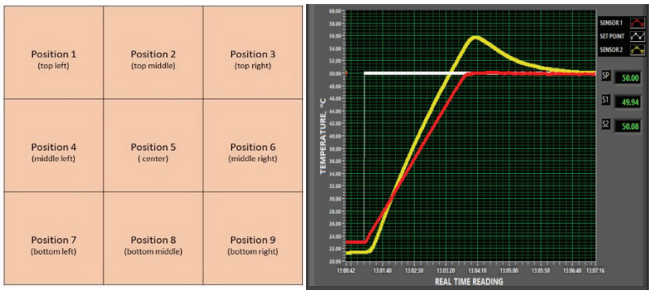


Fig. 8. Spectrometer positioning on the sample stage (left), Fast and accurate set point acquisition of the sample stage.

A. *Spectral Match*

Here the simulated spectrum was measured using the spectrometer, positioning it at the center of the stage. The recorded irradiance vs. wavelength data were divided into spectral ranges as required by the standard. The deviation percentages were calculated using Equation 1. The initial interval and the final interval had to be limited to 350-400 nm and 900-1035 nm, respectively, due to the spectrometer limitations. The respective deviations are shown in Table I, and it can be identified that all the deviations are within the Class A requirement which is less than ±25%. This proves that this simulator belongs to the Class A type in terms of the spectral match.

B. *Homogeneity*

This is calculated by measuring the total irradiance given out by the simulated spectrum at 9 different positions on the stage. In order to get a largest area consideration possible, the stage was divided into 9 symmetrical compartments as shown in Fig. 8 (left) and the spectrometer was positioned at the middle of each compartment. The obtained results are shown in Table 2.

With the use of Equation 2, we managed to obtain the factor of homogeneity as 1.963% which demonstrates that the deviation is less than 2% as per the requirement to be classified as a Class A simulator.

C. *Temporal Stability*

Here, both STI and LTI needed to be calculate separately. Hence, two set of experiments were carried out. For the STI, three rounds of spectrometer readings were taken. In each round 10 spectral readings were taken with 100 ms intervals for a complete 1 s. For the LTI, the same three rounds of measurements were carried out but with 10 s of time intervals for a complete 100 s. During the LTI measurements, it was made sure to start each round after letting the light source to warm up for 30 s to reduce the errors in measurements.

Using Equation 3, FTI and LTI percentage factors were obtained which are shown in Table III. To obtain a Class A certification under Temporal Stability, the STI and LTI deviation should be less than 0.5% and this is proven from the above results. This guarantees the constant emission of the LEDs and the halogen in our system over the period of measurements, as a Class A solar simulator in Temporal stability.

D. *Thermal Stage Calibration*

When the thermal stage calibration is considered, our main goal was to bring the thermal stage to the set point as soon as possible and maintain it at that value with minimum oscillation. Out of the three main damping processes (under damping, over damping, critical damping), critical damping was identified as the proper approach and accordingly PID parameters were optimized following the steps mentioned in the TC-720 controller user guide. Finally, as it is shown in Fig. 8 (right), we managed to achieve fast and reliable constant set point acquisitions with an oscillation less than 0.05ºC. Some of the important results are shown in Table III and Table IV

TABLE II. INTEGRATED IRRADIANCE MEASUERMENTS FOR THE HOMOGENEITY CALCULATION.

Position	Integrated total irradiance (mW/cm^2)
Position 1	65.33
Position 2	65.22
Position 3	64.48
Position 4	64.83
Position 5	64.27
Position 6	64.08
Position 7	63.27
Position 8	64.05
Position 9	62.82

TABLE III. IRRADIANCE DEVIATION BETWEEN SIMULATED SPECTRUM AND AM1.5G STANDARD SPECTRUM.

Round	STI (%)	LTI (%)
1	0.38	0.22
2	0.42	0.45
3	0.27	0.17
Average	0.356	0.28

TABLE IV. THERMAL STAGE TEMPERATURE VARIATION RESULTS WITH TIME (HEATING).

Sample Stage Temperature – SST (C^o)	Time taken to reach SST (s)	Max Oscillation (C^o)
20 to 30	35	0.05
30 to 40	48	0.05
40 to 50	60	0.15
50 to 60	72	0.25
60 to 70	90	0.30

TABLE V. THERMAL STAGE TEMPERATURE VARIATION RESULTS WITH TIME (COOLING).

Sample Stage Temperature – SST (C^o)	Time taken to reach SST (s)	Max Oscillation (C^o)
70 to 60	90	0.05
60 to 50	120	0.25
50 to 40	150	0.15
40 to 30	180	0.05
30 to 20	240	0.05
20 to 10	320	0.10
10 to 0	~1000	0.20
0 to -10	~2500	0.35
-10 to -20	-	-
-20 to -30	-	-

IV. VALIDATION

We are currently using an ORIEL LSH-7320 ABA LED solar simulator with 1 sun condition for the standard in-house *J-V* measurements and related experiments. A comparison between the *J-V* measurements obtained from this setup and measurements obtained from the newly developed Irradiance and Temperature Control Chamber was carried out to validate the system.

The following three types of devices were tested, each one a variation of a CdS/CdTe device with varying back contact designs as follows:

- Au Only
- Cu/Au
- $CuAlO_x$/Au

All devices (3 cm x 3 cm) were prepared for the measurements following the same scribing pattern. 10 different cells were measured under each case. It was made sure to maintain the temperature on the sample stage in the chamber similar to the room temperature used at the in-house measurement unit. The dry air system was not turned on as the temperature was around 22 ºC and hence humidity level had no impact on the experiment. Obtained results are listed in Fig 9.

A separate experiment was carried out on each device to showcase the validity of temperature effect given by the newly developed system on the solar cell parameters. Here a previously identified good cell on the standard device (Cu/Au) was used to measure the *J-V* parameters while changing the thermal stage temperature from 10 ºC intervals. As the thermal stage temperature varied through a wide range of temperatures from positive to negative, dry air supply was kept turned on throughout the experiment to maintain the same humidity conditions in the chamber and to avoid any frosting on the thermal stage during the measurements. Observations are listed in Table VI.

TABLE VI. *J-V-T* MEASUERMENTS

Temperature (C^o)	V_{OC} (mV)	J_{SC} (mA)	Efficiency (%)	FF
50	790	21.96	12.02	69.32
40	819	21.75	12.57	70.58
30	830	21.61	12.85	71.65
20	848	21.45	12.98	71.40
10	874	21.36	13.08	70.08
0	895	21.25	13.24	69.62
-10	909	21.12	13.26	69.12

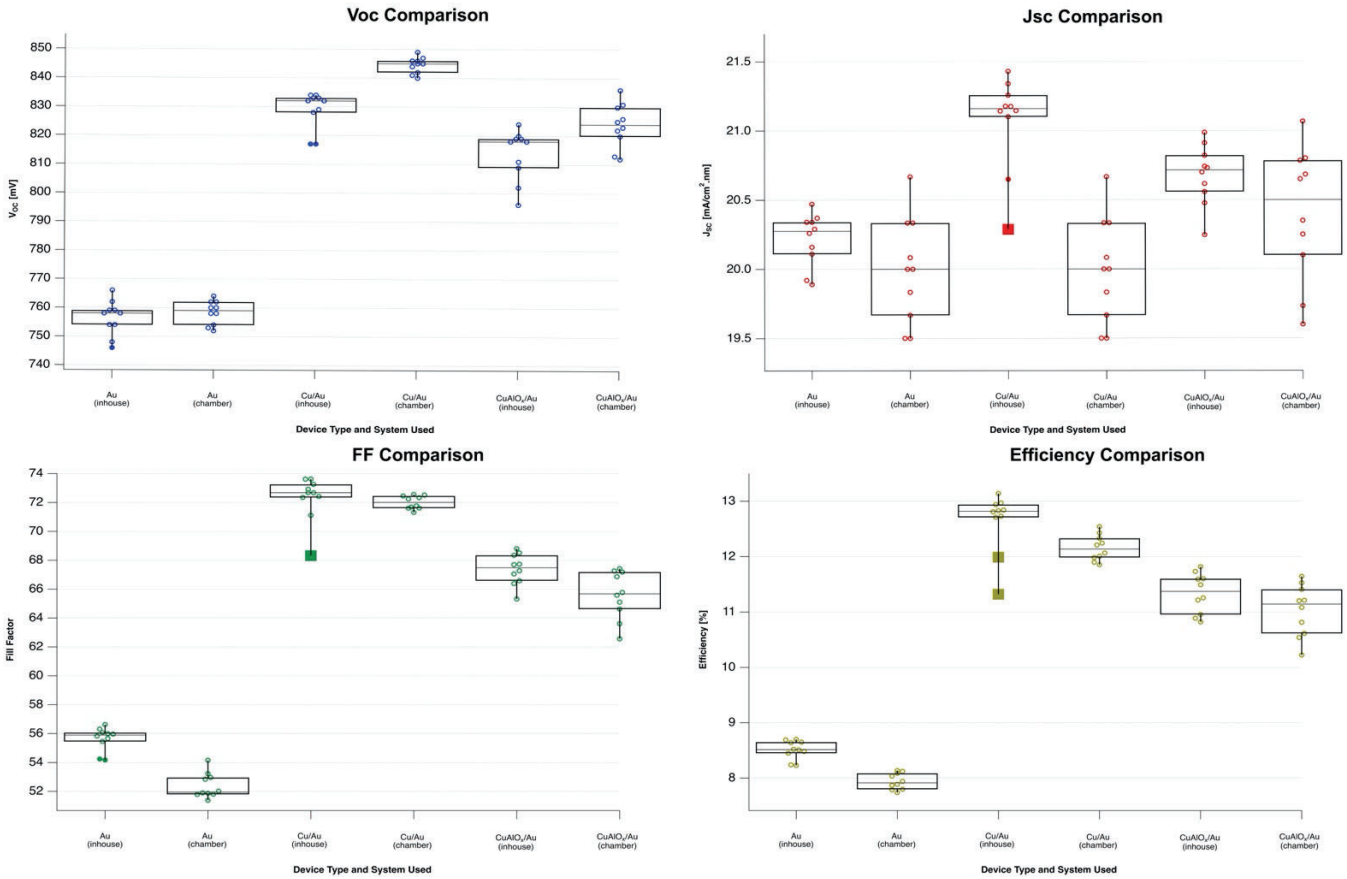


Fig. 9. Statistical distribution of device performance comparison between inhouse solar simulator and irradiance and temperature control chamber.

V. Discussion

In comparison with similar previous work and literature, this system consists of advance and accurate features over most of the common LED based solar simulators while maintaining the Class AAA solar simulator classification. Even though most of the systems are just LED based, this uses an advance hybrid multi array light system which consists of 9 types of LEDs and halogen, to simulate the spectrum. This allows an accurate emission of a wide spectral range, making the system usable over a wide range of solar cell testing applications. The capability to address each one of these lights separately adds considerable flexibility for simulated spectrum control and accuracy. The ability to concentrate and maintain the simulated spectrum uniformity over the total area of the sample stage has been improved due to the use of accurate mirror assembly. This is a significant advantage of this system compared to many other solar simulator systems used in the field. Having a fully closed and dark environment in the test chamber makes the experiment results more accurate as zero background lights can intrude and influence the measurements.

When the thermal stage is considered, it is highly responsive and accurate. With the capabilities such as achieving a wider range of temperature variation, temperature stability over time, minimum oscillation at the set point, etc. overcome most of the drawbacks which can be found in stand-alone *J-V-T* measurement units presented in literature. Use of bipolar devices (Peltiers) and a fully electrical system for the heating/cooling process has made it more convenient to control and modify the system with respect to the systems which use liquid nitrogen and/or heat lamps to control the temperature. The sensors used in the system can measure and control the solar cell temperature accurately compared to other systems found in the literature. Having a regulated dry air supply connected to the test chamber adds convenience for maintaining a constant humidity level inside the chamber, as critical when the temperature measurements are carried out which would otherwise result in condensation and frosting.

Having a single LabVIEW program to control each and every unit of the chamber makes things more efficient. When it comes to real experiments, capability of carrying out several *J-V-T* measurements within a wide range of negative and positive temperatures, under different spectrums, only by changing some values on the LabVIEW user interface can open new possibilities.

These separate units are integrated into a single chamber mainly focusing on the ease of use while limiting all the possible drawbacks as much as possible. From the initial designing phase to the final construction phase, all steps including selection of materials, assembling, sealing, wiring and many other things had

been carried out considering the durability and easy access of repairing/replacing of each and every part of the system.

VI. Conclusion

Irradiance and Temperature control chamber designing, construction, calibration and validation is presented here which can be used for *J-V* measurements under selective spectral and temperature conditions. The system consists of company-built advance components like the hybrid light source, TC-720 temperature controller, chiller unit, dry air supply, and in-house crafted and molded components such as aluminum profiles, panels, copper block, tubes and fittings.

Although there are many stand-alone systems to do solar simulations and *J-V-T* measurements separately, a system with the capability of both seems to be a breakthrough in solar cell research. Hence this project was developed and the final output has the capability of simulating AM1.5G spectrum maintaining a Class AAA qualification over a sample size as large as 10 cm x 10 cm while changing the temperature of the testing cell in a wide temperature range between -10°C and 70°C. A constant humidity level can also be maintained in the chamber with the help of the dry air supply attached. The system validation has been proven from the comparison carried out with results obtain using the in-house simulator.

Although one of the project goals was to achieve a negative temperature of -35°C, this target was not yet reached due to some constraints in the power supplies and Peltiers. Future modifications are focused on resolving this issue along with some other developments such as improvement of the AM1.5G simulation by reducing the spectral deviation, simulation of AM1.0/AM1.5D spectrum, automation of *J-V-T* measurements between predefined maximum and minimum temperatures, improvement of the humidity control process, improvements in the test chamber sealing to develop high vacuum environments in the chamber, etc. These will result in more reliable and accurate simulations and measurements in the future where this Irradiance and Temperature Control Chamber will bring out a whole new set of capabilities under *J-V-T* measurements in the field of solar cell research.

Acknowledgment

This report is based on research sponsored by Air Force Research Laboratory under agreement numbers FA9453-18-2-0037 and FA9453-19-C-1002, and by the U.S. DOE's Office of Energy Efficiency and Renewable Energy (EERE) under Solar Energy Technologies Office (SETO) Agreement DE-EE0008974. The U.S. Government is authorized to reproduce and distribute reprints for Governmental purposes notwithstanding any copyright notation thereon. Disclaimer: The views and conclusions contained herein are those of the authors and should not be interpreted as necessarily representing the official policies or endorsements, either expressed or implied, of Air Force Research Laboratory or the U.S. Government. The authors would like to thank Willard and Kelsey Solar Group for providing CdS/CdTe film stack samples.

References

[1] N. Taylor, "Equipment and basis of power measurements," in Guidelines for PV Power Measurement in Industry, 1st ed. Luxembourg: Office for Official Publications of the European Union, 2010, ch. 3, pp. 23–30.

[2] National Renewable Energy Laboratory. Accessed: Aug. 27, 2018. [Online]. Available: https://rredc.nrel.gov/solar/spectra/am1.5/

[3] Eduardo L pez-Fraguas , Jos M. S nchez-Pena , Senior Member, IEEE, and Ricardo Vergaz, "A Low-Cost LED-Based Solar Simulator"

[4] Green, M.A., Emery, K., Blakers, A.W., 1982. Silicon solar cells with reduced temperature sensitivity. Electron. Lett. 18,97

[5] Osterwald, C.R., Glatfelter, T., Burdick, J., 1987. Comparison of the temperature coefficients of the basic I–V parameters for various types of solar cells. In: Proceedings of 19th IEEE PVSC, 188.

[6] Wysocki, J.J., Rappaport, P., 1960. Effect of temperature on photovoltaic solar energy conversion. J. Appl. Phys. 31,571–577

[7] D. Kolberg, F. Schubert, N. Lontke, A. Zwigart, and D. M. Spinner, "Development of tunable close match LED solar simulator with extended spectral range to UV and IR," Energy Procedia, vol. 8, pp. 100–105,Apr. 2011.

[8] V. Esen, S. Sa˘glam, and B. Oral, "Light sources of solar simulators for photovoltaic devices: A review," Renew. Sustain. Energy Rev., vol. 77, pp. 1240–1250, Sep. 2017

Approved for public release; distribution unlimited.

Solution-Processed P-type Copper Gallium Oxide as a Back Buffer Layer for CdTe Solar Cells

Aesha P. Patel, Kamala Khanal Subedi, Dipendra Pokhrel, Ebin Bastola, Adam B. Phillips, Michael J. Heben, and Randy J. Ellingson

Wright Center for Photovoltaic Innovation and Commercialization, Department of Physics and Astronomy, The University of Toledo, 2801 Bancroft Street, Toledo, OH 43606, USA

***Abstract*—Here, we report the solution-based synthesis of $CuGaO_X$ thin film, and its optimization for application as a back buffer layer in CdS/CdTe solar cells. The $CuGaO_X$ composition was optimized for best results by varying copper source concentration and annealing time post spin-coating. Minority carrier lifetimes and device parameters were recorded. For glass-side illumination, the best cell exhibited an improved efficiency of 14.6% mainly due to a significant increase in V_{OC} (V_{OC} = 863 mV, FF = 74.4%, J_{SC} = 22.7 mA/cm^2) compared to the standard device (Cu/Au back contact) best cell efficiency of 13.0% (V_{OC} = 818 mV, FF = 75.9%, J_{SC} = 21.0 mA/cm^2).**

Keywords—back contact, CdTe solar cells, $CuGaO_X$, interface, thin film

I. Introduction

CdTe - a II-VI group material, featuring a direct bandgap of ~ 1.5 eV, high light absorption, and lower production costs, shows immense potential to compete with the conventional Silicon-based solar technology which currently dominates the terrestrial solar market share [1]. Hence, in the past decade, a proclivity towards improving the CdTe photovoltaic material system has been observed. While the theoretical power conversion efficiency (PCE) limit for CdTe as per Shockley-Queisser is about 32%, its current world record efficiency has reached 22.1% at laboratory scale [2].

Conventional Cu-doped CdTe has a deep work function of ~ 5.7 eV, with low p-type doping (10^{14} cm^{-3}). For typical metal contacts, this creates an efficiency-limiting downward-bending Schottky barrier at the back contact. Hence, finding a suitable high-performance back contact remains a big challenge. To improve the performance at the back contact, either chemical passivation is required to reduce surface recombination velocity or a p-type back buffer layer has to be incorporated which creates a positive initial Fermi level offset (IFLO) to create upward band bending at the back to reflect electrons toward the conduction band [3]. Several back-interface layers have been employed to increase PCE. Subedi *et al.* and Robinson *et al.* used chemical bath deposited $Cu_XZn_{1-X}S$ and sputtered $Cu_XZn_{1-X}S$ back contact to improve the CdTe device band alignment and efficiency, respectively [4], [5]. Subedi *et al.* witnessed an increase in fill factor and V_{OC} by using $CuAlO_X$ to improve CdTe efficiency, an effect they attributed to upward band bending at the back contact [6], [7]. Many have preferred copper (Cu)-based back contacts because an optimum amount of Cu doping enhances device efficiency [8]–[10]. Researchers believe that a Te-rich surface, obtained by chemical etching, evaporated Te buffer layer or by using Te nanowires [11]–[13], can also improve CdTe device performance.

Recently, we have investigated $CuGaO_X$ as a back buffer layer in CdTe. $CuGaO_X$ is a transparent, natural p-type, conductive material previously used as a hole transport layer for organic photovoltaics [14], [15]. This material was synthesized by a solution-based method and spin-coated on CdTe devices to prepare a back contact in order to investigate the device performance and corresponding minority carrier lifetimes.

II. Experimental Details

The CdTe solar panels in use were manufactured by Willard and Kelsey Solar Group by depositing CdS (120 nm) and CdTe (3 μm) through commercial vapor transport deposition (VTD) method onto the TEC^{TM}-15 glass substrates. To improve the grain growth and absorber passivation, $CdCl_2$ treatment was done by depositing a saturated $CdCl_2$-methanol solution onto the 1 x 1 sq. inch CdTe devices and annealing them at 387°C for 30 min in dry air.

For $CuGaO_X$ synthesis, 40 mmol each of $Cu(NO_3)_2{\bullet}3H_2O$ and $Ga(NO_3)_3{\bullet}H_2O$ were dissolved in 5 ml of dimethyl formamide (DMF) with varying Cu concentration (Cu source: 1%, 5%, 10%, 30%, 50%, and 100%). This precursor solution was stirred at a constant speed of 200 rpm for 5 min at room temperature. $CuGaO_X$ film deposition onto the $CdCl_2$ treated CdTe devices was carried out by a 2-step spin-coating process (run 1:1000 rpm for 10 s; run 2: 3500 rpm for 50 s) using 50 μl solution followed by annealing in air at 220°C for different annealing times: 3 min, 6 min, and 9 min. For device completion, 50 nm gold (Au) back contact was thermally evaporated at 1 Å/s. For a standard device, a Cu/Au back contact was fabricated by $CuCl_2$ treatment. The treatment followed Bastola *et al.* without further process optimization [16]. For Cu diffusion, these cells were annealed at 200°C for 20 min and completed with 50 nm of evaporated Au. For devices with $CuGaO_X$ back interface layer (FTO/CdS/CdTe/$CuGaO_X$/Au), $CuCl_2$ treatment was omitted. The devices were then scribed using a 532 nm laser to obtain an array of approximately 15 cells with a device area of 0.06 cm^2.

For completed devices, the *J-V* measurements were taken under simulated 1-sun AM1.5G solar irradiance spectrum conditions. External quantum efficiency (EQE) measurements were conducted on PV Instruments (model IVQE8-C) system.

Approved for public release; distribution unlimited.

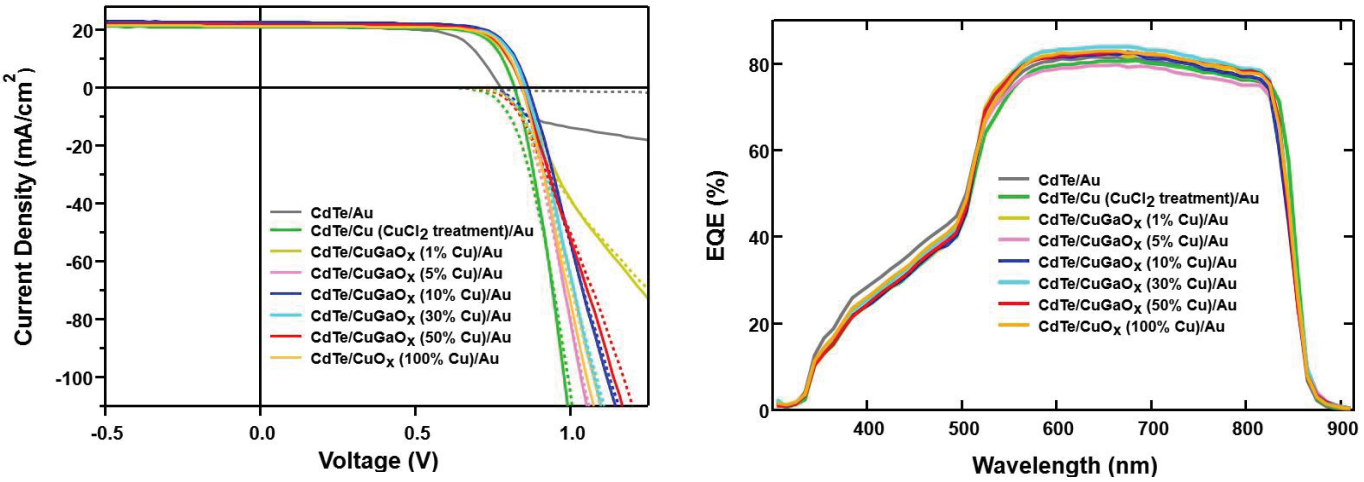


Fig. 1. (a) *J-V*, and (b) EQE measurements of the best CdTe solar cells with $CuGaO_X$ back buffer layer and their comparison with control devices with Au only and Cu/Au standard back contacts

TABLE I. DEVICE PARAMETERS FOR THE BEST AND AVERAGE OF CELLS. DEVICE AREA: 0.06 CM^2

Back contact configuration		***Voc*** **(mV)**	***Jsc*** **(mA/cm^2)**	***FF*** **(%)**	***η*** **(%)**
Au only	Best	775	21.2	68.5	11.3
	Average	764 ± 9	21.0 ± 0.4	68.3 ± 1.6	10.9 ± 0.3
Cu ($CuCl_2$ treated) / Au	Best	818	21.0	75.9	13.1
	Average	815 ± 5	20.6 ± 0.3	74.8 ± 3.0	12.6 ± 0.5
$CuGaO_X$ (1% Cu) / Au	Best	844	21.9	72.3	13.4
	Average	847 ± 4	21.5 ± 0.3	71.8 ± 0.7	13.1 ± 0.3
$CuGaO_X$ (5% Cu) / Au	Best	852	22.1	75.5	14.2
	Average	853 ± 2	21.8 ± 0.2	75.4 ± 0.3	14.0 ± 0.1
$CuGaO_X$ (10% Cu) / Au	Best	863	22.7	74.4	14.6
	Average	861 ± 2	21.7 ± 0.3	74.7 ± 0.3	14.0 ± 0.3
$CuGaO_X$ (30% Cu) / Au	Best	856	21.7	75.7	14.1
	Average	854 ± 2	21.5 ± 0.2	75.6 ± 0.2	13.9 ± 0.1
$CuGaO_X$ (50% Cu) / Au	Best	842	22.0	75.1	14.0
	Average	842 ± 3	21.8 ± 0.2	74.8 ± 0.5	13.8 ± 0.1
CuO_X (100% Cu) / Au	Best	842	21.3	76.9	13.8
	Average	846 ± 2	21.1 ± 0.2	76.3 ± 0.4	13.6 ± 0.1

Time-resolved photoluminescence (TRPL) measurements were conducted using a time-correlated single-photon counting (TCSPC) module with a 633 nm pulsed laser (~5ps pulse width) as the excitation source. For film-side and glass-side illumination, 20 MHz and 1 MHz repetition rates were employed, respectively.

III. RESULTS AND DISCUSSION

Fig. 1(a) and Fig. 3(a) summarize the device performance comparison between the best cells with $CuGaO_X$ back-interface layer (varying Cu concentration and post annealing time) and the devices with standard back contacts (Au only and Cu/Au). The champion device with η = 14.6% (V_{OC} = 863 mV, *FF* = 74.4%, and J_{SC} = 22.7 mA/cm^2) was obtained for $CuGaO_X$ buffer layer device with 10% Cu concentration annealed for 9 min post spin-coating (Fig. 3(b)). Compared to the devices with standard back contacts of Au (V_{OC} = 775 mV, *FF* = 68.5%, and J_{SC} = 21.2 mA/cm^2) and Cu/Au (V_{OC} = 818 mV, *FF* = 75.9%, and J_{SC} = 21.0 mA/cm^2), the relative improvement for the device using CdTe/$CuGaO_X$ (10% Cu)/Au configuration is about 43% and 22%, respectively. $CuGaO_x$ buffer mitigates the crossover effect by providing good surface passivation. External quantum efficiency (EQE) measurements were conducted to confirm the improved J_{SC} by the introduction of $CuGaO_X$ as depicted in Fig. 1(b). The parasitic absorption of the CdS window layer reduces current collection at the shorter wavelength region. From Table I, it is evident that $CuGaO_x$ (10% Cu)/Au device gives better average V_{OC} but $CuGaO_x$ (30% Cu)/Au gives higher average *FF*. Hence, to witness any improvement possibility in V_{OC} for $CuGaO_x$ (30% Cu)/Au device, annealing time post spin-coating was varied as shown in Fig. 3. $CuGaO_X$ (30% Cu) buffer annealed for 9 min slightly increases photocurrent collection in the wavelength region between 500-800 nm (Fig. 3(b)) along with significant increase in V_{OC} (Fig. 3(a)). Further optimization of the back buffer could only slightly improve the device efficiency to 15% because the filmstack is limited due to front

Approved for public release; distribution unlimited.

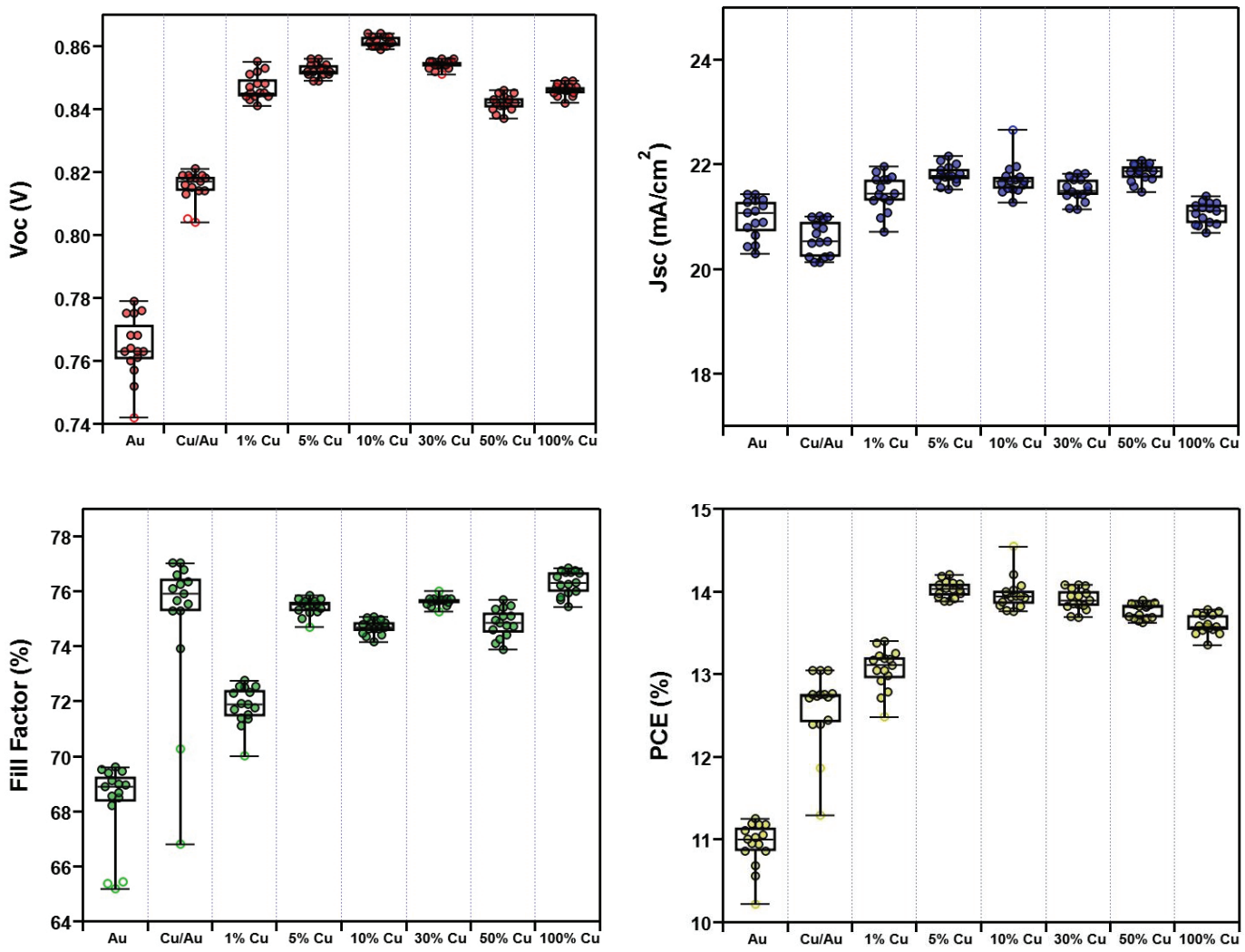


Fig. 2. Statistical distribution of V_{OC}, J_{SC}, FF, and η for CdTe cells with standard back contacts (Au only, and Cu/Au), and $CuGaO_X$/Au back contacts with varying Cu concentration

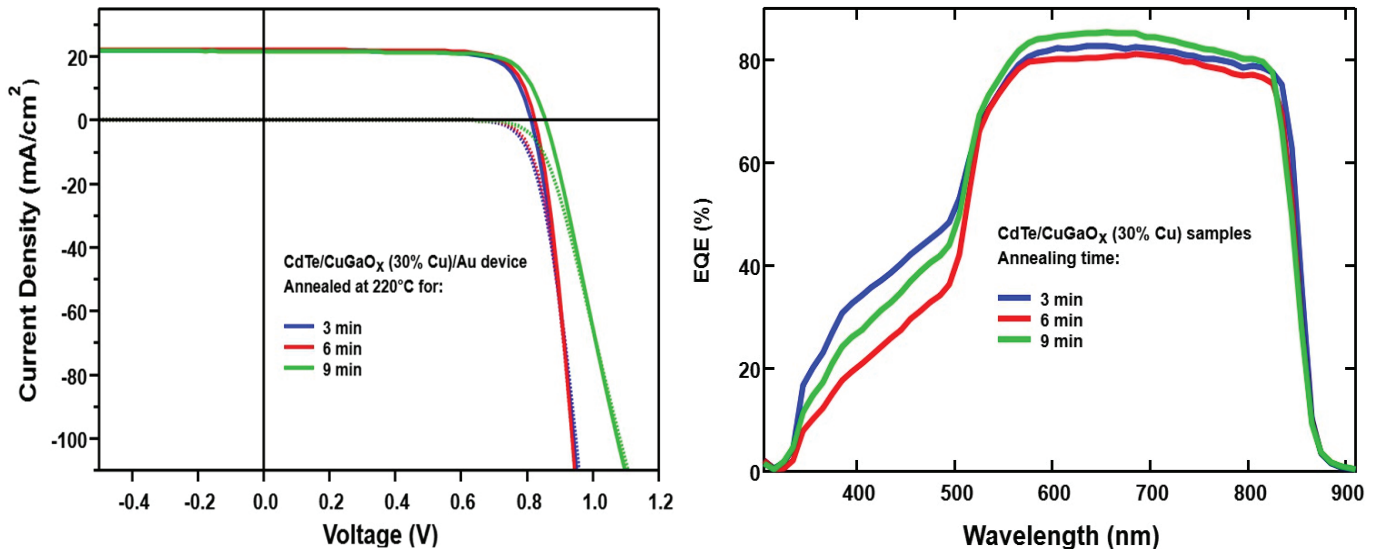


Fig. 3. (a) *J-V*, and (b) EQE measurements of CdTe/$CuGaO_X$ (30% Cu)/Au solar cell devices annealed at 220°C for different annealing time post spin-coating

Approved for public release; distribution unlimited.

TABLE II. DEVICE PARAMETERS FOR THE BEST AND AVERAGE CELLS WITH $CuGaO_x$ (30% CU)-VARYING ANNEALING TIME POST SPIN-COATING. DEVICE AREA: 0.06 CM^2

CuGaOx (30% Cu) annealed at 220°C for varying annealing time post spin-coating		***VOC* (mV)**	***JSC* (mA/cm2)**	***FF* (%)**	***η* (%)**
$CuGaO_X$ (30% Cu) – 3min	Best	813	21.9	75.8	13.5
	Average	805 ± 4	21.3 ± 0.4	74.3 ± 0.8	12.7 ± 0.3
$CuGaO_X$ (30% Cu) – 6 min	Best	823	22.2	76.9	14.0
	Average	825 ± 1	21.3 ± 0.5	76.3 ± 0.9	13.4 ± 0.4
$CuGaO_X$ (30% Cu) – 9 min	Best	856	21.7	75.7	14.1
	Average	854 ± 2	21.5 ± 0.2	75.6 ± 0.2	13.9 ± 0.2

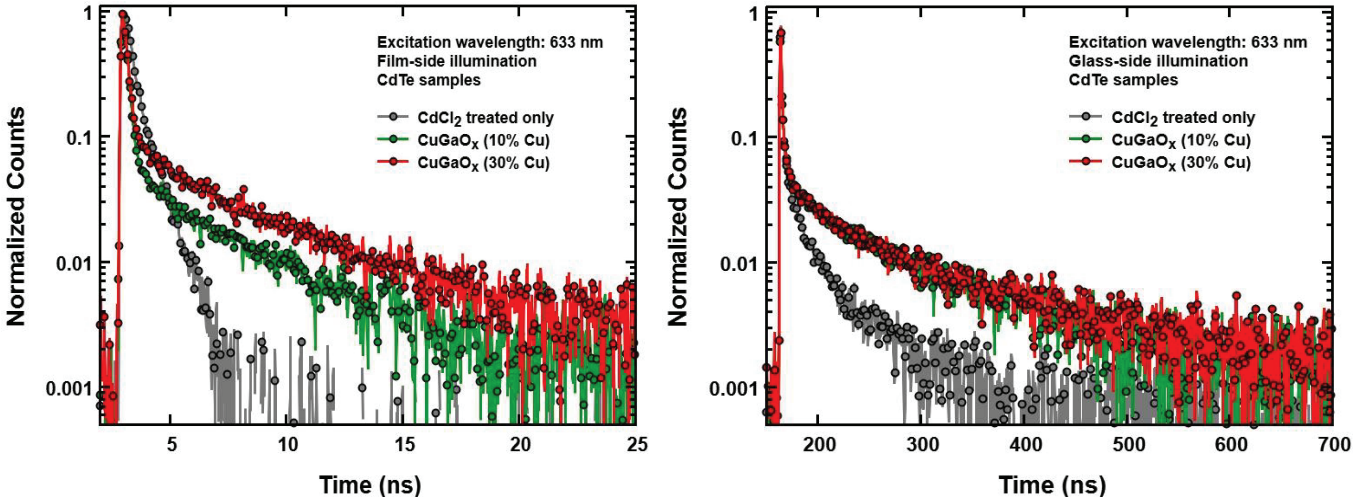


Fig. 4. TRPL measurements for CdTe/$CuGaO_X$ (10% and 30% Cu) from film side (633 nm laser excitation wavelength for repetition rate: 20 MHz) and glass side (633 nm laser excitation wavelength for repetition rate: 1 MHz) illumination

TABLE III. MINORITY CARRIER LIFETIMES FOR CDTE SAMPLES: $CdCl_2$ ONLY (STANDARD DEVICE) AND $CuGaO_X$ (10% AND 30% CU) BUFFER (CHAMPION DEVICE)

	CdTe samples	**τ_2 (ns)**	**Yield2 (%)**
Film-side illumination	$CdCl_2$ treated only	1.8	48.3
	$CdCl_2$/$CuGaO_X$ (10% Cu)	5.1	47.1
	$CdCl_2$/$CuGaO_X$ (30% Cu)	5.7	62.6
Glass-side illumination	$CdCl_2$ treated only	26.7	45.0
	$CdCl_2$/$CuGaO_X$ (10% Cu)	86.9	74.1
	$CdCl_2$/$CuGaO_X$ (30% Cu)	87.2	73.0

surface recombination [17]. The detailed summary of the best and average device parameters with a standard deviation for at least 15 cells can be found in Table I and Table II. Fig. 2 shows the statistical distribution of V_{OC}, J_{SC}, *FF*, and η for devices with standard and novel $CuGaO_X$ back contacts. The efficiency improvement for the champion device is mainly attributed to the significant increase in V_{OC}. Unlike Au devices, Cu/Au devices show no rollover effect in *J-V* as shown in Fig. 1(a). However, a crossover effect is visible for $CuCl_2$ devices between light and dark *J-V* curves in forward bias. Introducing $CuGaO_X$ (at 10% Cu) solves the crossover effect issue, thereby reducing the back-barrier height between CdTe and Au. As a result, V_{OC} increases significantly indicating a possibility that the work function of $CuGaO_X$ may be similar to that of CdTe. For Cu concentrations higher than 10%, $CuGaO_X$ films show a slight increase in *FF* along with a major decrease in V_{OC}. This behavior correlates with the reappearing crossover effect for higher Cu concentrations.

Fig. 4 shows the TRPL decay curves for film-side and glass-side illumination of $CdCl_2$-treated cells without and with the $CuGaO_X$ (10% and 30% Cu) back buffer layer. From Table III, it is evident that the minority carrier lifetimes (τ_2) increase significantly from front and back by the addition of $CuGaO_X$ back buffer layer in CdTe cells, proving it to be a competitive material for further research. The 30% $CuGaO_x$ buffer composition showed slightly higher carrier lifetimes than 10% buffer.

IV. CONCLUSION

P-type transparent $CuGaO_X$ has been successfully synthesized by a solution-based method and its application as a back buffer layer for CdTe solar cells has been discussed in this paper. For optimization studies, the Cu concentration was varied from 1% to 100% and annealing time post spin-coating was varied from 3 min to 9 min. The two best performing Cu concentrations for the $CuGaO_x$ back buffer were 10% and 30% annealed at 220°C for 9 min, out of which $CuGaO_x$ (10% Cu)/Au showed comparatively better average device performance and $CuGaO_x$ (30% Cu) buffer showed higher minority carrier lifetimes. This configuration improved V_{OC} by approximately

Approved for public release; distribution unlimited.

5.6% while maintaining similar J_{SC} and FF, indicating improved band alignment. Longer τ_2 lifetimes indicate reduced interface recombination at the back contact, which together with PV performance results demonstrates the potential for $CuGaO_X$ to serve as a transparent back buffer layer for bifacial and tandem CdTe devices.

ACKNOWLEDGMENT

This report is based on research sponsored by Air Force Research Laboratory under agreement numbers FA9453-18-2-0037 and FA9453-19-C-1002, and by the U.S. DOE's Office of Energy Efficiency and Renewable Energy (EERE) under Solar Energy Technologies Office (SETO) Agreement DE-EE0008974. The U.S. Government is authorized to reproduce and distribute reprints for Governmental purposes notwithstanding any copyright notation thereon. Disclaimer: The views and conclusions contained herein are those of the authors and should not be interpreted as necessarily representing the official policies or endorsements, either expressed or implied, of Air Force Research Laboratory or the U.S. Government. The authors would like to thank Willard and Kelsey Solar Group for providing CdS/CdTe film stack samples.

REFERENCES

[1] Fraunhofer Institute for Solar energy Systems and PSE Projects GmbH, "Photovoltaics Report," 2020.

[2] M. Green, E. Dunlop, J. Hohl-Ebinger, M. Yoshita, N. Kopidakis, and X. Hao, "Solar cell efficiency tables (version 57)," *Progress in Photovoltaics: Research and Applications*, vol. 29, no. 1, pp. 3–15, 2021, doi: 10.1002/pip.3371.

[3] G. K. Liyanage, A. B. Phillips, F. K. Alfadhili, R. J. Ellingson, and M. J. Heben, "The Role of Back Buffer Layers and Absorber Properties for >25% Efficient CdTe Solar Cells," *ACS Applied Energy Materials*, vol. 2, no. 8, pp. 5419–5426, 2019, doi: 10.1021/acsaem.9b00367.

[4] K. K. Subedi *et al.*, "Nanocomposite (CuS)x(ZnS)1-x thin film back contact for CdTe solar cells: Toward a bifacial device," *Solar Energy Materials and Solar Cells*, vol. 186, no. April, pp. 227–235, 2018, doi: 10.1016/j.solmat.2018.06.025.

[5] R. Woods-Robinson *et al.*, "Sputtered p-Type CuxZn1-xS Back Contact to CdTe Solar Cells," *ACS Applied Energy Materials*, vol. 3, no. 6, pp. 5427–5438, 2020, doi: 10.1021/acsaem.0c00413.

[6] K. K. Subedi, A. B. Phillips, M. J. Heben, and R. J. Ellingson, "Solution Based Cu-Doped Aluminum Oxide as a Back Interface Layer for CdTe Solar Cells," *Conference Record of the IEEE Photovoltaic Specialists Conference*, pp. 1–4, 2020.

[7] K. K. Subedi *et al.*, "Enabling Bifacial Thin Film Devices by Developing a Back Surface Field using CuxAlOy," *Nano Energy*, in press.

[8] E. Bastola, K. K. Subedi, K. P. Bhandari, and R. J. Ellingson, "Solution-processed Nanocrystal Based Thin Films as Hole Transport Materials in Cadmium Telluride Photovoltaics," *MRS Advances*, vol. 3, no. 41, pp. 2441–2447, 2018, doi: 10.1557/adv.2018.349.

[9] J. Li *et al.*, "Controlled activation of ZnTe:Cu contacted CdTe solar cells using rapid thermal processing," *Solar Energy Materials and Solar Cells*, vol. 133, pp. 208–215, 2015, doi: 10.1016/j.solmat.2014.10.045.

[10] K. K. Subedi *et al.*, "Bifacial CdS/CdTe Solar Cell using Transparent Barium Copper Sulfide as a Hole Transport Layer," *Conference Record of the IEEE Photovoltaic Specialists Conference*, pp. 185–188, 2019, doi: 10.1109/PVSC40753.2019.8980936.

[11] A. Moore, T. Song, and J. Sites, "Improved CdTe Solar-Cell Performance with An Evaporated Te Layer before The Back Contact," *MRS Advances*, vol. 2, no. 53, pp. 3195–3201, 2017, doi: 10.1557/adv.2017.403.

[12] D. Pokhrel, E. Bastola, K. K. Subedi, A. Phillips, M. J. Heben, and R. J. Ellingson, "Solution-Processed Copper Telluride Nanowire Thin Film as a Back-Buffer Layer to Cadmium Telluride Solar Cells," in *IEEE 47th Photovoltaic Specialists Conference (PVSC)*, 2020, pp. 2561–2563. doi: 10.1109/pvsc45281.2020.9300649.

[13] D. Pokhrel, E. Bastola, A. B. Phillips, M. J. Heben, and R. J. Ellingson, "Aspect ratio controlled synthesis of tellurium nanowires for photovoltaic applications," *Materials Advances*, vol. 1, no. 8, pp. 2721–2728, 2020, doi: 10.1039/d0ma00394h.

[14] R. Nagarajan *et al.*, "p-type conductivity in delafossite structure," *International Journal of Inorganic Materials*, vol. 3, no. 3, pp. 265–270, 2001, doi: https://doi.org/10.1016/S1466-6049(01)00006-X.

[15] J. Wang, V. Ibarra, D. Barrera, L. Xu, Y. J. Lee, and J. W. P. Hsu, "Solution Synthesized p-Type Copper Gallium Oxide Nanoplates as Hole Transport Layer for Organic Photovoltaic Devices," *Journal of Physical Chemistry Letters*, vol. 6, no. 6, pp. 1071–1075, 2015, doi: 10.1021/acs.jpclett.5b00236.

[16] E. Bastola, A. v. Bordovalos, E. Leblanc, N. Shrestha, M. O. Reese, and R. J. Ellingson, "Doping of CdTe using $CuCl_2$ Solution for Highly Efficient Photovoltaic Devices," *Conference Record of the IEEE Photovoltaic Specialists Conference*, pp. 1846–1850, 2019, doi: 10.1109/PVSC40753.2019.8980780.

[17] A. B. Phillips, G. K. Liyanage, F. K. Alfadhili, and M. J. Heben, "Understanding CdTe Performance with Engineered Front and Back Interfaces," *Conference Record of the IEEE Photovoltaic Specialists Conference*, pp. 777–782, 2019, doi: 10.1109/PVSC40753.2019.8980683.

Material Requirements for CdSe Wide Bandgap Solar Cells

Jared D. Friedl, Ramez Hosseinian Ahangharnejhad, Adam B. Phillips, and Michael J. Heben

Wright Center for Photovoltaic Innovation and Commercialization, Department of Physics and Astronomy, University of Toledo, Toledo, OH 43606

***Abstract* — CdSe has an ideal bandgap for the absorber of a top subcell in tandem solar cell configuration. With similar thermodynamic properties to CdTe as well as demonstrated low cost, high volume depositions for application in the manufacturing of CdTe photovoltaic (PV) devices, CdSe is expected to be a robust and reliable material for commercial PV if high quality materials can be fabricated. In this work, optical simulations via transfer matrix method and numerical simulations of device performance are used to determine key material conditions required to achieve high power conversion efficiency CdSe solar cells.**

I. Introduction

With growing energy demands, development of high power conversion efficiency (PCE) solar cells are critical. With champion PCEs of single junction solar cells nearing the Shockley-Queisser limit for photovoltaic (PV) PCE, multijunction solar cells offer an avenue to reach higher PCEs. One path towards high PCE tandem solar cells is the incorporation of perovskite subcells into the device. Due to versatility in fabrication and control of the material properties, namely in bandgap, high-PCE multijunction solar cells incorporating perovskites as the top subcell have been demonstrated. PCE values of 29.1% [1] and 27.7% [2] have been achieved for two- and four-terminal PK/Si [1] devices, respectively. For devices with all-thin-film stacks, efficiencies for devices in two- and four-terminal configurations of 24.2% [1] and 25.9% [3], respectively, for perovskite/CIGS and 24.8% [4] and 25% [5], respectively, for perovskite/perovskite devices have been reported. These PCEs are either comparable or better than those of the single junction counterparts of either absorber material. However, the stability issues concerning the perovskites have hindered their commercialization. In order for a material or device structure to have a successful commercialization track record, low degradation rates are critical. [6]

An alternative material for the top subcell of tandem devices may be CdSe. It has been shown that the performance of multijunction solar cells critically depends on the bandgap of the absorbers in the subcells. [7] For a multijunction device with two subcells the ideal top subcell has a bandgap of ~1.7 eV. [8] The bandgap of CdSe matches this requirement, and its combination with Si and CIGS can produce high PCEs without compromise in stability. Similarities in the thermodynamic properties of CdSe and CdTe suggest similar stability to already commercialized CdTe devices.

Additionally, phase stability problems observed for wide bandgap alloys of CdTe (e.g. CdZnTe, CdMgTe) caused by the $CdCl_2$ treatment [9], [10] are unlikely to occur for pure CdSe absorbers, and such an activation process is expected to be necessary. Furthermore, the fact that CdSe is currently deposited in commercial CdTe-based modules shows that the low cost vapor transport deposition [11] is amenable to CdSe deposition, and the cost to manufacture CdSe solar cells will be low.

However, CdTe solar cells famously have lower voltages than the theoretical expectations. For this reason, the record PCEs of CdTe solar cells have not matched those of perovskite, CIGS, and Si PV yet. Efforts on addressing the voltage problems of CdTe solar cells have shown that the low carrier lifetimes, [12] poor energetic band alignment, and high recombination at the interfaces can be the causes of this issue. [13] Therefore, proper understanding of the required material optical, structural, and electronic properties and their impact on overall performance is required.

In this contribution we investigate proposed CdSe devices in an effort to determine what material properties are required to achieve high efficiencies. We employ the transfer matrix method and one-dimensional charge transport principles via SCAPS to determine the required material thicknesses as well as defect properties at the bulk and the interfaces. For an 800 nm thick CdSe absorber, high-quality interfaces of CdSe with the hole-selective and electron-selective transport layers are shown to be critical for high V_{OC} and J_{SC}, respectively. V_{OC} exceeding 900 mV and PCE above 10% is shown to be possible over a relatively wide range of defect characteristics in the absorber and at the interfaces. Conditions necessary for V_{OC} as high as 1.3 V and J_{SC} as high as 18 mA/cm^2 are articulated.

II. Methods

A. Optical simulations

To build a proper understanding of the impact of thickness and optical losses on the photogenerated current in CdSe as a potential top subcell in a tandem device, optical analyses were performed. To this end, we considered the device structure shown in Fig. 1. Via transfer matrix method [14], [15], which uses measured refractive indices of every material in the device thin film stack [16], the absorption, reflection, and transmission through every interface and film were determined. Carrier generation density as a function of depth in the absorber material and the external quantum efficiency as a function of incident light wavelength were determined assuming that the internal quantum efficiency is 100% for varying absorber material thickness.

Approved for public release; distribution unlimited.

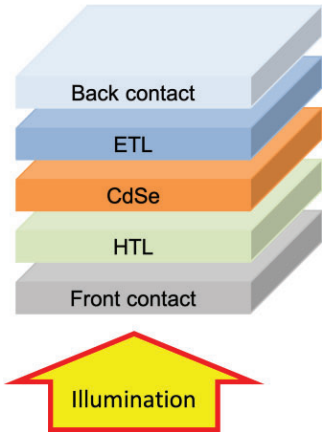


Fig. 1. Thin film stack of the CdSe device considered for the simulation work. CdSe layer is sandwiched between electron and hole transport layers (ETL and HTL).

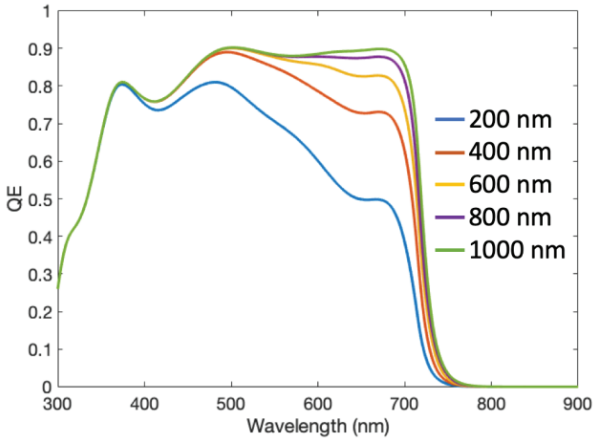


Fig. 2. Simulated EQE for varying CdSe absorber layer.

B. One-dimensional charge transport simulations

Numerical simulation (SCAPS) was used to simulate device performance. Material properties for CdSe were taken from [17]–[19] including a shallow donor density of 2.2e17 cm^{-3}. For electron and hole transport layers (ETL and HTL), TiO_2 and Spiro were considered. These materials have been used in a similar fashion as transport layers in perovskite devices to achieve high PCE. The electronic properties of these materials were taken from [20]–[25]. Carrier lifetimes of the CdSe material were adjusted via bulk defect densities and carrier capture cross sections. Another critical parameter that impacts the performance of CdTe solar cells is the surface recombination velocities (SRVs) at the interfaces of the absorber with the back contact (or buffer) and front junction. To introduce this factor into the current simulations, the interface recombination velocities were varied through total interface defect density at the interfaces implemented between absorber and transport layers.

III. Results

Results of the optical simulations are shown in Fig. 2 for varying CdSe absorber thickness. The results demonstrate that current increases as a function of thickness. For a 200 nm CdSe absorber, the photogenerated current density is 13.80 mA/cm^2. This value increases to 17.03, 18.21, 18.76, and 19.08 mA/cm^2 for 400, 600, 800, and 1000 nm CdSe absorber layers, respectively. The fractional gain in current reduces as the thickness increases, reaching ~3% and ~1% for increasing the thickness from 600 nm to 800 nm and 800 nm to 1 micron, respectively. This is potentially important for conditions where the generated carrier extraction is limited by short carrier lifetimes and reduction in thickness is critical for high voltages and fill factors.

To determine the expected performance of a CdSe device of the structure shown in Fig. 1, SCAPS simulations were performed. For these analyses, the generation profile as a function of depth determined via transfer matrix method for 800 nm CdSe was used. The analysis focused on the impact of carrier lifetimes in the absorber and interface defects at both sides of the CdSe. Due to lack of information on the defect density and carrier lifetimes of polycrystalline CdSe thin films post $CdCl_2$ treatment, lifetimes of both carriers were made equal and varied. For the interfaces, the SRVs at both sides were first made equal and varied, after which the effects of the SRV of each interface were treated individually.

Fig. 3 shows the simulated PCE, open circuit voltage (V_{OC}), short circuit current density (J_{SC}), and fill factor (FF) as a function of carrier lifetimes and interface SRVs under different conditions. Figure 3(a-d) shows these parameters for a cell whose interfaces between the absorber and charge transport layers are assigned the same generalized transport layer (TL) SRV. The PCE under this condition (Fig. 3a) shows some dependence on both lifetime and SRV up to about a lifetime of 100 ns, where bulk Shockley-Read-Hall (SRH) recombination becomes insignificant and efficiency can only be further improved by reduced SRV. Efficiencies above 14% are expected only for lifetimes above 100 ns and recombination velocities nearing 1 cm/s. Fig. 3b shows that V_{OC} is primarily interface-dependent, exhibiting a nominal increase of about 4 mV over a 5 order of magnitude lifetime improvement but an entire 100 mV for *each* order of magnitude reduction in SRV. V_{OC} above 1 V requires lifetimes above 1 ns and SRVs not much higher than 1 cm/s. Relaxing this threshold to 900 mV only requires lifetimes above 0.1 ns and SRVs below 10 cm/s. J_{SC} (Fig. 3c) exhibits the inverse dependencies of V_{OC}, showing nearly complete independence to SRV for lifetimes below ~2 ns, above which lifetime and SRV both play a part, until finally for lifetimes nearing 1 µs J_{SC} is purely interface-limited. J_{SC} exceeds 17 mA/cm^2 for high lifetimes and low SRV. Lastly, fill factor (Fig. 3d) reflects the same transition between dominance of recombination mechanisms as J_{SC}, with some SRV dependence even at lower lifetimes, until lifetimes above 100 ns eliminate the significance of SRH recombination.

Approved for public release; distribution unlimited.

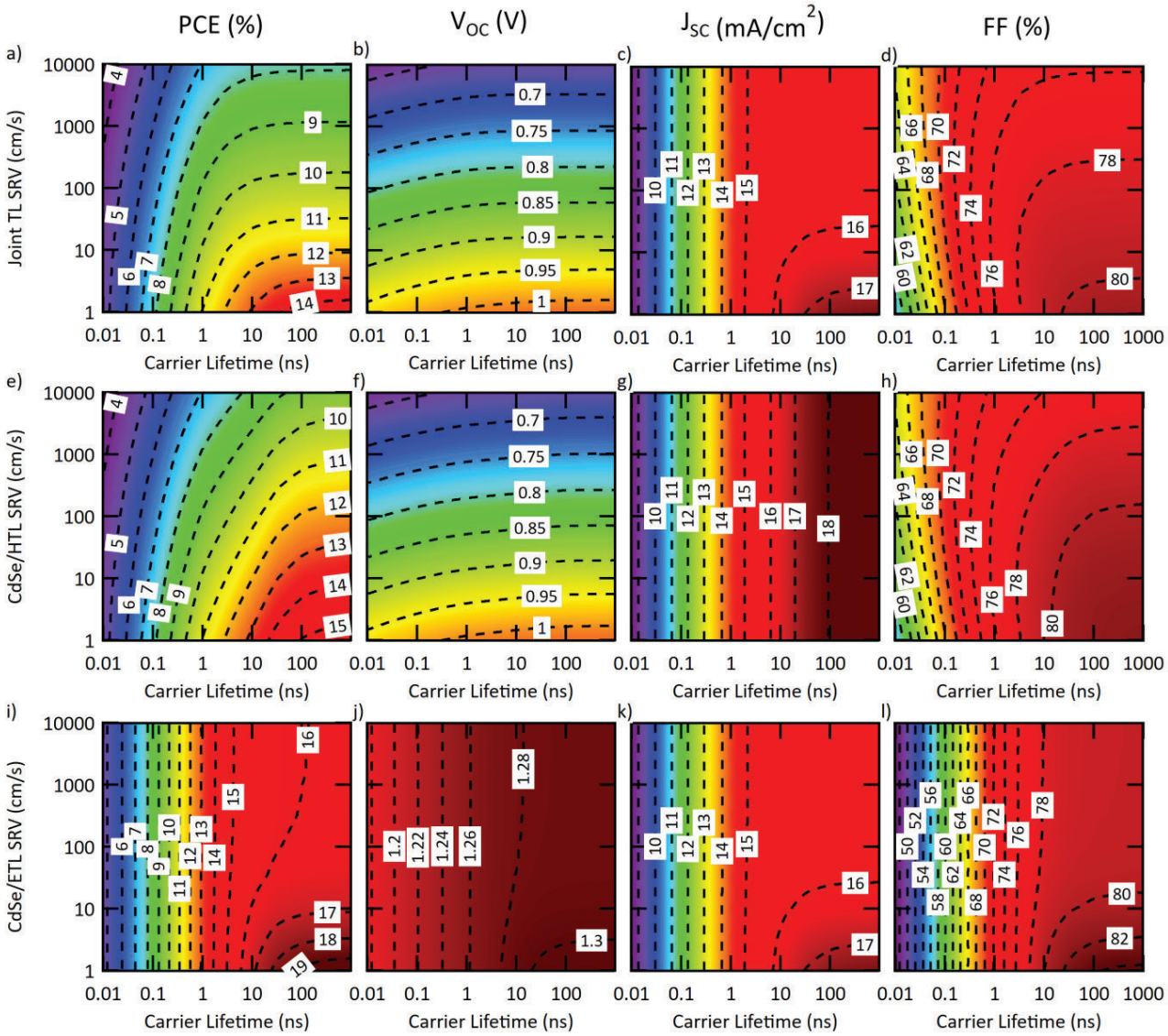


Fig. 3. PCE, V_{OC}, J_{SC} and FF are shown for CdSe devices as function of carrier lifetimes and surface recombination velocities. 3(a-d) shows these parameters for equal SRV at the CdSe/ETL and CdSe/HTL interfaces, while 3(e-h) shows them for an isolated CdSe/HTL interface and 3(i-l) for an isolated CdSe/ETL interface.

To more closely investigate the contribution of each individual absorber/transport layer interface to the SRV and lifetime dependencies just described, each transport layer's interface with the absorber was in turn "shut off," meaning that the SRV was reduced to such a degree (10^{-4} cm/s) that what interfacial recombination remains may essentially be purely attributed to the absorber/TL interface left "on." Fig. 3(e-h) thus isolates the impact of the SRV associated with the CdSe/Spiro-OMeTAD HTL interface, and Fig. 3(i-l) does likewise for the SRV associated with the CdSe/TiO_2 ETL interface.

Fig. 3e shows that the PCE dependence on the CdSe lifetime and the SRV at the CdSe/HTL interface somewhat resembles that of the PCE when the transport layer SRVs were not distinct, with slightly higher values due to the elevated CdSe/ETL interface passivation. The V_{OC} for an isolated CdSe/HTL interface (Fig. 3f) shows an even subtler deviation from the general TL SRV case, suggesting that this interface plays an outsized part in limiting the quasi-Fermi level separation that leads to high V_{OC}. This is expected due to the fact that CdSe has strong n-type doping, so that the junction formed between it and the p-type HTL represents the main p-n junction of the device, and a high density of interface states may impede the full development of a large built-in voltage. J_{SC}, alternately, in Fig. 3g shows no dependence on the CdSe/HTL SRV, even at the highest lifetimes, suggesting that the relative band bending at this interface remains large enough, no matter the SRV, that

current only ever bottlenecks at the other interface. Fill factor (Fig. 3h), like PCE, resembles that of the indistinct SRV scenario, with elevated values at higher lifetimes due to the removal of recombination at the CdSe/ETL interface.

When the CdSe/HTL interface is instead shut off, and the CdSe/ETL SRV varied, the absolute highest device performance is seen. Lifetime plays a singular role for every PV performance parameter up until about 1 or 2 ns lifetimes, regardless of SRV for the CdSe/ETL interface. As most generation occurs nearer to the HTL interface in this configuration appropriate for top tandem subcells, the absorber lifetime must first be high enough for a significant number of carriers to reach the ETL interface before significant recombination occurs there. As expected from the previous case, now with a fully passivated HTL interface, Fig. 3f shows that V_{OC}s are now much higher in general, above 1.2 V for lifetimes as low as 0.1 ns and exceeding 1.3 V, over 90% of the thermodynamic limit for CdSe, only for the highest lifetimes and lowest SRVs observed. For lifetimes exceeding 2 ns, when a significant amount of charge does reach the ETL interface, its SRV plays a role in limiting J_{SC} and fill factor via recombination. Comparing Fig. 3c and Fig. 3k, it is evident that J_{SC} is only ever limited by the CdSe/ETL interface. Conversely, the independence of fill factor to absorber lifetime for lifetimes below ~2 ns that fill factor dependence to SRV seen in this region of Fig. 3d was purely due to the CdSe/HTL interface.

IV. Conclusions

Results shown here indicate the potential of CdSe as an absorber for a top subcell of tandem solar cells. Further studies are needed to determine and, likely, improve the actual interface recombination velocities and the carrier lifetimes of the fabricated material, but the results presented here suggest reasonable efficiencies and V_{OC} greater than 900 mV may be achievable in the near term. Especially important are the materials chosen as charge transport layers, whose quality when interfaced with CdSe is imperative for high performance. Further improvements to the material properties by, for example, optimizing the $CdCl_2$ treatment to improve the lifetime, will only lead to higher device performance. Improved electrical and optical characterization of CdSe, as well as full-device implementation with a variety of accompanying materials, should provide further refinement to optoelectronic modeling and therefore more accurate projections and recommendations. As the results indicate, some hurdles faced by CdTe devices, such as proper band alignment, are not as challenging for CdSe. Even so, further studies on how such energetic properties may further contribute to device performance are necessary.

References

[1] "NREL Best Research-Cell Efficiencies," 2021. [Online]. Available: https://www.nrel.gov/pv/cell-efficiency.html.

[2] T. Duong *et al.*, "High Efficiency Perovskite-Silicon Tandem Solar Cells: Effect of Surface Coating versus Bulk Incorporation of 2D Perovskite," *Adv. Energy Mater.*, vol. 10, no. 9, pp. 1–15, 2020.

[3] D. H. Kim *et al.*, "Bimolecular Additives Improve Wide-Band-Gap Perovskites for Efficient Tandem Solar Cells with CIGS," *Joule*, vol. 3, no. 7, pp. 1734–1745, 2019.

[4] R. Lin *et al.*, "Monolithic all-perovskite tandem solar cells with 24.8% efficiency exploiting comproportionation to suppress Sn(ii) oxidation in precursor ink," *Nat. Energy*, vol. 4, no. 10, pp. 864–873, 2019.

[5] J. Tong *et al.*, "Carrier lifetimes of >1 μs in Sn-Pb perovskites enable efficient all-perovskite tandem solar cells," *Science (80-.).*, vol. 364, no. 6439, pp. 475–479, 2019.

[6] D. C. Jordan and S. R. Kurtz, "Photovoltaic Degradation Rates—an Analytical Review," *Prog. Photovoltaics Res. Appl.*, vol. 21, pp. 12–29, 2013.

[7] A. De Vos, "Detailed balance limit of the efficiency of tandem solar cells," *J. Phys. D. Appl. Phys.*, vol. 13, no. 83946, pp. 839–846, 1980.

[8] R. Hosseinian Ahangharnejhad *et al.*, "Irradiance and temperature considerations in the design and deployment of high annual energy yield perovskite/CIGS tandems," *Sustain. Energy Fuels*, vol. 3, no. 7, pp. 1841–1851, 2019.

[9] O. S. Martinez *et al.*, "Photovoltaic performance of a Cd1 - XMgxTe/CdS top-cell structure," *Thin Solid Films*, vol. 582, pp. 120–123, 2015.

[10] T. M. Shimpi *et al.*, "CdS barrier to minimize Zn loss during CdCl2 treatment of Cd-Zn-Te absorbers," *Sol. Energy*, vol. 173, no. June, pp. 1181–1188, 2018.

[11] S. E. Sofia, J. P. Mailoa, D. N. Weiss, B. J. Stanbery, T. Buonassisi, and I. M. Peters, "Economic viability of thin-film tandem solar modules in the United States," *Nat. Energy*, vol. 3, pp. 387–394, 2018.

[12] X. Zheng, E. Colegrove, J. N. Duenow, J. Moseley, and W. K. Metzger, "Roles of bandgrading, lifetime, band alignment, and carrier concentration in high-efficiency CdSeTe solar cells," *J. Appl. Phys.*, vol. 128, no. 5, 2020.

[13] G. K. Liyanage, A. B. Phillips, F. K. Alfadhili, R. J. Ellingson, and M. J. Heben, "The Role of Back Buffer Layers and Absorber Properties for >25% Efficient CdTe Solar Cells," *ACS Appl. Energy Mater.*, vol. 2, no. 8, pp. 5419–5426, 2019.

[14] L. A. A. Pettersson, L. S. Roman, and O. Inganäs, "Modeling photocurrent action spectra of photovoltaic devices based on organic thin films," *J. Appl. Phys.*, vol. 86, no. 1, pp. 487–496, 1999.

[15] R. Hosseinian Ahangharnejhad *et al.*, "Optical design of perovskite solar cells for applications in monolithic tandem configuration with CuInSe2 bottom cells," *MRS Adv.*, vol. 3, no. 52, pp. 3111–3119, 2018.

[16] M. M. Junda, C. R. Grice, Y. Yan, and N. J. Podraza, "Parametric Optical Property Database for CdSe1−xSx Alloys," *Electron. Mater. Lett.*, vol. 15, no. 4, pp. 500–504, 2019.

[17] S. Kasap and P. Capper, *Springer Handbook of Electronic and Photonic Materials*. 2017.

[18] O. Madelung, *Semiconductors Data Handbook*. 2012.

[19] X. Yang, C. Xu, and N. C. Giles, "Intrinsic electron mobilities in CdSe, CdS, ZnO, and ZnS and their use in analysis of temperature-dependent Hall measurements," *J. Appl. Phys.*, vol. 104, no. 7, p. 073727, 2008.

[20] A. K. Jena, A. Kulkarni, and T. Miyasaka, "Halide Perovskite Photovoltaics: Background, Status, and Future Prospects," *Chem. Rev.*, vol. 119, no. 5, pp. 3036–3103, 2019.

[21] D. Poplavskyy and J. Nelson, "Nondispersive hole transport in amorphous films of methoxy-spirofluorene-arylamine organic compound," *J. Appl. Phys.*, vol. 93, p. 341, 2003.

[22] G. Giorgi, J. I. Fujisawa, H. Segawa, and K. Yamashita, "Small Photocarrier Effective Masses Featuring Ambipolar Transport in Methylammonium Lead Iodide Perovskite: A Density Functional Analysis," *J Phys Chem Lett*, vol. 4, no. 24, pp. 4213–4216, 2013.

[23] C. Wehrenfennig, G. E. Eperon, M. B. Johnston, H. J. Snaith, and L. M. Herz, "High Charge Carrier Mobilities and Lifetimes in Organolead Trihalide Perovskites," *Adv. Mater.*, vol. 26, pp. 1584–1589, 2014.

[24] T. Minemoto and M. Murata, "Theoretical analysis on effect of band offsets in perovskite solar cells," *Sol. Energy Mater. Sol. Cells*, vol. 133, pp. 8–14, 2015.

[25] S. D. Stranks *et al.*, "Electron-hole diffusion lengths exceeding 1 micrometer in an organometal trihalide perovskite absorber," *Science (80-.).*, vol. 342, no. 6156, pp. 341–344, 2013.

Optimizing the Selenization of Sb_2Se_3 Absorbers to Improve the Film Quality and Solar Cell Performances

Suman Rijal, Zhaoning Song, Deng-Bing Li, Sandip S. Bista, and Yanfa Yan

Department of Physics and Astronomy, and Wright Center for Photovoltaics Innovation and Commercialization (PVIC), University of Toledo, Toledo, OH, 43606, USA

Abstract— **In this work, we study antimony selenide (Sb_2Se_3) thin film solar cells deposited by closed space sublimation followed by a post-deposition selenization process at different temperatures. Scanning electron microscopy and X-ray diffraction analyses are employed to investigate the effects of the selenization treatment on the structural properties of Sb_2Se_3 films. It is found that a proper selenization temperature leads to a high-quality Sb_2Se_3 film with the desired grain orientation and a benign Sb_2Se_3/Mo interface. After optimizing, we obtained Sb_2Se_3 solar cells with an improved power conversion efficiency from 3.66 to 7.07 %.**

Keywords—Sb_2Se_3, Solar cell, Annealing treatment, Selenization temperature

I. INTRODUCTION

The urgent need for low-cost, stable, low-toxic, and high efficiency drives the sustained research on thin-film photovoltaics with new absorber materials. The PV market is currently dominated by crystalline Si-based solar cells. However, this technology has several drawbacks, such as a long energy payback time, a low industrial production rate, and a high value of initial investment for the production facility. These technical drawbacks were tried to be removed by developing thin-film solar cells, e.g., Cu(In, Ga)(S, Se)2 (CIGSSe), CdTe, and lead halide perovskite solar cells, with impressive power-conversion efficiencies (PCEs) of 22.6%, [1] 22.1%, [2] and 25.5% [3] respectively. However, due to the concerns regarding the scarcity of Te, In, and Ga, and the toxicity of Cd and Pb, photovoltaics researchers are looking into the materials which are earth-abundance, low cost, and low-toxicity. Cu_2ZnSn (Se, $S)_4$ can be considered one of the most promising materials with low cost and non-toxic constituents. Unfortunately, Complex phase composition and carrier trapping defects hindered the further efficiency improvement in this material. Recently, simple chalcogenides (e.g., SnS, GeSe, and Sb_2Se_3) appeared as new alternatives with less complex, low-toxic and earth-abundant absorbers.

Among them, Sb_2Se_3 has appeared as a promising candidate either for single-junction solar cells or the bottom subcells for dual junction tandem devices due to its high absorption coefficient (10^5 cm^{-1}) and suitable bandgap (1- 1.3 eV) [4] . Besides, the properties of the earth-abundant, low-toxicity, and low-cost constituents (i.e., Sb and Se) make Sb_2Se_3 a very promising candidate to replace CIGS and CdTe for the long-term development of thin-film solar cells.

Despite decent material properties, the record efficiency of Sb_2Se_3 solar cells is only 9.2% [5], which is much lower than the theoretical limit exceeding 30% [6]. A high density of deep defects and a high recombination rate in Sb_2Se_3 films and at the interface are the main causes that hinder the improvement of device performances. The quality of Sb_2Se_3 absorbers can be improved through advancing deposition methods, doping engineering, and post-deposition annealing treatments which ultimately improve the device performances. Among them, a post-deposition annealing treatment is one of the most efficient methods to improve the film quality, e.g., by increasing the crystallinity, tuning the crystal orientation, and reducing the compensate defects concentration, which has shown several great benefits in CdTe and CIGS solar cells [7, 8]. The thermal evaporated CdS/Sb_2Se_3 solar cells have demonstrated an efficiency improvement from 2.6 to 3.7% when selenization was done at 200 ^oC [9]. Similarly, sputtered Sb_2Se_3 solar cell has shown an efficiency of 6.06% by tuning the post-selenization parameters [10]. Also, we were able to fabricate a Sb_2Se_3 solar cell with an efficiency of 6.43% [11] previously by optimizing the selenization temperature. The selenization treatment of Sb_2Se_3 films compensates the Se loss during the deposition, which reduces the V_{Se} related recombination [9] and also forms a thin $MoSe_2$ layer at the Sb_2Se_3/Mo interface, which helps to eliminate the Schottky barrier and reduces the recombination at the back interface [10]. Here, the effect of post-selenization on the Sb_2Se_3 film quality and device performances are investigated systematically.

II. EXPERIMENTAL DETAILS

Fig. 1 shows the schematic diagrams of a substrate-type Sb_2Se_3 solar cell and the close space sublimation (CSS) deposition equipment for depositing Sb_2Se_3 films. A 900 nm Mo layer was deposited on a cleaned glass substrate by DC-sputtering. After that, a 200 nm Sb_2Se_3 film was deposited as a seed layer with a source temperature (T_{sou}) of 500 ^oC and a substrate temperature (T_{sub}) of 315 ^oC according to our previous publication [12]. Then, the main Sb_2Se_3 absorber layer was deposited on top of the seed layer with T_{sou} and T_{sub} at 480 and 400 ^oC, respectively. During the deposition, pure nitrogen flow was supplied at a flow rate of 400 sccm to maintain a base

Approved for public release; distribution unlimited.

pressure of 231 mTorr. The thickness of the absorber layers was ~2 μm for a 6 min deposition. The obtained absorber layer was then selenized at temperatures from 350 to 425 °C in Ar with 100 mg selenium for 30 min to promote the recrystallization of Sb_2Se_3. After that, a 55 nm CdS buffer layer was deposited on top of the Sb_2Se_3 absorber layer using chemical bath deposition (CBD). A 50 nm high-resistive i-ZnO layer and a 250 nm aluminum doped zinc oxide (AZO) front contact layer were deposited by radio frequency (RF) sputtering. Lastly, a 200 nm Ag metal grid was deposited on the AZO layer via thermal evaporation. Before the measurement, the devices were mechanically scribed into individual cells with an active area of 0.2 cm^2.

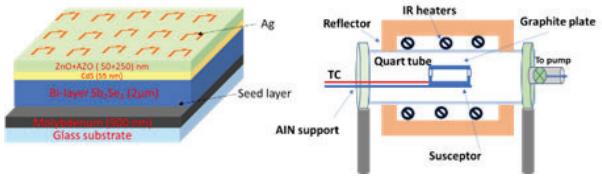


Fig. 1. Schematics of a) Sb_2Se_3 solar cells and b) CSS equipment.

III. Results and Discussions

Surface and cross-sectional SEM images of Sb_2Se_3 films annealed at various temperatures ranging from 375 to 425 °C are shown in Fig. 2. As expected, the grain size increases, and the porosity decreases with the increasing selenization temperature. For the sample annealed at 400 °C, Sb_2Se_3 grains with an average size of more than 1 μm were formed and distributed evenly over the sample surface. At a higher annealing temperature, i.e., 425 °C, larger grains with sizes of over 1.5 μm were formed, with a compact morphology and no observable voids. When the selenization temperature was further increased to 450 °C, the grain size increased to 3~5 μm, but voids with micrometer size appeared.

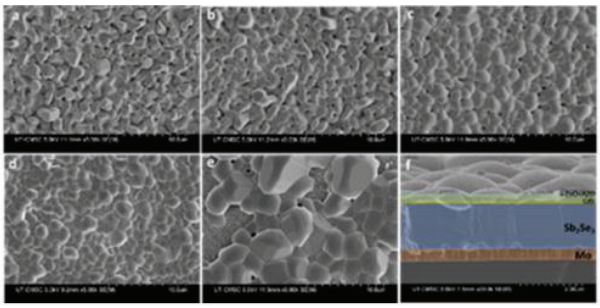


Fig. 2. Morphology evolution of Sb_2Se_3 thin films. Top-view of SEM images of Sb_2Se_3 thin films annealed at different selenization temperatures: (a) before annealing, (b)375 °C, (c) 400 °C, (d) 425 °C and (e) 450 °C. (f) Cross-sectional SEM image of a complete Sb_2Se_3 solar cell with the Sb_2Se_3 film selenized at 425 °C. Reproduced with permission from Ref [11]. Copyright 2021 American Chemical Society.

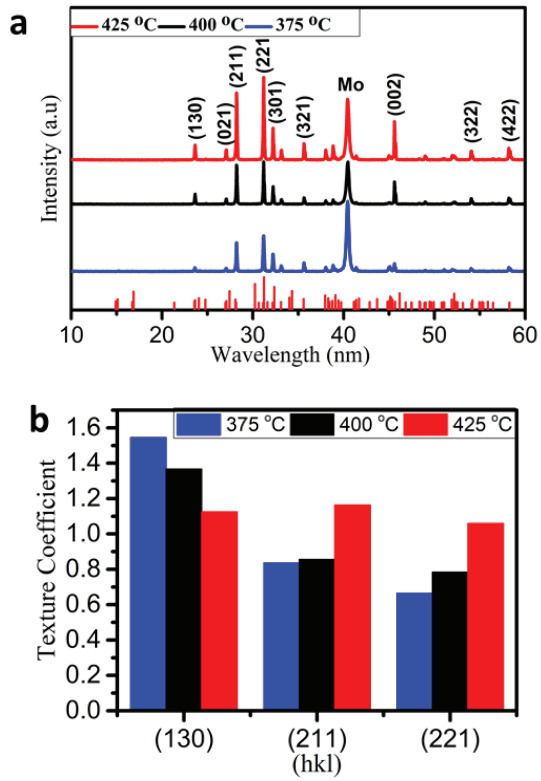


Fig. 3. (a) XRD patterns and (b) the calculated texture coefficients of Sb_2Se_3 thin films selenized at various temperatures. Panel (a) is reproduced with permission from Ref [11]. Copyright 2021 American Chemical Society.

XRD was used to investigate the crystal phases of the Sb_2Se_3 thin films deposited on the Mo-coated glass substrates. The XRD patterns of the unannealed and selenized Sb_2Se_3 thin films at different temperatures from 375 to 425 °C are shown in Fig. 3. All the diffraction peaks can be indexed to the orthorhombic phase of Sb_2Se_3 (JCPDS No. 97-008-5676) except the diffraction peak at 40.45°, which can be indexed to Mo underneath. The overall diffraction peak intensities of the films increase upon increasing selenization temperature, indicating the improved crystallinity. To study the film orientation qualitatively, texture coefficient (TC) for (130), (211), and (221) diffraction peaks were calculated using equation:[13]

$$TC(hkl)= \frac{\frac{I(hkl)}{Io(hkl)}}{\sum_{i=1}^{N}\frac{I(h_ik_il_i)}{Io(h_ik_il_i)}} \quad (1)$$

Where I(hkl) and I_O(hkl) are the diffraction peak intensities of (hkl) planes in the measured and standard XRD patterns of Sb_2Se_3 (JCPDS 97-008-5676), respectively. A large TC value of a diffraction peak indicates a preferred orientation along this particular direction [10]. Fig. 3b shows that the TC values of the (211) and (221) planes increase, whereas the TC of the (130) plane decreases with the increasing selenization temperature. Due to the unique 1-dimensional crystal structure of Sb_2Se_3, Sb_2Se_3 films with the (hkl, l≠0) peaks are preferred for better carrier transport and collection, thereby higher device performances, while the (hkl, l = 0) orientated Sb_2Se_3 films generally result in a high carrier transport barrier[10]. The improvement of TC values for the (211) and (221) planes for the

Approved for public release; distribution unlimited.

film annealed at 425 °C indicates that the more preferred Sb_2Se_3 film orientations can be obtained at a higher selenization temperature, predicting higher device performances.

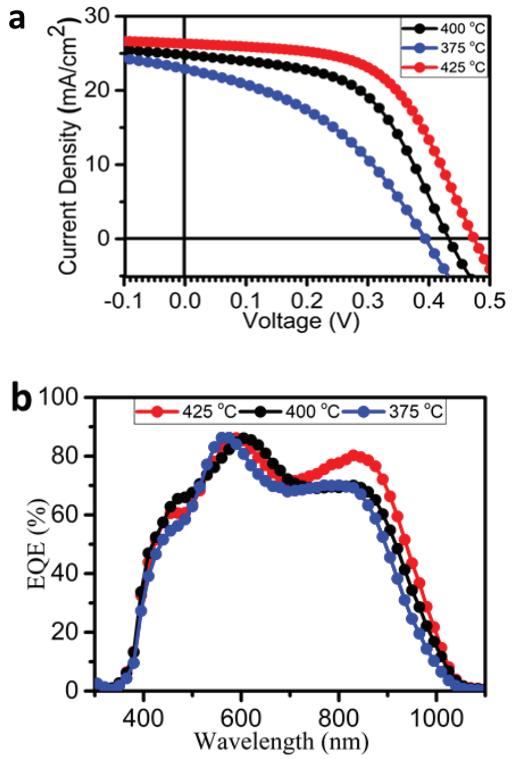


Fig. 4. (**a**) Current density-voltage (J-V) and (**b**) external quantum efficiency (EQE) curves of the Sb_2Se_3 solar cells grown under different selenization conditions. Reproduced with permission from Ref [11]. Copyright 2021 American Chemical Society.

TABLE I. The J-V parameters of champion Sb_2Se_3 solar cells selenized at different temperatures

Selenization Temp. (°C)	***V_{OC} (mV)***	***J_{SC} (mA/cm²)***	***FF (%)***	***PCE (%)***	***R_S (Ω·cm²)***	***R_{SH} (Ω·cm²)***
375	394	22.91	40.51	3.66	7.62	78.72
400	433	24.90	53.57	5.77	6.01	158.44
425	474	26.32	56.61	7.07	5.58	315.35

Substrate-type Sb_2Se_3 solar cells with a structure of Ag grid/ZnO:Al/ZnO/CdS/Sb_2Se_3/Mo/glass were fabricated to investigate the relation between Sb_2Se_3 film quality and device performances. Table 1 summarizes the photovoltaic parameters for devices prepared with Sb_2Se_3 films selenized at different temperatures (375, 400, and 425 °C). Comparing with the device selenized at 375 °C, the device selenized at 425 °C has an improved open-circuit voltage (V_{OC}) from 394 to 474 mV, an improved short-circuit current density (J_{SC}) from 22.91 to 26.32 mA/cm², and an improved fill factor (FF) from 40.51 to 56.61 %, respectively, yielding an overall PCE improvement from 3.6% to 7.07 %. The improvement of V_{OC} and FF can be attributed to the improved crystallinity, preferred orientation, and compact morphology of the Sb_2Se_3 films, as discussed above. Besides, the selenization treatment can also facilitate the formation of $MoSe_2$ between the Mo and Sb_2Se_3, which can help to improve the back-interface quality and reduce the Schottky barrier height. Higher selenization temperature can help to form a more compact $MoSe_2$ film at the back interface. This might be another reason for the improved device performance comparing with that with lower selenization temperatures. The external quantum efficiency (EQE) can further confirm the improvement of back surface quality (Fig. 4b). When the selenization temperature increases from 375 to 425 °C, the EQEs at longer wavelengths are higher, suggesting a better back contact between Mo and Sb_2Se_3.

IV. Conclusions

In conclusion, the impact of selenization temperature on the PV performance of Sb_2Se_3 was investigated. We found that the selenization temperature of 425 °C was beneficial to increase the grain size, crystallinity and orientation of the Sb_2Se_3 films. In addition, the Se loss during the CSS deposition can be compensated by the selenization process, which results in a reduced V_{Se} related recombination loss. Because of all of these benefits after selenization, a significant device performance improvement from 3.66 to 7.07 % is achieved.

V. Acknowledgments

The authors gratefully acknowledge funding support from the U.S. Air Force Research Laboratory, Space Vehicles Directorate, under Contract # FA9453-19-C-1002.

References

1 Jackson, P., Wuerz, R., Hariskos, D., Lotter, E., Witte, W., and Powalla, M.: 'Effects of heavy alkali elements in Cu (In, Ga) Se2 solar cells with efficiencies up to 22.6%', physica status solidi (RRL)–Rapid Research Letters, 2016, 10, (8), pp. 583-586

2 NREL, N.: 'Best Research-Cell Efficiency Chart', in Editor (Ed.)^(Eds.): 'Book Best Research-Cell Efficiency Chart' (US Department of Energy, 2019, edn.), pp.

3 Yoo, J.J., Seo, G., Chua, M.R., Park, T.G., Lu, Y., Rotermund, F., Kim, Y.-K., Moon, C.S., Jeon, N.J., and Correa-Baena, J.-P.: 'Efficient perovskite solar cells via improved carrier management', Nature, 2021, 590, (7847), pp. 587-593

4 Zeng, K., Xue, D.-J., and Tang, J.: 'Antimony selenide thin-film solar cells', Semiconductor Science and Technology, 2016, 31, (6), pp. 063001

5 Li, Z., Liang, X., Li, G., Liu, H., Zhang, H., Guo, J., Chen, J., Shen, K., San, X., Yu, W., Schropp, R.E.I., and Mai, Y.: '9.2%-efficient core-shell structured antimony selenide nanorod array solar cells', Nature Communications, 2019, 10, (1), pp. 125

6 Shockley, W., and Queisser, H.J.: 'Detailed balance limit of efficiency of p‐n junction solar cells', Journal of applied physics, 1961, 32, (3), pp. 510-519

7 Geethalakshmi, D., and Muthukumarasamy, N.: 'Effect of annealing on structural and optical properties of CdTe thin films', Journal of NanoScience and NanoTechnology, 2012, 1, (1), pp. P: 23-29
8 Marsillac, S., Zouaghi, M., Bernede, J., Nasrallah, T.B., and Belgacem, S.: 'Evolution of the properties of spray-deposited CuInS2 thin films with post-annealing treatment', Solar energy materials and solar cells, 2003, 76, (2), pp. 125-134
9 Leng, M., Luo, M., Chen, C., Qin, S., Chen, J., Zhong, J., and Tang, J.: 'Selenization of Sb2Se3 absorber layer: an efficient step to improve device performance of CdS/Sb2Se3 solar cells', Applied Physics Letters, 2014, 105, (8), pp. 083905
10 Li, Z., Chen, X., Zhu, H., Chen, J., Guo, Y., Zhang, C., Zhang, W., Niu, X., and Mai, Y.: 'Sb2Se3 thin film solar cells in substrate configuration and the back contact selenization', Solar Energy Materials and Solar Cells, 2017, 161, pp. 190-196
11 Rijal, S., Li, D.-B., Awni, R.A., Bista, S.S., Song, Z., and Yan, Y.: 'Influence of Post-selenization Temperature on the Performance of Substrate-Type Sb2Se3 Solar Cells', ACS Applied Energy Materials, 2021, 4, (5), pp. 4313-4318
12 Wang, L., Li, D.-B., Li, K., Chen, C., Deng, H.-X., Gao, L., Zhao, Y., Jiang, F., Li, L., Huang, F., He, Y., Song, H., Niu, G., and Tang, J.: 'Stable 6%-efficient Sb2Se3 solar cells with a ZnO buffer layer', Nature Energy, 2017, 2, pp. 17046
13 Sze, S.M., Li, Y., and Ng, K.K.: 'Physics of semiconductor devices' (John wiley & sons, 2021. 2021)

64th Annual Technical Conference Proceedings
Virtual Event: May 3 – 7, 2021
https://doi.org/10.14332/svc21.proc.0016
© 2021 Society of Vacuum Coaters (www.svc.org)
all rights reserved ISSN 0737-5921
ISBN 978-1-878068-41-5

Deposition Temperature Dependence of Optical and Structural Properties of Glancing Angle Deposited CdTe

Niva K. Jayswal, Dipendra Adhikari, Indra Subedi, Corey R. Grice, and Nikolas J. Podraza
Wright Center for Photovoltaics Innovation and Commercialization & Department of Physics and Astronomy, University of Toledo, Toledo, OH, 43606, USA

ABSTRACT

X-ray diffraction (XRD) patterns are compared for radio frequency (RF) sputtered glancing angle deposited (GLAD) CdTe films prepared on soda lime glass at 250°C and room temperature (RT) at different incident source flux angles (Φ) with respect to the substrate normal ranging from Φ = 0° - 80°. A smaller distribution of diffraction peaks are observed in high temperature deposited CdTe films at all glancing angles indicating more preferential crystallite orientation. Only the cubic (C) and mixed cubic + hexagonal (C + H) phases are observed in the XRD patterns for 250°C-deposited CdTe, while the hexagonal (H) phase has been observed at high Φ in RT CdTe. Crystallite size of polycrystalline CdTe films corresponding to the C(111)/H(002) diffraction peak located at 23.7° are calculated using Scherrer's equation showing that the high temperature films have larger crystallites. Complex dielectric function, $\varepsilon = \varepsilon_1 + i\varepsilon_2$, spectra are obtained from spectroscopic ellipsometry over the range of Φ and indicate sharper critical points with higher amplitudes compared to RT CdTe. In-plane compressive stress for high temperature and RT GLAD CdTe are observed through the shift of the lowest energy critical point relative to that of single crystal CdTe.

INTRODUCTION

Cadmium telluride (CdTe) is a very stable, cost effective, and high-performance absorber layer used in thin film photovoltaic (PV) devices [1]. CdTe has a bandgap of ~1.5 eV and when used as a PV absorber has achieved >22% efficiency [2]. However, in sputter deposited polycrystalline CdTe, recombination of photogenerated carriers in the absorber layer are efficient due to charge traps at grain boundaries, small crystallite size, and poor electronic quality of the film resulting in reduced electrical properties and reduced device performance [3]. Investigation of microstructural and optical properties of the CdTe absorbers are crucial to improve PV device efficiency. Polycrystalline CdTe thin films may exhibit both cubic zinc blende (C) and hexagonal wurtzite (H) phases which have been produced by pulsed laser deposition [4], physical vapor deposition [5], and RF magnetron sputtering [6]. Glancing angle deposition (GLAD) can be used to tailor both the phase structure and crystallite orientation by increasing the oblique source flux angle (Φ) between the substrate normal and the target normal [5,6]. In GLAD sputtering, the target material arrives to the substrate at an oblique angle relative to substrate normal. CdTe films deposited at room temperature (RT) at Φ > 40° exhibit mixed phase cubic + hexagonal (C + H) structures and some diffraction peaks corresponding only to the hexagonal phase, H(100), H(101), H(102), and H(103) [5,6].

The microstructural and optical properties are studied for radio frequency (RF) sputtered GLAD CdTe films prepared at a higher substrate temperature of 250°C to better correspond with high efficiency solar cells incorporating sputtered CdTe absorbers [6,7]. Here, we report the variation in microstructural properties in terms of crystallite orientation, phase structure, and crystallite size for films prepared at different Φ. Due to columnar structure formed during deposition at high Φ, different microstructures are formed due to atomic self-shadowing effects [5,6]. Optical properties of GLAD CdTe deposited at 250°C are determined in terms of complex dielectric function ($\varepsilon = \varepsilon_1 + i\varepsilon_2$) spectra by analyzing ellipsometric spectra and compared with that of GLAD CdTe films prepared at RT by Adhikari et al. [6].

EXPERIMENTAL DETAILS

GLAD polycrystalline CdTe thin films are prepared on soda lime glass substates at different Φ. GLAD sputtering involves an oblique angle between the normal extending from the centers of the sample and the sputtering target. CdTe films are fabricated at 250°C substrate temperature at Φ = 0°, 20°, 40°, 60°, and 80°. Glass substrates are cleaned ultrasonically for 90 mins in two 45 min steps with and without detergent in deionized water and then dried with nitrogen gas before deposition. To prepare CdTe at 250°C, glass substrates are heated for 70 mins in low argon flow of 5 SCCM at 15 mTorr pressure. High temperature CdTe films are prepared in argon flow of 23 SCCM at a pressure of 15 mTorr with a RF power of 100 W. X-ray diffraction (XRD) measurements (Raguku Ultima III diffractometer) are performed to study microstructural properties in terms of crystal phase structure, crystallite orientation,

Approved for public release; distribution unlimited.

64th Annual Technical Conference Proceedings
Virtual Event: May 3 – 7, 2021
https://doi.org/10.14332/svc21.proc.0016
© 2021 Society of Vacuum Coaters (www.svc.org)
all rights reserved ISSN 0737-5921
ISBN 978-1-878068-41-5

and crystallite size of all the samples. Optical characterization of the films are performed using a single rotating compensator multichannel ellipsometer (M-2000, J. A. Woollam Co.) [8,9]. Ellipsometric spectra are collected in spectral range 0.73 - 5.89 eV at 70° angle of incidence.

RESULTS AND DISCUSSION

XRD patterns of CdTe films deposited at 250°C at different Φ are shown in Figure 1. Diffraction peaks indexed to C(111) and C(311) planes of the cubic zinc blende crystal structure have been observed for all GLAD CdTe films. The C(220), C(400), and C(331) orientation peaks also exist for the film deposited at Φ = 0°. The C(222) peak is observed for Φ ≠ 0°. No peaks attributed to only the hexagonal phase are found in this series of films, although the H(002) and C(111), H(110) and C(220), and H(112) and C(311) overlap. The H(002)/C(111) and H(112)/C(311) peaks are observed for all Φ. These overlapping peaks imply that a mixed phase C+H structure is possible, however it is unlikely as peaks unique to solely the hexagonal phase are not observed in these films. Figure 2 compares XRD patterns for individual Φ GLAD CdTe prepared at RT and at 250°C. Room temperature XRD patterns have been previously reported in Adhikari et al. [6]. As shown in Figure 2, the crystallite orientations of 250°C-deposited films are different from RT deposited films for all Φ. Diffraction peaks corresponding to only the hexagonal phase are not observed for 250°C GLAD CdTe films whereas these peaks are observed for the films deposited at RT for Φ ≥ 40°. As shown in Figure 1, a wider distribution of crystallite orientations are observed for Φ = 0° whereas it is least for Φ = 40°. This implies that crystallites are randomly orientated at Φ = 0° and more preferentially oriented for Φ = 40° and other values of Φ resulting in increased crystallite size corresponding to certain orientations. Crystallite size is determined from XRD using Scherrer's equation,

$$d = \frac{k\lambda}{\beta \cos\theta}$$

where $k = 0.9$ is shape factor (dimensionless), λ is wavelength of x-ray, β is the full width half maxima of diffraction peak, and θ is the Bragg's angle or the diffraction angle. Diffraction peaks at $2\theta = 23.7°$ corresponding to C(111)/H(002) orientation crystallites are used to calculate crystallite size. Average crystallite sizes found in 250°C and RT deposited GLAD CdTe are compared in Figure 3. For 250°C-deposited CdTe, crystallite size is highest for the Φ = 40° film and lowest for the Φ = 0° due to lowest and highest distribution of crystallite orientations at Φ = 40 and 0°, respectively. Crystallite size of high temperature CdTe is larger than RT deposited CdTe due to more preferential orientation of crystallites at 250°C. At higher temperature, extra thermal energy facilitates the growth of the stable cubic phase as opposed to the metastable hexagonal phase. Also, the effect of atomic shelf-shadowing effect at higher Φ is decreased at high temperature due to extra thermal energy hindering formation of the tilt columnar structure and leading to larger crystallite sizes due to thermally enhanced diffusion of precursors on the surface [10].

Spectra in ε for polycrystalline CdTe films deposited on soda lime glass are obtained by applying a structural and parametric model to the measured ellipsometric spectra. The structural model consists of soda lime glass / bulk CdTe thin film / surface roughness, and the parametric model describing ε for polycrystalline CdTe consists of the sum of critical point (CP) parabolic band oscillators [11] and a Tauc-Lorentz oscillator [12]. All films are approximated as being isotropic. Surface roughness on top of the bulk CdTe is described by Bruggeman effective medium approximation [13] consisting of variable fractions of void (f_v) and bulk CdTe ($1-f_v$). Figure 4 compares spectra in ε for 250°C and RT GLAD CdTe prepared at Φ = 0° and 80°. The first three CPs represented as E_0, E_1, and $E_1+\Delta_1$ are found at 1.583 ± 0.009, 3.216 ± 0.127, and 4.126 ± 0.214 eV for Φ = 0° and 1.552 ± 0.007, 3.351 ± 0.120, and 4.315 ± 0.135 eV for Φ = 80° GLAD CdTe films prepared at high temperature. The CPs for crystalline CdTe are located at 1.49, 3.31, and 3.89 eV [14]. Film stress (X) is determined using a linear stress coefficient, $C_X(E_o)$ = 0.071 eV/GPa, relative to that of E_0 for single crystal CdTe [14]. In-plane compressive stress of 1.26 and 0.85 GPa are found in high temperature GLAD CdTe at Φ = 0° and 80°, respectively. RT GLAD CdTe have similar values with E_0 = 1.58 ± 0.01 and 1.54 ± 0.02 eV with corresponding compressive stress of 1.23 and 0.65 GPa for Φ = 0° and 80°, respectively. As shown in Figure 4, the CdTe films prepared at 250°C have sharper peaks with high amplitude compared to those prepared at RT due to the increased crystallite size of CdTe deposited at high temperature [15].

Approved for public release; distribution unlimited.

64th Annual Technical Conference Proceedings
Virtual Event: May 3 – 7, 2021
https://doi.org/10.14332/svc21.proc.0016
© 2021 Society of Vacuum Coaters (www.svc.org)
all rights reserved ISSN 0737-5921
ISBN 978-1-878068-41-5

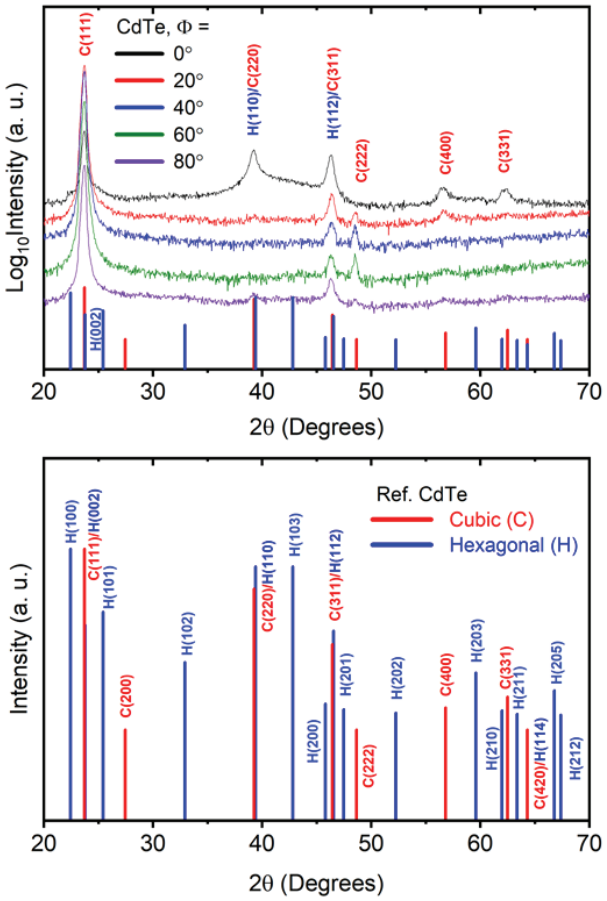
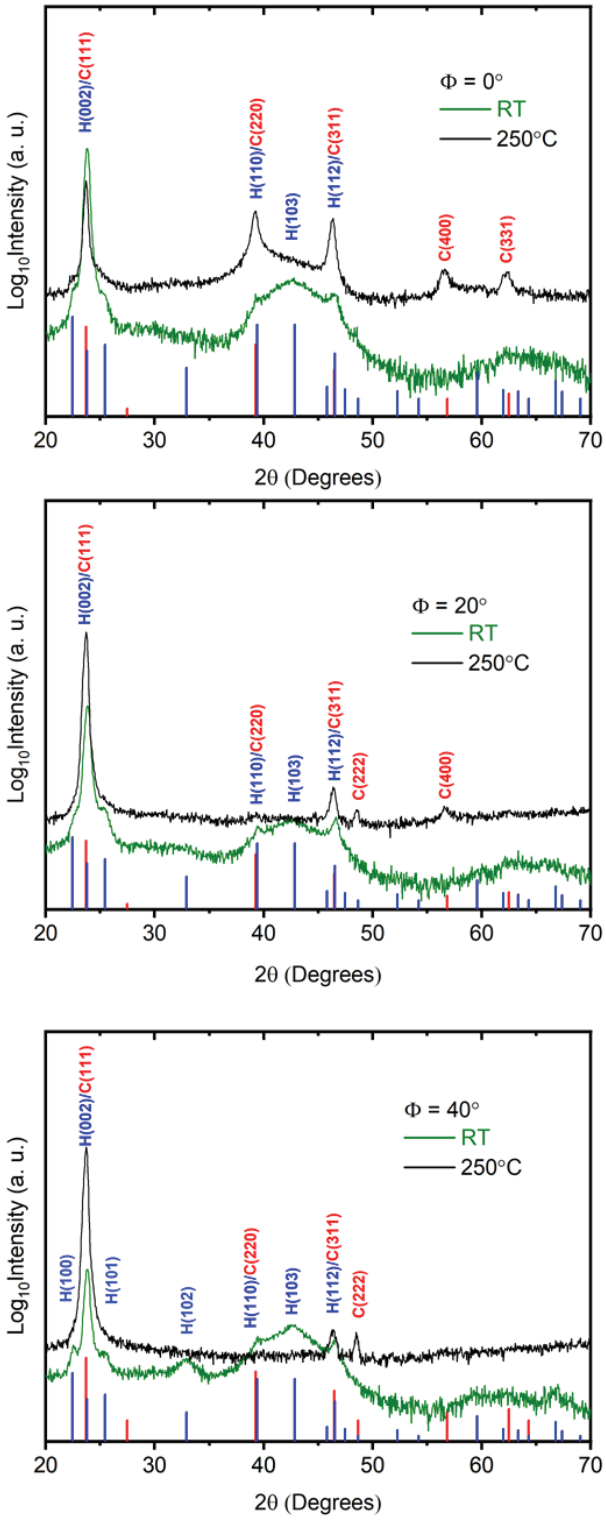


Figure 1. (top) X-ray diffraction (XRD) patterns of thin film CdTe deposited at different source flux angles (Φ) at 250°C substrate temperature. (bottom) Reference peaks for cubic zinc blend (C) CdTe (PDF# 97-010-8238) and hexagonal wurtzite (H) CdTe (PDF # 97-015-0941) are shown (MDI JADE software).



Approved for public release; distribution unlimited.

64th Annual Technical Conference Proceedings
Virtual Event: May 3 – 7, 2021
https://doi.org/10.14332/svc21.proc.0016
© 2021 Society of Vacuum Coaters (www.svc.org)
all rights reserved ISSN 0737-5921
ISBN 978-1-878068-41-5

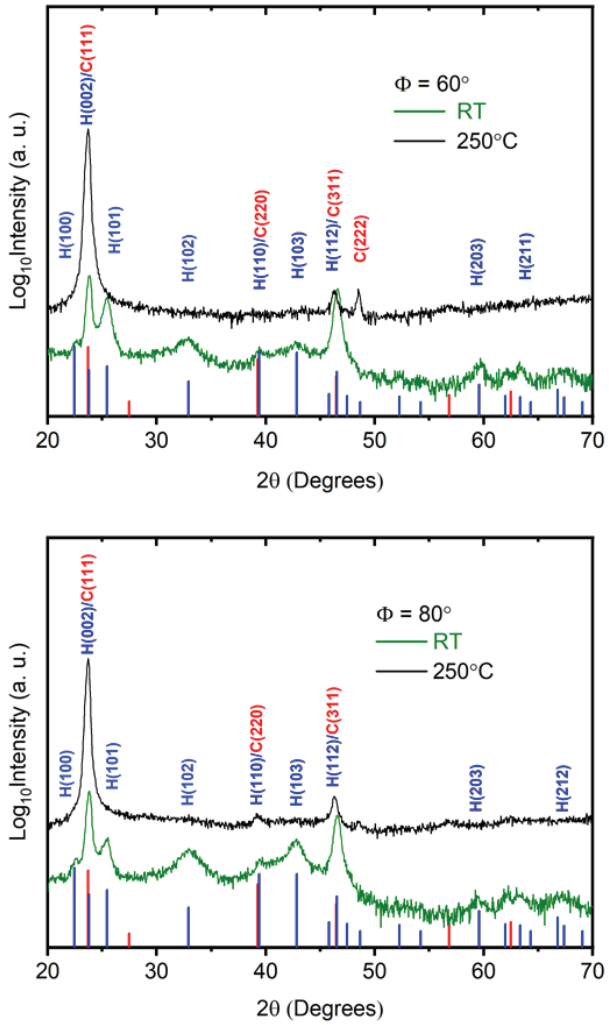


Figure 2. Comparison of XRD patterns of thin film CdTe deposited at different source flux angles (Φ = 0°, 20°, 40°, 60°, 80°) at RT and 250°C substrate temperatures.

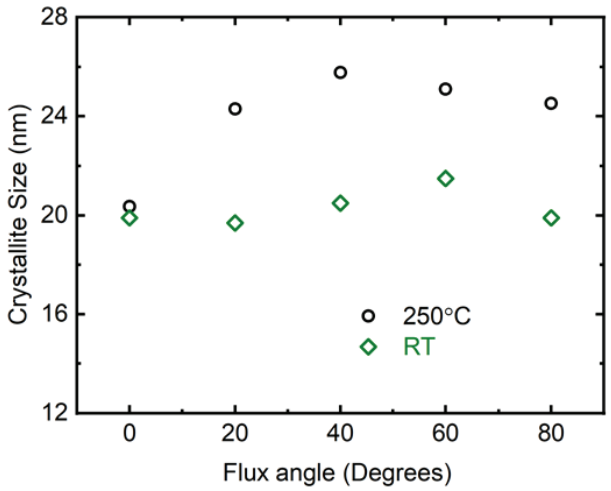


Figure 3. Crystallite size of CdTe deposited at different source flux angle and substrate temperature.

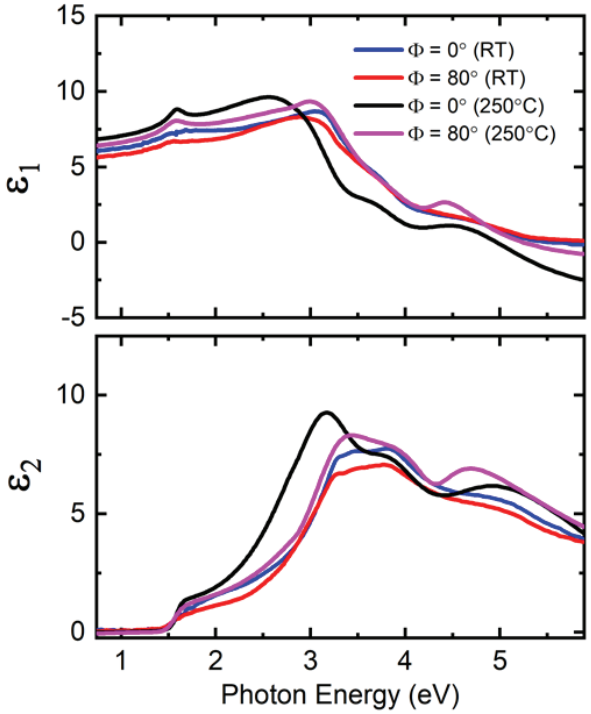


Figure 4. Comparison of complex dielectric function ($\varepsilon = \varepsilon_1 + i\varepsilon_2$) spectra of CdTe deposited at different flux angles at 250°C and RT.

Approved for public release; distribution unlimited.

https://doi.org/10.14332/svc21.proc.0016
© 2021 Society of Vacuum Coaters (www.svc.org)
all rights reserved ISSN 0737-5921
ISBN 978-1-878068-41-5

CONCLUSIONS

XRD studies of polycrystalline GLAD CdTe fabricated by RF sputtering at 250°C does not show diffraction corresponding to only the hexagonal crystal structure at any oblique source flux angle. High temperature CdTe films exhibits a lower number of diffraction peaks than RT CdTe and all peaks are either cubic or mixed phase (cubic + hexagonal). More preferential crystallite orientations, larger crystallite size, and the formation of the stable cubic phase over the metastable wurtzite phase occur at high temperature CdTe due to additional thermal energy increasing the diffusion length of precursors on the surface and facilitating a more thermodynamically stable crystal structure. The CP features in the complex optical response are sharper due to this increased crystallite size. Using high temperature GLAD CdTe as an interlayer in CdS/CdTe PV device is less likely to reduce lattice mismatch between the hexagonal wurtzite CdS n-type heterojunction partner and the cubic zinc blende CdTe p-type absorber as the hexagonal or mixed phase high Φ RT GLAD CdTe interlayer does [6]. Fabrication of the GLAD CdTe interlayer should be performed at lower temperatures and high Φ to promote the formation of the hexagonal phase while the remainder of the CdTe absorber may be deposited at higher temperature to promote larger crystallite size and improved electronic order.

ACKNOWLEDGEMENTS

This work is supported by National Science Foundation (NSF) Grant No. 1711534 and Air Force Research Laboratory under agreement number FA9453-18-2-0037 and FA9453-19-C-1002. The U.S. Government is authorized to reproduce and distribute reprints for Governmental purposes notwithstanding any copyright notation thereon. The views and conclusions contained herein are those of the authors and should not be interpreted as necessarily representing the official policies or endorsements, either expressed or implied, of Air Force Research Laboratory or the U.S. Government.

REFERENCES

1. M. Lingg, S. Buecheler, and A.N. Tiwari, “Review of $CdTe_{1-x}Se_x$ thin films in solar cell applications”, *Coatings*, *9*(8), pp. 520, 2019. https://doi.org/10.3390/coatings9080520
2. M.A. Green, E.D. Dunlop, J. Hohl-Ebinger, M. Yoshita, N. Kopidakis, and X. Hao, “Solar cell efficiency tables (version 56)”, *Prog. Photovolt: Res. Appl.*, *28*(NREL/JA-5900-77544), 2020. https://doi.org/10.1002/pip.3303
3. M. Tuteja, P. Koirala, S. MacLaren, R. Collins, and A. Rockett, “Direct observation of electrical properties of grain boundaries in sputter-deposited CdTe using scan-probe microwave reflectivity based capacitance measurements”, *Appl. Phys. Lett.*, *107*(14), pp. 142106, 2015. https://doi.org/10.1063/1.4932952
4. S.K. Pandey, U. Tiwari, R. Raman, C. Prakash, V. Krishna, V. Dutta, and K. Zimik, “Growth of cubic and hexagonal CdTe thin films by pulsed laser deposition”, *Thin solid films*, *473*(1), pp. 54-57, 2005. https://doi.org/10.1016/j.tsf.2004.06.157
5. M.H. Ehsani, H.R. Dizaji, S. Azizi, S.G. Mirmahalle, and F.H. Siyanaki, “Optical and structural properties of cadmium telluride films grown by glancing angle deposition”, *Phys. Scr.*, *88*(2), pp. 025602, 2013. https://doi.org/10.1088/0031-8949/88/02/025602
6. D. Adhikari, M.M. Junda, E. Bastola, P. Koirala, R.J. Ellingson, R.W. Collins, and N.J. Podraza, “Glancing angle deposited CdTe: Nanostructured films and impact on solar cell performance”, *Surf. Coat. Technol.*, *381*, pp. 125127, 2020. https://doi.org/10.1016/j.surfcoat.2019.125127
7. V.V. Plotnikov, A.C. Vasko, A.D. Compaan, X. Liu, K.A. R.M. Wieland, Zeller, J. Li, and R.W. Collins, “Magnetron sputtering for II-VI solar cells: Thinning the CdTe”, *Mater Res Soc Symp Proc*, *1165*, 2009. https://doi.org/10.1557/PROC-1165-M09-01
8. J. Lee, P.I. Rovira, I. An, and R.W. Collins, “Rotating-compensator multichannel ellipsometry: Applications for real time Stokes vector spectroscopy of thin film growth”, *Rev. Sci. Instrum.*, *69*(4), pp. 1800-1810, 1998. https://doi.org/10.1063/1.1148844
9. B. Johs, J. A. Woollam, C. M. Herzinger, J. N. Hilfiker, R. A. Synowicki, & C. L. Bungay, “Overview of variable-angle spectroscopic ellipsometry (VASE): II. Advanced applications”, *Proc. SPIE - Int. Soc. Opt. Eng.*, *10294*, 1029404, pp. 29-58, 1999. https://doi.org/10.1117/12.351667
10. C.M. Zhou, and D. Gall, “Competitive growth of Ta nanopillars during glancing angle deposition: Effect of surface diffusion”, *J. Vac. Sci. Technol. A*, *25*(2), pp. 312-318, 2007. https://doi.org/10.1116/1.2539328
11. D. E. Aspnes, "Modulation spectroscopy/electric field effects on the dielectric function of semiconductors", *Handbook on Semiconductors, Optical Properties of Solids* 2, pp. 109-154, 1980.
12. G.E. Jellison Jr, and F.A. Modine, “Parameterization of the optical functions of amorphous materials in the interband region”, *Appl. Phys. Lett.*, *69*(3), pp. 371-373, 1996. https://doi.org/10.1063/1.118064
13. H. Fujiwara, J. Koh, P.I. Rovira, and R.W. Collins, “Assessment of effective-medium theories in the analysis of nucleation and microscopic surface roughness evolution for semiconductor thin films”, *Phys. Rev. B*, *61*(16), pp. 10832, 2000. https://doi.org/10.1103/PhysRevB.61.10832
14. J. Li, J. Chen, and R.W. Collins, “Optical transition energies as a probe of stress in polycrystalline CdTe thin films”, *Appl. Phys. Lett.*, *99*(6), pp. 061905, 2011. https://doi.org/10.1063/1.3624536

Approved for public release; distribution unlimited.

64th Annual Technical Conference Proceedings
Virtual Event: May 3 – 7, 2021
https://doi.org/10.14332/svc21.proc.0016
© 2021 Society of Vacuum Coaters (www.svc.org)
all rights reserved ISSN 0737-5921
ISBN 978-1-878068-41-5

15. J. Chen, "Spectroscopic ellipsometry studies of II-VI semiconductor materials and solar cells", The University of Toledo, 2010.

FOR FURTHER INFORMATION

Prof. Nikolas J. Podraza
Department of Physics and Astronomy
University of Toledo
2801 W. Bancroft St.
Toledo, OH 43606 USA
419-530-4905
nikolas.podraza@utoledo.edu
www.weshinelightonstuff.com

View publication stats

Fabricating Efficient CdTe Solar Cells: The Effect of Cu Precursor

Deng-Bing Li, Sandip S. Bista, Rasha A. Awni, Kamala K. Subedi, Niraj Shrestha, Sabin Neupane, Manoj K. Jamarkattel, Zhaoning Song, Randy J. Ellingson, and Yanfa Yan*

Department of Physics and Astronomy, and Wright Center for Photovoltaics Innovation and Commercialization (PVIC), University of Toledo, Toledo, OH 43606, USA.

***Abstract*—Copper (Cu) is being widely used in CdTe solar cells to improve the p-type conductivity and reduce the back-barrier height. However, due to the defect compensate effect and the high spatial migration rate of Cu, the physical mechanism of Cu in CdTe is still a challenge. Here, three different Cu dopant source, metallic copper (Cu), and cuprous chloride (CuCl) and copper chloride ($CuCl_2$), are applied in ZMO/CdTe solar cells. Our results indicate that solution processed Cu treatment supplies lower Cu diffusion temperature and possibilities to reduce the Cu dosage and distribution profile in CdTe.**

Keywords—CdTe, Cu doping, Cu precursor, solar cell

I. Introduction

Cadmium Telluride (CdTe) solar cells are continuously attracting extensive attentions due to its successful commercialization[1]. In most of the efficient CdTe solar cells, copper (Cu) is applied as dopant to improve the hole concentration of CdTe film as well as to reduce the Schottky back-barrier height between CdTe and the back contact[2].

Although the incorperation of Cu significantly advances the CdTe solar cell performance, the precise control of Cu concentration and distribution are still a chellenges to maximize the device performance. For example, the immoderate incoperation of Cu can introduce interstitial defects (Cu_i) and other Cu related compensasion complexes, e.g., Cu_i-Cu_{Cd},[3] which would limit the apparent hole density improvement in CdTe film. Addtionally, Cu ions diffuse in high speed at grain boundaries in the form of Cu_i due to the high Cu solubility at grain boundaries,[4] reasonably reducing the long-term stability of CdTe solar cells[5]. More importantly, Cu at front interfaces, (e.g., CdS/CdTe and zinc magnesium oxide (ZMO)/CdTe interface), has been supposed to form recombination centers and shunt pathways, causing the degradation of device performance[6]. Thus, in premise of enough Cu concentration on the CdTe back surface, the Cu concentration and distribution in CdTe films should be well controlled to maximize device efficiency as well as the long-time stability.

Aiming to solve the issue caused by Cu, lots of approaches has been investigated, including metallic Cu[7], Cu_xTe[8], Cu doped ZnTe[9], CuSCN[10], CuCl[11], and $CuCl_2$[12]. Recently, $CuCl_2$ has been reported as a back contact for CdTe solar cells with a PCE of ~16%[12]. A group from Colorado State University achieved a PCE of 19.1% using CSS processed CuCl as Cu precursor for CdSeTe solar cells [11]. Our group also reported a PCE of 17.5% for pure CdTe solar cell with a solution processed CuCl treatment [13]. Here, solutions processed CuCl and $CuCl_2$ with same Cu concentration are compared with traditional metallic Cu. Our results indicate that solution processed CuCl and $CuCl_2$, with different Cu ionic valence state, deliver similar CdTe solar cell performances. Additionally, the devices with CuCl and $CuCl_2$ show outstanding improvement comparing to metallic Cu treated devices. The mechanisms of device performance improvement were further investigated, including the recombination at front interface, CdTe bulk and back interface through a suite of optical and electrical characterizations.

II. Evaluation abstract

The current density-voltage (J-V) and external quantum efficiency (EQE) curves of the devices with metallic Cu (named CdTe-Cu here after) and solution processed CuCl (named CdTe-CuCl here after) and $CuCl_2$ (named CdTe-$CuCl_2$ here after) as back contact is depicted in Figure 1. Both the CdTe-CuCl or CdTe-$CuCl_2$ devices show much higher performance than the CdTe-Cu devices, showing great advances for solution processed Cu treatment. The CdTe-Cu devices shows an maximum PCE of 12.9% with a V_{OC} of 0.837 V, a J_{SC} of 25.9 mA/cm^2, and a fill factor (*FF*) of 61.8%, while the CdTe-CuCl device delivers an efficiency of 17.5% with a V_{OC} of 0.862 V, a J_{SC} of 26.9 mA/cm^2, and a *FF* of 75.5% and the CdTe-$CuCl_2$ device delivers an efficiency of 16.7% with a V_{OC} of 0.851 V, a J_{SC} of 26.6 mA/cm^2, and a *FF* of 73.9%. The devices treated with solution processed CuCl and $CuCl_2$ show much higher quantum efficiencies in whole wavelength as shown in Figure 1b.

Approved for public release; distribution unlimited.

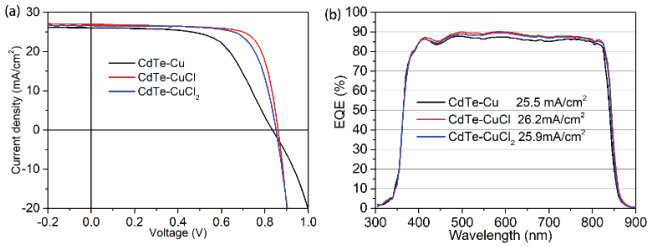


Fig. 1 (a) J-V and (b) EQE curves for devices with Cu metal and CuCl and $CuCl_2$ treatment.

It's worthy to notify that, as shown in Figure 1a, the CdTe-Cu device show clear distorted J-V curves at forward bias near V_{OC} (S-kink), indicating poor heterojunction properties at ZMO/CdTe interfaces. The reason of S-kind in ZMO/CdTe devices has been assigned to the large conduction band offset at ZMO/CdTe interface and low conductivity of ZMO film while performing $CdCl_2$ treatment in atmosphere with oxygen[14]. Here, the $CdCl_2$ treatment for all the devices are performed in oxygen-free atmosphere and the copper treatment procedure is the only variation during the device fabrication. According to our SCAPS simulation in the previous reports[14], with the same conduction band offset between ZMO and CdTe, the S-kink can be assigned to either the low ZMO film conductivity or the high acceptor-like trap state concentration. The S-kink in CdTe-Cu device is likely the conjoint results of the acceptor-like trap state at the front interface and the reduced ZMO film conductivity, which is caused by the over diffusion of Cu[14].

Different from the CdTe-CuCl and CdTe-$CuCl_2$ devices, a sever aggregation of Cu in the front interface and ZMO films was observed from the SIMS profile for the CdTe-Cu devices (Figure 2).[13] The Cu at CdS/CdTe interface has been supposed to form recombination centers and shunt pathways, causing the reduction and degradation of device performance.[6] While in the ZMO/CdTe devices, the accumulation of Cu at ZMO/CdTe interface would promote the formation of acceptor-like defects at the ZMO/CdTe interface. Additionally, the diffusion of Cu into the ZMO films would significantly decrease the ZMO films conductivity as reported by literature, yielding the presence of S-kink in CdTe-Cu devices[14]. while for the CdTe-CuCl and CdTe-$CuCl_2$ devices, the Cu activations can be performed by a rapid thermal annealing process at 160 ºC with ~150 times less Cu dosage according to our previous report, which can help to reduce the accumulation of Cu at front interface and inside ZMO film. Thus, the S-kink is absent in CdTe-CuCl and CuTe-$CuCl_2$ devices[13]. Rapid thermal annealing process has also been tried in ZMO/CdTe stacks with metallic Cu as doping source. Unfortunately, the traditional Cu activation process (200 ℃ for 20 min) always show higher device performance than the devices treated with rapid thermal annealing process when metallic Cu is used as Cu source, suggesting that ionic Cu (i.e., CuCl and $CuCl_2$) source shows lower Cu diffusion barrier and lower activation energy than metallic Cu. Similar phenomenon has also been demonstrated in group V doped CdTe solar cells[15].

In order to understand the origin of the performance improvement, series and shunt resistances (R_S and R_{SH}), ideality diode factor (A) and saturation current density (J_0) were extracted from the J-V curves according to Sites's method.[16]

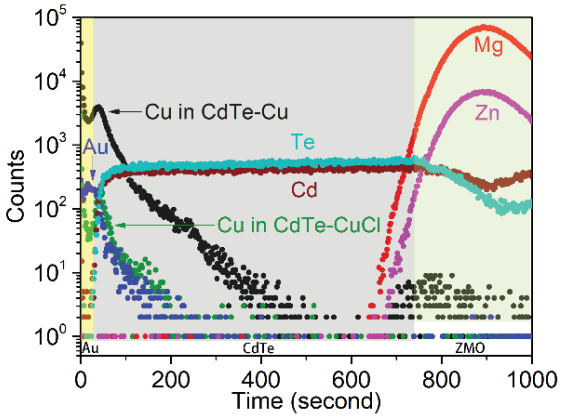


Fig. 2 Secondary ion mass spectroscopy (SIMS) depth profiles of the CdTe-Cu devices.

the CdTe-CuCl and CdTe-$CuCl_2$ devices show reduced R_S of 1.71 Ω cm² and 2.69 Ω cm², respectively, which is much lower than 9.83 Ω cm² for the CdTe-Cu device. The shunt resistances also show significant improvement from 1297 Ω cm² for CdTe-Cu device to 1455 Ω cm² for CdTe-CuCl and 1548 Ω cm² for CdTe-$CuCl_2$ device. The CdTe-Cu show an ideal factor exceeding 2, which is higher than the value of 1.55 in the CdTe-CuCl and 1.76 in the CdTe-$CuCl_2$ devices. J_0 is reduced from 1.1×10^{-6} for the CdTe-Cu device to 2.1×10^{-7} mA/cm² for the CdTe-CuCl device and 3.0×10^{-7} mA/cm² for the CdTe-$CuCl_2$ device. The reduction of both the A and J_0 values in the devices with the solution processed treatment imply the improvement of diode quality, which is beneficial to reduce the interface nonradiative recombination.

The J-V performance and diode quality analysis indicates that the CdTe-CuCl and CdTe-$CuCl_2$ devices show similar device performances. However, the devices treated with metallic Cu in solid phase show much lower device performance with poor diode quality. To further validate and investigate the effect of metallic Cu and ionized Cu in CdTe devices, a suite of characterizations was performed laterally. Due to the similar performances of the CdTe-CuCl and CdTe-$CuCl_2$ devices, CdTe-CuCl was chosen as the representative of ionized Cu treated devices to make comparison with the devices treated with the metallic Cu.

PL measurements were carried out for CdTe-Cu and CdTe-CuCl devices as shown in **Figure 4a**, both samples excited through the FTO glass side and CdTe film side show PL spectra with emission peak centered at 1.501 ± 0.003 eV but with different emission intensities.[17] In both glass and film sides, the CdTe-CuCl device shows higher PL intensities comparing to that for the CdTe-Cu device, indicating higher recombination rate at ZMO/CdTe and CdTe/Au interfaces in the CdTe-Cu device than that in the CdTe-CuCl device.[14] The TRPL results in Figure 4b further confirms this conclusion by showing a much higher carrier life time of 4.36 ns and 0.25 ns in CdTe-CuCl comparing to 0.19 ns and 0.04 ns in CdTe-Cu device when exicited from the glass side and film side, respectively.

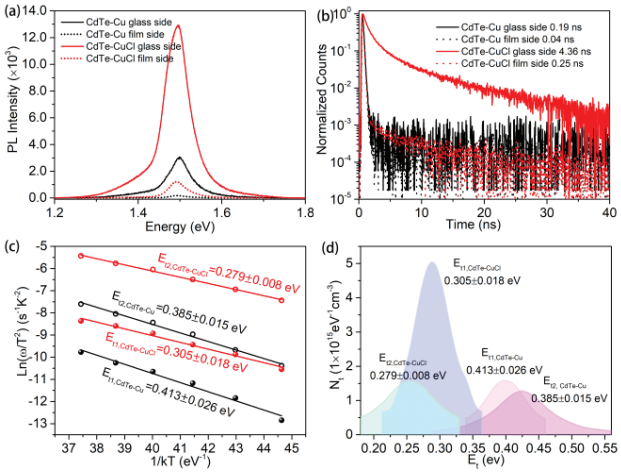


Fig. 3 Steady-state and time-resolved PL spectra of samples with (a) Cu metal and (b) CuCl solution treatment. For each sample, PL spectra were excited through the FTO glass side and CdTe film side with 633 nm laser excitation. (c) Arrhenius plots of admittance spectroscopy signature of CdTe-Cu and CdTe-CuCl devices. (d) Defects density and distribution in CdTe-Cu and CdTe-CuCl devices obtained from temperature-dependent admittance spectroscopy (TAS) measurement.

Besides the effect at ZMO/CdTe interface, the Cu profile at the rear of CdTe films of these two devices also show large difference. The CdTe-CuCl device shows much lower intensites comparing to that in the CdTe-Cu devices (Figure 2), indicating less Cu atoms localized at the back surface. This is attributed to the small dosage of Cu in CuCl solution as discussed above. This result can be further confirmed from the low temperature steady-state PL measurement excited from the film side as shown in Figure 4c. Similar emission profiles are observed in both CdTe-Cu and CdTe-CuCl films such as free excitonic peak at 1.594 eV,[18] DAP peak at 1.552 eV (recombination of some donor state to V_{Cd} acceptor) and its phonon replica,[19] and DAP peak at 1.454 eV (a DAP peak results due to the recombination of Cl donor to Cu_{Cd} acceptor) and its phonon replicas at ~20 meV[20]. The CdTe-CuCl device displays higher PL intensity at ~1.454 eV than CdTe-Cu device. This indicates higher number of Cu_{Cd} acceptor formed in CdTe-CuCl devices due to the reduction of the compensative defect formation, which is helpful for the carrier concentration improvement and, thus, the reduction of back barrier height,.

The defects states in CdTe-Cu and CdTe-CuCl devices were further investigated through thermal admittance spectroscopy measurements, from which, two defect activation energies (E_a) are extracted as shown in Figure 3c and d[7]. The CdTe-Cu device shows two activation energies with $E_{a1} = 0.413 \pm 0.008\ eV$, $E_{a2} = 0.385 \pm 0.010\ eV$, which are much higher than that in the CdTe-CuCl device with $E_{a1} = 0.305 \pm 0.018\ eV$, $E_{a2} = 0.279 \pm 0.008\ eV$. The reduction of these deep defects level might cause by the difference of defects formation mechanisms in these two kinds of Cu treatment. Besides the reduction of trap states level, both the recombination capture section and recombination velocity are also significantly decreased by several orders of magnitude in the CdTe-CuCl device. All these results can help to reduce the non-radiative recombination and improve the device performances.

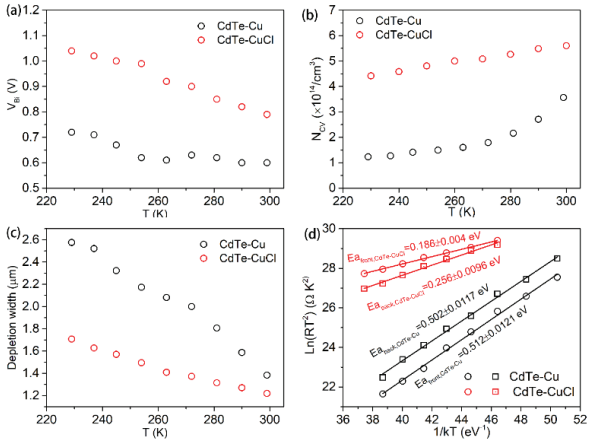


Fig. 4 (a) Build-in potential, (b) carrier concentration and (c) depletion width as a function of temperature calculated for the CdTe-Cu and CdTe-CuCl devices.

The Mott Schottky plots of temperature dependent capacitance-voltage (C-V) measurements were further carried out and the carrier concentration as a function of the distance from the p-n junction at different temperature, from which the build-in potential (V_{bi}), carrier concentration (N_A), and depletion width (W) at each temperature were extracted (Figure 4a-c) following the reported method[7]. For the CdTe-CuCl device, the V_{bi} increases from 0.80 to 1.04 V as temperature decreases from 300 to 230 K, which is much higher than that in the CdTe-Cu device (from 0.60 to 0.72 V). The more pronounced V_{bi} would benefit the carrier extraction and help to boost higher V_{OC}, which has been demonstrated by our device performances. The carrier density was calculated from the Mott-Schottky plot at zero bias. In both devices, the carrier densities decrease with the measuring temperature from 300 to 230 K and the CdTe-CuCl device show much higher carrier density at all temperatures, suggesting more efficient Cu incorporation than CdTe-Cu device. Due to the improved carrier density, the CdTe-CuCl device shows lower depletion width than the CdTe-Cu, indicating larger diffusion region in the device treated with CuCl. Fortunately, benefiting from the higher carrier density and decent carrier lifetime and improved defect properties, the carrier diffusion length improved, and the carrier collection efficiency show significant improvement as discussed above.

Another critical factor determines the carrier collection efficiency is the carrier transport barrier height at interface. Impedance spectroscopy (IS) measurement is capable to supply insights on the barrier height at both the front and back interfaces with proper equivalent circuit model of the diode in devices. Here, an nonideal equivalent circuit model with three subcircuits from our previous publication for ZMO/CdTe devices is used to fit the resistance at the front and back interfaces, which were used to estimate the barrier heights at both the front and back interface, respectively[21]. The calculated results about interface barrier heights are shown in Figure 4d. The CdTe-CuCl device show a back barrier of 0.256±0.0096 eV, which is much lower than 0.502±0.0017 eV in the CdTe-Cu devices, indicating higher hole concentration at the back of CdTe films and lower Shockley barrier height between CdTe and Au electrode. The reduction of back barrier height is responsible for the significantly improved V_{OC} and FF. Regarding the front barrier

height at the ZMO/CdTe interface, the CdTe-CuCl device shows a much lower value than that in the CdTe-Cu device (0.186±0.0004 eV for CdTe-CuCl vs. 0.512±0.0121 eV for CdTe-Cu). The reduction of both front and back barrier heights can be attributed to the desired low Cu dosage and gradient Cu profile, which is enabled through a solution processed CuCl treatment with a rapid thermal annealing process.

III. CONLUSIONS

A comparison among different Cu precursors (i.e., metallic Cu, CuCl and $CuCl_2$ solution) as doping source is performed on CdTe solar cells. The similar performance of the device with CuCl and $CuCl_2$ suggest that the valence states of Cu in solution show negligible effect on device performance. Both solutions processed CuCl and $CuCl_2$ treatment show significant improvement on device performance comparing to that with metallic Cu, suggesting more efficient Cu incorporation using Cu ionic compound than that in metallic state. The results also indicate that solution processed Cu treatment for CdTe solar cells enable lower dopant diffusion and activation temperature, lower Cu dosage and desired gradient Cu profile in CdTe film, resulting with improved electrical properties at interface and the bulk of the absorber and promising higher device performance. .

ACKNOWLEDGMENT

This work is supported by the U.S. Department of Energy's Office of Energy Efficiency and Renewable Energy (EERE) under Solar Energy Technologies Office (SETO) Agreement Number DE-EE0008974. Air Force Research Laboratory, Space Vehicles Directorate (contract # FA9453-18-2-0037 and FA9453-19-C-1002). We thank Dr. David Strickler from Pilkington North America Inc. for supplying us FTO coated substrates.

REFERENCES

[1] M. A. Green, Y. Hishikawa, E. D. Dunlop, D. H. Levi, J. Hohl-Ebinger, and A. W. Y. Ho-Baillie, "Solar cell efficiency tables (version 51)," *Progress in Photovoltaics: Research and Applications,* vol. 26, pp. 3-12, 2018.

[2] T. Ablekim, J. N. Duenow, X. Zheng, H. Moutinho, J. Moseley, C. L. Perkins, *et al.*, "Thin-Film Solar Cells with 19% Efficiency by Thermal Evaporation of CdSe and CdTe," *ACS Energy Letters,* vol. 5, pp. 892-896, 2020/03/13 2020.

[3] D. Krasikov and I. Sankin, "Defect interactions and the role of complexes in the CdTe solar cell absorber," *Journal of Materials Chemistry A,* vol. 5, pp. 3503-3513, 2017.

[4] J. Perrenoud, L. Kranz, C. Gretener, F. Pianezzi, S. Nishiwaki, S. Buecheler, *et al.*, "A comprehensive picture of Cu doping in CdTe solar cells," *Journal of Applied Physics,* vol. 114, p. 174505, 2013.

[5] D. Krasikov, A. Knizhnik, B. Potapkin, S. Selezneva, and T. Sommerer, "First-principles-based analysis of the influence of Cu on CdTe electronic properties," *Thin Solid Films,* vol. 535, pp. 322-325, 2013/05/15/ 2013.

[6] K. D. Dobson, I. Visoly-Fisher, G. Hodes, and D. Cahen, "Stability of CdTe/CdS thin-film solar cells," *Solar Energy Materials and Solar Cells,* vol. 62, pp. 295-325, 2000/05/15 2000.

[7] R. A. Awni, D.-B. Li, C. R. Grice, Z. Song, M. A. Razooqi, A. B. Phillips, *et al.*, "The Effects of Hydrogen Iodide Back Surface Treatment on CdTe Solar Cells," *Solar RRL,* vol. 3, p. 1800304, 2019.

[8] C. Li, H. Xu, K. Li, X. Ma, L. Wu, W. Wang, *et al.*, "CuTe Nanoparticles/Carbon Nanotubes as Back Contactfor CdTe Solar Cells," *Journal of Electronic Materials,* vol. 47, pp. 1250-1258, February 01 2018.

[9] C. A. Wolden, A. Abbas, J. Li, D. R. Diercks, D. M. Meysing, T. R. Ohno, *et al.*, "The roles of ZnTe buffer layers on CdTe solar cell performance," *Solar Energy Materials and Solar Cells,* vol. 147, pp. 203-210, 2016/04/01/ 2016.

[10] D.-B. Li, S. S. Bista, Z. Song, F. K. Alfadhili, R. A. Awni, N. Shrestha, *et al.*, "CuSCN as the Back Contact for Efficient ZMO/CdTe Solar Cells," *Materials,* vol. 13, p. 1991, 2020/04/24 2020.

[11] A. H. Munshi, J. Kephart, A. Abbas, J. Raguse, J. Beaudry, K. Barth, *et al.*, "Polycrystalline CdSeTe/CdTe Absorber Cells With 28 mA/cm^2 Short-Circuit Current," *IEEE Journal of Photovoltaics,* vol. 8, pp. 310-314, 2018.

[12] E. Artegiani, D. Menossi, H. Shiel, V. Dhanak, J. D. Major, A. Gasparotto, *et al.*, "Analysis of a novel CuCl2 back contact process for improved stability in CdTe solar cells," *Progress in Photovoltaics: Research and Applications,* vol. 27, pp. 706-715, 2019.

[13] D.-B. Li, S. S. Bista, Z. Song, R. A. Awni, K. K. Subedi, N. Shrestha, *et al.*, "Maximize CdTe solar cell performance through copper activation engineering," *Nano Energy,* vol. 73, p. 104835, 2020/07/01/ 2020.

[14] D.-B. Li, Z. Song, R. A. Awni, S. S. Bista, N. Shrestha, C. R. Grice, *et al.*, "Eliminating S-Kink To Maximize the Performance of MgZnO/CdTe Solar Cells," *ACS Applied Energy Materials,* vol. 2, pp. 2896-2903, 2019/04/22 2019.

[15] D.-B. Li, C. Yao, S. N. Vijayaraghavan, R. A. Awni, K. K. Subedi, R. J. Ellingson, *et al.*, "Low-temperature and effective ex situ group V doping for efficient polycrystalline CdSeTe solar cells," *Nature Energy,* 2021/06/24 2021.

[16] J. R. Sites and P. H. Mauk, "Diode quality factor determination for thin-film solar cells," *Solar Cells,* vol. 27, pp. 411-417, 1989/10/01/ 1989.

[17] P. J. Roland, N. R. Paudel, X. Chuanxiao, Y. Yan, and R. J. Ellingson, "Photoluminescence spectroscopy of Cadmium Telluride deep defects," in *2014 IEEE 40th Photovoltaic Specialist Conference (PVSC)*, 2014, pp. 3266-3271.

[18] X. Liu and A. D. Compaan, "Photoluminescence from Ion Implanted CdTe Crystals," *MRS Proceedings,* vol. 865, p. F5.25, 2005.

[19] J. Krustok, V. Valdna, K. Hjelt, and H. Collan, "Deep center luminescence in p-type CdTe," *Journal of Applied Physics,* vol. 80, pp. 1757-1762, 1996.

[20] J. P. Chamonal, E. Molva, and J. L. Pautrat, "Identification of Cu and Ag acceptors in CdTe," *Solid State Communications,* vol. 43, pp. 801-805, 1982/09/01/ 1982.

[21] R. A. Awni, D.-B. Li, Z. Song, S. S. Bista, M. A. Razooqi, C. R. Grice, *et al.*, "Influences of buffer material and fabrication atmosphere on the electrical properties of CdTe solar cells," *Progress in Photovoltaics: Research and Applications,* vol. 27, pp. 1115-1123, 2019.

ACS APPLIED ENERGY MATERIALS

www.acsaem.org Letter

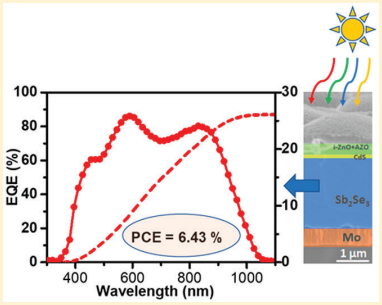
Influence of Post-selenization Temperature on the Performance of Substrate-Type Sb_2Se_3 Solar Cells

Suman Rijal, Deng-Bing Li, Rasha A. Awni, Sandip S. Bista, Zhaoning Song,* and Yanfa Yan*

Cite This: https://doi.org/10.1021/acsaem.1c00657 Read Online

ACCESS | Metrics & More | Article Recommendations | Supporting Information

ABSTRACT: Antimony selenide (Sb_2Se_3) solar cells are an environmentally friendly and cost-effective photovoltaic technology. In this work, we fabricate Sb_2Se_3 solar cells using closed-space sublimation followed by postdeposition selenization. We investigate the effects of the selenization temperature on the structural and morphological properties of Sb_2Se_3 films and photovoltaic performance of the corresponding devices. The results indicate that a proper selenization temperature is critical to achieving Sb_2Se_3 films with large grains, uniform morphology, high crystallinity, desired crystal orientations, and increased carrier density. By optimizing the selenization temperature, we obtained Sb_2Se_3 solar cells with a power-conversion efficiency of 6.43%.



KEYWORDS: *antimony selenide (Sb_2Se_3), thin film, solar cell, closed-space sublimation, annealing treatment, selenization temperature, power-conversion efficiency, PCE*

Downloaded via KING ABDULLAH UNIV SCI TECHLGY on May 14, 2021 at 20:37:29 (UTC).
See https://pubs.acs.org/sharingguidelines for options on how to legitimately share published articles.

The urgent need for high-efficiency, low-cost, low-toxicity, and stable solar cells drives the sustained research effort on thin-film photovoltaics (PVs) with new absorber materials. Crystalline Si-based solar cells are currently dominating the PV market. However, this first-generation PV technology has several drawbacks: a long energy payback time, a low industrial production rate, and a high value of initial investment for the production facility. Over the years, alternative low-cost thin-film PV technologies have been developed, including Cu(In, Ga)(S, Se)$_2$ (CIGSSe), CdTe, and lead halide perovskite solar cells, with power-conversion efficiencies (PCEs) of 22.6%,[1] 22.1%,[2] and 25.5%,[3] respectively, approaching the record efficiency of 26.5%[4] for crystalline Si solar cells. However, due to the concerns regarding the scarcity of Te, In, and Ga, and the toxicity of Cd and Pb, emerging photovoltaic materials with the merits of earth abundance, low cost, and low toxicity have been drawing intense attention in the past few decades.[5] $Cu_2ZnSn(Se, S)_4$ has been considered one of the most promising materials with these merits, such as a low cost and nontoxic constituents.[6] Unfortunately, a further efficiency improvement is hindered by its complex phase composition and carrier trapping defects.[7] Recently, simple binary chalcogenides (e.g., SnS,[8] GeSe,[9] Sb_2Se_3,[10] and $Sb_2(S,Se)_3$[11]) appeared as new alternatives with less complex, low-toxicity, and earth-abundant absorbers.[5]

Among them, Sb_2Se_3 is one of the most promising candidates as either single-junction solar cells or the bottom subcells for dual-junction tandem devices due to its high absorption coefficient (10^5 cm^{-1}) and suitable bandgap (1−1.3 eV).[5] In addition, the properties of the earth-abundant, low-toxicity, and low-cost constituents (i.e., Sb and Se) make Sb_2Se_3 a very promising candidate to replace CIGS and CdTe for the long-term development of thin-film solar cells.[5]

Despite decent material properties, the record efficiency of Sb_2Se_3 solar cells is only 9.2%,[10] which is much lower than the theoretical limit exceeding 30%.[12] This is mainly due to the relatively high density of deep defects in the absorber, which accelerated the recombination rate in Sb_2Se_3 films and at the interfaces.[13] To further improve device performance, the quality of Sb_2Se_3 absorbers should be improved through advancing deposition methods,[14,15] doping engineering,[16,17] and postdeposition annealing treatments.[18−20] Among them, the postdeposition annealing treatment has been demonstrated to be one of the most efficient methods for improving CdTe and CIGS solar cells. Typically, postdeposition annealing improves the absorber quality by increasing the crystallinity, tuning the crystal orientation, reducing the bulk trap density, and decreasing nonradiative recombination loss.[15] Some related studies have been done on the Sb_2Se_3 absorber layer. A selenization treatment at 200 °C for the thermal evaporated CdS/Sb_2Se_3 solar cells has demonstrated an efficiency improvement from 2.6% to 3.7%.[19] In another study, the

Received: March 5, 2021
Accepted: April 22, 2021

ACS Publications © XXXX American Chemical Society

Approved for public release; distribution unlimited.

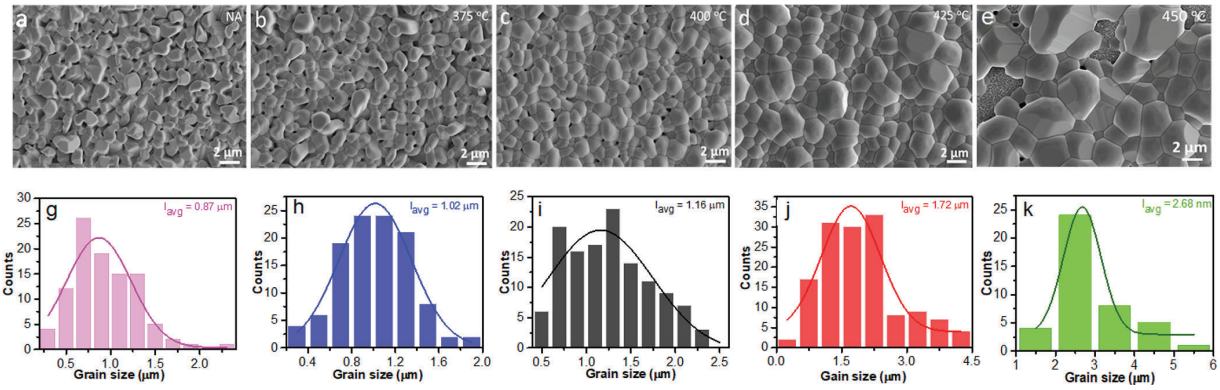


Figure 1. Top-view SEM images of Sb_2Se_3 thin films (a) without postdeposition annealing and annealed at different selenization temperatures, including (b) 375, (c) 400, (d) 425, and (e) 450 °C. The corresponding histograms of grain size distribution for Sb_2Se_3 thin films (g) without annealing and annealed at (h) 375, (i) 400, (j) 425, and (k) 450 °C.

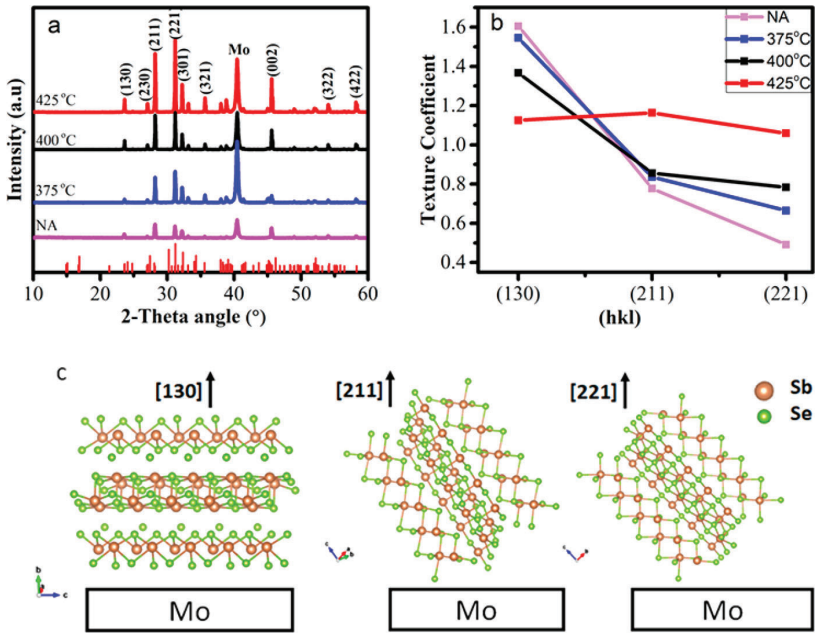


Figure 2. (a) XRD patterns and (b) the calculated texture coefficients of Sb_2Se_3 thin films without annealing and annealed at various temperatures. (c) Atomic structures of Sb_2Se_3 in particular crystal orientations.

selenization treatment of coevaporated Sb_2Se_3 films was found to improve conversion efficiency from 3.07% to 4.25%.[18] Similarly, sputtered Sb_2Se_3 solar cells with an efficiency of 6.06% have been achieved by tuning the post-selenization parameters.[18] An open-circuit voltage (V_{OC}) exceeding 500 mV has been achieved after selenizing the sputtered Sb_2Se_3 thin-film solar cells.[20] As known from the previous work, the selenization treatment of Sb_2Se_3 films can benefit the film quality and device performance in two ways: (1) compensating the Se loss during the deposition, which helps reduce the V_{Se} related recombination;[19] (2) forming a thin $MoSe_2$ layer at the Sb_2Se_3/Mo interface, eliminating the Schottky barrier and reducing the recombination at the back interface.[18]

In this work, we systematically investigated the impact of postdeposition annealing temperature on the structural and morphological properties of Sb_2Se_3 thin films deposited on Mo-coated glass substrates by closed-space sublimation (CSS) (Figure S1) and the PV performance of the corresponding solar cells. We found that, at an optimal temperature of 425 °C, Sb_2Se_3 thin films exhibit larger crystal grains, uniform surface morphology, desired crystal orientations, proper stoichiometry, and increased carrier density, leading to a champion PCE of 6.43% in our substrate-type Sb_2Se_3 solar cells.

To investigate the impact of selenization temperature on the microstructure of Sb_2Se_3 films, we used scanning electron microscopy (SEM) to examine the surface morphology of Sb_2Se_3 films without annealing and annealed at various temperatures ranging from 375 to 450 °C. Figure 1a–d shows that the grain size and compactness increase, whereas the porosity decreases with the increasing selenization temperature. The average grain size of Sb_2Se_3 films increased

https://doi.org/10.1021/acsaem.1c00657
ACS Appl. Energy Mater. XXXX, XXX, XXX−XXX

Approved for public release; distribution unlimited.

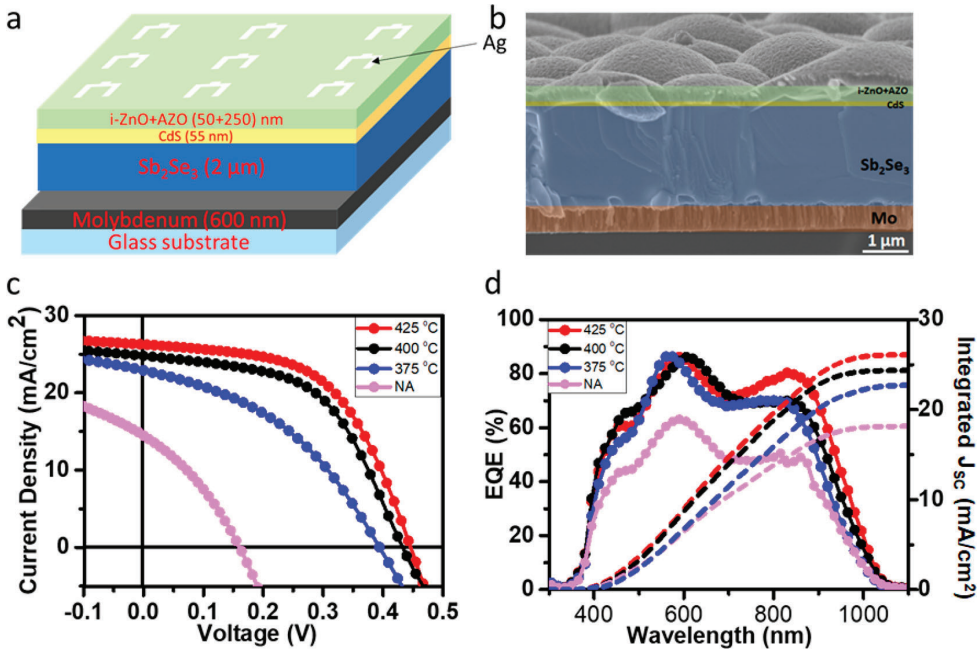


Figure 3. (a) Schematic device architecture and (b) cross-sectional SEM image of Sb_2Se_3 solar cells. (c) Current density−voltage (J−V) and (d) external quantum efficiency (EQE) and integrated J_{SC} curves of the Sb_2Se_3 solar cells prepared without annealing and annealed at different selenization temperatures.

from 0.87 μm for the unannealed film to 1.02, 1.16, and 1.72 μm after selenization at 375, 400, and 425 °C, respectively (Figure 1g−j). Moreover, the grain size distribution becomes narrower, and grains become more compact at higher temperatures. When a Sb_2Se_3 film was selenized at 450 °C, the average grain size further increased to 2.68 μm (Figure 1k). However, large voids with micrometer sizes appeared, and the film became discontinuous and nonuniform (Figure 1e). This deformation could be attributed to a combined effect of the loss of Se from the Sb_2Se_3 film at a high temperature,[21] the overgrowth of Sb_2Se_3 grains due to Ostwald ripening, and the thermal expansion coefficient mismatch among soda-lime glass ($>8 \times 10^{-6}$ K^{-1}),[22] Mo (4.8×10^{-6} K^{-1}),[23] and Sb_2Se_3 (3.7×10^{-5} K^{-1}).[24] Additionally, energy dispersive X-ray spectroscopy (EDS) results (Figure S2) reveal that the Sb_2Se_3 films without selenization and when overheated (450 °C) have a severely Se-deficient stoichiometry (Se/Sb = 1.33 and 1.32, respectively), whereas the films annealed at temperatures of 400 and 425 °C have Se/Sb ratios (Se/Sb = 1.43, and 1.44, respectively) closer to the stoichiometric Sb_2Se_3 film (Se/Sb = 1.5). A higher Se/Sb ratio is critical for Sb_2Se_3 solar cells because it helps reduce the nonradiative recombination related to the V_{Se} defects, particularly at Sb_2Se_3 ribbon edges and grain boundaries.[20,25−27] The optical transmittance measurement shows that all the annealed Sb_2Se_3 films have a bandgap of ~1.2 eV (Figure S3). Overall, the film annealed at 425 °C exhibits large and densely packed grains, uniform and smooth film morphology, and appropriate stoichiometry, which are desired properties for Sb_2Se_3 thin-film solar cells.

X-ray diffraction (XRD) was used to investigate the impact of selenization temperature on the structural properties of the Sb_2Se_3 thin films deposited on Mo-coated glass substrates. Figure 2a shows the XRD patterns of the Sb_2Se_3 thin films without annealing and annealed at different temperatures of 375, 400, and 425 °C. All of the diffraction peaks can be indexed to phase pure Sb_2Se_3 in an orthorhombic phase (JCPDS 97-008-5676) except the diffraction peak at 40.45°, which belongs to the Mo substrate underneath. The overall diffraction peak intensity of the Sb_2Se_3 films increases upon increasing selenization temperature, indicating improved crystallinity.

To study the impact of the annealing temperature on the crystal orientation qualitatively, texture coefficients (TCs) for the (130), (211), and (221) diffraction peaks were calculated using the equation

$$\mathrm{TC}(hkl) = \frac{I(hkl)}{I_o(hkl)} \Big/ \sum_{i=1}^{N} \frac{I(h_i k_i l_i)}{I_o(h_i k_i l_i)} \quad (1)$$

where $I(hkl)$ and $I_o(hkl)$ are the diffraction peak intensities of the (hkl) planes in the measured and standard XRD patterns of Sb_2Se_3 (JCPDS 97-008-5676), respectively. A high TC value of a diffraction peak indicates a preferred orientation along this particular direction.[18] It is worth noting that the CSS-deposited Sb_2Se_3 films on Mo show no XRD peaks below 20°, such as the (020) and (120) peaks, which are known to negatively correlate to the device performance.[25−27] Figure 2b shows that the TC values of the (211) and (221) planes increase, whereas the TC of the (130) plane decreases with the increasing selenization temperature. Due to the unique one-dimensional crystal structure of Sb_2Se_3 (Figure 2c), Sb_2Se_3 films with the (hkl, $l \neq 0$) orientations (e.g., oriented in the [211] and [221] directions) are preferred for better carrier transport and collection through the absorber layer. In contrast, (hkl, $l = 0$) oriented Sb_2Se_3 films (e.g., oriented in the [130] direction) consist of one-dimensional ribbons aligned in the direction parallel to the substrate (Figure 2c) and generally result in a high carrier transport barrier through

https://doi.org/10.1021/acsaem.1c00657
ACS Appl. Energy Mater. XXXX, XXX, XXX−XXX

Approved for public release; distribution unlimited.

the film thickness.[10,27] The increased TC values of the (211) and (221) planes for the film annealed at 425 °C indicate that the more preferred Sb_2Se_3 film orientations can be obtained at a higher selenization temperature (425 °C), predicting better device performances.

To study the impact of selenization temperature on solar cell performance, we fabricated several batches of Sb_2Se_3 solar cells with a substrate-type structure, i.e., Ag grid/ZnO:Al/i-ZnO/CdS/Sb_2Se_3/Mo/glass, as shown in Figure 3a. The cross-sectional SEM analysis of a typical device (annealed at 425 °C) shows a compact Sb_2Se_3 absorber layer comprising large grains with a size comparable with the film thickness (Figure 3b and Figure S4). The formation of large grains extended over the entire film thickness and free of horizontal grain boundaries is beneficial for the solar cell performance because of a low density of grain boundaries in the pathway of photoexcited charge carriers.

We measured $J-V$ performance of Sb_2Se_3 solar cells prepared under different selenization conditions and summarized the statistical distribution of the key device performance parameters from each annealing condition in Figure S5. Figure 3c shows the $J-V$ curves of the best-performing solar cells using the Sb_2Se_3 absorber layers prepared without annealing and annealed at different temperatures of 375, 400, and 425 °C. The detailed PV parameters of these champion devices are tabulated in Table 1. The unannealed Sb_2Se_3 cell shows very poor performance with a PCE of 1.85%, and a low V_{OC} of 285 mV, a low short-circuit current density (J_{SC}) of 18.6 mA/cm^2, and a low fill factor (FF) of 34.9%. The inferior PV performance is mainly attributed to small grain sizes, a high defect density due to pinholes and Se-poor stoichiometry, and undesired grain orientations. Selenization at an appropriate elevated temperature (375 to 425 °C) significantly increases the device performance. However, at a too high annealing temperature of 450 °C, the devices exhibit poor PV performance (Figure S6) due to the porous Sb_2Se_3 film morphology (Figure 1e). Overall, the annealing temperature of 425 °C leads to the best device performance. In a comparison with the device annealed at 375 °C, the device annealed at 425 °C has a V_{OC} improving from 394 to 446 mV, J_{SC} improving from 22.91 to 26.35 mA/cm^2, and FF improving from 40.51% to 54.90%, respectively, yielding an overall PCE improvement from 3.6% to 6.43%. The improvements in V_{OC} and FF are attributed to the improved crystallinity, preferred orientation, larger grain size, more compact and uniform morphology, and better stoichiometry of the Sb_2Se_3 films. Particularly, the increasing selenization temperature from 375 to 425 °C decreases the series resistance (R_S) from 7.6 to 4.3 Ω cm^2 and increases shunt resistance (R_{SH}) from 78.7 to 227.3 Ω cm^2 (Table 1), likely due to the improved through-film charge transport and reduced pinhole density and V_{Se} defects, which explain the increased FF. In addition, it is reported that a high selenization temperature can facilitate the formation of a compact $MoSe_2$ between the Mo and Sb_2Se_3, which can improve the back-interface quality and reduce the Schottky barrier height.[18,28] The improved J_{SC} was further evaluated by external quantum efficiency (EQE) measurements (Figure 3d). When the selenization temperature increases from 375 to 425 °C, EQE shows a significant improvement at longer wavelengths (700–1000 nm), suggesting improved absorber quality and a better back interface between Mo and Sb_2Se_3.

Furthermore, a capacitance–voltage ($C-V$) measurement was performed on the 375 and 425 °C annealed cells to understand the effect of selenization temperature on the V_{OC} and carrier concentration for Sb_2Se_3 solar cells. Figure 4a shows the Mott–Schottky plot ($1/C^2$ versus V) of cells prepared with these two devices. The built-in potential (V_{bi}) extracted from the Mott–Schottky plot at the intercepts with the x-axis was found to be 450 and 540 mV for the samples selenized at 375 and 425 °C, respectively, values which are consistent with the trend in V_{OC} values obtained from the $J-V$ measurement. The apparent net carrier concentration (N_{cv}) of the absorber layer was calculated by using the following equation:[29]

Table 1. $J-V$ Parameters of Champion Sb_2Se_3 Solar Cells without Annealing and Annealed at Different Selenization Temperatures

selenization temp (°C)	V_{OC} (mV)	J_{SC} (mA/cm^2)	FF (%)	PCE (%)	R_S (Ω cm^2)	R_{SH} (Ω cm^2)
NA	285	18.6	34.9	1.85	8.7	34.2
375	394	22.9	40.5	3.66	7.6	78.7
400	433	24.9	53.6	5.77	6	158.4
425	446	26.4	54.9	6.43	4.3	227.3
450	122	19.9	27.4	0.67	5.5	8.1

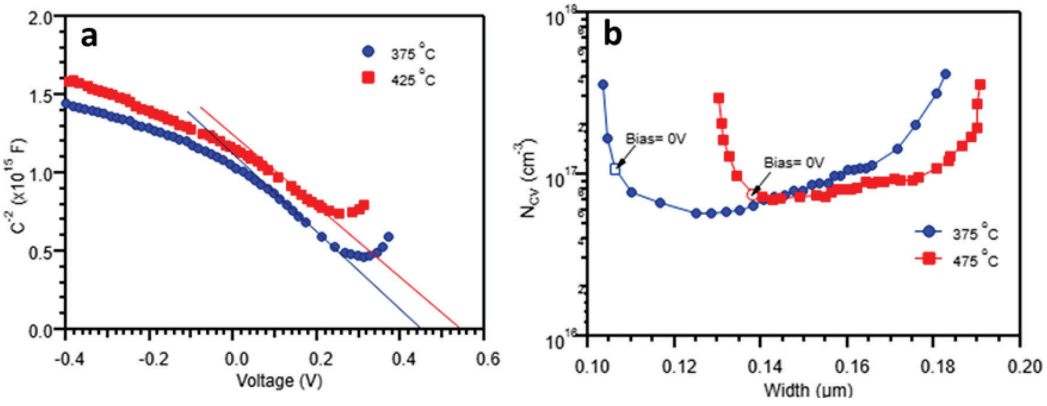


Figure 4. (a) $1/C^2$ versus V curves and (b) carrier density profiles of the Sb_2Se_3 cells selenized at 375 and 425 °C.

https://doi.org/10.1021/acsaem.1c00657
ACS Appl. Energy Mater. XXXX, XXX, XXX–XXX

Approved for public release; distribution unlimited.

$$N_{cv} = \frac{2}{q\varepsilon\varepsilon_o}\left[\frac{dC^{-2}(V)}{dV}\right]^{-1} \quad (2)$$

where ε and ε_o are the relative permittivity value of the Sb_2Se_3 films and the absolute permittivity of vacuum, respectively. The value of ε is considered to be 30 for Sb_2Se_3.[30] The distance from the front junction (χ) is calculated directly from $\chi = \varepsilon\varepsilon_o/C$, where C is the capacitance per unit area. The apparent net carrier densities of the Sb_2Se_3 films selenized at 375 and 425 °C are determined to be 5.69×10^{16} and 7.21×10^{16} cm^{-3}, respectively, as shown in Figure 4b. The change in V_{OC} due to the change in carrier density can be calculated by using the following equation.[18]

$$\Delta V_{OC} = \frac{K_B T}{q}\ln\left(\frac{N_2}{N_1}\right) \quad (3)$$

In this equation, N_1 and N_2 are the carrier densities of the film selenized at 325 and 425 °C, respectively, K_B is the Boltzmann's constant, and T is the temperature. By using eq 3, we found a negligible change (~6 mV) in the V_{OC} due to this small difference in carrier concentration. Therefore, in a comparison of the cells annealed at 425 and 375 °C, the increased V_{OC} of 50−100 mV is mainly due to the reduced recombination in the Sb_2Se_3 layer and its interfaces rather than the increased carrier concentration.

In conclusion, we investigated the impact of selenization temperature on the PV performance of substrate-type Sb_2Se_3 solar cells. We identified that the selenization temperature of 425 °C was beneficial to increase the grain size and crystallinity and improve the orientation of the Sb_2Se_3 films. In addition, the Se loss during the CSS deposition can be compensated by the selenization process, which results in a reduced V_{Se} related recombination loss. Because of all of these benefits of proper selenization, a significant device performance improvement from 1.85% to 6.43% is achieved. Further optimization on controlling the amount of Se during selenization could be the next step for improving the quality of the Sb_2Se_3 absorber layer and device performance.

■ ASSOCIATED CONTENT

Supporting Information

The Supporting Information is available free of charge at https://pubs.acs.org/doi/10.1021/acsaem.1c00657.

Experimental methods, a schematic image of the CSS system and temperature profile of the postdeposition selenization treatment, EDS analysis of Sb_2Se_3 thin films, transmittance spectra of Sb_2Se_3 thin films, top-view and cross-sectional SEM images of Sb_2Se_3 film annealed at 425 °C, statistic distributions of PV parameters for Sb_2Se_3 solar cells, and the $J-V$ curve of a 450 °C annealed cell (PDF)

■ AUTHOR INFORMATION

Corresponding Authors

Zhaoning Song − *Department of Physics and Astronomy, and Wright Center for Photovoltaics Innovation and Commercialization (PVIC), University of Toledo, Toledo, Ohio 43606, United States;* orcid.org/0000-0002-6677-0994; Email: zhaoning.song@utoledo.edu

Yanfa Yan − *Department of Physics and Astronomy, and Wright Center for Photovoltaics Innovation and Commercialization (PVIC), University of Toledo, Toledo, Ohio 43606, United States;* orcid.org/0000-0003-3977-5789; Email: yanfa.yan@utoledo.edu

Authors

Suman Rijal − *Department of Physics and Astronomy, and Wright Center for Photovoltaics Innovation and Commercialization (PVIC), University of Toledo, Toledo, Ohio 43606, United States;* orcid.org/0000-0002-7738-4917

Deng-Bing Li − *Department of Physics and Astronomy, and Wright Center for Photovoltaics Innovation and Commercialization (PVIC), University of Toledo, Toledo, Ohio 43606, United States;* orcid.org/0000-0003-4555-4894

Rasha A. Awni − *Department of Physics and Astronomy, and Wright Center for Photovoltaics Innovation and Commercialization (PVIC), University of Toledo, Toledo, Ohio 43606, United States*

Sandip S. Bista − *Department of Physics and Astronomy, and Wright Center for Photovoltaics Innovation and Commercialization (PVIC), University of Toledo, Toledo, Ohio 43606, United States*

Complete contact information is available at: https://pubs.acs.org/10.1021/acsaem.1c00657

Notes

The authors declare no competing financial interest.

■ ACKNOWLEDGMENTS

This material is based on research sponsored by the U.S. Air Force Research Laboratory under agreement numbers FA9453-18-2-0037 and FA9453-19-C-1002. The U.S. Government is authorized to reproduce and distribute reprints for Governmental purposes not withstanding any copyright notation thereon. The views and conclusions contained herein are those of the authors and should not be interpreted as necessarily representing the official policies or endorsements, either expressed or implied, of the U.S. Air Force Research Laboratory or the U.S. Government.

■ REFERENCES

(1) Jackson, P.; Wuerz, R.; Hariskos, D.; Lotter, E.; Witte, W.; Powalla, M. Effects of heavy alkali elements in Cu (In, Ga) Se2 solar cells with efficiencies up to 22.6%. *Phys. Status Solidi RRL* **2016**, *10*, 583−586.

(2) NREL. *Best Research-Cell Efficiency Chart*; US Department of Energy, 2019.

(3) Yoo, J. J.; Seo, G.; Chua, M. R.; Park, T. G.; Lu, Y.; Rotermund, F.; Kim, Y.-K.; Moon, C. S.; Jeon, N. J.; Correa-Baena, J.-P.; et al. Efficient perovskite solar cells via improved carrier management. *Nature* **2021**, *590*, 587−593.

(4) Green, M.; Dunlop, E.; Hohl-Ebinger, J.; Yoshita, M.; Kopidakis, N.; Hao, X. Solar cell efficiency tables (version 57). *Prog. Photovoltaics* **2021**, *29*, 3−15.

(5) Zeng, K.; Xue, D.-J.; Tang, J. Antimony selenide thin-film solar cells. *Semicond. Sci. Technol.* **2016**, *31*, No. 063001.

(6) Zhang, C.; Zhong, J.; Tang, J. Cu2ZnSn(S,Se)4 thin film solar cells fabricated with benign solvents. *Frontiers of Optoelectronics* **2015**, *8*, 252−268.

(7) Kumar, M.; Dubey, A.; Adhikari, N.; Venkatesan, S.; Qiao, Q. Strategic review of secondary phases, defects and defect-complexes in kesterite CZTS−Se solar cells. *Energy Environ. Sci.* **2015**, *8*, 3134−3159.

Approved for public release; distribution unlimited.

(8) Yun, H.-S.; Park, B.-w.; Choi, Y. C.; Im, J.; Shin, T. J.; Seok, S. I. Efficient Nanostructured TiO2/SnS Heterojunction Solar Cells. *Adv. Energy Mater.* **2019**, *9*, 1901343.
(9) Xue, D.-J.; Liu, S.-C.; Dai, C.-M.; Chen, S.; He, C.; Zhao, L.; Hu, J.-S.; Wan, L.-J. GeSe Thin-Film Solar Cells Fabricated by Self-Regulated Rapid Thermal Sublimation. *J. Am. Chem. Soc.* **2017**, *139*, 958−965.
(10) Li, Z.; Liang, X.; Li, G.; Liu, H.; Zhang, H.; Guo, J.; Chen, J.; Shen, K.; San, X.; Yu, W.; Schropp, R. E. I.; Mai, Y. 9.2%-efficient core-shell structured antimony selenide nanorod array solar cells. *Nat. Commun.* **2019**, *10*, 125.
(11) Wang, X.; Tang, R.; Jiang, C.; Lian, W.; Ju, H.; Jiang, G.; Li, Z.; Zhu, C.; Chen, T. Manipulating the Electrical Properties of Sb2(S,Se)3 Film for High-Efficiency Solar Cell. *Adv. Energy Mater.* **2020**, *10*, 2002341.
(12) Shockley, W.; Queisser, H. J. Detailed balance limit of efficiency of p−n junction solar cells. *J. Appl. Phys.* **1961**, *32*, 510−519.
(13) Lei, H. W.; Chen, J. J.; Tan, Z. J.; Fang, G. J. Review of Recent Progress in Antimony Chalcogenide-Based Solar Cells: Materials and Devices. *Sol. RRL* **2019**, *3*, 1900026.
(14) Wen, X.; Chen, C.; Lu, S.; Li, K.; Kondrotas, R.; Zhao, Y.; Chen, W.; Gao, L.; Wang, C.; Zhang, J.; et al. Vapor transport deposition of antimony selenide thin film solar cells with 7.6% efficiency. *Nat. Commun.* **2018**, *9*, 2179.
(15) Li, D.-B.; Yin, X.; Grice, C. R.; Guan, L.; Song, Z.; Wang, C.; Chen, C.; Li, K.; Cimaroli, A. J.; Awni, R. A.; et al. Stable and efficient CdS/Sb2Se3 solar cells prepared by scalable close space sublimation. *Nano Energy* **2018**, *49*, 346−353.
(16) Liang, G.; Chen, X.; Ren, D.; Jiang, X.; Tang, R.; Zheng, Z.; Su, Z.; Fan, P.; Zhang, X.; Zhang, Y.; Chen, S. Ion doping simultaneously increased the carrier density and modified the conduction type of Sb2Se3 thin films towards quasi-homojunction solar cell. *Journal of Materiomics* **2021**. DOI: 10.1016/j.jmat.2021.02.009
(17) Ma, Y.; Tang, B.; Lian, W.; Wu, C.; Wang, X.; Ju, H.; Zhu, C.; Fan, F.; Chen, T. Efficient defect passivation of Sb2Se3 film by tellurium doping for high performance solar cells. *J. Mater. Chem. A* **2020**, *8*, 6510−6516.
(18) Li, Z.; Chen, X.; Zhu, H.; Chen, J.; Guo, Y.; Zhang, C.; Zhang, W.; Niu, X.; Mai, Y. Sb2Se3 thin film solar cells in substrate configuration and the back contact selenization. *Sol. Energy Mater. Sol. Cells* **2017**, *161*, 190−196.
(19) Leng, M.; Luo, M.; Chen, C.; Qin, S.; Chen, J.; Zhong, J.; Tang, J. Selenization of Sb2Se3 absorber layer: an efficient step to improve device performance of CdS/Sb2Se3 solar cells. *Appl. Phys. Lett.* **2014**, *105*, No. 083905.
(20) Liang, G.-X.; Luo, Y.-D.; Chen, S.; Tang, R.; Zheng, Z.-H.; Li, X.-J.; Liu, X.-S.; Liu, Y.-K.; Li, Y.-F.; Chen, X.-Y.; Su, Z.-H.; Zhang, X.-H.; Ma, H.-L.; Fan, P. Sputtered and selenized Sb2Se3 thin-film solar cells with open-circuit voltage exceeding 500 mV. *Nano Energy* **2020**, *73*, 104806.
(21) Liu, X.; Chen, J.; Luo, M.; Leng, M.; Xia, Z.; Zhou, Y.; Qin, S.; Xue, D.-J.; Lv, L.; Huang, H.; et al. Thermal evaporation and characterization of Sb2Se3 thin film for substrate Sb2Se3/CdS solar cells. *ACS Appl. Mater. Interfaces* **2014**, *6*, 10687−10695.
(22) Hultqvist, A.; Salomé, P. M. P.; Fjällström, V.; Edoff, M.; Aitken, B.; Zhang, K.; Shi, Y.; Fuller, K.; Williams, C. K. Performance of Cu(In,Ga)Se2 solar cells using nominally alkali free glass substrates with varying coefficient of thermal expansion. *J. Appl. Phys.* **2013**, *114*, No. 094501.
(23) Lide, D. R. *CRC Handbook of Chemistry and Physics, 2003−2004*; CRC Press: Boca Raton, FL, 2003.
(24) Herrmann, M. G.; Stoffel, R. P.; Sergueev, I.; Wille, H.-C.; Leupold, O.; Ait Haddouch, M.; Sala, G.; Abernathy, D. L.; Voigt, J.; Hermann, R. P.; Dronskowski, R.; Friese, K. Lattice Dynamics of Sb2Se3 from Inelastic Neutron and X-Ray Scattering. *Phys. Status Solidi B* **2020**, *257*, 2000063.
(25) Guo, H.; Chen, Z.; Wang, X.; Cang, Q.; Jia, X.; Ma, C.; Yuan, N.; Ding, J. Enhancement in the Efficiency of Sb2Se3 Thin-Film Solar Cells by Increasing Carrier Concertation and Inducing Columnar Growth of the Grains (Solar RRL 3/2019). *Sol. RRL* **2019**, *3*, 1970033.
(26) Zhou, Y.; Wang, L.; Chen, S.; Qin, S.; Liu, X.; Chen, J.; Xue, D.-J.; Luo, M.; Cao, Y.; Cheng, Y.; Sargent, E. H.; Tang, J. Thin-film Sb2Se3 photovoltaics with oriented one-dimensional ribbons and benign grain boundaries. *Nat. Photonics* **2015**, *9*, 409−415.
(27) Tang, R.; Zheng, Z.-H.; Su, Z.-H.; Li, X.-J.; Wei, Y.-D.; Zhang, X.-H.; Fu, Y.-Q.; Luo, J.-T.; Fan, P.; Liang, G.-X. Highly efficient and stable planar heterojunction solar cell based on sputtered and post-selenized Sb2Se3 thin film. *Nano Energy* **2019**, *64*, 103929.
(28) Tang, R.; Chen, X.-Y.; Liang, G.-X.; Su, Z.-H.; Luo, J.t.; Fan, P. Magnetron sputtering deposition and selenization of Sb2Se3 thin film for substrate Sb2Se3/CdS solar cells. *Surf. Coat. Technol.* **2019**, *360*, 68−72.
(29) Sze, S. M.; Li, Y.; Ng, K. K. *Physics of Semiconductor Devices*; John Wiley & Sons, 2021.
(30) Luo, M.; Leng, M.; Liu, X.; Chen, J.; Chen, C.; Qin, S.; Tang, J. Thermal evaporation and characterization of superstrate CdS/Sb2Se3 solar cells. *Appl. Phys. Lett.* **2014**, *104*, 173904.

https://doi.org/10.1021/acsaem.1c00657
ACS Appl. Energy Mater. XXXX, XXX, XXX−XXX

Approved for public release; distribution unlimited.

The Journal of Chemical Physics ARTICLE scitation.org/journal/jcp

Kinetically driven island morphology in growth on strained Cu(100)

Cite as: J. Chem. Phys. 155, 074703 (2021); doi: 10.1063/5.0058926
Submitted: 3 June 2021 • Accepted: 2 August 2021 •
Published Online: 17 August 2021

View Online Export Citation CrossMark

Indiras Khatri,[a] Ehsan H. Sabbar,[b] Yunsic Shim,[c] and Jacques G. Amar[d]

AFFILIATIONS

Department of Physics and Astronomy, University of Toledo, Toledo, Ohio 43606, USA

[a]indiras.khatri@rockets.utoledo.edu
[b]**Current address:** Department of Electrical Engineering, University of Anbar, 11, Ramadi, Iraq. ehsan.sabbar@uoanbar.edu.iq
[c]yunsic.shim@utoledo.edu
[d]**Author to whom correspondence should be addressed:** jacques.amar@utoledo.edu

ABSTRACT

We study the effects of strain on the monomer and dimer diffusion mechanisms and island morphology during the growth of Cu on a biaxially strained Cu(100) substrate. We find an approximately linear dependence of the activation barriers on strain. In particular, while hopping is favored for compressive and/or small (<2%) tensile strain, for greater than 2% tensile strain, the exchange mechanism is favored. We then present the results of temperature-accelerated dynamics simulations of submonolayer growth at 200 K. For the case of 2% compressive strain we find that, as in previous kinetic Monte Carlo simulations of Cu/Ni(100) growth, the competition between island growth and multi-atom relaxation ("pop-out") events leads to an island morphology with a mixture of open and closed steps. At slightly higher coverage, island coalescence then leads to elongated islands. However, annealing leads to a significant decrease in the number of open steps. In contrast, for the case of 8% tensile strain, only one large strongly anisotropic island is formed. Surprisingly, we find that despite the large strain, the island anisotropy is not due to energetics but is instead due to anisotropic attachment barriers that favor the exchange-mediated attachment of monomers to corners over close-packed step-edges. An explanation for the asymmetry in attachment barriers is provided. Our results provide a new general kinetic mechanism for the formation of anisotropic islands in the presence of isotropic diffusion and tensile strain.

Published under an exclusive license by AIP Publishing. https://doi.org/10.1063/5.0058926

I. INTRODUCTION

Strain in submonolayer heteroepitaxial thin-film growth has been shown both experimentally[1–11] and theoretically[12–18] to lead to a variety of interesting morphological and structural effects. For example, in the case of Cu/Ni(100) growth (corresponding to 2.7% compressive strain), it has been found that strain and/or chemical effects lead to ramified islands as well as stacking faults (SFs).[2–4,7,9] Strain can also lead to additional morphological and structural effects in submonolayer growth, including the formation of 3D islands,[1,12] partial dislocations,[9] as well as transitions from isotropic to anisotropic islands with increasing island size.[5,8,11] In particular, continuum elasticity theory predicts that in equilibrium, the competition between step energy (which favors a compact shape) and strain energy may lead to a spontaneous shape transition from compact to elongated islands above a critical island size.[12,13]

Previously, we have carried out energetics calculations and on-lattice kinetic Monte Carlo (KMC) simulations of Cu/Ni(100) growth,[19] which indicated that the ramified islands observed experimentally are not due to energetics but instead are due to strain-induced kinetic effects, which lower the barriers for "pop-out" events, leading to ramified islands with a mixture of open ([100]) and closed ([110]) step-edges. More recently, we have used off-lattice temperature-accelerated dynamics (TAD) simulations of Cu growth on a Cu(100) substrate with 4% compressive strain in order to study the mechanisms for stacking fault (SF) formation. In this case, we found[20] that islands play a key role by lowering the barriers for substrate vacancy formation, while due to entropic effects, SF formation is both kinetically and thermodynamically favored at sufficiently high temperatures. These results indicate that the SF formation observed in Cu/Ni(100) islands is primarily due to strain rather than "chemical" effects.

Here, we first study the strain dependence of the activation barriers for Cu monomer and dimer diffusion via hopping and exchange on a biaxially strained Cu(100) substrate. As in previous calculations for Ag on strained Ag(100),[21] we find an approximately

Published under an exclusive license by AIP Publishing

Approved for public release; distribution unlimited.

linear dependence of the activation barriers on strain. In particular, while hopping is favored for compressive and/or small (<2%) tensile strain, for greater than 2% tensile strain, the exchange mechanism is favored.

We then present the results of TAD simulations of the submonolayer growth of Cu on strained Cu(100) at 200 K for both the case of 2% compressive and 8% tensile strain. For the case of 2% compressive strain, we find that, as in previous KMC simulations of Cu/Ni(100) growth, the competition between island growth and multi-atom "pop-out" events leads to an island morphology with a mixture of open and closed steps. At slightly higher coverage, island coalescence then leads to elongated islands as in Cu/Ni(100) growth. These results suggest that the primary cause of the ramified islands in Cu/Ni(100) growth is, in fact, strain rather than chemical effects.

In contrast, for the case of 8% tensile strain, only one large strongly anisotropic island is formed. Surprisingly, we find that despite the large strain, the island anisotropy is not due to energetics but is instead due to anisotropic attachment barriers that favor the exchange-mediated attachment of monomers to corners over close-packed step-edges. An explanation for the asymmetry in attachment barriers is also provided. Our results provide a new general kinetic mechanism for the formation of anisotropic islands in the presence of isotropic diffusion and tensile strain.

The organization of this paper is as follows: We first briefly discuss our TAD simulations in Sec. II and then present our results in Sec. III. Finally, in Sec. IV, we summarize our results.

II. SIMULATIONS AND CALCULATIONS

Our growth simulations and calculations of the strain dependence of the activation barriers for monomer and dimer diffusion were carried out using an embedded-atom method (EAM) potential[22] with a substrate consisting of six Cu(100) layers with width L = 10 a (where a is the lattice constant of Cu) with the three bottom layers held fixed. In order to include the effects of strain, the substrate was strained biaxially, with the misfit ranging from −6% (compressive strain) to +8% (tensile strain) while periodic boundary conditions were assumed in the in-plane directions. In order to study the dependence of the dominant transport mechanisms on strain, nudged elastic band calculations were carried out for both the case of hopping and exchange.

In order to simulate submonolayer growth on timescales close to experiment while also taking into account strain-induced activated events, our simulations were carried out using temperature-accelerated dynamics (TAD).[23–26] While we have already described this method in detail in Ref. 20, here we note that it involves the use of a basin-constrained molecular dynamics (MD) simulation at a high temperature T_{high} to accelerate the search for the next activated event that will occur at a low temperature T_{low}. In order to maximize the "boost" or acceleration, we have carried out our growth simulations at a relatively moderate value of T_{low} (T_{low} = 200 K), while the high-temperature MD simulations were carried out with T_{high} = 650 K. In our simulations, Cu atoms were deposited randomly with a deposition rate of 1 monolayer (ML)/s. While this deposition rate is still somewhat faster than that used in experiments, it is still many orders of magnitude slower than is typically used in molecular dynamics simulations. As already indicated, our growth simulations were carried for both the case of 2% compressive and 8% tensile strain.

III. RESULTS

A. Dependence of dominant diffusion mechanisms and barriers on strain

Figure 1 shows our results for the dependence of the activation barriers for monomer and dimer hopping and/or exchange on strain. As can be seen, in the absence of strain, monomer and dimer hopping dominate over exchange, while the barrier for dimer diffusion (0.49 eV) is actually slightly lower than that for monomer diffusion (0.51 eV). With increasing compressive strain, the activation barriers for hopping decrease further, while the barriers for exchange increase. As a result, for the case of compressive strain and/or less than 2% tensile strain, hopping dominates over exchange. In contrast, for greater than 2% tensile strain, the activation barriers for monomer and dimer exchange are smaller than for hopping. As a result, exchange dominates over hopping.

We note that these results are qualitatively similar to those previously found by Ratsch[21] for Ag monomer diffusion on Ag(100), while the approximately linear dependence on strain is also in good agreement with the theoretical prediction[14] that the activation barrier should depend linearly on misfit. In the case of monomer hopping, the increase in the activation barrier with increasing tensile strain may be explained[21] by the fact that this leads to a greater variation in the potential energy surface. In contrast, the decrease in the exchange barrier with increasing tensile strain is due to the fact that this leads to more space, which is needed for the exchange mechanism, and also weakens the strength of the interatomic bonds in the substrate layer.

B. Submonolayer growth with 2% compressive strain

Previously, we have carried out KMC simulations of Cu/Ni(100) growth[19] with the same deposition rate and island density as in experiments,[4,7] which were able to explain the observed ramified island morphology. However, due to the low experimental

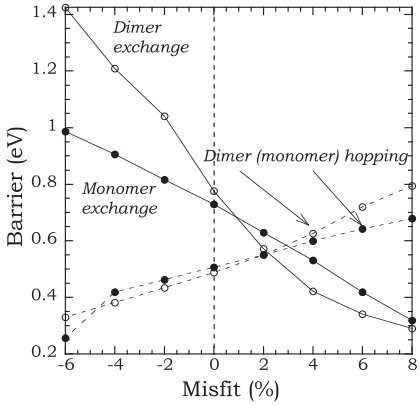


FIG. 1. Energy barriers for monomer and dimer hopping and exchange on strained Cu(100) as a function of misfit.

Published under an exclusive license by AIP Publishing

Approved for public release; distribution unlimited.

deposition rate (0.0015 ML/s) and island density and high growth temperature (250 K), we were unable to carry out full TAD simulations in this case. Accordingly, in order to compare with these results and also take into account all possible collective events that might not be included in KMC simulations, here we present the results of full TAD simulations for the case of 2% compressive strain at a somewhat lower temperature (T = 200 K) and higher deposition rate (1 ML/s).

Figure 2 shows the evolution of the island morphology in this case. As can be seen, once the coverage reaches 0.245 ML, there are two relatively large islands in the system. As in our previous kinetic Monte Carlo simulations of Cu/Ni(100) growth,[19] the two larger islands in Figs. 2(c) and 2(d) have a mixture of open ([100]) and closed ([110]) step-edges. As indicated by the arrows in Fig. 2, a variety of multi-atom in-plane pop-out events—whose barriers are significantly reduced due to strain—play an important role in determining the island morphology. The coalescence of the two small islands on the left-hand side of Fig. 2(a) to form the larger island in Fig. 2(b) also involves a large number of similar 2-, 3-, and 4-atom moves.

At a coverage of 0.285 ML [see Fig. 3(a)], the two large islands in Fig. 2(d) have coalesced to form one large elongated island with both open and closed step-edges, while at the end of deposition [0.305 ML, see Fig. 3(b)], four additional atoms have been deposited, two of which have attached to the island. Interestingly, the resulting elongated structure is similar in shape to but approximately one-third the size of some of the elongated islands obtained in KMC simulations of Cu/Ni(100) growth at 250 K with a much lower deposition rate (0.0015 ML/s) after 0.5 ML have been deposited.[19]

To study the morphological evolution of the large island over a longer timescale (10 s), we then annealed the system at 200 K with the heptamer removed to eliminate repetitive low-barrier edge-diffusion events. Figure 3(c) shows the island morphology after

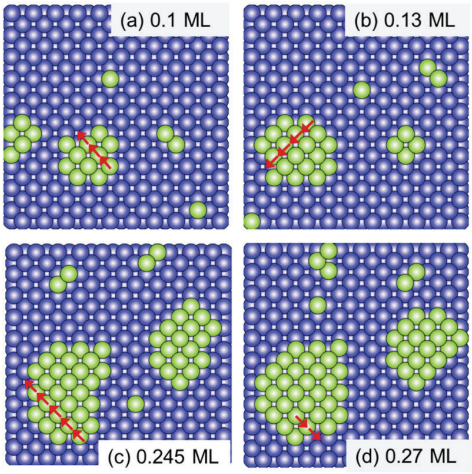


FIG. 2. Evolution of the system during growth of Cu on Cu(100) with 2% compressive strain. Also shown (arrows) are typical multi-atom pop-out events (see text). The corresponding barriers with (without) strain are (a) 0.32 (0.46) eV, (b) 0.43 (0.63) eV, (c) 0.46 (0.72) eV, and (d) 0.49 (0.79) eV.

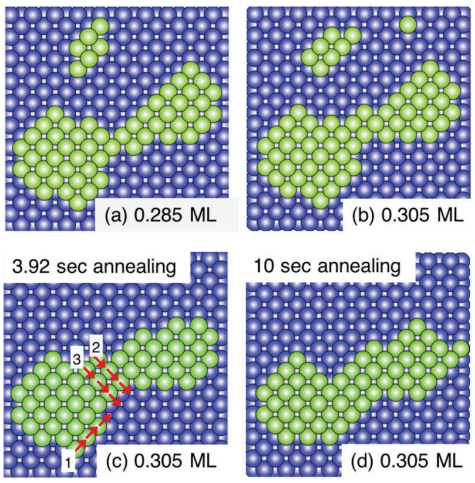


FIG. 3. (a) and (b) Same as Fig. 2 but at higher coverage. (c) and (d) Evolution of elongated island during annealing. Barriers with (without) strain for events indicated in (c) are (1) 0.62 (0.73) eV, (2) 0.44 (0.63) eV, and (3) 0.32 (0.51) eV.

3.92 s of annealing at which point the total system energy has been reduced by 0.76 eV. A portion of this reduction (0.13 eV) was due to island re-arrangement events that occurred during the first 1.85 s (just before the monomer attached to the island), while the system energy was further reduced by 0.51 eV after monomer attachment at a kink site. As a result of additional island re-arrangement events, the energy was then further reduced by an additional 0.12 eV. As an illustration of the typical re-arrangement events, also shown in Fig. 3(c) (arrows) are the next three events [(1)–(3)] that occur just after 3.92 s of annealing along with the corresponding activation barriers with and without strain. As can be seen, all of these moves correspond to three-atom events while the corresponding barriers are significantly reduced due to strain.

Figure 3(d) shows the final morphology after a full 10 s of annealing. While the number of open step-edges has been further reduced, the island remains elongated as previously found in KMC simulations of the annealing of ramified Cu/Ni(100) islands at 250 K for 10^3 s.[19] In addition, the total system energy has been reduced by an additional 0.32 eV. While the entire annealing process involved 230 activated events including monomer hopping, the overwhelming majority corresponded to collective events involving at least three atoms while the corresponding barriers ranged from 0.24 eV (monomer edge-diffusion) to 0.62 eV.

C. Submonolayer growth with 8% tensile strain

For comparison with our results for 2% compressive strain, we have also carried out TAD simulations of Cu/Cu(100) submonolayer growth for the case of 8% tensile strain. As indicated in Fig. 1, the dominant mechanisms for adatom transport in this case are monomer and dimer diffusion via exchange with the substrate. As can be seen in Fig. 4 (corresponding to the end of growth with 0.215 ML deposited), due to the relatively low barriers for monomer and dimer diffusion, only one island is formed. However, starting with a stable tetramer (atoms labeled "1" in Fig. 4), the island growth

Published under an exclusive license by AIP Publishing

Approved for public release; distribution unlimited.

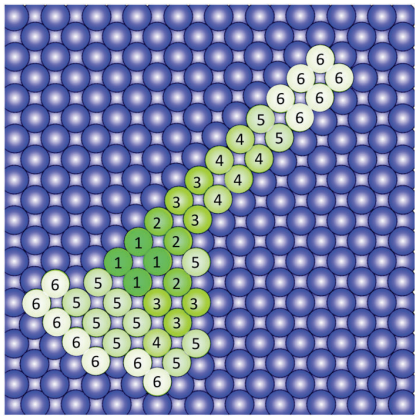


FIG. 4. Growth of the anisotropic island during deposition of Cu on Cu(100) with 8% tensile strain. Atom numbers correspond to the order of island attachment (see text).

becomes highly anisotropic. In particular, as indicated by the "atom numbers" in Fig. 4, which correspond approximately to the order of island growth, the island first forms an L-shape with both sides of the "L" of width equal to two atoms (see atoms labeled "1–3") and then grows along the "top" arm, forming an extended two-atom-wide rectangle, as well as at the "base."

One possible explanation for the strongly anisotropic island growth is that the strain energy contribution to the total energy is significantly lower for anisotropic islands than for compact islands, thus compensating for the gain in perimeter energy. This is consistent with previous work on strained island growth in which a transition from square islands to anisotropic islands was found[1,5,8,10–12,17] for sufficiently large island sizes. However, calculations that we have carried out for a variety of different island sizes and aspect ratios indicate that at least for islands with up to 256 atoms, both the energy and free energy[27] at 200 K are always smaller for isotropic (square) islands than for anisotropic islands with the same number of atoms. Similarly, we find that the energy and free energy at 200 K of an almost isotropic 43-atom island (corresponding to a compact 6 by 7 island with one edge atom) are significantly lower than the energy of the 43-atom island in Fig. 4. These results clearly indicate that the formation of an anisotropic island in our simulations is not due to energetics but is instead due to kinetics.

We now consider the kinetics of island growth. As can be seen in Fig. 5, while the barrier for monomer diffusion far away from the island [Fig. 5(a)] is 0.32 eV, the barrier for attachment to the two-atom-wide tip [Fig. 5(b)] is only 0.29 eV, corresponding to a "negative" attachment barrier. Similarly, the barrier for a monomer to attach to the "side" corner of the two-atom-wide tip (not shown) is also 0.29 eV, while the barrier for an exchange move from this corner to the front of the tip [Fig. 5(c)] is only 0.21 eV. In addition, the barrier for a second monomer to attach at one of the tip corners [Fig. 5(d)] is only 0.27 eV.

In contrast, the barrier for attachment to a close-packed step-edge away from a corner [see Fig. 5(e)] is significantly higher (0.37 eV). The activation barrier to approach one step away from a close-packed step-edge [0.36 eV, see Fig. 5(f)] is also higher than

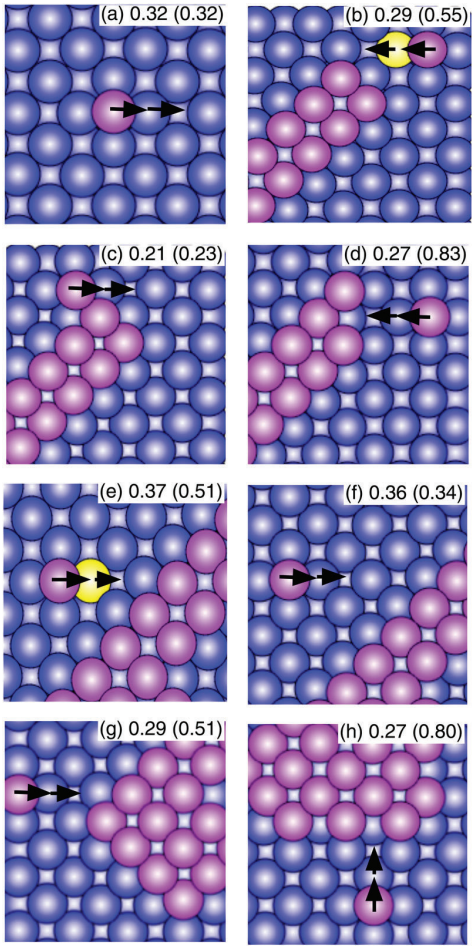


FIG. 5. Key forward and reverse (in parentheses) barriers (in eV) involved in anisotropic island growth for the case of 8% tensile strain: (a) monomer exchange on substrate, (b) monomer attachment at tip, (c) corner-rounding, (d) attachment of second monomer at the tip, (e) attachment to close-packed step-edge, (f) approach to close-packed step-edge, (g) corner attachment, and (h) attachment to open step-edge.

the monomer diffusion barrier, while the reverse barrier (0.34 eV) is lower than the forward barrier. As a result, atoms are repelled from the long close-packed step-edges shown in Fig. 4 and attracted to the two-atom-wide tip. In fact, in our simulations, only one atom attached to the upper close-packed step-edge of the island and that atom eventually migrated to the tip via two edge-diffusion moves with a barrier of 0.42 eV. These results clearly indicate that the growth of the two-atom-wide tip is strongly kinetically favored over sideways growth, thus explaining the island anisotropy.

Since Fig. 4 also indicates that significant island growth occurs in the lower half of the island, we have also calculated the corresponding attachment mechanisms and barriers. As can be seen in Fig. 5(g), the barrier for attachment at the bottom corner (0.29 eV) is

Published under an exclusive license by AIP Publishing

Approved for public release; distribution unlimited.

the same as for attachment at the tip [Fig. 5(b)]. In addition, the barrier for attachment at an open step-edge [0.27 eV, see Fig. 5(h)] is the same as for the attachment of a second atom at the tip [see Fig. 5(d)]. As a result, in addition to growth at the tip, the island also grows at the base via attachment at open steps and corner sites, followed by multi-atom re-arrangement moves to minimize the number of open steps.

We now consider the mechanism for the decrease in the activation barrier for attachment via exchange at a corner compared to that at a close-packed step-edge. Analysis of the local geometry indicates that in both cases, there are three substrate atoms in front of the attaching atom [yellow atoms in Figs. 5(b) and 5(e)]—one on each side of the final position and one in front. One of these substrate atoms has no island nearest-neighbors. However, in the case of attachment at a close-packed step-edge, the other two substrate atoms each have two island nearest-neighbor bonds, while in the case of attachment at a corner or tip, one of them has only one island nearest-neighbor bond. This implies that it is easier for nearby atoms to relax during the attachment process in the case of tip/corner attachment than during attachment at a close-packed step-edge, thus leading to a reduction in the tip/corner attachment barrier.

A similar argument also indicates that the energy reduction after tip/corner attachment should be larger than for attachment at a close-packed step-edge. In particular, we find that while attachment at a corner [Fig. 5(g)] decreases the system energy by ~0.26 eV, attachment at a closed step-edge away from a corner only decreases the energy by 0.14 eV. Thus, the difference in the final state energy between close-packed step-edge attachment and tip attachment (0.12 eV) is consistent with but somewhat larger than the corresponding difference in the energy barriers (0.08 eV). In contrast, in the absence of strain—for which the dominant diffusion mechanism involves hopping—the activation barriers for attachment at a two-atom-wide tip and a close-packed step-edge are the same (0.45 eV). Accordingly, square islands are both kinetically and energetically favored in this case.

IV. CONCLUSION

Using an EAM potential, we have studied the strain dependence of the Cu monomer and dimer diffusion mechanisms and activation barriers on a biaxially strained Cu(100) substrate. As in previous calculations for Ag on strained Ag(100),[21] we find an approximately linear dependence of the activation barriers on strain. In particular, we found that while hopping is favored for compressive and/or small (<2%) tensile strain, for greater than 2% tensile strain, the exchange mechanism is favored.

In order to compare with Cu/Ni(100) growth and also separate out chemical effects from strain effects as well as take into account all possible collective events that might not be included in KMC simulations, we have also carried out TAD simulations of submonolayer homoepitaxial Cu growth at 200 K for the case of 2% compressive strain. As in previous KMC simulations of Cu/Ni(100) growth,[19] the competition between island growth and multi-atom "pop-out" events was found to lead to an island morphology with a mixture of open and closed steps. We also found that at a coverage of 0.305 ML, island coalescence leads to elongated islands as in Cu/Ni(100) growth. These results suggest that the primary cause of the ramified islands in Cu/Ni(100) growth is, in fact, strain rather than chemical effects.

We have also studied the annealing process for longer times (10 s). Our simulations indicate that the primary relaxation processes involve a variety of multi-atom events involving three or more atoms whose barriers are significantly reduced due to strain and which tend to significantly reduce the number of open steps. These results clearly indicate that the island morphology during growth is due to a competition between island attachment (which leads to open step-edges) and multi-atom relaxation processes.

For comparison, we have also carried out TAD simulations of Cu/Cu(100) growth for the case of 8% tensile strain. In this case, due to the low barriers for monomer and dimer diffusion, the island density is relatively low and so only one large strongly anisotropic island was formed. Surprisingly, we found that despite the large strain, the island anisotropy is not due to energetics but is instead due to anisotropic attachment barriers that favor the exchange-mediated attachment of monomers to corners over close-packed step-edges. We note that anisotropic islands have also been observed in the growth of Co on the reconstructed Pt(111) surface corresponding to 9.7% tensile strain.[28] However, in this case, the anisotropy is a result of the Pt(111) reconstruction[29] that occurs in the absence of Co deposition and leads to highly anisotropic Co diffusion. In contrast, in our TAD simulations, we have isotropic diffusion and there is no surface reconstruction. Thus, our results provide a new kinetic mechanism for the formation of anisotropic islands in the presence of isotropic diffusion and tensile strain.

ACKNOWLEDGMENTS

This work was supported by NSF Grant No. DMR-1410840 and the Air Force Research Laboratory under Agreement No. FA9453-18-2-0037. We would also like to acknowledge a grant of computer time from the Ohio Supercomputer Center.

DATA AVAILABILITY

The data that support the findings of this study are available from the corresponding author upon reasonable request.

REFERENCES

[1] Y.-W. Mo, D. E. Savage, B. S. Swartzentruber, and M. G. Lagally, Phys. Rev. Lett. **65**, 1020 (1990).
[2] B. Müller, L. Nedelmann, B. Fischer, A. Fricke, and K. Kern, J. Vac. Sci. Technol. A **14**, 1878 (1996).
[3] B. Müller, B. Fischer, L. Nedelmann, A. Fricke, and K. Kern, Phys. Rev. Lett. **76**, 2358 (1996).
[4] B. Müller, L. Nedelmann, B. Fischer, H. Brune, J. V. Barth, and K. Kern, Phys. Rev. Lett. **80**, 2642 (1998).
[5] S. H. Brongersma, M. R. Castell, D. D. Perovic, and M. Zinke-Allmang, Phys. Rev. Lett. **80**, 3795 (1998).
[6] G. Medeiros-Ribeiro, T. I. Kamins, D. A. A. Ohlberg, and R. S. Williams, Phys. Rev. B **58**, 3533 (1998).
[7] B. Müller, L. P. Nedelmann, B. Fischer, H. Brune, J. V. Barth, K. Kern, D. Erdös, and J. Wollschläger, Surf. Rev. Lett. **5**, 769 (1998).
[8] W. Ma, R. Nötzel, H.-P. Schönherr, and K. H. Ploog, Appl. Phys. Lett. **79**, 4219 (2001).
[9] V. Fournée, J. Ledieu, T. Cai, and P. A. Thiel, Phys. Rev. B **67**, 155401 (2003).

Published under an exclusive license by AIP Publishing

Approved for public release; distribution unlimited.

[10]N. V. Medhekar, V. B. Shenoy, J. B. Hannon, and R. M. Tromp, Phys. Rev. Lett. **99**, 156102 (2007).
[11]M. S. J. Marshall and M. R. Castell, Phys. Rev. Lett. **102**, 146102 (2009).
[12]J. Tersoff and R. M. Tromp, Phys. Rev. Lett. **70**, 2782 (1993).
[13]A. Li, F. Liu, and M. G. Lagally, Phys. Rev. Lett. **85**, 1922 (2000).
[14]D. J. Shu, F. Liu, and X. G. Gong, Phys. Rev. B **64**, 245410 (2001).
[15]H. J. W. Zandvliet and R. van Gastel, Phys. Rev. Lett. **99**, 136103 (2007).
[16]J.-N. Aqua and T. Frisch, Phys. Rev. B **78**, 121305(R) (2008).
[17]Y. Li, M. Liu, D. Ma, D. Yu, X. Chen, X.-C. Ma, Q.-K. Xue, K. Xu, J.-F. Jia, and F. Liu, Phys. Rev. Lett. **103**, 076102 (2009).
[18]K. Liu, I. Berbezier, T. David, L. Favre, A. Ronda, M. Abbarchi, P. Voorhees, and J.-N. Aqua, Phys. Rev. Mater. **1**, 053402 (2017).
[19]Y. Shim and J. G. Amar, Phys. Rev. Lett. **108**, 076102 (2012).
[20]I. Khatri, E. H. Sabbar, Y. Shim, and J. G. Amar, Phys. Rev. Mater. **4**, 113403 (2020).
[21]C. Ratsch, Phys. Rev. B **83**, 153406 (2011).
[22]Y. Mishin, M. J. Mehl, D. A. Papaconstantopoulos, A. F. Voter, and J. D. Kress, Phys. Rev. B **63**, 224106 (2001).
[23]Y. Shim and J. G. Amar, J. Chem. Phys. **145**, 014105 (2016).
[24]M. R. Sørensen and A. F. Voter, J. Chem. Phys. **112**, 9599 (2000).
[25]D. Perez, B. P. Uberuaga, Y. Shim, J. G. Amar, and A. F. Voter, Annu. Rep. Comput. Chem. **5**, 79 (2009).
[26]R. J. Zamora, B. P. Uberuaga, D. Perez, and A. F. Voter, Annu. Rev. Chem. Biomol. Eng. **7**, 87 (2016).
[27]Our calculation of the free energy takes into account the vibrational entropy as in Ref. 20. While relatively small at 200 K, this contribution also tends to favor isotropic islands.
[28]P. Grütter and U. Dürig, Surf. Sci. **337**, 147 (1995).
[29]M. Bott, M. Hohage, T. Michely, and G. Comsa, Phys. Rev. Lett. **70**, 1489 (1993).

Published under an exclusive license by AIP Publishing

Approved for public release; distribution unlimited.

Journal of Alloys and Compounds 891 (2021) 161866

Contents lists available at ScienceDirect

Journal of Alloys and Compounds

journal homepage: www.elsevier.com/locate/jalcom

Correlating structure and orbital occupation with the stability and mechanical properties of 3d transition metal carbides

I. Khatri[a], N.J. Szymanski[a,b], B.B. Dumre[a], J.G. Amar[a], D. Gall[c], S.V. Khare[a,*]

[a] Department of Physics and Astronomy, University of Toledo, Toledo, OH 43606, USA
[b] Department of Materials Science and Engineering, University of California, Berkeley, Berkeley, CA 94720, USA
[c] Department of Materials Science and Engineering, Rensselaer Polytechnic Institute, Troy, NY 12180, USA

ARTICLE INFO

Article history:
Received 25 April 2021
Received in revised form 23 August 2021
Accepted 2 September 2021
Available online 10 September 2021

Keywords:
Coating materials
Crystal structure
Electronic properties
Phonons
Computer simulations
Mechanical properties

ABSTRACT

The development of novel transition metal carbides for improved hard coating technologies requires a detailed understanding of the factors influencing their stability and mechanical performance. To this end, we carried out first principles calculations based on density functional theory to tabulate the electronic structures, formation energies, and phonon dispersion curves of 3d transition metal carbides adopting zincblende, rocksalt, and cesium chloride structures. By analyzing the corresponding results, we outline a theoretical framework that describes how valence electron concentration and bonding configuration control the stability of these compounds. Many early transition metal carbides are predicted to be stable in the rocksalt and zincblende structures, enabled by filled bonding states, whereas the cesium chloride structure shows persistent instability. For compounds that are predicted to be stable, mechanical properties were investigated through calculation of elastic tensors, from which observable properties including Vicker's hardness and ductility were derived. A robust mechanical performance is shown to be correlated with complete filling of bonding orbitals as illustrated for rocksalt TiC and VC, which have calculated hardnesses of 25.66 and 22.63 GPa respectively. However, enhanced ductility and toughness can be achieved by allowing partial occupation of the antibonding states as in CrC, which has a relatively low Pugh's ratio of 0.51.
© 2021 Elsevier B.V. All rights reserved.

1. Introduction

Many transition metal carbides (TMCs), nitrides, and carbonitrides are known to display a wide range of remarkable physical and chemical properties [1–15]. These include but are not limited to exceptional hardness and wear resistance, robust stability at high operating temperatures, and high thermal conductivity [4]. Moreover, TMCs have been the subject of intense research interest in the fields of catalysis and surface science [16]. Detailed reviews of previous work on well-studied TMCs and their alloys can be found in Refs. [4–23]. Owing to their versatile properties, several TMCs have been considered for industrial applications involving hard coatings [24,25], refractory materials, conducting barriers, energy storage devices [26,27], catalytic agents [28], and potentially even high-temperature superconductors [29]. Depending on the application in focus, many previous studies have aimed to study the electronic structure and its influence on the bonding characteristics of the TMCs [9,19,30]. Because the underlying electronic structure may be tuned using both structure and composition, it is possible to fine-tune the materials by design. However, this requires a detailed understanding of the correlation between atomic-level electronic interactions and macroscopic properties. We therefore aim to build upon previous work [31,32] to illustrate a clear framework describing the factors influencing the stability and mechanical performance of TMCs.

Numerous studies have been conducted on TMCs using both experimental [33–36] and theoretical techniques, primarily focusing on the rocksalt structure which is most commonly adopted by these compounds [37–54]. With respect to their mechanical properties, Balasubramanian et al. [31] identified the valence electron concentration as a dominant factor controlling hardness and ductility across many rocksalt TMCs based on orbital filling. Using similar arguments, Häglund et al. [11] found that the cohesive energy in 3d TMCs is correlated with the filling of bonding and antibonding orbitals, with TiC showing the most exothermic cohesive energy of all compounds considered. Moving toward TMCs with higher group numbers, Singh et al. [42] reported that instability arises as metal-carbon bonds become weakened upon the increased filling of the

* Corresponding author.
E-mail address: sanjay.khare@utoledo.edu (S.V. Khare).

https://doi.org/10.1016/j.jallcom.2021.161866
0925-8388/© 2021 Elsevier B.V. All rights reserved.

Approved for public release; distribution unlimited.

antibonding orbitals, e.g., in CrC. This effect becomes more pronounced when dealing with the intermediate and late TMCs (FeC, CoC, and NiC), where previously reported mechanical properties imply relatively weak bonding [45].

While there has been extensive work done involving TMCs, a detailed and systematic investigation of 3d TMCs has not yet been reported across three unique cubic structures: rocksalt (RS), zinc-blende (ZB), and cesium chloride (CsCl). Here, we address this shortcoming by presenting the results of first principles calculations based on density functional theory. We specifically choose to focus on the electronic structures, formation energies, and phonon dispersion curves calculated for all ten 3d TMCs. We restrict our main analysis to cubic structures as those are suspected to balance good hardness and ductility, whereas materials with a hexagonal (wurtzite) structure tend to be brittle owing to a lack of slip planes [55,56]. Our calculated results comprise a theoretical guide that may be used to understand how valence electron concentration and bonding configuration each play a role in the stability of these compounds. In addition, we have also studied the mechanical properties of compounds that are predicted to be stable using calculated elastic tensors. Derived properties are then considered to reveal insight into the performance of the TMCs for hard coating applications.

In summary, we present results that imply the stability of seven TMCs in the ZB structure and five in the RS structure, whereas a persistent instability is observed in the CsCl configuration owing to its dense eight-fold coordination. As for the instabilities that arise through intermediate TMCs in the RS structure, metallic dimers are predicted to form as a direct result of strong d-d orbital overlap. This occurs due to an increased valence electron concentration, as well as a decrease in the metal−carbon bond strengths. In contrast, instabilities in the ZB structure are attributed to Jahn-Teller distortions [57–59] mediated by degenerate d orbital configurations in the tetrahedral ligand field. For the stable compounds, an increasing valence electron concentration leads to higher values of C_{11} and C_{12}, which in turn raises the bulk moduli across intermediate TMCs. In comparing RS versus ZB structures, the former is found to lead to higher shear resistance (and therefore much higher hardness) given that its bonding configuration enforces strong d-p orbital hybridization. From these results, we conclude that early TMCs adopting the RS structure are preferred for hard coating applications, confirming previous findings and removing the need for further investigation regarding alternative structures and compositions for this purpose. Among these compounds, a tradeoff is illustrated between hardness and ductility, which are predicted to be optimal in TiC and CrC respectively.

2. Computational methods

All density functional theory (DFT) calculations were carried out using the Vienna Ab initio Simulation package (VASP) [60–63]. The projector augmented wave (PAW) [64] method was utilized with exchange-correlation interactions treated by the generalized gradient approximation (GGA) in the Perdew-Burke-Ernzerhof (PBE) formalism [65]. For the early 3*d* transition metals Sc, Ti, and V, semi-core *s* and *p* electrons were included as valence states, whereas only semi-core *p* electrons were included for Cr and Mn. Only outer-core electrons were explicitly considered in the late transition metals Fe, Co, Ni, Cu, and Zn. A plane-wave basis set was constructed using a kinetic energy cutoff of 520 eV. Γ-centered grids of 4000 k-points per reciprocal atom (KPPRA) were employed for all calculations in the Brillouin zone [66,67]. Electron minimizations, for which Gaussian smearing of width 0.05 eV was used, were performed with a convergence criterion of 10^{-6} eV/atom as in previous work [68–70]. Spin-polarization was taken into account for all compounds. Four possible magnetic configurations were tested with respect to the transition metal ions: (i) non-magnetic ordering with each moment set to zero, (ii) ferromagnetic ordering with all moments aligned parallel, (iii) antiferromagnetic ordering with moments alternating along the [001] direction, and (iv) antiferromagnetic ordering with moments alternating along the [111] direction. For all compounds studied in this work, a non-magnetic or ferromagnetic configuration was identified to be the lowest-energy state – these ground states were used throughout the remainder of the calculations. Ionic relaxations were performed using a conjugate-gradient algorithm with a force constant criterion of 0.01 eV/Å as described in earlier works [71]. To precisely determine equilibrium lattice constants and bulk moduli, energies were computed for each compound at six volumes about the approximate energetic minima; these values were then fit to a Birch-Murnaghan equation of state [72,73].

To study the stability of each compound, we consider two key aspects: dynamics and energetics. Understanding the dynamical behavior of the structure is necessary to determine whether it is stable against perturbations; these include changes to the unit cell dimensions (strain), as well as collective atomic displacements (vibrational modes). To gain insight into the former, we calculated the independent elastic constants corresponding to the cubic crystal system (C_{11}, C_{12}, and C_{44}) by computing the energy of the unit cell under varied sets of strain and fitting the resulting values to a quadratic stress-strain relationship, as is described in detail throughout previous work [74–76]. From the elastic constants, stability against cell strain was determined using the Born criteria [77,78]:

$$C_{11} - C_{12} > 0,\ C_{11} + 2C_{12} > 0,\ \text{and}\ C_{44} > 0, \tag{1}$$

As for the effects of vibrational modes, we computed phonon dispersion curves along high-symmetry paths in the Brillouin zone. This was done by calculating the Hessian matrices for $5 \times 5 \times 5$ supercells using density functional perturbation theory (DFPT) [79] as implemented in VASP, with post-processing conducted via the PHONOPY [80] software. Compounds are deemed dynamically stable if all phonon frequencies are real, which implies that all atoms occupy positions corresponding to local energy minima. Should this condition hold, the next question is whether they are stable with respect to decomposition into competing phases, i.e., does the compound represent the energetic ground state. Here, we calculate the formation energy per atom of each binary carbide with respect to its constituent elemental ground states using the following equation:

$$\Delta E_F = \frac{E_{MC} - E_M - E_C}{2} \tag{2}$$

Accordingly, compounds with $\Delta E_F < 0$ are energetically preferable to the competing elemental phases, whereas compounds with $\Delta E_F > 0$ are energetically unstable. However, we note that such compounds may still be metastable assuming kinetic barriers are significant. The ground state structures of metal and carbon were used from Ref. [81].

To study the mechanical properties of the TMCs, we used the calculated elastic constants to obtain the bulk modulus (B), Cauchy pressure (P_c), shear modulus under the Voigt (G_V) and Reuss approximations (G_R) as well as Hill's arithmetic mean (G), Pugh's ratio (κ), Poisson's ratio (ν), and Young's modulus (Y) using the following equations:

$$B = (C_{11} + 2C_{12})/3 \tag{3}$$

$$P_c = C_{12} - C_{44} \tag{4}$$

$$G_V = [(C_{11} - C_{12}) + 3C_{44}]/5 \tag{5}$$

$$G_R = [5(C_{11} - C_{12})C_{44}]/(4C_{44} + 3C_{11} - 3C_{12}) \tag{6}$$

$$G = (G_V + G_R)/2 \tag{7}$$

Approved for public release; distribution unlimited.
794

$$\kappa = G/B \tag{8}$$

$$\nu = (3 - 2\kappa)/[2(3 + \kappa)] \tag{9}$$

$$Y = 9G/(3 + \kappa) \tag{10}$$

The Vickers hardness (H_V) was calculated using the following relation by Tian et al. [82]:

$$H_V = 0.92\kappa^{1.137}G^{0.708} \tag{11}$$

The Debye temperature (θ_D) was also calculated via the following relations:

$$\theta_D = \frac{h}{k_B}\left[\frac{3n}{4\pi}\left(\frac{N_A}{M}\rho\right)\right]^{\frac{1}{3}} v_m \tag{12}$$

$$v_m = \left[\frac{2}{3}\left(\frac{2}{v_t^3} + \frac{1}{v_l^3}\right)\right]^{\frac{-1}{3}},$$

$$v_t = \left(\frac{G}{\rho}\right)^{\frac{1}{2}}, \quad v_l = \left(\frac{3B + 4G}{3\rho}\right)^{\frac{1}{2}} \tag{13}$$

where h is Planck's constant, k_B is Boltzmann's constant, N_A is Avogadro's number, ρ is the mass density, M is the molecular weight of the primitive cell, and n is the number of atoms in the cell for which M is calculated. v_t, v_l, and v_m are the transverse, longitudinal, and mean speeds of sound respectively.

To relate the macroscopic properties of TMCs to their underlying electronic structure, we calculated the density of states for each compound using the tetrahedron method with Blochl corrections [83]. Densities were further separated into elemental and orbital components to highlight the effects of the ligand field present in each structure. The ionic characters of individual bonds were revealed using metal-to-carbon charge transfer calculated within Bader's division scheme [84–86], which partitions real space to quantitatively attribute charge to each atom. On the other hand, covalent interactions were studied using Crystal Orbital Hamiltonian Populations (COHP) calculations performed with the LOBSTER package [87–91], which separates electronic occupancies into bonding and antibonding states.

3. Results and discussion

3.1. Structure and stability

The calculated volumes (per formula unit) of the 3d transitional metal carbides (TMCs) in the ZB, RS, and CsCl structures are listed in Table 1, showing excellent agreement with previously reported [92–94] data where available. Analyzing trends in volume with respect to structure, we observe an inverse correlation between the volume and the coordination number of the underlying atomic arrangement. Namely, $V_{ZB} > V_{RS} > V_{CsCl}$ owing to their respective coordination numbers of four, six, and eight. As for the effect of chemistry, there exists a nearly parabolic relationship between the volume and group number in all structures. This trend is directly related to the size of the metal element, which decreases from the early to intermediate TMs, then increases from intermediate to late TMs. As displayed in Fig. S1 of the Supplementary Material, subtle deviations from the parabolic relationship can be attributed to variations in the degree of bonding covalency versus ionicity [95]. Those elements with a large number of unpaired d electrons (e.g., Mn and Fe) tend to exhibit bond lengths representative of their covalent radii [95], whereas those with fewer unpaired electrons more clearly adopt highly ionic bonds.

Calculated lattice parameters and elastic constants are listed in Table S1 and S2 of the Supplemental Material respectively, and are in good agreement with available experimental [96–99] and calculated [100] values. The calculated elastic constants are used to determine whether each compound is mechanically stable, i.e., if they satisfy the Born criteria [77,78] and are therefore able to withstand strain without undergoing a phase transformation. We find twenty total compounds to be mechanically stable; these include eight ZB, ten RS, and two CsCl structures. Interestingly, there appears to be a clear difference in the origin of mechanical instability in the ZB and CsCl configurations – the former exhibits a lower value of C_{11} than C_{12}, whereas the latter exhibits a negative value of C_{44}. This suggests that the ZB structures are prone to instabilities arising from normal (uniaxial) strain, whereas CsCl structures are more likely to transform via shear strain. This agrees with expectations based on the connectivity of each structure - the ZB arrangement favors strong directional and shear-resistant bonding but is less robust against uniaxial compression owing to its low atomic density. In contrast, the CsCl structure is amenable to isotropic bonding, which is much more susceptible to shearing instabilities, while its high density is more resistant to normal strain. An intermediate situation is found in RS, which is commonly adopted by compounds formed via strong covalent (directional) and ionic (isotropic) bonding, including titanium carbides and nitrides which are known to be exceptionally resistant to deformation. As a result of these hybrid bonding characteristics, all ten 3d TMCs are mechanically stable in the RS structure.

To further investigate stability, we calculated the phonon dispersion curves of all 3d TMCs. As summarized in Table 1, we identify seven compounds as dynamically stable in the ZB structure, five in the RS structure, and zero in the CsCl structure. The presence of imaginary frequencies, as shown in Fig. S2 of the Supplementary Material, shows the dynamical instability of all the carbides in CsCl structure. The persistent instability of TMCs in the densely packed CsCl structure arises from its 8-fold coordination, which is deleterious to covalently bound systems such as the carbides studied here. The CsCl structure, with an 8-fold coordination, is commonly adopted by ionic systems as it maximizes (minimizes) the electrostatic attraction (distance) between cations and anions with a radius mismatch ratio near 0.64, according to Pauling's rules. In addition, an 8-fold coordination with square antiprismatic geometry would require sp^3d^4 hybridization, which is rare owing to its high energy cost [101,102]. Indeed, previous works have demonstrated that TMCs may adopt the CsCl structure only at exceptionally high pressures, coupled with a transition to metallic bonding [103,104]. As we aim to focus only on materials which may be useful under ambient conditions, we exclude the CsCl structure from consideration for the remainder of this work. With respect to the RS and ZB structures, our calculations confirm the stability of the previously reported TMCs based on the early transition metals (e.g., ScC, TiC, VC, and CrC) [100]. Purely predictive findings are proposed for the intermediate and late TMCs.

To uncover the origin of instability throughout intermediate TMCs in the RS and ZB structures, we identify any regions of the Brillouin zone in which phonon modes exhibit imaginary frequencies. Intermediate TMCs in the RS structure are found to exhibit instabilities surrounding the L point, with $\vec{k} = \frac{2\pi}{a}(0.5, 0.5, 0.5)$. As illustrated for MnC in Fig. 1, the associated phonon mode yields an off-center displacement of the central transition metal atom toward an edge of the octahedral complex, therefore shortening the 2nd nearest-neighbor metal-metal bond. Specifically, the energy of the system is minimized when the separation between adjacent metal atoms is equal to 2.605 Å, reflecting the formation of Mn^{4+} dimers [105]. From an orbital occupation perspective, this effect can be related to the nominal d^1 configuration which Mn adopts owing to the tetravalent state of the carbides. Each metal ion contributes one electron to the metal-metal bond, therefore forming an energetically

Approved for public release; distribution unlimited.
795

Table 1
Calculated volumes (V), normalized per formula unit (f.u.), for all 3d transition metal carbides (TMCs) in the zincblende, rocksalt, and cesium chloride structures. Previously computed data, where available, are given for comparison. The mechanical and dynamical stability of each compound are also presented. "MS/MU" correspond to the mechanically stable/unstable according to the Born criteria and "DS/DU" correspond to the dynamically stable/unstable as indicated by fully real-valued phonon mode frequencies.

Compound	Zincblende		Rocksalt		Cesium chloride	
	V (Å^3/f.u.)	Stability	V (Å^3/f.u.)	Stability	V (Å^3/f.u.)	Stability
ScC	32.78	MU, DU	25.71 25.72[T,a]	MS, DS	23.81	MU, DU
TiC	26.50	MS, DS	20.40 20.37[T,a]	MS, DS	19.97	MU, DU
VC	23.04	MS, DS	18.08 18.03[T,a]	MS, DS	17.51	MU, DU
CrC	21.14	MS, DS	16.91 16.96[T,b]	MS, DS	16.12	MS, DU
MnC	20.06	MS, DS	16.31	MS, DU	15.33	MS, DU
FeC	19.27	MS, DS	15.95	MS, DU	15.00	MU, DU
CoC	19.50	MS, DS	16.14	MS, DU	15.48	MU, DU
NiC	20.60	MS, DU	16.82[T,a] 16.95	MS, DU	16.35	MU, DU
CuC	22.72	MU, DU	18.95	MS, DU	18.44	MU, DU
ZnC	25.72	MS, DS	21.31	MS, DS	21.06	MU, DU

[a] Ref. [92].
[b] Ref. [94].
[T] Computed value.

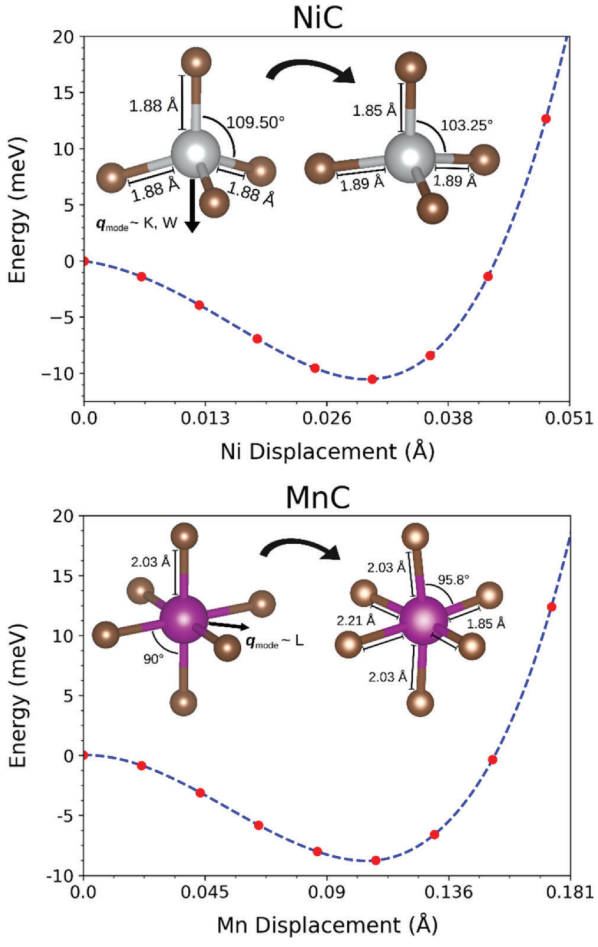


Fig. 1. Illustration of the energy landscapes, modulated along instabilities at high-symmetry points according to phonon dispersion calculations, for NiC (top) and MnC (bottom) in the zincblende and rocksalt structures respectively. Insets show local bonding configurations (tetrahedra and octahedra) before and after application of distortions. For the latter, bond lengths and angles corresponding to a minimum in energy are listed.

preferred singlet state. Based on our calculated maps of the electron localization function (i.e., ELF maps displayed in Fig. S9 of the Supplementary Material), the metal-metal interactions are mostly metallic in nature as electrons are delocalized between adjacent metal atoms with low ELF values (< 0.5) [106]. The effects of metallic dimerization are further illustrated by the projected electronic density of states displayed in Fig. 2. While the early TMCs exhibit complete occupation of the hybridized p-e_g orbitals and little to no occupation of the higher-energy p-t_{2g} orbitals, the latter frontiers display increasing occupation as the electron count is raised throughout the intermediate TMCs, including MnC and NiC. Since the apices of the t_{2g} orbitals lie directly between metal-carbon bonds within the octahedral coordination, they show some degree of overlap between the 2nd-nearest neighbor metal atoms. As a result, the initially non-bonding electrons occupying the t_{2g} orbitals begin to interact with one another, encouraging the formation of metal dimers. Moreover, the distortions associated with dimerization face only weak resistance from the exceedingly weak metal-carbon bonds found in the intermediate TMCs, as will be discussed in Section 3.2. These combined effects of increased metal-metal interactions and decreased metal-carbon strengths yield the dynamic instabilities found in the RS configurations of MnC, FeC, CoC, NiC, and CuC.

For compounds adopting the ZB structure, the origin of instability can be divided into two major categories: those occurring in ScC, an early TMC, and those occurring in the intermediate-to-late TMCs of Ni and Cu. The former case of ScC is characterized solely by elastic instabilities, as demonstrated by the aforementioned low value of C_{11} and equivalently the soft acoustic phonons surrounding the Γ zone-center shown in Fig. S3 of the Supplementary Material. In addition to the effects of connectivity and density discussed earlier in this Section, the instability of ScC can also be attributed to its unsaturated metal-carbon bonds, given that Sc may only contribute three valence electrons per atom. In contrast to the CsCl and RS structures, wherein respective metallic and ionic interactions may play a significant role, the ZB configuration relies heavily on covalent bonding. These bonds are insufficiently supported by the partially occupied orbitals in ScC, and therefore its structure is unstable with respect to cell distortions. In contrast, there is an excess of valence electrons available to participate in covalent bonding for both NiC and CuC, with nominal configurations of d^6 and d^7 respectively. Further distinguishing from ScC, these intermediate TMCs are prone to dynamic instabilities associated with imaginary phonon

Approved for public release; distribution unlimited.
796

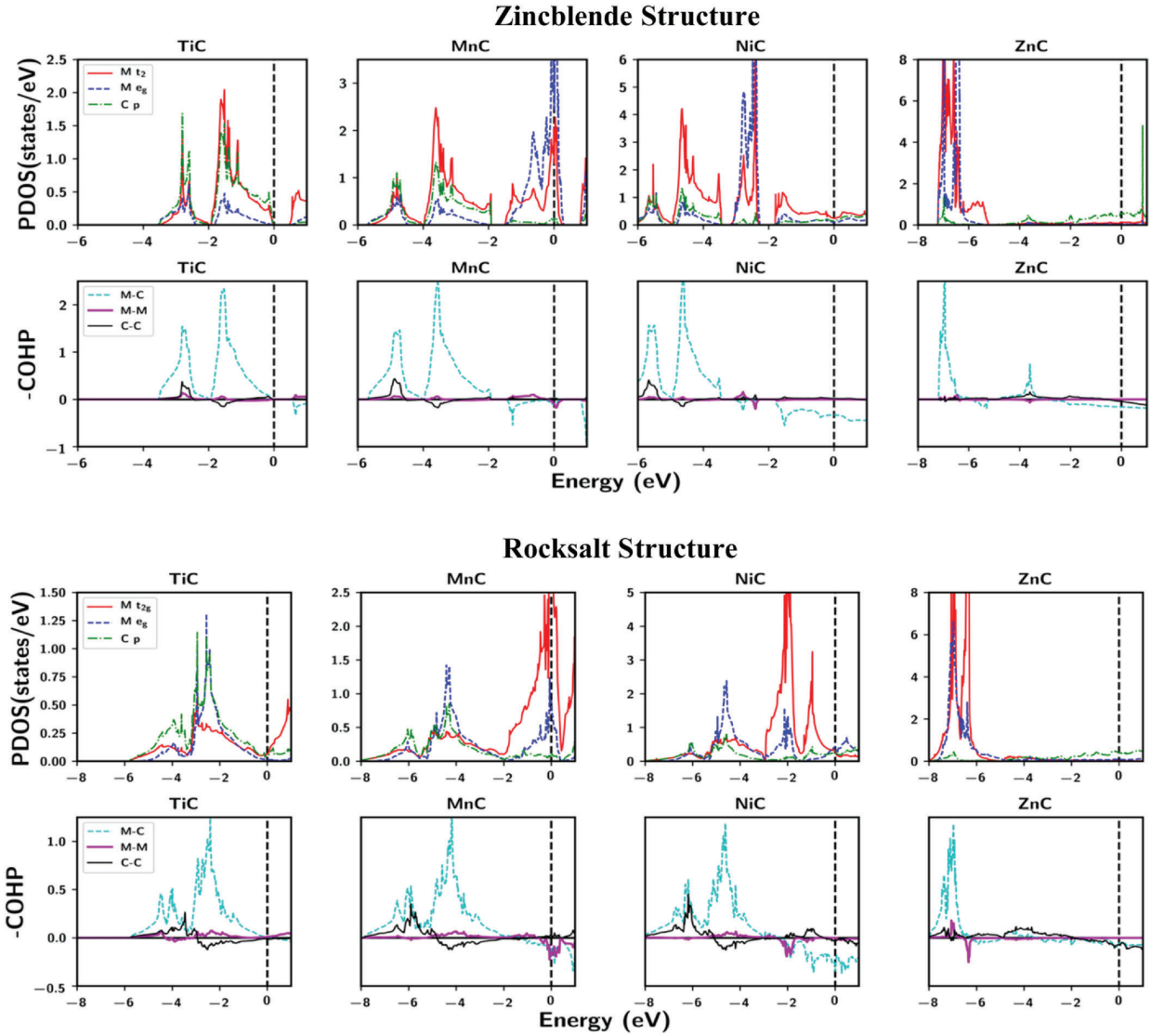


Fig. 2. Projected density of states (PDOS) and Crystal Orbital Hamiltonian Populations (COHP) of four unique TMCs spanning the 3d row. Compounds considered in the zincblende and rocksalt [113] structures are presented in the top and bottom panels respectively. For the PDOS, 3d densities are separated into t_{2g} and e_g components to illustrate the effects of crystal field splitting. In the COHP curves, covalent interactions among metal-carbon (M–C), metal-metal (M–M), and carbon-carbon (C–C) bonding pairs are shown. Positive and negative values of COHP represent bonding and antibonding respectively. For all plots, the Fermi energy is set to 0 eV.

frequencies surrounding the K and W points of the Brillouin zone, with coordinates of $\vec{k} = \frac{2\pi}{a}(0.75, 0.75, 0.0)$ and $\vec{k} = \frac{2\pi}{a}(0.5, 1.0, 0.0)$ respectively. By following the corresponding atomic displacements, we identify an off-center displacement of the central metal atom parallel and away from the direction of one of the coordinated carbon atoms, essentially flattening the tetrahedral complex. This effect, illustrated for NiC in Fig. 1, leads to a decrease in energy of 10 meV when the nickel atom is displaced by about 0.03 Å. The distortions found in NiC and CuC are suggestive of a Jahn-Teller instability [57–59]. In the tetrahedral ligand field of the ZB structure, the 3d orbitals are split into two low-energy *e* orbitals and three high-energy t_2 orbitals. When t_2 orbitals become sufficiently occupied, as in the d^6 configuration of NiC, there are three degenerate electron configurations possible. By Jahn-Teller distorting (i.e., by displacing the central atom and lowering the symmetry of the tetrahedral ligand field), a lower-energy configuration is adopted. This is further supported by the projected electron density of states, shown for NiC in Fig. 2, which display partially occupied, non-bonding t_2 orbitals near the Fermi level. These states are initially degenerate and high-energy in the ideal tetrahedral coordination. However, as the orbitals are only partially filled by the d^6 configuration of NiC, the total energy of the system can be decreased via the aforementioned displacement of the central metal atom, which serves to enhance hybridization between the t_2 and p orbitals of the three nearest carbon atoms. Accordingly, both NiC and CuC are unstable in the ZB structure, whereas earlier TMCs may retain their ideal tetrahedral geometries owing to their decreased electron count serving to mitigate the incentive for Jahn-Teller [59,107] distortions.

Lastly, we study the thermodynamic stability of the TMCs in each structure by calculating the formation energy with respect to the constituent elements in their ground states, with results displayed in Fig. 3. Agreeing with their previously discussed dynamic instability in the earlier paragraph, all compounds adopting the CsCl structure

Approved for public release; distribution unlimited.
797

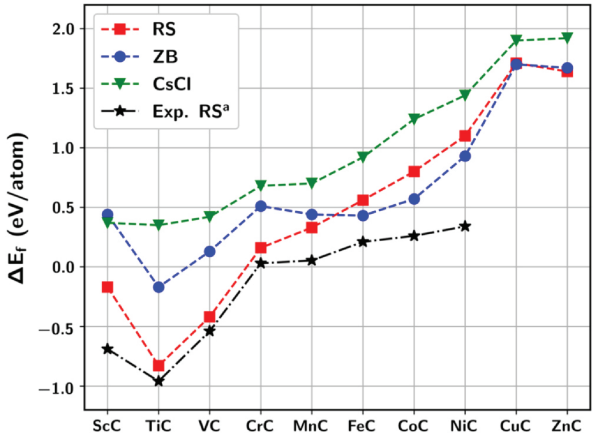


Fig. 3. Calculated formation energies of all 3d transition metal carbides in the rocksalt structure (RS), zincblende structure (ZB), and cesium chloride structures (CsCl). Symbols represent calculated values, whereas the lines represent interpolations plotted to highlight general trends. (a): Experimental formation energies are from Ref. [40].

are highly unstable with respect to decomposition, as signified by large, positive formation energies. In contrast, compounds in the RS and ZB structures generally exhibit much lower formation energies than those in the CsCl structure. Between these two configurations, RS is preferred for earlier TMCs owing to the substantial ionic character of their bonds, whereas ZB becomes energetically favorable for intermediate to late TMCs for which covalent interactions play a greater role. We emphasize that the vast majority of TMCs, regardless of structure, are thermodynamically unstable – agreeing with previous reports in the literature suggesting the difficulty to synthesize a variety of crystalline, stoichiometric carbides containing elements beyond Ti and Cr [40,46]. Indeed, the calculated stability and experimental synthesizability of TMCs are both restricted to the early transition metals. ScC, TiC, and VC are thermodynamically stable and experimentally synthesizable [108–110]. Although CrC is thermodynamically unstable, its formation energy is relatively low, and it can be accessed using low-temperature synthesis techniques [111].

Trends in formation energy across the period can be directly correlated with the effects d orbital filling, which influence the occupation of bonding and anti-bonding states. To more clearly illustrate this effect, we analyze the COHP curves displayed in Fig. 2 wherein positive values (above the y-axis) and negative values (below the y-axis) represent bonding and anti-bonding interactions respectively. First, ScC is shown to contain only partially filled bonding states resulting from the inability of Sc (s^2d^1) to contribute four electrons to its metal-carbon bonds. Despite this shortcoming, its high ionicity yields negative formation energies in the RS and ZB structures. Next, the increase in electron count allows all metal-carbon bonds to saturate as reflected by completely filled bonding states in the COHP curves. For this reason, TiC displays the lowest negative formation energy out of all TMCs studied here. From TiC on to the intermediate and late TMCs, the increasing electron count causes the antibonding states to become partially filled. These unfavorable interactions, mediated by electron repulsion, cause the formation energies to continuously increase moving from left to right across the period.

Subtle deviations from the monotonic trend in formation energy described above are observed in TMCs where magnetic ordering plays a significant role. Both MnC and FeC adopt a ferromagnetic ground state caused by a Stoner instability [112] in which the intra-atomic exchange and electronic occupation at the Fermi level become sufficiently strong such that ferromagnetic ordering is preferred. The ferromagnetic rearrangement of electrons allows the majority-spin M-M bonding states to become fully occupied (fall below the Fermi level), while the minority-spin M-M antibonding states become unoccupied (rise above the Fermi level). This is illustrated by our spin-polarized COHP plots provided in Fig. S8 of the Supplementary Material. A more in-depth analysis of ferromagnetic instabilities in RS TMCs can be found in our previous work [113].

Lastly, ZnC acts independently owing to its filled, nonbonding d shell, resulting in a slightly lower formation energy than the carbides of nearby metals. Because Zn has no unpaired electrons, it is more electropositive than nearby metals – e.g., Zn has an electronegativity of 1.66, whereas Cu has an electronegativity of 1.75 [114]. Therefore, the ionic contribution to the metal-carbon bonding is greater in ZnC than in TMCs with a comparable (lower) atomic number. Despite this difference, ZnC remains highly thermodynamically unstable, with an energy of 1.64 eV/atom above the convex hull formed by Zn and C.

As mentioned previously, we chose to focus on cubic structures as they are suspected to have promising mechanical properties. However, for the sake of completeness in our analysis, we also tested all ten TMCs in the hexagonal (wurtzite) structure, with the corresponding formation energies listed in Table S6 of the Supplementary Material. The results indicate the a hexagonal structure is preferred only for CrC and MnC. However, these still remain unstable with respect to decomposition into elemental ground states. We note that while most of the intermediate and late TMCs are thermodynamically unstable, many of those identified as dynamically stable may still be synthesizable using chimie douce techniques, which are commonly employed to access metastable states.

3.2. Bonding and mechanical properties

To study the mechanical properties, we look to the calculated elastic constants displayed in Fig. 4 and provide an explanation of any trends throughout the TMCs by analyzing their electronic structure. From the elastic constants, derived quantities including bulk moduli, shear moduli, Vicker's hardness, Cauchy's pressure, Poisson's ration and Pugh's ratio are listed in Table S2 of the Supplementary Material, and are in good agreement with available experimental [115,116] and calculated [33] values. The derived quantities such as bulk moduli, shear moduli, and Vicker's hardness are displayed in Fig. 5 to gain insight into directly observable properties. For both the ZB and RS structures, we find that increasing valence electron concentrations leads to higher values of C_{11} and C_{12} throughout many of the stable TMCs. These changes raise the bulk moduli across the intermediate TMCs, with maxima occurring at FeC and CrC in ZB and RS respectively, corresponding to calculated bulk moduli of 252.9 GPa and 326.4 GPa.

The observed correlation between bulk modulus and group number can be attributed to three effects. First, the introduction of additional valence electrons (beyond a configuration of d^0 in TiC) mediates increased filling of the antibonding states. In this respect, the PDOS plots in Fig. 2 illustrate that the Fermi level monotonically increases moving left to right across the periodic table, leading to enhanced occupation of the high-lying t_2 and e_g states in the ZB and RS structures respectively. From the COHP curves, these states are confirmed to be strongly antibonding in nature. Consequently, a higher occupation of the antibonding orbitals ensures that the structures are more resistant to compression given that such deformation will decrease the metal-carbon bond lengths and therefore raise the energy of the antibonding levels [117,118]. The changing occupation of the antibonding orbitals are quantified by integrating COHP curves below the Fermi level, yielding ipCOHP values whereby larger (more positive) values signify enhanced bonding and decreased antibonding. As shown in Table S7 in

Approved for public release; distribution unlimited.
798

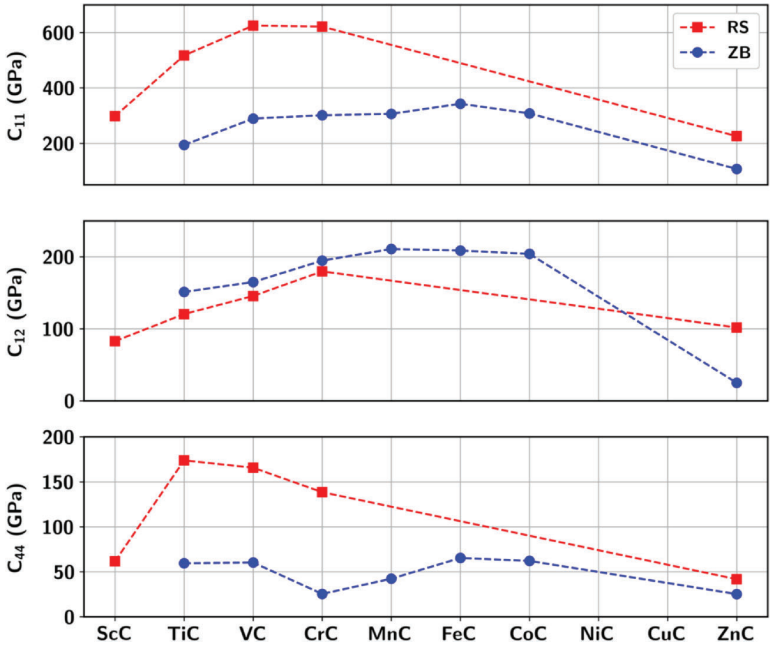


Fig. 4. Independent elastic constants (C_{11}, C_{12}, C_{44}) shown for all the stable/metastable compounds in the rocksalt structure (RS) and zincblende structure (ZB). Symbols represent calculated values, whereas the lines represent interpolations plotted to highlight general trends.

Supplemental Material, a maximum ipCOHP is achieved for TiC in both structures (2.23 eV and 1.55 eV for ZB and RS, respectively), whereas ipCOHP decreases across the later TMCs as the covalent interaction strength weakens. Second, the amount of electronic charge transferred between the metal and the carbon ions varies with the electronegativity of the TM. These changes, quantified by our Bader charge transfer values listed in Table S4 of the Supplemental Material, show that less charge is transferred between the ions in the late TMCs. Those TMCs with lower charge transfer tend to have higher bulk moduli as their attractive electrostatic force is decreased – hence, compression is favored less. Third, intermediate TMCs adopt structures with higher atomic densities owing to their short ionic radii. The increased strength of electrostatic repulsions acting across shorter distances encourages a more robust resistance to compression and therefore higher bulk moduli. In contrast, both electronic and steric effects lead to lower values of C_{11} and C_{12} in the

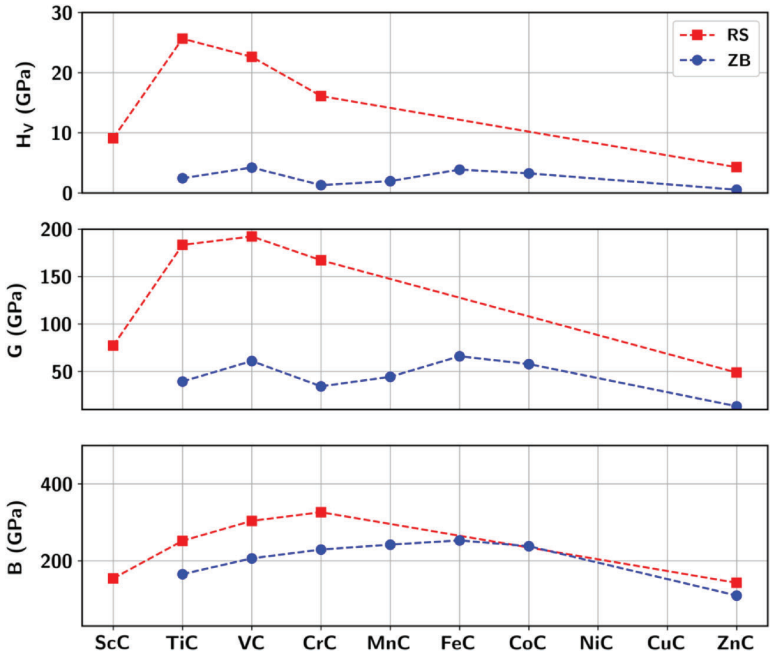


Fig. 5. Correlation of Vickers hardness (H_V), shear modulus (G), and bulk modulus (B) with increasing group number across all stable/metastable 3d TMCs in the rocksalt structure (RS) and zincblende structure (ZB). Symbols represent calculated values, whereas the lines represent interpolations plotted to highlight general trends.

Approved for public release; distribution unlimited.
799

late TMCs. ZnC, for example, has a filled d shell in which many of its valence electrons occupy non-bonding states as confirmed by the COHP curves shown in Fig. 2. The corresponding orbitals respond weakly to compression, thus contributing little to the mechanical properties. Moreover, the atomic density of ZnC is relatively low, further reducing its bulk modulus.

There appears to be a more subtle relationship between C_{44} and group number across the TMCs that correlate quite closely with the calculated formation energies. Initially, C_{44} exhibits a large increase from ScC to TiC owing to a complete filling of the bonding orbitals as shown in the PDOS and COHP curves. For RS-structured compounds beyond TiC, a clear monotonic decrease in C_{44} is observed with increasing group number due to enhanced filling of the antibonding orbitals. Electrons occupying these states favor shearing as it reduces overlap between σ orbitals mediating nearest-neighbor bonds in the RS structure, thereby lowering the energy of the antibonding levels. Moreover, an increased electron count favors shearing as it enhances d orbital overlap between TM neighbors, thereby enabling metal dimer formation as discussed in the previous section. This further contributes to low values of C_{44} in the intermediate-late TMCs. Interestingly, changes in C_{44} are somewhat different for TMCs adopting the ZB structure. In this case, C_{44} displays a minimum for CrC before increasing back to relatively high values across the intermediate TMCs with a maximum at FeC. Then, a return back to low C_{44} is shown for the late TMCs such as ZnC. We propose that magnetic ordering likely plays a large role in lowering the occupation of antibonding states in the intermediate TMCs, as the splitting of majority- and minority-spin states reduces Pauli repulsion between like electrons. Similar trends may indeed be observed throughout compounds in the RS structure. However, most intermediate TMCs are not stable in this structure and therefore cannot be reliably considered.

To further investigate the effect of structure on the resulting mechanical properties, we directly compare the elastic constants calculated for each compound adopting RS and ZB structures. Fig. 4 shows that C_{11} and C_{44} are consistently larger in the RS structure, C_{12} is more dominant in ZB. These differences arise from the underlying bonding configurations of each structure, as the direct σ overlap between metal d and carbon p orbitals in the RS structure ensure is highly resistant to uniaxial compression (C_{11}) and shearing (C_{44}). However, this same configuration is relatively dense and displays weaker resistance to transverse strain (C_{12}). In contrast, direct σ-bonding in the ZB structures requires some energy cost associated with hybridization as the original (atomic) d orbitals do not directly overlap with the carbon p orbitals. Furthermore, the tetrahedral coordination environments comprising the ZB structure are more readily distorted without causing substantial compression or elongation of individual bond lengths. These features lower the observed values of C_{11} and shearing C_{44}. Though, because compounds adopting the ZB structure have larger volumes, they readily accommodate volume dilation associated with higher values of C_{12}.

Differences in atomic interactions can also be illustrated through analysis of the phonon dispersion curves, which are plotted for TiC and ZnC in Fig. 6. Between RS and ZB structures, there are several key distinguishing features. First, the slope of the acoustic branch near the Γ point is higher in the RS structure for the early TMCs (as shown by TiC), which suggests increased hardness and is in good agreement with our calculated elastic constants. In contrast, ZnC has very soft (low-frequency and weakly sloped) acoustic phonon modes near Γ when adopting the RS structure, which reflects weaker metal-carbon bonding due to the filled 3d states as supported by our earlier COHP analysis. On the other hand, increased covalent interactions in the ZB structure stabilize a raised slope in the acoustic branches near Γ for ZnC. Second, while the RS phonon dispersion curves display large anomalies (e.g., deviations in the longitudinal acoustic mode along Γ-X) that indicate strong electron-phonon coupling, in

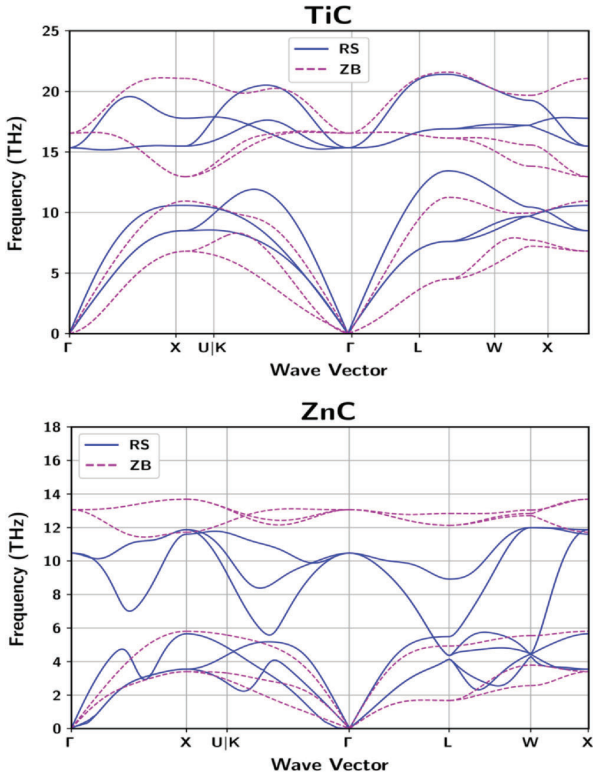


Fig. 6. Phonon dispersion curves for TiC and ZnC, each of which represents extrema in the valence electron concentration of all stable compounds. To illustrate dynamic differences arising from varying structural factors, individual curves are plotted for the rocksalt (RS) and zincblende (ZB) structures.

accordance with previous work [113], the ZB phonon dispersion curves display no noticeable anomalies. This highlights the difference in local interactions between metal d orbitals; electron-phonon coupling in RS is mediated by significant d-d overlap between nearest metal neighbors, whereas the distance between metal atoms in the ZB structure is too large to support any significant coupling via d-d interactions. Hence, unconventional superconductivity is suspected in the RS structure, but not in the ZB structure. Last, the optical frequencies of the ZB structure are shown to be higher than those in the RS structure for TiC and ZnC, possibly due to enhanced C-C interactions [119]. Despite the longer C—C bond lengths in the ZB structure relative to the RS structure, the tetrahedral coordination of the ZB structure is suspected to mediate stronger overlap of the *p* orbitals when compared to the octahedral coordination of the RS structure. This is supported by our calculated ipCOHP values, which show enhanced C-C interaction in the ZB structure (80 meV) relative to the RS structure (30 meV) for TiC. Interestingly, despite the increased mass mismatch between Zn and C (as opposed to Ti and C), significant acoustic/optical overlap is observed in RS-structured ZnC, further signifying the anomalous behavior of that compound due to its filled d shell and strong electron-phonon coupling.

Last, to consider these TMCs as applications in hard coatings, it is of interest to determine their hardness (measured by Vicker's hardness) and ductility. A material is expected to be ductile if its Pugh's ratio is below 0.5–0.6, its Poisson's ratio is above 0.25–0.28, and its Cauchy pressure is greater than zero [120]. Here, we find that TMCs maintain much higher values of Vicker's hardness in the RS structure as opposed to ZB. This difference can be traced back to the lower values of C_{44} found in the ZB structure as discussed in the previous paragraph, which preclude them from being used for high-

Approved for public release; distribution unlimited.
800

Table 2
Calculated Cauchy's pressure (P_c), Poisson's ratio (ν), and Pugh's ratio (κ) of each stable 3d transition metal carbides (TMCs) in the zincblende structure (ZB) and rocksalt structure (RS). Instability is denoted by "U". Since all TMCs are unstable in the cesium chloride structure (CsCl), the corresponding values are not presented here.

TMCs	$P_{c\ (GPa)}$		ν		κ	
	ZB	RS	ZB	RS	ZB	RS
ScC	U	21.4	U	0.29	U	0.50
TiC	91.6	- 53.5	0.39	0.21	0.24	0.73
VC	104.7	- 20.1	0.37	0.24	0.30	0.63
CrC	167.3	41.2	0.43	0.28	0.15	0.51
MnC	168.5	U	0.41	U	0.18	U
FeC	143.4	U	0.38	U	0.26	U
CoC	141.9	U	0.39	U	0.24	U
ZnC	82.1	60.2	0.44	0.35	0.12	0.34

hardness coating applications. As for the RS materials, a maximum hardness of 25.66 GPa is identified in TiC, matching with previous findings [121]. Though, both VC and CrC also display reasonably high hardnesses of 22.63 and 16.11 GPa respectively. Of these compounds, both TiC and VC are predicted to be brittle according to their reported values of Pugh's ratios, Poisson's ratios, and Cauchy pressures in Table 2. For the remaining stable TMCs, their properties instead show ductile behavior. Therefore, although TiC is the hardest material studied here, we propose that CrC may be preferred in applications where toughness is also required.

4. Conclusion

In summary, our work illustrates how valence electron concentration and structure play dominant roles in controlling the stability and mechanical performance of 3d TMCs. Across early TMCs adopting the RS structure, comprising the most widely studied systems, our findings confirm the importance of filled bonding states to enable robust stability and exceptionally high hardness. Furthermore, we build upon existing understanding to provide novel insight into the source of instability of the RS structure throughout the intermediate TMCs, which is shown to correlate with enhanced metal-metal interactions and weakened metal-carbon bonds. With regards to the ZB structure, our calculations reveal several new compounds that are metastable and potentially synthesizable if the thermodynamic ground state can be avoided (e.g., via chimie douce techniques). Although their mechanical properties are not as promising as those displayed by TMCs in the RS structure, they may warrant further investigation considering the possibility of potentially interesting and unexpected electronic properties. Lastly considering the CsCl structure, we predict that all 3d TMCs are unstable under ambient conditions owing to the dense eight-fold coordination that constitutes the local bonding environments in CsCl and that does not accommodate the highly covalent bonding in the carbides. Though, high-pressure studies may be worthwhile to investigate whether stabilization can be obtained through many of the TMCs. If this can be accomplished, there exists a possibility to find new and interesting properties such as unconventional superconductivity previously reported [113] in several RS TMCs.

Based on the findings presented above, we focus on the RS structure and propose several guiding principles for the design of novel TMCs that may be used in next-generation hard coating applications. First, to maximize hardness and stability, a valence electron count of four (e.g., TiC) is critical. In this case, covalent M-C interactions dominate owing to the completely filled bonding orbitals, whereas metallic M-M interactions are minimized because of the d^0 configuration (empty metal orbitals). Second, if ductility rather than hardness is to be optimized, then a valence electron count well beyond four is favorable. In this case, M-M interactions play a larger role as the non-bonding d orbitals become filled, which favor shearing deformations that allow the d orbitals to overlap. However, it is also important to prevent over-filling of the d orbitals so that the structure does not become dynamically unstable with respect to metal dimer formation (e.g., as in MnC). Third, to achieve tough materials with a balance between hardness and ductility, one may consider a valence electron count that is only slightly higher than four. Because an increase beyond four electrons causes enhanced ductility but worsened hardness, we suggest that an optimal tradeoff may be realized through ion substitution – e.g., between TiC and CrC. By forming solid solutions with controllable compositions, the mechanical properties may be fine-tuned by varying Ti-Cr content. Although past works suggest that high temperatures are necessary to form such solutions [122], alternative techniques such as high-energy ball milling or doping (e.g., high-entropy alloys) may be considered in the future.

CRediT authorship contribution statement

Indiras Khatri: Conceptualization (Lead), Formal analysis (Lead), Methodology (Lead), Software (Lead), Writing – original draft (Lead). **Nathan J. Szymanski:** Conceptualization (Equal), Investigating (Equal), Validation (Lead), Writing – review & editing (Equal). **Bishal Babu Dumre:** Methodology (Supporting). **Jacques G. Amar:** Funding acquisition (Lead), Project administration (Lead), Validation (Lead), Writing – review & editing: Supporting). **Daniel Gall:** Validation (Supporting), Writing – review & editing (Supporting). **Sanjay V. Khare:** Conceptualization (Supporting), Funding acquisition (Lead), Project administration (Lead), Writing – review & editing (Supporting).

Declaration of Competing Interest

The authors declare that they have no known competing financial interests or personal relationships that could have appeared to influence the work reported in this paper.

Acknowledgements

This material is based on research sponsored by Air Force Research Laboratory under agreement number FA9453-18-2-0037 and the National Science Foundation Division of Civil, Mechanical, and Manufacturing Innovation through grants 1629239 and 1629230. The U.S. Government is authorized to reproduce and distribute reprints for Governmental purposes notwithstanding any copyright notation thereon. We would also like to acknowledge a grant of computer time from the Ohio Supercomputer Center [123].

Disclaimer

The views and conclusions contained herein are those of the authors and should not be interpreted as necessarily representing the official policies or endorsements, either expressed or implied, of Air Force Research Laboratory or the U.S. Government.

Appendix A. Supporting information

Supplementary data associated with this article can be found in the online version at doi:10.1016/j.jallcom.2021.161866.

References

[1] L.E. Toth, Transition Metal Carbides and Nitrides, Elsevier, 2014.
[2] C. Kral, W. Lengauer, D. Rafaja, P. Ettmayer, Critical review on the elastic properties of transition metal carbides, nitrides and carbonitrides, J. Alloy. Compd. 265 (1998) 215–233.

Approved for public release; distribution unlimited.
801

[3] X. Zhou, D. Gall, S.V. Khare, Mechanical properties and electronic structure of anti-ReO3 structured cubic nitrides, M_3N, of d block transition metals M: an ab initio study, J. Alloy. Compd. 595 (2014) 80–86.
[4] J.G. Chen, J. Eng Jr., S. Kelty, NEXAFS determination of electronic and catalytic properties of transition metal carbides and nitrides: from single crystal surfaces to powder catalysts, Catal. Today 43 (1998) 147–158.
[5] S. Kodambaka, S.V. Khare, W. Swiech, K. Ohmori, I. Petrov, J.E. Greene, Dislocation-driven surface dynamics on solids, Nature 429 (2004) 49–52.
[6] H.H. Hwu, J.G. Chen, Surface chemistry of transition metal carbides, Chem. Rev. 105 (2005) 185–212.
[7] S. Kodambaka, S.V. Khare, V. Petrova, D.D. Johnson, I. Petrov, J.E. Greene, Absolute orientation-dependent anisotropic TiN (111) island step energies and stiffnesses from shape fluctuation analyses, Phys. Rev. B 67 (2003) 035409.
[8] L.I. Johansson, Electronic and structural properties of transition-metal carbide and nitride surfaces, Surf. Sci. Rep. 21 (1995) 177–250.
[9] H. Li, L. Zhang, Q. Zeng, K. Guan, K. Li, H. Ren, S. Liu, L. Cheng, Structural, elastic and electronic properties of transition metal carbides TMC (TM= Ti, Zr, Hf and Ta) from first-principles calculations, Solid State Commun. 151 (2011) 602–606.
[10] K. Zhang, K. Balasubramanian, B.D. Ozsdolay, C.P. Mulligan, S.V. Khare, W.T. Zheng, D. Gall, Growth and mechanical properties of epitaxial NbN (001) films on MgO (001), Surf. Coat. Technol. 288 (2016) 105–114.
[11] J. Häglund, G. Grimvall, T. Jarlborg, A.F. Guillermet, Band structure and cohesive properties of 3d-transition-metal carbides and nitrides with the NaCl-type structure, Phys. Rev. B Condens Matter 43 (1991) 14400–14408.
[12] S. Kodambaka, V. Petrova, S.V. Khare, D. Gall, A. Rockett, I. Petrov, J.E. Greene, Size-dependent detachment-limited decay kinetics of two-dimensional TiN islands on TiN (111), Phys. Rev. Lett. 89 (2002) 176102.
[13] N. Koutná, A. Brenner, D. Holec, P.H. Mayrhofer, High-throughput first-principles search for ceramic superlattices with improved ductility and fracture resistance, Acta Mater. 206 (2021) 116615.
[14] K. Balasubramanian, S.V. Khare, D. Gall, Energetics of point defects in rocksalt structure transition metal nitrides: thermodynamic reasons for deviations from stoichiometry, Acta Mater. 159 (2018) 77–88.
[15] F. Benesovsky, R. Kieffer, P. Ettmayer, Nitrides, Encycl. Chem. Technol. 15 (1981) 871–881.
[16] R. Levy, M. Boudart, Platinum-like behavior of tungsten carbide in surface catalysis, Science 181 (1973) 547–549.
[17] S.T. Oyama, Preparation and catalytic properties of transition metal carbides and nitrides, Catal. Today 15 (1992) 179–200.
[18] S.T. Oyama, Introduction to the Chemistry of Transition Metal Carbides and Nitrides, in the Chemistry of Transition Metal Carbides and Nitrides, Springer, 1996, pp. 1–27.
[19] J.A. Warner, S. Patil, S.V. Khare, K.C. Masiulaniec, Ab initio calculations for properties of MAX phases Ti_2TlC, Zr_2TlC, and Hf_2TlC, Appl. Phys. Lett. 88 (2006) 101911.
[20] S.K.R. Patil, N.S. Mangale, S.V. Khare, S. Marsillac, Super hard cubic phases of period VI transition metal nitrides: First principles investigation, Thin Solid Films 517 (2008) 824–827.
[21] L.L. Wang, S.V. Khare, V. Chirita, D.D. Johnson, A.A. Rockett, A.I. Frenkel, N.H. Mack, R.G. Nuzzo, Origin of bulklike structure and bond length disorder of Pt_{37} and Pt_6Ru_{31} clusters on carbon: Comparison of theory and experiment, J. Am. Chem. Soc. 128 (2006) 131–142.
[22] B.D. Ozsdolay, C.P. Mulligan, K. Balasubramanian, L. Huang, S.V. Khare, D. Gall, Cubic β-WNx layers: growth and properties vs N-to-W ratio, Surf. Coat. Technol. 304 (2016) 98–107.
[23] S.V. Khare, T. Einstein, Energetics of steps and kinks on Ag and Pt using equivalent crystal theory (ECT), Surf. Sci. 314 (1994) L857–L865.
[24] J. Musil, Hard and superhard nanocomposite coatings, Surf. Coat. Technol. 125 (2000) 322–330.
[25] M. Yasuoka, P. Wang, R. Murakami, Comparison of the mechanical performance of cutting tools coated by either a TiC_xN_{1-x} single-layer or a $TiC/TiC_{0.5}N_{0.5}/TiN$ multilayer using the hollow cathode discharge ion plating method, Surf. Coat. Technol. 206 (2012) 2168–2172.
[26] Y. Zhong, X. Xia, F. Shi, J. Zhan, J. Tu, H.J. Fan, Transition metal carbides and nitrides in energy storage and conversion, Adv. Sci. 3 (2016) 1500286.
[27] B. Anasori, M.R. Lukatskaya, Y. Gogotsi, 2D metal carbides and nitrides (MXenes) for energy storage, Nat. Rev. Mater. 2 (2017) 1–17.
[28] M. Nagai, T. Kurakami, Reverse water gas shift reaction over molybdenum carbide, J. Chem. Eng. Jpn. 38 (2005) 807–812.
[29] R. Zhan, X. Luo, Topologically nontrivial phases in superconducting transition metal carbides, J. Appl. Phys. 125 (2019) 053903.
[30] A.F. Guillermet, J. Häglund, G. Grimvall, Cohesive properties of 4d-transition-metal carbides and nitrides in the NaCl-type structure, Phys. Rev. B 45 (1992) 11557–11567.
[31] K. Balasubramanian, S.V. Khare, D. Gall, Valence electron concentration as an indicator for mechanical properties in rocksalt structure nitrides, carbides and carbonitrides, Acta Mater. 152 (2018) 175–185.
[32] Z.T. Liu, X. Zhou, S.V. Khare, D. Gall, Structural, mechanical and electronic properties of 3d transition metal nitrides in cubic zincblende, rocksalt and cesium chloride structures: a first-principles investigation, J. Phys. Condens. Matter 26 (2014) 025404.
[33] L. Wu, T. Yao, Y. Wang, J. Zhang, F. Xiao, B. Liao, Understanding the mechanical properties of vanadium carbides: nano-indentation measurement and first-principles calculations, J. Alloy. Compd. 548 (2013) 60–64.
[34] D.D. Koelling, G.O. Arbman, Use of energy derivative of the radial solution in an augmented plane wave method: application to copper, J. Phys. F: Met. Phys. 5 (1975) 2041–2054.
[35] A.F. Guillermet, G. Grimvall, Cohesive properties and vibrational entropy of 3d transition-metal compounds: MX (NaCl) compounds (X= C, N, O, S), complex carbides, and nitrides, Phys. Rev. B Condens Matter 40 (1989) 10582–10593.
[36] J.E. Krzanowski, R.E. Leuchtner, Chemical, mechanical, and tribological properties of pulsed-laser-deposited titanium carbide and vanadium carbide, J. Am. Ceram. Soc. 80 (1997) 1277–1280.
[37] R. Ahuja, O. Eriksson, J.M. Wills, B. Johansson, Structural, elastic, and high-pressure properties of cubic TiC, TiN, and TiO, Phys. Rev. B Condens. Matter 53 (1996) 3072–3079.
[38] S.H. Cai, C.W. Liu, Studies on the band structures of some layered transition metal dichalcogenides, J. Mol. Struct. (Theochem.) 362 (1996) 379–385.
[39] J.L. Calais, Band structure of transition metal compounds, Adv. Phys. 26 (1977) 847–885.
[40] J. Häglund, A. Fernández Guillermet, G. Grimvall, M. Körling, Theory of bonding in transition-metal carbides and nitrides, Phys. Rev. B Condens. Matter 48 (1993) 11685–11691.
[41] A. Neckel, Recent investigations on the electronic structure of the fourth and fifth group transition metal monocarbides, mononitrides, and monoxides, Int. J. Quantum Chem. 23 (1983) 1317–1353.
[42] D.J. Singh, B.M. Klein, Electronic structure, lattice stability, and superconductivity of CrC, Phys. Rev. B Condens. Matter 46 (1992) 14969–14974.
[43] L. Benco, Metal-to-metal bonding in transition metal monocarbides and mononitrides, J. Solid State Chem. 128 (1997) 121–129.
[44] K.K. Korir, G.O. Amolo, N.W. Makau, D.P. Joubert, First-principle calculations of the bulk properties of 4d transition metal carbides and nitrides in the rocksalt, zincblende and wurtzite structures, Diam. Relat. Mater. 20 (2011) 157–164.
[45] C. Paduani, Electronic structure and Fermi surfaces of transition metal carbides with rocksalt structure, J. Phys.: Condens. Matter 20 (2008) 225014.
[46] M.G. Quesne, A. Roldan, N.H. de Leeuw, C. Catlow, Bulk and surface properties of metal carbides: implications for catalysis, Phys. Chem. Chem. Phys. 20 (2018) 6905–6916.
[47] Y. Zhang, J. Li, L. Zhou, S. Xiang, A theoretical study on the chemical bonding of 3d-transition-metal carbides, Solid State Commun. 121 (2002) 411–416.
[48] A. Vojvodic, C. Ruberto, Trends in bulk electron-structural features of rocksalt early transition-metal carbides, J. Phys. Condens. Matter 22 (2010) 375501.
[49] J. Maibam, B. Indrajit Sharma, R. Bhattacharjee, R.K. Thapa, R.K. Brojen Singh, Electronic structure and elastic properties of scandium carbide and yttrium carbide: a first principles study, Phys. B: Condens. Matter 406 (2011) 4041–4045.
[50] A.F. Guillermet, J. Häglund, G. Grimvall, Cohesive properties and electronic structure of 5d-transition-metal carbides and nitrides in the NaCl structure, Phys. Rev. B Condens. Matter 48 (1993) 11673–11684.
[51] J.C. Grossman, A. Mizel, M. Côté, M.L. Cohen, S.G. Louie, Transition metals and their carbides and nitrides: trends in electronic and structural properties, Phys. Rev. B 60 (1999) 6343–6347.
[52] Y.H. Zhao, H.Y. Su, K. Sun, J. Liu, W.X. Li, Structural and electronic properties of cobalt carbide Co_2C and its surface stability: density functional theory study, Surf. Sci. 606 (2012) 598–604.
[53] F. Viñes, C. Sousa, P. Liu, J.A. Rodriguez, F. Illas, A systematic density functional theory study of the electronic structure of bulk and (001) surface of transition-metals carbides, J. Chem. Phys. 122 (2005) 174709.
[54] Y. Yang, H. Lu, C. Yu, J.M. Chen, First-principles calculations of mechanical properties of TiC and TiN, J. Alloy. Compd. 485 (2009) 542–547.
[55] M. Fukuichi, First-Principles Calculations on the Origin of Mechanical Properties and Electronic Structures of 3d, 4d, and 5d Transitional Metal Monocarbides, Department of Physics, Osaka University, 2019. ⟨https://doi.org/10.18910/72647⟩.
[56] S.F. Pugh, Relations between the elastic moduli and the plastic properties of polycrystalline pure metals, Philos. Mag. (1954) 823–843.
[57] C.E. Housecroft, A.G. Sharpe, Chapter 22: d-block metal chemistry: the first row elements, Inorganic Chemistry, 716, 2008.
[58] M.A. Halcrow, Jahn–Teller distortions in transition metal compounds, and their importance in functional molecular and inorganic materials, Chem. Soc. Rev. (2013) 1784–1795.
[59] D. Reinen, M. Atanasov, G. Nikolov, F. Steffens, Localand cooperative Jahn-Teller distortions of nickel (2+) and copper (2+) intetrahedral coordination, Inorg. Chem. (1988) 1678–1686.
[60] G. Kresse, Ab initiomolecular-dynamics simulation of the liquid-metal–amorphous-semiconductor transition in germanium, Phys. Rev. B 49 (1994) 14251–14269.
[61] G. Kresse, J. Furthmüller, Efficiency of ab-initio total energy calculations for metals and semiconductors using a plane-wave basis set, Comput. Mater. Sci. 6 (1996) 15–50.
[62] G. Kresse, J. Hafner, Ab initio molecular dynamics for liquid metals, Phys. Rev. B Condens. Matter 47 (1993) 558–561.
[63] G. Kresse, J. Furthmüller, Efficient iterative schemes for ab initio total-energy calculations using a plane-wave basis set, Phys. Rev. B Condens. Matter 54 (1996) 11169–11186.
[64] P.E. Blöchl, Projector augmented-wave method, Phys. Rev. B Condens. Matter 50 (1994) 17953–17979.
[65] J.P. Perdew, K. Burke, M. Ernzerhof, Generalized gradient approximation made simple, Phys. Rev. Lett. 77 (1996) 3865–3868.

Approved for public release; distribution unlimited.

802

[66] H.J. Monkhorst, J.D. Pack, Special points for Brillouin-zone integrations, Phys. Rev. B 13 (1976) 5188–5192.
[67] J.D. Pack, H.J. Monkhorst, Special points for Brillouin-zone integrations—a reply, Phys. Rev. B 16 (1977) 1748–1749.
[68] B.B. Dumre, N.J. Szymanski, V. Adhikari, I. Khatri, D. Gall, S.V. Khare, Improved optoelectronic properties in $CdSe_xTe_{1-x}$ through controlled composition and short-range order, Sol. Energy 194 (2019) 742–750.
[69] B.B. Dumre, D. Gall, S.V. Khare, Stability, and electronic and optical properties of ternary nitride phases of $MgSnN_2$: a first-principles study, J. Phys. Chem. Solids 153 (2021) 110011.
[70] I. Efthimiopoulos, I. Khatri, Z. Liu, S.V. Khare, P. Sarin, V. Tsurkan, A. Loidl, D. Zhang, Y. Wang, Universal link of magnetic exchange and structural behavior under pressure in chromium spinels, Phys. Rev. B 97 (2018) 184435.
[71] I. Efthimiopoulos, Z. Liu, M. Kucway, S.V. Khare, P. Sarin, V. Tsurkan, A. Loidl, Y. Wang, Pressure-induced phase transitions in the $CdCr_2Se_4$ spinel, Phys. Rev. B 94 (2016) 174106.
[72] H. Fu, D. Li, F. Peng, T. Gao, X. Cheng, Ab initio calculations of elastic constants and thermodynamic properties of NiAl under high pressures, Comput. Mater. Sci. 44 (2008) 774–778.
[73] F. Murnaghan, The compressibility of media under extreme pressures, Proc. Natl. Acad. Sci. USA 30 (1944) 244–247.
[74] N.J. Szymanski, Z. Liu, T. Alderson, N.J. Podraza, P. Sarin, S.V. Khare, Electronic and optical properties of vanadium oxides from first principles, Comput. Mater. Sci. 146 (2018) 310–318.
[75] Z.T. Liu, B.P. Burton, S.V. Khare, D. Gall, First-principles phase diagram calculations for the rocksalt-structure quasibinary systems TiN–ZrN, TiN–HfN and ZrN–HfN, J. Phys. Condens. Matter 29 (2017) 035401.
[76] V. Adhikari, Z. Liu, N.J. Szymanski, I. Khatri, D. Gall, P. Sarin, S.V. Khare, First-principles study of mechanical and magnetic properties of transition metal (M) nitrides in the cubic M_4N structure, J. Phys. Chem. Solids 120 (2018) 197–206.
[77] F. Mouhat, F.X. Coudert, Necessary and sufficient elastic stability conditions in various crystal systems, Phys. Rev. B 90 (2014) 224104.
[78] J.F. Nye, Physical Properties of Crystals: Their Representation by Tensors and Matrices, Oxford University Press, 1985.
[79] G. Kresse, D. Joubert, From ultrasoft pseudopotentials to the projector augmented-wave method, Phys. Rev. B 59 (1999) 1758–1775.
[80] A. Togo, I. Tanaka, First principles phonon calculations in materials science, Scr. Mater. 108 (2015) 1–5.
[81] L. Ward, A. Dunn, A. Faghaninia, N. Zimmermann, S. Bajaj, Q. Wang, J. Montoya, J. Chen, K. Bystrom, M. Dylla, K. Chard, M. Asta, K.A. Persson, G.J. Snyder, I. Foster, A. Jain, Matminer: an open source toolkit for materials data mining, Comput. Mater. Sci. 152 (2018) 60–69.
[82] Y. Tian, B. Xu, Z. Zhao, Microscopic theory of hardness and design of novel superhard crystals, Int. J. Refract. Hard Met. 33 (2012) 93–106.
[83] P.E. Blöchl, O. Jepsen, O.K. Andersen, Improved tetrahedron method for Brillouin-zone integrations, Phys. Rev. B Condens. Matter 49 (1994) 16223–16233.
[84] F.W. Biegler-könig, R.F.W. Bader, T.H. Tang, Calculation of the average properties of atoms in molecules. II, J. Comput. Chem. 3 (1982) 317–328.
[85] G. Henkelman, A. Arnaldsson, H. Jónsson, A fast and robust algorithm for Bader decomposition of charge density, Comput. Mater. Sci. 36 (2006) 354–360.
[86] E. Sanville, S.D. Kenny, R. Smith, G. Henkelman, Improved grid-based algorithm for Bader charge allocation, J. Comput. Chem. 28 (2007) 899–908.
[87] V.L. Deringer, A.L. Tchougréeff, R. Dronskowski, Crystal orbital Hamilton population (COHP) analysis as projected from plane-wave basis sets, J. Phys. Chem. A 115 (2011) 5461–5466.
[88] R. Dronskowski, P.E. Blöchl, Crystal orbital Hamilton populations (COHP): energy-resolved visualization of chemical bonding in solids based on density-functional calculations, J. Phys. Chem. 97 (1993) 8617–8624.
[89] S. Maintz, V.L. Deringer, A.L. Tchougréeff, R. Dronskowski, Analytic projection from plane-wave and PAW wavefunctions and application to chemical-bonding analysis in solids, J. Comput. Chem. 34 (2013) 2557–2567.
[90] S. Maintz, V.L. Deringer, A.L. Tchougréeff, R. Dronskowski, LOBSTER: a tool to extract chemical bonding from plane-wave based DFT, J. Comput. Chem. 37 (2016) 1030–1035.
[91] S. Maintz, M. Esser, R. Dronskowski, Efficient rotation of local basis functions using real spherical harmonics, Acta Phys. Pol. B 47 (2016) 1165.
[92] A. Jain, S.P. Ong, G. Hautier, W. Chen, W.D. Richards, S. Dacek, S. Cholia, D. Gunter, D. Skinner, G. Ceder, K.A. Persson, Commentary: the materials project: a materials genome approach to accelerating materials innovation, APL Mater. 1 (2013) 011002.
[93] M. Kavitha, R. Rajeswarapalanichmy, K. lyakutti, First principles study of structural, electronic superconducting and mechanical properties of titanium carbide, IJSER 5 (2014) 169–172.
[94] H.M. Tütüncü, S. Bağcı, G.P. Srivastava, A. Akbulut, Electrons, phonons and superconductivity in rocksalt and tungsten–carbide phases of CrC, J. Phys. Condens Matter 24 (2012) 455704.
[95] R.D. Shannon, D.B. Rogers, C.T. Prewitt, J.L. Gillson, Chemistry of noble metal oxides. III. Electrical transport properties and crystal chemistry of ABO_2 compounds with the delafossite structure, Inorg. Chem. 10 (1971) 723–727.
[96] R.W.G. Wyckoff, Cryst. Struct. 1 (1963) 85.
[97] P. Villars, L. Calvert, Pearson's Handbook of Crystallographic Data for Intermediate Phases, ASM, Cleveland, OH, 1985.
[98] B. Liu, X. Cheng, A metastable Cr carbide of NaCl structure formed by carbon-ion implantation into chromium films, J. Phys.: Condens. Matter 4 (1992) L265–L268.
[99] A.N. Christensen, The temperature factor parameters of some transition metal carbides and nitrides by single crystal x-ray and neutron diffraction, Acta Chem. Scand. 32 (1978) 89–90.
[100] E.K.K. Abavare, S. Dodoo, K. Uchida, G.K. Nkurumah-Buandoh, A. Yaya, A. Oshiyama, Indirect phase transition of TiC, ZrC, and HfC crystal structures, Phys. Status Solidi B 253 (2016) 1177–1185.
[101] D.L. Kepert, Aspects of the stereochemistry of eight-coordination, Prog. Inorg. Chem. (1978) 179–249.
[102] C.W. Haigh, Enumeration by pólya's theorem of the isomerism in eight-coordinate complexes in square antiprismatic, triangular dodecahedral and hendecahedral (bicapped trigonal prismatic) geometries, Polyhedron (1996) 605–643.
[103] P. Bhardwaj, Structural study of transition metal carbides, Acta Phys. Pol. A 122 (2012) 138–141.
[104] K. Kim, V. Ozoliņš, A. Zunger, Instability of the high-pressure CsCl structure in most III-V semiconductors, Phys. Rev. B 60 (1999) R8449–R8452.
[105] O.C. Gagné, F.C. Hawthorne, Bond-length distributions for ions bonded to oxygen: results for the transition metals and quantification of the factors underlying bond-length variation in inorganic solids, IUCrJ 7 (2020) 581–629.
[106] K. Chen, S. Kamran, Bonding characteristics of TiC and TiN, Model. Numer. Simul. Mater. Sci. 3 (2013) 7–11.
[107] R. Janes, E.A. Moore, Metal-ligand bonding, R. Soc. Chem. (2004).
[108] E.A. Juarez-Arellano, et al., Formation of scandium carbides and scandium oxycarbide from the elements at high-(P, T) conditions, J. Solid State Chem. (2010) 975–983.
[109] E. Zhang, et al., A study on the kinetic process of reaction synthesis of TiC: Part I. Experimental research and theoretical model, Metall. Mater. Trans. A (1999) 1147–11514.
[110] L. Wu, et al., Understanding the mechanical properties of vanadium carbides: nano-indentation measurement and first-principles calculations, J. Alloy. Compd. (2013) 60–64.
[111] S.M. Schmuecker, et al., Synthesis of metastable chromium carbide nanomaterials and their electrocatalytic activity for the hydrogen evolution reaction, Dalton Trans. (2017) 13524–13530.
[112] K.H.J. Buschow, F.R. Boer, Physics of Magnetism and Magnetic Materials 7 Kluwer Academic/Plenum, New York, 2003.
[113] N.J. Szymanski, I. Khatri, J.G. Amar, D. Gall, S.V. Khare, Unconventional superconductivity in 3d rocksalt transition metal carbides, J. Mater. Chem. C 7 (2019) 12619–12632.
[114] A.L. Allred, E.G. Rochow, A scale of electronegativity based on electrostatic force, J. Inorg. Nucl. Chem. 5 (1958) 264–268.
[115] V.P. Zhukov, V.A. Gubanov, O. Jepsen, N.E. Christensen, O.K. Andersen, Calculated energy-band structures and chemical bonding in titanium and vanadium carbides, nitrides and oxides, J. Phys. Chem. Solids 49 (1988) 841–849.
[116] P. Soni, G. Pagare, S.P. Sanyal, Structural, high pressure and elastic properties of transition metal monocarbides: a FP-LAPW study, J. Phys. Chem. Solids 72 (2011) 810–816.
[117] Y. Lang, et al., Enhanced hardness in transition-metal monocarbides via optimal occupancy of bonding orbitals, ACS Appl. Mater. Interfaces (2021) 14365–14376.
[118] S.H. Jhi, et al., Electronic mechanism of hardness enhancement in transition-metal carbonitrides, Nature (1999) 132–134.
[119] N.R. Rathod, S.K. Gupta, P.K. Jha, First-principles structural, electronic and vibrational properties of zinc-blende zirconium carbide, Solid State Commun. 169 (2013) 32–36.
[120] S.F. Pugh, Relations between the elastic moduli and the plastic properties of polycrystalline pure metals, Philos. Mag. 45 (1954) 823–843.
[121] A. Teber, F. Schoenstein, F. Têtard, M. Abdellaoui, N. Jouini, Effect of SPS process sintering on the microstructure and mechanical properties of nanocrystalline TiC for tools application, Int. J. Refract. Hard Met. 30 (2012) 64–70.
[122] D. Bandyopadhyay, R.C. Sharma, N. Chakraborti, The Ti-Cr-C (titanium-chromium-carbon) system, J. Phase Equilib. 20 (1999) 325–331.
[123] Ohio-Supercomputer-Center. ⟨http://osc.edu/ark:/19495/f5s1ph73⟩.

Approved for public release; distribution unlimited.
803

Structure, Electronic and Optical Properties of Ternary Nitride Phases of $MgSnN_2$: A First-principles Study

B. B. Dumre[a], D. Gall[c], S. V. Khare[a,*]

[a]Department of Physics and Astronomy, University of Toledo, Toledo, OH 43606, USA
[b]Department of Materials Science and Engineering, Rensselaer Polytechnic Institute, Troy, NY 12180, USA
*Corresponding Author: sanjay.khare@utoledo.edu

Published As: B. B. Dumre[a], D. Gall[b], S. V. Khare[a,*], Journal of Physics and Chemistry of Solids 153 (2021) 110011

Ohio Supercomputer Center

Approved for public release; distribution unlimited.
804

Introduction

- An experimental synthesis of disordered-rocksalt $MgSnN_2$ inspired this computational study [1].
- It has been introduced as a semiconductor material that can be suitable as an opto-electronic device, acting in short-wavelength region of visible range.
- It is synthesized using highly Earth-abundant and non-toxic metals (Mg and Sn) which are relatively cheaper and easy to recycle than other metals such as In and Ga which are used to prepare materials with similar properties.
- It's growth on multiple substrates (such as GaN) is made possible by congruent lattice parameters.
- We present here a thorough computational investigation of structural, mechanical and opto-electronic properties in disordered-rocksalt, disordered-wurtzite and orthorhombic crystal structures of $MgSnN_2$.

Computational Methods

- Vienna Ab initio Simulation Package (VASP) software used for simulation based on Density Functional Theory (DFT).
- DFT provides accurate prediction of ground state properties of a material.
- Generalized Gradient Approximation (GGA) pseudopotential used for computing structural and mechanical properties.
- Heyd-Scuseria-Ernzerhof (HSE06) functional utilized to calculate excited state optical properties and the band gap as they have been successful in doing so.

Structural Properties

- We substituted all 4a Wyckoff positions by two atoms each of Mg and Sn in a conventional cell of 8 atoms in the rocksalt structure, thereby forming a cation-disordered-rocksalt structure.
- Furthermore, all 4b Wyckoff positions were substituted by N or O atoms in different stoichiometries in order to account for the presence of oxygen impurities in the experimental work.
- Similarly, we randomly substituted Mg and Sn atoms in a 1:1 ratio in the 2a cationic Wyckoff positions, whereas substituted N atoms in the other two anionic 2b Wyckoff positions to create a cation-disordered-wurtzite crystal structure.
- We took an ordered orthorhombic crystal structure with 16 atoms in its conventional cell from Materials Project [2].
- Results for lattice constants for all these structures generated are given in Table 1.
- The structure of primary interest here, disordered-rocksalt, has a calculated lattice constant of 4.56 Å, close to the experimental value of 4.48 Å.
- The average bond lengths from Mg, Sn and N to the first nearest neighbors within disordered-rocksalt structure is 2.28 Å, due to its cubic symmetry. However, bond lengths of 2.12 Å and 2.09 Å are interchanged for Mg and Sn between orthorhombic and disordered-wurtzite crystal structures. The bond lengths at N at these two phases are 2.10 Å.
- Orthorhombic phase has a lower formation energy per formula unit, making it more stable than the other two phases of $MgSnN_2$.
- Despite being energetically metastable, disordered-rocksalt and disordered-wurtzite crystal structures appear to be mechanically and vibrationally stable.

Table 1. Lattice constants, formation energies, band gaps and effective masses in different crystal structures.

Material	Crystal Structure		Lattice Constants (Å)			Formation Energy (eV)	Band Gap (eV)		Effective Mass (m*)	
	Name	Space Group	a	b	c		GGA	HSE06	Electron (m_e/m_0)	Hole (m_h/m_0)
$MgSnN_2$	disordered rocksalt	P4/mmm	4.56, 4.48 [1]	= a	= a	−3.18	0	2.69; indirect, 2.3; direct [1]	0.26	2.15
$MgSnN_2$	disordered wurtzite	P3m1	3.44	= a	5.58	−3.64	2.47; direct	4.36; direct	0.69	4.75
$MgSnN_2$	orthorhombic	$Pna2_1$	5.54	5.97	6.94	−4.12	2.84; direct	4.86; direct	0.47	2.46
$MgSnN_{1.5}O_{0.5}$	disordered rocksalt	P4/mmm	4.63	= a	= a	−4.84	0	0	-	-
MgSnNO	disordered rocksalt	P4/mmm	4.71	= a	= a	−6.44	0	0	-	-
$MgSnN_{0.5}O_{1.5}$	disordered rocksalt	P4/mmm	4.77	= a	= a	−8.31	0	0	-	-
$MgSnO_2$	disordered rocksalt	P4/mmm	4.86	= a	= a	−9.94	0.01; indirect	1.01; direct	4.093	1.506

Mechanical Properties

- The bulk and shear moduli in the three phases decrease in the order: disordered-rocksalt > orthorhombic > disordered-wurtzite.
- The Pugh's ratio is 0.75 for the disordered-rocksalt structure and 0.49 for the other two phases.
- The Vickers hardness of the disordered-rocksalt structure of $MgSnN_2$ is 17.76 GPa, higher than those of the orthorhombic (7.59 GPa) and disordered-wurtzite (6.97 GPa) crystal structures. It is also higher than those of Si (11.77 GPa) [3] and CdTe (0.49 GPa) [4].

Vibrational Properties

- Phonon band structure and density of states (DOS) is plotted in Figure 1.
- For each structure, there is no phonon population below zero frequency, which clarifies that all the phonons are dynamically stable in these crystal phases.
- Further, we can distinguish that N gives rise to prominent peaks in the higher frequency range around 10 THz, the Mg peaks are around 5–10 THz, and the Sn peaks are below 5 THz in each of the crystal structures. This reflects the fact that lighter particles have higher vibrational frequencies than heavier ones.
- In the orthorhombic and disordered-wurtzite structures, a gap is apparent in the phonon bands, whereas no such gap is seen for the disordered-rocksalt structure that makes the formers to be used as sound filters and ideal mirrors, because any frequency within the gap will not propagate in the material, and hence will be reflected from its surface.

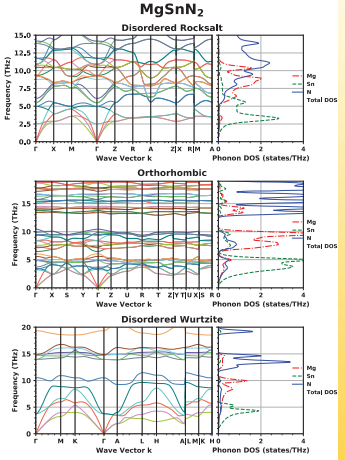


Figure 1. Comparison of phonon band structures and densities of states (DOS) per unit cell of $MgSnN_2$ for different crystal structures, computed using the GGA.

Electronic Properties

- Positive and negative values of projected Crystal Orbital Hamilton Populations (-pCOHP) plotted in Figure 2 correspond to the bonding and antibonding interactions respectively.
- As electronic states are loosely bound above the Fermi level in the conduction band, the (pCOHP) curves above the Fermi level are in antibonding states in all three crystal structures.
- The total net interactions in orthorhombic and disordered-wurtzite structures, shown in green dot-dashed lines, show that they are positively bonded, below the Fermi level.
- However, in the disordered rocksalt structure, the interactions of both Mg and Sn with N, as well as the total net interaction in the material, show an anti-bonding area between - 5 eV and - 2 eV.
- Thus, one may deduce that there is an instability in the disordered-rocksalt structure. This inference is supported by the highest formation energy of the disordered rocksalt structure, as given in Table 1, and the subsequent phonon contribution to the stability as given in Figure 1.
- Calculated band gap of 2.69 eV is comparable to an experimental gap of 2.3 eV for disordered-rocksalt as given in Table 1.
- Band gaps of $MgSnN_{2-x}O_x$ (x = 0.5, 1.0, 1.5) are 0 eV, whereas that of $MgSnO_2$ is 1.01 eV.
- Disordered-rocksalt structure has the lowest carrier effective masses compared to others.

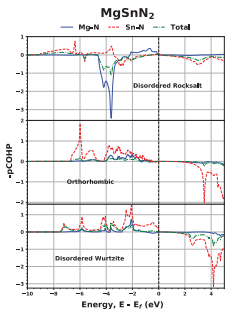


Figure 2. -pCOHP of all nearest-neighbors interactions in $MgSnN_2$ for different crystal structures. The Fermi energy is set to 0 eV.

Optical Properties

- Absorption of the disordered-rocksalt structure commences at 2.7 eV and then shows a steep rise from 3.2 eV to 3.5 eV.
- For the orthorhombic and wurtzite crystal structures, absorption barely starts up to 3.5 eV. Hence, there is no reflection from these crystal structures between 1 eV and 3.5 eV.
- Disordered-rocksalt structure may be used in the higher energy region of the visible range, whereas the other two structures could be used as window layers in solar cells.

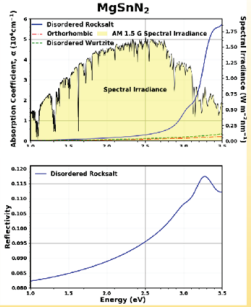


Figure 3. Absorption coefficient, α (top panel), and reflectivity (bottom panel) curves, left axis, of $MgSnN_2$ for different crystal structures computed using HSE06 functional. Standard AM 1.5 G solar spectral irradiance, right axis, is illustrated in the yellow shaded area along with the absorption curve.

Conclusion

- A computational study inspired by recent experimental synthesis of disordered-rocksalt $MgSnN_2$ has been carried out.
- The calculated lattice constant of 4.56 Å matches the experimental result of 4.48 Å.
- The calculated indirect band gap of 2.69 eV is comparable to an experimental direct gap of 2.3 eV.
- Band gaps of $MgSnN_{2-x}O_x$ (x = 0.5, 1.0, 1.5) are 0 eV, whereas that of $MgSnO_2$ is 1.01 eV.
- Rocksalt $MgSnN_2$ is mechanically and dynamically stable, thermodynamically metastable, and is suitable as a short-wavelength photovoltaic absorber material.

Acknowledgements

All computing for this project was performed at the Ohio Supercomputer Center (OSC). We thank our funding sources: The National Science Foundation Division of Civil, Mechanical, and Manufacturing Innovation through grants 1629230 and 1629239, the University Cooperative Agreement High Specific Power Multi-Junction Thin Film Photovoltaics under Contract # FA9453-18-2-0037.

References

[1] Kawamura, F., et al., *Synthesis of a novel rocksalt-type ternary nitride semiconductor $MgSnN_2$ using the metathesis reaction under high pressure.* European Journal of Inorganic Chemistry, 2020, **2020**(5): p. 446-451.
[2] Jain, A., et al., *Commentary: The Materials Project: A materials genome approach to accelerating materials innovation.* APL Materials, 2013, **1**(1): p. 11.
[3] Zanatta, J.P., et al., *Growth of HgCdTe and CdTe(331)B on germanium substrate by molecular beam epitaxy.* Applied Physics Letters, 1997, **71**(20): p. 2984-2986.
[4] Cole, S., M. Brown, and A.F.W. Willoughby, *The microhardness of $Cd_xHg_{1-x}Te$.* Journal of Materials Science, 1982, **17**(7): p. 2061-2066.

DISTRIBUTION LIST

DTIC/OCP
8725 John J. Kingman Rd, Suite
0944 Ft Belvoir, VA 22060-6218 1 cy

AFRL/RVIL
Kirtland AFB, NM 87117-5776 1 cy

Official Record Copy
AFRL/RVS/Alec Jackson 1 cy

Approved for public release; distribution unlimited.

--- This Page Intentionally Left Blank ---